HANDBOOK OF SURFACE SCIENCE VOLUME 2

SERIES EDITORS:

N.V. RICHARDSON

S. HOLLOWAY



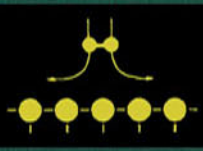

# Electronic Structure

K. Horn and M. Scheffler, volume editors

NORTH - HOLLAND

Handbook of Surface Science
Volume 2

# Handbook of Surface Science

*Series editors*

S. HOLLOWAY

*Surface Science Research Centre*
*Liverpool, UK*

N.V. RICHARDSON

*Director, Surface Science Research Centre*
*Liverpool, UK*




ELSEVIER
Amsterdam • Lausanne • New York • Oxford • Shannon • Singapore • Tokyo

Volume 2

# Electronic Structure

*Volume editors*

K. HORN

*Fritz-Haber-Institut der Max-Planck-Gesellschaft*
*Department of Surface Physics*
*Faradayweg 4-6*
*D-1000 Berlin 33, Germany*

and

M. SCHEFFLER

*Fritz-Haber-Institut der Max-Planck-Gesellschaft*
*Theory Department*
*Faradayweg 4-6*
*D-1000 Berlin 33, Germany*




2000
ELSEVIER
Amsterdam • Lausanne • New York • Oxford • Shannon • Singapore • Tokyo

ELSEVIER SCIENCE B.V.
Sara Burgerhartstraat 25, P.O. Box 211, 1000 AE Amsterdam, The Netherlands

© 2000 Elsevier Science B.V. All rights reserved.

This work is protected under copyright by Elsevier Science, and the following terms and conditions apply to its use:

Photocopying
Single photocopies of single chapters may be made for personal use as allowed by national copyright laws. Permission of the Publisher and payment of a fee is required for all other photocopying, including multiple or systematic copying, copying for advertising or promotional purposes, resale, and all forms of document delivery. Special rates are available for educational institutions that wish to make photocopies for non-profit educational classroom use.

Permissions may be sought directly from Elsevier Science Global Rights Department, PO Box 800, Oxford OX5 1DX, UK; phone: (+44) 1865 843830, fax: (+44) 1865 853333, e-mail: permissions@elsevier.co.uk. You may also contact Global Rights directly through Elsevier's home page (http://www.elsevier.nl), by selecting 'Obtaining Permissions'.

In the USA, users may clear permissions and make payments through the Copyright Clearance Center, Inc., 222 Rosewood Drive, Danvers, MA 01923, USA; phone: (978) 7508400, fax: (978) 7504744, and in the UK through the Copyright Licensing Agency Rapid Clearance Service (CLARCS), 90 Tottenham Court Road, London W1P 0LP, UK; phone: (+44) 171 631 5555; fax: (+44) 171 631 5500. Other countries may have a local reprographic rights agency for payments.

Derivative Works
Tables of contents may be reproduced for internal circulation, but permission of Elsevier Science is required for external resale or distribution of such material.
Permission of the Publisher is required for all other derivative works, including compilations and translations.

Electronic Storage or Usage
Permission of the Publisher is required to store or use electronically any material contained in this work, including any chapter or part of a chapter.

Except as outlined above, no part of this work may be reproduced, stored in a retrieval system or transmitted in any form or by any means, electronic, mechanical, photocopying, recording or otherwise, without prior written permission of the Publisher.
Address permissions requests to: Elsevier Science Global Rights Department, at the mail, fax and e-mail addresses noted above.

Notice
No responsibility is assumed by the Publisher for any injury and/or damage to persons or property as a matter of products liability, negligence or otherwise, or from any use or operation of any methods, products, instructions or ideas contained in the material herein. Because of rapid advances in the medical sciences, in particular, independent verification of diagnoses and drug dosages should be made.

First edition 2000

Library of Congress Cataloging in Publication Data
A catalog record from the Library of Congress has been applied for.

ISBN: 0-444-89291-5 (Volume 2)
ISBN: 0-444-82526-6 (Series)

♾The paper used in this publication meets the requirements of ANSI/NISO Z39.48-1992 (Permanence of Paper).
Printed in The Netherlands.

# General Preface

How many times has it been said that surface science has come of age? Rather than being a fledgling area of study, it is now patently clear that the investigation of solid surfaces and related interfacial problems is a unique field with profound implications for basic (dare one say academic!) scientific study and the understanding of materials. Surface science provides major support to many technologically ambitious industries. It is widely recognised that it underpins the fabrication of electronic devices but this also extends to any industry working in nanotechnology. Surface science makes significant contributions to product development and problem solving in many materials-based industries where surface finish, cleanliness, adhesion, wear or friction are important. An understanding of surface processes is vital in chemical industries because of the importance of heterogeneous catalysis and is likely to make major contributions to the growing optoelectronics and molecules sensing industries. In social terms, an improved understanding of surfaces will facilitate the development of better catalysts and sensors for improvement of our environment. Most recently, surface science has begun to make real contributions to the understanding of biological surfaces.

In this series, we have brought together some of the key players that have made seminal contributions to the study of solid surfaces and their interactions with foreign species. Because of the broad scope of surface science, even when restricted to the solid surfaces which we hope to cover in this series, we have been coerced into 'packaging' the subject in what is, it must be said, a rather arbitrary way. No doubt different editors would have chosen different themes around which to base individual volumes.

Following the first volume, which addressed the geometry of surfaces, this Volume 2 deals with the experimental determination and theoretical description of surfaces. Continuing developments in computer hardware have stimulated activity in electronic structure calculations from several different viewpoints and allowed more sophisticated systems to be contemplated by theorists. While theory provides a direct link between geometric structure and electronic properties, the distinction retains some validity in experimental studies of surfaces.

Volume 3 will address the dynamical aspects of surfaces and surface processes, reflecting in detail current understanding of energy exchange at surfaces and the part this plays in the adsorption and reaction of atoms and molecules at surfaces. Surface dynamics is, of course, intimately related to the geometric and electronic properties of the surface and while Volumes 1 and 2 address the equilibrium geometry and ground state electronic properties, Volume 3 pays particular attention to the response of surfaces to external stimulation.

In recognition of the important role that surface science has played in advancing our understanding of semiconductor surfaces and therefore our ability to exploit semiconductor surfaces in the electronics and, more recently, optoelectronics industries, Volume 4 will be targeted at their structure, electronic activity, growth, reactivity and passivation.

Taken as a set, the volumes of this series aim to provide an in-depth introduction to the world of surface and interfacial science and would be most suited for scientists having obtained a first degree in natural sciences.

*N.V. Richardson and S. Holloway*
*Surface Science Research Centre*
*Liverpool, UK*

# Preface to Volume 2

The chapters in this second volume of the "Handbook of Surface Science" deal with aspects of the electronic structure of surfaces as investigated by means of the experimental and theoretical methods of physics. The importance of understanding surface phenomena stems from the fact that for many physical and chemical phenomena, the surface plays a key role: in electronic, magnetic, and optical devices, in heterogenous catalysis, in epitaxial growth, and the application of protective coatings, for example. Thus a better understanding and, ultimately, a predictive description of surface and interface properties is vital for the progress of modern technology. An investigation of surface electronic structure is also central to our understanding of all aspects of surfaces from a fundamental point of view. Electronic states at surfaces govern the geometric structure, including relaxation and reconstruction phenomena (comprehensively covered in Volume 1). They dominate processes such as adsorption and molecular dissociation. Moreover, on semiconductors, they may render a surface semiconducting or metallic, depending on their density and energy, and they may not only affect the energy and spatial distribution of surface states, but also the chemical potential of the electrons at an interface in semiconductor junctions. Finally, surface electronic states are important in dynamic processes at surfaces to be covered in Volume 3 of this series. The nature of the surface chemical bond and the surface band structure is extensively covered in this volume; emphasis is placed on simple physical models in order to further an understanding of general trends.

When looking back at more than three decades of modern surface science, it is obvious that a tremendous progress in our knowledge of surface electronic structure has been achieved. Early studies often used work function change experiments, which had important applications, but generally were (and still are) difficult to interpret in terms of surface electronic states. An important step forward came with the introduction of valence level photoelectron spectroscopy in the 1960's. This technique is the basis, along with its counterpart of inverse photoemission, for much of our knowledge of occupied and unoccupied surface electronic band structures, extensively covered this volume. Surface states had been predicted as early as the 1930's, and their abundance, and influence on a variety of surface processes, such as phase transitions, for example, has become clear within the last decade. Moreover, the study of surface electronic states often involves an evaluation of the bulk electronic structure from which they are derived, such that an enormous increase of our knowledge of bulk band structure $E(\mathbf{k})$ has been achieved, employing the angle-resolved photoemission mode. In this way, surface science has been active in revitalising some aspects of solid state physics; indeed, many connections between bulk and surface electronic structure are apparent in the contributions to this volume. This mutual interconnection also

applies to surfaces and thin films, the electronic structure of which, for example in cases of quantization of bulk states through electron confinement, can be traced in detail. The very nature of surface science methods, their surface sensitivity, can be utilized in investigating the initial stages of interface formation.

The techniques of wave vector-resolved electronic state analysis, i.e. the characterization in reciprocal space, are beautifully complemented by the direct access to the distribution of electronic states in real space, through scanning tunnelling microscopy and spectroscopy. These methods give direct access to the distribution of electronic surface states in real space, and thus give evidence for surface state assignments in terms of specific atomic species at the surface. They also permit the observation of changes in electronic structure near steps, kinks, and defects in a manner that was thought quite impossible only a decade ago. While photoemission and scanning tunnelling microscopy and spectroscopy dominate electronic structure studies, we note that many other techniques such as optical and X-ray absorption and core level photoemission, for example, have also made important contributions to this field. Other techniques, such as X-ray emission spectroscopy, are emerging with the advent of third generation synchrotron radiation facilities.

These advances in experimental investigations have been aptly matched by an advancement of the theoretical treatment of surface electronic structure. Much of the complexity and novelty which makes surface science such an exciting field stems from the inherent low symmetry and reduced dimensionality. From the early empirical tight binding and model Hamiltonian calculations, we have witnessed the breakthrough of density-functional theory, in predicting not only the electronic structure for a given surface geometry, but to arrive, through total energy calculations, at the stable geometry assumed by a specific system. Even metastable geometries (often more important than stable ones in surface processes), transition states, and high-dimensional total energy surfaces can now be calculated, together with the phenomena of chemical bond formation and breakup. The success of such calculations in the various areas of surface science is documented in several chapters of this volume. Moreover, not only are these calculations able to describe the ground state, but they also permit a direct comparison with results from electron spectroscopies, through quasiparticle calculations, when extended by calculations of the self energy, or by time-dependent density functional theory. The challenge of understanding results from electron spectroscopies beyond the single particle picture, by taking into account the interaction between the emitted particle and the electron gas in the emission process, has also been taken up in a concerted effort between theory and experiment. Future studies will address surface processes under conditions of high ambient pressure and varying temperature such that one can decide between a thermal equilibrium situation or a special metastable state.

Surface science has reached a degree of maturity which permits to take a broad look at the goals achieved, and the challenges ahead, both in experiment and theory. We hope that the collection of chapters in this Handbook will serve this purpose for the electronic structure of solid surfaces. We would like to thank our colleagues and collaborators, who are personally acknowledged in the chapters, for their help in getting this volume written and published. Special thanks are due to Elsevier Science for their expert assistance, and their patience.

*K. Horn and M. Scheffler*

# Contents of Volume 2

*General Preface* . . . . . v
*Preface to Volume 2* . . . . . vii
*Contents of Volume 2* . . . . . ix
*Contributors to Volume 2* . . . . . xi

1. E. Wimmer and A.J. Freeman
*Fundamentals of the electronic structure of surfaces* . . . . . 1

2. J. Pollmann and P. Krüger
*Electronic structure of semiconductor surfaces* . . . . . 93

3. G. Borstel and J.E. Inglesfield
*Electronic states on metal surfaces* . . . . . 209

4. C.M. Bertoni, G. Roma and R. Di Felice
*Electronic structure of adsorbates on surfaces. Adsorption on semiconductors* . 247

5. M. Scheffler and C. Stampfl
*Theory of adsorption on metal substrates* . . . . . 285

6. F.J. Himpsel
*Experimental probes of the surface electronic structure* . . . . . 357

7. K. Horn
*Electronic structure of semiconductor surfaces* . . . . . 383

8. S.D. Kevan
*Surface states on metal surfaces* . . . . . 433

9. C.M. Schneider and J. Kirschner
*Magnetism at surfaces and in ultrathin films* . . . . . 511

10. H.-J. Freund and H. Kuhlenbeck
*Adsorption on metals* . . . . . 669

11. R. Ludeke
*The metal–semiconductor interface* . . . . . 749

12. R. Miranda and E.G. Michel
*Electronic structure of adsorbates on semiconductors* . . . . . 863

13. S.-Å. Lindgren and L. Walldén
*Some properties of metal overlayers on metal substrates* . . . . . 899

14. G.D. Mahan and E.W. Plummer
*Many-body effects in photoemission* . . . . . 953

Author index . . . . . 989
Subject index . . . . . 1049

# Contributors to Volume 2

*Carlo M. Bertoni*, Dipartimento di Fisica, Universita' di Roma "Tor Vergata", 00133 Roma, Italy. Present address: INFM and Dipartimento di Fisica Universita' di Modena e Reggio Emilia, Via Campi 213/A, 41100 Modena, Italy

*G. Borstel*, Department of Physics, University of Osnabrück, D-49069 Osnabrück, Germany

*Rosa Di Felice*, Dipartimento di Fisica, Universita' di Roma "Tor Vergata", 00133 Roma, Italy. Present address: INFM and Dipartimento di Fisica Universita' di Modena e Reggio Emilia, Via Campi 213/A, 41100 Modena, Italy

*Arthur Freeman*, Department of Physics and Astronomy, Northwestern University, Evanston, IL 60208-3112, USA

*H.-J. Freund*, Abteilung Chemische Physik, Fritz-Haber-Institut der Max-Planck-Gesellschaft, Germany

*Franz J. Himpsel*, Department of Physics, University of Wisconsin-Madison, 1150 University Avenue, Madison WI 53706-1390, USA

*Karsten Horn*, Department of Surface Physics, Fritz-Haber-Institut der Max-Planck-Gesellschaft, Faradayweg 4-6, D-14195 Berlin, Germany

*John Inglesfield*, Department of Physics and Astronomy, University of Wales Cardiff, PO Box 913, Cardiff, CF2 3YB, UK

*Steve D. Kevan*, Physics Department, University of Oregon, Eugene, OR, USA 97403

*Jurgen Kirschner*, Max-Planck-Institut für Mikrostrukturphysik, Am Weinberg 2, D-06120 Halle/Saale, Germany

*Peter Krüger*, Institut für Theoretische Physik II-Festkörperphysik, Universität Münster, D-48149 Münster, Germany

*H.J. Kuhlenbeck*, Abteilung Chemische Physik, Fritz-Haber-Institut der Max-Planck-Gesellschaft, Germany

*S.-Å. Lindgren*, Physics Department, Chalmers University of Technology, Göteborg, Sweden

*Rudi Ludeke*, IBM Research Division, T.J. Watson Research Center, P.O. Box 218, Yorktown Heights, NY, 10598, USA

*G.D. Mahan*, Department of Physics, University of Tennessee, Knoxville, USA

*Enrique Michel*, Departamento de Física de la Materia Condensada, and Instituto Universitario de Ciencia de Materiales "Nicolás Cabrera", Universidad Autónoma de Madrid, Madrid, Spain

*Rodolfo Miranda*, Departamento de Física de la Materia Condensada, and Instituto Universitario de Ciencia de Materiales "Nicolás Cabrera", Universidad Autónoma de Madrid, Madrid, Spain

*Ward Plummer*, Department of Physics, University of Tennessee, Knoxville, USA

*Johannes Pollmann*, Institut für Theoretische Physik II-Festkörperphysik, Universität Münster, D-48149 Münster, Germany

*Guido Roma*, Istituto Nazionale di Fisica della Materia, Dipartimento di Fisica, Universita' di Modena, 41100 Modena, Italy. Present address: CECAM, Ecole Normale Supérieure 46 Allée d'Italie, 69364 Lyon cedex 07, France

*Matthias Scheffler*, Fritz-Haber-Institut der Max-Planck-Gesellschaft, Faradayweg 4-6, D-14195 Berlin, Germany

*C.M. Schneider*, Institut für Festkörper- und Werkstofforschung Dresden, Helmholtzstr. 20, D-01069 Dresden, Germany

*Catherine Stampfl*, Fritz-Haber-Institut der Max-Planck-Gesellschaft, Faradayweg 4-6, D-14195 Berlin, Germany

*Lars Walldén*, Physics Department, Chalmers University of Technology, Göteborg, Sweden

*Erich Wimmer*, Institut Supérieur des Matériaux du Mans and Materials Design s.a.r.l., 72000 Le Mans, France

CHAPTER 1

# Fundamentals of the Electronic Structure of Surfaces

E. WIMMER

*Institut Supérieur des Matériaux du Mans*
*and Materials Design s.a.r.l.*
*72000 Le Mans, France*

A.J. FREEMAN

*Department of Physics and Astronomy*
*Northwestern University*
*Evanston, IL 60208-3112, USA*

© *2000 Elsevier Science B.V.*
*All rights reserved*

*Handbook of Surface Science*
*Volume 2, edited by K. Horn and M. Scheffler*

# Contents


1.1. Introduction . . . 3
1.2. Basic concepts of density functional theory . . . 4
1.2.1. The Kohn–Sham equations . . . 4
1.2.2. One-particle energies and work function . . . 10
1.2.3. Spin-polarized systems . . . 11
1.2.4. Beyond the local density approximation . . . 12
1.2.5. Relativistic effects . . . 14
1.2.6. Relativistic spin polarization and magnetization . . . 16
1.3. Surface models and computational approaches . . . 19
1.3.1. Geometric models . . . 19
1.3.2. Overview of computational methods . . . 21
1.3.3. Variational solution of the Kohn–Sham equations . . . 23
1.3.4. Self-consistency cycle and geometry optimizations . . . 24
1.3.5. Representation of wave functions for surfaces . . . 26
1.3.6. Specific computational implementations . . . 28
1.3.6.1. Full-potential linearized augmented plane wave (FLAPW) method . . . 28
1.3.6.2. Pseudopotential plane wave method . . . 33
1.3.6.3. Localized orbital methods . . . 38
1.3.6.4. Green's functions with localized orbitals . . . 42
1.4. Electronic states at surfaces . . . 45
1.4.1. Surface states and surface resonance state in nearly free-electron metals: Al(001) . . . 45
1.4.2. Theoretical 2p-core-level shift and crystal-field splitting at the Al(001) surface . . . 47
1.5. Charge density distributions at surfaces: surface states and surface resonances . . . 49
1.6. Surface potential and work function . . . 52
1.6.1. Origin of the work function . . . 52
1.6.2. Cesiation of W(001): work function lowering by multiple dipole formation . . . 56
1.7. Geometric structure and energetics of clean surfaces . . . 61
1.7.1. Surface relaxation on W(001): evidence for short-range screening . . . 62
1.7.2. Surface reconstructions and structural surface phase transitions: W(001) . . . 64
1.7.3. Surface energy of transition metals: W(001) and V(001) . . . 67
1.8. Semiconductor surfaces and adsorbates . . . 68
1.8.1. Structure of the Si(100) $2 \times 1$ surface . . . 69
1.8.2. Passivation of the Si(100) surface . . . 72
1.8.3. Importance of adsorbate–adsorbate interactions for As and Sb chemisorption on Si(100) . . . 75
1.9. Magnetism at surfaces and interfaces: spin–orbit induced magnetic effects . . . 75
1.9.1. Magneto-crystalline anisotropy . . . 76
1.9.2. Magneto-optical effects . . . 80
1.9.2.1. SMOKE . . . 80
1.9.2.2. Magnetic circular X-ray dichroism . . . 82
1.9.3. Conclusions on magnetic surface effects . . . 83
1.10. Summary and perspective on future developments . . . 84
References . . . 86

## 1.1. Introduction

The richness of physical and chemical properties of surfaces finds its fundamental explanation in the arrangement of atoms, the distribution of the electrons, and their response to external changes. For example, surface reconstructions such as that of the Si(001) surface are driven by electronic structure effects; the work function of a metal surface is determined by the extent to which electrons spill out into the vacuum region; enhanced magnetism at the surfaces of Fe and Ni is the consequence of surface-induced changes in the electronic structure of the metal atoms at the surface; adsorption, chemisorption, and chemical reactions on surfaces are the result of the fascinating dynamic relationship between positions of atoms, electronic structure, and total energy.

Therefore, the understanding and quantitative prediction of the electronic structure takes a central and fundamental role in today's concept of surfaces. As in the investigation of bulk solids and molecular systems, the quality and reliability of any electronic structure theory of surfaces hinges on the ability to describe the many-body interactions accurately enough to allow quantitative predictions of physical properties. On the other hand, the theory has to allow practical calculations at a reasonable computational effort on systems which are large enough so that realistic surface models can be studied. These two requirements, accuracy and practicality, continue to present a tremendous challenge to the theoretical/computational physicist and chemist.

Since the formulation of quantum mechanics in the 1920's, two major theoretical and computational approaches have emerged, namely Hartree–Fock theory and density functional theory. A third approach, quantum Monte Carlo, is promising but, so far, has remained limited to rather small systems. Because of its applicability to a wide range of systems including metallic, semiconducting, and insulating materials and its good balance between accuracy and computational efficiency, density functional theory has become the dominant approach for electronic structure calculations of surfaces. Therefore, this chapter focuses on density functional methods and their applications to surface problems. However, the reader should be aware that Hartree–Fock based approaches have also been successful in describing surface phenomena such as chemisorption using small clusters as surface models. Furthermore, Dovesi et al. (1992) have developed a Hartree–Fock program for periodic systems that can also be used to study surfaces. These approaches and their applications will not be discussed here. In addition, one should keep in mind that in the modeling and simulation of surface phenomena, electronic structure aspects constitute the most fundamental and deepest level of theory of atomic-scale simulations, but the study of surface phenomena involving hundreds of thousands of atoms and time-scales of microseconds and longer require radically different theoretical and computational approaches. These approaches remain also outside the scope of this chapter.

## 1.2. Basic concepts of density functional theory

### *1.2.1. The Kohn–Sham equations*

Hohenberg and Kohn (1964) and Kohn and Sham (1965) formulated a rather remarkable theorem which states that the total energy of a system such as a bulk solid or a surface depends only on the electron density of its *ground state*. In other words, one can express the total energy of an atomistic system as a functional of its electron density

$$E = E[\rho]. \tag{1.1}$$

The idea of using the electron density as the fundamental entity of a quantum mechanical theory of matter originates in the early days of quantum mechanics (Thomas, 1926; Fermi, 1928). However, in the subsequent decades, it was rather the Hartree–Fock approach (Hartree, 1928; Fock, 1930a, b) which was developed and applied to small molecular systems. Calculations on realistic solid state systems were then out of reach. Slater (1951) used ideas from the electron gas with the intention to simplify Hartree–Fock theory to a point where electronic structure calculations on solids became feasible. Slater's work, which led to the so-called $X\alpha$ method (Slater, 1974), has contributed tremendously to the development of electronic structure calculations. Today, Slater's $X\alpha$ method can be seen as an early, simplified form of density functional theory. The $X\alpha$ method is hardly used in present electronic structure calculations and therefore will not be further pursued in this chapter and we return now to the explanation of density functional theory.

The electron density is a scalar function defined at each point $\mathbf{r}$ in real space,

$$\rho = \rho(\mathbf{r}). \tag{1.2}$$

The electron density and the total energy depend on the type and arrangements of the atomic nuclei. Therefore, one can write

$$E = E\big[\rho(\mathbf{r}), \{\mathbf{R}_\alpha\}\big]. \tag{1.3}$$

The set $\{\mathbf{R}_\alpha\}$ denotes the positions of all atoms $\alpha$ in the system under consideration. Equation (1.3) is the key to the atomic-scale understanding of electronic, structural, and dynamic properties of matter. If one has a way of evaluating expression (1.3), one can, for example, predict surface reconstructions, the equilibrium geometry of molecules adsorbed on surfaces, and the cohesive energies of solids.

Furthermore, the derivative of the total energy (1.3) with respect to the nuclear position of an atom gives the force acting on that atom. This enables the efficient search for stable structures and, perhaps more importantly, the study of dynamical processes such as diffusion or the reaction of molecules on surfaces. Most of the considerations discussed in this book are based on the Born–Oppenheimer approximation in which it is assumed that the motions of the electrons are infinitely faster than those of the nuclei. In practice this means that the electronic structure is calculated for a fixed atomic arrangement and the atoms are then moved according to classical mechanics. This is a fairly good approximation for heavy atoms like W, but can cause significant errors for light atoms like H or Li.

In density functional theory, the total energy (1.1) is decomposed into three parts, a kinetic energy, an electrostatic or Coulomb energy, and a so-called exchange–correlation energy,

$$E = T_0 + U + E_{\mathrm{xc}}. \tag{1.4}$$

The most straightforward term is the Coulomb energy $U$. It is purely classical and contains the electrostatic energy arising from the Coulombic attraction between electrons and nuclei, the repulsion between all electronic charges, and the repulsion between nuclei

$$U = U_{\mathrm{en}} + U_{\mathrm{ee}} + U_{\mathrm{nn}} \tag{1.5}$$

with

$$U_{\mathrm{en}} = -e^2 \sum_{\alpha} Z_\alpha \int \frac{\rho(\mathbf{r})}{|\mathbf{r} - \mathbf{R}_\alpha|}\, \mathrm{d}\mathbf{r}, \tag{1.6}$$

$$U_{\mathrm{ee}} = e^2 \iint \frac{\rho(\mathbf{r})\rho(\mathbf{r}')}{|\mathbf{r} - \mathbf{r}'|}\, \mathrm{d}\mathbf{r}\, \mathrm{d}\mathbf{r}', \tag{1.7}$$

$$U_{\mathrm{nn}} = e^2 \sum_{\alpha\alpha'} \frac{Z_\alpha Z_{\alpha'}}{|\mathbf{R}_\alpha - \mathbf{R}_{\alpha'}|}, \tag{1.8}$$

where $e$ is the elementary charge of a proton and $Z_\alpha$ is the atomic number of atom $\alpha$. The summations extend over all atoms and the integrations over all space. Once the electron density and the atomic numbers and positions of all atoms are known, expression (1.6)–(1.8) can be evaluated by using the techniques of classical electrostatics.

The kinetic energy term $T_0$ is more subtle. In density functional theory, the "real" electrons of a system are replaced by "effective" electrons with the same charge, mass, and density distribution. However, effective electrons move as independent particles in an effective potential, whereas the motion of a "real" electron is correlated with those of all other electrons. $T_0$ is the sum of the kinetic energies of all effective electrons moving as independent particles. Often, one does not explicitly make this distinction between real and effective electrons.

If each effective electron is described by a single particle wave function $\psi_i$ then the kinetic energy of all effective electrons in the system is given by

$$T_0 = \sum_i n_i \int \psi_i^*(\mathbf{r}) \left[ -\frac{\hbar^2}{2m} \nabla^2 \right] \psi_i(\mathbf{r})\, \mathrm{d}\mathbf{r}. \tag{1.9}$$

Expression (1.9) is the sum of the expectation values of one-particle kinetic energies; $n_i$ denotes the number of electrons in state $i$. By construction, dynamical correlations between the electrons are excluded from $T_0$.

The third term of Eq. (1.4) includes all remaining complicated electronic contributions to the total energy and is called exchange–correlation energy, $E_{\mathrm{xc}}$. The most important

of these contributions is the exchange term. Electrons are fermions and obey the Pauli exclusion principle. In real space, the Pauli principle implies that, around each electron with a given spin, all other electrons with the same spin tend to avoid that electron. As a consequence, the average Coulombic repulsion acting on that electron is reduced. This energy gain is called exchange energy. Effectively each electron is surrounded by a positive exchange hole (Slater, 1951, 1974). It can be shown (Slater, 1974) that the total charge integrated over the entire exchange hole equals $+e$. By definition, the additional many-body interaction terms between electrons of opposite spin are called correlation energy.

As an illustration, the total energy of a single C atom is approximately $-1019$ eV, that of a Si atom $-7859$ eV and that of a W atom $-439634$ eV. The kinetic energy and the Coulomb energy terms are of similar magnitude but of opposite sign whereas the exchange–correlation term is about 10% of the Coulomb term and attractive for electrons (because the exchange-hole is positive). The correlation energy is smaller than the exchange energy, but plays an important role in determining the details in the length and strength of interatomic bonds. In fact, compared with the total energy, the binding energy of an atom in a solid or on a surface is quite small and lies in the range of about 1 to 8 eV. Energies involved in changes of the position of atoms on a surface can be even smaller. For example, only about 0.03 eV are required to flip an asymmetric Si-dimer on a reconstructed Si(001) surface from one conformation into another where the role of the upper and lower Si atom are reversed. It is a tremendous challenge for any theory to cope with such a range of energies. Density functional theory, as it turns out, comes amazingly close to this goal.

The Hohenberg–Kohn–Sham theorem, which is a central part of density functional theory, states that the total energy is at its minimum value for the ground state density and that the total energy is stationary with respect to first-order variations in the density, i.e.,

$$\left.\frac{\partial E[\rho]}{\partial \rho}\right|_{\rho=\rho_0} = 0. \tag{1.10}$$

In conjunction with the kinetic energy, we have introduced one-particle wave functions $\psi_i(\mathbf{r})$ which generate the electron density

$$\rho(\mathbf{r}) = \sum_i n_i \left|\psi_i(\mathbf{r})\right|^2. \tag{1.11}$$

As in the expression (1.9) for the kinetic energy, $n_i$ denotes the occupation number of the eigenstate that is represented by the one-particle wave function $\psi_i$. So far, one has a formally exact theory in the sense that no approximations have been made yet to the many-electron interactions. By construction, $\rho(\mathbf{r})$ in Eq. (1.11) is the *exact* many-electron density.

The goal of the next step is the derivation of equations that can be used for practical density functional calculations. Through Eqs. (1.9) and (1.11) we have introduced one-particle wave functions. A change of these wave functions corresponds to a variation in the electron density. Therefore, the variational condition (1.10) can be used to derive the conditions for the one-particle wave functions that lead to the ground state density. To this

end, one substitutes Eq. (1.11) in expression (1.10) and varies the total energy with respect to each wave function. This procedure leads to the following equations:

$$\left[-\frac{\hbar^2}{2m}\nabla^2 + V_{\text{eff}}(\mathbf{r})\right]\psi_i(\mathbf{r}) = \varepsilon_i\psi_i(\mathbf{r}) \tag{1.12}$$

with

$$V_{\text{eff}}(\mathbf{r}) = V_{\text{C}}(\mathbf{r}) + \mu_{\text{xc}}\big[\rho(\mathbf{r})\big]. \tag{1.13}$$

Equations (1.12) are called the Kohn–Sham equations. The electron density which corresponds to these wave functions is the ground state density which minimizes the total energy. The solutions of the Kohn–Sham equations form an orthonormal set, i.e.,

$$\int \psi_i^*(\mathbf{r})\psi_j(\mathbf{r})\,\mathrm{d}\mathbf{r} = \delta_{ij}. \tag{1.14}$$

This additional constraint is achieved by introducing Lagrange multipliers, $\varepsilon_i$ in Eq. (1.12). These "Lagrange multipliers" are effective one-electron eigenvalues and their interpretation will be discussed later. These eigenvalues are used to determine the occupation numbers $n_i$ by applying the Aufbau principle. The eigenstates are ordered according to increasing eigenvalues. For non-spin polarized systems each state is occupied by two electrons until all electrons are accommodated. In spin polarized systems, each state is occupied by at most one electron.

As a consequence of the partitioning of the total energy (1.4), the Hamiltonian operator in the Kohn–Sham equations (1.12) contains three terms, one for the kinetic energy, the second for the Coulomb potential, and the third for the exchange–correlation potential.

The kinetic energy term is the standard second-order differential operator of one-particle Schrödinger equations and its construction does not require specific knowledge of a system. In contrast, the Coulomb potential operator, $V_{\text{C}}(\mathbf{r})$, and the exchange–correlation potential operator, $\mu_{\text{xc}}$, depend on the specific electron distribution in the system under consideration.

The Coulomb or electrostatic potential $V_{\text{C}}(\mathbf{r})$ at point $\mathbf{r}$ is generated from the electric charges of all nuclei and electrons in the system. It can be evaluated directly in real space,

$$V_{\text{C}}(\mathbf{r}) = -e^2\sum_{\alpha}\frac{Z_\alpha}{|\mathbf{r}-\mathbf{R}_\alpha|} + e^2\int\frac{\rho(\mathbf{r}')}{|\mathbf{r}-\mathbf{r}'|}\,\mathrm{d}\mathbf{r}'. \tag{1.15}$$

In condensed systems it is more convenient to use Poisson's equation

$$\nabla^2 V_{\text{C}}(\mathbf{r}) = -4\pi e^2 q(\mathbf{r}) \tag{1.16}$$

to calculate the electrostatic potential. Here, $q(\mathbf{r})$ denotes both the electronic charge distribution $\rho(\mathbf{r})$ and the positive point charges of the nuclei at positions $\mathbf{R}_\alpha$.

The exchange–correlation potential is related to the exchange–correlation energy by

$$\mu_{\mathrm{xc}} = \frac{\partial E_{\mathrm{xc}}[\rho]}{\partial \rho}. \tag{1.17}$$

Equation (1.17) is formally exact in the sense that it does not contain any approximations to the complete many-body interactions. In practice however, the exchange–correlation energy (and thus the exchange–correlation potential) is not known and one has to make approximations.

As a consequence of the Kohn–Sham theorem, the exchange–correlation energy depends only on the electron density. As a simple and, as it turns out, surprisingly good approximation one can assume that the exchange–correlation energy depends only on the local electron density around each volume element $\mathbf{dr}$. This is called the local density approximation (LDA)

$$E_{\mathrm{xc}}[\rho] \approx \int \rho(\mathbf{r}) \varepsilon_{\mathrm{xc}}\big[\rho(\mathbf{r})\big]\,\mathrm{d}\mathbf{r}. \tag{1.18}$$

Figure 1.1 illustrates the basic idea. In any atomic arrangement such as a crystal, a surface, or a molecule, there is a certain electron density $\rho(\mathbf{r})$ at each point $\mathbf{r}$ in space. The LDA then rests on two basic assumptions: (i) the exchange and correlation effects come predominantly from the immediate vicinity of a point $\mathbf{r}$ and (ii) these exchange and correlation effects do not depend strongly on the variations of the electron density in the vicinity of $\mathbf{r}$. If conditions (i) and (ii) are reasonably well fulfilled, then the contribution from volume element $\mathbf{dr}$ would be the same as if this volume element were surrounded

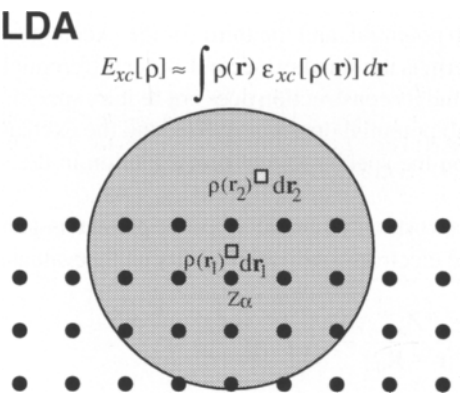


Fig. 1.1. Illustration of the local density approximation (LDA). The solid dots represent positions of atomic nuclei $\alpha$ with a nuclear charge $Z_\alpha$. $\rho(\mathbf{r}_1)$ and $\rho(\mathbf{r}_2)$ denote the electron density at points $\mathbf{r}_1$ and $\mathbf{r}_2$, respectively. In the LDA it is assumed that the exchange–correlation contribution from the volume element around $\mathbf{r}$ in the real case (left hand side) can be approximated by the same local contribution of a system where the electron density $\rho(\mathbf{r}_1)$ is the same anywhere outside as inside the volume element around $\mathbf{r}$ (right hand side). The analogous approximation is made to calculate the contribution from the volume element around $\mathbf{r}_2$. Note that the evaluation of the Coulombic terms involves the full inhomogeneity of the real electron density.

by a constant electron density of the same value as within **dr** (cf. Fig. 1.1). This is an excellent approximation for metallic systems, but represents quite a severe simplification in systems with strongly varying electron densities. In such cases one has to make a careful assessment of its validity. This will be illustrated in the context of specific examples which are discussed later.

A system of interacting electrons with a constant density is called a homogeneous electron gas. Substantial theoretical efforts have been made to understand and characterize such an idealized system. In particular, the exchange–correlation energy per electron of a homogeneous electron gas, $\varepsilon_{xc}[\rho]$, has been calculated by several approaches such as many-body perturbation theory (Hedin and Lundqvist, 1972) and quantum Monte Carlo methods (Ceperley and Alder, 1980). As a result, $\varepsilon_{xc}[\rho]$ is quite accurately known for a range of densities. For practical calculations, $\varepsilon_{xc}[\rho]$ is expressed as an analytical function of the electron density. There are different analytical forms with different coefficients in their representation of the exchange–correlation terms. These coefficients are not adjustable parameters, but rather they are determined through first-principles theory. Hence, the LDA is a first-principles approach in the sense that the quantum mechanical problem is solved without any adjustable, arbitrary, or system depended parameters. Table 1.1 shows an example of such local exchange–correlation terms. Note that there are two types of exchange–correlation terms, one for the energy and one for the potential. The energy, $\varepsilon_{xc}$, is needed to evaluate the total energy and the potential term, $\mu_{xc}$, is required for the Kohn–Sham equations. The two terms are related by

$$\mu_{xc} = \frac{\partial[\rho\varepsilon_{xc}(\rho)]}{\partial\rho} \tag{1.19}$$

which follows from Eqs. (1.17) and (1.18).

Table 1.1

Explicit forms for the local density exchange (Gáspár, 1954; Kohn and Sham, 1965) and correlation terms (Hedin and Lundqvist, 1972) for a non-spin polarized system. Exchange and correlation energies per electron are denoted by $\varepsilon$ and the corresponding potentials by $\mu$. Both quantities are given in Hartree atomic units (1 Hartree = 2 Rydberg = 27.21165 eV). The units for the electron density are number of electrons/(Bohr radius)$^3$

| | Energy | Potential |
|---|---|---|
| | $\varepsilon_{xc} = \varepsilon_x + \varepsilon_c$ | $\mu \dfrac{\partial(\rho\varepsilon)}{\partial\rho}$ |
| Exchange | $\varepsilon_x = -\dfrac{3}{2}\left(\dfrac{3}{\pi}\rho\right)^{1/3}$ | $\mu_x = -2\left(\dfrac{3}{\pi}\rho\right)^{1/3}$ |
| Correlation | $\varepsilon_c = -c\left[\left(1+x^3\right)\ln\left(1+\dfrac{1}{x}\right) + \dfrac{x}{2} - x^3 - \dfrac{1}{3}\right]$ | $\mu_c = -c\ln\left(1+\dfrac{1}{x}\right)$ |
| | $c = 0.0225, \quad x = \dfrac{r_s}{21}, \quad r_s = \left(\dfrac{3}{4\pi\rho}\right)^{1/3}$ | |

Using the explicit formulas given in Table 1.1, one can evaluate the exchange–correlation potential for any electron density $\rho(\mathbf{r})$. Thus, all terms of the effective one-particle operator in the Kohn–Sham equations are defined and one can proceed with a computational implementation. Before we present the various computational methods to solve the Kohn–Sham equations, we will discuss the interpretation of the one-particle eigenvalues of these equations.

### *1.2.2. One-particle energies and work function*

The fundamental quantities in density functional theory are the electron density and the corresponding total energy, but not the one-particle eigenvalues. However, the one-electron picture is so useful that one seeks to exploit the Kohn–Sham eigenvalues and one-particle wave functions as much as possible. The one-particle energies of effective electrons have been introduced in the derivation of the Kohn–Sham equations as Lagrange multipliers. The Kohn–Sham equations have the form of an eigenvalue problem in which each wave function has an associated eigenvalue $\varepsilon_i$ with an occupation number of $n_i$. Janak's theorem (Janak, 1978) provides a relationship between the total energy and these eigenvalues.

$$\varepsilon_i = \frac{\partial E}{\partial n_i} \tag{1.20}$$

The eigenvalue $\varepsilon_i$ equals the change of the total energy with the change of the occupation number of level $i$.

However, it is desirable to seek a more direct physical interpretation of these eigenvalues. Already before the formulation of present density functional theory, the one-electron picture has become widely used in solid state physics. For example, the distinction between a metal and an insulator is based on the analysis of the energy bands (energy bands are one-electron energies plotted as a function of different directions in reciprocal space); the characteristics of semiconductors and semiconductor/metal junctions are explained in terms of energy band structures; photoemission experiments are conveniently interpreted by a one-electron picture, often with quite reasonable quantitative agreement between theory and experiment. Furthermore, the analysis of the s, p, and d character of partial densities of states has become an extremely useful tool in the understanding of chemical bonding in alloys and compounds. While the direct interpretation of the Kohn–Sham eigenvalues as excitation energies often gives quantitative agreement with experimental photoemission spectra, there are significant differences in quantities such as energy band gaps in semiconductors. In fact, discrepancies of over a factor of two can be found between measured values and the LDA eigenvalues.

Such discrepancies between experimental excitation energies and differences between LDA eigenvalues are not necessarily a failure of the LDA, but rather an inappropriate interpretation of theoretical results. In the derivation of the Kohn–Sham equations given above, the effective one-particle eigenvalues were never required to be excitation energies! Only the total electron density and the corresponding total energy have rigorous meaning. It is possible, though, to use the results of density functional calculations as input into rigorous evaluations of excitation energies, as shown, for example, by Hybertsen and Louie (1987).

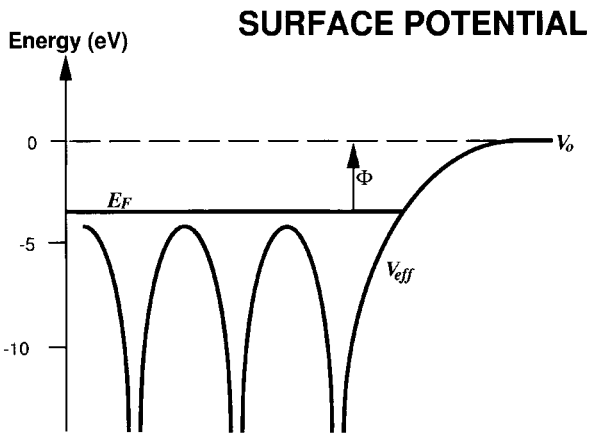


Fig. 1.2. Schematic representation of the effective one-electron potential in a cross section of a surface. The singularities of the effective potential mark the positions of atomic nuclei. Typical values for work functions are in the range 1–5 eV.

The highest occupied electronic level in a metallic system is called the Fermi energy or Fermi level, $E_F$. The nature of the electronic states at $E_F$ play a crucial role in determining materials properties such as electrical conductivity, magnetism, and superconductivity. On surfaces, the energy difference between $E_F$ and the electrostatic potential in the vacuum region, $V_0$, above the surface is the work function, $\Phi$ (cf. Fig.1.2). While in general the Kohn–Sham eigenvalues are not excitation energies, it can be shown (Schulte, 1977) that for a metallic system the highest occupied Kohn–Sham eigenvalue can be directly interpreted as the work function as shown in Fig. 1.2. Thus, the agreement between experimental and calculated work functions provides a good test for the quality of actual calculations. With present LDA approaches, the calculated values are typically within 0.1–0.2 eV of the experimental results. Work functions depend strongly on the geometry and nature of the surface and we will discuss some characteristic examples later in this chapter.

### *1.2.3. Spin-polarized systems*

So far, the discussion of density functional theory was restricted to non-spin-polarized cases. However, many systems such as magnetic transition metal surfaces or the dissociation of molecules on surfaces involve unpaired electrons or molecular radicals and thus require a spin-polarized method. In such systems, the number of electrons with "spin-up" can be different from that with "spin-down". Density functional theory has been generalized to accommodate spin-polarized systems which resulted in spin density functional theory with the local spin density (LSD) approximation (von Barth and Hedin, 1972; Gunnarson et al., 1972).

In the local spin density functional (LSDF) theory, the fundamental quantities are both the electron density, $\rho(\mathbf{r})$, and the spin density, $\sigma(\mathbf{r})$. The spin density is defined as the

difference between the density of the spin-up electrons and the density of the spin-down electrons

$$\sigma(\mathbf{r}) = \rho_\uparrow(\mathbf{r}) - \rho_\downarrow(\mathbf{r}) \tag{1.21}$$

with the total electron density

$$\rho(\mathbf{r}) = \rho_\uparrow(\mathbf{r}) + \rho_\downarrow(\mathbf{r}). \tag{1.22}$$

In LSDF theory, the exchange–correlation potential for spin-up electrons is in general different from that for spin-down electrons. Consequently, the effective potential (1.13) becomes dependent on the spin. Thus, the Kohn–Sham equations (1.12) in their spin-polarized form are

$$\left[-\frac{\hbar^2}{2m}\nabla^2 + V_{\text{eff}}^\sigma(\mathbf{r})\right]\psi_i^\sigma(\mathbf{r}) = \varepsilon_i^\sigma \psi_i^\sigma(\mathbf{r}), \quad \sigma = \uparrow \text{ or } \downarrow \tag{1.23}$$

with

$$V_{\text{eff}}^\sigma(\mathbf{r}) = V_{\text{C}} + \mu_{\text{xc}}^\sigma\big[\rho(\mathbf{r}), \sigma(\mathbf{r})\big]. \tag{1.24}$$

The exchange–correlation potential in LSDF theory depends on both the electron density and the spin density, as written in Eq. (1.24). There are two sets of single-particle wave functions, one for spin-up electrons and one for spin-down electrons, each with their corresponding one-electron eigenvalues. For the case of equal spin-up and spin-down densities, the spin density is zero throughout space and LSDF theory becomes identical with the LDF approach. Notice that in spin-polarized calculations, the occupation of single-particle states is 1 or 0, but there is still only one Fermi energy. In magnetic systems, the spin-up and spin-down electrons are often referred to as "majority" and "minority" spin systems. Table 1.2 gives an example of a commonly used local spin density exchange–correlation formula (von Barth and Hedin, 1972).

### *1.2.4. Beyond the local density approximation*

A large number of total energy calculations have shown that the LDA gives interatomic bond lengths within ±0.05 Å of experiment or better for a great variety of solids surface and molecules. However, two systematic trends have been found: (i) weak bonds are too short, for example the Ni–C bond in the Ni carbonyl $Ni(CO)_4$, the bond between two magnesium atoms (which are closed shell systems), and the length of hydrogen bonds such as that in the water dimer $H–O–H\cdots OH_2$; (ii) the binding energies calculated with the LDA are typically too large, sometimes by as much as 50% in strong bonds (Weinert et al., 1982) and even more in weak bonds.

Gradient-corrected density functionals as suggested by Perdew (1986), Becke (1988), and Perdew et al. (1992) seem to offer a remedy. The basic idea in these schemes is the inclusion of terms in the exchange–correlation expressions that depend on the gradient

Table 1.2

Explicit form of local spin density exchange–correlation terms (von Barth and Hedin, 1972). Energies and potentials are given in Hartree atomic units; the units for the electron and spin densities are number of electrons/(Bohr radius)$^3$. The electron gas density parameter $r_s$ is defined in Table 1.1

| | |
|---|---|
| Exchange–correlation energy | $\varepsilon_{xc}(\rho,\zeta) = \varepsilon_{xc}^{p}(\rho) + \left[\varepsilon_{xc}^{f}(\rho) - \varepsilon_{xc}^{p}(\rho)\right] f(\zeta)$ |
| | $\varepsilon_{xc}^{p} = \varepsilon_{x}^{p} + \varepsilon_{c}^{p}, \qquad \varepsilon_{xc}^{f} = \varepsilon_{x}^{f} + \varepsilon_{c}^{f}$ |
| | $\varepsilon_{x}^{p} = -\frac{3}{2}\left(\frac{3}{\pi}\rho\right)^{1/3}, \qquad \varepsilon_{x}^{f} = 2^{1/3}\varepsilon_{x}^{p}$ |
| | $\varepsilon_{c}^{p} = -0.0225\, F\left(\frac{r_s}{21}\right), \qquad \varepsilon_{c}^{f} = -0.01125\, F\left(\frac{r_s}{53}\right)$ |
| | $F(x) = \left(1+x^3\right)\ln\left(1+\frac{1}{x}\right) + \frac{x}{2} - x^3 - \frac{1}{3}$ |
| | $f(\zeta) = \frac{(1+\zeta)^{4/3} + (1-\zeta)^{4/3} - 2}{2^{4/3} - 2}$ |
| | $\zeta = \frac{\rho_\uparrow - \rho_\downarrow}{\rho}$ |
| Exchange–correlation potential | $\mu_{xc}^{\sigma} = A(\rho)\left(\frac{2\rho_\sigma}{\rho}\right)^{1/3} + B(\rho), \qquad \sigma = \uparrow \text{ or } \downarrow$ |
| | $A(\rho) = \mu_{x}^{p}(r_s) + \nu_c(r_s), \qquad B(\rho) = \mu_{c}^{p}(r_s) - \nu_c(r_s)$ |
| | $\mu_{c}^{p}(r_s) = -0.0225 \ln\left(1 + \frac{21}{r_s}\right)$ |
| | $\nu_c = -\frac{4}{3}\frac{1}{2^{1/3}-1}\left[0.01125\, F\left(\frac{r_s}{53}\right) - 0.0225\, F\left(\frac{r_s}{21}1\right)\right]$ |

of the electron density and not only on its value at each point in space. Therefore, these corrections are also sometimes referred to as "non-local" potentials. As example, Table 1.3 gives the form suggested by Becke (1988) for the exchange part and Perdew (1986) for the correlation.

While dissociation energies calculated with these corrections rival in accuracy the best post-Hartree–Fock quantum chemistry methods, gradient corrected density functional calculations are computationally much less demanding and more general. At present, gradient corrected density functionals have been studied mostly for molecular systems (e.g., Andzelm and Wimmer, 1992). The results are very encouraging and this approach could turn out to be of great value in providing quantitative thermochemical data on surface reactions, as needed, for example, in the design and optimization of chemical vapor deposition (CVD), gas separation, catalytic, and electrochemical processes.

Table 1.3

Gradient-correction to the total energy for exchange (Becke, 1988) and correlation (Perdew, 1986). Energies are given in Hartree atomic units; the units for the electron and spin densities are number of electrons/(Bohr radius)$^3$. The constant $b$ in Becke's formula is a parameter fitted to the exchange energy of inert gases. The explicit form of the functions $f$ and $g$ in Perdew's expression for the correlation energy is given in the original paper (Perdew, 1986)

| | $E_{\mathrm{GGA}} = E_{\mathrm{LSD}} + E_{\mathrm{x}}^{G} + E_{\mathrm{c}}^{G}$ |
|---|---|
| Gradient-corrected exchange (Becke, 1988) | $E_{\mathrm{x}}^{G} = b\sum_{\sigma}\int \frac{\rho_\sigma x_\sigma^2}{1+6bx_\sigma \sinh^{-1} x_\sigma}\,\mathrm{d}\mathbf{r}$ <br> $x_\sigma = \frac{\lvert\nabla\rho\rvert}{\rho_\sigma^{4/3}}, \quad \sigma = \uparrow \text{ or } \downarrow$ |
| Gradient-corrected correlation (Perdew, 1986) | $E_{\mathrm{c}}^{G} = \int f(\rho_\uparrow, \rho_\downarrow)\mathrm{e}^{-g(\rho)\lvert\nabla\rho\rvert}\lvert\nabla\rho^2\rvert\,\mathrm{d}\mathbf{r}$ |

The one-particle eigenvalues obtained from gradient-corrected exchange–correlation potentials are not significantly different from the LDA eigenvalues. Therefore, these potentials do not (and are not intended to) remove the discrepancy between calculated and measured energy band gaps. This is the objective of self-interaction corrections and other computationally more demanding approaches such as the GW method, which are discussed in later chapters.

### *1.2.5. Relativistic effects*

Electrons near an atomic nucleus achieve such high kinetic energies that relativistic effects become noticeable even for light atoms at the beginning of the periodic table. For elements with an atomic number above about 54 (Xe) these relativistic effects become quite important and should be included in electronic structure calculations. The relativistic mass enhancements of electrons near the nuclei lead to a contraction of the electronic charge distribution around the nuclei compared with a non-relativistic treatment. For atoms with about $Z > 54$ non-relativistic calculations therefore can overestimate bond lengths by 0.1 Å and more. Furthermore, relativistic effects change the relative energy of s-, p-, d-, and f-states which can have a significant impact on bonding mechanisms and energies. Relativistic effects lead to a spin–orbit splitting which is, for example, about 0.3 eV for the splitting between the $4f_{5/2}$ and $4f_{7/2}$ in Ce. For core states, the spin orbit splitting can be very large. For example, the $2p_{1/2}$ and the $2p_{3/2}$ core states in W are split by 1351 eV. Important effects on surfaces such as the Kerr rotation in magneto-optical devices or the X-ray dichroism involve spin–orbit splitting. Thus, a relativistic electronic structure theory is necessary. This is accomplished by solving the Dirac equations, as discussed, for example, in the textbooks by Bjorken and Drell (1964) and Messiah (1970). Within a spherically symmetric potential, the Dirac equations, like the non-relativistic Schrödinger equation, can be decomposed into a radial and angular part. For illustration, we show the

radial equations

$$\begin{aligned} -\frac{\mathrm{d}F_{nlj}(r)}{\mathrm{d}r} + \frac{\kappa}{r}F_{nlj}(r) &= \left[E - m + V_{\mathrm{eff}}(r)\right] \\ \frac{\mathrm{d}G_{nlj}(r)}{\mathrm{d}r} + \frac{\kappa}{r}G_{nlj}(r) &= \left[E + m + V_{\mathrm{eff}}(r)\right] \end{aligned} \tag{1.25}$$

$$\begin{array}{lllll} & s & p & d & f \ldots \\ l = & 0, & 1, & 2, & 3 \ldots \\ j = & \frac{1}{2}, & \frac{1}{2}, \frac{3}{2}, & \frac{3}{2}, \frac{5}{2} & \frac{5}{2}, \frac{7}{2} \cdots \\ \kappa = & -1, & 1, -2, & 2, -3, & 3, -4 \ldots \end{array}$$

$$\kappa = \begin{cases} -(l+1), & j = l + \frac{1}{2}, \\ +l, & j = l - \frac{1}{2}. \end{cases}$$

$F$ and $G$ are called the large and small component of the radial wave function. The quantum numbers $n$ and $l$ are equivalent to the non-relativistic case; $j$ labels spin–orbit-split states and is used as subscript to label states such as $2p_{1/2}$, $2p_{3/2}$ and the $4f_{5/2}$. The quantum number $\kappa$ is a convenient quantity used within relativistic computer programs. The radial part of the charge density is constructed from the large and small components by

$$\rho(r) = \sum_{nlj} n_{nlj}\left[|F_{nlj}(r)|^2 + |G_{nlj}(r)|^2\right]. \tag{1.26}$$

The correct treatment of exchange and correlation in a fully relativistic theory is a difficult problem and has not yet been completely resolved.

Koelling and Harmon (1977) have proposed a semi-relativistic (or scalar-relativistic) treatment. This approach involves an averaging over the spin–orbit splitting, but retains the kinematic effects. This restores most of the simplicity of a non-relativistic method, but still gives an excellent representation of the core electron distribution and the appropriate (spin–orbit averaged) energies of the valence electrons.

Pseudopotentials can also be used to mimic relativistic effects such as the contraction of the core electrons and to include relativistic effects in the shape of the pseudo-wave functions. Once the pseudopotentials are constructed, calculations of the valence electrons proceed in the same way as in the non-relativistic case. This approach is used in the pseudopotential plane wave method discussed below and also in some quantum chemical calculations.

### *1.2.6. Relativistic spin polarization and magnetization*

For magnetic phenomena in transition metals, rare earths and actinides, one is faced with both relativistic and spin-polarization effects. This is a difficult theoretical problem and we will show here the concepts and the approach taken by Weinert and Freeman (1983) in the study of the Knight shift of the Pt(001) surface.

Consider the coupling of Dirac particles of mass $m$ and charge $e$ to the electromagnetic field (we will be in the radiation gauge $\nabla \cdot A = 0$). We write

$$\hat{H} = \hat{H}_0 + \frac{1}{c}\int \hat{J}_\mu A^\mu \, \mathrm{d}\mathbf{r} \tag{1.27}$$

where $\hat{H}_0$ is the Hamiltonian in the absence of external fields and the four-current operator and four-potential are given by

$$\hat{J}_\mu = \left(c\hat{\rho}, \hat{\vec{J}}\right) = ec\hat{\bar{\psi}}(\mathbf{r})\gamma^\mu\hat{\psi}(\mathbf{r}), \tag{1.28}$$

$$A^\mu = \left(\Phi, \vec{A}_{\mathrm{ext}}\right). \tag{1.29}$$

[The notation follows the convention of Bjorken and Drell (1964, 1965).] Rajagopal and Callaway (1973), MacDonald and Vosko (1979), and Rajagopal (1978) have demonstrated that the Hohenberg–Kohn theorems on which DFT is based can be generalized to include relativistic effects. Moreover, these authors have shown that one can obtain Kohn–Sham single-particle equations of the form (MacDonald and Vosko, 1979)

$$\left\{c\vec{\alpha}\cdot\left[\vec{p} - \frac{e}{c}\vec{A}_{\mathrm{eff}}\right] + \beta mc^2 + eV_{\mathrm{eff}}(\mathbf{r})\right\}\phi_i(\mathbf{r}) = \varepsilon_i\phi_i(\mathbf{r}), \tag{1.30}$$

where the effective potentials are given by

$$V_{\mathrm{eff}}(\mathbf{r}) = \Phi(\mathbf{r}) + e\int \frac{n(\mathbf{r}')}{|\mathbf{r}-\mathbf{r}'|}\,\mathrm{d}\mathbf{r}' + \frac{\delta E_{\mathrm{xc}}[J_\mu]}{\delta J_0(\mathbf{r})}, \tag{1.31}$$

$$\vec{A}_{\mathrm{eff}}(\mathbf{r}) = \vec{A}_{\mathrm{ext}} - \frac{\delta E_{\mathrm{xc}}[J_\mu]}{\delta J(\mathbf{r})} \tag{1.32}$$

and $n(\mathbf{r})$ is the number density [or, in the notation used earlier, the electron density $\rho(\mathbf{r})$]. The exchange–correlation energy functional $E_{\mathrm{xc}}[J_\mu]$ contains magnetic effects through its dependence on the spatial components of the current.

If we are interested in spin effects, this approach is not appropriate since spin and kinetic effects are not separable. Following MacDonald and Vosko (1979) we take the non-relativistic viewpoint that the external fields (in analogy with non-relativistic spin density functional theory) couple only to the particle and spin densities,

$$\hat{H}_{\mathrm{ext}} = e\int :\hat{\bar{\psi}}(\mathbf{r})\gamma_0\hat{\psi}(\mathbf{r}): \Phi(\mathbf{r})\,\mathrm{d}\mathbf{r} - \frac{1}{2}\mu_{\mathrm{B}}\int :\hat{\bar{\psi}}(\mathbf{r})\sigma_{\mu\nu}\hat{\psi}(\mathbf{r}): F^{\mu\nu}_{\mathrm{ext}}(\mathbf{r})\,\mathrm{d}\mathbf{r}, \tag{1.33}$$

where $\mu_B$ is the Bohr magneton and

$$\sigma^{\mu\nu} = \frac{1}{2} i \left[\gamma^\mu, \gamma^\nu\right], \tag{1.34}$$

$$F^{\mu\nu} = \partial^\mu A^\mu - \partial^\nu A^\nu. \tag{1.35}$$

If we consider $A^\mu$ and $F^{\mu\nu}$ to be given classical objects with $F^{\mu\nu}$ having only spatial components, we have (MacDonald and Vosko, 1979)

$$\hat{H}_{\text{ext}} = e \int : \hat{\bar{\psi}}(\mathbf{r}) \gamma_0 \hat{\psi}(\mathbf{r}) : \Phi(\mathbf{r})\, d\mathbf{r} - \mu_B \int \left[ : \hat{\bar{\psi}}(\mathbf{r}) \vec{\sigma} \hat{\psi}(\mathbf{r}) : \right] \cdot \vec{B}\, d\mathbf{r}. \tag{1.36}$$

If we now define the magnetization density operator $\hat{\vec{m}}(\mathbf{r}) = \mu_B \hat{\bar{\psi}} \vec{\sigma} \hat{\psi}$, we can write

$$\hat{H}_{\text{ext}} = \int \left\{ \hat{\rho}(\mathbf{r}) \Phi(\mathbf{r}) - \left[ \vec{m}(\mathbf{r}) \cdot \vec{B} \right] \right\} d\mathbf{r}. \tag{1.37}$$

The first term contains the usual minimal electromagnetic coupling while the second term represents a coupling to the magnetic dipole moment only. This Hamiltonian leads to single-particle equations of the form

$$\left[ c \vec{\alpha} \cdot \vec{p} + \beta m c^2 + e V_{\text{eff}}(\mathbf{r}) - \mu_B \vec{\Sigma} \cdot \vec{U}_{\text{eff}}(\mathbf{r}) \right] \phi_i(\mathbf{r}) = \varepsilon_i \phi_i(\mathbf{r}), \tag{1.38}$$

where $V_{\text{eff}}(\mathbf{r})$ is given by Eq. (1.31) and the spin-density operator $\vec{\Sigma}$ and the effective magnetic potential are given by

$$\vec{\Sigma} = \begin{pmatrix} \vec{\sigma} & 0 \\ 0 & -\vec{\sigma} \end{pmatrix}, \tag{1.39}$$

$$\vec{U}_{\text{eff}} = \vec{B} + \frac{\delta E_{\text{xc}}}{\delta \vec{m}(\mathbf{r})}, \tag{1.40}$$

where $\vec{\sigma}$ denotes the $2 \times 2$ Pauli spinors. The number density $n(\mathbf{r})$ and magnetization density $\vec{m}(\mathbf{r})$ are given by

$$n(\mathbf{r}) = \sum_i \phi_i^\dagger(\mathbf{r}) \phi_i(\mathbf{r}), \tag{1.41}$$

$$\vec{m}(\mathbf{r}) = \mu_B \sum_i \left[ \phi_i^\dagger(\mathbf{r}) \vec{\Sigma} \phi_i(\mathbf{r}) \right], \tag{1.42}$$

where the sums are over all occupied (positive-energy) states.

If one takes the non-relativistic limit of Eq. (1.38) retaining the first relativistic correction, we obtain the familiar Pauli-type equation for a magnetic field coupling to the spins only (Baym, 1976)

$$\left[\left(\frac{p^2}{2m} - \frac{p^4}{8m^3c^2}\right) - \mu_B\vec{\sigma}\cdot\left(\vec{B} - \frac{1}{2mc}(\nabla V \times \vec{p})\right) + \left(eV + \frac{\hbar^2 e}{8m^2c^2}\nabla^2 V\right)\right]\psi = (\varepsilon - mc^2)\psi. \tag{1.43}$$

In this equation $\vec{B}$ and $V$ are the effective magnetic fields and potentials which include the exchange–correlation effects.

The set of self-consistent Eqs. (1.31) and (1.38)–(1.42), in principle, yields the correct charge and magnetization densities. Unfortunately, since the exact exchange–correlation functional is not known, one has to use the well-known local-density approximation. For metals such as Pt, relativistic corrections to the exchange and spin–orbit coupling do affect the Fermi surface, but the valence charge and spin densities are rather insensitive to these effects (MacDonald et al., 1981). Hence, one can treat the valence electrons scalar relativistically (Koelling and Harmon, 1977), i.e., including all kinematic relativistic effects except spin–orbit effects. In this way, one avoids the problems associated with solving the Dirac equation self-consistently for complex systems with large unit cells such as those encountered in surface systems. For the core electrons, on the other hand, the spin–orbit term can have large effects (especially for p functions), and hence one treats the core fully relativistically.

One is now left with the question of how to include magnetic and spin effects. The non-relativistic viewpoint implicit in the form of the coupling in Eq. (1.37) suggests treating these effects in an analogous way to the non-relativistic (local-) spin-density functional method, i.e., solving the standard spin-polarized equations but with the non-relativistic single-particle operator replaced by the scalar relativistic one. This prescription is obviously not exact, but only true in a perturbational sense. However, since we know that for light systems the relativistic equations must reduce to the standard non-relativistic results, there is justification for this approach. For the magnetic fields and Pt surfaces which Weinert and Freeman (1983) considered, the magnetization fraction (magnetization density divided by charge density) in the high-density (relativistic) core region is of the order $10^{-8}$–$10^{-6}$; hence a perturbational expansion in terms of this factor will converge quite rapidly. For the non-relativistic regions of space, this procedure reduces correctly to the standard spin-polarized one.

Using this approach, one is left with the question of how to obtain the magnetization density, or equivalently, the magnetization fraction, from the spin-polarized single-particle equations. In the non-relativistic limit one would define the relative magnetization $\zeta$ as

$$\zeta = \frac{|\vec{m}_{NR}|}{n} = \frac{n_\uparrow - n_\downarrow}{n_\uparrow + n_\downarrow}, \tag{1.44}$$

where $n_\uparrow(n_\downarrow)$ is the number density of up (down) electrons and $n = n_\uparrow + n_\downarrow$. Ramana and Rajagopal (1979) have considered the case of a relativistic spin-polarized electron gas and have obtained a relationship for the relativistic magnetization fraction $\xi$,

$$\xi = \frac{|\vec{m}|}{n} \tag{1.45}$$

using $\xi$ as a parameter (Ramana and Rajagopal, 1979).

$$\xi(\zeta) = \frac{1}{3}\zeta + \frac{1}{2\beta^3}\{\beta x(1+\beta^2 x^2)^{1/2} - \beta y(1+\beta^2 y^2)^{1/2} + \ln[\beta x + (1+\beta^2 x^2)^{1/2}] - \ln[\beta y + (1+\beta^2 y^2)^{1/2}]\}, \tag{1.46}$$

where $x = (1+\zeta)^{1/3}$, $y = (1-\zeta)^{1/3}$, and $\beta = \hbar k_F/(mc) = \alpha(3\pi^2 n)^{1/3}$ is a dimensionless relativistic expansion parameter depending on the density $n$. In the non-relativistic case ($\beta \to 0$) the ratio $\xi/\zeta$ approaches one, while in the extreme relativistic limit ($\beta \to \infty$) the ratio approaches $1/3$. This reduction of the relativistic magnetization fraction compared to the non relativistic case can be understood by noting (Ramana and Rajagopal, 1979) that the helicity, and not spin, is a good quantum number; hence, each electron has both a "spin-up" and "spin-down" part. Note that this result implies that it is impossible to have a fully polarized relativistic electron gas. Likewise, if one has an external magnetic field, the spin-quantization axis of an electron in its rest frame is not parallel to the external field.

One can use Eq. (1.46) locally to transform the spin densities obtained from the scalar relativistic equations into the relativistic magnetization densities. This relativistic correction in elements such as Pt is important only very near the nucleus where it yields a factor of approximately one-half, while already for distances of the order of 0.5 Bohr the correction is less than 1%.

## 1.3. Surface models and computational approaches

### *1.3.1. Geometric models*

One of the most crucial steps in computational science is the creation of relevant geometric models. Many, but by no means all phenomena in surface science are relatively short-range in nature. This makes it possible to choose geometric models which are small enough to be tractable by today's electronic structure methods yet still large enough to be physically meaningful. Systems containing of the order of 100 atoms per repeat unit can be treated on a first-principles level with today's programs and computer hardware. A particular choice depends on the physical or chemical question to be answered and each geometric model has its strengths and limitations. In the following, we will discuss the most common geometric models for electronic structure calculations of surfaces (cf. Fig. 1.3) and outline their range of applicability.

Conceptually the most satisfying surface geometry is that of a semi-infinite solid. This geometry can be used for the simple jellium model of surfaces. In the jellium model, the positive charge of the atomic nuclei is simply represented by a uniform constant positive

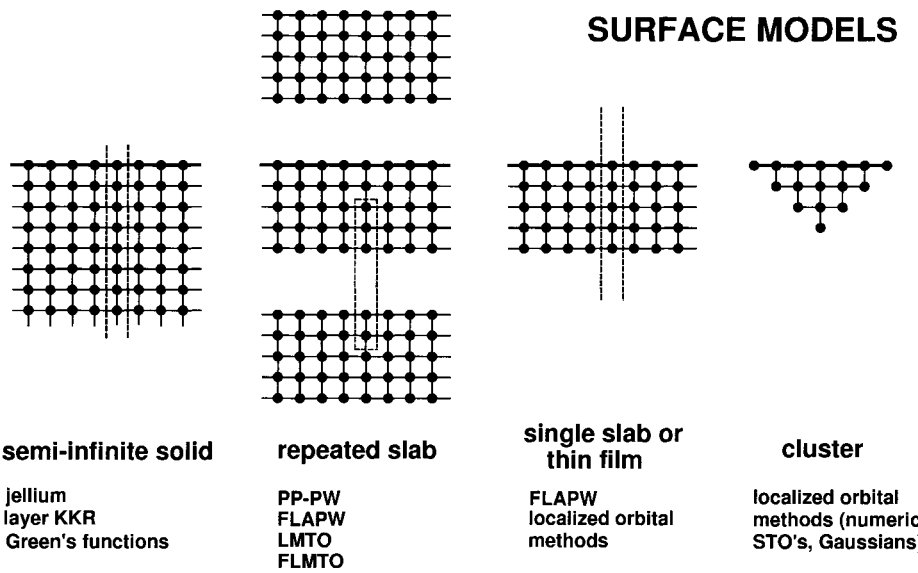


Fig. 1.3. Geometric models for practical surface calculations. The geometry of a semi-infinite solid is mainly used in jellium calculations and methods employing Green's functions and matching techniques. Standard band structure methods using three-dimensional periodicity can be directly applied to a repeated slab geometry. These standard methods include the pseudo-potential plane wave (PP-PW) methods, the full-potential linearized augmented plane wave (FLAPW) method, the linearized muffin-tin orbital (LMTO) method and the full potential LMTO method. The FLAPW method has been implemented for the single slab geometry, which also can be used with localized orbital methods. The cluster geometry is amenable for localized orbital methods with numerical functions, Slater-type orbitals (STO's) or Gaussians as basis set, as used for molecular quantum chemical calculations.

background inside the solid and zero outside an appropriately chosen surface plane. Effectively, the system is thus reduced to a one-dimensional problem and the distribution of the electrons are then calculated using density functional theory.

The use of a semi-infinite solid is much more difficult if a full three-dimensional solution of the density functional problem is attempted. However, it is reasonable to assume that any material becomes bulk-like at a certain distance away from the surface. A priori one does not know that distance, but experience shows that typically of the order of 10 atomic layers are sufficient. Hence, one can use the electronic structure of the bulk system, calculated with the three-dimensional periodicity, up to a plane about 10 atomic layers underneath the surface. In the top layers or "surface region", the electronic wave functions are then chosen to match the bulk states inside the solid and satisfy the vacuum boundary conditions above the surface. Green's functions techniques as used, for example, in the layer-KKR method (Korringa, 1947; Kohn and Rostoker, 1954; Cooper, 1973; Kar and Soven, 1975) provide the necessary mathematical apparatus to accomplish this matching procedure.

A simple, but effective geometric surface model is the repeated slab geometry (cf. Fig. 1.3). Thin films consisting of about 5 to 20 layers are repeated in the direction perpendicular to the surface. The layers are chosen thick enough to approach bulk-like behavior

near the center of each layer and the spacing is taken large enough so that any artificial interactions across the vacuum region between the slabs are minimized. About 10–20 Å are usually sufficient to fulfill this requirement. For such a geometry, any three-dimensional band structure method can be used. The most common approaches for three-dimensional band structure calculations are the pseudopotential plane wave method, the full-potential linearized augmented plane wave (FLAPW) method, and the linearized muffin-tin orbital (LMTO) method with its generalization to full potentials. Practical applications of these approaches are limited by the number of atoms in the three-dimensional supercell. Thus, a compromise needs to be found between slab thickness, spacing between the slabs, and computational effort.

One way to overcome at least one of these limitations is the use of a single-slab geometry (cf. Fig. 1.3). The slab still has be to be thick enough to achieve bulk-like behavior in its interior, but correct vacuum boundary conditions are fulfilled above and below the slab. It has been found that transition metal films as thin as five layers exhibit already the major characteristics of transition metal surfaces such as surface states and reasonable values for work functions while approaching bulk-like behavior near the center of the film. Simple metals such as Al require a larger number of layers, preferably more than about 10, to approach bulk like behavior in the interior.

Finally, surfaces can be modeled by finite clusters. This approach is being widely used for the investigation of chemisorption, since it allows the application of standard quantum chemistry programs. While reasonable structural information such as adsorption geometries can be obtained with relatively small clusters consisting of 10 or 20 atoms, much larger clusters of preferably well over 100 atoms are required to achieve reliable results for sensitive quantities such as adsorption energies or the distinction between different adsorption sites with similar energy. Large clusters pose serious computational challenges, especially for transition metals where the convergence of the self-consistency procedure (see below) can be rather slow. Finally, even for large clusters, termination effects can have unpredictable side effects.

### *1.3.2. Overview of computational methods*

Figure 1.4 provides an overview of the major choices between different surface electronic structure methods. If the system contains elements with atomic numbers greater than about 40, a scalar-relativistic or fully relativistic treatment is appropriate. Most surface electronic structure calculations are done either non-relativistically or on a scalar-relativistic level. The neglect of relativistic effects can be quite severe leading to an overestimation of bond distances of perhaps 0.1Å and incorrect ordering of energy bands.

Choices of specific geometric models and their space group symmetry are reflected in the effective potential operator. Symmetry such as an inversion center and mirror planes can greatly reduce the computational effort. In practical density functional implementations, the computational effort scales approximately with a third power or less in the number of atoms. If the number of inequivalent atoms of a system is reduced, for example, by a factor of 4, the computational time can thus be reduced by about 50 times.

The next major choice is between a non-spin polarized and a spin-polarized calculation. In most cases, structural information such as surface reconstructions or equilibrium geometries of adsorbates can be quite reliably obtained from non-spin polarized calculations.

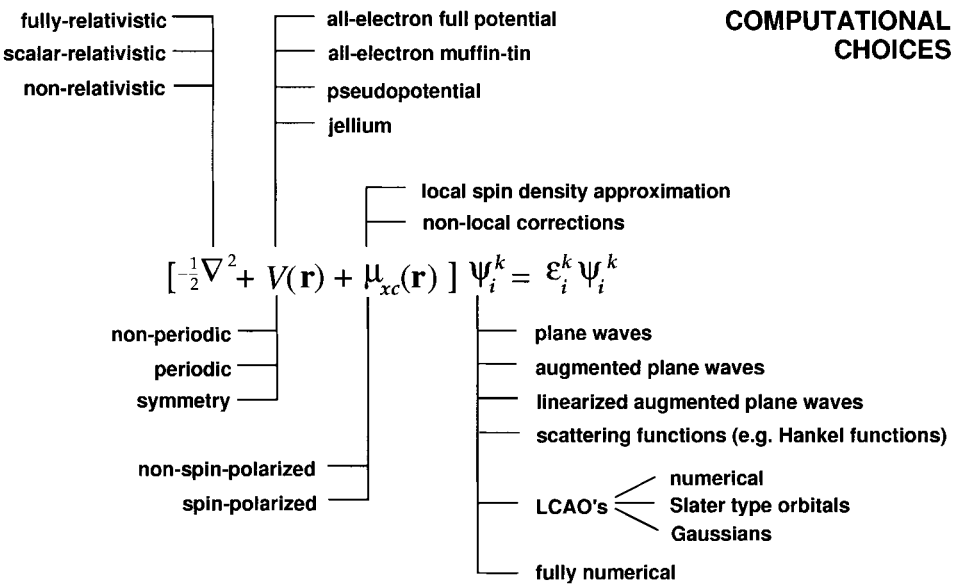


Fig. 1.4. Overview of theoretical and computational choices for the solution of the density functional one-particle equations.

Also the characteristic features of the charge density distribution and the work function differ usually little between non-spin polarized and spin-polarized treatments. Therefore, one often first performs non-spin polarized calculations followed by spin-polarization.

A characteristic feature of specific computational methods are the various simplifications to the form of the effective potential. In the most general case, the potential is constructed from all electrons and no additional approximation is made to its shape. In the late 1930's, the so-called muffin-tin approximation was introduced. In this approximation, the effective potential within a sphere around each atom is taken to be spherically averaged, thus resembling a free atom. In the remaining interstitial region of a solid, the potential is simply taken to be constant. This approximation can be generalized to surface calculations by adding in the region above the surface a potential which depends only on the distance from the surface, obtained by averaging the potential in planes parallel to the surface. Muffin-tin potentials are reasonable for densely packed metallic systems, but lead to uncontrolled errors if applied to more open structures. Both the full-potential and the muffin-tin potential approach are used in all-electron calculations.

Pseudopotentials are frequently employed for calculations on semiconductor surfaces. In this approximation, the core electrons and the Coulomb singularity from the atomic nuclei are replaced by a smooth pseudopotential around each atom. At a certain cut-off radius away from each atomic position, the pseudopotential becomes the actual effective potential. There are three major reasons for using pseudopotentials: (i) simple basis functions such as plane waves work well with pseudopotentials, (ii) there are fewer electrons thus simplifying the calculation, and (iii) relativistic effects which are mainly due to core electrons can be included in the pseudopotential. Together, these features lead to computa-

tionally highly efficient and relatively simple computational implementations. The major drawbacks of pseudopotentials are (i) an additional approximation is introduced, (ii) pseudopotentials for transition metals, rare earths, and actinides are possible in principle, but their effectiveness and accuracy has yet to be demonstrated, and (iii) properties and effects involving the core electrons such as core level shifts, hyperfine fields, and spin polarization of the core electrons are not directly accessible from pseudopotential calculations. For these reasons, both all-electron and pseudopotential methods have found their place in surface electronic structure theory.

A central part of any electronic structure calculation is the treatment of the exchange and correlation effects. Within density functional theory, the appropriate choices have to be made in the selection of the exchange–correlation potential operator. Earlier, we have discussed the local density approximation and its generalization to the spin-polarized case. The local density approximation is uniquely defined by Eqs. (1.17) and (1.18). However, different ways, such as many-body perturbation theory and quantum Monte Carlo methods, to evaluate the exchange–correlation energy in the homogeneous interacting electron gas have led to slightly different explicit forms for the exchange–correlation potentials. However, the deviations between these different forms are typically smaller than the discrepancies between calculated and experimental values. Thus, one can consider these potentials as practically equivalent.

As discussed earlier, there are several ways to include effects beyond the local density approximation. While improvements such as the density-gradient corrections to exchange and correlation have become rapidly popular in quantum chemistry calculations, their advantages and benefits for solid state and surface calculations are still a matter of discussion and ongoing research.

### *1.3.3. Variational solution of the Kohn–Sham equations*

The Kohn–Sham equations (1.12) have the form of one-particle eigenvalue equations

$$\mathbf{H}\psi_i(\mathbf{r}) = \varepsilon_i \psi_i(\mathbf{r}) \tag{1.47}$$

with the effective one-particle Hamilton operator

$$\mathbf{H} \equiv -\frac{\hbar^2}{2m}\nabla^2 + V_{\text{eff}}(\mathbf{r}). \tag{1.48}$$

Following standard mathematical techniques for solving eigenvalue problems, one can expand the unknown solutions $\psi_i(\mathbf{r})$ in a set of known functions, $\phi_j(\mathbf{r})$, with unknown linear coefficients, $c_{ij}$,

$$\psi_i(\mathbf{r}) = \sum_j c_{ij}\phi_j(\mathbf{r}). \tag{1.49}$$

These coefficients are determined through a variational procedure which leads to the solution of the following matrix problem

$$(\underline{\mathbf{H}} - \varepsilon\underline{\mathbf{S}})\mathbf{c} = \mathbf{0}. \tag{1.50}$$

$\underline{\mathbf{H}}$ and $\underline{\mathbf{S}}$ are the so-called Hamiltonian and overlap matrices with the following matrix elements

$$H_{ij} = \int \phi_i^*(\mathbf{r}) \left[ -\frac{\hbar^2}{2m} \nabla^2 + V_{\text{eff}}(\mathbf{r}) \right] \phi_j(\mathbf{r}) \, \mathrm{d}\mathbf{r}, \tag{1.51}$$

$$S_{ij} = \int \phi_i^*(\mathbf{r}) \phi_j(\mathbf{r}) \, \mathrm{d}\mathbf{r}. \tag{1.52}$$

$\varepsilon$ represents an eigenvalue and $\mathbf{c}$ are the coefficients of a solution represented as a column vector. In standard density functional calculations one diagonalizes the matrix $(\underline{\mathbf{H}} - \varepsilon \underline{\mathbf{S}})$. The dimension of the matrices is determined by the number of basis functions in the expansion (1.49).

### *1.3.4. Self-consistency cycle and geometry optimizations*

The effective potential in the Kohn–Sham equations (1.12) depends on the charge density, which is constructed from the one-particle wave functions. These wave functions are solutions of the Kohn–Sham equations. In other words, in order to set up the Kohn–Sham equations one needs to know their solutions. This problem is solved by an iterative, self-consistent procedure as shown in Fig. 1.5.

Start geometries for density functional calculations on surfaces are constructed either by using experimental data such as bulk lattice constants, from simpler computational approaches such as force field or semi-empirical methods, or from intuition. The start densities are then constructed from a superposition of atomic densities (calculated for individual free atoms or ions) or results from previous density functional computations are re-used.

The fundamental quantities of density functional theory are the electron density and, in the case of spin-polarized systems, also the spin density. With these quantities, and a given geometry, the Kohn–Sham equations are completely defined. Through the solution of Poisson's equation, the electrostatic Coulomb potential is obtained. Using an explicit form for the exchange–correlation potential as, for example, given in Table 1.1, the exchange–correlation potential operator is constructed. For a given variational basis set $\{\phi_j\}$, the Hamiltonian and overlap matrix elements can then be computed as indicated in Fig. 1.5. Subsequently, the matrix $\mathbf{H} - \varepsilon\mathbf{S}$ is diagonalized resulting in a set of one-particle eigenvalues and the variational expansion coefficients corresponding to each eigenvalue. Using these coefficients, the single-particle wave functions are synthesized and a new ("output") electron density can be calculated. To this end, the occupation of each state is determined by using Fermi–Dirac statistics. This means that the eigenvalues are sorted with increasing energy and all states are filled until the total number of electrons of the system is exhausted. In the case of systems with two-dimensional periodicity such as ordered surfaces, the synthesis of the charge density from one-particle wave functions involves the integration of the two-dimensional Brillouin zone in reciprocal space, as will be discussed in Subsection 1.3.5.

The new electron density is often referred to as "output" density indicating that each cycle in the self-consistency procedure essentially maps an "input" density into an "output"

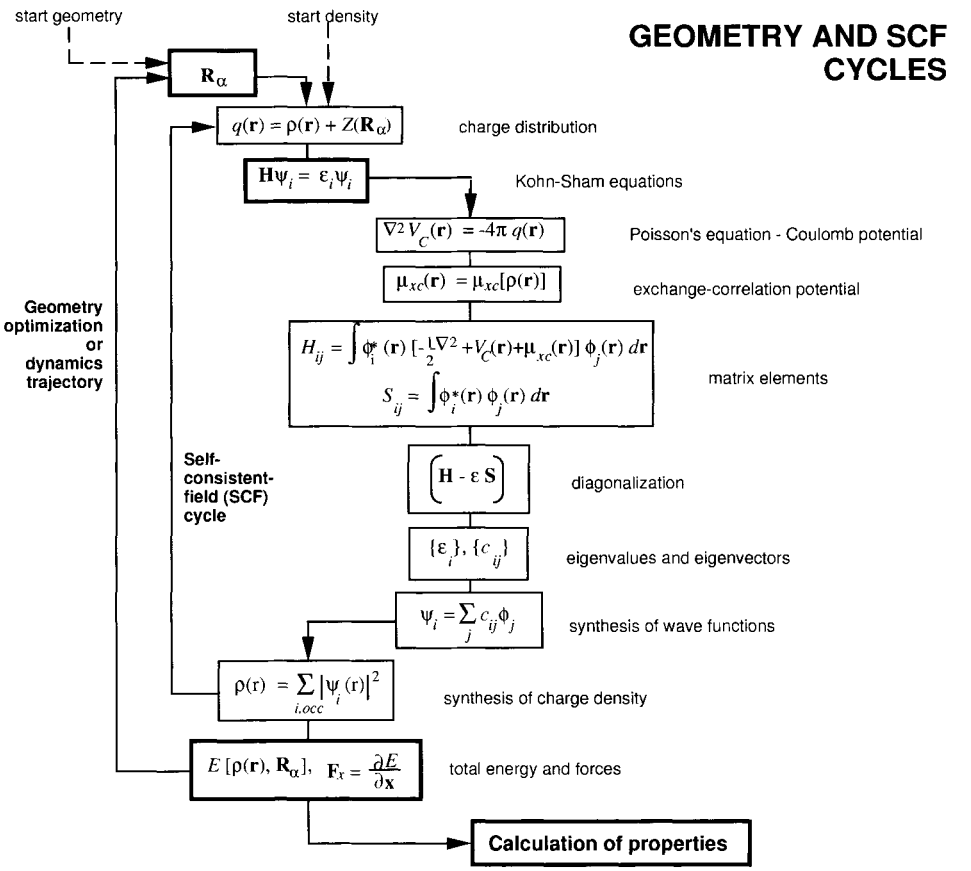


Fig. 1.5. Scheme of typical electronic structure calculations. The outer cycle represents the geometry optimization or other manipulation of the geometry such as dynamics trajectories or Monte Carlo procedures. The inner cycle is the self-consistency procedure to solve the Kohn–Sham equations. In methods such as the Car–Parrinello approach, both cycles are carried out simultaneously. The matrix diagonalization can be done either through explicit diagonalization or through iterative procedures. For simplicity, atomic units are used in the formulas.

density. By definition, self-consistency is achieved when the output density equals the input density. In practice, one iterates sufficiently long until the residual difference between the input and output densities does not cause any significant errors in the total energy or other properties of interest.

While this self-consistency procedure is straightforward in principle, practical calculations especially for magnetic systems are often plagued by aggravating convergence problems. If one would feed the full output density back as input density, the self-consistency process would quickly diverge. Therefore, many computational schemes have been devised to enable and accelerate convergence. The simplest method consists in mixing the output density with the input density, for example using 10% of the new output density, in order to construct the input density for the next iteration. In magnetic systems, feedback of

more than 3% can sometimes already lead to divergence. More sophisticated convergence and extrapolation schemes have thus been developed such as that suggested by Andersen (1965). In many non-magnetic systems, sufficient self-consistency can be reached within 10–20 cycles, but 50 steps or more may be necessary in more difficult cases.

Once self-consistency is achieved, the total energy and the forces on each atom can be calculated. Using this information, it is possible to optimize geometries, i.e., searching for minima or saddle points on the energy hypersurface. Geometries can be optimized by using only the total energy for various atomic arrangements. In practice, this is an extremely tedious process and only a few geometric parameters such as the lattice constant of a highly symmetric solid or the distance between an adsorbate atom and a surface can be optimized in this way. Knowledge of the forces on each atom greatly facilitates such geometry optimizations and makes it possible to relax many degrees of freedom simultaneously. In fact, quantum chemists have developed extensive experience with such methods (e.g., Schlegel, 1982) and this experience can be readily applied to surface calculations. Important optimization methods include steepest descent, conjugate-gradient, and the Broyden–Fletcher–Goldfarb–Shanno (BFGS) methods (Press et al., 1986). However, none of these methods can guarantee that the global minimum has been found. Thus, as the complexity and degrees of freedom of a system increase, molecular dynamics methods and Monte Carlo searches are a practical alternative.

To this end, an exciting and promising use of forces is the computation of dynamics trajectories. This enables the search for structural minima by simulated annealing techniques and, in principle, the computation of diffusion, phase transitions, and entire chemical reactions. However, the time-scales necessary to tackle these problems are in many cases far beyond the computational speed of present density functional calculations, but very encouraging first results have already been obtained.

The final geometries are then used for the calculation of properties which can be derived from the charge density, the potential, and the one-electron wave functions. The examples which will be discussed in later sections of this chapter as well as the other articles in this volume will give an overview of the structural, energetic, electronic, optical, and magnetic properties accessible through density functional calculations on surfaces.

### *1.3.5. Representation of wave functions for surfaces*

On surfaces, the three-dimensional periodicity of a crystal lattice is reduced to two-dimensional translational symmetry. Correspondingly, electronic wave functions are labeled by a two-dimensional $\mathbf{k}$-vector parallel to the surface, $\mathbf{k}^{\parallel}$, obeying a two-dimensional Bloch theorem

$$\psi_i\left(\mathbf{r}+\mathbf{T}^{\parallel},\mathbf{k}^{\parallel}\right)=\mathrm{e}^{\mathrm{i}\mathbf{k}^{\parallel}\cdot\mathbf{T}^{\parallel}}\psi_i\left(\mathbf{r},\mathbf{k}^{\parallel}\right). \tag{1.53}$$

Here, $\mathbf{T}^{\parallel}$ denotes a two-dimensional translation by integer multiples of the lattice vectors $\mathbf{a}_1$ and $\mathbf{a}_2$ in real space (cf. Fig. 1.6)

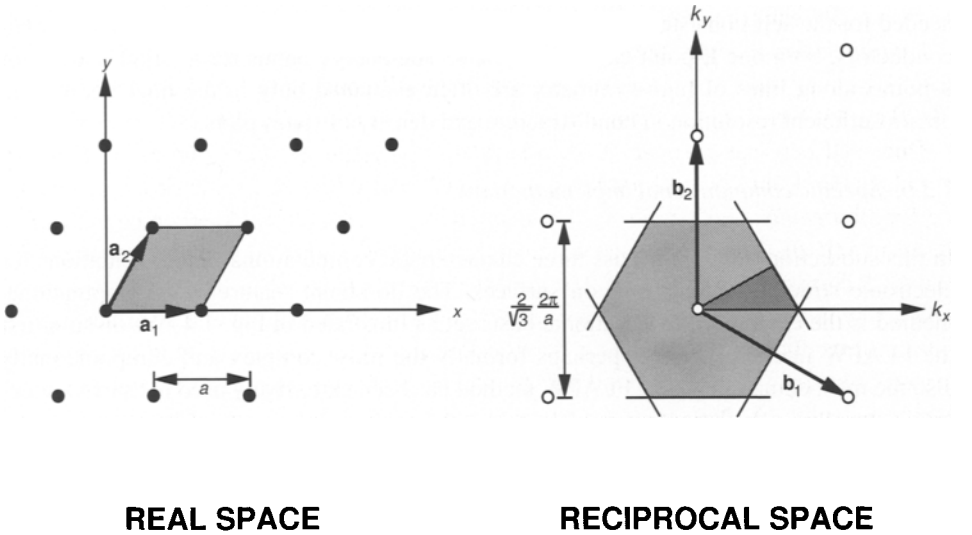


Fig. 1.6. Two-dimensional hexagonal lattice. The real space is shown on the left hand side with $\mathbf{a}_1$ and $\mathbf{a}_2$ denoting the translational vectors of the lattice. The unit cell is shaded. The right hand side shows the corresponding reciprocal lattice in the reciprocal or $\mathbf{k}$-space. The translational vectors of the reciprocal lattice are denoted by $\mathbf{b}_1$ and $\mathbf{b}_2$. The first Brillouin zone is shaded with the irreducible part shown darker.

In actual electronic structure calculations for surfaces or thin films with two-dimensional periodicity, the synthesis of the charge density from one-particle wave functions involves an integration over the first two-dimensional Brillouin zone (cf. Fig. 1.6).

$$\rho(\mathbf{r}) = \int_{\mathrm{BZ}} \theta\left[E_{\mathrm{F}} - \varepsilon_i\left(\mathbf{k}^{\parallel}\right)\right] \left|\psi_i\left(\mathbf{r}, \mathbf{k}^{\parallel}\right)\right|^2 \mathrm{d}\mathbf{k}^{\parallel}. \tag{1.54}$$

The step function $\theta$ insures that for each $\mathbf{k}$-point only occupied states below the Fermi energy $E_{\mathrm{F}}$ are counted. The labeling of wave functions by a $\mathbf{k}$-vector and the techniques of integrating over $\mathbf{k}$-space by using a finite $\mathbf{k}$-mesh are equivalent to standard electronic structure calculations for systems with three-dimensional translational symmetry. The theory and techniques are discussed in textbooks of solid state physics such as that of Ashcroft and Mermin (1976).

As mentioned earlier, the use of symmetry can greatly reduce the computational effort. For $\mathbf{k}$-space integrations this implies that only wave functions in the irreducible wedge of the Brillouin zone need to be calculated (cf. Fig. 1.6) and the contributions from symmetry-equivalent parts follow from the application of the appropriate symmetry operations.

Figure 1.5 discussed earlier contained an over-simplification since the $\mathbf{k}^{\parallel}$-label for wave functions and eigenvalues was not shown. Within each self-consistency cycle, the Kohn–Sham equations need to be solved not only once, but for each $\mathbf{k}$-point. The size of the Brillouin zone is inversely proportional to the size of the real-space unit cell. Thus, for complex systems with large two-dimensional unit cells, only a few $\mathbf{k}$-points are usually

needed for the self-consistency procedure. Especially for surfaces of insulators and semiconductors, even one **k**-point can be sufficient. The energy bands for a larger number of **k**-points along lines of high-symmetry are often evaluated only in the final iteration to obtain sufficient resolution in band structure and density of states plots.

### *1.3.6. Specific computational implementations*

In this subsection we will discuss three characteristic computational implementations for electronic structure calculations on surfaces. The dominant feature of a computational method is the choice of the variational basis set as illustrated in Fig. 1.4. We discuss first the FLAPW method which is perhaps formally the most complex and computationally also the most demanding. The FLAPW method has been extensively used for surface electronic structure calculations, it is often taken as benchmark because of its accuracy, and it shows all major features of surface electronic structure calculations. Subsequently, we will discuss the pseudopotential plane wave method which plays an important role in the study of semiconductor surfaces as well as in the combination of electronic structure theory and molecular dynamics. The third approach discussed here employs not analytical basis functions, but numerically generated atomic orbitals. This approach is closer to quantum chemical calculations and thus is playing an increasingly important role in the investigation of chemical reactions on surfaces.

#### *1.3.6.1. Full-potential linearized augmented plane wave (FLAPW) method*

The augmented plane wave (APW) method was introduced by Slater (1937). The basic idea is the partitioning of real space into spherical regions around atoms, so-called muffin-tin or atomic spheres, and an interstitial region (cf. Fig. 1.7). The dominant part of the effective potential inside the spheres has spherical symmetry and is constant in the interstitial region. Thus, one chooses as basis functions the solutions of Schrödinger's equations for these types of potentials, namely products of radial functions and spherical harmonics inside the atomic spheres and plane waves for the interstitial region. It is important to note that the muffin-tin potential is used here to construct the basis functions. Once such a basis set is defined, the solutions to *any* potential can be represented. A major step forward in the development of the APW method was the linearization of the eigenvalue problem (Koelling and Arbman, 1975; Andersen, 1975) by introducing two radial wave functions per angular momentum quantum number, which are the solutions of the radial Schrödinger equation, solved at fixed trial energies $E_l$

$$\frac{1}{2r}\frac{\mathrm{d}^2}{\mathrm{d}r^2}\left[ru_{nl}(r)\right] - \frac{l(l+1)}{2r^2}u_{nl}(r) + \left[E_l - V_{\mathrm{eff}}(r)\right]u_{nl}(r) + h_r u_{nl}(r) = 0 \qquad (1.55)$$

and the energy derivative of these radial solutions (Hartree atomic units are used here with $\hbar = m = e = 1$). The term $h_r$ is a semi-relativistic correction following Koelling and Harmon (1977).

In a single slab or thin film FLAPW approach (Krakauer et al., 1979a; Wimmer et al., 1981a; Weinert et al., 1982; Wimmer et al., 1985), one defines vacuum regions above and

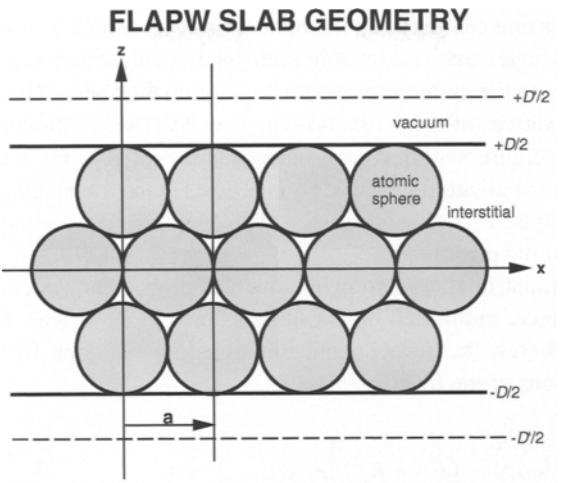


Fig. 1.7. Single slab or thin film geometry used in FLAPW calculations. The interstitial region extends between the two vacuum boundaries at $z = \pm D/2$. The vacuum regions above and below the film extend to $\pm\infty$. The arbitrary boundaries at $z = \pm D'/2$ are used to define a three-dimensional plane wave basis set within the interstitial region. These plane wave basis functions are not used in the region between $\pm(D'/2$ and $D/2)$. They are also not used inside the atomic spheres. The vector **a** denotes the two-dimensional translational basis vector parallel to the film surface.

below the slab as shown in Fig. 1.7. For the construction of the wave functions in these vacuum regions one uses only the $z$-dependent part of the potential, starting at $z = \pm D/2$. The explicit form of the FLAPW one-particle wave functions in the thin film geometry are thus

$$\psi_i(\mathbf{r}, \mathbf{k}^{\parallel}) = \sum_j c_{ij}\phi(\mathbf{r}, \mathbf{K}_j) \tag{1.56}$$

with

$$\mathbf{K}_j = \mathbf{k}^{\parallel} + \mathbf{G}_j. \tag{1.57}$$

$\mathbf{k}^{\parallel}$ is an arbitrary vector of the two-dimensional Brillouin zone and $\mathbf{G}_j$ is a three-dimensional lattice vector of the reciprocal space with its $k_x$ and $k_y$ components as integer multiples of the basis vectors $\mathbf{b}_1$ and $\mathbf{b}_2$. In the $z$-direction, an artificial periodicity between the boundaries at $z = \pm D'/2$ is used to define the third component of $\mathbf{G}_j$. With these definitions, the FLAPW basis functions $\phi(\mathbf{K}_j)$ are

$$\phi(\mathbf{r}, \mathbf{K}_j) = \begin{cases} \Omega^{-1/2} e^{i\mathbf{K}_j \cdot \mathbf{r}} \quad \text{for } \mathbf{r} \in \text{interstitial}, \\ \sum_{lm} \left[A^{\alpha}_{lm}(\mathbf{K}_j) u_j\left(E^{\alpha}_l, R_{\alpha}\right) + B^{\alpha}_{lm}(\mathbf{K}_j) \dot{u}_l\left(E^{\alpha}_l, r_{\alpha}\right)\right] Y_{lm}(\hat{r}_{\alpha}) \\ \quad \text{for } \mathbf{r} \in \text{sphere}\,\alpha, \\ \sum_q \left[A_q(\mathbf{K}_j) u_{\mathbf{k}q}(E_v, z) + B_q(\mathbf{K}_j) \dot{u}_{\mathbf{k}q}(E_v, z)\right] e^{i(\mathbf{k}^{\parallel} + \mathbf{K}^{\parallel}_q)\cdot \mathbf{r}} \\ \quad \text{for } \mathbf{r} \in \text{vacuum}. \end{cases} \tag{1.58}$$

$\Omega$ is the volume per unit cell between the boundaries at $z = \pm D/2$; $u_l(E_l, r)$ are solutions of the radial Schrödinger equations inside each sphere, calculated at a trial energy $E_l$ and classified according to the angular momentum quantum number $l$. The functions $\dot{u}_l(E_l, r)$ are the energy derivatives of these functions at $E = E_l$. The coefficients $A_{lm}$ and $B_{lm}$ are determined by the requirement that each plane wave, $\exp(i\mathbf{K}_j \cdot \mathbf{r})$, is continuous in value and radial derivative at all atomic sphere boundaries. Hence the matching coefficients $A_{lm}$ and $B_{lm}$ for each sphere $\alpha$ depend on $\mathbf{K}_j$. The functions $Y_{lm}$ are spherical harmonics centered at each atomic position.

The basis functions in the vacuum involve functions that depend only on the distance from the surface, multiplied by two-dimensional plane waves. Similar to the functions inside the spheres, the $z$-dependent functions are obtained from one-dimensional Schrödinger equations of the form

$$\left[-\frac{1}{2}\frac{\partial^2}{\partial z^2} + V_{\text{eff}}(z) - \left(E_\nu - K_q^2\right)\right] u_{\mathbf{k}q}(E_\nu, z) = 0. \tag{1.59}$$

$V(z)$ is the planar average of the effective potential perpendicular to the surface, $E_\nu$ are fixed energy parameters, and $\mathbf{K}_q^{\parallel}$ denote reciprocal lattice vectors of the two-dimensional lattice parallel to the surface. The matching coefficients $A_q(\mathbf{K}_j)$ and $B_q(\mathbf{K}_j)$ are chosen such that each basis function in the vacuum region is smooth in value and derivative (perpendicular to the surface) across the vacuum boundaries at $z = \pm D/2$.

Another way of looking at the FLAPW basis functions is the following. In the FLAPW method one uses numerical atomic-like functions in regions around the atoms and numerical functions for the vacuum region. These functions are joined together by plane waves. Continuity in value and derivatives throughout space, as required for any acceptable solution of Schrödinger's equation, is ensured by appropriate matching conditions. The radial functions in each atomic sphere depend on the actual spherical part of the effective potential, which varies from iteration to iteration in the self-consistency procedure. In standard FLAPW calculations, the radial functions are recalculated in each iteration. Typically functions up to $l = 8$ are used with two functions, $u(r)$ and $\dot{u}_l(r)$, for each $l$ value. Similarly, the $z$-dependent part of the vacuum potential is used to generate the basis functions in the vacuum region. Also these functions are recalculated as the form of the potential changes with the iterations. FLAPW basis sets can be systematically improved by increasing the cut-off for the maximum length of the reciprocal lattice vectors $\mathbf{G}_j$ and by increasing the highest $l$-component inside the atomic spheres. It has been found that for densely packed systems such as transition metal surfaces, about 50 basis functions per atom are needed.

In contrast, standard basis sets in quantum chemistry are not recalculated in each iteration (in fact, they are defined once and for all for each atom type) and usually functions up to $l = 2$ are used. This shows the high variational quality of FLAPW basis functions compared with other methods using fixed functions.

Unlike earlier implementations of the APW and LAPW method, no shape approximations to the charge density or the effective potential are made in the FLAPW method (Wimmer et al., 1981a). Both the charge density and the effective potential are represented by the same analytical expansions, i.e., a Fourier representation in the interstitial region

and an expansion in spherical harmonics inside the spheres. In the vacuum region, two-dimensional Fourier expansions in planes parallel to the surface are used. Thus, the charge density $\rho(\mathbf{r})$ is given by

$$\rho(\mathbf{r}) = \begin{cases} \sum_j \rho_j e^{i\mathbf{G}_j \cdot \mathbf{r}} & \text{for } \mathbf{r} \in \text{interstitial}, \\ \sum_{lm} \rho_{lm}^{\alpha}(r_\alpha) Y_{lm}(\hat{r}_\alpha) & \text{for } \mathbf{r} \in \text{sphere}\,\alpha, \\ \sum_q \rho_q(z) e^{i\mathbf{K}_q^{\parallel} \cdot \mathbf{r}} & \text{for } \mathbf{r} \in \text{vacuum}, \end{cases} \tag{1.60}$$

with an analogous representation of the effective potential. The coefficients $\{\rho_j, \rho_{lm}(r), \rho_q(z)\}$ are used in each iteration to create the Coulomb potential via the solution of Poisson's equation (1.16) and to synthesize the exchange–correlation potential (1.17). These coefficients of the input and output densities are also used to enable and accelerate the self-consistency procedure via mixing of the input and output density in each iteration.

In the FLAPW method Poisson's equation is solved by the following technique (Weinert, 1981; Wimmer et al., 1981a). The actual electron density inside the atomic spheres is replaced by a smooth pseudo-density which is constructed in such a way that the multipole moments outside the atomic spheres are identical to those of the actual density. The smooth pseudo-density is Fourier-transformed to a form which is analogous to the expansion of the interstitial charge density (1.60). In this representation, the solution of Poisson's equation is very simple yielding the correct electrostatic potential everywhere outside and on the surface of the atomic spheres. Using the correct potential on the surface of the atomic spheres and the original electron density inside each sphere, the correct potential can subsequently be calculated also inside the spheres by a Green's function method. The potential in the vacuum region is also obtained by a Green's function method involving one-dimensional integrations of the $z$-dependent part of the vacuum potential.

The exchange–correlation potential is evaluated on a real space grid and then fitted to analytic representations in each of the regions corresponding to the form of the wave functions in the various regions. Thus, the evaluation of the FLAPW matrix elements (cf. Fig. 1.5) can be done analytically. This is straightforward, but tedious both in programming effort and in computational demand. The difficulty arises from the fact that each function has to be integrated over certain regions of space.

The FLAPW method is an all-electron approach, but only the valence electrons are expanded in a variational basis set as described above. The core electron states, which are localized within the atomic spheres, are recalculated numerically in each iteration using a scheme equivalent to free atoms. Only the spherical part of the current FLAPW potential is used for these calculations. In the implementation mentioned above (Wimmer et al., 1981a), the core electrons are treated fully relativistically and a scalar-relativistic approach (Koelling and Harmon, 1977) is adopted for the valence states.

One of the most powerful capabilities of present density functional methods is the ability to predict the total energy as a function of nuclear positions. As discussed earlier, this allows the determination of important structural properties such as surface reconstructions,

adsorbate geometries, and, at least in principle, the simulation of diffusion and chemical reactions.

Once the total electron density, the effective potential, and the one-particle wave functions have been calculated, all terms necessary for the evaluation of the total energy are given, as can be seen from Eqs. (1.4)–(1.9). Measured on the scale of total energies originating from all electrons only very small and delicate energy differences determine the structural and chemical behavior of solids, surfaces, and molecules. For example, the energy change involved in the reconstruction of a surface can be eight orders of magnitude smaller than the absolute value of the total energy. Therefore, care has to be taken to ensure algorithmic and numerical stability.

The total energy capability has been implemented in the thin-film FLAPW method (Weinert et al., 1982) and applied to a number of systems including graphite monolayers (Weinert et al., 1982), monolayers of alkali (Wimmer, 1983), alkaline earth (Wimmer, 1984a) and transition metals (Wimmer, 1984b), and the relaxation and reconstruction of the W(001) surface (Fu et al., 1984; Singh et al., 1986; Fu and Freeman (1988); Singh and Krakauer (1988); Yu et al., 1992). These calculations as well as many other systematic studies described later in this chapter, demonstrate that the local density functional approach provides a surprisingly accurate tool for structural predictions of solids, surfaces, and molecules with a typical agreement of about $\pm 0.02$ Å between measured and calculated interatomic bond distances. However, the local density approximation overestimates the binding energy and underestimates the bond distance between weakly bound atoms such as a Mg dimer or in hydrogen bonds. Gradient corrections to the exchange and correlation terms, as discussed in Subsection 1.2.4, seem to overcome some of these limitations.

Now, it is known that a well optimized atomic structure – generally unknown for most low dimensional systems explored in the laboratory or modeled and studied theoretically for the first time – is a prerequisite for obtaining reliable predictions of their structural, electronic and magnetic properties. This is especially the case for transition metal systems with strong interfacial hybridization and exchange interactions. Of course, geometry optimizations are greatly facilitated if the forces on each atom are known. To this end, one has to differentiate the total energy with respect to the nuclear coordinates of each atom. In principle, this is straightforward, but the complexity of the LAPW basis functions makes this a rather tedious task and only recently has this feature been implemented for bulk solids by Yu et al. (1992) and Soler and Williams (1989). Following their work, Wu and Freeman (1994) have developed a highly precise and efficient procedure to determine the atomic forces based on the FLAPW thin film method. They have already applied this force approach for the determination of multilayer relaxation and reconstruction for a number of systems such as W(001), Fe(111), Mn/Fe(001), MgO(001) and 4d overlayers on MgO(001). The results on single layer relaxation show very good agreement between force and total energy results. In addition, they found that the forces are even numerically more stable with respect to charge self-consistency, a number of sample **k**-points, energy cutoff, etc., and thus are reliable to more digits.

Finally, there are other full potential and all-electron methods that can be applied to the study of surface electronic structures. In particular, the full-potential linearized muffin-tin-orbital (FP-LMTO) of Methfessel et al. (1989). Similar to the FLAPW method, the space is partitioned into spheres around atoms and the interstitial space. Inside the spheres,

both the FLAPW and FP-LMTO methods use atomic-like functions. The methods differ conceptually in the treatment of the interstitial region. Whereas plane waves are used in the FLAPW approach, localized functions derived from scattering theory such as Hankel functions are employed in the FP-LMTO method. Such an approach can be computationally more efficient for systems with open structures, but these localized functions do not offer a systematic convergence.

*1.3.6.2. Pseudopotential plane wave method*

The tightly bound "core" electrons close to a nucleus do not participate in the chemical bonding between atoms and they do not determine most of the electronic or optical characteristics of a material. For the study of most chemical, electronic, and optical properties it seems therefore appropriate to replace the core electrons as well as the nucleus itself by a pseudopotential which is constructed such that the valence electrons in the outer regions of each atom are not altered compared with all-electron calculations. This approximation is the basis of the pseudopotential method, which has become particularly successful in the investigation of electronic and structural properties of semiconductors. Originally (Phillips, 1958; Cohen and Heine, 1970), pseudopotentials were constructed semi-empirically to reproduce the key features of the energy band structure (such as the band gap). During the last decade, reliable pseudopotentials have been developed such as those by Hamann et al. (1979), Zunger and Cohen (1979a, b), Kerker (1980), and Bachelet et al. (1982) which are based on rigorous first principles.

Figure 1.8 shows a sketch of a pseudopotential with a corresponding pseudo wave function. At first one would expect that all core electrons and the nucleus can be replaced by one pseudopotential which is the same for all valence electrons. Such a form is called "local pseudopotential" and is particularly convenient for its computational implementation. It turns out, though, that valence wave functions with different angular momentum quantum number require different pseudopotentials. For example, in the case of the oxygen atom, the radial part of the O-2s function has to be orthogonal to the O-1s function whereas the O-2p function does not have a counterpart in the core region with the same angular momentum quantum number to which it has to be orthogonal. Hence, the pseudopotentials for the O-2s and O-2p functions are quite different. When this difference is taken into account, then the pseudopotentials depend not only on a spatial coordinate, but also on the angular momentum quantum number of the valence functions. This form is called "non-local pseudopotential".

It is reasonable to construct pseudopotentials such that outside a critical radius, denoted $R_c$ in Fig. 1.8, the pseudo-wave function and the all-electron wave function are identical. If the pseudo-wave function and the all-electron wave function have the same norm, i.e., the integral of the square of the wave function over all space is the same, then the corresponding pseudopotentials are called "norm-conserving".

If pseudopotentials are constructed such that they are smooth throughout the entire space of a system, the electron wave function can be expanded in a set of pure plane waves. This is mathematically elegant and greatly simplifies the writing of computer programs. In the pseudopotential approach, also the density of the valence electrons and the Coulomb potential are represented as an expansion in plane waves, i.e., as Fourier series, which makes the evaluation of the Hamiltonian matrix elements particularly convenient.

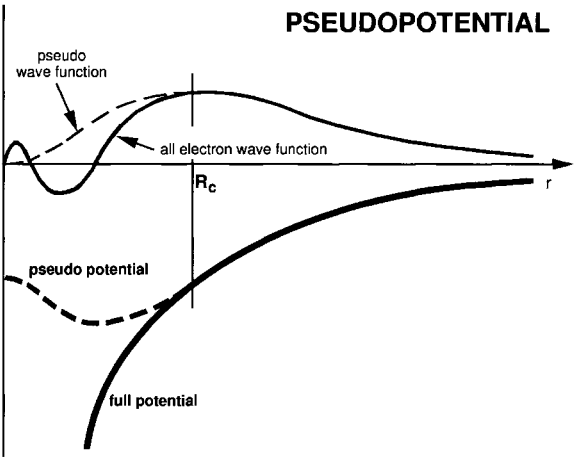


Fig. 1.8. Schematic representation of an atomic-like potential and wave function. "Full potential" denotes an effective one-electron potential containing the contribution of all electrons and the nuclear charge. One of the corresponding all electron wave functions is shown in the upper part of the figure. Dashed lines indicate a pseudopotential with a corresponding pseudo wave function. Outside the critical radius, $R_c$, the all-electron and pseudo functions are identical.

The variational expansion of electron wave functions in plane waves offers a systematic converge, but this convergence is slow. Typically about 100 plane waves are needed for each atom in the unit cell. When short bond distances and large interatomic distances occur in the same unit cell or if the pseudopotential for a certain atom in the unit cell is deep, the number of plane waves per atom can be much higher. If one uses a conventional self-consistency scheme as shown in Fig. 1.5, the diagonalization of the matrix $(\mathbf{H} - \varepsilon\mathbf{S})$ becomes a severe computational bottleneck for systems containing more than about 10 atoms per unit cell, because the dimension of this matrix is $N \times N$ with $N$ being the total number of basis functions and the computational effort of a conventional diagonalization increases as $N^3$.

The total number of basis functions can be reduced by using a mixed basis set (Louie et al., 1979) consisting of plane waves to describe the extended, smoothly varying parts of the wave functions, and localized functions such as Gaussians to capture the rapidly varying components of the wave functions near the nuclei. Such a mixed basis, however, destroys the mathematical simplicity of the matrix elements thereby losing some important advantages of a pure plane wave representation. For these reasons, substantial efforts have been devoted to develop alternative schemes. Today, so-called iterative methods based either on molecular dynamics (Car and Parrinello, 1985) or on a preconditioned conjugate gradient approach (Payne et al., 1986) have emerged as viable alternatives. In the following paragraphs, we will describe the basic concepts of these approaches. A more detailed discussion is given, for example, in a review by Payne et al. (1992).

The solution of an eigenvalue problem such as the Kohn–Sham equations (1.12) does not have to be done via a conventional diagonalization of a matrix, but one can exploit the variational principle differently. If one takes any normalized trial function, $\psi$, the vari-

ational principle implies that the expectation value of the Kohn–Sham Hamiltonian with such a trial function is greater than the lowest eigenvalue

$$\int \psi_1^*(\mathbf{r})\mathbf{H}\psi_1(\mathbf{r})\,\mathrm{d}\mathbf{r} \geqslant \varepsilon_0. \tag{1.61}$$

A priori, there is no particular prescription how this variation has to be done. One could, for example, expand the wave function $\psi$ in a set of plane waves

$$\psi(\mathbf{k},\mathbf{r}) = \sum_j c_j \mathrm{e}^{\mathrm{i}(\mathbf{k}+\mathbf{G}_j)\cdot\mathbf{r}} \tag{1.62}$$

then try random choices for the expansion coefficients $c_j$, scale the coefficients such that the wave function remains normalized

$$\int \psi_1^*(\mathbf{r})\psi_1(\mathbf{r})\,\mathrm{d}\mathbf{r} = 1 \tag{1.63}$$

and evaluate the integral (1.61) for each choice. The set of expansion coefficients which leads to the smallest expectation value (1.61) would be a viable solution. This procedure would have to be repeated for each $\mathbf{k}$ point in the Brillouin zone giving each time an eigenvalue $\varepsilon(\mathbf{k})$. The connection of all these eigenvalues would be the first energy band.

The next band would be obtained by a similar procedure, but one would have to ensure that the new wave function is orthogonal to the first one

$$\int \psi_2^*(\mathbf{r})\psi_1(\mathbf{r})\,\mathrm{d}\mathbf{r} = 0. \tag{1.64}$$

Similar steps would have to be taken to obtain all the other bands necessary to accommodate the valence electrons in the system. The orthogonalization of a newly constructed wave function to all previous wave functions at the $\mathbf{k}$-point is an essential part of this procedure. Once all the wave functions for a given Hamiltonian are found in this way, a new charge density and potential can be constructed from the new wave functions and the procedure repeated until the charge density does not change (within a convergence threshold) from one iteration to the next. In principle, one could thus solve the band structure problem without ever explicitly diagonalizing the secular matrix $(\mathbf{H} - \varepsilon\mathbf{S})$.

Of course, there are better ways to find the expansion coefficients than by a blind random procedure. Mathematically, one seeks to minimize the Kohn–Sham energy functional (1.4) which can be also written as

$$E = E\big[\{\psi_i\}, \{\mathbf{R}_\alpha\}, \{\mathbf{a}_j\}\big], \tag{1.65}$$

where $\{\psi_i\}$ are the Kohn–Sham single-particle wave functions, $\{\mathbf{R}_\alpha\}$ are the positions of the atoms in the unit cell, and the three translational vectors $\{\mathbf{a}_j\}$ define the shape and size of the unit cell. The wave functions $\{\psi_i\}$ are subject to the orthonormality constraint

$$\int \psi_i^*(\mathbf{r})\psi_j(\mathbf{r})\,\mathrm{d}\mathbf{r} = \delta_{ij}. \tag{1.66}$$

Car and Parrinello (1985) used ideas from classical and statistical mechanics to solve this minimization problem. If one considers the wave functions $\psi_i$ as objects that propagate through a space until they minimize the function (1.61), one can formulate a quasi-classical equation of motion. However, one needs to maintain orthonormality, which imposes a constraint on the "motion" of the wave functions. By using the formulation of classical Lagrangian mechanics, one arrives at the following equation of motion

$$\mu \frac{\partial^2}{\partial t^2} \psi_i = -\mathbf{H}\psi_i + \sum_j \Lambda_{ij} \psi_j . \tag{1.67}$$

The wave function $\psi_i$ is thus given a fictitious mass $\mu$. Its acceleration is caused by the "force" $-\mathbf{H}\psi_i$ and an orthonormality constraint, which could be thought of as an additional force influencing the propagation of the wave function $\psi_i$. By carrying out a molecular dynamics simulation where the temperature is slowly reduced ("simulated annealing"), each wave function $\psi_i$ eventually settles in a minimum or, in other words, becomes stationary, thereby minimizing the Kohn–Sham functional (1.65) without any explicit matrix diagonalization. The Hamiltonian operator $\mathbf{H}$ depends on the wave functions through the charge density and the potential. As the wave functions evolve, the operator $\mathbf{H}$ needs to be updated. It turns out that rather small time steps are required in the molecular dynamics of the wave functions, otherwise the system diverges. In this procedure the Kohn–Sham energy functional is solved indirectly.

Another alternative is the direct minimization of the Kohn–Sham energy functional using a scheme such as the preconditioned conjugate gradient approach (Payne et al., 1986 and 1992; Teter and Allan, 1987). The objective is again the minimization of the Kohn–Sham energy functional (1.65). Figure 1.9 shows a sketch of a generic function near its minimum and two procedures to locate the minimum by an iterative process.

In the steepest descent procedure one starts at an arbitrary point (e.g., point 1 in Fig. 1.9) and evaluates the gradient of the function. The negative of the gradient vector gives the direction of the steepest descent which is followed until a minimum is reached along this line. At that point, the procedure is repeated until the value can no longer be lowered within a given convergence threshold. Figure 1.9 shows that this is a reasonable, but not optimal search strategy. A more efficient approach is the conjugate gradient method, which starts like the steepest descent procedure searching along the line of steepest descent. In the following step, however, the new search direction contains information not only from the gradient at that point, but also from the previous gradient in the form

$$\mathbf{d}_m = \mathbf{g}_m + \gamma_m \mathbf{g}_{m-1} \tag{1.68}$$

with $\mathbf{d}_m$ being the search direction in step $m$ and $\mathbf{g}_m$ is the steepest descent direction at point $m$

$$\mathbf{g}_m = -\left.\frac{\partial F(\mathbf{x})}{\partial \mathbf{x}}\right|_{\mathbf{x}=\mathbf{x}_m} . \tag{1.69}$$

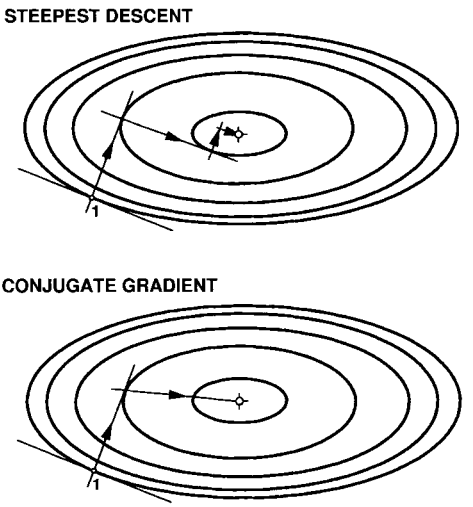


Fig. 1.9. Search for the minimum of a function using the steepest descent (upper panel) and a conjugate gradient approach (lower panel). In both cases the search begins at point 1. The conjugate gradient method converges faster.

The coefficient $\gamma_m$ is defined by

$$\gamma_m = \frac{(\mathbf{g}_m \cdot \mathbf{g}_m)}{(\mathbf{g}_{m-1} \cdot \mathbf{g}_{m-1})} \tag{1.70}$$

with the initial condition $\gamma_1 = 0$.

In the solution of the Kohn–Sham equations with the conjugate gradient method, the function $F$ to be minimized is the Kohn–Sham energy functional (1.65). The wave functions $\{\psi_i\}$ assume the role of the variable $\mathbf{x}$. The Hamilton operator $\mathbf{H}$ defines the gradient operator and thus the steepest descent direction $\mathbf{g}$. Conceptually, one starts with a trial wave function and proceeds with the conjugate gradient procedure until the wave function minimizes the Kohn–Sham functional. As in the molecular dynamics procedure, one has to maintain orthonormality of the wave functions. This is achieved by modifying the steepest descent direction accordingly. As one searches along a given line for the minimum energy, the charge density and potential of the Hamilton operator are updated corresponding to the changes in the wave functions under consideration. In practical calculations, one improves one band at a time in order to keep the computer memory requirements at a reasonable level. After a sweep over all bands the accuracy in the minimization procedure is tightened and each band is updated again.

In pseudopotential plane wave calculations each basis function corresponds to a certain kinetic energy given by

$$T_{\mathbf{G}} = -\frac{\hbar^2}{2m}|\mathbf{k} + \mathbf{G}|^2. \tag{1.71}$$

Each step in the conjugate gradient scheme tends to reduce errors in the trial wave function emphasizing a certain energy range. In order to ensure the proper weighting of the important low-energy (long wave length) components, convergence is improved by so-called preconditioning. The technique of preconditioning involves multiplying the steepest-descent vector by a preconditioning matrix as described by Payne et al. (1992).

The preconditioned conjugate gradient pseudopotential plane wave method overcomes the computational bottleneck of traditional diagonalization schemes caused by a large number of basis functions. With current computer technology, traditional diagonalization schemes are limited to several thousand basis functions. With the preconditioned conjugate gradient approach, it is possible to handle basis sets containing several hundred thousand plane waves.

In the discussion of the molecular dynamics method we have skipped an important point. Expression (1.65) shows that the total energy also depends on the position of the atoms and the shape and size of the unit cell. One of the key features of the Car–Parrinello scheme (Car and Parrinello, 1985) is the simultaneous evolution of the electronic wave functions and the nuclear coordinates. Using a simulated annealing procedure, one can thus optimize the geometry and the electronic structure within a unified procedure. Alternatively, this approach allows *ab initio* molecular dynamics by moving the atoms along dynamics trajectories determined by the quantum mechanical forces on each atom. The electronic wave functions are thus updated simultaneously as the positions of the atoms change.

It is possible to perform molecular dynamics also with the preconditioned conjugate gradient method. In this case, the forces on each atom are evaluated at the end of each conjugate gradient sequence and the atoms are moved along a dynamics trajectory. Each step in the Car–Parrinello molecular dynamics approach is faster than in the conjugate gradient approach, but smaller moves of the atoms are necessary to avoid divergence. Thus, both approaches are viable for the optimization of geometries and for carrying out *ab initio* molecular dynamics.

### *1.3.6.3. Localized orbital methods*

The full-potential linearized augmented plane wave method and the pseudopotential plane wave approach are particularly well suited for the calculation of clean surfaces or surfaces with high-coverage overlayers. Since these methods require periodicity, the study of low coverages of atoms or molecules interacting with surfaces would require very large unit cells and the computational effort would be high. The use of a cluster approach or, preferably, a cluster embedded in semi-infinite crystal are better suited for the investigation of chemically localized phenomena on surfaces such as chemisorption and surface reactions. Linear combinations of atomic orbitals have emerged as a successful approach to such localized systems and one can build on the experience gained in quantum chemistry during the past three decades.

Gaussian-type orbitals have become the standard in Hartree–Fock based quantum chemical calculations. Gaussians have convenient mathematical properties that make it possible to calculate efficiently the four-center integrals occurring in Hartree–Fock theory. However, Gaussian-type orbitals do not have the correct shape required by wave functions especially near the nucleus and also in the tails of the wave functions. Therefore, a tremendous effort

has been made by quantum chemists to construct appropriate combinations of Gaussians that mimic true wave functions. In density functional methods, these four-center integrals can be avoided and therefore there is no need for Gaussians and a range of alternatives have been explored. Among the possible alternatives, the use of numerical functions is particularly elegant and powerful. We will discuss here the concept of these numerical atomic orbitals, and will not elaborate on the use of Gaussians (Sambe and Felton, 1975; Dunlap, 1986; Salahub, 1987; Andzelm and Wimmer, 1992) or Slater-type orbitals (Averill and Ellis, 1973; Baerends et al., 1973; Rosén and Ellis, 1976; Versluis and Ziegler, 1988).

The concept of a localized orbital method is based on the fact that in condensed systems the electron wave functions maintain their atomic-like character to a large extent. Therefore, one can express the one-electron wave functions of a molecule, a surface, or a bulk solid as a linear combination of atomic orbitals $\phi_j(\mathbf{r})$

$$\psi(\mathbf{r}) = \sum_j c_j \phi_j(\mathbf{r}) \tag{1.72}$$

provided that enough variational freedom is given to the radial wave functions for the contraction or expansion caused by neighboring atoms. Each atomic orbital is constructed from a radial part and a spherical harmonic

$$\phi_j(\mathbf{r}) = R_{nl}(r) Y_{lm}(\theta, \varphi) \tag{1.73}$$

with $R(r)$ being the radial part of the wave functions depending on the principle quantum number $n$ and the angular momentum quantum number $l$. The functions $Y(\theta, \varphi)$ denote spherical harmonics labeled by the quantum numbers $l$ and $m$.

Within such an atomic-orbital basis, the radial contraction or expansion is made possible by the right choice of the radial functions $R_{lm}(r)$. It has been found that for each state such as those derived from O-2s or O-2p levels one should use at least two radial functions such as

$$\phi_{nl}^{(1)}(\mathbf{r}) = R_{nl}^{(1)}(r) Y_{lm}(\theta, \varphi), \quad \phi_{nl}^{(2)}(\mathbf{r}) = R_{nl}^{(2)}(r) Y_{lm}(\theta, \varphi). \tag{1.74}$$

The function $R^{(1)}(r)$ is obtained, for example, from a neutral atom and the function $R^{(2)}(r)$ from a positive ion. For a given pair of quantum numbers $n$ and $l$, the function of the positive ion is more contracted. Figure 1.10 gives an illustration of such a pair of wave functions.

In fact, such a construction of basis functions from pairs of radial functions with the same quantum numbers also underlies the basis functions of the FLAPW method and the LMTO method mentioned earlier. In FLAPW, one uses for each angular momentum quantum number an atomic-like radial wave functions calculated at a trial energy $E$ and a second radial function which is the energy derivative of the first function. In the LMTO method, one employs two radial wave functions per angular momentum quantum number corresponding to two different trial energies.

The DMol method (Delley, 1990, 1991) uses numerically generated atomic orbitals as basis functions and a self-consistent solution of the Kohn–Sham equations with a conven-

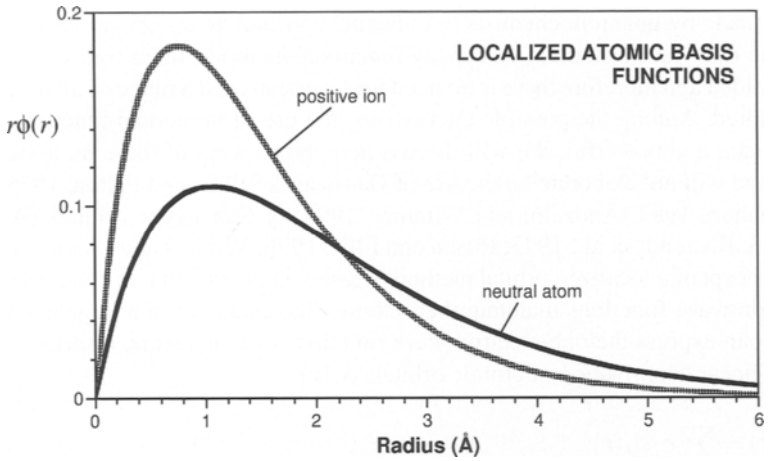


Fig. 1.10. Atomic wave functions as used to construct localized basis sets. Functions from a neutral atom and positive ions provide radial variational freedom. The functions shown above are hydrogen-like 2p wave functions.

tional matrix diagonalization. Because of the numerical representation of the basis functions, the Hamiltonian and overlap matrix elements are evaluated by a numerical integration outlined below. The Hamiltonian matrix elements are given by Eqs. (1.51) and (1.52). The following three integral types need to be evaluated:

$$T_{ij} = -\frac{\hbar^2}{2m}\int \phi_i^*(\mathbf{r})\nabla^2\phi_j(\mathbf{r})\,\mathrm{d}\mathbf{r}, \tag{1.75}$$

$$V_{ij} = \int \phi_i^*(\mathbf{r})V_{\mathrm{C}}(\mathbf{r})\phi_j(\mathbf{r})\,\mathrm{d}\mathbf{r}, \tag{1.76}$$

$$X_{ij} = \int \phi_i^*(\mathbf{r})\mu_{\mathrm{xc}}(\mathbf{r})\phi_j(\mathbf{r})\,\mathrm{d}\mathbf{r}. \tag{1.77}$$

In DMol, within numerically accuracy, $\phi_j(\mathbf{r})$ is an exact solution of the Kohn–Sham equation for atom $\alpha$

$$\left[-\frac{\hbar^2}{2m}\nabla^2 + V_{\mathrm{eff}}^{\alpha}(\mathbf{r})\right]\phi_j(\mathbf{r}) = \varepsilon_j^{\alpha}\phi_j(\mathbf{r}). \tag{1.78}$$

Therefore, the kinetic energy term $T_{ij}$ in Eq. (1.75) can be substituted by expressions involving the effective potentials and the eigenvalues of free atoms

$$\left[-\frac{\hbar^2}{2m}\nabla^2\right]\phi_j(\mathbf{r}) = \left[\varepsilon_j^{\alpha} - V_{\mathrm{eff}}^{\alpha}(\mathbf{r})\right]\phi_j(\mathbf{r}) \tag{1.79}$$

and

$$T_{ij} = \int \phi_i^*(\mathbf{r})\left[-\frac{\hbar^2}{2m}\nabla^2\right]\phi_j(\mathbf{r})\,\mathrm{d}\mathbf{r}$$
$$= \varepsilon_j^\alpha \int \phi_i^*(\mathbf{r})\phi_j(\mathbf{r})\,\mathrm{d}\mathbf{r} - \int \phi_i^*(\mathbf{r})\left[V_{\mathrm{eff}}^\alpha(\mathbf{r})\right]\phi_j(\mathbf{r})\,\mathrm{d}\mathbf{r}. \tag{1.80}$$

Therefore, the only type of integral to be solved is

$$I_{ij} = \int \phi_i^*(\mathbf{r}) f(\mathbf{r})\phi_j(\mathbf{r})\,\mathrm{d}\mathbf{r} \tag{1.81}$$

with $\phi_i(\mathbf{r})$, $\phi_j(\mathbf{r})$, and $f(\mathbf{r})$ being three-dimensional functions given on a numerical grid or $f(\mathbf{r}) = 1$ for the overlap integrals. The integral $I_{ij}$ can be approximated by

$$I_{ij} = \int \phi_i^*(\mathbf{r}) f(\mathbf{r})\phi_j(\mathbf{r})\,\mathrm{d}\mathbf{r} = \sum_p w_p \phi_i^*(\mathbf{r}_p) f(\mathbf{r}_p)\phi_j(\mathbf{r}_p), \tag{1.82}$$

where the sum extends over a discrete set of grid points $p$ on which the functions $\phi_i$, $\phi_j$, and $f$ are known and $w_p$ is the weight of each grid point. Sufficiently accurate numerical methods are available to carry out the integrals (1.82) requiring of the order of 1000 grid points per atom (Delley, 1990).

As described earlier, the self-consistency procedure requires the sequence:

$$\rho^i \to V^i \to \psi \to \rho^{i+1} \to V^{i+1} \to \ldots \tag{1.83}$$

The potential consists of an electrostatic part and the exchange–correlation part. Because of its nature, the exchange–correlation potential has to be evaluated on each grid point of a numerical grid. In the DMol approach, this grid for the exchange–correlation terms is the same as that for the numerical integration (1.82). Even in the methods using analytic basis functions such as Slater-type orbitals or Gaussians, the exchange–correlation terms involve grid-based numerical integrations while the electrostatic potential terms can be evaluated analytically.

The electrostatic potential is obtained either by solving Poisson's equation and then calculating the matrix elements (1.76) or by expanding the charge density in a set of analytical functions $g(\mathbf{r})$

$$\rho(\mathbf{r}) = \sum_q \rho_q g_q(\mathbf{r}). \tag{1.84}$$

The Coulomb integrals originating from electron–electron interactions are then evaluated explicitly as

$$U_{ij} = \sum_q \rho_q \iint \frac{\phi_i^*(\mathbf{r}) g_q(\mathbf{r}')\phi_j(\mathbf{r})}{|\mathbf{r} - \mathbf{r}'|}\,\mathrm{d}\mathbf{r}\,\mathrm{d}\mathbf{r}'. \tag{1.85}$$

In the DMol approach the former approach is taken. To this end, the charge density is projected onto a multi-center multi-polar expansion which enables the solution of Poisson's equation and hence the evaluation of the electrostatic potential on the numerical grid.

In localized orbital methods using Slater-type orbitals or Gaussians, the charge density is fitted to an auxiliary basis set and then integrals (1.85) are calculated. Therefore, analytic localized orbital methods are actually hybrids between analytic and grid-based numerical methods. Contrary to earlier expectations, analytic localized orbital methods still require numerical grids almost as dense as the grid for the exchange–correlation part of purely numerical orbital methods.

Localized orbital methods allow the calculation of forces, i.e., the derivatives of the total energy with respect to nuclear displacements. Contrary to the pseudopotential plane wave method, these forces are quite complicated involving terms that originate from the incompleteness of the localized basis sets. Atomic force determinations and attendant automatic geometry optimizations are now a standard, and powerful, feature of the DMol code.

Earlier, we have discussed the concept of pseudopotentials to eliminate the core electrons from the calculations. In principle, this approach can also be taken in methods using localized basis sets. Alternatively, one can freeze the wave functions of the core electrons and include only the valence states in the variational procedure. This reduces the size of the Hamiltonian matrix and thus saves computer time. However, the core and valence states need to remain orthogonal which requires explicit orthogonalization steps.

The power of localized basis sets comes from the fact that this approach works not only for clusters describing a surface, but there is now ample evidence (Delley, 1991; Andzelm and Wimmer, 1992) that such approaches give accurate geometries, vibrational frequencies, and binding energies for a wide range of organic, inorganic, and organometallic molecules, especially if non-local gradient corrections are included. Therefore, this approach lends itself particularly well to the study of chemical reactions of molecules on surfaces.

*1.3.6.4. Green's functions with localized orbitals*

The methods described so far require either a periodic system or a finite cluster. Both assumptions lead to undesired effects especially if one wants to understand the details of surface electronic structures, isolated defects on a surface, or the interactions of atoms and molecules with surfaces in the low-coverage limit. For these reasons, it would be desirable to have a method which can link the surface layers to a truly semi-infinite crystal and which can embed a localized area such as an adsorption site in an otherwise perfect system.

The Green's function approach offers this capability and it has been used for the calculation of semi-infinite crystals (Krüger and Pollmann, 1988, 1991; Scheffler et al., 1991) and for adsorption of single atoms on a semi-infinite crystal (Feibelmann, 1985). This approach is based on earlier work by Appelbaum and Hamann (1974) and by Appelbaum et al. (1975). It is also related to the wave function matching technique of Benesh and Inglesfield (1984) and to the work on bulk impurities by Zeller and Dederichs (1979) and bulk defects in semiconductors (Scheffler et al., 1981). Here, we describe the approach formulated by Krüger and Pollmann (1988, 1991) for calculating the electronic and structural properties of semi-infinite crystals.

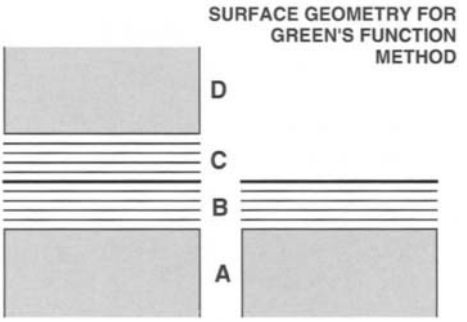


Fig. 1.11. Surface model used in the Green's functions scattering method. The left panel represents a perfect three-dimensional crystal with certain atomic layers shown explicitly. The right panel represents a semi-infinite solid with the atomic layers in region B being different from the bulk region A.

Conceptually, one starts with a perfect crystal which is periodic in three dimensions (cf. Fig. 1.11) and then removes one half of it, thus creating a surface parallel to certain atomic layers in the crystal. The one-electron wave functions for this system are built from localized atomic orbitals, $\phi_\alpha(\mathbf{r})$, which are combined to form layer-orbitals, $\chi_{\alpha\lambda}(\mathbf{q}, \mathbf{r})$,

$$\chi_{\alpha\lambda}(\mathbf{q}, \mathbf{r}) = N \sum_p e^{i\mathbf{q}\cdot(\mathbf{R}_p + \mathbf{R}_{\alpha\lambda})} \phi_\alpha(\mathbf{r} - \mathbf{R}_p - \mathbf{R}_{\alpha\lambda}). \tag{1.86}$$

Here, $N$ is a normalization factor, $\mathbf{q}$ denotes a reciprocal lattice vector parallel to the surface, $\mathbf{R}_p$ is a two-dimensional lattice vector parallel to the surface and $\mathbf{R}_{\alpha\lambda}$ is the position of atom $\alpha$ in layer $\lambda$. In practice, Krüger and Pollmann (1988) used a linear combination of Gaussian-type orbitals to construct the localized atomic orbitals. The one-particle wave functions in the Kohn–Sham equations are then expanded into these layer orbitals

$$\psi_i(\mathbf{q}, \mathbf{r}) = \sum_{\alpha\lambda} c^i_{\alpha\lambda} \chi_{\alpha\lambda}(\mathbf{q}, \mathbf{r}). \tag{1.87}$$

For a semi-infinite crystal, the variational solution of the Kohn–Sham equations would lead to an eigenvalue problem $(\mathbf{H} - \varepsilon\mathbf{S})$ in which the Hamiltonian and overlap matrices $\mathbf{H}$ and $\mathbf{S}$ are of infinite dimension because of the infinite number of layers involved. If a sufficiently thick surface region B is chosen (cf. Fig. 1.11), one can assume that in the bulk region A the layer-orbitals and the corresponding electron density in the semi-infinite crystal are the same as in the infinite three-dimensional crystal. This assumptions makes it possible to reduce the problem to a finite size.

The mathematical apparatus to accomplish this goal is referred to as the Green's function method. The Green's function corresponding to the Hamiltonian and overlap matrices $\mathbf{H}$ and $\mathbf{S}$ is given by

$$\big[E\mathbf{S}(\mathbf{q}) - \mathbf{H}(\mathbf{q})\big]\boldsymbol{G}(E, \mathbf{q}) = 1, \tag{1.88}$$

where

$$E = \varepsilon + \mathrm{i}\varepsilon' \tag{1.89}$$

is a complex energy constructed as a generalization of the real one-particle eigenvalues $\varepsilon$ of the original Hamiltonian. $\varepsilon'$ is an arbitrary, real and positive number. The Green's function contains the same information as the original Hamiltonian, just in a mathematically different form which turns out to be more convenient for handling the semi-infinite crystal.

The construction of the Green's function $\boldsymbol{G}(E, \mathbf{q})$ of the semi-infinite crystal is done by taking the following steps. First, the Green's function of the perfect three-dimensional crystal $\boldsymbol{G}^0(E, \mathbf{q})$ is obtained by using a standard bulk method and a localized basis. Next, one plane in the crystal is selected to become the surface. The three-dimensional crystal is conceptually decomposed into two semi-infinite crystals. Because of the localized nature of the orbitals, there are no interactions between the layer-orbitals in region A and D (cf. Fig. 1.11). The effect of the layer-orbitals in region C on those in region B and vice versa can be described as a perturbation $U^{\mathrm{I}}$ to a system in which there is no interaction between the semi-infinite crystals AB and CD. In other words, the term $U^{\mathrm{I}}$ decouples the three-dimensional crystal into two idealized semi-infinite crystals. Now the strength of the Green's function method becomes important: Knowledge of the Green's function $\boldsymbol{G}^0(E, \mathbf{q})$ of the full three-dimensional crystal and the perturbation $U^{\mathrm{I}}$ allows the evaluation of the Green's function $\boldsymbol{G}^{\mathrm{I}}(E, \mathbf{q})$ of the "ideal" semi-infinite crystal through the solution of the so-called Dyson equation:

$$\boldsymbol{G}^{\mathrm{I}}(E, \mathbf{q}) = \boldsymbol{G}^0(E, \mathbf{q}) + \boldsymbol{G}^0(E, \mathbf{q}) U^{\mathrm{I}} \boldsymbol{G}^{\mathrm{I}}(E, \mathbf{q}). \tag{1.90}$$

Notice that $\boldsymbol{G}^{\mathrm{I}}(E, \mathbf{q})$ does not contain any new physical information about the surface, but it is just an elegant way of recasting the problem so that the Green's function $\boldsymbol{G}^{\mathrm{I}}(E, \mathbf{q})$ can serve as a reference to the Green's function of the "real" surface. Both Green's functions have the same structure. In fact, $\boldsymbol{G}(E, \mathbf{q})$ of the "real" semi-infinite crystal differs from $\boldsymbol{G}^{\mathrm{I}}(E, \mathbf{q})$ only in the terms which originate from the finite region B. The transition from $\boldsymbol{G}^{\mathrm{I}}(E, \mathbf{q})$ to $\boldsymbol{G}(E, \mathbf{q})$ is expressed as a perturbation $U$ which is localized to region B. Once again, Dyson's equation can be used to calculate the effect of this perturbation

$$\boldsymbol{G}(E, \mathbf{q}) = \boldsymbol{G}^{\mathrm{I}}(E, \mathbf{q}) + \boldsymbol{G}^{\mathrm{I}}(E, \mathbf{q}) U \boldsymbol{G}(E, \mathbf{q}). \tag{1.91}$$

Because of the localization of $U$ to region B, only matrix inversions in the finite sub-space B have to be carried out (Krüger and Pollmann, 1988, 1991). This approach leads finally to the solution of the following matrix equation:

$$\boldsymbol{G}(E, \mathbf{q}) = \boldsymbol{G}^0(E, \mathbf{q}) + \boldsymbol{G}^0(E, \mathbf{q}) \begin{pmatrix} 0 & 0 \\ 0 & \mathbf{T}_{\mathrm{BB}} \end{pmatrix} \boldsymbol{G}^0(E, \mathbf{q}) \tag{1.92}$$

with

$$\mathbf{T}_{\mathrm{BB}}(E, \mathbf{q}) = \mathbf{U}_{\mathrm{BB}}(E, \mathbf{q}) \left[ 1 - \boldsymbol{G}^0_{\mathrm{BB}}(E, \mathbf{q}) \mathbf{U}_{\mathrm{BB}}(E, \mathbf{q}) \right]^{-1}. \tag{1.93}$$

While this Green's function approach is more complicated than supercell or cluster methods, Krüger and Pollmann (1988, 1991) have demonstrated its feasibility not only in the calculation of the surface electronic structure, but also as a tool for energy minimization through the calculation of forces with subsequent relaxation of the atomic positions.

## 1.4. Electronic states at surfaces

At a surface with its reduced coordination and lack of periodicity in the direction perpendicular to the surface, new features in the electronic band structure and new states (called surface states and surface resonance states) appear. This is best illustrated by means of some examples, including surfaces of Al (a nearly free electron metal), W (an extensively studied transition metal) and Si (the most important semiconductor material).

### *1.4.1. Surface states and surface resonance state in nearly free-electron metals: Al(001)*

A good example that illustrates some of the important physics at the surface of a nearly free-electron (NFE) metal is given in the pseudopotential calculations by Caruthers et al. (1973) and the all-electron LAPW results by Krakauer et al. (1978), using nine and thirteen layer aluminum films. The conduction electrons of aluminum resemble free electrons, but the Bragg scattering caused by the planes of Al atoms is sufficiently large to split some bands by more than 1 eV. A projection of these bands onto the two-dimensional surface Brillouin zone thus exhibits band gaps. The potential at the Al surface alters the energy of certain electronic levels such that they fall into these surface-projected band gaps, thus giving rise to surface states. Surface states decay exponentially towards the bulk, i.e., their **k**-vector perpendicular to surface is imaginary. In NFE metals, the decay can be rather slow and extend over ten and more layers. Towards the vacuum, surface states also decay exponentially as all other bound states. Surface resonance states have an enhanced amplitude near the surface region, but do not fall into absolute band gaps of the surface-projected energy band structure. In fact, inside the crystal, surface resonance states join bulk states. This picture emerges in a quantitative way from the rigorous surface electronic structure calculations by Krakauer et al. (1978) as discussed now in more detail.

Figure 1.12a shows surface-projected bulk free-electron bands, $E(\mathbf{k}_\parallel) = \frac{1}{2}(\mathbf{k}_\parallel + k_z\hat{\mathbf{z}} + \mathbf{G})^2$ for a few fixed values of $k_z$, the $z$ component of the three-dimensional Bloch momentum. Here, $\mathbf{k}_\parallel$ refers to a reciprocal lattice vector parallel to the surface and $\hat{\mathbf{z}}$ denotes a unit vector perpendicular to the surface. $\mathbf{G}$ is a three-dimensional reciprocal lattice vector corresponding to the primitive bulk Brillouin zone. In Fig. 1.12b we have reproduced from Caruthers et al. (1973) those projected bulk bands with the same values of $k_z$ as displayed in Fig. 1.12a. Absolute bulk band gaps are represented by the shaded regions. The band structure for a nine-layer Al(001) film as calculated by Krakauer et al. (1978) is shown in Fig. 1.12c. The plus and minus signs in Fig. 1.12c label states which are, respectively, symmetric and antisymmetric with respect to a reflection at the central plane of the film. The film bands, although seemingly complicated at first glance, are essentially free-electron-like as can be seen from the following. Turning on the bulk crystal potential causes bands

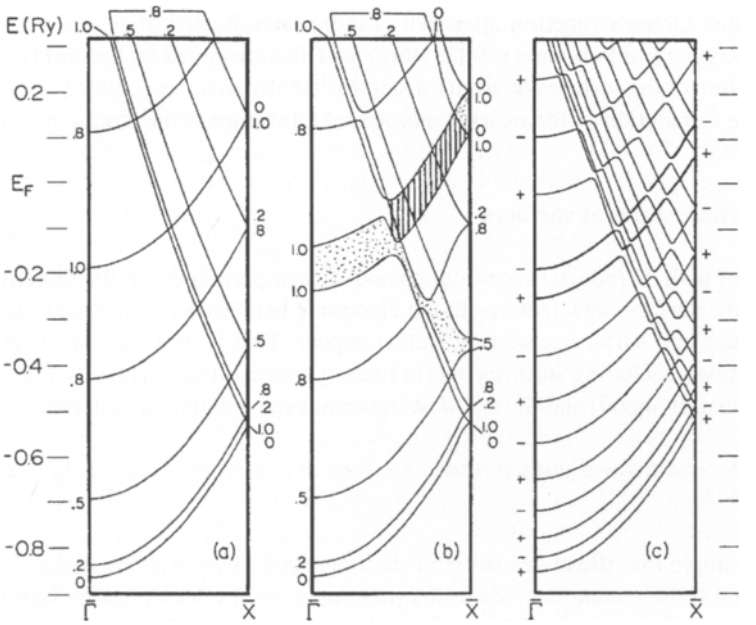


Fig. 1.12. (a) Free-electron bulk bands. (b) Projected bulk bands. Absolute bulk band gaps are represented by the shaded regions. A "partial" Bragg-reflection gap is represented by vertical cross hatching. (c) Band structure for a nine-layer Al(001) film. The relevant pair of the surface states and surface resonances are identified by the heavy lines. The numbers which label the bands in (a) and (b) represent values of $k_z$ in units of $2\pi/A$, where $A$ is the bulk lattice parameter.

with the same value of $k_z$ in Fig. 1.12a to repel one another (all the bands shown in Fig. 1.12 have the same two-dimensional $\bar{\Delta}_1$ symmetry and this causes bulk energy gaps to appear. The resulting band structure, pictured in Fig. 1.12b, remains predominantly parabolic as expected for a NFE metal like aluminum. Introducing the perturbation due to the presence of the surface destroys periodicity in the $z$ direction with the result that $k_z$ is no longer a good quantum number. Crossings of bulk bands with different $k_z$ in Fig. 1.12b must now become anticrossings in the film calculation, Fig. 1.12c. The only allowed crossings in Fig. 1.12c are between states of different $z$-reflection symmetry. As the film becomes thicker, however, $k_z$ is more nearly a "good" quantum number, and these additional sharp anticrossings begin to look more and more like true crossings. In view of these remarks, one can see the close similarity of the film bands (Fig. 1.12c) with the projected bulk bands (Figs. 1.12a, b).

The other new feature in the film calculation is the occurrence of surface states and surface resonances. For comparison with experiment, the relevant pair of surface states and surface resonances are identified in Fig. 1.12c by heavy lines which clearly have a free-electron-like dispersion. The surface states start at $\bar{\Gamma}$ and run up to about $\mathbf{k}_\parallel = (0.5, 0)$ within a region corresponding to the absolute bulk band gap in Fig. 1.12b. These surface states then persist as a pair of surface resonances into a region corresponding to the continuum of bulk states and within the partial Bragg reflection gap in Fig. 1.12b (represented

by the vertical crosshatching), again becoming true surface states as they enter the smaller absolute band gap near $\bar{X}$. Two pairs of surface states are found in this gap; one of these pairs is the continuation of the resonance states. While these surface states have been previously found, Krakauer et al. (1978) focused for the first time on the existence of the surface resonance. The dispersion of the heavy lines in Fig. 1.12c agrees extremely well with the experimental dispersion relation (Gartland and Slagsvold, 1978).

There is a fairly simple explanation for the occurrence of the surface state and surface resonance. Referring to Fig. 1.12b, the absolute bulk band gap which starts at $\bar{\Gamma}$ and continues to about $\mathbf{k}_{\parallel} = (0.5, 0)$ is, in a simple pseudopotential model, a Bragg-reflection gap due to the $V_{002}$ pseudopotential coefficient which splits the two degenerate free-electron states with $k_z = 1$ in Fig. 1.12a. While the absolute gap is narrowed and pulled down in energy near $\mathbf{k}_{\parallel} = (0.5, 0)$ (it continues downward to $\bar{X}$ as a $V_{111}$ absolute gap), the $V_{002}$ Bragg gap persists as a partial $V_{002}$ Bragg gap all the way up to the other absolute $V_{002}$ gap at $\bar{X}$. This partial Bragg gap is delimited by the two NFE-like states with $k_z = 1$ in Fig. 1.12b. It is a partial gap in the sense that, while it is embedded in a continuum of bulk plane-wave states of the type $(\mathbf{k} - \mathbf{G}_{111})$, there are no bulk plane-wave states of the type $(\mathbf{k})$ or $(\mathbf{k} - \mathbf{G}_{002})$ in this partial Bragg gap. Introducing the perturbation due to the presence of the surface has the effect, then, of pulling into this $V_{002}$ gap states from the continuum of $(\mathbf{k})$ and $(\mathbf{k} - \mathbf{G}_{002})$ states. In the region where it is an absolute Bragg gap, these states are true surface states, but in the region where it is a partial Bragg gap, these states are surface resonances, since they can mix with the continuum of $(\mathbf{k} - \mathbf{G}_{111})$ states. Inside the partial Bragg gap, the $(\mathbf{k})$ and $(\mathbf{k} - \mathbf{G}_{002})$ character of these states must be localized near the surface, since only $(\mathbf{k} - \mathbf{G}_{111})$ character is permitted deep into the bulk, and this favors the formation of a surface resonance.

The formation of surface resonances in partial Bragg reflection gaps in NFE metals is a particularly striking and illustrative example of a general mechanism which can also be present in more complex systems. Thus, one could generally expect to find surface resonances at points in the two-dimensional BZ where (in the corresponding projected bulk band structure for a single two-dimensional symmetry type, e.g., $\bar{\Delta}_1$, or $\bar{\Delta}_2$ along $\bar{\Gamma}$–$\bar{X}$) a bulk band edge of one "character" is embedded in a continuum of bulk states of another character (see Appelbaum and Hamann, 1976a, for a general review). While in NFE-like metals it is particularly easy to map such partial gaps (since the character of the bulk states is simply related to their plane-wave composition), a similar mapping for general systems requires inspection of projections of individual bulk bands.

### *1.4.2. Theoretical 2p-core-level shift and crystal-field splitting at the Al(001) surface*

As described later in this book, developments in surface-sensitive photoemission experiments using synchrotron radiation have stimulated the theoretical investigation of the electronic structure of surfaces. Aluminum is of particular interest since it provides the classic case of a nearly free-electron metal and the study of surface-induced effects on the 2p core levels gives insight into the effective screening near the metal–vacuum interface. From the rather slow decay of surface states towards the bulk one might conclude that the many other features of the electronic structure such as charge densities and effective potentials

differ for many layers near a surface from those in the bulk. This, however, does not seem to be the case. On the contrary, especially the charge density become bulk-like only a few atomic layers underneath a surface. Experimentally, this can be verified by core-level spectroscopy, which essentially probes the effective local potential near atoms. However, the full value of the experimental data can only be realized when reliable theoretical data are available for their interpretation. Again, the Al(001) surface provides an illustrative example.

Eberhardt et al. (1979) found from X-ray photoemission spectroscopy (XPS) measurements on an Al(001) surface that, quite surprisingly, the 2p line from the surface layers was not shifted within an experimental uncertainty of $\pm 40$ meV compared to the bulk signal, but the line for the surface signal was markedly broadened by 100–200 meV. These authors attributed the broadening to a crystal-field splitting of the initial states in the surface layer and supported this idea by a simple atomic model calculation.

Although a comprehensive interpretation of photoemission spectra has to take into account the complicated scattering mechanisms of the photoelectron, electron–hole interactions, secondary processes like Auger transitions, and many-body relaxation effects, the starting point of a theoretical investigation has to be an accurate calculation of the initial ground state. As it turns out in many cases, the electronic structure of the initial ground state alone determines the main features of the photoemission spectrum. Wimmer et al. (1981b) have carried out a self-consistent calculation for a nine-layer Al(001) film using the FLAPW method. During the self-consistency procedure all core states including the 2p states were treated fully relativistically. For the Al 2p states in the surface layer, the calculations give a shift to smaller binding energies of 120 meV accompanied by a crystal-field splitting of 38 meV for the $2p_{3/2}$ states. The core-level shift in the subsurface layer is decreased to 50 mRy and vanishes in the third layer. A pronounced crystal-field splitting is found only for the surface layer. Chiang and Eastman (1981) derived from surface-sensitive photoelectron partial yield spectra a 2p core-level shift of $\sim -57$ meV and a much smaller surface-sensitive broadening than did Eberhardt et al. (1979). Their layer-decomposed results indicate that both effects (shift and splitting) are important in analyzing the experimental data.

The FLAPW one-electron energy eigenvalues for the 2p core state including the crystal-field splitting as obtained by Wimmer et al. (1981b) are plotted in Fig. 1.13. It was found that the $2p_{1/2}$ and $2p_{3/2}$ levels in the surface layer compared to the central (bulk-like) layer are shifted by $\sim 120$ meV to smaller binding energies. A similar shift, although reduced to 50 meV, is also obtained for the subsurface layer (S-1). In the layer S-2, the surface induced shift is almost completely screened but there is still a slight oscillation in the layers S-2, S-3, and the central layer. The 1s and 2s core states show essentially the same shifts as the 2p levels. As expected, the crystal-field splitting is localized to the surface layer and almost no splitting is found for the subsurface layers. The accuracy of their calculation is indicated by the calculated work function of 4.53 eV which is in very good agreement with the experimental value of $4.41 \pm 0.03$ eV (Grepstad et al., 1976).

The theoretical FLAPW results, which show both a shift and a crystal-field splitting, permit a clarification of experiments. Whereas Eberhardt et al. (1979) overemphasized crystal-field effects in the analysis of their experiments and did not find a 2p shift, Chiang and Eastman (1981) did not take into account crystal-field effects in their fitting procedure.

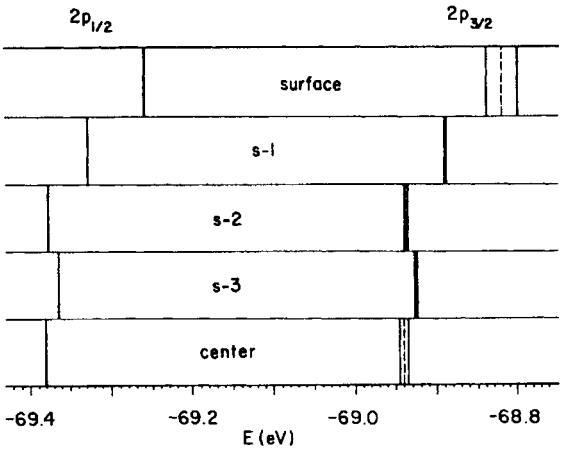


Fig. 1.13. FLAPW one-electron energy eigenvalues for the 2p core states in a nine-layer Al(001) film. The values are given with respect to the vacuum. The dashed lines are the values for the $2p_{3/2}$ states without crystal-field splitting.

Table 1.4

FLAPW one-electron energy eigenvalues for the core levels in a nine-layer Al(001) film. The values are given in eV with respect to the vacuum. The last column lists the crystal-field splitting of the $2p_{3/2}$ levels

| | $1s_{1/2}$ | $2s_{1/2}$ | $2p_{1/2}$ | $2p_{3/2}$ | Splitting |
|---|---|---|---|---|---|
| Surface | −1502.792 | −106.758 | −69.262 | −68.822 | −0.038 |
| S-1 | −1502.846 | −106.829 | −69.331 | −68.892 | 0.001 |
| S-2 | −1502.889 | −106.877 | −69.379 | −68.939 | 0.006 |
| S-3 | −1502.882 | −106.863 | −69.366 | −68.927 | 0.004 |
| Center | −1502.886 | −106.880 | −69.381 | −68.942 | 0.010 |

The calculations of Wimmer et al. (1981b) found that both effects are important for a proper analysis of the experimental data. Further, since only the $2p_{3/2}$ states show a crystal-field splitting, one should be able, in principle, to isolate crystal-field effects in the experimental spectra by comparing the $2p_{1/2}$ and the $2p_{3/2}$ spectra.

## 1.5. Charge density distributions at surfaces: surface states and surface resonances

Within a distance of only a few Ångströms, the charge density at a surface decays from quite high values in the bulk (especially for transition metal surfaces) to zero. This feature of the charge density is accompanied by a characteristic surface potential as was shown earlier in Fig. 1.2. The surface potential causes the appearance of surface states and surface resonance states which, in turn, then determine the surface charge density. Thus, electronic states which are localized near the surface are among the most prominent of the observed

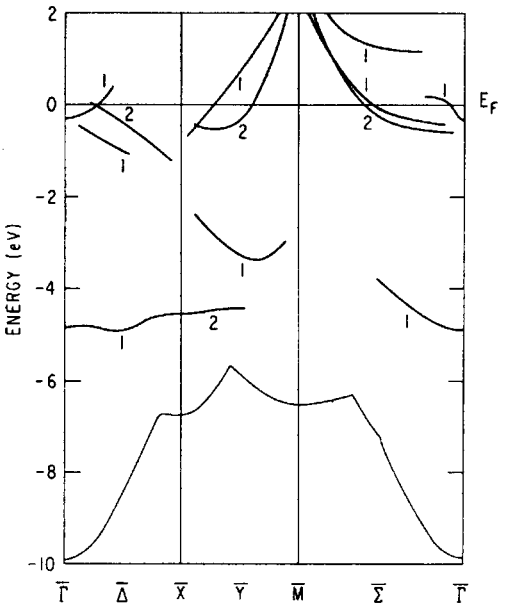


Fig. 1.14. Surface states and resonances for W(001) with a localization greater than 70% in the two outermost layers of the film. The bottom of the conduction band is outlined along the lower portion of the figure.

spectroscopic features. Experimentally, however, there is often little difference between surface states (SS), which decay exponentially into the bulk, and surface resonances (SR), which can be described as a hybrid of a true surface state and a bulk state. While SS and SR are relatively well understood on semiconductor and simple metal surfaces (cf. for example, Appelbaum and Hamann, 1976a), it is more recent that electronic structure calculations have been made to deal with the additional complexity arising from d electrons in noble and transition metal surfaces (see, for example, the reviews by Inglesfield, 1982 and by Wimmer et al., 1985).

Representative charge densities for the surface states and surface resonances, calculated for a thirteen-layer film of Al were determined by Krakauer et al. (1978). The decay constant for the symmetric surface state at $\bar{\Gamma}$ is in very good agreement with that given by Caruthers et al. (1973) for a 39-layer film. The surface state and surface resonance both exhibit essentially the same degree of localization near the surface. This accounts for the absence of any abrupt change in the experimentally observed (Gartland and Slagsvold, 1978) peak behavior due to the closing of the absolute bulk band gap near $\mathbf{k}_{\|} = (0.5, 0)$.

In the next example, we remain with metallic surfaces, but consider now the additional complexity that arises from the presence of localized d-states which occur together with the free-electron-like s- and p-states of transition metals such as W.

In their pioneering calculations, Posternak et al. (1980) investigated the W(001) surface using the LAPW thin film method. In order to highlight their results, we display in Fig. 1.14, along the high-symmetry directions, those SS and SR which have a localization greater than 70% in the two outermost layers of W(001). For ease of reference, the bot-

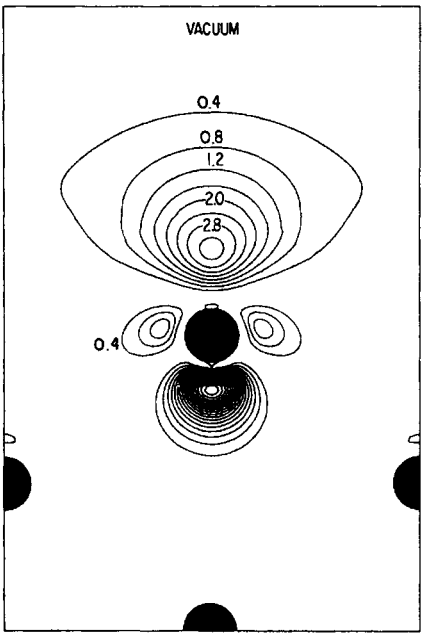


Fig. 1.15. Charge density contour plot for the very localized W(001) surface state 0.3 eV below $E_F$ at $\Gamma(\mathbf{k}_\parallel = 0)$. Successive contours are separated by 0.4 in units of electrons per bulk unit cell.

tom of the conduction band is plotted along the lower portion of the figure. An analysis of these results shows that they provide for the first time good agreement with detailed angle-resolved photoemission measurements of all three surface resonance bands observed.

(i) There is an extremely localized state just below $E_F$ near $\bar{\Gamma}$ which has a small upwards dispersion along $\bar{\Gamma}\bar{X}$ and $\bar{\Gamma}\bar{M}$ with $\bar{\Delta}_1$ and $\bar{\Sigma}_1$ symmetry in agreement with experiment. It disappears about one-third of the way between $\bar{\Gamma}\bar{X}$ and $\bar{\Gamma}\bar{M}$. This is the state which is seen as a sharp peak in photoemission spectra at normal exit. It is a true SS only at $\bar{\Gamma}$ where it exists in a bulk $\bar{\Delta}_1$ symmetry gap.

The $\bar{\Gamma}$ SS just below $E_F$ is extremely localized in the surface layer (~93%) and projects quite far out into the vacuum region (see Fig. 1.15). Thus, it is perhaps not surprising that the conditions for the formation of this state are quite sensitive to the behavior of the potential near the surface. The surface potential in turn depends on the delicate rearrangement of electronic charge at the surface which leads to the formation of the surface dipole barrier and the correct work function. It is most gratifying to see that today's sophisticated electronic structure methods can offer a rather remarkable accuracy in predicting work functions.

(ii) Posternak et al. (1980) also found a pair of SR (for $\mathbf{k}_\parallel \neq 0$) about 0.5 eV below the SS described above. Along the symmetry lines $\bar{\Gamma}\bar{X}$ and $\bar{\Gamma}\bar{M}$, one of the pair of SR is symmetric ($\bar{\Delta}_1$ and $\bar{\Sigma}_1$, respectively) and the other is antisymmetric ($\bar{\Delta}_1$ and $\bar{\Sigma}_1$, respectively) with respect to the corresponding mirror planes [a (100) plane along $\bar{\Gamma}\bar{X}$ and a (110) plane along $\bar{\Gamma}\bar{M}$]. Along the $\bar{\Gamma}\bar{M}$ direction these states have a small upward disper-

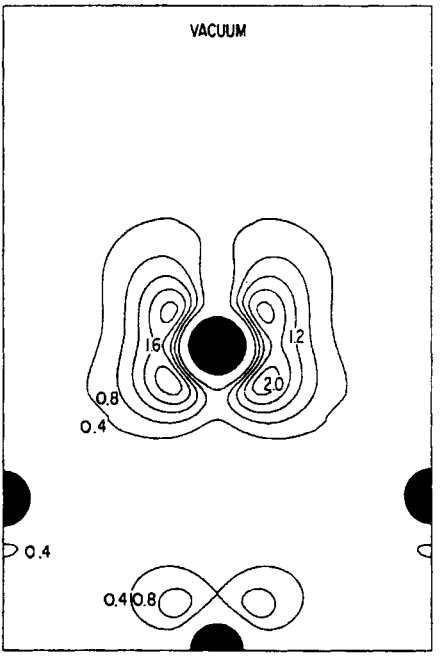


Fig. 1.16. Charge density for the $\Sigma_1$ surface resonance on W(001) near $E_F$ at $\mathbf{k}_\parallel = (0.5, 0.5)\pi/a$. Successive contours are separated by 0.4 in units of electrons per bulk unit cell.

sion (in agreement with experiment) cutting $E_F$ about half-way between $\bar{\Gamma}$ and $\bar{M}$. Along the $\bar{\Gamma}\bar{X}$ direction, however, these states have a small downward dispersion, whereas the experimentally determined dispersion is slightly upward toward $E_F$.

It is important to note that the $\bar{\Sigma}_2$ SR is about 20–25% more localized in the two outermost layers than is the $\bar{\Sigma}_2$ SR (below $E_F$, the localization in the topmost two layers is typically greater than 90% for the $\bar{\Sigma}_1$ SR). Contour plots for the $\bar{\Sigma}_1$ and $\bar{\Sigma}_2$ SR are shown in Figs. 1.16 and 1.17, respectively.

(iii) Finally, there is a low-lying SR with very flat dispersion along $\bar{\Gamma}\bar{X}$ and part of the way along $\bar{X}\bar{M}$ at about $-4.5$ eV. This state is also found part of the way along $\bar{\Gamma}\bar{M}$, but is much less localized and shows a greater dispersion. The symmetries are, respectively, $\bar{\Delta}_1$, $\bar{Y}_2$, and $\bar{\Sigma}_1$, in agreement with the experimentally determined ($\bar{\Delta}_1\bar{\Sigma}_1$) low-lying resonance.

## 1.6. Surface potential and work function

### *1.6.1. Origin of the work function*

The work function is defined (Wigner and Bardeen, 1935) as the difference in energy between a lattice with an equal number of ions and electrons, and the lattice with the same

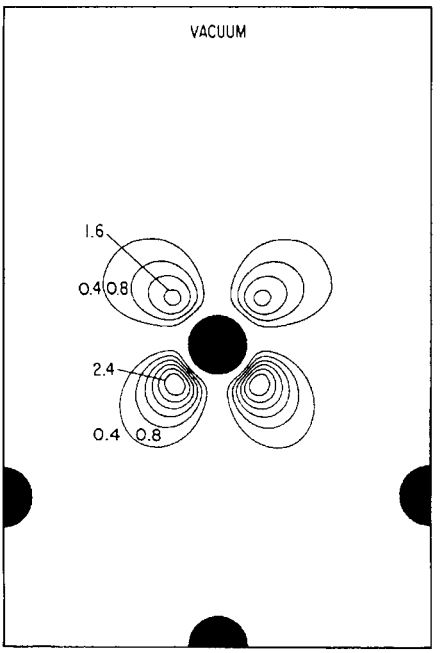


Fig. 1.17. Charge density for the $\Sigma_2$ surface resonance on W(001) near $E_F$ at $\mathbf{k}_\parallel = (0.5, 0.5)\pi/a$. Successive contours are separated by 0.4 in units of electrons per bulk unit cell.

number of ions, but with one electron removed. One of the first, and for several decades the most, sophisticated quantum-mechanical calculation of the work function was performed by Bardeen (1936). He employed a jellium model for the surface and solved the Hartree–Fock equations for the electron gas ($r_s = 4$), including a nonlocal (energy-dependent) form of the exchange and correlation potential. His results indicate that the surface barrier is due primarily to exchange and polarization forces, and that ordinary electrostatic forces play a minor role.

Three decades later, progress in many-body theory led to the formulation of density-functional theory which has been subsequently applied to the self-consistent solution of the jellium model for surfaces (Bennett and Duke, 1969; Smith, 1969; Lang, 1969). Using this approach, Smith (1969) calculated work functions and surface potentials systematically for a series of metals ranging from low-electron densities (alkali metals) to high densities typical for transition metals. His results confirm that the surface barriers are, in most cases, due to many-body effects, but dipole barriers are found to be small only for alkali metals, and become quite large for the transition metals.

The jellium-model calculations have been refined to give surface energies (Lang and Kohn, 1970) and work functions for different crystal faces by including the effect of the ion cores in a simple pseudopotential theory. Lang and Kohn (1971) gave the first rigorous demonstration that the original definition of the work function $\Phi$, as the energy difference between the systems with $N$ and $N - 1$ electrons is equivalent to $\Phi = \Delta - \mu$, where $\Delta$ is

the rise in mean electrostatic potential across the metal surface and $\mu$ is the bulk chemical potential of the electrons relative to the mean electrostatic potential in the metal interior. This expression is shown to include all many-body effects and in particular, that of the image force.

The pioneering calculation of Bardeen (1936) was later reassessed (Sahni and Ma, 1980) and work functions have been obtained for simple metals using the "displaced-profile change-in-self-consistent-field" approach, still remaining basically in the jellium model.

It then became apparent that realistic local-density calculations of the electronic structure of simple metal surfaces such as the Al(001) surface (Wimmer et al., 1981a) and also transition-metal surfaces such as Cu(001) (Gay et al., 1979; Smith et al., 1980) and W(001) (Posternak et al., 1980; Ohnishi et al., 1984) gave consistently good theoretical results for the work function, usually $\pm 0.2$ eV within the experimental value. Since the FLAPW method has been demonstrated to be one of the most accurate methods to solve fully self-consistently the local-density equations in the thin-film geometry, one therefore expects from this method work functions close to the local-density limit.

Two main criteria determine the work function (i.e., the energy of the Fermi level with respect to the vacuum): the electrostatic surface dipole due to the spill-out of electrons into the vacuum (described by the electrostatic Coulomb potential) and the many-body exchange and correlation effects as incorporated into the effective one-electron potential. Consider the surface dipole of the clean W(001) surface (Wimmer et al., 1982). The surface dipole can be visualized by comparing the charge density on the "real" W(001) surface with that of an "ideal" surface, which is constructed by cutting a bulk crystal along the boundaries of nearest-neighbor polyhedra without allowing any charge relaxation. The difference between the charge densities of the real and the ideal surface is due to the spill-out of electrons into the vacuum (Fig. 1.18). It is remarkable that the charge rearrangement involves essentially only the surface atoms and the influence of the vacuum boundary is mostly screened off already for the subsurface W layer. Associated with the charge-density

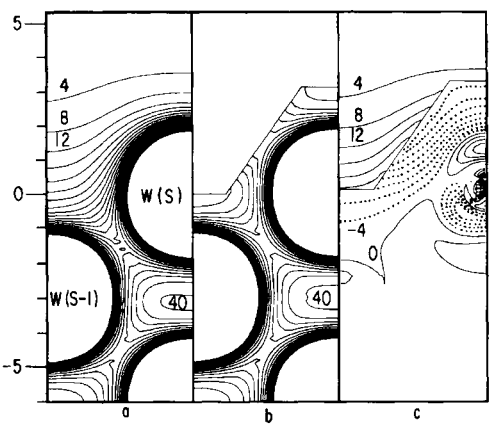


Fig. 1.18. Total charge density on (a) a clean W(001) surface, (b) an ideal surface, and (c) the difference between (a) and (b), in units of $10^{-3}$ electrons/(Bohr radii)$^3$.The dotted lines indicate a loss of electronic charge. The vertical scale gives the distance from the surface W atoms in Bohr radii.

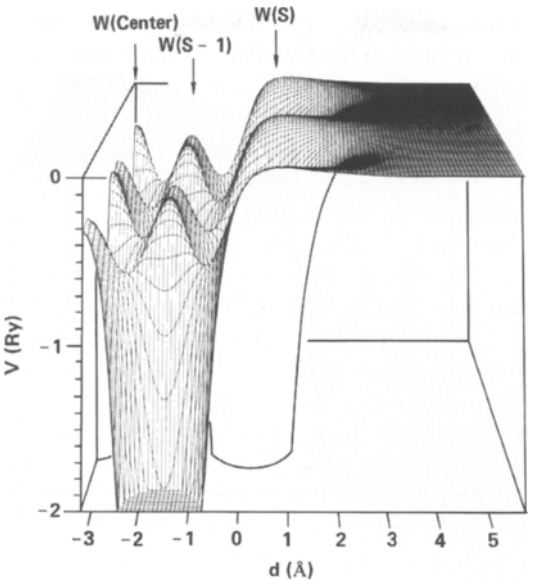


Fig. 1.19. Electrostatic Coulomb potential in the (110) plane normal to the surface for clean W(001).

difference shown in Fig. 1.18 is a surface dipole barrier of 5.5 eV. This is qualitatively in agreement with the result of Smith (1969) who finds that the electrostatic double layer is "quite large for the transition metals".

It should be noted, however, that the definition of the double layer is not unique. One could have (less realistically) defined an ideal surface by cutting the crystal at a plane halfway between two (001) planes and then compared with the real surface. In that case we would have obtained a much larger "spill-out dipole barrier" of 13.3 eV. The electrostatic Coulomb potential in the (110) plane perpendicular to the surface is shown in Fig. 1.19 in the form of a three-dimensional plot for the clean W(001) surface. It is interesting that regions of positive Coulomb potential are found between the surface atoms. This fact, which indicates a very strong screening, is related to the high, localized electronic density in the surface region.

This high density, on the other hand, leads to a large exchange–correlation potential which amounts to $-10$ eV in the interstitial region inside the metal and leads to the effective one-electron potential shown in Fig. 1.20 for the clean W(001) surface, which is much deeper than the Coulomb potential. In Fig. 1.20, the Fermi level is indicated by the hatched area and the work function $\Phi$ is drawn as the energy difference between the Fermi level and the vacuum zero. For the five-layer W(001) slab, the result is a value of 4.77 eV for the work function, which is slightly too high compared to the experimental value of $4.63 \pm 0.02$ eV (Billington and Rhodin, 1978). The small discrepancy is presumably due to a thickness effect of the film, since a seven-layer calculation (Ohnishi et al., 1984) with otherwise the same computational characteristics as this five-layer W(001) calculation gives a work function of 4.63 eV in agreement with experiment.

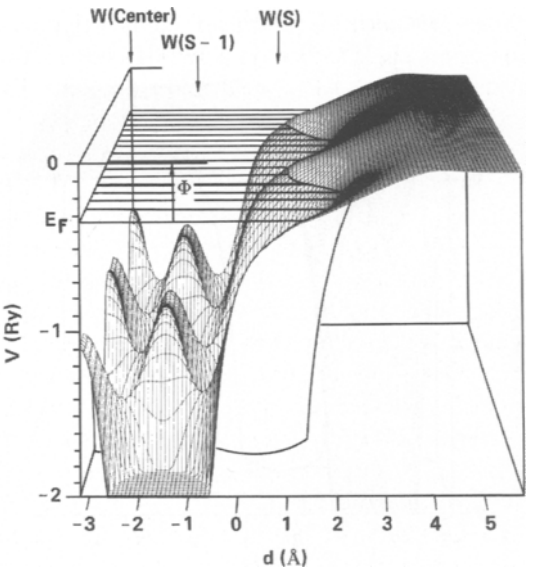


Fig. 1.20. Effective one-electron potential in the (110) plane normal to the surface for a clean W(001). $\Phi$ denotes the work function.

### *1.6.2. Cesiation of W(001): work function lowering by multiple dipole formation*

Work functions depend on the structure and chemical composition of a surface. For example, different crystallographic surfaces of the same metal or compound can have substantially different work functions. Chemical modifications of a surface can have even larger consequences. This is beautifully illustrated by the deposition of alkali overlayers such as sodium or cesium on transition metal surfaces.

Cesiated metal surfaces are important both for their prototypical properties and for their technological applications. Thus, the lowering of the work function by the deposit of an overlayer of Cs on a metal surface like W, first discovered by Kingdon and Langmuir (1923) and still widely used in a host of experiments, has widespread applicability in such areas as thermionic conversion (Hatsopoulos and Gyftopoulos, 1979), ion propulsion (Forbes, 1968) and recently as negative hydrogen (deuterium) ion sources for magnetic fusion reactors (Hiskes et al., 1976). Despite its long history and obvious importance, the mechanism for the work-function lowering was a classic challenge for theoretical treatment. Because of the complexity of rigorous calculations for this type of system, only calculations on a "jellium" model had been carried out to describe the work-function changes induced by alkali adsorption (Lang, 1971). Although these calculations give a qualitatively correct description of the work function changes, important structures due to the atomistic nature of the surface and interface atoms are not included in these calculations. In particular, an understanding of the role played by the rich, localized W d surface states (Posternak et al., 1980) requires a more detailed description of the surface.

Wimmer et al. (1982, 1983) presented results of the first rigorous, full self-consistent, all-electron calculation of Cs chemisorbed on a W(001) surface using the full-potential linearized augmented plane wave (FLAPW) method for thin films. The chemisorption process was characterized by comparing the results of independent self-consistent calculations for (1) a five-layer W(001) slab, (2) an unsupported Cs monolayer, and (3) Cs in a c(2 × 2) coverage on W(001) at distances ranging from 2.6 to 2.9 Å. They found that the reduction in the work function, $\Phi$, upon cesiation, arises from a multiple dipole formation at the surface and interface layers rather than from an ionic charge transfer from Cs into the surface. A characteristic feature of the clean W(001) surface is the pronounced spill-out of electrons from the surface layer into the vacuum, which lead to the formation of a strong surface dipole as discussed in the section above. This surface dipole is reduced in the cesiated system: Cs forms a metallic overlayer with its valence electrons polarized toward the W surface, thus reducing the spill-out into the vacuum. Correlated with the polarization of the Cs valence electrons, the Cs semicore 5p electrons were found to be markedly counterpolarized. Because of the strong metallic screening, changes in the electronic environment are localized to the Cs overlayer and the Cs/W interface layer. The net result of these polarizations is a reduction of the effective electrostatic surface barrier. As a result, all W states, and also the Fermi level, are shifted to smaller binding energies with respect to vacuum and consequently the work function is reduced by 2.0–2.5 eV, depending on the Cs–W distance used.

We have seen above how the spill-out of electrons on the clean surface defines the value of the work function. The alkali-induced change of the work function thus corresponds to a modification of this spill-out. This can be visualized by comparing the self-consistent charge density of the clean and cesiated surface. To this end, we take the total charge density of the cesiated W surface (Fig. 1.21) and subtract the charge density of the clean W surface as well as the charge density of a Cs monolayer (with the same Cs–Cs spacings as in the overlayer on the W surface. The resulting charge-density difference (Fig. 1.21) reveals the charge redistribution upon cesiation. Two main effects become obvious: (1) a loss of electrons in the region between and outside the Cs atoms combined with a pronounced increase in electronic charge near the surface W atoms and (2) a substantial polarization of the Cs 5p semicore electrons. Both effects are associated with the formation of dipole layers which influence the work function of the system. The region between and outside the Cs atoms is the domain of Cs valence electrons (originating in the bulk from the atomic 6s functions). Upon deposition of the Cs overlayer on the W surface, the Cs valence electrons are polarized towards the W surface leading to an increase of electronic charge in the interface region between the Cs and surface W atoms. An analysis of the projected density of states by atom type and orbital angular momentum for the clean and cesiated W surface reveals that the contribution from the surface W atoms remains the dominant component near the Fermi energy and that the Cs d character of the states near $E_F$ is greatly enhanced compared with that of an unsupported Cs monolayer. Together, these observations indicate a polarized metallic bond with a tendency towards the formation of a covalent bond between Cs and the surface W atoms.

We are now in a position to understand the changes in the electrostatic potential induced by the cesiation of the W surface. This potential is most conveniently displayed in the form of the Coulomb potential averaged over planes parallel to the surface. In Fig. 1.22 (lower

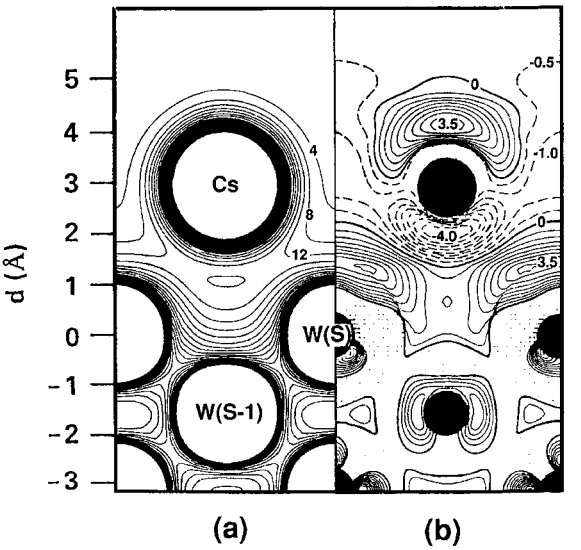


Fig. 1.21. (a) Total electronic charge density for Cs c(2 × 2) on W(001) and (b) the difference charge density between that of Cs/W and the superposed density of clean W(001) and a Cs monolayer in units of $10^{-3}$ electrons/(Bohr radii)$^3$. The vertical scale at the left gives the distance from the surface W atoms in atomic units.

panel) we show this averaged potential for the clean (solid lines) and the cesiated (broken lines) W surface together with the corresponding Fermi energies and work functions for a Cs–W distance of 2.6 Å. The analysis of these results reveals that the Coulomb potential near the W atoms is shifted by almost the same constant amount (2.00 eV) by which the work function is reduced ($\Phi = 2.77$ eV for the cesiated W(001) surface). This shift is caused by the change in the effective surface dipole layer: The polarization of the Cs valence electrons towards the surface W atoms gives rise to a dipole barrier which counteracts the original spill-out dipole and thus reduces the work function. By contrast, the dipole layer associated with the polarization of the Cs 5p semicore electrons acts in the same direction as the spill-out dipole and tends to increase the work function.

The resulting effect of these multiple dipole formations is a net reduction of the effective surface dipole and hence a lowering of the work function. The Cs-induced changes in the electrostatic potential, i.e., the formation of a dipole layer which counteracts the spill-out dipole, is shown in the upper panel of Fig. 1.22 in the form of the difference between the (planar-averaged) Coulomb potential of the cesiated system and the superposed Coulomb potentials of the clean W and the unsupported Cs monolayer. One observes clearly a dipole barrier due to the polarization of the Cs valence electrons and a superposed structure due to the Cs semicore 5p polarization. The net result is an almost constant shift by 2 eV inside the Cs/W interface region. Further, as found from independent self-consistent calculations for increases of W–Cs distances from 2.6 to 2.75 and 2.90 Å, there is an increase of the spatial extension of the polarized Cs overlayer and hence an enhancement of the counteracting dipole. As a result, the work function is further reduced to 2.55 and 2.28 eV, respectively.

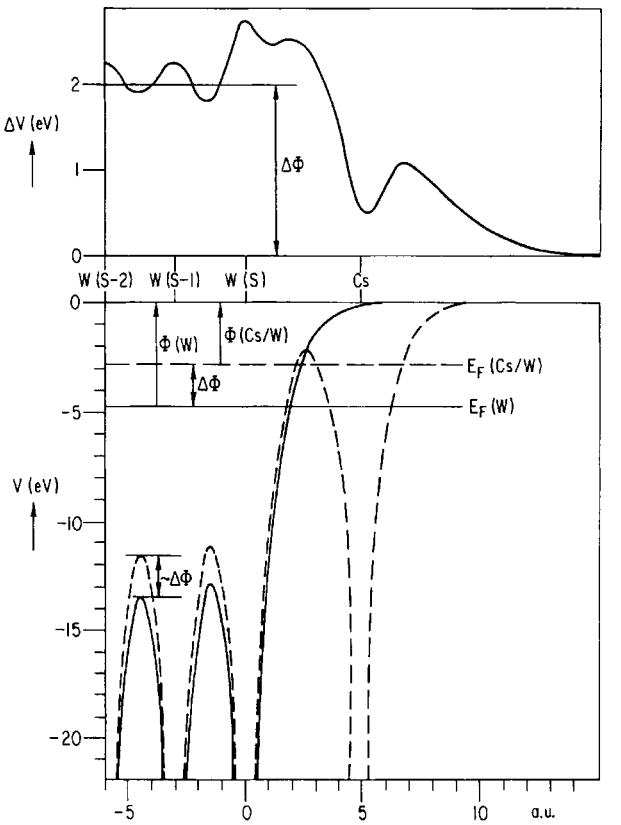


Fig. 1.22. Lower panel: Coulomb potential $V$ averaged in planes parallel to the surface for the clean (solid lines) and the cesiated (dashed lines) W(001) surfaces. Top panel: $V$(Cs/W) − [$V$(clean W) + $V$(Cs monolayer)]. $\Phi$(W) and $\Phi$(Cs/W) denote the work functions of the clean and cesiated W surface, respectively, and $\Delta\Phi$ is the lowering of the work function. The distance (height) of the Cs atoms to the surface W atoms is 2.60 Å.

The detailed structure of the Cs-induced potential barriers, represented in the form of a 3D plot in Fig. 1.23, demonstrates this situation very impressively. We recognize in Fig. 1.23 the 2-eV barrier originating from the polarization of the Cs valence electrons and the balcony-like structures due to the counterpolarization of the Cs 5p electrons. The plateau on the left-hand side of Fig. 1.23 represents the essentially constant shift of the potential in the interior of the system. The Coulomb potential of the cesiated W(001) surface, shown in Fig. 1.24, resembles that inside the clean W(001) surface (Fig. 1.19) except for the fact that it is shifted by 2 eV to higher energies. Since, as stated earlier, the exchange–correlation contribution to the potential inside the surface remains unaltered upon cesiation, the effective potential (Fig. 1.20) is shifted by the same amount (2 eV) as the Coulomb potential.

As a consequence, the Fermi energy is also shifted by 2 eV to higher energies with respect to the vacuum (compare Figs. 1.20 and 1.25) and thus the work function is lowered.

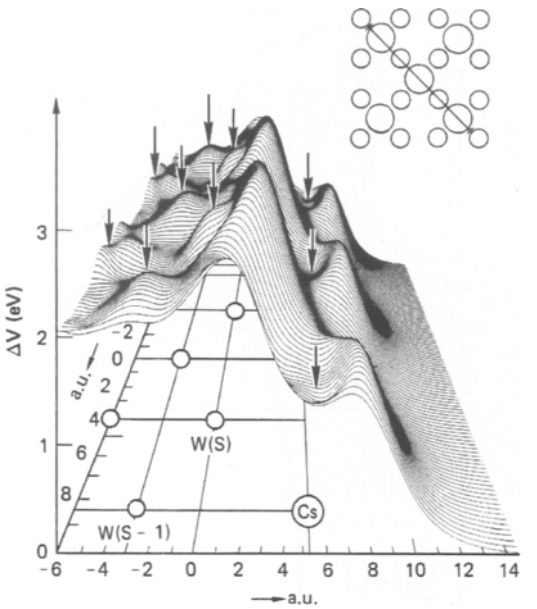


Fig. 1.23. Electrostatic Coulomb potential barrier originating from the polarizations in a c(2 × 2) Cs overlayer ($d = 2.6$ Å) on a W(001) surface (corresponding to the charge redistribution shown in Fig. 1.22) in the (110) plane perpendicular to the surface as indicated by the inset in the upper right corner.

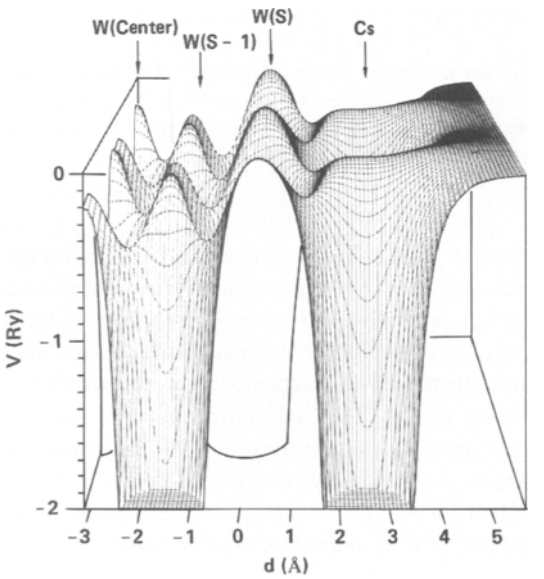


Fig. 1.24. Coulomb potential for c(2 × 2) Cs on W(001) ($d = 2.60$ Å) in the (110) plane perpendicular to the surface.

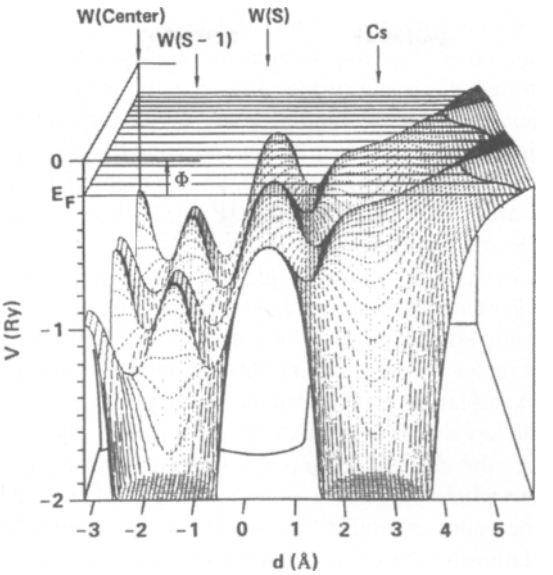


Fig. 1.25. Effective one-electron potential for c(2 × 2) Cs on W(001) ($d$ = 2.60 Å) in the (110) plane perpendicular to the surface. $\Phi$ denotes the work function of this system.

As the distance of the Cs atoms from the W surface is increased from 2.60 to 2.90 Å, the work function of the cesiated surfaces is changed markedly from 2.77 to 2.28 eV. The main reason seems to be that upon separation the thickness of the polarized Cs overlayer is extended and consequently its dipole moment increased, and this leads to a further lowering of the work function. It is important to note that the multiple dipoles which reduce the work function are essentially located outside the surface W atoms. Therefore, the simple classical dipole picture of a $Cs^+$ ion and its image charge inside the metal surface is inadequate.

We have cited these rigorous, self-consistent, all-electron, FLAPW studies in detail in order to show the complex nature of the multipole dipole formation mechanism by which the work function is lowered when a transition metal like W is cesiated. Unlike simple models, which ionize the Cs overlayer atoms by electron transfer into the W surface, Cs forms a metallic overlayer, which has its valence electrons strongly polarized and its 5p semicore shell dipole polarized oppositely. The charge redistribution is localized to the interface atoms and shows an enhancement of the electronic charge on the Cs side of the interface W atoms. The admixture of the directional character of Cs d-like charge and the persistent dominance of W d-like surface states near $E_F$ indicates a tendency towards a covalent Cs (s, d)–W (surface-d) bond. Together, these effects reduce the effective surface dipole barrier and bring about the dramatic reduction in the observed work function.

## 1.7. Geometric structure and energetics of clean surfaces

In the previous sections we have seen how the changes in the electronic density at a surface lead to the occurrence of new electronic levels such as surface states and surface resonance

states. Furthermore, we have discussed how adsorbates such as alkali metals modify the charge distribution and other properties such as the work function. Any rearrangement of the charge density around atoms at a surface also changes its bonding characteristics such as bonding geometries, bond lengths, binding energy, and vibrational properties. For these reasons, the determination of the geometric structures and the corresponding energetics of surfaces form a major part of present experimental and theoretical efforts with far reaching consequences in areas such as adhesion, coating, friction, catalysis, chemical vapor deposition, edging, electrochemistry, and corrosion.

The accurate prediction from first principles of structural and energetic properties of clean surfaces and adsorbate–surface interactions is perhaps one of the greatest triumphs of the present electronic structure theory of surfaces. While the exploitation of this capability constitutes a major recurring theme throughout this volume, we want to discuss here a few selected examples to demonstrate the underlying concepts of such calculations and to point out some key aspects. To this end, we will first discuss the phenomenon of surface relaxation, i.e., the change of interlayer spacings near a surface, then proceed to surface reconstructions where the surface atoms are displaced both laterally and vertically, and finally discuss the geometry and energetics of adsorbate atoms on surfaces. A common theme is the relationship between geometric changes and the underlying electronic structure effects.

### *1.7.1. Surface relaxation on W(001): evidence for short-range screening*

Relaxation and reconstruction play a fundamental role in the physics and chemistry of surfaces and thus have been the object of intense experimental efforts. Their observation in such diverse systems as semiconductors and clean and adsorbate-covered metal surfaces indicates that these structural changes can be considered to be the rule rather than the exception. In some cases such as the Al(110) (Nielsen et al., 1982), the Cu(110) (Adams et al., 1982) or the V(100) (Jensen et al., 1982) and Re(0101) (Davis and Zehner, 1980) surfaces, it has been possible to present experimental evidence for multilayer relaxation effects. Early theoretical attempts to calculate surface relaxation effects were limited to semiempirical tight-binding calculations (Allan and Lannoo, 1973; Treglia et al., 1983; Stephenson and Bullett, 1984) or to simplified model Hamiltonians (Barnett et al., 1983). The accurate experimental determination of multilayer relaxation effects have called attention to the need for precise theoretical determinations of the energetics and detailed information on the driving mechanism behind the observations.

First-principles self-consistent calculations have confirmed a damped oscillatory multilayer relaxation for the Al(110) surface (Ho and Bohnen, 1985). On the other hand, for the important class of transition-metal surfaces, no *ab initio* study of any surface multilayer relaxation had been reported until a decade ago and little was known about the energetics of such a process. For well-studied surfaces such as W(001), no multilayer relaxation has been observed and even the extent of the relaxation of just the first layer has been a matter of controversy: the values of the low-energy electron diffraction (LEED) analyses for this contraction vary between $(4.4 \pm 3)\%$ and $(11 \pm 2)\%$ (van Hove and Tong, 1976; Debe et al., 1977; Lee et al., 1977; Feder and Kirschner, 1978; Kirschner and Feder, 1979; Heilmann et al., 1979; Clarke and Marales De La Garza, 1980; Marsh et al., 1980). Backscattering–channeling experiments (Feldman et al., 1977) using MeV ions lead to the conclusion that

the value for the contraction does not exceed 6%. A spin-polarized LEED study (Feder and Kirschner, 1981) suggests a value of $(7.0 \pm 1.5)\%$.

The situation was sharply changed as a result of several local density studies. Here we illustrate this work with the results of Fu et al. (1984) on the energetics of the multilayer relaxation process on the W(001) surface employing a total-energy FLAPW approach (Weinert et al., 1982). They predicted a contraction of the topmost layer by 5.7% accompanied by an outward relaxation of the second and third layers leading to an increase of the second and third interlayer spacings by 2.4% and 1.2%, respectively. Surprisingly, they found that the relaxation of the second and third interlayer spacings does not influence the equilibrium spacing between the two topmost layers, i.e., keeping the inner layers unrelaxed leads to practically the same equilibrium distance between the first and second layer as is found for the fully relaxed system. Thus, the equilibrium between the adjacent layers appears to be governed by highly screened local interactions. This decoupling of the relaxation for the topmost and the inner layers is the more remarkable since 25% of the total relaxation energy of 0.06 eV originates from the relaxation of the inner layers.

In these calculations (Fu et al., 1984), the W(001) surface was described by a single-slab using five- and seven-layer films – thicknesses which have been demonstrated sufficient to describe accurately the electronic structure of this system. Here we first focus on relaxation effects only and later describe additional reconstruction effects as has been observed (Debe and King, 1977; Felter et al., 1977) for the low-temperature phase of the W(001) surface. As we shall see, although additional reconstruction effects modify somewhat the interlayer spacing between the surface and subsurface layers, they are very unlikely to change the overall mechanism and the multilayer relaxation results.

In order to explore the energy hypersurface which determines the multilayer relaxation process in the case of the five-layer film, the interlayer spacings between first and second ($d_{12}$) and second and third layer ($d_{23}$) were varied independently. For the seven-layer film three interlayer spacings, $d_{12}$, $d_{23}$, and $d_{34}$ were treated as independent quantities. The energy hypersurface is scanned by varying $d$ with a step width of 1.5% of the bulk lattice constant. Near the equilibrium geometry, these discrete points of the energy hypersurface are parabolically fitted as shown in Fig. 1.26. The root mean square (rms) value of this parabolic fit is less than 0.2 mRy showing that, as expected, the system behaves harmonically around its equilibrium positions. Furthermore, this small rms value demonstrates the high numerical precision and stability of the FLAPW approach.

Surprisingly, for all cases listed, Fu et al. (1984) find the same contraction $(5.5 \pm 0.5)\%$ for the topmost layer, i.e., independent of the assumed relaxation process underneath. This theoretical value is consistent with experimental results (Debe et al., 1977; Feldman et al., 1977; Feder and Kirschner, 1978; Heilmann et al., 1979; Clarke and Marales De La Garza, 1980; Marsh et al., 1980; Feder and Kirschner, 1981). For the relative change between the second and third layer, $\Delta_{23}$ Fu et al. (1984) predict an expansion of 2.4% and for $\Delta_{34}$ an expansion of 1.2%. The positive sign of $\Delta_{34}$ is unexpected, since intuitively one might expect an alternation of contractions and expansions upon going from the surface into the interior of the system as has been reported for the Al(110) surface (Nielsen et al., 1982; Ho and Bohnen, 1985).

The electronic origin of the relaxation on a transition-metal surface such as the W(001) surface may be understood by considering the simultaneous effects of bonding of local-

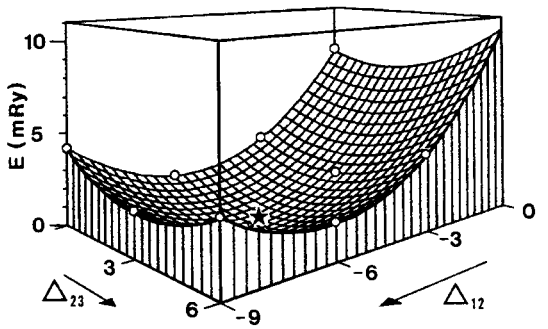


Fig. 1.26. Energy hypersurface for a seven-layer W(001) film as a function of the relative changes (in percent) of the first two interlayer spacings. For this plot, the third interlayer spacing is kept at its bulk value. The minimum in the total energy, indicated by the star, is set equal to zero, i.e., subtracting 226144.0175 Ry. The open circles indicate the geometries where self-consistent calculations have been performed.

ized d electrons and delocalized sp electrons. In the bulk of a transition metal, the bond formation driven by d electrons tends to decrease the interatomic distances while the free-electron-like sp electrons minimize their contribution to the total energy by expanding the lattice which decreases their kinetic energy. The balance between these two mechanisms leads to the bulk equilibrium geometry. At the surface, the d–d bonding between the surface and subsurface atoms is enhanced, i.e., the bond distance can be shortened, since the sp electrons can be pushed into the vacuum region above the surface. Thus, the binding energy is increased by enhanced d–d bonding while the sp electrons can maintain their low kinetic energy by extending further out into the vacuum. As a consequence of this increased spillout of electrons into the vacuum, the topmost interlayer spacing is contracted relative to the bulk layer spacing. This balance between these two mechanisms also results in a work function ($\Phi = 4.6$ eV) which shows very little variation (less than 0.14 eV) for all the relaxation processes studied. The enhancement of the d–d bonding increases $\Phi$, while the rearrangement of the sp electrons decreases the surface dipole layer as the surface layer spacing is contracted. Further, the surface relaxation energy, 0.06 eV, amounts to only 2% of the surface energy calculated by Fu et al. (1984). Thus, the surface relaxation mechanism does not lead to a significant change in the surface energy.

### *1.7.2. Surface reconstructions and structural surface phase transitions: W(001)*

The focus of much of the effort at understanding transition-metal surfaces has been directed at tungsten, which plays the same prototypical role for metal surfaces as does Si for semiconductor surfaces. Extensive investigations and considerable progress in elucidating a number of electronic structure properties have been made which have led to an understanding of the structural phase transition in W(001). Originally, Felter et al. (1977) suggested the possibility of an alternating displacement of the atoms perpendicular to the surface. Currently, the most widely accepted model to explain the observed reconstruction (Felter et al., 1977; Debe and King, 1979a, b) upon cooling below room temperature from

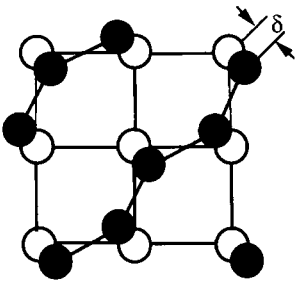


Fig. 1.27. Atomic displacements for $\mathbf{M}_5$ phonon with displacements in the ⟨110⟩ direction (open circles indicate bulk-like positions).

a $(1 \times 1)$ into a $c(2 \times 2)$ structure, is the alternating lateral displacements of W atoms along the ⟨110⟩ directions to form zig-zag chains with a $(\sqrt{2} \times \sqrt{2})R45°$ structure.

Theoretical model calculations based on two-dimensional surface response functions, (Krakauer et al., 1979b; Terakura et al., 1981), the matched Green's-function method (Inglesfield, 1979), lattice dynamics (Fasolino et al., 1980, 1981) and concluded that a reconstructed surface exists at low temperatures; however, a stable $(1 \times 1)$ surface was obtained with empirical tight-binding total-energy approaches (Treglia et al., 1983; Stephenson and Bullett, 1984).

Fu et al. (1984) presented the first all-electron local-density-functional (LDF) study of the surface reconstruction on the W(001) surface employing the FLAPW total energy approach. On the basis of the "frozen-phonon" method (adiabatic approximation), they studied lateral displacements via the longitudinal phonon mode $\bar{M}_5$ [$\mathbf{q} = (\pi/a)(1, 1)$, where $a = 3.16$ Å] which leads to a $(\sqrt{2} \times \sqrt{2})R45°$ structure (Fig. 1.27). The results support the conclusion that W(001) is reconstructed at low temperature according to the Debe and King (1977, 1979a, b) model with an in-plane displacement in the ⟨110⟩ direction by $0.18 \pm 0.01$ Å. Evidence was given that the strong coupling between surface states and $\bar{M}_5$ phonons near the Fermi level is the driving mechanism of this phase transition. The reconstructed surface was found to exhibit essentially no relaxation of the surface atoms and this demonstrated, for the first time, that surface reconstruction may act to suppress surface relaxation or even reverse the surface relaxation from a contraction into an expansion. The transition from the relaxed $(1 \times 1)$ phase into the reconstructed $c(2 \times 2)$ phase proceeds over a very flat region of the energy hypersurface before the system is stabilized in a shallow harmonic potential.

A simple physical picture emerged from these first all-electron total-energy calculations: the transition from the $p(1 \times 1)$ into the $c(2 \times 2)$ phase involves two competing effects – lowering of the total energy either by relaxation or by reconstruction. Surface relaxation barely reduces the density of states for the surface layer at $E_F$. On the other hand, a larger electronic energy is gained through the surface reconstruction by opening a surface band gap around $E_F$ which significantly reduces the density of states at the Fermi level. Therefore, the system tends to minimize its electronic energy by increasing the lateral atomic displacement and avoids the energetically unfavorable nuclear repulsion due

to the decreased atomic distances in the relaxed phase by expanding the first interlayer spacing. The result is that surface relaxation is suppressed for the reconstructed surface.

In a subsequent paper, Fu and Freeman (1988) considered the effects of multilayer relaxation on the reconstruction of the W(001) surface. Until then, the surface reconstruction had been considered as mostly confined to the surface layer, owing to the surface-layer-localized electronic states near $E_F$ (Krakauer et al., 1978; Ohnishi et al., 1984; Fu et al., 1984; Fu et al., 1985; Weinert et al., 1986; Singh et al., 1986) with a bulk-like structure assumed for the inner layers. Although the possibility of a reconstructed subsurface layer had been suggested, it was assigned an insignificant role in the surface energetics (Fasolino et al., 1980, 1987). While the multilayer relaxation is a well-established property for metallic surfaces (Fu et al., 1984) little was known about the energetics and mechanism behind a possible multilayer reconstruction. Its possible existence is, of course, considered essential for understanding surface properties and, in particular, for surface structural (such as low-energy electron-diffraction) and vibrational analyses.

In their paper, Fu and Freeman (1988) reported results of a of a local-density-functional total-energy study of the c(2 × 2) multilayer reconstruction on W(001) induced by the $\bar{M}_5$ ⟨11⟩ and $\bar{M}_5$ ⟨10⟩ soft-phonon modes. They found that the subsurface (S-1) layer is also reconstructed into the c(2 × 2) structure with a sizeable displacement amounting to one-fourth of that found for the surface atoms (0.22 Å for $\bar{M}_5$ ⟨11⟩ and 0.17 Å for $\bar{M}_5$ ⟨10⟩). The mechanism driving the (S-1) layer reconstruction is a combination of symmetry lowering and induced strain caused by the surface layer reconstruction. The surface multilayer reconstruction energies are 60 meV for $\bar{M}_5$ ⟨11⟩ and 30 meV for $\bar{M}_5$ ⟨10⟩ per surface and subsurface atom pair, which are twice those obtained by freezing the atoms of (S-1) layer at their bulk truncated positions. As a consequence, the characteristic vibrational frequency ($\omega_{\|}$ = 30 meV) associated with the reconstructed (S-1) layer atoms if found to be rigid, i.e., above the frequency of the bulk continuum. These results suggest that multilayer reconstruction, which is manifested as the "elastic" response of inner layers to the displaced surface atoms, should be considered as a universal property for the reconstructed metallic surfaces.

The more recent work on the multilayer relaxation and reconstruction of the W(001) surface by Yu et al. (1992) again using the FLAPW method is an example of the current state of the art in theoretical and computational surface physics. This tour de force work by Yu et al. (1992) is the culmination of a parallel line of research to that described above for the W(001) surface, which had obtained some different results (Singh et al., 1986; Singh and Krakauer, 1988). The approach by Yu et al. (1992) combined total energy and atomic force calculations on a seven layer slab which is repeated normal to the surface with vacuum regions equivalent to five atomic layers of W separating the slabs. We quote their results below.

The calculated reconstruction and relaxation parameters of the equilibrium geometry are given in Table 1.5, together with the results of the previous theoretical (Fu and Freeman, 1988; Legrand et al., 1986) and experimental (Altman and Estrup, 1988) work. Uncertainties associated with these values are estimated from the residual forces and are also given in Table 1.5. As described by Yu et al. (1992), there is an appreciable scatter in the values for the lateral shift of the surface atoms. Their value of $\delta(S) = 0.268$ Å is near the upper limit of the X-ray-diffraction experimental value, while that of Fu and Freeman (1988) of 0.22 Å is at the lower end of the experimental error range. This discrepancy already was

Table 1.5

Comparison of the theoretical and experimental lateral displacements of the surface and subsurface layer atoms and percentage change in the first- and second-interlayer spacings of the low-temperature W(001) from the bulk-truncated geometry (after Yu et al., 1992)

| | Theory | | | Experiment |
|---|---|---|---|---|
| | Yu et al. (1992) | Fu and Freeman (1988) | Legrand et al. (1986) | Altman and Estrup (1988) |
| $\delta$(S)(Å) | $0.268 \pm 0.005$ | 0.22 | 0.25, 0.18 | $0.24 \pm 0.025$ |
| $\delta$(S-1)(Å) | $0.048 \pm 0.002$ | 0.05 | 0.05 | $0.046 \pm 0.016$ |
| $\delta$(S-2)(Å) | $0.015 \pm 0.002$ | | | |
| $\delta$(S-3)(Å) | $0.006 \pm 0.002$ | | | |
| $\Delta_{12}$(%) | $-6 \pm 0.5$ | $-4$ | $-2.1, -1.5$ | $-4 \pm 10$ |
| $\Delta_{23}$(%) | $0.5 \pm 0.5$ | | $-0.9, -0.6, -0.3$ | |

present in earlier work (Fu et al., 1985; Singh et al., 1986; Fu and Freeman, 1988; Singh and Krakauer, 1988) that considered the reconstruction of the surface layer only. (The origin of the discrepancy is still unresolved). The result of Legrand et al. (1986) appears to be in better agreement with experiment. One must note, however, that the error bar of the experimental result is large enough to allow all of the theoretical results. Results of previous LEED experiments, which favor the smaller lateral shift, are undermined by the inherent assumption that the reconstruction is confined to the first layer and thus the comparison may not be very meaningful. The theoretical values for the lateral shift of subsurface atoms are in surprisingly good agreement with each other and with experiment. Further, Yu et al. (1992) find the lateral shift of the third and fourth to be 0.015 and 0.006 Å, respectively, with an uncertainty of 0.002 Å. The displacement of the center-layer atoms may be larger than what it should be as a result of the slab geometry. On the other hand, its small value suggests that finite-size effects do not affect the surface and subsurface layers significantly. Note that the results show an exponential decay of the lateral displacement with the distance from the surface, with the decay length being on the order of the interlayer distance.

### *1.7.3. Surface energy of transition metals: W(001) and V(001)*

The creation of a surface, for example by splitting a solid and separating it into two pieces, requires energy. This "surface energy" plays an important role in many physical and chemical processes on solid surfaces such as crystal and epitaxial growth, tribology, fracture, catalysis, and corrosion. Accurate experimental measurements of the surface energy are difficult to perform. In fact, such measurements are mostly constrained to the determination of surface energies at high temperatures and are subject to numerous errors due to surface-active contaminants. For example, although the tungsten surface has been the most studied metal surface in the last decade, the experimentally measured surface energies at high temperature scatter widely from 1.8 to 5 J/m$^2$. As another example, the surface energy of solid vanadium has not even been measured experimentally owing to the difficulty in preparing a clean surface because of oxygen contamination. Similarly, theoretical determinations of the surface energy face a formidable challenge. Previous theoretical efforts

focused on simple metals using either first-order pseudopotential perturbation theory (Lang et al., 1973) or nonperturbative variational methods (Monnier and Perdew, 1978). Only recently have first-principles calculations of the surface energy of such complex systems as the transition metals become feasible and realistic.

Fu et al. (1985) reported theoretical determinations of the surface energies of W(001) and V(001) using the FLAPW total-energy method. The W(001) and V(001) surfaces are described in a single slab geometry with five and seven atomic layers. (Because the slabs have two surfaces, the surface energy is one-half of the total-energy difference between a film and the corresponding value for the same number of atoms in a bulk crystal.) The convergence of the surface energy with respect to film thickness depends on how well the inner layers of the film approach the bulk. This was examined by comparing the total energy of the bulk atoms and the corresponding value obtained from the total-energy difference between the five- and seven-layer films. Thus, they incorporated results obtained with both the FLAPW thin-film method and an independent FLAPW bulk method (Jansen and Freeman, 1984) into the surface energy determinations.

In order to test the variation of the surface energy with respect to different forms of the exchange–correlation potential, both the Hedin and Lundqvist (1971) and the Wigner (Pines, 1963) exchange–correlation potentials have been used. The former is known to be more exact in the metallic density region, while the latter is more appropriate for diffuse regions such as those near the surface. The effect of the surface lattice relaxation was examined for both tungsten and vanadium. They used the experimental lattice constants of 3.16 Å for bulk bcc tungsten and 3.03 Å for bcc bulk vanadium in the calculations for the surface energy.

Their calculated values of the surface energies are 5.1 J/M$^2$ for W(001) and 3.4 J/m$^2$ for V(100), respectively. They find that (i) owing to the highly local screening interaction, the seven-layer films are thick enough to explore the surface energy of transition metals with a convergence better than 0.1 eV and (ii) the dominant contributions are from the surface and subsurface atoms.

The large values of the surface energies are related to the high density of surface states near the Fermi level. Significantly, the surface energies are found to be almost independent of the local exchange–correlation potentials employed. Because of the highly local screening at transition metal surfaces, the dominant contributions to the surface energies are from the surface and subsurface atoms. The surface relaxation and reconstruction (Fu et al., 1984, and Yu et al., 1992) energies are small, i.e., less than 2% of the W(001) surface energy and less than 4.5% of the V(001) surface energy. A comparison of the theoretical value at $T = 0$ K with the measured surface energies at high temperatures for W(001) supports a large surface entropy above 1000 K ($\Delta S \sim 1.5 \times 10^{-3}$ J/m$^2$deg). This implies large lattice anharmonicity and emphasizes the possible disordered nature of the W(001) surface at high temperatures.

## 1.8. Semiconductor surfaces and adsorbates

So far, we have mostly given as examples the structure and properties of metal surfaces. Semiconductor surfaces play an extremely important role in microelectronics and thus

many theoretical and computational studies have been focused on these systems. For this reason, special chapters of this Volume are devoted to semiconductor surfaces. Here we provide a few examples that show the concepts of a localized-orbital cluster approach to problems of surface structure and adsorbate–surface interactions.

Electronic and structural properties of the clean and metal adsorbed silicon surface continues as one of the most studied subjects in surface science. The motivation for this effort comes from both technological and fundamental scientific interest in the metal/silicon interface, which is especially important in the manufacture of electronic devices. The clean Si(100) surface shows a dominant $2 \times 1$ structure (Schlier and Farnsworth, 1959) although some higher-order structures (Lander and Morrison, 1962; Poppendieck et al., 1978; Cardillo and Becker, 1978, 1980; Ide and Mizutani, 1992; Uhrberg et al., 1992; Tromp et al., 1985; Hamers et al., 1986), such as $c(4 \times 2)$, $p(2 \times 2)$, $c(2 \times 2)$ and $c(4 \times 4)$, are also reported. The $2 \times 1$ reconstruction is generally believed to be due to Si dimer formation (Haneman, 1987; Wolkow, 1992).

### *1.8.1. Structure of the Si(100) 2 × 1 surface*

The structural and electronic properties of the clean reconstructed Si(100)$2 \times 1$ surface remain of considerable interest for both fundamental scientific and technological reasons. Although several models have been proposed for the Si(100)$(2 \times 1)$ reconstructed surface (Green and Seiwatz, 1962; Harrison, 1976; Schlier and Farnsworth, 1959; Phillips, 1973; Poppendieck et al., 1978; Seiwatz, 1964; Jona et al., 1977; Northrup, 1985), such as the dimer model (Schlier and Farnsworth, 1959; Phillips, 1973; Poppendieck et al., 1978), the vacancy model (Schlier and Farnsworth, 1959; Phillips, 1973; Poppendieck et al., 1978) and the conjugated-chain-type model (Seiwatz, 1964; Jona et al., 1977; Northrup, 1985) the early studies by Appelbaum et al. (1975, 1976b) and later calculations (Haneman, 1987; Appelbaum and Hamann, 1978; Kerker et al., 1978; Chadi, 1979; Ihm et al., 1980; Yin and Cohen, 1981; Verwoerd, 1981; Brink and Verwoerd, 1981; Krüger and Pollmann, 1988; Bechstedt and Reichardt, 1988; Zhu et al., 1989; Redondo and Goddard III, 1982; Pandey, 1984; Artacho and Yndurain, 1989; Abraham and Batra, 1985; Batra, 1990) all showed that the dimer model is the most favored model for the Si(100)$2 \times 1$ surface reconstruction.

However, the question whether the surface dimer is symmetric or asymmetric (e.g.., buckled dimer) (cf. Figs. 1.28a and b) remains open despite the large number of experimental and theoretical studies that have been performed. Early energy minimization calculations suggested an asymmetric dimerized structure on the surface (Chadi, 1979). Later studies (Ihm et al., 1980; Yin and Cohen, 1981; Verwoerd, 1981; Brink and Verwoerd, 1981; Krüger and Pollmann, 1988; Bechstedt and Reichardt, 1988; Zhu et al., 1989) also favored the asymmetric dimer result with some modifications of the Si coordinates. The asymmetric dimer model was however questioned by some other theoretical work (Redondo and Goddard, 1982; Pandey, 1984; Artacho and Yndurain, 1989; Abraham and Batra, 1985; Batra, 1990). Redondo and Goddard (1982) found from Hartree–Fock cluster calculations that the ground state of the symmetric dimer is 1.0 eV lower than the buckled dimer. Pandey (1984) found a substantial decrease in the surface total energy by introducing a $\pi$-bonded defect model based on the symmetric dimer and that an optimized symmetric dimer structure has an energy of 0.36 eV/dimer lower than the asymmetric

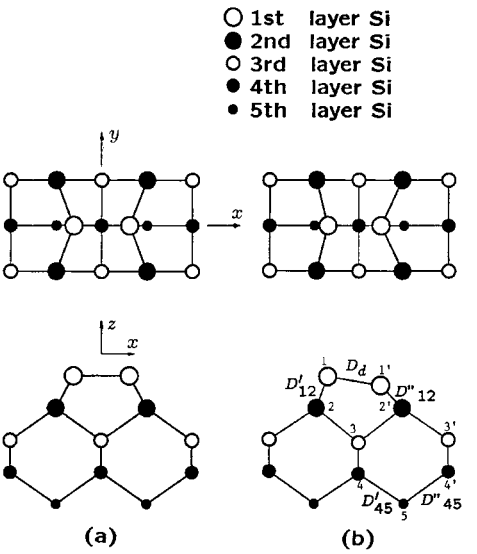


Fig. 1.28. Schematic diagram showing the dimer's atomic geometry on the Si(100)2 × 1 reconstructed surface. Each figure is given in top view from the [100] direction and side view from the [011] direction. The Cartesian coordinates $x$, $y$ and $z$ refer to the [011], [01$\bar{1}$] and [100] directions, respectively. (a) Symmetric dimer reconstruction, and (b) asymmetric dimer model.

dimer structure obtained by Yin and Cohen (1981). More recently, Artacho and Yndurain (1989) found, using a total energy and core-level-shift cluster model calculation, that an antiferromagnetic spin arrangement within the symmetric dimer lowers the total energy by 1.3 eV/dimer below the asymmetric dimer. The symmetric dimer model was also supported by calculations of Abraham and Batra (1985) and more recently by Batra (1990). These various calculations were done by utilizing tight binding (Chadi, 1979; Verwoerd, 1981; Brink and Verwoerd, 1981; Bechstedt and Reichardt, 1988), pseudopotential (Ihm et al., 1980; Yin and Cohen, 1981; Zhu et al., 1989; Pandey, 1984; Batra, 1990), Green's function (Krüger and Pollmann, 1988), and Hartree–Fock (Redondo and Goddard, 1982) methods with either slab (Chadi, 1979; Ihm et al., 1980; Yin and Cohen, 1981; Krüger and Pollmann, 1988; Bechstedt and Reichardt, 1988; Zhu et al., 1989; Pandey, 1984; Batra, 1990) or cluster models (Verwoerd, 1981; Brink and Verwoerd, 1981; Redondo and Goddard, 1982; Artacho and Yndurain, 1989) and with molecular dynamics simulations (Abraham and Batra, 1985). Some results were obtained with more elaborate slab models by optimizing the coordinates of several Si layers using total energy or force calculations (Yin and Cohen, 1981; Bechstedt and Reichardt, 1988; Zhu et al., 1989; Batra, 1990), since it was found experimentally (Yang et al., 1983; Holland et al., 1984) and theoretically (Appelbaum and Hamann, 1978; Yin and Cohen, 1981) that the surface dimerization is accompanied by a large relaxation of the substrate atoms. Finally, previous cluster calculations employed relatively small clusters which contain only 9 silicon atoms and 12 saturating hydrogen atoms. The results of these cluster calculations differ, however, with some favoring the symmetric dimer (Redondo and Goddard, 1982; Artacho and Yndurain,

1989), and others finding the asymmetric dimer to be more stable (Verwoerd, 1981; Brink and Verwoerd, 1981).

On the experimental side, ion scattering experiments with low energy (Anno et al., 1982) and medium energy (Tromp et al., 1981a, b, 1983) supported the buckled dimer model. In addition, Yang et al. (1983) proposed a dimer model based on low-energy electron diffraction (LEED) data in which the dimer can twist along the $y$ direction. However, this conclusion was questioned by Holland et al. (1984) who fitted their LEED data to yield an asymmetric dimer structure without a $y$ twist. Scanning tunneling microscopy (STM) studies by Tromp et al. (1985, 1986) showed that symmetric and asymmetric dimers could be present on the surface in roughly equal amounts. Using the same technique, Samsavar et al. (1989) found that most of the dimers on the Si(100) surface are non buckled, and that the buckling of the dimer occurs mainly near defects or steps. It has been suggested by Soukiassian (1994) that the existence of non buckled or buckled dimer surfaces is strongly dependent on the way the surface is prepared, and especially on the temperature. Their STM studies have shown that a symmetric dimer is formed on the clean Si(100) surface (Soukiassian et al., 1991).

As a result of these conflicting results, Tang et al. (1992) performed a detailed theoretical study including substrate relaxation on finite cluster models of a dimer on the Si(100)$2 \times 1$ reconstructed surface. They used fairly large clusters (up to 63 atoms) to reduce the effect of the boundary and obtained results for optimized structural models based on both total energy and force calculations. The short dimer bond length obtained by other authors (Yin and Cohen, 1981; Zhu et al., 1989; Pandey, 1984; Batra, 1990) was confirmed. It was found that the energy difference between the symmetric and asymmetric dimer is very small ($\sim$0.02 eV). This result is consistent for all three cluster models chosen. Therefore, they concluded that symmetric and asymmetric dimer structures may well coexist on the surface.

Specifically, Tang et al. (1992) calculated the force on the first four silicon layers and minimized the total energy of the cluster to obtain the optimized atomic geometry with minimum energy. The first layer Si atoms are found to relax inward by about 0.38 Å for the symmetric dimer, and 0.16 Å and 0.55 Å for the asymmetric dimer. The dimer bond length is 2.23 Å and 2.27 Å for the symmetric and the asymmetric dimer, respectively.

This work represents the first application of a density functional localized-orbital cluster approach (DMol) using its force capability to study the dimer model of the Si(100)$2 \times 1$ reconstructed surface. By using the convergence of the forces on atoms as a criterion for assessing cluster size effects, Tang et al. (1992) showed that a $Si_9H_{12}$ cluster (used in all previous studies) is too small to give adequate geometric information. However, the relative energy difference between the two dimers is less affected by the small size of clusters. The structure of the dimer was optimized for a $Si_{31}H_{32}$ cluster and it was found that the energy difference between the symmetric and asymmetric dimers is very small ($\sim$0.02 eV). Thus, the possibility that both dimers could coexist on the surface even at modest temperatures can not be ruled out. The dimer bond lengths predicted from the present calculation are 2.23 Å and 2.27 Å for the symmetric and the asymmetric dimer, respectively. For the symmetric dimer, the dimer atoms relax inward by 0.37 Å and for the asymmetric dimer, the dimer atoms relax inward by 0.16 Å and 0.55 Å, respectively.

### *1.8.2. Passivation of the Si(100) surface*

The Si(100) surface, even in its reconstructed form, is still chemically reactive since there is a dangling bond associated with each surface Si atom. There are many applications that require the Si surface to be less reactive and stable against contamination, oxidation, etc. (Uhrberg et al., 1986, 1987; Bringans et al., 1986; Olmstead et al., 1986). Thus, the search for adsorbates that can passivate the surface is an attractive and interesting subject of surface physics.

Great progress has been made in the last few years. Following the successful practice of a related Ge(111) passivation by As (Bringans et al., 1985), it was found that the same element can also passivate both the Si(111) (Olmstead et al., 1986; Uhrberg et al., 1987; Becker et al., 1988a, b) and Si(100) surfaces (Uhrberg et al., 1986; Bringans et al., 1986) and form a stable overlayer. Further, a similar effect was also achieved on the Si surface by using another group V metal, Sb, as an adsorbate (Rich et al., 1989; Richter et al., 1990). Other possible candidates, such as group VI elements, have also received considerable attention (Kaxiras, 1991; Weser et al., 1987; Krüger and Pollmann, 1990) and one element, S, has already demonstrated its ability to passivate the Ge(100) surface (Weser et al., 1987; Krüger and Pollmann, 1990).

The properties of clean and chemisorbed Si(100) surfaces are the focus of many theoretical and experimental studies. It is well known that the clean Si(100) surface reconstructs into a $(2 \times 1)$ structure by forming surface dimers that are arranged in parallel rows. The reconstruction of the Si(100) surface is stable upon chemisorption by many different kinds of atoms. However, the $(2 \times 1)$ reconstruction is removed by the adsorption of some group V metals such as As (Uhrberg et al., 1986; Bringans et al., 1986; Zegenhagen et al., 1988; Becker et al., 1988a, b) and Sb (Rich et al., 1989; Richter et al., 1990). Incidentally, As and Sb are also found to passivate the Si(111) surface (Becker et al., 1988a, b; Rich et al., 1989; Olmstead et al., 1986; Uhrberg et al., 1987). The possible restoration of Si(100) by adsorption of group VI elements was studied recently by Kaxiras (1990, 1991) and by Weser et al. (1987). For the Sb/Si(100) system, photoemission studies by Rich et al. (1989) found that the Si(100) surface shows bulk-like properties after Sb chemisorption suggesting an Sb-induced passivation of the Si(100)$(2 \times 1)$ surface. More recently, Richter et al. (1990) combined surface extended-X-ray-absorption fine structure (SEXAFS) with scanning tunneling microscopy (STM) measurements and showed that in addition to removing the surface reconstruction upon Sb chemisorption, Sb atoms occupy a modified bridge site and form dimer chains perpendicular to the Si dimer chains. Another group V element, As, displays a similar phenomenon (Uhrberg et al., 1986; Bringans et al., 1986; Zegenhagen et al., 1988; Becker et al., 1988a, b) when adsorbed on Si(100). The dimer formation of some III and IV metals were also observed by several groups for Al/Si(100) (Batra, 1989; Nogami et al., 1991), In/Si(100) (Rich et al., 1987; Baski et al., 1991a) and for Sn/Si(100) (Andriamanantenasoa et al., 1987; Rich et al., 1988; Baski et al., 1991b).

Until recently, the chemisorption of Sb on Si(100)$(2 \times 1)$ had not been studied theoretically and so the mechanism that drives its passivation and the formation of metal dimers on the surface was not clear. There exist a few theoretical studies of the symmetric As dimer on the Si(100) surface. Uhrberg et al. (1986) found that the symmetric As dimer model on Si(100) calculated by the pseudopotential method gives results in agreement with their

angle-resolved photoemission data. Shen and Matthai (1991) also studied the As dimer on Si(100) using an empirical tight binding method in the extended Hückel approximation and found that the passivation is due to the splitting of the density of states at $E_F$ into a filled bonding state and an antibonding state above $E_F$. Batra (1989) studied the stability of a group III metal dimer of Al on Si(100) using the pseudopotential approach and found that the Al dimers are stable on the ideal Si(100) surface rather than on the reconstructed surface.

Recently, Tang and Freeman (1992) reported a first principles study of the structural and electronic properties of Sb chemisorbed on Si(100) using the DMol method. The Hedin–Lundqvist exchange–correlation potential was used in the calculation. The frozen core approximation was employed for Si and Sb, but with the Sb-4d electrons treated fully in the self-consistent iterations. The basis set chosen for Si and Sb contains a double set of valence functions plus a single d polarization function. This basis set has been proved to be very good in studying the Si(100)(2 × 1) surface dimer model described earlier. For the bare (2 × 1) surface, a symmetric dimer arrangement is chosen in which the first layer Si atoms relax inward by 0.38 Å and the dimer bond length is 2.23 Å (Tang et al., 1992). Several different sizes of clusters are used to simulate both the (2 × 1) and (1 × 1) surface. Figure 1.29 shows three of these clusters. As usual, hydrogen atoms are used to saturate the Si dangling bonds at the cluster boundary and the Si–H bond length is taken to be 1.48 Å.

At first, Tang and Freeman (1992) studied the optimal adsorption site of a single Sb atom on Si(100)(2 × 1). This adsorption site is used in further studying the passivation of the Si(100)(2 × 1) surface. Four possible adsorption sites ("cave", "bridge", "valley bridge" and "pedestal") were simulated by four appropriate clusters ranging from $SbSi_9H_{12}$ to $SbSi_9H_{16}$. By examining the geometry of Si(100)(2 × 1) and the bond directions of the top layer Si atoms, the valley bridge and pedestal sites are seen to be unlikely. This is confirmed in the calculation. Experimentally (Richter et al., 1990), one Sb atom is expected to bond to two Si atoms. Again from geometrical considerations, the cave site seems to be the most favored since the dangling bonds of the nearest two dimer atoms point in the direction above the cave site. In fact, this site was used in interpreting the photoemission data for In/Si(100) (Rich et al., 1987), where the In atom was found to bond with two Si atoms.

Instead, Tang and Freeman (1992) found that the bridge site is the most stable among the four sites studied for single Sb atom adsorption. The chemisorption energy calculated for the bridge site is −3.26 eV which is 0.51 eV lower than for the cave site (−2.75 eV). The Sb–Si bond length at the bridge site (2.57 Å) is also very close to the experimental value (2.63 Å) (Richter et al., 1990). In comparison, the Sb–Si bond length at the cave site is 2.84 Å which is quite far from the experimental value.

Thus, the following understanding of the initial Sb deposition on a Si(100) surface is emerging: Sb atoms adsorbed on the bridge site of Si(100)(2 × 1) saturate the dangling bonds of the underlying Si dimer atoms, showing an unusual chemisorption site for Sb/Si(100). Tang and Freeman (1992) went further and considered a larger coverage by Sb using cluster models with up to 62 atoms. As a result, the Si dimer is broken when Sb is adsorbed on the cave site between two bridge sites which are already occupied by Sb atoms, resulting in a recovery of the (1 × 1) geometry. The Sb dimer is formed whenever there are two Sb atoms adsorbed on the nearest bridge site along a Si dimer row and it exists regardless of the geometry of the substrate, i.e., (2 × 1) or (1 × 1) geometry. The

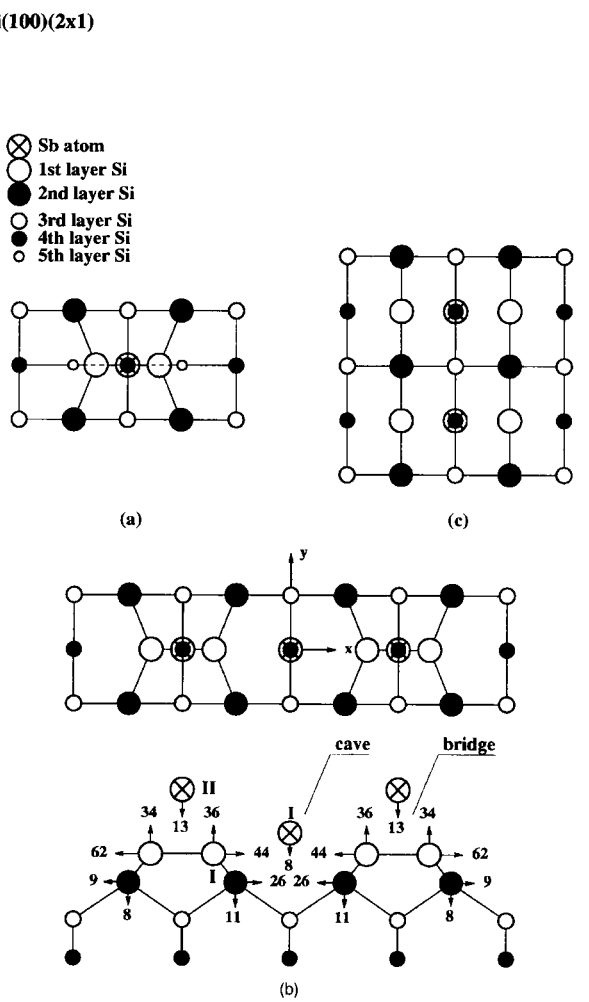


Fig. 1.29. Three cluster models used in the calculation. The Cartesian coordinates $x$ and $y$ refer to the [01−1] and [011] directions, respectively. Hydrogen atoms are not shown in the figures. (a) $Sb_1Si_{17}H_{20}$ cluster, (b) $Sb_3Si_{27}H_{32}$ cluster (given as a in top view from the [100] direction and a side view from the [011] direction). The values of atomic force on the Sb and the first two layers of Si atoms are shown in unit of $10^{-3} \sim$(Ry/a.u.), which Sb atoms are placed at 2.34 Å and 0.79 Å above the bridge and cave site respectively. (c) $Sb_2Si_{25}H_{28}$ cluster.

Sb–Sb, Sb–Si and the vertical distance between Sb and Si surface were found to be 2.93 Å, 2.61 Å and 1.73 Å, respectively – in excellent agreement with experiment (Richter et al., 1990). Finally, since the Sb dimer on Si(100)(2 × 1) is more stable than on Si(100)(1 × 1) at low coverage, they proposed that a temporary phase having Sb(2 × 2) structure may be seen at low coverage. These conclusions may extend to As/Si(100) for which the metal atom has electronegativity comparable with Sb.

### *1.8.3. Importance of adsorbate–adsorbate interactions for As and Sb chemisorption on Si(100)*

While theoretical studies focused on the electronic and structural properties of As and Sb dimers on Si, little attention was paid to the relationship of the chemisorption geometry of metals on Si(100) at initial deposition and at high coverage. Previous experimental and theoretical studies were usually conducted at relatively high metal coverage ($\geqslant 0.5$ ML) (Uhrberg et al., 1986; Bringans, 1986; Rich et al., 1989; Richter et al., 1990). As cited above, Tang and Freeman (1993a) showed that the Sb-induced passivation occurs when Sb is adsorbed on a cave site between two nearest bridge sites in adjacent Si dimer rows already occupied by Sb atoms. In a subsequent paper, Tang and Freeman (1993b) presented a detailed analysis of the chemisorption of As and Sb atoms on a Si(100) surfaces, again using first principles local density calculations with molecular cluster models. The chemisorption geometries are determined through comparison of single and two atom adsorption. The results show that As and Sb form dimers on the Si surface, and stay at a modified bridge site in agreement with experiment (Uhrberg et al., 1986; Bringans et al., 1986; Richter et al., 1990). They also found that calculations of single Sb atom adsorption do not give a correct description of the chemisorption geometry because of the lack of adsorbate–adsorbate interactions.

Briefly put, using the first principles DMol approach and cluster models up to 63 atoms, Tang and Freeman (1993b) showed that the single As prefers to stay on the bridge site of both the ideal and $2 \times 1$ reconstructed Si(100) surface, while single Sb atoms would occupy the hollow site on the ideal substrate and the bridge site on the reconstructed substrate. This leads to a contradiction with the experimental fact that As and Sb exhibit similar behavior on the Si surface. The key issue underlying the discrepancy was then shown to be the lack of adsorbate–adsorbate interaction in the single atom adsorption. By putting metal atoms on various adsorption sites and in different orientations, they found that the two metal atoms interact strongly and form dimers when they are at the modified bridge site along a direction perpendicular to the Si dimer rows. Because the metal dimer is favored in energy over the non-dimer configuration on both ideal and reconstructed surfaces, Tang and Freeman (1993b) concluded that the dimer structure is essential for these chemisorption systems.

## 1.9. Magnetism at surfaces and interfaces: spin–orbit induced magnetic effects

During the course of the last decade, low-dimensional magnetism of surfaces, interfaces and thin-films has matured into a major branch of modern condensed matter physics and is likely to open vast vistas for practical applications (Falicov et al., 1990; Bader, 1990; Mathon, 1988). The abrupt termination of the lattice or composition in these systems leads to a variety of new phenomena such as localized electronic surface states, magnetic moment enhancement, perpendicular magneto-crystalline anisotropy (MCA), complex magnetic ordering, etc. Fortunately today – as is spelled out later in Chapter 4 – it is possible

to synthesize and study thin films with either stable or metastable phases, and this has dramatically and importantly increased the range of materials that are magnetic and hence the challenges for understanding magnetism in low dimensional systems.

It is known that *ab initio* energy band methods, mainly the full-potential linearized augmented plane wave (FLAPW) method, based on local spin density (LSD) functional theory have played a very important role in the understanding and development of low-dimensional magnetism. As discussed by Schneider and Kirschner in Chapter 9, theoretical calculations predicted the large enhancement of the magnetic moment for 3d transition metal (TM) surfaces or TM ultra thin films deposited on inert substrates and possible magnetism in some normally non-magnetic materials; some of these predictions have already been verified experimentally. Stable magnetic structures, especially some antiferromagnetic (AFM) configurations, can now be predicted by comparing total energies and, in the same way, equilibrium atomic geometries and lattice relaxation (including surface and interface) can also be determined.

Wang et al. (1993) proposed and implemented a state-tracking procedure to treat the effects of spin–orbit coupling (SOC) with the FLAPW method. As a result, one can now obtain and we will describe here, (i) reliable MCA energies (although they are as small as a few tenths of an meV/atom) for real complex systems and (ii) magneto-optical Kerr effect (MOKE) and magnetic soft X-ray circular dichroism (MCD) spectra. Model analyses have been shown to provide a clear physical picture for these important phenomena previously thought to be very complex.

### *1.9.1. Magneto-crystalline anisotropy*

To determine the MCA, the SOC ($H^{\mathrm{sl}} = \xi\sigma \cdot \mathbf{L}$) must be included into the Hamiltonian. Here, $\xi$ denotes the coupling constant which depends on the gradient of the potential around each atom. In transition metal systems, since the SOC becomes extremely weak because of the quenching of the orbital angular momentum, a perturbative (rather than self-consistent) treatment based on a force theorem (Weinert et al., 1986) is usually adopted in MCA calculations, in which the SOC induced change of total energy is given by

$$E^{\mathrm{sl}}(\theta) = \sum_{\{O'\}} \varepsilon_i' - \sum_{\{O\}} \varepsilon_i . \tag{1.94}$$

A key problem is the definition of the set $\{O'\}$ of occupied states after SOC is introduced. In all previous calculations (Gay et al., 1986; Li et al., 1990), $\{O'\}$ was defined solely by comparing the eigenenergies, $\varepsilon_i'$, regardless of any information about their wave functions ("blind Fermi filling"). This definition, (i) results in a strong stochastic MCA energy distribution in the Brillouin zone with respect to the charge filling and (ii) violates its basic assumption, i.e., minimal change of the charge and spin densities required by the correct application of the force theorem. This is why earlier pioneering tight binding and even recent first principles theoretical studies of MCA actually resulted in seemingly more controversy than success.

Wang et al. (1993) proposed a state tracking technique to determine the set of occupied states $\{O'\}$ which can ensure the stability of the calculated MCA energy with respect to the

number of **k** points, electron filling and even the SOC scaling factor. They treat the $H^{\mathrm{sl}}$ in a second variational way in the space expanded by $\{\Psi_i\}$, i.e.,

$$\langle\Psi_i|H^0+H^{\mathrm{sl}}|\Psi_j\rangle=\varepsilon_i\delta_{ij}+\langle\Psi_i|H^{\mathrm{sl}}|\Psi_j\rangle \tag{1.95}$$

with the SOC perturbed state

$$\Psi_i'=\sum_j C_j^i\Psi_j. \tag{1.96}$$

Here, $\varepsilon_j$ and $\Psi_j$ are eigenvalues and wave functions obtained for the unperturbed Hamiltonian, $H^0$, using the regular FLAPW method. Whether the state $\Psi_i'$ should be considered occupied is determined by tracking its projection onto the occupied states by defining

$$P_i^{\mathrm{occ}}=\sum_{j\in\{O\}}|C_j^i|^2 \tag{1.97}$$

rather than using its energy $\varepsilon_i'$. Since $H^{\mathrm{sl}}$ is very weak, this definition does not introduce any ambiguity, i.e., the value of $P_i^{\mathrm{occ}}$ is either $> 99\%$ or $< 1\%$ (excluding degenerate state pairs which have no contribution to MCA). In this sense, the newly occupied states give almost the same spatial distribution of the charge and spin densities – which ensures the correct application of the force theorem. Furthermore, such a state-tracking procedure is done independently at each **k** point; hence, the randomness in the BZ can also be removed.

Wang et al. (1993) applied this state-tracking procedure to study the magnetic anisotropy of the Fe, Co and Ni monolayers, the Co/Cu(001) overlayer system and Cu/Co/Cu sandwiches. Some important results, including the background physics for the MCA, have been revealed. For a simple demonstration, we will discuss here why Co (in plane) and Fe (perpendicular) ultra thin films favor different MCA directions.

Simply put, the SOC induced energy changes for perpendicular and in-plane magnetizations can be written as

$$\Delta E(z)=-\xi^2\sum_{u_\downarrow}\left\{\sum_{o_\downarrow}\frac{|\langle u_\downarrow|L_z|o_\downarrow\rangle|^2}{\varepsilon_{u_\downarrow}-\varepsilon_{o_\downarrow}}-\sum_{o_\uparrow}\frac{|\langle u_\downarrow|L_x|o_\uparrow\rangle|^2}{\varepsilon_{u_\downarrow}-\varepsilon_{o_\uparrow}}\right\}, \tag{1.98}$$

$$\Delta E(x)=-\xi^2\sum_{u_\downarrow}\left\{\sum_{o_\downarrow}\frac{|\langle u_\downarrow|L_x|o_\downarrow\rangle|^2}{\varepsilon_{u_\downarrow}-\varepsilon_{o_\downarrow}}-\sum_{o_\uparrow}\frac{|\langle u_\downarrow|L_z|o_\uparrow\rangle|^2}{\varepsilon_{u_\downarrow}-\varepsilon_{o_\uparrow}}\right\}, \tag{1.99}$$

where $u$ and $o$ stand for unoccupied and occupied states, respectively. Due to the large exchange splitting (about 2 eV for Co and Fe), contributions from SOC between spin down states dominate these energy changes and thus we can simplify the MCA energy to

$$\Delta E^{dd}=E^{dd}(x)-E^{dd}(z)=\xi^2\sum_{o_\downarrow u_\downarrow}\frac{|\langle o_\downarrow|L_z|u_\downarrow\rangle|^2-|\langle u_\downarrow|L_x|o_\downarrow\rangle|^2}{\varepsilon_{u_\downarrow}-\varepsilon_{o_\downarrow}}. \tag{1.100}$$

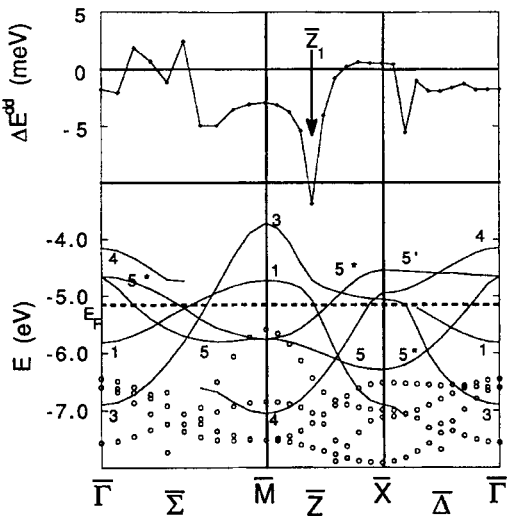


Fig. 1.30. MCA contribution of the SOC between the spin-down states, $E^{dd}$, of each **k**-point versus direction in the BZ correlated with the unperturbed spin-down band of the Co(001) free-standing monolayer ($a = 4.83$ a.u.). Band numbers 1, 3, 4, 5′ and 5″ stand for $z^2$, $z^2 - y^2$, $xy$, $yz$ and $xz$ states, respectively. Band 5 and 5* are hybridized $xz$ and $yz$ orbitals. Spin-up bands are plotted by empty circles showing the shift due to the exchange splitting. Only states with more than a 50% d component are shown.

Thus, if the coupling through $L_z$ is stronger, perpendicular magnetization prevails (positive MCA energy) and vice versa.

As an example of their results, we cite their first application to Co and Fe monolayers. The calculated band structure for the Co(001) monolayer is presented in the bottom panel of Fig. 1.30. There are two important SOC contributions, i.e., (i) states 5 and 5* through $L_z$ and (ii) states 1 and 5 (5*) through $L_x$. As clearly shown in the top panel of Fig. 1.31, SOC between 5 and 5* contributes a *positive* MCA energy along the $\bar{\Sigma}$ direction. However, in most parts of the Brillouin zone, SOC between 1 and 5 (5*) becomes stronger (resulting in a *positive* MCA energy) because of either the occupation of both 5 and 5* (around $\bar{M}$) or $|\varepsilon_1 - \varepsilon_5| < |\varepsilon_5 - \varepsilon_5|$ (along $\bar{\Delta}$). The calculated total MCA energy (integrated over the BZ) is $-1.35$ meV/atom for the free Co monolayer – indicating an in-plane magnetization. Note that in the middle of the $\bar{Z}$ line, states 1 and 5* become almost degenerate at $E_F$, which results in a singularity of the MCA energy as pointed out by an arrow. This so-called surface pair coupling requires special treatment in some cases. For Fe, the Fermi level shifts down by 0.5 eV. As a result, the predominant SOC will be between 5 and 5* (especially in the area around $\bar{M}$) and the MCA energy becomes positive in most of the BZ for the Fe monolayer. The calculated MCA energy for Fe monolayer (with the same lattice constant as that for the Co(001) monolayer) is 0.42 meV/atom – indicating a perpendicular magnetization.

Wang et al. (1993) have also determined the MCA energy for Cu/Co/Cu(001) and Pd/Co/Pd(001) sandwiches and have revealed the underlying physics. A five layer slab model was adopted to simulate the interfaces with the Co atom lying at the ideal position

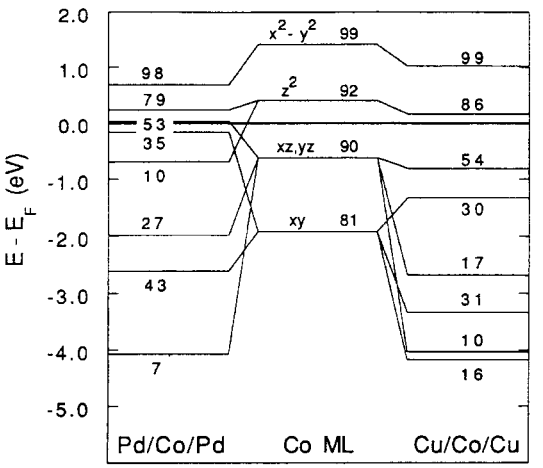


Fig. 1.31. Comparison of the effect of the Co–Pd and Co–Cu interface on the Co d electron state at **M**. Numbers are the percentage of the Co d component inside the Co muffin-tin spheres.

in the substrate lattices (without possible atomic relaxation). Summation over 66 **k**-points in the 1/8 irreducible two-dimensional BZ (corresponding to 400 **k**-points in the full BZ) was found to be sufficient to provide stable MCA energies.

Upon contact with a non-magnetic substrate at the interface, the energies and the wave functions of the Co-$d_{z^2}$ and Co-$d_{xz,yz}$ states (both point out of the plane) are changed by the interfacial hybridization. Figure 1.31 presents the energy positions of the hybridized states at $\bar{M}$ for Cu/Co/Cu(001) and Pd/Co/Pd(001) sandwiches and their components projected back to the states for the free standing Co monolayer. For the Cu/Co/Cu system, the out-of-plane $d_{xz,yz}$ states are pulled down by the Cu d-bands, while the Co-$d_{z^2}$ state remains almost unaffected since it separates far from the Cu-d bands in energy. By contrast, at the Co–Pd interface, both Co-$d_{xz,yz}$ and Co-$d_{z^2}$ states are strongly affected. A substantial component (53%) the Co-$d_{xz,yz}$ wave function is now in the hybridized states which are shifted upward by about 0.7 eV – already lying slightly above $E_F$.

These hybridizations are expected and indeed found to affect the strength of the SOC perturbation between the Co-$d_{xz,yz}$ and the Co-$d_{z^2}$ states and thus the MCA energy. Figure 1.32 gives the band filling dependencies of the MCA energies for the Cu/Co/Cu and Pd/Co/Pd sandwiches. For comparison, the MCA energy of a free standing Co monolayer is also shown in Fig. 1.32, which exhibits the band filling dependence typical for 3d transition metal monolayers. It is characterized by the strong negative peak at about half-occupation of the spin-down d band and a change of the MCA sign at a slightly smaller occupation.

Obviously, for Pd/Co/Pd the negative peak of the MCA is still as strong as for a free standing monolayer, but its position has been largely shifted to the larger band filling region. This behavior is caused mostly by the change of the upward shift of the out-of-plane $d_{xz,yz}$ bands (cf. Fig. 1.32) into the empty part and thus the reduction in the negative MCA energy results from the SOC (through $L_x$) between the Co-$d_{z^2}$ and Co-$d_{xz,yz}$ states. As a result, a positive MCA energy for Pd/Co/Pd, 0.55 meV (only SOC for Co atom), is

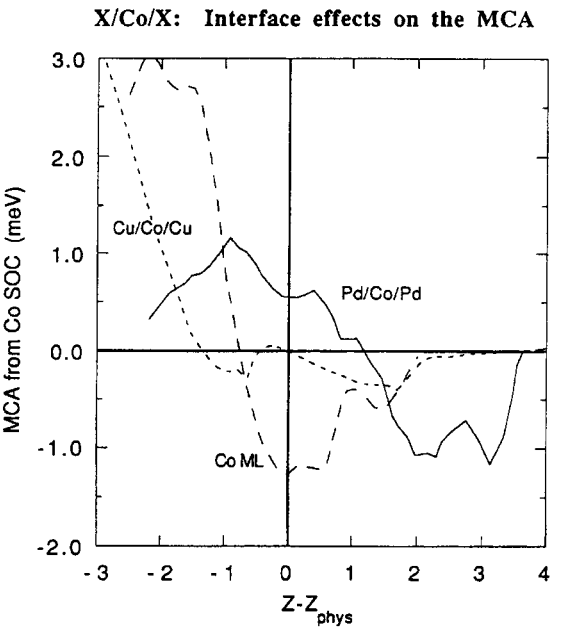


Fig. 1.32. Comparison of the effect of the Co–Pd and Co–Cu interface on the MCA contribution calculated when only the SOC inside the Co muffin-tin spheres is included. Results are plotted as a function of the number of valence electrons by employing a rigid band approximation. Long-dashed, short-dashed and solid lines are for Co ML, Cu/Co/Cu and Pd/Co/Pd sandwiches, respectively. (A Gaussian broadening with full width of 40 meV was employed.)

achieved at the physical value of band filling. This behavior is in some sense very similar to the origin of the positive MCA energy for a free standing Fe monolayer according to the relative position of the $d_{xz,yz}$ states with respect to $E_F$. In the case of a free standing Fe monolayer, the $d_{xz,yz}$ is empty because there is one less electron/atom, but for the Co/Pd interface, it is due to the upward shift of the bonding Co-$d_{xz,yz}$ states.

This behavior is in clear contrast to the behavior of the Co–Cu interface, where only the magnitude of the negative MCA energy peak is greatly reduced and the change of MCA sign is shifted to the region with lower band filling (short dashed line in Fig. 1.32) due to the downward shift of the out-of-plane bonding bands. This is expected since, as shown in Fig. 1.31, the Co-$d_{xz,yz}$ state is drawn down by the lower-lying Cu-I bands, while the Co-$d_{z^2}$ state remains almost unaffected.

### *1.9.2. Magneto-optical effects*

#### *1.9.2.1. SMOKE*

The surface magneto-optic Kerr effect (SMOKE) has recently been demonstrated to be a powerful in situ characterization probe of the magnetic and magneto-optic properties of magnetic films during the growth process (Bader, 1990). Now it is well accepted that the Kerr effect results mainly from the combined action of SOC and exchange interaction in

the process of interband transitions (Bennett and Stern, 1965; Cooper, 1965; Erskine and Stern, 1973; Wang and Callaway, 1974; Oppeneer et al., 1992) SOC acts as a magnetic field and thus breaks the symmetry between the absorption for left- and right-handed circularly polarized photons. The exchange interaction, on the other hand, separates the majority and minority spin states and allows a net rotation of the polarization plane of the incident light. Since the Kerr effect is determined by SOC perturbations on the wave functions (including states lying 10–20 eV above $E_F$), a very accurate treatment of both the semi-relativistic ground state properties (magnetic moment and band structures, etc.) and SOC perturbation are essential to obtain correct results theoretically.

For the most important physical case of SMOKE, i.e., the polar Kerr effect, both the magnetization and the incident wave vector are perpendicular to the surface. In this case, the macroscopic conductivity tensor $\sigma$ is well defined within ultra thin films and in bulk materials. The complex polar Kerr angle is given by

$$\Phi_K = \delta_K + i\varepsilon_K = \frac{-\sigma_{xy}}{\sigma_{xx}\sqrt{1 + i(4\pi\sigma_{xx}/\omega)}}, \tag{1.101}$$

where $\delta_K$ and $\varepsilon_K$ are the real rotation angle and ellipticity, respectively. The components of the conductivity tensor, $\sigma_{xx}$ and $\sigma_{xy}$, can be obtained from electronic properties such as band structure and the wave functions (including SOC) using the Kubo (1957) formula. In particular, the absorptive part of the off-diagonal element, to which the Kerr rotation angle depends most closely, can be expressed as

$$\omega\sigma_{xy}^{(2)} = \frac{\pi}{4V}\sum_{\alpha,\beta}\kappa_{\beta\alpha}\delta(\omega_{\beta\alpha} - \omega) \tag{1.102}$$

and

$$\kappa_{\beta\alpha} = 2i\left[\langle\beta|p_x|\alpha\rangle\langle\alpha|p_y|\beta\rangle - \langle\beta|p_y|\alpha\rangle\langle\alpha|p_x|\beta\rangle\right], \tag{1.103}$$

where $V$ is the volume of system, $p$ is the momentum operator and $|\beta\rangle$ and $|\alpha\rangle$ are occupied and unoccupied states, respectively.

Wu and Freeman (1994) developed an approach and a computer code to calculate Kerr effects for both bulk and thin film materials based on the FLAPW method. Their goal is to explore the physical origin of the Kerr effects on the microscopic level and, hopefully, to predict new magneto-optic materials. First results obtained for the Ni(001) surface (simulated by 1, 3 and 5 layer slabs) and bulk Ni show that the agreement between the calculated and measured curves for bulk Ni is acceptable considering that the existing experimental values are highly scattered (Buschow, 1988; Erskine, 1977). The first high peak in the experimental curve, hinted at by the high peak of the curve calculated for the surface layer, appears to contain mainly the surface contribution. In addition, they found that there is no simple (e.g., proportional) relationship between the intensity of the SMOKE signal and the magnetic moment for a given photon energy.

*1.9.2.2. Magnetic circular X-ray dichroism*

It is now apparent that the observation of soft X-ray magnetic circular dichroism (MCD) by Schültz et al. (1987), followed by important experimental and theoretical work (van der Laan et al., 1986; Chen et al., 1990, 1991; Baumgarten et al., 1990; Tobin et al., 1992; van der Laan et al., 1992; Smith et al., 1992) has led to the establishment of MCD as an exciting, and in some respects unique, new powerful tool for investigating the magnetism of transition and rare-earth metal systems. Compared to other techniques, the high element selectivity of MCD, is especially useful for identifying the magnetism from different specific atoms, e.g., in alloys, as impurities, at surfaces or interfaces (Idzerda et al., 1993a, b; Chen et al., 1993). It also offers potential applications for element-specific magnetic microscopy (Stöhr et al., 1993). Recently, as a result of new magneto-optical sum rules derived for X-ray MCD (Thole et al., 1992), considerable interest has centered on these measurements as a way to determine $\langle S_z \rangle$, the spin moment and $\langle L_z \rangle$ the orbital moment. It has also been stressed that MCD may be the only practical way to determine $\langle L_z \rangle$ in bulk and reduced dimensional systems.

These powerful sum rules, however, were derived from a simple model system, namely a single ion in a crystal field with the valence shell only partially filled. Thus, there is still some question as to the validity and range of applicability of this sum rule to real condensed matter systems such as transition metals with their strongly hybridized multiband structure. Wu et al. (1993) and Wu and Freeman (1994) reported results of detailed local density FLAPW studies of the X-ray MCD spectra in several transition metal bulk and surface systems in which both ground state and core excitations (treated as a supercell impurity) were investigated. We cite their work here as it represents an important new extension of LSD theory using the FLAPW approach to the study of magnetism in reduced dimensional systems such as surfaces and interfaces.

As is well known, MCD measures the difference in absorption between right- and left-circularly polarized incident light during the process of electric transitions from core states to unoccupied valence states. Due to the spin–orbit coupling (SOC) between valence states, the MCD signals of $\sigma_m (= \sigma_+ - \sigma_-)$ for the $L_2$ and $L_3$ absorption edge for 3d transition metals no longer cancel each other as they do in the absence of SOC where the integrated $L_2$ and $L_3$ signals are equal and opposite. Here, $\sigma_+$ and $\sigma_-$ represent the absorption cross sections for left-and right-circularly polarized light, respectively. The energy dependence of the cross sections, i.e., $\sigma_+$, $\sigma_-$ and $\sigma_z$, for electric dipole transitions from core to valence bands can be evaluated as

$$\sigma_n(E) = \frac{8\pi^2}{3} \int_{\mathbf{k}} |\langle \psi_c | p_n | \psi_v' \rangle|^2 \delta(E_v - E_c - E)\, \mathrm{d}\mathbf{k}, \quad n = +, -, z. \tag{1.104}$$

Obviously, the angular and spin momentum parts of the **p**-matrices result in the well-known selection rules: $\Delta l = \pm 1$, $\Delta m = \pm 1, 0$ and $\Delta S = 0$.

As stated in the MCD sum rules (Thole et al., 1992; Altarelli, 1993; Carra et al., 1992), integrations of the MCD and total absorption spectra relate directly to $\langle L_z \rangle$, $\langle S_z \rangle$ and $\langle T_z \rangle$ for the unoccupied states

$$\frac{I_m = \int_{L_3+L_2} \sigma_m \, \mathrm{d}E}{I_t = \int_{L_3+L_2} \sigma_t \, \mathrm{d}E} = \frac{C\langle L_z \rangle}{N_h = \int \rho(E)\, \mathrm{d}E} \tag{1.105}$$

and

$$\frac{I_s = \int[\sigma_s = \int(\sigma_{m,L_3} - \frac{c+1}{c}\sigma_{m,L_2})]\,\mathrm{d}E}{I_t = \int_{L_3+L_2}\sigma_t\,\mathrm{d}E} = \frac{\langle S_e\rangle = (A\langle S_z\rangle + B\langle T_z\rangle)}{N_h}, \tag{1.106}$$

where $\sigma_m = \sigma_+ - \sigma_-$ and $\sigma_t = \sigma_+ + \sigma_- + \sigma_z$, and the constants $A$, $B$ and $C$ are determined from the core and valence angular momenta $c$ and $l$ as $A = [l(l+1) - 2 - c(c+1)]6c$, $B = \{l(l+1)[l(l+1) + 2c(c+1) + 4] - 3(c-1)^2(c+2)^2\}/6cl(l+1)$ and $C = [l(l+1) + 2 - c(c+1)]/2l(l+1)$. Thus $A = 1/3$, $B = 7/3$ and $C = 1/2$ for $L$ adsorption edges in 3d transition metals. $\mathbf{T}$ is the spin magnetic dipole operator, i.e., $\mathbf{T} = 1/2[\mathbf{S} - 3\mathbf{r}(\mathbf{r}\cdot\mathbf{S})]$, ($T_z = S_z(1 - 3\cos^2\theta)^2$ for $\mathbf{S}$ aligned along the $z$ direction). The number of valence holes $N_\mathrm{h}$ can be obtained from an integration over the unoccupied density of states $\rho(E)$.

There are two assumptions in the derivation of the sum rules: (i) the radial matrix elements are constant for all transitions, and (ii) no hybridization exists between different $l$ shells (i.e., $l$ is a good quantum number). As is well-known, both assumptions fail in real materials and thus weak spd-hybridization (which affects both assumptions) is important for the validity of the sum rule. Since the effects of sp states are inherent in real materials and thus in the experimental spectra, the validity of these sum rules needs to be checked. To this end, FLAPW calculations were carried out to obtain both the MCD spectra ($I_m$, $I_s$ and $I_t$) and ground state properties ($\langle S_z\rangle$, $\langle L_z\rangle$, $\langle T_z\rangle$ and $N_\mathrm{h}$).

In a series of investigations, Wu et al. (1993) found that the main mechanism affecting the validity of the sum rules is the hybridization between the d states and the high-lying sp states. Significantly, the $I_t$ and $N_\mathrm{h}$ are not well defined quantities since they do not converge with respect to the upper-limit of the energy integration, and thus an arbitrary energy cut-off has to be applied in order to stay within the d band region. Wu et al. (1993) proposed a criterion for the choice of the energy cut-off, i.e., cut the integrations for $I_t$ and $N_\mathrm{h}$ at the energy where the MCD counterpart becomes acceptably close to zero. Based on this criterion, they adopted an energy cut-off of 6 eV above $E_\mathrm{F}$ for the calculated results for Fe, Co and Ni (bulk and surfaces).

They find that the orbital sum rule is valid within 10% for transition metal systems. In contrast, the spin sum rule deviates by as much as 15% for surface Fe and bulk Co, 27% for surface Co and 32% for bulk and 48% for surface Ni and thus the spin sum rule fails, especially for Ni systems. This is expected since the sp states not only contribute to the denominators ($I_t$ and $N_\mathrm{h}$), but also contribute to the numerators of Eqs. (1.105) and (1.106). Ni contains a much smaller number of d holes than Fe and thus the weight of sp states increases. The role of these states and thus the importance of the energy integration cut-off are seen from the fact that (i) the spin sum rule error for the surface Ni layer can be reduced to 15% by using an energy cut-off of only 3.0 eV, and (ii) well converged orbital and spin values (within 5% and almost independent of the assumed energy cut-off) can be obtained for all atoms by eliminating the sp contributions in the calculations.

### *1.9.3. Conclusions on magnetic surface effects*

From the results presented here and in Chapter 9 by Schneider and Kirschner, it is quite apparent that state-of-the-art *ab initio* FLAPW LSD electronic structure calculations have

achieved great success in the exciting field of thin film magnetism, both in explaining existing phenomena and, more importantly, in predicting the properties of new systems. Results obtained demonstrate that: (1) the lowered coordination number at clean metal surfaces leads to enhanced magnetic moments; (2) noble metal and MgO substrates do not affect the magnetism in most cases, but show significant effects on 4d overlayers; (3) the strong interaction (hybridization) with nonmagnetic transition metals diminishes (entirely in some cases) the ferromagnetism and usually leads to AFM ordering; (4) the core contribution to the Fermi contact hyperfine field (but not the total) is proportional to the local magnetic moment; (5) the magneto-crystalline anisotropy (MCA) can be predicted correctly using the state-tracking procedure; and (6) magneto-optical Kerr effect and magnetic circular dichroism (MCD) can be explained in the framework of interband transitions. In the future, electronic structure theory is expected to continue play an even more predictive role by considering more complex systems, by eliminating the limitation of the local spin density approximation and developing more efficient and precise methods.

## 1.10. Summary and perspective on future developments

The increasing technological importance of an in-depth understanding and control of surfaces, the development of fascinating experimental surfaces techniques such as the scanning tunneling microscope, the atomic force microscope, and advanced spectroscopic methods using synchrotron radiation have stimulated a tremendous interest in surfaces. Theoretical and computational methods have made critical contributions to this scientific and technological progress. The earlier stage of rather approximate and conceptual electronic structure calculations of surfaces has been superseded by the present phase of the increasingly accurate prediction of the electronic structure of surfaces. Density functional theory and its implementation in the form of sophisticated and powerful computational schemes such as the surface-FLAPW approach have made it possible to predict and explain electronic, optical, and magnetic effects arising from the reduced symmetry at surfaces. The prediction of surface states and surface resonance states as illustrated for surfaces of nearly-free-electron (e.g., aluminum) and transition metals (e.g., tungsten), the prediction of the work function lowering by adsorption, the prediction of magnetic anisotropy, and surface magnetism are vivid examples of these capabilities.

However, one of the most impressive successes of surface electronic structure calculations is the ability to predict the total energy and the forces on the surface atoms once the electronic structure is known. This total energy capability rests on an *ab initio* approach. No empirical or other system-specific parameters are necessary to predict surface geometries to within a few hundreds of an Ångström, thus opening the possibility to predict surface relaxations, surface reconstructions, adsorption geometries, and, in principle, the entire energy-hypersurface of atoms and molecules on surfaces. Impressive successes have already been achieved: for example, the quantitative explanation of surface diffusion, the reconstructions of the Si(111) and Si(001) surfaces and a detailed, quantitative picture of the energetics of the reconstruction of the W(001) surface. The theoretical and computational approaches used in these studies are maturing and are becoming increasingly

available to wider community of scientists and engineers as sophisticated, integrated software systems with graphical user interfaces for easy use, accessibility, and visualization of the results.

Most of these surface calculations, however, are focusing on static phenomena (at $T = 0$). During the coming decade and beyond, it can be expected that major efforts will be devoted to the study of dynamical phenomena such as diffusion, adsorption and desorption, and chemical reactions on surfaces as they occur in epitaxial growth, chemical vapor deposition, catalysis, electrochemistry, and corrosion. It is likely that one will recognize that present-day electronic structure approaches and implementations are many orders of magnitudes too slow to cope with the requirements of adequate statistical sampling. Despite this challenge of the time-scale, progress is being made. Parallel implementations of existing programs (Li et al., 1994) on massively parallel computers together with the continuing progress in computer hardware will lead to qualitatively new capabilities. On the other hand, there are still many opportunities to find new theoretical and computational approaches to handle surface phenomena. At present, the dominating first-principles approaches are the pseudopotential plane-wave methods, the full-potential linearized augmented plane-wave (FLAPW) methods, and localized orbital cluster models. Density functional theory is pervasive, while Hartree–Fock approaches are playing a smaller role in surface electronic structure calculations. Quantum Monte Carlo methods, which offer another approach to the electronic many-body problem are making progress, but are still quite far from being competitive with present density functional approaches.

There is clearly a need to build the bridge between highly accurate electronic structure methods, which will remain for some time static methods, and more simplified methods such as tight-binding or density matrix based approaches that have the potential to provide excellent survey tools, which can be used in conjunction with more accurate first-principles methods. It seems natural, to embed different levels of theory in one computational model so as to carry out the demanding accurate first-principles calculations only for that part of a system that really requires such a resolution, while less critical parts of a system could be treated on a lower level of theory. However, such hybrid schemes have met so far with only modest success, but clearly represent a development both necessary and urgent.

All aspects considered, we are witnessing a golden age of surface science, fueled by exciting discoveries and developments on both the experimental as well as on the computational side. The initial focus of electronic structure theory of surfaces has been on metallic surfaces and semiconductor surfaces, with a lesser emphasis on inorganic compounds, ceramics, and especially synthetic polymers. As the field of functional polymeric and ceramic materials continues to grow in technological importance, one can expect that many new developments in computational surface science will respond to these new opportunities and challenges.

In conclusion, a variety of exciting methods for surface electronic structure calculations have been developed and used to discover and understand new surface phenomena. However, we are just at the beginning and many beautiful (and perhaps entirely unexpected) discoveries have yet to be made. They are sure to give us not only a better scientific understanding and improved technological capabilities, but also a deeper appreciation of the endless richness of surface and interface phenomena.

*Acknowledgments*

We are grateful to many collaborators whose work we have cited. Special thanks are due to Ruqian Wu, Shaoping Tang, Fangyi Rao and Jennifer Bosak for their help with this chapter. Work at Northwestern University supported by the U.S. National Science Foundation (DMR grant No. 91-17818) and the U.S. Office of Naval Research (grant N00014-94-1-0030).

## References

Abraham, F.F. and I.P. Batra, 1985, Surf. Sci. **163**, L752.
Adams, D.L., H.B. Nielsen, J.N. Andersen, I. Stensgaard, R. Feidenhans'l and J.E. Sorensen, 1982, Phys. Rev. Lett. **49**, 669.
Allan, G. and M. Lannoo, 1973, Surf. Sci. **40**, 375.
Altarelli, M., 1993, Phys. Rev. B **47**, 597.
Altman, M.S. and P.J. Estrup, 1988, Phys. Rev. B **38**, 5211.
Andersen, D.G., 1965, J. Assoc. Comput. Mach. **12**, 547.
Andersen, O.K., 1975, Phys. Rev. B **12**, 3060.
Andriamanantenasoa, I., J.P. Lacharme and C.E. Sëbenne, 1987, Surf. Sci. **189/190**, 563.
Andzelm, J. and E. Wimmer, 1992, J. Chem. Phys. **96**, 1280.
Anno, M., Y. Hou, C. Oshima and Y. Ishizawa, 1982, Phys. Rev. Lett. **49**, 567.
Appelbaum, J.A. and D.R. Hamann, 1974, Phys. Rev. Lett. **32**, 225.
Appelbaum, J.A., G.A. Baraff and D.R. Hamann, 1975, Phys. Rev. Lett. **35**, 729.
Appelbaum, J.A., G.A. Baraff and D.R. Hamann, 1976b, Phys. Rev. B **14**, 588.
Appelbaum, J.A. and D.R. Hamann, 1976a, Rev. Mod. Phys. **48**, 479.
Appelbaum, J.A. and D.R. Hamann, 1978, Surf. Sci. **74**, 21.
Artacho, E. and F. Yndurain, 1989, Phys. Rev. Lett. **62**, 2491.
Ashcroft, N.W. and N.D. Mermin, 1976, Solid State Physics. Holt, Rinehart and Winston, New York.
Averill, F.W. and D.E. Ellis, 1973, J. Chem. Phys. **59**, 6412.
Bachelet, G.B., D.R. Hamann and M. Schlüter, 1982, Phys. Rev. B **26**, 4199.
Bader, S.D., 1990, Proc. IEEE **78**, 909.
Baerends, E.J., D.E. Ellis and P. Ros, 1973, Chem. Phys. **2**, 41.
Bardeen, J., 1936, Phys. Rev. **49**, 653.
Barnett, R.N., U. Landman and C.L. Cleveland, 1983, Phys. Rev. B **28**, 1685.
Baski, A.A., J. Nogami and C.F. Quate, 1991a, Phys. Rev. B **43**, 9316.
Baski, A.A., C.F. Quate and J. Nogami, 1991b, Phys. Rev. B **44**, 11167.
Batra, I.P., 1989, Phys. Rev. Lett. **63**, 1704.
Batra, I.P., 1990, Phys. Rev. B **41**, 5048.
Baumgarten, L., C.M. Schneider, H. Peterson, F. Schäfers and J. Kirschner, 1990, Phys. Rev. Lett. **65**, 492.
Baym, G., 1976, in: Lectures on Quantum Mechanics. Benjamin, New York, pp. 558–563.
Bechstedt, F. and D. Reichardt, 1988, Surf. Sci. **202**, 83.
Becke, A.D., 1988, Phys. Rev. A **38**, 3098.
Becker, R.S., T. Klitsner and J.S. Vickers, 1988a, J. Microscopy, **152**, 157.
Becker, R.S., B.S. Swartzentruber, J.S. Vickers, M.S. Hybertsen and S.G. Louie, 1988b, Phys. Rev. Lett. **60**, 116.
Benesh, G.A. and J.E. Inglesfield, 1984, J. Phys. C **17**, 1595.
Bennett, A.J. and C.B. Duke, 1969, in: Structure and Chemistry of Solid Surfaces, ed. G.A. Somorjai. Wiley, New York.
Bennett, H.S. and E.A. Stern, 1965, Phys. Rev. **137**, A448.
Billington, R.L. and T.N. Rhodin, 1978, Phys. Rev. Lett. **41**, 1602.
Bjorken, J.D. and S.D. Drell, 1964, in: Relativistic Quantum Mechanics. McGraw-Hill, New York.
Bjorken, J.D. and S.D. Drell, 1965, in: Relativistic Quantum Fields. McGraw-Hill, New York.

Brillson, L.J., 1982, Surf. Sci. Rep. **2**, 123.
Bringans, R.D., R.I.G. Uhrberg, R.Z. Bachrach and J.E. Northrup, 1985, Phys. Rev. Lett. **55**, 533.
Bringans, R.D., R.I.G. Uhrberg, M.A. Olmstead and R.Z. Bachrach, 1986, Phys. Rev. B **34**, 7447.
Brink, R.S. and W.S. Verwoerd, 1981, Surf. Sci. **154**, L203.
Buschow, K.H.J., 1988, in: Ferromagnetic Materials, Vol. 4, eds. E.P. Wohlfarth and K.H.J. Buschow. North-Holland, Amsterdam, p. 493.
Car, R. and M. Parrinello, 1985, Phys. Rev. Lett. **55**, 2471.
Cardillo, M.J. and G.E. Becker, 1978, Phys. Rev. Lett. **40**, 1148.
Cardillo, M.J. and G.E. Becker, 1980, Phys. Rev. B **21**, 1497.
Caruthers, E.B., L. Kleinman and G.P. Alldredge, 1973, Phys. Rev. B **8**, 4570.
Carra, P., 1992, Synch. Rad. News **5**, 21.
Ceperley, D.M. and B.J. Alder, 1980, Phys. Rev. Lett. **45**, 566.
Chadi, D.J., 1979, Phys. Rev. Lett. **43**, 43.
Chen, C.T., F. Sette, Y. Ma and S. Modesti, 1990, Phys. Rev. B **42**, 7262.
Chen, C.T., N.V. Smith and F. Sette, 1991, **43**, 6785.
Chen, C.T., Y.U. Idzerda, H.-J. Lin, G. Meigs, A. Chaiken, G.A. Prinz and G.H. Ho, 1993, Phys. Rev. B **48**, 642.
Chiang, T.-C. and D.E. Eastman, 1981, Phys. Rev. B **23**, 6836.
Clarke, L.J. and L. Marales De La Garza, 1980, Surf. Sci. **9**, 419.
Cohen, M.L. and V. Heine, 1970, Solid State Phys. **24**, 37.
Cooper, B.R., 1973, Phys. Rev. Lett. **30**, 1316.
Cooper, B.R., 1965, Phys. Rev. **137**, A1504.
Davis, H.L. and D.M. Zehner, 1980, J. Vac. Sci. Technol. **17**, 190.
Debe, M.K. and D.A. King, 1977, Phys. Rev. Lett. **39**, 708.
Debe, M.K. and D.A. King, 1979a, Phys. Rev. Lett. **39**, 708.
Debe, M.K. and D.A. King, 1979b, Surf. Sci. **81**, 193.
Debe, M.K., D.A. King and F.S. Marsh, 1977, Surf. Sci. **68**, 437.
Delley, B., 1990, J. Chem. Phys. **92**, 508.
Delley, B., 1991, J. Chem. Phys. **94**, 7245.
Delley, B. and D.E. Ellis, 1982, J. Chem. Phys. **76**, 1949.
Dovesi, R., V.R. Saunders and C. Roetti, 1992, CRYSTAL 92 User Manual. Univ. of Turin, Italy, and SERC Daresbury Laboratory, U.K.
Dunlap, B.I., J.W.D. Connolly and J.R. Sabin, 1979a, J. Chem. Phys. **71**, 3396.
Dunlap, B.I., J.W.D. Connolly and J.R. Sabin, 1979b, J. Chem. Phys. **71**, 4993.
Dunlap, B.I., 1986, J. Phys. Chem. **90**, 5524.
Eberhardt, W., G. Kalkoffen and C. Kunz, 1979, Solid State Commun. **32**, 901.
Erskine, J.L., 1977, Physica B **89**, 83.
Erskine, J.L. and E.A. Stern, 1973, Phys. Rev. B **8**, 1239.
Falicov, L.M., T.D. Pierce, S.D. Bader, R. Gronsky, K.B. Hathaway, H.J. Hopster, D.N. Lambeth, S.P. Parkin, G.A. Prinz, M. Salamon, I.K. Schuller and R.H. Victora, 1990, J. Mater. Res. **5**, 1299.
Fasolino, A., G. Santoro and E. Tosatti, 1980, Phys. Rev. Lett. **44**, 1684.
Fasolino, A., G. Santoro and E. Tosatti, 1981, J. Phys. C **6**, 846.
Fasolino, A. and E. Tosatti, 1987, Phys. Rev. B **35**, 4264.
Feder, R. and J. Kirschner, 1978, Phys. Status Solidi **45**, K117.
Feder, R. and J. Kirschner, 1981, Surf. Sci. **103**, 75.
Feibelmann, P.J., 1985, Phys. Rev. Lett. **54**, 2627.
Feldman, L.C., R.L. Kauffmann, P.J. Silverman, R.A. Zuhr and J.H. Barrett, 1977, Phys. Rev. Lett. **39**, 38.
Felter, T.E., R.A. Barker and P.J. Estrup, 1977, Phys. Rev. Lett. **38**, 1138.
Fermi, E., 1928, Z. Phys. **48**, 73.
Fock, V., 1930a, Z. Phys. **61**, 126.
Fock, V., 1930b, Z. Phys. **62**, 795.
Forbes, S.G., 1968, in: Jet, Rocket, Nuclear, Ion, and Electric Propulsion: Theory and Design, Vol. 7, ed. W.H.T. Loh, Applied Physics and Engineering. Springer-Verlag, New York, p. 442.
Fu, C.L. and A.J. Freeman, 1988, Phys. Rev. B **37**, 2685.

Fu, C.L., A.J. Freeman, E. Wimmer and M. Weinert, 1985, Phys. Rev. Lett. **54**, 2261.
Fu, C.L., S. Ohnishi, E. Wimmer and A.J. Freeman, 1984, Phys. Rev. Lett. **53**, 675.
Gartland, P.O. and B.J. Slagsvold, 1978, Solid State Commun. **25**, 489.
Gáspár, R., 1954, Acta Phys. Acad. Sci. Hung. **3**, 263.
Gay, J.G. and R. Richter, 1986, Phys. Rev. Lett. **56**, 2728.
Gay, J.G., J.R. Smith and F.K. Arlinghaus, 1979, Phys. Rev. Lett. **42**, 332.
Green, M. and R. Seiwatz, 1962, J. Chem. Phys. **37**, 458.
Grepstad, T.K., P.O. Gartland and P.T. Slagsvold, 1976, Surf. Sci. **57**, 348.
Gunnarsson, O., B.I. Lundqvist and S. Lundqvist, 1972, Solid State Commun. **11**, 149.
Hamann, D.R., M. Schlüter and C. Chiang, 1979, Phys. Rev. Lett **43**, 1494.
Hamers, R.J., R.M. Tromp and J.E. Demuth, 1986, Phys. Rev. B **34**, 5343.
Haneman, D., 1987, Rep. Prog. Phys. **50**, 1045.
Harrison, W.A., 1976, Surf. Sci. **55**, 1.
Hartree, D.R., 1928, Proc. Cambridge Philos. Soc. **24**, 89.
Hatsopoulos, G.N. and E.P. Gyftopoulos, 1979, Thermionic Energy Conversion. MIT Press, Cambridge, MA.
Hedin, L. and B.I. Lundqvist, 1971, J. Phys. C **4**, 2064.
Hedin, L. and S.J. Lundqvist, 1972, Phys. (France) **33**, C3–73.
Heilmann, P., K. Heinz and F. Muller, 1979, Surf. Sci. **89**, 84.
Hiskes, J.R., A. Karo and M. Gardner, 1976, J. Appl. Phys. **47**, 3888.
Ho, K.M. and K.P. Bohnen, 1985, Phys. Rev. B **32**, 3446.
Hohenberg, P. and W. Kohn, 1964, Phys. Rev. **136**, B864.
Holland, B.W., C.B. Duke and A. Paton, 1984, Surf. Sci. **140**, L269.
Hybertsen, M.S. and S.G. Louie, 1987, Phys. Rev. Lett. **58**, 1551.
Ide, T. and T. Mizutani, 1992, Phys. Rev. B **45**, 1447.
Idzerda, Y.U., C.J. Gutierrez, L.H. Tjeng, H.-J. Lin, G. Meigs and C.T. Chen, 1993a, J. Magn. Magn. Mater. **127**, 109.
Idzerda, Y.U., L.H. Tjeng, H.-J. Lin, C.J. Gutierrez, G. Meigs and C.T. Chen, 1993b, Surf. Sci. **287–288**, 741.
Ihm, J., M.L. Cohen and D.J. Chadi, 1980, Phys. Rev. B **21**, 4592.
Inglesfield, J.E., 1979, J. Phys. C **12**, 149.
Inglesfield, J.E., 1982, Rep. Prog. Phys. **45**, 223.
Janak, J.F., 1978, Phys. Rev. B **18**, 7165.
Jansen, H.J.F. and A.J. Freeman, 1984, Phys. Rev. B **30**, 561.
Jensen, V., J.N. Andersen, H.B. Nielsen and D.L. Adams, 1982, Surf. Sci. **116**, 66.
Jona, F., H.D. Shih, A. Ignatiev, D.W. Jepsen and P.M. Marcus, 1977, J. Phys. C **10**, L67.
Kar, N. and P. Soven, 1975, Phys. Rev. B **11**, 3761.
Kaxiras, E., 1990, in: Atomic Scale Calculations of Structure in Materials, eds. M.S. Daw and M.A. Schlüter, MRS Symp. Proc. No. 193, p. 143.
Kaxiras, E., 1991, Phys. Rev. B **43**, 6824.
Kerker, G., 1980, J. Phys. C **13**, L189.
Kerker, G.P., S.G. Louis and M.L. Cohen, 1978, Phys. Rev. B **17**, 706.
Kingdon, K.H. and I. Langmuir, 1923, Phys. Rev. **21**, 380.
Kirschner, J. and R. Feder, 1979, Surf. Sci. **79**, 176.
Koelling, D.D. and G.O. Arbman, 1975, J. Phys. F **5**, 2041.
Koelling, D.D. and B.N. Harmon, 1977, J. Phys. C **10**, 3107.
Kohn, W. and N. Rostoker, 1954, Phys. Rev. **94**, 1111.
Kohn, W. and L.J. Sham, 1965, Phys. Rev. **140**, A1133.
Korringa, J., 1947, Physica **13**, 392.
Krakauer, H., M. Posternak and A.J. Freeman, 1978, Phys. Rev. Lett. **41**, 1072.
Krakauer, H., M. Posternak and A.J. Freeman, 1979a, Phys. Rev. B **19**, 1706.
Krakauer, H., M. Posternak and A.J. Freeman, 1979b, Phys. Rev. Lett. **17**, 1885.
Krakauer, H., M. Posternak, A.J. Freeman and D.D. Koelling, 1981, Phys. Rev. B **23**, 3859.
Krüger, P. and J. Pollmann, 1988, Phys. Rev. B **38**, 10578.
Krüger, P. and J. Pollmann, 1990, Phys. Rev. Lett. **64**, 1808.

Krüger, P. and J. Pollmann, 1991, Physica B **172**, 155.
Kubo, R., 1957, J. Phys. Soc. Jpn., **12**, 570.
Lander, J. and J. Morrison, 1962, J. Chem. Phys. **37**, 729.
Lang, N.D. and W. Kohn, 1970, Phys. Rev. B **1**, 4555.
Lang, N.D. and W. Kohn, 1971, Phys. Rev. B **3**, 1215.
Lang, N.D., 1969, Solid State Commun. **7**, 1047.
Lang, N.D., 1971, Phys. Rev. B **4**, 4234.
Lang, N.D., 1973, Solid State Phys. **28**, 225.
Lee, B.W., A. Ignatiev, S.Y. Tong and M.A. Van Hove, 1977, J. Vac. Sci. Technol. **14**, 291.
Legrand, B., G. Treglia, M.C. Desjonqueres and D. Spanjaard, 1986, J. Phys. C **19**, 4463.
Levine, J.D., 1973, Surf. Sci. **34**, 90.
Li, C., A.J. Freeman, H.J.F. Jansen and C.L. Fu, 1990, Phys. Rev. B **42**, 5433.
Li, Y.S., M.A. van Daelen, M. Wrinn, D. King-Smith, J.M. Newsam, B. Delley, E. Wimmer, T. Klitsner, M.P. Sears, G.A. Carlson, J.S. Nelson, D.C. Allan and M.P. Teter, 1994, J. Computer-Aided Matl. Design **1**, 199.
Louie, S.G., K.-M. Ho and M.L. Cohen, 1979, Phys. Rev. B **19**, 1774.
MacDonald, A.H., J.M. Daams, S.M. Vosko and D.C. Koelling, 1981, Phys. Rev. B **23**, 6377.
MacDonald, A.J. and S.H. Vosko, 1979, J. Phys. C **12**, 2977.
Marsh, F.S., M.K. Debe and D.A. King, 1980, J. Phys. C **13**, 2799.
Mathon, J., 1988, Rep. Prog. Phys. **51**, 1.
Melmed, A.J., R.T. Tung, W.R. Graham and G.D.W. Smith, 1979, Phys. Rev. Lett. **43**, 1521.
Messiah, A., 1970, Quantum Mechanics, Vol. II. North-Holland, Amsterdam.
Methfessel, M., C.O. Rodriquez and O.K. Andersen, 1989, Phys. Rev. B **40**, 2009.
Monnier, R. and J.P. Perdew, 1978, Phys. Rev. B **17**, 2595.
Nielsen, H.B., J.N. Andersen, L. Petersen and D.L. Adams, 1982, J. Phys. C **15**, L1113.
Nogami, J., A.A. Baski and C.F. Quate, 1991, Phys. Rev. B **44**, 1415.
Northrup, J.E., 1985, Phys. Rev. Lett. **54**, 815.
Ohnishi, S., A.J. Freeman and E. Wimmer, 1984, Phys. Rev. B **29**, 5267.
Olmstead, M.A., R.D. Bringans, R.I.G. Uhrberg and R.Z. Bachrach, 1986, Phys. Rev. B **34**, 6041.
Onodera, Y. and M.J. Okazaki, 1966, Phys. Soc. Jpn. **21**, 2400.
Oppeneer, P.M., T. Maurer, J. Sticht and J. Kübler, 1992, Phys. Rev. B **45**, 10924.
Pandey, K.C., 1984, in: Proceedings of the 17th International Conference on the Physics of Semiconductors, eds. D.J. Chadi and W.A. Harrison. Springer, Berlin, p. 55.
Parr, R.G. and W. Yang, 1989, Density-Functional Theory of Atoms and Molecules. Clarendon, Oxford.
Payne, M.C., J.D. Joannopoulos, D.C. Allan, M.P. Teter and D.H. Vanderbilt, 1986, Phys. Rev. Lett. **56**, 2656.
Payne, M.C., M.P. Teter, D.C. Allan and J.D. Joannopoulos, 1992, Rev. Mod. Phys. **64**, 1045.
Perdew, J.P., 1986, Phys. Rev. B **33**, 8822.
Perdew, J.P., J.A. Chevary, S.H. Vosko, K.A. Jackson, M.R. Pederson, D.J. Singh and C. Fiolhais, 1992, Phys. Rev. B **46**, 6671.
Phillips, J.C., 1958, Phys. Rev. **112**, 685.
Phillips, J.C., 1973, Surf. Sci. **40**, 459.
Pines, D., 1963, Elementary Excitations in Solids. Benjamin, New York, Eq. (3.58).
Poppendieck, T.D., T.C. Gnoc and M.W. Webb, 1978, Surf. Sci. **75**, 287.
Posternak, M., H. Krakauer, A.J. Freeman and D.D. Koelling, 1980, Phys. Rev. B **21**, 5601.
Press, W.H., B.P. Flannery, S.A. Teukolsy and W.T. Vetterling, 1986, Numerical Recipes. Cambridge Univ. Press, Cambridge, p. 308.
Rajagopal, A.K. and J. Callaway, 1973, Phys. Rev. B **7**, 1912.
Rajagopal, A.K., 1978, J. Phys. C **11**, L943.
Ramana, M.V. and A.K. Rajagopal, 1979, J. Phys. C **12**, L845.
Ravenek, W. and E.J. Baerends, 1984, J. Chem. Phys. **81**, 865.
Redondo, A. and W.A. Goddard, III, 1982, J. Vac. Sci. Technol. **21**, 344.
Rich, D.A., A. Samsavar, T. Miller, H.F. Lin and T.-C. Chiang, 1987, Phys. Rev. Lett. **58**, 579.
Rich, D.H., T. Miller, A. Samsavar, H.F. Lin and T.-C. Chiang, 1988, Phys. Rev. B **37**, 10221.
Rich, D.H., T. Miller, G.E. Franklin and T.-C. Chiang, 1989, Phys. Rev. B **39**, 1438.

Richter, M., J.C. Woicik, J. Nogami, P. Pianetta, K.E. Miyano, A.A. Baski, T. Kendelewicz, C.E. Bouldin, W.E. Spicer, C.F. Quate and I. Lindau, 1990, Phys. Rev. Lett. **65**, 3417.
Rosén, A. and D.E. Ellis, 1976, J. Chem. Phys. **65**, 3629.
Sahni, V. and C.Q. Ma, 1980, Phys. Rev. B **22**, 5987.
Sahni, V., J.P. Perdew and J. Gruenebaum, 1981, Phys. Rev. B **23**, 6512.
Salahub, D.R., 1987, in: Ab Initio Methods in Quantum Methods in Quantum Chemistry – II, ed. K.P. Lawly. Wiley, New York, p. 447.
Sambe, H. and R.H. Felton, 1975, J. Chem. Phys. **62**, 1122.
Samsavar, A., E.S. Hirschorn, F.M. Leibsle and T.-C. Chiang, 1989, Phys. Rev. Lett. **63**, 2830.
Scheffler, M., Ch. Droste, A. Fleszar, F. Máca, G. Wachutka and G. Barzel, 1991, Physica B **172**, 143.
Scheffler, M., S.T. Pantelides, N.O. Lipari and J. Bernholc, 1981, Phys. Rev. Lett. **47**, 413.
Schlegel, B., 1982, J. Comp. Chem. **3**, 214.
Schlier, R.E. and H.E. Farnsworth, 1959, J. Chem. Phys. **30**, 917.
Schulte, F.K., 1977, Z. Physik B **27**, 303.
Schütz, G., W. Wagner, W. Wilhelm, P. Kienle, R. Zeller, R. Frahm and G. Materlik, 1987, Phys. Rev. Lett. **58**, 737.
Seiwatz, R., 1964, Surf. Sci. **2**, 473.
Shen, T.-H. and C.C. Matthai, 1991, J. Phys.: Condens. Matter **3**, 6169.
Singh, D. and H. Krakauer, 1988, Phys. Rev. B **37**, 3999.
Singh, D., S.-H. Wei and H. Krakauer, 1986, Phys. Rev. Lett. **57**, 3292.
Slater, J.C., 1937, Phys. Rev. **51**, 846.
Slater, J.C., 1951, Phys. Rev. **81**, 385.
Slater, J.C., 1974, Quantum Theory of Molecules and Solids, Vol. 4. McGraw-Hill, New York.
Smith, J.R., 1969, Phys. Rev. **181**, 522.
Smith, N.V., C.T. Chen, F. Sette and L.F. Mattheiss, 1992, Phys. Rev. B **46**, 1023.
Smith, J.R., J.G. Gay and F.J. Arlinghaus, 1980, Phys. Rev. B **21**, 2201.
Somorjai, G.A. and M.A. Van Hove, 1989, Prog. Surf. Sci. **30**, 201.
Soler, J.M. and A.R. Williams, 1989, Phys. Rev. B **40**, 1560.
Soukiassian, P., 1994, private communication.
Soukiassian, P. and J.A. Kubby, 1991, in: Structure of Surfaces – III, eds. S.Y. Tong, M.A. Van Hove, K. Tagayanaki and X. Xide, Springer Series in Surface Science, Vol. 24. Springer-Verlag, Berlin, p. 584.
Stephenson, P.C. and D.W. Bullett, 1984, Surf. Sci. **139**, 1.
Stöhr, J., Y. Wu, B.D. Hermsmeier, M.G. Samant, G.R. Harp, S. Koranda, D. Dunham and B.P. Tonner, 1993, Science **259**, 658.
Tang, S., A.J. Freeman and B. Delley, 1992, Phys. Rev. B **45**, 1776.
Tang, S. and A.J. Freeman, 1993a, Phys. Rev. B **47**, 1460.
Tang, S. and A.J. Freeman, 1993b, Phys. Rev. B **48**, 8068.
Terakura, I., K. Terakura and N. Hamada, 1981, Surf. Sci. **103**, 103.
Teter, M.P. and D.C. Allan, 1987, Phys. Rev. Lett. **59**, 1136.
Thole, B.T., P. Carra, F. Sette and G. van der Laan, 1992, Phys. Rev. Lett., 1943.
Thomas, L.H., 1926, Proc. Cambridge Philos. Soc. **23**, 542.
Tobin, J.G., G.D. Waddill and D.P. Pappas, 1992, Phys. Rev. Lett. **68**, 3642.
Tosatti, E., 1978, Solid State Commun. **25**, 637.
Treglia, G., M.-C. Desjonqueres and D. Spanjaard, 1983, J. Phys. C **16**, 2407.
Tromp, R.M., R.J. Hamers and J.E. Demuth, 1985, Phys. Rev. Lett. **55**, 1303.
Tromp, R.M., R.J. Hamers and J.E. Demuth, 1986, Phys. Rev. B **34**, 5343.
Tromp, R.M., R.G. Smeenk and F.W. Saris, 1981a, Phys. Rev. Lett. **46**, 939.
Tromp, R.M., R.G. Smeenk and F.W. Saris, 1981b, Solid State Commun. **39**, 755.
Tromp, R.M., R.G. Smeenk, F.W. Saris and D.J. Chadi, 1983, Surf. Sci. **133**, 137.
Tung, R.T., W.R. Graham and A.J. Melmed, 1982, Surf. Sci. **115**, 576.
Uhrberg, R.I.G., R.D. Bringans, R.A. Bachrach and J.E. Northrup, 1986, Phys. Rev. Lett. **56**, 520.
Uhrberg, R.I.G., R.D. Bringans, M.A. Olmstead, R.Z. Bachrach and J.E. Northrup, 1987, Phys. Rev. B **35**, 3945.
Uhrberg, R.I.G., J.E. Northrup, D.K. Biegelsen, R.D. Bringans and L.-E. Swartz, 1992, Phys. Rev. B **46**, 10251.

van der Laan, G., B.T. Thole, G.A. Sawatzky, J.B. Goedkoop, J.C. Fuggle, J.-M. Esteva, R. Karnatak, J.P. Remeika and H.A. Dabkowska, 1986, Phys. Rev. B **34**, 6529.
van der Laan, G., M.A. Hoyland, M. Surman, C.F.J. Flipse and B.T. Thole, 1992, Phys. Rev. Lett. **69**, 3827.
van Hove, M.A. and S.Y. Tong, 1976, Surf. Sci. **54**, 91.
Versluis, L. and T. Ziegler, 1988, J. Chem. Phys. **88**, 322.
Verwoerd, W.S., 1981, Surf. Sci. **99**, 581.
von Barth, J. and L. Hedin, 1972, J. Phys. C **5**, 1629.
Wang, C.S. and J. Callaway, 1974, Phys. Rev. B **8**, 4897.
Wang, D.-S., R. Wu and A.J. Freeman, 1993, Phys. Rev. Lett. **70**, 869.
Weinert, M., 1981, J. Math. Phys. **22**, 2433.
Weinert, M., E. Wimmer and A.J. Freeman, 1982, Phys. Rev. B **26**, 4571.
Weinert, M. and A.J. Freeman, 1983, Phys. Rev. B **28**, 6262.
Weinert, M., A.J. Freeman and S. Ohnishi, 1986, Phys. Rev. Lett. **56**, 2295.
Weser, T., A. Bogen, B. Konrad, R.D. Schnell, C.A. Schug and W. Steinmann, 1984, in: Proc. of the 18th Intl. Conf. on the Physics of Semiconductors, ed. O. Engström. World-Scientific, Singapore.
Weser, T., A. Bogen, B. Konrad, R.D. Schnell, C.A. Schug and W. Steinmann, 1987, Phys. Rev. B **35**, 8184.
Wigner, E. and J. Bardeen, 1935, Phys. Rev. **48**, 84.
Wimmer, E., 1983, J. Phys. F **13**, 2313.
Wimmer, E., 1984a, J. Phys. F **14**, 681.
Wimmer, E., 1984b, J. Phys. F **14**, 2613.
Wimmer, E., H. Krakauer, M. Weinert and A.J. Freeman, 1981a, Phys. Rev. B **24**, 864.
Wimmer, E., M. Weinert, A.J. Freeman and H. Krakauer, 1981b, Phys. Rev. B **24**, 2292.
Wimmer, E., A.J. Freeman, M. Weinert, H. Krakauer, J.R. Hiskes and A.M. Karo, 1982, Phys. Rev. Lett. **48**, 1123.
Wimmer, E., A.J. Freeman, J.R. Hiskes and A.M. Karo, 1983, Phys. Rev. B **28**, 3074.
Wimmer, E., H. Krakauer and A.J. Freeman, 1985, in: Advances in Electronics and Electron Physics, Vol. 65, ed. P.W. Hawkes. Academic Press, Orlando, p. 357.
Wolkow, R.A., 1992, Phys. Rev. Lett. **68**, 2636.
Wu, R., D. Wang and A.J. Freeman, 1993, Phys. Rev. Lett. **71**, 3581.
Wu, R. and A.J. Freeman, 1994, Phys. Rev. Lett. **73**, 1994.
Yang, W.S., F. Jona and P.M. Marcus, 1983, Phys. Rev. B **28**, 2049.
Ye Ling, A.J. Freeman and B. Delley, 1989, Phys. Rev. B **39**, 444, Fig. 1.
Yin, M.T. and M.L. Cohen, 1981, Phys. Rev. B **24**, 2303.
Yu, R., H. Krakauer and D. Singh, 1992, Phys. Rev. B **45**, 8671.
Zegenhagen, J., J.R. Patel, B.M. Kincaid, J.A. Golovchenko, J.B. Mock, P.E. Freeland, R.J. Malik and K.-G. Huang, 1988, Appl. Phys. Lett. **53**, 252.
Zeller, R. and P.H. Dederichs, 1979, Phys. Rev. Lett. **42**, 1713.
Zhu, Z., N. Shima and M. Tsukada, 1989, Phys. Rev. B **40**, 11868.
Zunger, A. and M.L. Cohen, 1979a, Phys. Rev. B **20**, 4082.
Zunger, A. and M.L. Cohen, 1979b, Phys. Rev. Lett. **56**, 2656.

This Page Intentionally Left Blank

CHAPTER 2

# Electronic Structure of Semiconductor Surfaces

J. POLLMANN and P. KRÜGER

*Institut für Theoretische Physik II-Festkörperphysik*
*Universität Münster*
*D-48149 Münster, Germany*

© *2000 Elsevier Science B.V.*
*All rights reserved*

*Handbook of Surface Science*
*Volume 2, edited by K. Horn and M. Scheffler*

# Contents


2.1. Introduction . . . 96
2.2. Semiconductor surface theory . . . 98
2.2.1. Basic theory . . . 98
2.2.2. Supercell method (SCM) . . . 100
2.2.3. Scattering-theoretical approach (STA) . . . 101
2.2.4. Surface bound states and resonances . . . 104
2.2.5. Calculational details of ab initio calculations . . . 106
2.2.6. Beyond LDA . . . 107
2.2.7. Improved LDA calculations for wide-band-gap semiconductors . . . 112
2.3. Basic properties of ideal surfaces . . . 116
2.3.1. Geometry-dependence of surface states . . . 116
2.3.2. Ionicity-dependence of surface states . . . 121
2.4. Surfaces of elemental semiconductors . . . 122
2.4.1. The Si(001) surface . . . 122
2.4.2. Comparison of the (001) surfaces of C, Si, Ge and $\alpha$-Sn . . . 129
2.4.3. The Si(111) surface . . . 136
2.4.3.1. Si(111)-(2 × 1) . . . 138
2.4.3.2. Si(111)-(7 × 7) . . . 139
2.4.4. The Ge(111) surface . . . 142
2.4.5. The C(111) surface . . . 144
2.4.6. The Si(110) surface . . . 146
2.5. SiC surfaces . . . 147
2.5.1. General mechanisms for the relaxation of ionic surfaces . . . 149
2.5.2. Nonpolar $\beta$-SiC(110) and 2H-SiC(10$\bar{1}$0) surfaces . . . 149
2.5.3. Polar (001) surfaces of $\beta$-SiC . . . 152
2.5.3.1. Si-terminated $\beta$-SiC(001)-(2 × 1) . . . 152
2.5.3.2. C-terminated $\beta$-SiC(001) surfaces . . . 155
2.5.4. The SiC(111) surface . . . 160
2.5.5. Polar (0001) surfaces of 6H-SiC . . . 160
2.5.5.1. Relaxed 6H-SiC(0001)-(1 × 1) surfaces . . . 161
2.5.5.2. Si-terminated 6H-SiC(0001)-($\sqrt{3} \times \sqrt{3}$) surfaces . . . 162
2.5.5.3. C-terminated 6H-SiC(0001)-($\sqrt{3} \times \sqrt{3}$) surfaces . . . 168
2.6. Surfaces of III-V semiconductors . . . 172
2.6.1. The nonpolar GaAs(110) surface . . . 172
2.6.2. Other nonpolar (110) III-V surfaces . . . 175
2.6.3. Polar GaAs surfaces . . . 178
2.6.3.1. Electron counting rule . . . 178
2.6.3.2. The GaAs(001) surface . . . 179
2.6.3.3. The GaAs(111) surface . . . 182
2.7. Surfaces of group III-nitrides . . . 183
2.7.1. Surfaces of cubic group III-nitrides . . . 183
2.7.1.1. Nonpolar surfaces of cubic group III-nitrides . . . 183

2.7.1.2. Polar surfaces of cubic group III-nitrides . . . . . 183
2.7.2. Surfaces of hexagonal group III-nitrides . . . . . 185
2.7.2.1. Nonpolar surfaces of hexagonal group III-nitrides . . . . . 185
2.7.2.2. Polar surfaces of hexagonal group III-nitrides . . . . . 187
2.8. Surfaces of II-VI semiconductors . . . . . 188
2.8.1. Nonpolar surfaces of cubic II-VI compounds . . . . . 190
2.8.2. Nonpolar surfaces of hexagonal II-VI compounds . . . . . 191
2.9. Summary . . . . . 195
References . . . . . 196

## 2.1. Introduction

Semiconductor surfaces are of basic importance both from a fundamental as well as an applied point of view. Their very intriguing physical properties and the wide range of their technological applications has been an ever increasing stimulus to fully understand their atomic and electronic structure on a microscopic level. We have witnessed exciting developments and applications of pretentious and fascinating surface-sensitive experimental techniques. Concomitantly with these developments, the field of atomic and electronic structure theory of semiconductor surfaces has matured within the last decade. It is nowadays possible by employing total energy minimization techniques to theoretically determine optimal surface structures with a good level of confidence and to self-consistently evaluate the respective surface electronic structure, in particular charge densities, energy bands and wave-vector resolved layer densities of states (LDOS) of surfaces with high precision.

Although structural and electronic properties of semiconductor surfaces have been studied for decades, a number of systems remain under debate because of their complex reconstruction behavior. While surfaces like Si(111) or GaAs(110) are well-understood, by now, others like (001) and (111) surfaces of compound semiconductors continue to attract large attention. In addition, new systems like surfaces of SiC or of group III-nitrides move into the focus of interest because of their potential for microelectronic devices. Likewise, surfaces of cubic and hexagonal II-VI semiconductors attract increasing interest because of their importance for optoelectronic devices and heterogeneous catalysis.

A wealth of studies based on the empirical tight-binding method (ETBM) has been carried out in the past and has yielded many beautiful qualitative results. In particular, these calculations easily allow to reveal trends in the relaxation or reconstruction behavior of surfaces and to identify the origin and physical nature of particular surface states. In consequence, such calculations have proven extremely useful for suggesting new structural models (cf. Chadi, 1978b, 1979b; Pandey, 1981). The results, however, critically depend on empirical parameters.

To arrive at a most quantitative description of structural, electronic and chemical properties of surfaces it has turned out mandatory to employ first-principles calculations. Here we concentrate on a discussion of *ab initio* calculations and their respective results, therefore. We focus on more recent results for prototypical systems that are under intensive study currently and use these results to develop a general picture of surface electronic properties of various classes of important semiconductors. In particular, we will relate the specific electronic features of particular surfaces to basic chemical and physical properties of the underlying bulk solids, as well as, to the atomic structure of these surfaces.

As to the atomic structure, we note at the very beginning that the physical properties of a particular solid sensitively depend on the considered solid. While this is a most trivial statement for bulk crystals it cannot be overstated in the context of surfaces. Particular

surfaces of a given bulk solid and their structural variants often constitute largely different systems because most physical properties of a surface sensitively depend on its specific atomic structure. In this respect, e.g., bulk Si and Ge have probably more in common than the Si(001)-(2 × 1) and the Si(111)-(7 × 7) surface. As a matter of fact, the actual electronic structure of a particular surface may be viewed as a 'fingerprint' of its specific atomic structure. In this sense, we will characterize a large number of different semiconductor surfaces in this chapter by their fingerprints. The sensitive atomic-structure dependence allows to observe a wealth of different spectroscopic results for different surfaces of the same bulk material in experiment. In theory, one needs to know as precisely as possible the structure of a particular surface before one can study its electronic, chemical, vibrational or magnetic properties with the prospect of arriving at results that are accurate enough to allow for a meaningful interpretation of experimental data. Discussing electronic properties of surfaces, therefore, necessitates to address their atomic structure, as well.

In this chapter, we certainly cannot give a full account of the entire history of the whole field. For summaries of by now 'classical' experimental and theoretical results, we refer the reader to the review articles by Hansson and Uhrberg (1988) and LaFemina (1992) and to a comprehensive monography by Mönch (1995). A fairly complete account on structural and electronic properties of semiconductor surfaces has been compiled in two recent volumes of Landolt-Börnstein (Chiarotti, 1993, 1994). In addition, the structure of surfaces, in general, and of semiconductor surfaces, in particular, is discussed in great depth in Volume I of this "Handbook of Surfaces". We mention, as well, a recent review by Duke (1996) in which the structural properties of semiconductor surfaces are discussed in conjunction with a number of principles that seem to govern semiconductor surface relaxation and reconstruction. For a full account on structural properties of the surfaces addressed in this chapter, we refer the interested reader to these publications. Here we will address surface structural properties in more detail only for those systems for which more recent progress has been achieved. The structure of 'well-known' surfaces will be summarized only very briefly in the respective sections.

In Section 2.2 we address currently used theoretical methods for semiconductor surface calculations as well as quasiparticle band structure calculations and calculations that take self-interaction and relaxation corrections into account. Following is a more general discussion of the geometry and ionicity dependence of salient surface features, highlighted for the case of geometrically ideal surfaces in Section 2.3. Ideal surfaces serve as a reference for the following discussions of relaxed and reconstructed surfaces of a host of technologically important semiconductor crystals. In our following discussions of actual results on real surfaces, we start out with surfaces of elemental semiconductors in Section 2.4. Next we address surfaces of the ionic group-IV semiconductor SiC in Section 2.5. We then move on to surfaces of common III-V compound semiconductors in Section 2.6 and discuss group III-nitride surfaces in Section 2.7, as well. Finally, we consider surfaces of II-VI compound semiconductors in Section 2.8. A short summary concludes this chapter in Section 2.9. Since many of the addressed surfaces have been studied more recently within the local density approximation (LDA) of density functional theory (DFT) or employing GWA, in cases, we will use respective results for most of our discussions.

## 2.2. Semiconductor surface theory

In this section, we first briefly address basic aspects of the theory of surfaces, in general, and discuss in some detail the methods most widely used currently for semiconductor surfaces, in particular. We then very briefly summarize a few important technical details of actual LDA calculations. Thereafter, we describe in some depth ways to go beyond the LDA by employing GW quasiparticle band structure calculations or by employing self-interaction- and relaxation-corrected (SIRC) pseudopotentials in LDA calculations.

### *2.2.1. Basic theory*

The calculation of electronic properties of semiconductor surfaces is as simple or as demanding, *in principle*, as bulk band-structure calculations for semiconductors. *In practice*, however, the treatment of surfaces is complicated by two obstacles. First, the translational invariance perpendicular to a surface is broken so that Bloch's theorem only allows to classify electronic surface states by a wave vector $\mathbf{k}_\parallel$ that is parallel to the surface. Second, and much more importantly, for many surfaces the actual configuration of atoms at or near the surface is *a priori* much less precisely known than that of the respective bulk solids. Since the electronic surface structure is very sensitively dependent on the surface atomic structure, as mentioned above, the calculation of surface electronic properties, in general, constitutes a coupled atomic and electronic structure problem.

Most current days surface electronic structure calculations deal with this situation by referring to density functional theory (Hohenberg and Kohn, 1964) within local density approximation (Kohn and Sham, 1965). Due to its formal and computational simplicity as well as due to its very impressive successes in describing ground-state properties of many-electron systems, DFT-LDA has become the dominant approach for calculating structural and electronic properties of bulk semiconductors (see, e.g., Lundqvist and March, 1983; Devreese and Van Camp, 1985; Pickett, 1985) and their surfaces. Within DFT-LDA the total energy of a surface system is given by:

$$E_{\text{tot}}\big(\rho, \{\mathbf{R}_i\}\big) = E_{\text{kin}} + E_{\text{el-ion}} + E_{\text{coul}} + E_{\text{xc}}^{\text{LDA}} + E_{\text{ion-ion}}, \tag{2.1}$$

with

$$E_{\text{kin}} = \sum_{s\mathbf{k}_\parallel} \int \psi_{s\mathbf{k}_\parallel}^*(\mathbf{r}) \left( -\frac{\hbar^2}{2m} \nabla^2 \right) \psi_{s\mathbf{k}_\parallel}(\mathbf{r})\, \mathrm{d}^3 r, \tag{2.2}$$

$$E_{\text{el-ion}} = \int V_{\text{el-ion}}\big(\{\mathbf{R}_j\}, \mathbf{r}\big) \rho(\mathbf{r})\, \mathrm{d}^3 r, \tag{2.3}$$

$$E_{\text{coul}} = \frac{e^2}{2} \iint \frac{\rho(\mathbf{r})\rho(\mathbf{r}')}{|\mathbf{r} - \mathbf{r}'|}\, \mathrm{d}^3 r\, \mathrm{d}^3 r', \tag{2.4}$$

$$E_{\text{xc}}^{\text{LDA}} = \int \rho(\mathbf{r}) f_{\text{xc}}^{\text{LDA}}\big(\rho(\mathbf{r})\big)\, \mathrm{d}^3 r, \tag{2.5}$$

$$E_{\text{ion-ion}} = \frac{e^2}{2} \sum_{i,j} \frac{\mathrm{Z}_i \cdot \mathrm{Z}_j}{|\mathbf{R}_i - \mathbf{R}_j|}. \tag{2.6}$$

Various approximations for $f_{\mathrm{xc}}^{\mathrm{LDA}}(\rho)$ have been discussed in Chapter 1 of this volume (Wimmer and Freeman, 2000). The total energy depends on the positions $\{\mathbf{R}_i\}$ of all atoms in the system and on the electronic charge density $\rho(\mathbf{r})$ which has to be calculated self-consistently.

Minimizing the total energy with respect to the total valence-charge density $\rho$ under the constraint of orthonormalized wave functions yields the Kohn–Sham equations (Kohn and Sham, 1965)

$$\begin{aligned}&\left\{-\frac{\hbar^2}{2m}\nabla^2 + V_{\mathrm{ion}}\big(\{\mathbf{R}_i\},\mathbf{r}\big) + V_{\mathrm{coul}}\big([\rho(\mathbf{r})],\mathbf{r}\big) + V_{\mathrm{xc}}\big([\rho(\mathbf{r})],\mathbf{r}\big)\right\}\psi_{s\mathbf{k}_\parallel}(\mathbf{r})\\ &\quad =: \left\{-\frac{\hbar^2}{2m}\nabla^2 + V_{\mathrm{eff}}\big(\{\mathbf{R}_i\},[\rho(\mathbf{r})],\mathbf{r}\big)\right\}\psi_{s\mathbf{k}_\parallel}(\mathbf{r}) = E_{s\mathbf{k}_\parallel}^{\mathrm{LDA}}\psi_{s\mathbf{k}_\parallel}(\mathbf{r}) \qquad (2.7)\end{aligned}$$

for the one-particle wave functions labeled by the quantum numbers $s$ and $\mathbf{k}_\parallel$. The effective one-particle potential in these equations is a sum of an ionic potential $V_{\mathrm{ion}}$, which is most often used in the form of a pseudopotential, the Coulomb potential $V_{\mathrm{coul}}$ and the exchange–correlation potential $V_{\mathrm{xc}}$.

Minimizing the total energy with respect to all structural degrees of freedom $\{\mathbf{R}_i\}$ of a semi-infinite surface system by eliminating the forces

$$\mathbf{F}_i = -\frac{\partial}{\partial \mathbf{R}_i} E_{\mathrm{tot}}\big(\{\mathbf{R}_j\}\big) = 0, \quad \forall \mathbf{R}_i \qquad (2.8)$$

yields the optimal surface atomic structure corresponding to a minimum of the total energy in configuration space (see, e.g., Ihm et al., 1979; Scheffler et al., 1985; Krüger and Pollmann, 1991a). The resulting minimum, in general, not necessarily needs to be a global minimum of the total energy.

Even if the actual atomic structure of the surface is known, one has to solve, in principle, the Kohn–Sham equation for a semi-infinite system self-consistently. Since the respective unit cell is infinitely long in the direction perpendicular to the surface, it contains infinitely many atoms. Thus any standard bulk-band structure method immediately leads to $\infty \times \infty$ matrices that need to be diagonalized. Since that cannot be achieved one recurs to either substitute geometries to simulate a surface or to alternative formal approaches which do not necessitate the diagonalization of Hamiltonian and overlap matrices. We briefly list the formal methods that are used to deal with this *geometry problem*:

- cluster method (CM)
- slab method (SM)
- super-cell method (SCM)
- wave-function-matching method (WMM)
- transfer-matrix method (TMM)
- embedding methods (EM)
- scattering-theoretical approach (STA)

The CM does not make full use of the symmetry of a surface system. The SM and SCM simulate a solid surface by relatively thin slabs (typically of the order of 10 atomic layers) either as a single slab (SM) or as a periodic repetition of slabs with sufficiently many

vacuum layers between the slabs in the direction perpendicular to the surface (SCM). In the latter case the problem reduces to a bulk-like calculation with a unit cell (the supercell) that is relatively large in the surface-perpendicular direction. The respective Brillouin zone is correspondingly flat so that the dispersion of the bands resulting in that direction can be ignored. The remaining methods, i.e., the WMM, the TMM, the EM and the STA all allow to treat truly semi-infinite systems, in principle. We use the label scattering-theoretical approach (STA) instead of scattering-theoretical method to avoid confusion with the well-established abbreviation for scanning-tunneling microscopy (STM).

All of these methods have been discussed in detail by Wimmer and Freeman (2000) in the Chapter 1 of this volume. Therefore, we only briefly summarize some basic formal aspects of the two methods most widely used in recent *ab initio* calculations for semiconductor surfaces, namely the SCM and the STA. In particular, the STA allows to identify *bona fide* bound surface states and surface resonances simply on a formal basis very clearly.

### 2.2.2. *Supercell method (SCM)*

Within the supercell method, the solution of Eq. (2.7) is achieved by expanding the wave functions in terms of plane wave basis sets (see, e.g., Schlüter et al., 1975) or of localized Gaussian orbital basis sets (see, e.g., Schröer et al., 1994; Sabisch et al., 1995). Semiempirical, local or nonlocal ionic pseudopotentials are used in the effective potential $V_{\text{eff}}$. Expanding the wave functions in terms of plane waves $|\mathbf{k}, \mathbf{g}\rangle$ and minimizing the energy with respect to the linear expansion coefficients yields a linear equation system given by:

$$\sum_{\mathbf{g}'} C^s_{\mathbf{g}'}(\mathbf{k}) \left\{ \left[ \frac{\hbar^2}{2m} (\mathbf{k}+\mathbf{g})^2 - E_s(\mathbf{k}) \right] \delta_{\mathbf{g},\mathbf{g}'} + V(\mathbf{k}+\mathbf{g}, \mathbf{k}+\mathbf{g}') \right\} = 0. \tag{2.9}$$

In this case no overlap matrix occurs, since plane waves form an orthonormal basis set. When the wave functions are expanded in terms of a localized orbital basis set $|\mathbf{k}, l\rangle$, the respective linear equation system is given by:

$$\sum_{l'} C^s_{l'}(\mathbf{k}) \left\{ H_{l,l'}(\mathbf{k}) - E_s(\mathbf{k}) S_{l,l'}(\mathbf{k}) \right\} = 0, \tag{2.10}$$

where in addition to the Hamiltonian matrix also an overlap matrix occurs since the localized orbitals at different atoms need not be orthogonal to one another (cf. Schröer et al., 1994; Sabisch et al., 1995). Since the supercell contains considerably more atoms than a typical bulk unit cell, the respective size of the occurring Hamiltonian and overlap matrices are correspondingly larger. Usually one employs some 200 plane waves per atom so that, e.g., a ten layer slab calculation for the Si(001)-$(2 \times 1)$ surface calls for $2 \times 10 \times 200 = 4000$ basis states leading to $4000 \times 4000$ matrices in Eq. (2.9) that need to be diagonalized. When Gaussian orbitals are employed some 20 basis states per atom yield sufficient accuracy in most cases so that $2 \times 10 \times 20 = 400$ orbitals are contained in the basis yielding $400 \times 400$ matrices in Eq. (2.10). The generalized eigenvalue problem defined by Eq. (2.10) is solved by first carrying out a Cholesky decomposition of the overlap matrix and then diagonalizing the correspondingly transformed Hamiltonian matrix (cf. Louie et al., 1979). Since

straightforward matrix diagonalizations involve $N^3$ operations, the plane wave approach for our example would necessitate about $10^3$ times as many operations as the localized orbital approach. But the numerical effort in such calculations is nowadays routinely reduced significantly by referring to iterative diagonalization techniques (Payne et al., 1992). Concerning the comparison between the two methods, it should be noted that the calculation of the matrix elements in the plane wave basis is almost trivial and increasing the basis set to convergence, if sufficient computer capacity is available, is very simple. For localized Gaussian orbital basis sets, the calculation of the matrix elements is more involved and increasing the basis set is not as straightforward as it is for plane waves. In any case, in the SCM the surface system is addressed as an entirely new system in its own right without making use of the solutions of the underlying bulk problem. Within this methodology, *bona fide* bound surface states can easily be determined but surface resonances do not readily result with very good resolution.

### *2.2.3. Scattering-theoretical approach (STA)*

Just by looking at the basic equations of the STA, a number of characteristic surface properties can easily be assessed. Therefore, it is very useful to address the formalism of the STA (Pollmann and Pantelides, 1978; Pollmann, 1980; Williams et al., 1982; Krüger and Pollmann, 1988, 1991a; Scheffler et al., 1991; Wachutka et al., 1992) in some detail. A closely related Green function approach – the embedding method – has been discussed in comparison with the STA by Inglesfield (1981, 1987) and by Benesh and Inglesfield (1984). The scattering-theoretical approach can be characterized by four specific features: (1) it fully incorporates the electronic properties of the underlying bulk crystal, (2) it treats a surface as a two-dimensionally periodic perturbation that is highly localized in the surface-perpendicular direction, (3) it allows to solve the geometry problem numerically exactly and (4) it yields bound states as well as resonances with an extremely high spectral resolution.

The starting point of this method is the bulk crystal described by the Hamiltonian $H^0$. Let us assume the bulk band structure problem

$$H^0\Phi_{n\mathbf{k}}(\mathbf{r}) = E_n(\mathbf{k})\Phi_{n\mathbf{k}}(\mathbf{r}) \tag{2.11}$$

to be solved. The one-particle wave functions are labeled by the quantum numbers $n$ and $\mathbf{k}$. Let the full Hamiltonian of a surface system be labeled $H$. Thus one has to solve

$$H\psi_{s\mathbf{k}_\parallel}(\mathbf{r}) = E_{s\mathbf{k}_\parallel}\psi_{s\mathbf{k}_\parallel}(\mathbf{r}). \tag{2.12}$$

To represent the wave functions and operators, so-called layer orbitals

$$\begin{aligned}\langle \mathbf{r} \mid \alpha, \mu, m; \mathbf{k}_\parallel \rangle &:= \psi_{\alpha,\mu,m}(\mathbf{k}_\parallel, \mathbf{r}) \\ &= \frac{1}{\sqrt{N_2}} \sum_l \mathrm{e}^{\mathrm{i}\mathbf{k}_\parallel(\boldsymbol{\rho}_l + \boldsymbol{\lambda}_\mu^m)} \phi_\alpha\left(\mathbf{r} - \boldsymbol{\rho}_l - \boldsymbol{\lambda}_\mu^m - \boldsymbol{\kappa}_m\right)\end{aligned} \tag{2.13}$$

are introduced, in which $\alpha$ labels the orbital type, $\mu$ labels the atoms in the layer unit cell and $m$ labels a particular layer. The vectors $\boldsymbol{\rho}_l$ span the two-dimensional surface Bravais

lattice, the vector $\lambda_\mu^m$ defines the position of the $\mu$-th basis atom in the unit cell on the $m$-th layer and $\kappa_m$ is the shortest distance between layer $m$ and the origin of the coordinate system.

A surface breaks translational invariance perpendicular to the surface so that only $\mathbf{k}_\parallel$ remains a 'good quantum number' and all bulk eigenstates with $(\{n\}, \mathbf{k}_\parallel, \{\mathbf{k}_\perp\})$ scatter at the surface. In consequence, all bulk states with different band indices $n$ and wave vectors $\mathbf{k}_\perp$ become mixed due to scattering at the surface. Equation (2.12) can most conveniently be solved by referring to the formalism of potential scattering theory (cf. Pollmann and Pantelides, 1978; Krüger and Pollmann, 1988, 1991a). In this approach a surface is formally described as a perturbation. We describe the basics of the formalism in a matrix representation. One seeks the Green functions or resolvents of the Schrödinger equations for the surface and bulk systems (Eqs. (2.12) and (2.11)), respectively. They are defined by

$$(ES - H)G = 1 \tag{2.14}$$

and

$$\left(ES^0 - H^0\right)G^0 = 1, \tag{2.15}$$

respectively, where $S$ and $S^0$ are the corresponding overlap matrices. The solutions of these equations are formally given by

$$G(E) = \lim_{\varepsilon \to 0^+} \{ES + \mathrm{i}\varepsilon - H\}^{-1} \tag{2.16}$$

and

$$G^0(E) = \lim_{\varepsilon \to 0^+} \left\{ES^0 + \mathrm{i}\varepsilon - H^0\right\}^{-1}, \tag{2.17}$$

respectively. For $G^0(E)$ one can easily write down the spectral representation

$$G^0(\mathbf{k}_\parallel, E) = \lim_{\varepsilon \to 0^+} \sum_{n\mathbf{k}_\perp} \frac{|n, \mathbf{k}_\parallel, \mathbf{k}_\perp\rangle\langle n, \mathbf{k}_\parallel, \mathbf{k}_\perp|}{E + \mathrm{i}\varepsilon - E_n(\mathbf{k}_\parallel, \mathbf{k}_\perp)} \tag{2.18}$$

since the bulk eigenvalues and eigenvectors are assumed to be known. We recognize that the discrete poles of $G^0$ on the real energy axis define the bulk eigenvalues and the residues determine the bulk eigenfunctions. Writing down the respective spectral representation for the surface Green function $G$ is useless at this point, since one does neither know the eigenvalues nor the eigenvectors of the surface problem. They are precisely what one is looking for eventually. Therefore, one makes use of an equation that allows to evaluate $G$ explicitly. If one rewrites Eq. (2.14) in the following form:

$$\left\{ES^0 - H^0 - \left[H - H^0 - E\left(S - S^0\right)\right]\right\}G =: \left(ES^0 - H^0 - U\right)G = 1 \tag{2.19}$$

it becomes most obvious that the perturbation matrix describing the surface is given by

$$U := H - H^0 - E(S - S^0). \tag{2.20}$$

This perturbation matrix creates the semi-infinite crystal and takes the surface reconstruction as well as the charge-density relaxations occurring at the surface into account explicitly. Most importantly, from a practicable point of view, the layer-orbital representation of the $U$-matrix yields nonvanishing matrix elements only in a very small subspace of the full Hilbert space of the problem. This is due to the fact that the *changes* in the charge density $\rho$ and in the effective potential $V_{\text{eff}}$ due to a surface are very strongly localized at and near the surface within a few layers. Thus in the layer-orbital representation, the surface-describing localized perturbation $U$ can be represented by a relatively small matrix. The size of this matrix is determined by the number of layers contributing to the surface perturbation and the number of orbitals per layer unit cell and thus depends on the type of band structure method and basis set used in the calculations. For the details of this formalism the interested reader is referred to (Krüger and Pollmann, 1988, 1991a).

Multiplying Eq. (2.19) from the left by the bulk Green function $G^0$ according to Eq. (2.17) immediately yields the Dyson equation for the surface Green function

$$G = G^0 + G^0 U G. \tag{2.21}$$

The formal solution of this equation is given by

$$G(E) = \{1 - G^0(E)U\}^{-1} G^0(E). \tag{2.22}$$

As in the bulk case, the discrete poles of $G(E)$ define the eigenvalues of the discrete states of the surface system. From Eq. (2.22) it becomes most obvious that the bulk eigenvalues enter the surface Green function $G$ as the poles of the bulk Green function $G^0$. The surface, in addition, can give rise to exponentially localized bound surface states that are determined by the new poles of the surface Green function contained in the first factor of Eq. (2.22), i.e., they are given by the zeros of the so-called Fredholm determinant

$$D(E_s) = \det|1 - G^0(E_s)U| = 0. \tag{2.23}$$

Iteration of Eq. (2.21) yields

$$G(E) = G^0(E) + G^0(E)T(E)G^0(E), \tag{2.24}$$

where the $T$ matrix is defined as

$$T(E) = U\{1 - G^0(E)U\}^{-1} = \{1 - UG^0(E)\}^{-1} U. \tag{2.25}$$

From Eq. (2.24) we easily recognize that the surface Green function separates into a bulk contribution $G^0$ and a surface contribution $G^0 T G^0$. The latter describes the scattering of

the bulk states (contained in $G^0$) at the surface (described by $T$). To clearly separate bulk from surface features is obviously trivial using Eq. (2.24).

The key quantity of the theory, in addition to the bulk Green function $G^0$, is the $T$ matrix. Since the surface perturbation $U$ is very localized in space, the $T$ matrix can be treated exactly. *The discrete poles and the continuous branch cuts of $G(E)$ in the complex energy plane contain full information on the electronic one-particle spectrum of the surface system.* Typical sizes of the perturbation matrix range from $20 \times 20$ to $400 \times 400$ depending on the actual problem considered and in particular on the type of reconstruction (short or long range, respectively).

The discrete poles of the surface Green function determine the energies of surface bound states, i.e., the states which are exponentially localized perpendicular to the surface. They are given by the zeros of the Fredholm determinant (Eq. (2.23)). Surface resonances are determined by the branch cuts and their energetic position can directly be determined by analysing the *changes* in the layer density of states induced by the surface. They are defined by:

$$\Delta N_{\alpha,\mu,m}(E) = N_{\alpha,\mu,m}(E) - N^0_{\alpha,\mu,m}(E) \tag{2.26}$$

and are given in terms of the Green function and overlap matrix as:

$$N_{\alpha,\mu,m}(\mathbf{k}_\parallel, E) =: N_l(\mathbf{k}_\parallel, E) = -\frac{2}{\pi} \lim_{\varepsilon \to 0^+} \operatorname{Im} \sum_{l'} G_{l,l'}(E + \mathrm{i}\varepsilon, \mathbf{k}_\parallel) S_{l',l}(\mathbf{k}_\parallel). \tag{2.27}$$

### 2.2.4. *Surface bound states and resonances*

Surface bound states can occur when $E_s$ resides in a gap of the bulk band structure and resonances can occur when $E_s$ overlaps in energy with the quasicontinuum of the bulk states, i.e., if $E_s$ is resonant with the bulk continuum. To properly define these discerning energy regions, it is necessary to take the wave vector $\mathbf{k}_\parallel$, which remains a 'good quantum number' at the surface, into account. From Eq. (2.18) we recognize that $E$ is resonant with the bulk spectrum when it is given by:

$$E = E_{\{n\}}\big(\mathbf{k}_\parallel, \{\mathbf{k}_\perp\}\big) =: E^{\mathrm{PBS}}(\mathbf{k}_\parallel). \tag{2.28}$$

If it does not fulfil this condition, $E$ resides in one of the gaps or pockets of the so-called projected band structure (PBS) of the underlying bulk crystal. The PBS results by projecting all band structure energies of the bulk crystal from the first bulk Brillouin zone (BBZ) for a given $\mathbf{k}_\parallel$ onto the surface Brillouin zone (SBZ).

The bulk band structure of Si and the result of this projection are shown for the case of the ideal Si(001) surface in Fig. 2.1. Band gaps in the bulk band structure give rise to band gaps in the PBS. In addition, in certain $\mathbf{k}_\parallel$ regions of the PBS so called 'pockets' or 'stomach gaps' can occur, in which exponentially localized bound surface states may exist. In the other regions of the PBS only surface resonances can occur. The point pattern in Fig. 2.1 highlights the density of projected bulk states, i.e., the one-dimensional bulk density of states resulting from bulk states with wave vectors perpendicular to the surface

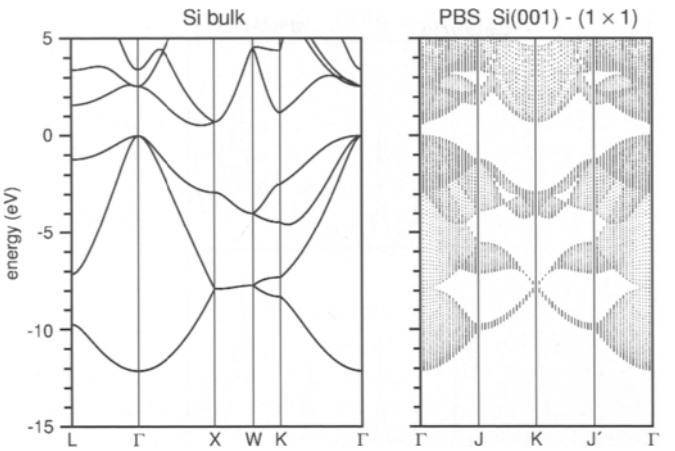


Fig. 2.1. LDA bulk band structure of Si (left panel) together with its projection onto the surface Brillouin zone (SBZ) of Si(001)-(1 × 1) (right panel).

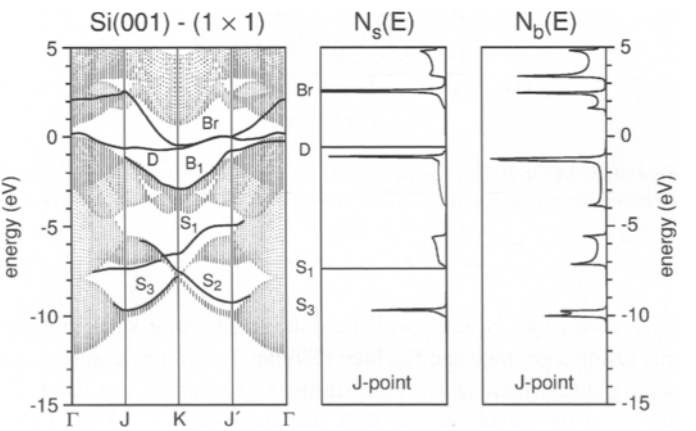


Fig. 2.2. Surface band structure of the geometrically ideal Si(001)-(1 × 1) surface and layer densities of states at the surface layer ($N_s$) and a bulk layer ($N_b$).

plane. In most of the following figures we will represent the PBS just by shaded areas, as is common use.

As an example, Fig. 2.2 shows the most salient bound states at the ideal Si(001) surface together with the layer density of states (LDOS) at the J-point of the SBZ on the surface layer ($N_s$) and on a bulk layer ($N_b$) of the semi-infinite system. Localized surface states are clearly to be seen in the band gaps or pockets ($\delta$-peaks) and surface resonances occur within the PBS. These show the smoothing of van Hove singularities at the surface and the typical 'band narrowing'.

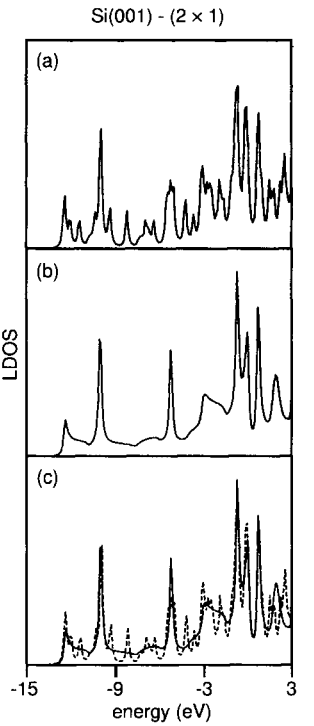


Fig. 2.3. Comparison of the LDOS at the Γ-point of Si(001)-(2 × 1) as resulting within (a) the supercell method (SCM), (b) the scattering theoretical approach (STA), and (c) direct comparison of both (Krüger and Pollmann, 1988).

Bound surface states can equally well be calculated using sufficiently thick slabs or employing semi-infinite geometries. Surface resonances, on the contrary are more easily and more precisely determined when semi-infinite geometries are used. To identify the different resolution of the SCM and the STA, we show in Fig. 2.3 the LDOS on the first layer of a (2 × 1)-reconstructed Si(001) surface at the center of the SBZ. The top panel shows the result of a calculation employing 12 atomic layers per supercell. The middle panel shows the result of an STA calculation employing the semi-infinite geometry. The bottom panel shows a direct comparison of the two results revealing a number of 'spurious peaks' in the slab LDOS.

### 2.2.5. *Calculational details of ab initio calculations*

Most of the results reviewed in this chapter have been calculated employing theoretical methods, the details of which have been described in detail elsewhere (see, e.g., Schlüter et al., 1975; Krüger and Pollmann, 1988; Schröer et al., 1994; Sabisch et al., 1995). Therefore, we only summarize the basic ingredients of these calculations. Most of current-days *ab initio* calculations for semiconductors are carried out within DFT-LDA

employing nonlocal, norm-conserving pseudopotentials as, e.g., suggested by Bachelet et al. (1982), by Gonze et al. (1991), or by Troullier and Martins (1991). These pseudopotentials are employed in separable form, as suggested by Kleinman and Bylander (1982). The exchange–correlation potential (XC) is usually taken into account in the Ceperley–Alder (1980) form as parameterized by Perdew and Zunger (1981) but the Wigner form (1934, 1937) has been used in cases as well. As basis sets to represent the wave functions, mostly plane waves or Gaussian orbitals are being used. Plane waves are certainly easier to handle but they lead to very large Hamiltonian matrices when supercell geometries are used to describe surface systems. For semi-infinite systems that can be described by potential scattering theory and Green's functions (Krüger and Pollmann, 1988, 1991a), plane waves are inadequate. In this case the calculations can be carried out very efficiently with Gaussian orbital basis sets. Total energies for the surface structure optimizations are by now routinely calculated self-consistently using the momentum-space formalism of Ihm et al. (1979). Optimal surface relaxations or reconstructions are determined within the supercell approach (Schlüter et al., 1975) or within the STA (Krüger and Pollmann, 1991a) by equilibrating the forces. When a Gaussian basis is employed, Pulay forces have to be taken into account in addition to the Hellmann–Feynman forces (Scheffler et al., 1985; Krüger and Pollmann, 1991a). Eliminating the forces iteratively is often achieved by employing the Broyden (1965) scheme. One moves all atoms in the unit cell until all forces vanish to within a prechosen accuracy level of, e.g., $10^{-3}$ Ry/a.u.

### *2.2.6. Beyond LDA*

So far we have discussed DFT-LDA calculations for semiconductor surfaces. As is well-known, DFT provides an exact formulation for the ground-state energy. Excitation energies, however, do not directly follow from DFT, since the one-particle eigenvalues in LDA are not formally interpretable as quasiparticle energies. The failures of such interpretations are well-known. Band gaps in semiconductors are typically underestimated by 30–50% and in particular cases like ZnO or Ge the gap is nearly (Schröer et al., 1993a) or even entirely closed (Bachelet and Christensen, 1985), respectively. These shortcomings in calculated band gaps and excited-state properties, in particular, can be overcome by quasiparticle band structure calculations (see, e.g., the very recent review by Aryasetiawan and Gunnarsson, 1998).

The basic formal development of first-principles methods for calculating quasiparticle energies and excited-state properties of solids has been put forward already some 30 years ago (Hedin, 1965; Hedin and Lundqvist, 1969). For semiconductors, the major difficulty stems from an adequate treatment of dynamical correlations of the electrons in a solid with an energy gap and with a strongly inhomogeneous charge density distribution. The basic object of the theory is a nonlocal, non-Hermitian and energy-dependent self-energy operator $\Sigma(\mathbf{r}, \mathbf{r}', E)$. In lowest approximation, $\Sigma$ is given as a product of the Green's function $G$ and the screened Coulomb interaction $W$. This approximation is referred to as GW approximation (GWA) (Hedin, 1965; Hedin and Lundqvist, 1969). In their landmark contributions to the field, Hybertsen and Louie (1986a, b) as well as Godby et al. (1988) developed practicable schemes for evaluating the many-body corrections within GWA and arrived at theoretical results which are in very good agreement with a whole

body of experimental data. Three elements in the theory were found to be crucial for the success: (1) a proper account of the nonlocality of the Green's function $G$, (2) the inclusion of the full dielectric matrix $\varepsilon$ in the screened Coulomb interaction $W$ and (3) an adequate treatment of dynamical effects in the screening. By now, a number of GW calculations have been reported confirming the originally found excellent agreement with experiment for many more bulk semiconductors and insulators. Even a number of surfaces (Zhu et al., 1989a, b, 1991a, b; Northrup et al., 1991; Northrup, 1993; Rohlfing et al., 1995a, b, c) and adsorbate systems (Hybertsen and Louie, 1987, 1988a, b; Hricovini et al., 1993; Rohlfing et al., 1996a, b) have been treated this way, to date, yielding results in very good agreement with photoemission and inverse photoemission data, as well.

GW calculations for sp-bonded semiconductors have been carried out using either plane wave or Gaussian orbital basis sets. Calculations employing relatively small Gaussian orbital basis sets yield essentially the same results as plane wave calculations if both are carried out to basis set convergence (see, e.g., Rohlfing et al., 1993, 1995a). For more complex systems like II-VI semiconductor compounds, which are characterized by cationic d-orbitals, the use of Gaussian orbital basis sets has turned out to be crucial for the practicability of the calculations (Rohlfing et al., 1995c, 1996a).

In this subsection, we briefly summarize the basic formalism of the GWA as it applies to bulk band structure calculations. The same formalism applies equally well to surface calculations, carried out within SCM, since the latter are just bulk band structure calculations for very large unit cells (see Subsection 2.2.2). As discussed in Subsection 2.2.1, ground-state properties of semiconductors and insulators can be calculated from first principles employing DFT-LDA. Its central aspect is the approximation of exchange–correlation effects by a potential $V_{\mathrm{xc}}(\mathbf{r})$ which depends on the local density $\rho(\mathbf{r})$. Within LDA, as discussed above, one has to solve the Kohn–Sham equation (see Subsection 2.2.1)

$$\left\{-\frac{\hbar^2}{2m}\nabla^2 + \hat{V}_{\mathrm{ps}}(\mathbf{r}) + e^2\int\frac{\rho(\mathbf{r}')}{|\mathbf{r}-\mathbf{r}'|}\,\mathrm{d}^3r' + V_{\mathrm{xc}}(\rho(\mathbf{r}))\right\}\psi_{n\mathbf{k}}(\mathbf{r}) = E_{n\mathbf{k}}^{\mathrm{LDA}}\psi_{n\mathbf{k}}(\mathbf{r}). \tag{2.29}$$

This equation is usually formulated for the valence electrons only. Therefore, the electron–ion interaction is described by a pseudopotential $\hat{V}_{\mathrm{ps}}$. This 'state of the art' method has been applied to many systems and the calculated ground-state properties, e.g., theoretical lattice constants and theoretical bulk moduli agree well with experimental data (Lundqvist and March, 1983; Devreese and Van Camp, 1985; Pickett, 1985; Jones and Gunnarsson, 1989). Usually, the Lagrangian parameters $E_{n\mathbf{k}}^{\mathrm{LDA}}$ in Eq. (2.29) are regarded as single-particle energies yielding quite reliable band structures, at least for the valence band states. Nevertheless, the LDA energy values are not exact single-particle energies. As mentioned already, all LDA band structures for semiconductors suffer from a too low fundamental gap. To obtain band structures with reliable energy values for the conduction bands as well quasiparticle corrections have to be taken into account.

The principles of the GWA which have been described by many authors (Hedin, 1965; Hedin and Lundqvist, 1969; Hybertsen and Louie, 1986a, b; Godby et al., 1988; von der Linden and Horsch, 1988) can be summarized as follows. The central quantity of the for-

malism is the single-particle Green's function as introduced by Hedin (1965) and Hedin and Lundqvist (1969)

$$G(\mathbf{r}, \mathbf{r}', E) = \sum_{n\mathbf{k}\sigma} \frac{\psi_{n\mathbf{k}\sigma}(\mathbf{r})\psi^*_{n\mathbf{k}\sigma}(\mathbf{r}')}{E - E_{n\mathbf{k}\sigma} + \mathrm{i}0^+ \mathrm{sign}(E_{n\mathbf{k}\sigma} - \mu)} \tag{2.30}$$

where $\mu$ is the chemical potential. The Green's function satisfies an equation which can be written in terms of one-particle wave functions as

$$\left\{-\frac{\hbar^2}{2m}\nabla^2 + \hat{V}_{\mathrm{ps}}(\mathbf{r}) + e^2 \int \frac{\rho(\mathbf{r}')}{|\mathbf{r} - \mathbf{r}'|} \mathrm{d}^3 r'\right\} \psi_{\mathbf{k}}(\mathbf{r}) + \int \Sigma(\mathbf{r}, \mathbf{r}', E_{n\mathbf{k}}) \psi_{n\mathbf{k}}(\mathbf{r}') \mathrm{d}^3 r' = E_{n\mathbf{k}} \psi_{n\mathbf{k}}(\mathbf{r}). \tag{2.31}$$

Again, this equation is usually formulated for the valence electrons only. As in LDA, the electron–ion interaction is described by a pseudopotential $\hat{V}_{\mathrm{ps}}$. Norm-conserving *ab initio* pseudopotentials are mostly used in these calculations for semiconductors.

The central difficulty connected with Eq. (2.31) is to find an adequate approximation for the self-energy operator $\Sigma(\mathbf{r}, \mathbf{r}', E)$. Within the GW approximation, it is calculated from the Green's function $G$ and the dynamically screened Coulomb interaction $W$:

$$\Sigma(\mathbf{r}, \mathbf{r}', E) = \frac{\mathrm{i}}{2\pi} \int \mathrm{e}^{-\mathrm{i}\omega 0^+} G(\mathbf{r}, \mathbf{r}', E - \omega) W(\mathbf{r}, \mathbf{r}', \omega) \mathrm{d}\omega. \tag{2.32}$$

The screened interaction $W$ can be written by introducing the inverse dielectric function. Within Fourier representation, one obtains

$$W_{\mathbf{G},\mathbf{G}'}(\mathbf{q}, \omega) = \varepsilon^{-1}_{\mathbf{G},\mathbf{G}'}(\mathbf{q}, \omega) \frac{4\pi e^2}{V} \frac{1}{|\mathbf{q} + \mathbf{G}|} \frac{1}{|\mathbf{q} + \mathbf{G}'|}. \tag{2.33}$$

Within the GW approximation, the dielectric function is calculated as follows:

$$\begin{aligned} \varepsilon_{\mathbf{G},\mathbf{G}'}(\mathbf{q}, \omega) = {} & \delta_{\mathbf{G},\mathbf{G}'} + 2\frac{4\pi e^2}{V} \frac{1}{|\mathbf{q} + \mathbf{G}|} \frac{1}{|\mathbf{q} + \mathbf{G}'|} \\ & \times \sum_{\mathbf{k}} \sum_{\substack{m \in \mathrm{Val} \\ n \in \mathrm{Con}}} \left( \int \psi^*_{m\mathbf{k}}(\mathbf{r}) \mathrm{e}^{-\mathrm{i}(\mathbf{q}+\mathbf{G})\mathbf{r}} \psi_{n,\mathbf{k}+\mathbf{q}}(\mathbf{r}) \mathrm{d}^3 r \right) \\ & \times \left( \int \psi^*_{m\mathbf{k}}(\mathbf{r}) \mathrm{e}^{-\mathrm{i}(\mathbf{q}+\mathbf{G}')\mathbf{r}} \psi_{n,\mathbf{k}+\mathbf{q}}(\mathbf{r}) \mathrm{d}^3 r \right)^* \\ & \times \left[ \frac{1}{E_{n,\mathbf{k}+\mathbf{q}} - E_{m\mathbf{k}} - \omega + \mathrm{i}0^+} + \frac{1}{E_{n,\mathbf{k}+\mathbf{q}} - E_{m\mathbf{k}} + \omega + \mathrm{i}0^+} \right]. \end{aligned} \tag{2.34}$$

The orthogonality of wave functions of different spins has been taken into account. Equation (2.34) corresponds to the random-phase approximation (RPA). Before inserting $\varepsilon$ into

Eqs. (2.32) and (2.33), these matrices have to be inverted with respect to the reciprocal lattice vectors $\mathbf{G}$ and $\mathbf{G}'$ to obtain the inverse dielectric matrices. It should be noted that time-ordered quantities instead of causal ones are required by the GW approximation.

In general, Eq. (2.31) has to be solved self-consistently with respect to the charge density $\rho(\mathbf{r})$ and the quasiparticle energies $E_{n\mathbf{k}}$. Usually, the self-energy operator is calculated approximately by taking the wave functions $\psi_{n\mathbf{k}}(\mathbf{r})$ and the band structure energies $E_{n\mathbf{k}}$ from LDA. Thus, both the Green's function $G$ and the dielectric matrix $\varepsilon$ are calculated from the respective LDA results. In the solution of Eq. (2.31) it turned out, e.g., for Si (Hybertsen and Louie, 1986a) that the eigenfunctions $\psi_{n\mathbf{k}}(\mathbf{r})$ are very similar to the LDA eigenfunctions $\psi_{n\mathbf{k}}^{\mathrm{LDA}}(\mathbf{r})$. This behavior is assumed to apply for all sp-bonded semiconductors that have been studied so far (the index LDA at the wave functions will be omitted, therefore, from now on). For semiconductors involving d-orbitals particular care of this point needs to be taken (see Rohlfing et al., 1995c). Taking into account that the wave functions satisfy the Kohn–Sham equation (Eq. (2.29)), one obtains from Eqs. (2.29) and (2.31) as a great simplification the relation

$$E_{m\mathbf{k}} = E_{m\mathbf{k}}^{\mathrm{LDA}} + \langle \psi_{m\mathbf{k}} | [\Sigma(E_{m\mathbf{k}}) - V_{\mathrm{xc}}] | \psi_{m\mathbf{k}} \rangle. \tag{2.35}$$

According to this equation, the LDA energy eigenvalues $E_{m\mathbf{k}}^{\mathrm{LDA}}$ are corrected by quasiparticle corrections. The self-energy operator $\Sigma$ describes exchange–correlation effects in the quasiparticle energies more successfully than the local, energy-independent exchange–correlation potential $V_{\mathrm{xc}}$ of the LDA. The difference between the two is treated as a perturbation.

The central problem of this scheme is the calculation of the self-energy operator, which is performed in terms of the diagonal matrix elements in Eq. (2.35), $\langle \psi_{m\mathbf{k}} | \Sigma(E) | \psi_{m\mathbf{k}} \rangle$, using the LDA wave functions. As can be seen from Eq. (2.32), this requires an integral with respect to the energy $\omega$. The dielectric matrices $\varepsilon_{\mathbf{G},\mathbf{G}'}(\mathbf{q}, \omega)$ have to be calculated and inverted for many values of $\omega$. This very time-consuming calculation has explicitly been carried out for some examples (Godby et al., 1988). Most often, however, plasmon-pole models (Hybertsen and Louie, 1986b; von der Linden and Horsch, 1988; Hott, 1991; Rohlfing et al., 1993, 1995a, b, c, 1996b) are used to approximately describe the dependence of $\varepsilon^{-1}(\omega)$ on the frequency $\omega$. In this scheme, only the calculation of the *static* dielectric matrix $\varepsilon_{\mathbf{G},\mathbf{G}'}(\mathbf{q}, \omega = 0)$ is required. The quadrature with respect to $\omega$ is carried out analytically. One can use the method of the dielectric band structure (Car et al., 1981; Baroni and Resta, 1986; von der Linden and Horsch, 1988) to introduce a plasmon-pole model. Considering that the static dielectric matrix $\varepsilon_{\mathbf{G},\mathbf{G}'}(\mathbf{q}, 0)$ is Hermitian, its real eigenvalues $\lambda_{\mathbf{q}l}$ and orthonormal eigenvectors $\phi_{\mathbf{G}}^{l}$ can be used to perform the inversion of the matrix. The eigenvalues of the related full dielectric matrix are assumed to be dependent on the frequency $\lambda_{\mathbf{q}l}(\omega)$ while the eigenvectors are independent of the frequency. For the inverse dielectric matrix one thus obtains

$$\varepsilon_{\mathbf{G},\mathbf{G}'}^{-1}(\mathbf{q}, \omega) = \sum_{l} \phi_{\mathbf{G}}^{l}(\mathbf{q}) \frac{1}{\lambda_{\mathbf{q}l}(\omega)} \left(\phi_{\mathbf{G}'}^{l}(\mathbf{q})\right)^{*}. \tag{2.36}$$

Within the plasmon-pole model, $\lambda_{\mathbf{q}l}(\omega)$ is given as (von der Linden and Horsch, 1988; Hott, 1991)

$$\lambda_{\mathbf{q}l}(\omega) = \left[1 + \frac{z_{\mathbf{q}l}\omega_{\mathbf{q}l}}{2}\left(\frac{1}{\omega - (\omega_{\mathbf{q}l} - \mathrm{i}0^+)} - \frac{1}{\omega + (\omega_{\mathbf{q}l} - \mathrm{i}0^+)}\right)\right]^{-1}. \tag{2.37}$$

The parameters $z_{\mathbf{q}l}$ and $\omega_{\mathbf{q}l}$ are to be determined by adjusting Eqs. (2.36) and (2.37) to the static dielectric matrix and by taking Johnson's sum rule (1974) into account. As a result, the diagonal matrix elements of the self-energy operator (cf. Eq. (2.35)) become

$$\begin{aligned}\langle\psi_{m\mathbf{k}}|\Sigma(E)|\psi_{m\mathbf{k}}\rangle = {} & \frac{4\pi e^2}{V}\sum_{\mathbf{q},\mathbf{G},\mathbf{G}'}\sum_{n}\frac{1}{|\mathbf{q}+\mathbf{G}|}\frac{1}{|\mathbf{q}+\mathbf{G}'|} \\ & \times\left(\int \psi^*_{m\mathbf{k}}(\mathbf{r})\mathrm{e}^{-\mathrm{i}(\mathbf{q}+\mathbf{G})\mathbf{r}}\psi_{n,\mathbf{k}+\mathbf{q}}(\mathbf{r})\,\mathrm{d}^3r\right)\left(\int \psi^*_{m\mathbf{k}}(\mathbf{r})\mathrm{e}^{-\mathrm{i}(\mathbf{q}+\mathbf{G}')\mathbf{r}}\psi_{n,\mathbf{k}+\mathbf{q}}(\mathbf{r})\,\mathrm{d}^3r\right)^* \\ & \times\begin{cases}\displaystyle\sum_l \phi^l_{-\mathbf{G}}(-\mathbf{q})\left(\phi^l_{-\mathbf{G}'}(-\mathbf{q})\right)^*\left[-1 + \frac{z_{-\mathbf{q}l}\omega_{-\mathbf{q}l}}{2}\frac{1}{E - E^{\mathrm{LDA}}_{n,\mathbf{k}+\mathbf{q}} + \omega_{-\mathbf{q}l}}\right] \\ \qquad \text{for } n \in \mathrm{Val} \\ \displaystyle\sum_l \phi^l_{-\mathbf{G}}(-\mathbf{q})\left(\phi^l_{-\mathbf{G}'}(-\mathbf{q})\right)^*\left[\frac{z_{-\mathbf{q}l}\omega_{-\mathbf{q}l}}{2}\frac{1}{E - E^{\mathrm{LDA}}_{n,\mathbf{k}+\mathbf{q}} - \omega_{-\mathbf{q}l}}\right] \\ \qquad \text{for } n \in \mathrm{Con}.\end{cases}\end{aligned} \tag{2.38}$$

Such GW calculations have been performed, e.g., for bulk diamond, Si, Ge, GaAs and cubic SiC by Rohlfing et al. (1993). Figure 2.4 highlights the type of agreement one obtains nowadays between theoretical bulk band structure results and experimental ARPES and KRIPES data for Si, Ge and GaAs, when the GW approximation is employed together with RPA dielectric matrices. Examples of GW results for semiconductor surfaces will be

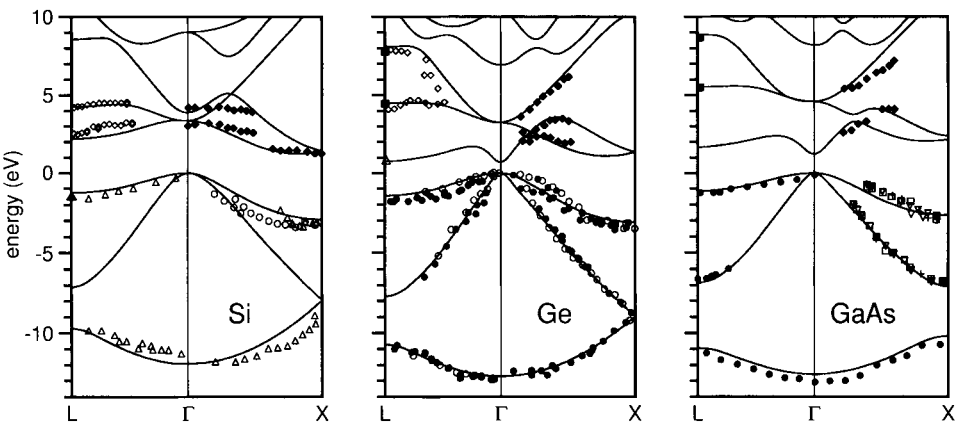


Fig. 2.4. GW quasiparticle bulk band structure of Si, Ge and GaAs (Rohlfing et al., 1993) in comparison with ARPES data (from Ortega and Himpsel, 1993; Chen et al., 1990).

discussed in the respective sections below revealing the type and the importance of the many body corrections on the surface electronic structure.

### 2.2.7. *Improved LDA calculations for wide-band-gap semiconductors*

In wide-band-gap semiconductors, like group III-nitrides or II-VI compounds, cationic d bands are of considerable importance. If the d electrons are treated as core electrons, calculated lattice constants badly underestimate the measured values by as much as 13% and 18%, e.g., for wurtzite structure ZnS and ZnO, respectively, while inclusion of the d electrons in the valence shell yields very accurate lattice constants (Schröer et al., 1993a, b; Vogel et al., 1995, 1996, 1997). Thus for a meaningful calculation of structural and electronic properties of surfaces of wide-band-gap semiconductors the d electrons have to be taken into account explicitly in the valence shell. Such calculations are very demanding because of the high spatial localization of the cationic d electrons. Even if the d electrons are properly taken into account, the results of LDA calculations employing standard nonlocal, norm-conserving pseudopotentials show distinct shortcomings. Not only is the band gap strongly underestimated. They also fail to accurately describe the strongly localized semicore d states and underestimate their binding energies. This is partially due to unphysical self-interactions contained in any standard LDA calculation and to the neglect of electronic relaxation. Especially in the case of group III-nitrides and II-VI semiconductors, the d electron bands have been found (Schröer et al., 1993a, b; Wei and Zunger, 1988; Martins et al., 1991; Xu and Ching, 1993; Yeh et al., 1994; Arai et al., 1995; Zhang et al., 1995b; Lambrecht and Segall, 1994; Fiorentini et al., 1993; Christensen and Gorczyka, 1994; Wright and Nelson, 1994; Surh et al., 1991; Rubio et al., 1993; Palummo et al., 1994; Vogel et al., 1995, 1996, 1997) to result some 3 eV too high in energy as compared to experiment (Ley et al., 1974; Lüth et al., 1976; Ranke, 1976; Zwicker and Jacobi, 1985; Weidmann et al., 1992). In consequence, their interactions with the anion p valence bands are artificially enlarged, falsifying the dispersions and band width of the latter and shifting them inappropriately close to the conduction bands. As a result, the LDA band gap underestimate for group III-nitrides and II-VI compounds is even significantly more pronounced than for elemental or sp-bonded III-V semiconductors. Using standard pseudopotentials for ZnO, e.g., one obtains $E_g^{th} = 0.23$ eV in LDA (Schröer et al., 1993a) as opposed to $E_g^{exp} = 3.4$ eV. It is, therefore, necessary to use an approach that is more accurate than the standard LDA for describing bulk and surface electronic properties of these compounds in order to arrive at quantitatively reliable results.

One could study such systems using quasiparticle band structure calculations (see Section 2.2.6) including semicore d electrons explicitly within the GW approximation. Such calculations have very recently been shown to be feasible for cubic bulk CdS (Rohlfing et al., 1995c) and ZnSe (Aryasetiawan and Gunnarson, 1996) but they are forbiddingly involved for compound semiconductor surfaces. Alternatively, one could try to extend the GW bulk calculations of Zakharov et al. (1994, 1995) to surfaces of the respective compounds. Those authors have reported plane wave GW calculations for a number of II-VI compounds simply treating the d electrons as core electrons and deliberately carrying out the GW calculations at the *experimental* lattice constants. This

way the calculations are not more involved than, e.g., those for sp-bonded III-V semiconductors yielding very good results for anion p valence bands and gap energies. But, of course, no assertion concerning the d band positions can be made on the basis of such calculations. In particular, the Hamiltonians used by Zakharov et al. (1994, 1995) are not perfectly suited for surface structure optimizations because of the omission of the d electrons.

A practicable and much more efficient alternative to largely overcome the above mentioned problems is to take dominant self-interaction and relaxation corrections into account. Self-interaction and relaxation effects contained in standard LDA calculations are largely responsible for the above mentioned deficiencies, as has been shown by Vogel et al. (1995, 1996, 1997). The authors construct *atomic* self-interaction and relaxation-corrected pseudopotentials (SIC- and SIRC-PPs) which are then transferred to bulk and surface calculations. A detailed derivation of SIC- and SIRC-pseudopotentials was given by Vogel et al. 1996. Therefore, here we only briefly summarize the basic ideas that have led to that approach. From the work of Perdew and Zunger (1981) on free atoms and ions it was well-known that self-interactions contained in standard LDA calculations, being most pronounced for tightly bound and highly localized states, give rise to significant misplacements of respective energy levels. In consequence, all-electron LDA calculations do not yield atomic binding energies correctly. Yet, it has become common use to construct standard pseudopotentials in such a way that they reproduce the results of respective all-electron calculations exactly. The construction procedure for pseudopotentials can, however, be refined and improved in order to describe wide-band-gap semiconductors more appropriately. Self-interaction–corrections including orbital relaxation can easily be incorporated (Perdew and Zunger, 1981) in electronic structure calculations for atoms within LDA or its spin-polarized variant, the LSD approximation. But even SIC-LSD calculations do not yield exact binding energies for all of the atomic states because they do not take *electronic* relaxation fully into account. Very accurate atomic binding energies can be obtained, however, within the so-called self-consistent field (SCF) approach (Hedin and Johansson, 1969). Binding energies are derived from well-defined total energy *difference* calculations ($\Delta$SCF) for ground states of neutral and ionized atoms avoiding problems originating from the neglect of electronic relaxation, as contained in standard LDA calculations, to a large extent. For solids, however, such $\Delta$SCF calculations are not practicable, to date.

If the SIC-formalism is extended to solids, it gives rise to orbital-dependent effective potentials breaking the translational invariance of the original Bravais lattice. Extended Bloch-orbitals lead to nearly homogeneous one-particle densities and to vanishing SIC contributions. Localized wave functions, on the contrary, can yield strong SIC contributions within full SIC-LSD calculations which are extremely demanding, however. To avoid the practical problems involved in such full SIC-LSD calculations for solids, the method has been applied previously in simplified forms (see, e.g., Majewski and Vogl, 1992a, b, and the references therein). More recently, full SIC-LSD calculations have been reported, e.g., for bulk transition metals, high-$T_c$ superconductors, Ce compounds, and transition-metal oxides by Svane and Gunnarson (1990), Svane (1992), Szotek et al. (1993, 1994), Arai and Fujiwara (1995), respectively. The work of these authors has clearly shown that self-interaction–corrections shift occupied d states significantly down in energy also in solids. Full SIC calculations, however, for group III-nitrides and II-VI compounds are

extremely involved for the bulk already and they are entirely out of reach for the respective surfaces, to date. It is possible, however, to correct for self-interactions and to take electronic relaxation into account within an alternative approach that is less involved. The respective, very efficient theoretical framework accounts for both effects in an approximate way and, nevertheless, accurately describes electronic and structural properties of wide-band-gap semiconductor compounds (Vogel et al., 1995, 1996, 1997). The basic idea of that approach is to construct *new pseudopotentials* that take self-interaction–corrections and electronic relaxation in the constituent *atoms* into account from the very beginning. Self-interactions in the atoms are accounted for in exactly the same way as described by Perdew and Zunger (1981) in their original SIC publication. In addition, electronic relaxation in the atoms is taken into consideration by referring to atomic $\Delta$SCF results. Once the pseudopotentials are constructed, they can be transferred to solids in an appropriate and well-defined way and can be employed in standard LDA codes. This approach is capable to overcome the above mentioned LDA problems and is, nevertheless, computationally not more involved than any current 'state of the art' LDA calculation. The electronic and structural properties calculated with these pseudopotentials are in gratifying agreement with a host of experimental data on group III-nitrides and II-VI compounds (Vogel et al., 1995, 1996, 1997). The SIC-PPs yield lattice constants that are slightly increased with respect to the usual LDA results. They are found to be in excellent agreement with a host of experimental data. For AlN, GaN, ZnS, CdS and CdSe they are even closer to experiment than standard LDA results. Also bulk moduli, as calculated using SIC-PPs are considerably closer to experiment than those calculated using standard pseudopotentials.

To give one example for the improvements brought about by the SIRC pseudopotentials in calculated bulk band structures, we show in Fig. 2.5 the band structure of wurtzite CdS as calculated using standard (left panel) and SIRC pseudopotentials (right panel). The left panel clearly reveals the above-mentioned shortcomings. The gap is underestimated by roughly 50%, the experimental p-band width is slightly underestimated and the calculated d bands result roughly 3 eV higher in energy than observed in experiment. The right panel shows that the d-bands are shifted down in energy considerably by the SIRC-PP and concomitantly the gap is opened up drastically. Actually, the gap energy and the d-band position are grossly improved with respect to the standard LDA results and they are now in excellent agreement with experiment. It should be noted at this point, that not only the downward shift of the d bands and the related reduction in p–d interactions open up the gap. In addition, the change in atomic s- and p-term values, resulting from the atomic SIRC calculation and entering the pseudopotentials, also contribute to the effect. In addition, we note in Fig. 2.5 that the dispersion and width of the S 3p valence bands become changed by the SIRC pseudopotential. They compare favorably with the high-symmetry-point ARPES data measured by Stoffel (1983), shown for comparison as well.

To further highlight the improvements achieved by our SIRC pseudopotentials in some more detail, we show in Fig. 2.6 a 'blow up' of a section of the valence bands of wurtzite CdS along the $\Gamma$–M line (see Fig. 2.5) and compare our standard pseudopotential (left panel) and SIRC-PP (right panel) results (Vogel et al., 1996) with more recent high-resolution ARPES data of Magnusson and Flodström (1988b). While the standard LDA results in the left panel do not coincide well with the data, the SIRC-PP results are in gratifying accord with the measured S 3p valence bands. The symmetry of the measured bands

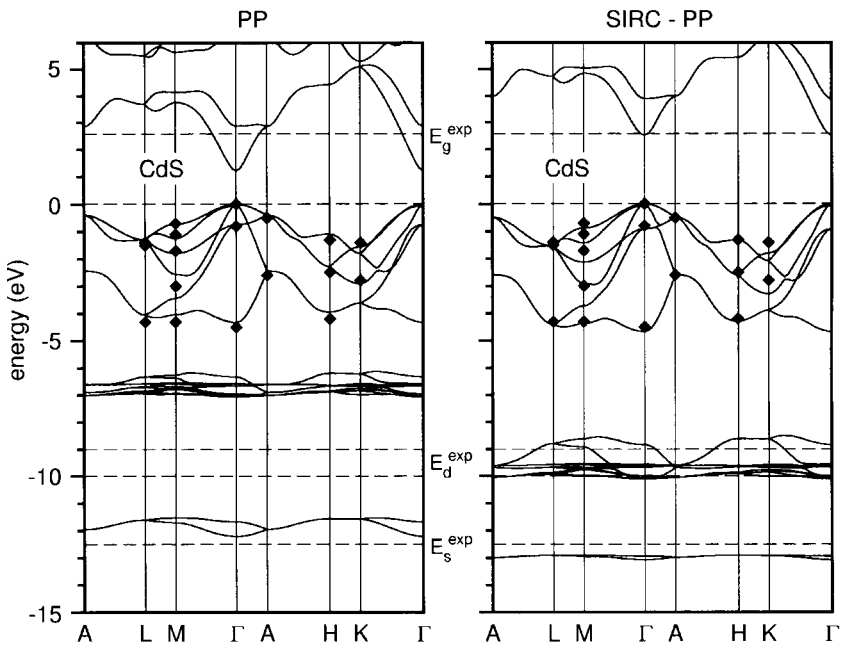


Fig. 2.5. Bulk band structure of wurtzite CdS as calculated within standard LDA (left panel) or using SIRC pseudopotentials (right panel) (Vogel et al., 1995) in comparison with ARPES data (Stoffel, 1983). The horizontal lines indicate the measured energy gap, the d-band width and the s-band position, respectively.

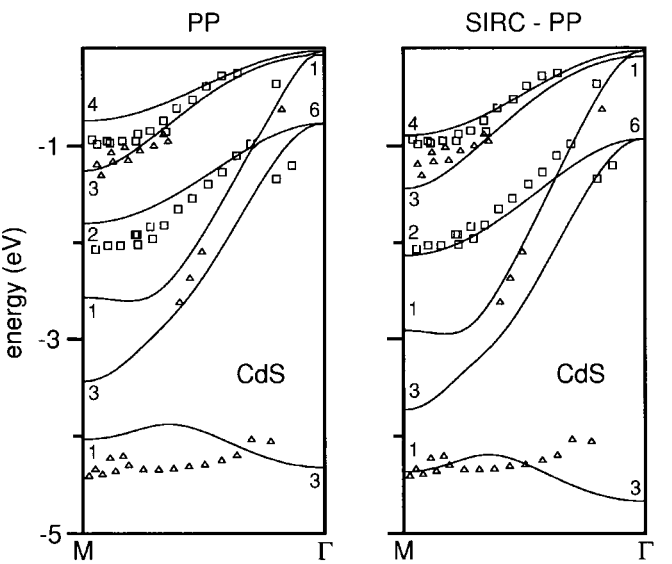


Fig. 2.6. Comparison of calculated and measured valence bands of wurtzite CdS. Standard LDA (left) and SIRC-PP (right panel) results (Vogel et al., 1995) are compared with polarisation- and angle-resolved PES data (Magnusson and Flodström, 1988a).

(△ even and □ odd with respect to the mirror plane) is in accord with the calculated bands (1,3 even and 2,4 odd), as well.

Similar improvements for a large number of zincblende and wurtzite group III-nitrides and II-VI compounds have been reported (Vogel et al., 1995, 1996, 1997). The SIC- and SIRC-PP approach thus overcomes the above-mentioned problems of standard LDA calculations for wide-band-gap compounds to a large extent. Since it is not more involved than any standard LDA calculation it can easily be applied to surfaces of these compounds employing the SCM. Respective applications will be discussed below.

## 2.3. Basic properties of ideal surfaces

Electronic properties of semiconductor surfaces sensitively depend on the atomic geometry at the surface and on the ionicity of the underlying bulk crystal as well as of the considered particular surface. In this section, we address the geometry- and ionicity-dependence of surface electronic features, in general. For this discussion, we use ideal surface geometries. *Geometrically ideal* surfaces are defined by truncating a perfectly periodic bulk solid at a given surface-parallel plane. The bulk atomic positions are kept fixed up to the surface so that the atomic structure of such ideal systems is exactly known. Most often they are not realized in nature but a thorough knowledge of their basic properties is a very helpful reference for a detailed understanding of the structural and electronic properties of related *real*, i.e., relaxed or reconstructed surfaces.

### *2.3.1. Geometry-dependence of surface states*

In Fig. 2.7 the surface band structures of the ideal Si(111), Si(110) and Si(001) surfaces resulting from empirical tight-binding calculations (Ivanov et al., 1980) are shown in direct comparison (upper panels) together with the corresponding surface unit cells (lower panels). Representative $sp^3$ hybrid lobes, which would exist on the corresponding planes in the bulk lattice, are shown as well. Breaking these bonds to create the ideal surfaces induces characteristic surface states. At the (111) surface, only *one* bond per surface unit cell needs to be broken. The remaining dangling hybrid energetically resides between the bonding (valence) and the antibonding (conduction) bands giving rise to *one* dangling bond band (D) within the gap energy region. Its dispersion is fairly week since the surface dangling bonds are separated by a bulk second-nearest neighbor distance and they interact only via $\pi$ interactions. At the (110) surface, *two* $sp^3$ bonds per surface unit cell need to be broken giving rise to two dangling hybrids which yield *two* dangling bond bands ($D_1$ and $D_2$) within the gap energy region. Their dispersion is small as well since neighboring dangling hybrids point in opposite directions. At the (001) surface, again *two* $sp^3$ bonds per unit cell need to be broken, but now they are localized at the same surface site. In consequence, the former hybrid bonds dehybridize into bridge-bond orbitals which are parallel to the surface and dangling-bond orbitals which are perpendicular to the surface plane (Appelbaum et al., 1975). As a result, the orbital character of the resulting surface states strongly differs from that of the original $sp^3$ bonds. A dangling bond (D) perpendicular to the surface with s, $p_z$ wave function character and a bridge bond (Br) lying in the surface plane

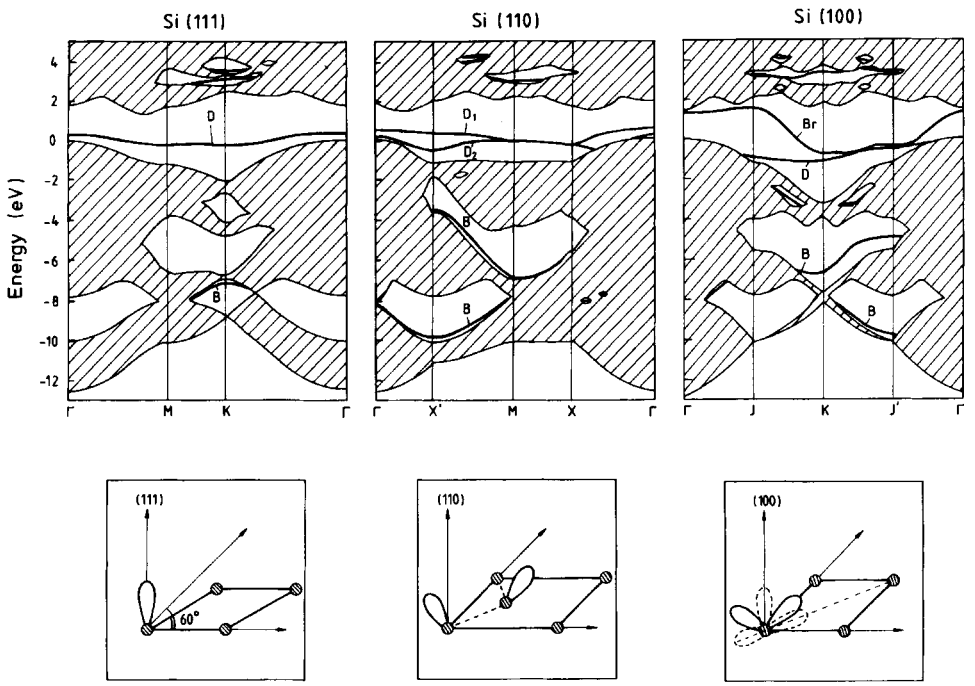


Fig. 2.7. Surface band structures of the geometrically ideal Si(111), Si(110) and Si(100) surfaces (Ivanov et al., 1980). Respective sections of the surface unit cells are shown in the lower panels.

with $p_x$, $p_y$ character result. They are shown schematically by dashed lines in the lower right panel. The D band shows only a week dispersion since the dangling bonds interact only via a second-nearest neighbor $\pi$ interaction, while the Br band shows considerable dispersion along particular $\mathbf{k}_\parallel$ directions due to a much stronger interaction between the bridge bonds. The outermost surface atoms form chains along the [110] direction and the bridge-bond orbitals are directed along the perpendicular [$\bar{1}$10] direction so that a strong $\sigma$ interaction occurs along that direction. Correspondingly, the dispersion of the Br band is strong along the Γ–J′ and J–K directions. The interaction of the bridge bonds along the [110] direction is of $\pi$ type. In consequence, the Br band dispersion is week along the Γ–J and K–J′ directions. Figure 2.7 clearly reveals that *semiconductor surface electronic states are very sensitive to the surface structure*. This fact, highlighted here for the three ideal low-index surfaces of Si, obtains equally well for all real relaxed or reconstructed semiconductor surfaces.

All three ideal Si surfaces are metallic because of the occurrence of unsaturated dangling bonds giving rise to partially filled bands. These unsaturated bonds can lower their energy by formation of new surface bonds between neighboring surface-layer atoms. This leads to a reconstruction of the surfaces, as will be discussed below.

In all three cases presented in the above comparison, back-bond states with predominant Si 3s character are found, in addition. To highlight the properties of this type of surface

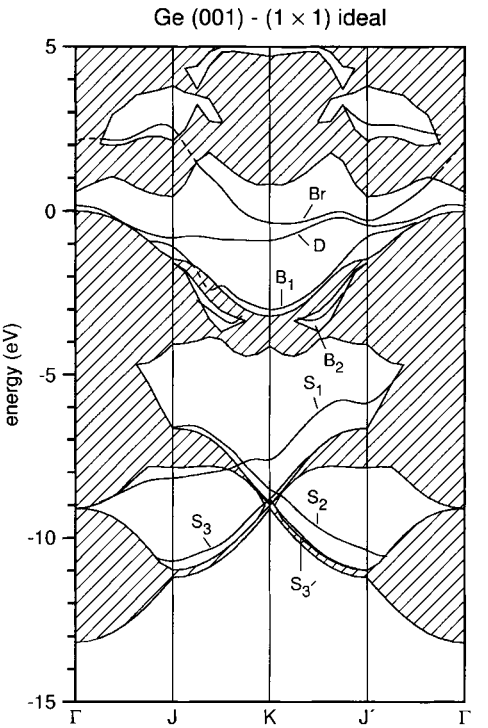


Fig. 2.8. Surface band structure of the ideal Ge(001)-(1 × 1) surface showing bridge bond (Br), dangling bond (D), back bond (B) and predominantly s-like (S) surface states (Krüger and Pollmann, 1991b).

states in some more detail and to give a comprehensive representation of the general type of information one obtains from current days 'state of the art' surface electronic structure calculations, we show in Fig. 2.8 the surface band structure of the ideal Ge(001)-(1 × 1) surface along high-symmetry lines of the (1 × 1) SBZ (Krüger and Pollmann, 1991b).

The shaded area represents the PBS. We have labeled the various states according to their physical origin and character. In the fundamental gap, there are the dangling-bond and the bridge-bond band. These bands are not fully occupied and they overlap in energy so that the ideal surface turns out to be metallic. The bands $B_1$ and $B_2$ stem from back-bond states. There are bands of s-like states below $-5$ eV, in addition. To highlight the spatial extent of the various states, we show in Fig. 2.9 LDOSs at the K-point of the SBZ for the first three layers and on a bulk layer, for comparison.

The bridge-bond and the dangling-bond states are localized mainly at the topmost layer, while the back-bond state $B_1$ is stronger at the second layer. The s-like states are split off from the bulk states near $-9$ eV. At the first layer, there occurs the largest perturbation of the charge density with respect to the unperturbed bulk situation. This leads to a large upward shift of $S_1$ with respect to the bulk bands. Electrons in the $S_1$ state are mainly localized on the first layer atoms, as can be seen in Fig. 2.10 where energy-resolved charge densities of the localized surface states at the K-point are plotted. Due to the electronic

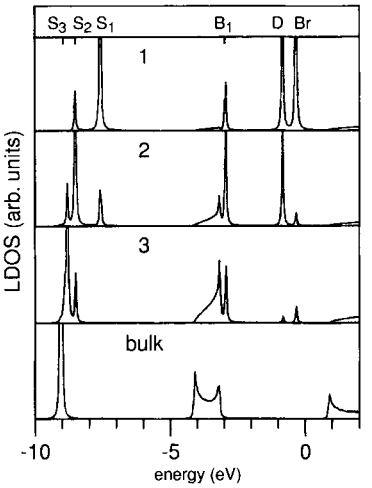


Fig. 2.9. Layer densities of states at the K-point of the SBZ of Ge(001)-(1 × 1). The states are labelled in accord with Fig. 2.8 (Krüger and Pollmann, 1991b).

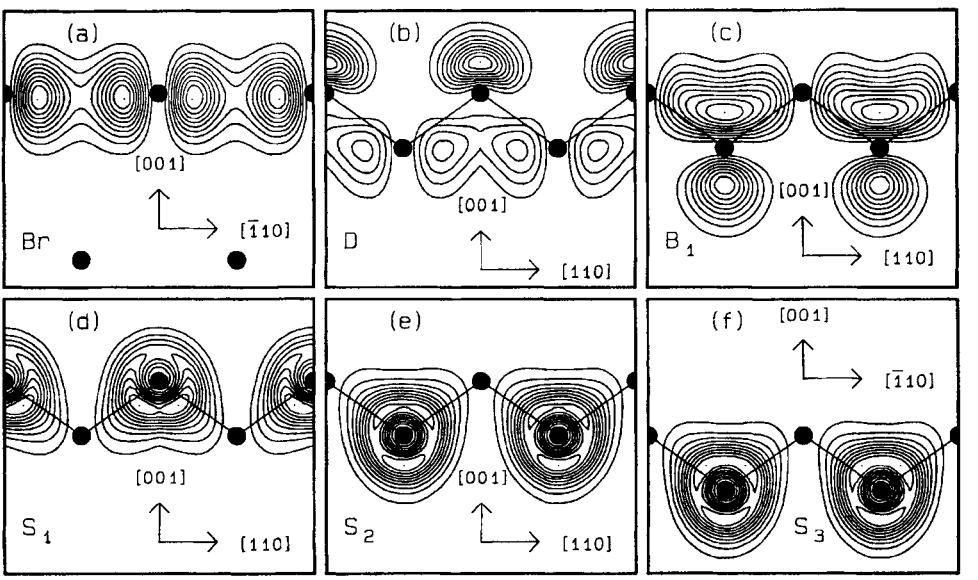


Fig. 2.10. Charge densities of salient surface states at the K-point of the SBZ of Ge(001)-(1 × 1) (Krüger and Pollmann, 1991b). For reference, see Figs. 2.8 and 2.9.

relaxation there are smaller perturbations of the potential at the second and third layer as well inducing the states $S_2$ and $S_3$. The charge densities of $S_1$–$S_3$ are not fully spherically symmetric but have bulges of charge maxima due to the interaction with nearest neighbors.

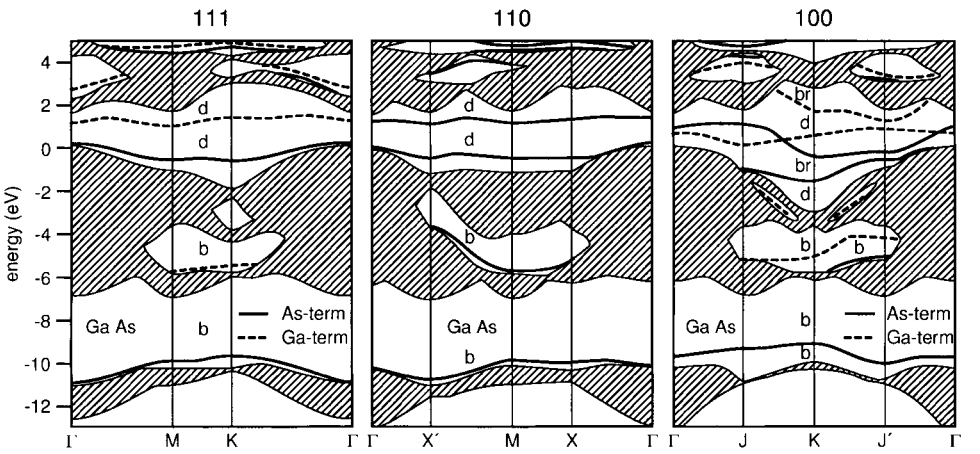


Fig. 2.11. Surface band structures of the ideal GaAs(111/$\bar{1}\,\bar{1}\,\bar{1}$), GaAs(110) and GaAs(100/$\bar{1}$00) surfaces (Ivanov et al., 1980).

The charge density of the Br state is $p_x$,$p_y$-like and forms bridges between second-nearest neighbor surface atoms. The dangling bond (D) has its charge density maximum in the vacuum region just above the surface layer. These selfconsistent results confirm the intuitive interpretation given above for the ideal Si surfaces. On the basis of ETBM calculations one does not obtain charge densities.

Simple correlations between broken $sp^3$ hybrid bonds and gap surface state bands, as discussed above for low-index faces of Si and Ge, are observed as well for most low-index semiconductor surfaces. To give one example, we present in Fig. 2.11 the surface band structures of the geometrically ideal low-index faces of GaAs as resulting from empirical tight-binding STA calculations (Ivanov et al., 1980). In a heteropolar crystal, there are two different (111) surfaces, namely the cation-terminated (often referred to as (111)) and the anion-terminated (often referred to as ($\bar{1}\bar{1}\bar{1}$)) surface. They are both polar surfaces, since they are either anion- or cation-terminated. At the (111) surface, only one bond per surface unit cell needs to be broken. The remaining dangling hybrids energetically reside between the bonding and the antibonding projected bulk bands giving rise to *one* dangling bond band (d) within the gap energy region in each case. The anion-derived band (d) resides lower in energy (close to the upper edge of the valence band projection) than the cation-derived band (d) which is close to the lower edge of the conduction band projection since the anion potential is stronger than that of the cation. They are separated in energy by roughly 1 eV due to the hetoropolarity of GaAs. The dispersion of these dangling bond bands is fairly week since the surface dangling bonds are again separated by a bulk second-nearest neighbor distance and they interact only via $\pi$ interactions. At the (110) surface, two $sp^3$ bonds per surface unit cell need to be broken giving rise to two dangling hybrids which yield *two* dangling bond bands (d) within the gap energy region. Their dispersion is small as well, since neighboring dangling hybrids point again in opposite directions. The upper one is cation-derived and the lower one is anion-derived, so that their energy location is similar to those of the two respective bands at the polar (111) and ($\bar{1}\bar{1}\bar{1}$) surfaces. At the

(001) surfaces, which are polar surfaces too, again two $sp^3$ bonds per unit cell need to be broken. They are localized at the same surface site, however. In consequence, they strongly interact and dehybridize. As a result, the orbital character of the resulting surface states strongly differs from that of the original $sp^3$ bonds. As at the Si(001) surface, a dangling bond (d) perpendicular to the surface with s, $p_z$ wave function character and a bridge bond (br) lying in the surface plane with $p_x$, $p_y$ character result. The respective bands for the anion-terminated surface are again lower in energy than those for the cation-terminated surface for the reasons given above.

### *2.3.2. Ionicity-dependence of surface states*

The surface-band structures shown in Figs. 2.7, 2.8 and 2.11 allow to address the ionicity dependence of salient surface features. To broaden the database for this discussion, we show in Fig. 2.12 the surface band structure of a prototypical wide-band-gap semiconductor CdS obtained from a self-consistent SCM calculation (Vogel, 1998). It is obvious from the figure that the ideal CdS($10\bar{1}0$) surface exhibits surface state bands that are qualitatively similar to those of the GaAs(110) surface. Quantitative differences, however, do occur due to the larger ionicity of CdS, as compared to GaAs. As to the influence of the ionicity, in general, first we note the differences in *bulk* band projections. With increasing ionicity from Si over GaAs to CdS the optical gap becomes increasingly larger. In addition, the pocket in the PBS of Si in the energy region from $-8$ eV to $-10$ eV opens up in GaAs forming the heteropolar (or ionic) gap. In CdS this ionic gap between S 3p and S 3s states is huge. In consequence, only in the energy range from 0 eV to about $-5$ eV sp-type valence bands occur. In addition, there are the projected Cd 4d semicore bands, of course, at the

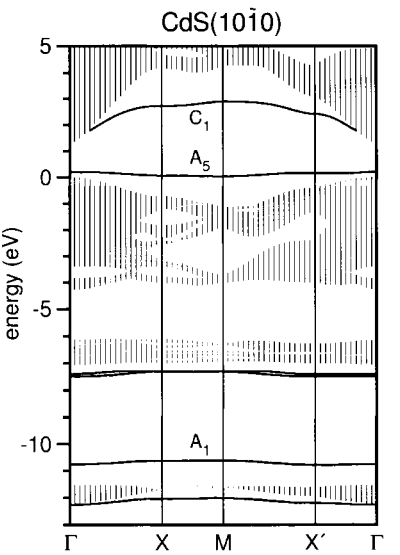


Fig. 2.12. Self-consistent surface band structure of the ideal CdS($10\bar{1}0$) surface (Vogel, 1998).

CdS(10$\bar{1}$0) surface. For the sake of this comparison, let us concentrate on nonpolar (110) or (10$\bar{1}$0) surfaces. Their surface band structures show salient dangling bond bands. For Si(110) they are partially degenerate (see Fig. 2.7) due to a particular glide plane symmetry (Jones, 1968) and show only a very small splitting due to the weak $\pi$ interaction of the dangling bonds. At GaAs(110), the respective bands are separated already by roughly 1 eV due to the different strengths of the Ga and As potentials, respectively. The movement of the anion-derived dangling bond band towards the projected valence bands and that of the cation-derived dangling bond band towards the projected conduction bands, as compared to Si(110), is due to the ionicity of GaAs. This effect is even more pronounced in the heteropolar ionic semiconductor CdS. Here the cation-derived dangling bond has become a Cd 4s resonance within the lower edge of the conduction band projection and the anion-derived dangling bond band has moved close to the projected upper edge of the valence bands. The energy separation between $A_5$ and $C_1$ at the CdS(10$\bar{1}$0) surface is much larger than for the respective dangling bond bands at the GaAs(110) surface. This is a direct consequence of the larger ionicity of CdS. In summary, we note that *the surface electronic structure is very sensitive to the ionicity of the underlying bulk solid.* By the same token, we will see below that changes in the ionicity of particular bonds at and near a surface occurring due to relaxation or reconstruction, have a marked influence on the actual surface electronic structure. Ionicity-induced trends, as discussed above for ideal surfaces, also obtain for real SiC, III-V, group III-nitride and II-VI surfaces, as will be discussed in detail below.

## 2.4. Surfaces of elemental semiconductors

Real semiconductor surfaces relax or reconstruct to reduce the number of unsaturated surface bonds and to minimize their total energy. In this section, we first address the Si(001) surface. Next we discuss structural and electronic properties of diamond, Ge and $\alpha$-Sn (001) surfaces in comparison with those of Si(001). We then turn to the Si(111), Ge(111) and C(111) surfaces. Finally, we briefly address the less-detailed studied Si(110) surface.

### *2.4.1. The Si(001) surface*

The Si(001) surface is one of the backbones of semiconductor technology. In consequence, it certainly belongs to the most important and most thoroughly studied semiconductor surfaces. There is a huge literature on both experimental and theoretical studies of this surface (see, e.g., the reviews by Haneman, 1987; Hansson and Uhrberg, 1988; LaFemina, 1992; Mönch, 1995; Duke, 1996). As pointed out in Subsection 2.3.1, the geometrically ideal Si(001) surface is not stable. It shows a dangling-bond and a bridge-bond state at each surface layer atom. The respective surface bands overlap in energy (see upper left panel of Fig. 2.7) giving rise to a metallic surface. Unsaturated surface bonds are energetically unfavorable and very reactive. Their number can easily be reduced by forming surface dimers (Chadi, 1979b; Hanemann, 1987). Neighboring surface-layer atoms move towards one another until a new chemical bond is formed. These dimers form rows at the surface (Hamers et al., 1986a, b). In the most simple case this gives rise to a (2 × 1) reconstruction

(Uhrberg et al., 1981; Johansson et al., 1990; Johansson and Reihl, 1992). The energy gain due to dimer formation relative to the geometrically ideal surface configuration is given by about 2 eV per dimer (see, e.g., Chadi, 1979b; Krüger and Pollmann, 1995; Ramstad et al., 1995).

In principle, the dimers can be oriented parallel to the surface plane yielding the so-called symmetric dimer model (SDM). The dangling bonds of the SDM form symmetric and antisymmetric linear combinations, referred to as $\pi$ and $\pi^*$ states, respectively, due to the mirror symmetry of the dimers. The dimers may, as well, be tilted with respect to the surface plane yielding the so-called asymmetric dimer model (ADM). The upper dimer atom in the ADM is usually referred to as 'up-atom' and the lower as 'down-atom'. There has been a long-standing discussion whether the Si(001) surface reconstructs in the SDM or ADM. The original motivation for the introduction of asymmetric dimers by Chadi (1979b) was the finding that empirical tight-binding band structure calculations which assumed a symmetric dimer reconstruction of Si(001)-(2 × 1) invariably resulted in a metallic surface in disagreement with the results of angle-resolved photoelectron spectroscopy (ARPES) data (Himpsel and Eastman, 1979). The picture of asymmetric dimers was supported, e.g., by core-level spectroscopy (CLS) (Himpsel et al., 1980b), surface-photovoltage (Mönch et al., 1981), LEED (Holland et al., 1984) and ion-scattering (Tromp et al., 1985) experiments. The CLS data showed two different Si 2p lines distinctly shifted with respect to the bulk line indicating that there are two atom positions at the surface with different electronic configurations. The charge-density relaxations within the dimers occurring in consequence of the tilting explain this finding. The results of the LEED and the ion scattering experiments could be explained much better on the basis of the ADM than the SDM. In scanning tunneling microscopy studies carried out later (Hamers et al., 1986b), the dimers appeared to be symmetric, however. These results questioned the appropriateness of the ADM, since they seemed to indicate a symmetric dimer reconstruction on a first glance. This experimental finding, however, is not necessarily in contradiction to asymmetric dimers at the surface. More recent studies of the dynamics of the surface have shown that the dimers may flip between their two opposite tilting directions (Dabrowski and Scheffler, 1992; Shkrebtii et al., 1995). At room temperature, this dimer-flipping happens on a time scale of $10^{-10}$–$10^{-8}$ seconds. Measurements that do not have the respective time-resolution are bound to find a symmetric appearance of the dimers which corresponds to an average of the two extreme tilt-directions. This rationalizes the fact that STM pictures taken at room temperature appear to evidence symmetric rather than asymmetric dimers. In addition, effects resulting from interactions between the scanning tip and the sample cannot be ruled out as well (Cho and Joannopoulos, 1993).

A large number of more recent experiments, partially carried out at very low temperatures (Jedrecy et al., 1990; Johansson and Reihl, 1992; Wolkow, 1992; Landemark et al., 1992; Fontes et al., 1993; Jayaram et al., 1993; Tochihara et al., 1994; Badt et al., 1994; Munz et al., 1995; Bullock et al., 1995), convincingly show that the dimers at the Si(001) surface are buckled. This is in agreement with the results of *ab initio* total energy LDA calculations (Yin and Cohen, 1981; Roberts and Needs, 1990; Kobayashi et al., 1992; Dabrowski and Scheffler, 1992; Ramstad et al., 1995; Krüger and Pollmann, 1988, 1995). Plane wave LDA calculations with relatively low cut-off energies yield significantly smaller tilt-angles. Only cut-off energies of 20 Ryd or more yield the tilt-angle

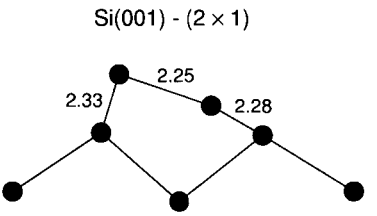


Fig. 2.13. Optimal surface structure of the Si(001)-(2 × 1) surface (Krüger and Pollmann, 1995). The bond lengths are given in Å.

convergently, as has been shown by Ramstad et al. (1995). The optimized structure of the Si(001)-(2 × 1) surface, as resulting from recent *ab initio* total energy calculations (Krüger and Pollmann, 1995; Ramstad et al., 1995) is shown in Fig. 2.13. The asymmetry of the dimers has two important consequences: first, the buckling opens up a Jahn-Teller like gap between the surface-induced dangling bond states yielding a semiconducting Si(001)-(2 × 1) surface for the ADM in agreement with experiment (Himpsel and Eastman, 1979; Landemark et al., 1992; Munz et al., 1995). Second, within the SDM, reconstructions more complex than the (2 × 1) cannot be rationalized. LEED experiments at temperatures below 200 K, however, clearly show spots that are related to c(4 × 2) and p(2 × 2) reconstructions (Poppendieck et al., 1978; Tabata et al., 1987). These higher reconstructions originate from different configurations of left- and right-tilted dimers. They give rise to small additional total energy gains of 0.05 eV per dimer from interactions between neighboring dimers in a dimer row and 0.003 eV per dimer from interactions of nearest neighbor dimers in two neighboring dimer rows (Ramstad et al., 1995). It turns out that the total energy is minimal if the dimer-tilt direction alternates along and perpendicular to the dimer rows. The resulting c(4 × 2) reconstruction is indeed observed at low temperatures (Popendieck et al., 1978; Tabata et al., 1987; Badt et al., 1994). The related energy gain is so small, however, that the ideal c(4 × 2) long range order is lost at higher temperatures. Tabata et al. (1987) have shown that the respective (1/4,1/2) LEED spots diminish above 150 K and vanish altogether at room temperature.

The two-dimensional dimer lattice of the surface with either right- or left-tilted dimers can easily be mapped onto a two-dimensional Ising model. From a renormalization group analysis of this model, a transition temperature $T_c = 250$ K for the structural phase transition from (2 × 1) to c(4 × 2) was obtained (Ihm et al., 1983). As to the long-range order, at room temperature only a nominal (2 × 1)-reconstruction persists (Uhrberg et al., 1981; Johansson et al., 1990; Johansson and Reihl, 1992). Yet, there remains a short-range correlation between the tilt-direction of the dimers in the dimer rows (Shkrebtii et al., 1995) favoring alternate tilting of neighboring dimers. This correlation is lost only at very high temperatures. As to the local structure of a single dimer, it can be expected that the asymmetry remains due to the asymmetry-induced energy gain of about 0.15 eV

The surface band structure of the Si(001)-(2 × 1) surface, as resulting from STA calculations (Krüger and Pollmann, 1993), is shown in Fig. 2.14. The tilting of the dimers leads to very significant consequences in the electronic structure of the surface. It gives rise to two distinctly different dangling bond states $D_{up}$ and $D_{down}$ (see Fig. 2.14). The buckling

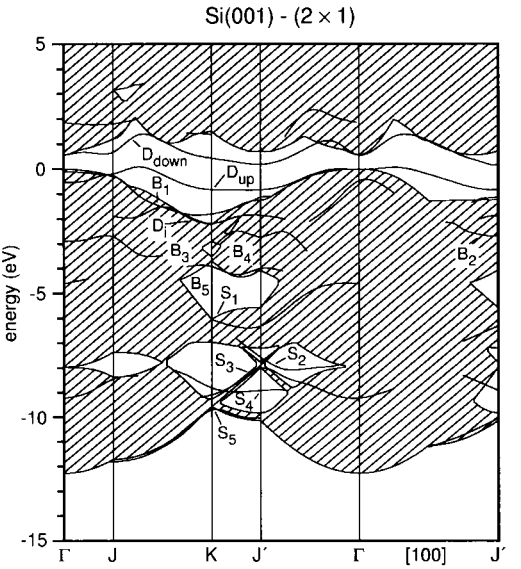


Fig. 2.14. LDA surface band structure of the Si(001)-(2 × 1) surface (Krüger and Pollmann, 1993).

lowers the energy of the $D_{up}$ state and raises the energy of the $D_{down}$ state. Since $D_{up}$ is occupied and $D_{down}$ is empty, this energetic lowering of $D_{up}$ leads to a lowering of the total energy. In consequence, the ADM is lower in energy than the SDM (see, e.g., Krüger and Pollmann, 1995). The respective energy gain is 0.14 eV per dimer. The resulting dimer bond length of 2.25 Å is somewhat smaller than the Si bulk bond length of 2.35 Å. Relative to their second-nearest-neighbor distance of 3.8 Å at the ideal surface, the atoms forming a dimer thus move much closer together at the reconstructed surface.

The surface band structure of the ADM exhibits a very rich spectrum of surface state bands (see Fig. 2.14) originating from dangling bonds, dimer bonds and backbonds. The states $S_1$–$S_5$ have backbond character and their wave functions are mostly s-like. The bands $B_1$–$B_5$ have backbond character as well, but the related states are strongly p-like with small s and d admixtures. Respective charge densities of salient surface states as resulting from STA calculations (Krüger and Pollmann, 1988) are shown in Fig. 2.15. Due to the reconstruction-induced symmetry-breaking of the ideal surface, the former dangling bond (D) and bridge-bond (Br) states (see upper right panel of Fig. 2.7) per (2 × 1) unit cell strongly interact at the reconstructed surface giving rise to bonding ($D_i$) and antibonding ($D_i^*$) dimer-bond bands and to the $D_{up}$ and the $D_{down}$ dangling bond bands, respectively, originating from the dangling bond states at the dimer up and down atoms. The strong localization of the charge density in the dangling bonds at the up and down atoms (see Fig. 2.15) confirms their identification as $D_{up}$ and $D_{down}$ states, respectively. The dimer bond state $D_i$, on the contrary, is strongly resonant in energy with bulk states (see Fig. 2.14) and is more extended in space accordingly (see Fig. 2.15). Nevertheless, the formation of a new and strong chemical bond between neighboring surface layer atoms in the dimer is clearly to be seen.

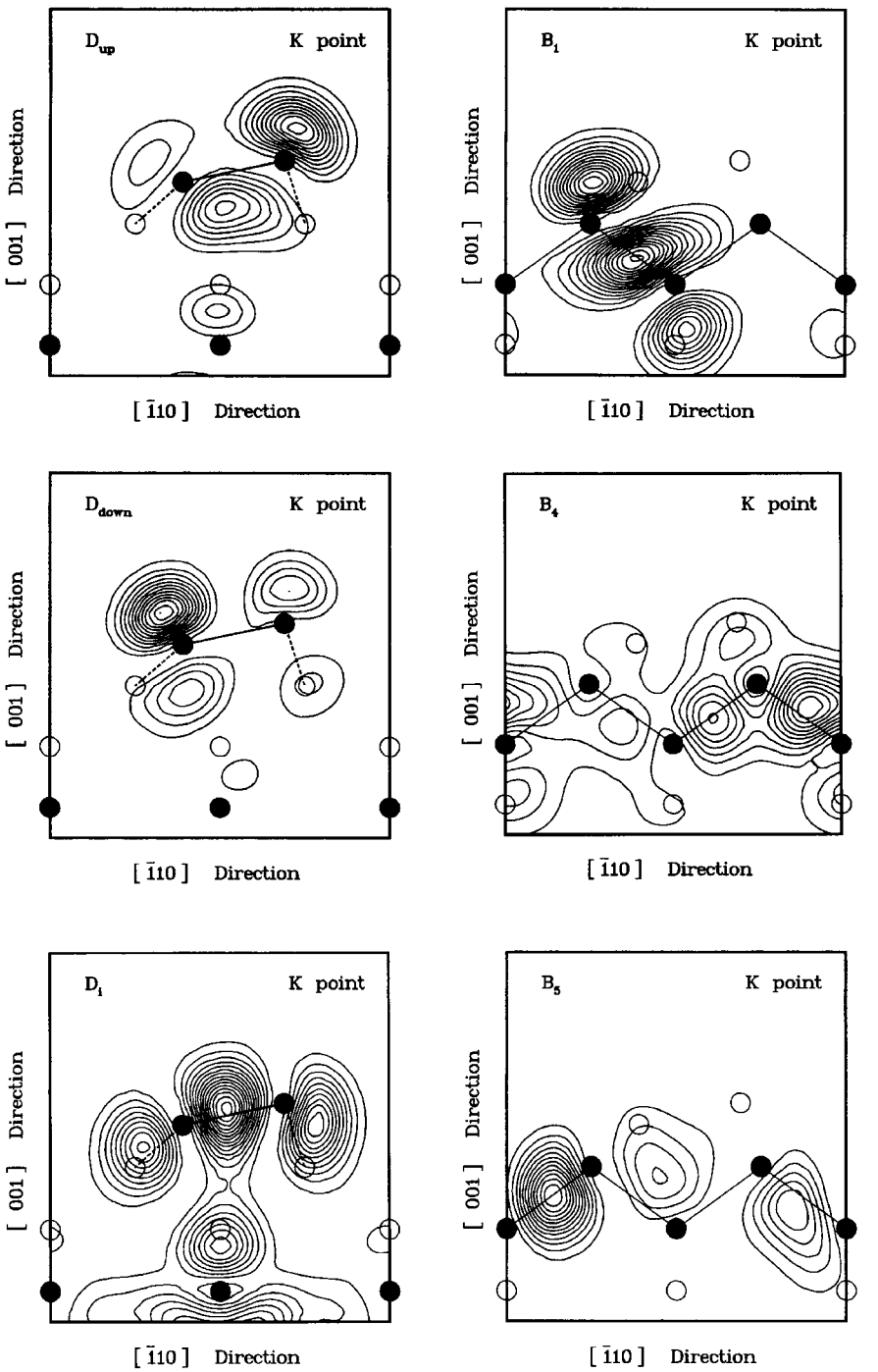


Fig. 2.15. Charge densities of salient surface states at the Si(001)-(2 × 1) surface (Krüger and Pollmann, 1988).

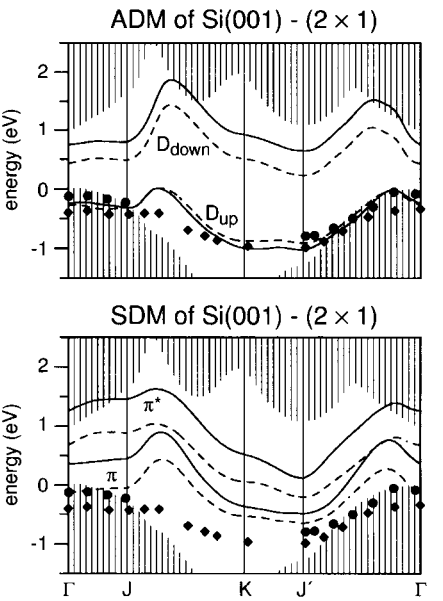


Fig. 2.16. Sections of the LDA (dashed lines) and GWA (full lines) surface band structures of the ADM (upper panel) and the SDM (lower panel) of Si(001)-(2 × 1) (from Rohlfing et al., 1995a) in comparison with ARPES data (Uhrberg et al., 1981, black squares and Johansson et al., 1990, full dots).

In Fig. 2.14 we again realize the strong influence of the surface geometry and the ionicity of the considered solid on the surface electronic structure. The reconstruction of the surface within the ADM yields $D_{up}$, $D_{down}$, $D_i$ and $D_i^*$ bands which are largely different from the respective D and Br bands at the ideal (001) surfaces of elemental semiconductors (cf. Fig. 2.8).

While the surface band structure in Fig. 2.14 nicely agrees with ARPES data, it fails to correctly describe measured surface gaps (Mönch et al., 1981; Chabal et al., 1983; Hamers and Köhler, 1989). This is related to the well-known shortcoming of the LDA which underestimates band gaps of bulk semiconductors and surfaces considerably. These problems can be overcome by carrying out quasiparticle band structure calculations as discussed in Subsection 2.2.6. In Fig. 2.16 we show the quasiparticle band structures for the SDM and the ADM of Si(001)-(2 × 1) as obtained by GW calculations employing Gaussian orbital basis sets (Rohlfing et al., 1995b). Respective LDA results are given by dashed lines for comparison. It should be noted at this point, that the band structures in Fig. 2.16 have been calculated using the supercell method for a supercell geometry with 8 atomic and 6 vacuum layers per supercell while that in Fig. 2.14 was calculated within the scattering theoretical approach for semi-infinite geometries. Figure 2.16 reveals two important results. First, we note that the SDM remains metallic even if the quasiparticle band structure is considered. This result together with the evidence from the above discussed total energy minimization calculations convincingly rules out the SDM. Second, we note that the $D_{up}$ band for the ADM hardly changes while the $D_{down}$ band strongly moves up in energy opening up the

LDA gap of only 0.2 eV to the GWA gap of 0.65 eV. The results in Fig. 2.16 have been obtained using a model dielectric matrix in the GW calculations (Rohlfing et al., 1995b). They are very close to those of full RPA calculation (Rohlfing et al., 1995a) yielding a surface gap of 0.7 eV. The calculated gap energies are eligible within the range of the experimental values of 0.44 eV from optical absorption spectroscopy (Chabal et al., 1983), 0.64 eV from surface photovoltage measurements (Mönch et al., 1981) and 0.9 eV from tunneling spectroscopy (Hamers and Köhler, 1989). One should take into account in this comparison, in particular, that in optical absorption spectroscopy excitonic effects may give rise to a smaller gap energy value. Surface photovoltage, on the contrary, yields the one-particle gap. Finally, the largest contribution to the tunneling current originates from surface states at the $\Gamma$ point since they are characterized by the slowest spatial decay into vacuum. The respective calculated gap energy at the $\Gamma$ point is 0.95 eV in close agreement with the scanning–tunneling spectroscopy result. The average direct gap between occupied and empty surface states in Fig. 2.16 is 1.8 eV. This value is close to the energy position of a pronounced EELS peak at 1.7 eV observed by Chabal et al. (1983).

Comparing the most pronounced measured surface-state band of the ADM with the calculated quasiparticle $D_{up}$ band (top panel of Fig. 2.16) it becomes obvious, that the calculated band width is somewhat larger than the experimental band width. In addition, there are further experimental features (cf. Landemark, 1993) which cannot be reconciled with the theoretical bands resulting for the (2 × 1) surface. Northrup (1993) has carried out GW calculations for the low temperature c(4 × 2) phase of Si(001). On the basis of a comparison of his results with ARPES data of Landemark (1993) it seems very likely that the above-mentioned features originate from c(4 × 2) islands at the nominal 2 × 1 room temperature surface. We note in passing that the observed opening of the surface gap due to quasiparticle corrections for the c(4 × 2) surface (0.48 eV) (Northrup, 1993) and for the 2 × 1 surface (0.50 eV) (Rohlfing et al., 1995a) is very close. STA calculations to evaluate the surface atomic and electronic structure for the semi-infinite c(4 × 2) surface have been carried out (Pollmann et al., 1996; Krüger, 1997). A small section of the respective band structure near the top of the valence bands is compared in Fig. 2.17 with ARPES data of Enta et al. (1990) and Landemark (1993). There is a very good agreement to be noted between the occupied bands of the LDA surface band structure of the c(4 × 2) surface and the data.

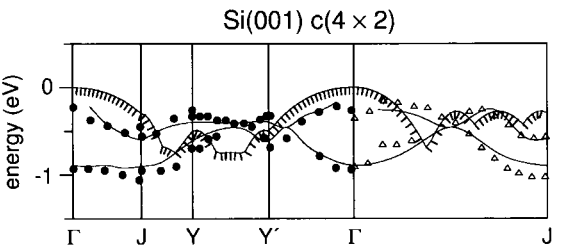


Fig. 2.17. Section of the surface band structure of Si(001)-c(4 × 2) in comparison with salient experimental ARPES data (black dots: Enta et al., 1990; triangles: Landemark, 1993).

### 2.4.2. *Comparison of the (001) surfaces of C, Si, Ge and α-Sn*

The origin and nature of dimer reconstructions at (001) surfaces of elemental semiconductors has been one of the most intensively discussed issues in semiconductor surface physics. Large efforts have concentrated on the Si(001) surface, as discussed above. Its reconstruction is the most subtle, as compared to those of the (001) surfaces of the other elemental semiconductors. By now, a consistent picture of the reconstruction of the (001) surfaces has emerged from a number of *ab initio* total energy minimization calculations the results of which are in very good agreement with a whole body of experimental surface structure and surface spectroscopy data. The optimal surface atomic structure of the C(001)-(2 × 1) and the Ge(001)-(2 × 1) surface resulting from a total energy minimization within the STA are shown in Fig. 2.18 in direct comparison with that of Si(001)-(2 × 1). Calculated dimer bond lengths and back bond lengths for these three surfaces resulting from *ab initio* calculations are compiled in Table 2.1.

The C(001)-(2 × 1) surface, which is of particular technological importance in the context of diamond thin film growth (Hamza et al., 1990), has been studied using self-consistent LDA calculations only fairly recently (Kress et al., 1994b; Furthmüller et al., 1994; Zhang et al., 1995a; Krüger and Pollmann, 1995). These investigations agreeingly find the SDM to be the equilibrium configuration of this surface. The dimer-bond length calculated within the STA (Krüger and Pollmann, 1995) is 1.37 Å. Previous empirical and

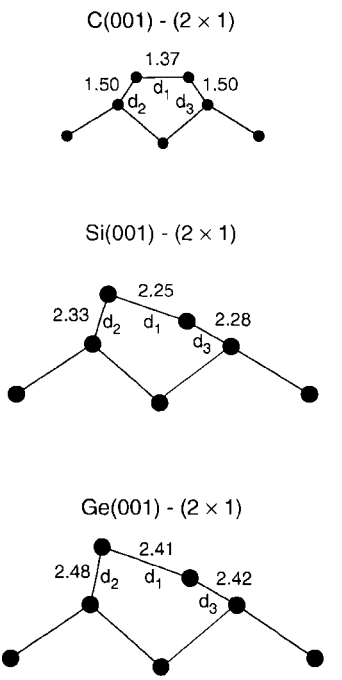


Fig. 2.18. Side views of energy-optimized configurations of the C(001)-, Si(001)-, and Ge(001)-(2 × 1) surfaces (Krüger and Pollmann, 1995). Bond lengths are given in Å.

Table 2.1

Tilt angle $\varphi$ (in °) and bond lengths $d_i$ (in Å; for their definition see Fig. 2.18) at the reconstructed C, Si, Ge and $\alpha$-Sn(001)-(2 × 1) surfaces from theoretical (T) and experimental (E) surface structure determinations

| | $\varphi$ | $d_1$ | $d_2$ | $d_3$ | T/E | Reference |
|---|---|---|---|---|---|---|
| C(001)-(2 × 1) | 0 | 1.37 | | | T | a |
| | 0 | 1.37 | 1.50 | 1.50 | T | b |
| | 0 | 1.37 | 1.50 | 1.50 | T | c |
| | 0 | 1.38 | | | T | d |
| Si(001)-(2 × 1) | 5 | 2.20 | | | E | e |
| | 7 | 2.21 | | | T | f |
| | 7 | 2.34 | | | E | g |
| | 8 | 2.25 | | | T | h |
| | 14 | 2.36 | | | E | i |
| | 14 | 2.27 | | | T | j |
| | 15 | 2.23 | | | T | k |
| | 18 | 2.26 | 2.34 | 2.29 | T | l |
| | 19 | 2.25 | 2.33 | 2.28 | T | c |
| | 19 | 2.25 | | | E | m |
| Ge(001)-(2 × 1) | 14 | 2.46 | | | T | n |
| | 15 | 2.48 | | | T | o |
| | 19 | 2.46 | | | T | p |
| | 19 | 2.41 | 2.48 | 2.42 | T | c |
| | 19 | 2.38 | | | T | q |
| | 20 | | | | E | r |
| | 21 | 2.44 | | | E | s |
| Sn(001)-(2 × 1) | 21 | 2.82 | | | T | t |

[a]Kress et al. (1994c).
[b]Furthmüller et al. (1994).
[c]Krüger and Pollmann (1995).
[d]Zhang et al. (1995a).
[e]Jayaram et al. (1993).
[f]Roberts and Needs (1990).
[g]Jedrecy et al. (1990).
[h]Yin and Cohen (1981).
[i]Tromp et al. (1985).
[j]Kobayashi et al. (1992).
[k]Dabrowski and Scheffler (1992).
[l]Ramstad et al. (1995).
[m]Bullock et al. (1995).
[n]Needles et al. (1987).
[o]Spiess et al. (1994).
[p]Cho et al. (1994).
[q]Jenkins et al. (1996).
[r]Culbertson (1986).
[s]Rossmann et al. (1992).
[t]Lu et al. (1998a).

semi-empirical calculations except for the non-selfconsistent LDA calculation by Yang et al. (1993) found symmetric dimers as well, with bond lengths ranging from 1.40 Å to 1.43 Å (see Jing et al., 1994). Experimental information on C(001)-(2 × 1) is currently still scarce. Lurie and Wilson (1977) have reported a (2 × 1) reconstruction after annealing at high temperature (above 1573 K) in ultra-high vacuum. No evidence for any higher order reconstructions such as the c(4 × 2) was seen in their work and in other investigations (Hamza et al., 1990). Thus there is no evidence for a ground state of correlated asymmetric dimers at the C(001) surface. The results of all recent first-principles structure

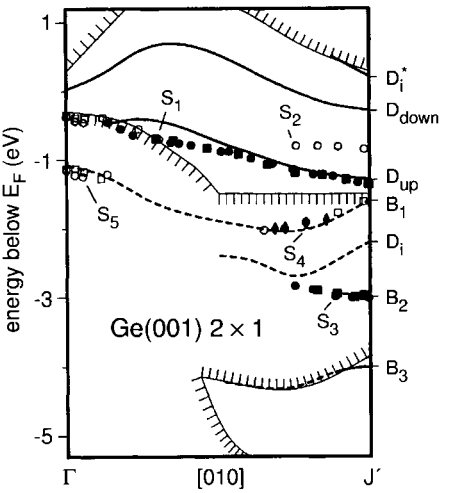


Fig. 2.19. Section of the surface band structure of the ADM of Ge(001)-(2 × 1) in comparison with experimental ARPES data (Landemark et al., 1990a).

optimizations completely agree on this finding and they are in excellent mutual agreement.

Recent results for the buckling angle and the dimer bond length at the Si(001)-(2 × 1) surface (see Table 2.1) are in good agreement (Kobayashi et al., 1992; Northrup, 1993; Krüger and Pollmann, 1995; Ramstad et al., 1995). Measured bond lengths spread over a wider range from 2.20 Å to 2.36 Å sensitively depending on the experimental method and on surface preparation (see Table 2.1). The relatively large scatter might be related to surface imperfections (dimer defects, etc.).

The studies of the Ge(001)-(2 × 1) surface have rather quickly converged to the ADM. Close agreement between the calculations and the experimental data (Landemark et al., 1990a) is obtained (see Fig. 2.19). The Ge(001)-(2 × 1) surface shows an asymmetric dimer reconstruction as well. Calculated bond length are given in Table 2.1. The values of 2.41 Å and of 19° for the dimer bond length and the tilt-angle, as obtained by Krüger and Pollmann (1995) in an STA calculation, are in good accord with those resulting from an *ab initio* SCM calculation by Needles et al. (1987) who obtained 2.46 Å and 14°, while Spiess et al. (1994) have determined a bond length of 2.48 Å and a buckling angle of 15° within an LDA cluster calculation. Culbertson et al. (1986) have measured a buckling angle of 20° while Rossmann et al. (1992) obtained best agreement with their X-ray diffraction data for a fit model with a dimer-bond length of 2.44 Å and a buckling angle of 21°.

Recent very detailed *ab initio* investigations (Lu et al., 1998a) of $\alpha$-Sn(001)-(2 × 1) have found that the dimers are strongly buckled at this surface. A buckling angle of 21° and a dimer-bond length of 2.82 Å was found.

The reconstruction mechanism at Si, Ge and $\alpha$-Sn(001) resembles that of the Jahn-Teller effect in molecules with a symmetry-degenerated ground state. At the considered surfaces, however, the dangling-bond bands of the SDM are not symmetry-degenerated.

Table 2.2

Calculated reconstruction-induced energy gain per dimer ($E_{rec}$) for the (001) surfaces of C, Si, Ge and $\alpha$-Sn in comparison with measured cohesive energies per bulk bond ($E_{coh}$). The results for C, Si and Ge are from Krüger and Pollmann (1995) and those for $\alpha$-Sn are from Lu et al. (1998a). $E_{asy}$ is the energy gain per dimer due to asymmetric as compared to symmetric dimer formation

| | $E_{rec}$ (eV) | $E_{coh}$ (eV) | $E_{asy}$ (eV) |
|---|---|---|---|
| C | 3.36 | 3.68 | |
| Si | 1.94 | 2.32 | 0.14 |
| Ge | 1.66 | 1.93 | 0.30 |
| Sn | 1.24 | 1.41 | 0.24 |

There is only an accidental degeneracy. Therefore symmetric dimers at (001) surfaces of group IV semiconductors are not necessarily unstable with respect to symmetry-breaking by dimer buckling. This is confirmed by the results for the C(001) surface for which the SDM is already semiconducting. An asymmetry of the dimers does not yield an energy gain. Therefore, the Jahn-Teller like transition does not occur at C(001)-(2 × 1) in agreement with experiment.

Characteristic energies of the reconstructed C, Si, Ge and $\alpha$-Sn(001)-(2 × 1) surfaces are compiled in Table 2.2 to highlight salient chemical trends in their reconstruction behavior. It is interesting to note that the reconstruction energy per surface unit cell $E_{rec}$ follows exactly the same trend as the cohesive energy per bulk bond $E_{coh}$. They mostly agree to within 0.3 eV. Thus $E_{rec}$ results in each case essentially from the formation of a new bond namely the dimer bond. The energy gain due to asymmetric as compared to symmetric dimer formation $E_{asy}$ is 0.14 eV for Si, 0.30 eV for Ge and 0.24 eV for $\alpha$-Sn(001)-(2 × 1). In consequence, the dimer flipping rate for Ge(001) is about $10^3$ times smaller than for the Si(001) surface at RT and thermally induced dimer flipping is strongly suppressed at the Ge(001)-(2 × 1) surface, therefore. This theoretical finding is supported by experimental results (Kubby et al., 1987). The energy gains per dimer at the Si(001)-(2 × 1) surface, as obtained from STA calculations 0.14 eV (Krüger and Pollmann, 1995) and from SCM calculations 0.12 eV (Dabrowski and Scheffler, 1992), 0.15 eV (Ramstad et al., 1995) and 0.14 eV (Northrup, 1993) are in gratifyingly close mutual agreement. The energy gain of 0.24 eV found by Lu et al. (1998a) for the asymmetric dimer reconstruction of the $\alpha$-Sn(001)-(2 × 1) surface nicely fits into the general picture outlined above.

The electronic surface band structure for the SDM of C(001)-(2 × 1) and for the SDM and ADM of Si and Ge (001)-(2 × 1) is shown in Fig. 2.20 in comparison with most recent ARPES data. Respective results for $\alpha$-Sn(001)-(2 × 1) (see Lu et al., 1998a) are very similar to those of the Si and Ge surfaces, as shown in the figure. The electronic properties of the SDM of the three surfaces in Fig. 2.20 are qualitatively similar but show drastic quantitative differences. In the SDM, two equivalent dangling bond orbitals per dimer occur. They exhibit a $\pi$-interaction giving rise to a bonding $\pi$-band and an antibonding $\pi^*$- band. The interaction between dangling bonds at neighboring dimers leads to a strong dispersion of these bands along the J–K and the $\Gamma$–J′ directions. The filled $\pi$ band and the empty $\pi^*$ band

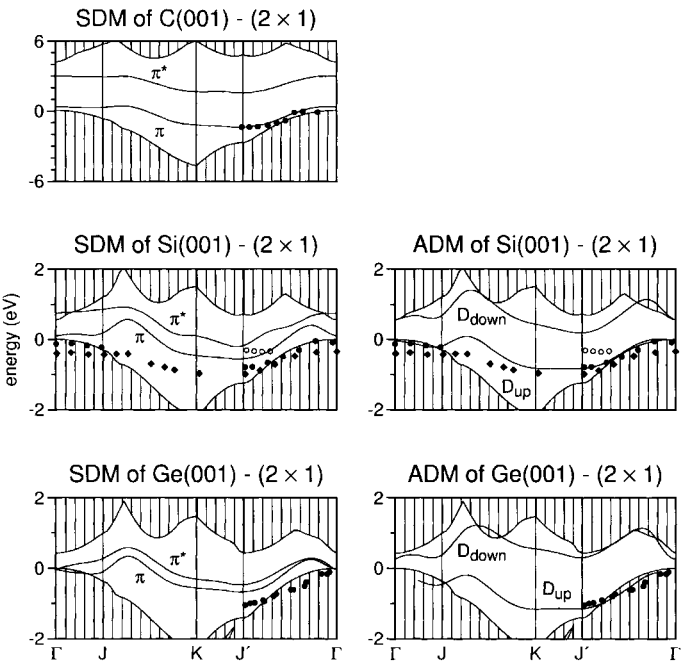


Fig. 2.20. Sections of the surface band structures (Krüger and Pollmann, 1995) for the SDM and ADM of C(001)-, Si(001)- and Ge(001)-(2 × 1) in comparison with salient experimental ARPES data by Graupner et al. (1997) for C(001)-(2 × 1), Uhrberg et al. (1981), squares and Johansson et al. (1990), circles for Si(001)-(2 × 1) and by Landemark (1994) and Landemark et al. (1990a) for Ge(001)-(2 × 1).

of C(001) are separated in energy by 1.2 eV. Thus the C(001) surface is semiconducting already in the SDM. For the SDM of the Si and Ge (001) surfaces, on the contrary, the $\pi$ and $\pi^*$ bands overlap and the surfaces turn out to be metallic, in marked contrast to experiment. In this case the Jahn-Teller like distortion occurs, as pointed out above, leading to asymmetric dimers in both cases. The asymmetry of the dimers in the ADM of Si and Ge (001) leads to a pronounced splitting of the two related bands $D_{up}$ and $D_{down}$, as can be seen in Fig. 2.20. There is a gap of 0.10 eV between the two bands at Si(001) and of 0.26 eV at Ge(001). In both cases the surface thus becomes semiconducting. The asymmetry yields an energy gain which stabilizes the buckled geometry. ARPES data from Uhrberg et al. (1981), Landemark et al. (1990a) and Graupner et al. (1997) are shown in Fig. 2.20, as well. There is much better agreement between the calculated electronic structure for the ADM of Si and Ge (001) with the respective ARPES data than for the SDM. The $\pi$ bands for the SDM of these surfaces are hard to reconcile with the measured dispersions and band widths of the most pronounced dangling-bond band in both cases. Conversely, the surface electronic structure for the SDM of C(001)-(2 × 1) is in very good agreement with the ARPES data of Graupner et al. (1997).

The reconstruction of the (001) surfaces of C, Si, Ge and $\alpha$-Sn reveal clear physical and chemical trends. C(001) is at the one limit showing symmetric dimers while Ge and

Table 2.3
Calculated dimer-bond lengths $d_l$ of C, Si, Ge (Krüger and Pollmann, 1995) and $\alpha$-Sn(001)-(2 × 1) (Lu et al., 1998a) in comparison with respective bulk-bond lengths $d_b$. Bond lengths for related molecules (with X = C, Si, Ge) are given in columns 4 and 5

| | $d_l$ (Å) | $d_b$ (Å) | $d_{H_3X-XH_3}$ (Å) | $d_{H_2X=XH_2}$ (Å) |
|---|---|---|---|---|
| C | 1.37 | 1.52 | 1.55 | 1.34 |
| Si | 2.25 | 2.33 | 2.33 | 2.15 |
| Ge | 2.41 | 2.42 | 2.40 | 2.30 |
| Sn | 2.82 | 2.81 | | |

$\alpha$-Sn(001) are at the other limit clearly showing asymmetric dimers. Si(001) resides at the border-line between these two extremes. From an analysis of the chemical nature of the reconstruction-induced dimer bonds a clear physical picture emerges (see Table 2.3).

At C(001)-(2 × 1), neighboring surface atoms form double-bonded dimers with a bond lengths of 1.37 Å, which is very close to the double-bond length of 1.34 Å in, e.g., the $C_2H_4$ molecule. At the Ge(001)-(2 × 1) surface they form single-bonded dimers whose bond length of 2.41 Å is close to the single-bond length of 2.40 Å in $Ge_2H_6$ molecules. The case of Si(001)-(2 × 1) resides in the middle of these two limiting cases. In consequence of the short dimer bond, the $\pi$-interaction between the dangling bonds at the C(001)-(2 × 1) surface is strong enough to clearly separate the $\pi$- and $\pi^*$-bands energetically. Thus the SDM of C(001)-(2 × 1) is already semiconducting and tilting the dimers does not lead to any additional energy gain. In contrast, in the SDM of Si and Ge(001)-(2 × 1), the $\pi$-interactions are not strong enough to open up a surface gap (see the left panels of Fig. 2.20). The very different behavior of the dimer-bond length $d_l$ at these surfaces can be traced back to the electronic properties of the constituent atoms. C-2p valence orbitals are more localized than C-2s orbitals since there are no p-states in the C core. Therefore p-like C orbitals are able to concentrate charge in the bonding region very efficiently leading to a strong tendency of $\pi$-bond formation. Actually it is the strong $\pi$- and $\sigma$-bonding between the occupied dimer states which strengthen the dimer bonds of C(001) so much that they become double bonds. For Si and Ge the tendency of forming $\pi$-bonds is clearly suppressed since in these materials the p-valence orbitals are more extended than the s-valence orbitals. The electrons in the occupied $D_{up}$ states of the ADM of Si and Ge (001) do not give rise to strong $\pi$-bonding and thus contribute only little to the dimer bonds. Therefore, double-bonds are not established at Si(001) and, in particular, not at Ge(001). The valence-charge density $\rho(\mathbf{r})$ (left panels) and valence-charge density *differences* $\Delta\rho(\mathbf{r})$ (right panels) contours in Fig. 2.21 confirm these notions. For C(001) there is a huge charge accumulation in the dimer bond region. This results from the C=C double bond formed by the $\sigma$- and $\pi$-orbitals of the C dimer atoms. The $\Delta\rho(\mathbf{r})$ contours for C(001) clearly show that the lobes of the dimer-bond charge density are oriented parallel to the bond direction. For Si and Ge (001), $\rho(\mathbf{r})$ shows a pronounced maximum in the dimer bond region residing slightly closer to the down atom in both cases. Contrary to the case of C(001), the bond lobes in the $\Delta\rho(\mathbf{r})$ contours for these two surfaces are oriented perpendicular to the bond direction.

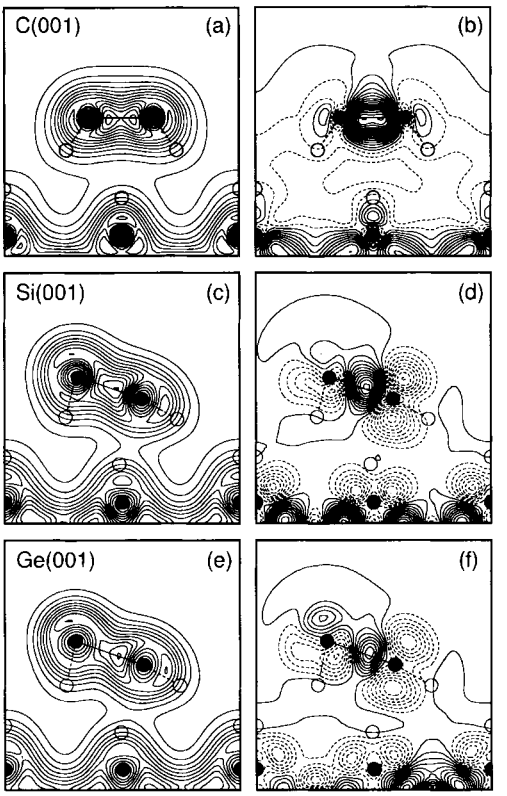


Fig. 2.21. Contours of total valence charge density $\rho(\mathbf{r})$ (a, c, e) and differences $\Delta\rho(\mathbf{r})$ between $\rho(\mathbf{r})$ and a superposition of atomic valence charge densities (b, d, f) for C, Si and Ge(001) (Krüger and Pollmann, 1995). The contour steps are 3 $e/\Omega$ ($\Omega$ is a volume of respective bulk unit cell) in (a, c, e) and 1 $e/\Omega$ in (b, d, f). Dashed contours denote negative charge differences.

From Fig. 2.21 it becomes fully apparent that the reconstruction of C(001) is qualitatively different from the extremly similiar reconstructions of Si(001) and Ge(001). This is related to the fact that both Si and Ge have p-orbitals in the core while they are missing in the core of C. Between Si and Ge (001) only quantitative differences occur. These chemical trends rationalize the specifically different reconstruction behavior of C(001) as opposed to Si and Ge (001) and they highlight the physical origins of the reconstruction behavior showing clear evidence for the SDM of the C(001) and for the ADM of the Si(001) and Ge(001) surfaces. For the same reasons, $\alpha$-Sn(001)-(2 $\times$ 1) shows the asymmetric dimer reconstruction (Lu et al., 1998a) as well.

Also in the case of Ge(001)-(2 $\times$ 1) the surface band structure (see the lower right panel of Fig. 2.20) is in reasonable agreement with ARPES data (Kipp et al., 1995, 1997; Skibowski and Kipp, 1994), but fails to correctly describe measured surface gaps (Kubby et al., 1987; Kipp et al., 1995, 1997; Skibowski and Kipp, 1994). In Fig. 2.22 we show the quasiparticle band structure for the ADM of Ge(001)-(2 $\times$ 1) as obtained

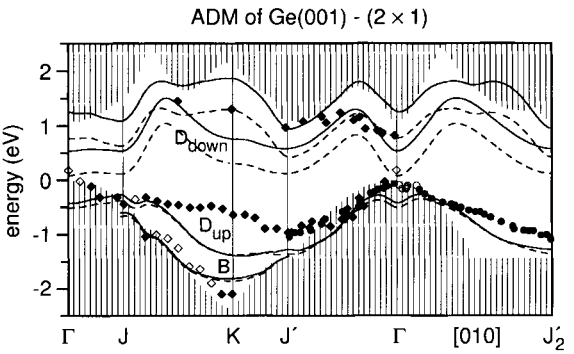


Fig. 2.22. Sections of the LDA (dashed lines) and GWA (full lines) surface band structure (Rohlfing et al., 1996b) of the ADM of Ge(001)-(2 × 1) in comparison with ARPES and KRIPES data (Kipp et al., 1995, 1997).

by GW calculations (Rohlfing et al., 1996b). Respective LDA results are given by dashed lines for comparison. We note that also at this surface, due to quasiparticle corrections, the $D_{up}$ band for the ADM hardly changes while the $D_{down}$ band strongly moves up in energy opening up the LDA gap of only 0.1 eV to the GWA gap of 0.55 eV. The calculated direct gap energy of 0.95 eV at the Γ point compares reasonably well with the gap of 0.9 eV as observed in scanning tunneling microscopy (Kubby et al., 1987). The calculated energies for direct transitions between occupied and empty states range from 0.6 eV to 2.0 eV while ARPES and KRIPES measurements (Kipp et al., 1995, 1997; Skibowski and Kipp, 1994) have observed a range of transition energies from 0.9 eV to 2.2 eV. Obviously, there is still some significant disagreement between the theoretical and experimental results in Fig. 2.22 that calls for further investigations.

### *2.4.3. The Si(111) surface*

The structure of the Si(111) surface has been resolved already in the 1980's. The different phases and the structural phase transitions of the Si(111) surface have been addressed in many reviews (see, e.g., Haneman, 1987; Hansson and Uhrberg, 1988; LaFemina, 1992; Chiarotti, 1993, 1994; Mönch, 1995; Duke, 1996; Volume I of this Handbook). We only summarize a few basic aspects in this chapter, therefore.

The (111) surface is the cleavage face of Si. An ideal truncation of the bulk crystal perpendicular to the [111] direction would result in a surface with either one (1DB surface) or three (3DB surface) dangling bonds per surface-layer atom depending on whether the truncation is made above or between one of the Si double-layers stacked along the [111] direction in the bulk. The 3DB surface is energetically less favorable than the 1DB surface, since the former has three broken bonds while the latter has only one. The ideal 1DB surface leads to a surface band structure with a half-filled dangling-bond band (D) inside the band gap (see Fig. 2.7). Since the respective dangling bond is unsaturated, the ideal surface is unstable with respect to more complex reconstructions. Although the ideal surface is unstable, (1 × 1) LEED patterns have been observed at very high temperatures or after impurity stabilization (Lander, 1964; Florio and Robertsen, 1970,

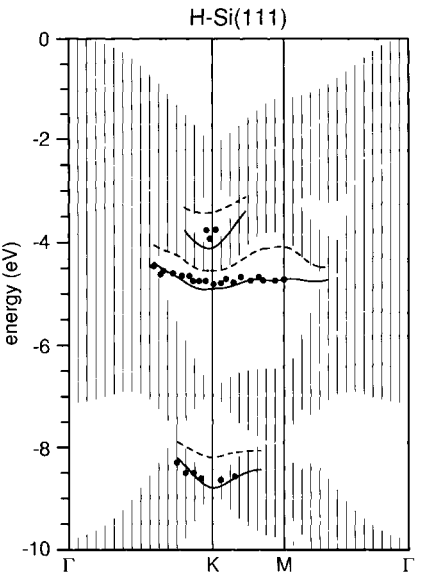


Fig. 2.23. Surface band structure of the H:Si(111)-(1 × 1) surface as resulting from LDA (dashed lines) and GWA (full lines) calculations (Rohlfing, 1996a) in comparison with experimental ARPES data (Hricovini et al., 1993).

1971; Hagstrum and Becker, 1973; Shih et al., 1976; Eastman et al., 1980; Chabal et al., 1981). Using wet chemical preparation techniques, it has become possible, as well, to prepare geometrically ideal Si(111)-(1 × 1) surfaces by adsorption of a monolayer of hydrogen. The adsorbed H atoms saturate the Si dangling bonds so that a fully passivated semiconducting surface results. The respective surface gap is free from surface states. The H-terminated Si(111)-(1 × 1) surface has been studied by GW quasiparticle calculations (Hricovini et al., 1993; Rohlfing, 1996a). The respective surface electronic structure is shown in Fig. 2.23 in comparison with ARPES data. The excellent agreement between the quasiparticle band structure and experiment confirms the ideal geometric structure of the underlying substrate surface. Further evidence for this structure is obtained from surface phonon measurements (Harten et al., 1988; Dumas and Chabal, 1992; Stuhlmann et al., 1992) and calculations (Sandfort et al., 1995; Miglio et al., 1988). The results of surface phonon calculations (Sandfort et al., 1995) employing a semiempirical total energy scheme (see, e.g., Mazur and Pollmann, 1990; Mazur et al., 1997) have been found in very good agreement with HREELS and HAS data for H:Si(111)-(1 × 1), fully confirming the (1 × 1) structure of the substrate surface.

The clean unreconstructed Si(1 × 1) surface is unstable. Ultrahigh vacuum cleavage below 603 K produces a (2 × 1) structure which transforms into a (7 × 7) structure upon annealing above 873 K (see, e.g., Mönch, 1995). This conversion is quite complex depending sensitively on preparation and annealing techniques. Further heating to above 1123 K yields a disordered (1 × 1) surface. We briefly address the (2 × 1) and (7 × 7) surfaces in the following two subsections.

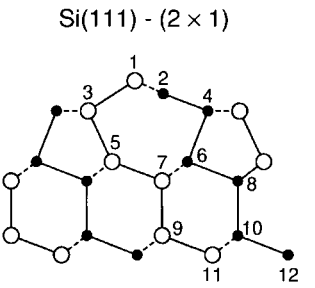


Fig. 2.24. Side view of the surface structure of the $\pi$-bonded chain model of Si(111)-(2 × 1) surface (Northrup and Cohen, 1982).

*2.4.3.1. Si(111)-(2 × 1)*

Initially, a buckling of the Si(111) top layer was thought to explain the (2 × 1) reconstruction of the surface (Haneman, 1961). Electronic properties resulting for this simple model, however, turned out to be at variance with CLS data (Himpsel et al., 1980a) and with measured bandwidths (Himpsel et al., 1981a; Uhrberg et al., 1982) for the dangling-bond bands. If the surface layers are only slightly buckeled, the surface dangling bonds remain at a relatively large distance (see the discussion in Subsection 2.3) so that no large dispersion of the dangling-bond bands results. Later on, the (2 × 1) reconstruction was proposed to consist of zigzag chains along a [110] direction which are connected to the underlying subsurface atoms by five- and seven-membered rings as opposed to the six-membered rings characteristic for the bulk structure of diamond-type crystals. The chains had to be tilted to account for the occurrence of two inequivalent surface atoms per unit cell in the CLS data (Himpsel et al., 1980b). If the Si crystal is cleaved so that only one bond per surface Si atom is broken (1DB surface), the $\pi$-bonded chain structure of Si(111)-(2 × 1) shown in Fig. 2.24 results. It was first predicted by Pandey (1981, 1982b) and confirmed later by a host of experimental and theoretical investigations (see the reviews by Haneman (1987) and Schlüter (1988)). Structure determinations have been performed using LEED (Himpsel et al., 1984b) and ion-scattering (Smit et al., 1985) and STS (Feenstra et al., 1987). First-principles total energy minimization calculations have confirmed these results (Northrup and Cohen, 1982, 1983; Northrup et al., 1991). STM studies (Stroscio et al., 1987; Feenstra et al., 1987) have confirmed the structure and the existence of $\pi$ and $\pi^*$ states associated with the dangling bonds at the atoms of the tilted chains.

In the $\pi$-bonded chain model all backbonds become fully saturated and the nearest-neighbor dangling bonds at the surface atoms exhibit a strong $\pi$ interaction yielding strongly dispersive bonding ($\pi$) and antibonding ($\pi^*$) dangling-bond bands. These $\pi$ and $\pi^*$ states have clearly been identified in STS data (Stroscio et al., 1987). The tilting of the surface chains renders neigboring surface atoms significantly inequivalent electronically so that the surface becomes semiconducting. While the dispersion of the $\pi$ and $\pi^*$ bands, as resulting from ETBM (Pandey, 1981, 1982b) and from DFT-LDA calculations (Northrup and Cohen, 1982) compares favorably with ARPES and KRIPES data, the calculated absolute energy position and the separation between the two bands (0.15 eV) shows the usual LDA shortcommings. To resolve this issue, Northrup et al. (1991) have studied the Si(111)-

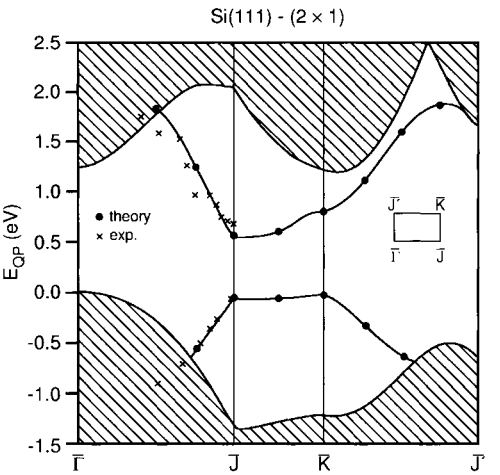


Fig. 2.25. Section of the surface band structure of the Si(111)-(2 × 1) surface as resulting from GWA (full dots) calculations (Northrup et al., 1991) with experimental data (Hricovini et al., 1993).

(2 × 1) surface by GW quasiparticle band structure calculations. Their results, shown in Fig. 2.25 show excellent correspondence with the data very convincingly confirming the $\pi$-bonded chain model for Si(111)-(2 × 1). The surface band gap of 0.62 eV, as resulting from these calculations, compares favorably with the value of about 0.45 eV, as obtained from multiple internal reflection spectroscopy (Chiaradia et al., 1984). The surface exciton, not considered in such calculations, might very well account for the remaining difference.

*2.4.3.2. Si(111)-(7 × 7)*

The Si(111)-(7 × 7) surface is the most complex and most famous clean surface structure in the history of surface science (Haneman, 1987; Schlüter, 1988; Mönch, 1995; Duke, 1996). This surface has a unit cell that is 49 times larger than that of the ideal Si(111)-(1 × 1) surface. Correspondingly, the SBZ of the former is 49 times smaller than that of the latter. In consequence, the dangling-bond band of the ideal (1 × 1) surface (see Fig. 2.7) becomes backfolded many times. In addition, the reconstruction-induced symmetry reduction gives rise to significant interactions between the backfolded bands so that an entirely new surface electronic spectrum results.

The by now generally accepted structural model for the Si(111)-(7 × 7) surface is the dimer-adatom-stacking-fault (DAS) model shown in Fig. 2.26. It was suggested on the basis of transition electron diffraction (TED) data by Takayanagi et al. (1985a, b) and is consistent with LEED (Tong et al., 1988), glancing-incidence X-ray diffraction (Robinson et al., 1986), X-ray reflectivity (Robinson and Vlieg, 1992), transmission electron diffraction (Twesten and Gibson, 1994), STM (Tromp et al., 1986) and RHEED (Ma et al., 1994) data. The DAS model has been convincingly confirmed by two independent DFT-LDA calculations employing Car–Parrinello molecular dynamics (Stich et al., 1992; Brommer et al., 1992). Both calculations yield basically the same structure showing that the (7 × 7) surface is only 0.06 eV per (1 × 1) unit cell lower in energy than the (1 × 1) surface. This

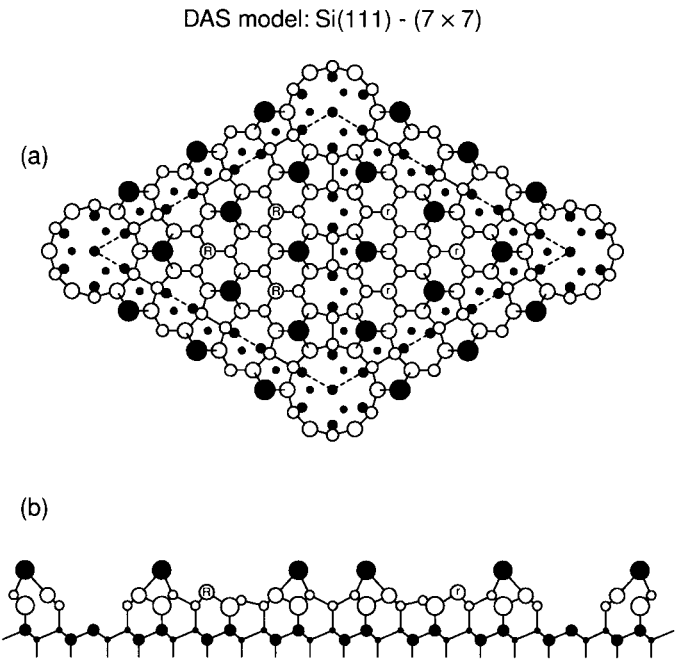


Fig. 2.26. Side view of the surface structure of the DAS model of the Si(111)-(7 × 7) surface (Takayanagi et al., 1985b).

small energy gain allows to rationalize that many competing phenomena eventually lead to the complex (7 × 7) structure. Earlier semiempirical total energy calculations by Qian and Chadi (1987b) had arrived already at virtually the same structure highlighting again the usefulness of the ETBM approach for addressing surface structures. The DAS model is characterized by the following features: it has 12 adatoms at the threefold hollow sites ($T_4$ sites), it has 6 first-layer atoms (the so-called restatoms) with a free dangling bond as at the ideal surface, it has 9 dimers per unit cell at the second layer, it has a corner hole with missing double-layer atoms and a stacking fault at the fourth layer. If the adatoms are covalently bonded to the first-layer atoms, there are 19 dangling bonds per unit cell localized at the 12 adatoms, the 6 restatoms and at the corner hole. As compared to the ideal surface, the number of the original 49 dangling bonds is thus reduced to only 19 at the (7 × 7) surface. The surface states associated with these dangling bonds lie near the Fermi level. They have all been observed by Hamers et al. (1987) using scanning tunneling spectroscopy (STS). Additional surface states associated with the stacking fault, the distorted backbonds and the dimer bonds occur.

The electronic structure of the (7 × 7) surface has a metallic character due to the odd number of electrons per unit cell (Demuth et al., 1983). It has been studied by EELS, ARPES and KRIPES investigations (cf. Demuth et al., 1983; Mårtensson et al., 1986, 1987; Nicholls and Reihl, 1987). Results of the ARPES and KRIPES studies are compiled in Fig. 2.27. Four bands of occupied and empty surface states have been observed that were

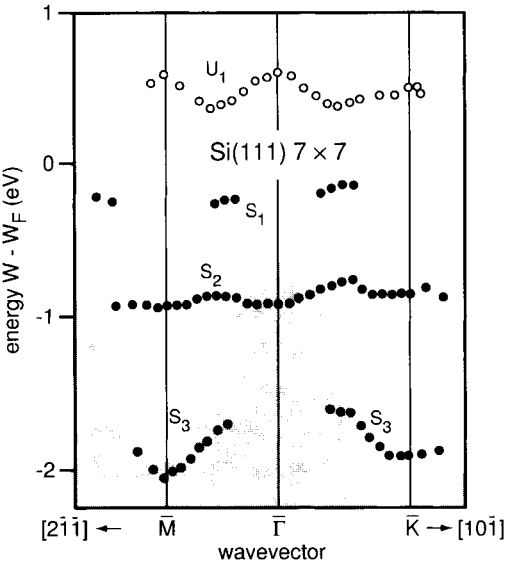


Fig. 2.27. Section of the surface band structure of the Si(111)-(7 × 7) surface as resulting from ARPES and KRIPES measurements (see, e.g., Mönch, 1995, p. 185).

found as well in the STS studies of Hamers et al. (1987). STS reveals the $S_1$ state to be localized at the adatoms. The same holds for the empty $U_1$ states. The band $S_1$ extends up to the Fermi level and it is this metallic band which pins the Fermi level at 0.7 eV above the top of the valence bands. STS correlated the almost dispersionless band $S_2$ with the six restatoms per unit cell. These states are well below the Fermi level and are thus completely occupied. The band $S_3$ originates from the backbonds at the adatoms as demonstrated by STS (Hamers et al., 1987). These experimental data were confirmed by ETBM calculations of Qian and Chadi (1987a, b) who evaluated layer densities of states for the DAS model yielding salient surface state peaks in good accord with the measured energy positions (see Table 2.4). The two papers on Car–Parrinello structure determinations of the DAS model

Table 2.4

Calculated (Qian and Chadi, 1987b) and measured (Mårtensson et al., 1986, 1987; Nicholls and Reihl, 1987) energy positions of salient surface states at the center of the SBZ of the Si(111)-(7 × 7) surface. All energies are referred to $E_F$

| | Experiment | Theory |
|---|---|---|
| Adatoms | $E_{U_1} = +0.5$ eV | $E_{U_1} = +0.8$ eV |
| | $E_{S_1} = -0.2$ eV | $E_{S_1} = \pm 0.0$ eV |
| Restatoms | $E_{S_2} = -0.8$ eV | $E_{S_2} = -0.9$ eV |
| Adatom backbonds | $E_{S_3} = -1.7$ eV | $E_{S_3} = -1.5$ eV |
| Corner hole | $-1.0\text{ eV} \leqslant E \leqslant -0.6$ eV | $E = -0.7$ eV |

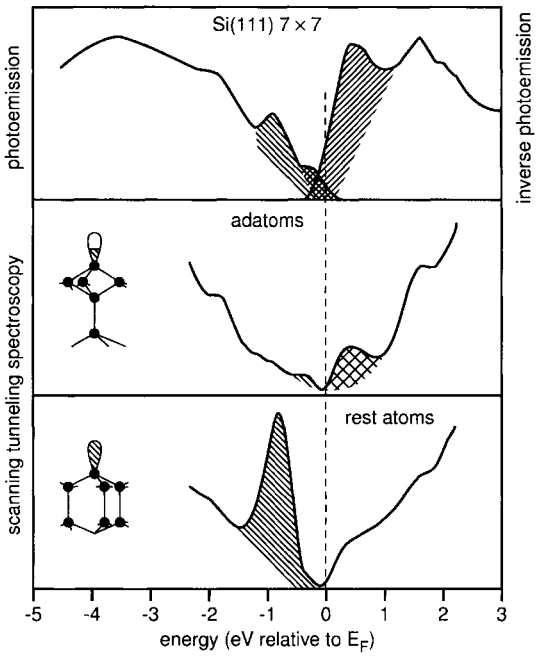


Fig. 2.28. Distribution of broken bond states at the Si(111)-(7 × 7) surface as observed in photoemission (see, e.g., Chiarotti et al., 1994, p. 379).

(Stich et al., 1992; Brommer et al., 1992), unfortunately, did not report the respective surface electronic structure which would have been most useful for comparisons with ARPES and KRIPES data. The distribution of broken bond surface states at the Si(111)-(7 × 7) surface is shown in Fig. 2.28.

### *2.4.4. The Ge(111) surface*

A fairly complete account on structural and electronic properties of Ge(111) surfaces has been given already in 1988 by Uhrberg and Hansson and more recent updates were presented by Mönch (1995) and Duke (1996). In this chapter, we only very briefly address Ge(111) surfaces, therefore. The Ge(111) surface exhibits a 2 × 1 reconstruction after cleavage at room temperature (Phaneuf and Webb, 1985; Becker et al., 1985). The cleavage face is metastable and transforms into a c(2 × 8) structure upon heating above 300 °C. The 2 × 1 surface shows the $\pi$-bonded chain reconstruction as suggested by Pandey (1981) for Si(111)-(2 × 1). Northrup and Cohen (1983), Zhu and Louie (1991a) and Takeuchi et al. (1991) have evaluated the structure of the Ge(111)-(2 × 1) surface in detail. A ball and stick model of the structure is shown in Fig. 2.29 clearly exhibiting the five- and seven-membered rings characteristic for this model.

The electronic structure of the $\pi$-bonded chain model, as resulting from the DFT-LDA calculations of Northrup and Cohen (1983) is compared in Fig. 2.30 with ARPES and KRIPES data of Nicholls et al. (1983, 1984) and of Nicholls and Reihl (1989).

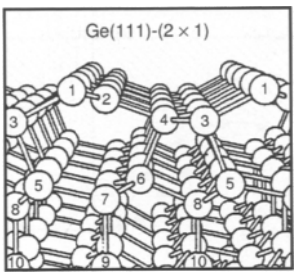


Fig. 2.29. Ball and stick model of the $\pi$-bonded chain structure of the Ge(111)-(2 × 1) surface as resulting from LDA total energy minimization calculations (Northrup and Cohen, 1983).

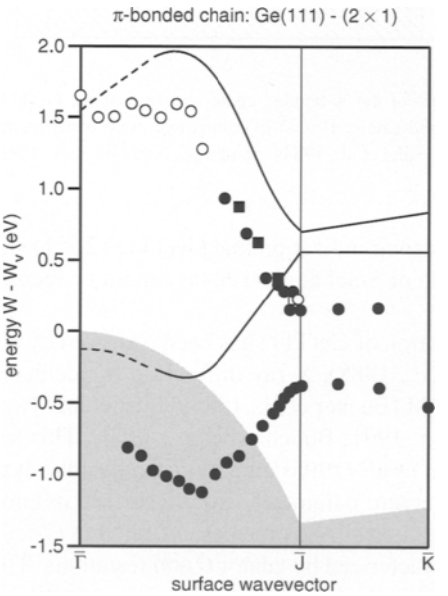


Fig. 2.30. Surface band structure of the $\pi$-bonded chain structure of the Ge(111)-(2 × 1) surface as resulting from LDA calculations (Northrup and Cohen, 1983) in comparison with experimental data (Nicholls et al., 1983).

There is good general agreement concerning measured and calculated band width as well as dispersion. The LDA results, however, show the usual shortcomings. The calculated bands reside considerably higher in energy than the measured bands and the surface band gap is underestimated. These shortcomings are again overcome by quasiparticle band structure calculations (Zhu and Louie, 1991a) yielding results in excellent agreement with part of the data as is most obvious from Fig. 2.31. The two sets of ARPES data in Fig. 2.31 give quite different band dispersions for the occupied surface states. The one by Nicholls et al. (1983, 1984) shows a highly dispersive occupied band with a band width of 0.8 eV. The other one by Solal et al. (1984a) only shows a 0.2 eV dispersion. The agreement between the theory (Zhu et al., 1991a) and the ARPES data of Nicholls et al. (1983,

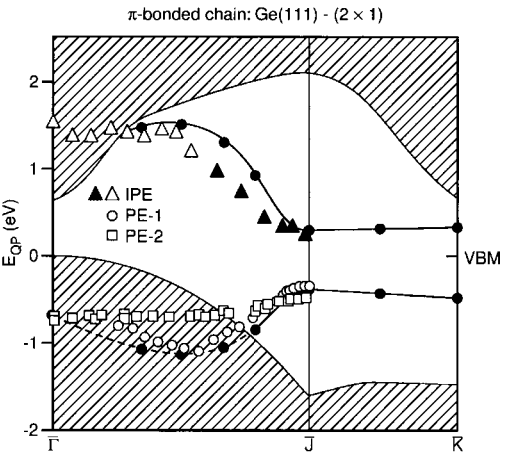


Fig. 2.31. Surface band structure of the $\pi$-bonded chain structure of the Ge(111)-(2 × 1) surface as resulting from GWA calculations (Zhu and Louie, 1991a) in comparison with experimental data (Nicholls et al., 1983, 1984, circles; Solal et al., 1984a, diamonds; Nicholls et al., 1989, triangles).

1984) is considered as a strong indication that Ge(111)-(2 × 1) shows the $\pi$-bonded chain structure, indeed. The data of Solal at al. (1984a) cannot be reconciled with the calculated quasiparticle bands.

The (2 × 8)-reconstruction of Ge(111) has been observed by LEED (Tong et al., 1990), ion scattering (Marée et al., 1988), X-ray diffraction (Feidenhans'l et al., 1988; van Silfhout et al., 1990) and STM (Becker et al., 1985; Klitsner and Nelson, 1991; Becker et al., 1989; Feenstra and Slavin, 1991; Bouchard et al., 1994). This surface has more recently been studied by Takeuchi et al. (1995) employing molecular dynamics calculations. The authors have reported structure parameters for the surface in good accord with the X-ray data of van Silfhout et al. (1990). As is the case of Si(111)-(7 × 7), also the reconstrution of Ge(111)-(2 × 8) is characterized by adatoms and restatoms. There are two adatoms and two restatoms per unit cell in this case. The dispersion of some salient surface state bands has been measured by Yokotsuka et al. (1984), Nicholls et al. (1986), Bringans et al. (1986) and Aarts et al. (1988). A compilation of these experimental results is given in earlier reviews (Hansson and Uhrberg, 1988; Mönch, 1995). To date, the electronic structure of the Ge(111)-(2 × 8) surface has not yet been calculated, to the best of our knowledge.

### *2.4.5. The C(111) surface*

The LEED pattern of the clean C(111) surface shows an apparent 2 × 2 translational symmetry which is commonly interpreted as arising from a superposition of three rotated 2 × 1domains (Pate, 1986; Sowa et al., 1988). There is general agreement that a $\pi$-bonded chain model as introduced by Pandey (1981) explains the reconstruction of this surface. Experimental evidence is based on ion scattering (Derry et al., 1986), ARPES (Himpsel et al., 1981c; Morar et al., 1986; Kubiak and Kolasinski, 1989) and sum-frequency-generation (SFG) spectroscopy (Chin et al., 1995). The general nature of the reconstruction has

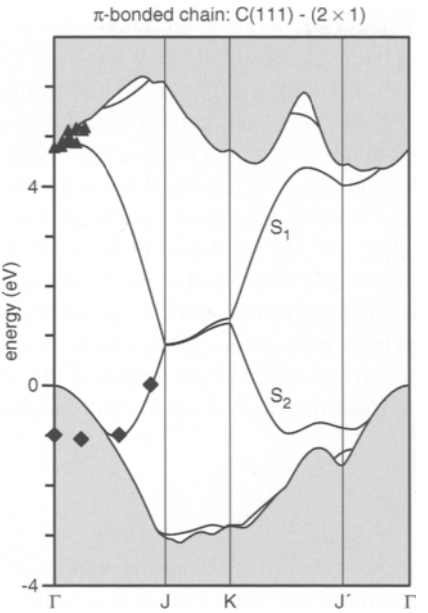


Fig. 2.32. Surface band structure of the $\pi$-bonded chain model of the C(111)-(2 × 1) surface (Scholze et al., 1996) in comparison with experimental data (Himpsel et al., 1981c, diamonds; Kubiak and Kolasinski, 1989, triangles).

been supported by a host of calculations (Pandey, 1982a; Vanderbilt and Louie, 1983, 1984; Chadi, 1984; Badzaig and Verwoerd, 1988; Zheng and Smith, 1991; Iarlori et al., 1992; Frauenheim et al., 1993; Davidson and Pickett, 1994; Kress et al., 1994a; Alfonso et al., 1995; Scholze et al., 1996; Kern et al., 1996). These investigations have been accompanied by a vivid and controversial discussion of the precise structure, such as chain dimerization or chain buckling, and the origin of the observed surface gap of at least 1 eV (Pepper, 1982). Different semiempirical and first-principles calculations have yielded conflicting evidence concerning dimerization and buckling of the chains and the nature and origin of the surface gap. More recently, it has been shown that both basis set convergence and **k**-point sampling are crucial for reliable calculational results (Scholze et al., 1996; Kern et al., 1996). In these calculations the undimerized and unbuckled $\pi$-bonded chain model is found to yield the lowest total energy with an energy gain of 1.40 eV per surface atom relative to the ideal surface. Dimerization of the chains had been invoked earlier (Iarlori et al., 1992) to explain the occurrence of the surface gap as resulting from a Peierls-type transition. For nearly undimerized and unbuckled $\pi$-bonded chains in the (2 × 1) Pandey reconstruction, the electronic LDA band structure exhibits no optical gap (see Fig. 2.32).

The data points for occupied states from ARPES (Himpsel et al., 1981c) and two-photon PES (Kubiak and Kolasinski, 1989) are found in good agreement with the results of the calculations. The seemingly good agreement for the upward dispersion of the occupied surface band from Γ to J, however, was assessed by the authors as being fortuitous. In agreement with the results of Vanderbilt and Louie (1983, 1984) and Alfonso et al. (1995)

the surface bands become nearly degenerate at the J point. Introducing dimerization makes the surface semiconducting but a gap of only 0.3 eV has been found at the J point (Iarlori et al., 1992). Again, these shortcomings might be related to the LDA. GW quasiparticle calculations (Kress et al., 1994a) have been carried out, therefore, showing strong quasiparticle shifts of the surface bands at $\Gamma$ in good agreement with experiment but not at the J-point. The calculated value of 0.25 eV is too small to explain the measured surface gap of at least 1 eV (Pepper, 1982). Nevertheless, these results are not yet fully conclusive since the standard perturbation approach, as employed in the GW approximation, may fail to describe surface states appropriately that result as nearly degenerate within LDA. Instead the full quasiparticle equations need to be solved to arrive at a definite answer. More recent DFT-LDA calculations by Scholze et al. (1996) and Kern et al. (1996) have confirmed that the $\pi$-bonded chains are symmetric and unbuckled in the $(2 \times 1)$ Pandey reconstruction. A final solution of the issue thus has to await a full quasiparticle calculation for the C(111)-$(2 \times 1)$ surface.

### *2.4.6. The Si(110) surface*

The ideal Si(110) surface shows two surface dangling-bond bands (see Fig. 2.7) which are not fully occupied. In consequence, the ideal surface is metallic. The unsaturated dangling bonds render the surface chemically reactive. It can lower its total energy by reconstruction. The reconstruction should give rise to a reduction of the number of unsaturated dangling bonds. The reconstruction of the Si(110) surface, as opposed to that of the other low-index faces of Si, has been investigated less intensively. Hansson and Uhrberg (1988) have summarized earlier investigations of structural properties and ARPES studies. Very recently, Packard and Dow (1997) and Menon et al. (1997) have investigated the Si(110) surface by semi-empirical calculations and STM studies. The surface shows complicated long-range reconstructions of $(5 \times 1)$ or $(16 \times 2)$ symmetry. A number of models, based on a face-centered stretched hexagon of Si adatoms as the main building block has been discussed in conjunction with the STM data (Packard and Dow, 1997). It was concluded that the $(16 \times 2)$ reconstruction is slightly more prevalent. So far, only the structure of this surface has been addressed by semiempirical calculations. No first-principles structure optimizations of the Si(110) surface have been reported, to date, and the electronic structure of this surface has not yet been investigated, at all.

The geometrically ideal Si(110)-$(1 \times 1)$ surface can be prepared when H is adsorbed, as has been shown very recently by Watanabe (1996). The author has investigated this system since hydrogen-terminated Si surfaces are of basic importance in surface science and semiconductor technology. Adsorbed hydrogen, e.g., has a strong influence on the Si growth process and hydrogenation of Si surfaces in solution as a final step of cleaning is a key technology to obtain oxygen-free stable surfaces. Watanabe (1996) has employed infrared spectroscopy with multireflection attenuated total reflection as well as polarized infrared transmission spectroscopy and has measured stretching and bending vibrations associated with H adsorbed on Si(110) formed in hydrofluoric acid and in hot deoxygenated water. The author concludes from his data that the Si surface is not reconstructed by hydrogenation in solution. The surface formed by hydrogenation in hot water was found to be approximately ideal and has shown a number of well-resolved surface-phonon modes.

The surface formed in hydrofluoric acid, on the contrary, showed several broad absorption features. These data have been interpreted using the results of surface-phonon calculations yielding a complete and detailed picture of the surface dynamics of the H:Si(110)-(1 × 1) adsorption system (Gräschus et al., 1997). Localized and resonant surface-phonon modes throughout the whole SBZ were found. A comparison of the theoretical results with the experimental Γ-point data for the bending and stretching modes (Watanabe, 1996) confirmed that the substrate surface is only marginally relaxed but not reconstructed.

## 2.5. SiC surfaces

SiC is a wide-band-gap compound semiconductor with very promising potential for applications in microelectronic and electrooptical devices (Davis, 1993; Choyke, 1990; Pensl and Helbig, 1990; Ivanov and Chelnokov, 1992; Harris, 1995; Bermudez, 1997). SiC surfaces have been studied theoretically (cf. Pollmann et al., 1997) by first-principles approaches only very recently and they are not covered at all, to date, in most of the reviews on semiconductor surfaces, mentioned in the introduction. The only exception is the monography by Mönch (1995). Therefore, we will address SiC and its surfaces in more detail in this chapter.

SiC occurs in an extremely large number of polytypes. Cubic 3C-SiC and hexagonal 6H-SiC seem to be the most important for technological applications. Cubic $\beta$-SiC, or 3C-SiC, has one Si and one C atom per bulk unit cell. Hexagonal $\alpha$-SiC occurs in 2H, 4H and 6H modifications depending on the stacking sequence of SiC bilayers along the crystal c-axis. They have $n$ Si and $n$ C atoms (with $n = 2$, 4 or 6) per bulk unit cell, respectively. In these cubic and hexagonal polytypes, the nearest-neighbor configuration of Si and C atoms is tetrahedral and the SiC bond length is close to 1.89 Å. Though being a group-IV semiconductor, SiC is fairly ionic due to the extreme disparity of the covalent radii of Si and C which originates from the largely different strengths of the Si and C potentials, respectively. The ionicity of cubic SiC amounts to $g = 0.475$ on the Garcia–Cohen scale (1993). The ionicity of SiC gives rise to an ionic gap within the valence bands of the bulk-band structure of all polytypes, very much like in heteropolar covalent III-V or heteropolar ionic II-VI compound semiconductors. The pronounced ionicity of the SiC bond stems from the different strengths of the C and Si potentials, giving rise to the very different covalent radii of C ($r_C = 0.77$ Å) and Si ($r_{Si} = 1.17$ Å). In addition, the electronegativity of C ($e_C = 2.5$) is considerably larger than that of Si ($e_{Si} = 1.7$). The stronger C potential, as compared to that of Si, leads to a charge transfer from Si to C so that the electronic charge density distribution along the SiC bond is strongly asymmetric (Sabisch et al., 1995). Therefore, Si atoms act as cations while C atoms act as anions in SiC. In consequence of the ionicity of SiC, there are nonpolar and polar SiC surfaces. Si and C layers alternate, e.g., along the [001]-direction of $\beta$-SiC and along the [0001]-direction of $\alpha$-SiC. Thus, there are two distinctly different SiC surfaces in each case which are usually referred to as Si- or C-terminated surfaces. Pashley's electron counting rule (see, e.g., Subsection 2.6.3.1) is less important for SiC than for III-V or II-VI surfaces since the nature of the ionicity in SiC is vastly different from that in III-V or II-VI semiconductors. While the ions in the latter bulk crystals have 3, 5, 2 or 6 valence electrons, respectively,

and respective ideal surface dangling bonds are occupied on average by 3/4, 5/4, 1/2 or 3/2 electrons, in SiC the situation is quite different. Here both Si and C have 4 valence electrons each and ideal surface dangling bonds are occupied by 1 electron.

When discussing structural and electronic properties of SiC surfaces in conjunction with those of the related Si or diamond surfaces it is important to have in mind that the bulk lattice constant $a_0 = 4.36$ Å of SiC is some 20% smaller than that of bulk Si ($a_0 = 5.43$ Å) and some 22% larger than that of bulk diamond ($a_0 = 3.57$ Å). In consequence, at Si- or C-terminated surfaces one encounters Si (C) orbitals on a two-dimensional lattice with a lattice constant that is much smaller (larger) than that of related Si (diamond) surfaces, respectively. This is of considerable relevance for the particular reconstruction of some SiC surfaces, as compared to those of related Si and diamond surfaces, respectively. Another important point to be noted in this context is the large difference in angular forces occurring at Si and C atoms when the tetrahedral bonds to their nearest neighbors become bent upon surface relaxation or reconstruction. They are much larger at C than at Si atoms so that structural changes of the bulk tetrahedral configuration around C atoms involve a much larger contribution to the reconstruction energy than for Si atoms. This fact strongly discerns Si- from C-terminated surfaces of cubic or hexagonal SiC and is one of the reasons for their distinctively different reconstruction behavior.

A number of SiC surfaces has been investigated within the last two decades by empirical and semi-empirical methods (Lee and Joannopoulos, 1982; Mehandru and Anderson, 1990; Craig and Smith, 1990, 1991; Lu et al., 1991; Badziag, 1990, 1991, 1992, 1995). Only more recently, prototype SiC surfaces have been addressed by 'state of the art' first-principles LDA (Wenzien et al., 1994a, b, c, 1995; Käckell et al., 1996a, b; Yan et al., 1995; Northrup and Neugebauer, 1995; Sabisch et al., 1995, 1996a, b, 1997b, 1998; Catellani et al., 1996; Pollmann et al., 1996, 1997) and GW quasiparticle (Sabisch et al., 1996a) calculations. By now, relaxed nonpolar $\beta$-SiC(110) (Wenzien et al., 1994a, b; Sabisch et al., 1995; Pollmann et al., 1996, 1997) and 2H-SiC($10\bar{1}0$) (Pollmann et al., 1996, 1997) surfaces as well as $\beta$-SiC(111) (Wenzien et al., 1994c, 1995), $\beta$-SiC(001) (Käckell, 1996a, b; Yan et al., 1995; Sabisch et al., 1996a; Pollmann et al., 1996, 1997; Catellani et al., 1996, 1998) and 6H-SiC(0001) (Northrup and Neugebauer, 1995; Sabisch et al., 1996b, 1997b, 1998; Pollmann et al., 1997) surfaces have been investigated. Most authors use the supercell method for treating SiC surfaces. It has turned out in these studies that employing a sufficiently large number of $\mathbf{k}_\parallel$ points is crucial for convergent surface-structure calculations. Using $\Gamma$-point sampling only is often not sufficient.

Experimentally, SiC surfaces have been investigated by LEED, Auger electron spectroscopy (AES), STM, atomic force microscopy (AFM), electron-energy loss spectroscopy (EELS), X-ray photoelectron spectroscopy (XPS), near-edge X-ray absorption fine structure (NEXAFS), core-level spectroscopy, photoelectron spectroscopy (PES), angle-resolved photoelectron spectroscopy (ARPES) and $\mathbf{k}_\parallel$-resolved inverse photoelectron spectroscopy (KRIPES). The current status of experimental research has recently been reviewed by Bermudez (1997) and Starke (1997), where a fairly complete account of the pertinent experimental literature may be found.

### *2.5.1. General mechanisms for the relaxation of ionic surfaces*

Basic physical mechanisms that contribute to the relaxation of heteropolar covalent or ionic semiconductor surfaces have been addressed, e.g., by Sabisch et al. (1995) and Pollmann et al. (1996). Structural rearrangements at semiconductor surfaces are driven by electron–electron Coulomb repulsions, by quantum mechanical hybridization effects and by classical Coulomb attractions (electrostatic interactions) between anions and cations occurring in heteropolar covalent and heteropolar ionic systems. The actual atomic configuration of a particular surface depends critically on the heteropolarity or ionicity, respectively and on the structure (cubic or hexagonal) of the underlying semiconductor. To reduce the Coulomb repulsion between electrons, in general, the more electronegative anions tend to stay as far as possible above the surface. Even in covalent systems, ionicity plays an important role, in that creation of a surface can give rise to a charge transfer between surface atoms so that some of these effectively behave as anions and others as cations. To optimize the hybridization energy, on the contrary, cations tend to move below the surface and to establish a planar $sp^2$-like bonding configuration with their three nearest neighbors. Finally the classical Coulomb attraction between anions and cations yields an optimal energy gain when their distance is as small as possible. In consequence, anions and cations can be expected to have a tendency to reside in the same plane. For more ionic systems, the dominance of the electrostatic attraction in the interplay between the three mechanisms leads to a bond contraction at the surface. The most important structural parameter characterizing the relaxation is the top-layer bond-rotation angle $\omega$. For more covalent systems, like the surfaces of III-V semiconductors, quantum mechanical hybridization effects dominate giving rise to relatively large bond-rotation angles $\omega$ and the anion-cation bond length is nearly preserved at the surface. If the systems become increasingly more ionic, like SiC or the group III-nitrides, the classical Coulomb attraction between anions and cations starts to dominate the relaxation process and the systems tend to form more planar cation-anion arrays at the surface with correspondingly smaller $\omega$ values. The anion-cation bond length in the surface layer is found to contract accordingly in these models. A bond-length-contracting rotation relaxation results in these cases. These notions apply, e.g., to a considerable number of nonpolar surfaces, as well. In general, the nonpolar (110) zincblende and $(10\bar{1}0)$, as well as, $(11\bar{2}0)$ wurtzite surfaces of SiC, of group-III nitrides and of II-VI compounds show an outward relaxation of the surface layer anions and an inward relaxation of the surface-layer cations. This rotation of the surface-layer bonds leads to a raising of the energetic position of empty cation-derived and a lowering of occupied anion-derived dangling-bond states. These general trends identified in this Section are born out by respective results for the specific systems discussed in this chapter.

### *2.5.2. Nonpolar $\beta$-SiC(110) and 2H-SiC$(10\bar{1}0)$ surfaces*

Both the cubic and the hexagonal modifications of SiC exhibit nonpolar surfaces like, e.g., the $\beta$-SiC(110) or the 2H-SiC$(10\bar{1}0)$ surface. These nonpolar surfaces, in general, are largely similar to the related GaAs(110) surface or the $(10\bar{1}0)$ surfaces of II-VI compounds, respectively (cf. Pollmann et al., 1996). Nonpolar SiC surfaces have not been investigated experimentally, to date. Recent self-consistent calculations of the nonpolar $\beta$-SiC(110)

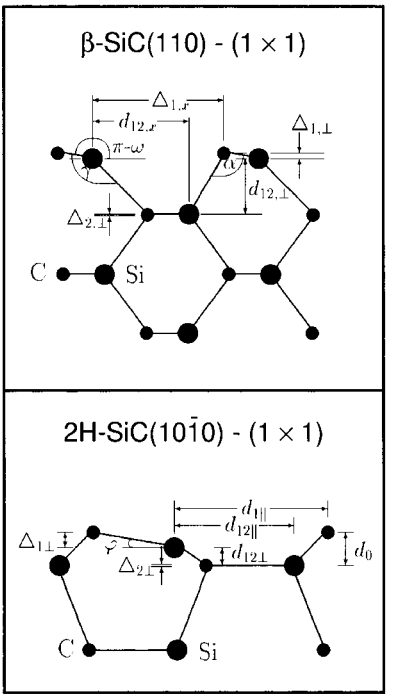


Fig. 2.33. Side view of the relaxed $\beta$-SiC(110)-(1 × 1) (top panel) and the relaxed 2H-SiC(10$\bar{1}$0)-(1 × 1) surface (bottom panel) (Pollmann et al., 1996).

surface (Wenzien et al., 1994a, b; Sabisch et al., 1995; Pollmann et al., 1996) yield excellent mutual agreement concerning the atomic structure. The nonpolar 2H-SiC(10$\bar{1}$0) surface has been studied, as well (Pollmann et al., 1997). In Fig. 2.33 we show side views of the optimized structures of both surfaces which are characterized by a bond-length contracting rotation-relaxation. The surface-bond contractions amount to 6% for $\beta$-SiC(110) and 9% for 2H-SiC(10$\bar{1}$0) with respect to the SiC bulk-bond length. The respective relaxation-induced energy gains are 0.64 eV and 0.71 eV for the two surfaces, respectively. They are very similar since the nearest-neighbor configuration of Si and C atoms is the same in both polytypes and only the second-nearest-neighbor configurations discern these structures. Wenzien et al. (1994b) found almost the same energy gain (0.63 eV) for the (110) surface. The relaxation-induced bond rotation at the surfaces is characterized by the tilt angle $\varphi$ and the relaxation angle $\omega$, respectively. The tilt angle $\varphi$ is the angle between the SiC surface-layer bonds and the surface plane. The relaxation angle $\omega$ results from a projection of the SiC bonds onto the drawing plane in Fig. 2.33. Since the SiC surface-layer bonds lie in the drawing plane for 2H-SiC(10$\bar{1}$0), $\omega$ and $\varphi$ are identical for the hexagonal surface while they are different for the cubic surface. For $\beta$-SiC(110), 8.2° and 16.9° is found for $\varphi$ and $\omega$, respectively, while they are equal and amount to only 3.8° at the 2H-SiC(10$\bar{1}$0) surface (Pollmann et al., 1996). Thus $\omega$ is much smaller at $\beta$-SiC(110) than at GaAs(110) where it amounts to about 30°. This is mainly due to the larger ionicity of SiC and to the more

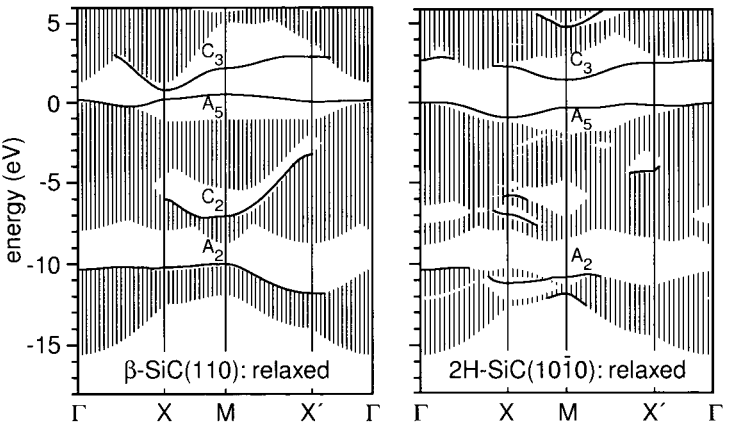


Fig. 2.34. Surface band structure of the relaxed $\beta$-SiC(110)-(1 × 1) (left panel) and the relaxed 2H-SiC(10$\bar{1}$0)-(1 × 1) surface (right panel). The projected bulk band structure is shown by the vertically shaded areas in each case (Pollmann et al., 1996).

pronounced asymmetry of the charge density along SiC bonds, as compared to GaAs (see Section 2.5.1, and Pollmann et al. (1997)). In addition, the C anion in SiC is a first row element whose covalent radius is much smaller than that of the cation Si. In GaAs both ions have similar covalent radii.

The surface electronic structure of the two nonpolar surfaces is shown in Fig. 2.34 together with the PBS. The calculated gap is some 50% smaller than the experimental gap as is usual in LDA results. Both surfaces exhibit pronounced anion-derived ($A_5$) and cation-derived ($C_3$) surface-state bands within the gap-energy region. We note in passing, that we had labeled respective states in Fig. 2.11 as d states to identify their dangling bond character and we have discussed in the respective subsection the origin (anion-derived or cation-derived, respectively) of these states. It has become common use, by now, to label these states as $A_5$ and $C_3$ so that we use that nomenclature in our following discussions. The energetic separation of these states is larger for the hexagonal than for the cubic surface since the bulk gap of 2H-SiC is considerably larger than that of 3C-SiC. Additional anion- and cation-derived surface-state bands occur within the projected bulk valence bands. As is obvious from Fig. 2.34, both nonpolar surfaces are semiconducting. Figure 2.35 reveals the origin and nature of the $A_5$ and $C_3$ dangling-bond states at the two surfaces. Clearly, $A_5$ is an anion-derived, i.e., a carbon-derived dangling-bond state while $C_3$ is a cation-derived, i.e., a Si-derived dangling-bond state. The respective states at the cubic and at the hexagonal surface are very similar due to the identical nearest-neighbor configuration of the two polytypes. Only the second- and third-nearest neighbor configurations discern the structures. For the same reason, the different lattices give rise to similar charge densities of the pronounced $A_5$ and $C_3$ surface states, as shown in Fig. 2.35. Comparing the surface electronic structure for the optimally relaxed configurations of these two nonpolar SiC surfaces with that of GaAs(110) (see Fig. 2.52) reveals that the band structure for the $\beta$-SiC(110) surface (left panel of Fig. 2.34) is very similar to that of GaAs(110), in general.

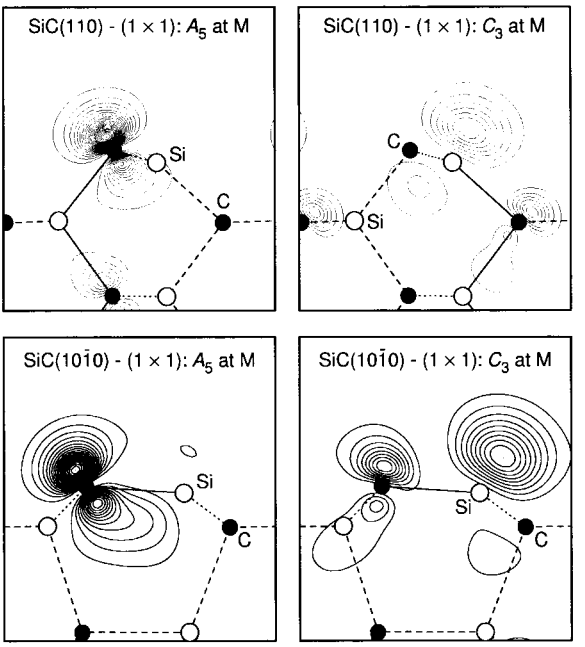


Fig. 2.35. Charge densities of the C- and Si-derived dangling-bond states $A_5$ and $C_3$ at the M-point of the relaxed $\beta$-SiC(110)-(1 × 1) (top panels) and the relaxed 2H-SiC(10$\bar{1}$0)-(1 × 1) surface (bottom panels). Bonds within (parallel to) the drawing plane are shown by full (dashed) lines. Bonds forming an angle with the drawing plane are shown by dotted lines (Pollmann et al., 1996).

### 2.5.3. *Polar (001) surfaces of $\beta$-SiC*

The current status of experimental research on structural and electronic properties of $\beta$-SiC(001) surfaces has recently been reviewed by Bermudez (1997). Within the past two decades several semi-empirical structure studies of SiC(001) surfaces have been carried out (Lee and Joannopoulos, 1982; Mehandru and Anderson, 1990; Craig and Smith, 1990, 1991; Lu et al., 1991; Badziag, 1992, 1995). More recently, a number of first-principles calculations have been reported (Käckell, 1996a, b; Yan et al., 1995; Sabisch et al., 1996a; Pollmann et al., 1996; Catellani et al., 1996, 1998; Lu et al., 1998b), as well. We first address the Si-terminated SiC(001)-(2 × 1) surface and then discuss (2 × 1), (1 × 2) and c(2 × 2) reconstruction models for the C-terminated $\beta$-SiC(001) surface.

#### 2.5.3.1. *Si-terminated $\beta$-SiC(001)-(2 × 1)*

Experimental data show (2 × 1), c(4 × 2), (3 × 2), and (5 × 2) reconstructions of the Si-terminated $\beta$-SiC(001) surface (Dayan, 1986; Kaplan, 1989; Powers et al., 1991; Parill and Chung, 1991; Hara et al., 1990, 1994; Semond et al., 1996; Aristov et al., 1997; Soukiassian et al., 1997; Bermudez, 1997). We basically restrict ourselves to a discussion of the (2 × 1) surface and conclude this subsection by some remarks on the c(4 × 2). A side view of the optimized geometry resulting from first-principles calculations (Sabisch, 1996a) is shown

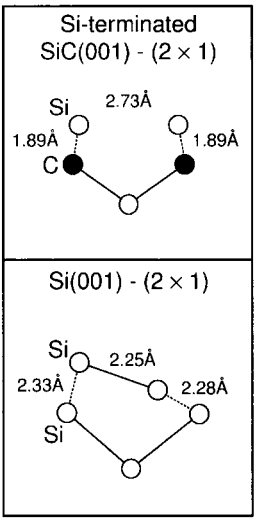


Fig. 2.36. Side views of the surface structure of Si-terminated $\beta$-SiC(001)-(2 × 1) (top panel) and of Si(001)-(2 × 1) (bottom panel) (Sabisch et al., 1996a).

in the top panel of Fig. 2.36 in direct comparison with that of the related Si(001)-(2 × 1) surface (Krüger and Pollmann, 1995). The reconstruction of the Si-terminated SiC(001)-(2 × 1) surface, obviously, is largely different from that of Si(001)-(2 × 1). This is related to the charge transfer from Si to C in SiC and to the fact that the lattice constant of SiC is about 20% smaller than that of Si. Dimer formation at the SiC surface involves much larger back-bond repulsions, therefore, as compared to the case of the Si surface. In addition, when Si surface dimers are to be formed at the Si-terminated SiC(001) surface, angular forces on the second layer C atoms are involved. These are much larger at the C atoms of the SiC surface than at the Si atoms of the Si surface so that strong dimer formation is prevented at the SiC surface. In the optimized structure the Si surface-layer atoms have moved only slightly towards each other with respect to the ideal surface, their distance amounting to 2.73 Å. *No Si surface dimers are formed* in marked contrast to the case of the Si(001)-(2 × 1) surface. The reconstruction-induced energy gain is only 0.01 eV per unit cell. This type of a very weak reconstruction agreeingly results from all convergent first-principles calculations (Käckell et al., 1996a, b; Sabisch et al., 1996a; Catellani et al., 1996).

A section of the surface electronic structure of the Si-terminated $\beta$-SiC(001)-(2 × 1) surface is shown in Fig. 2.37. There are four salient surface state bands in the gap-energy region. They originate from the dangling- and bridge-bond bands originally present at the ideal SiC(001) surface (see, e.g., Sabisch et al., 1996a). The nature and origin of these four bands become most apparent from the charge densities of the respective states shown in Fig. 2.37, as well. The occupied $\pi$ and $\pi^*$ states mainly result from symmetric and antisymmetric combinations of the former dangling-bond orbitals at the ideal surface while the empty $\sigma$ and $\sigma^*$ states result from symmetric and antisymmetric combinations of the former bridge-bond orbitals. The optimized structure leads to a semiconducting surface

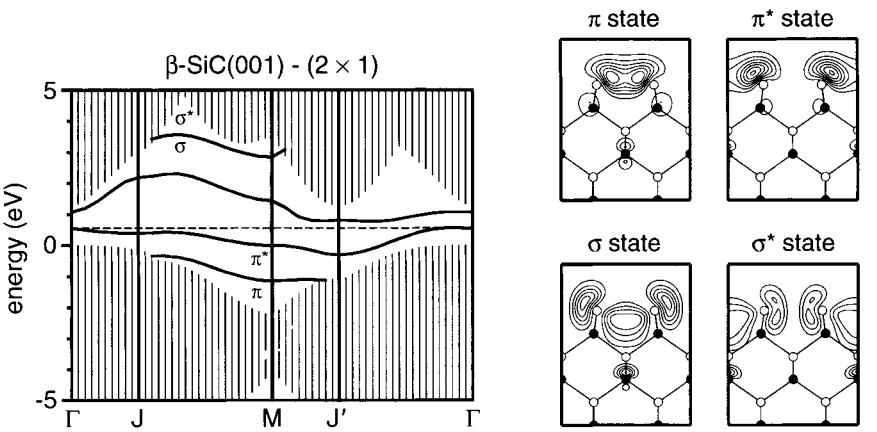


Fig. 2.37. Section of the surface band structure of $\beta$-SiC(001)-(2 × 1) (left panel) and charge densities of salient surface states at the K point of the (2 × 1) surface Brillouin zone shown in the $x$–$z$ plane containing the Si surface atoms (Pollmann et al., 1997).

already within LDA. A reconstruction of the Si-terminated SiC(001)-(2 × 1) surface, with dimers fully buckled as at the Si(001)-(2 × 1) surface, is energetically less favorable by 0.67 eV and has to be discarded as the optimal structure, therefore. Furthermore, it gives rise to a strongly metallic surface (cf. Sabisch et al., 1996a) in contrast to experiment (cf. Bermudez, 1997).

On the basis of TLEED data it was concluded that buckled dimers with a bond length of 2.31 Å are formed at the surface (Powers et al., 1991). This interpretation was supported by semi-empirical (Craig and Smith, 1990; Badziag, 1992, 1995) and by first-principles calculations (Yan et al., 1995). The results of more recent first-principles calculations (Käckell et al., 1996a, b; Sabisch et al., 1996a; Catellani et al., 1996) contradict this interpretation.

PES data clearly indicate the existence of two occupied surface-state bands which are referred to as "$V_1$" and "$V_2$" features (cf. Shek et al., 1994; Bermudez, 1997). $V_1$ occurs above the bulk valence band maximum and $V_2$ is observed roughly 1 eV below $V_1$. The calculated $\pi^*$ and $\pi$ bands in Fig. 2.37 appear to be closely related to these measured features. Both the absolute energy positions and, in particular, the energetic separation of about 1 eV between the calculated bands are well in accord with the data.

ARPES data on this surface have been published more recently (Käckell et al., 1997) and have been compared to theoretical results. There are considerable deviations between theory and experiment. KRIPES data seem not to be available on this surface to date. They would certainly be most useful to shed more light on the question of the actual surface reconstruction and to resolve the above mentioned discrepancy between theory and experiment. Interestingly enough, recent STM measurements on the c(4 × 2) surface (Soukiassian et al., 1997) and accompanying calculations have confirmed that the reconstruction of this SiC surface is significantly different from the reconstruction of the respective Si(001)-c(4 × 2) surface. This lends further support to the notion that Si-terminated SiC surfaces are strongly different from related Si surfaces and do not show strong Si surface dimers with a bond length as small as 2.31 Å.

First- and second-derivative EELS data on the SiC(001)-(2 × 1) surface have been reported (Kaplan, 1989; Bermudez, 1997). In the second-derivative spectra, three features are observed at relatively low transition energies of 1.8 eV, 3.1 eV and 4.7 eV. The latter feature seems to correspond to a peak observed in the first-derivative spectrum at 5.3 eV (Bermudez, 1997). Theoretical results (Sabisch et al., 1996a; Pollmann et al., 1997) are compatible with these data. When comparing theory and experiment one has to have in mind the LDA underestimate of band gaps. For $\beta$-SiC the calculated LDA gap is 1.28 eV (Sabisch et al., 1996a) while the measured gap is 2.41 eV. According to related GW results (cf. Sabisch et al., 1996a, and Fig. 2.42), it is to be expected that the occupied surface-state bands $\pi$ and $\pi^*$ (see Fig. 2.37) are not affected while the empty surface-state bands $\sigma$ and $\sigma^*$ are shifted up in energy by some 1.1 eV due to the quasiparticle corrections. From the surface-band structure in Fig. 2.37 one can easily extract ranges of possible transition energies. Taking into account the above-mentioned upward shift of the empty bands by quasiparticle corrections one can read off the following energy ranges for the four possible transitions: (1) 1.6 eV to 2.8 eV for $\pi^* \rightarrow \sigma$ transitions, (2) 3.0 eV to 3.8 eV for $\pi \rightarrow \sigma$ transitions, (3) 4.0 eV to 4.2 eV for $\pi^* \rightarrow \sigma^*$ transitions, and (4) 4.9 eV to 5.1 eV for $\pi \rightarrow \sigma^*$ transitions. The first and second of these ranges appear to have a higher spectral weight on their low-energy side, respectively. Thus the first could be related to the measured peak at 1.8 eV, the second to the measured peak at 3.1 eV and the fourth to the measured peaks at 4.7 eV or 5.3 eV in the second- or first-derivative spectra, respectively.

More recently, there is a lively discussion on the structure of the c(4 × 2) surface of SiC. Since this debate has not yet come to an entirely conclusive end, we refer the reader to the respective publications (Aristov et al., 1997; Catellani et al., 1998; Lu et al., 1998b).

### *2.5.3.2. C-terminated β-SiC(001) surfaces*

A number of structural models for the C-terminated $\beta$-SiC(001) surface has been suggested in the literature (Powers et al., 1991; Bermudez, 1995; Hara et al., 1990; Long et al., 1996; Bermudez, 1997). They comprise (2 × 1) or (1 × 2) row and c(2 × 2) staggered configurations of dimers or $C_2$ groups. The atomic structure of these models has been optimized by first-principles calculations (Käckell et al., 1996a, b; Yan et al., 1995; Sabisch et al., 1996a; Catellani et al., 1996; Pollmann et al., 1996). Top views of our optimized models are shown in Fig. 2.38.

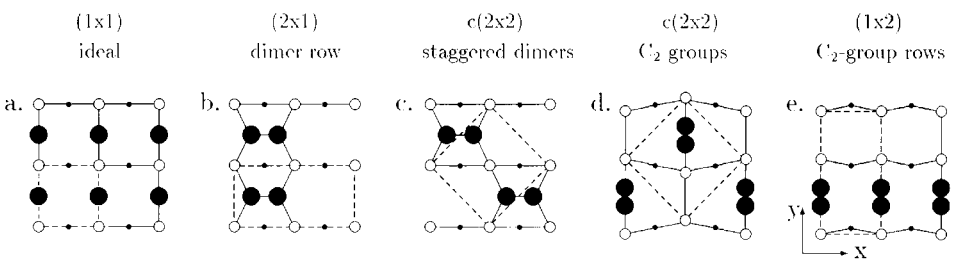


Fig. 2.38. Top views of the (1 × 1) ideal (a), the (2 × 1) dimer-row (b), the c(2 × 2) staggered-dimer (c), the c(2 × 2) staggered $C_2$-group (d), and (1 × 2) $C_2$-group-row configurations of the C-terminated $\beta$-SiC(001) surface. The unit cell is indicated by dashed lines in each case (Sabisch et al., 1996a).

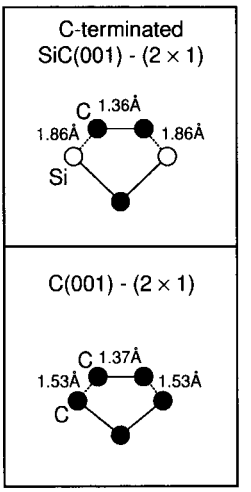


Fig. 2.39. Side views of the surface structure of C-terminated $\beta$-SiC(001)-(2 × 1) (top panel) and of C(001)-(2 × 1) (bottom panel) (Sabisch et al., 1996a).

In addition, Fig. 2.39 shows a side view of our optimized C-terminated SiC(001)-(2 × 1) dimer row structure (see Fig. 2.38b) in direct comparison with the structure of the related C(001)-(2 × 1) surface (Krüger and Pollmann, 1995). There is amazing similarity between these two reconstructions. In both cases strong surface dimers are formed. Their bond lengths of 1.36 Å and 1.37 Å, respectively, are very close to the C=C double-bond length in molecules like, e.g., $C_2H_4$. All arguments given in Section 2.5.3.1 against dimer formation at the Si-terminated surface work in favor of dimer formation at the C-terminated SiC(001)-(2 × 1) surface. At the latter surface, charge is transferred from the second layer Si atoms to the surface layer C atoms which reside at a surface lattice whose lattice constant is some 22% larger than that of C(001). So there is plenty of space for a full dimerization without invoking strong back-bond repulsions. In addition, surface-dimer formation now involves angular forces on the second-layer Si atoms which are much smaller than those at the second-layer C atoms of the Si-terminated surface. In consequence, C surface dimers are easily formed and the reconstruction-induced energy gain turns out be as large as 4.88 eV. This very strong surface reconstruction results as well from semi-empirical MINDO calculations (Craig and Smith, 1991).

The c(2×2) staggered-dimer structure of Fig. 2.38c is also characterized by C=C surface dimers with a double-bond length of 1.36 Å. The structure of this type of reconstruction results from all calculations in very close mutual agreement (cf. Sabisch et al., 1996a). The energy gain resulting from the different calculations differ to a certain extent. We have found a value of 4.73 eV and Käckell et al. (1996a, b) report a value of 4.36 eV, while Yan et al. (1995) have obtained 3 eV.

The c(2×2) staggered $C_2$-group reconstruction shown in Fig. 2.38d yields a reconstruction-induced energy gain of 4.76 eV. This value is only 0.12 eV smaller than that found for the (2 × 1) dimer-row structure. In the staggered $C_2$-group structure triple bonds between

surface C atoms with a bond length of only 1.22 Å are formed. The structure parameters resulting from different calculations for this configuration are in excellent agreement with one another (cf. Sabisch et al., 1996a).

The (1 × 2) $C_2$-group-row structure of Fig. 2.38e also exhibits surface triple bonds with a bond length of 1.22 Å and Si dimers on the second layer. This structure yields an energy gain of 4.58 eV relative to the ideal surface and turns out to be the least favorable of the four models in the calculations of Sabisch et al. (1996a).

Experiment has favored the c(2 × 2) $C_2$-group reconstruction on the basis of TLEED data (Powers et al., 1991). Long et al. (1996) have confirmed this conclusion by a polarization analysis of NEXAFS data. From the first-principles results for the C-terminated surfaces it appeares that theory slightly favores the (2 × 1) dimer-row structure. The energy gains for the different reconstructions are fairly close, however, their mutual difference being much smaller than the absolute gain with respect to the ideal surface. Thus a coexistence of domains of different reconstructions, as observed in experiment (Powers et al., 1991), depending on the particular sample preparation method used, is compatible with the theoretical results.

The electronic structure of these four models has been discussed in great detail by Käckell et al. (1996a, b), Sabisch et al. (1996a) and Pollmann et al. (1996, 1997). Here we only address the surface band structure of the two most probable reconstructions, namely the (2 × 1) dimer-row and the c(2 × 2) staggered $C_2$-group reconstructions. The band structures are shown in Fig. 2.40 in direct comparison. Both show a number of bands in the gap-energy region and back-bond bands within the PBS.

A pronounced band, S, occurs below the PBS in both cases originating from s orbitals on the C surface-layer atoms. The $P'_1$ and $P'_2$ bands (see left panel of Fig. 2.40) and the $P_1$ band (see right panel of Fig. 2.40) originate from C-Si backbonds having predominantely

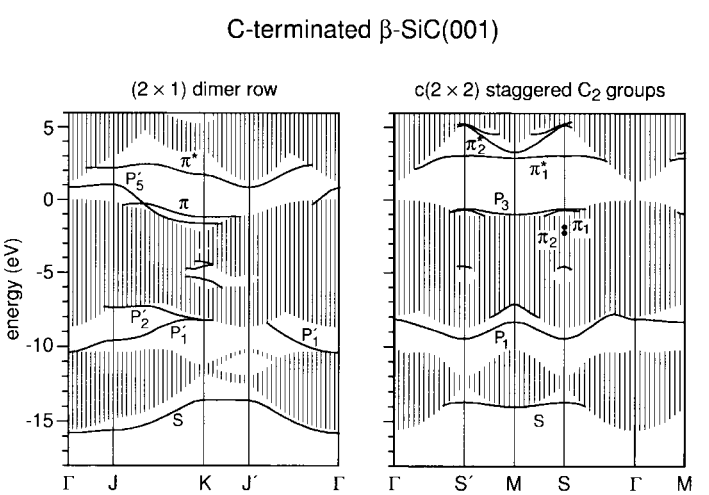


Fig. 2.40. Surface band structure of the (2 × 1) dimer row reconstructed (left panel) and the c(2 × 2) staggered $C_2$ group reconstructed (right panel) C-terminated $\beta$-SiC(001) surfaces. The projected bulk band structure is shown by the vertically shaded areas in each case (Pollmann et al., 1997).

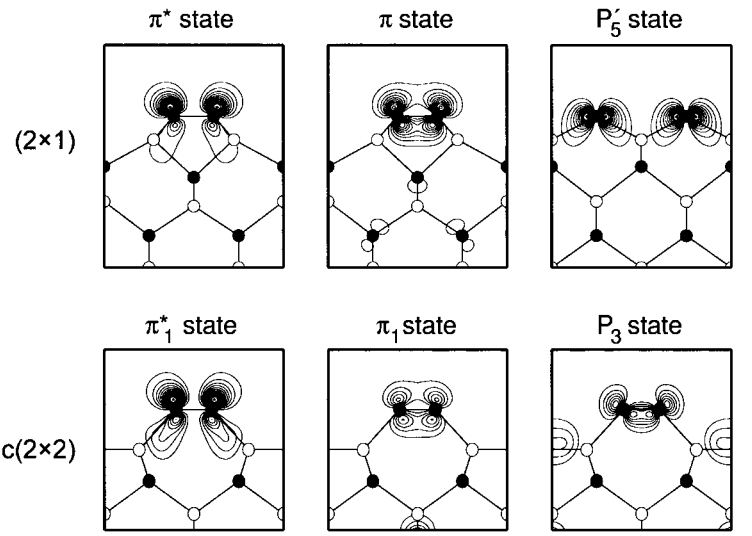


Fig. 2.41. Charge density contours of salient surface states at the C-terminated (2 × 1) dimer-row reconstructed (top panels) and the c(2 × 2) staggered-$C_2$-group reconstructed (bottom panels) C-terminated $\beta$-SiC(001) surfaces. The states $\pi^*$ and $\pi$ at the K point of the (2 × 1) SBZ are shown in the $x$–$z$ plane and $P'_5$ at the $\Gamma$ point is shown in the $y$–$z$ plane. The states $\pi_1^*$, $\pi_1$ and $P_3$ at the S point of the c(2 × 2) SBZ are drawn in the $y$–$z$ plane which is perpendicular to the surface and contains the $C_2$ groups (Pollmann et al., 1997).

p-wave-function character. The $\pi$ and $\pi^*$ bands in the gap-energy region of the (2 × 1) surface (see left panel of Fig. 2.40) are very similar to the related bands at the C(001)-(2 × 1) surface (see upper left panel of Fig. 2.20). They are separated in energy by roughly 1 eV and originate from symmetric ($\pi$) and antisymmetric ($\pi^*$) linear combinations of the dangling-bond orbitals at the dimer atoms (see the upper left and middle panel of Fig. 2.41). The $P'_5$ band is mostly occupied and originates from p states at the surface-layer C atoms (see upper right panel of Fig. 2.41). The (2 × 1) surface is marginally metallic (Sabisch et al., 1996a). Interestingly enough, the c(2×2) $C_2$-group reconstruction gives rise to a semiconducting surface already within LDA. The $\pi_1^*$ and $\pi_1$ states are antibonding and bonding states of the triply-bonded $C_2$ groups (see Fig. 2.41, two lower left panels). Their charge densities show amazing similarities with those of the $\pi^*$ and $\pi$ states at the (2 × 1) surface (see upper panels of Fig. 2.41) in spite of the fact that the lattice topology is quite different for the two surfaces. The former exhibits five-membered rings while the latter has seven-membered rings. The similarity of the respective states is a consequence of the fact that they are highly localized surface states whose properties are basically determined by the surface-layer atoms. The $P_3$ state originates from $p_y$ and $p_z$ orbitals at the $C_2$ groups and the second-layer Si atoms (see lower right panel of Fig. 2.41).

While the c(2 × 2) surface results already as semiconducting within LDA, the (2 × 1) surface is marginally metallic due to the occurrence of the $P'_5$ band. This metallicity, however, is an artefact of the LDA calculations (cf. Sabisch et al., 1996a). When quasiparticle corrections are included within the GW approximation, the gap opens up (see Fig. 2.42) and this surface becomes semiconducting, as well. Including respective quasiparticle cor-

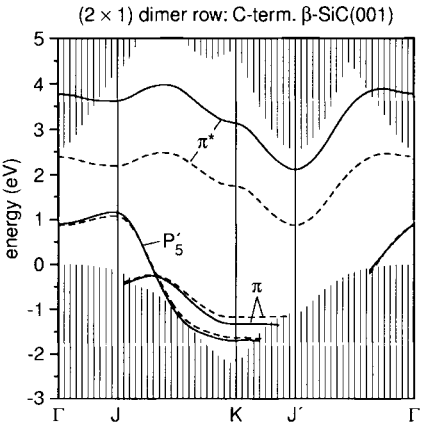


Fig. 2.42. Section of the surface band structure of the (2 × 1) dimer-row reconstruction of the C-terminated $\beta$-SiC(001) surface (see Fig. 2.38b) as resulting from LDA (dashed lines) and GWA (full lines) calculations (Sabisch et al., 1996a).

rections in the calculation of the surface band structure of the c(2 × 2) staggered $C_2$-group structure would increase the surface gap by about 1 eV in addition. Thus both reconstructions give rise to semiconducting surfaces with largely similar surface states (cf. Fig. 2.41).

The fact that the gap of the c(2 × 2) surface is clear from surface states is in good accord with photoemission measurements by Bermudez and Long (1995) and Semond et al. (1996) who did not observe surface states in the gap-energy region. In addition, there is no clear indication of surface states in the band gap in EELS data (cf. Kaplan, 1989; Bermudez, 1997). H-sensitive structure in EELS data has been observed (Bermudez and Kaplan, 1991) at about 4 eV and between 8 and 11 eV which is clearly due to surface exitations but an assignment of these features has not yet been given. From the right panel of Fig. 2.40, i.e., for the experimentally favored reconstruction, we read off possible transition energies of about 5 eV for $P_3 \rightarrow \pi_1^*$ transitions (including the gap correction of about 1 eV discussed in Subsection 2.5.3.2) and 12 eV for $P_1 \rightarrow \pi_1^*$ transitions. Neither one is close to the measured peak positions. The respective transition energies for the (2 × 1) dimer-row recontruction can directly be inferred from the left panel of Fig. 2.40 in conjunction with the quasiparticle surface band structure in Fig. 2.42 showing the correct experimental gap. Possible $\pi \rightarrow \pi^*$ transitions range from 3.5 eV to 4.4 eV. The maximum in the JDOS is to be expected near 4.2 eV. In addition, $P_2' \rightarrow \pi^*$ transitions range from 10 eV to 11 eV. These values are fairly close to the peak positions in the EELS data. But since we have merely estimated these transition energies in a very rough way, more or less good agreement with the EELS data should not be considered as a proof or disproof of one structural model as compared to the other.

To fully resolve the structure of the C-terminated SiC(001) surface, ARPES and KRIPES data are certainly needed for detailed comparisons with the calculated electronic structure.

### 2.5.4. The SiC(111) surface

The polar (111) surfaces of $\beta$-SiC are largely similar to the respective polar (0001) surfaces of 6H-SiC. The former have been studied within *ab initio* LDA by Wenzien et al. (1994c, 1995) and by Northrup and Neugebauer (1995). The latter authors have studied Si-terminated $\beta$-SiC(111)-($\sqrt{3} \times \sqrt{3}$)R30° surfaces which are largely equivalent to the respective hexagonal surfaces. Their calculations were intended to contribute to the discussion of structural and electronic properties of the hexagonal Si-terminated 6H-SiC(0001)-($\sqrt{3} \times \sqrt{3}$)R30° surface. We, therefore, discuss the related results in Section 2.5.5 on polar 6H-SiC surfaces further below.

The structure of the relaxed Si-terminated SiC(111)-(1 × 1) surface has been optimized by Wenzien et al. (1994a, 1995). Small vertical relaxations of the top layer have been found giving rise to an energy gain of 0.10 eV per unit cell. There is one half-filled dangling-bond band at the surface since the dangling bonds are not saturated. This result is very similar to what one obtains for the polar relaxed 6H-SiC(0001)-(1 × 1) surface (see Subsection 2.5.5.1). It is also very similar to the case of the Si(111)-(1 × 1) surface (see Section 2.3.1). Like the latter, also SiC(111)-(1 × 1) is metallic. The surface can reduce the number of unsaturated dangling bonds and its chemical reactivity by reconstruction. Significant energy lowering was obtained for a (2 × 2) vacancy-buckling model, very similar to those observed at GaAs(111) or ZnSe(111) surfaces (see Section 2.6.3.3).

### 2.5.5. Polar (0001) surfaces of 6H-SiC

The current status of experimental research on structural and electronic properties of hexagonal SiC surfaces has recently been reviewed by Starke (1997). Most reconstruction models for polar 6H-SiC(0001) surfaces involve Si or C adatoms or adsorbed Si or C trimers and are called adsorption-induced reconstructions, therefore. The respective Si- or C-terminated *substrate* surfaces are characterized by Si (C) top layer atoms with one dangling bond and three back bonds connecting them with their three nearest-neighbor C (Si) atoms on the second substrate layer. LEED, AES and EELS results are almost identical for corresponding reconstructions of the $\beta$-SiC(111) and the 6H-SiC(0001) surface (Kaplan, 1989) since the stacking sequence of Si–C bilayers in the cubic [111]-direction of $\beta$-SiC and in the hexagonal [0001]-direction of 6H-SiC are identical down to the eighth layer. Based on the indistinguishable LEED results for these two surfaces one can conclude that they are characterized by the same reconstruction geometry. Among the structures reported are (1 × 1), ($\sqrt{3} \times \sqrt{3}$)R30°, (3 × 3), ($6\sqrt{3} \times 6\sqrt{3}$)R30° and (9 × 9) configurations depending sensitively on temperature and on sample preparation. Different preparation methods appear to yield different reconstructions and, in general, the experimental structure data seem not to be entirely conclusive, yet (for details see Bermudez, 1997; Kaplan, 1989; Nakanishi et al., 1989; Starke et al., 1995; Schardt et al., 1995; Owman and Mårtensson, 1995; Li and Tsong, 1996; Starke, 1997).

First-principles investigations of polar hexagonal 6H-SiC(0001) surfaces have been reported recently (Northrup and Neugebauer, 1995; Sabisch et al., 1996a, 1997b, 1998). Northrup and Neugebauer (1995) have studied Si-terminated $\beta$-SiC(111)-($\sqrt{3} \times \sqrt{3}$)R30° surfaces which are largely equivalent to the respective hexagonal surfaces, as mentioned

above. Badziag (1990, 1992) has studied some of the (0001) surfaces by semi-empirical calculations.

*2.5.5.1. Relaxed 6H-SiC(0001)-(1 × 1) surfaces*

At the unreconstructed Si-terminated (1 × 1) surface there is usually a disordered layer of impurities like O which can be removed by annealing in UHV. The (1 × 1) structure of the C-terminated surface results from impurities at the surface, as well (Bermudez, 1997). Well-ordered unreconstructed 6H-SiC(0001) surfaces seem to have been investigated experimentally in some more detail only very recently (Starke, 1997; Hollering et al., 1997).

Atomic relaxations can occur only along the surface normal ($z$-direction) due to the hexagonal symmetry of the lattice. The most significant effect resulting from first-principles calculations is a pronounced inward relaxation of the top layer atoms for both surfaces. The respective decrease in the distance of the first two surface layers, as compared to its value at the ideal surfaces, amounts to −0.15 Å for the Si- and −0.25 Å for the C-terminated surface (Sabisch et al., 1997b). This is in good general accord with the structural results of Hollering et al. (1997). The calculated atomic relaxation on lower lying layers is very small. The calculations yield a relaxation-induced energy gain of 0.09 eV at the Si-terminated surface and a more than three times larger gain of 0.30 eV at the C-terminated surface. This energy difference originates from the larger relaxation of the C-face, as compared to that of the Si-face, and is again related to the difference in bond-bending angular forces at second-layer C or Si atoms, respectively. Structure parameters for the optimally relaxed Si- and C-terminated substrate surfaces are given by Sabisch et al. (1997b).

Figure 2.43 shows the surface band structure from Sabisch et al. (1997b) for the relaxed Si- and C-terminated 6H-SiC(0001)-(1 × 1) surfaces. For both surfaces there results one dangling-bond band in the gap-energy region very similar to the respective D band at the ideal Si(111) surface (see Fig. 2.7). These bands $D_{Si}$ and $D_C$ originate from dangling bonds localized at the Si or C top-layer atoms, respectively. Each of these dangling-bond bands is half filled since there is only one top layer atom per (1 × 1) unit cell in both cases. The

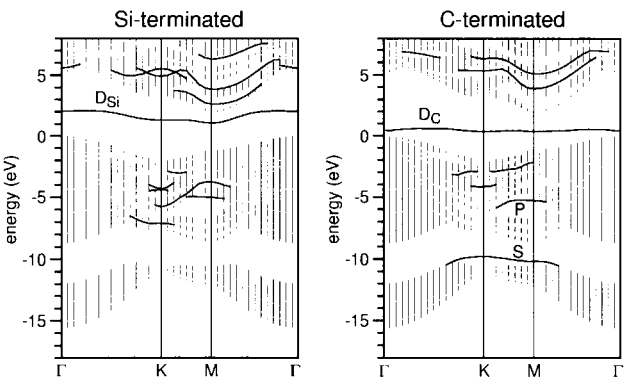


Fig. 2.43. Surface band structures of the relaxed Si-terminated (left panel) and C-terminated (right panel) 6H-SiC(0001)-(1 × 1) surfaces. The projected bulk band structure is shown by vertically shaded areas (Sabisch et al., 1997b).

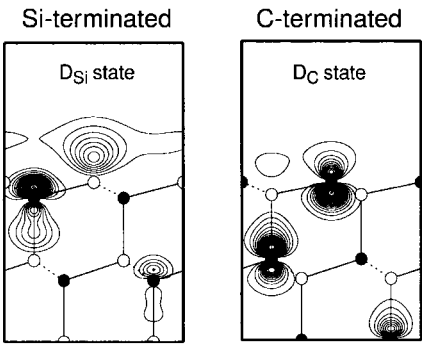


Fig. 2.44. Charge density contours of the dangling-bond states at the Γ-point of the relaxed Si-terminated (left panel) and C-terminated (right panel) 6H-SiC(0001)-(1 × 1) surfaces. The charge densites are presented for a side view of the relaxed structures (Sabisch et al., 1997b).

resulting band structures are thus metallic. This behavior is very similar to that of the ideal Si(111) surface, as discussed in Subsection 2.3.1. Comparing the energetic positions of $D_{Si}$ and $D_C$ it becomes obvious that $D_C$ occurs roughly 1.5 eV lower in energy than $D_{Si}$ which is due to the stronger C potential, as compared to that of Si. The ionicity of SiC gives rise to relative energy positions of these two bands which are similar to the related bands at the relaxed SiC(110) or GaAs(110) surfaces, respectively. The dispersion of $D_{Si}$ is more pronounced than that of $D_C$, because $D_{Si}$ is laterally more extended as can be seen in Fig. 2.44 showing charge density contours of these dangling bond states. Obviously, the dangling bonds are predominantly localized at the top-layer atoms and are oriented perpendicularly to the surface.

*2.5.5.2. Si-terminated 6H-SiC(0001)-($\sqrt{3} \times \sqrt{3}$) surfaces*

Owman and Mårtensson (1995) have investigated Si-terminated 6H-SiC(0001)-($\sqrt{3} \times \sqrt{3}$)R30° surfaces by STM. The authors observed images consistent with a structural model composed of 1/3 layer of Si or C adatoms in threefold-symmetric sites above the outermost Si–C bilayer, similar to the reconstructions observed for 1/3 monolayer of, e.g., Al, Ga, In or Pb on the Si(111) surface (Hamers, 1989; Nogami et al., 1987, 1988; Ganz et al., 1991). Similar structural models had been suggested by Kaplan (1989), before. From STM data alone, it is neither possible to identify which one of the elements (Si or C) constitutes the adatoms nor to determine in which of the two symmetry-allowed sites ($T_4$ or $H_3$) the adatoms are located. A mixture of adsorbed Si and C adatoms was excluded by Owman and Mårtensson (1995). But more complex structures like, e.g., trimers could not be excluded.

The $\sqrt{3} \times \sqrt{3}$ unit cell is three times as large as that of the relaxed surfaces and contains three atoms per layer unit cell in the substrate. Five adsorption models of the Si-terminated 6H-SiC(0001)-($\sqrt{3} \times \sqrt{3}$)R30° surface have been studied by first-principles calculations (Northrup and Neugebauer, 1995; Sabisch et al., 1997b). They are shown in Fig. 2.45 by top and side views. The structure parameters characterizing the different configurations are given in Fig. 2.45, as well. Si adatoms in $T_4$ (Fig. 2.45a) and $H_3$ (Fig. 2.45b) and C

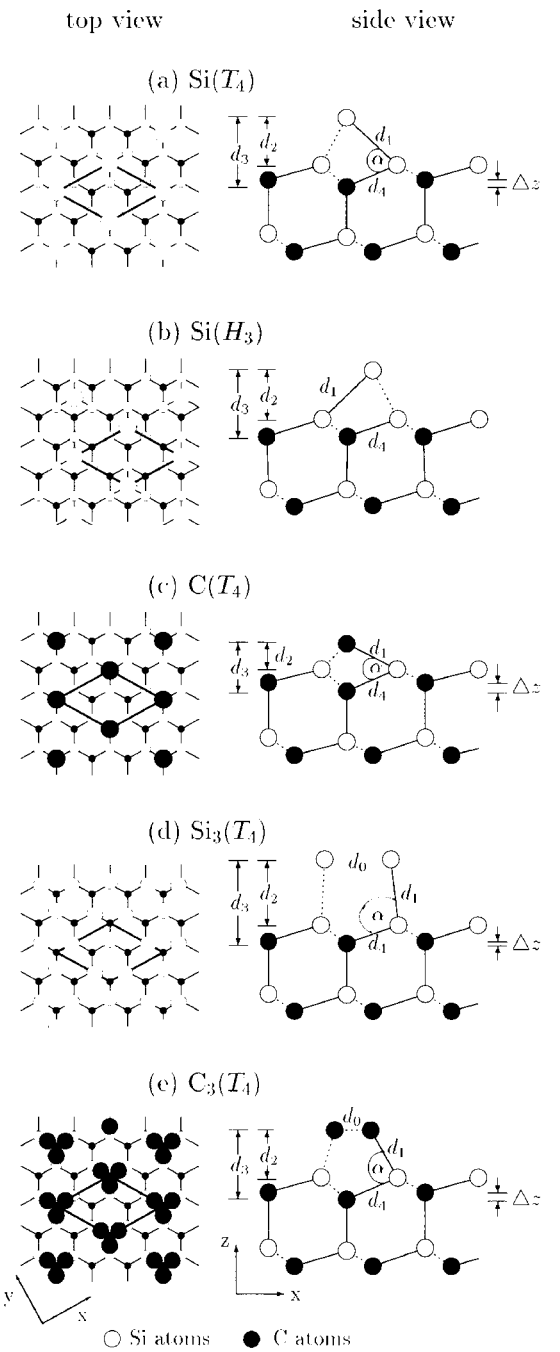


Fig. 2.45. Top and side views of the optimized ($\sqrt{3} \times \sqrt{3}$)R30° reconstructions of Si-terminated 6H-SiC(0001) surfaces. The $\sqrt{3} \times \sqrt{3}$ unit cells are indicated by heavy lines in the left panels. The structure parameters are introduced in the side views and their actual values are compiled in Table 2.5 (Sabisch et al., 1997b).

Table 2.5

Calculated optimal structure parameters (as defined in Fig. 2.45) for Si and C adatom, as well as, Si and C trimer reconstructions of Si-terminated 6H-SiC(0001)-($\sqrt{3} \times \sqrt{3}$)R30° surfaces (Sabisch et al., 1997b). The values in parentheses are the results of Northrup and Neugebauer (1995)

| | $Si(T_4)$ | $Si(H_3)$ | $C(T_4)$ | $Si_3(T_4)$ | $C_3(T_4)$ |
|---|---|---|---|---|---|
| $d_0$ (Å) | | | | 2.59 | 1.41 |
| $d_1$ (Å) | 2.41 (2.42) | 2.44 | 1.93 (1.98) | 2.39 | 1.92 |
| $d_2$ (Å) | 1.71 (1.75) | 1.73 | 0.92 (1.22) | 2.37 | 1.69 |
| $d_3$ (Å) | 2.50 | 2.36 | 1.70 | 3.03 | 2.46 |
| $d_4$ (Å) | 1.88 | 1.88 | 1.87 | 1.87 | 1.89 |
| $\Delta z$ (Å) | 0.25 (0.22) | | 0.31 (0.52) | 0.07 | 0.25 |
| $\alpha$ (°) | 70 | | 53 | 105 | 86 |

adatoms in $T_4$ positions (Fig. 2.45c) have been considered. In addition, Si and C trimers in $T_4$ positions (Figs. 2.45d, e) have been optimized. Adatoms in $T_4$ ($H_3$) positions reside above second (fourth) substrate-layer atoms (see, e.g., Figs. 2.45a, b). For shortness sake, we refer to the different configurations as $Si(T_4)$, $Si(H_3)$, $C(T_4)$, $Si_3(T_4)$ and $C_3(T_4)$, respectively. The optimal structures as resulting from total-energy minimization (Sabisch et al., 1997b) are drawn to scale in Figs. 2.45a–e. The respective structure parameters are given in Table 2.5.

In all five adsorption configurations the three substrate-surface dangling bonds per $\sqrt{3} \times \sqrt{3}$ unit cell become fully saturated by the adatoms. But now the adatoms have dangling bonds. Their number, however, is smaller than the number of the original dangling bonds at the clean substrate surface. In the configurations of Figs. 2.45a–c the number of dangling bonds is reduced by adatom adsorption to one third. In the case of the Si and C trimers (see Figs. 2.45d, e) the dangling-bond reduction sensitively depends on to which extent the dangling bonds at the trimer atoms become involved in chemical bonding. The newly established surface bonds $d_1$ in all five configurations have a bond length which turns out to be slightly larger than respective bulk bonds (2.33 Å for Si and 1.89 Å for SiC) and close to the sum of the covalent radii of the involved atoms ($r_C = 0.77$ Å and $r_{Si} = 1.17$ Å). The new surface bonds are significantly strained, however, since the respective bond angle $\alpha$ (see Fig. 2.45 and Table 2.5) is far from the tetrahedral angle of 109.5°. In all five configurations, the bond length $d_4$ between the first and second substrate layer atoms result as almost bulk-like. There is an important difference between the $T_4$ and $H_3$ configurations to be noted at this point. In the $T_4$ adatom configurations, the system can reduce its strain and increase the bond angle $\alpha$ by pushing down the second-layer C atom residing vertically below the adatom and lifting the other two C atoms in the $\sqrt{3} \times \sqrt{3}$ unit cell on the second substrate layer. In consequence, a buckling of the second substrate layer, characterized by $\Delta z$ (see Fig. 2.45 and Table 2.5) occurs. In the $H_3$ configuration, on the contrary, all three C atoms per unit cell on the second substrate layer are equivalent so that no buckling of the second layer can occur. Thus, strain relief can be accomplished much more efficiently in the $T_4$ than in the $H_3$ configuration.

In the optimized $Si(T_4)$ structure (see Fig. 2.45a) each Si adatom forms a bond of length $d_1 = 2.41$ Å (see Table 2.5) with each of the three Si substrate-surface layer atoms. By

pushing down the second layer C atom residing below the adatom and lifting the other two C atoms on the second substrate layer, the bond angle $\alpha$ results as 70°. This way, a buckling of $\Delta z = 0.25$ Å occurs. The results of Northrup and Neugebauer (1995) and of Sabisch et al. (1997b) for this configuration are in very close agreement (see Table 2.5).

In the optimized Si($H_3$) structure the bond lengths $d_1$, $d_2$ and $d_4$ are very similar to those at the optimized Si($T_4$) configuration. The discerning feature of the two is the buckling $\Delta z$ of the second substrate layer which is unequal zero only in the latter configuration. The Si($H_3$) configuration turns out to be energetically less favorable. The total energy of the Si($H_3$) configuration is higher by $\Delta E = 0.60$ eV per $\sqrt{3} \times \sqrt{3}$ unit cell as compared to the Si($T_4$) configuration in the results of Sabisch et al. (1997b) in very close agreement with the respective energy difference of $\Delta E = 0.54$ eV reported by Northrup and Neugebauer (1995).

In the optimized C($T_4$) configuration the bond length $d_1 = 1.93$ Å between C adatoms and Si substrate-surface layer atoms turns out to be smaller than the respective bond length $d_1 = 2.41$ Å in the Si($T_4$) configuration because of the smaller covalent radius of carbon. The distance of the C adatoms to the second-layer C atoms turns out to be only $d_3 = 1.70$ Å. In consequence, the buckling of the second substrate layer $\Delta z = 0.31$ Å is larger than that at the Si($T_4$) surface. Northrup and Neugebauer (1995) have obtained a similar bond length $d_1$ and even find a buckling of $\Delta z = 0.52$ Å in this case (see Table 2.5). The surface bonds in the C($T_4$) configuration are very strongly strained since $d_3$ is very small and $\alpha$ turns out to be only 53°. Because of their smaller covalent radius the C adatoms in C($T_4$) reside nearer to the Si substrate-surface layer atoms than the Si adatoms in Si($T_4$).

For Si trimers adsorbed in $T_4$ positions at the substrate surface, it is found that the individual Si atoms of the trimers move into new positions vertically above the Si substrate-surface layer atoms (see Fig. 2.45d). In the optimized configuration their distance $d_0 = 2.59$ Å is considerably larger than twice the covalent radius of Si or the Si bulk-bond length of 2.33 Å, respectively. This behavior is very similar, in general, to that observed at the Si-terminated $\beta$-SiC(001)-(2 × 1) surface having the same physical origin (cf. Section 2.5.3.1). The surface bonding configuration is now nearly tetrahedral resulting in an angle of $\alpha = 105°$ and a concomitantly small buckling $\Delta z = 0.07$ Å of the second substrate layer. The bond length $d_1$ between the Si adatoms and the Si substrate surface layer atoms of 2.39 Å is close to the bulk-bond length of Si and to the sum of the covalent radii of two Si atoms.

For C trimers adsorbed in $T_4$ positions the resulting bond length $d_1 = 1.92$ Å is again close to the sum of the covalent radii of C and Si. The three C trimer atoms saturate the substrate-surface dangling bonds and form C bonds with a bond length of $d_0 = 1.41$ Å. This value is between the length of C=C double bonds (1.36 Å) in molecules and C–C single bonds (1.52 Å) in bulk diamond. The bond angle $\alpha = 86°$ is closer to the tetrahedral angle than for the Si($T_4$) and C($T_4$) adatom geometries. Because of the smaller strain in the bonds, the buckling of the C atoms in the second substrate layer ($\Delta z = 0.25$ Å) is smaller than for the C($T_4$) structure ($\Delta z = 0.31$ Å).

To decide which one of these configurations is the most favorable surface structure one cannot directly compare the total energies of the different optimized adsorption models in a meaningful way since the number (one or three) and the species (Si or C) of the adatoms are different. Nevertheless, one can compare the different structures by referring

to the grandcanonical potential $\Omega$ at $T = 0$ K, as suggested by Qian et al. (1988b) and by Northrup and Froyen (1993)

$$\Omega = E - \sum_i \mu_i n_i . \tag{2.39}$$

The $\mu_i$ are the chemical potentials of atomic species $i$ and $n_i$ is the number of atoms $i$ in the system. If a system consisting of a SiC crystal and Si and C atoms in the gas phase is in thermodynamic equilibrium, the following relation holds:

$$\mu_{\mathrm{Si}} + \mu_{\mathrm{C}} = \mu_{\mathrm{SiC(bulk)}} . \tag{2.40}$$

In addition, the following relation holds:

$$\mu_{\mathrm{SiC(bulk)}} = \mu_{\mathrm{Si(bulk)}} + \mu_{\mathrm{C(bulk)}} - \Delta H_{\mathrm{f}} . \tag{2.41}$$

Here $\mu_{\mathrm{Si}}$ and $\mu_{\mathrm{C}}$ are the chemical potentials of the free atoms in the gas phase while $\mu_{\mathrm{Si(bulk)}}$, $\mu_{\mathrm{C(bulk)}}$ and $\mu_{\mathrm{SiC(bulk)}}$ are the chemical potentials of the atoms in the respective bulk crystals. Finally, $\Delta H_{\mathrm{f}}$ is the formation enthalpy of the SiC bulk crystal. The above relation allows one to eliminate $\mu_{\mathrm{C}}$ in the grandcanonical potential. Application of this scheme to SiC surfaces has been discussed in detail by Northrup and Neugebauer (1995) and Sabisch et al. (1997b). One can evaluate $\Omega$ as a function of the chemical potential of the involved Si atoms, alone. The formation enthalpy results as $\Delta H_{\mathrm{f}} = 0.51$ eV and $\Delta H_{\mathrm{f}} = 0.75$ eV in the calculations of Sabisch et al. (1997b) and of Northrup and Neugebauer (1995), respectively. The experimental value is 0.72 eV.

The chemical potential $\mu_{\mathrm{Si}}$ is restricted to the range (Qian et al., 1988b; Northrup and Froyen, 1993)

$$\mu_{\mathrm{Si(bulk)}} - \Delta H_{\mathrm{f}} \leqslant \mu_{\mathrm{Si}} \leqslant \mu_{\mathrm{Si(bulk)}} . \tag{2.42}$$

The result of the calculations by Sabisch et al. (1997b) is shown in Fig. 2.46. Obviously, C adatoms and C trimers are less favorable than the ideal Si-terminated surface. This result derives from the fact that C adatoms are too small to efficiently saturate the dangling bonds on the Si substrate surface layer atoms (Northrup and Neugebauer, 1995). In particular, the bonds between C adatoms and Si substrate-surface layer atoms are far from tetrahedral and they are thus strongly strained. The relaxation of the ideal surface slightly lowers the energy. Si($H_3$) and Si($T_4$) configurations are more favorable. The Si($T_4$) configuration is the lowest energy structure for all allowed $\mu_{\mathrm{Si}}$ values (Northrup and Neugebauer, 1995; Sabisch et al., 1997b). The energetic order of Si($T_4$) and C($T_4$) corresponds to the size of the bond-angle $\alpha$ which is 70° and 53°, respectively, in the two cases (see Table 2.5). Note that the change in $\Omega$ increases (decreases) for adsorbed C (Si) atoms as a function of $\mu_{\mathrm{Si}}$.

From this analysis one concludes that the Si-terminated 6H-SiC(0001) surface shows a $\sqrt{3} \times \sqrt{3}$ reconstruction if ample Si and C atoms are offered in the gas phase. This conclusion and the actual Si($T_4$) structure, as resulting from the calculations, are compatible with experimental data (Bermudez, 1997; Kaplan, 1989; Nakanishi et al., 1989; Starke et al., 1995; Owman and Mårtensson, 1995; Li and Tong, 1996).

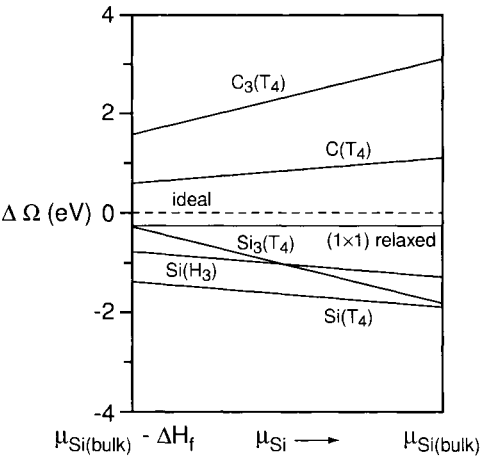


Fig. 2.46. Comparison of grand canonical potentials (relative to that of the ideal surface) for six different structural models (relaxation and five different reconstructions) of the Si-terminated 6H-SiC(0001)-($\sqrt{3} \times \sqrt{3}$)R30° surface as a function of the Si chemical potential $\mu_{Si}$ for the allowed range (Sabisch et al., 1997b).

The surface electronic structure for all discussed adsorption models of the Si-terminated 6H-SiC(0001)-($\sqrt{3} \times \sqrt{3}$)R30° surface has been calculated and discussed in detail by Northrup and Neugebauer (1995) and Sabisch et al. (1997b). The surface band structure and salient charge densities of the energetically most favorable Si($T_4$) configuration as calculated by Sabisch et al. (1997b) are shown in Fig. 2.47. Within the gap-energy region there are three bands of localized states. The bands $P_1$ and $P_2$ with $p_x$ and $p_y$ symmetry originate from the interaction of the Si($T_4$) adatoms with the Si substrate surface layer atoms. Their charge densities are largely similar in nature. The band D having mostly $p_z$-wavefunction character originates from the dangling-bond states localized at the Si($T_4$) adatoms (see middle panel of Fig. 2.47). These bands show a very small dispersion because the Si adatoms interact only very weakly since they have a very large distance of 5.32 Å. The D band is half filled since there is only one adatom per $\sqrt{3} \times \sqrt{3}$ unit cell so that the surface band structure is metallic.

Contrary to the theoretical results, recent ARPES (Johansson et al., 1996a) and KRIPES (Themlin et al., 1997) investigations have observed one band of occupied and one band of empty dangling-bond states in the gap-energy region. The authors of both references conclude on the basis of their data that the surface is semiconducting. This is an obvious contradiction between theory and experiment which calls for further investigations. One possible reason for the discrepancy could be the fact that the actual structure of this surface is more complex than was anticipated in the calculations, so far. If there were adatoms with three or five valence electrons at the surface instead of Si adatoms this would lead to semiconducting surfaces. In the first case one empty and in the second case one fully occupied dangling-bond band would result within the gap but certainly not both of them as observed in experiment (Johansson et al., 1996b; Themlin et al., 1997). Another possible explanation could be related to many-body correlation effects of the Hubbard-type in the very flat half-filled D band of Fig. 2.47 giving rise to a splitting of this band into two

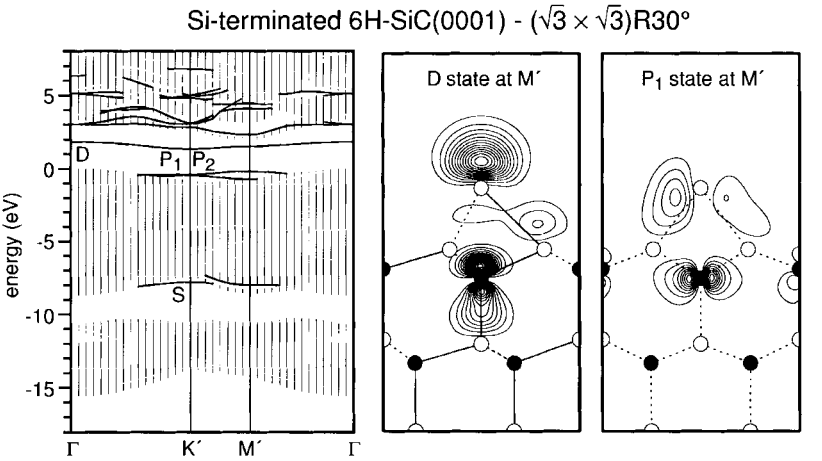


Fig. 2.47. Surface band structure of the Si-terminated 6H-SiC(0001)-($\sqrt{3} \times \sqrt{3}$)R30° surface for Si adatoms in $T_4$ position (see Fig. 2.45a) and charge density contours of salient surface states at the M′ point of the SBZ (Sabisch et al., 1997b). The charge density of the $P_1$ state is presented in the $y$–$z$ plane. The charge density of the D state is presented in the $x$–$z$ plane containing the middle Si–C zig-zag chain for Si adatoms in $T_4$ position (see Fig. 2.45a). The projected bulk band structure for the $\sqrt{3} \times \sqrt{3}$ SBZ is shown by vertically shaded areas.

bands. This would result in a fully occupied (lower Hubbard band) and an empty dangling-bond band (upper Hubbard band) within the gap energy region, as observed in experiment. Northrup and Neugebauer (1998) have carried out a calculation in this framework and have found results in good accord with the measured data.

*2.5.5.3. C-terminated 6H-SiC(0001)-($\sqrt{3} \times \sqrt{3}$) surfaces*

Several ($\sqrt{3} \times \sqrt{3}$)R30° reconstruction models of the C-terminated substrate surface have been investigated, to date. Si and C adatoms and adsorbed Si trimers have been considered (Sabisch et al., 1997b, 1998). The optimal structures as obtained from our total-energy minimization are shown in Figs. 2.48a–c by top and side views. The relevant structure parameters are defined in the figure and their actual values are compiled in Table 2.6. In the Si($T_4$) and C($T_4$) configurations (see Fig. 2.48a, b), the adatoms are bound to three substrate-surface layer atoms. The bond lengths $d_1$ (see Fig. 2.48 and Table 2.6) turn out to be somewhat larger than respective bulk-bond lengths of SiC (1.89 Å) and diamond (1.52 Å). In both configurations the resulting distances $d_2$ between adatoms and Si atoms in the second substrate layer are relatively small because of the very small covalent radius of C. In consequence, a large buckling $\Delta z$ of the second substrate layer results. The Si atoms on this layer show a much larger buckling than the C atoms on the corresponding second layer of the Si-terminated surface (see Table 2.5). This difference is again related to the differences in angular forces at C or Si atoms, respectively, involved in the reconstruction-induced bond bending.

Si trimers originally adsorbed in $T_4$ positions move upon energy minimization to ideal on-top positions above the C atoms at the substrate-surface layer and a geometrically ideal (1 × 1) structure results (see Fig. 2.48c). One should note, however, that the Si adatoms

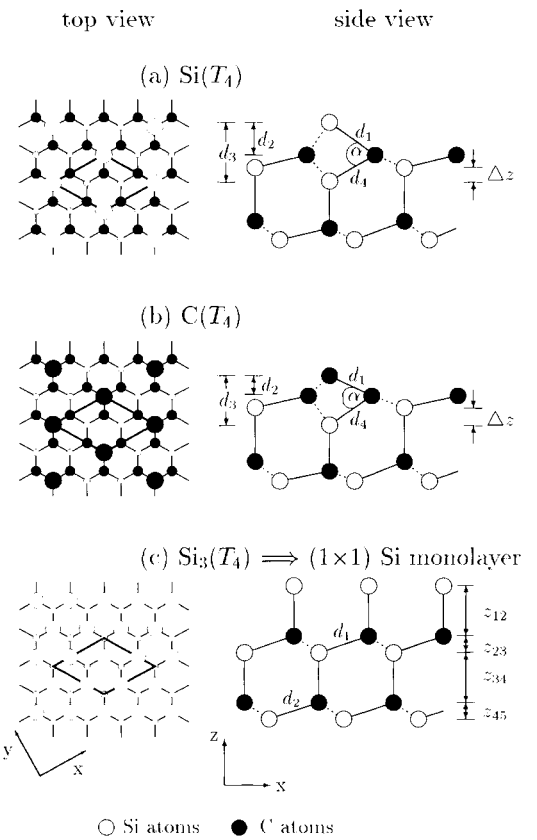


Fig. 2.48. Top and side views of the optimized ($\sqrt{3} \times \sqrt{3}$)R30° reconstructions of the C-terminated 6H-SiC(0001) surfaces (Sabisch et al., 1997b). The structure parameters are introduced in the side views (see also caption of Fig. 2.45). Their actual values are compiled in Table 2.6.

Table 2.6

Optimized structure parameters (as defined in Fig. 2.48) for the Si and C adatom and Si trimer reconstructions of C-terminated 6H-SiC(0001)-($\sqrt{3} \times \sqrt{3}$)R30° surfaces. Adsorption of Si trimers leads to an ideal (1 × 1) structure in which the Si surface atoms are one-fold coordinated with the C substrate-surface layer atoms and have three unsaturated dangling bonds each (3DB surface)

| | $Si(T_4)$ | $C(T_4)$ | $Si_3(T_4)$ |
|---|---|---|---|
| $d_0$ (Å) | | | 3.07 |
| $d_1$ (Å) | 2.04 | 1.66 | 1.88 |
| $d_2$ (Å) | 1.24 | 0.73 | 1.88 |
| $d_3$ (Å) | 2.21 | 1.86 | 2.51 |
| $d_4$ (Å) | 1.89 | 1.87 | 1.88 |
| $\Delta z$ (Å) | 0.50 | 0.68 | 0.00 |
| $\alpha$ (°) | 68 | 63 | 109.5 |

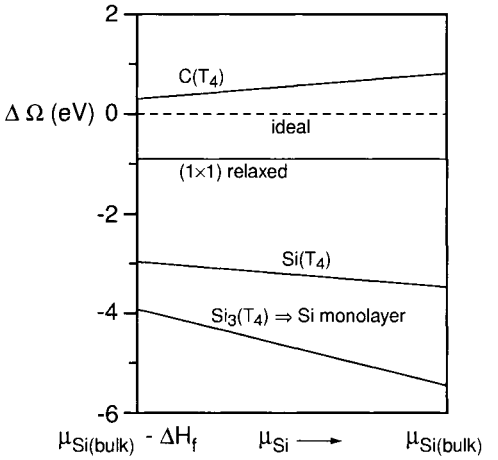


Fig. 2.49. Comparison of grand canonical potentials (relative to that of the ideal surface) for four different structural models (relaxation and three different reconstructions) of the C-terminated 6H-SiC(0001)-($\sqrt{3} \times \sqrt{3}$)R30° surface as a function of the chemical potential $\mu_{Si}$ for the allowed range (for details, see text) (Sabisch et al., 1997b).

are only one-fold coordinated to the substrate in this structure having three unsaturated dangling bonds each. It is a 3DB surface structure, therefore.

Figure 2.49 shows the change in the grandcanonical potential $\Omega$ relative to its value at the ideal surface for the investigated structures. As in the case of the Si-terminated substrate surface (cf. Fig. 2.46), C adatoms turn out to be less favorable than the ideal and the relaxed surface. The Si($T_4$) configuration is considerably more stable for all values of $\mu_{Si}$. The Si monolayer resulting from adsorbed Si trimers after energy minimization, amazingly enough, is energetically most favorable. In this case there are three equivalent adatoms per $\sqrt{3} \times \sqrt{3}$ unit cell while in the Si($T_4$) configuration there is only one adatom per unit cell. Comparing these two structures, one has to have in mind that in the first configuration three Si adatoms are adsorbed in ideal onefold-coordinated sites, having three dangling bonds each, while in the second configuration one Si adatom is adsorbed in a $T_4$ site of the $\sqrt{3} \times \sqrt{3}$ unit cell and two free Si atoms are in the gas phase. Although the Si($T_4$) adatom is stronger bound to the substrate than each Si adatom in the ideal (1 × 1) configuration, the monolayer system has the lower grandcanonical potential. These results clearly show that the investigated $\sqrt{3} \times \sqrt{3}$ structures of the C-terminated surface are no minimum configurations. Instead, an adsorbed Si monolayer turns out to be energetically much more favorable. Nevertheless, it seems obvious that such a monolayer cannot be the stable structure of this surface since each adlayer Si atom has three unsaturated dangling bonds in this (1 × 1) configuration. A more complicated reconstruction is instead to be expected. This conclusion is in accord with experiment which has observed (3 × 3) reconstructions of this surface (Nakanishi et al., 1989; Starke et al., 1995; Schardt et al., 1995). Only Li and Tsong (1996) have observed a $\sqrt{3} \times \sqrt{3}$ reconstruction in their STM investigations. They have annealed a (3 × 3) sample under a Si flux at 850 °C which changed into a $\sqrt{3} \times \sqrt{3}$ reconstruction after further annealing at 950 °C. Another possibility could be a $\sqrt{3} \times \sqrt{3}$

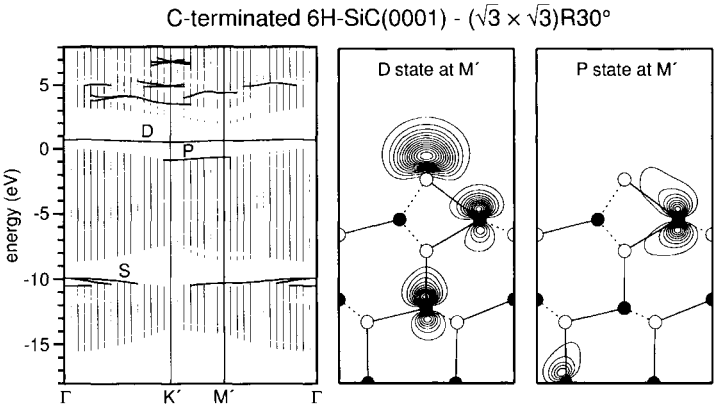


Fig. 2.50. Surface band structure of the C-terminated 6H-SiC(0001)-($\sqrt{3} \times \sqrt{3}$)R30° surface for Si adatoms in $T_4$ position (see Fig. 2.48a) and charge density contours of salient surface states at the M′ point of the SBZ (Pollmann et al., 1997). The charge densities are presented in the $x$–$z$ plane containing the middle Si–C zig-zag chain (see Fig. 2.45).

$B_5$ model, as discussed by Badziag (1990) and Li and Tsong (1996), in which Si adatoms are adsorbed in $T_4$ positions above the C-terminated surface and all second-layer substrate Si atoms are replaced by C atoms. Also impurity-stabilized (1 × 1) structures, as observed by Bermudez (1995), should be considered in this context.

The surface band structure of the optimized Si($T_4$) adatom configuration is shown in Fig. 2.50 together with charge density contours of the gap surface states. Surface band structures for the other models of the C-terminated 6H-SiC(0001) surface were given by Sabisch et al. (1997b, 1998). It is revealing to compare this surface band structure with that in Fig. 2.47. In the gap energy region, there occurs a fully occupied band P and a half filled dangling-bond band D. The D band in Fig. 2.50 is roughly 1 eV lower in energy than that in Fig. 2.47 originating from the stronger C potentials on the substrate-surface layer of the C-terminated substrate as compared to the Si potentials on the substrate-surface layer of the Si-terminated substrate. This is again an effect of the ionicity of SiC. The related charge density of the dangling-bond state D in Fig. 2.50 is localized at the Si($T_4$) adatoms and shows a strong coupling to the C atoms on the first and third substrate layers. This is significantly different from the character of the D state in Fig. 2.47.

In summary, relaxed nonpolar $\beta$-SiC(110) and 2H-SiC(10$\bar{1}$0) show bond-length contracting rotation-relaxations very much like the surfaces of other ionic wide-band-gap semiconductors. Cubic Si- or C-terminated polar $\beta$-SiC(001) surfaces show significantly different reconstructions. The C-terminated surfaces exhibit double-bonded C=C surface dimers very much like the C(001)-(2 × 1) surface while the Si-terminated surface shows a reconstruction that differs considerably from that of Si(001)-(2 × 1). The polar hexagonal 6H-SiC(0001)-(1 × 1) surfaces show a strong inward relaxation of the top layer towards the substrate, the relaxation being larger for the C- than for the Si-terminated surface. For the reconstructed polar Si-terminated 6H-SiC(0001)-$\sqrt{3} \times \sqrt{3}$ surface, adsorption of

Si adatoms in $T_4$ positions turns out to be most favorable. The polar C-terminated 6H-SiC(0001)-$\sqrt{3} \times \sqrt{3}$ surface appears to be no stable energy-minimum configuration.

The surface electronic structure for a number of these surfaces has been discussed in comparison with PES and EELS data. Nevertheless, many of the theoretical results are predictions, at the time being, since ARPES and KRIPES data on SiC surfaces are still fairly scarce, to date. Some of the theoretical results are in good accord with structure and electronic structure data but significant deviations between theory and experiment are found in cases, most noticeably for the structure of the Si-terminated $\beta$-SiC(001)-$(2 \times 1)$ surface and for the electronic structure of the 6H-SiC(0001)-$\sqrt{3} \times \sqrt{3}$ surfaces. More work seems necessary to resolve these issues.

## 2.6. Surfaces of III-V semiconductors

Among the low-index faces of semiconductors having zincblende structure, the (110) surfaces have been most intensively studied. They are the cleavage faces of these crystals and show electrostatic stability since each layer unit cell contains an equal number of anions and cations. Indeed, it turns out that the (110) surfaces only show relaxed $(1 \times 1)$ structures while the (001) and (111) surfaces show more complicated reconstructions. The atomic structure of nonpolar (110) surfaces of III-V semiconductors has been determined, e.g., by LEED (Kahn et al., 1978a, b; Meyer et al., 1979; Kübler et al., 1980; Duke et al., 1983; Tong et al., 1984; Puga et al., 1985), STM (Feenstra et al., 1987) and by theoretical structure optimizations (Chadi, 1979a; Pandey, 1982a; Srivastava et al., 1983; Schmeits et al., 1983; Mailhiot et al., 1984; Qian et al., 1988a; Alves et al., 1991; Sabisch et al., 1995). Geometrically ideal (001) and (111) III-V surfaces have either anions or cations in their surface layers, respectively (see Section 2.3.1). They are polar surfaces, therefore. Their ideal structure is unfavorable with respect to electrostatic energy and does not obey the 'electron counting rule' (Pashley, 1989). They show a variety of reconstructions.

### *2.6.1. The nonpolar GaAs(110) surface*

The nonpolar GaAs(110) surface is one of the most-intensively studied and one of the best well-known surfaces. Detailed accounts of the history of the determination of the relaxation of GaAs(110) have been given in various review articles (see, e.g., Duke, 1982, 1988a, b). It is the prototype for all (110) surfaces of the common III-V compound semiconductors. The atomic and electronic structure is currently believed to be known with a precision unequalled by any other semiconductor surface.

Cleaving III-V semiconductors perpendicular to the [110] direction, one dangling bond is created at each surface-layer anion and cation giving rise to two dangling-bond bands in the gap energy region (see Subsection 2.3.1). Since the anion is lower in energy than the cation, the cation-derived dangling bond is emptied and the respective charge is transferred into the anion-derived dangling bond. Concomitantly, a rehybridization of the three-fold coordinated surface atoms occurs. The cations prefer a planar-trigonal $sp^2$ configuration with their nearest neighbors while the anions prefer a pyramidal $s^2p^3$ configuration as in $PH_3$ or $AsH_3$ molecules. In consequence of this rehybridization, a relaxation of the (110)

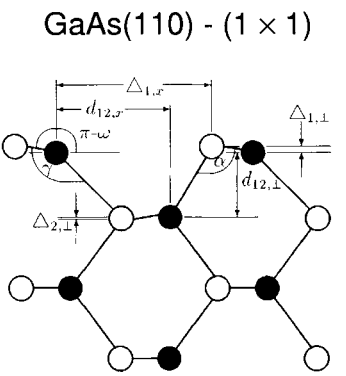


Fig. 2.51. Side view of the relaxed GaAs(110)-(1 × 1) surface defining the structural parameters characterizing the relaxation.

surfaces occurs by which the surface can lower its total energy. The (110) surfaces of III-V semiconductors are relaxed with their group V atoms (As, P, In) moving out of the surface plane and their group III atoms (Ga, In) moving below the surface plane towards the bulk. A respective rotation of the anion-cation bonds at the surface of about 30° occurs. The surface bond length is largely preserved in this process which is referred to as 'bond-length-conserving rotation relaxation'. Since there is one anion and one cation per (1 × 1) unit cell already at the ideal surface, this structural change retaining the (1 × 1) symmetry constitutes a relaxation.

The structure of the relaxed GaAs(110) surfaces is shown schematically by a side view in Fig. 2.51, where the structure parameters commonly used to characterize the relaxation (see, e.g., Duke et al., 1983; Tong et al., 1984) are defined, as well. The relaxation is characterized by the rotation of the As atoms out of the surface plane and of the Ga atoms below the surface plane giving rise to the bond-rotation angle $\omega$. The Ga–As bonds on the first subsurface plane counterrotate by a very small angle so that the vertical distance between the As and Ga subsurface layers is only 0.06 Å. In Table 2.7 we compare results for the structural parameters as obtained more recently from first-principles total energy minimization calculations (Alves et al., 1991; Sabisch et al., 1995) with LEED data (Duke et al., 1983; Tong et al., 1984). There is amazingly close agreement between theory and experiment. In the comparison, one should have in mind that LDA total energy minimization as employed in the calculations typically underestimates the lattice constants by some 1–2%. With this in mind, the agreement is even more impressive. These results confirm the well-known bond-length-conserving rotation relaxation model (Duke et al., 1983). GaAs(110) is the prototype example for a bond-length-conserving rotation relaxation governed mainly by the quantum mechanical hybridization mechanism as briefly discussed in Section 2.5.1.

The surface electronic structure of the ideal and the relaxed GaAs(110)-(1 × 1) surfaces are shown in Fig. 2.52 in direct comparison to highlight the effects of the surface relaxation on the surface electronic structure. It is obvious from the figure that the occupied anion-derived dangling-bond band $A_5$ moves to lower and the empty cation-derived dangling-bond band $C_3$ moves to higher energy upon relaxation clearing the gap from surface states

Table 2.7

Optimized structure parameters (as defined in Fig. 2.51) for the relaxed GaAs(110)-(1 × 1) surface, as resulting from recent *ab initio* calculations in comparison with experimental data

| GaAs(110) | a | b | c | d |
|---|---|---|---|---|
| $a_b$ (Å) | 5.56 | 5.54 | 5.65 | 5.65 |
| $d_b$ (Å) | 2.41 | 2.40 | 2.45 | 2.45 |
| $\Delta_{1,\perp}$ ($d_b$) | 0.28 | 0.29 | 0.28 | 0.28 |
| $\Delta_{1,x}$ ($d_b$) | 1.83 | 1.82 | 1.84 | 1.78 |
| $\Delta_{12,\perp}$ ($d_b$) | 0.59 | 0.60 | 0.59 | 0.60 |
| $\Delta_{12,x}$ ($d_b$) | 1.32 | 1.34 | 1.36 | 1.29 |
| $\Delta_{2,\perp}$ ($d_b$) | −0.04 | −0.04 | −0.02 | −0.01 |
| $\omega$ (°) | 30.20 | 30.60 | 31.10 | 28.00 |

[a]Alves et al. (1991). [c]Duke et al. (1983).
[b]Sabisch et al. (1995). [d]Tong et al. (1984).

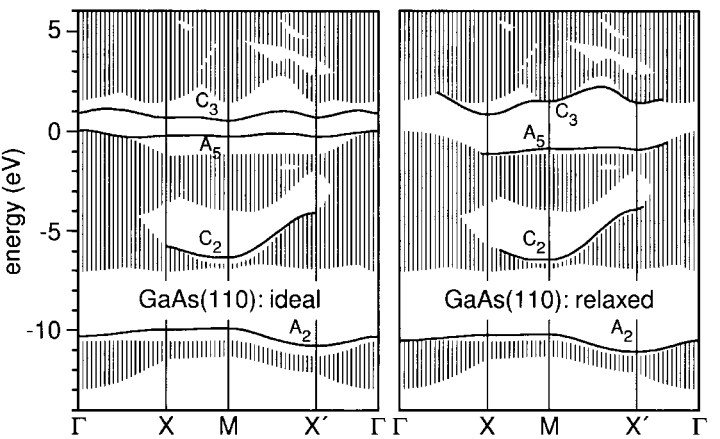


Fig. 2.52. Surface band structure of the ideal and the relaxed GaAs(110)-(1 × 1) surfaces. The PBS is shown by vertically shaded areas in each case (Sabisch et al., 1995).

and reducing the total energy. The energy gain per unit cell due to relaxation amounts to $\Delta E = 0.80$ eV. The surface is semiconducting.

Charge density contours of the $A_5$ and the $C_3$ states at the M-point of the SBZ are shown in the left and right panels of Fig. 2.53, respectively. The figures clearly reveal the localized nature and the origin of the related states. They are amazingly similar to respective states at the SiC(110)-(1 × 1) surface (see Fig. 2.35, for comparison). Calculated energy values of occupied surface states (see, e.g., Alves et al., 1991; Sabisch et al., 1995) are in excellent agreement with experimental data (see Table 2.8).

As discussed in Section 2.2.6, LDA calculations fail to yield the correct gap and, in consequence, place empty surface states too low in energy, as compared to experiment.

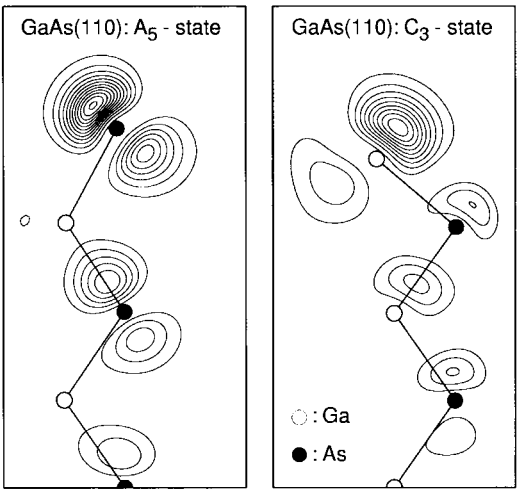


Fig. 2.53. Charge densities of the As- and Ga-derived dangling-bond states $A_5$ and $C_3$ at the M-point of the relaxed GaAs(110)-(1 × 1) surface (Sabisch et al., 1995).

Table 2.8
Comparison of calculated (Alves et al., 1991; Sabisch et al., 1995) and measured energies of salient surface states at the relaxed GaAs(110) surface

| | Alves et al. | Sabisch et al. | Experiment |
|---|---|---|---|
| $A_2(X)$ | −10.10 | −10.24 | −10.04[a], −11.0[b] |
| $A_3(X)$ | −3.73 | −3.68 | −3.7[c] |
| $A_5(X)$ | −1.02 | −1.11 | −1.2[a], −1.3[d] |
| $C_3(X)$ | 0.83 | 0.85 | 1.4[a], 1.7[e] |
| $C_1(M)$ | −6.97 | −7.00 | −7.0[f] |
| $C_2(M)$ | −6.42 | −6.51 | −6.6[a,c] |

[a]van Laar et al. (1977).
[b]Pandey et al. (1977).
[c]Williams et al. (1978).
[d]Huijser et al. (1978).
[e]Reihl et al. (1988).
[f]Knapp et al. (1976).

To resolve this issue for the case of GaAs(110), Zhu et al. (1989b) have investigated the surface by quasiparticle band structure calculations. Their results are shown in Fig. 2.54 in comparison with ARPES (Huijser et al., 1978) and KRIPES data (Straub et al., 1985a, b; Reihl et al., 1988).

### *2.6.2. Other nonpolar (110) III-V surfaces*

The electronic properties of the (110) surfaces of III-V compounds present strong similarities since these crystals all have zincblende structure and are isoelectronic. All materials are predicted to have surface states in the fundamental gap for the ideal unrelaxed surface

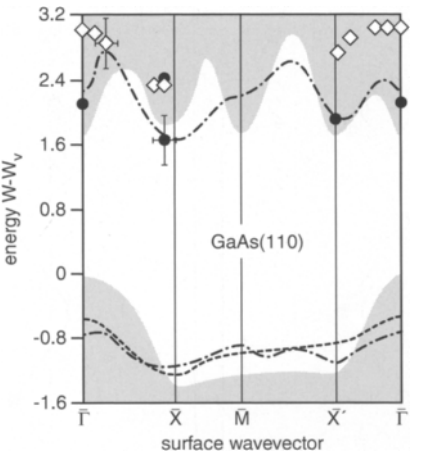


Fig. 2.54. Surface band structure of the relaxed GaAs(110) surface as resulting from GWA calculations (Zhu et al., 1989b) in comparison with experimental data (Huijser et al., 1978, dashed lines; Straub et al., 1985a, b, full dots; Reihl et al., 1988, diamonds).

due to the presence of unsaturated bonds (see, e.g., the discussion in Subsection 2.3.1). In all cases the surface relaxation is responsible for an almost complete removal of dangling-bond states from the gap (see, e.g., Fig. 2.52), with the noticeable exception of GaP for which most of the data indicate that the empty surface-state band is situated inside the gap energy region (Huijser et al., 1977; Guichar et al., 1979; Lassabatere et al., 1987; Manghi et al., 1990a, b) and GaSb where a tail of filled surface states has been observed above the valence band maximum (Manzke et al., 1987).

In a more recent DFT-LDA study, Alves et al. (1991) have investigated structural and electronic properties of the (110) surfaces of GaP, InP, GaAs and InAs. The resulting surface band structures of the GaP, InP, and InAs(110) surfaces are shown in Fig. 2.55 in direct comparison. They are very similar to the surface band structure (cf. Fig. 2.52 ) of GaAs(110).

Measured band gaps of the (110) surfaces at one high-symmetry point of the SBZ for the Ga and In compounds are shown in Fig. 2.56. They have been obtained from combined ARPES and KRIPES measurements (Carstensen et al., 1990). When comparing these experimental results with the calculated surface band structures (Figs. 2.52 and 2.55) one has to take the LDA band gap underestimation into consideration. On the contrary, the GW quasiparticle band structure for GaAs(110) in Fig. 2.54 shows a respective gap of 3.1 eV in good accord with the data. We do not address explicitly the calculation of ARPES and KRIPES spectra in this chapter. However, we would like to note in passing that important contributions to the analysis of photoemission and inverse photoemission spectra have been made by Schattke et al. (see, e.g., Schattke, 1997, and references therein).

More recently, Ebert et al. (1996) have studied electronic resonances at (110) surfaces of III-V semiconductors employing STM measurements and DFT-LDA calculations. The authors have shown that surface resonances have a marked influence on STM images. While the images at negative voltages are dominated as expected by the occupied dangling

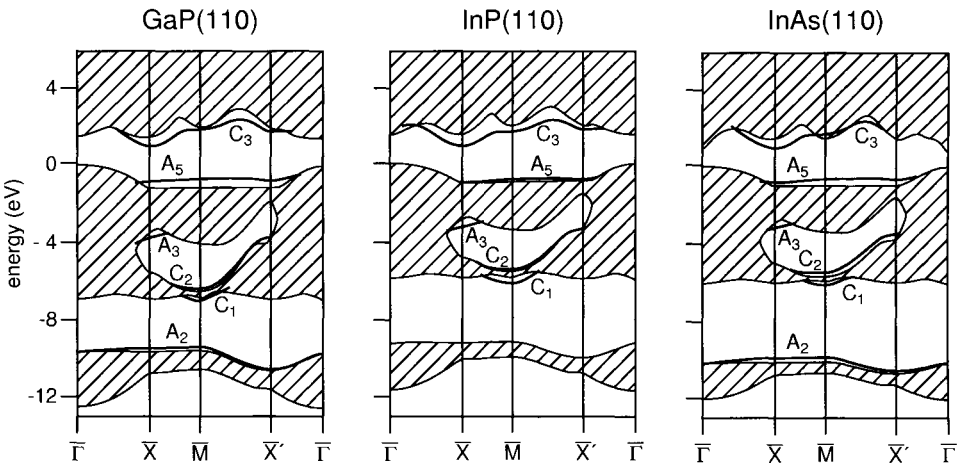


Fig. 2.55. Surface band structures of the relaxed (110)-(1 × 1) surfaces of GaP, InP, and InAs. The PBS is shown by shaded areas in each case (Alves et al., 1991).

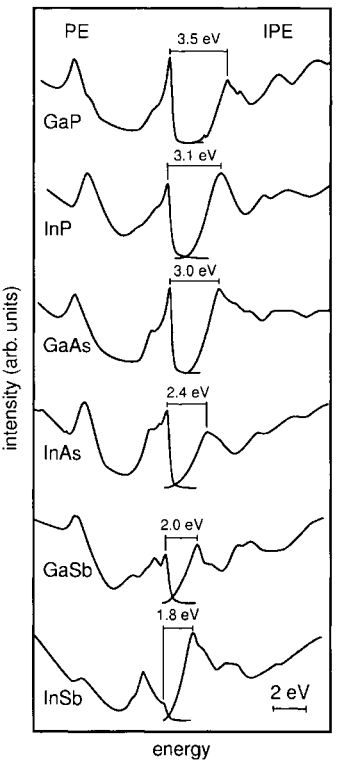


Fig. 2.56. Band gaps at the X′ point of the SBZ of the (110) surfaces of Ga and In compound semiconductors, as obtained from combined ARPES and KRIPES measurements (Carstensen et al., 1990).

bond state $A_5$, the empty state images are not governed by the empty dangling bond state $C_3$ but rather by empty resonances that lead to a 90° rotation of the apparent rows.

### 2.6.3. *Polar GaAs surfaces*

The understanding of the surface atomic and electronic structure of (111) and (001) compound semiconductor surfaces has advanced considerably during the past decade. As a result, the nature of the reconstructions of GaAs(001) and GaAs(111) are now known with a good degree of confidence. In their geometrically ideal (1 × 1) configuration, polar (001) and (111) surfaces of GaAs are metallic (see Section 2.3.1). The observed reconstructions on both surfaces, however, reveal nonmetallic surface band structures which can easily be understood in context of the electron counting rule (Pashley, 1989; see Section 2.6.3.1).

Structural properties of polar GaAs surfaces have been summarized in a number of reviews (Hansson and Uhrberg, 1988; LaFemina, 1992; Kahn, 1994; Mönch, 1995; Duke, 1996). We, therefore, restrict ourselves to a brief discussion of basic building blocks of the reconstructions occurring at these surfaces in the context of the electron counting rule and address the results of most recent DFT-LDA electronic structure calculations of the GaAs(001) surface (Schmidt and Bechstedt, 1996) in some detail.

#### 2.6.3.1. *Electron counting rule*

The nature of the reconstruction of, e.g., GaAs(111)-(2 × 2) and GaAs(001)-(2×4) can be rationalized in the context of the electron counting rule. The atomic arrangements of the surface atoms give rise to an ordered array of 1/4 of a monolayer of Ga vacancies at the Ga-rich GaAs(111)-(2 × 2) surface and As dimers and a missing dimer per unit cell at the As-stabilized GaAs(001)-(2×4) surface. Polar (001) and (111) surfaces of GaAs are metallic in their geometrically ideal (1 × 1) configuration (see Section 2.3.1). However, the observed reconstructions on both surfaces lead to nonmetallic surface band structures. This nonmetallicity has been used as an important condition for predicting the atomic structure of GaAs surfaces. It can be formalized into a simple 'electron-counting rule' (cf. Pashley, 1989). According to this rule, the stable surfaces of a III-V semiconductor such as GaAs correspond to those structures in which the number of 'donor-like' states (e.g., Ga dangling bonds) is as close as possible to the number of available 'acceptor-like' states (e.g., As dangling bonds). The rule ensures that the predicted surface structures are nonmetallic and nonpolar. Furthermore they are metastable at least, since the compensation of the donor electrons leaves no occupied states in the upper part of the gap which otherwise could easily induce other reconstructions. The nonpolarity condition for the stability of reconstructed polar surfaces was initially proposed by Harrison (1979). Obviously, the geometrically ideal (001) and (111) surfaces having only an anion- or a cation-derived dangling bond band, respectively, are in contradiction to the rule. They show strong reconstructions, therefore. To implement the electron-counting rule one employs fractional occupancies of the dangling bonds at the surface atoms. In the bulk, each group V anion contributes 5/4 electrons and each group III cation contributes 3/4 electrons to the tetrahedral heteropolar two-electron bonds. Each anionic (cationic) surface dangling bond at a III-V surface can be expected to contain 5/4 (3/4) of an electron. At the surfaces, due to the change in bonding configuration, a charge transfer from the cation to the anion occurs.

The surface cations thus behave as donors with each dangling bond donating 3/4 electron while the surface anion dangling bonds, originally occupied by 5/4 electrons, act as acceptors. The anion dangling bonds, thereby, can become fully occupied dangling bonds, if sufficiently many donor electrons are available. At the (110) surfaces of III-V semiconductors, there is a perfect balance between donor and acceptor centers. After the respective charge transfer the low energy group V orbitals are in a closed shell environment and the high energy group III orbitals are empty. The structures of all III-V and II-VI surfaces which have been determined up to now are consistent with this rule.

*2.6.3.2. The GaAs(001) surface*

The As-rich GaAs(001) surface shows (2 × 4) and c(4 × 4) reconstructions crucially depending on surface preparation conditions and temperature. Different (2 × 4) phases, the so-called $\alpha$, $\beta$, $\beta 2$ and $\gamma$ phases have been observed (Farrell and Palmstrøm, 1990; Hashizume et al., 1994, 1995). These phases have been studied by Chadi (1987), Northrup and Froyen (1993, 1994), Pashley et al. (1988a, b) and Biegelsen et al. (1990a, b). In an earlier study, an asymmetric dimer model for an As-terminated GaAs(001)-(2 × 1) surface has been investigated by Larsen et al. (1982). The calculations revealed (see Fig. 2.57) characteristic $D_{up}$ and $D_{down}$ as well as $D_i$ and $D_i^*$ states, as discussed for the (001) surfaces of elemental semiconductors (see Section 2.4.1). However, in this case both the $D_{up}$ and the $D_{down}$ bands occur close to the top of the projected valence bands due to the strong As potential. In this model, there are no Ga dangling bonds and no Ga dangling bond bands, accordingly. The model, however, contradicts the electron counting rule and is not in accord with the experimentally observed (2 × 4) reconstruction.

In a recent DFT-LDA calculation, Schmidt and Bechstedt (1996) have studied structural and electronic properties for a number of reconstruction models of the GaAs(001) surface from first-principles. The authors observed that all structural models that were energy optimized in their calculations are characterized by similar structural elements, namely As dimers at the surface with a dimer bond length of about 2.5 Å, dimer vacancies and a nearly planar configuration of the threefold coordinated second layer Ga atoms. In consequence, the resulting electronic properties of the surfaces have also similar features. The surface band structures are dominated by filled As dimer states and empty Ga dangling bond states close to the valence and conduction-band edges, respectively, in close general correspondence with the relaxed GaAs(110) surface.

Figure 2.58 schematically shows the $\beta$ structure of GaAs(001)-(2×4). It has three As dimers and one As dimer vacancy per surface unit cell. From considering the grandcanonical potential (see Section 2.5.5.2), Schmidt and Bechstedt (1996) find the $\alpha$ structure to be energetically most favorable in a relatively small range of the As chemical potential. It becomes unstable with respect to the $\beta 2$ structure in more As-rich conditions. The three-dimer $\beta$ structure turns out to be metastable. All of these models fulfil the electron counting rule. To address one example, the $\beta(2 \times 4)$ structure (see Fig. 2.58) exhibits three surface dimers and one dimer vacancy per (2 × 4) unit cell. Thus there are four Ga dangling bonds per unit cell on the respective second-layer Ga atoms which can donate 3/4 electrons each to the six dangling bonds at the three As dimers per unit cell. The As dimer atoms use 2.5 electrons to saturate their two backbonds and 1 electron to establish the dimer bonds. The remaining 1.5 electrons do not fully occupy the As dangling bonds. Since there are

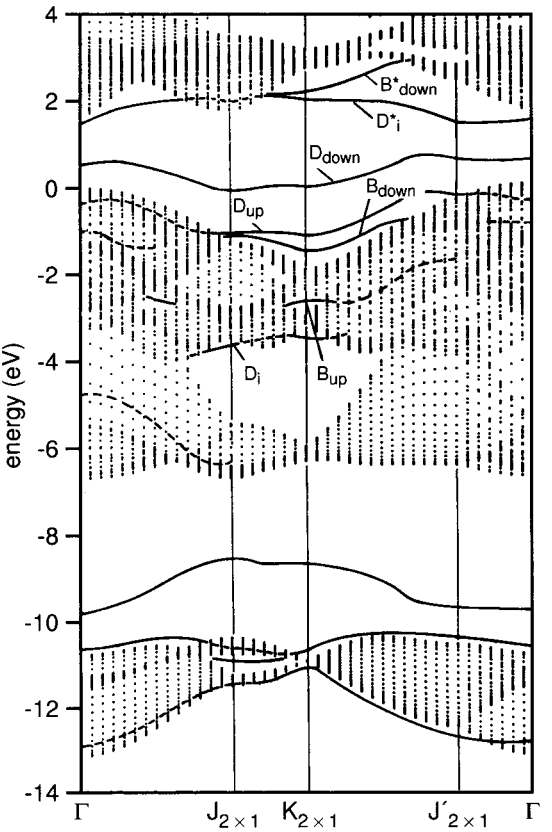


Fig. 2.57. Surface band structure of the asymmetric dimer model of the GaAs(001)-(2 × 1) surface (Larsen et al., 1982).

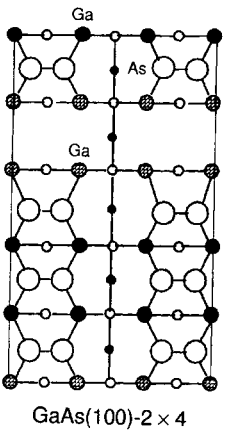


Fig. 2.58. Top view of the GaAs(001)-$\beta$(2 × 4) model of the reconstructed GaAs(001)-(2 × 4) surface (Chadi, 1991).

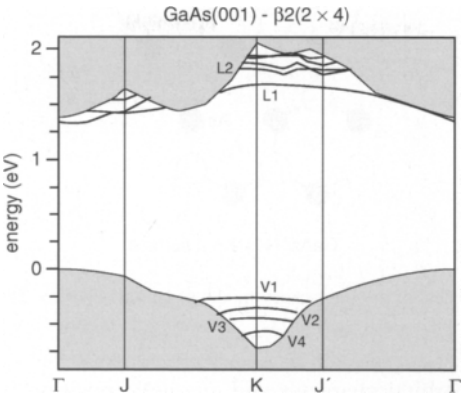


Fig. 2.59. Surface band structure of the reconstructed GaAs(001)-$\beta 2(2 \times 4)$ surface (Schmidt and Bechstedt, 1996).

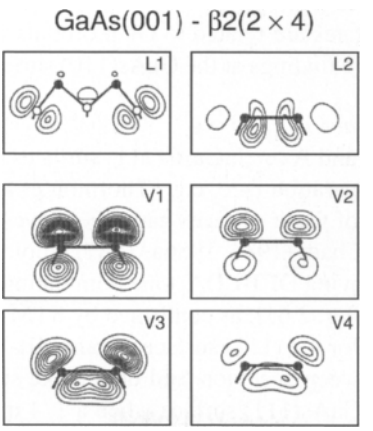


Fig. 2.60. Charge densities of salient surface states at the reconstructed GaAs(001)-$\beta 2(2 \times 4)$ surface (Schmidt and Bechstedt, 1996).

six dangling bonds in total per unit cell, three electrons are needed to saturate these bonds. Precisely three electrons can be provided by the four Ga dangling bonds ($4 \times 3/4$) mentioned above, so that full balance between acceptor and donor like states is accomplished. A semiconducting surface results (see Schmidt and Bechstedt, 1996). The same obtains for the $\beta 2$ structure favored by the authors. The respective surface band structure is shown in Fig. 2.59, and charge densities of salient surface states at the K-point are shown in Fig. 2.60. The features to be seen in Figs. 2.59 and 2.60 are characteristic for the surface electronic structure of all three models that have been considered by Schmidt and Bechstedt (1996). The highest occupied states $V_1$ and $V_2$ are related to antibonding $\pi^*$ combinations of $p_z$ orbitals at the As dimers. The energetic positions of these states are slightly below ($\beta 2$, see Fig. 2.59) or above ($\alpha$ and $\beta$, see Schmidt and Bechstedt, 1996) the bulk valence

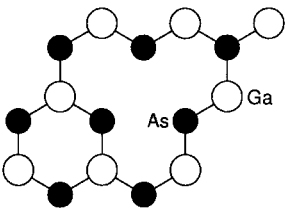


Fig. 2.61. Top view of the Ga vacancy model of GaAs(111)-(2 × 2) (Chadi, 1991).

band maximum. Their orbital character and energetic position is similar to the highest occupied surface state at the GaAs(110) surface (see Section 2.6.1). Energetically lower lying bound surface states arise from the corresponding As dimer $\pi$ bonds and perturbed $\sigma$ like Ga–As backbonds. These states are closely related to the $D_{up}$ and $D_{down}$ states at the GaAs(001)-(2 × 1) surface (see Fig. 2.57).

The lowest unoccupied states are related to Ga p orbitals which is also in close correspondence with the respective findings at the GaAs(110) surface.

*2.6.3.3. The GaAs(111) surface*

Numerous structures of Ga- and As-rich GaAs(111) surfaces have been observed depending critically on surface preparation (see, e.g., Thornton et al., 1994; Ranke and Jacobi, 1977). Structural properties of these surfaces have been investigated by total energy minimization in great detail by Chadi (1984, 1986a, 1987) employing ETBM and by Kaxiras et al. (1986, 1987a, b) employing DFT-LDA. One dominating structure is the GaAs(111)-(2 × 2) vacancy model (see Fig. 2.61), as confirmed by STM data (Haberern and Pashley, 1990). It has been observed for the (111) surface of other III-V compounds, as well (Bohr et al., 1985). A balance between acceptor- and donor-like surface states is easily established at the Ga-terminated GaAs(111) surface when a 1/4 monolayer of Ga vacancies is formed in a (2 × 2) configuration. As a result, the (2 × 2) unit cell contains three Ga atoms each with one dangling bond (donating 3/4 electrons) and an equal number of threefold-coordinated As atoms in the second layer (which can accept 3/4 electrons to fill their dangling bonds). As in the case of the (110) surface, a perfect balance between the donor and acceptor states is established this way. In consequence, the As dangling bonds become fully occupied while the Ga dangling bonds are emptied. Thus vacancy formation has the effect of transforming the surface from a polar metallic into a nonpolar semiconducting one. Its electronic structure shows strong resemblance to that of the nonpolar (110) surface. Occupied surface states at the GaAs(111)-(2 × 2) surface have, e.g., been observed by Bringans and Bachrach (1984a).

Formation of As vacancies seems not to occur at the As-terminated GaAs(111) surface, often referred to as GaAs($\bar{1}\bar{1}\bar{1}$), because it is energetically less favorable (Chadi, 1984; Kaxiras et al., 1987b). Instead As-trimers are observed in a (2 × 2) configuration but a number of other structures have been considered too. This As-trimer model containing completely occupied As dangling bonds only yields a semiconducting surface and is in accord with the electron counting rule (see, e.g., Duke, 1996).

## 2.7. Surfaces of group III-nitrides

Group III-nitrides and their surfaces are currently investigated very intensively worldwide. The large interest originates from their promising potential for short-wavelength light-emitting diodes, semiconductor lasers and optical detectors as well as for high-temperature, high-power, and high-frequency devices (Harris, 1995). They are strongly ionic wide-band-gap semiconductors, very much like SiC or the II-VI compounds. They form a continuous range of solid solutions so that electrooptical devices with specifically engineered band gaps from the visible to the deep UV seem at reach through alloying (Davis, 1993). The specific electronic properties of the nitrides are the very basis for these important applications. In view of this exciting challenge, theoretical studies of structural and electronic properties of nonpolar and polar surfaces of cubic and hexagonal group III-nitrides have been carried out very recently (Jaffe et al., 1996; Kádas et al., 1996; Northrup and Neugebauer, 1996; Yamauchi et al., 1996; Pandey et al., 1997; Northrup et al., 1997; Rapcewicz et al., 1997).

### *2.7.1. Surfaces of cubic group III-nitrides*

Both nonpolar and polar surfaces of cubic group III-nitrides have been studied very recently. While the relaxation of the former is fairly simple and straightforward, the latter exhibit more complex reconstruction behavior as could be expected on the basis of their large ionicity.

#### *2.7.1.1. Nonpolar surfaces of cubic group III-nitrides*

Mostly structural properties of AlN(110) and GaN(110) surfaces have been studied by Pandey et al. (1997) and Jaffe et al. (1996), respectively, employing all-electron Hartree–Fock total energy calculations. In both cases, the authors find bond-length-contracting rotation relaxations with a relatively small rotation angle. For AlN(110), Pandey et al. (1997) report a rotation angle $\omega = 8.8°$ and a bond contraction of about 7%. For GaN(110), Jaffe et al. (1996) have obtained a rotation angle $\omega = 6°$ and a bond contraction of about 7%. These findings are in general accord with what one would expect on the basis of the relaxation mechanisms discussed in Section 2.5.1. The nonpolar (110) surfaces of cubic group III-nitrides thus behave as respective surfaces of other wide-band-gap semiconductor compounds such as SiC or the II-VI compounds. Of course, small quantitative differences due to differences in ionicity do occur. The relaxations of these wide-band-gap semiconductors, however, show marked quantitative differences from the 30° bond-length-conserving rotation relaxation as observed for nonpolar (110) surfaces of common III-V semiconductors. Surface band structures for the relaxed (110) surface of the group III-nitrides, as resulting from 'standard' LDA calculations have been published recently (Grossner et al., 1998). A very recent result obtained in our group by *ab initio* SCM calculations which make use of SIRC pseudopotentials is shown for AlN(110) in Fig. 2.62.

#### *2.7.1.2. Polar surfaces of cubic group III-nitrides*

Geometrically ideal anion- or cation-terminated (001) and (111) surfaces of group III-nitrides are polar, metallic and unstable as is most obvious from our discussions in Sec-

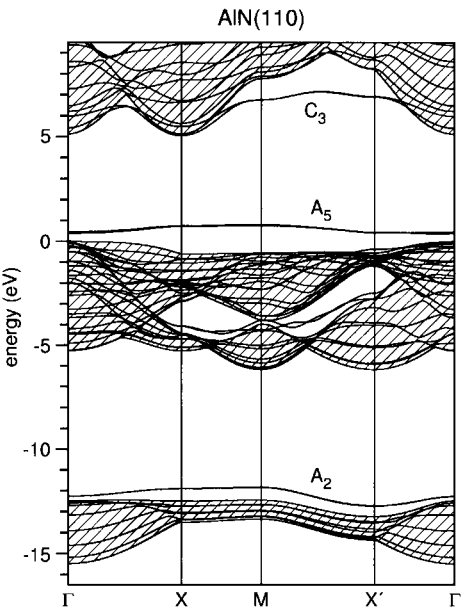


Fig. 2.62. Surface band structure of the relaxed AlN(110) surface as resulting from our recent LDA calculations employing SIRC pseudopotentials (Hirsch et al., 1998).

tion 2.3.2. They can be expected to show a rich variety of more complex long-range reconstructions, such as those discussed above for polar GaAs surfaces in Section 2.6.3. To date, the cubic BN(001) surface has been studied. A whole variety of conceivable reconstruction geometries of N-rich and B-rich surfaces ranging from $(2 \times 1)$ over $c(2 \times 2)$ to $(2 \times 4)$ and $(4 \times 2)$ dimer and bridge structures has been investigated in great detail by Yamauchi et al. (1996) employing DFT-LDA together with soft pseudopotentials. All of these surface reconstructions have been discussed in context of the electron counting rule and stable structures have been identified by referring to grandcanonical potential calculations (see Section 2.5.3). For a fairly wide range of the nitrogen chemical potential the N-terminated B(001)-$(2 \times 1)$ dimer structure turns out to be energetically most favorable. It is, however, metallic and is in obvious contradiction to the electron counting rule. In different narrower ranges of the nitrogen chemical potential, N-terminated or B-terminated BN(001)-$(2\times4)$ and BN(001)-$(4 \times 2)$ structures characterized by three N or B dimers, respectively, and a corresponding dimer vacancy are stable. These structures are very similar to the related GaAs(001) surfaces (see Section 2.6.3.2). They obey the electron counting rule and exhibit a semiconducting surface. It has been observed by Yamauchi et al. (1996) that the electrostatic energy plays the most important role in determining the stable structures of BN(001). This is in accord with the general mechanisms discussed in Section 2.5.1 since BN is highly ionic so that the electrostatic interaction should indeed dominate the reconstruction.

The electronic structure for quite a number of the reconstruction models of BN(001) has been evaluated and discussed in detail by Yamauchi et al. (1996). We refer the interested

reader to the original work. ARPES or KRIPES data have not been reported for BN(001), to date.

### *2.7.2. Surfaces of hexagonal group III-nitrides*

Both nonpolar and polar surfaces of hexagonal group III-nitrides have been studied very recently. While the relaxation of the former is again fairly simple and straightforward, the latter exhibit more complex reconstruction behavior, as well, as could again be expected on the basis of their large ionicity.

#### *2.7.2.1. Nonpolar surfaces of hexagonal group III-nitrides*

Unlike the case of zincblende-structure crystals, two stable cleavage faces occur for wurtzite compound semiconductors. These two faces, the $(10\bar{1}0)$ and $(11\bar{2}0)$ are nonpolar with equal numbers of surface cations and anions. They undergo a bulk-symmetry conserving relaxation. Since these compounds are fairly ionic, the length of the surface bonds is shortened upon relaxation. Thus one encounters bond-length-contracting rotation relaxations at these surfaces. The relaxed structures are in accord with Pashley's electron counting rule since there is an equal number of cation and anion dangling bonds at these surfaces. The more electronegative anion moves above and the more electropositive cation moves below the surface plane in agreement with the general relaxation mechanisms discussed in Section 2.5.1. Due to the large ionicity, electrostatic interactions dominate and the resulting relaxation angles are found to be relatively small.

AlN$(10\bar{1}0)$ and $(11\bar{2}0)$ surfaces have been studied by Pandey et al. (1997) and Kádas et al. (1996). GaN$(10\bar{1}0)$ has been studied by Jaffe et al. (1996) employing Hartree–Fock total energy calculations and by Northrup and Neugebauer (1996) employing DFT-LDA total energy minimization. The latter authors have also addressed the GaN$(11\bar{2}0)$ surface. The results of all of these studies confirm the general relaxation mechanism discussed in Section 2.5.1. Bond-length-contracting rotation relaxations with small relaxation angles ranging from 4.4°, over 6° to 7° are found for the systems studied. Concomitantly, respective surface bond contractions between 6% and 8% are found. Kádas et al. (1996) explicitly noted that the results of their Hartree–Fock total energy minimization calculations indicate, that ionicity is an important factor determining the extent of relaxation: the more covalent the solid, the larger are the effects of relaxation on its surface atomic structure.

The effects of the relaxation on the surface electronic structure are shown in Figs. 2.63 and 2.64 for the GaN$(10\bar{1}0)$ and the AlN$(11\bar{2}0)$ surface, respectively. In both cases, anion-derived dangling bond states occur near the top of the projected valence bands and cation-derived dangling bond states are found near the bottom of the projected conduction bands. They are significantly separated in energy since the anion potential is stronger than that of the cations. Like in the case of GaAs(110), SiC(110) or SiC$(10\bar{1}0)$, the relaxation gives rise to an upward shift in energy of the empty cation-derived dangling-bond band (labeled $S_{Ga}$ in Fig. 2.63) and to a downward shift of the occupied anion-derived dangling-bond band (labeled $S_N$ in Fig. 2.63). Similar general behavior is found for the AlN$(11\bar{2}0)$ surface in Fig. 2.64. After relaxation, the gap is free (see Fig. 2.63) or almost free (see Fig. 2.64) from surface states and the surfaces are clearly semiconducting. To date, no ARPES or KRIPES data have been published for any one of the nonpolar surfaces of the group III-nitrides, to the best of our knowledge.

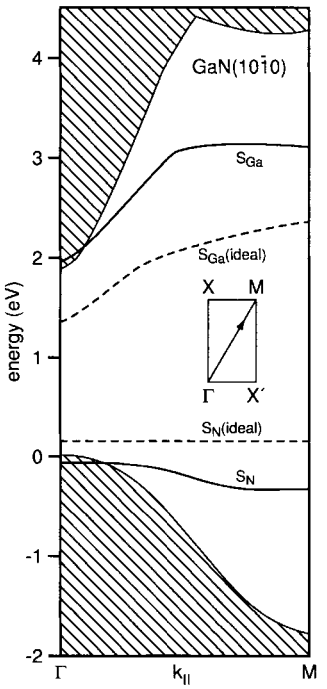


Fig. 2.63. Surface band structure (dashed lines for ideal surface and full lines for the relaxed surface) of GaN(10$\bar{1}$0) as resulting from LDA calculations (Northrup and Neugebauer, 1997).

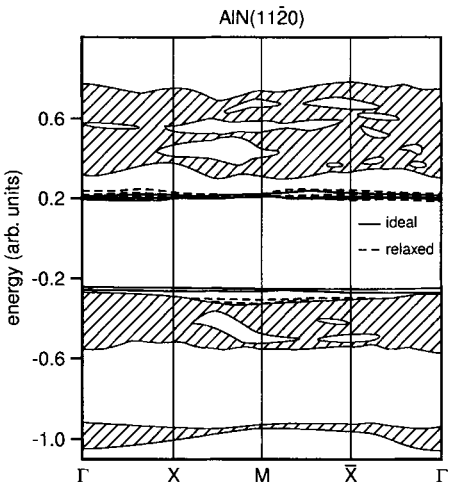


Fig. 2.64. Surface band structure (full lines for the ideal and dashed lines for the relaxed surface) of the AlN(11$\bar{2}$0) surface as resulting from LDA calculations (Kádas et al., 1996).

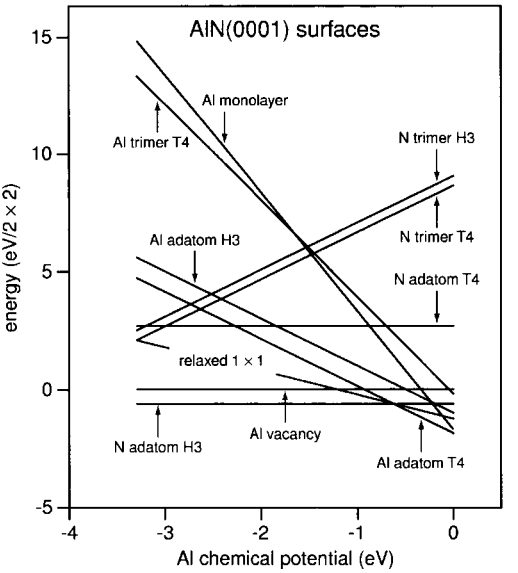


Fig. 2.65. Comparison of grand canonical potentials (relative to that of the ideal surface) for different structural models (relaxation and reconstructions) of the nominally Al-terminated AlN(0001) surface as a function of the Al chemical potential for the allowed range (Northrup et al., 1997).

### *2.7.2.2. Polar surfaces of hexagonal group III-nitrides*

In a recent DFT-LDA calculation, Northrup et al. (1997) have studied polar AlN(0001) and AlN(000$\bar{1}$) surfaces and Rapcewicz et al. (1997) have studied GaN(0001) surfaces. For AlN, structural models with 2 × 2 symmetry satisfying the electron counting rule, as well as metallic surfaces with 1 × 1 symmetry have been considered. For AlN(0001), both Al-$T_4$ and N-$H_3$ models are found to be stable in the allowed range of the Al and N chemical potential. The N-adatom structure is stable in N-rich conditions and the Al-adatom structure is most stable in Al-rich conditions. For the AlN(000$\bar{1}$) surface, the 2 × 2 Al-$H_3$ adatom model is stable in N-rich conditions while under Al-rich conditions an Al adlayer is favored. A summary of the grandcanonical potentials as a function of the chemical potential of Al for the structures investigated by Northrup et al. (1997) is shown in Fig. 2.65. The figure reveals the large number of competing structures that has been studied in great detail.

Small sections of the surface band structures of a number of models studied have been presented by Northrup et al. (1997). The relaxed AlN(0001) surface turns out to be metallic, as was to be expected. The (2 × 2) Al vacancy model turns out to be semiconducting and is in agreement with the electron counting rule very much like the closely related Ga vacancy structure of GaAs(111)-(2 × 2) surface (see Section 2.6.3.2). The most stable of these Al-rich surfaces, the Al-$T_4$ model gives rise to a semiconducting surface, as well. Rapcewicz et al. (1997) obtained similar results for these polar surfaces.

Neither LEED, nor STM nor ARPES or KRIPES data on polar hexagonal group III-nitride surfaces seem to be available. They would be most useful to identify the actual

structure realized under certain growth conditions. Certainly, a number of experimental investigations to be carried out in the near future will shed more light on the reconstructions of these surfaces.

## 2.8. Surfaces of II-VI semiconductors

II-VI compound semiconductors and their surfaces are currently studied intensively because of their paramount technological potential. Applications range from optoelectronic devices (e.g., blue lasers based on ZnSe heterostructures) to heterogeneous catalysis (e.g., oxide surfaces). For a basic understanding of the related phenomena and an optimization of materials for relevant processes ('band-structure-engineering') a quantitative knowledge of electronic and structural properties of these compounds, their surfaces and interfaces is needed.

Tetrahedrally coordinated II-VI semiconductors occur in the zincblende and wurtzite structure. Zincblende materials exhibit a single cleavage face, the (110) surface, consisting of equal numbers of anions and cations which form zig-zag chains directed along the $[1\bar{1}0]$ direction in the surface plane. Wurtzite materials exhibit two cleavage faces, the $(10\bar{1}0)$ and $(11\bar{2}0)$ surfaces, both consisting of equal numbers of anions and cations. The $(10\bar{1}0)$ surface consists of isolated anion–cation dimers backbonded to the layer beneath while the $(11\bar{2}0)$ surface consists of anion–cation chains analogous to those at the (110) zincblende surface but with four rather than two inequivalent atoms per surface unit cell.

The nonpolar surfaces of cubic and hexagonal II-VI semiconductors, the (110), $(10\bar{1}0)$ and $(11\bar{2}0)$ surfaces, respectively, have been studied most intensively. Therefore, we restrict ourselves to a discussion of these surfaces in this chapter. By now, it is well-appreciated that all three nonpolar surfaces show relaxed $(1 \times 1)$ structures but the actual structure parameters, in particular, the relaxation angles are still under investigation. The relaxed $(1 \times 1)$ surface structures are in full agreement with the electron counting rule. A number of experimental and theoretical investigations of these surfaces has been carried out over the years (see, e.g., Duke, 1992, 1996). Previous calculations have employed empirical tight-binding approaches (Chadi, 1979b; Lee and Joannopoulos, 1980, 1981; Ivanov and Pollmann, 1981; Wang et al., 1987a, b, 1988a, b, c). Comprehensive reviews of these empirical calculations and of experimental work on II-VI semiconductor surfaces have been presented more recently by Duke (1992, 1996). Surface structural models obtained from LEED intensity analyses and from empirical tight-binding calculations have been suggested by Duke and coworkers (Duke et al., 1984a, b, 1992; Wang et al., 1987a, b, 1988a, b, c). These models are characterized by an outward relaxation of the surface layer anions and an inward relaxation of the surface-layer cations. This rotation of the surface-layer atoms leads to a raising of the energetic position of empty cation-derived and a lowering of occupied anion-derived dangling-bond states very much like at the respective III-V compound semiconductor surfaces, as discussed in Section 2.6.1. It was concluded (see, e.g., Duke, 1992) as a universal feature of these relaxations that the tilt angle $\omega$ of the surface anion–cation bond with respect to the ideal surface is about $18° \pm 3°$ for the $(10\bar{1}0)$ surfaces and about $29° \pm 3°$ for the (110) surfaces (see Fig. 2.66). It is interesting to note, that a reasonable interpretation of the LEED data (Duke, 1984a, b)

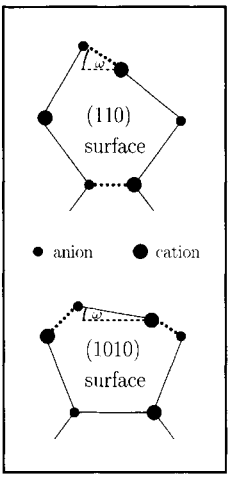


Fig. 2.66. Side views of relaxed (110) and (10$\bar{1}$0) surfaces of II-VI compound semiconductors. The structure parameters are defined as in Fig. 2.33.

Table 2.9

Calculated top-layer bond-rotation angles $\omega$ of zincblende (110) and wurtzite (10$\bar{1}$0) surfaces as resulting from DFT-LDA (Vogel et al., 1998; Vogel, 1998) and ETBM calculations in comparison with LEED data

| | DFT-LDA | ETBM | Experiment |
|---|---|---|---|
| (110) surfaces | | | |
| ZnS | 30.5 | 27.4[a] | 1.9[b], 28.0[b] |
| ZnSe | 31.3 | 28.7[c] | 4.0[f], 29.0[d] |
| ZnTe | 30.5 | | 28.0[e] |
| CdSe | 29.6 | | |
| CdTe | 37.5 | 28.1[f] | 30.5[e] |
| (10$\bar{1}$0) surfaces | | | |
| ZnO | 19.4 | 17.2[g] | 11.5[e] |
| CdS | 16.7 | 17.5[g] | |
| CdSe | 21.5 | 17.7[g] | 21.5[e] |

[a]Wang and Duke (1987a).
[b]Duke et al. (1984a).
[c]Wang et al. (1987b).
[d]Duke et al. (1984b).
[e]Duke (1988a).
[f]Wang et al. (1988b).
[g]Wang and Duke (1988c).

was also possible for relatively small rotation angles of the (110) surfaces of ZnS and ZnSe (about 2° and 4°, respectively).

The calculated electronic structure of the (110) and (10$\bar{1}$0) surfaces was found to show an anion-derived dangling-bond band near the top of the valence bands (Duke, 1992; Wang

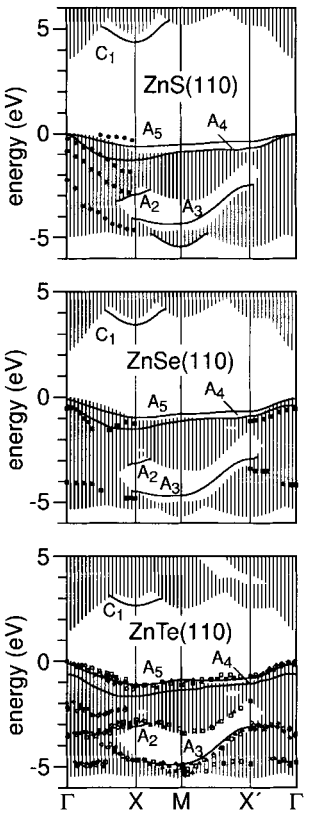


Fig. 2.67. Surface band structure of the relaxed ZnS(110), ZnSe(110) and ZnTe(110) surfaces, as calculated within LDA using SIRC pseudopotentials (Vogel, 1998) in comparison with ARPES data (ZnS(110): Barman et al., 1998; ZnSe(110): Qu et al., 1991b; ZnTe(110): Qu et al., 1991a).

et al., 1987a, 1988a). This latter finding has been confirmed by more recent *ab initio* calculations (Schröer et al., 1994; Vogel et al., 1998; Vogel, 1998). We also find local minima of the total energy for fairly small relaxation angles (6.8° for ZnS and 8.1° for ZnSe). The total energy gain related to these minima, however, is smaller than that of the optimal relaxations for angles near 30°.

### *2.8.1. Nonpolar surfaces of cubic II-VI compounds*

The nonpolar (110) surfaces of cubic II-VI compounds show a rotation relaxation which is similar, in general, to that of the GaAs(110) surface (see Figs. 2.51 and 2.66). The actual rotation angles at these surfaces are still under investigation. Those resulting from empirical and from *ab initio* calculations show some differences (Vogel, 1998). The fine details of the charge-density relaxations at these surfaces have an important effect on their relaxation.

Figure 2.67 shows a comparison of salient sections of the surface band structure of ZnS(110), ZnSe(110) and ZnTe(110). The electronic structure has been calculated em-

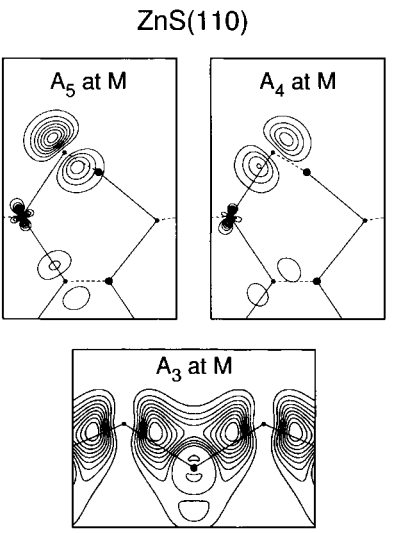


Fig. 2.68. Charge-density contours of salient surface states at the relaxed ZnS(110) surface, as calculated within LDA using SIRC pseudopotentials (Vogel, 1998).

ploying DFT-LDA together with SIRC pseudopotentials (see Section 2.2.7). In addition, ARPES data (ZnS(110): Barman et al., 1998; ZnSe(110): Qu et al., 1991a; ZnTe(110): Qu et al., 1991b) are shown for comparison. There is very good overall agreement between the calculated occupied bands and the data. In all three cases, a salient anion-p-derived dangling bond band is found. In addition, in all three cases a pronounced cation-derived empty dangling-bond band $C_1$ occurs close to the bottom of the projected conduction bands. The character of the most salient occupied states $A_3$, $A_4$ and $A_5$, is highlighted in respective charge-density plots in Fig. 2.68.

A comparison of DFT-LDA results (Vogel et al., 1998; see the left panel of Fig. 2.69) for the CdTe(110) surface with ARPES data of Magnusson and Flodström (1988b) shows significant systematic deviations, in particular with respect to the $A_2$ and $A_3$ bands (see also the ETBM results of Wang et al., 1988b). These deviations occur if spin–orbit interaction is neglected in the calculations.

On the contrary, if spin–orbit interaction is included, the valence band width of CdTe increases, the stomach gap in the PBS shifts down in energy and the surface state bands $A_2$ and $A_3$ shift accordingly. The resulting surface band structure (see right panel of Fig. 2.69) is found in good agreement with the data. Quantitative differences in the $A_4$ and $A_5$ bands remain to be resolved.

### *2.8.2. Nonpolar surfaces of hexagonal II-VI compounds*

Experimental and theoretical investigations of hexagonal surfaces of II-VI compounds have been reported as well. LEED studies of, e.g., ZnO($10\bar{1}0$) have been carried out by Duke et al. (1977, 1978). Early empirical tight-binding calculations for the surface electronic

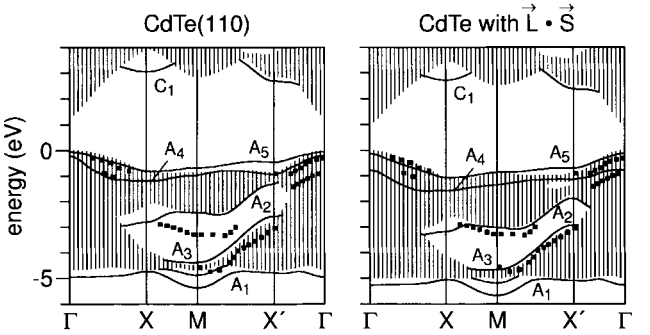


Fig. 2.69. Surface band structure of the relaxed CdTe(110) surface, as calculated within LDA without (left panel) and with (right panel) spin–orbit interaction using SIRC pseudopotentials (Vogel et al., 1998) in comparison with experimental data (Magnusson et al., 1988b).

structure of ZnO($10\bar{1}0$) have lead to strikingly different results for the surface bands in the gap energy region. Ivanov and Pollmann (1981), who used an empirical tight-binding Hamiltonian incorporating only Zn 4s and O 2p orbitals did not find dangling bond bands in the gap but only ionic resonances within the projected bulk bands. Wang and Duke (1987b), on the other hand, included Zn 4p orbitals in their Hamiltonian and found a dangling bond band of occupied O 2p states near the top of the projected bulk valence bands. To resolve this discrepancy, Schröer et al. (1994) have investigated the CdS($10\bar{1}0$) and ZnO($10\bar{1}0$) surfaces by *ab initio* DFT-LDA calculations employing standard pseudopotentials. They confirmed the results of Wang and Duke (1987b), as far as the O 2p dangling bond band is concerned. They found anion-derived dangling bond bands near the top of the valence bands for both surfaces.

In Fig. 2.70 we show the surface band structure of the relaxed CdS($10\bar{1}0$) surface as resulting with usual pseudopotentials (left panel) and with SIRC pseudopotentials (right panel). An anion-derived dangling bond band $A_5$ and two bands $A_4$ and $A_6$ are found near the top of the valence bands at the relaxed surface for both calculations. In the surface band structure calculated with SIRC pseudopotentials, the gap is opened up and the 4d bands are shifted down in energy to where they belong. Except for the $A_4$ and $A_5$ bands, the fundamental gap is free from surface states due to the large ionicity of this compound. Comparing the surface band structure in Fig. 2.70 with that of the relaxed 2H-SiC($10\bar{1}0$) surface in the right panel of Fig. 2.34, we observe a number of distinct differences. First, the heteropolar gap between the anion-derived s- and p-bands in II-VI semiconductors is much larger than in SiC due to the increased ionicity. Second, there is no empty dangling-bond band in the gap of the relaxed CdS($10\bar{1}0$) surface and the $A_5$ band is somewhat closer to the projected valence bands than at 2H-SiC($10\bar{1}0$) (see the right panel of Fig. 2.34). This is related to the larger ionicity and the concomitantly smaller covalent character of CdS, as compared to SiC. Third, in II-VI semiconductors there are occupied cationic d states whose energies reside between those of the anion s- and p-states. They give rise to d-bands between the anion p- and s-valence bands.

Although the self-consistent calculation of the surface electronic structure of ZnO($10\bar{1}0$) had confirmed the existence of an anion-derived dangling-bond band, the question re-

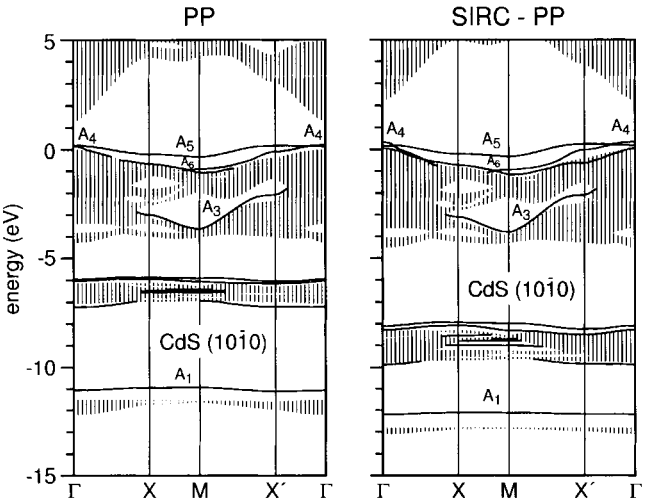


Fig. 2.70. Surface band structure of the relaxed CdS(10$\bar{1}$0) surface, as calculated within standard LDA (left panel) or using SIRC pseudopotentials (right panel).

mained whether the dangling bond states near the top of the valence bands are calculated accurately enough within standard LDA, since the LDA gap for, e.g., ZnO results as 0.23 eV as opposed to the experimental value of 3.4 eV. In addition no quantitative assertion of the influence of the Zn 3d states on the dangling-bond surface states could be made, since the former result some 3 eV too high in energy from DFT-LDA when standard pseudopotentials are used (see Section 2.2.7). To resolve this issue, the surface electronic structure of ZnO(10$\bar{1}$0), CdS(10$\bar{1}$0) and CdSe(10$\bar{1}$0) has been studied employing DFT-LDA together with SIRC pseudopotentials (Vogel et al., 1998; Vogel, 1998). The results of Schröer et al. (1994) concerning the oxygen-derived dangling bond band close to the top of the projected valence bands of ZnO(10$\bar{1}$0) have been confirmed.

There is very good agreement (see Table 2.10) between the structural results of ETBM (Wang et al., 1987b, 1988a) and DFT-LDA calculations (Vogel et al., 1998; Vogel, 1998). The structural relaxation of the three (10$\bar{1}$0) surfaces investigated is similar, in principle, to that of SiC(10$\bar{1}$0).

Small sections of the surface band structures of ZnO(10$\bar{1}$0), CdS(10$\bar{1}$0) and CdSe (10$\bar{1}$0), as resulting from SIRC-PP calculations, are compared with experimental data of Magnusson and Flodström (1988c) and of Wang et al. (1988b) in Fig. 2.71.

The existence of an anion-p-derived dangling bond band at the surface of II-VI semiconductors is firmly established by these results and the theoretical results are in very good agreement with the data. This holds in particular for the $A_3$, $A_4$ and the $A_6$ bands. The character of the most pronounced states $A_3$, $A_4$, $A_5$ and $A_6$ is shown by respective charge densities at the X′-point in Fig. 2.72. It is obvious from the figure, that all three states have strong $p_z$-contributions and should therefore be accessible to ARPES measurements. Nevertheless, the most pronounced $A_5$ band has not been observed in experiment, to date. The bands $A_3$, $A_4$ and $A_6$ are in excellent agreement with the ARPES data (Magnusson

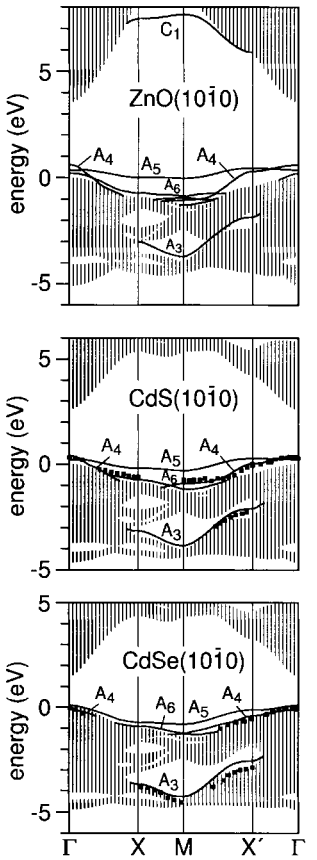


Fig. 2.71. Surface band structures of the relaxed (10$\bar{1}$0) surfaces of ZnO, CdS, and CdSe (Vogel et al., 1998) in comparison with ARPES data (CdS: Magnusson et al., 1988c; CdSe: Wang et al., 1988b).

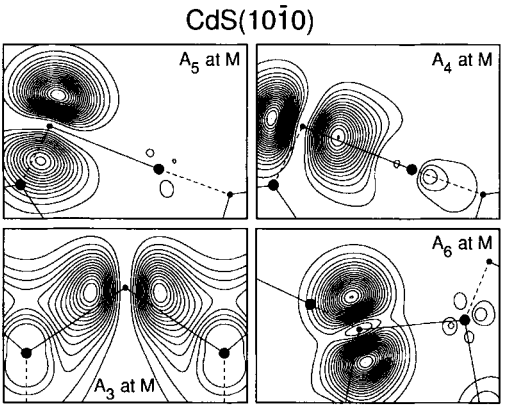


Fig. 2.72. Charge densities of salient surface states at the relaxed CdS(10$\bar{1}$0) surface (Vogel, 1998).

Table 2.10

Optimized structure parameters (as defined in Fig. 2.66) for the relaxed ZnO(10$\bar{1}$0), CdS(10$\bar{1}$0) and CdSe(10$\bar{1}$0) surfaces, as resulting from recent *ab initio* DFT-LDA calculations (Vogel et al., 1998) and from ETBM calculations (Duke, 1988a; Wang et al., 1987b, 1988b) in comparison with experimental data

| ZnO(10$\bar{1}$0) | DFT-LDA | ETBM | a | b |
|---|---|---|---|---|
| $\Delta_{1,\perp}$ (Å) | 0.24 | 0.20 | $0.2 \pm 0.15$ | $0.4 \pm 0.20$ |
| $\Delta_{2,\perp}$ (Å) | −0.05 | 0.00 | 0.00 | 0.00 |
| $d_{12,\perp}$ (Å) | 0.66 | 0.87 | 0.62 | 0.54 |
| $d_{1,\parallel}$ (Å) | 3.36 | 3.22 | $3.37 \pm 0.20$ | 3.24 |
| $d_{12,\parallel}$ (Å) | 2.81 | 2.61 | 2.41 | 2.61 |
| $d_0$ (Å) | 0.85 | 1.61 | 0.84 | 0.94 |
| $\omega$ (°) | 19.4 | 5.7 | $6.2 \pm 3$ | $11.5 \pm 5$ |
| CdS(10$\bar{1}$0) | DFT-LDA | ETBM | | |
| $\Delta_{1,\perp}$ (Å) | 0.69 | 0.74 | | |
| $\Delta_{2,\perp}$ (Å) | −0.15 | 0.08 | | |
| $d_{12,\perp}$ (Å) | 0.61 | 0.62 | | |
| $d_{1,\parallel}$ (Å) | 4.40 | 4.41 | | |
| $d_{12,\parallel}$ (Å) | 3.72 | 3.86 | | |
| $d_0$ (Å) | 1.15 | 1.19 | | |
| $\omega$ (°) | 16.7 | 17.9 | | |
| CdSe(10$\bar{1}$0) | DFT-LDA | ETBM | c | |
| $\Delta_{1,\perp}$ (Å) | 0.90 | 0.78 | $1.03 \pm 0.2$ | |
| $\Delta_{2,\perp}$ (Å) | −0.20 | 0.07 | $0.00 \pm 0.1$ | |
| $d_{12,\perp}$ (Å) | 0.53 | 0.64 | $0.41 \pm 0.2$ | |
| $d_{1,\parallel}$ (Å) | 4.66 | 4.59 | $4.60 \pm 0.2$ | |
| $d_{12,\parallel}$ (Å) | 4.03 | 4.04 | $3.89 \pm 0.2$ | |
| $d_0$ (Å) | 1.24 | | $1.24 \pm 0.2$ | |
| $\omega$ (°) | 21.5 | 17.7 | $23.0 \pm 3$ | |

[a]Duke et al. (1977).
[b]Duke et al. (1978).
[c]Duke (1992).

and Flodström, 1988c). Only in the case of ZnO(10$\bar{1}$0), an empty dangling-bond band ($C_1$) occurs but not at the CdS(10$\bar{1}$0) and CdSe(10$\bar{1}$0) surfaces.

## 2.9. Summary

In this chapter we have briefly discussed structural and electronic properties of a number of prototype semiconductor surfaces. The results of well-converged *ab initio* total energy minimization and electronic structure calculations were found to be in good agreement with available experimental data of surface structure determinations and high-resolution

surface spectroscopy results. In the cases where there are no experimental data available, they yield most useful predictions. The resulting structural and electronic properties have been analyzed and a general picture of the physical nature and origin of particular reconstruction or relaxation behavior has been developed. A clear physical picture of a number of important surfaces has emerged. Shortcomings of LDA results have been identified and it has been exemplified in cases how they can be overcome by GW quasiparticle band structure calculations or by LDA calculations that include most important self-interaction and relaxation corrections through the use of SIRC pseudopotentials. The good agreement of the theoretical results with most recent experimental data on these surfaces confirms the appropriateness and usefulness of most advanced 'state of the art' theoretical approaches for quantitative studies of well-ordered clean semiconductor surfaces.

*Acknowledgements*

It is our great pleasure to acknowledge members of our group who have contributed to the results on which we have based most of our discussions in this chapter. First of all, we thank Dr. Albert Mazur for numerous fruitful discussions and for his continuous and very competent support of our computing systems throughout the course of this work. Furthermore, we thank Dr. Ivan Ivanov, Dr. Albert Mazur, Dr. Michael Rohlfing, Dr. Magdalena Sabisch, Dr. Peter Schröer, Dr. Dirk Vogel, Dr. Gerd Wolfgarten and Dr. Klaus Würde for their commitment to the study of semiconductor surfaces. Our scientific research on clean surfaces in collaboration with all of them has been a great pleasure and a lot of fun throughout. In particular, we would like to acknowledge the Deutsche Forschungsgemeinschaft (Bonn, Germany) who has supported our research on semiconductor surfaces over many years by a large number of projects. Finally, one of the authors (JP) would like to acknowledge the almost everlasting patience of the editors and coauthors of this volume.

## References

Aarts, J., A.J. Hoeven and P.K. Larsen, 1988, Phys. Rev. B **37**, 8190.
Alfonso, D.R., D.A. Drabold and S.E. Ulloa, 1995, Phys. Rev. B **51**, 14669.
Alves, J.L.A., J. Hebenstreit and M. Scheffler, 1991, Phys. Rev. B **44**, 6188.
Appelbaum, J.A. and D.R. Hamann, 1973, Phys. Rev. Lett. **31**, 106.
Appelbaum, J.A. and D.R. Hamann, 1974, Phys. Rev. Lett. **32**, 225.
Appelbaum, J.A., G.A. Baraff and D.R. Hamann, 1975, Phys. Rev. B **11**, 3822.
Arai, M. and T. Fujiwara, 1995, Phys. Rev. B **51**, 1477.
Aristov, V.Yu., L. Douillard, O. Fauxchoux and P. Soukiassian, 1997, Phys. Rev. Lett. **79**, 3700.
Aryasetiawan, F. and O. Gunnarson, 1994, Phys. Rev. B **49**, 16214.
Aryasetiawan, F. and O. Gunnarson, 1995, Phys. Rev. Lett. **74**, 3221.
Aryasetiawan, F. and O. Gunnarson, 1996, Phys. Rev. B **54**, 17564.
Aryasetiawan, F. and O. Gunnarson, 1998, Rep. Prog. Phys. **61**, 237.
Aspnes, D.E., 1975, Phys. Rev. B **12**, 2297.
Bachelet, G.B. and N.E. Christensen, 1985, Phys. Rev. B **31**, 879.
Bachelet, G.B., D.R. Hamann and M. Schlüter, 1982, Phys. Rev. B **26**, 4199.
Badt, D., H. Wengelnik and H. Neddermeyer, 1994, J. Vac. Sci. Technol. B **12**, 2015.
Badziag, P., 1990, Surf. Sci. **236**, 48.
Badziag, P., 1991, Phys. Rev. B **54**, 11143.

Badziag, P., 1992, Surf. Sci. **269**, 1152.
Badziag, P., 1995, Surf. Sci. **337**, 1.
Badziag, P. and W.S. Verwoerd, 1988, Surf. Sci. **194**, 535.
Baldereschi, A. and E. Tosatti, 1979, Solid State Commun. **29**, 131.
Barman, S.R., S.A. Ding, G. Neuhoff, K. Horn, D. Wolfram and D.A. Evans, 1998, private communication.
Baroni, S. and R. Resta, 1986, Phys. Rev. B **33**, 7017.
Becker, R.S., J.A. Golovchenko and B.S. Swartzentruber, 1985, Phys. Rev. Lett. **54**, 2678.
Becker, R.S., B.S. Swartzentruber, J.S. Vickers and T. Klitsner, 1989, Phys. Rev. B **39**, 1633.
Benesh, G.A. and J.E. Inglesfield, 1984, J. Phys. C **17**, 1595.
Beres, R.P., R.E. Allen and J.D. Dow, 1982, Phys. Rev. B **26**, 5702.
Bermudez, V.M., 1995, Appl. Surf. Sci. **84**, 45.
Bermudez, V.M., 1997, Phys. Stat. Sol. (b) **202**, 447.
Bermudez, V.M. and R. Kaplan, 1991, Phys. Rev. B **44**, 11149.
Bermudez, V.M. and J.P. Long, 1995, Appl. Phys. Lett. **66**, 475.
Bertoni, C.M., O. Bisi, C. Calandra and F. Manghi, 1979, Inst. Phys. Conf. Ser. **43**, 191.
Biegelsen, D.K., R.D. Bringans, J.E. Northrup and L.-E. Swartz, 1990a, Phys. Rev. Lett. **65**, 452.
Biegelsen, D.K., R.D. Bringans, J.E. Northrup and L.-E. Swartz, 1990b, Phys. Rev. B **41**, 5701.
Bohr, J., R. Feidenhans'l, M. Nielsen, M. Toney, R.L. Johnson and I.K. Robinson, 1985, Phys. Rev. Lett. **54**, 1275.
Bouchard, A.M., G.C. Osbourn and B.S. Swartzentruber, 1994, Surf. Sci. **321**, 276.
Bringans, R.D. and R.Z. Bachrach, 1984a, Phys. Rev. Lett. **53**, 1954.
Bringans, R.D. and R.Z. Bachrach, 1984b, in: Proc. Int. Conf. Phys. Semicond., eds. D.J. Chadi and W.A. Harrison. New York, Springer-Verlag, p. 67.
Bringans, R.D., R.I.G. Uhrberg and R.Z. Bachrach, 1986, Phys. Rev. B **34**, 2373.
Bringans, R.D., 1990, in: Angle-Resolved Photoemission, ed. S.D. Kevan. Elsevier Scientific.
Brommer, K.D., M. Needles, B.E. Larson and J.D. Joannopoulos, 1992, Phys. Rev. Lett. **68**, 1355.
Broyden, C.G., 1965, Math. Comput. **19**, 577. See also D.D. Johnsson, 1988, Phys. Rev. B **38**, 12807.
Bullock, E.L., R. Gunnella, L. Patthey, T. Abukawa, S. Kono, C.R. Natoli and L.S.O. Johansson, 1995, Phys. Rev. Lett. **74**, 2756.
Calandra, C., F. Manghi and C.M. Bertoni, 1977, J. Phys. C.: Solid State Phys. **10**, 1911.
Car, R., E. Tosatti, S. Baroni and S. Leelaprute, 1981, Phys. Rev. B **24**, 985.
Car, R. and M. Parrinello, 1985, Phys. Rev. Lett. **55**, 2471.
Carstensen, H., R. Claessen, R. Manzke and M. Skibowski, 1990, Phys. Rev. B **41**, 9880.
Catellani, A., G. Galli and F. Gygi, 1996, Phys. Rev. Lett. **77**, 5090.
Catellani, A., G. Galli and F. Gygi, 1998, Phys. Rev. B **57**, 12255.
Ceperley, D.M. and B.J. Alder, 1980, Phys. Rev. Lett. **45**, 566.
Chabal, Y.J., R.J. Culbertson, L.C. Feldman and J.E. Rowe, 1981, J. Vac. Sci. Technol. **18**, 880.
Chabal, Y.J., S.B. Christman, E.E. Chaban and M.T. Yin, 1983, J. Vac. Sci. Technol. A **1**, 1241.
Chadi, D.J., 1978a, J. Vac. Sci. Technol. **15**, 631.
Chadi, D.J., 1978b, Phys. Rev. B **18**, 1800.
Chadi, D.J., 1979a, J. Vac. Sci. Technol. **16**, 1290.
Chadi, D.J., 1979b, Phys. Rev. B **19**, 2074.
Chadi, D.J., 1979c, Phys. Rev. Lett. **43**, 43.
Chadi, D.J., 1984, Phys. Rev. Lett. **52**, 1911.
Chadi, D.J., 1986a, Phys. Rev. Lett. **57**, 102.
Chadi, D.J., 1986b, J. Vac. Sci. Technol. A **4**, 944.
Chadi, D.J., 1987, J. Vac. Sci. Technol. A **5**, 834.
Chadi, D.J., 1991, in: Surface Physics and Related Topics, Festschrift für Xide Xie, eds. F.J. Yang, G.J. Ni, X. Wand, K.M. Zhang and D. Lu. World Scientific, Singapore.
Chadi, D.J. and M.L. Cohen, 1973, Phys. Rev. B **8**, 5747.
Chadi, D.J. and C. Chiang, 1981, Phys. Rev. B **23**, 1843.
Chan, C.T., D. Vanderbilt and S.G. Louie, 1986, Phys. Rev. B **33**, 2455.
Chang, C.S., I.S.T. Tsong, Y.C. Wang and R.F. Davis, 1991, Surf. Sci. **256**, 354.

Chang, K.J., S. Froyen and M.L. Cohen, 1983, Phys. Rev. B **28**, 4736.
Chang, K.J. and M.L. Cohen, 1987, Phys. Rev. B **35**, 8196.
Chelikowsky, J.R. and S.G. Louie, 1984, Phys. Rev. B **29**, 3470.
Chen, X.H., W. Ranke and E. Schröder-Bergen, 1990, Phys. Rev. B **42**, 7429.
Cheng, C., R.J. Needs and V. Heine, 1988, J. Phys. C **21**, 1049.
Cheong, B.H., J.J. Chang and M.L. Cohen, 1991, Phys. Rev. B **44**, 1053.
Chiang, T.-C., J.A. Knapp, M. Aono and D.E. Eastman, 1980, Phys. Rev. B **21**, 3513.
Chiang, T.-C., R. Ludeke, M. Aono, G. Landgren, F.J. Himpsel and D.E. Eastman, 1983, Phys. Rev. B **27**, 4770.
Chiaradia, P., A. Cricenti, S. Selci and G. Chiarotti, 1984, Phys. Rev. Lett. **52**, 1145.
Chiarotti, G. (ed.), 1993, in: Numerical Data and Functional Relationships in Science and Technology. Landolt-Börnstein, New Series Group III, Vol. 24a. Springer, Berlin.
Chiarotti, G. (ed.), 1994, in: Numerical Data and Functional Relationships in Science and Technology. Landolt-Börnstein, New Series Group III, Vol. 24b. Springer, Berlin.
Chin, R.P., J.Y. Huang and Y.R. Shen, 1995, Phys. Rev. B **52**, 5985.
Cho, J., S. Jeong and M.H. Kang, 1994, Phys. Rev. B **50**, 17139.
Cho, K. and J.D. Joannopoulos, 1993, Phys. Rev. Lett. **7**, 1387.
Choyke, W.J., 1990, in: The Physics and Chemistry of Carbides, Nitrides and Borides. Vol. 183, Nato Advanced Study Institute, Series E. Applied Sciences, ed. R. Freer. Kluwer, Dordrecht, p. 563.
Christensen, N.E. and I. Gorczyka, 1994, Phys. Rev. B **50**, 4397.
Craig, B.I. and P.V. Smith, 1989, Surf. Sci. **218**, 569.
Craig, B.I. and P.V. Smith, 1990, Surf. Sci. **233**, 255.
Craig, B.I. and P.V. Smith, 1991, Surf. Sci. Lett. **256**, L609.
Culbertson, R.J., L.C. Feldman and P.J. Silverman, 1980, Phys. Rev. Lett. **45**, 2043.
Culbertson, R.J., Y. Kuk and L.C. Feldman, 1986, Surf. Sci. **167**, 127.
Dabrowski, J. and M. Scheffler, 1992, Appl. Surf. Sci. **56**, 15.
Davis, R.F., Z. Sitar, B.E. Williams, H.S. Kong, H.J. Kim, J.W. Palmour, J.A. Edmond, J. Ryu, J.T. Glass and C.H. Carter, 1988, Mater. Sci. Eng. B **1**, 77.
Davis, R.F., 1993, Physica B **185**, 1.
Davidson, B.N. and W.E. Pickett, 1994, Phys. Rev. B **49**, 11253.
Dayan, M., 1986, J. Vac. Sci. Technol. A **4**, 38.
Demuth, J.E., B.N.J. Persson and A.J. Schell-Sorokin, 1983, Phys. Rev. Lett. **51**, 2214.
Derry, T.E., L. Smit and J.F. van der Veen, 1986, Surf. Sci. **167**, 502.
Devreese, J.T. and P. van Camp, 1985, in: Electronic Structure, Dynamics, and Quantum Structural Properties of Condensed Matter, eds. J.T. Devreese and P. van Camp, NATO-ASI-Series. Plenum, New York. Also references therein.
Drube, W., D. Straub and F.J. Himpsel, 1987, Phys. Rev. B **35**, 5563.
Duke, C.B., 1982, Surf. Sci. **11/12**, 1.
Duke, C.B., 1988a, J. Vac. Sci. Technol. A **6**, 1957.
Duke, C.B., 1988b, in: Surface Properties of Electronic Materials, eds. D.A. King and D.P. Woodruff. Elsevier, Amsterdam, pp. 69–118.
Duke, C.B., 1992, J. Vac. Sci. Technol. A **10**, 2032.
Duke, C.B., 1994, in: Festkörperprobleme/Advances in Solid State Physics, ed. R. Helbig. Vieweg, Braunschweig, pp. 1–36.
Duke, C.B., 1996, Chem. Rev. **96**, 1237.
Duke, C.B. and A.R. Lubinsky, 1975, Surf. Sci. **50**, 605.
Duke, C.B., A.R. Lubinsky, S.C. Chang, B.W. Lee and P. Mark, 1977, Phys. Rev. B **15**, 4865.
Duke, C.B., A. Paton, W.K. Ford, A. Kahn and G. Scott, 1981, Phys. Rev. B **24**, 3310.
Duke, C.B., A. Paton, A. Kahn and D.-W. Tu, 1984a, J. Vac. Sci. Technol. B **2**, 366.
Duke, C.B., A. Paton and A. Kahn, 1984b, J. Vac. Sci. Technol. A **2**, 515.
Duke, C.B., A. Paton and P. Mark, 1978, Phys. Rev. B **18**, 4225.
Duke, C.B., S.L. Richardson, A. Paton and A. Kahn, 1983, Surf. Sci. **127**, L135.
Duke, C.B. and Y.R. Wang, 1989, J. Vac. Sci. Technol. A **7**, 2035.
Dumas, P. and Y.J. Chabal, 1992, J. Vac. Sci. Technol. **10**, 2160.

Ebert, Ph., B. Engels, P. Richard, K. Schroeder, S. Blügel, C. Domke, M. Heinrich and K. Urban, 1996, Phys. Rev. Lett. **77**, 2997.
Eastman, D.E., F.J. Himpsel and J.F. van der Veen, 1980, Solid State Commun. **35**, 345.
Ebina, A., T. Unno, Y. Suda, H. Koinuma and T. Takahashi, 1981, J. Vac. Sci. Technol. **19**, 301.
Ebina, A. and T. Takahashi, 1982, J. Crystal Growth **59**, 51.
Enta, Y., S. Suzuki and S. Kono, 1990, Phys. Rev. Lett. **65**, 2704.
Farrell, H.H. and C.J. Palmstrøm, 1990, J. Vac. Sci. Technol. B **8**, 903.
Feenstra, R.M. and A.J. Slavin, 1991, Surf. Sci. **251/252**, 401.
Feenstra, R.M., J.A. Stroscio, J. Tersoff and A.P. Fein, 1987, Phys. Rev. Lett. **58**, 1192.
Feidenhans'l, R., J.S. Pederson, J. Bohr, M. Nielsen, F. Grey and R.L. Johnson, 1988, Phys. Rev. B **38**, 9715.
Fiorentini, V., M. Methfessel and M. Scheffler, 1993, Phys. Rev. B **47**, 13353.
Florio, J.V. and W.D. Robertson, 1970, Surf. Sci. **22**, 459.
Florio, J.V. and W.D. Robertson, 1971, Surf. Sci. **24**, 173.
Fontes, E., J.R. Patel and F. Comin, 1993, Phys. Rev. Lett. **70**, 2790.
Frauenheim, Th., U. Stephan, P. Blaudeck and D. Porezag, 1993, Surf. Sci. **295**, 340.
Furthmüller, J., J. Hafner and G. Kresse, 1994, Europhys. Lett. **28**, 659.
Ganz, E., I.-S. Hwang, F. Xiong, S.K. Theiss and J. Golovchenko, 1991, Surf. Sci. **257**, 259.
Garcia, A. and M.L. Cohen, 1993, Phys. Rev. B **47**, 4215 and 4221.
Godby, R.W., M. Schlüter and L.J. Sham, 1986, Phys. Rev. Lett. **56**, 2415.
Godby, R.W., M. Schlüter and L.J. Sham, 1988, Phys. Rev. B **37**, 10159.
Goldmann, A., P. Koke, W. Mönch, G. Wolfgarten and J. Pollmann, 1986, Surf. Sci. **169**, 438.
Käckell, P., F. Bechstedt, H. Hüsken, B. Schröter and W. Richter, 1997, Surf. Sci. **391**, 1183.
Gonze, X., R. Stumpf and M. Scheffler, 1991, Phys. Rev. B **44**, 8503.
Göpel, W., R.S. Bauer and G. Hansson, 1980, Surf. Sci. **99**, 138.
Göpel, W., J. Pollmann, I. Ivanov and B. Reihl, 1982, Phys. Rev. B **26**, 3144.
Gräschus, V., A. Mazur and J. Pollmann, 1997, Phys. Rev. B **56**, 6482.
Graupner, R., M. Hollering, A. Ziegler, J. Ristein, L. Ley and A. Stampfl, 1997, Phys. Rev. B **55**, 10841.
Grossner, U., J. Furthmüller and F. Bechstedt, 1998, Phys. Rev. B **58**, R1722.
Guichar, G.M., C.A. Sebenne and C.D. Thuault, 1979, J. Vac. Sci. Technol. **16**, 1212.
Gunnarsson, O. and R.O. Jones, 1980, Phys. Scr. **21**, 394.
Gygi, F., 1993, Phys. Rev. B **47**, 11692.
Haberern, K.W. and M.D. Pashley, 1990, Phys. Rev. B **41**, 3226.
Hagstrum, H.D. and G.E. Becker, 1973, Phys. Rev. B **8**, 1580.
Haight, R., J. Bokor, J. Tark, R.H. Storz, R.R. Freeman and P.H. Bucksbaum, 1985, Phys. Rev. Lett. **54**, 1302.
Haight, R. and J.A. Silberman, 1989, Phys. Rev. Lett. **62**, 815.
Hamann, D.R., 1981, Phys. Rev. Lett. **46**, 1227.
Hamann, D.R., 1989, Phys. Rev. B **40**, 2980.
Hamann, D.R., M. Schlüter and C. Chiang, 1979, Phys. Rev. Lett. **43**, 1494; 1984, Phys. Rev. B **32**, 393.
Hamers, R.J., 1989, Phys. Rev. B **40**, 1657.
Hamers, R.J., R.M. Tromp and J.E. Demuth, 1986a, Phys. Rev. B **34**, 5343.
Hamers, R.J., R.M. Tromp and J.E. Demuth, 1986b, Phys. Rev. Lett. **56**, 1972.
Hamers, R.J., R.M. Tromp and J.E. Demuth, 1987, Surf. Sci. **181**, 346.
Hamers, R.J. and U.K. Köhler, 1989, J. Vac. Sci. Technol. A **7**, 2854.
Hamza, A.V., G.D. Kubiak and R. Stuhlen, 1990, Surf. Sci. **237**, 35.
Haneman, D., 1961, Phys. Rev. **121**, 1093.
Haneman, D., 1987, Rep. Prog. Phys. **50**, 1045.
Hansson, G.V., 1990, Vacuum **41**, 583.
Hansson, G.V. and R.I.G. Uhrberg, 1988, Surf. Sci. Rep. **9**, 197.
Hara, S., W.F.J. Slijkerman, J.F. van der Veen, I. Ohdomari, S. Misawa, E. Sakuma and S. Yoshida, 1990, Surf. Sci. Lett. **231**, L196.
Hara, S., S. Misawa, S. Yoshida and Y. Aoyagi, 1994, Phys. Rev. B **50**, 4548.
Harrison, W.A., 1979, J. Vac. Sci. Technol. **16**, 1492.
Harris, G.L.,1995, in: Properties of Silicon Carbide, ed. G.L. Harris, EMIS Datareviews Series No. 13. INSPEC, London.

Harrison, W.A., 1980, Electronic Structure and the Properties of Solids. Freeman, San Francisco.
Harten, U., J.P. Toennies, Ch. Wöll, L. Miglio, P. Ruggerone, L. Colombo and G. Benedek, 1988, Phys. Rev. B **38**, 3305.
Hashizume, T., Q.K. Xue, J. Zhou, A. Ichimiya and T. Sakurai, 1994, Phys. Rev. Lett. **73**, 2208.
Hashizume, T., Q.K. Xue, A. Ichimiya and T. Sakurai, 1995, Phys. Rev. B **51**, 4200.
Hedin, L., 1965, Phys. Rev. **139**, A796.
Hedin, L. and S. Lundqvist, 1969, in: Solid State Physics: Advances in Research and Application, Vol. 23, eds. F. Seitz, D. Turnbull and H. Ehrenreich. Academic, New York, p. 1.
Hedin, L. and A. Johansson, 1969, J. Phys. B **2**, 1336.
Hellwege, K.-H. and O. Madelung (eds.), 1982, in: Semiconductors. Physics of Group IV Elements and III-V Compounds. Landolt-Börnstein, New Series, Group III, Vol. 17, Pt.a. Springer, Berlin.
Hellwege, K.-H. and O. Madelung (eds.), 1989, in: Semiconductors. Intrinsic Properties of Group IV Elements and III-V, II-VI, and I-VII Compounds. Landolt-Börnstein, New Series, Group III, Vol. 22, Pt.a. Springer, Berlin.
Hellwege, K.-H. and O. Madelung (eds.), 1982, in: Numerical Data and Functional Relationships in Science in Technology. Landolt-Börnstein, New Series Group III, Vols. 17a and 22a. Springer, Berlin.
Henk, J., W. Schattke, H.P. Barnscheidt, C. Janowitz, R. Manzke and M. Skibowski, 1989, Phys. Rev. B **39**, 13286.
Himpsel, F.J., 1982, Adv. Phys. **32**, 1.
Himpsel, F.J., 1990, Surf. Sci. Rep. **12**, 1.
Himpsel, F.J. and D.E. Eastman, 1979, J. Vac. Sci. Technol. **16**, 1297.
Himpsel, F.J., J.F. van der Veen and D.E. Eastman, 1980a, Phys. Rev. B **22**, 1967.
Himpsel, F.J., P. Heimann, T.-C. Chiang and D.E. Eastman, 1980b, Phys. Rev. Lett. **45**, 1112.
Himpsel, F.J., D.E. Eastman, P. Heimann, B. Reihl, C.W. White and D.M. Zehner, 1981a, Phys. Rev. B **24**, 1120.
Himpsel, F.J., P. Heimann and D.E. Eastman, 1981b, Phys. Rev. B **24**, 2003.
Himpsel, F.J., D.E. Eastman, P. Heimann and J.F. van der Veen, 1981c, Phys. Rev. B **24**, 7270.
Himpsel, F.J. and Th. Fauster, 1984a, J. Vac. Sci. Technol. A **2**, 815.
Himpsel, F.J., P.M. Marcus, R. Tromp, I.P. Batra, M.R. Cook, F. Jona and H. Liu, 1984b, Phys. Rev. B **30**, 2257.
Hirabayashi, K., 1969, J. Phys. Soc. Jpn. **27**, 1475.
Hirsch, G., P. Krüger and J. Pollmann, to be published.
Höchst, H. and I. Hernandez-Calderon, 1984, Phys. Rev. B **30**, 4528.
Hohenberg, P. and W. Kohn, 1964, Phys. Rev. **136**, B864.
Holland, B.W., C.B. Duke and A. Paton, 1984, Surf. Sci. **140**, L269.
Hollering, M., A. Ziegler, R. Graupner, B. Mattern, L. Ley, A.P.J. Stampfl and J.D. Riley, 1997, Diam. Relat. Mater. **6**; Heinz, K., to be published.
Horsky, T.N., G.R. Brandes, K.F. Canter, C.B. Duke, A. Paton, D.L. Lessor, A. Kahn, G. Horn, K. Stevens, K. Stiles and A.P. Mills, 1992, Phys. Rev. B **46**, 7011.
Hott, R., 1991, Phys. Rev. B **44**, 1057.
Hricovini, K., R. Günther, P. Thiry, A. Taleb-Ibrahimi, G. Indlekofer, J.E. Bonnet, P. Dumas, Y. Petroff, X. Blase, X. Zhu, S.G. Louie, Y.J. Chabal and P.A. Thiry, 1993, Phys. Rev. Lett. **70**, 1992.
Huang, M.-Z. and W.Y. Ching, 1993, Phys. Rev. B **47**, 9449.
Huijser, A. and J. van Laar, 1975, Surf. Sci. **52**, 202.
Huijser, A., J. van Laar and T.L. van Rooy, 1977, Surf. Sci. **62**, 472.
Huijser, A., J. van Laar and T.L. van Rooy, 1978, Phys. Lett. **65A**, 337.
Humphreys, T.P., G.P. Srivastava and R.H. Williams, 1986, J. Phys. C: Solid State Phys. **19**, 1259.
Hybertsen, M.S. and S.G. Louie, 1985, Phys. Rev. Lett. **55**, 1418.
Hybertsen, M.S. and S.G. Louie, 1986a, Phys. Rev. B **32**, 7005.
Hybertsen, M.S. and S.G. Louie, 1986b, Phys. Rev. B **34**, 5390.
Hybertsen, M.S. and S.G. Louie, 1987, Phys. Rev. Lett. **58**, 1551.
Hybertsen, M.S. and S.G. Louie, 1988a, Phys. Rev. B **37**, 2733.
Hybertsen, M.S. and S.G. Louie, 1988b, Phys. Rev. B **38**, 4033.
Iarlori, S., G. Galli, F. Gygi, M. Parrinello and E. Tosatti, 1992, Phys. Rev. Lett. **69**, 2947.
Ihm, J., S.G. Louie and M.L. Cohen, 1978, Phys. Rev. B **17**, 769.

Ihm, J., A. Zunger and M.L. Cohen, 1979, J. Phys. C **12**, 4409.
Ihm, J., M.L. Cohen and D.J. Chadi, 1980, Phys. Rev. B **21**, 4592.
Ihm, J., D.H. Lee, J.D. Joannopoulos and J.J. Xiong, 1983, Phys. Rev. Lett. **51**, 1872.
Inglesfield, J.E., 1981, J. Phys. C **14**, 3795.
Inglesfield, J.E., 1987, Prog. Surf. Sci. **25**, 57.
Ivanov, I., A. Mazur and J. Pollmann, 1980, Surf. Sci. **92**, 365.
Ivanov, I. and J. Pollmann, 1981, Phys. Rev. B **24**, 7275.
Ivanov, P.A. and V.E. Chelnokov, 1992, Semicond. Sci. Technol. **7**, 863.
Jaffe, J.E., N.M. Harrison and A.C. Hess, 1994, Phys. Rev. B **49**, 11153.
Jaffe, J.E., R. Pandey and P. Zapol, 1996, Phys. Rev. B **53**, R4209.
Janowitz, C., L. Kipp, R. Manzke and B.A. Orlowski, 1990, Surf. Sci. **231**, 25.
Jayaram, G., P. Xu and L.D. Marks, 1993, Phys. Rev. Lett. **71**, 3489.
Jedrecy, N., M. Sauvage-Simkin, R. Pinchaux, J. Massies, N. Greiser and V.H. Etgens, 1990, Surf. Sci. **230**, 197.
Jing, Z. and J.L. Whitten, 1994, Phys. Rev. B **50**, 2598.
Johansson, L.I., F. Owman and P. Mårtensson, 1996a, Phys. Rev. B **53**, 13793.
Johansson, L.I., F. Owman and P. Mårtensson, 1996b, Surf. Sci. Lett. **360**, L483.
Johansson, L.I., F. Owman and P. Mårtensson, 1996c, Surf. Sci. Lett. **360**, L478.
Johansson, L.I., F. Owman, P. Mårtensson, C. Persson and U. Lindefelt, 1996d, Phys. Rev. B **53**, 13803.
Johansson, L.S.O., R.I.G. Uhrberg, P. Mårtensson and G.V. Hansson, 1990, Phys. Rev. B **42**, 1305.
Johansson, L.S.O. and B. Reihl, 1992, Surf. Sci. **269/270**, 810.
Johnson, D.L., 1974, Phys. Rev. B **9**, 4475.
Jones, R.O., 1968, Phys. Rev. Lett. **20**, 992.
Jones, R.O. and O. Gunnarsson, 1989, Rev. Mod. Phys. **61**, 689.
Kádas, K., S. Alvarez, E. Ruiz and P. Alemany, 1996, Phys. Rev. B **53**, 4933.
Käckell, P., J. Furthmüller and F. Bechstedt, 1996a, Appl. Surf. Sci. **104/105**, 45.
Käckell, P., J. Furthmüller and F. Bechstedt, 1996b, Surf. Sci. **352–354**, 55.
Käckell, P., J. Furthmüller, F. Bechstedt, G. Kresse and J. Hafner, 1996c, Phys. Rev. B **54**, 10304.
Kahn, A., E. So, P. Mark and C.B. Duke, 1978a, J. Vac. Sci. Technol. **15**, 580.
Kahn, A., E. So, P. Mark and C.B. Duke, 1978b, J. Vac. Sci. Technol. **15**, 1223.
Kahn, A., 1994, Surf. Sci. **299/300**, 469.
Kaplan, R., 1988, J. Vac. Sci. Technol. A **6**, 829.
Kaplan, R., 1989, Surf. Sci. **215**, 111.
Katnani, A.D. and D.J. Chadi, 1985, Phys. Rev. B **31**, 2554.
Kaxiras, E., Y. Bar-Yam, J.D. Joannopoulos and K.C. Pandey, 1986, Phys. Rev. B **33**, 4406.
Kaxiras, E., Y. Bar-Yam, J.D. Joannopoulos and K.C. Pandey, 1987a, Phys. Rev. B **35**, 9625.
Kaxiras, E., Y. Bar-Yam, J.D. Joannopoulos and K.C. Pandey, 1987b, Phys. Rev. B **35**, 9636.
Kern, G., J. Hafner and G. Kresse, 1996, Surf. Sci. **366**, 464.
Kevan, S.D. and N.G. Stoffel, 1984, Phys. Rev. Lett. **53**, 702.
Kevan, S.D., 1985, Phys. Rev. B **32**, 2344.
Kipp, L., R. Manzke and M. Skibowski, 1995, Solid State Commun. **93**, 603.
Kipp, L., 1997, private communication.
Kleinman, L. and D.M. Bylander, 1982, Phys. Rev. Lett. **48**, 1425.
Klitsner, T. and J.S. Nelson, 1991, Phys. Rev. Lett. **67**, 3800.
Knapp, J.A. and G.P. Lapeyre, 1976, J. Vac. Sci. Technol. **13**, 757.
Kobayashi, K., Y. Morikawa, K. Terakura and S. Blügel, 1992, Phys. Rev. B **45**, 3469.
Kohn, W. and L.J. Sham, 1965, Phys. Rev. **140**, A1133.
Koke, P., A. Goldmann, W. Mönch, G. Wolfgarten and J. Pollmann, 1985, Surf. Sci. **152/153**, 1001.
Kress, C., M. Fiedler and F. Bechstedt, 1994a, in: Proceedings of the Fourth International Conference on the Formation of Semiconductor Interfaces, eds. B. Lengeler, H. Lüth, W. Mönch and J. Pollmann. World Scientific, Singapore, p. 19.
Kress, C., M. Fiedler and F. Bechstedt, 1994b, Europhys. Lett. **28**, 433.
Kress, C., M. Fiedler, W.G. Schmidt and F. Bechstedt, 1994c, Phys. Rev. B **50**, 17697.
Krüger, P., 1997, unpublished.

Krüger, P., A. Mazur, G. Wolfgarten and J. Pollmann, 1986, Phys. Rev. Lett. **57**, 1468.
Krüger, P. and J. Pollmann, 1988, Phys. Rev. B **38**, 10578.
Krüger, P. and J. Pollmann, 1990a, Phys. Rev. Lett. **64**, 1808.
Krüger, P. and J. Pollmann, 1990b, Vacuum **41**, 638.
Krüger, P. and J. Pollmann, 1991a, Physica B **172**, 155.
Krüger, P. and J. Pollmann, 1991b, Prog. Surf. Sci. **35**, 3.
Krüger, P. and J. Pollmann, 1993, Phys. Rev. B **47**, 1898.
Krüger, P. and J. Pollmann, 1994a, Phys. Rev. Lett. **72**, 1130.
Krüger, P. and J. Pollmann, 1994b, Appl. Phys. A **59**, 487.
Krüger, P. and J. Pollmann, 1995, Phys. Rev. Lett. **74**, 1155.
Kubby, J.A., J.E. Griffith, R.S. Becker and J.S. Vickers, 1987, Phys. Rev. B **36**, 6079.
Kubiak, G.D. and K.W. Kolasinski, 1989, Phys. Rev. B **39**, 1381.
Kübler, B., W. Ranke and K. Jacobi, 1980, Surf. Sci. **92**, 519.
Kulakov, M.A., G. Henn and B. Bullemer, 1996, Surf. Sci. **346**, 49.
Kulakov, M.A., P. Heuell, V.F. Tsvetkov and B. Bullemer, 1994, Surf. Sci. **315**, 248.
LaFemina, J.P., 1992, Surf. Sci. Rep. **16**, 133.
Lambrecht, W.R. and B. Segall, 1994, in: Properties of group III-nitrides, ed. J.H. Edgar, EMIS Datareviews Series, London, p. 125.
Landemark, E., 1993, Ph.D. Thesis, University of Linkøping, unpublished.
Landemark, E., L.S.O. Johansson, C.J. Karlsson and R.I.G. Uhrberg, 1990b, Vacuum **41**, 635.
Landemark, E., C.J. Karlsson, Y.-C. Chao and R.I.G. Uhrberg, 1992, Phys. Rev. Lett. **69**, 1588.
Landemark, E., C.J. Karlsson, L.S.O. Johansson and R.I.G. Uhrberg, 1994, Phys. Rev. B **49**, 16523.
Landemark, E., R.I.G. Uhrberg, P. Krüger and J. Pollmann, 1990a, Surf. Sci. Lett. **236**, L359.
Lander, J.J., 1964, Surf. Sci. **1**, 125.
Lander, J.J. and J. Morrison, 1962, Chem. Phys. **37**, 729.
Lander, J.J. and J. Morrison, 1966, Surf. Sci. **4**, 241.
Larsen, P.K., J.H. Neave and B.A. Joyce, 1981, J. Phys. C **14**, 167.
Larsen, P.K., J.H. Neave, J.F. van der Veen, P.J. Dobson and B.A. Joyce, 1983, Phys. Rev. B **27**, 4966.
Larsen, P.K., J.F. van der Veen, A. Mazur, J. Pollmann, J.H. Neave and B.A. Joyce, 1982, Phys. Rev. B **26**, 3222.
Lassabatere, L., 1987, in: Semiconductor Interfaces: Formation and Properties, eds. G. Le Lay, J. Derrien and N. Boccara. Springer-Verlag, Berlin, p. 239.
Lee, D.H. and J.D. Joannopoulos, 1980, J. Vac. Sci. Technol. **17**, 987.
Lee, D.H. and J.D. Joannopoulos, 1981, Phys. Rev. B **24**, 6899.
Lee, D.H. and J.D. Joannopoulos, 1982, J. Vac. Sci. Technol. **21**, 351.
Leung, K.T., L.J. Terminello, I. Hussain, X.S. Zhang, T. Hayashi and D.A. Shirley, 1988, Phys. Rev. B **38**, 8241.
Ley, L., R.A. Pollak, F.R. McFeely, S.P. Kowalczyk and D.A. Shirley, 1974, Phys. Rev. B **9**, 600.
Li, L. and I.S.T. Tsong, 1996, Surf. Sci. **351**, 141.
Long, J.P., V.M. Bermudez and D.M. Ramaker, 1996, Phys. Rev. Lett. **76**, 991.
Louie, S.G., K.M. Ho and M.L. Cohen, 1979, Phys. Rev. B **19**, 1774.
Lu, W., W. Yang and K. Zhang, 1991, J. Phys.: Condens. Matter **3**, 9079.
Lu, Z.-Y., G.L. Chiarotti, S. Scandolo and E. Tosatti, 1998a, Phys. Rev. B **58**, 13698.
Lu, W., P. Krüger and J. Pollmann, 1998b, Phys. Rev. Lett. **81**, 2292.
Lundqvist, S. and N.H. March, 1983, in: Theory of the Inhomogeneous Electron Gas, eds. S. Lundqvist and N.H. March. Plenum, New York. Also references therein.
Lurie, P.G. and J.M. Wilson, 1977, Surf. Sci. **65**, 453.
Lüth, H., G.W. Rubloff and W.D. Grobmann, 1976, Solid State Commun. **18**, 1427.
Ma, Y., S. Lordi, J.A. Eades and S. Ino, 1994, Phys. Rev. B **49**, 17448.
Magnusson, K.O., S.A. Flodström, P. Mårtensson, J.M. Nicholls, U.O. Karlson, R. Engelhardt and E.E. Koch, 1985, Solid State Commun. **55**, 643.
Magnusson, K.O. and S.A. Flodström, 1988a, Phys. Rev. B **38**, 1285.
Magnusson, K.O., S.A. Flodström and P.E.S. Persson, 1988b, Phys. Rev. B **38**, 5384.
Magnusson, K.O. and S.A. Flodström, 1988c, Phys. Rev. B **38**, 6137.
Mailhiot, C., C.B. Duke and Y.C. Chang, 1984, Phys. Rev. B **30**, 1109.

Mailhiot, C., C.B. Duke and D.J. Chadi, 1985a, Phys. Rev. B **31**, 2213.
Mailhiot, C., C.B. Duke and D.J. Chadi, 1985b, Surf. Sci. **149**, 366.
Majewski, J.A. and P. Vogl, 1992a, Phys. Rev. B **46**, 12219.
Majewski, J. A. and P. Vogl, 1992b, Phys. Rev. B **46**, 12235.
Manghi, F., C.M. Bertoni, C. Calandra and E. Molinari, 1981, Phys. Rev. B **24**, 6029.
Manghi, F., 1986, Phys. Rev. B **33**, 2554.
Manghi, F., E. Molinari, C.M. Bertoni and C. Calandra, 1982, Solid State Phys. **15**, 1099.
Manghi, F., R. Del Sole, A. Selloni and E. Molinari, 1990a, Phys. Rev. B **41**, 9935.
Manghi, F., P. Perfetti and B. Reihl, 1990b, Solid State Commun. **76**, 1371
Manzke, R., H.P. Barnscheidt, C. Janowitz and M. Skibowski, 1987, Phys. Rev. Lett. **58**, 610.
Marée, P.J.M., K. Nakagawa, J.F. van der Veen and R. Tromp, 1988, Phys. Rev. B **38**, 1585.
Mårtensson, P., A. Cricenti and G.V. Hansson, 1985, Phys. Rev. B **32**, 6959.
Mårtensson, P., A. Cricenti and G.V. Hansson, 1986, Phys. Rev. B **33**, 8855.
Mårtensson, P., W.-X. Ni, G.V. Hansson, J.M. Nicholls and B. Reihl, 1987, Phys. Rev. B **36**, 5974.
Martins, J.L., N. Troullier and S.-H. Wei, 1991, Phys. Rev. B **43**, 2213.
Mazur, A. and J. Pollmann, 1990, Surf. Sci. **225**, 72.
Mazur, A., B. Sandfort, V. Gräschus and J. Pollmann, 1997, in: Festkörperprobleme/Advances in Solid State Physics, Vol. 36, ed. R. Helbig. Vieweg, Braunschweig/Wiesbaden, p. 181.
Mehandru, S.P. and A.B. Anderson, 1990, Phys. Rev. B **42**, 9040.
Menon, M., N.N. Lathiotakis and A.N. Andriotis, 1997, Phys. Rev. B **56**, 1412.
Meyer, R.J., C.B. Duke, A. Paton, A. Kahn, E. So, J.L. Yeh and P. Mark, 1979, Phys. Rev. B **19**, 5194.
Meyer, R.J., C.B. Duke, A. Paton, J.L. Yeh, J.C. Tsang, A. Kahn and P. Mark, 1980a, Phys. Rev. B **21**, 4740.
Meyer, R.J., C.B. Duke, A. Paton, E. So, J.L. Yeh, A. Kahn and P. Mark, 1980b, Phys. Rev. B **22**, 2875.
Miglio, L., P. Ruggerone and G. Benedek, 1988, Phys. Scr. **37**, 768.
Miller, T., E. Rosenwinkel and T.-C. Chiang, 1983, Solid State Commun. **47**, 935.
Mönch, W., P. Koke and S. Krueger, 1981, J. Vac. Sci. Technol. **19**, 313.
Mönch, W., 1995, Semiconductor Surfaces and Interfaces, 2nd edn., Springer Series in Surface Science. Springer-Verlag, Berlin, Vol. 26.
Morar, J.F., F.J. Himpsel, G. Hollinger, J.L. Jordon, G. Hughes and F.R. McFeely, 1986, Phys, Rev. B **33**, 1346.
Muehlhoff, L., W.J. Choyke, M.J. Bozack and J.T. Yates, Jr., 1986, J. Appl. Phys. **60**, 2842.
Munz, A.W., C. Ziegler and W. Göpel, 1995, Phys. Rev. Lett. **74**, 2244.
Nakanishi, S., H. Tokutaka, K. Nishimori, S. Kishida and N. Ishihara, 1989, Appl. Surf. Sci. **41/42**, 44.
Needels, M., M.C. Payne and J.D. Joannopoulos, 1987, Phys. Rev. Lett. **58**, 1765.
Needels, M., M.C. Payne and J.D. Joannopoulos, 1988, Phys. Rev. B **38**, 5543.
Nicholls, J.M., G.V. Hansson, R.I.G. Uhrberg and S.A. Flodström, 1983, Phys. Rev. B **27**, 2594.
Nicholls, J.M., G.V. Hansson, U.O. Karlsson, R.I.G. Uhrberg, R. Engelhardt, K. Seki and E.E. Koch, 1984, Phys. Rev. Lett. **52**, 1555.
Nicholls, J.M., P. Mårtensson and G.V. Hansson, 1985, Phys. Rev. Lett. **54**, 2363.
Nicholls, J.M., G.V. Hansson, R.I.G. Uhrberg and S.A. Flodström, 1986, Phys. Rev. B **33**, 5555.
Nicholls, J.M. and B. Reihl, 1987, Phys. Rev. B **36**, 8071.
Nicholls, J.M. and B. Reihl, 1989, Surf. Sci. **218**, 237.
Nogami, J., S.-I. Park and C.F. Quate, 1987, Phys. Rev. B **36**, 6221.
Nogami, J., S.-I. Park and C.F. Quate, 1988, Surf. Sci. **203**, L631.
Northrup, J.E., 1985, Phys. Rev. Lett. **54**, 815.
Northrup, J.E., 1986, Phys. Rev. Lett. **57**, 154.
Northrup, J.E., 1993, Phys. Rev. B **47**, 10032.
Northrup, J.E. and M.L. Cohen, 1982, Phys. Rev. Lett. **49**, 1349.
Northrup, J.E. and M.L. Cohen, 1983, Phys. Rev. B **27**, 6553.
Northrup, J.E. and S. Froyen, 1993, Phys. Rev. Lett. **71**, 2276.
Northrup, J.E. and S. Froyen, 1994, Phys. Rev. B **50**, 2015.
Northrup, J.E., M.S. Hybertsen and S.G. Louie, 1989, Phys. Rev. B **39**, 8198.
Northrup, J.E., M.S. Hybertsen and S.G. Louie, 1991, Phys. Rev. Lett. **66**, 500.
Northrup, J.E. and J. Neugebauer, 1995, Phys. Rev. B **52**, R17001.

Northrup, J.E. and J. Neugebauer, 1996, Phys. Rev. B **53**, R10477
Northrup, J.E., R. Di Felice and J. Neugebauer, 1997, Phys. Rev. B **55**, 13878.
Northrup, J.E. and J. Neugebauer, 1998, Phys. Rev. B **57**, R4230.
Olde, J., G. Mante, H.-P. Barnscheidt, L. Kipp, J.-C. Kuhr, R. Manzke, M. Skibowski, J. Henk and W. Schattke, 1990, Phys. Rev. B **41**, 9958.
Olmstead, M.A., R.D. Bringans, R.I.G. Uhrberg and R.Z. Bachrach, 1986, Phys. Rev. B **34**, 6041.
Ortega, J.E. and F.J. Himpsel, 1993, Phys. Rev. B **47**, 2130.
Owman, F. and P. Mårtensson, 1995, Surf. Sci. **330**, L639.
Packard, W.E. and J.D. Dow, 1997, Phys. Rev. B **55**, 15643.
Palummo, M., L. Reining, R.W. Godby, C.M. Bertoni and N. Börnsen, Europhys. Lett. **26**, 607.
Pandey, K.C., J.L. Freeouf and D.E. Eastman, 1977, J. Vac. Sci. Technol. **14**, 904.
Pandey, K.C., 1981, Phys. Rev. Lett. **47**, 1913.
Pandey, K.C., 1982a, Phys. Rev. B **25**, 4338.
Pandey, K.C., 1982b, Phys. Rev. Lett. **49**, 223.
Pandey, K.C., 1983, Physica B **117/118**, 761.
Pandey, K.C. and J.C. Phillips, 1975, Phys. Rev. Lett. **34**, 1450.
Pandey, K.C. and J.C. Phillips, 1976, Phys. Rev. B **13**, 750.
Pandey, R., P. Zapol and M. Causá, 1997, Phys. Rev. B **55**, R16009.
Parill, T.M. and Y.W. Chung, 1991, Surf. Sci. **243**, 96.
Park, C.H., B.-H. Cheong, K.-H. Lee and K.J. Chang, 1994, Phys. Rev. B **49**, 4485.
Pashley, M.D., 1989, Phys. Rev. B **40**, 10481.
Pashley, M.D., K.W. Haberern, W. Friday, J.M. Woodall and P.D. Kirchner, 1988a, Phys. Rev. Lett. **60**, 2176.
Pashley, M.D., K.W. Haberern, W. Friday and J.M. Woodall, 1988b, J. Vac. Sci. Technol. B **6**, 1468.
Pate, B.B., 1986, Surf. Sci. **165**, 83.
Payne, M.C., J.D. Joannopoulos, D.C. Allan, M.P. Teter and D.H. Vanderbilt, 1986, Phys. Rev. Lett. **56**, 2656.
Payne, M.C., M.P. Teter, D.C. Allan, T.A. Arias and J.D. Joannopoulos, 1992, Rev. Mod. Phys. **64**, 1045.
Payne, M.C., N. Roberts, R.J. Needs, M. Needels and J.D. Joannopoulos, 1989, Surf. Sci. **211/212**, 1.
Pensl, G. and R. Helbig, 1990, in: Festkörperprobleme, Advances in Solid State Physics, Vol. 30, ed. U. Rössler. Vieweg, Braunschweig, p. 133.
Pepper, S., 1982, Surf. Sci. **123**, 47.
Perdew, J.P. and A. Zunger, 1981, Phys. Rev. B **23**, 5048.
Perfetti, P., J.M. Nicholls and B. Reihl, 1987, Phys. Rev. B **36**, 6160.
Phaneuf, R.J. and M.B. Webb, 1985, Surf. Sci. **164**, 167.
Phillips, J.C., 1973, in: Bonds and Bands in Semiconductors. Academic, New York.
Pickett, W.E., 1985, Comments Solid State Phys. **12**, 1.
Pollmann, J. and S.T. Pantelides, 1978, Phys. Rev. B **18**, 5524.
Pollmann, J., 1980, in: Festkörperprobleme, Advances in Solid State Physics, Vol. 20, Vieweg Braunschweig, p. 117.
Pollmann, J., R. Kalla, P. Krüger, A. Mazur and G. Wolfgarten, 1986, Appl. Phys. A **41**, 21.
Pollmann, J., P. Krüger and A. Mazur, 1987, J. Vac. Sci. Technol. B **5**, 945.
Pollmann, J. and P. Krüger, 1990, in: Proceedings of the 20th Int. Conf. Phys. Semiconductors. World Scientific, Singapore, p. 91.
Pollmann, J., P. Krüger, M. Rohlfing, M. Sabisch and D. Vogel, 1996, Appl. Surf. Sci. **104/105**, 1.
Pollmann, J., P. Krüger and M. Sabisch, 1997, Phys. Stat. Sol. (b) **202**, 421.
Poppendieck, T.D., T.C. Ngoc and M.B. Webb, 1978, Surf. Sci. **75**, 287.
Powers, J.M., A. Wander, P.J. Rous, M.A. van Hove and G.A. Somorjai, 1991, Phys. Rev. B **44**, 11159.
Powers, J.M., A. Wander, M.A. van Hove and G.A. Somorjai, 1992, Surf. Sci. Lett. **260**, L7.
Puga, M.W., G. Xu and S.Y. Tong, 1985, Surf. Sci. **164**, L789.
Pulay, P., 1977, in: Modern Theoretical Chemistry, ed. H.F. Schaefer. Plenum, New York, Vol. 4, pp. 153–185.
Qian, G. and D.J. Chadi, 1987a, J. Vac. Sci. Technol. A **5**, 906.
Qian, G. and D.J. Chadi, 1987b, Phys. Rev. B **35**, 1288.
Qian, G., R.M. Martin and D.J. Chadi, 1988a, Phys. Rev. B **37**, 1303.
Qian, G., R.M. Martin and D.J. Chadi, 1988b, Phys. Rev. B **38**, 7649.

Qu, H., P.O. Nilsson, J. Kanski and L. Ilver, 1989, Phys. Rev. B **39**, 5276.
Qu, H., J. Kanski, P.O. Nilsson and U.O. Karlsson, 1990, Vacuum **41**, 610.
Qu, H., J. Kanski, P.O. Nilsson and U.O. Karlsson, 1991a, Phys. Rev. B **43**, 9843.
Qu, H., J. Kanski, P.O. Nilsson and U.O. Karlsson, 1991b, Phys. Rev. B **44**, 1762.
Ramstad, A., G. Brocks and P.J. Kelly, 1995, Phys. Rev. B **51**, 14504.
Ranke, W., 1976, Solid State Commun. **19**, 685.
Ranke, W. and K. Jacobi, 1977, Surf. Sci. **63**, 33.
Ranke, W. and K. Jacobi, 1979, Surf. Sci. **81**, 504.
Rapcewicz, K., M.B. Nardelli and J. Bernholc, 1997, Phys. Rev. B **56**, R12725.
Reihl, B., T. Riester, M. Tschudy and P. Perfetti, 1988, Phys. Rev. B **38**, 13456.
Rich, D.H., T. Miller, G.E. Franklin and T.-C. Chiang, 1989, Phys. Rev. B **39**, 1438.
Roberts, N. and R.J. Needs, 1990, Surf. Sci. **236**, 112.
Robinson, I.K., W.K. Waskiewicz, P. Fuoss, J.B. Stark and P.A. Bennet, 1986, Phys. Rev. B **33**, 7013.
Robinson, I.K. and E. Vlieg, 1992, Surf. Sci. **261**, 123.
Rohlfing, D.M., J. Ellis, B.J. Hinch, W. Allison and R.F. Willis, 1989, Surf. Sci. **207**, L955.
Rohlfing, M., P. Krüger and J. Pollmann, 1993, Phys. Rev. B **48**, 17791.
Rohlfing, M., P. Krüger and J. Pollmann, 1995a, Phys. Rev. B **52**, 1905.
Rohlfing, M., P. Krüger and J. Pollmann, 1995b, Phys. Rev. B **52**, 13753.
Rohlfing, M., P. Krüger and J. Pollmann, 1995c, Phys. Rev. Lett. **75**, 3489.
Rohlfing, M., 1996a, Ph.D. Thesis, University of Münster.
Rohlfing, M., P. Krüger and J. Pollmann, 1996b, Phys. Rev. B **54**, 13759.
Rohrer, G.S. and D.A. Bonnel, 1991, Surf. Sci. Lett. **247**, L195.
Rossmann, R., H.L. Meyerheim, V. Jahns, J. Wever, W. Moritz, D. Wolf, D. Dornisch and H. Schulz, 1992, Surf. Sci. **279**, 199.
Rubio, A., J.L. Corkill, M.L. Cohen, E.L. Shirley and S.G. Louie, 1993, Phys. Rev. B **48**, 11810.
Sabisch, M., P. Krüger and J. Pollmann, 1995, Phys. Rev. B **51**, 13367.
Sabisch, M., P. Krüger, A. Mazur, M. Rohlfing and J. Pollmann, 1996a, Phys. Rev. B **53**, 13121.
Sabisch, M., P. Krüger, A. Mazur and J. Pollmann, 1996b, in: Proceedings of ICPS-23, eds. M. Scheffler and R. Zimmermann. World Scientific, Singapore, p. 819.
Sabisch, M., P. Krüger, A. Mazur and J. Pollmann, 1998, Surf. Rev. Lett. **5**, 199.
Sabisch, M., P. Krüger and J. Pollmann, 1997b, Phys. Rev. B **55**, 10561.
Sandfort, B., A. Mazur and J. Pollmann, 1995, Phys. Rev. B **51**, 7139.
Sauvage-Simkin, M., R. Pinchaux, J. Massies, P. Calverie, J. Bonnet, N. Jedrecy and I.K. Robinson, 1989a, Surf. Sci. **211/212**, 39.
Sauvage-Simkin, M., R. Pinchaux, J. Massies, P. Calverie, N. Jedrecy, J. Bonnet and I.K. Robinson, 1989b, Phys. Rev. Lett. **62**, 563.
Schardt, J., Ch. Bram, S. Müller, U. Starke, K. Heinz and K. Müller, 1995, Surf. Sci. **337**, 232.
Schattke, W., 1997, Prog. Surf. Sci. **54**, 211.
Scheffler, M., J.P. Vigneron and G.B. Bachelet, 1985, Phys. Rev. B **31**, 6541.
Scheffler, M., Ch. Droste, A. Fleszar, F. Maca, G. Wachutka and G. Barzel, 1991, Physica B **172**.
Schlüter, M., 1988, in: The Chemical Physics of Solid Surfaces and Heterogeneous Catalysis, eds. D.A. King and D.P. Woodruff. Elsevier, Amsterdam, Vol. 5, pp. 37–68.
Schlüter, M., J.R. Chelikowsky, S.G. Louie and M.L. Cohen, 1975, Phys. Rev. B **12**, 4200.
Schmeits, M., A. Mazur and J. Pollmann, 1981, Solid State Commun. **40**, 1081.
Schmeits, M., A. Mazur and J. Pollmann, 1983, Phys. Rev. B **27**, 5012.
Schmidt, W.G. and F. Bechstedt, 1996, Phys. Rev. B **54**, 16742.
Schnell, R.D., D. Rieger, A. Bogen, F.J. Himpsel, K. Wandelt and W. Steinmann, 1985, Phys. Rev. B **32**, 8057.
Scholze, A., W.G. Schmidt and F. Bechstedt, 1996, Phys. Rev. B **53**, 13725.
Schröer, P., P. Krüger and J. Pollmann, 1993a, Phys. Rev. B **47**, 6971.
Schröer, P., P. Krüger and J. Pollmann, 1993b, Phys. Rev. B **48**, 18264.
Schröer, P., P. Krüger and J. Pollmann, 1994, Phys. Rev. B **49**, 17092.
Semond, F., P. Soukiassian, P.S. Mangat and L. di Ciaccio, 1995, J. Vac. Sci. Technol. B **13**, 1591.
Semond, F., P. Soukiassian, A. Mayne, G. Dujardin, L. Douillard and C. Jaussaud, 1996, Phys. Rev. Lett. **77**, 2013.

Shek, M.L., K.E. Miyano, Q.-Y. Dong, T.A. Callcott and D.L. Ederer, 1994 J. Vac. Sci. Technol., A **12**, 1079.
Shirley, E.L., X. Zhu and S.G. Louie, 1992, Phys. Rev. Lett. **69**, 2955.
Shkrebtii, A.I., R. Di Felice, C.M. Bertoni and R. Del Sole, 1995, Phys. Rev. B **51**, 11201.
Shih, H.D., F. Jona, D.W. Jepsen and P.M. Marcus, 1976, Phys. Rev. Lett. **37**, 1622.
Skibowski, M. and L. Kipp, 1994, J. Electron Spectrosc. Relat. Phenom. **68**, 5576.
Smit, L., R.M. Tromp and J.F. van der Veen, 1985, Surf. Sci. **163**, 315.
Solal, F., G. Jezequel, A. Barski, P. Steiner, R. Pinchaux and Y. Petroff, 1984a, Phys. Rev. Lett. **52**, 360.
Solal, F., G. Jezequel, F. Houzay, A. Barski and R. Pinchaux, 1984b, Solid State Commun. **52**, 37.
Sorba, L., V. Hinkel, H.U. Middelmann and K. Horn, 1987, Phys. Rev. B **36**, 8075.
Soukiassian, P., F. Semond, L. Douillard, A. Mayne, G. Dujardin, L. Pizzagalli and C. Joachim, 1997, Phys. Rev. Lett. **78**. 907.
Sowa, E.C., G.D. Kubiak, R.H. Stulen and M.A. van Hove, 1988, J. Vac. Sci. Technol. A **6**, 832.
Spiess, L., A.J. Freeman and P. Soukiassian, 1994, Phys. Rev. B **50**, 2249.
Srivastava, G.P., 1982, Phys. Rev. B **25**, 2815.
Srivastava, G.P., I. Singh, V. Montgomery and R.H. Williams, 1983, J. Phys. C: Solid State Phys. **16**, 3627.
Srivastava, G.P. and D. Weaire, 1987, Adv. Phys. **26**, 463.
Starke, U., Ch. Bram, P.-R. Steiner, W. Hartner, L. Hammer, K. Heinz and K. Müller, 1995, Appl. Surf. Sci. **89**, 175.
Starke, U., 1997, Phys. Stat. Sol. (b) **202**, 475.
Stich, I., M.C. Pane, R.D. King-Smith, J.-S. Lin and L.J. Clarke, 1992, Phys. Rev. Lett. **68**, 1351.
Stoffel, N.G., 1983, Phys. Rev. B **28**, 3306.
Straub, D., V. Dose and W. Altmann, 1983, Surf. Sci. **133**, 9.
Straub, D., M. Skibowski and F.J. Himpsel, 1985a, Phys. Rev. B **32**, 5237.
Straub, D., L. Ley and F.J. Himpsel, 1985b, Phys. Rev. Lett. **54**, 142.
Straub, D., L. Ley and F.J. Himpsel, 1986, Phys. Rev. B **33**, 2607.
Stroscio, J.A., R.M. Feenstra and A.P. Fein, 1986, Phys. Rev. Lett. **57**, 2579.
Stroscio, J.A., R.M. Feenstra and A.P. Fein, 1987, J. Vac. Sci. Technol. A **5**, 838.
Stroscio, J.A., R.M. Feenstra, D.M. Newns and A.P. Fein, 1988, J. Vac. Sci. Technol. A **6**, 499.
Stuhlmann, Ch., H. Bogdány and H. Ibach, 1992, Phys. Rev. B **45**, 6786.
Surh, M.P., S.G. Louie and M.L. Cohen, 1991, Phys. Rev. B **43**, 9126.
Svane, A., 1992, Phys. Rev. Lett. **68**, 1900; ibid 1994, **72**, 1248.
Svane, A. and O. Gunnarson, 1990, Phys. Rev. Lett. **65**, 1148.
Szotek, Z. and W.M. Temmerman, 1993, Phys. Rev. B **47**, 4029.
Szotek, Z., W.M. Temmerman and H. Winter, 1994, Phys. Rev. Lett. **72**, 1244.
Tabata, T., T. Aruga and Y. Murata, 1987, Surf. Sci. **179**, L63.
Takahashi, T. and E. Ebina, 1982, Appl. Surf. Sci. **11/12**, 268.
Takai, T., T. Halicioglu and W.A. Tiller, 1985, Surf. Sci. **164**, 341.
Takayanagi, K., 1984, J. Microsc. (Oxford) **136**, 287.
Takayanagi, K., Y. Tanishiro, M. Takahashi and S. Takahashi, 1985a, J. Vac. Sci. Technol. A **3**, 1502.
Takayanagi, K., Y. Tanishiro, M. Takahashi and S. Takahashi, 1985b, Surf. Sci. **164**, 367.
Takeuchi, N., A. Selloni, A.I. Shkrebtii and E. Tosatti, 1991, Phys. Rev. B **44**, 13611.
Takeuchi, N., A. Selloni and E. Tosatti, 1995, Phys. Rev. B **51**, 10844.
Temmerman, W.M. and Z. Szotek, 1993, Phys. Rev. B **47**, 1184.
Themlin, J.-M., I. Forbeaux, V. Langlais, H. Belkhir and J.-M. Debever, 1997, Europhys. Lett. **39**, 61.
Thornton, J.M.C., P. Unsworth, M.D. Jackson, P. Weightmann and D.A. Woolf, 1994, Surf. Sci. **316**, 231.
Tochihara, H., T. Amakusa and M. Iwatsuki, 1994, Phys. Rev. B **50**, 12262.
Tong, S.Y., W.N. Mei and G. Xu, 1984a, J. Vac. Sci. Technol. B **2**, 393.
Tong, S.Y., G. Xu and W.N. Mei, 1984b, Phys. Rev. Lett. **52**, 1693.
Tong, S.Y., G. Xu, W.Y. Hu and M.W. Puga, 1985, J. Vac. Sci. Technol. B **3**, 1076.
Tong, S.Y., H. Huang, C.M. Wei, W.E. Packard, F.K. Men, G. Glander and M.B. Webb, 1988, J. Vac. Sci. Technol. A **6**, 115.
Tong, S.Y., H. Huang and C.M. Wei, 1990, in: Chemistry and Physics of Solid Surfaces, Vol. 8, eds. R. Vaneslow and R. Howe. Springer-Verlag, Berlin, p. 395.

Tromp, R.M., E.J. van Loenen, M. Iwami and F.W. Saris, 1982, Solid State Commun. **44**, 971.
Tromp, R.M., R.G. Smeenk, F.W. Saris and D.J. Chadi, 1983, Surf. Sci. **133**, 137.
Tromp, R.M., L. Smit and J.F. van der Veen, 1984, Phys. Rev. B **30**, 6235.
Tromp, R.M., R.J. Hamers and J.E. Demuth, 1985, Phys. Rev. Lett. **55**, 1303.
Tromp, R.M., R.J. Hamers and J.E. Demuth, 1986, Phys. Rev. B **34**, 1388.
Troullier, N. and J.L. Martins, 1991, Phys. Rev. B **43**, 1993.
Jenkins, S.J. and G.P. Srivastava, 1996, J. Phys.: Condens. Mat. **8**, 6641.
Twesten, R.D. and J.M. Gibson, 1994, Ultramicroscopy **53**, 223.
Tyc, S., 1994, J. Phys. I (Paris) **4**, 617.
Uhrberg, R.I.G., G.V. Hansson, J.M. Nicholls and S.A. Flodström, 1981, Phys. Rev. B **24**, 4684.
Uhrberg, R.I.G., G.V. Hansson, U.O. Karlsson, J.M. Nicholls, P.E.S. Persson and S.A. Flodström, 1982, Phys. Rev. Lett. **48**, 1032.
Uhrberg, R.I.G., G.V. Hansson, J.M. Nicholls, P.E.S. Persson and S.A. Flodström, 1985, Phys. Rev. B **32**, 2174.
Uhrberg, R.I.G., R.D. Bringans, M.A. Olmstead, R.Z. Bachrach and J. Northrup, 1987, Phys. Rev. B **35**, 3945.
van Bommel, A.J., J.E. Crombeen and A. van Tooren, 1975, Surf. Sci. **48**, 463.
van Camp, P.E., V.E. van Doren and J.T. Devreese, 1986, Phys. Rev. B **34**, 1314.
van Camp, P.E., V.E. van Doren and J.T. Devreese, 1988, Phys. Rev. B **38**, 12675.
van Laar, J. and J.J. Scheer, 1967, Surf. Sci. **8**, 342.
van Laar, J. and A. Huijser, 1976, J. Vac. Sci. Technol. **13**, 769.
van Laar, J., A. Huijser and T.L. van Rooy, 1977, J. Vac. Sci. Technol. **14**, 894.
van Silfhout, R.G., J.F. van der Veen, C. Norris and J.E. Macdonald, 1990, Farad. Discuss. Chem. Soc. **89**, 169.
Vanderbilt, D. and S.G. Louie, 1983, J. Vac. Sci. Technol. B **3**, 723.
Vanderbilt, D. and S.G. Louie, 1984, Phys. Rev. B **30**, 6118.
Vanderbilt, D., 1990, Phys. Rev. B **41**, 7892.
Vogel, D., 1998, Ph.D. Thesis, Universität Münster.
Vogel, D., P. Krüger and J. Pollmann, 1995, Phys. Rev. B **52**, R14316.
Vogel, D., P. Krüger and J. Pollmann, 1996, Phys. Rev. B **54**, 5495.
Vogel, D., P. Krüger and J. Pollmann, 1997, Phys. Rev. B **55**, 12836.
Vogel, D., P. Krüger and J. Pollmann, 1998, Surf. Sci. **402**, 774.
von der Linden, W. and P. Horsch, 1988, Phys. Rev. B **37**, 8351.
von Münch, W., 1982, in: Numerical Data and Functional Relationships in Science and Technology, eds. O. Madelung, M. Schulz and H. Weiss. Landolt Börnstein, New Series, Groups IV and III-V, Vol. 17, Pt. a. Springer, Berlin (see also references therein).
Wachs, A.L., T. Miller, T.C. Hsieh, A.P. Shapiro and T.-C. Chiang, 1985, Phys. Rev. B **32**, 2326.
Wachutka, G., A. Fleszar, F. Maca and M. Scheffler, 1992, J. Phys.: Condens. Mat. **4**, 2831.
Wang, C.S. and B.M. Klein, 1981, Phys. Rev. B **24**, 3393.
Wang, Y.R. and C.B. Duke, 1987a, Surf. Sci. **188**, L708.
Wang, Y.R. and C.B. Duke, 1987b, Surf. Sci. **192**, 309.
Wang, Y.R. and C.B. Duke, 1988a, Phys. Rev. B **37**, 6417.
Wang, Y.R., C.B. Duke, K. Stevens, A. Kahn, K.O. Magnusson and S.A. Flodström, 1988b, Surf. Sci. **206**, L817.
Wang, Y.R., C.B. Duke, K.O. Magnusson and S.A. Flodström, 1988c, Surf. Sci. **205**, L760.
Watanabe, S., 1996, Surf. Sci. **351**, 149.
Webb, M.B., 1988, J. Vac. Sci. Technol. A **6**, 115.
Wei, S.H. and A. Zunger, 1988, Phys. Rev. B **37**, 8958.
Weidmann, R., H.E. Gumlich, M. Kupsch and H.U. Middelmann, 1992, Phys. Rev. B **45**, 1172.
Wells, A.F., 1975, in: Structural Inorganic Chemistry. Clarendon, Oxford.
Wenzien, B., P. Käckell and F. Bechstedt, 1993, in: Proceedings of the 5th International Conference on Silicon Carbide and Related Materials, Washington, ed. M. Spencer, 1994, IOP Conf. Proc. No. 137. Institute of Physics and Physical Society, London, p. 223.
Wenzien, B., P. Käckel and F. Bechstedt, 1994a, Surf. Sci. **307–309**, 989.
Wenzien, B., P. Käckell and F. Bechstedt, 1994b, in: IOP Conf. Proc. No. 137. Institute of Physics and Physical Society, London, p. 223.
Wenzien, B., P. Käckell and F. Bechstedt, 1994c, in: Proceedings of ICPS-22, Vancouver 1994. World Scientific, Singapore, p. 389.

Wenzien, B., P. Käckell and F. Bechstedt, 1995, Surf. Sci. **331–333**, 1105.
Wigner, E., 1934, Phys. Rev. **46**, 1002.
Wigner, E., 1938, Trans. Faraday Soc. **34**, 678; 1937, Phys. Rev. **46**, 1002.
Williams, A.R., P.J. Feibelman and N.D. Lang, 1982, Phys. Rev. B **26**, 5433.
Williams, G.P., R.J. Smith and G.J. Lapeyre, 1978, J. Vac. Sci. Technol. **15**, 1249.
Wimmer, E. and A. Freeman, 2000, see Chapter 1 of this book.
Wolfgarten, G., P. Krüger and J. Pollmann, 1985, Solid State Commun. **54**, 839.
Wolkow, R.A., 1992, Phys. Rev. Lett. **68**, 2636.
Wolkow, R. and Ph. Avouris, 1988, Phys. Rev. Lett. **60**, 1049.
Wright, A.F. and J.S. Nelson, 1994, Phys. Rev. B **50**, 2159.
Xu, Y.-N. and W.Y. Ching, 1993, Phys. Rev. B **48**, 4335 (also references therein).
Yamauchi, J., M. Tsukuda, S. Watanabe and O. Sigino, 1996, Phys. Rev. B **54**, 5586.
Yan, H., A.P. Smith and H. Jónsson, 1995, Surf. Sci. **330**, 265.
Yang, S.H., D.A. Drabold and J.A. Adams, 1993, Phys. Rev. B **48**, 5261.
Yang, W.S., F. Jona and P.M. Marcus, 1982, Solid State Commun. **43**, 847.
Yang, W.S., F. Jona and P.M. Marcus, 1983, Phys. Rev. B **28**, 2049.
Yang, W.S. and F. Jona, 1984, Phys. Rev. B **29**, 899.
Yean, D.H. and J.R. Riter, 1971, J. Phys. Chem. Solids **32**, 653.
Yeh, Ch.Y., S.H. Wei and A. Zunger, 1994, Phys. Rev. B **50**, 2715.
Yin, M.T. and M.L. Cohen, 1981, Phys. Rev. B **24**, 2303.
Yokotsuka, T., S. Kono, S. Suzuki and T. Sagawa, 1981, Solid State Commun. **39**, 1001.
Yokotsuka, T., S. Kono, S. Suzuki and T. Sagawa, 1984, J. Phys. Soc. Jpn. **53**, 696.
Zakharov, O., A. Rubio, X. Blase, M.L. Cohen and S.G. Louie, 1994, Phys. Rev. B **50**, 10780.
Zakharov, O., A. Rubio and M.L. Cohen, 1995, Phys. Rev. B **51**, 4926.
Zhang, Z., M. Wensell and J. Bernholc, 1995a, Phys. Rev. B **51**, 5291.
Zhang, S.B., S.H. Wei and A. Zunger, 1995b, Phys. Rev. B **52**, 13975.
Zheng, X.M. and P.V. Smith, 1991, Surf. Sci. **253**, 395.
Zhu, X., S. Fahy and S.G. Louie, 1989a, Phys. Rev. B **39**, 7840.
Zhu, X., S.B. Zhang, S.G. Louie and M.L. Cohen, 1989b, Phys. Rev. Lett. **63**, 2112.
Zhu, X. and S.G. Louie, 1991a, Phys. Rev. B **43**, 12146.
Zhu, X. and S.G. Louie, 1991b, Phys. Rev. B **43**, 14142.
Zwicker, G. and K. Jacobi, 1985, Solid State Commun. **54**, 701.

CHAPTER 3

# Electronic States on Metal Surfaces

G. BORSTEL

*Department of Physics*
*University of Osnabrück*
*D-49069 Osnabrück, Germany*

J.E. INGLESFIELD

*Department of Physics and Astronomy*
*University of Wales Cardiff*
*PO Box 913, Cardiff, CF2 3YB, UK*

*© 2000 Elsevier Science B.V.*
*All rights reserved*

*Handbook of Surface Science*
*Volume 2, edited by K. Horn and M. Scheffler*

# Contents


3.1. Introduction . . . . . 211
Surface convention and units . . . . . 212
3.2. Theory of electron states at surfaces . . . . . 212
3.2.1. Effective potential and the surface barrier . . . . . 212
3.2.2. Surface states in multiple scattering theory . . . . . 214
3.2.2.1. General scattering formalism . . . . . 214
3.2.2.2. Model studies – Cu(111) . . . . . 217
3.2.2.3. Cu(100) . . . . . 220
3.2.3. Bulk states at the surface . . . . . 221
3.2.3.1. Bulk states in multiple scattering theory . . . . . 221
3.2.3.2. Local density of states at Cu(100) and Ni(100) . . . . . 224
3.3. Photoemission and surface electronic structure . . . . . 225
3.3.1. Theory of photoemission . . . . . 225
3.3.2. Calculating photoemission . . . . . 226
3.4. Results for selected systems . . . . . 227
3.4.1. Simple metals: Al . . . . . 227
3.4.2. Noble metals: Cu . . . . . 229
3.4.2.1. Cu(100) . . . . . 229
3.4.2.2. Cu(111) . . . . . 231
3.4.2.3. Corrugation effects . . . . . 233
3.4.2.4. Effective surface barriers . . . . . 234
3.4.3. Magnetic d-metals: Fe and Ni . . . . . 237
3.4.3.1. Fe(110) . . . . . 238
3.4.3.2. Ni surfaces . . . . . 240
3.5. First principles calculations of the image potential . . . . . 241
3.5.1. Image potential felt by a test charge . . . . . 241
3.5.2. Image potential felt by an electron . . . . . 241
References . . . . . 243

## 3.1. Introduction

Photoemission, inverse photoemission, two-photon photoemission and very-low-energy electron diffraction experiments have recently led to a renewed interest in the study of electron states at metal surfaces, particularly the surface states – states which are localized at the surface with energies in a local energy gap. In this contribution we study both occupied and unoccupied states. It is not our intention to give an exhaustive review of all the theoretical and experimental work which has been done in the last decades – instead, we will focus on some model surfaces, for which the physical aspects of the electron states can be worked out in some detail. These systems are Al as a typical nearly-free-electron metal, nonmagnetic Cu and the ferromagnets Fe and Ni as typical d-band systems.

The nature of electron states at the surface, particularly the possibility of surface states, is a consequence of breaking the bulk three-dimensional symmetry by cutting the solid in two. The bulk potential is connected via a potential barrier to the vacuum potential. On the solid side, the bulk potential is reached very quickly, within an atomic layer or so because of the short screening length in metals; on the vacuum side, the surface barrier asymptotically approaches the image potential, with important consequences for the surface states.

As usual in condensed matter physics, we use a one-electron or quasiparticle description, and we talk about the *effective* potential. An electron then feels the self-energy $\Sigma(\mathbf{r}, \mathbf{r}', E)$, a non-Hermitian, non-local, energy-dependent operator (Echenique and Pendry, 1990). The self-energy is defined within the many-body Green function formalism and takes into account all the dynamical exchange and correlation effects beyond the Hartree approximation (Fetter and Walecka, 1971). In another approach, density functional theory (DFT) shows that the ground state charge density and ground state energy can be constructed from the one-electron orbitals and eigenenergies of the Schrödinger equation containing a local, static effective potential (Lundqvist and March, 1983). This effective potential consists of the exchange–correlation potential $V_{\mathrm{XC}}(\mathbf{r})$ added on to the Hartree potential and the potential due to the nuclei. The asymptotic charge density extending into the vacuum, coming from states at the Fermi energy $E_{\mathrm{F}}$, is described correctly by $V_{\mathrm{XC}}$, in full DFT. Applications of DFT usually rely on the local density approximation (LDA), possibly with gradient corrections, allowing for *ab initio* calculations of the total effective potential and the surface barrier $V_{\mathrm{B}}(\mathbf{r})$ (Jennings and Jones, 1988).

For occupied and unoccupied electron states at metal surfaces with energies near $E_{\mathrm{F}}$, the DFT surface barrier $V_{\mathrm{B}}$ in principle gives an excellent description. Unfortunately, DFT in the LDA results in an incorrect asymptotic behaviour of $V_{\mathrm{B}}(\mathbf{r})$ in the vacuum region: at a large distance $|z|$ from the metal surface, $V_{\mathrm{B}}(\mathbf{r})$ in LDA decays exponentially, instead of varying proportional to $1/|z|$ like the image potential. This shortcoming of the usual LDA-DFT barrier potential prevents a fully *ab initio* description of the image-potential states, a class of unoccupied surface states with energies just below the vacuum level which are a consequence of the long-range image potential behaviour of the true surface barrier. Since

first-principles calculations of the surface barrier potential with a correct asymptotic behaviour have only recently become available for jellium (Eguiluz et al., 1992) and Al(111) (White et al., 1998) (Section 3.5), all practical calculations of image-potential surface states for real systems up till now have used models for the surface barrier which are parametrised in some way (Section 3.2.1), or interpolate between the LDA surface potential and the image potential (Section 3.2.3.2).

Fully self-consistent electronic structure calculations, within the framework of DFT (LDA), are carried out using a variety of basis functions – plane waves with pseudopotentials (Pickett, 1989), full-potential linearised augmented plane waves (LAPW's) (Wimmer et al., 1981; Weinert et al., 1982), and full-potential linearised muffin tin orbitals (LMTO's) (Methfessel et al., 1992) are most widely used both in the bulk and at surfaces. The surface breaks the periodicity in the $z$-direction, but this can be restored by considering a superlattice of slabs separated by vacuum – this enables standard codes to be used, which depend on three-dimensional periodicity. A disadvantage of slab methods from the point of view of considering surface-localised surface states is that the states on either side of the slab can interact, complicating the whole picture. Moreover, it is sometimes difficult to distinguish between surface resonances, which leak into the bulk, and the true surface states. Green function methods (Krüger and Pollmann, 1988), the embedding technique (Benesh and Inglesfield, 1984), and layer-scattering methods (layer-KKR) (MacLaren et al.,1990) enable the electronic structure of true semi-infinite systems to be calculated, and surface states can then be studied more precisely. We shall use the layer scattering methods to study conditions for the occurrence of surface states in Section 3.2.2, and these methods also enable photoemission spectra to be calculated for comparison with experiment (Section 3.3). The embedding method will be used in Sections 3.2.3.2 and 3.4.3.1 for full-potential studies of bulk states at the surface and image states.

*Surface convention and units*
Our convention is that the positive $z$-axis points into the semi-infinite crystal. We use atomic units, with $\hbar = e = m = 1, c = 137.036$.

## 3.2. Theory of electron states at surfaces

### *3.2.1. Effective potential and the surface barrier*

The potential felt by an electron outside a metal surface has, asymptotically, the image potential form:

$$V(z) = -\frac{1}{4|z - z_{\mathrm{im}}|}, \tag{3.1}$$

where $z_{\mathrm{im}}$ is the position of the image plane. A classical test charge also feels a potential of the same form, but with a different value of $z_{\mathrm{im}}$, as we shall discuss further in Section 3.5. The image potential is a consequence of the electron–electron interaction, and both the effective potential in exact DFT and the self-energy $\Sigma$ in the many-body Green function

approach vary like (3.1) (Eguiluz et al., 1992; White et al., 1998). The usual LDA approach for DFT unfortunately does not give the correct form of surface barrier, exponential decay into vacuum rather than (3.1), because in LDA the effective potential depends only on the local charge density. We shall see in this section how these deficiencies inherent in the LDA treatment can be rectified. It should be emphasised, however, that self-consistent LDA calculations give excellent work functions and surface energies, because the errors in the LDA surface barrier occur where the ground state electron density is very small. This was first pointed out by Lang and Kohn (1971) in their pioneering study of work functions and surface energies of jellium surfaces. We only need worry about the discrepancy when we consider electron states extending into vacuum, like the image-potential surface states, or deal with electron spectroscopies like LEED, photoemission and STM.

When the correct asymptotic behaviour of the surface barrier potential is needed, a long-range image tail can be fitted to the self-consistent LDA effective potential. A widely used parametrization of the surface barrier potential $V_B(z)$, connecting the bulk crystal potential with the vacuum potential, is the JJJ form devised by Jones, Jennings and Jepsen (Jones et al., 1984; Jennings et al., 1988)

$$V_B^{JJJ}(z) = \begin{cases} \dfrac{1-\exp[\lambda(z-z_{im})]}{4(z-z_{im})} & z < z_{im}, \\ \dfrac{V_{or}}{A\exp[-B(z-z_{im})]+1} & z \geqslant z_{im}. \end{cases} \tag{3.2}$$

The potential deep in the vacuum is taken as the energy zero. In this formula, the parameter $\lambda$ controls the transition from the image potential to $V_{or}$, the average potential inside the bulk crystal (the average has to be suitably defined, with the deep potential inside the muffin tins removed). The constants $A$ and $B$ are fixed by matching the potential and derivative at $z_{im}$. This potential has no variation parallel to the surface, but this is an adequate description for most spectroscopic applications.

Another widely used form of one-dimensional barrier potential was devised by Rundgren and Malmström (1977), with slightly more flexibility in functional form than the JJJ barrier. This is the one used in later analysis in this article, and it has the form:

$$V_B^{RM}(z) = \begin{cases} \frac{1}{4}(z-z_{im})^{-1} & z < z_A < z_{im}, \\ s_0 + s_1(z-z_A) + s_2(z-z_A)^2 + s_3(z-z_A)^3 & z_A < z < z_E, \\ V_{or} & z > z_E. \end{cases} \tag{3.3}$$

In this barrier the asymptotic regime $z < z_A$ is connected to $V_{or}$ by the third-order polynomial in $z$, spanning the range $z_A < z < z_E$. The polynomial coefficients are fixed through the requirement of continuity of $V_B^{RM}$ and its derivative. The RM barrier is determined by four parameters, $z_{im}$, $V_{or}$, $z_A$, and $z_E$. As compared to the JJJ barrier, it allows for slightly more flexibility in the transition range. Note that this transition range is $1/\lambda$ in $V_B^{JJJ}$ and $|z_A - z_E|$ in $V_B^{RM}$.

Both the JJJ and the RM barrier have a transition region, and continuous first derivatives with respect to the $z$-coordinate. This is advantageous, since a step in $V_B(z)$ gives rise to

spurious reflections. A simple long-range barrier with a step and no transition region is the truncated image barrier, which is still often used in model calculations:

$$V_B(z) = \begin{cases} \frac{1}{4}(z - z_{im})^{-1} & z < z_c < z_{im}, \\ V_{or} & z > z_c. \end{cases} \tag{3.4}$$

It introduces an image form far from the surface and truncates it at $z_c$, where $V_B(z_c) = V_{or}$. There are only two parameters, $z_{im}$ and $V_{or}$.

Surface state wave-functions and energies can be calculated very accurately using the embedding method, which builds in the effects of the substrate and the long range image tail in the vacuum while preserving the three-dimensional form of the barrier potential (Nekovee and Inglesfield, 1992). The surface state wave-functions are explicitly calculated in the "near-surface region", the region outside the surface atoms extending about 5 Å into the vacuum. An embedding potential matches the wave-functions onto the solution of the Schrödinger equation of the surface with the self-consistent LDA potential on the crystal side of the near-surface region; on the vacuum side an embedding potential matches the solutions on to Coulomb wave-functions. In the near-surface region itself, the effective potential interpolates between the self-consistent LDA barrier potential, and the image form (3.1).

### *3.2.2. Surface states in multiple scattering theory*

In this section, we present general conditions for the occurrence of localized surface states at clean surfaces, in the framework of multiple scattering theory. This is based on arguments originally developed by Echenique and Pendry (1978) and McRae (1979). Multiple scattering theory is widely used for calculating the surface electronic structure, and it also forms the basis for LEED and photoemission calculations.

#### *3.2.2.1. General scattering formalism*

In multiple scattering theory applied to surfaces, the solid is divided into atomic layers parallel to the surface. We start by considering the form of the wave-function $\phi(\mathbf{r}_\parallel, z)$ in the region between the topmost atomic layer at $z = 0$ and the surface barrier, where the effective potential can be assumed to be constant (this region can be as thin as we like):

$$\phi(\mathbf{r}_\parallel, z) = \sum_{\mathbf{g}} \{ d_{\mathbf{g}}^{+} \exp(i\mathbf{k}_{\mathbf{g}}^{+} \cdot \mathbf{r}) + d_{\mathbf{g}}^{-} \exp(i\mathbf{k}_{\mathbf{g}}^{-} \cdot \mathbf{r}) \}, \tag{3.5}$$

with

$$\mathbf{k}_{\mathbf{g}}^{\pm} = \left( \mathbf{k}_\parallel - \mathbf{g},\ \pm [2(E - V_{or}) - |\mathbf{k}_\parallel - \mathbf{g}|^2]^{1/2} \right). \tag{3.6}$$

Here $\mathbf{g}$ is a two-dimensional surface reciprocal lattice vector, and $V_{or}$ is the constant potential in this region (usually assumed to be the same as the bulk interstitial potential). The wavefield in (3.5) is a sum of two sets of plane waves, one set with coefficients $(d_{\mathbf{g}}^{-})$

headed away from the crystal towards the barrier, and the other set ($d_{\mathbf{g}}^{+}$) travelling away from the barrier. This is the general form of any wave-function in this region, describing both travelling waves from the bulk reflected by the surface and the surface states. In a surface state these two sets of waves reflect into each other with no transmission into the bulk (Echenique and Pendry, 1978; McRae, 1979). Denoting the reflection coefficients of the crystal by $r^{\mathrm{C}}_{\mathbf{g}\mathbf{g}'}$ and those of the barrier by $r^{\mathrm{B}}_{\mathbf{g}\mathbf{g}'}$, we have:

$$d_{\mathbf{g}}^{-} = \sum_{\mathbf{g}'} r^{\mathrm{C}}_{\mathbf{g}\mathbf{g}'} d_{\mathbf{g}'}^{+} \tag{3.7}$$

for reflection by the crystal, and

$$d_{\mathbf{g}}^{+} = \sum_{\mathbf{g}'} r^{\mathrm{B}}_{\mathbf{g}\mathbf{g}'} d_{\mathbf{g}'}^{-} \tag{3.8}$$

for reflection at the barrier. The requirement of self-consistency between (3.7) and (3.8) results in the condition for the existence of a surface state

$$\det\left(I - r^{\mathrm{C}} r^{\mathrm{B}}\right) = 0. \tag{3.9}$$

The surface barrier potential has the general form

$$V_{\mathrm{B}}(\mathbf{r}) = \sum_{\mathbf{g}} V_{\mathrm{B}\mathbf{g}}(z) \mathrm{e}^{\mathrm{i}\mathbf{g}\cdot\mathbf{r}_{\parallel}}, \tag{3.10}$$

where the contributions from the non-zero surface reciprocal lattice vectors correspond to surface corrugation. For many purposes – calculating LEED, photoemission, inverse photoemission, etc. – this corrugation may be neglected (Bartynski et al., 1985; Van Siclen, 1990), so (3.10) reduces to the one-dimensional form $V_{\mathrm{B}}(z)$. The matrix $r^{\mathrm{B}}_{\mathbf{g}\mathbf{g}'}$ then becomes diagonal in $\mathbf{g}$. For $\mathbf{k}_{\parallel}$ near the centre of the surface Brillouin zone and energies near the Fermi energy, beams with $\mathbf{g} \neq 0$ in (3.5) decay away from the crystal. Assuming that multiple scattering via these evanescent waves may be neglected, we obtain from (3.9)

$$1 - r^{\mathrm{C}}_{00} r^{\mathrm{B}}_{00} \equiv 1 - r_{\mathrm{C}} \exp(\mathrm{i}\phi_{\mathrm{C}}) r_{\mathrm{B}} \exp(\mathrm{i}\phi_{\mathrm{B}}) = 0. \tag{3.11}$$

This condition is fulfilled only when

$$r_{\mathrm{C}} = r_{\mathrm{B}} = 1, \tag{3.12}$$

$$\phi_{\mathrm{C}} + \phi_{\mathrm{B}} = 2\pi n, \tag{3.13}$$

where $n$ is zero or an integer. Equation (3.12) requires no transmission into continuum states, so surface states can only occur for energies $E$ in a bulk band gap ($r_{\mathrm{C}} = 1$) and below the vacuum level $E_{\mathrm{vac}}$ ($r_{\mathrm{B}} = 1$). This situation is depicted schematically in Fig. 3.1.

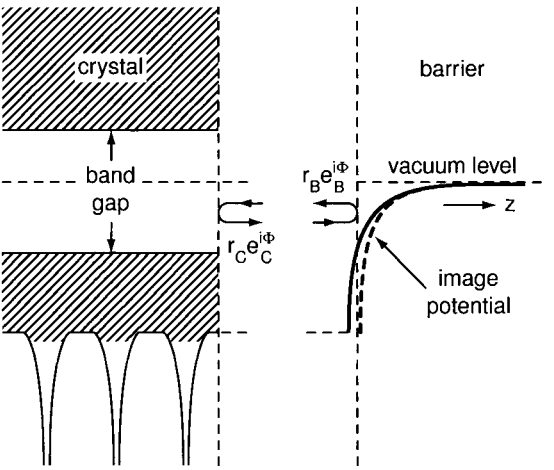


Fig. 3.1. Schematic potential in the vicinity of a crystal surface (Smith, 1985b).

If leakage into the continuum can occur because there is a bulk state at the same value of $E$ and $\mathbf{k}_{\|}$, a surface resonance can still occur when the wave-function peaks in the surface region. By the multiple scattering theory, the wave-function is proportional to:

$$\left| \frac{1}{1 - r^{\mathrm{C}}_{00} r^{\mathrm{B}}_{00}} \right| \tag{3.14}$$

so the surface resonance will occur at a minimum of

$$\left| 1 - r_{\mathrm{C}} \exp(\mathrm{i}\phi_{\mathrm{C}}) r_{\mathrm{B}} \exp(\mathrm{i}\phi_{\mathrm{B}}) \right|. \tag{3.15}$$

Conditions (3.12) and (3.13) are well-known from the theory of bound states in one-dimensional quantized systems. The quantum number $n$ in (3.13) has a precise mathematical meaning and gives the number of nodes of the corresponding eigenfunction for finite $z$ beyond the crystal edge. Equation (3.13) has been extensively used by Smith and coworkers (Smith, 1985a, b; Garrett and Smith, 1986). By assuming reasonable expressions for the energy-dependence of the phases $\phi_{\mathrm{B}}$ and $\phi_{\mathrm{C}}$, they were able to give a qualitatively correct picture of surface states within the s-p band gap of various metal surfaces and to derive useful quantitative trends. We present below a discussion of surface states on Cu(111) and Cu(100) within this simple one-beam multiple scattering model.

In the one-step model of photoemission (Section 3.3), the full reflection matrices $r^{\mathrm{C}}$ and $r^{\mathrm{B}}$ are calculated for the crystal and barrier potential in question. Minima in $|\det(I - r^{\mathrm{C}} r^{\mathrm{B}})|$ may then show up as maxima in the photocurrent. A peak in an angle-resolved photoemission spectrum can be identified as a surface state or resonance rather than a bulk transition, by the independence of initial state energy on photon energy; to distinguish between surface states and resonances we need to know whether the state lies in a bulk band gap or not.

*3.2.2.2. Model studies – Cu(111)*

In this section, we consider the condition for the existence of surface states on Cu(111), in the $L_{2'}$–$L_1$ band gap around the Fermi energy of the Cu bulk band-structure. The bulk band-structure in the ΓL direction projects onto $\bar{\Gamma}$ at the centre of the (111) surface Brillouin zone. We use various stages of approximations for the bulk potential and the surface barrier, and study their effects on the surface electronic structure.

The $L_{2'}$–$L_1$ band gap lies in the Cu s-p band, above the d-states, and is inverted – the p-like state (with symmetry $L_{2'}$) lies under the s-like state (with symmetry $L_1$). We shall treat the gap as nearly-free-electron-like, and then the solution of the Schrödinger equation inside the crystal ($z > 0$) at energy $E$ within the gap has the form (Smith, 1985b, 1988)

$$\psi_C(z) \propto \exp(-\gamma z)\cos\left(z\sqrt{2E_G} - \delta\right). \tag{3.16}$$

Here $E_G$ is the energy of the mid-point of the gap relative to the zero of energy, in this NFE model the average pseudopotential in the bulk crystal. The decay constant $\gamma$ of this solution at energy $E$ is given by the positive root of

$$\gamma^2 = 2\left[\left(V_G^2 + 4EE_G\right)^{1/2} - (E + E_G)\right]. \tag{3.17}$$

The phase $\delta$ is given by

$$\sin 2\delta = -\gamma\sqrt{2E_G}/V_G, \tag{3.18}$$

where $V_G$ is the Fourier component of the pseudopotential which gives rise to the gap. $V_G$ and $E_G$ are in fact model parameters which can be fitted to a regular band calculation. We note that (3.16), which is the solution of the Schrödinger equation going into the crystal at an arbitrary energy inside the gap, is not an eigenfunction of the system – it has not yet been matched onto the solution valid in the surface barrier region and vacuum.

We now find the crystal phase $\phi_C$, matching (3.16) onto plane waves at $z_0$, the position of the crystal edge. This gives the following equation for $\phi_C$ (Smith, 1985b)

$$\sqrt{2E}\tan\left(\frac{\phi_C}{2} - z_0\sqrt{2E}\right) = \sqrt{2E_G}\tan\left(\delta - z_0\sqrt{2E_G}\right) - \gamma. \tag{3.19}$$

Taking the origin at the centre of a surface atom, the inverted gap corresponds to positive $V_G$, and the phase $\delta$ in (3.18) varies between $-\pi/2$ at the bottom of the gap to 0 at the top. This corresponds to charge piling up between the atoms (p-like states) at the bottom of the gap and on the atoms (s-like states) at the top. As $E$ is close to $E_G$ in the gap, $\phi_C$ varies roughly between $-\pi$ and 0 through the gap.

The other ingredient in finding the surface states is the barrier phase $\phi_B$. This can be found by matching plane waves onto $\psi_B$, the solution of the Schrödinger equation at energy $E$, which is regular deep in vacuum

$$\phi_B = -2z_c\sqrt{2E} - 2\arctan\left(\frac{\psi_B'(z_c)}{\sqrt{2E}\psi_B(z_c)}\right), \tag{3.20}$$

where $z_c$ is the position of the matching plane, which can be different from $z_0$ (Fig. 3.1). At $E = 0$, $\phi_B$ is given by $-\pi$ independent of the barrier potential, but going up to the vacuum level $E_{vac}$ its behaviour depends on $V_B(z)$. For a short range $V_B$, $\phi_B$ stays finite, but for the long-range image potential varying like $1/|z|$, $\phi_B$ goes to $+\infty$ like $(E_{vac} - E)^{-1/2}$ as $E$ approaches $E_{vac}$. Combining this with what we know about $\phi_C$, this means that condition (3.13) for the existence of surface states can only be satisfied at a finite number of energies for a short-range barrier, but an infinite number of solutions will occur for a $1/|z|$ barrier if the band gap spans $E_{vac}$ – the Rydberg series of image potential surface states.

The simplest model for a surface barrier is the step potential half-way between atomic layers (Shockley, 1939) – that is, at $z_c = z_0 = -d/2$ with respect to the origin on the surface atoms where $d$ is the interlayer spacing. For $E$ in the band gap, $\sqrt{2E}$ is about $\pi/d$, so the first term in (3.20) is given approximately by $+\pi$. The argument of arctan in the second term is positive, so $\phi_B$ is positive but less than $\pi$ for energies in the band gap. Now $\phi_C$ varies between $-\pi$ and 0, so we conclude that for some energy in the band gap

$$\phi_C + \phi_B = 0 \tag{3.21}$$

and condition (3.13) for the occurrence of a surface state with $n = 0$ is satisfied. This state is the Shockley surface state, and as it is a direct consequence of the termination of the crystal, it is also called a crystal-induced state (Echenique and Pendry, 1978). The existence of this state in a NFE gap requires the inverted gap, with the p-state lying below the s-state. For a non-inverted gap with $V_G$ negative, $\phi_C$ varies between 0 and $\pi$ and the surface state condition is not satisfied. These conclusions remain essentially unchanged when $V_B$ is a general short-range barrier potential, and in realistic situations it is not possible to get more than the $n = 0$ solution for a NFE gap.

A simple and analytically tractable long-range barrier potential is the image potential with a cut-off at $z_c$ (3.4). The regular solution $\Psi(z, E)$ of the Schrödinger equation for $z < z_c$, where the electron feels the image potential, is the Whittaker function $W_{-is,1/2}(xe^{-i\pi})$ (Whittaker and Watson, 1973), with $x = -2ik_z(z - z_{im})$, $s = -0.25/k_z$, and taking $\mathbf{k}_\parallel = 0$, $k_z = [2(E - E_{vac})]^{1/2}$. The phase condition (3.13) is solved graphically in Fig. 3.2 for Cu(111), assuming two different positions for $z_{im}$. The values for $V_G$, $E_G$, and $E_F$ are taken from the band calculation of Burdick (1963) based on the Chodorow potential (1939), and the work function is 4.98 eV (Hölzl and Schulte, 1979). The results of such a phase analysis have been shown to be not very sensitive to the choice of the crystal edge $z_0$ (Ortuno and Echenique, 1986).

Figure 3.2 gives once again the $n = 0$ (crystal-induced) Shockley surface state, which we found with the simple step barrier. Physically this arises from the fact that the Shockley state is due to the termination of the crystal and, thus, its existence is independent of the nature of $V_B$. With the long-range potential, $\phi_B$ diverges as $E$ approaches the vacuum level, and if the energy gap spans $E_{vac}$ the phase condition (3.13) results in the full Rydberg series of image potential surface states with $n \geqslant 1$ (Johnson and Smith, 1983). The energies of these states are given by:

$$E_n = E_{vac} - \frac{1}{32(n + a_n)^2} \quad (n = 1, 2, 3, \ldots) \tag{3.22}$$

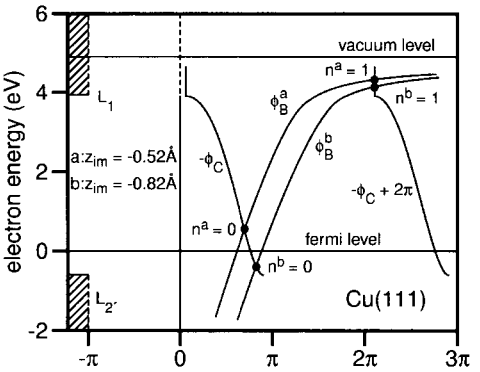


Fig. 3.2. Energy-dependence of the phases $\phi_C$ and $\phi_B$ in the multiple reflection theory of Cu(111) for an image potential with cut-off and the image plane at the position $z_{im}$. Solid circles denote the energies of the $n = 0, 1$ surface states (Borstel and Thörner, 1988).

which is the standard Rydberg series with $Z = 1/4$, this factor coming from the form of image potential and containing the quantum defect $a_n$. The quantum defect comes from the deviation of the potential from a pure Coulomb form and the boundary condition of matching the hydrogenic solution outside the surface onto the crystal solution of the Schrödinger equation inside – these effects are all contained in $\phi_B$ and $\phi_C$, of course. In this case, $E_{vac}$ lies above the top of the gap, and from Fig. 3.2 condition (3.13) is satisfied at energies overlapping with the continuum where true surface states cannot occur – rather, image potential surface resonances. Experimentally, the $n = 1$ image state actually lies just below the (calculated) band edge, and should then be a true surface state.

The typical behaviour of the surface state wave-functions $\Psi_n(z)$ is shown in Fig. 3.3. Beyond the crystal edge $z < z_0$ the $n = 0$ crystal-induced surface state exhibits an exponentially decaying tail without any nodes, just as the $n = 0$ Shockley surface state for a simple step barrier. $|\Psi_0|^2$ has its maximum near $z_0$, i.e., slight variations of the effective potential near the surface will have quite a large effect on the energetic position of the $n = 0$ state. By contrast, the $n = 1, 2$ image-potential states with one and two nodes for $z < z_0$, respectively, protrude far out into the vacuum region and are therefore only slightly affected by the bulk potential. As a variation of the effective crystal potential causes a change in the work function, this means that the image-potential states are essentially tied to the vacuum level.

For a consistent description of surface states at $\mathbf{k}_\parallel \neq 0$ within the multiple scattering theory we must restart from (3.9) and take care of including correctly all propagating plane waves in the basic expansion (3.5). According to (3.6) we have to take into account all beams for which $|\mathbf{k}_\parallel - \mathbf{g}|^2 \leqslant 2(E_{vac} - V_{or})$ ($\simeq 25$ eV for Cu(111)). A continuous transition from $\mathbf{k}_\parallel = 0$ ($\bar{\Gamma}$) to the boundary of the surface Brillouin zone requires at least two-dimensional matrices $r^B$ and $r^C$ in (3.9). In such a two-beam description, when $\mathbf{k}_\parallel$ is at a point of high symmetry, (3.9) splits into two one-dimensional equations and the phase condition (3.13) may be applied to each (Smith, 1985b).

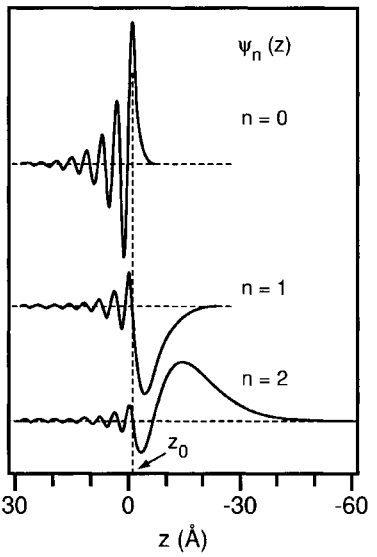


Fig. 3.3. Surface state wave-functions for an image-potential barrier (Dose, 1985).

*3.2.2.3. Cu(100)*

We now turn to the $X_{4'}$–$X_1$ gap in Cu(100) and consider again $\mathbf{k}_\parallel = 0$. The $X_{4'}$–$X_1$ gap occurs at a higher energy than $L_{2'}$–$L_1$, above the Fermi energy, with the vacuum level lying near the centre of the gap. This results in a Rydberg series of image potential states inside the gap. The crystal-induced state, on the other hand, becomes a resonance below the gap.

To understand this resonance, we go beyond the NFE approximation, calculating $\phi_C(E)$ and $r_C(E)$ from the realistic three-dimensional Chodorow potential (1939). The results are shown in Fig. 3.4 for energies around $X_{4'}$; to mimic damping effects, a small imaginary contribution of 0.05 eV has been added to the inner potential – this smooths out kinks in $\phi_C(E)$ and $r_C(E)$ at the band edge. Using the image potential barrier with the cut-off (3.4) to calculate $r_B(E)$, $|1 - r_C \exp(i\phi_C) r_B \exp(i\phi_B)|^2$, occurring in (3.15), has the variation shown in Fig. 3.5. The $n = 1$ image-potential surface state is clearly identified by the zero near 4 eV. By contrast, the crystal-induced surface state near 1.15 eV appears as an extremely weak minimum which can be identified only at an enlarged vertical scale (see insert in Fig. 3.5). At this energy, the reflection coefficient $r_C$ has already dropped to $\sim 0.4$, so the surface resonance must have a large bulk component. The crystal-induced resonance has been detected experimentally at 1.1–1.15 eV (Thörner et al., 1985; Woodruff et al., 1985).

A simple one-beam phase model in the two-band NFE approximation gives a qualitatively correct account of the physics of surface states in s-p gaps of metals. It is inadequate for detailed quantitative investigations through the surface Brillouin zone, and in the case of d-metals, it can be safely applied only to those band gaps where the character of the wave-functions is pure s-p-like. To study these more complex cases, we must resort to the full multiple scattering formalism, or use methods like embedding.

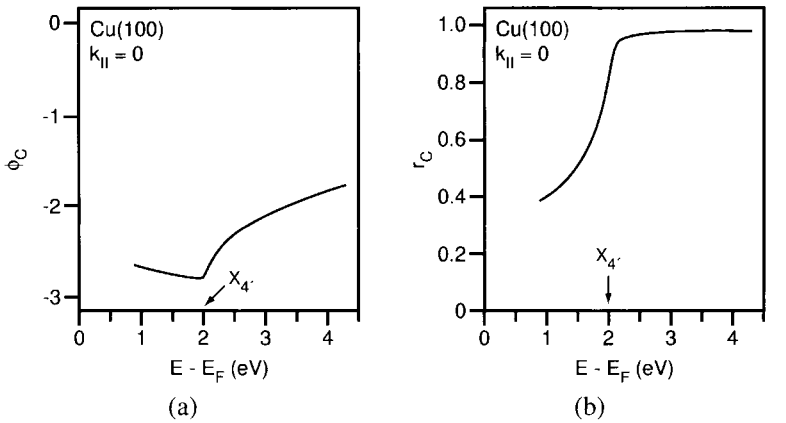


Fig. 3.4. Energy-dependence of the phase $\phi_C$ (a) and the modulus $r_C$ (b) of the reflection coefficient for Cu(100) near the lower gap edge $X_{4'}$ (Borstel and Thörner, 1988).

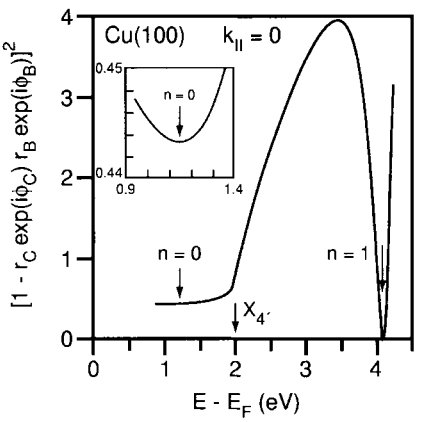


Fig. 3.5. Energy-dependence of $|1 - r_C \exp(i\phi_C) r_B \exp(i\phi_B)|^2$ in Eq. (3.15) for Cu(100) and an image potential barrier with cut-off ($z_{im} = -0.74$ Å) near the lower gap edge $X_{4'}$ (Borstel and Thörner, 1988).

### *3.2.3. Bulk states at the surface*

As well as the localized surface states, bulk states contribute to the surface charge density and density of states – each bulk state travelling towards the surface is reflected back by the surface barrier potential with an exponential decay into the vacuum. The surface resonances which we discussed above are in fact bulk states with an enhanced amplitude at the surface.

#### *3.2.3.1. Bulk states in multiple scattering theory*

Away from the surface barrier an electron feels the same potential as in the bulk, so we can build up a solution of the Schrödinger equation in this region from bulk solutions. If, for

example, we are working at $\bar{\Gamma}$ in the *surface* Brillouin zone for fcc (100), the bulk bands projecting onto this wave-vector lie along $\Gamma X\Gamma$ in the *bulk* Brillouin zone. As well as these travelling waves, there are also evanescent solutions of the bulk Schrödinger equation with the same reduced surface wave-vector – these are not allowed in the infinite crystal, but in the semi-infinite crystal we must consider additional solutions which decay exponentially away from the surface into the bulk. In fact, at energy $E$ and surface wave-vector $\mathbf{k}_\parallel$, for each surface reciprocal lattice vector $\mathbf{g}$ there is *either* one bulk wave-function travelling towards the surface and one travelling away from the surface *or* an evanescent wave-function decaying away from the surface (the corresponding solution increasing into the bulk is not allowed).

In the presence of the surface, each continuum state can be derived from a bulk state $\psi^-_{\mathbf{k}_\parallel,\mathbf{g}}$ travelling towards the surface, which is then reflected by the surface barrier potential into the waves $\psi^+_{\mathbf{k}_\parallel,\mathbf{g}}$ travelling away from the surface or decaying exponentially with the same reduced $\mathbf{k}_\parallel$ and energy $E$. We can write the full wave-function away from the surface barrier as

$$\phi_{\mathbf{k}_\parallel,\mathbf{g}} = \psi^-_{\mathbf{k}_\parallel,\mathbf{g}} + \sum_{\mathbf{g}'} \hat{r}^{\mathrm{B}}_{\mathbf{g},\mathbf{g}'} \psi^+_{\mathbf{k}_\parallel,\mathbf{g}'}, \tag{3.23}$$

where $\hat{r}^{\mathrm{B}}_{\mathbf{g},\mathbf{g}'}$ is the reflection matrix of the surface barrier in terms of bulk states rather than plane waves as in Section 3.2.2.1. In fact $\hat{r}^{\mathrm{B}}_{\mathbf{g},\mathbf{g}'}$ can be found in terms of the plane wave reflection matrices $r^{\mathrm{B}}_{\mathbf{g}\mathbf{g}'}$ and $r^{\mathrm{C}}_{\mathbf{g}\mathbf{g}'}$. If the crystal is divided into atomic layers, each bulk state $\psi^{\pm}_{\mathbf{k}_\parallel,\mathbf{g}}$ may be expanded in terms of plane waves in between the layers, as in (3.5), with expansion coefficients given by the band-structure calculation. Substituting back into (3.23), we can obtain a plane wave expansion of $\phi_{\mathbf{k}_\parallel,\mathbf{g}}$ in between the top layer of atoms and the surface barrier, and the requirement that the plane waves are reflected into one another by the barrier and the crystal determines $\hat{r}^{\mathrm{B}}_{\mathbf{g},\mathbf{g}'}$.

Working in terms of bulk states explicitly is formally very useful – it shows how the bulk states at the surface arise – and it has recently found application in the studies of transport properties of multilayer systems (Schep et al., 1997). However, the most widely used scattering method for surface applications is the layer-KKR (LKKR) (MacLaren et al., 1990) which uses a plane wave representation of the wave-function between atomic layers, just like in Section 3.2.2.1. The idea of LKKR is, first of all, to calculate the reflection and transmission matrices of a single atomic layer. In terms of these, the wave-function corresponding to a plane wave incident from the left is given by:

$$\begin{aligned} \phi(\mathbf{r}_\parallel, z) &= \exp\left(\mathrm{i}\mathbf{k}^+_{\mathbf{g}} \cdot \mathbf{r}\right) + \sum_{\mathbf{g}'} R_{\mathbf{g}\mathbf{g}'} \exp\left(\mathrm{i}\mathbf{k}^-_{\mathbf{g}'} \cdot \mathbf{r}\right) \quad z \text{ left of the layer} \\ &= \sum_{\mathbf{g}'} T_{\mathbf{g}\mathbf{g}'} \exp\left(\mathrm{i}\mathbf{k}^+_{\mathbf{g}'} \cdot \mathbf{r}\right) \qquad\qquad z \text{ right of the layer.} \end{aligned} \tag{3.24}$$

$R_{\mathbf{g}\mathbf{g}'}$ and $T_{\mathbf{g}\mathbf{g}'}$ can be found from the scattering properties (the $t$-matrix, in fact) of the individual atoms within the layer. The plane wave expansion in (3.24) is valid outside the layer itself, exactly as in (3.5).

Putting together two layers, with reflection and transmission matrices $R_1$, $T_1$, $R_2$, $T_2$, respectively, the transmission matrix $T_{1,2}$ of the combined system can be written symbolically as

$$T_{1,2} = T_1 P_{1,2} T_2 + T_1 P_{1,2} R_2 P_{2,1} R_1 P_{1,2} T_2 + \cdots, \tag{3.25}$$

where $P_{1,2}$, $P_{2,1}$ are free-electron Green functions describing the propagation of the wave from layer 1 to layer 2 and *vice versa*. The first term describes transmission through the first layer, propagation to the second layer, and then transmission through the second layer. The second term describes reflection at the second layer, propagation back to the first, subsequent reflection and propagation to the second layer, and finally transmission. An attractive aspect of one-dimensional stacking of the layers is that the series in (3.25) can be summed giving:

$$T_{1,2} = T_1 [1 - P_{1,2} R_2 P_{2,1} R_1]^{-1} P_{1,2} T_2. \tag{3.26}$$

Further layers can be added by repeating the process, and the reflection and transmission properties of as many layers as we like can be calculated. The process of adding layers converges if a little absorption is included in each layer, so that the reflection and transmission matrices of what is essentially a semi-infinite crystal can be found.

Rather than calculating individual wave-functions (3.24), the reflection and transmission properties are usually used to find the Green function $G(\mathbf{r}, \mathbf{r}'; E)$. This is given by the sum over states

$$G(\mathbf{r}, \mathbf{r}'; E) = \sum_i \frac{\phi_i(\mathbf{r}) \phi_i^*(\mathbf{r}')}{E - E_i}, \tag{3.27}$$

so the local density of states – the charge density of electrons at energy $E$ – is given by:

$$\sigma(\mathbf{r}; E) \equiv \sum_i |\phi_i(\mathbf{r})|^2 \delta(E - E_i) = -\frac{1}{\pi} \Im \mathrm{m}\, G(\mathbf{r}, \mathbf{r}; E). \tag{3.28}$$

From $\sigma$ we can obtain the charge density by integrating up to the Fermi energy, and the density of states by integrating over entire space. We shall see in Section 3.3 how the Green function enters the theory of photoemission.

It is particularly straightforward to calculate the Green function in the multiple scattering theory (MacLaren et al., 1990). $G$ at atomic site $\alpha$ can be written as

$$G^\alpha(\mathbf{r}, \mathbf{r}'; E) = -2\mathrm{i}\kappa \sum_L Z_L^\alpha(\mathbf{r}_<) S_L^\alpha(\mathbf{r}_>) - 2\mathrm{i}\kappa \sum_{L,L'} Z_L^\alpha(\mathbf{r}) \Gamma_{L,L'}^\alpha Z_{L'}^\alpha(\mathbf{r}'), \tag{3.29}$$

where $\kappa = \sqrt{2E}$ and $Z_L^\alpha$, $S_L^\alpha$ are the regular and irregular solutions of the radial Schrödinger equation at the site $\alpha$. This expression can be derived from the Dyson equation for $G$, and $\Gamma_{L,L'}^\alpha$ represents the scattering of the electrons by the surrounding atoms. $\Gamma_{L,L'}^\alpha$ can be found from the scattering within the layer of the atom, plus reflection from the surrounding planes – which we have already seen how to calculate.

*3.2.3.2. Local density of states at Cu(100) and Ni(100)*

The local density of states at the surface shows the most interesting behaviour around band edges. Figure 3.6 gives the local density of states (3.28) integrated through the near-surface region (Section 3.2.1), at $\mathbf{k}_{\|} = 0$ for Cu(100) and Ni(100), for energies spanning the $X_{4'}$–$X_1$ gap (Nekovee, private communication). These results were calculated using the embedding method described at the end of Section 3.2.1 (Benesh and Inglesfield, 1984) rather than the multiple scattering method we have just described, because the effects of the long range image potential can be incorporated very accurately in the embedding method. In fact the embedding potential for the bulk substrate was calculated in the framework of LKKR. The most obvious features in Fig. 3.6 are the image-potential states just below the vacuum level (the zero of energy here) – these show up as Lorentzians rather than sharp $\delta$-functions because $\sigma(\mathbf{r}; E)$ is calculated at the energy with a small imaginary part. These states show up particularly prominently, because they have their weight precisely in the near-surface region. It is interesting to note that the image states have almost exactly the same energy relative to $E_{\text{vac}}$ in both Cu and Ni, even though the work functions are significantly different (4.63 eV for Cu(100) and 5.30 eV for Ni(100)) – this illustrates the point made in Section 3.2.2.2 that the image states are tied to the vacuum level.

At the band edge below the vacuum level, the densities of states show a characteristic $(E_b - E)^{1/2}$ behaviour, where $E_b$ is the energy of the band edge. In the bulk, the density of states at a fixed wave vector parallel to the surface varies like $(E_b - E)^{-1/2}$, and the singularity becomes weakened at the surface. This behaviour is the same at all band edges. The Cu(100) surface density of states shows a peak just below the band edge, which is the weak surface resonance discussed in Section 3.2.2.3. On Ni(100), however, there is no surface resonance. On neither surface is there a crystal-induced surface state measured in

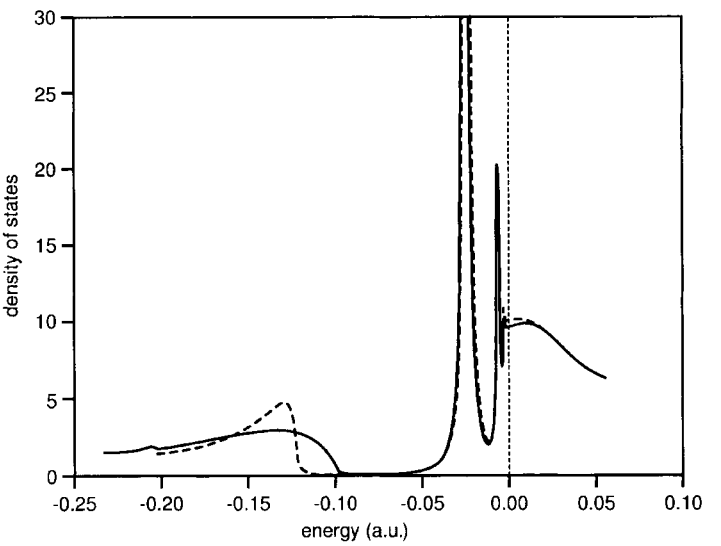


Fig. 3.6. Density of states at $\bar{\Gamma}$ in near-surface region for Cu(100) (dashed line) and Ni(100) (solid line).

the $X_{4'}$–$X_1$ band gap around $\bar{\Gamma}$ (Thörner et al., 1985; Woodruff et al., 1985; Goldmann et al., 1985a).

The behaviour at the vacuum level is interesting, as below $E_{\text{vac}}$ we have the infinite Rydberg series of image-potential surface states, and above there is a continuum of states associated with the vacuum (which are, however, reflected by the crystal within the band gap). From the figure we see that the surface density of states is in fact continuous across $E_{\text{vac}}$ when the discrete Rydberg series is broadened slightly by the imaginary part of the energy. With any broadening at all (and some broadening always occurs because of lifetime effects) we cannot see the vacuum level in the local density of states (Nekovee and Inglesfield, 1992)! This is a consequence of the Coulomb tail of the image potential, and similar effects are known in the optical spectrum of excitons. As we shall see in Section 3.4.1, the density of states is also continuous when the vacuum level lies inside a bulk energy band.

## 3.3. Photoemission and surface electronic structure

Angle-resolved photoemission provides a very powerful probe of occupied electron states, both bulk states, and states at the surface. A short mean free path of the emitted electrons, typically about 10 Å, together with a contribution to the transition matrix element from the surface potential barrier give the technique surface sensitivity. Most analyses of photoemission spectra rely on changing experimental variables such as photon frequency or polarization to distinguish between bulk and surface transitions in the spectra. However, an accurate and computationally viable theory of photoemission has been built up in recent years, which makes it easier to interpret the experimental spectra by comparison with theoretical curves.

The same theory is applicable to inverse photoemission for probing the unoccupied states – the only difference is a geometrical factor coming from phase space considerations.

### *3.3.1. Theory of photoemission*

In photoemission, the perturbation $\Delta$ due to the light field, frequency $\omega$, excites an electron from an initial state $i$, energy $E$, into some state which reaches the detector. The photoemitted state can be written as

$$\text{emitted state} = \int \mathrm{d}\mathbf{r}'\, G_2^+(\mathbf{r}, \mathbf{r}'; E+\omega)\langle \mathbf{r}'|\Delta|i\rangle, \tag{3.30}$$

where $G_2^+$ is the Green function propagating the excited electron; the superscript + indicates outgoing boundary conditions, and the subscript 2 means that it is evaluated at the energy $E + \omega$ of the excited state. The current going into states with wave vector $\mathbf{k}_\parallel$ parallel to the surface and energy $E + \omega$ can then be written as (Pendry, 1976, 1981; Hopkinson et al., 1980)

$$I(\mathbf{k}_\parallel, E+\omega) = -\frac{1}{\pi}\Im\mathrm{m}\langle \mathbf{k}_\parallel | G_2^+(E+\omega)\Delta G_1^+(E)\Delta^\dagger G_2^-(E+\omega)|\mathbf{k}_\parallel\rangle. \tag{3.31}$$

In this expression, $|\mathbf{k}_\parallel\rangle$ is the state $\exp(\mathrm{i}\mathbf{k}_\parallel\cdot\mathbf{r})\delta(z-z_0)$, a two-dimensional plane wave outside the solid onto which the Green function $G_2^{\pm}$ is projected. $G_1^+$ is the Green function at the initial state energy $E$, and it appears as $\Im\mathrm{m}\, G_1^+$ when initial states with energy $E$ are summed over.

The perturbation $\Delta$ is given by

$$\Delta = \frac{1}{2c}(\mathbf{A}\cdot\mathbf{p} + \mathbf{p}\cdot\mathbf{A}), \tag{3.32}$$

where $\mathbf{p}$ is the momentum operator and $\mathbf{A}$ is the magnetic vector potential. The screening of the electromagnetic field is in principle important at and above the plasmon frequency, but $\mathbf{A}$ is usually taken to be constant in actual calculations. $\Delta$ then simplifies to

$$\Delta = \frac{1}{c}\mathbf{A}\cdot\mathbf{p} \tag{3.33}$$

which, by commuting with the Hamiltonian, is equivalent to

$$\Delta = \frac{\mathrm{i}}{\omega c}\mathbf{A}\cdot\nabla V. \tag{3.34}$$

$V$ is the potential felt by the electrons, and this shows how the surface barrier potential with its rapid variation with $z$ gives rise to a contribution to photoemission. Surface photoemission is important for sp-bonded materials, where the pseudopotential is weak and, consequently, $\nabla V$ inside the atoms is small. It is most important for photoemission from surface states and resonances.

The formalism described here is sometimes called the "one-step" model, because the photocurrent is given by a single matrix element (3.31). This is in contrast with the earlier three-step model, in which photoemission was envisaged to take place in three stages – excitation of the electron from the valence (or core) state, propagation of the excited electron through the material, and, thirdly, transmission through the surface barrier. The present method is still essentially a one-electron theory, but some many-body effects can be treated via the Green functions. The self-energy of the hole left behind after photoemission, which can be included in $G_1^+$, has a real part shifting the one-electron bands and an imaginary part which describes the lifetime of the hole. Similarly, the mean free path of the photoelectron is described by the self-energy in the propagator $G_2^{\pm}$.

### *3.3.2. Calculating photoemission*

To calculate photoemission (3.31) is rewritten in the form (Hopkinson et al., 1980)

$$I(\mathbf{k}_\parallel, E+\omega) = -\frac{1}{\pi}\Im\mathrm{m}\int \mathrm{d}\mathbf{r}\langle\mathbf{k}_\parallel|G_2^+(E+\omega)|\mathbf{r}\rangle\Delta\langle\mathbf{r}|G_1^+(E)\Delta^\dagger G_2^-(E+\omega)|\mathbf{k}_\parallel\rangle. \tag{3.35}$$

The first term in the integral can be identified as the photoemission final state

$$\psi_2(\mathbf{r}) = \langle \mathbf{r} | G_2^-(E+\omega) | \mathbf{k}_\parallel \rangle. \tag{3.36}$$

This is the time-reversed LEED state: we shoot a beam of electrons with the projected wave vector $\mathbf{k}_\parallel$ and energy $E+\omega$ at the surface of the crystal and allow this to scatter, and then time-reverse (complex-conjugate) the resulting wave-function to obtain $\psi_2$. It can be easily found using the multiple scattering theory. The second term in (3.35) can be written as

$$\psi_1(\mathbf{r}) = \int \mathrm{d}\mathbf{r}'\, G_1^+(\mathbf{r}, \mathbf{r}'; E) \Delta^\dagger \psi_2(\mathbf{r}'), \tag{3.37}$$

where the expression $\Delta^\dagger \psi_2(\mathbf{r}')$ acts as a hole source, the hole being subsequently propagated by $G_1^+$. This term is also straightforward to evaluate. We should emphasise here that, although $\psi_2$ is the final state, $\psi_1$ is not the initial state in the Golden Rule sense; the initial state from which the photoemitted electron actually comes is contained in $G_1^+$.

With a muffin-tin form of the potential, we see from (3.34) that the contributions to $I(\mathbf{k}_\parallel, E+\omega)$ in (3.35) only come from the atomic potentials inside the muffin tins and the surface barrier. In the flat interstitial region between the $j-1$ and the $j$th atomic layers, the wave-functions in (3.35) can be expanded in the same form as (3.5):

$$\begin{aligned}
\psi_2(\mathbf{r}) &= \sum_{\mathbf{g}} \left\{ a_{j,\mathbf{g}}^+ \exp\left[\mathrm{i}\mathbf{k}_\mathbf{g}^+ \cdot (\mathbf{r} - \mathbf{c}_j)\right] + a_{j,\mathbf{g}}^- \exp\left[\mathrm{i}\mathbf{k}_\mathbf{g}^- \cdot (\mathbf{r} - \mathbf{c}_j)\right] \right\}, \\
\psi_1(\mathbf{r}) &= \sum_{\mathbf{g}} \left\{ b_{j,\mathbf{g}}^+ \exp\left[\mathrm{i}\mathbf{k}_\mathbf{g}^+ \cdot (\mathbf{r} - \mathbf{c}_j)\right] + b_{j,\mathbf{g}}^- \exp\left[\mathrm{i}\mathbf{k}_\mathbf{g}^- \cdot (\mathbf{r} - \mathbf{c}_j)\right] \right\},
\end{aligned} \tag{3.38}$$

where $\mathbf{c}_j$ is the local origin between the layers. The coefficients can most conveniently be found using the LKKR method (Pendry, 1974, 1976; Hopkinson et al., 1980). For finding the atomic contribution to $I(\mathbf{k}_\parallel, E+\omega)$, these plane wave expansions are matched on to atomic solutions at each atomic site. The surface barrier contribution is particularly simple if we take a step potential of height $V_0$. Then (3.35) becomes (Pendry, 1976)

$$I^{\mathrm{surf}}(\mathbf{k}_\parallel, E+\omega) = -\frac{A_z V_0}{\pi \omega c} \Im \mathrm{m} \sum_{\mathbf{g}} \left(a_{1,\mathbf{g}}^+ + a_{1,\mathbf{g}}^-\right)^* \mathrm{i} \left(b_{1,\mathbf{g}}^+ + b_{1,\mathbf{g}}^-\right). \tag{3.39}$$

The advantage of comparing the calculated spectra with experimental photoemission and inverse photoemission is that features can be unambiguously identified. In Section 3.4.2 this comparison is made for Cu(100) and Cu(111).

## 3.4. Results for selected systems

### *3.4.1. Simple metals: Al*

Aluminium is a typical nearly-free-electron metal, with small band gaps in the nearly-free-electron band structure. Crystal-induced surface states occur in many of these gaps

on the various surfaces. An extensive theoretical study of surface states and surface resonances has been recently published for three low-index surfaces of Al (Heinrichsmeier et al., 1993). The calculations use *ab initio* norm-conserving pseudopotentials within the LDA framework, and with slab geometry. On Al(100) there is a prominent surface state in the band gap induced by the (200) Fourier component of the pseudopotential. This state occurs near the bottom of the gap, and calculation puts it at 2.67 eV below the Fermi energy at $\bar{\Gamma}$ (Heinrichsmeier et al., 1993). It shows up very strongly in photoemission, at $2.8 \pm 0.2$ eV below $E_F$ (Levinson et al., 1983). On all three low-index surfaces, there is a rich structure of unoccupied surface states, particularly on Al(110) around $\bar{S}$ in the surface Brillouin zone. An interesting feature on Al(111) is a broad surface resonance in the $\bar{\Gamma}\bar{M}$ direction which crosses the Fermi energy and has been seen in both photoemission and inverse photoemission.

As the low index surfaces of simple metals like Al do not have a projected band gap at the vacuum level for $\mathbf{k}_\parallel = 0$ (Szmulowicz and Segall, 1981), we would not expect to find image surface states on these surfaces. However, inverse photoemission spectra from Al(111) show a spectral feature at $\bar{\Gamma}$, 0.5 eV below the vacuum level (Heskett et al., 1987, 1988), which was identified as an image state resonance. The problem, then, is to explain the origin of the electron reflectivity on the crystal side of the surface barrier. Exploring this issue, Lindgren and Walldén (1989) found a pronounced peak in the density of states of a jellium surface bounded by a truncated image potential barrier, in good agreement with the inverse photoemission measurements. However, when the truncated image potential was replaced by a more realistic JJJ barrier (Section 3.2.1) the peak in the surface density of states disappeared (Papadia et al., 1990). Subsequently Papadia et al. (1990) found that the Al potential produces enough reflectivity even far away from the band gap, for an image state surface resonance to appear on Al(111). This explanation for the observed structure was challenged by Schaich and Lee (1991), who calculated inverse photoemission from the jellium surface and found a peaked structure in the spectrum arising from matrix element behaviour rather than the surface density of states. Subsequent inverse photoemission and scanning tunneling spectroscopy experiments confirm the occurrence of the image state surface resonance on Al(111) (Yang et al., 1993).

The behaviour of the surface density of states on Al(100) at energies near the vacuum level has been studied by Nekovee and Inglesfield (1992) using the embedding method. The semi-infinite substrate, and the long-range image tail are included by adding embedding potentials onto the Hamiltonian for the near-surface region (extending 10 a.u. into the vacuum from the top of the surface atoms), and in this region itself the potential is interpolated between the asymptotic image form and the self-consistent LDA potential. The results for the density of states of the near-surface region are shown in Fig. 3.7 for $\mathbf{k}_\parallel = 0$. The peak at about $-0.28$ a.u. relative to the vacuum level is the Shockley surface state. Just below the vacuum level a whole series of image resonances occurs, the resonances sharpening up and becoming closer together as vacuum threshold is approached. The remarkable feature of these results is that the density of states of the image resonances joins smoothly on to the continuum of states above the vacuum zero, just as we found for the transition between image states and the continuum when a band gap straddles $E_{vac}$ (Section 3.2.3.2). This behaviour is characteristic of the long range image potential. With the LDA potential,

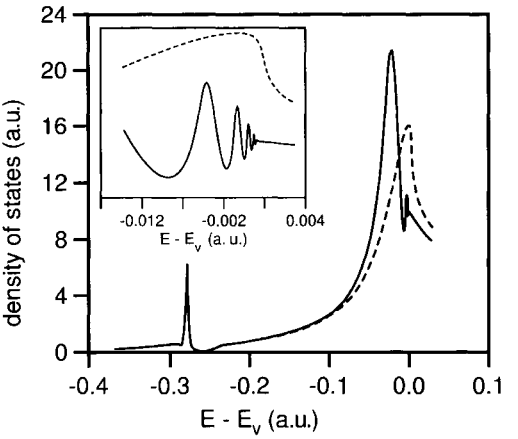


Fig. 3.7. Density of states at $\bar{\Gamma}$ in the near-surface region for Al(100). The solid line shows the results with an asymptotic image potential, and the dashed line with the LDA potential. The imaginary part of the energy is taken as 0.001 a.u., and the inset shows the results with an imaginary energy of 0.0001 a.u.

a single large peak is found in the density of states just below threshold, and at threshold the density of states has an infinite slope (Fig. 3.7).

### *3.4.2. Noble metals: Cu*

The low-index surfaces of Cu are probably the best studied experimentally systems, in photoemission for the occupied states (Courths and Hüfner, 1984), and both inverse photoemission (Dose, 1985) and two-photon photoemission (Steinmann and Fauster, 1993) for the unoccupied states. They have also been investigated theoretically with *ab initio* calculations. Thus a wealth of surface states is known for these systems. In the following sections we will discuss the Cu(100) and Cu(111) surfaces in more detail, and see what consequences can be drawn for the effective barrier potential from a systematic comparison between theory and experiment (Graß et al., 1993).

The theoretical spectra of electronic surface states on the Cu surfaces have been calculated with the theoretical model for photoemission described in Section 3.3. For the bulk muffin-tin potential of Cu the potential due to Chodorow (1939) was used. Damping processes within the one-step model are described by adding a constant imaginary part $iV_{oi}$ to the inner potential $V_{or}$, (3.6). For more details we refer to the original work (Graß et al., 1993).

#### *3.4.2.1. Cu(100)*

In Fig. 3.8, we present the projected bulk band structure for Cu(100) together with the experimentally observed and calculated inverse photoemission structure. The agreement between theory (denoted by solid circles) and experiment (open squares) is generally very satisfactory. Along $\Gamma XUL$ four empty surface states SR, $S_1$, $S_2$, $S_3$ and two unoccupied bulk states $B_1$, $B_2$ have been detected so far in IPE experiments (Graß et al., 1993). SR denotes the crystal-induced surface resonance associated with the $X_{4'}$–$X_1$ gap, and in the

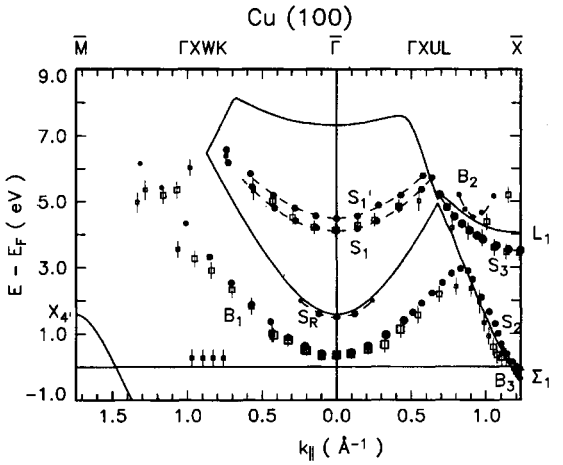


Fig. 3.8. Bulk bandstructure of Cu, projected onto the $\bar{\Gamma}$–$\bar{X}$ and $\bar{\Gamma}$–$\bar{M}$ directions of the surface Brillouin zone. Solid circles (open squares with error bars) denote calculated (measured) band dispersions. The size of the symbols indicates the intensity of transition. The band gaps of the projected bulk band structure are bounded by solid lines (Graß et al., 1993).

same gap $S_1$ is the first image-potential state (Sections 3.2.2.3, 3.2.3.2). $S_2$ and $S_3$ represent crystal-induced surface states derived from the $L_{2'}$–$L_1$ gap. $S_2$ becomes an occupied surface state near $\bar{X}$ and has been detected there in high-resolution photoemission spectroscopy (Kevan, 1983a).

Calculated IPE-spectra and the corresponding experimental data ($\hbar\omega = 9.7$ eV) are shown in Fig. 3.9 for different angles of electron incidence and photons emitted within the ΓXUL azimuth. The calculated spectra are found by convoluting the raw spectra with a Gaussian of 0.275 eV full width at half-maximum, to take the experimental resolution into account. Apart from the fact that the experimental spectra show a large fraction of secondary emitted photons, which are not taken into account in the calculations, the agreement between theory and experiment is generally very good. In particular, the polarization dependence of the intensity of the various peaks is well reproduced in the theory. A systematic comparison of all the calculated surface states at the zone centre $\bar{\Gamma}$ and boundary $\bar{X}$ with experimental data for Cu(100) is included in Table 3.1. The agreement between theory and experiment for the energetic positions and effective masses is within the error bars of the experiment.

The surface contribution to the current (of photons in inverse photoemission or electrons in photoemission) comes from photons polarised parallel to the surface normal (we conventionally take this as the $z$-direction) – this is because the surface barrier potential entering the matrix element (3.34) is predominantly $z$-dependent. It is in fact found that the surface state features in the calculated spectra shown in Fig. 3.9 are significant only with $z$-polarisation. This suggests that the bulk contribution to the current is very small, and that we really deal with surface features. In these calculations for Cu(100), a significant non-zero current for photons polarised in the surface plane is found only for the surface state $S_2$ at $\bar{X}$.

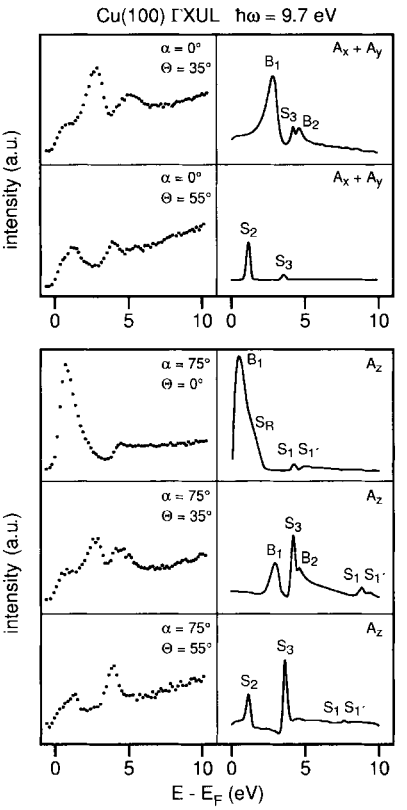


Fig. 3.9. Experimental (left) and theoretical (right) inverse photoemission spectra ($\hbar\omega = 9.7$ eV) for Cu(100) along the ΓXUL bulk mirror plane. $\Theta$ denotes the angle of electron incidence and $\alpha$ the photon detection angle (Graß et al., 1993).

In addition to the transitions discussed so far, the experimental IPE-spectra contain dispersionless features in the range 0–1.5 eV above the Fermi level. These features, which show up at all the three low-index surfaces of Cu, must be attributed to transitions into weak maxima of the three-dimensional density of states (DOS) in this energy range.

*3.4.2.2. Cu(111)*

Figure 3.10 shows the projected bulk band structure for Cu(111) together with all the calculated and experimentally observed IPE data. Three bulk states $B_1$, $B_2$, $B_3$, two image-potential surface states $S_1$, $S_1'$ in the $L_{2'}$–$L_1$ derived gap and two crystal-induced surface states $S_2$, $S_3$ in the $L_{2'}$–$L_1$ and $X_{4'}$–$L_1$ derived gap are identified. Again $S_2$ becomes an occupied surface state near $\bar{\Gamma}$ and is observable in high-resolution photoemission spectroscopy (Kevan, 1983c; Fischer et al., 1991).

The ΓXUL and ΓLKL azimuths shown in Fig. 3.10 are equivalent if only the surface layer is taken into account, but become non-equivalent for the bulk crystal. Pure surface

Table 3.1

Comparison of experimental and calculated binding energies and effective masses of surface states on Cu(100), Cu(110) and Cu(111) (Graß et al., 1993)

| Surface normal | Symmetry point | Type | $E - E_F$ (eV) (theor.) | $m^*/m_e$ (theor.) | $E - E_F$ (eV) (exp.) | $m^*/m_e$ (exp.) | References |
|---|---|---|---|---|---|---|---|
| | | | | | $4.13 \pm 0.20$ | | Schuppler et al. (1990) |
| (100) | $\bar{\Gamma}$ | $S_1$ | 4.10 | 0.990 | $4.00 \pm 0.20$ | $1.2 \pm 0.20$ | Dose et al. (1984) |
| | | | | | $4.06 \pm 0.02$ | $0.90 \pm 0.10$ | Steinmann (1989) |
| (100) | $\bar{\Gamma}$ | $S_1'$ | 4.48 | 1.010 | $4.45 \pm 0.02$ | | Steinmann (1989) |
| | | | | | 1.15 | | Woodruff et al. (1985) |
| (100) | $\bar{\Gamma}$ | $S_R$ | 1.50 | 0.427 | $1.20 \pm 0.30$ | | Schuppler et al. (1990) |
| | | | | | $1.48 \pm 0.06$ | | Wegehaupt et al. (1988) |
| (100) | $\bar{X}$ | $S_2$ | −0.065 | 0.076 | $-0.058 \pm 0.025$ | $0.067 \pm 0.01$ | Kevan (1983a) |
| (100) | $\bar{X}$ | $S_3$ | 3.52 | 0.630 | $3.60 \pm 0.20$ | $0.70 \pm 0.20$ | Donath et al. (1986) |
| | | | | | $3.45 \pm 0.20$ | | Schuppler et al. (1990) |
| (110) | $\bar{\Gamma}$ | $S_1$ | 4.54 | 0.98 | $4.28 \pm 0.35$ | | Reihl and Frank (1985) |
| | | | | | $4.39 \pm 0.15$ | | Straub and Himpsel (1986) |
| (110) | $\bar{\Gamma}$ | $S_1'$ | 4.74 | 0.99 | | | |
| (110) | $\bar{Y}$ | $S_2$ | −0.42 | 0.21 | $-0.393 \pm 0.025$ | $0.268 \pm 0.01$ | Kevan (1983b) |
| | | | | | $2.50 \pm 0.20$ | 1.10 | Bartynski et al. (1985) |
| (110) | $\bar{Y}$ | $S_3$ | 2.38 | 0.94 | $1.91 \pm 0.25$ | | Schuppler et al. (1990) |
| | | | | | $1.80 \pm 0.20$ | $0.80 \pm 0.20$ | Jacob et al. (1986) |
| (110) | $\bar{X}$ | $S_4$ | 1.96 | 0.248 | $2.09 \pm 0.20$ | | Schuppler et al. (1990) |
| | | | | | $2.00 \pm 0.40$ | | Reihl and Frank (1985) |
| (110) | $\bar{X}$ | $S_5$ | 5.36 | 1.49 | $5.63 \pm 0.20$ | | Schuppler et al. (1990) |
| | | | | | $5.40 \pm 0.40$ | | Jacob et al. (1986) |
| | | | | | $4.11 \pm 0.03$ | | Fischer et al. (1991) |
| (111) | $\bar{\Gamma}$ | $S_1$ | 4.06 | 0.89 | $4.05 \pm 0.05$ | $1.00 \pm 0.10$ | Kubiak (1988) |
| | | | | | $4.39 \pm 0.20$ | | Schuppler et al. (1990) |
| (111) | $\bar{\Gamma}$ | $S_1'$ | 4.68 | 0.98 | $4.63 \pm 0.05$ | $0.90 \pm 0.15$ | Kubiak (1988) |
| (111) | $\bar{\Gamma}$ | $S_2$ | −0.40 | 0.369 | $-0.389 \pm 0.025$ | $0.462 \pm 0.01$ | Kevan (1983c) |
| | | | | | $-0.39 \pm 0.02$ | 0.46 | Fischer et al. (1991) |
| (111) | $\bar{M}, \bar{M}'$ | $S_3$ | 0.98 | 0.031 | | | |

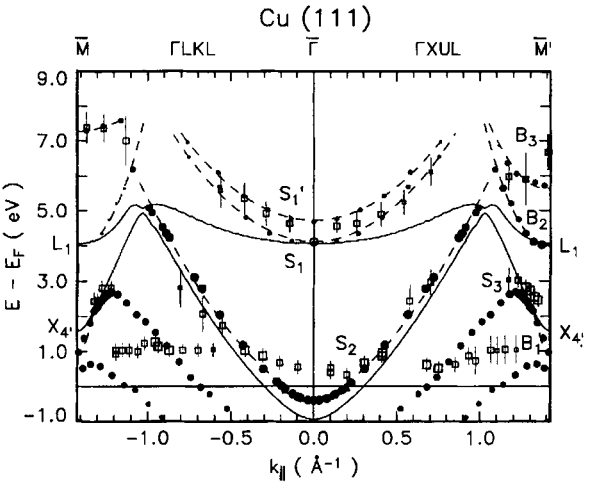


Fig. 3.10. Bulk band structure of Cu, projected onto the $\bar{\Gamma}$–$\bar{M}$ and $\bar{\Gamma}$–$\bar{M}'$ directions of the surface Brillouin zone. Solid circles (open squares with error bars) denote calculated (measured) band dispersions. The size of the symbols indicates the intensity of transition. The band gaps of the projected bulk band structure are bounded by solid lines (Graß et al., 1993).

states should thus behave symmetrically in both azimuths, whereas bulk states can exhibit an asymmetry. This is indeed the case in Fig. 3.10.

The calculated IPE-spectra and measured data ($\hbar\omega = 9.7$ eV) for Cu(111) are shown in Figs. 3.11 and 3.12 for the ΓXUL and ΓLKL azimuths, respectively. Again, theory and experiment agree very well. The non-equivalence of both azimuths for bulk states is clearly seen. This non-equivalence also occurs in the intensity of the surface state $S_3$ at larger values of electron incidence (i.e., for wave vectors near the surface Brillouin zone boundary). This suggests that this surface state has a considerable bulk weight, and this is confirmed by the fact that at $\bar{M}$ and $\bar{M}'$ $S_3$ has the largest intensity with in-plane photon polarisation of all the Cu(111) surface states. The energy and effective mass of surface states on Cu(111) are shown in Table 3.1 and again show agreement with the experiment essentially within experimental error bars. (We note that the energy of $S_3$ is not known exactly at the zone boundary.) As in the case of Cu(100), the experimental IPE data show weak dispersionless features in the energy range 0.5–1.5 eV above the Fermi level which correspond to DOS transitions.

### *3.4.2.3. Corrugation effects*

We define corrugation as the lateral variation of the barrier potential $V_B(\mathbf{r})$ in (3.10) with $\mathbf{r}_\parallel$. This effect is neglected in most LEED and photoemission calculations. The bulk crystal potential has a strong lateral variation, of course, but this is taken into account in the formalism of Section 3.3.

To judge the absolute importance of corrugation effects in the barrier, we consider the occupied surface state $S_2$ at the various surfaces, since this state has been measured with the highest resolution. A comparison of theory and experiment for $S_2$ is shown in Fig. 3.13.

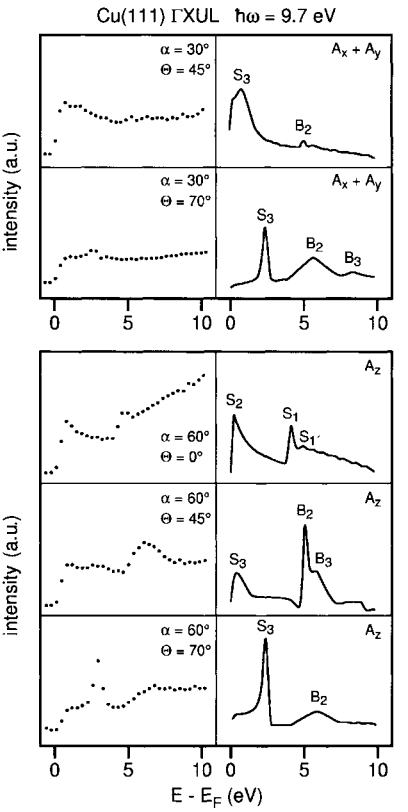


Fig. 3.11. Experimental (left) and theoretical (right) inverse photoemission spectra ($\hbar\omega = 9.7$ eV) for Cu(111) along the ΓXUL bulk mirror plane. $\Theta$ denotes the angle of electron incidence and $\alpha$ the photon detection angle (Graß et al., 1993).

The calculated energetic position of $S_2$ at the various symmetry points is always within the error bars of the experiment. Only the calculated effective mass of $S_2$ at Cu(110) and Cu(111) lies slightly outside the error bars, but whether this is a clear-cut indication for the importance of surface corrugation is not clear at present.

Some image-potential states can also be measured with a very high precision, using two-photon photoemission. This is the case for $S_1$ and $S_1'$ on the (100) and (111) surfaces of Cu (Fischer et al., 1991; Kubiak, 1988; Steinmann, 1989). From the agreement between theory and experiment in Table 3.1 for these states, we can conclude that no influence of surface corrugations is discernable in these cases. This conjecture is in agreement with a recent theoretical study of this problem (Van Siclen, 1990).

### *3.4.2.4. Effective surface barriers*

Effective $z$-dependent surface barriers $V_B(z)$ for the various Cu surfaces (Graß et al., 1993) are shown in Fig. 3.14. They are plotted with respect to the vacuum level $E_{vac}$ using the values of the work function $W$ given in Table 3.2; the zero of $z$ lies in the uppermost

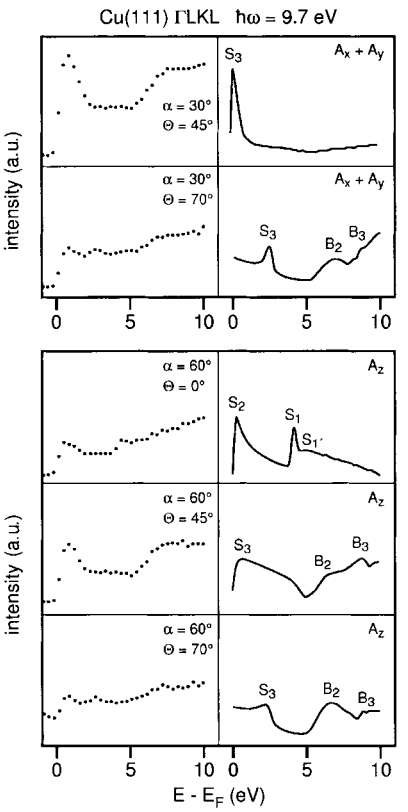


Fig. 3.12. Experimental (left) and theoretical (right) inverse photoemission spectra ($\hbar\omega = 9.7$ eV) for Cu(111) along the ΓLKL bulk mirror plane. $\Theta$ denotes the angle of electron incidence and $\alpha$ the photon detection angle (Graß et al., 1993).

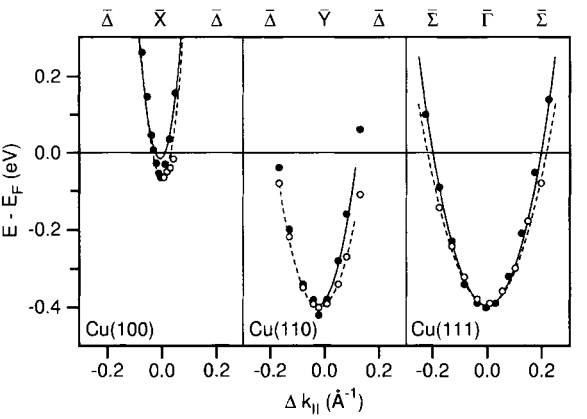


Fig. 3.13. Energetic position of surface state $S_2$ at various Cu surfaces. Solid (open) circles denote calculated (measured) band dispersions (Graß et al., 1993).

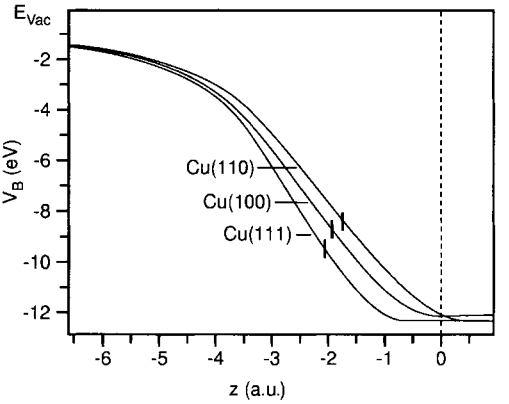


Fig. 3.14. Barrier potentials for Cu(111), Cu(100) and Cu(110) from the analysis of inverse photoemission, photoemission and two-photon photoemission data. The origin $z = 0$, marked by the dotted line, represents the centre of the first row of atoms. Different image planes are marked by solid short lines (Graß et al., 1993).

Table 3.2
Potential parameters for the barrier potentials of Cu(111), Cu(100) and Cu(110) (Graß et al., 1993)

| | Cu (111) | Cu (100) | Cu (110) |
|---|---|---|---|
| Work function, $W$ (eV) | 4.88[a] | 4.63[b] | 4.87[a] |
| Surface barrier potential, $V_{or}$ (eV) | −12.43 | −12.18 | −12.42 |
| Beginning of the polynomial region, $z_A$ (a.u.) | −3.611 | −3.974 | −4.066 |
| End of the polynomial region, $z_E$ (a.u.) | −0.522 | −0.008 | 0.577 |
| Length of the polynomial region, $\Delta z = \lvert z_A - z_E \rvert$ (a.u.) | 3.089 | 3.966 | 4.643 |
| Size of the surface unit cell, $A_E 10^{-2}$ (a.u.)$^2$ | 0.722 | 0.833 | 1.179 |
| One-half of interlayer distance, $d_{1/2}$ (a.u.) | 1.972 | 1.708 | 1.206 |
| Position of the image plane, $z_{im}$ (a.u.) | −2.047 | −1.932 | −1.762 |

[a]Straub and Himpsel (1986).
[b]Giesen et al. (1987).

layer of atoms. These potentials are of the Rundgren–Malmström (RM) type (3.3). The parameters $z_{im}$, $z_A$, $z_E$ and the polynomial transition range $\Delta z = |z_A - z_E|$ are listed in Table 3.2, together with the area of the surface unit cell $A_E$, half the interlayer spacing $d_{1/2}$, etc.

The quality of these barrier potentials, which represent best fits to experimental data, depends on the accuracy of the experimental measurements. To reproduce the measured data within the experimental resolution, especially the results from the high-resolution photoemission experiments (Kevan, 1983a, b, c) and two-photon photoemission experiments (Fischer et al., 1991; Kubiak, 1988; Steinmann, 1989; Wegehaupt et al., 1988), it was necessary to vary the most sensitive parameter $z_{im}$ up to the third digit. It should be noted that no relaxation of the outermost atomic surface layer has been taken into account in the present calculation. This neglect of relaxation effects seems to be justified on the

basis of LEED and ion scattering experiments on the low-index Cu surfaces (Van Hove et al., 1986).

From the data in Table 3.2, we see that $z_{\text{im}}$ moves toward the first layer of atoms and the transition range $\Delta z$ becomes larger as $A_E$ increases. This means that the most open surface, Cu(110), exhibits the strongest saturation of the image potential with an image plane lying nearest to the topmost layer. As a further consequence, the image force for a given value of $z$ outside the crystal is strongest for Cu(111) and weakest for Cu(110).

This general trend, that the image plane lies closer in for more open surfaces, is found in other studies of surface barrier parameters. There are three main approaches for finding $z_{\text{im}}$: the approach described here, in which potential parameters are used to fit experimental data on image states; fitting to self-consistent LDA-DFT potentials (Jennings et al., 1988; Smith et al., 1989); and first principles calculations of the image potential itself (described in Section 3.5). Fitting the JJJ form of the surface barrier potential (3.2) to planar averaged potentials, found from self-consistent LAPW slab calculations (Jennings et al., 1988), gives values for $z_{\text{im}}$ of $-2.40$ a.u. and $-2.33$ a.u. for Cu(100) and $-2.17$ and $-2.28$ a.u for Cu(110). These also show that $z_{\text{im}}$ moves in on the open surfaces, though the absolute values are farther out than in Table 3.2, $-1.93$ a.u. for Cu(100) and $-1.76$ for Cu(110). In fact, we would not expect the LDA-DFT fits to work particularly well, as the LDA potential does not explicitly contain the image potential. Smith et al. (1989) have used LDA-DFT fits to determine the parameters $V_{\text{or}}$ and $\lambda$ in the JJJ surface barrier potential (3.2), and have then found $z_{\text{im}}$ by fitting image state energies with a nearly-free-electron model of the bulk reflectivity. The simplicity of this model does not allow for the derivation of a definite set of barrier parameters, which work for all the observed surface states at a given surface. What can be obtained, however, are values averaged over the surface states included in the fitting procedure. In this way, the authors derived $\langle z_{\text{im}} \rangle = -2.27$ a.u. for Cu(111), $-2.18$ a.u. for Cu(100) and $-1.70$ a.u. for Cu(110). The fact, that the face dependence in these $\langle z_{\text{im}} \rangle$ values is more pronounced than the values given in Table 3.2, is understandable, since the two procedures work at quite different levels of theoretical refinement.

In Section 3.5, we shall discuss the origin of the image potential further, and how first principles determinations of $z_{\text{im}}$ are related to image state studies.

### *3.4.3. Magnetic d-metals: Fe and Ni*

Ferromagnetism is associated with a spin-splitting of the energy bands, both in the bulk and at the surface, and the techniques of spin-polarized photoemission and inverse photoemission have opened up the possibility of measuring the exchange splitting of surface states directly (Donath, 1989; Donath et al., 1990; Schneider et al., 1992; Starke et al., 1992). This magnetic splitting may serve as a sensitive probe of magnetic properties at and in the vicinity of magnetic surfaces. First-principles self-consistent local spin-density calculations predict that the magnetic moment in the topmost layer of magnetic 3d-transition metals is usually enhanced with respect to the bulk magnetic moment (Falicov and Morán-López, 1986; Wimmer et al., 1984; Wan and Freeman, 1981). This is due to the reduction in symmetry and coordination number at the surface, resulting in narrowed d-bands and enhancement of the paramagnetic density of states at the Fermi level. As an example, the magnetic moment in the top layer of Fe(110) is found to be $2.75\mu_{\text{B}}$, compared with $2.2\mu_{\text{B}}$ in the bulk (Nekovee et al., 1993).

The magnetic splitting of a surface state at a ferromagnet is the result of two effects (Nekovee et al., 1993): first, spin-up and spin-down surface states are scattered from different substrate potentials. This part of the splitting can be viewed as a bulk band structure effect, caused by a difference in the position of spin-up and spin-down bulk band edges. Second, the effective surface barrier potential experienced by an electron outside the metal will, in general, also be spin-dependent due to the exchange interaction near the crystal surface.

*3.4.3.1. Fe(110)*

Calculations of angle-resolved photoemission give a spin-split crystal-induced surface resonance on Fe(110) (Redinger et al., 1988). Its minority spin component has been identified at 0.5 eV below $E_F$ in spin-resolved photoemission experiments, though there is no experimental evidence for a majority spin feature (Vescovo et al., 1993). The most interesting experimental results are for the spin-split $n = 1$ image state, which has been found at about 0.7 eV below the vacuum level in inverse photoemission and two-photon photoemission (Himpsel, 1991; Fischer et al., 1992). The spin-splitting has been measured directly using spin-resolved inverse photoemission, and is found to be $57 \pm 5$ meV (Passek et al., 1995).

To analyse these experimental results, we first use the multiple scattering approach for surface states (Section 3.2.2.1). The ΓN direction of the bulk Brillouin zone projects onto the centre of the (110) surface Brillouin zone, and Fig. 3.15 shows the bulk band structure near N as a function of energy, together with the modulus $r_C$ and phase $\phi_C$ of the reflection coefficients for the semi-infinite crystal. The calculations correspond to $\mathbf{k}_{\|} = 0$, and include a small imaginary contribution $V_{oi} = -0.05$ eV in the spin-dependent effective bulk potential to describe damping effects. For both spins there is an effective gap where $r_C \simeq 1$ extending from $N_4$ (1.5 eV) to $N_1$ (9.36 eV) for the minority spin and from $N_3$, $N_{1'}$ (0.4 eV) to $N_1$ (7.78 eV) for the majority spin. The crystal phases $\phi_C$ extend for both spin systems from approximately $-\pi$ (lower gap edge) to approximately $-\pi/2$ (upper gap

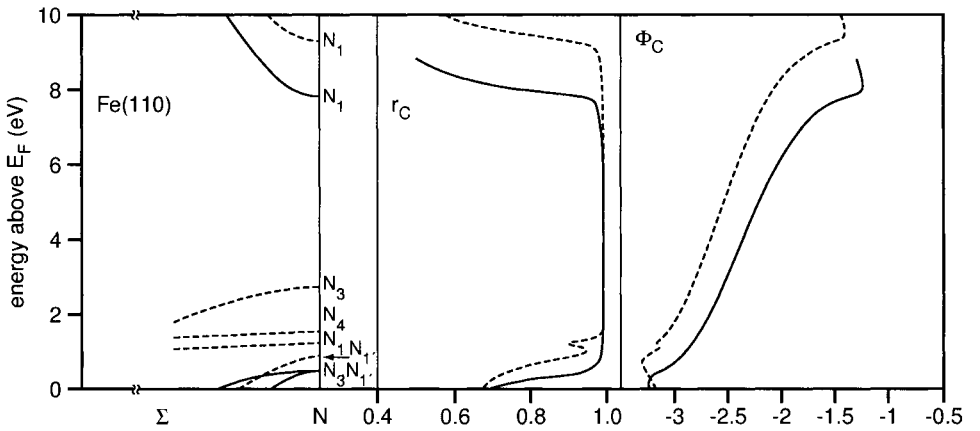


Fig. 3.15. Band structure (Moruzzi et al., 1978) and energy-dependence of the modulus $r_C$ and the phase $\phi_C$ of the reflection coefficient for Fe(110) (Borstel and Thörner, 1988). Dashed lines refer to minority spin, solid lines to majority spin.

edge), but are shifted against each other because of the spin-dependence of the effective bulk muffin-tin potential. The quite different behaviour of $\phi_C$, when compared to that in the two-band NFE model, is predominantly due to strong hybridization with d-states.

To investigate qualitatively the possibility of spin-split surface states on ferromagnets, we restrict ourselves to the energy region where $r_C \simeq 1$ for both spin systems. We shall assume a simple image potential barrier with cut-off ($W = 5.05$ eV (Pirug et al., 1980)), and a spin-independent image plane at $z_{im} = -0.39$ Å relative to the outermost atomic layer. This value is artificially chosen so that both crystal-induced and image-induced surface states occur in this energy range. The evaluation of the phase condition (3.13) for $\mathbf{k}_\parallel = 0$ is shown in Fig. 3.16. For the crystal-induced surface state a spin-splitting of 0.4 eV is obtained, whereas for the first image-potential state this splitting is 0.03 eV. The much smaller spin-splitting of the image state is due, in this phase picture, to a rapid variation of $\phi_B$ near the vacuum level.

The chosen value 0.39 Å for $|z_{im}|$ is much too small. For larger and more realistic values of $|z_{im}|$ the $n = 0$ spin-split Shockley surface state on Fe(110) moves below the lower gap edges, becomes a surface resonance and is eventually occupied. The energy of the $n = 1$ spin-split image-potential state is simultaneously lowered with respect to $E_{vac}$, which in turn results in an increase of the spin-splitting $\Delta_1$.

The spin-split image states on Fe(110) have been studied in a full-potential calculation based on the embedding method (Nekovee et al., 1993). The embedding potential replacing the surface and substrate is calculated from the Green function for the surface from the spin-polarised self-consistent surface calculation. In the vacuum beyond the near-surface region (which is taken typically to be 10 a.u. thick), it is assumed that the electrons feel the asymptotic image potential, taken to be spin-independent in this study; this semi-infinite vacuum is replaced by the Coulomb embedding potential. In the near surface region itself the potential is interpolated between the spin-polarised local density potential and the image potential.

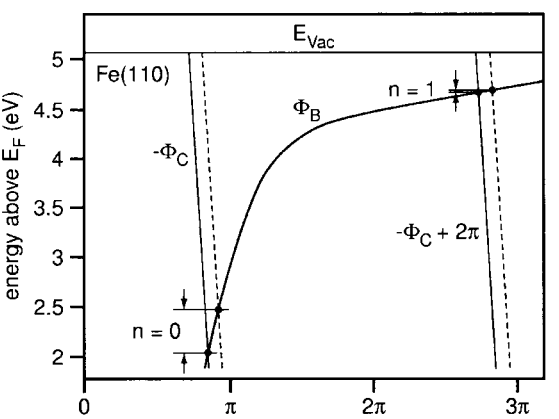


Fig. 3.16. Energy-dependence of $\phi_C$ and $\phi_B$ in the multiple scattering theory for Fe(110) for an image potential with cut-off ($z_{im} = -0.39$ Å). Dashed lines refer to minority spin, solid lines to majority spin. Filled circles indicate the energy of the $n = 0, 1$ surface states, arrows mark the spin-splitting (Borstel and Thörner, 1988).

The results of this calculation show a spin-splitting for the $n = 1$ image state of 55 meV in remarkable agreement with experiment (for once, the theory came before the spin-polarised measurement!). This splitting is primarily a result of coupling to the spin-polarised substrate via the embedding potential. The effect of the spin-polarised surface barrier turns out to be relatively small (about 20%) and of the opposite sign to the substrate contribution. The fact that the spin polarisation of the surface barrier works in the opposite way to the substrate can be traced to a sign reversal in the ground state spin density just outside the Fe(110) surface.

The question whether the image plane position $z_{\mathrm{im}}$ for an electron outside a ferromagnet is spin-dependent may be important for such an analysis. As *ab initio* calculations of the effective barrier potential with a correct long-range asymptotic behaviour have not yet been carried out for ferromagnetic materials, and the available experimental data do not allow for a determination of $z_{\mathrm{im}}^{\uparrow}$ and $z_{\mathrm{im}}^{\downarrow}$ so far, this question is still open. It is apparent that the classical image limit of the surface barrier, $V_{\mathrm{B}}(z) \rightarrow -1/|4z|$, is due to the Coulomb correlation effect and thus universal. But it is precisely the non-classical exchange interaction that shifts the image plane position $z_{\mathrm{im}}$ away from the jellium edge, and this differs for the two spins in a ferromagnetic system.

*3.4.3.2. Ni surfaces*

The experimental situation is quite clear for Ni surfaces (Donath, 1994), despite the fact that the exchange splitting in Ni is smaller than in Fe. On Ni(100) a crystal-induced surface state has been detected just below the Fermi energy, using photoemission, though its spin-structure was not determined (Plummer and Eberhardt, 1979; Erskine, 1980). An occupied surface state on Ni(110) was observed as a double-peak structure and interpreted as spin-split (Eberhardt et al., 1979). Spin-resolved inverse photoemission measurements have shown a spin-split crystal-derived surface state on Ni(110) (Donath, 1989; Donath et al., 1990), and on Ni(100) spin-splitting of a crystal-derived state around $\bar{\mathrm{X}}$ and of the $n = 1$ image state around $\bar{\Gamma}$. On Ni(111) the splitting of the $n = 1$ image state has been found to be 18 meV (Passek and Donath, 1992). These results have definitely ruled out the existence of magnetically dead surface layers at the low-index surfaces of Ni.

A particular interesting situation occurs for Ni(111): the $n = 0$ crystal-induced surface state was already detected in 1978 using ordinary photoemission, at 0.25 eV below the Fermi level (Himpsel and Eastman, 1978). In view of the well-documented $n = 1$ image state at 0.8 eV below the vacuum level (Goldmann et al., 1985b; Schuppler et al., 1990), the Ni(111) surface, therefore, seemed to exhibit at $\bar{\Gamma}$ a standard set of surface states, comparable to the Cu(111) case. Recently, however, spin-resolved inverse photoemission measurements on Ni(111) have revealed a second, spin-split, crystal-induced surface state close to the Fermi level, which around the $\bar{\Gamma}$ point is partly occupied (Donath et al., 1993) – for the majority spin. The observed exchange splitting is about 100 meV. As the majority spin component is cut off by $E_{\mathrm{F}}$, and the minority spin component is at least less occupied, this state is magnetic and will contribute to the surface magnetic moment of Ni(111). An indication that there might exist two crystal-induced surface states near $\bar{\Gamma}$ on Ni(111) had already been found in early calculations of photoemission and isochromat spectra for this surface (Borstel et al., 1985).

## 3.5. First principles calculations of the image potential

The surface barrier potential felt by an electron outside a metal surface varies asymptotically like the image potential (3.1), giving rise to the Rydberg series of image states which we have discussed earlier in this article. Precise measurements of the energies of these states give information about the form of the surface barrier, so it is important to understand the value of $z_{im}$, the position of the image plane from which the image potential is measured. This has consequences for interpreting LEED and STM, two spectroscopies in which the form of surface barrier is very important, as well as for the image states.

### *3.5.1. Image potential felt by a test charge*

An external classical test charge feels an image potential of the same form as (3.1), but with a different value of $z_{im}$ from the value for an electron. For the test charge, $z_{im}$ is given by the centre of gravity of the screening charge induced by a weak uniform external field – it is in fact the electrostatic origin of the surface, from which, for example, the separation of the plates in a capacitor should be measured.

There have been several calculations of the screening of a uniform field – this represents a rather small modification to the self-consistency part of the electronic structure calculation. The classic calculation by Lang and Kohn (1973) for jellium with the electron density of Al puts the image plane at $z_{im} = -1.6$ a.u. relative to the jellium edge (the edge of the chopped-off positive background), in other words, on the vacuum side of the surface. Subsequent calculations in which the full crystal potential is included give for Al(100) $z_{im} = -1.1$ a.u., for Al(111) $-0.95$ a.u. and $-0.81$ a.u., and for Al(110) $-1.5$ a.u. (Inglesfield, 1987; Lam and Needs, 1993), measured again with respect to the geometrical surface at which the crystal is chopped in two. These rather large variations with surface orientation become smaller when $z_{im}$ is measured from the plane of the top layer of atoms, giving (in the order of decreasing atomic density) for Al(111) $z_{im} = -3.16$ a.u., for Al(100) $-3.01$ a.u., and for Al(110) $-2.86$ a.u. Putting this all together, we see that the crystal lattice tends to pull the image plane in compared with the jellium surface, but $z_{im}$ tends to be tied to the atoms rather than the geometrical surface. There is still a variation of $z_{im}$ with the plane, and it tends to move in towards the crystal as the atomic density decreases. This is exactly the same trend found in the fits of image states shown in Table 3.2.

One of the few calculations on d-electron metals is for Ag(100), for which $z_{im} = -2.92$ a.u. relative to the top layer (Aers and Inglesfield, 1989). On this surface the energies of the image states have been fitted by a model surface barrier, and this gives a value of $-1.75$ a.u. (Smith et al., 1989). This value is not far from the value for Cu(100) presented in Table 3.2, and it suggests a clear difference between the image plane felt by the electron in the image state and that felt by the classical test charge.

### *3.5.2. Image potential felt by an electron*

Inside the solid, an electron is surrounded by the exchange–correlation hole in the electron distribution – an effect of the correlated motion of these indistinguishable particles. As the electron moves through the surface, the exchange–correlation hole becomes the image

charge, giving rise to the image potential. There are two frameworks for treating the effects of exchange–correlation on electrons. The first is density functional theory (Lundqvist and March, 1983), in which an electron feels a local, energy-independent exchange–correlation potential $V_{XC}(\mathbf{r})$ in addition to the Hartree potential of the electron charge density and the ionic potential. In DFT the individual wave-functions and their eigenenergies do not have an individual meaning – thus, the wave-functions are used to construct the ground state charge density, and the single-particle energies the total ground state energy, and it is only these ground state properties that are in principle given correctly by DFT. In fact the wave-functions are often treated as the wave-functions of the true single-particle excitations of the system – the quasiparticles – and the DFT single-particle energies as the quasiparticle excitation energies. As we know, $V_{XC}$ is usually found in the local density approximation, which does not describe the asymptotic image potential behaviour correctly, though the exact $V_{XC}$ must have the image form.

The other approach to tackling the many-body problem is to describe exchange–correlation by the self-energy $\Sigma(\mathbf{r}, \mathbf{r}', E)$ (Fetter and Walecka, 1971) – a non-local, energy-dependent potential which acts on the true quasiparticle wave function. The energy eigenvalues from the quasiparticle Schrödinger equation correspond to exact excitations of the system, in other words, the actual band structure. There is a well-defined approximation to find $\Sigma$, the GW approximation (Hedin and Lundqvist, 1969), which, although much more involved than density functional theory in the local density approximation, begins to be applied to real materials and real surfaces. The GW approximation does give the image potential correctly, and, of course, this is the image potential felt by the quasiparticles in image states, for example.

There is an integral equation which relates the exact $V_{XC}$ to $\Sigma$, and this was used by Eguiluz et al. (1992) to find $V_{XC}(\mathbf{r})$ at the surface of jellium with the density of Al, starting with a GW calculation of $\Sigma$. This gives $z_{im} = -0.72$ a.u. relative to the jellium edge, significantly closer to the edge than the image plane for the classical charge. The surface barrier potential with this $V_{XC}$ (a much more accurate potential than in LDA) gives rise to a Rydberg series of image resonances. Subsequent work has shown that the wave-functions and energies of these states are extremely close to the true quasiparticle states in the self-energy formalism. Moreover, the local potential acting on the quasiparticle wave-function, equivalent to the full non-local self-energy, can be defined by (Deisz et al., 1993):

$$V_{\text{eff}}(\mathbf{r})\psi_{\text{qp}}(\mathbf{r}) = \int \mathrm{d}\mathbf{r}'\, \Sigma(\mathbf{r}, \mathbf{r}', E)\psi_{\text{qp}}(\mathbf{r}'). \tag{3.40}$$

This turns out to be extremely close to the GW-derived $V_{XC}$, suggesting that $z_{im}$ for the effective electron in DFT and for the quasiparticle in the self-energy formalism are very close, but significantly different from the value for the classical charge.

Recently $\Sigma$ has been calculated for the Al(111) surface, including the atoms in the pseudopotential formalism (White et al., 1998). The equivalent local potential is again defined, and it is found that $z_{im} = -0.4$ a.u. relative to the geometrical surface. So the effect of the lattice is to move the image plane into the surface compared with jellium, the same trend as with the classical test charge. We must wait for full calculations of $\Sigma$ for d-electron metals for a proper comparison with image potential surface states as observed experimentally.

*Acknowledgements*

The financial support for this work by the Deutsche Forschungsgemeinschaft is gratefully acknowledged.

## References

Aers, G.C. and J.E. Inglesfield, 1989, Surf. Sci. **217**, 367.
Bartynski, R.A., T. Gustafsson and P. Soven, 1985, Phys. Rev. B **31**, 4745.
Benesh, G. and J.E. Inglesfield, 1984, J. Phys. C: Solid State Phys. **17** 1595.
Borstel, G., G. Thörner, M. Donath, V. Dose and A. Goldmann, 1985, Solid State Commun. **55**, 469.
Borstel, G. and G. Thörner, 1988, Surf. Sci. Rep. **8**, 1.
Burdick, G.A., 1963, Phys. Rev. **129**, 138.
Chodorow, M.I., 1939, Phys. Rev. **55**, 675.
Courths, R. and S. Hüfner, 1984, Phys. Rep. **112**, 53.
Deisz, J.J., A.G. Eguiluz and W. Hanke, 1993, Phys. Rev. Lett. **71**, 2793.
Donath, M., 1989, Appl. Phys. A **49**, 351.
Donath, M., 1994, Surf. Sci. Rep. **20**, 251.
Donath, M., V. Dose, K. Ertl and U. Kolac, 1990, Phys. Rev. B **41**, 5509.
Donath, M., M. Glöbl, B. Senftinger and V. Dose, 1986, Solid State Commun. **60**, 237.
Donath, M., F. Passek and V. Dose, 1993, Phys. Rev. Lett. **70**, 2802.
Dose, V., 1985, Surf. Sci. Rep. **5**, 337.
Dose, V., W. Altmann, A. Goldmann, U. Kolac and J. Rogozik, 1984, Phys. Rev. Lett. **52**, 1919.
Eberhardt, W., E.W. Plummer, K. Horn and J. Erskine, 1979, Phys. Rev. Lett. **45**, 273.
Echenique, P.M. and J.B. Pendry, 1978, J. Phys. C **11**, 2065.
Echenique, P.M. and J.B. Pendry, 1990, Prog. Surf. Sci. **32**, 111.
Eguiluz, A.G., M. Heinrichsmeier, A. Fleszar and W. Hanke, 1992, Phys. Rev. Lett. **68**, 1359.
Erskine, J.L., 1980, Phys. Rev. Lett. **45**, 1446.
Falicov, L.M. and J.L. Morán-López (eds.), 1986, Magnetic Properties of Low-Dimensional Systems. Springer-Verlag, Berlin.
Fetter, A.L. and J.D. Walecka, 1971, Quantum Theory of Many Particle Systems. McGraw-Hill, New York.
Fischer, R., N. Fischer, S. Schuppler, Th. Fauster and F.J. Himpsel, 1992, Phys. Rev. B **46**, 9691.
Fischer, N., S. Schuppler, R. Fischer, Th. Fauster and W. Steinmann, 1991, Phys. Rev. B **43**, 14722.
Garrett, R.F. and N.V. Smith, 1986, Phys. Rev. B **33**, 3740.
Giesen, K., F. Hage, F.J. Himpsel, H.J. Riess and W. Steinmann, 1987, Phys. Rev. **35**, 971.
Goldmann, A., M. Donath, W. Altmann and V. Dose, 1985a, Phys. Rev. B **32**, 837.
Goldmann, A., V. Dose and G. Borstel, 1985b, Phys. Rev. B **32**, 1971.
Graß, M., J. Braun, G. Borstel, R. Schneider, H. Dürr, Th. Fauster and V. Dose, 1993, J. Phys. Condens. Matter **5**, 599.
Hedin, L. and S. Lundqvist, 1969, Solid State Physics, eds. H. Ehrenreich, F. Seitz and D. Turnbull, Vol. 23. Academic Press, New York.
Heinrichsmeier, M., A. Fleszar and A.G. Eguiluz, 1993, Surf. Sci. **285**, 129.
Heskett, D., K.-H. Frank, K. Horn, E.E. Koch, H.-J. Freund, A. Baddorf, K.-D.Tsuei and E.W. Plummer, 1988, Phys. Rev. B **37**, 10387.
Heskett, D., K.-H. Frank, E.E. Koch and H.-J. Freund, 1987, Phys. Rev. B **36**, 1276.
Himpsel, F.J., 1991, Phys. Rev. B **43**, 13394.
Himpsel, F.J. and D.E. Eastman, 1978, Phys. Rev. Lett. **41**, 507.
Hölzl, J. and F.K. Schulte, 1979, Springer Tracts in Modern Physics, Vol. 85. Springer-Verlag, Berlin.
Hopkinson, J.F.L., J.B. Pendry and D.J. Titterington, 1980, Comput. Phys. Commun. **19**, 69.
Inglesfield, J.E., 1987, Surf. Sci. **188**, L701.
Jacob, W., V. Dose, U. Kolac, Th. Fauster and A. Goldmann, 1986, Z. Phys. B **63**, 459.

Jennings, P.J. and R.O. Jones, 1988, Adv. Phys. **37**, 341.
Jennings, P.J., R.O. Jones and M. Weinert, 1988, Phys. Rev. B **37**, 6113.
Johnson, P.D. and N.V. Smith, 1983, Phys. Rev. B **27**, 2527.
Jones, R.O., P.J. Jennings and O. Jepsen, 1984, Phys. Rev. B **29**, 6474.
Kevan, S.D., 1983a, Phys. Rev. Lett. **50**, 526.
Kevan, S.D., 1983b, Phys. Rev. B **28**, 2268.
Kevan, S.D., 1983c, Phys. Rev. B **28**, 4822.
Krüger, P. and J. Pollmann, 1988, Phys. Rev. B **38** 10578.
Kubiak, G.D., 1988, Surf. Sci. **201**, L475.
Lang, N.D. and W. Kohn, 1971, Phys. Rev. B **3** 1215.
Lang, N.D. and W. Kohn, 1973, Phys. Rev. B **7**, 3541.
Lam, S.C. and R.J. Needs, 1993, J. Phys. Condens. Matter **5**, 2101.
Levinson, H.J., F. Greuter and E.W. Plummer, 1983, Phys. Rev. B **27**, 727.
Lindgren, S.Å. and L. Walldén, 1989, Phys. Rev. B **40**, 11546.
Lundqvist, S. and N.H. March, 1983, Theory of the Inhomogeneous Electron Gas. Plenum Press, New York.
MacLaren, J.M., S. Crampin, D.D. Vvedensky, R.C. Albers and J.B. Pendry, 1990, Comput. Phys. Commun. **60**, 365.
McRae, E.G., 1979, Rev. Mod. Phys. **51**, 541.
Methfessel, M., D. Hennig and M. Scheffler, 1992, Phys. Rev. B **46**, 4816.
Moruzzi, V.L., J.F. Janak and A.R. Williams, 1978, Calculated Electronic Properties of Metals. Pergamon Press, New York.
Nekovee, M., private communication.
Nekovee, M., S. Crampin and J.E. Inglesfield, 1993, Phys. Rev. Lett. **70**, 3099.
Nekovee, M. and J.E. Inglesfield, 1992, Europhys. Lett. **19**, 535.
Ortuno, M. and P.M. Echenique, 1986, Phys. Rev. B **34**, 5199.
Papadia, S., M. Persson and L.-A. Salmi, 1990, Phys. Rev. B **41**, 10237.
Passek, F. and M. Donath, 1992, Phys. Rev. Lett. **69**, 1101.
Passek, F., M. Donath, K. Ertl and V. Dose, 1995, Phys. Rev. Lett. **75**, 2746.
Pendry, J.B., 1974, Low Energy Electron Diffraction. Academic Press, London.
Pendry, J.B., 1976, Surf. Sci. **57**, 679.
Pendry, J.B., 1981, J. Phys. C **14**, 1381.
Pickett, W.E., 1989, Comput. Phys. Rep. **9**, 115.
Pirug, G., G. Brodén and H.P. Bonzel, 1980, Surf. Sci. **94**, 323.
Plummer, E.W. and W. Eberhardt, 1979, Phys. Rev. B **20**, 1444.
Redinger, J., C.L. Fu, A.J. Freeman, U. König and P. Weinberger, 1988, Phys. Rev. B **38**, 5203.
Reihl, B. and K.H. Frank, 1985, Phys. Rev. B **31**, 8282.
Rundgren, J. and G. Malmström, 1977, J. Phys. C **10**, 4671.
Schaich, W.L. and J.T. Lee, 1991, Phys. Rev. B **44**, 5973.
Schep, K.M., J.B.A.N. van Hoof, P.J. Kelly, G.E.W. Bauer and J.E. Inglesfield, 1997, Phys. Rev. B **56**, 10815.
Schneider, R., K. Starke, K. Ertl, M. Donath, V. Dose, J. Braun, M. Graß and G. Borstel, 1992, J. Phys. Condens. Matter **4**, 4293.
Schuppler, S., N. Fischer, W. Steinmann, R. Schneider and E. Bertel, 1990, Phys. Rev. B **42**, 9403.
Shockley, W., 1939, Phys. Rev. **56**, 317.
Smith, N.V., 1985a, Appl. Surf. Sci. **22/23**, 349.
Smith, N.V., 1985b, Phys. Rev. B **32**, 3549.
Smith, N.V., 1988, Rep. Prog. Phys. **51**, 1227.
Smith, N.V., C.T. Chen and M. Weinert, 1989, Phys. Rev. B **40**, 7565.
Starke, K., K. Ertl and V. Dose, 1992, Phys. Rev. B **45**, 6154.
Steinmann, W., 1989, Appl. Phys. A **49**, 365.
Steinmann, W. and Th. Fauster, 1993, in: Laser Spectroscopy and Photochemistry on Metal Surfaces, eds. H.L. Dai and W. Ho. World Scientific, Singapore.
Straub, D. and F.J. Himpsel, 1986, Phys. Rev. B **33**, 2256.
Szmulowicz, F. and B. Segall, 1981, Phys. Rev. B **24**, 892.

Thörner, G., G. Borstel, V. Dose and J. Rogozik, 1985, Surf. Sci. **157**, L379.
Van Hove, M.A., W.H. Weinberg and C.-M. Chan, 1986, Low-Energy Electron Diffraction. Springer-Verlag, Berlin.
Van Siclen, C. DeW., 1990, Phys. Rev. B **41**, 8175.
Vescovo, E., C. Carbone, W. Eberhardt, O. Rader, T. Kachel and W. Gudat, 1993, Phys. Rev. B **48**, 285.
Wan, C.S. and A.J. Freeman, 1981, Phys. Rev. B **24**, 4364.
Wegehaupt, T., D. Rieger and W. Steinmann, 1988, Phys. Rev. B **37**, 10086.
Weinert, M., E. Wimmer and A.J. Freeman, 1982, Phys. Rev. B **26**, 4571.
White, I.D., R.W. Godby, M.M. Rieger and R.J. Needs, 1998, Phys. Rev. Lett. **80**, 4265.
Whittaker, E.T. and G.N. Watson, 1973, A Course of Modern Analysis. Cambridge University Press, London.
Wimmer, E., A.J. Freeman and H. Krakauer, 1984, Phys. Rev. B **30**, 3113.
Wimmer, E., H. Krakauer, M. Weinert and A.J. Freeman, 1981, Phys. Rev. B **24**, 864.
Woodruff, D.P., S.L. Hulbert, P.D. Johnson and N.V. Smith, 1985, Phys. Rev. B **31**, 4046.
Yang, S., R.A. Bartynski, G.P Kochanski, S. Papadia, T. Fondén and M. Persson, 1993, Phys. Rev. Lett. **70**, 849.

This Page Intentionally Left Blank

CHAPTER 4

# Electronic Structure of Adsorbates on Surfaces. Adsorption on Semiconductors

C.M. BERTONI*, G. ROMA** and R. Di FELICE*

*Istituto Nazionale di Fisica della Materia*
*Dipartimento di Fisica, Universita' di Modena, 4100 Modena, Italy*
*Dipartimento di Fisica, Universita' di Roma "Tor Vergata", 00133 Roma, Italy*

* *Present address: INFM and Dipartimento di Fisica*
*Universita' di Modena e Reggio Emilia*
*Via Campi 213/A, 41100 Modena, Italy*

** *Present address: CECAM, Ecole Normale Supérieure*
*46 Allée d'Italie, 69364 Lyon cedex 07, France*

© *2000 Elsevier Science B.V.*
*All rights reserved*

*Handbook of Surface Science*
*Volume 2, edited by K. Horn and M. Scheffler*

# Contents

4.1. Introduction . . . . . 249
4.2. A brief review of the methods of calculation . . . . . 251
4.3. Adsorption on Si(111). Remotion of reconstruction . . . . . 253
4.4. Adsorbates on Si(100)-(2 × 1)-like surfaces . . . . . 259
4.5. Adsorption on III-V cleavage surfaces and other surfaces . . . . . 261
4.6. Alkali metals on semiconductors . . . . . 267
4.7. Other metals on semiconductors and the early stages of Schottky-barrier formation . . . . . 272
4.8. A simple picture for surface bands and structure: the electron or hole counting-rule . . . . . 274
4.9. Core level spectroscopy and adsorbates . . . . . 278
4.10. Conclusions and perspectives . . . . . 280
References . . . . . 281

## 4.1. Introduction

Various theoretical and computational approaches have been used in the study of chemisorption on surfaces. In the seventies, it was particularly important to have a tool to interpret the results of photoemission spectroscopy, a technique rapidly evolving with the improvements of ultra-high vacuum, the evolution of photon sources (particularly synchrotron radiation) and the resolution of the analyzers. The electronic structure obtained for the adsorbate–surface system was directly compared with the energy distribution curves (EDC), to have an indirect check of the geometry of the adsorption process. The definition of some selected surface geometries, the calculation of their electronic structure, and the comparison with the photoemission data, were the three steps to examine both clean reconstructed surfaces and the surfaces with adsorbates. The explicit calculation of the electron wave functions and of the particle density of each electron state, localized in the substrate and adsorbate regions, could allow a microscopical understanding of the adsorption bond (see, for instance, Pandey et al., 1975). For this purpose, semiempirical approaches based on tight-binding parametrizations as well as on pseudopotential methods (even in approximate local form or in not well converged basis set) were the main tools. It was clear that in any case a successful theory had to account for the rearrangement of the charge density distribution self-consistently, eventually in an approximate way.

With the improvements of the computational methods and of the power of the hardware, the computation had to approach a variety of more and more complex systems with the accuracy of fully self-consistent calculations. In the early eighties, the main goal was to produce reliable results, not only for the band structure, but also for total energies and forces (Ihm et al., 1979). This goal was achieved by exploring the stability of assumed model geometries and by allowing the geometrical arrangement of the atoms to relax towards equilibrium, in successive computations. The minimum energy configuration of a system could be selected by comparing the total energies of different geometries included in a limited set of structures. The capability of the density functional theory in the local density approximation (DFT-LDA) was thus tested. This theory, which describes the ground state properties of systems of interacting electrons exactly, was originally formulated by Hohenberg and Kohn (1964) and by Kohn and Sham (1965); for a more recent extensive treatment see the excellent book by Dreizler and Gross (1990). Also the semiempirical methods (Chadi, 1984a) had to be implemented to include an estimate of the total energy as a function of the configuration parameters. In the meanwhile, more stringent comparisons to experimental results were made possible with the appearance of a direct microstructural probe: the scanning tunnelling microscopy (STM) (Binnig et al., 1983). The interest towards surface systems with adsorbates was renewed, and the possibility of using the STM in spectroscopical mode increased the need for reliable electronic structure calculations to interpret or to *simulate* STM images at a given bias voltage between the tip and the sample.

The need to understand the details of the band structure in the region around the gap put the problem of the underestimation of the gap itself, that is typical of DFT-LDA band structures even in the bulk of semiconductors. The failure of the Kohn–Sham eigenvalues in describing properly the excitation spectrum (electron or hole creation), within a theory which is designed to describe the ground state properties of the system, is well understood. The evaluation of the $\Sigma_{xc} - V_{xc}$ correction to the Kohn–Sham eigenvalues, in order to describe the one-particle excitation spectrum, has been done successfully in the GW approximation (Hedin, 1965) and a few surface calculations (also in presence of adsorbates) included these corrections recently (see, for instance, Northrup et al. (1991) for a calculation on a clean surface; Blase et al. (1994) for a calculation on an adsorption system).

The major improvements in the theory of surfaces and adsorbates came from the invention of the so-called *ab initio* molecular dynamics, or Car–Parrinello method (Car and Parrinello, 1985). This approach, when used as a global minimization scheme, allows to reach in the same computational procedure the self-consistent DFT electronic structure and the equilibrium atomic positions. When used as a real finite-temperature molecular dynamics, it allows to understand the driving forces that cause instabilities, modify the surface geometries upon adsorption, and cause transitions among different structures. The study of harmonic and anharmonic vibrations at surfaces are also accessible. Surface migration, defects and interactions at surfaces can be studied dynamically in the limits of the DFT framework. These developments (inclusion of many-body effects and use of first principles molecular dynamics) represent the most significant progress of the present decade and their application to a wide class of systems is far from being completed.

Despite the developments of the theoretical methods and of the computational resources on one side, and the refinements of experimental probes on the other, only few systems among semiconductor surfaces with adsorbates can be considered as definitely understood in geometry, electronic properties and dynamics. The refinement of the computational and experimental methods has often questioned the pre-existing interpretation. There are still living controversies, that will be quoted in the present review, about many widely studied systems.

In general, for semiconductor surfaces which exhibit a variety of surface reconstructions, the first question is how the reconstruction itself can influence adsorption as far the site, the symmetry of the bonding and the local reactivity are concerned. The second concern is the change of surface structure upon adsorption, the possible reduction of the reconstruction superstructure, the passivation and the existence of multiple metastable phases. We will be mainly interested in the *ordered adsorption*, upon which periodical structures are obtained. This facilitates the theoretical description by enabling the use of the methods of solid-state theory for periodic systems. The third aspect is the link between the geometry of the adsorption state and the electronic structure of the new surface system created. The evolution of the structure when one passes from the single overlayer to the growth of a full interface makes the problem interesting from a technological point of view as well.

In this chapter we will follow some selected cases among the wide literature that is continuously growing. In Section 4.2 we trace a brief review of the methods. In Section 4.3 we consider the adsorption of atoms on different reconstructed structures of Si(111), with particular attention to the hydrogenation of the cleaved metastable $(2 \times 1)$ surface and to the properties of the ideal H:Si(111) surface prepared by chemical etching. In Section 4.4

we present the current understanding of atomic adsorption (hydrogen and other light elements) on the (2 × 1)-Si(100) surface, with reference to passivation, stabilization, and heteroepitaxy. The adsorption of various elements (H, Cl, Sb, Se) on the surfaces of III-V compounds is treated in Section 4.5. Sections 4.6 and 4.7 are devoted to the adsorption of metals, with reference to the early stages of formation of the metal/semiconductor barrier. In Section 4.8 we illustrate a simple prescription which predicts the stability of a given surface structure on the basis of the enumeration of the surface bonds and dangling bonds, and we compare its predictions in some cases to first principles results. In Section 4.9 we consider the problems connected to the interpretation of the core level spectroscopy, which is a very precise tool for surface analysis. Section 4.10 is devoted to conclusions and perspectives.

## 4.2. A brief review of the methods of calculation

A reliable method for the description of the adsorption process of atoms or molecules at surfaces should correctly treat the adsorbate and the substrate separately. See, e.g., Spanjaard and Desjonquères (1990) for a valuable detailed formulation of the problem. In particular, one should be able to describe the two regimes of the adsorption process: (i) in *physisorption* the bonding energy is $|E_B| \leqslant 0.5$ eV and the adsorbate is bonded to the substrate by Van der Waals-type forces, due to dipole-dipole interactions; (ii) in *chemisorption* the bonding energy is $|E_B| \geqslant 0.5$ eV and the bond between the adsorbate and the substrate has chemical nature, that implies sharing or transfer of electrons.

In the large distance regime, much work can be done within the image charge description. However, when the adatoms approach the surface beyond a critical distance, the classical model of the image charge is no longer valid, because electron transfer can be fractionary and induce a *band widening* of the adsorbate electronic states.

Here we briefly sketch the different methods that have been successfully used in describing the adsorption process.

- The Anderson–Grimley–Newns Hamiltonian is

$$H = H_{\text{ads}} + H_{\text{subs}} + H_{\text{coupling}}.$$

It was first introduced by Anderson in 1961 to treat impurities and then revised by Grimley in 1967 and by Newns in 1976 to treat adsorption of atoms. It is a *many body* formulation that requires the model parameters from other sources. It can be solved in the Hartree–Fock approximation, which produces some unphysical results such as a variation of the Fermi-level and magnetic solutions. These limitations can be overcome by going beyond Hartree–Fock.

- Simple tight-binding models (see, e.g., Bassani et al., 1975) are based on a parametrization of the single-particle Hamiltonian in terms of neighbor interaction hopping integrals. In general the overlap terms are neglected. The parametrizations are usually obtained from a bulk one-electron band structure and transferred to a number of different geometries, with some approximate *ansatz* for the dependence on the distance. Originally conceived to describe the electronic structure, the method has been implemented to obtain total energy and forces. In this complete formulation it allows to calculate the binding

energy of an adsorbate as a function of its three spatial coordinates. From such calculations it is thus possible to extract all the information necessary to the structural (as well as electronic) characterization of the system: for instance, the most stable adsorption site and its energy, the bond length, the activation energy for surface diffusion, and the vibrational properties. The failure of this scheme is linked to the limits of the transferability of the potential parameters from the bulk to open geometries.

- Quantum chemistry methods can be used in a variety of approximations and developments reached by molecular calculations. The common aspect is the substitution of the substrate with an aggregate of atoms: the larger is the number of atoms included, the more accurate is the description of the crystal and of the continuum of its electronic states.
- Density functional theory in the local density approximation (Dreizler and Gross, 1990) gives the solutions of the one-electron equations, consistent with the evaluation of the effective potential due to the nuclei and to the electron charge distribution. The many-electron effects are described in the exchange–correlation energy density and potential. The calculations can be performed using different descriptions of the electron–ion interaction for the band structure calculations. The most common methods are: the pseudopotentials, the linear muffin-tin orbitals (LMTO) scheme, and the full-potential augmented plane waves approach. In the field of our interest, the pseudopotential approach is the most widely used. See Phillips and Kleinman (1959) for the original formulation, Bachelet et al. (1982) for the tabulation of first principles norm-conserving pseudopotentials for all the elements, Pickett (1988) for a review of their application. More recent developments of the pseudopotential approach can be found in Hamann (1989) and Vanderbilt (1990). In principle, within all the methods and with the help of Green-function techniques, it is possible to treat the case of a single atom (or molecule) adsorption, but the most common approach is to deal with periodic structures. The use of large surface unit cells can mimic the isolate atom adsorption or treat low depositions.

The use of appropriate basis functions, localized along the $z$ direction perpendicular to the surface plane, allows the description of the substrate, the surface, the adsorbate, and the vacuum region, through a single slab of atomic planes. By using delocalized plane waves as in the common pseudopotential methods, one adopts the *repeated slab method* to recover three-dimensional (3D) periodicity. The repeated slab unit cell is a 3D cell that must be so thick to describe properly the existence of the substrate and the vacuum, reducing the spurious interactions among the two surfaces of the slab of atomic planes. This last approach is also adopted in the total-energy-and-force method and in the Car–Parrinello method.

In this review, necessarily limited in view of the large amount of existing results, we consider selected examples of physical systems and we will mention some aspects of the employed methods during the discussion of each case. Excellent reviews can be found in the existing literature on the theoretical results for adsorbates on semiconductors. Let us remind the book by Bechstedt and Enderlein (1988) and the review paper on semiconductor surfaces, that also contains many references to adsorbates, by La Femina (1992).

### 4.3. Adsorption on Si(111). Remotion of reconstruction

The (111) cleavage surface of silicon exhibits a metastable (2 × 1) reconstruction described by the "$\pi$-bonded chain model" (Pandey, 1981), which definitely substituted in 1981, on the basis of energy bands considerations, the "buckling model" (Hanemann, 1961), previously conceived to explain reconstructions at diamond and zincblende surfaces. The "buckling model" accounted for the (2 × 1) geometry at the Si(111) surface in terms of alternating outermost atoms displacing inwards and outwards with respect to the ideal plane, with a rehybridization of the electronic states stabilizing the structure. Pandey's "$\pi$-bonded chain model" consists instead in the breaking of sixfold rings and the consequent formation of fivefold and sevenfold rings, with chains of $\pi$ bonds on the surface. In Fig. 4.1a a side view of the Pandey-like reconstruction is shown. Following the proposal of the model, calculations were performed to test its validity and to obtain quantitative geometrical parameters (see Pandey, 1982; Northrup and Cohen, 1982; Chadi, 1982). At variance with the originally proposed model in which the $\pi$-chains were lying on the surface plane, nowadays it is commonly accepted that they are substantially buckled, as it is shown, e.g., in an *ab initio* simulation (see Ancilotto et al., 1990) performed with the Car–Parrinello method (Car and Parrinello, 1985). The stable structure of the Si(111) surface, obtained by annealing at high temperature, is the (7 × 7) reconstruction (Takayanagi et al., 1985), which was

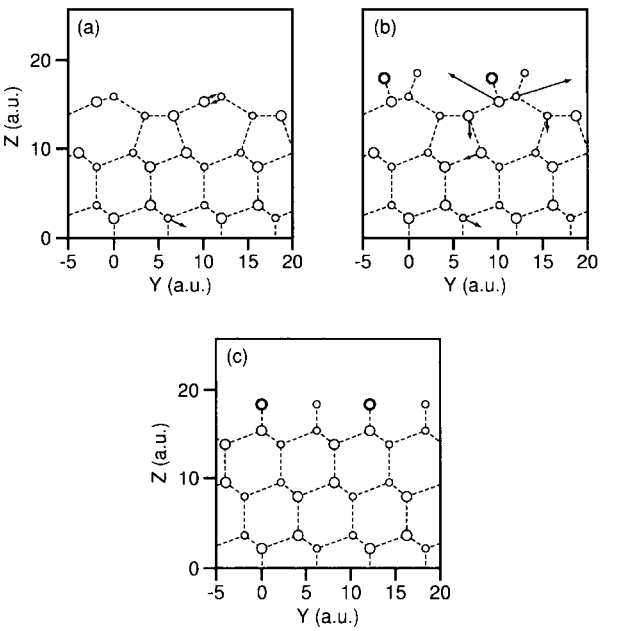


Fig. 4.1. Side view of Si(111) surface structures. Large (small) circles represent in-plane (out-of-plane) Si atoms. Large (small) double circles represent in-plane (out-of-plane) H atoms. (a) Clean reconstructed 2 × 1 surface. (b) H-covered reconstructed 2 × 1 surface; large forces tend to destroy the sevenfold and fivefold rings. (c) H-covered unreconstructed surface. Forces are shown with $|\mathbf{F}_{max}| = 7.6 \times 10^{-2}$ Ry/$a_0$. From Buongiorno Nardelli et al. (1992).

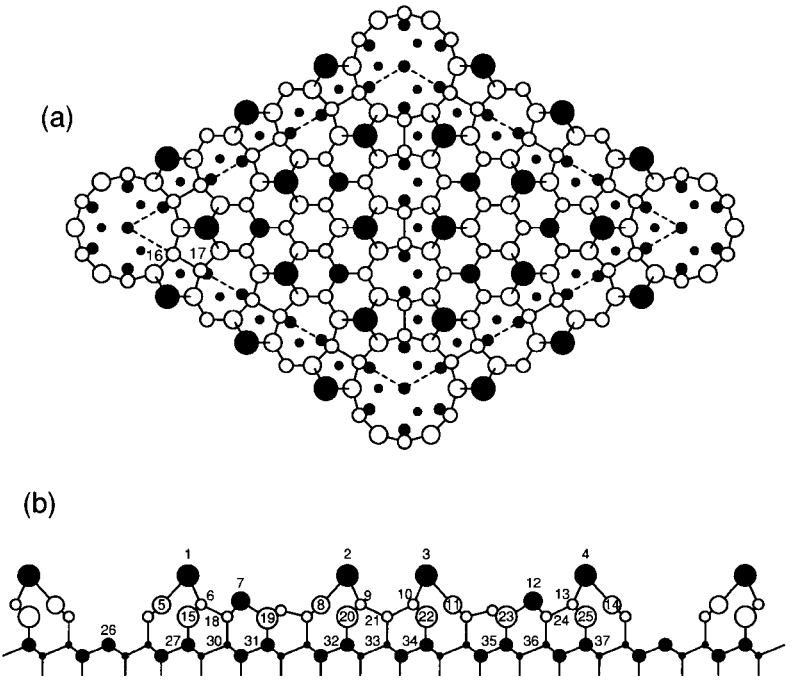


Fig. 4.2. (a) Top view and (b) side view of the Si(111)-( 7 × 7 ) surface. The atoms labeled 1–4 are the *adatoms*, those labeled 7–12 are the *rest atoms*, the atom labeled 26 is a *corner atom*. From Brommer et al. (1992).

also simulated through first principles calculations by Brommer et al. (1992) and Štich et al. (1992). In Fig. 4.2a, b a top view (side view) of the (7 × 7)-Si(111) cell is shown.

Here we want to consider the removal of the reconstruction at the Si(111) surface as a consequence of atom adsorption. The instability of the ideal bulk-terminated (1 × 1) geometry at the clean surface is due to the presence of one dangling bond per atom: the surface band arising from the dangling bonds is completely embedded in the Si bulk-gap, and the occupancy of one electron per atom gives origin to a half-filled band and consequently to a metallic system. The formation of sevenfold rings in the (2 × 1) reconstruction enables the approaching of atoms and the interaction between dangling bonds. An energetical stabilization, a lowering of the occupied electronic levels, and the opening of a gap follow.

The deposition of reactive atoms on the surface, e.g., hydrogen atoms, can saturate the dangling bonds, with a cancellation of the main driving mechanism towards reconstruction and a consequent stabilization of the ideal surface. This is intuitively clear, but it is interesting to investigate a lot of properties, such as the paths of the (2 × 1) → (1 × 1) transformation, the bond lengths and stretching frequencies of the adsorbates on the substrate, the electronic features, the stable geometry, the critical deposition, and many others. In the following, we will concentrate on hydrogen adsorption, mentioning some other interesting cases.

Hydrogen on cleavage surfaces of semiconductors is a prototypical chemisorption system, for the simplicity in understanding the action of the hydrogen atoms and in producing

well ordered structures through different experimental techniques (see Chabal et al., 1983; Burrows et al., 1988; Higashi et al., 1990). The structural features of this system have been clearly outlined via *ab initio* DFT-LDA calculations both in the total-energy-and-force (see Buongiorno Nardelli et al., 1992) and in the Car–Parrinello (see Ancilotto and Selloni, 1992) schemes. In the former approach the authors have studied a situation in the full monolayer (ML) regime of hydrogen coverage on the Si(111)-(1 × 1) surface. It comes out that the H–Si bond length minimizes the energy at 1.54 Å (Buongiorno Nardelli et al., 1992; Kaxiras and Joannopoulos, 1988) with the H atoms lying on top of the substrate atoms. The calculation of the atomic forces for such geometry shows that they are almost identically vanishing, indicating a metastable geometry (Fig. 4.1c). On the contrary, if one puts the H atoms on the Si atoms of the chains in the (2 × 1) Pandey-like reconstruction, the substrate atoms in these chains experience very large lateral forces which tend to destroy the $\pi$ bonds and recover the sixfold rings of the ideal (111) plane (Fig. 4.1b). Moreover, the calculation of the Si–Si bond lengths in the first layer and between the first and second layers in presence of a full hydrogen coverage shows that they are stretched in comparison to the clean surface, and the buckling is removed, so that the atoms on the outermost plane become all equivalent (Ancilotto and Selloni, 1992). Another possible structure resulting after hydrogen exposure of a Si(111)-(7 × 7) surface is the $SiH_3$-(1 × 1). This structure can form upon extraction of the top layer of Si atoms. As a consequence, Si atoms which have three dangling bonds each remain exposed. Each of them can bind to three H atoms, forming $SiH_3$ complexes (see Pandey et al., 1975; Zheng and Smith, 1993).

The stretching frequency of the H–Si bond is about 2022–2025 $cm^{-1}$ in the framework of DFT-LDA and pseudopotential methods, as found by Buongiorno Nardelli et al. (1992), Blase et al. (1994), Li and Vanderbilt (1992). Ancilotto and Selloni (1992) and Kaxiras and Joannopoulos (1988) report slightly lower values. Semiempirical calculations (Sandfort et al., 1994) are able to reproduce better the experimental determination (Higashi et al., 1990), giving 2080 $cm^{-1}$ against 2083 $cm^{-1}$ (bond-charge-model calculations by Harten et al., 1988, give ~2090 $cm^{-1}$). This is a strongly localized dispersionless mode (Sandfort et al., 1994), as is the bending mode of the same bond. The bending mode was reported by Harten et al. (1988) to show a noticeable dispersion, with frequency values ranging from ~564 $cm^{-1}$ to ~645 $cm^{-1}$: other determinations of its frequencies (Li and Vanderbilt, 1992; Kaxiras and Joannopoulos, 1988; Ancilotto and Selloni, 1992; Sandfort et al., 1994) fell in this same range, but found almost no dispersion. A two-phonon bound state was recently found for this system: it was first experimentally determined (Guyot-Sionnest, 1991) at a frequency of 90 $cm^{-1}$, deduced from the large measured anharmonicity, and then theoretically calculated (86.4 $cm^{-1}$) through a Hubbard-type phonon Hamiltonian in a first principles simulation (Li and Vanderbilt, 1992). A similar large anharmonicity was also found for the stretching vibration of H on C(111)-(1 × 1) (Zhu and Louie, 1992): in both cases it is due to the very light mass of hydrogen with respect to the substrate atoms, resulting in a large amplitude of the displacements. Concerning the whole phonon spectrum of the fully hydrogenated Si(111) surface, it is interesting to note the presence of the so-called Lucas mode (Harten et al., 1988; Sandfort et al., 1994), falling at ~460 $cm^{-1}$: this is a feature of the (111) surface of silicon (it also appears in the (2 × 1) reconstructed surface, as in Alerhand et al., 1985), not depending on perturbations induced from reconstructions or adsorbates. It is important here to underline that the quality of the infrared spectra is influ-

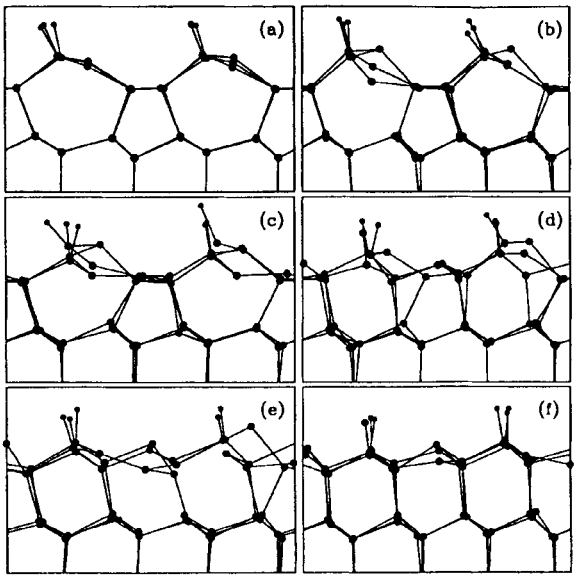


Fig. 4.3. The dereconstruction path of the 2 × 1 Si(111) surface upon coverage by half a monolayer of hydrogen. The average temperature of the two topmost Si layers in the simulations are (a) 200 K, (b) 800 K, (c) 900 K, (d) 800 K, (e) 600 K, (f) 300 K. From Ancillotto and Selloni (1992).

enced by the experimental technique used to prepare the surface. For instance, as pointed out by Dumas et al. (1990), broad spectra are obtained if the hydrogenated surface is produced from exposure of the cleaved surface to atomic hydrogen (Chabal et al., 1983). On the contrary, a single well-peaked Si–H stretching mode is obtained if the surface is chemically treated (Higashi et al., 1990) in high-pH HF solutions. Exposure to atomic hydrogen produces a disordered (1 × 1) structure with many defects, while the chemically prepared H:Si(111)-(1 × 1) surface is well ordered.

In Ancilotto et al. (1990), it was shown that the (1 × 1) → (2 × 1) transformation has a negligible activation energy. It is also interesting to have insight about the inverse process. This was studied through partial-coverage simulations of the system. One knows from LEED outcomes (e.g., from Schulze and Henzler, 1983) that the spots due to the (2 × 1) structure weaken during hydrogen exposure, becoming negligible at about 0.5 ML. It is natural to suppose that the dereconstruction process begins locally in regions with a large hydrogen concentration, and involves the whole surface when these regions overlap significantly. Ancilotto and Selloni (1992) have shown that the critical hydrogenation fraction at which this occurs is about 0.3 ML. They have also determined a path towards the removal of the reconstruction, which is facilitated at a low coverage configuration in which the H atoms are bonded to non nearest-neighbor surface atoms. In this situation, some atoms in the $\pi$-chains are allowed to have large displacements, they approach the second layer and form bonds with the atoms on the third layer. The result is a restoration of the sixfold rings characteristic of the ideally-terminated (111) plane (see Fig. 4.3c, d from Ancilotto and

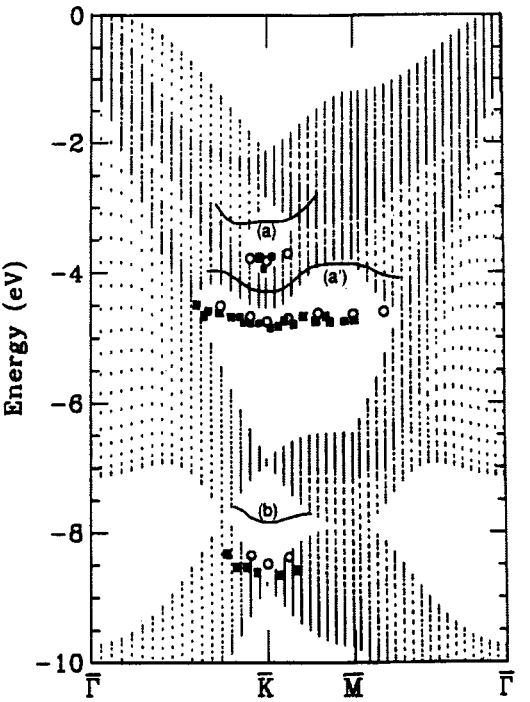


Fig. 4.4. Surface-state bands for the H:Si(111)-(1 × 1) surface, calculated within LDA (solid lines) and GW (open circles). The solid squares represent the experimental data. In the background is the GW projected bulk band structure for bulk Si. From Blase et al. (1994).

Selloni, 1992). In the same work it was also found that this path has a very low activation energy, and it should be allowed even at room temperature.

The electronic structure of the H:Si(111)-(1 × 1) can be obtained from first principles in the DFT-LDA scheme with pseudopotentials, as in Buongiorno Nardelli et al. (1992) and Blase et al. (1994). At the $\bar{M}$ point of the surface Brillouin zone (2DBZ) (at the center of the edges of the hexagons) there is a surface state in the valence band inside a gap at −3.86 eV, and two surface resonances in the conduction band at 2.83 and 4.14 eV. At the $\bar{K}$ point (at the corners of the hexagons) a clear surface state localized at the interface (−7.89 eV) and a surface state localized on the hydrogen atoms (−3.19 eV) exist; in the conduction band there is a resonance at 3.84 eV and a state at 2.23 eV. At the $\bar{\Gamma}$ point surface resonances are present in both the valence and the conduction bands. Summarizing the main features appearing in the valence bulk-band, three surface-localized bands are present, as pointed out by Blase et al. (1994) all mainly located around $\bar{K}$ (see Fig. 4.4); only one of them, the intermediate one, is present at $\bar{M}$. Its dispersion is overestimated in LDA, and the corresponding state at $\bar{M}$ is not correctly located, with an error much larger than the corresponding error for the system As:Si(111)-(1 × 1) (Becker et al., 1988), because of the strong localization of the wave-function on the hydrogen atoms. Blase et al. (1994) showed that self-energy corrections in the GW approximation (Hedin, 1965),

sensible to localization, give substantial shifts of the lower and intermediate bands, and improvement in the description of their dispersion.

Self-energy corrections in the GW approximation (Hedin, 1965) were also applied by, e.g., Becker et al. (1988) and by Hybertsen and Louie (1988), to investigate the electronic structure of the As:Si(111) system, in which the As atoms induce a $(1 \times 1)$ geometry, replacing the top silicon atoms in almost ideal positions, with only a slight outward relaxation. There are two main surface bands: one occupied, deriving from the As lone-pair, and the other empty, split off the continuum of bulk states near $\bar{\Gamma}$. For the As:Si(111) system, as for H:Si(111)-$(1 \times 1)$, GW corrections sensibly improve the agreement between theoretical calculations and experimental outcomes as concerning the electronic band structure (Hybertsen and Louie, 1988), since the self-energy calculation accounts for the quasi-particle energies which are measured in photoemission experiments.

The adsorption of chlorine on semiconductor surfaces has also been a matter of interest in the past, as this element is very electronegative and can easily saturate dangling bonds. The results of a recent simulation within the *ab initio* molecular dynamics approach, for a system made up with a $Cl_2$ molecule impinging on a Si(111)-$(2 \times 1)$ surface with a fixed initial energy (De Vita et al., 1993; Stich et al., 1994), have shown that $Cl_2$ dissociates. The path of the dissociation depends on the geometry of the initial configuration. Different reasonable starting positions for the molecule are above the $\pi$ chains or between adjacent chains. The intrachain bonds are likely very reactive, since they contain threefold coordinated silicon atoms which have rehybridized in order to saturate dangling bonds: a situation which brings them back to a $sp_3$ hybridization could be much favorable. For most cases taken into account the $Cl_2$ molecule immediately dissociates, giving origin to chemisorption of single atoms. However, for some initial conditions, there exists an intermediate *precursor state* for associative chemisorption, with the molecule bonded to the substrate. In this intermediate configuration, the Cl–Cl bond is largely stretched with respect to the free molecule, and it is subsequently broken by overcoming an energy barrier of about 0.9 eV. The breaking of the bond is driven by chemical processes, through a charge transfer to an antibonding molecular orbital.

Another typical example of molecule adsorption on the Si(111) surface is $NH_3$ on Si(111)-$(7 \times 7)$. The $(7 \times 7)$ reconstruction is the stable structure of the Si cleavage surface, reached after annealing the sample. The $NH_3$ molecule dissociates giving origin to a $H^+$ ion and a $NH_2^-$ radical. The maximum probability of chemisorption is on the corner hole atoms. The rest atoms and the adatoms are sites with lower probability of chemisorption (see, for instance, Wolkow and Avouris, 1988; Brommer et al., 1994). In the latter paper the reactivity of different surface sites is measured in terms of spatially integrated local softness, which is defined as the derivative of the charge density with respect to the chemical potential at fixed temperature and external potential. It is shown that this quantity is able to measure the reactivity of surface regions towards adsorbates of different kinds (donors or acceptors of electronic charge). Its value is calculated separately for reactants having positive or negative electronegativity difference with respect to the substrate, and it is thus possible to determine which are the sites of maximum reactivity for a given adsorbate species. In such a scheme it has been shown that H is likely to bind to a corner atom on the $(7 \times 7)$ cell, while substances like Pd, Ag and Li have maximum probability

to bind to the adatoms. This is a significant example of the amount of prediction that can be extracted from a DFT calculation.

Finally, we just mention a possible $\sqrt{3} \times \sqrt{3}$ reconstruction pattern which occurs at the (111) face of silicon when group-III, -IV or -V elements are deposited on the surface. This periodicity can manifest itself through a monomer or a trimer basic reconstruction, depending on the adsorbate. Ag seems to give origin to a trimer-based reconstruction in a missing top layer model (see Kirchner et al., 1994, 1995). Group-III adatoms form trimers and find place at the hollow sites of the top Si layer, while group-V adatoms behave like Ag (see, for instance, Nagayoshi (1993), where chemisorption of Sb on the Si(111)-(7 × 7) is treated).

### 4.4. Adsorbates on Si(100)-(2×1)-like surfaces

Before considering the adsorption process on the Si(100) surface, we give a brief account of the clean surface. The structure of the clean Si(100) surface has been the subject of a long standing controversy. It was evident since 1959, when Schlier and Farnsworth found a (2 × 1) LEED pattern, that the surface was reconstructed. The basic reconstruction mechanism is the formation of dimers, which accomplishes the saturation of half of the surface dangling bonds. The Si atoms of the last plane, having two dangling bonds each at the second-neighbor distance, are paired. Such a pairing takes place through a symmetry breaking (choice between the two possible directions of dimerization $\{0, 1, 1\}$ and $\{0, -1, 1\}$) and a considerable reduction of the distance between the two atoms in the pair, which becomes similar to the bulk first-neighbor distance. The content of the controversy is the buckling of the surface dimers. In the so-called *asymmetric dimer model* the dimers are buckled. One of the two Si atoms in each dimer moves outwards and the other inwards with respect to the bulk-terminated surface. For what concerns the electronic properties, the dimerization mechanism induces the presence of two surface bands in the gap of the projected bulk band structure (Bertoni, 1990). While these bands are degenerate for symmetric dimers, the buckling mechanism opens a gap between the two surface bands. The band corresponding to the dangling bond of the more external atom is filled and the other is empty. This is the general mechanism of gap-opening at surfaces. It easily implies an energy gain.

A number of accurate calculations, based both on DFT-LDA for repeated slabs and on the HF method for clusters (see, for instance, Tsuda et al., 1991), support the existence and relative stability of symmetric dimers. However, the most recent studies support the asymmetric dimer model. DFT-LDA pseudopotential investigations, and in particular those performed in the molecular dynamics CP approach, give buckled dimers. Furthermore, in agreement with the experimental data at low temperature, the correlated alternation of the sign of the buckling angle can give origin to long range reconstructions (e.g., the $p(2 \times 2)$ and the $c(4 \times 2)$ reconstructions) that correspond to local energy minima. Both the symmetric-dimer (SD) and asymmetric-dimer (AD) (2 × 1) geometries are not even local minima. A recent dynamical simulation (Shkrebtii et al., 1995) indicates that frequent flips of the buckling angles can occur even at room temperature. A microscopic description of a dimer flip, induced by the interaction with the tip of an atomic force microscope, is given by Cho and Joannopoulos (1995). Summarizing, it is well established

that the dimerization is the basic mechanism of the clean Si(100) reconstruction. Thus, the reconstructed surface will be called Si(100)-(2 × 1), despite the various possible complex arrangements of the order of buckled dimers.

*Hydrogenated Si(100) surface.* The (100) surface of silicon can be easily passivated by adsorption of atomic hydrogen. There is evidence of monohydride and di-hydride regimes at different H exposures and temperatures of the substrate. The adsorption along the dangling bonds of Si–Si dimers preserves the (2 × 1) reconstruction but alters the $\pi$ and $\pi^*$ orbitals of the clean surface. The length of the Si–Si bond increases and the symmetric dimer configuration is favored. A (1 × 1) phase can be obtained by adding 1 ML of H atoms. The dimers are broken and each Si atom at the surface is bonded to a couple of H atoms. A (3 × 1) phase has been also found. It has been explained as an ordered alternation along the dimer directions of $SiH_2$ and $Si_2H_2$ units. The earliest works for a theoretical description of the monohydride and di-hydride phases (Appelbaum et al., 1978; Ciraci and Batra, 1984) offered a good explanation of the stability of the structures and of the EDC features seen in photoemission experiments for the two phases. A mechanism to explain the release of molecular $H_2$ was suggested by Ciraci and Batra (1984) in terms of a transition from two neighboring di-hydrided Si and the H–Si-Si–H dimer configuration. More recently, a number of experimental results based on STM at low and intermediate coverages (Boland, 1991), and the evidence of a first-order desorption kinetics of $H_2$ (Sinniah et al., 1989), questioned these simple interpretations and encouraged a variety of detailed surface calculations in order to understand the energetics of H adsorption on Si(100) and to interpret the results of STM spectroscopy (Li et al, 1995; Uchiyama and Tsukada, 1993, 1994).

*Si(100) with group-V, -VI and -VII elements as adsorbates.* A surface structure with pure (2 × 1) periodicity, without the presence of more complex phases due to the ordered patterns of buckled dimers, can be obtained by depositing As or other group-V elements on Si(100) at 1 ML coverage. Each As atom is bonded to two surface Si atoms and to another As partner localized at a neighboring surface dimer. Two electrons per As atom are not involved in the bonds: they constitute lone pairs that occupy completely the surface state bands. This electronic distribution does not induce any inequivalence between the two As atoms in a pair, hence the As dimers are symmetric. The geometry of the substrate is not far from ideal already at the first Si sublayer. The As–As bond length is 2.55 Å, as obtained by Uhrberg et al. (1986) in a work which gives experimental evidence and theoretical explanation of the structure of the As:Si(100)-(2 × 1) passivated surface. Similar results are expected for P and Sb as overlayers. With the restoration of the ideal geometry of the underlying Si atoms and with the creation of a further layer of adsorbates, the direction of adsorbate dimers is rotated by 90° with respect to the original Si-dimers. As the preferential direction of the dimers is that of the surface steps, one observes this effect ((2 × 1) → (1 × 2) transition induced by adsorbate dimerization) only at sufficiently low temperature (less than 400 K). At higher temperature, surface diffusion is allowed, and as a consequence there is a reverse transition to the lower energy (2 × 1) phase (dimers parallel to the step edges). This effect, important for the study of GaAs heteroepitaxy on Si(100), which can start from As layer deposition, has been clarified trough a total-energy slab calculation with a fairly large number of atoms in a paper by Alerhand et al. (1991).

Upon adsorption of group-VI atoms, the ideal bulk termination of the surface is recovered. Both S and Se adsorption (Krüger and Pollmann, 1990, 1993a; Kaxiras, 1991) eliminate the $(2 \times 1)$ reconstruction and create an ordered $(1 \times 1)$ monolayer, for both the dimerized Ge(100) and Si(100) surfaces. The surface layer is inert and has the geometry of an ideal surface. Any other geometry, including exchange reactions between the adsorbate and the substrate, turns out to be energetically unfavorable.

Also oxygen adsorption at the full monolayer coverage recovers the $(1 \times 1)$ structure, provided it takes place in atomic form. A recent paper by Kirchner and Baerends (1994) about atomic oxygen adsorption on Ge(100), shows that at $\theta = 0.5$ ML one obtains an ordered chemisorption in the bridge position above the dimers with relaxation of the $(2 \times 1)$ reconstruction and at $\theta = 1$ ML a full coverage with $(1 \times 1)$ pattern.

Chemisorption of Cl is expected to take place along the dangling bonds of the dimers at the Si(100)-$(2 \times 1)$ surface. Water has the same behavior. Dissociation of $H_2O$ in $H^+$ and $OH^-$ allows the two species to bind at the two dangling bonds in a dimer (Bu and Rabalais, 1994). Figure 4.5 indicates schematically the bonding geometries in the considered cases.

## 4.5. Adsorption on III-V cleavage surfaces and other surfaces

The stable structure of the (110) cleavage surface of GaAs is well understood. The experiments have revealed the presence of relaxation in the first two layers (see, e.g., Feenstra and Fein, 1985), and the same result was obtained from calculations (see, e.g., Calandra et al., 1977; Qian et al., 1988; Di Felice et al., 1993 and references therein). In the $1 \times 1$ ideal unit cell there are 1 Ga and 1 As atoms, each with a dangling bond. The relaxation derives from a partial transfer of charge from the Ga dangling bond to the As dangling bond. The electronic structure of the ideal surface presents two dangling bond bands in the bulk gap. The lowest band is filled and has the dominant contribution from the As surface atoms. The highest band is empty and has the dominant contribution from the Ga surface atoms. The ideal surface is unstable with respect to a rotation–relaxation adjustment in which the As atoms in the outermost plane displace outwards, while the Ga atoms in the same plane displace inwards. This structural mechanism is accompanied by an electronic re-hybridization: the Ga atoms assume a threefold coordination and an $sp_2$-like hybridization. The relaxation process pushes the two surface bands out of the edges of the bulk gap. In the plane immediately below the surface a slight buckling of opposite sign appears, with the Ga atoms displaced outwards and the As atoms displaced inwards with respect to the ideal (110) plane. The buckling angles that the As–Ga bonds form with the ideal plane are very different at the surface plane and at the plane below the surface. The angle at the surface plane is $\sim 30°$, the angle at the sub-surface plane is $\sim -1°$. A side view of the clean GaAs(110) surface is shown in the upper part of Fig. 4.6. The parameters of the structure outlined in the figure, obtained via first principles calculations (see, e.g., Di Felice et al., 1993) are in good agreement with the experimental results (see, e.g., Duke et al., 1983) and with many other calculations.

H atoms are able to saturate the dangling bonds present at the clean GaAs(110) surface, inducing a derelaxation towards the ideal structure. Upon complete hydrogenation of the surface, the outer chains of GaAs pass from a large positive buckling to a small negative

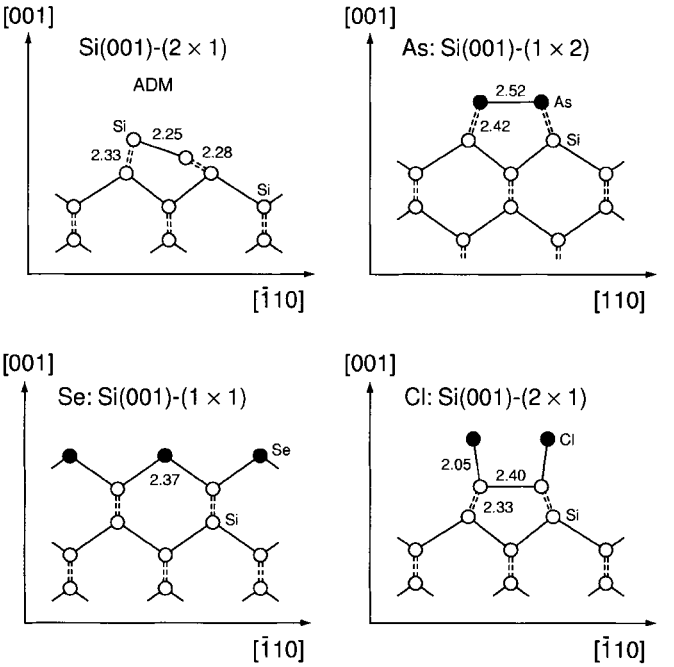


Fig. 4.5. Schematic side views of the energy-optimized configurations of Si(100) surfaces with different adsorbates. From Krüger and Pollmann (1993a).

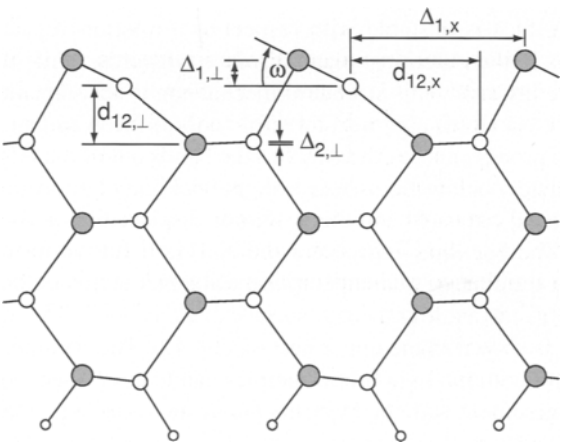


Fig. 4.6. Side view of the GaAs(110) supercell used in *ab initio* dynamical simulations by Di Felice et al. (1993). The upper face shows the optimized geometry of the clean relaxed surface. The lower face shows the optimized geometry of the surface with $\theta = 1$ ML hydrogen coverage. From Di Felice et al. (1993).

buckling (Ga moves outwards and As inwards with respect to the ideal (110) planes; see the bottom part of Fig. 4.6). This was shown in a Car–Parrinello simulation by Di Felice et al. (1993). The authors obtained the stable structure of the hydrogenated system in the full monolayer regime, with detailed microscopical information about the geometry: for example, the lengths of the Ga–H and the As–H bonds are 1.574 Å and 1.548 Å, respectively. They also performed a finite temperature dynamical simulation from which the stretching frequencies of the Ga–H and As–H bonds were extracted. The frequencies of these vibrational modes are underestimated by about 10% as compared to the energy-loss data by Lüth and Matz (1981) (a similar underestimation was previously found in a calculation performed in the same DFT-LDA scheme but in a *static* approach by Bertoni et al., 1990) and the phonon branches are almost flat along symmetry lines in the Brillouin zone. The discrepancy is partly due to the kinetic energy cutoff (12 Ryd) used in the plane-wave expansion of the electronic wave functions, which may give large errors in the description of the hydrogen potential. In the same work the authors also examined partial hydrogenation of the GaAs(110) surface, for coverage $\theta = 0.25$ ML. At this low coverage the surffface is not completely derelaxed, but the derelaxation takes place only locally where the H atoms are bonded to the substrate atoms. From a more recent unpublished work, it appears that the same local character of the derelaxation is maintained for a higher coverage of $\theta = 0.5$ ML. This manifests a very different action of hydrogen with respect to its action on the Si(111) surface, where it induces extended derelaxation at coverages as low as $\theta = 0.3$ ML (Ancilotto and Selloni, 1992).

The problem of Cl adsorption on the cleavage surfaces of III-V semiconductors was addressed several years ago by Margaritondo et al. (1979, 1981). For adsorption on a GaAs substrate, the EDC's observed in photoemission experiments were compared to the tight-binding electronic structure (local density of states at the surface layers and band dispersion). Margaritondo et al. assumed dissociative chemisorption of the $Cl_2$ molecules and examined different adsorption sites for the Cl atoms at coverage $\theta = 0.5$ ML. In particular, they considered the Cl atoms bonded to the As anions at the relaxed GaAs(110) surface, and either to the As anions or to the Ga cations at the ideal surface. The comparison was in favor of Cl–As bonding, and this outcome was interpreted as an effect of the surface relaxation and As rehybridization. The same effects were found for Cl adsorption on other relaxed cleavage surfaces such as GaSb(110) and InSb(110).

In 1985 this picture was confirmed by core-level X-ray photoemission spectroscopy by Schnell et al. (1985). More recently, these results have been questioned on the basis of a theoretical work on the electronic structure. Rincón et al. (1995) found an energy gain of 1.9 eV for the formation of the Cl–Ga bond and of 1.5 eV for the formation of the Cl–As bond. However, the simultaneous chemisorption of two Cl atoms on both Ga and As sites in the surface unit cell, gives a very large energy gain (4.5 eV). This result indicates that simultaneous adsorption on both Ga and As is largely favored. The method of calculation was based on rewriting the Hamiltonian for the interacting electrons in a linear combination of atomic orbitals (LCAO) basis, and describing the many body part in terms of an effective potential that is a function of the orbital occupancy in the spirit of the Kohn–Sham approach (see Garcia-Vidal et al., 1994). The stability of the double site adsorption configuration was confirmed through first principles calculations, both in a structural optimization study by Corkill and Chelikowsky (1996) and in a dynamical simulation by Marcellini et al. (1998).

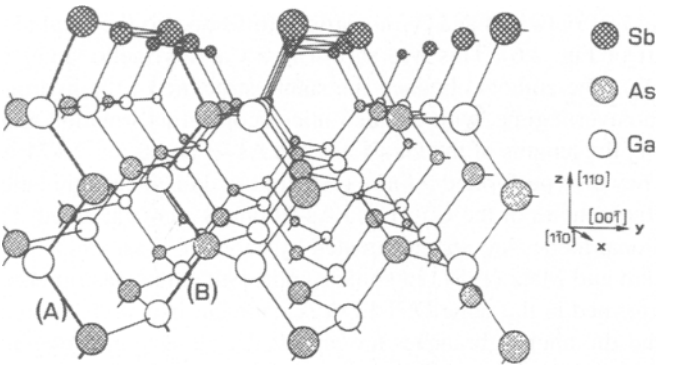


Fig. 4.7. Lateral view of the geometry of the Sb-covered GaAs(110) surface. From Bertoni et al., 1983.

On the experimental side, results from electron stimulated desorption (Troost et al., 1993) and from vibrational electron energy-loss spectroscopy (Pankratz et al., 1994) suggested the presence of both Cl–Ga and Cl–As bonds on the surface, even in the early stages of adsorption. Shuh et al. (1994) by an accurate remake of the initial experiments of valence- and core-level spectroscopy, obtained a confirmation of the strong signature of Cl–As bonding, but considered this aspect as a consequence of the etching of Ga by Cl, at the active Ga sites, occurring also at room temperature.

The formation of overlayers on compound semiconductors is a subject that attracted much interest in the past, since the beginning of surface science, especially with regard to the mechanism of the Schottky-barrier formation and to epitaxial growth. We shall limit our review to the examination of two examples: Sb and Se on GaAs(110). For the chemisorption of Sb, Duke et al. predicted in 1982, from the analysis of elastic low-energy electron diffraction data, that the Sb atoms at the monolayer completion reside in positions similar to those of the Ga and As atoms in the ideal (110) planes, forming zig-zag chains bonded to a nearly unrelaxed GaAs(110) surface. A three-dimensional view of four GaAs(110) planes with one Sb overlayer is shown in Fig. 4.7. Being the Sb–Sb bond distance larger than the Ga–As bond distance, there are distortions inducing a rearrangement of the Sb atoms in the surface chains to form angles of about 90° typical of the $p^2$ bonding. This picture was confirmed by Mailhiot et al. (1984, 1985), who calculated in the tight-binding scheme the geometrical parameters of the structure for the (110) surfaces of many different III-V semiconductor compounds. Moreover, they calculated the electronic surface-state eigenvalue spectra of the different surfaces examined using scattering-theory after Schmeits et al. (1983). They performed the electronic structure calculations separately for an isolated Sb chain, for the chain bonded to a non-polar surface, and for the chain bonded to a polar surface such as GaAs(110) or the others examined. They found essentially six features for the Sb chain. Two *non-bonding* s-derived states are not essentially affected by the substrate except for a removal of their degeneracy along $\bar{X}\bar{M}$. Two *intrachain bonding* p-*states* are also very slightly modified by adsorption on the polar substrate. Finally, two occupied bonding and two empty antibonding surface state bands, coming from p-states, largely interact with the substrate dangling bonds when the Sb chain is deposited on a

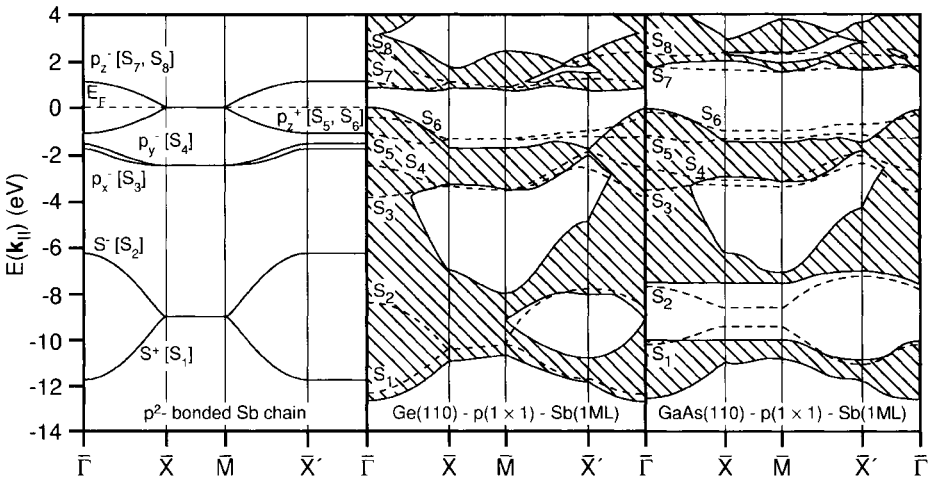


Fig. 4.8. Energy dispersions of (a) electronic states for isolated Sb chains, (b) Sb-derived surface states for Sb chains on Ge(110), (c) Sb-derived surface states for Sb chains on GaAs(110). From Mailhiot et al. (1984).

surface, forming hybrid Sb–substrate electronic states. These electronic states go into the continuum of bulk states and at their borders. These results are shown in Fig. 4.8 and they reproduce the outcome of a previous calculation by Bertoni et al. (1983) performed in a self-consistent local pseudopotential scheme. First principles calculations (Northrup, 1991; Schmidt et al., 1994) confirmed the *epitaxial continuous layered structure* for 1 ML of Sb atoms on GaAs(110).

The submonolayer coverage regime was also investigated, with the twofold purpose of understanding whether Fermi-level pinning may be induced by interface states, and of clarifying the growth mode of the overlayer. Manghi and Calandra in 1990, using a large surface unit cell, considered partial coverages with $\theta = 0.5$ ML (obtained removing one complete Sb chain every two Sb chains) and $\theta = 0.625$ ML (obtained truncating all the Sb chains). From the structural point of view, the $\theta = 0.625$ ML case gives origin to surface terraces. By calculating the electronic properties through a tight-binding Hamiltonian, they obtained that for $\theta = 0.5$ ML the system is semiconducting: the surface states penetrate into the bulk gap, but maintain an energy gap. On the contrary, for $\theta = 0.625$ ML the system resulted metallic, with a partially occupied state inside the bulk gap, localized at the Sb atoms situated at the edges of the truncated chains. This outcome is in contrast with the experiments (Feenstra and Møartensson, 1988), which predict the existence of a residual surface gap with pinning of the Fermi-level between the highest occupied and the lowest empty surface states, for a system Sb:GaAs(110) with terraces. In order to investigate the above discrepancy Magri et al. (1994) repeated the calculation for the 0.625 ML coverage with some new elements: they first performed an *ab initio* DFT-LDA calculation with pseudopotentials, reproducing the peak with metallic character. Then they considered again a simple tight-binding calculation, in order to have results on a localized basis, and finally used these localized wave functions in a Hubbard-like description of the system as exposed in the theory by Calandra and Manghi (1994). This approach is non-perturbative

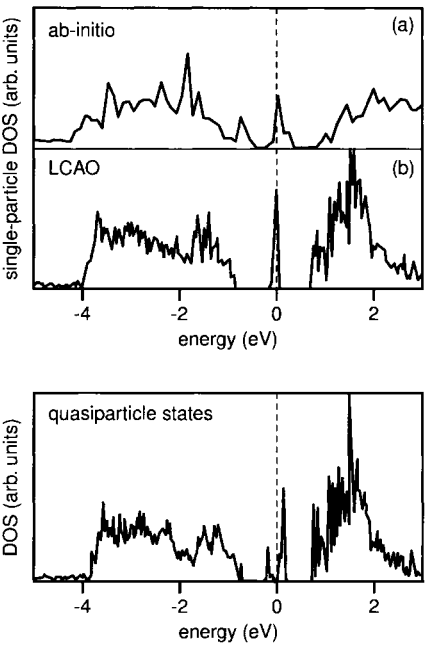


Fig. 4.9. The upper panel shows the single particle density of states of a system containing 0.625 ML of Sb atoms above the GaAs(110) surface. (a) Outcome of a first principles DFT-LDA calculation. (b) Outcome of an LCAO calculations. For the same system Sb(0.625 ML):GaAs(110), the lower panel shows the density of the quasiparticle states in the energy region around the optical gap obtained through a Hubbard-like Hamiltonian with the Coulomb parameter $U = 1.2$. The Fermi level position is indicated with a dashed line. From Magri et al. (1994).

and valid for any value of the Coulomb parameter $U$ in the Hubbard Hamiltonian. It consists of a configuration–interaction expansion of the many-body states of the interacting electrons where various configurations differ for the number of electron–hole pairs. With the inclusion of the Hubbard repulsion, the peak inside the bulk gap splits into two peaks separated by a small gap. Even if this surface gap is still underestimated with respect to the experimental data, its existence suggests the possibility that the system be a Mott–Hubbard insulator. In Fig. 4.9a, b the density of states obtained from the *ab initio* calculation and from the tight-binding Hamiltonian, respectively, are shown: the peak inside the bulk gap is clearly visible. In the lower panel of Fig. 4.9, the density of states exhibits the splitting of this peak, following the introduction of the Hubbard repulsion.

Schmidt et al. (1994) considered the partial coverage of antimony on the GaAs(110) surface, with first principles calculations for the optimization of the structure. They limited themselves to the coverage $\theta = 0.5$ ML, after considering also different selected geometries for $\theta = 1$ ML. They calculated the total energy of the system for many different positions of a single Sb atom on the elementary two-dimensional (2D) cell of the GaAs(110) surface. The outcome is a total energy surface which exhibits a sort of channel in the direction of the GaAs zig-zag chains, along which there are two minima separated by a very small energy barrier. In the direction perpendicular to the substrate chains the energy bar-

rier is much larger, inhibiting diffusion of antimony. In summary, Sb at the $\theta = 0.5$ ML coverage shows a tendency to clusterize, forming islands particularly developed in the $[\bar{1}10]$ direction. This result is in agreement with the STM measurements from Feenstra and Møartensson (1988).

Schmidt and Bechstedt (1994) performed a similar calculation of the total energy surface for Se on GaAs(110), considering a single Se atom on a GaAs(110)-$(2 \times 1)$ cell, with coverage $\theta = 0.25$ ML. They found two equivalent adsorption sites in interchain bridging positions, in which the Se atom sits at almost the same distance from the Ga and the As atoms. Differently from the case of Sb deposition, the energy barriers between two adsorption positions are almost equal in the directions parallel and perpendicular to the zig-zag chains, so that the movement of Se atoms at low temperature is prevented, and consequently an ordered structure at low coverages is not likely to be formed. In the 1 ML coverage case, the Se atoms seem to choose a geometry classified as *epitaxial on top structure*, forming chains just above the GaAs chains.

## 4.6. Alkali metals on semiconductors

In the field of metal/semiconductor systems, the adsorption of alkali metals on semiconductors (Si and GaAs) received particular attention. The adsorption takes place with no drastic change of the substrate geometry. The adsorption site is a symmetric site inside the surface cell.

These systems are of interest not only as relatively simple examples useful to understand the formation of metal–semiconductor interfaces, but also because of the strong reduction of the work function that is induced by alkali adsorption (i.e., oxidized alkali–GaAs systems have a negative electron affinity). Furthermore, the changes in the electronic structure following alkali chemisorption at different coverages, and the transfer of electrons into the empty surface band of the substrate to give a partially filled surface band, represent a possible surface example of Mott–Hubbard insulator.

It is evident from diffraction experiments that K and Na adsorption up to $\theta = 0.5$ ML or $\theta = 1$ ML coverages preserves the $(2 \times 1)$ periodicity of the Si(100) surface, and the existence of dimers in the top layer. Four possible adsorption sites (see Fig. 4.10a) must be considered: (i) the *bridge* position above the dimer $b$; (ii) the *pedestal* site $p$ above the third-plane Si atoms, which is a hollow site between two neighboring dimers along the dimer rows; (iii) the *valley-bridge* site $v$ above the third-plane Si atoms between the dimer rows; (iv) the *cave* site $c$ above the fourth-plane Si atoms between the dimer rows. First principles calculations performed with different methods have determined the electronic structure, the total energy and the atomic forces, as a function of the normal coordinate. Different alkali coverages were considered on relaxed or unrelaxed substrates. The different adsorption geometries are local minima of the total energy surface, and there is no agreement about the ground state for different adsorbates.

Levine suggested (1973) that the *pedestal* site was the most stable adsorption site for Cs on Si(100). Ishida et al. (1985), in the LCAO-$X\alpha$ scheme, calculated the surface bands for K adsorbed on the $p$ and the $b$ sites on a Si(100)-$(2 \times 1)$ surface with symmetric dimers. They obtained in both cases three bands inside the gap, resulting from the mixing

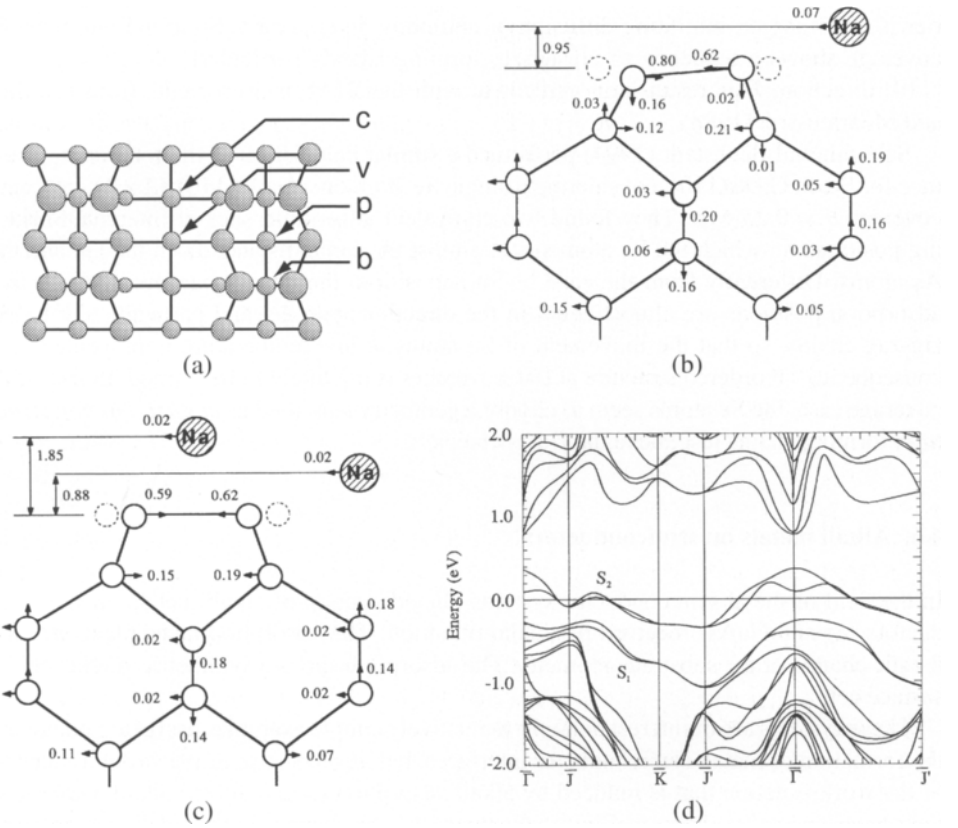


Fig. 4.10. (a) Top view of the Si(100)-2 × 1 surface showing the dimers on the outermost plane, as well as the positions of the atoms on the second, third, and fourth planes. The different alkali atom adsorption sites are indicated. (b) Side view of the geometry found by Kobayashi et al. (1992) for $\theta = 0.5$ Na coverage, with the Na atom at the $v$ adsorption site. (c) Side view of the geometry found by Kobayashi et al. (1992) for $\theta = 1$ Na coverage, with Na atoms at the $p$ and $v$ adsorption sites. (d) Band structure, including surface bands in the gap, obtained for the geometry of panel (b) ($E_F = 0$). From Kobayashi et al. (1992).

between the $\pi$, $\pi^*$ orbitals of the Si–Si dimers, and the orbitals of the adsorbate atoms. The motivation of that work was to discuss the plasmon dispersion relation in this surface system and the electronic structure calculation was just a step to this goal.

More recently, the literature about alkali adsorbates on semiconductor surfaces has reported DFT-LDA total-energy-and-force calculations, which included full optimization of different adsorption geometries and the simultaneous evaluation of the self-consistent electronic surface band structure. Among these works, Ling et al. (1989) performed calculations for clusters of different size to study a variety of adsorption geometries for K on Si(100)-(2 × 1). They used an approach based on a discrete variational method (Delley, 1990). The most stable structure turned out to be the $c$ site, with a K–Si distance of 3.22 Å between the adsorbed K atoms and the Si atoms of the surface dimers. A phase with each K atom at the $c$ sites forming chains, with very small zig-zag Peierls-like distortion to create

a surface band gap, was the suggested surface structure at the coverage of 1 K atom per Si dimer ($\theta = 0.5$ ML).

A further work by Spiess et al. (1993) using the same method, but with no constraints for substrate reconstruction, investigated the adsorption of Na confirming also for this adsorbate species the $c$ site as the preferred adsorption site. The energy difference between the stable adsorption geometry and the $c$ and $p$ adsorption geometries was 0.17 eV and 0.30 eV, respectively. For the Na atoms sitting at the $c$ and $p$ sites, the shortest Na–Si bond distance occurs for bonds between the adatoms and Si atoms of the outermost layer. For Na atoms sitting at the $v$ sites, the nearest Si atoms are found in the second layer. The structure obtained for the minimum energy configuration appeared consistent with the EXAFS results.

Batra (1991) approached the problem with the pseudopotential method and self-consistent DFT-LDA band calculation for a $(2 \times 1)$ supercell, exploring different geometries and optimizing the sub-layer geometry of two atomic planes for each choice. At $\theta = 0.5$ ML the most stable structure was found for adsorption at the $p$ site. The $c$ site resulted almost degenerate, while the $v$ site was energetically unfavored. For $\theta = 1$ ML (two atoms per Si-dimer) the $p$–$c$ and $p$–$v$ configurations were found to have the same formation energy. The surface resulted metallic (with a half-filled surface band) at $\theta = 0.5$ ML and semiconducting at $\theta = 1$ ML.

Other pseudopotential calculations (Terakura et al., 1992) presented a different outcome for the intermediate coverage. A preferential adsorption at the $v$ site for both Na and K, with a substantial increase of the dimer length, was found for $\theta = 0.5$ ML. The most stable structure for $\theta = 1$ ML was confirmed to be the $p$–$v$ combined adsorption geometry. Upon Na adsorption, the Si–Si dimer bond length increased from 2.26 Å to 2.42 Å and to 2.63 Å for $\theta = 0.5$ ML and $\theta = 1$ ML, respectively. The distance between Na at the $v$ site and first-layer Si atoms was 3.28 Å for both coverages examined. The distance between Na at the $v$ site and second-layer Si atoms was 3.10 Å and 3.06 Å for $\theta = 0.5$ ML and $\theta = 1$ ML, respectively. The distance between Na at $p$ site and first-layer Si atoms was 2.97 for $\theta = 1$ ML (see Fig. 4.10b, c). A number of other coverages were investigated with the use of a large $(2 \times 3)$ surface cell.

Despite the controversy about the relative stability of the different adsorption sites, the common feature resulting from all the mentioned self-consistent calculations is a considerable transfer of electron charge from the alkaline atoms towards the Si-dimers. We can summarize the electronic properties of the system in the presence of a band inside the gap ($S_2$), arising from the $\pi^*$ empty band of the clean Si surface, slightly modified by the presence of the adsorbed atoms. By increasing the amount of K coverage, there is a change in the orbital composition of this band but no new surface state appears in the same region of the gap. The alkali-derived band ($S_3$) remains higher in energy, inside the conduction band or in any case well separated from $S_2$. The Si-dimer $S_1$ band, mainly with $\pi^*$ orbital character, is shifted downwards to overlap the bulk valence band. The filling of the $S_2$ band increases up to completion for $\theta = 1$ ML.

Since the first steps of surface physics, there has been a huge interest in the interface between GaAs(110), the prototype of ionic semiconductor surfaces, and alkali metals (Na, K, Rb, Cs). There is no mixing and no reaction at the interface, and the structure of the substrate is preserved, with possible modifications to the relaxation of the clean surface

in the first layers. This non-destructive chemisorption process takes place even in the case of Cs, where the large size of the adsorbed atoms causes a superstructure of the adsorbed layer. Assuming a density of atom per layer equal to that of the (110) plane of the bcc structure, Cs can have a maximum coverage $\theta = 0.44$ ML, while for Na higher coverages up to $\theta = 1$ ML are allowed ($\theta = 1$ ML means two atoms of adsorbate for each molecular unit of GaAs).

In the case of Cs, Van Bommel and Crombeen (1979) observed a $c(4 \times 4)$ superstructure that can be interpreted as a $\theta = 9/16$ ML coverage obtained by a compressed (110) plane of Cs on top of the ideal geometry of the substrate. A $(3 \times 3)$ unit cell of Cs(110) was supposed to match a $(4 \times 4)$ cell of GaAs(110), not assuming any preferential site for adsorption.

The electronic structure of such a system has been described with a DFT self-consistent calculation within a model. The calculation assumed the discrete structure of the substrate through a pseudopotential calculation with a $(1 \times 1)$ surface cell and a jellium slab of the appropriate density on top of it below the vacuum region (Manghi et al., 1984). Despite the approximation, some peculiar features of the system were described in a satisfactory way. These are: (i) the existence of a partially filled band in the gap, resulting from the mixing between the 2D free electron bands of the overlayer and the Ga-like dangling bonds; (ii) the persistence of the surface core exciton evident in the loss-spectra; (iii) the pinning of the Fermi level and the reduction of the work function.

Some years later accurate total energy calculations have been applied to the case of Na on GaAs(110). Within the repeated supercell approach, with a $(1 \times 1)$ surface cell and without allowing for atomic relaxation of the substrate, Fong et al. (1989) studied the most stable adsorption geometries for $\theta = 0.5$ ML and $\theta = 1$ ML. We will recall here the results of a more recent and accurate work (Hebenstreit et al., 1991), which included full atomic relaxation for the substrate. In Fig. 4.11a the preferred adsorption sites in the surface unit cell are schematically indicated. In Fig. 4.11b a map of the energy surface as a function of the planar coordinates of a single adsorbate (Na with $\theta = 0.5$ ML) is reported. The total energy values across the surface are determined at each $(x, y)$ site, looking at the minimum value as a function of $z$. The energy surface in Fig. 4.11b exhibits a deep channel, rather flat at its bottom, parallel to the surface zig-zag atomic chains. The adsorption energy at the two sites differs by only 0.05 eV, but they are separated by a barrier of 0.20 eV along the bottom of the channel. At $\theta = 0.5$ ML with the Na atom at site 1 (Fig. 4.11a), the distance Na–Ga is 3.44 Å and the buckling of the first GaAs layer is reduced from 0.63 Å to 0.17 Å. This effect, together with the interaction between the Ga-localized dangling bond and the conduction states of Na, shifts the energy of the surface band (empty in the case of the clean surface) towards lower energy inside the gap. This band is consequently half-filled and is considerably flat, due the strong localization at the Ga site of the surface electron states at $\theta =$ 0.5 ML, with no overlap between neighboring sites. It has been pointed out that the character of this surface band is mainly determined by the dangling bond of Ga, not much affected by the interaction of the adsorbate, and the occupancy of this flat band is due to the electron transfer for the alkali metal, that contributes also to a slight shift of the band towards low energy inside the gap. The localized nature of this band together with the experimental indications of non metallic nature of this systems (GaAs(110)+alkali) by STM experiments (Whitman et al., 1991), suggested to Pankratov and Scheffler (1993) to reinterpret

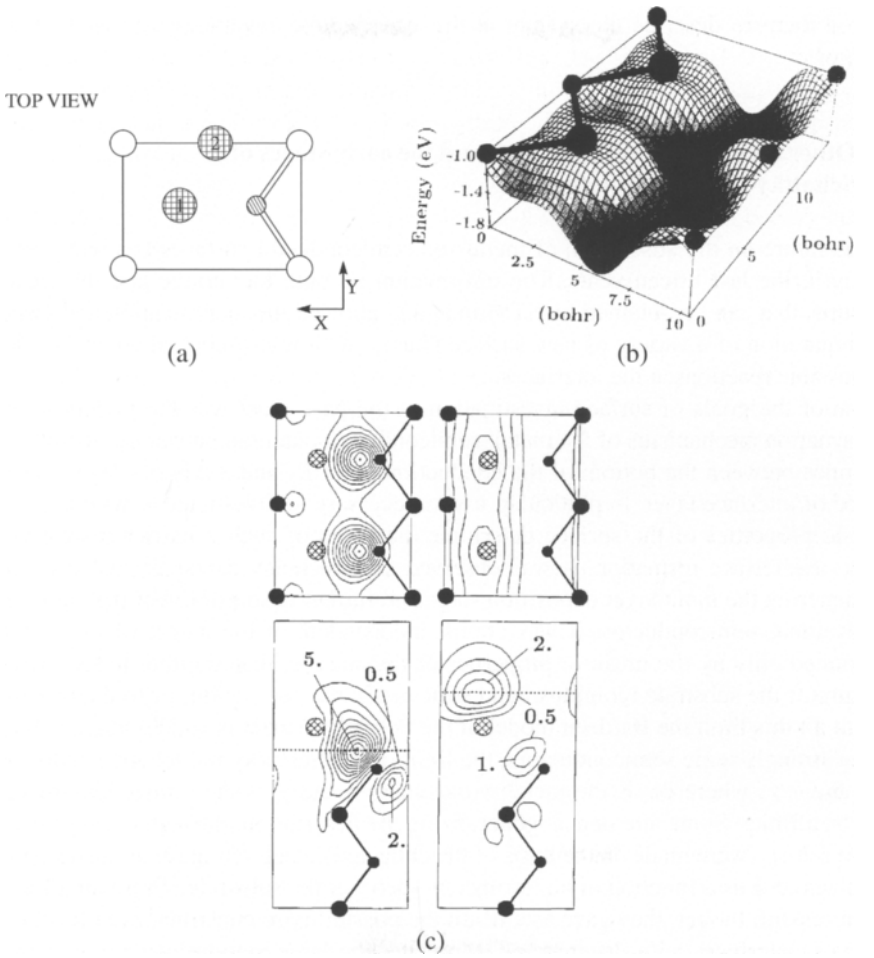


Fig. 4.11. (a) Top view of the GaAs(110) unit cell. Open circles indicate As atoms, hatched circles indicate Ga atoms, the crossed-hatched circles indicates the favored adsorption site for Ga. (b) Total energy surface of Na:GaAs(110) with coverage $\theta = 0.5$ ML. (c) Squared wave functions, at the $\bar{X}'$ point of the 2DBZ, of the surface state of the partially occupied band (left) and of the first occupied band (right). The upper plots are cross sections at the dotted lines indicated in the lower side views. From Hebenstreit et al. (1991).

the outcome of the DFT-LDA calculation of the surface electronic structure in terms of a Mott–Hubbard system. They described the dangling bond band by an effective Hamiltonian

$$H = \sum_{i \neq j} t_{ij} c_i^{\dagger} c_j + \frac{1}{2} U \sum_i n_i^2 + \sum_i \Delta_i n_i,$$

where $c_i$ ($c_i^{\dagger}$) is the destruction (creation) operator for state $i$, and $n_i = c_i^{\dagger} c_i$ is the number operator. The low values of $t_{ij} \leqslant 0.5$ eV compared to $U = 0.56$ eV and $\Delta = -0.21$ eV

allowed them to describe the system at the intermediate coverages as a Mott–Hubbard insulator.

### 4.7. Other metals on semiconductors and the early stages of Schottky-barrier formation

The literature on the adsorption of metals on semiconductor surfaces has widened enormously in the last fifteen years. The information on both the atomic and the electronic structures that can be obtained by STM imaging, allowed the identification and improved the preparation of a variety of new surface phases, with microscopical control of defects and possible reactions at the interfaces.

One of the goals of surface investigation in the past years was the understanding of the formation mechanisms of the metal–semiconductor potential barrier $\phi_b$, defined as the difference between the bottom of the conduction band $E_c$ and the Fermi level $E_F$, at the surface or interface layer. In particular, it was necessary to investigate to which extent the intrinsic properties of the surface determine the value of such a barrier since the early stages of interface formation. It was observed that, in many cases, the value of $\phi_b$ did not vary from the monolayer deposition stage and further adsorption. For the covalent and weakly ionic semiconductors it was almost independent of the nature of the metal and determined only by the intrinsic properties of the surface, linked either to the electronic structure of the substrate (complex band structure in the gap region) or to the presence of defects. In this limit the Bardeen model of the Schottky barrier is valid. On the other side, for the strongly ionic semiconductors, the limit of the Schottky model appeared to work: $\phi_b = \phi_m - \chi$, where $\phi_m$ is the metal work function and $\chi$ is the semiconductor surface electron affinity. Some attempts at generalizing the description, through a law of the form $\Delta\phi_b = S\Delta\phi_m$, were made on the basis of the collected data, looking for a rule determining the values of $S$ as a function of an intrinsic property of the substrate. These attempts were not successful. In fact, they gave as a result the possibility to construct, even for the same materials, interfaces with different $\phi_b$. Moreover the large amount of data have lost the evidence of the existence of systematic trends, emphasizing the role of the microscopic structure of each interface.

Among the metal/semiconductor systems, we consider here overlayers of Ag, Au and Pb on Si(111) and Ge(111), and overlayers of Al on GaAs(110). For the former class, a clear review has been recently given by Le Lay et al. (1994), and many theoretical calculations were performed.

The stable structures of Si and Ge (111) surfaces ($(7 \times 7)$ and $(2 \times 8)$ respectively), upon Ag and Au adsorption, evolve as a function of coverage and temperature towards different phases. A number of them have $(\sqrt{3} \times \sqrt{3})$-R30° periodicity.

Figure 4.12 shows the most realistic model for Ag:Si(111)-$(\sqrt{3} \times \sqrt{3})$-R30°, the honeycomb-chained triangle (HCT) model. It is obtained by removal of the top plane of Si atoms in the usual termination and addition of a metal overlayer. The Si atoms which remain exposed to the metal have three dangling bond each (instead of one dangling bond per surface atom for the usual termination). The formation of Si trimers reduces the high number of dangling bonds per surface atom from three to one. The residual dangling bonds

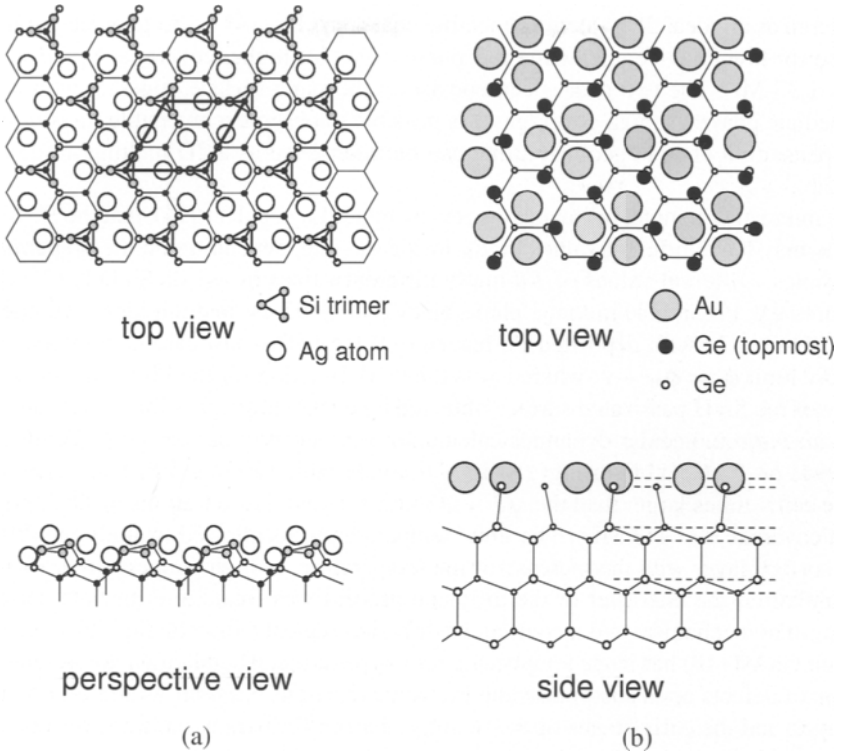


Fig. 4.12. (a) HCT model for the Ag:Si(111)-($\sqrt{3} \times \sqrt{3}$) structure. (b) Trimer model for the Au:Ge(111)-($\sqrt{3} \times \sqrt{3}$) structure. From Le Lay et al. (1994).

are used to form bonds with the deposited metal atoms. Although it requires the creation of a *missing top layer* configuration, this structure is rather stable. Total-energy calculations support the HCT model (Ding et al., 1991; Kirchner et al., 1994). The electronic structure exhibits an energy gap, due to bond saturation, and the calculated images of the tunnelling current, for the states just below and above the gap, are in agreement with the STM results at the appropriate values of the bias voltages.

The other structure indicated in Fig. 4.12 describes one of the phases of Au:Si(111)-($\sqrt{3} \times \sqrt{3}$)-R30°, as well as Ag and Au on Ge(111). Here the last plane of Si or Ge atoms is in the unusual *missing top layer* configuration, but Si or Ge atoms do not form trimers. The trimers are formed by the noble metal atoms that have a nearest neighbor distance shorter than in the previously considered geometry. The relevant difference between this geometry and the previous one is confirmed in the differences between their surface core level shifts. For Au on Si one finds a metallic behavior, like in the clean Si(111)-(7 × 7). The pinning of the Fermi level at 0.33 eV is due to the presence of a partially filled band, rather flat, in the lower part of the gap.

Pb on Si(111) and Ge(111) gives origin to a ($\sqrt{3} \times \sqrt{3}$) structure, with different phases at different coverages. Pb has no tendency to diffuse inside the substrate, hence it can be

considered as an ideal 2D system of metallic character. The $\sqrt{3} \times \sqrt{3}$ geometry can be an $\alpha$ phase for low Pb coverage, while a $\beta$ phase exists for higher coverage, e.g., $\theta = 1$ ML or $\theta = 1.33$ ML. The two phases can coexist on the same surface, together with a $4 \times 4$ intermediate phase. At high coverages it is possible to observe a reversible transition from the $\beta$ phase to a $(1 \times 1)$ geometry, that can be interpreted as a 2D melting around 200–300 °C.

It is interesting to note, following the review by Le Lay et al. (1994), that the Pb:Si(111) systems may have different values of $E_F$ inside the gap, depending on the preparation of the samples. Different values of $E_F$ imply different values of $\phi_b$. Pb:Si(111)-$(7 \times 7)$ has $\phi_b = 0.70$ eV, Pb:Si(111) in the $\beta$ phase gives $\phi_b = 0.93$ eV and the ideal hydrogenated H:Si(111)-$(1 \times 1)$ with deposited Pb has $\phi_b = 0.1$ eV. This last case corresponds to the Schottky limit $\phi_b = \phi_m - \chi$, where $\phi_m$ is the work function for the Pb metal and $\chi$ is the affinity of the Si–H passivated surface obtained by chemical preparation.

An *ab initio* molecular dynamics calculation was recently performed by Ancillotto et al. (1994) on Pb:Ge(111), using a slab of 6 layers with 12 Ge atoms per plane, with a surface cell 4 times larger than the $\sqrt{3} \times \sqrt{3}$ unit cell and with 16 atoms of Pb on top of it (dense coverage $\theta = 4/3$ ML). The finite temperature runs allowed to study the diffusion at the surface layer with the increase of the temperature: at high temperature ($\sim$800 K in the simulation) the character of the diffusion process was found intermediate between a jumping-like mechanism and a continuous diffusion typical of the 2D liquid.

Al on GaAs(110) has since long been a prototype of metal/semiconductor systems. The creation of defects upon adsorption, the exchange reactions between Al and Ga on the surface layer, and the early stages of the Schottky barrier formation, have been investigated. More recently, after the discovery of a new way of creating an abrupt, defect free, interface, Yi and Bernholc (1992) simulated successfully with *ab initio* molecular dynamics the atomic and cluster deposition of Al on GaAs(110).

The above examples are a small subset of the progress in the field of metal adsorption on semiconductor surfaces to create metal/semiconductor interfaces. This issue will be addressed more extensively elsewhere in this book. Our key concern in this section was to show how the structural properties and the dynamical processes can be treated at the same time of the electronic structure analysis to study the initial formation of the interfaces and their growth. The systematic application of *ab initio* molecular dynamics is particularly effective in this field of applications.

## 4.8. A simple picture for surface bands and structure: the electron or hole counting-rule

*The model.* The electron counting model (ECM) (Pashley, 1989) is a simple rule proposed to explain the reconstruction of some polar semiconductor surfaces and their tendency, during growth, to form islands elongated in preferred directions over the surface. It has been successfully applied to reconstructed surfaces with or without adsorbates.

The idea is to require that the surface is semiconducting by filling the dangling bonds of the more electronegative atoms and leaving empty those of the less electronegative atoms. For a tetrahedrally coordinated atom the number of electrons that we can use to fill the

dangling bonds is calculated assuming that it contributes to each bond with $Z_v/4$ electrons, $Z_v$ being the valence of the atom. If we have dimers on the surface we assume that the dimer bond receives one electron from each of the two atoms. Then we have to match the number of electrons not involved in the bonding with the underneath layer and the number of bonds that we have to fill.

There are cases where this rule is immediately fulfilled and there is no need for a reconstruction. This is the case for the (110) surface of III-V semiconductors. In the $(1 \times 1)$ surface unit cell of GaAs(110) we have a Ga atom providing $\frac{3}{4}$ of an electron and an As atom providing $\frac{5}{4}$ of an electron: the resulting two electrons fill completely the As dangling bond, leaving the Ga dangling bond empty, and thus we have a nonpolar, semiconducting surface. This configuration is responsible for the buckling relaxation.

However, for other III-V surfaces the $(1 \times 1)$ surface is not stable. For instance, the As-terminated GaAs(001)-$(2 \times 4)$ (Pashley et al., 1988; Pashley, 1988) surface has a unit cell containing three As dimers, the fourth lacking. As originally explained by Pashley, the dimer vacancy allows to fulfil the ECM. Each dimer bond hosts two of the five electrons provided by the two As ($\frac{5}{4} \times 2$ each As) leaving only $\frac{3}{2}$ electrons for each dangling bond. So we need one electron for each dimer; a dimer vacancy leaves 4 Ga atoms with a broken bond, providing $\frac{3}{4} \times 4 = 3$ electrons: then for three dimers we need one dimer vacancy to saturate the dangling bonds, giving the $(2 \times 4)$ reconstruction.

In a similar way it is possible to explain the $(2 \times 2)$ reconstruction of the GaAs(111) surface (Chadi, 1984a; Haberern and Pashley, 1990), where a gallium vacancy every three Ga atoms is needed to saturate the dangling bonds.

It must be pointed out that the simple ECM recipe, in spite of its valuable heuristic power, does not give unique solutions to the problem of surface reconstruction.

Nevertheless, the success in explaining these and other surface reconstructions (see Chadi, 1991) has suggested to use the ECM either in predicting new possible reconstructions (and then achieve quantitative information by means of first principles calculations) or in the interpretation of images obtained by STM or other experimental information about surfaces, involving vacancies, periodicity faults, islands growth, and adsorbed atoms, and their role in the stabilisation of surfaces.

*Passivation of (100) surfaces of III-V semiconductors.* A natural application of the ECM seems to be the passivation of a surface, since the requirement of a nonpolar, semiconducting character well applies to non-reactive surfaces. It frequently happens that the adsorption of atoms of a different species on a surface causes dereconstruction or at least allows smaller unit cells than for the clean surface. This can be explained, in certain cases, simply by bond filling arguments like those of the electron counting model.

The case of GaAs(100)-$(2 \times 4)$ was studied by Miyamoto and Nonoyama (1992), and by Nonoyama et al. (1993), for coverages of 0.5 ML and 1 ML of hydrogen. Their first principles calculations yield positive heat of formation for two $(2 \times 2)$ and one $(2 \times 1)$ surface unit cells with 0.5 ML coverage. These three reconstructions, that came out from a global minimization procedure, are all consistent with the counting rule, because the two H atoms are bonded to As. Thus, 5 electrons are provided by each As dimer – two electrons fill the dimer bond and two others go in each of the two As–H bonds, leaving one electron to fill completely the couple of dangling bonds of a nearby As dimer. In such a configuration the periodicity is reduced from $(2 \times 4)$ to $(2 \times 2)$; it can be reduced to $(2 \times 1)$

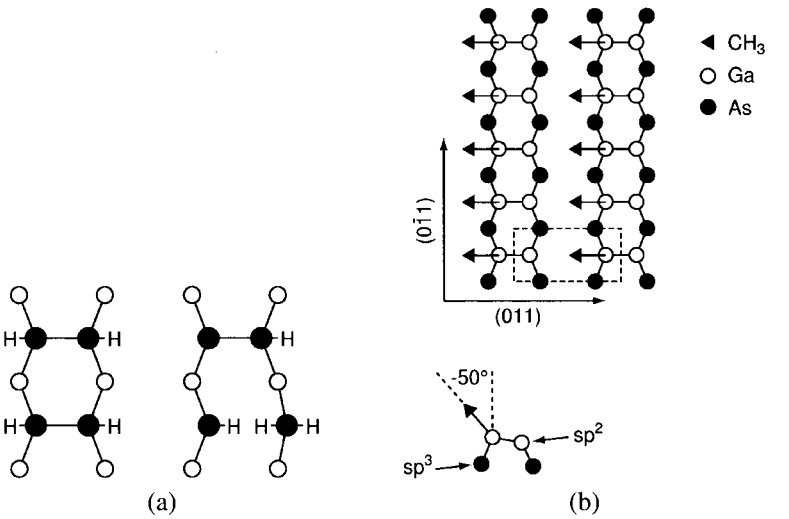


Fig. 4.13. (a) Two configurations for H on As-terminated GaAs(100) surface: the structure on the left is metallic, that on the right (which is energetically favored) fulfils the electron counting rule and is semiconducting. From Nonoyama et al. (1993). (b) Proposed structure for the Ga-terminated (100) surface of GaAs with $\frac{1}{2}$ ML of methyl groups. From Creighton (1994).

if each dimer has only one As–H bond (then H provides the electron that was lacking in each As dimer (2 × 1) unit of the clean surface).

Even more striking is the comparison of two unit cells in the monolayer regime; in Fig. 4.13a two possible bonding configurations for H in a (2 × 2) unit cell are shown. Only the second of the two configurations fulfils the requirements of the ECM, while the first has one excess electron for each As dimer with two As–H bonds. Although this arrangement has fewer dangling bonds, it is less stable both than both the other arrangement and the clean surface. Nonoyama and coworkers also found a stable 1.5 ML arrangement in agreement with the ECM.

In the framework of the ECM they also proposed a justification for the buckling of As dimers in some of the proposed reconstructions. In fact they claim that electrons in a dangling bond gain energy if they occupy an s-type orbital. This is possible if the backbond of the atom bearing the dangling bond leaves the s-orbital empty, that is if this bond is closer to a $\pi$ bond; this is achieved the closer the angle is to 90°. If then the energy loss for bond bending is less than the energy gain by the dangling bond electrons, some buckling is found.

A passivating mechanism similar to the previous one has been recently proposed by Creighton (1994) for the Ga-rich GaAs(100) surface, using methyl groups instead of hydrogen. Moreover, the adsorption of $\frac{1}{2}$ ML of $CH_3$ on the surface allows to stabilize the surface with a complete ML of dimerized gallium atoms. In fact, a (1 × 2) LEED pattern is observed, which is easily explained by the structure shown in Fig. 4.13b, where the ECM works perfectly. Each dimerized Ga atom has $\frac{1}{2}$ electron in its dangling bond: $CH_3$ binding to the substrate involves this electron, and leaves the Ga dangling bond empty.

The passivation of the (100) surfaces of III-V semiconductors can be also achieved by exposing them to group VI elements like S or Se. Instead of getting the lacking electron from H, we can substitute an As in the dimer with a group VI element and we still have a $(2 \times 1)$ unit cell where the electron counting gives no excess electrons. An empirical tight binding calculation (see Ren and Chang, 1990) has been done for this geometry, but no total energy comparison with the other calculated structures is made.

More recently, some measurements on the InP(001) surface (Gallet and Hollinger, 1993) have found a $(2 \times 1)$ reconstruction, but it seems that S–S dimers are formed, thus requiring an equal number of P–P dimers to rule out any charge imbalance; it is not clear how this could produce a $(2 \times 1)$ reconstruction.

The case of Se-passivated GaAs(001) surface is similar. STM measurements (Li and Pashley, 1994) give evidence of Se dimers, but unfortunately a $2 \times 1$ reconstruction with Se dimers that fulfils the ECM does not exist. The only possibility is a less strict fulfilment of the ECM, e.g., domains of the surface with only Se dimers alternated with domains with only As dimers.

*Other cases, the role of vacancies, periodicity faults.* There are many cases, other than III-V(100) surfaces, where some of the states appearing during adsorption on surfaces can be analysed in terms of the ECM. In this paragraph we will review some of them, pointing out where the ECM works and where it does not.

To continue with selenium on GaAs, we consider deposition on the GaAs(110) surface. First principles calculations in different coverage regimes ($\theta = \frac{1}{4}$ ML, $\frac{1}{2}$ ML, 1 ML) have been recently performed. A $2 \times 1$ reconstruction is stable for $\theta = \frac{1}{4}$ ML, and different $1 \times 1$ structures are stable for higher coverages (see Schmidt and Bechstedt, 1994). Although all the unit cells used were in agreement with the ECM, only the $2 \times 1$ structure with $\theta = \frac{1}{4}$ ML was found to be semiconducting, as predicted by Pashley's rule. This is in contrast with the experimental finding of a nonmetallic character of the surface with 1–2 ML of chemisorbed selenium.

Another study case, in which the ECM is only partly fulfilled, concerns the growth of Ge on GaAs(110). After several ML's of Ge are grown on GaAs(110), As atoms are found to form zig-zag chains (see Yang et al., 1992) and dotted chains (sequence of As dimers separated by a vacancy). The zig-zag chains are perfectly explained by the ECM as the As atoms in a chain provide one electron for each of the two chain bonds and another for the Ge backbond, leaving two electrons to fill the dangling bond. Also the dotted chains, that have been interpreted as aligned As dimer rows, are consistent with the ECM with a $1 \times 2$ unit cell. However, the proposed $3 \times 2$ unit cell is not consistent with the ECM.

The previous case is an example where the electron counting rule gives insights into features developed on surfaces during growth or adsorption, which are not necessarily complete reconstructions, but domains or islands where the rule is satisfied. Another case similar to these is worth mentioning, despite it is not really an adsorption process: we are speaking about the effect of Si-doping of the substrate on GaAs(001)-$(2 \times 4)$ surface. It has been observed by Pashley and Haberern (1991) that periodicity faults in the $(2 \times 4)$ reconstruction show up as shifts in the dimer chains (a dimer vacancy row bends, forming a kink). The density of these kinks in the surface grows linearly with the doping level, and this can be explained in terms of kinks acting as electron traps (in fact here the ECM is no longer satisfied).

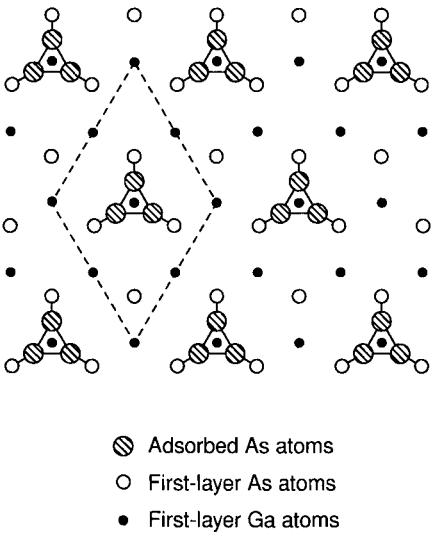


Fig. 4.14. Arsenic trimer model of GaAs(111)B-(2 × 2). The same structure had already been proposed for Sb on InSb(111). From Fu et al. (1994).

As the role of vacancies on the GaAs(111)-(2 × 2) surface has been explained by the ECM (Chadi, 1991; Haberern and Pashley, 1990), also the adsorption of atoms of the same type as those of the substrate can be explained by similar arguments, for the same surface. In Fig. 4.14 the As-trimer model proposed (see Biegelsen et al., 1990) for both adsorption of Sb on InSb(111)-(2 × 2) (Nakada and Osaka, 1991) and of As on GaAs(111)-(2 × 2) (Fu et al., 1994) is shown. It is easily verified that the electrons provided by the three adsorbed As atoms and by the four As atoms from the first layer are 20, exactly those needed to fill 3 As–As bonds, 3 trimer bonds, and 4 As dangling bonds (3 of the trimer and one of the remaining first layer As, not bonded to the trimer). As explained by Fu and coworkers, faults in periodicity (leading to neighboring trimer domains) act as donor or acceptor sites, as for kinks on Si-doped GaAs, providing a mechanism for Fermi level pinning by introducing levels in the surface gap.

It seems that the ECM does its best when it gives local informations about the neutrality of small structures that are joined to form bigger structures like the chains of the previous case or as the islands whose stability was explained in the original paper by Pashley (1989). The rule is not general, but even in those cases where it is not fulfilled, the explanation of why this happens gives insights in the structural and electronic properties of surfaces with adsorbed atoms. It does not avoid the need of structural minimization calculations, but it can offer guidelines or checks which are useful also in dealing with complex geometries.

## 4.9. Core level spectroscopy and adsorbates

The study of surface core-level shifts is a relevant tool to study surfaces and adsorbates. The power of this technique was enhanced by the increasing resolution in the energy of

the photoemitted electrons and of the incoming photons, and by the use of different photon energies to increase surface sensitivity.

The comparison with the theory, to interpret the outcomes of the measurements, requires more and more accuracy in the description of the surface core level shifts. The situation is generally more complex than that provided by the naïve interpretation in terms of *chemical shifts*. These shifts are easily interpreted for the case of a single adsorbate species which can sit on a surface in different oxidation states. An interesting example is the experimental study of the oxidation at heavy doses of $O_2$ of the Si(100) As-passivated surface (Rochet et al., 1995). From an accurate analysis of the Si $2p_{3/2}$ peak, it was possible to recognize multiple contributions. The different terms are: (i) the bulk contribution; (ii) the low-energy shift due to the sublayer Si atoms bonded to the dimers of the passivating As atoms; (iii) and the four terms due to Si atoms in different oxidation states localized in the surface regions where O atoms succeeded to overcome the passivating As layer. Different components are evident also in the As 3d peak. The highest-energy contribution comes from the residual dimers on the surface regions which remain efficiently passivated. There is a contribution from metallic As (probably small islands or clusters) with a a shift of $-0.4$ eV, and also the contributions from three different oxidation states (I, II, III) for the reacted part of the overlayer.

The above example is a clear case where the interpretation of the experiment is unambiguous. However, the quantitative understanding of the shifts and the interpretation of their sign may be a difficult task especially when the shifts are small and do not involve strong charge transfers. A meaningful case is the $c(4 \times 2)$ Si(100) structure, the phase observable at low temperature in the family of the "$(2 \times 1)$"-like reconstructions of Si(100). Landemark et al. (1992, 1993) were able to identify four different shifts with respect to the bulk values: the shifts at $+0.49$ eV and at $-0.06$ eV were attributed, respectively, to the upward and to the downward atoms in the surface Si dimers, the $-0.22$ eV shift was attributed to the Si atoms of the second layer, and there was an additional weak component at $+0.20$ eV. For the sign convention, the energy is referred to the kinetic energies of the outcoming electrons, and consequently to the binding energies. Similar results are obtained for the Ge(100) surface, where the contribution of the second layer is shifted upwards by 0.19 eV. Pehlke and Scheffler (1993) interpreted the results in terms of the corrections due to final state effects: the relaxation originated by the screening of the core hole must be added to the energy of the hole in the frozen configuration of other electrons. This correction can be different according to the different sites where the hole is created and in this case it is larger at the surface than in the bulk. This takes into account the particular electronic structure of the surface where the filled band is associated to the upward surface atoms and the empty band to the downward surface atoms. The hole localized on the downward atoms has the stronger screening effect.

In general, one could not expect that this variation in relaxation energy $\Delta E_c$ from site to site and the calculation of the shifts of the core single-particle level can take into account only the changes of the core orbital energy, due to the local values of the self-consistent potential. This has been done for instance in the calculation for overlayers on Si(111) (Ossicini et al., 1991, and reference therein). The results for the shifts at first and second layers are in good agreement with the experiments, for the deposition onto Si(111) of Na, Pb, Ca, Ca–F and $CaF_2$. The authors point out that these values, which are not corrected by the

$\Delta E_R$ shifts, but are obtained from the total self-consistent potential of the slab calculation in the LMTO scheme, are not reducible to simple charge transfers. The total potential is dependent also on the rearrangement of the charge distribution out of the site. On the contrary, the value of the core level shifts for the ideally terminated H:Si(111) surface (Buongiorno Nardelli et al., 1992) are not in agreement with the experimental results (Hricovini et al., 1993). The *many-body* effects on the evaluations of core level-shift as a function of surface site and geometry can be a relevant theme of future investigation on surfaces and adsorbates. In a recent work on As:Si(111), Johansson et al. (1995) have shown a strong effect of surface diffraction on the intensity of the surface components of core level photoelectron: the relative intensity of the surface peaks depends dramatically on the azimuth of detection.

## 4.10. Conclusions and perspectives

The controlled adsorption of atoms on semiconductor surfaces is able to produce ordered structures with interesting physical properties, from both points of view of applied physics and fundamental physics. The theoretical descriptions and the computational simulations, at the present level of evolution, can describe on the same basis both the structural properties (like the equilibrium configuration or the existence of multiple metastable phases), the electronic properties, and the driving forces of surface modifications. Some general picture, based on relatively simple rules to account for bond creation and counting, can be of considerable help to predict stable structures, but the first principles calculations are the ultimate resource to describe the different aspects of these systems in a reliable way. DFT based band computations, mainly applied in the repeated slab methods, are used to achieve this goal. Pseudopotential methods and LMTO are the tools that can be used more easily for this purpose. For a number of systems this approach is not satisfactory to describe the experiments that give the one-particle excitation spectrum, like direct and inverse photoemission. The evaluation of self-energy corrections, performed in the GW scheme, can account for the values of the surface gaps and the properties of surface electronic structure. In surface systems with higly localized electron states, the DFT-LDA approach and the itinerant band structure for electrons can be insufficient. With the use of Hubbard type Hamiltonians, to describe many body correlation effects, the transition to Mott–Hubbard insulators can be accounted for and this seems to be the case for alkali metals, and Sb at incomplete coverages, on III-V semiconductors.

The adoption of the appropriate tools to describe electron correlation in surface–adsorbate systems will play in the future the role that they already have in other fields of condensed matter theory. Another urgent need is to find a reliable way to calculate the core level shifts, including many body effects, to understand and to interpret in a quantitative way the amount of information existing in high resolution core level spectroscopy.

As shown in the recent development in the last five years, surface Car–Parrinello molecular dynamics is the way to treat on the same basis the electronic, structural, dynamical and statistical properties of surface–adsorbate systems. The new improvements of the method and of the computational tools to deal with large scale *ab initio* simulations will certainly provide a deeper insight on the subject.

## References


Alerhand, O.L., D.C. Allan and E.J. Mele, 1985, Phys. Rev. Lett. **55**, 2700.

Alerhand, O.L., J. Wang, J.D. Joannopoulos, E. Kaxiras and R.S. Becker, 1991, Phys. Rev. B **44**, 6534.

Ancilotto, F., W. Andreoni, A. Selloni, R. Car and M. Parrinello, 1990, Phys. Rev. Lett. **65**, 3148.

Ancilotto, F. and A. Selloni, 1992, Phys. Rev. Lett. **68**, 2640.

Ancilotto, F., A. Selloni and R. Car, 1994, Phys. Rev. B **50**, 15158.

Anderson, P.W., 1961, Phys. Rev. **124**, 41.

Appelbaum, J.A., G.A. Baraff, D.R. Hamann, H.D. Hagstrum and T. Sakurai, 1978, Surf. Sci. **70**, 659.

Bachelet, G.B., D.R. Hamann and M. Schlüter, 1982, Phys. Rev. B **26**, 4199.

Bassani, F. and G. Pastori Parravicini, 1975, in: Electronic States and Optical Transitions in Solids, ed. R.A. Ballinger. Pergamon, Oxford.

Batra, I.P., 1991, Phys. Rev. B **43**, 12322.

Bechstedt, F. and R. Enderlein, 1988, Semiconductor Surfaces and Interfaces. Akademie-Verlag, Berlin.

Becker, R.S., B.S. Swartzentruber, J.S. Vickers, M.S. Hybertsen and S.G. Louie, 1988, Phys. Rev. Lett. **60**, 116.

Bertoni, C.M., 1990, in: Interaction of Atoms and Molecules with Solid Surfaces, eds. V. Bortolani, N.H. March and M.P. Tosi. Plenum, pp. 155–200.

Bertoni, C.M., C. Calandra, F. Manghi and E. Molinari, 1983, Phys. Rev. B **27**, 1251.

Bertoni, C.M., M. Buongiorno Nardelli, F. Bernardini, F. Finocchi and E. Molinari, 1990, Europhys. Lett. **13**, 653.

Biegelsen, D.K., R.D. Bringans, J.E. Northrup and L.-E. Swartz, 1990, Phys. Rev. Lett. **65**, 452.

Binnig, G., H. Rohrer, Ch. Gelbel and E. Weibel, 1983, Phys. Rev. Lett. **50**, 120.

Blase, X., X. Zhu and S.G. Louie, 1994, Phys. Rev. B **49**, 4973.

Boland, J.J., 1991, Phys. Rev. Lett. **67**, 1539.

Brommer, K.D., M. Needels, B.E. Larson and J.D. Joannopoulos, 1992, Phys. Rev. Lett. **68**, 1355.

Brommer, K.D., M. Galván, A. Dal Pino, Jr. and J.D. Joannopoulos, 1994, Surf. Sci. **314**, 57.

Bu, H. and J.W. Rabalais, 1994, Surf. Sci. **301**, 285.

Buongiorno Nardelli, M., F. Finocchi, M. Palummo, R. Di Felice, C.M. Bertoni, F. Bernardini and S. Ossicini, 1992, Surf. Sci. **269/270**, 879.

Burrows, V.A., Y.J. Chabal, G.S. Higashi, K. Raghavachari and S.B. Christman, 1988, Appl. Phys. Lett. **53**, 998.

Calandra, C., F. Manghi and C.M. Bertoni, 1977, J. Phys. C: Solid State Phys. **10**, 1911.

Calandra, C. and F. Manghi, 1994, Phys. Rev. B **50**, 2061.

Car, R. and M. Parrinello, 1985, Phys. Rev. Lett. **55**, 2471.

Chabal, Y.J., G.S. Higashi and S.B. Christman, 1983, Phys. Rev. B **28**, 4472.

Chadi, D.J., 1982, Phys. Rev. B **26**, 4762.

Chadi, D.J., 1984a, Phys. Rev. Lett. **52**, 1911.

Chadi, D.J., 1984b, Phys. Rev. B **29**, 785.

Chadi, D.J., 1991, in: The Structure of Surfaces III, eds. S.Y. Tong, M.A. Van Hove, K. Takayanagi and X.D. Xie. Springer-Verlag, Berlin.

Cho, K. and J.D. Joannopoulos, 1995, Surf. Sci. **328**, 220.

Ciraci, S. and I.P. Batra, 1984, Surf. Sci. **178**, 80.

Corkill, J.L. and J.R.Chelikowsky, 1996, Surf. Sci. **53**, 12605.

Creighton, J.R., 1994, Appl. Surf. Sci. **82/83**, 171.

Delley, B., 1990, J. Chem. Phys. **92**, 508.

De Vita, A., I. Štich, M.J. Gillan, M.C. Payne and L.J. Clarke, 1993, Phys. Rev. Lett. **71**, 1276.

Di Felice, R., A.I. Shkrebtii, F. Finocchi, C.M. Bertoni and G. Onida, 1993, J. Electron Spectrosc. and Rel. Phen. **64/65**, 697.

Ding, Y.J., C.T. Chan and K.M. Ho, 1991, Phys. Rev. Lett. **67**, 1454.

Dreizler, R.M. and E.K.U. Gross, 1990, Density Functional Theory: An Approach to the Quantum Many-Body Problem. Springer-Verlag, Berlin.

Duke, C.B., A. Paton, W.K. Ford, A. Kahn and J. Carelli, 1982, Phys. Rev. B **26**, 803.

Duke, C.B., S.L. Richardson, A. Paton and A. Kahn, 1983, Surf. Sci. **127**, L135.

Dumas, P., Y.J. Chabal and G.S. Higashi, 1990, Phys. Rev. Lett. **65**, 1124.

Feenstra, R.M. and A.P. Fein, 1985, Phys. Rev. B **32**, 1394.
Feenstra, R.M. and P. Møartensson, 1988, Phys. Rev. Lett. **61**, 447.
Fong, C.Y., L.H. Yang and I.P. Batra, 1989, Phys. Rev. B **40**, 6120.
Fu, J., J. Kim, M.C. Gallagher, R.F. Willis and D.L. Miller, 1994, Surf. Sci. **318**, 349.
Gallet, D. and G. Hollinger, 1993, Appl. Phys. Lett. **62**, 982.
Garcia-Vidal, F.J., J. Merino and F. Flores, 1994, Phys. Rev. B **50**, 10537.
Grimley, T.B., 1967, Proc. Phys. Soc. **90**, 751; **92**, 776.
Guyot-Sionnest, P., 1991, Phys. Rev. Lett. **67**, 2323.
Haberern, K.W. and M.D. Pashley, 1990, Phys. Rev. B **41**, 3226.
Hamann, D.R., 1989, Phys. Rev. B **40**, 2980.
Hanemann, D., 1961, Phys. Rev. **121**, 1093.
Harten, U., J.P. Toennies, Ch. Wöll, L. Miglio, P. Ruggerone, L. Colombo and G. Benedek, 1988, Phys. Rev. B **38**, 3305.
Hebenstreit, J., M. Heinemann and M. Scheffler, 1991, Phys. Rev. Lett. **67**, 1031.
Hedin, L., 1965, Phys. Rev. **139**, A796.
Higashi, G.S., Y.J. Chabal, G. Trucks and K. Raghavachari, 1990, Appl. Phys. Lett. **56**, 656.
Ho, K.M., M.L. Cohen and M. Schlüter, 1977, Phys. Rev. B **15**, 3888.
Hohenberg, P. and W. Kohn, 1964, Phys. Rev. **136**, B864.
Hricovini, K., R. Günther, P. Thiry, A. Taleb-Ibrahimi, G. Indlekofer, J.E. Bonnet, P. Dumas, Y. Petroff, X. Blase, X. Zhu, S.G. Louie, Y.J. Chabal and P.A. Thiry, 1993, Phys. Rev. Lett. **70**, 1992.
Hybertsen, M.S. and S.G. Louie, 1988, Phys. Rev. B **38**, 4033.
Ihm, J., A. Zunger and M.L. Cohen, 1979, J. Phys. C **12**, 4409.
Ishida, H., N. Shima and M. Tsukada, 1985, Phys. Rev. B **32**, 6246.
Johansson, L.S.O., R. Gunnella, E.L. Bullock, C.R. Natoli and R.I.G. Uhrberg, 1995, to be published.
Kaxiras, E., 1991, Phys. Rev. B **43**, 6824.
Kaxiras, E. and J.D. Joannopoulos, 1988, Phys. Rev. B **37**, 8842.
Kirchner, E.J.J. and E.J. Baerends, 1994, Surf. Sci. **311**, 126.
Kirchner, E.J.J., E.J. Baerends and E. Vlieg, 1994, Surf. Sci. **304**, 12.
Kirchner, E.J.J., E.J. Baerends, G. te Velde and E. Vlieg, 1995, Surf. Sci. **330**, 113.
Kobayashi, K., Y. Morikawa, K. Terakura and S. Blügel, 1992, Phys. Rev. B **45**, 3469.
Kohn, W. and L.J. Sham, 1965, Phys. Rev. **140**, A1133.
Krüger, P. and J. Pollmann, 1990, Phys. Rev. Lett. **64**, 1808.
Krüger, P. and J. Pollmann, 1993a, Phys. Rev. B **47**, 1898.
Krüger, P. and J. Pollmann, 1993b, Progr. Surf. Sci. **42**, 351.
La Femina, J.P., 1992, Surf. Sci. Rep. **16**, 133.
Landemark, E., C.J. Karlsson, Y.C. Chao and R.I.G. Uhrberg, 1992, Phys. Rev. Lett. **69**, 1588.
Landemark, E., C.J. Karlsson, Y.C. Chao and R.I.G. Uhrberg, 1993, Surf. Sci. **287/288**, 529.
Le Lay, G. et al., 1994, Surf. Sci. **307–309**, 280.
Levine, J., 1973, Surf. Sci. **34**, 90.
Li, D. and M.D. Pashley, 1994, Phys. Rev. B **49**, 13643.
Li, G., Y.-C. Chang, R. Tsu and J.E. Greene, 1995, Surf. Sci. **330**, 20.
Li, X.-P. and D. Vanderbilt, 1992, Phys. Rev. Lett. **69**, 2543.
Ling, Y., A.J. Freeman and B. Delley, 1989, Phys. Rev. B **39**, 10144.
Lüth, H. and R. Matz, 1981, Phys. Rev. Lett. **46**, 1652.
Magri, R., F. Manghi and C. Calandra, 1994, in: Proceedings of the 22nd International Conference on the Physics of Semiconductors, ed. D.J. Lockwood. World Scientific, Singapure.
Mailhiot, C., C.B. Duke and D.J. Chadi, 1984, Phys. Rev. Lett. **53**, 2114; 1985, Phys. Rev. B **31**, 2213.
Manghi, F., C. Calandra, C.M. Bertoni and E. Molinari, 1984, Surf. Sci. **136**, 629.
Manghi, F. and C. Calandra, 1990, Vacuum **41**, 693.
Marcellini, A., C.A. Pignedoli, M. Ferrario and C.M. Bertoni, 1998, Surf. Sci. **402–404**, 47.
Margaritondo, G., J.E. Rowe, C.M. Bertoni, C. Calandra and F. Manghi, 1979, Phys. Rev. B **20**, 1538; 1981, Phys. Rev. B **23**, 509.
Miyamoto, Y. and S. Nonoyama, 1992, Phys. Rev. B **46**, 6915.

Nagayoshi, H., 1993, Surf. Sci. **282**, 163.
Nakada, T. and T. Osaka, 1991, Phys. Rev. Lett. **67**, 2834.
Newns, D.M., 1976, Phys. Rev. **178**, 1123.
Nonoyama, S., Y. Miyamoto, Y. Aoyagi and T. Sugano, 1993, Phys. Rev. B **47**, 7622.
Northrup, J.E. and M.L. Cohen, 1982, Phys. Rev. Lett. **49**, 1349.
Northrup, J.E., 1991, Phys. Rev. B **44**, 1349.
Northrup, J.E., M.S. Hybertsen and S.G. Louie, 1991, Phys. Rev. Lett. **66**, 500.
Ossicini, S., C. Arcangeli and O. Bisi, 1991, Phys. Rev. B **43**, 9823.
Pandey, K.C., 1981, Phys. Rev. Lett. **47**, 1913.
Pandey, K.C., 1982, Phys. Rev. Lett. **49**, 223.
Pandey, K.C., T. Sakurai and H.D. Hagstrum, 1975, Phys. Rev. Lett. **35**, 1728.
Pankratov, O. and M. Scheffler, 1993, Phys. Rev. Lett. **70**, 351.
Pankratz, J., H. Nienhaus and W. Mönch, 1994, Surf. Sci. **307**, 211.
Pashley, M.D., 1989, Phys. Rev. B **40**, 10481.
Pashley, M.D. and K.W. Haberern, 1991, Phys. Rev. Lett. **67**, 2697.
Pashley, M.D., K.W. Haberern, W. Friday, J.M. Woodall and P.D. Kirchner, 1988, Phys. Rev. Lett. **60**, 2176.
Pehlke, E. and M. Scheffler, 1993, Phys. Rev. Lett. **71**, 2338.
Phillips, J.C. and L. Kleinman, 1959, Phys. Rev. **116**, 287.
Pickett, W., 1988, Comput. Phys. Rep. **9**, 115.
Qian, G., R.M. Martin and D.J. Chadi, 1988, Phys. Rev. B **37**, 1303.
Ren, S.-F. and Y.-C. Chang, 1990, Phys. Rev. B **41**, 7705.
Rincón, R., F.J. García-Vidal and F. Flores, 1995, Surf. Sci. **320**, 297.
Rochet, F., C. Poncey, G. Dufour, H. Roulet, W.N. Rodrigues, M. Sauvage, J.C. Bouilliard, F. Sirotti and G. Panaccione, 1995, Surf. Sci. **326**, 229.
Sandfort, D., A. Mazur and J. Pollmann, 1994, Phys. Rev. B **51**, 7139.
Schlier, R.E. and H.E. Farnsworth, 1959, J. Chem. Phys. **30**, 917.
Schmeits, M., A. Mazur and J. Pollmann, 1983, Phys. Rev. B **27**, 5012.
Schmidt, W.G. and F. Bechstedt, 1994, Phys. Rev. B **50**, 17280; Phys. Rev. B **50**, 17651.
Schmidt, W.G., B. Wenzien and F. Bechstedt, 1994, Phys. Rev. B **49**, 4731; Surf. Sci. **307–309**, 235.
Schnell, R.D., D. Rieger, A. Bogen, R. Wandelt and W. Steinmann, 1985, Solid State Commun. **53**, 205.
Schulze, G. and M. Henzler, 1983, Surf. Sci. **124**, 336.
Shkrebtii, A.I., R. Di Felice, C.M. Bertoni and R. Del Sole, 1995, Phys. Rev. B **51**, 11201.
Shuh, D.K., C.W. Lo, J.A. Yarmoff, A. Santoni, L.J. Terminello and F.R. McFeely, 1994, Surf. Sci. **303**, 89.
Sinniah, K., M.G. Sherman, L.B. Lewis, W.H. Weinberg, J.T. Yates and K.C. Janda, 1989, Phys. Rev. Lett. **62**, 567.
Spanjaard, D. and M.C. Desjonquères, 1990, in: Interaction of Atoms and Molecules with Solid Surfaces, eds. V. Bortolani, N.H. March and M.P. Tosi. Plenum, New York.
Spiess, L., P.S. Mangat, S.-T. Tang, K.M. Shirm, A.J. Freeman and P. Soukiassan, 1993, Surf. Sci. **289**, L631.
Štich, I., M.C. Payne, R.D. King-Smith, J.-S. Lin and L.J. Clarke, 1992, Phys. Rev. Lett. **68**, 1351.
Štich, I., A. De Vita, M.C. Payne, M.J. Gillan and L.J. Clarke, 1994, Phys. Rev. B **49**, 8076.
Takayanagi, K., Y. Tanishiro, M. Takahashi and S. Takahashi, 1985, J. Vac. Sci. Technol. A **3**, 1502.
Troost, D., H.J. Clemens, L. Koenders and W. Mönch, 1993, Surf. Sci. **307**, 211.
Tsuda, M., T. Hoshino, S. Oikawa and I. Ohdomari, 1991, Phys. Rev. B **44**, 11241.
Uchiyama, T. and M. Tsukada, 1993, Surf. Sci. **295**, L1037.
Uchiyama, T. and M. Tsukada, 1994, Surf. Sci. **313**, 17.
Uhrberg, R.I.G., R.D. Bringans, R.Z. Bachrach and J.E. Northrup, 1986, Phys. Rev. Lett. **56**, 520.
van Bommel, A.J. and J.E. Crombeen, 1979, Surf. Sci. **49**, 308.
Vanderbilt, D., 1990, Phys. Rev. B **41**, R7892.
Whitman, L.J., A. Stroscio, R.A. Dragoset and R.J. Celotta, 1991, Phys. Rev. Lett. **66**, 1338.
Wolkow, R. and Ph. Avouris, 1988, Phys. Rev. Lett. **60**, 1049.
Yang, Y.-N., Y.S. Luo and J.S. Weaver, 1992, Phys. Rev. B **46**, 15395.
Yi, J.-Y. and J. Bernholc, 1992, Phys. Rev. Lett. **69**, 486.
Zheng, X.M. and P.V. Smith, 1993, Surf. Sci. **282**, 173.
Zhu, X. and S.G. Louie, 1992, Phys. Rev. B **45**, 3940.

This Page Intentionally Left Blank

CHAPTER 5

# Theory of Adsorption on Metal Substrates

M. SCHEFFLER and C. STAMPFL

*Fritz-Haber-Institut der Max-Planck-Gesellschaft*
*Faradayweg 4-6*
*D-14195 Berlin, Germany*

*© 2000 Elsevier Science B.V.*
*All rights reserved*

*Handbook of Surface Science*
*Volume 2, edited by K. Horn and M. Scheffler*

# Contents


5.1. Introduction . . . 287
5.1.1. The nature of the surface chemical bond: indeterminate concepts, yet useful . . . 288
5.1.2. What will be discussed and why, and what is missing . . . 289
5.2. Concepts and definitions . . . 290
5.2.1. Density of states . . . 291
5.2.2. Energies . . . 294
5.2.3. Binding energy at kink sites . . . 296
5.2.4. The surface energy barrier . . . 297
5.3. The tight-binding picture of bonding . . . 299
5.3.1. Adsorbate–substrate interaction . . . 299
5.3.2. Adsorbate band structure . . . 305
5.4. Adsorption of isolated adatoms . . . 309
5.4.1. Geometry . . . 310
5.4.2. Density of states $\Delta N(\epsilon)$ . . . 311
5.4.3. Electron density: $n(\mathbf{r})$, $\Delta n(\mathbf{r})$, and $n^{\Delta}(\mathbf{r})$ . . . 313
5.4.4. Surface dipole moments . . . 315
5.5. Alkali-metal adsorption: the traditional picture of *on-surface* adsorption . . . 317
5.5.1. The Langmuir–Gurney picture . . . 318
5.5.2. Coverage dependence of the work function . . . 319
5.5.3. Ionization of the adsorbate and screening by the substrate electrons . . . 320
5.5.4. Surface band structure . . . 322
5.6. Substitutional adsorption and formation of surface alloys . . . 324
5.6.1. Na on Al(001) . . . 326
5.6.2. Na on Al(111) . . . 329
5.6.3. Co on Cu(001) . . . 331
5.7. Adsorption of CO at transition metal surfaces – a model system for a simple molecular adsorbate . . . 333
5.8. Co-adsorption [the example CO plus O on Ru(0001)] . . . 335
5.9. Chemical reactions at metal surfaces . . . 337
5.9.1. The problem with "the" transition state . . . 337
5.9.2. Dissociative adsorption and associative desorption of $H_2$ at transition metals . . . 339
5.9.2.1. The potential-energy surface of $H_2$ at transition-metal surfaces . . . 340
5.9.2.2. The dynamics of $H_2$ dissociation at transition-metal surfaces . . . 342
5.10. The catalytic oxidation of CO . . . 345
5.11. Summary outline of main points . . . 350
References . . . 352

## 5.1. Introduction

The theory of adsorption has reached a level where it is possible to calculate free energies, as well as the electronic and atomic structure, of medium-sized systems with predictive accuracy. Such *ab initio* calculations (i.e., starting from the electronic structure) typically employ complicated methods and significant computational resources. Clearly, the methodological developments of recent years have been impressive, although further developments, enhancements, and speed-ups of such methods are still necessary. Acknowledging the predictive power of density-functional theory calculations, however, we also note that the need remains for finding explanations and developing simple concepts. Today's concepts are largely based on experience from gas-phase chemistry, as for example the concepts of electronegativity, HOMOs (highest occupied molecular orbitals), LUMOs (lowest unoccupied molecular orbitals), and the reactivity of open-shell systems. However, it is also clear that some concepts, which are powerful in the gas-phase chemistry of molecules, can be quite misleading when it comes to surfaces. One example is that of "the" transition state of a chemical reaction: For molecular chemistry this concept is typically useful, but for molecules at surfaces it turns out that the dimension of phase space is so high that not just one, but many transition states exist, and all of them may play a role (see Section 5.9).

What is needed now, and in the years to come, is to perform more predictive simulations of surface chemical reactions; but also the next step can and should be done, which is the development of *explanations* and *understanding*. For example, at this point we are not able to rationalize the factors that determine at which transition-metal surface a rotationally excited molecule will dissociate more easily than a molecule that is not rotationally excited (see Section 5.9.2). Also we are just starting to develop an understanding of why some adsorbates occupy a substitutional site, and not just simply adsorb *on* the surface, and why this geometry may change with coverage. Note that ten years ago substitutional adsorption of single adatoms was unheard of, but now, it is a well known and common phenomenon (see Section 5.6).

The discussion presented in this chapter is based on results from density-functional theory calculations. Rather than discussing details of these calculations, we simply use the results to show where we are on the way to attaining a rationalization of the factors which actuate the surface chemistry for different systems. This goal does not (and cannot) aim at a quantitative description, and it is clear that concepts, e.g., that of electronegativity, often do not withstand a quantitative analysis. However, describing the results in words and in a chemical language, is the basis on which "understanding" is built. Clearly, the quality (i.e., the nature or character) of an effect is linked to the quantitative numbers, and sometimes a small change in the quantity changes the quality. In this sense our goal is insecure. But we strongly believe that capturing the nature of a situation and understanding trends is the essence of "understanding". As we said above, theoretical surface science is now able to

do this, and some examples along this route already exist, some of which will be discussed in this chapter.

### 5.1.1. *The nature of the surface chemical bond: indeterminate concepts, yet useful ...*

A crude classification of adsorption distinguishes two classes, namely that of a very weak (van der Waals type) interaction between adsorbate and substrate (physisorption), where the adsorption energy is typically less than 0.3 eV per adsorbed particle (6.9 kcal $mol^{-1}$), and that of chemisorption, where the adsorption energy is larger.

For chemisorption systems there is a further classification of the nature of bonding which is frequently applied, although it is neither unique nor general. Nevertheless, it has some natural advantages and will also be applied in this chapter. It is based on a survey of electronic, electrical, vibrational, and thermal properties. Thus, altogether we will distinguish four different types of bonding:

1. van der Waals,
2. covalent,
3. metallic,
4. ionic.

As little the nature of bonds of types 2, 3, and 4 is well defined, that of van der Waals bonding is equally so. The concept of the van der Waals interaction is valid for large distances where orbitals do not overlap. It is due to electron-density fluctuations at the different atoms and the polarization that the fluctuations induce at the other atoms. However, at the equilibrium geometry of an adsorbate on a surface, the direct interaction of adsorbate and substrate orbitals is significant. This is indeed plausible as equilibrium geometries are determined by the interplay of attractive interactions and Pauli repulsion. As a consequence, at the bonding geometry of adsorbed noble-gas atoms which are regarded as exhibiting a van der Waals like bonding, and even more so at the turning point of noble-gas atom scattering at surfaces, the physics is largely determined by the interaction of orbitals and *static* polarization. Thus, *physisorption*, although implying a weak interaction strength, can induce a static dipole moment at the adsorbate (in particular for larger atoms, e.g., Xe), and the electrostatic interaction of this adsorbate dipole with the substrate contributes noticeably to the bond strength. Indeed, density-functional theory (DFT) calculations performed using either the local-density approximation (LDA) or the generalized gradient approximation (GGA) for the exchange–correlation interaction, which both lack a description of the nature of the van der Waals interaction, as this is intrinsically non-local, seem to give a reasonable description of adsorption of noble-gas atoms at surfaces (see, e.g., Brivio and Trioni, 1999). Nevertheless, it is not clear if the acting "overlap-modified dispersion forces" are described by the present exchange–correlation functionals with sufficient accuracy. In any case, what we like to emphasize is that even weak bonding can give rise to noticeable changes in the electrostatic field at the surface and therefore to changes in surface properties. We elaborate here on this discussion more than usual because the use of the above noted four bonding types has often caused confusion when they were interpreted literally. Knowing about the danger of over-interpreting the relevance of these concepts we still feel that the advantage of categorizing systems is important for identifying trends,

noting unusual effects, and for *scientific understanding* in general. In Sections 5.3, 5.4, and 5.5 we will continue this discussion with respect to ionic and covalent bonding.

Metallic bonding, also noted in the above list, is a special case of covalent interaction where the electron density is more delocalized and not (strongly) peaked between the atoms. In principle, the attractive interaction is due to the fact that the electrons act like a structure-less "glue" between the nuclei. This attraction is stabilized by a repulsive term due to the kinetic energy of the electrons, because electrons do not like to become localized, but instead, as a consequence of the Heisenberg uncertainty principle, they like to spread out. For *isolated* adatoms, the concept of metallic bonding is not very useful because metallic bonding, and the concept of delocalized electrons, requires a high coordination. Therefore we will not allude to this concept in Section 5.4 where isolated atoms are discussed, but we will in Sections 5.5.4 and 5.6 when we compare adlayers of different density and discuss the formation of a surface electronic band structure.

### *5.1.2. What will be discussed and why, and what is missing*

This chapter deals with various adsorbates on metal surfaces, where we focus on the electronic properties and the nature of the chemical bond. To some extent this also necessitates a discussion of the atomic geometries because the distances and directions between the atoms and their neighbors, determine which, and how, orbitals will hybridize. Just as one example we mention aluminum which is a nearly-free-electron metal. However, when an Al atom is placed in a certain local coordination, its s- and p-electrons can hybridize and form directional bonds. This is in fact well known even for bulk systems, as for example AlAs. This property of Al, namely being close to a covalent material, contributes to the low formation energy of surface vacancies at Al(111) (see Neugebauer and Scheffler, 1992) and is instrumental in the theoretical result that self diffusion at Al(001) proceeds via the atomic exchange mechanism (see Feibelman, 1990; Yu and Scheffler, 1997).

We will keep the discussion in this chapter simple and accentuate the *qualitative* nature of the various mechanisms. Nevertheless, we emphasize that all results discussed below are based on quantitative calculations performed using density-functional theory (DFT) (Dreizler and Gross, 1990). Indeed, the dialectic relation of quantity and quality will become obvious through several examples discussed below: Often a small quantitative difference in certain values will cause a significantly changed electronic and/or geometric structure and as a consequence a different bonding quality or nature.

The exchange–correlation functional employed in many of the studies discussed below is the local-density approximation (LDA), which gives a reliable description of geometries and the nature of the bond. In the more recent studies, which are presented in Sections 5.7–5.10, the generalized gradient approximation (GGA) is employed. For equilibrium geometries the GGA gives results similar to the LDA. For the description of chemical reactions, in particular of transition states, where the breaking of old bonds and making of new bonds occurs, the GGA is in fact mandatory, i.e., the LDA often gives even qualitatively incorrect results (see for example Hammer et al., 1994, and references therein).

For simplicity's sake, we restrict ourselves to close-packed substrate surfaces [mainly fcc (111) and fcc (001)]. The more open surfaces are typically close to a structural instability and therefore sometimes already reconstruct when clean, or when adsorbates are

added. We also limit the number of substrate materials with the view that this will ease the readability of the chapter. However, essentially all important mechanisms that we would like to discuss are represented by the systems presented.

Because of their large dipole moments and special role in various industrial applications, the discussion of alkali-metal adsorbates is addressed in particular detail. This presentation also focuses on the general properties; for more complete discussions we refer to some recent review papers, e.g., Stampfl and Scheffler (1995) and Adams (1996). Noble-gas adatoms[1] and f-electron systems are not discussed, and also for metallic substrates not all "classes" are covered: We concentrate on elemental substrates (only a few words are said about alloys) and consider low coverages, i.e., from a single adatom up to a full monolayer.[2]

As the properties of adsorbates on metals are manifold, we are unable to address all features which may be relevant in one or another situation. For example, core-levels and surface core-level shifts (with their interesting initial state and final state effects) are not mentioned (see, for example, Andersen et al., 1994; Methfessel et al., 1995; Hennig et al., 1996; Ganduglia-Pirovano et al., 1997, and references therein). The same is true for surface electric resistance, magnetism, and more.

Otherwise, we trust that the selection of systems is representative. It covers a small fraction of work done by us over the last several years on adsorption, co-adsorption, and chemical reactions. We note that similar work has also been published by other groups (see, e.g., Hammer and Nørskov, 1997, and references therein).

## 5.2. Concepts and definitions

This section starts with some general remarks and then collects definitions of important quantities which are typically calculated in theoretical work on adsorption and will be used later in this chapter.

Accurate knowledge of the geometry of the adsorbate and substrate atoms is a prerequisite for any additional analysis of the adsorbate properties, as for example the surface electronic structure, adsorbate-induced work function changes, and the chemical reactivity. The apparent hierarchy expressed in this sentence reflects the fact that the atomic structure is somewhat more directly accessible for experimental studies. Nevertheless, we emphasize that electronic and atomic structure are closely interconnected and do not consider it very useful to analyze "the chicken and the egg problem", i.e., to discuss whether the geometry creates the electronic structure or vice versa. In fact, we will stress in this chapter (particularly in Sections 5.5 and 5.6) that the same adsorbate can exhibit a different bonding character, depending on the adsorbate coverage and the local adsorbate geometry. We will discuss these aspects for special examples but note that these are *examples* which represent many systems; they are selected because they demonstrate the effects most clearly.

---

1 For a discussion of recent work on noble-gas atom adsorption see Bruch et al., 1997; Brivio and Trioni, 1999; Seyller et al., 1998; Petersen et al., 1996, 2000.

2 The coverage is defined in this chapter such that for $\Theta = 1$, the number of adatoms is the same as the number of atoms in the clean, unreconstructed surface.

### *5.2.1. Density of states*

An important quantity accessible in calculations, though not in experiments, is the local density of states

$$n(\mathbf{r}, \epsilon) = \sum_{i=1}^{\infty} |\varphi_i(\mathbf{r})|^2 \delta(\epsilon - \epsilon_i), \tag{5.1}$$

where $\varphi_i(\mathbf{r})$ are the single-particle eigenfunctions of the Kohn–Sham Hamiltonian. For those who like Green functions this is written as

$$n(\mathbf{r}, \epsilon) = -\frac{2}{\pi} \mathrm{Im}\, \mathcal{G}(\mathbf{r}, \mathbf{r}, \epsilon), \tag{5.2}$$

where $\mathcal{G}(\epsilon)$ is the retarded Green-function operator of the adsorbate system. The electron density is

$$n(\mathbf{r}) = \int_{-\infty}^{\infty} f(\epsilon, T) n(\mathbf{r}, \epsilon)\, \mathrm{d}\epsilon = \sum_{i=1}^{\infty} f(\epsilon_i, T) |\varphi_i(\mathbf{r})|^2, \tag{5.3}$$

with the Fermi distribution $f(\epsilon, T)$ at temperature $T$. Often, when the nature of a chemical bond is analyzed, electron density plots are shown, sometimes complemented with a discussion of charge transfer from atom A to atom B. We do not consider this approach so useful and emphasize that a small difference in the electron density sometimes implies a significantly different physical–chemical interaction. This is demonstrated in Fig. 5.1 which shows the electron density of bulk NaCl, that is a system, which is well accepted to have ionic bond character. However, even in this example the self-consistently calculated electron density (right) and that constructed by a superposition of electron densities of the

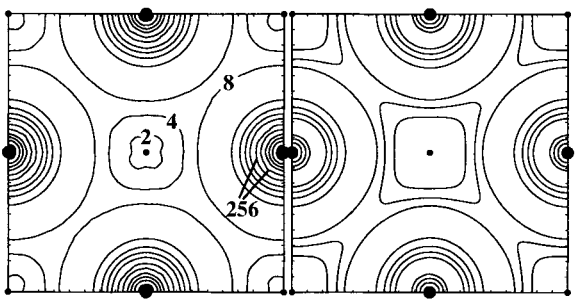


Fig. 5.1. Lines of constant electron density (valence only) for a NaCl crystal, the prototype of ionic bonding. Left: Result obtained by a superposition of the electron densities of *neutral* Na and Cl atoms. Right: Result from a self-consistent DFT-LDA calculation. The units are $10^{-3}$ bohr$^{-3}$. Large dots mark the positions of the Cl atoms, and small dots mark the Na atoms. Adjacent contour lines differ by a factor of 2. The maximum density for the non-self-consistent calculation (left) is $265 \times 10^{-3}$ bohr$^{-3}$ and for the self-consistent calculation (right) the highest density is $253 \times 10^{-3}$ bohr$^{-3}$ (from Bormet et al., 1994a).

*neutral* Na and *neutral* Cl atoms (left) differ only slightly, and just on the basis of inspecting $n(\mathbf{r})$ charge transfer can hardly be identified. The small changes brought about by the self-consistent rearrangement of electron density are that around the Na nucleus the charge density is very slightly decreased; but also at the Cl atom we see that the maximum of the electron density, which is rather close to the nucleus, becomes slightly lower. Thus, when one only inspects the electron density, even NaCl does not present a clear case for a system with ionic bonding. We emphasize that for low-symmetry situations, as for example a surface, this problem is even more pronounced. However, an analysis of the density of states (see, e.g., also Section 5.4.2) shows that it is indeed appropriate to describe the upper valence band in terms of Cl 3p and the lower conduction band in terms of Na 3s orbitals.

The example of Fig. 5.1 shows that despite the fact that the electron density can be considered the ruling quantity in density-functional theory, its inspection can be misleading. Sometimes, though not always, plots of density *differences*

$$\Delta n(\mathbf{r}) = n(\mathbf{r}) - n^0(\mathbf{r}) \tag{5.4}$$

give a better impression (see Sections 5.4 and 5.5.3). Here $n^0(\mathbf{r})$ is the electron density of the clean substrate where the geometry is (typically) chosen to be that of the adsorbate system. Also the *difference density*

$$n^{\Delta}(\mathbf{r}) = n(\mathbf{r}) - n^0(\mathbf{r}) - n^{\mathrm{Na},f_{3s}}(\mathbf{r}) \tag{5.5}$$

is often a helpful quantity. Here $n^{\mathrm{Na},f_{3s}}(\mathbf{r})$ is the (spherical) electron density of the partially ionized atom to be adsorbed, where the occupation of the valence level is given by the parameter $f_{3s}$. Just as an example, our indices here refer to a Na atom, where the valence level is 3s.

A typically more sensitive quantity is the density of states (DOS),

$$N(\epsilon) = \int n(\mathbf{r},\epsilon)\,\mathrm{d}\mathbf{r} = \sum_{i=1}^{\infty} \delta(\epsilon - \epsilon_i), \tag{5.6}$$

where the sum goes over all eigenstates of the Kohn–Sham Hamiltonian. The DOS gives a noticeable contribution to the electrons' kinetic energy

$$T_{\mathrm{s}}[n(\mathbf{r})] = \int_{-\infty}^{\infty} f(T,\epsilon) N(\epsilon)\,\epsilon\,\mathrm{d}\epsilon - \int V^{\mathrm{eff}}(\mathbf{r}) n(\mathbf{r})\,\mathrm{d}\mathbf{r}, \tag{5.7}$$

where $V^{\mathrm{eff}}$ is the effective potential of the Kohn–Sham Hamiltonian (see Chapter 1 of this book). We also note that a one-to-one correspondence exists between $N(\epsilon)$ and the electron density,[3] which (in addition to the argument of practicability and clarity) gives a premise to its use.

---

3 Obviously, as $N(\epsilon)$ defines the Kohn–Sham Hamiltonian, it also defines all ground-state and all excited-state properties.

Throughout this chapter we will follow the thinking that the nature of bonding is determined by the interaction of the orbitals at the different atoms involved, and thus, it is more clearly identified by an inspection of the DOS and/or by the adsorbate-induced change ($\Delta$DOS)

$$\Delta N(\epsilon) = N(\epsilon) - N^0(\epsilon), \tag{5.8}$$

where $N^0(\epsilon)$ is the DOS of the clean substrate where the geometry is typically chosen to be that of the adsorbate system. Furthermore, we note the state-resolved DOS, also called the projected DOS, as a very useful quantity:

$$N_\alpha(\epsilon) = \sum_{i=1}^{\infty} \left| \langle \phi_\alpha \mid \varphi_i \rangle \right|^2 \delta(\epsilon - \epsilon_i), \tag{5.9}$$

where $\phi_\alpha$ is a properly chosen localized function. The spatial distribution of the electron density is viewed as a consequence (not the origin) of the hybridization of different orbitals. The critic may argue that this is just (another) chicken–egg problem, and we agree with this assessment, i.e., our approach is simply taken because it is useful. We also note that information about $N_\alpha(\epsilon)$ can be obtained (though in a somewhat distorted way) from angle-resolved photoemission, inverse photoemission, and scanning tunneling spectroscopy.

Unlike the bond formation in molecular chemistry, the case of adsorption is one between very different partners: The adatom comes with discrete energy levels and few occupied states, but the substrate has a near-infinite number ($\sim 10^{23}$) of electrons. Thus, the valence level of the adparticle will interact with a semi-infinite continuum of levels $\epsilon \geqslant \epsilon_0$, where $\epsilon_0$ is the bottom of the substrate valence band. The location of the highest occupied level, the Fermi energy, is determined by the substrate. On a surface, a description of the chemical bonding in terms of an elementary discrete level scheme has therefore to be extended: Levels lying in the band region of the substrate receive a finite width. These broad levels are called adsorbate-induced resonances and they get filled up to the substrate Fermi level. The wave functions of these resonances can be understood to arise from the adsorbate orbitals. In an alternative view, the states of the clean surface are described as standing waves, incident from the bulk and reflected at the potential-energy barrier of the clean surface, with a node at the surface. An adsorbed particle modifies the reflection properties, which can be described by introducing an energy-dependent phase shift, $\delta_\alpha(\epsilon)$, describing the scattering of bulk states of a certain representation $\alpha$ by the adparticle. This phase shift is defined by (Callaway, 1964, 1967)

$$\tan \delta_\alpha(\epsilon) = \frac{-\operatorname{Im} D_\alpha(\epsilon)}{\operatorname{Re} D_\alpha(\epsilon)}, \tag{5.10}$$

where $D_\alpha$ is the determinant

$$D_\alpha(\epsilon) = \det\left\{1 - \mathcal{G}^0(\epsilon)\Delta V\right\}_\alpha, \tag{5.11}$$

$\mathcal{G}^0$ is the Green function of the bare substrate, and $\Delta V$ is the change in the potential due to the adsorbate

$$\Delta V = V^{\text{eff}}[n] - V^{\text{eff}}[n^0]. \tag{5.12}$$

The density of states, induced by the adparticle, is given by the derivative of the phase shift

$$\Delta N(\epsilon) = \frac{2d_\alpha}{\pi} \frac{\mathrm{d}\delta_\alpha(\epsilon)}{\mathrm{d}\epsilon}, \tag{5.13}$$

where $d_\alpha$ is the dimension of the representation $\alpha$. A resonance in $\Delta N(\epsilon)$ will occur at an energy close to that at which the phase shift $\delta_\alpha(\epsilon)$ increases through $\pi/2$ with increasing energy, i.e., where the real part of the determinant $D_\alpha$ vanishes. Close to this energy, $\epsilon_\alpha$, the induced density of states takes a Lorentzian line shape

$$\Delta N(\epsilon) = \frac{d_\alpha \Delta_\alpha}{\pi} \frac{1}{(\epsilon - \epsilon_\alpha)^2 - (\Delta_\alpha/2)^2} \tag{5.14}$$

The width of the resonance, $\Delta_\alpha$, is

$$\Delta_\alpha = \left[ \frac{2 \operatorname{Im} D_\alpha(\epsilon)}{(\mathrm{d} \operatorname{Re} D_\alpha(\epsilon)/\mathrm{d}\epsilon)} \right]_{\epsilon=\epsilon_\alpha} \tag{5.15}$$

We note the close similarity between Eq. 5.14 and the Anderson–Grimley–Newns model of chemisorption (Grimley, 1975; Muscat and Newns, 1978, 1979). On the lower energy side of the resonance, the phase of the reflected wave is shifted such that electron density is accumulated in the region of the adparticle–substrate bond, indicating that these states are bonding in character. On the higher energy tail of the resonance, the electron density in the bond region is reduced, indicating that these states are antibonding in character (Lang and Williams, 1978; Liebsch, 1978). However, if the interaction with the substrate is very strong, bonding and antibonding states will split apart: A bound state (or resonance) is then formed below the substrate band, which is bonding in character, and a broad (antibonding) resonance will appear in the valence band (see also the discussion of Fig. 5.4 in Section 5.3.1).

### *5.2.2. Energies*

We will assume that the dynamics of the electrons and the nuclei can be decoupled and that whatever the dynamics of the nuclei are, the electrons are in the electronic ground state of the instantaneous geometry. This is the Born–Oppenheimer approximation (Born and Oppenheimer, 1927; Born and Huang, 1954), which for adsorbates, and often also for chemical reactions, is well justified; for some reactions, and in particular for photochemistry, important violations of the Born–Oppenheimer approximation occur, but this is not the subject of this chapter. The *DFT total energy*, $E^{\text{total}}(T, V, N_{\text{A}}^{\text{nuc.}}, N_{\text{B}}^{\text{nuc.}}, \ldots, \{\mathbf{R}_I\})$, at temperature $T$, volume $V$, and composition $N_{\text{A}}^{\text{nuc.}}, N_{\text{B}}^{\text{nuc.}}, \ldots$, when studied as a function of the atomic coordinates, is often called the potential-energy surface (PES) because it

defines the potential-energy landscape on which the nuclei A, B, ... travel. It is related to an experimentally accessible quantity only in a restricted way: If, as is typically done, the self-consistent calculations are performed at constant volume, the *DFT total energy* corresponds to the Helmholtz free energy at zero temperature and neglecting zero-point vibrations. In general, the Helmholtz free energy is

$$F\left(T, V, N_{\mathrm{A}}^{\mathrm{nuc.}}, N_{\mathrm{B}}^{\mathrm{nuc.}}, \ldots, \{\mathbf{R}_I\}\right) = E^{\mathrm{total}}\left(T, V, N_{\mathrm{A}}^{\mathrm{nuc.}}, N_{\mathrm{B}}^{\mathrm{nuc.}}, \ldots, \{\mathbf{R}_I\}\right) + E^{\mathrm{vib.}}\left(T, V, N_{\mathrm{A}}^{\mathrm{nuc.}}, N_{\mathrm{B}}^{\mathrm{nuc.}}, \ldots, \{\mathbf{R}_I\}\right) - TS\left(T, V, N_{\mathrm{A}}^{\mathrm{nuc.}}, N_{\mathrm{B}}^{\mathrm{nuc.}}, \ldots, \{\mathbf{R}_I\}\right) \quad (5.16)$$

with the vibrational contribution noted as $E^{\mathrm{vib.}}$ and $S$ is the entropy. At a given volume $V$, the atomic geometry of stable or metastable configurations is determined by

$$\left(\frac{\partial F(T, V, N_{\mathrm{A}}^{\mathrm{nuc.}}, N_{\mathrm{B}}^{\mathrm{nuc.}}, \ldots, \{\mathbf{R}_I\})}{\partial \mathbf{R}_I}\right)_{T, V, N_{\mathrm{A}}^{\mathrm{nuc.}}, N_{\mathrm{B}}^{\mathrm{nuc.}}, \ldots} = 0, \quad (5.17)$$

and for a given pressure $p$ it is determined by

$$\left(\frac{\partial G(T, p, N_{\mathrm{A}}^{\mathrm{nuc.}}, N_{\mathrm{B}}^{\mathrm{nuc.}}, \ldots, \{\mathbf{R}_I\})}{\partial \mathbf{R}_I}\right)_{T, p, N_{\mathrm{A}}^{\mathrm{nuc.}}, N_{\mathrm{B}}^{\mathrm{nuc.}}, \ldots} = 0, \quad (5.18)$$

where

$$G\left(T, p, N_{\mathrm{A}}^{\mathrm{nuc.}}, N_{\mathrm{B}}^{\mathrm{nuc.}}, \ldots, \{\mathbf{R}_I\}\right) = F\left(T, V, N_{\mathrm{A}}^{\mathrm{nuc.}}, N_{\mathrm{B}}^{\mathrm{nuc.}}, \ldots, \{\mathbf{R}_I\}\right) + pV(T, p, N_{\mathrm{A}}^{\mathrm{nuc.}}, N_{\mathrm{B}}^{\mathrm{nuc.}}, \ldots, \{\mathbf{R}_I\}) \quad (5.19)$$

is the Gibbs free energy. If the system is in contact with a particle reservoir, for example, the sample is held in some gas phase, particles can be exchanged between the system and the reservoir. Then we have to add to Eq. (5.16) a term $-\sum_{\mathrm{X}} \mu_{\mathrm{X}} N_{\mathrm{X}}^{\mathrm{nuc.}}$, where $\mu_{\mathrm{X}}$ is the atom chemical potential of atom-type X, which can be controlled by external reservoirs, i.e., by the environmental conditions (partial pressure and temperature).

Later in this chapter we will study the *adsorption energy per adatom*. This is the difference of the total energy of the adsorbate system and the total energy of the clean substrate together with a corresponding number of free, neutral atoms. For *on-surface* adsorption this reads

$$E_{\mathrm{ad}}^{\mathrm{Na/Al(001)}} = -\left(E^{\mathrm{Na/Al(001)}} - E^{\mathrm{Al(001)}} - N_{\mathrm{Na}}^{\mathrm{nuc.}} E^{\mathrm{Na-atom}}\right) / N_{\mathrm{Na}}^{\mathrm{nuc.}}, \quad (5.20)$$

where $E^{\mathrm{Na/Al(001)}}$ is the total energy per adatom of the adsorbate system, $E^{\mathrm{Al(001)}}$ is the total energy of the clean Al(001) substrate, and $N_{\mathrm{Na}}^{\mathrm{nuc.}} E^{\mathrm{Na-atom}}$ is the total energy of $N_{\mathrm{Na}}^{\mathrm{nuc.}}$ free Na atoms that take part in the adsorption. We have used here as an example indices which refer to the adsorption of Na on Al(001), but translation to other systems is obvious.

Often adatoms are *not* adsorbed on the surface with only slight modification of the original surface structure, but instead adsorption may occur substitutionally. In this case the adatom kicks out an atom from the surface and takes its site. In thermal equilibrium the

kicked out atom is then re-bound at a kink site at a step (the binding energy at a kink site equals the bulk cohesive energy, which is shown in the next section).

For substitutional adsorption, the adsorption energy is defined essentially the same way as above, only that the kicked off surface atoms that are re-bound at kink sites, have to be accounted for as well. Each rebound kicked out atom contributes an energy equal to that of a bulk atom (see Section 5.2.3). Thus, for the substitutional adsorption the adsorption energy is

$$E_{\mathrm{ad}}^{\mathrm{Na/Al(001)-sub}} = -\big(E^{\mathrm{Na/Al(001)-sub}} + N_{\mathrm{Na}}^{\mathrm{nuc.}} E^{\mathrm{Al-bulk}} - E^{\mathrm{Al(001)}} - N_{\mathrm{Na}}^{\mathrm{nuc.}} E^{\mathrm{Na-atom}}\big)/N_{\mathrm{Na}}^{\mathrm{nuc.}}. \tag{5.21}$$

$E^{\mathrm{Al-bulk}}$ is the energy of an atom in a bulk crystal of aluminum and the quantity $E^{\mathrm{Na/Al(001)-sub}}$ in Eq. (5.21) is the total energy of the slab with the adatoms adsorbed in substitutional sites.

We end this section with a warning that may be relevant for *Surface Science* studies more often than typically appreciated. The energy quantities defined in this section are relevant if thermal equilibrium conditions are attained, but often this is not the case. Instead, a surface is studied which may be in a metastable state and this state hopefully corresponds to an equilibrium situation of the sample's history (at best). This somewhat unclear situation will hopefully improve in the future, when not just UHV studies are performed but also experiments under well controlled atmospheres. We also note that structures in *local* thermodynamic equilibrium, or metastable geometries can have a very long life time – just consider diamond (a metastable structure of carbon) for which at room temperature the phase transition to its ground-state crystal structure (graphite) is known to be rather slow. In particular, for multi-component materials, the stoichiometry at the surface requires exchange of atoms or molecules with some reservoirs and this can be hampered by significant energy barriers. Metal oxides represent an example which comes to mind, as in UHV, oxygen can desorb into the chamber, but with respect to the metal content at the surface, attaining the thermal-equilibrium stoichiometry is hampered (see, e.g., Wang et al., 1998).

### *5.2.3. Binding energy at kink sites*

As mentioned above, kicked out surface atoms may be re-bound at kink sites at steps. We will see that this is in particular relevant when we discuss below in this chapter the substitutional adsorption of alkali metal atoms and of cobalt. Therefore we now present a simple discussion of the energetics of substrate atoms at kink sites. Although we use a simplified model, we note that the conclusions are in fact valid in general.

The total energy of a many-atom system can be written as the sum over contributions assigned to the individual atoms,

$$E = \sum_{I=1}^{N^{\mathrm{nuc.}}} E_I. \tag{5.22}$$

$E_I$ is the energy contribution due to atom $I$. In an approximate way we can write $E_I = E_I(C_I)$, where $C_I$ is the number of nearest-neighbor atoms of atom $I$. This is a

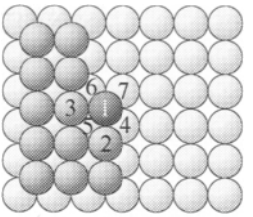


Fig. 5.2. View of a kink site at a step on an fcc (001) surface. The local coordination of an atom (labeled 1) adsorbed at a kink site $C_1$ changed from 0 (that of the free atom) to 6. For its six neighbor atoms (labeled 2, 3, 4, 5, 6, 7) the coordination numbers are increased by one, thus attaining the values: $C_2 = 7$, $C_3 = 8$, $C_4 = 10$, $C_5 = 12$, $C_6 = 11$, $C_7 = 9$.

simplified presentation of an approach which has many names (e.g., effective-medium theory, embedded-atom method, Finnis–Sinclair potentials, glue model) and which we all call *bond-cutting models*. The various implementations are similar but differ in the way the function $E(C)$ is represented. In the simplest, yet physically meaningful approach, the function $E(C)$ is roughly proportional to $\sqrt{C}$ (see Spanjaard and Desjonquères, 1990; Robertson et al., 1994; Payne et al., 1996; Methfessel et al., 1992b; Christensen and Jacobsen, 1992).

If we consider a single-element system and place an atom at a kink site at a step of an fcc (001) surface, the changes of the local coordination are as noted in Fig. 5.2. Putting this information into Eq. (5.22) and calculating the *change* in the total energy by placing an atom ($I = 1$) at a kink site (i.e., $E_{\text{ad}}^{\text{kink}} = -E^{\text{after}} + E^{\text{before}}$) gives

$$\begin{aligned} E_{\text{ad}}^{\text{kink}} = & - \big(E_1(6) + E_2(7) + E_3(8) + E_4(10) + E_5(12) + E_6(11) + E_7(9)\big) \\ & + E_1(0) + E_2(6) + E_3(7) + E_4(9) + E_5(11) + E_6(10) + E_7(8) \\ = & - E_5(12) + E_1(0). \end{aligned} \tag{5.23}$$

Thus, the adsorption energy at a kink site equals the cohesive energy. This result is in fact plausible if one considers that the adsorption at a kink site leaves the system essentially unchanged, because the kink site is simply moved by one atom and thus, the situation at the surface is physically not altered. Therefore the difference between the original and final situations is simply (and rigorously) the addition of one bulk atom, which has the energy $E(12)$.

### *5.2.4. The surface energy barrier*

We add some remarks on the behavior of the effective Kohn–Sham potential, $V^{\text{eff}}$ (see Eq. (5.7) and Fig. 5.3). The increase in $V^{\text{eff}}$ at the surface from its average bulk value up to the vacuum level is termed the surface barrier. Inside the solid, the potential $V^{\text{eff}}$ seen by an electron becomes attractive, due to the electrostatic potential of the ion cores, due to the electrostatic field of the surface–dipole layer, and due to the lowering of the electron

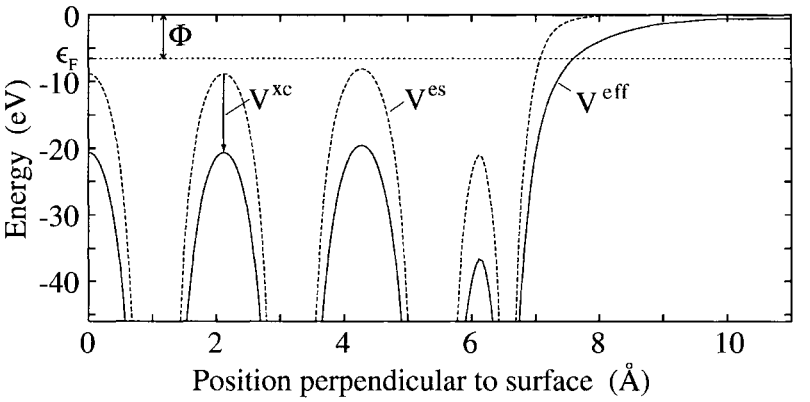


Fig. 5.3. The Kohn–Sham effective potential $V^{\text{eff}}$ (solid line) and the electrostatic potential $V^{\text{es}}$ (broken line) at an adsorbate-covered surface. In the example, which shows results for O/Ru(0001), the electrostatic potential in the bulk is below the Fermi level, but for substrates with low electron density it will be above.

energy by the formation of an exchange–correlation hole. For an electron in the vacuum region, the potential is described by the classical image effect

$$V^{\text{eff}}(z) = -\frac{1}{4\pi\varepsilon_0}\frac{(e^-)^2}{4(z-z_0)} \quad \text{for} \quad (z-z_0) \gtrsim 2\ \text{Å}, \tag{5.24}$$

where $z$ is the position of the electron, $z_0$ is the position of the reference plane of the image effect, and $\varepsilon_0$ is the vacuum dielectric function. Figure 5.3 shows the electrostatic potential and the effective one-particle potential at an adsorbate-covered surface. Here, $\Phi$ is the work function, $V^{\text{es}}$ is the electrostatic potential due to the electron density $n(\mathbf{r})$ and the nuclei, and $V^{\text{xc}}$ is the exchange–correlation potential. The latter is attractive and varies roughly as $n(\mathbf{r})^{1/3}$. The only surface contribution to the total height of the surface barrier is due to the electrostatic potential; the contribution of the exchange–correlation term to the height is a property of the bulk and not of the surface.

Nevertheless, the behavior of the potential at the surface is largely determined by the distortion of the exchange–correlation hole which stays behind as an electron passes through the surface region into the vacuum. In the local-density approximation, the exchange–correlation hole is assumed to be spherically symmetric and centered on the electron. Although both assumptions are, in general, incorrect, this approximation affects the potential $V^{\text{eff}}$ significantly only in the surface region. The local-density approximation therefore yields an exponential decrease of the effective potential near the surface rather than the $1/z$ behavior of the image effect. This inaccuracy of the local-density approximation appears to become noticeable well outside the surface region in the vacuum. Properties such as the ground-state electron density, the work function, or the surface energy seem to be relatively little affected (see, e.g., Methfessel et al., 1992a, b). The detailed shape of the barrier thus appears to be of less importance than its position and height.

The barrier affects individual electron wave functions. For example, reflection of electrons from the inner side of the barrier can give rise to surface resonances when the electron is trapped between the barrier and the rest of the crystal. In particular, the barrier position influences the energies of adsorbate states. For excited states, there are additional effects. Virtual surface resonances will appear, which in LEED, for example, show up as narrow peaks in the intensity versus voltage curves (McRae, 1971; Jennings, 1979). Furthermore, the wavelength of an electron is longer outside the crystal than inside. This yields the well-known refraction effect which broadens the angular range of emitted electrons in the vacuum region such that, at high polar angles, the electron current vanishes (see, for example, Scheffler et al., 1978). Another effect is found in the interaction of light with the surface: Photoabsorption, and hence photoemission, require a gradient in the potential. The surface barrier thus yields a special contribution to this excitation, called the surface photoeffect. For photoemission from adsorbates on transition metals, this contribution appears to be very small compared to that due to the ion core potentials. However, it can be important in systems where the valence electrons are nearly free electron-like, i.e., where their interaction with the ion cores is small. For excited states, the inner potential will be modified (also becoming complex) due to inelastic electron–electron interactions such as the excitation of electron–hole pairs, plasmons or surface plasmons, and dynamical corrections (e.g., a delay in the response of the electrons).

## 5.3. The tight-binding picture of bonding

### *5.3.1. Adsorbate–substrate interaction*

When an atom and a surface start to interact, the respective states mix and new states are created which have energy levels usually broadened and shifted with respect to the energy levels found in the uncoupled systems. Typically, the new states can still be related to the original ones, and Fig. 5.4 shows a schematic tight-binding description of the interaction of an atom with a transition metal surface. The free atom's electronic structure is noted in panel (b) of the figure, and the electronic structure of the substrate is sketched in panel (a). In principle we could choose any adatom we like for this discussion, but for ease we take hydrogen. Therefore the two levels of relevance, which result from solving the Kohn–Sham equation are the hydrogen 1s and hydrogen 2s levels; for simplicity we neglect contributions from the H 2p and other higher-lying states. We note that the highest occupied DFT-LDA (and DFT-GGA) Kohn–Sham eigenvalue should not be confused with ionization energy (see the discussion of Fig. 5.5 and Eq. (5.25) below). Instead, for partially occupied valence states it is roughly at the mid value of the ionization and affinity energies.

Different transition-metal substrates mainly differ in the width of the d-band, which increases from 3d to 4d to 5d; and they differ in the position of the Fermi level, which varies from the left to the right of the periodic table as follows: For the 4d series it is at the lower edge of the d-band for strontium, just below the top of the d-band for palladium, and about 3 eV above the upper edge of the d-band for silver. Thus, in the example of Fig. 5.4 we use the Fermi level $\epsilon_F$ corresponding to palladium.

At first we consider the role of the substrate s-band. When the adsorbate and the substrate interact, the hybridization of the adsorbate wave functions and the states of the sub-

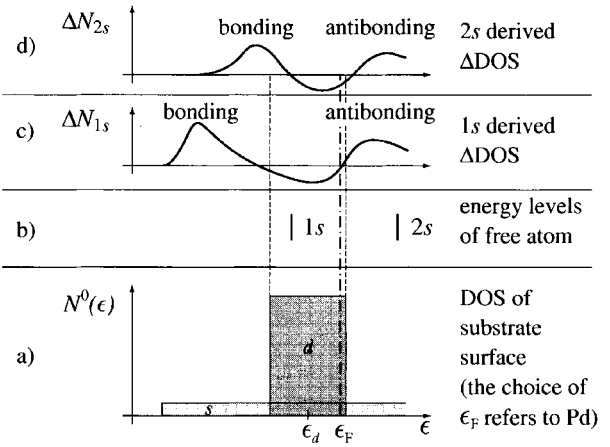


Fig. 5.4. Formation of adsorbate-induced peaks in the DOS. The bottom panel (a) shows the density of states for a transition metal before adsorption ($\epsilon_d$ is the center of the d-band). Panel (b) shows the Kohn–Sham energy levels of a free atom (here as an example, H). The interaction between the H 1s-level and the substrate s- and d-bands gives rise to a broadening and the formation of an antibonding level (above the d-band) and a bonding level (below the d-band) – see panel (c). Panel (d) shows that the interaction between the H 2s-level with the substrate s- and d-bands gives rise to a broadening and the formation of a bonding level (at about the lower edge of the d-band) and an antibonding level (at about the empty free atom 2s-level).

strate s-band gives rise to a broadening of the adsorbate levels, and the atomic levels will shift because the substrate Fermi level and the electron chemical potential of the atom become aligned. The latter will result in a fractional electron transfer (see the discussion of Fig. 5.5 below). An analysis of the wave-function character in such a broadened peak shows that the low-energy part of the peak belongs to states which have an increased electron density between the adsorbate and the substrate (such states are called "bonding"), and the high-energy part of the peak belongs to states which have a node between the adsorbate and the substrate (such states are called "antibonding"). The substrate s-electrons spill out most into the vacuum, and that is why the broadening (and shifting) of electronic levels is the first change that happens when an atom is brought toward a surface. Broadening implies a coupling of the formerly localized electrons of the adatom to the substrate, thus a delocalization. In fact, still neglecting (for the moment) the interaction of the adatom with the d-band, there are three contributions which affect the adatom levels:

(i) A shift which can go in either direction and which is caused by charge transfer or charge redistribution (or polarization) at the adatom. For partially occupied valence states it largely reflects an alignment of the adsorbate DOS with respect to the substrate Fermi level.

(ii) A shift toward lower[4] energies because the potential at the surface is lower than that in vacuum (cf. Fig. 5.3 and/or Chapter 1 of this book).

4 Our wording is chosen as such that "higher energy" of a bound electronic state means closer to the vacuum level, i.e., with respect to Fig. 5.4 or 5.12 the energy is more to the right. Obviously, "lower energy" then refers to an energy more to the left in these figures.

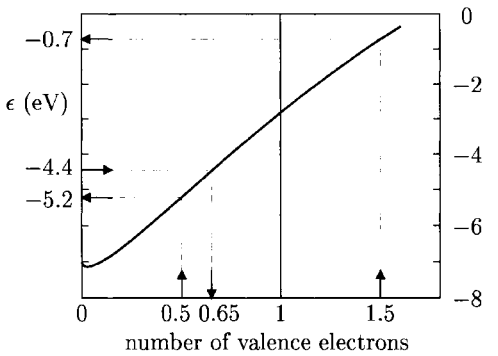


Fig. 5.5. Kohn–Sham energy level (DFT-LDA) of the 3s-state of Na as function of the number of valence electron: $f_{3s} = 0$ is the $Na^+$ ion, $f_{3s} = 1$ is the neutral atom, and $f_{3s} = 2$ is the $Na^-$ ion. For $f_{3s} = 0.5$ the eigenvalue gives the ionization energy (here 5.2 eV; the experimental result is 5.14 eV). For $f_{3s} = 1.5$ the eigenvalue gives the electron affinity (here 0.7 eV; the experimental result is 0.55 eV). If the eigenvalue were fixed by an electron reservoir to 4.4 eV, which is the Fermi level of Al(001), an occupation of 0.65 of the Na valence shell would result.

(iii) A contribution which implies a shift to lower[4] energies because the self-interaction (an artifact in DFT-LDA and DFT-GGA calculations) is smaller for the more extended states of the adsorbate than for the states in the free atom.

These broadened and shifted energies are called "renormalized atomic levels". The three contributions are indeed significant. As a consequence, a self-consistent treatment is crucial for calculating the adsorbate–substrate interaction.

We note that the self-interaction effect is strong when DFT-LDA energy levels are studied. But in total-energy *differences* it nearly cancels out. This is demonstrated in Fig. 5.5, which shows the DFT-LDA eigenvalue for the atomic Na 3s-state as function of its occupation. For the neutral Na atom the occupation is 1 and the energy level is at −2.8 eV. The extent to which a Kohn–Sham energy eigenvalue $\epsilon_k$ reflects the ionization energy, which is the minimum energy to remove an electron from the $k$-th level, depends on how strongly the eigenvalue depends on the occupation number $f(\epsilon_k, T)$. If this dependence is negligible, then the negative of the energy eigenvalue equals the ionization energy. This is the density-functional theory analogue of Koopmans' theorem in Hartree–Fock theory.

In general, the ionization energy ($I_k$) is defined by the total-energy difference of the neutral atom and the positively charged ion, and this can be read off from Fig. 5.5 as the energy at occupation 0.5. This approach only employs the mean-value theorem of integration

$$I_k = E^{N-1} - E^N = \int_N^{N-1} \frac{\mathrm{d}E^{N'}}{\mathrm{d}N'}\,\mathrm{d}N' = -\int_0^1 \epsilon_k(f_k)\,\mathrm{d}f_k \approx -\epsilon_k(f_k = 0.5). \tag{5.25}$$

It is called the Slater–Janak transition-state approach of evaluating total-energy differences (Janak, 1978), which works very well in LDA and GGA calculations (for a discussion of the general proof see Perdew and Levy, 1997; Kleinman, 1997; and references therein).

According to Fig. 5.5 the transition-state gives $I_k \approx 5.2$ eV, which agrees well with the experimental result for the ionization energy of 5.14 eV. Analogously we note that the highest occupied Kohn–Sham eigenvalue at occupation 1.0 agrees well with the mean value of the ionization and affinity energies.

The result shown in Fig. 5.5 is typical for all atoms. It demonstrates the importance of electron–electron correlation, though it is also largely due to self-interaction, an LDA artifact. Clearly, the measurable ionization energies (level at occupation 0.5) and the theoretical Kohn–Sham eigenvalue (level at occupation 1.0) are very different and should not be confused. Figure 5.5 also shows that typically only partial electron transfer is to be expected upon adsorption. If the substrate mainly plays the role of providing an electron reservoir, thus, the electron chemical potential is fixed by the substrate Fermi level, which for Al(001) is at 4.4 eV below the vacuum level, Fig. 5.5 then shows that the occupancy of the Na 3s-level will be adjusted to 0.65. Thus we obtain a partial ionization and a shift of the Na 3s-level, already from a study of the free-atom eigenvalue. This is fully in accord with what is suggested by the electronegativities of the atoms: $\kappa_{\mathrm{Na}} = 0.93$ and $\kappa_{\mathrm{Al}} = 1.61$.

We continue the discussion of Fig 5.4. At close distances of the adsorbate to the surface the *renormalized atomic levels* [i.e., the levels which result after the effects (i), (ii), and (iii)] will interact with the more localized d-states. Because the d-band is rather narrow and its width comparable to the interaction strength, the interaction will result in a splitting into the bonding states, $\psi_{\mathrm{b}} \approx (\varphi_{\mathrm{H\,1s}} + \varphi_{\mathrm{Pd\,4d}})$ and the antibonding states, $\psi_{\mathrm{a}} \approx (\varphi_{\mathrm{H\,1s}} - \varphi_{\mathrm{Pd\,4d}})$. The resulting adsorbate-induced density of states (DOS) for the H 1s-state is shown in panel (c) of Fig. 5.4. Panel (d) shows the corresponding result induced by the H 2s state. We note that the resulting peaks are close to the lower and upper edge of the d-band and inside the d-band the density is reduced, which simply reflects the fact that these states are shifted from inside the d-band to higher and lower energy upon hybridization with the adsorbate states.

Obviously, the bonding is strongest when bonding states are occupied and antibonding states remain empty. According to Fig. 5.4 this will happen when the Fermi level is in the middle of the d-band, as for example for Mo and Ru substrates.

Figure 5.6 describes the same physics as Fig. 5.4, but with an additional simplification: Now the broadening due to the substrate s-band is ignored and the d-band is replaced by just a single level, the d-band center. The energy levels of the "free" adatom are in fact the "renormalized levels", and therefore we tagged them in Fig. 5.6 with a tilde: $1\tilde{s}$, $2\tilde{s}$.

Deepening this discussion we show in Fig. 5.7 results of actual calculations where the distance dependence of the broadening and shift of the energy level is displayed for two qualitatively different systems: Na on Al(001) and O on Ru(0001). For both adatoms, Na and O, the ionization energy of the free atoms is below the Fermi level. In fact, the relevant "energy level" to be considered is not the ionization energy and also not the electron affinity, but the mean value of those two (or alternatively, the Kohn–Sham eigenvalue of the highest occupied state; cf. the discussion above). This mean value is plotted in Fig. 5.7: For the Na atom it is at $(5.1 + 0.5)/2\,\mathrm{eV} = 2.8$ eV and for the O atom it is at $(13.6 + 1.4)/2\,\mathrm{eV} = 7.5$ eV below vacuum. When the adatoms approach the surface, the substrate Fermi level acts as an electron reservoir. For Na this implies a partial charge transfer from the adsorbate to the substrate (see the discussion of Fig. 5.5 above). But for oxygen, with its initially rather deep level, this implies a partial charge transfer from the substrate to the adatom.

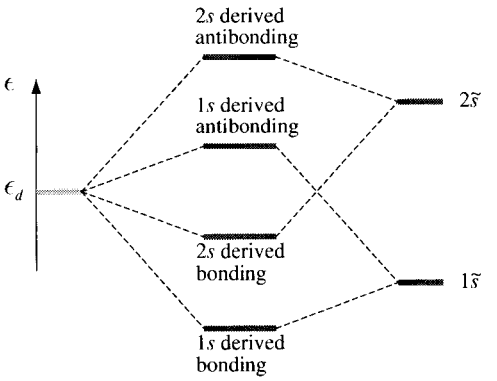


Fig. 5.6. Schematic summary of the content of Fig. 5.4. Left: the d-band-center energy of the clean substrate. Right: the *renormalized energy levels* of the free atom (i.e., after interaction with the s-band, but before interaction with the d-band). Middle: the resulting bonding and antibonding H 1s- and H 2s-derived levels on adsorption.

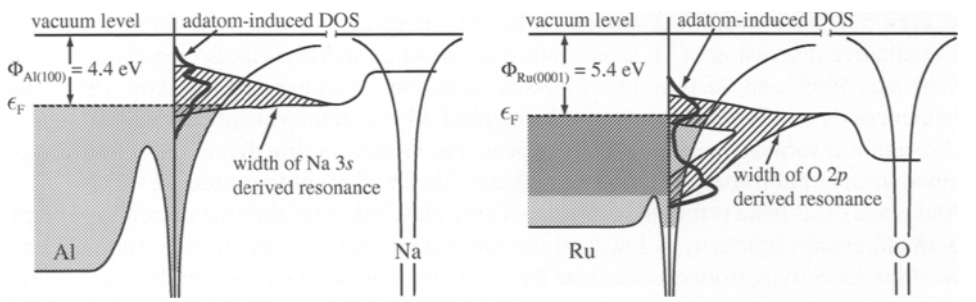


Fig. 5.7. Side view of the surface, and the adsorbate-induced change in the density of states as a function of distance. Two chemically distinct systems are displayed. Left: Na on Al(001). Right: O on Ru(0001). The dark gray region in right figure marks the occupied part of d-band of the Ru substrate. The energy levels noted for the atoms are the mean values of the ionization energy and electron affinity (Na: 2.8 eV, O: 7.5 eV), see text for details.

Upon close approach these partially ionized atoms interact with the substrate orbitals. For Na/Al(001) the DFT-LDA calculations predict a double peak structure, which has its main weight above the Fermi level, but with a tail reaching into the occupied states regime. For O/Ru(0001) the interaction is stronger because the adatom's equilibrium position is very close to the surface and the substrate d-states impart a strong covalent bond and a splitting into bonding and antibonding states. The left panel of Fig. 5.7 nicely reflects the Gurney description of alkali-metal adsorption, and the right panel of Fig. 5.7 displays the corresponding result for an "opposite" adsorbate, namely one with high electronegativity and a strong covalent adsorbate–substrate interaction.

The adsorbate-induced DOS (as shown in Fig. 5.4c, d) enables us to decide on the nature of the bond. Assuming that the antibonding states are at least partially empty we have chemical bonding of either covalent or ionic character. When the states of the occupied peak are predominantly derived either from adsorbate or substrate orbitals

the bonding character is called "ionic". When the wave-function character of the occupied states is derived by about the same amount from the substrate and the adsorbate the bond is called "covalent". The problem with this classification is in the assumption that a substrate and an adsorbate region can be defined and separated. However, for strong chemisorption situations it is typically not obvious how to assign electron density to the different atoms. Still the concepts are valuable and we will come back to them in Section 5.4. We note in passing that an intriguing way to assign electron density to individual atoms in a many-atom system was developed by Bader (1990, 1994, and references therein), but it is only now that these concepts are being used in solid-state calculations.

The concept behind the qualitative discussion presented in this section is essentially that of the Anderson–Grimley–Newns model for chemisorption (see, for example, Nørskov, 1990; Spanjaard and Desjonquères, 1990). The main difference is that free-atom levels are replaced by *renormalized* levels, that we have not introduced a restrictive assumption about electron correlation and the localization of the adsorbate–substrate interactions, and that we kept the discussion at a qualitative level. We believe that the approach sketched in Figs. 5.4, 5.6 is useful but should not be overinterpreted. It was used, for example, for a qualitative discussion of $H_2$ dissociation at transition metal surfaces (see Hammer and Scheffler, 1995; and Section 5.9). Nørskov et al. (see Hammer and Nørskov, 1997, and references therein) refined the approach and used it for a (semi-) quantitative discussion of adsorption at various transition metal surfaces. The results confirm the simple chemical picture that adsorption energies decrease with the d-band filling of the substrate (for $N_d \geqslant 5$). And when the d-band is full, the d-electrons only play little role; thus the adsorption energy is small, chemical activity is low, and the substrate is called noble. In fact, Hammer and Nørskov recently performed extensive DFT calculations of atomic and molecular adsorption at several metal surfaces and then used the above described approach to explain the main trends of bonding to metal surfaces in terms of the d-band filling. The crucial term in their approach is the adsorbate–substrate coupling matrix element. The latter depends on the adsorbate geometry (site and interatomic distances); unfortunately, but also quite obviously, this cannot be obtained from a simple Anderson–Gimley–Newns type of description.

As a warning remark we add that energy levels and the density of states, $N(\epsilon)$, are important ingredients of the total energy, but from the total-energy contribution

$$E^{\text{bands}} = \int_{-\infty}^{+\infty} f(\epsilon) N(\epsilon) \epsilon \, \mathrm{d}\epsilon, \tag{5.26}$$

it is typically not possible to decide on the strength of chemical bonding. The situation is different, when different geometries are compared and a frozen-potential approximation applied (the Andersen–Pettifor force theorem), as then (and only then) the other terms in the DFT total-energy expression cancel and *energy differences* based on Eq. (5.26) may give an approximate description (see Skriver, 1985, and references therein). In this context we note that many-atom systems tend to assume a geometry with an electron density as hard as possible, which means that either a band gap is opened or the density of states at the Fermi level is reduced. This may be viewed as a generalization of the Jahn–Teller theorem. In this sense $N(\epsilon)$, in particular its behavior at the Fermi level, is instructive.

### *5.3.2. Adsorbate band structure*

To discuss covalent interactions between adparticles on a surface, we consider an ordered adlayer which is in registry with a crystalline substrate. Such a system has two-dimensional translational symmetry and the eigenfunctions are two-dimensional Bloch states which are defined by their reduced $\mathbf{k}_{\|}$-vector (in the surface Brillouin zone) as well as by their energy. Figure 5.8 shows the surface Brillouin zones for the clean surface and for a c(2 × 2) adsorbate overlayer on the (001) face of an fcc metal. To obtain the bulk band structure projected onto the surface of a clean semi-infinite system, it is necessary to integrate over $k_z$ inside the bulk Brillouin zone and to shift regions outside the first two-dimensional Brillouin zone into its interior by a reciprocal lattice vector of the (two-dimensional) surface structure. This folding back of the $\mathbf{k}_{\|}$-resolved density of states of a clean, unreconstructed surface is indicated in Fig. 5.9a. The broken lines show the projection of the bulk Brillouin zone. Even for the clean surface, it is found that the surface Brillouin zone is usually smaller than the projection of the three-dimensional bulk Brillouin zone on the surface. For a periodic adlayer at fractional coverage, the surface Brillouin zone is further reduced compared with the clean surface, which again requires a shift of the $\mathbf{k}_{\|}$-resolved density of states of regions outside the new surface Brillouin zone into its interior, as shown in Fig. 5.9b. Because the back-folded density of states adds to the original one, the change in the $\mathbf{k}_{\|}$-resolved density of states is obviously quite large. We note, however, that this folding back is a purely mathematical effect. It takes into account the increase of the periodicity parallel to the surface but it is independent of the strength and the type of the physical mechanism causing this change in periodicity. The physical importance of this effect, i.e., the degree of the mixing of the wave functions involved in the surface region and in turn the question how strongly this effect will affect, for example, photoemission spectra, depends on the strength of the adsorbate–substrate interaction. We return to this back-folding effect in the discussion of Figs. 5.19 and 5.20 of Section 5.5.4 below.

The dispersion $\epsilon(\mathbf{k}_{\|})$ of the chemisorption-induced bands can be described in a simple tight-binding picture. It is appropriate to use a LCMO (linear combination of molecular orbitals) description where the MOs contain the interaction with the substrate as well as

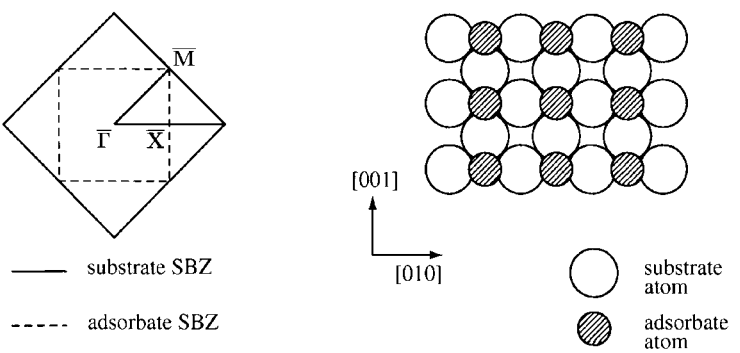


Fig. 5.8. The surface Brillouin zones (SBZs) and real-space lattice of a c(2 × 2) adlayer on an fcc (001) surface. The lettering of the symmetry points refers to the adsorbate SBZ.

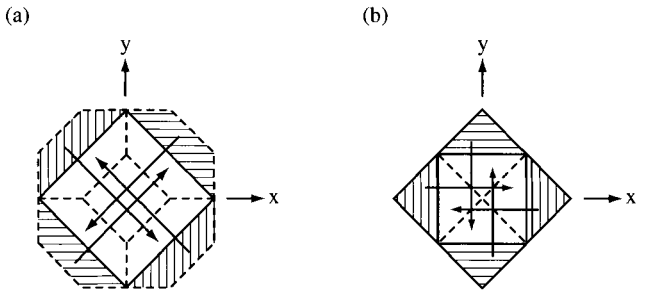


Fig. 5.9. (a) The relation between the surface Brillouin zone (full line) and the projection of the bulk Brillouin zone of an fcc substrate onto the (001) surface (broken line). Hatched regions have to be shifted by a surface reciprocal lattice vector into the first surface Brillouin zone, as indicated by arrows. (b) Surface Brillouin zone for the c(2 × 2) adsorbate layer, showing shift of hatched regions by (adsorbate) reciprocal lattice vectors.

the intra-adparticle mixing of wave functions. Because this method is very simple and gives a reasonable qualitative description, we consider it in more detail. Two-dimensional Bloch states are used as a basis

$$\chi_\alpha(\mathbf{r}, \mathbf{k}_\parallel) = \frac{1}{\sqrt{N^{\text{nuc.}}}} \sum_{\mathbf{R}_I}^{N^{\text{nuc.}}} e^{i\mathbf{k}_\parallel \mathbf{R}_I} \phi_\alpha(\mathbf{r} - \mathbf{R}_I), \tag{5.27}$$

where $\alpha$ labels the different (molecular) orbitals $\phi$ in the unit cell. The $\mathbf{R}_I$ are two-dimensional lattice vectors. The wave functions of the system are thus given by

$$\varphi(\epsilon, \mathbf{k}_\parallel, \mathbf{r}) = \sum_\alpha C_\alpha(\epsilon, \mathbf{k}_\parallel) \chi_\alpha(\mathbf{r}, \mathbf{k}_\parallel). \tag{5.28}$$

For the Hamilton matrix we find

$$H_{\alpha,\alpha'}(\mathbf{k}_\parallel) = \langle \chi_\alpha(\mathbf{k}_\parallel) | H | \chi_{\alpha'}(\mathbf{k}_\parallel) \rangle = \sum_{\mathbf{R}_I}^{N^{\text{nuc.}}} e^{i\mathbf{k}_\parallel \mathbf{R}_I} H_{\alpha,\alpha'}(\mathbf{R}_I) \tag{5.29}$$

with

$$H_{\alpha,\alpha'}(\mathbf{R}_I) = \langle \phi_\alpha(\mathbf{r}) | H | \phi_{\alpha'}(\mathbf{r} - \mathbf{R}_I) \rangle. \tag{5.30}$$

Because the basis (5.27) is usually not orthogonal, we get an overlap matrix

$$S_{\alpha,\alpha'}(\mathbf{k}_\parallel) = \langle \chi_\alpha(\mathbf{k}_\parallel) \mid \chi_{\alpha'}(\mathbf{k}_\parallel) \rangle = \sum_{\mathbf{R}_I}^{N^{\text{nuc.}}} e^{i\mathbf{k}_\parallel \mathbf{R}_I} S_{\alpha,\alpha'}(\mathbf{R}_I) \tag{5.31}$$

with

$$S_{\alpha,\alpha'}(\mathbf{R}_I) = \langle \phi_\alpha(\mathbf{r}) \mid \phi_{\alpha'}(\mathbf{r} - \mathbf{R}_I) \rangle. \tag{5.32}$$

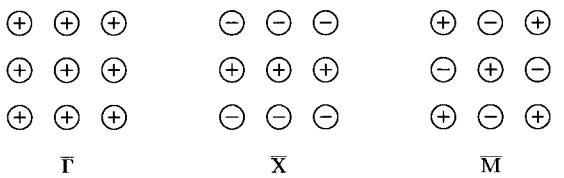


Fig. 5.10. Top view of a schematic representation of the two-dimensional Bloch states formed from atomic or molecular orbitals belonging to the $a_1$ representation of the $C_{4v}$ point group (s-like orbitals) at the high-symmetry points of the surface Brillouin zone (see Fig. 5.8 and Eq. (5.34)). We display a region of 9 adatoms. The sign of the orbital in the center $\mathbf{R}_0$ is chosen +, and the signs of other orbitals are then $e^{i\mathbf{k}_\parallel(\mathbf{R}_I-\mathbf{R}_0)}$ with $\mathbf{k}_\parallel$ defined by Eq. (5.34).

The Schrödinger equation is then

$$\sum_{\alpha'}\left\{\sum_{\mathbf{R}_I}^{N^{\text{nuc.}}} e^{i\mathbf{k}_\parallel\mathbf{R}_I}\left[H_{\alpha,\alpha'}(\mathbf{R}_I)-\epsilon(\mathbf{k}_\parallel)S_{\alpha,\alpha'}(\mathbf{R}_I)\right]\right\}C_{\alpha'}(\epsilon,\mathbf{k}_\parallel)=0 \tag{5.33}$$

and must be solved at each $\mathbf{k}_\parallel$. The zeros of the determinant of the matrix in the curly brackets in Eq. (5.33) give the dispersion $\epsilon(\mathbf{k}_\parallel)$. The required matrix elements $H_{\alpha,\alpha'}(\mathbf{R}_I)$ and $S_{\alpha,\alpha'}(\mathbf{R}_I)$ can be calculated numerically in some approximation (Bradshaw and Scheffler, 1979; Horn et al., 1978; Scheffler et al., 1979; Jacobi et al., 1980). Often, an empirical tight-binding calculation might be sufficient, which introduces the following three assumptions: (1) Orbitals $\phi_\alpha$ at different centers are orthogonal, the overlap matrix $S_{\alpha,\alpha'}(\mathbf{R}_I)$ is thus equal to one for $\alpha=\alpha'$ and $\mathbf{R}_I=(0,0)$ and zero otherwise. (2) Only nearest neighbors (sometimes also second nearest neighbors) are taken into account in the sum over $\mathbf{R}_I$ in Eq. (5.33). (3) The matrix elements are fitted to experimental results; usually there are only very few remaining.

We will illustrate this for the example of an adsorbate with s-like states in a c(2 × 2) overlayer on an fcc (001) surface ($p_z$-like states would behave the same way). The corresponding adsorption-induced MOs $\phi_\alpha$ belong to the $a_1$ representations of the $C_{4v}$ point group (we assume that the adsorbate occupies a fourfold symmetric site). We then have two parameters in Eq. (5.33): $H_{a_1,a_1}(0)$ and $H_{a_1,a_1}(\mathbf{R}_I)$. Figure 5.10 shows schematically the Bloch states according to Eq. (5.27) for the three high symmetry points of the surface Brillouin zone (see Fig. 5.8)

$$\bar{\Gamma}:\mathbf{k}_\parallel=(0,0),\qquad \bar{\mathrm{X}}:\mathbf{k}_\parallel=\frac{g}{2}(1,0),\qquad \bar{\mathrm{M}}:\mathbf{k}_\parallel=\frac{g}{2}(1,1), \tag{5.34}$$

where $g$ is the length of the first two-dimensional reciprocal lattice vector of the adlayer. Figure 5.10 has been constructed by placing orbitals of s-like symmetry at all the atoms (or molecules) of the adlayer (only 9 of them are shown in the figure). The phase factors of orbitals at different sites is $e^{i\mathbf{k}_\parallel\mathbf{R}_I}$ corresponding to the appropriate $\mathbf{k}_\parallel$-point in the surface Brillouin zone. An analysis of this figure already yields the qualitative band structure. At $\bar{\Gamma}$ the $a_1$-derived two-dimensional Bloch state is completely bonding in the adlayer, giving this state the lowest energy. At $\bar{\mathrm{M}}$ it is completely antibonding (highest energy), and at $\bar{\mathrm{X}}$,

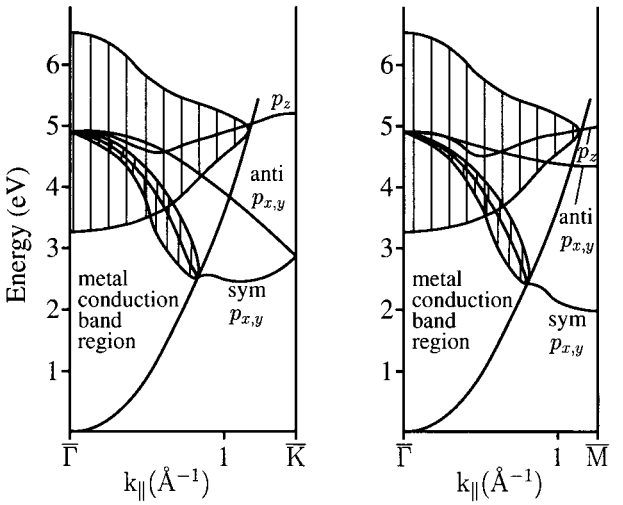


Fig. 5.11. Calculated band structure for a hexagonal (1 × 1) oxygen layer on a jellium substrate, simulating the Al(111) surface. Reproduced after Hofmann et al. (1979).

it is of mixed character. Thus, s-like adsorbate states give rise to an energy band which has the lowest energy at $\bar{\Gamma}$ and the highest energy at $\bar{M}$. The analogous discussion for $p_x$-, $p_y$-like states can be found in an earlier review article by Scheffler and Bradshaw (1983).

To discuss the interaction of an adsorbate with the s-band of the substrate, we consider in Fig. 5.11 as an example the adsorption of oxygen on jellium corresponding to a (1 × 1) overlayer on Al(111) (Hofmann et al., 1979), which has been calculated using the two-dimensional KKR method (Kambe and Scheffler, 1979). The crystallographic point group is $C_{6v}$ because the jellium model neglects the atomic structure of the substrate. Full lines show the center of the peaks; hatched regions indicate the width of the peaks. The strong dispersion of the levels is quite apparent. The width of the band structure (the dispersion of the full lines) indicates the extent of the splitting between states which are bonding with respect to neighboring adparticles and those which are antibonding, just as in the case of the tight-binding scheme discussed above. At $\bar{\Gamma}$ the $p_x$- and the $p_y$-derived Bloch states are degenerate because of the $C_{6v}$ symmetry and the splitting between the $p_z$- and $p_x$, $p_y$-derived states is very small. The O $2p_z$-induced level is broad but that derived from $p_x$, $p_y$ is sharp. This different behavior of the two levels can be explained in the following way. For an ordered overlayer in registry with the substrate, two-dimensional Bloch states of the overlayer can only hybridize with those of the substrate which have the same $\mathbf{k}_{\parallel}$ vector. The resulting wave functions inside the jellium can thus be given as a sum over plane waves propagating toward the surface and the reflected waves

$$\varphi(\epsilon, \mathbf{k}_{\parallel}, \mathbf{r}) = \sum_{\mathbf{g}} U_{\mathbf{g}}^{+} e^{i\mathbf{k}_{\mathbf{g}}^{+}\mathbf{r}} + U_{\mathbf{g}}^{-} e^{i\mathbf{k}_{\mathbf{g}}^{-}\mathbf{r}}. \tag{5.35}$$

Because the potential is constant inside the jellium, the $\mathbf{k}_{\mathbf{g}}^{\pm}$-vectors of these plane waves

are given by

$$\mathbf{k}_{\mathbf{g}}^{\pm} = \left(\mathbf{k}_{\parallel} + \mathbf{g}, \pm\sqrt{\frac{2m(\epsilon - V_0)}{\hbar^2} - (\mathbf{k}_{\parallel} + \mathbf{g})^2}\right), \tag{5.36}$$

where $\mathbf{g}$ are reciprocal lattice vectors of the (two-dimensional) surface Brillouin zone. Obviously, for $\mathbf{k}_{\parallel} = (0, 0)$ and a wave function which is antisymmetric with respect to a mirror plane of the system, the coefficients $U^{+}_{(0,0)}$ and $U^{-}_{(0,0)}$ vanish. At energies close to the bottom of the conduction band of the substrate, all the remaining terms have an imaginary value for $k_z$, which implies that these states decay exponentially normal to the surface. These are true surface states and have a sharp energy. In other words, we could say that at the bottom of the band the substrate states are s-like and thus do not have the correct symmetry in order to hybridize with $p_x$, $p_y$-like adsorbate levels at $\mathbf{k}_{\parallel} = (0, 0)$. Only at higher energies could these states also couple to bulk bands and broaden. Figure 5.11 also shows that the levels change their width with $\mathbf{k}_{\parallel}$ and become discrete when they lie outside the metal conduction band. We note the behavior of the symmetric $p_x$, $p_y$-derived band at the point at which it begins to hybridize with the substrate wave functions: just outside the metal conduction band region it bends slightly to lower[4] energies. Here it is purely bonding in character. At the same $\mathbf{k}_{\parallel}$ value, we note that the corresponding antibonding (broad) level occurs in the conduction band. When the band enters the conduction band, the bonding and the antibonding levels form one broad peak as mentioned above.

## 5.4. Adsorption of isolated adatoms

Calculations of isolated adatoms afford an analysis of the nature of the adsorbate–substrate bond without it being obscured by the influence of other adsorbates. In this section we will therefore summarize characteristic results of the adsorption of isolated atoms.

The calculations presented in the remaining part of this section were performed with the Green-function method, which provides the most accurate and efficient approach for calculating properties of truly isolated adatoms on extended substrates. For technical details of the method we refer the interested reader to the original papers (see in particular Bormet et al., 1994a; Lang and Williams, 1978; Bormet et al., 1994b; Wenzien et al., 1995; Scheffler et al., 1991; and references therein).

We consider group I, group IV, and group VII adsorbates, namely Na, Si, and Cl. By such a trend study of atoms from the left to the right side of the periodic table, a classification of the nature of the bond becomes rather clear, but we will also emphasize (again) the limitation and/or danger of "nature-of-bond" concepts. Three different substrates will be considered, namely,

- jellium with an electron density corresponding to aluminum,
- Al(111),
- Cu(111),

which enables us to identify the role of substrate s-, p-, and d-states. For the Al(111) and Cu(111) systems the adsorbates were placed in the fcc-hollow site. In this section we discuss on-surface adsorption; substitutional adsorption, where the adatom replaces a surface

atom, will be treated in Section 5.6, and subsurface adsorption will be briefly touched upon in Section 5.10.

### 5.4.1. Geometry

Table 5.1 gives the adsorbate heights $Z$ and effective radii $R$ of the adsorbates, as obtained from the distances between the adatom and its nearest-neighbor substrate atoms, using the substrate atomic radii from the bulk. Both the calculated heights and the effective radii (the bond length is given by the sum $R + R_{Al}$ or $R + R_{Cu}$) are found to be noticeably smaller for Al(111) than for the jellium substrate. This is due to the fact that jellium is devoid of any information concerning the atomic structure. Thus, the shell-like property of electrons, i.e., their s-, p-, d-like character is missing, which hinders the formation of directional orbitals in the substrate; and aluminum, despite its reputation of being a jellium-like system, is in fact a material with noticeable ability for covalent bond formation. On comparison of the results for adsorption on the Cu and Al substrates, it is found that the trend from jellium to aluminum continues: The effective radius of the studied adsorbates on Cu(111) is smaller than on Al(111). The smaller values reflect that bonding of the adsorbates is stronger on Cu(111) than on Al(111), which was identified as being due to the Cu d-electrons (Yang et al., 1994); although the top of the Cu d-band is about 2 eV below the Fermi level, the d-states play a noticeable role.

The results demonstrate that stronger bonds go together with shorter bondlengths. As noted above in Table 5.1 we considered a threefold coordinated adsorption site. For other sites with lower coordination the strength per individual bond will typically increase, because the same number of adsorbate electrons have to be distributed (by tunneling or hopping) over fewer bonds. As a consequence, the bond length will typically decrease. This does not mean that the binding energy will increase as well, because this is determined by *all* bonds. This correlation between local coordination and bond strength, and the correlation between bond strength and bond length is well known (see, e.g., Pauling, 1960; Methfessel et al., 1992a). But we also emphasize that when significant changes in hybridization

Table 5.1

Calculated geometrical parameters for adsorbed atoms from the left to the right side of the periodic table, and for different substrates. The height $Z$ is defined with respect to the center of the top substrate layer. The effective radii of the adatoms $R$ are evaluated by subtracting from the calculated bond lengths the radius of a substrate atom (as given by the inter-atomic distances in the bulk). Thus, we use $R_J = R_{Al} = 1.41$ Å and $R_{Cu} = 1.27$ Å. For the jellium substrate we assume the geometry of Al(111). Also noted as a percentage is the difference of the adatom radii with respect to that of the jellium calculation: $(R_J - R)/R_J$. The jellium results are from Lang and Williams (1978), the Al(111) results are from Bormet et al. (1994a) and the Cu(111) results are from Yang et al. (1994)

| Substrate | Na | | | Si | | | Cl | | |
|---|---|---|---|---|---|---|---|---|---|
| | $Z$ (Å) | $R$ (Å) | $\Delta R/R_J$ | $Z$ (Å) | $R$ (Å) | $\Delta R/R_J$ | $Z$ (Å) | $R$ (Å) | $\Delta R/R_J$ |
| Jellium | 2.79 | 1.82 | 0 | 2.37 | 1.46 | 0 | 2.52 | 1.59 | 0 |
| Al(111) | 2.69 | 1.73 | −5% | 1.95 | 1.13 | −22% | 2.09 | 1.24 | −22 % |
| Cu(111) | 2.43 | 1.56 | −14% | 1.68 | 0.96 | −34% | 1.78 | 1.03 | −35 % |

occur for different geometries, and/or when the system cannot attain the geometry of optimum bond angles, this simple picture breaks down.

### *5.4.2. Density of states* $\Delta N(\epsilon)$

As emphasized in Sections 5.1.1, 5.2.1, and 5.3, inspection of the adsorbate-induced change in the density of states $\Delta N(\epsilon)$ is particularly informative. Together with the knowledge of the position of the Fermi energy, it tells us whether the electronic states which are formed upon adsorption are occupied, unoccupied, or partially occupied, and this enables us to discern the nature of the chemical bond. Figures 5.12a and b show such results for adsorbates on Al(111) and on jellium. The adsorbates investigated in the work of Bormet et al. (1994a) (Fig. 5.12a) were Na, Si, and Cl, and in that of Lang and Williams (1978) (Fig. 5.12b) they were Li, Si, and Cl. The results of both of these calculations agree qualitatively and show the following: For both alkalis (Na and Li) the adsorbate resonance lies well above the Fermi level and is thus largely unoccupied. This indicates that the valence electron of the alkali metal atom (or part thereof) has been transferred to the substrate

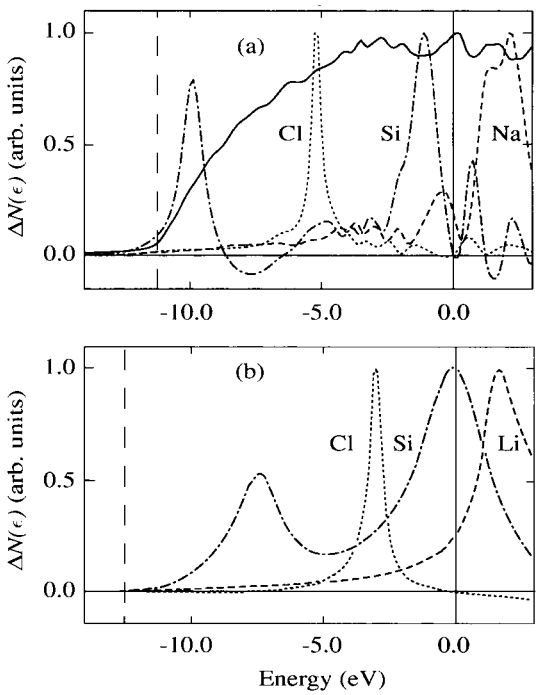


Fig. 5.12. Adsorbate-induced change of the density of states (cf. Eq. (5.8)) for three different adatoms (group I, IV, and VII of the periodic table) on an Al(111) substrate (top: a) and on jellium with an electron density corresponding to Al (bottom: b). For the Al substrate also the bulk density of states is displayed (the full line in figure a). The results are from Bormet et al., 1994a, (top), and from Lang and Williams, 1978, (bottom). The Fermi level $\epsilon_F$ is at the energy equal to zero. The vertical dashed line indicates the bottom of the band of the substrate.

and the adatom is partially positively charged. In an opposite manner, on adsorption of chlorine, the resonance in the curve corresponding to the Cl 3p resonance lies 5 eV below the Fermi level, and the Cl 3s peak is positioned even below the substrate valence band at about $-18$ eV, i.e., outside the energy range displayed in Fig. 5.12. This result implies that a transfer of electron density from the substrate to the Cl adatom has taken place; the adsorbed Cl atom is partially negatively charged. Thus, Li and Na constitute examples of positive ionic chemisorption and Cl is an example of negative ionic chemisorption.

For the adsorption of an isolated Si atom it can be seen from the jellium calculations that the Si 3p resonance lies just at the Fermi level, which implies that it is about half occupied. As noted in Sections 5.2.1 and 5.3.1, the states of the energetically lower half of the resonance are bonding between the adatom and the substrate and the energetically higher states are antibonding. Because the Fermi level cuts the p-resonance approximately at its maximum, the bonding nature of Si is covalent, i.e., the bonding states are filled and the antibonding states are empty. The results for atomistic (Al and Cu) substrates also show that the bond is covalent. In this case, however, more structure occurs in the DOS than in the jellium calculations. This arises because the atomic structure of the substrate leads to band-structure effects, clearly reflected by the structure of the bulk DOS at $\epsilon_F$ in Fig. 5.12a. As a consequence, adsorption of a covalent atom, such as Si, results in a splitting of the bonding and antibonding states, and the adatom density of states exhibits a minimum at the Fermi level (Bormet et al., 1994a). Similarly to the jellium substrate, also for Si/Al(111) the Fermi level cuts the Si 3p-induced DOS roughly in the middle. We note in passing that for Si on Al(111) (cf. Fig. 5.12a) the structure of the p-like adsorbate density of states is largely determined by the clean-substrate density of states: With the Green function $\mathcal{G}^0$ of the clean substrate, we find at maxima of $\mathrm{Im}\{\mathrm{Tr}(\mathcal{G}^0(\epsilon))\}$ minima of $\Delta N(\epsilon)$, and at minima of $\mathrm{Im}\{\mathrm{Tr}(\mathcal{G}^0(\epsilon))\}$ we find maxima (see Bormet et al., 1994a, for more details).

Despite the differences, which clearly exist between jellium and Al(111), we find for both systems that the adsorbate-induced change in the DOS confirms the expected picture for a chemisorbed adsorbate on a metal surface:

- Atomic levels of the adsorbate are broadened due to the hybridization with the extended substrate states (in particular the substrate s-states).
- Compared to the free atom DFT-LDA level[5] the adsorbate-induced peak is found at higher[4] energy for adsorbed Na, at about the same energy for adsorbed Si, and at lower energy for adsorbed Cl. The calculated shifts are $\Delta\epsilon(\mathrm{Na\,3s}) \approx +0.6$ eV, $\Delta\epsilon(\mathrm{Si\,3p}) \approx +0$ eV, $\Delta\epsilon(\mathrm{Cl\,3p}) \approx -0.5$ eV.

This trend also conforms to the finding that the ionic character of the adatoms changes from plus to minus when going from Na to Si to Cl. It reflects that partially occupied levels have to align with respect to the substrate Fermi level (contribution (i) discussed in Section 5.2). But fully occupied levels (such as the 3p states of the $Cl^-$ ion) are more affected by the surface potential (contribution (ii) discussed in Section 5.2).

---

5 For open-shell systems, which are discussed here, the DFT-LDA Kohn–Sham eigenvalue of the highest occupied level is a good estimate of the mean value of the ionization energy and the electron affinity (cf. Figs. 5.5, 5.7 and their discussion).

For a core (or semi-core) state the shift of an adsorbate level upon adsorption mainly reflects the effects (i) (due to the changed electrostatic potential caused by transfer or redistribution of valence electron density) and (ii) (due to the substrate surface potential). With respect to the latter, we note that core levels are affected more by the electrostatic part of the potential than by the full effective potential, because the change in the exchange–correlation potential for core electrons due to the substrate electrons is negligible: At the high electron density in the core region, the exchange–correlation potential is only weakly affected by the relatively slight increase in electron density due to the substrate valence electrons. The shift of core levels due to effects (i) and (ii) of Section 5.3.1 is the initial-state contribution of X-ray spectroscopy of the adsorbate core-level shift. The results of Fig. 5.12 reveal that the Si 3s semi-core level is shifted by 3.4 eV and the Cl 3s-level by only 1.67 eV toward lower[4] energy. For Si the shift largely reflects how the adatom core states feel the substrate potential. The shift of Cl is smaller because the Cl is positioned further away from the surface than Si, and because the electron transfer toward the Cl adatom implies a repulsive potential for the core and semi-core states implying a contribution shifting their energy levels to higher[4] energies.

### 5.4.3. *Electron density:* $n(\mathbf{r})$, $\Delta n(\mathbf{r})$, *and* $n^{\Delta}(\mathbf{r})$

The trend seen in the results of Fig. 5.12 is in accordance with what is expected from electronegativity considerations: Na is electropositive with respect to the neighboring Al atoms, i.e., it gives up an electron more readily than Al. Cl, on the other hand, is strongly electronegative on Al and electron transfer from Al to Cl should occur. Silicon has nearly the same (or slightly higher) electronegativity as Al.

The formation of bonding and antibonding levels, together with the position of the Fermi level, will be reflected in the electron density $n(\mathbf{r})$. With this hierarchy in mind it is useful to inspect *in addition* to the DOS (Fig. 5.12) the electron density and, what is more instructive, the electron-density *change*, i.e., comparing the adsorbate system and the uncoupled systems. Figure 5.13 shows the electron density of the valence states.

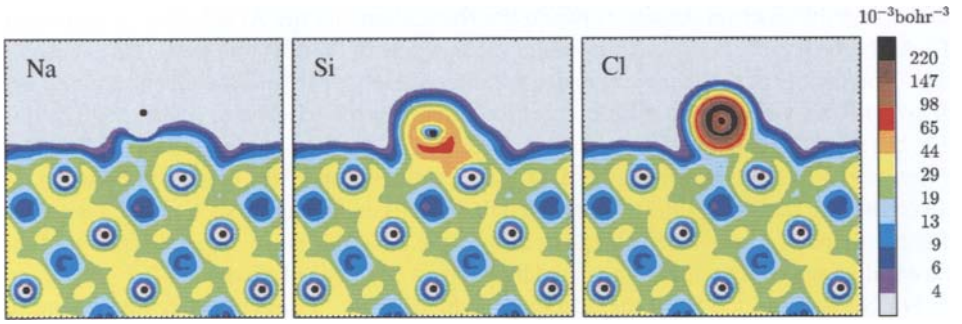


Fig. 5.13. Electron density (valence only), cf. Eq. (5.3), for three different adatoms (groups I, IV, and VII of the periodic table) on an Al(111) substrate. We display a cut along the $(1\bar{1}0)$ plane, perpendicular to the surface. The results are from Bormet et al. (1994a).

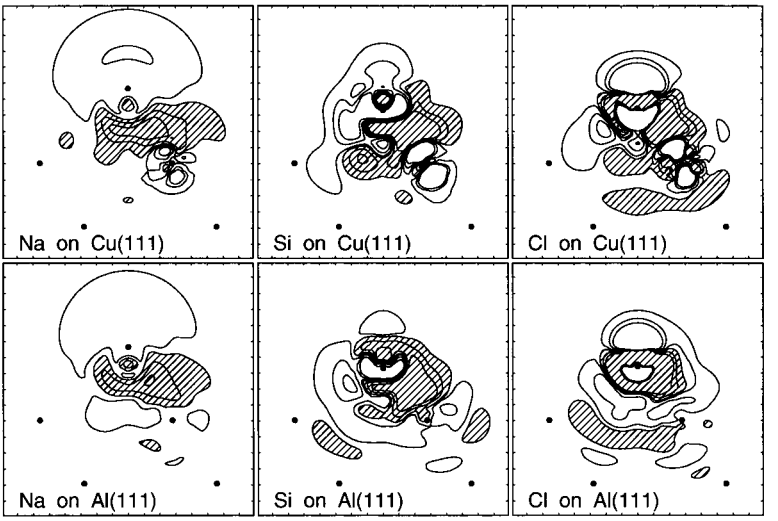


Fig. 5.14. Electron *difference density* $n^{\Delta}(\mathbf{r})$ (see Eq. (5.5)), considering for the free adatom the neutral charge state, for three different adatoms (group I, IV, and VII of the periodic table) on a Cu(111) substrate (top) and on an Al(111) substrate (bottom). We display a cut along the $(1\bar{1}0)$ plane, perpendicular to the surface. Densely hatched areas indicate accumulation of electron density [positive $n^{\Delta}(\mathbf{r})$]. Non-hatched areas correspond to electron depletion [negative $n^{\Delta}(\mathbf{r})$]. The positions of nuclei are marked by dots. Results are from Yang et al., 1994, (top), and Bormet et al., 1994a, (bottom).

In the case of sodium, the charge transfer from the adsorbate toward the substrate is clearly visible. From the vacuum side the sodium looks practically naked. Figure 5.13 may overemphasize this impression because it shows a wide range of electron density in order to be able to compare atoms from the left to the right of the periodic table. The first displayed contour has a very low value which supports (again) the description of Na as being a (partially) ionized adatom and that particles which approach the adsorbed Na from the vacuum side will experience the "naked" side of the adsorbate. Figure 5.13 also shows that the electron density between the Na adatom and the Al substrate is increased. Thus, charge has been displaced from the vacuum side of the Na atom toward the substrate side. The details of this charge transfer are more clearly visible in the electron *difference density* $n^{\Delta}(\mathbf{r})$, which is the difference of the density of the adsorbate system, displayed in Fig. 5.13, of the density of the clean surface, and of the free atoms (cf. Eq. (5.5)). This *difference density* is shown in Fig. 5.14. The maximum of $n^{\Delta}(\mathbf{r})$ is located between the adsorbate and the substrate. In a more detailed discussion given in Section 5.5.3 we show that the shape of this induced charge density is the quantum-mechanical realization of the classical image effect which is actuated by the partially ionized adsorbate.

For Si, as expected from the adsorbate-induced DOS, a directional covalent bond is present between the Si adatom and the nearest-neighbor substrate atom (see Figs. 5.13 and 5.14). Furthermore, it can be seen that the maximum of the charge density of the chemisorption bond is closer to the more electronegative Si atom. We also see a typical increase of electron density on the opposite side of the bonding hybrid.

In the case of Cl on Al the charge density distribution around the adsorbate is almost spherical, again supporting the picture we had derived from the DOS in Fig. 5.12 of a (partially) negatively charged adatom.

The results for the Al and Cu substrates show a number of similar features, and some interesting differences. Firstly, it can be noted that in each case the perturbation to the system caused by the adsorbates does not reach very far into the metal substrate. The interior is essentially identical to that of the clean surface for layers deeper than the second. We emphasize that this localization holds for the electron density *perturbation* but not for individual wave functions. For Na adsorption the results of Fig. 5.14 imply the building up of a surface dipole which locally decreases the work function. The opposite situation is found for Cl, which is negatively charged and sits on an adsorption site that is positively charged. In this case charge has moved from the substrate toward the Cl atom, and the local work function therefore will be increased relative to the value of the clean surface. For both substrates, Si appears covalently bound with a slight electron transfer toward the adatom. Comparing in more detail the results for Al and Cu, we see that there is more charge between the Na adatom and the top layer of the Cu substrate. Also, there is a greater depletion of charge at the vacuum side. These effects are consistent with the fact that the electronegativity difference between Na and Cu ($0.93 - 1.9 = -0.97$) is larger than that between Na and Al ($0.93 - 1.61 = -0.68$). The Si atom, which clearly forms a covalent bond with both substrates, is slightly more electronegative than Al (by 0.27). In this respect, it can be seen that more charge resides on the Si atom when adsorbed on Al than when on Cu for which the electronegativity difference is zero. In all cases for the adsorbates studied, the adsorption on Cu exhibits some structure in the valence-electron density change near the nucleus of the Cu atom closest to the adsorbate, which reflects the participation of the Cu d-electrons in the bonding.

### *5.4.4. Surface dipole moments*

A further interesting quantity obtainable in adsorption calculations is the change in the adsorbate induced dipole moment as a function of adsorbate height. In a naive picture one would expect that for ionic bonding the dipole moment $\mu$ changes linearly with the adatom height $Z_{ad}$. For a covalent bond the dipole moment should be approximately constant (for small variations of the adsorbate height). Indeed, we find that this picture applies. For Na we obtain a nearly linear increase of the dipole moment with increasing adsorbate height, and for Cl we obtain a decrease. The dynamic charge, which is the slope of $\mu(Z_{ad})$, is given in Table 5.2 and is in good agreement with the jellium calculations of Lang and Williams. These results support again the usefulness of the ionic pictures for Na and for Cl, and of the mainly covalent description of Si adatoms on Al(111).

A homogeneously distributed layer of adatoms induces an electric field due to the adatom induced dipoles. The dipole strength is related to the adsorbate induced change in the work function, $\Delta\Phi_{ad}$, by the Helmholtz equation:

$$\Delta\Phi_{ad} = \Theta\mu(\Theta)/\varepsilon_0. \tag{5.37}$$

We have seen (cf. Figs. 5.13 and 5.14 ) that adsorption on a metal surface only significantly affects the electron density of the bare metal substrate in the outermost layers.

Table 5.2
Dynamic charge $\partial\mu/\partial Z_{ad}$, as obtained for isolated adatoms on jellium, and from supercell calculations for adsorbates on Al(111) at a low coverage of $\Theta = 1/16$. The units are electron charges. The results are from Bormet et al. (1994a)

| Substrate | Adsorbate | | |
|---|---|---|---|
| | Na | Si | Cl |
| Jellium | +0.4 | +0.0 | −0.5 |
| Al(111) | +0.4 | −0.1 | −0.5 |

The spatial distribution of the electronic charge with respect to the adsorbate nuclei gives rise to a dipole moment which changes the work function. Furthermore, charge transfer toward (or away from) the adparticle, as well as a permanent dipole moment give rise to a long range repulsive electrostatic interaction between different adparticles. If this is the dominant lateral interaction, which is true in some cases at low coverage, it will further result in a depolarization of the adsorption-induced dipole moment with increasing coverage (Antoniewicz, 1978; Topping, 1927; Kohn and Lau, 1976).

It is convenient to illustrate this depolarization effect by considering the physisorption of rare gases. For these systems there is practically no charge transfer, and we only have to consider the static adsorbate dipole. For not too small adsorbate–substrate separation, we can calculate, using classical electrostatics, the dipole moment $\mu$ which enters Eq. (5.37). The dipole moment on each atom as a function of coverage is written as

$$\mu(\Theta) = \mu_{st} + \alpha\mathcal{E}_z(\Theta), \tag{5.38}$$

where $\mu_{st}$ is the static dipole moment of the adparticle alone, i.e., without considering the effect of screening by the metal conduction electrons and for $\Theta \to 0$. $\mathcal{E}_z(\Theta)$ is the component normal to the surface of the microscopic electric field at the adparticle under consideration and $\alpha$ is its polarisability. To calculate the field $\mathcal{E}_z(\Theta)$, it is necessary to take the image dipoles into account. Thus, as well as the direct dipole–dipole interaction, the dipole–image and image–image interactions must be considered. The actual dipole moment at coverage $\Theta$ then is

$$\mu(\Theta) = \frac{\mu_{st}}{1 + \alpha[T + V - 1/4D^3]}, \tag{5.39}$$

where $D$ is the distance of the adparticle dipole to the effective image plane, and $T$ and $V$ are lattice sums of the direct and the indirect interactions (see Scheffler and Bradshaw, 1983, for details). The dipole moment of an adparticle at zero coverage is thus given by

$$\mu_0 = \frac{\mu_{st}}{(1 - \alpha/4D^3)}. \tag{5.40}$$

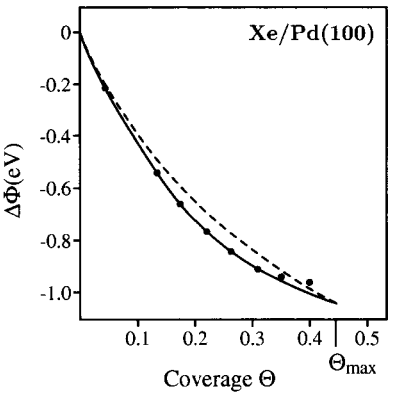


Fig. 5.15. Calculated work function change for the adsorption system Xe/Pd(001) as a function of coverage.[2] Solid line: lattice sums proportional to $\Theta^{3/2}$. Broken line: lattice sums proportional to $\Theta$. The points represent the experimental results of Palmberg (1971). After Bradshaw and Scheffler (1979).

Due to the screening by the substrate, the adatom-induced dipole moment is thus enhanced from the value $\mu_{st}$ to $\mu_0$. Equation (5.39) shows that with increasing coverage, i.e., increasing value of $T + V$, the particle is depolarized. Expressions similar to Eq. (5.39), but without the image terms ($V - 1/4D^3$) were proposed by Topping (1927) and Miller (1946). Equation (5.39) has been applied to the physisorption system Xe/Pd(001) (Bradshaw and Scheffler, 1979). Figure 5.15 shows measured and calculated changes in work function. $D$ has been taken to be 1.5 Å, and for the polarizability the gas phase value, $\alpha = 4$ Å$^3$, was used. For the monolayer obtained at $\Theta = 0.44$, the lattice sums are given by $T + V = 0.17$ Å$^{-3}$. The only remaining parameter is the dipole moment of the single adsorbed Xe atom, $\mu_0$. For the best fit to the experimental data, this is given by 0.93 Debye with the positive end away from the surface. At coverages between zero and $\Theta_{max}$, the lattice sums are either proportional to $\Theta^{3/2}$ (Topping, 1927), if an ordered array is present at every coverage, or proportional to $\Theta$ (Miller, 1946), if the adlayer is disordered. Both cases yield similar behavior and are shown in Fig. 5.15. We thus see that the work function does not change linearly with coverage but that depolarization causes a less rapid change at higher coverages.

## 5.5. Alkali-metal adsorption: the traditional picture of *on-surface* adsorption

In this section we discuss the traditional picture of alkali-metal adsorption. This implies that we consider situations where alkali-metal atoms adsorb *on the surface* without disrupting the substrate very much, which is in contrast to *substitutional* adsorption (see Section 5.6) where the adatom kicks out an atom from the substrate and takes its place. We recall that we discuss only the closed-packed substrate surfaces, namely fcc (111) and fcc (001). For more open surfaces, adsorbates, in particular alkali-metal atoms, can induce significant surface reconstructions. That substitutional adsorption at close-packed surfaces (and in more general terms, surface alloy formation) can happen even with adsorbates that

do not mix in the substrate bulk, was first found by Schmalz et al. (1991) in a combined study of surface extended X-ray absorption fine structure (SEXAFS) experiments and DFT total-energy calculations. This subject will be discussed in Section 5.6 below. In this section we discuss *on-surface* adsorption and note only in passing that in the past, several experiments have been interpreted inappropriately by incorrectly assuming an on-surface adsorbate geometry. We will take care that only those experiments are discussed below for which the adatom indeed sits on the surface. In fact, attaining the substitutional adsorbate geometry is hampered by an energy barrier, and therefore for low-temperature adsorption, adatoms are likely to stay on the surface. For the example discussed below, in which Na is at Al(001), the transition temperature is $T = 160$ K.

Substitutional adsorption has been observed for Na, K, and Rb on Al(111), where the tendency toward the substitutional adsorption seems to decrease with increasing adatom radius. Thus, for Cs substitutional adsorption has not been found.

### *5.5.1. The Langmuir–Gurney picture*

In the seminal work of Taylor and Langmuir in (1933) for the Cs/W system, it was shown that the work function of the clean surface is reduced by several electronvolts on Cs adsorption and that for thermal desorption at low coverage, almost all the Cs adatoms leave the surface as positive ions. In the light of such results, the alkali metal bond to the substrate was viewed as a spectacular example of ionic bonding akin to that in alkali halides (see also Naumovets, 1994). As discussed above (see Fig. 5.1), even in NaCl the nature of bonding is debatable, and it is therefore not a surprise that the question whether or not alkali-metal adsorption should be described in terms of ionic bonding has sometimes been raised. With all the warnings mentioned in Section 5.1 in mind, we argue (and already did so in Section 5.4) that the ionic picture is appropriate. For a more detailed analysis of the controversy about the ionic nature of the bond we refer to the publications of Scheffler et al. (1991) and Bormet et al. (1994a).

A simple picture of the interaction between alkali-metal atoms and a metal surface, and of the resulting chemisorption bond was proposed by Langmuir (1932). He assumed that the alkali-metal atom transfers its valence s-electron completely to the substrate. In a more rigorous theoretical description of alkali-metal adsorption Gurney, in 1935, proposed a quantum-mechanical picture applicable at low coverages, where the discrete s-level of the free alkali metal atom broadens and shifts, becoming partially emptied as a result of the interaction with the substrate states as it approaches the surface. Figure 5.7 (left) summarizes this view. The partially positively charged adatom then induces a negative screening charge density in the substrate surface giving rise to an adsorbate-induced dipole moment which naturally explains the reduction in the work function of clean surfaces.

The building up of such adsorbate-induced dipole moments also leads to the understanding that the dominant interaction between the adsorbates is repulsive and that the adatoms should form a structure with the largest possible interatomic distances compatible with the coverage. In this description it is expected that with increasing coverage the adsorbate–adsorbate distance gradually decreases, and the electrostatic repulsion between the adatoms increases. To weaken this repulsion, i.e., to lower the total energy, some fraction of the valence electrons flows back from the Fermi level of the metal to the adsorbate. Thus, a reduction of the adsorbate-induced dipole moment, i.e., depolarization

takes place. This picture of Langmuir and Gurney is fully supported by systematic studies of Lang and Williams, Bormet et al., and others, some of which were discussed in Section 5.4 above. If the coverage-dependent depolarization is strong and/or the nature of the adsorbate–substrate binding changes with the local coverage, it is also possible (and observed) that with increasing coverage a phase separation occurs into close-packed islands (also called "condensation") (Neugebauer and Scheffler, 1993; Over et al., 1995).

### *5.5.2. Coverage dependence of the work function*

In his earlier work, Lang (1971, 1973) studied the alkali metal-induced work-function change using the jellium model for the substrate and for the adsorbate layer. Despite the extremely approximate nature of this approach, the results demonstrated that many ground-state properties of metal surfaces and metal–adatom systems can be described in a physically transparent manner. As an example, we show in Fig. 5.16 the change in work function with increasing coverage (cf. footnote 2) for parameters corresponding to Na on aluminum (in the jellium approach; left side). The right side of the figure shows a calculation for Na on Al(001), which takes the atomic structure into account. We note that for coverages $\Theta_{\mathrm{Na}} \gtrsim 0.15$ the on-surface geometry is a metastable structure which only exists at temperatures below 160 K (Andersen et al., 1992; Aminpirooz et al., 1992).

The coverage dependence of the work function possesses a form similar to that often observed experimentally. It is explained as a consequence of the above-mentioned depolarization of the alkali metal-induced surface dipole-moment induced by continuous reduction of the adsorbate–adsorbate distance and corresponds to a rapidly decreasing work function at low coverage, reaching a minimum at about $\Theta = 0.1$ (Fig. 5.16, left) or $\Theta = 0.25$ (Fig. 5.16, right), and subsequently rising toward the value of the pure alkali metal.

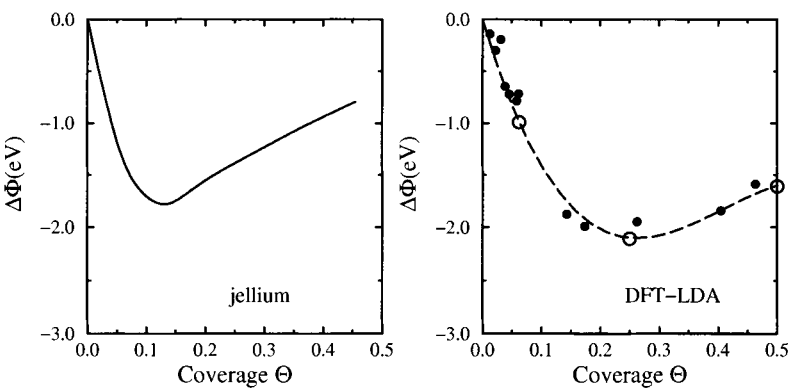


Fig. 5.16. Change in work function with increasing coverage (cf. footnote 2). Left: Results of Lang (1971) using a jellium on jellium model with parameters corresponding to Na on Al(001). Right: DFT-LDA calculations (open circles) for periodic Na adlayers on Al (001). Closed circles are experimental results from Porteus (1974) and Paul (1987), obtained by adsorption at low temperature ($T = 100$ K).

### 5.5.3. *Ionization of the adsorbate and screening by the substrate electrons*

We will now, for the moment, assume that we can neglect any effect due to the chemical interaction (i.e., hybridization of orbitals) upon adsorption and that the substrate mainly plays the role of providing an electron reservoir, i.e., fixing the electron chemical potential to its Fermi level. Using the Fermi-level position of Al(001), Fig. 5.5 shows that then the occupancy of the Na 3s-level will be 65%. Thus 35% of the Na 3s-electron is now in the substrate.

A partially ionized atom in front of a metal surface will not leave the metal electrons unaffected. To discuss this, we will at first sketch the quantum mechanical concept of screening at a metal surface which asymptotically, for large distances, includes the classical image effect. When a charged particle approaches a metal surface a screening charge will be created at the surface. The quantum-mechanical realization of the classical image effect is an induced electron density which has its center of gravity at the "effective metal surface", i.e., the image plane (cf. Lang and Williams, 1978). Thus, whereas in the classical description the electrostatic screening of a *point charge* at a distance $D$ in front of a metal surface is modeled by an image point charge inside the metal at a distance $-D$ away from the surface, the truth is that there is no image point charge inside the substrate but a charge density right at the surface (see Fig. 5.18b), which creates the same electrostatic field in the vacuum as the (fictitious) point charge of classical electrostatics.

Considering close-packed surfaces, the image-plane position (see Eq. (5.24)) is on the vacuum side of the center of the outermost atomic layer, because electrons spill out into the vacuum to lower their kinetic energy. At small distances (typically $d < 2$ Å) the justification of the image-plane concept gradually breaks down. However, it is still approximately valid, because metallic screening is still important. The concept can be approximately justified by assuming that for a charged system close to the surface, the image plane ($z_0$ in Eq. (5.24)) is displaced toward the substrate. This is what we have in mind when we use the term "image effect" in the following discussion. For a deeper discussion of this problem we refer to Scheffler and Bradshaw (1983), Finnis et al. (1995), and references therein.

Figure 5.17 shows that the description of partial ionization of the Na adatom and building up a screening charge in the substrate remains *qualitatively* valid when the alkali-metal atom is adsorbed. Figure 5.17 displays the *difference density* $n^{\Delta}(\mathbf{r})$ (cf. Eq. (5.5)) using a neutral atom ($f_{3s} = 1$). It can be seen that the upper half of the adsorbed Na atom has a negative $n^{\Delta}$ thus less electron density than the free, neutral alkali atom, and on the substrate side of the adatom there is an increase of electron density.

Figure 5.18a shows a plot of $n^{\Delta}(f_{3s} = 0.1)$, where $n^{\mathrm{Na}}$ (cf. Eq. (5.5)) is now taken from a self-consistent calculation for the partially ionized free atom. This picture looks very similar to the pure screening charge density which we obtain for an external point charge (see Fig. 5.18b). The shape of this screening charge density is very similar for a negative point charge and for a positive point charge, as long as the latter is sufficiently weak so that it cannot bind an electron. The magnitude of the contour lines nearly scale linearly with the magnitude of the external point charge. The similarity between Figs. 5.18a and b is quite surprising, because a Na-ion is – of course – different from a point charge. Nevertheless, the response of the metal is similar for both cases. The slight differences between Figs. 5.18a and b may be interpreted as an indication that some covalency and some s-$p_z$

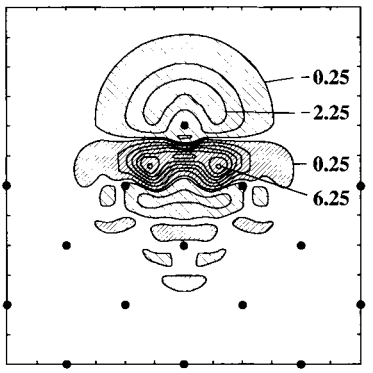


Fig. 5.17. Electron *difference density* $n^{\Delta}(\mathbf{r})$ for Na adsorbed on Al(001). For the definition of $n^{\Delta}$ see Eq. (5.5); $n^{\mathrm{Na}}$ is taken from a free, neutral atom. Units are $10^{-3}$ bohr$^{-3}$. The contour line spacing is $10^{-3}$ bohr$^{-3}$. Densely hatched areas indicate accumulation of electron density [positive $n^{\Delta}(\mathbf{r})$]. Sparsely hatched areas correspond to electron depletion [negative $n^{\Delta}(\mathbf{r})$]. The positions of nuclei are marked by dots (from Scheffler et al., 1991).

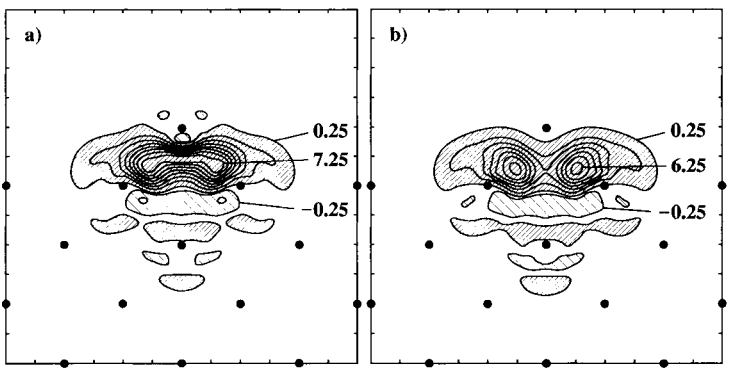


Fig. 5.18. Panel (a): Electron *difference density* $n^{\Delta}(\mathbf{r})$ for Na adsorbed on Al(001). For the definition of $n^{\Delta}$ see Eq. (5.5); $n^{\mathrm{Na}}$ is taken from a partially ionized, free Na atom ($f_{3s} = 0.1$). Units are $10^{-3}$ bohr$^{-3}$. The contour line spacing is $10^{-3}$ bohr$^{-3}$. Panel (b) shows the screening charge density of an external, positive point charge of $-0.09e^{-}$. Here the units are $10^{-4}$ bohr$^{-3}$. Densely hatched areas indicate accumulation of electron density [positive $n^{\Delta}(\mathbf{r})$]. Sparsely hatched areas correspond to electron depletion [negative $n^{\Delta}(\mathbf{r})$]. The positions of nuclei are marked by dots (from Scheffler et al., 1991).

mixing are present in the Na–Al(001) interaction, but these contributions are not very large. From the similarity of Figs. 5.18a and b we conclude that the "charge transfer picture" is indeed useful and appropriate to describe the physics of alkali adsorption at low coverage. However, charge transfer alone is not sufficient to understand the adsorbate–substrate interaction because the charge transfer actuates a significant change in the substrate surface electron density. We also note that the metal screening charge is largely located in front of the metal, i.e., between the adsorbate and the substrate (see Fig. 5.18b). As a consequence, the adsorbate-induced electron-density change cannot be divided *directly* into adsorbate and metal contributions.

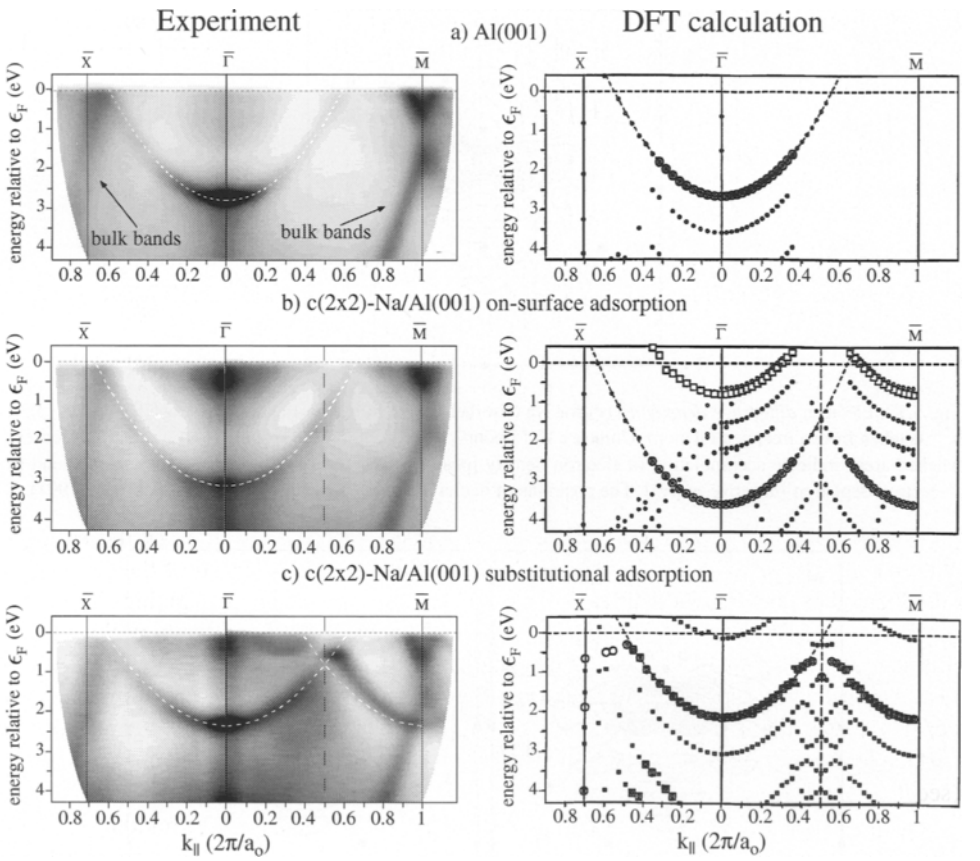


Fig. 5.19. Comparison of experimental (left panels) and calculated (right panels) surface band structures. The symbols used are such that squares and circles represent Na- and Al-derived bands, respectively (for a precise definition see the paper by Stampfl et al., 1998). Panels (a) show results for the clean Al(001) surface, panels (b) the on-surface hollow site, and panels (c) display results for the substitutional adsorption. The results are taken from Stampfl et al. (1998).

### *5.5.4. Surface band structure*

At low coverages the interaction between adsorbed alkali-metal atoms will originate from their strong dipole moments. As the coverage increases, wave functions will overlap and a surface electronic band structure will form. This band is of s-character and its dispersion was discussed in Section 5.3.2 above. In Fig. 5.19 we show experimental (left panels) and calculated (right panels) surface states/resonances for (a) the clean Al(001) surface, (b) the on-surface c(2 × 2)-Na/Al(001) structure, and (c) the substitutional c(2 × 2)-Na/Al(001) adsorbate structure (discussed in more detail in Section 5.6.1 below). Firstly, we note that there is good overall agreement between theory and experiment. The main, lower-lying band in each case is Al-derived, as indicated by the circles in the theoretical plot. The

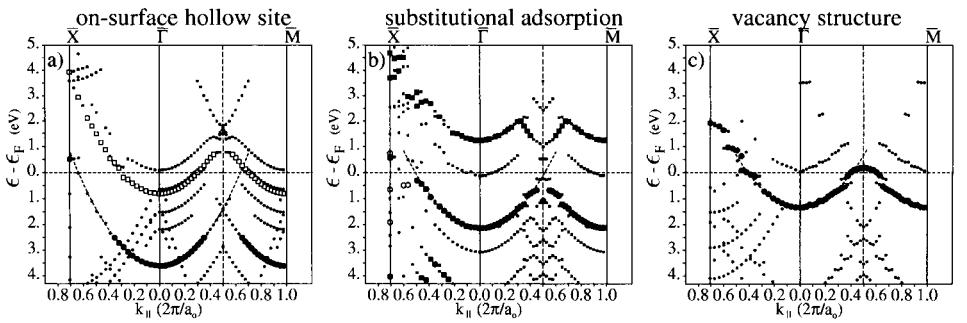


Fig. 5.20. Surface band structures of c(2 × 2) Na on Al(001) for (a) on-surface adsorption, (b) substitutional adsorption, and (c) the vacancy structure, including the energy range above the Fermi level. The symbols used are such that squares and circles represent Na- and Al-derived bands, respectively (for a precise definition see the paper by Stampfl et al., 1998).

bands represented by squares are Na-derived. Compared to the position of the surface-state band of the clean surface, it can be seen that the Al-derived band of the on-surface adsorbate phase lies around half an eV lower in energy. The mechanism giving rise to this downward shift is discussed below. Interestingly, the experimental results show clearly that this state does not have the c(2 × 2) periodicity of the adsorbates, but rather has kept the (1 × 1) periodicity of the clean surface (cf. Fig. 5.19a). Indeed, inspection of the electron density reveals that the on-surface adsorbate represents only a modest perturbation of the surface electronic structure, which cannot be resolved in the photoemission experiments (see the discussion of Fig. 5.9 above).

From the calculated bands of the on-surface adsorbate phase (right middle panel of Fig. 5.19), it can be seen that there is also a surface-state/resonance with an energy of about 0.7 eV below the Fermi level at $\bar{\Gamma}$. As indicated by the open squares, it is a Na-derived band (of Na 3s character). It crosses the Fermi level and is partly occupied. From Fig. 5.20, which shows the calculated band structure also in the region *above* the Fermi level, it can be seen that the part of the Na-derived band above $\epsilon_F$ exhibits a band structure with c(2 × 2) periodicity of the adsorbed Na layer. Thus the higher coverage of Na present in this phase, as compared to the situation of an isolated adatom, has given rise to the development of significant adsorbate–adsorbate bonding and band formation.

From construction of electron "difference density" plots (cf. Eq. (5.5)), that is, subtracting off from the total valence electron density of the system, the superposition of the electron densities of the clean Al substrate and the Na atoms (arranged in the same c(2 × 2) periodicity), it is found that due to Na adsorption there is an increase of electron density at the position of the surface-state band (the band of parabolic shape which has a lower energy at 2.8 eV in Fig. 5.19a, left and 3.2 eV in Fig. 5.19b, left), and from the region between the Na atoms electron density is depleted. These results, together with comparison of the band structure of a *free* c(2 × 2)-Na monolayer which has an electron occupancy *larger* than the Na-derived band seen in Fig. 5.19, suggests electron transfer occurs from the Na atoms directly into the pre-existing surface states of Al(001). Thus, the Na-induced structures seen in Fig. 5.19b, left (see the dark regions at $\bar{\Gamma}$) originate from a coupling

between the 3s-derived band of the free c(2 × 2) monolayer of Na and the surface-state band of the clean Al(001) surface. This may be understood as being due to the formation of bonding and antibonding states, leading to the downward shift of the Al-derived band with an increase in population and the upward shift of the Na-derived band with a decrease in population. Nevertheless, the electron density of the Al-derived band lies well below the smeared-out density of the Na-derived band, and also below the position of the Na atoms. Therefore the traditional picture of a thin metallic film covering a metallic substrate, as in the jellium model, remains qualitatively valid. We will see in the next section that this is *not* the case for the substitutional-adsorbate phase.

### 5.6. Substitutional adsorption and formation of surface alloys

Recent experimental and theoretical studies of the adsorption and co-adsorption of alkali metals on Al surfaces have shown that the traditional view of alkali-metal adsorption outlined in Section 5.5 above, is in fact, only part of the whole picture and that phenomena such as the following may occur:

1. The alkali-metal atoms may not necessarily assume highly coordinated sites on the surface.
2. The alkali-metal adatom may kick out surface substrate atoms and adsorb substitutionally. Substitutional adsorption has been shown in three cases to occur as the result of an irreversible phase transition from an "on-surface" site by warming to room temperature, without change in the periodicity of the surface unit cell or of the coverage, i.e., order-preserving phase transformations between metastable and stable structures occur.
3. The alkali-metal atom may switch site on variation of coverage.
4. Island formation may occur.
5. There may be a strong intermixing of the alkali-metal atom with the substrate surface, as for example the formation of a four-layer ordered binary surface alloy which was identified for Na on Al(111) at a coverage $\Theta_{Na} = 0.5$ (Stampfl and Scheffler, 1994c). Also ternary surface alloys form for the co-adsorption of Na ($\Theta_{Na} = 0.25$) with either of K, Rb, or Cs on Al(111) (Christensen et al., 1996).

Only some of these aspects will be discussed below. A comprehensive description of the updated, modern view of alkali-metal adsorption can be found in a special issue of Surface Reviews and Letters (SRL, 1995) which collected review papers of the key groups which were working on this subject. There, and also in Adams (1996), it is shown in greater detail than possible here that the adsorption and co-adsorption of alkali metals on Al surfaces exhibit a wealth of previously unexpected phenomena.

Although it is well known that many, though not all, materials mix and form alloys, up until recently intermixing was not considered to be very relevant for adsorption on close-packed surfaces. Thus, adsorbates on such surfaces were assumed to occupy on-surface sites. Figure 5.21a gives an example for Na on Al(001). It was also assumed that this view is justified, in particular, for systems where the adatom is insoluble in the bulk substrate. This standard picture was questioned in 1991 by a combined study of surface-extended X-ray adsorption fine-structure (SEXAFS) experiments and DFT total-energy

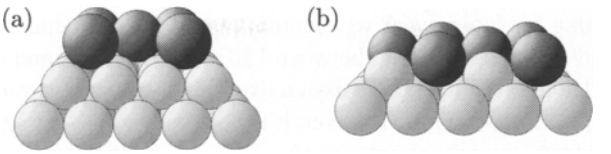


Fig. 5.21. Perspective view of the atomic structure of c(2 × 2)-Na on Al(001). Dark and light gray circles represent, respectively, Na atoms and Al atoms. (a) On-surface hollow site geometry and (b) substitutional geometry, where every second Al atom in the top unreconstructed Al layer has been kicked out.

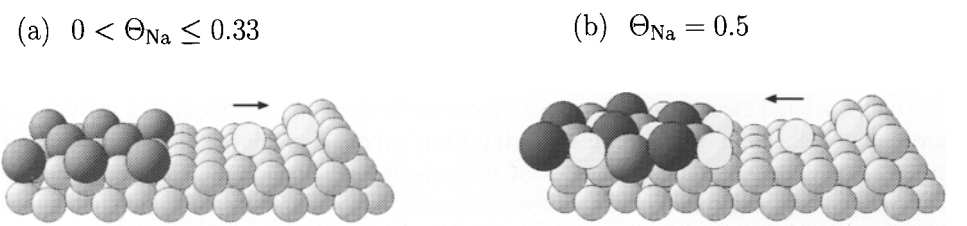


Fig. 5.22. Possible mass-transport scenario for substitutional adsorption and the formation of a surface alloy for the system Na/Al(111). (a) Island formation occurs with a $(\sqrt{3} \times \sqrt{3})R30°$ structure with Na atoms in substitutional sites, for coverages $0 < \Theta_{Na} \leq 1/3$: Every third Al atom is "missing"; Al atoms diffuse to steps. (b) Surface alloy formation with a (2 × 2) geometry implies diffusion of Al atoms back from steps.

calculations for the system Na on Al(111) (Schmalz et al., 1991); by now it is well established that often adatoms do not adsorb on the surface, but instead, it can be energetically favorable that they kick out atoms from the substrate and take their sites. The kicked out atoms then diffuse to a step (see Fig. 5.22a). The process may be kinetically hindered, but this hindrance may be overcome even at rather low temperatures, e.g., for Na on Al(001) for $T \geqslant 160$ K (Andersen et al., 1992; Aminpirooz et al., 1992) and/or by the heat of adsorption. Whether the solubility in the substrate bulk is low or even zero is of no relevance at all for substitutional adsorption. Atoms, which are too big to fit into a bulk vacancy, can still prefer to take a substitutional site, because at the surface bigger atoms can simply sit somewhat above the center of the created surface vacancy. Since 1991 many examples of substitutional adsorption have been reported, as for example K on Al(111) (Neugebauer and Scheffler, 1992, 1993; Stampfl et al., 1992, 1994a), Na on Al(001) (Stampfl et al., 1994b), Au on Ni(110) (Pleth Nielsen et al., 1993), Sb on Ag(111) (Oppo et al., 1993), Co on Cu(111) (Pedersen et al., 1997), Mn on Cu(001) (Rader et al., 1997), Co on Cu(001) (Nouvertné et al., 1999), to name a few. Thus, the phenomenon is not at all exotic, but rather general.

In this section we will discuss in particular three systems, Na on Al(001), Na on Al(111), and Co on Cu(001), as these exhibit qualitatively different behavior.

Alkali metal-induced surface reconstructions are well known on the more open surfaces (Somorjai and Van Hove, 1989; Barnes, 1994; Behm, 1989) as these clean surfaces are close to a structural instability (Heine and Marks, 1986). But that significant reconstruction can occur on close-packed fcc (111) and (001) surfaces had not been expected previ-

ously.[6] As a warning for future work we mention that for alkali-metal adsorbates, several studies, had found "good agreement" between LEED experiments and theory as well as band-structure calculations and photoemission experiments (this also was the case for the example discussed in this section). However, it is now known that the reported agreement was purely coincidental, and the concluded physical and chemical properties were grossly incorrect because the alkali-metal atoms were not sitting on the surface (cf. Fig. 5.21a), but in substitutional sites (cf. Fig. 5.21b). Consequently, the nature of the adsorbate chemical bond, the surface electronic structure, and the origin of the coverage dependence of the work function are in fact qualitatively different to what was assumed before 1992 (Andersen et al., 1992; Aminpirooz et al., 1992; Stampfl et al., 1994b; Berndt et al., 1995). Thus, good agreement between theory and experiment and/or a convincing physical picture are no guarantee that the description and trusted understanding is indeed correct.

The associated electronic properties of these surface atomic arrangements, perhaps not surprisingly, also exhibit behavior deviating from expectations based on early ideas. For example, experimental measurements of the change in work function as a function of alkali-metal coverage can be quite different to the "expected" form of Fig. 5.16 and the density of states induced by alkali-metal adsorbates may not correspond to that expected from the model of Gurney.

### *5.6.1. Na on Al(001)*

For Na on Al(001), the adsorption energy for the on-surface hollow site and the substitutional site as a function of adsorbate coverage is shown in Fig. 5.23. It can be seen that the on-surface hollow site is clearly preferred over the substitutional site at low coverages. Its adsorption energy rapidly decreases with increasing coverage indicating a strong repulsive interaction between the Na atoms. The adsorption energy for Na in the surface substitutional site depends much more weakly on coverage than for the on-surface site, and, in fact, the adsorption energy for the $\Theta = 0.5$ substitutional structure is more favorable than even that of the lower coverage substitutional structures.

These results are interpreted as follows: At low coverages, the on-surface adsorption in a homogeneous adlayer is the stable structure for low as well as high temperature, but for higher coverages, on-surface adsorption becomes metastable. For high temperature adsorption, or warming the substrate, the adatoms then switch to substitutional sites, forming islands with a c(2 × 2) structure. The phase transition from the on-surface hollow site to substitutional adsorption is indicated in Fig. 5.23 by the dashed line. This predicted behavior is in good accord with experimental studies, see, e.g., Fasel et al. (1996).

The widely differing adsorbate geometries and the strong dependence of them on coverage and temperature, as described above, means that the type of bonding and chemical properties of the adsorption system will vary significantly depending on these factors. In

---

6 The late 5d transition metals (Ir, Pt, Au) are exceptions to this rule. In these systems relativistic effects give rise to a substantial lowering of the s-band and a rather high surface stress. For the (001) surfaces, the desire to achieve a higher coordination in the top layer is indeed stronger than the cost of breaking (or stretching) some bonds between the first and second layer (see Fiorentini et al., 1993).

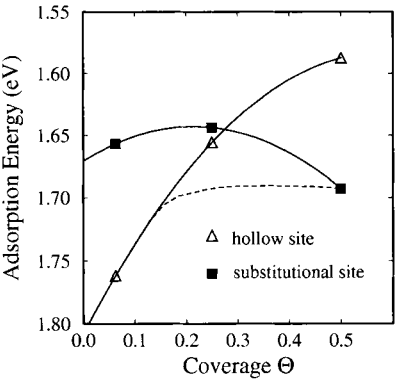


Fig. 5.23. Adsorption energy versus coverage for Na on Al(001) in the on-surface hollow site and in the surface substitutional site (from Stampfl and Scheffler, 1995).

this section we examine the electronic structure and bonding nature of the c(2 × 2) substitutional structure of Na on Al(001); that of the c(2 × 2) on-surface hollow structure was briefly touched upon already in Section 5.5.4.

Firstly, it can be noted from Fig. 5.19c for substitutional adsorption that the main band in the experimental results clearly exhibits a c(2 × 2) periodicity, in contrast to the on-surface hollow structure. This is due to the significantly reconstructed Al(001) surface. It can also be noticed that this band is higher in energy than the surface state band of the clean Al(001) surface. Furthermore, the Na-derived band, as clearly observed for the on-surface phase in Fig. 5.19b in a greater region around $\bar{\Gamma}$ below $\epsilon_F$, is nearly absent in the substitutional phase. However, from Fig. 5.20b which shows the same calculated band structure as in Fig. 5.19c, but where the energy region extends higher into the positive range, it can be seen that a significant Na-derived band (tagged by square symbols) lies well above the Fermi level, i.e., it is unoccupied. Figure 5.20c also shows the calculated surface state bands of the artificial c(2 × 2) vacancy structure. Here a strong Al-derived band can clearly be seen, its position being higher in energy than that of the clean surface. Similarly to the clean Al(001) surface, the maxima of charge density of the surface states for the vacancy structure lie on top of the uppermost surface Al atoms, having this time the c(2 × 2) periodicity. On adsorption of Na, as for the on-surface phase, this band shifts down in energy. The character of this Al-derived band is only slightly changed compared to that of the vacancy structure, which explains the well developed c(2 × 2) character of the band found in Fig. 5.19c.

In this case electron transfer occurs from the Na atoms into the surface state/resonance of the *vacancy structure*. Figure 5.24 (right panel) shows that electron charge has been transferred mainly from the region on top of the Na atoms into the region above the Al atoms, corresponding to the position of the surface states. Compared to the Na–Al bond length of Na in the on-surface hollow site, that in the substitutional geometry is approximately 4% (from DFT-LDA) and 11% (from LEED) shorter, indicating a larger ionicity of the bonding. The results discussed above, together with Fig. 5.24 (middle panel), which shows the regions where electron density has been increased due to Na adsorption, demon-

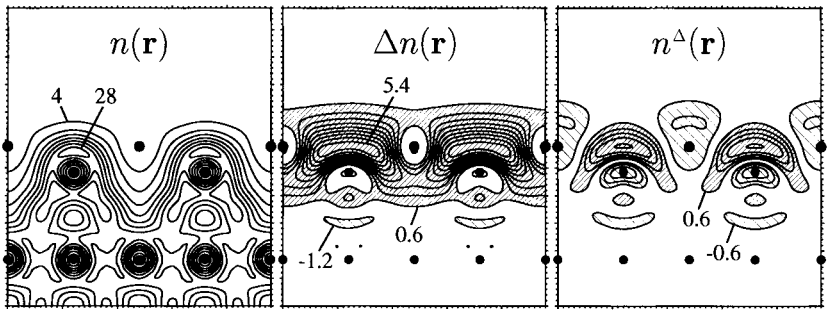


Fig. 5.24. Total valence electron density $n(\mathbf{r})$ (left panel), density difference $\Delta n(\mathbf{r})$ (middle panel), and the *difference density* $n^{\Delta}(\mathbf{r})$ for $f_{3s} = 1$ (cf. Eq. (5.5)) (right panel), of the substitutional geometry of the Na/Al(001) adsorbate system at $\Theta = 0.5$. The units are $10^{-3}$ bohr$^{-3}$. The results are from Stampfl et al. (1998).

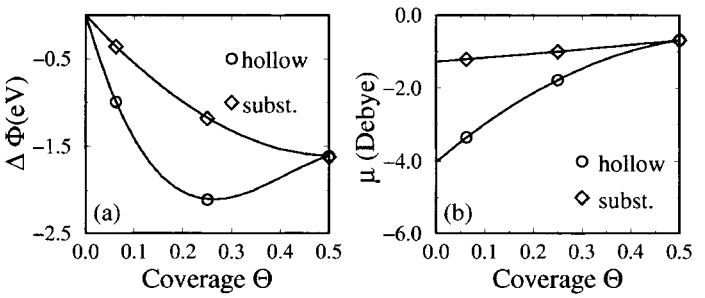


Fig. 5.25. Change in work function $\Delta\Phi$ and surface dipole moment $\mu$ as a function of coverage for Na in the substitutional (diamonds) and on-surface hollow sites (circles) for Na on Al(001) (from Stampfl and Scheffler, 1995).

strates that for the *substitutional* adsorption phase the Na adlayer *cannot* be regarded as a simple metal film on a metallic substrate, and the jellium model is not valid.

Another interesting property which yields insight into the bonding nature are the work function change and surface dipole moment. As discussed in Sections 5.5.1 and 5.5.2, for *on-surface* adsorption the characteristic change in the work function $\Delta\Phi(\Theta)$ with coverage is typically explained in terms of the Gurney picture and the "usual form" can be described reasonably well by assuming a jellium model. The work function change $\Delta\Phi$ and surface dipole moment $\mu$ are shown in Figs. 5.25a and 5.25b, respectively, as a function of coverage. For comparison, results for Na in the on-surface hollow structures are also displayed. As is consistent with the traditional picture of alkali-metal adsorption, there is a significant decrease of the surface dipole moment with increasing coverage for the on-surface site and the typical form of $\Delta\Phi(\Theta)$ is observed. The substitutional adsorption, on the other hand, exhibits a much weaker dependence. This reflects the fact that in the substitutional site the Na atoms sit lower in the surface and the repulsive adsorbate–adsorbate interaction is screened better.

As discussed above (cf. Fig. 5.23), under not too low temperature conditions a phase transition to c(2 × 2) islands occurs at coverage $\Theta \approx 0.15$; thus the local dipole moment will be fixed at the value of the c(2 × 2) phase and the work function change will vary linearly as $\Delta\Phi = \Theta\mu/\varepsilon_0$. At $\Theta = 0.5$ it is found that the values of $\mu$ (and $\Delta\Phi$) are the same for the on-surface and substitutional adsorption. This is in agreement with experiment, i.e., in all cases (theory and experiment) the value of $\Delta\Phi$ is 1.6 eV (Porteus, 1974; Paul, 1987).

### *5.6.2. Na on Al(111)*

The adsorption of Na on Al(111) was the first alkali metal on close-packed metal system that was discovered to assume substitutional adsorption. Further interesting and unanticipated phenomena were found to occur for higher Na coverages on this surface, in particular, the formation of a "four layer" surface alloy; the complex atomic geometry of which had foiled initial experimental attempts at its determination. This difficulty was related to its relative complexity, but was also due to conceptual barriers since such a structure was not expected to occur.

In Fig. 5.26 the adsorption energy of Na on Al(111) is displayed for various structures and coverages of Na in on-surface geometries (Fig. 5.26a) and in the substitutional site (Fig. 5.26b). For the latter, the adsorption energy is split into its constituents, namely, the binding energy and the surface vacancy formation energy. For on-surface adsorption, the theory indicates that for low coverages the hollow site is energetically most favorable and strong repulsive adsorbate–adsorbate interactions exist. A condensed (4 × 4) structure is seen to be energetically more favorable than homogeneous adlayers of Na for coverages larger than approximately $\Theta_{Na} = 0.1$. In the condensed phase, the coverage is $\Theta_{Na} = 9/16$ and the structure represents a densely packed hexagonal adlayer with nine Na adatoms per surface unit cell, all occupying different (mostly low symmetry) on-surface sites. Thus, the picture is that for very low coverages, the adsorbates occupy on-surface hollow sites

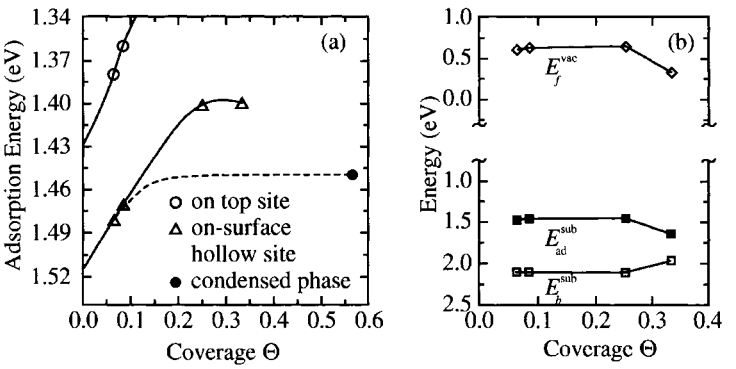


Fig. 5.26. (a) Adsorption energy versus coverage for Na in on top and fcc-hollow sites on Al(111). The dashed line marks the phase transition from the homogeneous adlayer into adatom islands with a condensed structure. (b) Adsorption energy $E_{ad}^{sub}$ and binding energy $E_b^{sub}$ for substitutional adsorption (cf. Eq. (5.21)), and vacancy formation energy $E_f^{vac}$ (from Neugebauer and Scheffler, 1993).

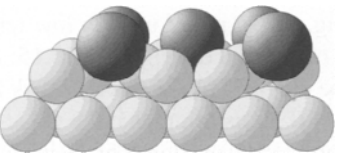

Fig. 5.27. Atomic geometry of the $(\sqrt{3} \times \sqrt{3})R30°$ substitutional structure of Na on Al(111). Dark and light gray circles represent Na and Al atoms, respectively.

and are uniformly distributed over the surface (homogeneous adlayers) but for coverages greater than about $\Theta_{Na} = 0.1$, island formation with the condensed structure and a $(4 \times 4)$ periodicity occurs as indicated by the dashed line. In this case it is energetically favorable to build up a metallic-like bonding between the adatoms and to reduce the ionic character of the adatom–substrate bonding.

For the case of substitutional adsorption it can be seen from Fig. 5.26b that the adsorption energy of the substitutional geometry is the most favorable for *all* structures investigated (note the different energy scales of Figs. 5.26a and 5.26b). In particular, substitutional adsorption with a $(\sqrt{3} \times \sqrt{3})R30°$ periodicity has *the* most favorable adsorption energy. It is therefore expected that a condensation into $(\sqrt{3} \times \sqrt{3})R30°$ islands with the Na atoms in substitutional sites occurs, beginning at very low coverages. The atomic structure is displayed in Fig. 5.27. The repulsive character of the binding energy for the $(\sqrt{3} \times \sqrt{3})R30°$ phase can be seen (cf. Fig. 5.26b) to be over-compensated for by the attractive interaction of the surface vacancies.

In Fig. 5.28 the difference between the electron density of the $(\sqrt{3} \times \sqrt{3})R30°$-Na/Al(111) phase and that of the underlying vacancy structure plus a free standing Na layer with also $(\sqrt{3} \times \sqrt{3})R30°$ periodicity is shown. It can be seen that due to Na adsorption, electron density has been displaced from the Na atoms toward the Al atoms of the substrate. As noted above, the reason for the favorable adsorption energy of Na in this structure is due to the particularly low vacancy formation energy; the reason for this has been attributed to the formation of covalent-like, in-plane bonding between the remaining top-layer Al atoms, the honey-comb arrangement of which is similar to that of graphite. The electronic structure of the reconstructed surface is found to be largely responsible for that of the $(\sqrt{3} \times \sqrt{3})R30°$-Na/Al(111) phase. In particular, new states close to the bottom of the Al valence band are found as well as broad unoccupied bands. In this case, the role of Na is apparently mainly to create the vacancy but not to modify very much the electronic structure of the vacancies (Wenzien et al., 1993).

On further deposition of 1/6 of a monolayer of Na onto the substitutional $(\sqrt{3} \times \sqrt{3})R30°$-Na surface, a $(2 \times 2)$ structure forms with two Na atoms per unit cell. As discussed above, the atomic geometry of this phase proved initially difficult to determine. Its correct structure was first proposed on the basis of DFT-LDA calculations (Stampfl and Scheffler, 1994c) and was subsequently confirmed by a LEED intensity analysis (Burchhardt et al., 1995). From consideration of the atomic structure of the $(2 \times 2)$ phase, it would seem that no mass transport is necessary in its formation, i.e., there is an Al atom missing due to the substitutional adsorption of Na, but there is an additional Al atom embedded between the Na atoms. However, the lower coverage $(\sqrt{3} \times \sqrt{3})R30°$ substitutional structure

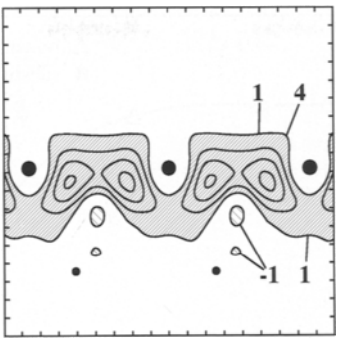


Fig. 5.28. Change of the electron density for $(\sqrt{3} \times \sqrt{3})R30°$-Na on Al(111) with Na in the substitutional site. The reference system is the $(\sqrt{3} \times \sqrt{3})R30°$ surface vacancy structure plus a free standing Na layer. The contours are displayed in a $(1\bar{2}1)$ plane. Substrate atoms are represented by small dots and Na atoms by large dots. The units are $10^{-3}$ bohr$^{-3}$ (from Neugebauer and Scheffler, 1992).

involves displacement of 1/3 of a monolayer of Al atoms, which are assumed to diffuse across the surface to be re-bound at steps. The results indicate, therefore, that formation of the $(2 \times 2)$ structure from the $(\sqrt{3} \times \sqrt{3})R30°$ structure involves the reverse process, that is, diffusion of 1/3 of a monolayer of Al atoms back from the steps which are used in the formation of the $(2 \times 2)$ structure. This process is depicted in Fig. 5.22b.

Interestingly, in a manner similar to that discussed above for the two substitutional structures of Na on Al(001) and Al(111), the *occupied* part of the surface band structure of the $(2 \times 2)$ Na-Al surface alloy can be explained largely in terms of the underlying Al structure. The latter corresponds to the reconstructed Al $(2 \times 2)$ vacancy layer *plus* the Al atom in the hcp-hollow site on this structure. In particular, a significant peak is observed at approximately 2 eV below the Fermi level. Analyzing the wave functions of this state at $\bar{\Gamma}$ shows that it is localized on top of the uppermost hcp-hollow Al atoms. For the surface alloy, in addition, unoccupied features are identified which are associated with the Na atoms, and at $\bar{\Gamma}$, they are centered above the uppermost Na atoms (Stampfl and Scheffler, 1994c).

### *5.6.3. Co on Cu(001)*

In the above sections it was shown that the substitutional adsorption of alkali-metal atoms is driven by the strong dipole moment of adatoms, a rather low formation energy of surface vacancies, and the fact that the adsorbate–adsorbate repulsion is reduced in the substitutional geometry. Thus, substitutional adsorption does not occur for single adatoms, but only when the coverage has reached a critical value where the adatom–adatom interaction becomes significant (cf. Fig. 5.23).

For cobalt adsorbed on Cu(001) the situation is different. Here the adatoms can assume a substitutional geometry at the lowest coverages and with increasing coverage a structural phase transition occurs toward the formation of close-packed islands. The difference compared to alkali-metal adsorption is due to the fact that cobalt, as a transition metal from the middle of the 3d series, likes to involve its d-electrons in the chemical binding. This implies that Co likes to assume a highly coordinated site. A single Co adatom on a Cu(001)

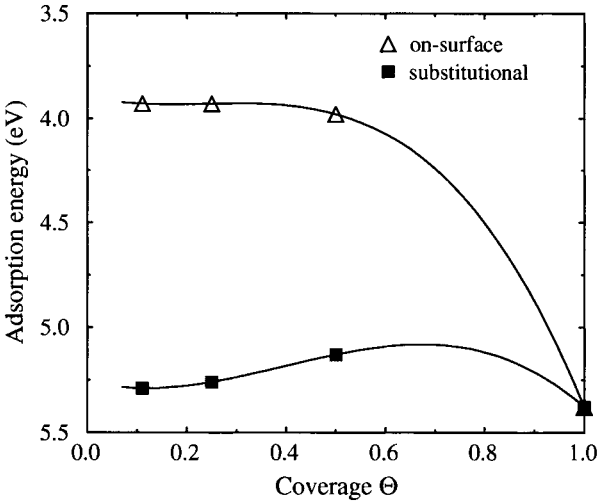


Fig. 5.29. Adsorption energy versus coverage for Co on Cu(001) in the on-surface hollow site and in the surface substitutional site (from Pentcheva and Scheffler, 2000).

surface in the on-surface hollow site has four Cu neighbors. However, in the substitutional site it is embedded in the electron density provided by eight Cu neighbors. Thus adsorption in a substitutional site (i.e., in a surface vacancy) is clearly more favorable than adsorption in an on-surface site. In fact, the energy difference between on-surface adsorption and into-surface-vacancy adsorption is larger than the energy to create a surface vacancy. Thus, single Co adatoms tend to kick out Cu atoms from the surface and assume their sites. We note that the Cu atoms taken out of the surface are re-bound at kink sites at steps where they attain the Cu-bulk cohesive energy (cf. Section 5.2.3). In this context it is also relevant that Cu adatoms on Cu(001) have a higher mobility than Co adatoms, which implies that thermal equilibrium with kink sites can be attained easily for Cu adatoms, but is hindered for Co adatoms.

Figure 5.29 shows the adsorption energies for on-surface and substitutional adsorption of Co. For low coverages substitutional adsorption is energetically favorable. For higher coverage it is still more energetically favorable for an open adlayer to adsorb substitutionally than on-surface, but the energetically lowest configuration is that of a close-packed Co islands. In other words, Fig. 5.29 tells us that substitutionally adsorbed Co atoms form strong bonds with their eight Cu neighbors. However, the strongest bonds are achieved when Co adatoms form close-packed Co islands. Thus, for higher coverages, and/or higher temperature, when Co adatoms perceive the existence of other Co atoms on the surface, isolated, substitutionally adsorbed Co atoms are predicted to leave their site and close-packed Co islands will be formed. In fact, recent DFT calculations predict that these islands preferentially will have a thickness of 2–3 Co layers and are capped by a Cu layer (Pentcheva and Scheffler, 2000).

## 5.7. Adsorption of CO at transition metal surfaces – a model system for a simple molecular adsorbate

The adsorption of a diatomic molecule on a surface represents the next degree of complexity with respect to the adsorption of a single atom and serves as a link to understanding the behavior of more complex molecular adsorbates, as well as to the important area of carbonyl chemistry. As such, CO adsorption has become a paradigm for the study of a simple molecular adsorbate on a surface and has been extensively studied both experimentally and theoretically, see, e.g., Hermann et al. (1987), Hoffmann (1988), Campuzano (1990), and references therein. This interest in CO adsorption also originates from the technological importance of oxidation catalysis (e.g., the car exhaust catalytic converter).

The three outer valence orbitals of a free CO molecule are sketched in Fig. 5.30. With decreasing ionization energies, these are the $5\sigma$ orbital (largely C 2s, C $2p_z$), the doubly degenerate $1\pi$ orbital (largely C $2p_x$, $p_y$, O $2p_x$, $p_y$) and the $4\sigma$ orbital (largely O 2s, O $2p_z$). The first unoccupied state, shown at the far right in the figure, is the antibonding C $2p_x$, $p_y$, O $2p_x$, $p_y$ ($2\pi^*$) orbital. The two most important orbitals are the $5\sigma$ and the $2\pi^*$ orbitals which correspond to the HOMO and LUMO, respectively (see Fig. 5.30). The notation here is that "$\sigma$" indicates orbitals that are rotationally invariant with respect to the inter-nuclear axis and "$\pi$" represents orbitals that are lacking this symmetry.

When CO is brought toward a metal surface the CO $5\sigma$ orbital is significantly perturbed by the hybridization with the substrate d-electrons. The energy of the $5\sigma$ orbital changes most strongly because the bonding to the substrate is governed by the interaction of this orbital. This gives rise to charge transfer from the CO $5\sigma$ orbital to the metal, but the metal gives charge back into the antibonding $2\pi^*$-CO orbital. This is called the donor–acceptor model for CO bonding (Blyholder, 1964, 1975), which is known from the metal carbonyls and is similar to the results for $H_2$ adsorption (see the discussion of Fig. 5.37 in Section 5.9.2 below). The back donation from the substrate into the $2\pi^*$-CO orbital

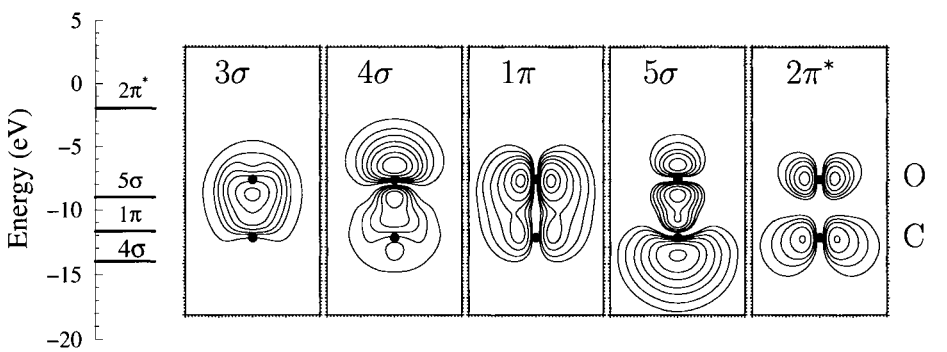


Fig. 5.30. Electron density of the valence molecular orbitals of a free CO molecule and their DFT-GGA Kohn–Sham eigenvalues (far left) with respect to the vacuum level. The lower and upper small black dots represent the positions of the C and O atoms, respectively. The first contour lines are at $8\times10^{-3}$ bohr$^{-3}$, except for the $2\pi^*$ orbital where it is $15 \times 10^{-3}$ bohr$^{-3}$, and the highest-valued contour lines are at 0.5, 0.3, 0.2, 0.15, and 0.15 bohr$^{-3}$ for the $3\sigma$, $4\sigma$, $1\pi$, $5\sigma$, and $2\pi^*$ orbitals, respectively.

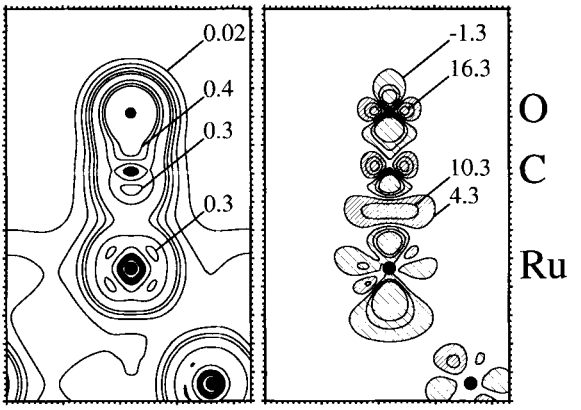


Fig. 5.31. Valence electron density (left) and *difference density* $n^{\Delta}(\mathbf{r})$ (cf. Eq. (5.5)) for the adsorption of CO in the on top site on Ru(0001). Units are bohr$^{-3}$ in the left panel and $10^{-3}$ bohr$^{-3}$ in the right panel.

weakens the bonding within the CO molecule and strengthens the bond to the substrate. At close distances the ordering of the $1\pi$- and the $5\sigma$-derived levels is reversed compared with the gas phase (see also the discussion of CO on Ni by Hermann and Bagus (1977), and of CO on Cu by Hermann et al. (1987)). In the Blyholder model the lower lying $4\sigma$ and $1\pi$ MOs (as well as the $3\sigma$ and of course the core states) are assumed not to play an important role in the CO–metal bond formation.

In the following we will use Ru(0001) as the substrate for the discussion of CO adsorption but note that the basic results are valid for other transition-metal substrates as well. In the left panel of Fig. 5.31 the valence electron density of CO in the on-top site on the Ru(0001) surface is shown, and in the right panel of Fig. 5.31 is the difference between the electron density of the CO/Ru(0001) system and the superposition of Ru(0001) and free molecular CO. From the latter, the electron redistribution can be seen to be in good general agreement with the Blyholder donor–acceptor model: Depletion is clearly seen from the $\sigma$ orbitals of CO and an increase in electron density into the $2\pi^*$ orbitals. Depletion can also be clearly noted from Ru states with $d_{z^2}$-like character, as well as a significant increase in electron density in the region of the adsorbate–substrate bond, i.e., between the C and Ru atoms. A similar behavior was found for CO on other substrates (see, e.g., Wimmer et al., 1985 and Bagus et al., 1986). It is pointed out that in addition, there is participation to the CO–metal bonding by the Ru atoms in the *second* layer.

The Kohn–Sham eigenvalues of the free CO molecule shift noticeably upon adsorption on the Ru(0001) surface; in particular, a significant downward shift of the $5\sigma$ orbital energy due to hybridization with Ru states, and also a small downward shift of the $4\sigma$ level is observed. The $1\pi$-level is changed only little, and the $2\pi^*$-level moves up in energy reflecting the increased occupation. Also, correspondingly, the development of antibonding states occurs. Thus, the behavior follows that of Section 5.3.1, and we realize that the effects (ii) and (iii) are apparently small for on-top adsorbed CO. In Fig. 5.32 the spatial distribution of some of these CO-derived states are displayed. It can be seen that the $3\sigma$ orbital remains unperturbed (compare with Fig. 5.30) by CO adsorption on the substrate

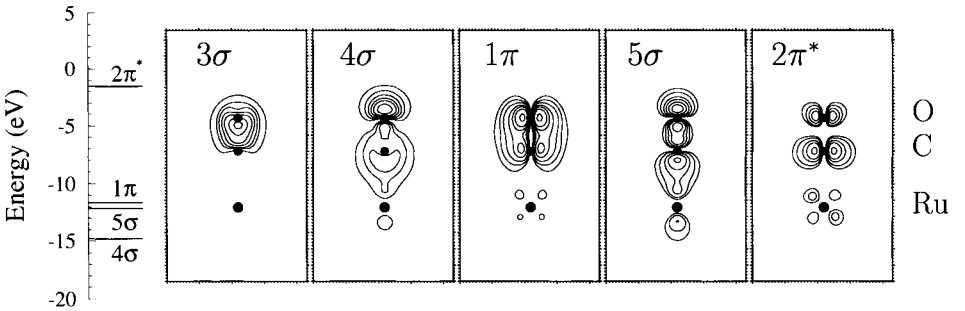


Fig. 5.32. Electron density distribution of the CO-derived states for CO adsorbed in the on-top site of Ru(0001) and their DFT-GGA Kohn–Sham eigenvalues (far left) with respect to the vacuum level. The black dots represent the positions of the O, C, and Ru atoms. The first contour lines are at $8 \times 10^{-3}$ bohr$^{-3}$, except for the $1\pi$ orbital where it is $4 \times 10^{-3}$ bohr$^{-3}$. The highest-valued contour lines are at 0.5 for the $3\sigma$ and $4\sigma$ orbitals and at 0.2, 0.3, and 0.09 bohr$^{-3}$ for the $1\pi$, $5\sigma$, and $2\pi^*$ orbitals, respectively.

since it lies significantly lower in energy and away from the surface. The $4\sigma$ orbital interacts with Ru $d_{z^2}$-like states, as does the strongly interacting $5\sigma$ orbital. The $1\pi$ orbital on the other hand interacts only weakly with the substrate. The unoccupied $2\pi^*$-orbital hybridizes with Ru states of $d_{xz}$- and $d_{yz}$-character. Certain of these adsorbate–substrate bonding states also have an antibonding partner (not shown), the weight of which resides predominately in the substrate.

We see therefore that the first-principles calculations support in general the Blyholder model, but that the details of the bonding are somewhat more complicated; similar observations have been pointed out and discussed in more detail by Hu et al. (1995) for first-principles studies of CO on Pd(110) and from experiments by Nilsson et al. (1997).

## 5.8. Co-adsorption [the example CO plus O on Ru(0001)]

A prerequisite to understanding heterogeneous catalytic reactions is knowledge of the behavior of the various reactants (e.g., the adsorption sites and binding energies), as well as their mutual interactions. The co-adsorption system ($m$CO + $n$O)/Ru(0001) represents a well-studied model system, not least due to the drive aimed at obtaining an understanding of the catalytic oxidation of CO by $O_2$, but also as a "simple" model system for oxidation catalysis in general. Despite the considerable interest, it is only recently that the detailed atomic structure of some of the phases of ($m$CO + $n$O) on Ru(0001) have been determined, and new ones discovered. Depending on the experimental conditions, co-adsorption of CO and O on Ru(0001) can form the following phases: $(2 \times 2)$-(1O + 1CO) [Kostov et al., 1992; Narloch et al., 1995], $(2 \times 2)$-(2O + 1CO) [Narloch et al., 1994], and $(2 \times 2)$-(1O + 2CO) [Schiffer et al., 1997]. These mixed ($m$CO + $n$O)/Ru(0001) surface structures are depicted in the top panel of Fig. 5.33.

For the first two structures, low-energy electron diffraction (LEED) intensity analyses have been performed: In the first phase, the O atoms occupy hcp sites and the CO molecule adsorbs in the on-top site. In the second phase, a restructuring induced by CO adsorption

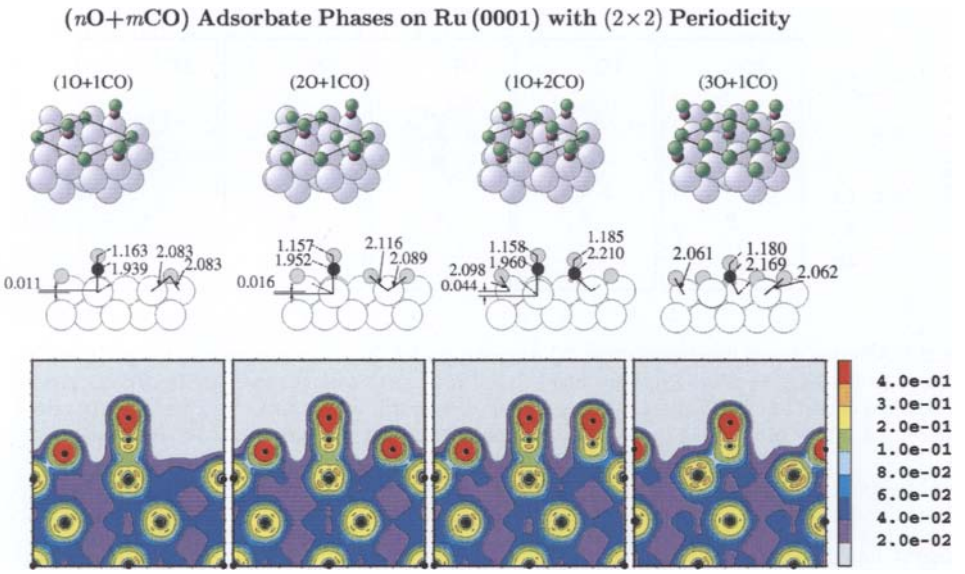


Fig. 5.33. Perspective and side views of the various phases of O and CO on Ru(0001). Large and small (green and red) circles represent Ru, O, and C atoms, respectively. The lower panel shows the electron density of the valence states. The contour lines are in bohr$^{-3}$ and distances are in Å (from Stampfl and Scheffler, 1998).

of the O atoms of the (2 × 1) (Lindroos et al., 1989) phase occurs: Half of the O atoms, initially occupying the hcp sites, switch to fcc sites and CO adsorbs again in the favored on-top site. For the (1O + 2CO) structure, there has been no LEED intensity analysis, but infrared absorption spectroscopy (IRAS) and X-ray photoelectron spectroscopy (XPS) experiments (Schiffer et al., 1997) indicate that the O atoms occupy hcp sites and the CO molecules occupy on-top and fcc sites.

To obtain insight into the behavior of these co-adsorption systems, DFT calculations have been carried out. The calculated atomic geometries are displayed in the middle section of Fig. 5.33. Good agreement with the LEED determined geometry was found for the first two of these phases for which comparison is possible (Stampfl and Scheffler, 1998). The calculations show that for the (2O + 1CO) structure, it is indeed energetically more favorable (by 0.59 eV) for half of the O atoms to occupy the less favorable fcc sites and CO to adsorb in the on-top site rather than maintaining the (2 × 1)-O arrangement and CO adsorbing in a hollow site. In addition to those phases that have been experimentally identified, the theory predicts the stability of another phase (Stampfl and Scheffler, 1998), namely (2 × 2)-(3O + 1CO)/Ru(0001), seen in the far right-hand-side of Fig. 5.33. The adsorption energy of CO in this structure is notably weaker than for CO in the on-top site; it is, however, still appreciably exothermic with a value of 0.85 eV. An important consideration concerning whether a structure can in fact form, is the kinetics. The possibility of kinetic hindering due to energy barriers induced by the adsorbed O atoms was investigated by calculating the total energy of CO at various distances above the hcp-hollow adsorption site, i.e., above the vacant O site of the (2 × 2)-3O/Ru(0001) structure. Incidentally, this

structure has recently been shown to represent a new stable phase of O on Ru(0001) (Kostov et al., 1997; Kim et al., 1998; Gsell et al., 1998). The calculations show that there is an energy barrier to adsorption of $\approx$0.35 eV. This implies that rather high CO pressures would be required in order to realize this structure experimentally. Similar calculations were carried out for the (1O + 2CO) phase for the CO molecule above the fcc site. It was found in this case there is also an energy barrier, but slightly smaller of about 0.2 eV, thus (at least partially) explaining the low sticking coefficient and the necessary high exposures found experimentally in order to create this phase (Schiffer et al., 1997).

The valence electron density of the various phases are also shown in Fig. 5.33. The oxygen atoms appear as the red (i.e., high electron density), almost spherical features. Both CO and O can be seen to induce a significant redistribution of the electron density of the top-layer Ru atoms. For CO in the hollow sites, it is apparent that the bond strength (per bond) is weaker than that for CO in the on-top site. In the hollow sites, however, CO forms *three* bonds with the metal surface so it is expected that they be longer and weaker. The calculations show nevertheless that the adsorption energy is significantly weaker in the hollow sites than in the on-top site for these structures; this is not the case for the clean surface where the energy difference is only about 0.04 eV. Thus, this significant energy difference is a consequence of the co-adsorbates. These ($m$CO + $n$O)/Ru structures depicted in Fig. 5.33, each possessing the same periodicity but with varying numbers of species and adsorption sites, represent an ideal model co-adsorption series for study by first-principles calculations. From analysis of the results of such calculations much can be learnt about the various interaction mechanisms at play.

## 5.9. Chemical reactions at metal surfaces

This section summarizes some basic aspects of the present understanding of the reactivity of surfaces. Here the term "reactivity" usually refers to the surfaces' ability to break bonds of an approaching molecule and to adsorb the fragments, which is often the rate limiting step in catalytic reactions. For example, in the ammonia synthesis it is the dissociation of $N_2$, and for various examples of oxidation catalysis (e.g., the catalytic oxidation of CO) it is the dissociation of $O_2$ (see Section 5.10 below). Just having referred to "catalysis" a word of warning is appropriate because industrial catalysis involves many more aspects than just dissociation of a certain molecule. Other aspects are "selectivity", which means that only the desired reaction should take place, and competing reactions yielding unwanted products are suppressed. Also the buffering of intermediate chemical products is important, as is the self-maintenance of the catalyst, the possible role of the catalyst's support and of promoters. And (often) it is important that no poisonous by-products are released.

### *5.9.1. The problem with "the" transition state*

We will discuss the surface reactivity in terms of molecules approaching the surface considering all relevant atomic coordinates. The total energy as function of the atomic coordinates is called the "potential-energy surface" (PES), cf. Section 5.2.2. It represents the energy surface on which the atoms will move. Whereas the electrons are assumed to be in

their ground state of the instantaneous geometry, the wave functions of the nuclei describe the details of the atoms' dynamics, i.e., the vibrations, rotations, center-of-mass translation, the scattering at the surface, the dissociation, and the surface diffusion of the fragments.

In order to keep the discussion simple we will discuss the situation of a molecular beam which is sent toward the surface, and in which the molecules have a certain center-of-mass kinetic energy, and are in a well defined vibrationally and rotationally excited state or the ground state. The probability of dissociation then is considered to be a measure for the surface reactivity. It contains

- information concerning the surface electronic structure, i.e., on the relevance of so-called frontier orbitals (Wilke et al., 1996, and references therein),
- information about the high-dimensional PES on which the approaching molecule travels toward the surface,
- the statistical average over many trajectories which finally determines with what probability the active sites at the surface are found and the molecule will dissociate, or if it will be reflected into the gas phase.

To discuss the dissociation probability of incoming molecules, it is often assumed that the reaction proceeds along a one-dimensional (or low-dimensional) reaction coordinate and that it will cross a well defined "transition state" (cf. Fig. 5.34). Then the reaction probability is given by an Arrhenius behavior with the energy barrier given by this transition state. While the concept behind Fig. 5.34 has proven useful (at least often) in gas-phase chemistry, it may be misleading for the description of surface chemical reactions. In particular, we note that the phase space for a molecule–surface reaction has very high dimensionality. For example, even in the simplest surface reaction, i.e., when $H_2$ molecules are sent toward the surface and if the substrate atoms do not move during the scattering event, the translations, vibrations and rotations of the two H atoms take place in a 6-dimensional configuration space, i.e., a 12-dimensional phase space. As a consequence, the assumption of "the" transition state, as depicted in Fig. 5.34 can be grossly misleading. Instead, many transition states exist, and which of them is taken with what probability depends on the details of the incident $H_2$ dynamics, i.e., the $H_2$ translational kinetic energy, and the vibrations and rotations. Consequently, a good treatment of the statistics of the many possible trajectories is mandatory.

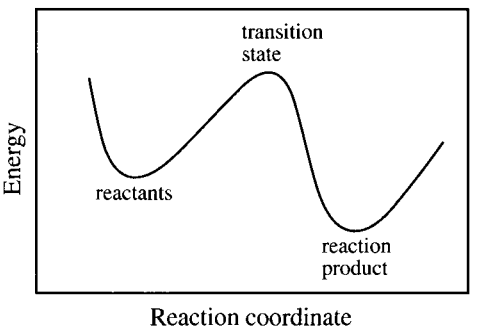


Fig. 5.34. Energetics of a chemical reaction in which reactants (their energy is that of the left minimum) reach the reaction product (energy of the right minimum) via a well defined transition state.

As noted in Section 5.2.2 we will restrict the discussion in this chapter to situations where the Born–Oppenheimer approximation is justified. Still, a severe problem remains, namely that knowledge of the high-dimensional PES barely exists. Up until recently only rough, and as we now know, often incorrect semi-empirical models were used, and these earlier studies of the dissociation dynamics were restricted in their dimensionality. For example, in the past the dissociation of $H_2$ was described in terms of only 2 or 3 coordinates (out of the six important coordinates), and the dependence of the PES on the other coordinates was simply neglected. The only reason for this simplification was that evaluating a PES using good-quality electronic structure theory is elaborate. Since about 1994 the situation has changed, i.e., several groups started to take into account the higher dimensionality (see Gross and Scheffler, 1998, and references therein). Though involved, even treating the six-dimensions of the two hydrogen atoms is not yet complete because in general it could happen that electronic excitations play a role in the scattering event which is outside the Born–Oppenheimer approximation, and furthermore, it is well possible that the dynamics of the substrate atoms will play a role. These concerns may not be very important for the systems studied so far, but for other systems they may well be relevant. With respect to the validity of the Born–Oppenheimer approximation we are not aware of a serious breakdown, although sometimes it has been speculated. For adsorbates at metal substrates, levels are typically broadened, which implies that excited states have a short life time and thus relaxation into the ground state configuration will be (nearly) instantaneous on the time scale of the nuclear motion. Obviously, for insulators and semiconductors the situation is different (see, e.g., the discussion in Gross et al., 1997). Also, the situation would be different if laser excitations are involved (i.e., photo-chemistry), but this is not the topic of this chapter.

### *5.9.2. Dissociative adsorption and associative desorption of $H_2$ at transition metals*

Dissociative adsorption (or the time-reversed process, which is associative desorption) is a dynamical process, and because of the high dimensionality of the PES, a proper treatment of the dynamics is indeed crucial. Typically the dynamics of atoms is treated classically, i.e., by Newton's equation of motions, but the underlying PES and the forces acting on the atoms are (or could be and should be) calculated by DFT. This is what is called "*ab initio* molecular dynamics". It started with the seminal work of Car and Parrinello (1985). The elegance of their approach appears to imply that typically it is not very efficient, and since their original paper several alternative (and numerically more efficient) formulations have been developed (see, e.g., Payne et al., 1992; Kresse and Furthmüller, 1996; Bockstedte et al., 1997; and references therein).

When the moving nuclei are hydrogen atoms, it is often necessary to treat also the nuclei as quantum particles. For such problems a rather involved, high-dimensional "*ab initio* quantum dynamics" method has been implemented (Gross et al., 1995, 1998; Kroes et al., 1997; and references therein). This is probably the most advanced approach and for heavy particles (obviously) it becomes identical to *ab initio* molecular dynamics.

In the following section we describe some general features of the PES and then we show examples which demonstrate the importance of a quantum dynamical treatment of

scattering and dissociation of molecules at surfaces. The dissociative adsorption of $H_2$ appears to be a very simple reaction. However, due to the quantum nature of the hydrogen nuclei, the actual processes are rather complex. Again, as always in this chapter, we will keep the discussion simple, and for more details we refer to papers by Gross and Scheffler (1998), Gross (1998) and Kroes (1999).

*5.9.2.1. The potential-energy surface of $H_2$ at transition-metal surfaces*

A good knowledge of the high-dimensional PES of the molecule–surface system is mandatory for a detailed understanding, as the PES rules the scattering and the dissociation. The high-dimensionality implies that the dynamics of the problem will be complex and therefore typically it will be impossible to analyze the PES by simply looking at it. In fact, looking at a PES with dimensionality equal to or higher than six is only possible in terms of cuts along planes in configuration space. Figure 5.35 shows three examples of what is usually called an "elbow plot" because it often looks like an elbow. The planes in configuration space are identified by the insets in the figure. Along these planes the height of the molecule $Z$ and the H–H distance $d_{H-H}$ is varied, and lines of constant potential energy are displayed. Obviously the cut through the PES shown in Fig. 5.35a looks very different to those in Figs. 5.35b, c.

If the $H_2$-surface distance (i.e., $Z$) is large the contour lines in Fig. 5.35 reflect the energetics of a free $H_2$ molecule, which has the equilibrium separation of 0.75 Å. We can also read off the nearly harmonic potential underlying the H–H vibration, which implies an $H_2$ zero-point energy of 0.26 eV, and a vibrational excitation energy of 0.52 eV.

Although the knowledge of one elbow plot is already much better than just knowing the transition state, as the latter is just one point in the whole configurations space, restricting the world to only one elbow ignores the fact that two H-atoms have six degrees of freedom, not just two. It is obvious from Fig. 5.35 that neglecting the high dimensionality, i.e., assuming that the elbows for different choices of $(X, Y, \theta_{H_2}, \phi_{H_2})$ are similar, is by no means justified.

We will now discuss one aspect of the PES which explains the general trend of the reactivity of different transition-metal surfaces. However we already like to add the warning that an appropriate (and reliable) analysis of chemical reactivity has to include a good *statistical treatment* of the *dynamics* of the atoms, which will be discussed in the next section.

Figure 5.35a shows that on Pd(001) there is at least one pathway toward dissociative adsorption which is not hindered by an energy barrier. In fact, if we inspect the PES for Rh (the left neighbor of Pd in the periodic table) [see Eichler et al., (1999a)] one sees that here the PES offers even more pathways without barriers: For molecules with their axis parallel to the surface almost all dissociation paths are non-activated. On the other hand, for Ag (the right neighbor of Pd) we find that all pathways toward dissociative adsorption are hindered by a significant energy barrier (Eichler et al., 1999a). This result simply reflects the higher chemical activity of the true transition metals compared to the noble metal silver. Figure 5.36 shows the PES of $H_2$ at Ag(001). The important aspect in comparing the (a) panels of Figs. 5.35 and 5.36 is not just that there is an energy barrier for the silver substrate, but *where this barrier is located* in configuration space: The lowest barrier (see Fig. 5.36) is found very close to the surface and at a H–H distance which is significantly stretched (by

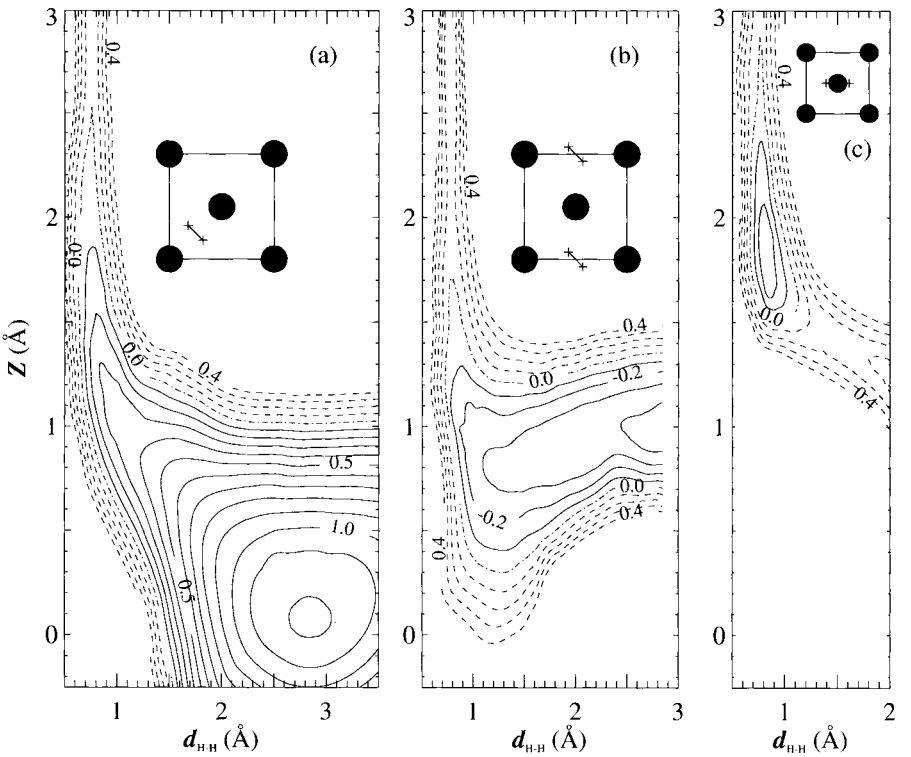


Fig. 5.35. Cut through the six-dimensional potential energy surface (PES) of an $H_2$ molecule above of Pd(001). We display "elbow plots" where $Z$ is the height of the $H_2$ center of mass over the surface, and $d_{H-H}$ is the distance between the two hydrogen atoms. Each cut is defined by the lateral $H_2$ center-of-mass coordinates in the surface unit cell and the orientation of the molecular axis, i.e., the coordinates $X, Y, \theta_{H_2}$, and $\phi_{H_2}$: The molecule is kept parallel to the surface ($\theta_{H_2} = 90°$) at an azimuthal orientation, $\phi_{H_2}$, and $X, Y$ coordinates shown in the insets. The units of the potential energy are eV and the interval between adjacent contour lines is 0.1 eV. The results are from Wilke and Scheffler (1996).

about 100%) compared to the free molecule. We also note in passing that the adsorption state of H on Ag(001) is only metastable, i.e., at a higher energy than the free $H_2$ molecule.

Keeping the problems with "the" transition state in mind (we will come back to it in the next section) we now analyze its properties. The fact that the transition state in Fig. 5.36 is found at small $Z$ and significantly stretched $d_{H-H}$ values implies that the H–H bond is nearly broken when the molecule has reached the top of the barrier. In fact, the detailed analysis of the wave functions of the $H_2$–surface system at the geometry of the barrier shows that the differences between different metals should be described in a covalent (or tight-binding) picture. Earlier attempts, which applied a description in terms of Pauli repulsion, and/or frontier orbitals of the unperturbed constituents do not account properly for the character and strength of the interaction: At the barrier we find that the interaction between the molecule and the substrate is already significant and the electronic states ruling the energetics are very different from those of

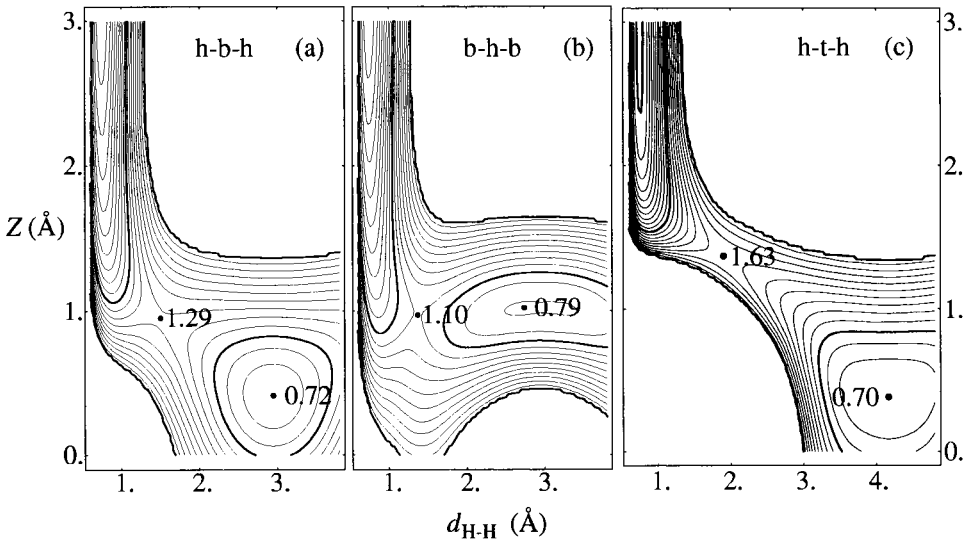


Fig. 5.36. The same as Fig. 5.35 but for $H_2$ at Ag(001). The results are after Eichler et al. (1999a) and private communication.

the clean surface. Figure 5.37 summarizes the view developed by Hammer et al. (1994, 1995) in their analysis of $H_2$ at Cu(111) and $H_2$ at NiAl(110) [see also the earlier study by Hjelmberg et al. (1979) for $H_2$ at jellium]. Because of obvious reasons, this figure looks similar to that in Section 5.3.1, but now the interacting particle is an $H_2$ molecule and the geometry is that of the transition state, and not of an adsorbate equilibrium configuration. At the transition state the interaction of the molecule with the surface has already produced a clear splitting into states which are bonding between the molecule and the substrate and which are antibonding. Assuming a substrate from the middle of the transition-metal series (e.g., Ru or Rh) implies that the low energy resonances, which are $\sigma_g$ and $\sigma_u$ derived, are filled with electrons. These states are bonding with respect to the molecule–substrate interaction and thus their filling implies an attraction of the molecule to the surface. But the filling of the $\sigma_u$ resonance also implies a weakening of the H–H bond. Thus, when the substrate Fermi-level is in the middle of the d-band, we understand that molecules are strongly attracted to the surface and at the same time the molecular bond is broken.

On the other hand, when the substrate Fermi level is well above the d-band, as for a noble metal, also the states which are antibonding with respect to the molecule–surface interaction get filled (the high energy DOS in panels (c) and (d) of Fig. 5.37). This implies that the net interaction between the molecule and the substrate is repulsive. Thus, an energy barrier is built up which hinders the dissociation.

*5.9.2.2. The dynamics of $H_2$ dissociation at transition-metal surfaces*

We have seen that the dissociative adsorption of $H_2$ at Pd(001) can proceed without an energy barrier. However, this holds only for few pathways; in particular, it is necessary that the molecule reaches the surface with an orientation parallel to the surface in order to be able to dissociate. Molecules arriving with an orientation of their axis perpendicular

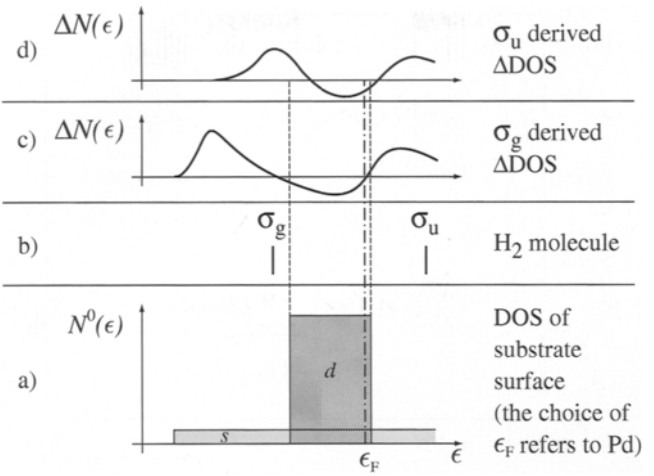


Fig. 5.37. Schematic description of the interaction of $H_2$ at the transition state toward dissociative adsorption at transition-metal surfaces. The bottom panel (a) shows the density of states for a transition metal before adsorption, and panel (b) shows the energy levels of a free $H_2$ molecule: the bonding state $[\phi_{\sigma_g} = \phi_{1s}(\mathbf{R}_1) + \phi_{1s}(\mathbf{R}_2)]$ and the antibonding state $[\phi_{\sigma_u} = \phi_{1s}(\mathbf{R}_1) - \phi_{1s}(\mathbf{R}_2)]$. The $\sigma_g$-level is filled with two electrons and the $\sigma_u$-level is empty. The interaction between the $H_2$ $\sigma_g$-level and the substrate s- and d-bands gives rise to a broadening and the formation of an antibonding level at about the upper edge of the d-band and a bonding level below the d-band, see panel (c). Panel (d) shows that the interaction between the $H_2$ $\sigma_u$-level with the substrate s- and d-bands gives rise to a broadening and the formation of a bonding level (at about the lower edge of the d-band) and an antibonding level (above the d-band).

to the surface will be reflected. In order to understand in more detail what goes on and to determine the probability of dissociation, it is necessary to calculate the dynamics along the high-dimensional PES. This has been done by Gross et al. (Gross et al., 1995, 1998). They treat also the hydrogen nuclei as quantum particles, and a comparison with a classical treatment of the dynamics showed in great detail, which quantum effects are important (mainly zero-point vibrations, and only little tunneling).

Figure 5.38 displays the sticking probability $S$ for two different substrates. The sticking probability is the probability that an incoming $H_2$ molecule dissociates and that the atoms then adsorb at the surface. One could also say that $(1 - S)$ is the probability that an incoming $H_2$ molecule gets reflected back into the vacuum. The calculated sticking curve exhibits many oscillations. This is not noise, but reflects the quantum nature of the dissociative adsorption and the scattering event: The reflected $H_2$ beams, which differ by reciprocal lattice vectors of the surface, and the rotationally and vibrationally excited beams are subject to quantum interferences. Thus, the oscillations have a quantum mechanical origin, and when the hydrogen nuclei were treated classically, they were absent. Similar oscillations are well known for other quantum mechanical scattering studies, such as the scattering of electrons (LEED) or that of He. We trust that at some time they will be also observed experimentally for the $H_2$ scattering at metal surfaces, but clearly such experiments are very demanding. More details on the nature of the quantum interference effects of $H_2$/Pd scattering can be found in the paper by Gross and Scheffler (1998). When the theoretical results were

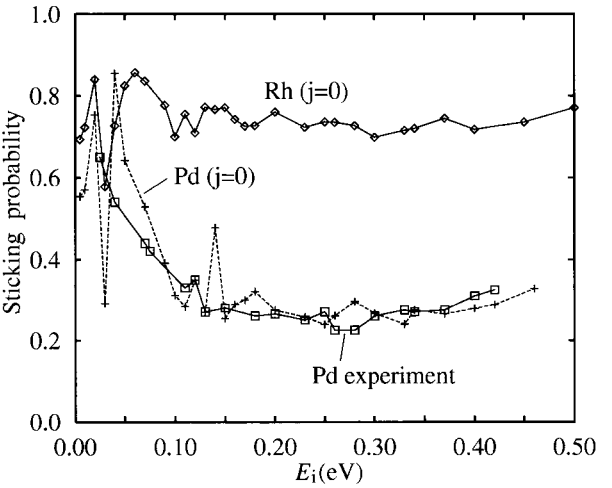


Fig. 5.38. Initial sticking probability versus kinetic energy for an $H_2$ beam under normal incidence on a clean Pd(001) and Rh(001) surface. The $H_2$ molecules are incident normal to the surface and are in their rotational and vibrational ground state. Theoretical results are from Eichler et al. (1999a), and the experimental data are from Rendulic et al. (1989).

broadened with the energy resolution of typical experiments, most of the oscillations were averaged out.

One unexpected and surprising result of Fig. 5.38 is that for low kinetic energies ($E_i < 0.05$ eV) the sticking probabilities for the Pd and Rh substrates are very similar (we recall that the PES of Rh offers many pathways with vanishing energy barriers toward dissociation but Pd only a few). Despite their differences in electronic structure (Pd is more noble than Rh) and the clear differences in the PESs, both substrates give an $S$ value as high as 75% for low $E_i$. In fact, this low energy range corresponds to the typical thermal kinetic energies. While for Rh the sticking probability always remains high, it decreases for Pd to about 25%.

The sticking probability for $H_2$ at Pd(001) starts at a high value and then it goes down; this is found in the theory as well as in the experimental data. Earlier, it had been suggested that this behavior is due to the existence of a precursor adsorption, where $H_2$ is trapped close to the surface from where it can undergo many attempts to dissociate. Whereas this concept is valid for some systems, the theoretical PES does not exhibit such a precursor state and thus, the explanation for this behavior of $S(E_i)$ must have a different origin. The analysis of the $H_2$ dynamics revealed that the effect is best described by the word "steering", which means the same as on the road. If one is going slowly, one will make it well along a curvy street. However, when one is going too fast one is pulled out of the curve. Thus, molecules which are approaching slowly will be able to follow a pathway along curvy valleys and find (along the high-dimensional PES) the way toward the point where they can dissociate without an energy barrier. They will dissociate even if their initial orientation is unfavorable (e.g., perpendicular to the surface) because they are steered toward a more favorable transition state geometry. On the other hand, fast molecules will

not be able to make it around all the curves. They will bump against an energy barrier and be reflected back into the gas phase.

Thus, the behavior we see for the Pd substrate which increases the sticking to nearly 75% at low energies of the $H_2$ beam, is truly a dynamical effect. In a static picture the high reactivity of Pd cannot be understood. The efficiency of steering depends on the speed of the incoming molecule and on the shape of the PES. Therefore, to evaluate the sticking probability, which we consider a good measure of the surface reactivity, it is important to consider all degrees of freedom and the dynamics of the nuclei. Obviously, as much as "steering" is important to understand the high reactivity of Pd at low $E_i$, for other systems, which on the grounds of the electronic structure alone may be expected to exhibit a high reactivity, an "anti-steering" may occur, which drives approaching molecules not toward the best transition state but against an energy barrier.

We add some words on the influence of rotations of the incoming molecule. For rapidly rotating molecules steering is suppressed because the molecules will quickly rotate out of favorable orientations for dissociation (so-called rotational hindering) (Darling and Holloway, 1994; Gross et al., 1996a, b, c). But, there is also a steric effect (Gross et al., 1995): molecules rotating in the so-called helicopter fashion (i.e., parallel to the surface) with $m = j$ dissociate more easily than molecules rotating in the so-called cartwheel fashion (i.e., perpendicular to the surface) with $m = 0$, because the helicoptering molecules have their axis already oriented preferentially parallel to the surface which is the most favorable orientation for dissociation. This orientation effect can be so strong that it even overcompensates the rotational hindering. Furthermore we note that, for example, the hindering effect of the rotational motion may be counterbalanced by the transfer of rotational energy to translational energy (see Eichler et al., 1999b, and Gross and Scheffler, 1996b, for more details).

## 5.10. The catalytic oxidation of CO

Just as the dissociative adsorption of $H_2$ discussed above in Section 5.9.2 may be regarded as the model system for studying the dynamics of the dissociative adsorption and associative desorption of small molecules, the CO oxidation reaction may be regarded as the most simple prototype model system of a surface heterogeneous catalytic reaction – a process involving molecular adsorption (chemisorption of CO is non-dissociative under the conditions of catalytic oxidation) and dissociative (atomic) adsorption, surface diffusion, surface reaction, and desorption of products. The oxidation of carbon monoxide has been extensively studied which is largely due to its technological importance (e.g., in car exhaust catalytic converters where the active components are transition metals such as Pt, Pd, and Rh) but is also related to its (relative) "simplicity" (Engel and Ertl, 1979, 1982; Bielánski and Haber, 1991; Peden, 1992, and references therein). Therefore there exists a large data-base concerning its macroscopic behavior and in these terms it is reasonably well understood. On a *microscopic* level, however, an understanding is still lacking. Steps in this direction have recently been made via first-principles calculations (Stampfl and Scheffler, 1997, 1999; Alavi et al., 1998; Eichler and Hafner, 1999). The results of one of these studies is briefly discussed below.

We first like to mention that the investigation of this type of surface process is more complex than that described above for $H_2$ dissociation; firstly significant substrate relaxations may be induced by CO and O adsorption, and the surface should not be treated as rigid. Secondly, the nature of the problem is different; here a "real" surface chemical reaction takes place where a product is formed that desorbs from the surface. So not only the coordinates of one adparticle need to be considered, but also those of the reacting partner, i.e., the problem has an even higher dimensionality.

Catalytic oxidation of CO at the ruthenium transition metal surface has been reported to exhibit unusual behavior compared to other transition metals when studied at high pressures (Peden, 1992, and references therein). In particular, the reaction rate over Ru for oxidizing conditions (i.e., at $CO/O_2$ pressure ratios $< 1$) is the highest of the transition metals considered. In contrast, under ultra-high vacuum conditions (UHV), the rate is by far the lowest. In addition, the kinetic data for the reaction over Ru (e.g., the temperature and pressure dependencies of the rate) deviate compared to the other metals and highest reaction rates occur for high oxygen concentrations at the surface. Interestingly, under these conditions, it was speculated that the reaction mechanism may proceed via an Eley–Rideal interaction (Peden et al., 1986, 1991), that is, a scattering reaction where a particle from the gas-phase reacts with an adsorbed species without adsorbing on the surface first. The usual mechanism by which reactions at surfaces take place is via the Langmuir–Hinshelwood mechanism where both species are adsorbed on the surface prior to reaction.

Under standard UHV conditions using $O_2$, the saturation coverage of O on Ru(0001) has been reported to be approximately half a monolayer. Recent studies employing $NO_2$ or very high exposures of $O_2$ have shown, however, that Ru(0001) can support higher coverages; namely ordered structures $(2 \times 2)$-3O (Kostov et al., 1997; Kim et al., 1998; Gsell et al., 1998) and $(1 \times 1)$-O (Stampfl et al., 1996), as had initially been predicted by DFT-GGA calculations (Stampfl and Scheffler, 1996), and that subsurface adsorption occurs after completion of the monolayer structure at elevated temperatures ($\approx$600 K) (Stampfl et al., 1996; Mitchell and Weinberg, 1996; Böttcher and Niehus, 1999). Subsurface oxygen can apparently occur as well as the formation of surface oxides[7], and surfaces with different domains of high oxygen concentration but different stoichiometry are assumed to actuate the high catalytic reactivity of Ru. Thus, the (apparent) oxygen saturation coverage noted above for low (or room) temperature UHV conditions and typical exposure by $O_2$ is solely due to kinetic hindering for $O_2$ dissociation.

The adsorption energy of O on Ru(0001) decreases notably with increasing coverage; in particular, for concentrations $\geqslant 1$ ML the bond strength is atypically weak compared to the lower coverage structures. This can be seen from Fig. 5.39. A good catalyst should actuate dissociation of $O_2$ but at the same time should not bind the dissociated entities too strongly, as then they have a good capability to diffuse and react. Too strongly bound constituents would have little reason to react at all. It is expected therefore that these weaker adsorption energies for $\Theta \geqslant 1$ will lead to an enhanced reaction rate of $CO_2$ formation. Indeed, re-

7 We note that the term "surface oxide" is not well defined, and in particular for Ru, which can exist in many oxidation states, it may be difficult, if not impossible, to distinguish between a 2–3 layer thick "surface oxide" and an on-surface plus sub-surface adsorbate phase.

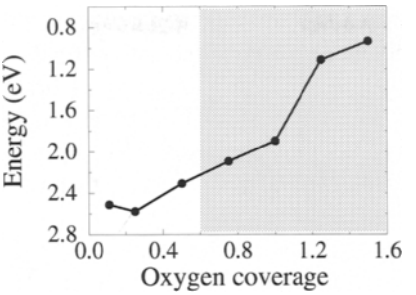


Fig. 5.39. Average adsorption energy of O on Ru(0001) for various coverages, with respect to 1/2 $O_2$. From Stampfl and Scheffler (1997).

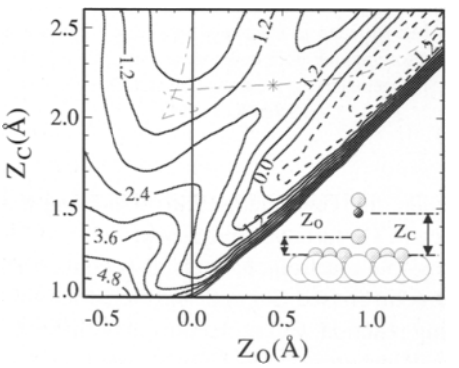


Fig. 5.40. Cut through the high-dimensional potential energy surface (PES) as a function of the positions of the C atom, $Z_C$, and the O adatom, $Z_O$ (see inset). The molecular axis is constrained to be perpendicular to the surface. Positive energies are shown as continuous lines, negative ones as dashed lines. The contour-line spacing is 0.6 eV. The dot-dashed line indicates a possible reaction pathway. From Stampfl and Scheffler (1997).

cent experimental studies of CO oxidation over Ru(0001) surfaces loaded with such high oxygen concentrations, have found even higher rates (Böttcher et al., 1997, 1999).

When a complete (1 × 1)-O structure is present, the calculations show that CO cannot adsorb. However, a scattering reaction of gas-phase CO with adsorbed oxygen (i.e., an Eley–Rideal mechanism) is possible, and the minimum energy barrier was found to be about 1.1 eV with a corresponding bent transition state geometry (Stampfl and Scheffler, 1997). Figure 5.40 shows an appropriate cut through the high-dimensional PES. The minimum barrier corresponds to a tilted CO molecular axis of about 131° as depicted in the inset of Fig. 5.41 which shows the corresponding energy diagram. It can be seen that due to the surface reaction there would be a significant energy gain of about 1.95 eV so that the produced $CO_2$ molecules would be highly energetic. Assuming this energy barrier would be the rate-limiting step of $CO_2$ formation via this mechanism, then an estimate of the reaction rate can be made using an Arrhenius-like equation. The prefactor being taken as the number of CO molecules hitting the surface per site per second at a given temperature and pressure. The rate obtained in this way was found to be significantly lower than that mea-

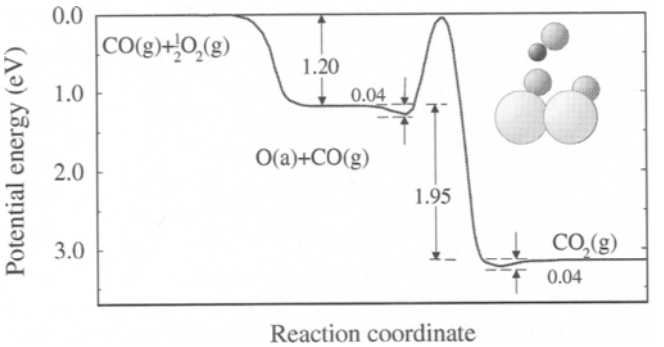


Fig. 5.41. Calculated energy diagram for a scattering reaction of gas-phase CO (Eley–Rideal mechanism) with an adsorbed O atom of the 1 ML phase on Ru(0001). Note, 1.20 eV is the energy required to remove one O atom (relative to 1/2 $O_2$) from the 1 ML structure as calculated in a (2 × 2) surface unit cell – or, equivalently, the energy gained by the system on adsorbing this atom in the vacant site, i.e., it is not the average adsorption energy at 1 ML as shown in Fig. 5.39. The geometry of the transition state is indicated in the inset. From Stampfl and Scheffler (1997).

sured experimentally (Peden and Goodman, 1986) indicating that this mechanism alone cannot explain the enhanced $CO_2$ turnover frequency.

To investigate other possible reaction channels, it is conceivable that there may be vacancies in the (1 × 1)-O adlayer (see Stampfl and Scheffler, 1997), e.g., created by the above mentioned scattering reaction. CO molecules may then adsorb at these vacant sites and react via a Langmuir–Hinshelwood mechanism (see Fig. 5.42). In Section 5.8 it was seen that there is an energy barrier for CO to adsorb in such a vacancy; however, at the high pressures and elevated temperatures employed in catalytic reactor experiments, it is expected that a barrier of such size can be readily overcome.

In view of the weaker CO–metal bond strength compared to that of the O–metal bond strength at this coverage, i.e., 0.85 eV compared to 2.12 eV[8] (with respect to gas phase 1/2 $O_2$), it may be expected that the energetically favorable reaction pathway is via movement of CO toward the O atom. Indeed, among the various pathways investigated, this turns out to be the case where the determined energy barrier is about 1.5 eV. Some selected geometries along the reaction path are shown in Fig. 5.43. We refer to Stampfl and Scheffler (1999) for further details.

It can be seen that at the transition state (also shown in the inset of Fig. 5.44), the C–O(a) bond[9] is almost parallel to the surface. The CO axis is bent away from O(a) yielding a bent CO–O(a) complex with a bond angle of 125°; similar to that found for the Eley–Rideal mechanism. The C–O(a) bond length is 1.59 Å (about 29% stretched compared to that in $CO_2$) and the CO bond length is 1.18 Å. At the transition state CO and O begin to lift-off the surface as they break their metal bonds in favor of developing a C–O(a)

8 Here 2.12 eV is the average adsorption energy of O at coverage $\theta = 0.75$ (cf. Fig. 5.39), i.e., corresponding to the (2 × 2)-3O structure.

9 O(a) labels the oxygen atom which is adsorbed to the metal substrate.

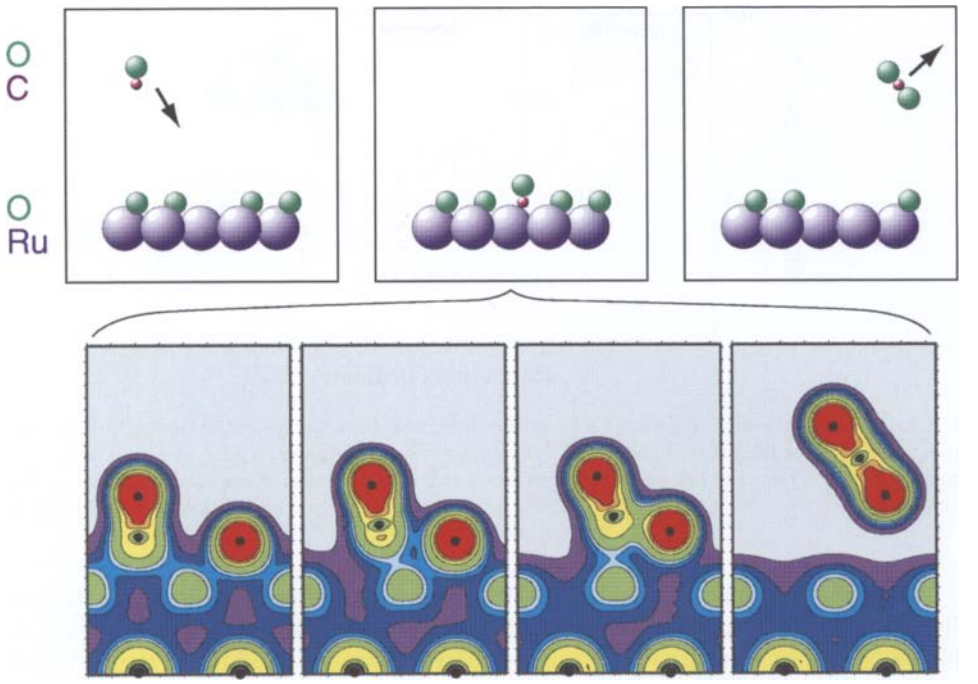


Fig. 5.42. Snapshots of the Langmuir–Hinshelwood reaction (top panel) of CO oxidation at Ru(0001). The bottom panels display the electron density distribution along a reaction path close to the transition states. The units are $\text{bohr}^{-3}$, and the colors and contours are the same as in Fig. 5.33.

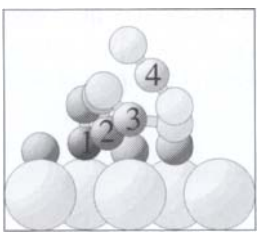


Fig. 5.43. Atomic positions along a reaction energy pathway to $CO_2$ formation. The large, small, and small (labeled) circles represent Ru, O, and C atoms, respectively. The numbers indicate the sequence along the reaction path.

bond. This behavior can also be seen from the corresponding valence electron density distribution shown in Fig. 5.42. The corresponding energy diagram is given in Fig. 5.44. In the work of Alavi et al. (1998) and Eichler and Hafner (1999) bent transition state geometries were also identified for the CO oxidation reaction over the Pt(111) surface for the case of low ($\Theta = 0.25$) oxygen coverages. Alavi et al. (1998) attributed the main contribution to the activation barrier to the weakening of the O-metal bond strength, which supports the general understanding in this respect.

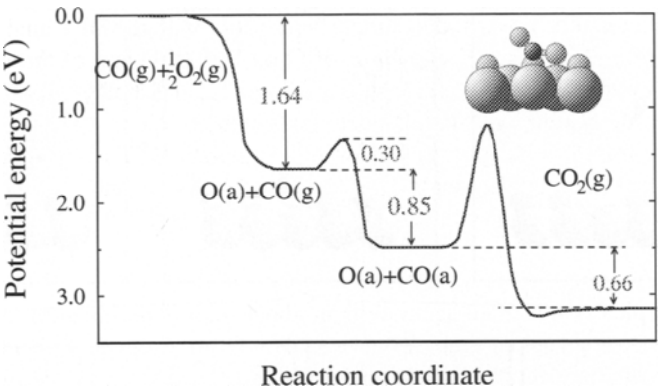


Fig. 5.44. Calculated energy diagram for a Langmuir–Hinshelwood reaction mechanism at Ru(0001) for high oxygen coverages on the surface. Note, 1.64 eV is the energy required to remove one O atom (relative to 1/2 $O_2$) from the (2 × 2)-3O structure – or, equivalently, the energy gained by the system on adsorbing this atom in an hcp site of the (2 × 1) structure, yielding the (2 × 2)-3O structure. The transition state is indicated in the inset (from Stampfl and Scheffler, 1999).

We end this section by noting that despite its high reactivity for CO oxidation, elemental Ru will not be used in automotive catalysts because a volatile Ru oxide exists which is highly poisonous. Nevertheless, trying to understand why Ru is so much more effective than other transition metals may help to design materials with similar properties as Ru. Furthermore, as noted above, there is an interesting and likely conceptionally important aspect of Ru studies: Ru can exist in many oxidation states and the result (see Fig. 5.39) that its surface region can be loaded with a high concentration of oxygen, poses the question whether it is appropriate to call the reactive surface an adsorbate system, or if it is more appropriate to call this a surface oxide (a $RuO_2$-like system in the present case). The highly reactive surface of O/Ru(0001) apparently is one with oxygen concentration much higher than $\Theta = 1$ and a coexistence of several domains of different stoichiometry.

## 5.11. Summary outline of main points

A deeper understanding of chemisorption, surface chemical reactions, and heterogeneous catalysis is currently one of the main aims of surface science (other important topics are, e.g., crystal growth, surface magnetism). In the context of this complex problem, the nature of the chemisorption bond, the energetics of adsorption, and adsorbate geometries and bond-lengths receive considerable attention. While several simple rules have been found to be useful as in the area of molecular chemistry, others should be applied with much caution. Below we summarize some of the findings discussed in this chapter in terms of a brief list:

1) Density-functional theory has evolved into an important tool for analyzing surface geometries. For example, the four-layer surface alloy of Na on Al(111) was first predicted and analyzed by DFT calculations (Stampfl and Scheffler, 1994c) and subsequently confirmed by a LEED intensity analysis (Burchhardt et al., 1995); in view of the high number

of structural parameters, it was indeed important to start with the DFT analysis. Similarly, the existence of a $(1 \times 1)$ ordered adlayer of O on Ru(0001) and of the $(2 \times 2)$-3O adlayer was first predicted by DFT calculations (Stampfl and Scheffler, 1996) with detailed specification of the geometry. And more examples exist.

2) In addition to providing accurate atomic geometries, DFT calculations also (and in particular) offer the potential of analysis of the underlying mechanisms which determine if and how a certain geometry can be attained and what the nature of the chemical bond is.

3) Whereas the geometry is (typically) well described by DFT-LDA and DFT-GGA calculations, the resulting *energies* must be taken with some more caution. Adsorption energies are typically not more accurate than about 0.2 eV per adatom. And we do not expect that new exchange–correlation functionals will improve this to better than 0.1 eV per adatom in the near future (the letter "A", as in LDA and GGA, will remain part of exchange–correlation functionals employed in actual DFT calculations). However, energy *differences* of chemically similar bonding situations (in particular energies of small distortions and phonons) are described with very high (possibly even meV) accuracy.

4) The influence of thermally induced vibrations of the substrate surface and adatoms is often ignored, even today. Still, it is quite clear that some geometries (e.g., the unreconstructed surface of Au(111), or the in-registry adsorption of Xe on fcc(111) surfaces) are stabilized by vibrational energy and entropy. We also mention that surface stress can be noticeably affected by the surface thermal expansion. Thus, sometimes it may be necessary to include the influence of thermal expansion in theoretical studies (see, e.g., Cho and Scheffler, 1997; Xie et al., 1999).

5) Unlike a chemical reaction in molecular chemistry, adsorption on a surface involves very unequal partners. For example, the substrate surface gives rise to broadening of adsorbate levels, has an infinite number of electrons, and fixes the electron chemical potential.

6) Despite item 5), electronegativity differences between adsorbate and substrate species appear to give a qualitatively correct description of the nature of the chemical bond.

7) Item 6) may hold less true for higher coverages when the adsorbate–adsorbate interaction becomes noticeable.

8) The correlation between local-coordination and bond-strength, as noted for molecules by Pauling, appears to be (typically) fulfilled for adsorbates. The energy per atom scales roughly proportional to the square root of the coordination. For covalent systems, some geometries may have a more favorable energy than that of this simple proportionality, e.g., when coordination numbers and/or bond-angles conform with the number of available valence electrons.

In this context we also re-emphasize that unexpected behavior of atoms can occur at surfaces (i.e., the discussed substitutional adsorption and alloy formation). At this time knowledge about the energetics of the underlying processes, as, e.g., the formation of surface vacancies and the adsorption of adatoms at step sites, is not sufficiently well developed that a prediction of the adsorbate site (in particular at low coverage) is possible without performing a DFT calculation.

9) The validity of a correlation between local coordination and bond-length (in principle a consequence of the local-coordination–bond-strength correlation), appears to be rarely fulfilled for adsorbates. This is due to the fact that geometries are quite constrained,

as the atoms of the substrate surface are well bonded to the rest of the substrate, and thus the adsorbate bonds may not succeed to attain their optimum bond angle. Thus, surface bonds my be subject to a "frustrated" hybridization of the adatom orbitals or the substrate–surface orbitals.

10) A metal surface attempts to reach charge neutrality on a rather short length scale. In fact, typically a perturbation is even slightly over-screened on the length scale of the nearest-neighbor distance and then the induced electron density is slowly decaying in an oscillatory manner. This highly localized screening is achieved by locally shifting valence electron density of states to higher or lower energies and thus changing the occupancy.

11) Reactivity concepts of molecular chemistry, which explore the electron density of the *unperturbed* partners, are only of limited value for dissociation at surfaces. It appears that the lowest energy transition states are (often) so close to the surface where the interaction is already so strong, that "new states" are formed, which differ considerably from the clean surface states and the free adatom orbitals. The filling of these "new states" (determined by the substrate Fermi level) rules (at least partially) the reactivity.

12) In addition to item 11) it is important to include the *dynamics* of the approaching molecules: It is not enough to know just the energy of the lowest-energy transition state, but it is important to know whether or not (or with what probability) the transition state will be found by an approaching molecule. This stresses the importance of the high dimensionality of the potential-energy surface on which an approaching molecule travels and of *the statistics*.

13) Some often used concepts still need qualification. For example, it is not clear how a term like that of a "surface oxide" or "surface hydride" describes a situation (or phase) which is different from an "adsorbate". Clearly, this problem only arises for high-coverage adsorption ($\Theta > 1$).

14) We trust that the future will bring more studies which are performed under finite pressure of a well defined atmosphere (getting out of the vacuum) and in which the temperature is changed systematically (warming up and cooling down). This will show which of the previous studies were concerned with a thermal equilibrium geometry and which dealt with a (possibly very special) metastable state.

*Acknowledgement*

We are grateful for the collaborations with many colleagues and friends, the results of whom have been discussed in this chapter. In particular we mention Jörg Bormet, Axel Gross, and Jörg Neugebauer, but this list could easily be extended. We thank Kristen Fichthorn, Klaus Hermann, and Karsten Reuter for helpful comments on the manuscript.

## References

Adams, D.L., 1996, Appl. Phys. A **62**, 123.

Alavi, A., P. Hu, T. Deutsch, P.L. Silvestrelli and J. Hutter, 1998, Phys. Rev. Lett. **80**, 3650.

Aminpirooz, S., A. Schmalz, N. Pangher, J. Haase, M.M. Nielsen, D.R. Batchelor, E. Bøgh and D.L. Adams, 1992, Phys. Rev. B **46**, 15594.

Andersen, J.N., M. Qvarford, R. Nyholm, J.F. van Acker and E. Lundgren, 1992, Phys. Rev. Lett. **68**, 94.

Andersen, J.N., D. Hennig, E. Lundgren, M. Methfessel, R. Nyholm and M. Scheffler, 1994, Phys. Rev. B **50**, 17525.

Antoniewicz, P.R., 1978, Phys. Status Solidi (B) **86**, 645.

Bader, R.F.W., 1990, Atoms in Molecules. A Quantum Theory, International Series of Monographs on Chemistry, Vol. 22. Oxford University Press, Oxford.

Bader, R.F.W., 1994, Phys. Rev. B **49**, 13348.

Bagus, P.S., K. Hermann, W. Müller and C.J. Nelin, 1986, Phys. Rev. Lett. **57**, 1496.

Barnes, C.J., 1994, in: The Chemical Physics of Solid Surfaces, Vol. 7, Phase Transitions and Adsorbate Restructuring at Metal Surfaces, eds. D.A. King and D.P. Woodruff. Elsevier, Amsterdam, p. 501.

Behm, R.J., 1989, in: Physics and Chemistry of Alkali Metal Adsorption, eds. H.P. Bonzel, A.M. Bradshaw and G. Ertl. Elsevier, Amsterdam, p. 111.

Berndt, W., D. Weick, C. Stampfl, A.M. Bradshaw and M. Scheffler, 1995, Surf. Sci. **330**, 182.

Bielański, A. and J. Haber, 1991, Oxygen in Catalysis. Dekker, New York, p. 472.

Blyholder, G., 1964, J. Phys. Chem. **68**, 2772.

Blyholder, G., 1975, J. Vac. Sci. Technol. **11**, 865.

Bockstedte, M., A. Kley, J. Neugebauer and M. Scheffler, 1997, Comput. Phys. Commun. **107**, 187.

Bormet, J., J. Neugebauer and M. Scheffler, 1994a, Phys. Rev. B **49**, 17242.

Bormet, J., B. Wenzien, J. Neugebauer and M. Scheffler, 1994b, Comput. Phys. Commun. **79**, 124.

Born, M. and R. Oppenheimer, 1927, Ann. Phys. **84**, 457.

Born, M. and K. Huang, 1954, in: Dynamical Theory of Crystal Lattices, eds. N.F. Mott and E.C. Bullard. Clarendon, Oxford, p. 420.

Böttcher, A. and Niehus, 1999, J. Chem. Phys. **110**, 3186.

Böttcher, A., Niehus, S. Schwegmann, H. Over and G. Ertl, 1997, J. Phys. Chem. **101**, 11185.

Böttcher, A., M. Rogozia, H. Niehus, H. Over and G. Ertl, 1999, J. Chem. Phys., accepted.

Bradshaw, A.M. and M. Scheffler, 1979, J. Vac. Sci. Technol. **16**, 447.

Brivio, G.P. and M.I. Trioni, 1999, Rev. Mod. Phys. **71**, 231.

Bruch, L.W., M.W. Cole and E. Zaremba, 1997, Physical Adsorption: Forces and Phenomena. Clarendon, Oxford.

Burchhardt, J., M.M. Nielsen, D.L. Adams, E. Lundgren, J.N. Andersen, C. Stampfl, M. Scheffler, A. Schmalz, S. Aminpirooz and J. Haase, 1995, Phys. Rev. Lett. **74**, 1617.

Callaway, J., 1964, J. Math. Phys. **5**, 783.

Callaway, J., 1967, Phys. Rev. **154**, 515.

Campuzano, J.C., 1990, in: The Chemical Physics of Solid Surfaces and Heterogeneous Catalysis, Vol. 3a: Chemisorption Systems, eds. D.A. King and D.P. Woodruff. Elsevier, Amsterdam, p. 389.

Car, R. and M. Parrinello, 1985, Phys. Rev. Lett. **55**, 2471.

Cho, J.-H. and M. Scheffler, 1997, Phys. Rev. Lett. **78**, 1299.

Christensen, O.B. and K.W. Jacobsen, 1992, Phys. Rev. B **45**, 6893.

Christensen, S.V., J. Nerlov, K. Nielsen, J. Burchhardt, M.M. Nielsen and D.L. Adams, 1996, Phys. Rev. Lett. **76**, 1892.

Darling, G.R. and S. Holloway, 1994, J. Chem. Phys. **101**, 3268.

Dreizler, R.M. and E.K.U. Gross, 1990, Density Functional Theory. Springer, Berlin.

Echenique, P.M. and J.B. Pendry, 1975, J. Phys. C **8**, 2936.

Eichler, A., J. Hafner, A. Gross and M. Scheffler, 1999a, Phys. Rev. B **59**, 13297.

Eichler, A., J. Hafner, A. Gross and M. Scheffler, 1999b, Chem. Phys. Lett. **311**, 1.

Eichler, A. and J. Hafner, 1999, Phys. Rev. B **59**, 5960.

Engel, T. and G. Ertl, 1979, J. Chem. Phys. **69**, 1267; Adv. Catal. **28**, 1.

Engel, T. and G. Ertl, 1982, in: The Chemical Physics of Solid Surfaces and Heterogeneous Catalysis, Vol. 4, Fundamental Studies of Heterogenous Catalysis, eds. D.A. King and D.P. Woodruff. Elsevier, Amsterdam, p. 73.

Fasel, R., P. Aebi, R.G. Agostino, L. Schlapbach and J. Osterwalder, 1996, Phys. Rev. B **54**, 5893.

Feibelman, P.J., 1990, Phys. Rev. Lett. **65**, 729.

Finnis, M.W., R. Kaschner, C. Kruse, J. Furthmüller and M. Scheffler, 1995, J. Phys.: Condens. Matter **7**, 2001.

Fiorentini, V., M. Methfessel and M. Scheffler, 1993, Phys. Rev. Lett. **71**, 1051; 1998, Phys. Rev. Lett. **81**, 2184.

Ganduglia-Pirovano, M.V., J. Kudrnovský and M. Scheffler, 1997, Phys. Rev. Lett. **78**, 1807.
Grimley, T.B., 1975, Prog. Surf. Membr. Sci. **9**, 71.
Gross, A., S. Wilke and M. Scheffler, 1995, Phys. Rev. Lett. **75**, 2718.
Gross, A. and M. Scheffler, 1996a, Chem. Phys. Lett. **256**, 417.
Gross, A. and M. Scheffler, 1996b, Prog. Surf. Sci. **53**, 187.
Gross, A., S. Wilke, and M. Scheffler, 1996c, Surf. Sci. **357/358**, 614.
Gross, A., M. Bockstedte and M. Scheffler, 1997, Phys. Rev. Lett. **79**, 701.
Gross, A. and M. Scheffler, 1998, Phys. Rev. B **57**, 2493.
Gross, A., 1998, Surf. Sci. Rep. **32**, 291.
Gsell, M., M. Stichler, P. Jacob and D. Menzel, 1998, Israel J. Chem. **38**, 339.
Gurney, R.W., 1935, Phys. Rev. **47**, 479.
Hammer, B., M. Scheffler, K.W. Jacobsen and J.K. Nørskov, 1994, Phys. Rev. Lett. **73**, 1400.
Hammer, B. and M. Scheffler, 1995, Phys. Rev. Lett. **74**, 3487.
Hammer, B. and J.K. Nørskov, 1997, in: Chemisorption and Reactivity on Supported Clusters and Thin Films, eds. R.M. Lambert and G. Pacchioni. Kluwer, Dordrecht, p. 285.
Heine, V. and D. Marks, 1986, Surf. Sci. **115**, 65.
Hennig, D., M.V. Ganduglia-Pirovano and M. Scheffler, 1996, Phys. Rev. B **53**, 10344.
Hermann, K. and P.S. Bagus, 1977, Phys. Rev. B **16**, 4195.
Hermann, K., P.S. Bagus and C.J. Nelin, 1987, Phys. Rev. B **35**, 9467.
Hjelmberg, H., B.I. Lundqvist and J.K. Nørskov, 1979, Phys. Scr. **20**, 192.
Hofmann, P., C. von Muschwitz, K. Horn, K. Jacobi, A.M. Bradshaw, K. Kambe and M. Scheffler, 1979, Surf. Sci. **89**, 327.
Hoffmann, R., 1988, Rev. Mod. Phys. **60**, 601.
Horn, K., M. Scheffler and A.M. Bradshaw, 1978, Phys. Rev. Lett. **41**, 822.
Hu, P., D.A. King, M.-H. Lee and M.C. Payne, 1995, Chem. Phys. Lett. **246**, 73.
Jacobi, K., C. von Muschwitz and K. Kambe, 1980, Surf. Sci. **93**, 310.
Janak, J.F., 1978, Phys. Rev. B **18**, 7165.
Jennings, P.J., 1979, Surf. Sci. **88**, L25.
Kambe, K. and M. Scheffler, 1979, Surf. Sci. **89**, 262.
Kim, Y.D., S. Wendt, S. Schwegmann, H. Over and G. Ertl, 1998, Surf. Sci. **418**, 267.
Kleinman, L., 1997, Phys. Rev. B **56**, 16029.
Kohn, W. and K.H. Lau, 1976, Solid State Commun. **18**, 553.
Kostov, K.L., H. Rauscher and D. Menzel, 1992, Surf. Sci. **278**, 62.
Kostov, K.L., M. Gsell, P. Jakob, T. Moritz, W. Widdra and D. Menzel, 1997, Surf. Sci. **394**, L138.
Kresse, G. and J. Furthmüller, 1996, Phys. Rev. B **54**, 11169.
Kroes, G.J., E.J. Baerends and R.C. Mowrey, 1997, Phys. Rev. Lett. **78**, 3583; 1998, Phys. Rev. Lett. **81**, 4781.
Kroes, G.J., 1999, Prog. Surf. Sci. **60**, 1.
Lang, N.D. and W. Kohn, 1971, Phys. Rev. B **3**, 1215.
Lang, N.D., 1971, Phys. Rev. B **4**, 4234.
Lang, N.D., 1973, Solid State Phys. **28**, 225.
Lang, N.D. and A.R. Williams, 1977, Phys. Rev. B **16**, 2408.
Lang, N.D. and A.R. Williams, 1978, Phys. Rev. B **18**, 616.
Langmuir, I., 1932, J. Am. Chem. Soc. **54**, 2798.
Liebsch, A., 1978, Phys. Rev. B **17**, 1653.
Lindroos, M., H. Pfnür, G. Held and D. Menzel, 1989, Surf. Sci. **222**, 451.
McRae, E.G., 1971, Surf. Sci. **25**, 491.
Methfessel, M., D. Hennig and M. Scheffler, 1992a, Phys. Rev. B **46**, 4816.
Methfessel, M., D. Hennig and M. Scheffler, 1992b, Appl. Phys. A **55**, 442.
Methfessel, M., D. Hennig and M. Scheffler, 1995, Surf. Rev. Lett. **2**, 197.
Miller, A.R., 1946, Proc. Cambridge Philos. Soc. **42**, 492.
Mitchell, W.J. and W.H. Weinberg, 1996, J. Chem. Phys. **104**, 9127.
Muscat, J.P. and D.M. Newns, 1978, Prog. Surf. Sci. **9**, 1.
Muscat, J.P. and D.M. Newns, 1979, Phys. Rev. B **19**, 1270.

Narloch, B., G. Held and D. Menzel, 1994, Surf. Sci. **317**, 131.
Narloch, B., G. Held and D. Menzel, 1995, Surf. Sci. **340**, 159.
Naumovets, A.G., 1994, in: The Chemical Physics of Solid Surfaces, Vol. 7, Phase Transitions and Adsorbate Restructuring at Metal Surfaces, eds. D.A. King and D.P. Woodruff. Elsevier, Amsterdam, p. 163.
Neugebauer, J. and M. Scheffler, 1992, Phys. Rev. B **46**, 16067.
Neugebauer, J. and M. Scheffler, 1993, Phys. Rev. Lett. **71**, 577.
Nilsson, A., N. Wassdahl, M. Weinelt, O. Karis, T. Weill, P. Bennich, J. Hasselström, A. Föhlisch, J. Stöhr and M. Samant, 1997, Appl. Phys. A **65**, 147.
Nørskov, J.K., 1990, Rep. Prog. Phys. **53**, 1253.
Nouvertné, F., U. May, M. Bamming, A. Rampe, U. Korte, G. Güntherodt, R. Pentcheva and M. Scheffler, 1999, Phys. Rev. B **60**, 14382.
Oppo, S., V. Fiorentini and M. Scheffler, 1993, Phys. Rev. Lett. **71**, 2437.
Over, H., H. Bludau, M. Gierer and G. Ertl, 1995, Surf. Rev. Lett. **2**, 409.
Palmberg, P.W., 1971, Surf. Sci. **25**, 598.
Paul, J., 1987, J. Vac. Sci. Technol. A **5**, 664.
Pauling, L., 1960, The Nature of the Chemical Bond and the Structure of Molecules and Crystals: An Introduction to Modern Structural Chemistry. Cornell University Press.
Payne, M.C., M.P. Teter, D.C. Allan, T.A. Arias and J.D. Joannopoulos, 1992, Rev. Mod. Phys. **64**, 1045
Payne, M.C., I.J. Robertson, D. Thomson and V. Heine, 1996, Philos. Mag. B **73**, 191.
Peden, C.H.F., D.W. Goodman, M.D. Weisel and F.M. Hoffmann, 1991, Surf. Sci. **253**, 44.
Peden, C.H.F. and D.W. Goodman, 1986, J. Phys. Chem. **90**, 1360.
Peden, C.H.F., 1992, in: Surface Science of Catalysis: In Situ Probes and Reaction Kinetics, eds. D.J. Dwyer and F.M. Hoffmann. Am. Chem. Soc., Washington DC.
Pedersen, M.O., I.A. Bonicke, E. Laegsgaard, I. Stensgaard, A. Ruban, J.K. Nørskov and F. Besenbacher, 1997, Surf. Sci. **387**, 86.
Pentcheva, R. and M. Scheffler, 2000, Phys. Rev. B, in print.
Perdew, J.P. and M. Levy, 1997, Phys. Rev. B **56**, 16021.
Petersen, M., P. Ruggerone and M. Scheffler, 1996, Phys. Rev. Lett. **76**, 995; 2000, Phys. Rev. B, submitted.
Pleth Nielsen, L., F. Besenbacher, I. Stensgaard, E. Lægsgaard, C. Engdahl, P. Stoltze, K.W. Jacobsen and J.K. Nørskov, 1993, Phys. Rev. Lett. **71**, 754.
Porteus, J.O., 1974, Surf. Sci. **41**, 515.
Rader, O., W. Gudat, C. Carbone, E. Vescovo, S. Blügel, R. Kläsges, W. Eberhardt, M. Wuttig, J. Redinger and F.J. Himpsel, 1997, Phys. Rev. B **55**, 5404.
Rendulic, K.D., G. Anger and A. Winkler, 1989, Surf. Sci. **208**, 404.
Robertson, I.J., D.I. Thomson, V. Heine and M.C. Payne, 1994, J. Phys. Condens. Matter **6**, 9963.
Scheffler, M., K. Kambe and F. Forstmann, 1978, Solid State Commun. **25**, 93.
Scheffler, M., K. Horn, A.M. Bradshaw and K. Kambe, 1979, Surf. Sci. **80**, 69.
Scheffler, M. and A.M. Bradshaw, 1983, in: The Chemical Physics of Solid Surfaces and Heterogeneous Catalysis, Vol. 2: Adsorption at Solid Surfaces, eds. D.A. King and D.P. Woodruff. Elsevier, Amsterdam, p. 165.
Scheffler, M., Ch. Droste, A. Fleszar, F. Máca, G. Wachutka and G. Barzel, 1991, Physica B **172**, 143.
Schiffer, A., P. Jakob and D. Menzel, 1997, Surf. Sci. **389**, 116.
Schmalz, A., S. Aminpirooz, L. Becker, J. Haase, J. Neugebauer, M. Scheffler, D.R. Batchelor, D.L. Adams and E. Bøgh, 1991, Phys. Rev. Lett. **67**, 2163.
Seyller, T., M. Caragiu, R.D. Diehl, P. Kaukasoina and M. Lindroos, 1998, Chem. Phys. Lett. **291**, 567.
Skriver, H., 1985, Phys. Rev. B. **31**, 1909.
Somorjai, G.A. and M.A. Van Hove, 1989, Prog. Surf. Sci. **30**, 201.
Spanjaard, D. and M.C. Desjonquères, 1990, in: Interaction of Atoms and Molecules with Surfaces, eds. V. Bortolani, N.H. March and N.P. Tosi. Plenum, New York, London, p. 255.
SRL, 1995, Surf. Rev. Lett. **2**, 315. A special issue of *Surface Review and Letters* devoted to alkali-metal adsorption, containing review articles by several groups.
Stampfl, C., M. Scheffler, H. Over, J. Burchhardt, M. Nielsen, D.L. Adams and W. Moritz, 1992, Phys. Rev. Lett. **69**, 1532.
Stampfl, C., M. Scheffler, H. Over, J. Burchhardt, M. Nielsen, D.L. Adams and W. Moritz, 1994a, Phys. Rev. B **49**, 4959.

Stampfl, C., J. Neugebauer and M. Scheffler, 1994b, Surf. Sci. **307/309**, 8.
Stampfl, C. and M. Scheffler, 1994c, Surf. Sci. **319**, L23.
Stampfl, C. and M. Scheffler, 1995, Surf. Rev. Lett. **2**, 317.
Stampfl, C. and M. Scheffler, 1996, Phys. Rev. B **54**, 2868.
Stampfl, C., 1996, Surf. Rev. Lett. **3**, 1567.
Stampfl, C., S. Schwegmann, H. Over, M. Scheffler and G. Ertl, 1996, Phys. Rev. Lett. **77**, 3371.
Stampfl, C. and M. Scheffler, 1997, Phys. Rev. Lett. **78**, 1500; J. Vac. Sci. Technol. A **15**, 1635; Surf. Sci. **377–379**, 808.
Stampfl, C., K. Kambe, R. Fasel, P. Aebi and M. Scheffler, 1998, Phys. Rev. B **57**, 15251.
Stampfl, C. and M. Scheffler, 1998, Israel J. Chem. **38**, 409.
Stampfl, C. and M. Scheffler, 1999, Surf. Sci. **433–435**, 119.
Taylor, J.B. and I. Langmuir, 1933, Phys. Rev. **44**, 423.
Topping, J., 1927, Proc. Roy. Soc. London Ser. A **114**, 67.
Wang, X.-G., W. Weiss, Sh.K. Shaikhutdinov, M. Ritter, M. Petersen, F. Wagner, R. Schlögl and M. Scheffler, 1998, Phys. Rev. Lett. **81**, 1038.
Wilke, S. and M. Scheffler, 1996, Phys. Rev. B **53**, 4926.
Wilke, S., M.H. Cohen and M. Scheffler, 1996, Phys. Rev. Lett. **77**, 1560.
Wenzien, B., J. Bormet, J. Neugebauer and M. Scheffler, 1993, Surf. Sci. **287/288**, 559.
Wenzien, B., J. Bormet and M. Scheffler, 1995, Comput. Phys. Commun. **88**, 230.
Wimmer, E., C.L. Fu and A.J. Freeman, 1985, Phys. Rev. Lett. **55**, 2618.
Xie, J., S. de Gironcoli, S. Baroni and M. Scheffler, 1999, Phys. Rev. B **59**, 970.
Yang, L., G. Vielsack and M. Scheffler, 1994, unpublished.
Yu, B.D. and M. Scheffler, 1997, Phys. Rev. B **56**, R15569.

CHAPTER 6

# Experimental Probes of the Surface Electronic Structure

F.J. HIMPSEL

*Department of Physics*
*University of Wisconsin-Madison*
*1150 University Avenue*
*Madison WI 53706-1390*
*USA*

*© 2000 Elsevier Science B.V.*
*All rights reserved*

*Handbook of Surface Science*
*Volume 2, edited by K. Horn and M. Scheffler*

# Contents

6.1. Concepts and overview . . . . . 359
6.2. Single quasiparticles: photoemission and inverse photoemission . . . . . 362
6.3. Pairs of quasiparticles and collective excitations: optical methods and electron energy loss . . . . . 367
6.4. Core levels . . . . . 371
6.5. Spectro-microscopy . . . . . 377
References . . . . . 380

## 6.1. Concepts and overview

According to density functional theory the electronic structure of a solid or surface in its ground state is fully characterized by the total charge density of its electrons. That is all one needs to know. The charge density can be measured by elastic scattering of particles, such as X-rays and electrons, without perturbing the ground state by adding energy to the electrons. In magnetic solids one needs additional spin information, which can be obtained from elastic neutron scattering. Fortunately, this is not the end of the story. In addition to the ground state there exist many excited states, which make condensed matter physics exciting. These play a role in most real-life situations, such as optical and transport properties. In addition to elastic scattering there is always a finite probability that a particle transfers some of its energy to a solid or a surface. In fact, one needs to excite an electron in a solid above the Fermi level, if one wants to determine its binding energy. Therefore, it is quite useful to ask the question, how the fundamental excited states of a solid, or quasiparticles, can be characterized in a systematic fashion. Some of these quasiparticles are mainly associated with atoms (e.g., photons), others with electrons, e.g., an extra electron in the solid, a hole, an electron–hole pair (exciton). That continues up to the limit of collective excitations, such as plasmons.

Quasi-particles are characterized by quantum numbers, which reflect symmetries of the solid. The quasiparticle energy $E$ is related to the invariance with respect to translation

Table 6.1
Selected spectroscopies for electronic states of surfaces

| Incoming Particle: | Outgoing Particle: Photon | Electron | Ion/Atom |
|---|---|---|---|
| Photon | Optical<br>Luminescence<br>Sum Frequency | Photoemission<br>Auger<br>Partial yield | Photon-stimulated<br>Desorption |
| Electron | Inverse Photoemission<br>Appearance Potential<br>Cathodoluminescence | Electron Energy Loss<br>Auger<br>Appearance Potential<br>Tunneling | Electron-stimulated<br>Desorption |
| Ion/Atom | Chemoluminescence | Ion Neutralization<br>Penning Ionization | Ion/Atom Scattering |

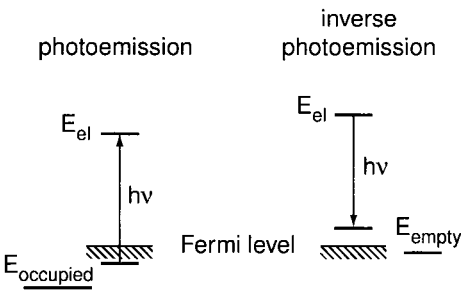


Fig. 6.1. Energy balance in photoemission and inverse photoemission.

Table 6.2
Connection between quantum numbers of electrons in a solid and experimental parameters in photoemission and inverse photoemission

| Quantum number | Relation | Experimental parameter |
|---|---|---|
| Energy, $E$ | $E = E_{\rm el} - h\nu$ | Photon energy, $h\nu$ |
| Momentum: | | |
| perpendicular, $k_\perp$ | $k_\perp$ ($E_{\rm el}, k_\parallel$), Upper band | Electron energy, $E_{\rm el}$ |
| parallel, $k_\parallel$ | $k_\parallel = k_\parallel^{\rm el} + g_\parallel$ | Electron momentum, $k_\parallel^{\rm el}$ |
| Spin, $\sigma$ | $\sigma = \sigma_{\rm el}$ | Electron spin, $\sigma_{\rm el}$ |
| Point group symmetry: | Selection rules using $\mathbf{A}, k_\perp, k_\parallel$ | Photon polarization, $\mathbf{A}$ |

For two-dimensional states at the surface the perpendicular momentum $k_\perp$ is not a good quantum number. $g_\parallel$ is a reciprocal surface lattice vector.

in time, the reduced momentum is related to the invariance with respect to translation by a lattice vector in a crystal. In addition, there are angular symmetries, given by the point groups, and spin. For measuring the quantum numbers of a quasiparticle, one may excite a solid with a photon, electron, ion or atom and look for outcoming particles. The corresponding grid in Table 6.1 contains many well-known surface spectroscopies. Each of them has different characteristics in probing quasiparticles. Here we will concentrate on simple quasiparticles, such as electrons and holes, and the corresponding probes. In this case there are two techniques which are distinguished by their ability to determine a complete set of quantum numbers. These are photoemission and inverse photoemission.

As shown in Fig. 6.1 and Table 6.2, photoemission and inverse photoemission have just enough measurement parameters to determine the quantum numbers of a hole and an electron in a solid. In both cases we have an upper state, which corresponds to the outgoing or incoming probe electron with kinetic energy $E_{\rm el}$, and a lower state, which is the hole or electron that we want to map out. Its energy is determined by subtracting the photon energy $h\nu$ from the kinetic energy $E_{\rm el}$ (Fig. 6.1). This energy balance is Einstein's formula for the photoelectric effect. To obtain the momentum of the lower state, i.e., its wave vector $\mathbf{k} = (k_\perp, k_\parallel)$, one needs the three momentum components of the electron in the upper state,

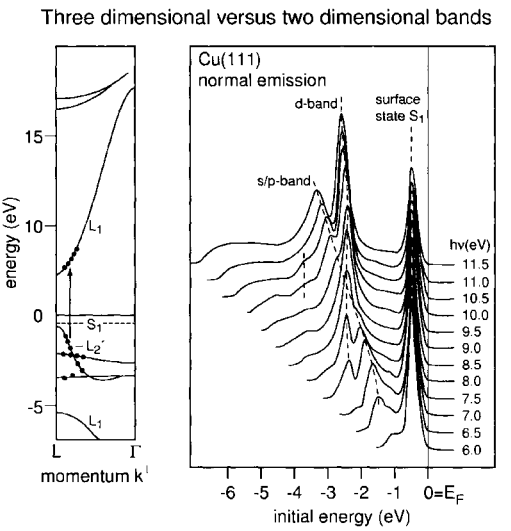


Fig. 6.2. Distinguishing surface states from bulk states in photoemission. The surface state $S_1$ does not change its energy when the perpendicular momentum is changed by varying the photon energy (arrow). It is located in a gap of bulk states (from Knapp et al., 1979; Himpsel, 1983).

e.g., two angles $\theta$, $\phi$ characterizing its parallel momentum $k_{\parallel}^{\mathrm{el}}$, and again the electron energy $E_{\mathrm{kin}}$. The parallel momentum is conserved up to a reciprocal surface lattice vector $g_{\parallel}$ for a crystalline surface, but the perpendicular momentum is not, due to the absence of periodicity in this direction. However, in practice there is a well defined relation between the perpendicular momenta of the probing electron and the lower state. It is determined by $E_{\mathrm{el}}(k_{\parallel}, k_{\perp})$ band dispersion of the bulk states that are accessible to the probing electron. With a fixed photon energy one can only access a single $k_{\perp}$ for a state of given energy $E$, and not its full $E(k_{\perp})$ band dispersion (compare the left hand side of Fig. 6.2). Therefore, one needs a tunable light source, such as synchrotron radiation, or a tunable photon detector to map three-dimensional electron states and to separate out two-dimensional states at surfaces. The spin quantum number in a ferromagnetic solid can be determined directly from the spin-polarization of the electrons, the point group symmetry can be inferred from the orientation of the vector potential $\mathbf{A}$ of the photon via dipole selection rules. The experimental and theoretical information about electronic states is usually summarized by energy band dispersions $E(\mathbf{k})$, where energy is plotted vs. momentum for different energy bands, which are distinguished by their spin and point group labels. Two-dimensional surface states (see Fig. 6.3) are distinguished from three-dimensional bulk states by the fact that the perpendicular momentum $k_{\perp}$ is not a good quantum number. As a consequence, surface states lack any perpendicular band dispersion $E(k_{\perp})$. This can be tested by varying $k_{\perp}$ with a tunable photon energy (see Fig. 6.2). Alternatively, one can map out the bulk band structure and check if a surface state indeed falls into a symmetry gap of the bulk bands. In real life the situation is not always so clear. There can be surface resonances, where a two-dimensional surface state hybridized with bulk states (Fig. 6.3). This happens quite often in semiconductors, where broken bond states retain strong surface character even in

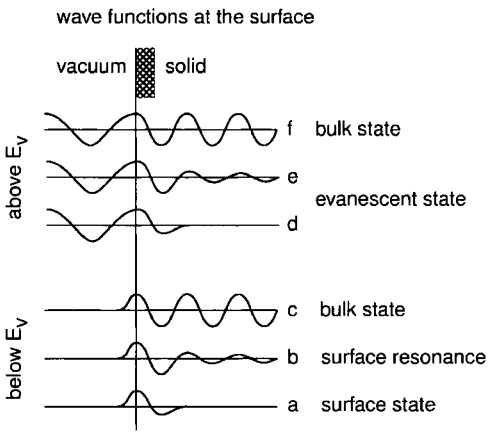


Fig. 6.3. Schematic representation of the electronic states involved in photoemission and inverse photoemission: d, e, f show wave functions of the external electron, a, b, c those of the state that is being probed. Various combinations of propagating and exponentially-damped wave functions are encountered (from Himpsel, 1983).

the presence of bulk states. Theorists have gone on to classifying surface resonances as surface states whenever their wave function is localized more than a certain percentage in the first layer (about 70%, depending on the theorist). Experimentalists do not have this luxury. Their localization criterium is the "crud test". By offering adsorbates to a suspected surface resonance one hopes to quench it or at least change its energy. However, the transmission of bulk electrons through the surface is also affected by the adsorbate, making the crud test somewhat ambiguous. Another way to identify surface states is by comparison with a spectroscopy that sees only the outermost layer. As shown in Fig. 6.4, scanning tunneling spectroscopy does provide the surface sensitivity to identify the surface resonances on the famous Si(111)7 × 7 surface (Binnig et al., 1983; Hamers et al., 1986; Wolkow and Avouris, 1988). In addition it makes it possible to assign the surface states to different types of surface atoms, e.g., so-called rest atoms with a lone pair, and adatoms with a nearly-empty broken bond orbital. While providing real space information, scanning tunneling spectroscopy loses $k$-space information due to the uncertainty principle. Nearly, all $\mathbf{k}$ vectors are able to contribute, with some weighting towards $k_{\|} = 0$.

In the following we will give representative examples of surface states and surface excitations, working our way up from single particles to collective excitations. Along the way we will encounter various experimental techniques, and discuss the features that optimize them for solving specific questions. After these simple model cases we turn to the real world of complex, disordered, and microstructured surfaces and interfaces. In this case one has to resort to measurement techniques involving core levels, which extract the remaining information on the local bonding and provide chemical identification.

## 6.2. Single quasiparticles: photoemission and inverse photoemission

Figure 6.4 shows a characteristic case, where angle-resolved photoemission with variable photon energy is used to probe surface states as well as bulk states (Knapp et al., 1979;

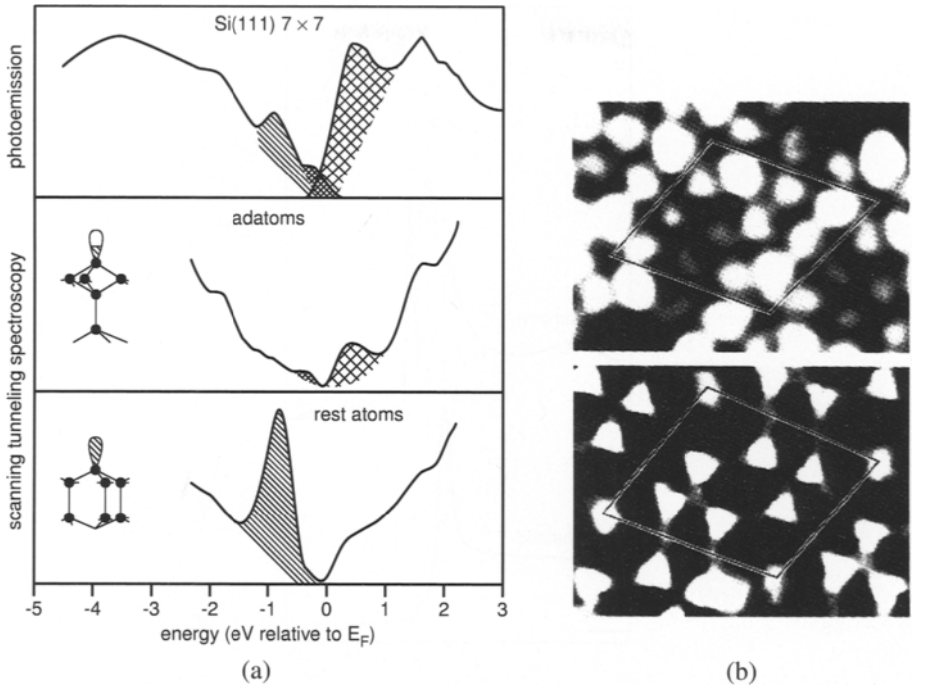


Fig. 6.4. Detecting surface states on silicon with photoemission, inverse photoemission, and scanning tunneling spectroscopy (from Himpsel, 1990; Wolkow and Avouris, 1988). Two types of broken bond states occur, a lone pair at the so-called rest atom sites, and a partially-filled state at the adatom sites (a). The two sites can be located by tunneling into empty states (b, top) or from occupied states (b, bottom) (from Hamers et al., 1986).

Himpsel, 1983; for reviews on angle-resolved photoemission see Plummer and Eberhardt, 1982; Himpsel, 1983; Freund and Neumann, 1988; Kevan, 1992; for inverse photoemission see Smith, 1988; Donath, 1989; Himpsel, 1990). The probing depth of photoemission and inverse photoemission typically covers around 5 Å, i.e., a few atomic layers, and thus makes them capable of seeing bulk states together with surfaces states. It is determined by the mean free path of the probing electrons (see Section 6.4). The spectra in Fig. 6.2 are all taken at a fixed parallel momentum ($k_\parallel = 0$), but with variable perpendicular momentum $k_\perp$. In a typical $E(k_\perp)$ band dispersion plot, as shown in Fig. 6.2, the perpendicular momentum of the upper state changes with energy according to the band dispersion of some bulk band. Therefore, $k_\perp$ can be changed by tuning the photon energy (arrow in Fig. 6.2). While a bulk state changes its energy with $k_\perp$ a surface state does not, since $k_\perp$ is not a good quantum number for a two-dimensional state. Therefore, it can be represented as horizontal line in the $E(k_\perp)$ band diagram, which emphasizes that the surface state wave function contains a whole spectrum of $k_\perp$ values. Indeed, such a surface state can be found in a gap of bulk bands in Fig. 6.2 (dashed line $S_1$). It shows up in the spectra as a peak that does not move when $k_\perp$ is changed by tuning the photon energy $h\nu$. All the other peaks move with $h\nu$, at least somewhat. Their perpendicular momentum $k_\perp$ is obtained simply by taking the energy of the photoelectron and looking where it intersects the up-

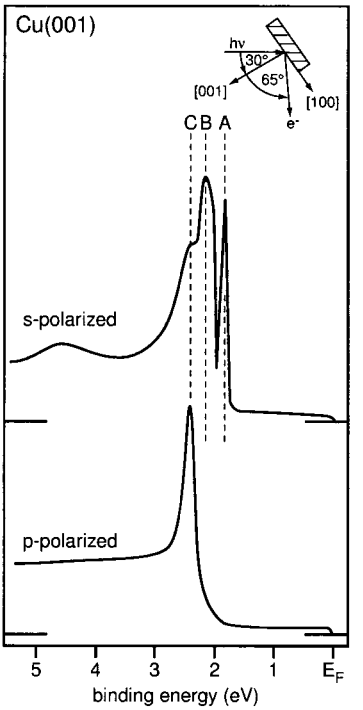


Fig. 6.5. Use of polarization selection rules to determine the symmetry of a surface state. States of even symmetry are detected with the electric field vector in the mirror plane (p-polarized), odd states with the electric field perpendicular (s-polarized). The surface state A has odd symmetry (from Kevan and Shirley, 1980).

per band (upper dots in Fig. 6.2 left). This procedure shows, in a nutshell, how bands are mapped with angle-resolved photoemission. It leaves out many details, such as absolute methods of determining $k_\perp$ (i.e., without a semiempirical upper band, as in Fig. 6.2) and lifetime broadening effects (for reviews see Himpsel, 1983; Kevan, 1992). A great number of band structure studies have been performed with this technique. They are compiled in Landolt–Börnstein (1989) for bulk bands. Only less comprehensive reviews of the data are available for surface states, e.g., for semiconductor surfaces in Hansson and Uhrberg (1988) and Himpsel (1990).

So far we have only considered the quantum numbers $E$ and $\mathbf{k}$. Figures 6.5 and 6.6 address angular symmetry and spin, respectively. The angular symmetry is characterized by the representations of the point group at a particular $\mathbf{k}$. The example in Fig. 6.5 (Kevan and Shirley, 1980) is particularly simple, reducing the symmetry to even and odd states with respect to a single mirror plane perpendicular to the surface. By detecting only photoelectrons in this mirror plane, and switching the direction of the electric field vector $\mathbf{A}$ from parallel to perpendicular with respect to the mirror plane, one excites even and odd states separately. This is a result of a simple dipole selection rule, which states that the product of initial state wave function, $\mathbf{A}$-vector, and final state wave function has to be even for a non-vanishing transition matrix element. Since the final state wave function can

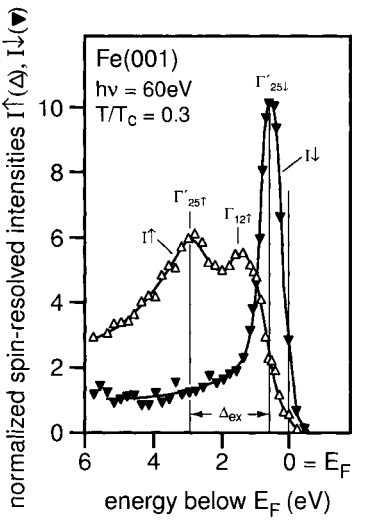


Fig. 6.6. Detecting spin in photoemission. The ferromagnetic exchange splitting $\Delta_{ex}$ between majority and minority spin sub-bands is characteristic of the magnetic properties (from Kisker et al., 1985).

only be even for photoelectrons coming out in the mirror plane, the symmetry of the initial state has to be equal to that of the **A**-vector. Similar selection rules apply for $k$-points with higher symmetry. They have been compiled in various places for bulk solids (Eberhardt and Himpsel, 1980; Benbow, 1980; Niles et al., 1992). At surfaces one generally can use the symmetry of the "rod" in $k$ -space obtained by adding arbitrary $k_\perp$ to the $k_\parallel$ value of the surface state. However, there are exceptions, such as the lowering of the six-fold symmetry of the hcp lattice along the (0001) axis to three-fold at the (0001) surface, and likewise for the the (100) axis of the diamond lattice.

The spin quantum number can be determined simply by measuring the electron spin in photoemission (Fig. 6.6, Kisker et al., 1985), or using a spinpolarized electron beam in inverse photoemission (Donath, 1989). As long as there is no spin-flip scattering by thermally-excited magnons or by impurity spins, one has spin-conservation in the photoemission process. The key quantity in spin-resolved measurements is the ferromagnetic exchange splitting between the majority and minority spin sub-bands. Experimentally it is far from trivial to detect spin or to produce spin-polarized electrons. Spin-detection typically reduces the signal by 3–4 orders of magnitude. A spin-polarized electron source requires touchy, negative affinity semiconductor surfaces as emitters.

The electronic structure of adsorbate-covered surfaces has its own characteristics. Typically, the molecular orbitals of the adsorbate react with broken bond orbitals of the substrate, forming bonding and antibonding combinations. A rather clear-cut case is shown in Fig. 6.7. For H absorption on Ti(0001) one has essentially the H 1s orbital reacting with a Ti $3d_{z^2}$ orbital (Feibelman et al., 1980). The latter can be seen on the clean surface as a surface state near the Fermi level. After H adsorption two surface states are observed, the upper corresponding to the antibonding combination (which has mostly Ti $3d_{z^2}$ character), the lower to the bonding (with mostly H 1s character). This type of interaction can

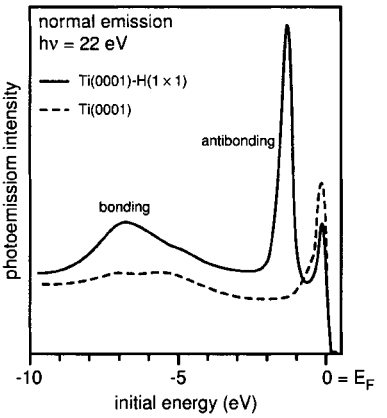


Fig. 6.7. Electronic states of adsorbates. Typically, bonding and antibonding combinations are formed between the adsorbate and substrate states. Here, the bonding state has mostly adsorbate character (H 1s), while the antibonding state resembles a surface state of Ti $3d_{z2}$ character (from Feibelman et al., 1980).

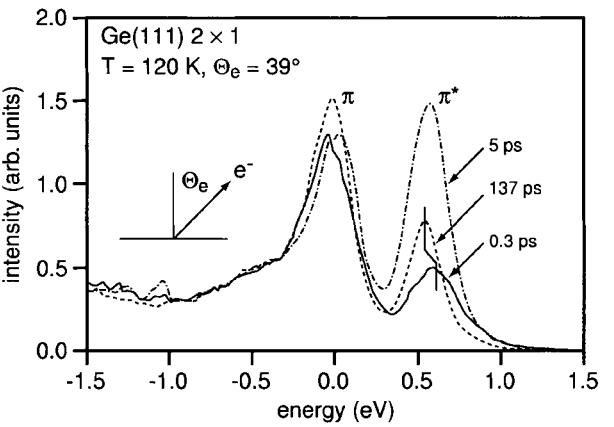


Fig. 6.8. Time-resolved photoemission showing the build-up and decay of electron population in the antibonding $\pi^*$ surface state of the cleaved Ge(111)2 × 1 surface. Electrons are first pumped into the normally unoccupied $\pi^*$ state with visible light and then probed by UV light after a certain delay time (from Baeumler and Haight, 1991).

be explored in great detail by pinpointing the character of the observed states with the use of band calculations.

With the push of fast lasers into the ultraviolet it is now possible to perform photoemission experiments on a sub-picosecond time scale in the pump-probe mode. This makes it possible to follow the decay of an electronic surface excitation in real time, instead of just looking at the decay product (e.g., luminescence, Auger electrons), or determining the lifetime broadening. The example in Fig. 6.8 (Baeumler and Haight, 1991) shows how electrons can be pumped into the conduction band of germanium where they relax in several picoseconds to the lowest possible state, i.e., the minimum of a surface state band in the gap.

## 6.3. Pairs of quasiparticles and collective excitations: optical methods and electron energy loss

Moving up on the scale of complexity we encounter pairs of quasiparticles, such as the electron–hole pairs in optical absorption, hole–hole pairs in Auger spectroscopy, and electron–electron pairs in appearance potential spectroscopy. Here we will limit our discussion to electron–hole pairs. They are involved in the determination of the band gap of semiconductors and insulators, i.e., the most fundamental quantity characterizing the electronic structure of these materials. The band gap can change quite dramatically at surfaces and interfaces. For example, the band gap at the $CaF_2$/Si (111) interface is more than twice as large as in Si, and five times smaller than in $CaF_2$ (Heinz et al., 1989). The gap can shrink substantially at semiconductor surfaces, e.g., by a factor of two on Si(111)-2 × 1 (Chiaradia et al., 1983), and all the way to zero on Si(111) 7 × 7 (see Fig. 6.4a). Conversely, a band gap can open up at the interface layer of a semi-metal with a semiconductor, such as the 0.7 eV gap of Bi on GaAs(110) (see Himpsel, 1990).

Here we use one of the classic semiconductor surfaces, i.e., cleaved Si(111)-2 × 1, to demonstrate various techniques for probing electron–hole pairs. This surface has a $\pi$-bonded chain structure, similar to that of polyacetylene, except for the absence of dimerization. If the chains were isolated from the bulk, there would be a half-filled, metallic $\pi$-band. At the surface the chains tilt, leading to two inequivalent atoms in the chain and to a separation of the $\pi$-band into bonding and antibonding portions, which are separated by a band gap of about 0.5 eV. The onset of optical transitions across the surface gap shows up very clearly in a variety of optical probes, such as differential reflectivity, surface photovoltage, and photothermal displacement (Fig. 6.9a, see Olmstead, 1987, for a review). In each case an extra trick had to be added to the optical probe in order to make it surface sensitive. In photothermal displacement spectroscopy one measures the slight thermal bulge (typically less than an Å) that the absorbed photons create at the surface (Olmstead and Amer, 1984; Olmstead, 1987), in surface photovoltage spectroscopy one detects subtle changes in the Fermi level position at the surface as the pinning states are being filled or depleted (Assmann and Mönch, 1980), and in differential reflectivity one measures the changes in reflectivity after quenching a surface transition by an adsorbate (Chiaradia et al., 1983). Optical spectroscopy can also be made surface-sensitive by using electrons for exciting optical transitions (e.g., in cathodoluminescence, see Viturro et al., 1986), or by detecting electrons that are emitted as decay products of an optical excitation (Auger and secondary electrons in optical absorption). We will come to that technique in the context of core level spectroscopy (Section 6.4).

Optical methods with their deep penetration are particularly useful for looking at surfaces exposed to various gases in a chemical reactor, and at buried interfaces. Two up-and-coming techniques utilize the symmetry lowering at the surface to enhance optical transitions at surfaces and interfaces and suppress the bulk signal. In the case of the Si(111)-2 × 1 surface there is a substantial in-plane anisotropy, due to its nearly one-dimensional, chain-like structure (Fig. 6.9b, Selci et al., 1985). Such a difference in the optical response parallel and perpendicular to the chains cannot be due to isotropic bulk silicon. Polarization modulation has been used to distinguish gallium- and arsenic-rich versions of the GaAs (100) surface during epitaxial growth by chemical vapor deposition (Aspnes et al., 1990,

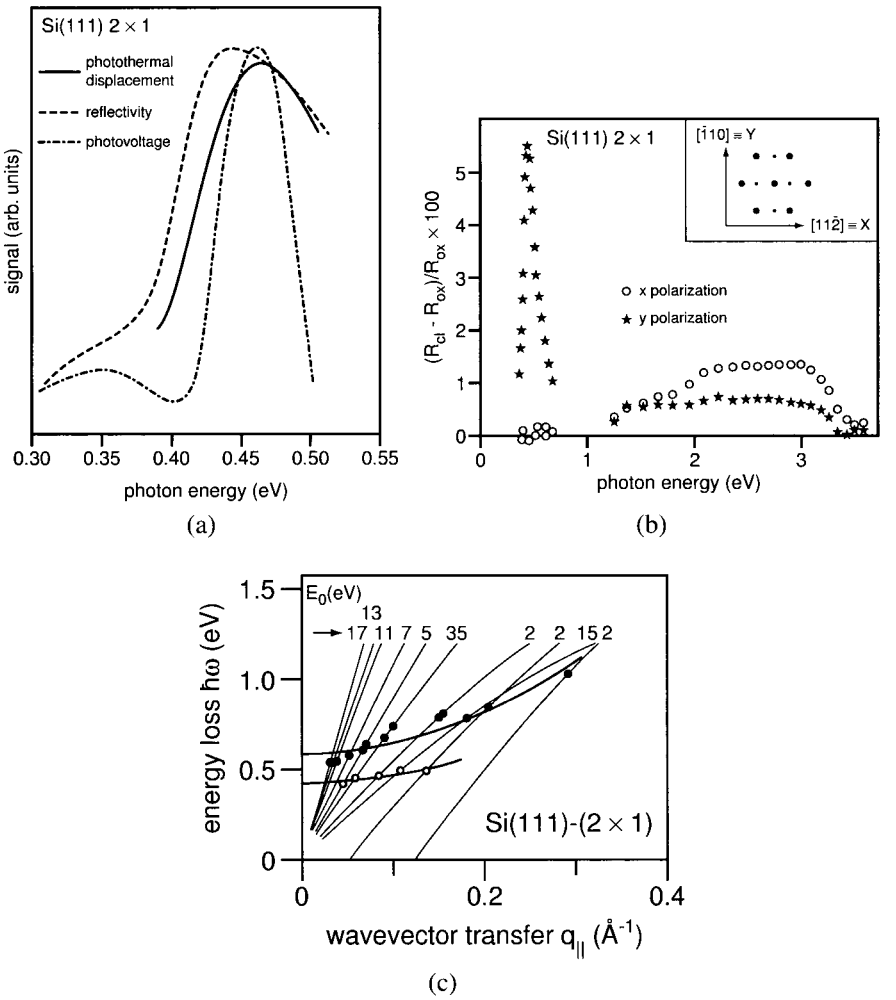


Fig. 6.9. Optical probes of surface states, showing the transition between the $\pi$ and $\pi^*$ surface states on Si(111)-2 × 1. The onset at 0.4–0.5 eV represents the surface band gap, which is less than half the size of the bulk gap of 1.1 eV (a, from Olmstead, 1987; Chiaradia et al., 1983; Assmann and Mönch, 1980; Olmstead and Amer, 1984). Due to the one-dimensional, chain-like arrangement of surface atoms there is a strong in-plane anisotropy of the transitions (b, from Selci et al., 1985). The momentum dependence of the $\pi$ to $\pi^*$ transition can he probed with electron energy loss spectroscopy (c, from Matz et al., 1983).

Fig. 6.10). The natural in-plane anisotropy of the GaAs(100) surface is amplified by the formation of Ga and As dimers at the surface, which reduce the number of broken bonds by a factor of two. The Ga and As dimers are rotated by 90° with respect to each other and have different optical excitation energies. Instead of the in-plane anisotropy one can also utilize the more common out-of-plane anisotropy of surfaces, and compare the absorption of light polarized parallel and perpendicular to the the surface. Another growing technique, i.e., op-

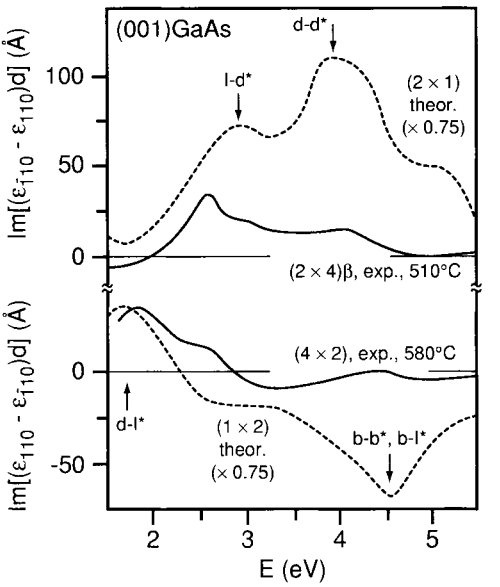


Fig. 6.10. In-plane anisotropy at GaAs(100) surfaces, measured by a polarization-modulation technique (from Aspnes et al., 1990). The structures are assigned to transitions involving surface states of Ga–Ga and As–As dimers, using a tight binding calculation (dashed).

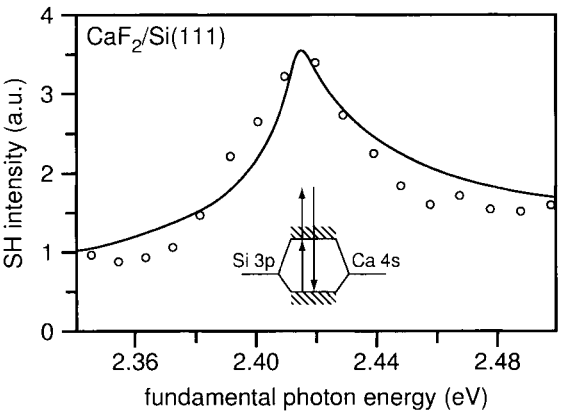


Fig. 6.11. Optical second harmonic generation at a buried $CaF_2$/Si(111) interface, showing transitions from the bonding to the antibonding combination of the Si and Ca interface orbitals. The line is the second harmonic signal calculated for a step-like onset of the absorption at an interface hand gap of 2.41 eV. This value is more than twice as large as the gap in Si and five times smaller than in $CaF_2$ (from Heinz et al., 1989).

tical sum frequency generation, senses the breaking of inversion symmetry at the surface (Fig. 6.11, Heinz et al., 1989). It is dipole-forbidden in inversion-symmetric bulk media, such as Si and $CaF_2$. This technique promises to become a very flexible tool for looking at

low-dimensional structures, separating not only two-dimensional from three-dimensional features, but also one-dimensional from two-dimensional features. There are three polarization vectors to play with, two for the incoming photons, one for the outgoing. They can be aligned in many different ways to dipole-select just about any geometry. For example, it has been shown that optical sum frequency generation can be very sensitive to the the electronic states at steps (Verheijen et al., 1991). Although most experiments have been performed at a fixed frequency up to now, the development of broadly tunable Ti-sapphire lasers should make it easier in the future to use the technique in the spectroscopic mode and gain direct information about the energy levels involved. Another natural extension would be towards time-resolved pump and probe experiments.

Many of the optical surface spectroscopies mentioned here have provided fundamental quantities of the surface electronic structure, such as the band gap in semiconductors. Naively, the onset of absorption may be taken as a measure of the gap. However, looking at a more detailed level one expects a series of discrete absorption lines converging towards the band gap, due to the formation of electron–hole pairs (excitons) near the band edge. In bulk semiconductors these lines can be resolved in great detail at low temperatures. At the Si(111)-2 × 1 surface one finds only a single peak (Fig. 6.9). Just the strongly-peaked lineshape of the surface absorption spectrum gives an indication that the interband absorption edge is enhanced by excitons near the interband threshold. Calculations as well as experiments indicate an electron–hole interaction in the order of 0.1 eV for this system, but both need to be pushed to their limits to provide definitive numbers. For core-to-valence transitions at semiconductor and insulator surfaces the electron–hole interaction is substantially larger, since the electron is much closer to a core hole than a valence hole. It reaches about 1 eV in core excitons of III-V compounds and several eV in ionic insulators.

A more indirect, but rather surface-sensitive method for exciting electron–hole pairs is electron energy loss spectroscopy. Compared to optical methods it has the additional capability of changing the wave vector $\mathbf{k}$ of the combined electron–hole pair by going off the specularly-reflected electron beam. Optical spectroscopy is limited to $k \approx 0$ due to the small momentum of the photons. Figure 6.8c shows an example of energy loss spectra versus momentum transfer, again for Si(111)-2 × 1 (Matz et al., 1983). The energy and momentum resolution in electron energy loss spectroscopy is generally better than in photoemission and inverse photoemission, making this technique well-suited for looking at sharp surface states close to the band edges, and at reconstructed surfaces with small unit cells in momentum space.

After considering single electrons and electron–hole pairs we may jump to the opposite limit, i.e., collective excitations, such as plasmons. Again, electron energy loss spectroscopy is well-suited for mapping out the fundamental energy-versus-momentum dispersions. This is shown in Fig. 6.12 (Tsuei et al., 1991) for the surface plasmon dispersion on potassium. Alkali metals represent some of the closest incarnations of "jellium", that structureless theoretical material which has made so many first principles calculations possible. The measurement in Fig. 6.12 shows that the surface plasmon energy is not fixed at $1/\sqrt{2}$ of the bulk plasmon energy, but varies with $k_{\parallel}$, in qualitative agreement with jellium calculations. These dispersion effects become even more pronounced in thin films, where additional multipole plasmon modes appear.

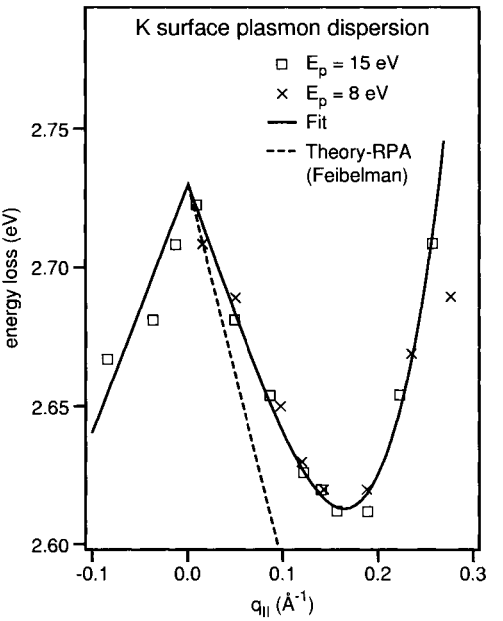


Fig. 6.12. Fundamental energy-versus-momentum band dispersion of surface plasmons, probed by angle-dependent election energy loss spectroscopy (from Tsuei et al., 1991).

Magnetic properties can be probed optically with elliptically-polarized light, i.e., the difference in the optical response to left- and right-handed light. There are many geometries, depending on the lineup of the magnetic field vector, the easy magnetic axis of the sample, the sample normal, and the direction and polarization of the light (see Chapter 9 by Schneider and Kirschner). Methods, such as the Kerr effect and magnetic circular dichroism are not surface probes *per se*, but they can exhibit monolayer sensitivity. Figure 6.13 shows a dramatic effect, where the addition of somewhat more than a monolayer to a magnetic structure completely changes its magnetic response (Qiu et al., 1992). The upper curve in Fig. 6.13 resembles the usual hysteresis curve of a ferromagnet, using the Kerr rotation of the polarization as a measure of the magnetization. The bottom curve is characteristic of antiferromagnetic coupling between the two magnetic layers, with no net magnetization at zero field, and the magnetization of both layers forced to line up by an external field. This technique has gained popularity for detecting the magnetic state of thin films, since it is much less cumbersome than spin-polarized electron spectroscopies. The surprising magnetic phenomena at surfaces and various techniques for probing them are reviewed by Himpsel et al. (1998).

## 6.4. Core levels

The structure and composition of many surfaces and interfaces encountered in technology is complex, and much too disordered for using angle-resolved photoemission to map the

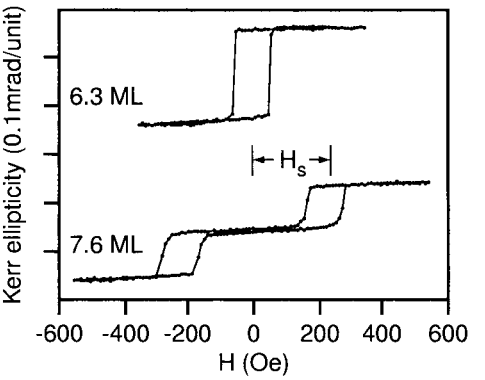


Fig. 6.13. Detecting magnetism with optical techniques by using the Kerr effect as a measure of the sample magnetization. In a sandwich of two Fe films enclosing a Mo film a switch of the coupling between the Fe layers from ferromagnetic (top) to antiferromagnetic (bottom) can be induced by adding only about a monolayer of Mo to the spacer film. At the switching field $H_S$ the antiferromagnetic layers are forced into ferromagnetic alignment by the external field (from Qiu et al., 1992).

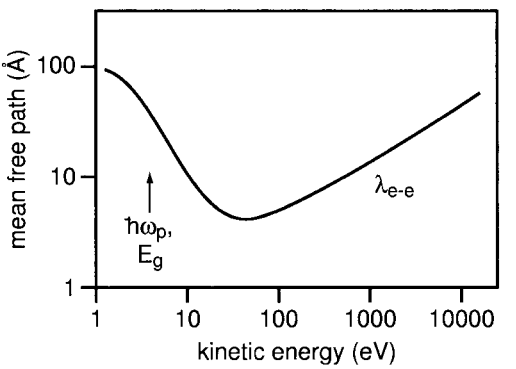


Fig. 6.14. Use of the energy-dependent mean free path of electrons for surface sensitive electron spectroscopies. At energies below the escape depth minimum certain excitations are no more accessible, such as electron–hole pairs and plasmons. At higher energies the larger velocity lengthens the mean free path.

valence band. When long-range order is lost one has to resort to simpler probing techniques and must concentrate on determining the short-range order and the local properties, e.g., coordination, valence, and oxidation state. Core levels are well-suited for this purpose. They are not affected by the loss of long-range order because of their localized nature. The core level binding energy has a simple relation with chemical properties, e.g., charge transfer and oxidation state, at least at metallic or semiconducting surfaces, where local differences in screening are small (see Himpsel et al., 1990).

The use of synchrotron radiation has given a great boost to the field. Monolayer surface sensitivity can be achieved by tuning the photon energy to 30–50 eV above threshold, where photoelectrons come out with the minimum escape depth (Fig. 6.14, Lindau

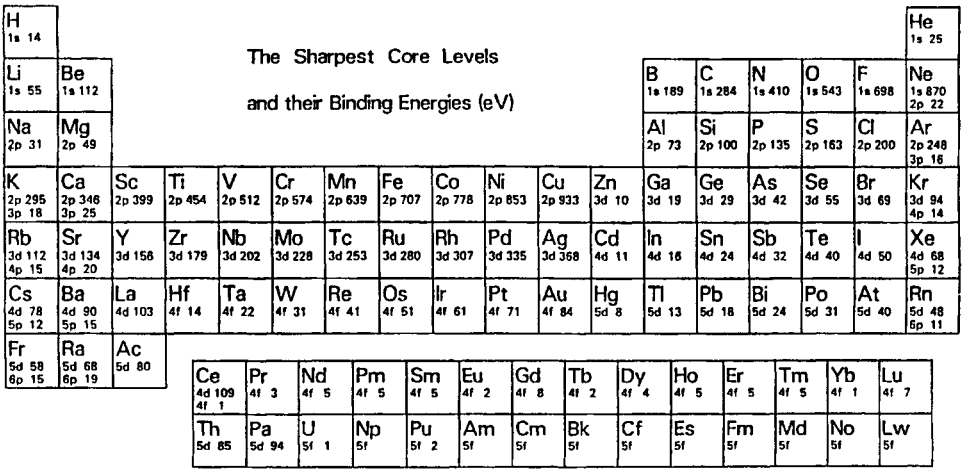


Fig. 6.15. Binding energies of the sharpest core levels of all the elements. A tunable light source with photon energies up to 1 keV is required to excite these core electrons to energies near the minimum escape depth.

and Spicer, 1974). At higher energy the electrons penetrate farther, at lower energy they lack energy for exciting electron–hole pairs or plasmons. The plasmon excitation threshold shows up in metals and semiconductors (e.g., Al and Si) as a strong increase in the escape depth below about 25 eV kinetic energy. The electron–hole pair threshold is particularly noticeable in insulators. At its minimum the escape depth can be as short as 3 Å (two layers) compared to about 20 Å (more than 10 layers) in conventional X-ray photoelectron spectroscopy (XPS). This short escape depth makes it possible to detect a monolayer of chemically altered atoms at a surface or an interface.

The photon-energy range for core level spectroscopy is determined by the binding energies of the sharpest core levels. Generally, these are the outermost shells with the highest angular momentum, i.e., 1s, 2p, 3d, 4f, as we progress through the Periodic Table. As shown in Fig. 6.15, their binding energies range up to 1 keV. Third generation undulator sources can access these core levels at their intrinsic limit. These elements include the organic group (C, O, N, F) and the 3d, 4d, 5d transition and noble metals, including magnetic materials, such as Cr, Mn, Fe, Co, Ni. Experiments have shown that inequivalent carbon atoms can be distinguished in organic compounds all the way up to polymers. Thus one can study their chemical reactions individually. In the following we will demonstrate the capabilities of core level spectroscopy for the Si 2p level, which is one of the most extensively studied core levels.

Core level shifts can have a variety of causes, such as charge transfer, relaxation, band bending, and photovoltage (Fig. 6.16, Egelhoff, 1987; Himpsel et al., 1990; Horn, 1990; Pehlke and Scheffler, 1993). Here, we are mainly interested in the chemical shift for atoms in the surface layer or at an interface. Band bending and photovoltage give rise to an overall shift of the spectrum relative to the Fermi level, since the probing depth is usually much shorter than the depth of the band bending region. Bulk and surface effects can easily be separated by taking spectra with different photon energies, corresponding to different

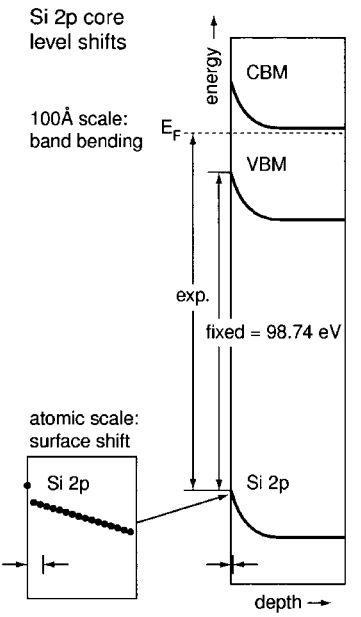


Fig. 6.16. Various types of core level shifts on a semiconductor surface. A typical probing depth of synchrotron radiation experiments (indicated by double-arrows) allows to distinguish the shifted core levels of the outermost atomic layer. Changes in band bending show up as an overall shift of the spectrum (from Himpsel et al., 1990).

electron escape depths. Near threshold one has a probing depth of about ten layers, whereas at $h\nu = 130$ eV one probes only two Si layers.

A classic problem in semiconductor physics is the bonding at the $SiO_2$/Si interface. After all, the extremely high electrical quality of this interface has spawned the dominant role of silicon technology in microelectronics. Many models of the $SiO_2$/Si interface have been constructed, but they are all hampered by the fact that $SiO_2$ is amorphous, and thus does not allow for a unique interface structure. However, the essentials of the local bonding can he extracted using core level spectroscopy. As shown in Fig. 6.17, oxygen pulls electrons away from Si and increases the binding energy of the Si core electrons by creating a positive electrostatic potential. One can clearly distinguish four discrete surface core levels for Si atoms at the interface. They are assigned to Si atoms bonding to one, two, three and four oxygen atoms, which may loosely be designated as $Si^{1+}$, $Si^{2+}$, $Si^{3+}$, and $Si^{4+}$. The latter is the bonding configuration of $SiO_2$, while the other three intermediate oxidation states are only stable at the interface. They disproportionate into Si and $SiO_2$ when prepared in bulk form. The relative abundance of the three intermediate oxidation states is a measure of the bond topology at the interface. It is sensitive to the crystallographic orientation (Fig. 6.17) and to the perfection of the interface. The integrated intensity of intermediate oxidation states is a measure of the interface width.

In general, the chemical core level shift is related roughly linearly to the charge transfer, as pointed out already in the early years of core level spectroscopy. Figure 6.18 gives an example for carbon compounds, where shifts of several eV are not unusual (Gelius et al.,

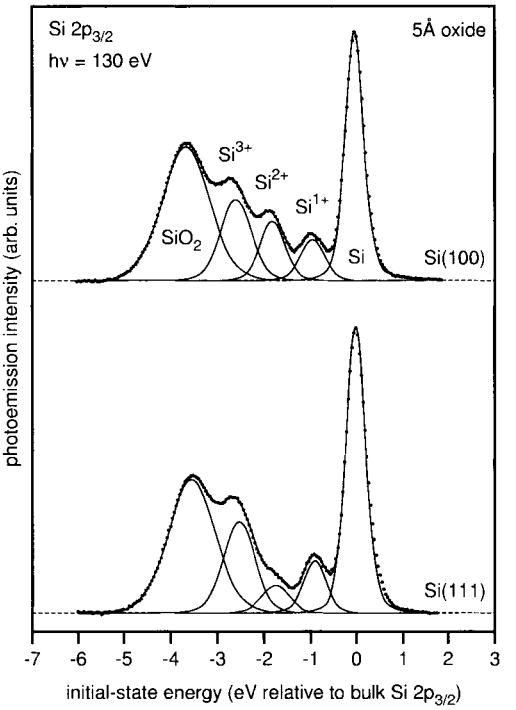


Fig. 6.17. Distinguishing all four oxidation states of silicon at $Si/SiO_2$ interfaces by their core level shifts. The different distributions for the two crystallographic orientations are a signature of different bond topologies. Only the Si $2p_{3/2}$ spin–orbit partner line is shown (from Himpsel et al., 1988).

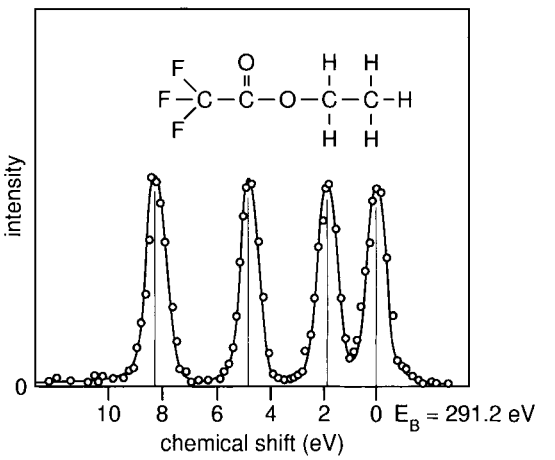


Fig. 6.18. Distinguishing inequivalent carbon atoms in organic molecules by their core level shifts. The shift is roughly proportional to the charge transfer and can be used to follow chemical reactions of each C atom in the molecule (from Gelius et al., 1974).

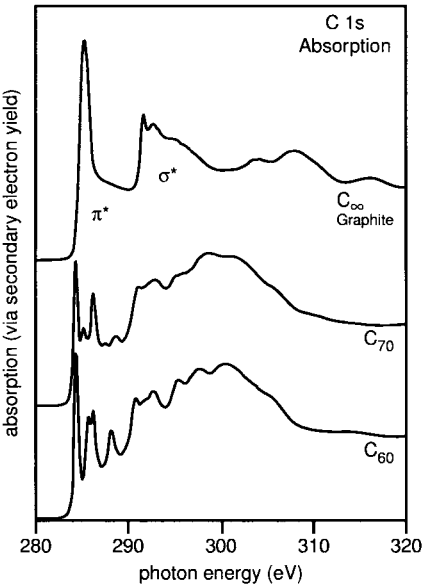


Fig. 6.19. C 1s absorption spectra of fullerenes and their infinite analog graphite measured by detecting secondary electrons. A manifold of unoccupied $\pi^*$ and $\sigma^*$ orbitals is seen, which still changes with the size of the clusters, even for molecules as large as 60 and 70 atoms (from Terminello et al., 1991).

1974). Together with an intrinsic line width of the C 1s level of less than 0.1 eV this sensitivity allows one to characterize the chemical state of C in organic compounds to quite some detail.

Another popular technique in organic surface chemistry is the use of the sharp 1s core levels of C, N, O as initial states for optical transitions into unoccupied states, such as the lowest $\pi^*$ and $\sigma^*$ orbitals (for a review see Stöhr, 1992). Surface sensitivity is achieved in so-called partial yield spectroscopy by detecting Auger or secondary electrons as decay product of the optical excitation, or even selecting the outermost layer with photodesorbed ions and atoms. Figure 6.19 shows for the case of fullerenes that one may encounter a wealth of well-defined antibonding orbitals, and that these are fairly sensitive to the bonding geometry (Terminello et al., 1991). Molecules as large as $C_{60}$ and $C_{70}$ are still distinct from each other in their orbital pattern, and have not converged to their infinite analog graphite. In small organic molecules the position of the antibonding orbitals is a sensitive function of the bond length, and can be used to detect the weakening of intra-molecular bonds in chemisorption reactions. The stronger the bond, the larger is the splitting between bonding and antibonding orbitals (Stöhr, 1992). The orientation of the adsorbed molecules can be inferred directly from the polarization dependence of the optical transitions via dipole selection rules.

While the coordination number of surface atoms does provide some structural information, it is often desirable to learn more about the atomic positions, e.g., bond angles and bond lengths, while keeping the chemical information from the core level shift. This can be accomplished via diffraction of core level photoelectrons by surrounding atoms. A variety

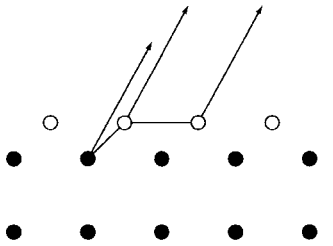

Fig. 6.20. Schematic of the concept of photoelectron holography (Barton, 1988). The photoelectron emitted directly from a core level acts as reference wave, the waves backscattered from neighbor atoms as object.

of diffraction geometries has been tested (see Fadley, 1990). There is a very elegant way to think about the information that can be obtained. It has been shown that the problem is mathematically similar to holography (Barton, 1988), whereby the electron-wave emitted directly from the core level represents the reference wave, and the waves scattered from neighbor atoms the object wave (Fig. 6.20). By measuring the interference pattern, i.e., the photoelectron emission pattern, one ought to be able to reconstruct the positions of the neighbor atoms around the emitter. The feasibility of this concept has been demonstrated, but in practice the effects of multiple scattering and unknown phase shifts complicate a quantitative analysis. They can be reduced to some degree by properly averaging over holograms taken at different photon energies (Terminello et al., 1993). Currently it appears that this method is helpful for a first look at an unknown atomic geometry. For a quantitative analysis it is necessary to simulate the photoemission pattern with a full-fledged multiple scattering calculation (Woodruff and Bradshaw, 1994).

## 6.5. Spectro-microscopy

Traditionally, microscopists have focused on atoms and have not been that interested in electronic information. Even such a basic property as the atomic number $Z$ of an atom could not be determined by most microscopes, including the transmission electron microscope (TEM) and the scanning tunneling microscope (STM), despite their atomic resolution. Several developments are rapidly changing the situation. On the atomic scale, scanning tunneling spectroscopy is able to detect valence states within a few eV of the Fermi level (for an overview of STM see Stroscio and Kaiser, 1993) and to provide chemical images (Jung et al., 1998). It thus provides essential information about chemically-active valence orbitals, such as the HOMO and LUMO, i.e., the highest occupied and lowest unoccupied molecular orbitals. Scanning transmission electron microprobes are now able to take high resolution energy loss spectra of a few atom columns (Batson, 1996). On a 100–1000 Å scale, photoelectron and soft X-ray microscopy are benefitting from a new, third generation of undulator-based synchrotron light sources with $10^4$ times the brilliance of existing sources. They are capable of element-resolved imaging by using core levels.

Scanning tunneling spectroscopy practically has a monopoly in identifying the electronic structure of defects at surfaces. By measuring the quantity $(\mathrm{d}I/\mathrm{d}V)/(I/V)$ with a modulation technique it is possible to get an approximation of the local density of states,

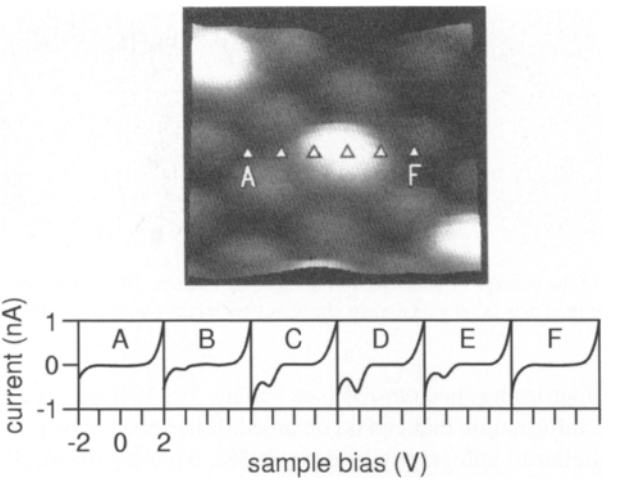


Fig. 6.21. Variation of the current–voltage characteristics of a scanning tunneling microscope tip when crossing a surface defect. A local extremum develops near the defect due to tunneling between discrete states at the defect and at the tip (from Avouris et al., 1990).

weighted preferably around zero parallel momentum ($I$ is current, $V$ is voltage between tip and sample). As shown in Fig. 6.3b, c the density of occupied and empty dangling bond orbitals can be seen for specific atoms (Hamers et al., 1986; Wolkow and Avouris, 1988). Together with the possibility of manipulating individual atoms at surfaces (Eigler and Schweizer, 1990) there are exciting prospects of hand-crafting electronic devices on the atomic scale (Aono, 1992). An example of a peculiar local electronic structure giving rise to interesting electrical characteristics is given in Fig. 6.21 (Avouris et al., 1990). As one approaches a boron-induced defect at a silicon surface, one finds that the current-versus-voltage $I(V)$ curves develop a local extremum, which is due to tunneling between two defect levels, one at the tip, the other at the sample. The negative differential resistance associated with this extremum might some day be used to start an oscillator, as done with more macroscopic tunnel diodes. It is interesting to note that at the atomic level the electronic structure of the tip becomes as important as that of the surface, requiring exquisite tip control for predictable device structures.

A whole variety of microscopes is being explored for element-resolved imaging, using the excitation of core levels with soft X-rays to achieve contrast. In general, one can distinguish scanning and imaging methods. The former focus a soft X-ray beam with Fresnel zone plates or multilayer-coated mirrors and scan the sample across it while detecting transmitted photons or emitted photoelectrons. With imaging methods the whole field of view is illuminated on the sample, and the emitted photoelectrons are accelerated and used to form a magnified image with standard electron microscope techniques. Using photoelectrons there are two ways to become element-selective, i.e., taking either the photon energy or the electron energy to pick out a particular core level. In the first case, one tunes into the core level absorption threshold and collects the whole photoelectron spectrum, in the latter case one selects a core-specific peak in the photoelectron spectrum. By fine-tuning into detailed

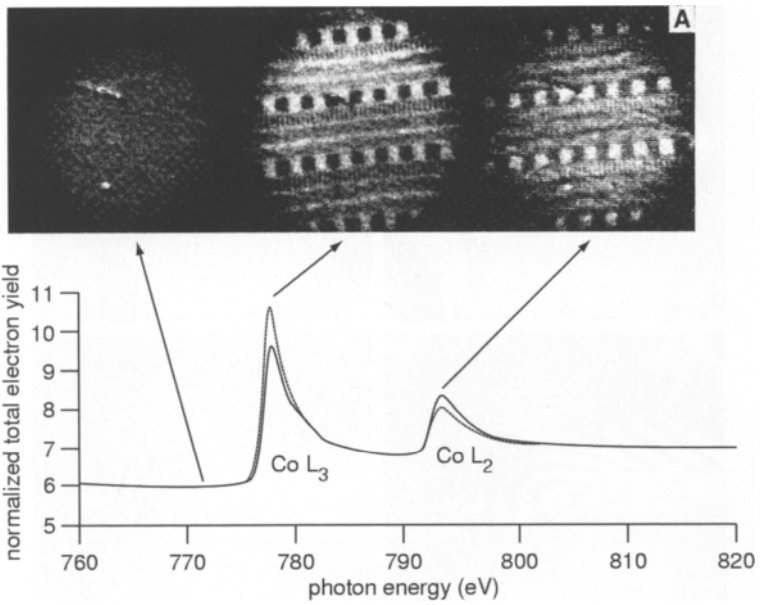


Fig. 6.22. Images of magnetic domains written onto a magnetic recording disk, taken with a photoelectron microscope and using circularly polarized soft X-rays. Magnetic circular dichroism leads to opposite magnetic contrast for the $L_3$ and $L_2$ absorption edges of Co (from Stöhr et al., 1993).

features of an absorption edge or into a chemically shifted core level peak one can, in addition, find out about the chemical state of a particular element (Ade et al., 1992). Although the limitations and relative merits of all these methods have yet to be sorted out, their potential can already be inferred from some of the available results. Figure 6.22 (Stöhr et al., 1993) shows that not only an element can be selected in this case by tuning into the Co 2p absorption edge, but also its magnetic orientation determined (by using the difference between left- and right-handed, circularly-polarized light). This way a bit pattern written onto a magnetic disc becomes visible. Since in today's applications most magnetic materials are ternary alloys, it is quite useful to have this element-specific magnetic information. With further improvements in resolution it should become possible to resolve the magnetic domain structure of each bit. Element-resolved microscopy has not only a promising future in the microelectronics area, but also in surface chemistry. Figure 6.23 shows that chemical reactions can develop very peculiar spatial (and temporal) patterns at surfaces, due to nonlinear phenomena (Rotermund et al., 1991; Rotermund, 1993). In this case the difference in the photoelectric threshold between O- and CO-covered platinum was used to generate contrast with near-threshold photons. There are many other micron-sized phenomena at surfaces that can be explored with an element-resolved microscope, such as nucleation and growth, steps, whiskers, etc. LEED microscopy has shown the way (Bauer et al., 1991), using low energy electron diffraction to generate contrast. With photoelectrons one can overcome the restrictions of having to look at crystalline substrates, and is able to tell the chemical identity of a structure.

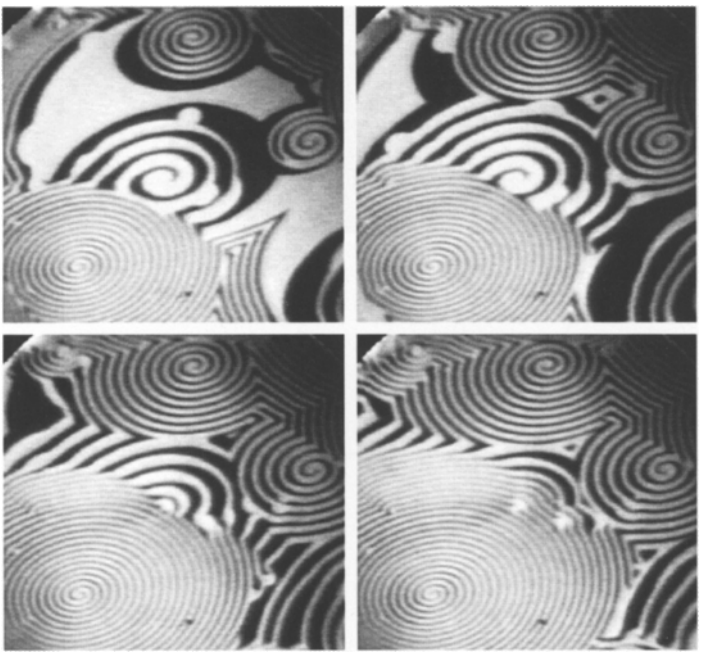

Fig. 6.23. Spatially-resolved surface chemical reactions probed with a photoelectron microscope that uses chemical variations in the work function to generate contrast (from Rotermund, 1993).

## References


Ade, H., X. Zhang, S. Cameron, C. Costello, J. Kirz and S. Williams, 1992, Science **258**, 972.

Aono, M., 1992, Science **258**, 5.

Aspnes, D.E., Y.-C. Chang, A.A. Studna, L.T. Florez, H.H. Farrell and J.P. Harbison, 1990, Phys. Rev. Lett. **64**, 192.

Assmann, J. and W. Mönch, 1980, Surf. Sci. **99**, 34.

Avouris, Ph., In-Whan Lyo, F. Bozso and E. Kaxiras, 1990, J. Vac. Sci. Technol. A **8**, 3405.

Barton, J.J., Phys. Rev. Lett. **61**, 1356.

Batson, P.E., 1996, J. Electron Microscopy **45**, 51.

Bauer, F., M. Mundschau and W. Swiech, 1991, J. Vac. Sci. Technol. B **9**, 403.

Baeumler, M. and R. Haight, 1991, Phys. Rev. Lett. **67**, 1153.

Benbow, R., 1980, Phys. Rev. B **22**, 3775.

Binnig, G., H. Rohrer, Ch. Gerber and E. Weibel, 1983, Phys. Rev. Lett. **50**, 120.

Chiaradia, P., C. Chiarotti, S. Selci and Z. Zhu, 1983, Surf. Sci. **132**, 62.

Donath, M., 1989, Appl. Phys. A **49**, 351.

Eberhardt, W. and F.J. Himpsel, 1980, Phys. Rev. B **21**, 5572; Phys. Rev. B **23**, 5650.

Egelhoff, W.F., 1987, Surf. Sci. Rep. **6**, 253.

Eigler, D.M. and E.K. Schweizer, 1990, Nature **344**, 524.

Fadley, C.S., 1990, in: Synchrotron Radiation Research: Advances in Surface Science, ed. R.Z. Bachrach. Plenum, New York.

Feibelman, P.J., D.R. Hamann and F.J. Himpsel, 1980, Phys. Rev. B **22**, 1734.

Freund, H.-J. and M. Neumann, Appl. Phys. A **47**, 3.

Gelius, U., E. Basilier, S. Svensson, T. Bergmark and K. Siegbahn, 1974, J. Electron Spectrosc. Relat. Phenom. **2**, 405.
Hamers, R.J., R.M. Tromp and J.E. Demuth, 1986, Phys. Rev. Lett. **56**, 1972.
Hansson, G.V. and R.I.G. Uhrberg, Surf. Sci. Rep. **9**, 197.
Heinz, T.F., F.J. Himpsel, F. Palange and E. Burstein, 1989, Phys. Rev. Lett. **63**, 644.
Himpsel, F.J., 1983, Adv. Phys. **32**, 1.
Himpsel, F.J., 1990, Surf. Sci. Rep. **12**, 1.
Himpsel, F.J., F.R. McFeely, A. Taleb-Ibrahimi, J.A. Yarmoff and G. Hollinger, 1988, Phys. Rev. B **38**, 6084.
Himpsel, F.J., B.S. Meyerson, F.R. McFeely, F. Morar, A. Taleb-Ibrahimi and J.A. Yarmoff, 1990, in: Proceedings of the Enrico Fermi School on Photoemission and Absorption Spectroscopy of Solids and Interfaces with Synchrotron Radiation. North-Holland, Amsterdam.
Himpsel, F.J., J.E. Ortega, G.J. Mankey and R.F. Willis, 1998, Adv. Phys. **47**, 511.
Horn, K., 1990, Appl. Phys. A **51**, 289.
Jung, T., F.J. Himpsel, R.R. Schlittler and J.K. Gimzewski, 1998, in: Scanning Probe Microscopy, Analytical Methods, ed. R. Wiesendanger. Springer, Berlin, p. 11.
Kevan, S.D., 1992, Angle-Resolved Photoemission. Elsevier, Amsterdam.
Kevan, S.D. and D.A. Shirley, 1980, Phys. Rev. B **22**, 542.
Kisker, E., K. Schröder, W. Gudat and M. Campagna, 1985, Phys. Rev. B **31**, 329.
Knapp, J.A., F.J. Himpsel and D.E. Eastman, 1979, Phys. Rev. B **19**, 4952.
Landolt–Börnstein, 1994, Numerical Data and Functional Relationships in Science and Technology, New Series, Group III, Vol. 23 a, b. Electronic Structure of Solids: Photoemission Spectra and Related Data, eds. A. Goldmann and E.-E. Koch. Springer, Berlin.
Lindau, I. and W.E. Spicer, 1974, J. Electron Spectrosc. **3**, 409.
Matz, R., H. Lüth and A. Ritz, 1983, Solid State Commun. **46**, 343.
Niles, D.W., D. Rioux and H. Höchst, 1992, Phys. Rev. B **46**, 12547.
Olmstead, M.A. and N.M. Amer, 1984, Phys. Rev. Lett. **52**, 1148.
Olmstead, M.A., 1987, Surf. Sci. Rep. **6**, 159.
Pehlke, E. and M. Scheffler, 1993, Phys. Rev. Lett. **71**, 2338
Plummer, E.W. and W. Eberhardt, 1982, Adv. Chem. Phys. **49**, 533.
Qiu, Z.Q., J. Pearson, A. Berger and S.P. Bader, 1992, Phys. Rev. Lett. **68**, 1398.
Rotermund, H.H., 1993, Surf. Sci. **283**, 87.
Rotermund, H.H., S. Jakubith, A. von Oertzen and G. Ertl, 1991, Phys. Rev. Lett. **66**, 3083.
Selci, S., P. Chiaradia, F. Ciccacci, A. Cricenti, N. Sparvieri and C. Chiarotti, 1985, Phys. Rev. B **31**, 4096.
Smith, N.V., Rep. Prog. Phys. **51**, 1227.
Stöhr, J., 1992, NEXAFS Spectroscopy, Springer Series in Surface Sciences, Vol. 25, eds. G. Ertl, R. Gomer and D. Mills. Springer-Verlag, New York.
Stöhr, J., Y. Wu, B.P. Hermsmeier, M.C. Samant, C.R. Harp, S. Koranda, D. Dunham and B.P. Tonner, 1993, Science **259**, 658.
Stroscio, J.A. and W.J. Kaiser, 1993, Methods of Experimental Physics, Vol. 27, Scanning Tunneling Microscopy. Academic Press, Boston.
Terminello, L.J., J.J. Barton and D.A. Lapiano-Smith, 1993, Phys. Rev. Lett. **70**, 599.
Terminello, L.J., D.K. Shuh, F.J. Himpsel, D.A. Lapiano-Smith, J. Stöhr, P.S. Bethune and C. Meijer, 1991, Chem. Phys. Lett. **182**, 491.
Tsuei, K.-D., F.W. Plummer, A. Liebsch, E. Pehlke, K. Kempa and P. Bakshi, 1991, Surf. Sci. **247**, 302.
Verheijen, M.A., C.W. van Hasselt and Th. Rasing, 1991, Surf. Sci. **251/252**, 467.
Viturro, R.E., M.L. Slade and L.J. Brillson, 1986, Phys. Rev. Lett. **57**, 487.
Wolkow, R. and Ph. Avouris, 1988, Phys. Rev. Lett. **60**, 1049.
Woodruff, D.P. and A.M. Bradshaw, 1994, Rep. Prog. Phys. **57**, 1029.

This Page Intentionally Left Blank

CHAPTER 7

# Electronic Structure of Semiconductor Surfaces

K. HORN

*Department of Surface Physics*
*Fritz-Haber-Institut der Max-Planck-Gesellschaft*
*Faradayweg 4-6*
*D-14195 Berlin, Germany*

*© 2000 Elsevier Science B.V.*
*All rights reserved*

*Handbook of Surface Science*
*Volume 2, edited by K. Horn and M. Scheffler*

# Contents


7.1. Introduction . . . . . 385
7.2. Elemental semiconductor surfaces . . . . . 386
7.2.1. The Si(100) surface . . . . . 386
7.2.2. Si(111) . . . . . 394
7.2.2.1. Si(111)-(2 × 1) . . . . . 394
7.2.2.2. The Si(111)-(7 × 7) reconstruction . . . . . 397
7.2.3. Ge(100) . . . . . 402
7.2.4. Ge(111) . . . . . 404
7.2.5. Diamond surfaces . . . . . 405
7.2.6. α-Sn . . . . . 407
7.3. Compound semiconductor surfaces . . . . . 407
7.3.1. The III-V compound semiconductors . . . . . 407
7.3.1.1. The (110) surface of zincblende compound semiconductors . . . . . 408
7.3.1.2. The (100) faces of III-V compound semiconductors . . . . . 419
7.3.1.3. Band bending and the 2D electron gas at InAs surfaces . . . . . 421
7.3.1.4. The group III nitrides . . . . . 424
7.3.2. The II-VI compound semiconductor surfaces . . . . . 424
7.3.3. Other compound semiconductor surfaces . . . . . 426
7.4. Conclusion and outlook . . . . . 427
References . . . . . 428

## 7.1. Introduction

Semiconductor surfaces have played a particularly important role in the investigation of the geometric and electronic structure of solid surfaces. A strong motivation for investigating semiconductor surfaces arises from the all-pervading use of semiconductor devices in the electronics industry. There is a direct connection between the development of ultra-high vacuum based experimental techniques for surface investigations and the emergence of semiconductor devices: in both fields, single crystalline samples with a high degree of cleanliness and atomic order right up to the surface or interface are used. With layer thicknesses in semiconductor devices approaching the region of a few atomic layers, such as in $SiO_2$ gate oxides or optoelectronic devices, an understanding of the atomic and electronic structure of surfaces and interfaces (Lüth, 1995) becomes increasingly important. From a technical point of view, many close connections between semiconductor surface research and device fabrication exist.

This chapter will describe the basic aspect of the electronic structure of several model surfaces of silicon, germanium, and the compound semiconductor surfaces, revealed by experimental techniques such as photoelectron spectroscopy, inverse photoemission and scanning tunneling microscopy/spectroscopy discussed in Chapter 6 by Himpsel. The main focus is on the microscopic electronic properties such as local charge distribution, surfaces states etc., but in a few cases a discussion of the so-called macropotential which may lead to band bending, as dealt with in more detail in the Chapter 11 by Ludeke, will be included. In the discussion, the close relation between geometric and electronic structure will become apparent, for example when a change in surface state occupation leads to surface reconstruction. This relation can be examined by combining the techniques of scanning tunneling microscopy and spectroscopy, which offer a means of determining electronic state characterization in real space, with experimental results from photoemission, permitting the determination of the energy–wave-vector relation $E(\mathbf{k})$ of electronic states, thus offering a complete description of surface electronic structure.

This chapter is organized as follows: first, the surfaces of elemental semiconductors are discussed. The features of tetrahedrally coordinated compound semiconductors such as the III-V and II-VI compounds are presented next. Finally, other materials such as the IV-IV compound semiconductors, e.g., SiC, as well as layered semiconductors, are briefly discussed. A summary and outlook conclude the chapter. The bulk electronic structure is only addressed where it is important for an understanding of the surface structure. The study of bulk band structures invariably accompanies investigations of surface states and resonances, since the experimental data, such as derived from photoelectron spectra, contain contributions from both bulk and surface. (For a critical discussion of semiconductor bulk band structure investigations, the reader is referred to the review by Leckey and Riley (1992) and references therein.) Frequent reference is made to theoretical investigations of semiconductor surface structure, as described in detail in Chapter 2 by Pollmann and

Krüger. An exhaustive overview of work performed in this field is not intended, and would be hardly feasible given the intense research effort; rather, specific examples which are thought to be representative for a class of semiconductors, or which demonstrate a certain experimental approach, are presented and discussed. Also, the historical development leading to our present state of knowledge will rarely be covered; this is described in detail in the textbook by Mönch (1995).

## 7.2. Elemental semiconductor surfaces

The elemental semiconductors play a central role in investigations of surface electronic structure, not only because silicon belongs to this class, but also since the bond in these solids is purely covalent. Many systematic aspects of "Bonds and Bands in Semiconductors" (Phillips, 1973) can be studied by considering the sequence from diamond with its band gap of 5.5 eV to the semimetallic $\alpha$-Sn. Here, emphasis will be put on studies of silicon surfaces, for which the largest and most detailed body of experimental and theoretical material has been obtained, with a somewhat shorter discussion of germanium, and a short note on diamond and $\alpha$-Sn. In the spirit of covering a few model systems only the properties of the low-index (100) and (111) surfaces of the elemental semiconductors will be dealt with.

### *7.2.1. The Si(100) surface*

Silicon surfaces have been extensively studied, and the (100) surface in particular, since this is the "device" surface that is used for most of silicon semiconductor device fabrication. The bulk truncated (100) surface would result in two dangling bonds per surface atom. This situation is energetically unstable; the reduction of the number of dangling bonds through reconstruction is a recurring theme in the formation of semiconductor surface structures. In Si(100), a pairing of neighboring atoms into dimers will occur, such that one dangling bond per surface atom is removed. Dimer formation leads to a doubling of periodicity along the direction of bond pairing, i.e., a $(2 \times 1)$ periodicity. On the fourfold symmetric (100) surface two domains of $(2 \times 1)$ periodicity occur, as observed in LEED experiments (Schlier and Farnsworth, 1959). These surface geometries are shown schematically in Fig. 7.1. Direct evidence in favor of the dimer reconstruction was obtained from scanning tunneling microscopy data; Tromp and coworkers obtained clear scanning tunneling microscopy (STM) images which showed the presence of surface dimers (Tromp et al., 1985). Figure 7.1 shows the pairing of surface atoms in models of symmetric and asymmetric dimers. While the former can only induce a $(2 \times 1)$ reconstruction, the latter can form an additional periodicity through periodic tilt angle repetition (Fig. 7.1b), leading to a $c(4 \times 2)$ reconstructed surface, which is indeed observed in low energy electron diffraction at low temperature. The two-dimensional asymmetric dimer lattice is a representation of the 2D Ising model, and a phase transition temperature of about 250 °C was calculated (Ihm et al., 1983). There is now convincing evidence that the dimers are indeed asymmetric, from a variety of experimental probes as well as extensive calculations as discussed at length by Pollmann and Krüger in Chapter 2; we will return to this topic in the discussion of the surface band structure of Si(100).

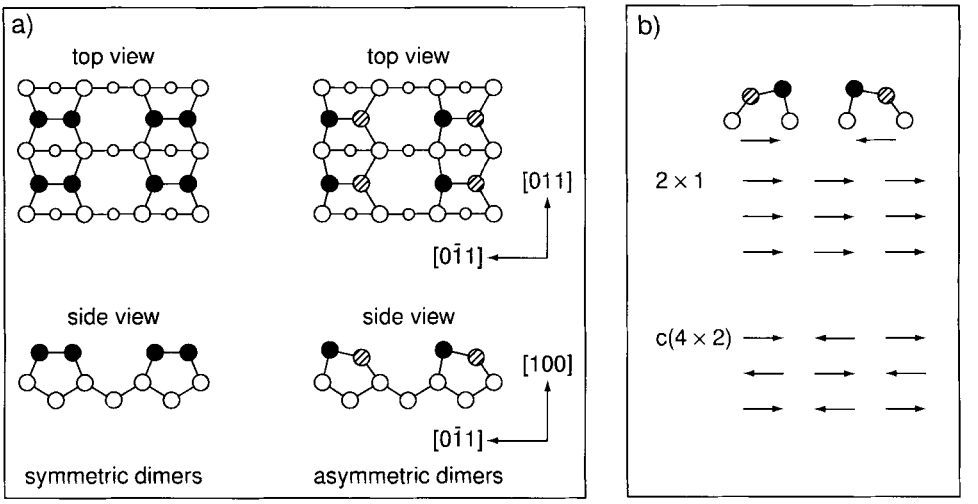


Fig. 7.1. (a) Ball- and stick-model of the symmetric and asymmetric dimer structure of Si(100)(2 × 1). (b) Arrangement of asymmetric dimers in an (2 × 1) and c(4 × 2) structure. Adapted from MacLaren et al. (1987).

The electronic charge rearrangement responsible for dimer formation will obviously be reflected in the energy and occupancy of surface states (Himpsel, 1994) and, in a more indirect way, in the number and magnitude of shifted surface core level lines. Evidence for surface state emission was already obtained in the early angle-integrated photoemission data by Rowe and Ibach (1974). For a more detailed comparison with band structure calculations, the momentum-resolved surface state energy, i.e., the surface band structure is needed. This can be obtained by angle-resolved photoemission as described in detail in Chapter 6. The determination of surface state dispersion on the Si(100)-(2 × 1) surface is complicated by the fact that the photoemission signal contains an incoherent superposition of emission from the two equivalent (2 × 1) domains, rotated by 90° with respect to one another, which are present on a normal Si(100) surface. However, there is one direction in the surface Brillouin zone which is equivalent for the two domains, along the [010] azimuth, and initial investigations have concentrated on these. Photoemission data of Himpsel and Eastman (1979) for this azimuth showed a dominant surface state structure at 0.7 eV below $E_F$ at the zone center, which dispersed towards higher binding energies, away from the valence band maximum for increasing $\mathbf{k}_{\|}$. There have been many subsequent angle-resolved photoemission studies, which are collected and discussed in Hansson and Uhrberg's review (1988, 1992), and also many surface band structure calculations which are discussed extensively in Chapter 2 by Pollmann and Krüger.

Dimerisation of the surface atoms leads to anisotropy in the surface bands, since the overlap between neighboring dangling bonds will be reduced along the direction of dimerisation, where the distances are twice as large as in the bulk-truncated surface, while they remain identical in the direction across the dimers. In order to clearly determine the dispersion along these two directions, and to identify the influence of dimerisation, the incoherent

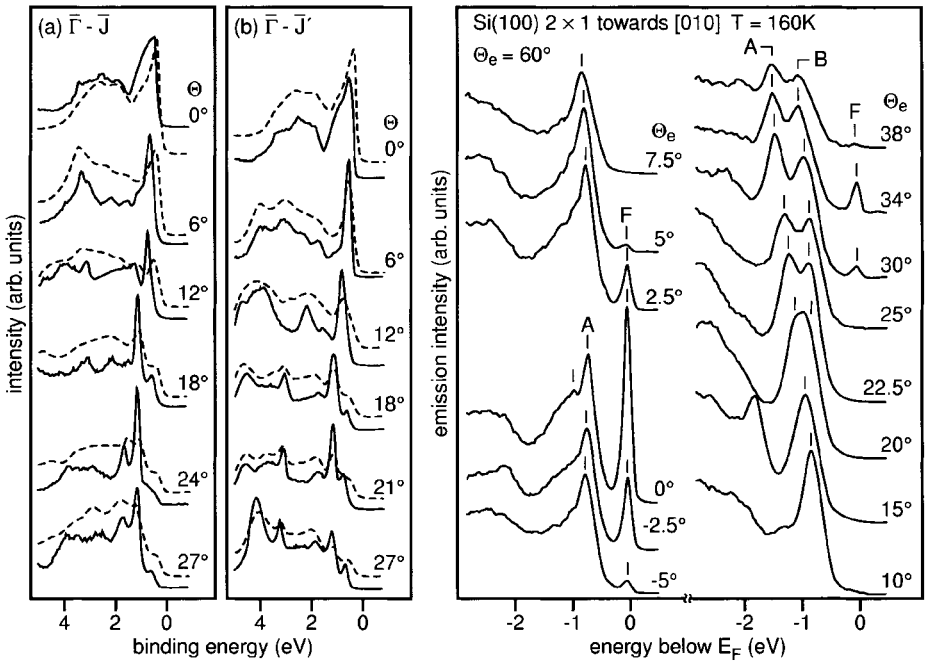


Fig. 7.2. (a) Angle-resolved valence level photoemission spectra from Si(100)-(2 × 1) (dashed lines) and c(4 × 2) surfaces (Enta et al., 1990a). (b) Spectra for a single domain Si(100)-(2 × 1) surface from a degenerately n-doped sample, exhibiting a feature above the valence band maximum (F) which is attributed to the normally unoccupied $D_{down}$ surface state. From Johansson et al. (1990), with permission. © 1990 American Physical Society.

superposition from the two coexisting domains has to be avoided, i.e., single domain (100) surfaces are needed. These can be prepared by cutting a Si surface oriented a few degrees away from the (100) azimuth, giving rise to surfaces with terraces separated by double height steps, such that the domains on all terraces have the same orientation (Bringans et al., 1986), or by growing layers of Si on Si(100) by molecular beam epitaxy followed by extensive annealing (Enta et al., 1990a). A complete map of the surface state dispersion can been derived in this way, e.g., in the studies by Enta et al. (1990a) and Johansson et al. (1990). Photoemission data by Enta et al. (1990a) are shown in Fig. 7.2a. The dashed lines are spectra from a single domain (2 × 1) surface, while the solid lines are for a low temperature c(4 × 2) surface. It is found that all spectral features become much sharper in the c(4 × 2) structure, which can only be partly accounted for by the reduced thermal broadening at low temperature. Along the $\bar{\Gamma}$–$\bar{J}$ direction, i.e., perpendicular to the dimer row, this effect is particularly strong. The dominating peak A near the valence band maximum is attributed to the dimer dangling bond surface state, and is found to disperse more strongly for the c(4 × 2) than for the (2 × 1) structure. Another band B is found to exhibit the dispersion expected from the c(4 × 2) surface Brillouin zone. A compilation of the photoemission results in terms of a surface band structure along the different directions of the surface Brillouin zone (Johansson et al., 1990) is shown in Fig. 7.3 together with a drawing

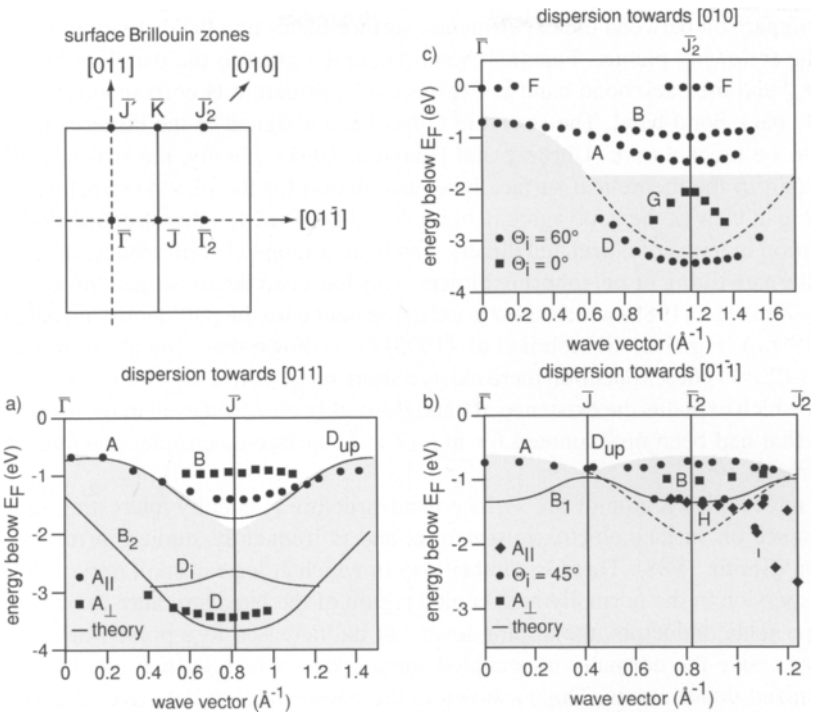


Fig. 7.3. Surface band structure of Si(100)-(2 × 1) along different directions in the surface Brillouin zone (shown in the top) as indicated. From Johansson et al. (1990), with permission.

of the surface Brillouin zone. Figure 7.3a gives the dispersion of features along the $\bar{\Gamma}$–$\bar{J}'$, i.e., the [011] direction, where the points marked A label a band which disperses by about 0.7 eV towards higher binding energies. The lines are from the band structure calculation for the (2 × 1) surface by Krüger et al. (1986). The shaded area represents the region of the projected bulk band structure. In the asymmetric dimer model, which has been supported by a large number of experimental and theoretical studies, the upper dimer atom is referred to as the "up-atom" and the lower as the "down-atom". This buckling opens up a Jahn–Teller-like gap between the states located on the up- and down-atom, resulting in two dangling bond bands, an occupied $D_{up}$ band and an empty $D_{down}$ band, yielding a semiconducting surface. The band characterized by the points marked A is the band due to the up-atoms on the asymmetric dimers, marked $D_{up}$ in Fig. 7.3.

Two other surface features labeled B and D are also observed; their surface character is suggested from the fact that all (including A) are completely removed by hydrogen adsorption when the Si(100)(2 × 1):H phase is formed, saturating the dangling bonds. Along the $\bar{\Gamma}$–$\bar{J}$ direction (Fig. 7.2b), feature A only shows a small dispersion; this suggests that A is indeed due to the dangling bond state since these are far apart along this direction. Feature B is also seen here, and another peak marked H is located about 1.3 eV below the VBM at $\bar{\Gamma}_2$.

A comparison between the experimental surface bands and band structure calculations gives the following picture. Features A and D are assigned to the dangling bond surface band $D_{up}$ and the back bond band $B_2$, respectively. Structure H corresponds to the calculated $B_1$ back bond band. The structure G has been assigned to the dimer band, but this seems to be inconclusive (Uhrberg and Hansson, 1991). Finally, the structure B has no counterpart in the theoretical surface band calculation for the $(2 \times 1)$ structure, which is surprising in view of the good agreement for A and D. However, this structure finds a ready explanation in terms of correlated dimers which are arranged "antiferromagnetically", i.e., in an alternate tilting of neighboring dimers. This has been demonstrated through calculations by Zhu et al. (1989) which show good agreement with the photoemission data by Enta et al. (1990a) (Fig. 7.2). Shkrebtii et al. (1995) have shown that even above the structural $c(4 \times 2)$-$(2 \times 1)$ phase transition there exists a short-range correlation between neighboring dimers, which explains the existence of band B, weakly observed even in room temperature spectra that had been unaccounted for in a $(2 \times 1)$ surface electronic structure (Hansson and Uhrberg, 1991).

The unoccupied region of the surface band structure is equally interesting in terms of its influence on surface electronic structure, and is frequently studied in inverse photoemission (Smith, 1988). There is another way in which at least a small part of the surface state dispersion in the normally unoccupied region of the band structure can be observed. In n-type semiconductors, the doping level can be increased to a point where the Fermi level lies above the normally unoccupied surface state which is then filled by electrons from ionized donor atoms. This is shown in the photoemission data from a degenerately n-doped Si(100) surface in Fig. 7.2b, recorded along the [010] direction (Johansson et al., 1990). There is an intense peak (marked F) above the valence band maximum in normal emission, which vanishes within a few degrees of polar angle away from normal emission. The surface state calculated to be related to the $D_{down}$ atoms (F) lies close to the conduction band minimum and, as $\mathbf{k}_{\parallel}$ is increased away from the $\Gamma$ point, disperses to higher binding energies; thus due to the filling it can be observed in a small region of $\mathbf{k}$ space around the zone center (Mårtensson et al., 1986) and at the zone boundary. Thus the basic features of surface state emission from Si(100) agree well with band structure calculations, and the magnitude of their dispersion agrees well with expectations from basic concepts. These data provide strong support for the asymmetric dimer model, and its prediction of a semiconducting Si(100)-$(2 \times 1)$ surface.

From the energies at which this surface state is observed, Mårtensson et al. conclude that this is the surface state which is responsible for determining the position ("pinning") of the Fermi level in n-type Si(100). They suggested that a similar observation in Ge(100) by Kevan and Stoffel (1984) is also related to surface state emission rather than defect state emission as previously believed; this is discussed in the Section 7.2.3 on Ge(100) below. The observation of surface state occupation by electrons from the conduction band in n-type samples demonstrates that the study of surface states has a bearing not only on the microscopic level interaction between surface atoms, but also on the determination of the macropotential of the surface in question, which manifests itself in the location of the surface Fermi level, i.e., in the magnitude of the work function at such surfaces.

Historically, many of the attempts to identify certain peaks and bands in the valence region on the basis of comparison with calculations were motivated by the search for a valid

structural model for a specific reconstruction as observed in low energy electron diffraction. The advent of a real space method for structure determination, e.g., the scanning tunneling microscope, the results of which often give important clues towards settling a dispute over surface structures, has made this pursuit less important. However, the understanding of bonding at semiconductor surfaces still takes important input from a determination of surface states and their dispersion. Another important tool for the elucidation of surface electronic structure from a rather different angle comes from an analysis of surface core level shifts in terms of surface charge rearrangement. Such studies are also important since changes induced by adsorption may serve to elucidate the mechanism of the chemisorption bond, and to identify specific adsorbate bonding sites; for this purpose an assignment of the clean surface core level lines is mandatory. While charge rearrangement in surfaces indeed gives rise to shifted core level lines, an understanding of the processes involved can be more complex than suggested from a simple initial state argument, however.

Consider the Si 2p core level spectrum in Si(100)-(2 × 1); this is also relevant to the controversy concerning symmetric vs. asymmetric dimers on Si(100). The Si 2p core level spectrum has been studied by many groups, and components shifted by the presence of surface atoms were discovered already in the early 80's (Himpsel et al., 1980). High resolution spectra from the (2 × 1) and c(4 × 2) surfaces of Si(100), the latter prepared by cooling the sample to 120 K are shown in Fig. 7.4, recorded by Landemark et al. (1992). Without any line shape analysis, the raw data reveal the presence of surface shifted components. The prominent peak S at lower binding energies is clearly evident, and shoulders on the main peak also; these are shown to increase as the photon energy is tuned to a more surface-sensitive situation, indicating that other surface-related features are also present in this region. It is often necessary to apply line shape analysis techniques to the spectra for an interpretation of the complex peak shapes that arise from a superposition of lines from atoms in the different environments, i.e., the surface and bulk atoms in the present context. These procedures are well established, and the necessary precautions that have to be taken in order to avoid spurious or misleading results are known (Wertheim and DiCenzo, 1986). In order to extract quantitative information, a line shape analysis based on Voigt functions was applied to the Si 2p spectra from Si(100)-(2 × 1). A fit with four components was found to give rise to systematic variations of peak energy with photon energy and was thus found to be deficient. Five line pairs (for the $2p_{1/2}$ and $2p_{3/2}$ spin–orbit-split components) were needed in order to result in the fit shown in Fig 7.4. Such fits depend to some extent on the input parameters for Lorentzian widths, related to the hole state lifetime, Gaussian width (representing, among others, thermal broadening, inhomogeneous broadening due to lateral variations of the pinning position, and instrumental broadening), branching ratio and spin–orbit splitting; some of these can be determined directly in the experiment, while for others a range of values has to be assumed. The fit by Landemark et al. results in one bulk component B, and four surface components S, C, SS, and S′, shifted by −485, −205, 62, and 220 meV with respect to the bulk line for the c(4 × 2) reconstruction; some variation occurred upon variation of the emission angle (higher surface sensitivity) and for the (2 × 1) surface. The identification drawn from these shifts and relative intensities related the peak S to the dimer atoms. The SS component exhibits a similar behavior than the S peak, and the latter is thus assigned to the up-atoms, while the former is related to the

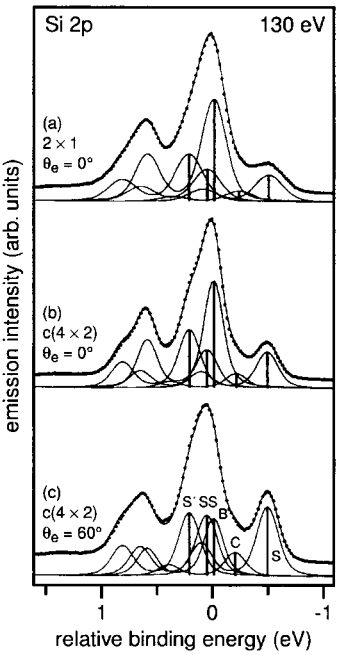


Fig. 7.4. (a) Line shape analysis of Si 2p core level spectra obtained from Si(100)(2 × 1) at room temperature (top), and from Si(100) c(4 × 2) at 120 K at a photon energy of 130 eV, for normal and off-normal emission as indicated. The S, C, SS, and S′ lines are located at 0.48, 0.20, −0.06, and −0.22 eV relative to line B, respectively. From Landemark et al. (1992), with permission. © 1992 American Physical Society.

down-atoms. S′ in this interpretation arises from second layer atoms, while an origin of C from surface defects could not be ruled out.

The presence of two lines from the dimer atoms strongly suggests that the dimer atoms are not equivalent, i.e., that the dimers on Si(100) in the c(4 × 2) structure are asymmetric. It is intriguing that the emission from the two dimer atoms is separated by such a large energy (about 550 meV). Surface core level shifts are generally interpreted in terms of initial state effects, i.e., a different "chemical" environment. In this model charge transfer from the down-atom to the up-atom would suggest that the S line is due to the up-atoms, but one would also expect that the down-atom line to be symmetrically shifted with respect to the bulk. However, what is omitted in the initial state picture is the response of the valence electrons to the creation of the core hole, i.e., relaxation effects (Hüfner, 1996), which may be different for surface and bulk atoms, and indeed different for inequivalent atoms on the surface. An interpretation for this effect, which is of general importance for surface core level shift analysis, has been given by Pehlke and Scheffler (1993). The authors calculated differences of the total energy of slabs containing core-excited atoms at different positions at the surface and in the bulk, using density functional theory and the local density approximation. They showed that not only is screening enhanced in the surface compared to the bulk, but also the screening of the core hole is different for the up-atom and the down-atom in the dimer. Consider the schematic diagram in Fig. 7.5a, which compares an assignment

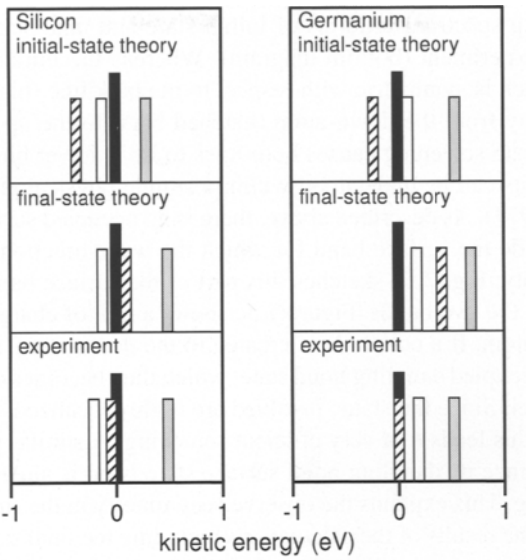


(a)

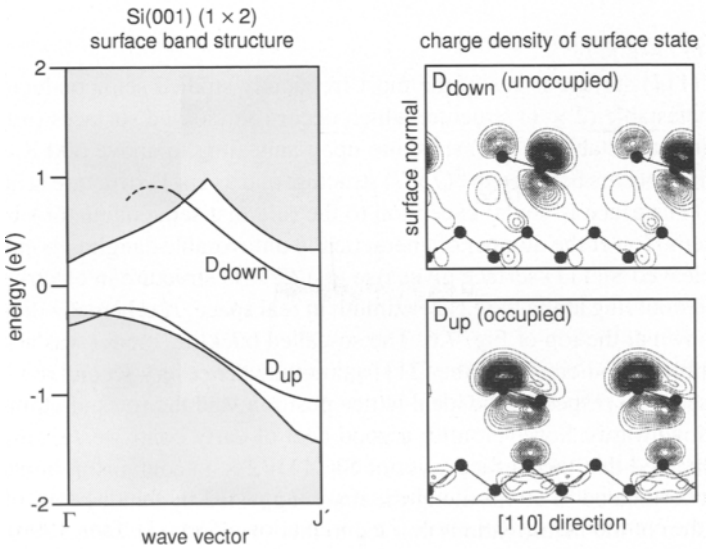


(b)

Fig. 7.5. (a) Schematic representation of the emission from bulk and surface atom core levels in photoemission from Si(100)-(2 × 1), according to an initial state calculation (top) and a final state calculation (center), compared to the experiment shown in Fig. 7.4. The black bar denotes the bulk Si 2p line, whereas the gray, hatched, and white bars correspond to emission from up-, down-, and second layer atoms. After Pehlke and Scheffler (1993). (b) Surface state band structure showing the up-atom and down-atom branches, the latter being unoccupied. The charge density of the two states is shown on the right. After Pehlke and Scheffler (1993), with permission.

© 1993 American Physical Society.

of lines in the Si 2p spectrum in terms of initial state and final state calculations, and a comparison with experiment (bottom diagram). Whereas the initial state theory gives a core level shift which is symmetric with respect to the bulk line (black) as expected from charge transfer away from the down-atom (hatched bars) to the up-atom (grey bars), an inclusion of final state screening causes both lines to lie at lower binding energy than the bulk line. The results can be understood within a simple physical picture (Schönhammer and Gunnarsson, 1977). As described above, there is an occupied surface band $D_{up}$ related to the up-atom, while the surface band for which the wave functions are localized at the down atoms is empty; Fig. 7.5b sketches this part of the surface band structure along the $\bar{\Gamma}$–$\bar{J}'$ direction with the two bands. Figure 7.5c shows a plot of charge distribution around the up- and down-atom. If a core hole is created in the down-atom, the induced potential pulls down the unoccupied dangling bond state, which then becomes occupied by electrons from the Fermi level. Since the states involved are highly localized, as shown by the diagram in Fig. 7.5b, this leads to a very efficient screening. A similar process cannot occur at the down-atom since its dangling bond surface state band is already occupied, leading to reduced screening. This explains the observed asymmetry in the shift from up-atom and down-atom lines. The results of the calculations including the final state effects are in very good quantitative agreement for Si(100) as shown schematically in Fig. 7.5a.

### *7.2.2. Si(111)*

#### *7.2.2.1. Si(111)-(2 × 1)*

The silicon (111) surface is easily the most frequently studied semiconductor surface. It exhibits a metastable (2 × 1) structure which occurs on cleaved surfaces (reference), and transforms into the stable (7 × 7) structure upon annealing to above 600 K. A reversible phase transition occurs between the (7 × 7) structure and a (1 × 1) structure at about 1130 K.

The Si(111) surface is not an exception to the rule that semiconductor surfaces reconstruct in order to lower the number of energetically unfavorable dangling bonds. The structure of the cleaved Si(111) surface gives rise to a (2 × 1) structure in electron diffraction, with a period doubling along the $[\bar{2}11]$ azimuth in real space. A schematic diagram for this surface is shown at the top of Fig. 7.6. The so-called buckling model was assumed to explain the double periodicity along the $[\bar{2}11]$ azimuth, where every second row of surface Si atoms is raised with respect to the ideal lattice position, and the rows of atoms in between are shifted downwards; however, after a good deal of early controversy, universal agreement was obtained that the surface layer of Si(111)-(2 × 1) contains $\pi$-bonded chains of locally $sp^2$-coordinated Si atoms along the lines suggested by Pandey (1981). For a thorough discussion of the investigations that led to this structure, see Mönch (1995). The $sp^2$ chain is a recurring motif in the surface structure of tetrahedrally coordinated semiconductors, and reflects the tendency of normally tetravalent, fourfold coordinated Si atoms to satisfy their fourfold valence in a threefold coordination, which can be understood from basic chemical principles as explained by Duke (1996).

The principal means of studying the electronic structure of Si(111)-(2 × 1) is again angle-resolved photoelectron spectroscopy and inverse photoemission, and as in the case of Si(100) the occurrence of equivalent domains leads to a superposition of features from three directions of the surface Brillouin zone in valence level spectroscopy. By exerting the

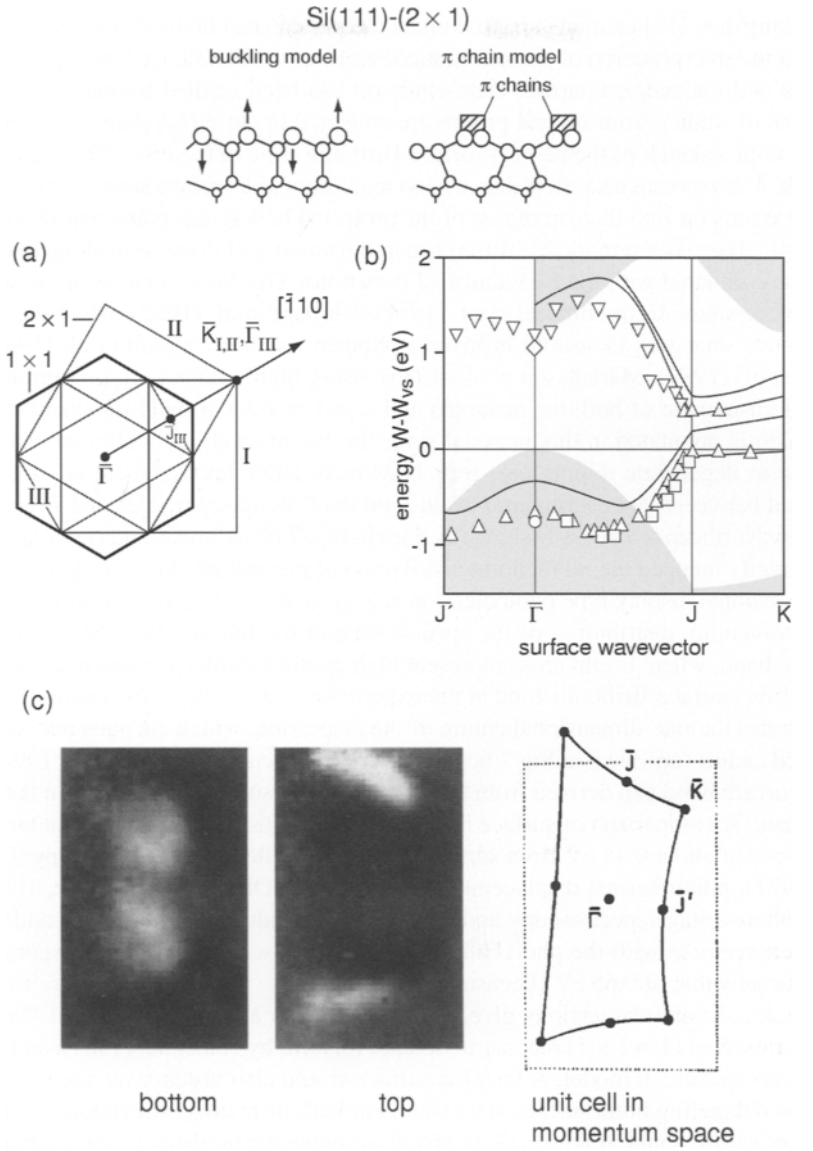


Fig. 7.6. (a) Geometry of the surface Brillouin zone of Si(111)-(2 × 1). (b) Energy dispersion of occupied and empty dangling bond surface states on cleaved Si(111)-(2 × 1) surfaces obtained by angle-resolved ultraviolet and inverse photoemission (after Mönch, 1995). Circles are data from Himpsel et al. (1981), squares from Uhrberg (1982), bottom triangles from Mårtensson et al. (1985), diamonds from Straub et al. (1985a), top triangles from Perfetti et al. (1987). Lines give the calculated dispersions by Northrup and Cohen (1982) (dashed) and Northrup et al. (1991) (full lines). Shaded areas give the projected bulk band region. (c) Emission intensity of the surface state band in Si(111)-(2 × 1) in momentum space of the bottom and the top of the band, recorded using a 2D display electron energy analyser. This set of data gives a graphic representation of the dispersion along the chains (up-down direction). From Himpsel (1994), with permission.

cleave along the [$\bar{2}11$] azimuth, single domain cleaves can be obtained, and this has greatly helped in the interpretation of surface-induced features in the valence level spectrum. The occupied and unoccupied surface state emission has been studied by many groups, and the results of studies from several groups are collected in the $E(k_{\parallel})$ diagram of Fig. 7.6b, together with a sketch of the $(2 \times 1)$ surface Brillouin zone in the inset. The identification of a peak in the spectra near the valence band maximum as a surface state is quite obvious, since it extends far into the gap region of the projected bulk bands (shown as shaded area) along $\bar{\Gamma}$–$\bar{J}$ . There is a remarkable difference in the amount of dispersion along the $\bar{\Gamma}$–$\bar{J}$ direction as compared with the $\bar{\Gamma}$–$\bar{J}'$ and $\bar{\Gamma}$–$\bar{J}$ directions. The determination of the occupied surface state stems from Himpsel et al. (1981), Uhrberg et al. (1982), while the unoccupied surface state was measured in inverse photoemission by Straub et al. (1985a) and Perfetti et al. (1987). Mårtensson et al. (1985), using highly doped n-type samples, measured the dispersion of both the occupied and a part of the normally unoccupied surface state which is populated in this material since the Fermi level lies within the conduction band due to degenerate doping (see refs. in Mönch, 1995, book). There is good overall agreement between the experimental results and the GW quasiparticle band structure calculated by Northrup et al. (1991) shown as lines in Fig. 7.6b. Himpsel and coworkers (1981, 1994) directly mapped the momentum distribution of the surface state through the use of a two-dimensional display type photoelectron energy analyzer. Figure 7.6c shows an image of the momentum distribution of the surface state at the top and the bottom of the surface state band, where bright areas represent high photoelectron emission intensity, with a sketch of the surface Brillouin zone in the experimental geometry. This result graphically demonstrates the one-dimensional nature of the dispersion, which changes only along the $\pi$-bonded chains (up-down in Fig 7.6c) and not perpendicular to it (Himpsel, 1994).

The surface band gap derived from the calculations is somewhat larger than the experimental data. A comparison of surface band gaps derived from several different techniques gives values of about 0.45 eV from surface differential reflectance spectroscopy (Chiarotti et al., 1971), photothermal displacement spectroscopy (Olmstead and Amer, 1984), and surface photovoltage spectroscopy and surface photoconductance (Assmann and Mönch, 1980) in agreement with the photoemission data, while scanning tunneling spectroscopy gives a larger value of 0.65 eV (Feenstra, 1991).

The surface band dispersions give strong arguments against the original "buckling" model for the Si(111)-$(2 \times 1)$ reconstruction put forward by Haneman (1961), and in favor of the $\pi$-bonded chain model. A buckled surface would also produce an occupied and an unoccupied dangling bond surface state band, but with little dispersion along the $\bar{\Gamma}$–$\bar{J}$ line of the surface Brillouin zone, since the dangling bonds remain at a fairly large distance, contrary to what is seen along the $\bar{\Gamma}$–$\bar{J}$ azimuth. The $\pi$-bonded chain model put forward by Pandey (1981, 1982), shown in Fig. 3.24 of Chapter 3, which explains the surface geometry of the $(2 \times 1)$ reconstruction in terms of five- and seven-membered rings, is able to fully account for the experimental surface band structure; it also explains the semiconducting character of the surface. In this model, bond breaking in the second layer is required, but the resulting zigzag pattern allows the dangling $p_z$ bonds of the topmost layer to form one-dimensional $\pi$ bonds such as in a one-dimensional organic molecule. Later structure determinations by LEED (Batra et al., 1985) and ion scattering (Smit et al., 1985a) have shown that while the basic features of the $\pi$-bonded chain model can be reconciled with

the data, only a considerable buckling of the outer chain gives good agreement with the data. This topic is extensively discussed in Mönch (1995) and Lüth (1995). The $\pi$-bonded chain model also explains the STM data of Feenstra et al. (1987).

In the $\pi$-bonded chain model all backbonds become fully saturated, and the nearest neighbor dangling bonds at the surface atoms exhibit a strong $\pi$ interaction yielding strongly dispersive bonding $\pi$ and antibonding $\pi^*$ dangling bond bands, as shown in the data and calculated dispersions of Fig. 7.6. There have been attempts to identify, beyond the dangling bond states, back-bond surface states, but this identification seems questionable (Uhrberg and Hansson, 1991).

The photoemission data by Mårtensson et al. (1985) for degenerately n-doped Si(111), where the normally unoccupied surface state is partly occupied, show that the position of the antibonding surface state is at the Fermi level, suggesting that this state is responsible for Fermi level pinning at the surface of such samples. The observation of the occupied and unoccupied surface states in one spectrum also permits the determination of the surface band gap as about 0.45 eV, in good agreement with optical absorption measurements cited above. The corresponding $\pi$–$\pi^*$ optical transitions are also clearly observed in high resolution electron energy loss (Matz et al., 1983) and infrared absorption experiments (Chiaradia et al., 1984). The latter provide a particularly convincing argument in favor of the $\pi$-bonded chain model since there is a strong polarization dependence of the optical transition matrix element, where light polarized normal to the chains cannot excite the transition, whereas light polarized in parallel can; this result cannot be explained by the buckling model.

*7.2.2.2. The Si(111)-(7 × 7) reconstruction*

Ever since the (7 × 7) surface reconstruction of Si(111), which is obtained by annealing a clean Si(111) surface, was first observed by Schlier and Farnsworth in 1959, it has been a challenge for the understanding of surface reconstructions. Many different models have been proposed over the years, but only with the aid of scanning tunneling microscopy (Binnig et al., 1983), ion scattering (Bennet et al., 1983) and transmission electron diffraction (Takayanagi et al., 1985) a model was formulated in terms of dimers (D), adatoms (A), and a stacking fault (S) as structural building blocks. This so-called dimer-adatom-stacking fault or DAS model, which agrees with all experimental results, has so far stood the test of time. It has 12 adatoms, 6 so-called rest-atoms, 9 dimers, and one corner hole per surface unit cell, and there is a stacking fault in one half of the unit cell (see Fig. 2.26 in Chapter 2). The model is also in quantitative agreement with a LEED analysis (Tong et al., 1988) and with two independent density functional calculations (Stich et al., 1992; Brommer et al., 1992). The driving force of surface reconstructions, i.e., the reduction of dangling bonds, is also making itself felt here. A crucial role is played by the adatom–rest-atom mechanism (Meade and Vanderbilt, 1989). The number of dangling bonds is reduced by adatoms, each of which saturates three broken bonds, but introduces only one new dangling bond. However, it is not energetically favorable to saturate all surface dangling bonds by adatoms, i.e., in a $\sqrt{3} \times \sqrt{3}$ structure, because of the distortion of bond lengths and angles. Thus another important aspect of this reconstruction, the presence of rest-atoms, comes into play. Charge is transferred from the adatom to the rest-atom, influencing the surface band structure and the number and energy of surface core levels. Dangling bonds reside on the adatoms, rest-

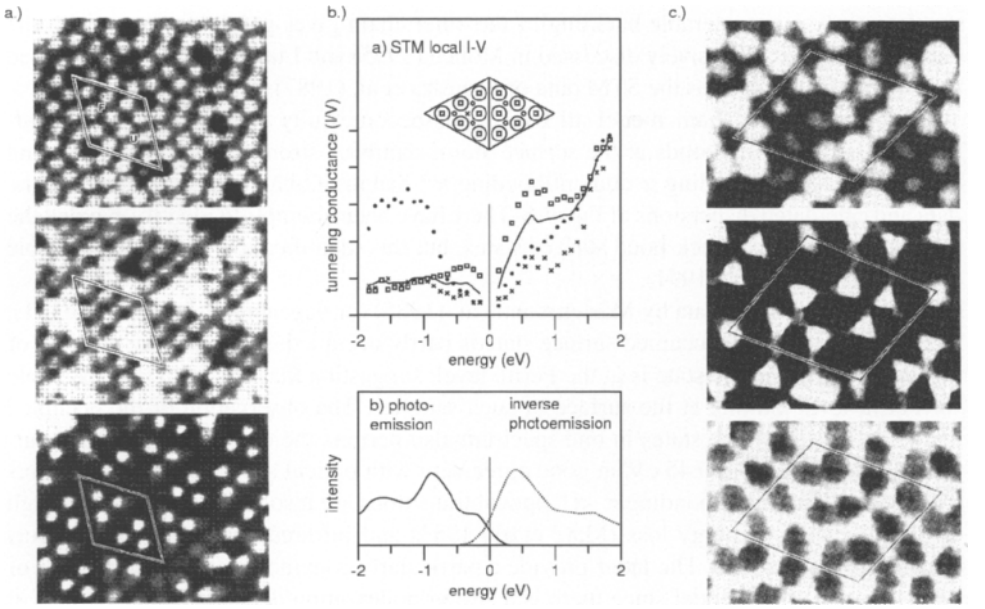


Fig. 7.7. (a) STM topograph of the Si(111)-(7 × 7) surface, acquired at a bias of +2 V (top). The center and bottom panels show a current image recorded at +1.45 and −1.45 V. (b) Constant-distance conductivity-bias spectra for Si(111)-(7 × 7) averaged over one unit cell (solid line) and at selected locations in the unit cell. From Hamers et al. (1986). The lower diagram shows the corresponding photoemission (solid line, Himpsel and Fauster, 1984) and inverse photoemission (dashed line, Fauster and Himpsel, 1983) spectra. (c) Difference STM images from Si(111)-(7 × 7) (Hamers et al., 1986) for an average bias of −0.35 V (top), −0.8 V (middle) and −1.7 V (bottom), showing the contributions from the adatoms, rest-atoms and backbond states, respectively. From Hamers et al. (1986), with permission. © 1986 American Physical Society.

atoms and the corner hole atom, thus 19 dangling bonds in all compared with 49 in the (1 × 1) unit cell. The energy gain by removing dangling bonds is also offset by the energy costs of a stacking fault and corner holes. The fact that not all dangling bonds are saturated is also reflected in the fact that the (7 × 7) surface is metallic (Demuth et al., 1983).

The determination of the electronic structure of a surface reconstruction as intriguing as Si(111)-(7 × 7) has obviously been the topic of many investigations, notably photoelectron spectroscopy and inverse photoemission (Mönch, 1995). However, in view of the complexity of this reconstruction, and the small surface Brillouin zone, an assignment of surface states in terms of the structural building blocks is difficult. An breakthrough in the assignment of electronic states to the building blocks of the reconstruction was achieved by Hamers et al. (1986) through bias-dependent scanning tunneling microscopy and spectroscopy results, which gave a direct assignment of the different occupied and unoccupied levels in terms of the atoms on which the corresponding states are located. The top panel of Fig. 7.7a shows a constant current STM image of the (7 × 7) surface at +2.0 V (i.e., tunneling into unoccupied surface states), showing 12 protrusions due to the adatoms. The center and bottom panel shows a simultaneously acquired image recorded at +1.45 and −1.45 V, respectively. The sampling of unoccupied surface states at +1.45 V reveals a

specific difference between the faulted half (top part of the unit cell in the figure) and the unfaulted half, the conductance being higher in the former. Tunneling out of occupied states at $-1.45$ V shows six protrusions, assigned to the rest-atoms. By measuring the tunnel current at different bias during scanning, with the feedback loop of the STM disabled, $I/V$ spectra can be recorded, which can be translated into identification of surface states being related to specific atom sites. This is shown in Fig. 7.7b, where tunneling spectra at different locations of the $(7 \times 7)$ unit cell are indicated by the different symbols. On the basis of these data, the steep onset of conductance beyond $-0.8$ eV is found to stem from the rest-atoms, while the increase just below $E_F$ and at about 0.5 eV occurs above the twelve adatoms; these states on the adatoms are also strong in the unoccupied region. They straddle the Fermi level and thus are responsible for the metallic nature of the $(7 \times 7)$ surface. These features are directly related to peaks seen in photoelectron spectroscopy and inverse photoemission (Himpsel and Fauster, 1984) (center part of Fig. 7.7b). A comparison of the laterally averaged $I/V$ characteristics measured by STM is shown in the bottom panel, demonstrating the similarity of features in scanning tunneling spectroscopy and the photoemission technique.

These features become even clearer when considering the difference between images recorded at different bias voltages (Fig. 7.7c, from Hamers et al., 1986). In the top panel, a difference image centered at $-0.35$ V reveals the dangling bond states located at the adatoms and shows that each of the four types of adatoms (faulted half, unfaulted half, center and corner hole adatoms) have a slightly different density of states on them. The center panel ($-0.8$ eV) shows the rest-atoms located between the adatoms and emission from the adatom at the bottom of the "corner hole". The observation of dangling bond states located on the rest-atoms, with the mirror symmetry across the lines connecting both sets of corner holes, implies reflection symmetry also in the layer beneath the adatoms and directly indicates the presence of a stacking fault in one half of the unit cell. The third image ($-1.7$ V) shows a network pattern surrounding the adatoms where the Si–Si back bonds are expected and also a diffuse circular path at the corner hole where additional back bonds are exposed to the vacuum. This spatial distribution shows that the state observed at $-1.75$ eV in photoemission is a back bond state. These data are a superb demonstration of the capabilities of the scanning tunneling microscope to reveal the location of surface states on specific atom sites.

The surface Brillouin zone of the $(7 \times 7)$ structure has a diameter that is only 1/7th of the nonreconstructed $(1 \times 1)$ surface, such that one would expect the dangling bond band to be folded back seven times into the $(7 \times 7)$ surface Brillouin zone (SBZ). This process yields a manifold of bands that lie close to each other, producing a continuous distribution within the bulk band gap, i.e., a metallic character of the surface. Angle-resolved spectra by Mårtensson et al. (1987) showed three surface-related structures, the dispersion of which were followed in high resolution photoemission experiments at low sample temperature (Fig. 7.8a, Uhrberg et al., 1998). The $S_1$ surface state peak is located less than 0.2 eV below the Fermi level and the high energy cutoff is very similar to a Fermi edge in metals. This metallic character of the $(7 \times 7)$ surface has also been found in electron energy loss experiments where a strong broadening of the elastic peak is observed that results from a continuum of transitions between states straddling the Fermi level (Backes and Ibach, 1981). The state $S_2$ is located within the projected bulk band gap over the most part of the

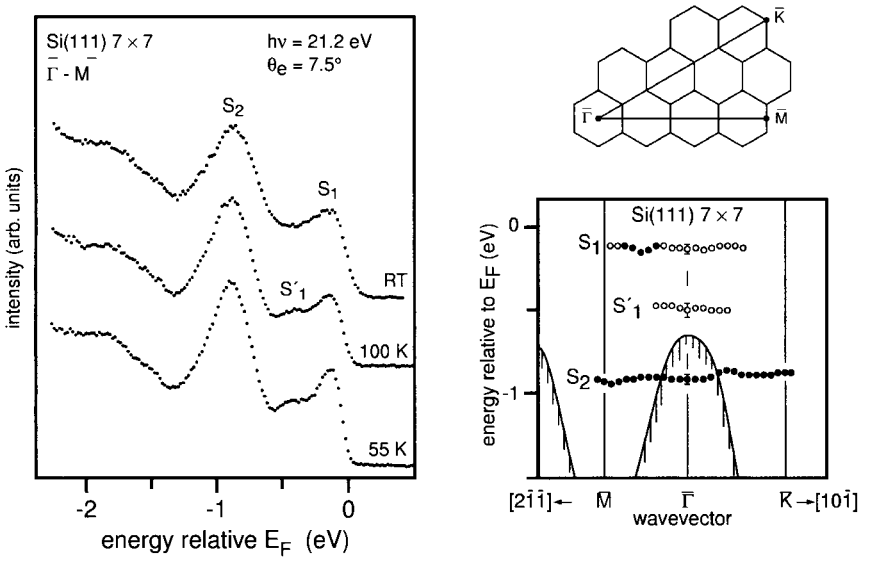


Fig. 7.8. (a) Angle-resolved photoemission spectra from Si(111)(7 × 7) for angles along the $\bar{\Gamma}$–$\bar{M}$ azimuth, and (b) dispersion of surface states for Si(111)-(7 × 7) in two directions of the surface Brillouin zone. From Uhrberg et al. (1998), with permission. © 1998 American Physical Society.

SBZ (Fig. 7.8b). This feature is assigned in accordance with the STM data of Hamers et al. (1986) to the dangling bonds on the rest-atoms, which indeed are quite far apart and from which no dispersing state is expected. The additional state observed between $S_1$ and $S_2$, named $S_1'$, is attributed to the adatom states near the corner holes by comparison with theoretical calculations of Fujita et al. (1991).

Northrup (1986) has performed calculations for (111) surfaces with a $\sqrt{3} \times \sqrt{3}$ and (2 × 2) surface periodicity, which contain the basic building blocks of the (7 × 7) DAS surface; for example, the (2 × 2) model has a threefold coordinated adatom and one rest-atom per unit cell. For this geometry, three surface states are found, all with appreciable s-$p_z$ dangling bond character are found. Their assignment to adatom and rest-atom states is in excellent agreement with the STM conclusions discussed above, and the energy positions and dispersions compare well with the results shown in Fig. 7.8b.

In the case of Si(100), the shape of the Si 2p core level emission was found to reflect the electronic structure of the surface; thus one might ask to what extent the Si 2p core level line shape of the much more complex Si(111)-(7 × 7) surface can be related to the charge distribution among the surface atoms. A set of bulk- and surface-sensitive spectra from Si(111) is shown in Fig. 7.9a (Paggel et al., 1994). The bottom, bulk-sensitive spectrum exhibits two well separated main lines from the bulk, with some extra emission in the valley between them. Going to more surface-sensitive conditions it is seen that surface emission dominates the spectrum. This is probably not surprising since the reconstruction affects at least two complete layers of the surface. Extra peaks and inflections such as

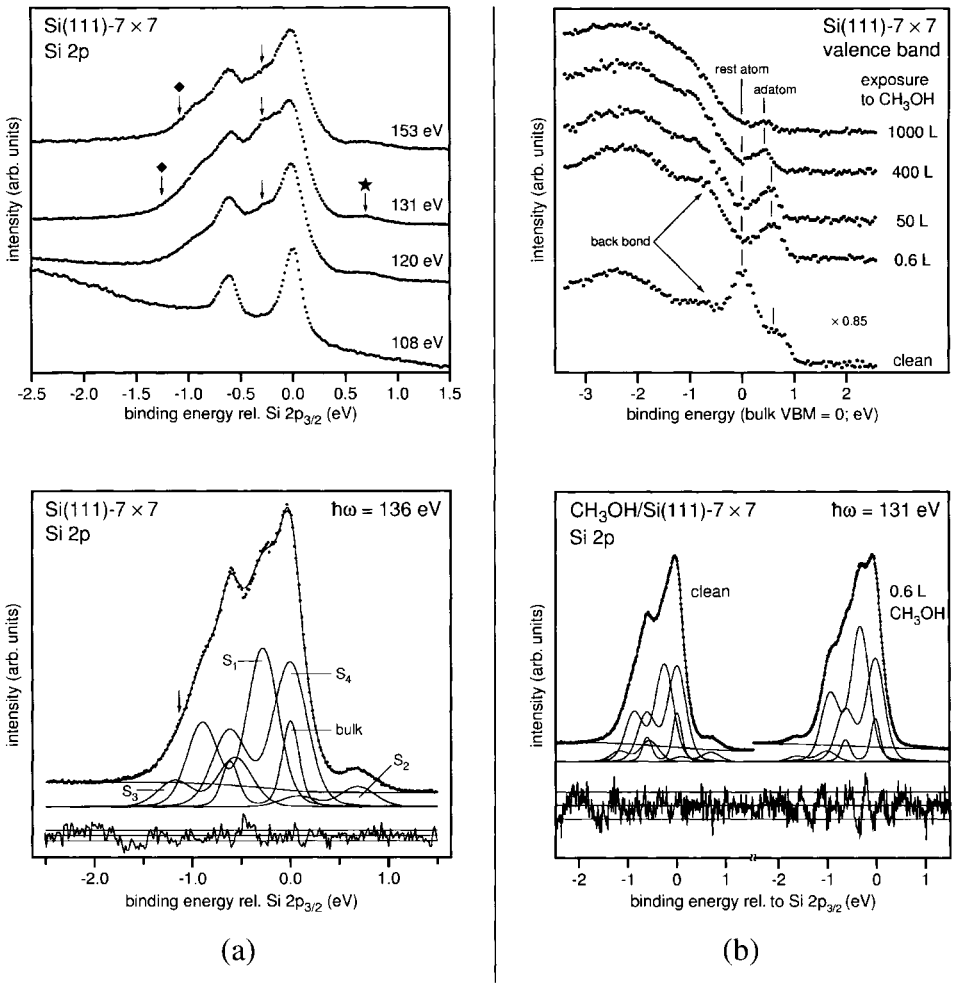


Fig. 7.9. (a) Top panel: Si 2p core level spectra from Si(111)-(7 × 7), demonstrating the increasing surface sensitivity for higher photon energies. Bottom: line shape analysis of emission from Si(111)-(7 × 7) in terms of one bulk line and four surface-induced lines (Paggel et al., 1994 © American Physical Society). (b) Top: valence level spectra from Si(111)-(7 × 7) for the clean surface and after exposure to different doses of methanol, indicating the preferential removal of the surface state due to the rest atoms. Bottom: the same for the Si 2p core level, showing that the $S_2$ component at low binding energy is preferentially extinguished by methanol adsorption. From Piancastelli et al. (1997), with permission. © 1997 American Physical Society.

those marked by the star and diamond indicate additional components. The lower part of Fig. 7.9a shows a line shape analysis in terms of one bulk-derived and four surface-derived lines which, as seen from the residual at the bottom, give a good description of the line shape; in fact, this model describes the line shape over a photon energy range of about 60 eV, form the most bulk-sensitive to the most surface-sensitive spectra. From this model,

an assignment of the different lines in terms of adatoms ($S_3$), rest-atoms ($S_2$), and the atoms bonded to rest-atoms and adatoms ($S_1$); the atoms of the first bulk-like layer and the dimer atoms are assigned to $S_4$. This assignment was arrived from the relative intensities of the lines, compared to the number of atoms of the respective species, taking into account that the intensities exhibit a considerable variation with kinetic energy, probably due to diffraction effects. Several models have been put forward to describe the difficult region around the bulk lines (Paggel et al., 1994; Karlsson et al., 1994; LeLay et al., 1994) and it is fair to say that modeling this region involves a certain amount of ambiguity. However, the controversial point regarding the assignment of the peak $S_2$ at low binding energy can be clarified. Here, Carlisle et al. (1993) put forward an assignment in terms of adatoms, in contrast to what is expected from an initial state charge transfer argument. This would predict that emission from the adatoms, which transfer charge to the rest-atoms, occurs at the highest binding energy, while the line due to the rest-atoms, which receive this charge, occurs at the lowest binding energy. The assignment by Paggel et al. (1994), Karlsson et al. (1994) and LeLay et al. (1994), based on high resolution studies of the lines to these two species, conforms with expectations from the straightforward initial state picture. This is thought to apply here, in contrast to what was observed in the case of Si(100). Final state effects depend on the availability of empty states above $E_F$, and the only species which have such states associated to them are the adatoms; thus line energies from the other species will not be affected by final state effects.

There is a rather more direct way of testing the assignment of core level line components to the different building blocks of the (7 × 7) structure. In a recent core and valence level photoemission study of Si(111)-(7 × 7) (Piancastelli et al., 1997) it was found that methanol adsorption causes (a) the $S_2$ level to disappear, and (b) the surface state emission assigned to the rest-atoms on the basis of bias-dependent STM images and scanning tunneling spectroscopy (STS) above to be extinguished. These two spectra are shown in Fig. 7.9b. This simultaneous disappearance of the line in the valence region and the removal of the $S_2$ level is interpreted in terms of a site-selective adsorption bond between the methoxy radical on the rest-atoms, whereas the adatoms states are largely unaffected in the early stages of this chemisorption process. It demonstrates that $S_2$ is caused by the rest-atoms, which receive charge from the adatoms in the (7 × 7) reconstruction.

### *7.2.3. Ge(100)*

Among the elemental semiconductor surfaces, Ge has played a less important role in surface studies, although there has been a renewed interest recently, possibly brought about by the attempts to use Ge–Si alloys or superstructures in semiconductor devices. Again, we address the Ge(100) electronic structure first, with an emphasis on the similarities and differences between Si and Ge. The Ge(100) surface also exhibits a (2 × 1) surface reconstruction in LEED (Schlier and Farnsworth, 1959), and in analogy to the data discussed above, this is attributed to dimer formation in order to reduce the number of dangling bonds. These dimers are also thought to be asymmetric, as explained by Pollmann and Krüger in Chapter 2. Taking this analogy further, we would then expect to see surface state bands from the down- and up-atom on the dimers, with the latter being occupied and accessible in photoemission. A surface state near $E_F$, i.e., above the valence band maximum was

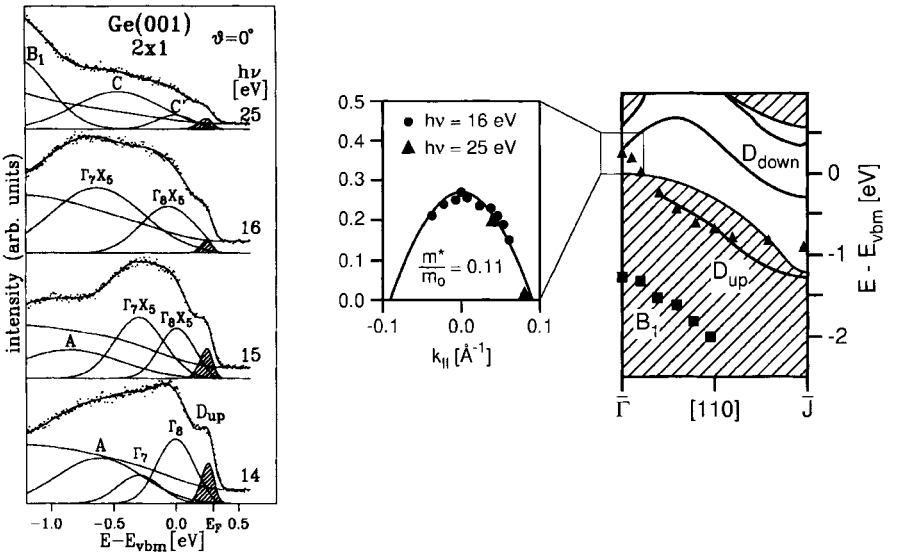


Fig. 7.10. Left: valence level spectra from Ge(100)-(2 × 1) in normal emission for different photon energies, showing the contributions from the bulk bands and the dangling bond surface state $D_{up}$ assigned to the up-atoms. Right: dispersion of the dangling bond surface state near the center of the surface Brillouin zone (left) and along the $\bar{\Gamma}$–$\bar{J}$ direction. From Kipp et al. (1995), with permission.

indeed observed by Kevan and Stoffel (1984). This surface emission was attributed to defects in the low temperature c(4 × 2) reconstruction, a view which was later challenged by Johansson et al. (1989) as mentioned above, in terms of an explanation as a normally empty surface state band which is partly filled by electrons from the conduction band in n-type material. Recent spectra by Kipp et al. (1995) on nominally undoped Ge(100), recorded in very high angular and energy resolution, are in disagreement with both the above interpretations. Rather, they show that the region near the valence band maximum can be interpreted in terms of bulk and surface emission, with the latter, derived from the $D_{up}$ surface state giving rise to a sharp peak at the Fermi energy. Their data are shown in Fig. 7.10. The surface state, which is identified from an absence of dispersion with the normal component of the wave vector, is seen to disperse strongly downwards within the first 0.1 $Å^{-1}$ away from the surface Brillouin zone center. The dispersion with $\mathbf{k}_{\|}$ has a parabolic shape that can be modeled by an effective mass of $m^* = 0.11 m_{el}$ and at the zone boundary is located about 1 eV below the VBM. Such dispersion is incompatible with either defect states or emission from a normally unoccupied surface state band. One remaining problem is the shape of the band dispersion around $\bar{\Gamma}$. Density-functional calculations by Krüger et al. (1986) predict that this surface state has resonance character and that it is located well inside the valence band at the point, whereas Kipp et al. (1995) identify it as a proper surface state which gives this surface a metallic character, as seen from the sharp cutoff in the spectra at the surface state emission (Fig. 7.10). This discrepancy, which awaits clarification, demonstrates the need for high angular and energy resolution to distinguish specific states in the photoemission spectra.

### 7.2.4. Ge(111)

The surfaces of the elemental semiconductors exhibit considerable similarities, as we have seen in the case of Si(100) and Ge(100) above. These also pertain to the metastable Si(111)-(2 × 1) and Ge(111)-(2 × 1) surfaces which are prepared by cleaving and only convert into the stable configuration upon annealing. These surfaces share many features and a detailed discussion is not necessary here – the interested reader is referred to accounts such as presented in Mönch (1995). The situation is different for the stable phases of the (111) surfaces; the stable Si(111) structure is the (7 × 7) as discussed at length above, while the stable Ge(111) has a (2 × 8) unit mesh. In both reconstructions a crucial role is played by the adatom–rest-atom mechanism (Meade and Vanderbilt, 1989); about 3/4 of the (1 × 1) surface dangling bonds are saturated by "adatoms", while extra electrons are mainly captured away by the remaining 1/4 of surface atoms named "rest-atoms". In the simplest adatom–rest-atom structure, with a (2 × 2) or c(2 × 4) unit cell, charge transfer between the adatoms and the rest-atoms leads to filled and empty surface state bands, all partly filled dangling bonds are eliminated and the surface is stable. The situation is somewhat more complex for the Si(111) surface which has additional building blocks such as the surface dimers and the corner hole. The Ge(111)-(2 × 8) surface is conceptually much simpler since, as shown in the schematic diagram in the top of Fig. 7.11, it consists of alternating (2 × 2) and c(4 × 2) subunits which contain adatoms and rest-atoms. The fact that this surface is less complex than the Si(111)-(7 × 7) surface has made it amenable to *ab initio* calculations of the surface structure and its electronic properties (Takeuchi et al.,

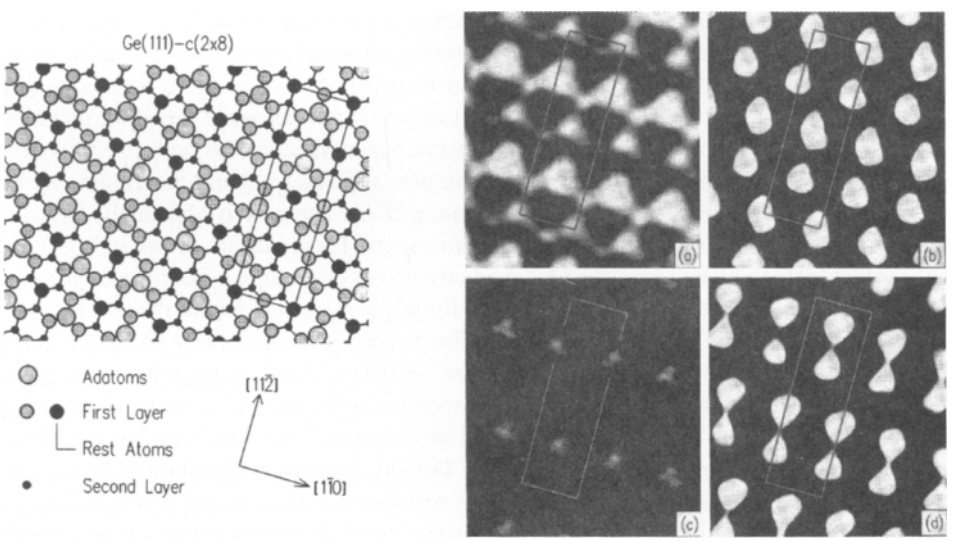


Fig. 7.11. Left: schematic drawing of the Ge(111)-(2 × 8) surface reconstruction, with adatoms indicated by the large shaded circles, and rest-atoms by the smaller circles. Right: STM images recorded at a bias of −0.7, 1.2, −0.6, and +1.5 V, respectively, showing the rest-atom emission with varying intensity (a)–(c) and the adatoms (d). From Hirschorn et al. (1992). © American Physical Society.

1992) and a comparison with angle-resolved photoemission and scanning tunnelling spectroscopy data. By performing *ab initio* molecular dynamics calculations (with adatoms) and allowing the five topmost Ge layers to move, the authors arrived at a structure which has a slight asymmetry in the surface unit cell, explaining the combination of the $(2 \times 2)$ and $c(2 \times 4)$ structural subunits. This is reflected in the STM images shown on the right-hand side of Fig. 7.11 (Hirschorn et al., 1992). The image in Fig. 7.11a shows emission from rest-atoms at a bias voltage of $-0.7$ V, but it is obvious that the rest-atoms in the unit cell are not equally bright, suggesting a significant asymmetry between the neighbouring rest-atoms along the $[11\bar{2}]$ direction; additional maxima correspond to the locations of the adatom dangling bonds. Figure 7.11b shows an image taken at $-1.2$ V bias, where the rest-atoms (shown as black disks in the schematic drawing) dominate the image. In Fig. 7.11c a constant background has been subtracted from Fig. 7.11a, such that half of the rest-atoms are no longer visible, demonstrating that the two neighbouring rest-atoms are not at the same apparent height. Finally, the adatoms dominate the image at a bias of $-1.5$ V in Fig. 7.11d. This set of data gives an impressive assignment of the surface states to the atoms in the surface reconstruction, and clearly show the asymmetry which leads to the $c(2 \times 8)$ unit cell. While the stable Si(111) and Ge(111) surfaces share common building blocks, details in the geometric arrangement result in qualitative differences of the surface electronic structure: Si(111)-$(7 \times 7)$ is metallic (see above), while Ge(111)-$(2 \times 8)$ is semiconducting. This conclusion is drawn from a comparison of angle-resolved photoemission (Aarts et al., 1988), inverse photoemission (Himpsel, 1990), and scanning tunnelling spectroscopy data (Feenstra and Slavin, 1991) with the results of the calculations (Takeuchi et al., 1992).

### *7.2.5. Diamond surfaces*

Studies of diamond surfaces have been motivated by the unique properties of this material, such as high hole mobilities, high heat conductivity, and the large band gap (5.5 eV), all of which hold promise for interesting technological applications. This material has recently received renewed interest since it is now possible to produce large area thin films by chemical vapour deposition techniques. Diamond is also interesting from a fundamental point of view in the discussion of the origin and nature of surface reconstructions, for example, in the (100) surface. As discussed in more detail in Section 2.4.2 of Chapter 2, the idea that the asymmetric reconstruction of the (100) surfaces of the elemental semiconductors can be understood in terms of a Jahn–Teller splitting of a symmetry degenerate ground state is questionable. There is apparently only an accidental degeneracy in the dimer states, and thus the symmetric dimers of the (100) surfaces are not necessarily unstable with respect to symmetry breaking by dimer buckling. Thus while total energy calculations show the presence of asymmetric dimers on Si(100) and Ge(100), for the C(100) surface already the symmetric dimer structure is semiconducting. The energy gain derived from asymmetric dimer formation is calculated to be near zero for diamond and rises to about 0.6 eV through group IV to $\alpha$-Sn. This view is supported by a comparison of experimental and calculated surface band structures as discussed in Chapter 2. The filled $\pi$ and empty $\pi^*$ bands of C(100) are separated by about 1.2 eV, whereas they overlap in Si(100) and Ge(100) for the symmetric dimer model. The corresponding photoelectron spectra for an as-prepared and

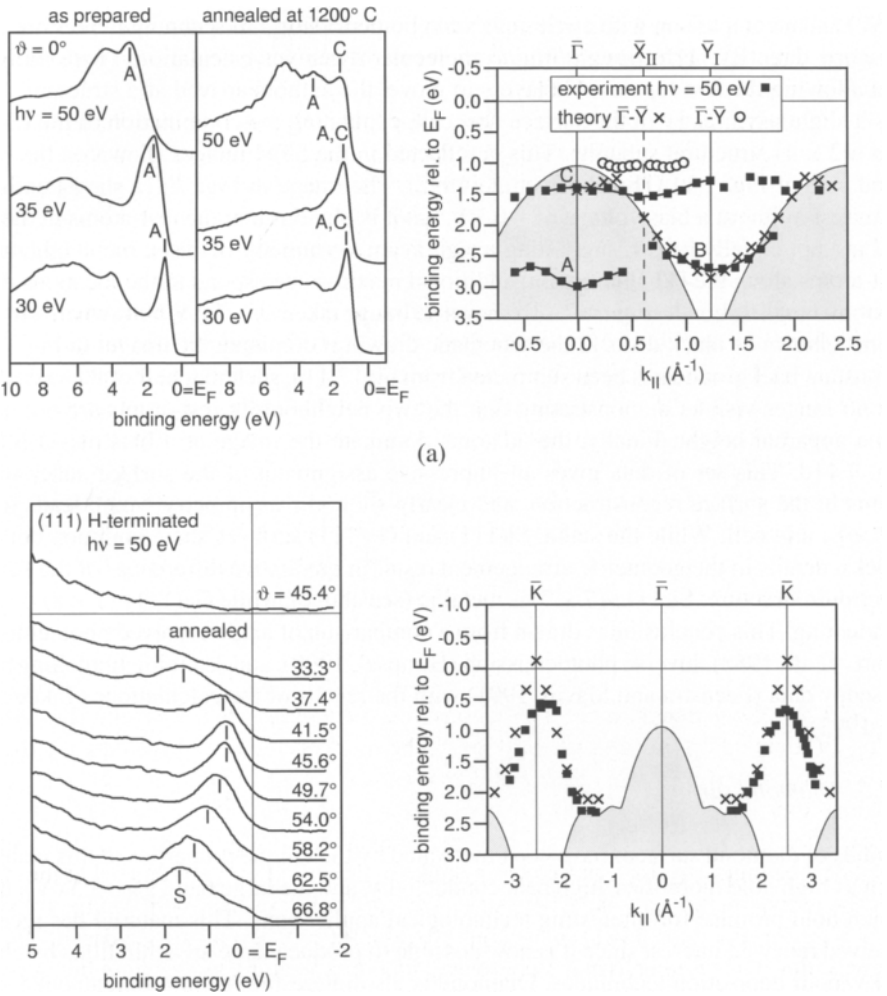


Fig. 7.12. (a) Spectra from an as-prepared (left) and a clean C(100) surface, showing that peak A is due to bulk emission. The dispersion of surface emission is shown in the surface Brillouin zone and compared with a calculation by Furthmüller et al. (1996). (b) Surface state dispersion in C(111) for the clean surface; a spectrum from the hydrogen-terminated surface is shown for comparison in the top. The surface band exhibits about 1.5 eV dispersion near the K point of the surface Brillouin zone. From Graupner et al. (1997). © American Physical Society.

an annealed, i.e., clean diamond (100) surface are shown in the upper portion of Fig. 7.12a. The spectra from the as-prepared surface show a strong peak A, which disperses with the normal component of the electron wave vector, i.e., it is bulk-derived. The other peaks B and C are due to surface states, as evident from a comparison of as-prepared and annealed surfaces. Their dispersion, which is quite different along the symmetry directions, indicates that C is most likely from the domain which has the large distance between dimers, while

peak B exhibits a strong dispersion with the right periodicity to represent dispersion along the short direction. The data are in good agreement with values calculated for symmetric dimers by Furthmüller et al. (1996).

The diamond (111) surface shows the (2 × 1) reconstruction that is observed also in cleaved Si(111) and Ge(111) surface, and there is general agreement that the $\pi$-bonded chain model (Pandey, 1981) explains this structure also. However, this reconstruction is also the stable one – more complex clean surface reconstructions do not seem to exist for C(111). Unfortunately, the problem of overlapping domains occurs here also. Graupner et al. (1997) have measured the dispersion of surface state bands in C(111) along the $\bar{\Gamma}$–$\bar{K}$ direction; see the surface Brillouin zone diagram in Fig. 7.6. The spectra are shown on the left-hand side of Fig. 7.12b, where the top diagram for hydrogen-terminated C(111) demonstrates that the leading peak is surface-derived. The dispersion of this peak is plotted in terms of $E(\mathbf{k}_{\|})$ on the right-hand side of Fig. 7.12b. Again, there are ambiguities in data interpretation because of the overlapping domains, but the strongly dispersing feature in the data is well reproduced by the theory (see Chapter 2, Fig. 2.20) which is based on undimerized, $\pi$-bonded chains. The experimental dispersion remains at least 0.5 eV below $E_F$, i.e., the surface is semiconducting in agreement with EELS experiments by Pepper (1982). Theory also predicts that the surface is semiconducting already in the symmetric dimer structure.

### *7.2.6. α-Sn*

In order to follow trends in reconstructions and the surface state structure through the group IV elemental semiconductors, it would be most desirable to have data for the last semiconductor of this group, i.e., $\alpha$-Sn. Few studies are available, however, because of the problems associated with the preparation of $\alpha$-Sn surfaces. Sn undergoes a phase transition from the semimetallic zincblende $\alpha$-phase to the metallic $\beta$-Sn phase at 13 °C. This largely precludes the preparation of surfaces from bulk single crystal samples, such that thin films must be grown on lattice-matched samples. Well-ordered layers of $\alpha$-Sn can be grown on InSb(100) (Farrow et al., 1981) and CdTe(100) (Höchst and Hernandez-Calderon, 1983) at temperatures much higher than the phase transition temperature, the $\alpha$-phase being probably stabilized by the substrate lattice, and the (2 × 1) symmetry of the surface is observed also here as in all cases of the elemental group IV semiconductors. Theoretical studies of Lu et al. (1998) have shown that the surface dimers are also buckled in this surface with a buckling angle of 21° – the largest among the group IV semiconductors. However, while a photoemission determination of the bulk band structure along the $\bar{\Gamma}$–$\bar{X}$ direction was performed (Middelmann et al., 1987), no experimental $k$-resolved studies of surface bands are available as yet.

## 7.3. Compound semiconductor surfaces

### *7.3.1. The III-V compound semiconductors*

Compound semiconductors form an important class of materials because they possess, unlike the elemental semiconductors silicon and germanium, a direct band gap and can thus

be utilized for optoelectronic applications such as light-emitting diodes, semiconductor lasers and photodetectors. We concentrate first on the compound semiconductors of the groups III and V of the Periodic Table, i.e., compounds consisting of boron, aluminum, gallium, and indium as cations and nitrogen, phosphorus, arsenic, and antimony as anions. Most of these compounds crystallize in the zincblende (sphalerite) lattice, with the notable exception of the group III nitrides AlN, GaN, and InN, for which the wurtzite structure is energetically lower (see, for example, the article by Lambrecht and Segall, 1994, and references therein).

As we have seen in the previous chapter, semiconductor surfaces tend to react to the breaking the directional bonds at the surface, with the formation of "dangling bonds", by reconstructing, such that the surface geometry is changed from the bulk environment and even the periodicity may change. This gives rise to reconstructions of varying complexity, examples of which are described, together with the underlying mechanisms, by Duke (1996) in Volume I of this Handbook. For compound semiconductor surfaces, the reconstruction depends also on the surface stoichiometry, such that the size of the unit cell and the atom locations depend strongly on the cation/anion ratio. This is not a problem in the (110) surface which is non-polar, having the same number of cations and anions in the surface plane. It is also a "natural" study object from a surface science point of view, since it is the cleavage planes of the zincblende lattice, and can thus be prepared by cleaving in vacuum without problems of cleaning or deviation from stoichiometry. We thus take this example to start our discussion of the electronic structure of semiconductor surfaces.

*7.3.1.1. The (110) surface of zincblende compound semiconductors*

The atomic geometry of the (110) surface of zincblende type semiconductors is shown in Fig. 7.13. On the left-hand side the unreconstructed surface is shown; the zigzag chain of bonds between surface anion and cations parallel to the surface is clearly visible. Each surface anion has two bonds to surface cations and one back bond to a second layer cation; an analogous situation applies to the cations. Since the anion dangling bond is lower in energy than the cation dangling bond state (see also the discussion by Pollmann and Krüger in Chapter 2) charge is transferred to lower the total energy. Thus the anion dangling bond state is completely filled, such that the surface, which would be metallic with a half filled anion and cation dangling bond band, becomes semiconducting. Because of the missing charge in the cation, this atom moves inward to arrive at a geometry which is closer to $sp_2$. This process causes a surface relaxation in which the symmetry of the surface is maintained, but the bond angles are changed because of rehybridization.

The surface relaxation, depicted on the right-hand side of Fig. 7.13, is characterized by a tilt of the surface cation-anion bond which leaves the bond lengths unaffected. This surface relaxation, which has been intensely studied in the past, is discussed in detail by Duke (1996). The tilt angle $\omega$ turns out to be very similar for all zincblende-type compound semiconductors studied (Duke, 1996), with a small inward relaxation of the top layer and an outward relaxation of the second layer. Even more generally, the structures of the zincblende (110) surfaces may be regarded for all such semiconductors in that the surface bond lengths scale with the spectroscopic ionicity of the bulk compound (Duke, 1996).

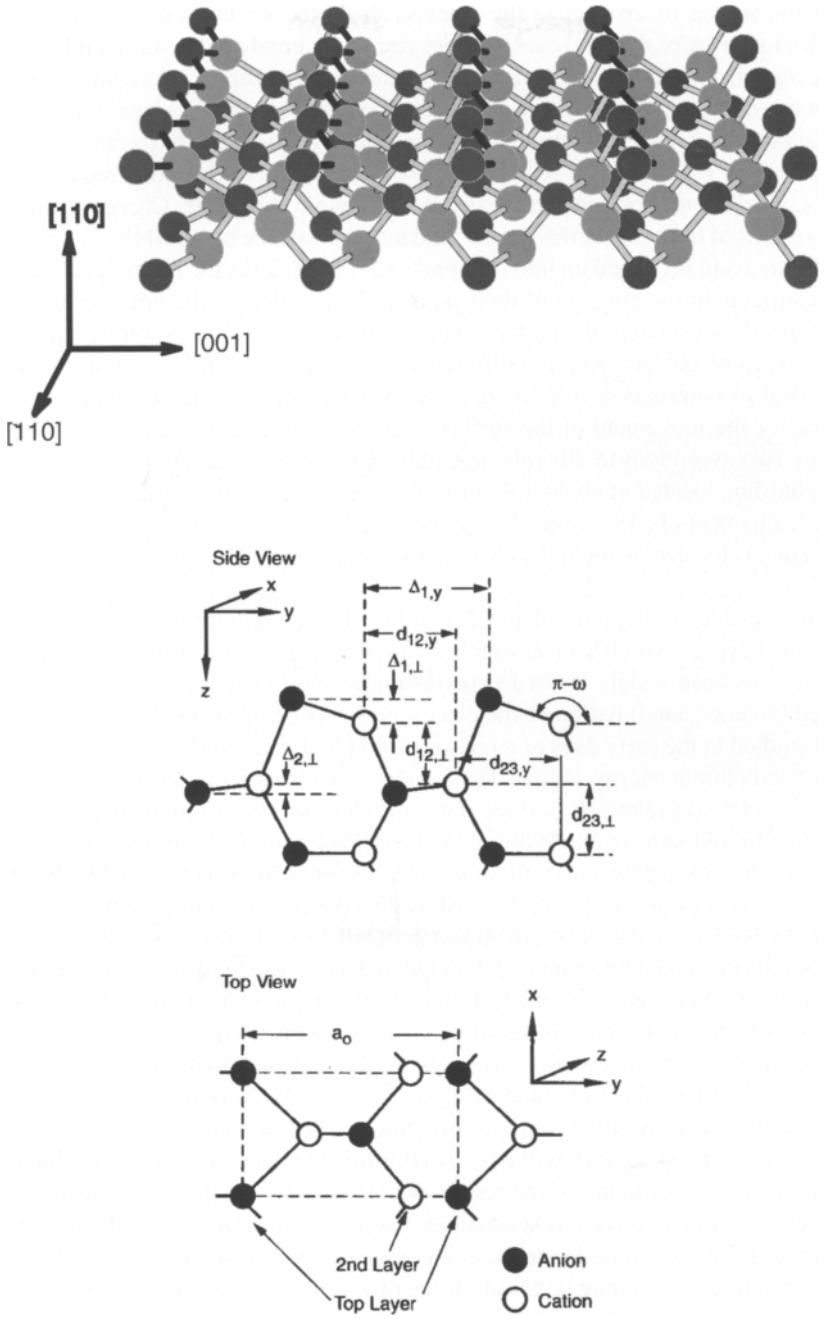


Fig. 7.13. Geometric structure of the (110) surface of zincblende-type III-V semiconductors, with a schematic display of the bond-angle rotation relaxation (after Duke, 1996).

It is interesting to investigate the valence electronic structure of this surface which, through a lowering of the total energy, gives rise to the bond angle rotation relaxation. The fully occupied anion dangling bond surfaces states and the empty cation states are expected to form two-dimensional surface state bands. These have been calculated with an increasingly sophisticated range of methods by many groups; an overview of recent results is given in Chapter 2 by Pollmann and Krüger. For GaAs(110), one of the most frequently studied surfaces, a calculated surface band structure is shown in Fig. 2.52. Charge rearrangement leads to a shift of the anion surface state band into the valence band, while the empty cation surface state band is pushed up into the conduction band. Thus the Fermi level of the clean relaxed surface, in the absence of defects, is at the position of the bulk Fermi level, and no band bending occurs at the surface. This result was arrived at experimentally, through measurements of contact potential differences between n- and p-type samples, only after a great deal of controversy (see the discussion in Mönch, 1995), and provided clear-cut evidence for the movement of the surface state bands out of the fundamental band gap. There are two exceptions to this rule: in GaSb(110), the anion dangling bond surface state is thought to be located at about 150 meV above the valence band maximum (Manzke et al., 1987; Zhang et al., 1993; see also below), while in GaP(110) the unoccupied (cation) surface state is located at about 0.4 eV below the conduction band minimum (Straub et al., 1985a).

Let us consider a mapping of the 2D surface band structure by angle-resolved photoemission from GaAs(110) first, which material, being the most important one for applications, has been widely studied experimentally and theoretically. The features of the occupied (valence band) region of the electronic structure of the GaAs(110) surface were already studied in the early days of angle-resolved photoemission, by Huijser et al. (1978), using a fixed photon energy source. The authors consider their spectrum to be dominated by four sets of peaks related to surface state emission (in contrast to the band structure determination of Williams et al. (1986), which consider them to be dominated by bulk state emission). The origin of some of these peaks has remained obscure, but with hindsight it is clear that the leading peak can be attributed to the anion dangling bond surface state. The data by Huijser et al. (1978) are shown in Fig. 7.14 for energies near the valence band maximum. Its dispersion is compared with the results of a quasiparticle calculation below.

Comparisons between surface electronic structure calculations have frequently been used to distinguish between models of surface reconstruction, as discussed in more detail in the section on silicon surfaces. With the advent of reliable structurally sensitive techniques this aspect has lost some of its significance. What remains important, though, is a comparison with specific electronic structure predictions such as the magnitude of the surface state band gap, and we will return to this topic at the end of this section.

From the above example and the results of calculations (Chapter 2) we have seen that, while there are several surface related states, the most prominent ones, which also exhibit clear surface state (as opposed to surface resonance) character, are the dangling bond states. We will therefore concentrate on these for the rest of the discussion. A characterization of the energy–momentum relation for the occupied surface state in GaAs(110) was shown above. With the advent of scanning tunneling microscopy, it became possible to study the charge distribution in real space. This relies on the fact that the anion and cation dangling bond surface states are localized on the respective atom species, as evident from Fig. 2.53

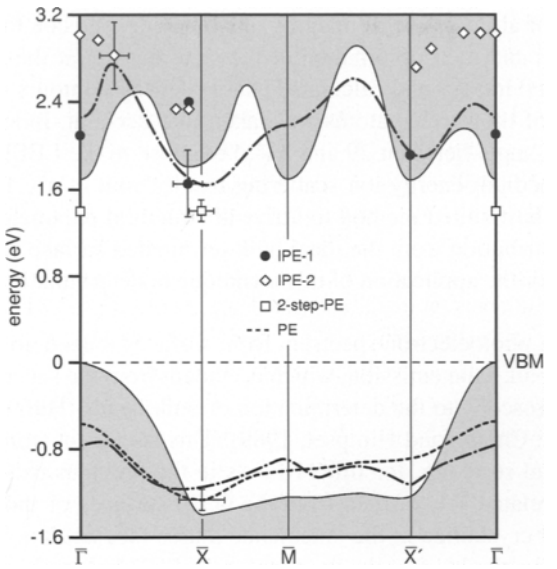


Fig. 7.14. Energy dispersion of surface state bands for GaAs(110) recorded with 16.8, 21.2 and 40.8 eV photons. From Huijser et al. (1978), with permission.

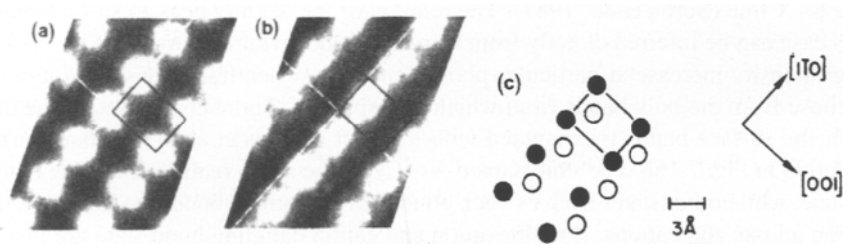


Fig. 7.15. Constant current STM images from GaAs(110), acquired at sample voltages of (a) 1.9 and (b) −1.9 V. The surface height is given by a grey scale, ranging (a) from 0 to 0.83 Å (black) and (b) from 0 to 0.65 Å (white). (c) Top view of the surface atoms. Arsenic atoms are represented by open circles and Ga atoms by closed circles. The rectangle indicates a unit cell, whose position is the same in all three figures. From Feenstra (1987), with permission. © 1987 American Institute of Physics.

in Chapter 2. Thus, by tunneling at positive and negative bias, the unoccupied and occupied densities of states at the surface are sampled, respectively. On the basis of the charge transfer arguments outlined above, the image should then reflect the cation and anion dangling bond surface states, which in real space are offset from one another by roughly the distance of the respective cation and anion zigzag rows. That this is indeed borne out by experiment is shown in the data by Feenstra et al. (1987) in Fig. 7.15, where a clear shift is observed between the lateral positions of the topographic maxima for positive and negative bias. This shift is readily understood in terms of our charge transfer concept above and was supported by calculations of the contours of the density of states (Feenstra et al., 1987).

This nice example of atom-selective imaging obviously depends on the spatial separation of the surface states and their domination of the state density at the surface. Agreement between experimental images and calculated charge density contours was best if the bond rotation relaxation of the surface atoms was taken into account. Indeed, the best fit was found for a rotation angle between 29 and 31°, i.e., close to the LEED (see references in Kahn, 1983) and medium energy ion scattering result (Smit et al., 1985a). While STM probably is not the best-suited method to arrive at structural parameters, the fact that the density of states distribution from the ideal bulk-terminated surface is not in good agreement is reassuring for the application of this technique to determinations of surface charge distributions.

The features in a photoelectron spectrum from surfaces indeed arise from a combination of surface *and* bulk state emission, which is evident from the successful application of photoelectron spectroscopy to the determination of bulk bands (Hüfner, 1996; Inglesfield and Plummer, 1992; Chiang and Himpsel, 1989). This is evident from our second example of a surface band structure, for InP(110). As in the previous example of GaAs(110) and in the closely related sets of data from the (110) surfaces of those II-VI compound semiconductors that crystallize in the zincblende lattice (see Section 7.3.2), spectra from InP(110) exhibit a multitude of peaks down to about 6 eV below the valence band maximum. A prominent leading peak near the valence band maximum is generally related to the anion dangling bond surface state as in the case of GaAs, while other peaks clearly relate to bulk band transitions, and have been used to map the bulk band structure of InP along the $\bar{\Gamma}$–$\bar{K}$–$\bar{X}$ line (Sorba et al., 1987). The relation of the leading peak to surface emission in this case can be inferred directly from its resonant behavior as shown in Fig. 7.16a, i.e., strong intensity increase at particular photon energies, when transitions from it coincide with those from the bulk bands from which it is split off (Sorba et al., 1987). The dispersion of the surface bands is compared with a recent (Engels et al., 1997) band structure calculation in Fig. 7.16b. The state named $A_5$ ($C_3$) is the anion (cation) dangling bond surface state, while other states such as back bond (bb) and bridge bond (br) states are shared between anions and cations. Both the anion and cation dangling bond state are inside the bulk bands at the zone center and only acquire surface state character away from it. Fair agreement between theory and experiment is found for the dispersion of the phosphorus dangling bond state. Other experimental bands, particularly the one extending into the so-called stomach gap, are not so well reproduced by the calculation; this point is discussed also in Section 7.3.3 and in Chapter 2. However, the overall trend, while different in small details, is qualitative similar to the one for GaAs(110) shown above, supporting the earlier discussion of charge transfer among anions and cations being characteristic for the entire class of materials.

While these data suggest a similarity of electronic structure among the III-V semiconductors, there seem to be differences in detail as revealed by bias-dependent scanning tunneling microscopy data by Ebert et al. (1996). In particular, it appears that tunneling into the unoccupied dangling bond surface state alone cannot explain the STM data at positive bias, but that empty surface resonances, which have a different spatial distribution, must be taken into account also. Their data for InP(110) in Fig. 7.17 show the same lateral offset in the topographical maxima of the STM images as seen by Feenstra et al. (1987) for GaAs(110). However, when tunneling into the unoccupied region of the band structure a

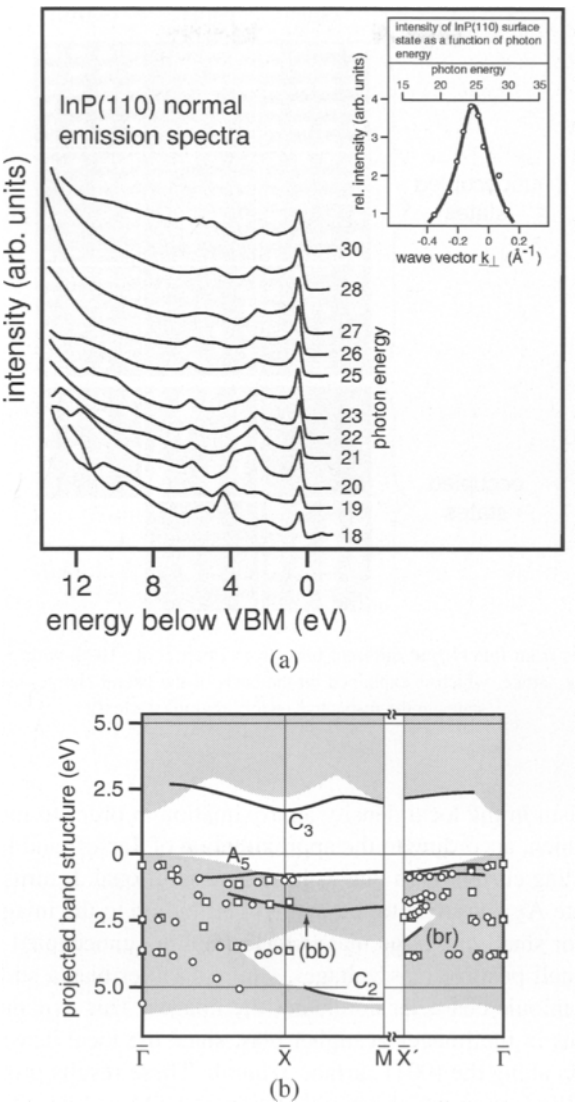


Fig. 7.16. (a) Set of normal emission spectra from InP(110) recorded at different photon energies as indicated. The inset shows the intensity variation of the leading peak with photon energy around 27 eV, demonstrating that this peak is surface-derived. From Sorba et al. (1987). (b) Experimental surface band structure data for InP(110), from data similar to those shown in Fig. 7.16, compared with a recent density functional surface band structure calculation, from Ebert (1999).

rotation of the chain structure in the STM images occurs, seen for example in going from 1.9 to 3.2 V bias. Quantitatively, the ratio of STM image corrugations along the (001) and (110) azimuths shows large variations in the unoccupied states, while little variation is found in the occupied part. The authors performed slab calculations based on the density

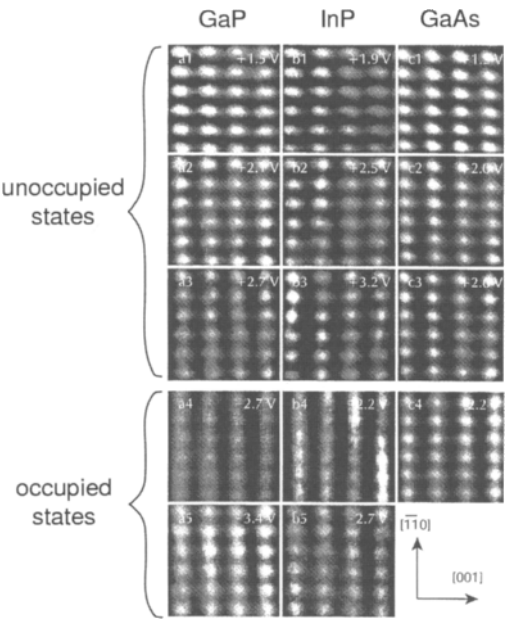


Fig. 7.17. STM images from InP(110) at different bias (from Ebert et al., 1996, with permission), showing an apparent rotation of the lattice, which is explained on the basis of the lateral charge distribution of the surface states in the respective energy region (see text).

functional formalism in the local density approximation in order to model the local density of states to which, according to the approximation of Tersoff and Hamann (1983) the variation of tunneling current with bias voltage is proportional. It turns out that the anion dangling bond state $A_5$ gives rise to the major contribution to the images in the occupied electronic states for small *and* large bias voltages, but the unoccupied surface state $C_3$ is only imaged at small positive bias voltages, while at larger bias a surface resonance $C_4$ which has partly anionic character dominates the images. This explains the apparent rotation of the chains in the images at higher bias, since the local density of states shows chain-like contours along the [001] surface azimuth. These results provide an impressive demonstration of the way in which a combination of STM and density of states calculations can identify contributions to the surface electronic structure. The observed rotation of image periodicity also occurs in GaAs(110) and GaP(110), strengthening the notion of close similarity in the surface electronic structure of the III-V compound semiconductors.

We have discussed above how charge rearrangement in surface reconstructions and, in fact, any charge rearrangement in adsorption and interface formation, can be inferred from core level photoemission spectroscopy. This technique is sensitive to the chemical environment around each atom, with a number of caveats (Hüfner, 1996), and by choice of the respective core level line charge rearrangements around different atoms can be investigated separately. Spectra from GaAs(110), InP(110) and GaP(110) surfaces are shown in Fig. 7.18 as an example of such surface core level shifts (Eastman et al., 1980; Wilke

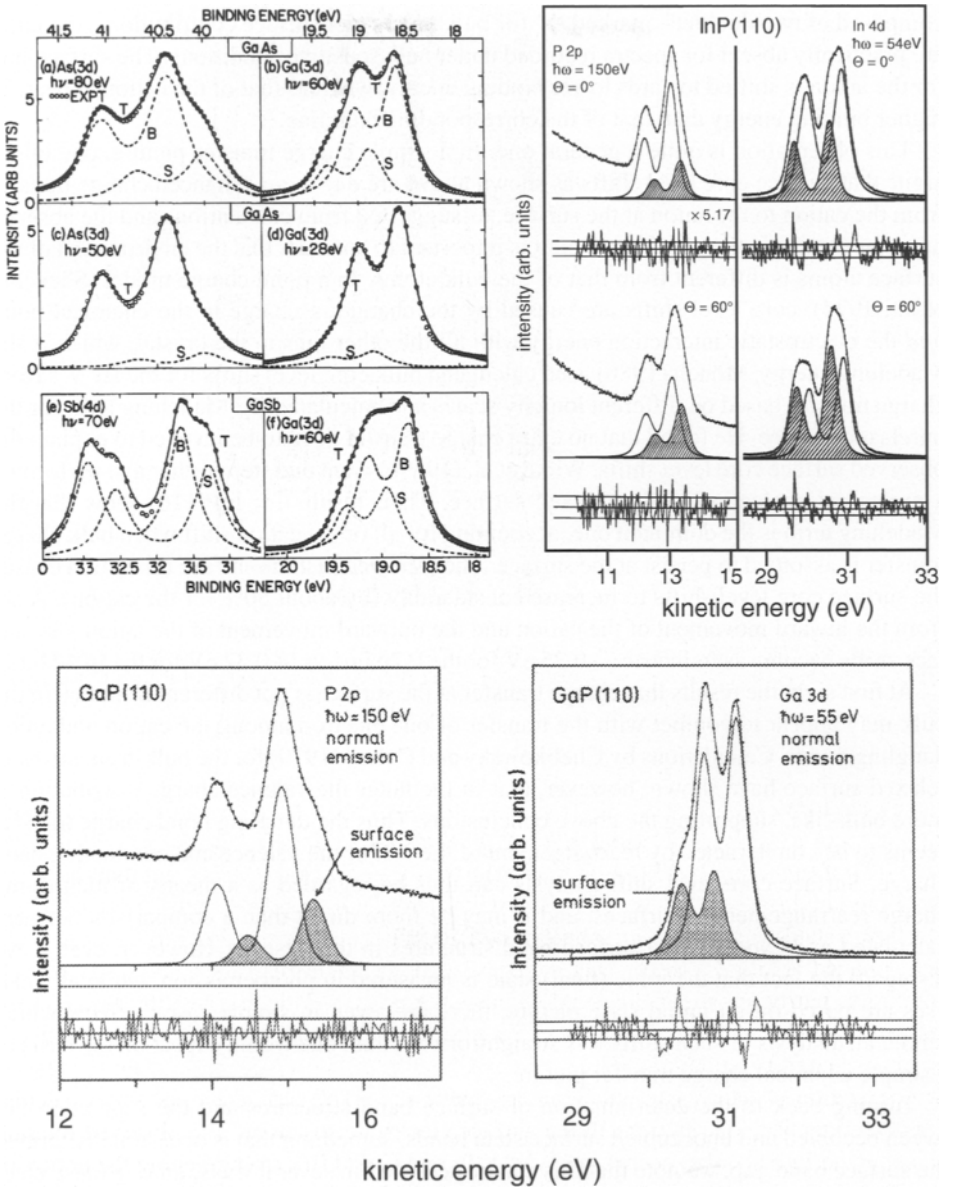


Fig. 7.18. Surface core level shifts in GaAs(110) and GaSb(110) (from Eastman et al., 1980) as well as InP(110) and GaP(110) (Wilke et al., 1989b; Chassé et al., 1993).

et al., 1989b; Chassé et al., 1993). Variation of surface sensitivity is achieved by tuning the kinetic energy to near threshold and near the escape depth minimum for the line in question. For the Ga and As 3d lines this shows that the spin–orbit split pair of lines is

composed of two doublets, marked 'b' for bulk and 's' for surface contributions; the latter are practically absent for spectra recorded under bulk sensitive conditions. The surface line for the anion is shifted towards lower binding energy, whereas that of the cation appears at higher binding energy than that of the corresponding bulk line.

This observation is quite a general one. In a simple charge transfer picture, one might argue that surface core level shifts as shown above are due to an enhanced charge transfer from the cation to the anion at the surface, as suggested from calculations and the absence of surface states in the gap. However, it is important to consider that the environment of the surface atoms is different from that of the bulk atoms. In a point charge model (Shevchik et al., 1974), core level shifts are caused by the change in charge in the chemical bond *and* the electrostatic interaction energy with all the other ions in the crystal, which is the Madelung energy. Mönch (1986) used calculated bulk core level shifts for the III-V's from charge transfer based on different ionicity scales and calculated the Madelung term for the unrelaxed surface. He found that no extra charge transfer need to be invoked to explain the observed surface core level shifts. Wilke et al. (1989b) went one step further and performed a numerical evaluation of the relaxed surface. Their results for InP(110) show that the Madelung term is the dominant one, accounting for all of the cation shift when bulk charge transfer is assumed to persist at the surface. They showed that the surface relaxation causes the surface core level shifts to increase considerably (by about 50% for the cation). Also, from the inward movement of the cation and the outward movement of the anion, the surface shifts become asymmetric ($-0.25$ eV for the P 2p line vs. $+0.32$ eV for the In 4d line).

At first sight the results that charge transfer at the surface is not different from that in the bulk may appear to conflict with the transfer of one electron among the cation and anion dangling bonds. Calculations by Chelikowsky and Cohen (1979) for the bulk-truncated and relaxed surface have shown, however, that in the latter the valence charge distribution is more bulk-like, supporting the above conclusions. Thus the dangling bond charge transfer seems to be counteracted by rearrangement of the rest of the valence and conduction band charge. Surface core level shift analysis can thus be regarded as a means of identifying charge rearrangement at surfaces, and it may be more direct than a comparison between calculated and experimental surface band structures in this respect. However, even if we disregard the fact that the ionic (final) state is measured in photoemission, while all analyses are based on an initial state picture, there are, even in simple cases, effects which render an analysis of such shifts less straightforward than one would expect on the basis of a simple chemical charge transfer picture.

Turning back to the determination of surface band structures and the separation between occupied and unoccupied surface state bands, something that is occasionally termed the surface band gap, we note that this can be achieved in several ways, among these electron energy loss spectroscopy, optical absorption, and scanning tunneling spectroscopy. It can also be achieved by combining photoelectron and inverse photoemission to measure the energies of the occupied and unoccupied dangling bond states. This has been carried out in a very convincing manner by Carstensen et al. (1990). Consider the specific case of GaSb(110), where results are shown for different points of the surface Brillouin zone in Fig. 7.19. As evident from both the photoemission and inverse photoemission spectra, surface-related emission is rather weak at the $\bar{\Gamma}$ and $\bar{\mathrm{M}}$ points, but sharp peaks near the onset of the spectra for the $\bar{\mathrm{X}}$ and $\bar{\mathrm{X}}'$ points show that it is quite pronounced there, an ob-

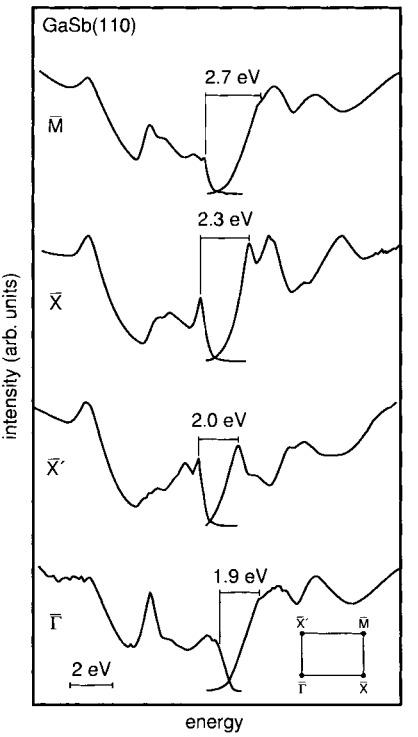


Fig. 7.19. Angle-resolved photoelectron spectroscopy and inverse photoemission results at different points of the surface Brillouin zone for GaSb(110). After Carstensen et al. (1990), with permission.

servation that is found in all semiconductors. In agreement with what was presented above, the occupied dangling bond state is inside or close the projected bulk bands at the $\bar{\Gamma}$ and $\bar{M}$ points, such that its emission overlaps with bulk state emission. Therefore, it is not easy to extract the band gap information from the rather lower emission intensity of the surface state at $\bar{\Gamma}$. This is clearly a consequence of the low transition matrix element at the particular photon and electron energy chosen, since emission from surface states can be enhanced as we have seen in the case of InP above (Sorba et al., 1987). However, in regions of the surface Brillouin zone where the surface states are split off from the bulk bands, for example, at $\bar{X}$ and $\bar{X}'$, surface state emission appears as sharp peaks, and here the surface band gap can be measured with rather higher precision. A direct comparison between experimental spectra and (ground state) band structure calculations is not possible, of course, due to the fact that the ionic state is measured in the photoemission and inverse photoemission techniques as outlined in Chapter 6 by Himpsel. Also, the ground state density functional calculations suffer from the well-known problem of underestimating the size of the band gap (see Chapter 2 by Pollmann and Krüger). For the GaAs(110) surface a quasiparticle band structure calculation was performed by Zhu et al. (1989) which takes care of such problems, and reasonable agreement between the experimental band gaps across the surface Brillouin zone and the calculations was found.

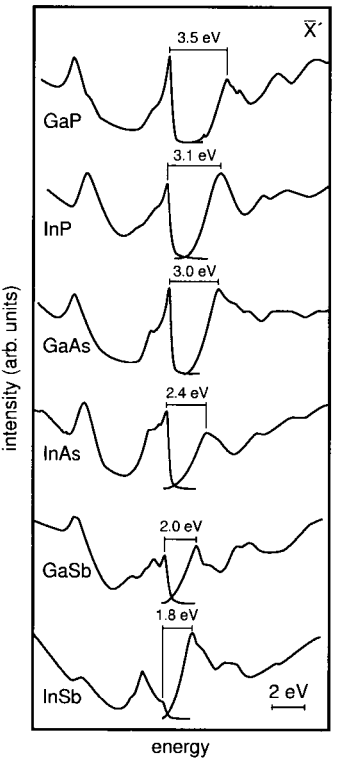


Fig. 7.20. Surface band gaps at the $\bar{X}$ point of the surface Brillouin zone, from a combination of photoemission and inverse photoemission spectra of the (110) surfaces of InSb, GaSb, InAs, GaAs, InP, and GaP. After Carstensen et al. (1990), with permission.

The study of surface band gaps was extended to the entire class of III-V semiconductor surfaces by Carstensen et al. (1990). Their experiment has the particular advantage that a common energy reference for the two spectroscopies was established. Figure 7.20 shows the spectra for the (110) surfaces of GaP, InP, GaAs, InAs, GaSb, and InSb at the $\bar{X}'$ point of the surface Brillouin zone. In all cases it is evident that the anion-derived surface state gives rise to a clear peak, while the cation-derived feature in some cases is a rather broad line with a large slope at lower energies which cannot entirely be attributed to the lower resolution of the IPS experiment. The trend of increasing surface state band gap from $\Gamma$ over $\bar{X}'$ to $\bar{X}$ and $\bar{M}$ again is found for all III-V semiconductors. The surface band gap for the (100) surface of these materials at the surface Brillouin zone center and the $\bar{X}'$ point is considerably larger than the fundamental bulk band gap, but the increase from InSb to GaP has roughly the same slope. The trend as observed by a combination of photoelectron spectroscopy and inverse photoemission agrees well with measurements of optical excitations if excitations between states at the zone boundary are taken into account. There is also good overall agreement with scanning tunneling spectroscopy studies of the (110) surfaces of these semiconductors by Feenstra (1994).

*7.3.1.2. The (100) faces of III-V compound semiconductors*

The clean (100) surfaces of compound semiconductors, for which we again take GaAs(100) as the most intensely studied example, are not terminated in the ideal bulk-truncated configuration rather. Instead, they exhibit a number of different reconstructions which depend on elemental composition of the surface, i.e., the ratio of anion to cation atoms. This composition can be modified by annealing in vacuum (Cho, 1971; Drathen et al., 1978), by adjustment of Ga and As fluxes in molecular beam epitaxy (MBE) growth, thermal treatment of arsenic-capped surfaces etc. Thus, with increasing annealing temperature, a sequence of $(2 \times 4)$, $(1 \times 6)$, $c(6 \times 4)$, $(3 \times 1)$, $(4 \times 1)$ and $c(8 \times 2)$ superstructures is observed in electron diffraction. The mechanism responsible for the formation of these reconstructions, i.e., energy minimization through electronic charge rearrangement, can be understood in terms of the principles laid down by Duke (1996), and in particular the so-called electron counting rule extensively discussed by Pollmann and Krüger in Chapter 2. Briefly, this rule (also called autocompensation, see Harrison, 1979) requires that the number of donor-like states is as close as possible to the number of acceptor-like states, such that the surfaces are non-polar and nonmetallic (see Section 2.3.2.2 of Chapter 2 for details). As a consequence, reconstructions tend to saturate surface dangling bonds or to convert them into non-bonding states. This leads to charge transfer at the surface from the cation-derived dangling bond states (usually at higher energy) to the anion dangling bond states, just as in the case of the (110) surfaces discussed above.

In GaAs(100), where each surface atom has two dangling bonds, a reduction of the number of dangling bond states can be achieved by two atoms forming a surface bond, i.e., a dimer. Thus the number of dangling bonds is reduced by 50%; a similar process takes place at the silicon (100) surface as described above. This process was suggested as an explanation for the reconstructions (Cho, 1976; Larsen, 1982; see also references in Mönch, 1995, for details). Various ways to group dimers in order to explain the different reconstructions were put forward. A clear demonstration that this basic assumption is correct was provided by the STM investigations of Biegelsen et al. (1990a, b, c), where large ordered arrays of dimers were found, and based on these observations reliable real-space models could be formulated. Thus it was found that the $c(2 \times 8)$ structure differs from the $(2 \times 4)$ only in that adjacent unit cells are shifted by half a superlattice constant along one azimuth. Real space models could also be constructed for other reconstructions observed (e.g., the $(4 \times 4)$ structure (Biegelsen et al., 1990b). Calculations of the electronic structure are discussed in Chapter 2; density functional calculations yield lowest energies for those structures which fulfil the electron counting rule in all cases. Schmidt and Bechstedt (1996) found that all structures that were energy-optimized had similar structural elements, i.e., arsenic dimers, dimer vacancies, and a nearly planar configuration of the second layer gallium atoms.

In spite of several theoretical treatments, experimental investigations of the electronic structure of GaAs(100) have been rather scarce. Larsen et al. (1982) performed angle-resolved photoemission studies of GaAs(100) surfaces grown by MBE. They obtained data from the $(2 \times 4)$ phase of GaAs and analyzed them in terms of a $(2 \times 1)$ surface Brillouin zone since the data showed this to be the dominant periodicity, i.e., along the $[1\bar{1}0]$ azimuth, the same azimuthal direction as the As dangling bonds on the bulk truncated surface. The spectra exhibit a set of surface-related features in the region from 0 to 3 eV below the

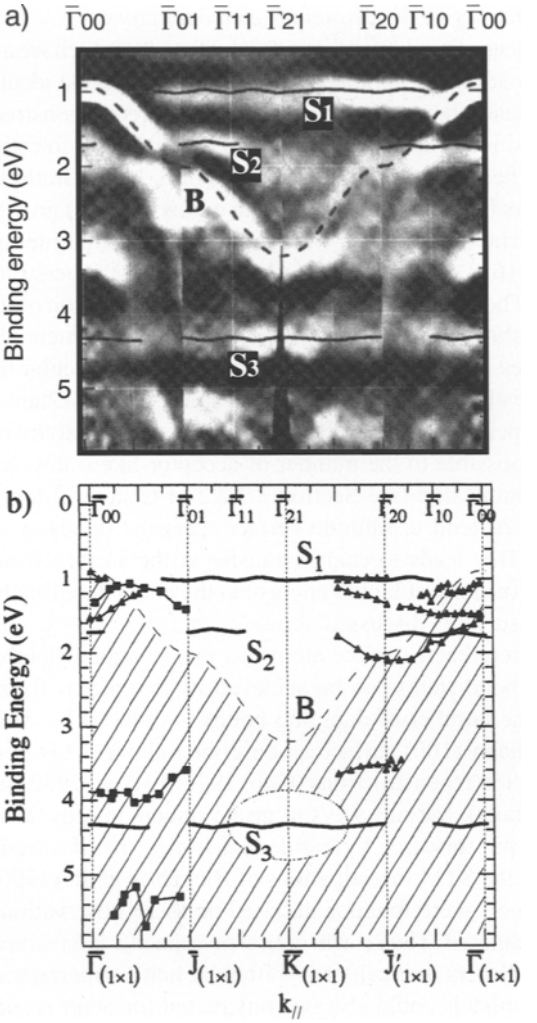


Fig. 7.21. Valence level photoemission data for InP(100)-(2 × 4), plotted in terms of intensity distributions (top), and the respective surface band structure (bottom). The (1 × 1) surface Brillouin zone boundaries are given at the bottom, and for the (2 × 4) in the top. The bulk- (B) and surface ($S_1$–$S_3$)-derived emissions are indicated in the intensity diagram. The data for InP (solid lines) are compared with the surface band structures of GaAs(100)-(2 × 4) from Larsen et al. (1982) (triangles) and for InAs(100)-(2 × 4) by Håkansson et al. (1997) (squares), with permission.

valence band maximum. The upper surface bands show a weak dispersion, while the peak at 3 eV ($S_4$) hardly disperses at all (see Fig. 7.21). The authors compared their data with calculations from the scattering theoretical method based on an extended tight binding description of the GaAs bulk crystal. They found that in the region 0–1.5 eV below the VBM a number of surface-related features are indeed identified in the calculations, the dispersion of which is not directly described by the theory.

These data can be compared with results from other (2 × 4) reconstructed compound semiconductor surfaces, such as the InAs(100)-(2 × 4) from Håkansson et al. (1997) and InP(100)-(2 × 4) from Huff et al. (1998). The data by Huff et al. for the valence band emission from InP(100)-(2 × 4) are displayed in an interesting valence band imaging technique in Fig. 7.21, where the peaks in the spectrum are displayed in a grey scale diagram. The intense (white regions) bulk- (B) and surface ($S_1$–$S_3$)-derived emissions are indicated in the intensity diagram. The data for InP (solid lines) are compared with the surface band structures of GaAs(100)-(2 × 4) from Larsen et al. (1982) (triangles) and for InAs(100)-(2 × 4) by Håkansson et al. (1997) (squares). For GaAs(100) and InAs(100), it is known from STM images (Avery et al., 1995; Yamaguchi and Horikoshi, 1995) that their surface geometric structures are very similar, consisting of an extended array of As dimers. Although the InAs and GaAs surface bands have different binding energies, both exhibit dispersions which indicate their delocalized character. The surface states on the InP(100)-(2 × 4) surface, on the other hand, are almost dispersionless (Fig. 7.21). This result suggests that the elements of the InP(100)-(2 × 4) unit cell are more localized than those of the GaAs or InAs surfaces. Evidence for differences in the structure of InP(100)-(2 × 4) compared with those of GaAs and InAs also comes from STM images which suggest differences in the local geometric structure, and from optical measurements (see the discussion in Huff et al., 1998). These results call for structure-dependent valence band calculations to provide more information on the local geometry and electronic interaction between the building blocks of the (2 × 4) reconstruction.

*7.3.1.3. Band bending and the 2D electron gas at InAs surfaces*

So far we have been mainly concerned with the electronic potential at a microscopic, atomic scale. However, in semiconductors the macroscopic potential can vary over large distances because of the low carrier concentration. Thus if the surface of a semiconductor carries intrinsic surface states in the gap, such as the silicon surfaces, the Fermi level at the surface will in general have a different energy than in the bulk and, consequently, a band bending ensues. Such band bending can also be caused by extrinsic surface states brought about by adsorbates and defects, which will also induce a band bending. Adsorption of foreign atoms onto (110) surfaces of the III-V compound semiconductors induces a depletion layer, i.e., an upwards band bending on n-type material (see the discussion in Mönch, 1995). The notable exception to this rule is InAs where an accumulation layers on n-type and inversion layers on p-type material are observed. This effect is thought to be the reason for many unusual properties of interfaces involving InAs (Olson et al., 1996). This direction of band bending offers a way to study charge accumulation layers and the dynamics of excited electrons in the two-dimensional electron gas below the surface (Karlsson et al., 1998). In fact, InAs was the first material in which quantization of charge in near-surface layers was demonstrated and for which the first measurements of subband energies were performed (Tsui, 1970). Such 2D systems, which are buried under oxide layers, can generally only be studied by methods such as Hall effect or optical spectroscopy. A degenerate 2D electron gas at the surface offers a system in which details of the subbands can be studied by means of surface sensitive methods.

On the clean InAs(111)-(2 × 2) surface, a downwards band bending is induced, possibly by surface defect states, and the creation of an accumulation layer is observed directly

in angle-resolved photoemission, as seen in the spectra by Ölsson et al. (1996) shown in Fig. 7.22a. They exhibits a small peak at about 0.3 eV above the valence band maximum (measured both by means of the common linear extrapolation method, and by reference to the binding energy of a shallow core level). The small peak has a high kinetic energy cutoff at the position of the Fermi level. This peak shows a strong dispersion with $\mathbf{k}_{\|}$, passing through the Fermi level within a few percent of the $\mathbf{k}_{\|}$ value of the surface Brillouin zone boundary. It shows a strong resemblance to the emission from the conduction band minimum seen in the heavily doped Si surfaces occur, in which occupation of the states around the conduction band minimum by degenerate doping. A straightforward reasoning demonstrates that the peak in InAs(111)-(2 × 2) is derived from bulk states. The surface Brillouin zone for the (111) surface is larger than the corresponding hexagonal area of the bulk Brillouin zone, i.e., the LKW surface. Thus a surface-related feature should be seen at the $\bar{\Gamma}$ point of the first and second surface Brillouin zone, while a bulk-derived feature should not be observed at the second $\bar{\Gamma}$ point. This is exactly what is observed in the corresponding spectra also shown in Fig. 7.22a, demonstrating that the peak is indeed derived from bulk states at the CBM. Similar features showing the formation of a downward band bending are also observed on other InAs surfaces.

The formation of charge accumulation layers on InAs cannot be due to unoccupied surface states since they are far above the conduction band minimum in InAs. The reason for the unusual position for the Fermi level (the "pinning" position) is caused by the fact that the "effective midgap energy" (Tersoff, 1984) in InAs is above the conduction band minimum. This is due to the unusual band structure of InAs, in which the lowest conduction band turns down well below the average conduction band minimum (Tersoff, 1985). For the states within the accumulation layer, two subbands are supposed to be filled at densities of about $10^{12}$ cm$^{-2}$. On cleaved InAs(110), the initial flat band situation can be reverted into a downward band bending by very small amounts of adsorbate deposition (Chen et al., 1989) or even just the presence of cleavage step defects, and rather large values for the band bending have been found (Aristov et al., 1993). Aristov et al. (1995) have studied such accumulation layers in n- and p-type InAs(110), and their data are displayed in Fig. 7.22b. The small peak in the overview spectrum (bottom) is shown in more detail in the close-up spectrum, and after deposition of about 0.01 monolayer of Cs a sharp emission for p-type material is clearly seen (marked 2-p). For n-type material the shape is much broader, and two peaks can be distinguished; these are assigned to the first and second subband in the quantum well. Model calculations which take the amount of band bending as input predict only one subband for p-type and two for n-type material. The emergence of the characteristic line shape seen in the experiment can be understood in terms of the schematic diagram on the right-hand side of Fig. 7.22b, where the effective density of states of the 2D states is shown, and the influence of the Fermi function, and the convolution with a Gaussian representing the instrumental resolution leads to the observed line shape. Strictly speaking, the 2D gas is not a surface property in the sense that we have used so far in this chapter, since it extends up to about 200 Å into the bulk region; however, it is induced by a surface process, and its presence in clean surfaces can be used in experiments concerning properties such as the dynamics of the 2D electron gas (Karlsson et al., 1998).

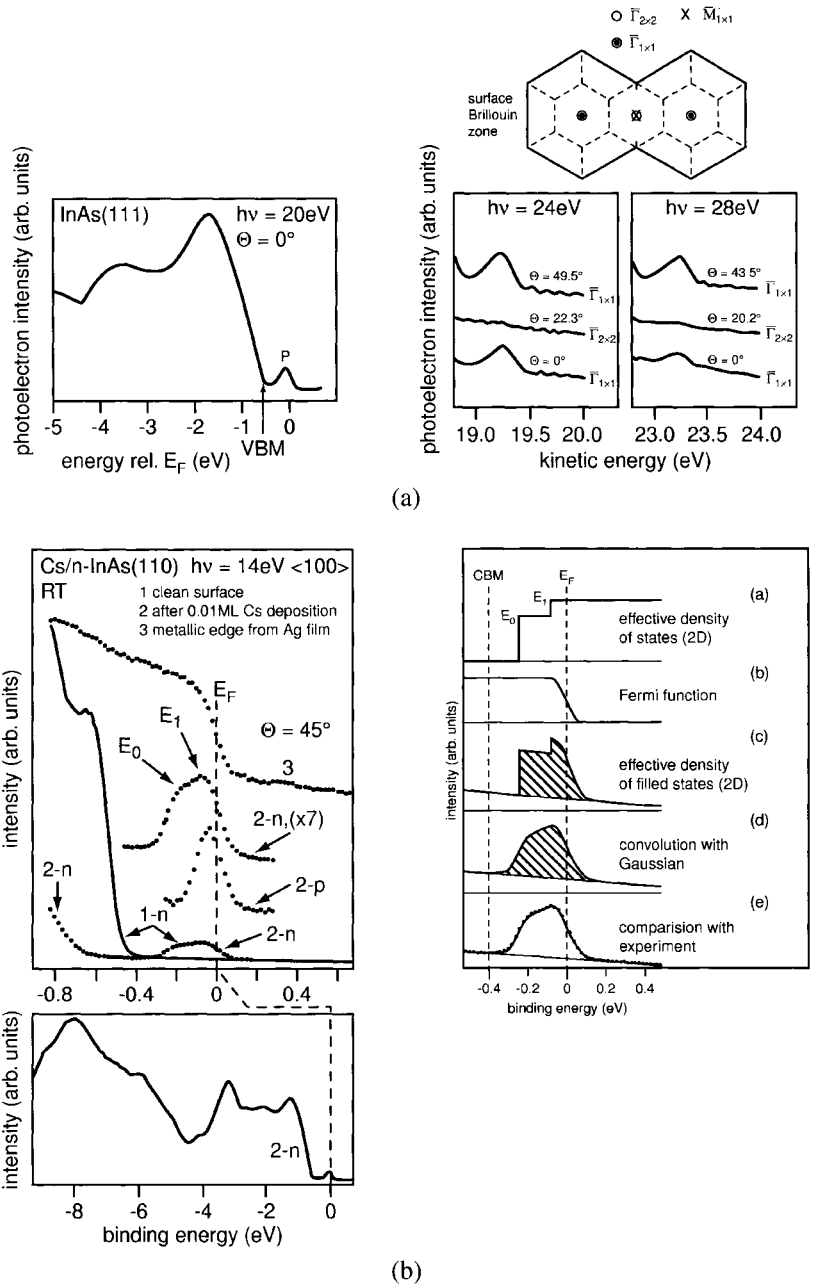


Fig. 7.22. (a) Photoemission spectrum from InAs(111), which exhibit a small peak near the Fermi energy. This peak appears only at the $\bar{\Gamma}$ points of the (1 × 1) surface Brillouin zone, showing that it is derived from bulk conduction band states, supporting the interpretation in terms of a 2D electron gas. From Ölsson et al. (1996). (b) Set of spectra from n- and p-type InAs(110) surfaces with 1% of a monolayer of Cs adsorbed, showing the emission due to the 2D electron gas; one subband is occupied in the case of p-type material, while two subbands can be discerned in n-type material. From Aristov et al. (1995), with permission.

*7.3.1.4. The group III nitrides*

There has recently been a revival in the investigation of the surface properties of the group III nitrides AlN, GaN, and InN, due to their optoelectronic properties which permit to use them in light-emitting devices in the blue-green region of the spectrum (Strite and Morkoç, 1992). Interest from a surface point of view is enhanced by the fact that all materials in this group have to be prepared by molecular beam epitaxy or metal-organic chemical vapor deposition since bulk samples are not widely available (Lambrecht and Segall, 1994). Important progress in understanding the similarities and differences between the nitrides and the other III-V compound semiconductor surfaces has recently been made from a number of theoretical calculations. However, progress in experimental studies has been hampered by the difficulty in preparing clean and well-ordered surfaces of the group III nitrides. From the STM work of Smith and coworkers (Smith et al., 1997) it appears that *in situ* preparation by MBE or MOCVD is mandatory, and few groups have so far mastered the additional experimental effort. Photoemission studies have so far concentrated on the bulk band structure of the wurtzite and cubic material, from angle-resolved studies of GaN(0001) and GaN(100) and (110) surfaces (Dhesi et al., 1997; Ding et al., 1996). A feature in the spectra from GaN(0001)-(1 × 1) near the valence band maximum has been assigned to a surface state by Dhesi et al. (1997). A feature near the valence band maximum of AlN(0001) has also been identified as surface-related (Wu and Kahn, 1999). However, an extensive study of the changes in electronic structure accompanying the various observed reconstructions (Smith et al., 1997), and the different terminations that have been calculated to be stable, is awaiting progress in the widespread availability of surface preparation methods leading to well-defined nitride surfaces.

*7.3.2. The II-VI compound semiconductor surfaces*

The surfaces of the II-VI compound semiconductors are interesting study subjects because of the larger ionicity of the constituent bonds, and the possibility of optoelectronic applications in the blue-green region of the spectrum. A number of studies of the surfaces of ZnSe (Xue et al., 1998; Qu et al., 1991a), CdTe (Magnusson et al., 1988; Janowitz et al., 1990; Qu et al., 1991b; Khazmi et al., 1992), CdSe and CdS (Magnusson et al., 1987, 1988, 1998) have been performed using angle resolved photoemission and inverse photoemission. In view of the fact that some of the II-VI semiconductors crystallize in the wurtzite structure, e.g., CdSe and CdS, but can be grown in the cubic phase by pseudomorphic growth on suitable substrates (Wilke, 1989a; Neuhold, 1995), a comparison of band structures for the two crystal phases can be carried out (Stoffel, 1983; Stampfl, 1997). The electronic structure of those II-VI compound semiconductor surfaces which crystallize in the zincblende lattice is expected to exhibit similar features than those of the III-V materials. This is in fact borne out by a comparison such as shown in Figure 2.67 of Chapter 2, where calculated band structures for the surface bands of the (110) surfaces of ZnS, ZnSe and ZnTe are shown and compared to experimental data. Qu et al. (1991a, b) have undertaken an extensive study of the surface-induced features from ZnSe(110), ZnTe(110) and CdTe(110); their method includes an investigation of the 3D bulk bands also. They note that this forms an important basis for surface state identification, since most surface-induced states are found to be resonances of underlying bulk states. Thus those peaks which cannot be attributed to bulk band transitions along $\bar{\Gamma}$–$\bar{K}$–$\bar{X}$ and are not due to density-of-state

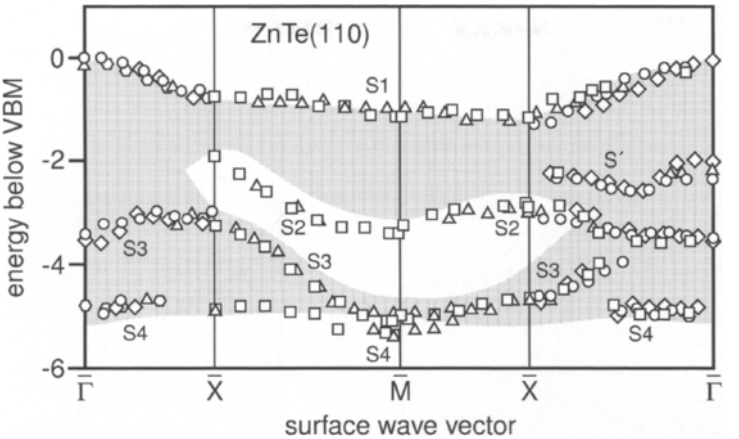


Fig. 7.23. Surface band structure of ZnTe(110). After Qu et al. (1991a), with permission.

features are assigned to surface emission. Finally, angle-dependent spectra are recorded for several different photon energies, which is a critical test since bulk band transitions are expected to shift with photon energy. For ZnTe(110), the $E(\mathbf{k}_\parallel)$ dispersion was measured at photon energies of 23, 25, 27, 31 and 41 eV, corresponding to a range of $k_\perp$ of 0.7 $\text{Å}^{-1}$, i.e., half the distance between $\Gamma$ and X, a considerable variation. These data are shown in Fig. 7.23. The shaded region indicates the projected bulk band region, and it is seen that, except for $S_2$ and possibly for $S_1$, the surface states clearly fall into this region. A comparison with surface band structure calculations such as shown in Fig. 2.65 of Chapter 2 for ZnSe(110) and ZnTe(110), or that of Schmeits (1990) shows that some of the calculated surface bands match well with the experimental data, but that others have no counterpart in the experiments. Disagreement is particularly obvious in the region near the VBM, where the calculations have two bands running fairly parallel in $k_\parallel$-space, while the experiments for some surfaces have only one. Two surface-induced features near the valence band maximum were found in a study of ZnS(110) layers grown through molecular beam epitaxy on GaP(110) surfaces by Barman et al. (1998) which included a mapping of the 3D bulk bands. The spectra (Fig. 7.24) exhibit several features which disperse with $\mathbf{k}_\parallel$, and from the symmetry of the dispersion they can be clearly attributed to surface states. The surface band structure is compared to a recent calculation within the self-interaction and relaxation scheme which is also discussed in Chapter 2. The notion of two surface bands near the valence band maximum seems to be in conflict with the generally accepted picture of one dangling bond state on the anion. The strongly dispersing feature is interpreted in the calculations as due to the in-plane surface bond, while the rather weakly dispersing feature is assigned to the dangling bond feature. In view of the apparent conflict with a large body of experimental and theoretical data for the (110) surfaces of the other II-VI and III-V surfaces (see Chapter 2), a more extensive investigation is clearly desirable.

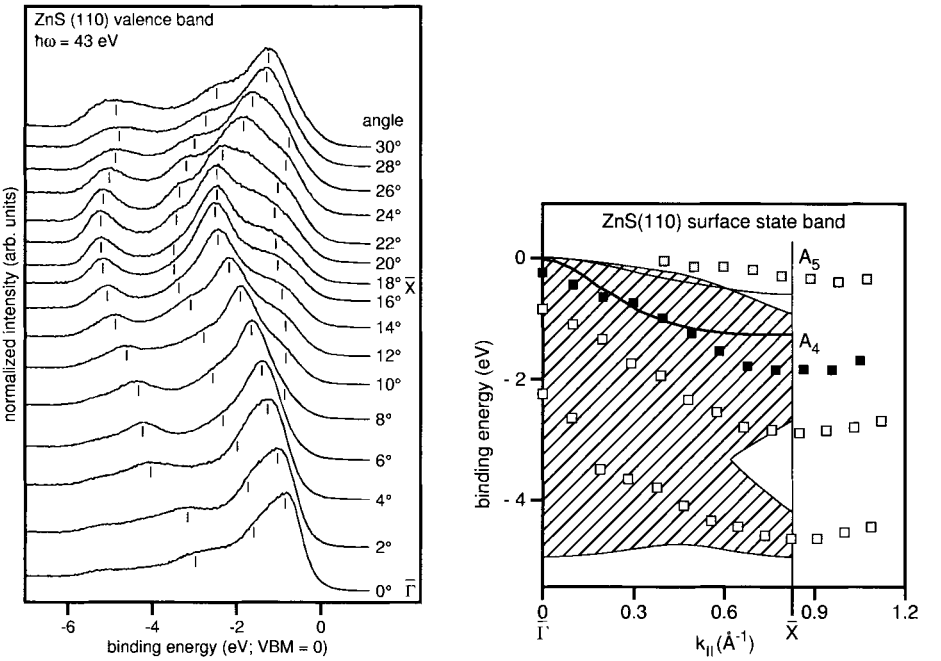


Fig. 7.24. Left: Angle-resolved spectra from a ZnS(110) surface for different polar emission angles. Right: plot of surface state energies within the surface Brillouin zone, showing two features near the valence band maximum. From Barman et al. (1998), with permission. © American Physical Society.

### *7.3.3. Other compound semiconductor surfaces*

There are a large variety of compound semiconductors which have attracted interest in view of their specific properties related to electronic or optoelectronic applications. Among these is silicon carbide, which, being a group IV-IV compound, has interesting properties; its wide gap renders it suitable for high-power, high temperature applications (Pensl and Helbig, 1990). One problem that has so far prohibited widespread applications of SiC is the fact that it crystallizes in a number of different polytypes. Cubic or $\beta$-SiC has one Si and one carbon atom per unit cell, in a zincblende lattice, while the hexagonal phase most commonly exists in the so-called 2H, 4H and 6H modifications, where the number indicates the number of Si and C atoms per unit cell. Although SiC is a group IV semiconductor, the bond between silicon and carbon has a strong ionic component due to the large electronegativity difference, leading to an ionic gap in the band structure. However, the nature of the ionic bond is quite different from that of the III-V and II-VI compound semiconductors since there is no difference in valence electron number among the constituents in SiC. Depending on stoichiometry, the SiC surfaces show a multitude of surface reconstructions in LEED as described by Bermudez (1997). Work has concentrated on the (100) surface of the cubic phase and the (0001) surface of the hexagonal phases. The consequences of the particular bonding type in SiC for the surface electronic structure are presented by Poll-

mann and Krüger, and are discussed in relation with available experimental information, in Section 2.5 of Chapter 2, and thus will not be covered here.

Another important class of compound semiconductors are the layered compound semiconductors. These were among the first systems to be studied in angle-resolved photoemission, and a clear-cut demonstration of the method of "band mapping" was in fact performed (Smith et al., 1974; see his interesting account on the "prehistory of angular-resolved photoemission" in Yu and Cardona, 1996). The band structure of layered compound semiconductors is much simpler than that of the elemental or zincblende/wurtzite compound semiconductors since they consist basically of strong bonds within the layers, while only weak bonding forces act between layers, thus making the band structure essentially two-dimensional. This is also the general result found in experimental band structure studies of the materials in this class, such as $MoSe_2$ and $MoS_2$ (Coehoorn et al., 1987), $WSe_2$ (Finteis et al., 1997; Traving et al., 1997), InSe (Larsen et al., 1977), GaSe (Thiry et al., 1977) and others. Due to the weak bonding between the layers no proper surface states are expected.

## 7.4. Conclusion and outlook

What are the achievements and challenges when we look back at more than 25 years of surface electronic structure studies of semiconductors? The relation between surface reconstruction and surface electronic states in the low index surfaces of the elemental semiconductors has been convincingly explained, from a combination of experimental results and modern electronic structure calculations. This is not only important for an understanding of these particular systems, but for the entire field in general, since many of the processes leading to specific reconstructions and band arrangements are recurring themes in other semiconductor surfaces. Progress in understanding the surface electronic states of the more complex reconstructions of GaAs and other compound semiconductor surfaces will no doubt progress with improved knowledge of the surface geometry. The challenges from a materials point of view lie in surfaces such as those of the group III nitrides, but progress that has been made in similarly complex materials such as SiC give rise to the expectation that this problem will be solved in time. From the point of view of the experimental technique, an important challenge in photoelectron spectroscopy continues to be the correct evaluation of the valence band maximum, which is not only important for a determination of a proper level of reference for comparisons with theory, but also for barrier height determinations in studies of metal–semiconductor interfaces and semiconductor heterojunctions. The still widely used practice of using an extrapolation of intensity at the leading edge of the spectrum will increasingly be replaced by identifying the bulk-derived band-to-band transitions at the valence band maximum (Manzke et al., 1987), even though this may involve the identification of overlapping surface state emission first. This will help to improve the determination of surface band structures and to provide an accurate data set for comparisons with theory. Third generation synchrotron light sources with their increased resolution and flux, and new electron energy analyzers will help to achieve this goal. It is also hoped that progress in attributing specific surface states to specific entities on the semiconductor surface, so beautifully demonstrated in the early examples of scanning tunneling spectroscopy for Si(111) (Hamers et al., 1986) and GaAs(110) (Feenstra

et al., 1987) will be made in other systems. The field of semiconductor surface electronic structure investigations has certainly matured considerably, but it is also true that much work remains to be done.

*Acknowledgements*

Some of the work described here was supported by the Bundesministerium für Bildung, Forschung und Technologie as well as the Deutsche Forschungsgemeinschaft. This work has benefited from conversations with Ph. Ebert, G. Neuhold, S.R. Barman, Th. Chassé, and M. Scheffler.

## References

Aarts, J., A.-J. Hoeven and P.K. Larsen, 1988, Phys. Rev. B **37**, 8190.
Aristov, V.Yu., G. LeLay, Le Tranh Vinh, K. Hricovini and J.E. Bonnet, 1993, Phys. Rev. B **47**, 2138.
Aristov, V.Yu., G. Le Lay, M. Grehk, V.M. Zhilin, A. Taleb-Ibrahimi, G. Indelkofer and P. Soukiassian, 1995, Surf. Rev. Lett. **2**, 723.
Assmann, J. and W. Mönch, 1980, Surf. Sci. **99**, 34.
Avery, A.R., D.M. Holmes, J. Sudikono, T.S. Jones and B.A. Joyce, 1995, Surf. Sci. **323**, 91.
Backes, U. and H. Ibach, 1981, Solid State Commun. **40**, 575.
Barman, S.R., S.-A. Ding, G. Neuhold, K. Horn, D. Wolfframm and D.A. Evans, 1998, Phys. Rev. B **58**, 7053.
Batra, I.P., F.J. Himpsel, P.M. Marcus, R.M. Tromp, M.R. Cook, F. Jona and H. Lin, 1985, in: Structure of Surfaces. Springer-Verlag, Berlin, p. 285.
Bennet, P.A., L. Feldman, Y. Kuk, E.G. McRae and J.E. Rowe, 1983, Phys. Rev. B **28**, 3656.
Bermudez, V., 1997, Phys. Status Sol. B **202**, 407.
Biegelsen, D.K., L.E. Swartz and R.D. Bringans, 1990a, J. Vac. Sci. Technol. A **8**, 280.
Biegelsen, D.K., R.D. Bringans, J.E. Northrup and L.E. Swartz, 1990b, Phys. Rev. B **41**, 5701.
Biegelsen, D.K., R.D. Bringans, J.E. Northrup and L.E. Swartz, 1990c, Phys. Rev. Lett. **65**, 452.
Binnig, G., H. Rohrer, Ch. Gerber and E. Weibel, 1983, Phys. Rev. Lett. **50**, 120.
Bringans, R.D. and R.Z. Bachrach, in: Synchrotron Radiation Research: Advances in Surface Science. Plenum Press.
Bringans, R.D., R.I.G. Uhrberg, M.A. Olmstead and R.Z. Bachrach, 1986, Phys. Rev. B **34**, 7447.
Brommer, K.D., M. Needels, B.E. Larson, J.D. Joannopoulos, 1992, Phys. Rev. Lett. **68**, 1355.
Carlisle, J.A., M.T. Sieger, T. Miller and T.-C. Chiang, 1993, Phys. Rev. Lett. **71**, 2955.
Carstensen, H., R. Claessen, R. Manzke and M. Skibowski, 1990, Phys. Rev. B **41**, 9880.
Chadi, D.J., 1979, Phys. Rev. Lett. **43**, 43.
Chassé, T., M. Alonso, R. Cimino, W. Theis, W. Braun and K. Horn, 1993, Appl. Surf. Sci. **64**, 329.
Chelikowsky, J.R. and M.L. Cohen, 1979, Phys. Rev. B **20**, 4150.
Chen, Y., J. Hermanson and G.J. Lapeyre, 1989, Phys. Rev. B **39**, 12682.
Chiang, T.-C. and F.J. Himpsel, 1989, Electronic Structure of Solids: Photoemission Spectra and Related Data, Vol. III/23a. Landolt-Börnstein, Numerical Data and Functional Relationships in Science and Technology. Springer-Verlag, Berlin, Chapter 2.1.
Chiaradia, P., A. Cricenti, S. Selci and G. Chiarotti, 1984, Phys. Rev. Lett. **52**, 1145.
Chiarotti, G., S. Nannarone, R. Pastore and P. Chiaradia, 1971, Phys. Rev. B **4**, 3398.
Cho, A.Y., 1976, J. Appl. Phys. **47**, 2841.
Cho, A.Y, 1971, J. Appl. Phys. **42**, 2074.
Coehoorn, R., C. Haas, J. Dijkstra, C.F.J. Flipse, R.A. de Groot and A. Wold, 1987, Phys. Rev. B **35**, 6195.
Demuth, J.E., B.N.J. Persson and A.J. Schell-Sorokin, 1983, Phys. Rev. Lett. **51**, 2214.
Ding, S.-A., G. Neuhold, J.H. Weaver, P. Häberle, K. Horn, O. Brandt, H. Yang and K. Ploog, 1996, J. Vac. Sci. Technol. A **14**, 819.

Dhesi, S.S., C.B. Stagarescu, K.E. Smith, D. Doppalapudi, R. Singh and T.D. Moustakas, 1997, Phys. Rev. B **56**, 10271.
Drathen, P., W. Ranke and K. Jacobi, 1978, Surf. Sci. **77**, L162.
Drube, W., D. Straub and F.J. Himpsel, 1987, Phys. Rev. B **35**, 5563.
Duke, C.B., 1996, in: Handbook of Surface Science, Vol. 1, ed. W. Unertl. North-Holland, Amsterdam, Chapter 6.
Eastman, D.E., T.-C. Chiang, P. Heimann and F.J. Himpsel, 1980, Phys. Rev. Lett. **45**, 656.
Ebert, Ph., 1999, Surf. Sci. Rep. **33**, 121.
Ebert, Ph., B. Engels, P. Richard, K. Schroeder, S. Blügel, C. Domke, M. Heinrich and K. Urban, 1996, Phys. Rev. Lett. **77**, 2997.
Engels, B., P. Richard, K. Schroeder, S. Blügel, Ph. Ebert and K. Urban, 1997, Phys. Rev. B.
Enta, Y., S. Suzuki and S. Kono, 1990a, Phys. Rev. Lett. **65**, 2704.
Enta, Y., S. Suzuki, S. Kono and T. Sakamoto, 1990b, J. Phys. Soc. Jpn. **59**, 657.
Farrow, R.F.C., D.S. Robertson, G.M. Williams, A.G. Cullis, G.R. Jones, I.M. Young and P.N.J. Dennis, 1981, J. Cryst. Growth **54**, 507.
Feenstra, R.M., 1991, Phys. Rev. B **44**, 13791.
Feenstra, R.M., J.A. Stroscio, J. Tersoff and A.P. Fein, 1987, Phys. Rev. Lett. **58**, 1192.
Feenstra, R.M. and A.J. Slavin, 1991, Surf. Sci. **251/252**, 401.
Feenstra, R.M., 1994, Phys. Rev. B **50**, 4561.
Finteis, T., M. Hengsberger, T. Straub, K. Fauth, R. Calessen, P. Auer, P. Steiner, S. Hüfner, P. Blaha, M. Vögt, M. Lux-Steiner and E. Bucher, 1997, Phys. Rev. B **55**, 10400.
Fujita, M., H. Nagayoshi and A. Yoshimori, 1991, Surf. Sci. **242**, 229.
Furthmüller, J., J. Hafner and G. Kresse, 1996, Phys. Rev. B **53**, 7334.
Graupner, R., M. Hollering, A. Ziegler, J. Ristein and L. Ley, 1997, Phys. Rev. B **55**, 10841.
Håkansson, M.C., L.S.O. Johansson, C.B.M. Andersson, U.O. Karlsson, L. Ö. Olsson, J. Kanski, L. Ilver and P.O. Nilsson, 1997, Surf. Sci. **374**, 73.
Hamers, R.J., R.M. Tromp and J.E. Demuth, 1986, Phys. Rev. Lett. **56**, 1972.
Haneman, D., 1961, Phys. Rev. **121**, 1093.
Hansson, G.V. and R.I.G. Uhrberg, 1988, Surf. Sci. Rep. **9**, 197.
Hansson, G.V. and R.I.G. Uhrberg, 1992, in: Angle-Resolved Photoemission, Theory and Current Applications, ed. S.D. Kevan. Elsevier, Amsterdam.
Harrison, W., 1979, J. Vac. Sci. Technol. **16**, 1492.
Himpsel, F.J., 1994, Surf. Sci. **299/300**, 535.
Himpsel, F.J. and D.E. Eastman, 1979, J. Vac. Sci. Technol. **16**, 1297.
Himpsel, F.J. and Th. Fauster, 1983, J. Vac. Sci. Technol. A **1**, 1111.
Himpsel, F.J., P. Heimann and D.E. Eastman, 1981, Phys. Rev. B **24**, 2003.
Himpsel, F.J. and Th. Fauster, 1984, J. Vac. Sci. Technol. A **2**, 815.
Himpsel, F.J., P. Heimann, T.-C. Chiang and D.E. Eastman, 1980, Phys. Rev. Lett. **45**, 1112.
Himpsel, F.-J., 1990, Surf. Sci. Rep. **12**, 1.
Hirschorn, E., D.S. Lin, F.M. Leibsle, A. Samsavar and T.-C. Chiang, 1992, Phys. Rev. B **44**, 1403.
Höchst, H. and I. Hernandez-Calderon, 1983, Ann. Isr. Phys. Soc. **6**, 333.
Huff, W.R.A., M. Shimomura, N. Sanada, G. Kaneda, T. Takeuchi, Y. Suzuki, H.W. Yeom, T. Abukawa, S. Kono and Y. Fukuda, 1998, Phys. Rev. B **57**, 10132.
Hüfner, S., 1996, Photoelectron Spectroscopy, 2nd edn. Springer-Verlag, Berlin.
Huijser, A., J. van Laar and T.L. van Rooy, 1978, Phys. Lett **65** A, 337.
Ihm, J., D.H. Lee, J.D. Joannopoulos and J.J. Xiong, 1983, Phys. Rev. Lett. **51**, 1872.
Inglesfield, J.E. and E.W. Plummer, 1992, in: Angle-Resolved Photoemission, ed. S.D. Kevan. Elsevier, Amsterdam.
Janowitz, C., L. Kipp, R. Manzke and B.A. Orlowski, 1990, Surf. Sci. **231**. 25.
Johansson, L.S.O., E. Landemark, G.V. Hansson and R.I.G. Uhrberg, 1989, Surf. Sci. **211/212**, 578.
Johansson, L.S.O., E. Landemark, G.V. Hansson and R.I.G. Uhrberg, 1990, Phys. Rev. B **42**, 1305.
Kahn, A., 1983, Surf. Sci. Rep. **3**, 193.
Karlsson, C.J., E. Landemark, Y.-C. Chao and R.I.G. Uhrberg, 1994, Phys. Rev. B **50**, 5767.
Karlsson, H., G. Ghiaia and U.O. Karlsson, 1998, Surf. Sci. Lett. **407**, L687.

Kevan, S.D. and N.G. Stoffel, 1984, Phys. Rev. Lett. **53**, 702.
Khazmi, Y., J. Kanski, P.O. Nilsson, Z. Lin, M.C. Håkansson and U.O. Karlsson, 1992, Surf. Sci. **269/270**, 844.
Kipp, L., R. Manzke and M. Skibowski, 1995, Solid State Commun. **93**, 603.
Krüger, P. and J. Pollmann, 1995, Phys. Rev. Lett. **74**, 115.
Krüger, P., A. Mazur, J. Pollmann and G. Wolfgarten, 1986, Phys. Rev. Lett. **57**, 1486.
Lambrecht, W.R.L. and B. Segall, 1994, in: Properties of the Group III Nitrides, ed. J.H. Edgar. EMIS Datareviews Series, London, p. 125.
Landemark, E., C.J. Karlsson, Y.-C. Chao and R.I.G. Uhrberg, 1992, Phys. Rev. Lett. **69**, 1588.
Larsen, P.K., J.F. van derVeen, A. Mazur, J. Pollmann, J.H. Neave and B.A. Joyce, 1982, Phys. Rev. B **26**, 3222.
Larsen, P.K., J.H. Neave, J.F. van derVeen, P.J. Dobson and B.A. Joyce, 1983, Phys. Rev. B **27**, 4966.
Larsen, P.K., S. Chiang and N.V. Smith, 1977, Phys. Rev. B **15**, 3200.
Leckey, R.C.G. and J.D. Riley, 1992, Crit. Rev. Solid State Mat. Sci. **17**, 307.
LeLay, G., 1995, Prog. Surf. Sci. **48**, 145.
LeLay, G., M. Göhtelid, T.M. Grehk, M. Björkquist, U.O. Karlsson and V.Y. Aristov, 1994, Phys. Rev. B **50**, 14277.
Lu, Z.-Y., G.L. Chiarotti, S. Scandolo and E. Tosatti, 1998, Phys. Rev. B **58**, 13698.
Lüth, H., 1995, Surfaces and Interfaces of Solids, 3rd edn. Springer-Verlag, Berlin.
MacLaren, J.M., J.B. Pendry, P.J. Rous, D.K. Saldin, G.A. Somorjai, M.A. van Hove and D.D. Vvedensky, 1987, Surface Crystallographic Information Service: A Handbook of Surface Structures. Reidel, Dordrecht, 352 pp.
Magnusson, K.O. and S.A. Flodström, 1988, Phys. Rev. B **38**, 6137.
Magnusson, K.O., S.A. Flodström and P.E.S. Persson, 1988, Phys. Rev. B **38**, 5384.
Magnusson, K.O., U.O. Karlsson, D. Straub, S.A. Flodström and F.J. Himpsel, 1987, Phys. Rev. B **36**, 6566.
Magnusson, K.O.M., G. Neuhold, D.A. Evans and K. Horn, 1998, Phys. Rev. B **57**, 8945.
Manzke, R., H.P. Barnscheidt, C. Janowitz and M. Skibowski, 1987, Phys. Rev. Lett. **58**, 610.
Mårtensson, P., A. Cricenti and G.V. Hansson, 1985, Phys. Rev. B **32**, 6959.
Mårtensson, P., A. Cricenti and G.V. Hansson, 1986, Phys. Rev. B **33**, 8855.
Mårtensson, P., W.-X. Ni, G.V. Hansson, J.M. Nicholls and B. Reihl, 1987, Phys. Rev. B **36**, 5974.
Matz, R., H. Lüth and A. Ritz, 1983, Solid State Commun. **46**, 343.
Meade, R.D. and D. Vanderbilt, 1989, Phys. Rev. B **40**, 3905.
Middelmann, H.-U., L. Sorba, V. Hinkel and K. Horn, 1987, Phys. Rev. B **35**, 718.
Mönch, W., 1986, Solid State Commun. **58**, 215.
Mönch, W., 1995, Semiconductor Surfaces and Interfaces, 2nd edn. Springer, Berlin.
Neuhold, G., K. Horn, K.O. Magnusson and D.A. Evans, 1995, J. Vac. Sci. Technol. A **13**, 666.
Northrup, J.E., 1986, Phys. Rev. Lett. **57**, 154.
Northrup, J.E. and M.L. Cohen, 1982, Phys. Rev. Lett. **49**, 1349.
Northrup, J.E., M.S. Hybertsen and S.G. Louie, 1991, Phys. Rev. Lett. **66**, 500.
Olmstead, M. and N.M. Amer, 1984, Phys. Rev. Lett. **52**, 1148.
Ölsson, L.Ö., C.B.M. Andersson, M.C. Håkansson, J. Kanski, L. Ilver and U.O. Karlsson, 1996, Phys. Rev. Lett. **76**, 3626.
Paggel, J.J., W. Theis, K. Horn, Ch. Jung, C. Hellwig and H. Petersen, 1994, Phys. Rev. B **50**, 18686.
Pandey, K.C., 1981, Phys. Rev. Lett. **47**, 1913.
Pandey, K.C., 1982, Phys. Rev. Lett. **49**, 223.
Pehlke, E. and M. Scheffler, 1993, Phys. Rev. Lett. **71**, 2338.
Pensl, G. and R. Helbig, 1990, in: Festkörperprobleme: Advances in Solid State Physics, ed. U. Rössler. Vieweg, Braunschweig.
Pepper, S.V., 1982, Surf. Sci. **123**, 47.
Perfetti, P., J.M. Nicholls and B. Reihl, 1987, Phys. Rev. B **36**, 6160.
Phillips, J.C., 1973, Bonds and Bands in Semiconductors. Academic Press, New York.
Piancastelli, M.N., J.J. Paggel, M. Hasselblatt, Ch. Weindl and K. Horn, 1997, Phys. Rev. B **58**, 12737.
Qu, H., J. Kanski, P.O. Nilsson and U.O. Karlsson, 1991, Phys. Rev. B **43**, 14589.
Qu, H., J. Kanski, P.O. Nilsson and U.O. Karlsson, 1991a, Phys. Rev. B **44**, 1762.
Qu, H., J. Kanski, P.O. Nilsson and U.O. Karlsson, 1991b, Phys. Rev. B **43**, 9843.
Rowe, J. and H. Ibach, 1974, Phys. Rev. Lett. **32**, 421.

Schlier, R.E. and H.E. Farnsworth, 1959, J. Chem. Phys. **30**, 917.
Schmeits, M., 1990, Surf. Sci. **251**, 389.
Schmidt, W.G. and F. Bechstedt, 1996, Phys. Rev. B **54**, 16742.
Schönhammer, K. and O. Gunnarsson, 1977, Solid State Commun. **23**, 691.
Shevchik, N.J., J. Tejeda and M. Cardona, 1974, Phys. Rev. B **9**, 2627.
Shkrebtii, A.I., R. Di Felice, C.M. Bertoni and R. Del Sole, 1995, Phys. Rev. B **51**, 11201.
Smit, L., T.E. Derry and J.F. van der Veen, 1985a, Surf. Sci. **150**, 245.
Smit, L., R.M. Tromp and J.F. van der Veen, 1985b, Surf. Sci. **163**, 315.
Smith, A.R., R.M. Feenstra, D.W. Greve, J. Neugebauer and J.E. Northrup, 1997, Phys. Rev. Lett. **79**, 3934.
Smith, N.V., M.M. Traum and F.J. DiSalvo, 1974, Solid State. Commun. **15**, 211.
Smith, N.V., 1988, Rep. Prog. Phys. **51**, 1227.
Sorba, L., V. Hinkel, H.U. Middelmann and K. Horn, 1987, Phys. Rev. B **36**, 8075.
Stampfl, A.P.J., Ph. Hofmann, O. Schaff, A.M. Bradshaw, 1997, Phys. Rev. B **55**, 9679.
Stoffel, N.G., 1983, Phys. Rev. B **28**, 3306.
Straub, D., L. Ley and F.J. Himpsel, 1985a, Phys. Rev. Lett. **54**, 142.
Straub, D., M. Skibowski and F.J. Himpsel, 1985b, J. Vac. Sci. Technol. A **3**, 1484.
Stich, I., M.C. Payne, R.D. King-Smith, J.-S. Lin, 1992, Phys. Rev. Lett. **68**, 1351.
Strite, S. and H. Morkoç, 1992, J. Vac. Sci. Technol. B **10**, 1237.
Takahashi, T. and E. Ebina, 1982, Appl. Surf. Sci. **11/12**, 268.
Takayanagi, K., T. Tanishiro, M. Takahashi and S. Takahashi, 1985, J. Vac. Sci. Technol. A **3**, 1502.
Takeuchi, N., A. Selloni and E. Tosatti, 1992, Phys. Rev. Lett. **69**, 648.
Tersoff, J. and D.R. Hamann, 1983, Phys. Rev. Lett. **50**, 1998.
Tersoff, J., 1984, Phys. Rev. Lett. **52**, 465.
Tersoff, J., 1985, Phys. Rev. B **32**, 6968.
Thiry, P., Y. Petroff, R. Pinchaux, C. Guillot, Y. Ballu, J. Lecante, J. Paigné and F. Levy, 1977, Solid State Commun. **22**, 685.
Tong, S.Y., H. Huang, C.M. Wei, W.E. Packard, F.K. Men, G. Glander and M.B. Webb, 1988, J. Vac. Sci. Technol. A **6**, 615.
Traving, M., M. Boehme, L. Kipp, M. Skibowski, F. Starrost, E.E. Krasovski, A. Perlov and W. Schattker, 1997, Phys. Rev. B **55**, 10392.
Tromp, R.M., R.J. Hamers and J.E. Demuth, 1985, Phys. Rev. Lett. **55**, 1303.
Tsui, D.C., 1970, Phys. Rev. Lett. **24**, 303.
Uhrberg, R.I.G. and G.V. Hansson, 1991, Crit. Rev. Solid State Mat. Sci. **17**, 133.
Uhrberg, R.I.G., G.V. Hansson, J.M. Nicholls and S.A. Flodström, 1982, Phys. Rev. Lett. **48**, 1032.
Uhrberg, R.I.G., T. Kaurila and Y.-C. Chao, 1998, Phys. Rev. B **58**, R1730.
Wang, Y.R., C.B. Duke, K. Stevens, A. Kahn, K.O. Magnusson and S.A. Flodström, 1988, Surf. Sci. **206**, L817.
Wertheim, G.K. and S.B. DiCenzo, 1986, J. Electron Spectrosc. Relat. Phenom. **40**, 301.
Wilke, W.G., R. Seedorf and K. Horn, 1989a, J. Vac. Sci. Technol. **B 7**, 807.
Wilke, W.G., V. Hinkel, W. Theis and K. Horn, 1989b, Phys. Rev. B **40**, 9824.
Williams, G.P., F. Cerrina, G.J. Lapeyre, J.R. Anderson, R.J. Smith and J. Hermanson, 1986, Phys. Rev. B **43**, 5548.
Wu, C.I. and A. Kahn, 1999, Appl. Phys. Lett. **74**, 546.
Xue, J.Y., A.P.J. Stampfl, D. Wolfframm, D.A. Evans, M. Hollering, L. Ley, J.D. Riley and R.C.G. Leckey, 1998, Surf. Sci. **401**, L401.
Yamaguchi, H. and Y. Horikoshi, 1995, Phys. Rev. B **51**, 9836.
Yu, P.Y. and M. Cardona, 1996, Fundamentals of Semiconductors. Springer-Verlag, Berlin.
Zhang, X.D., R.C.G. Leckey, J.D. Riley, J. Faul and L. Ley, 1993, Phys. Rev. B **48**, 5300.
Zhu, Z., N. Shima and M. Tsukuda, 1981, Phys. Rev. B **24**, 2303.
Zhu, X., S.B. Zhang, S.G. Louie and M.L. Cohen, 1989, Phys. Rev. Lett. **63**, 2112.

This Page Intentionally Left Blank

CHAPTER 8

# Surface States on Metal Surfaces

S.D. KEVAN

*Physics Department*
*University of Oregon*
*Eugene, OR, USA 97403*

*© 2000 Elsevier Science B.V.*
*All rights reserved*

*Handbook of Surface Science*
*Volume 2, edited by K. Horn and M. Scheffler*

# Contents

8.1. Introduction . . . . . 435
8.2. Surface state phenomena on low-index metals surfaces . . . . . 438
8.2.1. Surface states on low index copper surfaces . . . . . 438
8.2.2. Surface electronic structure of Be(0001) . . . . . 447
8.2.3. Surface electronic structure of Al(001) and Al(111) . . . . . 454
8.2.4. Surface electronic structure of Ta(011) . . . . . 457
8.3. Interaction of surface states on metals with adsorbed atoms . . . . . 461
8.3.1. Alkali adsorption on Cu(111) . . . . . 463
8.3.2. Lithium adsorption on Be(0001) . . . . . 467
8.3.3. Adsorption of monovalent atoms on Ta(011) . . . . . 470
8.3.4. Chemisorbed layers and the theory of random alloys . . . . . 474
8.4. Non-adiabatic effects and surface electronic structure . . . . . 476
8.4.1. Fermi contours, intraband excitations, and zone center phonons . . . . . 481
8.4.2. Vibrational damping on Mo(001)–2H and W(001)–2H . . . . . 485
8.4.3. Vibrational damping and phonon anomalies . . . . . 487
8.4.4. Reconstruction of W(001) and Mo(001) . . . . . 490
8.5. Lateral interactions and adsorbate periodicities . . . . . 494
8.5.1. Ordering and reconstruction for O/Mo(011) and O/W(011) . . . . . 496
8.5.2. Peierls instability in thallium chains on Cu(001) . . . . . 500
8.6. Concluding remarks . . . . . 503
References . . . . . 504

## 8.1. Introduction

Sixty years ago, not long after the initial development of the band theory of solids, interest in surface-related perturbations to this theory arose. The concept of an electronic surface state, that is, a state at an energy in a bulk band gap and having a wave function localized near the surface barrier, was born (Tamm, 1932; Maue, 1935; Goodwin, 1939a, b, c; Shockley, 1939). Since that time, the existence of surface states of one type or another has been invoked to explain a diverse array of surface phenomena ranging from Fermi level pinning and Schottky barrier formation to mediation of adsorbate lateral interactions and damping of adsorbate vibrations. In the past twenty years, aided by the routine availability of ultrahigh vacuum and the contemporaneous development of an alphabet soup of experimental and computational probes of surface properties, our understanding of surface state phenomena has progressed from conjecture to become a true science. This chapter provides a general, though certainly not encyclopedic, review of these conceptual developments in the experimental study of surface states located on metal surfaces. More complete treatments of the experimental, theoretical, and computational aspects of the surface electronic structure of metals may be found in other reviews and in previous chapters of this book (Plummer and Eberhardt, 1982; Kevan and Eberhardt, 1992; Inglesfield, 1981a, 1987; Davison and Levine, 1970; Prutton, 1984; Davison and Streslicka, 1992; Forstmann, 1978; Himpsel, 1985; Smith and Kevan, 1991a).

The first experimental evidence for the existence of a surface state on a metal surface came from early measurements of the energy distribution of electrons field emitted from a W(001) tip (Swanson and Crouser, 1967a, b). In actual fact, originally these measurements were interpreted in terms of a bulk rather than a surface effect and it was not until some time later that the precise identification of a surface state was accomplished (Plummer and Gadzuk, 1970; Waclawski and Plummer, 1972; Feuerbacher and Fitton, 1972). The original spectral evidence, presented in Fig. 8.1, provides one of the paradigms still used today. The figure shows curves from a clean and contaminated surface – the so-called "crud test" – wherein the particular sensitivity of surface states to contamination is clearly revealed. It is not surprising that the combination of this metal with this technique should provide such a proving ground in this area. The field of surface science was essentially born on studies of tungsten due primarily to the simplicity of preparing its surfaces, and techniques related to field emission were some of the first generally applied. Indeed, surface states on clean metal surfaces were identified several years before similar states on semiconductor (i.e., silicon) surfaces (Eastman and Grobman, 1972; Wagner and Spicer, 1972). Unfortunately, the complexity of the electronic structure of a 5d transition metal precluded a thorough understanding of the observed surface state until the mid 1980's when relativistic effects could be adequately included in modern calculations of surface band structures (Mattheiss and Hamann, 1984).

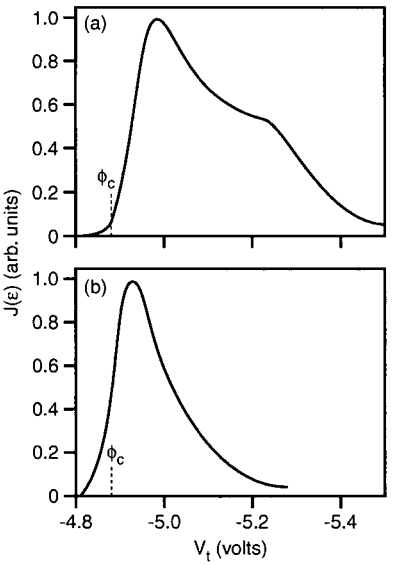


Fig. 8.1. Early field emission energy distribution curves collected from a (a) clean and (b) ZrO-contaminated tungsten tip of (001) orientation. The disappearance of a high-energy shoulder in the lower curve provided the first evidence for the existence of a surface state on a clean metal surface. From Swanson and Crouser (1967a).

Soon after the discovery of the W(001) surface state, a much simpler state was discovered on Cu(111) (Gartland and Slagsvold, 1975). The power of a new technique, angle-resolved photoemission (ARP), in the study of surface electronic structure became apparent in part through the work of Gartland and Slagsvold. This technique, which has been the subject of several previous chapters in this book, allows systematic variation of energy and momentum so that dispersion relations may be easily measured. It also can be applied to any conductor without need of forming a field emission tip. Figure 8.2 reproduces the original ARP work on this system, and the sensitivity to contamination or surface disorder of the emission feature near 0.4 eV binding energy relative to the Fermi energy is clearly evident. This and related surface states on noble metal surfaces have provided an excellent and enduring focus for experiments and computations as described further in previous chapters and in the next section. At present, low index single crystal surfaces of a wide array of metals have been successfully studied using ARP, and many surface bands have been detected and studied.

The Cu(111) state mentioned above and also a closely related state on Au(111) have recently been the subject of what is undoubtedly a crowning achievement in the characterization of surface states on metals, that is, their direct observation in real space using scanning tunneling microscopy (STM) (Crommie et al., 1993; Hasegawa and Avouris, 1993). In principle this would be very difficult for a perfect surface since the band velocity of these traveling states is much too high to allow a "snap shot" to be taken with the STM. A uniform charge density would therefore be observed. For an imperfect surface, however, this problem can be overcome. The relevant results, shown in Fig. 8.3 for Cu(111), are

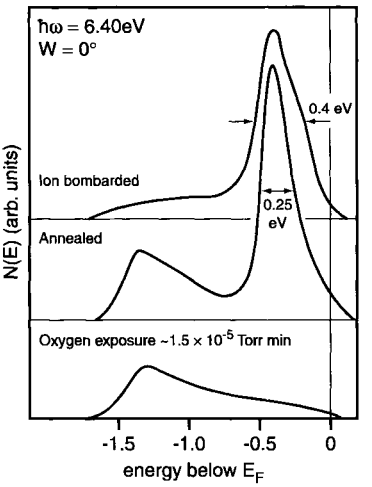


Fig. 8.2. ARP spectra collected from a clean (middle), ion bombarded (top), and contaminated (bottom) Cu(111) surface at a photon energy of 6.4 eV. The feature at ~0.4 eV binding energy exhibits substantial sensitivity to contamination and also passes other tests to confirm that it arises from a surface state. From Gartland and Slagsvold (1975).

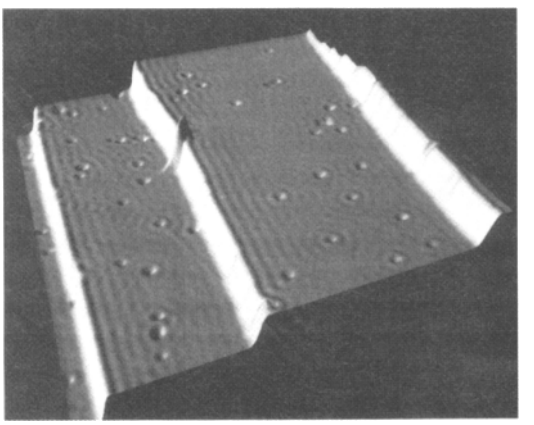

Fig. 8.3. Constant current STM image of Cu(111) collected at a positive bias of 0.1 Volt. The sample was at 4 K. Linear and circular standing waves observed near steps and point defects, respectively, arise from scattering of electrons in the surface state from Fig. 8.2. From Crommie et al. (1993).

both visually revealing and indicative of many interesting future possibilities. The figure shows a constant current STM image of Cu(111) collected at a positive bias of 0.1 V and a tunneling current of 1 nA. Near steps and point defects, the 2D traveling Bloch waves associated with the surface band are scattered into standing waves with a periodicity of ~15 Å which are clearly visible in the figure. The periodicity of the standing wave can be varied by changing the bias on the tip, thereby sampling a different initial state energies.

These charge-density-oscillations may be loosely viewed as energy-resolved Friedel oscillations (Friedel, 1954) and are thus intimately associated with electronic screening. As such they can play a role in determining the potential energy surface describing the lateral interaction energy between adsorbed atoms or between steps on the surface (Lau and Kohn, 1978; Einstein, 1991; Johansson, 1979). In essence, the surface-state-mediated interaction arises from the overlap of standing wave fields from neighboring imperfections. For magnetic impurities, similar standing waves would be related to the exchange splitting of the substrate sp-band, an integral part of the RKKY interaction (Ruderman and Kittel, 1954; Yoshida, 1957; Van Vleck, 1962).

Following a brief description of experimental aspects of characterizing surface states on metals and the impact these activities have had upon calibrating computational procedures, the focus of this chapter will be upon the way in which surface states can and do impact metal surface properties like those described in the previous paragraph. How do surface states participate in bonding to adsorbates? How can they mediate lateral interactions and help to determine adsorbate periodicities or the metallic character of a surface? Are surface states dynamically "active"? That is, are they involved significantly in surface dynamical processes such as charge exchange and energy transfer? These are the kinds of questions which will occupy researchers in the field for years to come.

## 8.2. Surface state phenomena on low-index metals surfaces

The emphasis of this review is upon surface states on nominally clean metal surfaces. Moreover, we focus mainly upon states located energetically near the Fermi level, $E_F$. We have narrowed the focus in this way because many of the questions posed at the end of the previous section are particularly pertinent to states near $E_F$. For this reason, we initiate our discussion using as examples states on low index copper surfaces and Be(0001) where a direct relationship between the bulk Fermi surface and the surface Fermi contours can be drawn. We continue our discussion of surface states with Al(001), where one would hope things would be equally simple. Finally, we conclude with a discussion of Ta(011) to assess the extent to which ideas derived from simple metals can be easily extended to transition metals.

### *8.2.1. Surface states on low index copper surfaces*

Like any defect state, a true surface state exists in a band gap. Unlike most other defect states, however, a surface state exists in periodic manifold, that is, it is localized near a surface with two-dimensional periodicity. For this reason, the "gap" in which a surface state exists need not be absolute. Rather, there need only be a gap in the bulk band structure at a given momentum parallel to the surface plane along a line in momentum space normal to this plane. This is why so many surface bands have been observed on metal surfaces despite the fact that there generally exists no absolute gap in the bulk band structure.

A good and often-studied example is Cu(111). Figure 8.4 shows the calculated bands for this metal along the [111] direction (Papaconstantopoulos, 1986). There exists a large gap which spans from about a 1 eV below $E_F$ to about 4 eV above $E_F$. This gap lies primarily in the sp manifold and arises principally from the relatively large $V_{111}$ pseudopotential

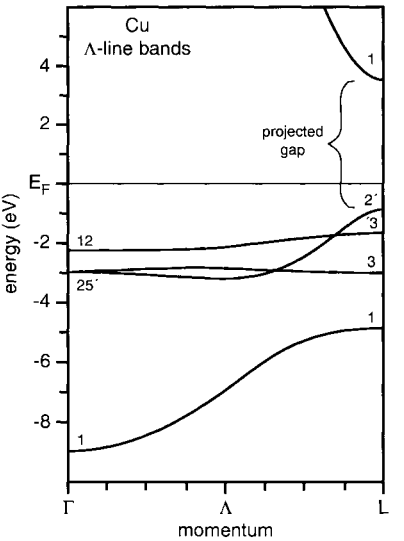


Fig. 8.4. Calculated bulk band structure of copper along the [111] direction. Note the absence of states from 0.9 eV below $E_F$ to ~4.0 eV above $E_F$, a condition that can lead to a surface state at the center of the Cu(111) SBZ (calculated using the code in Papaconstantopoulos, 1986).

coefficient in the noble metals. It is in this sense that the Cu(111) surface supports a "simple" surface state: it can be understood semiquantitatively using simple pseudopotential-based models which largely ignore the more complicated d-bands, as discussed in the chapter by Borstel and Eguiluz and elsewhere (Inglesfield, 1981a; Smith, 1985a; Weinert et al., 1985; Kevan, 1986a; Chen and Smith, 1987). The [111] direction is perpendicular to the (111) surface plane, and its component parallel to that plane is zero. Thus we can say that there is a projected band gap near $E_F$ at the center of the Cu(111) surface Brillouin zone (SBZ), i.e., near where the two dimensional component of the wave vector $\mathbf{k}_{\|}$ parallel to the surface plane is $(0, 0)$. Similar projections (either calculated or experimental) along lines at different $\mathbf{k}_{\|}$ indicate that this gap slowly closes for momenta further out into the SBZ.

The ARP spectra shown in Fig. 8.2 distinguish a feature at a binding energy of ~0.4 eV relative to $E_F$ for emission normal to the surface. Normal emission implies that the component of the final state photoelectron's momentum parallel to the surface plane is zero, independent of its energy. Using a 2D crystal momentum conservation relation similar to that operative in surface diffraction techniques, we deduce that the initial state associated with this feature also lies at $\mathbf{k}_{\|} = (0, 0)$. Given this combination of energy relative to $E_F$ and parallel momentum, the feature must lie within the projected gap discussed in the previous paragraph and is thus very likely a surface state. Moreover, the feature is "quenched" by adsorption of impurities, as indicated by the results of the "crud test" in Fig. 8.2. Finally, other results have shown that the energy of this feature depends only on parallel momentum, that is, it is a 2D state. These three "tests" – location in a projected gap, particular sensitivity to contamination, and dependence only upon parallel momentum – have become the paradigms for assignment of surface electron states using ARP.

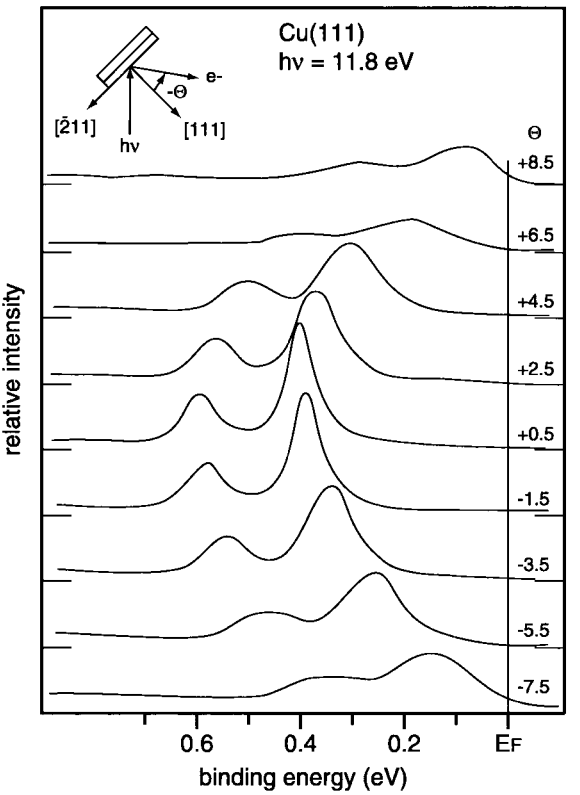


Fig. 8.5. High resolution spectra of the Cu(111) surface state as a function of emission angle using Ar I resonance radiation. Note the obvious parabolic dispersion about normal emission and thus about the center of the SBZ. The surface state is doubled due to the doublet character of the Ar I radiation. From Kevan (1983a).

The next logical step in characterizing a surface state is to measure its dispersion relation as a function of parallel momentum. The aforementioned parallel momentum conservation condition makes this is straightforward using ARP since the kinetic energy $E_K$ and the polar emission angle $\vartheta$ map directly into the magnitude of the photoelectron's parallel momentum using the kinematic relationship (Plummer and Eberhardt, 1982; Himpsel, 1985)

$$\mathbf{k}_{\|}\ (\text{Å}^{-1}) = 0.512\sqrt{E_K(\text{eV})}\sin(\vartheta). \tag{8.1}$$

The dispersion relation for the Cu(111) surface state was first determined by Gartland and Slagsvold (1975). Spectra which have lead to the most accurate determination to date are given in Fig. 8.5 (Kevan, 1983a; Tersoff and Kevan, 1983). These were collected using a high resolution analyzer coupled to a noble gas resonance lamp operating with the Ar I doublet, so the surface feature is seen doubled. The parabolic dispersion of the surface state is clearly evident up to the point where the feature disappears at $E_F$. Spectra like these can easily be converted using Eq. (8.1) into the dispersion relation shown in Fig. 8.6. The

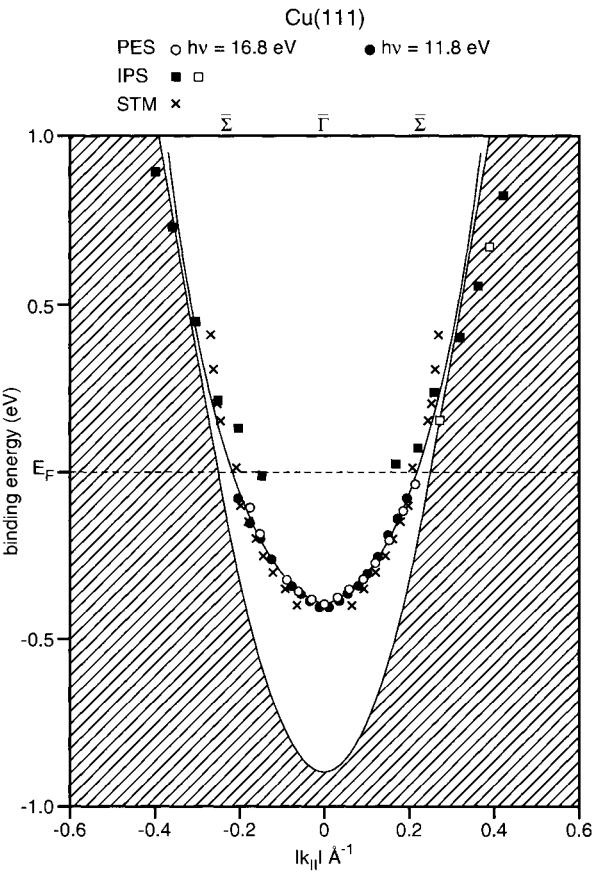


Fig. 8.6. Experimental and calculated dispersion relation for the Cu(111) zone-center surface band near $E_F$. Solid circles ● are ARP experimental points (Kevan, 1983a); ▲: inverse photoemission experimental points (Hulbert et al., 1985); ■: STM experimental points (Crommie et al., 1993); Solid curve: parabolic fit to ARP results; Dotted curve: parabolic fit to STM results; Dashed curve: calculated result (Euceda et al., 1983a). The shaded region is the experimentally-determined projected bulk continuum.

experimental points are accurately modeled using a parabolic band with an effective mass of 0.46 times the free electron mass $m_e$, and a band minimum 0.39 eV below $E_F$. Above the Fermi level the dispersion relation has been determined using inverse photoemission (Jacob et al., 1986; Hulbert et al., 1985). These results, also shown in Fig. 8.6, connect smoothly to the photoemission results.

The dispersion relation of this state has also been determined from the STM results mentioned in the Introduction (Crommie et al., 1993). In this case, one measures the periodicity of the standing wave, which gives directly the parallel wave vector at an energy related to the tip bias. Results from this determination are also given in Fig. 8.6. The parameters of the parabolic dispersion relation derived from this technique, band origin 0.44 eV below $E_F$ and effective mass of $0.38m_e$, are similar to those determined from ARP, though

not identical. One difference between the two data sets is that the latter was determined at 4 K, while the former was determined at 300 K. The binding energy of this state is known to increase as the temperature decreases (Knapp et al., 1979a), but the magnitude of this effect cannot explain a 50 meV shift in band origin, nor can it explain the observed difference in effective mass. The relaxation and screening processes operative in tunneling are very different from those in photoemission. It is likely that these many body effects explain the different results from these two determinations. Support for this conclusion is supplied by the observation that the Fermi wave vectors determined by the two techniques are identical, to within experimental error. Since the photohole self energy corrections go to zero near $E_F$, one should expect the Fermi wave vectors to be technique independent. A more precise explanation for the differences in effective mass and band origin energy awaits further theoretical effort.

The dashed curve in Fig. 8.6 gives the dispersion relation for this surface band calculated with fully self-consistent local-density-approximation (LDA) calculations (Euceda et al., 1983a). The band minimum lies at a binding energy of 0.58 eV, and the effective mass is $0.37m_e$. These parameters, while close to experiment, are nonetheless systematically different. These results are qualitatively similar to those for the measured and calculated bulk bands of alkali metals (Jensen and Plummer, 1985). LDA-based calculations of the electronic structure of metals tend to predict larger band widths and smaller effective masses than measured by ARP, an effect which might be improved by modifications to the LDA to include self energy corrections in the region of an inhomogeneous electron gas, the so-called gradient corrections (Hedin and Lundqvist, 1969; Hybertson and Louie, 1985, 1986; Northrup et al., 1986; Godby et al., 1987). As for the alkali metals, the calculated Fermi wave vector for the surface band is nearly identical to those measured by the two experiments. For the bulk alkalis, this equivalence is ensured by charge neutrality since the volume of the Fermi sphere is related to the total electronic charge. Taken together these results suggest that the energy and mass of the surface state are related to maintaining charge neutrality of the surface layers. The situation is clearly more complicated than in that bulk alkali metals, however, where charge neutrality is exact and only a single valence band is partially occupied. In principle, a surface layer need not be precisely charge neutral. However, if a good choice is made for the real-space integration volume, most metal surfaces are essentially neutral since any significant charge separation will be screened by the metallic electrons. Even assuming charge neutrality of the Cu(111) surface layers, however, there is still more than one band in the surface region: the surface state itself and bulk band from which it is derived. In principle a calculation could shift charge from one of these to the other while maintaining neutrality. It is thus relevant and important to compare not only the calculated surface band, but also the associated bulk continuum. This is an important and often overlooked shortcoming of calculations which use the slab geometry, since bulk states are not accurately reproduced without also carrying out a true bulk calculation using, for example, the self-consistent potential for the middle layer of the slab. The calculation for Cu(111) reported the edges of the bulk continua calculated in this way (Euceda et al., 1983a). The bottom of the continuum at $\bar{\Gamma}$ was deduced to lie 0.88 eV below $E_F$, while the experimental value is 0.75 eV (Gartland and Slagsvold, 1975; Lindau and Wallden, 1971). We thus see that the *splitting* of the surface band from the bottom of the bulk continuum is excellently reproduced in this case.

Despite the slight differences between experimental and calculated band masses and minimum energies, useful conclusions may be drawn from the measured dispersion relations. For example, the density of states, $g_{2D}(E)$, for a 2D parabolic electron band of effective mass $m^*$ above the band minimum is constant and equal to $m^*/\pi\hbar^2$ (Ashcroft and Mermin, 1976). For the state on Cu(111) with $m^* \approx 0.4m_e$, this translates to $g_{2D}(E_F) \approx 0.1$ electrons/eV/atom. This should be compared to the calculated sp density of states at $E_F$ for bulk copper of ~0.15 electrons/eV/atom (Papaconstantopoulos, 1986). The local density of states at the surface of this single surface band must be comparable to that in the bulk continuum with which it is associated since, if the surface is neutral, the sum of these two ought to sum roughly to the total bulk sp density of states. The impact of the charge division between bulk and surface states upon surface charge neutrality and the dynamical response of the surface region to external perturbations should thus not be underestimated. This simple argument ignores the significant delocalization of the charge in this surface band into the first few layers of the bulk metal. In other words, $g_{2D}(E)$ is not a "local density of states" (LDOS) in the usual sense. Rather, it is the LDOS over an area of one unit cell integrated along the surface normal.

ARP can be used to estimate the degree to which the surface state wave function penetrates the bulk layers (Louie et al., 1980; Kevan, 1986b; Kevan et al., 1985a; Hsieh et al., 1987). It is instructive to see qualitatively how this is done. The simple surface states considered here can be roughly considered to be composed of a damped oscillatory wave inside the crystal matched to a monotonically decaying wave outside. To zero order, the angle-resolved photoemission intensity is a measure of the Fourier transform of the initial state wave function at a wave vector given by that of the final state photoelectron. If we consider the emission intensity of a surface state as a function of final momentum normal to the surface at fixed parallel momentum, then we can approximately map the momentum distribution of the surface state wave function normal to the surface. A highly localized surface state will have a broad momentum distribution, while a state which significantly penetrates the bulk will have large intensity over only a narrow range of momenta.

The data in Fig. 8.7 present the relative emission intensity of the Cu(111) surface state at $\mathbf{k}_\parallel = 0$ as a function of normal momentum $k_\perp$ or equivalently, photon energy (Louie et al., 1980). The results indicate that the surface state under consideration is intermediate between the two extremes described above. Application of more careful models indicates a penetration length of ~5 Å, a result in reasonably good accord with calculations (Euceda et al., 1983a; Kevan, 1986b; Kevan et al., 1985a; Hsieh et al., 1987; Appelbaum and Hamann, 1978). Moreover, both these experimental results and the calculations indicate that a substantial fraction (~one third) of the charge in this state is localized in a lobe outside the surface plane. Thus a better representation of the LDOS at $E_F$ for this state is ~0.03 electrons/eV/surface atom, a number which still is 20% of the bulk sp density of states at $E_F$. The d-like surface bands discussed later in this chapter are often more highly surface-localized than the states considered here, and the contribution of these to surface properties can be correspondingly more pronounced.

The above discussion concerning the density of states at $E_F$ ignores another very important aspect of this problem, that is, the phonon enhancements of $g(E_F)$ (Ashcroft and Mermin, 1976; Ziman, 1960, 1970). These can be substantial, even for a simple metal where transport properties are dominated by sp electrons. The above comparison was ap-

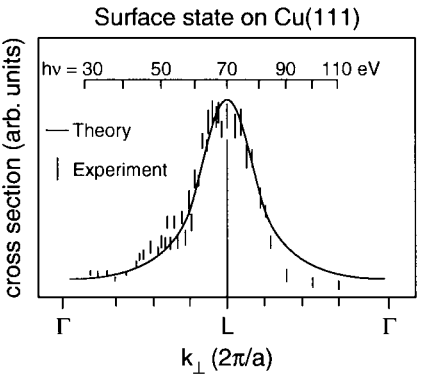


Fig. 8.7. Normalized ARP intensity of the Cu(111) surface state near $E_F$ at normal emission as a function of momentum normal to the surface. Note the intensity maximizes near an L point of the bulk band structure, confirming that the surface state exists in the projected gap at the L point. The width of the intensity distribution reflects the decay length of the surface state into the bulk. From Louie et al. (1980).

propriate since both the calculated bulk density of states and the experimentally derived partial surface density of states ignored the effect of the electron–phonon interaction upon the electronic density of states. Indeed, the surface band shown in Fig. 8.6 should be distorted by this interaction at energies within the Debye energy $\hbar\omega_D$, of $E_F$. That this is not seen is probably a reflection of limitations of the experimental techniques used. The Debye energy of copper is $\hbar\omega_D \sim 20$ meV. Correspondingly, the momentum range over which the deviations should be observable is $\hbar\omega_D/v_F \sim 0.005$ Å$^{-1}$, where the Fermi velocity $v_F \sim 4$ eV/Å$^{-1}$ can be determined from the dispersion relation. These energy and momentum scales were not accessible to the experiments reported in Fig. 8.6, although they may be in the near future. Observation of these electron–phonon-interaction induced distortions of a surface band would be a significant accomplishment since they are the "precursor" to formation of a superconducting gap.

The discussion of Fermi wave vectors in the preceding paragraph suggests that it might be useful to discuss the intrinsic surface states on low index copper and other noble metal surfaces in terms of the well-known Fermi surfaces for these metals (Halse, 1969). Figure 8.8, which shows a section of the experimentally determined copper Fermi surface in the ΓLUX plane of the bulk Brillouin zone, demonstrates this graphically. The nearly spherical Fermi surface for monovalent metals leads to a roughly circular cross section which is interrupted in the noble metals by well-known "necks" which contact the hexagonal faces of the Brillouin zone near the L-point. These result directly from the zone boundary hybridizational gap near $E_F$ in Fig. 8.4 discussed previously. If the Fermi surface is projected onto the (111) SBZ, this neck forms a projected gap, that is, there is a region near zone center where no points on the Fermi surface project. A Fermi contour associated with a surface localized electronic state can exist in this gap. The edges of this projected gap are represented in Fig. 8.6 by the limits of the projected bulk continuum at $E_F$. Indeed, the accurately measured dimension of the neck of the bulk Fermi surface was used in constructing this bulk band projection. The surface state discussed above does indeed form

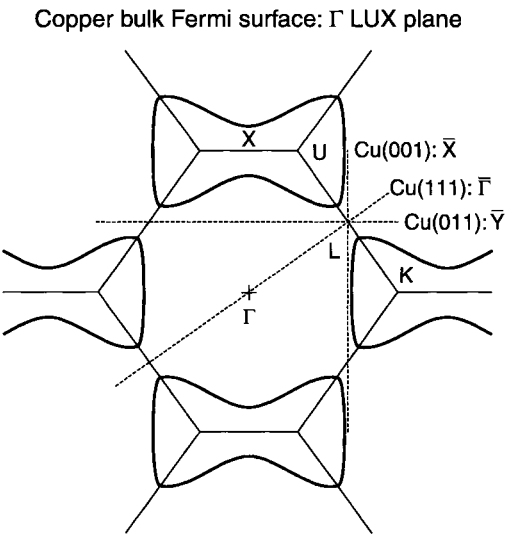


Fig. 8.8. Cross section of the bulk copper Fermi surface in the ΓLUX plane of the bulk Brillouin zone. The well-known necks near the L-points are readily apparent. These necks project as shown to form well-defined gaps onto all three low-index copper surfaces, and these gaps all support intrinsic surface states. Data taken from Halse (1969).

such a contour which lies entirely within the projected gap. The neck of the bulk Fermi surface and the surface Fermi contour have been measured to be highly isotropic about the [111] direction and the center of the SBZ, respectively (Kevan, 1986a).

Gaps are also observed when the section of the Fermi surface shown in Fig. 8.8 is projected along lines parallel to other high symmetry directions. For example, the length of the dog-bone-shaped hole pocket centered on the X point of the bulk Brillouin zone is slightly less than one half the projected momentum-space repeat distance along the [110] direction. This implies that projecting along lines parallel to the [001] direction will lead to a gap bounded by two separate "dog bone" structures, as shown in the Fig. 8.8. This gap exists at the $\bar{X}$ point of the SBZ on Cu(001), where a surface state might be expected to exist. Spectra indicating the existence of such a state are presented in Fig. 8.9 (Kevan, 1983a). The surface state (again seen doubled due to the use of the Ne I resonance lamp radiation) exists very close to $E_F$. It is thus energetically very narrow due to the limited phase space for radiationless decay of the final state photohole. As for Cu(111), the dispersion relation for this level has been measured and is shown in Fig. 8.10. The dashed curve in this figure is the result of an LDA-based self-consistent slab calculation of the Cu(001) surface electronic structure (Euceda et al., 1983a). The agreement between measured and calculated dispersion relations is perhaps better than one might expect, given the inherent limitations of LDA-based calculations in describing excited state properties discussed above and in previous chapters (Hedin and Lundqvist, 1969; Hybertson and Louie, 1985, 1986; Northrup et al., 1986; Godby et al., 1987). However, if we accept the arguments explored in the case of Cu(111) concerning the significant contributions of a surface band

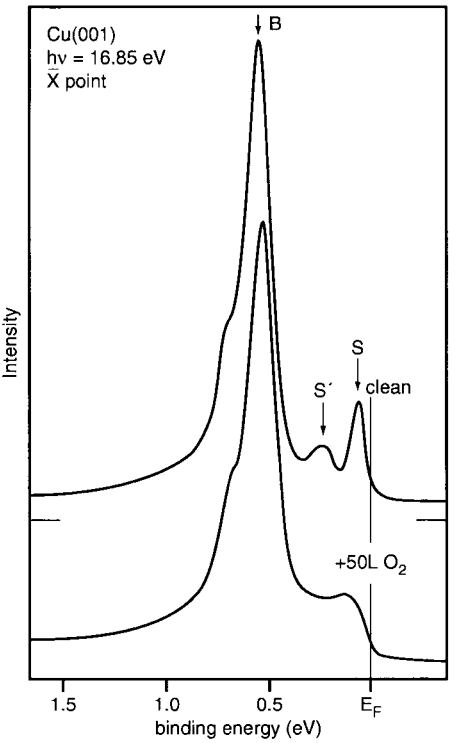


Fig. 8.9. High resolution ARP spectra of the Cu(001) surface in the vicinity of the $\bar{X}$ point of the SBZ collected using Ne I resonance radiation. Features labelled S and S′ very close to the Fermi level are the same surface state, seen doubled due to the presence of two closely spaced photon energies. The feature labelled B is attributed to the associated bulk band 6. From Kevan (1983a).

to the local density of states near a surface, this agreement between experiment and theory may be qualitatively understood. A self-consistent calculation of surface electronic structure will allow a surface band near $E_F$ to adjust to an energy to achieve approximate charge neutrality of the surface layers. This then requires that the area of the SBZ enclosed by a surface Fermi contour be well-predicted by calculations even if the dispersion relation itself is poorly reproduced. In the present instance, the surface band never deviates significantly below $E_F$, so the part of the dispersion relation probed by ARP will also be fairly well-described by the calculation.

At present, well-defined surface states associated with the zone-boundary hybridization at the L-point of the bulk Brillouin zone have been observed near $E_F$ on nearly every low index noble metal surface (Kevan et al., 1985a; Kevan and Gaylord, 1987; Heimann et al., 1977, 1979; Smith, 1985a; Johnson, 1992). Similar states have also been observed above $E_F$ on some surfaces of transition metals from the right side of the periodic chart (Smith, 1985a; Johnson, 1992; Dose, 1985). These have provided a very useful testing ground for both first principles computations in addition to the simple semiclassical phase analysis models presented in the chapter by Borstel and Eguiluz (Inglesfield, 1981a; Smith, 1985a;

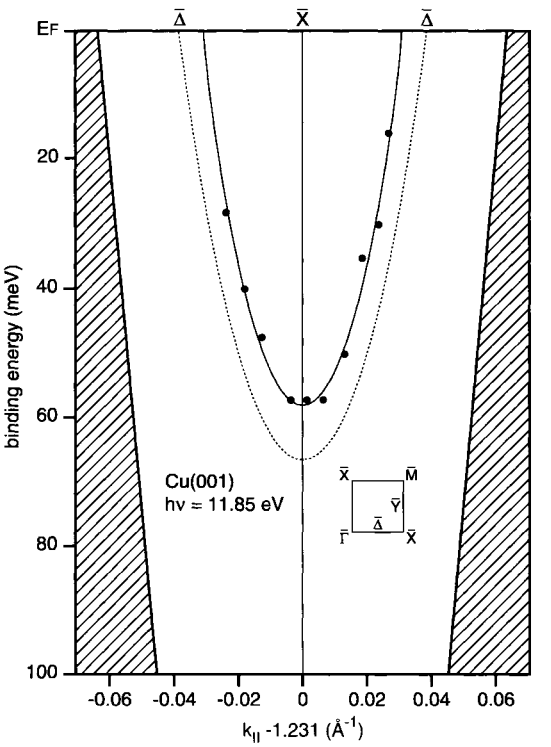


Fig. 8.10. Experimental and calculated dispersion relation for the Cu(001) $\bar{X}$ surface state near $E_F$. Experimental points are from Kevan (1983a); the solid curve is a parabolic fit to the experiment, and the dashed curve is the result of a calculation from Euceda et al. (1983a).

Weinert et al., 1985; Kevan, 1986a; Chen and Smith, 1987). In general these states are fairly well-described by existing theory. They will very likely continue to provide useful challenges to theory in the future from the perspective of trying to understand the excitation properties and the role of many-body effects in the photoemission process.

### *8.2.2. Surface electronic structure of Be(0001)*

Divalent metals present some interesting challenges that are not present in their monovalent counterparts. For example, a divalent solid is an insulator at appropriately large spacing, even in the single-particle picture. Group IIA and IIB elements are all metals in bulk form under normal conditions due to overlap between the first and second valence bands. This results from an interplay between hybridizational band width and the size of hybridizational band gaps. A stronger pseudopotential could open larger gaps, thereby forcing the entire first band below $E_F$ and rendering an insulating state (Mott, 1990). Alternatively, reducing the coordination number naturally decreases the band width and might also lead to an insulating state. Experimental results exist, for example, that indicate that a submono-

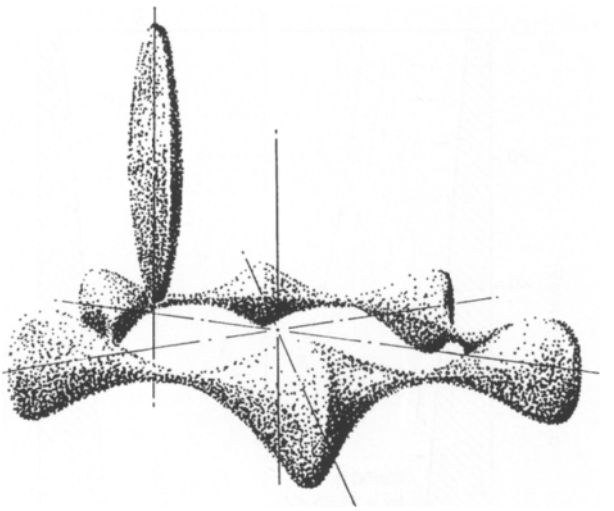

Fig. 8.11. Bulk Fermi surface of beryllium from Loucks and Butler (1964). Note the large projected gaps along lines perpendicular to the basal plane.

layer of alkaline earths adsorbed on Mo(112) and of mercury adsorbed onto copper and nickel are nonmetallic (Katrich et al., 1992; Dowben and Lagraffe, 1990; Dowben et al., 1991; Zhang et al., 1992). Reduced coordination near a surface normally makes the surface local density of states narrower than that of the bulk, and speculation has arisen that the surfaces of divalent metals might be insulating.

Of the alkaline earth metal surfaces, both the Be(0001) and Mg(0001) have received considerable experimental attention (Karlsson et al., 1982, 1984; Jensen et al., 1984; Bartynski et al., 1985, 1986; Watson et al., 1990, 1993). The former is closer to being an insulator. That is, the bulk density of states at $E_F$ is smaller for Be. Some studies of this surface are reviewed here. The bulk Fermi surface reproduced in Fig. 8.11 provides a graphic indication of how close beryllium is to being an insulator (Loucks and Butler, 1964). The relatively strong pseudopotential reduces the free electron Fermi surface to a thin hole "coronet" and six small electron "cigars" around the periphery of the hexagonal Brillouin zone. When the bulk Fermi surface is projected onto the (0001) SBZ, there is a very large projected gap which covers nearly the entire zone. One might expect that this gap to support a surface Fermi contour, and indeed it does. Among the elemental alkaline earth metals, beryllium exhibits anomalously large overall band widths and hybridizational band gaps. A useful and conceptually simple explanation for this behavior has been proposed (Hannon et al., 1993; Hannon, private communication). Beryllium has no p-symmetry core levels, so the p-like pseudopotential is thus strongly attractive. This leads, in some structures, to favorable hybridization with neighboring atoms thereby helping to overcome the energy required to promote a 2s electron into a 2p orbital to form a bond. The enhanced band width and band gaps naturally result.

The spectra in Fig. 8.12 were collected from a clean Be(0001) surface as a function of emission angle or $\mathbf{k}_{\|}$ in the $\bar{\Sigma}$ mirror plane of the surface Brillouin zone (Bartynski et al.,

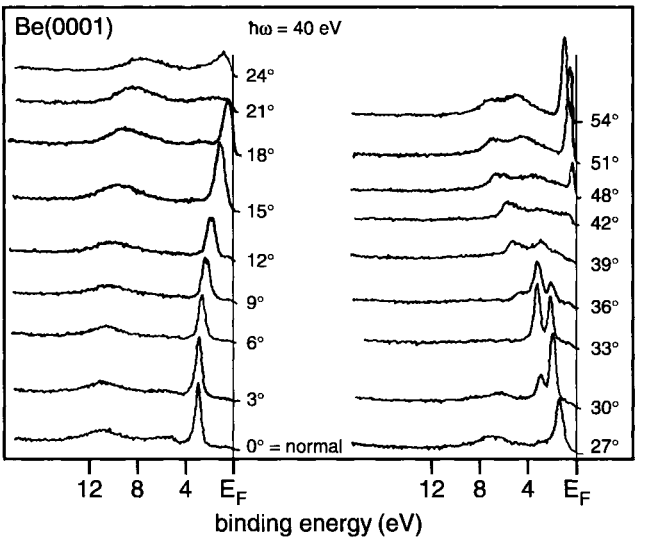


Fig. 8.12. ARP spectra collected from Be(0001) as a function of emission angle at a photon energy of 40 eV in the $\bar{\Gamma} \rightarrow \bar{M}$ azimuth. The large feature near 2.8 eV binding energy at normal emission is an intrinsic surface state with a parabolic dispersion relation centered in the SBZ. From Bartynski et al. (1985).

1985). Using the tests described in the previous section, the intense feature observed at normal emission has been determined to be a surface state. Much like Cu(111), a parabolic upward dispersion is indicated by the spectra collected at oblique emission angles. The dispersion relation derived from these spectra is given in Fig. 8.13 along with a projection of the calculated bulk band structure. The surface band is seen to lie in a large projected gap. In accord with Fig. 8.11, near the Fermi level this gap spans nearly the entire SBZ. The effective mass of the surface band is $m^* \sim 1.29 m_e$ (Watson et al., 1990), and it crosses $E_F$ outside the projection of the bulk Fermi surface to form a well-defined nearly circular surface Fermi contour. Using the simple ideas presented in the previous section, this band contributes a partial density of states at $E_F$ of 0.23 electrons/eV/atom. This is a factor of 5–10 larger than the calculated bulk density of states at $E_F$ (Jensen et al., 1984; Nilsson et al., 1974; Wilk et al., 1978). It is clearly not appropriate to think of the Be(0001) surface as being less metallic than bulk beryllium. This conclusion is provided even more substance by the existence of a second band near $E_F$ in the vicinity of the $\bar{M}$ point of the SBZ, as observed in Figs. 8.12 and 8.13. This band, however, crosses into the bulk continuum just below $E_F$ so its impact upon $g_{2D}(E_F)$ is not easy to quantify.

The spectra in Fig. 8.14 indicate moreover that the zone center surface state on Be(0001) is fairly surface-localized (Bartynski et al., 1985). These were collected at normal emission, i.e., $k_\parallel = 0$, as a function of photon energy, or equivalently, $k_\perp$. Aside from a large intensity oscillation near $\hbar\omega = 20$ eV which is related to plasmon enhancements of the photoemission intensity rather than to delocalization of the surface state wave function, the surface state intensity exhibits a smooth and monotonic dependence upon photon energy. This suggests that the surface state does not penetrate significantly into the bulk, at least at zone

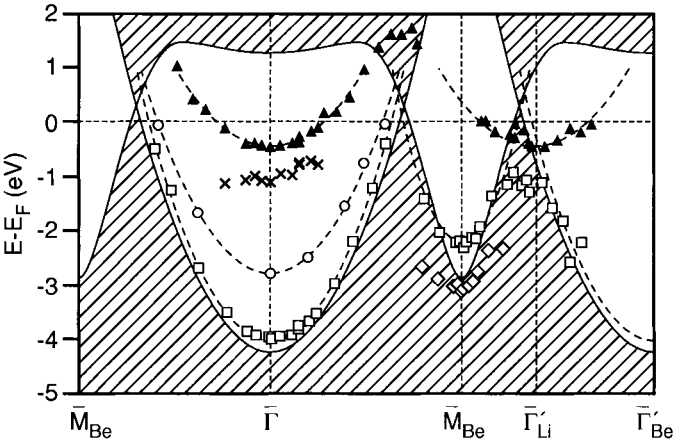


Fig. 8.13. Experimental and calculated dispersion relations for intrinsic surface states on clean Be(0001) (filled circles) and also after adsorption of a monolayer of lithium (open squares). The extrinsic Li-induced band is also shown (open circles). Experimental points below and above $E_F$ were determined with ARP and inverse photoemission, respectively (Bartynski et al., 1985) and (Watson et al., 1990). The latest calculated result from Feibelman (1992) is also shown (filled triangles, ▲). Dashed curves give the fitted parabolic dispersion relations.

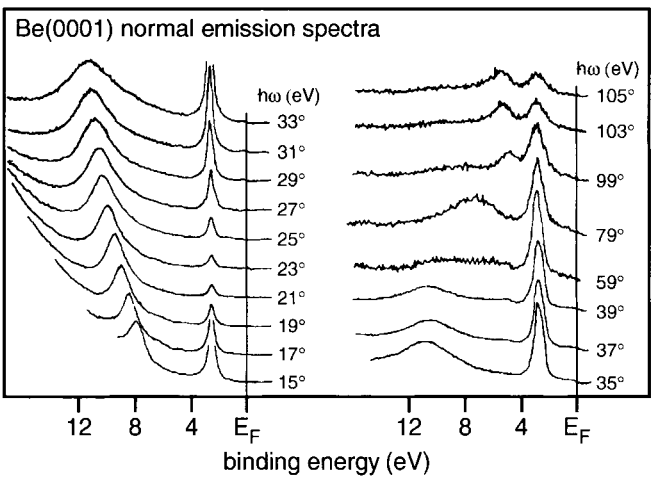


Fig. 8.14. ARP spectra of Be(0001) collected at normal emission as a function of photon energy (Bartynski et al., 1985). The intensity of the zone center surface state is observed to decrease monotonically as a function of photon energy, implying that the state is highly surface-localized.

center. By contrast, other data for the surface bands observed near $\bar{M}$ imply that these penetrate significantly into the bulk and thus make a much-reduced contribution to the surface LDOS at $E_F$. Simple pseudopotential-based models predict that the bulk penetration depth scales inversely with both the magnitude of the gap and also the energy separation from the bulk band edge (Goodwin, 1939a; Inglesfield, 1981a; Smith, 1985a; Kevan, 1986a).

For the zone center state on Be(0001), these are both large numbers and the surface state is predicted to be highly localized to the surface layer. There is discord among self-consistent slab calculations concerning the degree of localization of these states. An early calculation of a 3-layer slab found that the charge density contours for the surface state near $\bar{\Gamma}$ resembles an sp-like orbital projecting from and highly localized to the surface plane (Boettger and Trickey, 1986). A more recent calculation of a thicker slab found this state to be less surface localized, but that the states near $\bar{\mathrm{M}}$ are very highly localized (Feibelman, 1992).

The relatively large local density of states near $E_{\mathrm{F}}$ on Be(0001) bears some similarity to the situation on a narrower band transition metal or a semiconductor surface (Kevan and Eberhardt, 1992; Hansson and Uhrberg, 1992). In these cases, formation of a surface breaks "bonds" formed by relatively localized orbitals. These broken bonds form bands which would often be fairly narrow, thereby leading to a large local density of states at the surface. In many instances, this situation leads to an electronic instability which can cause surface reconstruction or formation of unusual magnetic structures. This overall similarity is really just qualitative, however. The surface band on Be(0001) is several volts wide and is thus comparable to a bulk band width in a simple metal. The Fermi velocity of the surface band is quite high and the likelihood of non-adiabatic interactions is correspondingly reduced. Indeed, recent measurements of the surface phonon dispersion relations on Be(0001) find no indication of phonon anomalies or incipient surface reconstruction (Hannon, private communication). The high surface/bulk density of states ratio results simply from the reduced dimensionality of the surface band. It is interesting, however, that this metal surface would be predicted to have radically different dielectric properties form the bulk material, a fact which suggests numerous experiments.

For example, recent core level photoemission results for Be(0001) report the observation of four distinct core levels, a very unusual result for a close-packed surface (Johansson et al., 1993). These have been assigned to the bulk and first three surface layers of the crystal. The original interpretation of these results invoked enhanced screening by 2p-derived charge in beryllium, that is, the anomalously large shifts were interpreted in terms of a final-state screening effect. The enhanced screening was attributed to the aforementioned attractive p-symmetry pseudopotential (Aldén et al., 1993). This interpretation would imply similarly anomalous behaviors on all low index beryllium surfaces, but recent results on Be($10\bar{1}0$) apparently do not support this expectation (Plummer, private communication). A better explanation invokes core holes which are differentially screened according to their separation from the highly metallic outermost surface layer. While many of the unusual properties of beryllium and its surfaces (including ultimately the surface band on Be(0001)) might result from the attractive p-symmetry pseudopotential (Hannon et al., 1993; Feibelman, 1992; Davis et al., 1992), the anomalous core level spectra on Be(0001) are apparently only indirectly related.

Thus far we have ignored an important facet of interpreting ARP spectra. That is, we have assumed that it is a simple matter to reduce spectra like those in Figs. 8.5 and 8.12 to the dispersion relations in Figs. 8.6 and 8.13. This in principle cannot be done accurately without understanding the underlying line shapes since these are intricately coupled to our ability to determine the "energy" of a given peak. Unfortunately, while significant progress has been achieved (Claessen et al., 1992; Inglesfield and Plummer, 1992), a complete theoretical understanding of valence band photoemission line shapes has not been developed

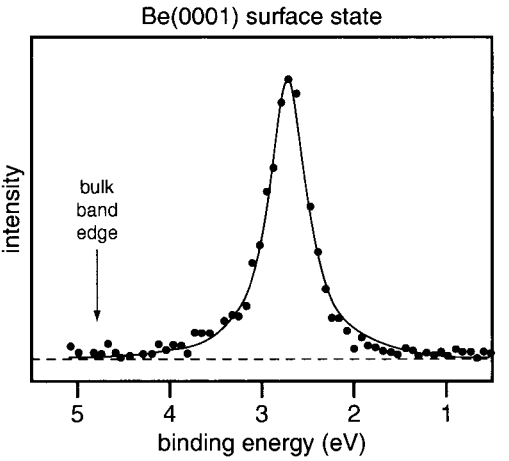


Fig. 8.15. Nonlinear least squares fit of a spectrum of the Be(0001) surface state at normal emission to a single Lorentzian with a smooth background. From Bartynski et al. (1985).

(Smith, 1992). The simplest models are phenomenological in nature. These treat the line shape as a convolution of the impact of the inverse lifetimes of the final state photoelectron $\Gamma_e$ and photohole $\Gamma_h$ (Pendry, 1978; Knapp et al., 1979a; Thiry et al., 1979). Often these are assumed to convolute to yield a Lorentzian line shape of width $\Gamma$. At normal emission, a simple relationship can easily be derived which expresses the width $\Gamma$ in terms of $\Gamma_e$ and $\Gamma_h$ and the band velocities of the hole and electron states normal to the surface plane, $v_h$ and $v_e$, respectively,

$$\Gamma = \frac{\Gamma_h + (v_h/v_e)\Gamma_e}{1 - v_h/v_e}. \tag{8.2}$$

An intrinsic surface state provides a good test of these models, since $v_h$ is zero for a true 2D state so that $\Gamma = \Gamma_h$. Figure 8.15 indicates that these simple ideas provide a good starting point for understanding the surface state on Be(0001). This figure presents a spectrum of the Be(0001) state at normal emission fitted to a single Lorentzian line shape (Bartynski et al., 1985). That the fit is fairly good implies that the dispersion relation in Fig. 8.13, which simply plots the maximum of the peak in each ARP spectrum as a function of $k_{\|}$, is indeed meaningful.

Jellium theory predicts that the photohole inverse lifetime should increase monotonically below $E_F$ due to the increasing phase space for radiationless filling of a photohole (Hedin and Lundqvist, 1969; Hedin, 1965; Lundqvist, 1969). Qualitatively, this is the reason why the surface state at on Cu(001) is observed to be fairly narrow ($\Delta E \sim 20$–$30$ meV at a binding energy of ~60 meV), while that considered on Cu(111) is slightly broader ($\Delta E \sim 50$–$60$ meV at a binding energy of 400 meV), and that considered here on Be(0001) is still broader ($\Delta E \sim 430$–$450$ meV at a binding energy of 2.8 eV). Attempts to verify the detailed functional dependence of the hole inverse lifetime upon the separation from $E_F$

(Lundqvist, 1969), even in the simple model systems discussed here, have met with limited success (Kevan, 1983a; Jensen et al., 1984; Levinson et al., 1983). A more complete treatment really should not rely on phenomenological models based upon hole and electron lifetimes, but should rather fit ARP spectra directly to an assumed, fundamentally sound line shape (Inglesfield and Plummer, 1992). Some encouraging progress in this area has been reported for the quasi-2D metal $TiTe_2$ (Claessen et al., 1992). The weakness of this experiment was that the small dispersion normal to the surface was not taken into account in the course of fitting ARP spectra of the Ti(3d) manifold very close to $E_F$. Near $E_F$, the hole inverse lifetime approaches zero and the second term in Eq. (8.2) will dominate the line width and line shape, even for a quasi-2D material (Smith, 1992). Experiments like that reported by Claessen et al. (1992), ought to be repeated for intrinsic surface bands as they cross the Fermi level. The precise characteristics of the valence band photoemission line shape remains an ill-defined issue which continues to limit the information that can be attained from a photoemission spectrum.

There have been three first-principles, self-consistent, LDA-based slab calculations for Be(0001) (Boettger and Trickey, 1986; Feibelman, 1992; Chulkov et al., 1987). The dashed curve in Fig. 8.13 shows the result of the latest of these for Be(0001) (Feibelman, 1992). For the surface state centered in the SBZ, this predicts a band minimum 2.77 eV below $E_F$ at $\bar{\Gamma}$, with an effective mass of $1.15m_e$. There is thus a small deviation from the reported experimental effective mass, but the match between the experimental and calculated dispersion relations is nonetheless excellent. This calculation also predicted a work function in fair accord with experiment, and, most importantly, explained the unusual outer layer expansion for this surface. An earlier calculation of a three layer slab was very much at odds with these experimental results, placing the minimum at 2.0 eV and the effective mass at $1.03m_e$ (Boettger and Trickey, 1986). The third calculation produced results intermediate between these two (Chulkov et al., 1987). These results indicate that, even for simple metals like beryllium, some care must be exercised in order to produce calculated results which can be usefully compared to experiment. A good way to understand the divergence of the three calculations is in terms of the size of the Fermi contour produced by this band. The most recent calculation predicted $k_F$ in close accord with the experimental value, while the older calculation predicted a value for $k_F$ two-thirds the magnitude of experiment. This means that the band from the earlier calculation would hold less than one half the charge of the experimental one. The bulk state/surface state interplay which maintains approximate surface layer charge neutrality is really very different in the two calculations.

A final important aspect of these calculations is the placement of the surface band relative to the bulk band edge. Surprisingly, the most recent calculation, which matched the experimental dispersion relation for the surface band so well, places the bottom of the bulk continuum nearly 0.5 eV lower than experiment (Feibelman, 1992). This is a difficult result to understand, since it tends to imply that the self-energy corrections which are handled by current LDA codes work better for 2D bands than for 3D bands. Presumably, if the calculation were artificially modified to move the bulk band up so that it matches experiment, the surface band would follow and would thus be too high. One interpretation of these observations is that the calculation has two systematic errors, e.g., incorrect handling of quasiparticle states and exclusion of a gradient correction in the vicinity of the surface, which cancel for the surface band but not for the bulk. Even more surprisingly,

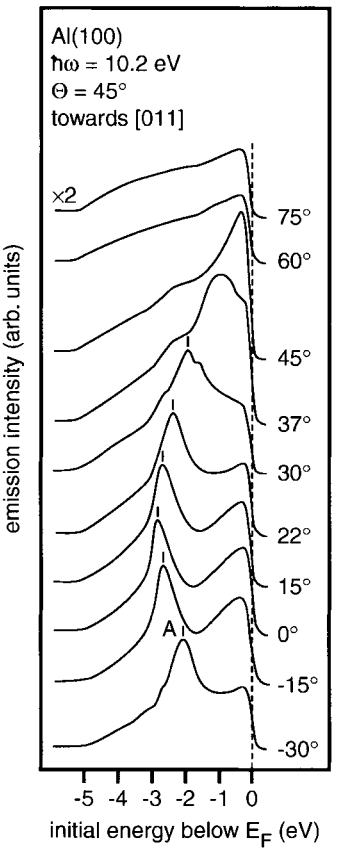


Fig. 8.16. ARP spectra of Al(001) as function of emission angle at a photon energy of 11.8 eV in the (01$\bar{1}$) azimuthal direction. The peak at a binding energy of 2.75 eV is an intrinsic surface state located very close to the bottom of a projected band gap at the X point of the bulk Brillouin zone (from Kevan et al., 1985a).

this mismatch between experimental and calculated splitting of the surface band from the bulk continuum seems to be improved for the generally more complicated noble metals, as discussed earlier.

### *8.2.3. Surface electronic structure of Al(001) and Al(111)*

The copper and Be(0001) states discussed above are simple in an additional sense that has not yet been discussed. That is, they exist in large projected gaps at an energy which is well-removed from any bulk band edge. The appropriate energy scale which determines whether a given state is "well-removed" from a band edge is the natural line width or, for a surface state, the inverse lifetime of the photohole state, $\Gamma_h$. States on aluminum do not satisfy the criterion of being "well-removed", and another level of complexity ensues. Superficially this is surprising. Aluminum is a classic nearly-free-electron metal which has

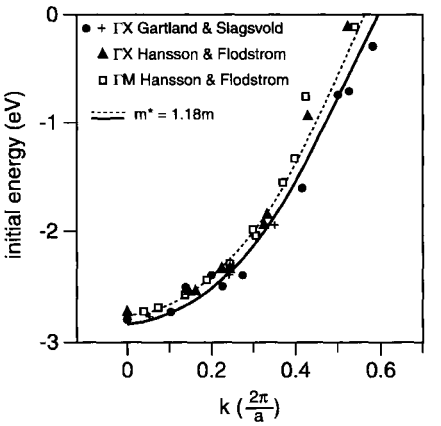


Fig. 8.17. Experimental dispersion relation for the Al(001) surface band. The surface state dispersion relation is from Hansson and Flodstrom (1978), while the experimentally determined continuum is from Levinson et al. (1983).

a relatively weak pseudopotential. One might expect everything to be simple. Below we briefly describe how this is not really true.

Figure 8.16 presents ARP spectra of the clean Al(001) surface as a function of emission angle in the $\bar{\Delta}$ mirror plane of the SBZ (Kevan et al., 1985a). The feature observed at a binding energy of 2.75 eV at normal emission has been determined to be a surface state located in a gap opened by zone boundary hybridization at the X point of the bulk Brillouin zone (Hansson and Flodstrom, 1978; Gartland and Slagsvold, 1978). Figure 8.17 presents the dispersion relation derived from similar data (Hansson and Flodstrom, 1978), plotted on an experimentally-determined projection of the bulk continuum (Levinson et al., 1983). The state has an effective mass of 1.18 times the free electron mass, and is split from the bottom edge of the bulk continuum by only ~0.1 eV. Unlike the states on Cu(111) and Be(0001), the projected gap does not extend up to $E_F$ since it is truncated by a band having an origin in a higher Brillouin zone. The surface band becomes less distinct as it approaches $E_F$. Two early calculations predicted dispersion relations for this state which matched the experimental relation very well (Caruthers et al., 1973; Spanjaard et al., 1979). The calculated position of the state in the projected gap differs from the measured position by ~0.5 eV, that is, as discussed previously for Be(0001) the bulk band edge was too low by nearly 0.5 eV. For this reason, the calculation predicted a much higher degree of surface localization than is measured by experiment.

This mismatch between theory and experiment has motivated two additional calculations for this system. These are reviewed since they adopt different approaches to solve problems associated with slowly decaying surface state wave functions. In systems like Al(001) where the separation of the state from the bulk continuum is small, the surface states decay very slowly into the bulk of the material and the accuracy of the slab geometry becomes suspect. One of these calculations employed an embedding procedure to calculate, from first principles, a true semiinfinite system (Benesh and Inglesfield, 1986). This technique will be discussed again in the next section. The second subsequent calculation

Table 8.1

Summary of experimental and calculated results for surface states on a few simple metal surfaces. $k_0$ is the symmetry point near which the surface band is located, $E_S(k_0)$ and $m^*/m_e$ are its corresponding energy and effective mass at that point, $k_F - k_0$ is the separation of the Fermi wave vector from the symmetry point, and $E_B(k_0)$ is the energy of the bottom of the corresponding projected bulk band gap

| | | Cu(111) | Cu(001) | Be(0001) | Al(001) |
|---|---|---|---|---|---|
| | $k_0$ | $\bar{\Gamma}$ | $\bar{X}$ | $\bar{\Gamma}$ | $\bar{\Gamma}$ |
| Experimental | $E_S(k_0)$ | 0.39(1) | 0.06(1) | 2.80(5) | 2.75(5) |
| | $m^*/m_e$ | 0.46(1) | 0.16(2) | 1.29(3) | 1.18(2) |
| | $k_F - k_0$ | 0.22(1) | 0.05(1) | 0.94(2) | |
| | $E_B(k_0)$ | 0.75 | 0.45 | 4.50(5) | 2.83(5) |
| Calculated | $E_S(k_0)$ | 0.58 | 0.07 | 2.77 | 2.67 |
| | $m^*/m_e$ | 0.37 | 0.20 | 1.15 | 1.11 |
| | $k_F - k_0$ | 0.24 | 0.06 | 0.94 | |
| | $E_B(k_0)$ | 0.88 | 0.47 | 5.0 | 2.90 |
| References | | Kevan (1983a), Euceda et al. (1983a) | Kevan (1983a), Euceda et al. (1983a) | Bartynski et al. (1985), Watson et al. (1990), Feibelman (1992) | Levinson et al. (1983), Kevan et al. (1985a), Heinrichsmeier et al. (1993) |

used a different approach to solve this problem (Heinrichsmeier et al., 1993). That is, relatively thin slabs were calculated fully self consistently. These slabs were then expanded by adding additional layers in the middle having the same self consistent potential as the most bulk-like layer in the original slab. The energy eigenvalues of the expanded slab were then determined without the necessity of self consistency. Both calculations locate the surface state accurately with respect to the bulk continuum, and the latter reported a dispersion relation in excellent accord with measurement.

The close proximity of the bulk band edge leads to another anomalous characteristic of this state and a closely related one on Al(111) (Kevan et al., 1985a). The width of the Al(001) surface band is ~0.4 eV at zone center. Thus the lifetime-broadened state overlaps the bulk continuum significantly. On Al(111), the gap is only ~0.4 eV wide and the corresponding surface state is observed to have an energy width of ~1.5 eV. This unusual phenomenon implies an unusual Fano-like coupling to the bulk continuum in the final state. On both surfaces, the observed line shape is asymmetric and cannot be easily fitted using any of the standard line shapes used in valence and core level photoemission. One of the above calculations focused upon this point in some detail and produced, from first principles, an asymmetric line shape closely resembling that observed experimentally.

Before proceeding with discussion of more complicated transition metal surfaces, it is useful to summarize the results presented so far for simple and noble metals. Table 8.1 gives the relevant parameters – relevant symmetry point in the SBZ, experimental and calculated energy at the symmetry point, experimental and calculated effective mass about the symmetry point, and energy of the associated bulk continuum at the symmetry point –

for the surfaces discussed above. A few trends are apparent, though not universally observed. In all cases, the existence of surface states is well predicted. The calculated energy at the symmetry point is generally somewhat lower than observed experimentally. This is compensated by a slightly smaller calculated effective mass so that the calculated and experimental Fermi wave vectors are normally within experimental error of one another. This is identical, for example, to results for the bulk bands on simple alkali metals (Jensen and Plummer, 1985). The bulk continuum is also generally placed too low in energy as compared to experiment with the result that the splitting between the bulk continuum and the surface band is often too large in the calculation.

Ultimately these systematic disagreements between experiment and theory must be understood in terms of limitations within the calculation. The limitations of making direct comparisons between LDA-calculated bands and bands determined by photoemission are well-known and have been emphasized elsewhere and also in several chapters of this book (Hedin and Lundqvist, 1969; Hybertson and Louie, 1985, 1986; Northrup et al., 1986; Godby et al., 1987). It would be tempting search for systematics in the magnitude of disagreement between experiment and LDA-based theory as a function of binding energy of the surface state. That is, the state on Cu(001) is nearly exactly predicted by theory and lies very close to $E_F$, the agreement is less exact for Cu(111) where the binding energy is $\sim$0.4 eV, and the disagreement, at least in terms of the splitting between the bulk and surface states, is quite serious for Be(0001) where the binding energy is 2.8 eV. One of the computations for Be(0001) (Boettger and Trickey, 1986) attributes some of these discrepancies to spurious self-interaction characteristic of the LDA method, an effect which is largest for states far from $E_F$ having highly localized wave functions. In this sense, the Be(0001) state is a very stringent test of such calculations. The wave functions are fairly localized to the surface plane, yet the degree of delocalization parallel to the plane is manifested by the large band width. One would expect therefore a large differential correction for this band near its minimum relative to its Fermi crossing. This still does not simply explain, however, the inconsistency in surface-bulk splitting.

### *8.2.4. Surface electronic structure of Ta(011)*

In order to ease the transition to the more complicated systems discussed below, it is useful to present results from a transition metal surface which nearly satisfies the criteria for being "simple". For this we choose Ta(011) since it provides results which are prototypical of many transition metals in several respects. Tantalum is a BCC metal and thus the (011) surface is the closest packed low index plane. The surface is apparently stable to reconstruction. Among the transition metals, the effect of electronic correlation should be nearly minimized for Ta since it lies near the lower left corner of the transition series. Most importantly from our perspective is its simple band structure along the bulk $\Gamma \rightarrow N(\Sigma)$ line, as shown in Fig. 8.18 (Papaconstantopoulos, 1986). This line, which projects onto the center of the (011) SBZ, exhibits a large projected gap. If we consider only states of even symmetry and thus exclude the odd symmetry bands, the gap is formed by hybridization of two bands which extends from just below $E_F$ downward to a binding energy of over 4 eV. This is qualitatively similar to the situation on Be(0001), except that the gap exists within the predominantly Ta(5d) manifold. We wish to determine the extent to which the simple ideas outlined previously can be applied to this somewhat more complicated situation.

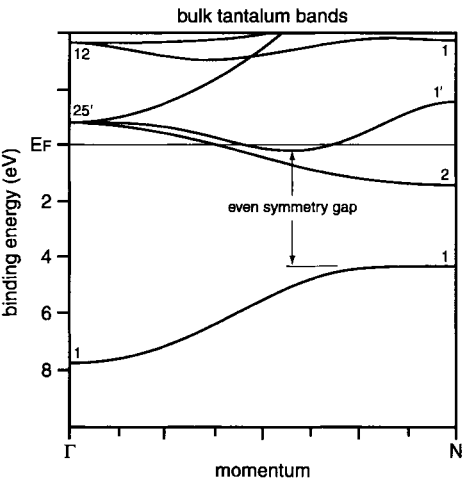


Fig. 8.18. Calculated bulk tantalum band structure along the Σ line of the BCC Brillouin zone. Note the large even-symmetry gap extending from just below $E_F$ to ~4 eV below $E_F$ (calculated using the code in Papaconstantopoulos (1986)).

Figure 8.19 presents spectra from clean Ta(011) as a function of emission angle in the $\bar{\Delta}$ azimuthal direction at $h\nu = 48$ eV (Kneedler et al., 1990, 1991). The intense feature as a binding energy of 0.4 eV near normal emission passes the tests to be labeled a surface state of even symmetry. In actual fact, the state is weakly coupled to the underlying odd-symmetry continuum by the spin–orbit interaction and should more accurately be labeled a surface resonance. For our purposes, however, this distinction is not important. As a function of emission angle or, equivalently using Eq. (8.1), $k_{\|}$, the feature is observed to be nearly dispersionless out to an emission angle of ~8° at which point the spectra become complex. These results are presented graphically in Fig. 8.20. There are several obvious distinctions from the surface states observed on Cu(111) and Be(0001). On Ta(011) the surface band splits from the top of the gap and the effective mass is nearly infinite. One would not be tempted to try to model this state using the simple pseudopotential-based models which have been described in the chapter by Borstel and Eguilez and elsewhere (Inglesfield, 1981a; Smith, 1985a; Weinert et al., 1985; Kevan, 1986a; Chen and Smith, 1987). This is not surprising since this state is predominantly of Ta(5d) character. The flatness of the band implies a $\delta$-function-like density of states, i.e., this state behaves qualitatively like a core level. Other experiments have shown that the tantalum surface core level shifts are generally negative, i.e., the surface core levels are more tightly bound than those of the bulk (van der Veen et al., 1981, 1982; Guillot et al., 1984, 1985). We can think of this surface state very roughly as a "5d core level" very close to $E_F$ which splits downward in energy from the bulk "core level continuum". Paradigmatic tight-binding LCAO or Hückel models for the existence of surface states on narrow band metals have been developed and could be applied here in place of the pseudopotential models mentioned above (Tamm, 1932; Goodwin, 1939a; Kevan and Eberhardt, 1992; van Hoof et al., 1992). Further support for this approximate interpretation is provided by the

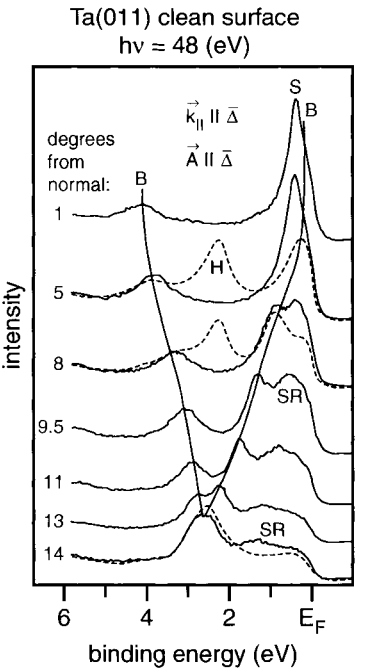


Fig. 8.19. ARP spectra of Ta(011) as a function of emission angle at a photon energy of 48 eV in the $\bar{\Delta}$ azimuthal direction. The narrow feature just below $E_F$ near normal emission is a surface state of $d_{z^2}$ symmetry (from Kneedler et al., 1991).

weak and monotonic photon energy dependence of the surface state emission intensity, implying a significant degree of surface localization. Similar states have been observed and characterized on a variety of other transition metal surfaces.

The most interesting aspect of these results for Ta(011) is the region near 8–10° emission angle in Fig. 8.19 and its relation to charge neutrality. These spectra map onto the region of the dispersion relation where the surface state band intersects the bulk continuum (Kevan and Eberhardt, 1992; Kneedler et al., 1990, 1991). A surface state which is degenerate with a continuum is referred to as a surface resonance. It is a resonance in the classic sense of being energetically broadened and shifted in energy by virtue of having a finite lifetime through tunneling into the continuum. Surface states in general and that on Ta(011) specifically offer the unusual opportunity to observe a well-defined defect state merge with its associated continuum. Given the results discussed above for Al(001) and Al(111), we might expect unusual phenomena to occur when this happens.

The original interpretation of the spectra in Fig. 8.19 was in terms of an avoided crossing between surface and bulk bands (Kneedler et al., 1990). Indeed, careful examination of the evolution of the surface sensitive feature led to this conclusion. Near zone center the surface feature lies at higher binding energy than the bulk feature, while beyond ~0.30 $Å^{-1}$ the order is clearly reversed. Recent calculations question this conclusion, however, with an equally interesting interpretation (van Hoof et al., 1992). Specifically, the surface state near

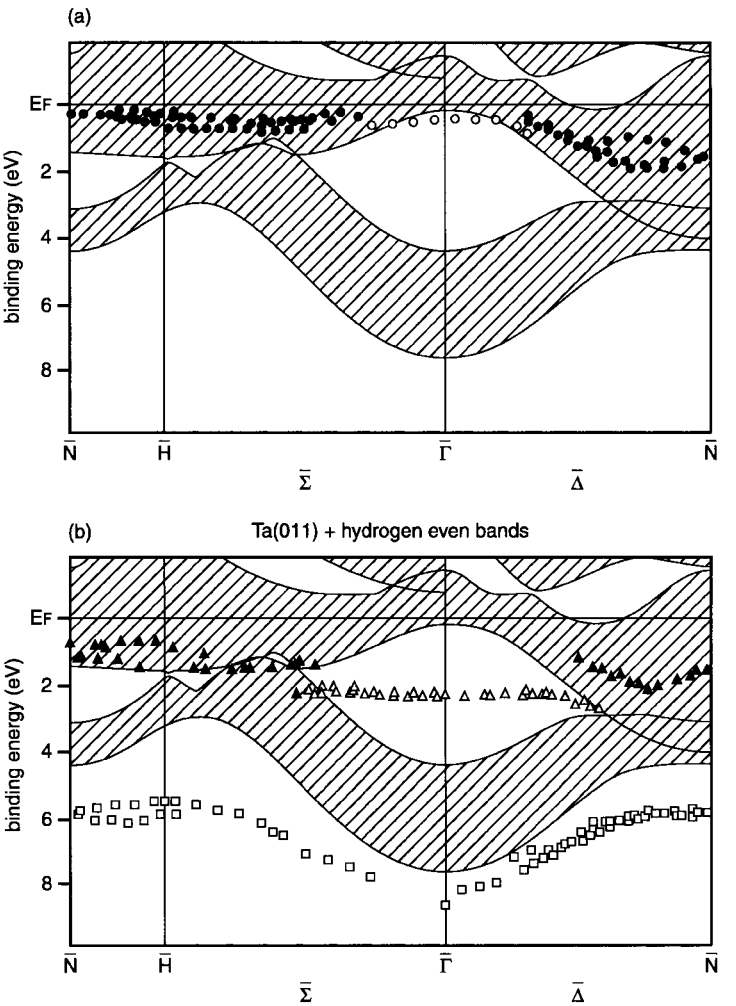


Fig. 8.20. Experimental surface band structures of (a) clean and (b) hydrogen-saturated Ta(011) in the mirror symmetry planes. The shaded region is a projection of the bulk band structure of even symmetry onto the SBZ (from Kneedler et al., 1991).

zone center and the surface resonance beyond 0.20 $Å^{-1}$ have different dominant orbital characters. The state is essentially $d_{z^2}$ in character and thus extends into the vacuum like a "dangling bond", while the resonance is mixed $p_z$ and $d_{yz}$. They are thus not directly related by an avoided crossing since in that case the orbital character would be the same. Rather, the surface resonance splits from a "hidden" band edge embedded in the projected continuum seen in Fig. 8.20.

Figure 8.21 shows the results of the calculation of the surface electronic structure of Ta(011) (van Hoof et al., 1992). We include it both to indicate the level of agreement be-

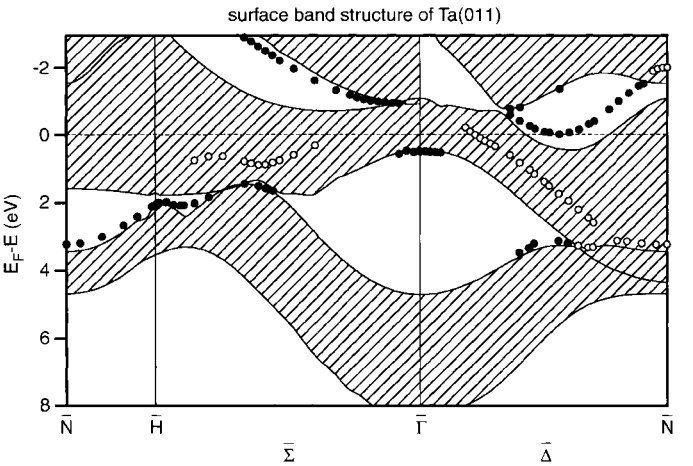


Fig. 8.21. Surface band structure of Ta(011) in the symmetry planes calculated using an embedding technique so that surface resonances can be precisely calculated. Only even mirror-plane symmetry bands are shown (from van Hoof et al., 1992).

tween calculation and experiment for this fairly complicated 5d transition metal and also to provide an example of one of the current states of the art in this area of computational physics (Inglesfield, 1981a, 1988; Inglesfield and Benesh, 1988). Like the calculations discussed previously for copper and beryllium, most calculations of surface electronic structure are carried out on a slab consisting of a finite number of layers. This leads to a discrete eigenvalue spectrum at each value of $k_{\|}$. Clearly it can be difficult in these situations even to distinguish surface states from bulk states. By their very nature, it is particularly difficult to characterize surface resonances. In the past 5–6 years, an embedding procedure has been perfected whereby the electron states in the vicinity of a surface are constrained to connect smoothly onto bulk states so that a true semiinfinite system can be calculated. Among other things, this has allowed new and very useful insights to be drawn between the topology of bulk bands as a function of $k_{\|}$ and the resulting surface electronic structure. The calculation predicted the resonant broadening of the surface resonance with reasonable accuracy. The calculation on Ta(011) provides a beautiful example of this.

## 8.3. Interaction of surface states on metals with adsorbed atoms

The previous section demonstrated that surface states and resonances contribute significantly to the total charge density at the metal–vacuum interface. They hence play an important role in a variety of surface processes, not the least of which are chemisorption, catalysis, and related phenomena. The direct observation of how a surface band responds to the adsorption of atoms or molecules provides an excellent opportunity to study the chemisorption bond, momentum by momentum. In this section we review a few experiments in this area which provide a useful basis upon which an understanding can be built.

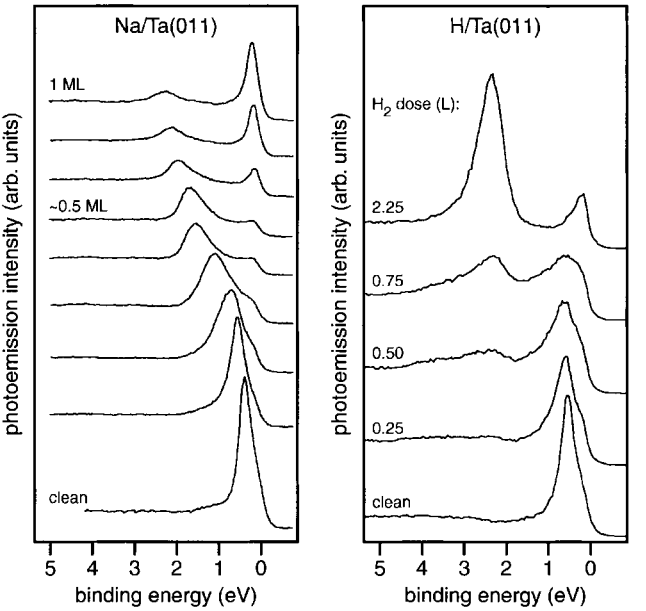


Fig. 8.22. ARP spectra of Ta(011) as a function of sodium (left) and hydrogen (right) dose at normal emission. Note that the surface state just below $E_F$ shifts smoothly to higher binding energy as sodium is deposited, but that it is extinguished and replaced by a separate feature at 2 eV higher binding energy upon hydrogen exposure (from Kneedler et al., 1991, 1995).

A fundamental issue in this area is the ability to forge a connection between delocalized electron bands in momentum space, the quantities normally measured by ARP, and localized bonds in real space, the simplest way to conceptualize chemisorption. Figure 8.22 provides a graphic illustration of the complexity of this problem. This show ARP spectra collected at normal emission from Ta(011) as a function of (a) hydrogen exposure (Kneedler et al., 1991), and (b) sodium exposure (Kneedler et al., 1995). These are both monovalent adsorbed atoms and thus one might hope to see unified behavior. Of key interest is the surface band located near $E_F$ discussed in the previous section. Recall that this is composed of $d_{z^2}$ dangling bond orbitals. In a chemical sense, these are the "frontier orbitals" in the reaction to form a chemisorption bond. That the associated energy band is flat implies that these orbitals do not interact with each other significantly and we can think of each unit cell as being roughly independent. As observed on many transition metal surfaces (Feibelman et al., 1980; Eberhardt et al., 1981), the surface band is quenched monotonically as the hydrogen coverage increases, that is, is passes the crud test. We cannot truly destroy a wave function and, more precisely, the electrons in this band end up in a more tightly bound bonding level which appears at a binding energy of 2.4 eV. This level grows continuously as hydrogen is adsorbed. The resulting modified band is also nearly dispersionless, so once again we should be able to think of non-interacting orbitals. These results present a very localized picture in which we are able to measure the energy levels of more or less isolated reaction centers.

As first observed for the W(001) and Mo(001) surfaces (Soukiassian et al., 1985) and later on Ta(001) (Cousty and Riwan, 1987), the situation upon alkali adsorption is less straight-forward. The surface state shifts continuously in energy as the sodium coverage increases. Simultaneously, the band develops a measurable dispersion with an effective mass near the free electron mass upon completion of the first layer. We clearly cannot think of isolated reaction centers in this case, as the disordered alkali layer interacts globally to modify the entire surface band. Even though the hydrogen and the alkalis are both monovalent, there is no obvious unifying theme in how they interact with these model surface states. Stranger still is the observation that, on many transition metal surfaces, hydrogen adsorption quenches some surface states and resonances while shifting others. We will see examples of this in Section 8.4 for hydrogen adsorption on W(011) and Mo(011).

We will return to these Ta(011) results later in this section. First, however, we explore how simple metals interact with alkalis since this provides a useful framework for continuing discussion of transition metal adsorption. We generally are not too concerned here with the adsorption of full or ordered layers. Rather, we are interested in understanding the dilute limit where the isolated adsorbate-surface state interactions are of major importance.

### *8.3.1. Alkali adsorption on Cu(111)*

Due to their weak pseudopotential, many of the properties of simple metals can be understood in terms of the jellium model. This is particularly true of the alkalis. For this reason, a good zero-order model for alkali adsorption is in terms of the adsorption of thin, variable-density layers of jellium (Lang and Williams, 1976, 1978; Benesh and Hester, 1988; Aruga and Murata, 1989; Ishida and Terakura, 1988; Ishida, 1989). One might hope that these models are particularly relevant for adsorption on simple metals.

The first detailed ARP study of the impact of alkali adsorption on a simple surface state was for Cs/Cu(111) (Lindgren and Walldén, 1978, 1980a, b). The main results are shown in Fig. 8.23. This shows ARP spectra collected at normal emission and for binding energies close to $E_F$ as a function of cesium coverage. The surface state discussed in Section 8.2.1 is observed to shift continuously to higher binding energy with increasing coverage. Surprisingly, this behavior is qualitatively similar to that observed for Na/Ta(011) in Fig. 8.22b even though the surface bands are of radically different spatial and orbital character. The shifting behavior for Cs/Cu(111) can be understood quantitatively using the simple pseudopotential-based phase model discussed in the chapter by Borstel and Eguilez and elsewhere (Inglesfield, 1981a; Smith, 1985a; Weinert et al., 1985; Kevan, 1986a; Chen and Smith, 1987). Much like a simple particle in a box problem where the energy of the lowest eigenstate decreases as the magnitude of the potential well decreases, the energy of the surface state decreases as the vacuum barrier decreases. More quantitatively, the energy of the surface state is determined by matching between a decaying oscillatory wave inside the crystal and a wave decaying approximately exponentially outside the crystal. The simplest model matches the phase of non-propagating solutions of the nearly-free-electron model inside the crystal to the semiclassical phase associated with the image potential outside the crystal. As the work function is lowered upon alkali adsorption, the wave function decays more slowly outside the surface, thereby changing the matching condition and lowering the energy of the surface state.

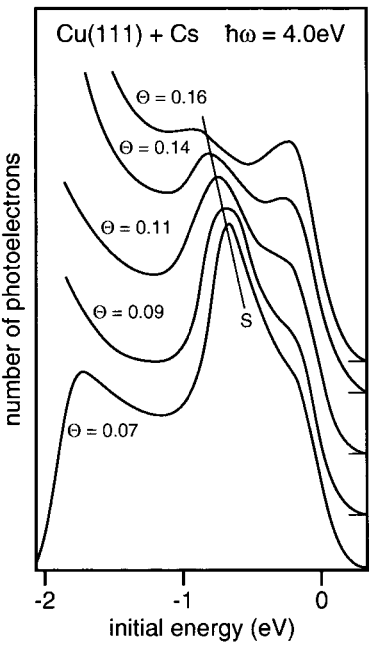


Fig. 8.23. ARP spectra of Cu(111) collected at normal emission as a function of cesium coverage at a photon energy of 4.0 eV. Note that the surface state just below $E_F$ shifts smoothly to higher binding energy as a function of cesium coverage (from Lindgren and Walldén, 1978).

Depending on the detailed assumptions made, these simple models predict that the Cu(111) surface state will shift downward initially at low coverage at a rate about 10% that of the work function decrease (Smith, 1985a; Weinert et al., 1985; Kevan, 1986a), while experiment measures this ratio to be typcally 10–15% (Lindgren and Walldén, 1978, 1980a, b, 1988; Kevan, 1986a). The important conclusion to be drawn is that a significant fraction of the underlying physics in Fig. 8.23 may be understood almost entirely by ignoring any detailed local interactions around the alkali. The important parameter is simply the work function. This is ultimately why the simple phase models work so well. Self-consistent calculations of surface electronic structure invest much effort in allowing the charge in the surface region to redistribute in such a way that one predicts the correct work function, while the phase models use this as an input parameter. For simple surface states like those in the noble metal sp-band gaps, the chemisorption of alkalis is, to zero order, modeled by the chemisorption of a jellium layer which simply modifies the work function and perhaps also alters the potential in the barrier region (Hamawi et al., 1991).

An issue of enduring popularity which is related to the above discussion is the degree to which the adsorbed alkali atoms "transfer" their valence electron to the surface at low coverage (Watson et al., 1990; Lang and Williams, 1976, 1978; Aruga and Murata, 1989; Ishida and Terakura, 1988; Ishida, 1989; Muscat and Newns, 1978; Wimmer et al., 1983; Riffe et al., 1990; Horn et al., 1988). The very old Langmuir and Gurney models were based essentially upon this premise and are able to provide qualitative insight into many

aspects of alkali adsorption (Langmuir, 1932, 1933; Topping, 1927; Gurney, 1935). Several recent experiments and calculations have questioned the validity of this model. While ARP results cannot by themselves measure the spatial distribution of charge, the amount of charge transferred into a particular surface band can easily be determined. When coupled to calculations, this could provide a useful probe of alkali adsorption.

We use as an example results for K/Cu(111) which are more complete than those for cesium adsorption, as explained further below (Kevan, 1986a). The goal is to measure the amount of charge donated into the Cu(111) sp-surface state as a function of alkali coverage in the low density limit. This is necessarily a positive number since the surface band shifts downward in energy as a function of coverage. The surface density of electrons in a 2D band is simply given by $n_{2D} = k_F^2/2\pi$, where $k_F$ is the 2D Fermi wave vector. $k_F$ can be easily extrapolated from the dispersion relations measured by ARP, as discussed in the previous section. This extrapolation must take into account both the shift of the band minimum and the variation of the effective mass upon alkali adsorption since, as the surface band moves toward the bulk continuum, its mass converges on that of the edge of the continuum. Using the energy and mass parameters in (Kevan, 1986a), we determine that the change in surface state charge density $\Delta n_{2D}$ varies linearly with the work function, to lowest order

$$\Delta n_{2D}(\Delta\varphi) - \Delta n_{2D}(0) < 0.002\,\Delta\varphi, \tag{8.3}$$

where $\Delta n_{2D}$ is in $\text{Å}^{-2}$ and $\Delta\varphi$ is in eV. Using the low-density variation of the work function with coverage (~20 eV/monolayer) and the area of the unit cell, we determine that $\Delta n_{2D} \sim 0.2 n_{2D}$ (K) at low potassium density $n_{2D}$ (K). Since the alkalis are monovalent, this implies that roughly 20% of the alkali valence charge becomes "associated" with the copper surface state. To determine whether this means that this fraction of the alkali charge is transferred, in real space, to the copper surface will require more detailed calculations.

The discussion in this section thus far has focused entirely upon the "jellium-like" character of alkalis adsorbed onto Cu(111). Close examination of Fig. 8.3 indicates that this cannot be a complete description. In the STM image are seen adatoms of some sort which are surrounded by standing wave halos formed by scattering of electrons bound in the sp surface state. Given their large adsorption dipole, adsorbed alkali atoms will certainly scatter electrons in the surface band thereby leading to lateral heterogeneity similar to that seen in Fig. 8.3. Since at low density the alkalis atoms are disordered, this heterogeneity will in principle destroy the momentum eigenstates of the valence electrons near the surface. A close examination of the ARP spectra for K/Cu(111) at low density provides useful insight in this direction. Figure 8.24 shows ARP spectra of the sp surface state collected at $k_\parallel = 0.15$ $\text{Å}^{-1}$, i.e., at a point where the band velocity is non-zero, as a function of alkali coverage (Kevan, 1986a). In addition to shifting to higher binding energy, the surface state peak broadens monotonically as a function of coverage. While the shift is fairly well-described by the simple phase models, the broadening clearly is not. Rather, it is caused by the lateral heterogeneity discussed above. The electrons are endowed with a mean-free-path $\lambda$ due to random elastic (or possibly inelastic) scattering off the adsorbed potassium atoms. Since the layer is disordered, the scattering events randomize the phase of the electron waves, thereby broadening the momentum by $\Delta k \sim 1/\lambda$. The non-zero band velocity

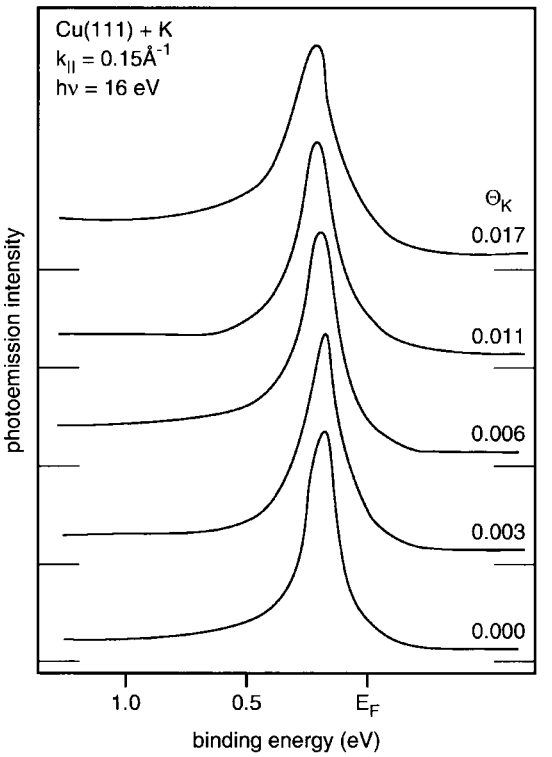


Fig. 8.24. ARP spectra of Cu(111) slightly off normal at a photon energy of 16 eV as a function of potassium coverage. Note that the systematic shift to higher binding energy, as observed in the previous figure, and is accompanied by broadening of the surface state as a function of potassium coverage. The latter of these indicates the importance of scattering of the surface state electrons off the adsorbed atoms and the consequent destruction of momentum as a good quantum number (from Kevan, 1986a).

leads to an energy broadening $\Delta E = v_{||} \Delta k$. These data provided an estimate of the size of the cross section (actually a length in this 2D problem) for electrons in the surface band scattering off adsorbed potassium atoms (Kevan, 1986a). It would be useful to correlate real-space images like those in Fig. 8.3 with these ARP results to provide a more complete picture of alkali adsorption on simple surfaces.

Finally, we discuss the relationship between these results for the adsorption of alkalis onto Cu(111) and various theories used to calculate or to model the electronic structure of bulk alloys. The relationship comes from associating A-atoms with adsorption sites occupied by an alkali and B-atoms with empty sites. We can then consider the form of the surface band resulting from this "surface alloy". The simplest theory which might be applied is the rigid band model in which the overall electronic band structure does not change, but the occupancy might (Seitz, 1940; Mott and Jones, 1936; Jones and March, 1973). Since copper and the alkalis are both monovalent, this theory actually predicts no spectral changes. More importantly, it has been well-established that alkali adsorption at low density on several different surfaces induces a feature well above $E_F$ which is roughly

associated with the alkali ionization level (Watson et al., 1993; Frank et al., 1989; Matthew et al., 1991; Tang and Heskett, 1993). This "extra" density of states is not predicted by rigid band theory. A slight improvement is offered by the "virtual crystal approximation" (VCA) in which case a random binary crystalline alloy $A_xB_{1-x}$ is replaced by a lattice of pseudoatoms having a weighted average scattering potential (Jones and March, 1973). Such a virtual crystal of pseudoatoms is periodic and thus the electronic structure can be calculated using conventional one-electron theory. The fact that ARP experiments observe a fairly well-defined dispersion relation for a system of randomly adsorbed alkali atoms suggests that this approximation might be a reasonable first approximation. Indeed, the VCA could probably be used to predict the continuous shift of the surface band as a function of coverage. However, neither the alkali-induced density of states above $E_F$ nor the systematic spectral broadening discussed above would be predicted by this model and thus the VCA is not conceptually correct for this system. Mean field theories of the electronic structure of bulk alloys such as the coherent potential approximation (CPA) or the average t-matrix approximation (ATA) can be conceptually applied with more success (Jones and March, 1973; Ehrenreich and Schwartz, 1976). For example, in the CPA method, the broadening results from a non-hermitian Hamiltonian which yields complex energy eigenvalues. That is, the self energy of the bands is complex due to a finite rate of disorder-induced elastic scattering from one perfect-crystal momentum eigenstate into others. We will return to this relationship between alkali and hydrogen chemisorption and the CPA method below.

### *8.3.2. Lithium adsorption on Be(0001)*

The system Li/Be(0001) has recently provided some very interesting results which are discussed briefly here (Watson et al., 1990, 1993). The motivation for these measurements was similar to that discussed in the last section concerning the degree of charge transfer from the alkali. A completely ionized alkali would not be "metallic" in the usual sense of possessing a finite density of states at the Fermi level. Since beryllium is a metal with a low bulk density of states at $E_F$ and indeed a large projected gap at $E_F$, it was thought that the issues of charge transfer and metallicity might be particularly apparent in this system.

Similar to observations for alkalis adsorbed onto Cu(111), adsorption of lithium onto Be(0001) shifts the surface band observed on the clean surface in Figs. 8.12 and 8.13 down in energy continuously as a function of coverage (Watson et al., 1990). At saturation, the band lies near the bottom of the projected gap. $k_F$ has increased slightly, indicating like Cu(111) that an increased amount of charge ($\sim$0.37 electrons/lithium atom) is held within this band. The effective mass has decreased to a value nearly equal to that of the bulk band edge. That this convergence of the surface band effective mass on that of the bulk band edge is not so clearly observed for K/Cu(111) reflects simply that the overall alkali-induced shift of the state is much smaller so that the final energy is not so close to the bulk band edge. Unlike the alkali/Cu(111) systems, the large magnitude of the shift of the intrinsic surface band cannot be explained quantitatively in terms of the simple pseudopotential models which use as input only the work function. The reason for this assertion lies in the binding energy of the surface state relative to the vacuum level. As the work function is decreased upon alkali adsorption, the change in the surface barrier at the energy of the surface band, which lies $\sim$7 eV lower in energy, will be very small. Correspondingly, the change in

the surface state energy due to the work function variation would be very small, that is, comparable to that observed and calculated for K/Cu(111). The larger energetic shift in this system must then be explained in terms of bonding interactions between the alkali atoms and the more highly surface-localized state. We examine these effects in more detail in Section 8.3.4.

It is instructive to think of the observations concerning effective masses of surface bands in the context of complex band structures (Heine, 1963, 1969; Pendry and Forstmann, 1970). Similar to effective mass theory, this theory involves a simple analytical continuation of the perfect-crystal band structure into the complex momentum plane. An imaginary component of momentum $q$ leads to wave functions which expand or decay exponentially with this exponential constant. For perfect bulk systems these are eliminated by application of the boundary conditions since they cannot be normalized for an infinite crystal. They must, however, be retained near a defect (i.e., a surface) since the exponentially increasing wave function can be trapped inside the surface plane. One of the predictions of complex band structure as applied to surface bands is that the effective mass of a surface state will vary smoothly between extremes given by the masses of the projected bulk continua at the bottom and top of the gap (Kevan, 1986a). In the vicinity of a band edge, the evanescent decay length ($\sim 1/q$) of the state increases in proportion to the inverse of the square root of the energy separation of the state from the band edge. These predictions imply that we could induce a smooth transition between a localized surface state and bulk state if we could change the boundary conditions sufficiently to force a state out of the gap. Treating adsorbed alkalis within the jellium model is equivalent to allowing this flexibility to change boundary conditions while not otherwise destroying momentum. For Li/Be(0001), the change is nearly sufficient to force the surface state-bulk state transition. The variation of effective mass and evanescent decay length have been measured for K/Cu(111), with results which are qualitatively though not quantitatively matched by the simplest predictions of complex band structure (Kevan, 1986a).

It is also useful to think about the comparison between theory and experiment for the dispersion relation of the surface state on the clean Be(0001) surface in the context of complex band structure (Bartynski et al., 1985; Watson et al., 1990, 1993). The effective mass of the top of this projected gap is fairly large, while that of the bottom is nearly $m_e$. Complex band structure predicts a smooth and calculable variation between these extremes for the effective mass for a surface state at any energy within the gap. The observed effective mass of $1.29m_e$ (Watson et al., 1990), and the more recently calculated value of $1.15m_e$ (Feibelman, 1992) for the clean surface state are roughly in accord with this expectation, while the effective mass of $1.0m_e$ derived in the older calculation is not (Boettger and Trickey, 1986). While the concept of complex band structure is certainly not rigorous in the simple application discussed here, it can provide a useful qualitative guide.

We now return to the issue which originally motivated measurements on the Li/Be(0001) system, that is, metallicity. By metallicity we mean the degree of delocalization of adsorbate charge parallel to the surface. The above discussion pertained to modifications of the surface state on the clean surface upon adsorption of lithium. There is no doubt that this surface state, which is predominantly of Be(2s) and Be(2p) character, is metallic and delocalized parallel to the surface. It has a well-defined dispersion relation, a finite density of states at $E_F$, and a large Fermi velocity. From a local point of view,

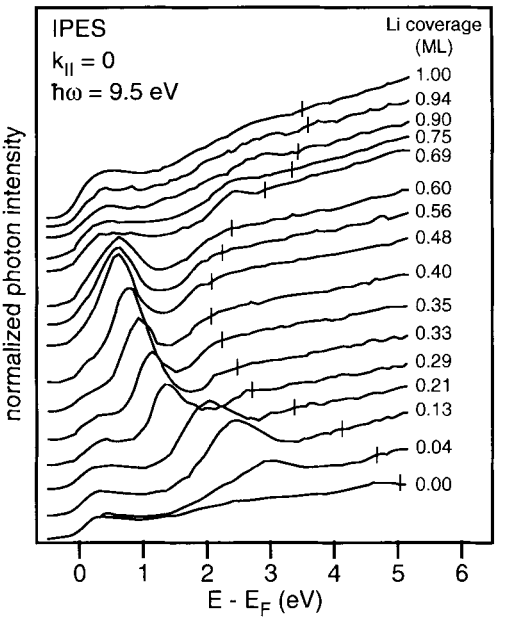


Fig. 8.25. Inverse photoemission spectra of Be(0001) as a function of lithium coverage. Note the appearance of a lithium-induced feature well-above $E_F$ at low coverage which shifts down smoothly in energy as the coverage increases, but crosses $E_F$ discontinuously at a coverage at which the overlayer orders (from Watson et al., 1993).

the energetic shifts discussed above must be explained by mixing some Li(2s) level into this surface band. It is thus reasonable to conclude that the Li(2s) level is delocalized and metallic parallel to the surface plane as well. If this were true, there should be a well-defined Li(2s) density of states at $E_F$. The experimenters searched unsuccessfully, using both photoemission to probe the occupied states and inverse photoemission to probe the unoccupied states, to detect this density of states (Watson et al., 1993). As shown in Fig. 8.25, at low density, the only adsorbate-induced feature detected was $\sim$3 eV above $E_F$ and was concluded to have a significant amount of Li(2s) character. This conclusion is qualitatively similar though quantitatively different from the simple Gurney model wherein the Li atoms are nearly completely ionized at low density and the ionization level lies well above $E_F$. The more sophisticated Lang and Williams jellium calculations make a similar prediction and place the partially-occupied alkali s-level much closer to $E_F$ than is observed experimentally (Lang and Williams, 1976, 1978). In Fig. 8.25, the induced feature is observed to move down in energy as the lithium coverage is increased. Simultaneously, the effective mass of the associated band decreases from $\sim 3m_e$ at 0.1 monolayers to $\sim 1.5m_e$ at 0.19 monolayers. Upon completion of the first monolayer, the lithium forms an incommensurate overlayer. As shown in Fig. 8.13, a dispersive feature having an effective mass of $1.8m_e$ is observed at zone center 0.47 eV below $E_F$. This feature is metallic and very likely has significant Li(2s) character.

The transition between the extreme of a localized, unoccupied level and a delocalized metallic band is the most interesting aspect of these experiments. Figure 8.25 shows that

the induced feature moves smoothly down in energy to ~0.6 eV above $E_F$ and then simply decreases in intensity. At about the same coverage, the occupied level begins to appear at zone center at a binding energy of 0.47 eV. The experimenters associate the transition from non-metallic to metallic with an ordering transition in the overlayer which occurs at the same coverage (Watson et al., 1993). There is then a coexistence regime between a low density/disordered/non-metallic phase and a high density/ordered/metallic phase. The conclusion is supported with careful LEED and core level photoemission studies. It has also recently been predicted by first-principles calculations (Neugebauer and Scheffler, 1993). If proven true, this analysis would point the way toward a very novel and fruitful area of surface physics.

Finally, we discuss briefly the dispersion relation for the lithium-induced band just below $E_F$. As mentioned above, this exhibits an effective mass of $1.8m_e$ and has a band origin 0.47 eV below $E_F$. These results were used to speculate about the possible role of many-body effects in thin alkali films (Watson et al., 1990). First note that, within the incommensurate hexagonal unit cell of the lithium overlayer, this lithium-induced band holds much less that one electron per lithium atom. Even including the charge deposited into the intrinsic surface band, accounting for the full "extra" alkali electron is not possible. The rest of the charge must be hybridized with other beryllium bulk and/or surface states in the surface region. The effective mass of a free-standing lithium layer is calculated to be very close to $1.0m_e$, so the measured effective mass at first appears to be anomalously high. In the context of complex band structure discussed above (Kevan, 1986a; Heine, 1969; Pendry and Forstmann, 1970), however, this effective mass is nearly to be expected if we allow the lithium 2s band to feel the underlying beryllium pseudopotential. Finally, an unusual "avoided crossing" is observed in Fig. 8.13 between this lithium-induced band near the center of the second SBZ for the incommensurate structure and the intrinsic surface bands near $\bar{M}$. All three of these observations indicate substantial Li(2s)-beryllium valence band hybridization and thus serve to emphasize further the similar qualitative conclusion drawn from the magnitude of the energetic shift of the surface band. The magnitude of these alkali/substrate interactions and how they vary as a function of alkali and of alkali coverage remains an active field of investigation.

### *8.3.3. Adsorption of monovalent atoms on Ta(011)*

We now return to the results in Fig. 8.22 to try to attain a qualitative understanding of the interaction between monovalent atoms and a model transition-metal surface state band. While the previous discussion has focused upon systems with weak pseudopotentials, this is not appropriate for transition metals. It is useful to approach these results, at least in the low density regime where the adsorbate atoms are weakly interacting, in terms of tight-binding models.

We begin with a discussion of the bands for saturated H/Ta(011) given in Fig. 8.20. (Kneedler et al., 1991). We see a tightly bound hydrogen-induced feature split off below the valence band with a band width of ~2 eV. This band is commonly observed upon adsorption of hydrogen on early transition metal surfaces (Kevan and Eberhardt, 1992; Feibelman et al., 1980; Eberhardt et al., 1981). Like a similar band in bulk hydrides, it has significant H(1s) character, although calculations generally show substantial hybridization

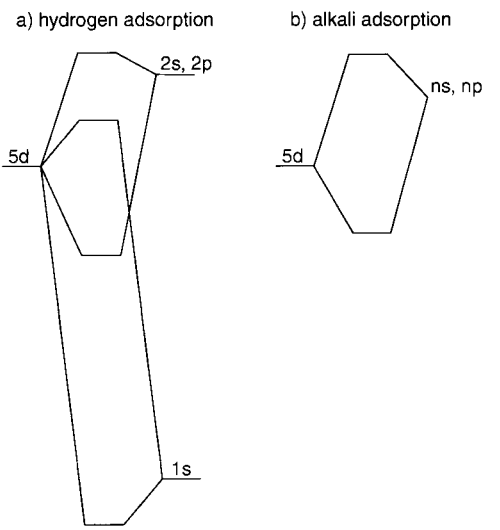


Fig. 8.26. A rough, covalent description of bonding between monovalent atoms and the narrow 5d surface band on Ta(011). (a) For hydrogen adsorption, the H(1s) lies near the bottom of the tantalum valence band so the mixing with the surface state will be minimal. Indeed, much of the bonding is associated with interaction between the H(1s) and Ta(6s, 6p) levels (not shown). Very roughly, the next higher level results from a bonding combination between the surface band and higher hydrogen levels. (b) For alkali adsorption, the ns, np orbital lies close in energy to the surface band (particularly at higher coverage) so that a strongly mixed 5d-(ns, np) hybrid orbital can be formed.

with the substrate sp band. At higher energy, in the middle of a large gap, a very flat band is observed. As discussed previously, this is simply the clean surface band shifted by covalent binding to the hydrogen atoms. The covalent effects are very roughly described by the diagram in Fig. 8.26a. This shows formation of the predominantly H(1s) split-off band with some admixture of tantalum levels, along with its antibonding component above $E_F$ having the opposite orbital character. Also shown is the formation of a bonding orbital between the narrow Ta(5d) surface band and, predominantly, the higher hydrogen (e.g., 2s, 2p) atomic orbitals. This bonding combination gives rise to the feature observed in the middle of the gap.

Aside from the obvious coverage-dependent differences observed in Fig. 8.22 between hydrogen and sodium adsorption, it is clear that Fig. 8.26a must be modified to describe the bonding between alkalis and tantalum. The alkali ionization levels are not nearly as tightly bound as the H(1s). Consequently, no "split-off" state is observed below the tantalum bands, e.g., for one monolayer of alkalis on Ta(011), as shown in Fig. 8.27. The level in the middle of the large gap observed in these bands, in the simplest covalent picture, must be derived from a bonding combination of the alkali(ns,np) ionization orbitals and the Ta(5d) surface state. As such, they correspond more directly to the H(1s) split-off state than to the predominantly H(2s, 2p)–Ta(5d) bonding level which is coincidentally bound by a similar energy. This rough model is supported by the systematically decreasing extent to which the Ta(5d) surface state is shifted by monolayer adsorption of heavier alkalis. The

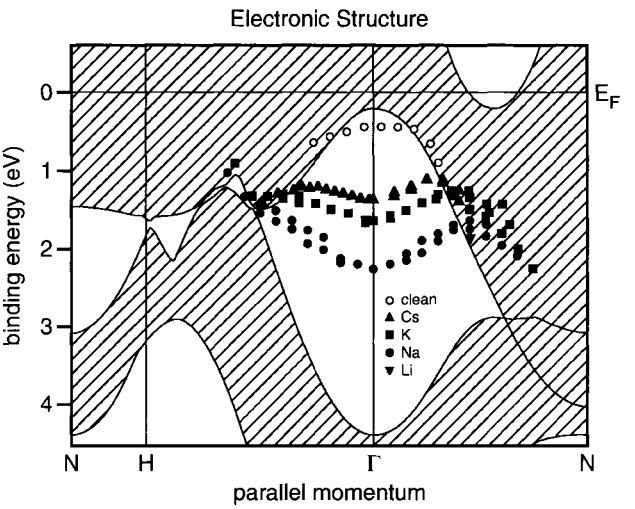


Fig. 8.27. Occupied surface bands for monolayer coverage of several alkalis adsorbed onto Ta(011) as determined by ARP. The band in the middle of the projected gap is the clean surface band shifted by alkali adsorption. Note that the initially dispersionless clean surface band acquires substantial dispersion upon completion of the alkali layers, providing further for 5d-ns orbital hybridization (from Kneedler et al., 1995).

ionization level shifts up in energy as one moves down the alkali series, and the resulting Ta(5d)–alkali(ns-np) bonding level is consequently predicted and observed to lie at higher energy as well.

It is useful to search for a unifying picture of the shifting behavior of the tantalum surface state upon adsorption of alkalis (Fig. 8.22) which might shed some light upon the bonding character, at least at low density. This has been proposed as follows (Kneedler et al., 1995). Consider an alkali s orbital at energy $\varepsilon_s$ interacting with a tantalum d orbital at energy $\varepsilon_d$. These interact *via* a hopping integral $H_{sd}$. Following Harrison (Harrison, 1980), define an average energy $\varepsilon_{av} = (\varepsilon_s + \varepsilon_d)/2$, a splitting between the atomic orbitals $\Delta = (\varepsilon_s - \varepsilon_d)/2$, and a splitting between the d orbital and the bonding orbital $\delta E = \varepsilon_d - \varepsilon_b$. The energy of the covalent bonding orbital is then $\varepsilon_b = \varepsilon_{av} - (H_{sd}^2 + \Delta^2)^{1/2}$, or, solving for the hybridization integral,

$$H_{sd} = \left(\delta E^2 + 2\delta E\,\Delta\right)^{1/2}. \tag{8.4}$$

We insert a coverage dependence by setting $\varepsilon_s$ equal to the coverage-dependent work function. In Fig. 8.28 we plot $H_{sd}$ calculated using Eq. (8.4) as a function of $\delta$E. By Eq. (8.4) this must initially behave as $\delta E^{1/2}$, as observed in the figure. Also, since $\delta E$ approaches zero smoothly as the coverage approaches zero, we must have that $H_{sd} \to 0$ in the zero coverage limit, as also observed in the figure. This condition on $H_{sd}$ is often defined as the limit of "ionic binding" since there is no hopping from one atom to the other (Harrison, 1980). We have thus devised a mathematical description with which the term "ionic" can be applied to alkali adsorption. Moreover, we see that this limit is only truly valid at zero

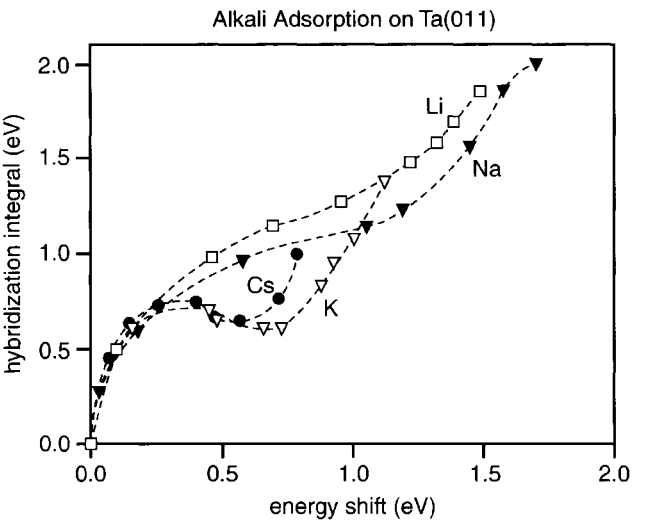


Fig. 8.28. Simple unifying model for the shift of the Ta(011) clean surface band upon alkali adsorption, as explained in the text (from Kneedler et al., 1995).

coverage since otherwise $H_{sd} \neq 0$ and the binding is partially covalent. Note that this ionic limit is ensured by the smoothly shifting behavior observed for d-like surface states on a variety of transition metal surfaces. Note also that this ionic limit implies nothing about the distribution of charge between the adsorbed alkali atoms and the surface. Finally, note that the model implicitly treats the alkali layer as jellium which would have a fairly narrow one electron bandwidth at low density, but which would impact the surface band in a distributed fashion. The results for Li/Be(0001) imply that this is an approximation which deserves further attention. We return to this point in the next section.

Perhaps the most surprising feature observed in Fig. 8.28 is that, at low density, all the alkalis appear to lie on the same curve up to a coverage of typically 0.1 monolayers. This implies that the hopping integrals are roughly alkali-independent. At first sight this is a surprising conclusion since the ionization orbitals are very different in size. Unlike the conclusions in the previous paragraph, this conclusion is dependent upon the placement of $\varepsilon_s$ which determines $\varepsilon_{av}$ in Eq. (8.4). A tempting alternative is to set $\varepsilon_s$ to the atomic values for the alkali ionization levels, perhaps shifted by image charge screening near the metal surface (Lang and Williams, 1976, 1978). Aside from eliminating the coverage dependence from the simple model, this assignment ignores the more global impact of alkalis upon the surface properties in terms of the work function change. One would expect, more or less in line with the Gurney model (Gurney, 1935), that the unhybridized alkali ionization level should be tied to work function and thus to shift toward $E_F$ as the coverage increases. Setting it to an energy which is only proportional to the coverage-dependent work function would also lead to the unified low coverage behavior observed in Fig. 8.28.

A further indication of the complexity of the adsorption of alkalis on transition metal surfaces is indicated by the observation that the feature which was assigned to the Ta(5d) surface state–alkali(ns,np) bonding hybrid forms a band with a decreasing effective mass

as the alkali coverage increases (Kneedler et al., 1995). In Fig. 8.27, it is seen that the band has a curvature characterized by an effective mass of $\sim m_e$ upon completion of a full monolayer for all the alkalis. This clearly emphasizes the increasing degree of lateral interaction with increasing coverage, since the tantalum surface band on the clean surface was essentially flat.

The assignment of the narrow feature located just below $E_F$ in Fig. 8.22 which begins to grow at a sodium coverage corresponding to the work function minimum is less obvious in terms of specific covalent interactions. Like the results for Li/Be(0001) in Fig. 8.13, this band is observed over a narrow region of the surface Brillouin zone and thus holds significantly less than one electron. It does begin to grow below $E_F$ at the work function minimum for all alkalis, but its energy is not constant above the threshold. The above discussion implies that it should not be simply called "the sodium 3s band" which would be predicted from the Gurney model at high density (Gurney, 1935), and which has been concluded in studies of alkali adsorption on simple metals (Watson et al., 1990; Horn et al., 1988). An attractive possibility is that it corresponds roughly to the Ta(5d)–Na(3s,3p) antibonding combination. Support for this is offered by the observation that the band shifts slightly upward for heavier alkalis. However, the fact that the feature is not observed until fairly high density brings into the question a simple covalent assignment which neglects the lateral interactions between the alkalis which are so clearly evident in the more tightly bound feature. This feature near $E_F$ is always energetically very close to the tantalum band edge and to the energy of the clean-surface band. It clearly must have a substantial Ta(5d) component.

### *8.3.4. Chemisorbed layers and the theory of random alloys*

The electronic structure of a disordered chemisorbed layer is determined, in principle, by the positions of the adsorbed atoms. We know, however, that the measured electronic structure and the resulting surface properties do not depend on the specific configuration of adsorbed atoms. This implies that the one needs to average the various adsorbate configurations, weighted to take account of the probability that a particular configuration occurs. Of course, these weightings are determined by the underlying electronic structure, implying that some level of self-consistency is necessary. As discussed briefly in Section 8.3.1, there is a direct correspondence between this problem and the electronic structure of bulk random alloys (Mott and Jones, 1936; Jones and March, 1973; Ehrenreich and Schwartz, 1976). The diverse and interesting properties exhibited by bulk alloys provide ample motivation for trying to apply, at least conceptually, some of these bulk computational approaches to the chemisorption problem.

The simplest theories of bulk alloys, rigid band theory and the virtual crystal approximation, provide useful insight in some systems (Seitz, 1940). For example, the smooth shift of the surface bands on Cu(111) and Be(0001) upon alkali adsorption can be roughly understood by an approximately rigid shift of the surface bands relative to the bulk continuum, which is tied to the bulk Fermi level. Thus the band is filled not by increasing the Fermi level but rather by shifting its energy relative to the bulk-determined Fermi level. A similar phenomenon is observed for the H/Mo(011) and H/W(011) systems discussed in the next section. However, as noted above these theories have fundamental flaws in treating

the chemisorption problem. For example, the systematic variation of the surface band effective mass is not simply incorporated. Neither are the observed H(1s) split-off band and the unoccupied alkali (ns) level observed in many systems. We therefore turn to theories based upon the coherent potential approximation which has been particularly successful in treating the electronic structure of bulk alloys. Our discussion is necessarily brief and elementary; many more detailed discussions of this theory are available (Jones and March, 1973; Ehrenreich and Schwartz, 1976).

Modern implementation of the CPA method is essentially a self-consistent mean-field theory for electronic structure of random alloys. The theory is Green-function based and thus provides most easily the total or local density of states. The simplest CPA model of a random $A_xB_{1-x}$ alloy provides useful insight and is discussed here. The system is parameterized with a single band, tight-binding Hamiltonian, which in second quantized notation is given by (Jones and March, 1973; Velicky et al., 1968)

$$H = \sum_n |n\rangle \varepsilon_n \langle n| + \sum_{n \neq m} |n\rangle t_{mn} \langle m|. \tag{8.5}$$

The first sum contains the diagonal on-site energies $\varepsilon_n$, which can have one of two values, $\varepsilon_A$ or $\varepsilon_B$. The second term contains the off-diagonal hybridization integrals $t_{mn}$ which are assumed to be site- and composition-independent. This implies that the pure A and B crystals have equal one-electron band widths $W$. The key parameters in this theory are $\delta = (\varepsilon_A - \varepsilon_B)/W$ and the concentration $x$. The limit $\delta \to 0$, corresponding to closely-spaced site energies and/or large band width, leads to virtual-crystal behavior. The density of states of the alloy shifts smoothly as a function of composition $x$ between those for pure A and pure B. There is no splitting of the density of states into distinct "predominantly A" and "predominantly B" manifolds. This latter observation delineates the failure of the simplest VCA theory in most chemisorption problems.

The other extreme, $\delta \to \infty$, corresponds to widely-spaced site energies and/or very narrow band widths. The simple model Hamiltonian in Eq. (8.5) actually does not predict what is clearly the correct density of states in this limit. One can think of this limit in terms of core levels, in which case one would expect to observe well-separated features in the total density of states lying at energies slightly shifted from $\varepsilon_A$ and $\varepsilon_B$ due to chemical-shift-like effects. Such effects are local so that the core levels will appear to be split or broadened, corresponding to the different possible local environments near a given atom. The orbital character of these two density of states features remains essentially pure A and pure B.

As is often the case, most interesting is the intermediate regime, $\delta \sim 1$. In this case, for small $x$ an impurity band of dominant A character splits from the dominant B-like density of states and grows monotonically as a function of $x$. This is similar, for example, to the behavior of the predominantly Li(2s) level observed above $E_F$ for Li/Be(0001). The central energies of these two density of states features shift smoothly as a function of composition, and the magnitude of these shifts depend upon the details of the model. We thus can describe qualitatively results for surface states which shift upon varying alkali coverage with the simultaneous appearance of a split-off alkali level above $E_F$ within the context of this simple model. The different behaviors between H/Ta(011) and Na/Ta(011) in Fig. 8.22

can also be understood in terms of different values of $\delta$. The Na(3s) level is much closer in energy to the Ta(5d) surface band than the H(1s) level. Also, the Na(3s) orbital is larger and more highly interacting than the (1s), so that the effective hybridization integrals are larger. Both of these observations will make an effective $\delta$ much larger for H/Ta(011) than for Na/Ta(011). Upon hydrogen adsorption, the Ta(5d) manifold to splits into two components which correspond, presumably, to tantalum surface sites which are either occupied or unoccupied by hydrogen atoms. We also observe a well-defined predominantly H(1s) split-off band. The simple model obviously breaks down in some important respects, such as the Ta(6s,6p)–H(1s) hybridization. By contrast, the smaller value of $\delta$ for Na/Ta(011) makes the spectral evolution more gradual for this system.

Clearly there is much room for a better and more complete theory in treating data such as these. The benefit will be an better understanding of surface alloys and perhaps the prediction of novel surface properties. For example, in the CPA method, the Hamiltonian is non-hermitian so that the energy eigenvalues are complex. That is, the self energy of the bands is complex due to a finite rate of disorder-induced elastic scattering. This is synonymous with the broadening of the Cu(111) surface band upon potassium adsorption observed in Fig. 8.24. In turn this implies that the ARP line shape in random alloys and disordered chemisorbed layers contains useful information that might be extracted if better CPA-based theories were to be applied and if other contributions to the line shape were better understood. Finally, we emphasize that the CPA method is just a mean-field method. This implies intrinsic limitations associated with short- or intermediate-range order. Various efforts to improve the CPA method, such as the cluster-CPA method (Bishop and Mookerjee, 1974; Mookerjee, 1975), may be important and useful in interpreting surface results.

## 8.4. Non-adiabatic effects and surface electronic structure

The Born–Oppenheimer approximation underlies much of our intuition about the equilibrium structure and properties of molecules and solids. With the exception of the brief discussions about electron–phonon-interaction-induced wiggles in bands crossing $E_F$ and of phonon anomalies, all of our discussion to this point has implicitly made this approximation since we have ignored nuclear motion entirely. At the heart of the Born–Oppenheimer approximation is the assertion that electrons respond effectively instantaneously on the time scale of nuclear motion. This leads to the separability of electronic and nuclear degrees of freedom in the Hamiltonian for a polyatomic system. Solution of the resulting electronic Hamiltonian leads to an eigenvalue spectrum which depends parametrically upon nuclear coordinates and thus to the concept of an adiabatic potential energy surface. In thermodynamics, "adiabatic" implies the absence of heat flow. In the context of the present discussion, it implies absence of dissipation of energy from the electronic manifold into the nuclear motion, and *vice versa*. Strict validity requires that nuclear velocities be infinitesimally small.

Many interesting dynamical phenomena require some degree of breakdown of the Born–Oppenheimer approximation. In molecular and solid systems, the static and dynamic Jahn–Teller effects, for example, cannot be explained within the confines of the

Born–Oppenheimer approximation (Bersuker and Polinger, 1989). These phenomena have counterparts in condensed phase systems, for example, in the observation that many ionic transition metal compounds are distorted from symmetric configurations (Cox, 1987; Goodenough, 1972). Their extension to non-zero momentum results in charge density wave formation and Peierls-like distortions (Peierls, 1964; Rice, 1975). Probably the most spectacular example of the breakdown of the adiabatic approximation is traditional superconductivity which is driven by the electron–phonon interaction. In many of these effects, the non-adiabaticity is removed by formation of a new, lower symmetry ground state and under normal conditions the system is adiabatic. Typically, the lower symmetry removes an electronic degeneracy. This provides the key to understanding the circumstances under which the Born–Oppenheimer approximation may not be valid. The important factor is not simply the velocity of the electrons relative to the nuclei as suggested in the previous paragraph. Rather, if the lowest energy electronic excitations are comparable in energy to that of typical lattice excitations then energy transfer from one manifold to the other, i.e., dissipation, is allowed. Thus the adiabatic approximation is always suspect in metals where the lowest energy electronic excitation is by definition zero (Ashcroft and Mermin, 1976).

A good example of the interplay between low energy electronic excitations and vibrational degrees of freedom is offered by the BCS-theory prediction of the critical temperature $T_c$ of a traditional superconductor (Ziman, 1972)

$$k_B T_c = 1.13\hbar\omega e^{-1/[V_0 g(E_F)]}. \tag{8.6}$$

$V_0$ is the average electron–phonon coupling strength, $\omega$ is a typical phonon frequency, and $g(E_F)$ is the density of states at the Fermi level. $T_c$ can be viewed as an approximate measure of the strength of non-adiabaticity involved in forming the superconducting state. We see that this strength increases as any or all of $\omega$, $V_0$, or $g(E_F)$ increase. This observation makes qualitative sense in terms of the criteria for the validity of the Born–Oppenheimer approximation. These comments, and indeed even Eq. (8.4), are also applicable to other non-adiabatic phenomena such as the Peierls distortion (Peierls, 1964; Rice, 1975).

As the dimensionality of a system decreases, the possibility of unusual features in $g(E_F)$ becomes progressively more important. The density of states near a band edge of a 3D system is generally smooth, that of a 2D system normally has a discontinuity in slope, while that of a 1D system is singular (Rice, 1975; Wilson et al., 1975). For this reason, one might expect greater impact from non-adiabatic effects at surfaces than in bulk media. Surprisingly, only a few surface systems have been found to exhibit dramatic breakdowns of the adiabatic approximation (Chabal, 1985, 1986, 1988; Reutt et al., 1988; Hirschmugl et al., 1990; Ryberg, 1989). It is not clear whether this paucity of examples results simply from a lack of appropriate surface techniques having sensitivity to non-adiabatic phenomena. It would be difficult, for example, to measure the superconducting properties of a of a clean surface in the absence of bulk interference.

A few excellent examples of significant breakdown of the adiabatic approximation in surface systems have been reported. For example, the resistivity of conductors requires energy to flow from electronic to nuclear vibrational degrees of freedom. An unusual yet relevant example of this phenomenon is offered by numerous studies of the resistivity of

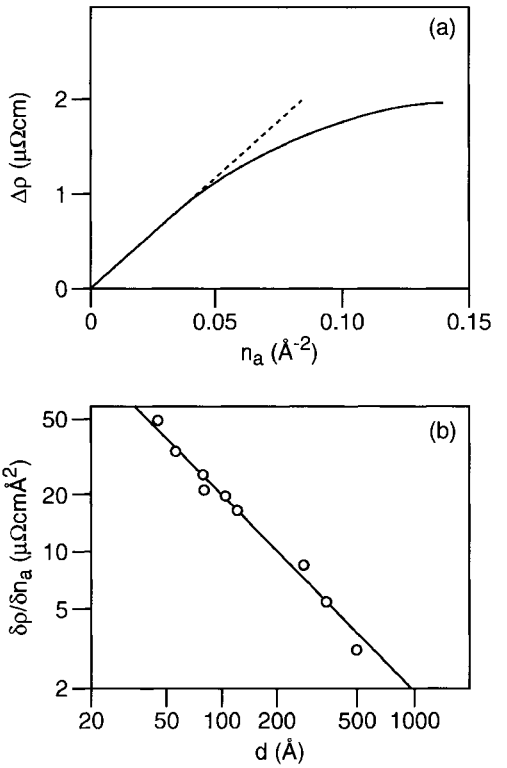


Fig. 8.29. Measured change in resistivity of a thin Ni(111) film as a function of adsorbed CO density. The linear variation at low density is similar to Matheison's rule for the resistivity of dilute bulk alloys. The presence of this increased resistivity must be attributed to the flow of energy between the electron gas and the lattice (from Persson et al., 1991).

thin films upon adsorption of atoms or molecules. An example is given in Fig. 8.29, which shows the resistivity of a crystalline, nominally clean Ni(111) film as a function of adsorbed CO coverage (Wissman, 1975; Persson et al., 1991). At low density, the resistivity is observed to increase linearly from the zero-coverage value. This is similar to Matheisen's rule which explains the linear dependence of the bulk resistivity of dilute alloys upon concentration of the dilute component. While the magnitude of the resistivity can be determined by elastic scattering of carriers, the existence of resistivity obviously requires dissipation in the form of inelastic scattering off vibrations. The results in Fig. 8.29 have been explained in terms of inelastic scattering of conduction electrons off the adsorbate frustrated translational modes parallel to the surface. A relation between this phenomenon and damping of the same adsorbate vibrations through creation of electron hole pairs has been proposed (Persson et al., 1991).

The data in Fig. 8.29 demonstrate the flow of energy from an electron gas into a phonon bath. The opposite phenomenon, adsorbate vibrational damping, can be and has been observed directly by measuring with high resolution the adsorbate vibrational spectrum. The

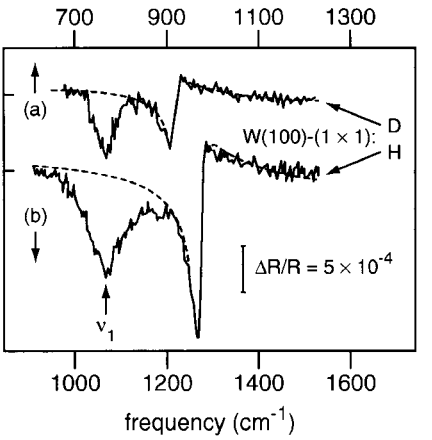


Fig. 8.30. Infrared reflection absorption spectrum of W(001)-2H and W(001)-2D. The mode near 1200 $cm^{-1}$ on the former exhibits a substantially asymmetric line shape, implying significant electronic damping of the adsorbate vibration (from Chabal, 1985).

first observed example of this is shown in Fig. 8.30 which gives the infrared reflection–absorption spectrum of hydrogen and deuterium adsorbed onto W(001) (Chabal, 1985, 1986; Reutt et al., 1988). In each case, two modes are observed. One mode has a fairly broad and symmetric line shape while the other is narrow and distinctly asymmetric. Zhang and Langreth showed that this asymmetric, derivative-like line shape is the signature of vibrational damping by excitation of electron-hole pairs (Langreth, 1985, 1986; Zhang and Langreth, 1989a, b). The underlying physics is similar to that of a Fano resonance in atomic physics (Fano, 1961). In the present case, a discrete vibrational mode is coupled to an underlying electron–hole pair continuum, and interference between these two degenerate excitation channels leads to the derivative-like absorption line shape. The degree of asymmetry in the lines in Fig. 8.30 was determined to imply a strong breakdown of adiabaticity. The original reference (Chabal, 1985) concluded that the mode showing this effect was actually an overtone of the so-called "wag" mode, that is, a zone center mode with eigenvector oriented approximately parallel to the surface plane but perpendicular to the two nearest neighbor tungsten atoms. The study also detected a broad absorption which was ascribed to an underlying electronic excitation. A later example of non-adiabatic damping of adsorbate vibrations was reported for CO/Cu(001), the results of which are shown in Fig. 8.31 (Hirschmugl et al., 1990). Again two modes are observed, one of which shows a asymmetric derivative-like line shape. In this case, there is actually an anti-absorption resonance, that is, the absorption is decreased near the center of the vibrational mode. The vibrational mode assigned to this feature was the frustrated rotational mode. The physics underlying these and other vibrational relaxation results for CO/Cu(001) has been examined in detail and with a good deal of success using *ab initio* calculations of a cluster model (Head-Gordon and Tully, 1992a, b).

There currently is significant interest in providing a uniform framework within which results like those in Figs. 8.29–8.31 can be understood. It is interesting and perhaps

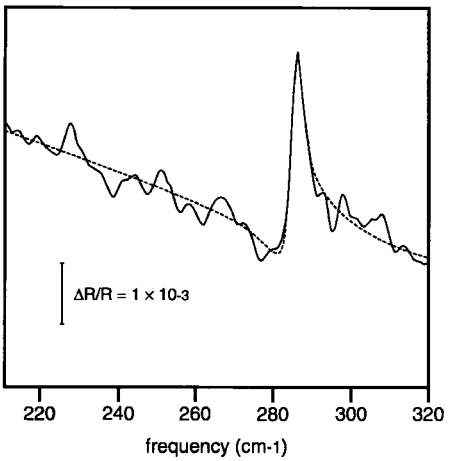


Fig. 8.31. Infrared reflection absorption spectrum of a saturation coverage of CO adsorbed onto Cu(001). The existence of an asymmetric anti-absorption resonance, like Fig. 8.30, implies breakdown of the adiabatic approximation (from Hirschmugl et al., 1990).

significant that in all cases the vibrational mode showing the most pronounced breakdown of the adiabatic approximation were frustrated modes with significant amplitude parallel to the surface. Normally such modes are difficult to observe with any technique, particularly infrared reflection–absorption spectroscopy, and it might be concluded that they acquire significant oscillator strength through coupling to electronic excitations. It is also useful to distinguish the participation of interband from intraband excitations in adsorbate vibrational damping. In order to have an energetic degeneracy between a zone center vibrational mode and an interband electron–hole pair excitation, the two bands must come very close in energy. Bands of opposite symmetry can cross and thus are of arbitrarily small separation, but this can only happen over a narrow region along symmetry lines and generally in the absence of strong spin–orbit interaction. The crossing must also occur very close to $E_F$ or the electron–hole pair excitation would be disallowed by Fermi–Dirac statistics. In short, the likelihood of simple surface band–surface band excitations participating in adsorbate vibrational damping is very small. In the diagram in Fig. 8.32, the interband electron–hole pair continuum is shown schematically to lie at higher energy than a typical zone-center adsorbate vibrational mode. If we have an ordered layer and thus need to consider the adsorbate vibration to be an extended, zone center phonon mode, the situation for intraband excitations is only slightly better. The intraband electron–hole pair continuum must always occupy a region of energy–momentum space below a line passing through the origin (Pines, 1963). A zone center adsorbate vibrational mode such as those in Figs. 8.30 and 8.31 lies at finite frequency but zero wave vector and there is thus no degeneracy. The only way for intraband excitations to participate in zone-center adsorbate vibrational damping is for the adsorbed layer to be imperfect so that momentum need not be conserved in the electron–hole pair excitation. This may be the primary weakness of the aforementioned cluster approach which was applied to CO/Cu(001).

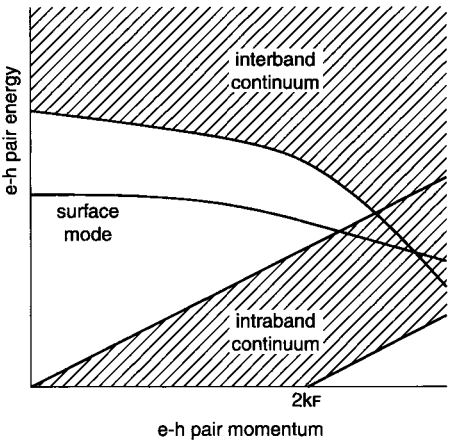


Fig. 8.32. Schematic of interband and intraband electron–hole pair continua. The surface mode might be an adsorbate phonon dispersion curve. In most instances, at zone center this mode will be degenerate with neither of the continua.

### *8.4.1. Fermi contours, intraband excitations, and zone center phonons*

Equation (8.3), which relates the change in occupation of a surface band to a change in work function for potassium adsorbed onto Cu(111), suggests the beginning of a mechanism through which energy in a zone-center adsorbate vibrational mode can be dissipated (Gaylord et al., 1989a). Consider a slow rigid translation of the potassium layer away from the surface plane by a distance $\Delta z$. The adsorption dipole and thus also the work function will change by some amount. Equation (8.3) implies that the number of electrons in the surface band below $E_F$ will also change. This makes sense because in the limit $\Delta z \rightarrow \infty$ the surface band will lie at the clean surface limit and will thus hold fewer electrons. For small $\Delta z$, $\Delta\Phi/\Delta z$ will be constant. Equation (8.3) implies then that $\Delta n_s/\Delta z$ will also be constant, or the occupation of the surface band varies approximately linearly with the vertical position of the adsorbate layer.

If instead we now allow the layer to oscillate normal to the surface at frequency $\omega$, which is obviously just the zone center optic phonon mode, the number of electrons in the surface band will also oscillate. If $\omega$ is small, the electronic manifold will remain in the ground state, that is, we will achieve the adiabatic limit. Stated differently, the electrons will oscillate in phase with the phonon mode. As $\omega$ increases, the electron gas may not be able to stay precisely in phase. An out of phase component implies dissipation, that is, transfer of energy from the phonon mode into the electron gas. This model is very similar to textbook models for AC conductivity (Ashcroft and Mermin, 1976; Ziman, 1972). In that case, the Fermi surface oscillates in the direction and at the driving frequency of the applied AC field. In the present discussion, the Fermi surface "breaths" at the frequency of the phonon mode. Electronic damping is often included using a phenomenological scattering time $\tau$, which determines the degree to which the electrons can stay in phase. Damping might arise in this case from surface imperfections and would endow the conductivity with

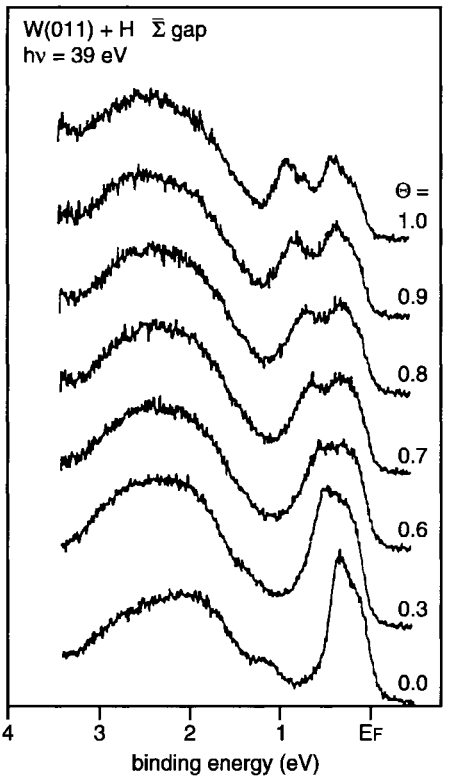


Fig. 8.33. ARP spectra of W(011) as a function of hydrogen coverage at a photon energy of 39 eV and at a momentum along the $\bar{\Sigma}$ symmetry line. Two surface features are observed on the clean surface, one at a binding energy of ~1.1 eV and another at ~0.3 eV. The former is observed to disappear from the spectrum upon adsorption, while the latter simply shifts smoothly to higher binding energy as a function of coverage (from Gaylord and Kevan, 1988).

a Drüde-like component (Ashcroft and Mermin, 1976). If $\tau$ is large, implying very low resistivity, the out-of-phase response will be small and the non-adiabatic effects should not be serious. We thus find once again that intraband electron–hole pair excitations can support non-adiabatic interactions only in the presence of imperfections. This type of damping mechanism can be operative for any surface state–adsorbate combination when 1) the surface band brackets the Fermi level and thus has a well-defined Fermi contour, and 2) the surface band shifts smoothly with adsorbate position, which might be correlated to the work function as discussed above. This shifting behavior can be operative in the dilute limit where, often, the adsorbate layer is disordered so that the momentum conservation problem associated with intraband transitions is in principle circumvented.

Results for H/W(011) and H/Mo(011) indicate that some surface bands on these systems also satisfy these criteria. Figure 8.33 shows spectra for W(011) as a function of hydrogen coverage (Gaylord and Kevan, 1988; Jeong et al., 1989a). The clean surface spectrum at the bottom exhibits two well-defined surface features, one of which is rapidly quenched upon

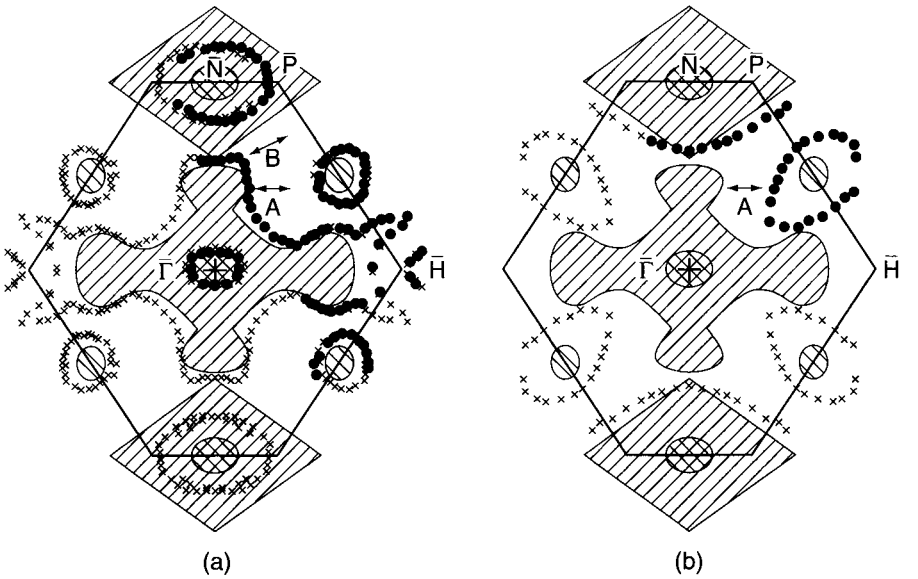


Fig. 8.34. Fermi contours for (a) clean and (b) hydrogen-covered W(011) determined using ARP from Gaylord et al. (1989a). The filled circles are actual measurements, while the open circles are deduced by symmetry. The shaded regions are the projection of the bulk Fermi surface from Girvan et al. (1968).

adsorption of hydrogen. This is similar to the "large $\delta$" behavior of H/Ta(011), although the resulting bonding level is not visible in this system. The other surface state shifts monotonically downward in energy with increasing hydrogen coverage and thus satisfies the second criterion outlined above. Both of these bands cross $E_F$ on the clean surface and thus produce the well-defined Fermi contours observed in Fig. 8.34a (Gaylord et al., 1989a, b), plotted together with a projection of the experimental bulk Fermi surface onto the (011) SBZ (Girvan et al., 1968). The three elliptical contours are associated with the first band and are thus removed upon hydrogen adsorption. The irregular electron contour is associated with the second surface band and thus expands smoothly with increasing coverage, in qualitatively similar fashion to the alkali/Cu(111) and Li/Be(0001) systems. Ultimately the contour converges on its image in the second zone and undergoes a topological change to form two closed hole pockets as shown in Fig. 8.34b. These changes are mirrored by the bulk continuum at energies slightly above $E_F$ (Jeong et al., 1989a), reflecting qualitatively the rigid-band-like behavior mentioned in Section 8.3.4. Figure 8.35 shows the measured change in the magnitude of $k_F$ for a particular segment of the Fermi contours as a function of coverage. The smooth variation of $k_F$ is interrupted by a change in slope near a coverage corresponding to where the surface reconstructs (Gaylord et al., 1989a, b; Chung et al., 1986; Altmann et al., 1987). This coverage is not simply related to the coverage at which the topological change mentioned above occurs. Figure 8.35, when applied to the above analysis implies that the zone center hydrogen vibrational mode oriented perpendicular to the surface plane might be damped by intraband electron–hole pair excitations across this contour.

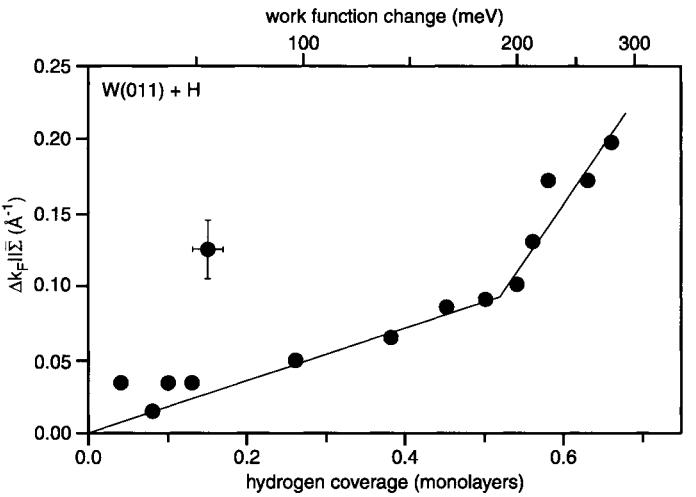


Fig. 8.35. Magnitude of the change in $k_F$ along the line labeled A in Fig. 8.34 as a function of hydrogen coverage on W(011). Upper abscissa indicates the corresponding work function change (from Gaylord et al., 1989a).

While this prediction has not been seriously tested, such behavior does not necessarily imply a strong breakdown of adiabaticity in adsorbate vibrational damping. In many instances the breakdown may not be very serious. By this we mean, for example, that the vibrational spectrum will not necessarily be very asymmetric as observed for one of the two features in Fig. 8.30. Though not directly applicable, Eq. (8.6) provides some useful insight in this respect. For example, one certainly expects the adiabatic approximation to be more valid for low than for high frequency vibrations. Non-adiabatic effects should thus be maximal for adsorbed hydrogen, and the likelihood of there being a strong breakdown on adiabaticity for the vibration of heavier alkalis is small. Also, a higher density of states at $E_F$ will naturally lead to greater deviations from the adiabatic limit. Another way to look at this is that $g(E_F)$ is inversely related to the Fermi velocity, and fast electrons are more likely to respond adiabatically. Both the alkali/copper and H/W(011) and Mo(011) systems have bands with fairly large Fermi velocities, so that the impact of non-adiabatic effects may not be pronounced in the vibrational spectrum, even though energy is being dissipated fairly efficiently. The electron–phonon coupling strength $V_0$ is generally less intuitive. However, in the simple model discussed above, the fundamental coupling of a translation of the adsorbate layer to the occupancy of a 2D electron gas is related to this parameter.

The spectra shown in Figs. 8.30 and 8.31 correspond to parallel vibrational modes, while the analysis given above was for a mode oriented normal to the surface. The coupling is may not be very strong for parallel modes. To date, direct correlation between the strongly non-adiabatic damping of an adsorbate vibrational mode and the surface electronic structure through the mechanism outlined above has not been reported. However, the cluster calculations for vibrational damping in CO/Cu(001) are very similar in spirit to this model (Head-Gordon and Tully, 1992a, b).

### *8.4.2. Vibrational damping on Mo(001)–2H and W(001)–2H*

As implied in the previous paragraphs, the results for W(001)–2H in Fig. 8.30 are not well-explained by non-adiabatic coupling to intraband electron–hole pair excitations (Chabal, 1985, 1986; Reutt et al., 1988). There is no surface band near $E_F$ that satisfies the second criterion described above. Moreover, the vibrational mode is almost certainly oriented parallel to the surface so that coupling through the work function change will not be very significant. Finally, the observed non-adiabatically damped mode is sharpest and its asymmetry is most well-defined as the perfection of the saturated layer is improved. Defects and imperfections appear to mask rather than enhance the degree of non-adiabaticity.

While there is no surface band that shifts smoothly with coverage for this surface, there is a hydrogen-induced level very close to $E_F$, as indicated for W(001)–2H in Fig. 8.36, which may be relevant to the observed vibrational damping (Smith and Kevan, 1990). This state and a similar one on Mo(001)–2H (Smith and Kevan, 1991b) are apparently associated with the saturated surface and lie less than 200 meV below $E_F$. While it is difficult to measure an accurate dispersion relation for these levels, is possible to plot the region of the surface Brillouin zone within which the state is observed, as shown in Fig. 8.37 for Mo(001)–2H. We see that the feature is observed over much of the zone, implying a small

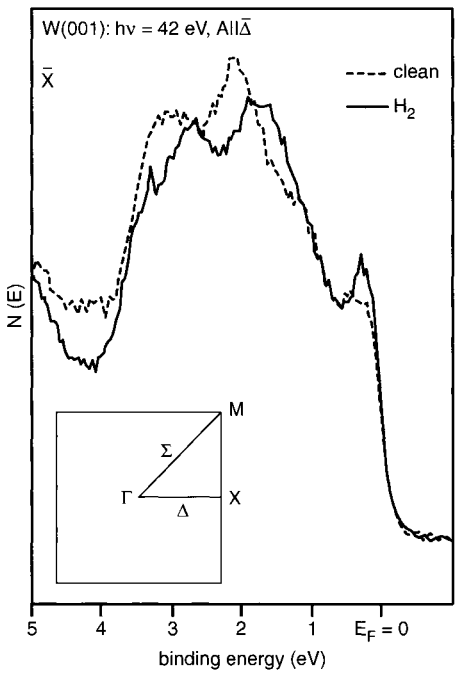


Fig. 8.36. Clean (dashed curve) and hydrogen-covered (full curve) ARP spectra for W(001)–2H collected at a photon energy of 42 eV and sampling states near the $\bar{X}$ point of the SBZ. Note the presence of a hydrogen-induced peak very close to $E_F$ which is well-placed to cause the observed adsorbate vibrational damping in this system (from Smith and Kevan, 1990).

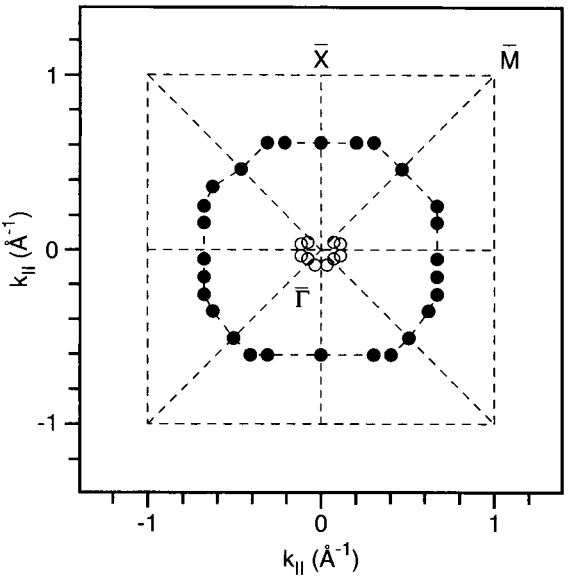


Fig. 8.37. Region of the SBZ over which a narrow feature below $E_F$ on Mo(001)–2H is observed using ARP (from Smith and Kevan, 1991b).

Fermi velocity and thus a very high density of states at $E_F$, estimated to be ~2/eV/atom compared to a bulk value of less than 0.5/eV/atom. In actual fact, the feature is a surface resonance over much of the zone. That its width is fairly small implies that it is not coupled strongly to bulk states. It should be considered to be a weakly coupled resonance approximately centered at $E_F$.

These qualities are not very different from those used in the original model by Zhang and Langreth to predict asymmetric adsorbate vibrational line shapes in the presence of a strong violation of the adiabatic approximation (Langreth, 1986; Zhang and Langreth, 1989a, b). In their model, the electronic density of states consisted of a smooth continuum punctuated by a $\delta$-function component less than one vibrational frequency from $E_F$. The non-adiabatic effects arose from a degeneracy between the vibration and electronic excitations into or out of the density of states anomaly. The key features which support non-adiabatic vibrational coupling are then 1) a narrow feature in the electronic density of states located within the vibrational energy of $E_F$, and 2) comparatively slow transfer of charge into and out of this feature.

A qualitative conjecture has been proposed which, given a measured surface electronic structure, allows prediction of which adsorbate modes might exhibit anomalous damping (Kneedler et al., 1991). It is difficult to slow electronic transitions sufficiently to produce non-adiabatic effects. That is, even if the second criterion in the previous section is satisfied, the rate of filling and emptying a given surface band near $E_F$ is still generally fast compared to typical vibrational frequencies. Consideration of a symmetry or near-symmetry effect is useful. Ignoring the spin–orbit interaction, surface bands at momenta in a mirror plane may be classified as either odd or even symmetry upon reflection. At

such momenta, a surface band can then be considered to be a pure state even though it is energetically degenerate with a continuum of the opposite symmetry. For example, this was discussed previously for the Ta(011) clean surface state near zone center. The degeneracy in energy and momentum between a band of one symmetry and the continuum of the opposite symmetry allows odd symmetry vibrations to decay by exciting an electron–hole pair having overall odd symmetry. In essence, the unshaded area in Fig. 8.32 can be filled by such surface band–bulk continuum electron–hole pair excitations. One might expect the rate of such damping to be comparable to the vibration itself, leading naturally to non-adiabatic effects. The precision of this conjecture is decreased by the presence of the spin–orbit interaction which mixes even and odd symmetries. However, the magnitude of this interaction is comparable to that of the adsorbate vibrational energy, so that elastic resonant exchange of electrons between the state and the continuum assisted by the spin–orbit interaction will occur at a rate which is comparable to the vibration itself. The conjecture is also only valid for electronic states along the symmetry lines, a region which constitutes a vanishingly small area of the surface Brillouin zone. However, off the symmetry lines the mixing of even and odd symmetries is often not very large and the same argument as for the spin–orbit interaction holds. This conjecture has recently been applied to photoemission results for the hydrogen-covered Ta(011) surface, although vibrational data for this system are not yet available (Kneedler et al., 1991). A similar symmetry analysis was used in the cluster calculations of CO/Cu(001) to model the widely different rates of damping for the different adsorbate modes (Head-Gordon and Tully, 1992a, b). Those calculations were non-relativistic and also clearly were not subject to constraints of momentum conservation discussed above.

### *8.4.3. Vibrational damping and phonon anomalies*

Our discussion so far has focused upon zone center vibrations localized primarily within the adsorbate layer. While this obviously can be extended to intrinsic (clean surface) zone center phonons, there is substantial interest also in investigating non-adiabatic effects at non-zero momentum. It is apparent from Fig. 8.32 that a phonon mode away from the zone center can decay either by interband or intraband electron–hole pair excitations. The issues then revert to the density of states and matrix element issues in Eq. (8.6). Such non-adiabatic damping of phonon modes can lead to Kohn anomalies (Kohn, 1959; Chan and Heine, 1973) in phonon dispersion curves and, if these anomalies are severe, to reconstruction through a mechanism similar to the Peierls distortion (Peierls, 1964; Rice, 1975). These issues will be the subject of the next section. Presently we are interested in the existence and strength of the anomalies themselves.

A graphic depiction of how a phonon anomaly is generated in a 2D system is given in Fig. 8.38 which shows a schematic of a 2D Fermi contour. Assume that this is an electron orbit so that occupied levels are enclosed. A phonon having very little energy can decay by exciting an electron from any location just inside the contour to any location just outside. Momentum conservation requires that the vector matching the electron and hole states be equal, within a reciprocal lattice vector, to the phonon momentum, as indicated by the vector $\mathbf{q}_1$. This condition reduces substantially the number of phonon modes that can decay by exciting a single electron–hole pair within this band. Of the subset of allowed momenta,

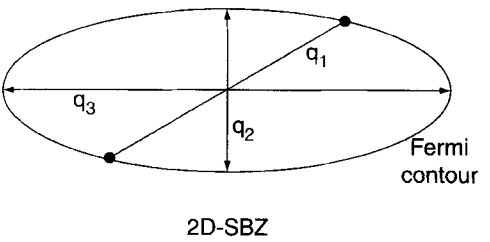


Fig. 8.38. Schematic description of how a Kohn anomaly can arise in a 2D metallic system. The elliptical curve is a schematic Fermi contour which lies entirely within the first 2D Brillouin zone, assumed to be of rectangular symmetry. The vectors $\mathbf{q}_1$, $\mathbf{q}_2$, and $\mathbf{q}_3$ couple states on the Fermi contour and thus can provide a channel for dissipating energy in a low energy mode at these wave vectors. Density of states arguments imply that the strongest anomaly will be observed at $\mathbf{q}_2$.

the joint density of states for electron–hole pair formation is maximal for excitations which span states near points on the Fermi contour which have parallel tangents. It is further enhanced by minimizing the curvature of the contour itself, so the strongest Kohn anomaly will be observed at point $\mathbf{q}_2$, and a somewhat weaker anomaly will be observed at $\mathbf{q}_3$, and no significant anomaly will be observed at $\mathbf{q}_1$. Mathematically, these ideas are contained in the Lindhard expression for the generalized susceptibility for an electron gas (ignoring matrix elements) (Ashcroft and Mermin, 1976; Ziman, 1960, 1972)

$$\chi(\mathbf{q},\omega)=\sum_{\mathbf{k},\mathbf{G}}\frac{f(\mathbf{k}+\mathbf{q}+\mathbf{G})-f(\mathbf{k})}{\varepsilon(\mathbf{k})-\varepsilon(\mathbf{k}+\mathbf{q}+\mathbf{G})+\hbar\omega}. \tag{8.7}$$

For small frequency $\omega$, $\chi(\mathbf{q},\omega)$ can be large when $\varepsilon(\mathbf{k}+\mathbf{q}+\mathbf{G})\cong\varepsilon(\mathbf{k})$. The Fermi factors $f(\mathbf{k}+\mathbf{q}+\mathbf{G})$ and $f(\mathbf{k})$ in the numerator require that one of these states be occupied while the other be unoccupied, and the only way a singularity can occur is if both energies are near $E_F$. Phonon anomalies are thus driven by singularities or near-singularities in the generalized susceptibility so that the system responds significantly for small driving force. The density of states arguments discussed above arise from converting the sum to an integral. Clearly dimensionality plays an important role in determining the structure of the joint density of states, a fact which suggests that such anomalies should be more severe in reduced-dimensional systems. Indeed, such anomalies play a major role in the structure and dynamical properties of quasi-1D and -2D metals (Rice, 1975; Wilson et al., 1975).

The first experimental evidence for the existence of an anomaly in a surface phonon dispersion curve was for Pt(111) (Harten et al, 1985; Neuhaus et al., 1986). Later analysis which concluded that the previous assignment was probably in error (Kern et al., 1986a, b; Bortolani et al., 1989) was supported by a contemporaneous measurement of the surface Fermi contours (Di et al., 1991, 1992), and it is presently thought that this surface is free of significant phonon anomalies.

More recent work on W(110)–H and Mo(110)–H have provided some of the best examples of a well-defined phonon anomaly in a surface system (Hulpke and Lüdeke, 1991, 1992, 1993). The dispersion curves along three different azimuthal directions for W(110)–H are shown in Fig. 8.39. A very deep anomaly is observed at $q\sim 0.9$ Å$^{-1}$ along

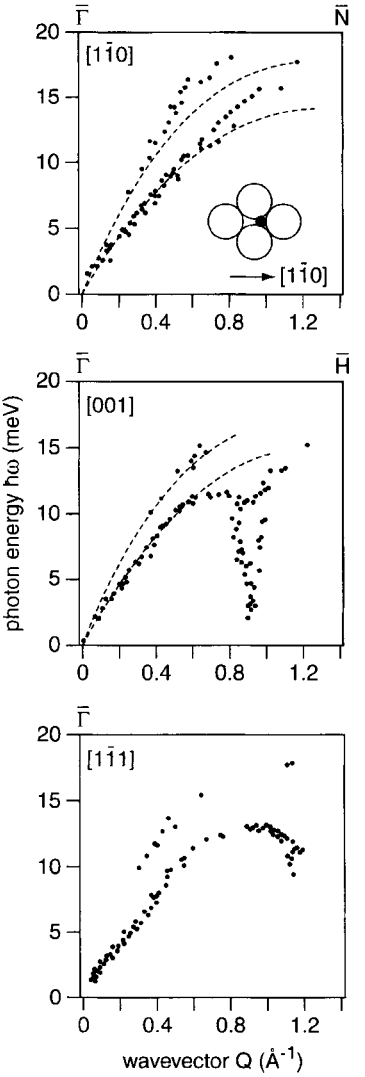


Fig. 8.39. Experimental surface phonon dispersion relations determined using inelastic helium scattering for saturation coverage of hydrogen on W(011) along three different directions in the SBZ. Note the very deep anomaly observed along the $\bar{\Gamma} \rightarrow \bar{H}$ ($\bar{\Sigma}$) azimuth (from Hulpke and Lüdeke, 1991).

the (001) or $\bar{\Sigma}$ azimuth. The anomaly is observed to persist off the $\bar{\Sigma}$ axis with a constant component along $\bar{\Sigma}$. That is, line of anomalous phonon wave vectors is perpendicular to $\bar{\Sigma}$ at a perpendicular distance from $\bar{\Gamma}$ of $\sim$0.9 Å$^{-1}$. If this anomaly is driven by the mechanism discussed above, a Fermi contour on the hydrogen-saturated surface which is also a straight line and which is separated from its image either in the same or a neighboring Brillouin zone by 0.9 Å$^{-1}$ would be required. Such a one-dimensional contour is not

observed in Fig. 8.34b. While it possible that another previously undetected contour exists on this surface, there is very little one-dimensional character in either the bulk or surface electronic structure of tungsten. The source of the anomaly observed in Fig. 8.39, the existence of which has been confirmed using inelastic electron scattering (Ibach, private communication) is a source of current study and speculation. The observed phonon anomalies have been the subject of considerable work since this chapter was originally written, and are now considered to be prototypical examples of anomalies driven by nested segments of the surface Fermi contours. Contours calculated from first principles for Mo(011)+H differed from those shown in Fig. 8.34b somewhat, and indicated the appropriate nesting (Bungaro et al., 1995; Kohler et al., 1995). Later experimental on W(011)+H results have expanded further upon this question by identifying a splitting of the nested contours caused by the spin-orbit interaction and predicting an unusual spin structure within the associated band (Rotenberg and Kevan, 1998).

### *8.4.4. Reconstruction of W(001) and Mo(001)*

As mentioned in the previous section, a phonon anomaly which is sufficiently severe will lead to a reconstruction of the surface through a mechanism similar to the Peierls distortion. The original Peierls instability was proposed for a simple, 1D metal having a half-filled band (Peierls, 1964). Such a system can lower its total electron energy by forming dimers, thereby doubling the size of the real-space unit cell and forming gaps at the Fermi level. This energy gain is linear in the magnitude of the distortion, while the elastic energy increases quadratically in its magnitude. Thus small distortions are always favored in a 1D metal. These ideas can easily be extended to other (even incommensurate) filling factors since the wave vector of the reconstruction is simply given by $2k_F$, i.e., the wavevector of the phonon anomalies discussed in the previous section. The extension to a 2D metal is non-trivial due to the possibility of competing long-range antiferromagnetic order, i.e., spin-density-waves vs. charge-density-waves (Liu et al., 1992; Mazumdar, 1987, 1989; Tang and Hirsch, 1988, 1989). This issue has been actively pursued in relation to the high temperature superconductors.

In spite of these complications, several quasi-2D metals do in fact exhibit reconstructions which are, to zero order, described as Peierls instabilities (Wilson et al., 1975), and these observations have naturally lead to the suggestion that surface reconstructions can be driven by a similar mechanism. An enduring and often controversial focus in this respect has been provided by the W(001) and Mo(001) surfaces (Debe and King, 1977, 1979; Felter et al., 1977; King, 1983; Pick et al., 1989; Hildner et al., 1991).These surfaces reconstruct to c(2 × 2) and very similar $(7\sqrt{2} \times \sqrt{2})$R45° structures, respectively, when cooled below room temperature. We discuss these reconstructions briefly here from the perspective of non-adiabaticity since they provide sobering examples of how difficult real systems are and also of how paradigmatic models can often be misleading. The reader is referred to previous reviews for a more detailed accounting of these reconstructions (Kevan and Eberhardt, 1992; Inglesfield, 1987; Smith and Kevan, 1991a; Inglesfield, 1985).

The driving forces for these reconstructions have been controversial since their first unambiguous observation in 1977. Models proposed to explain the reconstructions can be broadly defined as invoking either "localized" or "delocalized" electronic instabilities.

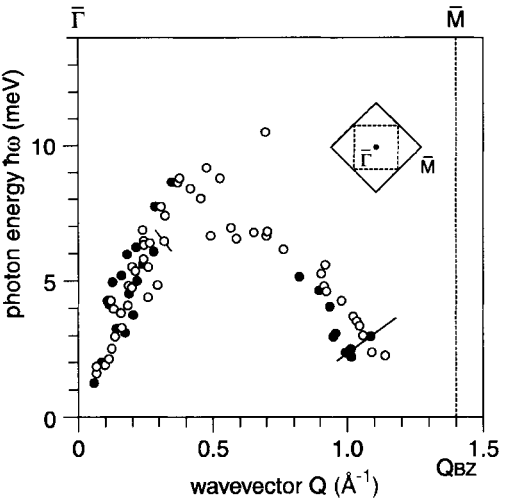


Fig. 8.40. Surface phonons dispersion relations on clean W(001) measured using inelastic helium scattering at different surface temperatures $T_S \sim 450$ K (open circles) and $T_S \sim 280$ (filled circles). Note the dramatic softening one phonon branch near (but not precisely at) the $\bar{M}$ point of the SBZ (from Ernst et al., 1987).

The former class is a generalization of a dynamical Jahn–Teller distortion which results in formation of localized bonding orbitals between neighboring atoms along the (110) azimuthal direction (King, 1983; Inglesfield, 1979; Singh and Krakauer, 1988; Campuzano et al., 1981; Barker et al., 1978). The delocalized mechanism is essentially a Peierls distortion which is preceded at higher temperature by a Kohn anomaly at a wave vector which spans segments of the surface Fermi contours (Tosatti, 1978; Inglesfield, 1978; Krakauer et al., 1979; Fasolino et al., 1980; Campuzano et al., 1980; Holmes and Gustafsson, 1981; Wang and Weber, 1987; Wang et al., 1988). In the present context, it is important to note that both of these paradigms require non-adiabatic interactions. Indeed, the fact that the reconstructed surfaces appear only below some temperature provides a very strong indication that this is the case. Our goal is thus to examine the extent to which ARP can help to understand the non-adiabatic interactions involved.

The delocalized mechanism is more easily tested since it makes predictions which can be tested experimentally. Firstly, the phonon dispersion curves ought to exhibit substantial softening at the wave vector appropriate for the reconstruction. The measured phonon dispersion curves for W(001) are shown in Fig. 8.40 (Ernst et al., 1987, 1989; Hulpke and Smilgies, 1989). Substantial softening is indeed observed near the $\bar{M}$ point of the SBZ, corresponding to the observed c(2 × 2) reconstruction. The softening apparently does not occur precisely at the $\bar{M}$ point, implying that the mechanism may not lead to a commensurate structure. Elastic helium diffraction does in fact observe some incommensurability for this surface and also on Mo(001) at temperatures slightly above the respective ordering temperatures (Ernst et al., 1987, 1989; Hulpke and Smilgies, 1989; Salanon and Lapujoulade, 1986; Schweizer and Rettner, 1989). This incommensurability fits very nicely into a delocalized model and might (Reinecke and Ying, 1991; Han and Ying, 1992) be taken as proof of its validity if not for the fact that neither electron, neon

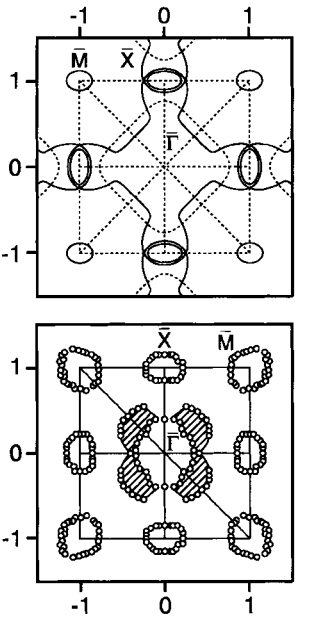


Fig. 8.41. Surface Fermi contours for W(001) determined using ARP. The two closed elliptical orbits are hole orbits and are not well-placed to be associated with the c(2 × 2) reconstruction. The shaded region is not precisely a Fermi contour, as explained in the text, but is apparently associated with driving the structural instability (from Smith et al., 1990).

atom, nor X-ray diffraction observes the incommensurate structures (Debe and King, 1977, 1979; Barker et al., 1978; Schweizer and Rettner, 1989; Estrup et al., 1989). Various suggested sources for this difference have been proposed, but none is yet generally accepted (Estrup et al., 1989). The delocalized mechanism also requires the existence of well-defined, heavily nested Fermi contours which are separated by the wave vector of the reconstruction. The most recently measured Fermi contours for W(001) are shown in Fig. 8.41 (Smith et al., 1990; Elliott et al., 1991). These exhibit well-defined hole pockets centered around the $\bar{M}$ and $\bar{X}$ points of the SBZ in addition to diffuse structures roughly centered on the $\bar{\Sigma}$ line. The former are not appropriately placed to drive the reconstruction, while the latter are. That the latter is a diffuse structure results from the complexity of the ARP spectra in this region. A feature is observed very close to $E_F$ over this entire shaded region and could in principle significantly impact the generalized susceptibility at momenta near the $\bar{M}$ point through Eq. (8.7). The fact that the shaded regions are centered somewhat closer to $\bar{\Gamma}$ than to $\bar{M}$ suggests that the maximum susceptibility might be slightly incommensurate, in support of the atom diffraction measurements. While these Fermi "contours" appear to provide support for the delocalized mechanism, they do not really refute the localized mechanism either. A truly local mechanism ignores momentum entirely and would thus predict a narrow feature near $E_F$ over the entire zone. This would be split by the formation of local bonds in the reconstruction, leading to a lower total electronic energy. The shaded region in Fig. 8.41 does not fill the entire zone, but it is not

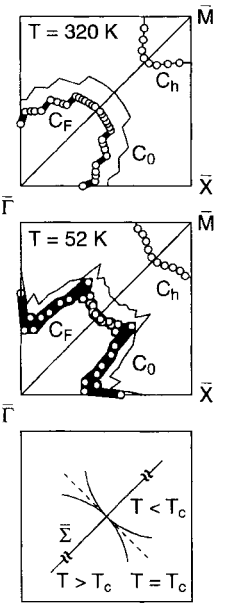


Fig. 8.42. Experimentally determined Fermi contours for clean Mo(001) at $T > T_c$ and $T < T_c$. The shift and change in curvature of the contour at low temperature near the middle of the $\bar{\Gamma} \rightarrow \bar{M}$ line is taken to support the delocalized, charge-density-wave mechanism for the observed reconstruction (from Chung et al., 1992).

a single contour either. The results provide a conceptual middle ground between the two competing paradigms in which some combination of local and nonlocal interaction leads to instability and reconstruction. Recent calculations which endow electron–phonon interaction matrix elements with substantial momentum dependence support this interpretation. The issue of "localized" vs. "delocalized" is largely one of semantics, since the real system is more complicated than any simple paradigmatic model.

The experiment reported in Fig. 8.41 was performed at room temperature on the disordered W(001) surface. Recent measurements of Mo(001) have been accomplished in both the disordered and ordered phases (Chung et al., 1992; Shin et al., submitted). The Fermi contours from these measurements, presented in Fig. 8.42, exhibit some similarities and some differences to those reported previously. The study reports sharper Fermi crossings and thus a smaller diffuse region than that corresponding to Fig. 8.41. The contour also is observed to curve toward zone center more than reported previously. Most importantly, however, the curvature of the contour in the SBZ appears to change sign as the temperature is lowered through the ordering temperature. This was taken to be compelling support for the delocalized mechanism.

These experiments demonstrate that ARP can provide some useful input in understanding non-adiabatic effects at surfaces. The information is not at a level of precision that allows, for example, detailed investigation of the electron–phonon interaction. Future improvements in the technique may allow the necessary increase in sensitivity to allow such measurements.

## 8.5. Lateral interactions and adsorbate periodicities

As mentioned in the Introduction, Fig. 8.3 provides a graphic illustration of one type of a substrate's contribution to lateral interaction potential energy between surface steps or adsorbed particles. While each step scatters the Cu(111) surface state discussed in Section 8.2.1 into a linear standing wave, each adatom produces a standing wave halo. Related effects have been observed previously using both STM and field ion microscopy (Chen and Tsong, 1990; Brune et al., 1990). The identity of the adatoms cannot be determined using these techniques, but the standing wave halos will be generic to all point defects and thus will always contribute to lateral interactions. When two adatoms or steps are close together, the corresponding standing waves interfere in much the same way as waves in a ripple tank. This interference will naturally contribute an energetic interaction which oscillates in magnitude as a function of separation. In the introduction, these standing waves were called energy-resolved Friedel oscillations. By this we mean that the full interaction potential between adsorbed atoms would require integration over all occupied states, while the STM samples states at a particular energy. Since the wave vector and thus the wavelength of the oscillations varies with energy, this integration will average some of the structure observed in Fig. 8.3. However, the sharp cut-off of the integration at the Fermi wave vector implies that the oscillations will persist as Friedel oscillations which are characterized by a wave vector of $2k_F$ (Friedel, 1954; Lau and Kohn, 1978; Einstein, 1991).

In the literature such behavior is commonly referred to as a "through-surface" or "substrate-mediated" interaction. Other mechanisms for through-surface interactions exist, e.g., phonon-mediated interactions (Prybyla et al., 1987; Tiersten et al., 1989, 1991), which play a dominant role on insulating and semiconducting surfaces, and have been suggested to play a significant role on metal surfaces as well. This mechanism normally does not lead to potentials which oscillate in sign like those considered here. Through-surface interactions are inherently complex and difficult to treat from first principles. There is, for example, no reason to expect these through-surface interactions to be pairwise additive when more than two atoms are involved (Einstein, 1979, 1991). Effects related to Friedel oscillations (Friedel, 1954) provide the basis for a variety of interesting phenomena in the bulk metals such as the long-range coupling between magnetic impurities through the RKKY interaction (Ruderman and Kittel, 1954; Yoshida, 1957; Van Vleck, 1962). Clearly such interactions should play a major role at surfaces as well. Given the density-of-states arguments in the previous section, one should also expect unusual behaviors if 2D surface bands are involved.

The character of these charge density oscillations and their impact, for example, on the ordering of adsorbed particles or steps and the energetics and kinetics of adsorption and coadsorption, has been the subject of significant theoretical effort (Lau and Kohn, 1978; Einstein, 1979, 1991; Johansson, 1979; Grimley, 1967; Einstein and Schrieffer, 1973; March, 1987; Muscat, 1987; Feibelman, 1989; Redfield and Zangwill, 1992; Bradshaw and Scheffler, 1979). The ordering patterns formed by adsorbed atoms are commonly observed to have periodicities larger than the range of local bonding interactions. Through-space multipole interactions are also generally too weak to produce the observed structures and the corresponding phase diagrams. Some other longer range interaction is required, and through-surface interactions have been implicated. Due to the difficulty of calculat-

ing extended but non-periodic systems, these treatments have relied heavily upon model Hamiltonians, ranging from tight-binding, News-Anderson-like theories (Muscat, 1987) to jellium models (Lau and Kohn, 1978; Johansson, 1979; March, 1987). At present, no first-principles, self-consistent calculations are available which have tried to determine, for example, the lateral pair potential (or pseudo-pair potential if we explicitly include the substrate) between adsorbed particles. A recent review of the status of these efforts has been provided by Feibelman (1989) and, as the available computational power increases, the prospects for substantial improvements in this area exists. The semiempirical models have provided various qualitative conclusions, some of which have been applied to interpret experimental results (Joyce et al., 1987; March, 1989). For example, at lateral distances $R$ much larger than both the screening length and also the distance to the image plane, particles adsorbed on a metal surface having a well-defined 3D Fermi surface are predicted to experience an oscillatory lateral interaction potential which decreases in magnitude as $1/R^5$. This fairly rapid decrease would generally lead to minor perturbations upon the properties of the adsorbed layer. However, at shorter distances, the decay is less rapid ($\sim 1/R^3$) and a larger contribution is expected. Most importantly from our perspective, the $1/R^5$ decrease is predicted to change to $1/R^2$ in the presence of a 2D surface band with a well-defined Fermi contour. Similar to the discussion in the previous section concerning phonon anomalies, this change is purely a result of the qualitatively different densities of states for a 2D vs. 3D band. Surface states can thus dramatically impact how atoms interact on surfaces.

An important aspect of the lateral interaction problem is that relatively weak interactions have a pronounced impact on the properties of an adsorbed layer. This is particularly true of regions of attractive interaction potential. In lattice gas theory, for example, an attractive site interaction energy of $\sim$100 K will have a pronounced impact upon kinetic and thermodynamic properties at temperatures of several hundred Kelvin. 100 K corresponds to an energy of 8 meV, which, on the scale of chemical bonding energies, is very small. This sensitivity of macroscopic properties to weak energetic interactions will place great demands on the accuracy of a complete first principles calculation of the lateral interaction energy surface which proposes to examine a specific system in detail. More importantly, even the relatively weak and rapidly decaying oscillatory through-surface interactions discussed above can play a major role in macroscopic properties of the adsorbed film.

An example of how a weak attractive interactions can play a central role in a simple surface kinetic process is offered by Fig. 8.43 (Peterson and Kevan, 1990, 1991; Wei and Kevan, to be published). This plots the isothermal and isosteric desorption rate constant as a function of coverage for the system CO/Cu(011). A key feature of this figure is the way in which the isotherms flatten at lower temperature. This is the signature of a phenomenon called kinetic compensation in which the coverage-dependent activation energy for desorption and the prefactor are correlated in such a way that the rate constant is nearly coverage-independent (Galwey, 1977; Peacock-Lopez and Suhl, 1982; Sommer and Kreuzer, 1982; Doyen, 1987). These data were analyzed with a quasiequilibrium theory which provides an insightful picture of how attractive lateral interactions can lead to such behavior. At equilibrium, the desorption rate constant is proportional to the activity of the adsorbed phase. The activity is simply the exponential of the chemical potential $\mu$ which in turn is a function of coverage and temperature. In direct analogy to the Boyle

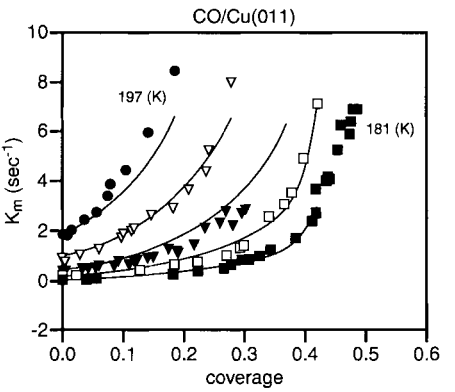


Fig. 8.43. Isothermal, nearly isosteric desorption rate constant for CO/Cu(011) as a function of coverage. The flattening of these isotherms is the signature of kinetic compensation, which in turn is driven by the presence of weakly attractive long-range lateral interactions between neighboring molecules (from Peterson and Kevan, 1991).

temperature for an imperfect gas, there will be a temperature at which the coverage dependence of $\mu$ disappears, to first order. This results from a competition between short-range repulsive interactions and weak, long-range attractive interactions. The Boyle temperature, or, by analogy, the compensation temperature, scales roughly with the magnitude of the attractive interaction, and the impact of the attractive well can be observed at substantially higher temperatures.

### *8.5.1. Ordering and reconstruction for O/Mo(011) and O/W(011)*

The temperature-coverage phase diagrams for the systems O/W(011) and O/Mo(011) have been extensively studied experimentally (Wang et al., 1978; Bauer et al., 1976; Bauer and Engel, 1978; Bauer and Poppa, 1979, 1983; Witt and Bauer, 1986; Grzelakowski et al., 1989) and have thus provided systems with which to test and upon which to apply a battery of modern lattice gas statistical techniques (Ching et al., 1978; Kaski et al., 1983; Rikvold et al., 1984; Dünweg et al., 1991). In these models, adatoms are attached by strong and usually harmonic forces to particular surface sites. The lateral interaction potential energy surface is approximated by discrete interactions between neighboring sites. It is straightforward to show that, if these interactions are pairwise additive, the resulting phase diagram will be symmetric about the coverage at which half the adsorption sites are occupied (Einstein, 1979, 1991). The degree to which this is not the case has often been used as evidence for non-pairwise additive interactions, although other shortcomings of the lattice gas model, such as the assumption of harmonic forces binding atoms to a particular site and the discretizing of the interaction potential itself, can also lead to such behavior (Persson, 1989a, b).

The measured phase diagram for O/W(011) is shown in Fig. 8.44a. There are three ordered phases, a (2 × 1) phase at 0.5 monolayers, a (2 × 2) phase at 0.75 monolayers, and a (1 × 1) phase at full monolayer coverage. The phase diagram is thus seen to ex-

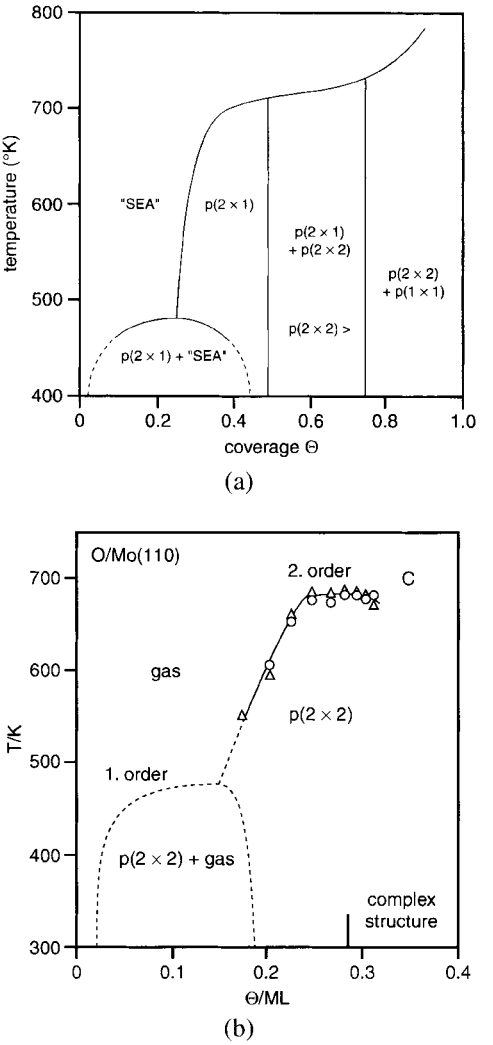


Fig. 8.44. One possible temperature–coverage phase diagram for O/W(011). Note the substantial asymmetry about half-monolayer coverage, which has been taken as evidence for non-pairwise additive lattice gas interactions (from Wang et al., 1978).

hibit a serious asymmetry about half monolayer coverage since a p(2 × 2) ordered phase is not observed 0.25 monolayer. Molybdenum and tungsten are similar metals and often exhibit similar bulk and surface properties. One is thus surprised that the phase diagram for O/Mo(011) exhibits substantial differences from that shown in Fig. 8.44b. There is an ordered (2 × 2) phase observed at 0.25 but not 0.75 monolayers. Complex patterns are observed near 0.3 monolayers for O/Mo(011) (Witt and Bauer, 1986; Grzelakowski et al., 1989), but on W(011) this lies in a coexistence region between the (2 × 1) phase and

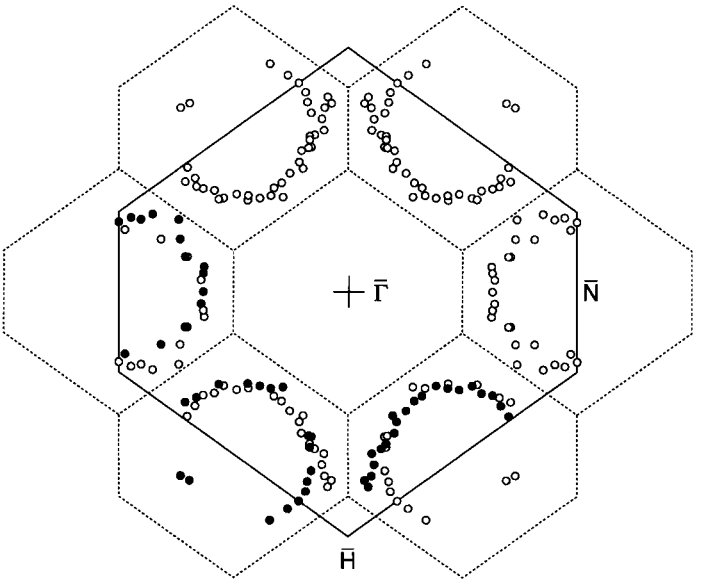


Fig. 8.45. Fermi contours for Mo(011)–(2 × 2)O at a coverage of 0.25 monolayers. The filled circles are actual measurements, while the open circles are deduced by symmetry. The solid lines are the boundaries of the (1 × 1) SBZ, while the dotted lines are those of the (2 × 2) SBZ (from Dhar and Kevan, to be published).

a dilute phase. In both systems, ordered phases, the (2 × 2) for O/Mo(011) and the (2 × 1) for O/W(011), are observed well below the correct nominal coverage, suggesting the prevalence of attractive lateral interactions even for nearest neighbor sites. The source of these interactions is not well understood. Lattice gas theories utilizing mean-field theory and finite-size scaling of both Monte Carlo simulations and transfer matrix techniques have been applied and have successfully modeled these data (Rikvold et al., 1984; Dünweg et al., 1991). It was found that interactions out to fifth neighbors and non-pair trio interactions were required to provide a good fit to the experimental phase diagrams. These efforts serve to distinguish the two primary shortcomings of such theories. Specifically, one does not *a priori* know which trio, quartet, etc. interactions to include, and one has no real insight in interpreting the derived lattice gas interaction energies.

Figure 8.45 shows the measured surface Fermi contours for Mo(011)–(2 × 2)O at 0.25 monolayers coverage (Dhar and Kevan, to be published). As was observed for H/W(011) in Fig. 8.34, three hole pockets on the clean surface are extinguished upon oxygen exposure while an irregular electron pocket simply grows until it merges with its image in the second SBZ to form two well-defined hole pockets along the edges of the SBZ. These persist well above a coverage of 0.25 monolayers. At that coverage, the pockets are nearly the same size and shape, although there is no reason by symmetry why this needs to be the case. Also shown in Fig. 8.45 are the SBZ boundaries for the (2 × 2) superlattice. The hole pockets are centered in these superlattice zones. This situation, through Eq. (8.7), implies what might be called a "giant" Peierls distortion. Unlike a typical Peierls distortion where only a small segment of Fermi contour is coupled to its image, each point on one of the

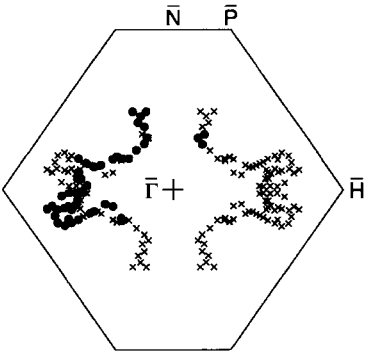


Fig. 8.46. Fermi contours for W(011)–(2 × 1)O at a coverage of 0.5 monolayers. The filled circles are actual measurements, while the open circles are deduced by symmetry. The solid lines are the boundaries of the (1 × 1) SBZ, while the dotted lines are those of the two differently oriented (2 × 1) SBZ's. Note the small but consistent wiggles in the contour as it crosses a (2 × 1) zone boundary (from Dhar and Kevan, to be published).

contours has a tangent which is parallel to the tangent of a point on the other contour which is separated by a reciprocal lattice vector for the (2 × 2) net. This provides a logical and purely electronic driving force for producing a (2 × 2) ordering pattern at 0.25 monolayers for O/Mo(011). This will involve attractive interactions in second-neighbor sites and thus to the tendency to form islands. By contrast, the Fermi contours do not support such a mechanism for O/W(011), and not low-coverage (2 × 2) phase is observed. Figure 8.46 shows Fermi contours for W(011)–(2 × 1)O at 0.5 monolayer coverage. In this system, once again the hole pockets on the clean surface (Fig. 8.34a) are extinguished while the electron pocket grows upon oxygen adsorption. The electron pocket initially merges with its image and then at higher coverage, after the work function change has reversed direction, the contours separate again to leave one electron pocket. At no point are the there two hole pockets which are strongly coupled through the "giant" Peierls distortion discussed above to form a (2 × 2) phase.

These two data sets then provide an explanation for at least one of the differences observed between the two phase diagrams. They do not provide any rationale for the higher-coverage features in the phase diagrams. These phases all involve placing oxygen atoms on nearest neighbor sites, and the influence of short-range interactions will be correspondingly greater. Most importantly, the energetics of a Fermi-contour-driven ordering pattern cannot in any simple way be separated into discrete, pairwise additive lattice gas energies. This non-pair behavior is typical of metallic cohesion in general and should thus not be surprising.

Recently, a weaker, longer range reconstruction of the (2 × 2)O/Mo(011) surface has been observed (Grzelakowski et al., 1989). In this case, at temperatures below ~200 K, weak seventh-order diffraction spots were observed along the (01$\bar{1}$) direction. The Fermi contours in Fig. 8.45 are compatible with such a reconstruction through a normal Peierls distortion. That is, the width of the two hole pockets is ~3/7 of the width of the (1 × 1) SBZ along the (01$\bar{1}$) direction, a fact which favors 7-fold periodicity. To date, no such

long-range reconstruction has been observed for O/W(011), and none is predicted by the data in Fig. 8.46.

It is interesting to speculate upon the generality of such long-range reconstructions which are perhaps driven by screening anomalies. The seventh order diffraction spots for O/Mo(011) are quite weak and their observation required, in addition to operation below room temperature, a low energy electron diffraction system optimized for single particle detection. The fact that other similar reconstructions have not been observed thus does not mean that they do not exist. This system may be fairly optimal for such a reconstruction. The oxygen atoms adsorb in or near the long-bridge site. Thus the restoring force for displacements along the $(01\bar{1})$ direction is small, and a correspondingly small electronic screening anomaly would lead to reconstruction.

### *8.5.2. Peierls instability in thallium chains on Cu(001)*

We have chosen to close this chapter with results from a system where intrinsic surface states, or states modified by adsorption like those described in previous sections, apparently play a minor role. However, the Tl/Cu(001) system has provided some tantalizing results which are central to the theme of this and the previous section (Binns and Norris, 1982, 1991; Binns et al., 1984, 1986). They are thus described briefly here even though the relevant states involved are extrinsic Tl(6s/6p)-derived rather than intrinsic-Cu(4s/4p)-derived which have been modified by adsorption. Like the results for O/Mo(011) discussed above, these results serve to emphasize both that careful measurements of relatively simple systems can lead to interesting and useful results and also that some care must be exercised when examining states very close to $E_F$.

Like several Pb/Cu systems (Sepulveda and Rhead, 1977), the Tl/Cu(001) system exhibits a rich variety of ordered phases. These result from an interplay between the relatively large sizes of these atoms compared to the underlying copper lattice and the developing electronic structure near $E_F$. Neglecting the latter effects, one would expect the Pb and Tl atoms to prefer to occupy particular high coordination adsorption sites. At higher coverage, however, one enters an interesting regime where this is not possible due to repulsive overlap of the Tl or Pb charge densities. Incommensurate or long-range commensurate structures result where more than one type of site is necessarily occupied. An excellent series of papers by Binns and coworkers (Binns et al., 1984, 1986; Binns and Norris, 1982, 1991) describes these phases for Tl/Cu(001) in detail and also explores the corresponding electronic structures. The two most relevant phases for our purposes are shown schematically in Fig. 8.47. These exist over narrow coverage ranges near $\vartheta = 0.60$ and $\vartheta = 0.67$ monolayer. Similar to numerous alkali/semiconductor adsorption systems (Whitman et al., 1991; Hashizume et al., 1990; Hasegawa et al., 1990), both exhibit substantial one-dimensional character within the overlayer. Also like the alkali/semiconductor systems, the source of this quasi-1D alignment of adatoms is not completely understood. A mechanism involving electron- or phonon-mediated through-substrate interactions, perhaps similar to that discussed in the previous section, must be involved. If we simply accept that the structures are quasi-1D in nature, then interesting issues concerning structural stability, that is, the possibility of a Peierls distortion, arise. The one-dimensionality is also plainly evident in the electronic structure since little dispersion is observed in the Tl(6s/6p) bands normal to the chains of adatoms (Binns et al., 1984,

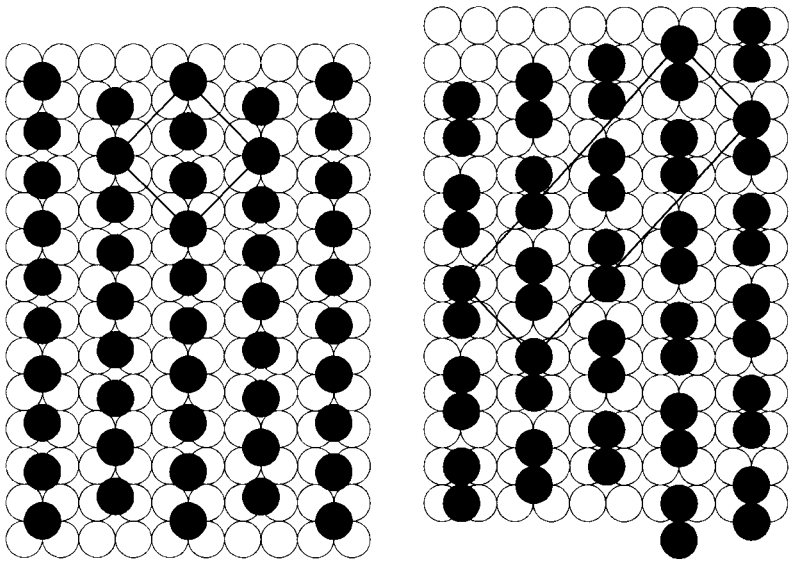


Fig. 8.47. Proposed 1D chain structures for thallium adsorbed onto Cu(001) at low temperature at a coverage of 0.60 (a) and 0.67 (b) monolayer (from Binns and Norris, 1991).

1986). The Peierls model holds that any 1D metal will be distorted. Since the Tl(6s/6p) band is partially occupied, we might anticipate that structures in this coverage regime would all be distorted in a fashion related to the resulting linear Fermi contours. In the figure, it appears that Tl atoms in the higher coverage regime are paired while those in the low coverage regime are not. The conclusion is that the $\vartheta = 0.60$ structure is not Peierls-distorted, while that at $\vartheta = 0.67$ monolayer is. This difference was related to the subtle effects discussed above: at $\vartheta = 0.60$, a greater proportion of the thallium atoms are in the preferred adsorption site than at $\vartheta = 0.67$. Thus the "restoring force", which would otherwise preclude reconstruction, will be weaker at the latter coverage which will consequently be more prone to undergo a Peierls distortion. This argument is similar in spirit to that invoking the small restoring force for displacements along the $(01\bar{1})$ direction for O/Mo(011) discussed above. In both cases, the substrate has a pronounced impact upon the behavior of the electronic instability. In this sense, the Tl/Cu(001) system is not one-dimensional in the strict sense since the thallium layer is attached to a two-dimensional surface, which in turn is attached to a bulk crystal. This simple observation has on occasion been overlooked in trying to apply these simple paradigms to surface and adsorbed layer reconstruction.

Unlike the O/Mo(011) system, Tl/Cu(001) is more amenable to detailed study of the electronic bands involved in driving the reconstruction. This is because O/Mo(011) exhibits the $(2 \times 2)$ and seven-fold reconstruction at very low coverage due to island formation driven by attractive lateral interactions, while the Tl/Cu(001) system exhibits different structures at coverages that are not very different so that comparative studies are possible. Figure 8.48 shows the measured 2D dispersion relations of the Tl(6p) band at $\vartheta = 0.67$

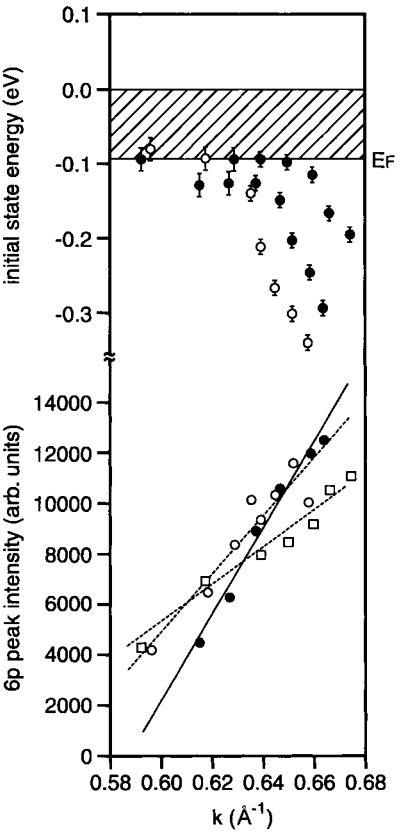


Fig. 8.48. Measured Tl(6p) bands for Tl/Cu(001) at various coverages and temperatures. Open squares are for 0.60 monolayer at 100 K, filled circles are for 0.67 monolayer at 100 K, open circles are for 0.67 monolayer at 300 K. Bottom part of the figure shows the measured intensity of the Tl(6p) feature. The shaded region at the top is inaccessible due to limited resolution (from Binns and Norris, 1991).

at low temperature where a well-defined, Peierls-distorted periodicity is observed and at room temperature where a $(1 \times 1)$ pattern is observed, and also at $\vartheta = 0.60$ at low temperature where a well-defined structure exists that is not Peierls-distorted (Binns and Norris, 1991). The results at $\vartheta = 0.67$ are more-or-less temperature-independent, indicating the existence of moderate-range order (to which ARP is sensitive) well above the disordering temperature. The dispersion relations for both of these are shifted downward and curved more substantially away from $E_F$ than the curve for $\vartheta = 0.60$, indicating the existence of a gap estimated to be 0.25 eV near the Fermi level. The presence of the gap was also surmised and its magnitude was estimated by measuring the Tl(6p) ARP peak intensity as the band crossed the Fermi level. The gap is determined to be correctly positioned in momentum space to correspond to the observed reconstruction, that is, the wave vector of the reconstruction is given by the vector spanning the Fermi crossings which are eliminated by gap formation.

Even using careful procedures to analyze these data, the magnitude of the gap and the detailed behavior of the band near the gap was difficult to determine using ARP. The shaded region in Fig. 8.48 provides the authors' estimate of the region over which their dispersion relations are unreliable due to distortion of the peak by the presence of the Fermi cutoff. This problem can only be partially solved by improving the experimental resolution, since there are other mechanisms beyond those discussed in Section 8.2 e.g., multi-phonon excitation (Dhar and Kevan, 1990), disorder-induced broadening (Kevan, 1983a; Tersoff and Kevan, 1983, etc.) which can and do lead to substantially broadened photoemission features. These results indicate one of the real limitation of ARP in such studies. The problem is exacerbated by our crude current understanding of ARP line shapes which makes detailed fitting procedures (particularly near $E_F$) of dubious value (Smith, 1992). If some of these problems could be overcome, it seems certain that many systems will provide a rich variety of results like those discussed here for O/Mo(011) and Tl/Cu(001).

## 8.6. Concluding remarks

With one or two significant reservations, the basic understanding of surface state phenomena on simple metal surfaces is very sound. By this we mean that calculations have good qualitative and fair quantitative predictive power for the existence of surface states and for their characteristics. The quantitative aspects are continually improving through implementation of, for example, the GW and related computational approaches (Hybertson and Louie, 1985, 1986; Northrup et al., 1986; Godby et al., 1987). We can expect continued incremental improvements in this area in the future.

We therefore close by returning to questions which were posed in the Introduction which were more closely connected to currently popular issues in other areas of surface physics and chemistry. In these there is room for substantial advances in the future. These have been discussed in the course of this chapter and are here further delineated:

- There is a need for a much improved understanding of disorder at surfaces. Disordered and glassy solids provide one of the major focuses of modern condensed matter physics (Mott, 1990). It is impossible to prepare a surface which comes close to the perfection of bulk media, and the impact of surface disorder of all sorts on chemical and physical properties cannot be underestimated. We do not know, for example, when and if electron states at surfaces are "localized" in the Anderson sense. One way to approach this problem is from the perspective of Section 8.3, that is, to treat the surface as a random alloy and to try to apply CPA-like theories to the chemisorption problem. This will need to be coupled to a better understanding of the ARP line shape so that all the information in an ARP spectrum can be used. What does it really mean when an intrinsic surface state shifts smoothly upon adsorption? The band might continue to bracket the Fermi level, but this does not necessarily mean that the resulting band will transport charge. Does the idea of a "mobility edge" for a surface or interfacial state have meaning?
- The connection between studies of surface states on metals and the fundamentals of surface chemical physics will come through a better understanding of and theoretical treatment for non-adiabatic effects at surfaces. By this we mean that a chemical reaction by definition requires a concerted interaction between electronic and vibrational degrees

of freedom, and this interaction in turn requires some degree of violation of the Born–Oppenheimer approximation. Our understanding of non-adiabatic phenomena at surfaces is more-or-less at the level of model Hamiltonians, similar to Zhang and Langreth's treatment of adsorbate vibrational damping (Zhang and Langreth, 1989a, b). What is needed is to extend calculations like these using "real" electronic structures. The Hartree–Fock calculations of Head-Gordon and Tully provide a major step in this direction (Head-Gordon and Tully, 1992a, b). These need to be extended to periodic systems so that the relevance of momentum conservation for zone-center adsorbate vibrations can be evaluated and also so that phonon damping and anomalies at non-zero momentum can be calculated and related to experiment.

- Finally, the connection between bands and bonds, that is, momentum space and real space, remains problematic. This issue is at the heart of much of the current focus upon alkali adsorption, but really extends much further. There are many relatively simple yet surprising observations in surface systems which must be explained by small changes in charge distribution. For example, despite the many similarities between the electronic structures of W(011) and Mo(011) discussed in Section 8.4, the work function of the former decreases upon hydrogen adsorption, while that of the latter increases. Overall, the difference is about 0.5 eV at saturation coverage. This requires only a very slight charge realignment which is not well understood at present. The relationship between this difference and the fact that W(011) undergoes the $(1 \times 1)$ reconstruction while Mo(011) does not is not yet clear (Chung et al., 1986; Altmann et al., 1987). More generally, the bond vs. bands problem is related issues of cohesion of the surface and of adsorbed layers. The "decohesion" of an alkali layers recently discussed by Neugebauer and Scheffler (1993) provides an excellent example of this.

Not surprisingly, most of these issues will be best studied by coupling ARP results to results from several other experimental probes and also to extensive calculations. To our knowledge, for example, there has never been a high resolution ARP spectrometer directly coupled to a surface infrared reflection–absorption apparatus. It is rare even for a high resolution electron scattering spectrometer to be coupled to an ARP spectrometer. For this reason, the vibrational and electronic properties of a clean or adsorbate-covered surface are rarely probed on precisely the same surfaces.

*Acknowledgement*

Part of this work was supported by the U.S. Department of Energy, Division of Materials Science under grant DE-FG06–86ER45275. I gratefully acknowledge numerous helpful comments from E.W. Plummer concerning this chapter.

## References

Aldén, M., H.L. Skriver and B. Johansson, 1993, Phys. Rev. Lett. **71**, 2457.

Altmann, M., J.W. Chung, P.J. Estrup, J.M. Kosterlitz, J. Prybyla, D. Sahu and S.C. Ying, 1987, J. Vac. Sci. Technol. A **5**, 1045.

Appelbaum, J.A. and D.R. Hamann, 1978, Solid State Commun. **27**, 881.

Aruga, T. and Y. Murata, 1989, Prog. Surf. Sci. **31**, 61.

Ashcroft, N.W. and N.D. Mermin, 1976, Solid State Physics. Holt, Rinehardt, and Winston, New York.
Barker, R.A., P.J. Estrup, F. Jona and P.M. Marcus, 1978, Solid State Commun. **25**, 375.
Bartynski, R.A., E. Jensen, T. Gustafsson and E.W. Plummer, 1985, Phys. Rev. B **32**, 1921.
Bartynski, R.A., R.H. Gaylord, T. Gustafsson and E.W. Plummer, 1986, Phys. Rev. B **33**, 3644.
Bauer, E. and T. Engel, 1978, Surf. Sci. **71**, 695.
Bauer, E. and H. Poppa, 1979, Surf. Sci. **88**, 31.
Bauer, E. and H. Poppa, 1983, Surf. Sci. **127**, 243.
Bauer, E., H. Poppa and Y. Viswanath, 1976, Surf. Sci. **58**, 517.
Benesh, G.A. and J.R. Hester, 1988, Surf. Sci. **194**, 567.
Benesh, G.A. and J.E. Inglesfield, 1986, J. Phys. C **19**, L543.
Bersuker, I.B. and V.P. Polinger, 1989, Vibronic Interactions in Molecules and Crystals. Springer-Verlag, Berlin.
Binns, C., M.-G. Barthés-Labrousse and C. Norris, 1984, J. Phys. C **17**, 1465.
Binns, C., D.A. Newstead, C. Norris, M.-G. Barthés-Labrousse and P.C. Stephenson, 1986, J. Phys. C **19**, 829.
Binns, C. and C. Norris, 1982, Surf. Sci. **115**, 395.
Binns, C. and C. Norris, 1991, J. Phys.: Condens. Matter **3**, 5425.
Bishop, A.R. and A. Mookerjee, 1974, J. Phys. C **7**, 2165.
Boettger, J.C. and S.B. Trickey, 1986, Phys. Rev. B **34**, 3604.
Bortolani, V., A. Franchini, G. Santoro, J.P. Toennies, C. Woll and G. Zhang, 1989, Phys. Rev. B **40**, 3524.
Bradshaw, A.M. and M. Scheffler, 1979, J. Vac. Sci. Technol. **16**, 447.
Brune, H., J. Wintterlin, G. Ertl and R.J. Behm, 1990, Europhys. Lett. **13**, 123.
Bungaro, C., S.D. Gironcoli and S. Baroni, 1995, Phys. Rev. Lett. **77**, 2491.
Campuzano, J.C., J.E. Inglesfield, D.A. King and C. Somerton, 1981, J. Phys. C: Solid State Phys. **14**.
Campuzano, J.C., D.A. King, C. Somerton and J.E. Inglesfield, 1980, Phys. Rev. Lett. **45**, 1649.
Caruthers, E., L. Kleinman and G.P. Alldredge, 1973, Phys. Rev. B **8**, 4570.
Chabal, Y.J., 1985, Phys. Rev. Lett. **55**, 845.
Chabal, Y.J., 1986, J. Electron Spectrosc. **38**, 159.
Chabal, Y.J., 1988, Surf. Sci. Rep. **8**, 211.
Chan, S.-K. and V. Heine, 1973, J. Phys. F: Metal Phys. **3**, 795.
Chen, C.T. and N.V. Smith, 1987, Phys. Rev. B **35**, 5407.
Chen, C.-L. and T.T. Tsong, 1990, Phys. Rev. Lett. **64**, 1417.
Ching, Y.W., D.L. Huber, M.G. Lagally and G.-C. Wang, 1978, Surf. Sci. **77**, 550.
Chulkov, E.V., V.M. Silkin and E.N. Shirykalov, 1987, Surf. Sci. **188**, 287.
Chung, J.W., S.C. Ying and P.J. Estrup, 1986, Phys. Rev. Lett. **56**, 749.
Chung, J.W., K.S. Shin, D.H. Baek, C.Y. Kim, H.W. Kim, S.K. Lee, C.Y. Park, S.C. Hong, T. Kinoshita, M. Watanabe, A. Kakizaki and T. Ishii, 1992, Phys. Rev. Lett. **69**, 2228.
Claessen, R., R.O. Anderson, J.W. Allen, C.G. Olson, C. Janowitz and W.P. Ellis, 1992, Phys. Rev. Lett. **69**, 808.
Cousty, J. and R. Riwan, 1987, Europhys. Lett. **3**, 1119.
Cox, P.A., 1987, The Electronic Structure and Chemistry of Solids. Oxford University Press, Oxford.
Crommie, M.F., C.P. Lutz and D. Eigler, 1993, Nature **363**, 524.
Davis, H.L., J.B. Hannon, K.B. Ray and E.W. Plummer, 1992, Phys. Rev. Lett. **68**, 2632.
Davison, S.G. and J.D. Levine, 1970, Solid State Phys. **25**, 1.
Davison, S.G. and M. Steslicka, 1992, Basic Theory of Surface States. Clarendon Press, Oxford.
Debe, M.K. and D.A. King, 1977, Phys. Rev. Lett. **39**, 708.
Debe, M.K. and D.A. King, 1979, Surf. Sci. **81**, 193.
Dhar, S. and S.D. Kevan, 1990, Phys. Rev. B **41**, 8516.
Dhar, S. and S.D. Kevan, to be published.
Di, W., K.E. Smith and S.D. Kevan, 1991, Phys. Rev. B **43**, 12062.
Di, W., K.E. Smith and S.D. Kevan, 1992, Phys. Rev. B **45**, 3652.
Dose, V., 1985, Appl. Surf. Sci. **22/23**, 338.
Doyen, G., 1987, in: Structure and Dynamic of Surfaces, eds. W. Schomers and P. von Blanckenhagen. Springer, Berlin.
Dowben, P.A. and D. Lagraffe, 1990, Phys. Lett. A **144**, 193.
Dowben, P.A., D. Lagraffe, D. Li, G. Vidali, L. Zhang, L. Dottl and M. Onellion, 1991, Phys. Rev. B **43**, 10677.

Dünweg, B., A. Milchev and P.A. Rikvold, 1991, J. Chem. Phys. **94**, 3958.
Eastman, D.E. and W.D. Grobman, 1972, Phys. Rev. Lett. **28**, 1378.
Eberhardt, W., F. Greuter and E.W. Plummer, 1981, Phys. Rev. Lett. **46**, 1085.
Ehrenreich, H. and L.M. Schwartz, 1976, in: Solid State Physics, eds. H. Ehrenreich, F. Seitz and D. Turnbull. Academic, New York.
Einstein, T.L., 1979, in: Chemistry and Physics of Solid Surfaces, ed. R. Vanselow. CRC, Boca Raton.
Einstein, T.L., 1991, Langmuir **7**, 2520.
Einstein, T.L. and J.R. Schrieffer, 1973, Phys. Rev. B **7**, 3629.
Elliott, G.S., K.E. Smith and S.D. Kevan, 1991, Phys. Rev. B **44**, 10826.
Ernst, H.-J., E. Hulpke and J.P. Toennies, 1987, Phys. Rev. Lett. **58**, 1941.
Ernst, H., E. Hulpke and J.P. Toennies, 1989, Europhys. Lett. **10**, 747.
Estrup, P.J., I.K. Robinson and J.C. Tully, 1989, Surf. Sci. **215**, L297.
Euceda, A., D.M. Bylander and L. Kleinman, 1983a, Phys. Rev. B **28**, 528.
Euceda, A., D.M. Bylander, L. Kleinman and K. Mednick, 1983b, Phys. Rev. B **27**, 659.
Fano, U., 1961, Phys. Rev. **124**, 1866.
Fasolino, A., G. Santoro and E. Tosatti, 1980, Phys. Rev. Lett. **44**, 1684.
Feibelman, P.J., 1989, Ann. Rev. Phys. Chem. **40**, 261.
Feibelman, P.J., 1992, Phys. Rev. B **46**, 2532.
Feibelman, P.J., D.R. Hamann and F.J. Himpsel, 1980, Phys. Rev. B **22**, 1734.
Felter, T.E., R.A. Barker and P.J. Estrup, 1977, Phys. Rev. Lett. **38**, 1138.
Feuerbacher, B. and B. Fitton, 1972, Phys. Rev. Lett. **29**, 786.
Forstmann, F., 1978, in: Photoemission and the Electronic Properties of Solids, eds. B. Feuerbacher, B. Fitton and R.F. Willis. Wiley, New York.
Frank, H.-J. Sagner and D. Heskett, 1989, Phys. Rev. B **40**, 2767.
Friedel, J., 1954, Adv. Phys. **3**, 446.
Galwey, A.K., 1977, Adv. Catal. **26**, 247.
Gartland, P.O. and B.J. Slagsvold, 1975, Phys. Rev. B **12**, 4047.
Gartland, P.O. and B.J. Slagsvold, 1978, Solid State Commun. **25**, 489.
Gaylord, R.H. and S.D. Kevan, 1988, Phys. Rev. B **37**, 8491.
Gaylord, R.H., K. Jeong and S.D. Kevan, 1989a, Phys. Rev. Lett. **62**, 203.
Gaylord, R.H., K. Jeong and S.D. Kevan, 1989b, J. Vac. Sci. Technol. A **7**, 2203.
Girvan, R.F., A.V. Gold and R.A. Phillips, 1968, J. Phys. Chem. Solids **29**, 1485.
Godby, R.W., M. Schlüter and L.J. Sham, 1987, Phys. Rev. B **35**, 4170.
Goodenough, J.B., 1972, Prog. Solid State Chem. **5**, 145.
Goodwin, E.T., 1939a, Proc. Cambridge Philos. Soc. **35**, 205.
Goodwin, E.T., 1939b, Proc. Cambridge Philos. Soc. **35**, 221.
Goodwin, E.T., 1939c, Proc. Cambridge Philos. Soc. **35**, 232.
Grimley, T.B., 1967, Proc. Roy. Soc. London **90**, 751.
Grzelakowski, K., I. Lyuksyutov and E. Bauer, 1989, Surf. Sci. **216**, 472.
Guillot, C., P. Roubin, J. Lecante, M.-C. Desjonquères, G. Tréglia, D. Spanjaard and Y. Jugnet, 1984, Phys. Rev. B **30**, 5487.
Guillot, C., D. Chaveau, P. Roubin, J. Lecante, M.-C. Desjonquères, G. Treglia and D. Spanjaard, 1985, Surf. Sci. **162**, 46.
Gurney, R.W., 1935, Phys. Rev. **47**, 479.
Halse, M.R., 1969, Philos. Trans. Roy. Soc. London, Ser. A **265**, 50.
Hamawi, A., S.Å. Lindgren and L. Walldén, 1991, Phys. Scripta **T39**, 339.
Han, W.K. and S.C. Ying, 1992, Phys. Rev. B **46**, 1849.
Hannon, J.B., R.L. Sameth, E.J. Mele and E.W. Plummer, 1993, submitted to Phys. Rev. Lett.
Hannon, J.B. Private communication.
Hansson, G.V. and S.A. Flodstrom, 1978, Phys. Rev. B **18**, 1562.
Hansson, G.V. and R.I.G. Uhrberg, 1992, in: Angle-Resolved Photoemission, ed. S.D. Kevan. Elsevier, Amsterdam.
Harrison, W.A., 1980, Electronic Structure and Properties of Solids. Freeman, San Francisco.

Harten, U., J.P. Toennies, C. Woll and G. Zhang, 1985, Phys. Rev. Lett. **55**, 2036.
Hasegawa, Y. and P. Avouris, 1993, Phys. Rev. Lett. **71**, 1071.
Hasegawa, Y., I. Kamiya, T. Hashizume, T. Sakuri, H. Tochihara, M. Kubota and Y. Murata, 1990, Phys. Rev. B **41**, 9688.
Hashizume, T., Y. Hasegawa, I. Kamiya, T. Ide, I. Sumita, S. Huodo, T. Sakuri, H. Tochihara, M. Kubota and Y. Murata, 1990, J. Vac. Sci. Technol. A **8**, 233.
Head-Gordon, M. and J.C. Tully, 1992a, Phys. Rev. B **46**, 1853.
Head-Gordon, M. and J.C. Tully, 1992b, J. Chem. Phys. **95**, 3939.
Hedin, L., 1965, Phys. Rev. A **139**, 796.
Hedin, L. and S. Lundqvist, 1969, in: Solid State Physics, eds. F. Seitz, D. Turnbull and H. Ehrenreich. Holt, Reinhardt, and Winston, New York.
Heimann, P., H. Miosga and H. Neddermeyer, 1979, Phys. Rev. Lett. **42**, 801.
Heimann, P., H. Neddermeyer and H.F. Roloff, 1977, J. Phys. C **10**, L17.
Heine, V., 1963, Proc. Phys. Soc. **81**, 300.
Heine, V., 1969, in: The Physics of Metals, ed. J.M. Ziman. Cambridge University, London.
Heinrichsmeier, M., A. Fleszar and A.G. Eguiluz, 1993, Surf. Sci. **285**, 129.
Hildner, M.L., R.S. Daley, T.E. Felter and P.J. Estrup, 1991, J. Vac. Sci. Technol. A **9**, 1604.
Himpsel, F.J., 1985, Adv. Phys. **32**, 1.
Hirschmugl, C.J., G.P. Williams, F.M. Hoffmann and Y.J. Chabal, 1990, Phys. Rev. Lett. **65**, 480.
Holmes, M.I. and T. Gustafsson, 1981, Phys. Rev. Lett. **47**, 443.
Horn, K., A. Hohlfeld, J. Somers, T. Lindner, P. Hollins and A.M. Bradshaw, 1988, Phys. Rev. Lett. **61**, 2488.
Hsieh, T.C., P. John, T. Miller and T.-C. Chiang, 1987, Phys. Rev. B **35**, 3728.
Hulbert, S.L., P.D. Johnson, N.G. Stoffel, W.A. Royer and N.V. Smith, 1985, Phys. Rev. B **31**, 6815.
Hulpke, E. and J. Lüdecke, 1991, Surf. Sci. **272**, 289.
Hulpke, E. and J. Lüdecke, 1992, Phys. Rev. Lett. **68**, 2846.
Hulpke, E. and J. Lüdecke, 1993, Surf. Sci. **287/288**, 837.
Hulpke, E. and D.-M. Smilgies, 1989, Phys. Rev. B **40**, 1338.
Hybertson, M.S. and S.G. Louie, 1985, Phys. Rev. Lett. **55**, 1418.
Hybertson, M.S. and S.G. Louie, 1986, Phys. Rev. B **34**, 5390.
Ibach, H. Private communication.
Inglesfield, J.E., 1978, J. Phys. C: Solid State Phys. **11**, L69.
Inglesfield, J.E., 1979, J. Phys. C: Solid State Phys. **12**, 149.
Inglesfield, J.E., 1981a, in: The Chemical Physics of Solid Surfaces, eds. D.A. King and D.P. Woodruff. Elsevier, Amsterdam.
Inglesfield, J.E., 1981b, J. Phys. C **14**, 3795.
Inglesfield, J.E., 1985, Prog. Surf. Sci. **20**, 105.
Inglesfield, J.E., 1987, Prog. Surf. Sci. **25**, 57.
Inglesfield, J.E., 1988, Phys. Rev. B **37**, 6682.
Inglesfield, J.E. and G.A. Benesh, 1988, Surf. Sci. **200**, 135.
Inglesfield, J.E. and E.W. Plummer, 1992, in: Angle-Resolved Photoemission, ed. S.D. Kevan. Elsevier, Amsterdam.
Ishida, H., 1989, Phys. Rev. B **40**, 1341.
Ishida, H. and K. Terakura, 1988, Phys. Rev. B **38**, 5752.
Jacob, W., V. Dose, U. Kolac, T. Fauster and A. Goldmann, 1986, Z. Phys. B – Condensed Matter **63**, 459.
Jensen, E., R.A. Bartynski, T. Gustafsson, E.W. Plummer, M.Y. Chou, M.L. Cohen and G.B. Hoflund, 1984, Phys. Rev. B **30**, 5500.
Jensen, E. and E.W. Plummer, 1985, Phys. Rev. Lett. **55**, 1912.
Jeong, K., R.H. Gaylord and S.D. Kevan, 1989a, J. Vac. Sci. Technol. A **7**, 2199.
Jeong, K., R.H. Gaylord and S.D. Kevan, 1989b, Phys. Rev. B **39**, 2973.
Johansson, P., 1979, Solid State Commun. **31**, 591.
Johansson, L.I., H.I.P. Johansson, J.N. Andersen, E. Lundgren and R. Nyholm, 1993, Phys. Rev. Lett. **71**, 2453.
Johnson, P.D., 1992, in: Angle-Resolved Photoemission, ed. S.D. Kevan. Elsevier, Amsterdam.
Jones, W. and N.H. March, 1973, Theoretical Solid State Physics. Wiley, New York.

Joyce, K., A. Martin-Rodero, F. Flores, P.J. Grout and N.H. March, 1987, J. Phys. C **20**, 3381.
Karlsson, U.O., S.A. Flodstrom, R. Engelhardt, W. Gadeke and E.E. Koch, 1984, Solid State Commun. **49**, 711.
Karlsson, U.O., G.V. Hansson, P. Persson and S.A. Flodstrom, 1982, Phys. Rev. B **26**, 1852.
Kaski, K., W. Kinzel and J.D. Gunton, 1983, Phys. Rev. B **27**, 6777.
Katrich, G.A., V.V. Klimov and I.N. Yakovkin, 1992, Ukr. Phys. J. **37**, 429.
Kern, K., R. David, R.L. Palmer, G. Comsa and T.S. Rahman, 1986a, Phys. Rev. B **33**, 4334.
Kern, K., R. David, R.L. Palmer, G. Comsa and T.S. Rahman, 1986b, Surf. Sci. **178**, 537.
Kevan, S.D., 1983a, Phys. Rev. Lett. **50**, 526.
Kevan, S.D., 1983b, Phys. Rev. B **28**, 2268.
Kevan, S.D., 1986a, Phys. Rev. B **34**, 6713.
Kevan, S.D., 1986b, Phys. Rev. Lett. **57**, 2975.
Kevan, S.D., 1986c, Surf. Sci. **178**, 229.
Kevan, S.D., 1986d, Phys. Rev. B **33**, 4364.
Kevan, S.D. and R.H. Gaylord, 1987, Phys. Rev. B **36**, 5809.
Kevan, S.D., N.G. Stoffel and N.V. Smith, 1985a, Phys. Rev. B **31**, 3348.
Kevan, S.D., N.G. Stoffel and N.V. Smith, 1985b, Phys. Rev. B **31**, 1788.
Kevan, S.D. and W. Eberhardt, 1992, in: Angle-Resolved Photoemission, ed. S.D. Kevan. Elsevier, Amsterdam.
King, D.A., 1983, Phys. Scripta **T4**, 34.
Knapp, J.A., F.J. Himpsel, A.R. Williams and D.E. Eastman, 1979a, Phys. Rev. B **19**, 2844.
Knapp, J.A., F.J. Himpsel and D.E. Eastman, 1979b, Phys. Rev. B **19**, 4952.
Kneedler, E., D. Skelton, K.E. Smith and S.D. Kevan, 1990, Phys. Rev. Lett. **64**, 3151.
Kneedler, E., K. Smith and S.D. Kevan, 1991, Phys. Rev. B **44**, 8233.
Kneedler, E., A.B. Andrews, Won-Kok Choi and S.D. Kevan, 1995, Phys. Rev. B **51**, 1823.
Krakauer, H., M. Posternak and A.J. Freeman, 1979, Phys. Rev. Lett. **43**, 1885.
Kohler, B., P. Ruggerone, S. Wilke et al., 1995, Phys. Rev. Lett. **74**, 1387.
Kohn, W., 1959, Phys. Rev. Lett. **2**, 393.
Lang, N.D. and A.R. Williams, 1976, Phys. Rev. Lett. **37**, 212.
Lang, N.D. and A.R. Williams, 1978, Phys. Rev. B **18**, 616.
Langmuir, I., 1932, J. Am. Chem. Soc. **54**, 2788.
Langmuir, I., 1933, Phys. Rev. **43**, 224.
Langreth, D.C., 1985, Phys. Rev. Lett. **54**, 126.
Langreth, D.C., 1986, Phys. Scripta **35**, 185.
Lau, K.H. and W. Kohn, 1978, Surf. Sci. **75**, 69.
Levinson, H.J., F. Greuter and E.W. Plummer, 1983, Phys. Rev. B **27**, 727.
Li, D., J. Zhang, S. Lee and P.A. Dowben, 1992, Phys. Rev. B **45**, 11876.
Lindau, I. and L. Walldén, 1971, Solid State Commun. **9**, 209.
Lindgren, S.Å. and L. Walldén, 1978, Solid State Commun. **28**, 283.
Lindgren, S.Å. and L. Walldén, 1980a, Solid State Commun. **34**, 671.
Lindgren, S.Å. and L. Walldén, 1980b, Phys. Rev. B **22**, 5967.
Lindgren, S.Å. and L. Walldén, 1988, Phys. Rev. B **38**, 3060.
Liu, J.N., X. Sun, R.T. Fu and K. Nasu, 1992, Phys. Rev. B **46**, 1710.
Loucks, T.L. and P.H. Butler, 1964, Phys. Rev. **133A**, 819.
Louie, S.G., P. Thiry, R. Pinchaux, Y. Petroff, D. Chandesris and J. Lecante, 1980, Phys. Rev. Lett. **44**, 549.
Lundqvist, B.I., 1969, Phys. Status Solidi **32**, 273.
March, N.H., 1987, Prog. Surf. Sci. **25**, 229.
March, N.H., 1989, Phys. Rev. B **39**, 1385.
Mattheiss, L.F. and D.R. Hamann, 1984, Phys. Rev. B **29**, 5372.
Matthew, J.A.D., F.P. Netzer and G. Astl, 1991, Surf. Sci. Lett. **259**, L757.
Mauc, A.W., 1935, Z. Phys. **94**, 717.
Mazumdar, S., 1987, Phys. Rev. B **36**, 7190.
Mazumdar, S., 1989, Phys. Rev. B **39**, 12324.
Mookerjee, A., 1975, J. Phys. C **8**, 29.
Mott, N.F. and W. Jones, 1936, Theory of the Properties of Metals and Alloys. Oxford University Press, Oxford.

Mott, N.F., 1990, Metal-Insulator Transitions. Taylor & Francis, London.
Muscat, J., 1987, Prog. Surf. Sci. **25**, 211.
Muscat, J.P. and D.N. Newns, 1978, Prog. Surf. Sci. **9**, 1.
Neugebauer, J. and M. Scheffler, 1993, Phys. Rev. Lett. **71**, 577.
Neuhaus, D., F. Joo and B. Feuerbacher, 1986, Surf. Sci. **165**, L90.
Nilsson, P.O., G. Arbman and T. Gustafsson, 1974, J. Phys. F **4**, 1937.
Northrup, J.E., M.S. Hybertson and S.G. Louie, 1986, Phys. Rev. Lett. **59**, 819.
Papaconstantopoulos, D.A., 1986, Handbook of the Band Structure of Elemental Solids. Plenum, New York.
Peacock-Lopez, E. and H. Suhl, 1982, Phys. Rev. B **26**, 3774.
Peierls, R.E., 1964, Quantum Theory of Solids. Clarendon, Oxford.
Pendry, J.N., 1978, in: Photoemission and the Electronic Structure of Solids, eds. B. Feuerbacher, B. Fitton and R.F. Willis. Wiley, New York.
Pendry, J.B. and F. Forstmann, 1970, J. Phys. C **3**, 59.
Persson, B.N.J., 1989a, Solid State Commun. **70**, 215.
Persson, B.N.J., 1989b, Solid State Commun. **70**, 211.
Persson, B.N.J., D. Schumacher and A. Otto, 1991, Chem. Phys. Lett. **178**, 204.
Peterson, L.D. and S.D. Kevan, 1990, Phys. Rev. Lett. **65**, 2563.
Peterson, L.D. and S.D. Kevan, 1991, J. Chem. Phys. **94**, 2281.
Pick, S., M. Tomásek and M.U. Luchini, 1989, Chem. Phys. Lett. **164**, 345.
Pines, D., 1963, Elementary Excitations in Solids. Benjamin, New York.
Plummer, E.W. Private communication.
Plummer, E.W. and W. Eberhardt, 1982, in: Advances in Chemical Physics. Wiley, New York.
Plummer, E.W. and J.W. Gadzuk, 1970, Phys. Rev. Lett. **25**, 1493.
Prutton, M., 1984, Electronic Properties of Surfaces. Hilgar, Bristol.
Prybyla, J.A., P.J. Estrup, S.C. Ying, Y.J. Chabal and S.B. Christman, 1987, Phys. Rev. Lett. **58**, 1877.
Redfield, A.C. and A. Zangwill, 1992, Phys. Rev. B **46**, 4289.
Reinecke, T.L. and S.C. Ying, 1991, Phys. Rev. B **43**, 12.
Reutt, J.E., Y.J. Chabal and S.B. Christman, 1988, Phys. Rev. B **38**, 3112.
Rice, T.M., 1975, in: Low-Dimensional Cooperative Phenomena, ed. H.J. Keller. Plenum, New York.
Riffe, D.M., G.K. Wertheim and P.H. Citrin, 1990, Phys. Rev. Lett. **64**, 571.
Rikvold, P.A., K. Kaski, J.D. Gunton and M.C. Yalabik, 1984, Phys. Rev. B **29**, 6285.
Rotenberg, E. and S.D. Kevan, 1998, Phys. Rev. Lett. **80**, 2905.
Ruderman, M.A. and C. Kittel, 1954, Phys. Rev. **96**, 99.
Ryberg, R., 1989, in: Molecule Surface Interactions, ed. K.P. Lawley. Wiley, New York.
Salanon, B. and J. Lapujoulade, 1986, Surf. Sci. **173**, L613.
Schweizer, E.K. and C.T. Rettner, 1989, J. Vac. Sci. Technol. A **7**, 1937.
Seitz, F., 1940, The Modern Theory of Solids. McGraw-Hill, New York.
Sepulveda, A. and G.A. Rhead, 1977, Surf. Sci. **66**, 436.
Shin, K.S., C.Y. Kim, J.W. Chung, S.C. Hong, S.K. Lee, C.Y. Park, T. Kinoshita, M. Watanabe, A. Kakizaki and T. Ishii, submitted to Phys. Rev. B.
Shockley, W., 1939, Phys. Rev. **56**, 317.
Singh, D. and H. Krakauer, 1988, Phys. Rev. B **37**, 3999.
Smith, K.E., G.S. Elliot and S.D. Kevan, 1990, Phys. Rev. B **42**, 5385.
Smith, K.E. and S.D. Kevan, 1990, Phys. Rev. Lett. **64**, 567.
Smith, K.E. and S.D. Kevan, 1991a, Ann. Rev. Solid State Chem. **21**, 49.
Smith, K.E. and S.D. Kevan, 1991b, Phys. Rev. B **43**, 1831.
Smith, N.V., 1985a, Phys. Rev. B **32**, 3549.
Smith, N.V., 1985b, Appl. Surf. Sci. **22/23**, 349.
Smith, N.V., 1992, Comments Condens. Mat. Phys. **15**, 263.
Sommer, E. and H.J. Kreuzer, 1982, Phys. Rev. Lett. **49**, 61.
Soukiassian, P., R. Riwan, J. Lecante, E. Wimmer, S.R. Chubb and A.J. Freeman, 1985, Phys. Rev. B **31**, 4911.
Spanjaard, D., D.W. Jeppsen and P.M. Marcus, 1979, Phys. Rev. B **19**, 642.
Swanson, L.W. and L.C. Crouser, 1967a, Phys. Rev. Lett. **16**, 389.

Swanson, L.W. and L.C. Crouser, 1967b, Phys. Rev. **163**, 622.
Tamm, 1932, Phys. Z. Sowjet **1**, 732.
Tang, D. and D. Heskett, 1993, Phys. Rev. B **47**, 10695.
Tang, S. and J.E. Hirsch, 1988, Phys. Rev. B **37**, 9546.
Tang, S. and J.E. Hirsch, 1989, Phys. Rev. B **39**, 12327.
Tersoff, J. and S.D. Kevan, 1983, Phys. Rev. B **28**, 4267.
Thiry, P., D. Chandesris, J. Lecante, C. Guillot, R. Pinchaux and Y. Petroff, 1979, Phys. Rev. Lett. **43**, 82.
Tiersten, S.C., T.L. Reinecke and S.C. Ying, 1989, Phys. Rev. B **39**, 12575.
Tiersten, S.C., T.L. Reinecke and S.C. Ying, 1991, Phys. Rev. B **43**, 12045.
Topping, J., 1927, Proc. Roy. Soc. London, Ser. A **114**, 67.
Tosatti, E., 1978, Solid State Commun. **25**, 637.
van der Veen, J.F., P. Heimann, F.J. Himpsel and D.E. Eastman, 1981, Solid State Commun. **37**, 555.
van der Veen, J.F., F.J. Himpsel and D.E. Eastman, 1982, Phys. Rev. B **25**, 7388.
van Hoof, J.B.A.N., S. Crampin and J.E. Inglesfield, 1992, J. Phys.: Condens. Matter **4**, 8477.
Van Vleck, J.H., 1962, Rev. Mod. Phys. **34**, 681.
Velicky, B., S. Kirkpatrick and H. Ehrenreich, 1968, Phys. Rev. **175**, 747.
Waclawski, B.J. and E.W. Plummer, 1972, Phys. Rev. Lett. **29**, 783.
Wagner, L.F. and W.E. Spicer, 1972, Phys. Rev. Lett. **28**, 1381.
Wang, G.-C., T.-M. Lu and M.G. Lagally, 1978, J. Chem. Phys. **69**, 479.
Wang, X.W., C.T. Chan, K.M. Ho and W. Weber, 1988, Phys. Rev. Lett. **60**, 2066.
Wang, X.W. and W. Weber, 1987, Phys. Rev. Lett. **58**, 1452.
Watson, G.M., P.A. Bruhwiler, E.W. Plummer, H.-J. Sagner and K.-H. Frank, 1990, Phys. Rev. Lett. **65**, 468.
Watson, G.M., P.A. Bruhwiler, H.J. Sagner, K.H. Frank and E.W. Plummer, 1993, submitted to Phys. Rev. Lett.
Wei, D.-S. and S.D. Kevan, to be published.
Weinert, M., S.L. Hulbert and P.D. Johnson, 1985, Phys. Rev. Lett. **55**, 2055.
Whitman, L.J., J.A. Stroscio, R.A. Dragoset and R.J. Celotta, 1991, Phys. Rev. Lett. **66**, 1338.
Wilk, L., W.R. Fehlner and S.H. Vosko, 1978, Can. J. Phys. **58**, 266.
Wilson, J.A., F.J. DiSalvo and S. Mahajan, 1975, Adv. Phys. **24**, 117.
Wimmer, E., A.J. Freeman, J.R. Hiskes and A.M. Karo, 1983, Phys. Rev. B **28**, 3074.
Wissman, P., 1975, in: Surface Physics, ed. G. Höler. Springer, Berlin.
Witt, W. and E. Bauer, 1986, Ber. Bunsenges Phys. Chem. **90**, 248.
Yoshida, K., 1957, Phys. Rev. **106**, 893.
Zhang, Z.Y. and D.C. Langreth, 1989a, Phys. Rev. Lett. **59**, 2211.
Zhang, Z.Y. and D.C. Langreth, 1989b, Phys. Rev. B **39**, 10.
Ziman, J.M., 1960, Electrons and Phonons. Clarendon Press, Oxford.
Ziman, J.M., 1970, Electrons in Metals. Taylor & Francis, London.
Ziman, J.M., 1972, Principles of the Theory of Solids. Cambridge University, Cambridge.

CHAPTER 9

# Magnetism at Surfaces and in Ultrathin Films

C.M. SCHNEIDER

*Institut für Festkörper- und Werkstofforschung Dresden*
*Helmholtzstr. 20, D-01069 Dresden, Germany*

J. KIRSCHNER

*Max-Planck-Institut für Mikrostrukturphysik*
*Am Weinberg 2, D-06120 Halle/Saale, Germany*

*© 2000 Elsevier Science B.V.*
*All rights reserved*

*Handbook of Surface Science*
*Volume 2, edited by K. Horn and M. Scheffler*

# Contents


9.1. Introduction . . . 514
9.1.1. Bulk magnetism in retrospect . . . 514
9.1.2. Surface magnetism: A new interdisciplinary research discipline . . . 516
9.2. Basic concepts in the magnetism of surfaces and thin film systems . . . 520
9.2.1. The ground state electronic structure ($T = 0$ K) . . . 520
9.2.1.1. A bulk ferromagnet . . . 520
9.2.1.2. A semi-infinite magnetic crystal . . . 534
9.2.1.3. Ultrathin films: 2-dimensional entities . . . 540
9.2.2. Magnetism at $T > 0$ K . . . 543
9.2.2.1. Magnetic excitations in the bulk . . . 543
9.2.2.2. Surfaces and thin films . . . 545
9.2.3. Magnetic anisotropies . . . 549
9.2.3.1. The bulk . . . 549
9.2.3.2. Surfaces and thin films . . . 554
9.3. Probing surface magnetism with spin-polarized electrons . . . 559
9.3.1. Description of polarized electrons . . . 560
9.3.2. Polarized electron sources . . . 562
9.3.3. Spin polarimeters . . . 567
9.4. Scattering of spin-polarized electrons from magnetic surfaces . . . 576
9.4.1. Elastic scattering (SPLEED) . . . 578
9.4.1.1. Magnetic structure analysis . . . 580
9.4.1.2. Temperature dependence of the surface magnetization in the spin-wave regime . . . 581
9.4.1.3. Critical phenomena at surfaces . . . 583
9.4.1.4. Magnetic size effects in ultrathin films . . . 584
9.4.1.5. Interlayer coupling in magnetic trilayers . . . 585
9.4.2. Inelastic scattering (SPEELS) . . . 586
9.4.2.1. Stoner excitations at magnetic surfaces . . . 589
9.4.2.2. Stoner excitations in ultrathin films . . . 592
9.4.2.3. Stoner excitations and magnetic ordering . . . 592
9.5. Emission of spin-polarized electrons from ferromagnets . . . 594
9.5.1. Some general remarks on spin-polarized photoelectron spectroscopies . . . 594
9.5.2. Analysis of valence electronic states . . . 601
9.5.2.1. Spin-split bulk band structures . . . 601
9.5.2.2. Magnetic surface states . . . 605
9.5.2.3. Electronic hybridization and magnetic interface states . . . 612
9.5.2.4. Quantum well-states . . . 616
9.5.2.5. Experimental results on the limits of the Stoner–Wohlfarth model of itinerant ferromagnetism . . . 623
9.5.3. Magnetism and element specificity . . . 629
9.5.3.1. Spin-polarized core level photoemission . . . 631
9.5.3.2. Spin polarized Auger electrons . . . 633
9.5.4. Magnetic dichroism . . . 636

9.5.5. Magnetic dichroism in the angular distribution of photoelectrons (MDAD) . . . . . 641
9.5.5.1. MDAD in core-level spectroscopy . . . . . 641
9.5.5.2. MDAD in valence electronic states . . . . . 650
References . . . . . 662

## 9.1. Introduction

### *9.1.1. Bulk magnetism in retrospect*

Magnetism has fascinated mankind since its discovery many centuries before the Christian era. The most intriguing aspect about this phenomenon is its close relation to specific materials. Nature provides us with a number of minerals whose unique property is a magnetic order over macroscopic distances, resulting in a permanent magnetic orientation within the material. The historical example for these substances is the mineral magnetite, a mixture of the iron oxides FeO and $Fe_2O_3$. The access to natural deposits of these minerals gave plenty of opportunity to observe the effect of magnetic interactions, for instance, the attraction of pieces of iron to magnetite, long before a systematic experimental approach in natural sciences attempted even a qualitative understanding of these phenomena. Empirical experience even led to first elementary but important applications of magnetism. The maybe most far-reaching of these applications employed the orientation of a piece of magnet in the earth magnetic field for the purpose of navigation. Predecessors of the modern pivot-type compass seem to have been in use in ancient China as early as 1000 B.C. Although there may be a considerable uncertainty about the circumstances of the discovery of magnetism and the date of its first application (Mattis, 1988), its impact on the development of mankind in many – not only technological – respects is undisputed.

With the rising knowledge of quantitative interrelations in physics and the accompanying mathematical tools the interpretation of magnetic phenomena shifted slowly from metaphysical to more analytical reasoning. An important milestone in this process was marked by the observation that electric currents can generate magnetic fields. This observation opened the way to a quantitative treatment of magnetic phenomena within the framework of classical electrodynamics, i.e., on the basis of Maxwell's equations (Maxwell, 1891). The concept of a magnetic field interacting with matter, thereby producing mechanical forces and electrical currents forms the basis for most technological applications of magnetism in every day live, ranging from electrical power engineering over communication technology up to magnetic recording. The success of this "macroscopic" approach, however, cannot hide the fact that the *property* magnetism is treated only in a phenomenological way. The magnetic state of a material enters Maxwell's equations only by means of a "proportionality factor", the magnetic susceptibility $\chi$, which describes the response of solid matter to an external magnetic field $H$ (Jackson, 1972). This approach allows a definition of various classes of magnets, for instance, distinguishing materials with a long-range spontaneous magnetic order (ferro-, ferri-, and antiferromagnets) from others which order only in an applied field (dia- and paramagnets). It cannot give insight into the origin of these different types of magnetism. A microscopic picture, i.e., the understanding of the physical processes that give rise to the various magnetic phenomena in solids, had to await the advent of modern quantum mechanics in the first half of this century.

It appears to be a particular irony of nature that one of the oldest phenomena known in natural sciences took the longest time to be understood and to be explained quantitatively. From today's standpoint the reason for the delayed progress must certainly be attributed to the intimate connection between magnetism and the electronic structure of matter. In order to appreciate the achievements on the way to a microscopic understanding of solid state magnetism, it is useful to review the main obstacles which had and still have to be overcome. First, the total magnetic moment of a piece of solid matter, and hence it's magnetization, is made up from the magnetic moments of individual electrons. Aside from orbital contributions, the magnetic moment of each electron is mainly determined by its *spin*. Originally, the quantum number spin was introduced somewhat artificially into the Schrödinger equation to explain the fine structure in atomic spectra. A first principles treatment of the electron spin, however, requires the framework of relativistic quantum mechanics and can only be given within Dirac's theory (Dirac, 1927). Second, the formation of a long-range magnetically ordered ground state in the material is driven by the so-called *exchange interaction*. This spin-dependent Coulomb-type interaction is essentially a consequence of the collective behavior of a Fermion system and as such a purely quantum mechanical phenomenon. In other words, there is no way to explain magnetism in a solid within classical physics. An adequate treatment of the electronic structure calls for appropriate many-particle descriptions. A number of theoretical procedures have been based on mean-field approaches, thus reducing the situation to an effective one-electron problem. The probably most famous representative of this class of theories is known as the Stoner–Wohlfarth model of ferromagnetism (Wohlfarth, 1953). Mean field approaches based on density functional theory with local spin density approximation nowadays yield a reasonably good description of the ferromagnetic ground state, i.e., at $T = 0$ K (Moruzzi et al., 1978). Yet, they usually fail to reliably predict the excited states, which are probed in many experiments. Third, the magnetic moments are found to be more or less strongly coupled to the crystal lattice, giving rise to preferred spatial orientations of the magnetization in crystalline materials. These *magnetic anisotropies* are crucial for practically all applications of magnetic materials in modern technology, ranging from permanent magnets to magnetic recording. One of the forces causing these anisotropies is a further spin-dependent interaction in solids, the spin–orbit coupling. Although this has been known for a long time, magnetic anisotropies are still very difficult to predict from first principles calculations. This is because they are due to extremely small energy variations ($\sim 10^{-4}$ eV per atom) upon rotation of the magnetization with respect to the lattice. Finally, a further complication arises from the observation that, depending on the material, different types of electrons may be responsible for the magnetism. Rare earth magnets, for instance, can be well understood by assuming the magnetic moments (and hence the f-electrons, which give rise to the magnetic moment) to be localized at the individual lattice points (localized magnets). In addition to the spin magnetic moment there may be considerably large orbital contributions. Due to the spatial localization f-electron magnets can often be described in atomic-like pictures. In the second class of so-called itinerant ferromagnets, with the classical examples Fe, Co and Ni, the same electrons which are responsible for the magnetic moment participate in the metal bonding and in transport phenomena. These d-electrons are to a strong degree delocalized and the orbital contributions to the magnetic moment are very small. The understanding of itinerant magnetism requires band theory approaches.

The sharp distinction into localized and itinerant magnets represents only the two extreme aspects, of course. In reality, any electronic system will reveal a mixture of localized and itinerant contributions. A unified picture of magnetism which will be able to treat all these various aspects on an equal footing is still in the evolutionary state.

### *9.1.2. Surface magnetism: A new interdisciplinary research discipline*

The importance of the surface comes from the fact that it represents the boundary of a solid to the ambient environment. The presence of a boundary has two important implications. First, it means a loss of bulk translational symmetry at the surface. It should be recalled that the concept of periodicity in crystalline materials leads to important simplifications in the quantitative description of lattice dynamics and electronic structures. Breaking this periodicity by introducing a surface must consequently alter these properties and give rise to novel physical phenomena. The influence on lattice dynamics is thoroughly treated in Volume 1 of this Handbook, whereas the electronic structure is the main topic of the present volume. Given the strong interdependence between electronic structure and magnetism, new magnetic effects may be expected at surfaces as well. Second, the surface is in direct contact with the environment and will usually undergo chemical reactions. Under ambient conditions this often causes the formation of oxide layers, in the case of iron the most widely known and often disliked being rust. The above situation illustrates one of the fundamental demands in surface physics: prior to the study of their properties, the surfaces must be brought into a well-defined state first. This task requires non-trivial efforts and became feasible only with the technological advances in the generation of extremely good (ultrahigh) vacua ($p < 10^{-9}$ mbar) in the 60's and early 70's. It was not until then that the interest in solid state physics shifted from bulk properties to the behavior at the surface, leading to the advent of the new field of surface science. Similarly, the availability of ultrahigh vacua (UHV) played a very important role in the development of the physics of thin films. The UHV environment permitted not only the preparation of atomically clean substrate surfaces, but also the deposition of clean and well-defined films by means of molecular beam epitaxy (MBE). The physics of surfaces and thin films is thus often grouped under the same roof, since many experimental methods and theoretical concepts are equally applicable in both cases.

Very similar considerations hold for the field which we refer today to as surface magnetism. As it deals with surface *and* thin film aspects, the discipline would be more appropriately (and more correctly) characterized as the *physics of low-dimensional magnetic systems*. Nevertheless, for reasons of brevity and coherence, we will continue to use the expression surface magnetism. From its first beginnings in the late 1960's, surface magnetism must be regarded as a truly interdisciplinary research direction, reconciling aspects from both surface science and magnetism. This becomes immediately clear when looking back into some of the early experimental results. Stimulated by the prediction of a peculiar magnetic behavior at surfaces (Néel, 1954), Liebermann et al. investigated thin Nickel films and reported the surface to consist of magnetically "dead" layers (Liebermann et al., 1969, 1970). Fortunately, the results were soon afterwards proven to be a consequence of the surface being contaminated by adsorbates – otherwise a field such as surface magnetism may have never evolved. This early example illustrates the connection between magnetism and

chemical condition of the surface, thus pointing out the importance of the surface science aspect.

The interdisciplinary character of surface magnetism allows one to choose between two different approaches to a given problem, starting either from magnetism or surface science – a choice most often dictated by the personal background. This situation brings with it a large variety of experimental procedures, which consequently fall into two classes: (i) techniques from bulk magnetism which have been modified and adapted to the requirements in surface magnetism, and (ii) genuine surface science techniques which have been "upgraded" to magnetic sensitivity. The modus operandi starting from magnetism was pioneered by Gradmann and coworkers who applied torsion oscillation magnetometry to study the magnetic anisotropy in thin Ni films (Gradmann, 1966). The surface physics approach to magnetism is closely connected to the work of Busch and Siegmann who demonstrated the emission of polarized electrons from magnetic surfaces (Busch et al., 1969), thus laying the foundation to the development of a number of spin-polarized electron spectroscopies. It must be pointed out, however, that these two procedures are not mutually interchangeable, as each of them can access only certain aspects in surface magnetism. For a concise description of the magnetic behavior at surfaces one must exploit the synergy effects by combining results from both surface physical and magnetic techniques. Achieving this synergy is sometimes a painstaking procedure, due to the fact that the magnetism and surface physics community do often speak different languages.

One should not get the impression, however, that surface magnetism is just a more or less exotic area kept alive by the curiosity of some unworldly scientists. On the contrary, there is a very close link to applications, in particular when it comes to magnetism at interfaces and in thin film systems (Bader, 1990; Falicov et al., 1990). It is justified to say that a major incentive for basic research in surface magnetism comes from the demands of information technology. One of the primary demands is the increase of the information capacity in mass storage devices, which implies an increase of the areal information density (usually measured in bits/cm$^2$ or bits/inch$^2$) on the storage medium. As a consequence, the size of the individual information unit (bit) must be reduced. Each bit is written as single magnetic domain which has a certain magnetic stray field. It is partly due to this stray field that bits cannot be made arbitrarily small and must have sufficient separation from each other, in order to minimize crosstalk. These limits are already within reach with longitudinal recording media (those in which domains are magnetized parallel to the plane of the medium) developed today. A significant improvement is expected from so-called perpendicular recording in which case the domains are magnetized perpendicular to the media surface. The storage medium – be it a magnetic tape, a hard disk, or a magneto-optical disk – is usually manufactured as a thin-film system on a polymer or metal substrate. One of the tasks is therefore to develop thin layers with suitable magnetic properties which are able to sustain very small domains with a magnetization vector normal to the surface. Surface magnetism aspects are becoming very important in solving this task.

A smaller average bit size causes a smaller magnetic stray field. As a consequence, one encounters increasing problems with the signal processing, because the head of the mass storage device picks up the stored information via the stray field. Within given limits the read-out signal of a hard disk drive can be somewhat improved by reducing the flying height of the read head. Driven by the need for a higher signal-to-noise ratio, the tradi-

tionally employed inductive heads (already being produced in thin-film technology) are therefore successively replaced by so-called anisotropic magnetoresistive (AMR) heads since the early 1990's (Tsang et al., 1998). In an MR read head the bit's stray field causes a change in resistance rather than induces a voltage. Being a transport property magnetoresistance involves the electrons at the Fermi level. In itinerant ferromagnets these are the same electrons which are spin-split and responsible for the magnetism. Magnetoresistance arises due to a small difference in the scattering probabilities for spin-up and spin-down electrons. The resulting effects of this spin-polarized transport are small in most bulk materials, usually of the order of $10^{-4}$ and less. The highest AMR values of up to 2% are found in Permalloy films (Daughton, 1999).

Magnetoresistance is a nice example for highlighting the impact of a basic research field such as surface magnetism on the development of novel technologies and their commercial exploitation. In the late 1980's, experiments on magnetic multilayers revealed a "giant magneto-resistance" (GMR) effect which is 2–3 orders of magnitude higher than the AMR values found previously. GMR is observed, for instance, in superlattices in which neighboring ferromagnetic layers are separated by a non-magnetic interlayer and have mutually opposite magnetization directions (Baibich et al., 1988; Binasch et al., 1989). This magnetic arrangement is called an "antiferromagnetically" coupled multilayer, in contrast to a ferromagnetic coupling in which situation the magnetization in adjacent ferromagnetic layers is pointing into the same direction. For an electrical current flowing parallel or perpendicular to the layers, the resistance is high for the antiferromagnetic coupling and low for the ferromagnetic one. In order to understand this behavior in a very simple picture one has to keep in mind that the states "spin-up" and "spin-down" are defined by the direction of the local magnetization within the layer. As a consequence, electrons traveling through an antiferromagnetically coupled superlattice have a spin-up character in one ferromagnetic layer and spin-down in the adjacent ones. Having the "wrong" spin when passing from a given layer to the next one increases the scattering and results in a higher resistance. The magnetoresistance becomes "giant" by adding up the contributions from all the layers and the interfaces in a superlattice or multilayer, thereby reaching values of more than 100% in Co/Cu multilayers (Parkin et al., 1991). Whether such a multilayer exhibits a ferromagnetic or antiferromagnetic interlayer coupling can be controlled by carefully tuning the thickness of the nonmagnetic spacer layer. It is thus mandatory to control the properties of these artificially generated structures on a nano- or even atomic-scale level. From the arguments given above the advantage of using GMR in magnetic recording – but not only there – is immediately clear. Magnetic sensors employing giant magnetoresistance have already entered the market and hard disk drives with GMR-based reading heads are becoming commercially available now.[1] Note that the time between the first observation of the effect in research laboratories and its exploitation in technical devices is less than 10 years.

Spin-polarized transport phenomena may be seen as only one facet of a larger area called *magnetoelectronics*. It is concerned with the interesting topic of incorporating magnetic elements into semiconductor integrated circuits. The underlying idea is to exploit the

1 During the year 1998 the first hard disk drives with an areal density of 2.7 Gb/in$^2$ and a total capacity of 16.8 Gb became available.

spin state of the conduction electrons in an itinerant ferromagnet as an additional degree of freedom. In analogy to a transistor which is essentially a current valve, one may develop, for instance, so-called spin-valves which can serve as building-blocks for magnetic transistors. In a bipolar magnetic transistor which has already been shown to be feasible (Monsma et al., 1995), the spin-polarized current through the device may be modulated by the magnetization direction of either the emitter or collector. Another device of considerable interest is a new type of computer memory, the so-called magnetic random access memory (magnetic RAM or MRAM) (Pohm et al., 1988). The main advantage of a RAM is that data can be stored and retrieved at very high rates. However, the information kept in the memory is volatile and must be "refreshed" periodically. This drawback could be overcome by magnetic RAM, in which the information is stored permanently in the magnetic layer. Another device that has been proposed and still awaits to be realized is a magnetic field effect transistor (MFET) (Datta and Das, 1990).

The examples discussed above may give a – limited – impression of the role that surface magnetism has played in recent research and development.[2] In addition to giving the reader a flavor of the field it may also serve as a means to justify our selection of topics in the present article. Describing all the various facets of surface magnetism would easily fill a whole book by itself. The present volume, however, is centered around the surface electronic structure. Because the electronic structure – as we have outlined above – is at the basis of magnetism, we would like to focus our contribution to this aspect. We are well aware that this deliberate restriction leaves aside numerous very interesting topics, for example, the wide field of critical magnetic phenomena, transport effects or issues related to the magnetic microstructure (micromagnetism). Nevertheless, whenever these aspects may become important in the understanding of experimental results on the electronic structure, we will include them in the discussion.

Our approach to surface magnetism puts a certain weight on the experimental side. We will discuss the interesting magnetic phenomena always in close connection with the background of the various experimental techniques used to measure them. It is important to consider the properties and limitations of these techniques in order to know (i) which aspects of the magnetic behavior are probed and (ii) how reliable the conclusions are. Nevertheless, many readers may not be familiar with the various concepts used in bulk magnetism, for instance, magnetic anisotropies. Because many of these concepts appear – in a modified form – also in surface magnetism, we found it necessary to devote a Section 9.2 to their short description, thereby pointing out the differences between bulk and surface magnetism. In Section 9.3 we give a short introduction into the physics of the generation and analysis of spin-polarized electrons. Sections 9.4 and 9.5 concentrate on the scattering and emission of spin-polarized electrons as very sensitive probes for the magnetic behavior and the electronic structure at surfaces.

---

2 For a more detailed description of the situation as of 1995 the reader may be referred to the April issue of *Physics Today* [Physics Today **48**(4), (1995)].

## 9.2. Basic concepts in the magnetism of surfaces and thin film systems

It has been emphasized in the introduction that surfaces and thin films often exhibit new and surprising magnetic phenomena. These new phenomena arise because of distinct differences between a low-dimensional and the corresponding bulk system with respect to the electronic structure, geometric arrangement of the atoms or magnetic interactions. We do not assume that the reader is fully familiar with the different facets of magnetism in bulk materials. The following section is therefore meant to stand as a brief introduction into some key aspects, which are important to understand the main differences between bulk and surface magnetism. We will point out these differences and qualitatively discuss their physical consequences. A concise discussion of the topics related to bulk magnetism which are touched in this chapter can be found in a number of excellent textbooks (Kneller, 1962; Chikazumi, 1964; Herpin, 1968).

### *9.2.1. The ground state electronic structure ($T = 0$ K)*

#### *9.2.1.1. A bulk ferromagnet*

Understanding magnetic properties of materials on the basis of their electronic structure has always been one of the major challenges in materials science. A significant progress over the years provides us nowadays with a quite accurate description of the magnetic ground state at $T = 0$ K, at least for bulk systems. It is thus possible to explore the intimate interrelation between magnetism and electronic structure and employ this knowledge in predicting trends in the magnetic behavior. Despite this achievement there are still numerous unsolved problems. Theories that give a good description of the ground state often break down at $T > 0$ K and are thus useless for the thermally excited state of the electronic system. Even more important, a unified approach for the magnetism in solids does not yet exist. This means, we have to know the details of the electronic system first, before we can select from the variety of models the one which might be most appropriate for the specific case.

Historically, ferromagnets are divided into two classes, the "localized" and "itinerant" ferromagnets. In a localized ferromagnet the magnetic moments are predominantly made up from unpaired electrons in localized wave functions. These states are confined to the lattice site and do not participate in the chemical bonding, thus being more or less atomic-like. The magnetic moment which consists of spin and orbital contributions is therefore essentially an atomic quantity, and can to first order often be deduced from Hund's rules. This situation is found in rare earth materials with 4f or 5f electronic configurations. The corresponding magnetic system has been successfully described by assuming a crystalline lattice with magnetic moments or spins localized at the lattice points. This is the starting point for a number of spin lattice models as the so-called Heisenberg and Ising systems, to name only the two most prominent ones. We will come back to this approach and particularly to the Heisenberg model in the discussion of magnetic spin systems at elevated temperatures ($T > 0$ K).

A much more complex situation is found in itinerant ferromagnets. The magnetic moment in these materials is due to delocalized electrons close to the Fermi level which participate in the chemical bonding and in transport phenomena. These conduction electrons

correspond to band states in the solid and can be therefore adequately treated only by electronic band theories. Classical examples for itinerant ferromagnets are the 3d-elements Fe, Co, Ni, and their alloys. The strong interaction and hybridization that characterizes conduction electrons implies far-reaching consequences for the magnetism. First, itinerant magnetism is a truly collective phenomenon, as it depends on the entire ensemble of electrons in the valence bands of the solid. Second, the presence of a magnetically ordered ground state is due to the exchange interaction, which favors the alignment of neighboring spins. This alignment may be parallel as in ferromagnets, antiparallel as in anti-ferromagnets, or even more complicated as, for example, helical spin structures in rare earth materials. Third, characteristic magnetic quantities, such as the magnetic moment or the saturation magnetization, cannot be related to atomic properties, but must be deduced from band structure calculations.

The distinction into "localized" and "itinerant" magnets seems to be very convenient. It is, however, only partly true and should therefore be taken as a guideline only. In reality, a magnetic material will exhibit both itinerant as well as localized aspects. As an example, we refer again to the lanthanides. The magnetic moments of the ferromagnetic 4f materials are not entirely determined by Hund's rules. The localized 4f electrons hybridize to a certain degree with conduction electrons of s, p or d orbital character. The hybridization causes deviations of the magnetic moment or the saturation magnetization from the atomic value. Let us take the example of Gadolinium which has a half-filled 4f-shell. In this case, Hund's rules yield a total spin $S = \frac{7}{2}$, a total orbital angular momentum $L = 0$, and thus a total angular momentum of $J = \frac{7}{2}$, resulting in an atomic magnetic moment of $\mu_{\text{at}} = 7\mu_{\text{B}}$. The respective experimental value which includes the conduction electron contribution to the magnetic moment is $\mu_{\text{exp}} = 7.63\mu_{\text{B}}$ (Legvold, 1980). Obviously the entire electronic system must be taken into account to arrive at an adequate description. A second counterexample is the successful application of spin wave theory to the 3d ferromagnets in order to analyze the temperature dependence of the magnetization close to $T = 0$ K. The basis for the spin wave theory is a Heisenberg type spin system. This means that we must somewhat detail our simple picture of itinerant and localized ferromagnets. Keeping this refinement in mind, we may still further use the above terminology. In the following, we will discuss in more detail the relationships between itinerant ferromagnetism and electronic band structure. This is important not only for the general understanding, but for the interpretation of the experimental examples, that will be discussed in the remainder.

The complication in itinerant magnetism arises through the high degree of electronic correlations in the narrow bands which form the electronic structure. A general treatment of this situation has been proposed by Hubbard (1963)

$$H = \sum_{ij\sigma} t_{ij} c_{i\sigma}^{+} c_{i\sigma} + U \sum_{i} n_{i\downarrow} n_{i\uparrow} = H_t + H_U. \tag{9.1}$$

The Hubbard-Hamiltonian $H$ describes a set of electrons which move via hopping across a lattice and are subject to Coulomb interactions between the electrons. Accordingly, the first term in (9.1) describes the hopping of electrons with spin $\sigma$ between the lattice sites $i$ and $j$. The probability of the hopping process is given by $t_{ij}$. The expression is written in the second quantization formalism, with $c_{i\sigma}^{+}$ and $c_{i\sigma}$ denoting the

annihilation and creation operators for an electron with spin $\sigma$ on lattice site $i$. The second term contains the Coulomb repulsion of the electrons, with its strength being defined by the parameter $U$. Equation (9.1) represents an approach for a single band and considers as an approximation only the effective Coulomb repulsion between electrons at the same lattice site. Despite this relatively simple structure, the Hubbard Hamiltonian has no general solution, which is the major shortcoming of this approach. The difficulty lies in the correct description of the various nearest and next nearest neighbor interactions involved. To circumvent this problem, at least partly, the interactions may be approximated by their average value. One thus arrives at the mean field version of the Hubbard model, the well-known Stoner–Wohlfarth model (Wohlfarth, 1953, 1980). Implemented in state-of-the-art band structure calculations, the Stoner–Wohlfarth model yields quite accurate predictions for the ferromagnetic ground state at $T = 0$ K. As a main drawback it usually fails to describe the excited state at elevated temperatures. The critical temperatures for long-range ferromagnetic ordering, the so-called Curie temperature $T_C$, as extracted from these band structure calculations, are much higher than the experimental values. In was not until recently that very elaborate calculations beyond the mean field approximation became available (Nolting et al., 1989). These studies are so far restricted to Ni and suggest that a realistic Hubbard model may yield a better treatment of the electronic system at finite temperature.

The advantage of the Stoner–Wohlfarth model, despite its drawbacks, is its simplicity, which allows an intuitive access to the fundamental aspects of band ferromagnetism, for example, the spin-split band structure or the role of the density of states. According to the Stoner model the magnetic interaction between itinerant electrons is mediated via a molecular field, which is determined by the macroscopic sample magnetization. Since a mean field approach implies the magnetization to be the same at each atom, it its equal to the local magnetization $M$ (per atom)

$$M = \mu_B \int^{E_F} \left[D^{\uparrow}(E) - D^{\downarrow}(E)\right] \mathrm{d}E. \tag{9.2}$$

The magnetization is defined as the difference in the density of states for spin-up and spin-down electrons, $D^{\uparrow}(E)$ and $D^{\downarrow}(E)$, respectively. $\mu_B$ denotes the Bohr magneton as atomic unit for the magnetic moment. $M$ interacts with the electron system in such a way that spin-up electrons experience a more attractive and spin-down electrons a more repulsive potential. This can be written as an additional term in the exchange–correlation potential that enters the band structure calculation

$$V_{xc}^{\uparrow\downarrow} = V_{xc}^{0} \mp \frac{1}{2} I M. \tag{9.3}$$

$I$ denotes the interaction parameter, and $V_{xc}^{0}$ the exchange–correlation potential without the magnetic interaction. The exchange–correlation potential represents an average over the many-particle interactions. The spin-dependent part of the potential leads to a splitting

and a shift of the energy eigenvalues with respect to the spin-independent case. The energy shift is in opposite directions for eigenvalues connected to spin-up and spin-down states

$$\varepsilon^{\uparrow\downarrow}(\mathbf{k}) = \varepsilon(\mathbf{k}) \mp \frac{1}{2} I M. \tag{9.4}$$

Equation (9.4) describes a spin-induced splitting of the electronic bands as a consequence of the exchange interaction $I$. In the very simple picture discussed above this spin or exchange splitting is a constant of the value $IM$. This basically means we can envision the ferromagnetic band structure as being constructed by doubling the paramagnetic bands and shifting them by $\mp\frac{1}{2}IM$ with respect to the Fermi level. The exchange splitting in the above model is the same for all energy eigenstates and does not depend on the symmetry of the electronic state. In reality, it varies with $E(\mathbf{k})$ and the symmetry character of the electronic wave function.

Note that Eq. (9.4) is strictly valid only at $T = 0$ K, for the following reason. Experience tells us that the macroscopic magnetization of a sample is not a constant but decreases monotonically with increasing temperature and finally disappears when $T$ approaches the Curie temperature $T_C$. Assuming the same behavior for the parameter $M$ in Eq. (9.4) we end up with a temperature-dependent exchange splitting. In the Stoner model the condition $M \overset{T \to T_C}{\longrightarrow} 0$ thus requires the spin-split band structure to continuously collapse into the paramagnetic one at $T \geqslant T_C$. This property raised a quite controversial dispute, as it was found to be incompatible with some experimental findings reporting a magnetic moment persisting even above the Curie temperature. In particular, the Stoner model is unable to reproduce the Curie–Weiss behavior of the magnetic susceptibility observed in Fe and Ni. This apparent contradiction is then explained in the framework of the so-called fluctuating band theory. This approach assumes first of all that the magnetic moment and the spin-split band structure do not break down at the Curie temperature, but remain locally well-defined. The spatial orientation of the magnetic moment, however, fluctuates in both time and space. Any temporally or spatially averaging experimental technique will therefore measure a macroscopic magnetization $M = 0$. This way, we retain a spin-split band structure and a local magnetic moment even above the Curie temperature. This is another example for the complicated relationship between electronic structure and itinerant magnetism.

The Stoner model, as one of its assets, yields a simple criterion for the existence of a stable ferromagnetic state in terms of quantities related to the electronic structure:

$$I \cdot D(E_F) > 1. \tag{9.5}$$

The exchange and correlation interaction $I$ is essentially of *intraatomic* origin and its value depends thus strongly on the element. The paramagnetic density of states at the Fermi level $D(E_F)$ is related to *interatomic* interactions, and is consequently strongly affected by the number and spatial separation of nearest neighbor atoms. It should be emphasized that the Stoner criterion Eq. (9.5) directly reflects the interrelation between electronic structure and magnetism in itinerant systems, as it connects the existence of a ferromagnetically ordered ground state with the density of states. It is therefore very useful in the qualitative estimate of the way changes in the electronic structure might affect the itinerant magnetism.

The physics behind the Stoner criterion may be understood in terms of an energy balance between the kinetic energy of the electron system and the so-called exchange energy. In a non-magnetic material all spins are aligned antiparallel. In order to achieve a parallel orientation of spins, the electrons which undergo a "spin flip" have to occupy higher lying states according to the Pauli exclusion principle. This means an increase of the total kinetic energy in the electron system. At the same time, electrons with parallel spin are on average further away from each other, which results in a reduced Coulomb repulsion. This effect arises from the so-called Fermi hole – a zone of reduced probability to find an electron of the same spin – that each electron carries around with it. The Fermi hole is another consequence of the Pauli principle and entirely a quantum mechanical effect in the many-electron system. The reduced electrostatic Coulomb repulsion between electrons of the same spin with respect to the antiparallel spin alignment is called exchange energy. This interpretation gives the somewhat abstract concept of exchange interaction $I$ a more tangible meaning. It is now clear that whenever the increase in kinetic energy is overcompensated by a gain in electrostatic energy, the system will spontaneously develop a stable state with a number of aligned spins, i.e., a magnetically ordered ground state. It becomes also intuitively clear why the density of states at the Fermi level is important in this process. A high value of $D(E_F)$ means that a large number of occupied and empty states in the vicinity of the Fermi level are available for this "spin flip" process. Therefore each spin-flip requires only a small amount of energy. If $D(E_F)$ is small the available states directly at the Fermi level will be quickly occupied and the energy needed for the parallel alignment of further electrons will strongly increase. Given the same total change in potential energy, a system with a high density of states at the Fermi level will therefore allow a much higher number of parallel spins than a system with a low value of $D(E_F)$. In fact, quantitative calculations indicate that the density of states is likely to be the most important parameter in the Stoner criterion whereas the value of the exchange interaction is very similar for different transitions metals ($I \sim 1$ eV).

In the following we will inspect some of the results from realistic band structure calculations for the example of Ni metal. Contemporary approaches determine the electronic structure in the framework of density functional theory (Kohn and Sham, 1965; Freeman and Wu, 1991). The mean-field approximation enters the formalism by the so-called local spin density approximation (LSDA), in which many-particle interactions are expressed in terms of the above exchange–correlation potential $V_{xc}$. The non local part in $V_{xc}(\mathbf{r})$ is approximated by a local potential, often derived from the exchange and correlation interactions in a homogeneous electron gas of equal density (Barth and Hedin, 1972). This is done in order to obtain equivalent single particle equations which can then be solved self-consistently. The resulting energy eigenvalues, in a strict sense, are not identical with the single particle energies which form the band structure. In fact, only the total energy calculated for the system can be directly compared to experimental values. Experience shows, however, that the energy eigenvalues calculated within the LSDA agree surprisingly well with experimental findings. This agreement is the only rationale that relates the calculated electronic states to the experiment. Figure 9.1 shows the density of states for paramagnetic nickel disregarding spin–orbit coupling effects (Moruzzi et al., 1978). We see the flat sp-like contribution at the bottom of the conduction band corresponding to almost free-electron-like (parabolic) bands. The pronounced structures are due to flat weakly dispers-

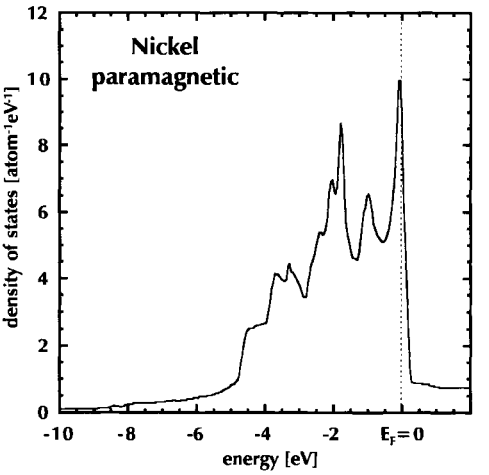


Fig. 9.1. Density of states (DOS) for paramagnetic Ni metal. (Taken from Moruzzi et al., 1978.)

ing bands of predominantly d-like electronic character. Important for the fulfillment of the Stoner criterion is the high density of states at the Fermi level. It is the reason for the ferromagnetically ordered ground state in Ni. The distinct problem in the spin-split calculations is the choice of a proper form for $V_{xc}^{\uparrow\downarrow}$. Again nickel may serve as an instructive example. For a considerable period of time experiment and theory differed by about a factor of two in the value for the exchange induced band splitting. This discrepancy was finally removed by the choice of a modified exchange–correlation potential (Eckardt and Fritsche, 1987). The spin-split densities of states for spin-up and spin-down electrons obtained from this calculation are reproduced in Fig. 9.2. It is obvious that the gross features in both spin channels are very similar, but shifted with respect to each other on the energy scale. The energy shift is most pronounced in the vicinity of $E_F$, i.e., for the d-like electronic states, and considerably smaller at the bottom of the conduction band. At a closer look the fine structure in the DOS curves appears different for both spin states. Since the Fermi energy must have the same value for spin-up and spin-down states, there are more occupied spin-up than spin-down states. This is, of course, the origin of the magnetic moment according to Eq. (9.1). It also explains the convention to designate spin-up and spin-down states as majority and minority states, respectively. The spin-split DOS curves also reflect another peculiarity of nickel, namely the almost complete occupation of the majority spin states. Only the minority spin states exhibit a significant contribution above $E_F$. This means that the magnetic moment in nickel is essentially determined by the unoccupied density of states, or, as it is sometimes said, by the "holes" in the conduction band. Such a magnetic system is often referred to as saturated or "strong" ferromagnet. In this sense also cobalt is a strong ferromagnet, in contrast to the weak ferromagnet iron.

The exchange induced splitting of the electronic states in a ferromagnet can also be understood from a different point of view, invoking the symmetry properties of the system in the framework of group theory. This approach is of considerable advantage in the understanding of the electronic band structure, and we will therefore go into some details.

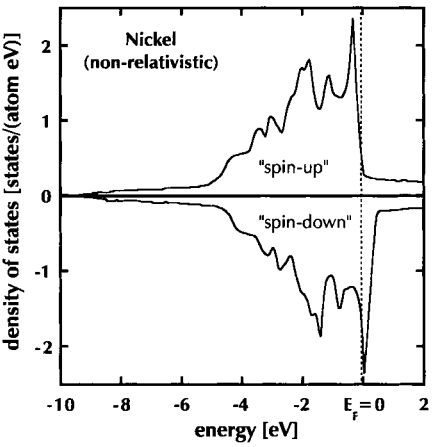


Fig. 9.2. Spin-split density of states calculated for ferromagnetic Ni without spin–orbit coupling. Taken from Eckardt and Fritsche (1987).

The starting point for this approach is the fact that all spatial symmetries of an electronic system are reflected in the Hamiltonian $H$ by virtue of the crystal potential $V(\mathbf{r})$

$$H\varphi(\mathbf{r}) = \left(-\frac{\hbar^2}{2m}\nabla^2 + V(\mathbf{r})\right)\varphi(\mathbf{r}) = E\varphi(\mathbf{r}). \tag{9.6}$$

In a paramagnetic crystal, for example, which could be described by a Hamiltonian like in Eq. (9.6) we have a set of spatial symmetry operations which form a group and describe the behavior of the crystal under rotations, reflections, translations and inversion. The same symmetry operations apply to the potential $V(\mathbf{r})$. For two reasons, this symmetry-based approach is very useful. First, it can be employed to reduce the efforts in the diagonalization of Eq. (9.6) by limiting the set of possible eigenfunctions. Secondly, it permits a labeling of the individual electronic states according to the so-called irreducible representations of this particular group. These labels are usually applied to distinguish the various bands in the electronic structure of a solid. In the standard notation they take the form $A_i$, in which A denotes a high symmetry point or direction in the bulk Brillouin zone, and the index numbers the appropriate irreducible representation. With respect to the discussion of band structures further below, we will examine the example of a cubic (001) axis, which is referred to as the $\Delta$-line, i.e., the line interconnecting the center of the BZ, $\Gamma$, with the high symmetry point X. Along this line we find four different irreducible representations, namely $\Delta_1$, $\Delta_2$, $\Delta_{2'}$, $\Delta_5$. These are used to distinguish the bands along this symmetry line. By means of compatibility relations, one may connect these representations with their atomic counterparts. One thus finds that a $\Delta_1$ is constructed of wave functions with predominantly s-like atomic character, whereas a $\Delta_5$ band contains mostly d-like atomic states. In order to avoid unnecessary confusion, we would like to discourage the use of atomic symmetry notations in the context of electronic bands in favor of the appropriate crystal related notation. This is, however, not consistently carried out in the available literature. In particular in

connection with LCAO band structure calculations one is often tempted to use the atomic designations.

Another symmetry property of a paramagnetic crystal, the time-reversal symmetry, is not as obvious, and therefore often not explicitly mentioned. But it is the combination of spatial inversion and time-reversal symmetry that leads to some fundamental requirements for the energy eigenstates in paramagnetic materials:

$$E(\mathbf{k}) = E(-\mathbf{k}), \tag{9.7}$$

$$E(\mathbf{k}, \uparrow) = E(\mathbf{k}, \downarrow). \tag{9.8}$$

Equation (9.8) describes the 2-fold spin-degeneracy in a paramagnet and is the direct consequence of the system being unaffected by time-reversal. This changes, as soon as the crystal is subject to magnetic interactions. The appropriate Hamiltonian will then take a form

$$(H_0 + H_B + H_{EX})\varphi(\mathbf{r}, \sigma) = E\varphi(\mathbf{r}, \sigma) \tag{9.9}$$

with $H_0$ containing Eq. (9.6), $H_B$ describing the interaction of the electrons with an external magnetic field, and $H_{EX}$ denoting the exchange interaction. The wave functions $\varphi(\mathbf{r}, \sigma)$ in (9.9) depend not only on the coordinates in real space $\mathbf{r}$, but also explicitly on the spin coordinate $\sigma$. They are therefore written as two-component "spinors". In the presence of a magnetic field, time reversal is no longer a symmetry operation of the electronic system, causing the symmetry of the respective Hamiltonian to be lowered. In almost all cases, the introduction of extra symmetry-reducing interactions in the Hamiltonian causes a splitting of formerly degenerate electronic states. The magnetic field acts only on the spins, but not on the spatial parts of the wave functions, by introducing a spin quantization axis. This quantization axis breaks the rotational symmetry in spin space, and the spin degeneracy is lifted. This is reflected in the band structure by the observation that minority and majority bands appear to be completely independent from each other. In other words, they form two independent sets of bands, which do not interact (as long as we stay in the non-relativistic limit). That is easily recognized by the fact that bands of the same spatial symmetry, but opposite spin character are allowed to cross. There is no formation of an anticrossing regime indicative of a hybridization between the bands. This can be seen very clearly in a calculated band structure of nickel, the (100) or $\Delta$-direction of which is reproduced in Fig. 9.3. Majority and minority spin bands are plotted on top of each other and labeled according to the group theoretical scheme mentioned above. The energy shift between spin-up and spin-down bands of the same symmetry character, the exchange splitting, is quite obvious. The value of the exchange splitting is not a constant, but depends on the $\mathbf{k}$ vector of the electrons, and also on the orbital character, i.e., the symmetry character of the specific electronic state. The energy splitting $\Delta E_{xc}(\mathbf{k})$ is much larger for d-states, than for sp-type bands. But since we are still within the Stoner model, even in the present case $\Delta E_{xc}(\mathbf{k})$ is directly connected to the average magnetization $M$, only in a wave vector and symmetry dependent way. We also note that the independence of spatial and spin parts of the electronic wave functions are furthermore illustrated by the fact that the "magnetic"

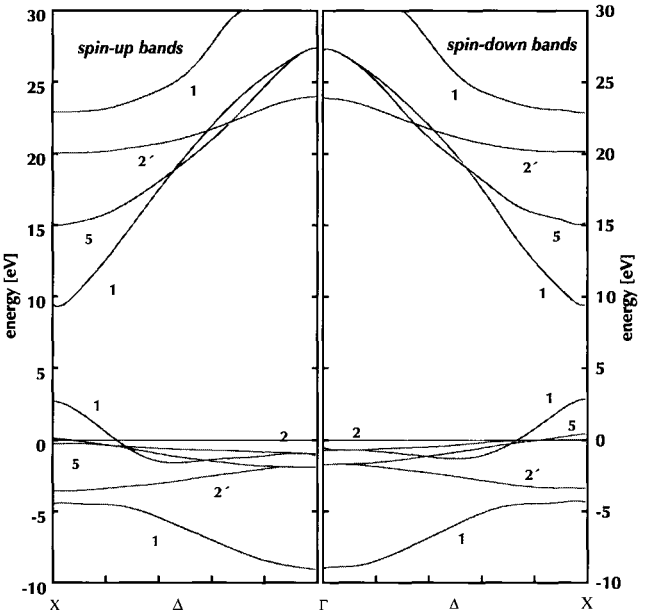


Fig. 9.3. Spin-split band structure of ferromagnetic Ni along the (001) or Δ direction without spin–orbit coupling (taken from Eckardt and Fritsche, 1987). The bands are labeled according to their single-group symmetry representation.

quantization axis may assume any arbitrary orientation in real space without affecting the exchange splitting or the band structure.

Up to this point we have implicitly assumed that the only spin-dependent mechanism in the electronic system arises from the exchange interaction. Although this approximation suffices to explain the presence of a spin-split band structure and the basic concept of itinerant magnetism, it does not yet give us the complete picture. Just as in the atomic case, there is spin–orbit coupling as a second spin-dependent interaction which affects the electronic states. Spin–orbit coupling is very important for the phenomenon of magnetic anisotropies. We will come back to this aspect in more detail in Subsection 9.2.1.3. Here we are mainly interested in the changes of the electronic structure. Formally we have to add another term $H_{SO}$ which includes the effect of spin–orbit coupling to the Hamiltonian in Eq. (9.9)

$$(H_0 + H_B + H_{EX} + H_{SO})\varphi(\mathbf{r}, \sigma) = E\varphi(\mathbf{r}, \sigma), \tag{9.10a}$$

$$(H_0 + H_{SO})\varphi(\mathbf{r}, \sigma) = E\varphi(\mathbf{r}, \sigma) \tag{9.10b}$$

with Eq. (9.10b) describing the nonmagnetic case. For the sake of clarity, we will consider the nonmagnetic electron system first. This is not only an academic exercise, because the effects due to spin–orbit coupling in non-magnetic materials can be experimentally verified by means of spin-polarized electron spectroscopies (Schneider and Kirschner, 1995). Using the symmetry-based approach, we can already qualitatively predict the influence of

the additional term $H_{SO}$. It couples the spatial and the spin parts of the electronic wave functions, $\mathbf{r}$ and $\sigma$, leaving them no longer as independent variables. As the most important consequence, the coupling removes the rotational symmetry in spin-space, because the spatial parts of the wave functions have preferred directions in real space. The symmetry properties of the electronic system are therefore lowered and we have to expect a splitting of degenerate states and additional electronic hybridizations. For the purpose of illustration we turn again to the $\Delta$ direction in an fcc crystal. Figure 9.4a reproduces schematically a set of electronic bands along $\Delta$ which are similar to the situation observed, for example, in copper. For simplicity, only the three uppermost bands of the type $\Delta_1$, $\Delta_2$, and $\Delta_5$ are shown. The band structure does not yet contain spin–orbit coupling and thus refers to the situation described by Eq. (9.6). The energy splitting induced by spin–orbit coupling is schematically depicted in Fig. 9.4b. Along (001) only the band of $\Delta_5$ spatial symmetry is two-fold degenerate and may therefore split. This degeneracy is of spatial origin and should not be confused with the spin or Kramers degeneracy. In addition, the symmetry of each band changes from the purely spatial (non-relativistic) one to the relativistic one. Because the symmetry of the spin–orbit coupled electronic system is lower, the number of irreducible representations is smaller, too. There are only two relativistic representations, namely $\Delta_6$ and $\Delta_7$, in contrast to the four non-relativistic ones ($\Delta_1$, $\Delta_2$, $\Delta_{2'}$, $\Delta_5$). $\Delta_6$ and $\Delta_7$ are often called double-group representations. The correspondence between the single-group and double-group representations is indicated in Fig. 9.4b, too. Note that the label of the representation includes the spatial symmetry type as a superscript and the double-group symmetry as a subscript. Because of the lower number of relativistic representations and the higher total number of bands, there are crossing points between bands of the same symmetry, for instance, $\Delta_6$. These crossing points, however, are not allowed and avoiding them leads to extended hybridization regions. The band structure drawn in Fig. 9.4b therefore does not correspond to any realistic case and is only shown for pedagogical purposes. The bands depicted in Fig. 9.4c finally include the hybridization regions and approximately describe the relativistic band structure found in a 3-d metal like copper. The electronic bands marked by heavy lines correspond to states which are probed in a photoemission experiment with the highest possible experimental symmetry (normal incidence, normal emission) as a consequence of non-relativistic and relativistic dipole selection rules (see Section 9.5). There are two anti-crossing regions of the type $\{\Delta_6^1 \mid \Delta_6^5\}$, one of which is responsible for a rather large band gap midway from $\Gamma$ to X, and a third hybridization zone of the type $\{\Delta_7^2 \mid \Delta_7^5\}$. Looking back to Fig. 9.4a it is obvious that already in paramagnetic crystals spin–orbit coupling leads to an increased complexity of the electronic structure.

We can use the same arguments developed above to understand the situation in a ferromagnetic material with a spin-split electronic structure. A ferromagnet is characterized by an internal spin quantization axis given by its magnetization $\mathbf{M}$. Coupled to the spatial part of the wave functions, the spin quantization axis can no longer point into arbitrary directions. Instead it assumes preferred directions in space, which may coincide with particular crystalline axes. This behavior is known as "magneto-crystalline" anisotropy, and we will come back to it below. Staying for the moment with the (001) surface, we are more concerned with the changes in the band structure. In analogy to the non-magnetic case, the reduced symmetry upon inclusion of spin–orbit coupling splits each $\Delta_5$ band of minority and majority spin character into two states. The symmetry of the resulting bands

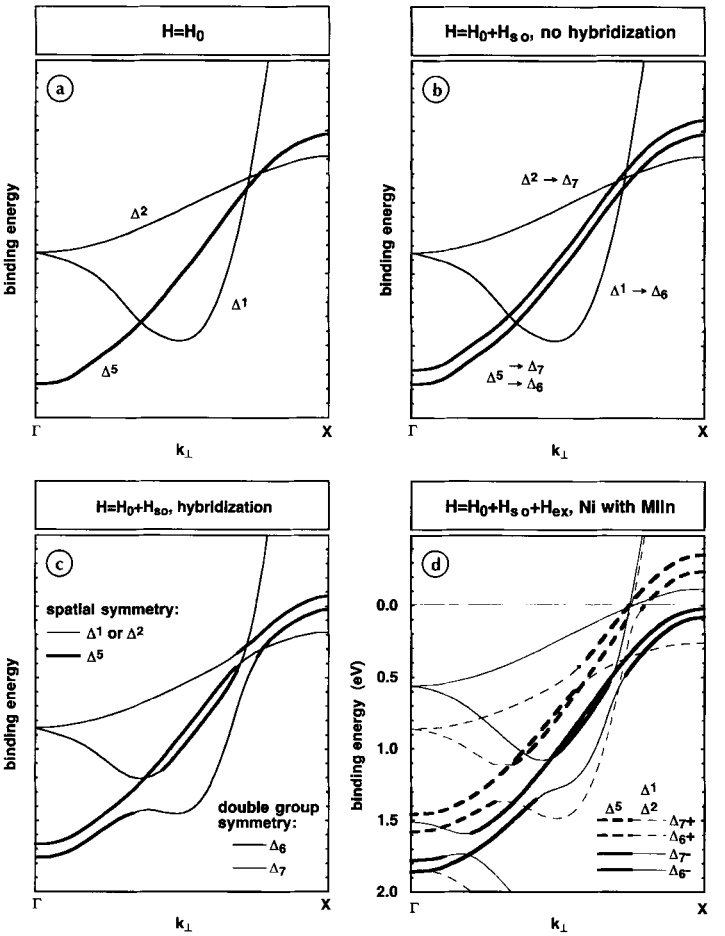


Fig. 9.4. Evolution of the electronic structure of an fcc d-band metal along the Δ direction under the influence of spin-dependent interactions: (a) without spin-dependent interactions; (b) band splitting due to a change in symmetry character induced by the spin–orbit coupling; (c) formation of anticrossing points due to hybridization of bands of the same relativistic symmetry (the electronic bands shown are adapted from a calculation for Cu by Eckardt et al., 1984); (d) result of a realistic band structure calculation for Ni including spin–orbit interaction and exchange coupling on an equal footing (after Scheunemann et al., 1994). For explanation of the symmetry labels see text. The heavy lined portions of the bands are those visible in an normal emission, normal incidence photoemission experiment.

can be adequately described by magnetic double-group representations or magnetic co-representations (Falicov and Ruvalds, 1968). We will adopt another notation proposed by Henk et al. (1996). For reasons of simplicity, we assume the magnetization being oriented along the surface normal. In this case the rotational symmetry with respect to the surface normal is preserved, but mirror operations are destroyed by the presence of the vector **M**. The spatial symmetry is thus reduced from $C_{4v}$ to $C_4$, and the relativistic symmetries can still be classified by the double-group representations $\Delta_6$ and $\Delta_7$. The spin-splitting is tak-

ing into account by defining the representations $\Delta_n^+$ and $\Delta_n^-$ which distinguish different spin characters. For the $\Delta_5$ bands, we therefore end up with the following scheme:

$$\Delta_5 \Rightarrow \left\{ \begin{array}{l} \xrightarrow{\text{exchange}} \left\{ \begin{array}{l} \Delta_5^{\uparrow} \\ \Delta_5^{\downarrow} \end{array} \right\} \\ \xrightarrow{\text{spin–orbit}} \left\{ \begin{array}{l} \Delta_6^5 \\ \Delta_7^5 \end{array} \right\} \end{array} \right\} \Rightarrow \left\{ \begin{array}{l} \Delta_6^+ \\ \Delta_6^- \\ \Delta_7^+ \\ \Delta_7^- \end{array} \right\}. \tag{9.11}$$

This notation makes a clear connection between systems with and without exchange induced splittings, but has also a certain disadvantage. Note that although the superscripts (+) and (−) distinguish between spin-up and spin-down states, the assignment of a superscript to a specific spin character is determined by the spatial symmetries. This is caused by the fact that in a relativistic ferromagnet the spin is no longer conserved. The total angular momentum replaces the spin as a good quantum number. This is an important point when the question of electronic hybridization is encountered, because a hybridization between spin-up and spin-down bands is no longer forbidden. This brings us to an important property of a relativistic ferromagnet: even bands of opposite spin character may hybridize. We will thus find regions along a band where the expectation value of $\sigma$ along $\mathbf{M}$ is no longer well-defined and can even assume values close to zero. It must be emphasized that under these circumstances the concept of exchange splitting becomes somewhat questionable, as it is based on pure spin states.

A short comment shall be given on our approach by using Hamiltonians. Equation (9.10a) which describes a Hamiltonian acting on two-component spinors is obtained by starting from a simple Schrödinger equation, that is from non-relativistic quantum mechanics, and adding terms which describe relativistic effects, such as spin–orbit coupling and the electron spin itself. A more rigorous but theoretically much more involved way of treating the electron spin may start from relativistic quantum mechanics, which describes the motion of electrons in an electromagnetic field via the Dirac equation (Dirac, 1927)

$$\left[i\hbar\partial_t + e\Phi - c\underline{\underline{\alpha}} \cdot \left(-i\hbar\vec{\nabla} + e/c \cdot \mathbf{A}\right) - \underline{\underline{\beta}}mc^2\right]\Psi = 0 \tag{9.12}$$

with the vector potential $\mathbf{A}$ and the scalar potential $\Phi$. $\underline{\underline{\alpha}} = (\alpha_x, \alpha_y, \alpha_z)$ and $\underline{\underline{\beta}}$ are ($4 \times 4$) matrices, which act on the four-component spinor $\Psi$. Equation (9.12) describes the relativistic behavior of spin $s = 1/2$ particles. In case that the kinetic and potential energies of the particles are both small compared to $mc^2$, (9.12) may be discussed in the non-relativistic limit. In this situation only two components of the spinor $\Psi$ are significant and we end up with the Pauli equation for an electron with spin (Kessler, 1985)

$$\Bigg(\underbrace{\frac{1}{2m}\left(\mathbf{p} - \frac{e}{c}\mathbf{A}\right)^2 + e\Phi}_{H_0} \underbrace{-e\frac{e\hbar}{2mc}\boldsymbol{\sigma} \cdot \mathbf{B}}_{H_B} \underbrace{+\mathrm{i}\frac{e\hbar}{4m^2c^2}\mathbf{E} \cdot \mathbf{p}}_{H_D} \underbrace{-\frac{e\hbar}{4m^2c^2}\boldsymbol{\sigma} \cdot (\mathbf{E} \times \mathbf{p})}_{H_{SO}}\Bigg)\varphi = W\varphi. \tag{9.13}$$

Note that this expression is similar to Eq. (9.11), except for two terms. $H_{EX}$ is missing, instead a term $H_D$ appears. $H_D$ denotes a relativistic energy correction, the so-called Darwin term. The Darwin term renormalizes the energy scale, but does not change the symmetry properties of the electronic system. It has therefore been omitted in Eq. (9.11). The term $H_{EX}$ is yet missing because (9.12), (9.13) describe only a single-electron system, with $\Psi$ and $\varphi$ being four- and two-component one-electron spinors, respectively. In order to include the exchange interaction, it is necessary to derive the Dirac equation for a many electron system. This is done within a relativistic version of the density functional theory. Only in this case which may be called a fully relativistic approach, spin–orbit coupling and exchange interaction can be treated on an equal footing. In analogy to the nonrelativistic case, the relativistic density functional formalism leads to a set of relativistic Kohn–Sham equations with a suitable expression for the exchange–correlation potential (Gay and Richter, 1994).

In the following, we will use results from a realistic band structure calculation in order to illustrate band splitting and hybridization phenomena in ferromagnets discussed above. For this purpose, again the band structure for Nickel along the $\Delta$ direction is depicted in Fig. 9.4d. The bands have been calculated within a Dirac scheme for a magnetization oriented parallel to the surface normal, that is, along $\Delta$. Despite the doubled number of bands, we still find similarities to Fig. 9.4c. This is not surprising as in analogy to the nonmagnetic case hybridizations are expected to occur at crossing points of the type $\{\Delta_6^1 \mid \Delta_6^5\}$ and $\{\Delta_7^2 \mid \Delta_7^5\}$. The hybridization takes place between bands of both spin characters leading to a significant reduction of the spin expectation value in the hybridization gap. In the extreme case, the expectation value of $\boldsymbol{\sigma}$ may indeed vanish at the hybridization point. It should be noted, however, that hybridization occurs only between bands belonging to either double-group symmetry $\Delta_6$ or $\Delta_7$. A band mixing between these two double-group representations is not allowed, because the magnetization vector being parallel to the low-index direction still ensures a relatively high symmetry of the system.

A further peculiarity of a relativistic spin-polarized electronic system can also be deduced from symmetry considerations. Because of the coupling between orbital and spin parts of the electronic wave functions, the direction of the magnetization is tied to specific crystalline axes. As a consequence, previously equivalent axes differ in their symmetry properties. In other words, directions parallel and perpendicular to the magnetization are characterized by different electronic structures. As mentioned above, for a magnetization pointing along the surface normal $\langle 001 \rangle$, the four-fold rotational symmetry is still preserved. The magnetization $\mathbf{M}$ is an axial vector and any mirror operation on a plane containing $\mathbf{M}$ will change $\mathbf{M} \rightarrow -\mathbf{M}$. Under these circumstances, we have the same set of spatial symmetries as in a paramagnet or non-relativistic ferromagnet, being the reason for our use of the double-group labels $\Delta_6$ and $\Delta_7$. This changes if the magnetization is oriented in-plane, say along $\langle 010 \rangle$, and thus perpendicular to the direction of observation. The rotational symmetry is broken and reduced to a 2-fold axis if combined with time reversal. We also have two mirror-planes containing the surface normal. The first one contains the magnetization and the mirror operation must be followed by a time reversal operation in order to achieve spatial mirror symmetry. The second one is perpendicular to $\mathbf{M}$ and therefore remains a "true" mirror-plane. From the viewpoint of symmetry the in-plane magnetized (001) surface effectively behaves like a (011) system. In fact, group-theoretical considera-

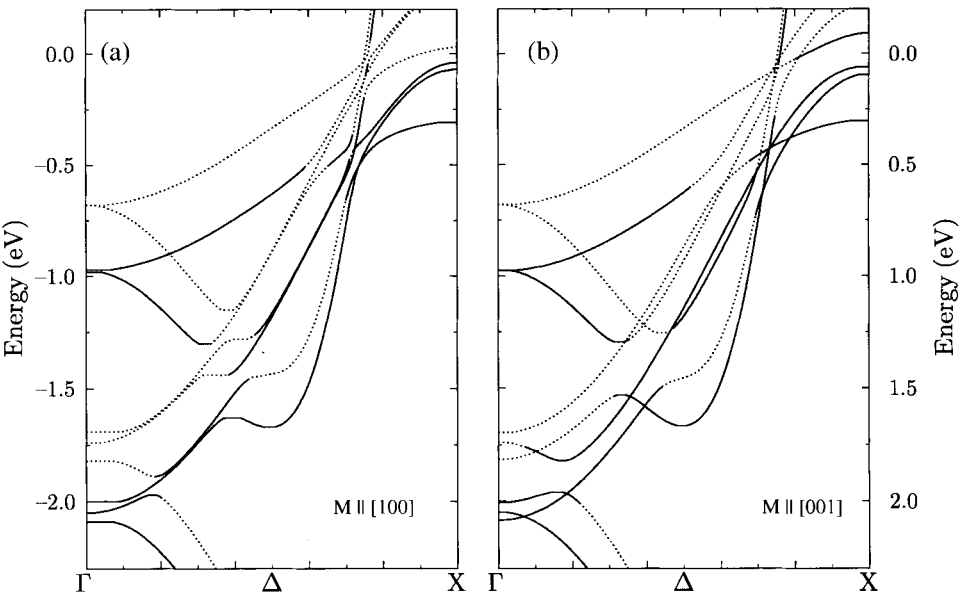


Fig. 9.5. Relativistic band structure of Ni metal along the [001] direction for a spatial orientation of the magnetization vector **M**, (a) within the surface along the [100] axis, and (b) along the surface normal (Henk, private communication).

tions show the electronic states to be classified according to the irreducible representations along the (011) axis or $\Sigma$ direction. Because of the lower spatial symmetry, the $\Sigma$ direction has four non-relativistic irreducible representations ($\Sigma_1$, $\Sigma_2$, $\Sigma_3$, $\Sigma_4$) but only one double-group representation $\Sigma_5$. Already in paramagnets a strong intermixing of bands along the (011) direction is therefore observed (Venus et al., 1986). The same can be expected for a ferromagnet with a (001) surface and in-plane orientation of the magnetization vector, $\mathbf{M} \perp \mathbf{n}$. In this case we have two representations $\Sigma_5^+$ and $\Sigma_5^-$, corresponding to spin-up and spin-down states. A fully relativistic calculation for an in-plane magnetized Ni(001) surface is shown in Fig. 9.5a, side-by-side to the case $\mathbf{M} \parallel \mathbf{n}$ for the same surface. Clearly the two band structures are non-equivalent and reflect the different symmetries in the electron system. The orientation of **M** determines the details like the magnitude of energy splittings and the degree of electronic hybridization. A closer inspection of Fig. 9.5a shows only very few remaining crossing points, but a large number of hybridization gaps, in contrast to the findings in Fig. 9.5b. This is exactly what we expect for a system of lower symmetry.

The results of the symmetry-based approach already point towards an intimate interdependence between electronic structure and the so-called magneto-crystalline anisotropy (MCA). The magneto-crystalline anisotropy describes the finding that the spontaneous magnetization at $T = 0$ points towards a certain crystalline direction. Rotating the magnetization away from this direction costs energy. Phenomenologically, the energy term of the magnetization reorientation can be described as a function of the directional cosines, i.e., $E = E(\cos\theta, \cos\phi)$, with $\theta$ and $\phi$ being the polar and azimuthal angles in a crystal-

based coordinate system. We will come to a more detailed discussion of this phenomenon in Section 9.2.3. Here we are only interested in the role of the electronic structure. The spin–orbit coupling being a possible origin for magnetic anisotropies was already suggested in the fifties (Van Vleck, 1937). Subsequent theoretical analyses have shown that there should indeed be a small variation of the total energy of the system with the orientation of the magnetization. The fact that the magnetization orients itself such that the total energy is minimized explains the existence of a magnetocrystalline anisotropy. A reliable theoretical prediction, however, is hampered by the extremely small anisotropy related changes ($\sim 10^{-6}$ eV/atom) on top of a large total energy ($\sim 10^{6}$ eV). This is far from being a non-trivial problem and still not completely solved today.

Turning to realistic *ab initio* band structure calculations, the scenario of a relativistic ferromagnet requires exchange interaction and spin–orbit coupling to be treated on an equal footing. This can only be done in the framework of the Dirac theory, leading to a so-called fully relativistic formalism. It must not be confused with so-called scalar-relativistic approaches, which generally include relativistic corrections like the Darwin or mass-velocity term. These corrections lead only to a re-normalization of the energy scale, without changing the hybridization and spin character of the electronic states. An intermediate step represents scalar-relativistic calculation which include spin–orbit coupling as a perturbation, and at least qualitatively show the effects of band splitting and hybridization. On the highest level of sophistication, the starting point for the calculation is no longer a Schrödinger or Pauli equation with two-component spinors, but the Dirac equation with the full four-component spinors. Thereby spin-dependent interactions are included from the beginning, and none of them is treated as a perturbation. The combined influence of spin–orbit and exchange interaction on the electronic bands along the (001) direction in Ni is shown in Fig. 9.4 for two orthogonal directions of magnetization. A comparison to the scalar-relativistic results in Fig. 9.3 clearly emphasizes the increased complexity in the bands between the Fermi level and $-2$ eV binding energy. There are more hybridization points and a higher number of bands in particular at the $\Gamma$ point. These findings are congruent with the conclusions drawn from our symmetry considerations. Whereas Fig. 9.4a shows the results for a high symmetry direction $\Delta$ along the magnetization **M**, Fig. 9.4b gives the bands along a high symmetry direction $\Delta$ perpendicular to **M**. We recall that in the absence of spin–orbit coupling the two electronic structures should be identical. Yet we clearly see differences in the details of the bands. Hybridization gaps and band splittings are changed, additional band crossings appear, and a different spin mixing is found at many hybridization points.

Whether or not the above complexity of the band structure can be disentangled by the experiment remains to be seen. New experimental methods such as photoelectron spectroscopies exploiting magneto-dichroic phenomena might hold the key to the solution of this task.

*9.2.1.2. A semi-infinite magnetic crystal*

In order to see the changes introduced by the presence of a surface, it is useful to recall some basic results about the electronic structure of solids emerging from the tight-binding approximation (Ashcroft and Mermin, 1976). If individual atoms are joined together to form a solid material, the atomic wave functions overlap and split in energy. In a solid

material this situation leads to the formation of energy bands. The closer the atoms or the higher the number of nearest neighbors, the higher is the spatial overlap of the electronic wave functions and the wider the resultant energy band. During this process, bands made up from s-, p- or d-orbitals may partly occupy the same energy eigenvalues and thus cause level crossings. These level crossings lead to hybridizations between bands of different orbital character. In the case of transition metals the main contribution to the density of states comes from the d-like electronic states, since these form relatively flat bands. We focus our attention onto the d-band width $W_d$ and the hybridization among the d-electrons (d–d) and with the sp-electrons (sp–d).

The presence of the surface imposes a boundary condition on the electronic system. In addition to the changes in the bulk-truncated electronic states, this causes the development of new electronic states which are localized at the surface. For nonmagnetic materials this case is thoroughly treated throughout this book. We therefore only list some properties of these surface electronic states. The corresponding wave functions can travel parallel to the surface, which means that surface states have a dispersion with $\mathbf{k}_\parallel$, the component of the electron wave vector $\mathbf{k}$ parallel to the surface. We may distinguish two cases of surface states. First, surface electronic states which exist entirely in the band gaps (either an absolute band gap or a gap between bands of a certain symmetry) of the bulk band structure. These states are usually referred to as surface states. Secondly, states which overlap with bulk electronic states and are usually termed surface resonances. These labels have to be used with some caution, though, as the character of the electronic states may be changing throughout reciprocal space. Depending on its dispersion, an electronic state can be a surface state at one point of the Brillouin zone, but may become a surface resonance at other $\mathbf{k}$-points.

The above surface-induced states are – in a simplistic view – located *within* the crystal (for the moment we neglect the spill-out of the electron wave functions and the charge density into the vacuum and assume the surface to be a sharp boundary). Now consider a free electron in front of the (conductive) surface. The electrostatic field of this electron has to fulfill well-defined boundary conditions at the surface which lead to the build-up of an image charge in the interior of the crystal (Jackson, 1972). If there are now bulk states available to which the electron can couple to, the attractive Coulomb interaction of the free electron with its own image charge results in the formation of a potential well in front of the surface. The potential well may contain bound electronic states, the so-called image potential states (McRae, 1979). An electron occupying one of these image potential states therefore has its wave function localized *outside* the crystal. In order to distinguish image potential states from the surface electronic states within the crystal, the latter are sometimes referred to as crystal-induced surface states.

In ferromagnets, both kinds of surface states are spin-split by the exchange interaction, just as their bulk counterparts. This means that we will find majority and minority spin type surface states. In particular surface states in the vicinity of the Fermi level can have a profound effect on the surface magnetism. Recalling the essence of the Stoner criterion Eq. (9.5), the existence and strength of the itinerant ferromagnetism is determined by the density of states at the Fermi level. Changes in $D^{\uparrow\downarrow}(E_F)$ due to surface states can therefore sensitively influence the magnetic properties. In particular, an increase of $D^{\uparrow\downarrow}(E_F)$ due to

Table 9.1
Coordination numbers $N$ and calculated spin magnetic moments for a free Fe atom, a free standing Fe monolayer (Fu et al., 1985), a bcc-Fe(100) and Fe(110) surface, and Fe bulk (Fu et al., 1985)

| | $\mu_{\text{atom}}$ | $\mu_{\text{mono}}$ | $\mu_{\text{S}}^{(100)}$ | $\mu_{\text{S}}^{(110)}$ | $\mu_{\text{bulk}}$ |
|---|---|---|---|---|---|
| $\mu_{\text{B}}$/atom | 4 | 3.2 | 2.88 | 2.43 | 2.15 |
| $N$ | – | 4 | 4 | 6 | 8 |

surface states can enhance a tendency towards ferromagnetism and increase the magnetic moment of the surface atoms.

In comparison to the bulk crystalline structure, the number of nearest neighbors is smaller at the surface. The reduced coordination number must therefore lead to a reduced band width $W_{\text{d}}$. In a zeroth order approximation the density of states may be assumed inversely proportional to the d-band width

$$D(E_{\text{F}}) \sim \frac{1}{W_{\text{d}}}. \tag{9.14}$$

Recalling the energy balance argument from the Stoner–Wohlfarth model, we see that the smaller the value of $W_{\text{d}}$ (and thus, the higher the paramagnetic density of states at the Fermi level), the smaller is the energy required for the transition to the ferromagnetic state. In other words, a small value of $W_{\text{d}}$ favors the existence of ferromagnetism. This leads us to the first important conclusion: since the reduced coordination number at the surface yields a narrowing of $W_{\text{d}}$, one should expect an *enhancement* of the magnetism (Mathon, 1988a). In terms of an experimentally accessible quantity, this means that the magnetic moment, $\mu_{\text{S}}(T = 0\ \text{K})$ in the surface layer will be enhanced with respect to the bulk value $\mu_{\text{Bulk}}(T = 0\ \text{K})$. Moreover, since the coordination number depends on the atomic arrangement at the surface, $\mu_{\text{S}}(T = 0\ \text{K})$ should also depend on the crystallographic orientation of the surface. This is precisely, what is found in *ab initio* calculations for iron. The (100) surface in bcc-Fe is more open than the (110) surface, hence, the magnetic moment is higher (Table 9.1). According to the above considerations, a crystal may be, in an extreme case, non-magnetic in the bulk, but ferromagnetic at the surface. This last hypothesis still lacks experimental confirmation. There is, however, some indication from recent experiments that ultrathin films of Ru on graphite may indeed develop a ferromagnetic order (Pfandzelter et al., 1995).

The above model describes the situation reasonably well, as long as both the majority and minority spin d-bands are not completely filled. This is strictly true only for iron. For Ni and also Co, however, this approach is no longer valid. The reason is that the majority spin d-bands in both materials are completely filled, and the magnetism is practically determined by the unoccupied minority states ("holes"). A reduction of the d-band width and the associated shift of the Fermi energy will therefore decrease the number of holes, and according to Eq. (9.14) *reduce* the magnetic moment. This apparent discrepancy comes from the fact that our picture above considered – for reasons of simplicity – only the d-like

contribution to the bulk density of states, and implied the number of d-electrons to be constant. In reality, the situation is more complicated, in particular, because the number of d-electrons varies with the local environment of the atom. This is mainly due to the following effects. First, at the surface we have surface state contributions to the density of states. A higher density of states – as compared to the bulk – at the right position on the energy scale can result in an enhanced moment, otherwise it might even cause a reduction of the moment. Secondly, the band narrowing at the surface causes a transfer of electrons from sp- to d-states, and at the same time a sp–d dehybridization. These two mechanisms counteract each other, but yield a net increase (decrease) of the number of majority (minority) d-electrons in Ni. According to Eq. (9.14) this results in a higher magnetic moment.

On the basis of these qualitative arguments given above, we can conclude that we should expect increased magnetic moments at the surface of itinerant ferromagnets. *Ab initio* calculations which have been carried out in recent years indeed support this conclusion. There is a pronounced trend in the size of the magnetic moment upon the effective coordination number (see Table 9.1). The above considerations give only a very rudimentary picture. In reality, the situation is much more complicated. As became apparent in the case of Ni, it is not only the d-band width, which determines the magnetic phenomena, but rather details in the density of states in the vicinity of the Fermi level. These details depend strongly on the real structure of the surface, for example, the presence of surface relaxations or reconstructions.

Some remarks shall be made on the available calculations. The biggest problem encountered in the theoretical description of a semi-infinite electronic system is the loss of translational symmetry normal to the surface and the boundary conditions imposed by the surface. The complexity of this case makes it virtually impossible to calculate a true semi-infinite system. One had therefore to look for approximations to this situation. A very successful approach is the so-called slab geometry: the semi-infinite crystal is "replaced" by a thin slab of several atomic layers with vacuum on either side (Wimmer et al., 1981; Weinert et al., 1982). This way one creates a second surface but gains reflection symmetry at the center plane of the slab, if both surfaces are made equal. The essential point is to make the slab thick enough, in order to separate the two surfaces and minimize "crosstalk" between the surface electronic states. Because of the short screening lengths in transition metals, slabs of 5–9 atomic layers are considered as sufficient to reproduce the same electronic structure for the central layer as is found for the entire crystal in bulk calculations. This screening effect is apparent in Fig. 9.6 which shows the layer-resolved density of states for the individual planes in a 5-layer slab. The differences in both the majority and minority spin DOS are much less pronounced between the second and central layer than between the surface and the neighboring layers. The comparison also shows the narrowing of the surface DOS for both spin channels, consistent with a narrowing of the band width $W_d$.

A similar projection onto planes has to be done with the individual electronic states in order to separate surface states from "bulk" states. We note that the states related to the slab bulk may also be termed as "quantum-well states", since the slab with vacuum on either side in principle represents a particle in a box system. The boundary conditions for the potential in $z$-direction are defined by a surface potential barrier, that interconnects the bottom of the potential well with the vacuum level. In $x$- and $y$-direction we can still exploit the usual periodic boundary conditions due to the lattice potential like in the three-dimensional

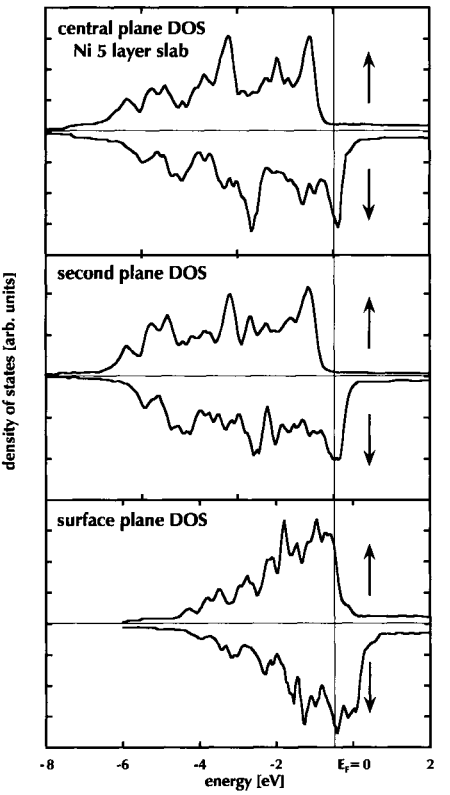


Fig. 9.6. Calculated layer- and spin-resolved density of states in a 5 layer Nickel slab (after Zhu et al., 1984).

case. The resulting calculated electronic dispersion curves look usually very complicated. Since we are mainly interested in surface electronic states, the dispersion curves are plotted in the two-dimensional Brillouin zone, as a function of $\mathbf{k}_{\parallel}$, the wave vector component parallel to the surface. For reasons of clarity these bands are often separated into sets with even or odd parity with respect to the surface normal. In a ferromagnet one additionally distinguishes between majority and minority states, finally resulting in four individual panels. These have to be superimposed to yield the total band structure. The results of such a calculation for a 5 layer Ni slab are reproduced in Fig. 9.7 (Zhu et al., 1984). It shows the dispersion of the states along the $\bar{\Delta}$ direction in the surface Brillouin zone. Only those states marked by circles have a probability of the electron to be found at the surface by more than 60%. They may therefore be considered surface states. In this calculation it has not been distinguished between surface states and surface resonances, i.e., states which hybridize with the bulk bands. The present example for the $Ni_5$ slab shows an accumulation of surface states close to the Fermi level. These states may be responsible – via a change in the total density of states compared to the bulk situation – for an increase of the magnetic moment. In this particular case the calculation predicts an enhancement of the surface magnetic moment by 8% over the center plane or bulk value of $0.56\mu_B$ (Zhu et al.,

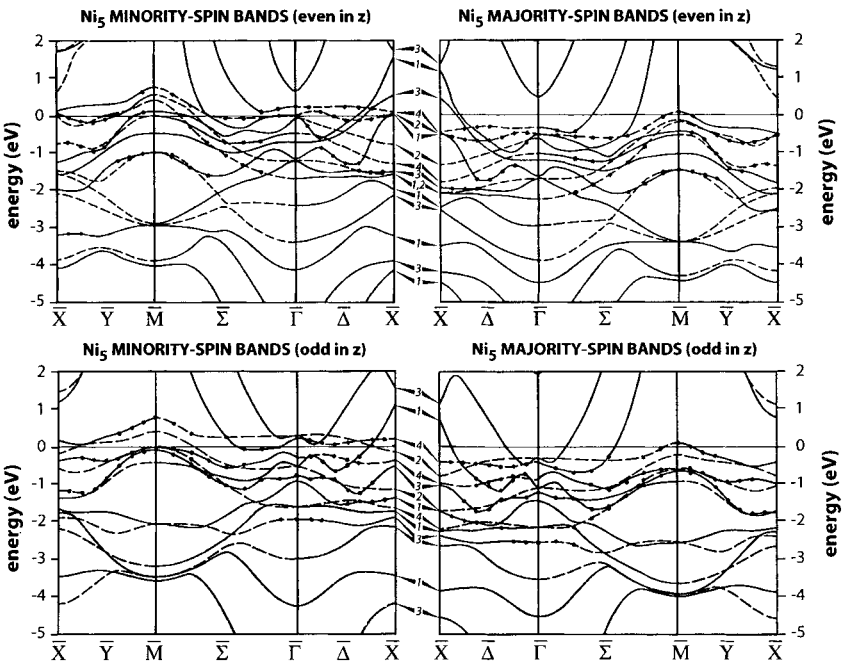


Fig. 9.7. Spin-resolved surface electronic states in a 5 layer Nickel slab. The states are distinguished according to their spin character (majority or minority) and their parity with respect to a mirror operation at the surface plane (even or odd) (after Zhu et al., 1984).

1984). The number of slab (or quantum-well) states increases with the number of lattice planes in the slab and eventually converges against the projected bulk band structure of the 3 dimensional infinite solid. The only way to identify the true surface states in this maze of electronic bands is to analyze the probability density of finding a specific state in a given plane, e.g., the surface layer.

Another interesting information that can be extracted from these electronic structure calculations is the spatial spin density distribution at the surface. Again nickel represents a very interesting case (Fig. 9.8) (Wimmer et al., 1984). One notes first that the majority spin density is essentially confined to the lattice sites, whereas a significant amount of the minority spin density is found in the interstitial regions between the atoms. This behavior is related to the fact that the majority bands of nickel are almost completely filled, and therefore the major part of the spin-up DOS is located well below the Fermi level. These electrons have a more localized character. The Fermi level cuts the minority DOS in the vicinity of a peak (Fig. 9.2). Both occupied and unoccupied spin-down states around the Fermi level are thus available. These states participate in electrical conductivity and are consequently more delocalized. The second observation concerns the behavior of the spin-density in the surface layer (S). The majority spin density is still concentrated at the lattice sites. The missing nearest neighbors, however, lead to an oval deformation of the spatial distribution, allowing the spin-up density to extend slightly further away from

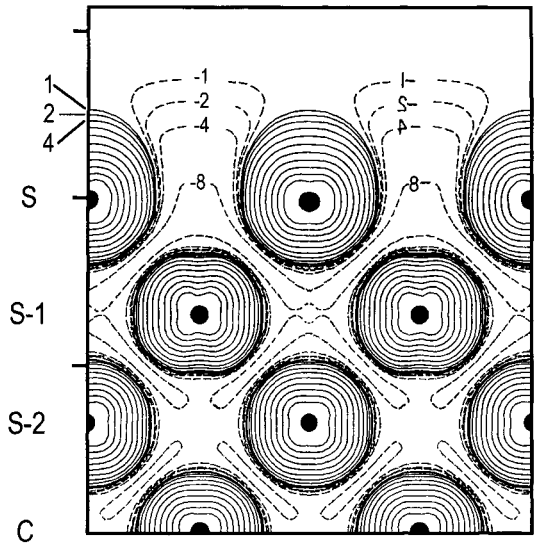


Fig. 9.8. Spin density of a 7-layer Ni(001) slab in the (100) plane perpendicular to the surface in units of $10^{-4}$ $e/(\text{a.u.})^3$. After Wimmer et al. (1984). The solid (broken) lines indicate majority (minority) spin states.

the surface atoms. This effect is much more pronounced for the minority spin density in the interstitial region, which seems to "spill" out into the vacuum region. Beyond a certain distance from the surface, the minority spin density may become dominant. A hypothetical probe able to measure the magnetic response as a function of the distance from the surface should therefore find a change in sign when approaching the surface. This situation in nickel is somewhat peculiar and differs from the one in iron and cobalt. In particular in iron a significant part of the spin-up states is crossing the Fermi level and exhibits a more delocalized character. As a consequence, the spill-out of the minority spin DOS in the interstitial surface region is partly compensated by a similar spill-out of the majority spin DOS.

The above examples underline the importance of both bulk and surface states for the surface magnetism. At the same time, they point out the limits of the qualitative discussion that we gave at the beginning of this section and in which surface states had not been included. Their presence and influence in a given system cannot be predicted without the help of sophisticated electronic structure calculations.

*9.2.1.3. Ultrathin films: 2-dimensional entities*

We will now turn to the question of the electronic structure in ultrathin film systems. Ultrathin films may basically be considered as a two-dimensional electronic system bounded by two *inequivalent* interfaces. These are the film surface and the film-substrate interface. We thus have a very similar situation as in the slab geometry discussed in the previous section. Therefore a qualitative discussion may expand on the arguments developed for treating the surface. Let us assume for the moment an ideal two-dimensional system, in which we neglect the substrate-film interaction. Such a system can be represented by a "free-standing"

monatomic layer. This corresponds very closely to our slab picture. What will happen to the magnetism in this case? Depending on the actual geometrical arrangement of the atoms within the layer, the coordination number may be even lower than for a surface atom of the same material. The monolayer should then exhibit an even higher magnetic moment than the surface, closer to the atomic value. This is indeed predicted by calculations for these idealized systems (Noffke and Fritsche, 1981).

Unfortunately the experimental realization of such systems is not nearly as perfect as their numerical simulation. There is always a substrate required in order to support the films. On the one hand, this turns out to be an important virtue. The crystalline structure of the substrate may largely influence the structure of the growing film. By choosing an appropriate template one may stabilize metastable lattice structures which are otherwise not accessible under ambient conditions. It is in particular the curiosity about the unknown magnetic properties of these metastable systems that fuels the current interest in surface magnetism. On the other hand, the intimate physical contact between substrate and film inevitably gives rise to electronic hybridizations. Localized electronic states may form at the substrate-film interface and influence the magnetic properties. These complications have all to be taken into account, when investigating electronic states in ultrathin magnetic films.

In the light of the above discussion we may formally distinguish between four types of electronic states in a thin film system. These are (i) surface states (including image potential states); (ii) interface states; (iii) localized film states (quantum well states); (iv) delocalized (hybridized) states whose wave function extends on both sides of the interface. Each of these electronic states gives a particular contribution to the density of states and may therefore affect the magnetism of the whole system. Of particular interest in this context are the states localized at the interface and the electronic hybridization. Interface states are thought to be responsible for interface related magnetic anisotropies. The origin of these anisotropies may be a change in the ratio between spin and orbital momentum. This can be induced by a different strength of the spin–orbit interaction, on either side of the interface. This situation arises, for example, if a 3-d ferromagnet is grown on a high-Z substrate, such as Pd, Pt or W. The electronic hybridization, on the other hand, may induce a spin-splitting and therefore a net magnetic moment in the substrate. In other words, we have a transfer of magnetic moment across the interface. In most cases, where non-magnetic substrates are involved this proximity effect is found to be small, but non-negligible. The possibility of a substrate magnetic moment induced by the ferromagnetic overlayer has been pointed out very early for Ni-films on Cu(100) (Wang et al., 1982). Note that the slab geometry in these thin film calculations again requires a mirror symmetry with respect to the center plane of the slab. That means we have an overlayer on each side of the slab. The effect of the electronic hybridization is clearly seen by comparing the Ni surface magnetic moments for a 1 and 2 ML Ni film. The calculation yields $0.39\mu_B$ for the Ni monolayer and $0.68\mu_B$ for the Ni bilayer (at $T = 0$ K). Also the subsurface layer in the 2 ML Ni film which is in direct contact with the Cu substrate has its magnetic moment reduced to about $0.47\mu_B$ (Wang et al., 1982). One might argue that Ni has already a relatively small bulk magnetic moment and may therefore react very sensitively to electronic perturbations by a substrate. In fact, similar calculations for Co mono- and bilayers on the same substrate show a considerably different picture (Wu and Freeman, 1992). The magnetic moment

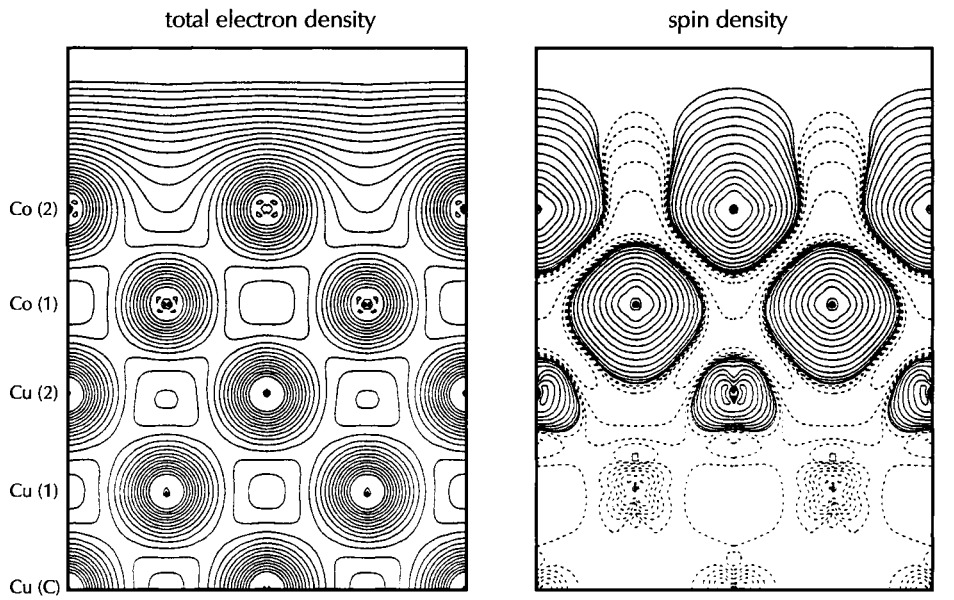


Fig. 9.9. Valence charge (a) and spin density distribution (b) in an epitaxial Co bilayer on a Cu(001) substrate (after Wu and Freeman, 1992). The solid and broken lines in (b) denote a majority and minority type spin density, respectively.

of the monolayer is calculated to $1.78\mu_B$ and thus slightly higher than the bulk value of $1.65\mu_B$. Obviously, the moment enhancement at the surface and the hybridization with the Cu substrate counteract each other, still resulting in a magnetic moment which is smaller than at the surface of Co bulk ($1.85\mu_B$) (Li and Freeman, 1988). In a bilayer, however, the magnetic moment of the interfacial layer reaches only $1.5\mu_B$. Obviously the strong enhancement of the surface magnetic moment is responsible for the peculiar behavior of the Co monolayer. The induced magnetic moment in the interfacial Cu layer, however, is only of the order of 0.02–0.03 $\mu_B$. This is a small but still measurable value. In a spatial map of the spin density the induced magnetic moment shows up as a majority spin contribution at the interfacial Cu atoms (Fig. 9.9).

It is only by means of this type of calculations that one can fully comprehend the complicated interrelations between electronic structure and magnetism. The theoretical efforts also led to a number of predictions concerning monolayer magnetism of materials which are otherwise non-magnetic in the bulk. The basics of these predictions can be easily understood by the same qualitative arguments developed above. In a monolayer we have less nearest neighbors of the same kind and the density of states will be more narrow than in the comparable bulk situation. Eventually this may lead to distribution of the states around the Fermi energy such that the Stoner criterion might be fulfilled. The monolayer of the respective material may then exhibit a magnetic ground state. This ferromagnetic state disappears quickly with increasing film thickness as the density of states approaches the bulk situation. A ferromagnetic ground state for a number of 4d- and 5d-transition metal mono-

layers on Ag- and Au-substrates has been predicted recently (Eriksson et al., 1991; Zhu et al., 1991; Blügel, 1992). The prediction for these particular systems still awaits experimental confirmation (Liu and Bader, 1991). The latter is complicated by the fact that the magnetism in such a monolayer is a very fragile physical property. It is easily affected by external influences, such as the actual structure of the film on the substrate or its morphology. Although it is commonly accepted by now that film imperfections play a substantial role in thin film magnetism, the specific nature and influence of the defects is still a matter of discussion. The inclusion of film imperfections in the theoretical approaches is difficult. On the one hand, the few available theoretical results indicate the promotion of ferromagnetic order in 4d-overlayers by structural defects (Turek et al., 1995). On the other hand, a roughening of the substrate–film interface due to interdiffusion or exchange mechanisms is held responsible for the absence of ferromagnetic order in Rh/Ag(001) (Schmitz et al., 1989; Mulhollan et al., 1991). This is a situation in which one has to be fully aware of the fact, that the thin film system investigated in the experiment might not behave nearly as ideal as assumed in the theoretical model and the reality in experiment is still an important topic in thin film magnetism. Much less complications should be expected in substrate–film combinations, in which the surface free energies are such that interdiffusion or interface roughening is highly improbable to occur. Indeed, very recently experimental evidence for ferromagnetic order in Ru monolayers on C(0001) was reported (Pfandzelter et al., 1995). The magnetic behavior, being strikingly different from that found for Ru layers grown on metallic substrates, was attributed to a rather flat film growth and the negligible electronic interaction with the substrate. Whether this result is valid only for a singular system, or maybe indicates a general tendency cannot be decided on the basis of the present data. Nevertheless, it opens interesting perspectives for future investigations.

### *9.2.2. Magnetism at $T > 0$ K*

#### *9.2.2.1. Magnetic excitations in the bulk*

It is well known from experiment that each ferromagnetic system exhibits a characteristic temperature $T_C$ at which the long-range ferromagnetic order finally breaks down. Similarly, there exists a critical temperature $T_N$ for the long-range magnetic order in an antiferromagnet. $T_C$ is commonly denoted "Curie temperature", whereas $T_N$ is termed "Néel temperature". The energy which is deposited into the system at $T > 0$ K obviously causes elementary excitations which counteract the magnetic order. For the moment we will concentrate on ferromagnets where one finds two types of magnetic excitations. The dominant elementary processes at low temperatures consist of collective excitations of the magnetic spin system. By analogy to lattice vibrations ("phonons") one may define spin waves or "magnons". These magnons may be regarded as elementary modes of spin lattice excitations. There are, however, the following important differences with respect to phonons. First, the motion of an individual spin is determined by rotational degrees of freedom, instead of translational ones as in the case of phonons. This is due to the fact that the interacting field (for example, the molecular field) exerts a torque on the magnetic moment induced by the spin. Secondly, the dynamic response of the spin system is determined by two interactions: the relatively short-ranged exchange interaction and long-range magnetic dipolar forces. The behavior of spin waves can be described by both classical and quantum

mechanical approaches. On the one hand, in a classical limit based on a continuum model this leads to the Landau–Lifshitz equations of motion

$$\frac{1}{\gamma}\frac{\mathrm{d}\mathbf{M}}{\mathrm{d}t} = \mathbf{M} \times \mathbf{H}_{\mathrm{eff}} \tag{9.15}$$

with $\gamma = \gamma_{\mathrm{e}}\frac{g}{2}$ being the gyromagnetic ratio ($g$ denotes the Landé factor and $\gamma_{\mathrm{e}} = 1.76 \times 10^{11}\ \mathrm{T}^{-1}\mathrm{s}^{-1}$ represents the value for a free electron). The effective field $\mathbf{H}_{\mathrm{eff}}$ which acts on the local magnetization $\mathbf{M}$ includes contributions from internal mechanisms and external driving forces due to the measuring process

$$\mathbf{H}_{\mathrm{eff}} = \mathbf{H}_0 + \mathbf{H}(t) + \mathbf{H}_{\mathrm{an}} + \mathbf{H}_{\mathrm{ex}}. \tag{9.16}$$

$\mathbf{H}_0$ and $\mathbf{H}(t)$ denote the external field and the time-dependent perturbation introduced by an experimental method, respectively. $\mathbf{H}_{\mathrm{an}}$ describes the field contribution due to magnetic anisotropies, and $\mathbf{H}_{\mathrm{ex}}$ the exchange field caused by the rotation of neighboring spins. The dipolar interactions are contained in the anisotropy field $\mathbf{H}_{\mathrm{an}}$.

On the other hand, if the localized aspect of the magnetic moment is emphasized, one usually takes recourse to a spin lattice. We recall from Section 9.2.1, that such a system can be described by a Heisenberg model. This results in a quantum mechanical approach to magnons. The Heisenberg Hamiltonian $H$ for a three dimensional isotropic system takes the general form

$$H = -\sum_{(n,m)} J_{nm}\mathbf{S}_n\mathbf{S}_m - g\mu_{\mathrm{B}}\mathbf{H}\sum_n \mathbf{S}_n. \tag{9.17}$$

The summation is usually restricted to the interaction between neighboring pairs $(n, m)$ of spins and the interaction parameter $J_{nm}$ is assumed to have the same value $J > 0$ fork the ferromagnetic system. The second term includes the interaction of the individual spins with a (mean) external field. Assuming only nearest neighbor interactions, spin waves can be identified with the eigenfunctions to (9.17). Both the quantum mechanical (9.17) and classical treatment (9.15) yield the same dispersion relations for the spin waves. For small wave vectors $\mathbf{q}$ one obtains a quadratic spin wave dispersion in cubic systems

$$E \approx 2JSa^2q^2 = Dq^2. \tag{9.18}$$

The Heisenberg model connects the so-called spin wave stiffness $D$ to the microscopic quantities $J$ and $S$ ($a$ denotes the nearest neighbor distance). In the classical model, the spin wave stiffness is related to macroscopic quantities such as the saturation magnetization $M_{\mathrm{S}}$ and the bulk exchange parameter $A$[3]

$$D = \frac{2A}{M_{\mathrm{S}}}. \tag{9.19}$$

3 In the macroscopic model of a magnetic crystal the magnetization vectors in neighboring lattice planes are coupled by a phenomenological "exchange interaction" $J$. Within the Heisenberg model this exchange interaction may be related to the spin–spin coupling $\sim S_i S_j$. Nevertheless, it should not be confused with the

As has been mentioned above, spin waves are important to describe the temperature dependence of the magnetization in the low temperature limit. The deviation of the saturation magnetization from its value $M_S(0)$ at $T = 0$ K follows the Bloch law

$$M(T) = M(0)\left(1 - B_b T^{3/2} - O\left(T^{5/2}\right)\right) \tag{9.20}$$

assuming (9.18) to hold. The parameter $B_b$ is a materials constant and specific for the particular bulk system. The validity of the Bloch $T^{3/2}$ law has been proven for a number of materials.

The second mechanism to dissipate energy in a ferromagnetic electron system involves single particle excitations or electron–hole pairs. These excitations can take place between bands of the same spin character or may involve a spin flip. The latter case results in an electron–hole pair with opposite spins and is called a "Stoner excitation". The spectral dependence of Stoner excitations depends strongly on details of the electronic structure, such as the value of the exchange splitting $\Delta E_{xc}(\mathbf{k})$, the shape of the bands in the vicinity of the Fermi level, the electron density, etc. For the very simple case of the homogenous three dimensional electron gas (parabolic shape of the bands), the qualitative form of the dispersion $E(|\mathbf{q}|)$ is reproduced in Fig. 9.10. The shaded area gives the continuum of the Stoner excitations. We have to distinguish two situations: (i) the exchange splitting shifts the bottom of the minority band, i.e., $\Delta E_{xc} > E_F$. The Stoner excitation involving the lowest energy takes place from the Fermi level to the bottom of the minority spin band. $E(|\mathbf{q}|)$ therefore exhibits a gap at low excitation energies. (ii) $\Delta E_{xc} > E_F$, i.e., the minority spin band is partly occupied. Stoner excitations can take place in the vicinity of the Fermi level for arbitrary energies for a certain interval of wave vectors. The gap at $|\mathbf{q}| = 0$ must persist, since it corresponds directly to the exchange splitting.

In the same diagrams we have included the quadratic dispersion relation of the magnons. It is thus obvious that in both cases the dispersion relations overlap at higher $q$ values. This causes an interaction between the two excitations. In other words, an energy transfer from spin waves to Stoner excitations and vice versa becomes possible. This is the reason, why spin wave spectra from 3d transition metals show a quadratic dispersion behavior only for small $q$ values and exhibit deviations and a significant broadening of the spectral features at higher $q$ (Paul et al., 1988). These interrelation shows that both spin waves and Stoner excitations are necessary to understand the behavior of band magnets at elevated temperature. The fact that the Stoner model describes the temperature dependence solely by single particle excitations and completely neglects spin fluctuations is usually taken as the reason for it's failure at higher temperatures.

### *9.2.2.2. Surfaces and thin films*

In order to see how the surface affects spin waves we can again use the analogy between phonons and magnons. Because of the missing nearest neighbors the surface spin feels

---

quantum mechanical exchange interaction described by the exchange integral $I$. Based on the phenomenological quantity $J$, the parameter $A$ is a measure of the stiffness of the system against a rotation of the magnetization vector between neighboring lattice planes. It is therefore an important quantity in micromagnetism, because together with the anisotropy constant it determines the width of magnetic domain walls. It also enters the last term in (9.16) as $\mathbf{H}_{ex} = \frac{2A}{M_S^2}\nabla^2\mathbf{M}$.

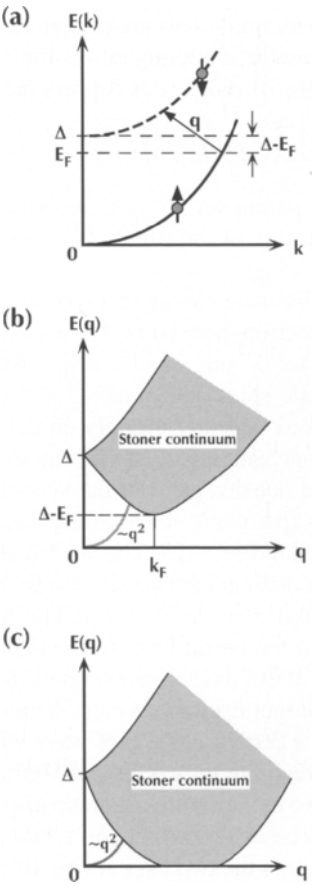


Fig. 9.10. Schematic combination of collective (spin wave) and single-particle excitations (Stoner excitations) in a ferromagnet. (a) Stoner excitations into a completely empty spin-down band. The minimum energy transfer required is thus $\Delta - E_F$. (b) Range of Stoner excitations in the $E(q)$ diagram compared to the spin wave dispersion $E \sim q^2$ for the case shown in (a). (c) The same as in (b), but for partially filled minority spin band.

different dipolar and exchange interactions than in the bulk. This will in general change the spin wave amplitude and energy at the surface compared to the bulk value. The corresponding modes are still bulk magnons which are perturbed in the vicinity of the surface. On the one hand, a reasonable assumption would be that the magnetic interaction between surface and bulk spins is weaker than between bulk spins, because of a smaller number of nearest neighbors. Since the interaction $J$ is directly proportional to the spin wave stiffness $D$ (Eq. (9.19)) this is often referred to as a 'softening' of the spin wave modes at the surface. On the other hand, we recall that the magnetism at the surface may be enhanced, which would lead to a 'hardening' of the spin wave modes. Predictions about the change of the spin wave modes at the surface therefore require a detailed knowledge of magnetic conditions. In order to get at least a certain idea of the geometrical influence of the surface,

a very simplified picture is often used. The spin waves at the surface are treated as truncated bulk modes, and any exchange coupling across the surface is neglected ("free-end" boundary condition). The spin waves then take the form of standing waves with antinodes at the surface. Because of the free-end boundary condition their mean deviation at the surface is twice as big as in the bulk (Mills and Maradudin, 1967). As a result, the temperature dependence of the surface magnetization close to $T = 0$ K is still described by a Bloch like law

$$M_S(T) = M_S(0)\left(1 - B_S T^{3/2}\right), \tag{9.21}$$

with the parameter $B_S = 2B_b$. It must be stressed that (9.21) is the result of rather strong approximations and care must be exercised in a comparison with experimental data. Indeed, the experiment often yields much higher values for $B_S$ indicating a stronger reduction of the surface magnetization with temperature (for example, see Walker et al., 1984; Korecki and Gradmann, 1986). A softening or hardening of the spin wave modes at the surface is only one mechanism that may lead to discrepancies between theory and experiment. There is, of course, also the possibility that the surface spins interact with each other. This may give rise to new spin wave modes with characteristic energies, which are localized at the surface and decay exponentially into the bulk. In analogy to surface phonons one can speak of these modes as surface magnons. The role of surface magnons in the magnetic behavior of the surface is a matter of extensive theoretical and experimental efforts.

We can use the same ideas as above to describe a thin film. As the main difference two surfaces and the resulting confinement have to be taken into account. The solution of the problem with the appropriate boundary conditions (Rado and Weertman, 1959) predicts two types of spin waves with completely different properties (Grünberg, 1989). In order to understand this result, we must recall that in the classical picture (Eq. (9.16)) spins (or magnetic moments) are interacting through two mechanisms: the short-ranged exchange coupling (described by the parameter $A$) and the long-ranged magnetic dipole interaction. Spin waves with large wavelengths (small $\mathbf{q}$) have predominantly dipolar character, because neighboring spins are only slightly canted and the exchange contribution may be neglected. At higher $\mathbf{q}$ values, the exchange contribution becomes more and more important. In a semi-infinite crystal, both kinds of spin waves can propagate in arbitrary directions, as long as the boundary conditions at the surface are satisfied. As mentioned in the context of Bloch's law (9.21), they may also form standing waves with antinodes at the surface. But this situation changes markedly in a thin film. The two-dimensional confinement eliminates the long wavelength modes from propagating along the surface normal. Only the exchange dominated modes are still able to form standing waves perpendicular to the film plane, provided that the wave vector component perpendicular to the surface $q_\perp$ is large enough to satisfy the resonance condition

$$q_\perp = \frac{n\pi}{t} \tag{9.22}$$

with the film thickness $t$. The lowest order ($n = 1$) spin wave has antinodes on each side of the film and a node in the center (Fig. 9.11a).

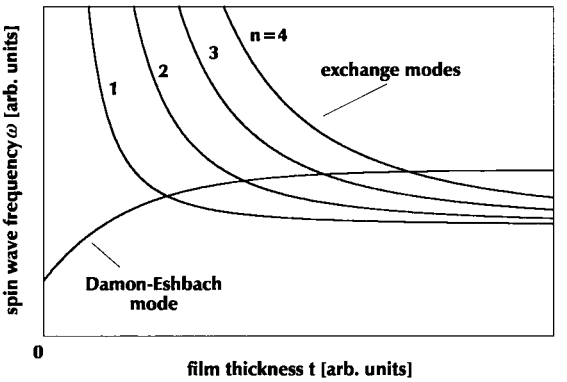


Fig. 9.11. Amplitude distributions for standing spin waves (a) and Damon–Eshbach spin wave modes (b) in an ultrathin film.

The confinement does not entirely exclude the presence of dipolar spin waves. It rather leads to modes with peculiar physical properties, the so-called Damon–Eshbach modes (Damon and Eshbach, 1961). These modes are localized in the surface with a wave vector $q_\parallel$ parallel to the surface plane. The spin wave amplitude is largest at the surfaces and decays exponentially into the interior of the film. In addition, Damon–Eshbach modes propagate only perpendicular to the direction of the saturation magnetization $M_S$, with a defined sense of revolution about the film. $M_S$ must lay within the film plane. This behavior is illustrated in Fig. 9.11b, depicting the mode profiles for a Damon–Eshbach mode with counterclockwise sense of revolution.

The above separation into exchange-dominated and dipolar spin wave modes is a consequence of the reduced dimensionality of a magnetic thin film. Both types of spin waves are employed in Brillouin light scattering (BLS) in order to investigate the magnetization dynamics and magnetic anisotropy fields in thin film systems. The spin wave frequency depends very sensitively on the film thickness $d$, the magnitude and direction of an applied field $H_0$, the saturation magnetization $M_S$, and particularly magnetic anisotropies. For example, the spin wave frequency $\omega$ varies characteristically with the film thickness $t$ like

$$\omega^2 \sim M_S^2\left(1 - \exp(2q_\parallel t)\right) \tag{9.23}$$

for the Damon–Eshbach modes, and like

$$\omega \sim \frac{2A}{M_S}\left(\frac{\pi}{t}\right)^2 n^2 \tag{9.24}$$

for the exchange-dominated standing wave modes. The thickness dependences $\omega(t)$ are schematically depicted in Fig. 9.12. For more detailed information on spin waves in ultrathin films and layered systems, the reader is referred to the excellent review articles by (Cochran, 1994; Hillebrands and Güntherodt, 1994).

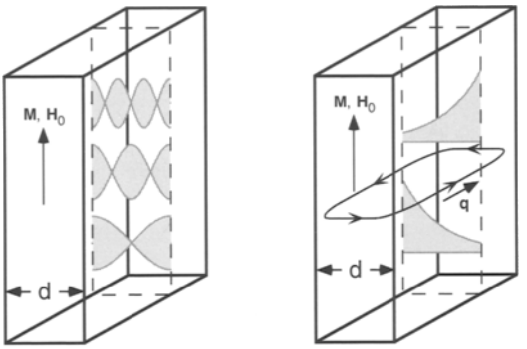


Fig. 9.12. Variation of the spin wave frequency $\omega$ with the film thickness $d$ for Damon–Eshbach (b) and exchange-dominated spin wave modes (a). The standing waves are labeled by the number of knots $n$.

### *9.2.3. Magnetic anisotropies*

#### *9.2.3.1. The bulk*

The response of the magnetization to an external field in crystalline materials usually exhibits pronounced spatial dependencies. In iron, for example, a much lower external field is needed to orient the magnetization along a {100} direction, than along a {110} or {111} direction. The {100} axis is therefore called an "easy" axis of magnetization. A "hard" axis denotes the one that requires the highest field for a complete magnetization reversal (Fig. 9.13). The anisotropic behavior of the magnetization vector is one of the central issues in bulk and surface magnetism. This is to a large extent due to the fact that magnetic anisotropies are vitally required in practically any technical application of magnetism. Without the anisotropic response of the magnetization there would be no magnetic domains, and thus no magnetic tape or storage device. The understanding of magnetic anisotropies, however, requires extensive basic research, since there is a large variety of different mechanisms involved. This is particularly true at surfaces and in thin films, where the situation is even more complicated than in the bulk.

The anisotropic behavior depicted in Fig. 9.13 is due to the coupling of the electron spin to the spatial part of the wave function, and hence to the crystal lattice, and is often referred to as magneto-crystalline or crystal anisotropy. Phenomenologically, crystal anisotropies are discussed within the framework of thermodynamics as an extra term to the free energy. This term is written either as an expansion into spherical harmonics, or as a power series into successive powers of the directional cosines $\alpha_i$, which describe the angles between magnetization and crystalline axes

$$E_{\mathrm{an}}^{\mathrm{V}} = c_0 + \sum_{i,j} c_{ij}\alpha_i\alpha_j + \sum_{i,j,k,l} c_{ijkl}\alpha_i\alpha_j\alpha_k\alpha_l + \cdots \tag{9.25}$$

We wish to emphasize that this description of magnetic anisotropies is purely phenomenological, and its expansion in directional cosines is arbitrary. The physical origin of the

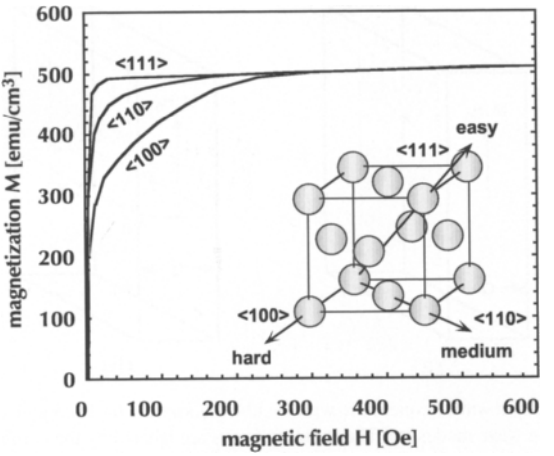


Fig. 9.13. Magnetization curves for disk-shaped nickel single crystals along different crystallographic axes (after Kaya, 1928).

magnetocrystalline anisotropy can only be understood on the basis of first-principles electronic structure calculations. Once being sufficiently advanced, these calculations should predict energy surfaces as a function of the external field direction in relation to crystalline directions. At present the accuracy of these calculations is sometimes not high enough to predict even the correct sign of the bulk magneto-crystalline anisotropy.

Due to symmetry arguments (time reversal) only even powers of $\alpha_i$ can appear in (9.25). The number of independent coefficients is greatly reduced by exploiting the symmetry operations of the crystal lattice. As an example, we will consider the cubic system. There, the anisotropy energy takes the following form:

$$E_{\mathrm{an}}^{\mathrm{V}} = K_0 + K_1\left(\alpha_1^2\alpha_2^2 + \alpha_2^2\alpha_3^2 + \alpha_3^2\alpha_1^2\right) + K_2\alpha_1^2\alpha_2^2\alpha_3^2 + K_3\left(\alpha_1^2\alpha_2^2 + \alpha_2^2\alpha_3^2 + \alpha_3^2\alpha_1^2\right)^2 + \cdots \tag{9.26a}$$

$K_0$ is usually neglected as only the change of $E_{\mathrm{an}}^{\mathrm{V}}$ with angle is of interest. In practice, $K_3$ is already much smaller than $K_1$ and $K_2$, and the first two terms are thus sufficient to describe the anisotropic behavior of the magnetization. It is important to note that due to the cubic symmetry the sum over all second order contributions is a constant. As a consequence, the first nonvanishing term in the angular variation is already of forth order in angle. The form of (9.26a) is thus a peculiarity of the cubic symmetry. In systems with a lower symmetry, for example, an axial one, second order terms prevail. Therefore, the analogous expression of (9.26a) for a hexagonal lattice reads

$$E_{\mathrm{an}}^{\mathrm{V}} = K_0 + K_1\sin^2\Theta + K_2\sin^4\Theta + \left(K_3 + K_3'\cos(6\Phi)\right)\sin^6\Theta + \cdots \tag{9.26b}$$

where $\Theta$ and $\Phi$ denote the angle with respect to the a and c axes, respectively. Equation (9.26b) is used to describe the crystal anisotropy in hcp cobalt. Unfortunately, a comparison of Eqs. (9.26a, b) also points out an inconsistency in the labeling of the anisotropy

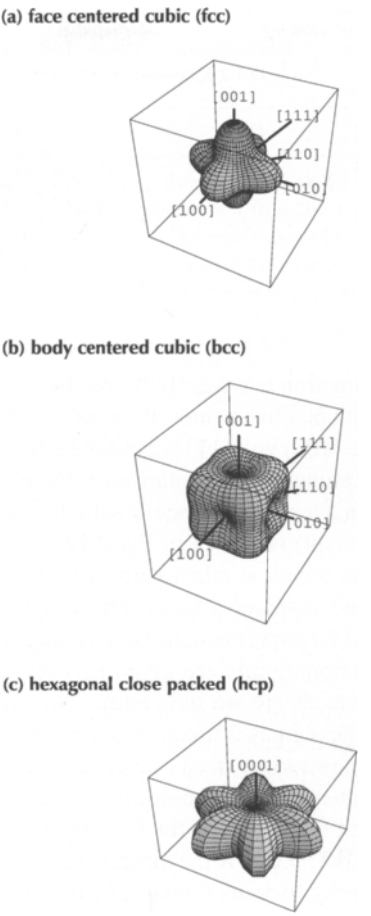


Fig. 9.14. Energy surfaces depicting bulk magneto-crystalline anisotropies in cubic systems with ⟨111⟩ (a) and ⟨001⟩ easy axes (b), and a hexagonal system with a ⟨0001⟩ easy axis (c).

constants $K_i$. $K_1$, for instance, is associated with the fourth order in angle in the cubic system, but with the second order in angle in the hexagonal lattice. It would be more reasonable to label the anisotropy constants according to the power of the angle $\Theta$ or $\alpha$ in the associated expressions. The notation used in (9.26a, b), however, has a long-standing tradition in bulk magnetism, which we will henceforth adapt in order to avoid additional confusion.

Equations (9.26a) basically describe an energy surface the shape of which directly reflects the arrangement of hard and easy axes of magnetization. The results for two different sets of anisotropy constants $K_1$ and $K_2$ are shown in Fig. 9.14, using a spherical reference system $(E, \Theta, \Phi)$. The surface in Fig. 9.14a is obtained if $K_1$ is chosen to be negative and $K_2 < \frac{9}{4}|K_1|$ (Bozorth, 1936). Apparently, this choice determines the {111} crystalline axes in the lattice as easy directions of magnetization, whereas the highest energy is obtained

Table 9.2
Magneto-crystalline anisotropy constants for bulk iron and nickel at $T = 4.2$ K (Escudier, 1975)

| | $K_1$ | $K_2$ |
|---|---|---|
| bcc-Fe | $5.84 \times 10^5$ erg/cm$^3$ | $1.96 \times 10^3$ erg/cm$^3$ |
| | $4.02 \times 10^{-6}$ eV/atom | $1.44 \times 10^{-8}$ eV/atom |
| fcc-Ni | $-12.83 \times 10^5$ erg/cm$^3$ | $5.78 \times 10^5$ erg/cm$^3$ |
| | $-8.63 \times 10^{-6}$ eV/atom | $3.95 \times 10^{-6}$ eV/atom |

along the {100} axes. This situation is typically found, for instance, in face centered cubic nickel. If $K_1$ and $K_2$ have both positive values, the energy surface takes the shape depicted in Fig. 9.14b. In this case, the {100) and {111} crystalline directions interchange their roles as easy and hard axes. A prominent representative of this class of anisotropic magnets is bcc bulk iron. The situation in a hexagonal system with the easy direction of magnetization along the c-axis (e.g., hcp cobalt) is shown in Fig 2.12c. Without the anisotropic contribution within the basal plane which is taken care of by the term determined by $K_3$ the energy surface would take the shape of a torus. The surfaces in Fig. 9.14 show a rather exaggerated view. For Fe and Ni experimentally determined values of the anisotropy constants $K_1$ and $K_2$ in conventional units are given in Table 9.2. It must be pointed out, however, that anisotropy constants are strongly temperature dependent, and may not only change their value but also the sign as a function of temperatures. As a consequence, the easy axis of magnetization may switch from one crystallographic axis to another, as it is known, for instance, to happen in cobalt (Tebble and Craik, 1969). In hcp-Co the easy axis of magnetization points along the c-axis of the hexagonal unit cell only at low temperatures. Between $T = 515$ K and $T = 600$ K the magnetization direction continuously rotates towards the basal plane, thereby forming a cone of easy directions around the c-axis. At around $T = 740$ K, the material undergoes a structural hcp-fcc phase transition, and the easy axis changes again to the {111} direction (Tebble and Craik, 1969).

Consulting textbooks on bulk magnetism (for example, Chikazumi, 1964, or Cullity, 1972) concerning the topic of magnetic anisotropy, one is often confronted with a rather complex picture. In addition to crystalline anisotropy, one finds treatments of a shape or dipolar, a strain-induced, a magnetoelastic anisotropy, etc. This situation is caused by the phenomenological approach which tends to look at each influence on the magnetic anisotropy as an individual physical effect. As a consequence, there is a confusing variety of anisotropy constants. Such a treatment may be useful for technical applications of magnetism, but is unacceptable as soon as the understanding of the physical mechanisms is the issue. From a "first principles" point of view, magnetic anisotropy means the coupling of the electron spin or the spin magnetic moment to a real space reference system. There are only two interactions, by means of which such a coupling can be achieved. The first one is the spin–orbit interaction which couples the spin **S** to the orbital moment **L** (see the term $H_{SO} \sim \mathbf{L} \cdot \mathbf{S}$ in Eq. (9.13)) and gives rise to the magneto-crystalline anisotropy discussed above. The second one is of purely dipolar nature and couples the spin or total magnetic moment $\sigma$ to the external magnetic field **B** (see the term $H_B \sim \sigma \cdot \mathbf{B}$ in Eq. (9.13)).

The field **B** may either be generated by the neighboring magnetic moments in a cluster or lattice, or by a truly external source. The dipole interaction is the reason for the "shape anisotropy" which should better be called a "demagnetization anisotropy". For any given shape of the magnetized body, the system tries to minimize the magnetic stray field and thus its magnetostatic energy. Only in a spherical object the magnetization vector may point into an arbitrary direction. A long cylinder, however, will always be easier to magnetize along its axis than perpendicular to it. This geometry effect is taken care of by the demagnetizing factor $D_M$ (being a second rank tensor for more complicated geometries). A very important geometry for our topic of thin films and surfaces is that of an infinitely extended 2-dimensional sheet, in which case $D_M = 4\pi$ and the magnetostatic energy density $E_{\text{dip}}$ may be written as

$$E_{\text{dip}} = -2\pi M_S^2 \cdot \sin^2 \Theta = K_S^V \cdot \sin^2 \Theta. \tag{9.27}$$

Popular units for $E_{\text{dip}}$ are erg/cm$^3$, more seldom eV/atom. The use of the latter units, however, should be encouraged because it allows a direct comparison of the strength of the various anisotropy contributions, as we will see below. Note that the angle $\Theta$ in (9.27) is measured from the surface normal of the sheet. Because $M_S^2$ is always positive it follows that the phenomenological anisotropy constant $K_S^V$ must always be negative. The energy becomes minimal at $\Theta = \pi/2$, corresponding to a magnetization oriented parallel to the sheet. This makes the surface normal a hard axis, a result that can be intuitively understood. Assume a two-dimensional lattice of magnetic moments which are all aligned with the surface normal. In this case each magnetic moment contributes to the stray field. If the magnetic moments lie in the plane of the sheet, however, only the magnetic moments along the circumference of the sheet are responsible for the stray field. With the saturation magnetization for bulk iron, $M_S = 1714$ emu/cm$^3$, $K_S^V$ takes the value of $-1.92 \times 10^7$ erg/cm$^3$ ($-1.41 \times 10^{-4}$ eV/atom). This value more than an order of magnitude larger than the bulk crystal anisotropy $K_1$ (Table 9.2).

The description of magnetic anisotropies in realistic systems must include two other important physical effects, namely magnetoelasticity and magnetostriction (Chikazumi, 1964). These describe the interactions between the elastic properties of a crystal lattice and the magnetization. A change of the interatomic distances may induce a change of the magnitude and/or direction of the magnetization vector (magnetoelasticity), or a nonzero magnetization is causing a change in the local atomic environment (magnetostriction). Qualitatively, it is easy to see how, for instance, magnetostriction can give rise to a magnetic anisotropy. A change in the geometrical arrangement of the next nearest neighbors leads to a change in the direction and length of the atomic bonds, and consequently to the spatial distribution of the electronic wave functions. Due to spin–orbit coupling, this change is transferred back to the spin system and thus the magnetization. The system will finally assume a new configuration of minimal total energy with a different spatial orientation of the magnetization. Although this is often called a magnetostrictive anisotropy, it is important to realize that the underlying physical mechanism is spin–orbit coupling. By similar arguments basically all phenomenologically distinguished types of magnetic anisotropy can be traced back to spin–orbit and/or dipolar interactions.

*9.2.3.2. Surfaces and thin films*

The cubic symmetry which gives rise to the particular form of (9.25) is only preserved in the bulk. Atoms at the surface are no longer in a highly symmetric environment, such that the second order terms in Eq. (9.25) become non-zero (please note that the shape anisotropy of a thin sheet in (9.27) is already the first example for such a behavior). As was first pointed out by L. Néel, this loss of cubic symmetry must give rise to an extra anisotropy contribution, the "surface anisotropy" (Néel, 1954). Néel proposed a so-called pair bonding model in which the direction of the magnetic moment at a given lattice site is determined by the orientation and length of the chemical bond to the next nearest neighbor atom. This ansatz invokes spin–orbit coupling as the main physical origin of the surface anisotropy. Although primarily intended to describe the behavior of localized magnetic moments at the surface, models based on Néel's idea are still proving very useful in the understanding of anisotropic effects even in itinerant ferromagnets. The surface contribution to the magneto-crystalline energy for a {100} plane which has a tetragonal symmetry may be written in an appropriate reference system as (see, for instance, Heinrich and Cochran, 1993)

$$E_{\mathrm{an}}^{\mathrm{S}} = K_1^{\mathrm{S}} \sin^2 \Theta + \left(K_2^{\mathrm{S}} + K_2'^{\mathrm{S}} \cos(4\Phi)\right) \sin^4 \Theta + \cdots \tag{9.28}$$

$\Theta$ denotes the angle between magnetization and surface normal, $\Phi$ gives the orientation within the surface plane. The leading term in (9.28) is of second order in angle, which is a direct consequence of the altered geometry. The tetragonal symmetry of the system is reflected in the presence of two higher order anisotropy constants, $K_2^{\mathrm{S}}$ and $K_2'^{\mathrm{S}}$. $K_2^{\mathrm{S}}$ describes an anisotropy contribution perpendicular to the surface, whereas $K_2'^{\mathrm{S}}$ stands for the four-fold in-plane anisotropy. Similar expressions can be derived for the orthorhombic and hexagonal symmetries associated with the {011}, {111} or {0001} surfaces. The form of the equation obtained for the hexagonal surface symmetry is very similar to (9.26b). In many laboratory situations the surface anisotropy is sufficiently described by the lowest order terms, i.e., $K_1^{\mathrm{S}}$. The higher order terms $K_2^{\mathrm{S}}$ become important, however, if additional in-plane contributions are considered, or if several terms $\sim \sin^2 \Theta$ are canceling each other, so that the higher order contributions are dominating the magnetic behavior. Although we were only mentioning surfaces, the same concept can be used to describe a magnetic anisotropy originating from interfaces between two different materials (interface anisotropy).

The most interesting case occurs if $K_1^{\mathrm{S}} > 0$. Following the arguments in the discussion of (9.27), a positive sign of the anisotropy constant $K_1^{\mathrm{S}}$ is related to an easy axis of magnetization along the surface normal. The corresponding energy surface given by (9.28) is illustrated in Fig. 9.15a. If no in-plane components to the surface anisotropy were present, the energy surface would resemble a simple torus. For our choice of the higher order anisotropy constants $K_2^{\mathrm{S}}$ and $K_2'^{\mathrm{S}}$ we obtain a pronounced four-fold in-plane anisotropy, with hard axes along the [100], [$\bar{1}$00], [010], and [0$\bar{1}$0] directions. The shape of the energy surface is, of course, directly reflecting the crystallographic symmetry of the surface. Using the appropriate counterparts to Eq. (9.28), similar angular dependencies may be plotted for the (111) and (011) surfaces (Figs. 9.15b, and c). In each case, a positive value of $K_1^{\mathrm{S}}$ leads to an easy axis along the surface normal.

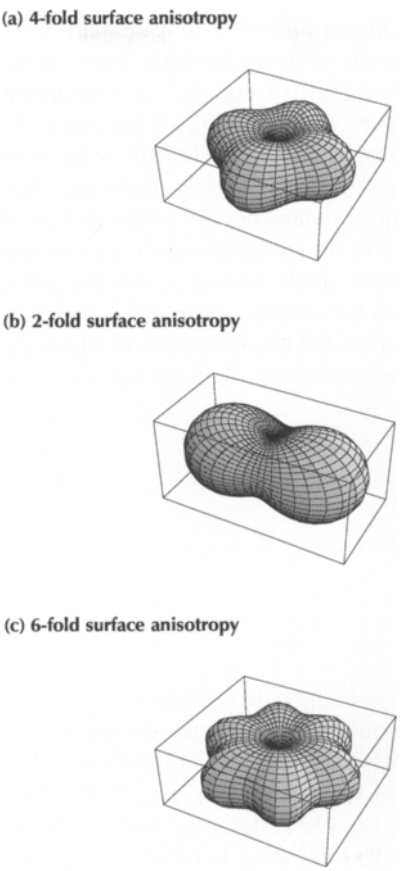


Fig. 9.15. Energy surfaces depicting surface magneto-crystalline anisotropies for the three low-index surfaces: {001} (a), {011} (b), and {111} (c). The easy axis points in all cases along the surface normal.

The surface term becomes particularly important in ultrathin film systems. Considering the different units ($K_1^S$ is given in energy per unit area, $K_1$ in energy per unit volume), the total anisotropy contribution to the free energy of a thin film is often written as

$$E_{an} = E_{an}^V + \frac{2}{t} E_{an}^S \quad \text{or} \quad t \cdot E_{an} = t \cdot E_{an}^V + 2E_{an}^S. \tag{9.29}$$

The film thickness $t$ may be given, for example, in monatomic layers (monolayers). The factor 2 accounts for the fact that the system has two interfaces, namely substrate–film and surface–vacuum. In most cases, these interfaces will differ substantially from each other, resulting in different values for $E_{an}^S$. This situation is only approximately taken care of by the factor 2. The second notation in (9.29) particularly stresses the point that together with the film thickness the bulk anisotropy energy of the film increases, whereas the surface anisotropy energy remains constant. As a consequence, the bulk term $t \cdot E_{an}^V$ usually

dominates the magnetic behavior of thicker films and the surface contribution can be neglected. This can be drastically different for films in the monolayer range. Experimental values of $|K_1^S|$ range between 0.1 to 1 erg/cm$^2$, corresponding to $10^{-4}$–$10^{-3}$ eV/surface atom. Comparing these values with Table 9.2, it becomes clear that in monolayer films the surface anisotropy may easily dominate the bulk term. In the case $K_1^S > 0$, the energy minimum is located at $\Theta = 0$ (Fig. 9.15). This means that the surface anisotropy by itself favors a magnetization vector oriented normal to the surface. As long as this perpendicular surface anisotropy prevails, the film will exhibit a perpendicular remanence below the magnetic ordering temperature. With increasing film thickness, however, the bulk contribution, that is, in most cases the demagnetizing field, will gain more and more influence. Let us consider for the moment the ideal situation in which shape and surface anisotropy terms $\sim \sin^2 \Theta$ are balancing each other. With the aid of (9.27) and (9.28), (9.29) becomes then

$$K_{\text{eff}} = K_S^V + \frac{2}{t} K_1^S. \tag{9.30}$$

At a certain critical thickness $t_c$,

$$t_c = -\frac{2K_1^S}{K_S^V}, \tag{9.31}$$

given by the condition $K_{\text{eff}} = 0$, the bulk contribution is finally overwhelming the surface anisotropy, and the magnetization flips into the film plane. One thus observes a so-called reorientation of the magnetization vector as a function of film thickness. This behavior has indeed been observed in various systems, e.g., Fe/Cu(100) (Pappas et al., 1990) and Fe/Ag(100). Unfortunately, Eq. (9.31) describes only an idealized case, in which the system becomes magnetically isotropic at $t_c$. In other words, exactly at the critical thickness, we have a transition from an anisotropic magnet to an isotropic Heisenberg magnet. The question whether or not this case has any experimental realizations is more of academic nature. As we have seen in the discussion of Eq. (9.28), the surface anisotropy contains also higher order terms which will eventually determine the magnetic behavior at $t_c$, thus preventing the system from becoming isotropic (Fritzsche et al., 1994). The magnetic processes leading to the spin-reorientation transition are therefore much more complex than suggested by the simple form of Eq. (9.31) and still not yet fully understood.

In order to illustrate the magnitude of the various anisotropy constants in a common reference system (meV/atom) at least for one system, we have chosen the {001} surface of bulk bcc Fe (Fig. 9.16). As already indicated in Table 9.2, the bulk magnetic anisotropy of iron is characterized by the phenomenological constants $K_1^V$ to $K_3^V$. $K_2^V$ and $K_3^V$ are already more than 3 orders of magnitude smaller than $K_1^V$. The uniaxial anisotropy introduced by the demagnetizing field of a monolayer ($K_S^V = -0.14$ meV/atom) is seen to be significantly larger than the bulk magneto-crystalline contributions. The most prominent contribution, however, comes from the surface. Gay and Richter calculated the value of $K_1^S = 0.38$ meV/atom for an Fe(001) monolayer (Gay and Richter, 1986). This is more than twice the demagnetizing field of the monolayer. Recalling the rather simplified discussion of the spin-reorientation transition, one would thus expect an Fe film of up to 4–5

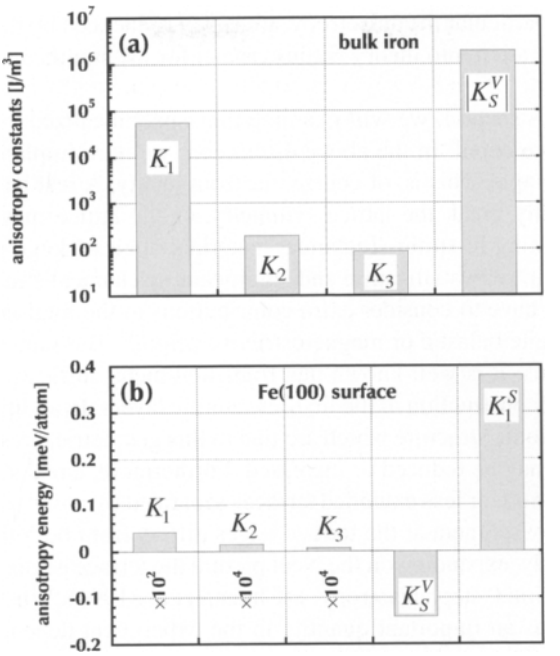


Fig. 9.16. Graphical representation of the numerical values for the various bulk and surface anisotropy constants known for iron. (a) Comparison of the bulk magnetocrystalline anisotropy constants $K_1$, $K_2$, and $K_3$, to the shape anisotropy constant for a thin plate $K_S^V$. (Note the logarithmic scale.) (b) Comparison of the values in the top panel to the anisotropy contribution of the Fe(100) surface as calculated by Gay and Richter (1986). The value of $K_S^V$ represents that of an Fe monolayer.

monolayers to develop an out-of-plane magnetic anisotropy (on the basis of (9.31)). In fact, experiments on Fe films on Ag(001) observed a perpendicular magnetization which turned into the film plane at above 2 monolayers. This discrepancy to the crude model is not surprising. It clearly indicates that the two interfaces Fe–vacuum and Fe–Ag have different magnetic properties. However, a later calculation for the magnetic anisotropy of an Fe monolayer on Ag(001) gave a result of only $K_1^S = 0.07$ meV/atom, being far to small to overcome the demagnetization energy of the monolayer (Gay and Richter, 1987). Even if one assumes the anisotropies at the two interfaces to be drastically different, this may only explain a perpendicular magnetization in the Fe bilayer, but not the monolayer film. This ambivalent result is symptomatic for the current situation. Although the magnetic anisotropies at the surface or in ultrathin films are significantly larger than the bulk values, it is still very difficult to obtain reliable results from first principle calculations and any agreement between experiment and theory still has the taste of fortuity. It must be emphasized, however, that this difficulties do not arise solely from the mathematical procedures and physical approximations employed in the theory. The systems investigated in the experiment must be thoroughly characterized with respect to their crystalline structure, surface topography, surface chemical composition (adsorbates), and strain fields. The mag-

netic properties, in particular the anisotropy, are easily influenced by these parameters, and their proper incorporation into theory is thus crucial for the significance of the theoretical predictions.

At the end of this section, we will examine the aspect idealized vs. realistic thin film system in some more detail. In the above discussion, we have implicitly presupposed an ideal, defect-free sample. This is, of course, far from reality. A real bulk crystal may have defects, which locally break the lattice symmetry, or the lattice may be subject to mechanical stress resulting in strain. Technical materials often undergo plastic deformation processes resulting in recrystallization and significant mechanical strain fields. In each of these cases we will have to consider extra contributions to the total magnetic anisotropy, for example, of magnetoelastic or magnetostrictive origin.[4] The same is true for surfaces and thin film systems. It is well-known that transition metal surfaces often show a structural relaxation or reconstruction in the first few atomic layers. In addition to the inevitable changes in the electronic structure which are tied to this geometrical restructuring, existing strain in the lattice may be reduced or increased. Furthermore, a real surface is not ideally flat, but consists of more or less extended terraces separated by mono- or polyatomic steps. The local atomic environment at the terrace edges differs from both the bulk and the flat surface. Consequently, expanding on the Néel picture the terrace edges will have their own anisotropy contribution ("step anisotropy") (Chuang et al., 1994). Whether or not this step anisotropy appears as an important quantity in the experiment depends on the particular circumstances. The situation in ultrathin films is even more complicated, since they must be grown on a template. This has two important consequences. First, the topology of the template (terrace size, step density, step height, etc.) is of importance for the magnetic behavior of the thin film. In the extreme case, this may lead to substrate-induced anisotropies in the film as has been demonstrated for Co/Cu and Fe/W stepped surfaces (Berger et al., 1992; Chen and Erskine, 1992). Secondly, the inescapable lattice mismatch between a template and the film can result in an anisotropic distortion of the film's crystalline structure. At the same time, one has to take the influence of a compressive or tensile stress in the film into account. Under particular circumstances, strain-induced magnetoelastic contributions to the total magnetic anisotropy may cause a perpendicular magnetization of the film. This can finally lead to an "inversion" of the spin reorientation transition, i.e., the magnetization vector rotates out of the film plane with increasing film thickness. This behavior is observed for thin Ni films on Cu(100) (Schulz and Baberschke, 1994; Farle et al., 1997). The quantitative analysis of these phenomena is often hampered by the fact that magnetic key parameters, such as saturation magnetization, anisotropy constants, or magnetoelastic coefficients are not yet known accurately enough for many thin film systems.

Apart from it's importance in technology, anisotropies play a key role for the existence of ferromagnetism in low-dimensional systems. Consider an ultrathin film consisting of a single layer of magnetic atoms. Depending on the spatial orientation of the magnetic moments, we can use the following models for a quantitative description. In the 2-d Ising model, the magnetic moments are all aligned along a common direction. In other words, the

4 Note that we have switched to the phenomenological picture again in order to make contact to the traditional practice in magnetism. Of course, each of these "extra" contributions to the magnetic anisotropy can be traced back to either spin–orbit coupling or a dipolar origin.

2-d Ising system is highly anisotropic. This model can be exactly solved (Onsager, 1944; McCoy and Wu, 1973), predicting a stable state with long-range ferromagnetic order for $T > 0$ K. In contrast to this stands the 2-d Heisenberg model, which imposes no spatial orientation on the magnetic moments and is thus totally isotropic. In their famous theorem, Mermin and Wagner (1966) showed that a ferromagnetic solution exists only for $T = 0$ K and the ordered state is destroyed by arbitrarily small thermal excitations. This means that the absence of any anisotropy is not compatible with any long-range ferromagnetic order at finite temperature. Recalling the arguments about the various mechanisms that can lead to anisotropies in thin film systems, it is still a matter of dispute whether or not there exists an unambiguous experimental realization of the 2-d Heisenberg model. In contrast to theory which can easily treat free-standing monolayers, the experimenter still needs a template to support the film, and therefore has to deal with its implications. Mermin and Wagner note, that as soon as anisotropies are allowed, the main postulate of the model is no longer fulfilled, and the theorem breaks down, then permitting long-range order. Some recent theoretical investigations connect the critical temperature $T_c$ for ferromagnetic ordering to magnetic anisotropies in the system (Bander and Mills, 1988; Erickson and Mills, 1991). This interplay between magnetic anisotropy and ferromagnetic ordering is another example for the importance of adapting theories to the treatise of more realistic systems instead of idealized mathematical models.

## 9.3. Probing surface magnetism with spin-polarized electrons

We stated in the introduction that surface magnetism is a field of uniquely interdisciplinary character. Methodologies derived from conventional magnetism are important to interpret the magnetic behavior, e.g., anisotropies or domain formation, of low-dimensional systems, but yield no or very little information about the interrelation between magnetism and electronic structures. In order to understand the basic physical mechanisms that cause magnetism, we need probes sensitive to the electronic states, in particular, in the near-surface region. This is where surface science has its domain. It offers an arsenal of methods specifically developed for this purpose. They are mostly based on the interaction of charged or neutral particles with the electronic charge distribution at the surface. In order to be sensitive to the uppermost layers only, the incident particles must have a small transverse energy component, i.e., the fraction of the kinetic energy $E_{kin}$ associated with the motion normal to the surface. With electrons, for example, this surface sensitivity is achieved at low kinetic energies $E_{kin} < 1$ keV, limiting the information depth to only 5–30 Å. With ion or neutral atoms one often uses grazing incidence techniques to reach this goal.

Among all these procedures which have found entrance into surface magnetism, electron-based techniques are the most popular and wide-spread ones. The reason is that they already possess an inherent magnetic sensitivity, if only the electron spin is taken into account as an experimentally accessible quantity. All processes involving the diffraction, scattering or emission of low energy electrons from magnetic surfaces contain a magnetic contribution, describing the specific interaction of the electron spin with the magnetic moments or spin distributions at the surface. Provided that the nature of the particular interaction event is understood, this information can be extracted and interpreted. In order to

be able to exploit this source of information we will need to either prepare a primary electron beam with defined spin polarization, or analyze the spin polarization of the electrons leaving the sample, or even do both.

A structural characterization of surfaces is most often done by the elastic scattering of electrons: low energy electron diffraction (LEED). The spin-polarized version employed in surface magnetism is termed SPLEED and yields information about the magnetic structure of the sample. In spin-polarized electron energy loss spectroscopy (SPEELS) also the inelastically scattered electrons are taken into account and analyzed with respect to their momentum vector and spin polarization (complete scattering experiment), or only with respect to their momentum (incomplete experiment). In both cases, one obtains information about magnetic single-particle excitations (Stoner excitations) and the physics of the spin-dependent scattering mechanisms, but the electronic structure enters the problem in a largely integrated manner. A very detailed picture of the valence electronic structure, by contrast, is given by angle-resolved ultraviolet photoelectron spectroscopies (ARUPS), in particular, if the experiments are performed with synchrotron radiation. With an additional spin-analysis of the photoelectrons (SPARUPS), the occupied majority and minority spin bands throughout the Brillouin zone may be precisely mapped. This is necessary to understand the role of the exchange interaction in itinerant electron systems. At higher photon energies, core levels become accessible, the investigation of which is the regime of X-ray photoelectron spectroscopy (XPS) and its spin-polarized version (SPXPS). The spin polarization of core photoelectrons carries local and element specific information about the magnetism. The same holds for spin polarized Auger electrons from ferromagnets (spin polarized Auger electron spectroscopy), which can be excited by both light and a primary electron beam. The magnetism is usually determined not only by the occupied, but also the unoccupied electronic states. These may be tested by inverse photoemission spectroscopy (IPES) or Bremsstrahlung isochromat spectroscopy (BIS). The spin polarized version (SPIPES) requires a polarized electron beam to be directed onto the sample. Finally, analyzing the spin polarization of the lowest energy secondaries in an electron emission experiment may serve for the purposes of magnetometry and domain imaging.

The above compilation illustrates the variety of different aspects in surface magnetism that can be approached by electron-based experiments. In the following section we will briefly discuss the procedures and devices used to produce and analyze spin polarized electrons. As a prerequisite of this discussion we give a short compilation of the basic equations which describe an ensemble of spin polarized electrons. For a more comprehensive introduction into the mathematical formalism, the reader is referred to the monograph written by Kessler (1985). A comprehensive review on spin polarized electron sources and detectors may be found in Kirschner (1985c, d).

### *9.3.1. Description of polarized electrons*

Elementary quantum mechanics teaches us that the intrinsic magnetic moment $\boldsymbol{\mu}$ of an electron can be expressed in terms of a quantum number $\mathbf{S}$, the electron spin

$$\mu_S = -g \cdot \mu_B \cdot \mathbf{S}.$$

The spin itself has no classical analogue and can be adequately described only in the framework of relativistic quantum mechanics. We have already pointed out in Section 9.2 that a rigorous treatment of electrons moving in an electromagnetic field can only be given by the Dirac equation (Eq. (9.12)). The appropriate wave functions of the Dirac equation are four-component spinors $\Psi$. This approach is rigorously carried through in contemporary electronic structure calculations. From the didactic point of view, however, a four-component spinor is not exactly a conspicuous quantity if it comes to the discussion of electronic wave functions. Whenever applicable, one therefore tries to reduce the problem to a more manageable form. Provided that the kinetic and potential energies of the particles are both small compared to $mc^2$, the Dirac equation can be treated in the non-relativistic limit. Instead of the four-component spinor $\Psi$ we are then left with two-component spinors $\varphi$. The resulting mathematical description is given by the Pauli equation (see Eq. (9.13)).

Any arbitrary spin function $\varphi$ may be expressed by the following basis in the two-dimensional spin space

$$\varphi = \begin{pmatrix} a \\ b \end{pmatrix} = a|\alpha\rangle + b|\beta\rangle = a\begin{pmatrix} 1 \\ 0 \end{pmatrix} + b\begin{pmatrix} 0 \\ 1 \end{pmatrix}. \tag{9.32}$$

The spin polarization $\mathbf{P}$ is determined by the expectation value of the spin operator $\underline{\underline{\sigma}}$, which may be expressed by the Pauli matrices

$$\sigma_x = \begin{pmatrix} 0 & 1 \\ 1 & 0 \end{pmatrix}, \quad \sigma_y = \begin{pmatrix} 0 & i \\ i & 0 \end{pmatrix}, \quad \sigma_z = \begin{pmatrix} 1 & 0 \\ 0 & -1 \end{pmatrix}. \tag{9.33}$$

The observable quantity in experiments is the $z$-component of the polarization vector along a given quantization axis. Using (9.32) and (9.33) yields its expectation value

$$\langle P_z \rangle = \frac{\langle \varphi | \sigma_z | \varphi \rangle}{\langle \varphi | \varphi \rangle} = \frac{|a^2| - |b^2|}{|a^2| + |b^2|}. \tag{9.34}$$

In a real experiment we will not work with a single electron, but rather with an electron beam made up from a large number of electrons with different spin polarizations. Such a partially polarized electron ensemble may be viewed as an incoherent superposition of pure spin states $\mathbf{P}_v$ with relative proportions $g_v$. Thus the spin polarization of the beam becomes

$$\mathbf{P} = \sum_v \mathbf{P}_v g_v. \tag{9.35}$$

The electron system may be equivalently described by the density matrix $\underline{\underline{\rho}}$

$$\underline{\underline{\rho}} = \sum_v g_v |\varphi_v\rangle\langle\varphi_v| \tag{9.36}$$

which yields the following expressions for the spin polarization and its $z$-component of the above ensemble

$$\mathbf{P} = \frac{\mathrm{Tr}(\underline{\underline{\rho}}\,\underline{\underline{\sigma}})}{\mathrm{Tr}(\underline{\underline{\rho}})}, \quad P_z = \frac{\mathrm{Tr}(\underline{\underline{\rho}}\sigma_z)}{\mathrm{Tr}(\underline{\underline{\rho}})}. \tag{9.37}$$

Conversely, it follows

$$\frac{\underline{\underline{\rho}}}{\mathrm{Tr}(\underline{\underline{\rho}})} = \frac{1}{2}(\underline{\underline{1}} + \mathbf{P}\underline{\underline{\sigma}}). \tag{9.38}$$

The density matrix may be diagonalized by transforming the coordinate system such that the $z$-axis coincides with the spin polarization vector and $\underline{\underline{\rho}}$ takes the form

$$\underline{\underline{\rho}} = \sum_v g_v \begin{pmatrix} |a_v|^2 & 0 \\ 0 & |b_v|^2 \end{pmatrix} = \frac{1}{N_\alpha + N_\beta} \begin{pmatrix} N_\alpha & 0 \\ 0 & N_\beta \end{pmatrix} \tag{9.39}$$

with $N_\alpha$ and $N_\beta$ being the number of electrons in state $|\alpha\rangle$ and $|\beta\rangle$, respectively. With (9.37) the spin polarization along a quantization axis becomes simply the normalized difference between the occupation numbers of the $|\alpha\rangle$ and $|\beta\rangle$ spin states

$$P = \frac{(N_\alpha - N_\beta)}{(N_\alpha + N_\beta)}. \tag{9.40}$$

With an appropriate experiment, we will be able to measure the spin polarization $P$ and the intensity $N = N_\alpha + N_\beta$. We can thus determine the occupation numbers by means of

$$N_\alpha = \frac{N}{2}(1 + P), \quad N_\beta = \frac{N}{2}(1 - P). \tag{9.41}$$

Equations (9.41a, b) form the basis for the analysis of spin resolved electron beam experiments.

### *9.3.2. Polarized electron sources*

The basic properties of a spin polarized electron source should be: (i) high degree of spin polarization (ideally 100%); (ii) easy to operate; (iii) compatible with the other experimental constraints. In order to fulfill at least some of these requirements, a variety of polarized sources have been developed during the last two decades in both atomic and surface physics, depending on the primary field of application. As we are concerned with surface magnetism, in the following only sources compatible with the UHV environment needed in surface physics investigations will be of interest.

The standard electron sources in surface physics consist of a piece of material, which is heated (thermionic emission), irradiated with light (photoemission), or subjected to strong electrostatic fields (field emission) in order to emit electrons. Each of these mechanisms

has been thoroughly inspected in the past for electron spin dependencies. In order to exhibit a spin dependence, the excitation process must explicitly include a spin dependent interaction. This can be either spin–orbit coupling in non-magnetic or exchange interaction in ferromagnetic materials. Since thermionic emission represents the most convenient electron source in surface science, it was near at hand to look for a spin polarized counterpart. Thus, some work has been devoted to the study of thermionic emission from ferromagnets. There are, however, two serious problems to overcome. First, a high temperature of the emitter will always reduce the spin polarization in the electron beam due to thermal disordering of the spin ensemble. Secondly, the ferromagnetic order in a material breaks down at the Curie temperature. The high temperatures required for a reasonable current density of emitted electrons exceed in most cases the Curie temperature of the respective material. No practical solution to these problems has been proposed yet.

In contrast to thermionic cathodes, field emission sources can be operated at room or even cryogenic temperatures. A high electrostatic field at the surface pulls down the surface potential barrier, thus creating a potential well. Electrons in the uppermost occupied levels close to $E_F$ will have a certain probability to tunnel through the well into the vacuum, where they are extracted by the external field. A spin-dependence in the tunneling process that may lead to a spin-polarized field emission current can most likely occur in ferromagnetically ordered materials. In a very simple picture this will happen in a material in which the density of states at $E_F$ distinctly differs for spin-up and spin-down electrons. Indeed, for a variety of ferromagnets such as Fe and Gd, a net spin polarization in the field emission current has been observed (Hofmann et al., 1967; Chrobok et al., 1977; Landolt and Campagna, 1978; Landolt and Yafet, 1978). In a different approach, a W tip covered with a thin layer of EuS was successfully used (Müller et al., 1972). EuS is a semiconductor, which becomes ferromagnetic at $T \leqslant 20$ K. Below this temperature the conduction band is spin-split with the majority (spin-up) electrons having the lower energy. At the W/EuS interface majority type electrons from W "see" a lower effective potential barrier for the tunneling step into the EuS majority conduction bands than the minority type carriers do for the corresponding process. Since the tunneling probability depends exponentially on the barrier height, the EuS layer works as a very efficient spin filter. Polarization values as high as 90% have been observed with this type of field emitter (Müller et al., 1972). Unfortunately, the advantage of a high source polarization is counteracted by a number of shortcomings. In general, field emission sources yield a beam of a high brightness, i.e., they offer a small source area, usually from metal tips. This, in turn, limits the total current obtainable. Moreover, they are very delicate devices and may involve substantial difficulties in the every-day operation (see, for example, the need for cryogenic temperatures in the EuS system). In most of the applications involving electron scattering or spectroscopies, a high current has priority over the spot size and the beam brightness. This is the reason why spin-polarized field emission sources are not in wide-spread use. Nevertheless, certain applications, for example, spatially resolving techniques, may exploit the characteristic properties of a field emission source.

The presently most popular source of polarized electrons is based on photoemission from gallium arsenide. It is relatively inexpensive and reliable. Its use still requires some experimental skills and knowledge in surface chemistry, as the GaAs surface must be prepared in certain manner. Among the three electron emission mechanisms, photoemission is the only one able to select electrons from states with a defined angular momentum.

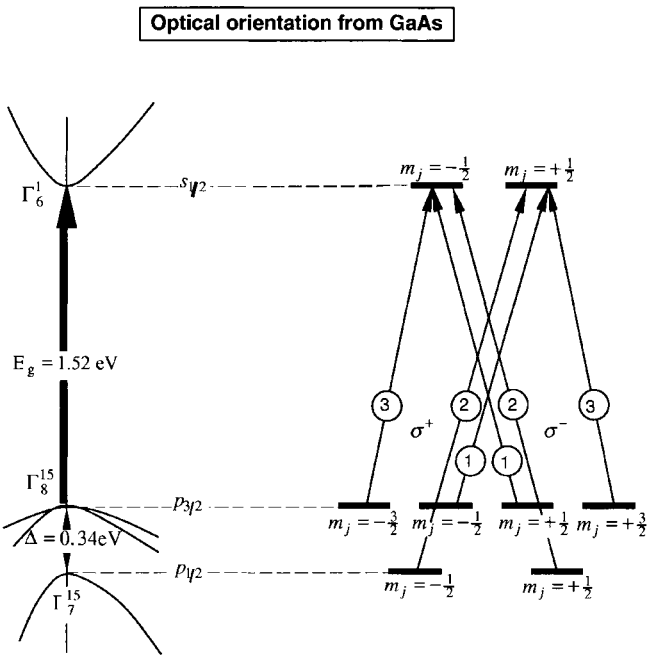


Fig. 9.17. Optical orientation with circularly polarized light from GaAs. Left panel: Electronic bands in GaAs close to the Γ point showing the energy gap $E_g$ and the spin–orbit splitting Δ. The symmetry of the electronic states can be approximated by the atomic wave functions indicated on the right. Right panel: Term scheme according to the atomic notation with transitions induced by right-hand (solid line) and left-hand circularly polarized light (broken line). The circled numbers give the relative transition probabilities.

This is because the electronic interband transition between the initial (occupied) and final (empty) state are governed by optical selection rules, which act on the spatial part of the electronic wave function. In order for these selection rules to work, certain polarization characteristics of the exciting radiation are needed. The spin-dependence in photoemission from GaAs arises from spin–orbit coupling in the initial states, which connects up and down spins with different orbital wave functions. The use of circularly polarized light permits dipole allowed transitions with a defined change in angular momentum, $\Delta l = 1$, and magnetic quantum number, $\Delta m_l = \pm 1$. By tuning to the proper transitions, one spin character is preferentially excited and this leads to a spin polarization of the electrons in the final state. This process is often referred to as "optical spin orientation", though this may cause a slight misunderstanding. It must be emphasized that the light does not interact directly with the electron spin, as the electromagnetic fields associated with the photon (at least for photon energies $h\nu < 1$ keV are too small. The light interacts only with the orbital part of the electron wave function, and the spin-dependence comes in only indirectly by spin–orbit coupling.

In order to see, how this mechanism works for GaAs, we have to inspect the details of the electronic band structure. The relevant section around the center of the bulk Brillouin zone (Γ-point) shows that GaAs is a direct band gap semiconductor (Fig. 9.17). The bottom

of the conduction band and the top of the valence bands are found at the same $\mathbf{k}$ value (in this case $\mathbf{k} = 0$), thus favoring direct (vertical, i.e., $k$-conserving)) interband transitions. The bottom of the conduction band is located at $\Gamma_6^1$. The valence bands are spin–orbit split ($\Delta = 0.34$ eV) into a doubly degenerate state at $\Gamma_8^{15}$ and a single state at $\Gamma_7^{15}$. In order to avoid confusion, we use the standard relativistic notation to label the electronic states. The relativistic double group is indicated by the subscript, whereas the superscript refers to the non-relativistic single group character. The excitation of polarized electrons is to the interband transition from $\Gamma_8^{15}$ to $\Gamma_6^1$ and requires a photon energy of $E_g = 1.52$ eV, which can be well matched with the light of a suitable GaAs laser diode. A group theoretical analysis of the relativistic selection rules governing the transition $\Gamma_8^{15} \rightarrow \Gamma_6^1$ predict a spin polarization of +50% for excitation with circularly polarized light of negative helicity ($\zeta^-$) (Wöhlecke and Borstel, 1981a). The selection rules also predict the spin polarization to change its sign but to retain the same absolute value of the electron spin polarization upon helicity reversal. Thus, the spin direction in the electron beam can be very conveniently flipped between up and down by simply switching from left hand to right hand circularly polarized light, and vice versa.

The reason for the theoretical limit of 50% spin polarization of the GaAs source is the 2-fold degeneracy of the bands at $\Gamma_8^{15}$, which hybridizes states of different symmetry character. The effect of this hybridization can be seen in the following rather simple evaluation. Since the $\Gamma$-point has the highest (cubic) symmetry in the Brillouin zone, the wave functions can be approximated by atomic-like orbitals (in other words, the cubic symmetry is approximated by a spherical one). In this case the following analogies to atomic wave functions can be made for the symmetry characters

$$\Gamma_6^1 \Rightarrow s_{1/2},$$
$$\Gamma_7^{15} \Rightarrow p_{1/2},$$
$$\Gamma_8^{15} \Rightarrow p_{3/2}.$$

Each of these states consists of a certain number of sublevels, distinguished by their $m_J$ values. The corresponding level scheme is given in Fig. 9.17, together with the possible transitions induced by circularly polarized light. Let us concentrate on the case of excitation with light of negative helicity. The requirement $\Delta m_J = -1$ limits the possible transitions between states $|j, m_J\rangle$ to

$$\left|\frac{3}{2}, \frac{3}{2}\right\rangle \rightarrow \left|\frac{1}{2}, \frac{1}{2}\right\rangle,$$
$$\left|\frac{3}{2}, \frac{1}{2}\right\rangle \rightarrow \left|\frac{1}{2}, -\frac{1}{2}\right\rangle.$$

The final states $|\frac{1}{2}, \frac{1}{2}\rangle$ and $|\frac{1}{2}, -\frac{1}{2}\rangle$ are pure spin states. The total spin polarization in the final state is therefore only determined by the relative strength of the transition matrix elements. Evaluation of the transition probabilities gives a ratio of 1/3 for the transitions from $m_J = 1/2$ and $m_J = 3/2$, respectively (Pierce and Meier, 1976). The resulting spin

polarization in the final state is then $P = (3 - 1)/(3 + 1) = 0.5$, just as predicted from group theory. It is obviously the $m_J = 1/2$ transition that contributes with the "wrong" spin character and thus precludes a 100% spin polarization. The latter can only be reached, if the states at $\Gamma_8^{15}$ were split in energy, so that the hybridization is reduced and a single transition can be selected. It may be noted from Fig. 9.17 that the degeneracy is indeed lifted away from the $\Gamma$-point due to a lower symmetry. These transitions become accessible at higher photon energies. Unfortunately, the wave functions also change if one leaves the $\Gamma$-point, and the spin polarization decreases (Pierce and Meier, 1976). If the photon energy is high enough to induce transitions from $\Gamma_7^{15}$, the spin polarization may be even reduced to zero. This is because transitions of the type $|\frac{1}{2}, \frac{1}{2}\rangle \rightarrow |\frac{1}{2}, -\frac{1}{2}\rangle$ (or more correctly $\Gamma_7^{15} \rightarrow \Gamma_6^1$) yield a spin polarization of $-100\%$ and contribute with a relative strength of 2 (Pierce and Meier, 1976). The polarization that is actually achieved in the experiment ranges between 25% and 30%.

Because the degeneracy at $\Gamma_8^{15}$ is due to the high symmetry of the crystal lattice, it could be removed by lowering the symmetry in a controlled manner. This has become feasible in recent years by the significant advances in the fabrication of semiconductor materials. Different approaches have been successfully pursued, for example, superlattices or strained GaAs epilayers on a suitable substrate. Both of these approaches indeed led to a significant increase in the photoelectron spin polarization. Values of more than 85% have been repeatedly reported (Nakanishi et al., 1991). As a caveat, the quantum efficiency of these devices is often 2 to 3 orders of magnitude lower than that of the common GaAs photocathodes, thus reducing the effective current densities. This can be somewhat compensated by using more powerful lasers, but limiting the thermal load on the crystal may then become a non-trivial problem. In terms of counting statistics in an electron spectroscopy or scattering experiment the performance of the photoemitter can be described by the so-called figure of merit $S$, calculated from the quantum yield $I$ and the source polarization $P$

$$S = P^2 I. \tag{9.42}$$

For strained GaAs epilayers, for example, one obtains values of $S = 7 \times 10^{-5}$, as compared to $S = 10^{-3}$ for standard GaAs sources. Further investigations on this problem are highly motivated by applications of these devices in high energy physics, e.g., in cases where the electron spin polarization is the dominant parameter.

So far, we have only considered the excitation step. This yields a spin polarized electron ensemble above the Fermi level, but these electrons are yet unable to leave the GaAs crystal. The reason for this is the energetic position of the vacuum level, which lies about 4 eV above the bottom of the conduction band. Fortunately, this electron affinity can be reduced to zero or even made negative by an appropriate treatment of the surface. The following recipe has been found to reliably yield a stable and reliable negative electron affinity (NEA) GaAs photocathode. The starting material is a heavily p-doped GaAs crystal. In a first step, the clean and annealed surface is covered with a thin layer of cesium. This already reduces the electron affinity close to zero. The adsorbed cesium is the subsequently oxidized, thereby forming $Cs_2O$. The vacuum level in the cesium oxide overlayer is finally lower than the conduction band in GaAs and the electron affinity becomes effectively negative. In order to optimize the cathode performance, the above procedure is

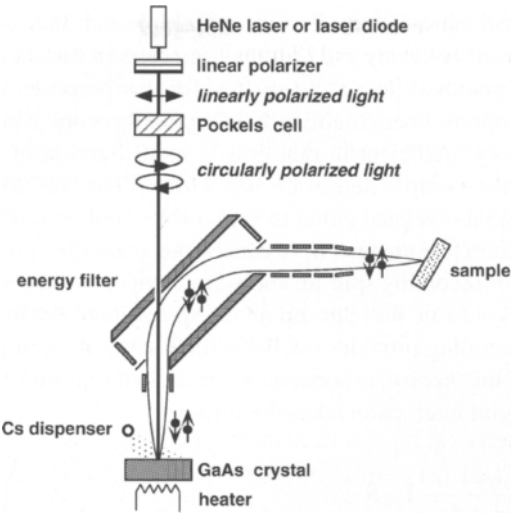


Fig. 9.18. Layout of a transversely spin-polarized electron gun based on optical orientation from GaAs.

repeated several times. With carefully prepared GaAs photoemitters, an electron spin polarization of up to 40% at currents of 100 $\mu$A can be achieved. The discrepancy between the experimental values and theoretical predictions for the photoelectron spin polarization must be attributed to spin-flip scattering processes, which the electrons undergo on their way to the GaAs surface and through the cesium oxide overlayer.

The technical layout of a GaAs polarized electron source (see Fig. 9.18) is very similar to conventional electron guns from the electron optical point of view. Certain provisions have to be made, however, for the *in situ* preparation of the GaAs crystal. This includes cesium dispensers, a heating and optional cooling facility, and optionally some means to clean the GaAs surface by ion bombardment. This can all be accommodated in a small containment. The GaAs surface is irradiated with a laser beam, preferably at normal incidence, as the electron spin quantization axis is determined by the photon spin. Normally incident light ensures a defined vector of the spin polarization normal to the surface and parallel to the electron momentum. This is often referred to as a longitudinally polarized source. In a transversely polarized source the beam is deflected by 90°, using electrostatic devices. As long as the electric fields are small, the electron spin remains unaffected. The polarization of the laser beam, and hence the electron beam, is reversed by means of an electro-optical modulator. Care has to be taken with the alignment of the optical axes, to insure that after switching the polarization the light beam still irradiates the same area on the GaAs crystal. Otherwise, this may cause different deflections of the electron beam leading to spurious asymmetries in the subsequent scattering experiment.

### *9.3.3. Spin polarimeters*

In analogy to the situation in conventional optics, the degree of spin polarization in an electron beam is not a directly measurable quantity. It has to be translated by an appropriate

device, the analyzer or spin polarimeter, into a proportional intensity signal or intensity difference. Practically all presently used spin polarimeters in surface physics involve spin-dependent scattering processes at a solid surface for this purpose. Therefore, in contrast to conventional light optics where highly efficient polarizers are available, a electron spin analyzer is usually very inefficient in that only a small fraction of the incident electron beam finally reaches the electron detector (channeltron). The spin-dependent contribution to the scattering potential is related either to spin–orbit coupling (non-magnetic materials) or exchange interaction (ferromagnets). It causes the scattering probability into a given solid angle to differ for incoming spin-up and spin-down electrons. As a consequence, the intensity of the outgoing beam will depend on the spin state of the incoming one.

Since spin–orbit coupling provides the basis for a series of spin polarimeters, we will discuss this scattering mechanism in some more detail. In the atomic case with it's spherical symmetry, the spin–orbit interaction takes the form

$$V_{SO} = \frac{1}{2m^2c^2r}\frac{1}{r}\frac{dV(r)}{dr}\mathbf{L}\cdot\mathbf{S} \tag{9.43}$$

with $r$ denoting the radius of the electron orbit in the classical picture. In a scattering process, $r$ describes the distance of the electron from the scattering center. The angular momentum $\mathbf{L}$ is then determined by the wave vectors of the incoming ($\mathbf{k}$) and the scattered electron ($\mathbf{k}'$), and points normal to the scattering plane spanned by $\mathbf{k}$ and $\mathbf{k}'$. $V_{SO}$ may be regarded as an additive contribution to the Coulomb part of the scattering potential. Because of the dot product in (9.43), spin-up and spin-down electrons with the same trajectories experience a different total scattering potential

$$V_{\pm} = V_0 \pm |V_{SO}|. \tag{9.44}$$

This results in spin-dependent scattering cross sections $\sigma(\Theta)$, i.e., the probability that an electron is scattered into a solid angle around $\Theta$. An example is given in Fig. 9.19, in which $\sigma^{\uparrow\downarrow}(\Theta)$ (upper panel) for the scattering of a 300 eV electron beam from Hg atoms is shown. The electron wave vector is comparable to the size of the atom, which gives rise to the interference-type behavior of $\sigma^{\uparrow\downarrow}(\Theta)$. The difference between the scattering cross sections for spin-up and spin-down electrons is easily visible, and becomes most pronounced in the vicinity of the minima in $\sigma^{\uparrow\downarrow}(\Theta)$. Because of this cross section argument, even an unpolarized primary beam becomes polarized during the scattering event, provided the scattered intensity is analyzed with sufficient angular resolution. The polarization in this case is simply connected to the cross sections as

$$P(\Theta) = \frac{\sigma^{\uparrow}(\Theta) - \sigma^{\downarrow}(\Theta)}{\sigma^{\uparrow}(\Theta) + \sigma^{\downarrow}(\Theta)} \tag{9.45}$$

and displayed in the lower panel of Fig. 9.19. It also follows immediately that

$$P(\Theta) = -P(-\Theta) \tag{9.46}$$

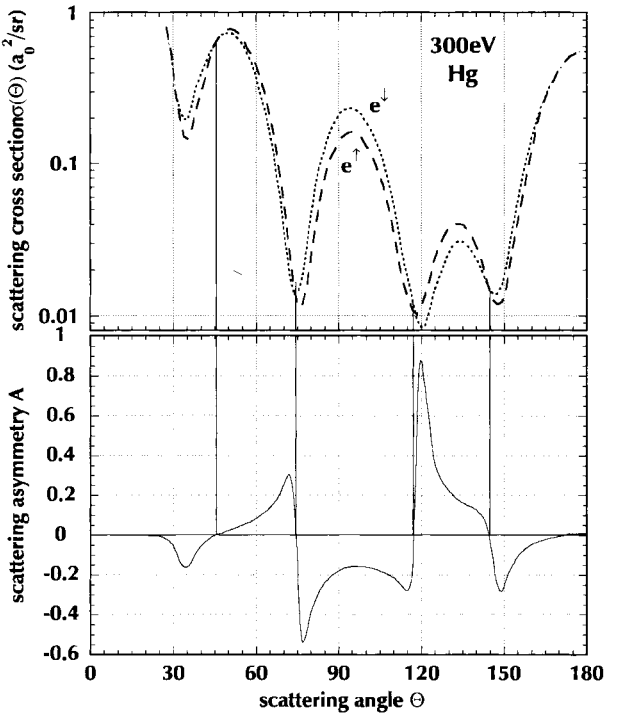


Fig. 9.19. Spin-dependent scattering from Hg atoms as a function of the scattering angle $\Theta$. Top: Scattering cross sections for the spin of the incoming electron parallel (dashed line) and antiparallel (dashed-dotted line) to the normal of the scattering plane. Bottom: Resulting asymmetry $A(\Theta)$ of the scattered electrons for a completely polarized primary electron beam (taken from Kessler, 1985).

as the dot product in (9.43) changes sign if the electron passes the atom on the other side and is scattered into the angle $-\Theta$. We thus have a "left–right asymmetry" in the polarization of the scattered electrons. The intensities scattered into the directions $\Theta$ and $-\Theta$ are still equal, because the unpolarized beam is composed of the same number of spin-up and spin-down electrons. If the incoming beam is already (partially) polarized, however, this situation changes. Spin-up and spin-down electrons are scattered with different probabilities resulting in different intensities at $\Theta$ and $-\Theta$. This gives rise to a left–right asymmetry in the scattered intensity proportional to the polarization of the primary beam.

The spherical symmetry of the electrostatic potential in the atomic case requires that the vector of the orbital momentum $\mathbf{L}$ is entirely defined by the electron wave vectors. This is different in crystalline materials, at least for valence electronic states which are strongly affected by the periodic potential of the crystal lattice. They experience more or less pronounced deviations from the spherical symmetry due to the chemical bonding between neighboring atoms. As a consequence, also the lattice symmetries, such as mirror planes or rotational axes enter the problem and affect the orientation of $\mathbf{L}$ in the scattering from solid surfaces. We will come back to this point when we discuss the class of low-energy spin polarimeters.

In order to employ the left–right asymmetry as a measure of the vector quantity spin polarization, three requirements have to be met. First, the scattering process must define a spin quantization axis, which determines the orientation of up and down spins in the three-dimensional space. In the above case this is obviously the angular momentum **L**, which is always normal to the scattering plane as determined by the wave vectors of the primary and scattered electrons. Secondly, the proportionality factor connecting the spin-polarization with the intensity or intensity asymmetry, the so-called analyzing power, has to be known precisely. Thirdly, the "zero line" of the detector must be carefully determined. According to the scheme discussed above, a polarization measurement could in principle be performed by measuring the intensity of the incoming beam, and the intensity scattered into a defined solid angle. The primary intensity is seldom precisely known which directly affects the accuracy of the zero-line. In particular the last requirement is therefore almost impossible to match with this simple procedure.

The common practice is therefore to determine the electron spin polarization from an intensity difference by exploiting the relation (9.46). The qualitative arguments concerning the left–right asymmetry can be cast into a quantitative form by explicitly calculating the differential cross section for the elastic scattering of a polarized electron beam starting from the Dirac equation. The variation of the cross section $\sigma(\Theta, \Phi)$ as a function of the two scattering angles can be written as (Kessler, 1985)

$$\sigma(\Theta, \Phi) = I(\Theta)\left[1 + S(\Theta)\mathbf{P} \cdot \mathbf{n}\right]. \tag{9.47}$$

The angle $\Theta$ is measured with respect to the wave vector of the incoming electron **k**, whereas $\Phi$ describes the position in a plane normal to **k**. The unit vector **n** defines the normal to the scattering plane. In fact, Eq. (9.50) describes the modulation of the scattered intensity $I(\Theta)$, being the sum of the spin-up and spin-down contributions, by a spin-polarization dependent term. As is evident from the preceding discussion, this spin-dependent term must contain the dot product between the polarization of the incident beam **P** and the normal of the scattering plane (the only contribution that varies with $\Phi$). The whole physics of the spin-dependent scattering process is hidden in the "Sherman function" $S(\Theta)$, which is determined by the (complex) scattering amplitudes for the spin-up and spin-down electrons. The Sherman function describes the analyzing power of the scattering process. A further inspection of Eq. (9.47) shows that for a given scattering geometry there exist two orthogonal scattering planes. This permits the simultaneous measurement of two components of the spin-polarization vector.

The spin-dependent scattering from a spherically symmetric potential is also known as "Mott scattering" (Mott and Massey, 1965), and spin polarimeters based on this physical mechanism are consequently termed Mott detectors. As far as atoms are concerned, the spherical symmetry is given already at low primary energies. Using a gaseous target in a spin-polarimeter is possible but impractical because of the low density of scattering centers. For a solid target, however, the primary energy must be sufficiently high, i.e., in the range of 20–150 keV, in order that the non-spherical contributions to the electrostatic potential may be neglected. In addition, the target is chosen to be a thin foil in order to reduce the amount of multiple scattering within the material. The maximum Sherman function is obtained for a single scattering event, whereas multiple scattering impairs the polarization

sensitivity. Prior to their spin polarization analysis in a Mott detector the electrons must therefore be accelerated to the proper scattering energy by strong electrostatic fields. On the one hand, this is one of the major disadvantages of this type of spin polarimeters, as the high voltages employed require particular safety measures with respect to electrical insulation. As a consequence, high energy spin detectors are relatively bulky and more or less stationary installations. On the other hand, highly energetic electrons may more easily tolerate poor vacuum conditions and the resulting "dirty" surface of the scattering target. This is certainly an advantage in experiments which do not necessarily require UHV conditions. The scattering target in a high energy Mott detector is usually a gold foil. This choice of material combines a high atomic number ($Z = 79$) with the possibility to produce extremely thin foils so that both the forward and backscattered electrons can be measured. An absolute determination of the polarization requires the knowledge of the effective Sherman function $S_{\text{eff}}$ for the particular scattering conditions (angle, energy, energy window, etc.). $S_{\text{eff}}$ is frequently obtained by measuring the asymmetry for different foil thicknesses $t$ and extrapolating the results to vanishing thickness, i.e., the ideal case without multiple scattering. The asymmetry $A(t \rightarrow 0)$ is then related to the calculated effective Sherman function.

In recent years some efforts have been devoted to the development of Mott detectors working at lower energies, the so-called medium energy or "mini" Mott polarimeters. Several designs operating in the 20–40 keV region have been proposed (Dunning et al., 1987; Tang et al., 1988). In addition, a variety of materials, among them uranium ($Z = 92$) (Pappas and Hopster, 1989) and thorium ($Z = 90$) (McClelland et al., 1989), have been tested as potential candidates for spin-analyzing targets. A comparison of the different detector performances is often done in terms of the so-called figure of merit $F$. The scattered intensities are usually measured by means of single electron counting devices (channeltrons or multichannel plates). The experimental uncertainty of the spin polarization is thus determined mainly by the counting statistics. In this situation the figure of merit is defined by (Kessler, 1985)

$$F = S_{\text{eff}}^2 \frac{I}{I_0}, \tag{9.48}$$

where $I/I_0$ describes the reflectivity of the scattering process. This criterion should be used with some precaution, however, as several other aspects concerning the actual operation (reproducibility, reliability, long term stability, handling, etc.) might be of higher priority in practice. At least with respect to the figure of merit, the medium energy Mott detectors do usually not reach the performance of the high energy version (see Table 9.3). Despite their reduction in size, even the "mini Motts" require some compromise in the experimental set-up.

In particular for angle- and energy-resolving electron spectroscopies it is important to be able to independently vary the electron emission angle. This means the spectrometer must be moveable on a goniometer stage with respect to the sample. A combination of this capability with a spin-polarization analysis can be done in two ways. The first method employs a sophisticated lens system behind the energy analyzer in order to guide the electrons into a stationary spin detector. The second, more versatile method requires a small,

Table 9.3
Comparison of the performance of different types of electron spin polarimeters

| Type | Scattering mechanism | Scattering energy | Spin sensitivity $S$ | Reflectivity $R$ | Figure of merit $F$ |
|---|---|---|---|---|---|
| HE-Mott | s.o. | 100 keV | 0.2–0.3 | n.a. | $2 \times 10^{-4}$ [b] |
| Mini-Mott | s.o. | 30 keV | 0.18 | $4 \times 10^{-4}$ | $1.3 \times 10^{-5}$ [a] |
| LEED | s.o. | 100 eV | 0.27 | $1 \times 10^{-3}$ | $1.6 \times 10^{-4}$ [b] |
| DELS | s.o. | 150 eV | 0.11 | n.a. | $1 \times 10^{-4}$ [c] |
| VLEED | exch. | 11 eV | 0.21 | $8 \times 10^{-2}$ | $3.2 \times 10^{-3}$ [d] |

[a] Pappas and Hopster (1989). [c] Erbudak and Ravano (1983).
[b] Kirschner and Feder (1979). [d] Tillmann et al. (1989).

light-weight spin-polarimeter that can be attached directly to the exit of the electron spectrometer. Both spin-detector and spectrometer may then be moved as a unit. This need led to the development of a variety of low energy spin-analyzing devices, which operate at scattering energies below 200 eV. A spin polarimeter based on the diffraction of low energy electrons (LEED detector) (Kirschner and Feder, 1979) may serve as a particularly illustrative example of this class in the following. The combination of angle- and energy-resolving electron spectrometer with the "add on" spin polarimeter is shown in Fig. 9.20. The central part of the LEED detector comprises a W(001) surface. The material tungsten combines a high atomic number ($Z = 74$), which implies a strong spin–orbit coupling, with a well-established procedure to reproducibly obtain an atomically clean surface. The (001) face has the particular advantage of a four-fold rotational symmetry. The incoming electron beam hits the surface at normal incidence with a primary energy of about $E_p = 104$ eV. At this energy diffracted beams up to the second order are able to leave the crystal and may be observed either by a conventional LEED system or by more sophisticated devices, such as the position sensitive single electron detector indicated in Fig. 9.20. Together with the primary electron beam, each pair of nominally equivalent beams defines a scattering plane. Because of the four-fold symmetry of the surface we have two orthogonal scattering planes, one for the group of {02} beams and {20} beams, respectively. The family of the second order diffracted beams is the most interesting, as they show a pronounced spin dependence. If the primary beam is spin-polarized perpendicular to the scattering plane of the {02} beams, for example, the intensity of the (02) is no longer equal to that of the $(0\bar{2})$ beam. This left/right asymmetry $A$ is proportional to the component of the spin polarization vector normal to the scattering plane

$$A = \frac{I_{(02)} - I_{(0\bar{2})}}{I_{(02)} + I_{(0\bar{2})}}. \tag{9.49}$$

The proportionality factor $S$, the spin sensitivity (which should not be confused with the Sherman function in the Mott scattering), between the measured asymmetry $A$ and spin polarization $P$ is usually determined by a suitable procedure (for example, a double scattering

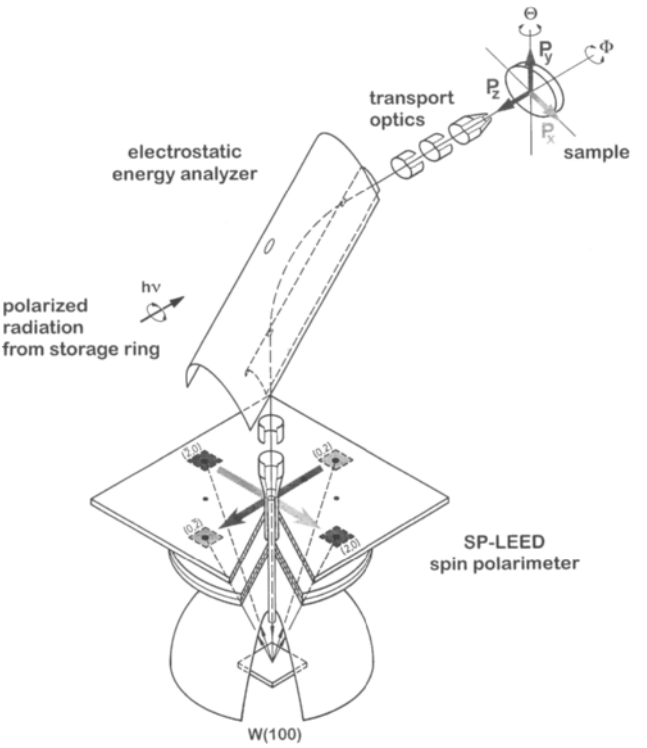


Fig. 9.20. Layout of an electron spectrometer with integrated SPLEED type spin-polarization detector.

experiment (Kirschner and Feder, 1979)) or by calibration against a detector of known spin sensitivity

$$P = \frac{1}{S} A. \tag{9.50}$$

By evaluating the left/right asymmetries in both the {02} and {20} beams two orthogonal components of the spin polarization vector may be determined concomitantly. In fact, this is a feature common to the type of spin polarimeters based on spin–orbit coupling effects. The analyzing power of the above LEED detector at the nominal scattering energy of $E_p = 104$ eV is $S = 27\%$. This means that an incoming electron beam which is 100% polarized along one of the spin-sensitive axes will yield a 27% intensity asymmetry in the appropriate pair of diffracted beams. The reflectivity $R$ for a {02} beam under the given conditions is

$$R = \frac{I_{(02)}}{I_0} = 10^{-3}. \tag{9.51}$$

Based on the numbers given above, the performance of the LEED spin polarimeter is characterized by a figure of merit $F = 1.6 \times 10^{-4}$. It has to be kept in mind, however, that

contrary to the Mott detector the SPLEED polarimeter is particularly adapted to UHV conditions. The nominal spin sensitivity is obtained only with a clean W(001) surface. Adsorbates from the residual gas can easily be removed by a simple heat treatment. The crystal is heated for a very short time ("flashed") to 1600 K or 2500 K in order to desorb carbon monoxide or oxygen, respectively. This procedure interrupts the experiment for about one minute. At a residual gas pressure of $10^{-10}$ mbar the SPLEED polarimeter can be operated with intervals of more than one hour between cleaning cycles without any significant degradation in performance (Sawler and Venus, 1991).

Two other types of low energy spin polarimeters based on spin–orbit related scattering mechanisms have been proposed. The first one is the so-called absorbed current detector (Erbudak and Ravano, 1981). It differs from all other spin polarimeters in that the electron current from the detector surface to ground rather than the reflected (scattered) intensity is measured. It's operating principle is based on the fact that the secondary electron yield varies as a function of the energy of the primary beam and usually exhibits a zero-crossing. This means that for a particular energy $E_0$ in the range of some 100 eV the net current equals zero because the secondary electron yield reaches unity. There is another zero-crossing at much higher energies ($E_0 \sim 10$ keV), which is of no interest for the present discussion. Experiments on ferromagnets (Siegmann et al., 1981) and high-$Z$ nonmagnetic materials (Erbudak and Ravano, 1981) have shown the low-energy zero-crossing to appear at different energies $E_0^{\uparrow}$ and $E_0^{\downarrow}$ depending on the spin polarization of the primary beam. For an evaporated polycrystalline gold film, the energy difference between $E_0^{\uparrow}$ and $E_0^{\downarrow}$ has been found to 1.2 eV, the angle of incidence of the primary beam being 35°. The direction of the primary beam together with the surface normal span a scattering plane, the normal of which defines the spin quantization or spin-sensitive axis of the detector. At normal incidence of the primary beam the spin-dependent contribution to the absorption disappears, because of symmetry considerations (Erbudak and Müller, 1981). In order to use the above mechanism as a spin polarimeter, the working point of the device has to be set to the zero-crossing $E_0$ for a completely unpolarized beam. Any arbitrary spin-polarization with a component along the quantization axis of the detector will then yield a non-zero current reading. In the vicinity of $E_0$ the relation between current and polarization is to a good approximation linear. It may be noted that under the above geometrical conditions only one component of the spin-polarization vector may be measured at a time. In terms of a figure of merit values of up to $F = 1.1 \times 10^{-4}$ have been reported for this type of device (Erbudak and Ravano, 1983).

The distinctive advantage of the absorbed current detector is certainly the combination of spin polarimetry with a simple current measurement. At the same time this feature allows only a narrow range of potential applications. Even with lock-in techniques the current detection limit is of the order of $10^{-15}$ A. Electron spectroscopy experiments often have to work with currents at the detector which are one or two orders of magnitude smaller, so that only single electron counting devices are applicable in these cases. A serious drawback, however, is the observed instability of the zero-point $E_0$. The energy position of $E_0$ may drift with time due to adsorption of residual gases. UHV conditions are therefore required, a clean polycrystalline Au surface can be easily evaporated onto a suitable template.

In particular the finding of a spin-dependence in the current absorbed on a polycrystalline Au surface soon raised the question, whether or not a spin-dependence might also

show up in the electrons scattered from this surface. The existence of such an effect was confirmed and led to the development of a low-energy diffuse scattering spin polarimeter (Unguris et al., 1986). The central part comprises a polycrystalline Au surface which serves as a scattering target for polarized electrons of about 150 eV kinetic energy. Due to the spin–orbit coupling in the valence electronic states of Au the scattering process becomes spin-dependent, resulting in a left/right asymmetry. The scattering geometry is very similar to that of the SPLEED detector except for the absence of any crystalline axes. The scattering planes and thus the quantization axes of the detector are therefore defined by the position and arrangement of the electron detectors (like in a Mott polarimeter). The similarity in the scattering geometries also explains the similar technical realization of the diffuse scattering detector with respect to the SPLEED polarimeter, the main difference being the planar geometry of the grids. The diffuse scattering exhibits a spin sensitivity of $S = 15\%$ at scattering angles of about 135°. This is comparable to values obtained in other devices. Unfortunately, the reflectivity at these conditions is only of the order of $R \approx 10^{-5}$, which would result in a very low figure of merit. By accepting large solid angles of the backscattered electrons, the situation can be significantly improved. In fact, the total area of the anode is divided into four quadrants of equal size. Although this geometry "smears out" the scattering angle, the loss in spin sensitivity is overcompensated by the gain in the reflected intensity, at least in terms of the figure of merit. A value of $F = 10^{-4}$ has been reported for this set-up (Unguris et al., 1986).

We have already pointed out at the beginning of this section that spin polarimeters based on spin–orbit coupling involve scattering processes from high-$Z$ materials. The reason for using heavy metals such as gold, tungsten, or uranium is the relative strength of the spin–orbit interaction. If we take the energy difference between spin–orbit split levels as a measure of the strength of the interaction we find, for example, a splitting of about 0.8–1 eV in the valence bands of Au or W. Comparing this to the typical exchange splitting in ferromagnetic Fe of the order of 2 eV, we may draw the conclusion that even larger effects in spin-dependent scattering from ferromagnets should be expected. Consequently, a great effort has been put into the investigation of elastic and inelastic scattering phenomena from magnetic surfaces (Kirschner, 1985b). Scattering asymmetries up to 30–40% have been found in elastic scattering, for example, for Fe(110) (Gradmann et al., 1983). Such extremal values mostly coincided with a very small reflected intensity and were therefore not suited for applications in a polarization analysis. Recently elastic scattering effects at very low kinetic energies have been reported, which combine both a reasonable spin sensitivity and a high intensity in the reflected beam (Tillmann et al., 1989; Fahsold et al., 1992). In these experiments electrons with a kinetic energy of $E \sim 10$ eV are scattered off an Fe surface. The reason for the spin dependence in the above process is the spin-splitting of the band edges in the unoccupied part of the band structure. Electrons entering the solid at the particular kinetic energy find a much higher density of unoccupied majority spin states. Thus the probability for minority spin electrons to be reflected is higher than for majority electrons. The spin-sensitive or quantization axis of this scattering process is the direction of the remanent magnetization $\mathbf{M}$ in the surface. We thus do not observe a left/right asymmetry, but a magnetic asymmetry. This magnetic asymmetry is due to an intensity change when the direction of $\mathbf{M}$ is flipped from a parallel ($I^{\uparrow\uparrow}$) to an antiparallel

orientation ($I^{\uparrow\downarrow}$) with respect to the spin-polarization of the incident electron beam. The spin polarization may then be extracted from the scattering asymmetry as

$$P = \frac{1}{S}\frac{I^{\uparrow\uparrow} - I^{\uparrow\downarrow}}{I^{\uparrow\uparrow} + I^{\uparrow\downarrow}}. \tag{9.52}$$

With a scattering energy of $E = 10.6$ eV, a scattering asymmetry of $S = 21\%$ and a reflectivity of $R \approx 0.1$ have been reported for Fe(100) (Tillmann et al., 1989). Simply calculating the figure of merit on the basis of these numbers yields a value of $F = 3.2 \times 10^{-3}$. Even more suitable parameters are found for the Fe(110) surface, where a scattering energy of $E = 5$ eV yields $S = 20\%$ and $R \approx 0.2$, resulting in a figure of merit of $F = 8 \times 10^{-3}$ (Fahsold et al., 1992). These results are somewhat misleading, however, as the scattering asymmetry has to be determined from two subsequent measurements for $I^{\uparrow\uparrow}$ and $I^{\uparrow\downarrow}$, and not simultaneously as in most other polarimeters. Taking this into account reduces the above value by a factor of two. This is still an order of magnitude larger than any other spin detector based on spin–orbit coupling.

Each concept is accompanied by certain drawbacks and the magnetic spin polarimeter is no exception to this rule. First, the definition of a quantization axis by the remanent sample magnetization implies that only one component of the spin-polarization vector can be measured at a time. Secondly, the surfaces of the ferromagnetic transition metals are usually much more reactive than those of, for example, gold. Therefore an UHV environment is mandatory for the proper functioning of the device. Thirdly, a clean iron surface cannot be obtained by a simple heat treatment, as in the case of tungsten. Provisions have to be made for cleaning the surface by ion bombardment. Even using Fe films instead of a bulk crystal surface brings only marginal improvement to the situation. The films must have a good crystalline structure and should thus be epitaxially grown *in situ* onto a suitable substrate, because the spin dependent scattering mechanism is a band structure effect. This also requires some efforts in substrate preparation and the thin film growth. As long as these complications are not overcome, the magnetic spin polarimeter will be a more or less stationary device. Its coupling to a rotatable energy analyzer may turn out to be difficult.

## 9.4. Scattering of spin-polarized electrons from magnetic surfaces

The interaction of energetic electrons with a crystalline surface is a complex process, as is seen in the energy distribution of the backscattered electrons (Fig. 9.21). First, one finds a pronounced peak at the kinetic energy of the incident electrons $E_0$. These electrons have been elastically scattered without any energy loss. Their spatial intensity distribution carries mainly information about the surface crystalline structure. This property is exploited in low energy electron diffraction (LEED) experiments. Then depending on the energy $E_0$ and the energy spread $\Delta E$ of the incident electrons, various elementary excitations of either the solid, or the individual atom become accessible to the experiment. If the energy and the energy spread of the incident electrons is rather small, we will be able to observe energy losses due to the excitation of lattice vibrations at the surface, so-called surface phonons. The typical energy loss related to a surface phonon is of the order of $\Delta E \cong 10$ meV. It

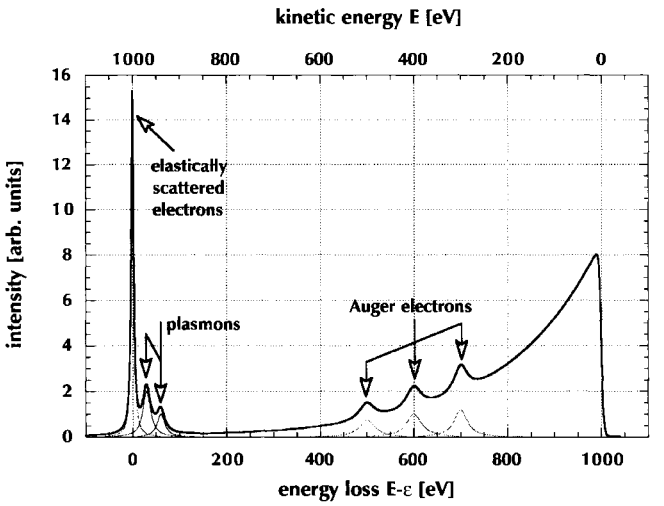


Fig. 9.21. Schematic electron energy loss spectrum of electrons scattered off a surface. The spectral features correspond to plasmon excitations and Auger transitions. The successive increase of the loss intensity towards low kinetic energies is due to a cascade of low-energy secondary electrons. Note that with the energy width of the elastically scattered beam as drawn, vibrational excitations (phonons) and energy losses due to electron–hole pair excitations are too close to the primary energy and cannot be resolved.

therefore requires very good energy and momentum resolution in both the incident and the analyzed electron beam. The respective experimental method is termed high resolution electron energy loss spectroscopy (HREELS) (Ibach and Mills, 1982). It has been used widely to determine the dispersion relation of surface phonons and in the vibrational spectroscopy of adsorbates. Under the same experimental conditions the energy of the primary beam is sufficient to generate single particle excitations. These are electrons from the occupied part of the density of states which gain energy during a scattering process and are lifted into empty states above the Fermi level. Finally, at larger energy loss we observe collective excitations of the electronic structure, so-called plasmons. The energy transfer required is of the order of $\Delta E \cong 10$–$30$ eV.

At the low energy end of the electron spectrum we usually observe a strong increase in the intensity down to very low kinetic energies. This is the region of the "true" secondary electrons, which are created in the course of a large number of inelastic scattering events and have just enough energy left to pass the surface barrier. Low-energy secondary electrons are usually created in large numbers and turned out to be particularly useful in the imaging of surfaces by scanning electron microscopy (SEM). The energy regime between the quasi-elastically scattered electrons and the true secondaries is dominated by Auger excitations. Because of their elemental specificity Auger electrons are widely employed for determining the chemical composition at the surface (Auger electron spectroscopy, AES) (Ertl and Küppers, 1985).

In a number of pioneering experiments, practically each type of the electrons listed above has been shown to carry a characteristic information about various aspects and quan-

titites of the magnetism at surfaces. A nagging exception,* however, is the observation of magnons which seem to have a very low cross section compared to phonons (Gokhale and Mills, 1994). In the following paragraph we will concentrate on electrons which are scattered either elastically or suffer only a small energy loss of $\Delta E \leqslant 1$ eV. Taking the spin of the primary and/or secondary electrons explicitly into account will bring us to the spin-polarized versions of LEED and EELS.

### *9.4.1. Elastic scattering (SPLEED)*

It is well-known from conventional LEED that the angular distribution of the elastically scattered (diffracted) electrons carries information about the spatial arrangement of atoms at the surface. A basic understanding of electron diffraction from a surface is already accomplished within the single scattering or kinematical approach. In order to extract the full wealth of information and come to a quantitative description of the diffracted intensities, however, a sophisticated theoretical formalism has to be employed. The reason for this is the strong electron–electron interaction which results in important contributions from multiple scattering processes. This means that only gross structural features such as the symmetry and the in-plane lattice constant at the surface or the presence of superstructures can be directly extracted from LEED data. A quantitative analysis that reveals details and yields reliable numerical values usually starts with a structural model, on the basis of which dynamical scattering calculations are carried out. The result of these calculations is a set of intensity vs. energy curves for various low and higher order diffraction spots. The degree of agreement between experiment and theory is then obtained from suitable least-squares criteria. By means of this procedure, atomic distances, relaxations and reconstructions at the surface can be determined with a quite high degree of numerical accuracy. The element specificity of the atomic scattering factor even allows the determination of elemental concentrations, for example, at alloy surfaces (Gauthier et al., 1987).

Considering the above arguments, a "magnetically sensitive" version of LEED should not only be able to determine the position and local geometry of surface atoms, but additionally yield information about the size, orientation, and arrangement of magnetic moments at the surface and in the near-surface layers. By analogy to conventional LEED essentially sensing the charge density distribution at the surface, one may expect magnetic LEED to map the surface spin density distribution. The magnetic contribution to the electron scattering originates from the exchange interaction and manifests itself in the electron spin, hence the term SP-LEED. In a typical SP-LEED experiment we will measure the intensity and polarization of the diffracted beam as a function of the primary energy, diffraction angle, and spin orientation of the primary electron with respect to the sample magnetization. As already discussed in Section 9.3.1 for the example of the ferromagnetic spin-polarimeter, the diffracted intensity will change with a reversal of the primary electron spin or the sample magnetization, given a spin-polarized incoming beam. The magnetic contribution in the diffraction process is thus contained in the intensity asymmetry. In the general case, however, the intensity asymmetry observed is not directly proportional to the

---

* Note added in proof: A recent publication on spin-polarized electron energy loss spectroscopy of ultrathin Fe-films reports a first evidence of spin wave related spectral signatures (Plihal et al., 1999).

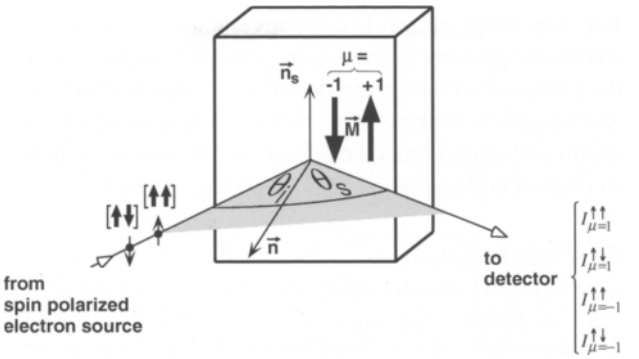


Fig. 9.22. Principles of a SPLEED experiment with transversely polarized electrons on a magnetic surface.

magnetic interaction. As we have seen in Section 9.3.1, there will be an additional complication as the scattering of electrons at a ferromagnetic surface is not determined solely by the exchange interaction, but also the spin–orbit coupling (the SPLEED spin polarimeter is the particular example). On the one hand, spin–orbit induced effects can be avoided, for example, by choosing a particular experimental geometry. If the spin of the primary electron lies parallel to the scattering plane (longitudinal polarization), intensity asymmetries related to spin–orbit coupling must vanish because of symmetry considerations (Celotta et al., 1979). On the other hand, the spin–orbit induced asymmetry contains valuable information about structural details, in particular in high-$Z$ elements, and may thus be of interest (Dunning and Walters, 1985). A second geometry has therefore been successfully applied, in which the spin is oriented perpendicular to the scattering plane (Fig. 9.22). It is necessary in this case to measure all permutations of the orientation of magnetization and electron spin relative to the normal of the scattering plane

$$A_\mu = \frac{I_\mu^{\uparrow\uparrow} - I_\mu^{\uparrow\downarrow}}{I_\mu^{\uparrow\uparrow} + I_\mu^{\uparrow\downarrow}}, \quad \mu = \{-1, +1\}, \tag{9.53}$$

$\mu = +1$ and $\mu = -1$ denote a sample magnetization oriented parallel and antiparallel, respectively, to the normal of the scattering plane. To a good approximation, the spin–orbit and exchange induced contributions, $A_{SO}$ and $A_{ex}$, to the total intensity asymmetry can then be separated by forming the following expressions (Alvarado et al., 1982c):

$$A_{ex} = \frac{1}{2}(A_{+1} - A_{-1}), \quad A_{SO} = \frac{1}{2}(A_{+1} - A_{-1}). \tag{9.54}$$

This method permits the simultaneous investigation of exchange and spin–orbit related effects.

With respect to the various possible set-ups in SPLEED one may distinguish between incomplete and complete scattering experiments. An incomplete experiment uses either an unpolarized primary beam and measures the polarization of the diffracted electrons, or the incoming electrons are spin-polarized and only the intensity asymmetry in the diffracted

beams is measured. The latter version is currently the most popular one. In the complete scattering experiment, the primary beam is spin-polarized and both the intensity and spin-polarization of the scattered electrons are determined. This method, of course, gives the most detailed results on the scattering processes, but requires the largest technical efforts due to the combination of spin-polarized electron source and spin-polarimeter in the sense of a double diffraction experiment (Kirschner and Feder, 1979).

*9.4.1.1. Magnetic structure analysis*

Up to now, detailed SPLEED investigations have been carried out on a number of single crystal surfaces such as Ni(100) (Celotta et al., 1979; Alvarado et al., 1982a–d), Ni(110) (Abraham and Hopster, 1987), and Fe(110) (Waller and Gradmann, 1982). As has been outlined in Section 9.2.1, the magnetic moment at the surface of a ferromagnet may differ significantly from the bulk value, giving rise to a magnetization profile normal to the surface. Such a profile should be reflected in the SPLEED results. Extensive theoretical analyses of the above experimental data seem to confirm this idea. In the case of Ni(100) they suggest a small enhancement of the surface magnetic moment of the order of 5% (Feder et al., 1983; Porter and Matthew, 1989). Larger effects have been extracted from the Fe(110) results, pointing towards a surface magnetic moment enhanced over the bulk value by more than 30% (Tamura et al., 1990). As in conventional LEED, the reliability and accuracy of the conclusion increases significantly with the size of the data set. In particular for the determination of magnetization profiles at the surface it is necessary to obtain an acceptable agreement between experiment and theory for the full data basis and not only a subset. How close theory comes to reproduce the experimental results from first-principles calculations may be seen in the work of Ormeci et al. for the Fe(110) surface (Ormeci et al., 1990, 1991).

The existence of enhanced surface magnetic moments is a generally accepted fact nowadays. A quantitative determination of the resulting magnetization profile by SPLEED, however, is still hampered by the large experimental and computational effort. This is very likely the reason, why SPLEED does not yet play a similar role in surface magnetism, as LEED does in conventional surface physics. On the other hand, there are a number of applications of spin-polarized electron diffraction in surface magnetism, which do not necessarily require a back-up by complex multiple scattering theories. These applications are simply exploiting the fact that a non-zero exchange asymmetry $A_{ex}$, observed in a given scattering condition, is connected to a non-zero remanent magnetization $M_R$ of the sample. Taking $A_{ex}$ as a measure for $M_R$, one may thus perform a qualitative kind of surface magnetometry.[5] For this purpose, $A_{ex}$ is measured as a function of the sample temperature $T$, for example. The dependence $A_{ex}(T)$ reflects the temperature dependence of the surface magnetization and may thus be used to determine the Curie temperature $T_c$ and the critical behavior in the vicinity of $T_c$. In the following we will review some of these applications.

---

5 Although there is a proportionality $A_{ex} \sim M_R$, the proportionality factor is not exactly known. Moreover, it may vary between different experimental situations, for instance, as a function of sample temperature. Particular attention must be paid to this fact, if a quantitative argument on the magnetism is relied on the behavior of $A_{ex}$.

*9.4.1.2. Temperature dependence of the surface magnetization in the spin-wave regime*
We recall from our introductory discussion in Section 9.2.2 that the temperature dependence of the magnetization in the low temperature limit is mainly determined by spin wave excitations. This situation is described by the Bloch law (Eq. (9.20)) with its characteristic $T^{3/2}$ dependence. Figure 9.23 compares the temperature variation of the bulk and surface magnetization for a metallic glass $Ni_{0.4}Fe_{0.4}B_{0.2}$ (Pierce et al., 1982). Both data sets follow indeed a Bloch-like power law, but it is obvious that the magnetization at the surface decays much faster with temperature than in the bulk. This result clearly states the effect of the surface on the magnetism, because according to the argument of Mills and Maradudin (1967) mentioned in Subsection 9.2.2.2, such a behavior should be due to the fact that the spin waves are subject to a free end boundary condition at the surface. Their average deviation is thus twice as large as in the bulk

$$\left\{1 - \frac{M_{S,surf}(T)}{M_{S,surf}(0)}\right\} = \alpha\left\{1 - \frac{M_{S,bulk}(T)}{M_{S,bulk}(0)}\right\} \tag{9.55}$$

with $\alpha = 2$ at low temperatures. In the case of $Ni_{0.4}Fe_{0.4}B_{0.2}$, however, one finds an even higher value, namely $\alpha = 3$. First of all, one should note that Fig. 9.23 does not compare exactly the same physical quantities. Bloch's law describes the temperature behavior of the saturation magnetization $M_S$, whereas the scattering asymmetry in SPLEED is proportional to the remanent magnetization $M_R$. The condition $M_S = M_R$ is fulfilled only for more or less rectangular hysteresis loop. Such loops are often found at low temperatures and a rounding of the loops causing $M_S < M_R$ is limited to the vicinity of $T_c$. If we assume $M_S = M_R$ in the present case another mechanism must be responsible for the above deviation.

We recall from Subsection 9.2.1.2 that the magnetic moment at ferromagnetic surfaces should be enhanced in many cases. Theory connects this surface enhancement of the mag-

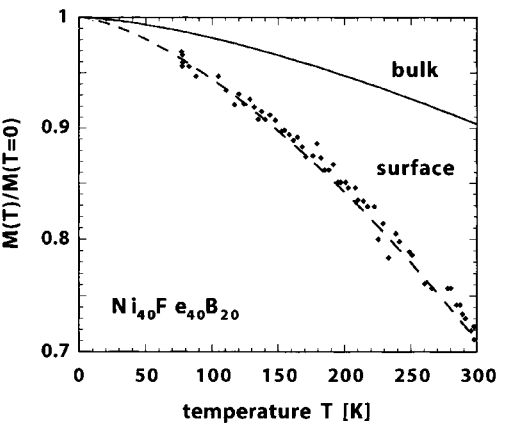


Fig. 9.23. Temperature dependence of the scattering asymmetry in FeNiB in the spin-wave regime (taken from Pierce et al., 1982). The solid line indicates the bulk behavior as obtained from magneto-optical Kerr effect measurements.

netic moment with a reduction of the exchange coupling parameter[6] $J_S$ at the surface (Mathon, 1988b). Because the quantity $J_S$ in turn determines the spin wave stiffness (see Eq. (9.18)) this process leads to a "softening" of the spin wave spectrum. In other words, the unexpectedly fast decay of the magnetization could be related to a change in the spin wave spectrum due to an altered exchange coupling at the surface. It was pointed out quite early, however, that a softening of the magnetic coupling within a surface layer should not affect the initial form of Bloch's law (Mills, 1970). This result is reproduced by recent theories which still find $\alpha = 2$ for a weakened coupling within the surface plane (Mathon and Ahmad, 1988; Mathon, 1988b). This leaves only the direction perpendicular to the surface as a possible origin. In fact, the same theories state a significant increase in $\alpha$ if a reduction of the magnetic coupling *normal* to the surface is assumed. The model assumes a weakened coupling between the surface layer and underlying bulk, leading to a formation of a two-dimensional density of spin-wave states in the surface layer. In the intermediate temperature range it is these two-dimensional spin-waves which determine the temperature dependence $M_S(T)$. The influence of the bulk spin-waves is found to be limited to the low-temperature regime of $\sim$1% of the Curie temperature (Mathon, 1988b). On the basis of this theory the results of Pierce et al. can be explained by assuming the magnetic coupling between the surface layer and the bulk to be only 30% of the bulk interlayer coupling.

This result requires some critical remarks. First of all, the suggested reduction in the magnetic coupling of 70% would be a tremendous effect, predicting the surface to be almost independent from the bulk (from a magnetic point of view). Secondly, limiting the softening of the spin waves to the uppermost layer represents a drastic simplification of the actual problem. A more realistic approach should consider a continuous profile of the coupling normal to the surface, similar to the magnetization profile. Nevertheless, the value of the model is that it points out the effects of a spin-wave softening as such on the temperature dependence of the surface magnetization. Regarding the classical approach of Mills and Maradudin (1967), who assumed a parabolic dispersion of the spin-wave band, the above result stresses that a detailed knowledge of the actual spin-wave dispersion curve is needed for a proper description at higher temperatures. Another deficiency of the above model by Mathon et al. is its phenomenological nature. Clearly missing is a microscopic mechanism which can be held responsible for an altered magnetic coupling in the surface layers. For this purpose one must establish a link between the electronic structure at the surface and the spin-wave spectrum. Given the complexity of the problem this is a difficult and not yet accomplished undertaking. Any appropriate approach should include bulk and surface anisotropies which have a considerable influence on the spin-wave stiffness. For the magnetic glasses, such as $Ni_{0.4}Fe_{0.4}B_{0.2}$, this is probably only of minor relevance, because they are magnetically soft and almost isotropic. In addition, the state of the surface itself with respect to chemical composition and structure is of substantial importance. Experiments on a $NiFeB_{0.5}$ surface showed, for example, that the prefactor $\alpha$ may be varied between 2 and 5 by a minuscule adsorption of Ta atoms (Mauri et al., 1988). The highest value of $\alpha \approx 5.4$ was observed for a coverage of 1/2 ML Ta. In fact, the initial experiment by Pierce et al. reported a measurable carbon contamination at the surface, which raises

6 Note that the use of an exchange coupling parameter $J_S$ implies a Heisenberg type spin lattice model as in Eq. (9.17).

the question whether or not the adsorbate was responsible for the increase in $\alpha$. It is clear that the surface electronic structure will be modified by the presence of adatoms of a different chemical species. The above result for the Ta adatoms is a clear indication for an adsorbate-induced change of the spin-wave behavior. Further theoretical and experimental work is required to establish the relationship between surface electronic structure and the spin-wave spectrum.

*9.4.1.3. Critical phenomena at surfaces*

The Curie temperature $T_c$ in a ferromagnet (or the Neél temperature $T_N$ in an antiferromagnet) marks the breakdown of the long-range magnetic order. The behavior of the ordering parameter magnetization in the vicinity of the critical temperature is described by a power law of the form

$$M_S(T) \sim |T - T_c|^{\beta}. \tag{9.56}$$

The critical exponent $\beta$ is a characteristic quantity that reflects the universality class of a given magnetic system. For a 3-d Heisenberg model, for example, one calculates a critical exponent of $\beta \approx 0.365$. A 3-d Ising system is characterized by $\beta \approx 0.325$, which changes to $\beta = 1/8$ in two dimensions. An experimental determination of $\beta$ may help to classify the magnetic system under investigation. The value of $\beta$ not only indicates whether a spin system behaves Ising or Heisenberg like, but may yield information about the actual dimensionality with respect to the magnetism. In order to be able to determine critical exponents by SPLEED, a strictly linear proportionality between the exchange asymmetry and the surface magnetization is required. Extensive theoretical investigations have shown that this proportionality indeed exists, but is limited to a narrow temperature range around $T_c$ (Feder and Pleyer, 1982).

Investigations of the critical behavior have been carried out, for example, on Ni surfaces (Alvarado et al., 1982a). Instead of the bulk exponent $\beta$, however, a different critical exponent $\beta_1$ for a semi-infinite system has been determined

$$A_{ex} \sim M_1(T) \sim (T_c - T)^{\beta_1} \tag{9.57}$$

with $M_1(T)$ denoting the magnetization in the surface layer. A compilation of experimental data for various scattering angles and primary energies yielded an average value of $\beta_1 \approx 0.81$ (Fig. 9.24). This is compatible with a semi-infinite Heisenberg spin system ($\beta_1 = 0.81$–$0.88$), whose 3-d counterpart gives a good description of the critical behavior of the bulk magnetization in nickel. Unfortunately, competing models, such as the Ising ($0.776 \leqslant \beta_1 \leqslant 1.13$) or the XY-model ($0.79 \leqslant \beta_1 \leqslant 0.93$) have similar critical exponents and must therefore be considered as well, so that an unambiguous answer cannot be given by the experiments in Fig. 9.24.

Another finding that emerges from the above Ni data is the close agreement of the critical temperature $T_{C,S}$ determined from the $A_{ex}(T)$ curves with the bulk Curie temperature $T_{C,B} = 627$ K. Within the experimental accuracy, one finds $T_{C,S} \approx T_{C,B} \pm 4$ K (Alvarado et al., 1982a). Such a result cannot necessarily be expected, considering the reduced coordination numbers and altered magnetic interactions at the surface. Indeed, investigations of

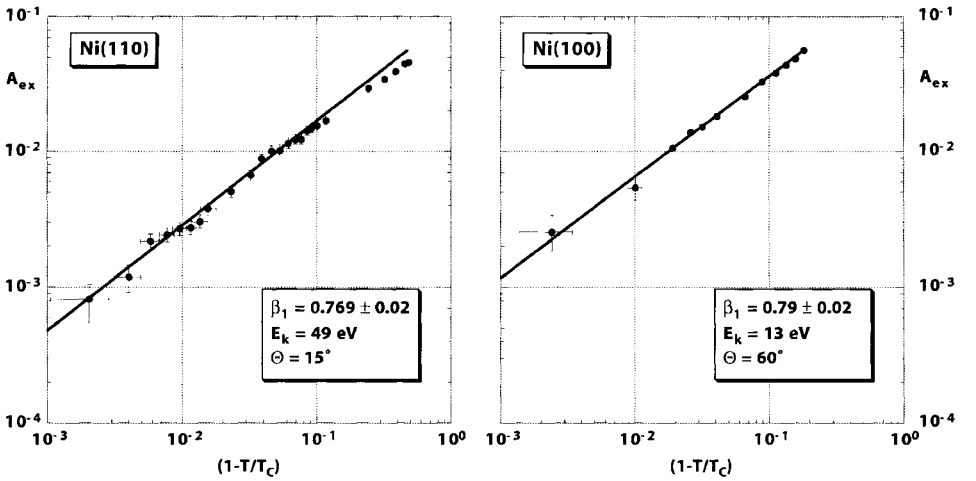


Fig. 9.24. Critical behavior of the exchange asymmetry in the vicinity of $T_c$ at different Ni surfaces (taken from Alvarado et al., 1982a).

the surface magnetism in rare earth materials show a dramatically different picture. A well-known example is the Gd(0001) surface, which shows a magnetic order at the surface well above the bulk critical temperature (Rau, 1983; Weller et al., 1985a, b; Rau et al., 1986). A surface critical temperature as high as $T_{C,S} \approx 315$ K has been reported, as compared to a bulk value of $T_{C,B} = 293$ K. A similar behaviour has been found on Tb(0001) surfaces (Rau and Jin, 1988; Rau et al., 1988), suggesting that this might be a more general property of rare earth magnetic systems. The origin of this enhanced surface magnetic order is tentatively attributed to an enhanced coupling in the topmost rare earth layer. Note, that this interpretation in turn implies a reduced coupling between the surface layer and the bulk just as we have discussed Subsection 9.4.1.2.

*9.4.1.4. Magnetic size effects in ultrathin films*

So far we have considered only semi-infinite magnetic systems in order to concentrate on surface-induced effects. In ultrathin magnetic films, in particular those grown on non-magnetic substrates, we also have to take into account the interface and the dimensionality. Systems with a reduced dimension exhibit striking new aspects in the critical behavior. Within the framework of scaling theory a pronounced variation of the magnetic ordering temperature with the film thickness $t$ has been predicted (Barber, 1983). This "finite size scaling" should follow a power law with a shift exponent $\lambda$ (Allan, 1970)

$$\frac{T_c(t) - T_{C,B}}{T_{C,B}} \sim C_0 t^{-\lambda}. \tag{9.58}$$

The existence of this behavior was proven in the pioneering work of Gradmann et al. on Ni films (Gradmann et al., 1985). The shift exponent $\lambda$ is closely related to the exponent of the

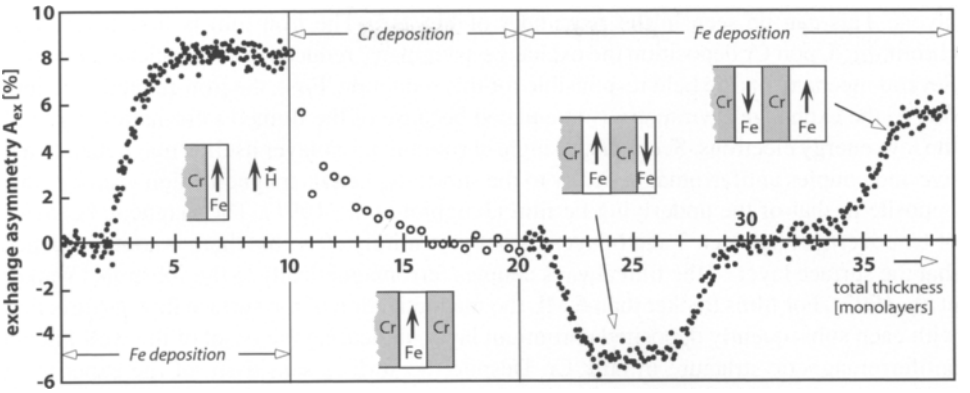


Fig. 9.25. Left panel: Development of ferromagnetic order in Fe-films on Cr(100). The exchange asymmetry $A_{ex}$ in the $(2\bar{2})$ beam is measured as a function of film thickness during the iron deposition at $T = 390$ K. The primary energy was set to $E = 73$ eV and the angle of incidence was $\Theta = 29°$ with respect to the surface normal. Above an Fe coverage of 2 ML one clearly observes the onset of ferromagnetism in the film, giving rise to a non-zero exchange asymmetry (which reflects the behavior of the remanent magnetization). Center panel: Reduction of the exchange asymmetry from the 10 ML Fe film upon subsequent Cr deposition. Because the magnetism in the Fe layer is not significantly influenced by the Cr cover, the behavior of $A_{ex}$ reflects the surface sensitivity of the experiment. Right panel: Antiparallel magnetic coupling of the second Fe layer through the Cr interlayer, which can be seen by the reversed sign of $A_{ex}$. The variation of the exchange asymmetry in the thickness regime above 25 ML is determined by the complicated coupling behavior of the two Fe films. From Carbone and Alvarado (1987).

correlation length, $\nu = 1/\lambda$, and may thus serve as a further indication of the universality class of the given magnetic system.

The thickness dependence of the Curie temperature in ultrathin films has an interesting consequence. Ultrathin films are usually grown epitaxially under UHV conditions and with the template kept close to room temperature. Measuring the exchange asymmetry in SPLEED under the above circumstances during the growth process directly shows the onset of ferromagnetic order at a critical thickness $t_c$. Below this thickness the Curie temperature is less than room temperature, and no long range magnetically ordered state can be achieved, corresponding to a zero exchange asymmetry. At the critical thickness $t_c(T)$ long-range ferromagnetic order sets in. This leads to a steady increase in the exchange asymmetry with film thickness until the coverage exceeds the information depth of the low energy electrons, causing the exchange asymmetry to show a saturation behavior. An example for this behavior is given in Fig. 9.25, monitoring the growth of iron on a Cr(100) surface by means of the exchange asymmetry (Carbone and Alvarado, 1987).

### *9.4.1.5. Interlayer coupling in magnetic trilayers*

The sign of the exchange asymmetry at a given diffraction condition is unambiguously connected to the direction of the remanent magnetization. A magnetization reversal causes a sign change in $A_{ex}$, which is essentially the reason why spin–orbit and exchange induced effects in the scattering asymmetry can be separated. The sign of the exchange asymmetry can therefore serve as an indicator of the coupling character between two ferromagnetic

layers. This can be seen in the remainder of Fig. 9.5. The iron film is first covered by chromium. Upon Cr deposition the exchange asymmetry reduces in a complicated manner. Several mechanisms are held responsible for this reduction. First, the iron-related contribution to the exchange asymmetry is attenuated because of the limited information depth of the low-energy electrons. Secondly, a single chromium monolayer itself is magnetically active and couples antiferromagnetically to the substrate, i.e., its magnetization vector points opposite to that of the underlying Fe film (Jungblut et al., 1991). The magnetic behavior of Cr coverages between 2 and 6 layers is not yet entirely clear, but there is some evidence that the surface layer of the film always couples ferromagnetically to the substrate (Walker et al., 1992). For films thicker than 6 ML the magnetization of the surface flips its direction with each subsequently deposited chromium layer, indicating the onset of the well-known antiferromagnetic structure in bulk Cr. Despite the surface sensitivity of the experiment the exchange asymmetry will be the average value over 2–3 atomic layers and thus close to zero, due to the alternating magnetization vector in the neighboring lattice planes. This explains the disappearance of $A_{ex}$, at a Cr coverage of about 10 ML.

For a subsequent coverage with Fe we find again a non-zero exchange asymmetry, but with the opposite sign. This finding leads to two important conclusions: (i) there is a magnetic coupling of two ferromagnetic layers through an antiferromagnetic interlayer; (ii) the negative sign of $A_{ex}$, indicates that the magnetization vector in the top Fe film is oriented oppositely to the bottom one, i.e., the coupling is antiferromagnetic for this particular thickness of the Cr interlayer. The thickness of the spacer layer is the important parameter in this phenomenon, since a number of studies have proven that the coupling character changes several times between ferromagnetic and antiferromagnetic coupling as a function of the interlayer thickness (Grünberg et al., 1986; Purcell et al., 1991; Unguris et al., 1991). It is therefore often referred to as oscillatory exchange or interlayer coupling, and has been found in the meantime in a large variety of systems including practically all 3d, 4d and 5d elements as interlayer materials (Parkin, 1994). We will go into some more detail on the likely electronic origin of the interlayer coupling in Section 9.5.4.

### *9.4.2. Inelastic scattering (SPEELS)*

The surface sensitivity of electron spectroscopy and scattering methods is due to the small inelastic mean free path of low-energy electrons. This comes about by the strong interaction of the electrons with the solid, which is mediated via a number of energy loss mechanisms involving phonons, plasmons, and electronic intra-/interband transitions. These excitations can be analyzed spectroscopically by taking an energy spectrum of the backscattered electrons. This is the basic principle of energy electron loss spectroscopy (EELS) which has found wide applications in the investigation of vibrational excitations at surfaces.

The individual loss mechanisms not only cause corresponding structures in the energy spectrum, but are also reflected in the angular distribution of the inelastically backscattered electrons (Ibach and Mills, 1982). Centered around the direction of the specular reflection one finds the so-called "dipolar cone". These are electrons which have suffered energy losses with a rather small momentum transfer. They are scattered from long-ranged dipolar fields in front of the surface, caused, for example, by charge density fluctuations due to elementary excitations in the solid. These excitations may be optical phonons, plasmons, or

relaxations in the electronic system associated with interband transitions. Another origin of these dipolar fields are vibrational excitations of adsorbates which lead to fluctuating dipole moments. In particular the latter loss channel is the basis for the success of EELS investigations in adsorbate physics. Besides the dipolar scattered intensity, a non-zero intensity contribution is also found at rather high scattering angles, corresponding to a large momentum transfer. This is the regime of the so-called "impact scattering". The impact scattering process is caused by short-ranged interactions within the surface. Therefore, in contrast to the dipolar scattering mechanism, the impact scattering requires the electrons to enter the solid before any energy loss event can occur. The dominant elementary excitation in this regime is the production of electron–hole pairs due to electronic interband transitions.

Recalling the situation in low energy electron diffraction, we can ask, of course, whether or not spin-dependent effects can be observed in the inelastic electron scattering from ferromagnets, too. A spin-dependent energy loss can show up in two different ways, namely as a one-step and as a two-step process. In the one step process, the energy loss occurs during a single spin-dependent and inelastic scattering event. This is the process we are mostly interested in. In the two-step mechanism, the electron undergoes an elastic spin-dependent diffraction step first, and subsequently suffers a spin-independent inelastic scattering process. Potential candidates for spin-dependent energy loss mechanisms in the sense of the one-step process are plasmons, electron–hole pairs, and, of course, the magnetic counterpart to phonons, the magnons or spin waves. Plasmons are predicted to have only minimal polarization effects (Helman and Baltensperger, 1980). Due to experimental limitations, out of the remaining two elementary excitations up to now only electron–hole pairs have been reliably identified and shown to have a spin dependence. We will therefore concentrate on this process in the following.

In analogy to SP-LEED we can perform two kinds of spin-polarized EELS experiments, an "incomplete" and a "complete" scattering experiment. Both require a spin-polarized primary beam, but in the complete experiment we measure the change in the spin-polarization of the primary electrons in addition to the exchange asymmetry in the intensity spectrum. Since only a complete scattering experiment yields a detailed picture of the spin-dependent scattering events, we will go into some details of this method. The basic observation in an EELS experiment is the following: We send in a spin-polarized electron with a definite kinetic energy $E_0$, which is scattered off the remanently magnetized surface. We then observe another electron at a smaller energy $E_0 - \varepsilon$, the spin-polarization of which is changed with respect to the primary beam. It is essential now to realize that the electron after the scattering event is not identical with the primary one, but the result of an exchange process. This becomes obvious if we go through the scattering process step by step. First, the primary electron enters the solid and occupies an electronic state in the empty part of the band structure above the vacuum level. As we have a ferromagnetic sample, both the occupied and unoccupied bands are spin-split due to the exchange interaction. The spin-splitting in the high energy empty states, however, is generally much smaller than in the occupied states and therefore often neglected. The electron then thermalizes down to the Fermi energy via elementary excitations (phonons, plasmons, etc.). In the vicinity of the Fermi level, the spin-splitting is important and leads to different densities of states for the majority (spin-up) and minority (spin-down) electrons. As a characteristic feature of a ferromagnet the

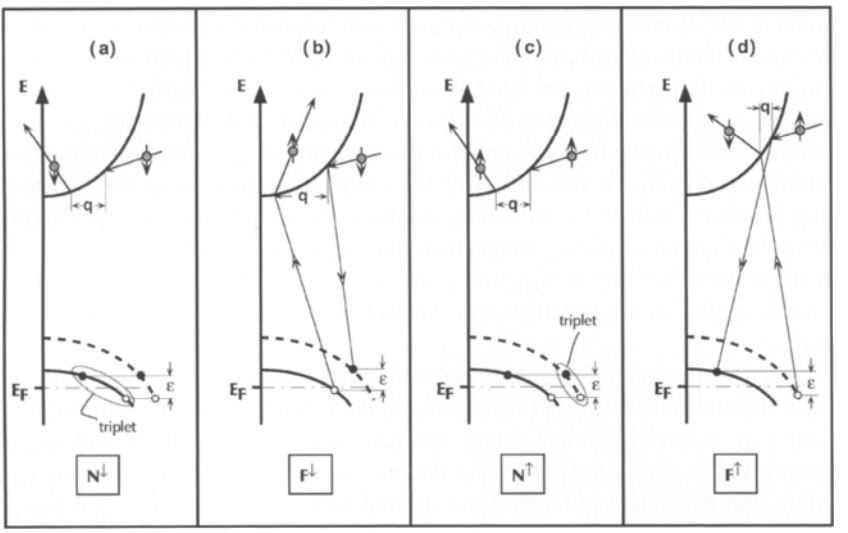


Fig. 9.26. Schematic representation of flip (F) and non-flip (N) electron energy loss processes associated with electron–hole pair generation (for reasons of simplicity, the exchange-splitting in the upper states is neglected). One distinguishes non-flip spin down (a), flip spin-down (b), non-flip spin up (c), and flip spin-up processes (d). In non-flip processes (a) and (c) either a majority or minority spin electron–hole pair can be excited. The scattered electron and the electron excited above the Fermi level form a singlet or a triplet state. At low primary energies the probability for triplet scattering is expected to be small.

empty minority DOS is always higher than the majority one (Section 9.2.1). With a certain probability, which depends on the density of the empty states of the right spin character, the deexcitation takes place in a single step and the energy is transferred to an electron in an occupied spin state. This electron is then lifted above the vacuum level, where it may leave the crystal with a kinetic energy $E_0 - \varepsilon$ towards the detector. We assume that no spin-flip occurs during the deexcitation process of the primary and the excitation of the secondary electron. After the scattering process the electronic system of the solid is left with an electron above and a hole below the Fermi level. The energy difference or loss $\varepsilon$ corresponds to the creation energy of the electron–hole pair. Depending on the spin character of the primary and secondary electrons we can have different situations, each leading to a separate contribution to the scattered intensity. Suppose, we have a spin-up primary electron. The secondary electron can have either spin-up or spin-down character. We denote the first case a "non-flip" process with a rate $N^{\uparrow}$, and the second case a "flip" process (because the spin of the outgoing electron is reversed with respect to the primary one), which takes place with a rate $F^{\uparrow}$ (Fig. 9.26). For flip processes we are left with an electron and a hole of opposite spin character, hence a Stoner excitation. Similarly, for a down-spin primary electron we have the flip and non-flip rates $F^{\downarrow}$ and $N^{\downarrow}$.

In the following we will be mostly interested in the flip processes because they are a measure of the elementary electronic excitations in a ferromagnet, the Stoner excitations. In this case the energy loss $\varepsilon$ represents the energy difference between the electron in the unoccupied minority spin band and the hole in the majority spin band. In general, electron

and hole have different **k**-vectors and the energy difference $\varepsilon$ does therefore not directly correspond to the exchange splitting of the bands (which refers to the same wave vector). The difference in the wave vectors of electron and hole is reflected in the momentum change **q** of the outgoing electron. A realistic experiment measures a mixture of the various flip and non-flip rates. According to Yin and Tosatti (1981), the rates can be composed in the following manner to yield the intensity asymmetry and spin-polarization in an experiment:

$$A_{\text{in}}(E_0, \varepsilon, \mathbf{q}) = \frac{(N^{\uparrow} + F^{\uparrow}) - (N^{\downarrow} + F^{\downarrow})}{(N^{\uparrow} + F^{\uparrow}) + (N^{\downarrow} + F^{\downarrow})}, \tag{9.59}$$

$$P_{\text{in}}(E_0, \varepsilon, \mathbf{q}) = \frac{(N^{\uparrow} + F^{\downarrow}) - (N^{\downarrow} + F^{\uparrow})}{(N^{\uparrow} + F^{\downarrow}) + (N^{\downarrow} + F^{\uparrow})}. \tag{9.60}$$

From these two equations we can immediately draw two important conclusions. First, even from a knowledge of both $A_{\text{in}}$ and $P_{\text{in}}$ only the differences in the flip and non-flip rates can be determined, but not the individual rates. Second, some magnetic information can already be extracted from a measurement of the inelastically scattered intensities via $A_{\text{in}}$. This situation calls for an "incomplete" scattering experiment involving a polarized primary electron beam and a conventional detector for the scattered electrons.

*9.4.2.1. Stoner excitations at magnetic surfaces*

In order to see how the energy losses due to an electron–hole pair creation show up in a SPEELS spectrum discussion an experimental example is most appropriate. This example is given in Fig. 9.27 showing the energy loss spectra from a Ni(110) surface. The experiment was carried out in the incomplete fashion, using a polarized primary beam and measuring the intensity asymmetry upon spin reversal of the primary beam or sample magnetization reversal. The upper panel of Fig. 9.27 depicts the intensity distributions in the specularly reflected beam as a function of energy loss for spin-up ($I^{\uparrow}$) and spin-down electrons ($I^{\downarrow}$), clearly showing a difference at energy losses above 100 meV. The spectra $I^{\uparrow}$ and $I^{\downarrow}$ are used to calculate the scattering asymmetry

$$A_{\text{in}}(E_0, \varepsilon, \mathbf{q}) = \frac{I^{\uparrow} - I^{\downarrow}}{I^{\uparrow} + I^{\downarrow}}. \tag{9.61}$$

The resulting asymmetry spectrum (Fig. 9.27b) is characterized by a pronounced energy loss dependence with a broad extremum between 200 and 300 meV energy loss. A magnetization reversal preserves the shape of the curve, but changes the sign, thereby proving the predominant magnetic origin of the observed asymmetry. The experimental asymmetry is rescaled on the right-hand side to correct for the incomplete polarization of the primary beam. A small difference in the curves when the magnetization is reversed is due to the influence of spin–orbit coupling.

How can this result be related to Stoner excitations? After all, the spectrum does not exhibit a sharp feature at about 300–400 meV, which might be inferred from the discussion above and should be related to the exchange splitting. The spectral resolution of the experiment of 35 meV is high enough to prevent a broadening of such a feature beyond the level

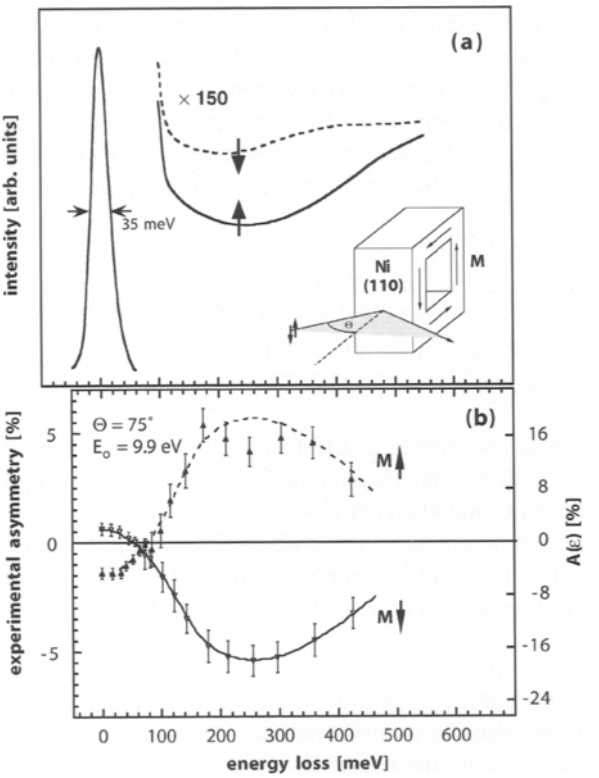


Fig. 9.27. Spin-polarized electron energy loss spectroscopy from Ni(110). (a) Typical electron energy loss spectra for spin-up and spin-down primary electrons, corrected for the finite polarization of the GaAs source. The measurements have been made in the indicated geometry (inset) in the specular beam at room temperature. (b) Intensity asymmetry distributions for the two directions of the magnetization. The asymmetry $A(\varepsilon)$ is scaled to a completely polarized primary beam.

of recognition. In order to explain this surprising finding we have to look into some details of the Ni band structure and the excitation process. First of all, a close inspection of the Ni density of states (DOS) or band structure (Figs. 9.2 and 9.3) reveals that there are only very few majority spin states above the Fermi level. This is due to the high band filling and the small exchange splitting in Ni. We can therefore neglect the spin-up flip rate $F^{\uparrow}$, which is a considerable simplification. Second, results from other experiments indicate that the two non-flip rates are nearly equal with only a weak energy dependence (Abraham and Hopster, 1987). Under these circumstances one deduces from Eq. (9.53)

$$A_{\mathrm{in}}(E_0, \varepsilon, \mathbf{q}) \propto -F^{\downarrow}. \tag{9.62}$$

The flip rate $F^{\downarrow}$, however, describes the creation of minority electron–majority hole pairs across the Fermi level, i.e., a Stoner excitation. For an experiment on the specular beam the asymmetry distribution should therefore indeed reflect the creation rate of Stoner ex-

citations at $\mathbf{q} = 0$. The condition $q = 0$ ensures that only vertical Stoner excitations are selected, but these can occur at any wave vector throughout the bulk Brillouin zone. The exchange splitting depends on $\mathbf{k}$, too, giving each individual electron–hole pair a different value for the energy loss. In other words, the measuring process samples different values of the exchange splitting, and the resulting asymmetry must be interpreted as the probability distribution of a local exchange splitting at the Fermi surface. In the absence of an energy and $\mathbf{k}$-dependence of the transition matrix elements, the asymmetry would be directly comparable to the Stoner density of states at $|\mathbf{q}| = 0$ (Kirschner, 1985b). Further experimental data are needed to clarify this point. In the meantime, the above results state the maximum of the asymmetry curve to be associated with the average exchange splitting in the Ni band structure of the order of 0.3 eV. This value agrees with the predictions from band structure calculations, if electronic correlations are properly accounted for. We will come back to this point in Section 9.5.

In order to judge the application of SPEELS to other systems than Ni it is important to recall the approximation made in the above case. First, Ni is a saturated ferromagnet with only very few majority spin holes. This was the reason for our neglect of the spin-up flip rate $F^{\uparrow}$. In Fe, for example, a significant part of the spin-up bands reaches above $E_F$. Thus the $F^{\uparrow}$ flip rate will become important. It is mandatory in such a situation to perform a complete scattering experiment, i.e., measuring both the flip and non-flip rates. An early experiment on Fe proved that the flip rates $F^{\uparrow}$ and $F^{\downarrow}$ are of the same magnitude, and that the $F^{\uparrow}$ contribution must be taken into consideration for the correct evaluation of the data (Kirschner, 1985a). It is also worthwhile to note, that the partial flip-rates in this experiment showed consistently a maximum at about 2 eV energy loss (Fig. 9.28), corresponding to the calculated d-band exchange splitting in iron.

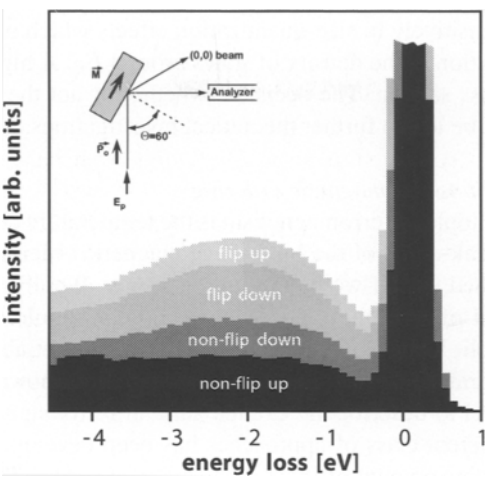


Fig. 9.28. Complete scattering experiment on Fe(110), showing the decomposition into the individual flip and non-flip rates. The energy of the primary beam was chosen as $E_p = 21$ eV, and the magnetization was along the ⟨100⟩ direction (Kirschner, 1985a).

*9.4.2.2. Stoner excitations in ultrathin films*

The averaging view of SPEELS with respect to the electronic structure of a ferromagnet can be employed to learn more about the electronic states in systems of reduced dimensions. Many of the physical properties change with the reduction of the dimensionality. The obvious question is, how this reduction will affect the spectrum of the Stoner excitations. Only a few results in this direction have been published so far (Idzerda et al., 1988; Kämper et al., 1992). A relatively extended complete scattering study has been carried out for the Co/Cu(100) system (Kämper et al., 1992). Cobalt in the fcc structural modification, which is of interest here, may be regarded as an intermediate case between Fe and Ni. It is not a saturated ferromagnet, but the number of empty spin-up states is significantly smaller than in Fe. Nevertheless, the results of Kämper et al. on a 20 ML film still show a sizable $F^{\uparrow}$ contribution. This comes by the fact that the experiment detected electrons away from the specular beam in order to put more emphasis on the impact scattering and thus on the Stoner excitations. The shoulder in both flip rates $F^{\uparrow}$, $F^{\downarrow}$ is found at 0.8 eV energy loss and associated with the average exchange splitting. This value must be compared with a d-band splitting of $\Delta E_{ex} \approx 1.2$ eV observed in spin-resolved photoemission (Schneider et al., 1991).

At a coverage of 20 ML the electronic structure of the film is essentially bulk-like and size-quantization effects play only a minor role. According to the results in Kämper et al. (1992), however, the shape of the intensity asymmetry and the partial flip rates remains almost the same down to coverages of 2 ML. The absolute value of the scattering asymmetry, in contrast, was reduced by a factor of 2, mainly due to an assimilation of the two flip-rates. This latter effect was unlikely to be caused by a reduced Curie temperature of the 2 ML film, as the choice of the measuring temperature of 80 K ensured $T < 0.3 \cdot T_c(t)$. Among several other mechanisms, an increased scattering from free-electron like Stoner excitations has been invoked. These excitations involve a hole of a given spin in the d-bands and an electron of opposite spin in the sp- (free electron like) state. These free-electron like states respond more sensitively to size-quantization effects which may lead to extra structures in the sp-contribution to the density of states around $E_F$. A higher DOS at $E_F$ means a higher scattering cross section. The decision, whether or not the above effect is due to size-quantization must be left to further theoretical investigations.

*9.4.2.3. Stoner excitations and magnetic ordering*

A particular intriguing topic in ferromagnetism is the temperature dependence of the magnetic ordering. The break-down of the long-range magnetic order at $T \geqslant T_c$ is an experimentally well-established fact. If we believe in the Stoner–Wohlfarth model of ferromagnetism, the breakdown of the long-range magnetic order should be accompanied by a collapse of the spin-split bands. Consequently, the ferromagnet above $T_c$ should behave electronically like a paramagnet like, say, copper. Also well-known, however, is the failure of the Stoner model to describe the excited state in ferromagnets, in particular close to $T_c$. Therefore a different class of approaches has been developed, having in common the prediction of a varying amount of short-range magnetic order. The short-range order is established by a locally defined exchange-split band structure.

As long as we have exchange-split electronic states, we should be able to observe Stoner excitations. It therefore appears that spin-resolved electron energy loss spectroscopy may

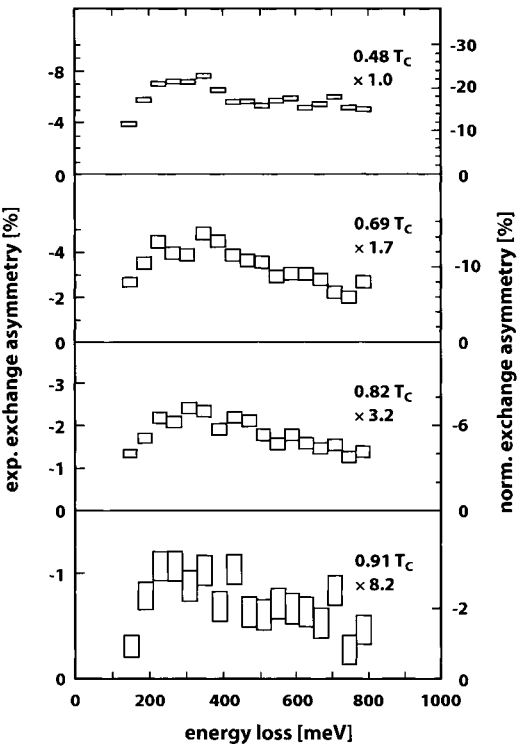


Fig. 9.29. Temperature dependence of the exchange asymmetry in SPEELS from a Ni(011) surface. Deviating from the situation in Fig. 9.27, the primary energy was set to $E_p = 4$ eV, the angle of incidence was chosen $\Theta = 60°$, and the spectra were measured 5° off the specular direction. The sample temperature during the measurement is given in fractions of the Curie temperature $T_c$ for bulk Ni. The spectra have been rescaled by a factor indicated in each panel, so that the area under each curve is the same as that at $T/T_c = 0.48$ (Kirschner and Langenbach, 1988).

be a suitable tool to discriminate between the persistence and the disappearance of a spin-splitting. This was the motivation for a number experiments intended to answer this question. Again, results from Ni may serve as an instructive example (Fig. 9.29) (Kirschner and Langenbach, 1988). The graph depicts the exchange asymmetry measured at different temperatures approaching $T_c$. The spectrum at $T \approx 0.5 \cdot T_c$ exhibits essentially the same features as already discussed in Section 9.4.2.1. The magnitude of the asymmetry curve is larger, though, because exchange effects have been emphasized by measuring in slightly off-specular direction. It is obvious that the shape of the spectra does not change with increasing temperature. In particular, the maximum of the asymmetry remains at the same energy loss around 300 meV even at $T > 0.9 \cdot T_c$. The gradual collapse of the exchange-split bands predicted by the Stoner model should show up in the spectra as a change of the spectral shape and a shift of the curve maximum to smaller energy losses. In contrast, the data in Fig. 9.29 give a strong indication of an almost unchanged exchange-split band structure up to $T_c$. Although the experiments have not been extended above $T_c$ – which

would be meaningless for an incomplete scattering set-up – the available results strongly support the application of local-band scheme to Ni at and above $T_c$. It must be kept in mind, however, that the integrating nature of a SPEELS experiment restricts the statement to the averaged band structure at the Fermi surface. A local collapse of the exchange splitting at limited regions in **k**-space cannot be excluded. This may explain the apparent discrepancy of the above results to findings from **k**-selective methods, such as direct and inverse photoemission techniques. We will come back to this point in more detail in Section 9.5.2.4.

Similar experiments on the question of magnetic order can be and have been performed on thin films. For this purpose the particular property of a thickness dependent $T_c$ in thin films comes at hand. By choosing thin enough films the Curie temperature might be pushed down to room temperature or even lower. As a particular aspect of a complete scattering experiment, its application is not limited to the regime below $T_c$. This has been demonstrated for fcc-Co films on Cu(100) (Kämper et al., 1992). A quantity that can be measured above $T_c$, besides the total flip and non-flip rates, is the so-called depolarization. This describes the spin-polarization of the scattered electron at energy loss $\varepsilon$ normalized to the spin-polarization of the elastically scattered electrons. Comparing the behavior of the depolarization in Co films below and above $T_c$, the authors concluded on the persistence of a local magnetic order above the critical temperature. In addition, the spin-resolved loss spectra from films below and above $T_c$ showed essentially the same features. These findings suggest that also fcc-Co exhibits a short-range magnetic order and thus a local spin-split band structure in some region above the Curie temperature. This conclusion agrees with spin-resolved photoemission results (see Section 9.5.2.5).

## 9.5. Emission of spin-polarized electrons from ferromagnets

### *9.5.1. Some general remarks on spin-polarized photoelectron spectroscopies*

Photoelectron spectroscopy (PES) has become a standard tool in the investigation of occupied electronic states. In particular its angle-resolving variant (ARPES) has been widely and successfully employed to lay a basis to our current understanding of the electronic band structure in solids. This development has been greatly supported by the availability of dedicated synchrotron radiation facilities, which enabled the experiments to be carried out with nearly continuously variable excitation energies. With respect to the empty (unoccupied) electronic states the same holds for inverse photoelectron spectroscopy (IPES) or Bremsstrahlen isochromate spectroscopy (BIS), which involves the reverse process to the photoemission event, although the development was not as spectacular. Both techniques and their physical background have been described in a number of books and review articles (see, for example, Feuerbacher et al., 1978; Himpsel, 1983; Hüfner, 1988; Smith, 1988). It will thus suffice to reproduce the essential results which are important for the understanding of the spin-polarized versions and their application to problems in surface magnetism.

In photoemission we are exciting an electron from an occupied state into an empty state above the vacuum level by means of a photon of sufficiently high energy. This interband transition is governed by optical selection rules. This means that the polarization state of the incident light and the symmetry character of the occupied and unoccupied electronic

states determine the transition probability. In a single particle picture the occupied state is often termed "initial" state, whereas the empty state is referred to as "final" state. The excited electron then somehow leaves the crystal and is analyzed by an appropriate electron spectrometer. In inverse photoemission we basically reverse the sequence of events. The electron is injected into the solid with a defined kinetic energy and wave vector. It will occupy a state in the empty part of the band structure above the vacuum level $E_{\text{vac}}$. With a certain probability the "hot" electron can decay into an empty state at the Fermi level $E_{\text{F}}$ within a single event, thereby emitting a photon which leaves the crystal and can be analyzed by a photon detector. The deexcitation transition is determined by the same selection rules as in the direct photoemission process. An important difference appears in the cross sections for the direct and inverse photoexcitation process. The cross section for the radiative deexcitation transition is a factor of about $10^{-5}$–$10^{-3}$ smaller than the one for the corresponding direct photoemission process (Smith, 1988). This is essentially due to the difference in the phase space cell available for the creation of an electron and a photon.

Both the direct and inverse photoemission process follow the same laws for energy and momentum conservation

$$E_f = E_i + h\nu, \tag{9.63}$$

$$\mathbf{k}_f = \mathbf{k}_i + \mathbf{q}. \tag{9.64}$$

In the UV regime ($h\nu \leqslant 35$ eV) the photon momentum $\mathbf{q}$ is negligible. Under these circumstances the transitions take place at the same $\mathbf{k}$ point in the Brillouin zone and are therefore said to be "vertical" transitions. It has to be kept in mind, however, that the momentum conservation is only fulfilled modulo a reciprocal lattice vector $\mathbf{G}$.

We will now look in some more detail into the process of direct photoemission. Most of the arguments developed hold in a similar fashion for the description of the inverse process. A rigorous treatment must take the photoemission process as one single event. Several of these so-called "one-step" theories have been developed over the last two decades with increasing degree of refinement and sophistication. The final state of the photoelectron in these approaches is considered to be a "time-reversed LEED state" (Pendry, 1975). Such a treatment corresponds to the inclusion of the multiple scattering events in the solid and at the surface, which the electron undergoes after the optical transition and before being registered in the spectrometer. The output of a typical one-step photoemission calculation yields a spectrum that may be more or less directly compared to the experimental one. This approach has two major drawbacks. Firstly, seen from the didactic point of view, the one-step approach largely masks the physics behind the photoemission process. Secondly, because of the considerable computational complexity, the calculations cannot cover any experimental situation whatever and have been carried out only for selected examples.

These are some of the reasons why a much simpler model of photoemission is still very popular and in wide-spread use among experimentalists. The photoemission process in a solid can be intuitively broken down into a sequence of five events, each of which can be treated separately (Fig. 9.30):

(1) Transmission of the incident light through the surface.

(2) Penetration of the light through the solid.

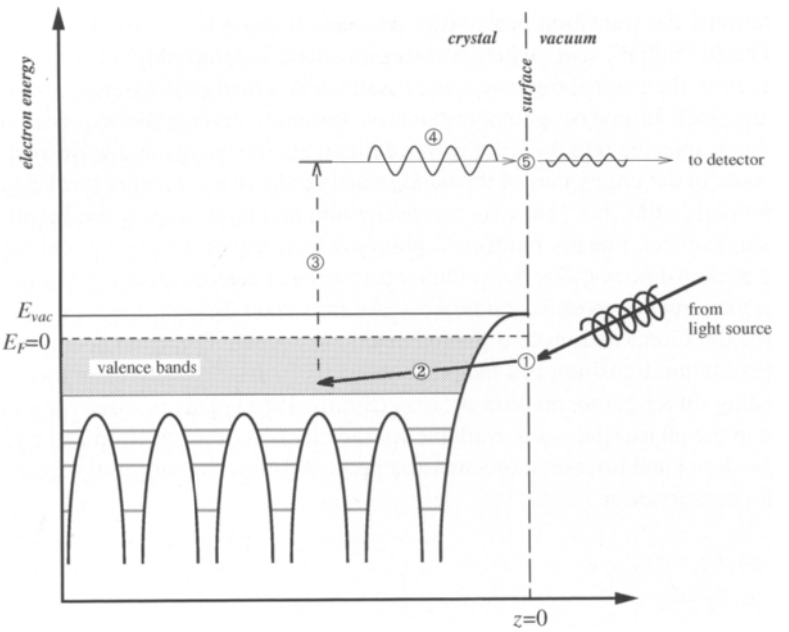


Fig. 9.30. Schematic picture of the three-step model of photoemission. For explanation see text.

(3) Excitation of the photoelectron (interband transition).
(4) Transport of the "hot" electron to the surface.
(5) Escape of the photoelectron through the surface.

Steps (1) and (2) describe the interaction of the light with the solid and are commonly treated within the classical macroscopic dielectric theory (metal optics) by means of Fresnel's equations (Whitaker, 1978). This is, of course, already a non-trivial approximation, since the microscopic distribution of the electromagnetic field in the near-surface region is completely neglected. Because the light wavelength $\lambda$ in UV photoemission experiments ($\lambda \sim 400$ Å at 30 eV) is much larger than the interatomic distances ($\sim$5 Å), the vector potential $\mathbf{A}$ is usually assumed to be constant in the near-surface region where the excitation takes place. This leads to the so-called "dipole approximation" in which the light operator $\mathbf{O}$ takes the simple form

$$\mathbf{O} \sim \mathbf{A} \cdot \mathbf{p}, \quad \text{or alternatively,} \quad \mathbf{O} \sim \mathbf{e} \cdot \mathbf{r} \tag{9.65a, b}$$

with $\mathbf{p}$ denoting the electron momentum operator and $\mathbf{e}$ the polarization vector of the light. Already at this point, one has to distinguish between UV and soft X-ray photoemission, as the above argument becomes questionable at higher excitation energies ($\lambda \sim 25$ Å at 500 eV). The vector potential must then be considered as a spatially varying quantity $\mathbf{A}(r)$ (Levinson et al., 1979).

After the excitation (3) the photoelectron must leave the crystal in order to arrive at the detector (steps (4) and (5)). If (3) to (5) are viewed as independent events, one ends

up with the well-known "three-step" model of photoemission, which has been originally proposed by Fan (1945), and underwent a series of refinements over the years (Mayer and Thomas, 1957; Spicer, 1958; Himpsel, 1983). The above effective single-electron picture within the three-step model represents the simplest approach to the analysis of photoemission data. On the one hand, despite its rigorous approximations, the three-step model has been, and still is, applied with a surprising success, to obtain a qualitative interpretation of photoemission results. This is particularly true for its spin-dependent version, which has been developed at the beginning of the 80's (Wöhlecke and Borstel, 1984). It allowed a symmetry-resolved investigation of the electronic bands in non-magnetic materials, exploiting the mechanism of optical orientation. In our discussion of the experimental data, we will often refer to this approach, if no *ab initio* calculations for the specific system exist.

The actual photoexcitation process is often considered to be the most important step in photoemission. We will therefore inspect the corresponding theoretical background more closely. The excitation lifts an electron from an occupied state below the Fermi energy up to an unoccupied state above the vacuum level. Expressed in a more formal way, the excitation corresponds to an electronic transition between two eigenstates of the $N$-electron system. If the disturbance of the electronic system by the light wave is small, the problem can be treated in first order perturbation theory. The contribution of a particular transition to the photocurrent is then expressed in a Fermi's golden rule form as

$$I(E_i, E_f, h\nu) \sim \left|\langle \Psi_f^N | \mathbf{O} | \Psi_i^N \rangle\right|^2 \delta\left(E_f^N - E_i^N - h\nu\right). \tag{9.66}$$

$E_f^N$ and $E_i^N$ are the energies of the initial and final $N$-electron state $\Psi_i^N$ and $\Psi_f^N$. Note that the meaning of initial and final state are different in the many electron picture. The term initial state refers to the $N$-electron system in the ground state and the final state describes the $(N-1)$-electron system after the excitation has taken place. The total photocurrent is given by the sum over all possible initial and final states

$$I(h\nu) = \sum_{i,f} I\left(E_f^N, E_i^N, h\nu\right). \tag{9.67}$$

This expression contains all correlation effects in the $N$-electron system, and in particular the interaction of the excited electron and the remaining $N-1$ electrons. These many-electron states are either of atomic-like, localized nature in the case of core level excitations, or have a Bloch-like character if valence bands are concerned. Therefore the further theoretical treatment differs.

Let us concentrate in more detail on the case of UV or valence band photoemission. In order to make the problem more manageable, one usually expresses the many-particle eigenstates in terms of single particle states $|\Phi\rangle$ and energies $\varepsilon$. This procedure is carried out in the "sudden" approximation, which assumes an almost negligible interaction between photoelectron and the remaining $N-1$ electron system during excitation. Equation (9.67) then becomes

$$I(h\nu) \sim \sum_{i,f} \left|\langle \Phi_f | \mathbf{O} | \Phi_i \rangle\right|^2 A_{ii}(\varepsilon_f - h\nu). \tag{9.68}$$

$A_{ii}$ is called the spectral function of the hole state and contains the many-body correlation effects. These are observed as energy shifts of the spectral feature with respect to the ground state due to the interaction of the photoelectron hole with the electron system, and as broadening of the line width. If these correlation effects are also neglected, $A_{ii}$ reduces to a series of delta functions and one arrives at the simple single-electron model of the excitation process

$$I(h\nu) \sim \sum_{i,f} \left|\langle \Phi_f | \mathbf{O} | \Phi_i \rangle\right|^2 \delta(\varepsilon_f - \varepsilon_i - h\nu). \tag{9.69}$$

The eigenstates $|\Phi\rangle$ are Bloch functions and are therefore characterized by the wave vector $\mathbf{k}$ and band index $n$. The electronic transition, which leads to the spectral features described by the energy conservation $h\nu = \varepsilon_f - \varepsilon_i$, takes place within the band structure of the solid. For the analysis of photoelectron spectra, the energies $(\varepsilon_f, \varepsilon_i)$ are thus compared to the dispersion relations $E(\mathbf{k})$ obtained in self-consistent band structure calculations. Most of these calculations include electronic correlations in the ground state by means of a mean field approach, the so-called local density approximation. It should be pointed out that within this single particle picture the terms initial and final state have a different meaning. They indicate the position of the electron on the energy scale in the ground state electronic structure, i.e., initial state refers to the occupied state below $E_F$, and final state denotes the unoccupied state in which the photoelectron is excited. The strength of each transition is determined by the dipole matrix elements $|\langle \Phi_f | \mathbf{O} | \Phi_i \rangle|$. Whether or not a transition takes place depends on the specific form of the wave functions and the dipole operator. Group theoretical analyses (Hermanson, 1977; Eberhardt and Himpsel, 1980) have proven that the very existence of a matrix element is determined only by the symmetries of the electronic states and the light operator. It can therefore be described by a set of dipole selection rules, whereby the symmetries of electronic states are classified by irreducible representations of the appropriate point group (Seghadat and Cracknell, 1974).

In the absence of spin-orbit coupling the inclusion of a spin-splitting in Eq. (9.69) is straightforward. Since the spin is independent of the spatial coordinates and we assume spin-flips to be absent during the excitation step, the spin character is preserved during the optical excitation. The total photocurrent $I(h\nu)$ thus decomposes into a majority and minority spin contribution. With additional summation indices $s, s'$ for the spin in the initial and final state the total photocurrent then becomes (using the orthogonality of the spin states)

$$I(h\nu) \sim \sum_{i,f,s,s'} \left|\langle \Phi_f | \mathbf{O} | \Phi_i \rangle\right|^2 \delta(\varepsilon_f - \varepsilon_i - h\nu)\delta_{s,s'}. \tag{9.70}$$

Equation (9.70) describes the simplest case. Transitions take place only within the subbands of majority or minority spin character. Independent of the spin, the transition probability (dipole matrix elements) is determined by the spatial part of the wave function. This means that the same selection rules as in the nonmagnetic case apply. Because of the spin splitting in the initial and final states, which in general is different, the transitions take place at different $\mathbf{k}$ values. A schematic view of the excitation process is given in Fig. 9.31.

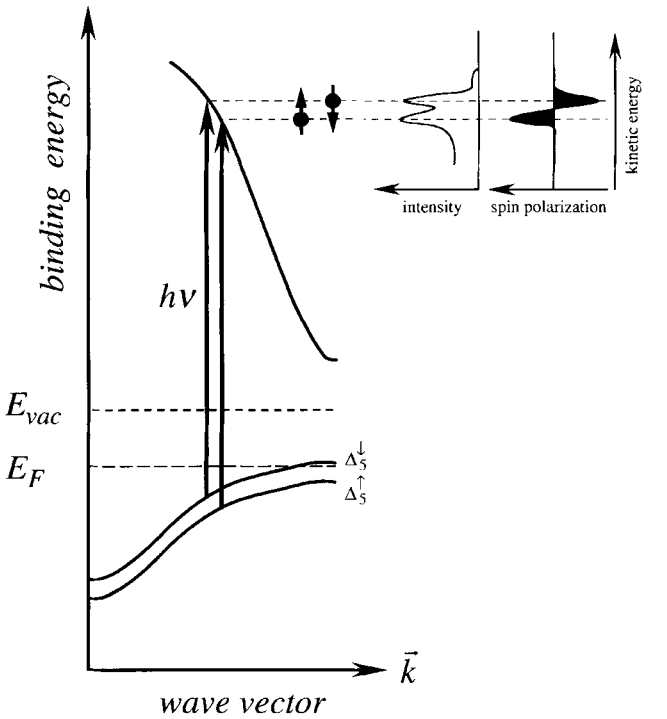


Fig. 9.31. Spin-polarized photoexcitation in a ferromagnet in the absence of spin–orbit coupling.

Therefore, under some circumstances one may be able to observe only one of the two transitions. In the ideal (non-relativistic) case, the spin polarization of the transitions is supposed to be +100% for majority electrons and −100% for minority electrons, because the initial states can be taken as pure spin states. In reality, the spin polarization observed in the experiment is often lower. Several mechanisms may be held responsible for this reduction. First of all, magnetic domain formation in the sample. Since the experiment can generally not be done in an applied magnetic field of sufficient strength to align domains, the sample has to be remanently magnetized. Remanence, however, may differ from magnetic saturation, only the latter being equivalent to a single domain state. The spin character – majority or minority – is determined with respect to the quantization axis defined by the vector of the remanent magnetization **M**. If the sample area where the spectroscopy information is collected from contains several magnetic domains, the average magnetization appears to be smaller than the magnetization in the individual domains and so does the spin polarization. Second, the electron spins are subject to thermal fluctuations, as the experiment is often carried out at ambient temperature. Third, the spectral features are broadened due to inelastic scattering, life time, and correlation effects. Depending on the size of the exchange splitting, the individual features may partially overlap, thereby again reducing the spin polarization. Finally, we have to consider spin–orbit coupling which causes a mixing of spin-up and spin-down states and may thus change the spin characters of the initial

and final state significantly. Nevertheless, spin-polarization values close to 90% have been reported in some experiments.

We can use the same formalism to understand the basics of spin-resolved inverse photoemission. The electron that enters the ferromagnetic crystal from the vacuum has to be spin-polarized for this purpose, i.e., it is usually generated from a GaAs source. Depending on its spin orientation relative to the sample magnetization **M**, it occupies an empty state within either the minority or majority band structure. Since the exchange splitting of the states far above the Fermi level is usually very small, the energies of the spin-up and spin-down excited states is approximately the same. The subsequent radiative decay of the electron down to the Fermi level is possible only for one type of spins, because a band of the correct spatial symmetry and spin character is required at the Fermi energy. Since the photon analyzer is often set to a fixed energy (a Geiger–Müller type counting device), the kinetic energy of the incoming electrons must be varied in order to get a high rate for the radiative decay in the other spin channel. The radiative transitions are governed by the same selection rules as in the direct photoemission case. There are, however, two important differences between direct and inverse photoemission which should not be ignored. Firstly, the process of radiative decay is not exactly the inverse of the photoemission event, because both initial and final states are located above the Fermi level, whereas the initial state in photoemission is located below $E_F$. The correct theoretical description of inverse photoemission requires a second quantization formalism in order to properly include the creation and spontaneous emission of the photon (Pendry, 1981). It can be shown, though, that a first-order perturbation treatment of this situation still leads to a golden rule type expression for the transition probability with a transition matrix element $M_{fi}$

$$M_{fi} = \langle \psi_f | \mathbf{O} | \psi_i \rangle \tag{9.71}$$

with $|\psi_i\rangle$ and $|\psi_f\rangle$ denoting the high energy and the low energy state in the decay process, respectively. The second difference between direct and inverse photoemission concerns the many-particle aspect. In inverse photoemission we add an electron to the system, i.e., $N \rightarrow (N + 1)$. The final state of the system from the many-electron point of view therefore differs by two electrons ($(N - 1)$ vs. $(N + 1)$). An equivalent treatment of direct and inverse photoemission is only justified as long as electronic correlation effects can be neglected. Up to now most of the analyses of inverse photoemission data are carried out under the assumption of a single-particle excitation. Within this one-electron picture the inclusion of the electron spin in order to treat spin-polarized inverse photoemission is just as straightforward as in direct photoemission. The above states $|\psi_i\rangle$ and $|\psi_f\rangle$ become in this case two-component Pauli spinors.

Inverse photoemission is very useful to investigate empty surface states. The reason is that most metals (in particular 3d ferromagnets) have a low density of states above the Fermi-level or even band gaps along certain crystallographic directions. Surface states will be located in these band gaps and can therefore be analyzed without a strong background of bulk states. This is usually more difficult to achieve in the occupied part of the band structure.

So far we have restricted ourselves to low energy excitations, i.e., to bulk interband transitions in an energy regime of several ten electron volts around the Fermi level. This is

the domain of spin- and angle-resolved photoemission and inverse photoemission, respectively. In recent years there was considerable effort involved in introducing magnetic sensitivity in the high energy version of photoelectron spectroscopy. By accessing the strongly bound and localized core levels one gains elemental selectivity. Because of the high binding energies of these level (e.g., ~700 eV for Fe 2p) the photon momentum can no more be neglected. Regardless of an angular resolution in the experiment, the excitation step already averages over a considerable fraction of the bulk Brillouin zone. Since the initial state is localized, this has no further consequence for the analysis of the core level itself. Of course, at the same time we are exciting electrons from less strongly bound core levels (for example 3p, 3s) and also from the valence bands. These are mostly affected by this **k**-averaging process, and the corresponding spectra reflect more the density of states rather than individual states at a well-defined **k**-value. The final state in this excitation process is a band state of the solid some 10 or 100 eV above the Fermi level, i.e., a time-reversed LEED state. If the core state is spin-split due to exchange interaction, the emitted photoelectron should be spin-polarized, just as in the case of valence state photoemission.

An additional complication in this high energy excitation process arises by the hole that is left behind in the core. Electrostatic interaction between the core hole and the remaining $N - 1$ electron system leads to a renormalization of the binding energy scale. This many-body effect is of course present in every photoemission process. Since the energies involved in core-level excitation are considerably higher than for valence band photoemission, many-particle effects show often up more clearly. A nice example are the satellite structures observed in Ni-core level photoemission. The decay of the core hole occurs via Auger transitions from higher-lying levels. If the outgoing photoelectron is spin-polarized, then the remaining hole must be spin-polarized, too. As a consequence, the emitted Auger electrons might carry a spin-polarization as well.

### *9.5.2. Analysis of valence electronic states*

In this section we will discuss some experimental results obtained with direct or inverse spin-polarized photoemission techniques. The emphasis is laid on the various aspects in the valence electronic structure of ferromagnetic systems. We will give experimental evidence for the ideas developed in Section 9.2.1.

#### *9.5.2.1. Spin-split bulk band structures*

The first task of a photoemission experiment must be to prove or disprove our picture of the spin-split band structure that emerges from the band structure calculations. There have been numerous approaches to this problem by conventional photoemission techniques, which were not always conclusive in this respect. In particular the question of a 3-dimensional band dispersion, indicative of a bulk band structure, was difficult to answer. The reason for this problem is in fact the high density of states at the Fermi-level of a ferromagnet. The hole lifetime is thus very short, leading to a significant lifetime broadening of the individual spectral features. The broadening increases with distance from the Fermi level, washing out the features at higher binding energy. Changes in the position of these features as a function of the excitation energy are difficult to see under these circumstances. Furthermore, a conventional experiment may identify the spin-character of a spectral feature

only through a comparison to the calculation, which does not always result in a definite and correct answer. An unambiguous band mapping of a ferromagnet electronic structure can only be achieved by spin-polarized spectroscopies. The first of this type of experiments dates back to the end of the 70's, when dedicated synchrotron radiation facilities became available. The use of synchrotron radiation facilitates the studies significantly, because the high photon flux at least partly compensates the intensity loss due to the spin polarization analysis. A spectrum from an Fe(100) surface may serve to underline the advantage of spin-resolution. The intensity spectrum – which is usually recorded together with the spin polarization and corresponds to the result of a conventional experiment – exhibits two individual spectral features (Fig. 9.32a). The energy separation of these peaks is comparable to the calculated value of the exchange splitting in the Fe 3d bands (~2 eV). This suggests that these peaks originate from an exchange–split pair of electronic states. A direct experimental confirmation of this assignment comes from the spin-polarization **P** (Fig. 9.32b). The spectrum of **P** shows a negative value at the Fermi level $E_F$, consistent with a minority spin character. With increasing distance to $E_F$ the polarization changes sign and assumes a relatively high positive value of ~60%. The positive sign of **P** corresponds to a majority spin character. The polarization spectrum has additional structure, for example, a dip at $E_B = 2$ eV. In order to obtain in detail the spin character of the individual transitions in the intensity spectrum, one calculates the so-called "partial intensities". These reflect the spin-up and spin-down contributions to the total intensity. Partial intensities $I^{\uparrow}$ and $I^{\downarrow}$, total intensity $I$ and spin polarization $P$ are related to each other by

$$I^{\uparrow} = \frac{I}{2}(1+P), \quad I^{\downarrow} = \frac{I}{2}(1-P) \tag{9.72}$$

(compare Eqs. (9.41a, b)). The result of these operations shows very clearly that the two dominant peaks in the intensity distribution are indeed of opposite spin character (Fig. 9.32c). In addition, a third peak in the majority channel becomes visible between 1 and 2 eV binding energy. At a photon energy of $h\nu = 60$ eV the transitions take place at the center of the bulk Brillouin zone, i.e., at $\Gamma$. Comparing the experimental binding energy values to a band structure calculation, the peaks can be associated with transitions from $\Gamma_{25}^{\downarrow}$, $\Gamma_{12}^{\uparrow}$ and $\Gamma_{25}^{\uparrow}$ initial states (in the order of increasing binding energy). The minority type $\Gamma_{12}^{\downarrow}$ state is not seen, because it is located above the Fermi level.

A band mapping experiment in a normal emission geometry on the same surface essentially reproduced the calculated dispersion of the bands along the $\Gamma$–$\Delta$–H direction in iron. The spectra were also found to be consistent with predictions from non-relativistic one-step photoemission calculations (Feder et al., 1984). It has to be taken into account, however, that both the band structure and photoemission calculation are carried out for the ferromagnetic ground state, i.e., $T = 0$ K, whereas the experiment takes place at room temperature. In addition, the photoemission process essentially probes an $(N-1)$ excited electron system, and not the ground state. Perfect agreement between theory and experiment should therefore not be expected and may be accidental. Nevertheless, the results show that our picture of the spin-split electronic bulk band structure is essentially correct.

Another example proves that we can extend the above approach also to the electronic states in an ultrathin film of several monolayers thickness. The system in questions consists

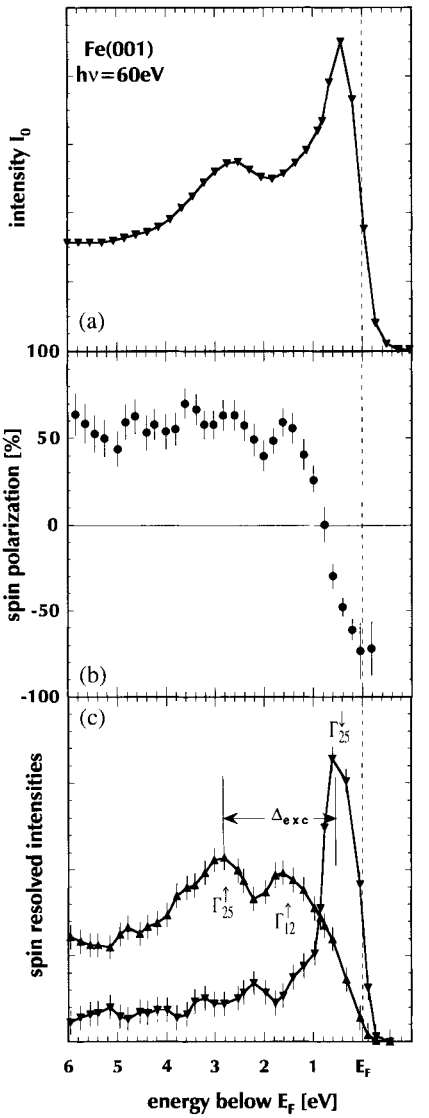


Fig. 9.32. Spin-polarized photoemission from Fe(100). Spin-integrated intensity (a), spin polarization (b), and (c) partial intensities of spin-up (▲) and spin-down character (▼) (taken from Kisker et al., 1984).

of 5 atomic layers of Co on a Cu (100) substrate. The Co atoms assume an fcc-like crystalline structure in registry with the underlying Cu lattice. In bulk materials the fcc-phase exists only at high temperatures. The film is thus a metastable system that is otherwise not accessible to electron spectroscopic investigations. In the absence of electronic structure calculations for the 5 ML film the band mapping results have been compared to a bulk band structure calculation. The calculation included exchange and spin–orbit coupling on

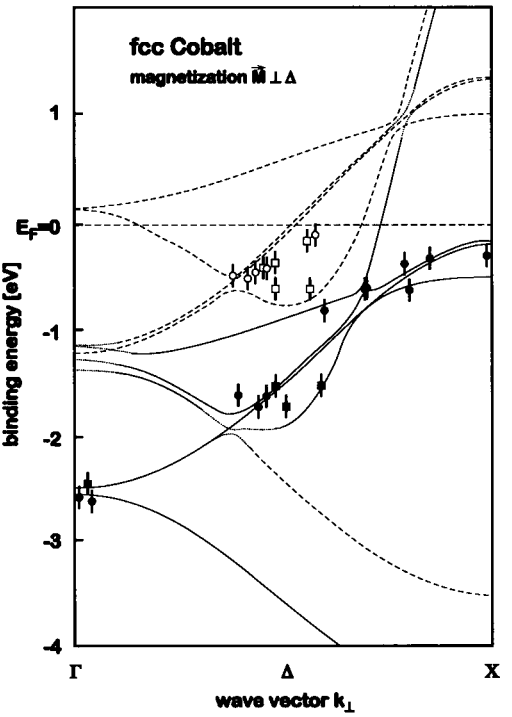


Fig. 9.33. Spin-resolved band mapping from Co(001). The samples have been 5 ML films of fcc-Co grown on Cu(100). The experimental data points for majority (closed) and minority spin states (open symbols) are compared to a fully-relativistic band structure calculation. The experiment was carried out in normal emission geometry for normally incident light (●, ○) and for a light incidence of $\Theta = 64°$ (■, □). Taken from Schneider et al. (1991).

an equal footing, i.e., was carried out in a fully relativistic formalism. This should be of minor importance for the moment as we are interested first of all in the exchange-related effects. Since the films had a (001) crystalline orientation and the experiment comprised a normal emission geometry, states along the Γ–Δ–X line in the fcc bulk Brillouin zone are tested. The experimentally observed dispersion compares surprisingly well with the calculated bulk bands, although the mean value of the exchange-splitting seen in the experiment is somewhat smaller (Fig. 9.33). This reduction can be partly accounted for by the tetragonal distortion of the films as a consequence of the in-plane lattice mismatch of ~2%. The lateral mismatch leads to a compression of the vertical interlayer distances resulting in band shifts close to $E_F$. The important conclusion from this experiment is, however, that a 5 ML thick film obviously reproduces quite closely the band dispersion expected from the respective bulk material. In other words, a few atomic layers only suffice to reproduce the gross features of the bulk electronic structure of a metal. This finding may be regarded as an independent experimental justification for the screening length argument that is used to introduce the slab geometry in electronic structure calculations.

On the basis of the currently available experimental and theoretical material, our understanding of the magnetic ground state in terms of the bulk electronic structure can be

considered quite reasonable. This is particularly true for materials with a large exchange-splitting, such as Fe and Co. In the case of Ni, as mentioned in Section 9.2.1, there was a considerable discrepancy between the theoretically predicted and experimentally found value of the spin-splitting. It was suspected that correlation effects might be responsible for this. Basically they enter the problem at two different points. Firstly, there is the electronic correlation in the ground state which is included in the band structure calculation via the exchange–correlation potential. Secondly, the electronic correlations are different for the excited system (photoelectron and remaining hole). The latter can of course only be modeled in a photoemission, but not in a ground state band structure theory. Whereas the second mechanism is certainly not negligible, particularly in systems with relatively narrow d-bands, such as Ni, the main contribution has been seen to stem from the ground state correlations. Eckardt et al. (Eckardt and Fritsche, 1987) employed a more sophisticated expression for the exchange–correlation potential. This resulted in a reduction of the exchange splitting by almost a factor of two coming into good agreement with the experimental value. More recently Nolting et al. (1989) calculated the electronic structure of Ni within a very elaborate Hubbard scheme, thereby using a completely different approach to the electronic correlations. The value of the exchange splitting that emerges from this calculation is actually quite close to the experiment and to the results of Eckardt et al. (Eckardt and Fritsche, 1987). The remaining difference must be certainly attributed to the difference between ground and excited state.

*9.5.2.2. Magnetic surface states*

The question of surface states in Fe and their role in magnetism has first been tackled at the beginning of the 80's by conventional photoemission (Turner et al., 1982; Turner and Erskine, 1983, 1984). Although a number of surface related features were identified at that time, they could not unambiguously be associated with minority or majority spin states. The same is true for Ni where also surface states were found using the customary criteria. Because of their temperature dependence some of these states were suggested to be spin-split (Plummer and Eberhardt, 1979; Eberhardt et al., 1980; Erskine, 1980), but a final confirmation had to wait for appropriate spin-resolved experiments. First results from spin-polarized direct photoemission for Fe and inverse photoemission for Ni became available at the beginning of the 90's. In order to illustrate the difficulties associated with the identification of magnetic surface states, we start out with the example of the Fe(100) surface. Two spin-resolved photoemission experiments have studied different types of surface states. In the work of Brookes et al. (1990), the spectra of clean Fe showed a minority spin feature at relatively high binding energies (~2.5 eV below $E_F$) (Fig. 9.34). The peak reacted very sensitively to the presence of adsorbates, which is one criterion for discriminating surface states. It furthermore dispersed only as a function of $k_\parallel$, the electron wave vector component parallel to the surface, being another indication for a surface state. Since we know the spin-character of the feature we are already a big step in front of the information drawn from conventional photoemission. This surface related feature is obviously exchange- (spin-) split, so the question appears where its majority spin counterpart can be found in the spectra. There is, in fact, no indication of a similar spin-up feature at higher binding energy, even if the exchange splitting is not assumed to agree with the average bulk value. This absence of a majority spin type surface state is consistently found

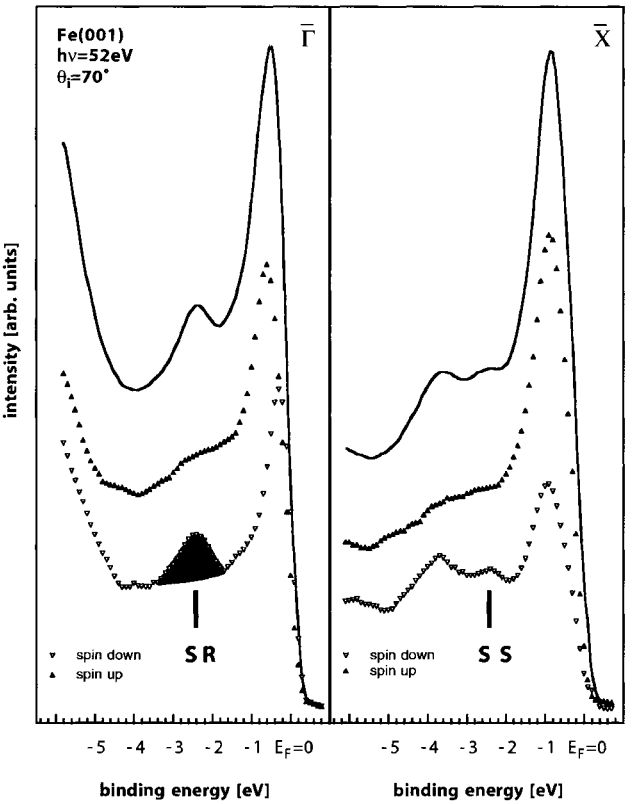


Fig. 9.34. Spin-split surface state on Fe(001) at the center of the surface Brillouin zone ($\bar{\Gamma}$) and at the zone boundary ($\bar{X}$). SR stands for surface resonance, whereas SS denotes the surface state. The surface state appears in the minority spin partial intensity spectra ($\nabla$), but not in the majority spin channel ($\blacktriangle$). Taken from Brookes et al. (1990).

at different $k_{\|}$ points along the $\bar{\Gamma}$–$\bar{X}$ axis in the surface Brillouin zone. The minority type surface state does not only disperse with $k_{\|}$, but shows a strong variation in the intensity of the spectral feature. This is the maximum information that can be drawn from the experiment.

Any further conclusion on the properties of the tentative surface states must refer to support from theory. Slab calculations indeed predict an energetic position and dispersion of the minority type surface state in reasonable agreement with the experiment (Fig. 9.35). An inclusion of the projected bulk bands reveals in addition that a true surface state exists only for approximately the second half of the SBZ. For the first half of the distance between $\bar{\Gamma}$ and $\bar{X}$ the state overlaps with the minority bulk bands, and thus forms a surface resonance. The calculation also yields surface-related states of majority spin character, which are predicted at 1.5–1.7 eV higher binding energies than the respective minority type band. It is interesting to note that this splitting is smaller than the average exchange splitting experimentally observed in the Fe bulk bands of $\Delta_5$ symmetry ($\Delta E_{ex} \sim 2.3$ eV in the above

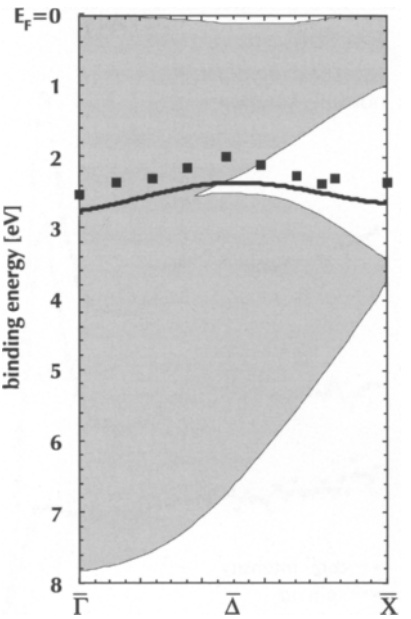


Fig. 9.35. Theoretical predictions for the minority spin-type surface state in Fe(001). The shaded area corresponds to the projected minority spin bulk bands. Taken from Brookes et al. (1990).

spectra). This indicates that the exchange-splitting of the surface-related electronic states does not necessarily agree with the bulk value. The question remains why the majority spin counterpart is not seen in the experiment, neither at $\bar{\Gamma}$ nor at $\bar{X}$. Theory suggests that the majority state is significantly broadened and therefore weaker in intensity due to hybridization with the majority spin bulk states, which are spread out over a larger energy range than the corresponding minority spin states.

The above surface states are located far below the Fermi level and are thus unlikely to have a strong influence on the magnetic moment of Fe. Surface states close the Fermi level should have much more impact in this respect. At excitation with high photon energies, however, these states are difficult to discern because of the dominant bulk-band emission from Fe close to $E_F$. This problem can be circumvented by taking advantage of the large gap in the final state bands along the Γ–Δ–H direction in Fe. At a photon energy below 18 eV, the emission can take place only via evanescent final states, and the intensity of bulk interband transitions is drastically suppressed. Data taken by Vescovo et al. (1993) show a pronounced peak at the Fermi level (Fig. 9.36), which is effectively quenched by minor quantities of oxygen. This feature was already observed in earlier investigations (Turner and Erskine, 1983), and was attributed to a surface state, because of its adsorption sensitivity and missing dispersion with $k_\perp$. By comparison to electronic structure calculations it was finally assigned to arise from a minority spin-split surface state. It is obvious that this earlier identification based on conventional photoemission cannot be kept in the light of the spin-resolved results which unequivocally indicated a majority spin character. This

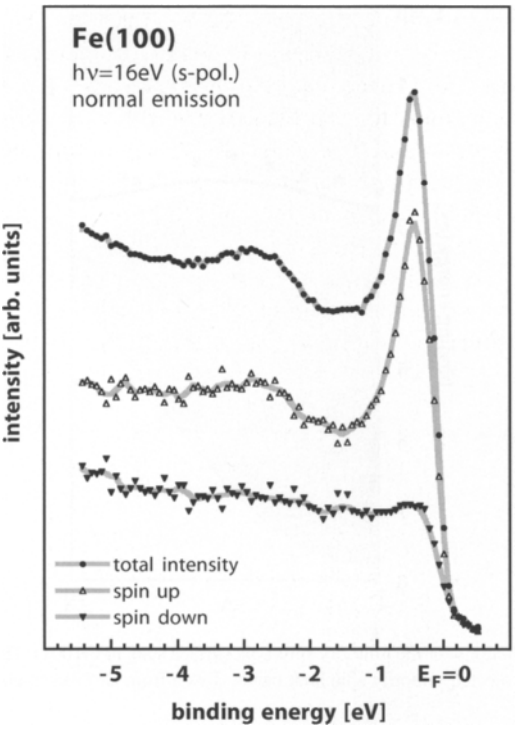


Fig. 9.36. Spin-polarized surface state on Fe(100) observed in band-gap photoemission at the center of the surface Brillouin zone. The surface state is located at the Fermi level and of majority spin character (△) (by Vescovo et al., 1993).

finding points out, how important an independent source of information – in this case the spin-polarization – can be in the analysis of spin-split electronic states.

Although the surface-related nature of the peak at $E_F$ is no matter of dispute, its role in the electronic structure is by no means clear. On the one hand, spin-polarized slab calculations do not produce surface states anywhere close in binding energy. On the other hand, the existence of a majority type surface resonance close to the Fermi level is predicted in a photoemission calculation for Fe (Feder et al., 1984). There is clearly some discrepancy, which needs further theoretical work to be resolved.

With respect to the role of surface states, the smaller exchange splitting in Ni leads to a completely different situation. The majority spin bands in Ni are practically filled and the magnetism is essentially determined by the unoccupied minority states. Any changes of the magnetic moment at the surface which might be connected to a change of the surface electronic structure are most likely to show up in the unoccupied part of the band structure. In addition the empty bulk bands have a gap close above $E_F$. This is an almost ideal configuration for observing surface states. The method of choice for this task is inverse photoemission with spin resolution. Results are available now for the three principal low-indexed faces of Ni. These investigations found spin-split empty surface states in all three cases.

A particularly interesting situation arises on the (111) surface. The experiments revealed a surface state which is partly occupied and should thus be connected directly to the magnetism of the Ni surface. This surface state is located in the sp-gap centered around $\bar{\Gamma}$ in the surface Brillouin zone. It almost touches the Fermi level at $\bar{\Gamma}$ and disperses upwards along the edge of the sp-gap towards $\bar{K}$. The exchange splitting of this state amounts up to 100 meV. The spin-resolved IPE spectra taken at $\bar{\Gamma}$ suggest that the majority spin state dives below the Fermi level and is thus partly occupied (Fig. 9.37). Because of the exchange splitting the minority state is slightly higher, but although it may also be located partly below $E_F$, its occupancy is smaller. Since the surface state dispersion around $\bar{\Gamma}$ is small, the corresponding contribution to the density of states is relatively high. Subsequent studies showed a reduction of the exchange splitting of this surface state upon oxygen adsorp-

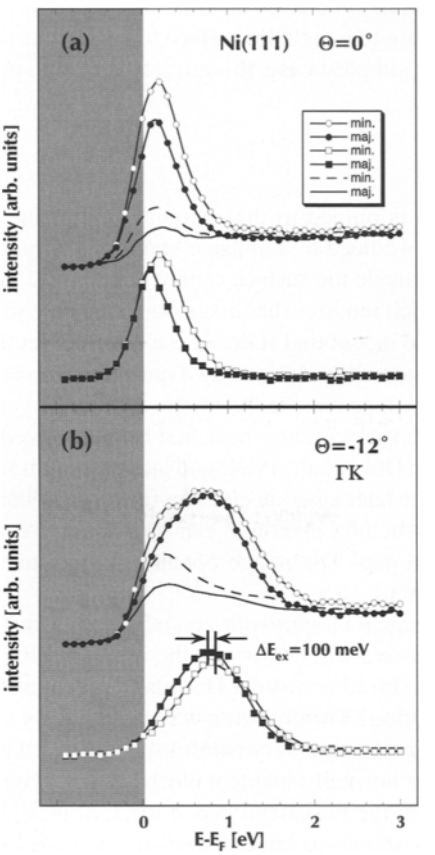


Fig. 9.37. Surface state observed in inverse photoemission from Ni(111). The state is probed at the center of the surface Brillouin zone (a) and along the $\bar{\Gamma}\bar{K}$ direction (b). The surface contribution is extracted by subtracting spectra after adsorption of 0.9L CO (lines without data points) from those of the clean surface. The resulting difference spectra (bottom set of spectra in each panel) clearly show the spin-splitting of approximately $\Delta E_{ex} =$ 100 meV. After Donath et al. (1993).

tion. Moreover, the state was found to shift away from the Fermi level, thereby becoming entirely unoccupied. No longer contributing to the DOS at $E_F$, it was concluded to be henceforth irrelevant for the surface magnetic moment. Whether or not the reduction of the magnetism observed upon adsorption of $O_2$ or CO can be directly related to these subtle changes in the surface electronic structure, can only be decided by further experiments.

The type of surface state that we have discussed so far is commonly termed "crystal-induced" surface state. This expression refers to the origin of these states being the regular crystal electronic structure. The electron wave functions are confined to the surface region, because these states are located within gaps of the bulk band structure. Both bulk and surface electronic states are ground state properties of the semi-infinite crystal and may be deduced from the density functional formalism. There is a second kind of electronic states localized at the surface, however, which is not contained in the ground state picture. These are the so-called "image-potential induced" surface states. These states owe their existence to the electrostatic interaction of an electron with its image charge in a conducting surface. If we bring an electron close to a metallic surface, it will be attracted in the Coulomb field of its image charge. In the simplest case, this attractive "image potential" can be written as

$$V(z) = -\frac{e^2}{4\pi\varepsilon_0}\frac{1}{4z}. \tag{9.73}$$

The image potential well is pinned to the vacuum level of the crystal. In order to form bound states in this well we need a "repulsive" part in the interaction. This is given, for example, if the electron outside the surface cannot couple to Bloch states of the bulk band structure. In this case, which requires the image potential state to fall into a bulk band gap, the electron can be trapped in a bound state. These image potential states are described by a Rydberg-like series and are characterized by a quantum number $n$. Their wave functions are localized several Ångströms outside the topmost atomic layer.

Image potential induced surface states have first been observed in inverse photoemission (Johnson and Smith, 1983; Dose et al., 1984) and later also with two-photon photoemission (Fischer et al., 1990). In the later case, an electron from a bulk band state is excited into the band gap close to $E_{vac}$ by the first photon. It can couple to the evanescent part of an image potential state in the band gap. The image potential state thus occupied is subsequently probed by the second photon.

Considering the importance of spin-split crystal induced surface states for the surface magnetism, the question arises whether or not the image potential states are participating in the magnetism as well. In other words: Do image potential states on a ferromagnetic surface exhibit a spin-splitting? This question was conclusively answered not before 1992, when Passek and Donath performed very careful spin-resolved inverse photoemission experiments on Ni(111). For normally incident electron they observed an $n = 1$ image potential state associated with the bulk band gap at the L point of bulk Brillouin zone. This image potential state was shown to have a spin-splitting of about 18 meV (Passek and Donath, 1992). This energy difference between the majority and minority type $n = 1$ image potential state is dramatically smaller than the average exchange splitting in bulk Ni ($\Delta E_{ex} \approx 300$ meV). A second number for comparison may be the exchange-splitting of a crystal induced surface state on the (110) surface which is found in the same band gap at the L point ($\Delta E_{ex} \approx 180$ meV) (Donath, 1989).

Two physical mechanisms have been discussed as a possible origin of the exchange-splitting in the image potential states. First, the position of the band edge differs for spin-up and spin-down states. In other words, the size of the bulk band gap and its energy position are spin-dependent. Consequently, also the reflection of the electron wave function becomes spin-dependent and the electron in the image potential state experiences a spin-dependent potential in the crystal (Borstel and Thörner, 1988). This results in a spin-splitting of the image potential states with the majority (minority) type state at higher (lower) binding energy. Note that this model involves the bulk spin-split electronic structure only. The exchange splitting in the image potential state is determined by the overlap of the image state wave function with the bulk states. The higher the overlap (i.e., the closer the electron to the surface), the higher the exchange splitting in the image potential state. Thus, states with $n = 1$ have the largest spin-splitting. This approach is reasonable only if the surface magnetic properties are very close to the bulk ones.

As a second mechanism a spin-dependence of the surface potential barrier has been invoked by the band-narrowing at the surface, which shifts the majority spin DOS further below $E_F$. The image potential states therefore interact with a surface electronic DOS of predominant minority character. The resulting energy shifts of the spin-up and spin-down image states are thus partially compensating the bulk-induced exchange-splitting.

If the exchange splitting of the image potential states is mediated by the bulk exchange, one should expect higher values of the spin-splitting for Fe and Co. No spin-resolved data on Fe are available yet. For Co, however, spin-split image states have been observed recently (Bode et al., 1994). The experiments were carried out on a Co($10\bar{1}0$) surface. The authors observed two $n = 1$ image potential states with splittings of about $\Delta E = 125$ meV and 100 meV, respectively, at the $\bar{Y}$ point of the surface Brillouin zone (Fig. 9.38). The appearance of two states is attributed to a corrugation of the surface which affects the surface potential and leads to a reduction of spatial symmetries. The resulting lifting of degeneracies causes a level-splitting (Smith, 1985; Chen and Smith, 1987). Unfortunately, calculations of a spin-dependent surface barrier are available for Fe(110) (Nekovee et al., 1993), but have not yet been carried out for any other surface or material. It is therefore unclear whether or not the predictions for Fe(110) may be relevant for the interpretation of the data from Co($10\bar{1}0$). As a qualitative result, at least, the calculation proves that the spin-dependent surface barrier may indeed contribute to the image state exchange splitting on Fe(110) (Nekovee et al., 1993). By contrast to common belief, however, this contribution was found to have the opposite sign of the bulk induced contribution, thereby effectively diminishing the exchange splitting of the image state. This surprising result is due to the location of the image potential state in front of the surface. The spin-split density of states at $E_F$ in the bulk has a predominant majority spin character. We have already shown in Section 9.2 that the spin-up electron density is more localized at the atom whereas the spin-down charge density dominates in the interstitial regions, leading to a "spill-out" of minority spin electrons at the surface. The comparably higher delocalization of the spin-down electrons leads to an effective minority spin DOS in front of the surface. This effect may even be enhanced.

To what extent the exchange-splitting of the image potential states is influenced by the surface barrier must therefore be left to further investigations. Seen from a different

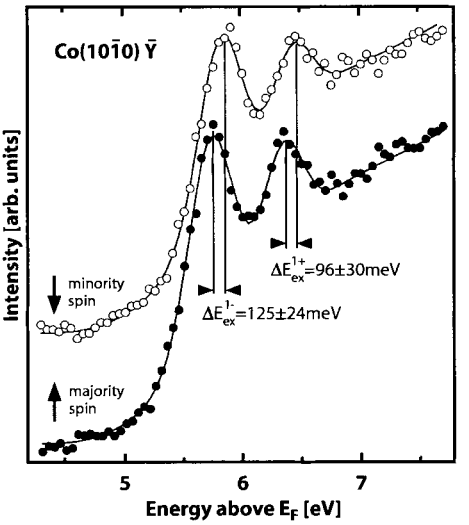


Fig. 9.38. Spin-split image potential states observed in inverse photoemission from Co(10$\bar{1}$0) at the $\bar{Y}$ point of the surface Brillouin zone. The surface corrugation causes a symmetry-induced splitting of the $n = 1$ image potential state into two levels with $n = 1^+$ and $n = 1^-$ (by Bode et al., 1994).

perspective, however, the experimental investigation of spin-split image potential states may lead to an improved understanding of the surface barrier and its spin-dependence.

*9.5.2.3. Electronic hybridization and magnetic interface states*

Whereas the identification of electronic surface states in the experiment is still relatively straightforward, the situation is much more complicated for states located at the boundary between overlayer and substrate. There are numerous experimental obstacles that have to be overcome. First of all, due to their localized nature interface states should only exhibit a dispersion with $k_\parallel$, similar to a surface state. At the same time, however, it will be much less affected by the actual condition of the surface layer, for example, structural reconstructions or the presence of adsorbates. A much bigger influence on the appearance of interfacial electronic states will come from the quality of the interface, of course, its sharpness and cleanliness. Being buried under the overlayer these aspects are notoriously difficult to characterize by surface sensitive techniques. In order to be able to investigate the interface with low energy electron spectroscopies, the overlayer must be kept sufficiently thin so that the signal is not washed out by too high a contribution from inelastic processes. Taking into account the very small inelastic mean free path values of low energy electron, this limits the usable coverages to about 2–3 monatomic layers. The question arises, of course, how much overlayer is needed, before the interface states have fully developed. Presently, there is no simple answer that can be given from experiment.

The motivation for investigating interfacial states goes clearly beyond the pure electronic aspect. Interface states are the direct consequence of the simple fact that two different materials have been joined together at a chemical and/or structural boundary. The formation of chemical bands along this boundary is immanent and must lead to an electronic

hybridization of states from both sides. A hybridization always includes subtle changes in the electronic density of states, which in turn might affect the magnetic properties of a film. This situation becomes very important in stacked film sequences, so-called multilayers or superlattices, with a high number of interfaces. One would like to know to what extend particular magnetic properties, for example, magnetic anisotropies, are caused by the interface and how they are related to the electronic structure. First steps into this direction have been made recently.

Concluding from the above arguments, it becomes clear that any experimental characterization of prospective interfacial states must be accompanied by appropriate theoretical calculations, in order to avoid ambiguities. Unfortunately these calculations are not readily available. As a consequence only very few interfacial systems are reasonably well understood. One of those is the Pd–Fe system, on which we will concentrate in the following for mainly two reasons. Firstly, both experimental and theoretical data are available. Secondly, the electronic structure of the interface has been analyzed, so to speak, from two points of view, namely by growing Fe-films on Pd single crystals, and vice versa (Rader et al., 1992, 1994). In both cases a pseudomorphic growth of the first two monolayers on (100) oriented surface has been reported. Structural and morphological complications between Fe on Pd(100) and Pd on Fe(100) may thus in a first order approximation be neglected. Of course, there is a lattice mismatch of about 4.3% between the surfaces mesh of bcc-iron and fcc-palladium. The different lattice structure causes a 45° rotational epitaxy, with the Pd-film stretched and the Fe-film compressed, respectively, in order to accommodate the above lattice mismatch.

Let us first concentrate on the case Pd on Fe(100). Spin-polarized photoemission revealed that Pd coverages of at least up to two monolayers possess magnetically induced spin polarization in the Pd-related spectral features (Rader et al., 1992). This indicates an induced magnetic moment in the Pd film. The spin-polarization disappears with increasing film thickness, which may lead to the conclusion, that the magnetic moment is only induced in the interfacial and adjacent Pd layer. One has to take into account, however, that with the coverage also the electronic structure of the Pd "slab" as a whole changes, which still leaves room for alternative interpretations of the photoemission data. Nevertheless, to find an induced magnetic moment in Pd should not be too surprising, recalling the fact that bulk Pd is actually very close to fulfill the Stoner criterion. This causes a high magnetic susceptibility and thus a high magnetic polarizability of Pd. It is therefore reasonable to assume that the ferromagnetic order in the Pd-overlayer is indeed caused by the magnetism of the Fe substrate. The alternative to this interpretation would be that Pd on its own forms a ferromagnetically ordered state due to the reduction of the natural lattice constant. In ferromagnets this mechanism often leads to an increase of the magnetic moment. Neither experimental data from Pd films on other substrates nor theoretical investigations give any support to this alternative. It is thus the ferromagnetism in the iron substrate that drives the Pd overlayer into a ferromagnetic ground state. This "magnetic coupling" must be obviously mediated by electronic states which are common to both materials.

Within the band model the ferromagnetism of the Pd overlayer should express itself in a spin-splitting resolvable by spin-polarized photoemission. To identify this spin-splitting turned out to be a major undertaking. This is illustrated by the results for a monatomic Pd overlayer (Fig. 9.39). The spin-resolved spectrum exhibits some Fe-related features close

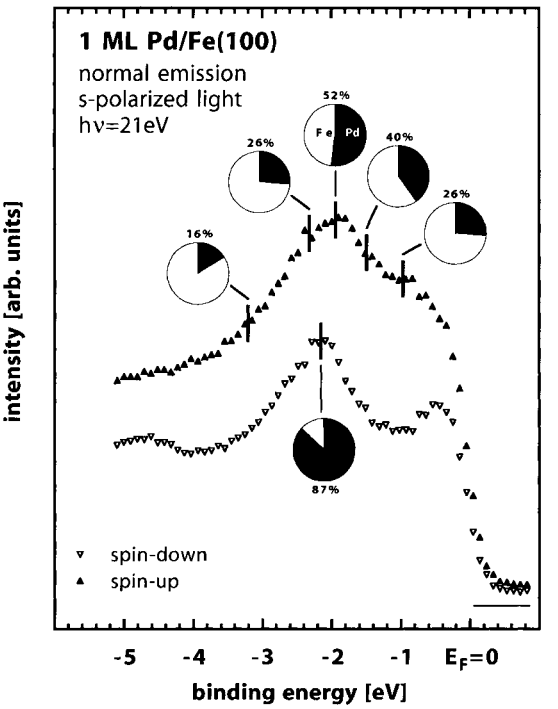


Fig. 9.39. Electronic hybridization in the Pd/Fe(100) system. Experimental spectra for spin-up (▲) and spin-down partial intensities (▽) are compared to predictions from an *ab initio* calculation with respect to the energy position of the $\bar{\Gamma}_5$ states (vertical bars) and the amount of Pd character (pie charts). The energy positions obtained from theory have been shifted by 0.5 eV towards higher binding energy. Taken from Rader et al. (1992).

to the Fermi level, and a number of peaks in both spin channels at higher binding energy. From the evolution of these peaks with the Pd coverage they are identified as of Pd origin. A single well-defined Pd-related peak appears only in the minority spin channel, whereas the majority spin spectrum consists of a rather broad distribution with internal structure. It is thus not clear where the spin-up counterpart of the peak in the minority spin spectrum, which involves a $\bar{\Gamma}_5^{\downarrow}$ initial state, should be located. This question could only be solved by the help of electronic structure calculations, in which the probability of finding an electron in the Pd or in the interfacial Fe layer was determined. The following picture emerges. The $\bar{\Gamma}_5^{\downarrow}$-related feature at 2.1 eV binding energy is indeed predominantly of Pd character with an Fe contribution of about 13%. The features in the majority spin spectrum, however, have an entirely mixed Fe–Pd character, with the Pd contribution reaching a maximum value of ~50%. In other words, the majority spin states of the Pd layer are strongly hybridized with the Fe bands, whereas the minority states are localized at the Pd atoms. The same conclusion on the hybridization was drawn from a comparison of the layer-resolved density of states taken from a Pd/7Fe(100)/Pd slab calculation. The reason for the difference is the large exchange splitting of iron which shifts a significant part of the minority density of states in iron above the Fermi level. It is therefore clear that the exchange-splitting of

the Pd states, although difficult to discern in the experimental data, must be significantly smaller than in Fe. The magnetic moment for the Pd layer is predicted to $0.29\mu_B$, whereas the interfacial Fe layer should have an enhanced magnetic moment of $2.69\mu_B$. This enhancement could be due to, for example, an increase in the orbital part of the moment due to the larger spin–orbit coupling in a 4d-metal.

Let us now turn to the inverse problem, namely Fe-films on Pd(100). Of course, the system is not entirely symmetric to the one dealt with above, as we have to keep in mind the effects of reduced dimensionality on the magnetism, in particular a reduced magnetic ordering temperature. For Pd/Fe(100) the magnetism was entirely determined by the bulk iron substrate. Nevertheless, a single monolayer of iron on Pd(100) has been reported to show ferromagnetism at room temperature. Experiments on ferromagnetic Fe films with 1–2 ML thickness are thus feasible. The photoemission results from this system exhibited a Pd surface state (Fig. 9.40), the spectral fingerprint of which is still preserved upon deposition (Rader et al., 1994). This behavior is totally inconsistent with the usual behavior of a surface state, reacting very sensitively to adsorption of a foreign material. In addition, the feature had no correspondence with bulk Fe results and did not change its position with the coverage. The idea of an Fe related quantum well state must therefore be dismissed. Again appropriate theoretical support helped to find the proper origin of this peak. Slab calculations for the clean and with 1 ML Fe covered Pd(100) substrate, reproduce first of all the Pd surface state which is located in a band gap. In this very same gap also falls a majority spin state $A^{\uparrow}$ of the iron overlayer (Fig. 9.41). Being within the band gap it can therefore not couple to bulk states and must be localized within the uppermost layers. Its minority spin counterpart $A^{\downarrow}$ is already above the Fermi level. A closer theoretical analysis reveals that the probability of finding an electron in the state $A^{\downarrow\uparrow}$ in the Fe or the interfacial Pd layer is about 50%. We thus have a very similar situation as for Pd/Fe(100): A majority spin state is localized at the interface and reflects a strong hybridization between Pd and Fe electronic states. The calculations show also that this state contributes significantly to the majority spin DOS and is thus partly held responsible for the induced magnetic moment in Pd. The predictions from theory are in agreement with spin-resolved photoemission experiments.

The system Fe/Pd represents a particular situation because of the high magnetic moment of Fe, and the high magnetic polarizability of Pd. But on the background of the available experimental and theoretical results it seems to be an exemplary case for the understanding of the 4d–3d hybridization, the formation of interface states and their role in the magnetism of thin film systems. Studies have also been carried out for a large number of other 3d, 4d, and 5d transition and noble metal combinations and different crystal orientations (Weber et al., 1992). An induced magnetic moment may even be found in a 3d–3d hybridization, for example in Co on Cu, and vice versa. For Co/Cu multilayer structures a magnetic moment in the Cu 3d electrons as high as $0.05\mu_B$ has been reported (Samant et al., 1994; Pizzini et al., 1995). Accompanying calculations again limit the magnetic moment to the interfacial region, with a fast decay into the nonmagnetic material.

In conclusion, the observation of magnetic interface states is a clear indication that the presence of a substrate can have profound effects on the electronic structure of a magnetic overlayer. Any realistic view of a magnetic thin film must therefore take this aspect into account.

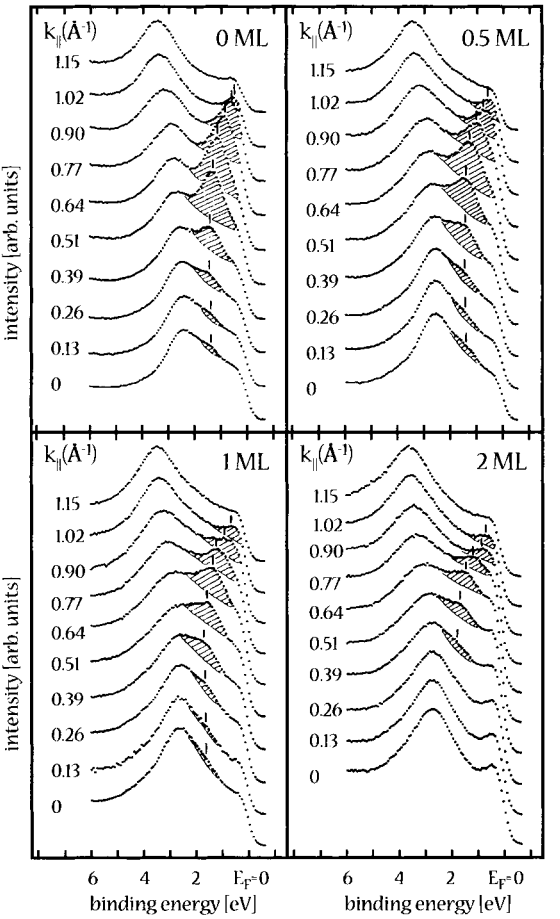


Fig. 9.40. Surface and interface states in the Fe/Pd(100) system. Change in the angle-resolved photoemission spectra taken at $h\nu = 40$ eV with increasing Fe coverage. The values of $k_{\parallel}$ refer to 1 eV binding energy. The hatched regions mark the Pd surface state (a) and the Pd–Fe interface state (b–d) (by Rader et al., 1994).

### *9.5.2.4. Quantum well-states*

Classical textbook quantum mechanics teaches us that a particle in an infinitely high potential well develops a spectrum of discrete energy eigenvalues. If we reduce the potential height to a finite value, we will still find some states confined within the potential well. A physical realization of this situation is an ultrathin film being infinitely extended in the lateral dimensions, but only a limited number of atoms thick. As long as any electronic interaction with a supporting substrate or a cover layer is neglected the electronic structure of the film is described by a set of so-called quantum well states. Quantum well states have been known for some time in semiconductor physics, and have even reached the level of technological importance, e.g., in quantum well laser diodes. In metals this quantum size effect has long been somewhat passed by, probably because it was believed that the

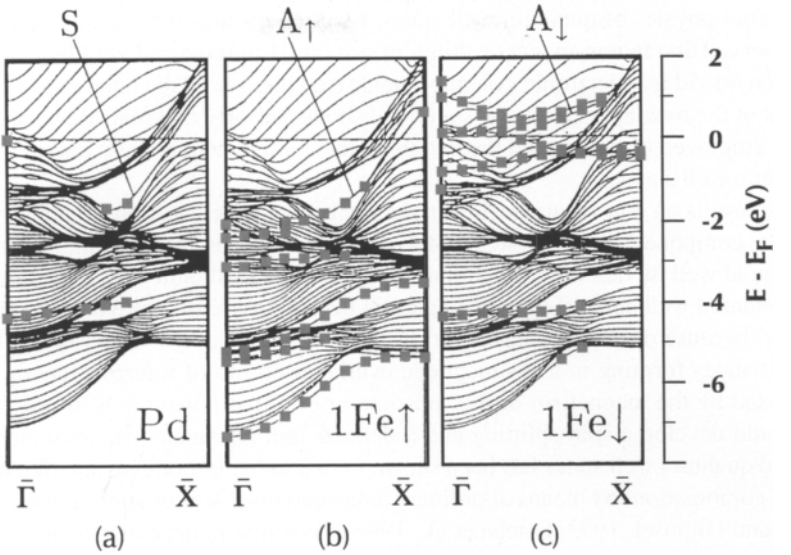


Fig. 9.41. Theoretical predictions for the $E(\mathbf{k}_{\|})$ diagram of the $\bar{\Delta}_1$ states in a 25-layer Pd(100) slab (a), majority (b) and minority spin (c) $\bar{\Delta}_1$ states in a 1Fe/25Pd(100) slab. The squares in (a) mark states which are more than 50% localized in the top-most Pd layer (Pd surface states). In (b) the squares indicate states which are more than 50% localized at the interfacial Fe and Pd atoms (Fe–Pd interface states). Taken from Rader et al. (1994).

itinerant nature of the electronic states in typical metals would not allow an effective localization. This may be true for polycrystalline materials, but not for single crystals which usually exhibit well-defined band gaps along certain crystallographic directions. Band gaps act as a barrier for electrons from another material in the same energy range, and may therefore lead to a confinement of particular electronic states. A second reason for the delayed activity in the field of quantum well states in metals is more of experimental nature. The preparation of metallic thin film systems had to reach the same high level of quality achieved earlier in the growth of layered semiconducting structures. This became possible by the improved preparation and characterization techniques developed in the 80's.

Being eigenstates of a quasi-two-dimensional electronic system, quantum well states should show dispersion only with $k_{\|}$, the wave vector component parallel to the film. They share this property with surface and interface states, which leads us to the question how quantum well states can be distinguished from the other two types of electronic states. Again we may refer to the simple model of a finite width and height potential well. It turns out that the number of bound eigenstates is connected to the width and the height of the potential well. If we keep the height constant, the number of states is still determined by the width. That means for a given width – which corresponds to the thickness of a film – we will have a discrete set of bound states. Upon adding another atomic layer, the wave functions in the well alter and the states change their energy position with respect to the bottom of the well. As a consequence, spectral features related to particular electronic states should shift on the energy scale as a function of the film thickness. The use of a simple potential well model renders this prediction very qualitative, but has the advantage of pointing out

the essential physics of quantum well states. Electronic states with such a behavior have been observed first in non-magnetic thin film systems (Lindgren and Walldén, 1987). Later studies on 4d–5d iso-electronic systems emphasized the role of the band gaps for the confinement of the overlayer electronic states and showed clearly that realistic band structures must be employed to understand the details of the confinement process and the formation of quantum well states.

These results on non-magnetic films naturally bring up the question what may happen if one of the components in the system is ferromagnetic. In this case, expanding on the simple potential well model, minority and majority spin states should "see" a different height of the potential well and different band gaps in the electronic structure of the nonmagnetic neighbor, because of the exchange splitting. One may also ask, whether or not the quantum well states forming in a nonmagnetic overlayer on top of a ferromagnetic substrate are affected by the magnetism of the substrate or even participate in it. In the latter case they should develop a spin-splitting and a defined spin character. The existence of these predicted quantum well states has been shown for a number of nonmagnetic/ferromagnetic material combinations by means of ordinary direct and inverse photoemission spectroscopy (Ortega and Himpsel, 1992; Ortega et al., 1993). As a first rather transparent example we turn to the Ag–Fe system. Silver films can be grown on a Fe(100) substrate with good structural quality, because of the almost perfect lateral lattice parameter match and the low surface free energy of silver. The unit cells of fcc-Ag(100) films on bcc-Fe(100) are rotated by 45° relative to each other. We recall from Section 9.5.1.1 that thicker films of, say, more than 4–5 ML already exhibit a bulk-like electronic structure. For this case we can base our argumentation on the bulk band structures of both materials. Comparing the Ag and Fe bulk bands along the (100) or $\Gamma$–$\Delta$–$X$ direction (see, for example, the compilations by Moruzzi et al., 1978, or Papaconstantopoulos, 1986) we immediately note several peculiarities (Fig. 9.42). Firstly, the Ag 4d bands of $\Delta_2$ and $\Delta_5$ symmetry are located at rather high binding energies ($E_B \sim 4$ eV), whereas the Fe 3d bands of the same symmetry extend from $E_B \sim 2$ eV up to above the Fermi level. This energetic separation inhibits electronic hybridization between these bands. Secondly, the Fe bands of $\Delta_1$ symmetry ("sp-like" states) have an extended sd-hybridization gap in both the spin-up and spin-down bands. In the minority bands the band reaches across the Fermi level. The majority spin sd-gap, however, is entirely confined to the occupied states, its upper border being located about 1 eV below $E_F$. The difference in the minority and majority spin sd-gaps offers a possible mechanism for a *spin-dependent* confinement of Ag electrons. Each state in the Ag bands is occupied by electrons of either spin. In order to leave the potential well of the Ag overlayer the electrons must occupy states which are hybridized with the Fe bands. For the Ag $\Delta_1$ states close to the Fermi level a hybridization is possible only for electrons with spin-up character. These electrons correspond to majority type electrons in Fe for which states electronic hybridization is supported by the smaller sd-gap. We thus end up with the following situation: Only spin-down electrons of the $\Delta_1$ band are completely confined to the overlayer and form "true" quantum well states, but spin-up electrons can pass the interface between substrate and film. The interface acts, so to speak, as a "spin filter" with a selective transmission for spin-up electrons. The hybridization of the corresponding Fe- and Ag-states may also involve a certain transfer of magnetic moment to the Ag overlayer, giving rise to a spin-polarization and eventually a spin-splitting in the quantum well states.

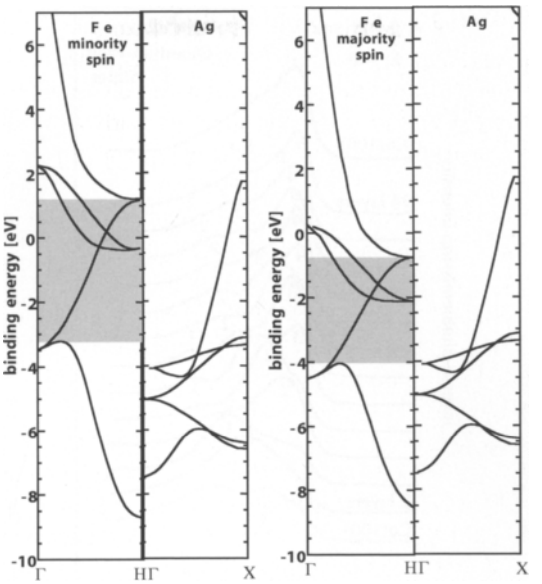


Fig. 9.42. Comparison of the band structures of bcc-Fe(100) and Ag(100) for spin-up and spin-down electronic states. The shading marks regions in the band structure where the density of sp-like states in Fe, and consequently the hybridization between Fe and Ag related sp-states is small.

According to this simplified picture one should expect the "true" quantum well states in the Ag overlayer to be of predominantly minority spin character. Due to the Ag–Fe hybridization the majority spin states should be much less confined and should consequently behave more like bulk crystal states. Qualitatively this model can indeed explain some findings from spin-polarized photoemission experiments on the Ag/Fe(100) system by Brookes et al. (1991). With increasing Ag coverage the authors observe the formation of several discrete spectral features with predominantly minority spin character. These minority type quantum well states shift towards the Fermi level with increasing overlayer thickness. It is interesting to note that the quantum well state associated with the 1 ML Ag coverage is actually very close to the minority spin surface state of the clean Fe surface which has been discussed in Section 9.5.2.2. We obviously find here a parallelism to the situation in Fe/Pd, where the surface state developed into an Fe–Pd interface state. This suspicion is indeed supported by tight binding calculations performed for the Fe–Ag system and which reproduce both the surface state on the clean Fe surface and the quantum well states in the Ag overlayer (Smith et al., 1994). The surface state is seen to hybridize with the Ag quantum well state, thereby forming a mixed interface/quantum well state at very low coverage. When the film gets thicker the electronic wave function extends more and more into the Ag overlayer causing the state to develop a quantum well character. At the same time the state is pushed towards the Fermi level and eventually leaves the majority spin type sd-hybridization gap. The wave function can then couple to Fe spin-up bulk states and the confinement for majority electrons is lifted. This mechanism could explain the absence of majority spin quantum well states in the photoemission spectra.

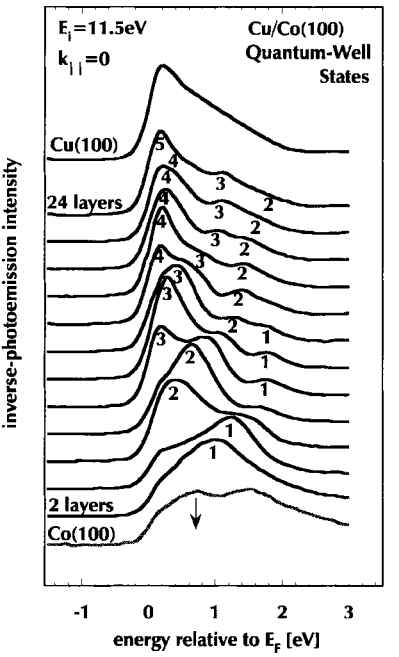


Fig. 9.43. Dispersion of quantum well states in the Cu/Co(100) system with increasing Cu coverage observed with inverse photoemission. The experiment was performed with a primary beam of energy $E_i = 11.5$ eV at normal incidence. The individual states are labeled by their quantum number $n$, ranging from 1 to 5 in the above example (taken from Ortega and Himpsel, 1992).

For several reasons electronic structure calculations are of vital importance for the understanding of quantum well states. First, our simple picture based on the bulk bands must break down in the monolayer regime. The electronic structure will then be entirely determined by quantum size effects. Second, the character of an electronic state in a complex interaction scheme with a substrate can only be deduced from a close comparison of experiment and *ab initio* theory. Third, in most other material combinations, there are no extensive band gaps as in Fe/Ag. Consequently, other mechanisms must be found for the confinement. Finally, the symmetry character of the quantum well states is found to contain both s- and d-like contributions (Wang et al., 1982). A mixed wave function must have a different confinement behavior than a pure s-state. The distinction of quantum-well states into sp- and d-related species is thus based more on convenience rather than on strict grounds.

As another example, we discuss some results for Cu-films on Co(100), mostly because the Cu/Co combination is the currently most investigated and best understood system. The Co(100) substrate crystal is realized by a thicker layer of fcc-Co epitaxially grown on a Cu(100) single crystal. Quantum well states in the Cu overlayer have first been observed in conventional inverse photoemission (Ortega and Himpsel, 1992; Ortega et al., 1993). The respective spectra exhibit a strong variation in the shape and structure with the Cu coverage (Fig. 9.43). A close inspection of the spectra reveals a whole series of individual quantum-well states (labeled by the number in the graph). With increasing coverage each

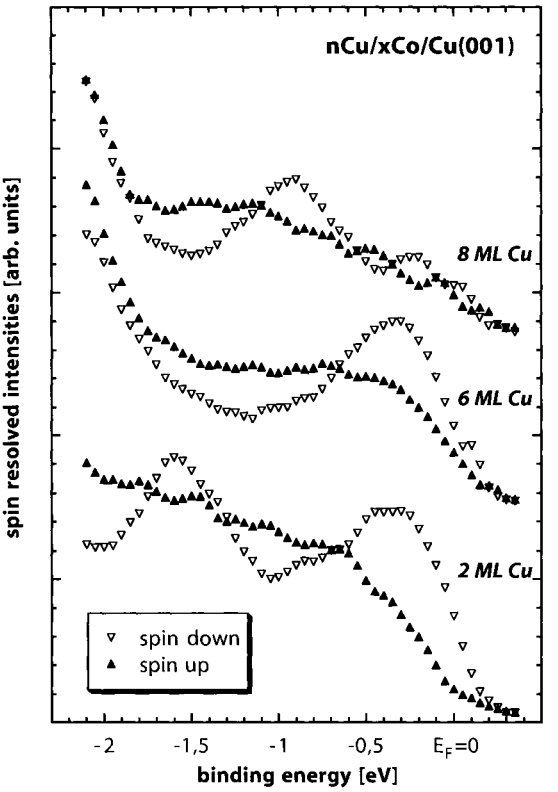


Fig. 9.44. Spin-resolved photoemission from quantum well states in Cu layers on Co(100), showing the dispersion and the minority spin character of the quantum well states in the Cu film. After Garrison et al. (1993).

state is seen to shift away from the Fermi level to make room for the appearance of the next state. Some states in the vicinity of $E_F$ may even shift from the occupied to the empty part of the band structure. This Fermi level crossing is seen in the combination of direct and inverse photoemission results. Subsequent spin-resolved photoemission investigations proved these states to be spin-polarized and partly exchange-split (Carbone et al., 1993; Garrison et al., 1993). An example for this behavior is given in Fig. 9.44, showing pronounced minority spin type quantum well states at coverages of 2 ML and 8 ML copper. If the thickness of the film becomes high enough, the individual states overlap and merge into a spectrum close to the bulk Cu result.

From the viewpoint of electronic structure, the situation in Co/Cu is considerably more complicated. Bulk fcc-Co has sd-hybridization gaps in both the minority and majority spin bands. A smaller exchange splitting combined with a higher band filling and a different position of the sd-gap in fcc lattice structures brings the hybridization gaps for both spin directions below the Fermi level. In other words, Co/Cu along the (100) direction does not exhibit a strict confinement for the $\Delta_1$-like electronic wave functions in the Cu overlayer. The dominance of quantum well states in the experiments, particularly in the inverse pho-

toemission, however, clearly proves that a certain confinement of electronic states takes place. Recalling the simple potential trough we know that the potential step at the border of the well causes a partial confinement due to a non-vanishing reflectivity, which causes even wave functions at high energies to be partly reflected. One can imagine that the potential step at the interface of two different materials acts in a similar manner. States of defined spatial symmetries may be confined if the reflectivity of the potential step for this particular wave function is high enough. We can consider this as a local band gap for states of a particular symmetry character. This situation has important implications for the understanding and theoretical modeling of these quantum well states. First of all, the formation of quantum well states will be determined by details of the electronic structure at the interface. This case cannot be adequately treated by the bulk approach that we employed in the Fe/Ag case. In addition, the absence of total band gaps gives a much higher chance for electronic hybridization, and thus a mixed symmetry character of the wave functions, as is also observed in the Cu/Co system (Johnson et al., 1994). Finally, requiring only partial confinement for the formation of a QWS means that a higher number of states may fulfill the criterion. As a consequence, a higher number of QWS states has to be expected. The analysis of such a complex situation can be largely facilitated by supporting *ab initio* calculations. For the Cu overlayers on Co(100), for example, both the observed thickness dependence of the energy position and the exchange splitting of $\Delta E \propto 0.16$ eV are nicely reproduced in the theory (Nordström et al., 1995). Furthermore, the calculation predicts not only sp-type QWS associated with the $\Delta_1$ bands in bulk Cu, but also a set of d-like states at higher binding energy which are related to the $\Delta_5$ Cu bands. The latter states have not yet been positively identified in the experiment. The observation of d-like QWS states has been reported, however, for various layered system containing Fe and Co in combination with noble metals along the (111) direction (Hartmann et al., 1993).

Although quantum-well states are an intriguing topic in itself they are also of importance in a very interesting magnetic phenomenon, namely the so-called oscillatory interlayer coupling. It appears if two ferromagnetic layers are exchange-coupled through a non-magnetic spacer layer, for example, Co/Cu/Co. Depending on the interlayer thickness, the two ferromagnets will either have their magnetization vectors pointing the same way, or into opposite directions. The first case refers to a ferromagnetic, the second to an antiferromagnetic coupling character. With an increase of the spacer layer thickness the coupling character usually switches several times between the two cases. The oscillation of the coupling character has a defined period on the thickness scale. A variety of theoretical approaches has been developed in order to explain this behavior. Among the early ones were those favoring an RKKY type interaction between the two ferromagnetic layers. In the RKKY model the exchange interaction is mediated via the polarization of the conduction electrons in the nonmagnetic material. As electrons at the Fermi level have the strongest contribution this involves the topology of the Fermi surface. The Fermi surface in crystalline materials is no longer spherical and only electrons with a defined Fermi wave vector $\mathbf{k}_F$ can participate in the interaction. For a number of systems, including Co/Cu, this simple model gave qualitatively a reasonable interpretation. Theory predicted, for example, the presence of two different oscillation periods in Co/Cu/Co along the (100) direction. The total oscillation in the interlayer coupling should be a superposition of a long-period and a short-period contribution, arising from extremal spanning vectors at the belly and the neck of the Cu

Fermi surface, respectively. Whereas the long period of $\lambda \propto 5$–6 ML was reported from the beginning, the short period of $\lambda \propto 2$ ML was found only in later experiments, presumably due to a better film quality. The important result of the comparison between theory and experiment, however, is the indication that the coupling character must be somehow related to the electrons at $E_F$.

The connection between the interlayer coupling and quantized electron states comes by the observation that the long period in the coupling reappears in a particular manner in the thickness dependence of the quantum well states. It corresponds closely to the difference between the coverages at which the $n$th and $(n + 1)$th quantum well state cross $E_F$. We recall that the interaction with the ferromagnetic substrate renders these states spin-polarized. Therefore, each time a state crosses $E_F$ we will observe a change in the spin density at $E_F$. An oscillatory variation of the polarization at the Fermi level with a period of $\lambda \propto 5$–6 ML has been indeed observed in the experiment (Carbone et al., 1993). In addition, we have to take into account that the states at $E_F$ have a predominant sp-character, thus being strongly delocalized. A spin-polarized, delocalized electron system, however, is the core of the RKKY model and explains why this approach was relatively successful. The consistency of the picture is a strong indication that the sp-like quantum well states at the Fermi level play a dominant role in the interlayer coupling. Experimentally, an oscillating spin density at $E_F$ whose period corresponds to the respective interlayer coupling has been found for a number of other systems, too (Rampe et al., 1995).

#### *9.5.2.5. Experimental results on the limits of the Stoner–Wohlfarth model of itinerant ferromagnetism*

Calculated electronic structures like those discussed in Section 9.2.1 refer almost all to the ground state, i.e., $T = 0$, where only zero-point fluctuations have to be considered. The experiment, by contrast, is carried out at finite temperature, often under ambient thermal conditions, $T = 300$ K. This does not pose a significant problem for the comparison of experiment and theory, as long as the Curie temperature of the ferromagnet under investigation is high. With respect to room temperature, this criterion is fulfilled for 3-d bulk ferromagnets (Fe: 1044 K; Co: 1388 K; Ni: 627 K) (Wohlfarth, 1980). We see that for Ni, a room-temperature experiment probes a state already half-way up to $T_C$. Since the temperature dependence of the magnetization **M** is still very small in this region, we still have a saturation magnetization of more than 90% of the ground state value (Cullity, 1972). For rare earth materials the Curie temperature is usually much lower and requires cryogenic temperatures to approximate the ground state. The same may be true, however, for ultrathin films of 3-d transition metals. The reduced dimensionality leads to a reduced Curie temperature, which may be as low as 300 K for a film of a few atomic layers (Schneider et al., 1990).

The Stoner–Wohlfarth model of itinerant ferromagnetism connects the exchange-induced spin-splitting to the macroscopic magnetization **M**. Because the magnetization disappears at $T_C$, within the model also the exchange–splitting should vanish, causing the spin-split band structure to transform itself continuously into a paramagnetic one above $T_C$. On the other hand, it is well known that the magnetic ordering temperatures calculated from Stoner–Wohlfarth based electronic structures are much to high. One reason for this failure may be that the models often include only thermally activated spin fluctuations. In the re-

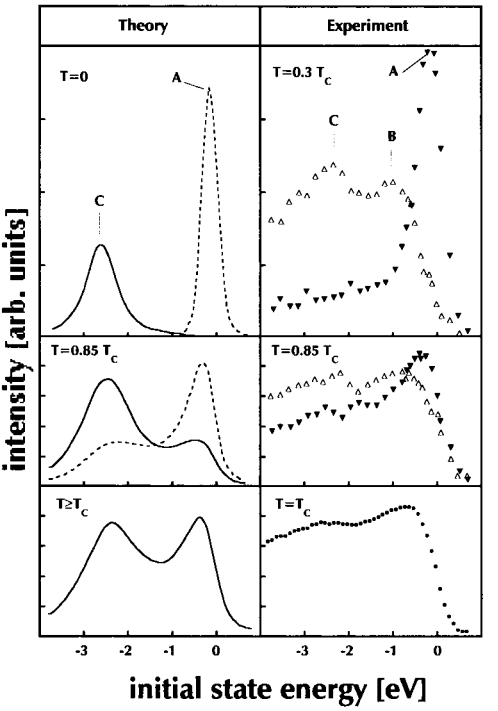


Fig. 9.45. Spin-resolved photoemission from Fe(001) below and at the Curie temperature $T_C$. The experimental data (right-hand panel) are compared to theoretical predictions from the fluctuating band model. Taken from Haines et al. (1985).

gion close to $T_C$, however, high energy single-particle excitations such as electron–hole pairs (Stoner excitations) may become of importance. These are usually neglected. One may therefore also put the prediction of a temperature-dependent spin-splitting at variance. In fact, this question, which is important for our basic understanding of ferromagnetism, has initiated a number of experiments with quite controversial results and interpretations. Most of the controversies centered around Ni, whereas Fe seemed to be a clear-cut case. Results on Co became only available very recently for thin films, because the structural phase transition hcp $\rightarrow$ fcc forbade high-temperature investigations on single crystals.

Most of the experimental results reported on spin-resolved photoemission from Fe are consistent with a persistence of the ferromagnetic spin-splitting even at temperatures significantly above $T_C$. In other words, the electronic structure of iron at $T_C$ does not behave "Stoner-like". An example for the experimental results is shown in Fig. 9.45 showing spin-resolved photoemission spectra below and at $T_C$. It is apparent that the spectral features in the minority and majority channel keep their energetic distance within the accuracy of the experiment. At $T_C$ the macroscopic magnetization has collapsed and we have no more a macroscopic quantization axis for the electron spin. Nevertheless, the spin-integrated spectrum still shows two peaks at the approximate positions of the $\Gamma_{25}^{\uparrow}$ and $\Gamma_{25}^{\downarrow}$ related emission features. This suggests that there is still an exchange-split electronic structure

at $T_C$. It cannot be excluded that the spin-splitting is somewhat smaller than at low temperature, but there is obviously no merging of the two peaks which would correspond to a total disappearance of the exchange splitting. This finding is also consistent with inverse photoemission investigations. These revealed in addition that the temperature variation in the band structure seems to be strongly $k$-dependent. Both collapsing and non-collapsing band behaviors were found at different points of the bulk Brillouin zone.

The new concept invoked to explain the "deviation" from the Stoner-like behavior is the fluctuating band theory. The basic idea of the fluctuating band model is the persistence of a locally well-defined exchange-split band structure with a non-zero magnetic moment, and thus a spin-quantization axis. This quantization axis, however, fluctuates in both time and space. A macroscopically averaging method – averaging in time and space – therefore yields a vanishing magnetic moment in accordance with the observation of a zero spin-polarization. The photoemission or inverse photoemission process takes place within a spin-split band structure. It has been shown that both the collapsing and non-collapsing band situation can be explained within the framework of the fluctuating band model. The interesting question that remains is that of the size of the regions with a locally defined spin-split band structure. From theoretical analysis of spin-resolved photoemission data the length of this short-range magnetic order was determined to at least $\lambda = 4$ Å. This means in a simplifying picture that a "cluster" of atoms with the diameter $\lambda$ is magnetically ordered to yield a finite magnetic moment. There is little doubt now that the electronic structure of Fe at and above $T_C$ is consistent with the results from the fluctuating band theory and is not Stoner-like.

Because of the considerably smaller exchange-splitting, the situation in Ni might be different. Although the Curie temperature for Ni as predicted from the Stoner-model is way too high, there could still be a Stoner-like collapse of the bands. The exchange-splitting in Ni is of the order of 300 meV, and small energy shifts of the spectral features which are of minor importance in the case of iron, can have a strong effect on the spectra in nickel. It is therefore much more difficult to decide on the question of short range magnetic order in Ni. There is a number of direct and inverse photoemission results, which report a collapse of the exchange splitting at $T_C$, but only a part of them is consistent with the fluctuating band theory. It predicts that in particular weakly dispersing ("flat") band the spin-splitting is preserved at $T_C$, whereas in strongly dispersing bands a temperature dependent collapse may be observed. Some work has thus been concentrated on the behavior of such weakly dispersing states in the Ni band structure. It was found that even spectral features related to these flat bands merged at approaching $T_C$, in disagreement with the fluctuating band picture. We restrict ourselves to only one example of the Ni(110) surface close to the W-point (Fig. 9.46). The optical transition at the energy of the photon detector (9.4 eV) involves the $Z_2$-band along X–W. This band is very flat and only partly occupied and therefore directly responsible for the magnetism in Ni. Temperature-dependent changes in the spin-splitting which are connected to a reduction of the local magnetic moment should be easily observable under these circumstances. Indeed, the spectra exhibit a temperature-dependent shift of the inverse photoemission peaks associated with the $Z_2^{\uparrow}$ and $Z_2^{\downarrow}$ band. The $Z_2^{\uparrow}$ band is located right below the Fermi level and gives therefore rise to only a weak feature in the spectrum. With increasing temperature, however, it gains intensity. This behavior can be interpreted as a shift of parts of the band across the Fermi level from above.

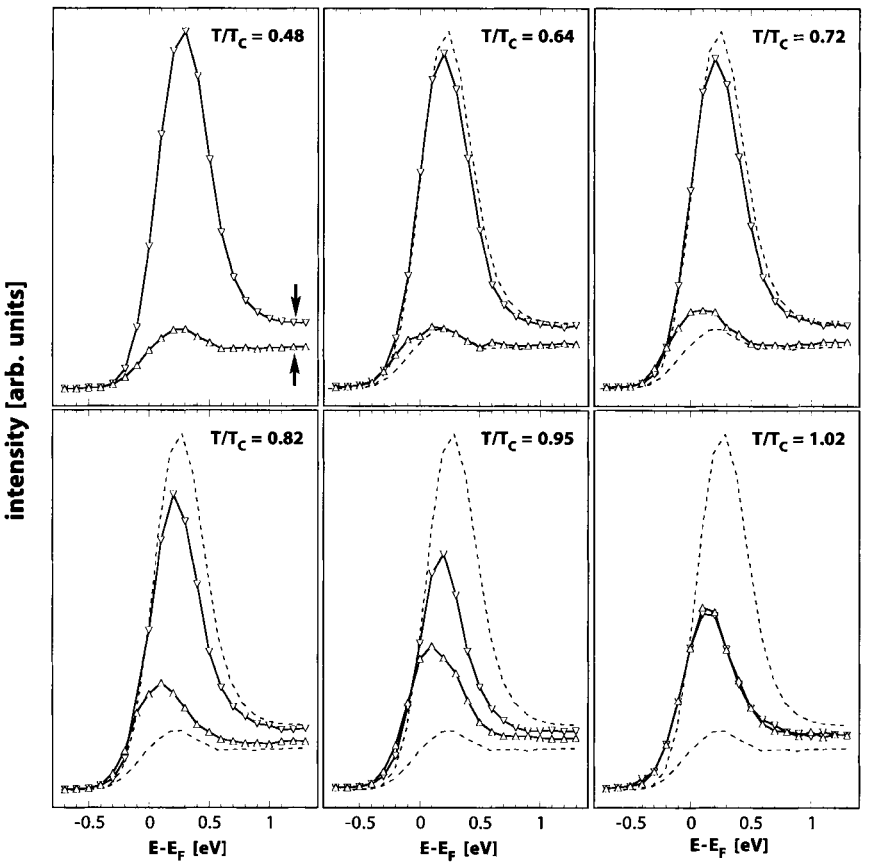


Fig. 9.46. Spin-resolved inverse photoemission from Ni as a function of temperature. Left panel: Spin-split band structure of Ni at $T = 0$ along K–X–W. Transitions from $Z_4$ into $Z_2$ bands at $h\nu = 9.4$ eV are indicated by the solid (minority spin) and dashed vertical lines (majority spin). Right panels: Spin-resolved inverse photoemission spectra corresponding to the transitions marked in the band structure taken at various temperatures between room and the Curie temperature. The spectra at a given temperature may be compared directly to the room temperature data ($T/T_C = 0.48$) given by the broken lines. Taken from Donath and Dose (1989).

Furthermore one observes the center of gravity of the curves to shift in energy towards the Fermi level and relative to each other. The analysis of these spectra is relatively complex, as the broadening of the Fermi function with increasing temperature may subtly alter the peak position by shifting the spectral weight. Taking this aspect into account the analysis of the data yielded a merging of the $Z_2^{\uparrow}$ and $Z_2^{\downarrow}$ related features in a Stoner-like manner. We note that an investigation of energy losses due to Stoner excitations, an approach corresponding to an averaging over the Brillouin zone, did not reveal evidence for a reduction of the mean exchange splitting (see Section 9.5.2).

The above inverse photoemission data were later supported by an electronic quasiparticle band structure calculation of Ni, involving an elaborate Hubbard approach (Nolting

et al., 1989). It has already been mentioned that the Hubbard model allows a better treatment of the electronic correlations than its mean field version, the Stoner model. Since electronic correlations are at the heart of ferromagnetism, one may expect a better description of magnetic properties at elevated temperatures. Indeed, the above calculations yield a Curie temperature and thermodynamic behavior in surprisingly close accordance with the experiment. The exchange-split band structure, however, is found to be strongly temperature-dependent, with all the bands collapsing into a paramagnetic electronic structure above $T_C$. Interestingly, the disappearance of the exchange splitting in the calculation is not accompanied by a loss of the magnetic moment. On the contrary, the *local* magnetic moment is found to be practically temperature-independent in the calculation. This result may sound like a contradiction, because the exchange splitting in an itinerant ferromagnet is the origin of the magnetic moment (see Section 9.2.1.1).[7] What it means is that although we are dealing with an itinerant ferromagnet, we are suddenly confronted with a localized aspect in the band magnetism of Ni (which may be emphasized by the particular choice of the above Hubbard model). In other words, the magnetism in Ni should to a certain extent behave like, for example, a Heisenberg ferromagnet. It should be noted in this context that the critical behavior of the magnetization in bulk Ni follows a Heisenberg model. It is thus clear that both itinerant and local aspects play a role in the magnetism of Ni.

Let us concentrate for a moment on the localized aspects. In a Heisenberg type model we have individual spins or magnetic moments localized at lattice sites. These moments are subject to thermally driven fluctuations. Below $T_C$, these moments are ferromagnetically coupled resulting in a long-range ferromagnetic order. At and above $T_C$, the magnetic moments disorder completely and not even a short-range order persists, except for a weak correlation between nearest neighbor moments. This is essentially the picture that underlies the "disordered local moment" model (DLM). The DLM theory may be seen as the antipode of the fluctuating band approach. Up to now, there exists no unified approach, which would allow a continuous interpolation between these two extreme cases. Any itinerant ferromagnet will display both itinerant and localized aspects, which may manifest themselves in the amount or degree of short-range magnetic order. It may be high, as in Fe, or small as in Ni, or somewhere in between. In fact, the presently available data support the existence of a short range magnetic order in Ni. These are, for example, the above mentioned SPEELS experiments (Kirschner and Langenbach, 1988; Hopster and Abraham, 1989), or very recent spin-resolved photoemission investigations of the 6 eV satellite structure in Ni (Kakizaki et al., 1994). Although all of these experiments suggest the presence of a short range magnetic order, none of them can determine its magnitude.

The third of the 3d ferromagnets, cobalt, has long been inaccessible to investigations with surface sensitive techniques at $T_C$. The main reasons were the high Curie tempera-

---

7 In order to understand this apparent contradiction, we must carefully distinguish between itinerant and localized views of the same quantity, in this case the magnetic moment. In the itinerant picture built by the Stoner model, the magnetic moment is due to the collective behavior of the electrons. In a spin lattice, the magnetic moment is localized at the lattice site, and the breakdown of the long-range ferromagnetic order occurs by random rotation of the moments at neighboring sites. The global magnetic moment or magnetization of the material vanishes, but the local magnetic moment at the site is preserved. As has been mentioned, the itinerant and the localized models are two extreme views of quantum magnetism, and any realistic system will probably show contributions from both.

ture, and the structural phase transition from hcp → fcc, which would cause an irreversible recrystallization of an hcp single crystal. Only by epitaxial stabilization of the fcc phase on a Cu(100) substrate, such studies became feasible. There remains, however, still a problem with the maximum allowable temperature, as the system is thermodynamically stable only below 500 K. Above this limit, which is of course much lower than the bulk Curie temperature, Cu diffuses to the surface and forms a partial cover layer thereby changing the magnetic properties (Schmid et al., 1993). In this situation a peculiar property of ultrathin film systems, namely the strong thickness dependence of the Curie temperature, comes to help. If the film is sufficiently thin the Curie temperature drops below the critical limit for the onset of interdiffusion. For Co films of 2 monatomic layers thickness, the Curie temperature is found to be in the vicinity of room temperature (Schneider et al., 1990). The 2 ML Co film is of course not equivalent to a bulk crystal, but one may expect that the essential aspects of a temperature-dependent band structure can be studied in this system as well. This point of view is supported by the finding, that experimentally determined exchange splitting in 2 ML fcc-Co films at cryogenic temperatures ($\Delta E_{ex} = 1.2$ eV) agrees with the value observed in 5 ML films, which in turn is consistent with bulk band structure calculations. This rather large value as compared to Ni suggests a behavior closer to iron than to Ni. A spin-resolved photoemission experiment carried out on such an ultrathin film system indeed found evidence for a short-range magnetic order. In particular, it ruled out the possibility of a Stoner-like paramagnetic band structure above $T_C$. This was achieved by exciting the photoelectrons with circularly polarized light and exploiting the effect of "optical spin orientation". This process has already been discussed in Section 9.2.3 in conjunction with the GaAs polarized electron source. Excitation from spin–orbit split bands in paramagnets produces spin-polarized photoelectrons. In a normal emission, normal incidence geometry the spin-polarization is oriented perpendicular to the surface. The magnetization in the Co-films, on the other hand, is oriented within the film plane, a behavior which is attributed to magneto-elastic contributions to the anisotropy (Chuang et al., 1994). The orthogonality of the two spin-quantization axis is the important ingredient in the experiment. If the ferromagnetic band structure of Co collapses into a paramagnetic one above $T_C$, then excitation with circularly polarized light should produce a spin-polarization in the Co-related spectral features. Such a behavior, however, has not been found (Fig. 9.47). Neither an in-plane nor a normal spin-polarization component could be discerned at $1.1T_C$, in clear contrast to the expectations from the Stoner picture. This finding can be understood in terms of the local band theory. In a locally spin-split band structure the symmetry of the bands differs from that of the equivalent bands in a paramagnet, because of the exchange contribution. This affects the relativistic selection rules, which determine the process of optical orientation. The conclusion of short-range magnetic order in fcc-Co was also confirmed by SP-EELS experiments on similar films, which reported an almost thickness (and thus temperature) independent shape of energy loss curves (Kämper et al., 1992). On the basis of the presently available data also fcc-Co appears to be an itinerant ferromagnet with an appreciable amount of short-range magnetic order above $T_C$. Detailed studies of the temperature-dependence of the bands at specific $k$-points by direct or inverse photoemission are yet missing. With respect to the series Fe, Co, Ni, however, Fe and Co do certainly exhibit short-range magnetic order at $T_C$ in accordance with a fluctuating band

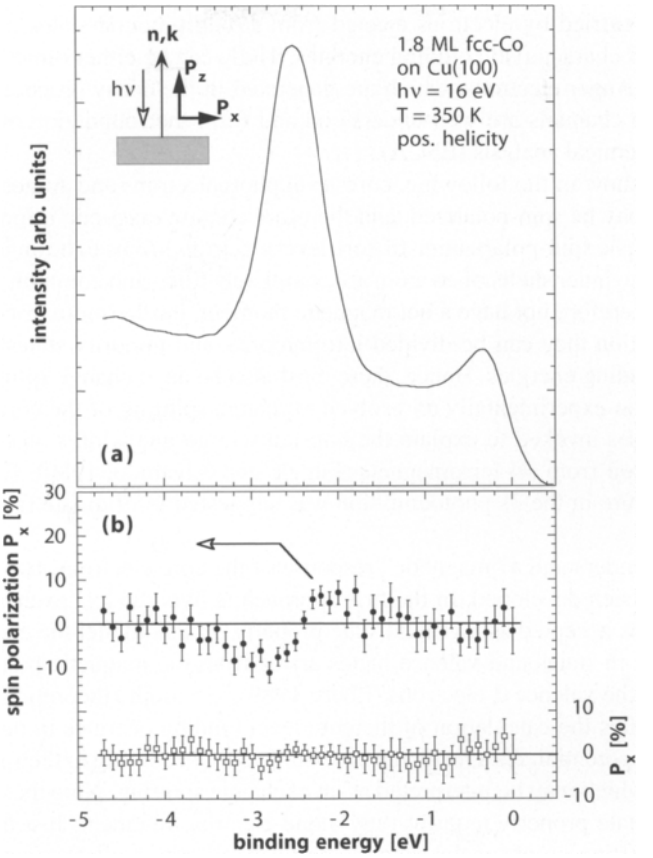


Fig. 9.47. Spin-resolved photoemission from Co ultrathin films above the Curie temperature $T_C$. The normally emitted spin-polarized electrons are generated by optical spin-orientation using normally incident circularly polarized light of positive helicity. Their polarization vector is oriented along the surface normal ($P_z$). Below the Curie temperature the Co films a remanently magnetized in-plane ($P_x$). The broken line in (b) indicates the spin-polarization component that should be expected from optical spin-orientation from paramagnetic fcc-cobalt.

model. Only Ni, because of its lower exchange splitting and high sensitivity to electronic correlations, is not a clear-cut case and may need further investigations.

### *9.5.3. Magnetism and element specificity*

The investigation of spin-polarized valence electronic states can yield a deep insight into the electronic origin of magnetism. Since the itinerant electrons are probed, a discrimination between the contributions from different elements in the interface region or in an alloy becomes possible only under very special circumstances. This is an inherent disadvantage, if one is interested in the magnetic response of a particular constituent. In this situation an element specific probe with additional magnetic sensitivity is needed. Element-specific

information is carried by electrons ejected from strongly bound states, i.e., core levels, because of their characteristic binding energies. These can be either direct core-level photoelectrons, or Auger electrons, which are generated in the decay process of a core hole. Both excitation channels are well-understood and form the foundation of electron spectroscopy for chemical analysis (ESCA).

As we will show in the following, core-level photoelectrons and Auger electrons from ferromagnets may be spin-polarized, and therefore contain magnetic information. At first glance, an intrinsic spin-polarization of core level electrons seems to be an impossible finding. After all, the inner shells of an atom are completely filled and common wisdom tells us that they can therefore not have a net magnetic moment. Furthermore, if core states show a spin-polarization they can be divided into majority and minority states with necessarily different binding energies. Hence, there must also be an exchange splitting in the core states. In fact, an experimentally unresolved exchange splitting of the core lines was one of the hypotheses invoked to explain the unusually large line widths observed in 2p and 3p photoemission from 3d ferromagnets (Fuggle and Alvarado, 1980). Even earlier, the multiplet structure in the 3s photoemission was suggested to originate from an exchange splitting.

In order to understand a "magnetic" response of the core electrons, two competing approaches have been developed. In the first approach, a hypothetical exchange splitting of the core levels is accepted as a ground state property. In this model the exchange interaction between core states and valence bands arises from the magnetic polarization of the inner shells by the valence d-electrons (Ebert, 1989).[8] From the theoretical point of view, this model implies the calculation of the core level binding energies in the presence of a spin-dependent potential. As a result the core-states split according to their magnetic quantum numbers, which may be interpreted as an exchange splitting. Note that the calculation of the ground state property requires only a one-electron treatment. Just the opposite situation is the starting point for the second approach, a many-body treatment. The ground state refers to the system before the excitation and is characterized by $N$ electrons. After the excitation the system is left with $N-1$ electrons and a core hole. The electrostatic interaction between the core hole and the $N-1$ electron system leads to a rescaling of the binding energies and may give rise to satellite structures in the spectra. It is the Coulomb interaction between the polarized d-electrons and the core hole that causes the "exchange" splitting in core levels in this model. In other words, the photoemission process itself is responsible for the level splitting via the removal of the ejected electron. An appropriate treatment of this scenario requires many-body calculations which are usually carried out for atomic-like systems. By means of these many body theories, satellite structures in core level photoemission, for example the famous 6 eV satellite in Ni, have been successfully explained. They are particularly useful to determine the multiplet structures in the spectra from rare earth materials. In the remainder of this section, we will give some examples for spin-polarized core level photoelectrons and Auger electron emission, and their interpretation on the basis of the above models.

---

8 Each shell is magnetically polarized by the valence electrons and the neighboring shells, whereby the individual field contributions can be of either sign. The sum over all inner-shell fields is ~20% of the larger individual contributions and constitutes the magnetic hyperfine field at the nucleus.

*9.5.3.1. Spin-polarized core level photoemission*

For a long time the explicit spin-analysis of core-level photoelectrons was hampered by technical problems, in particular the lack of brilliant light sources. It took until 1988 before the first spin-resolved spectra from Fe 3p taken with synchrotron radiation using an undulator were reported (Carbone and Kisker, 1988). Soon afterwards, a number of experiments on different systems was carried out, but these were all limited to the "shallow" core levels 3p and 3s. It could be experimentally proven that the Fe 3s states are indeed spin-split and the multiplet structure is associated with distinct majority and minority spin states (Carbone et al., 1990). The more strongly bound (deeper) core levels like 2p and 2s have been first accessed by means of laboratory experiments, using high power X-ray sources (Klebanoff et al., 1993).

We will restrict ourselves to only one example of the application of spin-polarized core level photoemission, emphasizing the aspect of elemental specificity. The system in question comprised Cr films on an Fe(100) surface. If the thickness of the Cr overlayer is sufficiently low, i.e., of the order of 1 or 2 atomic layer, photoemission from the Fe substrate is still reasonably high. The situation is particularly favorable for the 3p levels, because the Fe and Cr lines are only about 10eV in binding energy apart (Fe 3p: ~52 eV; Cr 3p: ~42 eV). They can therefore be measured side-by-side in a single spectrum (Fig. 9.48). The first remarkable finding is the strong background polarization in the spectra. This polarization which is of majority type spin character is a property of the secondary electron background in ferromagnets. The inelastic collision events in the low energy secondary electron cascade are spin-dependent, and lead to a majority spin polarization. The polarization depends on the kinetic energy and shows even an enhancement at very low secondary electron energies which may reach values of more than 50% in Fe (see Section 9.4). The polarized secondary electron background is a problem immanent to spin-polarized high energy spectroscopies. The second observation concerns the sign and size of the polarization in the individual 3p lines compared to iron. The polarization in the Cr 3p line is smaller and of opposite sign. In order to understand this finding we have to recall some properties of bulk chromium which is an antiferromagnet. Along the {001} direction the crystal is usually considered to consist of individual lattice planes with a uniform magnetization, whereby the magnetization direction in neighboring layers is pointing into opposite directions. This picture is not entirely correct, because the spatial variation of the magnetization is determined by an incommensurate spin density wave, the wavelength of which is slightly larger than the lattice parameter along [001]. Provided that the experiment averages over several layers, the specific situation in Cr should therefore not give rise to a net spin-polarization in an electron emission experiment. The finding of a nonzero spin-polarization in a 1 ML film indicates the presence of a long-range ferromagnetic order in the overlayer. Whether or not this order is predominantly induced by the iron substrate or may be an intrinsic property of a chromium monolayer cannot be deduced from this experimental result.[9] The opposite sign of the spin-polarization clearly indicates that the magnetization in the Cr layer is oriented antiparallel to the magnetization in the Fe substrate. The Cr monolayer thus couples antiferromagnetically to the Fe-template, as already concluded from SP-LEED experiments on this particular system (Carbone and Alvarado, 1987). The smaller intrinsic

9 The Neél temperature of bulk Chromium is around $T_N = 310$ K (Bacon, 1961).

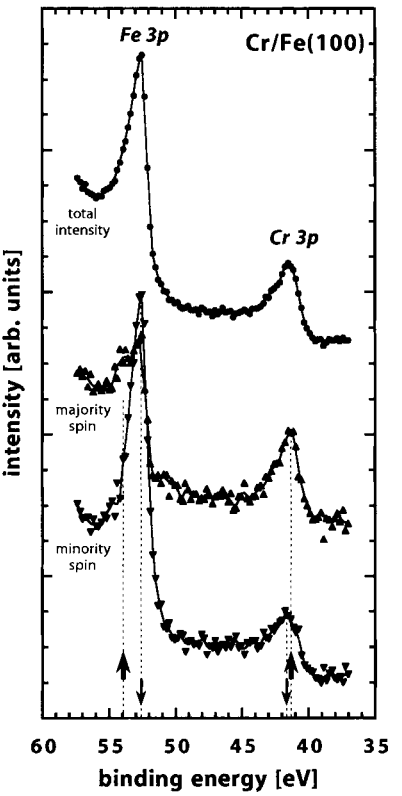


Fig. 9.48. Antiparallel coupling of a Cr monolayer to the Fe(100) substrate seen with spin-resolved core level photoemission. The total intensity distribution (●) reflects the emission from the Cr and Fe 3p levels. The partial intensities of spin-up (▲) and spin-down character (▼) show a dominant spin-down peak on the low binding energy side of the Fe 3p emission. In the Cr 3p spectrum the corresponding feature exhibits a spin-up character, thus directly indicating the opposite orientation of the magnetic moments between Cr and Fe.

spin-polarization in the Cr 3p line (roughly a factor of 2 smaller than Fe) has been interpreted in terms of a reduced magnetic moment in Cr of about 0.5–1 $\mu_B$ on the basis of model calculations (Hillebrecht et al., 1992). There is, however, no straightforward relationship between spin polarization and magnetic moment, which could serve as a reliable basis for an element specific magnetometry. The power of spin-resolved core-level photoemission is therefore limited to qualitative magnetic investigations for the time being.

For thicker Cr overlayers, the polarization in the Cr 3p line is diminished, and disappears at roughly 2 ML. This is interpreted as the second Cr monolayer coupling antiferromagnetically to the bottom layer yielding a net magnetic moment of the bilayer close to zero. This configuration already corresponds to the antiferromagnetism found in bulk chromium along (001). The spin polarization of the Cr 3p line remains zero for coverages above 2 ML, supporting the idea of an antiferromagnetic coupling of the individual Cr layers. This picture is consistent with SP-EELS data of the Cr/Fe system.

Because of the atomic excitation character of XPS, spin-resolved core level spectroscopy probes the *local* magnetic aspect, i.e., the magnetism in the neighborhood of the photoemitting atom. It is therefore particularly suited to investigate alloy materials. The main limitations of spin-resolved core-level spectroscopy are the low count rates, which can only partly be compensated by devices delivering a high photon flux, such as wiggler and undulators at synchrotron radiation facilities. The use of conventional light sources implies very long accumulation periods which make this method somewhat unattractive. In addition, explicit spin resolution is getting more and more competition from a class of methods involving a physical effect termed "magnetic dichroism". We will discuss these techniques in more detail in Section 9.5.4.

*9.5.3.2. Spin polarized Auger electrons*

The Auger process which is an important channel in the decay of the core hole is intrinsically a many-electron problem. It involves at least two electrons and the core hole, resulting in a rather complicated theoretical description of the transition. From the experimental point of view, spin-resolved Auger electron spectroscopy is facilitated by the fact that the core hole can be generated by a primary electron beam of high intensity. The loss in countrate due to the spin analysis can thus be compensated – in certain limits – by an increase of the primary beam current. However, an increase of the primary electron flux inevitably increases the secondary electron background. Like in spin-resolved XPS, background subtraction procedures are required to obtain the true spin-polarization of the Auger electrons.

In order to study the mechanisms involved in the Auger process, let us start with an example. Fig. 9.49 displays the spin-polarization in the region of the prominent LMM Auger transitions in iron (Allenspach et al., 1987). It is obvious that the spin polarization is determined by a monotonic increase towards lower kinetic electron energies. In addition, one observes a number of distinct features which, by comparison to the intensity spectra, are associated with the individual Auger transitions. After subtraction of the polarized background, the effective Auger electron polarization ranges between $-8$ and $+27\%$, depending on the transition in question. Because of the many-particle nature of the Auger process, theoretical interpretations of the Auger electron spin polarization have only been given in the framework of atomic-like many-body approaches. From the three LMM transitions, only the $L_3M_{23}M_{23}$ line exclusively involves core levels. After excitation of the 2p electron, the core hole is filled by a 3p electron and another 3p electron is ejected as an Auger electron. The final state of this process is an atom with two holes in the 3p shell. The two holes can form a singlet or triplet state, giving rise to a multiplet structure in the Auger electron spectrum. From the experiment, the singlet state exhibits a positive sign of the spin-polarization like the other LMM transitions, whereas the triplet state is characterized by a negative spin polarization. Based on the fact that the 3d electrons are not directly involved in the Auger process it was concluded that only the exchange interaction between the 3d electrons and the 3p and 2p holes, respectively, is responsible for the spin polarization. According to a model by Kotani and Mizuta, both the 3d–3p and 3d–2p interaction seem to be necessary to explain the experimental results (Kotani and Mizuta, 1984). The possibility of a ground state splitting due to an exchange interaction with the valence d-electrons has not been considered in these treatments up to now.

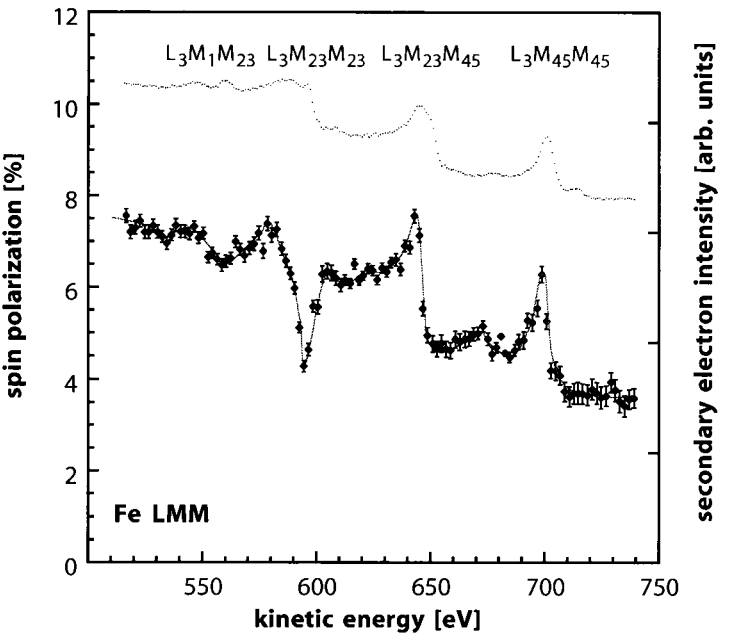


Fig. 9.49. Intensity and spin polarization distribution, $I(E)$ and $P(E)$, of secondary electrons from Fe(100), excited with primary electrons of 2500 eV kinetic energy. The spectral features correspond to the Fe LMM Auger transitions (after Allenspach et al., 1987).

The other two LMM transitions result in either one hole ($L_3M_{23}M_{45}$) or two holes ($L_3M_{45}M_{45}$) in the core electron system. This case is even more complicated to model, because the localized (atomic like) character of the core states and the itinerant nature of the 3d electrons has to be taken into account on an equal footing. Therefore the models describing the $L_3M_{23}M_{23}$ process cannot be simply transferred to other Auger excitation channels. In the absence of more sophisticated approaches, the spin-polarization is often described by a self-convolution of the occupied density of states. This is only possible, however, if correlation effects can be neglected. Within limits, this seems to be an appropriate approximation for the high energy Auger lines. It is no longer applicable in the case of the low energy and highly intense super-Coster–Kronig transitions, in particular if satellite structures are concerned.

More insight into the relevant mechanisms is gained by comparison of the results for iron and nickel. As it turns out, the Ni LMM Auger spin polarization is much smaller (about an order of magnitude) than that of the corresponding line in Fe. This finding is argued to be due to the almost filled 3d shell of nickel. In an atomic model, the ground state of Ni is often described as a $3d^9$ configuration, with a relatively narrow d-band width. In the presence of a core hole, electronic correlation effects pull the unoccupied part of the d-band below the Fermi level, resulting in a $3d^{10}$ configuration in the excited state. The $3d^{10}$ state has no spin magnetic moment left and the spin polarization should disappear. This case may be almost realized in the experiment and reflects the importance of correla-

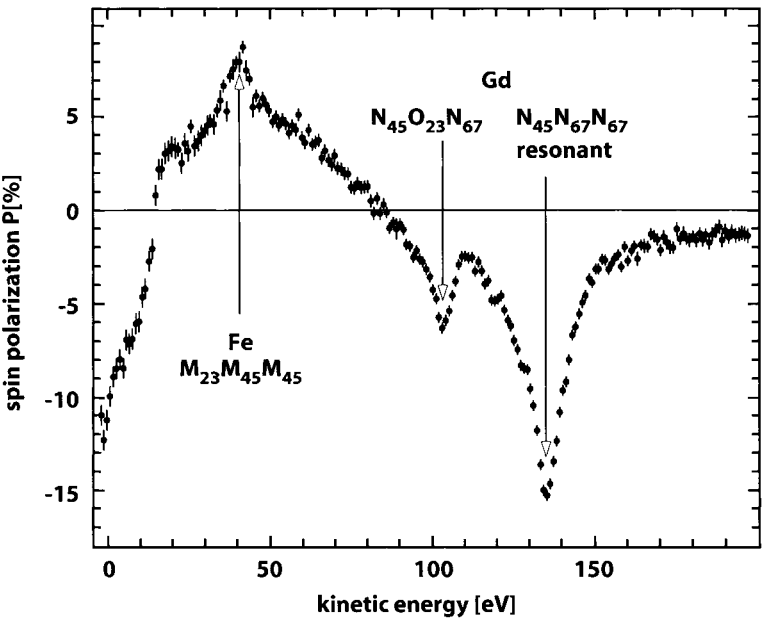


Fig. 9.50. Spin-resolved Auger electron spectroscopy on a Gd film (2.4 Å thick) on a Fe(100) surface. Indicated are the low-energy Auger transitions in Fe and Gd (by Landolt et al., 1986).

tion effects. The fact that the experiment still observes a residual polarization is attributed to the presence of resonant Auger excitations of the type 2p $\rightarrow$ 3d. In this case the spin polarization is determined by the many-particle correlation effects rather than a ground state property. An example for spin-polarized Auger electron spectroscopy that exploits the element specificity of the method is given in Fig. 9.50. A monolayer of Gd has been evaporated onto a Fe(100) surface. By measuring the close-lying Fe MMM and Gd NNN super-Coster–Kronig (sCK) transitions which involve 3d and 4f electrons, one obtains a magnetic fingerprint of the system. Since the sCK Auger electrons reflect – to a certain extent – the band polarization, the sign of the polarization indicates the relative orientation of the Fe and Gd magnetic moments. In the present case, the Gd sCK emission has a negative spin polarization as compared to the positive value in the Fe sCK line. These finding indicates that the Gd overlayer is ferromagnetically ordered, with its moments aligned antiparallel to the Fe magnetization. Similar to the system Fe/Cr, we find an antiferromagnetic coupling between the 3d template and the 4f overlayer. Further studies of the thickness and temperature dependence of the Gd Auger electrons reveal an interesting property of the system. The magnetism of the Gd adlayer seems to be predominantly determined by the Fe substrate. For example, for the 1 ML coverage of Gd a critical temperature of 800 K is found, considerably higher than the bulk Curie temperature of Gd ($T_{C,B} = 293$ K), but still lower than the corresponding value for bulk iron ($T_{C,B} = 1043$ K): One is thus led to the conclusion that the Gd layer together with the adjacent Fe surface layers forms a magnetic system, which is partly decoupled from the Fe bulk. It develops a magnetic or-

dering temperature comparable to that of FeGd alloys. A similar behavior is found even for submonolayer coverages of Gd, supporting the idea of a predominant 3d–4f exchange interaction in the system. Increasing the Gd coverage beyond the limit of ~2 ML, however, leads to a reduction in the NNN Auger electron spin polarization. Obviously the 4f–4f exchange is taking over and slowly establishes the bulk Gd magnetic properties. If the film is thick enough (for example, around 15 ML) the magnetic ordering takes place around the bulk $T_C$ of Gd.

### *9.5.4. Magnetic dichroism*

Considering the experimental complexity associated with an explicit spin-polarization analysis, in particular in the field of core-level spectroscopy, some efforts have been devoted to the development of alternatives. The aim was to obtain magnetic information from simple measurements of the photoelectron intensity distribution. This way much higher count rates are available, enabling a better spectral resolution and shorter acquisition times in the experiment. In developing such a technique, two steps were necessary. In order to set the proper background, it is instructive to recall that in conventional light scattering a magnetic effect on the intensity of a reflected light beam in the visible part of the light spectrum is well-known as the (transverse) magneto-optical Kerr effect (MOKE). Loosely speaking, we must therefore first look for a high energy counterpart of the classical Kerr effect. Second, this "high-energy Kerr effect" should not only be visible in the reflected light, but also in the photoelectrons emitted. The first step was taken at the end of the 80's when observations in X-ray absorption spectroscopy with linear and circularly polarized light indeed reported a magnetic response in the absorption cross section (van der Laan et al., 1986; Schütz et al., 1987). The absorption at the edges varied in a characteristic manner when the orientation between sample magnetization **M** and the light polarization was changed. In analogy to conventional light optics these phenomena have been termed "magnetic dichroism", with a suffix indicating the type of light polarization involved in the experiment. For experiments with circularly polarized X-rays one often uses the acronyms MCD, MXD, or MCXD, whereas MLD or MLXD refers to an effect induced by the linear polarization. In particular the MCXD effect has quickly matured into an element-selective probe of magnetism (Chen et al., 1993). It must be pointed out that the large information depth of the X-rays renders MCXD a bulk-sensitive probe suitable for magnetic multilayers and alloys. An apparent surface sensitivity can be achieved in ultrathin film systems, in which overlayer and substrate consist of different elements. In order to achieve a genuine surface sensitivity, emitted electrons rather than transmitted or reflected photons must be investigated. This can be done either by collecting all emitted electrons in front of the sample (total electron yield), or by measuring the photocurrent from sample to ground.

For didactic purposes we will focus in this section on the magnetic dichroism in photoabsorption, before we move on to magneto-dichroic photoemission experiments in Section 9.5.5. In order to understand the basic physics behind the phenomenon magnetic dichroism we restrict ourselves to the effect induced by circularly polarized light which is intuitively the easiest to understand. The important point is that both spin-dependent interactions, exchange and spin–orbit coupling, have to be taken into account in the electronic excitation. In Section 9.2 we have emphasized the importance of spin–orbit coupling for the "fine structure" of the electronic bands. But up to now we have implicitly

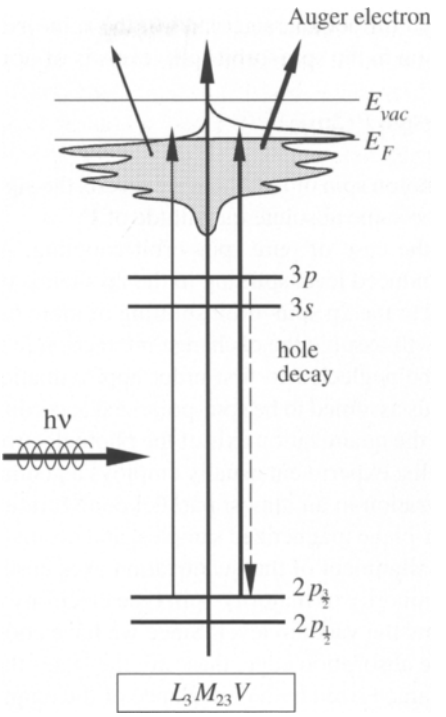


Fig. 9.51. Schematic picture of magnetic circular dichroism (MCD) in the photoabsorption. Also indicated is a possible decay channel for the core hole which leads to Auger electron emission involving an LMV transition.

assumed that spin–orbit coupling is of negligible influence on the photoexcitation process itself. For the understanding of magnetic-dichroic phenomena this simplification no longer holds. On the contrary, magnetic dichroisms arise due to an interplay between exchange interaction and spin–orbit coupling in the electronic states involved in the optical transition. This is, in fact, exactly what should be expected from a high-energy counterpart of the classical Kerr effect. The interplay between the two spin-dependent interactions gives rise to spin-dependent excitation mechanisms, which effectively act as a kind of "internal" spin detector. As a consequence, the magnetism in the system is already reflected in an intensity spectrum. This makes magnetic dichroism particularly attractive for core level spectroscopy.

Let us take the example of the $L_{2,3}$ absorption edge in a 3d ferromagnet, which involves the excitation of electrons from the 2p shell (Fig. 9.51). The 2p shell is split into two levels, $2p_{3/2}$ and $2p_{1/2}$, due to spin–orbit coupling. If we excite electrons from these levels with circularly polarized, they will be spin-polarized. This is the same mechanism of optical spin-orientation that we already know from the GaAs spin-polarized electron source. Optical spin-orientation is in fact a very general phenomenon that occurs as soon as we have a non-vanishing spin–orbit splitting either in the occupied, in the unoccupied state, or in both. The quantization axis of the excited electron is given by the photon spin $\zeta$ or the

photon wave vector **q**. Two further characteristics of the spin-orientation are:

(i) the spin-polarization in the spin–orbit split levels is of opposite sign, i.e.,

$$\mathrm{sgn}\left[P(2p_{1/2})\right] = -\mathrm{sgn}\left[P(2p_{3/2})\right] \tag{9.74}$$

(ii) a reversal of the photon spin or light helicity reverts the sign of the spin-polarization in each level, but keeps the same absolute magnitude of **P**.

These rules hold for the case of pure spin–orbit coupling. As we have seen in Section 9.5.3, the exchange induced level splitting in the 2p shell is of the order of 0.5 eV and therefore small compared to the 2p spin–orbit splitting of more than 10 eV for Fe, Co, and Ni. For the moment, we will assume the exchange interaction in the 2p shell to be a small perturbation, which can be neglected to first order approximation. The electrons excited from the 2p levels may thus assumed to be spin-polarized according to the above scheme of optical orientation. Since the quantization axis of the photoelectron spin-polarization is defined by the photon spin, the experiment usually employs a geometry which brings photon spin and sample magnetization in an almost parallel configuration. This means a grazing incidence geometry for in-plane magnetized samples, and normal incidence for perpendicular magnetization. This alignment of the quantization axes ensures that the photoexcited electrons can be seen as minority or majority-spin type electrons with respect to the empty exchange split states below the vacuum level. Since we have chosen the excitation to take place in the vicinity of the absorption edge, these are the states the core electron is excited into. A ferromagnet is characterized by an imbalance of the empty spin-up and spin-down states. Excited electrons of majority spin character thus find less available empty states than minority spin electrons.

For a fixed sample magnetization we can reverse the spin character of the electrons excited from a given level by simply inverting the helicity of the incident light. The electrons which assume a majority spin for one helicity, become minority spin for the other helicity. Consequently, for a given level, say, the 2p core states, this effect leads to a change in absorption probability with a helicity reversal. The helicity that produces majority spin electrons from the $2p_{1/2}$ levels, generates minority spins from the $2p_{3/2}$ levels, and vice versa. The sign of the change in the absorption cross section of the two levels upon helicity reversal is thus mutually opposite. In a typical absorption experiment one measures the absorption cross section as a function of photon energy for both light helicities and/or directions of sample magnetization. The magneto-dichroic signal is usually defined as the difference of the two spectra for opposite magnetization or helicity. The results of such an experiment are often interpreted by means of so-called "sum rules". These sum rules relate the magneto-dichroic signal or its integrated value to the spin and orbital magnetic moments of the specific element for which the absorption edge has been investigated (van der Laan et al., 1992). The possibility to determine magnetic moments with elemental selectivity is the driving force behind the increasing popularity of this technique.

A magnetic dichroism in the absorption cross section translates directly into a "dichroism" in the core hole density. All decay processes of the core hole will therefore reflect the magnetic dichroism. These are in particular the Auger transitions, leading to emitted electrons with the highest kinetic energy in the electron spectrum. In other words, the Auger electron yield will depend on the relative orientation of sample magnetization and photon

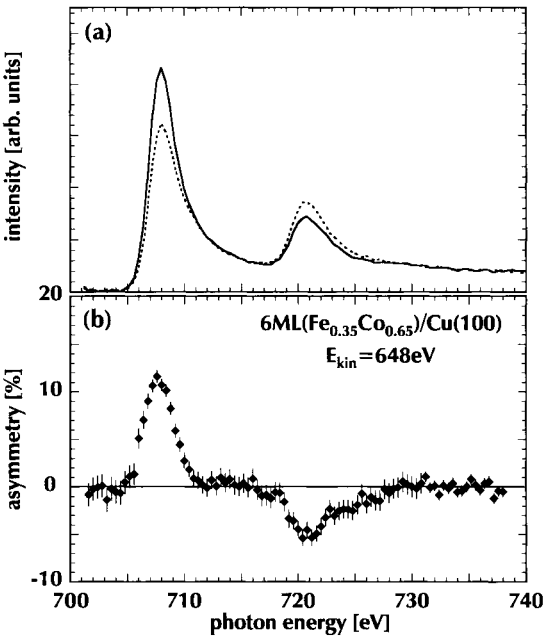


Fig. 9.52. MCD in the Auger LMV yield measured on an ultrathin FeCo alloy film grown on Cu(100). This spectrum shows the characteristic fingerprint of $L_{2,3}$ MCD spectra, namely the opposite sign of the magneto-dichroic signal at the $L_2$ and $L_3$ absorption edge.

spin. Hence, it will exhibit a magnetic circular dichroism, as has been experimentally confirmed recently (Schneider et al., 1993). An example for this effect is given in Fig. 9.52, depicting the MCD signal in the Fe Auger electrons from an $Fe_xCo_{1-x}$ alloy film. This result clearly shows a characteristic feature of the $L_{2,3}$ spectra, namely the opposite sign of the intensity asymmetry at the $L_2$ and $L_3$ absorption edge. The Auger electrons may suffer energy losses due to inelastic scattering, before they leave the crystal. A consequence of this energy transfer to the electron system of the solid is the generation of a secondary electron cascade. The total number of secondary electrons integrated over the half-space in front of the sample and the full range of kinetic energies), the so-called total yield, is to a first order approximation proportional to the number of primary electrons.[10] The magnetic dichroism is thus also found in total electron yield experiments (Chen et al., 1990). Using the emitted electrons rather than the reflected or transmitted light as a signal lends the method a certain surface sensitivity. This has been exploited in a number of edge spectroscopies, for example, EXAFS and SEXAFS. It must be pointed out, however, that the highest surface sensitivity is achieved in the case of the Auger electrons, which have not yet suffered energy losses. The information depth can then be estimated by means of the universal curve for the inelastic mean free path lengths (Seah and Dench, 1979). For a low-

10 At grazing incidence the penetration length of the light perpendicular to the surface becomes comparable to the electron mean free path leading to saturation effects (see, for example, Dunn et al., 1995).

energy secondary electron in an MCD experiment the *magnetic* information depth may be much larger. The reason is that the magnetic signal in the secondary electron current is determined by the primary electron or the core hole.

To understand this, let us consider a primary electron that undergoes a single scattering event in the neighborhood of the core where it was ejected from, thereby generating a high-energy secondary electron. The latter has sufficient kinetic energy to generate further secondaries far away from the position of the first scattering event. The low-energy secondary electrons which finally reach the detector and contribute most to the total yield may therefore be excited far away from the position of the original core hole. As a consequence, the magnetic information depth using the low-energy secondary electrons in a MCD experiment may be much larger than that of the high-energy primaries. This situation is in sharp contrast to a spin-polarized experiment with secondary electrons. The enhancement of the spin-polarization at low kinetic energies is a result of the spin-dependent scattering processes. An experiment that measures this spin-polarization yields the magnetic information contained in the final scattering events in the secondary electron cascade. In order to be able to leave the crystal, these electrons may therefore undergo only further elastic scattering. The spin-polarization of the low-energy secondaries thus probes the magnetism at the surface. The comparison of the physical mechanisms governing MCD in the electron yield and spin-polarized secondary electron emission clearly points out towards an important issue: Considerable care has to be taken in the choice of the electrons probed in a particular experiment in order to arrive at comparable physical results.

With respect to the signal strength in magnetic circular dichroism the $L_{2,3}$ edge in the 3d ferromagnets represents a particularly fortunate case. The combination of a strong spin–orbit coupling in the 2p core levels and a strong exchange interaction in the empty valence states below the vacuum level yields a large magneto-dichroic signal of more than 20%. This may be compared to the first MCD investigations which have been carried out at the K edges of iron (Schütz et al., 1987). Since the K-edge absorption involves a 1s-core level (i.e., $\mathbf{L} = 0$), the spin–orbit coupling can enter only via the final state. This means that both the spin–orbit coupling *and* the exchange interaction in the empty Fe 3d states determine the magnitude of the magneto-dichroic signal. Because spin–orbit coupling in these states is small – the splittings are less than 100 meV – the magnetic dichroism observed reached values of the order of $10^{-4}$ only. The other extreme is represented by the 4f states in the rare earths. They combine a large spin–orbit coupling in the 4f states with a considerably large exchange coupling in the empty DOS below the vacuum level. This gives rise to magneto-dichroic effects up to 70% and more (Starke et al., 1993).

The technical simplicity of total electron yield measurements paired with a certain surface sensitivity makes MCD experiments in the soft X-ray regime very attractive for element-selective studies of magnetic phenomena in layered systems. In metallic systems the magnetic information depth is of the order of 20 Å and thus gives the technique access to buried layers. It is important to point out that this total electron yield approach is not limited to spectroscopic investigations. The low energy secondary electrons which constitute the dominant contribution to the total electron yield are also used in laterally resolving techniques, the so-called electron emission microscopy (EEM) (Bauer and Telieps, 1988). It is thus relatively straightforward to exploit MCD in a photoelectron emission microscope for magnetic imaging purposes. The first experiment of this kind imaged magnetic domains

written into a thin film material employed in hard disk storage devices (Stöhr et al., 1993). The potential of this magnetic imaging approach was highlighted by further studies which were able to resolve magnetic domain walls and access the issue of magnetic interlayer coupling in buried films (Schneider, 1997; Schneider et al., 1997).

### *9.5.5. Magnetic dichroism in the angular distribution of photoelectrons (MDAD)*

In this section we will turn to the physics of magneto-dichroic effects that occur above the absorption edges. In this case the photoelectron is excited into a nearly free-electron like state far above the vacuum level, or more accurately in the language of photoemission theory, into a time-reversed LEED state. The excitation process differs in two important aspects from the situation treated in Section 9.5.4. First, the photoelectron wave vector **k** comes into play and represents an explicit observable in the experiment. Second, the exchange interaction in the final state (seen in a one-electron picture) is usually small and thus negligible. The origin of magneto-dichroic effects in direct photoemission must therefore be sought in the properties of the initial state. Because of the relevance of the photoelectron wave vector **k** in an angle-resolved photoemission experiment this class of magneto-dichroic effects is known as magnetic dichroism in the angular distribution of photoelectrons (MDAD). An additional letter usually indicates the polarization of the exciting radiation. C and L stand for circularly and linearly polarized light, respectively.

#### *9.5.5.1. MDAD in core-level spectroscopy*

We will first turn to the MDAD effects observed in the photoemission from strongly bound levels. In this case we can develop a qualitative, physically transparent picture, in particular for processes observed with circularly polarized light. The example of choice will be the 2p core level photoemission from iron in order to make contact to the discussion of the $L_{2,3}$ photoabsorption. The fact that iron has a relatively broad 3d band permits the use of a single-particle point of view. The situation would be more complicated for Ni, where many-particle interactions give rise to distinct spectral satellites in the photoemission process. This is a consequence of a much more narrow 3d band.

It has been pointed out in Section 9.5.4 that the spin–orbit coupling in the 2p levels is responsible for the optical spin-orientation of the photoelectron upon excitation with circularly polarized light. This process leads to a spin-polarization of opposite sign in the $2p_{1/2}$ and $2p_{3/2}$ photoelectrons. The electron spin-quantization axis is defined by the photon spin. A reversal of the photon spin (or the helicity) reverses the photoelectron spin polarization, but does not affect the photoelectron intensity distribution (Fig. 9.53a). This situation is found, however, only if the various electronic states in the $2p_{1/2}$ and $2p_{3/2}$ levels are energetically degenerate, which implies a non-magnetic material. As we already know from spin-resolved core level photoemission, the core states of ferromagnets are in fact spin-split, too. For the moment, we are not interested in whether this splitting may be a ground-state or a final state property in the sense of a many particle treatment, because this aspect is irrelevant for the main argument. We therefore simply assume that this splitting exists already in the ground state of a single-particle picture. Since the experiment proves that the exchange induced splitting is much smaller than the spin–orbit splitting in Fe 2p, the exchange interaction can be regarded as a perturbation, which we will explicitly consider in the following, in contrast to our discussion in Section 9.5.4. Each of the

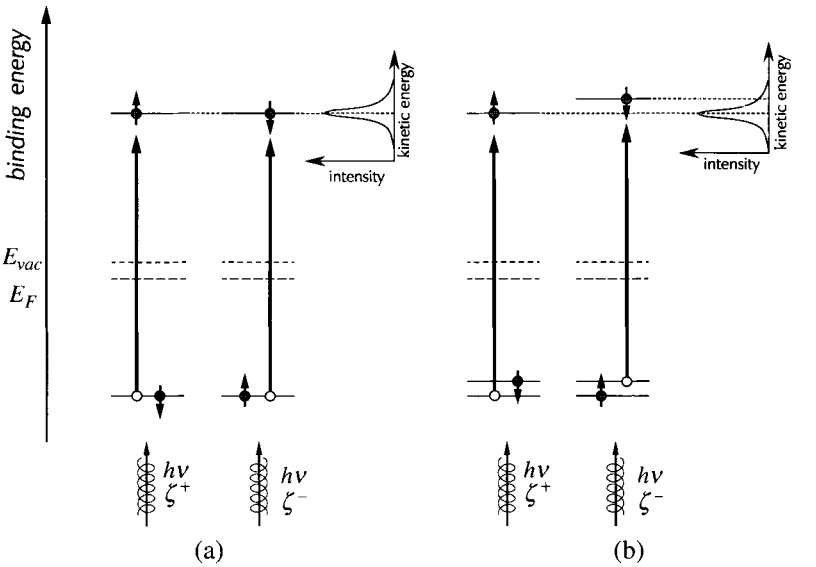


Fig. 9.53. The application of the principles of optical spin-orientation to ferromagnets explains the origin of the intensity asymmetry in magnetic circular dichroism in photoemission (MCDAD). Optical orientation from non-magnets (a) and from ferromagnets (b).

two 2p states will split into a series of spin-polarized sublevels. The sublevels are characterized by definite azimuthal quantum numbers $m_J$ and energy eigenvalues $E_{m_J}$ (Ebert, 1989). Strictly speaking the total angular momentum $J$ is no longer a "good" quantum number, because the magnetic interaction hybridizes the $2p_{1/2}$ and $2p_{3/2}$ core state wave functions. But since the spin–orbit coupling dominates the exchange contribution the labels $p_{1/2}$ and $p_{3/2}$ may still be applied. Within this perturbational approach the ground state spin-polarization of the sublevels, i.e., the expectation $\langle\sigma_z\rangle$ along the magnetic field axis, can easily be deduced from the Clebsch–Gordan coefficients of the appropriate unperturbed wave functions (Zare, 1988). The fractional values of $\langle\sigma_z\rangle$ in Table 9.4 reflect the influence of the spin–orbit coupling. Pure spin states ($\langle\sigma_z\rangle = \pm 1$) which are a prerequisite to define an exchange splitting appear only for $m_J = \pm\frac{3}{2}$. This suggests that the assignment of an exchange splitting as, for example, done in spin-resolved core level photoemission experiments has to be looked at with some caution.

In order to see how this ground state arrangement of spin-polarized levels can give rise to a magnetic dichroism in the emitted photoelectrons, we choose a particular geometry. We assume the circularly polarized light to impinge on the sample along the axis defined by the sample magnetization **M**. For an in-plane magnetization this requires grazing incidence, whereas normal incidence is used for a magnetization perpendicular to the sample surface. Thereby we create a situation in which the two vectors **M** and photon spin $\boldsymbol{\zeta}$ are mutually parallel or antiparallel. The wave vector of the emitted electron, **k**, is not yet taken into account for the sake of simplicity. Let us consider the $2p_{3/2}$ level and in particular the pure spin states $m_J = \pm\frac{3}{2}$. In the definition of quantum magnetism these states represent

Table 9.4
Expectation values of the magnetic moment $\langle\sigma_z\rangle$ along the magnetic field axis for the spin-orbit split 2p core levels

| $\langle\sigma_z\rangle$ | $2p_{1/2}$ | $2p_{3/2}$ |
|---|---|---|
| $+\frac{3}{2}$ | | $+1$ |
| $+\frac{1}{2}$ | $-\frac{1}{3}$ | $+\frac{1}{3}$ |
| $-\frac{1}{2}$ | $+\frac{1}{3}$ | $-\frac{1}{3}$ |
| $-\frac{3}{2}$ | | $-1$ |

a majority ($m_J = \frac{3}{2}$) and a minority spin state ($m_J = -\frac{3}{2}$). The helicity of the c.p. light should be such that spin-up electrons will be excited in the non-magnetic case. In the perturbational approach we can assume the same relativistic dipole selection rules to hold. The ($m_J = \frac{3}{2}$) level is populated by spin-up electrons, and the photoexcitation can take place in agreement with the optical selection rules. The ($m_J = -\frac{3}{2}$) state has the "wrong" spin character, and transitions from this state should be strongly suppressed. Thus we expect a high transition probability from the state ($m_J = \frac{3}{2}$) at energy $E_1$ and a low transition probability for ($m_J = -\frac{3}{2}$) at $E_2$ (Fig. 9.53b).

In other words, the spin character of the initial state is now reflected in the photoemission *intensity* from the respective sublevels. This is the principle of magnetic dichroism. A magnetization reversal $\mathbf{M} \rightarrow -\mathbf{M}$ interchanges ($m_J = \frac{3}{2}$) and ($m_J = -\frac{3}{2}$) at the energy eigenvalues $E_1$ and $E_2$. This means $E_1$ ($E_2$) is associated with a spin-down (spin-up) state. Consequently, an excitation with the same light polarization leads to a high transition probability at $E_2$, but a low one at $E_1$. The same result is achieved if the magnetization is kept the same, but the circular polarization of the light is switched (Fig. 9.53b). Note that in the experiment the change of the transition probabilities appears as an apparent energy shift of the spectral feature investigated. If we now compare the two hypothetical spectra for the two magnetization directions or light polarizations, we find an intensity difference which has the same absolute value but the opposite sign for the energy levels $E_1$ and $E_2$. Normalized to the sum of the spectra this results in an intensity asymmetry or magneto-dichroic signal. We can conclude that the observed magnetic dichroism arises from a competition of the quantization axes introduced by the magnetization $\mathbf{M}$ and the photon spin $\boldsymbol{\zeta}$, both acting on the electrons in the occupied state.

This simple qualitative model, which still draws on the experience made in absorption experiments is sufficient to point out the essential physics in the class of MDAD effects. The dichroic signal arises due to an optical spin-orientation from a spin-split – and therefore already spin-oriented – electronic state. This result can be generalized to itinerant electronic states and the excitation with arbitrary light polarization, as we will see in more detail below. With respect to experiments with circularly polarized light on the Fe 2p core levels (Baumgarten et al., 1990), the arguments given above can at least qualitatively ex-

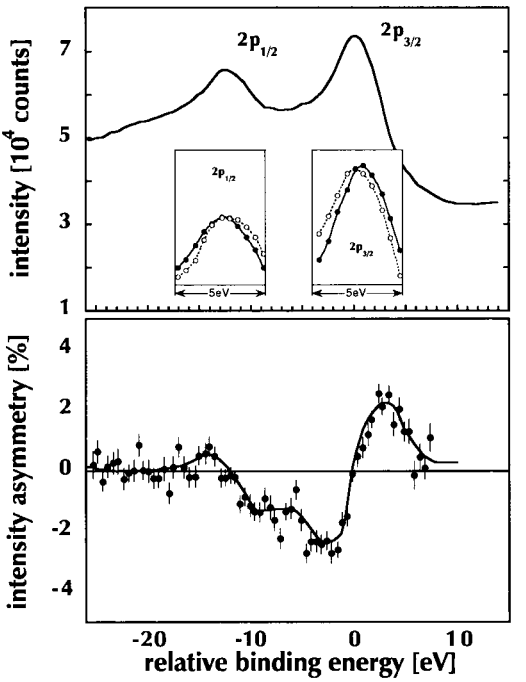


Fig. 9.54. Magnetic circular dichroism in core-level photoemission from ferromagnetic iron. Top panel: Total intensity distribution of the 2p photoemission lines. Bottom panel: Intensity asymmetry or magneto-dichroic signal. Insets: Magnified regions of the $2p_{1/2}$ and $2p_{3/2}$ lines showing the difference in the spectra upon magnetization reversal.

plain the experimental findings (Fig. 9.54). In this experiment, a grazing incidence geometry was chosen, in order to align the photon spin $\zeta$ with the in-plane magnetization of the Fe(110) surface. The spectra acquired for the two opposite directions of magnetization exhibit distinctly different binding energies for the spectral features, in accordance with the apparent energy shifts predicted by our simple picture. The "shift" of the spectral features upon magnetization reversal, however, goes into opposite directions for the $2p_{1/2}$ and $2p_{3/2}$ levels (see insets of Fig. 9.54). This leads to a characteristic form of the intensity asymmetry (bottom panel in Fig. 9.54) and rules out the possibility of experimental artifacts due to magnetic stray fields.

A more elaborate theoretical treatment, which explicitly calculates the transition probabilities gives a better insight into the behavior of the individual $m_J$ sublevels (Ebert et al., 1991). These are too close in binding energy to be resolved in the experiment. From this calculation emerges that, of course, all four sublevels contribute to the photocurrent, but with different spectral weights. A reversal of the helicity $\zeta$ or sample magnetization **M** inverts the sequence of the spectral weights, leading to the observed shift of the center of gravity of the photoemission peak on the binding energy scale (Fig. 9.55). The calculation reproduces essentially the spectral variation of the experimental intensity asymmetry, but the absolute values are too large by a factor of 6. A part of this discrepancy must be

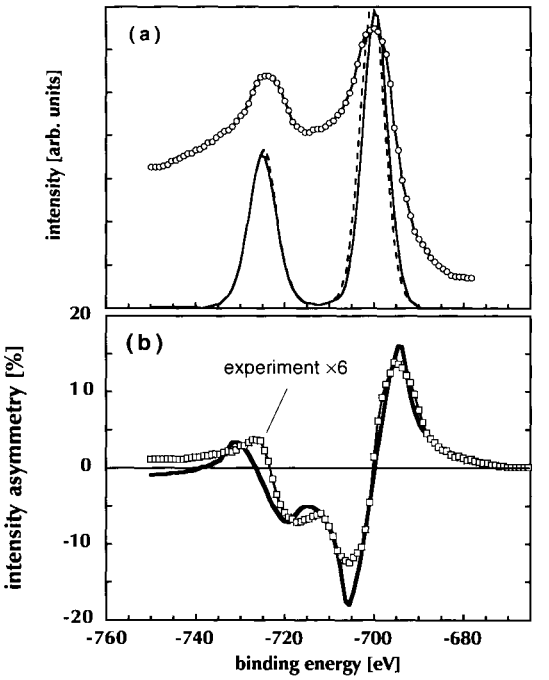


Fig. 9.55. Comparison of calculated and experimental MCDAD spectra. (a) Total experimental intensity (circles) and theoretical intensity distributions for opposite magnetization directions (solid and broken line). (b) Experimental (squares) and theoretical intensity asymmetry distribution (solid line). The experimental result has been multiplied by a factor 6 to scale with the theoretical prediction.

attributed to the neglect of a background of inelastically scattered electrons in the theoretical spectra, and to the assumption of a 100% circular polarization (estimated value of the degree of circular polarization in the experiment $P_c \sim 70\%$ (Petersen et al., 1992)). The experimental spectra purposely have not been "corrected" with respect to any of these two effects, which both tend to reduce the experimentally observed asymmetry. But even taking these reductions into account leaves about a factor of 2 between experiment and theory. Considering the approximations made in the theoretical modeling of the experiment, the result certainly indicates a very reasonable agreement.

It must be emphasized that the above theoretical treatment by Ebert et al. (1991) does not comment on any variations of the magneto-dichroic signal with the emission direction of the photoelectrons, i.e., the wave vector **k**. The reason for this is that **k** was not treated as an independent variable, but rather integrated over as in an absorption process. In this case, the only variation of the magneto-dichroic signal left is the one with the angle between photon spin $\zeta$ and sample magnetization **M**, following a simple dot product $A \sim \zeta \cdot \mathbf{M}$. Subsequent experiments showed, however, that the magnetic dichroism in photoemission is in fact strongly dependent on the emission direction of the photoelectrons (Schneider et al., 1992; Venus et al., 1993). In particular, a strong magnetic dichroism was observed in experimental geometries, where it should vanish according to the predictions

from absorption-based theories. One may thus imagine that the above remaining discrepancy of a factor of 2 between experiment and theory could be also due to the neglect of the angular variation of the magneto-dichroic signal. A theoretical approach is needed that puts more emphasis on the photoelectron wave vector **k** as an independent experimental parameter.

In a next step, we will therefore consider the explicit nature of the one-electron final state, described by the photoelectron wave vector **k**. In a correct theoretical description the final state must be identified with a time-reversed LEED state, thus implying the use of an appropriate scattering formalism. Since we cannot go into details of this theoretical approach, the interested reader is referred to the work by, for example, Pendry or Feder (Pendry, 1975; Feder, 1985). It may suffice to know at this point that the dipole transition probability, i.e., the strength of the dipole matrix element

$$M_{fi} = \langle f|\mathbf{O}|i\rangle \tag{9.75}$$

depends on the details of the final state $|f\rangle$. The photoelectron current into a specific emission direction in space, **k**, is therefore made up by the sum over the contributions from each sublevel $m_J$

$$I(\mathbf{k}, \mathbf{q}, \zeta, \mathbf{M}) = \sum_{m_J} M_{fi}(m_J) = \sum_{m_J} \langle \psi(\mathbf{k})|\mathbf{O}(\mathbf{q}, \zeta)|\phi(M_J)\rangle. \tag{9.76}$$

In this expression, $\langle\psi(\mathbf{k})|$ and $|\phi(m_J)\rangle$ denote the final and initial state wave functions, respectively, and $\mathbf{O}(\mathbf{q}, \zeta)$ describes the light operator, which in the general case depends on the photon wave vector **q** and the state of circular polarization $\zeta$ (for the case of an arbitrary light polarization we have to replace $\zeta$ by a suitable combination of basis vectors). Since the photoemission intensity in Eq. (9.76) depends explicitly on the $m_J$, a magnetization reversal will give rise to a magnetic dichroism which can be written as

$$D^{\mathrm{M}}(\mathbf{k}, \mathbf{q}, \zeta) = I(\mathbf{k}, \mathbf{q}, \zeta, \mathbf{M}) - I(\mathbf{k}, \mathbf{q}, \zeta, -\mathbf{M}). \tag{9.77}$$

This dichroism depends also explicitly on the wave vector **k**, and is thus termed MCDAD. This has the important consequence, that the strength of the dichroic signal $D^{\mathrm{M}}$ varies with the emission direction of the photoelectron. This variation has been experimentally shown first in MCDAD from the Fe 2p levels. It marks the crucial difference between the MD and MDAD effects. This can be seen even more clearly by considering a specific example: The complicated angular dependencies along arbitrary directions simplify considerably, if the emission takes place in a mirror plane of the crystal or even close to high symmetry directions. In this case the final state wave function takes a totally symmetric form. This means in terms of spherical harmonics $Y_{l,m}$ that only states with $m = 0$ couple to the plane waves traveling to the detector. Under these circumstances, the angular dependence takes the following form

$$A(\mathbf{k}, \mathbf{q}, \mathbf{M}) = \frac{4(\mathbf{q}\cdot\mathbf{M}) - 6(\mathbf{q}\cdot\mathbf{k})(\mathbf{k}\cdot\mathbf{M})}{5 - 3(\mathbf{q}\cdot\mathbf{k})^2} \tag{9.78a, b}$$

for the maximum asymmetry of the $2p_{1/2}$ peak (Venus et al., 1993). The inspection of Eq. (9.78a, b) clearly reveals the dichroic asymmetry to be mainly determined by the interplay of two terms in the numerator, the first one not being **k**-dependent. It essentially describes the geometrical relationship between sample magnetization **M** and the photon wave vector **q** (or equivalently, the photon spin $\zeta$) involved in the MD absorption process. The second term carries the angular variation and makes the asymmetry a complicated function of **k**. This term may cancel or even overcompensate the first one, thus changing the sign of the dichroic asymmetry. This result is of considerable importance if the sign of the magnetic dichroism is supposed to indicate the spatial orientation of the magnetization vector **M**. A further remark concerns the behavior of Eq. (9.78a, b) under an integration over **k**. In this limit the simple relation $A = \mathbf{q} \cdot \mathbf{M}$ is recovered, which describes the behavior of the magnetic-dichroic asymmetry at the absorption edge. In other words, the effect in direct photoemission is only visible with angular resolution and vanishes in any angle-integrated experiment. Finally, it shall be pointed out that Eq. (9.78a, b) also describes the magneto-dichroic asymmetry in the emission characteristics of a free atom. It may thus be deduced already from an atomic model (Cherepkov, 1994; Thole and Laan, 1994; van der Laan, 1995). The reason is that both in the atomic case as well as in the emission along a high symmetry direction in a solid the same spherical harmonics of $m = 0$ are important. This permits the application of an atomic approach for this particular crystalline geometry. As soon as **k** is allowed to point along an arbitrary direction in the crystal, the atomic approach breaks down, as linear combinations of $Y_{l,m}$ with different $m$ have to be included. This relationship between atomic and crystalline approach explains results reported on polycrystalline materials (Boeglin et al., 1993). The respective experiment incoherently adds up the contributions from (many) individual crystallites, thus averaging over all possible spatial orientations. The resulting anisotropy in the MCDAD signal corresponds approximately to the one predicted by the spherically symmetric model.

So far we have concentrated on MDAD induced by circularly polarized light. At this stage, MCDAD may be regarded as the magnetic counterpart of the phenomenon of optical orientation with circularly polarized light. This analogy between optical orientation and magnetic dichroism is not limited to circular light, but can be carried on even further. Recent theoretical work on optical orientation from nonmagnetic materials predicted spin-polarization with linearly polarized light in the valence bands (Tamura et al., 1989; Tamura and Feder, 1991). Some of these predictions have been already experimentally verified (Schmiedeskamp et al., 1988). Considering the fact that unpolarized light may be seen as an incoherent superposition of s- and p-polarized linear contributions, these effects may also be accessible with unpolarized radiation. Also this aspect has been confirmed by experiment recently (Irmer et al., 1992). In addition, there have been both theoretical predictions and experimental confirmations of optical orientation with unpolarized light from atomic levels. In each of these cases, the spin-polarization vector **P** obeys a certain geometrical relation with respect to the reaction plane spanned by the direction of light incidence **q** and the wave vector **k** of the emitted electron. If these arguments can be transferred to magnetic systems, we can expect to observe magneto-dichroic phenomena also with linearly polarized or unpolarized light. In fact, the characteristic angular variations of these effects can already be derived on the basis of symmetry considerations (Venus, 1994).

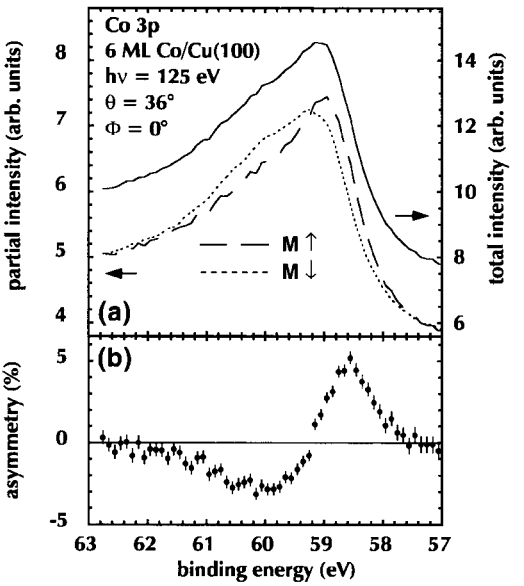


Fig. 9.56. Linear magnetic dichroism (LMDAD) from the Co 3p levels: (a) summed-up intensity distribution (solid line) and individual spectra for opposite magnetization directions (dotted and broken line), (b) resulting intensity asymmetry spectrum.

If we take, for example, p-polarized light at grazing incidence, and normal photoelectron emission, the spin-polarization vector due to optical spin-orientation stands perpendicular to the reaction plane (Tamura and Feder, 1991). A magnetic material with its magnetization **M** oriented along the same direction as **P** in the nonmagnetic case should then exhibit a magnetic dichroism, i.e., LMDAD. This conclusion can be drawn simply from our above argument of competing quantization axes. A corresponding type of LMDAD has indeed been discovered recently in 3p core level photoemission from iron with both linearly polarized and unpolarized light (Roth et al., 1993; Hillebrecht and Herberg, 1994). An example for LMDAD in Co is given in Fig. 9.56. Because spin–orbit and exchange coupling in the Co 3p levels are of comparable strength, the individual sublevels have a lesser separation in binding energy and thus overlap in the final spectra. The asymmetry distribution is characterized by a single plus/minus feature. We note that a decomposition into $3p_{1/2}$- and $3p_{3/2}$-states is no longer justified, because the states are strongly hybridized.

Both atomic-like and symmetry-based theories relate the linear magnetic dichroism to an interference of optical transitions that involve orthogonal light polarizations. Expanding on the derivation of Venus (1994), for an experimental geometry with the photon wave vector **q** within a mirror plane of the crystal, normal emission, and magnetization **M** orthogonal to the reaction plane, the linear dichroism can be written as

$$\begin{aligned} D_{\mathrm{L}}^{\mathrm{M}}(\mathbf{q},\mathbf{k},\pi) &= I(\mathbf{k},\mathbf{q},\pi,\mathbf{M}) - I(\mathbf{k},\mathbf{q},\pi,-\mathbf{M}) \\ &= 2\sin(2\Theta)\cos\Phi \cdot \mathrm{Re}\left[M_z^* \cdot M_y\right] \end{aligned} \tag{9.79}$$

with

$$M_z^* = \langle \psi_i(\mathbf{M}) | z | \psi_f(\mathbf{k}) \rangle \tag{9.80a}$$

and

$$M_y = \langle \psi_f(\mathbf{k}) | y | \psi_i(\mathbf{M}) \rangle. \tag{9.80b}$$

$M_z^*$ and $M_y$ the transition matrix elements with a component of the electric field vector along the surface normal $z$, and along the mirror plane of the crystal $y$. The angles $\Theta$ and $\Phi$ denote the angle of light incidence with respect to the surface normal, and the angle between the reaction plane and the mirror plane of the crystal, respectively. For $\Phi = 0°$, the reaction plane coincides with the mirror plane and the magnetization **M** is oriented normal to both. The dichroic signal is essentially determined by the interference of $M_z^*$ and $M_y$. The particular angular dependence in Eq. (9.79) has been confirmed experimentally (Kuch et al., 1995).

When introducing the electron wave vector dependence of the magnetic dichroism, we adopted a solid state point of view. This implies a one-step photoemission treatment in which the one-electron final state is represented by a time-reversed LEED state. Recently, an alternative interpretation based on photoelectron diffraction formalisms became popular, emphasizing the aspects of a localized picture. We know from the above theoretical arguments that already the emission from a single atom with a spatially oriented magnetic moment will yield a MDAD signal in photoemission. This has experimentally been verified in a system of laser-oriented atoms (von dem Borne et al., 1997). The photoelectron wave emerging from the emitter atom in a crystal lattice is scattered at the neighboring atoms. The interference between direct and scattered waves results in an photoelectron intensity modulation pattern which reflects the spatial arrangement of the atoms in the neighborhood of the emitter. This process is well understood and widely used for structural analyses at solid surfaces (Fadley, 1987). If the neighboring atoms carry a magnetic moment, however, not only the intensity distribution but also the magnetic dichroism – being an intensity difference – is strongly modulated as a function of wave vector **k**, leading to the complex angular variations mentioned above (Idzerda and Ramaker, 1993). With this approach it was possible to explain in detail the fine structure observed in MLDAD measurements from the 3p levels in single-crystalline Fe (Hillebrecht et al., 1995). These results clearly prove that the core level MDAD signal from a solid consist of an atomic and a crystalline contribution.

The exploitation of MDAD effects as element-selective probes of magnetic phenomena at surfaces are now becoming increasingly popular. Since the experiments can be carried out with rather conventional ESCA spectrometers and even unpolarized light, MDAD is maturing into a valuable tool in the field of surface magnetism. Recent investigations of electronic correlation effects (Schneider et al., 1996) and magnetization profiles in layered systems (Gao et al., 1998) underline the potential of this technique. Even quantitative analyses of surface magnetic phenomena in terms of a surface magnetometry are coming within reach (Liberati et al., 1999)

*9.5.5.2. MDAD in valence electronic states*

Whereas in core levels the presence of an exchange-induced energy splitting has been proven just recently, it is a well-established property of the valence bands in the 3d-ferromagnets. As outlined in Subsection 9.5.2.1, photoemission from a spin-split ground state will yield spin-polarized electrons in the final state, independent of the light polarization. The initial state can be identified from the magnitude and the sign of the photoelectron spin polarization. This is entirely correct only in the limit of vanishing spin–orbit coupling. We have already seen in Section 9.2 that the proper inclusion of spin–orbit coupling leads to rather complex band structures and hybridization, even between bands of opposite spin character. Experimentally, the presence and importance of spin–orbit coupling in the valence electronic structure of the 3d-ferromagnets could be proven only indirectly by magnetometric measurements.[11] We recall from Section 9.2, that spin–orbit interaction in the 3d valence bands is held responsible for the magneto-crystalline anisotropies observed in Fe, Co, and Ni.

Because the simultaneous presence of spin–orbit and exchange coupling in the electronic states involved in the optical transition is a necessary requirement for the occurrence of MDAD phenomena, one should expect to see these effects also in photoemission from the spin-split valence bands. Figure 9.57 gives an example for MCDAD from Co in a normal emission geometry. The samples are ultrathin films of five monatomic layers that had been stabilized by molecular beam epitaxy onto Cu(100) substrates. Spin-resolved band mapping experiments (see Fig. 9.33) yielded a bulk-like dispersion of the bands in close agreement with relativistic bulk band structure calculations for fcc-Cobalt (Schneider et al., 1991). The films are remanently magnetized along one of the in-plane [110] directions, which represent the easy axes of magnetization. The circularly polarized light was incident under $\Theta = 64°$ with respect to the surface normal. Experiments on Ag(100) and Cu(100) have shown that under these conditions, a spin-polarization component parallel to the reaction plane, i.e., the (110) directions, is generated by optical spin orientation (Schneider and Kirschner, 1995). The spectral feature at $E_F$ corresponds to emission from the minority d-bands of $\Delta_5^{\downarrow}$ character. It can easily be seen that the spectrum changes its shape and also the energy position of the maximum after a reversal of the helicity $\zeta$. These differences translate into an intensity asymmetry given in the bottom panel, causing a pronounced structure. The second set of panels in Fig. 9.57 displays the results for a similar experiment with $\Theta = -64°$. Obviously, the intensity asymmetry preserves its shape but reverses sign. Further experiments, which are not reproduced here, show the magneto-dichroic signal to disappear for normally incident light (i.e., $\mathbf{M} \perp \boldsymbol{\zeta}$). The peak-to-peak asymmetry may reach values of 8%. Considering the fact that there is almost no background in the valence band spectra and the degree of circular polarization was about 90% (Schäfers et al., 1985), this magneto-dichroic signal is significantly smaller than its high-energy counterpart seen in the core levels. Similar experimental data became available recently also for bulk Fe, bcc Fe and hcp Co films (Bansmann et al., 1992).

A first-principles interpretation of the MCDAD data in the valence band region poses a serious challenge to theory. A theoretical treatment of the electronic structure, which is

11 The contribution of an orbital magnetic moment can be seen, for instance, in the deviation of the $g$-factor from the ideal value $g = 2$.

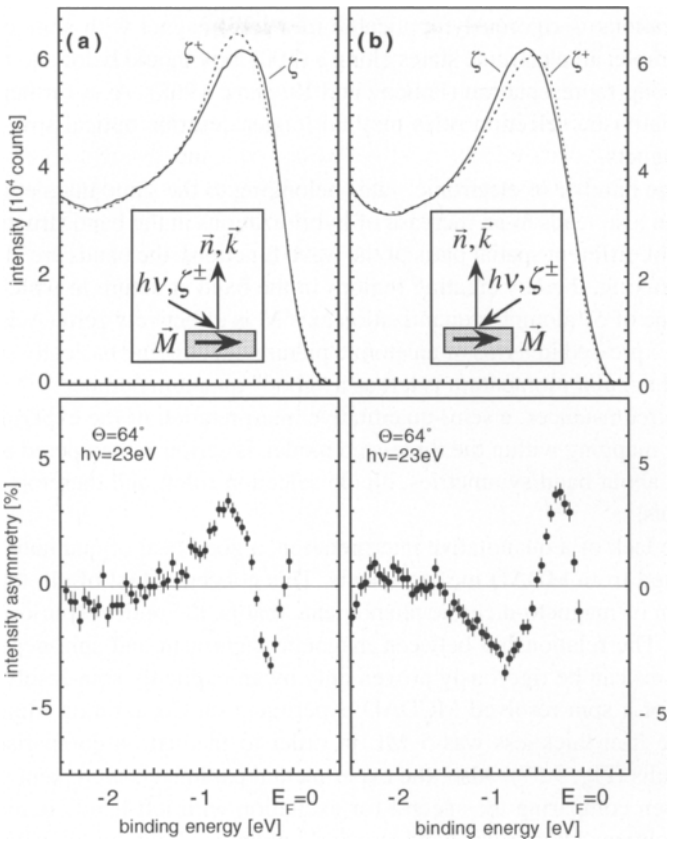


Fig. 9.57. Magnetic circular dichroism in valence band photoemission from the Co 3d bands for opposite angle of incidence. Top panels: Intensity spectra for opposite helicities of the circularly polarized light. Bottom panels: Intensity asymmetry distributions.

the first step in a photocurrent calculation, must take into account both exchange and spin–orbit coupling on an equal footing (see Section 9.2). Qualitatively, this situation leads to a number of implications, which considerably complicate the interpretation of valence band photoemission spectra from ferromagnets:

1. Spin–orbit coupling destroys the independence of the spin-split band structure from the spatial orientation of **M**. If **M** points along a particular high-symmetry direction, previously equivalent directions are no longer equivalent (Joshua, 1991). This means that the Brillouin zone of the magnetic problem is significantly larger than that of the corresponding non-magnetic problem. This complicates the computational procedure in the determination of band structures.
2. The electronic states in ferromagnets without spin–orbit coupling can be classified by their single-group character. When considering spin–orbit coupling only, we can divide the electronic states into various double-group characters. Neither of these two

classifications is rigorously applicable in a ferromagnet with spin–orbit coupling. For example, all electronic states along a (100) axis should belong to the same magnetic group representation (Falicov and Ruvalds, 1968). As a further consequence even relativistic selection rules may no longer describe optical spin-orientation in ferromagnets.

3. The large number of electronic states belonging to the same magnetic group representation also leads to an increase of hybridizations in the band structure. Besides a mixing of different spatial parts of the wave functions, the bands are also affected by a spin-mixing, thereby creating regions in the band structure in which the expectation value of $S_z$ along the quantization axis **M** is effectively zero (Ackermann et al., 1984). Expressed in terms of an atomic picture, this finding basically states that only the total angular momentum is left as a "good" quantum number.

Under these circumstances, a semi-quantitative interpretation of the experimental results, that is, a band mapping within the three-step model, is seriously hampered by the absence of knowledge about band symmetries, dipole selection rules, and therefore the transition matrix elements.

Despite the lack of a quantitative interpretation, a good deal of qualitative information can be extracted from MDAD measurements. This concerns, first of all, the basic physical mechanism of magneto-dichroic phenomena, that is, the optical spin-orientation from ferromagnets. The relationship between magnetic dichroism and spin-dependent excitation mechanisms can be rigorously proven only by an explicitly spin-resolving approach. An example for a spin-resolved MCDAD experiment on Co ultrathin films is displayed Fig. 9.58. The film thickness was 5 ML in order to facilitate a comparison with spin-integrated results (Fig. 9.57). Also, the experimental parameters were kept the same as in Fig. 9.57. When comparing the spectra for excitation with left-hand circularly polarized light to those obtained with right-hand circularly polarized light, both similarities and distinct differences are visible. First, the overall shape of the spin-polarization spectra (lower panel) is similar in that the spin-polarization close to the Fermi level is strongly negative and changes sign at about $-0.8$ eV binding energy. From the sign of the spin-polarization, one deduces the peak at $E_F$ (Fig. 9.58) to be of predominantly minority spin character, followed by a broader distribution of majority electrons at higher binding energies. Nevertheless, in going from Fig. 9.58a to b, the reversal of light helicity introduces subtle changes in the spin polarization spectra. These changes are the direct manifestation of a spin-dependent photoexcitation process. They show up even more clearly in the partial intensities with majority ($\uparrow$) and minority ($\downarrow$) character (upper panels). The strong minority spin-peak at $E_F$ seen with $\zeta^-$ light reduces upon excitation with $\zeta^+$ light, whereas the majority spin contribution increases. Note that no differences between the $\zeta^-$ and $\zeta^+$ spectra would exist in the absence of spin–orbit coupling. Because the two partial intensities sum up to the spin-integrated intensity distribution, the height and energy position of the dominant peak is different for $\zeta^-$ and $\zeta^+$. These differences result in a magneto-dichroic asymmetry essentially like the one shown in Fig. 9.57. This result establishes the correlation between magnetic dichroism and spin-dependent excitation mechanisms.

The above example involves initial states of the type $\Delta_5^{\downarrow}$ (in the non-relativistic notation). In the absence of spin–orbit coupling, the wave function of the minority spin initial

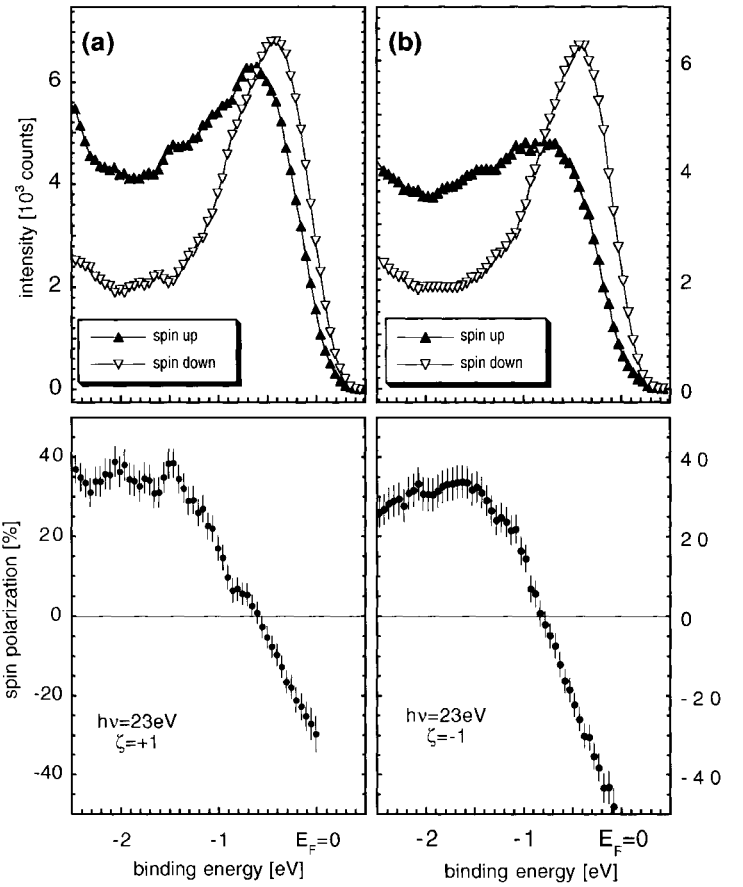


Fig. 9.58. Spin-resolved magnetic circular dichroism in the valence band photoemission from the Co 3d states. Top panels: partial intensities of majority (▲) and minority spin character (▽). Bottom panels: spin polarization spectra. Note the change in the partial intensity curves when changing from positive (a) to negative helicity (b).

state may be simply represented by independent spatial and spin parts

$$\psi_i = \varphi(\mathbf{r})|\beta\rangle. \tag{9.81}$$

Spin–orbit coupling splits the $\Delta_5$ bands of each spin-character by a small amount. To a first order approximation, it may thus be regarded as a perturbation. At the same time it causes an admixture of the opposite spin-character, which is particularly strong in regions of the band structure where bands of opposite spin-character hybridize. Because the spin–orbit split wave functions differ in their spatial parts, we have instead of Eq. (9.81)

$$\begin{aligned} \psi_i^1 &= a\varphi_1^1(\mathbf{r})|\alpha\rangle + b\varphi_2^1(\mathbf{r})|\beta\rangle, \\ \psi_i^2 &= c\varphi_1^2(\mathbf{r})|\alpha\rangle + d\varphi_2^2(\mathbf{r})|\beta\rangle \end{aligned} \tag{9.82}$$

with complex coupling coefficients $a$, $b$, $c$, and $d$. The transition probabilities for the individual $\varphi_j^i$ are not the same and depend on the helicity of the exciting radiation. Due to the coupling of the spatial and spin parts of the electronic wave function, the partial intensity of a given spin character changes upon excitation with $\zeta^-$ and $\zeta^+$ light, finally giving rise to the apparent energy shifts observed in the spin-integrated intensities. In contrast to the situation described in 9.5.5.2, the main effect results from the differences in the spatial parts of the wave function rather than the energy splitting of neighboring levels. The discussion that led to Eq. (9.82) is only valid as long as the spatial symmetry group is not altered by the presence of the magnetization. This is only the case for crystals with a magnetization oriented normal to the surface, because the rotational symmetry around the surface normal is preserved (i.e., $C_{4v}$ for the above example of a (100) surface).

For in-plane magnetized surfaces with (100) orientation the symmetry is lowered and may be described by the magnetic point group $2mm$. With respect to spatial symmetries, we are left with a two-fold rotational axis, equivalent to a (110) surface. Inclusion of spin–orbit coupling leads to a strong hybridization of all electronic states along this axis even in the nonmagnetic case, because there is only one relativistic (double-group) representation, $\Sigma_5$. Instead of Eq. (9.82), the wave functions must therefore be described by a linear combination of spatial parts transforming as representations along the $\Sigma$ line

$$|\varphi\rangle = a|\Sigma_1\rangle|\sigma\rangle + b|\Sigma_2\rangle|-\sigma\rangle + c|\Sigma_3\rangle|-\sigma\rangle + d|\Sigma_4\rangle|\sigma\rangle \tag{9.83}$$

with the complex coupling coefficients $a$ to $d$ and $\sigma$ denoting the vector of the Pauli spin matrices. As a further consequence of the lowered symmetry, we must apply the appropriate selection rules. For the situation described in the above MCDAD experiment, we will excite transitions from initial states with $\Sigma_1$, $\Sigma_3$ and $\Sigma_4$ single-group symmetry (nonrelativistic selection rules). Relativistic selection rules for the (110) direction cannot predict even the sign of the spin polarization due to optical orientation (Wöhlecke and Borstel, 1981c). A comparison of the non-relativistic and relativistic dipole selection rules indicates that the transition matrix elements are determined by a complex hybridization of the type $\{\Sigma_1, \Sigma_3, \Sigma_4\}$. Without a detailed knowledge of how the spatial parts of the individual states change along a given band in a fully relativistic treatment, one cannot hope to extract more information from the spectra within the three-step model.

This conclusion also holds for magnetic dichroism experiments with linearly polarized light. Basically, the same symmetry arguments which led to the magnetic dichroism described by Eq. (9.79) also predict a non-zero magnetic dichroism in valence band photoemission (Feder and Henk, 1996). The non-magnetic counterpart, namely optical spin-orientation with linearly polarized light at oblique incidence, has already been proven to exist (Schmiedeskamp et al., 1991; Tamura and Feder, 1991). The experimental geometry requires the magnetization $\mathbf{M}$ to be oriented perpendicular to the plane of incidence. The symmetry arguments, however, do not give insight into the microscopic origin of the magnetic dichroism. Recently an extensive experimental and theoretical analysis of MLDAD from an in-plane magnetized system became available for the Fe(110) surface (Rampe et al., 1998). The in-plane magnetized (110) surface represents the system of lowest symmetry among the low-indexed surfaces. With the magnetization vector $\mathbf{M}$ pointing along the $[\bar{1}10]$ in-plane direction, the nonmagnetic $C_{2v}$ ($2mm$) symmetry is reduced to the point

group $m$ which contains only the identity operation and a mirror plane perpendicular to **M** as spatial symmetry operations. The experiments by Rampe et al. are corroborated by an analytical theory (Henk et al., 1996) and one-step photoemission calculations. The results clearly show that the observed MLDAD signal is closely related to spin–orbit induced hybridization gaps in the electronic band structure leading to interference effects. A sizable MLDAD arises only at points in the band structure where initial state bands with $\Sigma_1$ and $\Sigma_3$ spatial symmetry character cross in the non-relativistic case. Spin–orbit coupling lifts the degeneracy and generates hybridization gaps. In the vicinity of the gaps one finds optical transitions from states with $\Sigma_1$ and $\Sigma_3$ spatial symmetry taking place simultaneously into the same final state band. The interference between the transitions involving $\Sigma_1$ and $\Sigma_3$ spatial parts finally leads to the observed magnetic linear dichroism. Consequently, in contrast to the findings in the case of MCDAD, the microscopic origin for MLDAD is an interference phenomenon between competing optical interband transitions.

Of course, an experimentalist would like to interpret his or her data qualitatively in terms of a simple bulk interband transition scheme within the three-step model of photoemission. This may in fact be achieved for a situation in which the magnetization is oriented perpendicular to the surface, because a higher spatial symmetry is preserved. For the above case of a (100) surface one is thus left with a four-fold rotational symmetry about the surface normal. The electronic states may therefore still be characterized by the representations of the non-magnetic double groups (i.e., $\Sigma_6$ and $\Sigma_7$) in the sense of Eq. (9.82). As a consequence, one may argue within the framework of non-relativistic and relativistic selection rules along the $\Delta$ line, although additional hybridizations and spin-mixing must be taken into account (Henk et al., 1996). Before we discuss experimental results, we will turn to a theoretical simulation for the above case first. Recently, magnetic dichroism and spin-polarization effects have been calculated for normal emission from Ni(100) within a fully relativistic one-step treatment (Scheunemann et al., 1994). The resulting spin-integrated and spin-resolved spectra are displayed in Fig. 9.59 together with a fully-relativistic bulk band structure, which served as an input in the photoemission calculation. The real part of the final state band is shifted towards $E_F$ by the photon energy ($h\nu = 21.22$ eV). Comparing the crossing points between the initial and final state bands with the energy positions of the calculated spectral features, one finds a one-to-one correspondence. In other words, basically all spectral features can be interpreted in terms of bulk interband transitions. We thus recover an access to these phenomena by means of the three-step model of photoemission. The crossing points in the band structure are numbered from "a" to "f" in the sequence of decreasing binding energy (Fig. 9.59a). In order to see how the three-step model can help to qualitatively understand the spectra, let us consider the transitions "a" and "b" in some detail. These transitions show an interesting behavior. In the spin-resolved spectra with linearly polarized light (Fig. 9.59d), transition "a" is associated with a minority type feature whereas transition "b" results in a majority type spin in the final state. In the band structure, however, the respective initial states have a predominant majority ("a") and minority spin character ("b"), indicated by the solid and dotted line type, respectively. Note, however, that in this figure a majority (minority) state does not necessarily have a expectation value $\langle s_z \rangle = \pm 1$, but instead will vary between $0 \leqslant \langle s_z \rangle \leqslant 1$ ($-1 \leqslant \langle s_z \rangle \leqslant 0$) along the band. This spin-mixing is a consequence of spin–orbit coupling, and so is the apparent excitation of the "wrong" spin character in the transitions "a" and "b". Writing

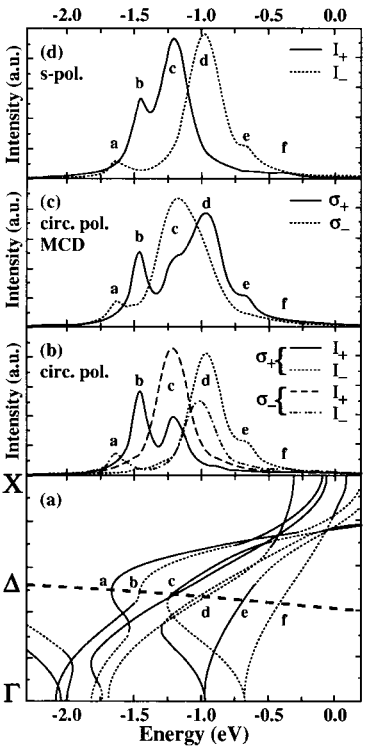


Fig. 9.59. Theoretical predictions for MCDAD spectra from perpendicularly magnetized Ni. (a) Relativistic bulk band structure along [001] for occupied states with dominant majority (solid) and minority spin character (dotted). Empty state bands of predominantly $\Delta_6^1$ spatial symmetry (dashed-dotted) have been shifted downwards by the photon energy $\hbar\omega = 21.22$ eV. (b) Spin-resolved normal emission spectra $I_+$ and $I_-$ and spin-integrated spectra (c). Both sets of spectra have been calculated at $\hbar\omega = 21.22$ eV for normally incident circularly polarized light of positive and negative helicity ($\zeta^+$ and $\zeta^-$). (d) Corresponding $I_+$ and $I_-$ spectra for s-polarized light. Crossing points between occupied and unoccupied bands and the corresponding spectral features are labeled a, ..., f (by Scheunemann et al., 1994).

the wave functions in the sense of Eq. (9.82) we have

$$\begin{aligned} |\psi_a\rangle &= a\left|\Delta_{6,a}^1\right\rangle|+\rangle + b\left|\Delta_{6,a}^5\right\rangle|-\rangle, \\ |\psi_b\rangle &= c\left|\Delta_{6,b}^1\right\rangle|-\rangle + d\left|\Delta_{6,b}^5\right\rangle|+\rangle \end{aligned} \tag{9.84}$$

with $|\Delta_{6,i}^1\rangle$ and $|\Delta_{6,i}^5\rangle$ denoting the spatial parts in the double group notation. $|+\rangle$ and $|-\rangle$ denote the spin character with respect to the quantization axis **M** (i.e., the surface normal). The spin-mixing determined by the complex coefficients $a$, $b$ ($c$, $d$) is such that the expectation value is $\langle s_z\rangle$ positive (negative) for $|\psi_a\rangle$ ($|\psi_b\rangle$). Next, we have to consider the dipole selection rules for normal emission

$$\Delta_6^1 \rightarrow \Delta_6^1, \quad \Delta_6^5 \rightarrow \Delta_6^1. \tag{9.85}$$

Since the electric field vector has only a component parallel to the surface, only $\Delta_6^5$ initial states are allowed (according to the non-relativistic selection rules). Thus, only the contributions in $|\psi_a\rangle$ and $|\psi_b\rangle$ transforming like $\Delta_6^5$ have non-vanishing transition matrix elements. The spin character in the initial state is preserved during the excitation, because the dipole operator acts only on the spatial parts of the wave function, but does not affect the spin directly (this is strictly true only in weak electromagnetic fields). As a consequence, the final state reflects the spin character of the $\Delta_6^5$ admixture in the initial state, and not the expectation value $\langle s_z \rangle$ of the initial state.

A similar situation is found for the transitions "e" and "f". The initial states contain a mixture of $\Delta_7^2$ and $\Delta_7^5$. In normal emission, only initial $\Delta_7^5$ states are allowed. Again the $\Delta_7^5$ states are connected to the "wrong" spin characters, that is to the admixture of opposite spin. In the final state one therefore observes again a spin-character, which is opposite to the one of the initial state band.

The case at points "c" and "d" is more complicated. At each point there is a spin–orbit split pair of states, the more (less) strongly bound having $\Delta_6$ ($\Delta_7$) double group symmetry. Each of these states is a mixture of $\{\Delta_6^1, \Delta_6^5\}$ and $\{\Delta_7^2, \Delta_7^5\}$ spatial symmetries, respectively. As in the cases discussed above, each spatial part of the wave function is connected to a distinct spin character

$$
\begin{aligned}
|\psi_{c,1}\rangle &= a_1 |\Delta_6^1| - \rangle + b_1 |\Delta_6^5| + \rangle, \\
|\psi_{c,2}\rangle &= a_2 |\Delta_7^2| - \rangle + b_2 |\Delta_7^5| + \rangle, \\
|\psi_{d,1}\rangle &= a_3 |\Delta_6^1| + \rangle + b_3 |\Delta_6^5| - \rangle, \\
|\psi_{d,2}\rangle &= a_4 |\Delta_7^2| + \rangle + b_4 |\Delta_7^5| - \rangle.
\end{aligned}
\tag{9.86a–d}
$$

Since only the spatial parts transforming like $\Delta_6^5$ and $\Delta_7^5$ have non-vanishing matrix elements in the chosen geometry, transition "c" ("d") will lead to a majority (minority) spin photoemission. This is consistent with the calculated spin polarization spectra (Fig. 9.59a). If we want to know the response of the system to circularly polarized light, we have to consider the relativistic selection rules and their spin dependence (Wöhlecke and Borstel, 1981b). For a non-magnetic system with the same experimental geometry, these predict

$$
\begin{aligned}
&\Delta_6^5 \xrightarrow{\zeta^+} \Delta_6^1 | + \rangle, \\
&\Delta_7^5 \xrightarrow{\zeta^+} \Delta_6^1 | - \rangle
\end{aligned}
\tag{9.87a, b}
$$

and interchanged spin expectation values in the final state for $\zeta^-$ light, respectively. Inspection of (9.86a–d) with respect to (9.87a, b) shows that only $|\psi_{c,1}\rangle$ and $|\psi_{d,2}\rangle$ initial states are compatible in both spatial and spin part of the wave function. For excitation with $\zeta^-$ light, $|\psi_{c,2}\rangle$ and $|\psi_{d,1}\rangle$ have the correct combination of spatial and spin part. In addition to this selection of wave functions by the polarization of the incident light – which is the magnetic analogue to the optical orientation – the absolute magnitude of the dipole matrix element differs for the individual transitions. Both effects, optical selection of neighboring states and different transition strengths contribute to the calculated MCDAD signal (Fig. 9.59c).

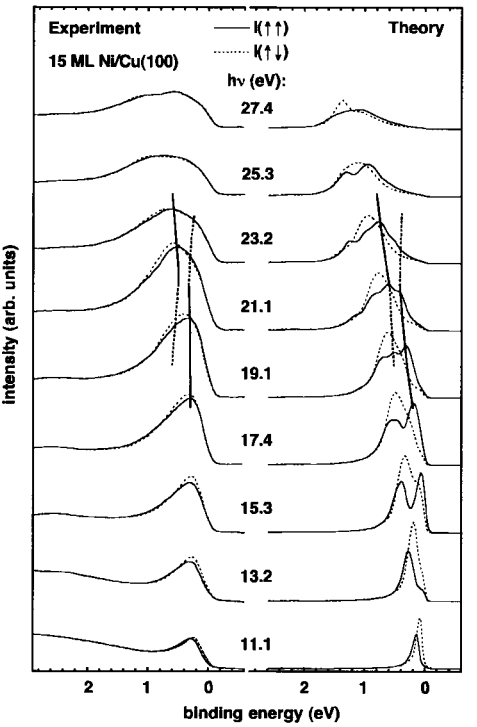


Fig. 9.60. Comparison of experimental (left hand row) and theoretical MCDAD spectra (right hand row) from perpendicularly magnetized Ni. Left: Experimental MCDAD spectra obtained in a normal incidence and normal photoelectron emission geometry as a function of photon energy $h\nu$. Shown are the intensity distribution curves for a magnetization direction **M** parallel (solid line) and antiparallel (dotted line) to the incoming light (or equivalently, the light helicity vector $\zeta$). Right: Theoretically predicted intensity distribution curves calculated within a fully relativistic photoemission formalism. The vertical lines indicate the occurrence of a hybridization region as explained in the text (from Kuch et al., 1996).

Stimulated by these predictions Kuch et al. (1996) were the first to investigate MCDAD in Ni(100) in the highly symmetric geometry (light incidence and electron emission direction both normal to the surface). The difficulty of having a magnetization direction perpendicular to the surface was overcome by using 15 ML thick Ni films on a Cu(100) substrate instead of a Ni single crystal. At this thickness, the Ni films exhibit a remanent magnetization normal to the film plane due to a dominating magnetoelastic contribution to the magnetic anisotropy (Schulz and Baberschke, 1994). The photoemission results are reproduced in Fig. 9.60. Because of the highly symmetric arrangement, the magnetic dichroism is represented by the difference between the intensity spectra for magnetization **M** parallel ($I[\uparrow\uparrow]$) and antiparallel to the light helicity $\zeta$ ($I[\uparrow\downarrow]$). The experimental spectra show a clear dispersion of the photoemission peaks with photon energy indicative of a pronounced 3-dimensional band structure. Using the model of direct interband transitions, the individual spectral features can be interpreted on the basis of the calculated fully relativistic Ni band structure in Fig. 9.5b. In fact, even a hybridization regime, marked by

the vertical lines, can be mapped out. The hybridization occurs between states of $|\Delta_7^5+\rangle$ and $|\Delta_7^2+\rangle$ symmetry. As in the nonmagnetic case the states have different spatial symmetries, but belong to the same relativistic representation $|\Delta_7+\rangle$ and are thus not allowed to cross. From these two states only the $|\Delta_7^5+\rangle$ admixture contributes to the photoemission spectrum, which leads to a doubling of the spectral features within the hybridization zone. In Fig. 9.60 the experimental spectra are also compared to fully relativistic photoemission calculations (the same code has been used to calculate the results in Fig. 9.59). The authors have refrained from broadening the calculated spectra as to mimick the experimental results as close as possible. Therefore, the individual features contributing to the spectra in the hybridization region are nicely resolved. Each of these features can be unambiguously related to an interband transition involving a certain initial state symmetry character. Apart from a steeper dispersion of the theoretical spectra which is probably due to an underestimate of electronic correlation effects, the agreement between experimental and theoretical intensity spectra is remarkable.

In order to highlight the connection between initial state symmetry and interband transition we discuss the results for $h\nu = 21.1$ eV in more detail (Fig. 9.61). In the bottom panel (a) the calculated Ni band structure from Fig. 9.59a is reproduced, this time displaying the bands according to their relativistic symmetry. The dash-dotted line represents the final state bands, shifted downwards in energy by $h\nu$. The exchange splitting of the final state bands is not resolved on this scale. The intersections of this line with $\Delta_5$-containing bands mark the positions in $k$-space where transitions for $h\nu = 21.1$ eV occur. The vertical lines connect the band structure in panel (a) to the result of a spin-resolved photoemission calculation, shown in panel (b). Each of the four bands with $\Delta_5$ spatial symmetry gives rise to a peak in one of the four partial spectra of Fig. 9.61b. In addition, in the $\Delta_7+$ spectra a peak at 0.45 eV binding energy appears. This is a consequence of electronic hybridization between $\Delta_7^5+$ and $\Delta_7^2+$ states, as discussed before. It leads to the simultaneous presence of $\Delta_5$ spatial symmetry in two $\Delta_7+$ bands in the hybridization region, which is about at the position where the transitions at $h\nu = 21.1$ eV take place. Similarly, a bump in the $\Delta_6-$ spectra at 1.2 eV is correlated to hybridization between $\Delta_6^5-$ and $\Delta_6^1-$ states around 1 eV binding energy.

In a spin-integrating photoemission experiment using circularly polarized excitation one observes spectra like the ones shown in Fig. 9.61c. The intensity spectra for parallel and antiparallel alignment of light helicity and magnetization are related to the spin-resolved spectra and thus to the initial states by

$$I[\uparrow\uparrow] \propto I\{\Delta_7+\} + I\{\Delta_6-\},$$
$$I[\uparrow\downarrow] \propto I\{\Delta_7-\} + I\{\Delta_6+\}. \qquad (9.88a, b)$$

The theoretical spectra in Fig. 9.61c were obtained by summing the appropriate pairs of spectra from Fig. 9.61b, using Eq. (9.88a, b). These spectra can already be compared to the experimental data and are used to finally calculate the theoretically predicted dichroism $A = I[\uparrow\uparrow] - I[\uparrow\downarrow]$ (Fig. 9.61d). Despite the contributions from four transitions, one notes a plus/minus/plus shape in the asymmetry at this photon energy, but the plus-peak at the higher binding energy side is very small. The reason for that is found in the details of

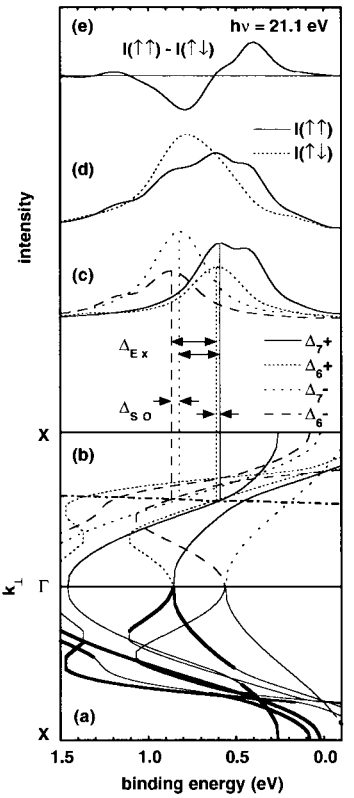


Fig. 9.61. Theoretical analysis of the MCDAD observed at $h\nu = 21.1$ eV. (a) Calculated fully relativistic Ni band structure from Fig. 9.59b for perpendicular magnetization. The bands are now distinguished by their relativistic double group symmetry $\Delta_7+$, $\Delta_6+$, $\Delta_7-$, and $\Delta_6-$. The final state band, shifted down by 21.1 eV, is shown as a dash-dotted line. The vertical lines mark crossing points of the shifted final state band with four initial bands of predominantly $\Delta_5$ spatial symmetry. The influence of spin–orbit ($\Delta_{SO}$) and exchange interaction ($\Delta_{EX}$) on the energetic separation of these bands is indicated by arrows. (b) Spin-resolved photoemission spectra for $h\nu = 21.1$ eV photon energy, calculated with the same parameters as the band structure of panel (a). The spectra are labeled according to the underlying initial-state bands. (c) Calculated photoemission intensity spectra for parallel ($I[\uparrow\uparrow]$, solid line) and antiparallel ($I[\uparrow\downarrow]$, dotted line) alignment of light helicity and magnetization direction. The spectra are related to the spin-resolved spectra in (b) by Eq. (9.88a, b). (d) Difference of the two curves in (c), showing the dichroism $A$. Taken from Kuch et al. (1996).

the band structure. At 21.1 eV photon energy the bands are probed at a position where the contribution from the lower lying band at 1.2 eV binding energy due to $\Delta_6^5-/\Delta_6^1-$ hybridization is rather small, and the higher lying $\Delta_6-$ band is shifted upwards in energy so that it nearly is degenerate with the $\Delta_7-$ band. This is also well seen by comparing Figs. 9.61a and b. This small energetic separation between the $\Delta_6-$ and $\Delta_7-$ contributions leads to nearly coinciding peaks in $I[\uparrow\uparrow]$ and $I[\uparrow\downarrow]$, and thus to the reduction of the plus feature in the difference spectra at the high binding energy side. This result clearly emphasizes that a qualitative understanding of MCDAD data is already possible on the

basis of simple assumptions. The full information contained in the asymmetry spectra, however, is not accessible without the help of appropriate photoemission calculations.

The above discussion of the Ni(100) case may suffice as an example for the interpretation of MDAD data on the basis of the three-step model of photoemission. It already shows some important effects that occur in a fully-relativistic treatment of photoemission from ferromagnets, e.g., the excitation of seemingly "wrong" spin characters. One must keep in mind, though, that the fully-relativistic treatment comes closest to the reality, whereas a non- or scalar-relativistic treatment contains more stringent approximations.

Finally, two other aspects must be mentioned in the context of MDAD phenomena. First, the three-step model inherently neglects contributions from surface and half-space states. These states are responsible, however, for a variety of optical orientation processes that occur with linearly polarized light on non-magnetic surfaces (Tamura et al., 1987; Tamura and Feder, 1991). Thus they are also important for the detailed understanding of MDAD effects in ferromagnetic systems (Henk et al., 1994, 1996). Their role can only be studied by means of one-step calculations. The application of the three-step model is reserved to MCDAD from bulk states, in analogy to the situation found in optical spin-orientation from non-magnetic materials. Second, the MDAD signal depends in a non-trivial way on the wave vector of the photoelectron. The angular dependence can be interpreted by a symmetry-based formalism like the one developed by Venus (1993, 1994), as long as spin–orbit coupling in the final state can be neglected. Unfortunately, changing the electron pick-off angle away from the surface normal gives rise to two competing effects that may alter or even mask the MDAD signal. First, spin–orbit coupling in the final state leads to a spin-dependent transmission of electrons through the surface potential barrier. These so-called transmission effects have their origin in a matching of the Bloch spinors within the crystal to the free-electron wave in the vacuum. This matching is different for spin-up and spin-down states, if the emission direction is inclined to the surface normal and the final state is affected by spin–orbit coupling (Oepen et al., 1986; Schneider and Kirschner, 1995). Spin-dependent transmission takes the form of an intensity asymmetry, that is a dichroic effect, and may be distinguished from MDAD only by a different dependence on the exciting energy. Second, if the experimental geometry is chosen such that it defines a chirality (i.e., $\mathbf{q}$, $\mathbf{k}$, and $\mathbf{M}$ are non-coplanar), contributions from another dichroic effect, CDAD, have to be expected (Schönhense, 1990). With respect to the dichroic signal, a reversal of the light helicity ($\zeta^+ \rightarrow \zeta^-$) and a magnetization reversal ($\mathbf{M} \rightarrow -\mathbf{M}$) are no longer equivalent. Because the physical mechanism behind the CDAD effect involves only dipole-allowed transitions and no spin-dependent processes, the resulting intensity asymmetries may be several times larger than those in MCDAD experiments. Particular care has to be taken in order to select the various contributions to the dichroic signal under these conditions. For example, the operation ($\mathbf{M} \rightarrow -\mathbf{M}$) gives only the magnetic-dichroic signal (MCDAD), whereas ($\zeta^+ \rightarrow \zeta^-$) contains a mixture of CDAD and MCDAD (Venus, 1994). Despite these difficulties, some recent experiments carried out at off-normal emission of the photoelectrons have shown that by a proper choice of the experimental geometry magnetic dichroism in photoemission reveals a considerably detailed picture of the electronic structure of a ferromagnetic system (Venus, 1997; Venus et al., 1997).

Magneto-dichroic phenomena in valence band photoemission may become an attractive alternative to explicitly spin-resolving techniques, provided that adequate theoretical support is available. By exploiting the different physics involved in MCDAD and MLDAD it may even be possible to select between bulk and surface electronic states and study their properties individually. A considerable development in this field may be expected for the future.

*Acknowledgements*

The authors wish to express their gratitude for many fruitful discussions and suggestions to: A.S. Arrott, S. Blügel, J.F. Cochran, A. Dittschar, M. Donath, H. Ebert, R. Feder, B. Heinrich, J. Henk, F.U. Hillebrecht, H. Hopster, Y.U. Idzerda, P.D. Johnson, W. Kuch, G. van der Laan, M.-T. Lin, D.T. Pierce, O. Rader, F. Schäfers, G. Schönhense, H.C. Siegmann, D. Venus, M. Zharnikov.

Thanks are due to Miss V. Vahland and Miss P. Menck for typesetting the manuscript and patiently including the continuous stream of changes.

## References

Abraham, D.L. and H. Hopster, 1987, Phys. Rev. Lett. **59**, 2333.
Ackermann, B., R. Feder and E. Tamura, 1984, J. Phys. F: Met. Phys. **14**, L173.
Allan, C.A.T., 1970, Phys. Rev. B **1**, 352.
Allenspach, R., D. Mauri, M. Taborelli and M. Landolt, 1987, Phys. Rev. B **35**, 4801.
Alvarado, S. F., M. Campagna, F. Ciccacci and H. Hopster, 1982a, J. Appl. Phys. **53**, 7920.
Alvarado, S.F., M. Campagna and H. Hopster, 1982b, Phys. Rev. Lett. **48**, 51.
Alvarado, S.F., R. Feder, H. Hopster, F. Ciccacci and H. Pleyer, 1982c, Z. Phys. B: Condens. Matt. **49**, 129.
Alvarado, S.F., H. Hopster and M. Campagna, 1982d, Surf. Sci. **117**, 294.
Ashcroft, N.W. and N.D. Mermin, 1976, Solid State Physics. Saunders College, Philadelphia.
Bacon, G.E., 1961, Acta Crystallogr. **14**, 823.
Bader, S.D., 1990, Proc. IEEE **78**, 909.
Baibich, M.N., J.M. Broto, A. Fert, F.N.V. Dau, F. Petroff, P. Etienne, G. Creuzet, A. Friederich and J. Chazelas, 1988, Phys. Rev. Lett. **61**, 2472.
Bander, M. and D.L. Mills, 1988, Phys. Rev. B **38**, 12015.
Bansmann, J., C. Westphal, M. Getzlaff, F. Fegel and G. Schönhense, 1992, J. Magn. Magn. Mater. **104–107**, 1691.
Barber, M.N., 1983, in: Phase Transitions and Critical Phenomena, eds. C. Domb and J.L. Lebowitz. Academic Press, London.
Barth, U.V. and L. Hedin, 1972, J. Phys. C: Solid State Physics **5**, 1629.
Bauer, E. and W. Telieps, 1988, in: Surface and Interface Characterization by Electron Optical Methods, eds. A. Howie and U. Valdrè. Plenum, New York, p. 195.
Baumgarten, L., C.M. Schneider, F. Schäfers, H. Petersen and J. Kirschner, 1990, Phys. Rev. Lett. **65**, 492.
Berger, A., U. Linke and H.P. Oepen, 1992, Phys. Rev. Lett. **68**, 839.
Binasch, G., P. Grünberg, F. Saurenbach and W. Zinn, 1989, Phys. Rev. B **39**, 4828.
Blügel, S., 1992, Phys. Rev. Lett. **68**, 851.
Bode, S., K. Starke, P. Rech and G. Kaindl, 1994, Phys. Rev. Lett. **72**, 1072.
Boeglin, C., E. Beaurepaire, B. Carrière, K. Hricovini and G. Krill, 1993, in: Proceedings Materials Research Society Symposium. Pittsburgh, Pennsylvania.
Borstel, G. and G. Thörner, 1988, Surf. Sci. Rep. **8**, 1.
Bozorth, R.M., 1936, Phys. Rev. **50**, 1076.

Brookes, N.B., Y. Chang and P.D. Johnson, 1991, Phys. Rev. Lett. **67**, 354.
Brookes, N.B., A. Clarke, P.D. Johnson and M. Weinert, 1990, Phys. Rev. B **41**, 2643.
Busch, G., M. Campagna, P. Cotti and H.C. Siegmann, 1969, Phys. Rev. Lett. **22**, 597.
Carbone, C. and S.F. Alvarado, 1987, Phys. Rev. B **36**, 2433.
Carbone, C., T. Kachel, R. Rochow and W. Gudat, 1990, Z. Phys. B: Condens. Matt. **79**, 325.
Carbone, C. and E. Kisker, 1988, Solid State Commun. **65**, 1107.
Carbone, C., E. Vescovo, O. Rader, W. Gudat and W. Eberhardt, 1993, Phys. Rev. Lett. **71**, 2805.
Celotta, R.J., D.T. Pierce, G.C. Wang, S.D. Bader and G.P. Felcher, 1979, Phys. Rev. Lett. **43**, 728.
Chen, C.T., Y.U. Idzerda, H.-J. Lin, G. Meigs, A. Chaiken, G.A. Prinz and G.H. Ho, 1993, Phys. Rev. B **48**, 642.
Chen, C.T., F. Sette, Y. Ma and S. Modesti, 1990, Phys. Rev. B **42**, 7262.
Chen, C.T. and N.V. Smith, 1987, Phys. Rev. B **35**, 5407.
Chen, J. and J.L. Erskine, 1992, Phys. Rev. Lett. **68**, 1212.
Cherepkov, N.A., 1994, Phys. Rev. B **50**, 13813.
Chikazumi, S., 1964, Physics of Magnetism. Wiley, New York.
Chrobok, G., M. Hofmann, G. Regenfus and R. Sizmann, 1977, Phys. Rev. B **15**, 429.
Chuang, D.S., C.A. Ballentine and R.C. O'Handley, 1994, Phys. Rev. B **49**, 15084.
Cochran, J.F., 1994, in: Ultrathin Magnetic Structures, eds. B. Heinrich and J.A.C. Bland. Springer-Verlag, Berlin, p. 222.
Cullity, B.D., 1972, Introduction to Magnetic Materials. Addison–Wesley, Reading, MA.
Damon, R.W. and J.R. Eshbach, 1961, J. Phys. Chem. Solids **19**, 308.
Datta, S. and B. Das, 1990, Appl. Phys. Lett. **56**.
Daughton, J.M., 1999, J. Magn. Magn. Mater. **192**, 334.
Dirac, P.A.M., 1927, Proc. Roy. Soc. A **114**, 243.
Donath, M., 1989, Appl. Phys. A **49**, 351.
Donath, M. and V. Dose, 1989, Europhys. Lett. **9**, 821.
Donath, M., F. Passek and V. Dose, 1993, Phys. Rev. Lett. **70**, 2802.
Dose, V., W. Altmann, A. Goldmann, U. Kolac and J. Rogozik, 1984, Phys. Rev. Lett. **52**, 1919.
Dunn, J.H., D. Arvanitis, N. Mårtensson, M. Tischer, F. May, M. Russo and K. Baberschke, 1995, J. Phys.: Condens. Matt. **7**, 1111.
Dunning, F.B., L.G. Gray, J.M. Ratliff, F.-C. Tang, X. Zhang and G.K. Walters, 1987, Rev. Sci. Instrum. **58**, 1706.
Dunning, F.B. and G.K. Walters, 1985, in: Polarized Electrons in Surface Physics, ed. R. Feder. World Scientific, Singapore, p. 289.
Eberhardt, W. and F.J. Himpsel, 1980, Phys. Rev. B **21**, 5572.
Eberhardt, W., E.W. Plummer, K. Horn and J. Erskine, 1980, Phys. Rev. Lett. **45**, 273.
Ebert, H., 1989, J. Phys.: Condens. Matt. **1**, 9111.
Ebert, H., L. Baumgarten, C.M. Schneider and J. Kirschner, 1991, Phys. Rev. B **44**, 4406.
Eckardt, H. and L. Fritsche, 1987, J. Phys. F **17**, 925.
Eckardt, H., L. Fritsche and J. Noffke, 1984, J. Phys. F: Met. Phys. **14**, 97.
Erbudak, M. and N. Müller, 1981, Appl. Phys. Lett. **38**, 575.
Erbudak, M. and G. Ravano, 1981, J. Appl. Phys. **52**, 5032.
Erbudak, M. and G. Ravano, 1983, Surf. Sci. **126**, 120.
Erickson, R.P. and D.L. Mills, 1991, Phys. Rev. B **43**, 11527.
Eriksson, O., R.C. Albers and A.M. Boring, 1991, Phys. Rev. Lett. **66**, 1350.
Erskine, J.L., 1980, Phys. Rev. Lett. **45**, 1446.
Ertl, G. and J. Küppers, 1985, Low Energy Electrons and Surface Chemistry. VCH, Weinheim.
Escudier, P., 1975, Ann. Phys. (Paris) **9**, 125.
Fadley, C.S., 1987, Physica Scripta **T17**, 39.
Fahsold, G., M.S. Hammond and J. Kirschner, 1992, Solid State Commun. **84**, 541.
Falicov, L.M. et al., 1990, J. Mater. Res. **5**, 1299.
Falicov, L.M. and J. Ruvalds, 1968, Phys. Rev. **172**, 498.
Fan, H., 1945, Phys. Rev. **68**, 43.
Farle, M., W. Platow, A.N. Anisimov, P. Poulopoulos and K. Baberschke, 1997, Phys. Rev. B **56**, 5100.
Feder, R., 1985, in: Polarized Electrons in Surface Physics, ed. R. Feder. World Scientific, Singapore.

Feder, R., S.F. Alvarado, E. Tamura and E. Kisker, 1983, Surf. Sci. **127**, 83.
Feder, R. and J. Henk, 1996, in: Spin–Orbit Influenced Spectroscopies of Magnetic Solids, eds. H. Ebert and G. Schütz. Springer-Verlag, Berlin, p. 85.
Feder, R. and H. Pleyer, 1982, Surf. Sci. **117**, 285.
Feder, R., A. Rodriguez, U. Baier and E. Kisker, 1984, Solid State Commun. **52**, 57.
Feuerbacher, B., B. Fitton and R.F. Willis, eds., 1978, Photoemission and the Electronic Properties of Surfaces. Wiley, New York.
Fischer, N., S. Schuppler, T. Fauster and W. Steinmann, 1990, Phys. Rev. B **42**, 9717.
Freeman, A.J. and R.-Q. Wu, 1991, J. Magn. Magn. Mater. **100**, 497.
Fritzsche, H., J. Kohlhepp, H.J. Elmers and U. Gradmann, 1994, Phys. Rev. B **49**, 15665.
Fu, C.L., A.J. Freeman and T. Oguchi, 1985, Phys. Rev. Lett. **54**, 2700.
Fuggle, J.C. and S.F. Alvarado, 1980, Phys. Rev. A **22**, 1615.
Gao, X., M. Salvietti, W. Kuch, C.M. Schneider and J. Kirschner, 1998, Phys. Rev. B **58**, 15426.
Garrison, K., Y. Chang and P.D. Johnson, 1993, Phys. Rev. Lett. **71**, 2801.
Gauthier, Y., R. Baudoing, M. Lundberg and J. Rundgren, 1987, Phys. Rev. B **35**, 7867.
Gay, J.G. and R. Richter, 1986, Phys. Rev. Lett. **56**, 2728.
Gay, J.G. and R. Richter, 1987, J. Appl. Phys. **61**, 3362.
Gay, J.G. and R. Richter, 1994, in: Ultrathin Magnetic Structures, eds. J.A.C. Bland and B. Heinrich. Springer-Verlag, Berlin, p. 21.
Gokhale, M.P. and D.L. Mills, 1994, Phys. Rev. B **49**, 3880.
Gradmann, U., 1966, Ann. Phys. **17**, 91.
Gradmann, U., R. Bergholz and E. Bergter, 1985, Thin Solid Films **126**, 107.
Gradmann, U., G. Waller, R. Feder and E. Tamura, 1983, J. Magn. Magn. Mater. **31–34**, 883.
Grünberg, P., 1989, in: Light Scattering in Solids, eds. M. Cardona and G. Güntherodt. Springer-Verlag, Berlin.
Grünberg, P., R. Schreiber, Y. Pang, M.B. Brodsky and H. Sowers, 1986, Phys. Rev. Lett. **57**, 2442.
Haines, E.M., R. Clauberg and R. Feder, 1985, Phys. Rev. Lett. **54**, 932.
Hartmann, D., W. Weber, A. Rampe, S. Popovic and G. Güntherodt, 1993, Phys. Rev. B **48**, 16837.
Heinrich, B. and J.F. Cochran, 1993, Adv. Phys. **42**, 524.
Helman, J.S. and W. Baltensperger, 1980, Phys. Rev. B **22**, 1300.
Henk, J., S.V. Halilov, T. Scheunemann and R. Feder, 1994, Phys. Rev. B **50**, 8130.
Henk, J., T. Scheunemann, S.V. Halilov and R. Feder, 1996, J. Phys.: Condens. Matt. **8**, 47.
Hermanson, J., 1977, Solid State Commun. **22**, 9.
Herpin, A., 1968, Théorie du Magnétisme. Presses Universitaires de France, Paris.
Hillebrands, B. and G. Güntherodt, 1994, in: Ultrathin Magnetic Structures, eds. B. Heinrich and J.A.C. Bland. Springer-Verlag, Berlin, p. 258.
Hillebrecht, F.U. and W.-D. Herberg, 1994, Z. Phys. B: Condens. Matt. **93**, 299.
Hillebrecht, F.U., H.B. Rose, T. Kinoshita, Y.U. Idzerda, G. van der Laan, R. Denecke and R. Ley, 1995, Phys. Rev. Lett. **75**, 2883.
Hillebrecht, F.U., C. Roth, R. Jungblut, E. Kisker and A. Bringer, 1992, Europhys. Lett. **19**, 711.
Himpsel, F.J., 1983, Adv. Phys. **32**, 1.
Hofmann, M., G. Regenfus, O. Schärpf and P.J. Kennedy, 1967, Phys. Lett. **25 A**, 270.
Hopster, H. and D.L. Abraham, 1989, Phys. Rev. B **40**, 7054.
Hubbard, J., 1963, Proc. Roy. Soc. A **276**, 238.
Hüfner, S., 1988, Introduction to Photoemission Spectroscopy. Springer-Verlag, Berlin.
Ibach, H. and D.L. Mills, 1982, Electron Energy Loss Spectroscopy and Surface Vibrations. Academic Press, New York.
Idzerda, Y.U., D.M. Lind, D.A. Papaconstantopoulos, G.A. Prinz, B.T. Jonker and J.J. Krebs, 1988, Phys. Rev. Lett. **61**, 1222.
Idzerda, Y.U. and D.E. Ramaker, 1993, Mat. Res. Soc. Symp. Proc. **313**, 659.
Irmer, N., R. David, B. Schmiedeskamp and U. Heinzmann, 1992, Phys. Rev. B **45**, 3849.
Jackson, J.D., 1972, Classical Electrodynamics. Wiley, New York.
Johnson, P.D., K. Garrison, Q. Dong, N.V. Smith, D. Li, J. Mattson, J. Pearson and S.D. Bader, 1994, Phys. Rev. B **50**, 8954.

Johnson, P.D. and N.V. Smith, 1983, Phys. Rev. B **27**, 2527.
Joshua, S.J., 1991, Symmetry Principles and Magnetic Symmetry in Solid State Physics. IOP, Bristol.
Jungblut, R., C. Roth, F.U. Hillebrecht and E. Kisker, 1991, J. Appl. Phys. **70**, 5923.
Kakizaki, A., J. Fujii, K. Shimada, A. Kamata, K. Ono, K.-H. Park, T. Kinoshita, T. Ishii and H. Fukutani, 1994, Phys. Rev. Lett. **72**, 2781.
Kämper, K.-P., D.L. Abraham and H. Hopster, 1992, Phys. Rev. B **45**, 14335.
Kaya, S., 1928, Science Reports Tohoky University **17**, 639.
Kessler, J., 1985, Polarized Electrons. Springer-Verlag, Berlin.
Kirschner, J., 1985a, Phys. Rev. Lett. **55**, 973.
Kirschner, J., 1985b, Inelastic electron scattering by ferromagnets, in: Polarized Electrons in Surface Physics, ed. R. Feder. World Scientific, Singapore.
Kirschner, J., 1985c, Polarized Electrons at Surfaces. Springer-Verlag, Berlin.
Kirschner, J., 1985d, Sources and detectors for spin polarized electrons, in: Polarized Electrons in Surface Physics, ed. R. Feder. World Scientific, Singapore.
Kirschner, J. and R. Feder, 1979, Phys. Rev. Lett. **42**, 1008.
Kirschner, J. and E. Langenbach, 1988, Solid State Commun. **66**, 761.
Kisker, E., K. Schröder, M. Campagna and W. Gudat, 1984, Phys. Rev. Lett. **52**, 2285.
Klebanoff, L.E., D.G. van Kampen and R.J. Pouliot, 1993, Mat. Res. Soc. Symp. Proc. **313**, 589.
Kneller, E., 1962, Ferromagnetismus. Springer-Verlag, Berlin.
Kohn, W. and L.J. Sham, 1965, Phys. Rev. A **140**, 1133.
Korecki, J. and U. Gradmann, 1986, Hyperfine Interactions **28**, 931.
Kotani, A. and H. Mizuta, 1984, Solid State Commun. **51**, 727.
Kuch, W., A. Dittschar, K. Meinel, M. Zharnikov, C.M. Schneider and J. Kirschner, 1996, Phys. Rev. B **53**, 11621.
Kuch, W., M.-T. Lin, W. Steinhögl, C.M. Schneider, D. Venus and J. Kirschner, 1995, Phys. Rev. B **51**, 609.
Landolt, M., R. Allenspach and M. Taborelli, 1986, Surf. Sci. **178**, 311.
Landolt, M. and M. Campagna, 1978, Surf. Sci. **70**, 197.
Landolt, M. and Y. Yafet, 1978, Phys. Rev. Lett. **40**, 1401.
Legvold, S., 1980, in: Ferromagnetic Materials, ed. E.P. Wohlfarth. North-Holland, Amsterdam, p. 183.
Levinson, H.L., P.J. Feibelman and E.W. Plummer, 1979, Phys. Rev. Lett. **43**, 52.
Li, C. and A.J. Freeman, 1988, J. Magn. Magn. Mater. **75**, 53.
Liberati, M., G. Panaccione, F. Sirotti, P. Prieto and G. Rossi, 1999, Phys. Rev. B **59**, 4201.
Liebermann, L.N., J. Clinton, P.M. Edwards and J. Mathon, 1970, Phys. Rev. Lett. **25**, 232.
Liebermann, L.N., D.R. Fredkin and H.B. Shore, 1969, Phys. Rev. Lett. **22**, 539.
Lindgren, S.Å. and L. Walldén, 1987, Phys. Rev. Lett. **59**, 3003.
Liu, C. and S.D. Bader, 1991, Phys. Rev. B **44**, 12062.
Mathon, J., 1988a, Rep. Prog. Phys. **51**, 1.
Mathon, M., 1988b, Physica B **149**, 31.
Mathon, J. and S.B. Ahmad, 1988, Phys. Rev. B **37**, 660.
Mattis, D.C., 1988, The Theory of Magnetism. Springer-Verlag, Berlin.
Mauri, D., D. Scholl, H.C. Siegmann and E. Kay, 1988, Phys. Rev. Lett. **61**, 758.
Maxwell, J.C., 1891, Treatise on Electricity and Magnetism. Dover, New York.
Mayer, H. and H. Thomas, 1957, Z. Phys. **147**, 419.
McClelland, J.J., M.R. Scheinfein and D.T. Pierce, 1989, Rev. Sci. Instrum. **60**, 683.
McCoy, B. and T.T. Wu, 1973, The Two-Dimensional Ising Model. Harvard, Cambridge.
McRae, E.G., 1979, Rev. Mod. Phys. **51**, 541.
Mermin, N.D. and H. Wagner, 1966, Phys. Rev. Lett. **17**, 1133.
Mills, D.L., 1970, Phys. Rev. B **34**, 1775.
Mills, D.L. and A.A. Maradudin, 1967, J. Phys. Chem. Solids **28**, 1855.
Monsma, D.J., J.C. Lodder, T.J.A. Popma and B. Dieny, 1995, Phys. Rev. Lett. **74**, 5260.
Moruzzi, V., J.F. Janak and A.R. Williams, 1978, Calculated Electronic Properties of Metals. Pergamon, New York.
Mott, N.F. and H.S.W. Massey, 1965, The Theory of Atomic Collisions. Clarendon, Oxford.
Mulhollan, G.A., R.L. Fink and J.L. Erskine, 1991, Phys. Rev. B **44**, 2393.

Müller, N., W. Eckstein, W. Heiland and W. Zinn, 1972, Phys. Rev. Lett. **29**, 1651.
Nakanishi, T., H. Aoyagi, H. Horinaka, Y. Kamiya, T. Kato, S. Nakamura, T. Saka and M. Tsubata, 1991, Phys. Lett. A **158**, 345.
Néel, L., 1954, J. Phys. Radium **15**, 225.
Nekovee, M., S. Crampin and J.E. Inglesfield, 1993, Phys. Rev. Lett. **70**, 3099.
Noffke, J. and L. Fritsche, 1981, J. Phys. C **14**, 89.
Nolting, W., W. Borgiel, V. Dose and T. Fauster, 1989, Phys. Rev. B **40**, 5015.
Nordström, L., P. Lang, R. Zeller and P.H. Dederichs, 1995, Europhys. Lett. **29**, 395.
Oepen, H.P., K. Hünlich and J. Kirschner, 1986, Phys. Rev. Lett. **56**, 496.
Onsager, L., 1944, Phys. Rev. **65**, 117.
Ormeci, A., B.M. Hall and D.L. Mills, 1990, Phys. Rev. B **42**, 4524.
Ormeci, A., B.M. Hall and D.L. Mills, 1991, Phys. Rev. B **44**, 12369.
Ortega, J.E. and F.J. Himpsel, 1992, Phys. Rev. Lett. **69**, 844.
Ortega, J.E., F.J. Himpsel, G.J. Mankey and R.F. Willis, 1993, Phys. Rev. B **47**, 1540.
Papaconstantopoulos, D.A., 1986, Handbook of the Band Structure of Elemental Solids. Plenum, New York.
Pappas, D.P. and H. Hopster, 1989, Rev. Sci. Instrum. **60**, 3068.
Pappas, D.P., K.-P. Kämper and H. Hopster, 1990, Phys. Rev. Lett. **64**, 3179.
Parkin, S.S.P., 1994, in: Ultrathin Magnetic Structures, eds. B. Heinrich and J.A.C. Bland. Springer-Verlag, Berlin, p. 132.
Parkin, S.S.P., Z.G. Li and D.J. Smith, 1991, Appl. Phys. Lett. **58**, 2710.
Passek, F. and M. Donath, 1992, Phys. Rev. Lett. **69**, 1101.
Paul, D.M., P.W. Mitchell, H.A. Mook and U. Steigenberger, 1988, Phys. Rev. B **38**, 580.
Pendry, J.B., 1975, J. Phys. C: Solid State Phys. **8**, 2413.
Pendry, J.B., 1981, J. Phys. C: Solid State Phys. **14**, 1381.
Petersen, H., F. Schäfers and W. Braun, 1992, BESSY.
Pfandzelter, R., G. Steierl and C. Rau, 1995, Phys. Rev. Lett. **74**, 3467.
Pierce, D.T., R.J. Celotta, J. Unguris and H.C. Siegmann, 1982, Phys. Rev. B **26**, 2566.
Pierce, D.T. and F. Meier, 1976, Phys. Rev. B **13**, 5484.
Pizzini, S., A. Fontaine, C. Giorgetti, E. Dartyge, J.-F. Bobo, M. Piecuch and F. Baudelet, 1995, Phys. Rev. Lett. **74**, 1470.
Plihal, M., D.M. Mills and J. Kirschner, 1999, Phys. Rev. Lett. **82**, 2579.
Plummer, E.W. and W. Eberhardt, 1979, Phys. Rev. B **20**, 1444.
Pohm, A.V., J.S.T. Huang, J.M. Daughton, D.R. Krahn and V. Mehra, 1988, IEEE Trans. Magn. **24**, 3117.
Porter, S.J. and J.A.D. Matthew, 1989, J. Phys.: Condens. Matt. **1**, SB13.
Purcell, S.T., W. Folkerts, M.T. Johnson, N.W.E. McGee, K. Jager, J.A.D. Stegge, W.B. Zeper, W. Hoving and P. Grünberg, 1991, Phys. Rev. Lett. **67**, 903.
Rader, O., C. Carbone, W. Clemens, E. Vescovo, S. Blügel, W. Eberhardt and W. Gudat, 1992, Phys. Rev. B **45**, 13823.
Rader, O., E. Vescovo, J. Redinger, S. Blügel, C. Carbone, W. Eberhardt and W. Gudat, 1994, Phys. Rev. Lett. **72**, 2247.
Rado, G.T. and J.R. Weertman, 1959, J. Phys. Chem. Solids **11**, 315.
Rampe, A., G. Güntherodt, D. Hartmann, J. Henk, T. Scheunemann and R. Feder, 1998, Phys. Rev. B **57**, 14370.
Rampe, A., D. Hartmann, W. Weber, S. Popovic, M. Reese and G. Güntherodt, 1995, Phys. Rev. B **51**, 3230.
Rau, C., 1983, J. Magn. Magn. Mater. **31–34**, 874.
Rau, C. and C. Jin, 1988, J. Phys. (Paris), 1627.
Rau, C., C. Jin and M. Robert, 1988, J. Appl. Phys. **63**, 3667.
Rau, C., C. Schneider, G. Xing and K. Jamison, 1986, Phys. Rev. Lett. **57**, 3221.
Roth, C., F.U. Hillebrecht, H.B. Rose and E. Kisker, 1993, Phys. Rev. Lett. **70**, 3479.
Samant, M.G. et al., 1994, Phys. Rev. Lett. **72**, 1112.
Sawler, J. and D. Venus, 1991, Rev. Sci. Instrum. **62**, 2409.
Schäfers, F., W. Peatman, A. Eyers, C. Heckenkamp, G. Schönhense and U. Heinzmann, 1985, Rev. Sci. Instrum. **57**, 1032.
Scheunemann, T., S.V. Halilov, J. Henk and R. Feder, 1994, Solid State Commun. **91**, 487.

Schmid, A.K., D. Atlan, H. Itoh, B. Heinrich, T. Ichinokawa and J. Kirschner, 1993, Phys. Rev. B **48**, 2855.
Schmiedeskamp, B., N. Irmer, B. Vogt and U. Heinzmann, 1991, Appl. Phys. A **53**, 418.
Schmiedeskamp, B., B. Vogt and U. Heinzmann, 1988, Phys. Rev. Lett. **60**, 651.
Schmitz, P.J., W.-Y. Leung, G.W. Graham and P.A. Thiel, 1989, Phys. Rev. B **40**, 11477.
Schneider, C.M., 1997, J. Magn. Magn. Mater. **175**, 160.
Schneider, C.M., P. Bressler, P. Schuster, J. Kirschner, J.J.D. Miguel and R. Miranda, 1990, Phys. Rev. Lett. **64**, 1059.
Schneider, C.M., R. Frömter, C. Ziethen, W. Swiech, N.B. Brookes, G. Schönhense and J. Kirschner, 1997, Mat. Res. Soc. Symp. Proc. **475**, 381.
Schneider, C.M., K. Holldack, M. Kinzler, M. Grunze, H.P. Oepen, F. Schäfers, H. Petersen, K. Meinel and J. Kirschner, 1993, Appl. Phys. Lett. **63**, 2432.
Schneider, C.M. and J. Kirschner, 1995, Critical Reviews in Solid State and Materials Sciences **20**, 179.
Schneider, C.M., W. Kuch, U. Pracht, A. Chassé and J. Kirschner, 1996, Phys. Rev. B **54**, R15618.
Schneider, C.M., P. Schuster, M. Hammond, H. Ebert, J. Noffke and J. Kirschner, 1991, J. Phys.: Condens. Matt. **3**, 4349.
Schneider, C.M., D. Venus and J. Kirschner, 1992, Phys. Rev. B **45**, 5041.
Schönhense, G., 1990, Physica Scripta **T31**, 255.
Schulz, B. and K. Baberschke, 1994, Phys. Rev. B **50**, 13467.
Schütz, G., W. Wagner, W. Wilhelm, P. Kienle, R. Zeller, R. Frahm and G. Materlik, 1987, Phys. Rev. Lett. **58**, 737.
Seah, M.P. and W.A. Dench, 1979, Surf. Interf. Anal. **1**, 1.
Seghadat, A.K. and A.P. Cracknell, 1974, Physica **71**, 615.
Siegmann, H.C., D.T. Pierce and R.J. Celotta, 1981, Phys. Rev. Lett. **46**.
Smith, N.V., 1985, Phys. Rev. B **32**, 3549.
Smith, N.V., 1988, Rep. Prog. Phys. **51**, 1227.
Smith, N.V., N.B. Brookes, Y. Chang and P.D. Johnson, 1994, Phys. Rev. B **49**, 332.
Spicer, W., 1958, Phys. Rev. **112**, 114.
Starke, K., E. Navas, L. Baumgarten and G. Kaindl, 1993, Phys. Rev. B **48**, 1329.
Stöhr, J., Y. Wu, M.G. Samant, B.D. Hermsmeier, G. Harp, S. Koranda, D. Dunham and B.P. Tonner, 1993, Science **259**, 658.
Tamura, E. and R. Feder, 1991, Europhys. Lett. **16**, 695.
Tamura, E., R. Feder, G. Waller and U. Gradmann, 1990, Phys. Status Solidi B **157**, 627.
Tamura, E., W. Piepke and R. Feder, 1987, Phys. Rev. Lett. **59**, 943.
Tamura, E., W. Piepke and R. Feder, 1989, J. Phys.: Condens. Matt. **1**, 6469.
Tang, F.-C., X. Zhang, F.B. Dunning and G.K. Walters, 1988, Rev. Sci. Instrum. **59**, 504.
Tebble, R.S. and D.J. Craik, 1969, Magnetic Materials. Wiley–Interscience, London.
Thole, B.T. and G. van der Laan, 1994, Phys. Rev. B **49**, 9613.
Tillmann, D., R. Thiel and E. Kisker, 1989, Z. Phys. B: Condens. Matt. **77**, 1.
Tsang, C.H., R.E. Fontana, T. Lin, D.E. Heim, B.A. Guerney and M.L. Williams, 1998, IBM J. Res. Develop. **42**, 103.
Turek, I., J. Kudrnovsky, M. Sob, V. Drchal and P. Weinberger, 1995, Phys. Rev. Lett. **74**, 2551.
Turner, A.M., Y.J. Chang and J.L. Erskine, 1982, Phys. Rev. Lett. **48**, 348.
Turner, A.M. and J.L. Erskine, 1983, Phys. Rev. B **28**, 5628.
Turner, A.M. and J.L. Erskine, 1984, Phys. Rev. B **30**, 6675.
Unguris, J., R.J. Celotta and D.T. Pierce, 1991, Phys. Rev. Lett. **67**, 140.
Unguris, J., D.T. Pierce and R.J. Celotta, 1986, Rev. Sci. Instrum. **57**, 1314.
van der Laan, G., 1995, Phys. Rev. B **51**, 240.
van der Laan, G., M.A. Hoyland, M. Surman, C.F. Flipse and B.T. Thole, 1992, Phys. Rev. Lett. **69**, 3872.
van der Laan, G., B.T. Thole, G.A. Sawatzky, J.B. Goedkoop, J.C. Fuggle, J.M. Esteva, R. Karnatak, J.P. Remeika and H.A. Dabkowska, 1986, Phys. Rev. B **34**, 6529.
van Vleck, J.H., 1937, Phys. Rev. **52**, 1178.
Venus, D., 1993, Phys. Rev. B **43**, 6144.
Venus, D., 1994, Phys. Rev. B **49**, 8821.

Venus, D., 1997, Phys. Rev. B **56**, 2661.
Venus, D., L. Baumgarten, C.M. Schneider, C. Boeglin and J. Kirschner, 1993, J. Phys.: Condens. Matt. **5**, 1239.
Venus, D., J. Garbe, S. Suga, C. Schneider and J. Kirschner, 1986, Phys. Rev. B **34**, 8435.
Venus, D., W. Kuch, M.-T. Lin, C.M. Schneider, H. Ebert and J. Kirschner, 1997, Phys. Rev. B **55**, 2594.
Vescovo, E., O. Rader and C. Carbone, 1993, Phys. Rev. Lett. **47**, 13051.
von dem Borne, A., T. Dohrmann, A. Verweyen, B. Sonntag, K. Godehusen and P. Zimmermann, 1997, Phys. Rev. Lett. **78**, 4019.
Walker, J.C., R. Droste, G. Stern and J. Tyson, 1984, J. Appl. Phys. **55**, 2500.
Walker, T.G., A.W. Pang, H. Hopster and S.F. Alvarado, 1992, Phys. Rev. Lett. **69**, 1121.
Waller, G. and U. Gradmann, 1982, Phys. Rev. B **26**, 6330.
Wang, D.-S., A.J. Freeman and H. Krakauer, 1982, Phys. Rev. B **26**, 1340.
Weber, W., D.A. Wesner, D. Hartmann and G. Güntherodt, 1992, Phys. Rev. B **46**, 6199.
Weinert, M., E. Wimmer and A.J. Freeman, 1982, Phys. Rev. B **26**, 4571.
Weller, D., S.F. Alvarado and M. Campagna, 1985a, Physica **130B**, 72.
Weller, D., S.F. Alvarado, W. Gudat, K. Schröder and M. Campagna, 1985b, Phys. Rev. Lett. **54**, 1555.
Whitaker, M.A.B., 1978, J. Phys. C **11**, L151.
Wimmer, E., A.J. Freeman and H. Krakauer, 1984, Phys. Rev. B **30**, 3113.
Wimmer, E., H. Krakauer, M. Weinert and A.J. Freeman, 1981, Phys. Rev. B **24**, 864.
Wöhlecke, M. and G. Borstel, 1981a, Phys. Status Solidi B **107**, 653.
Wöhlecke, M. and G. Borstel, 1981b, Phys. Rev. B **23**, 980.
Wöhlecke, M. and G. Borstel, 1981c, Phys. Rev. B **24**, 2857.
Wöhlecke, M. and G. Borstel, 1984, in: Optical Orientation, eds. F. Meier and B.P. Zakharchenya. North-Holland, Amsterdam, p. 424.
Wohlfarth, E.P., 1953, Rev. Mod. Phys. **25**, 211.
Wohlfarth, E.P., 1980, in: Ferromagnetic Materials, ed. E.P. Wohlfarth. North-Holland, Amsterdam.
Wu, R.-Q. and A.J. Freeman, 1992, J. Magn. Magn. Mater. **116**, 202.
Yin, S. and E. Tosatti, 1981, International Centre for Theoretical Physics, Miramare, Trieste, Italy.
Zare, R.N., 1988, Angular Momentum. Wiley, New York.
Zhu, M.J., D.M. Bylander and L. Kleinman, 1991, Phys. Rev. B **43**, 4007.
Zhu, X.-Y., J. Hermanson, F.J. Arlinghaus, J.G. Gay, R. Richter and J.R. Smith, 1984, Phys. Rev. B **29**, 4426.

CHAPTER 10

# Adsorption on Metals

H.-J. FREUND and H. KUHLENBECK

*Abteilung Chemische Physik*
*Fritz-Haber-Institut der*
*Max-Planck-Gesellschaft*

*© 2000 Elsevier Science B.V.*
*All rights reserved*

*Handbook of Surface Science*
*Volume 2, edited by K. Horn and M. Scheffler*

# Contents


10.1. Introduction . . . . . 671
10.2. Alkali adsorption . . . . . 677
10.3. Chalcogenide adsorption . . . . . 679
10.4. Hydrogen adsorption . . . . . 689
10.5. Carbon monoxide adsorption . . . . . 693
10.6. Nitrogen adsorption . . . . . 715
10.7. Carbondioxide adsorption . . . . . 718
10.8. Ethylene adsorbates . . . . . 722
10.8.1. Symmetry considerations and ethylene–substrate interaction . . . . . 722
10.8.2. Ordered ethylene overlayers . . . . . 725
10.9. Benzene adsorbates . . . . . 728
10.9.1. Symmetry considerations on the molecule–substrate interaction in a dilute disordered layer of $C_6H_6$/Ni(111) . . . . . 729
10.9.2. Ordered layers: $C_6H_6$/Ni(111) and $C_6H_6$/Os(0001) . . . . . 733
10.9.3. Symmetry considerations on molecule–substrate interaction in a dilute disordered layer of $C_6H_6$ of Ni(110) . . . . . 735
10.9.4. Ordered overlayer: $C_6H_6$/Ni(110) . . . . . 736
10.10. Co-adsorbates . . . . . 738
References . . . . . 742

## 10.1. Introduction

Irving Langmuir (1881–1957) may be looked at as one of the founders and promoters of modern surface science and its applications, and in particular he is one of the pioneers in adsorption studies on solid surfaces (Langmuir, 1918; Kingdom and Langmuir, 1923; Villars and Langmuir, 1931; Taylor and Langmuir, 1933). Adsorption on transition metal substrates has been interesting in Langmuir's days and it remains to be an interesting topic at present (Ertl and Küppers, 1985; Zangwill, 1988; Henzler and Göpel, 1991). The question is: How does an atom bind to a transition metal surface and what are the consequences for the electronic levels of the combined systems? Answer: It depends! Some limiting cases are depicted in Fig. 10.1, where we consider one electron levels. In Fig. 10.1a the atomic level is sharp as long as the atom is far away from the surface. The metal is represented by a potential well. This particular situation may for example represent an alkali metal atom on a free electron metal surface. As the atom approaches the metal we observe two effects (Lang, 1971; Muscat and Newns, 1978). The level changes its energy position and it increases its width considerably. Generally, the level changes its position because it feels the additional potential of the metal. The second effect, i.e., the increase in width is due to the reduced residence time of the electron on the atomic level as soon as hopping or hybridization with the metal levels becomes possible. Obviously, we have placed the atomic level in an energetic position so that it lies within the region of the metal band. The atomic level which was occupied in the free atom case, is energetically placed upon interaction with the metal completely or partly – depending on its width – above the Fermi level of the metal. Then, the electron density on the atom changes. In the present case a larger fraction of the electronic charge on the atom is transferred towards the metal. The adsorbate substrate bond is formed including a pronounced dipole pointing from the positively charged adsorbate towards the negatively charged metal surface. For alkali metal atoms bonding to transition metal, this discussion goes back to R.W. Gurney in 1935 (Gurney, 1935) and it has very recently been revisited with modern *ab initio* computer methods by Scheffler and his group (see Chapter 5). If the resonance ends up fully below the Fermi level (Fig. 10.1b), the charge transfer contribution is reduced.

So far we have assumed that the coupling between adsorbate and metal is only rather weak. If we increase the coupling we eventually form a "surface molecule" characterized by two features split off from the metal band. The two features shown in Fig. 10.1c may be looked at as a bonding and an antibonding combination of the wave functions of adsorbate and metal level. Depending on the relative position of the adsorbate level with respect to the metal both or only one of the two split off resonances is occupied.

In summary, bonding of an atom to a metal surface leads either to a shift of the atomic level and a considerable increase in width, or to the split off of a bonding and an antibonding level. The wide level may overlap the Fermi level so that the position of the Fermi level within the level determines the electronic density on the adsorbate. This model of

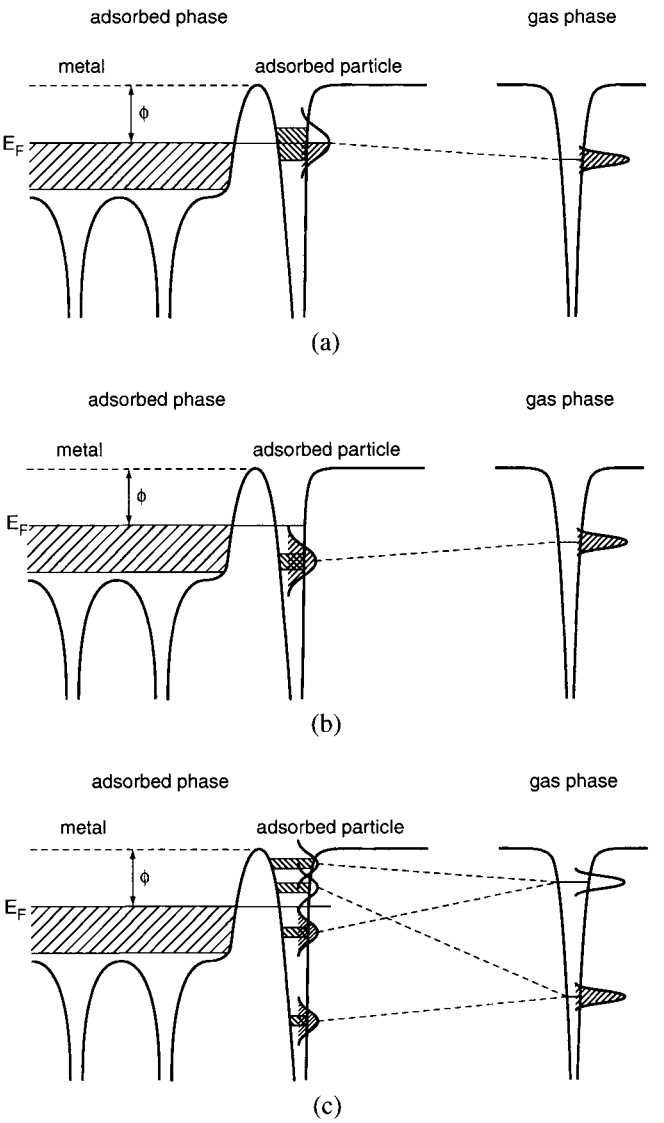


Fig. 10.1. Energy levels of free atoms (right) and atoms adsorbed on a metallic surface (left). (a) Partly occupied adsorbate level, (b) fully occupied adsorbate level, (c) interaction of an atom having an occupied and an unoccupied orbital with the valence band and the conduction band of the metal.

the adsorbate bonding is based on the so called Anderson–Grimley–Newns Hamiltonian (Anderson, 1961; Grimley, 1967; Newns, 1969; Spanjaard and Desjouqueres, 1990).

Another model describing the interaction of an isolated adsorbate and a clean surface which has been mainly developed for molecular, in particular for CO adsorption is called the Blyholder model (Blyholder, 1964, 1974) and is based primarily on molecular orbital

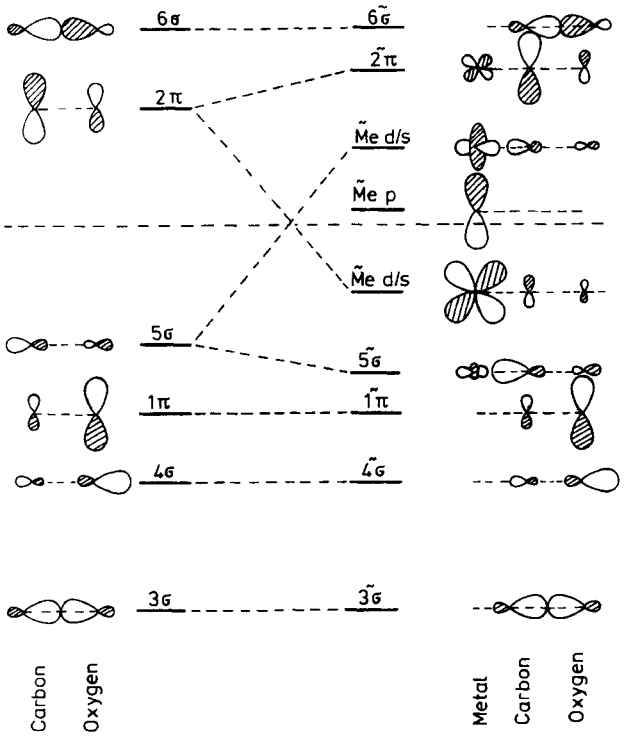


Fig. 10.2. The Blyholder model for the interaction of a CO molecule with a transition metal surface (Blyholder, 1964, 1974).

theory. It carries much of the essentials of the "surface molecule" aspect of the Anderson–Grimley–Newns Hamiltonian (Anderson, 1961; Grimley, 1967; Newns, 1969). In fact it is the "surface molecule" model. The essentials of the Blyholder model are summarized in Fig. 10.2. Assume an atom or a molecule has a doubly occupied non degenerate ($\sigma$-symmetry) and an empty degenerate ($\pi$-symmetry) orbital. The molecule interacts with its occupied orbital with the occupied and unoccupied orbitals of the metal. The interaction between occupied orbitals leads to a non-bonding Pauli repulsion. The interaction between occupied and unoccupied orbitals on the other hand leads to a bonding interaction. The interaction of the molecule's unoccupied orbital with the occupied metal orbitals belongs to the latter category and is important to understand the rather strong CO-metal bond. Since the occupied and the unoccupied orbital of the metal belong to different irreducible representations the coupling with the metal involves two independent subsets of metal orbitals, occupied and unoccupied. The synergetic interaction of substrate and adsorbate levels in the case of CO involves the $5\sigma$ and $2\pi$ levels and has been termed $\sigma$-donation and $\pi$-back-donation. This notation was introduced into surface science by Blyholder in 1965 and has been named after him although it has great similarities to the so called Dewar–Chatt–Duncanson model (Dewar, 1951; Chatt and Duncauson, 1953) well known in the discussion of the electronic structure of transition metal complexes since the early fifties.

Several modifications to the model have been proposed concerning in particular the relative importance of the donation and backdonation contributions to the metal molecule bond. It appears in several cases the $\pi$-backdonation channel dominates. Once again, the Blyholder model and its modifications may be mapped onto the surface molecule solution of the Anderson–Grimley–Newns-Hamiltonian in spite of the controversial discussion that has taken place in the literature in the past (Gumhalter et al., 1988).

The notion so far has assumed the interaction of a single adsorbate species with a bare metal surface. However, in general we have to deal with a finite coverage of the surface. In Langmuirs picture of adsorption (Langmuir, 1918; Kingdom and Langmuir, 1923; Villars and Langmuir, 1931; Taylor and Langmuir, 1933) the adsorbed particles occupy the lattice points of a two-dimensional substrate with equal probability and with hard wall potentials between the adsorbed particles, preventing double or multiple occupancy of any particular site and a well defined adsorption energy typical of the site. As a result saturation would be characterized by $\Theta = 1$ and the formation of a true $1 \times 1$ adsorbate layer. Obviously, the formation of ordered layers with coverages far below $\Theta = 1$ are more the exception than the rule and are a direct consequence of the existence of rather long reaching "softer" interaction potentials (Somorjai and Van Hove, 1979). Intermolecular interaction potentials may be either attractive or repulsive and may be classified into direct and indirect interactions. Direct interactions involve dipole–dipole (multipole–multipole) and orbital overlap interactions, and are often repulsive. On the other hand, indirect interactions mediated through the metal surface may be either attractive or repulsive depending on distance and surface sites, i.e., the kind of charge modification of the electronic structure of the substrate by the adsorbate (Koutecky, 1958; Grimley, 1960, 1971; Einstein and Schieffer, 1973). The interplay of the interadsorbate interaction potential and the adsorption energy of the isolated adsorbate with the clean substrate finally determines the observed structure of an ordered layer. In other words, the structure of the ordered layer depends on the heat of adsorption and the coverage.

A way to understand bonding in adsorbates on metals is to study their geometric and electronic structure experimentally and theoretically. Figure 10.3 shows a schematic representation of the electronic structure of an adsorbate as it develops from an isolated adsorbed atom into a two-dimensionally ordered adsorbate. Briefly, we have chosen the example representing a chalcogen atom like oxygen in a fourfold site on a (100) surface. The three fully occupied 2p-orbitals are situated well below the Fermi energy. They are split into a degenerate ($p_x$, $p_y$) set of orbitals and a non degenerate $p_z$ orbital as shown on the right hand side of Fig. 10.3. The relative position of the two levels is determined by the strengths of interaction with the substrate. If we, on the contrary, assume that there is no interaction between adsorbate and substrate but consider exclusively interadsorbate interaction we arrive at a situation depicted on the left hand side of Fig. 10.3: An adsorbate band structure develops. The last step in the formation of the full adsorbate–substrate band structure is to interact the adsorbate band structure with the metal, which is depicted in the central panel of Fig. 10.3. Order is particularly important because in the case of two-dimensionally well ordered overlayers the wave vector parallel to the surface ($\mathbf{k}_\parallel$) is a good quantum number, and therefore energy dispersions as a function of $\mathbf{k}_\parallel$ may be observed experimentally. Consequently, it is possible to carry out angle dependent inelastic electron spectroscopic measurements to determine the $\mathbf{k}_\parallel$ dependence of the particular elementary excitation. If

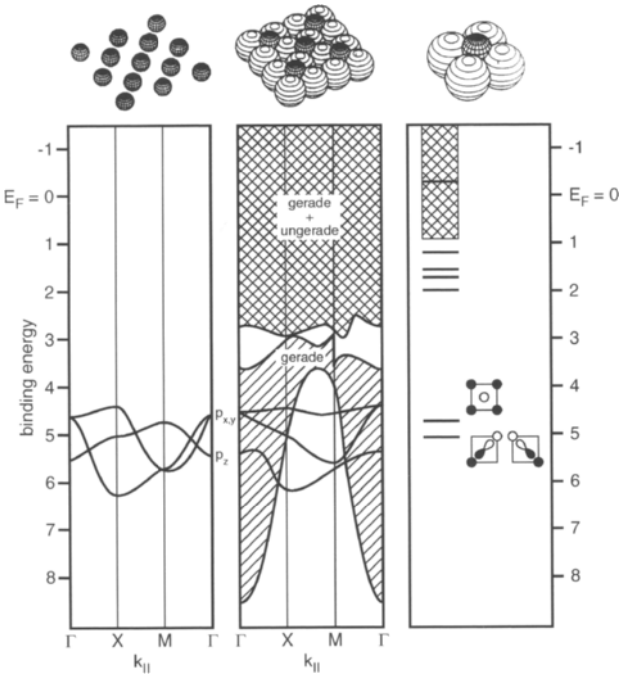


Fig. 10.3. Schematic one-electron diagrams of the valence electrons of a small chalcogen/metal cluster (right), an unsupported chalcogen c(2 × 2) adlayer (left), and a chalcogen c(2 × 2) adlayer on the surface of a transition metal (center).

we use, for example, electron energy loss spectroscopy we get the photon dispersion relations (Szeftel et al., 1983; Toennies, 1991) or the plasmon dispersion relations, etc. (Fink, 1992). If we perform angle resolved photoelectron spectroscopic (ARUPS) measurements we get the "band structure" of the ordered layer, or better the dispersion relations of the ion states of the system (Kevan, 1992). The experimentally determined band structure can be connected with the intermolecular interaction potential through theoretical modeling. Briefly, in the simplest form of the band structure formulation, the tight-binding approximation, the bandwidth is determined by the strength of the intermolecular interaction as probed by the particular molecular orbital (ion state) under consideration (Jones, 1975). If it is possible to identify a particular ion state of a molecule in ordered layers of different coverage densities, i.e., varying intermolecular distances, then we are in a position to determine ion state specific intermolecular interaction parameters as a function of intermolecular distance (Freund and Neumann, 1988). The last point is particularly interesting: Take diatomic molecules with localized orbitals. Assume the molecules interact on one end only with the surface and form an ordered layer. Ionization of an orbital localized on the far end of the molecules away from the surface most likely will lead to a dispersion relation predominantly determined by the direct, or "through space", interaction (Greuter et al., 1983). If on the other hand we choose to ionize an orbital localized on the near end of the molecules close to the surface, we are going to measure a dispersion relation determined

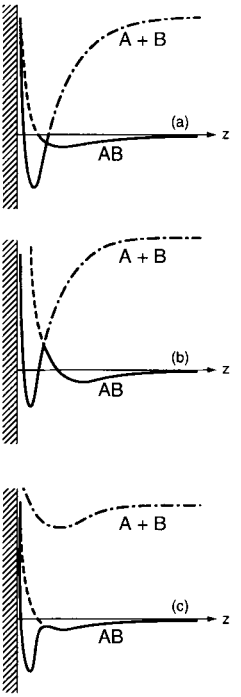


Fig. 10.4. Schematic diagrams of the potential energy of an adsorbate/substrate complex appropriate to three different state configurations: (a) dissociative chemisorption, (b) dissociative chemisorption with a physisorbed precursor, (c) molecular chemisorption (Lennard-Jones, 1932).

by direct as well as indirect, "through bond", interaction of the molecules (Heskett et al., 1985a). It is therefore possible to use measured ion state specific dispersion relations to study intermolecular interaction mechanisms. It must be understood, however, that experimentally determined band dispersions are excited state properties and intermolecular potentials are usually considered to be ground state properties. Up to this point we have assumed that the adsorbate has been formed somehow. However, the question of how an atomic adsorbate layer forms is important.

Atomic adsorption often occurs through binding a molecule from the gas phase which subsequently dissociates to form the adsorbate. This means that there is the question of molecular precursors for atomic adsorption. This energetic scenario has been discussed early by Lennard-Jones and others (Lennard-Jones, 1932), and a schematic representation is shown in Fig. 10.4. A molecule AB approaches a surface along the $z$-axis. In Fig. 10.4a the situation characteristic for dissociative adsorption is shown. The potential well for the adsorbed atoms is considerably deeper than that for the adsorbed molecules and there is no or a very small activation energy between the associative and the dissociative well. In Fig. 10.4b the activation energy is larger so that the molecular adsorbate is a real precursor for dissociative adsorption. Figure 10.4c represents the potential energy well for molecular chemisorption. Dissociative adsorption is unfavorable in this case. In principle these exam-

ples already represent the simplest cases of a reactive system and it is quite obvious that the potential energy hypersurface is the key ingredient in understanding chemical reaction on solid surfaces. The question of chemical reactivity is intimately connected with adsorption dynamics which is a topic finding increasing attention in recent years (Ertl, 1982).

We have organized the present chapter in such a way that we have chosen several well studied examples that represent the limiting cases of our present state of understanding surface–adsorbate bonding. Alkali-metal adsorption is meant to be an example for a system where a resonance near the Fermi energy of the substrate is formed. Chalcogen adsorption leads to a resonance below or at the lower end of the metal valence bands. An intermediate case is the adsorption of atomic hydrogen. Although the simplest of all adsorbates it leads to rather complicated changes in the energy distribution of metal levels and a qualitative discussion is often difficult. From the discussion of atomic adsorbates we shall turn to the study of molecular adsorbates. The largest data set on electronic structure exists for CO adsorption and some aspects, in particular the Blyholder model, shall be exemplified on the basis of this. After a few comments on the electronic structure of other di- and tri-atomic adsorbates we discuss more complex molecular adsorbates, the largest being aromatic ring compounds. Finally we shall comment on coadsorbate systems.

## 10.2. Alkali adsorption

In 1935 Gurney (1935) proposed the quantum mechanical model which has been shortly referred to in the introduction. According to this model the valence s level of a free alkali atom broadens and shifts while the atom approaches a free electron like metal, becoming partially emptied when the surface is reached. Thus the adsorbed alkali atom is positively charged, which may be traced back to the electropositive nature of alkali metals. This charge introduces a negative image charge in the substrate and the resulting dipole reduces the workfunction of the system considerably. When the coverage of alkali atoms on the surface is increased, the repulsive interaction of the dipoles comes into play, inducing a partial depolarization of the alkali ions; i.e., part of the charge flows back from the metal substrate to the alkali ions. This mechanism leads to a dependence of the workfunction on coverage as displayed in Fig. 10.5: a steeply decreasing workfunction at low coverages, a minimum at intermediate coverage and, due to depolarization, an increasing workfunction at higher coverage. Workfunction curves of this type have been found experimentally for many alkali/metal systems (Bonzel et al., 1989; Horn et al., 1988). For a long time the Gurney model has been considered to be valid. Later theoretical and experimental studies suggested that there was practically no charge transfer from the adsorbate to the substrate, but instead a polarization of the adsorbate and the adsorbate/substrate bond should be responsible for the experimentally observed workfunction decrease upon alkali deposition (Ishida, 1988, 1990; Riffe et al., 1990).

More recent studies (Stampfl and Scheffler, 1995; Stampfl, 1996; Burchhardt et al., 1995) indicate that the Gurney model is valid at low alkali coverage, but needs to be modified at higher coverage since it does not take into account the formation of ordered overlayers, phase transitions within the overlayers, and alloy formation. Model systems which have been theoretically and experimentally extensively studied (Stampfl and Scheffler, 1995; Stampfl, 1996; Burchhardt et al., 1995) are alkali atoms on Al(111). Some results

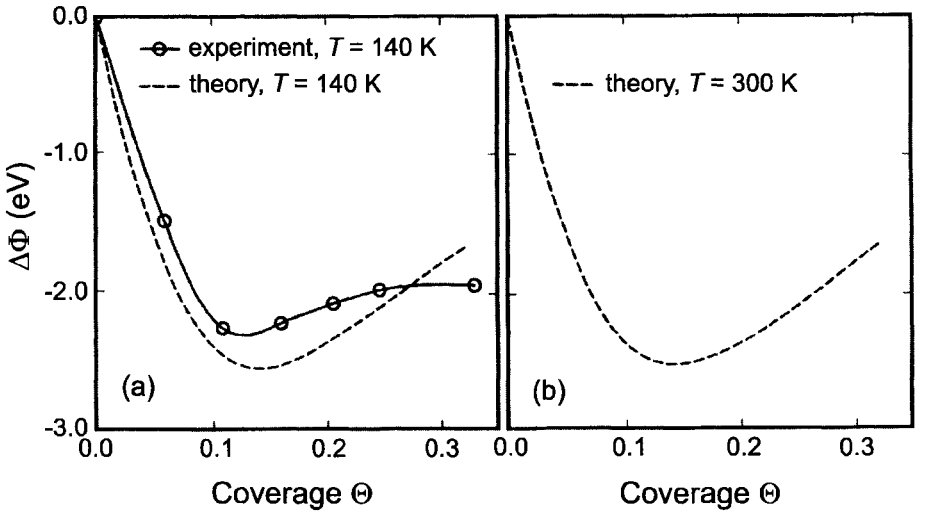


Fig. 10.5. Calculated (dashed line) (Stampfl and Scheffler, 1995) and measured (full line with open circles) (Horn et al., 1988) workfunction change with coverage for K on Al(111).

shall be repeated here. For these systems the Gurney model is valid at coverages below about $\Theta = 0.1$ (Stampfl and Scheffler, 1995). In this coverage regime the overlayer consists of randomly distributed atoms with negligible interaction. For K on Al(111) at low temperature (below 220 K) and coverages above $\Theta = 0.15$ $(\sqrt{3} \times \sqrt{3})R30°$ islands form on the surface (Stampfl and Scheffler, 1995). The lateral bonding in these island is mainly metallic and the ionicity of the adatoms is considerably reduced as compared to the low coverage regime. Neither the formation of a metallic bond nor the formation of the ordered adlayer is explained by the Gurney model (Gurney, 1935), although the reduced ionicity is in line with this model. When the same adsorption experiment is performed at temperatures above 220 K, a different process occurs. At such temperatures the thermal energy is high enough to overcome the activation barrier for replacement of aluminum atoms in the first layer by potassium atoms. This means that aluminum atoms are kicked out of the surface layer and the remaining holes are filled with alkali atoms, again forming a $(\sqrt{3} \times \sqrt{3})R30°$ structure (Stampfl et al., 1992). According to calculations (Stampfl and Scheffler, 1995) the potassium atoms are charged in this configuration. However, due to the embedding of the alkali atoms into the surface the length of the resulting dipole is small, so that the net dipole moment is not much different from the one observed for the $(\sqrt{3} \times \sqrt{3})R30°$ layer formed at lower temperature, giving rise to similar workfunction vs. coverage curves. Views of the $(\sqrt{3} \times \sqrt{3})R30°$ structures formed below and above 220 K are displayed in Fig. 10.6. Substitutive adsorption is not unique for potassium; similar observations have also been made for sodium (Stampfl et al., 1992) and rubidium atoms (Nielsen et al., 1994). According to calculations silver and copper are also candidates for substitutive adsorption of alkalis (Polatoglu et al., 1993), making this process a candidate for a rather general phenomenon.

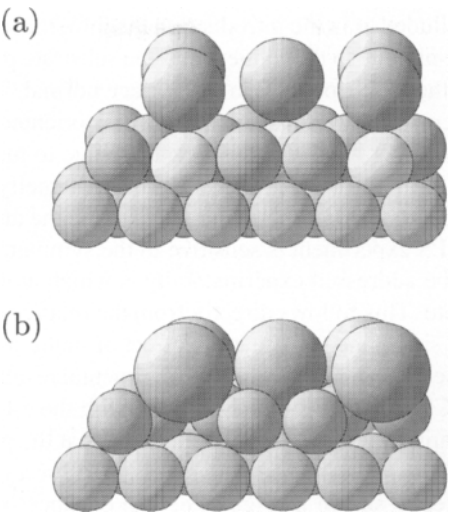


Fig. 10.6. Perspective view of the atomic structure of ($\sqrt{3} \times \sqrt{3}$)R30° K/Al(111) (Stampfl and Scheffler, 1995). (a) K atoms are in ontop sites on the surface (low temperature adsorption). The first Al layer is slightly buckled due to interaction with the adatoms. (b) Substitutional geometry where the Al atoms which were beneath the K atoms in (a) have been kicked out.

## 10.3. Chalcogenide adsorption

Oxygen adsorption has been studied for a long time. One of the most frequently studied systems is c(2 × 2)O/Ni(100) (Starke et al., 1988; Chubb et al., 1990). Nevertheless oxygen adsorbate systems are complicated in the sense that often different ordered structures coexist. Even oxide formation starts at rather low oxygen coverages (Brundle and Broughton, 1990). Therefore we shall discuss the bonding of chalcogens to metal surfaces by using sulphur adsorbates as examples. Atomic chalcogenides are characterized by the valence configuration $ns^2np^4$ and exhibit due to their electronegativity, the tendency to withdraw electrons from more electropositive bonding partners (Plummer and Eberhardt, 1982). These electrons then fill the chalcogenide valence shell. This is true in particular for oxygen but in a reduced form also in the case for the heavier chalcogenides. The first ionization potential for oxygen is 13.6 eV (Radzig and Smirnov, 1985), for sulphur it is 10.4 eV (Radzig and Smirnov, 1985). Taking into account a work function of approximately 5 eV we expect oxygen emission at about 8 eV below and at about 5 eV below the Fermi energy sulphur emission. For transition metals this is an energy range of small density of states. Mixing between adsorbate levels and substrate levels is comparably small. The wave functions conserve to a large extend their atomic character and interpretation is thus straight forward. Consider sulphur chemisorption on a Ni(100) surface. From structural studies it is well known that chalcogen atoms in general reside in four fold hollow sites on Ni(100) surfaces (Demuth et al., 1973). This is a situation very similar to the schematic diagram shown

in Fig. 10.3. As briefly alluded to in the introduction the threefold degenerate 2p orbitals of the chalcogenide atoms split due to the influence of the substrate potential. Let us choose a coordinate system with the $z$-axis parallel to the surface normal. The $p_z$-orbitals then feel a different potential as compared with the $p_x/p_y$-orbitals oriented parallel to the surface. The $p_x/p_y$ orbitals on the other hand remain degenerate due to the four fold symmetry of the site. The splitting of the 3p orbitals in a level with $a_1$-symmetry ($p_z$) and a level with e-symmetry ($p_x/p_y$) may be evaluated experimentally because the angular distribution of the photocurrent in an ARUPS experiment is sensitive to the symmetry of the involved states. The question, that may be addressed experimentally is which atomic level interacts more strongly with the substrate. This follows directly from the relative energetic position of the two levels if we assume simultaneously that the effect of many particle contributions and final state screening is the same for both levels. Experimental results are shown in Fig. 10.7 (Plummer et al., 1980). Clearly, the feature associated with the e-level is situated at higher binding energy as compared with the $a_1$-level, indicating that the $p_x/p_y$ orbitals do interact more strongly with the substrate. The spectra are recorded for a p(2 × 2)S/Ni(100) layer. Its structure is schematically shown in Fig. 10.8. The distance of the individual sulphur atoms is large enough to suppress strong direct lateral interactions. Therefore the result can be taken as characteristic for an individual sulphur atom. It is immediately obvious that this line of reasoning cannot be completely correct because in the absence of lateral interaction there were no ordered layer formation. On the other hand the lateral interaction leads to identical adsorption sites which is very useful for the following symmetry analysis: Briefly, the photoionization cross-section is proportional to the square of the dipole matrix element between the initial and the final state of the ionization process (Freund and Neumann, 1988; Plummer and Eberhardt, 1982; Hermanson, 1977)

$$I \propto \left| A_0 \langle \varphi_f | A p | \varphi_i \rangle \right|^2. \tag{10.1}$$

Firstly, it has to be remembered that $\varphi_f$ is the final state after electron excitation consisting of the ion state ${}^{N-1}\Psi_{e,E}$ and the emitted electron $\Phi_e(n)$, and that $\varphi_i$ represents the neutral ground state of the system. $A_0$ is the constant vector potential. Since $\mathbf{p}$ is a one electron operator the matrix element can be rewritten as (Cederbaum and Domcke, 1977)

$$I \propto \left| \Sigma \langle \Phi_e(n) | \mathbf{p}_n | \Phi_{\mathbf{k}}(n) \rangle \langle {}^{N-1}\Psi_{e,E} | a_{\mathbf{k}} \varphi_i \rangle \right|^2, \tag{10.2}$$

where $a_{\mathbf{k}}$ and $\Phi_{\mathbf{k}}(n)$ are the annihilation operator and the one electron wave function of the electron that is being emitted, respectively. These $\Phi_{\mathbf{k}}(n)$ are called initial states in the following.

The first matrix element determines the angular distribution pattern, the second matrix element defines the absolute value and contains the internal degrees of freedom of the system, e.g., the line widths (Cederbaum and Domcke, 1977). The sum takes all possible ion states ${}^{N-1}\Psi_{e,E}$ into account and explains the existence of satellite structure (Cederbaum and Domcke, 1977). Since we are interested in ARUPS, much of the discussion will concentrate on the first matrix element. Secondly, in order to evaluate whether this matrix element is nonzero, and thus leads us to expect a finite photoelectron current into a specific direction in space, symmetry arguments can be used (Hermanson, 1977). In principle the

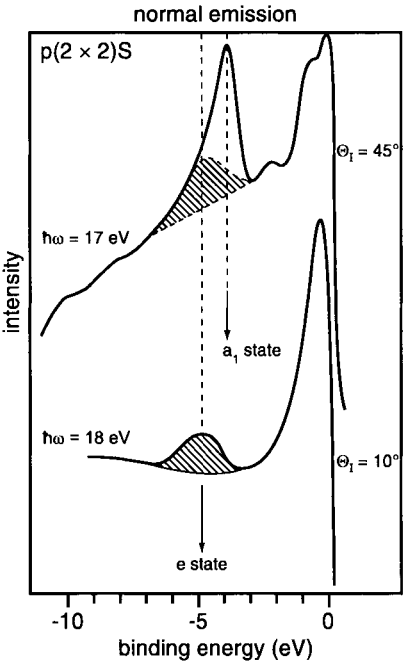


Fig. 10.7. Photoelectron spectra of p(2 × 2)S/Ni(100) recorded in normal emission for two different light incidence angles ($\Theta_i$) (Plummer et al., 1980).

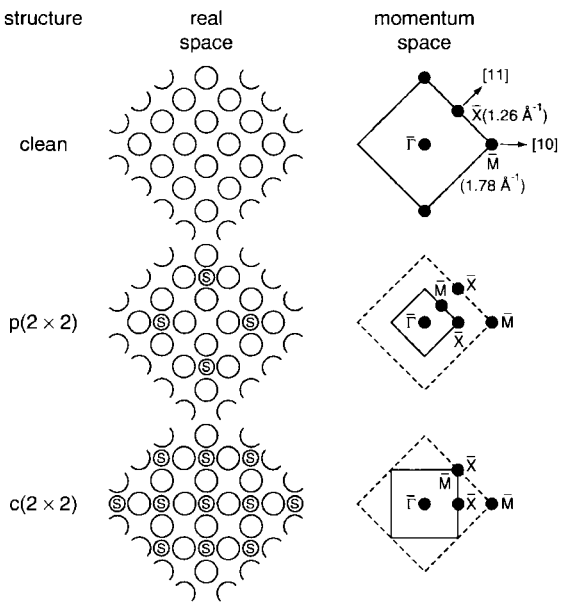


Fig. 10.8. Real space and $k$-space lattices of Ni(100), p(2 × 2)S/Ni(100), and c(2 × 2)S/Ni(100) (Plummer et al., 1980).

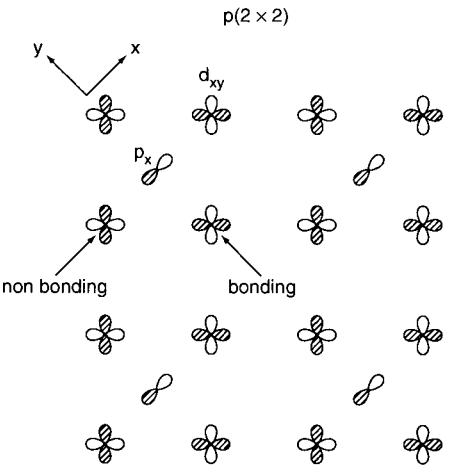


Fig. 10.9. Schematic orbital diagram of a possible S3p–Ni3d interaction for p(2 × 2)S/Ni(100).

space group of the adsorbate under consideration has to be chosen, and then we have to classify the wave functions according to its irreducible representations. Often, it is sufficient to consider one specific symmetry operation belonging to the point group, instead of all possible symmetry operations, in order to predict the angular variations of electron emission.

In the present case the layer has p(2 × 2) structure, i.e., the system has fourfold symmetry with four symmetry planes at 45° angles (Demuth et al., 1973). If we place the electron detector perpendicular to the surface, final states that lead to an observable signal must be even with respect to reflection at the mirror plane. In other words they have $a_1$ symmetry. If we chose the photon incidence for polarized light such that the electric field vector is either parallel (e-symmetry) or perpendicular ($a_1$-symmetry) to the surface plane, then initial states with e-symmetry emit in the former, initial states with $a_1$-symmetry emit in the latter case into the direction of the detector. This is the typical approach for the analysis of photoemission spectra.

We now come back to our specific example. In our case the $p_x/p_y$ are more strongly bound than the $p_z$ state. This is not a trivial result, because naively we might assume that the $p_z$ level is the more strongly bound level because it is oriented towards the substrate. A detailed analysis shows, however, that the fourfold hollow site is the reason for the level sequence. The chalcogen atom in the hollow site is above a Ni atom in the second layer and thus relatively close to the first layer. This leads to a strong interaction parallel to the surface as schematically shown in Fig. 10.9. In this diagram the overlap between a chalcogen $p_x$-orbital and the metal $d_{xy}$ orbitals is indicated. Please note that the presence of the adsorbate leads to a reduction of the size of the Brillouin zone. The Brillouin zone boundary of the clean substrate is folded back onto the Γ point of the new reduced Brillouin zone. Consequently, not in all wave functions the metal orbitals are in phase at Γ.

Let us consider next another S/Ni(100) system where at a higher sulphur coverage interadsorbate interactions become more important (Plummer et al., 1980). At a coverage

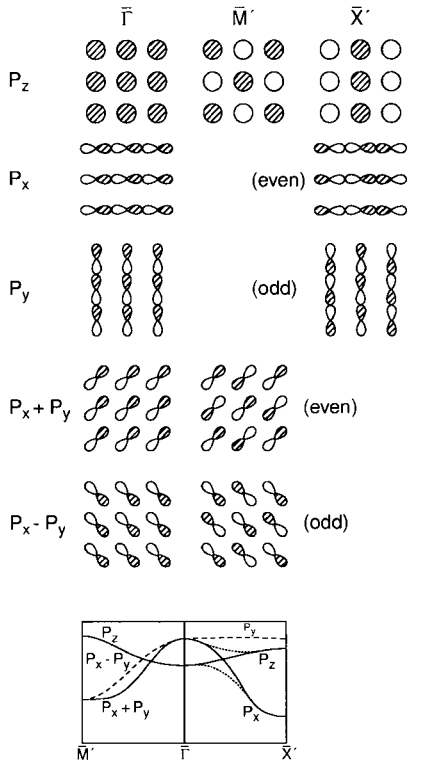


Fig. 10.10. Two-dimensional representation of $p_x$, $p_y$ and $p_z$ derived wave functions at different high symmetry points in $k$-space (Plummer and Eberhardt, 1982).

of $\Theta \sim 0.5$ sulphur forms a c(2 × 2)S/Ni(100) overlayer. If the intermolecular interaction potential is large enough to demand consideration of the two-dimensional crystal periodicity, the overlap of adsorbate wave functions is sufficient to produce two-dimensional Bloch states $\Psi_k$ and to make a band description of the electronic structure more appropriate (Horn et al., 1978a). Then the one-electron wave function at a lattice site $\mathbf{R}_1$ is related to the wave function at site $\mathbf{R}_2$ by:

$$\Psi_k(\mathbf{R}_1) = \Psi_k(\mathbf{R}_2) \exp\left[i\mathbf{k}_{\|}(\mathbf{R}_1 - \mathbf{R}_2)\right] \tag{10.3}$$

where $\exp[i\mathbf{k}_{\|}(\mathbf{R}_1 - \mathbf{R}_2)]$ gives the phase difference between the two sites for a state specified by the two-dimensional wave vector $\mathbf{k}_{\|}$. A schematic representation of this system is shown in Fig. 10.10. Let us consider first the free unsupported sulphur layer. We only consider the 3p niveous of sulphur. We can qualitatively estimate the band structure expected on the basis of nearest neighbour interactions only. The schematic wave functions of the c(2 × 2) layer are shows at three critical points Γ, X, M of the Brillouin zone (Plummer et al., 1980). The $p_z$ orbital transforms at Γ according to $a_1$, the $p_x/p_y$ orbitals belong to the irreducible representation e. The two-dimensional wave function that may be formed

through combinations of $p_z$ orbitals is strongly bonding at $\Gamma$. The two-dimensional wave functions based on the $p_x$ and $p_y$ orbitals indicate strongly antibonding character at $\Gamma$. Note that due to the orbital degeneracy we may either consider the pure $p_x/p_y$ components or linear combinations $p_x + p_y$ and $p_x - p_y$. On the way from $\Gamma \rightarrow$ M the phase relation between the atomic orbitals change. At M the two-dimensional wave functions derived from $p_z$ are antibonding. This is the reason why the $p_z$ derived band disperses from higher to lower binding energies. Due to the lower symmetry the $p_x$ and $p_y$ bands are no longer degenerate along $\Gamma$–M. They disperse towards higher binding energies on the way to M. The dispersion of the $p_x/p_y$ bands are considerably larger than the one of the $p_z$ derived bands. This is caused by the weaker interaction of the $p_z$ orbitals as compared with the $p_x/p_y$ orbitals which are directed towards each other. In the direction $\Gamma \rightarrow$ X the situation is quite analogous for the $p_z$ orbitals, i.e., the antibonding character of the two-dimensional wave function increases. On the contrary the $p_x$ and $p_y$ bands have considerably different energies because the $p_x$ band at X is strongly bonding while the $p_y$ band remains antibonding at X. Coming back to the $\Gamma$ point we realize from Fig. 10.3 that in the present situation the $p_z$ orbital is situated at higher binding energies than the e orbital derived form $p_x/p_y$. This is reversed with respect to the p(2 × 2) structure. While in the case of the p(2 × 2) structure coupling between adsorbate and substrate determines the sequence, the relative position of $a_1$ and e levels at $\Gamma$ is dominated by the interadsorbate interactions. The symmetry of the unsupported layer is $D_{4h}$. If we now bring this layer in contact with the substrate we destroy the symmetry of the layer in the sense that the system has no longer $D_{4h}$ but rather $C_{4v}$ symmetry. This induces hybridization between the $p_z$ and the $p_x$ derived bands along $\Gamma \rightarrow$ X and $\Gamma \rightarrow$ M. A hybridization gap is formed as indicated. At the same time the adsorbate levels mix with the levels of the substrate and a diagram as indicated in the middle panel of Fig. 10.3 results schematically. The same experiments that were shown in Fig. 10.7 for the p(2 × 2) structure are depicted in Fig. 10.11 for the c(2 × 2)S/Ni(100) structure (Plummer et al., 1980). The spectra taken in normal emission indicate that the sequence deduced from the unsupported layer survives when interaction with the substrate is switched on. In order to judge this statement in more detail, the band structure has to be determined via an angle resolved measurement. In our example we can try to probe the bands of various symmetries by choosing different measurement geometries. In order to detect the dispersion of odd bands within a mirror plane perpendicular to the surface we orient the electric field vector of the exciting radiation perpendicularly towards this mirror plane and place the detector within the plane. In this geometry only odd initial states are detected and their dispersion can be determined experimentally. If on the other hand, we place the electric field vector within the mirror plane we may record the dispersion of the even bands. In Fig. 10.11 the results of such measurements along the $\Gamma \rightarrow$ M direction are included. We find that in the present case not only the qualitative behaviour is correctly predicted but even the size of the dispersions is described semiquantitatively by the above predictions. One may conclude that the intermolecular interactions in sulphur adsorbates are dominated by direct sulphur–sulphur contacts.

The systems discussed so far involved chalcogenide adsorption without massive restructuring of the substrate. If we turn from the close packed (100) surface towards the more open (110) surfaces and choose as an adsorbate the more reactive oxygen we find examples where adsorption is accompanied by a pronounced reconstruction of the substrate (Bader

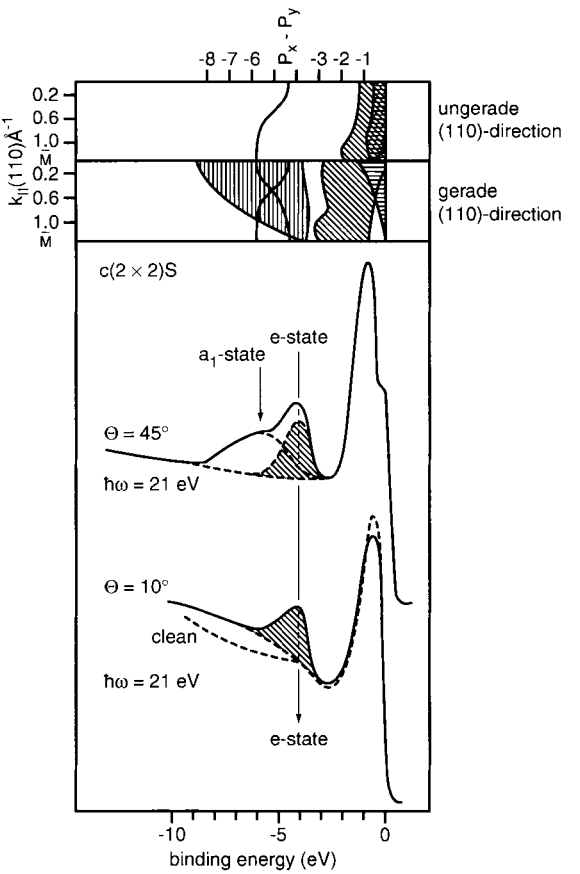


Fig. 10.11. Photoelectron spectra of c(2 × 2)S/Ni(100) recorded in normal emission for two different light incidence angles ($\Theta_i$) (Plummer et al., 1980).

et al., 1987; Coulman et al., 1990; Wintterlin et al., 1991). Oxygen adsorption on Cu(110) is a rather well studied adsorption system which has recently gained even more attention as it is to a certain extend a model system to study the electronic structure of high temperature superconductors. Upon exposure of oxygen to a Cu(110) surface a p(2 × 1) LEED pattern is observed which is caused by the so called "missing row" reconstruction, schematically shown in Fig. 10.12 in comparison with the unreconstructed surface. The (110) surface is characterized by two different bridging sites, namely the "short" bridge along ($1\bar{1}0$) and the "long" bridge along (001). Oxygen occupies the long bridge sites of every second row. Then the row of Cu atoms between the oxygen containing rows is missing. Another way of looking at this situation is to take the unreconstructed surface and add O–Cu–O–Cu rows at the appropriate periodicity along the substrate (100) direction. This "added" row description (Coulman et al., 1990; Wintterlin et al., 1991) may even be the more appropriate description if we consider the mechanism of formation and growth of this structure

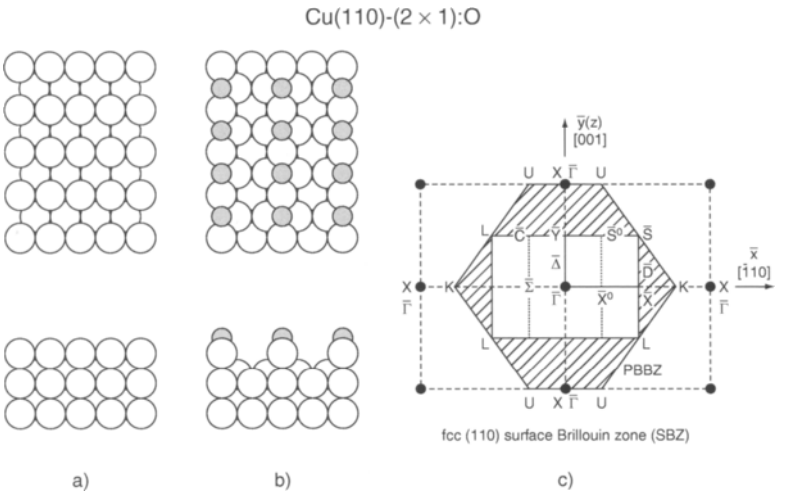


Fig. 10.12. Geometric structure of the clean Cu(110) surface (a), of O(2 × 1)/Cu(110) (b), and the Brillouin zone of O(2 × 1)/Cu(110) (c).

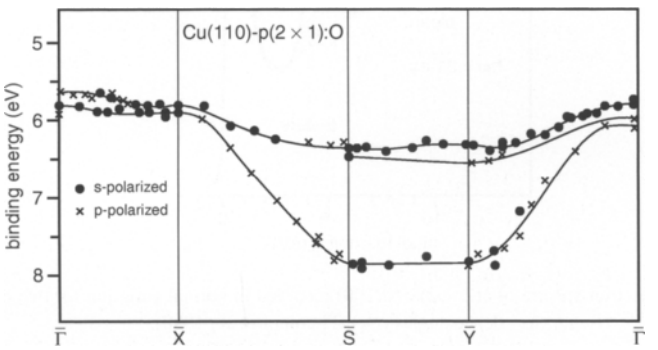


Fig. 10.13. Dispersion of oxygen 2p-derived bonding bands for several Brillouin zone directions of the reconstructed surface. Data from (Didio et al., 1984; Courths et al., 1986, 1987; Jacob et al., 1986; Courths, private communication; Goldmann, 1992). ΓY is oriented along [001], i.e., along the oxygen chains, while ΓX is oriented along [1$\bar{1}$0]. S bisects X–X and Y–Y, respectively, in the extended zone scheme.

as revealed through scanning tunneling microscopy. It is clear from what has been said that the electronic structure of the system has a certain degree of one dimensionality. The Brillouin zone of the system is shown in Fig. 10.12 and it is indicated how the Brillouin zone of the adsorbate is connected with the one of the unreconstructed surface. The electronic structure, i.e., the measured dispersions in the occupied energy region, is shown in Fig. 10.13 (Didio et al., 1984; Courths et al., 1987; Jacob et al., 1986). The one dimensionality is clearly evident from the experimental dispersions: there are unusually large (1.85 eV) dispersions measured along ΓY and XS. These are directions (see Fig. 10.12) along the (001) azimuth. The very large dispersions are hard to explain just on the basis

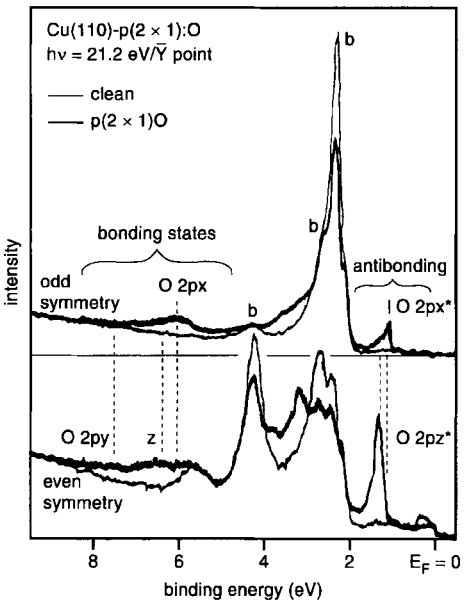


Fig. 10.14. ARUPS spectra taken with linearly polarized HeI radiation at the Y point of the surface Brillouin zone. For definition of coordinates see text. From Courths et al., 1986; Courths, private communication; Goldmann, 1992.

of pure oxygen-oxygen interactions because the distance is 3.5 Å. Probably quite strong Cu–O–Cu–O interactions must be considered. In contrast to this there is very little dispersion (< 0.3 eV) along ΓX and SY. The dispersions shown in Fig. 10.13 represent the three oxygen 2p derived resonances situated below the Cu d-band and they are related to the features discussed for the sulphur adsorbates in the last section. Due to the particular electronic structure of the coin metals there is a range of about 2 eV between the Fermi energy and the onset of the d-band density which is dominated by s-band density. Due to the relatively low intensity of the s-band features it is possible to detect adsorbate induced states that are the antibonding analogs to the features below the d-band. Typical spectra recorded for even and odd symmetry states at Y are shown in Fig. 10.14 (Courths et al., 1986; Courths, private communication; Goldmann, 1992).

The surface coordinates $y$ ($x$) are oriented along (perpendicular to) the Cu–O chains, while $z$ is defined along the surface normal. Using linearly polarized light and the appropriate nonrelativistic dipole selection rules, the orbital symmetry of all five occupied bands could be uniquely determined. In the upper part of Fig. 10.14 s-polarized light (vector potential $A_0$ along X) was used to project out the odd states. The lower part reveals the even orbitals since p-polarized radiation (A in $yz$-plane) was incident. A summary of all experimental dispersion curves along ΓY is shown in Fig. 10.15 (Didio et al., 1984; Courths et al., 1987; Jacob et al., 1986). The orbital symmetry at Y from bottom (−7.8 eV) to $E_F$ is $y$, $z$, $x$, $z$ and $x$. Also included is an empty band observed by inverse photoemission spectroscopy (Jacob et al., 1986). Note that these dispersion curves exhibit the periodicity of the

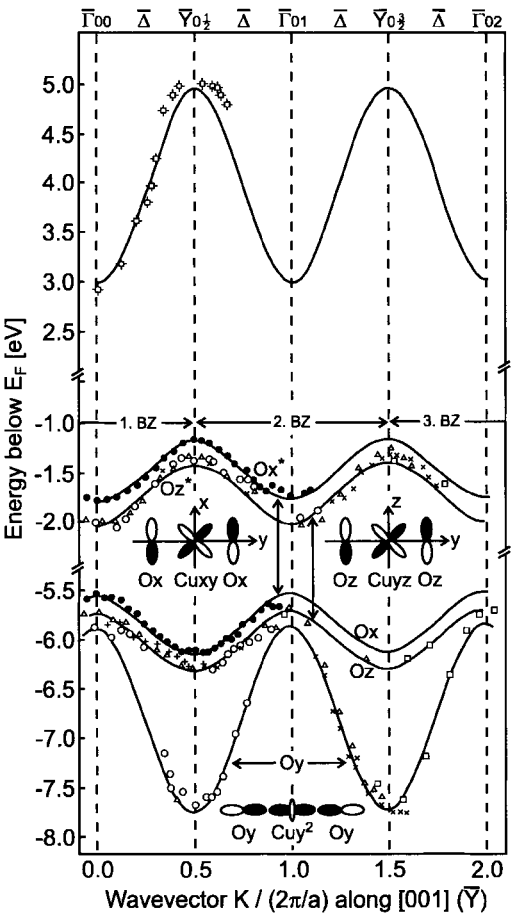


Fig. 10.15. Experimentally determined band structure of the adsorbate induced bands of the O(2 × 1)/Cu(110) adsorbate system (Didio et al., 1984; Courths et al., 1986, 1987; Jacob et al., 1986; Courths, private communication; Goldmann, 1992).

substrate lattice constant along Y, in agreement with the proposed structure model. The adsorption site is reflected in the number of bands: the $C_{2v}$ point group symmetry of the long-bridge site dictates a splitting of the 2px and 2py levels at Γ, which is clearly observed. Figure 10.15 immediately shows that the observed dispersion curves represent an oxygen–copper bond: in case of an exclusive linear O–O bond all three oxygen derived bonding (or antibonding) bands would not run in parallel. Courths et al. (Courths et al., 1986, 1987; Courths, private communication; Goldmann, 1992) have shown that all six dispersion curves may be modelled assuming O2p and Cu3d/4s orbitals to form Cu–O bonds in a linear O–Cu chain along $y$. Figure 10.16 shows a schematic molecular orbital diagram for the formation of Cu–O bonds from five degenerate 3d and a non degenerate 4s orbital of Cu and three degenerate 2p orbitals of O. Due to the $C_{\infty v}$ symmetry of the system the

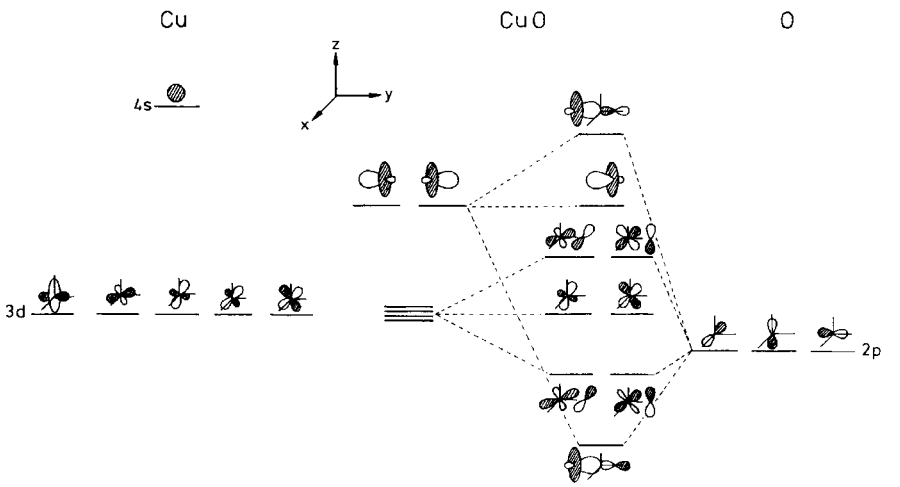


Fig. 10.16. Schematic molecular orbital diagram for a Cu–O bond on the basis of 5 Cu3d, 1 Cu4s, and 3 O2p orbitals. The energy scale is arbitrary.

4s and the $3d_{y^2}$ orbitals hybridize. Upon interaction bonding and antibonding combinations are formed. The energy split is large for the one $\sigma$-type interaction due to the large overlap of the atomic orbitals. The $\pi$-type interactions are smaller and thus the splitting of the doubly degenerate $d_{yz}$–$p_z$ and $d_{yx}$–$p_x$ combinations is considerably smaller. The two $d_{z^2-x^2}$ and $d_{xz}$ orbitals transform according to $\sigma$-symmetry and have no oxygen counterparts. They are thus nonbonding with respect to the Cu–O interaction. The same is true for the second $\sigma$-interaction of the $3d_{y^2}$/4s hybrids and caused by the very small overlap with respect to the Cu–O bond. If we fill this schematic diagram in Fig. 10.16 with 15 electrons (Cu:11 + O:4) the antibonding $\sigma$-combination is empty, and the non-bonding $3d_{y^2}$/4s combination is the highest molecular orbital. This diagram is the starting point for the qualitative discussion of the band structure: The strong bonding and antibonding $\sigma$-orbitals lead to pronounced dispersions along $\Gamma$Y and XS with opposite signs. These dispersions are about three times as larger as those of the $\pi$-bands. The parallel dispersions are explained by the phase relations. In other words, the observed dispersions are compatible with the electronic structure of linear chains, which are only weakly altered by interaction with the substrate.

Summarizing, the experiments indicate that the electronic structure of the O(2 × 1)/Cu(110) adsorbate system may be interpreted on the basis of linear Cu–O chains weakly interacting with the substrate.

## 10.4. Hydrogen adsorption

The adsorption of hydrogen has been discussed in great detail on various substrates in the past (Christmann, 1988). One of the main issues has been the dissociation mechanism. On most surfaces hydrogen adsorbs dissociatively at room temperature. However, the sticking

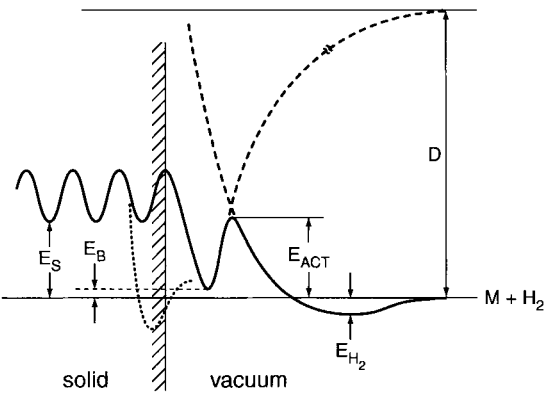


Fig. 10.17. Characteristic potential energy surface of H and $H_2$ on simple metals.

probability varies to a large extent (Retter et al., 1985; Kleyn et al., 1982). While for copper the sticking probability is low if the molecule is not translationally or vibrationally excited, the sticking probability for nickel is considerably higher. The picture that has evolved explaining these findings may be summarized on the basis of the potential energy diagram shown in Fig. 10.17. $H_2$ from the gas phase may adsorb into a molecular state before it, after surmounting an activation barrier, the height of which depends on the substrate, dissociates into an atomic adsorbate state. Again, depending on the substrate the hydrogen atom may be localized at the surface, i.e., when the barrier for absorption is large. If the barrier for absorption is small (dotted line) hydrogen atoms will diffuse into the bulk forming a hydride (Sprunger and Plummer, 1991).

In recent years a clear picture for the microscopic interactions influencing the barrier between molecular and atomic hydrogen has emerged (Harris and Andersson, 1985): There are two important ingredients. Firstly, when a molecule approaches a metal surface there will be a Pauli repulsion between the closed shell hydrogen molecule and the more diffuse electrons of the substrate. This, in fact, is the reason for the existence of the activation barrier. The size of this barrier is then, secondly, reduced depending on the electronic structure of the substrate. Consider Ni as opposed to Cu. Ni has a $d^9s^1$ and Cu a $d^{10}s^1$ configuration in the metal. Therefore, in Ni the diffuse electron may fill the hole in the d-shell and thus reduce the molecule-metal Pauli repulsion thus reducing the activation barrier. Then the molecule may come in closer, and form Ni–H bonds. While this may happen for Ni it will not happen for Cu because there is no hole in the d-shell, and therefore the activation barrier remains high.

There have been considerable experimental efforts which we shall summarize in the following to try to understand the electronic structure of hydrogen adsorbates. The model system to study would be hydrogen on simple metal surfaces (Sprunger and Plummer, 1991). Due to the complications in the controlled preparation of simple metal surfaces experiment is far behind the theoretical description (Hjelmberg, 1979; Yu and Lam, 1988; Lundquist et al., 1979). Only recently have several groups start to tackle this problem experimentally (Sprunger and Plummer, 1991) and I presume that in the near future some interesting

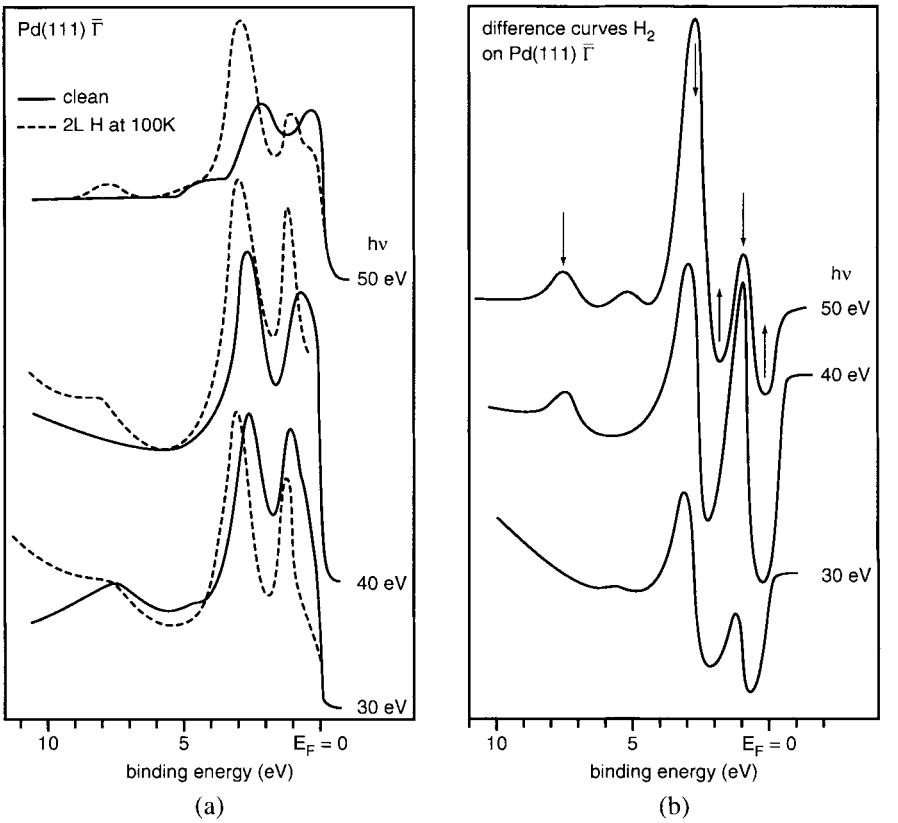


Fig. 10.18. (a) Energy distribution curves of clean Pd(111) (solid line) and H/Pd(111) (dashed line). (b) Difference spectra (Eberhardt et al., 1981).

results will energe from these studies. It may be stated, however, that the adsorption behaviour of hydrogen on simple metals also follows the scheme outlined in Fig. 10.17. The activation for dissociation seems to be high and the important parameter controlling the adsorption mode of atomic hydrogen appears to be the conduction electron density ($r_S$). As a function of this parameter it is found that atomic hydrogen is adsorbed on high density metal, such as Be and Al, but for low density metals, such as Na, the hydrogen is absorbed into the bulk forming a hydride. Intermediate cases like Mg may have characteristic features of both limiting cases (Sprunger and Plummer, 1991).

A system where the electronic structure has been studied in some detail is the system H/Pd(111), which we shall discuss below in more detail (Eberhardt et al., 1981; Eberhardt and Plummer, 1983; Shinn, 1986; Shinn and Madey, 1984, 1985).

In Fig. 10.18a electron distribution curves taken in normal emission are shown for several photon energies (Starke et al., 1988; Chubb et al., 1990). The full lines represent the clean surfaces and the broken lines represent the spectra of the surface after saturating the surface with hydrogen at 100 K. The feature at 7.8 eV is easily identified as due to a H1s

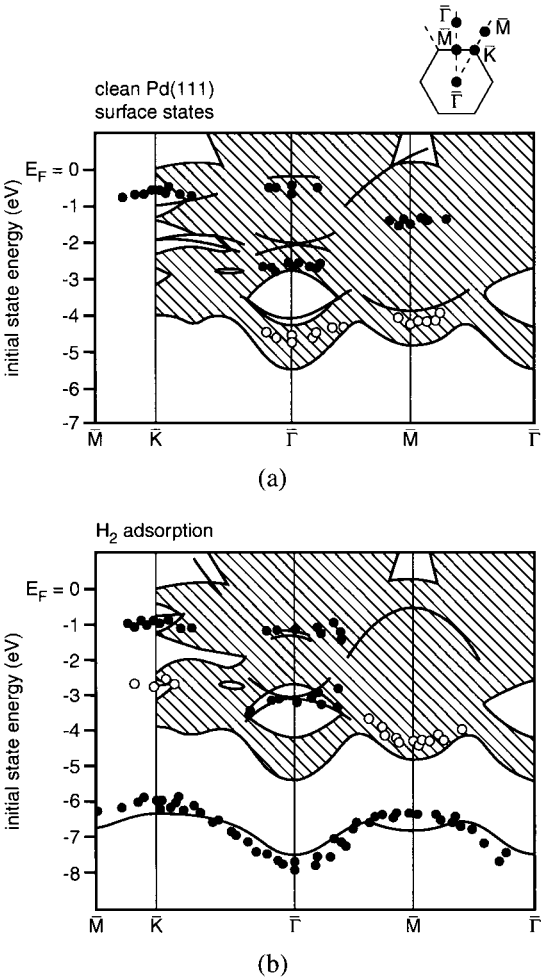


Fig. 10.19. Surface state of clean Pd(111) (a) and one monolayer H on Pd(111) (b). The projected band structure of Pd(111) is indicated by the hatched areas (Eberhardt and Plummer, 1983; Eberhardt et al., 1983).

induced state while the other differences between clean and covered surface are not as easy to assign. In order to get more insight we show in Fig. 10.18b the difference curves. There are systematic changes: While a peak at 1.2 eV appears, the feature at 0.5 eV binding energy is attenuated. In addition there is a decrease at 2.7 eV binding energy and an intensity increase at 3.2 eV. These changes are observed independent of photon energy. Theoretical calculations have been performed and are compared with the experimental observations in Fig. 10.19 (Eberhardt and Plummer, 1983; Eberhardt et al., 1983). The hatched areas indicate the projected bulk band structure. Calculated surface states are shown as fat lines, filled and open circles represent experimental measurements. There is relatively good agreement between experiment and theory. However, a detailed discussion of the bonding characteristics is still rather complicated and we shall not go into the details. This last example

shows that in particular in these systems a discussion of the bonding between adsorbate and substrate is only possible if theoretical calculations are directly available.

## 10.5. Carbon monoxide adsorption

No diatomic adsorbate system has been investigated and analysed in such detail as carbon monoxide adsorbates. This means that much of the fundamental aspects of bonding in molecular chemisorption systems can be demonstrated using experimental results on CO adsorbate systems (Freund and Neumann, 1988). However, certain aspects can be illustrated by including results on other diatomics such as $O_2$ and $N_2$. With the exception of very few examples, e.g., CO on Cr(110) (Shinn, 1986; Shinn and Madey, 1984, 1985), CO on Fe(100) (Saiki et al., 1989) and CO on Mo(100) (Zaera et al., 1985), where the molecule lies flat on the surface, CO is bound vertically towards transition metals if the adsorption energy is characteristic for a chemisorption system (Freund and Neumann, 1988; Plummer and Eberhardt, 1982). Figure 10.20 illustrates on the basis of one electron level diagrams, much in the same spirit as done in Fig. 10.3 for the atomic adsorbate, how the molecule substrate and intermolecular interaction potential determine whether local or global symmetry dominates. Since ARUPS, as will be shown further below, allows us to study symmetry properties of the electronic states of adsorbate systems, it may be possible to disentangle via ARUPS in favourable cases which of these two types of interactions dominates and how they are active in the adsorbate.

We begin the discussion with comments about the molecule substrate interaction. The relevant interactions are described within the "surface molecule" model according to Blyholder. As alluded to above we can look at this process from the view point of the molecule as a $\sigma$-donation-$\pi$-backdonation process. This means that the distribution of electrons among the subsystems, i.e., CO molecule and metal atom, in the metal–CO-cluster is considerably different as compared with the non-interacting subsystems. For example, the electron configuration of the metal atom in the cluster may be different from the isolated metal atom, or the electron distribution within the CO molecule bonded towards the metal atom may look more like the electron distribution of an "excited" CO molecule rather than the ground state CO molecule (Kao and Messmer, 1985). Nevertheless, as a consequence of the relatively weak molecule–substrate interaction only certain electronic levels of the sub-systems are strongly influenced, so that it appears to be justified to classify the electronic levels of the interacting adsorbate system according to the nomenclature used for the isolated subsystems. Naturally, the distortions of the molecular as well as the metal levels are reflected by changes in the ionization energies of those levels, their ionization probabilities, and the line shapes of the ionization bands. Figure 10.21 shows a set of angle resolved, normal emission valence electron spectra of CO adsorbates on different single crystal surfaces (Turner et al., 1970; Eberhardt and Freund, 1983; Schmeisser et al., 1985; Freund et al., 1983; Allyn, 1978; Odörfer, 1987). The binding energy ($E_B = h\nu - E_{Kin}$) refers to the vacuum level. The region where we expect emission from the three outer valence levels of CO, i.e., the $5\sigma$, $1\pi$, and $4\sigma$ levels (see Fig. 10.20) is shown, and most of the following discussion will concentrate on these levels. From the bottom to the top the heat of adsorption increases from 19 kJ/mol to 142 kJ/mol (Weast, 1973,

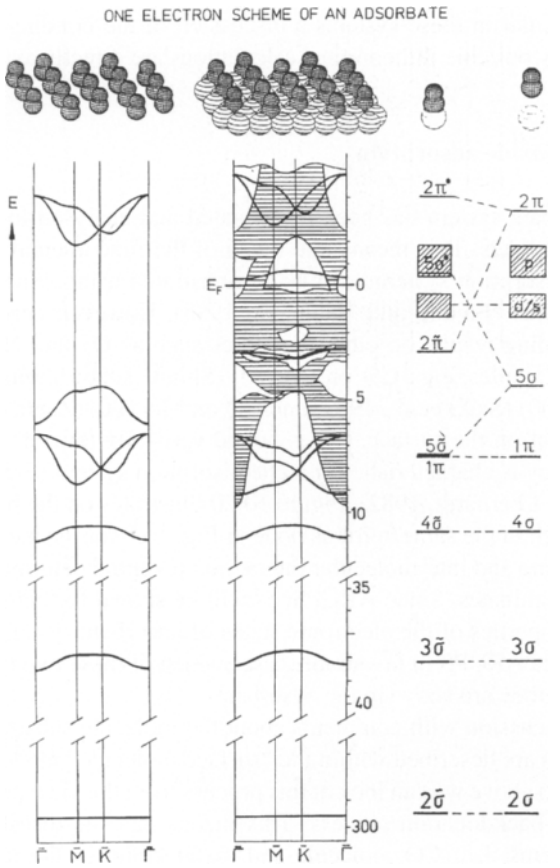


Fig. 10.20. Schematic one-electron level diagrams for diatomic molecules (CO) interacting with a transition metal surface. The level scheme for a molecule–metal cluster (right) is correlated with the band scheme of a free unsupported molecular layer (extreme left) and the band scheme of the quasi-two-dimensional adsorbate (middle). The band structure of the metal projected onto the surface is schematically shown as the hatched area.

1974; Elhiney et al., 1976; Kessler and Thieme, 1977; Christmann et al., 1974; Conrad et al., 1974). This is accompanied by changes in the adsorbate spectra as compared to the gas and solid phase spectra which are shown for comparison. There are several interesting differences in binding energies, line intensities and line shapes between gas, condensed and adsorbate phases, which we shall comment on in the following. In order to do so we have to cover many different aspects such as symmetry considerations, relaxation energies, line widths, shake-up satellites, and so on. We shall use Fig. 10.21 as a guide line to discuss the various aspects as they occur in going from the gas phase via weakly chemisorbed to strongly chemisorbed adsorbates.

In CO/Ag(111) at $T = 20$ K CO is physisorbed as documented by the small $E_{ad} =$ 19 kJ/mol (Elhiney et al., 1976). This explains why a spectrum similar to condensed CO is observed for this adsorbate. The splittings in the $4\tilde{\sigma}$ and $5\tilde{\sigma}$ emissions are connected

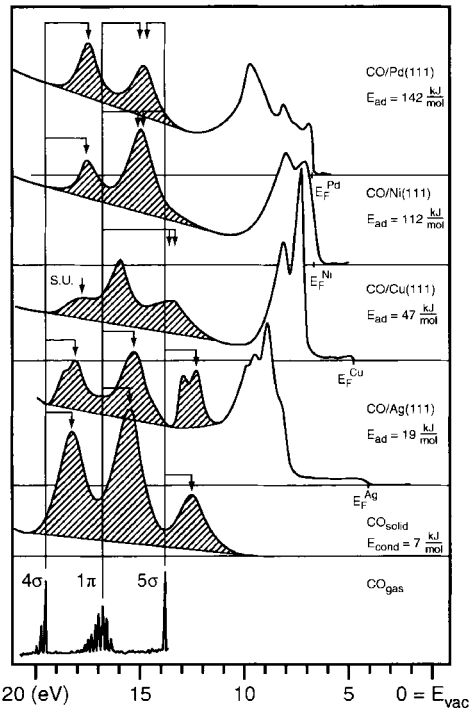


Fig. 10.21. Set of normal emission CO adsorbate spectra (Turner et al., 1970; Eberhardt and Freund, 1983; Schmeisser et al., 1985; Freund et al., 1983; Allyn, 1978; Odörfer, 1987). (S.U. – shake-up satellite.)

with the formation of a two-dimensional overlayer as will be discussed further below. In comparison with the gas phase, however, rather dramatic changes are observed upon condensation and physisorption, namely a shift of about 1 eV towards lower binding energies and a considerable increase in line width which destroys the vibrational structure observed in the gas phase. Very recently new results for weakly adsorbed $N_2$ layers have been reported and we shall come back to this topic in the section on $N_2$ adsorption. Chiang et al. (1980) found shifts by comparing the photoelectron spectra of CO, adsorbed on a metal surface (Al(111)), and of CO adsorbed on the same surface precovered with a monolayer of Xe, assisting as a spacer between metal and CO. The bands shift towards higher binding energies, and appear to exhibit smaller line widths when well separated from the surface. Theories have been developed that allow one to understand these observations on the basis of hole hopping and relaxation together with adsorbate–surface vibrations within the condensed quasi-two- or three-dimensional molecular solids (Duke, 1978; Duke et al., 1978; Gadzuk et al., 1982). The shift of the band to lower binding energy is a consequence of the electronic relaxation in the final ion state, which is considerably more pronounced when the molecule is bound to a readily polarizable medium, because metal electrons screen the positive charge introduced by the ionization process more effectively than do the electrons on the isolated molecule. The more pronounced screening stabilizes the final hole

state relative to the initial state, which lowers the binding energy as observed. Measured temperature dependences of line widths in molecular solids and model systems support the developed theoretical ideas (Gadzuk et al., 1982; Salaneck et al., 1980). It is likely that other processes, for example Auger decay or other radiationless decay mechanisms, contribute to these line widths as well (Sandell, 1993; Bjørneholm, 1992).

If the heat of adsorption increases to about 47 kJ/mol (Kessler and Thieme, 1977) (weak chemisorption), like, for example, in the case of a CO adsorbate on a Cu(111) surface, the features in the spectrum shift and the intensities of the lines are altered considerably with respect to the physisorbate. The line widths, on the other hand, are quite comparable in both systems. Three lines are still found, but their assignment is, as we shall see further below, quite different from the one for the condensed molecular solid.

Before we discuss how ARUPS establishes this assignment let us first turn towards the spectra of the strongly chemisorbed adsorbate systems, i.e., CO/Ni(111) and CO/Pd(111), which are only two examples out of a wealth of experimental data (Greuter et al., 1983; Shinn, 1986; Shinn and Madey, 1984, 1985; Saiki et al., 1989; Zaera et al., 1985; Allyn et al., 1977a; Horn et al., 1978a; Kuhlenbeck et al., 1986; Jensen and Rhodin, 1983; Miranda et al., 1984; Horn et al., 1979; Borstel et al., 1980; Hofmann et al., 1982, 1985; Heskett et al., 1985a; Steinkilberg, 1977; Braun et al., 1979; Kuhlenbeck, 1984; Seabury et al., 1980; Rieger et al., 1984; Apai et al., 1976; Smith et al., 1976). In the case of strong chemisorption the spectra show two bands, the binding energies of which are rather independent of the particular system under consideration, but are shifted by more than 2 eV to lower values with respect to the gas phase. ARUPS has been instrumental to show that these two CO induced bands are really caused by three CO ion states, and that the CO molecules are oriented with their axes parallel to the surface normal (Allyn et al., 1977a). Figure 10.22b shows an angular distribution pattern for the $4\sigma$ ion state intensity of a CO/Pd(111) adsorbate as recorded with an elliptical mirror analyser employing polarized synchrotron light (Miranda et al., 1984). The polarization plane is placed along the 0°/180° azimuth, i.e., the horizontal line in the angular coordinate diagram shown in Fig. 10.22a. With respect to the Pd(111) surface this corresponds to a mirror plane of the system. Figure 10.22c shows a quasi-three-dimensional plot of the emission intensity distribution (shaded areas on the half-sphere) as a function of azimuthal ($\phi$) and polar ($\theta$) angles in direct relation to the geometric structure of the molecular adsorbate (Freund and Neumann, 1988, 1992). The angular distribution pattern clearly shows how the symmetry of the adsorbate wave function with respect to this mirror plane determines the angular distribution of the emitted electron current. If we classify the wave functions of the electron $\phi_e$ and $\phi_k$, (see Eq. (10.2)) as well as the momentum operator $p$ "even" or "odd" with respect to this mirror plane, we are in the position to differentiate between "even" and "odd" initial states by choosing certain light polarizations and detecting the angular distribution pattern (see above) as long as spin orbit interaction is not important (Borstel et al., 1981). For the above given situation the light polarization direction is within the mirror plane. This corresponds to even symmetry of the momentum operator. Therefore, initial states with even symmetry will emit into the direction of the mirror plane because the final states have to be even in order for the matrix element not to vanish. In principle, one would expect a finite emission probability along the whole mirror plane. In the present case, however, one has to take into account the cylindrical symmetry of a CO molecule, bonded linearly towards the metal surface. Even initial

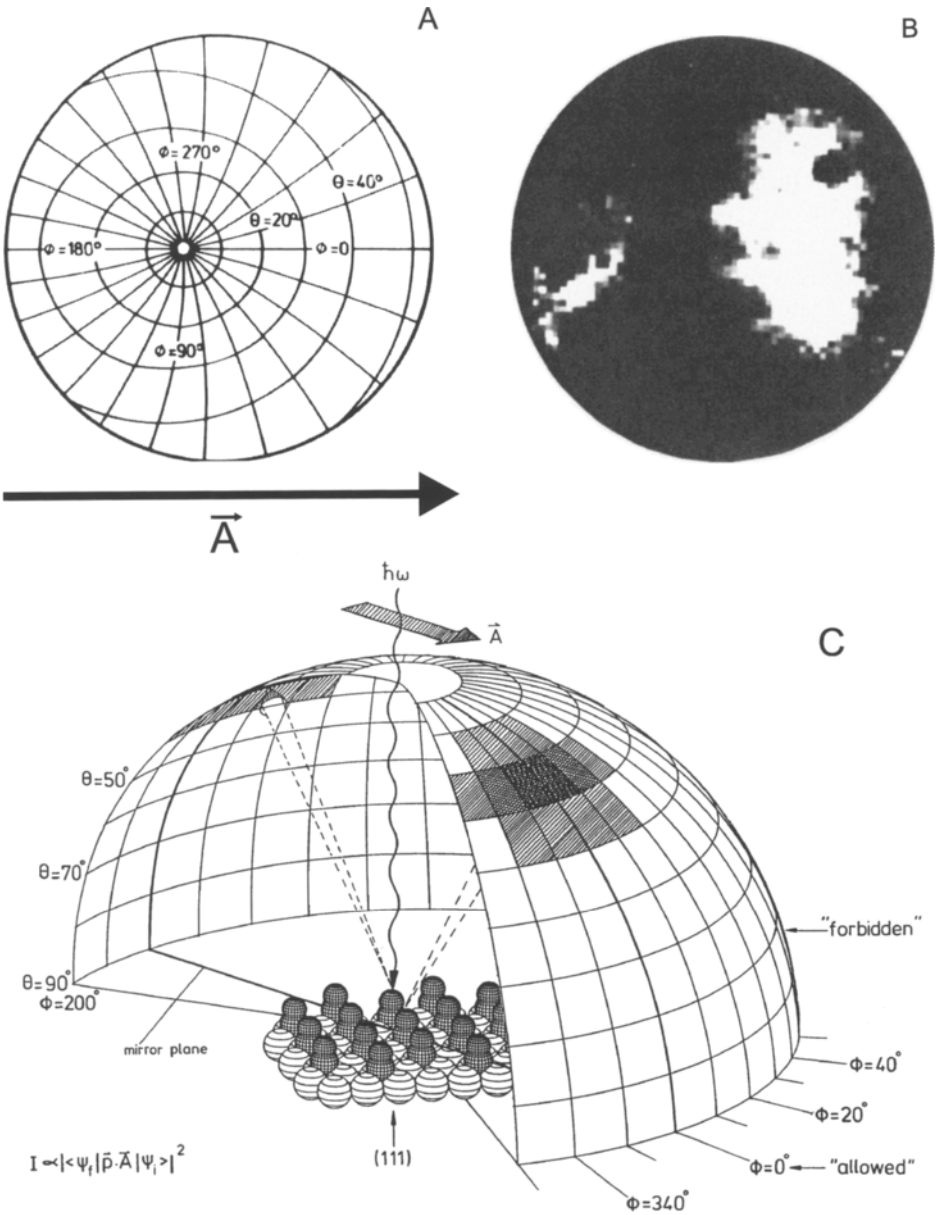


Fig. 10.22. CO $4\sigma$ emission intensity from CO/Pd(111) as recorded with an elliptical mirror analyser (Miranda et al., 1984). (a) Polar diagram, the direction of the light polarization vector is indicated by an arrow. (b) Intensity distribution pattern. Light regions correspond to high emission current. (c) Quasi three-dimensional representation of the relation between geometric structure of the adsorbate and the measured $4\sigma$ emission intensity as a function of $\Phi$ and $\Theta$. The emission intensity is given by the shaded areas.

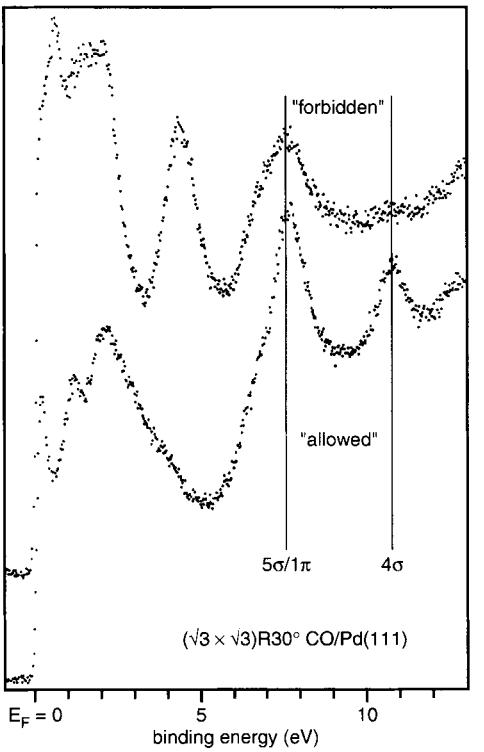


Fig. 10.23. ARUP-spectra of CO/Pd(111) in "forbidden" and "allowed" geometry (see text). The CO induced features are marked. The light polarization was placed along a Pd(210) mirror plane.

states of a cylindrical molecule cannot emit into a direction given by the plane perpendicular to the mirror plane which contains the light polarization vector. This latter property can easily be understood if we remember that any plane in a cylindrical system containing the cylindrical axis is a symmetry plane. Combining this property with the fact that the momentum operator is odd with respect to this second plane means that there cannot be any emission of even states into this direction. Therefore, in order to fulfill both conditions simultaneously, we do not expect an intense CO-4$\sigma$ emission along the surface normal for light polarized in the surface plane. 4$\sigma$ emission along the surface normal can only be achieved by using a light polarization perpendicular to the surface plane because in this case the momentum operator is even with respect to any plane perpendicular to the surface plane. If we combine the considerations so far we verify the above angular distribution pattern.

As a consequence of the outlined behaviour of even initial states, we expect a complementary behaviour of odd initial states. This is exactly what is observed experimentally and is shown as a set of electron distribution curves – which is the usual way to look at ARUP-spectra – in Fig. 10.23. In this figure the complementary behaviour of $\sigma$- and $\pi$-emissions, which was first observed by Lapeyre et al. (Smith et al., 1976) and later by Plummer and coworkers (Allyn et al., 1977a) is obvious: If we record a spectrum perpendicular (so-called "forbidden" geometry) to the incidence plane we do not observe emission in the

region of the $4\sigma$ level but only in the region of the $5\sigma/1\pi$ levels. Note, that the $1\pi$-ion state of CO has two degenerate components, one of which always transforms according to the even representation. Thus, we expect to see the one odd component of the $1\pi$-ion state. A spectrum recorded with the analyser placed within the incidence plane, the so called "allowed" geometry, show all states with even symmetry. From Fig. 10.23 it is clear that the band at 8 eV below the Fermi energy (Fig. 10.21) contains two states, i.e., the $1\pi$ and the $5\sigma$ ion states. Their energies are, in contrast to the gas phase, nearly (within a few tenths of an eV) degenerate in the adsorbate. This is a situation, predicted by the simple one-electron level scheme in Fig. 10.20. It is due to the donation of the $5\sigma$ carbon lone pair into empty metal levels, thus stabilizing the CO $5\sigma$-level with respect to the $1\pi$-level which is not as intimately involved in the molecule–metal interaction for linear metal–molecule bonding.

The logic so far has been that we have assumed a geometry of the adsorbate site, thus knowing the symmetry of the system, i.e., CO perpendicular to the surface plane, and have verified this via an analysis of the angular photoemission spectra. Usually, the arguments are turned around, namely, the observed angular behaviour is used to deduce an adsorbate site symmetry.

The adsorbate induced features exhibit, in addition to the described angular dependences (Davenport, 1976), characteristic photon energy dependences, which, when recorded in an angle dependent fashion, can be used to get further information about adsorbate site geometry (Allyn et al., 1977a). Figure 10.24 shows a plot of the intensity of the $4\sigma$ ion state as a function of photon energy. The data have been recorded for the system CO/Co(0001) (Greuter et al., 1983) for three different electron emission angles. The observed resonance feature is caused by the so-called shape resonance, which is well known from CO gas phase studies (Plummer et al., 1977). It can be traced back to a molecular final state of $\sigma$ symmetry in the ionization continuum, quasi-bound by a centrifugal barrier in the molecular potential. Its symmetry confines the electron emission direction to the molecular axis, and directs the $4\sigma$ emission out of the oxygen end of the molecule. This means that for the case of a molecule oriented along the surface normal, carbon-end bound to the surface, the resonance should peak along the surface normal.

Experimentally, we find in Fig. 10.24 the expected behaviour, i.e., a pronounced attenuation of the resonance intensity for off normal emission, which corroborates the assumed adsorbate orientation. Another interesting property of this resonance is its coherent-forward-emission character (Gustafsson, 1980). Coherent-forward-emission leads to an oscillatory behaviour of the photoionization cross-section. The periodicity is determined by the distance of the interfering sources, which are in the present case the carbon and oxygen atoms participating in the ion state wave function under consideration ($4\sigma$). Examples are shown in Fig. 10.25 for the system CO/Pd(111) (Geisler et al., 1996). At a photon energy of 35 eV the resonance corresponding to the one shown in Fig. 10.24 is found. As predicted by theoretical calculations (Gustafsson, 1980), at about 95 eV and 220 eV a second and a third feature with larger widths and smaller amplitudes are observed. Potentially, the energy separation can be used to estimate the CO bond length in adsorbates as proposed by Gustafsson (1980). For the $5\sigma$ emission the second and third features are missing due to back scattering.

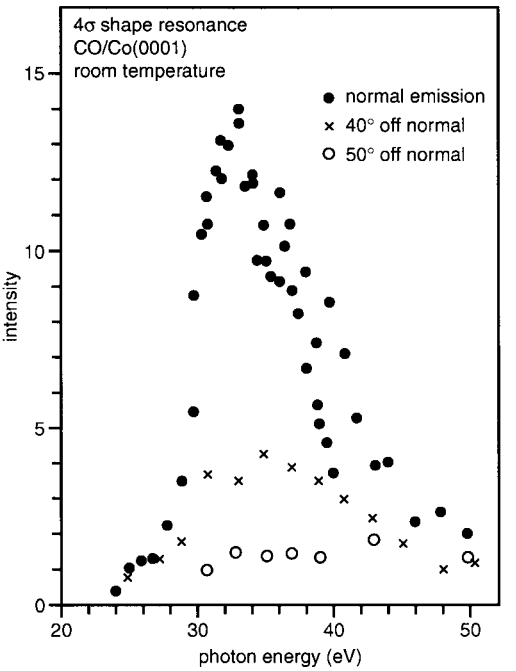


Fig. 10.24. Intensity variations of the $4\sigma$ intensity in CO/Co(0001) as a function of photon energy. Filled circles refer to normal emission, open circles and crosses to off-normal emission as indicated (Greuter et al., 1983).

If we apply the geometry sensitive experiments, just presented, to investigate the geometric structure of physisorbed molecules, for example CO/Ag(111) (Schmeisser et al., 1985), Fig. 10.21, or CO/Al(111) (Chiang et al., 1980), we find that the orientation of the molecular axis is not, like in the chemisorbates perpendicular, but rather parallel to the surface. The reason is that due to the electronic structure of the substrate, not enough energy can be gained via the above mentioned $\sigma$-donor-$\pi$-acceptor interaction, for which a vertical orientation is a necessary prerequisite. As we shall see further below, intermolecular interactions are rather important to understand the electronic structure of physisorbates.

At this point we can return to the assignment and analysis of the spectra of the weakly chemisorbed system. The assignment of the spectrum of the CO/Cu(111) system, given in Fig. 10.21 indicates that the considerations presented so far are not complete and sufficient to explain all experimental findings. It has been shown theoretically that for weakly chemisorbed systems so called shake up excitations accompanying the "normal" electron emission have to be considered (Hermann et al., 1981; Messmer and Lamson, 1979; Freund and Plummer, 1981; Saddei et al., 1980; Schönhammer and Gunnarsson, 1978; Mariani et al., 1982; Wendin, 1981; Umbach, 1982; Martensson and Nilsson, 1990; Sandell, 1993; Bjørneholm, 1992). These shake-up excitations are manifestations of the fact that the ionization process is a rather complicated many-electron process (Cederbaum and Domcke, 1977; Wendin, 1981). They can be assigned to electron excitations in addition to electron emission. Their intensity is determined by the second matrix element in Eq. (10.2) whose

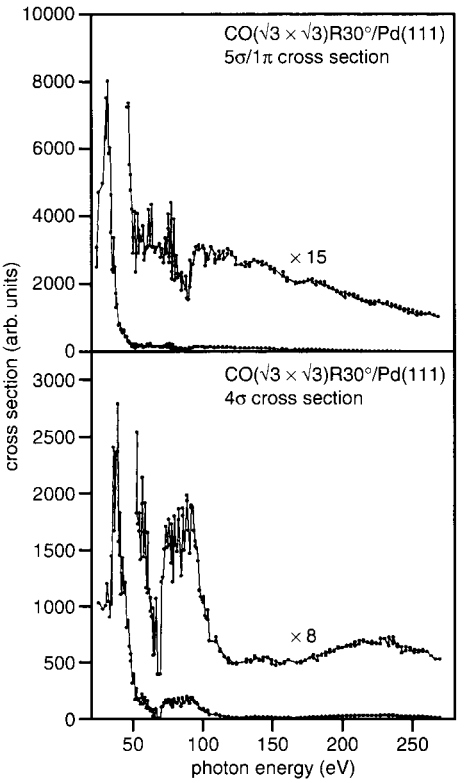


Fig. 10.25. Cross sections of the CO valence orbitals of $(\sqrt{3} \times \sqrt{3})$R30° CO/Pd(111) as a function of the photon energy (Odörfer, 1987).

magnitude is governed by the projection of the wave function of the shake-up state ${}^{N-1}\Psi_{e,E}$ onto the "frozen" ion state $a_k\varphi_i$. Shake-up intensities are rather low for chemisorbed and for physisorbed systems but reach the maximum for intermediate metal–molecule coupling, i.e., weak chemisorption (Messmer and Lamson, 1979; Freund and Plummer, 1981; Saddei et al., 1980; Schönhammer and Gunnarsson, 1978; Mariani et al., 1982; Umbach, 1982; Martensson and Nilsson, 1990). Again, ARUPS can be employed to support the assignment as given in Fig. 10.21 for the CO/Cu(111) system. If the most intense CO features were due to $1\pi$ emission, as might be suspected by comparing the spectra of the CO/Cu(111) system with CO/Ag(111), a resonance behaviour for this particular peak would not be allowed. Horn et al. (Mariani et al., 1982) showed that both bands at higher binding energy are due to states of $\sigma$ symmetry by investigating the shape resonance discussed above. The $4\sigma$ ion state as well as the accompanying shake-up transition exhibited parallel resonance behaviour as expected according to the assignment in Fig. 10.21. A spectrum rather similar to the one of the CO/Cu system, but with even slightly more intense satellite structure, has been found for the system CO/Au (Sandell, 1993; Bonzel, private communication). In the latter system the adsorption energy is between the one for CO/Ag

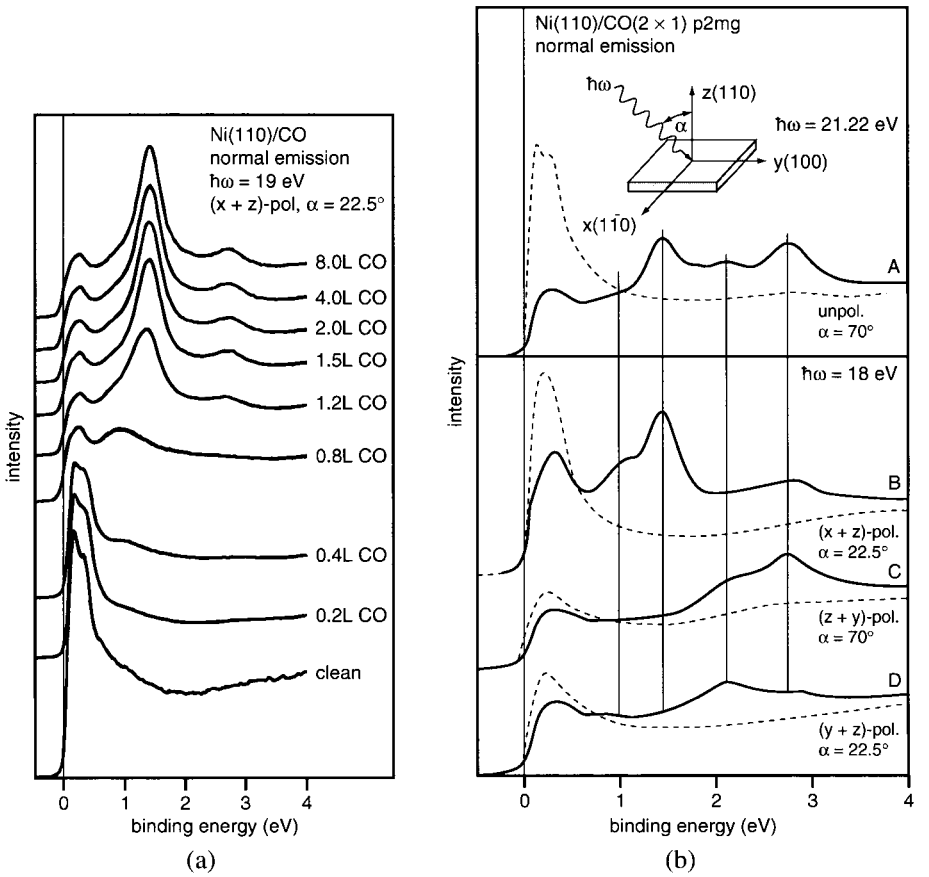


Fig. 10.26. (a) Normal emission ARUPS spectra of CO on Ni(110) as a function of coverage. (b) ARUP-spectra in normal emission for different light polarization directions of CO(2 × 1)p2mg/Ni(110) (full lines) in comparison with the clean Ni(110) surface (broken lines) in the region of the metal emissions (Kuhlenbeck et al., 1989).

and CO/Cu which leads us to expect more intense satellites, and corroborates the ideas presented.

In our discussion so far we have only considered the molecule induced peaks at binding energies higher than the metal states, i.e., those states that correspond to "molecular" ion states. However, as is obvious from Fig. 10.20 there are levels of the adsorbate system within the region of the metal projected density of states, due to the coupling of unoccupied molecular states to occupied metal states. There have been several attempts to identify these states (Smith et al., 1980; Boszo et al., 1983; Kuhlenbeck et al., 1987). The most recent one was done on the system CO(2 × 1)p2mg/Ni(110), whose structure will be discussed in detail in connection with intermolecular interactions (Kuhlenbeck et al., 1986). Figure 10.26a shows how these states develop as a function of coverage. The symmetry and high CO density of the system with highest coverage allows to measure the adsorbate induced peaks in the d-band region of the Ni substrate (Kuhlenbeck et al., 1987). Figure 10.26b shows a

selected set of spectra that demonstrate the intensity, symmetry and energy position of the CO induced, d-like states for this system. The spectra of the clean surface are given as dashed curves for comparison. The usually dominant CO molecular ionizations (Kuhlenbeck et al., 1986) are not shown in this figure. The various peak intensities are strongly polarization dependent, and, together with the measured dispersion, discussed in the section intermolecular interactions, support an assignment of these features to CO-$2\pi$–Ni-3d states. We shall come back to these states further down.

To complete the picture of the electronic structure we consider as the next step intermolecular interactions. As an introduction to the quasi two-dimensional band structure of molecular overlayers we discuss the band dispersions and the symmetry properties of a hexagonal overlayer (Greuter et al., 1983) of CO molecules on a fcc(111) surface as shown in Fig. 10.20.

We can illustrate the qualitative features of the dispersion by plotting schematically the real parts of a tight-binding wave function in real space for values of $k$ corresponding to high symmetry points in reciprocal space. Figure 10.27a shows the real- and reciprocal-space unit cells for the hexagonal structure. The real and reciprocal lattices have two mirror planes: one along the $\Gamma$–M–$\Gamma$ line (in reciprocal space) and the other one along the line $\Gamma$–K–M–K. The wave functions along these lines will be even (a′) or odd (a″). Figure 10.27b illustrates the phases of a $\sigma$ and the two $\pi$ states at $\Gamma$ and M. The discussion of band dispersions is analogous to the one discussed for sulphur on Ni(100) in Fig. 10.8 and we refer to literature for details. The dispersions connected with the wave functions are the ones shown in Fig. 10.20 on the left hand side.

Such dispersions can be determined via ARUPS. Figure 10.27c shows a comparison of calculated dispersions for the $4\sigma$-derived band with measured $4\sigma$ dispersions of CO/Co(0001) adsorbates in $\Gamma$–M direction in two hexagonal $(\sqrt{3} \times \sqrt{3})$R30° and $(2\sqrt{3} \times 2\sqrt{3})$R30° layers (Freund and Neumann, 1992). We have artificially set the lengths of the two Brillouin zones equal for a more convenient comparison. Due to the smaller CO–CO distance in the $(2\sqrt{3} \times 2\sqrt{3})$R30° layer, the overlap of the $4\sigma$-CO wave functions increases, and concomitantly, the band width increases. Figure 10.27c illustrates that the increase in band width can be quantitatively reproduced by simple tight binding calculations in the case of $4\sigma$ derived bands. In the present case the comparison can be made directly because the number of nearest neighbours is the same in both systems. If, on the other hand, we want to compare dispersions in hexagonal and quadratic systems, the observed band widths have to be corrected for the different number of nearest neighbours. Such a correction is straightforward on the basis of simple tight binding considerations. The result of such a comparison for several different adsorbate systems is shown in Fig. 10.28 (Freund et al., 1983; Allyn et al., 1977a; Horn et al., 1978a, b, 1979; Kuhlenbeck et al., 1986; Jensen and Rhodin, 1983; Greuter et al., 1983; Miranda et al., 1984; Hofmann et al., 1982, 1985; Heskett et al., 1985a; Rieger et al., 1984; Odörfer et al., 1988; Batra et al., 1979; Seaburg et al., 1981; Heskett, private communication; Schneider et al., 1988). The data points follow an exponential dependence on the nearest neighbour distance with a decay length on 1.25 Å if we disregard the CO–K co-adsorbate for the moment. This strongly supports the conclusion that the $4\sigma$ dispersion is caused by direct CO–CO overlap. Intuitively, this is reasonable, because the $4\sigma$-CO level is not strongly involved in the metal substrate bonding. At the same time we expect a completely different behaviour for the

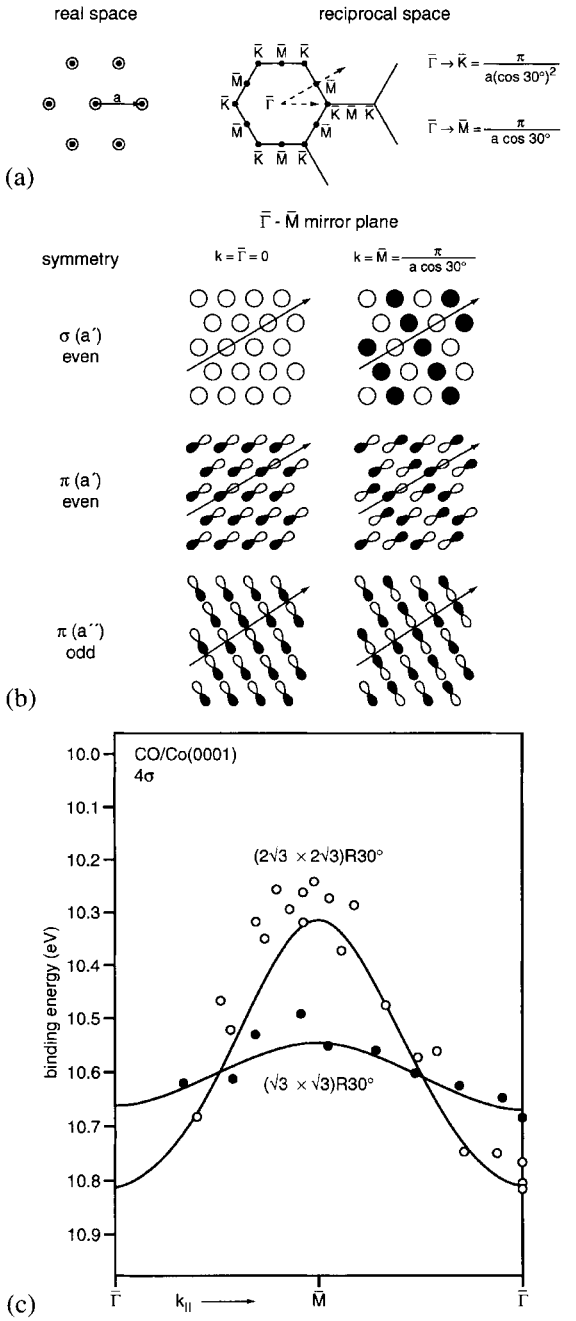


Fig. 10.27. Schematic two-dimensional wave functions of a hexagonal CO layer along the Γ–M direction. (a) Real and reciprocal space representation of the hexagonal layer, (b) wave functions, (c) comparison of experimental and theoretical dispersions for two CO overlayers on Co(0001) of varying CO density (Freund and Neumann, 1992).

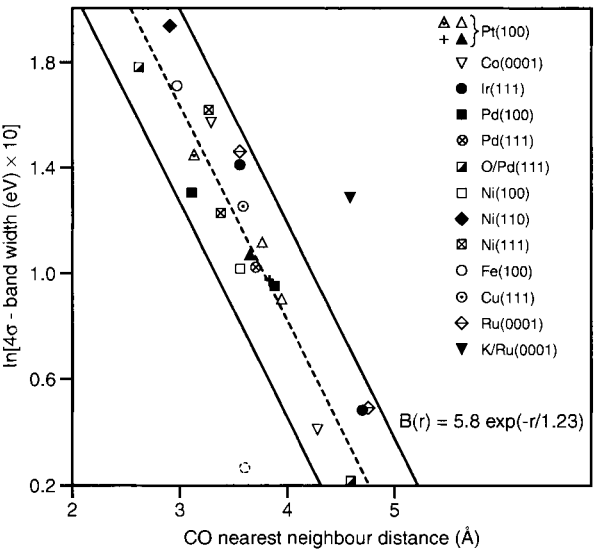


Fig. 10.28. Observed $4\sigma$ bandwidths as a function of intermolecular separation. Six nearest neighbours are used as reference (Greuter et al., 1983; Freund et al., 1983; Allyn et al., 1977a; Horn et al., 1978a, b, 1979; Kuhlenbeck et al., 1986; Jensen and Rhodin, 1983; Miranda et al., 1984; Hofmann et al., 1982, 1985; Heskett et al., 1985a; Rieger et al., 1984; Odörfer et al., 1988; Batra et al., 1979; Seaburg et al., 1981; Heskett, private communication; Schneider et al., 1988).

$5\sigma$ level, because in this case the interaction with the substrate as indicated in the middle of Fig. 10.20 should have a marked influence on measured dispersion. There is no such linear dependence of the observed band width as a function of CO–CO distances as for the $4\sigma$ level (Heskett et al., 1985a). A similar plot as for the $4\sigma$ level exhibits no particular functional dependence, which may be an expression of the participation of indirect through substrate interactions in intermolecular interaction. Care has to be exercised not to jump to this conclusion prematurely, because, due to the stabilization of the $5\sigma$ level into the region of the $1\pi$ level (see Fig. 10.20) we expect strong $5\sigma/1\pi$ hybridization effects which have to be taken into account in the prediction of band dispersions (Greuter et al., 1983).

There are only very few cases, where the complete band structure in the $5\sigma/1\pi$ region has been determined. One such example, which shall be considered in the following, is the system CO(2 × 1)p2mg/Ni(110) (Kuhlenbeck et al., 1986). In this system the coverage is $\Theta = 1$, and the lateral stress is particularly demanding. Figure 10.29 shows a model of this structure. The interesting structural feature is the glide plane along the densely packed rows ($(1\bar{1}0)$ azimuth) of the Ni(110) surface. The unit cell of this overlayer contains two CO molecules, which leads to peculiar consequences for the ARUP-spectra. Figure 10.30 shows the full band structure of the system including the unoccupied part. The occupied part was determined by measuring the binding energies of the CO induced features as a function of the electron emission angle along two azimuths with respect to the Ni(110) substrate, i.e., the $[1\bar{1}0]$ and the [001] directions. Together with the experimental data (Kuhlenbeck et al., 1986, 1989; Schneider et al., 1990; Memmel et al., 1989; Rangelov

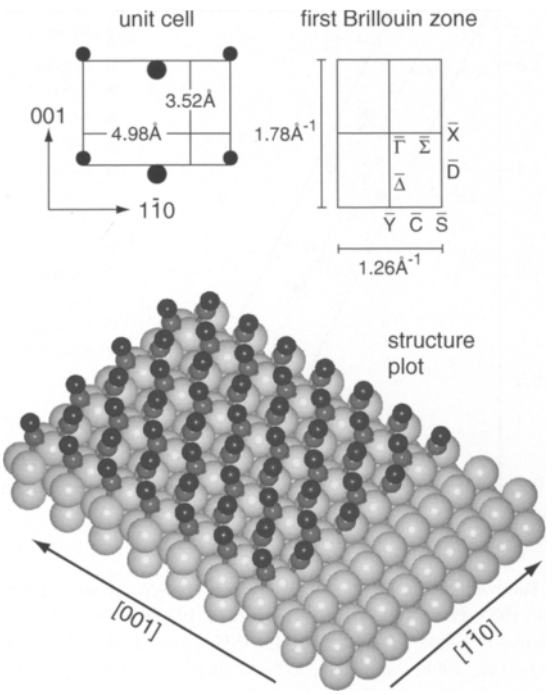


Fig. 10.29. Schematic representation of the CO(2 × 1)p2mg/Ni(110) structure, the unit cell and the surface Brillouin zone (Kuhlenbeck et al., 1986).

et al., 1991) we have plotted the result of a band structure calculation where the position of the lowest occupied $4\sigma^+$-valence orbital (see below) has been shifted to agree with experiments and the tilt angle has been used as a parameter. The best fit resulted for a tilt angle of 17° with respect to the surface normal. On the right hand side of the collected dispersion data we show a set of photoelectron spectra at the $\Gamma$ point (normal emission). Clearly, the number of outer valence features which are bound at binding energies above 6 eV is larger than four, which would be the maximum number of features for a single molecule within the unit cell ($5\sigma$, $4\sigma$ and two $1\pi$ components). This indicates that the unit cell contains more than one molecule (Kuhlenbeck et al., 1986). The region of the energetically well separated $4\sigma$-emissions shows a splitting into two features consistent with two molecules in the unit cell.

For a description of the band structure the wave functions of a single molecule are therefore not appropriate. However, linear combinations

$$\chi_1 = c_1|\mathrm{CO}^1\rangle + c_2|\mathrm{CO}^2\rangle \quad \text{(symmetric)},$$
$$\chi_2 = c_1|\mathrm{CO}^1\rangle - c_2|\mathrm{CO}^2\rangle \quad \text{(antisymmetric)} \tag{10.4}$$

of molecular CO wave functions located at the positions of the two molecules within the unit cell allow one to construct two-dimensional adlayer wave functions that transform

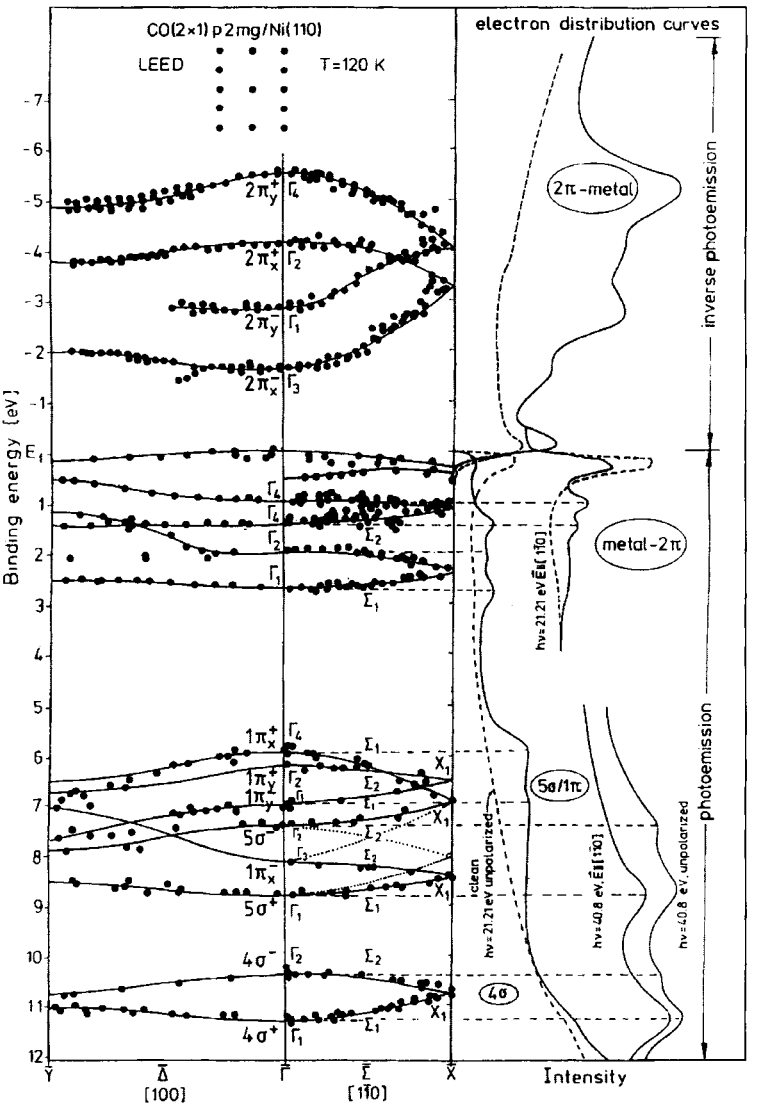


Fig. 10.30. Occupied and unoccupied band structure for CO(2 × 1)p2mg/Ni(110). In the right panel some typical electron distribution curves are shown (Kuhlenbeck et al., 1986; Memmel et al., 1989; Rangelov et al., 1991).

according to p2mg symmetry and which give rise to bands (E vs. $\mathbf{k}_\parallel$) easy to label by their irreducible representations at the points of high symmetry. Figure 10.31 schematically shows two-dimensional adlayer wave functions at Γ, X, and Y based on $\sigma$ molecular wave functions. The unit cell is indicated, $\chi_1$ and $\chi_2$ are plotted. Consider Fig. 10.31a to represent the $4\sigma$-orbitals of CO. Unlike the case of one molecule per unit cell leading to a single band per non-degenerate molecular orbital (MO) in the Brillouin zone, we have two

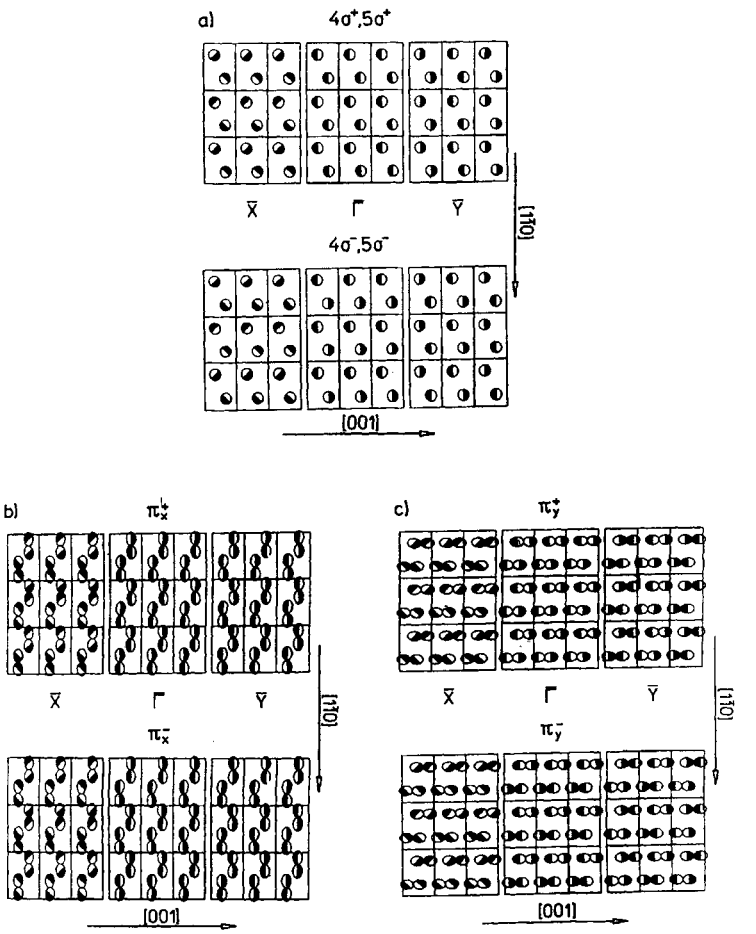


Fig. 10.31. Schematic representation of the $\sigma$(a) and $\pi$(b, c) derived wave functions of the CO overlayer for different **k**-points. Each orbital lobe is half hatched. The direction of the line separating open and hatched part of the lobe marks the phase of the respective molecular wave function. In the zero phase situation the direction of the separating line points along the [1$\bar{1}$0] direction and the left part of the lobe is hatched.

bands in the present case, namely, one associated with the symmetric, the other one with the antisymmetric combination of molecular orbitals. In the band structure the bands are labelled '+' and '−', respectively. At Γ the splitting of the two $4\sigma$ derived bands is about 0.85 eV, caused by the strong lateral interaction. In the symmetric combination all MOs have the same phase, i.e., the two-dimensional wave function is strongly bonding which leads to a stabilization on a binding energy scale compared to a laterally non-interacting adsorbate. The antisymmetric combination at Γ is antibonding with respect to the direction of the glide plane [1$\bar{1}$0], but bonding with respect to the [001] direction. The interaction is stronger along the close packed [1$\bar{1}$0] direction leading to a net destabilization on a binding energy scale. If we follow the bands in $\mathbf{k}_{\parallel}$-space along Γ–X (the Σ direction),

the '+' band increases, while the '−' band decreases in energy until they are degenerate at X. Figure 10.31a allows us to visualize the situation: at X the phase between adjacent unit cells changes by 180° along [1$\bar{1}$0]. Consequently, for the symmetric combination this yields a two-dimensional wave function with phase changes only between rows in [001] direction. For the antisymmetric combination a similar wave function results is evident from Fig. 10.31a. In fact, these wave functions are degenerate. As was shown by Hund (1936) the bands have to be degenerate on the entire line X–S, which is perpendicular the glide plane (see Fig. 10.29), i.e., the line perpendicular to the glide plane. Clearly, the wave function plots indicate that the energy position of the bands at X has to be intermediate between the energies at Γ since there is increasing antibonding character for the symmetric combination while there is loss of antibonding character for the asymmetric combination. At Y the wave functions and thus the bands are non-degenerate energetically, since the spacial separation between sites of equal phase is larger for the '−' than for the '+' band. The splitting at Y is 0.3 eV, which should be compared with 0.85 eV at Γ. In order to specify the character of the wave functions within the band structure plot the irreducible representations of the wave functions are indicated.

Next we consider the region of the band structure of occupied levels at lower binding energies, namely, the region of the $5\sigma$ and $1\pi$ molecular orbitals. Due to the low symmetry of the overlayer $5\sigma$ and $1\pi$ derived adlayer bands are allowed to hybridize. The solid lines in this region (Fig. 10.30) refer to the bands after hybridization has been taken into account, while the dotted lines refer to the non-hybridized bands. We start the discussion by first considering the band dispersion neglecting hybridization. Clearly the dispersion of the nonhybridized $5\sigma$-bands should be similar to the $4\sigma$-dispersion. In fact, this is our result. The splittings calculated for various symmetry points, however, differ considerably. This is expected since the spatial extent of the $5\sigma$ molecular orbitals is different form the $4\sigma$ molecular orbitals. This aspect has been discussed in detail by Greuter et al. (Freund and Neumann, 1988). Compared with the $4\sigma$-bands the $5\sigma$-bands show a splitting of 1.35 eV at Γ and 0.63 eV at Y since the $5\sigma$ molecular orbitals are more diffuse than the $4\sigma$ molecular orbitals.

The dispersion associated with the nonhybridized $1\pi$ molecular orbitals is, due to their twofold degeneracy on the molecular level, slightly more complicated than the $\sigma$ band dispersions. Since the global symmetry of the adlayer is only twofold, the two $1\pi$-components cannot be degenerate and, due to the formation of symmetric and asymmetric combinations, give rise to four bands at Γ. In order to label the bands, we have chosen $x$ to denote the component in [1$\bar{1}$0], $y$ to denote the component in [001] direction. The wave functions belonging to the $x$ components are shown in Fig. 10.31b. Again, symmetric and antisymmetric phase relations are identical to those for the $\sigma$-bands shown in Fig. 10.31a. Unlike the $\sigma$-bands, however, the antibonding combination is symmetric (+) and the bonding combination is antisymmetric (−) in the $1\pi$-case. As outlined above, the + or − signs refer to phase factors within the unit cell, while bonding and antibonding refer to the interaction of the wave functions within the unit cell: an in-phase combination of two $\pi$ functions is antibonding and thus energetically destabilized, the out-of-phase combination of two $\pi$ functions is bonding and thus energetically stabilized. In other words, $\pi$ bands associated with phase factors + and − are energetically reversed with respect to the $\sigma$-bands. The splitting between + and − bands differs for the $x$ and $y$ components, in agreement with

Table 10.1
Dipole selection rules for CO(2 × 1)p2mg

| Electric field vector **E** orientation | Initial state bands | | |
|---|---|---|---|
| | Symmetry | Molecular assignment | Symmetry |
| $E_{\parallel}[1\bar{1}0]$: $z$-polarization | $\Gamma_1$ | $4\sigma^+, 5\sigma^+, 1\pi_y^-$ | $\Gamma_1$ |
| $E_{\parallel}[001]$: $y$-polarization | $\Gamma_2$ | $4\sigma^-, 5\sigma^-, 1\pi_y^+$ | $\Gamma_2$ |
| – | $\Gamma_3$ | $1\pi_x^-$ | $\Gamma_3$ |
| $E_{\parallel}[1\bar{1}0]$: $x$-polarization | $\Gamma_4$ | $1\pi_x^+$ | $\Gamma_4$ |

expectations since the lateral interactions along $[1\bar{1}0]$ are much stronger than along [001]. The magnitudes of the splitting are 2.1 eV and 0.78 eV at $\Gamma$, respectively. At $\Gamma$, $1\pi_x^+$, $1\pi_x^-$, $1\pi_y^+$ and $1\pi_y^-$ all belong to different irreducible representations. At X the bands degenerate pairwise for the same reason as the $\sigma$-bands. The bonding character of the wave functions at X is clearly higher for the $x$-component than for the $y$-component as is evident from Fig. 10.31b and Fig. 10.31c. Along the $\Sigma$ line there are only two irreducible representations. The bands are labelled according to Litvin's compatibility relations (Litvin, 1983, 1984). The $1\pi_y^-$ band has the same symmetry as the $1\pi_x^+$ band along $\Sigma$, leading to a very small gap around the crossing point. The gap is very small since the interaction is "weak" for topological reasons. Perpendicular to the $\Sigma$ direction, namely in the $\Delta$ direction, the $\pi$-bands, like the $\sigma$-bands, are not degenerate at the zone boundary. Figure 10.31c shows on the right hand side that the $1\pi_y^-$ band is, in addition to its bonding character in [001], antibonding along $[1\bar{1}0]$. The $1\pi_y^+$-band is bonding in both directions.

$\sigma/\pi$-hybridization can only occur if the bands of $\sigma$ and $\pi$ parentage transform according to the same irreducible representations. Along $\Gamma$–X, i.e., in the $\Sigma$-direction, the $1\pi_x^-$-band hybridizes with the $5\sigma^-$-band, shifting the energetic position of the point of degeneracy. Note that the degeneracy at X is not lifted by $\sigma/\pi$-hybridization. However, it is evident that the hybridized band structure is considerably different from the nonhybridized one. At $\Gamma$, for instance, the $\sigma/\pi$-hybridization leads to reversal of the $1\pi_x^-$ and $5\sigma^-$ binding energies.

So far we have discussed the development of the band structure without explicit reference to the experimental observations. The basis for an experimental analysis is Table 10.1 where the dipole selection rules for the p2mg system at $\Gamma$ are summarized. At $\Gamma$ the symmetry is $C_{2v}$ and the symmetry selection rules shown in Table 10.1 may be applied. Because the final state of the electron must be totally symmetric ($\Gamma_1$) there is evidence for a $\Gamma_2$- and a $\Gamma_1$-state in the range of the $4\sigma$-ionization if we compare the spectra recorded with polarized (electric field vector **E** parallel to the $[1\bar{1}0]$ direction) and unpolarized light in Fig. 10.30. The symmetry restrictions for the $4\sigma^-$- and $4\sigma^+$-bands hold in the same way for the $5\sigma^-$- and $5\sigma^+$-band. The comparison of the same two spectra supports this conclusion. If the photon energy is smaller, i.e., around 20 eV the cross section of the $\pi$ derived components becomes more prominent. The $\pi$ derived $\Gamma_4$-band at lowest binding energy can be well used to demonstrate that the symmetry of the ordered overlayer is p2mg and not p1g1.

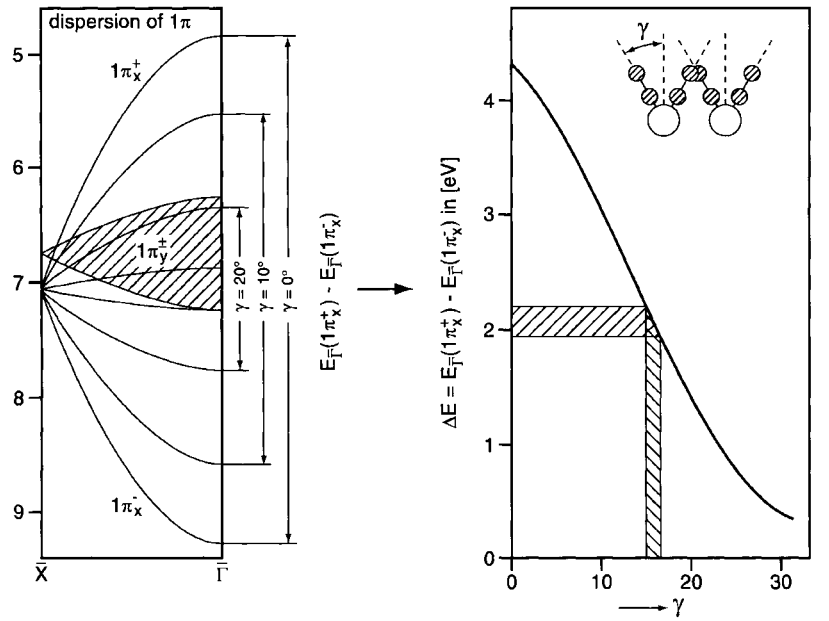


Fig. 10.32. Calculated $1\pi$-bandwidths as a function of the tilt angle of the molecular axis ($\gamma$) with respect to the surface normal. In the right hand panel the observed splitting is used to deduce a tilt angle (Kuhlenbeck et al., 1986).

The splitting of the $1\pi$-levels has been discussed above and the experimental data basically corroborate the conclusions as is evident from Fig. 10.30. The strong splitting of the $1\pi_x$ components can be used – and has been used – to estimate the CO tilt angle of the CO molecules. The procedure can be visualized with the help of Fig. 10.32. In the left panel we show the dispersion of the $1\pi_y$- and the $1\pi_x$-bands as a function of the tilt angle $\gamma$. The $1\pi_y$-bands disperse within the hatched area for the considered angular variations. We use the $1\pi_x$-bands as an example because for these bands the angular variations are largest and the fitting procedure is rather precise. For $\gamma = 0°$ the splitting is calculated to be $\approx$4 eV between the bands belonging to the bonding and the antibonding combination. Note that for $\gamma = 0°$ the glide plane disappears and we reach a p(1 × 1) structure. In this case the unit cell contains only one molecule, and therefore, instead of having a splitting at $\Gamma$ into two bands, the size of the Brillouin zone doubles. However, for comparison we have folded back the bands into a reduced zone, identical to the one of the p2mg structure. Clearly, as soon as we allow the CO molecules to avoid each other by tilting the splitting decreases dramatically, until we reach agreement with the experimentally observed splitting of 2.2 eV at $\gamma = (17 \pm 2)°$. This is graphically shown in the panel on the right-hand side of Fig. 10.32. This strong variation of the $1\pi_x$-splitting is a consequence of the strong variation of intermolecular overlap as a function of $\gamma$. The splitting of the $1\pi$-levels in the range of occupied orbitals should be compared with the corresponding splitting of the $2\pi$-orbitals in the unoccupied range show in Fig. 10.30. The experimental results have been taken from

inverse photoemission studies by (Memmel et al., 1989; Rangelov et al., 1991). The observed splitting for both the $2\pi_x$ (3.8 eV) and the $2\pi_y$ (1.2 eV) components is considerably larger than observed for the $1\pi$-levels. This may be caused again by substrate mediated interaction due to $2\pi$-backdonation but an additional role may be played by the $2\pi$-wave functions themselves which are expected to be considerably more diffuse as compared with the $1\pi$-levels. This point can be supported through a very nice series of experiments performed by Bertel and coworkers (Rangelov et al., 1991) on three isomorphic structures, i.e., CO(2 × 1)p2mg/Ni(110), CO(2 × 1)p2mg/Pd(110), and CO(2 × 1)p2mg/Pt(110) where the intermolecular CO spacing varies and also the substrate mediated interaction changes. The comparison between the Ni and the Pd systems reveal that the splitting in the $2\pi$ manifold is slightly smaller for Pd due to the increase in CO–CO separation. For Pt the situation is more complicated. Here it has been shown that the metal molecule interaction has a stronger $5\sigma$ donation component than for Pd and Ni (Tüshaus et al., 1987). This in turn would lead to the shift of the $5\sigma$-metal antibonding component in the unoccupied region while for Ni and Pd both the bonding and antibonding combinations are occupied.

A direct observation of the substrate mediated interaction is possible for the system CO p2mg on Ni(110) by following the CO induced features in the region of the metal band structure, i.e., between the Fermi energy and a binding energy of 3 eV (Kuhlenbeck et al., 1989). In this energy range Fig. 10.30 shows bands which exhibit dispersions of up to 0.5–1.0 eV indicating a substantial contribution via this type of interaction. A way to investigate the substrate mediated intermolecular interactions may be the analysis of the dispersion of the above mentioned molecule induced changes in the region of the metal-substrate ionizations (see solid lines in the region of the projected band structure in Fig. 10.20). Such an analysis has been carried out for the CO(2 × 1)p2mg/Ni(110) system [110]. Before the dispersions are analysed we have to ensure that the bands are really localized at the surface of the solid, i.e., the CO$2\pi$–Ni3d features should not exhibit a dispersion as a function of photon energy in normal emission, which is the usually applied criterion for a surface state. Once this has been done, we can determine the dispersion via off normal emission and vary the photon energy such that we choose an appropriate cross section of the feature under consideration. The result of such a very tedious analysis has been carried out by Kuhlenbeck et al. (1987, 1989) and is shown in Fig. 10.33 for two directions of the surface Brillouin zone. There are two important qualitative features of the dispersion curves. First, there are no band gaps at the zone boundary X, which – as Hund pointed out in 1936 (Hund, 1936) – is a consequence of the glide plane in the $\Sigma$ direction. Secondly, the lower well resolved band can be fitted closely with a tight binding type curve (full lines). A detailed discussion, for which we refer to the original literature (Kuhlenbeck et al., 1987), reveals a rather clear picture of the nature of the CO$2\pi$–Ni3d interaction. For the case Ni(110) this interaction creates new surface resonances positioned from 1 to 2.7 eV below the Fermi energy with the appropriate symmetry and intensity. We have not found direct indications of the $5\sigma$-metal antibonding combination, although we also cannot exclude its existence in this energy range. This picture seems to be quite incompatible with a model where the CO$2\pi$ orbital close to the Fermi level is resonantly broadened by interaction with the metal. The tails of this broadened band would extend below the Fermi energy and therefore create a degree of $2\pi$ occupancy. In the "surface molecule" model, on the other hand we have a $2\pi$ level, the width of which is not very important, far above the Fermi energy as

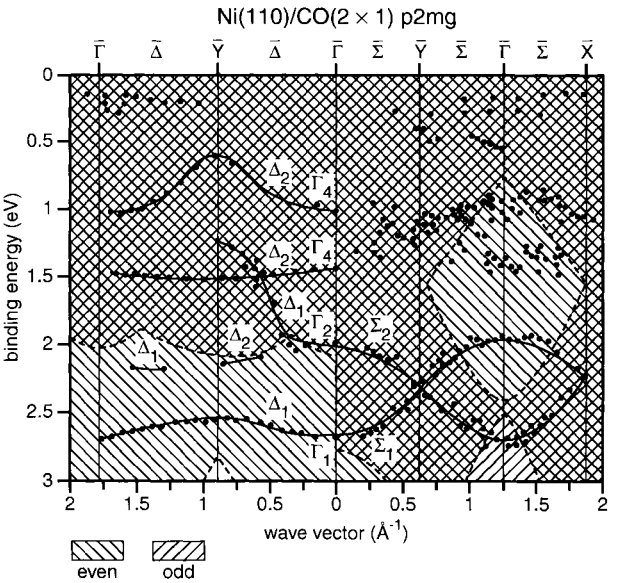


Fig. 10.33. Measured dispersions of the $2\pi$-d wave functions plotted on top of the calculated bulk band structure projected onto the [110] surface. The projection has been done separately for even and odd bands (Kuhlenbeck et al., 1989).

the molecule approaches the surface. This level (or the symmetry adapted combination of levels) mixes into the metal levels because there is a finite overlap between them. Since the overlap is a matter of symmetry it determines which of the metal bands will couple with the CO$2\pi$. The question which of the $2\pi$-induced bands are actually observed is then determined by the strength of the CO$2\pi$-metal coupling, and will depend upon the nature of the metal, the crystal face, and the structure of the CO layer.

The examples for dispersions in quasi two-dimensional systems were chosen so far from the many examples of strongly chemisorbed systems. One question is what happens to the dispersions when weakly chemisorbed or physisorbed systems are considered. The latter case is easy: Fig. 10.34 shows the dispersions measured via ARUPS for the system CO/Ag(111) (Schmeisser et al., 1985). We know from the previous section that in this system the CO molecules are oriented with their axis parallel to the surface. It is known from LEED studies that CO molecules physisorbed on graphite form herring-bone structures (Diehl and Fain, 1983) as shown in the inset in Fig. 10.34. Such structures again belong to nonsymmorphic space groups with two molecules in the unit cell. This is the reason why the molecular ionization bands appear as split in two components, i.e., a bonding and an antibonding combination at $\Gamma$. From symmetry considerations it is clear that these two bands are degenerate at the zone boundary. The splitting is larger for the $\sigma$ levels than for the $\pi$ level, which is not unreasonable on the basis of intermolecular overlap considerations. A particularly interesting observation has been made for this system if the temperature is increased. These physisorbed overlayers are known to undergo order–disorder transitions (Diehl and Fain, 1983). The CO molecules are then no longer locked into a herring-bone structure but rotate freely on their site. This destroys the nonsymmor-

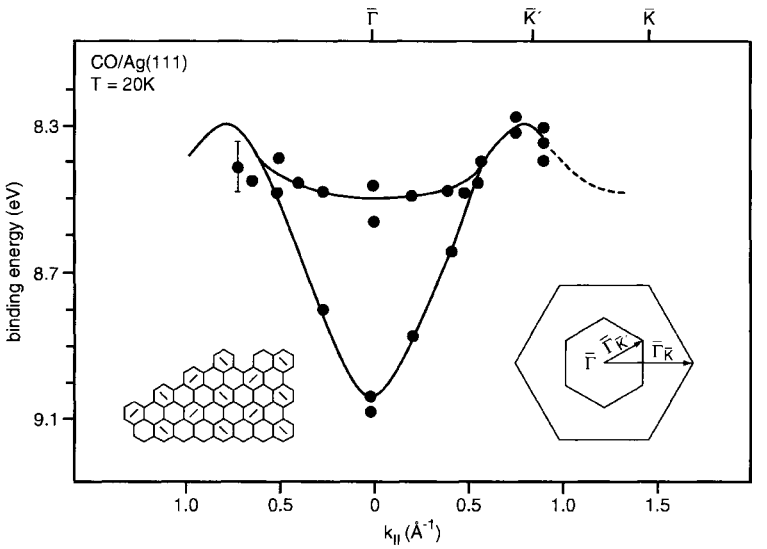


Fig. 10.34. Measured dispersion the $5\sigma$ CO levels of CO/Ag(111) (Schmeisser et al., 1985).

phic structure and, concomitantly, the splitting of the $\sigma$ levels disappears. CO/Ag(111) is a system where ARUPS can be used to study phase transitions in quasi-two-dimensional systems (Schmeisser et al., 1985).

In the case of weakly chemisorbed systems the situation is slightly more complicated. The reason for this complication is the shake-up structure identified in the previous section (Freund et al., 1983). Figure 10.35 shows the dispersions for the system $(\sqrt{7} \times \sqrt{7})$CO/Cu(111), for which Fig. 10.2 showed an electron distribution curve (Freund et al., 1983). In this case the CO molecules are oriented perpendicular to the surface as in the case of the strongly chemisorbed systems. While the integrated $5\sigma/1\pi$ dispersion is compatible with other CO overlayer systems, the $4\sigma$ dispersion is considerably smaller than expected for the given intermolecular separation. The observed value is represented in Fig. 10.28 by the dashed circle. The shake-up which is – as noted above – associated with the $4\sigma$ ionization shows almost no dispersion, but a slight variation in relative intensity with respect to the $4\sigma$ ionization. There are sum rules (Hedin, 1979; Lundquist, 1967, 1968, 1969) relating intensity and ionization energy of the peaks in the observed spectral function with the quasi-particle energy. These sum rules are of the type

$$\varepsilon_k^{\mathrm{HF}} = \int_{-\infty}^{\infty} \omega A(\omega, k)\, \mathrm{d}\omega. \tag{10.5}$$

We can apply this sum rule to the observed data and regain a dispersion shown as the open circles in Fig. 10.35. This renormalized $4\sigma$ band widths can now be favourably compared with the values measured for the strongly chemisorbed systems. This shows that it is the ionization process that introduces the deviations in the observed band widths and not a different intermolecular interaction potential in this case.

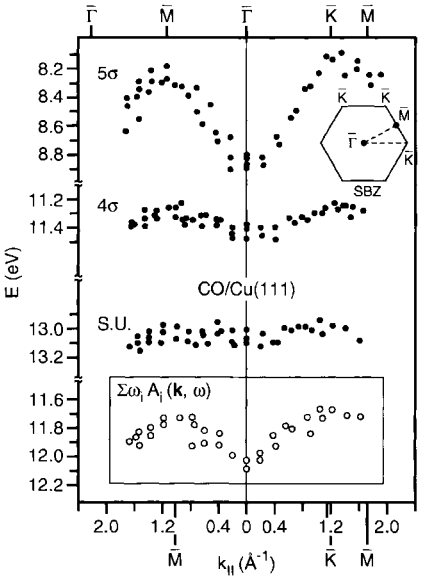


Fig. 10.35. Measured dispersion of the CO induced levels of the system CO/Cu(111). The renormalized dispersion of the $4\sigma$-levels is plotted as open circles (Freund et al., 1983).

## 10.6. Nitrogen adsorption

$N_2$ on Fe(111) has been the model system to investigate the mechanism of ammonia synthesis (Ertl, 1983). It is known that $N_2$ dissociation is the rate limiting step, and that there exist molecular precursor states for dissociation where $N_2$ has been presumed to be side-on bonded to the iron surface (Grunze et al., 1984). Via ARUPS a strongly inclined $N_2$ species was identified (Freund et al., 1987) in addition to a vertically bound $N_2$ species which only exists at lower temperature. Figure 10.10 shows a set of angle resolved spectra at low temperature (vertically bound $N_2$) and higher ($T = 110$ K) temperature ($N_2$ bond inclined). Figure 10.36 reveals the $\sigma$-shape resonance in normal emission for $z$-polarized light at $T < 77$ K. Figure 10.36 shows a $\sigma$ resonance, but only in off-normal emission for $s$-polarized light (compare left and right part of this figure) at $T = 110$ K, supporting the proposed inclined geometry in the second case.

Very similar observations have been made in a very detailed study by Shinn (1990) on $N_2$ bonding on Cr(110). Figure 10.37 shows a correlation of the outer valence ionizations of $N_2$ adsorbates including those where the $N_2$ molecule is bound "end-on" to the metal (b) and two where the molecule is $\pi$-bonded "side-on" to the metal surface. There are only slight differences between the two groups as compared with the gas phase and physisorbates (a). The reason for this similarity is still not quite clear. One might expect some major differences, in particular the $1\pi_u$ level should be split. However, there is no convincing experimental evidence for this. One reason may be that the mixing of the levels, especially in the highly asymmetric bonding sites on the Fe(111) surface, is so strong that a definitive differentiation between the two $\sigma$ levels and the $1\pi_u$ component with $\sigma$

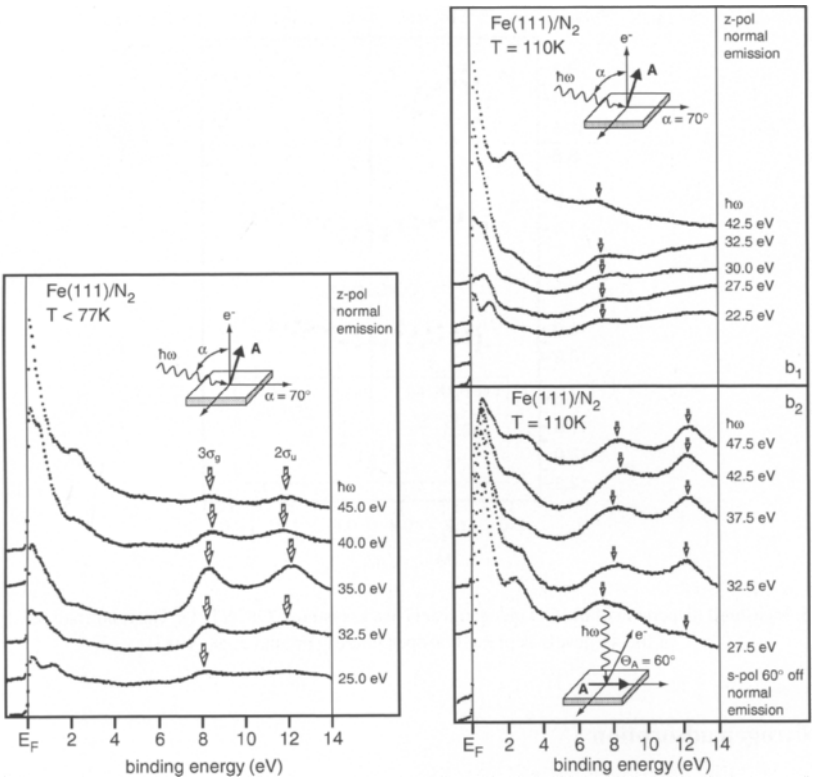


Fig. 10.36. ARUPS-spectra of $N_2$/Fe(111) for grazing light incidence and normal emission (left panel), and s-polarization (near normal incidence, right panel) and two electron emission angles: ($b_1$) normal emission; ($b_2$) off-normal (60°) emission. For each measurement geometry typical spectra at different photon energies are plotted (Freund et al., 1987).

symmetry is not possible. Another interesting feature can be demonstrated on the basis of the present results. Both, the $3\sigma_g$ as well as the $2\sigma_u$ state exhibit the shape resonance behaviour, while in the gas phase the $\sigma_g$ resonance is symmetry forbidden. The reason is very simple: the inversion symmetry of the homonuclear $N_2$ molecule is broken upon adsorption which makes the final resonance state accessible to both $\sigma$ states. This was demonstrated earlier by Horn et al. (1982) for the system $N_2$/Ni(110). In contrast to the case $N_2$/Fe(111) where $N_2$ dissociates at low temperature ($T > 140$ K), $N_2$-metal coupling is usually rather weak (Heskett et al., 1985a; Horn et al., 1982; Umbach et al., 1980; Dowben et al., 1984; Breitschafter et al., 1986). This leads to the existence of rather intense shake-up structure as noted for several $N_2$-transition metal systems (Heskett et al., 1985a; Horn et al., 1982; Umbach et al., 1980; Dowben et al., 1984; Breitschafter et al., 1986; Schichl et al., 1984; Messmer, 1984; Freund et al., 1985). The experimental findings are corroborated by several theoretical calculations (Heskett et al., 1985a; Horn et al., 1982; Umbach et al., 1980; Dowben et al., 1984; Breitschafter et al., 1986; Schichl et al., 1984; Messmer, 1984; Freund et al., 1985).

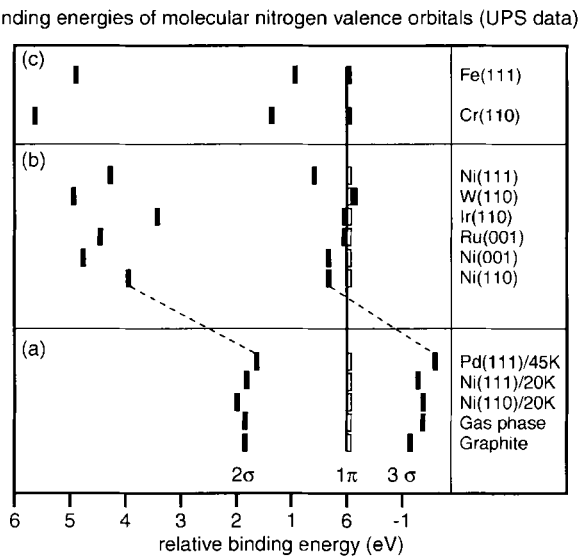


Fig. 10.37. Relative UPS molecular binding energies plotted with respect to the $N_2(1\pi_u)$ peak: (a) physisorption systems and gas phase, (b) weak chemisorption systems, and (c) strong chemisorption systems (Freund et al., 1987).

In the introduction we alluded to the question of line widths in weakly bound molecules. We shall deepen this aspect slightly at this point because Umbach and his group (Höfer et al., 1990), as well as Jacobi and coworkers (Bertolo et al., 1991) have recently presented interesting data for $N_2$ molecules adsorbed on a monoatomic Xe spacer layer on a metal surface. Figure 10.38 shows the region of the $N_2$ ionizations and indicates the pronounced vibrational structure in the $1\pi_u$ derived band. We note in passing that the splitting of the $3\sigma_g$ band in the present system is similar to observations in $N_2$ layers on graphite and CO layers on Ag, discussed above. The observed vibrational line shape of the $1\pi_u$ ionization cannot be reproduced by just convoluting the gas-phase data with the appropriate broadening function. Instead, both the vibrational progression of $N_2^+$ as well as of neutral $N_2$ had to be included, indicating that the hole life time is finite and the hole hops to another molecule in the physisorbed layer. From the fits a life time may be estimated to $(2\text{–}3)\times 10^{-15}$ s. The hopping of the hole is most effective for those levels between which the overlap is largest. This can be experimentally shown by taking the spectra as a function of incidence angle. $N_2$ is oriented with its axis parallel to the surface plane and thus the $1\pi_u$ splits into components parallel and perpendicular to the surface. At normal light incidence the $1\pi_u$ component parallel to the surface may lead to normally emitted electrons. At growing light incidence angle the perpendicular component leads to normal emission. Due to the larger overlap of the $1\pi_u$ component parallel to the surface the hopping is more effective for those levels. Therefore at near normal incidence the neutral contribution to the spectrum increases considerably. This is demonstrated by Fig. 10.38.

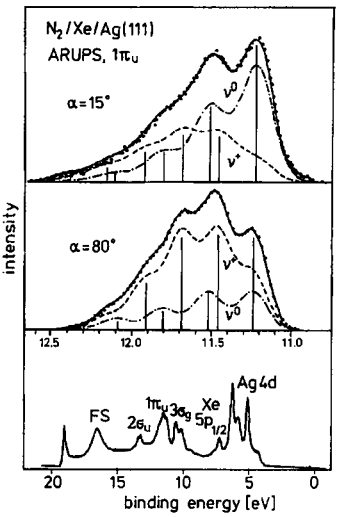


Fig. 10.38. Photoelectron spectra of $N_2$/Xe/Ag(111). At the bottom the full spectrum taken with a photon energy of 23 eV is shown. FS denotes a final state peak which appears at a fixed kinetic energy irrespective of the photon energy. It is due to the unoccupied $1\pi_g$ level. The other panels show spectra of the $1\pi_u$ state recorded in normal emission. For the spectrum at the top the light incidence angle was $\alpha = 15°$ and for the spectrum in the center it was $\alpha = 80°$ (Bertolo et al., 1991).

## 10.7. Carbondioxide adsorption

$CO_2$ has been the subject of many surface science studies (Bartos et al., 1987a, b; Freund et al., 1987; Peled and Asscher, 1987; Asscher et al., 1988; Brosseau et al., 1991; D'Evelyn et al., 1986; Walsh, 1913; Freund and Messmer, 1986; Wambach et al., 1991). Besides simple molecular physisorption also under certain circumstances transformation into a bent anionic species has been observed (Bartos et al., 1987a, b; Freund et al., 1987; Peled and Asscher, 1987; Asscher et al., 1988; Brosseau et al., 1991; D'Evelyn et al., 1986; Walsh, 1913; Freund and Messmer, 1986; Wambach et al., 1991). The latter cases are $CO_2$/Ni(110) (Bartos et al., 1987a, b), $CO_2$/Fe(111) (Freund et al., 1987), $CO_2$/Re(0001) (Peled and Asscher, 1987; Asscher et al., 1988), and $CO_2$/Pd(110) (Brosseau et al., 1991). Since the results are rather similar we will concentrate in the following on one of these systems, i.e., $CO_2$/Ni(110). A series of ARUPS spectra as a function of temperature is shown in Fig. 10.39. By comparison with the gas-phase spectrum (Turner et al., 1970) one finds that at $T = 80$ K $CO_2$ is molecularly adsorbed with out significant changes of the electronic structure. Angular-dependent measurements have shown that $CO_2$ adsorbs in a lying down geometry at this temperature (Bartos et al., 1987a, b). Upon heating the intense features in the photoelectron spectrum gradually fade away until at $T = 200$ K a spectrum (e) is observed that could neither be assigned to $CO_2$ nor to CO or O (confer Fig. 10.39). Further heating leads to a dissociation of this species into CO+O as indicated by spectrum (f) so that the species leading to spectrum (e) may be viewed as a precursor for $CO_2$ dissociation. On the basis of *ab initio* calculations this species has been assigned to bent anionic $CO_2^-$

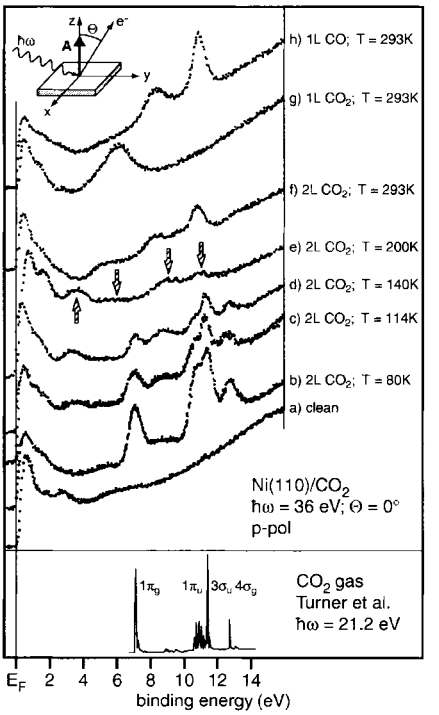


Fig. 10.39. Photoelectron spectra of a $CO_2$/Ni(110) adsorbate at various temperatures in comparison with the clean surface (a), an oxygen covered surface (g), and a CO covered surface (h). At the bottom a spectrum of $CO_2$ in the gas phase is shown (Turner et al., 1970).

which has also previously been proposed from the results of molecular-beam experiments on different metal surfaces (D'Evelyn et al., 1986). It is formed by an electron transfer from the substrate to the $CO_2$ molecule. According to the Walsh rules (Walsh, 1913) the molecular axis is no longer linear but bent, as is also the case for $NO_2$ which is isoelectronic to $CO_2^-$. The assignment of the $CO_2^-$ valence band features on the basis of *ab initio* calculations is shown in Fig. 10.40. Generally, all $CO_2$ levels shift to lower binding energy. The feature at about 3.5 eV ($6a_1$), which is not observed in the spectrum of linear $CO_2$, is due to the extra electron which is located at the carbon atom of the $CO_2^-$ anion. The respective level is unoccupied in linear $CO_2$. Angular dependent measurements indicate that the symmetry of the $CO_2^-$ anion is most likely $C_{2v}$. In this context the $CO_2^-$ molecules may bond to the substrate via the carbon atom (carbon end-down) or the oxygen atoms (carbon end-up). Due to the unpaired electron at the carbon end this species is rather reactive. Using HREELS it could be shown that the $CO_2^-$ anions readily react to form formate upon hydrogen exposure (Wambach et al., 1991). Formate differs from $CO_2^-$ only by a hydrogen atom which is bonded to the carbon atom. For steric reason it is therefore rather likely that $CO_2^-$ bonds to the substrate via the oxygen atoms since otherwise the molecule would have to turn around to form formate. This result is consistent with the behaviour of the work function which increases upon $CO_2^-$ formation.

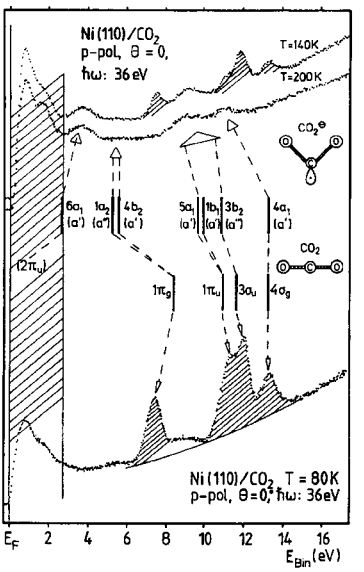


Fig. 10.40. Assignment of the photoelectron spectra of $CO_2$ at 80 K, 140 K, and 200 K and adsorbed $CO_2^-$ on the basis of *ab initio* calculations (Freund and Messmer, 1986).

The bonding of formate to Ni(110) and Cu(110) has recently been studied by several groups (Lindner et al., 1987; Hofmann and Menzel, 1987; Peyerimhoff, 1967; Woodruff et al., 1988; Puschmann et al., 1985; Madix et al., 1983; Jones et al., 1988; Jones and Richardson, 1989). Surface formate may be formed by adsorption of formic acid with subsequent annealing at temperatures above $T = 270$ K. Photoelectron spectroscopy (ARUPS) has been employed to deduce the orientation of the surface formate species. In Fig. 10.41 a set of ARUPS spectra taken from Hofmann and Menzel (1987) is shown. The spectra have been taken for different light incidence angles and polarizations, but always detecting the electrons along the surface normal. The assignment of the spectral features within the coordinate system of an isolated adsorbate molecule is indicated in the figure. Assuming a $C_{2v}$ geometry of the adsorbate complex the dipole operator transforms according to the irreducible representations b1, b2 and a1 of the adsorbate/substrate complex for $x$, $y$ and $z$ polarized light, respectively. For a light incidence angle of 65° with respect to the surface normal the $z$-component of the light is stronger than for 20°. Therefore orbitals with a1 symmetry are expected to emit stronger in spectra (c) and (d) than in spectra (a) and (b). By changing the azimuth of the **A**-vector of the light from $[1\bar{1}0]$ to [001] it is possible to differentiate between b1 and b2 orbitals. Orbitals with b2 symmetry should emit when the light contains a component polarized along [001] ($y$) whereas orbitals with b1 symmetry may be ionized by light polarized along $[1\bar{1}0]$ ($x$). The observed intensity variations observed in Fig. 10.41 are compatible with formate ions that are standing upright on the surface with the molecular plane oriented along the $[1\bar{1}0]$ azimuth. The same geometry has been deduced by Bradshaw and co-workers from their data (Lindner et al., 1987). This is also in agreement with the results of an X-ray absorption study by Puschmann et al.

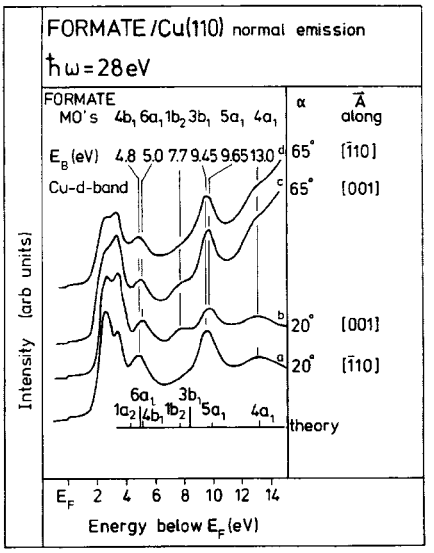


Fig. 10.41. Normal emission spectra of formate on Cu(110) taken for different polarizations of the incident light in normal emission (Hofmann and Menzel, 1987). At the bottom the assignment of the photoelectron peaks as derived from theoretical work (Peyerimhoff, 1967) is indicated.

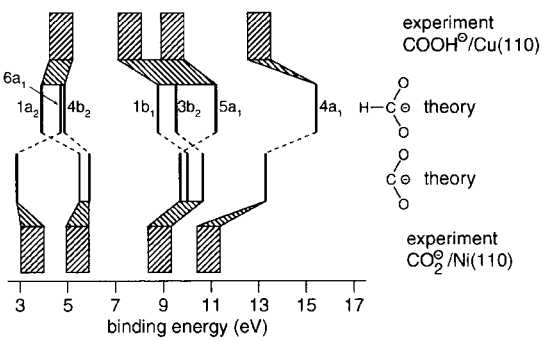


Fig. 10.42. Energy level diagram showing the correlation between the energy levels of $COOH^-$ and $CO_2^-$. The theoretical and experimental data have been taken from D'Evelyn et al. (1986); Hofmann and Menzel (1987) and Bartos et al. (1987a, b); Hofmann and Menzel (1987), respectively.

(Kimura et al., 1981) and a photoelectron diffraction study by Woodruff et al. (Woodruff et al., 1988; Puschmann et al., 1985). The influence of the adsorbate/substrate interaction on the binding energies of the valence levels indicates that for formate on Cu(110) the bonding to the substrate occurs via oxygen coordination. This is compatible with the proposed geometry of the $CO_2^-$ anion on Ni(110).

We see in Fig. 10.42 the direct comparison between the $CO_2^-$ and $CHO_2^-$ orbital energies (Bartos et al., 1987a, b; Freund et al., 1987; Peled and Asscher, 1987; Asscher et al., 1988; Brosseau et al., 1991; D'Evelyn et al., 1986; Walsh, 1913; Freund and Mess-

mer, 1986; Wambach et al., 1991; Hofmann and Menzel, 1987) and we may undertake a direct correlation of the observed ion states on the basis of the available molecular orbital calculations. The hydrogen-carbon bond formation leads to a stabilization of the totally symmetric orbitals with respect to all other orbitals. The effect is most pronounced for the low energy $4a_1$ orbital. In this case the stabilization effect may clearly be deduced from the experimental data.

## 10.8. Ethylene adsorbates (Sheppard, 1988)

Rather complete studies of the electronic structure of more complex adsorbate systems, such as chemisorbed hydrocarbons are relatively rare. Very recently, Steinrück and co-workers (Weinelt et al., 1992a, b) published an interesting study of ethylene adsorption on Ni(110) where the aspect of local and global symmetry has been discussed. We want to summarize their results in the following.

Saturation coverage of Ni(110) by $C_2H_4$ at $T = 120$ K results in a c(2 × 4) LEED pattern. This pattern represents a very dense layer containing two molecules per unit cell (i.e., $\Theta = 0.5$) as revealed through coverage determination with temperature programmed desorption (TPD) (Weinelt et al., 1992a).

The primary task, though, as in the case of the CO adsorbates, is the determination of the local symmetry of the molecule at the surface. This is done for a dilute ethylene layer ($\Theta \sim \Theta_{sat}/2$) where lateral interactions are not important. We shall see that the local geometry prevails in the dense layer. There are indications from high resolution electron energy loss spectroscopy (HREELS) that the ethylene species is di-$\sigma$-bonded as opposed to $\pi$-bonded with the C–C-axis parallel to the surface and that the site symmetry is actually lower than $C_{2v}$ (Stroscio et al., 1984). Theoretical results, however, indicate that the adsorbate bonding is quite similar in both the di-$\sigma$-bonded and the $\pi$-bonded cases, i.e., $\pi$-donation from $C_2H_4$ to the substrate is stronger as compared to $\pi$*-backdonation (Hofmann et al., 1985) from the substrate towards the $C_2H_4$ molecule.

### *10.8.1. Symmetry considerations and ethylene–substrate interaction*

Angle resolved photoemission spectra of the dilute layer are shown in Fig. 10.43 (Weinelt et al., 1992a). The photon energy of 30 eV was chosen to optimize the intensity of the adsorbate induced features. For comparison the angle integrated photoelectron spectrum of gas phase ethylene (Kimura et al., 1981) including assignment is plotted. The spectra have been aligned at the $3a_g$ and $1b_{3u}$ levels (gas phase nomenclature) as is frequently done in the literature (Weinelt et al., 1992a). The comparison reveals that the adsorbate spectrum is characteristic of a molecularly adsorbed species. It also shows that the $1b_{2u}$ ion-state is shifted by 1.1 eV to higher binding energies. This is by far the largest differential shift observed in this system. The shape of the ethylene orbitals in the gas phase is plotted in Fig. 10.44 (Jorgensen and Salem, 1974). It shows that the $1b_{2u}$ orbital is characteristic for a $\pi$-bond. The large shift indicates that the main interaction of the molecule with the surface takes place through this orbital.

The site symmetry and the orientation of the adsorbed ethylene molecules in the dilute layer can be derived from the polarization, polar angle and azimuthal dependences

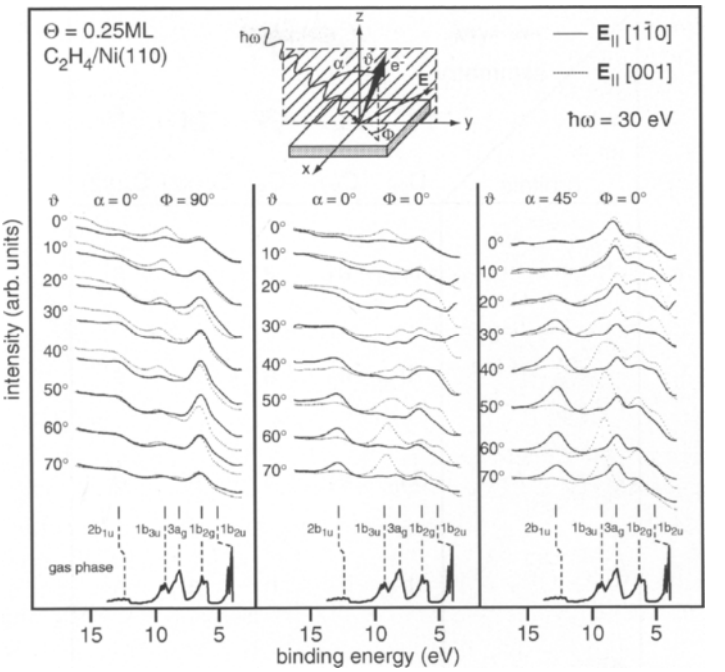


Fig. 10.43. Angle resolved electron distribution curves for a dilute $C_2H_4$ layer on Ni(110) in comparison to the gas phase (Weinelt et al., 1992a).

of the observed ionization bands, which are shown in Fig. 10.43 and are discussed below. Figure 10.44 shows how the irreducible representations of the molecular orbitals in the isolated molecule correlate with the corresponding irreducible representations when ethylene is bound to the surface in four different point group symmetries of the hypothetical sites. The real-space geometries corresponding to the site symmetries are shown in Fig. 10.44. Due to the twofold symmetry of the Ni(110) surface there are two possibilities for a $C_s$ site as indicated.

There is an important experimental detail in the experiments by Steinrück et al. (Weinelt et al., 1992a, b) that must be mentioned at this point. The electron analyzer allows to measure angular distributions of electrons by means of multichannel detection techniques including normal emission also at light incidence normal to the surface (Engelhardt et al., 1981a, b). At these particular experimental conditions two bands ($3a_g$ at 8.0 eV and $1b_{2u}$ at 5.0 eV) show no normal emission intensity for normal incidence, but rather strong normal emission for incidence at 45°, with detection in the plane of incidence. It is clear from Fig. 10.44 that this experimental observation is strong evidence for a basically flat lying geometry. Both orbitals $3a_g$ and $1b_{2u}$ belong to the totally symmetric representation in any considered point group and are only allowed in normal emission for a nonvanishing $z$-component of the electric field vector. Note that both orbitals show rather weak emission for normal incidence if the electrons are detected in a plane perpendicular to the incidence plane. This detection geometry is called "forbidden" geometry for diatomic adsorbates as

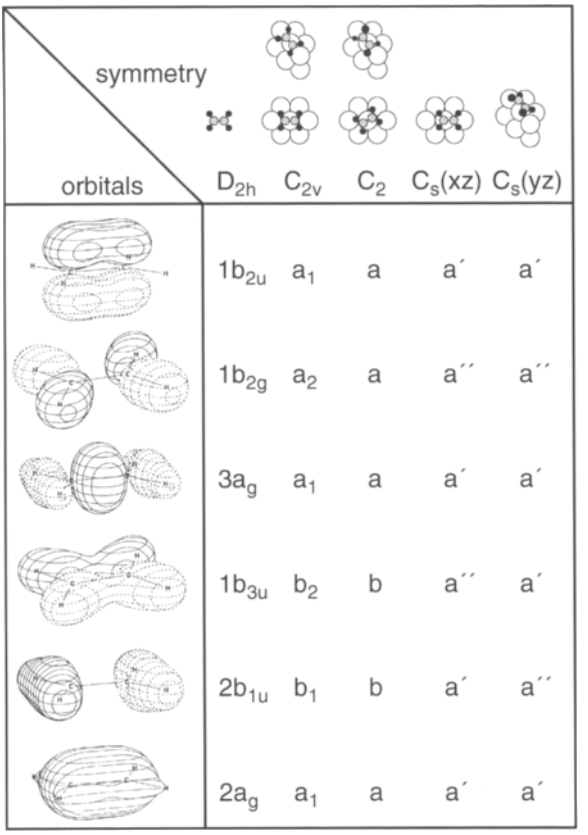


Fig. 10.44. Correlation table of ethylene orbital symmetries in the gas phase with those in varying adsorbed phases on Ni(110).

discussed above. The azimuthal orientation can be extracted from the intensity variations in the $2b_{1u}$ (12.7 eV) and $1b_{3u}$ (9.2 eV) emission (see Fig. 10.43). These states transform according to the $b_1$ and $b_2$ representations if $C_{2v}$ point group symmetry is assumed. They exhibit opposite intensity variations if the plane of light incidence is changed from [001] to [1$\bar{1}$0]. The $b_1$ state shows strong emission in the [001] plane and weak emission in the [1$\bar{1}$0] plane, while the $b_2$ is weak along [001] and strong along [1$\bar{1}$0], respectively. Figure 10.44 shows that the $b_2$ orbital has a node along the C–C axis, while the $b_1$ orbital has a node perpendicular to the C–C axis. Consequently, if the electric field vector points along the C–C axis the orbital with the node perpendicular to the C–C axis ($b_1$) should lead to normal emission intensity, and if the electric field vector is oriented perpendicular to the C–C axis the $b_2$ orbital should yield electron ejection in normal direction from Fig. 10.43 it is therefore quite obvious that the C–C axis of the $C_2H_4$ molecule is to a first approximation oriented along the [1$\bar{1}$0] azimuth. However, the intensities do not completely go to zero in the appropriate directions indicating that the alignment is not perfect. In other words, the symmetry of the adsorption complex is lower than $C_{2v}$. This is also in line with intensity

variations observed for the $1b_{2g}$ (6.2 eV) ion state which belongs to the $a_2$ representation in point group $C_{2v}$. In fact, a detailed analysis shows that the observed intensity of the $a_2$ ion state in normal emission can only be explained by either a slight tilting of the C–C axis, a lower symmetry adsorption site or a twisting of the molecule. Steinrück et al. (Weinelt et al., 1992a, b) exclude the former due to the vanishing normal emission intensity of the $3a_g(a_1)$ ion state and therefore favour a lower adsorption site, i.e., slightly displaced from a high symmetry adsorption site or twisting of the molecule as shown in Fig. 10.44.

Rösch and co-workers have analyzed the bonding via cluster calculations (Weinelt et al., 1992a, b) on the basis of the local-density functional approach. Their analysis shows that the molecule substrate interaction follows the standard description of olefin bonding towards transition metal atoms: $\pi$-donation to the metal and backdonation from the metal into the $\pi^*$-orbital of $C_2H_4$. However, the calculations do not allow discrimination between the two main adsorption modes, $\pi$ or di-$\sigma$.

### *10.8.2. Ordered ethylene overlayers*

After having discussed the local site geometry as determined via ARUPS on a dilute $C_2H_4$ layer we come back to the study of the layer at saturation coverage. Steinrück et al. (Weinelt et al., 1992a, b) showed that for the strongly laterally interacting $C_2H_4$ layer the local site is similar to the dilute layer so that we do not have to discuss the spectra in detail in this case.

From the variation of the binding energy with the emission angle, the two-dimensional band structure of the saturated ethylene layer can be evaluated. The two-dimensional band structure has been determined along the two high-symmetry directions of the substrate, i.e., $[1\bar{1}0]$ and [001]. Note that these directions are not necessarily mirror planes of the adsorbate Brillouin zone. The LEED Brillouin zone is shown in Fig. 10.45. The structure of the layer derived from this pattern is shown in the same figure. The molecules are put in the proposed asymmetric adsorption sites and are aligned along the $[1\bar{1}0]$ direction with 5 Å separation. Molecules in neighbouring rows are shifted with respect to each other by 1.25 Å. This results in translational equivalence at every fourth row, i.e., a $c(2 \times 4)$ structure. The ARUPS measurements combined with molecular dynamics simulations reveal that the active intermolecular $C_2H_4$ potentials lead to a band structure which is not directly compatible with the Brillouin zone derived from the LEED pattern (Weinelt et al., 1992a, b). The plot of the data $E_B$ vs. $\mathbf{k}_{\|}$ is shown in Fig. 10.46. Some high symmetry points in the extended Brillouin zone scheme deduced from the LEED pattern are indicated at the top of Fig. 10.46, and it is quite obvious that the observed band dispersions do not follow the true Brillouin zone symmetry. The observed band structure may be explained if the interaction of the molecule with the substrate is neglected for all but the $\pi$ $(1b_{2u})$ ion state and the molecules are displaced with respect to each other in neighbouring rows as indicated in the middle panel of Fig. 10.47. In other words the periodic potential leading to the fourfold repeat unit is not important. The molecular dynamics simulations energetically favour this interpretation. It is known from other hydrocarbons that the intermolecular interaction is dominated by the repulsive hydrogen–hydrogen interactions which are minimized in the geometry shown in the middle panel of Fig. 10.47 with respect to the other two limiting cases (left and right panels in Fig. 10.47). Without consideration of the substrate

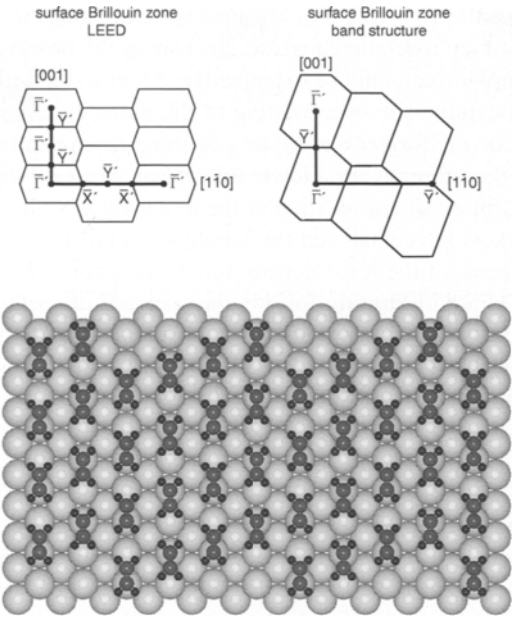


Fig. 10.45. Brillouin zones of the c(4 × 2)$C_2H_4$/Ni(111) system as observed with LEED (on the left) and as determined via band structure measurements (on the right). A real space model is included (Weinelt et al., 1992a, b).

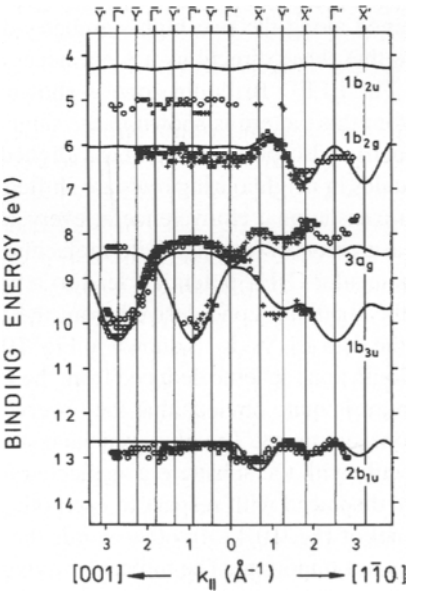


Fig. 10.46. Measured band structure for the system c(4 × 2)$C_2H_4$/Ni(111). Points of high symmetry according to the LEED Brillouin zone (top) and the band structure Brillouin zone (bottom) are indicated (Weinelt et al., 1992a, b).

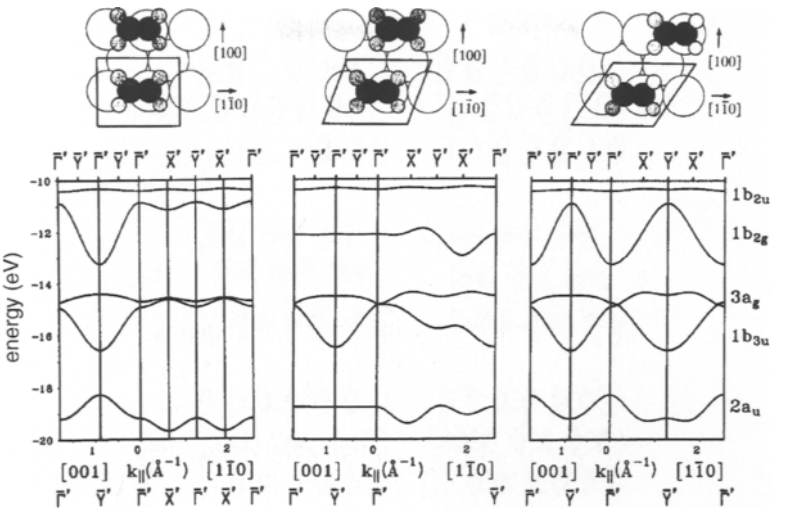


Fig. 10.47. Calculated band structures for three different lateral arrangements of $C_2H_4$ molecules (Weinelt et al., 1992a, b).

the adsorbate unit cell only contains a single molecule. The unit cell in reciprocal space is shown in Fig. 10.45. The experimentally chosen [001] and [1$\bar{1}$0] directions of the substrate are included in the figure. They do not represent high symmetry directions in the adsorbate mesh, but rather the paths from $\Gamma$ to Y along [1$\bar{1}$0]. The calculated band structure along these paths for the energetically favoured arrangement is depicted in Fig. 10.47 middle panel and may be directly compared with the calculated band structures for other geometries. If we now compare the calculated band structure with the measured data, as done in Fig. 10.46, we find very good agreement for four out of five ion states. The only noticeable exception is the $b_{2u}$ ion state which couples the ethylene molecule to the substrate. It is obvious that none of the other considered geometries (left and right panels) would yield a band structure that agrees with experiment anywhere near to this one. The dispersions observed can be explained on the basis of nearest neighbour interactions. Let us consider for simplicity the [001] direction. The highest binding energy ion state has $b_{1u}$ symmetry. The molecular wave function can be taken from Fig. 10.44. For a two-dimensional array of molecules (Fig. 10.48a) the relative phases lead to a mainly nonbonding wave function at $\Gamma$. If the relative phases of the molecule rows change at Y, the nonbonding character is not changed. Consequently, there is no dispersion of this orbital along the [001] direction. The two-dimensional wave function derived from the $1b_{3u}$ orbital as shown in Fig. 10.48b is strongly antibonding at $\Gamma$. Upon going to the zone boundary along [001] the wave function becomes strongly bonding, therefore leading to strong downward dispersions. In the case of the $3a_g$ derived wave function (see Fig. 10.48c), it is essentially nonbonding or weakly bonding at $\Gamma$. At Y it remains basically nonbonding or weakly antibonding. The $1b_{2g}$ orbital leads to a two-dimensional wave function as depicted in Fig. 10.48d. The overall character is nonbonding at $\Gamma$ and it remains nonbonding at Y. We do not expect any strong dispersion for this orbital. The $b_{2u}$ orbital couples to the substrate and thus we

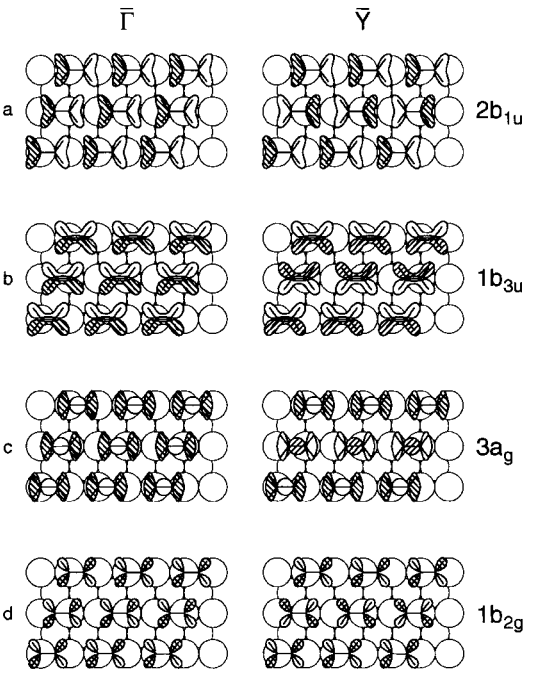


Fig. 10.48. Schematic two-dimensional wave functions for the ethylene overlayer for the center (left) and the border (right) of the Brillouin zone: (a) $2b_{1u}$, (b) $1b_{3u}$, (c) $3a_g$, (d) $1b_{2g}$.

cannot expect correspondence to the simple band structure calculation on an unsupported layer. Similar arguments hold for the other directions but they are slightly more involved because the $[1\bar{1}0]$ direction is not a high symmetry direction within the adsorbate structure.

Summarizing this section it has been demonstrated that a close packed ethylene overlayer exhibits a pronounced band structure which is completely determined by nearest neighbour interactions. The overall structure documented in the band structure is determined via ARUPS. Calculations on a free unsupported ethylene layer completely account for the observations. It should be noted that independent of the packing of the molecules, $C_2H_4$ occupies almost certainly a nonsymmetric surface site and interacts with the surface through its $\pi$-electrons. The band derived from the $\pi$-electron level does not follow the calculated band structure. It behaves like a localized state created via interaction with the substrate. The interaction with the substrate is documented predominantly in a more pronounced differential binding energy shift of this ion state.

## 10.9. Benzene adsorbates

Even more complex systems which nevertheless have been extensively studied during recent years are the various benzene adsorbates. Out of the many investigations performed so far (see, e.g., Table 10.2, Steinrück et al., 1989; Bertolini et al., 1977; Huber et al., 1991a, b; Ramsey et al., 1991; Jakob and Menzel, 1988; Bertel et al., 1986; Chiang et al., 1988;

Table 10.2
Ordered benzene overlayers on metal substrates

| Substrate | Structure | $\Theta$ (ML) | References |
|---|---|---|---|
| Ni(111) | $(\sqrt{7} \times \sqrt{7})$R19.1° | 0.143 | Steinrück et al. (1989)<br>Huber et al. (1991b) |
| Ni(100) | c(4 × 4) | 0.125 | Bertolini et al. (1977) |
| Ni(110) | c(4 × 2) | 0.250 | Huber et al. (1991a)<br>Ramsey et al. (1991) |
| Ru(0001) | $(\sqrt{7} \times \sqrt{7})$R19.1° | 0.143 | Jakob and Menzel (1988) |
| | $(2\sqrt{3} \times 2\sqrt{3})$R30° | 0.083 | Jakob and Menzel (1988) |
| Rh(111) | $(2\sqrt{3} \times \sqrt{3})$rect | 0.166 | Bertel et al. (1986)<br>Chiang et al. (1988)<br>Markert and Wandelt (1985)<br>Mate et al. (1986, 1988) |
| | $(\sqrt{19} \times \sqrt{19})$23.4° | 0.159 | Neuber et al. (1991)<br>Neuber (1992) |
| | $(\sqrt{7} \times \sqrt{7})$R19.1° | 0.143 | Koel et al. (1984) |
| | $(2\sqrt{3} \times 2\sqrt{3})$R30° | 0.083 | Uhlenbrock (private communication) |
| Pd(110) | c(4 × 2) | 0.250 | Netzer (1990) |
| Pd(100) | c(4 × 4) | 0.125 | Hofmann et al. (1981) |
| Ag(111) | (3 × 3) | 0.111 | Dudde et al. (1990) |
| Os(0001) | $(\sqrt{7} \times \sqrt{7})$R19.1° | 0.143 | Graen et al. (1990) |
| | $(\sqrt{21} \times \sqrt{21})$R10.9° | 0.19 | Neuber (private communication) |
| Ir(111) | (3 × 3) | 0.111 | Mack et al. (1985)<br>Nieuwenhuys et al. (1976) |
| Pt(100) | c(4 × 4) | 0.125 | Richardson and Palmer (1982) |

Markert and Wandelt, 1985; Mate et al., 1986, 1988; Neuber et al., 1991; Neuber, 1992, private communication; Koel et al., 1984; Uhlenbrock, private communication; Netzer, 1990; Hofmann et al., 1981; Dudde et al., 1990; Graen et al., 1990; Mack et al., 1985; Nieuwenhuys et al., 1976; Richardson and Palmer, 1982; Huber et al., 1991b, for a selection of structures) only rather few contain detailed band structure studies.

We shall review in the following data gained on adsorbates on (111) faces and choose as an example the Ni(111) (Steinrück et al., 1989; Huber et al., 1991a) and Os(0001) (Graen et al., 1990) surfaces. To further discuss the determination of further azimuthal ordering we turn then to the analysis on a surface with twofold symmetry, i.e., Ni(110) (Huber et al., 1991a).

### *10.9.1. Symmetry considerations on the molecule–substrate interaction in a dilute disordered layer of $C_6H_6$/Ni(111) (Huber et al., 1991b)*

For Ni(111) Huber et al. (1991b) have determined the structure for dilute layers of $C_6H_6$ from angle resolved photoemission. Figure 10.49 shows the comparison of the angle integrated spectrum for a disordered $C_6H_6$ layer at $\Theta = 0.1$ ML ($\Theta_{sat} = 0.143$ ML) with the gas phase spectrum (Turner et al., 1970). The assignment of the observed spectral features

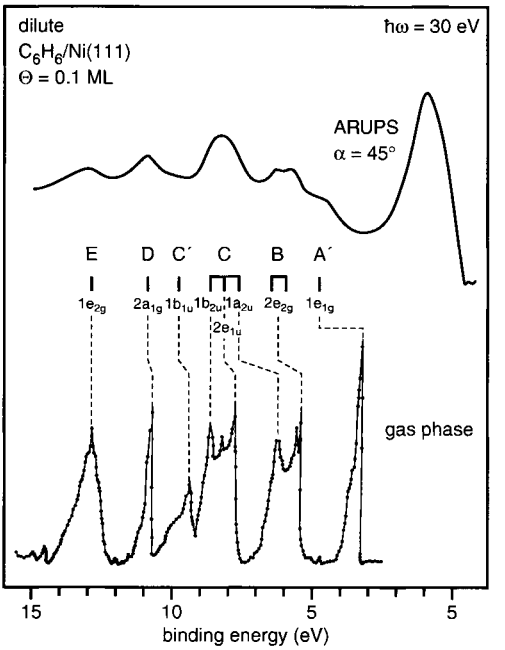


Fig. 10.49. Angle integrated photoelectron spectrum for a dilute $C_6H_6$/Ni(111) system (Huber et al., 1991b) in comparison with the gas phase (Turner et al., 1970).

in the adsorbate to the bands of the gas phase photoelectron spectrum has been discussed in detail by many authors (Steinrück et al., 1989; Bertolini et al., 1977; Huber et al., 1991a, b; Ramsey et al., 1991; Jakob and Menzel, 1988; Bertel et al., 1986; Chiang et al., 1988; Markert and Wandelt, 1985; Mate et al., 1986, 1988; Neuber et al., 1991; Neuber, 1992, private communication; Koel et al., 1984; Uhlenbrock, private communication, Netzer, 1990; Hofmann et al., 1981; Dudde et al., 1990; Graen et al., 1990; Mack et al., 1985; Nieuwenhuys et al., 1976; Richardson and Palmer, 1982). The shifts observed between gas and adsorbate phase strongly suggest that the interaction between molecule and substrate basically involves the $\pi$ electrons of benzene as is well known from transition metal benzene complexes, i.e., $(C_6H_6)Cr$ (Cotton and Wilkinson, 1980). Of course, the symmetry of the molecule, which is $D_{6h}$ in the gas phase is reduced upon interaction with the substrate at least to $C_{6v}$. If there is moderate interaction between molecule and substrate the threefold symmetry of the substrate is likely to reduce the sixfold molecular symmetry to a threefold $C_{3v}$ symmetry. The three symmetry planes may either correspond to the $\sigma_v$ or the $\sigma_d$ symmetry planes of the sixfold symmetry. On a surface with twofold symmetry the point group could be further reduced to $C_{2v}$. Figure 10.50 contains a correlation table for the molecular orbitals symmetries of $C_6H_6$ according to the various point groups. The + and − signs correspond to allowed and forbidden normal emission of the electrons for the two limiting light polarization directions, i.e., in the ring plane $(x, y)$ and perpendicular to the ring plane $(z)$. Due to the broad peaks in the adsorbate spectrum some ion states are su-

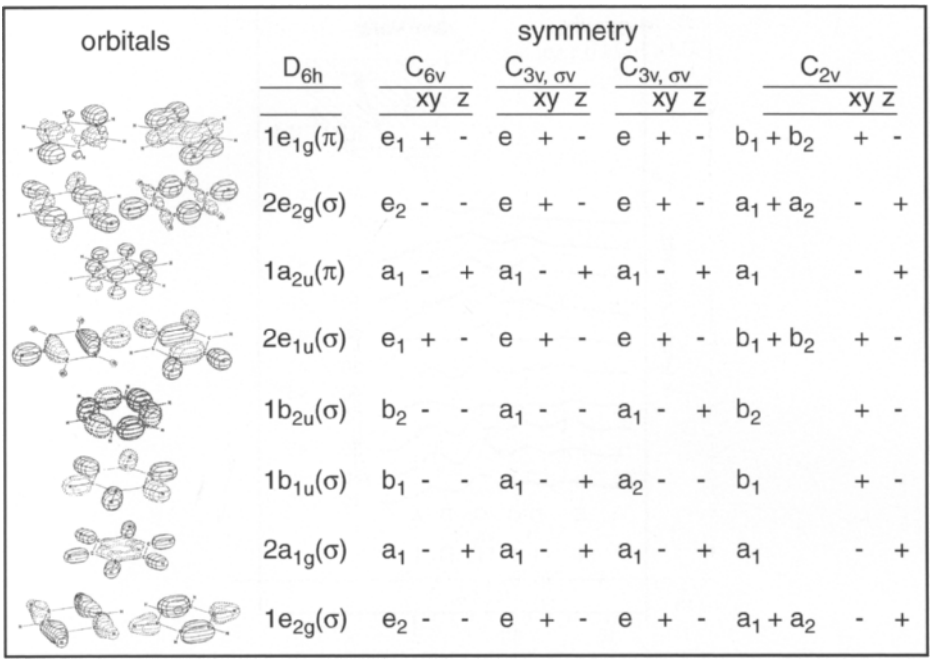


Fig. 10.50. Correlation table of the orbital symmetries of $C_6H_6$ in the gas phase ($D_{6h}$) with those in different adsorbed phases on Ni(111). The + and − signs denote whether the orbitals can be excited with light polarized along the $xy$ or the $z$ directions.

perimposed. The bands in the experimental spectrum are therefore labelled in alphabetical order. Figure 10.50 can be used to establish the symmetry of the adsorption site by evaluating the experimental data shown in Fig. 10.51. The spectra show negligible emission from the $2a_{1g}$ orbital for $\alpha = 0$, i.e., normal incidence and normal emission, but strong emission for $\alpha = 45°$, i.e., a non vanishing $z$-component of the light. Together with the fact that the $b_{1u}$ state shows no normal emission for both light incidence angles this proves that the ring plane is oriented parallel to the surface. From the observation that the $1b_{1u}$ state shows negligible emission at all angles whereas the $1b_{2u}$ orbital is rather intense we conclude that the detector is placed in the $\sigma_d$ mirror plane of the molecule, indicating that this plane acts as a mirror plane for the molecular symmetry. This is then compatible with a $C_{3v}(\sigma_d)$ symmetry of the adsorbate complex. Since the spectra have been collected along the $[1\bar{1}0]$ direction of the substrate, Steinrück et al. (Huber et al., 1991b) concluded that the benzene molecules are azimuthally oriented with the carbon–hydrogen bonds pointing along the $[2\bar{1}1]$ directions of the substrate as shown in Fig. 10.52a. The alternative local structure with $C_{3v}(\sigma_v)$ symmetry favoured by a recent cluster calculation, shown also in Fig. 10.51a is less likely but cannot completely be ruled out because measurements were only performed in one azimuth. Thus the structure marked $C_{3v}(\sigma_d)$ depicted in Fig. 10.52a is assumed to represent the interaction of an isolated benzene molecule with a Ni(111) surface.

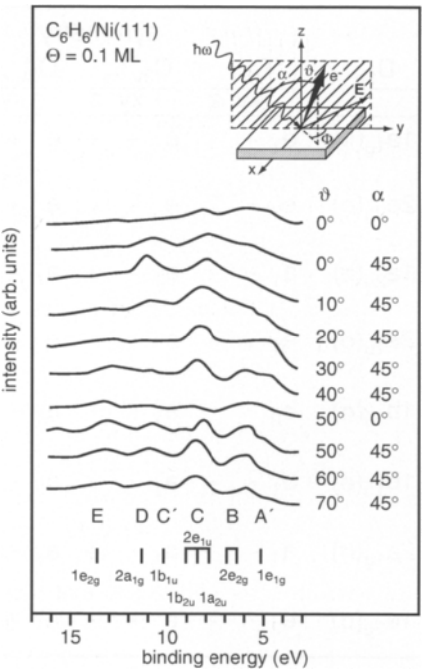


Fig. 10.51. Angle resolved electron distributions curves for a dilute $C_6H_6$ layer on Ni(111) (Huber et al., 1991b).

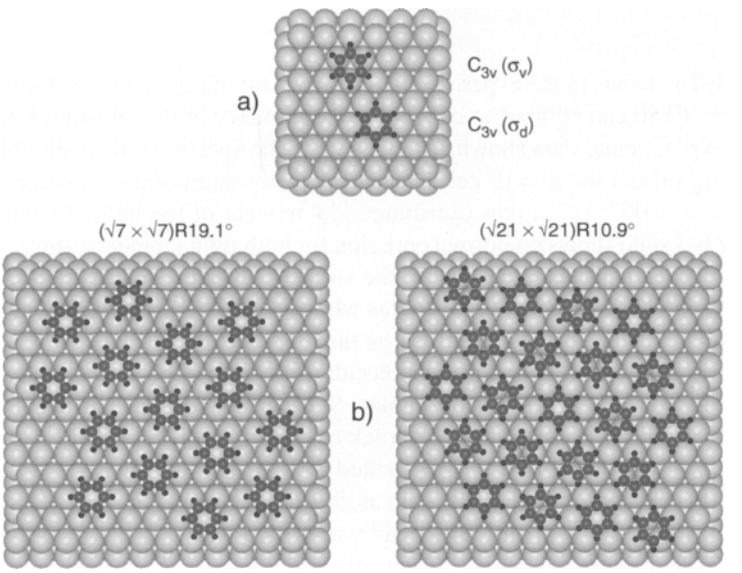


Fig. 10.52. Schematic representation of some $C_6H_6$ structures on (111) surfaces: (a) two possible adsorption sites of isolated $C_6H_6$ molecules; (b) left panel: $(\sqrt{7} \times \sqrt{7})$R19.1° structure model, right panel: $(\sqrt{21} \times \sqrt{21})$R10.9° structure model.

### *10.9.2. Ordered layers: $C_6H_6$/Ni(111) (Huber et al., 1991b) and $C_6H_6$/Os(0001) (Graen et al., 1990)*

$C_6H_6$ on Ni(111) as well as on Os(0001) which are examples of close packed surfaces of a fcc and a hcp metal, form ordered overlayers of the type $(\sqrt{7} \times \sqrt{7})$R19.1° and sometimes, i.e., on Os(0001), even more close packed layers of $(\sqrt{21} \times \sqrt{21})$R10.9° structure. Models of these structures are shown in Fig. 10.52b. The angle resolved spectra of a saturated $(\sqrt{7} \times \sqrt{7})$R19.1° $C_6H_6$ on Ni(111) exhibit characteristic differences if compared with those of the dilute layer (Huber et al., 1991b). The spectra (not shown) indicate strong emission from the $1b_{2u}$ ion state except at particular angles. Huber et al. (1991b) take this as indications that the detection plane is no longer the $\sigma_d$ mirror plane of adsorbed $C_6H_6$. An explanation would be an azimuthal rotation of the molecule due to strong lateral interactions. Figure 10.52b shows an anticipated model of the benzene layer keeping the adsorption site determined for the dilute layer, but allowing for a rotation by 30°.

Experimental evidence for strong lateral interaction is gained from the observation of dispersion of some of the ion states. Intermolecular interaction between planar hydrocarbon is mainly mediated through the hydrogen–hydrogen interaction. Therefore one expects those ion states to show the strongest effect that have considerable wave function coefficients at the hydrogen positions. Figure 10.50 shows that there are several candidates. However, for a clear experimental identification of the dispersion an energetically isolated level should be used in order to avoid problems with overlapping levels. We consider the system $(\sqrt{7} \times \sqrt{7})$R19.1° $C_6H_6$ on Os(0001) (Graen et al., 1990). In Fig. 10.53 the dispersions of the $2a_{1g}$ level are plotted for two photon energies along the direction indicated in the inset. The two possible domains of the overlayer are indicated. There exists a common direction $\Gamma \rightarrow A$ in both domains along which the experiments have been performed. Tight-binding calculations on an unsupported benzene layer have been performed in which the relative arrangement of the molecules within the layer has been varied in order to simulate the probable structures shown in Fig. 10.54a. Two extreme cases have been chosen, i.e., a parallel arrangement (Fig. $10.54b_1$), and an "interlocked" arrangement (Fig. $10.54b_2$).

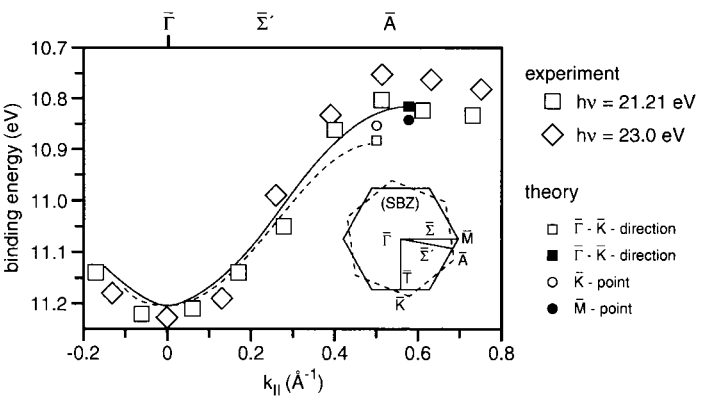


Fig. 10.53. Dispersion relation for the $2a_{1g}$ ion state of the system $C_6H_6(\sqrt{7} \times \sqrt{7})$R19.1°/Os(0001) (Graen et al., 1990).

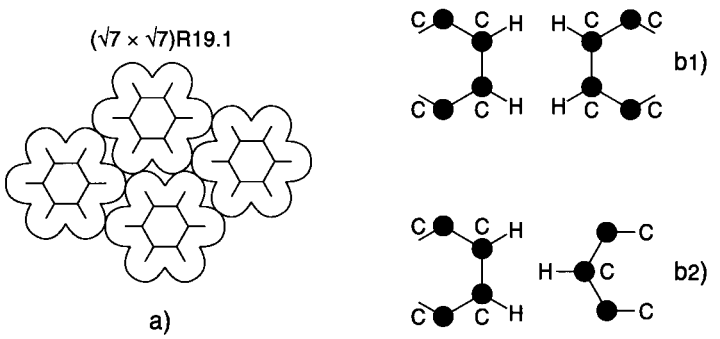


Fig. 10.54. Arrangement of the $C_6H_6$ molecules in the $(\sqrt{7} \times \sqrt{7})R19.1°$ structure (a) schematic representation of molecules in van der Waals contact, ($b_1$) eclipsed arrangement of two $C_6H_6$ molecules, ($b_2$) staggered arrangement of two $C_6H_6$ molecules.

Figure 10.54a obviously represents an intermediate case where the repulsion between interacting molecules is minimized. The calculated dispersion curves (Graen et al., 1990) are included in Fig. 10.53. They correspond to the two azimuthal directions, i.e., $\Gamma \rightarrow K$ and $\Gamma \rightarrow M$ applying intermolecular interaction parameters derived from the geometries shown in Fig. 10.54$b_1$ and Fig. 10.54$b_2$. The energy position of the band at the M point is always higher than at the K point, independent of the absolute value of the interaction parameter. The former value can be estimated almost quantitatively via a simple procedure: we consider a parallel arrangement of $C_6H_6$ moieties (Fig. 10.54$b_1$). On both molecules an $2a_1$-orbital is placed. The overlap between the two molecules will be dominated by the overlap of the adjacent hydrogen atomic orbitals. The reason is that the overlap depends exponentially on the distance. A calculation of the interaction parameter $\beta$ yields 0.045 eV. Since the band constructed from the $2a_{1g}$-levels is of $\sigma$-type, we expect a band dispersion from high binding energy at $\Gamma$ to lower binding energy at the zone boundary. In the simplest version of the tight-binding theory the band dispersion of a $\sigma$-type band in $\Gamma$–M and $\Gamma$–K direction are given by $9\beta$ and $8\beta$, respectively. This yields 0.4 eV and 0.36 eV if we use the above mentioned $\beta$ value. Those values are very close to the dispersion plotted in Fig. 10.53 as a result of the full calculation. A similar estimate can be made for the other geometry in Fig. 10.54$b_2$. This yields 0.36 eV and 0.32 eV, respectively. In conclusion we realize that the observed dispersion can be explained on the basis of simple considerations. Very similar results have been gained for the system $(\sqrt{7} \times \sqrt{7})R19.1°$ $C_6H_6$/Ni(111) and $(\sqrt{19} \times \sqrt{19})R23.4°$ $C_6H_6$/Rh(111). The observed dispersions are basically the same as for the Os(0001) surface layer and have been interpreted in a similar way by Huber et al. (1991b) and Neuber (1992).

Graen and Neumann (Graen, 1991; Graen and Neumann, private commun.) have also determined the dispersion for a more densely packed layer with a $(\sqrt{21} \times \sqrt{21})R10.9°$ structure (Fig. 10.52b). Here the bandwidth increases due to the shorter nearest neighbour distance. With such data one may now establish a bandwidth vs. distance plot quite similar to the one presented for CO adsorbates (Neuber, 1992; Graen, 1991; Graen and Neumann, private communication).

### *10.9.3. Symmetry considerations on molecule–substrate interaction in a dilute disordered layer of $C_6H_6$ of Ni(110) (Huber et al., 1991a)*

A different situation is found for the adsorption of $C_6H_6$ on Ni(110). An ordered approximate c(4 × 2) structure forms for saturation coverage which shows pronounced intermolecular interactions. Before we discuss the band structure, the interaction of a $C_6H_6$ molecule with the surface of twofold symmetry has to be discussed. A priori, one might expect that the molecules are no longer adsorbed in a flat geometry due to the troughs of the surface, different from other close packed surfaces. In fact, such a tilt has been proposed for $C_6H_6$ on Pd(110) (Netzer et al., 1988) while on other surfaces such as Pt(110) (1 × 2) (Surman et al., 1987), Cu(110) (Bader et al., 1986) and Ag(110) (Kelemen and Fischer, 1981; Liu et al., 1990) flat lying geometries have been suggested. Huber et al. (1991a) have recently presented a very detailed study on the adsorption geometry of $C_6H_6$ on Ni(110). The dilute layer corresponds to a coverage of ~0.1 monolayer which is half of the saturation coverage. The layer is disordered. A series of angle resolved spectra is shown in Fig. 10.55. A parallel orientation of the molecule is concluded from the fact that the $2a_{1g}$ state is only observed for $\alpha = 45°$ and normal emission but at no emission angle in a plane perpendicular to the plane of light incidence. This means that the mirror planes of the benzene molecule must coincide with the [001] and [1$\bar{1}$0] directions of the substrate which is a strong indication of an azimuthally oriented benzene molecule. The $1a_{2u}$ ion state behaves similarly and corroborates the above conclusion. Obviously, the adsorbate complex seems to exhibit $C_{2v}$ symmetry. Consequently, the doubly degenerate e-levels should split. By comparing the normal emission spectra for normal incidences obtained at the two different

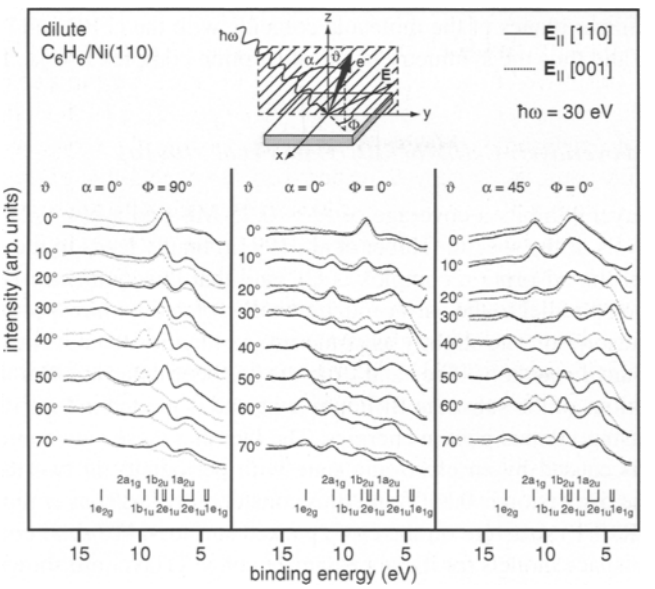


Fig. 10.55. Angle resolved electron distribution curves for a dilute $C_6H_6$/Ni(110) system (Huber et al., 1991a).

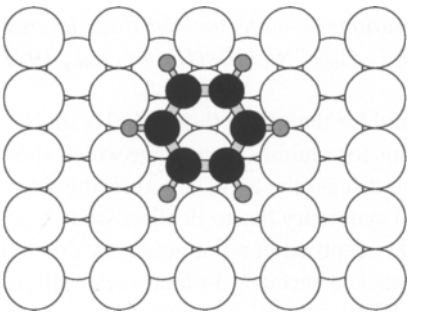

Fig. 10.56. Schematic representation of a single $C_6H_6$ molecule interacting with a Ni(110) surface.

azimuths there are indications (e.g., at 7.8 eV and 8.1 eV) for a split $2e_{1u}$ level. A characteristic angular intensity is exhibited by the $1b_{1u}$ ion state. Its intensity is very weak for the polarization of the light along the $[1\bar{1}0]$ azimuth but very strong for the light polarization parallel to [001]. Taking into account that for $\alpha = 45°$ the emission of the $1b_{1u}$ ion state is large along [001] and strongly attenuated along $[1\bar{1}0]$ corroborates the orientation of the molecule with its corners along the [001] direction. The behaviour of the $1b_{2u}$ ion state is in full agreement with this conclusion. It is therefore very likely that the symmetry of the adsorbate site is $C_{2v}$. We should note at this point that not all levels can be simply analyzed according to the above rules. For example the $2e_{2g}$ level shows a splitting which is due to a Jahn-Teller effect (Herzberg, 1966; Köppel et al., 1988; Eiding et al., 1991; Neumann et al., 1985), also known from the free molecule. Summarizing so far we realize that the plane of the molecule is parallel to the surface and the corners are oriented along the [001] direction. The mirror planes of the molecule coincide with the $[1\bar{1}0]$ and [001] directions of the substrate and thus the symmetry of the adsorption complex is $C_{2v}$. This is depicted in Fig. 10.56.

### *10.9.4. Ordered overlayer: $C_6H_6$/Ni(110) (Huber et al., 1991a)*

The saturated layer exhibits a coverage of $\Theta \sim 0.25$ ML and a c(4 × 2) LEED pattern. A detailed analysis of the spectra (Huber et al., 1991a) finally leads to the conclusion that the symmetry of the adsorption complex is $C_1$, and that this symmetry is achieved by a molecule oriented parallel to the surface, azimuthally rotated with respect to the $[1\bar{1}0]$ direction and an adsorption site slightly asymmetric. As mentioned above, the $2a_{1g}$ ion state exhibits significant dispersions. The band structure has been determined along the two high symmetry directions of the substrate Brillouin zone and is plotted in Fig. 10.57. Data have been obtained using various photon energies. The fact that these data coincide shows that the dispersion is caused by an electronic state with periodicity in two dimensions. The magnitude of the dispersion is 0.8 eV and thus considerably larger as compared with, e.g., the $(\sqrt{7} \times \sqrt{7})$R19.1° structure on the close packed surfaces. We shall come back to this point later. Real space models for the approximate c(4 × 2) layer are shown in Fig. 10.58. Figure 10.58a shows the situation if the molecules were not rotated with respect to the geometry in the dilute layer. Obviously, the van der Waals areas overlap strongly indica-

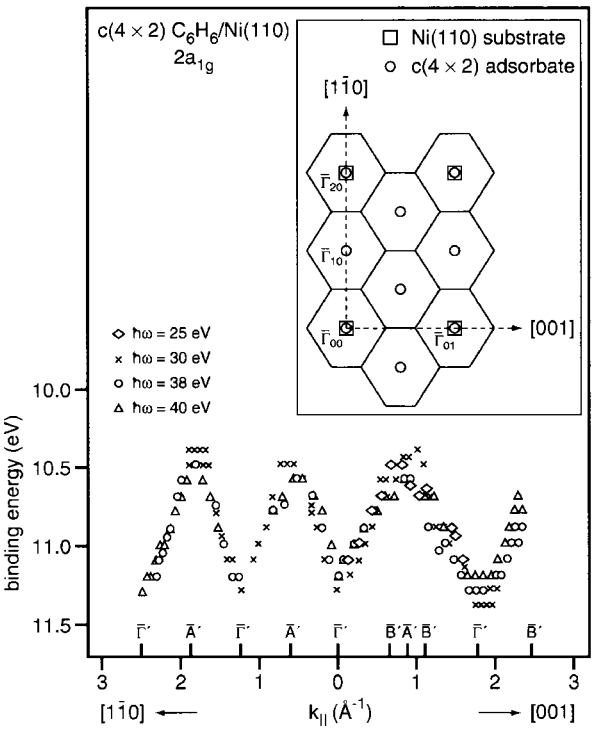


Fig. 10.57. Measured dispersion for a c(4 × 2) $C_6H_6$/Ni(110) system along two directions in **k**-space as indicated in the inset (Huber et al., 1991a).

tive of strong steric repulsion. While the geometry in Fig. 10.58b is sterically favourable, the molecule wants to assume the local geometry as in Fig. 10.58a. The arrangement in Fig. 10.58c is therefore a compromize with reduced steric repulsion and a geometry reasonably close to the local geometry. Such an arrangement has also been favored via a force field calculation by Fox and Rösch (1991).

As mentioned above, the dispersion in the present system is by a factor of two larger as compared to $C_6H_6$ on Ni(111) (Richardson and Palmer, 1982) and Os(0001) (Graen et al., 1990). This must result from the significantly closer packing of the molecules. For $C_6H_6$ on Ni(110) the coverage of $\Theta = 0.25$ ML corresponds to a unit cell area of 35.2 Å$^2$ with a nearest neighbour distance of 6.11 Å. This should be compared with a unit cell area of 37.6 Å$^2$ for the $(\sqrt{7} \times \sqrt{7})$R19.1° structure and a coverage of $\Theta = 0.143$ ML for Ni (111). The 6–7% denser packing in the layer obviously has a strong nonlinear response. This is due to the fact that the intermolecular overlaps scale exponentially with distance and in addition the local arrangement is such that the repulsive interaction between the hydrogen atoms is rather large. This effect has been discussed above for the $(\sqrt{7} \times \sqrt{7})$R19.1° structure. Clearly, the interaction energy of a single $C_6H_6$ molecule with the metal surface must be rather strong to tolerate the considerable intermolecular repulsions in the layer which in turn leads to the pronounced band structure effects in this system.

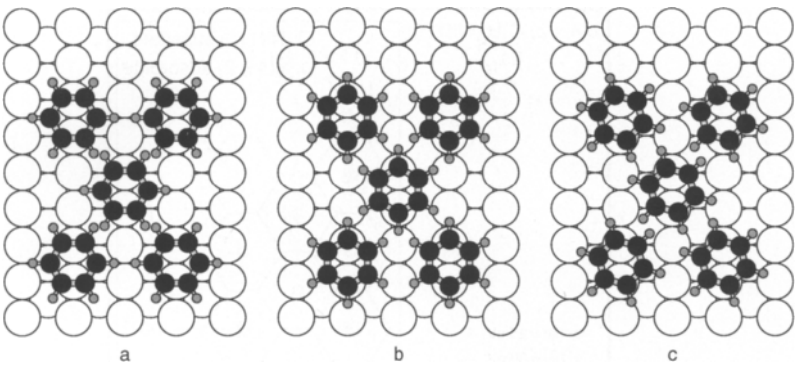


Fig. 10.58. Schematic representations of the relative arrangements in a c(4 × 2) $C_6H_6$/Ni(110) layer: (a) assuming the same site as in the dilute layer, (b) rotation by 30° with respect to the orientation in the dilute layer, (c) arrangement intermediate between (a) and (b).

## 10.10. Co-adsorbates

The adsorption of atomic hydrogen induces marked changes in the electronic structure of co-adsorbed CO on Ni(100), as was recently shown with ARUPS by Bradshaw and his group (Klauser et al., 1987; Hayden et al., 1987; Kulkarni et al., 1991). This is shown in Fig. 10.59 where spectra of a pure CO (a), a H+CO co-adsorbate, with both gases exposed to saturation coverage (b), and a H+CO co-adsorbate, the so-called $\Sigma$-state (c), where the hydrogen coverage is lower than in case (b) are presented. The spectra are taken with polarized synchrotron radiation at non-normal emission and a light incidence angle of 45° with respect to the surface normal. In spectra (a) and (b) we find the normal behaviour documented in Fig. 10.21. This is typical for strongly chemisorbed CO molecules oriented perpendicular to the surface plane. In spectrum (c), however, there are indications of weak satellite structure on the high binding energy side of the $4\sigma$ ionization. This is in line with the finding that the adsorption energy (Goodman et al., 1980) of the $\Sigma$-state of CO+H/Ni(100) is considerably weaker as compared to CO/Ni(100), and is similar to CO/Cu(100) (Allyn et al., 1977a), where we expect intense satellite structure similar to CO/Cu(111) (Fig. 10.21) (Freund et al., 1983) discussed above. The orientation of the CO axis in the $\Sigma$-state has been shown to be perpendicular to the surface plane.

CO–alkali-co-adsorbates (Bonzel, 1988) are the most frequently tackled co-adsorbate systems with ARUPS. Several different metal surfaces have been studied (Bonzel, 1988). The most complete sets of ARUP-spectra exist for Ru(001) and Cu(100) surfaces (Eberhardt et al., 1985; Heskett and Plummer, 1986; Heskett et al., 1985a, 1986; Weimer and Umbach, 1984; Weimer et al., 1985; Wurth et al., 1986). Some important conclusions have been drawn from these studies which were partially in contrast to existing models of CO–alkali interaction at the time (Goodman et al., 1980). As monitored by the angular distribution pattern and the peaking of the shape-resonance the CO orientation with respect to the surface normal does not change upon alkali co-adsorption independent of alkali-coverage, except for a thick alkali film (Eberhardt et al., 1985; Heskett and Plummer, 1986; Heskett et al., 1985a, 1986; Weimer and Umbach, 1984; Weimer et al., 1985; Wurth et al., 1986).

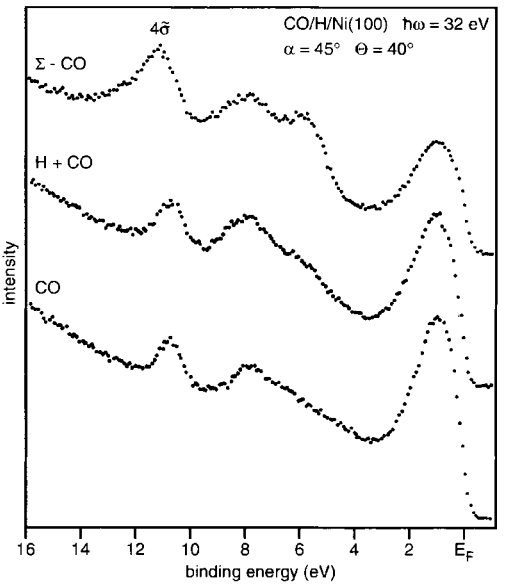


Fig. 10.59. Typical photoemission spectra for the CO/H/Ni(100) system at high emission angle showing the increase in intensity in the satellite region of the $4\tilde{\sigma}$ feature (Klauser et al., 1987; Hayden et al., 1987; Kulkarni et al., 1991).

In the case of the alkali–CO-co-adsorbates on Cu surfaces (Heskett and Plummer, 1986), interesting variations in the shake up structure have been observed by Heskett and Plummer (1986) as shown in Fig. 10.60, where both the pure CO and the co-adsorbate spectra are presented for comparison. As outlined above, the decrease of the satellite intensity can be a sign of stronger or weaker metal–CO coupling. Since, however, there are still only two CO bands we must conclude that the metal–CO-bond strength actually increases. In addition to this variation of the CO–metal bond strength direct CO–alkali short range interactions involving the alkali-s- and the CO-$1\pi$-orbitals have been postulated (Fox and Rösch, 1991). Figure 10.61 shows two sets of spectra, one for the pure CO adsorbate, equivalent to Fig. 10.21, and another one for the alkali-co-adsorbate. The spectra in the so-called "allowed" geometry are fairly similar, but in the "forbidden" geometry they are substantially different. The $1\pi$ peaks in spectra (b) and (c) are located at different energies and the $4\sigma$ peak for CO/K has more residual intensity than expected for an unperturbed, perpendicularly adsorbed CO molecule. The shift of the $1\pi$ level in the CO/K-system to lower binding energy is similar to that observed on Pt(111) (Kiskinova et al., 1983) or on Fe(110) (Brodén et al., 1979). The fact that $\sigma$ states are visible in the "forbidden" geometry may be caused by a slight tilting of the CO molecule or be due to the immediate vicinity of the K species, such that the symmetry of the coadsorbed CO molecule is broken. The spectra of the K/CO system are interestingly similar to those of systems like CO/Fe(111) (Freund et al., 1987). This may mean that in the latter case similar interactions, i.e., between the CO $1\pi$ and the metal surface are active. Very often alkali co-adsorption leads to stronger molecule–surface interactions (Bonzel, 1988), but there are cases where the

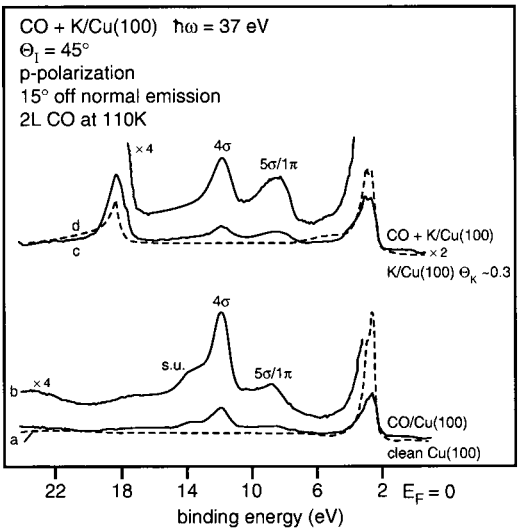


Fig. 10.60. Photoelectron spectra for CO/Cu(100) ($\Theta_{CO} = 0.5$) and CO+K/Cu(100) ($\Theta_K = 0.3$, $\Theta_{CO} = 0.3$) in comparison. The spectra of the CO free system are shown as broken lines (Heskett and Plummer, 1986).

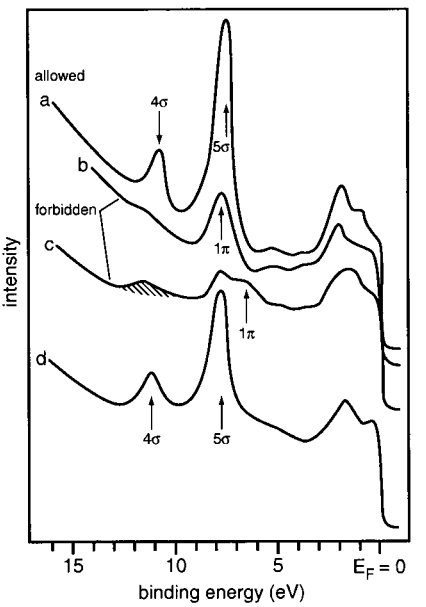


Fig. 10.61. Photoelectron spectra in "allowed" and "forbidden" geometry for CO/Ru(001) (c and d) and CO+K/Ru(001) ($\Theta_K = 0.33$) (a and b) (Eberhardt et al., 1985).

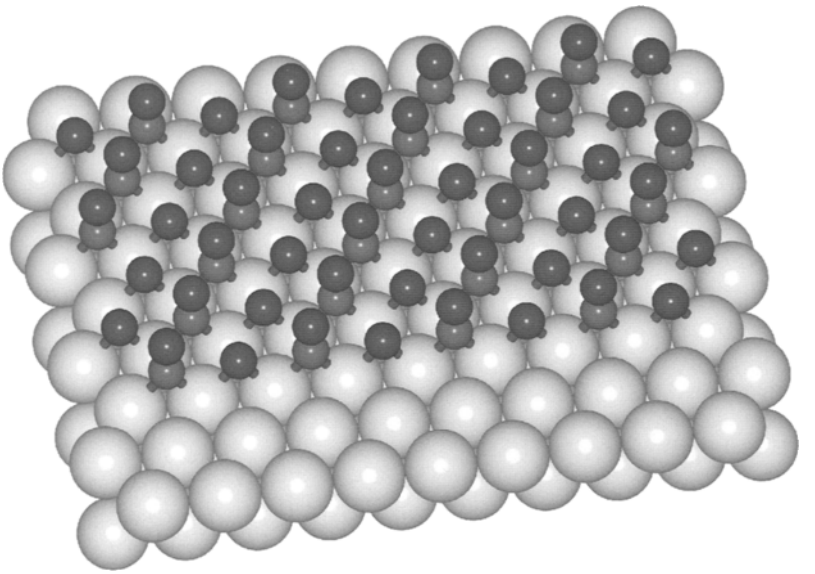

Fig. 10.62. Schematic representation of the structure of the (2 × 1)CO+O/Pd(111) coadsorption system.

opposite effect is observed. For example, small amounts of alkali precoverages lead to a very strong repulsive interactions with $N_2$ and attenuates $N_2$ adsorption by a factor of 4 while the electronic structure of the adsorbed $N_2$ appears to be the same as without alkali precoverage (Kiskinova et al., 1983). ARUPS was used to prove this (DePaola et al., 1987), and it has been interpreted as an indication for long range alkali-$N_2$ repulsion. Tentatively, a lack of d-$\pi$-backdonation in the case of $N_2$-transition metal bonding has been argued to be the reason for this behaviour (DePaola et al., 1987).

Many other alkali co-adsorbates have been studied using photoelectron spectroscopy (Bonzel, 1988). A use of angular resolution, on the other hand, has only been reported in a few cases. An ordered CO/O co-adsorbate on Pd(111) has been studied using ARUPS (Odörfer et al., 1988). Figure 10.62 shows a schematic picture of the structure proposed to explain the observed (2 × 1) LEED pattern. Early angle integrated photoemission results (Conrad et al., 1978) were basically reproduced. The co-adsorption of oxygen shifts the positions of the $4\sigma$ and $5\sigma/1\pi$ bands to higher binding energies. This has been taken as evidence for a strong oxygen CO interaction. The $4\sigma$ dispersion is, however, basically caused by the strong lateral interaction along the CO rows. The ARUPS study shows that the $4\sigma$ dispersion, as presented in Fig. 10.28 is in line with those of pure CO adsorbates. Therefore, if there is any distortion of the wave function then it is smaller than in the case of K/CO adsorbates. Further comparison with other pure CO adsorbates on Pd(111) revealed that the observed chemical shift of the CO peaks can be explained exclusively via CO–CO interaction. Therefore, the reason for the high tendency of the CO+O/Pd(111) system to form $CO_2$ well below room temperature (Conrad et al., 1978) must be due to CO–CO and O–O repulsive interactions rather than strong attractive CO–O interactions within the adsorbate.

*Acknowledgements*

We thank the Deutsche Forschungsgemeinschaft, the Bundesministerium für Forschung und Technologie, the Ministerium für Wissenschaften und Forschung des Landes Nordrhein-Westfalen and the Fonds der chemischen Industrie for support. Many coworkers have contributed over the years. Their names are mentioned in the references. We would like to thank Heiko Hamann for a critical reading of the manuscript.

## References

Allyn, C.L., 1978, Thesis, University of Pennsylvania.
Allyn, C.L., T. Gustafsson and E.W. Plummer, 1977a, Chem. Phys. Lett. **47**, 127.
Allyn, C.L., T. Gustafsson and E.W. Plummer, 1977b, Solid State Commun. **24**, 531.
Anderson, R.W., 1961, Phys. Rev. **124**, 41.
Apai, G., R.S. Wehner, R.W. Williams, J. Stöhr and D.A. Shirley, 1976, Phys. Rev. Lett. **37**, 1497.
Asscher, M., C.T. Kao and G. Somorjai, 1988, J. Phys. Chem. **92**, 2711.
Bader, M., J. Haase, K.-H. Frank, C. Ocal and A. Puschmann, 1986, J. Phys. (Paris) Coll. **C8**, 491.
Bader, M., J. Haase, A. Puschmann and C. Ocal, 1987, Phys. Rev. Lett. **59**, 2435.
Bagus, P.S., K. Hermann and C.W. Bauschlieher, Jr., 1984, J. Chem. Phys. **80**, 4378; 1984, J. Chem. Phys. **81**, 1966.
Bartos, B., H.-J. Freund, H. Kuhlenbeck and M. Neumann, 1987a, Kinetics of Interface Reactions, eds. M. Grunze and H.-J. Kreuzer, Springer Series in Surface Science, Vol. 8. Springer-Verlag, Berlin, p. 164.
Bartos, B., H.-J. Freund, H. Kuhlenbeck, M. Neumann, H. Lindner and K. Müller, 1987b, Surf. Sci. **179**, 59.
Batra, I.P., K. Hermann, A.M. Bradshaw and K. Horn, 1979, Phys. Rev. B **20**, 801.
Bertel, E., G. Rosina and F.P. Netzer, 1986, Surf. Sci. **172**, L515.
Bertolini, J.C., G. Dalmei-Imelik and J. Rousseau, 1977, Surf. Sci. **67**, 478.
Bertolo, M., W. Hansen and K. Jacobi, 1991, Phys. Rev. Lett. **67**, 1898.
Björneholm, O., 1992, Ph.D. Thesis, Uppsala University.
Blyholder, G., 1964, J. Phys. Chem. **68**, 2792;
Blyholder, G., 1974, J. Vac. Sci. Technol. **11**, 865.
Bonzel, H.P., private communication.
Bonzel, H.P., 1988, Surf. Sci. Rep. **8**, 43.
Bonzel, H.P., A.M. Bradshaw and G. Ertl (eds.), 1989, Physics and Chemistry of Alkali Metal Adsorption. Elsevier, Amsterdam.
Borstel, G., M. Neumann, G. Seitz and W. Braun, 1980, in: Proc. 4th Intern. Conf. Solid Surf., Vol. 1, p. 357.
Borstel, G., M. Neumann and M. Wöhlecke, 1981, Phys. Rev. B **23**, 3121.
Boszo, T., I. Arias, T.E. Yates, R.M. Martin and H. Metiu, 1983, Chem. Phys. Lett. **94**, 243.
Braun, W., G. Meyer-Ehmsen, M. Neumann and E. Schwarz, 1979, Surf. Sci. **89**, 354.
Breitschafter, M.J., E. Umbach and D. Menzel, 1986, Surf. Sci. **178**, 725.
Brodén, G., G. Gaffner and H.P. Bonzel, 1979, Surf. Sci. **84**, 295.
Brosseau, R., T.H. Ellis and H. Wang, 1991, Chem. Phys. Lett. **177**, 118.
Brundle, C.R. and J.Ch. Broughton, 1990, in: The Chemical Physics of Solid Surfaces and Heterogeneous Catalysis, Vol. 3, eds. D.A. King and D.P. Woodruff. Elsevier, Amsterdam, p. 131.
Burchhardt, J., M.M. Nielsen, D.L. Adams, E. Lundgren, J.N. Andersen, C. Stampfl, M. Scheffler, A. Schmalz, S. Aminpirooz and J. Haase, 1995, Phys. Rev. Lett. **74**, 1617.
Cederbaum, L.S. and W. Domcke, 1977, Adv. Chem. Phys. **36**, 205.
Chatt, J. and C.A. Duncauson, 1953, J. Chem. Soc. **3**, 2939.
Chiang, S., R.J. Wilson, C.M. Mate and H. Ohtani, 1988, J. Microsc. **152**, 567.
Chiang, T.C., G. Kaindl and D.E. Eastman, 1980, Solid State Commun. **36**, 25.
Christmann, K., 1988, Surf. Sci. Rep. **9**, 1.
Christmann, K., O. Schober and G. Ertl, 1974, J. Chem. Phys. **60**, 4719.

Chubb, S.R., P.M. Marcus, K. Heinz and K. Müller, 1990, Phys. Rev. B **41**, 5417.
Conrad, H., G. Ertl, J. Koch and E.E. Latta, 1974, Surf. Sci. **43**, 462.
Conrad, H., G. Ertl and J. Küppers, 1978, Surf. Sci. **76**, 323.
Cotton, F.A. and G. Wilkinson, 1980, Advanced Inorganic Chemistry, 4th edn. Wiley, New York.
Coulman, D.J., J. Wintterlin, G. Ertl and R.J. Behm, 1990, Phys. Rev. Lett. **64**, 1761.
Courths, R., private communication.
Courths, R., B. Cord, H. Wern and H. Saalfeld, 1986, BESSY Annual Report, p. 203.
Courths, R., B. Cord, H. Wern, H. Saalfeld and S. Hüfner, 1987, Solid State Commun. **63**, 619.
Davenport, J.W., 1976, Thesis, University of Pennsylvania; Davenport, J.W., 1976, Phys. Rev. Lett. **36**, 945.
Demuth, I.E., D.W. Jepsen and P.M. Marcus, 1973, Phys. Rev. Lett. **31**, 540.
DePaola, R.A., F.M. Hoffmann, D. Heskett and E.W. Plummer, 1987, Phys. Rev. B **35**, 4236.
D'Evelyn, M.P., A.V. Hamza, G.E. Gidowski and R.J. Madix, 1986, Surf. Sci. **167**, 451.
Dewar, M.J.S., 1951, Bull. Soc. Chem. Fr. **18**, C71.
Didio, R.A., D.M. Zehner and E.W. Plummer, 1984, J. Vac. Sci. Technol. A **2**, 852.
Diehl, R.D. and S.C. Fain, 1983, Surf. Sci. **125**, 116.
Dowben, P.A., Y. Sakisaka and T.N. Rhodin, 1984, Surf. Sci. **147**, 89.
Dudde, R., K.H. Frank and E.E. Koch, 1990, Surf. Sci. **225**, 267.
Duke, C.B., 1978, Surf. Sci. **70**, 674.
Duke, C.B., W.R. Salaneck, F.-J. Fabisch, J.J. Ritsko, H.R. Thomas and A. Paton, 1978, Phys. Rev. B **18**, 5717.
Eberhardt, W. and H.-J. Freund, 1983, J. Chem. Phys. **78**, 700.
Eberhardt, W., F. Greuter and E.W. Plummer, 1981, Phys. Rev. Lett. **46**, 1085.
Eberhardt, W., F.M. Hoffmann, R. DePaola, D. Heskett, I. Strathy, E.W. Plummer and H.R. Moser, 1985, Phys. Rev. Lett. **54**, 1856.
Eberhardt, W., S.G. Lonie and E.W. Plummer, 1983, Phys. Rev. B **28**, 465.
Eberhardt, W. and E.W. Plummer, 1983, Phys. Rev. B **28**, 3605.
Eiding, J., W. Domcke, W. Huber and H.-P. Steinrück, 1991, Chem. Phys. Lett. **180**, 133.
Einstein, T.L. and J.R. Schrieffer, 1973, Phys. Rev. B **7**, 3629.
Engelhardt, H.A., W. Bäck, D. Menzel and H. Liebl, 1981a, Rev. Sci. Instr. **52**, 835.
Engelhardt, H.A., A. Zartner and D. Menzel, 1981b, Rev. Sci. Instr. **52**, 1161.
Ertl, G., 1982, Ber. Bunsenges. Phys. Chem. **86**, 425.
Ertl, G., 1983, J. Vac. Sci. Technol. A **1**, 1247.
Ertl, G. and J. Küppers, 1985, Low Energy Electrons and Surface Chemistry. Verlag Chemie, Weinheim.
Fink, J., 1992, Transmission Electron Energy Loss Spectroscopy, in: Unoccupied Electronic States, Vol. 69, Topics in Applied Physics, eds. J.C. Fuggle and J.E. Inglesfield. Springer-Verlag, Berlin, p. 203 and references therein.
Fox, T. and N. Rösch, 1991, Surf. Sci. **256**, 159.
Freund, H.-J., B. Bartos, R.P. Messmer, M. Grunze, H. Kuhlenbeck and M. Neumann, 1987, Surf. Sci. **185**, 187.
Freund, H.-J., H. Behner, B. Bartos, G. Wedler, H. Kuhlenbeck and M. Neumann, 1987, Surf. Sci. **180**, 550.
Freund, H.-J., W. Eberhardt, D. Heskett and E.W. Plummer, 1983, Phys. Rev. Lett. **50**, 768.
Freund, H.-J. and R.P. Messmer, 1986, Surf. Sci. **172**, 1.
Freund, H.-J., R.P. Messmer, C.M. Kao and E.W. Plummer, 1985, Phys. Rev. B **31**, 4848.
Freund, H.-J. and M. Neumann, 1988, Appl. Phys. A **47**, 3.
Freund, H.-J. and M. Neumann, 1992, in: Angle Resolved Photoemission, ed. S.D. Kevan, Studies in Surface Science and Catalysis, Vol. 74. Elsevier, p. 319.
Freund, H.-J. and E.W. Plummer, 1981, Phys. Rev. B **23**, 4859.
Gadzuk, J.W., S. Holloway, K. Horn and C. Mariani, 1982, Phys. Rev. Lett. **48**, 1288.
Geisler, H., J. Wambach, H. Kuhlenbeck, H.-J. Freund, M. Neuber and M. Neumann, 1996, J. Electron Spectrosc. Relat. Phenom. **77**, 33.
Goldmann, A., 1992, in: Angle Resolved Photoemission, ed. S.D. Kevan, Studies in Surface Science and Catalysis, Vol. 74. Elsevier, p. 291.
Goodman, D.W., J.T. Yates and T.E. Madey, 1980, Surf. Sci. **93**, L135.
Graen, H.H., 1991, Thesis, Universität Osnabrück.
Graen, H.H., M. Neuber, M. Neumann, G. Odörfer and H.-J. Freund, 1990, Europhys. Lett. **12**, 173.

Graen, H.H. and M. Neumann, private communication.
Greuter, F., D. Heskett, E.W. Plummer and H.-J. Freund, 1983, Phys. Rev. B **27**, 7117.
Grimley, T.B., 1960, Adv. Catal. **12**, 1.
Grimley, T.B., 1967, Proc. Phys. Soc. **90**, 751; **92**, 776.
Grimley, T.B., 1971, Ber. Bunsenges. Phys. Chem. **75**, 1003.
Grunze, M., M. Golze, W. Hirschwald, H.-J. Freund, H. Pulm, U. Seip, N.C. Tsai, G. Ertl and F. Küppers, 1984, Phys. Rev. Lett. **53**, 850.
Guerney, R.W., 1935, Phys. Rev. **47**, 479.
Gumhalter, B., K. Wandelt and Ph. Avouris, 1988, Phys. Rev. B **37**, 8048.
Gustafsson, T., 1980, Surf. Sci. **94**, 593.
Höfer, U., M.J. Breitschafter and E. Umbach, 1990, Phys. Rev. Lett. **64**, 3050.
Hayden, B.E., R. Klauser and A.M. Bradshaw, 1987, Surf. Sci. **183**, L279.
Harris, J. and S. Andersson, 1985, Phys. Rev. Lett. **55**, 1383.
Hedin, L., 1979, Phys. Sci. **21**, 477.
Henzler, M. and W. Göpel, 1991, Oberflächenphysik des Festkörpers Teubner Studienbücher, Stuttgart.
Hermann, K., P.S. Bagus, C.R. Brundle and D. Menzel, 1981, Phys. Rev. B **24**, 7025.
Hermanson, J., 1977, Solid State Commun. **22**, 9.
Herzberg, G., 1966, Molecular Spectra and Molecular Structure, Vol. 3, Electronic Spectra and Electronic Structure of Polyatomic Molecules. Van Nostrand–Reinhold, New York.
Heskett, D., private communication.
Heskett, D. and E.W. Plummer, 1986, Phys. Rev. B **33**, 2322.
Heskett, D., E.W. Plummer, R.A. DePaola and W. Eberhardt, 1986, Phys. Rev. B **33**, 5171.
Heskett, D., E.W. Plummer, R.A. DePaola, W. Eberhardt and F.M. Hoffmann, 1985a, Surf. Sci. **164**, 490.
Heskett, D., I. Strathy, E.W. Plummer and R.A. DePaola, 1985b, Phys. Rev. B **32**, 6222.
Hjelmberg, H., 1979, Surf. Sci. **81**, 539.
Hofmann, P., S.R. Bare and D.A. King, 1982, Surf. Sci. **117**, 245.
Hofmann, P., J. Gossler, A. Zartner, M. Glanz and D. Menzel, 1985, Surf. Sci. **161**, 303.
Hofmann, P., K. Horn and A.M. Bradshaw, 1981, Surf. Sci. **105**, L260.
Hofmann, P. and D. Menzel, 1987, Surf. Sci. **191**, 353.
Horn, K., A.M. Bradshaw, K. Hermann and I.P. Batra, 1979, Solid State Commun. **31**, 257.
Horn, K., A.M. Bradshaw and K. Jacobi, 1978a, Surf. Sci. **72**, 719.
Horn, K., J.N. Di Nardo, W. Eberhardt, H.-J. Freund and E.W. Plummer, 1982, Surf. Sci. **118**, 465.
Horn, K., A. Hohlfeld, J. Somers, Th. Lindner, P. Holling and A.M. Bradshaw, 1988, Phys. Rev. Lett. **61**, 2488.
Horn, K., M. Scheffler and A.M. Bradshaw, 1978b, Phys. Rev. Lett. **41**, 822.
Huber, W., M. Weinelt, P. Zebisch and H.-P. Steinrück, 1991a, Surf. Sci. **253**, 72.
Huber, W., P. Zebisch, T. Bornemann and H.-P. Steinrück, 1991b, Surf. Sci. **258**, 16.
Hund, F., 1936, Z. Phys. **99**, 119.
Ishida, H., 1988, Phys. Rev. B **38**, 8006.
Ishida, H., 1990, Phys. Rev. B **42**, 10899.
Jacob, W., V. Dose and A. Goldmann, 1986, Appl. Phys. A **41**, 145.
Jakob, P. and D. Menzel, 1988, Surf. Sci. **201**, 503.
Jensen, E.S. and T.N. Rhodin, 1983, Phys. Rev. B **27**, 3338.
Jones, H., 1975, The Theory of Brillouin Zones and Electronic States in Crystals. North-Holland, Amsterdam.
Jones, T.S. and N.V. Richardson, 1989, Surf. Sci. **211/212**, 377.
Jones, T.S., N.V. Richardson and A.W. Joshi, 1988, Surf. Sci. **207**, 2948.
Jorgensen, W.L. and L. Salem, 1974, Orbitale Organischer Moleküle. Verlag Chemie, Weinheim.
Kao, C.M. and R.P. Messmer, 1985, Phys. Rev. B **31**, 4835.
Kelemen, S.R. and T.E. Fischer, 1981, Surf. Sci. **102**, 45.
Kessler, J. and F. Thieme, 1977, Surf. Sci. **67**, 405.
Kevan, S.D. (ed.), 1992, Angle Resolved Photoemission: Theory and Current Applications, Vol. 74, Studies in Surface Science and Catalysis. Elsevier, Amsterdam (and references therein).
Kimura, K., S. Katsumata, Y. Achiba, T. Yamakaki and S. Iwata, 1981, Handbook of HeI Photoelectron Spectra of Fundamental Organic Molecules. Halsted, New York.

Kingdom, K.H., 1923, I. Langmuir, Phys. Rev. **21**, 380.
Kiskinova, M., G. Pirug and H.P. Bonzel, 1983, Surf. Sci. **133**, 321.
Klauser, R., M. Surman, Th. Lindner and A.M. Bradshaw, 1987, Surf. Sci. **183**, L279.
Kleyn, A.W., A.C. Luutz and D.J. Auerbach, 1982, Surf. Sci. **117**, 33.
Koel, B.E., J.E. Crowell, C.M. Mate and G.A. Somorjai, 1984, J. Phys. Chem. **88**, 1988.
Köppel, H., L.S. Cederbaum and W. Domcke, 1988, J. Chem. Phys. **89**, 2023.
Koutecky, J., 1958, Trans. Faraday Soc. **54**, 1038.
Kuhlenbeck, H., 1984, Diplomarbeit, Universität Osnabrück.
Kuhlenbeck, H., M. Neumann and H.-J. Freund, 1986, Surf. Sci. **173**, 194.
Kuhlenbeck, H., H.B. Saalfeld, U. Buskotte, M. Neumann, H.-J. Freund and E.W. Plummer, 1989, Phys. Rev. B **39**, 3475.
Kuhlenbeck, H., H.B. Saalfeld, M. Neumann, H.-J. Freund and E.W. Plummer, 1987, Appl. Phys. A **44**, 83.
Kulkarni, S.K., J. Somos, A.W. Robinson, D. Ricken, Th. Lindner, P. Hollins, G.J. Lapeyre and A.M. Bradshaw, 1991, Surf. Sci. **259**, 70.
Lapeyre, G.J., J. Anderson and R.J. Smith, 1979, Surf. Sci. **89**, 304.
Lang, N.D., 1971, Solid State Commun. **9**, 1015.
Langmuir, I., 1918, J. Am. Chem. Soc. **40**, 1361.
Lennard-Jones, J.E., 1932, Trans. Farad. Soc. **28**, 333.
Lindner, Th., J. Somers, A.M. Bradshaw and G.P. Williams, 1987, Surf. Sci. **185**, 75.
Litvin, D.B., 1983, Thin Solid Films **106**, 203.
Litvin, D.B., 1984, J. Phys. C **17**, L37.
Liu, A.C., J. Stöhr, C.M. Friend and R.J. Madix, 1990, Surf. Sci. **235**, 107.
Lundquist, B.I., 1967, Phys. Cond. Mater. **6**, 193, 203.
Lundquist, B.I., 1968, Phys. Cond. Mater. **7**, 117.
Lundquist, B.I., 1969, Phys. Cond. Mater. **9**, 2236.
Lundquist, B.I., O. Gunnarsson, H. Hjeemberg and J.K. Nyrvkor, 1979, Surf. Sci. **89**, 196.
Mack, J.U., E. Bertel and F.P. Netzer, 1985, Surf. Sci. **159**, 265.
Madix, R.J., J.L. Gland, G.E. Mitchell and B.A. Sexton, 1983, Surf. Sci. **125**, 481.
Mariani, C., H.-U. Middelmann, M. Iwan and K. Horn, 1982, Chem. Phys. Lett. **93**, 308.
Markert, K. and K. Wandelt, 1985, Surf. Sci. **159**, 24.
Martensson, N. and A. Nilsson, 1990, J. Electron Spectrosc. Relat. Phenom. **52**, 1.
Mate, C.M., B.E. Bent and G.A. Somorjai, 1986, J. Electron Spectrosc. Relat. Phenom. **39**, 205.
Mate, C.M., C.-T. Kao and G.A. Somorjai, 1988, Surf. Sci. **206**, 145.
McElhiney, G., H. Papp and J. Pritchard, 1976, Surf. Sci. **54**, 617.
Memmel, N., G. Rangelov, E. Bertel, V. Dose, K. Kometer and N. Rösch, 1989, Phys. Rev. Lett. **63**, 1884.
Messmer, R.P. and S.H. Lamson, 1979, Chem. Phys. Lett. **65**, 465.
Messmer, R.P., 1984, J. Vac. Sci. Technol. A **2**, 899.
Nielsen, M.M., J. Burchhardt, D.L. Adams, E. Lungren and J.N. Andersen, 1994, Phys. Rev. Lett. **72**, 3370.
Miranda, R., K. Wandelt, D. Rieger and R.D. Schnell, 1984, Surf. Sci. **139**, 430.
Muscat, J.P. and D.M. Newns, 1978, Surf. Sci. **74**, 355.
Netzer, F.P., 1990, Vacuum **41**, 49.
Netzer, F.P., G. Rangelov, G. Rosina, H.B. Saalfeld, M. Neumann and D.R. Lloyd, 1988, Phys. Rev. B **37**, 10399.
Neuber, M., private communication.
Neuber, M., 1992, Thesis, Universität Osnabrück.
Neuber, M., S. Witzel, C. Zubrägel, H.H. Graen and M. Neumann, 1991, Surf. Sci. **251/252**, 911.
Neumann, M., J.U. Mack, E. Bertel and F.P. Netzer, 1985, Surf. Sci. **155**, 629.
Newns, D.M., 1969, Phys. Rev. **178**, 1123.
Nieuwenhuys, B.E., D.I. Hagen, G. Rovida and G.A. Somorjai, 1976, Surf. Sci. **59**, 155.
Odörfer, G., 1987, Diplomarbeit, Universität Erlangen-Nürnberg.
Odörfer, G., E.W. Plummer, H.-J. Freund, H. Kuhlenbeck and M. Neumann, 1988, Surf. Sci. **198**, 331.
Peyerimhoff, S.D., 1967, J. Chem. Phys. **47**, 349.
Peled, H. and M. Asscher, 1987, Surf. Sci. **183**, 201.
Plummer, E.W. and W. Eberhardt, 1982, Adv. Chem. Phys. **49**, 533.

Plummer, E.W., T. Gustafsson, W. Gudat and D.E. Eastman, 1977, Phys. Rev. A **15**, 2339.
Plummer, E.W., B.P. Tonner, N. Holzwarth and A. Liebsch, 1980, Phys. Rev. B **21**, 4306.
Polatoglu, H.M., M. Methfessel and M. Scheffler, 1993, Phys. Rev. B **48**, 1877.
Puschmann, A., J. Maase, M.D. Crapper, C.E. Riley and D.P. Woodruff, 1985, Phys. Rev. Lett. **54**, 2250.
Radzig, A.A. and B.M. Smirnov, 1985, Reference Data on Atoms, Molecules and Ions, Vol. 31, Springer Series in Chemical Physics. Springer-Verlag, Berlin.
Ramsey, M.G., D. Steinmüller, F.P. Netzer, T. Schedel, A. Santaniello and D.R. Lloyd, 1991, Surf. Sci. **251/252**, 979.
Rangelov, G., N. Memmel, E. Bertel and V. Dose, 1991, Surf. Sci. **251/252**, 965.
Rettner, C.T., H.E. Pfnür and D.J. Auerbach, 1985, J. Chem. Phys. **84**, 4163.
Richardson, N.V. and N.R. Palmer, 1982, Surf. Sci. **114**, L1.
Rieger, D., R.D. Schnell and W. Steinmann, 1984, Surf. Sci. **143**, 157.
Riffe, D.M., G.K. Wertheim, P.H. Citrin, 1990, Phys. Rev. Lett. 64, 571.
Saddei, D., H.-J. Freund and G. Hohlneicher, 1980, Surf. Sci. **95**, 257.
Saiki, R.S., G.S. Herman, M. Yamada, J. Osterwalder and C.S. Fadley, 1989, Phys. Rev. Lett. **63**, 283.
Salaneck, W.R., C.B. Duke, W. Eberhardt, E.W. Plummer and H.-J. Freund, 1980, Phys. Rev. Lett. **45**, 280.
Sandell, A., 1993, Thesis, Uppsala University.
Schichl, A., D. Menzel and N. Rösch, 1982, Chem. Phys. **65**, 225.
Schichl, A., D. Menzel and N. Rösch, 1984, Chem. Phys. Lett. **105**, 285.
Schmeisser, D., F. Greuter, E.W. Plummer and H.-J. Freund, 1985, Phys. Rev. Lett. **54**, 2095.
Schneider, C., H.-P. Steinrück, P. Heimann, T. Pache, M. Glanz, K. Eberle, E. Umbach and D. Menzel, 1988, Verhdl. DPG O-24.4.
Schneider, C., H.-P. Steinrück, T. Pache, P.A. Heimann, D.J. Coulman, E. Umbach and D. Menzel, 1990, Vacuum **41**, 730.
Schönhammer, K. and O. Gunnarsson, 1978, Solid State Commun. **26**, 399.
Seaburg, C.W., E.S. Jensen and T.N. Rhodin, 1981, Solid State Commun. **37**, 383.
Seaburg, C.W., T.N. Rhodin, M. Traum, R. Benbow and Z. Hurych, 1980, Surf. Sci. **97**, 363.
Sheppard, N., 1988, Ann. Rev. Phys. Chem. **39**, 589 and references therein.
Shinn, N.D., 1986, J. Vac. Sci. Technol. A **4**, 1351.
Shinn, N.D., 1990, Phys. Rev. B **41**, 9771.
Shinn, N.D. and T.E. Madey, 1984, Phys. Rev. Lett. **53**, 2481.
Shinn, N.D. and T.E. Madey, 1985, J. Chem. Phys. **83**, 5928.
Shinn, N.D. and K.-L. Tsang, 1990, J. Vac. Soc. Technol. A **8**, 2449.
Smith, R.J., J. Anderson and G.J. Lapeyre, 1976, Phys. Rev. Lett. **37**, 1081.
Smith, R.J., J. Anderson and G.J. Lapeyre, 1980, Phys. Rev. B **22**, 632.
Somorjai, G.A. and M.A. Van Hove, 1979, Adsorbed Monolayers on Solid Surfaces, Vol. 38, Structure and Bonding. Springer-Verlag, Berlin.
Spanjaard, D. and M.C. Desjouqueres, 1990, in: Interactions of Atoms and Molecules with Solid Surfaces, eds. V. Bertolani, N.H. March and M.P. Tosi. Plenum, New York, p. 255.
Sprunger, P.T. and E.W. Plummer, 1991, Chem. Phys. Lett. **187**, 559.
Stampfl, C. and M. Scheffler, 1995, Surf. Rev. Lett. **2** 317.
Stampfl, C., 1996, Surf. Rev. Lett. **3**, 1567.
Stampfl, C., J. Burchhardt, M. Nielsen, D.L. Adams, M. Scheffler, H. Over, W. Moritz, 1992, Phys. Rev. Lett. **69**, 1532.
Starke, U., P.L. de Andres, D.K. Saldin, K. Heinz and J.B. Pendry, 1988, Phys. Rev. B **38**, 12277.
Steinkilberg, M., 1977, Thesis, Technical University München.
Steinrück, H.-P., W. Huber, T. Pache and D. Menzel, 1989, Surf. Sci. **218**, 293.
Stroscio, J.A., S.R. Bare and W. Ho, 1984, Surf. Sci. **148**, 499.
Surman, M., S.R. Bare, P. Hofmann and D.A. King, 1987, Surf. Sci. **179**, 243.
Szeftel, J.M., S. Lehwald, H. Ibach, T.S. Rahman, J.E. Black and D.L. Mills, 1983, Phys. Rev. Lett. **51**, 268.
Taylor, J.B., 1933, I. Langmuir, Phys. Rev. **44**, 423.
Toennies, J.P., 1991, Experimental Determination of Surface Phonons by Helium Atoms and Electron Energy Loss Spectroscopy, Vol. 21, Springer Series in Surface Science. Springer-Verlag, Berlin, p. 111.

Turner, D.W., C. Baker, A.D. Baker and C.R. Brundle, 1970, Molecular Photoelectron. Spectroscopy. Wiley, New York.
Tüshaus, M., E. Schweizer, P. Hollins and A.M. Bradshaw, 1987, J. Electron Spectrosc. Relat. Phenom. **44**, 305.
Uhlenbrock, S., private communication.
Umbach, E., 1982, Surf. Sci. **117**, 482.
Umbach, E., A. Schichl and D. Menzel, 1980, Solid State Commun. **36**, 93.
Villars, D.S., 1931, I. Langmuir, J. Am. Chem. Soc. **53**, 486.
Walsh, A.D., 1913, J. Chem. Soc. 2266.
Wambach, J., G. Illing and H.-J. Freund, 1991, Chem. Phys. Lett. **184**, 239.
Weast, R.C., 1973, CRC Handbook of Chemistry and Physics, The Chemical Rubber Comp., 54th edn.
Weimer, J.J. and E. Umbach, 1984, Phys. Rev. B **30**, 4863.
Weimer, J.J., E. Umbach and D. Menzel, 1985, Surf. Sci. **159**, 83.
Weinelt, M., W. Huber, P. Zebisch, H.-P. Steinrück, M. Pabst and N. Rösch, 1992a, Surf. Sci. **271**, 539.
Weinelt, M., W. Huber, P. Zebisch, H.-P. Steinrück, B. Reichert, U. Birkenheuer and N. Rösch, 1992b, Phys. Rev. B **46**, 1675.
Wendin, G., 1981, Structure and Bonding, Vol. 45. Springer-Verlag, Berlin.
Wintterlin, J., R. Schuster, D.J. Coulman, G. Ertl and R.J. Behm, 1991, J. Vac. Sci. Technol. B **9**, 902.
Woodruff, D.P., C.F. McConville, A.L.D. Kilcoyne, Th. Lindner, J. Somers, M. Surman, G. Paolucci and A.M. Bradshaw, 1988, Surf. Sci. **201**, 228.
Wurth, W., J.J. Weimer, E. Hudeczek and E. Umbach, 1986, Surf. Sci. **173**, L619.
Yu, R. and P.K. Lam, 1988, Phys. Rev. B **37**, 8730.
Zaera, F., E. Kollin and J.L. Gland, 1985, Chem. Phys. Lett. **121**, 464.
Zangwill, A., 1988, Physics at Surfaces. Cambridge University Press, Cambridge.

This Page Intentionally Left Blank

CHAPTER 11

# The Metal–Semiconductor Interface

R. LUDEKE

*IBM Research Division*
*T.J. Watson Research Center*
*P.O. Box 218, Yorktown Heights*
*NY, 10598, USA*

*© 2000 Elsevier Science B.V.*
*All rights reserved*

*Handbook of Surface Science*
*Volume 2, edited by K. Horn and M. Scheffler*

# Contents


11.1. Introduction . . . 751
11.2. Basic concepts of the Schottky barrier . . . 752
11.2.1. Historical development . . . 752
11.2.2. Models for the Schottky barrier . . . 758
11.2.2.1. Metal induced gap states models . . . 758
11.2.2.2. Defect models . . . 764
11.2.2.3. Defects and metallic states: the delocalization model . . . 766
11.3. Schottky barrier properties and their measurement . . . 770
11.3.1. Schottky barrier capacitance . . . 770
11.3.2. Current transport . . . 772
11.3.2.1. Image force lowering of $\Phi_{sb}$ . . . 772
11.3.2.2. Thermionic emission model . . . 775
11.3.2.3. Internal photoemission . . . 779
11.3.2.4. Ballistic electron emission spectroscopy . . . 780
11.3.3. Photoemission methods . . . 780
11.3.3.1. Core level photoemission: band bending . . . 781
11.3.3.2. Photoemission spectroscopy: the role of surface photovoltage . . . 784
11.3.3.3. Core level photoemission: chemistry . . . 785
11.3.4. Schottky barrier formation and properties: case studies . . . 788
11.3.4.1. Spectroscopic studies of gap states . . . 788
11.3.4.2. Band bending: the role of metallic states . . . 792
11.3.4.3. Schottky barrier trends . . . 795
11.4. Ballistic electron emission microscopy . . . 799
11.4.1. Basic concepts . . . 799
11.4.2. Experimental technique . . . 803
11.4.2.1. STM/BEEM requirements and limitations . . . 803
11.4.2.2. UHV BEEM system . . . 805
11.4.3. Models of BEEM transport . . . 809
11.4.3.1. Planar tunneling theory . . . 809
11.4.3.2. Momentum conserving transport: the Bell–Kaiser model . . . 812
11.4.3.3. Quantum mechanical transmission effects . . . 818
11.4.3.4. Issues of transverse momentum conservation . . . 819
11.4.3.5. BEEM transport under conditions of nonconservation of $k_t$ . . . 821
11.4.3.6. First-principles computation of BEEM transport . . . 823
11.4.3.7. Image force, electric field and phonon scattering effects . . . 826
11.4.3.8. Monte Carlo methods . . . 830
11.4.4. Experimental BEEM results . . . 831
11.4.4.1. Threshold spectroscopies of metal–Si interfaces . . . 831
11.4.4.2. Threshold spectroscopies of metal–compound-semiconductor interfaces . . . 837
11.4.4.3. Energetic BEEM . . . 847
11.4.5. Summary and future prospects . . . 854
References . . . 855

## 11.1. Introduction

The importance of the metal–semiconductor (M–S) contact as a viable and fundamental electronic circuit element continues unabated. Its use affects all aspects of electron devices from non-rectifying or ohmic contacts necessary to apply power and sense electronic signals, to gate electrodes to control current flow in metal–semiconductor field-effect transistors (MESFET). The latter, as well as applications in photovoltaic devices, permeable chemical sensors, current rectifiers and radiation detectors, among others, rely on the more common, nonohmic or rectifying property of the M–S contacts. This property is a consequence of the formation of a potential barrier, or Schottky barrier, in the region of the semiconductor adjacent to the metal, that favors electrical current flow in one direction across the interface, but inhibits it in the opposite direction. This property is not only useful in devices, but is routinely applied in the laboratory to characterize materials properties such as dopant concentrations and profiles, as well as ionization levels of defects and impurities in semiconductors. In spite of the wide range of applications of the M–S contacts, there remain aspects in the basic understanding of the physical principles underlying the rectifying or Schottky behavior that demand further studies and clarification. To a certain degree the demand for further understanding depends on the person asked. Many theorists are satisfied with the present understanding of the physics underlying the Schottky barrier phenomenon, contending that the proposed models are able to give estimates of the barrier heights within a few tenth of an electron volt of measured barrier heights, which are in the 0.5 to 1.5 eV range for most semiconductors. However, this degree of uncertainty is totally unacceptable to VLSI circuit designers and device modelers who would only accept empirically determined barrier heights obtained using actual processing conditions during manufacture. This dichotomy of perception points to the difficulties in describing the relevant parameters that determine the Schottky behavior in a predictable manner. On the one hand the theorist can only aspire to describe or model a system that is nearly ideal, in that the metal and semiconductor, as well as their interface can be represented by defect free crystallographic media, although the metal is often represented as the ideal, but fictitious "jellium" metal. On the other hand, most if not all M–S systems are far from such an idealistic representation, and it is generally believed that the actual Schottky barrier height is often strongly influenced by deviations from ideality, which can take the form of simple crystallographic mismatch to strong interdiffusion and chemical compound formation. This reality has dissuaded theoretical activity in this area in recent times, not necessarily because of computational or mathematical difficulties, but rather due to a lack of M–S interfaces that are crystallographically speaking nearly perfect (although a few silicide-Si interfaces fall in this category), or are at least characterized well enough for modelling. The latter points to the experimental difficulties in determining the structural and chemical composition of the interface and particularly the role of defects, as well as assessing their influence on the electronic properties of the M–S interface. Nevertheless,

significant progress has been achieved over the last decade in the chemical and structural characterization of the interface to allow a better understanding of the role of the various physical properties that ultimately determine the Schottky barrier. In addition, novel applications of the scanning tunneling microscope (STM) have provided new insights into the formation process of the M–S interface during its nascent phase. An STM based spin-off technique, ballistic electron emission microscopy or BEEM, allows both the determination of Schottky barrier heights with unprecedented precision and spatial resolution, and the investigation of physical phenomena underlying electron transport across M–S interfaces. New applications of established techniques, such as cathodoluminescence, provide additional information on defect states in the semiconductor near the interface. Another direction that aids the understanding of the M–S interfaces falls under the name of interface engineering, i.e., the deliberate attempts to modify the structure and/or composition of the semiconductor at the interface or its vicinity in order to affect the Schottky barrier heights. Ideally these modifications are in the form of a well delineated narrow region of width of one to a few monolayers. The resulting changes in barrier height can be directly related to a particular mechanism influencing the potentials at the interface, provided that the intended changes at the interface are subsequently verified.

This chapter is intended to give an overview of the physics underlying the metal–semiconductor contact, while at the same time focus on recent developments in analytical techniques and how these bare on our understanding of the M–S contact, in particular on the electronic and the all important transport properties associated with this ubiquitous electronic device. Particular emphasis will be given to ballistic electron emission microscopy or BEEM, as this relatively recent technique opens up new perspectives on important transport issues across M–S interfaces. By necessity we will restrict the subject matter to well characterized M–S systems made up from semiconductors that are uniformly doped and devoid of intentional band gap modifications. Although of considerable technological significance, such engineered interfaces are beyond the scope of this article. The interested reader can refer to the excellent reviews by Capasso (1987), Gossman and Schubert (1993), Streetman and Shi (1992) and Shen et al. (1992). This restricted choice is dictated by a perceived need for a critical up-to-date survey of this field, yet bounded by the limitation of length in a field that still generates over 500 publications per year. Although this review will be largely tutorial and generally self-sufficient, the reader is encouraged to consult the many excellent and general books and reviews on the subject.

## 11.2. Basic concepts of the Schottky barrier

### *11.2.1. Historical development*

The first documented evidence for asymmetric behavior of current flow between two different materials was reported by Brown (1874), who observed a polarity dependent resistivity when electrodes of various metals were pressed against natural and synthetic metal sulfide samples. Confirmations soon followed by Adams and Day (1876) for Se. The "cat's whisker" concept of a metal wire in contact with a lead sulfide crystal rendered the discovery into practice as a rectifier (detector) of electromagnetic waves, which accelerated the

rapid growth of radio communications in the 1920's. A silicon point contact rectifier was patented by Pickard (1906) and a plate rectifier made of cuprous oxide was patented and described by Grohndal (1925, 1926). Although an understanding of the rectification principles had to await the concept of the electronic band structure of solids in the 1930's, Brown (1876) had already speculated on its origins, attributing the observations to a surface layer of high resistivity. This concept was vastly expanded upon by Schottky and co-workers (1929, 1931) who demonstrated that the voltage drop across a Cu–$Cu_2O$ interface not only occurred in a narrow region near the interface, the so-called "blocking layer", but that its width increased with reverse bias. Modelling the interface as a simple parallel plate capacitor, they were able to deduce the width of the unbiased blocking layer to be $\sim 0.3\ \mu$m. This width definitely excluded a tunneling mechanism as a plausible explanation of the rectification process, as Wilson (1932) had proposed soon after the concept of the band structure model of semiconductors had been developed. It was not until the late 1930's that the concept of a potential barrier in terms of a band structural picture was independently proposed by Schottky (1938) and by Mott (1938). Mott postulated that the origin of the barrier was due to the difference in work functions of the metal and semiconductor, which, upon intimate contact, drives a charge redistribution at the interface that equilibrates the chemical potential. Mott's view of the barrier region was based on the assumption that it was devoid of charge (absence of ionized donors for an n-type semiconductor), so that the potential varied linearly with distance. In contrast to this view, Schottky proposed the now universally accepted view that the barrier region contained a uniform distribution of stationary, charged impurities, thus formalizing the concept of a depletion region whose existence he had stipulated years earlier.

These concepts may be illustrated in a one-dimensional representation of the metal–semiconductor system before and after intimate contact. Figure 11.1 depicts the energy diagrams for an isolated metal, characterized by the work function $\phi_m$, and for a non-degenerately doped n-type semiconductor characterized by a band gap energy $E_g$ and an electron affinity $\chi_s$. Upon intimate contact, the Fermi levels in the two materials must equalize, which is accomplished in the present case by a flow of electrons from the semiconductor into the metal. These electrons leave behind an equal but positive charge of the ionized impurities from which they have emanated. The consequence of this mobile charge depletion in the semiconductor and the accumulation of the transferred charge onto the metal at the interface is the establishment of an electric field $\mathcal{E}$ that makes it energetically costly for an electron to approach the interface. In terms of the one-dimensional band structure representation this energy cost can be represented as an upward bending of the bands. For holes, on the other hand, the band bending would be downward. The situation after the Fermi levels have equalized is shown in Fig. 11.1b. The region over which the bands are not flat is the depletion or space charge region postulated by Schottky. Its width $w$ depends on the amount of band bending, the dopant concentration and the dielectric constant of the semiconductor. The width $w$ can be readily calculated by solving the one-dimensional Poisson equation

$$\frac{\partial^2 V}{\partial z^2} \equiv -\frac{\partial \mathcal{E}}{\partial z} = -\frac{\rho(z)}{\varepsilon_s \varepsilon_0},$$

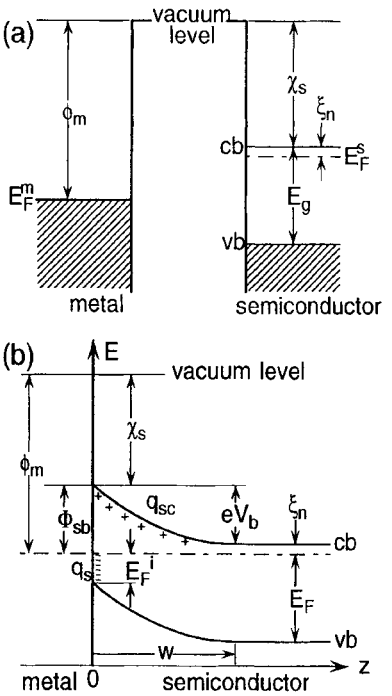


Fig. 11.1. One-dimensional energy diagram of the near-surface region of a metal and a n-type semiconductor before contact (a), and at equilibrium following intimate contact of the two surfaces (b). The latter represents the Schottky–Mott limit, i.e., an absence of dipole producing interface states, so that the Schottky barrier height $\Phi_{sb} = \phi_m - \chi_s$.

where $z$ is the coordinate normal to the interface, being positive in the semiconductor, $\rho(z)$ the charge density in the depletion region, $\varepsilon_0$ the permittivity of free space and $\varepsilon_s$ the dielectric constant of the semiconductor. Values $\varepsilon_s$ for some semiconductors are listed in Table 11.1. In the absence of other charges, e.g., compensating acceptor states or free carriers within the depletion layer (low temperature approximation), $\rho(z) = eN_D^+$, where $e$ is the charge of the electron and $N_D^+$ is the ionized donor density. Generally it is assumed that $N_D^+ = N_D$, the donor density, which is represented in the present solution by a uniform positive background charge instead of a random distribution of discrete charges. The first integration of the Poisson equation with the boundary condition $\mathcal{E}(w) = 0$ yields,

$$\mathcal{E}(z) = \frac{eN_D}{\varepsilon_0 \varepsilon_s}(z - w) = \mathcal{E}_m\left(\frac{z}{w} - 1\right), \tag{11.1a}$$

where $\mathcal{E}_m \equiv eN_D w/(\varepsilon_0 \varepsilon_s)$ is the magnitude of the maximum field at the interface. The second integration with the additional boundary condition $V(w) = 0$ gives

$$V(z) = \mathcal{E}_m\left(z - \frac{z^2}{2w} - \frac{w}{2}\right). \tag{11.1b}$$

Table 11.1
Some basic parameters for Si, Ge, GaAs and GaP

| | Si | Ge | GaAs | GaP |
|---|---|---|---|---|
| Lattice const. $a_0$ (Å) at 300 K | 5.431 | 5.646 | 5.653 | 5.450 |
| Energy gap $E_g$ (eV) at 300 K | 1.12 | 0.66 | 1.42 | 2.27 |
| Cond. band min.: symmetry & loc. | Δ[100] | L[1111] | Γ[000] | Δ[100] |
| Cond. band longitudinal mass $m_l/m_0$ | 0.92 | 1.59 | 0.063 | 0.91 |
| Cond. band transverse mass $m_{st}/m_0$ | 0.19 | 0.082 | 0.063 | 0.25 |
| Valence band heavy hole mass $m_{hh}/m_0$ | 0.49 | 0.34 | 0.50 | 0.67 |
| Valence band light hole mass $m_{lh}/m_0$ | 0.16 | 0.043 | 0.076 | 0.17 |
| Cond. band density of states $N_c$ ($cm^{-3}$) | $2.8 \times 10^{19}$ | $1.04 \times 10^{19}$ | $4.7 \times 10^{17}$ | $1.7 \times 10^{19}$ |
| Valence band dens. of states $N_v$ ($cm^{-3}$) | $1.04 \times 10^{19}$ | $6.0 \times 10^{18}$ | $7.0 \times 10^{18}$ | $1.48 \times 10^{19}$ |
| Dielectric constant $\varepsilon_s$ | 11.9 | 16.0 | 13.1 | 11.1 |
| Electron affinity $\chi_s$ (eV) | 4.13 | 4.06 | 4.13 | 3.75 |

These equations illustrate the linear dependence of $\mathcal{E}$ and the quadratic dependence of the potential $V$ on $z$. The band bending illustrated in Fig. 11.1 is given by $-|e|V(z)$ measured relative the band edges for $z > w$. It is maximum for $z = 0$: $eV_b = we\mathcal{E}_m/2$, from which we derive the expression for $w$

$$w = \left(\frac{2\varepsilon_0\varepsilon_s eV_b}{e^2N_D}\right)^{1/2}. \tag{11.2a}$$

At finite temperatures thermally excited electrons penetrate into the positively charged space charge region of an n-type semiconductor. This alters the charge balance whose net effect is a lowering of the band bending by $kT$. Thus at finite temperatures and for $eV_b \gg kT$ (Rhoderick and Williams, 1988)

$$w = \left[\frac{2\varepsilon_0\varepsilon_s(eV_b - kT)}{e^2N_D}\right]^{1/2} = L_D\left[2(eV_b/kT - 1)\right]^{1/2}, \tag{11.2b}$$

$L_D$, given by

$$L_D = \left(\frac{\varepsilon_s\varepsilon_0 kT}{e^2N_D}\right)^{1/2} \tag{11.3}$$

is the Debye length and represents a characteristic screening length in the semiconductor (Seeger, 1989). For the depicted unbiased junction, charge neutrality requires that the (negative) surface charge $q_s$ be compensated by the (positive) ionized donor charge in the depletion region, thus $q_s = -eN_Dw$. Substituting for $w$ from Eq. (11.2b),

$$q_s = -\left[2\varepsilon_s\varepsilon_0 N_D(eV_b - kT)\right]^{1/2} = -\left[2\varepsilon_s\varepsilon_0 N_D(\Phi_{sb} - \xi_n - kT)\right]^{1/2}. \tag{11.4}$$

Table 11.2

Dopant (donor) concentration dependent parameters for Si, GaAs and GaP. Generic Schottky barrier heights of 0.7, 0.8 and 1.2 eV were assumed for Si, GaAs and GaP, respectively, for the determination of band bending, image force effects and effective Schottky barrier heights

| | Si | | | GaAs | | | GaP | | |
|---|---|---|---|---|---|---|---|---|---|
| $N_d$ (cm$^{-3}$) | $10^{15}$ | $10^{17}$ | $10^{19}$ | $10^{15}$ | $10^{17}$ | $10^{19}$ | $10^{15}$ | $10^{17}$ | $10^{19}$ |
| $L_D$ (Å) | 1310 | 131 | 13.1 | 1370 | 137 | 13.7 | 1260 | 126 | 12.6 |
| $w$ (Å) | 7340 | 834 | 90 | 9430 | 1010 | 106 | 10600 | 1130 | 117 |
| $\xi_n$ (meV) | 265 | 146 | 55 | 160 | 65 | 0 | 252 | 140 | 63 |
| $\Phi_{sb}$ (eV) | 0.7 | 0.7 | 0.7 | 0.8 | 0.8 | 0.8 | 1.2 | 1.2 | 1.2 |
| $eV_b$ (eV) | 0.435 | 0.554 | 0.645 | 0.640 | 0.735 | 0.800 | 0.948 | 1.060 | 1.137 |
| $\delta z_i$ (Å) | 52 | 15.4 | 4.7 | 46 | 14.0 | 4.3 | 43 | 13.3 | 4.1 |
| $\delta\Phi_i$ (meV) | 12 | 39 | 129 | 12 | 39 | 127 | 15 | 49 | 157 |
| $\Phi_{sb}$ (eV) | 0.688 | 0.661 | 0.571 | 0.788 | 0.761 | 0.673 | 1.185 | 1.151 | 1.043 |

In the second equality of this equation use was made of the relation $\Phi_{sb} = eV_b + \xi_n$ between $V_b$ and the Schottky barrier height $\Phi_{sb}$, where $\xi_n$ is the energy between the Fermi level $E_F$ and the conduction band minimum in the bulk of the semiconductor, $\Phi_{sb}$ represents the minimum energy barrier an electron has to overcome to go from the metal to the semiconductor. The surface charge necessary to produce band bending of $\sim$1 V for $N_D \sim 10^{18}$ cm$^{-3}$ is $q_s \sim 10^{12}|e|$ cm$^{-2}$, or roughly one-electronic charge per 1000 surface atoms. Doping-concentration dependent values of $L_D$, $\xi_n$ and $w$ for Si, GaAs and GaP are shown in Table 11.2.

The magnitude or height of the barrier for an n-type semiconductor was proposed by Mott (1938) to be

$$\Phi_{sb} = \phi_m - \chi_s, \tag{11.5}$$

where $\phi_m$ is the work function of the metal and $\chi_s$ is the electron affinity of the semiconductor, i.e., the energy of the lowest empty conduction band state relative to the vacuum level. Equation (11.5) is based on strictly electrostatic arguments and assumes an absence of pre-existing surface charges in the semiconductor, that is, no initial band bending prior to junction formation, as well as an absence of charged interface states following the junction formation. The prediction of Eq. (11.5) that the barrier height for a given semiconductor varies directly with the metal work function is not observed for the most common, narrow band gap semiconductors. In fact, the relatively weak dependence on $\phi_m$ observed for Si and other covalent semiconductors prompted Bardeen (1947) to suggest that a large density of states at the interface could account for the observations by accommodating the charge redistribution without significantly affecting the position of $E_F^i$, the Fermi level relative to the band edge at the interface. He then proposed that the needed interface density of states arises from the intrinsic electronic states at the surface of the semiconductor, i.e., the large density ($\sim 10^{15}$ cm$^{-2}$) associated with the dangling bonds at the surface. The independence of $\Phi_{sb}$ on $\phi_m$ is now referred to as the Bardeen limit. In contrast, Eq. (11.5) is termed the Mott limit. The premise that the interface states in Bardeen's proposal derive

from the intrinsic semiconductor surface states was however challenged by Heine (1965), who contended that these states become resonances or virtual states due to their interaction with the metallic states. The metallic states, on the other hand, decay exponentially into the semiconductor band gap, which establishes an interface density of states into which charge can flow. This flow establishes an interface dipole that readily adjusts to differences in $\phi_m$ without appreciably affecting $E_F^i$. This model has become known under the label of MIGS, for metal induced gap states. Variation of it have been formulated over the years by Louie and Cohen (1976), Tejedor et al. (1977), Mele and Joannopoulos (1978), Tersoff (1984), Masri (1990), and others.

The notion of a weak metal dependency of $\Phi_{sb}$ is mostly restricted to the more covalent semiconductors like Ge, Si and the Ga and In containing III-V compound semiconductors. It was already realized by Schottky and coworkers (1942) that $\Phi_{sb}$ for Se varied linearly with $\phi_m$ but at a rate less than that predicted by Eq. (11.5). A linear dependence on $\phi_m$ was also reported for Si and other semiconductors (Cowley and Sze, 1965). These authors, as well as Heine (1965), proposed a description that would bridge the Bardeen and Mott limits. The model assumes: (1) the presence of a thin interface layer of width $\delta$ of order of an Ångström and of unspecified composition that is transparent to electron motion but capable to support a potential across it; and (2) the presence of interface states (acceptors for n-type semiconductors) of constant density $D_i$ states/cm$^2$ eV in the band gap, whose distribution is a step function beginning at an energy $E_i$ above the valence band edge. An energy diagram is shown in Fig. 11.2. The charge $q_i$ in the interface states is determined by the position of the Fermi level at the interface $E_F^i$, relative to $E_i$ and is given by $q_i = -eD_i\,(E_F^i - E_i)$. Both quantities, like $E_F$ in the semiconductor, are measured relative the valence band maximum.The equivalent charge density at the semiconductor interface is the sum of $q_i$ and the charge in the space charge region, given by Eq. (11.4). An equal, but opposite charge $q_m$ is established on the metal surface: $q_m = q_i - q_s$. As will be discussed in Section 11.2.2.2, the large screening effects of the charge in the metal results in $q_i \gg q_s$,

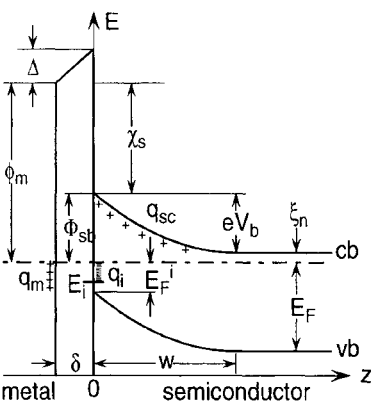


Fig. 11.2. Energy diagram of a metal/n-type semiconductor contact in the presence of acceptor states at the semiconductor side of the interface. These are filled to the Fermi level by an interface charge $q_i$, which is separated by a narrow interface layer of width $\delta$ from and equal but opposite charge $q_m$ residing on the metal surface.

so that $q_s$ can be neglected. The potential $\Delta$ across the interface layer, or dipole potential, is obtained by Gauss' law: $\Delta = eq_m\delta/\varepsilon_i$, where $\varepsilon_i$ is the permittivity of the interface region. Substituting for $q_m$ and using $E_F^i = E_g - \Phi_{sb}$, where $E_g$ is the band gap energy, one obtains $\Delta \approx e^2 D_i \delta(E_g - E_i - \Phi_{sb})/\varepsilon_i$. By inspection of Fig. 11.2, $\Delta = -\phi_m + \chi_s + \Phi_{sb}$, from which we can solve for an expression for $\Phi_{sb}$

$$\Phi_{sb} = \gamma(\phi_m - \chi_s) + (1 - \gamma)(E_g - E_i), \tag{11.6}$$

where $\gamma$ is given by

$$\gamma = \frac{\varepsilon_i}{\varepsilon_i + e^2 D_i \delta} \tag{11.7}$$

and may be viewed as an interface index that measures the effectiveness of the interface states to maintain a given charge in the presence of the dielectric screening by the interface layer. It can also be expressed as $\gamma = \partial\Phi_{sb}/\partial\phi_m$. The Bardeen limit is reached when $D_i$ is very large, whereas the Mott limit applies for a small $D_i$. A similar expression to $\gamma$ is the index of interface behavior $S = \delta\Phi_{sb}/\delta X_m$ (Kurtin et al., 1969). This parameter relates changes in $\Phi_{sb}$ to changes in $X_m$, the electronegativity of the metal. This definition avoids difficulties related to parameters of mixed surface and bulk contributions, such as work functions, that exhibit different values for different surface terminations (Hölzl and Schulte, 1979). Based on extensive Schottky barrier data, Kurtin et al. (1969) obtained a nearly bimodal distribution of $S$ when plotted against the electronegativity difference $\Delta X_s$ of the constituent atoms of the semiconductor. Their plot suggested an important role of the ionicity of the semiconductor in determining $S$ and $\Phi_{sb}$, but Schlüter (1978) reevaluated the data and concluded that saturation effects were not evident as originally reported by Kurtin et al. (1969). A similar distribution was reported for $S$ plotted against the heat of compound formation (Brillson, 1978) that lead to the suggestion that the interface chemistry plays a controlling role in the Schottky barrier formation. Considerable theoretical activity followed the phenomenological disclosures by Cowley and Sze and by Kurtin et al., all of them casting the interface density of states and the resulting dipole in terms of MIGS models (Yndurain, 1971; Louie et al., 1976, 1977; Tejedor et al., 1977; Mele and Joannopoulos, 1978; Zhang et al., 1986; Masri, 1990).

### *11.2.2. Models for the Schottky barrier*

#### *11.2.2.1. Metal induced gap states models*

It is instructive to discuss this model in terms of a one-dimensional (1-D) picture, as much of the physics is retained without adding the complexity of the three-dimensional case. Let us consider first a one-dimensional two-band model derived for a 1-D periodic potential $U(z) = U\cos(Kz)$, where $K = 2\pi/a_0$ is a reciprocal lattice vector with $a_0$ representing the real space periodicity (lattice constant). Near the Brillouin zone boundary at $K/2 = \pi/a_0$, the free electron bands open up a gap of width $2|U|$ centered about $E_0 = \hbar^2\pi^2/(2ma_0^2)$ (Ashcroft and Mermin, 1976). The shape or dispersion of the bands is strongly modified in the vicinity of the Brillouin zone boundary by $U$. It is convenient to express this

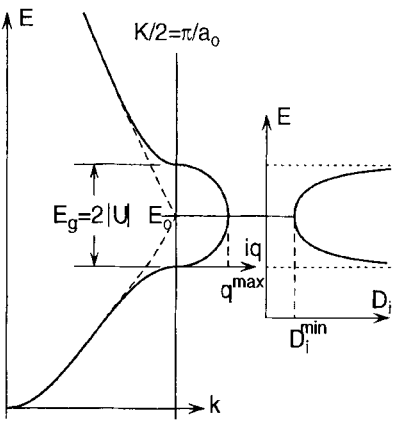


Fig. 11.3. Energy band diagram (left) for an one-dimensional periodic potential, and the resulting density of virtual gap states $D_i$ (right) to which metallic states can couple at a metal–semiconductor interface.

dispersion in terms of a momentum vector $q$ measured relative to $K/2$. Solution of the one-dimensional Schrödinger equation then yields

$$E = E_0 + E_q \pm (U^2 + 4E_0E_q)^{1/2} \tag{11.8}$$

with $E_q = \hbar^2q^2/(2m)$. The band dispersions are shown in Fig. 11.3 in the reduced zone representation. For an infinite chain, as assumed thus far, the Schrödinger equation allows physically meaningful solutions only for $q$ real. However, for a finite periodic chain, solutions with imaginary wave vector i$q$ are possible in the gap region at the chain's end, or "surface". These solutions are termed virtual gap states, and are represented by wave functions of the type (Tejedor et al., 1977):

$$\psi_s(z) \sim e^{-qz}e^{i|Kz+\phi|/2}, \tag{11.9}$$

where $\phi$ is a phase factor. For $q$ imaginary, we deduce from Eq. (11.8) that

$$\frac{\hbar^2q^2}{2m} \leqslant \frac{U^2}{4E_0}. \tag{11.10}$$

The variation of i$q$ in the band gap region is shown in Fig. 11.3. When the semiconductor is in close contact with a metal, metal wave functions of the appropriate energy and wave vector couple into the virtual gap states (Heine, 1965). The resulting hybrid states, called metal induced gap states, tail into the semiconductor over a distance given by the probability density $|\psi_s(z)|^2 \sim e^{-2qz}$ of the virtual gap states. This simple two-band model does not take into account the total three-dimensional charge density of the valence states of the semiconductor that would tend to screen the penetrating MIGS. We can fix this in ad-hoc

fashion by including a dielectric constant $\varepsilon_s$. A density of states associated with the MIGS is given by

$$D_i = \int e^{-2qz} n_m(E)\, dz \approx \frac{n_m(E)}{2q\varepsilon_s}, \tag{11.11}$$

where $n_m(E)$ is the volume density of states per unit energy of the metal. It is not expected to vary strongly with energy for free electron metals. The functional form of $D_i$ is shown in Fig. 11.3. The divergence at the band edges is a consequence of the one-dimensional model. The minimum in $D_i$ occurs near $E_0$ for $q = q^{max}$, which from Eq. (11.10) is

$$D_i^{min} \approx \frac{2^{1/2}\hbar n_m E_0^{1/2}}{m^{1/2}\varepsilon_s E_g}, \tag{11.12}$$

where $E_g = 2U$ is the energy gap of the semiconductor. Equation (11.12) predicts that $D_i$ is inversely proportional to the gap energy. Consequently the interface index $\gamma$, defined by Eq. (11.7), increases with $E_g$ (and increasing ionicity) in qualitative agreement with observations by Kurtin et al. (1969). The ratio $D_i^{min}/n_m$ can be interpreted as a mean penetration depth $\delta_s$ of the MIGS at midgap

$$\delta_s \approx \frac{2^{1/2}\hbar E_0^{1/2}}{m^{1/2}\varepsilon_s E_g}. \tag{11.13}$$

Estimates of $\delta_s \approx 1.1$ Å for Si and 0.7 Å for ZnS are obtained by assuming a generic effective valence band width $E_0 \approx 12.5$ eV (Harrison, 1980), as well as bulk dielectric constants and $E_g$'s equal to the minimum energy gap.

A similar "U"-shaped distribution for $D_i$ can be obtained by a different approach to the MIGS concept. It is known from adsorption theory that discreet valence states in an atom become energy broadened resonances when the atom is in the immediate vicinity of a metal surface (Gadzuk, 1967). The source of the broadening is a lifetime effect due to the finite probability that an electron in the formerly stationary state of the free atom can tunnel into the continuum of states of the metal. The lifetime $\tau$ can be calculated by a "golden rule" time dependent perturbation approach

$$1/\tau = \frac{2\pi}{h}|H_{if}|^2 \rho_f, \tag{11.14}$$

where $H_{if}$ is the matrix element of the perturbing potential, and $\rho_f$ is the density of final unperturbed states (Merzbacher, 1970). The lifetime broadening $\Gamma = h/\tau$ is of the order of 1 eV for atoms adsorbed on metals (Gadzuk, 1967). Dangling bond states on the free surface of a semiconductor are stationary states as well, and should exhibit a behavior in the presence of metallic states similar to atomic levels. The ensuing delocalization of the dangling bond states is schematically shown in Fig. 11.4. The states near the bottom of the conduction band represent empty states derived from empty dangling bonds, whereas the shaded band near the top of the valence band represents filled states derived from the

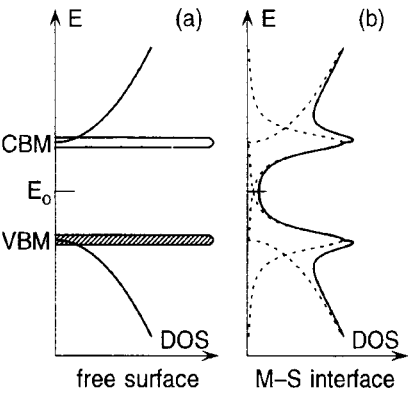


Fig. 11.4. Schematic representation of the density-of-states (DOS) at a semiconductor surface (a), with empty and filled surface states shown as narrow bands. These broaden into resonances in the presence of metallic states at the metal–semiconductor interface (b). In this simplified picture the broadening of the conduction and valence band edges near the interface has been neglected.

filled dangling bond states. The empty and filled band concept is retained in the resonances, with a crossover of these characteristics occurring at $E_0$. This approach was used by Mele and Joannopoulos (1978) to calculate a broadening of $\Gamma \approx 1$ eV for Si(111) dangling bond states in the presence of a "jellium" metal with electron densities similar to Al. They further estimated a value for $D_i \approx 0.64$ states/eV per surface Si atom, which is in excellent agreement with results obtained by Louie et al. (1977) using pseudopotential theory.

The work of Louie et al. (1977) represents the most sophisticated calculations to date of the M–S interface in the framework of the MIGS concept. Using a "jellium" model to describe the Al layer in contact with Si(111), GaAs(110), ZnSe(110) and ZnS(110) surfaces, a selfconsistent pseudopotential method was used to calculate barrier heights, the interface density of states in the band gap and the penetration of the tails of the MIGS into the semiconductor. The charge distribution of the penetrating MIGS is shown in Fig. 11.5. The results clearly show that for the wide band gap and more ionic semiconductors the penetration of the MIGS is reduced. A similar conclusion is indicated by the simple two band-model (Eq. (11.13)), which predicts values in fair agreement with those of Fig. 11.5. The local density of states as a function of energy for atomic layers parallel to the interface, progressing from the Al (regions I–III) through the interface (region IV) and into the Si (regions V and VI) is shown in Fig. 11.6 (Louie and Cohen, 1976). The filling-in of the Si band gap due to the MIGS is clearly seen for the interface layer (region IV), with some evidence of their penetration seen as well in the next layer (region V). Also evident in region III is the penetration of Si valence band states into the Al, which results in a delocalization of the Al states at the bottom of the Al valence band.

Much of the earlier theoretical work concerned itself with calculating $D_i$ and then $\gamma$ (Eq. (11.7)) or the index of interface behavior

$$S \equiv \frac{\partial \Phi_{sb}}{\partial X_m} = \frac{A}{1 + e^2 D_i \delta / \varepsilon_0}, \tag{11.15}$$

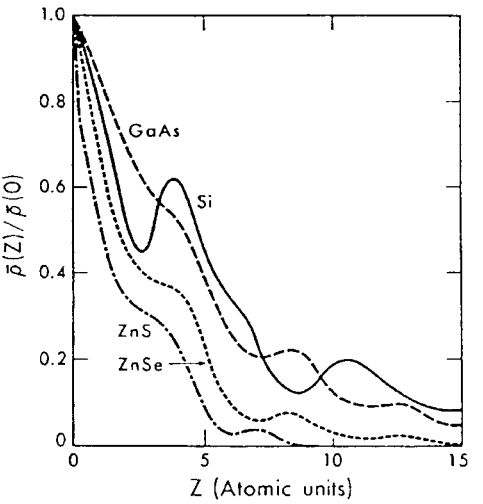


Fig. 11.5. Charge distributions of the penetrating tails of the metal induced gap states (MIGS) in the semiconductor gap. $\bar{\rho}(z)$ is the total charge density for these states averaged parallel to the interface. $z = 0$ is at the edge of the jellium core that represents the metal (after Louie et al., 1977, with permission).

where $A$ is an empirically determined constant in the range of 2.0–3.0, with a best estimate of 2.86 proposed by Schlüter (1978). Various approaches have been suggested to estimate $\delta$ (Heine, 1965; Louis et al., 1976; Louie et al., 1977; Schlüter, 1978; Ihm et al., 1978). Following Schlüter (1978),

$$\delta = \delta_m + \delta_s, \tag{11.16}$$

where $\delta_m \approx 0.5$ Å represents a typical screening length in the metal and $\delta_s$ is given by Eq. (11.13). More precise values were obtained by Louie et al. (1977) for the semiconductors shown in Fig. 11.5. Thus $\delta \approx 1.2$–2 Å, or approximately the width of a monolayer.

The calculation of $\Phi_{sb}$ is a much more difficult task than calculating $\gamma$ and $S$. The fundamental problem lies in establishing a datum for a common lineup of states on both sides of the junction, a problem of substantial difficulty even for lattice matched heterojunctions of two similar semiconductors. For M–S interfaces the concept of the charge neutrality level was first proposed by Tejedor et al. (1977). Although in principle a property of the bulk semiconductor (Tersoff, 1984), its concept is best understood at a surface or interface, where its position in the band gap marks the energy at which the virtual gap states exhibit equal admixture of valence and conduction band character. In our simple band picture the charge neutrality level $E_0$ is located near midgap in Fig. 11.3. To first order the density of states at the charge neutrality level is large enough to keep the Fermi level in its vicinity independent of the metal. Based on this view, Tersoff (1984) argued that by calculating $E_0$ for the 3-D band structure one could obtain the canonical value for $\Phi_{sb}$. Indeed, his calculated values fall well within the range of $\Phi_{sb}$ reported for different metals on a number of common semiconductors.

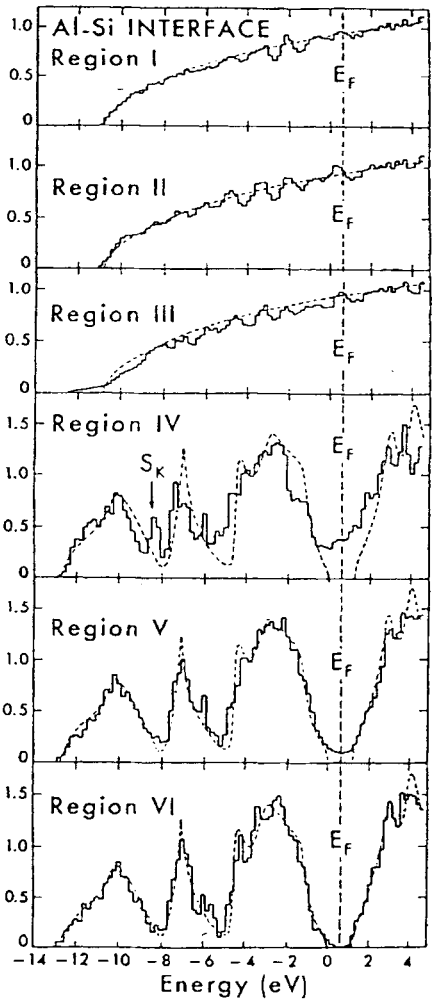


Fig. 11.6. Local density-of-states for slices or regions parallel to the aluminum–silicon interface. Regions I and II in the Al, and V and VI in the Si are mostly bulk-like. The interface is between regions III and IV. The width of each slice is equal to the Si bond length of 2.35 Å (after Louie and Cohen, 1976, with permission).

A general problem with the MIGS models is their inability to predict barrier heights of a given semiconductor for different metals. The reasons for this are multifold, ranging from neglect of interactions between a realistic "non-jellium" metal and the semiconductor at the interface, to the modification of the semiconductor band structure by the metallic states. Both these points should have metal-dependent effects on the interface density of states. The role of many body effects, including exchange and correlation effects, on the semiconductor band structure has been explored by Inkson (1972, 1973, 1974), who predicted a collapse or closure of the semiconductor band gap in the vicinity

of the metal. Recently, Charlesworth et al. (1993) readdressed this issue for a more realistic M–S system, namely Al/GaAs(110), and concluded that the band gap narrowing occurred predominantly due to image force effects in the conduction band. Their role in affecting the position of $E_F^i$, and hence $\Phi_{sb}$ was not addressed. Band structure calculations for realistic M–S interfaces have been presented for the epitaxial $NiSi_2$/Si(111) system by a number of groups (Das et al., 1989; Fujitani and Asano, 1990; Ossicini et al., 1990; Stiles and Hamann, 1991a) to explain the different $\Phi_{sb}$ values of 0.65 and 0.79 eV reported by Tung (1984) for type A and type B interfaces, respectively. These two interfaces differ only by a 180° lattice rotation about the interface normal that leaves intact the nearest neighbor bonding coordination of atoms at the interface. These efforts, as well as calculations for another lattice matched M–S interface, the $CoSi_2$/Si(111) system (Stiles and Hamann, 1991b), represent the sole examples to date of modeling M–S interfaces of known structural composition.

*11.2.2.2. Defect models*

Most of the studies of the formation of the metal–semiconductor interface were made on vacuum cleaved (110) surfaces of the tetrahedraly coordinated group III-V and to a lesser extent on the II-VI compound semiconductors. The basis for this was the observation by Huijser et al. (1977) that most well cleaved surfaces exhibited little band bending, which indicates an absence of both intrinsic and extrinsic surface states in the band gap. Thus defect levels generated by deposition of metal atoms or non-metallic adsorbates could induce band bending if charged. The band bending can readily be determined spectroscopically by photoemission or with a Kelvin probe that measures changes in the surface potential. As was pointed out in the discussion following Eq. (11.4), band bending of 1 V corresponds approximately to one electronic charge per $10^3$ surface atoms, which readily allows monitoring of (charged) surface coverages as small as $10^{-4}$ of a monolayer. Nearly all studies of band bending as a function of metal coverage on well cleaved surfaces (see Section 11.3.3.1) indicated that most band bending had ceased at coverages of a monolayer or less, and that frequently its magnitude appeared to be independent of the metal. The term "pinned" Fermi level has been used to describe this invariance of the final position of $E_F^i$. When first reported by Lindau et al. (1978) for some III-V semiconductors, this apparent work function independence of $\Phi_{sb}$ prompted Spicer et al. (1979) to attribute the origin of the pinning to defects. Moreover, they observed a slightly lower ~0.2 eV "pinning" position for p-type semiconductors. The "pinning" positions were interpreted in terms of defects states (acceptors for n-type and donors for p-type semiconductors) that were native or intrinsic to the semiconductor, as their energy, or more precisely $E_F$ at the interface did not change with the metal. Spicer et al. (1980) referred to this interpretation as the universal defect model. It was suggested that such defects were generated during the formation process of the M–S interface. Specific defects that were proposed include anion vacancies (Daw and Smith, 1981) and antisite defects (Allen and Dow, 1981), e.g., anion on a cation site in a III-V compound semiconductors.

However, it was pointed out by Zur et al. (1983) that differences in "pinning" positions for n- and p-type reported by Spicer et al. (1979, 1980) were only possible for low metallic coverages for which the metallic character, also referred to as metallicity, of the overlayer had not yet been established. In this case the charged defect density necessary for the

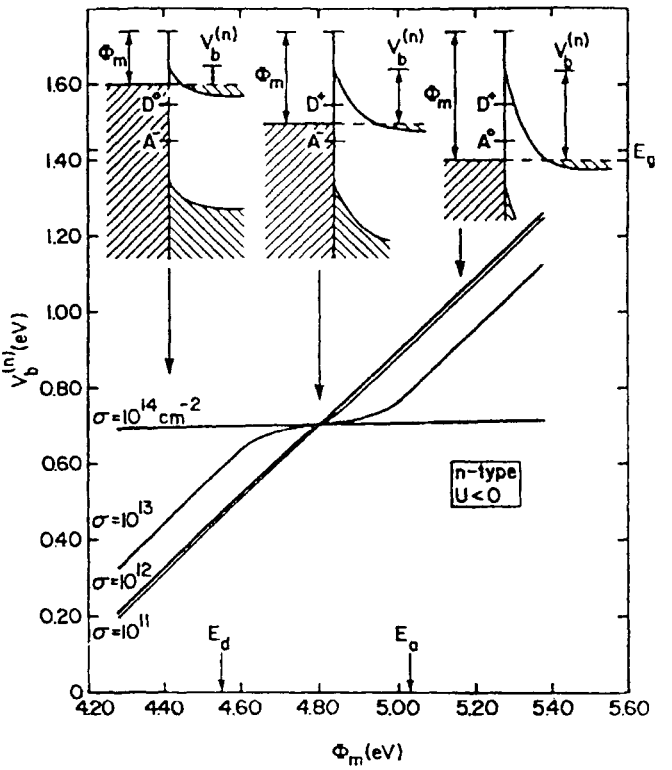


Fig. 11.7. Barrier height $V_b$ for n-GaAs as a function of metal work function for various densities of interface charge centers $\sigma$. Each charge center is allowed three charge states: acceptor (−), neutral or donor (+). A negative $U$ potential is assumed. The levels of the charged center are $E_a = E_g/3$ and $E_d = 2E_g/3$ (after Duke and Mailhiot, 1985, with permission).

observed band bending, obtained with Eq. (11.4), is $\sim 10^{-12}|e|\,\mathrm{cm}^{-2}$. On the other hand, for a completed metallic layer Zur et al. pointed out that $E_F^i$ for the n- and p-type material should be within 50 meV, and much less if there is a large density of interface states. This conclusion affirms the experimentally observed gap sum rule, that is, the sum of the Schottky barrier heights for a given metal on an n-type and p-type semiconductor equals the energy gap of the semiconductor. They further noted that because of screening by the metallic states, a substantially larger defect charge density is required at the interface than for the free surface case, a conclusion reached as well by Duke and Mailhiot (1985). Model calculations by both groups, based on arbitrarily positioning the defect centers 5–10 Å from the interface, gave similar results on the required number of charged defects ($\sim 10^{14}$ cm$^{-2}$) necessary to maintain a band bending of $\sim 1$ eV. The dependence of the Schottky barrier height on the metal work function in the presence of defect levels of density $\sigma$ is shown in Fig. 11.7 (Duke and Mailhiot, 1985). The particular defect chosen in this calculation is a 3-state level with charge states $+e$ (donor), $-e$ (acceptor) and 0 (neutral), with the donor state $D^0$ lying higher in the band gap than the acceptor state $A^0$, as schematically shown in the

insets of Fig. 11.7. The defects are assumed to be located within a distance $d = 10$ Å from the interface. In their absence or for low densities $E_F^i$, or equivalently $\Phi_{sb} = E_g - E_F^i$, is determined by the potential difference $\phi_m - \chi_s$, which represents the Schottky–Mott limit as indicated by the straight line in Fig. 11.7. If $\sigma$ is large ($\sim 10^{14}$ cm$^{-2}$) the potential difference is compensated by the formation of an interface dipole $d\sigma^{\pm}$ of sufficient strength to keep $E_F^i$ pinned between the two ionization levels of the defect (center diagram). For intermediate densities, e.g., $10^{13}$ cm$^{-2}$, the dipole is only able to compensate part of the potential difference up to $|\phi_m - \chi_s - \Phi_{sb}| = e^2 d\sigma^{\pm}/\varepsilon\varepsilon_0$. Once all acceptors or donors are charged (left and right inserts of Fig. 11.7), additional changes of the potential difference $\phi_m - \chi_s$ will cause the Fermi level to move freely within the band gap, but above the donor or below the acceptor levels, at a rate equal to the change in the potential difference $\phi_m - \chi_s$. That is, the Schottky–Mott picture is regained. In this model, both acceptor and donor states are required to provide the symmetric response shown in Fig. 11.7. Other shapes result for different donor and acceptor distributions and/or different level schemes (Zur et al., 1983; Duke and Mailhiot, 1985).

An important conclusion of the above discussion is that an interface defect density of $\sim 10^{14}$ cm$^{-2}$ is required to render $\Phi_{sb}$ relatively insensitive to variations in $\phi_m$. This density, if associated with a specific native defect should be observable by spectroscopic techniques; however, thus far no observation directly attributable to native defects have been reported. Instead, the evidence for states in the band gap region observed spectroscopically by photoemission and inverse photoemission (Schäffler et al., 1987a) and with cathodoluminescence (Viturro et al., 1986) indicates a strong metal dependence of their origin. This will be further discussed in Section 11.3.

Most of the earlier band bending studies suggested that the role of the metal was secondary to the formation of the Schottky barrier. However, upon a more careful analysis of the line shape of the photoemission core level signal to exclude chemical effects, it was discovered that additional band bending could take place following the establishment of metallic characteristics in the overlayer of some M–S systems (details will be given in Section 11.3.4.2). The metallic character in the forming metal overlayer is usually determined by the appearance of a metallic Fermi edge in the conduction band photoemission spectrum. Subsequent to this additional, metal-promoted band bending the Fermi level positions at the interface for n- and p-type material coincided, as predicted by Zur et al. (1983). These experiments demonstrated for the first time the importance of the metallic character in the overlayer. However, these observations can be affected by band bending induced by the photon flux used in the experiments (see Section 11.3.3.3). The onset of metallic character in the overlayer opens an interesting question, namely that of the role of MIGS in determining the Schottky barrier height in the presence of a large density of defect states at the interface. Although this question remains largely open, a simple model that addresses some aspects of this important issue will be discussed in the next section.

*11.2.2.3. Defects and metallic states: the delocalization model*

The realization that both defects and the presence of the metal are important to the formation process of the Schottky barrier led Ludeke et al. (1988) to assess their combined role. It was already known from the work by Gadzuk (1967) that the discrete valence levels of an isolated atom would assume a broadened energy distribution, termed a resonance,

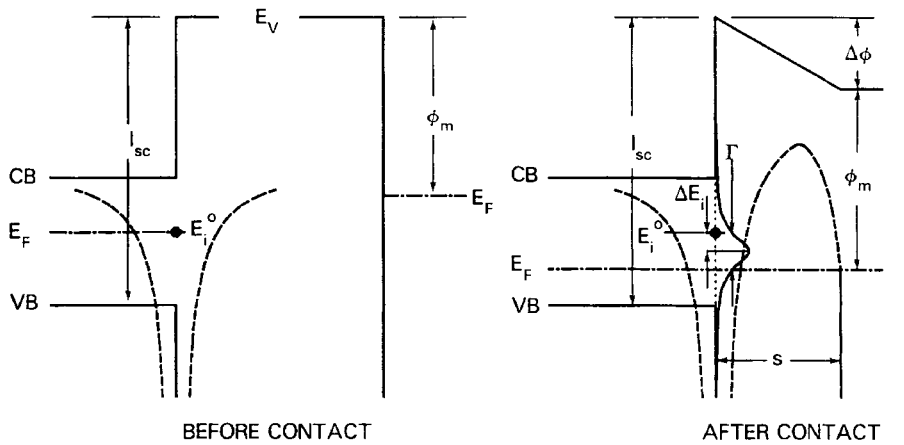


Fig. 11.8. Energy diagrams for a semiconductor with a surface impurity level $E_i^0$ prior (left panel) and after contacting a metal characterized by a work function $\phi_m$. The impurity level broadens by an amount $\Gamma$ in the presence of the metal and shifts by $\Delta E_i$ due to screening (image force) effects. The dashed line represents the potential of the impurity (after Ludeke, 1989).

when the atom was adsorbed on a metal surface. For such an adatom the valence orbitals can couple to the metallic states, thereby allowing electrons to tunnel between adatom and metal, which limits their life or residence time in the (perturbed) atomic orbitals. As a result of the uncertainty principle the energy level is no longer discrete or well defined, corresponding to an infinite lifetime in the isolated atom, but broadens into a resonance of width $\Gamma_0 \approx 1$ eV.

The situation is analogous to the above for a localizes impurity level in the semiconductor band gap, also referred to a "deep" level, when the impurity is located at or near the metal–semiconductor interface. A "deep" impurity has many of the characteristics of an atom (Jaros, 1982), but with a level structure that is narrower than that of an atom because of the screening of the dielectric medium of the semiconductor that is absent for an adatom on the free metallic surface. The dielectric response due to the valence charge of the semiconductor will more effectively reduce or screen the penetration the metallic states, thereby increasing the lifetime of the impurity level and narrowing the energy width of the resonance. An energy diagram depicting a generic impurity level of energy $E_0$ at the semiconductor surface before and after contact with the metal is shown in Fig. 11.8. It can be shown that the broadening upon delocalization of the impurity level in the presence of the metal can be described by a Lorentzian energy distribution (Ludeke et al., 1988)

$$\rho_i(E) = \frac{1}{\pi} \frac{\Gamma/2}{\{E - [E_i^0 - \Delta E_i(q_{\text{eff}})]\}^2 + (\Gamma/2)^2}, \tag{11.17}$$

where $\Gamma$ is the full width half maximum broadening parameter and $\Delta E_i$ is an image force correction arising from the screening of an effective charge $q_{\text{eff}}$ residing in the delocalized impurity state by the electrons in the metal. It is generally much smaller than $E_i^0$, and may

be neglected. $\rho_i$ may be looked at as a local density of states that can accommodate up to one electronic charge, i.e., $\int_{-\infty}^{\infty} \rho_i(E)\,dE = 1$. Since the level is no longer localized the average charge $q_{eff}$ residing in the resonance can assume a value less than one. Its value will be determined by the equilibrium conditions after intimate contact between metal and semiconductor has been established. At equilibrium the Fermi level $E_F$ is constant throughout the system, which generally can be achieved only through a charge redistribution at the interface. For the situation shown in Fig. 11.8, charge from the metal must flow into the resonance, leaving a positive counter charge at the metal surface. This establishes a dipole potential $\Delta\phi$ at the interface of sufficient magnitude to equilibrate the Fermi level in the absence of an external field. Hence at equilibrium the Fermi level is given by

$$E_F = I_{sc} - \phi_m - \Delta\phi, \tag{11.18a}$$

where $I_{sc}$ represents the ionization energy of the semiconductor. The measured values of $I_{sc}$ and $\phi_m$ for free surfaces contain contribution from both the bulk or internal portion of the crystal and from the surface (dipole contribution), whereas in Eq. (11.18a) only the internal contribution should be included. However, since $I_{sc}$ and $\phi_m$ always appear here as differences, the surface contributions, which are comparable (Duke and Mailhiot, 1985), nearly cancel when the experimental values are used in the calculations. The dipole potential $\Delta\phi = 4\pi N_i e^2 q_{eff}\lambda_{eff}$, where $N_i$ is the areal density of impurity sites on the semiconductor side of the interface and $\lambda_{eff}$ is the effective separation between $q_{eff}$ and its counterpart near the positive ion cores of the metal. It is given by $\lambda_{eff} \approx s/\varepsilon + \lambda_{TF}$, where $\lambda_{TF}$ is the Fermi–Thomas screening length, $s$ the separation between the impurity site and the metal surface and $\varepsilon$ an effective dielectric function (Louie et al., 1977). The effective charge $q_{eff}$ at the defect site can be obtained by integrating $\rho_i(E)$: $q_{eff}\int_{-\infty}^{\infty} f_F(E)\rho_i\,dE$, where $f_F(E)$ is the Fermi function. The low temperature limit is assumed for convenience and simplicity, for which integration of Eq. (11.17) gives

$$q_{eff} \overset{T\to 0}{=} \int_{-\infty}^{E_F} \rho_i(E)\,dE = \frac{1}{\pi}\left[\tan^{-1}\frac{E_F - (E_i^0 - \Delta E_i(q_{eff}))}{\Gamma/2} + \frac{\pi}{2}\right]. \tag{11.19}$$

Both the Fermi energy, now explicitly written as

$$E_F = (I_{sc} - \phi_m) - 4\pi\lambda_{eff}e^2 N_i q_{eff} \tag{11.18b}$$

and $\Delta E_i$ depend on $q_{eff}$, so that Eqs. (11.18b) and (11.19) must be solved self-consistently. The image force lowering $\Delta E_i(q_{eff})$ can be approximated by the image force potential (Newns, 1969; Inkson, 1971): $q_{eff}^2 e^2/4\varepsilon(s + \lambda_{TF})$. As we will determine, $q_{eff} \lesssim 0.1$ for most metals, so that $\Delta E_i(q_{eff})$ in most cases is negligible.

Reasonable estimates of all parameters in Eqs. (11.18b) and (11.19) can be made with the exception of $E_i^0$, which in principle is different for each metal induced impurity state. Experimentally its values fall within a few tenth of an eV of midgap for GaAs, for which a model calculation will be presented next (Ludeke et al., 1988; Ludeke, 1989). The simplifying assumption was made that $E_i^0$ lies 0.71 eV above the valence band maximum and is independent for all metals on GaAs. The electrically active density of defect states $N_i$

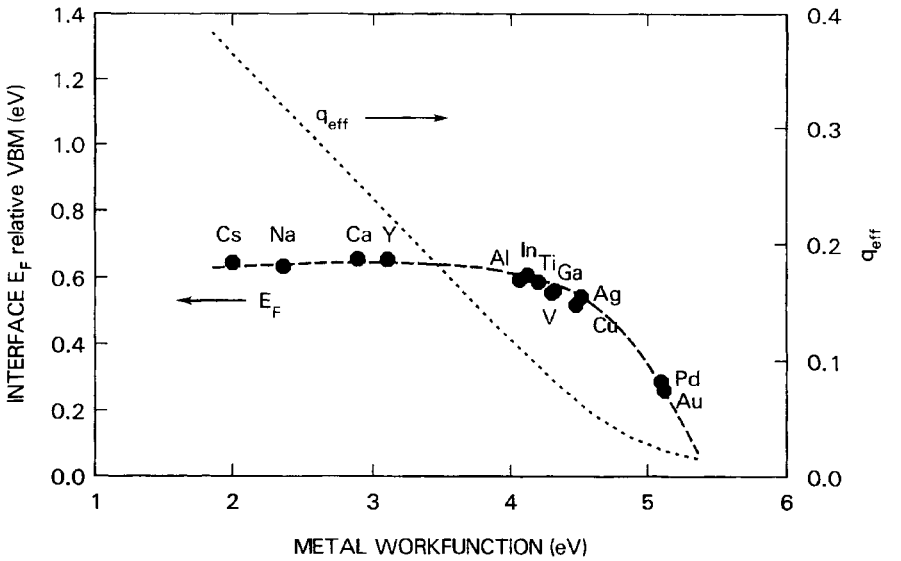


Fig. 11.9. Metal work function dependence of the interface Fermi level position for GaAs: solid circles and dashed line are predictions of the delocalization model for a midgap defect level. The dotted line represents the effective charge $q_{\text{eff}}$ in units of the electron charge residing at each defect site. The density of defect sites $N_i$ was assumed to be 1/2 ML or $4.43 \times 10^{14}$ cm$^{-2}$ (after Ludeke, 1989).

was taken to be limited to 1/2 ML ($4.43 \times 10^{14}$ cm$^{-2}$ for GaAs(110)). With $\lambda_{\text{eff}} = 1$ Å, $I_{\text{sc}} = 5.56$ eV and values of $\Gamma$ ranging from 0.016 eV for Cs to 0.081 eV for Cu, $q_{\text{eff}}$ and $E_{\text{F}}$ were calculated for a number of metals on GaAs. The results are shown in Fig. 11.9. The dashed line through the data points are solutions of Eqs. (11.18a) and (11.19) with a single value of $\Gamma = 0.062$ eV, which is the average of the values for the different metals. The near coincidence of the curve and data points indicates a somewhat weak dependence of the solution on the broadening parameter. The model predicts a non-linear dependence of $E_{\text{F}}$ on $\phi_{\text{m}}$ (or the electronegativity $X_{\text{m}}$ which is linearly related to $\phi_{\text{m}}$). For $\phi_{\text{m}} \lesssim 4$ eV the curve is essentially flat, although a slight rise in $E_{\text{F}}$ is predicted with increasing $\phi_{\text{m}}$. This rise is a consequence of the slight dominance of image force contributions due to the relatively large $q_{\text{eff}}$ for the low $\phi_{\text{m}}$ metals. The values of the effective charges are shown in Fig. 11.9 as well. As can be seen, their values for $\phi_{\text{m}} > 4$ eV are quite small, so that the resonances are essentially neutral, and Coulombic effects in general can be neglected. Also in this range the position of $E_{\text{F}}$ drops rapidly in the band gap as $\phi_{\text{m}}$ increases. The reason for this behavior is that only a small charge transfer is required to equalize the potentials. This charge density occupies only a fraction of the local density of states, thereby keeping $E_{\text{F}}$ positioned low in the Lorentzian tails. The predictions of the delocalization model will be compared with experimental results in Section 11.3.4.3.

The essential conclusions of this model is that defect states within one or two monolayers of the M–S interface, the region where such defects are most likely to be generated by the fabrication process of the contact, will be strongly modified by the metallic states. This modification broadens the former defect/impurity levels into resonances ~0.1 eV wide

while still retaining aspects of a near midgap impurity level. That is, the metal states are not capable to screen out completely the impurity states and their existence in the modified form, if of sufficient density, must be reckoned with in any complete Schottky barrier model. In addition, the nature of the resonance obviates the need for separate donor and acceptor impurity levels that otherwise need to be invoked if sole reliance is made of buried defect states, as discussed in the previous section.

## 11.3. Schottky barrier properties and their measurement

In this section we will discuss electronic and transport properties of Schottky barriers and how these properties can be extracted from experimental data. Only nearly ideal systems will be considered here; by this is meant that the semiconductor has a single homogeneously distributed dopant level, is lightly to moderately doped, the space charge layer is devoid of charge traps and there is an absence of any interlayer other than that due to interface reactions between the metal and the virgin semiconductor surface. Exceptions to this ideality and their bearing on understanding the M–S interface behavior will generally be noted, but further details will only be found in referenced material.

The experimental methods discussed in this section are grouped into Schottky barrier determining methods that include capacitance, transport, and internal photoemission techniques, and spectroscopic methods that include photoemission and inverse photoemission spectroscopies, contact potential methods and cathodoluminescence. The latter group is primarily used to characterize M–S interface properties, such as the electronic structure, interfacial chemistry, and their changes during the formation of the interface. Among these methods, core level photoemission spectroscopy can gather information on both band bending and chemistry during interface formation. All of these methods are well established and known techniques, and only limited space will be devoted to their description. The newest of the techniques, ballistic electron emission microscopy (BEEM), will be featured in Section 11.4.

### *11.3.1. Schottky barrier capacitance*

As already realized by Schottky and Deutschmann (1929) the M–S contact consists of two charge regions of opposite polarity, the interface charge $q_s$ and the stationary charge of the ionized dopant atoms in the depletion region, that are separated by the dielectric medium of width $w$ of the semiconductor. When a bias $V$ is applied across the junction both $q_s$ and $w$ change by an amount determined by replacing $V_b$ with $(V_b - V)$ in Eqs. (11.2) and (11.4). A schematic representation of an M–S contact under forward ($V > 0$) and reverse ($V < 0$) biases is shown in Fig. 11.10. The differential capacitance $C \equiv A_d|\partial q_s|/\partial V$ for the M–S junction of area $A_d$ can be readily obtained by differentiating Eq. (11.4) after this substitution. The result is

$$C = A_d\left[\frac{e\varepsilon_s\varepsilon_0 N_D}{2(V_b - V - kT/e)}\right]^{1/2} = \frac{\varepsilon_s\varepsilon_0 A_d}{w}. \tag{11.20}$$

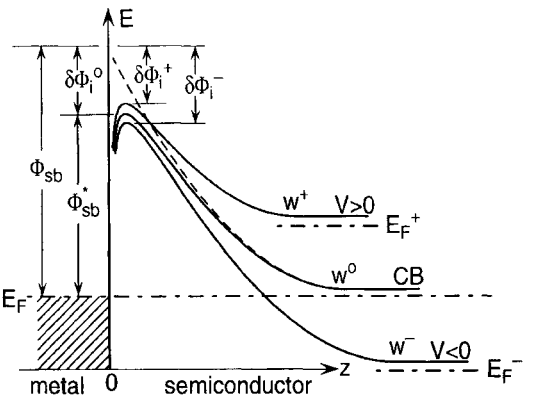


Fig. 11.10. The metal–semiconductor contact under zero, positive and negative bias showing the changes in the depletion width $w$ and the Schottky barrier lowering $\delta\Phi_i$ with bias $V$.

Thus a measurement of the differential capacitance $C$ by a suitable ac methods yields $V_b$ and consequently $\Phi_{sb}$ ($\Phi_{sb} = eV_b + \xi_n$). Equation (11.20) may be recast to a form convenient for graphic determination of $\Phi_{sb}$

$$\frac{1}{C^2} = \frac{2(\Phi_{sb} - \xi_n - eV - kT)}{A_d^2 e^2 \varepsilon_s \varepsilon_0 N_D}. \tag{11.21}$$

Thus plotting $1/C^2$ as a function of the reverse bias should give a straight line whose intercept $V_i$ for $1/C^2 = 0$ gives the Schottky barrier height

$$\Phi_{sb} = eV_i + \xi_n + kT. \tag{11.22}$$

$\xi_n$ can be calculated by established statistical methods from the known dopant concentration, their ionization energy and the temperature (Sze, 1981). Representative values are listed in Table 11.2 for Si, GaAs and GaP.

Such a plot is illustrated in Fig. 11.11 for three Schottky diodes on n-type GaAs(110) that were cleaved in UHV prior to the deposition of the metals, as reported by McLean and Williams (1988). Similar results were also reported by Newman et al. (1986) also on vacuum cleaved surfaces and by Waldrop et al. (1984) on GaAs(100) surfaces heat cleaned in UHV. These values are incorporated in Table 11.3. From Eq. (11.21) it is readily discerned that the slope is proportional to $1/N_d$, so that the data in Fig. 11.11 suggests a fairly uniform dopant concentration (a range of (6–12) $\times$ $10^{16}$ cm$^{-3}$ was calculated from the slopes). In fact the differential capacitance method is used to measure dopant profiles.

The accuracy of determining the barrier heights by $C$–$V$ measurements has been discussed by Goodman (1963), who also extended the analysis to include corrections when the semiconductor is degenerately doped (Goodman and Perkins, 1964). For M–S junctions that exhibit variations in local values of $\Phi_{sb}$ the capacitance method yields an average barrier height weighted by the relative surface areas over which the values are spread.

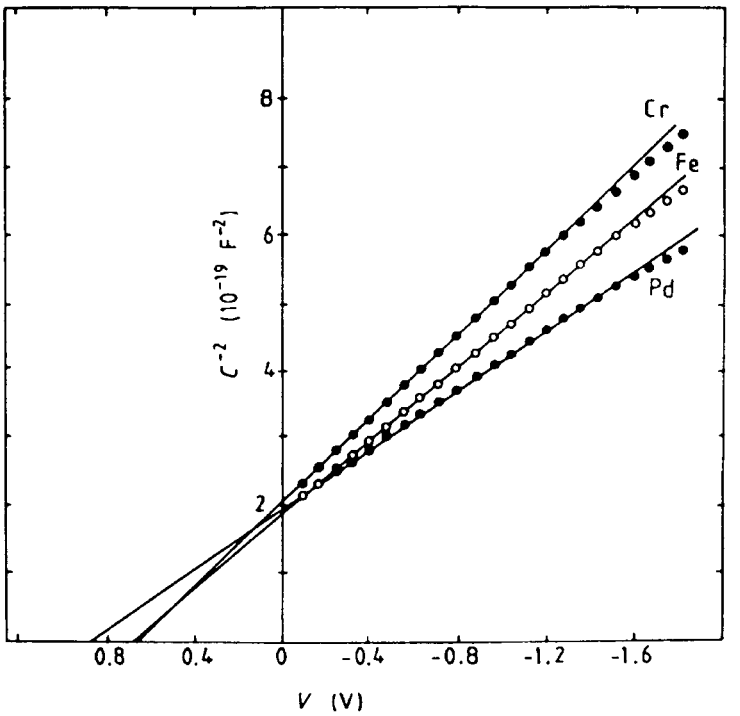


Fig. 11.11. Voltage dependence of the inverse square of the differential capacitance $C$ for Cr, Fe and Pd Schottky diodes fabricated on clean GaAs(110) surfaces prepared by cleaving. A dopant concentration lying in the (6–12) $\times$ $10^{16}$ $cm^{-3}$ range was extracted from the slopes of the curves (after McLean and Williams, 1988, with permission).

### *11.3.2. Current transport*

#### *11.3.2.1. Image force lowering of $\Phi_{sb}$*

The representation of the M–S interface has thus far been static, that is, mobile carriers in the semiconductor have been physically separated by a distance $w$ from the metal. This is no longer the case during transport as electrons or holes cross the M–S interface. In its vicinity, but still in the semiconductor, an electron (or hole) affects, through the Coulomb interaction, the charge distribution of the conduction electrons in the metal, which respond by trying to screen the perturbing field of the electron. The resulting force $F(z)$ can be represented by the classic concept of the image force (Jackson, 1975) and is equal to the attractive force between the charged particle at position $z$ relative to the interface plane ($z = 0$) and an equal charge of opposite polarity at $-z$

$$F(z) = \frac{-e^2}{4\pi\varepsilon_0\varepsilon_s(2z)^2} = \frac{-e^2}{16\pi\varepsilon_0\varepsilon_s z^2}. \tag{11.23}$$

Table 11.3
Schottky barriers for n-type GaAs diodes prepared by metal deposition in UHV on oxide free (100) surfaces and vacuum cleaved (110) surfaces

| | GaAs(100)[a] | | GaAs(110)[b] | | GaAs(110)[c] | |
|---|---|---|---|---|---|---|
| Metal | *I–V* | *C–V* | *I–V* | *C–V* | *I–V* | *C–V* |
| Cu | 0.96 | 0.96 | 0.84 | 0.88 | 0.87 | 0.94 |
| Pd | 0.91 | 0.93 | 0.89 | 0.95 | 0.85 | 0.88 |
| Ag | 0.90 | 0.89 | 0.90 | 0.95 | 0.89 | 0.97 |
| Au | 0.89 | 0.87 | 0.92 | 0.99 | 0.92 | 1.02 |
| Al | 0.85 | 0.84 | 0.80 | 0.94 | 0.82 | 0.88 |
| Ti | 0.83 | 0.83 | 0.78 | 0.82 | | |
| Pb | 0.80 | 0.91 | | | | |
| Bi | 0.77 | 0.79 | | | | |
| Ni | 0.77 | 0.91 | 0.73 | 0.78 | 0.77 | 0.82 |
| Cr | 0.77 | 0.81 | 0.70 | 0.76 | 0.67 | 0.72 |
| Fe | 0.72 | 0.75 | 0.70 | 0.76 | | |
| In | | | 0.78 | 0.82 | | |
| Sn | | | 0.79 | 0.82 | 0.77 | 0.83 |
| Sb | | | 0.72 | 0.78 | | |
| Y | | | 0.74 | 0.80 | | |
| V | | | 0.72 | 0.76 | | |
| Mn | | | 0.72 | 0.78 | 0.72 | 0.75 |
| Co | | | 0.70 | 0.75 | | |
| Na | | | 0.70 | 0.79 | | |

[a]Waldrop (1984). Includes an +0.04 eV image force correction for the *I–V* data.
[b]McLean and Williams (1988).
[c]Newman et al. (1986).

The potential energy $\phi_i$ of the electron in its image field is $\phi_i = \int_\infty^z F(\zeta)\,d\zeta$. Its total energy $\Phi(z)$ is the sum of this energy and that due to band bending as expressed through the electric field in the space charge layer (Eq. (11.1a)). For electrons $\Phi(z)$ is measured relative to the conduction band minimum at the M–S interface ($z = 0$), as shown in Fig. 11.12. It is given by

$$\Phi(z) = -\frac{e^2}{16\pi\varepsilon_0\varepsilon_s z} - e\mathcal{E}_m(1 - z/w)z. \tag{11.24}$$

$\Phi(z)$, as well as its two components are schematically shown in Fig. 11.12. $\Phi(z)$ reaches a maximum that is lower by $\delta\Phi_i$ than its value at $z = 0$ that corresponds to the Schottky barrier height $\Phi_{sb}$. This lowering of the Schottky barrier is called the Schottky effect or image force lowering. The position of the effective Schottky barrier height is also moved from the interface into the semiconductor by a distance $\delta z_i$. $\delta z_i$ is obtained by finding the maximum of Eq. (11.24), i.e., setting $\delta\Phi_i(z)/dz = 0$. As we shall see, $\delta z_i \ll w$, so that to a good approximation the differentiation yields

$$\frac{-e^2}{16\pi\varepsilon_0\varepsilon_s\delta z_i^2} + e\mathcal{E}_m = 0,$$

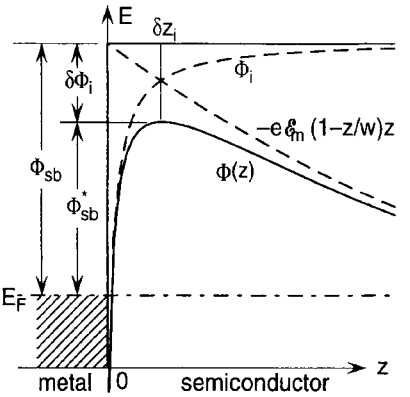


Fig. 11.12. Schematic representation of the lowering $\delta\Phi_i$ of the the Schottky barrier potential at a metal–semiconductor interface arising from the inclusion of the image potential $\phi_i$. $\delta z_i$ marks the distance from the interface where the modified Schottky barrier height is maximum.

from which

$$\mathcal{E}_m = \frac{e}{16\pi\varepsilon_0\varepsilon_s\delta z_i^2}. \tag{11.25a}$$

Substituting for $\mathcal{E}_m$ (Eq. (11.1a)) and $w$ (Eq. (11.2b)), and solving for $\delta z_i$:

$$\delta z_i = \frac{1}{4}\left[\frac{e^2}{2\pi^2\varepsilon_0\varepsilon_s N_D(eV_b - kT)}\right]^{1/4} = \frac{1}{4}\left[\frac{e^2}{2\pi^2\varepsilon_0\varepsilon_s N_D(\Phi_{sb} - \xi_n - kT)}\right]^{1/4} \tag{11.25b}$$

Substituting $\delta z_i$ into Eq. (11.24) gives

$$\delta\Phi_i = \frac{e^2}{16\pi\varepsilon_0\varepsilon_s\delta z_i} + e\mathcal{E}_m\delta z_i = \frac{e^2}{8\pi\varepsilon_0\varepsilon_s\delta z_i} \tag{11.26a}$$

by using Eq. (11.25a). Substituting for $\delta z_i$ from Eq. (11.25b) gives

$$\delta\Phi_i = \left[\frac{e^6 N_D(\Phi_{sb} - \xi_n - kT)}{8\pi^2\varepsilon_0^3\varepsilon_s^3}\right]^{1/4}. \tag{11.26b}$$

As given here Eqs. (11.25b) and (11.26b) apply only for zero bias. If a bias $V$ is applied, with $V > 0$ corresponding to forward bias that lowers the band bending, $V_b$ should be replaced by $(V_b - V)$ in Eqs. (11.25b) and (11.26b). Representative values of $\delta\Phi_i$ and $\delta z_i$ are shown in Table 11.2. The values for $\delta\Phi_i$ obtained from Eq. (11.26b) are probably overestimates, as the classical implementation of screening affects only the charged particle embedded in a dielectric medium and not the effect of metallic screening on the medium

itself. More realistic considerations of screening that incorporate exchange and correlation effects in a non-classical framework suggests that the valence and conduction bands of the semiconductor themselves are severely altered in the immediate vicinity of the metal in the form of a narrowing of the band gap, or closure (Inkson, 1973, 1974). Charlesworth et al. (1993) used the local density approximation to obtain estimates for the band gap narrowing for the Al/GaAs interface. They find that the downward band bending of the conduction band is less within 5 Å of the interface than that obtained by using the classical image force, yet comparable to it for distances farther from the interface. In contrast, the valence band remained essentially flat as compared to the strong upward bending predicted by the classical approach. It would thus appear that the classical method is a good approximation to estimate image force lowering for all but the most heavily doped semiconductors, for which $\delta z_i \lesssim 5$ Å.

*11.3.2.2. Thermionic emission model*

In the simplified picture of an M–S contact to a moderately doped semiconductor of sufficient mobility that scattering in the depletion region is small, electron transport across the interface can be envisioned as a thermally activated process with negligible contribution from a diffusion current. A transport description in terms of a diffusion process is seldom encountered in the form originally proposed by Schottky, although modifications of the thermionic emission model to include some contributions from a diffusion current have been proposed (see, for example, Sze, 1981, and Rhoderick and Williams, 1988). The current density $J_{s\to m}$ of electrons emitted from the semiconductor into the metal assumes a particularly simple form if the following assumptions are made: (i) the barrier height $\Phi_{sb} \gg kT$, which allows the use of Maxwell–Boltzmann statistics; (ii) the carriers are in equilibrium at the M–S interface (the emission plane); and (iii) the transmission probability across the M–S interface is unity. With these assumptions $J_{s\to m}$ is given by the product of the mean thermal velocity $\overline{v_z}$ of the electrons impinging onto the emission plane along the interface normal and their density $n$ at an energy corresponding to the top of the barrier (Bethe, 1942; Sze, 1981)

$$J_{s\to m} = e\overline{v_z}n = e(kT/2\pi m_s)^{1/2} N_c \exp\left[-(\Phi_{sb} - eV)/kT\right], \tag{11.27}$$

where $m_s$ is the effective mass of the conduction electron in the semiconductor and

$$N_c = 2\left(2\pi m_s kT/h^2\right)^{3/2} \tag{11.28}$$

is the conduction band density of states. In the absence of image force effects the emission plane is the metallurgical M–S interface, otherwise it is the plane parallel to it at $z = \delta z_i$, the position of the barrier maximum ($\Phi_{sb} - \delta\Phi_i$). A thermally activated current $J_{m\to s}$ will also flow from the metal into the semiconductor. The barrier $\Phi_{sb}$ may be assumed independent of the bias $V$ in the present model (we will deal shortly with the situation where this is not strictly true), for which case $J_{m\to s}$ is bias independent as well. Since no net current flows at zero bias $J_{m\to s} \equiv J_{s\to m}(V = 0)$. Then for a diode junction area $A_d$ the net current is

$$I(V) = A_d J(V) = A_d(J_{m\to s} + J_{s\to m}), \tag{11.29a}$$

which upon substitution with Eq. (11.27) becomes

$$I(V) = A_d A^* T^2 \exp(-\Phi_{sb}/kT)\left[\exp(eV/kT) - 1\right], \tag{11.29b}$$

where

$$A^* = 4\pi m_s e k^2/h^3 \tag{11.30}$$

is called the effective Richardson constant, in analogy to the Richardson constant for thermionic emission into vacuum for a free electron metal, to which it is identical except for the use of the free electron mass $m$. Thus

$$A^* = \frac{m_s}{m} A = 120 \frac{m_s}{m} A/\mathrm{cm}^2\mathrm{K}^2. \tag{11.31}$$

For a zone centered conduction band $A^*$ depends only on the isotropic effective mass $m_s$. However, for semiconductors such as Ge and Si with multiple conduction band minima at high symmetry points in reciprocal space, the effective mass $m_s$ also depends on the orientation of the effective mass tensor relative to the interface, as only the mass components perpendicular to the interface affects transport. Crowell (1965) has calculated the appropriate $A^*$ for variously oriented interfaces for Ge and Si; values of $A^*$ for different orientations generally agree within $<10\%$.

The inclusion of image force lowering of $\Phi_{sb}$ into the transport formalism discussed above adds a bias dependence of the effective Schottky barrier height $\Phi^*_{sb}$, since with an applied bias $V$ Eq. (11.26b) becomes

$$\delta\Phi_i = \left[\frac{e^6 N_D(\Phi_{sb} - eV - \xi_n - kT)}{8\pi^2 \varepsilon_0^3 \varepsilon_s^3}\right]^{1/4}. \tag{11.29c}$$

This effect is schematically shown in Fig. 11.10 for both forward and reverse bias conditions. Other sources for a bias dependence of the barrier height include the presence of an insulating interlayer and tunneling phenomena for highly doped semiconductors; both subjects have been discussed by Rhoderick and Williams (1988) and will not be considered further here. The effective $\Phi^*_{sb} = \Phi_{sb} - \delta\Phi_i$ can be expressed in a form linear in $V$ by a Taylor expansion of Eq. (11.29c), and keeping only terms to the first order. Thus

$$\Phi^*_{sb} = \Phi_{sb} - \delta\Phi_i^0 + \frac{\delta\Phi_i^0 eV}{4(\Phi_{sb} - \xi_n - kT)} = \Phi_{sb} - \delta\Phi_i^0 + \alpha eV, \tag{11.32}$$

where $\delta\Phi_i^0$ is the image force lowering $\delta\Phi_i$ for zero bias. In a more general sense, $\alpha$ can be expressed as

$$\alpha = \frac{\partial\Phi^*_{sb}}{\partial V} \tag{11.33}$$

and implies inclusion of voltage dependences in addition to those from image force effects. Substituting Eq. (11.32) into Eq. (11.29b) gives

$$I(V) = A_d A^* T^2 \exp\left[-(\Phi_{sb} - \delta\Phi_i^0 + \alpha V)/kT\right]\left[\exp\left(\frac{eV}{kT}\right) - 1\right], \tag{11.34a}$$

which can be written as

$$I(V) = I_0 \exp\left(\frac{eV}{nkT}\right)\left[1 - \exp\left(\frac{-eV}{kT}\right)\right]. \tag{11.34b}$$

Here

$$I_0 = A_d A^* T^2 \exp\left[-\frac{(\Phi_{sb} - \delta\Phi_i^0)}{kT}\right] \tag{11.35}$$

is called the saturation current, and

$$\frac{1}{n} \equiv 1 + \alpha = 1 + \frac{\partial \Phi_{sb}^*}{\partial V} \tag{11.36}$$

is called the ideality factor. For biases $V \gtrsim 3kT/e$,

$$I(V) = I_0 \exp\left(\frac{eV}{nkT}\right). \tag{11.34c}$$

In the preceding the assumption was made that an electron crossing the interface did so with unit probability. This assumption is not justifiable since an electron, assuming it has sufficient energy to overcome the barrier, can nevertheless be scattered back because of the necessary quantum mechanical description of the transmission process, which leads to a transmission probability $f_Q < 1$. In addition phonon scattering within the M–S interface region can contribute to additional reflections and consequently a lowering of the transmission probability due to phonon scattering $f_p$ to less than unity. Both phenomena are important for a complete understanding of transport phenomena across M–S structures, yet difficult to quantify for a real system. Moreover, the two quantities are dependent on both the electric field in the depletion region and on the kinetic energy of the electron, although in combination there is a tendency of a weaker energy dependence (Crowell and Sze, 1967). This topic will again be discussed in Section 11.4. Their influence can nevertheless be incorporated into the transport equations by redefining the effective Richardson constant

$$A^{**} = f_p f_Q A^* \tag{11.37}$$

which is adequate within the domain of validity of the thermionic emission theory. If a diffusion current is not negligible a more complicated expression for both $I_0$ (Eq. (11.35)) and $A^{**}$ is necessary (Sze, 1981; Rhoderick and Williams, 1988). For electrons in Si $A^* \approx$

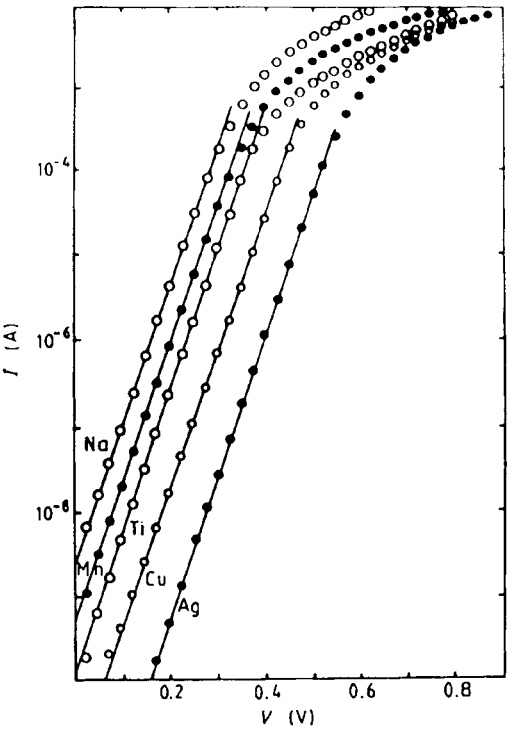


Fig. 11.13. $I$–$V$ characteristics of indicated metal–GaAs(110) Schottky diodes. The 0.5 mm diameter metal dots were deposited on freshly prepared surfaces cleaved in UHV (after McLean and Williams, 1988, with permission).

252 A/cm$^2$ K$^2$ (Crowell, 1965) and $A^{**} \approx 112$ A/cm$^2$ K$^2$ (Andrews and Lepselter, 1970). The corresponding values for GaAs are $A^* \approx 8.6$ A/cm$^2$ K$^2$ and $A^{**} \approx 4.4$ A/cm$^2$ K$^2$ (Crowell and Sze, 1966b).

To obtain the effective Schottky barrier height from $I$–$V$ measurements, the current is plotted on a logarithmic scale as illustrated in Fig. 11.13. Straight lines drawn through the $I$–$V$ curves show that they intersect the data points over a current range of at least four decades, which is a strong indication that the $I$–$V$ characteristics are dominated by thermionic emission. The saturation at higher forward biases is due to a voltage drop across the combined series resistances of the bulk of the semiconductor and the back contact. From Eq. (11.34c), $\ln I = \ln I_0 + eV/nkT$, so that the straight line current axis intercept for $V = 0$ gives the experimental saturation current $I_0^e$. It's slope gives directly the value of $n$. Hence, through Eq. (11.35),

$$\Phi_{sb}^* = \Phi_{sb} - \delta\Phi_i = kT\left\{\ln(A_d A^{**} T^2) - \ln I_0^e\right\}. \tag{11.38}$$

Equation (11.38) assumes knowledge of $A^{**}$. Actually its precise value need not be known since even an error by a factor of 3 produces an error in $\Phi_{sb}$ of only $kT$ (0.025 eV at room temperature). $A^{**}$ can be obtained experimentally by measuring the $I$–$V$ characteristics as

a function of temperature: as can be seen from Eq. (11.35), a plot of $\ln I_0/A_d T^2$ vs. $1/T$ should give a straight line with an extrapolated intercept of the ordinate at $1/T = 0$ equal to $\ln A^{**}$ (Rhoderick and Williams, 1988). Such procedure is warranted only if precision to less than $\pm 0.01$ eV in the value of $\Phi_{sb}$ is required. The attainment of such precision is also premised on high quality $I$–$V$ characteristics with linear current dependencies on $V$ over many orders of magnitude (in a logarithmic plot) and ideality factors $\lesssim 1.03$. Reliable values for $n$ as low as 1.01 have been reported for diodes of epitaxial Al/GaAs(100) grown by molecular beam epitaxy under exacting UHV conditions (Missous et al., 1986). In general, for any degree of confidence in the results of Schottky barrier measurements by $I$–$V$ methods the ideality factor should be less than 1.1.

For M–S diodes that exhibit variations in $\Phi_{sb}^*$, e.g., from incomplete reactions or contaminations at the interface, the $I$–$V$ method provides a value of $\Phi_{sb}^*$ that is heavily weighted by the lowest $\Phi_{sb}^*$, provided that the regions of lowest $\Phi_{sb}^*$ are of an extent larger than the depletion width $w$ to avoid "pinch-off" effects (Tung, 1991). This sensitivity to the lowest $\Phi_{sb}^*$ values is a direct consequence of the exponential dependence of $I_0$ on $\Phi_{sb}^*$ (Eq. (11.35)). Details of data analysis for M–S diodes with variations in Schottky barrier heights have been discussed by Sullivan et al. (1991), Werner et al. (1991) and Tung (1992).

*11.3.2.3. Internal photoemission*

An electron current across a M–S interface can also be generated by photoexcitation of electrons in the metal. Only electrons with energy $> \Phi_{sb}^*$ will make it across the barrier, with the electric field of the depletion layer assuring that they are collected as a photocurrent in the semiconductor. The method has the advantage that edge leakage effects, often problems in less than ideal Schottky diodes, can be eliminated by selective area illumination of the M–S junction area. In addition photoresponse measurements can be carried out under essentially zero bias conditions, thus avoiding some of the bias dependent problems discussed in conjunction with $I$–$V$ methods. In fact the method has been used by Sze et al. (1964) to measure the Schottky barrier heights as a function of applied bias, from which they deduced the field dependence of the image force correction $\delta\Phi_i$, as well as the effective dielectric constant $\varepsilon_s$ used in Eq. (11.26b), which turned out to be that of the semiconductor, as expected.

The theory of internal photoemission in a M–S diode is a simple adaptation of Fowler's (1931) theory for the photocurrent emitted into vacuum by metal surfaces under illumination. Fowler's model is based on a metal with a constant density of electron states and the assumption of momentum conservation for the escaping photoelectrons. He derived the following expression for the photoresponse $R$, i.e., the photocurrent per absorbed photon of energy

$$R = \frac{2\sqrt{2}\pi m^{3/2} k^2 T^2}{h^3 (E_F + \phi)^{1/2}} \left\{ \frac{\pi^2}{6} + \frac{\mu^2}{2} - \left( e^{-\mu} - \frac{e^{-2\mu}}{4} + \frac{e^{-3\mu}}{6} \right) - \cdots \right\}, \qquad (11.39a)$$

which is valid for $\mu \geqslant 0$, where $\mu = (h\nu - \phi)/kT$ and $\phi$ represents the barrier height (work function); $E_F$ is the Fermi energy of the metal. For sufficiently low temperatures

and/or large $h\nu$ so that $\mu \gtrsim 5$, and the further assumption that $(E_F + \phi) \gg h\nu/2$, which is invariably the case for Schottky barrier measurements, $R$ becomes

$$R \propto (h\nu - \phi)^2. \tag{11.39b}$$

Thus a plot of $\sqrt{R}$ vs. $h\nu$, a so-called Fowler plot, should yield a straight line whose intercept with the energy axis gives $\Phi^*_{sb}$. In practice the Fowler plot deviates from linearity for energies close to threshold. This limits the accuracy over which a straight line can best fit the data since in general the plot becomes nonlinear again for photon energies exceeding the band gap $E_g$ because of photoabsorption in the semiconductor. The shape of the photoresponse near threshold is also influenced by thermal effects and transmission probabilities arising from quantum mechanical effects and phonon scattering, as already mentioned in the previous section. The influence of quantum mechanical transmission on measured threshold energies was addressed by Anderson et al. (1975), who concluded that corrections to $\Phi^*_{sb}$ of as much as a few tens of meV were necessary. De Sousa Pires et al. (1984) have described computer aided fitting procedures to enhance the accuracy of extracting $\Phi^*_{sb}$ from Fowler plots.

*11.3.2.4. Ballistic electron emission spectroscopy*

In this transport-based method, which will be fully described in Section 11.4, the transmission into the semiconductor of electrons injected by an STM tip at the surface of a thin metal overlayer is monitored as a function of the STM tip bias. When the tip bias, which is measured relative to the Fermi energy in the metal, exceeds the effective Schottky barrier height $\Phi^*_{sb}$ some of the electrons will reach the semiconductor to be detected as a collector current. The collector current thus increases for biases exceeding a threshold voltage that equals $\Phi^*_{sb}$. To obtain the latter, the voltage dependence of the collector current is compared to theoretical predictions. Although these depend slightly on the assumptions used in developing the current models, the resulting fits give routinely threshold values with relative and absolute precision of better than $\pm 10$ and $\pm 30$ meV, respectively. Together with an unprecedented lateral resolution of the order of 1 nm, this spectroscopy offers exciting new areas of investigations related to transport and Schottky barrier phenomena. As for internal photoemission this method is preferentially used on unbiased M–S interfaces, which avoids the problems of voltage dependent variations in $\Phi^*_{sb}$. Unlike internal photoemission, however, the energy of the carriers is essentially unlimited, thereby allowing the investigation of hot electron phenomena relevant to a variety of transport issues related to M–S structures.

*11.3.3. Photoemission methods*

Photoemission spectroscopy has proven itself to be the most versatile technique used in the characterization of M–S interfaces. Although the least precise of the Schottky barrier measurement techniques described here, virtually all information of the development of the electronic structure during the formative stages of the M–S interface, i.e., for metal coverage from submonolayer to several monolayers, and of the ensuing interfacial chemistry has been obtained by photoemission spectroscopy. An introductory survey of the technique can be found in Chapter 8 of this volume. The technique is particularly powerful if

the photon source is synchrotron radiation emanating from a storage ring (Koch, 1983). Its intense and broad spectral photon flux, when passed through suitable monochromators, provides a highly monochromatic photon source with an energy spread $\lesssim$50 meV that is tunable to energies exceeding hundreds electron volts. The ability to adjust the photon energy allows not only the photoexcitation of electron core levels with large binding energies, but a choice of the kinetic energy $E_K$ of the photoemitted electrons as well. In a metal $E_K = h\nu - E_B + E_F$, where the binding energy $E_B$ of the electron is measured relative to the Fermi energy $E_F$. Since the electron mean free path in a solid depends strongly on its kinetic energy, as schematically shown in Chapter 8, Fig. 8.14, adjusting $E_K$ by varying $h\nu$ provides a means of selecting the width of the region below the surface from which photoelectrons can escape into the vacuum and be detected. Thus a selection of kinetic energies in the range of 30–50 eV achieves maximum surface sensitivity that permits the observation of spectral features of surface and near surface atoms and their changes with surface modifications. It is also very informative to follow changes in the shape of spectra arising from the photoexcitation of the valence electrons. These spectra, often referred to as electron distribution curves or EDC, reflect changes of valence band and/or density of states features. Examples of such changes include the appearance of emission structure in the forbidden gap region of a semiconductor as metal atoms are deposited. Initially these may appear as isolated impurity atoms, which upon further deposition agglomerate to eventually become a metal, with the appearance of the characteristic step structure at the Fermi energy (Fermi edge) signalling the establishment of metallic properties.

*11.3.3.1. Core level photoemission: band bending*

The binding energy of an electron in a particular quantum state of an isolated atom corresponds to the energy to remove the electron an infinite distance from the atom, leaving a positively charged ion behind. If the electron derives from a deep, non-valence electron level, the positive charge is referred to as a core hole. In a solid the binding energy is modified by an additional Coulomb correction or screening of the core hole, a correction that arises from the response of the valence charge contributed by the neighboring atoms of the photoexcited atom (Cardona and Ley, 1979). This net valence charge reflects the bonding or chemical environment of the atom. Changes in the valence charge are in turn reflected as changes in binding energies (and kinetic energies) of the photoelectrons and form the basis of photoelectron spectroscopy as a tool for chemical identification (e.g., ESCA for Electron Spectroscopy for Chemical Analysis). Changes in the binding energy due to valence charge redistributions are often called chemical shifts.

In a semiconductor, as we have seen, a small surface charge can drastically affect the band bending. Since such small charges will not affect the screening or chemical environment of an atom in the semiconductor, no chemical shift will result. The binding energy thus remains fixed relative to an internal reference level, which for non-metallic solids is generally taken to be the top of the valence band. In a photoemission experiment the Fermi level of the system, which includes the sample and detector, is a reference level that remains constant. Kinetic energies of emitted photoelectrons, which are measured relative to the Fermi level, will change if there are changes in band bending, as all electron energy levels, including core levels, moves rigidly relative to the Fermi level. An energy diagram depicting these changes for an n-type semiconductor is shown in Fig. 11.14. The

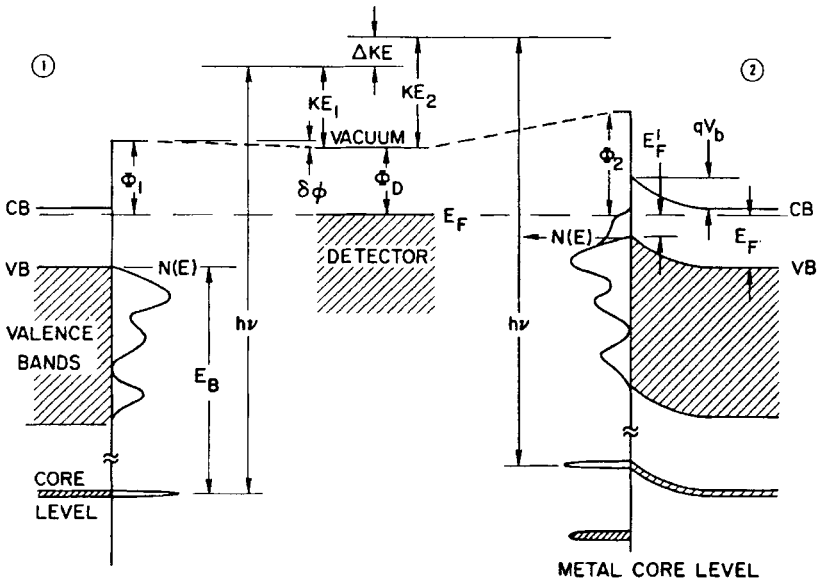


Fig. 11.14. Energy level diagram of a photoemission experiment of a clean semiconductor surface, panel 1, and after metal coverage, panel 2. Kinetic energies of the photoelectrons (*KE*) are measured relative the vacuum level at the detector (center). Since the Fermi level is constant, changes in band bending $qV_b$ translate to corresponding changes $\Delta KE$ in the kinetic energies of the photoelectrons.

left side shows a semiconductor whose bands remain flat to the surface, which happens in the absence of a surface charge. A photoelectron excited from a core level of the semiconductor by the absorption of a photon of energy $h\nu$ will exhibit a kinetic energy $KE_1$ relative to the vacuum level at the detector. With the adsorption of atoms – here assumed to be metal atoms – acceptor states will be generated in the band gap that upon charging will cause band bending, as shown on the right hand side. Since all electron states bend up together the photoelectron excited from this "raised" level will exhibit a kinetic energy $KE_2$ shifted to higher energies by $\Delta KE$ that exactly matches the change in band bending. For p-type semiconductors the bands bend downward with the addition of a positive surface charge at donor sites; this causes a decrease in the kinetic energies of the core level photoelectrons relative to their flat band values. It should be noted that neither the electron affinity $\chi_s$ (Fig. 11.1) nor the ionization energy ($\chi_s + E_g$) of the semiconductor changes with a change of the surface charge; they only change if in addition a surface dipole layer is present (Troost et al., 1987). Core levels are chosen to measure the changes in kinetic energy because their relatively narrow spectral width and well understood line shape allows for excellent data fits that result in determinations of shifts with errors of $\lesssim \pm 20$ meV. In addition the unique energy signature of core levels for different elements assures in general that an overlap of spectral features of semiconductor and metal overlayer does not occur. This is not the case for the valence electrons.

In an ideal scenario for measuring $\Phi_{sb}$ by photoemission core level spectroscopy one starts with a clean semiconductor surface devoid of band bending, as shown on the left

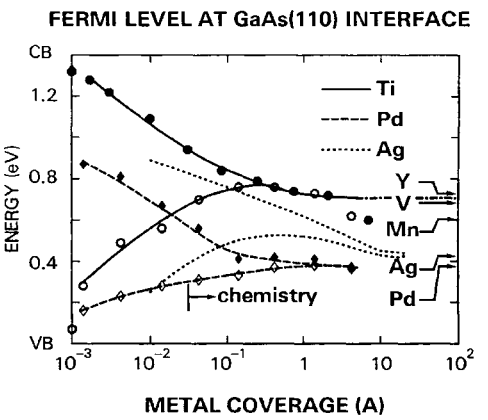


Fig. 11.15. The evolution of the Fermi level position at the GaAs(110)–metal interface with metal coverage for Ti, Pd and Ag deposited on vacuum cleaved p-type (bottom branches) and n-type GaAs (top branches). The two branches coincide after metallic character in the overlayer has been established. The thick coverage position of the Fermi level is noted on the right for a number of other metals on GaAs(110) (after Ludeke et al., 1987).

side of Fig. 11.14. This flat band situation is only achieved on exceptionally well cleaved surfaces of some compound semiconductors, such as the tetrahedrally bonded GaAs(110), InAs(110) and GaSb(110) (Huijser et al., 1977). Cleavage induced defects may cause some band bending. These defects are frequently donors and cause band bending on n-doped samples, with little or no band bending occurring for p-doped samples. Consequently, it is good practice to measure the photoemission core level spectra and valence band EDC's for clean surfaces of both dopant types. A measured kinetic energy difference in the core level spectra equal to $E_g - \xi_n - \xi_p$ will indicate flat band conditions for both substrates. For differences less than this value caution must be exercised, although often it is assumed that slight deviations of order 0.1–0.2 eV are due to band bending in the n-type sample. After the quality of the starting surfaces has been established metal atoms are deposited in a series of steps starting from less than 0.01 monolayers (ML) and continuing until the spectral features of the semiconductor are too weak for a reliable measurement of their kinetic energies, which usually occurs for coverages exceeding 5 ML (~10 Å). Spectra are taken after each deposition step. After extraction of the changes in kinetic energy these are plotted as function of metal coverage, as shown in Fig. 11.15. The plot represents the position of $E_F^i$ relative to the band edges of the semiconductor (GaAs), and assumes that the band was initially flat for the p-type samples, as the differences in *KE* for the two types of clean surfaces were always less than $E_g$. It should be noted that at sufficiently large coverages the Fermi levels for the n- and p-type samples coincide and remain constant relative to the semiconductor band edges. The Schottky barrier height for n-type material is the distance of the final position of $E_F^i$ relative to the conduction band, that for p-type relative to the valence band. The closure rate of the positions of $E_F^i$ for the two doping types with metal coverage is largely dominated by the morphology of the metal on the surface. Weakly interacting metal atoms such as Ag, with large surface mobilities at room temperature, tend to form clusters that are tenth of nanometers apart. Although the position

of $E_F$ underneath these clusters may already be in or near its final position, that in the free region between the clusters will tail towards the band edges, an exact surface analogy of the band bending into the bulk. Since the photoemission experiment measures an average position of $E_F$, its final value will not be attained until the uncovered regions of the surface shrink to sizes much smaller than the depletion width $w$. Tang and Freeouf (1984) have modeled the average position of $E_F^i$ as a function of surface donor/acceptor concentration. An additional point to notice in Fig. 11.15 is that some data points for the largest coverage of Ti lie off the extrapolated curve for the final position of $E_F^i$. The reason for this is an inability to extract precise kinetic energy changes for metals that chemically react strongly with the semiconductor substrate. This interaction distorts the core level lineshape due to the emergence of reaction products whose core level signature is chemically shifted from that of the atom bonded in the semiconductor. Such complications are a large source for errors in obtaining reliable values for $\Phi_{sb}$.

Because of uncertainties in establishing both $E_F^i$ relative to the band edges for the clean surface and the precise position of the bulk core level components affected by chemistry for larger coverages, the error in determining $\Phi_{sb}$ by core level photoemission spectroscopy is conservatively estimated at $\pm 0.1$ eV, with a reduction by a factor 2 to 3 for optimal cases for which these problems have been reduced or eliminated. The uncertainty of the position of $E_F^i$ for the clean surface may be reduced by accurately establishing the position of the bulk valence edge in the EDC's relative to $E_F$ of the system. This is accomplished by convoluting the instrumental broadening with the theoretical density of states, as proposed by Kraut et al. (1980). $E_F$ or more precisely the kinetic energy that corresponds to the $E_F$ of the system is obtained from the metallic Fermi edge of the EDC after full coverage of a metallic layer on the semiconductor has been achieved. This method of obtaining the initial band bending is limited, however, to photon energies for which interfering contributions from surface states near the band edge are negligible. At these energies, which are typically several hundred eV, the instrumental resolution is also lower, which adversely affects the accuracy of the measurements. In addition, but particularly for the more bulk sensitive energies, band bending evaluations must include corrections due to changes in band bending over the sampling depth of the measurement (Tang and Freeouf, 1984). Such corrections, given by $\Delta\Phi_{sb} \approx \lambda(2N_D\Phi_{sb}/\varepsilon_s\varepsilon_0)^{1/2}$, where $\lambda$ is the photoelectron escape depth, are always additive to $\Phi_{sb}$ (Prietsch et al., 1988).

Most of the measured band bending occurs for coverages $<0.1$ Å (0.05 ML), the results in Fig. 11.15 being typical. This lead to the suggestion that the Schottky barrier was formed before the metallic characteristics were established and that the presence of the metal was incidental (Spicer, 1979).

*11.3.3.2. Photoemission spectroscopy: the role of surface photovoltage*

The band bending in a semiconductor can be influenced by radiation of energy $h\nu > E_g$ through the so-called surface photovoltage (SPV) effect, and thus affect the precision of determining the band bending in a photoemission experiment. This effect, in its own right a useful spectroscopic tool (Assmann and Mönch, 1980; Clabes and Henzler, 1980), is a consequence of photocarriers generated in the depletion region of the semiconductor during illumination. The built-in electric field separates the electrons and holes, with the minority carriers moving to the interface where they partly compensate the interface charge

balance. The consequence is a decrease in the band bending, analogous to the application of an external bias (the photovoltage). The SPV effect was known to influence binding energies and band bending for some time (Margaritondo et al., 1980; Demuth et al., 1986), but its effect on the position of $E_F^i$ during metallization, particularly at low temperatures, was not appreciated until the work by Hecht (1990). The net implication of the SPV effect is that the photoemission experiment measures a band bending that is less than measured in darkness by another method, for example, by contact potential measurements with a Kelvin probe (Mao et al., 1992; Linz et al., 1993). The photovoltage is dependent on the intensity of the illumination, the initial (dark) band bending, the temperature and the doping concentration of the semiconductor. Its role has been quantified by Hecht (1990, 1992), and by Bauer et al. (1991), who concluded that the SPV is probably negligible at room temperature and for highly ($<10^{18}$ cm$^{-3}$) doped semiconductors during the formative phase of the M–S contact. Once a continues metallic film has formed the SPV is shorted and is of no further concern. Assessments of the role of SPV in photoemission experiments during the Schottky barrier formation process have been presented by Horn (1992) and by Mao et al. (1992).

*11.3.3.3. Core level photoemission: chemistry*

To illustrate the chemical information contained in a photoemission experiment we will follow the evolution of the core levels with metal coverage. We take as our example Ti deposited in UHV on freshly cleaved GaAs(110) surfaces. Representative spectra of the the Ga-3d and As-3d core levels on an n-type sample are shown in Fig. 11.16. The d-core levels are chosen because of their large photoionization cross section (Yeh and Lindau, 1985) compared to the s- and p-levels. An energy dependent background contribution due to inelastically scattered photoelectrons, assumed to be proportional to the integral under the raw data, has been subtracted (Wertheim and Citrin, 1978). The spectra of both As-3d and Ga-3d for the clean surface consist of a pair of spin–orbit-split subspectra, with a well known intensity or branching ratio of 3 : 2 for the $j = 5/2$ and $j = 3/2$ d-electrons. This ratio is not affected by subsequent spectral changes. The larger of the subspectra for the clean surface arises from atoms in the bulk, the smaller from atoms at the surface (Eastman et al., 1980). The surface atoms have a valence electron distribution that is different from bulk because of the removal of one nearest neighbor for surface atoms on the (110) surface of tetrahedrally bonded semiconductors (for further detail see Chapter 7). Since the As and Ga atoms on the surface have different electron affinity, the As surface atoms attract some of the charge from the Ga surface atom, resulting in the observed chemical shifts in the spectra, with the larger than bulk charge surrounding the As atoms resulting in a chemical shift to smaller binding energies (or equivalently larger kinetic energies) and the opposite for the Ga surface atoms. Hence their position on opposite sides of the bulk spectrum. Their size relative to the bulk component is an indication of the surface sensitivity of the measurement. If taken at the same kinetic energy this ratio must be the same for the two core levels, a fact not too infrequently ignored in reported spectral decompositions. The decomposition of spectra is done by computer aided least squares fitting routines. The fundamental lineshape consists of a Lorentzian, representing the intrinsic, lifetime broadened spectral shape, that is convoluted with a Gaussian, which describes instrumental broadening and other broadenings arising from inhomogeneous distributions in the sample. Once

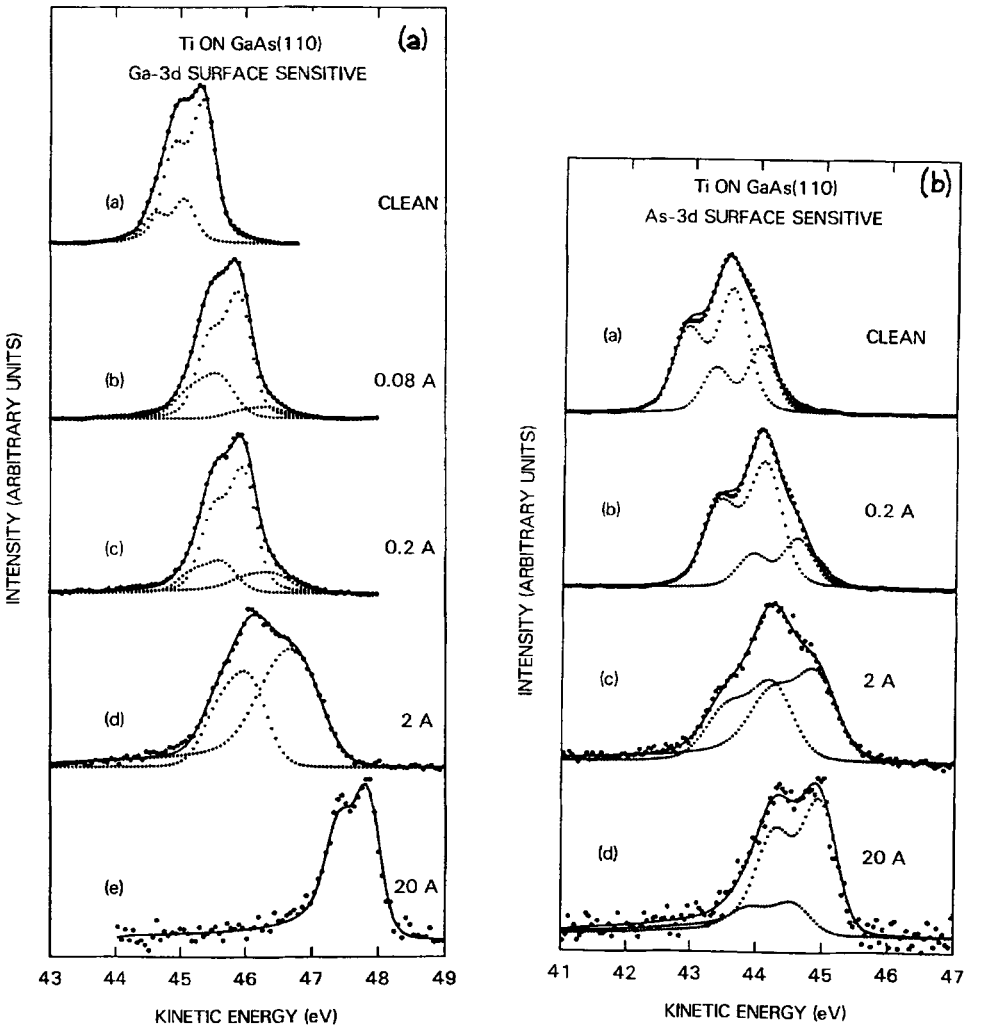


Fig. 11.16. The evolution of the Ga-3d (left panel) and As-3d (right panel) core level photoemission spectra with Ti deposited on n-type GaAs(110). The solid line, which overlies the experimental data (large dots), is the sum of computer generated spectral components (small dots). In spectra (a) of both panels the major component is due to atoms in the bulk, whereas the minor component arises from the surface atoms (after Ludeke and Landgren, 1986).

a clean spectrum is fitted, parameters such as the spin–orbit splitting, branching ratios and Lorentzian widths remain unchanged.

Noticeable changes in the spectra occur already for small coverages of the metal. The most obvious is a shift to higher kinetic energies of the entire spectrum, which is a result of band bending. In addition a weak shoulder appears on the high kinetic energy side of the Ga-3d spectrum (curve b). This component grows as the surface component weakens with

coverage, eventually dominating the spectrum at the highest coverages. The new component is due to elemental Ga that has been replaced in the surface by the more electropositive Ti, in what is called an exchange reaction. The increasing intensity of this component makes it progressively more difficult to extract the bulk component due to the Ga in GaAs, which is the marker for the measurement of the kinetic energy changes and hence band bending. The replaced Ga atoms aggregate into metallic Ga clusters. Their metallic character places an additional burden on the spectral decomposition, as the line shape of this component is no longer symmetrical. The asymmetric lineshape, which is broadened to lower kinetic energies, is the consequence of energy losses incurred by the emerging photoelectrons from low energy excitations of electrons near the Fermi level of the metallic Ga. The resulting line shape has been described by Doniach and Sunjic adjust (1970) (see also Wertheim and Citrin, 1978). Its omission in the analysis of band bending phenomena at M–S interfaces can lead to serious errors (Ludeke, 1986). The As-3d core level also depicts changes that are of a chemical origin. In the case shown for Ti/GaAs in Fig. 11.16, a single additional spectral component suffices to reproduce the experimental data. In this case the bulk component can be followed to larger coverages than for Ga-3d. This situation is, however, not always the case, as multiple As components in the core level spectra are needed to fit spectra for other metal, e.g., Ce (Weaver et al., 1985), Pd (Ludeke and Landgren, 1986) and Co (Xu et al., 1987) on GaAs(110).

The strong chemistry implied by the data above is not unique to Ti on GaAs. With the exception of the alkali metals and perhaps Ag, Pb and In, most of the other metals react in a varying degree with the semiconductor when deposited on the surface at room temperature. For the binary semiconductors, the metal-adsorbate atom generally replaces the cation in an exchange reaction, which was first observed for Al deposited on GaAs(110) by Brillson et al. (1979). On the GaAs(100) surface the exchange reaction was observed to be delayed until Al nucleated into clusters, with the heat of nucleation being attributed to trigger the reaction (Ludeke and Landgren, 1981; Zunger, 1981). In some cases the metal adsorbate replaces the anion, as for example Au atoms replacing Sb on the GaSb(110) surface, as reported by Lindau et al. (1978). However, generally both elemental constituents form reaction products with the metal adsorbates, as discussed above for Ti/GaAs(110). Thus on InP(110) surfaces Al (McLean et al., 1988), the noble and near-noble metals (Brillson et al., 1982; Petro et al., 1984) and transition metals (Aldau et al., 1988) induce exchange reactions with the formation of free In and a complicated phosphorous chemistry for the transition metals (Aldau et al., 1988). On GaP(110) surfaces evidence for interface reactions have been reported by Brillson et al. (1987), Chiaradia et al. (1987) and Miyano et al. (1990) with clear evidence for metal-Ga exchange reactions. Detailed lineshape analyses, including the asymmetric Doniach and Sunjic broadening of the Ga-3d core level for metallic Ga, were reported by Trafas et al. (1989) for Ti, Pd, Ag and Au; by Alonso et al. (1990) for Ag, In and Al; by Ludeke et al. (1990b) for Cu, Ag and Au; by Ludeke et al. (1990c) for V and Y; and by Evans et al. (1992) for Pt. With the exception of In, Ga, Sn and Bi all other metals reacted to varying degrees with the GaP. The metal induced chemistry for other surface orientations and for alloys of group III-V and II-VI semiconductors have been reviewed by Brillson (1985, 1992). Interfaces formed at low substrate temperatures, typically $>77$ K, exhibit comparable chemistry to interfaces formed at room temperature. However, the morphology is much

different due the limited surface mobility of the adsorbate atoms. This work has been reviewed by Kahn et al. (1989) and by Spicer et al. (1989). A novel approach to reduce interface reactivity consists of depositing metals at low temperatures ($\approx$60 K) on thin Xe layers condensed on cleaved GaAs(110) surfaces (Waddill et al., 1990). The metal atoms cluster on top of the Xe layer, whence they are gently deposited onto the GaAs(110) surface by evaporating the Xe layer upon warming. Although no evidence for disruption of the GaAs surface was found, the method, nevertheless, does not produce at this time smooth films that homogeneously cover the GaAs(110) surfaces, as is readily ascertained from the persistence of the surface components in both the As-3d and Ga-3d spectra for all coverages reported ($\lesssim$40 Å). For maximum coverages $E_F^i$ was found to be metal dependent for p-type GaAs(110), whereas it was invariant and located $\sim$0.3 eV below the conduction band edge for n-type GaAs. Although not understood, this unusual behavior appears now, in view of the lightly doped n-type material used, to be explainable by the ubiquitous surface photovoltage (SPV) effect.

### *11.3.4. Schottky barrier formation and properties: case studies*

In the following we will present experimental findings that support basic underlying concepts of the Schottky barrier formation process. Although specific cases, they reflect what is believed to be a universality in Schottky barrier phenomena. Most of the results discussed will be based on techniques detailed above. However, there are several other surface sensitive spectroscopies that are used to study the developing M–S interface to coverages of about a monolayer, such as contact potential differences (CPD) spectroscopy (Mao et al., 1992), STM spectroscopy (Feenstra and Stroscio, 1993; Stroscio and Feenstra, 1993) and inverse photoemission spectroscopy (see Chapter 8, and Himpsel, 1990). Except for specific results, no further details will be given concerning these techniques.

#### *11.3.4.1. Spectroscopic studies of gap states*

The existence of charged states in the semiconductor band gap at the M–S interface is largely inferred from their electrostatic consequences of inducing band bending. Direct spectroscopic measurements are generally hampered by a lack of sensitivity and/or by a degree of uncertainty that the detected interface states are actually the ones determining $E_F^i$. This situation, particularly grave for the fully developed M–S interface, is somewhat alleviated for the partially covered semiconductor surface. For submonolayer coverages the presence of adsorbate induced states has been verified by cathodoluminescence spectroscopy (Viturro et al., 1986), by two-photon (pump-probe) photoemission spectroscopy (Haight and Bokor, 1986), through inverse and conventional photoemission spectroscopies (Schäffler et al., 1987a, b) and by STM spectroscopy (Feenstra, 1989a, b). On a microscopic scale STM spectroscopy has had a convincing impact on the origin and locality of gap states generated by adsorbates and defects on the surface (Feenstra and Stroscio, 1993; Stroscio and Feenstra, 1993). An example for small Au clusters evaporated onto a cleaved GaAs(110) surface is shown in Fig. 11.17. The topographic image shows the Au clusters on the darker background of the bare GaAs surface, with the labeled marks indicating the positions where the spectra in the lower part of the figure were acquired. The spectra are shown in a normalized differential conductivity representation that closely resembles the

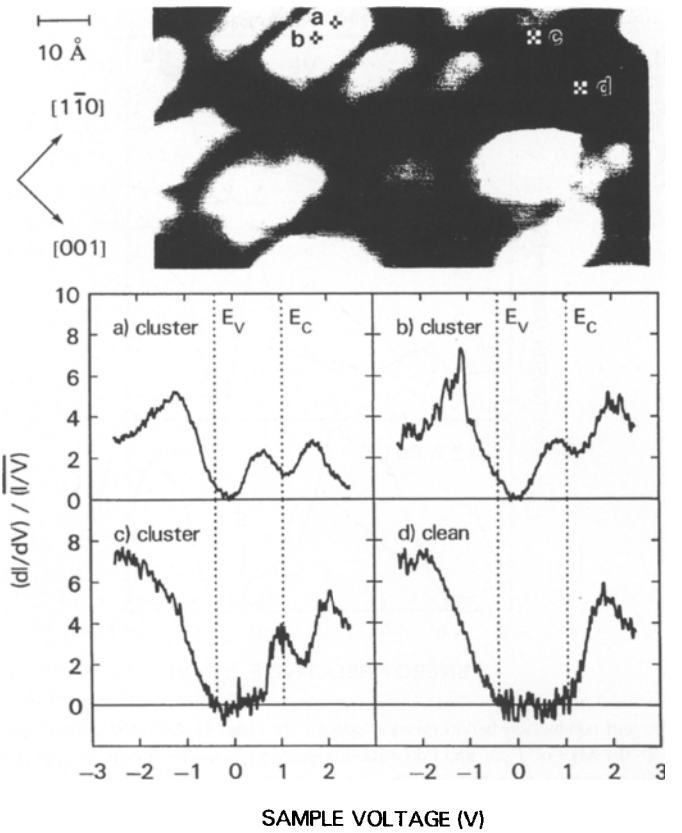


Fig. 11.17. Top: 100 × 55 Å$^2$ STM image of 0.25 ML Au on the GaAs(110) surface. The lettered crosses in the image mark the location at which the correspondingly lettered spectra shown in the bottom panels were acquired (after Feenstra, 1989a, with permission).

density of states in the surface region. Spectral features taken at negative sample voltage (electron extraction by the STM tip) correspond to filled states, those taken at positive voltages (electron injection) correspond to empty states. Spectrum (d), taken on the bare surface away from the clusters, is representative of the clean GaAs(110) surface; it exhibits a zero conductivity region ~1.4 V wide that represents the band gap of GaAs. Spectra (a) and (b), taken on a Au cluster, show a broad peak in the upper part of the band gap, as well as an enhanced state-density in the valence band that extends up into the band gap region. Even at the edge of the cluster, spectrum (c), state-density is enhanced relative to clean surface by a hybridization of Au and GaAs conduction band states, a clear indication of the perturbing influence of adsorbate atoms on the local density of states. At larger coverages the clusters merge into larger islands whose density of states progressively fill in the gap region and eventually approaches that of the metal (Feenstra, 1989b). These state densities are representative of the surface region of the Au islands, and *not* that of the immediate M–S interface region, which is inaccessible to all presently known spectroscopies. Similar

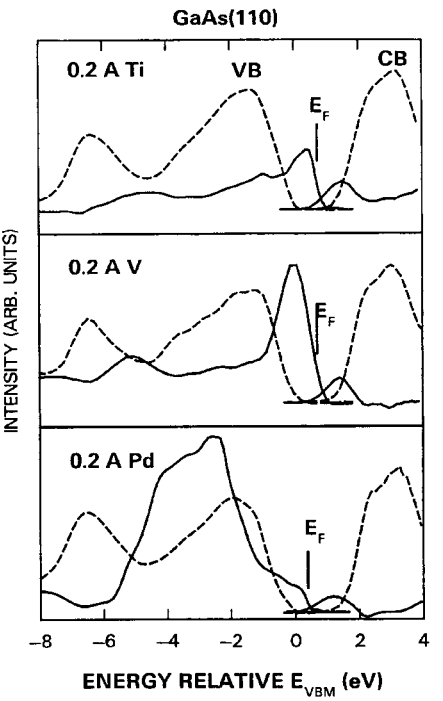


Fig. 11.18. Valence and conduction band emission spectra for clean GaAs(110) surfaces (dashed curves) and for low coverages (~0.1 ML) of Ti, V and Pd (solid curves). The latter are differential spectra that include the subtraction of the clean surface contributions. The valence band spectra (filled states) were obtained by photoemission, the conduction band spectra (empty states) by inverse photoemission. Both filled and empty "extrinsic" states derived from d-electrons of the transition metals are observed in the band gap region of the GaAs (after Schäffler et al., 1987a).

Au-derived states for comparable submonolayer coverages on heavily doped p-GaAs(110) had previously been observed by Haight and Bokor (1986). They detected these states by photoemitting electrons that had been pumped into them by low energy photons from lower lying valence electron states. Their spectra indicated a broadened state density in the gap that was peaked ≈0.5 eV above the valence band edge. This value is lower by 0.2–0.3 eV from those shown in Fig. 11.17, but undoubtedly are of the same origin.

Photoemission from filled and inverse photoemission from empty metal-induced gap states have been reported for submonolayers of transition metals on GaAs (Schäffler et al., 1987a) and InP (Schäffler et al., 1987b). Their results are shown in Fig. 11.18 for 0.2 Å (~0.1 ML) coverages of Ti, V and Mn. The experimental data, shown as solid lines, represent difference spectra between the clean and metal-exposed surfaces. The bulk DOS are shown as dotted lines. Clearly extra emission is observed in the band gap region, with the photoemission-detected filled states on the low energy side of $E_F$, and the empty states, observed with inverse photoemission, on the opposite side. These states are so readily observable because their origin derives from the 3-d states of the transition metals, which have a large photoionization cross section. Their presence is detectable for substantially

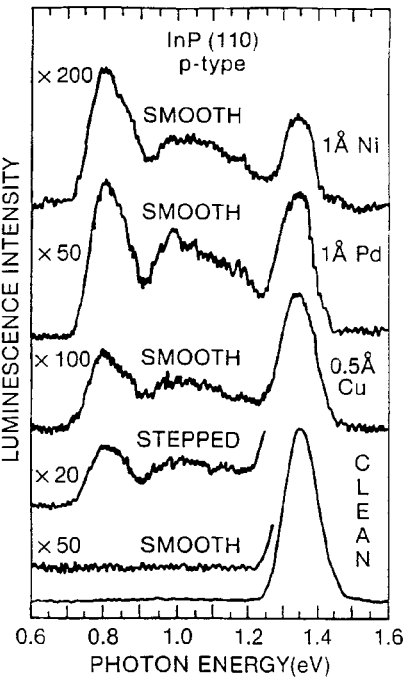


Fig. 11.19. Cathodoluminescence spectra of mirror-like, clean p-type InP(110) surfaces before (bottom spectrum) and after submonolayers of Ni, Pd and Cu were deposited. The "stepped" spectrum was obtained from a cleaved surface that exhibited such structure (after Viturro et al., 1986, with permission).

lower coverages, at which time evidence of their exchange reaction with the Ga atoms in GaAs is also present. That these atoms form gap states is not at all surprising since as substitutional atoms in III-V and II-VI semiconductors the transition metals are well known to form near-midgap impurity levels (Vogel and Baranowski, 1985; Clerjaud, 1985). For larger coverages the d-electron emission continues to intensify and eventually assumes the shape of the bulk transition metal This emission totally disguises that from the immediate M–S interface, whose evolution with coverage, as for STM spectroscopy, cannot be investigated.

Some evidence of the spectral evolution, and consequently that of the electronic structure, can be surmised from luminescence experiments (Viturro et al., 1986). Examples of spectra obtained by cathodoluminescence with 1 kV electrons for submonolayer coverages of metals on InP(110) surfaces are shown in Fig. 11.19. The spectrum for the clean surface, shown at the bottom, exhibits only spectral features close to band gap energies. The deposition of metals yields spectra characterized by relatively strong luminescence peaks at energies near 0.8 eV and a broader feature with peak intensities around 1 eV. The nature of the responsible states is not known; they may be acceptor states lying below midgap ($E_g = 1.35$ eV for InP) or donor states lying above midgap. The latter is more consistent with values of $\Phi_{sb}$ of 0.37–0.54 eV (Barret and Maaref, 1993; Newman et al., 1985), although it would imply that these states also exhibit acceptor character. As such

their recombination radiation, if it exists, should be at much lower energies and beyond detectability of the instrument. The spectral features remain for thicker coverages, although the 0.8 eV peak generally dominates (Viturro et al., 1986). Although some correlation between $\Phi_{sb}$ and spectral features in cathodoluminescence exists (Brillson, 1992), a basic question concerns the relationship of the radiative centers observed by luminescence and the states responsible for determining $E_F^i$ and consequently $\Phi_{sb}$. One could reasonably argue that the centers that support radiative recombination are somewhat removed from the immediate vicinity of the metal and are thus different from those containing the bulk of the interface charge. Some indication for this comes from capacitance spectroscopy of metal–InP(110) diodes prepared, as those for the cathodoluminescence studies, in UHV (Barret and Maaref, 1993). This spectroscopy measures the changes in capacitance arising from changing the interface charge with applied bias and is thus capable of determining the approximate distribution of the interface charge (Muret and Deneuville, 1982). Barret and Maaref (1993) observed interface states 0.37 eV below the conduction band edge of InP, a value that did not depend on the metal (Au, Ag, Pd and Al were studied). They speculated that these states were the ones responsible for the Schottky barrier.

*11.3.4.2. Band bending: the role of metallic states*

We have shown that reactive metals can induce surface states in the semiconductor band gap and that these cause $E_F^i$ to assume a value close to that of the fully formed M–S diode. Moreover, this occurs for coverages that are frequently much less than a ML, for which the dispersed metal atoms do not exhibit any metallic characteristics. The question then arises as to the role of the metal: is its presence necessary besides acting as a metallurgical support or as a low resistance electrical contact? The negative response was the view taken by Lindau et al. (1978) and Spicer et al. (1979) to propose that defect induced interface states were solely responsible for determining $\Phi_{sb}$. Moreover, since the position of $E_F^i$ measured by core level spectroscopy appeared to be independent of the metal adsorbate species, they suggested that a defect native to the semiconductor was responsible, a concept that is known as the unified defect model. Nearly all subsequent investigations, however, observed variations in $E_F^i$ for different metals. The role of the metallic characteristics of the overlayer in determining the final position of $E_F^i$ is less obvious, but clear indications have emerged in recent years that the role of the metal is other than a mere contact. In principle, as the overlayer becomes metallic, a charge redistribution takes effect at the interface because of metallic screening, as was discussed in Section 11.2.2. To reiterate, in the presence of the metal a larger interface charge is necessary to maintain electrostatic balance (Zur et al., 1983; Duke and Mailhiot, 1985). If the density of interface states is sufficiently large, the additional charge can be accommodated without affecting the position of $E_F^i$ in a measurable way. On the other hand, if the density of interface states is low the additional charge required may force the position of $E_F^i$ to be affected in a measurable way. Changes in $E_F^i$ that are correlated with the onset of metallic characteristics have been noted in the literature (Prietsch et al., 1988; Stiles and Kahn, 1988; Ludeke et al., 1988; Mao et al., 1992; Linz et al., 1993).

An example of the evolution of the surface Fermi level from low coverages through the formation of the metallic layer is shown in Fig. 11.20 for the rare earth Tm deposited on GaAs(110) cleaved surfaces under UHV conditions. The data was obtained from the core

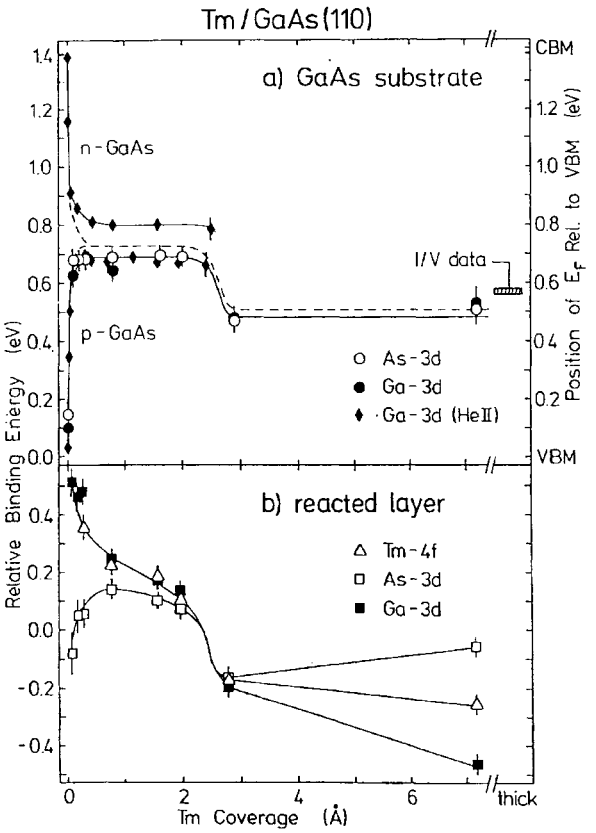


Fig. 11.20. Binding energy shifts of indicated core levels as function of thullium coverage on p-type (lower branch in panel a) and n-type GaAs(110) (upper branch in panel a). Panel (b) depicts the shifts in the reacted interface region, with shifts beyond 2.6 Å of Tm coverage being attributed to changes in chemical composition or coordination. The dashed line in panel (a) represents the common position of $E_F$ relative the valence band edge for n- and p-type GaAs (right hand scale) obtained after correction of the finite sampling depths of the photoemission process (after Prietsch et al., 1988, with permission).

level shifts of the bulk Ga-3d and As-3d levels. After the typical initial band bending for both n- and p-doped samples at low coverages, constant positions for $E_F^i$ were reached for coverages up to ~2.5 Å, which may be associated with Tm induced impurity levels. It should be noted that Tm, as so many other metals, reacts with the GaAs surface via an exchange reaction with the Ga. The reaction was easily discernible for coverages of 0.2 Å. The apparent separation of $E_F^i$ for n- and p-type samples has been interpreted as the result of the finite sampling depth of the experiment over which there is enough band bending to affect the determination of $E_F$ at the surface. The dashed line represents the correction for the finite sampling depth. For coverages beyond 2.5 Å $E_F^i$ for both n- and p-doped surfaces drops an additional 0.2 eV. This drop coincides with the appearance of metallic character in the Tm layer, as deduced from the emergence of a metallic Fermi edge in the valence

band EDC's. The new position of $E_F^i$ was attributed to the formation metal induced gap states.

The movement of $E_F^i$ with onset of metallic characteristics is particularly pronounced if both metal deposition and photoemission band bending measurements are performed at low temperatures (Stiles et al., 1987; Cao et al., 1987). Much of that band bending, particularly for n-doped material, can be attributed to surface photovoltage effects (see Section 11.3.3.3). For heavily doped p-type GaAs, Mao et al. (1992) have argued, based on photoemission and contact potential measurements, that the surface photovoltage effect is negligible. Cimino et al. (1992), on the other hand, argue that for heavily doped p-GaAs at low temperatures it is primarily charging of the semiconductor surface that contributes to strong band bending, the charging being induced by the photoemitted electrons whose charge is not entirely compensated from the bulk of the semiconductor (see also discussions by Horn, 1992).

At room temperature, however, the further relocation of the interface Fermi level with onset of metallic characteristics is a real effect for GaAs, as well as GaP. For moderately to heavily doped GaP even room temperature may not suffice to suppress SPV effects (Alonso et al., 1990), so that the observed changes in $E_F^i$ with the appearance of the metallic Fermi edge (Alonso et al., 1990; Ludeke et al., 1990a) are smaller than measured. On the other hand, Linz et al. (1993) showed that Cs deposition on GaP(110) at 80 K, with band bending probed by contact potential difference and ionization threshold methods to avoid SPV effects, clearly revealed a change in $E_F \sim 0.4$ eV following the appearance of a Fermi edge in the photoemission spectrum. They attributed the change in $E_F^i$ to the emergence of metal induced gap states that take over the role played by Cs induced gap states for coverages below the onset of metallic behavior.

What is clear from these studies is that metallic states do play an important role in determining the final position of $E_F^i$. What is not clear is the fate of the interface states that played such an important role in determining $E_F^i$ prior to the onset of metallic behavior. If these were true adsorbate-induced states, as for example in a non-interactive system, then the adsorbate atoms would merge with the metal as the coverage increases; as a result the adsorbate states would disappear and would be replaced by the emerging metal induced gap states. But such weakly interacting systems are the exception. If interface gap states are formed as a result of chemical reactions that produce impurity or defects that are not in immediate contact with the emerging metal interface, then the question of the role of the metal becomes rather complicated. If the defect levels are sufficiently removed from the interface so as not to overlap with the metallic wave functions, then the final position of $E_F^i$ depends on the density of defects: if too low ($<10^{13}$ cm$^{-2}$) the metal induced gap states will determine $E_F^i$. On the other hand, if their density is much larger ($>10^{14}$ cm$^{-2}$) $E_F^i$ will be determined by the defect level. This approach was used by Zur et al. (1983) and by Duke and Mailhiot (1985) to calculate the position of $E_F^i$. However, to assume defect states some 6 Å from the interface and no other ones of comparable densities closer to the interface does not appear to be realistic. More likely, a large density of impurity/defect states are within the immediate vicinity (~1–3 ML) of the metal, in which case the metallic states modify the defects states. The modified defect states are no longer spatially localized to the M–S interface as their wave functions have been hybridized with those of the metal, which results in a broadening of the energy levels (Section 11.2.2.3). This approach was taken by

Ludeke et al. (1988, 1989) to explain Schottky barrier trends and the observed changes in $E_F^i$ with onset of metallic characteristics. However, all of these model calculations assume the existence of at most two discrete levels with well defined binding energies in the band gap and at specific locations in the interface region. This oversimplification of the defect structure at the M–S interface, although a mathematical convenience, is the consequence of our ignorance of the structural and chemical complexity of most M–S interfaces. This complexity makes an assessment of the nature and role of electrically active interface states and a determination of their location extremely challenging. It is safe to say at this time that the role of defects at the M–S interface is not well understood.

*11.3.4.3. Schottky barrier trends*

Correlation studies of Schottky barrier heights with a variety of physical or chemical parameters of the semiconductors have been a part of the field for at least as far back as Schottky's (1940) observation that the zero bias resistance $R_0$ of different metal–Se contacts scaled with the work function of the metals ($R_0 = (\partial I/\partial V)^{-1}$ for $V = 0$, which, by use of Eq. (11.29b), leads to $\ln R_0 \propto \Phi_{sb}$). Thermodynamic correlations included observations that the heats of formation of transition metal silicides scale with $\Phi_{sb}$ (Andrews and Phillips, 1975), as do the lowest melting eutectic temperatures (Ottaviani et al., 1981). For binary compound semiconductors Brillson (1978) and Williams et al. (1979) reported that $\Phi_{sb}$ exhibited a nearly bimodal distribution when plotted against the heats of reaction between the metal and the semiconductor anion (column V or VI element), with the more reactive metals forming lower barrier heights on n-type semiconductors. These chemical trends can be qualitatively understood in that compound formation at the reactive M–S interfaces leads to electronic characteristics, such as the effective work function and electrononegativity, that are in between those of the constituents. Particularly for the compound semiconductors that generally do not form single metallic phases like the silicides, there is the additional complication that the reacted interface will probably be quite inhomogenous and full of defects, so that a large density of interface states is present. These two effects tend to lead to Schottky barrier heights that do not depend strongly on the metal work function and exhibit "average" values. For unreactive metals on the other hand, $E_F^i$ is freer to move over a broader range, which leads to high barrier values for the noble metals and lower barriers for the alkali metals on n-type semiconductors. Thus correlation studies of this type are only indirectly related to the microscopic parameters that underlie Schottky barrier physics.

More frequently the barrier heights are plotted against the metal work function or its electronegativity. A propensity exists among workers in the field to choose electronegativity in an attempt to establish a standard for ordering metals according to an intrinsic electronic potential or level, that does not include the surface dipole contribution inherent in work functions. However, at least for polycrystalline metals an empirical relationship between the Pauling electronegativity $\chi$ and the work function $\phi_m = 2.3\chi + 0.34$ (eV) is observed that applies reasonably well to most metals (Gordy and Thomas, 1956; Yamamoto et al., 1974). These parameters are more basic than the thermodynamic entities, but are still representative of a well defined system, such as a pure metal or a stoichiometric compound, situations that are only met infrequently for real systems. Let us illustrate this point with a plot of $\Phi_{sb}$ versus the electronegativity for a variety of metals and silicides on

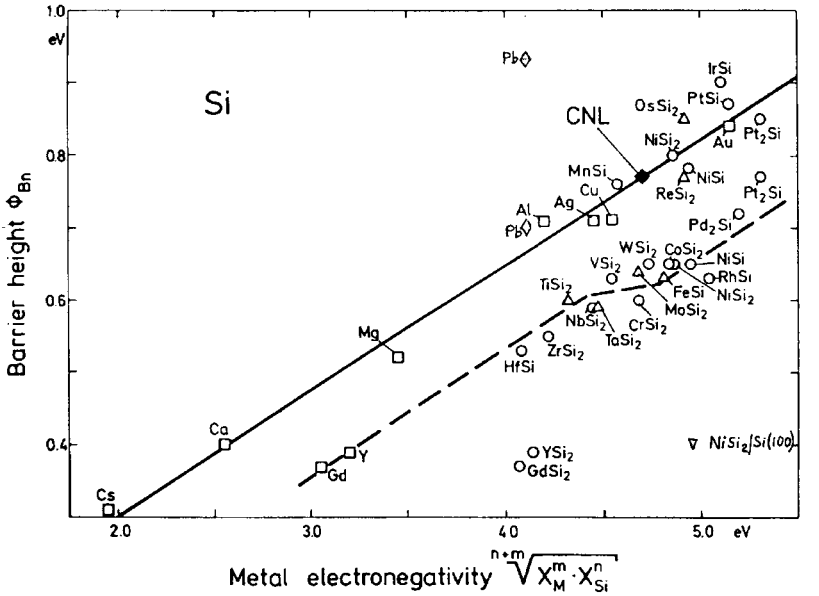


Fig. 11.21. Schottky barrier heights for n-type Si for metal-Si and silicide-Si contacts plotted against their electronegativities. The charge neutrality level (CNL) was determined by Tersoff (1984). Adapted from Mönch (1990), with permission. The data for Pb (Heslinga et al., 1990) and for $NiSi_2$/Si(100) (Tung et al., 1991) were added.

Si, as shown in Fig. 11.21. The Miedema electronegativity $\chi$ was chosen because it is based on a scale derived from chemical trends in the properties of metallic alloys and compounds (Miedema et al., 1980). Since this scale relates linearly to the Pauling electronegativity (Mönch, 1990), $X = 1.93\chi + 0.87$, the conclusions reached from such correlation studies do not change if the Pauling scale, or for that matter the work functions, are used. For the silicides of type $M_mSi_n$ in Fig. 11.21 a geometric mean $X \equiv (X_M^m X_{Si}^n)^{1/(m+n)}$ was used (Freeouf, 1980). The data in Fig. 11.21 falls approximately into two groups, one bounded by the solid line, the other straddling the dashed line. The solid line is a least square fit through 15 data points. The fact that Tersoff's (1984) charge neutrality level (CNL) also falls on this line has been used by Mönch (1987) to argue in favor of a MIGS interpretation: a metal less electronegative than Si would cause electrons to flow into the MIGS in order to establish an interface dipole necessary to equilibrate the Fermi level, thus raising it relative to the valence band and decreasing $\Phi_{sb}$ for n-type Si. The reverse occurs for metals that are more electronegative than Si. The additional assumption was made that the metals near this line also produce a low density of interface defect states, so that the Fermi level is not controlled (pinned) by them if their density is $\lesssim 10^{13}$ cm$^{-2}$. On the other hand Mönch (1987) argued that some metals and most silicides do produce densities of defect states of order ($\sim 10^{14}$ cm$^{-2}$) near midgap (indicated by the low sloped region of the dashed line in Fig. 11.21) that largely determine the position of $E_F^i$. According to the models of Zur et al. (1983) and of Mailhiot and Duke (1985), a variation of $E_F^i$ with $\phi_m$ similar to the dashed

line in Fig. 11.21 is expected (see Section 11.2.2.2). The equality of the slopes for the two segments to that of the solid line supports the contention that a similar mechanism, such as MIGS, determines the dependence of $\Phi_{sb}$ on $X$. However, a calculation of the slope based on a realistic Si band structure and a suitable model for the metal has yet to be attempted.

As suggestive as these trends may appear towards an understanding in terms of a universal model, there are nevertheless perturbing trends that imply that such a simplistic picture is not complete. The details of the interface structure appears to be important in at least several prominent examples of epitaxial systems, and further examples may emerge as unique interfacial arrangements can be prepared and identified. $NiSi_2$/Si(111), the first of such systems to be identified and studied (Tung, 1984), exhibits Schottky barrier heights on n-type Si of 0.65 and 0.79 eV for A- and B-type interfaces, respectively. These differ only by a 180° rotation about the interface normal of the $NiSi_2$ lattice relative to the Si(111) substrate, with the atoms at the interface retaining their coordination. These differences in barrier heights have been corroborated on a microscopic scale by BEEM (Fernandez et al., 1991a), as well as by theoretical calculations (Das et al., 1989; Fujitani and Asano, 1990; Ossicini et al., 1990; Stiles and Hamann, 1991a), although it has also been proposed that the differences could be attributed to differences in interface defect densities (Kikuchi, 1989). Additional support for a structural dependence comes from the work of Tung et al. (1991) for epitaxial $NiSi_2$/Si(100), for which $\Phi_{sb} = 0.40$ eV was reported for uniform planar films on n-type Si(100); in contrast non-ideal films that contained ⟨111⟩ oriented facets at the interface yielded more conventional values of 0.66 eV. Epitaxial $CoSi_2$/Si has also been reported to exhibit a wide range of $\Phi_{sb}$ values that range from 0.27 eV (Sullivan et al., 1993) to 0.8 eV (Jimenez et al., 1990) that cannot be explained by a simple defect model. Another example of apparent structural influence on the Schottky barrier height comes from the non-reactive Pb/Si(111) system, for which electrical measurements of epitaxial Pb/Si(111)$7 \times 7$ yielded a value of $\Phi_{sb} = 0.70$ eV, whereas for Pb deposited on the Pb-stabilized Si(111)$\sqrt{3} \times \sqrt{3}$ structure yielded a surprisingly high value of 0.93 eV (Heslinga et al., 1990). The Pb depositions occurred at room temperature, although the $\sqrt{3} \times \sqrt{3}$ structure is attained by heating the Si(111) surface covered with a monolayer of Pb to 300 °C. Such unusually large barrier heights have been corroborated by photoemission experiments, which in general yield even higher values (LeLay et al., 1989; Carlisle et al., 1992; Weitering et al., 1992). Valence band photoemission spectra for the monolayer covered ($7 \times 7$) and ($\sqrt{3} \times \sqrt{3}$) surfaces reveal a filled surface state band ~0.1 eV above the valence band maximum that was attributed by Weitering et al. (1992) as being responsible for determining the surface Fermi level. Theoretical studies suggest as well the existence of Pb-induced interface states near the bottom of the band gap that strongly depend on the bonding configuration of the Pb on the Si(111) surface (Ossicini and Bernardini, 1992). Lastly, it is worth mentioning that for Hg on hydrogen terminated p-type Si(111)–H surfaces a value of $\Phi_{sb} = 0.90$ eV was reported, which corresponds to a value of only 0.22 eV for n-type Si, clearly beyond the range of values plotted in Fig. 11.21 (Wittmer and Freeouf, 1992). This system is representative of an extremely non-interactive system, with the hydrogen passivating the surface and shielding the Si from the immediate influence of metallic state. Thus $E_F^i$ appears to be controlled by neither defect states nor MIGS; it is perhaps not a coincidence that $\Phi_{sb}$ agrees rather well with the prediction of the simple Schottky model (Eq. (11.5)).

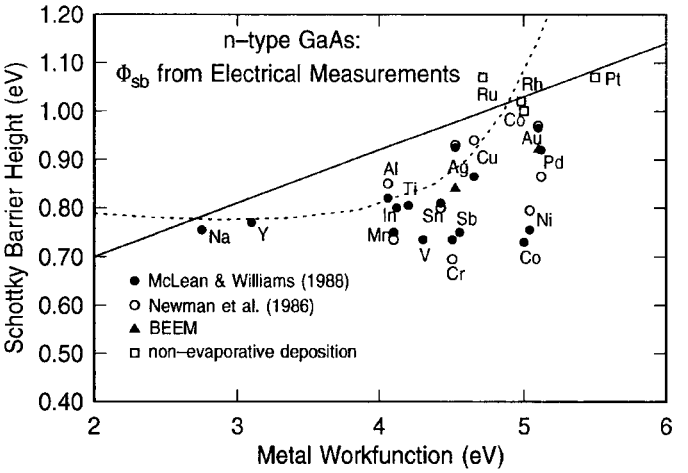


Fig. 11.22. Schottky barrier heights for metal–GaAs contacts plotted against the metal work function. Contacts for all but the non-evaporative deposition cases were fabricated on vacuum cleaved GaAs(110) surfaces followed by *in situ* metallization.

As a second example of a correlative representation of Schottky barrier data we illustrate in Fig. 11.22 barrier heights for n-type GaAs obtained from electrical measurements. The bulk of the data is for vacuum cleaved and thermal deposited metal contacts on (110) surfaces (McLean and Williams, 1988; Newman et al., 1986). For simplicity of viewing the $I-V$ and $C-V$ values for each metal were averaged. The data are quite scattered and do not follow any strong trends, although in general large work function metals lead to higher barrier values. Also shown in this figure as a solid line is the phenomenological limit expected for $\Phi_{sb}$ by the MIGS model for low ($\lesssim 10^{13}$ cm$^{-2}$) defect densities, as envisioned by Mönch (1990). As for Si above, barrier heights falling substantially below this line are probably dominated by defect states at the M–S interface, a view entirely consistent with the strong reactivity of most metals with GaAs, as discussed in Section 11.3.3.3. Further support for this view is suggested by the higher $\Phi_{sb}$ values obtained for plated metal contacts, shown in Fig. 11.22 by open squares. The studies by both Hashizumi et al. (1992, 1994) for electroplated Pt and by Ludwig et al. (1993) for electroless plated Rh on GaAs(100) surfaces resulted in higher barrier heights and a reduction in interface states, as determined by transient capacitance spectroscopy, compared to interfaces prepared by evaporation of the metal. Similar results have been obtained when the metal was evaporated onto conventionally cleaned GaAs(100) wafers held near 77 K (Shi and Anderson, 1992): for Au $C-V$ and $I-V$ determinations of $\Phi_{sb}$ yielded values of 1.02 and 0.97 eV, respectively. An estimate of the variation of $\Phi_{sb}$ with metal work function for an interface density of states dominated by a single defect level of density $\sim 4 \times 10^{14}$ cm$^{-2}$ is shown by the dashed line (Ludeke, 1989; see also Section 11.2.2.3). The large discrepancies between simple models and many measured barrier heights point clearly to the present inadequacy in our understanding of the microscopic nature of realistic interfaces. Their electronic characteristics are controlled by the local defect structure that is modified by the presence of

the metal, which in turn has properties that are affected both by chemical deviations from its pure form and by its local structure.

Plots similar to the above have also been reported for InP by Mönch (1990) and for GaP by Linz et al. (1993). For GaP the scatter of the data is comparable to GaAs. For InP, on the other hand, only Ag lies in close proximity of the expected upper boundary determined by the empirical MIGS model of Mönch (1990). However, recent reports for metals deposited on InP(100) wafers cooled to near 77 K revealed substantial enhancements in $\Phi_{sb}$ of up to 0.5 eV over room temperature prepared samples. The barriers heights, determined from $I$–$V$ curves of fair quality factors, were surprisingly high, with values of 0.96 and 0.86 eV reported for Pd and Au, respectively (Shi et al., 1991). These values fall beyond the boundary of the MIGS model, which may have to be reassessed.

## 11.4. Ballistic electron emission microscopy

### *11.4.1. Basic concepts*

The technique of ballistic electron emission microscopy (BEEM) is an elegant application of the scanning tunneling microscope (STM) realized by Kaiser and Bell (1988) to investigate electron transport across metal–semiconductor (M–S) interfaces with unprecedented spatial resolution. They monitored the current collected in a semiconductor (Si) covered with a thin, ~100 Å thick Au layer that was scanned by the STM. When the STM tip bias relative to the Au film exceeded a threshold value $V_0$ a current was observed emanating from the semiconductor. This current, sometimes termed the BEEM current, is more often called the collector current $I_c$, due to a functional resemblance of the experimental arrangement to a transistor structure. In the spectroscopy mode the STM scan is stopped and $I_c$ is measured as the tip bias $V_T$ is ramped with the tunnel current $I_T$ injected by the STM tip held constant. An early spectrum is shown in Fig. 11.23. The bias of the STM tip is such that electrons are injected into the metal surface, whence they reach the semiconductor after crossing the metal layer without scattering (ballistically). When the STM tip is scanned, there is the option of using both the STM feedback signal for imaging – the conventional STM imaging mode – and the collector current. The resulting image in the latter case is the BEEM image. An example of a BEEM image, taken simultaneously with the STM topographic image for a $CoSi_2$ film grown epitaxially on Si(111)(7 × 7) is shown in Fig. 11.24. In contrast to most images of non-epitaxial M–S interfaces, this BEEM image has clear correlations with topographic features in the STM image. Among these are the sharply contrasted monoatomic surface steps running diagonally across the topographic image and the faint network of lines attributed to dislocations in the $CoSi_2$ that show a remarkable contrast enhancement in the BEEM image. Most of the other random structure in the BEEM image has no equivalent in the STM image and represents changes of unknown origin in the transmission properties of the electrons as they traverse the metal film and enter the semiconductor. From the highly delineated contrast changes in the BEEM image, one would conclude that these are not due to changes in the barrier potential – the Schottky barrier – at the M–S interface, as these would not occur over distance much smaller than the Debye length (Eq. (11.3)) or ~50 Å for the doping of the semiconductor. To understand the origin of spatially varying collector current intensities, one must understand the

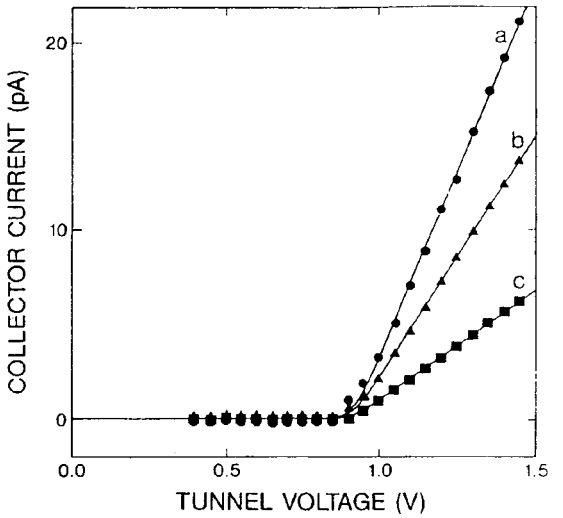


Fig. 11.23. BEEM spectra of the collector current $I_c$ as a function of the applied tip bias $V_T$ for a 100 Å Au layer on n-type Si(100). Spectra a (dots), b (triangles) and c (squares) were measured at constant tunnel currents $I_T$ of 0.87, 0.57 and 0.27 nA, respectively. The solid lines represent fits with calculated spectra, from which a barrier height or threshold potential $eV_0 = 0.92$ eV was obtained (after Kaiser and Bell, 1988, with permission).

complete transport process from injection to detection. Models of the transport processes will be discussed in Section 11.4.3.

As an introduction, it is worthwhile to look at a qualitative cartoon of the experimental setup and a corresponding energy diagram These are shown in Fig. 11.25. The STM tip operates in a constant current mode, here shown with a tip bias that corresponds to electron injection. The bias voltage $V_T$ is applied between tip and metal film, represented by a circular dot, by means of a contact electrode or wire. In this lies the major difference between BEEM and a regular STM, which has its circuit completed through the substrate, the semiconductor crystal in the present example. In BEEM the semiconductor substrate is partly isolated through the blocking characteristics of the Schottky barrier, so that part or all of the injected tunnel or tip current $I_T$ flows through the metal film and returns to ground through the BEEM contact. If $V_T$ exceeds a threshold voltage $V_0$ that corresponds to the Schottky barrier height, some of the injected electrons may traverse the metal ballistically (i.e., without scattering) to be collected in the semiconductor. For the noble metals the ballistic mean free path for energies of a few volts is of the order of a few hundred Ångströms (Cowley and Sze, 1965). Consequently BEEM spectroscopy probes the fully formed M–S interface and its results are representative and comparable to those obtained by $C$–$V$ and $I$–$V$ methods. On the other hand BEEM is also capable of characterizing transport through extremely thin (<10 Å) metal films (Bauer et al., 1993a, b; Ludeke and Bauer, 1993, 1994), and is thus capable of addressing issues previously restricted only to surface sensitive techniques, such as photoemission spectroscopy.

Like other spectroscopies, BEEM is characterized by its own unique attributes, transport properties in this case, that need to be understood in order to maximize the useful

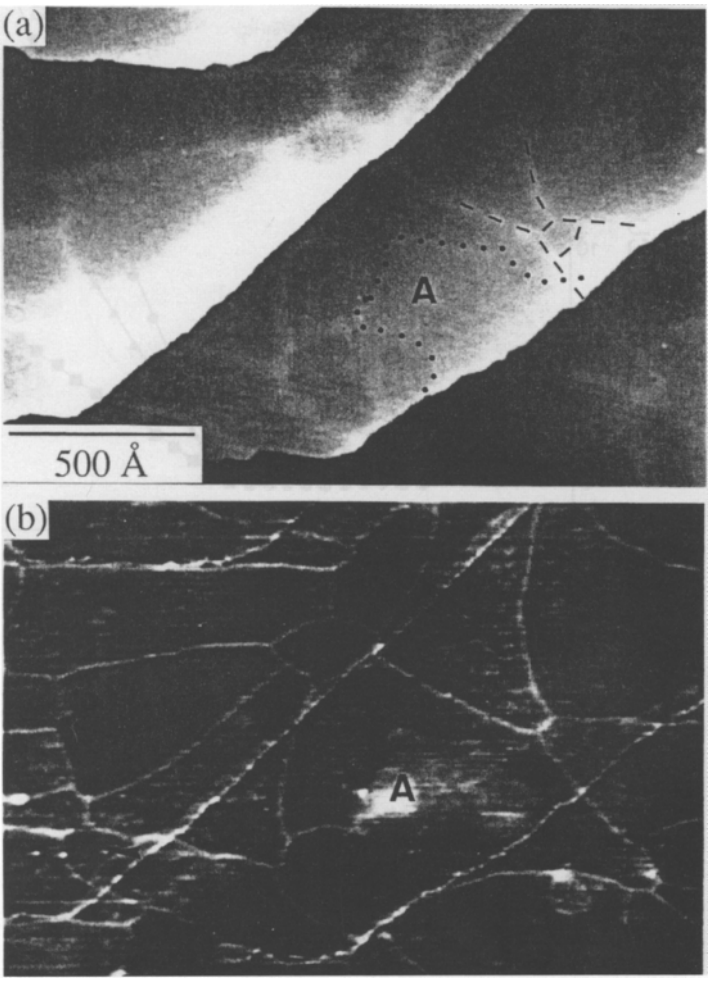


Fig. 11.24. STM topograph (a) and simultaneously recorded BEEM image (b) for a 25 Å epitaxial $CoSi_2$ layer on n-type Si(111) ($V_T = -2$ V, $I_T = 5$ nA). A portion of the weakly delineated dislocation network in the topograph is indicated by dashed lines. Brighter areas in the BEEM image correspond to larger collector currents $I_c$, which in the image varied over a range of ~150 pA (dark) to ~200 pA (bright). Region "A" and small stripes along the surface steps exhibit $2 \times 1$ surface reconstructions that enhance the transmission. The arrow in the lower left corner of (b) indicates an atomic scale surface point-defect that is not resolved in the topographic image (after Sirringhaus et al., 1994, with permission).

information that can be extracted from the BEEM images and spectra. The energetics of the transport process are schematically shown in the bottom panel of Fig. 11.25. The STM tip is represented schematically on the left by a metal with a Fermi energy $E_F$, which is raised relative to that of the metal overlayer by the tip bias $V_T$. The tunnel gap is shown as a trapezoidal barrier. The potential at the M–S interface is shown in the conventional representation. The complete description of the transport can be divided into three steps:

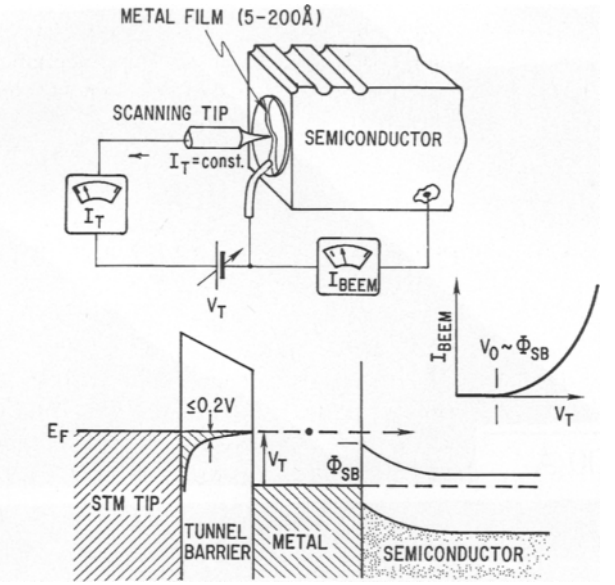


Fig. 11.25. Top: schematic view of a BEEM experiment. Bottom: corresponding energy diagram with the STM tip biased for electron injection ($V_T < 0$) into an n-type semiconductor. The $I_c$ vs. $V_T$ curve depicts a power law dependence above a threshold potential $V_0$.

injection, transport through the metal base and collection in the semiconductor. This sequence of events is closely related to transport in transistor structures, in particular the metal base transistor (Luryi, 1990).

Here we will briefly sketch the main features of the transport process, leaving the details for later sections. Current transport from the STM tip to a nearby crystalline surface of a metal (injection) is a complicated process that requires detailed knowledge of the geometry and composition of both tip and metal surface. Approximations in treating this problem include a spherical tip over a periodic lattice (Tersoff, 1990), a periodic tip over a periodic lattice (García et al., 1983) and a single atom tip over a "jellium" metal (Lang et al., 1989). These approaches do not lend themselves readily to a straightforward evaluation of the collector current. Instead the simpler approach assuming a planar tunneling geometry will be used. The tunneling probability, in this case, is represented by a simple exponential expression in terms of the barrier height and width (Simmons, 1964). Transport through the metal is generally assumed ballistic, that is a fraction of the electrons injected by the tip reach the metal–semiconductor interface without scattering. The simplest way to treat electron collisions or scattering is to assume that each such event prevents the electron from reaching the interface. Models that include an energy dependent probability of not scattering, $\sim e^{-w/\lambda_b(E)}$, where $\lambda_b(E)$ is the ballistic mean free path and $w$ the metal film thickness, have been reported by Ludeke et al. (1991) and Bauer et al. (1993a). Transport across the M–S interface and collection in the semiconductor assumes in general conservation of transverse momentum (Bell and Kaiser, 1988) and may include quantum mechan-

ical transmission probabilities (Ludeke et al., 1991) and phonon scattering effects in the semiconductor (Lee and Schowalter, 1991). When transverse momentum conservation is assumed for all three transport steps, then to the lowest order in a power series expansion, the collector current is

$$I_c \propto e(V_T - V_0)^2 \tag{11.40}$$

if quantum mechanical transmission is not included (Bell and Kaiser, 1988), or

$$I_c \propto e(V_T - V_0)^{5/2} \tag{11.41}$$

if it is included (Ludeke et al., 1991). On the other hand, Lee and Schowalter (1991) have argued that the inclusion of phonon scattering tends to cancel the additional 1/2 power due to quantum mechanical transmission, thus reverting the power dependency back to a square law. A schematic plot of the $I_c$–$V_T$ characteristics is shown in Fig. 11.25.

### *11.4.2. Experimental technique*

#### *11.4.2.1. STM/BEEM requirements and limitations*

For BEEM the STM should exhibit all the attributes of a state of the art instrument. From an operational point of view, a well designed STM is stable to conventional external vibrations and electrical influences common in an average laboratory. The criteria for achieving this are too numerous and complex to be included here. The interested reader should refer to the article by Park and Barrett (1993) or the book by Chen (1993) and references therein. In addition, a BEEM instrument should be optimized against thermal drifts that arise from temperature gradients across any of the elements connecting the sample and the STM tip, including support structure. Acquisition times for BEEM are typically an order of magnitude slower than for comparable STM procedures, either spectra or topographs, due to the lower signal strength (currents) in BEEM, which are in the picoampere range. Methods to minimize thermal drifts include use of material with matching thermal expansion coefficients, small dimensions and a symmetric design. Thermal drifts should be less than 1 Å/s, and preferably much lower than this, since spectra are typically taken within a few seconds. For these conditions the tip is unlikely to drift across a major topographic feature, such as a facet, which otherwise could affect $I_c$ as noise or sudden intensity changes (Prietsch and Ludeke, 1991a). It is also possible to compensate electronically for thermal drifts by determining the drift rate from known features on sequential topographic images and superimposing a suitable voltage ramp on the scanning piezos to cancel the drift (Feenstra, 1989a).

The salient difference between STM and BEEM is the additional amplifier connected to the semiconductor and the grounding contact to the metal overlayer that allows biasing the STM tip relative to the metal film. The amplifier should be a low-noise operational amplifier with a sensitivity at least a factor of 100 greater than that used to amplify the STM tunnel current. The current noise generated by an operational amplifier is extremely sensitive to the value of the resistance $R_L$, actually the load, connected to the input of the amplifier. The resulting noise current is $I_n = V_n/R_L$, where $V_n$ is the rms noise voltage of

the amplifier. For a typical $V_n = 10^{-6}$ V, $R_L$ should be greater than $10^6$ Ω for the noise current to be $<1$ pA. The source of $R_L$ is the zero bias resistance of the M–S contact, including any leakage resistance. If the latter is negligible, unfortunately not always the case, the zero bias resistance is calculable from the parameters of the M–S contact. Differentiating Eq. (11.29b) yields

$$R_0 = \left|\frac{\partial I}{\partial V}\right|^{-1}_{V=0} = \frac{h^3 \exp[\Phi_{sb}/kT]}{4\pi e^2 m_s kT A_d}. \tag{11.42}$$

Representative values of $R_0$ for GaAs, Si and GaP diodes of areas $A_d = 1$ mm$^2$ and 0.01 mm$^2$ are shown in Fig. 11.26 as a function of $\Phi_{sb}$. Three sets of curves represent $R_0$ for junctions at 77, 200 and 300 °K. Since $R_0$ should preferably exceed 1 MΩ, the curves provide an indication of the lowest $\Phi_{sb}$ that can be measured with good signal-to-noise ratios. In practice somewhat lower resistances can still be used provided longer acquisition times are used to average out the noise. Figure 11.26 clearly demonstrates the advantage of reducing the junction temperature to measure low barrier heights. This approach was used by Bell et al. (1990) to study low barriers for Au on p-type GaAs. The alternative is to decrease the junction area. Several schemes have been utilized. The simplest is evaporation through a mask, which is particularly attractive for UHV-prepared samples, but is limited to ~100 μm dimensions if the BEEM contact is to be made *in situ* as well. For smaller junction areas some sort of external lithographic process is essential. A scheme reported by several workers entails etching of small windows into thin $SiO_2$ films deposited on

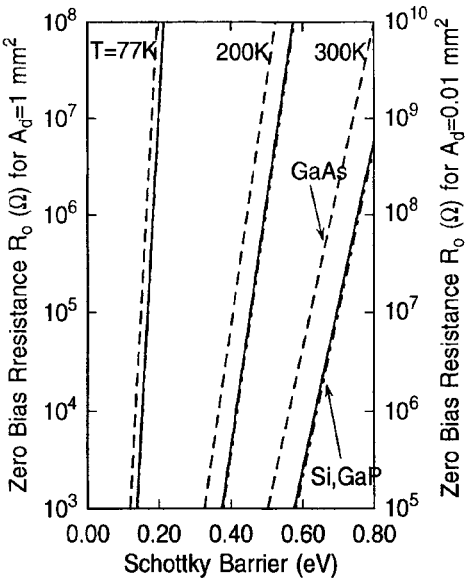


Fig. 11.26. Zero bias resistance of a Schottky diode as a function of barrier height for GaAs, GaP and Si at 77, 200 and 300 K. Calculations based on the thermionic emission model, with no allowances made for edge leakage.

Si substrates (Fernandez et al., 1991a; Hallen et al., 1991) or Si-Ge alloys (Davies et al., 1992). The metal is subsequently evaporated over the patterned $SiO_2$ layer. The BEEM contact is made to the metal where it overlies the oxide layer. A third method, reported by Fowell et al. (1992), consists of making mesa structures by first depositing all necessary layers, including the metal, and subsequently creating the desired structure through an etching process. This method has the advantage that the interfaces can be fabricated in the controlled cleanliness of an UHV chamber. Moreover, the mesa structure also reduces leakage currents that may otherwise render the sample unmeasurable.

*11.4.2.2. UHV BEEM system*

A description will be given of the author's system that was designed specifically for BEEM use. The principal design criteria were as follows: (a) UHV compatibility to investigate a broad range of materials; (b) vibration isolation equivalent to state-of-the-art STM's for atomic resolution microscopy; (c) sample exchangeability through an interlock to an adjacent UHV preparation/analysis chamber; (d) *in situ* STM tip cleaning and exchange to avoid venting; (e) externally controlled triaxial motion of BEEM grounding wire for precise positioning on small area M–S contacts; (f) low thermal drifts; and (g) reduction of electrical noise and pickup to allow measurements of sub-picoamp BEEM currents.

*Mechanical description.* The STM consists of a tubular scanning piezo that is mounted on a Macor platform or sled, as schematically illustrated in Fig. 11.27. The sled is driven by a push rod attached to a linear motion motor, specifically an Inchworm™ manufactured by Burleigh Instruments, Inc., Fishers, NY, that is mounted beneath the Macor support structure. Macor was used throughout the support structure, including a top plate that is not

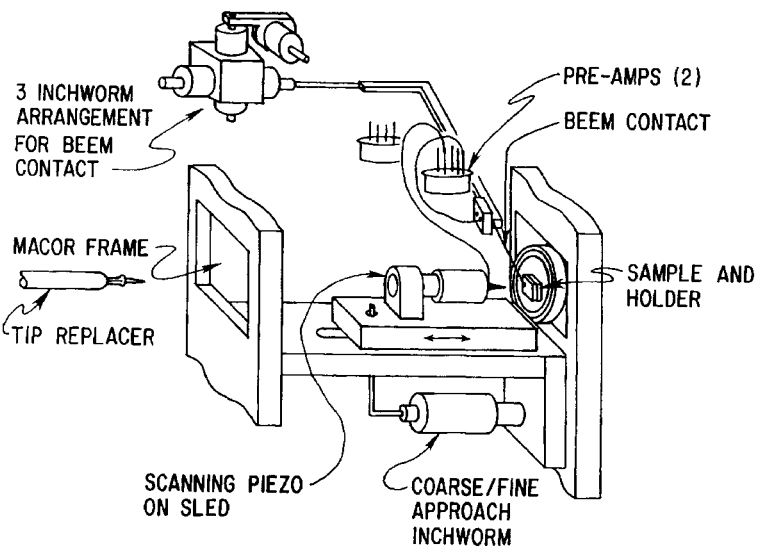


Fig. 11.27. Schematic view of the principal elements of the author's BEEM apparatus. A similar apparatus is described by Prietsch (1992).

shown in Fig. 11.27, because of its machinability and its match to the thermal expansion coefficient of the piezo scanner. The STM sled is guided by three stainless steel bearings, mounted in cups beneath the sled, that track in three parallel V-shaped grooves cut into sapphire spacers recessed into the bottom plate. The Inchworm is used for both coarse and fine approach of the tip to the sample surface. The STM tip assembly consists of a 0.007″ W wire that is spot welded to a holder. The tip is sharpened by electrolytically etching the W wire in a 1.6 molal solution of KOH in water. Tips can be exchanged in UHV by their removal and replacement through the body of the tubular scanner by means of a linear motion device or wobble stick. Up to ten tips are stored in a tip magazine that also contains a position at which the tip can be thermally cleaned by electron-beam heating. This is achieved by placing the tip at the center of a single loop W filament to which a negative bias of ~250 V is applied relative to the grounded tip. The filament current is adjusted until a few mA of emission results.

The circular sample holder (~3/4″ in diameter) is held by three point bayonet mounts on both the STM and the transfer rod. This arrangement permits easy and relatively smooth sample transfers between introduction chamber, sample preparation chamber and the STM. A variety of different sample shapes, from notched bars for cleaving to direct current heated wafers, can be used with this design. The receptacle for the substrate holder on the STM is mounted on a Macor frame that is electrically isolated. The frame can be coarsely adjusted along two orthogonal directions perpendicular to the axis of the piezo scanner, which is accomplished by two screwdrivers mounted on rotary feedthroughs. This action is necessary to position a desired area on the sample surface in front of the STM tip, as the latter can only be moved along its axial direction.

The STM in its Macor cage is mounted beneath a circular stainless steel platform that is hanging from a spring suspension system. The platform supports the operational amplifiers, feedback resistors, connectors for the wiring and the BEEM contact manipulator. The latter consists of three triaxialy mounted miniature Inchworms to which a bent lever arm is attached whose end lies in the vicinity of the sample. An electrically isolated Pt–Rh wire, attached to the end of the lever, can thus be manipulated with great precision and gentleness onto the metal contact of the sample.

The suspension system for the STM stage is composed of two stages, each of which consists of three springs about 15 cm in length. The first stage, which is also eddy current damped is attached to an 8″ UHV flange. The resonance frequency of this combination is about 1 Hz at the STM stage. Further damping and vibration isolation is achieved by Viton spacers between springs and spring supports, and by Viton wedges to anchor the extensive wiring passing through the two platforms at the end of each suspension stage. The platforms can be raised and locked mechanically by an axial lifter, thereby allowing sample and tip changes and coarse sample positioning, as well as facilitating removal of the instrument from the UHV chamber.

*Electronics and control.* In order to minimize electrical pickup, the operational amplifiers that preamplify the STM and BEEM currents and their feedback resistors are mounted in UHV in close proximity to the tip and sample. The electrical diagram is shown in Fig. 11.28. The hermetically sealed operational amplifiers and glass encapsulated resistors are UHV compatible. To prevent pickup from the scanning piezo it was necessary to

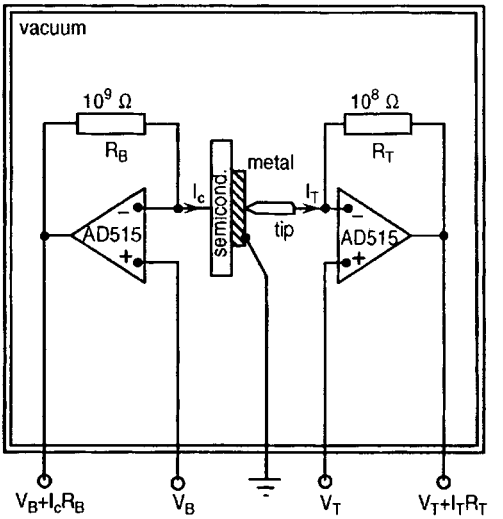


Fig. 11.28. Electrical diagram of STM/BEEM preamplifier circuits in the UHV chamber.

surround it with a cylindrical shield that is biased at the tip potential. All wiring was Kepton coated magnet wire. The system pressure after a mild, overnight bake out at ~100 °C was typically in the 1–2 × $10^{-10}$ Torr range.

The output of the tip amplifier is $V_T + I_T R_T$, and that of the BEEM current amplifier $V_B + I_c R_B$, where $V_B$ is the bias voltage optionally applied across the M–S junction and $R_T$, $R_B$ are the values of the feedback resistors. Generally $V_B$ will be zero, although a small bias may be applied to compensate for leakage or pickup currents. These biases are subtracted in the external control electronics prior to further signal processing. A simplified block diagram of the external STM/BEEM control electronics is shown in Fig. 11.29. This unit is under either manual or computer control. A novel feature is that all digital control signals coming from the personal computer, an IBM PS/2 Model 80, are linked to the digital to analog converters (DAC) via optoisolators to minimize digital noise pickup by the analog circuitry, as well as to prevent ground loop problems. Optoisolators are also used for the digitized output signals sent to the computer. The unit supplies the bias voltages and power for the STM and BEEM amplifiers in vacuum, the analog signal for the high voltage amplifier that drives the piezo scanner, the signals to and from the lock-in amplifier, as well as the digital output signal to the inchworm controller during tip approach.

In standard fashion, the tunnel-current signal is passed through a logarithmic amplifier and compared to a preset value. If a discrepancy exists due to a changing tip–sample separation, a difference signal is fed to the high voltage (HV) amplifier that drives the axial ($z$) direction of the scanning piezo, with the resulting change in the tip–sample position re-establishing a constant tip current. The difference signal, which is directly proportional to the change in tip–sample distance, is passed through an analog to digital (A/D) converter, whose output is subsequently used by the computer to image the topographic changes of the surface in the STM microscopy mode. If a collector or BEEM current $I_c$ is present,

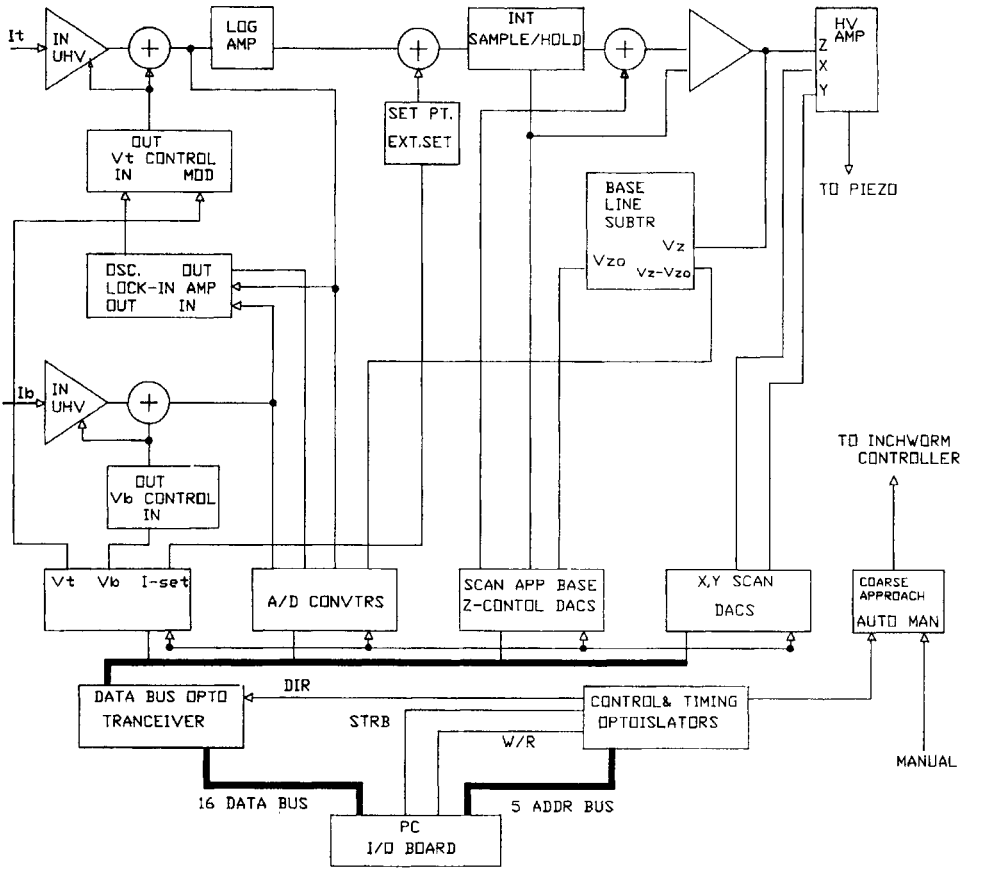


Fig. 11.29. Functional diagram of control and signal processing circuitry of a STM/BEEM system.

it may likewise be converted to a digital signal and used to generate a simultaneously recorded BEEM image. In the spectroscopy mode the scanning is interrupted. During STM spectroscopy the feedback loop is broken and $I_T$ is measured as $V_T$ is changed over a predetermined range. A derivative signal $dI_T/dV_T$ is obtained by applying a small ac bias to the tip and routing the tunnel current signal through a lock-in amplifier (Stroscio and Feenstra, 1993). In BEEM spectroscopy, the scanning is likewise interrupted, but the feedback, and hence a constant $I_T$, is maintained as the tip voltage is ramped. If desired, derivative acquisition modes are also possible (Lee et al., 1993).

Computer control of the electronics is menu based, with different menus for automatic tip approach, data acquisition and data analysis. In the spectroscopy mode of data acquisition, spectra can be taken in either the hot key mode at spontaneously chosen locations during the raster scan, or at a preselected grid of points on the scanned area. The latter mode was generally preferred, with grids of 16 to 36 spectra comprising a convenient data set. A spectrum consists typically of several hundred points, with each point sampled many

times to improve the signal-to-noise ratio. With a minimum practical bandwidth of 10 Hz and input noise voltage of ~4 $\mu$V p-p over a 0.1–10 Hz band width, the output current noise is $I_{\text{noise}} \sim 4 \times 10^{-6}/\sqrt{n}R_0$, where $n$ is the product of the sampling number and any additional point averaging after the data has been taken. Thus to achieve a noise current $I_n < 1$ pA p-p for $R_0 = 1$ M$\Omega$ $n$ should exceed 16. In practice the noise voltage is somewhat larger and values of $\lesssim 50$ are normally used. Typical acquisition times per spectrum are in the range of 5–20 seconds.

### *11.4.3. Models of BEEM transport*

#### *11.4.3.1. Planar tunneling theory*

Consider a simple rectangular barrier of height $\Phi$ separating two free-electron like metal regions of infinite lateral extent. An electron in the metal with energy $E_z < \Phi$ impinging on one side of the barrier has a wave function in the barrier region of the form $\psi \propto e^{-\kappa z}$, where $\kappa \approx [2m(\Phi - E_z)]^{1/2}/\hbar$ is the attenuation of $\psi$ in the barrier and $z$ is the direction normal to the barrier. The current emerging beyond the barrier of width $s$ is $I \propto |\psi|^2 = e^{-2\kappa s}$. The exponential term may be thought of as the probability for the electron to traverse the barrier. For a barrier $\Phi(z)$ of more general shape between two metals the tunneling probability $D(E_z)$ is given in the WKB approximation by (Bohm, 1951)

$$D(E_z) = \exp\left\{-\frac{2}{\hbar}\int_{S_1}^{S_2}\left[2m(\phi(z) + E_F - E_z)\right]^{1/2} dz\right\}, \tag{11.43}$$

where the integration limits represent the classical turning points. For convenience we have expressed here the barrier height $\phi(z) \equiv \Phi(z) - E_F$ relative to the Fermi energy $E_F$ of the metal. The current density of electrons that tunnel through the barrier in one direction is given by

$$\begin{aligned} J_z &= \frac{2e}{(2\pi)^3}\int D(E_z) f_F(E)\left[1 - f_F(E + eV_T)\right] v_z \, d^3k \\ &= \frac{2e}{(2\pi)^3\hbar}\iint D(E_z) f_F(E)\left[1 - f_F(E + eV_T)\right] d^2k_t \, dE_z, \end{aligned} \tag{11.44}$$

where $v_z = \hbar k_z/m$ is the velocity of the electrons in the $z$-direction normal to the barrier, $f_F$(E) and $f_F(E + eV_T)$ are Fermi functions, $V_T$ is the applied potential across the tunnel barrier and $k_t$ is the momentum component transverse to the $z$-direction, i.e., parallel to the barrier that lies in the $x$–$y$ plane. A similar expression for the tunnel current density in the opposite direction is obtained by exchanging the two Fermi functions. The difference of the two current densities is the net tunnel current density $J_T$,

$$J_T = \frac{2e}{(2\pi)^3\hbar}\int_0^\infty dE_z\left[f_F(E) - f(E + eV_T)\right]\int_{k_t} d^2k_t D(E_z). \tag{11.45}$$

A simple form for the tunneling probability $D(E_z)$ can be obtained by assuming that the barrier width is independent of the electron energy and equal to its value at $E_F$. With this assumption Simmons (1963) showed that Eq. (11.43) can be replaced by

$$D(E_z) \approx \exp\left[-A(E_F + \overline{\phi} - E_z)^{1/2}\right], \tag{11.46}$$

where

$$\overline{\phi} = \frac{1}{2}\int_{S_1}^{S_2} \phi(z)\,dz, \qquad A = \frac{2\beta s(2m)^{1/2}}{\hbar}. \tag{11.47}$$

$\beta$ is a correction factor close to 1, so that $A = 1.02s\ (\text{eV})^{-1/2}$. Simmons (1963, 1964) considered several shapes of the barrier, including the influence of image force lowering. Inclusion of the image force results in expressions that are not amenable to a closed form solution. Instead, we consider here a trapezoidal barrier that results when the applied bias $V_T$ between the electrodes is included

$$\phi = \overline{\phi} - \frac{eV_T}{2}. \tag{11.48}$$

Substituting $\phi$ for $\overline{\phi}$ in Eq. (11.46), we obtain

$$D(E_z) \approx \exp\left[-A\left(E_F + \overline{\phi} - \frac{eV_T}{2} - E_z\right)^{1/2}\right]. \tag{11.46a}$$

Within the framework of energy and momentum conservation and for $T = 0$, Eq. (11.45) can be separated into integrals spanning two ranges of $E_z$: $0 \leqslant E_z \leqslant (E_F - eV_T)$ and $(E_F - eV_T) \leqslant E_z \leqslant E_F$ to give (Floyd and Walmsley, 1978)

$$\begin{aligned} J_T = {} & \frac{4\pi m_{mt} e}{h^3}\int_{E_F - eV_T}^{E_F} D(E_z)\,dE_z \int_0^{E_F - E_z} dE_t \\ & + \frac{4\pi m_{mt} e}{h^3}\int_0^{E_F - eV_T} D(E_z)\,dE_z \int_{E_F - eV_T - E_z}^{E_F - E_z} dE_t, \end{aligned} \tag{11.49}$$

where $m_{mt}$ is the component of the effective mass tensor of the metal in the plane of the barrier, and where use was made of the relationship

$$d^2k_t = 2\pi k_t\,dk_t = \frac{2\pi m_{mt}}{\hbar^2}\,dE_t. \tag{11.50}$$

Integration over $dE_t$ yields:

$$J_T = \frac{4\pi m_{mt} e}{h^3}\left[eV_T\int_0^{E_F - eV_T} D(E_z)\,dE_z + \int_{E_F - eV_T}^{E_F} D(E_z)(E_F - E_z)\,dE_z\right]. \tag{11.51}$$

Upon further integration with $D(E_z)$ given by Eq. (11.46a), we obtain the tunnel current density (Wolf, 1985):

$$J_T = \frac{e}{2\pi h s^2}\left\{\phi \exp\left(-A\phi^{1/2}\right) - (\phi + eV_T)\exp\left[-A(\phi + eV_T)^{1/2}\right]\right\}. \tag{11.52}$$

Here $\phi$ is given by Eq. (11.48). Equation (11.52) represents the tunnel current density of a planar junction of infinite lateral extent. It is reasonable to ask if this expression is representative of the tunnel current for an STM tip with a radius of curvature of atomic dimensions. The answer seems to be a surprising, but qualified yes. For small values of $V_T$ the exponential terms in Eq. (11.52) can be expanded to give

$$J_T = \frac{(2m_{mt})^{1/2}e}{sh^2}\,\bar{\phi}^{1/2}\mathrm{e}^{-A\bar{\phi}^{1/2}}\left[eV_T + O\left(e^3V_T^3\right)\right]. \tag{11.53}$$

Analogous expressions for the term linear in $V_T$ were obtained for two different STM tip models by Tersoff and Hamann (1983) and by García et al. (1983), the latter group obtaining a factor $1.07A$ in the exponent, which they attributed to the curvature of their tip–surface geometry that is absent in the planar geometry. Thus planar tunneling theory is expected to give a fair representation of properties such as the angular distribution of the electrons and the energy distribution curve. An approximate angular distribution may be obtained from Eq. (11.46a) since the tunneling probability is the only function that exhibits strong intensity variations with parameter changes. The transverse energy component at maximum energy ($E_F$) is given by $E_t = E_F - E_z = E_F \sin^2\theta$. For angles of incidence $\theta$ relative to the barrier normal $\vec{z}$, such that $E_F \sin^2\theta \ll \bar{\phi} - eV_T/2$, Eq. (11.46a) can be expanded to give an angular attenuation function (Prietsch, 1992; Bauer et al., 1993a):

$$D(\theta) \approx \exp\left[\frac{-AE_F\sin^2\theta}{2(\bar{\phi} - eV_T/2)^{1/2}}\right] \tag{11.54a}$$

with a standard deviation

$$\Delta\theta = \left[\frac{(\bar{\phi} - eV_T/2)^{1/2}}{AE_F}\right]^{1/2}. \tag{11.54b}$$

$\Delta\theta$ represents the angle of the tunneling cone in which 68% of the injected electrons are contained. Using numbers that are typical for an experiment with a W tip on Au, e.g., $E_F = 5.6$ eV, $\bar{\phi} = 3$ eV (García et al., 1983), and $V_T = 1$ V, for which $s \sim 6$ Å (Becker et al., 1985), $\Delta\theta \sim 12°$. The angle within which the current is $1/2I_T$ is 8.3°. For comparable $s$, Lang et al. (1989) calculate a containment angle for $1/2I_T$ of 12.2° for a more realistic single Na atom tip in front of a jellium metal ($r_s = 2$). Since Eq. (11.54) suggests that $\Delta\theta \sim 0$ for $V_T \sim 6$ V ($s \sim 10$ Å), whereas Lang et al.'s model predict a $\delta\theta \sim 8.6°$, one is led to conclude that planar tunneling theory underestimates the beam divergence. It is, nevertheless quite contained. In a similar vein one can also determine the energy spread

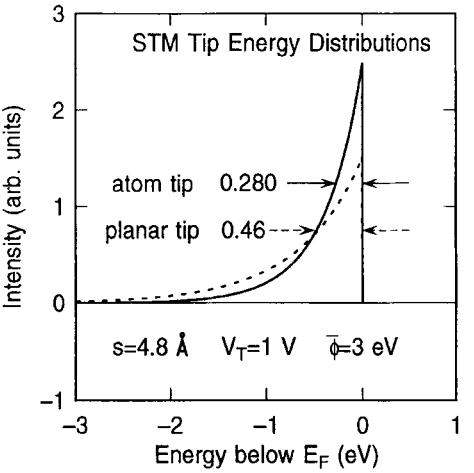


Fig. 11.30. Energy distributions of electrons crossing the tunnel barrier for a STM tip in close proximity to a metal surface: the solid line is based on a single atom tip model (Lang et al., 1989); the dashed line is based on planar tunneling theory.

(at FWHM) of the electrons in $I_T$, represented by $\delta E_{1/2} = E_F - E_z$ for which Eq. (11.46a) reduces to half:

$$\delta E_{1/2} = \frac{1.39(\overline{\phi} - eV_T/2)^{1/2}}{A}. \tag{11.55}$$

For $\overline{\phi} = 3$ V, $s = 4.8$ Å and $V_T = 1$ V, $\delta E_{1/2} = 0.46$ eV, which is somewhat larger than the value of 0.28 eV calculated with comparable parameters by Lang et al. (1989) for a single atom tip. A comparison of an electron distribution curve obtained from the planar theory and that for a single atom tip is shown in Fig. 11.30.

*11.4.3.2. Momentum conserving transport: the Bell–Kaiser model*

The first comprehensive model of electron transport in a BEEM experiment was proposed by Bell and Kaiser (1988). Their model is based on planar tunneling theory for electron injection by the STM tip and the assumption of both energy and the transverse momentum conservation for subsequent transport to and across the interface. These assumptions lend themselves to a closed form expression of the collector current density $J_c$ identical to Eq. (11.45)

$$J_c = \frac{2e}{(2\pi)^3\hbar} \int dE_z\, D(E_z) \int_{k_t} d^2k_t \left[ f_F(E) - f_F(E + eV_T) \right]. \tag{11.56}$$

The difference in the solutions of $J_c$ and $J_T$, e.g., Eq. (11.52), arises from the more restricted phase space requirements imposed on the injected electrons in order to overcome the Schottky barrier and be collected in the semiconductor. The obvious restriction is that

their energy must exceed that of the barrier energy $eV_0$, whereas a second restriction results from the general mismatch of the effective masses of the electrons in the metal and the semiconductor. These restriction will be reflected in the integration limits of Eq. (11.56), which will be discussed next. As an aside, Eq. (11.56) assumes that every electron that meets the phase space criteria will be collected in the semiconductor, that is, the transmission coefficient for the interface is unity and energy independent. We will show later the effect on $I_c$ of relaxing this assumption.

We will discuss next the integration limits set on Eq. (11.56) for transport over a step potential $eV_0$ that represents the Schottky barrier height. All conduction bands are assumed to have zone centered minima and be free-electron like with effective masses that may be anisotropic. In this case the kinetic energies can be expressed as $E = \sum_i (\hbar^2 k_i^2/2m_i)$. In the following the subscripts $z$, t will refer to components along the interface normal and transverse to it, respectively. Electrons injected with a bias $V_T$ into the metal have an energy $E_m = \mu + eV_T - (E_F - E)$, where the energy variable $E = E_z + E_t$ is measured relative to the bottom of the conduction band of the tip, whose Fermi energy is $\mu$. For simplicity we assume both that $\mu = E_F$, the Fermi energy of the metal film, in which case $E_m = eV_T + E_z + E_t$, and that the effective mass $m_m$ in the metal is isotropic, so that $E_m = \hbar^2(k_z^2 + k_t^2)/2m_m$. In the semiconductor the energy $E_s = \varepsilon_z + \varepsilon_t + eV_0$, where $\varepsilon_{z,t} = \hbar^2 \kappa_{z,t}^2/2m_{sz,st}$. $m_{sz,st}$ and $\kappa_{z,t}$ represent respectively the effective mass and momentum components. From the assumptions of energy conservation ($E_m = E_s$) and transverse momentum conservation, which implies that $\varepsilon_t = (m_m/m_{st})E_t$, an expression for $\varepsilon_z$ is obtained:

$$\varepsilon_z = e(V_T - V_0) - E_F + E_z - E_t\left(\frac{m_m - m_{st}}{m_{st}}\right). \tag{11.57}$$

For a finite collector current it is necessary that $\varepsilon_z \geqslant 0$. This places a constraint on $E_t$, which from Eq. (11.57) is

$$E_t \leqslant \left(\frac{m_{st}}{m_m - m_{st}}\right)(eV_T - e_0 V - E_F + E_z). \tag{11.58}$$

A $k$-space representation of the Fermi sphere and the phase space of electrons that meet the energy and transverse momentum conservation conditions is shown in Fig. 11.31. Electrons in the phase space bounded by the constant energy surfaces $E_F$ and $E_F - e(V_T - V_0)$ and with $k_z \geqslant 0$ have sufficient energy to to be collected in the semiconductor, but momentum conservation limits the allowed states only to the phase space bounded by the shaded area. This area is actually a three-dimensional hyperboloid determined by Eq. (11.58) expressed in momentum coordinates. Its volume is proportional to $J_c$, Eq. (11.56), which will be evaluated next.

The maximum value of $E_t$, $E_{max}$, represents the upper limit for the integration over $d^2k_t = (2\pi m_m/\hbar^2)\,dE_t$ in Eq. (11.56). Its lower limit is 0. Thus

$$E_{max} = \left(\frac{m_{st}}{m_m - m_{st}}\right)(eV_T - eV_0 - E_F + E_z). \tag{11.59}$$

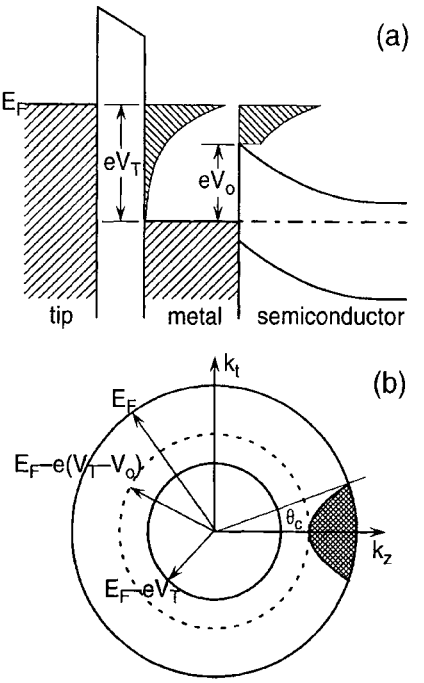


Fig. 11.31. (a) Energy distribution of electrons reaching an n-type semiconductor. (b) Energy–momentum representation of electrons reaching the semiconductor assuming parabolic, zone centered conduction bands for both metal and semiconductor. The shaded area represents the phase space of electrons allowed to reach the semiconductor. Scattering in the metal is ignored. $\theta_c$ represents the maximum angle, relative the interface normal, for transmission into the semiconductor. Electrons of energies $< E_F$ are restricted to smaller angles of incidence.

The limits for integration for $E_z$ in Eq. (11.56) are its lowest energy

$$E_{\min} = E_F - e(V_T - V_0) \tag{11.60}$$

and $\infty$. By use of Eq. (11.50) for $d^2k_t$ and with the integration limits Eq. (11.56) becomes:

$$J_c = \frac{2em_m}{(2\pi)^2\hbar^3}\int_{E_{\min}}^{\infty} dE_z\, D(E_z)\int_0^{E_{\max}} dE_t\big[f_F(E) - f_F(E+eV)\big]. \tag{11.61a}$$

The Fermi function is defined as:

$$f_F(E) = \big[1 + e^{(E-E_F)k_BT}\big]^{-1}. \tag{11.62}$$

For $T \to 0$ K,

$$J_c = \frac{2em_m m_{st}}{(2\pi)^2\hbar^3(m_m - m_{st})}\int_{E_{\min}}^{E_F} dE_z D(E_z)(eV_T - eV_0 - E_F + E_z). \tag{11.61b}$$

In a BEEM experiment the tunneling current is held constant by varying the tip-to-surface distance $s$. Variations in $s$ have a pronounced effect on $J_c$ due to the exponential dependence of $D(E_z)$ on $s$, as shown in Eqs. (11.46a) and (11.47). The effects of variations in $s$ can largely be cancelled by normalizing Eq. (11.61) with Eq. (11.45), or with its solution Eq. (11.52), since temperature effects are negligible for $V_0 > V_T \gg k_B T$. This normalization also cancels the area dependence so that the currents can be expressed as actual currents, rather than current densities:

$$I_c = I_T \frac{\int_{E_{min}}^{\infty} dE_z D(E_z) \int_0^{E_{max}} dE_t T(E)[f_F(E) - f_F(E + eV_T)]}{\int_0^{\infty} dE_z D(E_z) \int dE_t [f_F(E) - f_F(E + eV_T)]}. \tag{11.63}$$

For completeness we have inserted here an energy dependent transmission function $T(E)$ that will be discussed further in Section 11.4.3.3. For the remainder of this section we will assume $T = 1$.

In order to make comparisons with experimental BEEM spectra, it is common practice to integrate Eq. (11.63) numerically with a computer. It is however possible to obtain analytical solutions over a narrow $(V_t - V_0) \ll 1$ V range for $T \approx 0$ K. The exponent in $D(E_z)$ of Eq. (11.46a) can be approximated by $A(E_F + \phi - E_z)^{1/2} \approx A\phi^{1/2}[1 + (E_F - E_z)/2\phi]$, which allows Eq. (11.63) to be readily integrated. After expansion of the exponential terms and with the linearized expression Eq. (11.53) for the denominator one obtains:

$$I_c = \frac{m_{st} m_m^{1/2} s I_T e^{AeV/4\bar{\phi}^{1/2}}}{(m_m - m_{st})\hbar(2\bar{\phi})^{1/2} eV_T} \left[ (eV_T - eV_0)^2 - \frac{A}{6\bar{\phi}^{1/2}} (eV_T - eV_0)^3 + \cdots \right]. \tag{11.64}$$

From the first term of the expansion in $eV_T - eV_0$ the B–K model gets its sometime alternate name of "square law". The coefficient of the cubic term is $\approx 0.5$ for $\bar{\phi} \sim 3$ eV and $A \sim 6(e^{1/2}V^{1/2})$, so that a 10% correction occurs already for $V_T - V_0 = 0.2$ V. Clearly, fits to data with just the quadratic term is a poor approximation, with errors compounded by the inherent poorer signal-to-noise in the immediate threshold region over which such narrow range fits would be attempted. Since to a good approximation $s$ is linear in $V_T$ for constant $I_T$, both from Eq. (11.53) and for more realistic tip geometries (Tersoff and Hamann, 1983; García et al., 1983), their ratio in the prefactor of Eq. (11.64) is a constant. However, the prefactor $\exp(AeV_T/4\bar{\phi}^{1/2})$, which arises from the bias dependence of the tunnel barrier $\phi$ (Eq. (11.48)), adds a bias dependence to $I_c$ that is quite pronounced. If we take, for example, the experimentally determined relationship $s \sim 5.9 + 0.7V_T$ (Å) (Becker et al., 1985; Binnig et al., 1985) and a $\bar{\phi} = 3$ eV, a 50% increase in $V_T$ from 0.8 V to 1.2 V results in a 53% increase in $I_c$ from this exponential term alone. Furthermore, it is not known if the bias lowering of the tunnel barrier described by Eq. (11.48) is a good description for a real STM tip, a lack of information that adds additional uncertainty to the modelling of $I_c$ within the framework of planar tunneling theory.

Additional insights into the BEEM transport process, particularly with respect to the angular dependence of transmission across the interface, can be obtained from the BK model. Equation (11.58) can be recast as

$$E_t \leqslant \frac{m_{st}}{m_m}(eV_T - eV_0 - E_F + E). \tag{11.65}$$

The limitations on $E_t$ effectively determine the maximum or critical angle of incidence $\theta_c$ relative to the interface normal for which electrons are still able to cross the barrier and be collected. The angle of incidence is defined through $\sin^2\theta_i \equiv E_t/E_m$, and becomes a maximum at maximum kinetic energy, i.e., $E = E_F$. For this condition $E_m = eV_T + E_F$ and $E_t = (m_{st}/m_m)e(V_T - V_0)$. Hence, we obtain (Bell and Kaiser, 1988)

$$\sin^2\theta_c = \frac{m_{st}}{m_m}\frac{e(V_T - V_0)}{eV_T + E_F}. \tag{11.66}$$

Because of energy and $k_t$ conservation, as the angle of incidence $\theta_i$ increases the energy component $\varepsilon_z$, and consequently $\kappa_z$, of the electron in the semiconductor diminishes. That is, with increasing $\theta_i$ the electron in the semiconductor undergoes a refraction process. An angle of refraction $\theta_r$, defined through $\sin^2\theta_r \equiv \varepsilon_t/(\varepsilon_z + \varepsilon_t)$ can now be evaluated for electrons with energies $E = E_F$:

$$\sin\theta_r = \frac{m_m}{m_{st}}\left[\frac{eV_T + E_F}{e(V_T - eV_0)}\right]^{1/2}\sin\theta_i = \frac{\sin\theta_i}{\sin\theta_c}. \tag{11.67}$$

This equation represents the analog of Snell's law in optics.

The critical angle is quite small and is particularly extreme for small values of $m_{st}$ which severely limits the phase space of states in the metal that match states of equal $E$ and $k_t$ in the semiconductor. For the Si(100) surface, for example, for which $m_{st} = 0.19m_0$, Eq. (11.60) predicts a $\theta_c \sim 5.3°$ for $(V_T - V_0) = 0.3$ V, $V_0 = 0.7$ V and $E_F = 5.6$ eV. This is substantially narrower than the spread of the injected electrons discussed in conjunction with Eq. (11.54b). Even for $(V_T - V_0) = 1$ V, $\theta_c < 10°$. Thus the majority of the injected electrons are excluded from collection for the conventional low bias ranges ($V_T < 2$ V) used in many BEEM experiments, provided, of course, that conservation of transverse momentum is strictly obeyed. In this case, any additional scattering in the metal film will reduce further the number of electrons within the acceptance cone of $\theta_c$.

We have discussed thus far only electron injection into metal–n-type-semiconductor structures. Hole injection from the STM tip to the metal base and thence to the semiconductor is a complementary process for p-doped material, which physically corresponds to electron extraction. However, the process is not identical to electron injection, for which the reference of the electron distribution function is the Fermi level of the tip (Fig. 11.31a), whereas for hole injection it is the Fermi level of the metal layer, as shown in Fig. 11.32a. As a consequence the injected electrons have an intensity largely determined by the maximum in the distribution function, whereas for holes the distribution begins at $eV_0$ below its peak at the Fermi level. Consequently, for comparable experimental conditions the hole BEEM current is expected to be weaker than the electron BEEM current. Expressions for

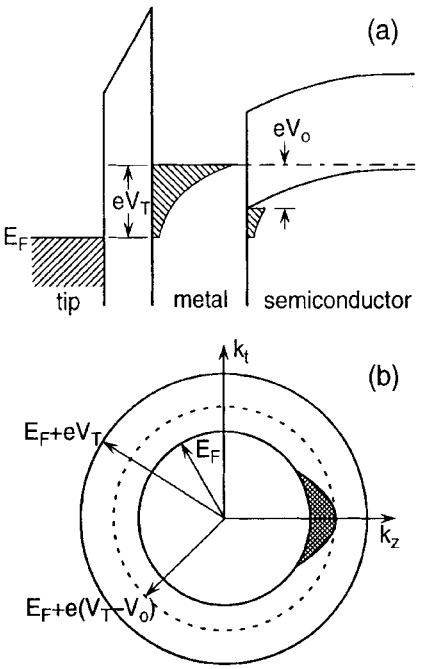


Fig. 11.32. (a) Energy distribution of holes reaching a p-type semiconductor. Note that the hole distribution is "clipped" below the maximum in the distribution, which renders the collector current for hole transport to be less than that for electron transport. (b) Energy–momentum representation of holes reaching the semiconductor assuming parabolic, zone centered valence bands for both metal and semiconductor. The shaded area represents the phase space of holes allowed to reach the semiconductor. Scattering in the metal is ignored.

the collector current similar to those for electrons are readily obtained. The equivalent of Eq. (11.59) for hole injection, based again on energy and $k_t$ conservation, is

$$E^h_{\max} = \left(\frac{m^{\mathrm{h}}_{\mathrm{st}}}{m_{\mathrm{m}} + m^{\mathrm{h}}_{\mathrm{st}}}\right)\left[E_{\mathrm{F}} + e(V_{\mathrm{T}} - V_0) - E_z\right]. \tag{11.68}$$

The limits for integration over $E_z$ are $E_{\mathrm{F}}$ and $E_{\mathrm{F}} + e(V_{\mathrm{T}} - V_0)$. The h superscripts are reminders that the parameters refer to holes. The $k$-space representation of allowed phase space is shown in Fig. 11.32b together with the Fermi sphere of the tip. The outer sphere represents the limit of filled electron states in the metal into which holes can transfer. Based solely on energy conservation, the phase space between the inner shells and for $k_z > 0$ meets the conditions for electron transfer (collection) into the semiconductor. When $k_t$ conservation is imposed, the allowed phase space reduces to the paraboloid marked by the cross hatched region, which is determined by Eq. (11.68). The critical angle can be expressed in similar fashion as for electrons. One readily obtains (Bell et al., 1993):

$$\sin\theta_{\mathrm{c}} = \frac{m^{\mathrm{h}}_{\mathrm{st}}}{m_{\mathrm{m}}}\frac{e(V_{\mathrm{T}} - V_0)}{E_{\mathrm{F}} - eV_{\mathrm{T}}}. \tag{11.69}$$

*11.4.3.3. Quantum mechanical transmission effects*

We have assumed so far that electrons that satisfy the phase space requirements dictated by energy and transverse momentum conservation will be collected in the semiconductor. This implies that the transmission probability is both energy independent and unity. From quantum mechanics it is, of course, well known that an electron can suffer reflections at a potential step of height $\phi$ even when its kinetic energy $E > \phi$. In the simplest one-dimensional case the transmission coefficient $T \sim 4[(E-\phi)/E]^{1/2}$ for $E \gg E - \phi$. In electron transport over a step potential separating two regions with different electron effective masses, such as exemplified by the zone centered conduction bands of the metal–semiconductor junction treated thus far, the problem is more complex. In addition to the continuity of wave functions $\psi$ the additional boundary condition that the net current is conserved must be satisfied. The latter condition implies that $(\partial\psi_1/\partial z)/m_1 = (\partial\psi_2/\partial z)m_2$ be satisfied at the interface between regions 1 and 2 (BenDaniel and Duke, 1966), where $\psi_{1,2}$ are suitable one-particle wave functions representing electrons of effective masses $m_{1,2}$. With these boundary conditions it is readily shown that the transmission coefficient for an abrupt step reduces to (Ludeke et al., 1991)

$$T(E) = \frac{4k_{\mathrm{mz}}k_{\mathrm{sz}}}{m_{\mathrm{mz}}m_{\mathrm{sz}}(k_{\mathrm{mz}}/m_{\mathrm{mz}} + k_{\mathrm{sz}}/m_{\mathrm{sz}})^2}. \tag{11.70}$$

Here the momentum components along $z$ in the metal ($k_{\mathrm{mz}}$) is given by:

$$k_{\mathrm{mz}} = \left[\frac{2m_{\mathrm{mz}}}{\hbar^2}(eV + E_z)\right]^{1/2} \tag{11.71a}$$

and for the semiconductor ($k_{\mathrm{sz}}$), from Eq. (11.57):

$$k_{\mathrm{sz}} = \left[\frac{2m_{\mathrm{sz}}}{\hbar^2}\left(E_z - E_{\mathrm{F}} + eV - eV_0 - \frac{m_{\mathrm{mt}} - m_{\mathrm{st}}}{m_{\mathrm{st}}}E_{\mathrm{t}}\right)\right]^{1/2}. \tag{11.71b}$$

It should be noted that the equations apply for off-normal incidence, with tangential momentum being conserved across the interface. $T(E)$ can then be inserted into the $\mathrm{d}E_{\mathrm{t}}$ integrand of Eqs. (11.61) or (11.63) to calculate numerically $I_{\mathrm{c}}$ or $J_{\mathrm{c}}$.

For the threshold region Eq. (11.61) can be integrated analytically with $T(E)$ being approximated by:

$$T(E) \sim \frac{4m_{\mathrm{mz}}k_{\mathrm{sz}}}{m_{\mathrm{sz}}k_{\mathrm{mz}}} = 4\left[\frac{m_{\mathrm{mz}}}{m_{\mathrm{sz}}}\frac{E_z - E_{\mathrm{F}} + eV - eV_0 - \frac{m_{\mathrm{mt}}-m_{\mathrm{st}}}{m_{\mathrm{st}}}E_{\mathrm{t}}}{eV + E_z}\right]^{1/2}. \tag{11.72}$$

With the simplifying assumptions used to derive the B–K expression Eq. (11.64) and that the effective mass in the metal ($m_{\mathrm{mz}} = m_{\mathrm{mt}} = m_{\mathrm{m}}$) is isotropic, integration by parts of Eq. (11.63) yields for $T = 0$ K:

$$I_c \approx \frac{2^{1/2} m_m m_{st} s I_T e^{AeV_T/4\bar{\phi}^{1/2}}}{(m_m - m_{st}) m_{sz}^{1/2} \hbar \bar{\phi}^{-1/2} e V_T} \frac{(eV_T - eV_0)^{5/2}}{(E_F + eV_0)^{1/2}} \left\{ 1 - \frac{Ae}{7\phi^{1/2}} (V_T - V_0) + \cdots \right\}. \tag{11.73}$$

Thus Eq. (11.73) predicts a $(V_T - V_0)^{5/2}$ dependence near threshold that differs from the B–K model's square law by the $1/2$ order derived from the transmission factor $T(E)$. The prefactor for the $7/2$ power term is about 0.5, so that significant corrections arise from the latter term for $e(V_T - V_0) > 0.2$ eV. Consequently the same caveat in the use of a single $5/2$ power term applies as for the use of only the quadratic term in the B–K model. Additional factors affecting the energy dependence of the transmission coefficient, such as electric field-effects and optical phonon scattering, will be discussed in Section 11.4.3.7.

*11.4.3.4. Issues of transverse momentum conservation*

The model calculations for the collector current in the two previous sections implicitly assume conservation of the transverse momentum component $k_t$ of the electrons crossing the metal–semiconductor interface. This implies basic assumptions on the perfection of the interface and on specifics of the band structure of the metal and semiconductor. Of these, the assumption of interface perfection is the more tenuous. Implicit to $k_t$ conservation lies the assumption that the periodicity of the lattice of both materials parallel to the interface is the same, which is referred to as a coherent interface. In this case the Bloch states on both sides of the interface can be expanded in terms of identical reciprocal lattice vectors. A lack of coherency in the periodicity across the interface has the effect of mixing states of different $k_t$. That is, the electron upon crossing the interface will undergo a change in $k_t$ or scatter. This is referred to as a breakdown in conservation of transverse momentum. Another way to represent this situation is to envision two band structures of discommensurate periodicity in the repeated zone scheme, which are projected onto the common interface plane: any state of a given energy and $k_t$ in one band will eventually match, in some distant period, an allowed state of the same energy and different crystal momentum in the second band. Other states of the same energy and different momenta will be reached at other periods. Thus all possible states of equal energy in the second medium are accessible to an electron that was in a well defined state in the first medium. The second factor in the assumption of $k_t$ conservation implies that the band structure of both the metal and semiconductor are not only free electron like, but that their conduction band minima are at the center of the Brillouin zone (BZ). This is valid for many metals, for all of the group II-VI and several group III-V semiconductors. The III-V semiconductors GaP and AlAs, as well as the group IV semiconductors diamond, Si and Ge are indirect band gap semiconductors, with their conduction band minima not at the zone center but at high symmetry points at or near the BZ boundary (see Table 11.1). These minima exhibit in general band curvatures – and hence effective masses – that are extremely anisotropic (Seeger, 1989), with constant energy surfaces that are oblate spheroids. An example for Si and GaP is shown in Fig. 11.33. Both of these materials have their conduction band minima along the six $\Delta$ (001) reciprocal lattice directions, with that of Si at 0.85X, where $X = 2\pi/a_0$, and $a_0$ is the lattice parameter (5.43 Å for Si). For Si or GaP in contact with a free electron like metal that has a zone centered conduction band, the question arises of how the electron can transfer from a given metallic state to a conduction band state in the semiconductor and yet satisfy

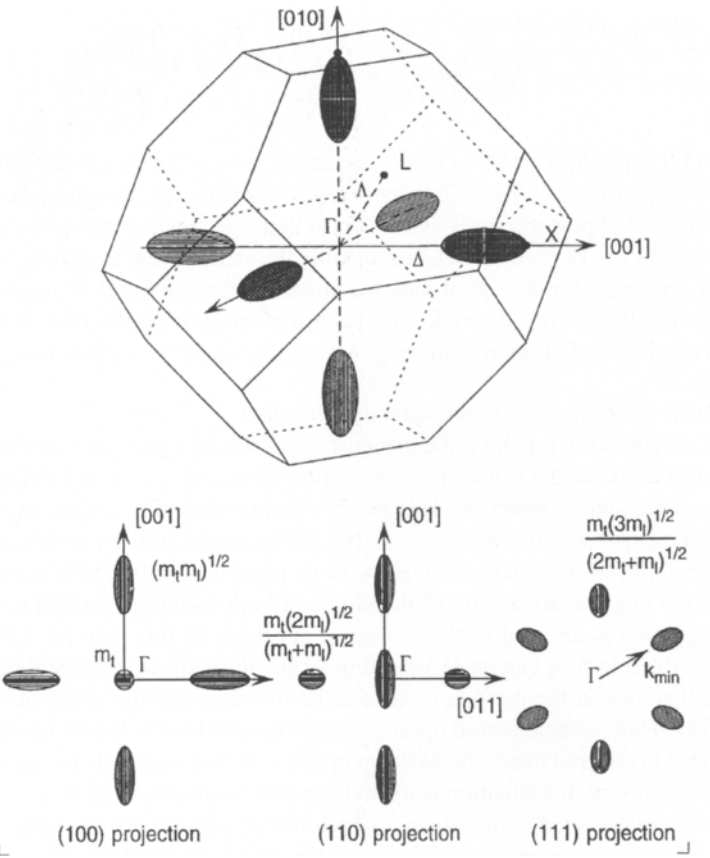


Fig. 11.33. Top: first Brillouin zone of the diamond structure showing the oblate spheroids for the conduction band minima for Si and GaP. Bottom: projection of the spheroids onto the (100), (110) and (111) planes of the reciprocal lattice. The areas of the projections are proportional to the longitudinal ($m_l$) and transverse ($m_t$) components of the effective masses, as shown next to the projections.

$k_t$ conservation. The answer is quite straightforward if one remembers that the momentum component perpendicular to the interface $k_z$ is not conserved for an electron crossing the interface. Since only $k_t$ matters for momentum conserving transmission, the allowed states in the semiconductor are represented by projecting the three-dimensional band structure onto a reciprocal lattice plane perpendicular to $k_z$. Three projections of constant energy surfaces for the Si (or GaP) conduction band states onto the (100), (110) and (111) surface Brillouin zones are shown schematically in Fig. 11.33. Thus for both the (100) and (110) oriented Si (or GaP) interfaces there are conduction band states in the neighborhood of the zone center into which electrons can transfer. The (110) projection is anisotropic and arises from the projection of an ellipsoid lying on a {010} direction parallel to the interface in the second BZ. For the (111) interface there are no allowed states projected onto the zone center of the surface BZ. For this case, if $k_t$ were to be conserved, an electron in the

metal would have to have a minimum value of $k_t^{min} = (0.85p)(2\pi/a_0) \sim 0.8$ Å$^{-1}$, where $p = (2/3)^{1/2}$ is a geometric correction for the projection onto the (111) plane. For Au (Fermi vector $k_F = 1.21$ Å$^{-1}$) on Si(111) such a value of $k_t$ implies an angle of incidence $\theta_i = \sin^{-1}(k_t^{min}/k_F) \sim 41°$. As discussed in Section 11.4.3.1, the angular distribution of electron injected by the tip is closer to 10°, so that few of the electrons meeting the energy criteria for collection have the necessary $k_t$ as well. Thus for a perfect metal–semiconductor system no collector current should be observed for surface orientations for which the conduction band minima of the indirect band gap semiconductor do not project onto the center of the surface BZ. Besides the Si(111) surface, the Ge(100) and Ge(110) surfaces are further examples, since for Ge the conduction band minima lie on the ⟨111⟩ reciprocal lattice directions.

Imperfections in the metal–semiconductor system will invalidate the restrictions imposed by the absence of conduction band states at the center of the surface BZ. Thus defects, e.g., point defects, dislocations and grain boundaries, and impurity atoms in the metal can potentially scatter the electrons in the metal out of the injection cone and into a direction with the appropriate $k_t$ for transmission into the semiconductor. However, it is not obvious if this is a viable mechanism in an actual BEEM experiment since injection occurs on an atomic scale and into well defined crystallites of the metal, which for the noble metals, at least, are not heavily defected. Phonon scattering is potentially another mechanism for transferring momenta to the electrons. However, the ratio of film thickness (10–100 Å) to electron–phonon mean-free-path $\lambda_p$ in the metal, which are in the range of 100–570 Å (Sze et al., 1966, see also values for $\lambda_\sigma$ listed in Table 11.4), is generally much less than one, making electron–phonon scattering an unlikely event in the metal film. Similarly, it is unlikely that an electron with $k_t \approx 0$ would partially penetrate into the band gap of Si and thence be scattered by a phonon since the penetration depth is only $\approx 1$ Å (Eq. (11.13)), whereas $\lambda_p \sim 60$ Å for Si. The most plausible mechanism for transferring electrons into noncentered minima is through scattering at a discommensurate or defective interface, as discussed above. Angular randomization through multiple passages and reflections at the interfaces is another possibility.

*11.4.3.5. BEEM transport under conditions of nonconservation of $k_t$*

We will assume that the interface disorder is such that scattering is isotropic, that is all angles are equally likely. The total energy of the electrons is assumed to be conserved, with a maximum of $eV_T + E_F$ on the metal side of the interface, and $e(V_T - V_0)$ on the semiconductor side, as shown in Fig. 11.34. Electrons entering the semiconductor can find propagating states only if scattered into any of the conduction band pockets of allowed states surrounding the locations of the CBM in $k$-space. Their surfaces of constant energy are ellipsoids, as shown in Fig. 11.33. Their projections onto the interface plane encloses an area given by $\pi \bar{k}_s^2 = 2\pi m_s e(V_T - V_0)\hbar^2$, where $m_s$ is the isotropic effective mass for a circular equivalent to the ellipsoid's projection. The magnitude of $m_s$ depends on the orientation of the semiconductor interface (Ludeke and Bauer, 1993). Thus for the conduction band ellipsoids of Si or GaP (Fig. 11.33), $m_s$ for the (111) and (100) projections are $m_{(111)} = (3m_l)^{1/2}m_t/(m_l + 2m_t)^{1/2}$ and $m_{(100)} = m_t + 4(m_t m_l)^{1/2}$, respectively, where $m_l$ and $m_t$ are the longitudinal and transverse mass components. For Si these masses assume the values $m_{(111)} = 0.28m_0$ and $m_{(100)} = 0.31m_0$. The area of the projections relative to

Table 11.4

Summary of Schottky barrier heights obtained with BEEM for listed metals deposited on vacuum cleaved n-type GaP(110). Results from three fitting procedures are listed, with estimated errors of ±0.02 eV. For comparison results quoted by conventional electrical methods are also shown. The last four columns list the metal parameters used for the BEEM fits. Italicized numbers in third column are the preferred BEEM results

| Metal | $\Phi_{sb}$ by BEEM (eV)[a] | | | $\Phi_{sb}$ (eV)[b] | $\phi_m$ (eV) | $E_F$ (eV) | $\lambda_\sigma$ (Å) | $K$ (Å/eV$^{1/2}$) |
|---|---|---|---|---|---|---|---|---|
| | Square law | 5/2 law | 5/2 + scatt. | IV or CV[b] | Ref.[c] | Ref.[d] | Eq. (11.77a) | Eq. (11.77b) |
| Mg | 1.08 | 1.03 | *1.07* | | 3.66 | 7.15 | 278 | 2.84 |
| Ag | 1.30 | 1.26 | *1.31* | 1.14–1.44 | 4.26 | 5.49 | 570 | 3.57 |
| Al | 1.28 | 1.23 | *1.24* | 1.16 | 4.28 | 11.7 | 180 | 1.95 |
| Bi | 1.18 | 1.12 | *1.14* | | 4.34 | – | | |
| Cr | 1.32 | 1.29 | *1.31* | 1.18 | 4.5 | 8.01 | 116 | 2.13 |
| Cu | 1.27 | 1.21 | *1.25* | 1.26–1.44 | 4.65 | 7.05 | 323 | 2.84 |
| Ni | 1.14 | 1.06 | *1.11* | 1.04–1.30 | 5.15 | 6.91 | 597 | 1.87 |
| Au | 1.45 | 1.41 | *1.46* | 1.30–1.52 | 5.1 | 5.58 | 400 | 3.57 |

[a]Ludeke et al. (1991), Ludeke (1993). [b]Lei et al. (1979), Tam and Chot (1986), Laperashvili and Nakashidze (1985). [c]Hölzl and Schulte (1979). [d]Harrison (1980).

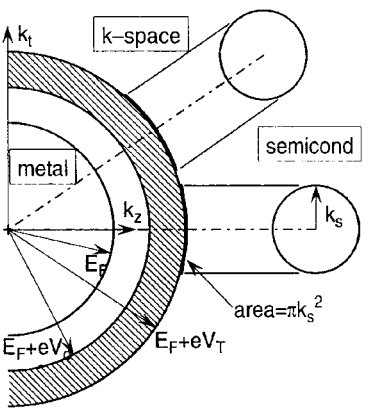


Fig. 11.34. Phase space restrictions for transport across the M–S interface when transverse momentum is not conserved. Only electrons that scatter within the projection of the conduction band spheroids can propagate in the semiconductor.

the area of an adjusted Fermi sphere, defined by the maximum in kinetic energy in the metal, determines the fraction of the scattered electrons at the interface that meets the conditions for propagation in the semiconductor. This fraction is simply $\tau = \eta\pi\bar{k}_s^2/2\pi(k_m^{max})^2$ where $\eta$ is the number of equivalent conduction band minima of the semiconductor and $k_m^{max} = [2m_m(E_F + eV_T)/\hbar^2]^{1/2}$. For a single, zone centered CBM this expression is identical to the previously discussed acceptance cone derived with $k_t$ conservation (Eq. (11.66)). $\tau$ is defined thus far only for a single energy, specifically the maximum kinetic energy $E_F + eV_T$. In real situations such a delta function representation must be replaced by a

distribution function $f_T(\varepsilon)$, whose origin for BEEM is the tunneling probability of electrons injected by the STM tip into the metal. $\varepsilon$ is a variable measured relative to $E_F + eV_T$. The convolution of $\tau$ with $f_T(\varepsilon)$ and the Fermi function $f_F(\varepsilon)$ gives the total fraction of electrons collected in the semiconductor at finite temperatures and for no carrier losses in the metal:

$$\tau_0(eV) = \frac{\eta m_s}{2m_m} \int_{-e(V_T - V_0)}^{\infty} \frac{T(\varepsilon) f_F(\varepsilon) f_T(\varepsilon)(eV_T - eV_0 + \varepsilon)}{E_F + V_T + \varepsilon} \, d\varepsilon, \tag{11.74}$$

where we have included for completeness an interfacial transmission factor $T(\varepsilon)$, to be further discussed in Section 11.4.3.7, that includes both quantum mechanical and electron–phonon scattering effects. The functional form of the numerator in Eq. (11.74) with $T = \text{const.}$ and $f_T(\varepsilon)$ replaced by $D(E_z)$ is in fact quite similar to the $k_t$ conserving BK model, for example Eq. (11.61b), in that both approaches involve integration over a linear energy term. The major difference between the two models concerns the role of the distribution function $f_T(\varepsilon)$ on the spectral shape in the threshold region. In planar tunneling theory this function, actually $D(E_z)$, has an energy distribution that is broader than expected for a more realistic "atom" tip, as shown in Fig. 11.30. The consequence of this is that the integrated intensity of Eq. (11.61b) increases more slowly towards a linear dependence on $eV_T$ above threshold, than does the narrower "atom" tip distribution. If $f_T$ can be represented by a delta function, then $I_c \propto (V_T - V_0)$ at $T = 0$ K. The question whether the linear dependence is approached in actuality depends more on the energy range of validity of effective mass theory and the absence of inelastic scattering in the metal film that can also affect the spectral shape. For a single atom tip $f_T(\varepsilon)$ is a near-exponential distribution function that is peaked at the Fermi level of the tip (Lang et al., 1989). At 0 K it exhibits a full width at half maximum $E_{1/2} = 0.120$ eV for a tip-to-surface distance of 15 Å and $E_{1/2} = 0.280$ eV for a distance of 4.5 Å and bias of 1 V. The latter conditions are close to those used in experiments. With $\varepsilon$ measured relative to $E_F + V$, the single atom tip function can be described well by a simple exponential expression:

$$f_T(\varepsilon) = \frac{|\ln 0.5|}{E_{1/2}} \exp\left(\frac{|\ln 0.5|\varepsilon}{E_{1/2}}\right), \tag{11.75}$$

which has been normalized such that $\int f_T(\varepsilon) \; f_F(\varepsilon) \, d\varepsilon = 1$.

Equation (11.74) is relatively free of parameters as compared to the $k_t$ conserving models. This has the advantage that quantitative comparisons can be made to experimental results, a task that is complicated for the planar tunneling models due to the general lack of knowledge of the parameters associated with the tunnelling process, e.g., effective barrier heights, the tunneling gap, and their dependence on tip bias.

*11.4.3.6. First-principles computation of BEEM transport*

In the models presented thus far it was tacitly assumed that both the metal and the semiconductor band structure could be represented each by a single parabolic band (effective mass approximation). This may be a good approximation for most semiconductors and free-electron like metals over a narrow energy range spanning a few tenth of an eV. However, most metals are not free electron like, among which fall the technologically important

transition metals. Furthermore, it is often desirable to assess interface transport over an energy range that exceeds the range of parabolic behavior. This goal is a formidable task that is presently restricted to unstrained (i.e., lattice matched) coherent interfaces of defect free materials. Systems that approach this ideality are very few, among them a few silicides, e.g., $CoSi_2$ and $NiSi_2$, on Si and perhaps some transition and rare earth intermetallic phases on III-V semiconductors (Palmstrøm and Sands, 1993).

Calculations of the collector currents for $NiSi_2$ and $CoSi_2$ have been reported by Stiles and Hamann (1991a, b) and for $CoSi_2$ by Reuter et al. (1998a, b). The collector current is equal to the integral of the electron flux $\rho_i$ incident on the metal–semiconductor interface multiplied by the transmission probability $T(n, k_t, E)$ that an electron in each state will be transmitted across the interface:

$$I_c = \frac{e}{(2\pi)^3\hbar}\int_0^{V_t} dE \int d^2k_t \sum_n \rho_i(n, E, k_t, V_t, s)T(n, k_t, E), \tag{11.76}$$

where $n$ refers to states of equal $E$ and $k_t$. The second integration is over the interface BZ. In order to evaluate the transmission probability the band structure of the metal overlayer and the semiconductor must be known. The overlap of the three-dimensional band structures projected onto the interface BZ provides a criteria for the magnitude of the transmission probability. This is illustrated for the $CoSi_2$/Si(111) interface in Fig. 11.35, which

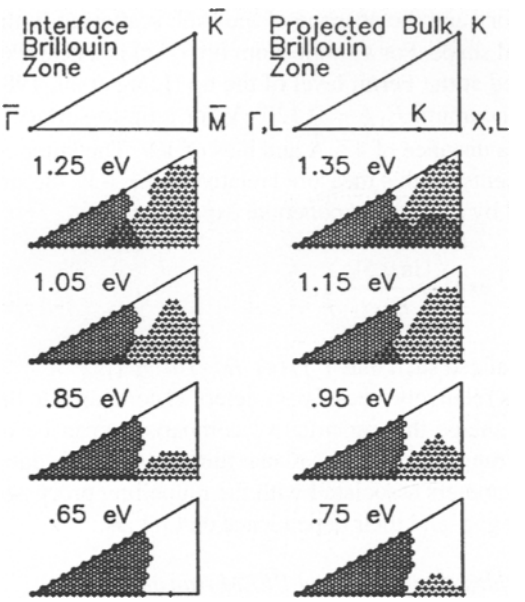


Fig. 11.35. Phase space for electron transmission through the commensurate $CoSi_2$/Si(111) interface. The panels show the irreducible wedge of the interface Brillouin zone (BZ) of both the $CoSi_2$ and the Si. For each calculated wave vector in the interface BZ an open circle denotes that there is at least one state in the $CoSi_2$ and a plus sign that there is at least one state in the Si for the energies marked next to each wedge (after Stiles and Hamann, 1991b, with permission).

depicts the energy ($eV_T$) dependent distribution of $CoSi_2$ and Si conduction band states in an irreducible segment of the interface BZ. At 0.65 eV, which corresponds to the Schottky barrier height, there are plenty of $CoSi_2$ states in the BZ, but only one for Si that corresponds to the conduction band minimum at 0.85X of the projected bulk BZ. Yet there is no overlap of states of equal $E$ and $k_t$, and if the latter is conserved, there will be no electrons allowed to cross the interface. This lack of overlap persists to ~0.85 eV. Only beyond this energy is transmission allowed. This curious delay in the onset of transmission, based strictly on $k_t$ conservation, was indeed confirmed experimentally by Kaiser et al. (1991), and is a striking demonstration of $k_t$ conservation for a nearly ideal, commensurate interface. At still higher energies the area of overlap steadily increases mostly due to an increase in the projected Si states. Between 1.25 and 1.35 eV the overlap increases mainly due to the availability of additional states in the $CoSi_2$. To a first approximation the transmission probability can be assessed at a given energy from the ratio of overlapping states to the number of states in the $CoSi_2$. Stiles and Hamann (1991b) refer to this as the kinematic model, which can be improved somewhat by adjusting the transmission probability per overlapping states according to the ratio of their degeneracies. In reality, of course, the transmission probability per state depends also on the matching of the wave functions, in a fashion analogous to the treatment of the step potential barrier in Section 11.4.3.3. This requires the calculation of the wave functions and their matching in value and derivative at the interface. This procedure was outlined for $NiSi_2$ by Stiles and Hamann (1989). Detailed results of such a "dynamical" model are shown in Fig. 11.36 for the A and B interfaces of $NiSi_2$/Si(111). These calculations not only postdict the difference in Schottky barrier height between the two types of interfaces (Tung, 1984), but also predict strongly

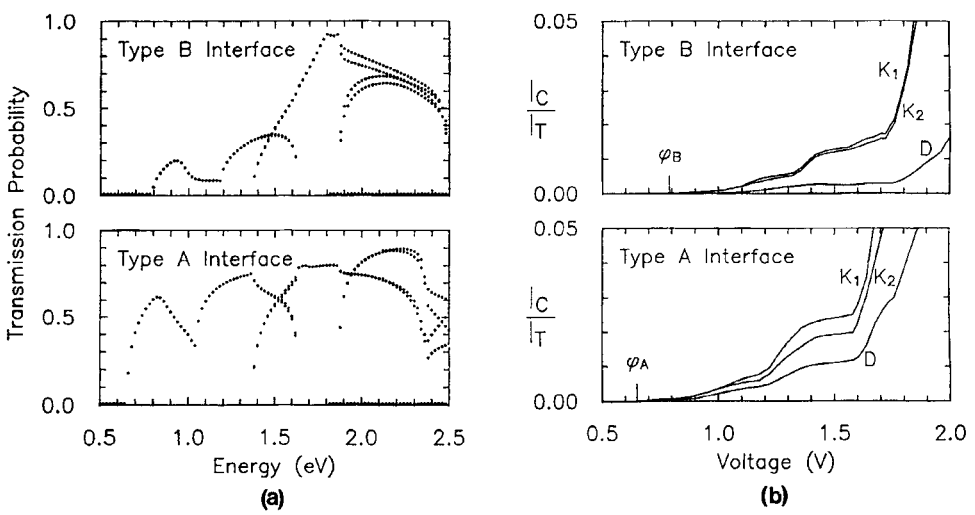


Fig. 11.36. (a) Transmission probabilities for electrons in $NiSi_2$ incident on a $NiSi_2$/Si(111) interface. The electrons have the same parallel wave vector as the Si conduction band minimum. (b) Calculated BEEM current for $NiSi_2$/Si(111) interfaces. $I_C/I_T$ is plotted as a function of the tip bias for two kinematic models ($K_1$ and $K_2$) and for the full dynamic model (D) (after Stiles and Hamann, 1991a, b, with permission).

differing transmission coefficients. It should be mentioned that the kinetic models give the same values for each interface, which are also larger than those obtained by the dynamical model. The structure arises largely from kinematic effects, with the probability at each threshold increasing proportionally to the square root of the energy, as expected from basic quantum mechanical considerations (Section 11.4.3.3).

In order to calculate $I_c$ the distribution of the electrons $\rho_i$ must be known. In the absence of any scattering in the metal film that may perturb the angular and energetic distributions, $\rho_i$ is equal to the distribution of the electrons injected by the STM tip. Calculation of this distribution from first principles is a formidable task that depends on the band structure and morphology of both tip and metal surface, as well as on the previously discussed details of tip–surface separation, barrier potential and shape, etc. In order to circumvent these problems, Stiles and Hamann (1991a, b) use a planar tunneling approach similar to the one discussed for the tunnel current in Section 11.4.3.1. Solutions for the collector current for A- and B-type $NiSi_2$/Si(111) interfaces are shown in Fig. 11.36b for both kinematic and dynamic treatment of the transmission probability. For the B interface the dynamic model predicts a very low transmission ratio up to 1.8 V, which follows the trend observed in the transmission probability in Fig. 11.36a. The authors acknowledge the limitations of assumption made in the model, particularly in the description of the injection process, and suggest that additional uncertainties can be removed from the spectra by taking BEEM spectra in the constant height mode and by analyzing the derivatives ratio $(dI_c/dV_T)/(dI_T/dV_T)$ rather than the $I_c/I_T$ ratio usually measured in the constant $I_T$ feedback mode (Stiles and Hamann, 1991a). An additional complexity in BEEM transport through the metal has recently been raised by Reuter et al. (1998a, b), who showed that preferred crystallographic directions exist – determined by the details of the band structure – in both Au (Reuter et al., 1998a) and $CoSi_2$ (Reuter et al., 1998b) along which the injected electrons propagate in narrow beams.

*11.4.3.7. Image force, electric field and phonon scattering effects*

As discussed in Section 11.3.2.1 an electron entering the semiconductor across the M–S interface is subject to additional forces due to the electric field in the depletion region and the screening effects of the metal (image forces). In the treatment of ballistic transport thus far we have neglected these effects and assumed an abrupt potential step at the interface. Once in the semiconductor, an electron may in addition to the quantum mechanical reflection be scattered back into the metal by optical phonons. The probability that the electron returns to the metal is enhanced if the scattering occurs in the region between the potential maximum at $\delta z_i$ and the M–S interface. These dynamic effects are difficult to treat in a rigorous manner and do not lend themselves to analytic expressions from which $I_c$ and the Schottky barrier can be quickly calculated. Nevertheless, their effects appear to be important under certain conditions, which will be outlined in this subsection.

The quantum mechanical transmission function in the presence of image forces and electric fields has been treated by Crowell and Sze (1966a) using numerical methods in the solution of a one-dimensional wave equation. In one of their models they "remove" the singularity of the image force term (Eq. (11.24)) at $z = 0$ by replacing the potential in the vicinity of the M–S interface with a smoothly decaying exponential with a characteristic Thomas–Fermi screening length $\lambda_{TF} = 0.55$ Å. Their approach consisted of a numerical

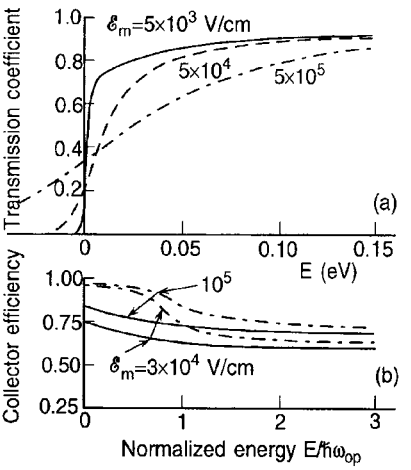


Fig. 11.37. (a): Energy dependence of the quantum mechanical transmission probability for electrons crossing the Au/Si interface for indicated constant electric fields (adapted from Anderson et al., 1975). The fields of $5 \times 10^3$, $5 \times 10^4$ and $5 \times 10^5$ V/cm correspond to maximum depletion layer fields $\mathcal{E}_m$ (Eq. (11.1a)) for $N_d = 10^{14}$, $10^{16}$ and $10^{18}$ cm$^{-3}$, respectively, under zero bias. (b) Collector efficiency after electron–phonon scattering in Si of a metal/Si Schottky contact at 300 K (solid lines) and 100 K (broken lines). The energy in units of $\hbar\omega_{op} = 0.35$ eV is measured relative the potential energy maximum in the Si (adapted from Crowell and Sze, 1967).

Taylor series calculation of two independent solutions of the Schrödinger equation over the region within the potential maximum and the M–S interface where a WKB solution was inaccurate. By matching the wave functions and their derivatives to WKB solutions far from the M–S interface the appropriate combination of the two independent solutions were obtained. Errors in the Taylor expansion were subsequently pointed out and corrected by Anderson et al. (1975), whose results of the quantum mechanical transmission for the Au–Si interface are shown in Fig. 11.37a for various constant internal fields. These fields arise from applied biases to the junction as well as from the internal fields due to the space charge region; the latter fields vary linearly with the distance from the M–S interface (Eq. (11.1a)). If no bias is applied to the junction the field that controls the interface transmission may be approximated by $\mathcal{E}_m$, since typical distances involved in the calculation of the transmission, e.g., optical phonon scattering lengths, are much smaller than the width $w$ of the depletion region. Hence the fields may be expressed in terms of equivalent doping levels that would produce such a field for a given Schottky barrier. These effective doping levels are indicated in the caption of Fig. 11.37a. For low fields, which correspond to low doping concentrations, the potential maximum at $\delta z_i$ is shifted into the semiconductor, a situation that represents a "soft" onset of the potential. The consequence of such a smooth potential is that the transmission coefficient rises rapidly above threshold, and may even exhibit a resonance enhancement (Crowell and Sze, 1967). For progressively higher fields $\delta z_i$ diminishes (Table 11.2) and the potential step becomes more abrupt, which results in a transmission function that rises more slowly above threshold. A higher effective mass similarly retards the rise in the transmission function above threshold (Crowell and Sze, 1966a). Based on these considerations, the formulation of $I_c$ with quantum mechanical reflection

presented in Section 11.4.3.3 represents a limiting case for heavily doped semiconductors and/or with large effective masses ($m_{sz} \gtrsim 1m$). At the other extreme, e.g., low doped GaAs ($m_s = 0.072m$) and Si, the soft potential profile would lead to a "5/2 power" dependence that saturated much faster than predicted by Eq. (11.70). Consequently, for these low doped semiconductors an expression for $I_c$ with constant transmission, e.g., Eqs. (11.63) or (11.74), should be used for fits to data that extend over a bias range of more than a few tenths of a volt above threshold.

As pointed out above, phonon scattering in the semiconductor may inhibit an electron from being collected. This process may occur if the electron gets scattered out of the acceptance cone and/or looses enough energy through phonon emission that the loss of $\hbar\omega_{op}$, the optical phonon energy, reduces the kinetic energy below that of the barrier. The latter process is particularly effective at low temperatures (negligible phonon absorption), for energies that exceed $eV_0$ by a few times the optical phonon energy $\hbar\omega_{op}$ (62 meV for Si) and for low internal fields (doping) such that the position of the barrier maximum $\delta_{zi} \gtrsim \lambda_{op}$, the effective mean free path for electron–phonon scattering. These conditions promote the emission of one or more phonon before the electron reaches the potential maximum with energy insufficient to overcome it. For Si at room temperature $\lambda_{op} \sim 65$ Å and varies very little for electron energies $>2\hbar\omega_{op}$ (Crowell and Sze, 1965b); its value at low temperatures is infinite for kinetic energies below $\hbar\omega_{op}$. At higher temperatures, including room temperature, scattering processes are dominated by phonon absorption, which results in a reduction of the energy dependence of the phonon-mediated transmission probability or collection efficiency, as it is sometimes called. These concepts have been quantified by Crowell and Sze (1965b) in a simple one-event scattering model that includes both image force effects and an applied electric field of constant strength. The model is based on calculating the probability $P(s)$ that the electron reaches a distance $s$ from the interface. $P(s) = P_b(s) + P_\theta(s)$, where $P_b(s)$ is the probability of not scattering (ballistic passage), and $P_\theta(s)$ is the probability that if scattered the electron is collected within an acceptance cone of half aperture $\theta$. $P_\theta(s) \approx 0$ for $s > \delta z_i$. The limits on the acceptance angle were defined as $\theta = \pi/2$ at $s = \delta z_i$ and $\theta = \pi$ for $s \gg \delta z_i$, that is, for large $s$ even electrons scattered back towards the interface are assumed to be collected. The collection efficiency $\alpha_c$ is defined as $P(s)$ averaged over a Maxwellian distribution of the electron source: $\alpha_c = \int_E^\infty P(s, E)\exp(-E/kT)\,dE/kT$, where $E$ represents the kinetic energy of the incident electrons relative to the energy maximum of the barrier. The results of the calculation of $\alpha_c$ for Si at 100 K and 300 K are shown in Fig. 11.37b (Crowell and Sze, 1967), for which a value for $s = \delta z_i + \lambda_{op}$ was assumed. Similar curves for Ge and GaAs, also calculated by these authors, exhibit a larger energy dependence at room temperature that is a direct consequence of their lower optical phonon energies ($\hbar\omega_{op} \approx 0.35$ eV). The higher values of $\alpha_c$ at low energies for the 100 K case is a consequence of the low probability for scattering by phonon absorption and the dominance of phonon emission, as discussed above. The higher collector efficiency at larger fields is the results of a decreasing $\delta z_i$ relative to $\lambda_{op}$.

An analogous approach that simulates three-dimensional phonon scattering in a one-dimensional model was proposed by Lee and Schowalter (1991). In this scheme the effective mean free path of an electron in the semiconductor travelling at an angle $\theta$ relative to the interface normal was defined through $\lambda_{op}\cos\theta$, i.e., the projection of $\lambda_{op}$ onto $\vec{z}$. The assumption was made that any phonon scattering renders the electron uncollectable,

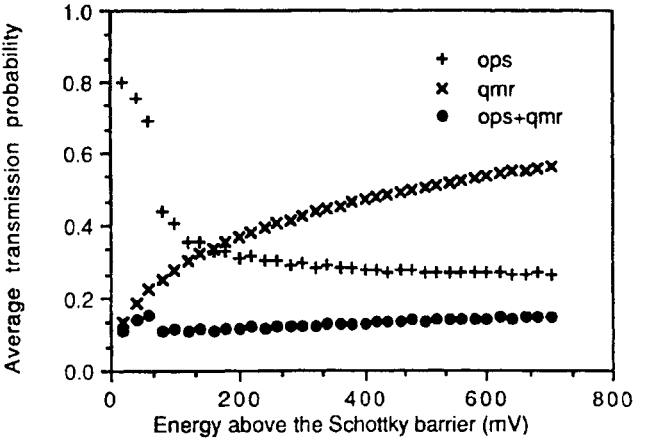


Fig. 11.38. Energy dependence of the average transmission probability at 300 K per incident electron impinging on a metal/Si interface within the critical angle cone. Curve of plus symbols (ops) considers only optical phonon scattering in the Si; curve of ×'s (qmr) considers only quantum mechanical reflection; curve of solid symbols includes both scattering mechanisms (after Lee and Schowalter, 1991, with permission).

or equivalently in terms of the probabilities, $P(s,\theta) \approx P_b\ (\delta z_i, \theta)$. This relationship is formally obtained from the Crowell and Sze (1965b) model by setting $s = \delta z_i$, which automatically ignores the $P_\theta(s)$ term discussed in the previous paragraph. Lee and Schowalter (1991) then calculated the transmission probability due to optical phonon scattering by averaging $P(s,\theta)$ over all angles within the acceptance cone for collection $\theta_c$. $\theta_c$ is defined by Eq. (11.66), with the additional assumption of equal effective masses in the metal and semiconductor. The results of their calculation for Si at 300 K and $\delta z_i = 70$ Å ($N_D = 2 \times 10^{14}$ cm$^{-3}$) are shown in Fig. 11.38. The considerably lower transmission probability as compared to the Crowell and Sze results is a combination of the lower fields and the neglect of forward scattering into the acceptance cone. It should be pointed out that the calculations are to be viewed as qualitative results. The values obtained are most likely underestimates of the transmission or collection efficiencies for Si, as the model neglects optical phonon scattering into the equivalent conduction band states located elsewhere in phase space. For both models, it is more difficult to assess the neglect of more than one scattering process and the omission of scattering by acoustic phonons, although a two scattering event calculation for low temperatures (no phonon absorption) indicated a slight enhancement in the transmission coefficient for low fields as compared to single phonon scattering (Crowell and Sze, 1965a).

The net transmission coefficient combining quantum mechanical reflection and phonon effects is taken as the product of the two, which assumes that these events are statistically independent. Examples are shown in Fig. 11.38 for Si from the work of Lee and Schowalter (1991). Because of the decrease in phonon scattering probability with energy and a corresponding increase in the quantum mechanical transmission, there is a cancellation that results in a near featureless net transmission for the low field case (low doping). The net transmission is again underestimated, not only because of the low estimate of the

phonon term discussed above, but also because of neglect of secondary reflections at the M–S interface for electrons that have been scattered back towards the semiconductor. This is important just above threshold where the quantum mechanical transmission is low (high reflectivity), since the process is independent on the direction of motion of the electron.

*11.4.3.8. Monte Carlo methods*

The models and theories discussed above for the collector current are either oversimplified, but with the advantage that relatively simple analytical expressions lend themselves to quick analysis, or overly complex requiring extensive, computer intensive band structure calculations. Even the latter are not amenable for easy inclusion of scattering processes, tip injection issues, etc. that can affect the spectral shape. Scattering in particular, whether in the metal, at the interface or in the semiconductor is difficult to treat since these events destroy the coherence or phase information that is inherent in the models discussed so far. A statistical approach, on the other hand, that traces an individual electron from injection by the STM tip until detected or rendered part of the base current is a viable alternative of calculating $I_c$. Such approach is the Monte Carlo method (Jacoboni and Reggiani, 1983). In Monte Carlo simulations of $I_c$ in BEEM (Schowalter and Lee, 1991; Bauer et al., 1993a) the trajectory of an electron of given kinetic energy injected by the tip is randomly assigned to an injection angle within the predictions of tunneling theory (planar tunneling theory has been used so far, using Eq. (11.54a). In the metal the electron may undergo elastic and inelastic scattering, each event described by its own, energy dependent mean free path $\lambda_e(E)$ and $\lambda_i(E)$. In practice, the energy dependence described by Crowell and Sze (1967) is used for elastic scattering:

$$\lambda_e = \lambda_\sigma (E/E_F)^2, \tag{11.77a}$$

where $\lambda_\sigma$ is the mean free path for electron conductivity. It is given by the ratio of the size effect and the resistivity of the metal (Bass, 1982). For inelastic (electron–electron) scattering, the expression derived by Quinn (1962) is used:

$$\lambda_i = K \frac{E_F^{3/2} E}{(E - E_F)^2}, \tag{11.77b}$$

with

$$K \equiv \frac{14.5\beta^{3/2}}{m_m^{1/2}[\tan^{-1}\beta^{-1/2} + \beta^{1/2}/(1+\beta)]},$$

where $\beta = 0.166 r_s$, $r_s$ being the radius of a sphere (in units of the Bohr radius) equal to the volume per conduction electron of the metal (Ashcroft and Mermin, 1976).

The trajectories following a scattering event, including that of secondaries, are assumed to be randomly distributed (isotropic). Following a collision, a random selection of the new path direction is made. If this path reaches the interface, it may be collected if the trajectory falls within the collection cone (Eq. (11.66)) and the electron has sufficient energy to

overcome the Schottky barrier. If the electron is collected a new electron, randomly "injected" by the tip, is traced. Otherwise, the electron is reflected and its path traced through subsequent scattering events to its demise or eventual collection. Each added event opens up a new parameter space of possibilities that have to be followed, which makes the Monte Carlo technique extremely demanding on computational time. If the electron returns to the metal surface it is assumed to scatter isotropically and thence to resume its quest to be collected or be eliminated due to insufficient energy. For transmission across the M–S interface, an energy dependent, quantum mechanical transmission factor (Eq. (11.70)) was included by Bauer et al. (1993a), who furthermore added the possibility of carrier multiplication arising from collected electrons of sufficient energy to create electron–hole pairs in the semiconductor. Schowalter and Lee (1991), on the other hand, included a transmission factor that consisted of an energy independent attenuation that included electron–phonon scattering in the semiconductor, as well as quantum mechanical transmission (Fig. 11.38). In the Monte Carlo simulations the same number of electrons for each bias value are traced, thereby directly simulating the constant $I_T$ mode used in data collection.

It should be emphasized that these Monte Carlo simulations do not contain new physical concepts, rather they allow evaluation of complex, statistically independent events that cannot be combined in simpler formalisms. Their accuracy is only as rigorous as the assumption made for each step of the process. Thus far in Monte Carlo simulations of BEEM transport these assumptions include planar tunneling theory for electron injection, effective mass theory limited to single, zone-centered bands for both metal and semiconductor, and oversimplified transmission characteristics at the M–S interface. Although more quantitative perhaps than previously discussed models based on similar assumptions, the value in Monte Carlo simulations will lie in future improved calculations that treat the events during transport in physically more realistic fashion.

### *11.4.4. Experimental BEEM results*

In this section we will present and discuss experimental results of BEEM studies that represent not only typical features for a number of metal–semiconductor systems, but includes applications that go beyond the initial visions of the technique. Among these, we include interface modifications and the investigation of bulk related hot electron effects in metals and semiconductors.

#### *11.4.4.1. Threshold spectroscopies of metal–Si interfaces*

*11.4.4.1.1. Au/Si.* This M–S combination represents the most widely studied system due to the inertness of Au that allows ambient BEEM studies. In addition Au makes abrupt interfaces with Si – thereby minimizing scattering effects – and has long electron mean free paths so that relatively thick, pin hole free layers can be used for the base. Representative $I_c$ vs. $V_T$ spectra for Au on n- and p-type Si(100), doped to (2–3) $\times$ $10^{15}$ $cm^{-3}$, under forward and reverse tip biases are shown in Fig. 11.39 (Bell et al., 1990, 1991). The data, indicated by dots for n-type (top panels) and p-type Si (bottom panels), were taken at 77 K by immersing the samples into liquid nitrogen. The low temperature is necessary to suppress the substantial thermionic current that is present at room temperature because of the low barrier heights in the p-type samples. The inserts show the energy diagram for

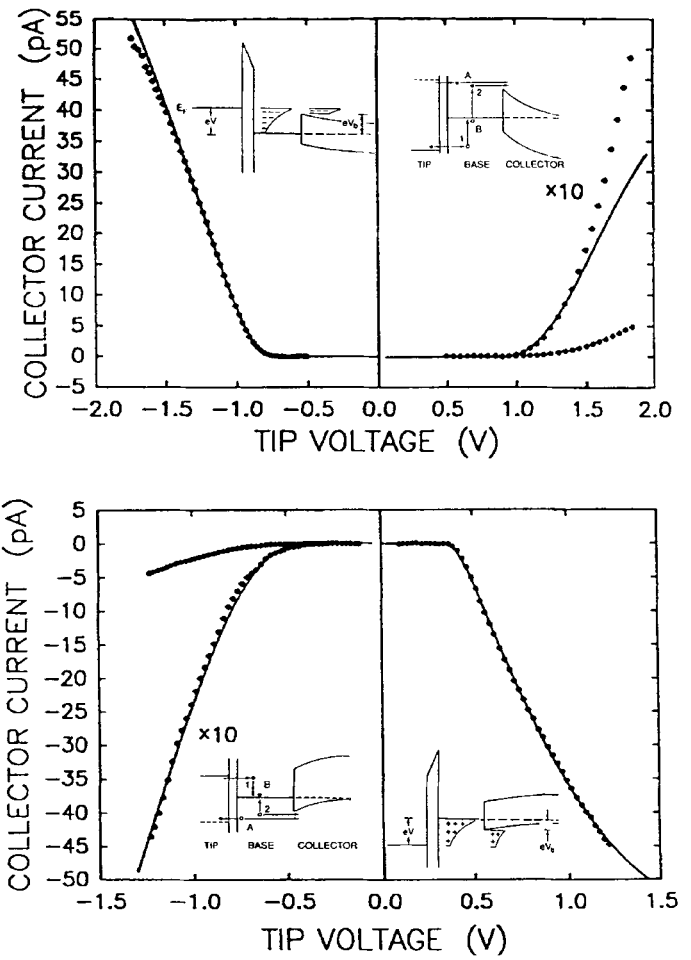


Fig. 11.39. BEEM spectra for Au/Si(100) contacts at 77 K. The insets in each panel show the energy diagrams under bias conditions used during data acquisition (after Bell et al., 1991, with permission).

each bias situation during data collection. Panels (a) and (d) represent electron and hole injection on n- and p-type samples, respectively, that is the conventional BEEM bias mode for majority carrier injection. The fits to these spectra, shown by the solid lines, were made with the B–K model discussed in Section 11.4.3.2, in particular by numerical integration of Eq. (11.63), with the adjustable parameters being the barrier height $eV_0$ and an arbitrary, but energy independent multiplication factor. Values for $eV_0$ of 0.82 eV and 0.35 eV were obtained from the fits of n-doped and p-doped samples, respectively, which add up to the expected band gap energy of Si of 1.17 eV at 77 K (Sze, 1981). Panels (b) and (c) represent reverse bias conditions that would result in minority carrier injection, specifically, hole injection into the n-type sample and electron injection into the p-type sample. The resulting collector current would be opposite to that for majority carrier injection. However,

this is not observed, as $I_c$ for each dopant type exhibits the same polarity irrespective of the polarity of the tip bias. This indicates that majority carrier transport occurs in the semiconductor regardless of the carrier type injected by the STM tip. The explanation proposed by Bell et al. (1990) is based on energetic or "hot" carrier scattering in the metal, specifically an Auger-mediated generation process of the appropriate majority carrier. These events are schematically shown in the inserts of panels (b) and (c). For hole injection, or more appropriately electron extraction from the metal, shown in (b), the hole is neutralized by an electron form near the Fermi level of the metal (process 1). The energy released is transferred to a second electron, the "Auger" electron (process 2), which may overcome the Schottky barrier and be collected if energy requirements and momentum conservation are satisfied. The same process, but starting with a hot electron injected into the conduction band of the metal and ending up with a hot hole in the valence band can occur for p-type samples, as illustrated in panel (c). The energy threshold for each of these processes is the same as for the respective majority carrier injection, as is readily discernible from the spectra in the top or bottom panels. The onset and spectral shape appears "softer" for the reverse or Auger BEEM. Indeed inclusion of the scattering processes within the framework of the B–K model yields a dependence of $I_c \propto (eV_T - eV_0)^4$ (Bell et al., 1991). The solid lines in panel (b) and (c) are fits using this theory. The thresholds obtained are the same as for majority carrier injection. An 9/2 power term near threshold would be expected if quantum mechanical transmission were included. The good fits obtained without inclusion of quantum mechanical transmission appears to be the consequence of both the low doping concentration that leads to a soft barrier profile, and the large optical phonon energies that results in partial compensation of the energy dependencies of the two ingredients to the net transmission function, as discussed in Section 11.4.3.7.

The quality of the fits in Fig. 11.39 do not necessarily obviate consideration of quantum mechanical transmission effects. Their inclusion consistently gave better fits in the immediate threshold region (0.8–0.9 eV) than fits with the B–K model in UHV study at 77 K by Henderson et al. (1993) for Au/Si(100). Their samples had an even lower dopant concentration ($\sim 10^{14}$ cm$^{-3}$) than those used by Bell et al. (1990). However, both fits above 1 eV deviated equally, albeit at opposite sides, from the experimental data. This deviation, which occurs sooner than that in Fig. 11.39, is somewhat surprising since Henderson et al.'s model includes an energy dependent correction to the effective mass that accounts for the non-parabolicity in the Si conduction band. These observations suggest that other, yet to be identified factors contribute to the spectral shape. Since comparable preparation methods and metal film thicknesses were used, the discrepancy appears to originate in the modelling of the transport related properties of the Si.

BEEM studies on Au/Si(111) interfaces were reported by Schowalter and Lee (1991) and by Palm et al. (1993) for Si substrates that had been dipped in HF prior to the Au evaporation in a conventional vacuum system. The HF treatment terminates the Si surface with hydrogen that renders it reasonably inert (passivated) against ambient oxidation (Burrows et al., 1988). Schowalter and Lee (1991) also made a comparison study between Si(100) and Si(111) substrates and reported remarkably similar spectra on these two surfaces. As discussed in Section 11.4.3.4, under the assumption of $k_t$ conservation and in the absence of appreciable scattering in the metal, little or no collector current should be observed for Au/Si(111) because of a lack of overlapping states between the Si conduction band states,

which are near the boundary of the interface BZ (Fig. 11.33d), and those of the Au, which to a good approximation are free electron like and centered in the BZ even for energies ~1 eV above $E_F$ (Cracknell, 1984). Schowalter and Lee (1991) proposed that the spectral similarity for the two Si orientations arises from multiple, predominantly elastic scattering in the Au film that gives an electron multiple chances to scatter into the acceptance cone. This process is enhanced by their assumption of a high (80%) reflection coefficient at the M–S interface (Fig. 11.38) for electrons with trajectories inside the acceptance cone. A Monte Carlo simulation, as outlined in Section 11.4.3.8, that includes multiple scattering in the metal and all six Si conduction bands produced the best agreement to their data. An unspecified model that considered no $k_t$ conservation resulted in a vastly poorer fit, with a predicted $I_c$ that rises in nearly linear fashion from a threshold at 0.80 eV. In view of the incommensurate nature of the Au–Si interfaces (even a 45° relative rotation in the (100) planes produces a 6% lattice mismatch) it is surprising that the assumption of nonconservation of $k_t$ gives such poor agreement when, intuitively, it should be the primary cause for the observed similarities in the Au/Si(111) and Au/Si(100) spectra. This point will be readdressed in the next section for Pd on Si(111) and Si(100) surfaces. An alternative explanation for a finite $I_c$ for Au/Si(111) has recently been proposed by Reuter et al. (1998a), who suggest that a fan-out of the injected electrons along preferred crystallographic directions in the Au provides the necessary conditions for their collection in the nonzonecentered conduction bands of Si.

Subsequently Davies and Craighead (1994) measured for the first time threshold variations for a Au/Si(100) interface under reverse bias conditions. The observed decrease in the threshold voltage with increasing bias was consistent with the bias dependent lowering of the Schottky barrier by image potential effects (Eq. (11.29c)). This effect has generally been ignored in the stated threshold values obtained by BEEM, a practice generally adopted in the reporting of nearly all Schottky barrier heights measured by transport techniques.

*11.4.4.1.2. Pd on Si.* The role of scattering on the ballistic transport properties for Si(111) and Si(100) interfaces with Pd was addressed by Ludeke and Bauer (1993, 1994). Thickness dependent BEEM spectra on both Si surfaces orientations exhibited comparable intensities and spectral features over the investigated thickness range of 8–92 Å. The data for a nominally 8 Å Pd film on Si(100) and one of 12 Å on Si(111) are depicted in Fig. 11.40a. It was noted that these thicknesses are much less than the electron mean free paths (which were also measured, as discussed in Section 11.4.4.3.2) and that the Pd surfaces were locally flat on an atomic scale, which precludes electron injection at large angles relative to the mean surface normal. These observations were used to argued in favor of interface scattering as the dominant mechanism that allows the injected electrons to reach conduction band minima throughout the Si BZ. The model used to calculate $I_c$ was described in Section 11.4.3.5, with the assumption that the interfacial transmission factor $T(eV_0 - eV_T + \varepsilon)$ is an energy independent fitting factor. This assumption, also used by Schowalter and Lee (1991), is based upon the unique cancellation effects of the phonon scattering and quantum mechanical transmission functions for low doped Si, as discussed in Section 11.4.3.7. It should be noted that the areas of the projections of the conduction band ellipsoids onto the interface plane are not identical for the two orientations, which is reflected in the magnitudes of the effective transverse masses: $m_{(111)} = 0.28m_0$

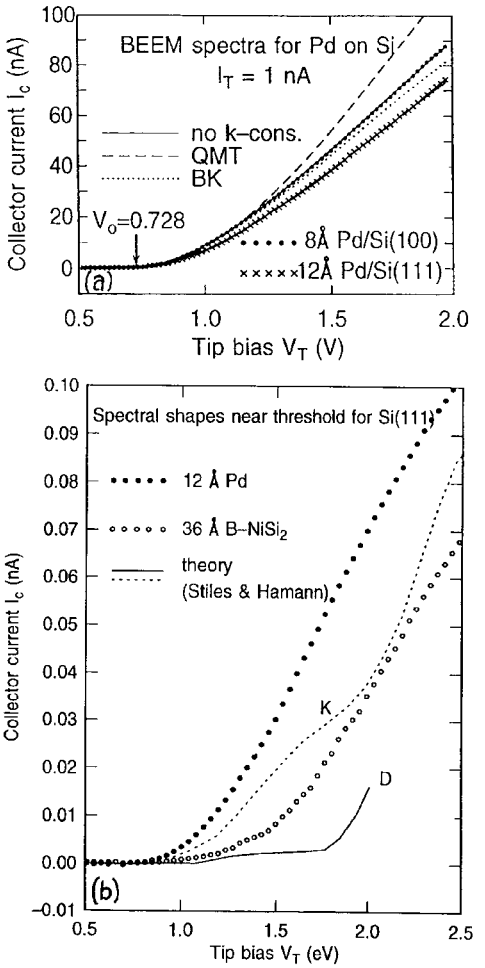


Fig. 11.40. (a) BEEM spectra for Pd on Si(100) and Si(111) and various attempts at fitting the data (symbols): solid line through data points is a fit with model that assumes momentum is not conserved; BK is a fit with the Bell–Kaiser model and QMT one that in addition includes quantum mechanical transmission effects (after Ludeke and Bauer, 1993). (b) BEEM spectra for Pd/Si(111) (dots) and for an epitaxial B-type $NiSi_2$/Si(111) interface compared with kinematic (K) and dynamic (D) model calculations of Stiles and Hamann (1991b) for the B-type $NiSi_2$/Si(111) interface.

and $m_{(100)} = 0.31m_0$. In addition a tip function in Eq. (11.74) with $E_{1/2} = 0.280$ eV was used for the fits, which are shown by the solid lines in Fig. 11.40a. Thus the difference in intensities between the two spectra stems primarily from the orientational differences, as expressed through the effective masses, and less ($\sim 1/3$) from differences in film thickness. Identical thresholds or effective Schottky barrier heights of 0.73 eV were obtained from the fits for both orientations. A transmission factor of $T = 0.7$ was obtained as well, which is somewhat larger than the 0.5 value estimated theoretically by Crowell and Sze (1967), but considerably larger than the value of 0.2 used by Schowalter and Lee (1991). The fits are

exceedingly good over the bias range shown. For comparison fits with the assumption of $k_t$ conservation that includes quantum mechanical transmission, as well as with the simpler B–K model are also shown. The fits were optimized to match the data in the immediate threshold region.

*11.4.4.1.3. Silicide–Si interfaces.* These are technologically important interfaces, among which the $NiSi_2$/Si(111) and $CoSi_2$/Si(111) interfaces are the best understood systems in terms of full band structural descriptions (Section 11.4.3.6). These include the observed differences in $\Phi_{sb}$ for the A-type and B-type $NiSi_2$/Si(111) interfaces. However, the first BEEM measurements by Hasegawa et al. (1991) reported no difference in threshold energies and only a 10% difference in the magnitude of $I_c$ for A and B type $NiSi_2$ patches on their samples, which were prepared *ex-situ*. In contrast, BEEM measurements by Fernandez et al. (1991a) on $NiSi_2$ prepared *in situ* on comparably doped n-type Si ($\lesssim 10^{15}$ cm$^{-3}$) gave values of 0.71 eV and 0.84 eV for the A- and B-type oriented grains found in their their samples. These numbers are are close to the reported values of 0.65 eV and 0.79 eV obtained from $I$–$V$ and $C$–$V$ measurements on macroscopic samples (Tung, 1984). Differences of ~30% in BEEM currents were reported between A- and B-type interfaces, which are significantly below the predictions by Stiles and Hamann (1991a, b) that are shown in Fig. 11.36b. A more favorable comparison between these predictions and measured values is shown in Fig. 11.40b, for a 36 Å B-type $NiSi_2$/Si(111). The measured curve (open circles) falls between the predictions of the kinematic (K) and the dynamic (D) models. The dynamic model predicts a strong suppression of $I_c$ for tip biases below 1.8 V, which is qualitatively observed, albeit constrained to lower biases, in the experimental curve. This suppression is made obvious when comparing the measured intensities to that of a 12 Å Pd film, also shown in the figure. The latter interface, as was discussed in the previous section, is dominated by interface scattering that enhances the spectral intensities. From this comparison one can derive at the conclusion that interface scattering is less pronounced for the $NiSi_2$/Si(111) system and that $k_t$ conservation is at least a partially valid concept. This notion is supported by contrast enhancements in BEEM images in the form of bright halos surrounding isolated atom clusters of Si adsorbed on the $NiSi_2$ surface (Bauer and Ludeke, 1994b). The halos are explained in terms of disturbances of the local potential that causes the electrons to be scattered into the appropriate off-normal acceptance cones, a process that cannot take place on the atomically smooth flats between the clusters.

Low temperature experiments on n- and p-type $CoSi_2$ were reported by Kaiser et al. (1991) on *ex-situ* prepared samples measured in an $N_2$ ambient. The 77 K temperature is necessary to reduce thermionic emission in the low barrier samples. The measured Schottky barrier heights were 0.46 eV and 0.67 eV for p- and n-type substrates, respectively. The latter value was actually obtained from photoresponse measurements, as the BEEM spectra for the n-type samples most frequently exhibited thresholds near 0.85 eV. However, lower barrier heights were also measured, but less frequently. These shifts in threshold from the expected 0.67 eV to the observed 0.85 eV are consistent with the theoretical calculation of the transmission function for electron transport across $CoSi_2$/Si(111) interfaces. As discussed in Section 11.4.3.6, and illustrated in Fig. 11.35, there is a lack of overlap of conduction band states with the same transverse momentum component between the $CoSi_2$ and the Si(111), which persists until an energy of 0.85 eV is reached. This is a remarkable

agreement between theory and experiment and implies $k_t$ conservation in the experiment, as well. This in turn suggests that scattering in the silicide is unimportant, a fact supported by the observation that for Auger-mediated BEEM spectra for $CoSi_2$ on n-type Si, which entails the generation of an isotropic distribution of electron in the silicide, the correct 0.65 eV threshold is observed. Presumably, some degree of scattering in the $CoSi_2$ could explain the occasional observation of thresholds lower than 0.85 eV. The agreement with theory extends reasonably well to absolute magnitudes for one of the kinematic models of Stiles and Hamann (1991b). A dynamical calculation was not presented. The agreement suggests a high degree of interface perfection, at least on a local scale. This view is supported by the recent BEEM images, shown in Fig. 11.24, of stress relieved $CoSi_2$ layers epitaxially grown *in situ* on Si(111) (Sirringhaus et al., 1994). The stress due to lattice misfit is partially relieved through the formation of networks of dislocations. These induce surface deformations that are measurable as faint white lines in the STM topograph, as illustrated in Fig. 11.24a (Stalder et al., 1991). The dashed lines mark a segment of the dislocations. The BEEM image (b), on the other hand, shows a sharply delineated network of enhanced contrast emanating from the dislocations. These enhancements in contrast are consistent with the notion of $k_t$ conservation for the regions bounded by the dislocations, the latter providing the scattering source that facilitates the transfer of electrons into the otherwise largely inaccessible conduction band states of the Si surface steps and other surface irregularities provide similar scattering centers. The BEEM spectra reported by Sirringhaus et al. (1994) and by Meyer and von Känel (1997) did not exhibit the delayed thresholds at 0.85 eV reported by Kaiser et al. (1991), but consistently yielded values of 0.66 eV. In recent BEEM measurements at 77 K reported by Sirringhaus et al. (1995), a dependence of $\Phi_{sb}$ on the crystallographic orientation of the silicide/Si interface was observed for $CoSi_2$ epitaxially deposited on n-type Si(100). Two grain orientation were observed for the $CoSi_2$; the (100) oriented grains exhibited a threshold at $0.74 \pm 0.04$ eV, whereas the (110) grains one at $0.58 \pm 0.04$ eV. Substantially larger collector currents were also observed for the (110) oriented grains. Neither the threshold nor the transmission differences are presently understood.

*11.4.4.2. Threshold spectroscopies of metal–compound-semiconductor interfaces*

*11.4.4.2.1. Metal–GaAs interfaces, including AlAs interlayers.* As a direct band gap semiconductor with an energy gap of 1.42 eV, GaAs is well suited for BEEM investigations at room temperature. Indeed, GaAs together with Si were the first semiconductors investigated by BEEM (Kaiser and Bell, 1988). Although initially the surfaces were prepared by chemically etching, subsequent BEEM studies were made on substrates on which appropriately doped buffer layers of GaAs(100) were grown by molecular beam epitaxy (MBE). *In situ* deposition of Au, however, resulted in ohmic M–S contacts of low resistance that were unsuitable for BEEM studies (Kaiser et al., 1989). To circumvent this, the MBE grown surfaces were first oxidized in water, followed by an HCl dip in an inert $N_2$ ambient to remove the oxide and then reintroduced into UHV for the Au deposition. BEEM spectra for samples of Au on both n-type GaAs (Hecht et al., 1989) and p-type GaAs (Hecht et al., 1990) have been reported. Only the results on n-type GaAs will be discussed here. Au is known to react moderately on MBE-grown GaAs(100) surfaces, with outdiffusion into the growing Au film occurring for both As (Kobayashi et al., 1985) and Ga (Kaiser et al.,

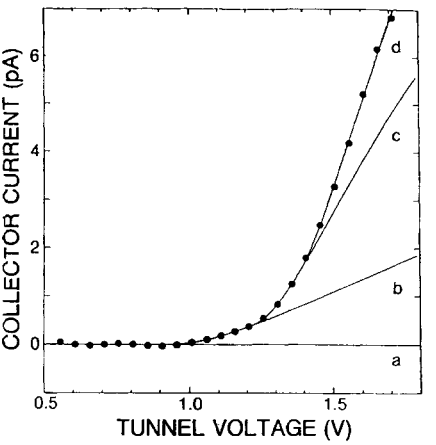


Fig. 11.41. BEEM spectrum for an Au/AlAs/GaAs(100) structure and attempts to fit the data (symbols) with the Bell–Kaiser model shown as solid lines (Eq. (11.63), with $T(E)$ constant). Fitted curve (b) assumes a single threshold, (c) two thresholds and (d) three thresholds. 5.6 Å AlAs layer is transparent to the electrons and acts as a diffusion barrier between the Au and GaAs (after Hecht et al., 1989, with permission).

1989). The resulting heterogeneity of the interface is reflected in the BEEM images, which revealed areas of irregular shapes of finite and zero collector currents for biases of 1.5 V. These areas appear largely unrelated to topographic surface features that were recorded simultaneously (Hecht et al., 1989), and therefore were attributed to subsurface and interface irregularities that can lead to a complete suppression of $I_c$. The interface reaction can be largely suppressed by an intervening AlAs layer, an observation also reported by Brillson et al. (1980) for thin Al interlayers between Au and a cleaved GaAs(110) surface. The resulting BEEM and topographic images were more uniform and exhibited none of the collector current suppression observed for the directly contacted interfaces. A typical BEEM spectrum for electrons on a structure consisting of a double layer of AlAs(100) (5.6 Å) between Au and GaAs(100) is shown in Fig. 11.41. This spectrum does not exhibit the smooth shape observed for Si, but consists of a composite of three components, curves b, c and d, with thresholds at 0.92, 1.20 and 1.36 eV (Hecht et al., 1989). The three thresholds are attributed to electron transfer into the GaAs conduction band minima at $\Gamma_1$, corresponding to the direct gap, as well as into the $L_1$ and $X_1$ conduction band minima located at the L and X symmetry points of the BZ boundary. BEEM spectroscopy on similarly prepared structures with AlAs interlayer thicknesses to 50 ML (140 Å) were reported by by Kaiser et al. (1993). The 50 Å layer is thick enough to prevent direct tunneling into the GaAs. From multiple thresholds in the spectra they were able to determine a value of 0.2 eV for the separation of the conduction bands at $X_1$ and $L_1$ in AlAs, for which the lowest conduction band minima lie near the six X points of the BZ.

In contrast to the ohmic behavior reported by Kaiser et al. (1989), Fowell et al. (1991) observed rectifying characteristics suitable for BEEM studies for *in situ* prepared Au contacts on MBE grown GaAs(100). They report as well the existence of two additional thresholds in their BEEM spectra at energies 0.26 eV and 0.41 eV above $eV_0 = 0.82$ eV. The

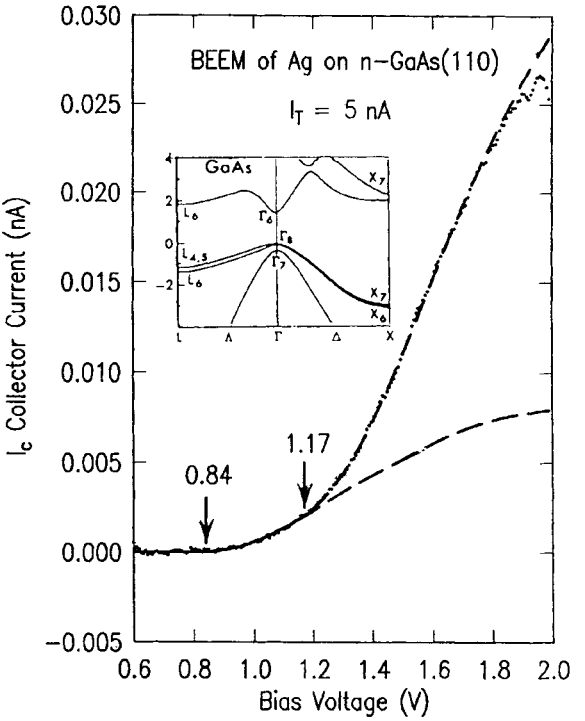


Fig. 11.42. BEEM spectrum (dots) for Ag/GaAs(110) sample prepared by cleavage and deposition in UHV. A proper fit requires a minimum of two thresholds at 0.84 and 1.17 V. A single threshold fit is shown by the lower dashed curve, which fits the data only up to 1.2 V. The inset depicts the band diagram for GaAs with labeled principal critical points.

higher thresholds appear as breaks in the slope of an $I_c^{1/2}$ vs. $V_T$ plot. The three thresholds were also attributed to electron transfer into the $\Gamma_1$, $X_1$ and $L_1$ conduction band minima of GaAs. Although the $\Gamma$ and X points map onto the zone center of the two-dimensional interface BZ for a (100) projection, the L point does not, as can be easily ascertained from Fig. 11.33. This implies that scattering in the Au or at the interface is appreciable in order to account for the strong threshold attributed to the L-point at 1.20 eV, a view that is consistent with the observations for Au and Pd on Si discussed in Section 11.4.4.1. Other means of repressing the Au–GaAs reaction and interdiffusion have been discussed by Talin et al. (1993), who pretreated the GaAs(100) surfaces with $(NH_4)_2S$ prior to the Au deposition. BEEM spectra for such treated interfaces revealed more uniform fundamental thresholds that were at higher energies than for samples treated with $NH_4OH$.

A BEEM spectrum for a 200 Å Ag film on cleaved n-type GaAs(110) is shown in Fig. 11.42, and represents the only reported BEEM spectrum for this surface. Cleavage, Ag deposition and spectral studies were made in UHV without intervening exposure to the ambient. This process generally resulted in diodes with unusable high leakage currents that were also observed for other metals, including Au. However, unlike Au, Ag is not

reactive on the GaAs(110) surface to within the sensitivity limits of synchrotron excited photoemission spectroscopy (Ludeke et al., 1983). The fit to the spectrum was made with Eq. (11.63), but included the quantum mechanical transmission function, as well as the attenuations due to scattering in the metal (Eqs. (11.77)) in the numerator of the integrand. The inclusion of the latter was necessary for a satisfactory fit, and indicates that scattering in the Ag film is pervasive. The inclusion of quantum mechanical transmission is justified for GaAs because optical phonon scattering, which can partially cancel the energy dependence of the transmission function (see Section 11.4.3.7) is essentially energy independent above $\hbar\omega_{op} = 0.036$ eV (Crowell and Sze, 1967). The fit in Fig. 11.42 could not be made with a single threshold, but required an additional threshold 0.33 eV higher in energy. No justification could be made to add a third threshold as in the case for Au/GaAs(100) discussed above. The 0.33 eV is an intermediate value to the reported Γ–L and Γ–X band separations of 0.28 eV and 0.47 eV reported by Drouhin et al. (1985) and of 0.30 eV and 0.39 eV measured by Bachelet and Christensen (1985). Scattering in the Ag film would allow access of the electron to the L point in the GaAs. Hence the observed second threshold arises from electrons transmitted into both L and X points, which cannot be differentiated due to the less than optimal signal-to-noise ratio.

*11.4.4.2.2. Metal–GaP(110) interfaces.* These interfaces represents the most diversified metal–semiconductor combinations studied to date with BEEM. The advantages of GaP for such studies include its wide band gap (2.26 eV at 300 K) that aids in the attainment of Schottky barriers in excess of 1 eV for n-type GaP, and its easy cleaving properties along the (110) crystallographic face that allow simple sample preparation in UHV. GaP has a band structure similar to Si, that is, it is an indirect semiconductor with conduction band minima along the Δ[(001)] directions of reciprocal space. Two of its six minima project onto the (110) interface Brillouin zone (Fig. 11.33), thereby allowing direct $k_t$-conserving electron transfer from a zone centered conduction band of the metal, such as that assumed for the simple metals. However, this is a rather simplistic view since most metals are known to react with GaP, thereby precluding the existence of a coherent interface that arguably could support the notion of transverse momentum conservation. This reactivity has been extensively documented in the literature (Chiaradia et al., 1987; Brillson et al., 1987; Trafas et al., 1989; Ludeke et al., 1990a, b; Miyano et al., 1990). In spite of the dubious quality of the metal–GaP interfaces, $k_t$ conservation has been assumed to be valid in all data fitting schemes reported thus far. However, as discussed in Section 11.4.4.1.2 and illustrated in Fig. 11.40b, this assumption does not produce a significantly different threshold fit from the nonconserving model. The samples for all reported BEEM studies of metals on GaP were prepared, as well as measured at room temperature in an UHV.

A variety of simple, transition and noble metals on cleaved GaP(110) surfaces have been investigated with BEEM. Representative spectra are shown in Fig. 11.43 as dotted curves, which have been displaced vertically for pictorial clarity. Two types of fits are shown for each spectra. The data for the metals shown fall below the solid curves of the fits in the higher range of $V_T$. This behavior clearly obviates the need for multithreshold fits as used for GaAs, although for Cr, shown in the insert (b) of Fig. 11.49, it was necessary to use two thresholds. The fits represent numerical solutions of Eq. (11.63) that include quantum mechanical transmission (Eq. (11.72)). Its inclusion is partly justified by the high doping

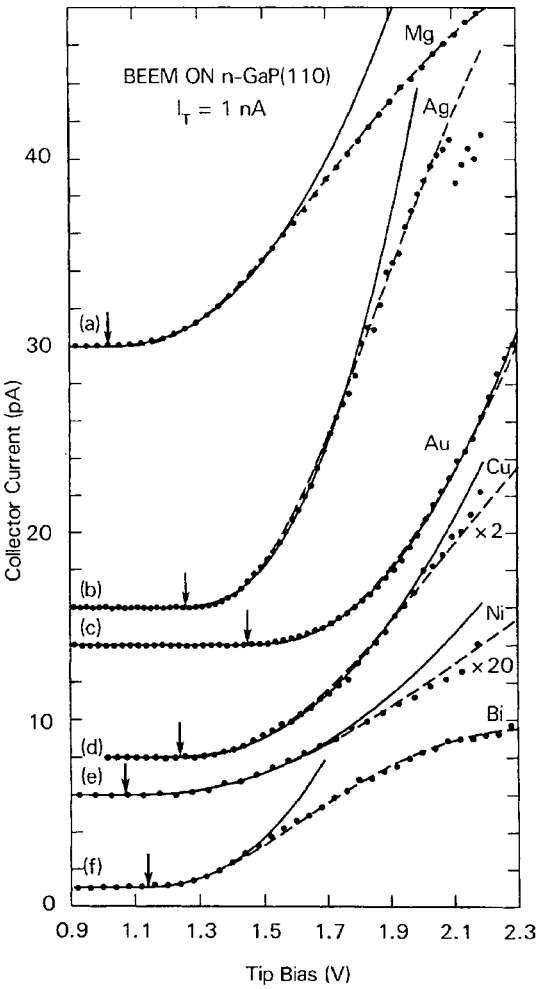


Fig. 11.43. BEEM spectra (dots) for metals on GaP(110): (a) 80 Å Mg, (b) 200 Å Ag, (c) 60 Å Au, (d) 150 Å Cu, (e) 50 Å Ni and (f) 100 Å Bi. All samples were prepared by cleavage and metal deposition in UHV. Two types of fits are shown: the solid line fits were made with Eq. (11.72), the dashed line fits considered in addition scattering in the metal (after Ludeke et al., 1991).

($\sim 10^{18}$ cm$^{-3}$) of the GaP that results in abrupt potential changes at the interface (Section 11.4.3.7). The dashed curves include in addition attenuations of the electron current arising from elastic and inelastic scattering in the metal, which was achieved by incorporating Eqs. (11.77a, b) into the numerator of Eq. (11.63). The quality of the fits is improved with this addition. However, the inclusion of scattering also affects the value of $V_0$ obtained with the fits. This effect is clearly shown in Fig. 11.44 for the case of a thick 200 Å Bi layer on GaP. The dashed and solid lines are again with and without the inclusion of scattering, the corresponding arrows mark the respective thresholds, which differ by 20

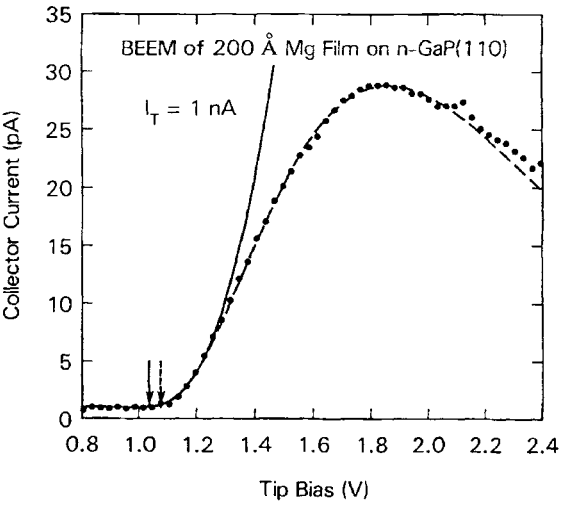


Fig. 11.44. BEEM spectrum (dots) for a 200 Å Mg film on GaP(110). A proper fit (dashed line) requires the inclusion of electron scattering in the Mg layer, which is neglected in the fit shown by the solid line. Inclusion of scattering also affects the threshold value, shown here by a dashed arrow (after Ludeke et al., 1991).

meV. The thresholds obtained from the fits, as well as the scattering parameters, are listed in Table 11.4. For comparison we also show Schottky barrier heights obtained by other techniques. One noteworthy observation in these studies was the extreme uniformity of barrier heights measured for a given metal across the sample and from sample to sample. The noticeable exception was Al. As shown in Fig. 11.45, thresholds varying from 1 to 1.38 eV were observed. A value of $1.24 \pm 0.03$ eV was observed most frequently, and was assumed to represent this interface. On the question of repeatability, it should be mentioned that similar BEEM studies by Bauer et al. (1993a) reported threshold values for Mg of 0.92 eV and for Au of 1.11 eV, which are, respectively, 0.11 and 0.3 eV lower than those reported by Prietsch and Ludeke (1991a) for comparable film thicknesses. The value of 1.11 eV for Au is puzzling as it is clearly outside the range obtained by other measurements, as shown in Table 11.4.

The surface topography of most of the metals used in the BEEM studies is rough on the atomic scale. In most instances the surface morphology exhibits a granularity that is smallest for Cr, with a grain size ~50 Å (Ludeke, 1993c), and largest for the noble metals, with grain sizes exceeding 100 Å (Ludeke and Prietsch, 1991; Bauer et al., 1993a). Features in the BEEM images for these interfaces are generally due to a combination of topographic, scattering and transmission effects and are difficult to interpret. At the other extreme is Bi, which forms terraces hundreds of Ångströms in extent that are atomically flat (Prietsch et al., 1991). An intermediate case is Mg, which forms smooth grains on the GaP, as shown in Fig. 11.46a. The grains are separated from adjacent ones of different height by clearly delineated boundary regions. These boundary regions are not just steps, but exhibit a region of slope 10–30 Å wide, as can be clearly seen by the gradient image of the topographic image, shown in Fig. 11.46b. Here black represents zero gradient and indicates the extent

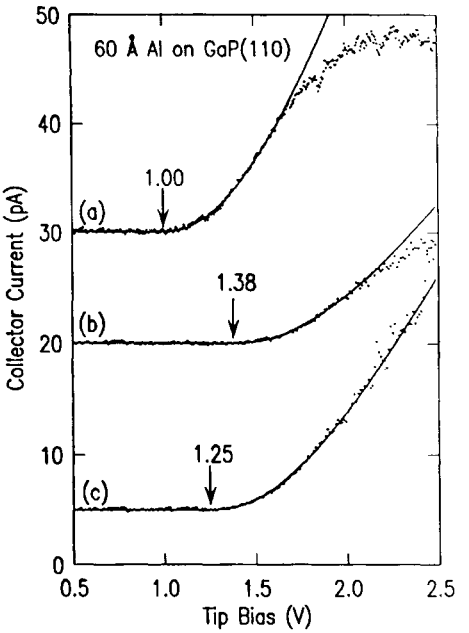


Fig. 11.45. Position dependent threshold variations for a 60 Å Al film deposited on n-type GaP(110), an unusual observation for metal–GaP(110) contacts (after Ludeke, 1993a).

of the flatness of the grains. Image (c) is the BEEM image taken simultaneously with the topographic image. The light areas represent regions of high $I_c$, whereas in the black areas $I_c < 8$ pA. The low current areas are attributed to tunnel current injection at the grain boundaries, where the surface between grains is inclined relative to the planar surface of the grains. Consequently, the electron trajectories at the grain boundaries are inclined as well relative to the surface normal of the grains, which are assumed to be parallel to the M–S interface. If the slope at the grain boundary is comparable to the critical angle of the acceptance cone (Eq. (11.66)), few electrons will be able to cross the interface. The notion of the acceptance cone is not dependent on the assumption of $k_t$ conservation, as was pointed out in the discussion leading to Eq. (11.74). A few details in the BEEM image, such as the series of dark spots in the left center of the image, are not correlated to topographic features on the surface, and appear to be due to defects at the interface or in the Mg film. A simple extension of the planar tunneling model (Eq. (11.73)) for injection at a surface gradient $\theta$ gives an expression for the collector current (Ludeke and Prietsch, 1991):

$$I_c \propto \frac{(eV_T - eV_0)^{5/2}}{(E_F - eV_0)^{1/2}} - \frac{2(m - m_{st})^{1/2} \sin\theta}{m_{st}} (eV_T - eV_0)^2.$$

Fits to spectra near threshold were made with this expression, with values of $\theta$, the only variable, obtained from topographic contours at the location of spectral measurements. The fits agreed well with the measured spectral intensities taken at a number of locations with

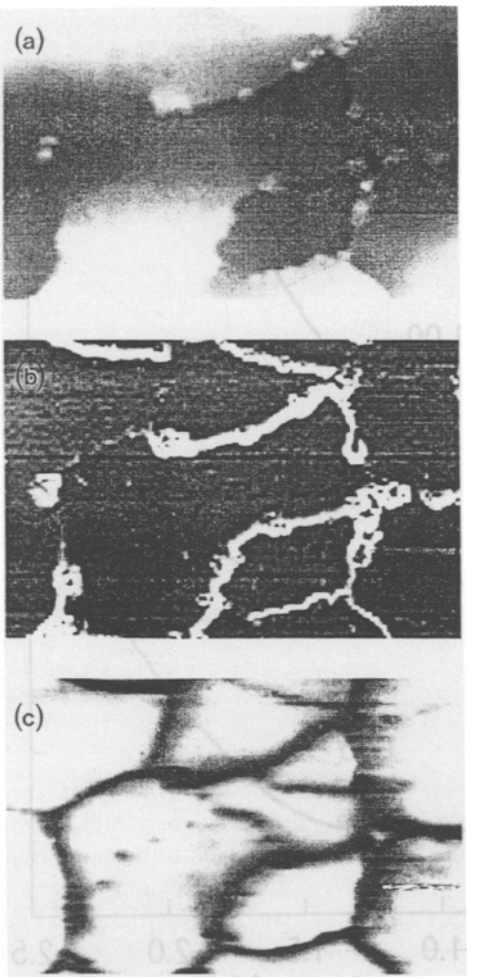


Fig. 11.46. STM topograph (a) and BEEM image (c) for a 200 Å Mg film deposited on n-type GaP(110). Panel (b) is a gradient image of (a) that highlights the weakly discernible grain boundaries in (a). The boundaries consist of risers with large gradients (bright lines) that clearly match the low collector current regions in the BEEM image. Ranges of black-white image contrast: (a) 12 Å, (b) 0–30% and (c) 8–28 pA. $V_T = 2.0$ V, $I_T = 5$ nA (after Prietsch and Ludeke, 1991a).

different surface gradients for Au on GaP (Prietsch and Ludeke, 1991a). More recently Bauer et al. (1993a) also reported strong anticorrelations between surface gradients and $I_c$ for a 12 Å Au film on GaP. Using Monte Carlo simulations of $I_c$ that include gradient effects, with gradients obtained from the topographic images as input, they obtained good agreement between calculated and measured $I_c$ along the corresponding contour line of the BEEM image. This topographic origin of BEEM image contrast, sometimes referred to as "search light" effect (Lee at al., 1993), has only recently been observed for Si, namely

for the coherent $NiSi_2$/Si(111) (Bauer and Ludeke, 1994b) and $CoSi_2$/Si(111) (Sirringhaus et al., 1994) systems. Previous failures to observe this effect for other metal–Si systems can be attributed to the strong scattering effects at the interface that randomize any prior directionality of the electron beam.

*11.4.4.2.3. Au–CdTe interfaces.* Variations of up to 1 eV have been reported in Schottky barriers heights for different metals on CdTe (Dharmadasa et al., 1987). Even for the same metal (Au and Sb) changes in $\Phi_{sb}$ as large as 0.2 eV have been observed for diodes prepared on Br-etched CdTe(100) surfaces (Dharmadasa et al., 1989). It was stipulated by Fowell et al. (1990) that these variations could be attributed to regions of low barrier heights dispersed among areas of larger barrier height, and thus amenable to BEEM investigations. The measured $\Phi_{sb}$ for a particular diode would then depend on the relative abundance of regions with low barrier heights, which can vary among different diodes. For their BEEM experiment, Fowell et al. (1990) deposited 200 Å of Au on $5 \times 10^{16}$ $cm^{-3}$ n-doped CdTe (Debye length $L_D \approx 170$ Å), and took BEEM spectra every 100 Å along a rectangular grid pattern. Fits to the spectra with the B–K model indicated variations in the thresholds of as much as 0.3 eV between adjacent points. Variations of such magnitude appear to be inconsistent with potential gradients expected from a uniformly doped substrate for the given large $L_D$. Of course, strong fluctuations in local doping could appreciably decrease $L_D$, thereby allowing larger gradients. Nevertheless, the results indicate that the Au/CdTe interface is extremely inhomogeneous in the distribution of the interface potential, which qualitatively explains the variations in $\Phi_{sb}$ observed for different Au/CdTe diodes.

*11.4.4.2.4. Heterojunctions.* The determination of the energy difference of conduction or valence bands across a semiconductor heterojunction, or band offset, is an important aspect of heterojunction characterization, and ultimately of device performance. Traditional measurement techniques, similar to those used to obtain the Schottky barrier, give values averaged over macroscopic dimensions. As for the M–S contact investigated with BEEM, it would be highly instructive to obtain the band offsets on a microscopic scale, as well as investigate aspects of the electron transport across heterojunctions and the influence thereon of microscopic features at or near the interface. This approach was taken by Shen et al. (1991) (see also Fowell et al., 1992) to investigate MBE grown heterojunctions consisting of ~100 Å of InAs (n-doped to $10^{18}$ $cm^{-3}$) epitaxially grown onto n-type GaAs(100) substrates doped to $10^{16}$ $cm^{-3}$. For this thickness, the InAs is expected to be nearly relaxed, the strain due to the 7% lattice mismatch with GaAs being reduced by the formation of a two-dimensional network of misfit dislocations (Woodall et al., 1983). It was hoped that evidence of misfit dislocations could be observed in the BEEM images. However, contrast in their BEEM images was dominated by thickness fluctuations of the Au overlayer and by irregular features more consistent with interface irregularities than with line dislocations. It is expected that superior sample preparations will reduce the background contrast and make the observation of the dislocations possible.

The energy diagram of the InAs–GaAs heterojunction for doping levels corresponding to the experimental conditions is shown in the insert of Fig. 11.47. For the doping level used, the InAs is degenerately doped, with the Fermi level lying in the conduction band by an amount $\Delta_1 \approx 0.05$ eV. The barrier height $\phi_b$ is determined experimentally, either

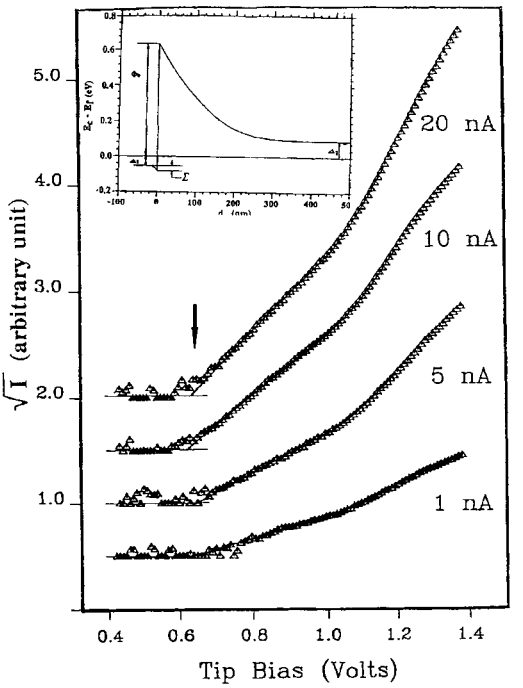


Fig. 11.47. BEEM spectra, presented as the root of the collector current, recorded for different values of tunnel-current (1, 5, 10, 20 nA) for a Au/InAs/GaAs heterojunction structure. The arrow marks the position of the effective barrier potential $\Phi$. Curves are displaced vertically for clarity. Inset: calculated profile for the heterojunction (after Shen et a., 1991, with permission).

from $I$–$V$ measurements on diodes (Shen et al., 1991) or by BEEM spectroscopy. Spectra for the latter are shown in Fig. 11.47, where $I_c^{1/2}$ is plotted rather than the more conventional $I_c$. A value for $\phi_b = 0.63$ eV was determined from the intersection of the essentially linear segment and the base line. This value is in good agreement with that obtained from $I$–$V$ measurements on conventional diodes prepared in the same way, except for a thicker Au overlayer. To obtain the conduction band offset $\Delta E_c$, the band bending $\Sigma$, as well as $\Delta_1$ must be added to $\phi_b$. $\Sigma$ was calculated by solving the Poisson equation, and entails a small additional correction of 0.04 eV. The value of $\Delta E_c = 0.72$ eV thus obtained is somewhat smaller than previously reported values of 0.89 eV obtained by photoemission spectroscopy (Kowalzcyk et al., 1982; Moison et al., 1989). The latter experiments were made on substantially thinner InAs films that probably were under higher strain. Values of $\phi_b$ varied by $\lesssim$0.06 eV among many locations measured over the interface area, indicating that the interface potential of this interface is reasonably homogeneous on a lateral scale. MBE grown InAs overlayers on GaAs have recently been used as base contacts in lieu of the metal (Heer et al., 1999), which greatly enhanced the transmitted current. A theoretical description of BEEM to the study of buried heterojunctions has been given by Smith and Kogan (1996).

MBE grown GaAs/$Al_xGa_{1-x}As$/GaAs(100) structures were used by O'Shea et al. (1994) to measure the conduction band offsets as a function of alloy composition $x$. The 100 Å AlGaAs layer was buried 100 Å below the GaAs surface, with a further narrow doping region ($\delta$-doping) burried 500 Å below the surface. The purpose of the p-type $\delta$-doping layer is to taylor a flat potential profile across the GaAs region in the outer 500 Å of the structure. This allows a direct determination of the band offsets with BEEM by merely determining the threshold shifts as a function of alloy composition for different samples, a procedure that is difficult by conventional bias driven transport measurements. Room temperature values of the conduction band offsets obtained were 0.19 and $0.33 \pm 0.03$ eV for $x = 0.21$ and 0.42, respectively. A study over a broader Al concentration range was recently reported by Cheng et al. (1997). O'Shea et al. (1996) reported the conduction band offsets in ordered GaInP/GaAs heterostructures.

*11.4.4.3. Energetic BEEM*

Thus far only threshold phenomena in the range $V_T \lesssim 2$ V have been discussed. However, a variety of interesting physical phenomena occur at somewhat higher energies, which is also the regime of tip induced surface modifications. There is little evidence for tip induced changes in the metal overlayer or at the M–S interface for biases $\lesssim 2$ V. For higher biases, the tip can induce morphological changes of the surface (Mamin et al., 1990; Uchida et al., 1993). This is, of course, undesirable if BEEM spectroscopy of the M–S structure is the intent. On the other hand, local modification of the surface or interface morphology for large tip currents or high field conditions is an emerging field in its own right (Uchida et al., 1993), and BEEM could evolve as a suitable diagnostic tool to assess the modifications and their effect on vertical electron transport. An example of interface modification will be discussed in the next subsection. The remainder of this section will emphasize the spectroscopic aspects of hot electron transport under high bias conditions.

*11.4.4.3.1. Interface modifications.* Hallen et al. (1991, 1992b) reported BEEM images for Au layers on Si that exhibited enhanced and suppressed regions of collector currents induced by tip bias changes. The effect was observed on both Si(111) and (100) surfaces. This so-called stressing is accomplished by momentarily stopping the raster scan and ramping or pulsing $V_T$ to $\gtrsim 2$ V. The suppression of $I_c$ was observed upon applying a tip bias $\gtrsim 3$ V to samples which had been dipped in HF prior to metallization and which exhibited remnant submonolayer contamination. An increase in the grain size of the Au at the stressing site was also noted. The size of the nearly circular region of suppressed $I_c$ and the corresponding Au mound depended on the tip bias. This suppression was attributed to electron induced enhancement in the interdiffusion between Au and Si at the interface. The interdiffused layer is believed to be a strong electron scatterer (Hallen et al., 1991). In subsequent experiments, Hallen et al. (1992b) introduce a thin 1–2 monolayer of C or carbon-based buffer layer between the Au and Si. This layer acts as a diffusion barrier that also enhances electron scattering, which in turn decreases the interfacial transmittance. For moderate voltage stressing near 2 V, they observed in the BEEM image regions of enhanced $I_c$ a few nanometers in extent surrounding the tip position, but without evidence of changes in the surface topography of the Au. They interpreted the observations, supported by model calculations, in terms of a charge (dosage) dependent replacement of the C layer

with Au. Making an analogy with electron stimulated desorption, this process entails the generation of Au "adsorbates" replacing C atoms at the interface. The Au vacancies and the replaced C atoms diffuse away. The coalescing or nucleating Au atoms form a terrace that enhances the transmittance because of a thickness reduction of the C layer.

In strong contrast, yet supportive of the role of interface contaminants in beam induced mixing, are the investigations by Cuberes et al. (1994a, b) of Au films on *in situ* prepared Si(111)-7 × 7 surfaces, for which the application of tip biases to 8 V did not alter the surface morphology nor the transmissivity of the stressed region. Furthermore, the surface morphology of the Au was different from the grainy and irregular shapes reported for Au films deposited on chemically prepared Si(111) surfaces. Under optimal UHV conditions the Au films exhibited a morphology consisting of circularly shaped and flat topped terraces several monolayers high. Photoemission studies also revealed that the Au/Si interface was abrupt.

*11.4.4.3.2. Energetic BEEM spectroscopy.* As the maximum tip bias is increased beyond the 1.5 to 2 V range used for conventional spectroscopy, several hot electron phenomena are likely to become increasingly important to the transport process. These include enhanced electron–electron scattering in the metal, which reduces the inelastic mean free path $\lambda_i$ (Eq. (11.77b) and electron–hole pair generation in the semiconductor. Both processes are shown schematically in the energy diagram of Fig. 11.48. For $eV_T \gtrsim 2\Phi_{sb}$ the electrons injected into the metal and inelastically scattered there, will produce secondary electrons of sufficient energy to overcome the Schottky barrier. Since primary and secondary electrons are expected to be isotropically distributed following the collisions, only a small fraction will scatter into the acceptance cone of the semiconductor. Because the latter is small just above threshold, a noticeable increase in $I_c$ is not expected above $V_T = 2\Phi_{sb}$, although

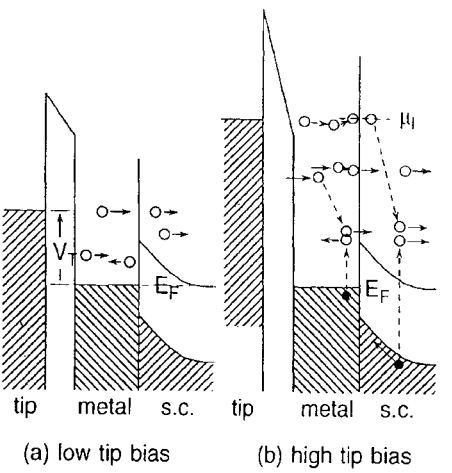


Fig. 11.48. Energy diagrams of electron transit during BEEM: (a) Conventional BEEM picture representing the coherent limit with no scattering in the metal. (b) Under high-bias conditions: elastic and inelastic scattering dominates in the metal, whereas impact ionization is the main scattering mechanism in the semiconductor. Electrons and holes are represented by open and filled circles, respectively.

slowly rising contributions to $I_c$ from this scattering mechanism may be present at substantially higher biases. An energetic electron entering the semiconductor can scatter there inelastically by exciting an electron from the valence band into the conduction band of the semiconductor. The hole left in the valence band gets accelerated towards the M–S interface by the electric field in the depletion layer of the n-type semiconductor shown in Fig. 11.48. At the same time the excited and scattered electrons move away from the interface due to the same field. The hole will be neutralized at the interface. The reverse is true for hot holes in a p-type semiconductor. Thus each hot carrier de-excited by electron–hole pair generation will generate two majority carriers. The scattering process is assumed to be energy and momentum conserving (Bude, 1991). The minimum or threshold energy for a conduction band electron to create an electron–hole pair is $E_{th} = E_e + E_g + E_h + E_s$, where $E_g$ is the band gap, $E_e$ and $E_h$ are the energies of the valence electron excited into the conduction band and that of the hole left behind, respectively, and $E_s$ is the energy of the scattered primary electron. For free-electron-like valence and conduction bands of equal mass, their momenta at threshold are collinear and equal. The assumption of momentum conservation leads to $k_{th} = k_e + k_h + k_s = 3k$, or $E_{th}^{1/2} = 3E^{1/2}$. Consequently, $E_e = E_h = E_s = E$ and $E_{th} = E_g + 3E$, which leads to the simple relation:

$$E_{th} = \frac{3}{2} E_g. \tag{11.78}$$

More complicated expressions have been derived by Hauser (1966) for indirect band gap semiconductors with unequal electron and hole masses. If only energy were conserved, $E_{th} = E_g$. However, Eq. (11.78) appears to be the preferred relationship that accounts for the observed pair creation energies in many semiconductors (Klein, 1968). Drummond and Moll (1971) have calculated the quantum yield $\gamma$, the probability that a hot electron de-energizes through electron–hole pair production, for single pair production in Si. The model calculations, which included the full silicon band structure, showed that the quantum yield rises rapidly from zero to nearly unity ~2 eV above the threshold for pair production. Similar conclusions were reached by Alig et al. (1980) for a much simpler two-band, free-electron model that was not restricted in energy and thus included the possibility of multiple pair production.

In BEEM spectroscopy, evidence for impact ionization was reported for GaP by Ludeke (1993b, c) and Bauer et al. (1993a). A representative spectrum for a 50 Å Cr film on GaP(110) is shown in Fig. 11.49a. The double hump structure was interpreted as resulting from phase space limitations (density-of-states effects) in the GaP (Ludeke, 1993b). However, subsequent fits that take into account electron–hole pair generation in the GaP indicates that a substantial contribution to $I_c$ in the second hump derives from impact ionization. The quantum yield $\gamma$ for this process was obtained with the model of Alig et al. (1980). The mostly ballistic primary component $I_p$ of $I_c$ is obtained from $I_p = I_c/(1+\gamma)$ and is shown in curve (ii). The structure in this component, consisting of a weak shoulder and the salient peak near 5.5 V, can be attributed to density-of-states effects in the GaP. The contribution to $I_c$ due to impact ionization is $I_c - I_p$ and is shown in curve (iii) of Fig. 11.49a. It exhibits a threshold at $V_T = 4.7$ V, which upon subtracting $\Phi_{sb} = 1.3$, results in a $KE$ of 3.4 eV that is very close to $1.5E_g$ for GaP ($E_g = 2.26$ eV). Bauer et al.

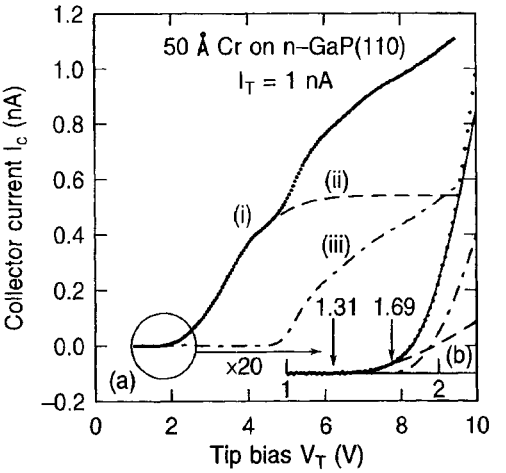


Fig. 11.49. BEEM spectra for Cr on GaP(110): (a) Single, broad bias scan of $I_c$ (curve i) and decomposition into primary component $I_p$ (ii) and secondary component due to impact ionization (iii). b) Expanded and magnified (×20) threshold region of curve (i): dots represent the experimental data; solid line is a fit with two current components with thresholds at 1.31 V (dashed curve) and 1.69 V (dash-dotted curve) (adapted from Ludeke, 1993, and Ludeke and Bauer, 1994).

(1993a) assigned a similar high energy threshold near 4 V to impact ionization. Their spectra for Au and Mg films on n-type GaP(110) are shown in Fig. 11.50. By means of Monte Carlo simulations the authors decomposed the spectra into components attributed to ballistic electrons, elastically and inelastically scattered electron, and contributions from impact ionization in the GaP. It should be noted that in this work, as well as that for Cr/GaP in Fig. 11.49, no evidence for a threshold due to inelastic scattering in the metal is observed. Evidence for impact ionization in GaP involving hot holes has been reported as well for positive tip biases (electron extraction), with a threshold near 4 V (Ludeke, 1993c).

The first direct measurement of the quantum yield over a wide (~7 eV) energy range has been reported by Bauer and Ludeke (1994a) for Si. BEEM spectroscopy was employed on thin $NiSi_2$ films grown epitaxially on n-type Si(111)-7 × 7 surfaces. These films displayed occasional pinholes, typically a few hundred Å in diameter, in which remnants of the 7 × 7 surface reconstruction were observed. The long-known metallic properties of this surface (Erbudak and Fischer, 1972) provides sufficient conductivity to allow BEEM spectroscopy. The BEEM current in the pinholes exhibited a dramatic enhancement of over an order of magnitude larger than that on the adjacent 26 Å $NiSi_2$ layer for $V_T \lesssim 2.5$ V. A spectrum taken in the pinhole is shown Fig. 11.51a. Its well delineated structure, which reaches a momentary plateau at 2.5 V beyond which a second threshold due to the onset of impact ionization is clearly revealed, is in strong contrast to the more washed out features reported for spectra taken on the $NiSi_2$ layer. Such spectra are strongly affected by band structure effects in the silicide and scattering at the interface, which makes a quantitative analysis of impact ionization critically dependent on the models used to describe the transport process. This difficulty is overcome for the spectra taken in the pinholes. The first plateau in

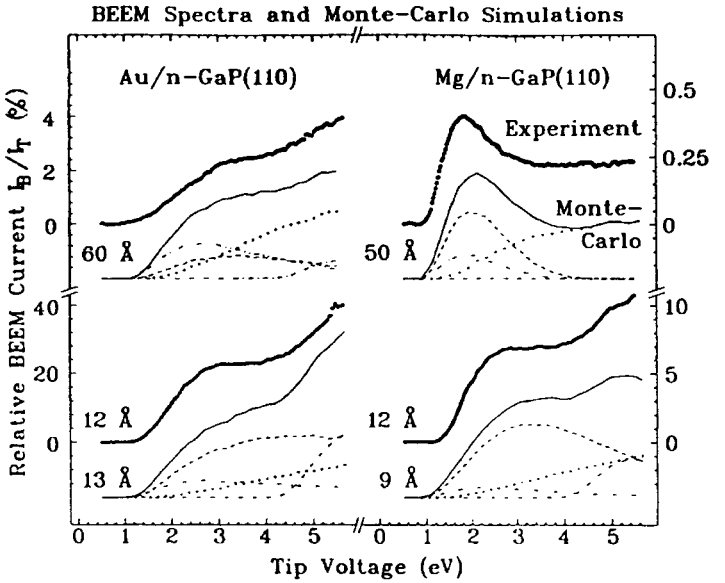


Fig. 11.50. BEEM spectra (filled circles) and Monte Carlo simulations (solid curves) for indicated thicknesses of Au and Mg layers deposited on n-type GaP(110). The simulated curves are composed of contributions from unscattered, ballistic electrons (dashed), only elastically scattered electrons (dash-dot-dotted), inelastic, including secondary, electrons (dotted), and additional electrons created by impact ionization (dash dotted) (Bauer et al., 1993a, with permission).

the raw spectrum (1) of Fig. 11.51a is due to the finite tunnel current, that is, the condition has been reached for which the acceptance cone is wider than the divergence of the injected electrons and the transmission function has reached a maximum value. $I_c$ up to this point can be simulated by use of Eq. (11.63) with the inclusion of quantum mechanical transmission as given by Eq. (11.70). The solution, adjusted to best fit the data to ~3 V rather than just the threshold region, is given by curve (2). This curve represents the primary component of $I_c$, that is, the BEEM current in the absence of carrier multiplication by impact ionization. Its maximum value of $0.73I_T$, a result of the fit, represents the maximum in the transmission function and is assumed to remain constant for higher energies. This value is substantially higher than previous estimates of ~0.5 (Crowell and Sze, 1967) and ~0.2 (Lee and Schowalter, 1991) discussed in Section 11.4.3.7. This discrepancy appears to be the consequence of an overestimate of phonon backscattering effects, rather than an underestimation of the quantum mechanical transmission function, although the latter is estimated low as well by Lee and Schowalter (1991), as shown in Fig. 11.38. The value of 0.73 represents the first direct measurement of the limiting value of the transmission factor. The surplus current due to impact ionization is obtained by subtracting curve (2) from (1), and is shown in curve (3) of Fig. 11.51. Its magnitude normalized by the saturation value of the primary $I_c$, i.e., $0.73I_T$, represents the quantum yield, which is plotted as the dotted curve in Fig. 11.51b. For this plot the the abscissa refers to the kinetic energy $e(V_T - V_0)$ relative to the bottom of the Si conduction band. The quantum yield tends to saturate above

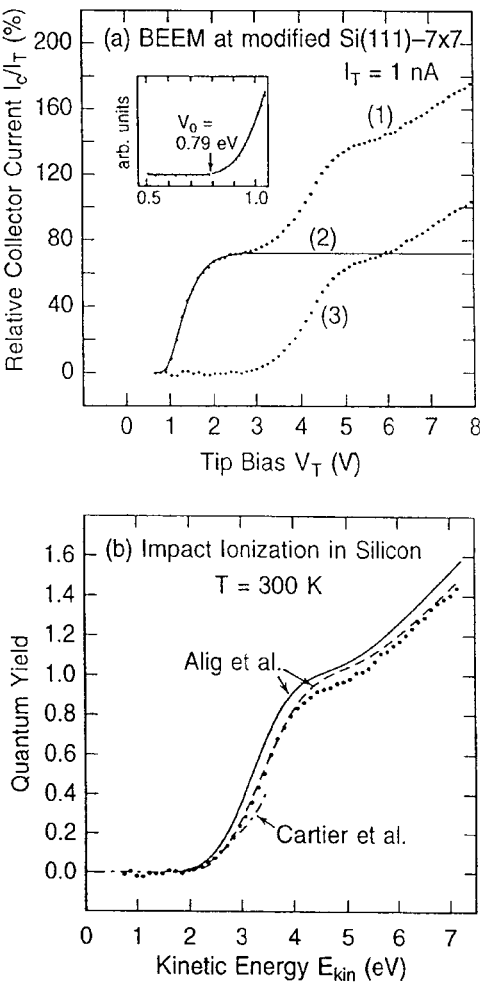


Fig. 11.51. (a) Representative BEEM spectrum (curve 1) taken in a pinhole of a 22 Å thick B-type $NiSi_2$ film. The spectrum is decomposed into a primary-electron part (curve 2) and a secondary-electron part resulting from impact ionization (curve 3). The threshold region of a BEEM spectrum taken in the same area is plotted in the inset. The arrow indicates the threshold position. (b) Quantum yield (dots) as a function of kinetic energy in Si, calculated from the above two subspectra by dividing curve 3 by curve 2. The solid, dashed, and dash-dotted lines represent results of theoretical calculations by Alig et al. (1980) and by Cartier et al. (1993). After Bauer and Ludeke (1994a, b).

4 eV and reaches a value near unity at an energy of 4.5 eV, beyond which it rises again. This second threshold is attributed to impact ionization processes that create two electron–hole pairs.

Comparison with two models are given as well in the figure. The one by Cartier et al. (1993), based on Monte Carlo simulations by Fischetti and Laux (1988) that include full band structural treatments, is based on a multi-component Keldysh-type expression for the

ionization rate with thresholds at 1.2, 1.8 and 3.35 eV. The agreement of the model with the BEEM data is excellent in the ionization threshold region to kinetic energies of 2.8 eV. The second model, that of Alig et al. (1980), is based on the calculation of the probabilities that a hot electron creates exactly 0, 1, 2, ..., electron–hole pairs in a two-band, free electron-like semiconductor. It is essentially a model free of adjustable parameters, which requires as inputs the energy gap $E_g$, the optical phonon frequency, the ionization threshold (assumed as $1.5E_g$) and an empirically determined parameter $A$, universal for most semiconductors. A is proportional to the ratio of the matrix elements for electron scattering by phonon emission and by impact ionization, and a value of 5.2 $eV^3$ was found to produce best agreement between model calculations of the pair creation energy and experimental estimates for many semiconductors. The solid line in Fig. 11.51b represents a fit with this model for $A = 5.2$ $eV^3$, $E_g = 1.12$ eV and $\hbar\omega_{op} = 0.063$ eV. Although the calculated quantum yield is somewhat larger than the experimental data, the overall description of the spectral shape is surprisingly good for such a simple model. The dashed line in Fig. 11.51 is obtained for $A = 7.5$ $eV^3$. An increase in $A$ represents a higher rate of phonon scattering relative to scattering through impact ionization.

Energetic BEEM spectroscopy has also been applied to determine the inelastic ($\lambda_i$) and elastic ($\lambda_e$) mean free paths in thin metal films (Ludeke and Bauer, 1994). The method entails measuring BEEM spectra over a broad bias range for a number of film thicknesses $w$ that span a range from $w \ll \lambda_B$ to $w \gg \lambda_B$. Here $\lambda_B$ is the ballistic mean free path defined by $1/\lambda_B = 1/\lambda_i + 1/\lambda_e$. For a given $V_T$ the net transmission, i.e., $I_c/I_T$, is plotted as a function of $w$. The resulting attenuation plots for Pd films on n-type Si are shown in Fig. 11.52. The curves are characterized by essentially linear segments (in the logarithmic sense) at the larger values of $w$ that are reminiscent of conventional attenuation curves, but markedly deviate from linearity for smaller $w$. The source of this behavior is the changing role of elastic scattering as the thickness decreases. A simple random walk model was developed that assumed mean progression steps of $\lambda_e/2$ towards or away from the M–S interface following each elastic collision in the metal film. An inelastic collision was assumed to remove the electron from being collected. With the boundary conditions that the initial penetration of the injected electrons is $\lambda_e$ from the vacuum interface and that the latter has unit reflectivity for any electrons scattered back to it, the probability $p$ for an electron to reach the M–S interface is:

$$p \approx e^{-w/\lambda_B} + (1 - e^{-w/\lambda_e})e^{-4w^2/\lambda_e\lambda_i}. \tag{11.79}$$

Its slope, $d(\ln p)/dw$, approaches $-1/\lambda_i$ and $-1/\lambda_B$ in the limits of very small ($\lesssim$10 Å) and very large ($\gtrsim$50 Å) widths, respectively. The collector current is proportional to this probability. The proportionality factor depends on the reflectivity $r_i$ at the M–S interface (a fitting parameter) and the probability $p_r$ that the electron gets redirected from the metal back to the interface after a reflection. $p_r = p_1 + p_2 + p_3 + \cdots$ has contributions from multiple scatterings in the metal of which only the term $p_1$ for a single elastic scattering event is important. Thus $p_r \approx p_1 = 0.5\exp(-2\lambda_e/\lambda_i)$. Allowing for multiple reflections back into the metal, the ratio of $I_c/I_T$ can be expressed as:

$$\frac{I_c}{I_T} = \frac{(1 - r_i)}{(1 - r_i p_r)} p. \tag{11.80}$$

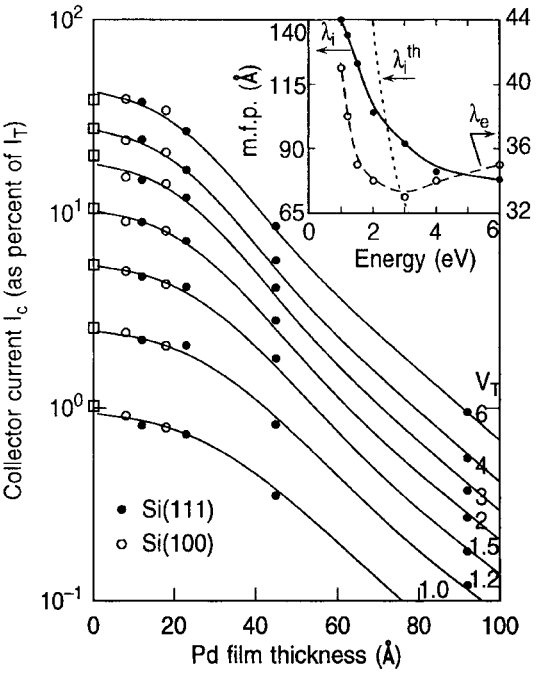


Fig. 11.52. Thickness dependence of $I_c$ for electron injection into Pd films on Si(100) and Si(111) for indicated tip biases $V_T$ Lines are fits with Eqs. (11.79) and (11.80). The electron mean free paths $\lambda_e$ and $\lambda_i$ obtained from the fits are plotted in the insert.

A unique combination of $\lambda_e$, $\lambda_i$ and $r_i$ is used to fit the experimental attenuation curves. The fits are shown as solid lines in Fig. 11.52. The values of $\lambda_e$ and $\lambda_i$ obtained from the fits are shown in the inset. $r_i$ was found to decrease from 0.997 at 1 eV to 0.920 at 6 eV. Also shown in the inset are the theoretical values for $\lambda_i^{th}$ obtained with Eq. (11.77b) (Quinn, 1962), which does not include d-band effects that are expected to significantly alter $\lambda_i$ (Quinn, 1962, 1963; Crowell and Sze, 1967). The agreement between experiment and theory is realtively poor. Although a smaller experimental $\lambda_i$ can be attributed to defects in the nonideal Pd films, its larger than predicted values for the higher energies appear to reflect problems with the theory.

### *11.4.5. Summary and future prospects*

In the preceding many examples were presented showing concrete new results that heretofore were obtainable only with difficulty, or not at all, with other spectroscopic tools. They show the power of this relatively new spectroscopic and microscopic application of the STM and, by implication, the future potentials of BEEM and BEEM spectroscopy. Although investigations of Schottky barrier related issues near threshold biases will undoubtedly command the widest application of BEEM for a long time, a number of specialized application will continue to grow, and new ones will undoubtedly emerge. Energetic

BEEM is expected to continue to impact our understanding of hot electron related issues. As shown, these are mostly "bulk" phenomena, and future directions will undoubtedly encompass new semiconductors, including wide band gap materials and insulators. Initial results of transmission properties across metal–insulator–semiconductor structures, e.g., Au/$CaF_2$/Si(111) (Cuberes et al., 1994a) and Pt/$SiO_2$/Si(100) (Ludeke et al., 1995), suggest BEEM to be a promising new technique to investigate transport and defect phenomena in insulators on an atomic scale. Transmission properties across man-made structures have received but scant attention with BEEM, but future directions there look very promising (Narayanamurti, 1998). Such phenomena as quantum interference, refraction and resonance transmission effects are likely candidates for investigation by BEEM (Henderson et al., 1991a, b), and offer the unique opportunity to characterize electron transport effects and the influence thereon of materials parameters, including defects, with unprecedented lateral resolution. Recent publications support this prognosis, thus image contrast effects due to quantum interference effects have been clearly identified for the first time in BEEM images for $CoSi_2$ layers on Si(111) taken at 77 K (Lee et al., 1994). Low temperature studies in general will enhance these effects, as well as allow threshold studies for M–S systems with low barriers. Temperature dependent transport studies through quantum confinement structures consisting of a thin GaAs layer sandwiched between two AlGaAs layers have also been reported recently (Sajoto et al., 1995). Several bound states of the GaAs quantum well were identified in the $d^2I_c/dV_T^2$ spectra. Single InAs Self Assembled Quantum Dots (SAD) embedded in a Au/GaAs interface were investigated with BEEM spectroscopy by Rubin et al. (1996). The understanding of transport phenomena in BEEM is largely constrained at present by the limited understanding of some fundamental aspects of the transport process. In particular the roles of the band structure and of wave function symmetry across the M–S interface, as well as the roles of defects, phonon and impurity scattering remains to be clarified. At present most of our understanding of the transport processes are based on theories and approaches developed a quarter century ago. The field would greatly benefit from a reevaluation of the premises underlying these models and from new theoretical endeavors than go beyond the simpler theories of the past.

## References

Aldau, C.M., I.M. Vitomirov, F. Xu and J.H. Weaver, 1988, Phys. Rev. B **37**, 6019.
Alig, R.C., S. Bloom and C.W. Struck, 1980, Phys. Rev. B **22**, 5565.
Allen, R.E. and J.D. Dow, 1981, J. Vac. Sci. Technol. **19**, 383.
Allongue, P. and E. Souteyrand, 1987, J. Vac. Sci. Technol. B **5**, 1644.
Alonso, M., R. Cimino, Ch. Maierhofer, Th. Chassé, W. Braun and K. Horn, 1990, J. Vac. Sci. Technol. B **8**, 955.
Anderson, C.L., C.R. Crowell and T.W. Kao, 1975, Solid State Electron. **18**, 705.
Andrews, J.M. and M.P. Lepselter, 1970, Solid State Electron. **13**, 1011.
Andrews, J.M. and J.C. Phillips, 1975, Phys. Rev. Lett. **35**, 56.
Ashcroft, N.W. and N.D. Mermin, 1976, Solid State Physics. Holt, Rinehart and Winston, New York, p. 152.
Assmann, J. and W. Mönch, 1980, Surf. Sci. **99**, 34.
Bachelet, G.B. and N.E. Christensen, 1985, Phys. Rev. B **31**, 879, and references therein.
Bardeen, J., 1947, Phys. Rev. **71**, 717.
Bethe, H.A., 1942, MIT Radiation Lab Report 43-12.
Barret, C. and H. Maaref, 1993, Solid State Electron. **36**, 879.

Bass, J., 1982, in: Landolt-Börnstein New Series, Group III, Vol. 15a: Metals: Electronic Transport Phenomena, ed. J. Bass and K.H. Fischer. Springer-Verlag, Berlin, pp. 92–142.
Bauer, A., M. Prietsch, S. Molodtsov, C. Laubschat and G. Kaindl, 1991, J. Vac. Sci. Technol. B **9**, 2108.
Bauer, A., M. Prietsch, M.T. Cuberes and G. Kaindl, 1993a, J. Vac. Sci. Technol. B **11**, 1584.
Bauer, A., M.T. Cuberes, M. Prietsch and G. Kaindl, 1993b, Phys. Rev. Lett. **71**, 149.
Bauer, A. and R. Ludeke, 1994a, Phys. Rev. Lett. **72**, 928.
Bauer, A. and R. Ludeke, 1994b, J. Vac. Sci. Technol. B **12**, 2667.
Becker, R.S., J.A. Golovchenko and B.S. Swartzentruber, 1985, Phys. Rev. Lett. **55**, 987.
Bell, L.D. and W.J. Kaiser, 1988, Phys. Rev. Lett. **61**, 2368.
Bell, L.D., M.H. Hecht, W.J. Kaiser and L.C. Davis, 1990, Phys. Rev. Lett. **64**, 2679.
Bell, L.D., W.J. Kaiser, M.H. Hecht and L.C. Davis, 1991, J. Vac. Sci. Technol. B **9**, 594.
Bell, L.D., W.J. Kaiser, M.H. Hecht and L.C. Davis, 1993, in: Methods of Experimental Physics, Vol. 27, ed. J.A. Stroscio and W.J. Kaiser. Academic Press, San Diego.
Bell, L.D., A.M. Milliken, S.J. Manion, W.J. Kaiser, R.W. Fathauer and W.T. Pike, 1994, Phys. Rev. B **50**, 8082.
BenDaniel, D.J. and C.B. Duke, 1966, Phys. Rev. **152**, 683.
Binnig, G., K.H. Frank, H. Fuchs, N. García, H. Rohrer, F. Salvan and A.R. Williams, 1985, Phys. Rev. Lett. **55**, 991.
Bohm, D., 1951, Quantum Theory. Prentice Hall, Englewood Cliffs, NJ.
Brillson, L.J., 1978, Phys. Rev. Lett. **40**, 261.
Brillson, L.J., R.Z. Bachrach, R.S. Bauer and J. McMenamin, 1979, Phys. Rev. Lett. **42**, 397.
Brillson, L.J., C.F. Brucker, G. Margaritondo and N.G. Stoffel, 1980, J. Phys. Soc. Jap. **49**, 1089.
Brillson, L.J., C.F. Brucker, A.D. Katnani, N.G. Stoffel, R. Daniels and G. Margaritondo, 1982, J. Vac. Sci. Technol. **21**, 564.
Brillson, L.J., 1985, in: Handbook of Synchrotron Radiation, Vol. 2, ed. G.V. Marr. North-Holland, Amsterdam.
Brillson, L.J., R.E. Viturro, M.L. Slade, P. Chiaradia, D. Kilday, M.K. Kelly and G. Margaritondo, 1987, Appl. Phys. Lett. **50**, 1379.
Brillson, L.J., 1992, in: Surfaces and Interfaces: Atomic-Scale Structure, Band Bending and Band Offsets, ed. P.T. Landsberg. Elsevier, Amsterdam.
Brown, F., 1874, Pogg. Ann. **153**, 556.
Brown, F., 1876, Sitzungsber. Naturforsch. Gesell. (Leipzig), p. 49.
Bude J., 1991, in: Monte Carlo Device Simulation: Full Band and Beyond, ed. K. Hess. Kluwer Academic, Boston.
Burrows, V.A., Y.J. Chabal, G.S. Higashi, K. Raghavachari and S.B. Christman, 1988, Appl. Phys. Lett. **53**, 998.
Cao, R., K. Miyano, T. Kendelewicz, K.K. Chin, I. Lindau and W.E. Spicer, 1987, J. Vac. Sci. Technol. B **5**, 998.
Capasso, F., 1987, in: Heterojunction Band Discontinuities, eds. F. Capasso and G. Margaritondo. North-Holland, Amsterdam.
Cardona, M. and L. Ley, 1979, in: Photoemission in Solids I, eds. M. Cardona and L. Ley. Springer-Verlag, Berlin.
Carlisle, J.A., T. Miller and T.-C. Chiang, 1992, Phys. Rev. B **45**, 3400.
Cartier, E., M.V. Fischetti, E.A. Eklund and F.R. McFeely, 1993, Appl. Phys. Lett. **62**, 3339.
Charlesworth, J.P.A., R.W. Godby and R.J. Needs, 1993, Phys. Rev. Lett. **70**, 1685.
Chen, C.J., 1993, Introduction to Scanning Tunneling Microscopy. Oxford University Press, New York.
Cheng, X.-C., D.A. Collins and T.C. McGill, 1997, J. Vac. Sci. Technol. A **15**, 2063.
Chiaradia, P., L.J. Brillson, M.L. Slade, R.E. Viturro, D. Kilday, N. Tache, M. Kelly and G. Margaritondo, 1987, J. Vac. Sci. Technol. B **5**, 1075.
Cimino, R., A. Giarante, M. Alonso and K. Horn, 1992, Appl. Surf. Sci. **56–58**, 151.
Clabes, J. and M. Henzler, 1980, Phys. Rev. B **21**, 625.
Clerjaud, B., 1985, J. Phys. C **18**, 3615.
Cowley, A.M. and S.M. Sze, 1965, J. Appl. Phys. **36**, 3212.
Cracknell, A.P., 1984, in: Landolt-Börnstein New Series, Group III, Vol. 13c: Metals: Phonon States, Electron States and Fermi Surfaces, ed. A.P. Cracknell. Springer-Verlag, Berlin, p. 47.
Crowell, C.R., 1965, Solid State Electron. **8**, 395.
Crowell, C.R. and S.M. Sze, 1965a, Solid State Electron. **8**, 673.

Crowell, C.R. and S.M. Sze, 1965b, Solid State Electron. **8**, 979.
Crowell, C.R. and S.M. Sze, 1966a, J. Appl. Phys. **37**, 2683.
Crowell, C.R. and S.M. Sze, 1966b, Solid State Electron. **9**, 1035.
Crowell, C.R. and S.M. Sze, 1967, in: Physics of Thin Films, Vol. 4, eds. G. Hass and R.F. Thun. Academic Press, New York, p. 325.
Cuberes, M.T., A. Bauer, H.J. Wen, M. Prietsch and G. Kaindl, 1994a, Appl. Phys. Lett. **64**, 2300; J. Vac. Sci. Technol. B **12**, 2646.
Cuberes, M.T., A. Bauer, H.J. Wen, D. Vandré, M. Prietsch and G. Kaindl, 1994b, J. Vac. Sci. Technol. B **12**, 2422.
Davies, A., J.G. Couillard and H.G. Craighead, 1992, Appl. Phys. Lett. **61**, 1040; J. Vac. Sci. Technol. B **10**, 3112.
Davies, A. and H.G. Craighead, 1994, Appl. Phys. Lett. **64**, 2833.
Das, G.P., P. Blöchl, O.K. Andersen, N.E. Christensen and O. Gunnarsson, 1989, Phys. Rev. Lett. **63**, 1168.
Daw, M.S. and D.L. Smith, 1981, Solid State Commun. **37**, 205.
Demuth, J.E., W.J. Thompson, N.J. DiNardo and R. Imbihl, 1986, Phys. Rev. Lett. **56**, 1408.
De Sousa Pires, J., P.A. Tove and D. Donoval, 1984, Solid State Electron. **27**, 1029.
Dharmadasa, I.M., A.B. McLean, M.H. Patterson and R.H. Williams, 1987, Semicond. Sci. Technol. **2**, 404.
Dharmadasa, I.M., J.M. Thornton and R.H. Williams, 1989, Appl. Phys. Lett. **54**, 137.
Doniach, S. and M. Sunjic, 1970, J. Phys. C **3**, 285.
Drouhin, H.J., C. Hermann and G. Lampel, 1985, Phys. Rev. B **31**, 3859.
Drummond, W.E. and J.L. Moll, 1971, J. Appl. Phys. **42**, 5556.
Duke, C.B. and C. Mailhiot, 1985, J. Vac. Sci. Technol. B **3**, 1170.
Eastman, D.E., T.-C. Chiang, P. Heimann and F.J. Himpsel, 1980, Phys. Rev. Lett. **45**, 656.
Erbudak, M. and T.E. Fischer, 1972, Phys. Rev. Lett. **29**, 732.
Evans, D.A., T.P. Chen, Th. Chassé, K. Horn, M. von der Emde and D.R.T. Zahn, 1992, Surf. Sci. **269/270**, 979.
Feenstra, R.M., 1989a, Phys. Rev. Lett. **63**, 1412.
Feenstra, R.M., 1989b, J. Vac. Sci. Technol. B **7**, 925.
Feenstra, R.M. and J.A. Stroscio, 1993, in: Methods of Experimental Physics, Vol. 27, eds. J.A. Stroscio and W.J. Kaiser. Academic Press, San Diego.
Fernandez, A., H.D. Hallen, T. Huang, R.A. Buhrman and J. Silcox, 1990, Appl. Phys. Lett. **57**, 2826.
Fernandez, A., H.D. Hallen, T. Huang, R.A. Buhrman and J. Silcox, 1991a, J. Vac. Sci. Technol. B **9**, 590.
Fernandez, A., H.D. Hallen, T. Huang, R.A. Buhrman and J. Silcox, 1991b, Phys. Rev. B **44**, 3428.
Fischetti, M.V. and S.E. Laux, 1988, Phys. Rev. B **38**, 9721.
Floyd, R.B. and D.G. Walmsley, 1978, J. Phys. C: Solid State Phys. **11**, 4601.
Fowell, A.E., R.H. Williams, B.E. Richardson and T.-H. Shen, 1990, Semicond. Sci. Technol. **5**, 348.
Fowell, A.E., R.H. Williams, B.E. Richardson, A.A. Cafolla, D.I. Westwood and D.A. Woolf, 1991, J. Vac. Sci. Technol. B **9**, 581.
Fowell, A.E., A.A. Cafolla, B.E. Richardson, T.-H. Shen, M. Elliot, D.I. Westwood and R.H. Williams, 1992, Appl. Surf. Sci. **56–58**, 622.
Fowler, R.H., 1931, Phys. Rev. **38**, 45.
Freeouf, J.L., 1980, Solid State Commun. **33**, 1059.
Fujitani, H. and S. Asano, 1990, Phys. Rev. B **42**, 1696.
Gadzuk, J.W., 1967, Surf. Sci. **6**, 133.
García, N., C. Ocal and F. Flores, 1983, Phys. Rev. Lett. **50**, 2002.
Goodman, A.M., 1963, J. Appl. Phys. **34**, 329.
Goodman, A.M. and D.M. Perkins, 1964, J. Appl. Phys. **35**, 3351.
Gordy, W. and W.J.O. Thomas, 1956, J. Chem. Phys. **24**, 439.
Gossman, H.J. and E.F. Schubert, 1993, Crit. Rev. Solid State & Material Sci. **18**, 1.
Grohndahl, L.O., 1925, U.S. Patent 1640335.
Grohndahl, L.O., 1926, Phys. Rev. **27**, 813.
Hallen, H.D., A. Fernandez, T. Huang, R.A. Buhrman and J. Silcox, 1991, J. Vac. Sci. Technol. B **9**, 585.
Haight, R. and J. Bokor, 1986, Phys. Rev. Lett. **56**, 2846.
Hallen, H.D., A. Fernandez, T. Huang, J. Silcox and R.A. Buhrman, 1992a, Phys. Rev. B **46**, 7256.
Hallen, H.D., T. Huang, A. Fernandez, J. Silcox and R.A. Buhrman 1992b, Phys. Rev. Lett. **69**, 2931.

Harrison, W.A., 1980, Electronic Structure and the Properties of Solids. Freeman, San Francisco.
Hasegawa, Y., Y. Kuk, R.T. Tung, P.J. Silverman and T. Sakurai, 1991, J. Vac. Sci. Technol. B **9**, 578.
Hashizumi, T., H. Hasegawa, T. Sawad, A. Grub and H.L. Hartnagel, 1992, in: Extended Abstracts of the 1992 Int. Conf. on Solid State Devices and Materials, 26–28 August, 1992, Tsukuba, Japan, p. 257.
Hashizumi, T., G. Schweeger, N.J. Wu and H. Hasegawa, 1994, J. Vac. Sci. Technol., to be published.
Hauser, J.R., 1966, J. Appl. Phys. **37**, 507.
Hecht, M.H., L.D. Bell, W.J. Kaiser and F.J. Grunthaner, 1989, Appl. Phys. Lett. **55**, 780.
Hecht, M.H., 1990, J. Vac. Sci. Technol. B **8**, 1018; Phys. Rev. B **41**, 7918.
Hecht, M.H., 1992, Phys. Rev. B **43**, 12102.
Hecht, M.H., L.D. Bell, W.J. Kaiser and L.C. Davis, 1990, Phys. Rev. B **42**, 7663.
Heer, R., J. Smoliner, G. Strasser and E. Gornik, 1999, Surf. Interface Anal. **27**, 517.
Heine, V., 1965, Phys. Rev. **138**, A1689.
Henderson, G.N., T.K. Gaylord and E.N. Glytsis, 1991a, Proc. IEEE **79**, 1643.
Henderson, G.N., T.K. Gaylord, E.N. Glytsis, P.N. First and W.J. Kaiser, 1991b, Solid State Commun. **80**, 591.
Henderson, G.N., P.N. First, T.K. Gaylord and E.N. Glytsis, 1993, Phys. Rev. Lett. **71**, 2999.
Heslinga, D.R., H.H. Weitering, D.P. van der Werf, T.M. Klapwijk and T. Hibma, 1990, Phys. Rev. Lett. **64**, 1589.
Himpsel, F.J., 1990, Surf. Sci. Rep. **12**, 1.
Hölzl, J. and F.K. Schulte, 1979, Solid Surface Physics, Springer Tracts in Modern Physics, Vol. 85, ed. G. Höhler. Springer-Verlag, Berlin.
Horn, K., 1992, Appl. Surf. Sci. **56–58**, 271.
Huijser, A., J. van Laar and van Rooy, 1977, Surf. Sci. **62**, 472.
Ihm, J., S.G. Louie and M.L. Cohen, 1978, Phys. Rev. Lett. **40**, 1028.
Inkson, J.C., 1971, J. Phys. C **4**, 591.
Inkson, J.C., 1972, J. Phys. C **5**, 2599.
Inkson, J.C., 1973, J. Phys. C **6**, 1350.
Inkson, J.C., 1974, J. Vac. Sci. Technol. **11**, 943.
Jackson, W.D., 1975, Classical Electrodynamics, 2nd edn. Wiley, New York.
Jacoboni, C. and L. Reggiani, 1983, Rev. Mod. Phys. **55**, 645.
Jaros, M., 1982, Deep Levels in Semiconductors. Hilger, Bristol.
Jimenez, J.R., L.J. Schowalter, L.M. Hsiung, K. Rajan and S. Hashimoto, 1990, J. Vac. Sci. Technol. A **8**, 3014.
Kahn, A., K. Stiles, D. Mao, S.F. Horng, K. Young, J. McKinley, D.G. Kilday and G. Margaritondo, 1989, in: Metallization and Metal–Semiconductor Interfaces, ed. I.P. Batra. NATO ASI Series **B195**. Plenum, New York, p. 163.
Kaiser, W.J. and L.D. Bell, 1988, Phys. Rev. Lett. **60**, 1406.
Kaiser, W.J., L.D. Bell, M.H. Hecht and F.J. Grunthaner, 1989, J. Vac. Sci. Technol. B **7**, 945.
Kaiser, W.J., M.H. Hecht, R.W. Fathauer, L.D. Bell, E.Y. Lee and L.C. Davis, 1991, Phys. Rev. B **44**, 6546.
Kaiser, W.J., M.H. Hecht, L.D. Bell, F.J. Grunthaner, J.K. Liu and L.C. Davis, 1993, Phys. Rev. B **48**, 18324.
Kikuchi, A., 1989, Phys. Rev. B **40**, 8024.
Klein, C.A., 1968, J. Appl. Phys. **39**, 2029. See also discussion in Alig et al., 1980.
Kobayashi, K.L.I., N. Watanabe, T. Narusawa and H. Nakashima, 1985, J. Appl. Phys. **58**, 3758.
Koch, E.E., D.E. Eastman and Y. Farge, 1983, in: Handbook of Synchrotron Radiation, Vol. 1a, ed. E.E. Koch. North-Holland, Amsterdam.
Kowalczyk, S.P., W.J. Schaffer, E.A. Kraut and R.W. Grant, 1982, J. Vac. Sci. Technol. **20**, 705.
Kraut, E.A., R.W. Grant, J.R. Waldrop and S.P. Kowalczyk, 1980, Phys. Rev. Lett. **44**, 1620.
Kurtin, S., T.C. McGill and C.A. Mead, 1969, Phys. Rev. Lett. **22**, 1433.
Lang, N.D., A. Yacoby and Y. Imry, 1989, Phys. Rev. Lett. **63**, 1499.
Laperashvili, T.A. and G.A. Nakashidze, 1985, Sov. Phys. Tech. Phys. **30**, 433.
Lee, E.Y. and L.J. Schowalter, 1991, J. Appl. Phys. **70**, 2156.
Lee, E.Y., B.R. Turner, L.J. Schowalter and J.R. Jimenez, 1993, J. Vac. Sci. Technol. B **11**, 1579.
Lee, E.Y., H. Sirringhaus and H. von Känel, 1994, Phys. Rev. B **50**, 14714.
Lei, T.F., C.L. Lee and C.Y. Chang, 1979, Solid State Electron. **22**, 1035.
Le Lay, G., K. Hricovini and J.E. Bonnet, 1989, Appl. Surf. Sci. **41/42**, 25.
Liehr, M., P.E. Schmid, F.K. Le Goues and P.S. Ho, 1985, Phys. Rev. Lett. **54**, 2139.

Lindau, I., P.W. Chye, C.M. Garner, P. Pianetta, C.Y. Su and W.E. Spicer, 1978, J. Vac. Sci. Technol. **15**, 1332.
Linz, R., H.J. Clemens and W. Mönch, 1993, J. Vac. Sci. Technol. B **11**, 1591.
Louie, S.G. and M.L. Cohen, 1976, Phys. Rev. B **13**, 2461.
Louie, S.G., J.R. Chelikowsky and M.L. Cohen, 1977, Phys. Rev. B **15**, 2154.
Louis, E., F. Yndurain and F. Flores, 1976, Phys. Rev. B **13**, 4408.
Ludeke, R. and G. Landgren, 1981, J. Vac. Sci. Technol. **19**, 667.
Ludeke, R., T.-C. Chiang and T. Miller, 1983, J. Vac. Sci. Technol. B **1**, 581.
Ludeke, R. and G. Landgren, 1986, Phys. Rev. B **33**, 5526.
Ludeke, R., 1986, Surf. Sci. **168**, 290.
Ludeke, R., G. Hughes, F. Schäffler, F.J. Himpsel, D. Rieger, D. Straub and G. Landgren, 1987, in: Proc. 18th Int. Conf. on Physics of Semiconductors, Stockholm, 1986, ed. O. Engström. World Scientific, Singapore, p. 287.
Ludeke, R., G. Jezequel and A. Taleb-Ibrahimi, 1988, Phys. Rev. Lett. **61**, 601; J. Vac. Sci. Technol. B **6**, 1277.
Ludeke, R., 1989, in: Metallization and Metal–Semiconductor Interfaces, ed. I. Batra, NATO ASI Series **B195**. Plenum, New York, p. 39; Phys. Rev. B **40**, 1947.
Ludeke, R., M. Prietsch, A.B. McLean and A. Santoni, 1990a, J. Vac. Sci. Technol. B **8**, 964.
Ludeke, R., A.B. McLean and A. Taleb-Ibrahimi, 1990b, Phys. Rev. B **42**, 2982.
Ludeke, R., M. Prietsch, A.B. McLean and A. Santoni, 1990c, J. Vac. Sci. Technol. B **8**, 964.
Ludeke, R., M. Prietsch and A. Samsavar, 1991, J. Vac. Sci. Technol. B **9**, 2342.
Ludeke, R., 1993a, unpublished.
Ludeke, R., 1993b, Phys. Rev. Lett. **70**, 214.
Ludeke, R., 1993c, J. Vac. Sci. Technol. A **11**, 786.
Ludeke, R. and A. Bauer, 1993, Phys. Rev. Lett. **71**, 1760.
Ludeke, R. and A. Bauer, 1994, J. Vac. Sci. Technol. A **12**, 1910; Physica Scripta **T55**, 90; J. Vac. Sci. Technol. A **13**, to be published.
Ludeke, R., A. Bauer and E. Cartier, 1995, Appl. Phys. Lett. **66**, 730; J. Vac. Sci. Technol. B **13**, No. 4.
Ludwig, H., G. Heymann and P. Janietz, 1986, J. Vac. Sci. Technol. B **4**, 485.
Ludwig, M.H., E. Meyer, G. Heymann and T. Chassé, 1993, Appl. Surf. Sci. **68**, 445.
Luryi, S., 1990, in: High-Speed Semiconductor Devices, ed. S.M. Sze. Wiley, New York, p. 419.
Mamin, H.J., P.H. Guethner and D. Rugar, 1990, Phys. Rev. Lett. **65**, 2418.
Mao, D., A. Kahn, G. Le Lay, M. Marsi, Y. Hwu and G. Margaritondo, 1992, Appl. Surf. Sci. **56–58**, 142.
Margaritondo, G., L.J. Brillson and N.G. Stoffel, 1980, Solid State Commun. **35**, 277.
Masri, P., 1990, Phys. Rev. Lett. **64**, 208.
McLean, A.B. and R.H. Williams, 1988, J. Phys. C **21**, 783.
McLean, A.B., I.T. McGovern, C. Stephens, W.G. Wilke, H. Haak, K. Horn and W. Braun, 1988, Phys. Rev. B **38**, 6330.
Mele, E.J. and J.D. Joannopoulos, 1978, Phys. Rev. B **17**, 1528.
Merzbacher, E., 1970, Quantum Mechanics, 2nd edn. Wiley, New York.
Meyer, T. and H. von Känel, 1997, Phys. Rev. Lett. **78**, 3133.
Miedema, A.R., P.F. de Chatel and F.R. de Boer, 1980, Physica **100B**, 1.
Missous, M., E.H. Rhoderick and K.E. Singer, 1986, J. Appl. Phys. **60**, 2439.
Miyano, K.E., R. Cao, T. Kendelewicz, A.K. Wahi, I. Lindau and W.E. Spicer, 1990, Phys. Rev. B **41**, 1076.
Moison, J.M., C. Guille, M. Van Rompay, F. Barthe, F. Houzay and M. Bensoussan, 1989, Phys. Rev. B **39**, 1772.
Mönch, W., 1970, Surf. Sci. **21**, 443.
Mönch, W., 1987, Phys. Rev. Lett. **58**, 1260.
Mönch, W., 1988, Phys. Rev. B **37**, 7129.
Mönch, W., 1990, Rep. Prog. Phys. **53**, 221.
Mott, N.F., 1938, Proc. Cambridge Philos. Soc. **34**, 568.
Muret, P. and A. Deneuville, 1982, J. Appl. Phys. **53**, 6289.
Narayanamurti, V., 1998, Proc. SPIE – Int. Soc. Opt. Engng. **3287**, 152.
Newman, N., T. Kendelewicz, L. Bowman and W.E. Spicer, 1985, Appl. Phys. Lett. **46**, 1176.
Newman, N., M. van Schilfgaarde, T. Kendelewicz, M.D. Williams and W.E. Spicer, 1986, Phys. Rev. B **33**, 1146.
Newns, D.M., 1969, J. Chem. Phys. **50**, 4572.

Niedermann, P., L. Quattropani, K. Solt, A. Kent and Ø. Fischer, 1992, J. Vac. Sci. Technol. B **10**, 580.
O'Shea, J.J., T. Sajoto, S. Bhargava, M.A. Chin and V. Narayanamurti, 1994, J. Vac. Sci. Technol. B **12**, 2625.
O'Shea, J.J., C.M. Reaves, S.P. Den Baars, M.A. Chin and V. Narayanamurti, 1996, Appl. Phys. Lett. **69**, 3022.
Ossicini, S., O. Bisi and C.M. Bertoni, 1990, Phys. Rev. B **42**, 5735.
Ossicini, S. and F. Bernadini, 1992, Solid State Commun. **82**, 863.
Ottaviani, G., 1981, J. Vac. Sci. Technol. **18**, 924.
Palm, H., M. Arbes and M. Schulz, 1993, Appl. Phys. A, Solid Surf. A **56**, 1; Phys. Rev. Lett. **71**, 2224.
Palmstrøm, C.J. and T. Sands, 1993, in: Contacts to Semiconductors, ed. L.J. Brillson. Noyes, Park Ridge, NJ.
Park, S.-I. and R.C. Barrett, 1993, in: Methods of Experimental Physics, Vol. 27, eds. J.A. Stroscio and W.J. Kaiser. Academic Press, San Diego.
Petro, W.G., T. Kendelewicz, I.A. Babalola, I. Lindau and W.E. Spicer, 1984, J. Vac. Sci. Technol. A **2**, 835.
Prietsch, M., M. Domke, C. Laubschat and G. Kaindl, 1988, Phys. Rev. Lett. **60**, 436; Phys. Rev. B **38**, 10655.
Prietsch, M. and R. Ludeke, 1991a, Phys. Rev. Lett. **66**, 2511.
Prietsch, M. and R. Ludeke, 1991b, Surf. Sci. **251/252**, 413.
Prietsch, M., A. Samsavar and R. Ludeke, 1991, Phys. Rev. B **43**, 11850.
Prietsch, M., 1992, Ballistic Electron Emission Microscopy (BEEM) Applied to Study the Electronic Structure of Metal/Semiconductor Interfaces, Habilitationsschrift, Institut für Experimental Physik, Freie Universität Berlin, unpublished.
Quattropani, L., K. Solt, P. Niedermann, I. Maggio-Aprile, Ø. Fischer and Pavelka, 1993, Appl. Surf. Sci. **70/71**, 391.
Quinn, J.J., 1962, Phys. Rev. **126**, 1453.
Quinn, J.J., 1963, Appl. Phys. Lett. **2**, 167.
Reuter, K., P.L. de Andrés, F.J. García-Vidal, D. Sestovic, F. Flores and K. Heinz, 1998a, Phys. Rev. B **58**, 14036.
Reuter, K., F.J. García-Vidal, P.L. de Andrés, F. Flores and K. Heinz, 1998b, Phys. Rev. Lett. **81**, 4963.
Rhoderick, E.H. and R.H. Williams, 1988, Metal–Semiconductor Contacts, 2nd. edn. Clarendon, Oxford.
Rubin, M.E., G. Medeiros-Ribeiro, J.J. O'Shea, M.A. Chin, E.Y. Lee, P.M. Petroff and V. Narayanamurti, 1996, Phys. Rev. Lett. **77**, 5268.
Sajoto, T., J.J. O'Shea, S. Bhargava, D. Leonard, M.A. Cin and V. Narayanamurti, 1995, Phys. Rev. Lett. **74**, in press.
Schäffler, F., G. Hughes, W. Drube, R. Ludeke and F.J. Himpsel, 1987a, Phys. Rev. B **35**, 6328.
Schäffler, F., W. Drube, G. Hughes, R. Ludeke, D. Rieger and F.J. Himpsel, 1987b, J. Vac. Sci. Technol. A **5**, 1528.
Schlüter, M., 1978, Phys. Rev. B **17**, 5044.
Schmid, P.E., 1985, Helv. Phys. Acta **58**, 371.
Schottky, W., 1938, Naturwiss. **26**, 843.
Schottky, W. and W. Deutschmann, 1929, Phys. Z. **30**, 839.
Schottky, W., 1939, Z. Phys. **113**, 367.
Schottky, W., 1940, Phys. Z. **41**, 570.
Schottky, W., 1942, Z. Phys. **118**, 539.
Schowalter, L.J. and E.Y. Lee, 1991, Phys. Rev. B **43**, 9308.
Seeger, K., 1989, Semiconductor Physics, an Introduction, 4th edn. Springer-Verlag, New York.
Shen, T.-H., M. Elliot, A.E. Fowell, A.A. Cafolla, B.E. Richardson, D. Westwood and R.H. Williams, 1991, J. Vac. Sci. Technol. B **9**, 2219.
Shen, T.-H., M. Elliot, R.H. Williams, D.A. Woolf, D.I. Westwood and A.C. Ford, 1992, Appl. Surf. Sci. **56–58**, 749.
Shi, Z.Q., R.L. Wallace and W.A. Anderson, 1991, Appl. Phys. Lett. **59**, 446.
Shi, Z.Q. and W.A. Anderson, 1992, Solid State Electron. **35**, 1427.
Simmons, J.G., 1963, J. Appl. Phys. **34**, 1793.
Simmons, J.G., 1964, J. Appl. Phys. **35**, 2655.
Sirringhaus, H., E.Y. Lee and H. von Känel, 1994, Phys. Rev. Lett. **73**, 577; J. Vac. Sci. Technol. B **12**, 2629.
Sirringhaus, H., E.Y. Lee, U. Kafader and H. von Känel, 1995, in: PCSI Conference Proceedings, J. Vac. Sci. Technol., to be published.
Smith, D.L. and S.M. Kogan, 1996, Phys. Rev. B **54**, 10354.
Spicer, W.E., P.W. Chye, P.R. Skeath and I. Lindau, 1979, J. Vac. Sci. Technol. **16**, 1422.

Spicer, W.E., I. Lindau, P.R. Skeath and C.Y. Su, 1980, J. Vac. Sci. Technol. **17**, 1019.
Spicer, W.E., R. Cao, K. Miyano, C. McCants, T.T. Chiang, C.J. Spindt, N. Newman, T. Kendelewicz, I. Lindau, E. Weber and Z. Liliental-Weber, 1989, in: Metallization and Metal–Semiconductor Interfaces, ed. I.P. Batra, NATO ASI Series **B195**. Plenum, New York, p. 139.
Stalder, R., H. Sirringhaus, N. Onda and H. von Känel, 1991, Appl. Phys. Lett.**59**, 1960.
Stiles, K., A. Kahn, D.G. Kilday and G. Margaritondo, 1987, J. Vac. Sci. Technol. B **5**, 987.
Stiles, K. and A. Kahn, 1988, Phys. Rev. Lett. **60**, 440.
Stiles, M. and D. Hamann, 1989, Phys. Rev. B **40** 1349.
Stiles, M. and D. Hamann, 1991a, Phys. Rev. Lett. **66**, 3179.
Stiles, M. and D. Hamann, 1991b, J. Vac. Sci. Technol. B **9**, 1394.
Streetman, B.G. and Y.C. Shih, 1992, J. Vac. Sci. Technol. B **10**, 296.
Stroscio, J.A. and R.M. Feenstra, 1993, in: Methods of Experimental Physics, Vol. 27, eds. J.A. Stroscio and W.J. Kaiser. Academic Press, San Diego.
Sullivan, J.P., R.T. Tung and M.R. Pinto, 1991, J. Appl. Phys. **70**, 7403.
Sullivan, J.P., R.T. Tung, D.J. Eaglesham, F. Schrey and W.R. Graham, 1993, J. Vac. Sci. Technol. B **11**, 1564.
Sze, S.M., 1981, Physics of Semiconductor Devices, 2nd edn. Wiley, New York.
Sze, S.M., C.R. Crowell and D. Kahng, 1964, J. Appl. Phys. **35**, 2534.
Sze, S.M., C.R. Crowell, G.P. Carey and E.E. La Bate, 1966, J. Appl. Phys. **37**, 2690.
Talin, A.A., R.S. Williams and K.L. Kavanagh, 1993, Mat. Res. Soc. Symp. Proc. **281**, 653.
Tam, N.T. and T. Chot, 1986, Phys. Status Solidi **93**, K 91.
Tang, J.Y.-F and J.L. Freeouf, 1984, J. Vac. Sci. Technol. B **2**, 459.
Tejedor, C., F. Flores and E. Louis, 1977, J. Phys. C: Solid State Phys. **10**, 2163.
Tersoff, J. and D.R. Hamann, 1983, Phys. Rev. Lett. **50**, 1998.
Tersoff, J., 1984, Phys. Rev. Lett. **52**, 465; Phys. Rev. B **30**, 4874.
Tersoff, J., 1990, Phys. Rev. B **41**, 1235.
Trafas, B.M., F. Xu, M. Vos, C.M. Aldao and J.H. Weaver, 1989, Phys. Rev. B **40**, 4022.
Troost, D., L. Koenders, L.-Y. Fan and W. Mönch, 1987, J. Vac. Sci. Technol. B **5**, 1119.
Tung, R.T., 1984, Phys. Rev. Lett. **52**, 462; J. Vac. Sci. Technol. B **2**, 465.
Tung, R.T., 1991, Appl. Phys. Lett. **58**, 2821.
Tung, R.T., A.F.J. Levi, J.P. Sullivan and F. Schrey, 1991, Phys. Rev. Lett. **66**, 72.
Tung, R.T., 1992, Phys. Rev. B **45**, 13509.
Uchida, H., D. Huang, F. Grey and M. Aono, 1993, Phys. Rev. Lett. **70**, 2040.
Viturro, R.E., M.L. Slade and L.J. Brillson, 1986, Phys. Rev. Lett. **57**, 487.
Vogel, P. and J.M. Baranowski, 1985, Acta Phys. Polon. **A67**, 133.
Waddill, G.D., I.M. Vitorimov, C.M. Aldao, S.G. Anderson, C. Capasso, J.H. Weaver and Z. Liliental-Weber, 1990, Phys. Rev. B **41**, 5293.
Waldrop, J.R., 1984, Appl. Phys. Lett. **44**, 1002; J. Vac. Sci. Technol. B **2**, 445.
Weaver, J.H., M. Grioni, J.J. Joyce and M. del Giudice, 1985, Phys. Rev. B **31**, 5290.
Weitering, H.H., A.R.H.F. Ettema and T. Hibma, 1992, Phys. Rev. B **45**, 9126.
Werner, J.H., H.H. Guttler and U. Rau, 1991, J. Appl. Phys. **69**, 1522.
Wertheim, G.K. and P.H. Citrin, 1978, in: Photoemission in Solids I, eds. M. Cardona and L. Ley. Springer-Verlag, Berlin. Care must be excercised in a background subtraction, particularly in the case of a metal.
Williams, R.H., R.R. Varma and V. Montgomery, 1979, J. Vac. Sci. Technol. **16**, 1418.
Wilson, A.H., 1932, Proc. Roy. Soc. **A136**, 487.
Wittmer, M. and J.L. Freeouf, 1992, Phys. Rev. Lett. **69**, 2701.
Woodall, J.M., G.D. Pettit, T.N. Jackson, C. Lanza, K.L. Kavanagh and J.W. Mayer, 1983, Phys. Rev. Lett. **51**, 1783.
Wolf, E.L., 1985, Principles of Electron Tunneling Spectroscopy. Oxford University Press, New York.
Xu, F., J.J. Joyce, M.W. Ruckman, H.-W. Chen, F. Boscherini, D.M. Hill, S.A. Chambers and J.H. Weaver, 1987, Phys. Rev. B **35**, 2375.
Yamamoto, S., K. Susa and U. Kawabe, 1974, J. Chem. Phys. **60**, 4076.
Yeh, J.J. and I. Lindau, 1985, Atomic Data and Nuclear Data Tables **32**, 1.
Yndurain, F., 1971, J. Phys. C: Solid State Phys. **4**, 2849.

Zhang, S.B., M.H. Cohen and S.G. Louie, 1986, Phys. Rev. B **34**, 768.
Zunger, A., 1981, Phys. Rev. B **24**, 4372.
Zur, A., T.C. McGill and D.L. Smith, 1983, Phys. Rev. B **28**, 2060.

CHAPTER 12

# Electronic Structure of Adsorbates on Semiconductors

R. MIRANDA and E.G. MICHEL

*Departamento de Física de la Materia Condensada*
*and Instituto Universitario de Ciencia de Materiales "Nicolás Cabrera"*
*Universidad Autónoma de Madrid*
*Madrid, Spain*

*© 2000 Elsevier Science B.V.*
*All rights reserved*

*Handbook of Surface Science*
*Volume 2, edited by K. Horn and M. Scheffler*

# Contents

12.1. Introduction . . . . . 865
12.2. Adsorption of hydrogen . . . . . 867
12.2.1. Adsorption of hydrogen on Si(111)7 × 7 . . . . . 867
12.2.2. Adsorption of hydrogen on Si(100)2 × 1 . . . . . 872
12.2.3. Adsorption of hydrogen on III-V semiconductors . . . . . 874
12.3. Oxidation of silicon surfaces . . . . . 875
12.3.1. Oxidation of Si(111)7 × 7 . . . . . 875
12.3.2. Oxidation of Si(100)2 × 1 . . . . . 877
12.3.3. Oxidation of III-V semiconductors . . . . . 878
12.4. Adsorption of other species . . . . . 879
12.4.1. Adsorption of water . . . . . 879
12.4.2. Nitridation . . . . . 880
12.4.3. Adsorption of other elements and compounds . . . . . 882
12.5. Surface passivation . . . . . 883
12.6. Adsorption of halogens . . . . . 886
12.6.1. Introduction . . . . . 886
12.6.2. Adsorption-site symmetry and polarization effects . . . . . 887
12.6.3. Group IV + halogens . . . . . 888
12.6.4. Group III-V compounds + halogens . . . . . 892
12.7. Adsorption of $C_{60}$ . . . . . 892
12.8. Conclusions and outlook . . . . . 893
References . . . . . 893

## 12.1. Introduction

A general overview of the electronic structure of adsorbates on semiconductors is not easy to construct. Ideally, one would like to determine experimentally and understand theoretically the trends of adsorption kinetics, saturation coverages, adsorption sites, bond lengths, charge transfer, type of bonding and electronic states, since all these topics are interwoven. Reviews on several of these aspects are available (Williams et al., 1980; Mönch, 1990). Here, we restrict ourselves to a tutorial description of the electronic structure of some model adsorbate/semiconductor systems. The most widely used experimental techniques to gain information on the occupied and empty electronic states are ultraviolet photoemission spectroscopy (UPS) (Himpsel, 1983) and inverse photoemission spectroscopy (IPS) (Himpsel, 1990), respectively. By measuring energy and angular distributions of photoemitted electrons, one obtains density of states and electronic band dispersions $E(\mathbf{k})$. Using large photon energies, core-level excitations and the corresponding chemical information, are also accessible (Hüfner, 1996).

The invention of the scanning tunneling microscope (STM) and its development as an spectroscopic tool (Stroscio and Kaiser, 1993) has allowed investigators to probe the spatial distribution of electronic properties at the atomic level. Spatial mapping of the distribution of electronic states with the STM is possible by recording $I$–$V$ curves at selected positions on the surface, obtaining the differential conductivity $\mathrm{d}I/\mathrm{d}V$ and normalizing to $I/V$. The resulting quantity, $(\mathrm{d}I/\mathrm{d}V)/(I/V)$, is proportional to the local density of states (Stroscio and Kaiser, 1993).

A look at the literature suffices to realize that for a number of years the experimental data for nominally identical systems, e.g., H/Si(111) or $O_2$/GaAs(110), have been contradictory and a systematic picture was absent. There are good reasons for this controversy. First, electronic structure and adsorption geometry are strongly interdependent. Most semiconductor surfaces reconstruct and the corresponding atomic structure has been elucidated only recently. Second, the spectroscopic techniques available, such as photoemission spectroscopies (PES) or inverse photoemission (IPS) average over $10^{12}$–$10^{14}$ atomic sites on the surface. Surface homogeneity at comparable scales is then very important to analyze the electronic spectra. However, it is difficult to prepare in a repetitive fashion semiconductor surfaces which are clean and homogeneous over these lateral scales, unless one has experimental techniques able to characterize the surface at the required level.

Luckily, the situation started to change in recent years. STM topographs can characterize the cleanliness and perfection of a surface at a scale not previously achievable by standard techniques like Auger electron spectroscopy (AES) and low energy electron diffraction (LEED), while recording local spectroscopic information. In this way, connection to averaging spectroscopies can be achieved. An example of the importance of a combined characterization of "clean" semiconductor surfaces is given in Figs. 12.1 and 12.2. Following a common method to prepare a $7 \times 7$ reconstructed Si(111) surface, the sample was

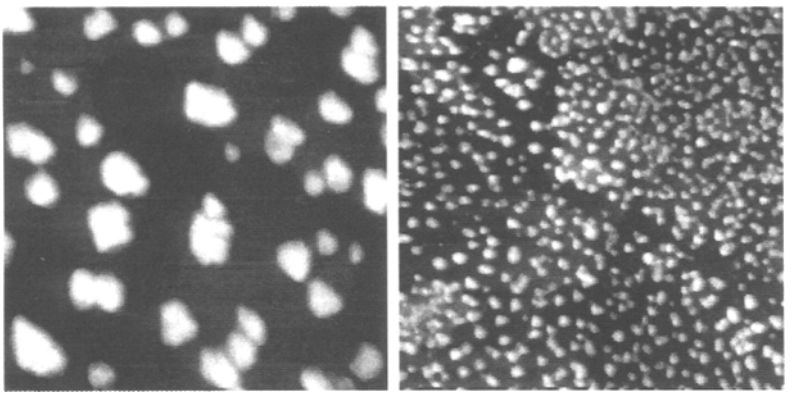

Fig. 12.1. STM images of a flashed Si(111) 7 × 7 surface (left, 2700 × 2700 Å$^2$, right 10200 × 10200 Å$^2$). The white protrusions are SiC clusters.

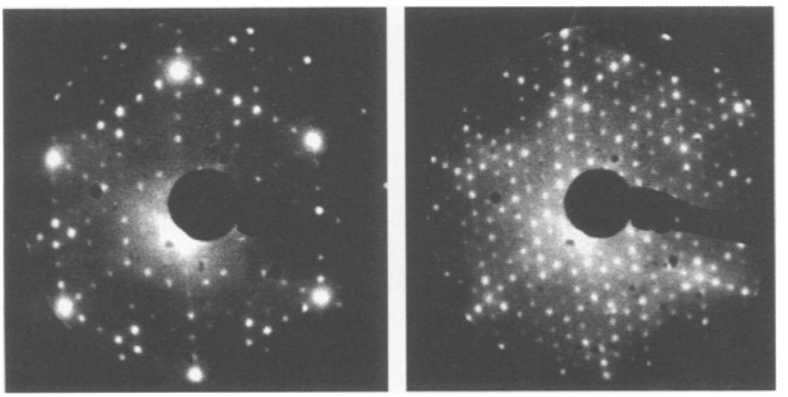

Fig. 12.2. LEED patterns corresponding to the surface shown in Fig. 12.1. Left, 30 eV, right, 60 eV.

cleaned by flashing out the native oxide in UHV conditions. The LEED pattern is reproduced in Fig. 12.2. It corresponds to a good quality 7 × 7 reconstruction. The AES spectrum indicates that the sample was clean within the sensitivity of AES, that is, the C/Si ratio of the peaks was 1/150, just at the level of noise of the electron spectrometer. The large scale STM images reproduced in Fig. 12.1, however show that 15% of the surface is covered by SiC clusters 30 Å-high, with a density of 6.5 × $10^{10}$ cm$^{-2}$. Zooming in between the clusters shows that the 7 × 7 reconstruction is present in these regions (Vazquez de Parga, 1992). It is quite obvious that extracting information on adsorption onto this Si(111)-7 × 7 surface from averaging techniques may result difficult.

In recent years the combination of PES, IPS and topographic and spectroscopic STM has started to yield a consistent picture of adsorption on some semiconductor surfaces. The summary of our present knowledge is the following: the chemical reactivity of semiconductor surfaces is determined by the dangling bonds, i.e., the surface states. Adsorbates

form chemical bonds with semiconductor surfaces in an attempt to saturate the dangling bonds. This process is accompanied by local deformations of bond angles that modify the strain energy of the surface. Stable structures result when the strain energy is overcompensated by the energy gain resulting from the saturation of the dangling bonds. In general, simple electron counting arguments are enough to find a reasonable starting point for the adsorption site and resulting surface electronic structure. In the case of homopolar semiconductors, as silicon or germanium, the truncated $sp^3$-bonds give rise to surface states in the band gap between valence and conduction band. Their dispersion depends on the orbital symmetry at the surface, and they are strongly affected by defects and adsorbates. Thus, the adsorption of hydrogen or the formation of a $SiO_2$/Si interface completely eliminate the electronic states from the band gap. This process takes place through formation of strong bonds and displacement of the corresponding dangling bonds into the valence band. Both the intrinsic electronic surface states of the clean surface and the molecular orbitals of the adsorbate are involved in this process. A similar behavior is found for adsorption on many heteropolar-covalent semiconductors, as GaAs, InP, etc. These materials also exhibit surface states (not always in the bulk band gap in this case). The surface states can be classified in a simplified model as coming from anion or from cation $sp^3$-orbitals (Mönch, 1990). Their exact location in energy depends on the local geometry, giving rise in some cases to strong energy dispersions with parallel momentum that is detected by angular resolved photoelectron spectroscopy (ARPES) (Himpsel, 1983).

In the following we shall concentrate in some selected examples which mostly represent old, but still relevant, problems.

## 12.2. Adsorption of hydrogen

Semiconductor surfaces, in particular Si, are inert with respect to exposures to $H_2$ molecules (Pretzer and Hagstrum, 1966), which have a large dissociation energy of 4.52 eV. Hydrogen atoms, on the other hand are easily adsorbed on Si and the bonding strength is 3.9 eV (notice that a Si–Si bond amounts to 2.32 eV). Accordingly, hydrogenation is usually achieved by exposing the sample to $H_2$ pressures in the presence of hot tungsten filaments, which dissociate $H_2$ into H atoms. The filaments are placed close to the sample and the intensity passing through them is carefully controlled. Since, in most cases, the actual rate of arrival of H atoms to the surface is not known, the exposure is usually given in Langmuirs ($1\ L = 1 \times 10^{-6}$ Torr s) of $H_2$, but one has to keep in mind that actual H exposures in different laboratories can be difficult to compare. The use of sources specially designed to produce atomic hydrogen is also possible, and in this case a more accurate control of the exposure can be achieved.

### *12.2.1. Adsorption of hydrogen on Si(111)7 × 7*

The Si(111) $7 \times 7$ reconstructed surface is a prototype (Schlier and Farnsworth, 1959). Its metallic character and atomic structure, given by the dimer–adatom–stacking fault model (Takayanagi et al., 1985), are widely accepted. The electronic structure is described in detail elsewhere in this book. Three occupied surface states, $S_1$, $S_2$ and $S_3$ are detected in

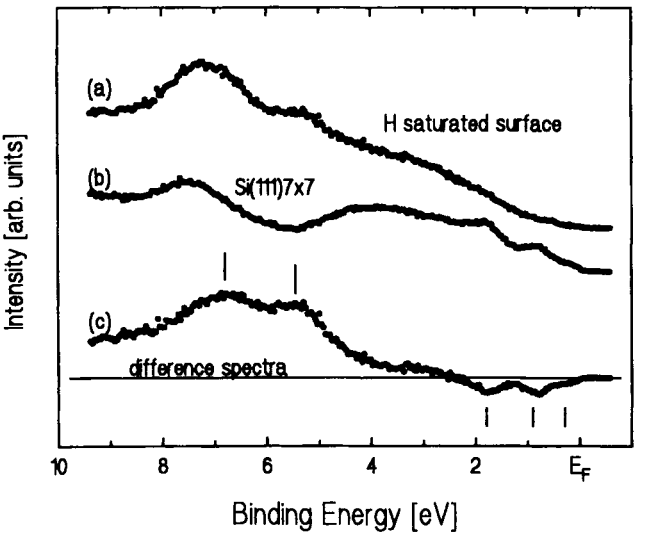


Fig. 12.3. Angle-integrated ultraviolet photoemission spectra of clean Si(111) 7 × 7 and a hydrogen-saturated Si(111):H "7 × 1" surface. The difference spectrum shows the lost surface state emission and the peaks due to Si–H bonds. The spectra have been taken with a photon energy of 21.2 eV.

angle-integrated PES (Himpsel and Fauster, 1984; Uhrberg et al., 1985; Chrost et al., 1995) (see Fig. 12.3) and IPS data (Himpsel and Fauster, 1984; Fauster and Himpsel, 1983). ARUPS studies show that the bands corresponding to $S_1$ and $S_2$ are quite flat, indicating that these features are highly localized in real space and atomiclike, as expected for isolated dangling bonds. STM has identified the spatial location of these surface states (Hamers et al., 1986). The state $S_1$, producing the metallic edge at the Fermi level and with a maximum at −0.3 eV corresponds to a half-filled dangling bond state located at the adatoms that form part of the 7 × 7 reconstruction. The state $S_2$, appearing as a well defined peak at −0.9 eV, is the filled dangling bond state situated on the rest atoms, while $S_3$, the filled surface state at −1.8 eV, is related to the backbonds between the Si adatoms and the three Si atoms directly underneath (Hamers et al., 1986). The intensity of the state $S_1$ is a good test of the quality of the surface reconstruction in Si(111).

Saturation exposure of Si(111) 7 × 7 to atomic hydrogen produces the Si(111):H 7 × 1 structure with a coverage of 1.25 ML (Culbertson et al., 1982). The effect of saturation hydrogenation on the valence band spectrum of Si(111) 7 × 7 is illustrated also in Fig. 12.3. The features associated to the surface states $S_1$, $S_2$ and $S_3$ do not appear in the spectrum of the saturated surface. In fact, the formation of covalent Si–H bonds completely removes the surface states of Si(111) 7 × 7 (Chrost et al., 1995; Ibach and Rowe, 1974; Sakurai and Hagstrum, 1975; Eastman et al., 1979). In the difference spectra, two hydrogen-induced peaks appear at −5.45 and −6.8 eV with respect to the Fermi level. Hydrogen is the simplest adsorbate with only one s-electron. Calculations for the monohydride Si(111):H 1 × 1 surface (Schlüter and Cohen, 1978) have been performed quite long ago and indicate that the state at −5.45 eV is the Si–H bonding state (the corresponding antibonding state ap-

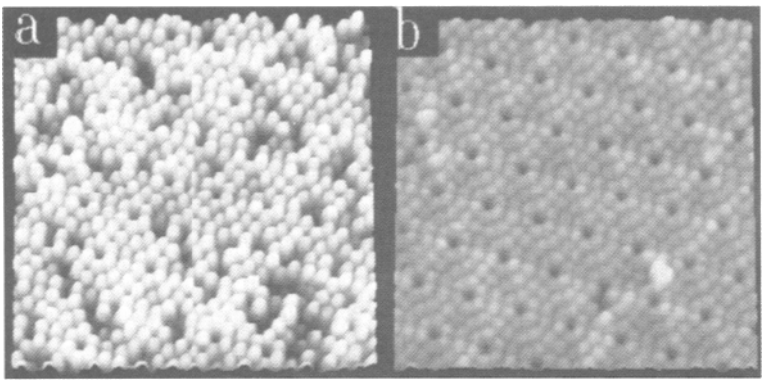


Fig. 12.4. STM topographs of the surface following a low coverage exposure to H atoms. The area is $200 \times 200$ Å$^2$, recorded at $+1$ V (left) and $+3$ V (right). From Boland (1991b).

pears at +3.5 eV, i.e., above the Fermi level). The feature at −6.8 eV corresponds to the bulk Si sp-band emission (at −7.4 eV in the clean crystal), enhanced and shifted to lower binding energy.

The sequence of the hydrogenation reaction can be summarized as follows: the adsorption initiates at the corner-hole dangling bonds, as first shown by infrared reflection spectroscopy (Chabal, 1983), then the dangling bonds of adatoms start to become saturated with hydrogen. The backbonds of the Si atoms are under strong tensile stress and are, thus, also easily attacked by hydrogen. Accordingly, surface states $S_1$ and $S_3$ disappear first from the UPS spectrum. After removal of the Si adatoms, the restatoms are saturated and the $S_2$ states vanish. This sequence of events has been visualized by STM. Figure 12.4 shows STM images recorded after submonolayer exposure to hydrogen (Boland, 1991b). The images show the disappearance of both occupied and empty adatom dangling bonds, as indicated by some adatoms turning dark during exposure (Tokumoto et al., 1990; Sakurai et al., 1990; Sakurai and Hagstrum, 1976; Boland, 1993). It turns out that the Si adatoms remain at their original $T_4$ site for these low hydrogen exposures. Only the dangling bond $S_1$ has been removed from the energy window imaged by the STM due to Si–H bond formation. The "lost" Si adatom reappears in the images at sample bias voltages above 2.2 eV, which image the empty states. The reappearance of the reacted adatoms is due to the broadening of the antibonding Si–H state induced by hybridization with conduction band states.

Figure 12.5 reproduces scanning tunneling spectroscopy data recorded at selected sites on the $7 \times 7$ unit cell before and after hydrogen exposure (Boland,1991b; Sakurai et al., 1990; Sakurai and Hagstrum, 1976). For the clean surface, occupied surface states are visible as peaks for negative sample bias, while empty dangling bonds are detected at positive sample bias. The spectrum obtained over the dark adatoms does not show the filled and empty dangling bonds characteristic of the clean surface. Furthermore, the spectrum recorded over the restatoms (only visible as saddle points in the filled state images) proves that some occupied restatom dangling bonds ($S_2$ state in Fig. 12.3) have been also eliminated at this early stage of the hydrogenation reaction. The empty dangling bonds at 0.5 eV

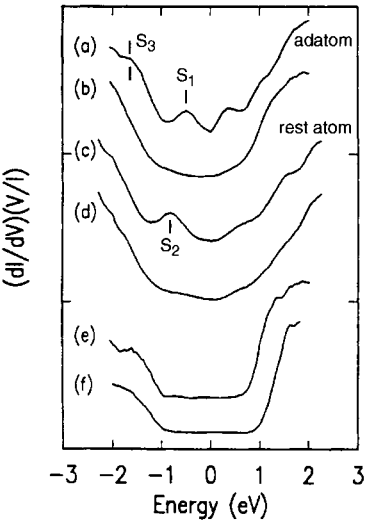


Fig. 12.5. $I$–$V$ curves recorded over specific sites of the surface: (a) unreacted adatom, (b) reacted adatom, (c) unreacted rest-atom, (d) reacted rest-atom. On the saturated surface (e) and (f) were recorded over an isolated adatom and a restlayer atom, respectively. From Boland (1991b).

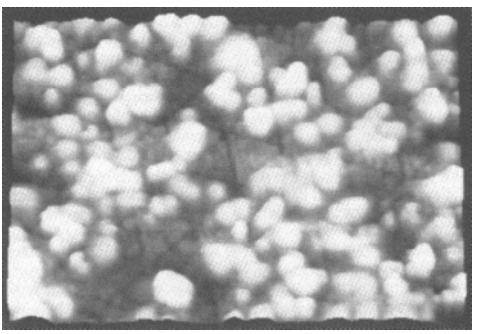

Fig. 12.6. STM topograph of the saturated surface recorded at a sample bias of +2 V. The area shown corresponds to 230 × 130 Å$^2$. From Boland (1991b).

above the Fermi level have been observed to disappear during hydrogenation by means of IPS (Bouzidi et al., 1992) and ELS (Eastman et al., 1979), while the removal of the occupied dangling bonds was shown before by means of UPS (Ibach and Rowe, 1974; Sakurai and Hagstrum, 1975; Eastman et al., 1979). At this stage of the reaction the surface coverage is 0.4 ML and the reaction with the adatoms has led to limited etching of the Si adatoms and binding to the dangling bonds of the next layer.

The room temperature (RT) saturated surface is imaged in Fig. 12.6 (Boland, 1991b). Many adatoms have been removed from their original sites, allowing the underlying (intact) layer of restatoms to be visible. The adatoms have rebonded to form clusters. Some of the

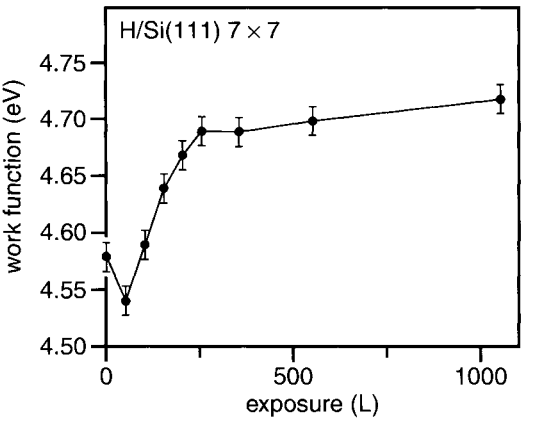


Fig. 12.7. Photoelectric work function changes corresponding to the process of adsorption of H on Si(111)7 × 7. From Chrost et al. (1995).

Si adatoms are etched away from the surface since $SiH_3$ and $SiH_4$ desorption occurs during hydrogen exposure at RT (Boland, 1993). Obviously, the surface is far from an ideally H-terminated Si(111). Thus, detailed comparison with theory is difficult.

The corresponding work function changes are reproduced in Fig. 12.7 (Chrost et al., 1995). The clean Si(111)7 × 7 surface has the Fermi level pinned at the surface and a work function of 4.58 ± 0.01 eV. Exposure to 50 L of hydrogen reduces slightly the work function, while further exposures up to 350 L increase it by 150 meV. Notice that the work function change is not saturated at 350 L exposure. It rather continues with a slow increase up to the largest exposure employed (1100 L). For exposures up to 100 L, no changes are detected in the LEED pattern, which is still 7 × 7. At larger exposures the LEED pattern shows the disappearance of the fractional order spots, except those connecting the 1 × 1 spots. This is referred to as the "7 × 1" or "7 × 7" structure (Sakurai and Hagstrum, 1975). ARUPS measurements indicate that the monohydride phase is formed on the Si(111):H 7 × 1 surface (Karlsson et al., 1990). The evolution of the work function can be understood easily: H is more electronegative than Si. H-induced surface dipoles will then have the negative charge outwards, producing a work function increase. The initial decrease is probably due to the elimination of the band bending.

The thermal desorption process of atomic hydrogen chemisorbed at RT on Si(111) represents an additional test of the capability of UPS to quantify the density of surface states. In effect, STM images prove that an undisturbed 7 × 7 surface is not fully recovered after complete desorption of hydrogen at 750 K, since limited etching of the Si adatom layer leading to $SiH_3$ and $SiH_4$ desorption occurs during hydrogen exposure at RT (Boland, 1993). The effect of annealing the H-saturated RT surface to increasing temperatures is shown in Fig. 12.8 (Boland, 1993). The intensity of the H-related emission at −5.4 eV increases at 520 K before any desorption of hydrogen is detected. This might be related to some reordering of the adlayer. The desorption is noticeable at 650 K (Chrost et al., 1995) where the surface states are detected again and the Si–H peak disappears. Hydrogen

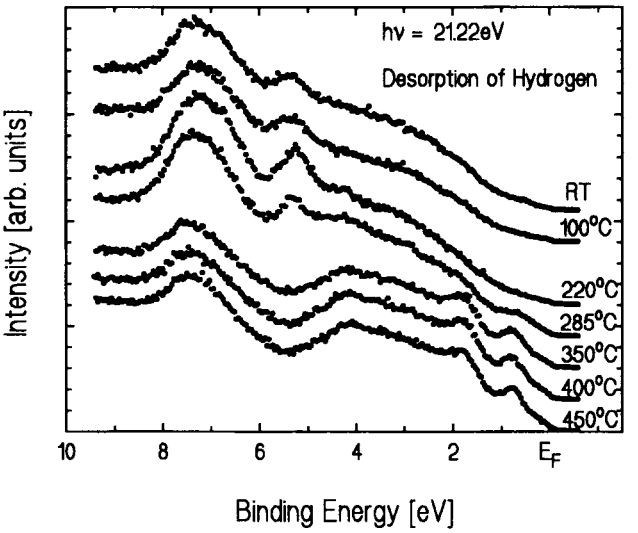


Fig. 12.8. Angle-integrated UPS spectra taken during desorption of hydrogen from the Si(111) surface. Note the reappearance of the surface states above 650 K. The intensity of $S_1$, however, is smaller than in the case of Fig. 12.3.

desorbs completely at 750 K leaving behind a residually disrupted Si(111) 7 × 7 surface, as judged from the reduced intensity of the adatom surface state $S_1$. STM, LEED and UPS show that a perfect 7 × 7 surface is obtained only after annealing to 900 K, which allows for recreation of an ordered layer of Si adatoms by surface diffusion.

### *12.2.2. Adsorption of hydrogen on Si(100)2 × 1*

In contrast to Si(111) 7 × 7, both UPS and STS studies show that the clean Si(100) 2 × 1 surface is semiconducting. The reconstruction consists in tilted Si–Si dimers forming chains on the surface. The STS spectrum of the clean surface reproduced in Fig. 12.9 (Boland, 1991a) shows an occupied state at −0.9 eV and the unoccupied counterpart at 0.5 eV above the Fermi level. The states are the bonding and antibonding combinations derived from the $\pi$ interaction of the dimer dangling bonds.

At low exposures, hydrogen atoms react at RT with the dangling bonds of Si(100) 2 × 1 yielding the 2 × 1 monohydride surface shown schematically in Fig. 12.10, where the dimer structure still exists (Sakurai et al., 1990; Sakurai and Hagstrum, 1976). The dimers, however, are no longer tilted but they become symmetric. This removes the dimer-related surface dipole and then changes the ionization energy of the surface. This is the reason behind the observation illustrated in Fig. 12.11 of a work function decrease during hydrogenation of Si(100) 2 × 1 (Oura et al., 1990; Koke and Mönch, 1980). Because of the larger electronegativity of H (2.2) with respect to Si (1.9), H-induced dipoles will exist with the negative charge outwards. Considering the surface density of dipoles, the work function is expected to increase by +0.8 eV. The reported negative work function change of −0.4 eV reflects the difference between the decrease in the ionization energy (1.14 eV) produced by

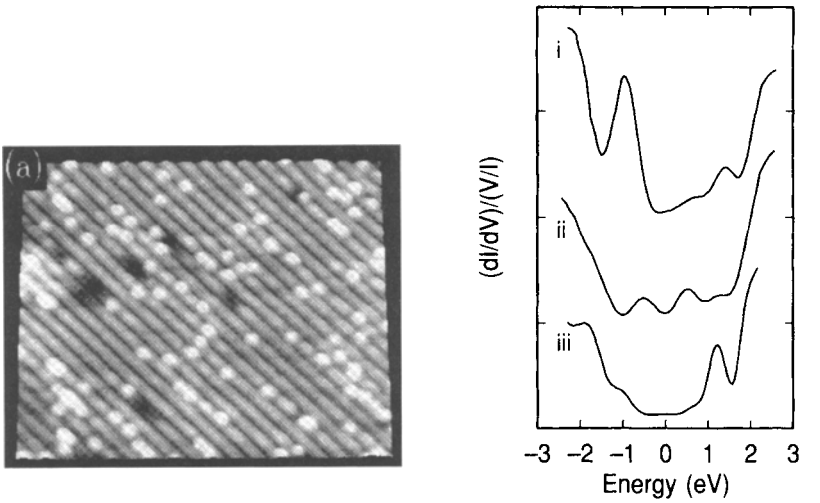


Fig. 12.9. Left panel: Si(100) surface following a submonolayer exposure to atomic hydrogen at 295 K. Right panel: STS spectra recorded at different sites of the Si(100) surface: (i) unreacted dimer site, (ii) bright ball-like site, (iii) dark well-resolved dimer site. From Boland (1991a).

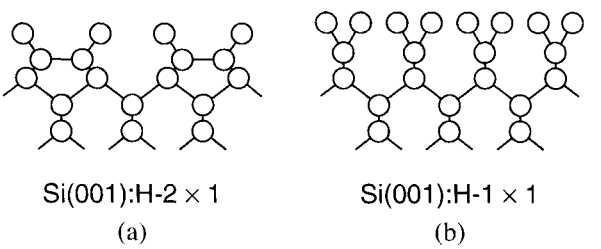


Fig. 12.10. Schematic representation of a monohydride (a) and dihydride (b) Si(100) surfaces.

the symmetrization of the dimers and the increase due to the Si–H surface dipole. A similar observation has been reported for H/GaAs(110), another surface where tilted dimers exist (Koke and Mönch, 1980).

The initial stages of the reaction are illustrated by the STM image of Fig. 12.9. In addition to unreacted dimer rows, bright, ball-like spots and dark dimers are seen. The corresponding STS spectra for the different reacted sites are displayed in Fig. 12.9 also. The bright features reveal two states at +0.5 and −0.5 eV due to unpaired dangling bonds that remain after reaction of the dimer with one hydrogen atom. The dark spots present an empty state at +1.2 eV, assigned to dimers reacted with two H atoms. For larger exposures of hydrogen, the uptake reaches a coverage of 1 ML and the LEED pattern changes to 1 × 1 (Sakurai et al., 1990; Sakurai and Hagstrum, 1976). The LEED analysis shows the surface to be bulk-like. The dimer bonds are broken and the two dangling bonds per surface atom are saturated with hydrogen. The resulting dihydride structure is also depicted in Fig. 12.10.

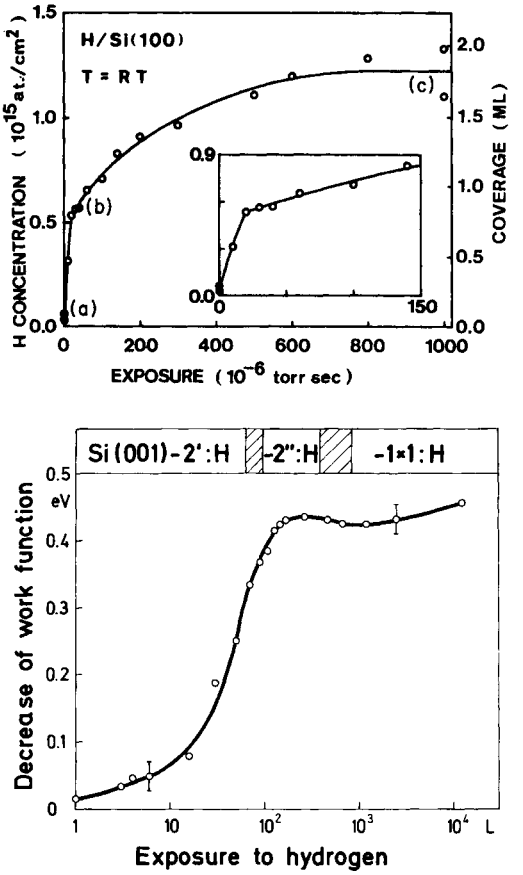


Fig. 12.11. Upper panel: hydrogen concentration (coverage) on a Si(100)2 × 1 surface vs. exposure (from Oura et al., 1990). Lower panel: work function change and LEED patterns vs. exposure to atomic hydrogen (exposure given in equivalent Langmuirs of molecular hydrogen). From Koke and Mönch (1980).

### *12.2.3. Adsorption of hydrogen on III-V semiconductors*

We consider now the adsorption of hydrogen on III-V semiconductors, and in particular on GaAs(110), the best studied example. Cleaved GaAs (110) surfaces are 1 × 1 reconstructed by forming chains of Ga–As dimers tilted away from the horizontal. The empty dangling bonds are localized in the protruding Ga atoms, while the occupied dangling bonds are located on the As atoms. Both kinds of surface states are energetically placed outside the bulk band gap and the bands are flat up to the surface.

In the first interaction step, atomic hydrogen is chemisorbed on both Ga and As atoms (del Pennino et al., 1993), surface acceptors are induced in the bulk band gap and the GaAs(110) surface derelaxes, with final positions close to those of the bulk terminated surface (Ruocco et al., 1995). The occupied As dangling bonds disappear from the UPS spectra, the Ga empty dangling bonds are also saturated during hydrogenation. The Ga–H

and As–H bonding levels are well below the valence band edge and doubly occupied. The antibonding As–H level is the surface acceptor level. The ionization energy decreases by 1.2 eV.

In a second stage, the substrate is dissociated into metallic Ga and $AsH_3$ molecules, and the surface is disordered (Sorba et al., 1990). Thus, the initial adsorption stage does not differ much from the phenomenology of Si surfaces, but in the second stage the Ga–As bonds are broken to a much larger extent than in Si.

In recent years a number of experiments on hydrogen adsorption on GaAs(100) have also been carried out (Pahlke et al., 1996). Atomic hydrogen was expected to modify the surface in a simple way by saturating the dangling bonds, but the interaction turned out to be complex and is not yet fully understood (Kawabe, 1995). Nevertheless, the practical use of H as a surfactant for the growth of GaAs (Pahlke et al., 1996) and InAs on GaAs(100) (Yong et al., 1995) ensures further future work on this system.

## 12.3. Oxidation of silicon surfaces

The formation and properties of the $SiO_2$–Si interface is one of the most investigated subjects in surface science (Engel, 1993). This is because silicon device technology is largely based on the unique ability to fabricate $SiO_2$/Si interfaces with electrically active interface states densities of less than 1 defect per $10^4$–$10^5$ interfacial bonds (Balk, 1988). Due to this reason it has been long desired to control the oxidation process at atomic level. This goal is crucial to obtain oxide layers atomically flat with controlled thickness (Balk, 1988). Many experimental and theoretical works have been devoted to the understanding of the reaction process. For a detailed account on the literature on this subject we refer the reader to Engel (1993). One of the most debated topics are the atomistic processes involved in the initial stages of the reaction. The first step of the reaction is dissociation of the oxygen molecule. This is also the rate limiting step in most models. The existence of a molecular precursor is now established, but it is not yet clear which are the first steps of atomic oxygen chemisorption (Weldon et al., 1997). This issue is now of high interest since the device dimensions have decreased so much that one oxide monolayer represents about 1/3 of the whole gate oxide (Weldon et al., 1997).

A lot of information has been obtained by measuring the valence band of partially oxidized silicon, and comparing it to theoretical calculations (Höfer et al., 1989b; Dujardin et al., 1994). The Si 2p-core level has also provided a lot of information of the oxidation process (Hollinger and Himpsel, 1983; Mascaraque et al., 1997). As shown in Fig. 12.12, Si atoms bonded to one, two, three or four O atoms exhibit Si 2p-core level with binding energy shifts of ~0.95 eV per O atom (Mascaraque et al., 1997). First-principles investigations support this image (Pasquarello et al., 1996).

### *12.3.1. Oxidation of Si(111)7 × 7*

Many studies were devoted in the past to the investigation of the initial stages of oxygen reaction with Si(111)7 × 7, and in particular to the existence of a molecular precursor for the oxidation reaction. Some years ago it was found using high resolution electron energy

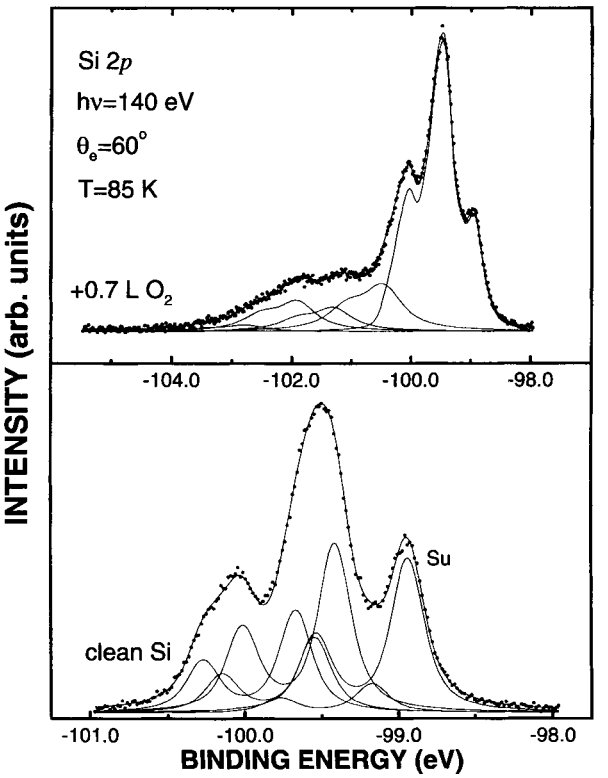


Fig. 12.12. Lower panel: deconvolution of the Si 2p-core level from a clean surface in different components. Upper panel: deconvolution of the Si 2p-core level after exposure to 0.7 L oxygen (from Mascaraque et al., 1997).

loss spectroscopy (HREELS) that at the initial stage of adsorption, most of the oxygen is dissociated, and occupies on-top sites (Si–O) and bridge sites (Si–O–Si) (Edamoto et al., 1985). X-ray photoemission spectroscopy (XPS) results at low temperature have provided evidence for a molecular precursor state (Höfer et al., 1989a, b; Morgen et al., 1989). The negatively charged, superoxide-like, bridging molecule is formed by a process of "harpooning" whereby electrons from the adatom dangling bonds tunnel to the $2\pi^*$ affinity level of the neutral oxygen molecule. Incident molecules probe the surface on a physisorbed precursor until they get trapped by harpooning at sites of high density of occupied states at the Fermi level, i.e., at corner-adatom sites. The molecular chemisorbed species has a lifetime of 14 min at 300 K and 60 min at 150 K. The molecular or atomic nature of adsorbed oxygen is reflected in the peaks appearing in the valence band. For atomic oxygen there is a single major peak in the UPS spectrum due to $\pi$-bonded O $p_x$, $p_y$ at about $-6$ eV. Molecularly chemisorbed oxygen is characterized by two peaks with O $2p_z$ character at $-11$ and $-3.5$ eV (Schubert et al., 1993).

STM images such as displayed in Fig. 12.13 have shown the existence of two different reaction stages, which appeared as "bright" or "dark" sites in the pictures (Avouris, 1990;

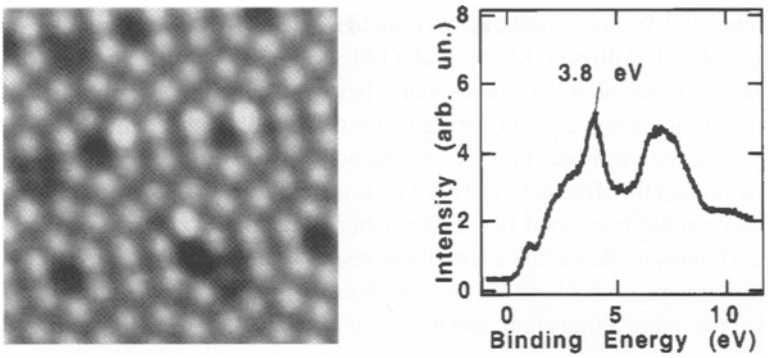


Fig. 12.13. Upper panel: 70 × 70 Å$^2$ STM topograph of a 0.15 L $O_2$ exposed Si(111)7 × 7 surface. Lower panel: UPS spectrum of a 0. 3L exposed Si(111)7 × 7 surface. From Dujardin et al. (1994).

Avouris and Wolkow, 1989; Avouris and Lyo, 1991; Avouris et al., 1991; Neddermeyer, 1996). Detailed tight-binding slab calculations (Schubert et al., 1993; Lyo and Avouris, 1991) identified the initial "bright" site with an oxygen atom inserted in one of the adatom backbonds, while the "dark" site was explained by one oxygen atom on-top and a second one in backbond position. More recently, it has been found that the molecular precursor has a much longer lifetime (Dujardin et al., 1994; Sakamoto et al., 1996), ranging between 400 min and 1500 min, depending on exposure and sample. The STM and valence band photoemission results shown in Fig. 12.13 (Dujardin et al., 1994, 1996) supported that the "bright" STM site corresponds to molecular oxygen, in particular the peak at −3.8 eV below the Fermi energy is a molecular band of O $2p_z$ character and that these molecular sites react very efficiently with further oxygen molecules (and residual $H_2O$) to produce the "dark" site, that was associated to various states of dissociated oxygen (Dujardin et al., 1994, 1996). The shorter lifetimes reported before were attributed to residual $H_2O$, which might explain the well-known effect of even trace amounts of $H_2O$ on accelerating the thermal oxidation of Si by oxygen.

### *12.3.2. Oxidation of Si(100)2 × 1*

High-resolution electron loss spectroscopy (HREELS) (Schaefer and Göpel, 1985) results suggested that oxygen atoms are inserted in the Si backbonds, bridging between the top and second layer Si atoms, followed by further adsorption of oxygen at the same Si atom. Surface-extended X-ray-absorption fine-structure (SEXAFS) (Incoccia et al., 1987) supported the existence of bridging sites between the two top layers, but also between dimers in the top Si layer. STM has been used also to analyze the oxidation process at room temperature (RT) and has provided a wealth of information on the reaction process (Avouris, 1990; Avouris and Wolkow, 1989; Avouris and Lyo, 1991; Avouris et al., 1991; Kliese et al., 1992; Udagawa et al., 1992). However, a conclusive assignment of the observed phenomena to precise adsorption or reaction events has not yet been reached. Again the main change after exposing the surface to oxygen is the appearance of bright spots in the STM pictures. Their identification, however, is controversial. While Avouris (Avouris,

1990; Avouris and Wolkow, 1989; Avouris and Lyo, 1991; Avouris et al., 1991) identified the spots as ejected Si dimers, Kliese et al. (1992) suggested that they are a weakly bound oxygen species, either atomic or molecular. They found also small protrusions at the earliest stages of oxidation, frequently bridging between two neighboring dimer rows. These protrusions induced local buckling. From a theoretical point of view this interface has recently been studied by Miyamoto (1992) who found three metastable sites, the most stable being an oxygen atom inserted in the dimer bond. Other sites found were the on-dimer and the backbond site. At variance with these results, Uchiyama and Tsukada (1997) have proposed that the most stable site is the backbond on the lower dimer atom, followed by backbond of the upper dimer atom, and finally an oxygen atom bridging between the two Si atoms of a dimer. The thermodynamics of the oxygen insertion and migration has been calculated by Stefanov and Raghavachari (1997). They found that the dimer bond is the initial target of O entry and an oxygen-inserted dimer was proposed as the most likely structure at low temperature. At higher temperatures, an asymmetrically oxidized dimer unit with three oxygen atoms inserted into the Si–Si bonds at the same Si was the dominant feature.

### *12.3.3. Oxidation of III-V semiconductors*

The interaction between oxygen and III-V semiconductors has been investigated for many years. We shall review next the most studied substrate, GaAs. The adsorption of oxygen on cleaved GaAs(110) induces surface acceptors and proceeds via a rather slow kinetics. At room temperature, an exposure of 1 mbar is needed to get 1 ML coverage (Ranke and Jacobi, 1979; Kraus et al., 1989). The sticking probabilities are in the range of $10^{-5}$ to $10^{-6}$ (Bartels and Mönch, 1990; Alonso et al., 1985; Ranke et al., 1982), much smaller than on Si(111)$2 \times 1$. Oxygen is adsorbed dissociatively above 60 K, as evidenced by the formation of Ga- and As-oxides. The mechanisms proposed do not differ much from those of silicon surfaces, but the existence of two chemically different atoms provides with two distinct targets for oxygen atoms. $Ga_2O$ is desorbed at temperatures around 800 K (Ranke and Jacobi, 1979; Landgren et al., 1984; Tone et al., 1992). The oxidation process depends critically on the experimental conditions. For instance, the presence of excited oxygen molecules in the gas enhances very much the oxidation rate (Kraus et al., 1989). Illumination or X-ray irradiation of the surface may influence both the oxidation rate and the chemical properties of the oxide (Bartels and Mönch, 1990; Bartels et al., 1983; Hiratani et al., 1990; Taneya et al., 1990; Anderson et al., 1990; Seo et al., 1990). This high sensitivity to the experimental conditions has hindered the elucidation of the oxidation process. In recent studies (Verheij et al., 1995a, b), it was found that oxygen adsorbs in molecular form on GaAs(100) below ~370 K. Annealing above 425 K gave rise to an irreversible disordering process concomitant with the dissociation of the incident oxygen molecules (Verheij, 1997). Adsorption on GaAs(100) above 470 K gives rise to direct oxygen dissociation. It was proposed that oxygen adsorbs initially in molecular form. Then, a reaction of oxygen molecules and surface atoms (stimulated by temperature, photons or electrons) produces defects, where incident oxygen molecules are rapidly dissociated.

## 12.4. Adsorption of other species

### *12.4.1. Adsorption of water*

Studies on $H_2O$ adsorption on silicon and germanium were started in the 60's. Early work has been reviewed by Meyer and Spaarnay (1975). In brief, early gas volumetric studies of $H_2O$ uptake by crushed germanium demonstrated an initial fast adsorption of which the saturation point was labeled monolayer coverage. Later studies showed that it in fact corresponded to somewhat less than one monolayer (Meyer and Spaarnay, 1975). The adsorption was deemed dissociative, and this was supported by the observation of the $H_2$ evolution upon annealing. Henzler and Topler (1973) performed extensive LEED and Auger studies on the adsorption of $H_2O$ on Ge(111) surface. A few percent of saturation coverage removed the LEED superstructures ($2 \times 1$ or $c(2 \times 8)$). Later studies (Sinharov and Henzler, 1975) revealed that for low coverage, only molecular $H_2O$ was desorbed from the $2 \times 1$ surface, compared with $H_2O$ and $H_2$ from the $c(2 \times 8)$ surface, but it could not be concluded from the data whether the mechanism was dissociative or non-dissociative. For high coverages on the $c(2 \times 8)$, the mechanism was dissociative. Fujiwara and co-workers (Fujiwara and Ogata, 1979; Fujiwara, 1981) have interpreted their photoemission, Auger and EELS results in the non-dissociative model (for Si(111)$7 \times 7$), with a single state of adsorption up to 850 °C. The photoemission spectra of the saturated surface were interpreted in terms of the molecular orbitals of $H_2O$. Other authors have pointed out the difficulty to distinguish in UPS molecular orbitals from a mixture of OH and H dissociatively adsorbed (Buchel and Lüth, 1979). STM results (Avouris and Lyo, 1991) are consistent with a dominant dissociative chemisorption on the adatoms. The hydroxyl groups tend to form islands on the surface. Electron energy loss spectroscopy (EELS) (Nishijima et al., 1986; Ibach et al., 1982; Kobayashi et al.,1983; Schäfer et al., 1984), infrared spectroscopy (Chabal and Christmann, 1984), and valence band photoemission (Poncey et al., 1995) have supported also dissociative chemisorption.

We may note that the number of studies devoted to the adsorption of water on high-symmetry surfaces is small. Conflicting results were reported concerning the adsorption on Si(100). HREELS (Ibach et al., 1982) and ellipsometric studies (Meyer and Spaarnay, 1975) conclude that water adsorbs dissociatively on Si(100) at RT, while other UPS studies (Schmeisser, 1984; Schmeisser et al., 1983) favored molecular adsorption at RT. It was claimed that water was monomerically physisorbed at 100 K on Si(100), without hydrogen bonding between water molecules for coverages below 0.5 ML, at variance with adsorption on metallic substrates. The UPS spectra show the emission peaks, attributed to water molecular orbitals ($b_2$, $a_1$, $b_1$). The width of the two peaks at higher binding energies give information on the water–water interaction. The surface state emission is quenched after 0.5 L exposure, and a strong work function decrease takes place ($-0.95$ eV). The conflicting results on the nature of adsorption at RT (or after warming) have been solved in favor of a predominantly dissociative adsorption at RT, forming SiH and SiOH (Thiel and Madey, 1987; Waltenberg and Yates, 1995; Struck et al., 1997; Ranke, 1996). STM images show that the two dangling bonds are occupied simultaneously as the result of each chemisorption event (Andersohn and Köhler, 1993), and that these occupied sites can be resolved into atomic features of different intensities (Chander et al., 1993b). Dissociative

chemisorption represents the favored process from a thermodynamic point of view, but involves an activation energy. Thus, also molecular chemisorption can be observed. Adsorption at low temperature takes place molecularly. Upon warming to RT the spectrum changes to indicate dissociation in Si–H and Si–OH species. Further annealing leaves only O chemisorbed. Weldon et al. (1997) have found that the Si–Si dimer bond is the target for the initial insertion of oxygen into the Si(100)2 × 1 surface, following $H_2O$ exposure and annealing. They reported also the observation of HSi–SiH, HSi–O–SiH, and HSi–O–Si(O)H dimers.

The adsorption of $H_2O$ has been investigated on III-V (110) surfaces as well (Buchel and Lüth, 1979). Two distinct molecular phases were observed. For adsorption at 180 K a physisorption-like state is observed. For room temperature adsorption, a shift in the orbitals suggests that the molecule is chemisorbed with the $b_1$ oxygen lone pair next to the surface, thus causing band bending of the n-GaAs sample. This behavior is analogous to the Si(100) case, the only difference being that further adsorption at RT causes a change in the UPS spectrum so that it looks similar to the spectrum obtained at 180 K. A concomitant shift of the work function by 1 eV was detected, suggesting the following interpretation: a reordering of $H_2O$ molecules takes place, so that the dipole field is directed towards the surface. The two adsorption phases on GaAs are also seen in surface photovoltage measurements. By contrast Ranke et al. (1987) reported that $SH_2$ adsorption on GaAs(110) is molecular. Dudzik et al. (1995) proposed a dissociative model at high coverages.

### *12.4.2. Nitridation*

The nitridation of silicon surfaces has been extensively studied for more than thirty years. The growth of silicon nitride ($SiN_x$ ($x \leqslant 4/3$)) is important from the point of view of electronic applications. Thermal nitridation with $N_2$ gas was primarily used, but it was found that a too high temperature ($\geqslant 1200\,^{\circ}C$) was required to obtain a continuous film (Ito et al., 1978a). More reactive species, such as $NH_3$ (Ito et al., 1978b; Mrarka et al., 1981) and plasma-excited $NH_3$ (Ito et al., 1981) were used instead of $N_2$, resulting in a better quality silicon nitride film. More recently, atomic N has also been employed (Tabe and Yamamoto, 1997). The adsorption of $NH_3$ on Si(111) 7 × 7 results in dissociation of the molecules even at temperatures as low as 100 K (Kubler, 1987; Boszo, 1988), giving rise to $NH_2 + H$. The most reactive sites correspond to the rest atoms of the 7 × 7 reconstruction (Lyo and Avouris, 1991).

Figure 12.14 (Avouris et al., 1990) reproduces UPS spectra during annealing of an adsorbed layer from 90 K to 1000 K. At 350 K, the spectrum shows peaks characteristics of dissociated $NH_3$. In fact, H, $NH_2$, and NH species are detected at the surface. The STM image of Fig. 12.15 (Avouris et al., 1990) shows a real space image of the adsorption process. Most of the adatoms, except the corner hole adatoms at the edge of the 7 × 7 unit cell, have disappeared. Deposition of B on Si(111) 7 × 7 and annealing results in a $\sqrt{3} \times \sqrt{3}R30^{\circ}$ surface which is semiconducting according to UPS and STM (Lyo et al., 1989). In order to reduce the strain energy of the 7 × 7 reconstructed surface, B atoms occupy substitutional sites underneath the Si adatoms in $T_4$ positions (Kaxiras et al., 1990). In this way the transfer of electrons from the Si surface adatoms to the B atom empties the dangling bonds and the surface is semiconducting. Adsorption of $NH_3$ onto this passivated surface results

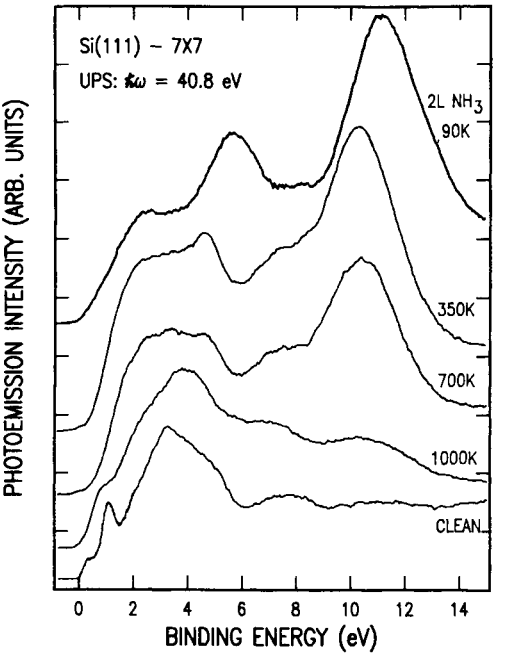


Fig. 12.14. He II valence photoemission of the surfaces produced by the interaction of clean Si(111)7 × 7 with 2 L $NH_3$ at 90 K, followed by annealing at the indicated temperatures. From Avouris et al. (1990).

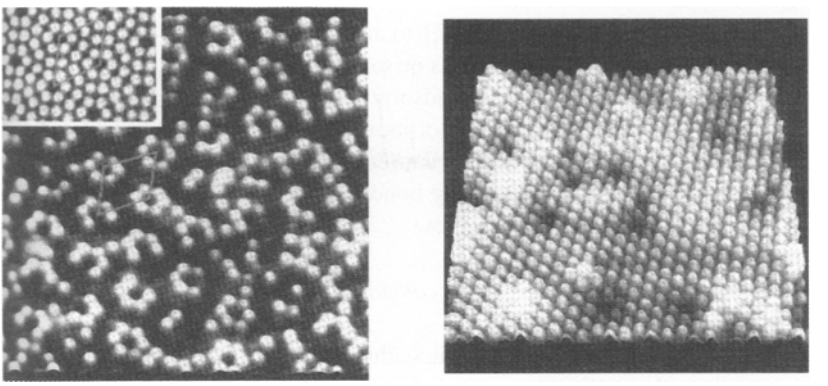

Fig. 12.15. Left: STM topograph of a Si(111)7 × 7 exposed to 5 L of $NH_3$ at 300 K. Inset: topograph of a clean Si surface. Right: STM topograph of a B/Si(111)-$\sqrt{3} \times \sqrt{3}$R30° surface exposed to ~400 L of $NH_3$ at 300 K. From Avouris et al. (1990).

now in bonding of the molecule via donation of the lone pair at N atoms to the empty dangling bond of the surface (Avouris et al., 1990). This is demonstrated in Fig. 12.16 where the UPS spectra show only reversible molecular adsorption. The STM image of Fig. 12.15

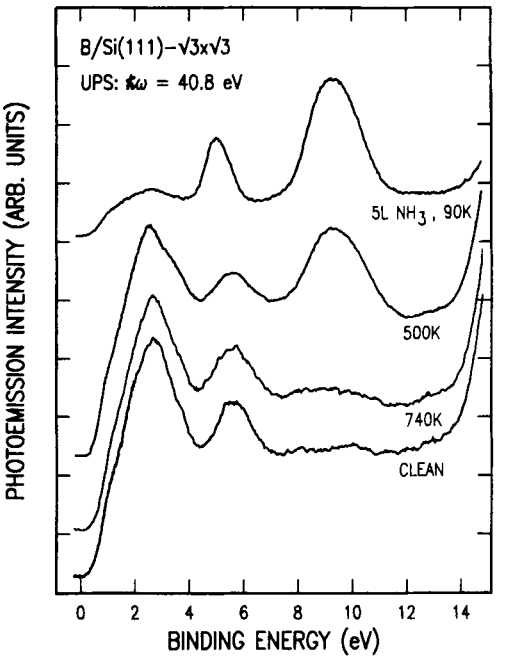


Fig. 12.16. He II valence photoemission of the surfaces produced by the interaction of B/Si(111)-$\sqrt{3} \times \sqrt{3}$R30° with 5 L $NH_3$ at 90 K, followed by annealing at the indicated temperatures. From Avouris et al. (1990).

proves that the surface has not reacted at RT to an exposure of 400 L of $NH_3$. Note that the STM visualizes in this case the Si adatoms on top of the B layer.

At variance with silicon surfaces, the adsorption of ammonia on clean germanium surfaces is molecular (Ranke, 1995). The adsorption properties change with the substrate orientation due to the different orbital distribution in each case. A strong interaction was reported (Ranke, 1995) with the dangling bonds of the Ge(100)2 × 1 dimers, that were found to be the preferential adsorption sites.

### *12.4.3. Adsorption of other elements and compounds*

Due to the growing interest of II-VI semiconductors, the adsorption of S on Si surfaces has been investigated as a first step to a II-VI/Si epitaxy (Kaxiras, 1991; Moriarty et al., 1993b; Metzner et al., 1997). As on metallic substrates, S is adsorbed in a well ordered fashion giving rise to new surface reconstructions (Metzner et al., 1997). It seems that a competition between substrate dangling bond filling and S–S interactions gives rise to a complex chemisorption behavior on Si(111) (Metzner et al., 1997). The adsorption of S on Si(100)2 × 1 has been studied in several works (Moriarty et al., 1993a; Papageorgopoulos and Kamaratos, 1996). While Moriarty et al. (1993a) proposed that the substrate 2 × 1 reconstruction is preserved after S adsorption, Papageorgopoulos and Kamaratos (1996) suggested that the surface reverted to 1 × 1 after adequate dosing.

$SH_2$ adsorption on Si and Ge has been studied only in few cases. Gas volumetric studies on crushed germanium favor dissociative adsorption, while energy loss studies indicate molecular adsorption (in the case of Si(111)7 × 7). Several superstructures have been reported after annealing the $SH_2$ overlayer on Ge(111), and this is in fact a method to deposit the chalcogen on the surface. Adsorption of $SH_2$ on the (110) surfaces of III-V semiconductors has been reviewed recently (Dudzik et al., 1995). Adsorption on InP, GaP and GaAs does not differ much, except for the adsorption temperatures needed. The adsorption of $SH_2$ is dissociative. The surface anion receives a proton, while the S atoms remains bonded to the surface cation.

Several other adsorbates have been investigated due to their importance in the growth of in situ doped Si thin films as well as optoelectronic materials on Si. One relevant example is the adsorption of phosphine $PH_3$, that has been analyzed using STM (Boszo and Avouris, 1991) and molecular beam techniques (Maity et al., 1995). The adsorption on Si(111)7 × 7 affects the 7 × 7 reconstruction, giving rise to a P-substituted 1 × 1 structure. This effect is interesting because the 1 × 1 structure is much more reactive, and gives rise to a kind of "autocatalytic" effect (Maity et al., 1995). The adsorption of many other molecules mainly on Si substrates has been investigated as well. In general, the surface dangling bonds act as reaction active sites, and are actively involved in the chemisorption process. In some cases, Si–Si bonds can be broken (in particular, intra dimer bonds) (Widdra et al., 1995).

## 12.5. Surface passivation

The modification of the dangling bonds present on clean semiconductor surfaces produces important differences in their adsorption behavior. The basic rule explaining the behavior of adsorbates on semiconductor surfaces is that adsorbates saturate dangling bonds. Provided that the adsorbate–substrate bond is strong enough, suitable adsorbates may passivate the surface against reaction with other gases such as oxygen. This simple idea has been used in recent years to produce many different passivation methods. Furthermore, an adequate passivating layer is able to eliminate the surface states completely. Further epitaxial growth would produce layers free of interface states, which would exhibit improved electronic properties (Saiz-Pardo et al., 1996).

An inert Si surface is extremely important as substrate for MBE or CVD applications, since a flat passivated surface may allow the formation of devices with atomically abrupt interfaces of macroscopic dimensions. A complete passivation of Si(111) surfaces can be obtained by dipping the samples in aqueous HF solutions (Higashi et al., 1990; Jakob et al., 1991; Dumas and Chabal, 1991). For basic solutions, the resulting surface is hydrogen-terminated and shows a 1 × 1 LEED pattern of outstanding quality. The surface is strain free and homogeneous over a fairly large lateral scale.

The nature of the 1 × 1 phase can be studied analyzing the Si 2p-core level. In the (7 × 7) reconstruction, the existence of several inequivalent atoms gives rise to many different surface components in the core level, which makes a direct assignment difficult. On the contrary, the line shape observed for the 1 × 1 phase is much simpler (Hricovini et al., 1993; Karlsson et al., 1994), with only two dominant components that can be attributed to surface and bulk atoms. Thus the 1 × 1 surface is simply the bulk terminated surface with

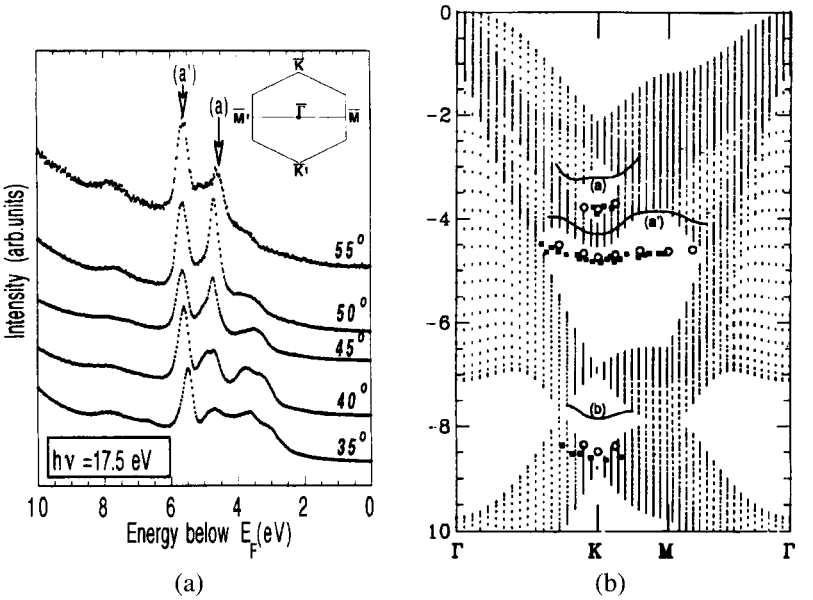


Fig. 12.17. Left: representative photoemission spectra of the Si(111) 1 × 1 surface obtained at $h\nu = 17.5$ eV as a function of polar emission angle. Right: surface bands calculated using the LDA (full lines) and the GW (open circles) methods. The experimental points are represented by solid black squares, and the background shows the projection of the bulk Si(111) bands. The energy scale is in eV and the zero is at the top of the valence band. From Hricovini et al. (1993).

all the dangling bonds saturated by hydrogen atoms. The ionization energy of Si(111):H 1 × 1 is 6.6 eV, i.e., 1.3 eV larger than the value for clean Si(111) 7 × 7. The hydrogen atoms adsorb on top with a bond length of 1.48 Å and because of their small size the mutual depolarization of Si–H dipoles can safely be ignored. The calculated value of the change in the ionization energy amounts to +1.1 eV, close to the experimental one.

Angle-resolved photoemission spectra of such a samples are shown in Fig. 12.17 (Hricovini et al., 1993; Karlsson et al., 1994). The corresponding surface bands are plotted in Fig. 12.17 together with quasiparticle energy dispersions calculated using a self-energy approach based in the GW method described elsewhere in this volume. The agreement between experiment and theory is excellent. Since there are no dangling bonds available, hydrogen-terminated Si surfaces are extremely passive against reaction with molecular oxygen, as proven by the uptake data shown in Fig. 12.18. The initial sticking coefficient is strongly reduced with respect to clean Si(111): irrespective of surface orientation, $10^{25}$ $O_2$ molecules per $cm^2$ result in no oxygen uptake.

Although hydrogen is the most widely used adsorbate for passivation purposes, several other elements may act as passivants as well. Adsorption of chlorine on Si(111) 7 × 7 at 850 K is capable of removing the Si adatoms leaving the underlying restatom layer intact (Villarrubia and Boland, 1989). Figure 12.19 shows the resulting surface. Chlorinated surfaces are basically unreactive towards oxygen exposure, even at 630 °C or towards water adsorption (Wise et al., 1996; Klyachko et al., 1997).

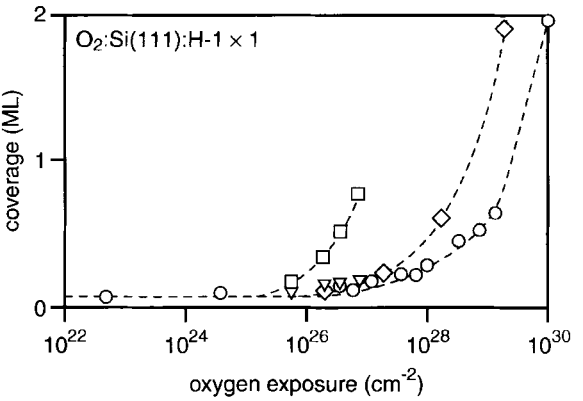


Fig. 12.18. Reactivity vs. molecular oxygen of Si(111)- and Si(100):H-1 × 1 surfaces: ▽ data from Thornton and Williams (1989), □ data from Gräf et al. (1990), ○ data from Stockhausen et al. (1992).

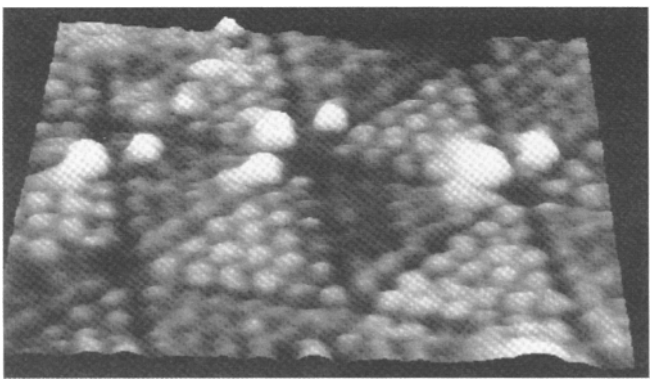

Fig. 12.19. STM topograph of a Si(111) surface after a saturation exposure to chlorine and anneal cycle. The area corresponds to 89 × 96 $Å^2$ at 3 V. From Villarrubia and Boland (1989).

Hydrogen passivated Si surfaces exhibit several interesting properties, based on the lack of surface states pinning the Fermi level and the drastically reduced surface energy. The possibility of growing metallic films on top of these interfaces has been tested recently in several studies. Surface passivation influences the mode of growth, inducing island formation (Nishiyama et al., 1996; Shen et al., 1997; Copel and Tromp, 1994; Murano and Ueda, 1996; Naitoh et al., 1996), or the growth of epitaxial films (Horn-von Hoegen and Golla, 1996; Ohba et al., 1997; Ababou et al., 1995). In principle, the formation of a Schottky barrier without surface state pinning could be studied also by this method. Nevertheless, and depending on the nature of the metal, partial reaction with the substrate can be of importance. Thus, while alkali metals behave in an almost ideal way (Grupp and Taleb-Ibrahimi, 1998a), Au destroys partially the passivating layer (Grupp and Taleb-Ibrahimi, 1998b).

Surface passivation by adsorbates plays a major role in the preparation of surfaces of III-V semiconductors. For instance, good quality GaAs(100) surfaces are usually prepared

by *in situ* MBE growth. In most cases, not much surface analytic equipment is available in MBE chambers. Thus, GaAs is usually passivated using an arsenic cap, that allows even ambient transfer (Resch-Esser et al., 1996).

## 12.6. Adsorption of halogens

### *12.6.1. Introduction*

The chemisorptive properties and electronic structure of halogens on solids have been a subject of interest since the mid-seventies, as a field inserted in the more general goal of understanding the gas-solid reactions, and the formation of solid interfaces (King and Woodruff, 1984). In the case of semiconducting substrates, most of the works have been devoted towards understanding the oxidation reaction, since it plays a crucial role in the determination of the properties of many microelectronics components. Nevertheless, the heterogeneous nature of oxide interfaces (Hollinger and Himpsel, 1983) complicated the task of finding the answers to the fundamental physical questions open: the role played by the detailed surface geometry in the reaction process, the factors determining the oxide growth mode, and the geometric and electronic properties of the grown oxide itself. Thus, halogen atoms (which usually form well-ordered overlayers on semiconductors) appeared as adequate model systems to study the chemisorption of highly electronegative elements on semiconducting substrates. In fact, the nominal monovalency of halogens, and the strong periodic trends expected, make them ideal probes for surface studies. On the other hand, halogen-semiconductor interfaces revealed themselves as a field of great technological interest. For instance, F or Cl adsorption plays a key role in many technologically important processes, such as reactive ion etching and chemical vapor deposition. Good examples are the usual method to produce epitaxial Si layers in gas-phase epitaxy, where silicon is deposited through the destruction of chlorsilanes on the substrate surface, or the selective silicon etch in a plasma reactor (through reaction with $CF_4$ or $NF_3$) (Oehrlein, 1992; Flammt and Donnelly, 1981). The initial lack of interest can be certainly attributed to the corrosive nature of these elements, which may difficult of even prevent some types of studies. During the eighties a large number of fundamental works was devoted to the adsorption of fluorine, chlorine, bromine and iodine on silicon and GaAs substrates, studied as the initial step of the etching process. The nature of these interfaces is also relevant to understand passivated surfaces, a topic which has deserved widespread attention in the last few years. Since halogens are among the most reactive elements of the periodic table, once a semiconducting surface has reacted with a layer of halogens, the surface remains in many cases passivated against reaction with any other element, which obviously opens many ways to novel applications.

The nature of the chemical bonding of the atoms of interest at an interface is governed by the electronic configuration near the surface, and also by the atomic positions of both adatoms and substrate atoms (symmetry and interatomic distances). These two types of properties, geometric and electronic, and deeply related, since changing the position of an adatom changes its chemical bonding, with a corresponding change in electronic configuration, and vice versa. Generally speaking, structural techniques such as LEED (Jona et

al., 1982), SEXAFS (Citrin et al., 1983; Citrin, 1987), XSW (Funke and Materlik, 1987) or more recently STM (Villarrubia and Boland, 1989), are employed to obtain information on the geometric structure of surfaces. In the case of halogen/semiconductor surfaces, these techniques have been applied recently as well, but a significant part of the information was obtained by photoemission (see below), making use of the sensitivity of the electronic cross section of the different orbitals to polarization effects. Thus, halogen/semiconductor interfaces are a nice example of how photoemission can be employed to obtain geometric information, i.e., how deeply electronic and geometric structure are interconnected, a circumstance very often undervalued.

### *12.6.2. Adsorption-site symmetry and polarization effects*

Two high-symmetry sites are possible for a halogen atom to adsorb on a semiconductor of (111) orientation (Schlüter and Cohen, 1978) (see Fig. 12.20): the so-called onefold covalent site (on top) and the threefold ionic site (either $H_3$ or $T_4$). Taking the $z$ axis perpendicular to the surface plane, in the on top site, a bond of $\sigma$ type is formed between the partially filled substrate dangling-bond (belonging to the $sp^3$ hybridization of Si atoms), and the halogen $p_z$ orbital. The bonding splits off the $p_z$ orbital, so that $p_x$ and $p_y$ orbitals behave at first approach as lone-pairs, and do not participate in the chemical bond. In principle, at least two photoemission peaks should be observed, one for the $p_z$ orbital, and one for $p_x$ and $p_y$ orbitals (Schlüter and Cohen, 1978).

On the other hand, in the adsorption geometry of the threefold site, the adatom sits equidistant to three substrate atoms. Thus, three Si dangling bonds (from $sp^3$ hybridization) are involved in the bonding. In this geometry, the overlapping of $p_z$ orbital with the dangling bonds is lesser than in the on top site, and thus the corresponding photoemission peak should appear at smaller binding energy than in the on top case.

In conclusion, we may expect the appearance of two peaks in the photoemission spectra: one corresponding to the $p_z$ orbital and one corresponding to the $p_x$ and $p_y$ orbitals. The appearance of the $p_z$ orbital at a greater (smaller) binding energy would indicate the occupation of the onefold (threefold) site. Given the two peaks, the problem is to assign

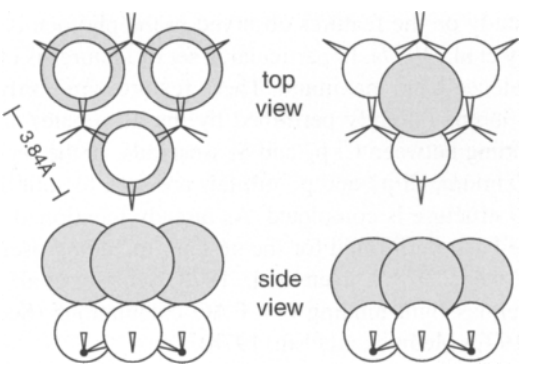


Fig. 12.20. Side and top views of a $T_4$ (right) and on top (left) site on a Si(111) surface.

them to the corresponding orbitals. This can be easily done provided the symmetry of the peaks can be experimentally determined, which is easy to do using polarization selection-rule effects (Plummer and Eberhardt, 1982). When polarized light is used, if it is normally incident to the surface (i.e., its electrical vector is parallel to the surface), then excitation from $p_z$-like orbitals is forbidden (assuming plane-wave final states). Conversely, when the electrical vector has some component perpendicular to the plane of the surface, excitation from $p_z$-like orbitals can occur. For some examples see next section.

### *12.6.3. Group IV + halogens*

The interaction of halogens with group IV semiconductors has been extensively studied because of the technological importance of dry etching processes (Winters and Coburn, 1992), but also because its fundamental interest (Farrel, 1984; Williams, 1984). At room temperature, $F_2$ etches, while the other gasses ($Cl_2$, $Br_2$ and $I_2$) saturate the surface (Villarrubia and Boland, 1989; Citrin, 1987; Funke and Materlik, 1987; Engstrom et al., 1988; Seel and Bagus, 1983, 1984; Schnell et al., 1985; Whitman et al.,1990; Boland and Villarrubia, 1990a, b; Michel et al., 1991). The simplest situation is found when Cl is deposited on the cleaved Si(111)2 × 1 surface. Information coming from different experimental techniques and theoretical calculations exist since several years (Rowe et al., 1977; Larsen et al., 1978; Pandey et al., 1977; Mednick and Lin, 1978; Schlüter et al., 1978). A 1 × 1 structure is formed, with one Cl atom per Si atom on the surface. Using the polarization selection-rule, the adsorption site has been determined by Schlüter et al. (1978). Using s- and p-polarized synchrotron light, they could observe the effects explained above (Fig. 12.21). Two major peaks are observed experimentally in the ultraviolet photoemission. With s-polarized light, the peak at larger binding energy (7–8 eV from the valence band maximum) decreased in intensity compared with p-polarization, the behavior predicted for a one-fold site. The result was further supported by comparing the experimental spectra with theoretical calculations. Angle-resolved studies by Larsen et al. (1978) have further supported this assignment. Keeping the polarization degree fixed, the angular dependencies of the photoemission peak intensity and energy position were measured. The observed dispersions of Cl-induced surface energy bands were in good agreement with calculations based on the one-fold model.

A more detailed study on the features observed in the photoemission spectra can also be performed (Pandey et al., 1977). In particular, a set of features is observed in the region of 2 eV below the valence-band maximum. These features are partly due to p-like back-bonding states of Si atoms (slightly perturbed by the adsorbate), and $\sigma$-bonding states corresponding to bonding between Cl $p_z$ and Si s-orbitals. In the region of 4–6 eV below the valence-band maximum, Cl $p_x$ and $p_y$ orbitals are seen to split due to Cl–Cl interactions, once the 1 × 1 structure is completed. As already mentioned, a variety of theoretical calculations have been performed for the system, including pseudopotential calculations (Schlüter and Cohen, 1978; Larsen et al., 1978; Schlüter et al., 1978), and semiempirical and first-principles tight-binding or LCAO calculations (Seel and Bagus, 1983, 1984; Pandey et al., 1977; Mednick and Lin, 1978).

The adsorption of Cl atoms on Si(111)7 × 7 gives rise to a weakening of the 7 × 7 LEED spots. At saturation coverage, only the 7th order spots nearby the 1st order spots remain (the

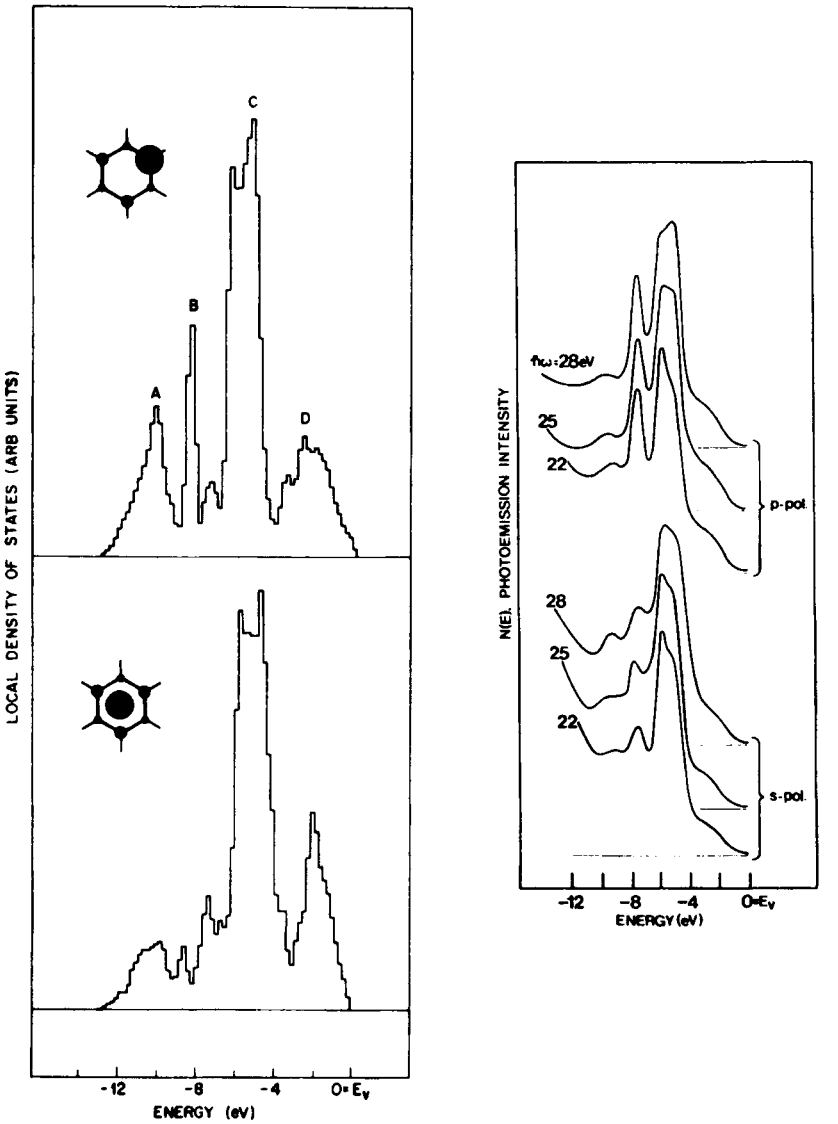


Fig. 12.21. Left: calculated density of states for a Si(111) surface covered with a Cl layer in top and three-fold sites. Right: experimental photoemission spectra of cleaved Si(111)–Cl employing s- and p-polarized photons of energies 22, 25, and 28 eV. From Schlüter et al. (1978).

so-called "7 × 1" pattern, similar to the pattern observed after hydrogen exposure) (Pandey et al., 1977). The pattern can be reproduced by 1 × 1 islands separated by the troughs commonly observed between the 7 × 7 unit cells. This hypothesis has been confirmed by STM results (Fig. 12.19) (Villarrubia and Boland, 1989). The photoemission spectra are

very similar to those obtained in the case of the $2 \times 1$ surface, although the polarization effects are much smaller. When Cl atoms are deposited on Si(111)$7 \times 7$, the reconstruction is destroyed, and significant mass transport takes place, as has been beautifully shown by STM work (Villarrubia and Boland, 1989). The whole process is temperature activated, and annealing or deposition at elevated temperature is necessary to get a completely-covered, well-ordered Si(111)$1 \times 1$ surface, formed by a layer of Cl atoms saturating the dangling bonds of the substrate. Additional information exists coming from LEED (Rowe et al., 1977; Pandey et al., 1977), SEXAFS (Citrin et al., 1983; Citrin, 1987), and theoretical calculations. All these studies have stressed the importance of annealing processes in order to improve the ordering of the halogen atoms on the surface, which might otherwise present different adsorption geometries. STM results have shown the importance of effects of this type (Villarrubia and Boland, 1989). Theoretical studies for these system have favored covalent bonding. The results of Rowe et al. (1977) indicated the possible presence on the surface of other adsorption sites in addition to the on top site. Schnell et al. (1985) have studied the chemisorption of Cl on Si(111)$7 \times 7$ analyzing also the Si 2p-core level. Their work clearly shows the appearance at RT of Si atoms with multiple Cl atoms bonded to them. After annealing at moderate temperatures, only monochloride species are observed. In this case, the polarization selection rules were employed to study the symmetry of the bands formed after a well-ordered Cl layer had been produced. The results favored adsorption at on top sites, in agreement with SEXAFS results. The two-dimensional dispersion $E(\mathbf{k})$ was directly mapped, together with the band dispersion of the chlorine induced states. The main result was the observation of the non-dispersing $\sigma$- and s-bands, in contrast with the $\pi$ bands (formed by the non-bonding Cl bonds). The results were compared with both pseudopotential calculations by Larsen et al. (1978) for this surface and self-consistent LCAO calculations by Batra (1979) for a free Cl layer, to demonstrate the effect of the adsorbate–substrate interaction on the band structure. The agreement with the experiments was reasonably good, although several effects were observed. In particular, the theoretical binding energies are larger than the experimental values. The adsorbate–surface interaction releases the degeneracy at the $\overline{\mathrm{K}}$ point of the free Cl monolayer. Generally speaking, the dispersions observed support a $1 \times 1$ surface Brillouin zone.

Studies involving the Ge(111) surface are less frequent (Michel et al., 1991; Göthelid et al., 1997). In spite of the similarity of both surfaces, Schlüter and Cohen have shown that the adsorption site in this case is threefold ionic (Schlüter and Cohen, 1978). In this case, upon going from p- to s-symmetry, only an asymmetrical narrowing of the main Cl-induced peak was observed, which is compatible with threefold adsorption geometry. At variance with the Si(111) surface, no strongly-localized, $\sigma$-like states were observed in this case.

The adsorption of halogens on Si(100)$2 \times 1$ has also been studied. In these case, several adsorption sites of different symmetry are possible. The surface is formed by pairs (dimers) of Si atoms, with dangling bonds pointing towards a direction at $\sim 54°$ from the surface. Rowe et al. (1977) studied this surface using LEED and photoemission polarization effects. The $2 \times 1$ reconstruction was still present after Cl adsorption. No polarization effects were observed in the angle-integrated peaks, but changes were detected in the angle-resolved normal-emission spectra. To explain the observation, a model including some bonding character for $p_x$- and $p_y$-orbitals, and mixing with $p_z$-orbitals, was successful. The degree

of mixing is consistent with a bonding geometry where Cl–Si bonds are not perpendicular to the surface, suggesting that the bond direction is close to the initial dangling bond direction. This results have been supported by ESDIAD (Yates et al., 1993), XSW (Eteläniemi et al., 1991), electron stimulated desorption (Simpson and Yarmoff, 1996), and SEXAFS (Thornton et al., 1989) measurements. In fact, if a systematic analysis of the bond direction is done, it is easy to observe that the bond angle increases as the halogen atomic size does, supporting that halogen–halogen repulsion is the driving force behind the bond angle tilting. Johansson et al. (1990) have performed extensive angle-resolved photoemission investigations on Cl:Si(100)2 × 1. The interpretation of the observed bands was difficult, even after detailed theoretical calculations (Krüger and Pollmann, 1993; Craig and Smith, 1992).

Halogen atoms (excluding F) can hardly penetrate the surface at room temperature, since the penetration barrier is high (Seel and Bagus, 1983, 1984; Bagus, 1985). This explains the saturation behavior during adsorption. Once saturation is reached, a passivating halogen layer is formed on the surface. Such halogen-covered surfaces have been reported to be stable against exposure to atmospheric pressure (specially for water-free environments) during periods of the order of days. As the protective layer can be removed by annealing, such passivated surfaces are interesting for different applications. In contrast, fluorine atoms are able to penetrate the surface, break silicon-silicon bonds, and etch the surface, even at room temperature. Thus, the electronic structure of F/Si(111) surfaces is less straightforward, because in this case a reaction layer coexists with chemisorbed F atoms. The F/Si(100) interface has been studied by Engstrom et al. (1989), and F/Si(111) by Lo et al. (1993). They found that the reaction process is characterized by four different regimes. In the first step, fluorination and etching of the 7 × 7 reconstruction takes place. In the second step, a quasiequilibrium reaction layer is formed (~1 ML thick), which acts as a passivating layer. The etching reaction proceeds through a third step, consisting in the disordering of the substrate and formation of a deeper reaction layer. Finally, a steady-state etching is reached when the reaction layer is completed. Interestingly, the etching process proceeds through the formation of defects which facilitate the amorphisation of Si. Amorphous Si is much easily etched than crystalline Si (whose Si–Si bonds cannot be broken by F atoms). Core-level X-ray photoelectron spectroscopy provides with a detailed information on how the reaction layer is built up when the Si 2p peak is detected with high surface sensitivity (Lo et al., 1993).

Generally speaking, all halogens behave in a similar way, although the heaviest elements (Br and I) need higher fluxes and/or surface temperatures to attain analogous surface ordering. In this case, mixed layers containing Si atoms bonded to different numbers of halogen atoms are frequently observed by X-ray photoemission spectroscopy (XPS). The valence band presents non-dispersing features, which is generally an indication of worse ordering. Annealing promotes the formation of smoother interfaces, but in the case of heavy halogens the whole process may be prevented because halogen desorption appears at rather low temperatures. Thus, deposition at elevated temperatures is needed in order to achieve well-ordered layers. The role of temperature and surface defects has been investigated using the STM (Chander et al., 1993a; Rioux et al., 1994, 1995).

### *12.6.4. Group III-V compounds + halogens*

The (110) surfaces of III-V compounds, such as GaAs, provide interesting substrates for chemisorption. In the bulk, a (110) layer contains both cations and anions in equal proportions. Therefore, as a first approach, bonding of halogen adatoms to either or both the anion or the cation substrate atoms must be considered. On the basis of electronegativity, one may argue that the cation should be the preferred binding site. Alternatively, steric considerations would possibly favor the anion as the preferred site, since the actual GaAs(110) surface is relaxed in a such a way that the anion atoms are outside, and cation atoms inside the surface. Margaritondo et al. (1979, 1981) have performed detailed studies on the electronic structure of Cl adsorbed on GaAs, GaSb, and InSb. Angle-integrated photoemission results were compared to semiempirical calculations for the local density of states for several adsorption geometries. Three Cl-induced features were observed in the spectra, which approximately resemble those observed in the Si(111) case. Nevertheless, for all III-V surfaces, no significant polarization effects were observed. Margaritondo et al. (1979, 1981) considered several adsorption geometries and surface relaxations, allowing also the bond length to change. The best agreement was found for a reconstructed surface such that the anion atoms are relaxed outwards (as in the clean GaAs case) from the bulk position, and Cl atoms are bonded to the anions, with a bond length contracted by 5–10% with respect to the sum of atomic radii. Both the intensity comparison and the absolute values of the observed binding energies were considered to account for the model. The polarization effects expected for some peaks could not be observed due to the weakness of the emissions under the available experimental conditions. Photoemission results by Troost et al. (1987) suggested that Cl bonds also to Ga atoms. More recent results supported adsorption on both Ga and As atoms (Gu et al., 1992), in agreement with other findings for F (McLean et al., 1989).

Patrin and Weaver's (1993) STM work has recently shown how GaAs is etched by Br and Cl. The authors have found different regimes depending on the halogen flux and the substrate temperature, which in fact parallel the behavior of multilayer growth. In particular, an overlayer of $1 \times 1$ symmetry is formed initially, with halogen features localized within the rectangle formed by four As atoms and on top of As atoms. Halogen atoms tend to coalesce and form chains, and when the flux is increased, multilayer etching takes place. A higher temperature facilitates surface ordering, and etch through step retreat is observed.

## 12.7. Adsorption of $C_{60}$

Since the discovery of fullerenes (Kroto et al., 1985), their outstanding electronic properties have received widespread attention (Hebard et al., 1991; Rosseinsky et al., 1991; Holczer et al., 1991). The growth of well ordered layers of $C_{60}$ on Au(111) (Wilson et al., 1990) made it possible the investigation of mono- and multilayers of $C_{60}$ of high crystalline quality. The interaction of the molecule with the substrate was supposed to be of van der Waals type. Later on, the adsorption of $C_{60}$ was studied on many metals and semiconductors (Si, GaAs, GaSe, GeS). The main conclusion was that there are significant electronic (Modesti et al., 1993) and vibrational changes (Suto et al., 1997) in the molecule as a consequence

of the adsorption process. This suggests that the nature of the bond should be more complex, and thus it was proposed that the bond is ionic (Suto et al., 1997). The formation of well-ordered layers has made it possible the use of angle-resolved photoemission to study the surface electronic bands (Gerstenblum et al., 1994). There is an overall broadening of the $C_{60}$ characteristic structures when adsorbed on a semiconductor. It has been attributed to a symmetry reduction after adsorption that releases in part the levels degeneracy (Gerstenblum et al., 1994). The analysis and understanding of the complex phenomenology of this system is a topic of current research (Rudolf et al., 1997).

## 12.8. Conclusions and outlook

The electronic structure of adsorbate covered semiconductors is a fascinating field of current research. While the most relevant features of simple adsorbates have already been elucidated, the behavior of more complex molecules is investigated nowadays. This research is expected to continue in the future in view of its importance from both applied (microelectronics) and fundamental points of view (self-organization, organic thin films, etc.).

*Acknowledgments*

This work was supported by DGES (Spain) under Grant. No. PB97-0031.

## References

Ababou, Y., R. Masut, A. Yelon and S. Poulin, 1995, Appl. Phys. Lett. **66**, 3352.
Alonso, M., F. Soria and J.L. Sacedón, 1985, J. Vac. Sci. Technol. A **3**, 1598.
Andersohn, L. and U. Köhler, 1993, Surf. Sci. **284**, 77.
Anderson, S.G., T. Komeda, J.M. Seo, C. Capasso, G.D. Waddill, P.J. Benning and J.H. Weaver, 1990, Phys. Rev. B **42**, 5082.
Avouris, P. and I.W. Lyo, 1991, Surf. Sci. **242**, 1.
Avouris, Ph., 1990, J. Phys. Chem. **94**, 2246.
Avouris, Ph., I.W. Lyo and F. Boszo, 1991, J. Vac. Sci. Technol. B **9**, 424.
Avouris, Ph., I.W. Lyo, F. Boszo and E. Kaxiras, 1990, J. Vac. Sci. Technol. A **8**, 3405.
Avouris, Ph. and R. Wolkow, 1989, Phys. Rev. B **39**, 5091.
Bagus, P.S., 1985, Mater. Res. Soc. Symp. Proc. **38**, 179.
Balk, P. (ed.), 1988, The $SiO_2$ System, Vol. 32, Materials Science Monographs. Elsevier, Amsterdam.
Bartels, F. and W. Mönch, 1990, Vacuum **41**, 667.
Bartels, F., L. Surkamp, H.J. Clemerns and W. Mönch, 1983, J. Vac. Sci. Technol. B **1**, 756.
Batra, I.P., 1979, J. Vac. Sci. Technol. **16**, 1359.
Boland, J.J., 1993, Adv. Phys. **42**, 129.
Boland, J.J., 1991a, Phys. Rev. Lett. **67**, 1539.
Boland, J.J., 1991b, Surf. Sci. **244**, 1.
Boland, J.J. and J.S. Villarrubia, 1990a, Phys. Rev. B **41**, 9865.
Boland, J.J. and J.S. Villarrubia, 1990b, Science **248**, 838.
Boszo, F., 1988, Phys. Rev. B **39**, 3937.
Boszo, F. and Ph. Avouris, 1991, Phys. Rev. B **43**, 1847.
Bouzidi, S., F. Coletti, J.M. Debever, P.A. Thiry, P. Dumas and Y.J. Chabal, 1992, Phys. Rev. B **45**, 1187.

Buchel, M. and H. Lüth, 1979, Surf. Sci. **87**, 285.
Chabal, Y.J., 1983, Phys. Rev. Lett. **50**, 1850.
Chabal, Y.J. and S.B. Christman, 1984, Phys. Rev. B. **29**, 6974.
Chander, M., Y.Z. Li, J.C. Patrin and J.H. Weaver, 1993a, Phys. Rev. B **47**, 13035.
Chander, M., Y.Z. Li, J.C. Patrin and J.H. Weaver, 1993b, Phys. Rev. B **48**, 2493.
Chrost, J., J.J. Hinarejos, E.G. Michel and R. Miranda, 1995, Surf. Sci. **330**, 34.
Citrin, P.H., 1987, Surf. Sci. **184**, 109.
Citrin, P.H., J.E. Rowe and P. Eisenberger, 1983, Phys. Rev. **28**, 2299.
Copel, M. and R. Tromp, 1994, Appl. Phys. Lett. **65**, 3102.
Craig, B.I. and P.V. Smith, 1992, Surf. Sci. **262**, 235.
Culbertson, R.J., L.E. Feldman, P.J. Silverman and R. Haight, 1982, J. Vac. Sci. Technol. **20**, 868.
del Pennino, U., C. Mariani, A. Amoddeo, R. Biaggi, F. Proix and C. Sebenne, 1993, J. Phys. Cond. Matt. **5**, 6613.
Dudzik, E., C. Müller, I.T. McGovern, D.R. Lloyd, A. Patchet, D.R.T. Zahn, T. Johal and R. McGrath, 1995, Surf. Sci. **344**, 1.
Dujardin, G., G. Comtet, L. Hellner, T. Hirayama, M. Rose, L. Philippe and M.J. Besnard-Ramage, 1994, Phys. Rev. Lett. **73**, 1727.
Dujardin, G., A. Mayne, G. Comtet, L. Hellner, M. Jamet, E. Le Goff and P. Millet, 1996, Phys. Rev. Lett. **76**, 3782.
Dumas, P. and Y.J. Chabal, 1991, Chem. Phys. Lett. **181**, 537.
Eastman, D.E., F.J. Himpsel, J.A. Knapp and K.C. Pandey, 1979, in: IOP Conf. Proc. No. 43. Institute of Physics, London, p. 1059.
Edamoto, K., H. Kobayashi, M. Onchi and M. Nishijima, 1985, J. Chem. Phys. **83**, 428.
Engel, T., 1993, Surf. Sci. Rep. **18**, 91; and references therein.
Engstrom, J.R., M.M. Nelson and T. Engel, 1988, Phys. Rev. B **37**, 6563.
Engstrom, J.R., M.M. Nelson and T. Engel, 1989, Surf. Sci. **215**, 437.
Eteläniemi, V., E.G. Michel and G. Materlik, 1991, Surf. Sci. **251/252**, 483.
Farrell, H.H., 1984, in: The Chemical Physics of Solid Surfaces and Heterogeneuos Catalysis, eds. D.A. King and D.P. Woodruff. Elsevier, Amsterdam.
Fauster, Th. and F.J. Himpsel, 1983, J. Vac. Sci. Technol. A **1**, 1111.
Flammt, D.L. and V.M. Donnelly, 1981, Plasma Chem. Plasma Proc. **1**, 317.
Fujiwara, K., 1981, J. Chem Phys. **75**, 5172; Surf. Sci. **108**, 14.
Fujiwara, K. and H. Ogata, 1979, Surf. Sci. **72**, 1200.
Funke, P. and G. Materlik, 1987, Surf. Sci. **188**, 378.
Gerstenblum, G. et al., 1994, Phys. Rev. B **50**, 11981.
Göthelid, M., G. Lelay, C. Wigren, M. Björqvist and U.O. Karlsson, 1997, Surf. Sci. **371**, 264.
Gräf, D., M. Gruncner and R. Schulz, 1990, J. Appl. Phys. **68**, S155.
Grupp, C. and A. Taleb-Ibrahimi, 1998a, J. Vac. Sci. Technol. A **16**, 1.
Grupp, C. and A. Taleb-Ibrahimi, 1998b, Phys. Rev. B **57**, 6258.
Gu, C., Y. Chen, T.R. Ohno and J.H. Weaver, 1992, Phys. Rev. B **46**, 10197.
Hamers, R.J., J.E. Demuth and R.M. Tromp, 1986, Phys. Rev. Lett. **56**, 1972.
Hebard, A.F. et al., 1991, Nature **350**, 600.
Henzler, M. and J. Topler, 1973, Surf. Sci. **40**, 388.
Higashi, G.S. et al., 1990, Appl. Phys. Lett. **56**, 656.
Himpsel, F.J., 1983, Adv. Phys. **32**, 1.
Himpsel, F.J., 1990, Surf. Sci. Rep. **12**, 1.
Himpsel, F.J. and Th. Fauster, 1984, J. Vac. Sci. Technol. A **2**, 815.
Hiratani, Y., Y. Ohki, Y. Sugimoto, K. Akita, M. Taneya and H. Hidaka, 1990, Jpn. J. Appl. Phys. **29**, L1360.
Höfer, U., P. Morgen and W. Wurth, 1989a, Phys. Rev. B **40**, 1130.
Höfer, U., A. Puschmann, D. Coulmann and E. Umbach, 1989b, Surf. Sci. **211**, 948.
Holczer, K. et al., 1991, Science **252**, 222.
Hollinger, G. and F.J. Himpsel, 1983, J. Vac. Sci. Technol. **1**, 640.
Horn-von Hoegen, M. and A. Golla, 1996, Phys. Rev. Lett. **76**, 2953.

Hricovini, K. et al., 1993, Phys. Rev. Lett. **70**, 1992.
Hüfner, S., 1996, Photoelectron Spectroscopy. Springer.
Ibach, H. and J.E. Rowe, 1974, Surf. Sci. **43**, 481.
Ibach, H., H. Wagner and D. Bruchman, 1982, Solid State Commun. **42**, 457.
Incoccia, L., A. Balerna, S. Cramm, C. Kunz, F. Senf and I. Storjohann, 1987, Surf. Sci. **189/190**, 453.
Ito, T., S. Hijiya, T. Nozaki, H. Arakawa, M. Shinoda and Y. Fukukawa, 1978a, J. Electrochem. Soc. **125**, 449.
Ito, T., T. Nozaki, H. Arakawa and M. Shinoda, 1978b, Appl. Phys. Lett. **32**, 330.
Ito, T., I. Kato, T. Nozaki, T. Nakamura and H. Ishikawa, 1981, Appl. Phys. Lett. **38**, 370.
Jakob, P. et al., 1991, Appl. Phys. Lett. **59**, 2968.
Johansson, L.S.O., R.I.G. Uhrberg, R. Linsday, P.C. Wincott and G. Thornton, 1990, Phys. Rev. B **42**, 9543.
Jona, F., J.A. Strozier, Jr. and W.S. Yang, 1982, Rep. Prog. Phys. **45**, 527.
Karlsson, C.J., E. Landemark, L.S.O. Johansson, U.O. Karlsson and R.I.G. Uhrberg, 1990, Phys. Rev. B **41**, 1521.
Karlsson, C.J., F. Owman, E. Landemark, Y.C. Chao, P. Mårtensson and R.I.G. Uhrberg, 1994, Phys. Rev. Lett. **72**, 4145.
Kawabe, M., 1995, J. Crystal Growth **150**, 370.
Kaxiras, E., 1991, Phys. Rev. B **43**, 6824.
Kaxiras, E., K.C. Pandey, F.J. Himpsel and R.M. Tromp, 1990, Phys. Rev. B **4**, 1262.
King, D.A. and D.P. Woodruff (eds.), 1984, The Chemical Physics of Solid Surfaces and Heterogeneuos Catalysis. Elsevier, Amsterdam.
Kliese, R., B. Röttger, D. Bast and H. Neddermeyer, 1992, Ultramicroscopy **42–44**, 824.
Klyachko, D.V., P. Rowntree and L. Sanche, 1997, Surf. Sci. **389**, 29.
Kobayashi, K., T. Kubota, M. Onchi and M. Nishijima, 1983, Phys. Lett. A **95**, 345.
Koke, P. and W. Mönch, 1980, Solid State Commun. **36**, 1007.
Kraus, P., W. Nunes Rodrigues and W. Mönch, 1989, Surf. Sci. **219**, 107.
Kroto, H., J.R. Heath, S.C. O'Brien, R.F. Curl and R.E. Smalley, 1985, Nature **318**, 162.
Krüger, P. and J. Pollmann, 1993, Phys. Rev. B **47**, 1898.
Kubler, L., 1987, Surf. Sci. **183**, 503.
Landgren, G., R. Ludeke, Y. Jugnet, J.F. Morar and F.J. Himpsel, 1984, J. Vac. Sci. Technol. B **2**, 351.
Larsen, P.K., N.V. Smith, M. Schlüter, H.H. Farrell, K.M. Ho and M.L. Cohen, 1978, Phys. Rev. B **17**, 2612.
Lo, C.W., D.K. Shuh, V. Chakarian, T.D. Durbin, P.R. Varekamp and J.A. Yarmoff, 1993, Phys. Rev. B **47**, 15648.
Lyo, I.W. and P. Avouris, 1991, Science **253**, 173.
Lyo, I.W., E. Kaxiras and Ph. Avouris, 1989, Phys. Rev. Lett. **63**, 1261.
Maity, N., L.Q. Xia, S.E. Roadman and J.R. Engstrom, 1995, Surf. Sci. **344**, L1201.
Margaritondo, G., J.E. Rowe, C.M. Bertoni, C. Calandra and F. Manghi, 1979, Phys. Rev. B **20**, 1538.
Margaritondo, G., J.E. Rowe, C.M. Bertoni, C. Calandra and F. Manghi, 1981, Phys. Rev. B **23**, 509.
Mascaraque, A., C. Ottaviani, M. Capozi, M. Pedio and E.G. Michel, 1997, Surf. Sci. **377–379**, 650.
McLean, A.B., L.J. Terminello and F.R. McFeely, 1989, Phys. Rev. B **40**, 11778.
Mednick, K. and C.C. Lin, 1978, Phys. Rev. B **17**, 4807.
Metzner, H., Th. Hahn and J.H. Bremer, 1997, Surf. Sci. **377–379**, 71.
Meyer, F. and M.J. Spaarnay, 1975, in: Surface Physics of Phosphors and Semiconductors, eds. C.G. Scott and C.E. Reed. Academic Press, London.
Michel, E.G., Th. Pauly, V. Eteläniemi and G. Materlik, 1991, Surf. Sci. **241**, 111.
Miyamoto, Y., 1992, Phys. Rev. B **46**, 12473.
Modesti, S., S. Cesarini and P. Rudolf, 1993, Phys. Rev. Lett. **71**, 2469.
Mönch, W., 1990, Rep. Prog. Phys. **53**, 221.
Morgen, P., U. Höfer, W. Wurth and E. Umbach, 1989, Phys. Rev. B **39**, 3270.
Moriarty, P., L. Koenders and G. Hughes, 1993a, Phys. Rev. B **47**, 15950.
Moriarty, P., L. Koenders, G. Hughes and O. Jusko, 1993b, Phys. Rev. B **47**, 15950.
Mrarka, S.P., C.C. Chang and A.C. Adams, 1981, J. Electrochem. Soc. **126**, 370.
Murano, K. and K. Ueda, 1996, Surf. Sci. **357–358**, 910.
Naitoh, M., A. Watababe and S. Nishigaki, 1996, Surf. Sci. **357–358**, 140.
Neddermeyer, H., 1996, Rep. Prog. Phys. **59**, 701; and references therein.
Nishijima, N., K. Edamoto, Y. Kubota, S. Tanaka and M. Onchi, 1986, J. Chem. Phys. **84**, 6458.

Nishiyama, A. et al., 1996, Surf. Sci. **350**, 229.
Oehrlein, G.S., 1992, IBM J. Res. Dev. **36**, 140.
Ohba, Y. et al., 1997, Appl. Surf. Sci. **113**, 448.
Oura, K., J. Yamane, K. Umezawa, M. Naitoh, F. Shoji and T. Hanawa, 1990, Phys. Rev. B **41**, 1200.
Pahlke, D., M. Arens, N. Esser, D.T. Wang and W. Richter, 1996, Surf. Sci. **352–354**, 66.
Pandey, K.C., T. Sakurai and H.D. Hagstrum, 1977, Phys. Rev. B **16**, 3648.
Papageorgopoulos, A. and M. Kamaratos, 1996, Surf. Sci. **352–354**, 364.
Pasquarello, A., M.S. Hybertsen and R. Car, 1996, Phys. Rev. B **53**, 10942.
Patrin, J.C. and J.H. Weaver, 1993, Phys. Rev. **48**, 17913.
Plummer, E.W. and W. Eberhardt, 1982, Adv. Chem. Phys. **49**, 533.
Poncey, C., F. Rochet, G. Dufour, H. Roulet, F. Sirotti and G. Panaccione, 1995, Surf. Sci. **338**, 43.
Pretzer, D.D. and H.D. Hagstrum, 1966, Surf. Sci. **4**, 265.
Ranke, W., 1995, Surf. Sci. **342**, 281; and references therein.
Ranke, W., 1996, Surf. Sci. **369**, 137.
Ranke, W. and K. Jacobi, 1979, Surf. Sci. **81**, 504.
Ranke, W., H.J. Kuhr and J. Finster, 1987, Surf. Sci. **192**, 81.
Ranke, W., Y.R. Xing and G.D. Shen, 1982, Surf. Sci. **120**, 67.
Resch-Esser, U., N. Esser, D.T. Wang, M. Kuball, J. Zegenhagen, B.O. Fimland and W. Richter, 1996, Surf. Sci. **352–354**, 71.
Rioux, D., R.J. Pechman, M. Chander and J.H. Weaver, 1994, Phys. Rev. B **50**, 4430.
Rioux, D., F. Stepniak, R.J. Pechman and J.H. Weaver, 1995, Phys. Rev. B **51**, 10981.
Rosseinsky, M.J. et al., 1991, Phys. Rev. Lett. **66**, 2830.
Rowe, J.E., G. Margaritondo and S.B. Christman, 1977, Phys. Rev. B **16**, 1581.
Rudolf, P., G. Gerstenblum and R. Caudano, 1997, J. Phys. IV France **7**, C6-137.
Ruocco, A., M. Biagini, A. di Bona, N. Gambacorti, S. Valeri and S. Nannarone, 1995, Phys. Rev. B **51**, 2399.
Saiz-Pardo, R., R. Rincon, P.L. Andres and F. Flores, 1996, Appl. Surf. Sci. **92**, 362.
Sakamoto, K., S. Suto and W. Uchida, 1996, Surf. Sci. **357–358**, 514.
Sakurai, T. and H.D. Hagstrum, 1975, Phys. Rev. B **12**, 5349.
Sakurai, T. and H.D. Hagstrum, 1976, Phys. Rev. B **14**, 1539.
Sakurai, T. et al., 1990, J. Vac. Sci. Technol. A **8**, 259.
Schäfer, J.A. and W. Göpel, 1985, Surf. Sci. **155**, 535.
Schäfer, J.A., F. Stucki, D.J. Frankel, G.J. Lapeyre and W. Göpel, 1984, J. Vac. Sci. Technol. B **2**, 359.
Schlier, R.E. and H.E. Farnsworth, 1959, J. Phys. Chem. **30**, 917.
Schlüter, M. and M.L. Cohen, 1978, Phys. Rev. B **17**, 716.
Schlüter, M., J.E. Rowe, G. Margaritondo, K.M. Ho and M.L. Cohen, 1978, Phys. Rev. Lett. **37**, 1632.
Schmeisser, D., 1984, Surf. Sci. **137**, 197.
Schmeisser, D., F.J. Himpsel and G. Hollinger, 1983, Phys. Rev. B **27**, 7813.
Schnell, R.D., D. Rieger, A. Bogen, F.J. Himpsel, K. Wandelt and W. Steinmann, 1985, Phys. Rev. B **32**, 8057.
Schubert, B., P. Avouris and R. Hoffmann, 1993, J. Chem. Phys. **98**, 7593; **98**, 7606.
Seel, M. and P.S. Bagus, 1983, Phys. Rev. B **28**, 2023.
Seel, M. and P.S. Bagus, 1984, Phys. Rev. B **29**, 1070.
Seo, J.M., S.G. Anderson, T. Komeda, C. Capasso and J.H. Weaver, 1990, Phys. Rev. B **42**, 5082.
Shen, T.C., C. Wang and J. Tucker, 1997, Phys. Rev. Lett. **78**, 1271.
Simpson, W.C. and J.A. Yarmoff, 1996, Surf. Sci. **359**, 135.
Sinharov, S. and M. Henzler, 1975, Surf. Sci. **51**, 75.
Sorba, L., M. Pedio, S. Nannarone, S. Chang, A. Raisanen, A. Wall, P. Philip and A. Franciosi, 1990, Phys. Rev. B **41**, 1100.
Stefanov, B.B. and K. Ragavachari, 1997, Surf. Sci. **389**, L1159-L1164.
Stockhausen, A., T.U. Kampen and W. Mönch, 1992, Appl. Surf. Sci. **56–58**, 795.
Stroscio, J.A. and W.J. Kaiser (eds.), 1993, Methods of Experimental Physics, Vol. 27, Scanning Tunneling Microscopy. Academic Press, Boston.
Struck, L.M., J. Eng, Jr, B.E. Bent, G.W. Flynn, Y.J. Chabal, S.B. Chrstman, E.E. Chaban, K. Raghavachari, G.P. Williams, K. Radermacher and S. Mantl, 1997, Surf. Sci. **380**, 444.

Suto, S., K. Sakamoto and T. Wakita, 1997, Phys. Rev. B **56**, 7439.
Tabe, M. and T. Yamamoto, 1997, Surf. Sci. **376**, 99.
Takayanagi, K., Y. Tanishiro, M. Takahashi and S. Takahashi, 1985, J. Vac. Sci. Technol. A **3**, 1502.
Taneya, M., Y. Sugimoto, H. Hidaka and K. Akita, 1990, J. Appl. Phys. **67**, 4297.
Thiel, P.A. and T.E. Madey, 1987, Surf. Sci. Rep. **7**, 211.
Thornton, J.M.C. and R.H. Williams, 1989, Semicond. Sci. Technol. **4**, 847.
Thornton, G., P.L. Wincott, R. McGrath, I.T. McGovern, F.M. Quinn, D. Normn and D.D. Vvedensky, 1989, Surf. Sci. **211/212**, 959.
Tokumoto, H. et al., 1990, J. Vac. Sci. Technol. A **8**, 255.
Tone, K., M. Yamada, Y. Ide and Y. Katayama, 1992, Jpn. J. Appl. Phys. **31**, L721.
Troost, D., L. Koenders, L.Y. Fan and W. Mönch, 1987, J. Vac. Sci. Technol. B **5**, 1119.
Uchiyama, T. and M. Tsukada, 1997, Phys. Rev. B **55**, 9356.
Udagawa, M. et al., 1992, Ultramicroscopy **42–44**, 838.
Uhrberg, R.I.G., G.V. Hansson, J.M. Nicholls, P.E.S. Persson and S.A. Flodstrom, 1985, Phys. Rev. B **31**, 3805.
Vazquez de Parga, A.L., 1992, Ph.D. thesis, Universidad Autónoma de Madrid, Spain.
Verheij, L.K., 1997, Surf. Sci. **387**, 160.
Verheij, L.K., M.K. Freitag and F. Wiegerhaus, 1995a, Surf. Sci. **334**, 105.
Verheij, L.K., M.K. Freitag and F. Wiegerhaus, 1995b, Surf. Sci. **342**, 47.
Villarrubia, J.S. and J. Boland, 1989, Phys. Rev. Lett. **63**, 306.
Waltenberg, H.N. and J.T. Yates, Jr., 1995, Chem. Rev. **95**, 1589.
Weldon, M.K., B.B. Stefanov, K. Raghavachari and Y.J. Chabal, 1997, Phys. Rev. Lett. **79**, 2851.
Whitman, L.J., S.A. Joyce, J.A. Yarmoff, F.R. McFeely and L. Terminello, 1990, Surf. Sci. **232**, 297.
Widdra, W. et al., 1995, Phys. Rev. Lett. **74**, 2074.
Williams, R.H., G.P. Srivastava and I.T. McGovern, 1980, Rep. Prog. Phys. **43**, 1357.
Williams, R.H., 1984, in: The Chemical Physics of Solid Surfaces and Heterogeneuos Catalysis, eds. D.A. King and D.P. Woodruff. Elsevier, Amsterdam.
Wilson, R.J. et al., 1990, Nature **348**, 621.
Winters, H.F. and J.W. Coburn, 1992, Surf. Sci. Rep. **14**, 161; and references therein.
Wise, M.L., O. Sneh, L.A. Okada and S.M. George, 1996, Surf. Sci. **364**, 367.
Yates, J.T., Jr., C.C. Cheng, Q. Gao and W.J. Choyke, 1993, Surf. Sci. Rep. **19**, 79.
Yong, J.C., Y. Okada and M. Kawabe, 1995, J. Crystal Growth **150**, 497.

This Page Intentionally Left Blank

CHAPTER 13

# Some Properties of Metal Overlayers on Metal Substrates

S.-Å. LINDGREN and L. WALLDÉN

*Physics Department*
*Chalmers University of Technology*
*Göteborg, Sweden*

*© 2000 Elsevier Science B.V.*
*All rights reserved*

*Handbook of Surface Science*
*Volume 2, edited by K. Horn and M. Scheffler*

# Contents


13.1. Introduction . . . . . 901
13.2. Vibrations . . . . . 903
13.2.1. Submonolayers . . . . . 903
13.2.2. Multilayers . . . . . 907
13.3. Electrons . . . . . 910
13.3.1. Surface states . . . . . 910
13.3.1.1. Surface states on clean metals . . . . . 910
13.3.1.2. Metal adsorption induced shifts of surface states . . . . . 912
13.3.2. Quantum well states for monolayers . . . . . 914
13.3.2.1. The proper work function . . . . . 921
13.3.2.2. Electronic structure of the overlayer . . . . . 923
13.3.2.3. Resonances in monolayers . . . . . 924
13.3.3. Quantum well states in multilayers . . . . . 925
13.3.3.1. Oscillatory thickness dependence . . . . . 927
13.3.3.2. Bulk band dispersion . . . . . 929
13.3.3.3. Emission intensities . . . . . 935
13.3.3.4. Spin-polarized quantum well states . . . . . 938
13.3.4. Oscillatory second harmonic generation . . . . . 940
13.3.5. Core level binding energies . . . . . 942
13.4. Concluding remarks . . . . . 946
References . . . . . 947

## 13.1. Introduction

The present interest in metal overlayers on metal substrates is due to their unique properties some of which are of practical importance. From a fundamental point of view the interest is motivated by the fact that there are well behaved systems which allow the thickness dependence of physical properties to be examined in a layer by atomic layer fashion for thicknesses ranging from one atomic layer. An important part of such work is the characterization of the structure as well as the electronic and vibrational excitations. As far as electronic and vibrational states are concerned the main difference between an extended solid and a thin film is that the confinement results in the break-up of the quasicontinuum of wave numbers allowed for the thick sample into a discrete set of values. For metals the study of quantum well type electronic states has developed slowly from the early observations by Jaklevic et al. (1971, 1975). They observed tunneling into such states in a thin metal film electrode of a metal/insulator/metal sandwich. However, regarding the effort and rate of development semiconductors have been in focus as quantum well structures due to the obvious technical applications of the their properties (Esaki, 1992).

At present the potential use of recently observed magnetic properties of metal multilayers for the development of components for the information industry provides strong stimulus for further work (Falicov, 1992, and references therein). Thin films with the quality needed for quantum well states to be observed are of interest for the study of phenomena involving short spatial periods such as charge or spin density waves. These waves and in particular the spin density waves are of immediate interest for understanding some of the magnetic properties of metal film structures such as the periodic change with Cu film thickness of the coupling between two Fe films separated by the Cu film from ferro to antiferromagnetic (Heinrich et al., 1990; Bennett et al., 1990). Many electronic properties are expected to have an oscillatory thickness dependence with an amplitude that decreases as the film becomes thicker and the finite level spacing becomes insignificant for the property of interest. If the film thickness could be varied continuously the work function of a free electron like metal is expected to oscillate with a period given by the appearance of new filled energy levels at regular thickness intervals (Schulte, 1976). In practice this spatial period, $\pi/k_F$, may be masked by the fact that the thickness can be varied only in units of the atomic layer thickness. However, an oscillatory thickness dependence has been observed for transport properties such as the electrical resistivity (Jalochowski et al., 1992a), the Hall coefficient (Jalochowski et al., 1996) and the superconducting transition temperature (Orr et al., 1984). Another recently observed manifestation of the thickness dependent electronic structure is that the step height between the terraces on the surface of a metal film has an oscillatory dependence on the film thickness if the step height is monitored by He atom scattering (Braun and Toennies, 1997; Crottini et al., 1997). Finally we mention the strong oscillatory thickness dependence of the second harmonic generation observed

for alkali metal overlayers where the period is due to the spatial period of Friedel-type charge density waves at optical frequencies (Song et al., 1988).

In recent work quantum well states and resonances have been observed for a number of metal films, often noble or simple metal films, deposited on metal substrates using standard techniques such as photoemission (Lindgren and Walldén, 1980a, 1987, 1988a, b; Miller et al., 1988, 1994; Mueller et al., 1989, 1990; Watson et al., 1990; Brookes et al., 1991; Clemens et al., 1992; Fischer et al., 1991, 1992b, 1993; Ortega et al., 1993; Jalochowski et al., 1992a; Beckmann et al., 1993; Smith et al., 1994; Patthey and Schneider, 1994), inverse photoemission (Jacob et al., 1987; Heskett et al., 1987, 1988; Frank et al., 1989; Dudde et al., 1990, 1991; Woodruff and Smith, 1990; Watson et al., 1990; Memmel et al., 1991, 1993; Himpsel, 1991; Ortega and Himpsel, 1992, 1993), as well as two photon photoemission (Fischer et al., 1991, 1992b, 1993) and spin resolved photoemission (Brookes et al., 1991; Clemens et al., 1992; Garrison et al., 1993; Carbone et al., 1993). Discrete vibrational states have been detected by inelastic He scattering (Benedek et al., 1992; Hulpke et al., 1996; Luo et al., 1996). The results obtained for a few simple metal overlayer systems with He scattering provide a rather complete picture of the thin film vibrational modes at different thicknesses. Unique with this method, apart from a high energy resolution, is that the dispersion can be measured over a large range of parallel wave vectors including the center of the Brillouin zone.

A large amount of work has been devoted to the study of alkali metal monolayers. This is motivated by their technical use as surface additives that modify the reactive properties of surfaces and by the low work function values obtained with a resulting enhancement of electron emission (Bonzel et al., 1989; Bonzel, 1987). From a fundamental standpoint the interest is due to the role, since long, of alkali metal atom adsorption on a metal surface as a prototype example of simple chemisorption (Gurney, 1935; Muscat and Newns, 1978; Lang and Williams, 1978; Gunnarsson et al., 1980; Holmström, 1987). The interest is continuing due in part to the difficulty of obtaining consensus regarding how the adsorbate–substrate bond is best described. More specifically there has been a discussion whether the adsorbate should be described as partially ionic or as polarized but essentially neutral (Ishida and Terakura, 1988; Ishida, 1989a, b, 1990; Ishida and Persson, 1990; Horn et al., 1988a; Riffe et al., 1990; Modesti et al., 1990; Lindgren et al., 1990; Benesh and King, 1992; Scheffler et al., 1991). The existence of this discussion is a manifestation of the lack of experimental probes that can provide information on the charge density distribution around an adsorbed atom.

Another reason for the focus on alkali metal monolayers is that for some of these the adsorbate at low and intermediate monolayer coverages is uniformly distributed with a well defined nearest neighbor distance that can be varied over a relatively large range simply by changing the surface coverage. Recent work has demonstrated that the structure in many cases is more complicated than previously expected and this explains the large present interest focused on the structure of alkali metal monolayers (for reviews see Müller, 1989; Tang et al., 1991; Fisher and Diehl, 1992; Diehl and McGrath, 1995, 1996). Here we will describe only a few structures of interest for the discussion below of vibrational and electronic properties. One of the unexpected results is that rather than occupying high coordination hollow sites the larger of the alkali metal atoms are on some substrates found to occupy low coordination on top sites on weakly corrugated surfaces

at near saturation coverage. Among these cases are Cu(111)–(2 × 2)Cs (Lindgren et al., 1983), Cu(111)–(2 × 2)K (Adler et al., 1993), Ru(0001)–(2 × 2)Cs (Over et al., 1992), Ni(111)–(2 × 2)K (Fischer et al., 1992aa), Al(111)–K (Stampfl et al., 1992). In other cases the substrate surface disrupts to provide substitutional sites for the alkali metal atoms and this disruption may occur only if a certain temperature or threshold coverage is exceeded. For Al(111)/Na a $(\sqrt{3} \times \sqrt{3})$ structure forms at room temperature with a third of the Al atoms in the uppermost atomic layer of the substrate is replaced by Na (Schmalz et al., 1991; Kerkar et al., 1992). A Na atom is bigger than an Al atom and therefore has its center above the center of the top layer Al atoms.

For Cu(111)/Li at room temperature substitutional sites become occupied if monolayer coverage is exceeded and at a coverage corresponding to 1.15 ML a (2 × 2) structure forms with both adsorbed and substitional Li (Mizuno et al., 1995). One third of the Li atoms occupy substitutional sites in the uppermost substrate layer where 1/4 of the Cu atoms are replaced by Li. If the Cu(111) substrate is at 170 K there is no evidence of substitution.

Substitutional sites leading to quasi one-dimensional structures with close packed rows of K atoms separated by a distance which depends on the surface coverage have been observed via STM (Schuster et al., 1991) for Cu(110)/K in a study of the well known missing row reconstruction of this surface (for a review see Behm, 1989). Chain like structures are observed also for other systems such as Pb and Tl adsorbed on Cu(100) (Binns et al., 1992). Of particular interest for the Tl system is the observation of dimerized chains, a band gap about the Fermi energy and a preliminary indication of surface superconductivity at temperatures above 200 K (Binns et al., 1992).

## 13.2. Vibrations

### *13.2.1. Submonolayers*

Vibrational excitations of metal overlayer systems have been studied mainly with electron energy loss spectroscopy (EELS) and inelastic He atom scattering. EELS has been used to study the vibrations perpendicular to the surface of alkali metal atoms adsorbed in submonolayer amounts on low index Cu surfaces (Astaldi et al., 1990; Rudolf et al., 1990; Lindgren et al., 1990, 1996; Mizuno et al., 1992; Hamawi et al., 1992), on Ni(111) (Chiarello et al., 1995), on Al(111) (Nagao et al., 1995), on Ru(0001) (He and Jacobi, 1996), on Pt (Hannon et al., 1997). An early observation of this vibration was made by dePaola et al. in a study of K/CO coadsorption on Ru(0001) (dePaola et al., 1985). As an example of EELS results the loss spectrum observed for Cu(111)/Na at low alkali metal coverage is shown in Fig. 13.1. The characteristic loss energy for the perpendicular vibration is 21 meV. With He atom scattering the vibration parallel to the surface was detected and as may be expected this has a much lower loss energy (5.7 meV at 70 K) (Ellis and Toennies, 1993; Graham et al., 1997). Vibrations perpendicular to a substrate surface have been observed also for Cu(100)/Ca (Rudolf et al., 1993). A general comment is that the database is small and the vibrational properties poorly understood. The coverage dependence observed for the vibration frequency is not understood at all and the EELS cross section varies with coverage in a manner which is explained only in qualitative terms.

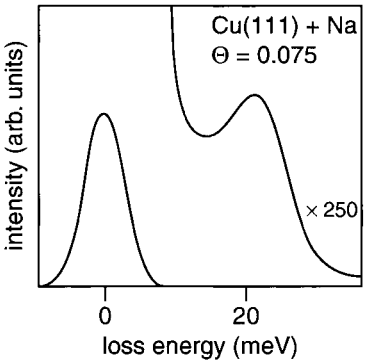


Fig. 13.1. Electron energy-loss spectrum obtained in the specular direction at 5 eV primary electron energy and 60° incidence angle from Cu(111) covered by 20% of a full monolayer of Na. The loss peak at 21 meV is ascribed to Na vibrations perpendicular to the surface. From Lindgren et al. (1990).

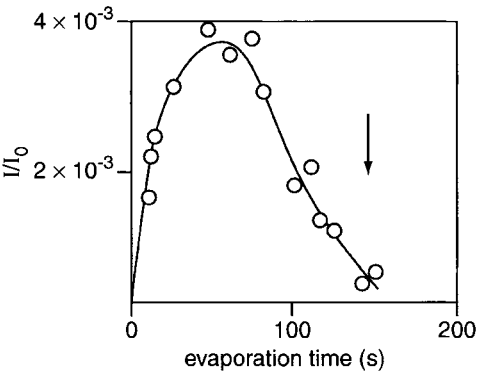


Fig. 13.2. Intensity relative to the elastic intensity of the 21 meV loss peak observed for Na covered Cu(111) plotted versus the Na evaporation time. The arrow marks the time needed to obtain the minimum value for the work function, which is found at around half of full monolayer coverage. From Lindgren et al. (1990).

Common for the EELS observations is that the excitation of the perpendicular vibration gives a loss peak with an intensity that varies strongly with coverage and is easily detected only for coverages below around 60% of a full monolayer (Fig. 13.2). An exception to this is found for Pt(111)/K (Hannon et al., 1997). For this system the loss peak, at 22 meV loss energy, is observed also at higher submonolayer coverages but this may be associated with the change with time of the spectra recorded at coverages in this range. With time a strong loss peak develops at 28 meV. With support from calculations of the vibration frequency and from STM observations this characteristic loss energy was initially assigned to the vibrational excitation of subsurface K atoms occupying sites in the second Pt layer. Recently however, based on additional experimental data, the authors have revised their interpretation and instead associate the loss peak with the formation of a KOH compound after dissociation of residual water molecules (Klünker et al., 1999). The revised assignment is in concordance with earlier experiments when a similar change with time of EEL spectra

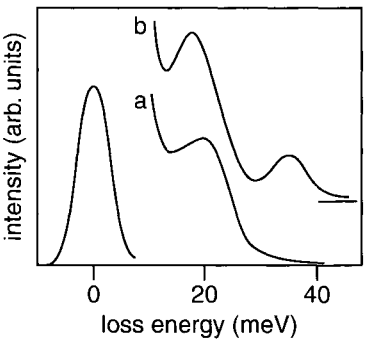


Fig. 13.3. Electron energy-loss spectra for Cu(111) covered by around 15% of a full monolayer of Na (curve a) and then exposed to enough water vapor that the intensity of the loss peak at 36 meV has saturated (curve b). The intensity in the loss region is magnified by a factor of 100 relative to the elastic intensity. From Lindgren et al. (1993).

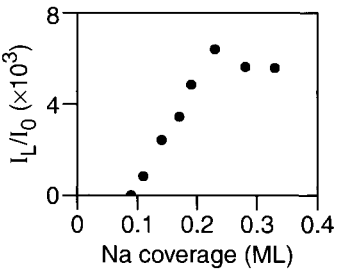


Fig. 13.4. Intensity $I_L$ of the water vapour exposure induced loss peak at 36 meV relative to the elastic peak intensity $I_0$ plotted versus the precoverage of Na on a Cu(111) substrate. The loss intensity is measured after an exposure which produces saturation of the loss intensity. From Lindgren et al. (1993).

for alkali metal adsorbates has been observed due to uptake of residual water vapor. For Cu(111)/K it was noted that with time a strong loss peak is found at 26 meV in addition to the 13 meV loss peak recorded soon after the K deposition (Svensson et al., 1993). For Cu(111)/Na water vapor exposure induces a peak at 36 meV loss energy (Fig. 13.3). Contamination due to residual water vapor is often a problem in experiments on alkali metal overlayers. Of some practical interest in connection with experiments on these adsorbates is that this difficulty for some systems is not met with if the alkali metal coverage is kept below a threshold value. In the case of Cu(111)/Na the EEL spectrum shows that the uptake of water vapor proceeds rapidly only if the alkali metal coverage exceeds a threshold value of around 0.1 ML (Fig. 13.4) (Lindgren et al., 1993). Similar submonolayer thresholds for water uptake have been observed for alkali metal covered Ru(001) held at elevated temperature (Semancik et al., 1986; Pirug et al., 1991).

The coverage dependence of the loss energy shows no common behaviour like that observed for the intensity. For Ru(0001)/Cs (He and Jacobi, 1996), Cu(111)/Li (Lindgren et al., 1996) and Pt(111)/K (Hannon et al., 1997) the vibration frequency increases when

more alkali metal is adsorbed. For Ru(0001)/Cs the loss energy is 6.5 meV at low coverage and 8.5 meV at intermediate monolayer coverage, while for Cu(111)/Li and Pt(111)/K the corresponding values shift from 38 meV and 17 meV to 43 meV and 22 meV, respectively. For Cu(111)/Na, K as well as for Cu(100)/Ca, on the other hand, the loss energy (13 meV for K, 21 meV for Na, 23 meV for Ca) is nearly independent of the coverage. For the alkali metal adsorbates the vibrational energies are thus not simply related to the adsorption energies which for these systems are found to decrease markedly as the monolayer coverage is increased (Gerlach and Rhodin, 1970). The calculated frequency for Na adsorbed on a jellium with the electron density of Al is 18 meV at low coverage and decreases almost linearly with coverage to around 13 meV when the monolayer is full (Ishida and Morikawa, 1993). At low coverage the estimated frequency is thus in fair agreement with the measured values for Na on Cu surfaces (Astaldi et al., 1990; Lindgren et al., 1990). An upshift of the frequency with increasing coverage like that observed for Ru(0001)/Cs and Cu(111)/Li is expected when dipole–dipole interactions are important (Ibach and Mills, 1982). The observed shifts are however much larger than predicted using reasonable values for the polarizability and the dynamic charge. For Ru(0001)/Cs He and Jacobi estimate that dipole coupling explains approximately 25% of the observed shift.

If Na or Li is deposited on Al(111) (Nagao et al., 1995) much lower loss energies (12 meV and 18 meV, respectively) are measured at small and intermediate monolayer coverage than with Cu as substrate. For Na, and probably for Li, the reason for this difference is that the alkali metal atoms assume substitutional sites in the uppermost atomic layer of the Al(111) substrate. In both cases an ordered structure $(\sqrt{3} \times \sqrt{3})$R30° is formed with 1/3 of the Al atoms replaced by the alkali metal atoms. For Al(111)/Na this substitutional structure is well established (Schmalz et al., 1992; Kerkar et al., 1992). The frequency measured for the Al(111)$(\sqrt{3} \times \sqrt{3})$R30°–Na agrees well with the value obtained from ab initio calculations (Neugebauer and Scheffler, 1992). The sensitivity of EELS to surface reconstructions is nicely illustrated also by the results reported by Rudolf et al. (1990, 1991) for alkali metal covered Cu(110). Alkali metal atoms induce $(1 \times 3)$ and $(1 \times 2)$ missing row reconstructions of this surface (for a review see Behm, 1989) if the sample is at room temperature but not when it is cooled to 90 K. At the lower temperature the loss energy characteristic of the alkali metal vibration is found to be higher by around 2.5 meV for both Li and K.

An interesting quantity obtained from EELS is the dynamic ionic charge $q_{\mathrm{dyn}}$ which is determined by the loss peak intensity assuming that the loss is due to dipole scattering (Andersson et al., 1980). The dynamic charge $q_{\mathrm{dyn}} = \mathrm{d}\mu/\mathrm{d}z$ is a measure of the dependence of the adsorbate induced dipole moment $\mu$ on the atom–surface distance $z$. When this is evaluated at low alkali metal coverage the dynamic charge is in the cases studied so far a large fraction of the charge unit. For Li, Na and K values of around $0.5e$ are obtained while for Ru(0001)/Cs (He and Jacobi, 1996) the dynamic charge was determined to be $1.1e$. The dynamic charge is of interest for the discussion regarding how the bond between an adsorbed alkali metal atom and a metal surface is best described, whether the adsorbate should be regarded as partly ionic due to a charge transfer to the substrate or as essentially neutral but strongly polarized. Prior to the advent of EELS data the discussion was based mainly on measured work function changes and core level shifts. The adsorbate induced dipole moment obtained from the work function change is not sufficient to discriminate

between the two suggestions and core level shifts are not easily interpreted for overlayer systems. The information added by EELS is that the dynamic charge determined from the loss intensity is rather close to the static charge obtained from the work function change (for a review see Aruga and Murata, 1989). In cases when an adsorbate carries nearly the same charge when it vibrates as when it is at rest and this charge is a sizeable fraction of the electronic charge the determined charge could serve as an empirical measure of the degree of ionic character. On this point one should also note that the measured dynamic charges are in good agreement with calculations of the dependence of the induced dipole moment on the distance from the surface (Lang and Williams, 1978; Holmström, 1987).

The value of the dynamic charge discussed above is obtained from the loss peak intensity at low alkali metal coverage. As the coverage is increased there is a mutual depolarization of the dipoles, static as well as dynamic. The reduction of the dynamic charge with increasing coverage is sufficiently strong to give an intensity maximum at a coverage of around 0.2 ML (Fig. 13.2). The gradual decrease of the loss intensity for coverages higher than this may therefore be explained by the transformation from a partly ionic adsorbate at low coverage to a metal overlayer with an electron density at full monolayer nearly equal to that of the bulk alkali metal. For the metal monolayer the field from the incident beam will therefore be screened. The decrease of the excitation probability may therefore be ascribed to the combined effect of a loss of ionicity and an increased screening as the alkali metal coverage increases (Lindgren et al., 1996).

The high loss intensity for a dispersed adsorbate and the low intensity for a full monolayer means that EELS can be used to monitor whether an adsorbate is dispersed or forms islands. Both growth modes were observed in a recent study of Cu(100)/Ca (Rudolf et al., 1993). If the substrate is at room temperature the EELS and work function data are quite similar to those observed for alkali metal submonolayers. The characteristic loss energy is 23 meV and the dynamic charge is estimated to be 0.8–1.0$e$. If, during Ca deposition, the substrate is kept at 110 K a loss peak is still observed but the intensity is an order of magnitude lower than at room temperature (RT). On warming to room temperature the spectrum transforms irreversibly to the one characteristic of deposition onto Cu(100) held at RT. The low loss intensity observed after deposition on the cold surface indicates that a dominating fraction of the Ca atoms form islands.

### *13.2.2. Multilayers*

As indicated by the vanishing EEL intensity observed for alkali metal adsorbates at high monolayer coverages the cross section for excitation of vibrational surface modes is small for a metal at the low impact energies (<5 eV) normally used unless in special cases, such as Cu(110) and Ni(110) (Stroscio et al., 1986), when there are dipole active surface phonons. At higher impact energies (>100 eV) the situation becomes more favorable (Lehwald et al., 1983) and EELS has been used to resolve thin film modes for Cu(100)/Fe (Daun et al., 1988) Cu(100)/Co (Mohamed et al., 1989), and Cu(100)/Ni (Stuhlmann and Ibach, 1989; Shen et al., 1991). Since we are here interested mainly in simple metal overlayers and since three such systems, Cu(100)/Na (Benedek et al., 1992; Luo et al., 1996), Ni(100)/K and Cu(111)/Cs (Hulpke et al., 1996) are better characterized than other metal overlayer systems with respect to the vibrational properties we focus attention on the results obtained for these.

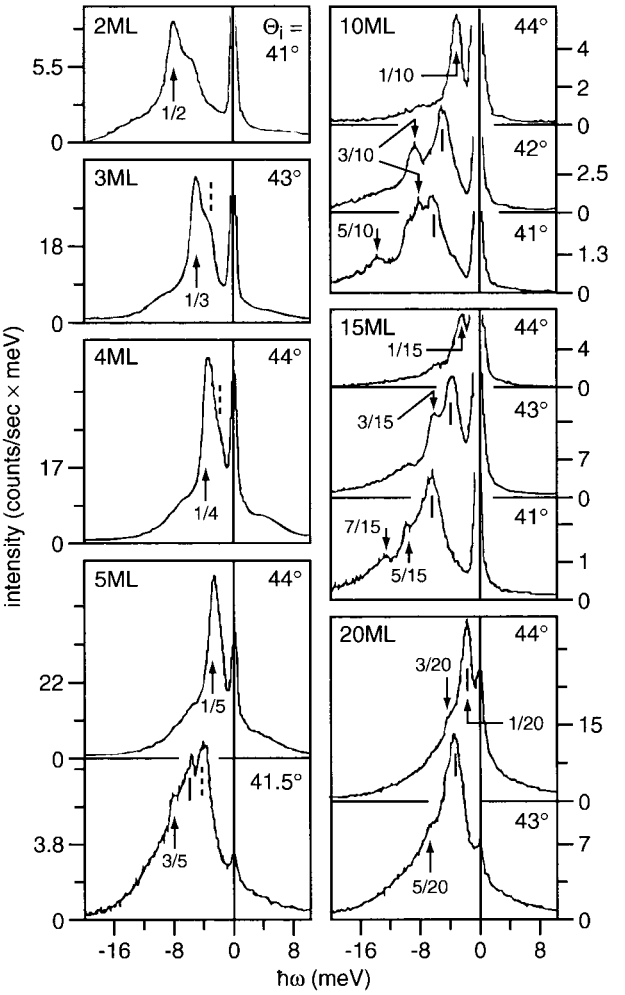


Fig. 13.5. Inelastic He-atom energy transfer spectra of ultrathin Na-films on Cu(100) for $N = 2$ to 20 monolayers (ML) along a ⟨100⟩ direction of the substrate. Each fraction $(2n - 1)/N$ labels the $n$th organ-pipe mode. The Rayleigh modes of the substrate (broken bar) and of the film (solid bar) are also indicated. From Benedek et al. (1992).

The thin film modes for the alkali metal overlayers were detected by inelastic He atom scattering and the results can be explained, at least qualitatively, in appealingly simple terms. Unique with the results is that the dispersion can be measured over a large range of lateral wave vectors including the center of the surface Brillouin zone. The quantized vibrational modes expected for a metal film were first observed for 2–20 ML of Na on Cu(100) (Benedek et al., 1992) (Fig. 13.5). The observed longitudinal standing waves were labeled organ-pipe modes by the authors. As for an open ended pipe the frequencies are given by an odd integer law. The waves have a node at the surface of the stiffer substrate and

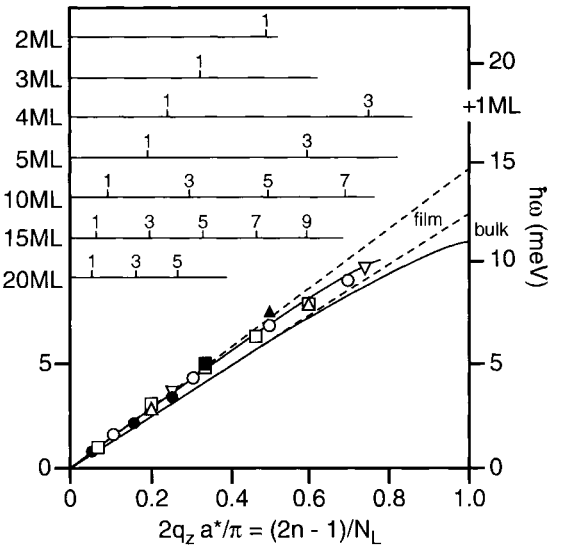


Fig. 13.6. The dispersion for the $Q = 0$ organ-pipe modes as function of the reduced wave vector normal to the surface. Different symbols correspond to different thicknesses, as indicated by the above "keyboard". The corresponding monolayer frequency is also given (+). The dispersion along ⟨110⟩ of the longitudinal mode of bulk sodium is shown for comparison (solid line) (Wood et al., 1962). The broken straight lines give the slope at $q_z = 0$. From Benedek et al. (1992).

a maximum at the vacuum interface. The vibrational standing wave states are analogous to the states, discussed below, of valence electrons confined to a thin metal overlayer. The quantized phonon and electron states both provide a unique opportunity to determine the dispersion of the overlayer metal in the perpendicular direction. For the determination of the dispersion the energy of the electron or the phonon is measured (Fig. 13.5) while the wave vector is obtained from the phase condition satisfied by the waves. For an organ-pipe mode the wave vector is $q_z = \pi(n - 1/2)/d$, where $d$ is an effective thickness. From the phase condition and the measured energy losses Benedek et al. (1992) determined the dispersion of phonons along the direction normal to the sample (Fig. 13.6).

While the results can thus be qualitatively understood in simple terms the measured frequencies at $\Gamma$ are higher by 10–20% than estimated by model calculations using force constants obtained from the phonon dispersion of bulk Na (Luo et al., 1996). This is ascribed to the structural distortion and compression of the lattice resulting from the mismatch at the metal-metal interface as thin films of close packed atomic layers adjust to the Cu(100) substrate. For Ni(100)/K and Cu(111)/Cs the measured frequencies suggest that the strain is substantially reduced as the films become thicker (Hulpke et al., 1996), while for Cu(100)/Na the frequencies remain high in the thickness range studied. For Cu(111)/Cs the phase velocity in the perpendicular direction decreases with increasing thickness and is close to the sound velocity of the alkali metal after five atomic layers have been deposited while for Ni(100)/K the corresponding thickness is around 10 ML. Striking with the thin film modes of the alkali metals is the weak lateral dispersion for some of the modes

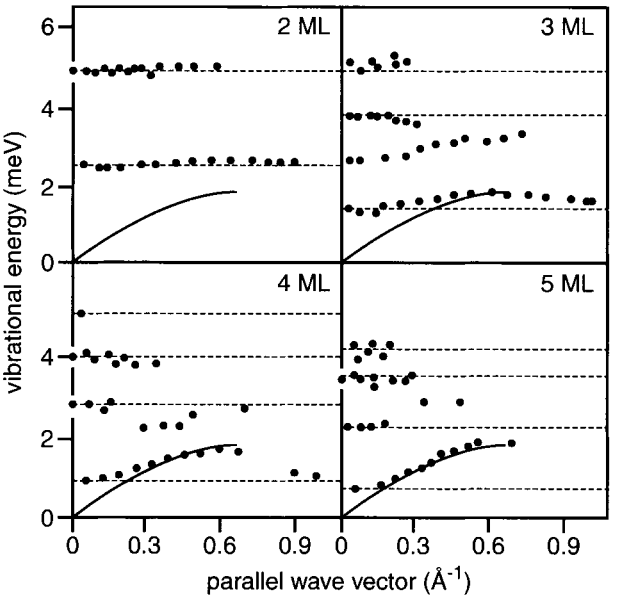


Fig. 13.7. Vibrational energy versus parallel wave vector for vibrational thin film modes observed by inelastic He atom scattering for Cu(111)/Cs. The full drawn lines indicate the lowest bulk phonon band. From Hulpke et al. (1996).

(Fig. 13.7). In the calculations by Luo et al. (1996) this flatness is reproduced and the authors suggest that for the structure at hand only weak second nearest neighbor interactions will contribute to the dispersion for these modes.

## 13.3. Electrons

### *13.3.1. Surface states*

#### *13.3.1.1. Surface states on clean metals*

During the last twenty years electronic surface states on metals and semiconductors have been studied extensively primarily by photoelectron and inverse photoelectron spectroscopy. The states appear in the potential well between the vacuum barrier and the effective barrier towards the interior of the crystal if this has a band gap in the energy range of interest. The tail into vacuum and the oscillating tail in the crystal may combine to form a state when the phase condition $\Phi_B + \Phi_C = 2\pi m$ satisfied, where $\Phi_B + \Phi_C$ are the phase shifts at the vacuum barrier and towards the interior of the crystal, respectively, while $m$ is an integer (Echenique and Pendry, 1978). A few Å into the vacuum the potential barrier is described by the image potential. With this $1/z$-potential a hydrogen-like series of states appear within an eV of the vacuum level. If the crystal barrier is assumed to be infinite and the entire vacuum barrier is taken to be an image barrier then the energies of the surface

state series are 1/16 of the energies of the hydrogen atom. The energy separation is thus small between the higher members of this series compared to the inverse life time typical of bulk states at energies near the vacuum level. In spite of this the entire series may still be resolved. The reason for this is that an electron in a Rydberg state avoids being scattered by spending most of its time far outside the metal, a region of space where there are few electrons to collide with. The states extend further into vacuum the higher the quantum number is. It was shown that if the first few members of the series survive as separate states when electron scattering is taken into account then also the whole series should be expected to remain resolved.

The existence of this Rydberg series on metal surfaces was first demonstrated by electron reflectivity spectra measured (Adnot and Carette, 1977) and calculated (Rundgren and Malmstrom, 1977) for energies just above diffraction thresholds. At these energies electrons can propagate along the surface under repeated reflections between the surface barrier and the bulk (for reviews see McRae, 1979; Jones and Jennings, 1988). The interference obtained in this shallow surface layer produces an oscillatory component in the electron reflectivity spectrum. The oscillations become more rapid near the threshold reflecting the fact that the image barrier then becomes wider. While the electron reflectivity spectra thus showed that the Rydberg series exists the method does not allow the energies of the states to be determined directly from the experiments. The energies can be measured by other techniques such as inverse photoemission (Johnson and Smith, 1983; Dose et al., 1984; Straub and Himpsel, 1984; Reihl et al., 1984) and two photon photoemission (Giesen et al., 1985; Kubiak, 1988).

The characteristic features of image barrier states on clean metal surfaces are by now rather well known. The main reason for the above brief summary is that similar states were recently observed for metal overlayer systems (Fischer et al., 1991, 1992b, 1993) and these will be discussed further in a following section. Surface states are usually labeled image potential states if, for $k_{\|} = 0$, the energy is within around 1 eV of the vacuum level. For energies further below the vacuum level the energy dependence of the phase shift on the crystal side, $\Phi_C$ becomes as or more important and the surface states are then referred to as crystal induced surface states. Also for a discussion of the states appearing in thin metal overlayers, especially for monolayers, the electronic structure of the clean metal surface is a good starting point. Particularly useful for an understanding of the states appearing in thin metal overlayers is the simplified phase analysis used by Smith (1985, 1988) and Chen and Smith (1987) to account for the energies of the much studied surface states appearing in the s,p-band gaps of noble and transition metals. The main advantage of the phase analysis is that it is simple, allows crystal induced and image barrier states to be treated on the same footing and that the energies obtained are in surprising agreement with the observations. Of main present interest is that the phase analysis can be easily extended to estimate the energies of the quantum well states appearing in overlayers of simple metal on a metal substrate. The mileage gained by this phase analysis is important considering the fact that for most overlayer systems there are still very few first principle type calculations of the electronic structure to compare the experimental results with.

The phase analysis is made by assuming that the s,p-bulk bands can be described by a two band model from which the phase shift $\Phi_C$ is calculated. If the surface barrier is taken to be an image barrier the phase shift $\Phi_B$ is approximately given by

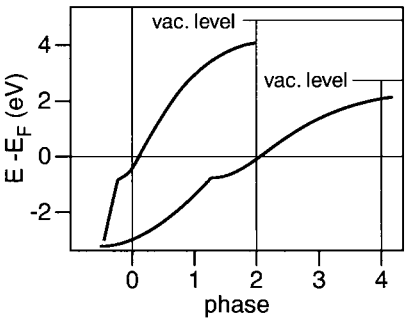


Fig. 13.8. The curve to the left shows the sum (in units of $\pi$) of the barrier phase shifts, $\Phi_B + \Phi_C$ calculated for energies within the Cu s,p-band gap at the L symmetry point. The gap extends from 0.8 eV below $E_F$ to 4.2 eV above $E_F$. A discrete Cu(111) surface state is obtained at the energy where the sum is zero. The curve to the right shows the phase shift sum, $\Phi_B + \Phi_C + 2\Phi_D$ obtained for a Cu(111) crystal covered by one full monolayer of Na. The details of the calculations are discussed in a following section of this paper. From Lindgren and Walldén (1988b).

$\Phi_B = \sqrt{3.4eV/(E_V - E)} - 1$, where $E_V$ is the vacuum level. With a slightly greater effort the phase shift at the image barrier can be obtained from the solutions to the wave equation in the image barrier region. The wave function is here the Whittaker function $W_{k,1/2}(x)$. Here $x = (z - z')(E_V - E)^{1/2}(2a_0\sqrt{0.85eV})^{-1}$, where $k^2 = 0.85eV/(E_V - E)$. $a_0$ is the Bohr radius and $z'$ is the position of the image plane. $W_{k,1/2}(x)$ is easily evaluated using an integral representation for $k < 1$ and a recursion relation to obtain energies corresponding to $k > 1$ (Slater, 1960).

The results of such a phase analysis for the Cu(111) surface is shown in Fig. 13.8. The curve to the left shows the variation with energy of the sum of the barrier phase shifts, $\Phi_B + \Phi_C$. The phase shift $\Phi_C$ varies by $\pi$ over the band gap which extends from 0.8 eV below the Fermi energy to 4.1 eV above the Fermi energy. For $m = 0$ the phase condition is satisfied for an energy somewhat below the Fermi level and this state is the often studied surface state observed at 0.4 eV below the Fermi edge in photoemission spectra recorded in the normal direction (Gartland and Slagsvold, 1975). Away from the center of the Brillouin zone the surface band runs nearly parallel to the bulk band describing the dispersion across the neck of the Cu Fermi surface (Heimann et al., 1979; Kevan, 1983). The curve to the right, as will be discussed below, shows the phase shift sum for Cu(111) covered with 1 ML of Na.

If the crystal has no band gap near the vacuum level there may appear a series of image potential induced surface resonances rather than surface states. Such resonances are observed even for free electron like metals such as Al(111) with only a weak electron reflectivity due to the bulk potential (Heskett et al., 1987, 1988; Yang et al., 1993).

*13.3.1.2. Metal adsorption induced shifts of surface states*

If the metal surface is covered by an adsorbate this often produces a major rearrangement of the electronic level structure and the surface states of the clean crystal surface no longer appear. One way of finding out whether an observed state is a surface state is to expose

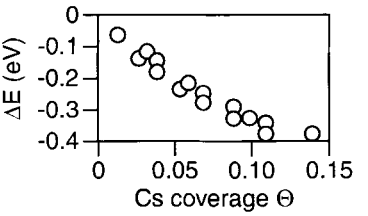


Fig. 13.9. Energy shift for $k_{\|} = 0$ of a Cu(111) surface state upon Cs adsorption. Full monolayer Cs coverage corresponds to $\theta = 0.25$.The shift is obtained from photoemission spectra recorded in the normal direction. From Lindgren and Walldén (1979).

the surface to some reactive gas, which usually makes a surface state disappear. If the adsorbate is a simple metal the behaviour is often different. When alkali metal or Ba atoms are adsorbed on Cu(111) (Lindgren and Walldén, 1978, 1979, 1980a, 1987, 1988b; Kevan, 1986), Li on Be(0001) (Watson et al., 1990) or Cs on W(100) or Ta(100) (Soukiassian et al., 1985) surface states of the metal crystal are still observed but appear at energies which shift gradually as the adsorbed amount is changed.

In the case of Cu(111) such a gradual shift is observed for the surface state 0.4 eV below $E_F$ discussed above (Fig. 13.9). The surface band shifts to lower energy upon adsorption such that at around half of full monolayer coverage it nearly coincides with its parent bulk band which at the L point of the bulk Brillouin zone is 0.8 eV below the Fermi level. If the band shifts downwards rigidly this means that it becomes more populated due to the alkali metal adsorption and that it thus is involved in the charge transfer between the substrate and the adsorbate. To some extent the band however changes its mass as it shifts to a lower energy and the amount of charge transferred to the surface band is uncertain due to the difficulty in measuring accurately the occupied area of the surface Brillouin zone (Kevan, 1986).

When the shifting Cu(111) surface state is observed by photoemission one notes that the intensity of the emission decreases as alkali atoms are adsorbed on the surface (peak S in Fig. 13.10). At first glance this may then be taken as an indication that the conditions become less favorable such that the state only exists over a shrinking fraction of the surface. However, largely the reduced intensity can be understood as a result of a smaller excitation probability for the state after its energy has shifted so that it lies closer to the bulk band. That a reduced intensity may be expected is realized by observing that as the surface band comes closer to the bulk band describing the dispersion across the neck of the Cu Fermi surface the wave function of the surface state becomes more like the wave function of the bulk states. These bulk states are not observed in a photoemission experiment with any appreciable intensity unless special photon energies are chosen such that direct optical transitions to a higher electron energy band are possible. One thus expects the surface state emission intensity to become progressively reduced as the state approaches the bulk band from which it is derived.

Further support for the view that it is the energy shift of the state which produces the reduced emission is obtained by first adsorbing an alkali metal to shift the energy downwards and then expose the sample to oxygen. This exposure makes the band shift back to higher

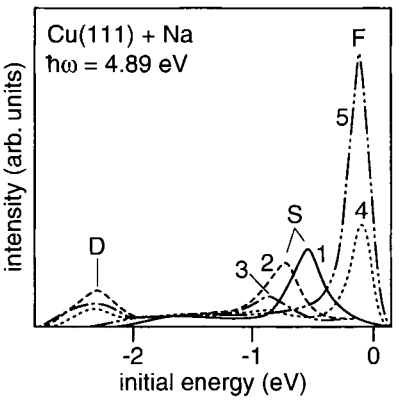


Fig. 13.10. Photoelectron energy spectra recorded along the surface normal at 4.9 eV photon energy for different coverages of Na on Cu(111). The numbers by the spectra indicate the evaporation times in minutes. One full monolayer corresponds to around five minutes evaporation time. Peak F is due to the discrete Na overlayer state characteristic of one full Na monolayer while S is due to the Cu(111) surface state in the L gap. The surface state shifts to lower energy due to the Na adsorption. Peak D is due to the highest Cu 3d band. From Lindgren and Walldén (1980a).

energies and then also the intensity of the emission is observed to increase (Lindgren and Walldén, 1979). Within the phase analysis a shift to lower energy may be expected from the lowering of the surface barrier. Another probable effect of the adsorbate is that the vacuum barrier has shifted in space towards vacuum making the potential well wider and this will also reduce the energy of the state (Chen and Smith, 1987; Ahlqvist, 1979).

Recently it was demonstrated that strain in an epitaxial film can shift the energy of a surface state appreciably (Neuhold and Horn, 1997). Photoemission spectra from 50 Å thick epitaxial Ag(111) films on Si(111)-(7 × 7) did not show the surface state peak close below the Fermi edge characteristic of an Ag(111) crystal and of Ag(111) films prepared on, for example, highly oriented pyrolytic graphite (Patthey and Schneider, 1994). The missing peak is found to appear after a small Cs deposit and shifts as described above for Cu(111)/Cs when the coverage is further increased (Fig. 13.11). The results indicate that the energy of the surface state is upshifted by 0.15 eV to an energy slightly above the Fermi level for the film grown on Si(111). The shift and depopulation of the state is ascribed the strain in the film due to the mismatch with the Si lattice. Of present interest is that the ability to shift surface states by alkali metal adsorption is crucial for the information gained.

### *13.3.2. Quantum well states for monolayers*

Quantum well states may appear in thin metal overlayers on a metal which has a band gap at the energies and parallel wave vectors of interest. The states are formed by valence electrons in the overlayer which are reflected back and forth between the vacuum barrier and the overlayer/substrate interface. The states satisfy the phase condition $\Phi_B + \Phi_C + 2\Phi_D = 2\pi m$, where $\Phi_D$ is the phase change as the electrons propagate across the interior of the thin film. For metal overlayer systems quantum well type states were first observed by

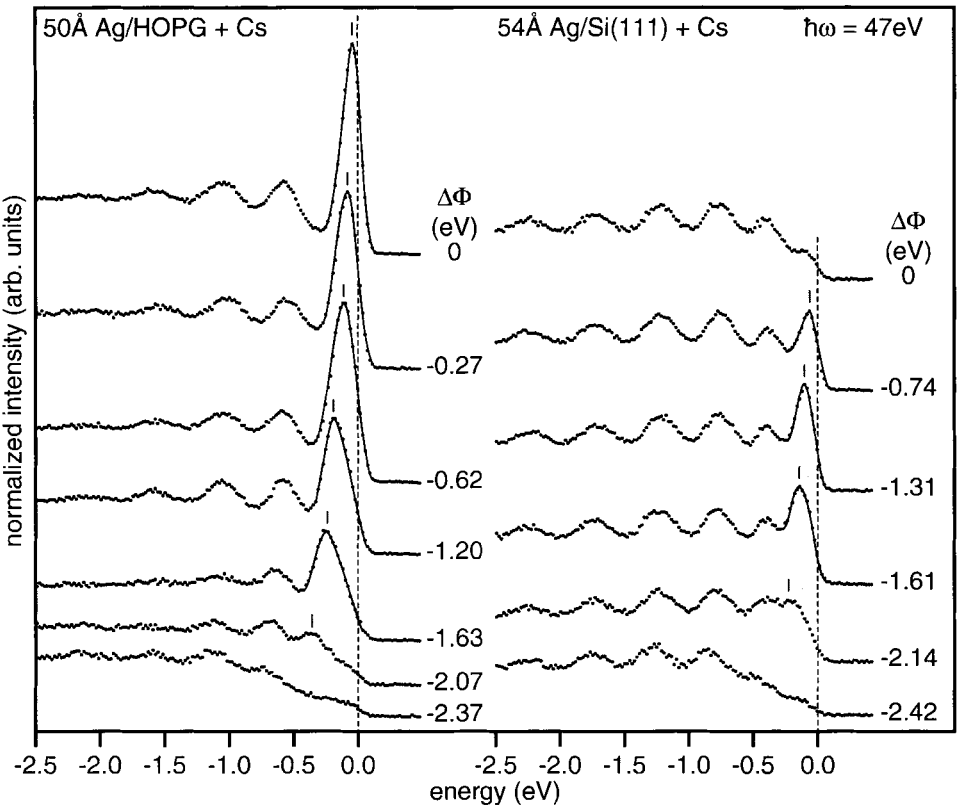


Fig. 13.11. Photoelectron energy spectra of Ag(111) films on HOPG (left) and on Si(111) (right) covered with submonolayer quantities of Cs. The gray bars indicate the positions of the emission peak due to the surface state. The state shifts to lower energy with increasing Cs coverage. For the film deposited on Si(111) the results indicate that the state is above the Fermi level at zero Cs coverage. From Neuhold and Horn (1997).

photoemission from alkali metal monolayers on a Cu(111) crystal (Lindgren and Walldén, 1980a, 1987). When a full monolayer of Na, K or Cs is adsorbed on Cu(111) a state appears near the Fermi energy at the center of the surface Brillouin zone (Lindgren and Walldén, 1980a, 1987; Fischer et al., 1991, 1992b, 1993). It is this state which gives the strong peak labeled F in Fig. 13.10. A simple model potential can be used to estimate the energy of this state. An image potential vacuum barrier is cut off by a constant potential in the interior of the film (Fig. 13.12). On the crystal side the phase shift is obtained from the two-band model for the Cu energy bands. With the constant potential in the film chosen to be that of bulk Na (6 eV below the vacuum level) the only remaining parameter is the thickness of the film and this can be adjusted to obtain the experimentally observed energy. Once the thickness has been determined the model potential can be used to predict the energies of empty overlayer states not observed in photoemission. The curve to the right in Fig. 13.8 shows the estimate made from the model potential of the variation with energy of the phase shift sum for Cu(111) covered with 1 ML Na. Compared with the model used by Smith

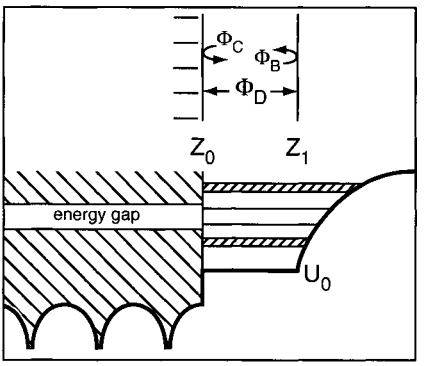


Fig. 13.12. Schematic drawing of the model potential used to estimate the energies of quantum well states formed in alkali metal mono- and multilayers adsorbed on a Cu(111) crystal (from Hamawi et al., 1991). Horizontal lines in the well mark discrete states formed in the energy range of the substrate gap. Resonances below and above the gap are indicated by shaded stripes.

(1985) for clean metal surfaces the only difference is that for the overlayer case there is a spacer layer with constant potential between the crystal and the vacuum barrier.

If, for the moment, life time broadening is ignored there will for the alkali metal monolayers on Cu(111) be a whole series of quantum well states extending to the vacuum level. A number of these empty states have been observed in two photon photoemission spectra. Due to the results obtained with this method by Fischer et al. (1991, 1993) and Fischer et al. (1992b) alkali metal monolayers on Cu(111) are now better characterized than any other metal quantum well type system. For Na on Cu(111) three empty states have been resolved, labeled $J_1$, $J_2$ and $J_3$ in Fig. 13.13. Considering the crudeness of the model potential used to predict the energies of these states there is a surprising agreement with the measured values. The lowest empty state for Cu(111)/Na was predicted to have an energy 0.5 eV below EV while the measured energy is 0.64 eV.

More interesting is the fact that states as high as this in energy can actually be resolved. The results suggest that even for some overlayer systems a whole Rydberg-like series will be obtained. As for clean crystal surfaces the series is due to the image potential character of the vacuum barrier close to the vacuum level. The life times should however be shorter for overlayer states than for surface states. Twice on every round-trip between the substrate surface and the vacuum barrier the electron occupying an overlayer state passes through the thin film in which the electron density is high and the scattering strong. As the overlayer is made thicker one therefore expects the life time broadening to increase and at some critical thickness the series will no longer be resolved. It is not clear whether this decay of the Rydberg series can be monitored experimentally since it may be obscured by the appearance of resonances associated with the vacuum barrier of the overlayer. Such resonances are detected for Al(111) (Heskett et al., 1987, 1988; Yang et al., 1993) as mentioned above and these might appear also for alkali metal surfaces.

The spectra shown in Fig. 13.10 give the impression that the monolayer state (peak F) remains at constant energy as the Na coverage increases. However, using a 1mW HeCd

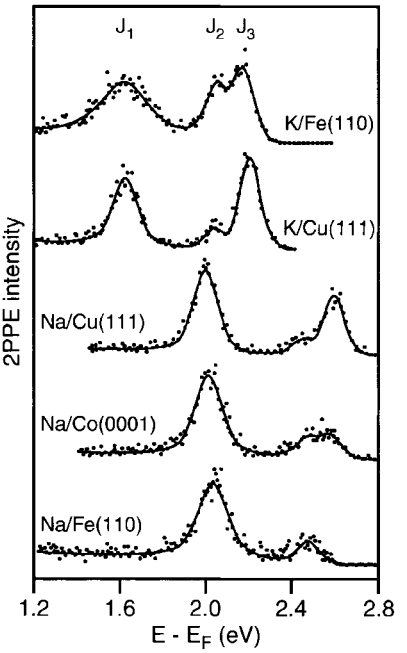


Fig. 13.13. Two-photon-photoemission spectra in the normal emission for a single layer of Na and K on different substrates. On each system a series of unoccupied states $J_1$, $J_2$, $J_3$ can be seen. The photon energies for the different spectra are 2.214 eV for K/Fe(110), 2.275 eV for K/Cu(111), 2.640 eV for Na/Cu(111), 2.583 eV for Na/Co(0001) and 2.280 eV for Na/Fe(110). For most systems the photon energy was chosen for resonant, efficient excitation at the third state $J_3$. From Fischer et al. (1993).

laser ($h\nu = 3.82$ eV) as light source and a high energy resolution spectrometer ($\Delta E =$ 5 meV) it is observed that the state shifts gradually to lower energy as the coverage is increased until the monolayer becomes full (Carlsson et al., 1997). With this light source the intensity is sufficient to probe states in a range extending to around $8kT$ above the Fermi level. Since states far above the Fermi level are not usually probed in photoemission experiments we show in Fig. 13.14 how such states appear in the spectra taking results obtained for 2 ML of Na on Cu(111) at room temperature and 165 K as an example. At room temperature one observes a doublet which may suggest that there is emission from two different states. The line shape is however well accounted for by one lifetime broadened peak 100 meV above the Fermi level modulated by the Fermi cut off function Fig. 13.15. Further evidence for this is given by the strong intensity reduction of the high energy shoulder when the temperature is reduced to 170 K. Notable is that the intensity decreases markedly also at initial state energies below the Fermi level (Fig. 13.14). This is mainly due to the reduced line width at the lower temperature. In the lower panel the spectra have been divided by the Fermi–Dirac distribution to display the emission features more clearly.

For Cu(111)/Na in the monolayer coverage range the advantage of high resolution and intensity is that the spectra reveal that the monolayer state shifts gradually with increasing

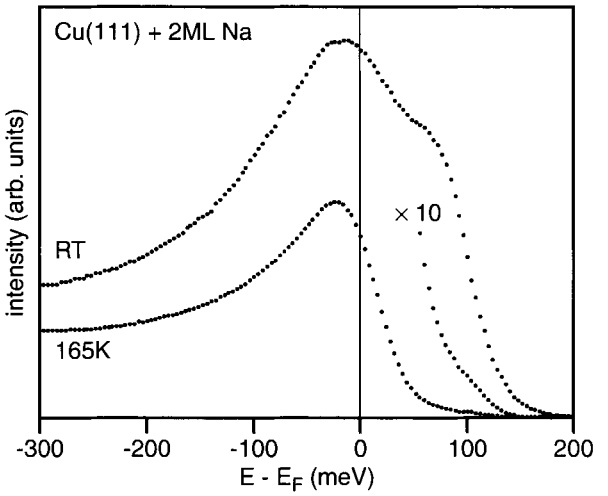


Fig. 13.14. Photoelectron energy spectra recorded for $h\nu = 3.82$ eV along the surface normal of Cu(111) covered with 2 ML of Na with the sample at RT (upper curve) and at 165 K. The high energy shoulder prominent in the RT spectrum is due to emission of electrons out of a discrete quantum well state 0.1 eV above the Fermi level. At 165 K the occupation of the state is reduced and the shoulder weaker. From Carlsson et al. (1997).

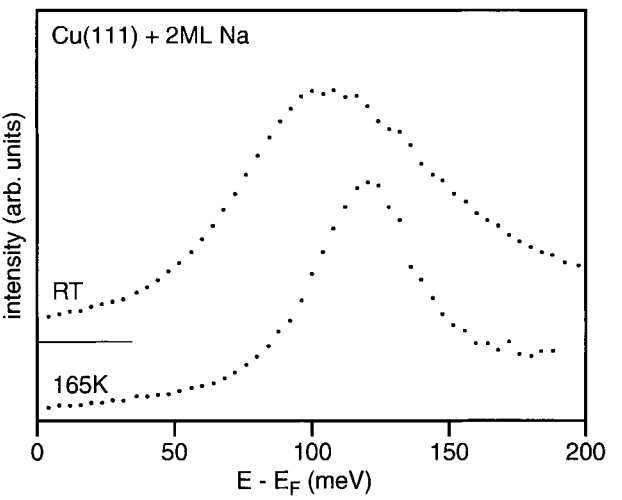


Fig. 13.15. The spectra in Fig. 13.14 multiplied by $1 + \exp(E - E_F/kT)$. From Carlsson et al. (1997).

coverage from energies above the Fermi level to the energy 100 meV below EF observed at 1 ML after passing the Fermi level at 0.85 ML (Fig. 13.16). In Fig. 13.17 the energy of this state and the energy of an empty state observed by two photon emission is plotted versus coverage. Though there is a small gap between the energy ranges covered by the two methods the results suggest that over a wide coverage range the Na monolayer can be

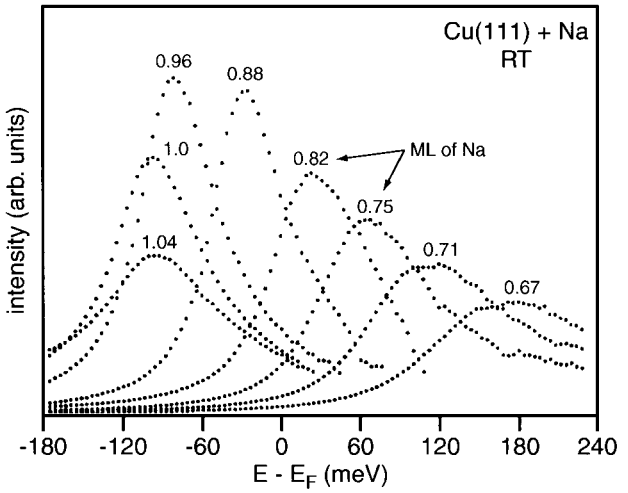


Fig. 13.16. Electron energy spectra obtained as in Fig. 13.14. The sample is a Cu(111) crystal covered with the different amounts of Na indicated in the diagram. From Carlsson et al. (1997).

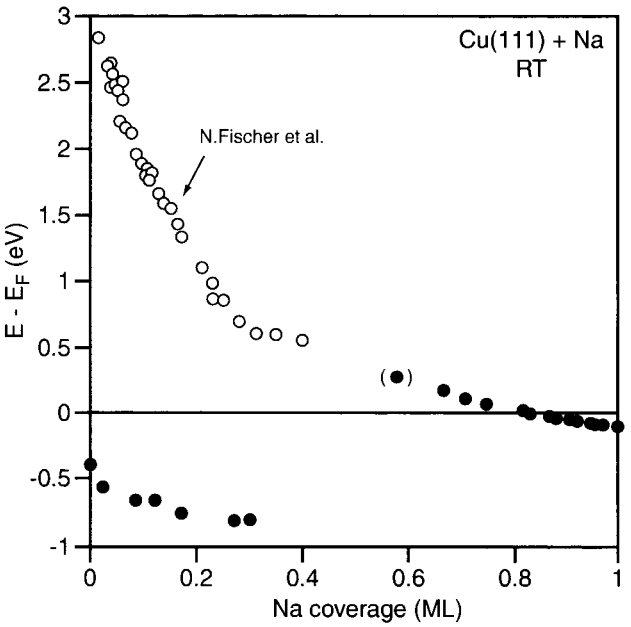


Fig. 13.17. Energy versus Na coverage on Cu(111) for states observed by photoemission (filled circles) (Carlsson et al., 1997) and two photon photoemission (open circles) (Fischer et al., 1994). The point marked with parentheses is not an observed peak position but obtained from a fit of a Lorentzian to the observed low energy tail of the emission line.

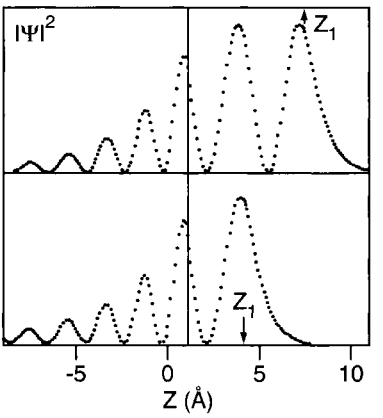


Fig. 13.18. Electron charge distribution obtained with the simplified model potential for the overlayer state near below the Fermi energy for a Na monolayer on Cu(111) (lower curve) and for an expected overlayer state just above the Fermi level for a two atomic layers thick Na film on Cu(111). From Lindgren and Walldén (1988b).

regarded as a continuously tunable quantum well. The energy downshift of the state ending up with an energy 100 meV below the Fermi level reflects the different ways the potential well is modified at low and high coverages. The rapid downshift at low coverages is mainly due to the decrease of the work function, which passes a minimum at around 0.5 ML. In the high coverage range the upshift expected from the work function increase is more than compensated for by the fact that the monolayer becomes more attractive as more Na atoms fill the layer. An estimate of the energy shift in high coverage range was made by assuming that the overlayer can be regarded as metal slab with an electron density that increases in proportion to the coverage to a density and well depth equal to that of bulk Na at 1 ML coverage (Lindgren and Walldén, 1988a). The downshift predicted from this simple model is 65% of the measured.

Photoemission and inverse photoemission data for Be(0001)/Li in the submonolayer range (Watson et al., 1994) are as pointed out by the authors similar to those reported for Cu(111)/Na. The comparison between the two systems was then based on results obtained for Cu(111)/Na which did not reveal the gradual downshift of the quantum well state from the unoccupied to the occupied energy range. Had this shift not been observed the data for Cu(111)/Na would have suggested that an abrupt change of the level structure in a small coverage range and similar change of the electronic structure is suggested by the results available for Be(0001)/Li. The interpretation given is that the change of the level energy marks the onset of a nonmetal to metal transition in the overlayer. While data obtained with higher resolution would be useful in this case we note that a difference between the two systems is indicated by core level spectra. For Be(0001)/Li two Li 1s-core level peaks are resolved with the intensity transferred from one to the other in the coverage range of the suggested transition, while for Cu(111)/Na a single Na 2p-level is observed in the monolayer range (Shi et al., 1993).

An overlayer state is a hybrid with the electronic charge shared by two different metals. On the sides of the standing wave in the overlayer there is an oscillating tail in the

substrate and a tail into vacuum, which is exponentially damped for filled states. At energies close below the vacuum level the weight is shifted into vacuum due to the long range image potential and then also this tail is osculating in the manner of hydrogen like wave functions. For an adsorbed monolayer a filled state may distribute its charge such that there is as much charge residing in the tail into the substrate as there is in the overlayer. In Fig. 13.18 is shown how the electronic charge is deposited by the state observed close below the Fermi energy at the center of the surface Brillouin zone for 1 ML Na on Cu(111) and for the state 100 meV above the Fermi level observed for 2 ML of Na as shown in Fig. 13.15. The electron distribution has been obtained from the model potential described above (Fig. 13.12). Theoretical calculations of the charge distribution and/or the dispersion of quantum well states have been reported for example for Au(100)/Ag, Cu(100)/Co (Pe'rez-Diaz and Munoz, 1996), Au(111)/Ag (Jaskolski et al., 1991), Fe(100)/Ag (Crampin et al., 1996), Li in vacuum (Boettger and Trickey, 1992), Be, Na, Mg, K, Ca, Rb, Sr in vacuum (Boettger and Trickey, 1989), Li, Na, K, Rb, Cs (Wimmer, 1983), Be, Mg, Ca, Sr, Ba in vacuum (Wimmer, 1984), Pb in vacuum (Saalfrank, 1992).

In the measurements the hybrid character is demonstrated by the dispersion of the overlayer states. To estimate the band mass of an electron moving along the surface of an alkali metal overlayer one may again use a free electron potential for the overlayer and obtain the energies at different values for the parallel wave vectors. One then has to take into account that the crystal band gap varies with $k_{\parallel}$. The use of a free electron potential for the overlayer is motivated by the fact that the bands obtained from a full band structure calculation are quite free electron like for a monolayer of an alkali metal (Wimmer, 1983). This procedure was used by Memmel et al. (1993) for Na on Ni(110) and the dispersion obtained in this manner was found to agree quite well with the dispersion measured by inverse photoemission (Fig. 13.19).

*13.3.2.1. The proper work function*

One of the interesting results of the two photon photoemission experiments on alkali metal covered substrates concerns the relevance of the work function as this is conventionally measured via the low energy cut off of emission spectra. For image barrier surface and overlayer states the vacuum level is the natural reference energy. If one could change the work function uniformly over the sample surface one would expect the image barrier states to shift by very nearly the same amount. Some slight difference between the shift of the vacuum level and the barrier states may be expected due to the energy dependence of the phase shift produced by the bulk band gap.

When looked at in detail with the high energy resolution obtained in the two photon photoemission experiment the two shifts are found by Fischer et al. (1993) to be significantly different. The explanation suggested by the authors for the difference is that even for carefully prepared samples there may be lateral variations of the surface barrier due to defects, contamination and growth of a second atomic layer over parts of the surface. While the work function is conventionally measured via the slowest electron leaving the sample the series of image barrier states converges towards the highest energy allowing an electron to remain in the sample. In the two photon photoemission experiment this highest energy can be obtained with respect to the Fermi energy with a high accuracy by measuring the energy relative to the Fermi level for image barrier overlayer states close to the high

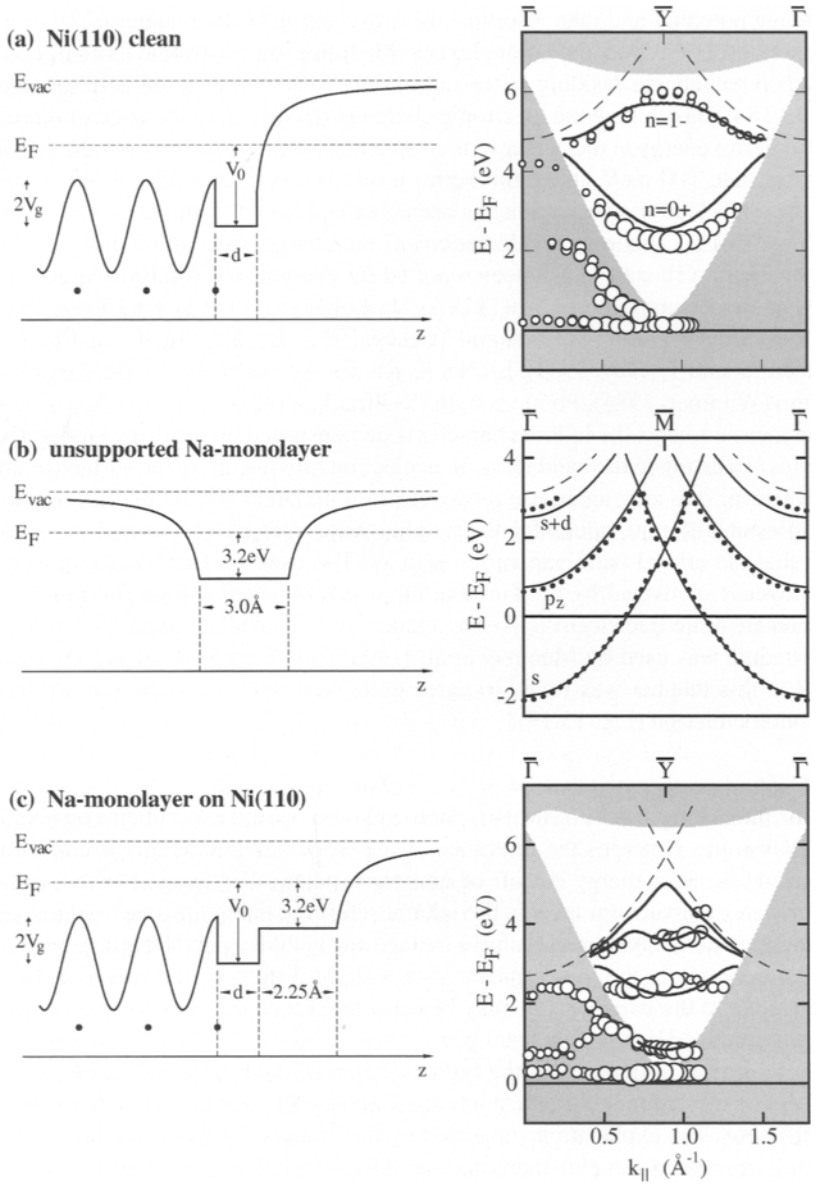


Fig. 13.19. Model potentials (left) used for calculations of surface and overlayer state energies for (a) the clean Ni(110) surface, (b) an unsupported Na monolayer in vacuum and (c) a Na monolayer on Ni(110). Open circles in the diagrams to the right denote experimental data points, solid lines the results of the calculations. Dotted lines in (b) are from a full band calculation by Wimmer (1983). The size of the experimental points indicates the observed intensities. From Memmel et al. (1993).

energy limit. The work function value obtained in this manner, labeled the proper work function by the authors, is then representative of that part of the surface which produces the observed series of image barrier type overlayer states.

The proper work function values determined by Fischer et al. (1993) as described above are found to be independent of whether the substrate is Cu(111), Fe(110) or Co(0001). For a Na monolayer it is 2.69 eV and for a K monolayer it is 2.27 eV. By contrast the conventionally measured values differ by around 0.2 eV for Na (2.77 eV with Cu(111) as substrate and 2.58 eV on Co(0001).

*13.3.2.2. Electronic structure of the overlayer*

The results obtained for the alkali metal monolayers suggest that the simple model potential for the alkali metal overlayer is a portable object that can be used to predict the energies of overlayer states for free electron like metal monolayers adsorbed on a metal with a band gap. It may not be very surprising that an image barrier cut off by a constant potential is a reasonable first approximation to describe a simple metal overlayer. Rather unexpected, however, is the observation made by Chen and Smith (1989) that with this type of potential one may account quite well for electron energy bands above EF for oxygen covered Cu surfaces. For this kind of an adsorbate the electronic structure is usually discussed in terms of a local orbital picture. As noted by the authors the results suggest that the possibility of quantum well type resonances need to be eliminated before adsorbate induced features in inverse photoemission spectra can be identified with local bonding configurations of substrate–adsorbate orbitals.

Even though the overlayer states observed for Cu(111)/Na and the simple model used to account for them can serve as a good example of quantum well type states for simple metal systems the experiments still provide only a fragmentary picture of the electronic structure of the adsorbate system. This is clear from the fact that the only band which is partly filled does not extend more than 0.1 eV below the Fermi energy, which means that the occupied fraction of the energy band corresponds only to approximately 5% of an electron per Na atom. The occupancy is estimated from the measured dispersion (Fischer et al., 1991) and using the Brillouin zone for a close packed Na monolayer. Since the Na atoms at full monolayer coverage are expected to be nearly neutral the photoemission spectra obtained so far provide little information about the remaining, major part of the Na valence electron.

The state appearing near the Fermi energy at gamma is the lowest discrete quantum well state for the alkali metal overlayer. For the formation of such states the substrate must have a band gap that can provide a high electron reflectivity at the overlayer/substrate interface. For energies outside the band gap the electrons in the overlayer will form resonances rather than discrete states. In the case of Cu(111) this means that for energies more than 0.8 eV below the Fermi level the alkali metal valence electrons are expected to form a resonance. It is this expected resonance which is occupied by the alkali metal valence electron. The experiments made so far provide no information of this resonance.

A more complete picture of the filled part of the electronic structure is obtained for Li adsorbed on Be(0001) (Watson et al., 1990). At the center of the surface Brillouin zone the projected bulk band gap of the substrate extends 4.3 eV below the Fermi energy and therefore one more filled discrete state may form (Fig. 13.20). From the increase of the occupied area in $k$ space upon Li adsorption it was found that 0.7 electrons per Li atom

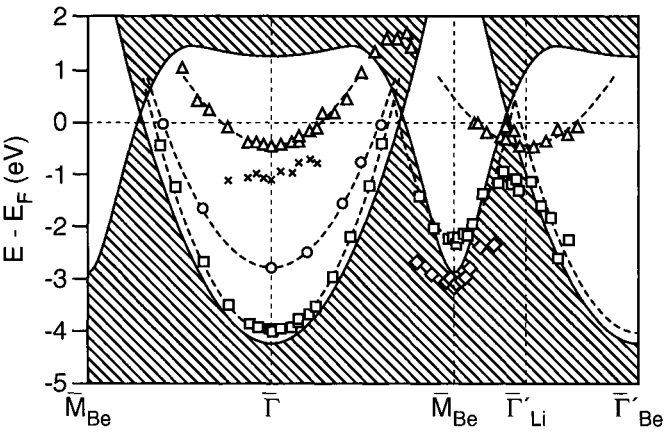


Fig. 13.20. Two-dimensional dispersion for both clean Be(0001) and a saturated monolayer of Li on Be(0001). The measured dispersion of the clean Be SS (surface state) is shown by the circles while the squares (triangles) show the dispersion of the downshifted Be SS (Li band) for the Li-covered surface. Dashed lines are fit to the data in the first Brillouin zones. Dashed lines in the second Brillouin zones represent fits in the first Brillouin zones shifted by the appropriate reciprocal lattice vector. From Watson et al. (1990).

can be accounted for. Out of this 0.33 electrons come from the increase of the occupied area of a Be(0001) surface band which shifts to lower energy as the Li is adsorbed. As pointed out by the authors it is not obvious that one may sum up charge in this manner since the Li overlayer is incommensurate with the substrate. In theory this lack of periodicity means that no surface Brillouin zone is defined. In the case of Be(0001)/Li the upper filled state (0.47 eV below EF, at $k_{\parallel} = 0$ in Fig. 13.20) is however largely confined to the overlayer while the electrons in the lower state reside mainly on the substrate side of the overlayer/metal interface. Therefore there are effectively two different Brillouin zones and these were used to estimate the occupancy.

*13.3.2.3. Resonances in monolayers*

As mentioned above photoemission, which is a rather generally applicable method of obtaining information about the valence electron structure of solids, has not given any information on the energy and dispersion of the resonance expected for a full atomic layer of alkali metal on top of a Cu(111) surface. A similar resonance would be expected also for a full monolayer of alkali metal on Cu(100) and on Al(111). In the case of Al(111) the resonance is expected to be located well below the Fermi edge at the center of the surface Brillouin zone (Ishida, 1989a; Salmi and Persson, 1989). In both cases the experimental spectra show a triangular shaped emission peak at the Fermi edge (Walldén, 1985; Horn et al., 1988a). From the observed coverage and photon energy dependence of the photoemission spectra for Na on Cu(100) the emission was ascribed the surface photoelectric effect (Walldén, 1985). This surface barrier induced emission is found for Al to produce a triangular shaped emission peak at the Fermi edge (Levinson and Plummer, 1981). According to theory the peak should be as wide as the filled part of the valence band. Experimentally the peak width is only a small fraction of this, around 2 eV for Al and 1 eV for Na.

While the theory of the surface photoelectric effect (Feibelman, 1982) is found to account well for the photon energy dependence of the cross section the energy distribution of the photoemitted electrons is poorly understood. To some extent the absence of the resonance expected for Na on Al(111) may be explained by the fact that the theoretical calculation was based on the assumption that the Na atoms are adsorbed on the surface and not in the substitional sites observed experimentally.

Uncharacteristically photoemission as well as other methods have failed to give any information also about other valence electron resonances expected for free electron like metal adsorbates. One interesting failure is that the occupied part of the well known s,p-resonance suggested by Gurney (1935) for an adsorbed alkali metal atom has not, as far as we know, been observed by any direct spectroscopic method. For some time it was believed that a peak near the Fermi edge of He* deexcitation spectra is due to this resonance (Woratschek et al., 1985) but these results have now obtained a different interpretation (Hemmen and Conrad, 1991).

For empty overlayer resonances the spectroscopic methods have been more successful. By inverse photoemission Heskett et al. (1987, 1988) observed such a resonance for a $(2 \times 2)$ Na overlayer on Al(111) located 0.9 eV below the vacuum level. This resonance can be understood in terms of a simple model with one free electron metal slab on top of a free electron metal substrate. The potential step at the junction gives an electron reflectivity which is sufficient to produce a peak in the $k$-resolved density of electronic state at an energy near the experimentally observed one (Salmi and Persson, 1989). The structure of Na/Al(111) is now known to be more complicated than assumed in the calculations. Qualitatively the same results are however expected for any overlayer with a considerably larger electron density in the substrate than in the overlayer.

### *13.3.3. Quantum well states in multilayers*

The first observation of quantum well states in thin metal films were made via tunneling experiments (Jaklevic et al., 1971; Jaklevic and Lambe, 1975). The films were prepared by evaporation onto an Al substrate which had been oxidized prior to the deposition in order to obtain a thin insulating spacer layer suitable for the tunneling experiment. The sample was then annealed at a temperature which gave a preferential orientation and placed in a cryostat for the $I-V$ measurements, which were made at liquid helium and $LN_2$ temperatures. Results were reported for several metals (Au, Ag, Mg and Pb) with film thicknesses ranging between around a hundred and a thousand Angström. The lower limit is set by the requirement that the film must serve as an electrode in the tunneling sandwich. As shown in Fig. 13.21 there is an oscillatory component in the current through the sandwich when the current is recorded versus the voltage across it. The separation between the energies of the standing wave states in the film is given by the separation between the peaks in the tunneling characteristic. The results were used to determine the dispersion of bulk electrons in an energy range of a few eV about the Fermi energy. These beautiful experiments demonstrated convincingly that the quantum size effect can be observed for metals. One reason why the method has not become popular as a tool for probing quantum well states is probably that only modest quantum size effects are expected at the rather large film thicknesses required.

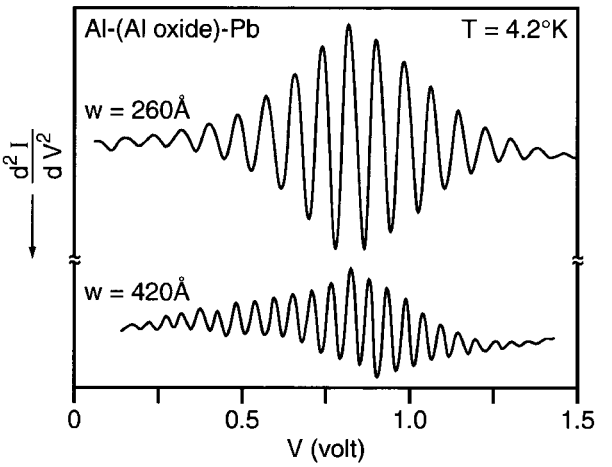


Fig. 13.21. Experimental plots of $d^2I/dV^2$ versus voltage for 260 Å and 420 Å Pb films in an Al–(Al oxide)–Pb tunneling sandwich. From Jaklevic and Lambe (1975).

By photoemission and inverse photoemission quantum well type overlayer states for two or more atomic layers thick films and the related oscillations in electron reflectivity spectra (Thomas, 1970; Jonker et al., 1983) have been observed for several overlayer/metal substrate combinations. Photoemission and inverse photoemission measurements have been reported for Cs and Ba adsorbed on Cu(111) (Lindgren and Walldén, 1987, 1988a), Na on Cu(111) (Carlsson et al., 1994, 1995), Na on Ag(111) (Carlsson et al., 1996), Na, K, Rb and Cs on Cu(100) (Woodruff and Smith, 1990), Ag on Cu(111) and on Au(111) (Miller et al., 1988; Mueller et al., 1989, 1990), Ag on Au(111) (Beckmann et al., 1993; Beckmann, 1996), Ag on Fe(100) (Brookes et al., 1991), Co on Cu(100) (Clemens et al., 1992), Cu on Fe(100) and on fcc Co(100), Ag and Au on Fe(100), Fe on Au(100) and Co on Cu(100) (Ortega et al., 1993), Ag on Ni(111) (Miller et al., 1994), Cu on Co(001) (Johnson et al., 1994), Ag on graphite (Patthey and Schneider, 1994), Hg on W(110) (Zhang et al., 1994). With two photon photon–electron spectroscopy, image potential states have been observed for 0–10 ML of Au on Pd(111) (Fischer and Fauster, 1995) and for Fe and Co on Cu(100) (Wattaner and Fauster, 1996). Using semiconductors as substrates thin film states have been observed for Ag on Si(111) (Wachs et al., 1986; Neuhold and Horn, 1997), Na on Si(100) (Hamawi and Walldén, 1992) and Pb and Pb/In on Si(111) (Jalochowski et al., 1992a). In the case of noble metals thin films of Ag and Au have been stacked on top of each other with alternating Ag and Au layers and this has allowed states to be observed which are ascribed to surface states appearing in the band gaps of the superlattice (Miller and Chiang, 1992). Using angle and spin resolved photoemission exchange split spin-polarized s,p-states in a non-magnetic overlayer on a magnetic substrate have been observed for Ag on Fe(100) (Brookes et al., 1991) and for Cu on fcc Co (100) (Carbone et al., 1993). For Co on Cu(100) this method revealed an enhanced exchange splitting at the center of the Brillouin zone for thicknesses less than 5 atomic layers Clemens et al. (1992). For Fe(110)/Pd spin resolved photoemission detected spin-split states for 1 and 2 ML thick overlayers (Weber

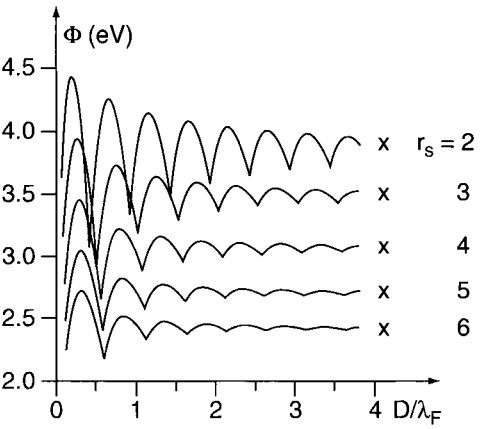


Fig. 13.22. Work functions versus $D/\lambda_F$ for electron densities corresponding to $r_S = 2, 3, \ldots, 6$. $D$ denotes the film thickness and $\lambda_F$ the Fermi wavelength. The crosses on the right hand side of the curves give the work functions calculated by Lang and Kohn (1971) for a half space model corresponding to infinite thickness. From Schulte (1976).

et al., 1991). In a more complicated geometry states in ultra-thin Cu films separated from the Cu(100) substrate by a an epitaxial Co wedge (0–11 Å) were studied with angle and spin-polarized photoemission (Li et al., 1995).

*13.3.3.1. Oscillatory thickness dependence*

The obvious reason for the study of quantum well states and resonances in thin films is the possibility to monitor the change in the electronic structure of a solid when the thickness is changed layer by atomic layer and correlate this with various properties observed for thin films. Several electronic properties are expected to depend on the thickness in an oscillatory manner. An instructive example of this is given by the thickness dependence of the work function calculated by Schulte (1976) for a slab of jellium in vacuum. As the film is made thicker all states shift to lower energies. At regular thickness intervals new states therefore become occupied. An estimate of the thickness increase needed to bring another level below EF is obtained by assuming the potential to be constant and the vacuum barriers to be infinite. The electron energy is then given by $E = \hbar^2(k_\parallel^2 + k_\perp^2)/2m$, where $k_\parallel = n\pi/d$. This gives a period $\lambda_F^2$ for the low energy edge (at $k_\parallel = 0$) of new bands to be pulled below the Fermi level. The same thickness period is obtained for the work function variations (Fig. 13.22). In this case the oscillations are due to the shifting balance between the number of electrons with a relatively high energy and the number with a low energy. States with energies close below the Fermi level have long tails and spill out charge far into vacuum. The large dipoles associated with the high energy states will therefore lead to an increase of the work function as the low energy edge of a an electron energy band becomes occupied. A small additional increase of the thickness will mean that more states with a relatively high energy become filled and the work function increases. This increase is however balanced and eventually overcome by the shorter vacuum tail obtained when

the band moves to lower energy. The result is a periodic variation with the period given by the thickness increase needed for new states to become filled.

Another characteristic of the $e\Phi$ oscillations is that they are damped. The damping is due to the smaller amplitude of the states as these are normalized to a wider potential well. If the well is wide enough that many energy bands already extend below EF then the appearance of yet another filled state does not change the charge distribution in the film as much as when there are only few filled states. For a real metal the oscillations will often be masked due to the fact that the thickness can not be changed infinitesimally. What remains to be observed is therefore a beating between the inherent spatial period $\lambda_F^2$ such as calculated by Schulte and the sampling period given by the atomic layer thickness (Feibelman, 1983). An oscillatory work function ascribed to the quantum size effect was observed by Marliere (1990) in an experiment where In is deposited on a Au(111) substrate and the work function changes are measured both by the Kelvin method and the diode method.

Recent results show that the variation with thickness of the electron spill out can be monitored by He atom scattering. In two experiments the apparent step height measured with this method is found to have an oscillatory thickness dependence for Pb films on Cu(111) (Braun and Toennies, 1997) and on Ge(100) (Crottini et al., 1997). The step height seen with this method is the vertical distance between the turning points of He atoms reflected by adjacent terraces. The He atom–surface interaction energy is proportional to the electron density and strong enough that the turning point falls on the vacuum tail of the electron density profile at a position determined by how far the tail extends into vacuum. The apparent step height is measured via the interference in the reflected specular beam intensity between the waves reflected from areas of the film which are $N$ and $N + 1$ atomic layers thick. From the oscillations recorded when beam energy is varied a step height is obtained. When this procedure is repeated for films with different thickness the step height is found to have an oscillatory thickness dependence as shown for Cu(111)/Pb in Fig. 13.23. The measured values (open circles) are shown together with values estimated from a model calculations.

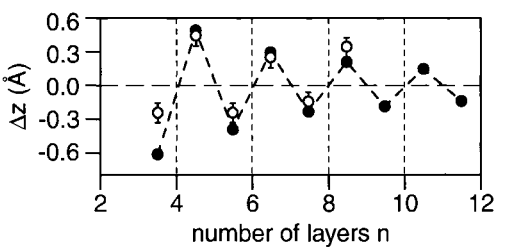


Fig. 13.23. The thickness dependence of the apparent step height measured by He atom scattering for Cu(111)/Pb. The values obtained from the oscillatory period of the specular reflectivity measured versus beam energy are indicated by open circles. Filled circles show theoretical estimates of the apparent step height. From Braun and Toennies (1997).

*13.3.3.2. Bulk band dispersion*

Of fundamental interest is that as for organ-pipe phonon modes the measured overlayer state energies can be used to determine the bulk band dispersion of the overlayer metal in the direction perpendicular to the sample. Photoemission, especially in its angle resolved version, is the standard method to probe the bulk and surface band structure of solids. With the advent of this method (Gustafsson et al., 1971) much new information has been obtained regarding the surface and bulk bands of solids. A difficulty with the method is that the dispersion can not be mapped directly from the measured spectra. The crux is that there is no conservation rule that allows the perpendicular component of the wave vector inside the sample to be determined from the wave vector measured for the emitted electron. The parallel wave vector is conserved and this makes the method well suited for measurement of the dispersion of overlayer and surface states.

Lacking a conservation rule to obtain the wave vector bulk band determinations by photoemission are often based on some assumption that allows the wave vector to be calculated. The final state bands may for example be assumed to be free electron like and often this is a reasonable assumption. One way to solve the problem is to record spectra for different crystal surfaces. If the same optical transition can be monitored for two different surfaces two $k_{\parallel}$ values may be determined (one for each surface) and this is enough to calculate the wave vector inside the crystal (Kane, 1964). The method has been demonstrated (Courths and Hüfner, 1984) but it has not been practiced much probably due to the expected difficulty of assuring that the same optical event is observed for the two crystals.

For samples with overlayer states the bulk band dispersion perpendicular to the surface can be determined if the measurements are made for a number of different and known thicknesses. The method was demonstrated for Cs on Cu(111) (Lindgren and Walldén, 1988a, b) using spectra such as shown in Fig. 13.24 and has been applied to a few systems (Lindgren and Walldén, 1989a; Mueller et al., 1990; Ortega et al., 1993; Beckmann et al., 1993). It is based on the observation that $k_{\perp}$ can be obtained by repeated use of the phase condition satisfied by the states. If two overlayer states are observed to have the same energy but appear at different thicknesses the barrier phase shifts can be eliminated and the perpendicular wave vector is given by $\pi(m_1 - m_2)/(d_1 - d_2)$. The wave vector is thus obtained if the thicknesses can be measured and the correct quantum numbers can be assigned to the observed states. In practice two overlayer states will not have the same energy. The spatial period $\Delta d = d_1 - d_2$ may then be obtained as the horizontal distance between smooth curves drawn through the points of a plot of the overlayer state energies versus the overlayer thickness, such as shown in Fig. 13.25 for Cs on Cu(111). The quantum numbers assigned to the states are indicated in the diagram. To obtain the expression for the perpendicular wave vector it was assumed that the barrier phase shifts only depend on the energy and not on the thickness. If data can be obtained for a sufficient range of thicknesses then several periods $Ad$ may be observed and it then becomes possible to check whether the barriers depend on the thickness. From the energies measured for hexagonal Cs layers on Cu(111) the dispersion shown in Fig. 13.26 was obtained using data for films, which are three atomic layers or thicker and in this thickness range there is no indication of any strong thickness dependence for the barrier phase shifts. Also shown in Fig. 13.26 is the energy dependence obtained for the sum of the barrier phase shifts.

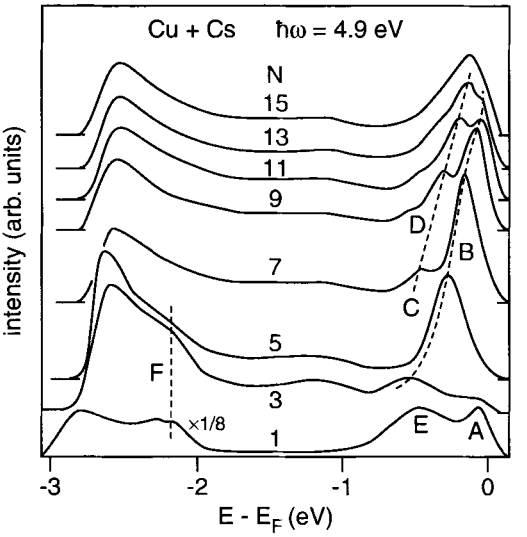


Fig. 13.24. Photoelectron energy spectra recorded along the surface normal at a photon energy of 4.9 eV from Cu(111) covered by the number of atomic Cs layers indicated in the diagram. A, B, C and D are emission features due to discrete overlayer states while E and F are due to the substrate. From Lindgren and Walldén (1988a).

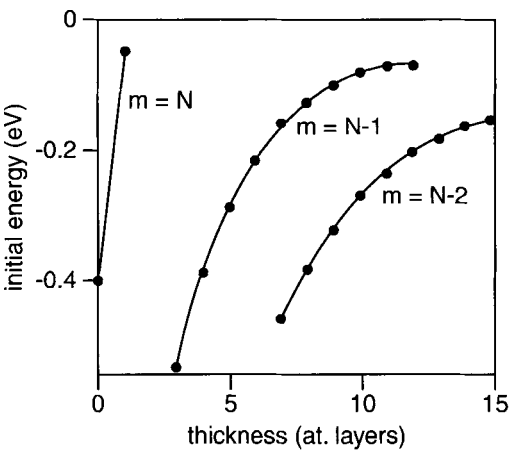


Fig. 13.25. The energy relative to $E_F$ of overlayer states observed for Cs on Cu(111) plotted against the coverage in units of atomic layers $N$. Indicated in the diagram are also the quantum numbers $m$ assigned to the states. From Lindgren and Walldén (1988a).

Alternatively the period can be obtained by adjusting the spectrometer to record the intensity at a certain energy and observe the oscillatory intensity as the film thickness varies. The latter procedure was used to obtain the dispersion of the s,p-bands of Cu, Ag and Au from inverse photoemission measurements from the resonances formed in overlayers of these metals deposited on Fe and Co substrates (Ortega et al., 1993).

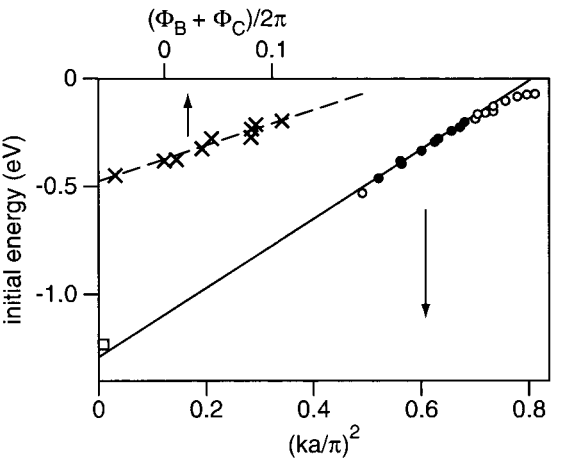


Fig. 13.26. The energy relative to $E_F$ of observed overlayer states for Cs on Cu(111) plotted (as crosses) against $\Phi_B + \Phi_C$ (upper scale). The dashed line is used to obtain values for $\Phi_B + \Phi_C$ outside the measured energy range. Along the lower scale the energy relative to $E_F$ is plotted (as circles) against $(ka/\pi)^2$, where $k$ is the perpendicular wave vector and $a$ is the Cs interlayer distance. Empty circles are used when $\Phi_B + \Phi_C$ has been obtained by extrapolation. The square on the vertical axis indicates the band bottom calculated by In-Whan Lyo and Plummer (1988). From Lindgren and Walldén (1988a).

Among the results obtained for the bulk band structure we first focus attention on the detailed investigation of the electronic structure of Ag in the Fermi surface neck region (Mueller et al., 1990). According to the authors a careful measurement of the overlayer state energies from spectra such as shown in Fig. 13.27 can be used to determine details of the Fermi surface with a better accuracy than obtained with standard techniques such as the de Haas–van Alphen method. Fig. 13.28 shows a portion of the Fermi surface contour obtained from the photoemission measurements on Ag covered Cu(111) by Mueller et al. (1990). Loly and Pendry (1983) suggested that measurements on overlayer systems will remove the limits to accurate electron energy band determinations. The main advantage with overlayers is that the emission peaks are broadened only by the hole lifetime. The narrow emission peaks obtained for an overlayer system means that the energy can be determined with a high degree of accuracy. For thick samples the emission peaks are broadened to an extent which depends upon the final state as well as the initial state life times and the dispersion of each of the two bands involved in the optical transition.

In practice the limit to accurate $E(\mathbf{k})$ determination will often be set by the uncertainty regarding the thickness of the overlayer. Even for films that grow largely in a layer by layer fashion the front may show a number of incomplete atomic layers as discussed by Jalochowski et al. (1992a). The overlayer state spectrum will then be characteristic of a weighted thickness average. Even when the thickness varies laterally by several atomic layers distinct energies may be resolved but then only for $k$-vectors in limited intervals around certain $k$-values. This case was discussed in detail by Jaklevic and Lambe (1975). These particular $k$-vectors are determined from the condition that the energy is the same or nearly the same for a film consisting of, let us say, a rather large number $N$ of atomic layers

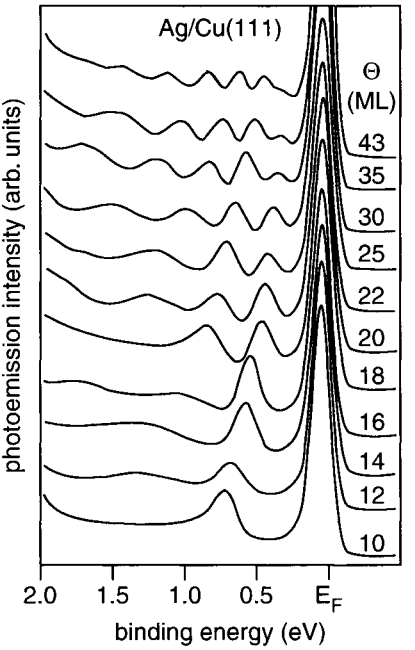


Fig. 13.27. Normal emission spectra taken, with 10 eV photon energy, at different Ag coverages on Cu(111). The binding energy scale is referred to the Fermi level $E_F$ and the coverage is expressed in terms of Ag(111) monolayers (ML). From Mueller et al. (1990).

as for a film with $N+n$ atomic layers, where $n$ is a relatively small number compared to $N$. If, for the moment, we ignore the barrier phase shifts in the phase condition this means that $2k_\perp Nd = 2m_1\pi$ and $2_\perp(N+n)d = 2m_2\pi$. By subtraction one finds that the standing waves with $k$ vectors given by $\pi/d$ times the ratio between two integers may be expected to give sharp overlayer states even when the film has uneven thickness.

When only few atomic layers are adsorbed it is often possible to determine the thickness directly from the measured spectra. During continued metal deposition an emission peak may appear representative of one atomic layer and the peak is then assumed to have its maximum intensity at the completion of the first atomic layer. Clearly this determination is not exact since the second layer could start to form before the first layer is complete. The intensity maximum is however expected to occur when as large as possible a fraction of the surface is covered by one atomic layer. When the quantum well is narrow the deposition of one more atomic layer usually produces a new overlayer state emission peak, which is well separated in energy from the peak observed prior to the addition of the new atomic layer. This is shown, for example, by the spectra obtained for one, two and three atomic layers of Ag on Fe(100) (Brookes et al., 1991) (Fig. 13.29). Cs on Cu(111) gives another example of this. Here one state is observed close to EF when there is one atomic layer on the surface. For two atomic layers the phase condition cannot be satisfied for any energy between EF and the lower edge of the Cu band gap, while for three atomic layers a state appears 0.55 eV below EF. An advantage of this procedure for thickness determinations is

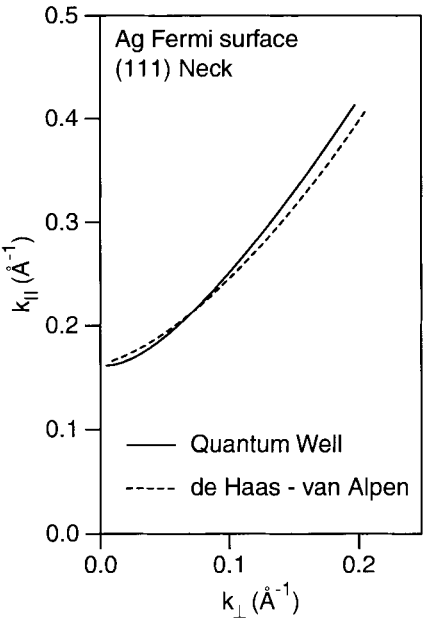


Fig. 13.28. The Ag Fermi surface (solid curve) contour determined from the quantum well state photoemission. The dashed curve represents results obtained from de Haas–van Alphen measurements. From Mueller et al. (1990).

that no detailed knowledge about the electronic structure of the overlayer metal is required. Another method can be used for films which are sufficiently thick that the energy separation, AE, between the states is small enough such that two or more states are observed in the same spectrum. If the dispersion is known for the overlayer metal and the energy dependence of the barrier phase shifts can be ignored in the energy range of interest the thickness $d$ can be estimated from $d\,\Delta E = \pi\,\mathrm{d}E/\mathrm{d}k$ (Hamawi and Walldén, 1992).

At higher metal coverages the spectra change less upon the addition of one more atomic layer and this means that the emission peaks appear to shift in a continuos manner as more metal is adsorbed. The shift to a higher energy for the peaks observed in Figs. 13.25 and 13.29 as the film becomes thicker may be confusing. As a quantum well widens one expects states to move to lower energies. If one could monitor a state with a certain quantum number and increase the thickness of the Cs and Ag layers in a continuous manner then one would find the energy to shift downwards with a rapid rate such that approximately one new state would become populated for each new atomic layer deposited. The observed small shift to higher energy is the result of the sampling of the rapidly changing energy level structure at discrete thickness intervals. For the two metals one then finds that a state with quantum number $m$ for a stack of $N$ atomic layers has slightly lower energy than the state with quantum number $m+1$ in a film consisting of $N+1$ atomic layers. The thickness period $\Delta d$ is the stroboscopic like beating observed when the fast thickness dependence of the electronic structure is sampled at the discrete intervals given by the atomic layer thickness. This is illustrated in Fig. 13.30 by the thickness dependence of the energies

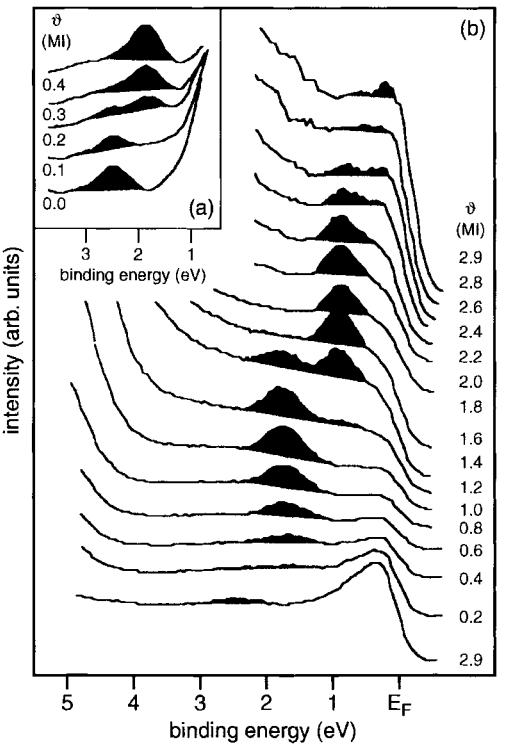


Fig. 13.29. Normal-emission angle-resolved photoemission spectra for Fe(100)/Ag at a photon energy of 52 eV and p-polarized light ($\Phi_i = 70°$, showing the evolution of the spectra with increasing silver overlayer thickness in monolayers (ML) for (a) the low coverage regime 0–0.4 ML and (b) coverages up to around 3 ML. From Brookes et al. (1991).

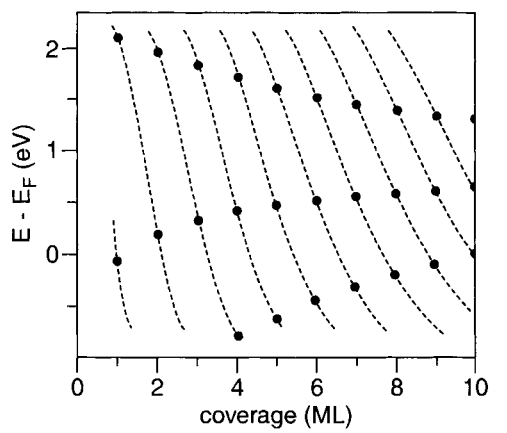


Fig. 13.30. Energies estimated for discrete overlayer states for Na on Cu(111) drawn against the thickness given in units of atomic layers. The dashed curves show the rapid thickness dependence expected if the thickness could be varied in a continuous manner. From Lindgren and Walldén (1989a).

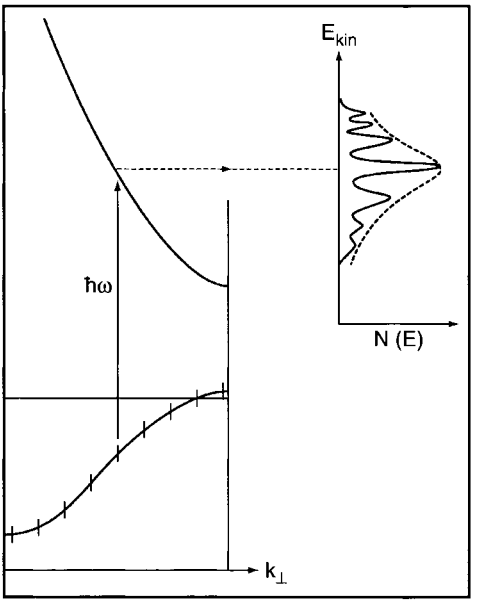


Fig. 13.31. Schematic drawing indicating the difference between the angle resolved photoemission spectrum obtained for a thin film (full drawn) and a thick sample (dashed).

predicted for Na overlayers on Cu(111) using the simplified model potential discussed above (Lindgren and Walldén, 1989a). One advantage of making dispersion measurements via thin films is that the photon energy can be chosen with some freedom. With a bulk sample the photon energy has to be adjusted to the energy required for the transitions between two bulk bands. To be able to probe the transitions over the entire zone this usually means that the photon energy has to be varied over a wide range. When thin films are used the only demand is that the emission intensity for the overlayer state is sufficient to distinguish the state from the background. Schematically the spectra characteristic of a thick sample and a thin film are expected to differ approximately as shown in Fig. 13.31. The spectrum for the thick film is an envelope to the thin film spectra. In the thin film case one may be able to resolve emission peaks far out in the wings of the intensity envelope.

*13.3.3.3. Emission intensities*

Characteristic of quantum well states is that the amplitude of the states becomes smaller as the electronic charge is spread over a wider well. This result of the normalization condition is directly reflected by the lower intensity of the peaks recorded in photoemission spectra as the film thickness increases. The emitted intensity is determined by the amplitude of the states within the shallow escape depth of the photoemitted electrons. The intensity fall off with increasing thickness should therefore be universal for several atomic layers thick films. For films thinner than this, when the thickness is comparable to the escape depth, the intensity may reflect the total optical transition probability of the overlayer state electrons. For free electron like metal overlayers the optical transition rate is expected to be small in

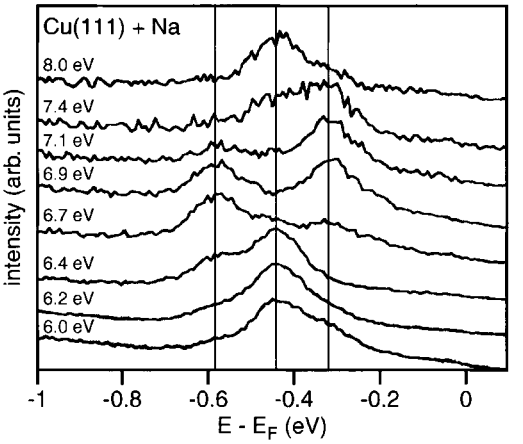


Fig. 13.32. Photoemission spectra recorded at different photon energies along the surface normal of Cu(111) covered with an Na film having an average thickness of 6 ML. The three peaks are due to quantum well states characteristic of 5- (the peak at $E_1 - E_F \approx -0.58$ eV), 6- (−0.44 eV) and 7-ML-thick (−0.32 eV) parts of the film. From Carlsson et al. (1995).

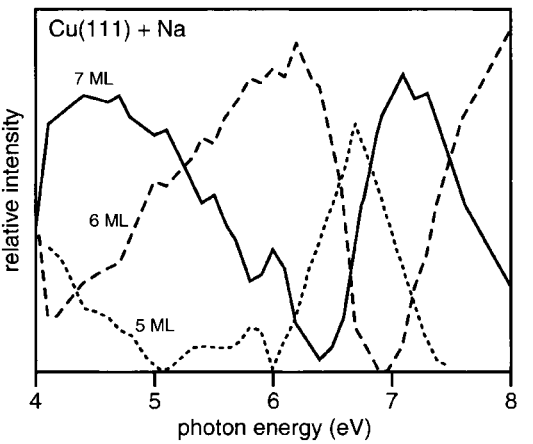


Fig. 13.33. Photon energy dependence of the relative intensities of the three quantum well state peaks shown in Fig. 13.32. From Carlsson et al. (1995).

the interior of the film. The contributions from the tails then become important. Depending on the choice of photon energy the emission may be dominated by the tail on the vacuum side or by the tail on the substrate side of the overlayer/substrate interface. If both tails contribute with comparable strength the interference in the photoemission matrix element will give an oscillatory intensity for the quantum well state when the photon energy is varied.

Strong cross section oscillations are observed for discrete states characteristic of Na overlayers on Cu(111), Figs. 13.32 and 13.33 (Carlsson et al., 1995). The overlayer is nominally 6 ML thick but the thickness is not uniform and quantum well states character-

istic of 5, 6 and 7 ML thick areas of the film is observed. In this case the tail in the substrate is similar to the tail of the surface state on the clean Cu(111) surface and this state gives strong emission at low photon energies. The rapid oscillations observed indicate that the two interfering sources are far apart and that the tails of the states thus are important. Compared to the heavier alkali metals the mean free path is long for Na (around 10 Å in the measured energy range) (Smith et al., 1993), making the emission due to the tail of the quantum well state in the substrate particular strong for this metal. Notable in Fig. 13.32 is that the intensity of the 6 ML state is out of phase with the intensities of the 5 and 7 ML states. This reflects the odd–even like character of the states. For these states $m = N$ and the number of nodes in the film is equal to the number of atomic layers. The out of phase variation for the intensity of odd–even states in a quantum well was predicted by Adawi (1964). An attempt to account for the observed cross section variation in simple terms was not successful. The observed variation with photon energy is approximately twice as rapid as that obtained by assuming interference between the back and front sides of the film. If the theoretically estimated self-energy correction for Na metal (Hedin and Lundqvist, 1969) is taken into account the discrepancy is reduced but only by 1/3. A realistic prediction of the cross section would furthermore have to include a calculation of the field in the film. For a thin film of alkali metal the response to the incident light is expected to deviate markedly from that calculated from the local-optics model if the photon energy is below the plasmon energy of the overlayer metal (Liebsch, 1991; Ishida and Liebsch, 1992).

For Ni(111)/Ag an oscillatory photoemission cross section is observed for resonant overlayer states (Miller et al., 1994). For this system, in contrast to Cu(111)/Na, a main contribution to the intensity comes from the interior of the film. The films studied were 10 ML and thicker which means that the free mean path is smaller than the thickness and the contribution from the back side therefore unimportant. Using a simple model the cross section variations shown in Figs. 13.34 and 13.35 is well reproduced. Also in this case the odd–even character of the states is reflected by the cross section. In Fig. 13.35 the characteristic out of phase variation is shown by the three resonances observed for the 18 ML thick film. That oscillations with a thickness dependent period is observed even though the contribution to the intensity from the back side is unimportant is due to the thickness dependent level spacing and the energy spread of the resonant levels. A resonance is not observed at constant initial energy when the photon energy is varied (Fig. 13.34). The matrix element varies across the resonance and the variation is different for different photon energies such that the photoemission peak is observed to slide from one side of the resonant energy to the other as the photon energy is varied. When as in Fig. 13.35 the intensity is recorded at a constant initial energy this peak position variation is emphasized. The results demonstrate the importance of the matrix element for the photoemission line shape produced by overlayer resonances. Even more complicated line shape changes are observed when there are contributions to the intensity not only from the interior of the overlayer. For 2 ML on Ag(111) and Cu(111) a split photoemission peak is observed for a resonance due to out of phase contributions from the overlayer and the bulk of the substrate (Carlsson et al., 1996).

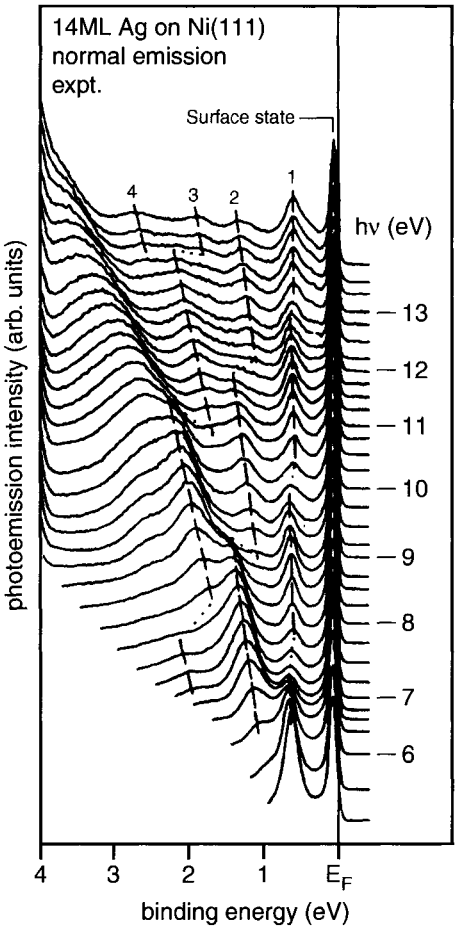


Fig. 13.34. Normal-emission photoelectron spectra for a 14 ML thick Ag film on Ni(111). Scans are shown for each 1/4 eV photon energy from 5.5 to 13.75 eV. The binding energy is referred to the Fermi level $E_F$. The dashed lines are guides to the eye showing the peak shifts. From Miller et al. (1994).

### *13.3.3.4. Spin-polarized quantum well states*

Recently it was suggested (Ortega and Himpsel, 1992; Ortega et al., 1993) that the thickness period of the oscillatory magnetic coupling between magnetic films separated by a non-magnetic metal spacer layer is determined by the periodic appearance of overlayer states near EF in the nonmagnetic film. The importance of considering the effects of the confinement on the states in the spacer layer had been pointed out in theoretical work and has been discussed extensively in the literature (Edwards et al., 1991, 1994; Ehrlich, 1993). Essential experimental evidence to support the role given the quantum well states is the observation by Brookes et al. (1991) via angle and spin-resolved photoemission that the overlayer states for Ag on Fe(100) (Fig. 13.29) indeed are formed by minority spin electrons (Fig. 13.36). As the Ag thickness is increased from one to three

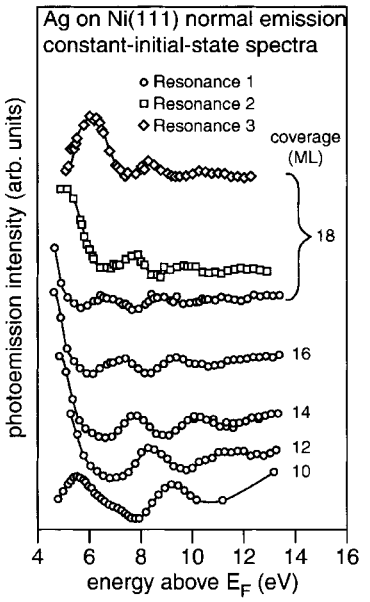


Fig. 13.35. Constant-initial-state spectra for Ag films on Ni(111). The data points are connected by smooth curves. The bottom five curves are results for the $n = 1$ peak (see Fig. 13.34) for five different film thicknesses as indicated. The top three curves are for the $n = 1$–3 peaks for a film thickness of 18 ML. From Miller et al. (1994).

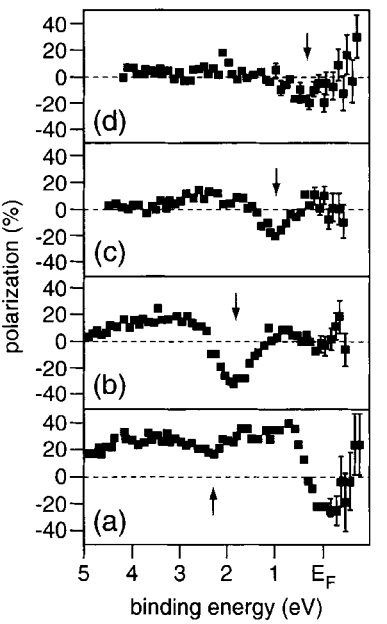


Fig. 13.36. Spin-polarization spectra taken at normal emission, $h\nu = 52$ eV and $\Phi_i = 70°$ for (a) clean Fe(100) and with silver overlayers, (b) 1 ML, (c) 2 ML and (d) 3 ML thick. The arrows mark the positions of the peaks in the photoemission spectra shown in Fig. 13.29 for each coverage. From Brookes et al. (1991).

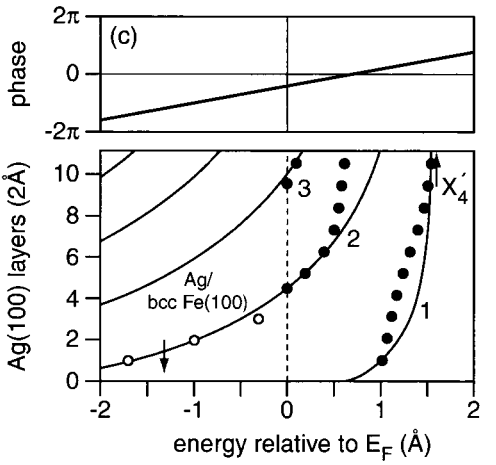


Fig. 13.37. Energy of empty overlayer states for Ag on Fe(100) (full circles). The open circles show the energies of the filled, spin-polarized overlayer states observed by Brookes et al. (1991). From Ortega et al. (1993).

layers the overlayer state energy approaches $E_F$ and as more than three atomic layers are adsorbed the corresponding state can be observed above $E_F$ by inverse photoemission (Ortega et al., 1993) (Fig. 13.37). The spin polarization of the Ag quantum well state is explained by the fact that the phase condition satisfied by an overlayer state in this case depends on the spin of the electron (Brookes et al., 1991). The reason for this is that the substrate s,p-band gap of the spin band structure occurs at different energies for the two spin bands. Hence the phase shift $\Phi_C$ will depend on the spin of the electron. Moreover, at energies near $E_F$ there is a band gap only for the minority spin states. This means that only minority spin electrons are able to form discrete overlayer states while the majority electrons can only form resonances.

Since states near $E_F$ are expected to be responsible for the magnetic coupling the thickness period for the appearance of spin polarized states with energies near the Fermi level is of obvious interest. From the phase condition applied to states at EF one obtains $\pi/\Delta d = \pi/a - k_F$, where a is the atomic layer thickness. With a weaker thickness dependence for the density at $E_F$ of majority spin states, which have a less well defined energy, the spin density modulations may be expected to reflect those of the minority spin electrons. The spin density is then found to be modulated with a characteristic wave vector $2(\pi/a - k_F)$ the factor 2 originating from the squaring of the wave function to obtain the density of electrons. For Ag the period so obtained is 5, 6 atomic layers which can be compared with an experimental value of 5–6 atomic layers (Celinski et al., 1993). While the period obtained from the overlayer state model thus is in the right range a detailed evaluation would have to include a summation over all $k_{\|}$ values. The period will depend on $k_{\|}$ more or less strongly depending on the shape of the Fermi surface.

### *13.3.4. Oscillatory second harmonic generation*

For nonmagnetic free electron like metal films short periods, similar to those mentioned above for the magnetic coupling, have been found in the optical second harmonic genera-

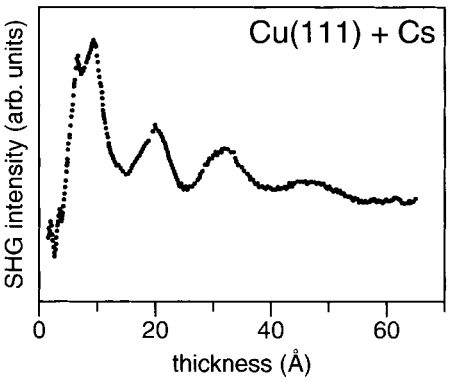


Fig. 13.38. Optical second harmonic intensity measured for Cs covered Cu(111) when light with $\lambda = 1064$ nm from a pulsed laser is incident at an angle of 570. The strong enhancement relative to the substrate signal and the oscillatory thickness dependence is observed only for p-polarized incident light. From Hamawi et al. (1991).

tion (SHG) (Song et al., 1988; Liebsch, 1987; Hamawi et al., 1991; Lindgren and Walldén, 1992; Plummer et al., 1989; Kempa et al., 1988), for a review of optical SHG applied to surfaces (see Richmond et al., 1988). While spin density waves are of interest for the magnetic coupling the rapid thickness oscillations observed for the SHG is ascribed to Friedel type charge density oscillations. In the magnetic case the observed period is a beating between the true period of the spin polarization, $2k_F$, and the spatial sampling period given by the atomic layer thickness. Also the SHG oscillations have considerably longer period than the static Friedel period $\lambda_F^2$ but in this case this is assigned to the appearance of a longer period when the optical frequency range is reached (Song et al., 1988; Plummer et al., 1989; Liebsch, 1987). The wavelength is frequency dependent and is expected to become smaller as the frequency is increased. For Rb on Ag(110) a thickness period of 22 Å is measured at a wave length of 1064 nm for the incident light, while it is 12 Å at 532 nm. At the shorter wave length the oscillations have a smaller amplitude. For Cs on Cu(111) (Hamawi et al., 1991) the wavelength is 14 Å at 1064 nm (Fig. 13.38) while for 532 nm incident wave length no oscillations are resolved. According to one theoretical estimate (1987) the wavelength of the Friedel-oscillation is given by $hk_F/m\omega$, which for Cs ($k_F = 0.65$ Å$^{-1}$) and $h\nu = 1.17$ eV is 26 Å. Another estimate, by Kempa et al. (1988) gives a wavelength of 37 Å.

For adsorbed alkali metals the strong coverage dependence starts already in the monolayer coverage range (Tom et al., 1986). For Cs on Cu(111) there is a strong increase of the SHG at a coverage of 15% of a full monolayer if light with $\lambda = 1064$ nm is used (Fig. 13.39). The sharp increase was ascribed to an onset at this coverage of inter-surface-band transitions (Lindgren and Walldén, 1992). In the case of clean Ag(110) such transitions are observed to produce a strong enhancement of the SH intensity (Urbach et al., 1992). For the clean Cu(111) surface the separation between the highest filled and the lowest empty surface bands is too big (more than 4 eV) for one or two photon optical transitions to occur with $\lambda = 1064$ nm. As alkali metal is adsorbed the work function is reduced and this means that the empty image barrier states and the filled surface states will come closer

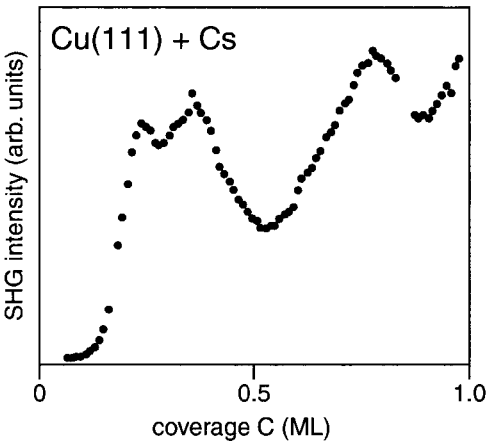


Fig. 13.39. Optical second harmonic intensity versus coverage for Cs on Cu(111) for p-polarized incident light with $\lambda = 1064$ nm and an incidence angle of 57°. The substrate was rotated to an azimuthal angle which produced the maximum intensity for the second harmonic intensity from the substrate. From Lindgren and Walldén (1992).

in energy. The onset of SH intensity is assigned to two photon transitions into the lowest of the surface barrier states. The doublet character of the SHG peak at around 0.2 ML is assigned to the splitting between the lowest empty barrier state and the remainder of the series of image potential states.

The high sensitivity of the SH signal to the polarizability of an adsorbate can be exploited to monitor structure changes. This was demonstrated for Al(111)-($\sqrt{3} \times \sqrt{3}$)R30°–K (Wang et al., 1995). If this structure is taken from $LN_2$ to room temperature the K atoms change from atop to substitutional sites with the long range order preserved (Stampfl et al., 1992; Andersen et al., 1992a). The structure change, which is complete at around 220 K, gave a drop of the SH intensity by a factor of 3 with the light source used ($\lambda = 1064$ nm, 100 ps pulses, 75 MHz repetition rate, 400 mW average power).

### *13.3.5. Core level binding energies*

The binding energy of a given core level depends on the local surrounding of the atom. As a result core level binding energies can provide qualitative structural information. With the development of high resolution (50–100 meV) core level spectroscopy much new information about the local atomic order becomes available. Simply by counting the number of components found for a certain core level qualitative information can be obtained, which is useful as guidance for quantitative structure determinations. The recent Na 2p and Al 2p photoemission spectra recorded for Al(111)/Na provide examples of this use of core level spectroscopy (Andersen et al., 1992a, 1993). When Na is deposited at room temperature the (2 × 2) structure formed at 0.5 ML surface coverage is ascribed to a surface alloy involving two surface layers (Fig. 13.40, topmost spectra). Compared to the clean substrate there are, for the (2 × 2) structure, two new levels for each Al 2p spin–orbit component, which shows that there are at least two new Al sites with different local surroundings.

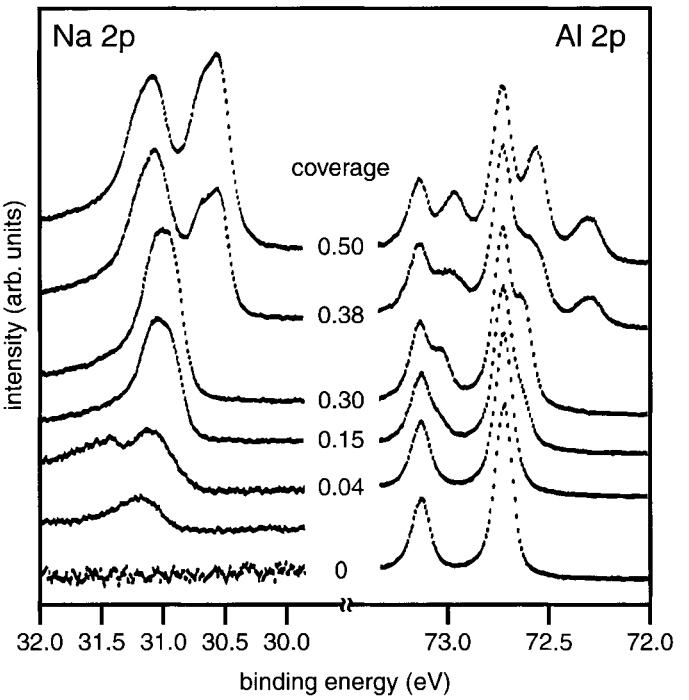


Fig. 13.40. Na and Al 2p core level spectra for different submonolayer coverages after deposition of Na on Al(111) at room temperature. The spectra are measured at 100 K. At 0.5 ML a (2 × 2) structure is formed by a surface alloy with both Al and Na in the two top atomic layers. At 0.3 ML the order is ($\sqrt{3} \times \sqrt{3}$) with Na atoms occupying substitutional sites in the uppermost substrate layer. From Andersen et al. (1993).

Upon deposition onto a $LN_2$ cooled substrate the Na atoms reside on top of the substrate and in that case no additional Al 2p peaks are observed, only a small shift (by 0.07 eV) (Fig. 13.41). The Na 2p spectra of the (2 × 2) structure show two components separated by around 0.5 eV (Fig. 13.40), which shows that there are at least two Na sites. This means that the (2 × 2) structure is not due to three rotated domains of a (2 × 1) structure as had been suggested previously. The two components are instead ascribed to Na atoms in two layers with also Al atoms in both of these layers. At low coverages the spectra obtained after deposition at room temperature are similar to those measured when the substrate is held at $LN_2$ temperature which indicates that the intermixing is not important at low coverages. For the Al(111)-($\sqrt{3} \times \sqrt{3}$)R30° Na structure formed at 0.33 ML with Na atoms in substitutional sites there is only one Na 2p-core level peak, at 31 eV, and one adsorbate induced Al 2p peak shifted by 0.13 eV to lower binding energy with respect to the original substrate peak (Fig. 13.40). At low temperature when Na remains on top of the substrate the Na 2p-level has 0.2 eV lower binding energy than observed at room temperature for the substitutional sites and at the same coverage (Fig. 13.41). A shift in the other direction would be expected since the common observation is that the binding energy is higher for a site with lower coordination. The inconsistency is ascribed to the formation of islands

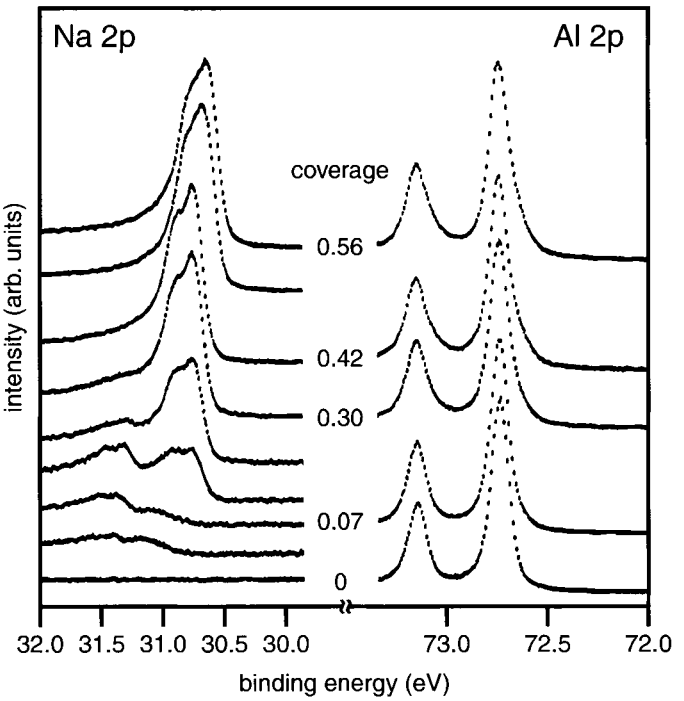


Fig. 13.41. Na and Al 2p core level spectra for various submonolayer coverages after deposition of Na on Al(111) at 100 K. From Andersen et al. (1993).

on the cooled surface such that the surface density of adatoms is locally higher than the average coverage given in Fig. 13.41.

With the high resolution achieved small shifts due to the different local surroundings thus give useful information also when the origin of the shifts is not well understood. Traditionally core level shifts have been used to estimate the amount of valence charge on an atom. For metal overlayers there seems to be no straightforward relationship between the core level binding energy and the valency of the atom in its initial state (Egelhoff, 1987). One reason for this is that the binding energy depends on how efficiently the core hole of the excited atom is screened. In general it is difficult to separate the initial state effects from final state effects, which is necessary for a determination of initial state properties. This is certainly true for the small shifts discussed above for Al(111)/Na and Al(111) covered by other alkali metals. (For the alkali metal covered Al(111) surface the largest shift of the Al 2p-level obtained when the adsorbate resides on top of the substrate rather than in the topmost substrate layer is 0.14 eV, which is the shift found for Cs (Andersen et al., 1993).) The comment is however valid also for the somewhat larger shifts, of around 1 eV, observed over the monolayer coverage range for the core levels of an alkali metal adsorbed on a noble and transition metal substrate. The usual observation is that the core level binding energy (Riffe et al., 1990; Andersen et al., 1993; Shi et al., 1993; for a compilation of results see Björneholm et al., 1989) or the excitation threshold measured by EELS (Andersson and

Jostell, 1975; Lindgren and Walldén, 1980b) is higher at low coverage when the adsorbate is partly ionic than at high monolayer coverage when the adlayer has properties expected for a thin metal slab. It is not known whether the decrease of the binding energy is due mainly to more charge on the adsorbate or to a more efficient screening of the core hole as the nearest neighbors come closer. That the binding energy is not always closely related to the charge on an adsorbed atom is demonstrated by the results obtained when a full monolayer of Cs on Cu(111) is exposed to oxygen. Upon oxygen adsorption the Cs atoms loose their valence electrons. This is indicated by the energy shift of a plasmon loss peak in EELS, the reduced intensity of Auger-emission involving Cs valence electrons and the vanishing of a photoemission peak due to the alkali metal valence electrons (Lindgren and Walldén, 1980b). For the ionic Cs adsorbate produced by the oxygen adsorption the Cs Sp threshold and binding energy is found to be even lower (by 0.8 eV) than for the full Cs monolayer.

The recent discussion regarding the relevance of the charge transfer picture for alkali metal adsorption systems was stimulated on the experimental side by the observation of unexpectedly small core level shifts for the surface atoms of the substrate when alkali metal atoms are adsorbed (Riffe et al., 1990). The small shifts were ascribed to a small charge transfer to the substrate. The question is whether there is a problem with the charge transfer model or with the interpretation of the spectra. While, as discussed in a previous section, the EEL spectra provide strong support for the view that the adsorbate carries a charge the core level spectra give little evidence for an increased charge in the core region of the atoms in the surface layer of the substrate. What is needed for a complete picture of the charge transfer to be obtained is an identification of the valence states on the receiving end of the electron transfer. As discussed above such states have indeed been observed but only in a couple of cases. Both for Be(0001) (Watson et al., 1990) and for Cu(111) (Lindgren and Walldén, 1978, 1979) partly occupied surface bands are found to shift in energy upon alkali metal adsorption in a gradual manner and in a direction, which allows the bands to accommodate additional electrons. In the two cases where one has observed substrate states involved in establishing the charge balance at the interface these states are thus modified upon adsorption in a way, which is consistent with the charge transfer model.

While the core level spectra of alkali metal overlayers are difficult to understand in any detail there are other cases for which the core level components are widely separated and for which there is no doubt that there are atoms on the surface having distinctly different electron configurations. The results obtained for Sm on Cu(100) (Fäldt and Myers, 1983, 1984, 1986) or Mo(110) (Stenborg et al., 1989a, b) are examples of this. Here the Sm appear in both divalent ($4f^6$) and trivalent ($4f^5$) forms with an energy separation between the $3d_{5/2}$ levels of around 8 eV. Each of these components show a modest coverage dependence for the core level binding energy. The intensity ratio, however, varies strongly with the surface coverage suggesting that the atoms are divalent when there are few of them while at high monolayer coverage the intensity ratio observed for Cu(100)/Sm corresponds to a mean valency of 2.7 (Fäldt and Myers, 1984). This is thus a change of valency that may be monitored via the recorded intensities rather than from energy shifts. The discussion regarding Sm overlayers has concerned mainly whether the mixed valency is homogenous and fluctuating or heterogeneous involving compound formation with the substrate.

While Sm atoms in a full monolayer thus have a high valency the atoms in the surface layer of a two atomic layer thick film are divalent (Stenborg et al., 1989a), which is also the valency characteristic of the surface layer of a thick Sm film (Wertheim and Crecelius, 1979; Johansson, 1979; Lang and Baer, 1979; Allen et al., 1980). This changeover in valency was observed via valence band photoemission spectra recorded for Sm (0001) films grown layer by layer on a Mo(110) substrate. Particularly interesting is that the surface reconstructs forming a $(5 \times 5)$ LEED pattern indicative of a 25% expansion of the interatomic distances in the topmost hexagonal layer. The reconstruction is induced by the difference in valence and thereby in size of surface and bulk atoms. The divalent Sm atom is estimated to have a radius which is 15% larger than the radius of the trivalent atom (Rosengren and Johansson, 1982).

## 13.4. Concluding remarks

Recent work has demonstrated that metal overlayers on a metal substrate are excellent objects for the study of quantum confinement of electrons as well as phonons. Merely by observing the thickness dependence of the energies for discrete states and resonances unique information can be obtained about the dispersion of electrons and phonons in the overlayer metal. In the case of electrons it appears, somewhat paradoxically, that the most accurate determination of bulk band structure can be made via measurements on ultra-thin films. This applies to favorable cases when strain in the epitaxial overlayer is insignificant. He atom scattering as well as photoemission data show that phonon as well as electron states can be significantly shifted by strain in the overlayer.

To understand the transport properties of thin metal films, which is a subject of strong present interest, spectroscopic information about electron states near the Fermi level is of particular interest. This is demonstrated by the important role played by spin- and angle-resolved photoemission for explaining the magneto-transport properties of thin film systems. Measurements made with high energy resolution furthermore show that discrete quantum well states near below and above the Fermi level can give narrow, hole lifetime limited photoemission lines. This means that it is possible to monitor, via the energy as well as line width and line shape, how such states are affected by imperfections, structure changes and adsorbates. In current electron spectroscopic work structure changes, such as the onset of intermixing with the substrate, has been studied mainly via core level shifts. EELS, at the low incident energies usually used, is applicable in the monolayer coverage range and the rather few results reported so far show that the vibrational frequency and cross section both are sensitive to the structure.

Many of the interesting observations made so far for thin films have been made with overlayers of simple metals which has the advantage that the electronic structure and its thickness dependence can be understood in simple terms at least semi-quantitatively. This is as expected for films which are sufficiently thick that the electronic level structure approaches that of an infinite solid. The results obtained with one and two photon photoemission demonstrate that simple models may be used also for the more complicated situation obtained for few atomic layers thick films, when the interfaces are important.

## References


Adawi, I., 1964, Phys. Rev. **114**, A788.

Adler, D.L., I.R. Collins, X. Liang, S.J. Murray, G.S. Leatherman, K.-D. Tsuei, E.E. Chaban, S. Chandavarkar, R.C. McGrawth, R.D. Diehl and P.H. Citrin, 1993, Phys. Rev. B **48**, 17445.

Adnot, A. and J.D. Carette, 1977, Phys. Rev. Lett. **38** 1084.

Ahlqvist, P., 1979, Solid State Commun. **31**, 1029.

Allen, J.W., L.I. Johansson, I. Lindau and S.B.M. Hagstrom, 1980, Phys. Rev. B **21**, 1335.

Andersen, J.N., E. Lundgren, R. Nyholm and M. Qvarford, 1992a, Phys. Rev. B **46**, 12784.

Andersen, J.N., E. Lundgren, R. Nyholm and M. Qvarford, 1993, Surf. Sci. **289**, 307.

Andersen, J.N., M. Qvarford, R. Nyholm, J.F. van Acker and E. Lundgren, 1992b, Phys. Rev. Lett. **68**, 94.

Andersson, S. and U. Jostell, 1975, Faraday Discuss. Chem. Soc. **60**, 255.

Andersson, S., B.N.J. Persson, T. Gustafsson and E.W. Plummer, 1980, Solid State Commun. **34**, 473.

Aruga, T. and Y. Murata, 1989, Progr. Surf. Sci. **31**, 61.

Astaldi, S., R. Rudolf and S. Modesti, 1990, Solid State Commun. **75**, 847.

Beckmann, A., M. Klaua and K. Meinel, 1993, Phys. Rev. B **48**, 1844.

Beckmann, A., 1996, Surf. Sci. **349**, L95.

Behm, R.J., 1989, in: Physics and Chemistry of Alkali Metal Adsorption, eds. H.P. Bonzel, A.M. Bradshaw and G. Ertl. Elsevier, Amsterdam.

Benedek, G., J. Ellis, A. Reichmuth, P. Ruggerone, H. Schief and J.P. Toennies, 1992, Phys. Rev. Lett. **69**, 2951.

Benesh, G.A. and D. King, 1992, Chem. Phys. Lett. **191**, 315.

Bennett, W.R., W. Schwarzacher and W.F. Egelhoff, 1990, Phys. Rev. Lett. **65**, 3169.

Binns, C., C. Norris and M.-G. Barthes-Labrousse, 1992, Physica Scripta **T45**, 283; and references therein.

Björneholm, O., A. Nilsson , J.N. Andersen and C. Wigren, 1989, Surf. Sci. **211/212**, 470.

Boettger, J.C. and S.B. Trickey, 1989, J. Phys. Condens. Matter. **1**, 4323.

Boettger, J.C. and S.B. Trickey, 1992, Phys. Rev. B **45**, 1363.

Bonzel, H.P., 1987, Surf. Sci. Rep. **8**, 43.

Bonzel, H.P., A.M. Bradshaw and G. Ertl (eds.), 1989, Physics and Chemistry of Alkali Metal Adsorption. Elsevier, Amsterdam.

Braun, J. and J.P. Toennies, 1997, Surf. Sci. **384**, L858.

Brookes, N.B., Y. Chang and P.D. Johnson, 1991, Phys. Rev. Lett. **67**, 354.

Carbone, C., E. Vescovo, O. Rader, W. Gudat and W. Eberhardt, 1993, Phys. Rev. Lett. **71**, 2805.

Carlsson, A., S.-A. Lindgren, C. Svensson and L. Walldén, 1994, Phys. Rev. B **50**, 8926.

Carlsson, A., D. Claesson, S.-A. Lindgren and L. Walldén, 1995, Phys. Rev. B **52**, 11144.

Carlsson, A., D. Claesson, S.-A. Lindgren and L. Walldén, 1996, Phys. Rev. Lett. **77**, 346.

Carlsson, A., B. Hellsing, S.-A. Lindgren and L. Walldén, 1997, Phys. Rev. B **56**, 1593.

Celinski, Z., B. Heinrich and J.F. Cochran, 1993, J. Appl. Phys. **73**, 5966.

Chen, C.T. and N.V. Smith, 1987, Phys. Rev. B **35**, 5407.

Chen, C.T. and N.V. Smith, 1989, Phys. Rev. B **40**, 7487.

Chiarello, G., A. Cupolillo, A. Amoddeo, L.S. Caputi, L. Papagno and E. Colavita, 1995, Phys. Rev. B **52**, 4752.

Clemens, W., T. Kachel, O. Rader, E. Vescovo, S. Blugel, C. Carbone and W. Eberhardt, 1992, Solid State Commun. **81**, 739.

Courths, R. and S. Hüfner, 1984, Phys. Rep. **112**, 53.

Crampin, S., S. De Rossi and F. Ciccacci, 1996, Phys. Rev. B **53**, 13817.

Crottini, A., D. Cvetko, L. Floreano, R. Gotter, A. Morgante and F. Tommasini, 1997, Phys. Rev. Lett. **79**, 1527.

Daun, W., C. Stuhlmann and H. Ibach, 1988, Phys. Rev. Lett. **60**, 2741.

dePaola, R.A., J. Hrbek and F.M. Hoffmann, 1985, J. Chem. Phys. **82**, 2484.

Diehl, R.D. and R. McGrath, 1995, Surf. Rev. Lett. **2**, 387.

Diehl, R.D. and R. McGrath, 1996, Surf. Sci. Rep. **23**, 43.

Dose, V., W. Altmann, A. Goldmann, U. Kolac and J. Rogozik, 1984, Phys. Rev. Lett. **52**, 1919.

Dudde, R., K.-H. Frank and B. Reihl, 1990, Phys. Rev. B **41**, 4897.

Dudde, R., L.S.O. Johansson and B. Reihl, 1991, Phys. Rev. B **44**, 1198.

Echenique, P.M. and J. Pendry, 1978, J. Phys. C: Solid State Phys. **LI**, 2065.

Edwards, D.M., J. Mathon, R.B. Muniz and M.S. Phan, 1991, Phys. Rev. Lett. **67**, 493.
Edwards, D.M., J. Mathon and R.B. Muniz, 1994, Phys. Rev. B **50**, 16066.
Egelhoff, W.F., 1987, Surf. Sci. Rep. **8**, 253.
Ehrlich, A.C., 1993, Phys. Rev. Lett. **71**, 2300.
Ellis, J. and I.P. Toennies, 1993, Phys. Rev. Lett. **70**, 2118.
Esaki, L., 1992, Physica Scripta **T42**, 102.
Falicov, L.M., 1992, Physics Today **45**, No 10, 46; and references therein.
Feibelman, P.J., 1982, Progr. Surf. Sci. **12**, 287.
Feibelman, P.J., 1983, Phys. Rev. B **27**, 1991.
Fisher, D. and R.D. Diehl, 1992, Phys. Rev. B **46**, 2512.
Fischer, R. and Th. Fauster, 1995, Phys. Rev. B **51**, 7112.
Fischer, D., S. Chandavarkar, I.R. Collins, R.D. Diehl, P. Kaukasoina and M. Lindroos, 1992a, Phys. Rev. Lett. **68**, 2786.
Fischer, N., S. Schuppler, R. Fischer, R. Fauster and W. Steinmann, 1991, Phys. Rev. B **43**, 14722.
Fischer, N., S. Schuppler, R. Fischer, R. Fauster and W. Steinmann, 1993, Phys. Rev. B **47**, 4705.
Fischer, N., S. Schuppler, T. Fauster and W. Steinmann, 1994, Surf. Sci. **314**, 89.
Fischer, R., N. Fischer, S. Schuppler, Th. Fauster and F.J. Himpsel, 1992b, Phys. Rev. B **46**, 9691.
Frank, K.-H., H.-J. Sagner and D. Heskett, 1989, Phys. Rev. B **40**, 2767.
Fäldt, A. and H.P. Myers, 1983, Solid State Commun. **48**, 253.
Fäldt, A. and H.P. Myers, 1984, Phys. Rev. Lett. **52**, 1315.
Fäldt, A. and H.P. Myers, 1986, Phys. Rev. B **33**, 1424; **34**, 6675.
Garrison, K., Y. Chang and P.D. Johnson, 1993, Phys. Rev. Lett. **71**, 2801.
Gartland, P.O. and B.J. Slagsvold, 1975, Phys. Rev. B **12**, 4047.
Gerlach, R. L. and T.N. Rhodin, 1970, Surf. Sci. **19**, 403.
Giesen, K., F. Hage, F.J. Himpsel, H.J. Riess and W. Steinmann, 1985, Phys. Rev. Lett. **55**, 300.
Graham, A.P., F. Hofmann, J.P. Toennies, L.Y. Chen and S.C. Ying, 1997, Phys. Rev. Lett. **78**, 3900.
Gunnarsson, O., H. Hjelmberg and J.K. No'rskov, 1980, Physica Scripta **22**, 165.
Gurney, R.W., 1935, Phys. Rev. **47**, 2798.
Gustafsson, T., P.-O. Nilsson and L. Walldén, 1971, Phys. Lett. **37A**, 121.
Hamawi, A. and L. Walldén, 1992, J. Vac. Sci. Technol. B **10**, 1914.
Hamawi, A., S.-A. Lindgren and L. Walldén, 1991, Physica Scripta **T 39**, 339.
Hamawi, A., S.-A. Lindgren, C. Svensson and L. Walldén, 1992, Acta Physica Polonica **81**, 7.
Hannon, J.B., M. Giesen, C. Klünker, G. Schulze Icking-Konert, D. Stapel, H. Ibach and J.E. Müller, 1997, Phys. Rev. Lett. **78**, 1094.
He, P. and K. Jacobi, 1996, Phys. Rev. B **53**, 3658.
Hedin, L. and S. Lundqvist, 1969, in: Solid State Physics, Vol. 23, ed. H. Ehrenreich. Academic Press, New York.
Heimann, P., J. Hermanson, H. Miosga and H. Neddermeyer, 1979, Surf. Sci. **85**, 263.
Heinrich, B., Z. Celinski, J.F. Cochran, W.B. Muir, J. Rudd, Q.M. Zhong, A.S. Arrot, K. Myrtle and J. Kirschner, 1990, Phys. Rev. Lett. **64**, 673.
Hemmen, R. and H. Conrad, 1991, Phys. Rev. Lett. **67**, 1314.
Heskett, D., K.-H. Frank, E.E. Koch and H.-J. Freund, 1987, Phys. Rev. B **36**, 1276.
Heskett, D., K.-H. Frank, K. Horn, E.E. Koch, H.-J. Freund, A. Baddorf, K.-D. Tsuei and E.W. Plummer, 1988, Phys. Rev. B **37**, 10387.
Himpsel, F.J., 1991, Phys. Rev. B **44**, 5966.
Hiroshi, Iwasaki, B.T. Jonker and R.L. Park, 1985, Phys. Rev. B **32**, 643; and references therein.
Holmström, S., 1987, Physica Scripta **36**, 529.
Horn, K., A. Hohlfeld, J. Somers, Th. Lindner, P. Hollins and A.M. Bradshaw, 1988a, Phys. Rev. Lett. **63**, 1536.
Horn, K., A. Hohlfeld, J. Somers, Th. Lindner, P. Hollins and A.M. Bradshaw, 1988b, Phys. Rev. Lett. **55**, 1231.
Hulpke, E., I. Lower and A. Reichmuth, 1996, Phys. Rev. B **53**, 13901.
Ibach, H. and D.L Mills, 1982, Electron Energy Loss Spectroscopy and Surf. Vibrations. Academic Press, New York.
In-Whan, Lyo and E.W. Plummer, 1988, Phys. Rev. Lett. **60**, 1558.
Ishida, H., 1989a, Phys. Rev. Lett. **63**, 1535.

Ishida, H., 1989b, Phys. Rev. B **39**, 5492.
Ishida, H., 1990, Phys. Rev. B **42**, 10899.
Ishida, H. and A. Liebsch, 1992, Phys. Rev. B **45**, 6171.
Ishida, H. and Y. Morikawa, 1993, Surf. Sci. **291**, 87.
Ishida, H. and B. Persson, 1990, Phys. Rev. B **42**, 3171.
Ishida, H. and K. Terakura, 1988, Phys. Rev. B **42**, 5752.
Jacob, W., E. Bertel and V. Dose, 1987, Phys. Rev. B **35**, 5910.
Jaklevic, R.C. and J. Lambe, 1975, Phys. Rev. B **12**, 4146.
Jaklevic, R.C., J. Lambe, M. Mikkor and W.C. Vassell, 1971, Phys. Rev. Lett. **26**, 88.
Jalochowski, M., H. Knoppe, G. Lilienkamp and E. Bauer, 1992a, Phys. Rev. B **46**, 4693.
Jalochowski, M., E. Bauer, H. Knoppe and G. Lilienkamp, 1992b, Phys. Rev. B **45**, 13607.
Jalochowski, M., M. Hoffmann and E. Bauer, 1996, Phys. Rev. Lett. **76**, 4227.
Jaskolski, W., V.R. Velasco and F. Garcia-Moliner, 1991, Physica Scripta **43**, 337.
Johansson, B., 1979, Phys. Rev. B **19**, 6615.
Johnson, P.D., K. Garrison, Q. Dong, N.V. Smith, Li. Dongqi, J. Mattson, I. Pearson and S.D. Bader, 1994, Phys. Rev. B **50**, 8954.
Johnson, P.D. and N.V. Smith, 1983, Phys. Rev. B **27**, 2527.
Jones, R.O. and P.J. Jennings, 1988, Surf. Sci. Rep. **9**, 165.
Jonker, B.T., N.C. Bartelt and R.L. Park, 1983, Surf. Sci. **127**, 183.
Kane, E.O., 1964, Phys. Rev. Lett. **12**, 17.
Kempa, K., A. Liebsch and W.L. Schaich, 1988, Phys. Rev. B **38**, 12645.
Kerkar, M., D. Fischer, D.P. Woodruff, R.G. Jones, R.D. Diehl and B. Cowie, 1992, Phys. Rev. Lett. **68**, 3204; Surf. Sci. **278**, 246.
Kevan, S.D., 1983, Phys. Rev. Lett. **50**, 526.
Kevan, S.D., 1986, Surf. Sci. **178**, 229.
Klünker, C., C. Steimer, J.B. Hannon, M. Giesen and H. Ibach, 1999, Surf. Sci. **420**, 25.
Kubiak, G.D., 1988, Surf. Sci. **201**, L475.
Lang, J.K. and Y. Baer, 1979, Solid State Commun. **31**, 945.
Lang, N.D. and W. Kohn, 1971, Phys. Rev. B **3**, 1215.
Lang, N.D. and A.R. Williams, 1978, Phys. Rev. B **18**, 616.
Lehwald, S., M. Jszeftel, H. Ibach, T.S. Rahman and D.L. Mills, 1983, Phys. Rev. Lett. **50**, 518.
Levinson, H.J. and E.W. Plummer, 1981, Phys. Rev. B **24**, 628.
Li, D., J. Pearson, J.E. Mattson, S.D. Bader and P.D. Johnson, 1995, Phys. Rev. B **51**, 7195.
Liebsch, A., 1987, Phys. Rev. B **36**, 7379.
Liebsch, A., 1991, Phys. Rev. Lett. **67**, 2858.
Lindgren, S.-Å. and L. Walldén, 1978, Solid State Commun. **28**, 283.
Lindgren, S.-Å. and L. Walldén, 1979, Surf. Sci. **89**, 319.
Lindgren, S.-Å. and L. Walldén, 1980a, Solid State Commun. **34**, 671.
Lindgren, S.-Å. and L. Walldén, 1980b, Phys. Rev. B **22**, 5967.
Lindgren, S.-Å. and L. Walldén, 1987, Phys. Rev. Lett. **59**, 3003.
Lindgren, S.-Å. and L. Walldén, 1988a, Phys. Rev. Lett. **61**, 2894.
Lindgren, S.-Å. and L. Walldén, 1988b, Phys. Rev. B **38**, 3060.
Lindgren, S.-Å. and L. Walldén, 1988c, Phys. Rev. B **38**, 10044.
Lindgren, S.-Å. and L. Walldén, 1989a, Surf. Sci. **211/212**, 394.
Lindgren, S.-Å. and L. Walldén, 1989b, J. Phys. Condens. Matter **1**, 215.
Lindgren, S.-Å. and L. Walldén, 1991, Surf. Sci. **257**, L619.
Lindgren, S.-Å. and L. Walldén, 1992, Phys. Rev. B **45**, 6345.
Lindgren, S.-Å., L. Walldén, J. Rundgren, P. Westrin and J. Neve, 1983, Phys. Rev. B **28**, 6707.
Lindgren, S.-Å., C. Svensson and L. Walldén, 1990, Phys. Rev. B **42**, 1467.
Lindgren, S.-Å., C. Svensson and L. Walldén, 1993, Chem. Phys. Lett. **205**, 391.
Lindgren, S.-Å., C. Svensson, L. Walldén, A. Carlsson and E. Wahlström, 1996, Phys. Rev. B **54**, 10912.
Loly, P.D. and J. Pendry, 1983, J. Phys. C: Solid State Phys. **16**, 423.
Luo, N.S., P. Ruggerone and J.P. Toennies, 1996, Phys. Rev. B **54**, 5051.

Marliere, C., 1990, Vacuum **41**, 1192.
McRae, E.G., 1979, Rev. Mod. Phys. **51**, 541.
Memmel, N., G. Rangelov, E. Bertel and V. Dose, 1991, Phys. Rev. B **43**, 6938.
Memmel, N., G. Rangelov and E. Bertel, 1993, Surf. Sci. **285**, 109.
Miller, T. and T.-C. Chiang, 1992, Phys. Rev. Lett. **68**, 3339.
Miller, T., A. Samsavar, G.E. Franklin and T.-C. Chiang, 1988, Phys. Rev. Lett. **61**, 1404.
Miller, T., A. Samsavar and T.-C. Chiang, 1994, Phys. Rev. B **50**, 17686.
Mizuno, S., H. Tochihara, T. Kadowaki, H. Minagawa, K. Hayakawaand I. Toyoshima, 1992, Surf. Sci. **264**, 103.
Mizuno, S., H. Tochihara, A. Barbieri and M.A. Van Hove, 1995, Phys. Rev. B **51**, 7981.
Modesti, S., C.T. Chen, Y. Ma, G. Meigs, P. Rudolf and F. Sette, 1990, Phys. Rev. B **42**, 5381.
Mohamed, M.H., J.S. Kim and L.L. Kesmodel, 1989, Surf. Sci. **220**, L687.
Mueller, M.A., T. Miller and T.-C. Chiang, 1990, Phys. Rev. B **41**, 5214.
Mueller, M.A, A. Samsavar, T. Miller and T.-C. Chiang, 1989, Phys. Rev. B **40**, 5845.
Müller, K., G. Besold and K. Heinz, 1989, in: Physics and Chemistry of Alkali Metal Adsorption, eds. H.P. Bonzel, A.M. Bradshaw and G. Ertl. Elsevier, Amsterdam.
Muscat, J.P. and D.M. Newns, 1978, Progr. Surf. Sci. **9**, 1.
Nagao, T., Y. Lizuka, M. Umeuchi, T. Shimazaki and C. Oshima, 1995, Surf. Sci. **329**, 269.
Neugebauer, J. and M. Scheffler, 1992, Phys. Rev. B **46**, 16067.
Neuhold, G. and K. Horn, 1997, Phys. Rev. Lett. **78**, 1327.
Orr, B.G., H.M. Jaeger and A.M. Goldmann, 1984, Phys. Rev. Lett. **53**, 2046.
Ortega, J. and F.J. Himpsel, 1992, Phys. Rev. Lett. **69**, 844.
Ortega, J.E., F.J. Himpsel, G.J. Mankey and R.F. Willis, 1993, Phys. Rev. B **47**, 1540.
Over, H., H. Blandau, M. Skottke-Klein, G. Ertl, W. Moritz and C.T. Campell, 1992, Phys. Rev. B **45**, 8638.
Patthey, F. and W.D. Schneider, 1994, Phys. Rev. B **50**, 17560.
Perez-Diaz, J.L. and M.C. Munoz, 1996, Phys. Rev. B **53**, 13583.
Plummer, E.W., K.-D. Tsuei, K.-J. Song and R. Murphy, 1989, in: Physics and Chemistry of Alkali Metal Adsorption, eds. H.P. Bonzel, A.M. Bradshaw and G. Ertl. Elsevier, Amsterdam.
Pirug, G., C. Ritke and H.P. Bonzel, 1991, Surf. Sci. **257**, 50.
Reihl, B., K.H. Frank and R.R. Schlittler, 1984, Phys. Rev. B **30**, 7328.
Richmond, G.L., J.M. Robinson and V.L. Shannon, 1988, Progr. Surf. Sci. **28**, 1.
Riffe, D.M., G.K. Wertheim and P.H. Citrin, 1990, Phys. Rev. Lett. **64**, 571.
Rosengren, A. and B. Johansson, 1982, Phys. Rev. B **26**, 3068.
Rudolf, P., C. Astaldi, A. Bianco and S. Modesti, 1993, Phys. Rev. B **47**, 4123.
Rudolf, P., C. Astaldi, G. Cautero and S. Modesti, 1991, Surf. Sci. **251/252**, 127.
Rudolf, P., C. Astaldi and S. Modesti, 1990, Phys. Rev. B **42**, 1856.
Rundgren, J. and G. Malmström, 1977, Phys. Rev. Lett. **38**, 836.
Saalfrank, P., 1992, Surf. Sci. **274**, 449.
Salmi, L.-A. and M. Persson, 1989, Phys. Rev. B **39**, 6249.
Scheffler, M., Ch. Droste, A. Fleszar, F. Maca, G. Wchutka and G. Barzel, 1991, Physica B **172**, 143.
Schmalz, A., S. Aminpirooz, L. Becker, J. Haase, J. Neugebauer, M. Scheffler, D.R. Batchelor, D.L. Adams and E. Borgh, 1991, Phys. Rev. Lett. **67**, 2163.
Schulte, F.K., 1976, Surf. Sci. **55**, 427.
Schuster, R., J.V. Barth, G. Ertl and R.J. Behm, 1991, Phys. Rev. B **44**, 13689.
Semancik, S., D.L. Doering and T.E. Madey, 1986, Surf. Sci. **176**, 165.
Serena, P.A. and N. Garcia, 1991, Surf. Sci. **251/252**, 866.
Shi, X., D. Tang, D. Heskett, K.-D. Tsuei, H. Ishida, Y. Morikawa and K. Terakura, 1993, Phys. Rev. B **47**, 4014.
Shen, Y., S.Y. Ta, J.S. Kim, M.H. Mohamed and L.L. Kesmodel, 1991, Phys. Rev. B **43**, 6788.
Slater, L.J., 1960, Confluent Hypergeometric Functions. Cambridge University Press, Cambridge.
Smith, N.V., 1985, Phys. Rev. B **32**, 3549.
Smith, N.V., 1988, Rep. Prog. Phys. **51**, 1227.
Smith, N.V., N.B. Brookes, Y. Chang and P.D. Johnson, 1994, Phys. Rev. B **49**, 332.
Smith, N.V., G.K. Wertheim, A.B. Andrews and C.-T. Chen, 1993, Surf. Sci. **282**, L359.
Song, K.J., D. Heskett, H.L. Dai, A. Liebsch and E.W. Plummer, 1988, Phys. Rev. Lett. **61**, 1380.

Soukiassian, P., R. Riwan, J. Lecante, E. Wimmer, S.R. Chubb and A.J. Freeman, 1985, Phys. Rev. B **31**, 4911.
Stampfl, C., M. Scheffler, H. Over, J. Burchhardt, M. Nielsen and D.L. Adams, 1992, Phys. Rev. Lett. **69**, 1532.
Stenborg, A., J.N. Andersen, O. Björneholm, A. Nilsson and N. Mårtensson, 1989a, Phys. Rev. Lett. **63**, 187.
Stenborg, A., O. Björneholm, A. Nilsson and N. Martensson, 1989b, Phys. Rev. B **40**, 5916.
Straub, D. and F.J. Himpsel, 1984, Phys. Rev. Lett. **52**, 1922.
Stroscio, J.A., M. Persson, S.R. Bare and W. Ho, 1986, Phys. Rev. Lett. **54**, 1428.
Stuhlmann, C. and H. Ibach, 1989, Surf. Sci. **219**, 117.
Svensson, C., S.A. Lindgren and L. Walldén, 1993, J. Electron Spectrosc. **64/65**, 483.
Tang, D., D. Mcllroy, X. Shi, C. Su and D. Heskett, 1991, Surf. Sci. **225**, L497.
Thomas, R.E., 1970, J. Appl. Phys. **41**, 5330.
Tom, H.W.K., C.M. Mate, X.D. Zhu, J.E. Crowell, Y.R. Shen and G.A. Somorjai, 1986, Surf. Sci. **172**, 466.
Urbach, L.E., K.L. Percival, J.M. Hicks, E.W. Plummer and H.-L. Dai, 1992, Phys. Rev. B **45**, 3769.
Wachs, A.L., A.P. Shapiro, T.C. Hsieh and T.-C. Chiang, 1986, Phys. Rev. B **33**, 1460.
Wallauer, W. and Th. Fauster, 1996, Phys. Rev. B **54**, 5086.
Walldén, L., 1985, Phys. Rev. Lett. **54**, 943.
Wang, J., Z.C. Ying and E.W. Plummer, 1995, Phys. Rev. B **51**, 5590.
Watson, G.M., P.A. Bruhwiler, E.W. Plummer, H.-J. Sagner and K.-H. Frank, 1990, Phys. Rev. Lett. **65**, 468.
Weber, W., D.A. Wesner, G. Güntherodt and U. Linke, 1991, Phys. Rev. Lett. **66**, 942.
Wertheim, G.K. and G. Crecelius, 1979, Phys. Rev. Lett. **40**, 813.
Wimmer, E.W., 1983, J. Phys. F **13**, 2313.
Wimmer, E.W., 1984, J. Phys. Met. Phys. L **4**, 681.
Wood, A.D.B., B.N. Brockhouse, R.N. March, T. Stewart and R. Browers, 1962, **128**, 1112.
Woodruff, D.P. and N.V. Smith, 1990, Phys. Rev. B **41**, 8150.
Woratschek, B., W. Sesselmann, J. Kuppers, G. Ertl and H. Haberland, 1985, Phys. Rev. Lett. **55**, 611.
Yang, S., R.A. Bartynski, G.P. Kochanski, S. Papadia, T. Fonden and M. Persson, 1993, Phys. Rev. Lett. **70**, 849.
Zhang, J., D. Li and P.A. Dowben, 1994, J. Phys. Condens. Matter **6**, 33.

This Page Intentionally Left Blank

CHAPTER 14

# Many-body Effects in Photoemission

G.D. MAHAN and E.W. PLUMMER

*Department of Physics*
*University of Tennessee*
*Knoxville, USA*

© 2000 Elsevier Science B.V.
All rights reserved

*Handbook of Surface Science*
*Volume 2, edited by K. Horn and M. Scheffler*

# Contents

14.1. Introduction . . . . . 955
14.2. Electron–electron interaction . . . . . 956
14.3. Photoemission . . . . . 971
14.4. Electron–phonon interactions . . . . . 983
References . . . . . 985

## 14.1. Introduction

Remarkable progress has been made in the understanding of the electronic structure of surfaces, both experimentally and theoretically. On the experimental side the development and utilization of synchrotron-based angle-resolved photoemission (Kevan, 1992) has opened up the investigation of the occupied band structure of the bulk and of the surface. Angle-resolved photoemission has become to band structure what X-ray scattering is to structure and inelastic neutron scattering is to lattice dynamics. It is the only experimental technique capable of directly mapping the energy bands of a solid over an extended energy range. Inverse photoemission and two photon photoemission have revealed the unoccupied band structure between the Fermi energy and the vacuum level. Theory both of the photoemission process and of electronic structure of solids has made equivalent progress during this period (Surh et al., 1988; Northrup et al., 1989; Louie, 1994). The emergence of the High-Tc materials has focused the attention of the scientific community on the technique of angle-resolved photoemission (Kevan, 1992) and on the need for higher resolution measurements. According to Phil Anderson in his Physics Today article about the High-Tc materials, 'photoemission is the smoking gun' (Anderson, 1991). In fact there are many papers now appearing, analyzing in detail the line shape in a photoemission spectra, arguing that the data show exotic behavior, such as non-Fermi liquid behavior (Manzke et al., 1989; Olson et al., 1990; Shen et al., 1993; Anderson et al., 1993; Anderson and Ren, 1994), Kondo resonance (Allen et al., 1986; Patthey et al., 1990; Allen, 1992; Tjeng et al., 1993), etc. Anderson has argued that many of the reduced dimensionality systems should exhibit non-Fermi liquid behavior (Anderson, 1990; Anderson and Ren, 1994) which can be described as a Luttinger liquid (Luttinger, 1960; Mattis and Lieb, 1963; Haldane, 1981). This article is intended to outline in detail the many-body effects in the photoemission spectra so that truly exotic behavior can be correctly recognized when it occurs. There is no doubt that single particle theory qualitatively reproduces many of the features seen in the angle-resolved photoemission spectra from solids, and consequently should be the starting point for any many-body theory. This chapter will describe the characteristics of the self-energy of an electron, based on calculations for an interacting electron gas, and compared to data for the simple s-p bonded metals. Section 14.2 describes the electron–electron interaction and the form of the self-energy, while Section 14.3 folds in the self-energy interaction with a single particle theory of photoemission. In Section 14.3 we will illustrate the effect of the self-energy on the observed photoemission spectra, stressing the interplay between the imaginary and real parts of the self-energy and the existence of important sum rules. Finally, the last Section 14.4 will describe the self-energy for states very close to the Fermi energy where electron–phonon coupling becomes important.

## 14.2. Electron–electron interaction

Electron–electron interactions are the largest interaction for most electrons in nearly free-electron metals. They determine the lifetime of quasiparticle excitations, and provide the largest contribution to the self-energy (Quinn and Ferrell, 1958; DuBois, 1959; Lundqvist, 1967, 1968; Hedin and Lundqvist, 1969, 1971; Mahan, 1990). In this section we give a detailed discussion of how one calculates these interactions and their effect on photoemission spectra. In the following section we discuss how electron–electron interactions change the measured spectra in photoemission. We will confine our discussion to metals whose electrons behave as if they are nearly free, i.e., the interactions are small. These are metals whose conduction band are composed of the chemical bonding of s- and p-orbitals. The properties of metals with highly correlated motion, composed of d- and f-orbitals, are discussed in earlier chapters.

An important function is the *self-energy* of an electron, which is denoted by the symbol $\Sigma(k, E)$ and depends on the wave vector $k$ and energy $E$ of the electron. This complex function has real and imaginary parts which are denoted by the subscripts (1, 2)

$$\Sigma(k, E) = \Sigma_1(k, E) + \mathrm{i}\Sigma_2(k, E). \tag{14.1}$$

In a noninteracting system the particles have no scattering and $\Sigma = 0$. The eigenstates live forever, and the band energy is given exactly as a function of wave vector: for free particles one has $\varepsilon_k = k^2/2m$. If the particles have interactions through which they can gain or lose energy, such as with phonons or with each other, the eigenstates have a nonzero lifetime. Excitations are called 'quasiparticles' and are not sharply defined in either momentum or energy space. Now we must treat energy $E$ and wave vector $k$ as independent variables for the quasiparticles. The zero of energy is taken to be the chemical potential. For quasiparticles with positive energy, the excitations above the chemical potential have properties similar to electrons. For excitations at negative energies, they are the holes in the Fermi sea.

The symbol $A(k, E)$ denotes the spectral function. It is the probability that an electron has energy $E$ and wave vector $k$. The spectral function inevitably occurs in any summation over energy and wave vector. For example, the density of states $N(E)$ is the number of energy states with energy $E$, while $n_k$ is the number of electrons with wave vector $k$. We list these expressions as well as several moments (Mahan, 1990):

$$N(E) = \int \frac{\mathrm{d}^3k}{(2\pi)^3} A(k, E), \tag{14.2}$$

$$n_k = \int \frac{\mathrm{d}E}{2\pi} A(k, E) n_{\mathrm{F}}(E), \tag{14.3}$$

$$n_{\mathrm{F}}(E) = \frac{1}{\mathrm{e}^{\beta E} + 1}, \tag{14.4}$$

$$1 = \int \frac{\mathrm{d}E}{2\pi} A(k, E), \tag{14.5}$$

$$\varepsilon_k = \int \frac{\mathrm{d}E}{2\pi} E A(k, E). \tag{14.6}$$

The symbol $n_F(E)$ is the Fermi–Dirac occupation number in terms of the temperature $\beta = 1/k_B T$. The integral in (14.5) shows that the integral over $E$ of the spectral function is always unity, regardless of the interactions. The first moment in (14.6) yields the particle energy $\varepsilon_k$ which the electron would have without electron–phonon or electron–electron interactions. It is the dispersion obtained in a band structure calculation.

The spectral function is given in terms of the self-energy

$$A(k, E) = \frac{-2\Sigma_2(k, E)}{(E - \varepsilon_k - \Sigma_1(k, E))^2 + \Sigma_2^2}. \tag{14.7}$$

The imaginary part $\Sigma_2 < 0$ so that $A > 0$ for any values of $(k, E)$. When there is no scattering, and $\Sigma_2 = 0$, then $A(p, E)$ becomes a delta function and there is only one value of energy for each value of $k$. Equation (14.7) provides the interpretation of the self-energy. The interpretation is easy if $\Sigma(k, E)$ is a constant. Then $A(k, E)$ has a Lorentzian shape as a function of energy. $\Sigma_2$ is the width of the Lorentzian which is its energy uncertainty. The uncertainty principle relates the energy uncertainty to the lifetime $\tau$ of the quasiparticle

$$\Gamma = \frac{\hbar}{\tau} = -2\Sigma_2. \tag{14.8}$$

We use the symbol $\Gamma$ to denote this energy uncertainty. Similarly the real part of the self-energy $\Sigma_1$ changes the energy of the electron. The peak of the spectral function is the most likely value of energy for a given wave vector. For a Lorentzian shape this peak occurs at $E_k = \varepsilon_k + \Sigma_1$. The real part of the self-energy changes the energy of the quasiparticle.

The self-energy $\Sigma(k, E)$ from electron–electron interactions is not a constant. Nevertheless we retain the same interpretation: the real part represents a change in energy of the quasiparticle, while the imaginary part determines the energy uncertainty and lifetime. Figure 14.1 shows the real and imaginary self-energies of electrons in some simple metals as calculated by Shung et al. (1987) using the jellium model which neglects the crystal structure.

The energy has been put 'on the mass shell' which means $E_k = \varepsilon_k$. The imaginary self-energy vanishes at $k/k_F = 1$ since the imaginary self-energy, from electron–electron interactions, vanishes on the Fermi surface at zero temperature. The kink in the curve at about $k/k_F \approx 2$ is due to the emission of plasmons. When the electron is excited above the Fermi surface with enough energy to emit a real plasmon, then its energy uncertainty increases dramatically and the mean free path decreases correspondingly. There is a corresponding cusp in the real part of the self-energy. Both the real and imaginary parts of the self-energy vanish slowly with increasing wave vector.

Earlier we mentioned that energy was measured with respect to the chemical potential $\mu$. The relative energy is

$$\xi_k = \varepsilon_k - \mu_0, \tag{14.9}$$

where $\mu_0 = \hbar^2(3\pi^2 n_0)^{2/3}/2m$ is the chemical potential of the noninteracting Fermi gas at zero temperature. Including electron–electron interactions changes the value of the energy of the electron. It also changes the chemical potential. At zero temperature the new

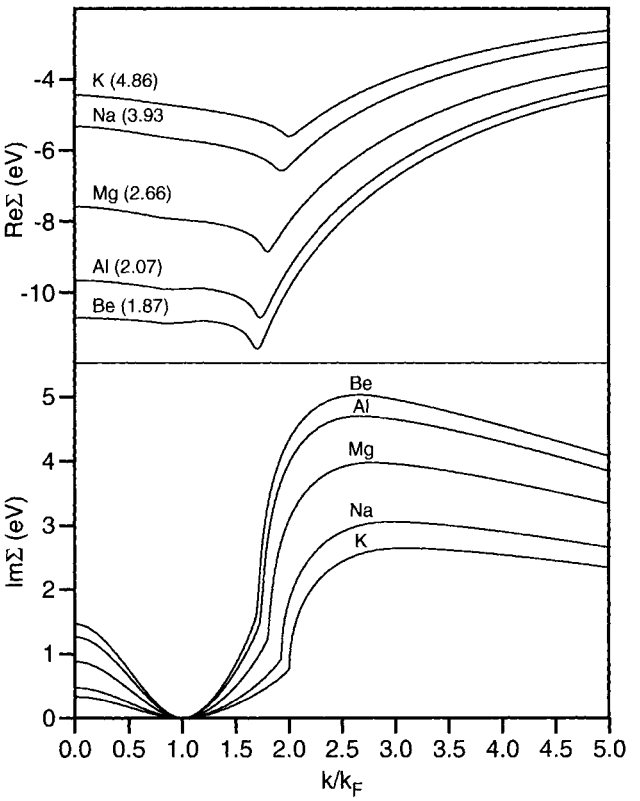


Fig. 14.1. Real $\Sigma_1$ and imaginary $\Sigma_2$ self-energies of electrons in some simple metals as calculated by Shung et al. (1987). The energy is chosen to be $E = \varepsilon_k - \mu$.

chemical potential is

$$\mu = \mu_0 + \Sigma_1(k_F, \varepsilon_{k_F}), \tag{14.10}$$

$$\tilde{\xi} = \varepsilon_k + \Sigma_1(k, \varepsilon_k) - \mu. \tag{14.11}$$

The chemical potential is adjusted for the contribution to the self-energy. The chemical potential is determined by the density of conduction electrons $n_0$. At zero temperature the electrons occupy a sphere in $k$-space whose volume is $n_0$ and whose radius is $k_F = (3\pi^2 n_0)^{1/3}$. The interactions do not change the number of electrons, and therefore do not change the volume or radius of the sphere. This is accomplished by having the net self-energy $\Sigma_1(k, \varepsilon_k) - \Sigma_1(k_F, \varepsilon_{k_F})$ vanish at the chemical potential. This simple argument is exact if $\Sigma_2 = 0$. However, even including it ($\Sigma_2 \neq 0$) does not cause any significant change in (14.10) as shown by Frota (Frota and Mahan, 1992).

Figure 14.2 shows the self-energy effects graphed three ways for sodium along the $\Gamma$ to N directions in the Brillouin zone. The graph (a) has the noninteracting energy bands. The dashed horizontal line is the chemical potential. The vertical arrows denote two optical

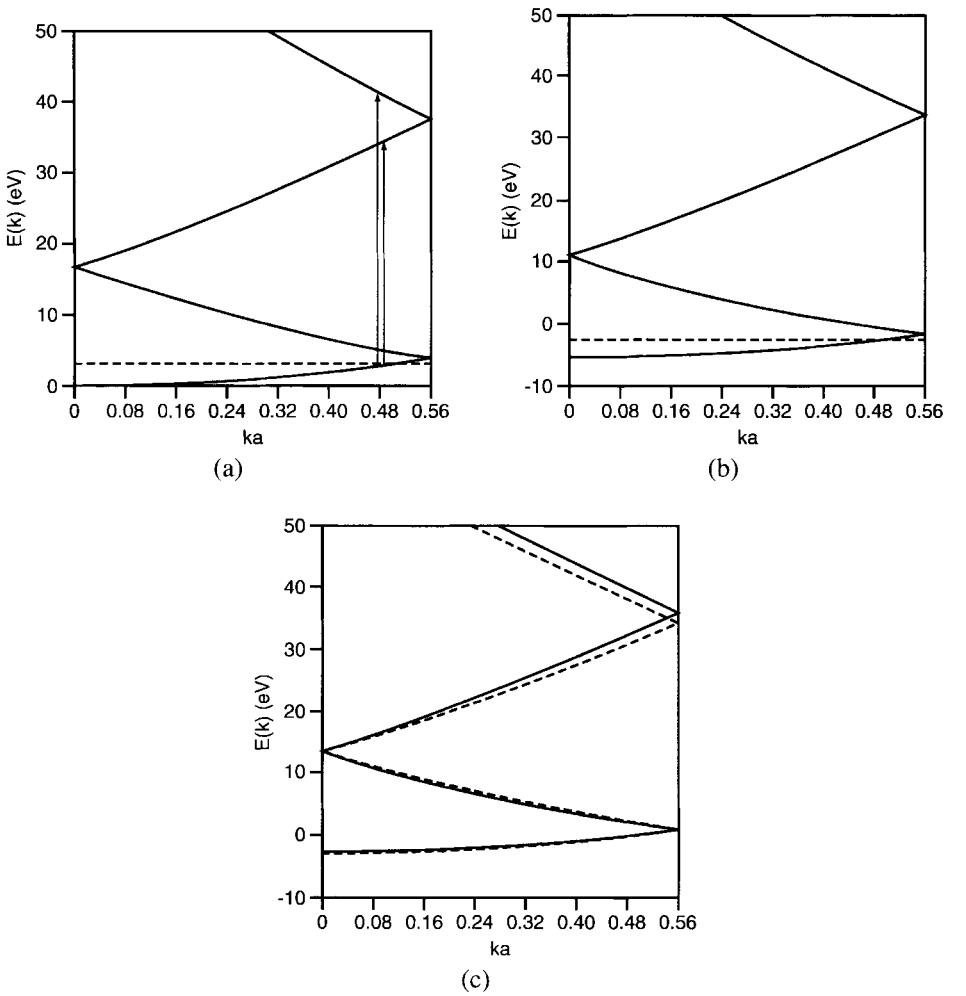


Fig. 14.2. (a) The the free electron band structure of sodium in the (011) direction. (b) Shows the bands corrected for the self-energy from electron–electron interactions. In (c) the curves with and without self-energy are superimposed. The dashed line are the noninteracting bands, while the solid line includes the real part of the self-energy. They have been normalized so that both chemical potentials are at zero energy.

transitions at the Fermi energy, and are discussed in the following section. In (b) the bands include the real part of the self-energy $\Sigma_1$ from electron–electron interactions. In (c) the two bands, with and without $\Sigma(k, E)$ are superimposed. The two chemical potentials are aligned. The dashed lines are the noninteracting bands, while the solid line includes the interactions. The two sets of curves separate at higher energy, which is due to the self-energy decreasing with higher wave vector.

The solid line has a higher energy than the dashed line at $k = 0$. This is because the self-energy is larger in magnitude at the chemical potential than at the bottom of the band.

Table 14.1
Table of bandwidths (eV) for the nearly free electron metals (adopted from Watson, 1992)

| Metal | Free electron | LDA | Quasiparticle (RPA)[a] | Quasiparticle (LDA) | Shung Mahan | Experiment |
|---|---|---|---|---|---|---|
| Be | 14.2 | 11.2[c] | 11.1 | | | 11.1[c] |
| Al | 11.7 | 11.1[d] | 10.8 | 10.0[b] | 10.7 | 10.7[h] |
| Mg | 7.1 | 6.8[e] | 6.5 | | | 6.1[e] |
| Li | 4.7 | 3.45[b] | 3.15 | 2.84[b] | | 2.86[i] |
| Na | 3.24 | 3.24[f] | 2.96 | 2.52[b] | 2.65 | 2.65[j] |
| K | 2.12 | 2.27[g] | 1.80 | 1.58[g] | 1.5 | 1.60[k] |

[a]RPA self-energy calculations from Hedin and Lundqvist (1969) are added to LDA bandwidths.
[b]LDA self-energies of Northrup et al. (1989) are added to LDA bandwidths.
[c]Jensen et al. (1984b).
[d]Singhal and Callaway (1977).
[e]Bartynski et al. (1986).
[f]Ching and Callaway (1975).
[g]Surh et al. (1988).
[h]Levinson et al. (1983).
[i]Watson (1992).
[j]Lyo (1988).
[k]Itchkawitz et al. (1990).

The electron–electron interactions cause an apparent band narrowing defined as

$$\Delta W = \Sigma_1(0,0) - \Sigma_1(k_F, \varepsilon_{k_F}). \tag{14.12}$$

This band narrowing was first calculated accurately in 1965 by Hedin (1965) with Lindhard screening and by Rice (1965) with Hubbard screening. Recent calculations (Mahan and Sernelius, 1989; Frota and Mahan, 1992) give very similar results. Photoemission experiments indicate a larger band narrowing in simple metals than given by the theory. Table 14.1 compares the photoemission measurements with free electron theory, single particle band calculations of the band width from three different quasiparticle calculations, which will be discussed in the next section.

A simple but beautiful example of the distortion of the bands above the Fermi energy caused by the structure in the self-energy displayed in Fig. 14.1 was measured by Jensen et al. (1984b). They measured the first unoccupied band in Be in the $\Gamma$ to A direction (along the c axis) in the energy range where the plasmon excitation is causing the rapid increase in $\Sigma_2$ (Fig. 14.1). Since the real and imaginary parts of the self-energy are coupled through a Kramer–Kronig relationship there is structure in the real part of $\Sigma(k, E)$ at this energy. Figure 14.3a shows the measured band compared to the single particle band. Figure 14.3b shows the difference between the measurement and the single particle calculation, which is the real part of the self-energy. The solid line is the calculation of the self energy by Hedin and Lundqvist (1971). The comparison between theory and experiment shows that the structure is similar in magnitude, position and width, but there seems to be a phase problem. The disagreement between the theory and experiment in this case is most likely a result of

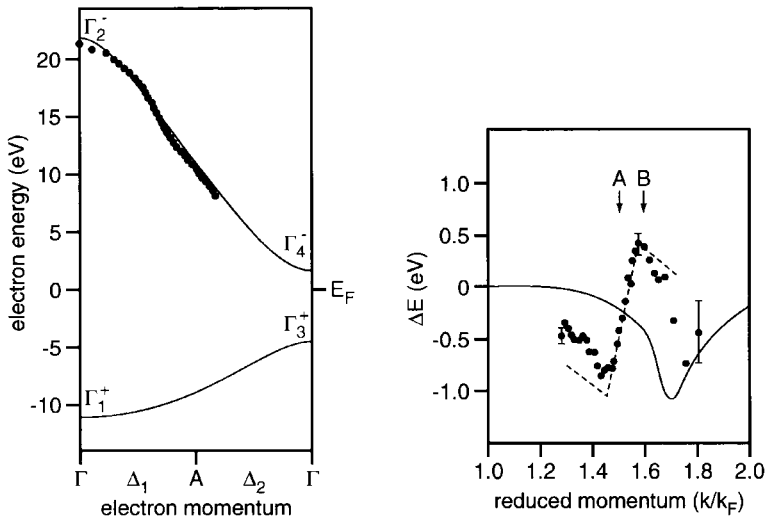


Fig. 14.3. (a) Band-structure of Be along the Δ axis in the energy range of the occupied and first unoccupied bands (Jensen et al., 1984b). The lower curve is the empirically determined occupied band while the upper curve is the calculated final band (Chou et al., 1983). (b) The difference between theory and experiment shown in (a). The solid line is the calculate self-energy correction to the free electron bands for an electron gas with the Be average density (Hedin and Lundqvist, 1971). $k_F$ in Be is 1.94 $Å^{-1}$.

the interaction of the plasmons with interband transitions. The arrow marked A is the wave vector in Be where the final band has an energy with respect to the Fermi energy equal to the plasmon energy. Arrow B is the predicted wave vector for a free electron gas with the density of Be. A second example of the importance of the self-energy on the position and shape of the final bands will be given in the next section when the photoemission from K and Na is discussed. This topic is discussed further in the next section.

Optical transitions are vertical in wave vector space since the photon wave vector is generally too small to be important. This statement becomes incorrect for X-rays, where the photon wave vector is similar in magnitude to that of the electron. For the visible and ultraviolet, one can write the following relations between the initial $k_i$ and final $k_f$ wave vectors of the electron in the reduced Brillouin zone

$$k_i = k_f, \tag{14.13}$$

$$\bar{\xi}_{k_i} + \hbar\omega = \bar{\xi}_{k_f}. \tag{14.14}$$

The electron self-energies are in the energies in (14.14). The importance of this fact is discussed in the next section, where we also indicate how to include the imaginary part of the self-energy in the photoemission.

Now we discuss the method of calculating the electron self-energy. Most calculations of this quantity evaluate the screened exchange energy. There are several ways to do this, each with increasing levels of sophistication.

We use the formalism for nonzero temperature (Mahan, 1990). During the calculations it is convenient to denote the particle energy by the complex quantity $ik_n = 2\pi i k_B T(n + 1/2)$. We employ a four-vector notation where $k$ denotes $(ik_n, \vec{k})$ and the wave vector is $\vec{k}$. Similarly, a summation over $k$ denotes a summation over the energy integer $n$ and an integral over the three-dimensional wave vector.

The first calculation was done by Quinn and Ferrell (1958) who evaluated $\Sigma(k, \xi_k)$: the energy was not treated as an independent variable, but its value was chosen to be 'on the mass shell' which means $E = \xi_k$. Independent calculations by Hedin (Hedin, 1965; Hedin and Lundqvist, 1969, 1971), Rice (1965), and Lundqvist (Lundqvist, 1967, 1968; Hedin and Lundqvist, 1971) first evaluated $\Sigma(k, E)$ for screened exchange. They did different calculations. We first describe the method of Hedin and Lundqvist

$$\Sigma(k, ik_n) = -\sum_q G(k+q)W(q), \tag{14.15}$$

$$G(p) = \frac{1}{ip_n - \xi_p}, \tag{14.16}$$

$$W(q) = \frac{v_q}{\varepsilon(q)}, \tag{14.17}$$

$$\varepsilon(q) = 1 - v_q P_0(q), \tag{14.18}$$

$$v_q = \frac{4\pi e^2}{q^2}. \tag{14.19}$$

The electron Green's function is denoted by $G(p)$ and the screened electron–electron interaction is denoted by $W(q)$. The factor $v_q$ is the Fourier transform of the Coulomb interaction. The factor $P_0(q)$ is the electron polarization in its most basic form, which is given in textbooks (Mahan, 1990). The dielectric function $\varepsilon(q)$ above is called the random phase approximation which is abbreviated as RPA. The right-hand side of (14.15) cannot be evaluated analytically, but requires large computer programs. Eventually one analytically continues $ik_n \to E + i\eta$, where $\eta$ is infinitesimal. Then the self-energy is the retarded one, with real and imaginary parts as described above.

The real part of self-energy, when on the mass shell in Fig. 14.1, is a rather smooth function of energy. However, when one fixes $k$ and plots the self-energy as a function of energy $E$, there is much structure. This behavior is due to plasmons. They have a large energy, and the interaction of the electron with this excitation causes much energy dependence in the self-energy. In Fig. 14.4 we show three sets of curves from Frota and Mahan (1992) which are similar to results in Hedin and Lundqvist (1969). In (a) we show the real and imaginary self-energy for an electron with $r_s = 5$ (e.g., potassium) as a function of $E$ for a fixed value of wave vector $k$. Solid line is RPA and dots are GW$\Gamma$. The two theories agree quite well. The straight line is the relative energy of noninteracting particle $E - \varepsilon_k$; peaks in spectral function occur where this line crosses the real part of the self-energy. With no self-energy the spectral function peaks where this crosses zero. In (b) we show the spectral function for the same three wave vectors. For $k = k_F$ there is a delta function at $E = 0$ which is indicated by a dotted vertical line. Peak at lowest energy is the plasmon satellite of the quasiparticle. In (c) we show the density of states $N(E)$ obtained by

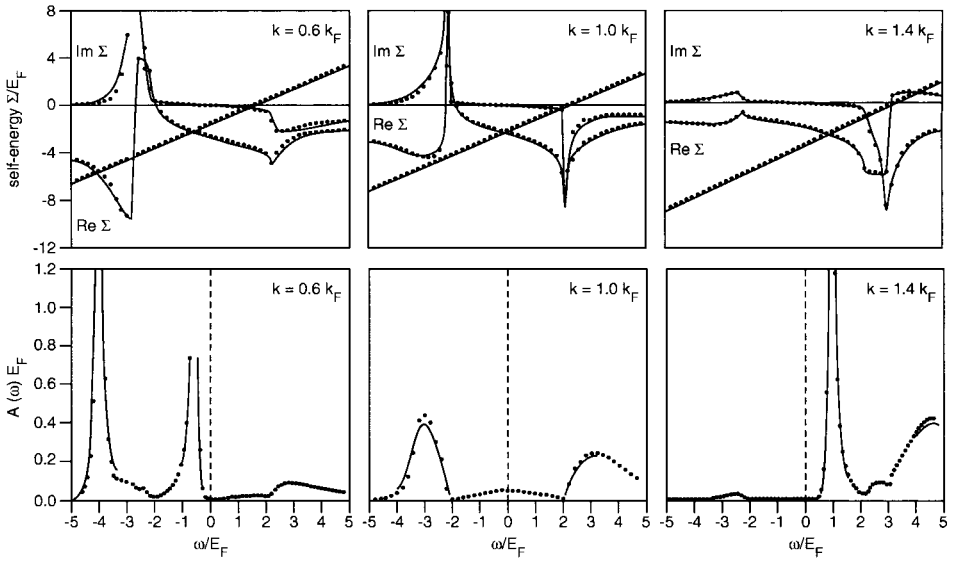


(a) and (b)

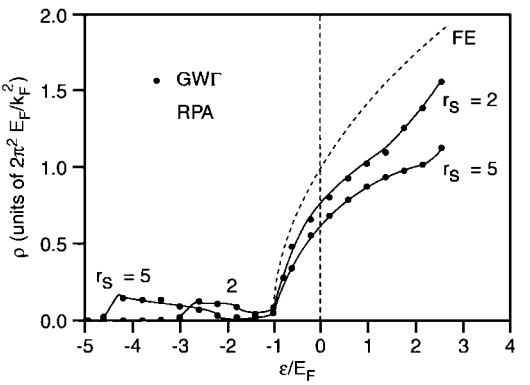


(c)

Fig. 14.4. The efects of electron–electron interactions in a metal with $r_s = 5$. (a) $\Sigma_1(k_F, E)$ and $\Sigma_2(k_F, E)$, straight line is $E - \varepsilon_k$. (b) $A(k, E)$ peaks where line crosses $\Sigma_1$. (c) Density of states $N(E)$. From Frota and Mahan (1992).

integrating over all wave vectors. The solid line includes electron–electron interactions, while the dashed line is for a noninteracting system where the chemical potential has been put into alignment. The interacting density of states has two remarkable features. The first is the structure below the band edge. About 22% of the electrons in the conduction band are at this energy beneath the minimum of the conduction band. This happens because an electron of energy $E$ emits a plasmon of energy $\hbar\omega_p$ and has energy $E - \hbar\omega_p$. This is a virtual process, and the plasmon is reabsorbed. The calculations show that this virtual

process occurs about 22% of the time! The extra structure beneath the conduction band has been named the 'plasmeron'. The other conspicuous feature of the interacting density of states $N(E)$ is that it is much reduced at the chemical potential. Since the electrons spend 22% of their time emitting a plasmon, then they are away from the chemical potential that amount and the density of states is lower there. Theorists define the 'renormalization constant' $Z$ as the fractional reduction in the density of states, at the Fermi surface, due to the interaction with the plasmon. In simple metals values of $Z$ are 0.7–0.8. Electrons spend the time $Z$ being good quasiparticles at the Fermi surface, and an amount roughly $1 - Z$ being a plasmon energy lower. There is no corresponding plasmon satellite in $N(E)$ at $\hbar\omega_p$ above the chemical potential. An electron can only absorb a plasmon if they already exist. This is unlikely since they are not previously thermally excited due to their high energy.

Equation (14.6) can be used to measure the dispersion of excitations on a surface, by measuring the spectral function at each wave vector. The wave vectors are selected using angular-dependent photoemission. Here we describe an example of this technique.

In a solid it is hard to measure the spectral function using photoemission because the hole and hot electron spectral functions are convoluted. For example, it is difficult to determine whether a plasmon satellite structure such as that shown in the lower left-hand panel of Fig. 14.4 is a consequence of the screening of the hole or the energy loss of the excited electron escaping from the solid. This complication can be removed by using gas phase molecules.

The properties of the spectral weight function described in Fig. 14.4 for an interaction electron gas can be illustrated with two examples taken from the photoelectron spectra of molecules. It is difficult to prove that the satellite peak seen in the angle-resolved photoemission spectra of a simple metal is a 'plasmeron' or just the plasmon excited by the photoexcited electron on its way out of the solid. Measurements on dilute gas phase molecules eliminates the concern about inelastic processes for the excited electron. Freund et al. (1981) demonstrated the sum rule on the spectral weight function given by Eq. (14.6), by studying the photoelectron spectra from the O1s level of CO, as a free molecule and bound to a metal atom in the carbonyl $Fe(CO)_5$. Figure 14.5 shows the O1s region of the photoelectron spectra from CO (bottom) and $Fe(CO)_5$ (top). There is a 3.3 eV reduction in the binding energy of the main O1s peak in the carbonyl compared to the CO molecule, but a single particle calculation predicts very little change in energy. The shift is caused by all of the new excitation channels present in the carbonyl which dramatically changes the self-energy. This statement can be checked by calculating the sum rules described by Eqs. (14.5) and (14.6). The measurements were made at the same pressure and incident X-ray flux so the sum rule on the intensity could be checked. The sum of the intensity over the region of the shake-up is the same for CO as for the carbonyl within 7%. Nearly 30% of the intensity in the main line for the carbonyl has been 'borrowed' by satellite lines. The first moment of the spectral weight for CO occurred at 546.4 eV while the corresponding moment for carbonyl was at 546.1 eV. The 0.3 eV difference could be error or a real chemical shift.

In the previous example the hole state is localized on the oxygen atom (core level) so there is no band dispersion and consequently $k$ is not a good quantum number in Eq. (14.6). Freund performed a second experiment to test the sum rules, but this time $k$ resolved (Freund et al., 1983). In this experiment the dispersion of the CO valence levels was measured

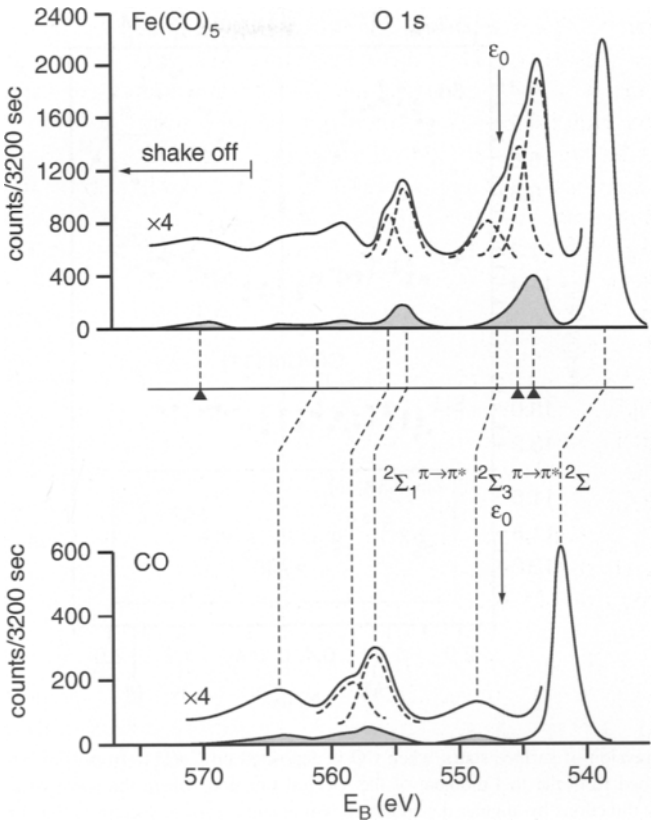


Fig. 14.5. Photoemission spectra (Freund et al., 1981) from molecular CO (lower) and CO in carbonyl (upper). The two curves have an area that integrates to unity, and a first moments which are very similar.

for an ordered array of CO molecules on a Cu(111) substrate. The bonding of CO to a copper surface is weaker than to most transitions substrates creating a unique situation where satellite lines appear on the valence excitation just like they did in the core level spectra shown in Fig. 14.5. Figure 14.6 shows the measurements of the dispersion of the CO induced levels in two directions of the surface Brillouin zone. The lowest binding energy level, 5s, is the bonding orbital and consequently is in intimate contact with the copper surface. This level displays the proper dispersion, both from a symmetry perspective and from comparison to single particle calculations (~0.7 eV dispersion from theory). In contrast the 4s level displays a small dispersion, less than 0.15 eV compared to the theoretical prediction of 0.36 eV. A new peak appears in this spectra approximately 2 eV below the 4s level, which is the satellite line created in the excitation process. This is equivalent to the spectral function calculated in Fig. 14.4 (bottom left) except the excitation is not a plasmon but an excited state of the molecule. The bottom panel of Fig. 14.6 is the $k$ resolved first moment (Eq. (14.6)) for the 4s level and the shake-up level. The dispersion in the first moment is exactly what was calculated in a single particle calculation.

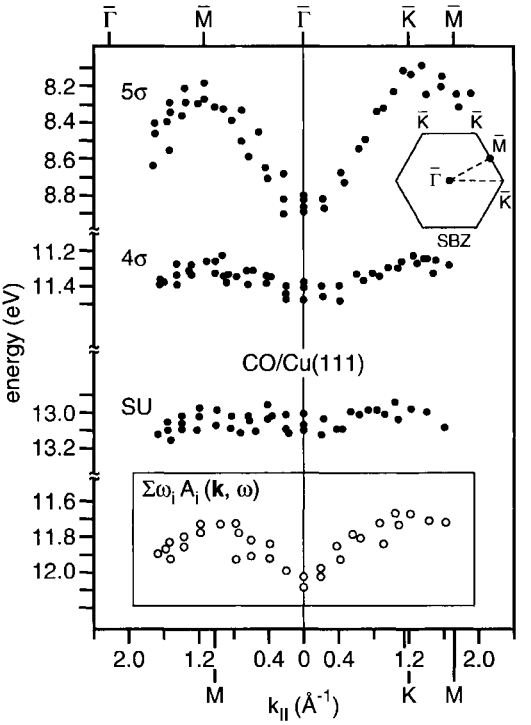


Fig. 14.6. The dispersion of surface states when CO is deposited on Cu(111) from (Freund et al., 1983). The dispersion is obtained from the first moment of the spectral function, where the wave vector is varied in two different symmetry directions by angular dependent measurements. Typical spectra in Fig. 14.4. Open circles at bottom are obtained by applying the $k$ resolved sum rule of (14.6). The data were accumulated at two photon energies (40 and 50 eV) to eliminate effects of cross section.

The sum rule on the intensity and on the first moment should be checked for all photoemission measurements on highly correlated systems such as the cuprates. It would be interesting to try this band mapping on surfaces where there are dilute adsorbates, and where electron localization is postulated. The mapping would show whether the electron had energy bands.

Each conduction electron, in its motion through the metal, manages to keep the other electrons a small distance away. This repulsion is accomplished by the exclusion principle for electrons of like spin, and by correlation for electrons of opposite spin. Hubbard showed (Mahan, 1990) that this exclusion has an important consequence on the dielectric function: it modifies the electronic polarization $P_0(q)$. Most theories employ the approximation that the Hubbard form of the dielectric function is

$$\varepsilon_{\rm H}(q) = 1 - v_q \Gamma(q) P_0(q), \tag{14.20}$$

$$\Gamma(q) = \frac{1}{1 + G_{\rm H}(q) v_q P_0(q)}. \tag{14.21}$$

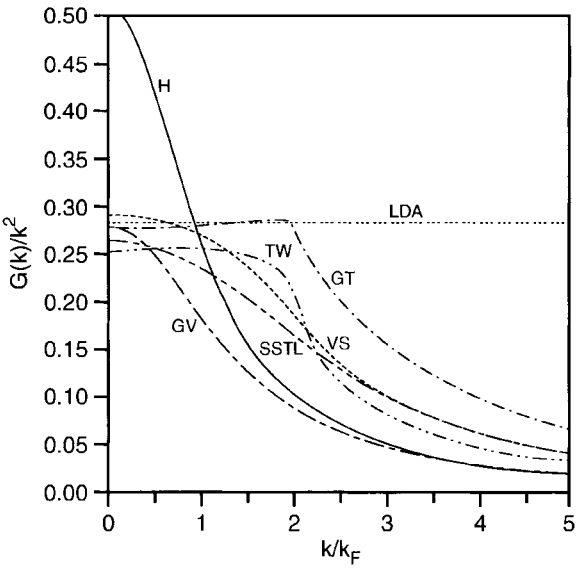


Fig. 14.7. Hubbard local field correction $G_{\mathrm{H}}(q)/q^2$ for several proposed functions. H: Hubbard (1963), GV: Geldart and Vosko (1966), GT: Geldart and Taylor (1970), SSTL: Singwin et al. (1970), TW: Tiogo and Woodruff (1970), VS: Vashishta and Singwi (1972).

The factor $G_{\mathrm{H}}(q)$ is called the 'Hubbard local field correction'. It is not a Green's function. Generally $G_{\mathrm{H}}(q)$ is approximated as a function only of the wave vector $\vec{q}$. Various forms have been proposed which are reviewed elsewhere (Mahan and Subbaswamy, 1990; Mahan, 1994). If $x = k/k_{\mathrm{F}}$ then the original Hubbard form is $G_{\mathrm{H}} = x^2/2(1 + x^2)$. Geldart and Vosko proposed $G_{\mathrm{H}} = x^2/2(2 + x^2)$ while Vashishta and Singwi proposed $G_{\mathrm{H}} = A[1 - \exp(-Bx^2)]$ where $A$ and $B$ are functions of density. All choices go as $G_{\mathrm{H}} \sim x^2$ at small wave vector and to a constant at large wave vector. Figure 14.7 shows a plot of $G_{\mathrm{H}}(x)/x^2$ for many different theories. RPA has $G_{\mathrm{H}} = 0$ whereas LDA usually takes $G_{\mathrm{H}} = Cx^2$ where $C$ is a constant which depends on density.

The phrase 'local-field correction' has its origins in the Lorentz–Lorenz dielectric function for induced dipoles in an insulators. For cubic lattices it has the form

$$\epsilon = 1 + \frac{4\pi\alpha}{1 - 4\pi\alpha/3}, \tag{14.22}$$

where $\alpha$ is the polarizability per unit volume. The numerator $4\pi\alpha$ is the average polarization per unit volume. The denominator contains the correction $4\pi\alpha/3$ which comes from summing the local dipoles in the vicinity of any one of them. This latter term is a 'local-field correction'. Our Hubbard dielectric function has exactly the same form. The numerator $-v_q P_0(q)$ is equivalent to $4\pi\alpha$ (recall $P_0 < 0$) and is the average response of the system of conduction electrons. The denominator contains the factor $G_{\mathrm{H}}(q)v_q P_0(q)$ which corrects for the local environment of the electron – now the local-field correction is due to the exchange–correlation hole.

One type of theory is called the (Mahan, 1994) 'GW Approximation' which will be called 'GWA'. The RPA theory used by Hedin and Lundqvist (Hedin, 1965; Hedin and Lundqvist, 1969, 1971) is a type of GWA which is quite good. As far as we know it gives accurate results for most quantities. Another kind of GWA uses the form for $\Sigma(k)$ in (14.15) with the Hubbard form for the dielectric function $\epsilon(q)$ in the denominator of (14.17). The justification is that the Hubbard dielectric function is better than RPA so use it. Unfortunately, this theory gives poor results (Mahan and Sernelius, 1989).

Years ago DuBois (1959) discussed the calculation of the self-energy of the electron. He classified higher-order contributions as either vertex diagrams or self-energy diagrams. The former increase the answer and the latter decrease the answer. In each order of perturbation theory there is much cancellation between these two kinds of contributions. The correct answer is only obtained by keeping the same amount of both kinds of contributions. Kadanoff and Baym (1961, 1962) called this the 'conserving approximation'. Ward identities (Mahan, 1992) can be used to group the two kinds of terms. These theories tell us that if we are going to add Hubbard corrections to the dielectric function, while calculating the self-energies, then the vertex term must also be included. This gives a theory which is called GW$\Gamma$

$$\Sigma(k, \mathrm{i}k_n) = -\sum_q G(k+q) W_{\mathrm{H}}(q) \Gamma(q), \tag{14.23}$$

$$W_{\mathrm{H}}(q) = \frac{v_q}{\varepsilon_{\mathrm{H}}(q)}, \tag{14.24}$$

$$W_{\mathrm{H}}\Gamma = \frac{v_q}{\varepsilon_f(q)}, \tag{14.25}$$

$$\varepsilon_f(q) = 1 - (1 - G_{\mathrm{H}}) v_q P_0(q). \tag{14.26}$$

The $\Gamma(q)$ is the same function as in (14.21). The combination $W_{\mathrm{H}}\Gamma$ produce an expression which appears to have an effective dielectric function $\varepsilon_f(q)$.

This type of theory was first done by Rice (1965). His results were very similar to Hedin's. The GW$\Gamma$ theory gives most results quite close to RPA (Frota and Mahan, 1992). As an example, Fig. 14.8 gives a calculation (Mahan and Sernelius, 1989) of the band narrowing for three theories as a function of electron density $n_0 a_{\mathrm{B}}^3 = 3/(4\pi r_s^3)$. The solid line is calculated using GW$\Gamma$ and the result is quite close to that using RPA. The third curve labeled $\Gamma = 1$ is a GWA using a Hubbard dielectric function but no additional factor of $\Gamma$ in the numerator of (14.23). The error in this calculation is quite large. Early LDA calculations on metals and semiconductors made GWA calculations with a Hubbard correction in the dielectric function but no correction in the numerator: they omitted the $\Gamma$ in GW$\Gamma$. They are probably similarly inaccurate.

At small values of energy one finds that

$$\Sigma(k_{\mathrm{F}}, E) = -\alpha E - \mathrm{i}\beta E^2. \tag{14.27}$$

Where $\alpha$ is a small dimensionless constant giving the slope of the real part of the self-energy near the Fermi energy as shown in Fig. 14.4. It is related to the renormalization coefficient $Z = 1/(1+\alpha)$. The constant $\beta$ gives the coefficient of the $E^2$ term in the

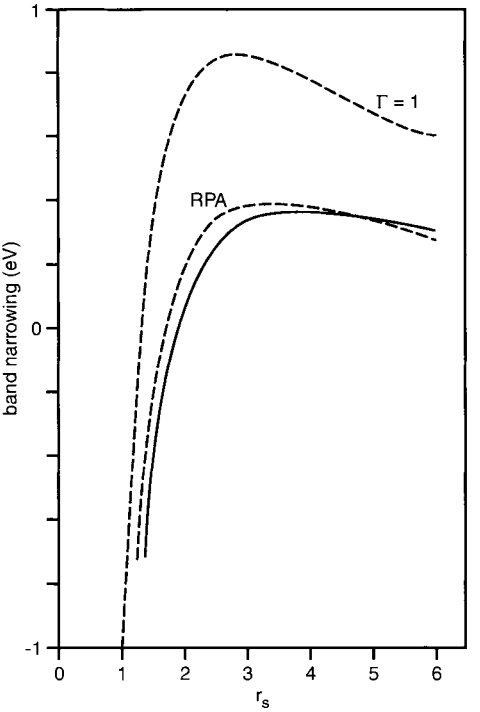


Fig. 14.8. Theoretical band narrowing in free electron metals as a function of density. Dashed curve is RPA and solid line is a GWΓ theory with a Hubbard dielectric function. Curve labeled "$\Gamma = 1$" is a GW theory. From Mahan and Sernelius (1989).

imaginary part. Claessen et al. (1992) found that this form of the self-energy predicted quite well the line shapes found in angular-resolved photoemission from $TiTe_2$. Here $\beta = 40/\text{eV}$ which is larger than found in most materials.

So far our discussion has been on the method of calculating the self-energies of electrons in a jellium model with neither ions nor a periodic potential. Nowadays, with big computers, computational theorists are using similar techniques to include self-energy corrections in realistic calculations of bulk and surface states of actual materials (Eguiluz and Quong, 1995). The initial calculations were done using the *Local Density Approximation* (LDA) (see Mahan and Subbaswamy, 1990) where the exchange and correlation effects were included approximately as a local function $V_{xc}(n(\vec{r}))$ of the electron density $n(\vec{r})$. The self-consistent set of equations to be solved for the electron density are

$$\varepsilon_\lambda \psi_\lambda(\vec{r}) = \left[-\nabla^2 + U(\vec{r}) + V_H(\vec{r}) + V_{xc}\big(n(\vec{r})\big)\right]\psi_\lambda(\vec{r}), \tag{14.28}$$

$$n(\vec{r}) = \sum_\lambda \left|\psi_\lambda(\vec{r})\right|^2, \tag{14.29}$$

$$V_H(\vec{r}) = 2\int d^3r' \frac{n(\vec{r}\,')}{|\vec{r} - \vec{r}\,'|} \tag{14.30}$$

and $U(\vec{r})$ is the potential from the ions or nuclei while $V_{\rm H}$ is the Hartree potential from the other electrons. The first equation describes a Schrödinger-type equation for the orbitals $\psi_\lambda(\vec{r})$. The density is found self-consistently by summing over all states $\lambda$ which are occupied by electrons. The form of the exchange–correlation potential $V_{\rm xc}$ is taken from the homogeneous electron gas.

LDA produces an electron density $n(\vec{r})$ which is quite realistic. However, there is no reason to expect that the eigenvalues $\varepsilon_\lambda$ correspond to actual energy states in the solid or atom. In fact, it is found that they do not. If one does a band structure for a semiconductor, then the energy gap between the conduction and valence bands is predicted to be much smaller than the experimental value. A similar problem is found in trying to calculate the dispersion of surface states on solids. This is called 'The band gap problem'. Louie and coworkers (Northrup et al., 1989; Louie, 1994) found that more realistic energy bands could be obtained by using a more realistic form for the exchange and correlation energy

$$V_{\rm xc}\psi_\lambda(\vec{r}) \rightarrow \int {\rm d}^3r'\, \Sigma(\vec{r},\vec{r}',\varepsilon_\lambda)\psi_\lambda(\vec{r}'), \tag{14.31}$$

$$\Sigma(\vec{r},\vec{r}',\varepsilon_\lambda) = {\rm i}\int \frac{{\rm d}\omega}{2\pi} G(\vec{r},\vec{r}',\varepsilon_\lambda-\omega)W(\vec{r},\vec{r}',\omega), \tag{14.32}$$

$$G(\vec{r},\vec{r}',E) = \sum_n \frac{\psi_n(\vec{r})\psi_n^\dagger(\vec{r}')}{\varepsilon_\lambda - E + {\rm i}\eta}. \tag{14.33}$$

The exchange–correlation potential is now expressed as a spatial integral over the self-energy $\Sigma(\vec{r},\vec{r}',\varepsilon_\lambda)$ which is an energy integral over the Green's function and the interaction $W$. Note that this is a GWA. All of these functions now depend upon position. Otherwise they are the natural extension of the above formulas for jellium. The screened interaction $W$ can be calculated using RPA, in which case one has to solve the integral equation

$$W(\vec{r}_1,\vec{r}_2,\omega) = \frac{1}{r_{12}} + \int \frac{{\rm d}^3r_3\,{\rm d}^3r_4}{r_{13}} P(\vec{r}_3,\vec{r}_4,\omega)W(\vec{r}_4,\vec{r}_2,\omega), \tag{14.34}$$

$$P(\vec{r}_1,\vec{r}_2,\omega) = \sum_{nm} \frac{n_n - n_m}{\varepsilon_n - \varepsilon_m + \omega + {\rm i}\eta} \psi_n^\dagger(\vec{r}_1)\psi_m(\vec{r}_1)\psi_n(\vec{r}_2)\psi_m^\dagger(\vec{r}_2). \tag{14.35}$$

This calculation is far more numerical work than the LDA equations, because of the integral equations. But it gives a far better answer. Figure 14.9 from Louie (1994) shows the quasiparticle energy bands on the (111) surface of silicon which has been covered with a monolayer of As. The As saturates the dangling bonds and prevents reconstruction. The dashed curve is LDA while the solid curves are the quasiparticle bands (labeled QP) using the above formalism.

All theories for the self-energy in simple metals include only the role of charge fluctuations. This is what we include in screened exchange. The contribution of spin fluctuations is ignored. Contrast this to theories of the Hubbard model for strongly correlated systems, where theorists include spin fluctuations and ignore charge fluctuations! A better procedure is to include both spin and charge fluctuations in all theories, whether jellium or strongly

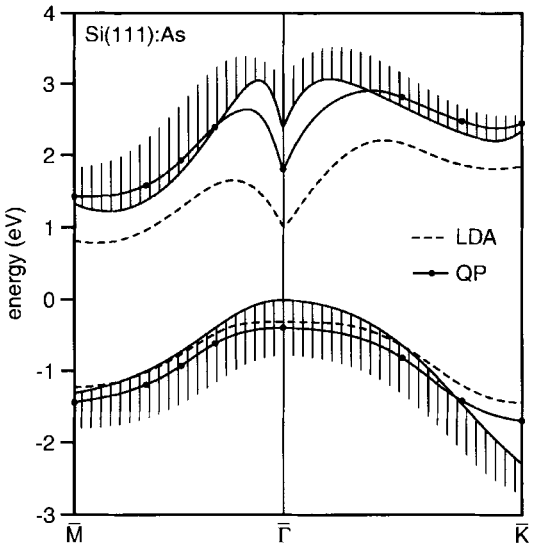


Fig. 14.9. Surface electron states on Si(111):As as calculated by Louie et al. (1994). Dashed lines by LDA are not as accurate as the quasiparticle calculations using the full nonlocal interaction for exchange and correlation.

correlated systems. For jellium, everyone who has examined the contribution of spin fluctuations has concluded they are small. Although this appears to justify their omission, we should remark that everyone who calculates them has a different way of doing it. There is no generally accepted method of including spin fluctuations in the homogeneous electron gas.

## 14.3. Photoemission

In photoemission a photon of frequency $\omega$ enters the solid and causes an electron of energy $E$ to leave the surface in a direction defined by a bit of solid angle $\mathrm{d}\Omega$. The interaction between the photon and the electron is given by the $\vec{p}\cdot\vec{A}$ interaction which we write as

$$\delta V = \frac{e}{2mc}\left[\vec{p}\cdot\vec{A} + \vec{A}\cdot\vec{p}\right], \tag{14.36}$$

where $A(\vec{r})$ is the vector potential from the photons and $\vec{p}$ is the momentum operator of the electrons. The rate of optical absorption is calculated using the 'Golden Rule' of quantum mechanics in terms of the matrix element $M$

$$W = 2\pi \sum_{if} |M|^2 \delta(E_i + \omega - E_f), \tag{14.37}$$

$$M = \int \mathrm{d}^3 r\, \psi_f^{\dagger}(\vec{r})\, \delta V\, \psi_i(\vec{r}). \tag{14.38}$$

Define the $z$-direction as normal to the surface so that $\vec{r} = (\vec{\rho}, z)$. The initial wave vector is $(k_z, \vec{k})$ and the final wave vector is $(p_z, \vec{p})$. Now the vector component of wave vector denotes the two components parallel to the surface. The wave functions parallel to the surface are plane waves $\exp(i\vec{k} \cdot \vec{\rho})$ for the initial state and $\exp(i\vec{p} \cdot \vec{\rho})$ for the final state. They remain undamped even when scattering causes a finite mean free path. This is an important point. When the electron leaves the solid, there is no scattering outside so the wave function is a plane wave with no damping. The plane wave outside must match perfectly to the wave function inside. So along the surface, there is no damping inside for the parallel component of the wave function. Of course, the wave function along the $z$-direction will be damped by interactions. The argument that the wave function along the surface remains undamped, even when there is absorption, is quite familiar from optics where it also applies to the wave functions of photons and to the electromagnetic fields.

The wave function of the final state $\psi_f(\vec{r})$ corresponds to an electron leaving the surface. When we take its Hermitian conjugate, that corresponds to the wave function of an electron coming into the solid from outside. The $z$-component of this incoming wave function is denoted as $\phi_f^>(z)$. That the matrix element is calculated with a wave function for an incoming wave is a standard result in scattering theory. It was first used in photoemission by Mackinson (Mackinson, 1949; Adawi, 1964) for the surface effect and by Mahan (1970) for the volume effect.

Assume the surface has an area $S$ and the solid has a thickness $L$ in the $z$-direction. The wave function for the initial and final states can be written as

$$\psi_i(\vec{r}) = \sqrt{\frac{2}{SL}}\phi_i(z)e^{i\vec{k}\cdot\vec{\rho}}, \tag{14.39}$$

$$\psi_f^\dagger(\vec{r}) = \frac{1}{\sqrt{SL}}\phi_f^>(z)e^{-i\vec{p}\cdot\vec{\rho}}. \tag{14.40}$$

The $z$-components of the wave functions, $\phi_i(z)\phi_f^>(z)$ are evaluated numerically. Usually one uses a surface potential $V(z)$ of the type first calculated for jellium by Lang and Kohn (1970). In photoemission, the state $\phi_i(z)$ describes an electron bound in the solid, while the incoming state $\phi_f^>(z)$ describes an unbound electron. In the interior of the solid, at large positive distances, they are normalized

$$\phi_i(z) \to \sin(k_z z + \delta), \tag{14.41}$$

$$\phi_f^>(z) \to Te^{ik_z' z}, \tag{14.42}$$

where $\delta$ is the surface phase shift and $T$ is the transmission factor for an electron entering the solid from the outside.

In (14.36) the symbol $\vec{p}$ denotes a momentum operator. Its components parallel to the surface operate on the plane wave components and bring down a factor of $\vec{k}$. However, the $z$-integral yields zero since $\phi_i$ and $\phi_f^>$ are orthogonal. The only nonzero component of the gradient operator in $\vec{p}$ is the $z$-component. We can effectively replace (14.36) by the expression

$$\delta V = \frac{e}{2mc}\left[p_z A_z(z) + A_z(z)p_z\right]. \tag{14.43}$$

The vector potential $A_z(z)$ does depend upon $z$ in the surface region. It exhibits Friedel oscillations into the interior. This dependence lessens at higher photon frequency. We make an approximation and treat $A_z(z)$ as a constant. Another approximation is that the operator $p_z$ is replaced by the derivative of the potential. One starts with the time derivative of the momentum operator

$$\frac{\partial p_z}{\partial t} = \mathrm{i}[H, p_z]. \tag{14.44}$$

On the left, the time variation of interest is $\exp(-\mathrm{i}\omega t)$, so the left side is $-\mathrm{i}\omega p_z$. On the right, $p_z$ commutes with the kinetic energy term, but not the potential energy term. We find $\mathrm{i}\omega p_z = \mathrm{d}V(z)/\mathrm{d}z$. This simple relationship is valid in an interacting system. The matrix element in (14.38) is now

$$M = \frac{\sqrt{2}\mathrm{i}}{m\omega L}\delta_{\vec{k}=\vec{p}}\left(\frac{e}{c}A_z\right)\bar{M}, \tag{14.45}$$

$$\bar{M} = \int_{-\infty}^{\infty} \mathrm{d}z\, \phi_f^{>}(z)\frac{\mathrm{d}V(z)}{\mathrm{d}z}\phi_i(z). \tag{14.46}$$

Define $F$ as the photon flux in units of photons per second. It is determined by the incident light in the photoemission experiment. It is related to the vector potential

$$\left(\frac{e}{c}A_z\right)^2 = \frac{4\pi\alpha\hbar^2(\hat{e}\cdot\hat{z})^2}{S\omega}F, \tag{14.47}$$

where $\hat{e}$ is the polarization vector of the incident light and $\alpha$ is the fine structure constant. We collect our results so far

$$W = \frac{(4\pi\hat{e}\cdot\hat{z})^2\alpha\hbar F}{m^2\omega^3}\frac{1}{SL^2}\sum_{if}|\bar{M}|^2\delta_{\vec{k}=\vec{p}}\delta(\varepsilon_k + \hbar\omega - \varepsilon_p). \tag{14.48}$$

Define $I = eW$ as the current of electrons in amperes. We change the summations over initial and final states to continuous integrals

$$\frac{1}{SL^2}\sum_{if}\delta_{\vec{k}=\vec{p}} = \frac{1}{(2\pi)^4}\int \mathrm{d}^3k \int \mathrm{d}^3p\, \delta^2(\vec{k}-\vec{p}). \tag{14.49}$$

Set $\mathrm{d}^3p = p^2\,\mathrm{d}p\,\mathrm{d}\Omega$ and take the factor of $\mathrm{d}\Omega$ to the left. The integral over $\mathrm{d}p$ eliminates the delta function of energy conservation. We find for the current per unit solid angle

$$\frac{\mathrm{d}I}{\mathrm{d}\Omega} = \frac{e\alpha F}{\pi^2 m\omega^3\hbar}\int \mathrm{d}^3k\, p\,\delta^2(\vec{k}-\vec{p})|\bar{M}|^2. \tag{14.50}$$

This is our basic formula (Mahan, 1970, 1990) for the intensity of electrons emitted from a solid as a function of the incident flux of photons.

The matrix element $\bar{M}$ contains an integral over the electron potential energy $V(z)$. In a three-dimensional solid we write this potential as

$$V(\vec{r}) = V_s(z) + \sum_{\vec{G}} V_g e^{i\vec{G}\cdot\vec{r}}. \tag{14.51}$$

The first term is the surface potential which confines the electrons to the metal and prevents bound electrons from leaking out. Its contribution to the photoemission is called the *surface effect*. In the early days of photoemission, everyone thought that this was the most important term. Nearly all of the early theories calculated just this contribution (Mitchell, 1934; Hill, 1938; Mackinson, 1949; Adawi, 1964). The second term contains a summation over the reciprocal lattice vectors $\vec{G}$. It is due to the periodic potential of the metal ions. Photoemission from this term alone is called the *volume effect*. Only in modern times have experimentalists identified this term as the largest contribution in most metals.

Since the mean free path of the excited electrons is rather short, only those electrons excited near the surface can exit the solid. In many experiments the majority of electrons come only from the first two atomic layers. In that case the surface and volume effects are both important. In squaring the matrix element, it is important to consider possible interference between the surface and volume effects. Such interference occurs if the solid is oriented so that there is a reciprocal lattice vector $\vec{G}$ which points normal to the surface, in the $\hat{z}$-direction. This is the case in the alkalis if the surface is (110). Furthermore, if one is measuring only electrons which are emitted normal to the surface, one can accurately simplify the above expressions to

$$\frac{dI}{d\Omega} = \frac{e\alpha F}{\pi^2 m\omega^3\hbar}\int dk_z\, p_z |\bar{M}|^2, \tag{14.52}$$

$$V(\vec{r}) = V_s(z) + \sum_{G_z} V_g e^{iG_z z}. \tag{14.53}$$

The first calculation of Shung and Mahan (1986, 1988) on the photoemission of sodium use a theory of this type. The mean free path of the excited electrons were include in a phenomenological way by using for $\phi_f^>$ the expression

$$\phi_f^>(z) = T e^{ik_z' z - z/\ell}, \tag{14.54}$$

where $\ell$ is the mfp of the electron as deduced from $\ell = -Z\Sigma_2/v_z$ where $Z$ is the renormalization coefficient and $v_z$ the Fermi velocity in the $z$-direction. Later calculations (Shung et al., 1987) included the self-energy effects in a more accurate manner.

We wish to include the effects of the electron self-energy on both the initial and final state of the electron during the photoemission process (Shung et al., 1987). We do that in the following fashion. We return to the original definition in (14.37) and (14.38) and write

these expressions as

$$I = \frac{2\pi e}{\hbar}\int \mathrm{d}^3 r_1\, \delta V(\vec{r}_1)\int \mathrm{d}^3 r_2\, \delta V(\vec{r}_2) \times \sum_i \psi_i(\vec{r}_1)\psi_i^\dagger(\vec{r}_2)\sum_f \psi_f^>(\vec{r}_2)\psi_f^{>\dagger}(\vec{r}_1)\,\delta(E_i+\hbar\omega-E_f). \tag{14.55}$$

We insert the spectral functions in the summations over $i$ and $f$. In the summation over initial states

$$\sum_i \psi_i(\vec{r}_1)\psi_i^\dagger(\vec{r}_2) \to \int \mathrm{d}E \sum_i \delta(E-\varepsilon_i)\,\psi_i(\vec{r}_1)\psi_i^\dagger(\vec{r}_2). \tag{14.56}$$

The delta function in energy conservation is replaced by the spectral function. Then one does in integral over components parallel to the surface.

$$\sum_i \psi_i(\vec{r}_1)\psi_i^\dagger(\vec{r}_2) \to \int \frac{\mathrm{d}E}{2\pi} A(\vec{r}_1,\vec{r}_2,E), \tag{14.57}$$

$$A(\vec{r}_1,\vec{r}_2,E) = \int \frac{\mathrm{d}^2k}{(2\pi)^2}\mathrm{e}^{\mathrm{i}\vec{k}\cdot(\vec{\rho}_1-\vec{\rho}_2)}A(z_1,z_2;\vec{k},E), \tag{14.58}$$

$$A(z_1,z_2;\vec{k},E) = \int \frac{\mathrm{d}k_z}{2\pi}\phi(k_z,z_1)\phi(k_z,z_2)A(k_z,\vec{k},E), \tag{14.59}$$

$$A^>(z_1,z_2;\vec{k},E) = \int \frac{\mathrm{d}k_z}{2\pi}\phi^>(k_z,z_1)\phi^{>*}(k_z,z_2)A(k_z,\vec{k},E). \tag{14.60}$$

Using these functions, we can write the integral for the current as

$$I = \frac{2\pi e}{\hbar}\int \mathrm{d}^3 r_1\, \delta V(\vec{r}_1)\int \mathrm{d}^3 r_2\, \delta V(\vec{r}_2) \times \int \mathrm{d}E\, A(\vec{r}_1,\vec{r}_2,E-\hbar\omega)A^>(\vec{r}_2,\vec{r}_1,E). \tag{14.61}$$

The functions $\phi(k_z,z)$ are the initial states which were called $\phi_i(z)$ earlier. Similarly, $\phi^>(k_z,z)$ is the final state which is incoming. The spectral function $A(k_z,\vec{k},E)$ is the same one which we discussed in the previous section on electron–electron interactions. It provides the broadening ($\Sigma_2$) and the energy shift ($\Sigma_1$) as a function of wave vector and energy. By summing the eigenstates over wave vector we define the position dependent function $A(\vec{r}_1,\vec{r}_2,E-\hbar\omega)$ for the initial states and $A^>(\vec{r}_1,\vec{r}_2,E)$ for the final incoming states.

In writing the above expression for the current, we have used the derivative definition of the potential $\delta V(\vec{r})$

$$\delta V(\vec{r}) = \frac{\mathrm{i}e}{mc\omega}\vec{A}(\vec{r})\cdot\vec{\nabla}V(\vec{r}). \tag{14.62}$$

Here the symbol $\vec{A}(\vec{r})$ refers to the vector potential. The advantage of using this form for $\delta V$ is that it can be put anywhere without regard to the ordering of other functions. In the earlier definition, which contained a gradient on the wave function, the ordering of the gradient operator was important.

The present technology is to measure the energy of the photoemitted electrons. It is easy to take a functional derivative of (14.61) with respect to $\mathrm{d}E$ to obtain the current per unit energy

$$\frac{\mathrm{d}I}{\mathrm{d}E} = \frac{2\pi e}{\hbar}\int \mathrm{d}^3 r_1\, \delta V(\vec{r}_1) \times \int \mathrm{d}^3 r_2\, \delta V(\vec{r}_2)\, A(\vec{r}_1, \vec{r}_2, E-\hbar\omega) A^{>}(\vec{r}_2, \vec{r}_1, E). \tag{14.63}$$

Since the experimentalist measures the final energy $E$ of the electron then that is fixed. Similarly, the initial energy must be $E-\hbar\omega$. Thus the initial and final energies are known. The function $A(\vec{r}_1, \vec{r}_2, E-\hbar\omega)$ expresses the fact that the interactions actually smear the wave vector, and not the energy. The integrals over wave vectors in $A(\vec{r}_1, \vec{r}_2, E-\hbar\omega)$ allow a range of values to contribute to the emitted electron state.

Usually the angular distribution is also measured, and then we need the current per unit energy per unit solid angle. The solid angle comes from the final electrons, and is contained in the definition of $A^{>}$

$$A^{>}(\vec{r}_1, \vec{r}_2, E) = \int \frac{\mathrm{d}^3 p}{(2\pi)^3} \mathrm{e}^{\mathrm{i}\vec{p}\cdot(\vec{\rho}_1-\vec{\rho}_2)} \phi^{>}(p_z, z_1)\phi^{>}(p_z, z_2) A^{>}(p_z, \vec{p}, E), \tag{14.64}$$

$$\mathrm{d}^3 p = p^2 \mathrm{d}p\, \mathrm{d}\Omega, \tag{14.65}$$

$$\frac{\mathrm{d}^2 I}{\mathrm{d}E\, \mathrm{d}\Omega} = \frac{e}{(2\pi)^2\hbar}\int \mathrm{d}^3 r_1\, \delta V(\vec{r}_1) \int \mathrm{d}^3 r_2\, \delta V(\vec{r}_2) A(\vec{r}_1, \vec{r}_2, E-\hbar\omega) \times \int p^2\, \mathrm{d}p\, \mathrm{e}^{\mathrm{i}\vec{p}\cdot(\vec{\rho}_1-\vec{\rho}_2)} \phi^{>}(p_z, z_1)\phi^{>*}(p_z, z_2) A^{>}(p_z, \vec{p}, E). \tag{14.66}$$

When the photoemission is measured normal to the surface then we can again simplify the above integral. Only the dependence in the $z$-direction is relevant and one can do the integrals over variables which are parallel to the surface. This brings us to the expression

$$\frac{\mathrm{d}^2 I}{\mathrm{d}E\, \mathrm{d}\Omega} = \frac{2e\alpha F}{(2\pi)^3\hbar^2\omega^3 m^2}\int p^2\, \mathrm{d}p\, A(p, E) \times \int \mathrm{d}z_1 \int \mathrm{d}z_2 \frac{\mathrm{d}V(z_1)}{\mathrm{d}z_1}\frac{\mathrm{d}V(z_2)}{\mathrm{d}z_2} \phi^{>}(p_z, z_1)\phi^{>*}(p_z, z_2) A(z_1, z_2; \vec{0}, E-\hbar\omega). \tag{14.67}$$

This expression is useful for calculating many-body effects in photoemission measured normal to the surface. The integral on the right is four-dimensional.

In the prior section we discussed the calculation of correlation functions such as the Green's function. We quoted DuBois (1959) in remarking that if one is going to add self-energies to the Green's functions, then one must also add vertex corrections to provide the

proper cancellation. Here we have violated that rule. We have only added self-energies in the employment of spectral functions. A better calculation would also add vertex corrections. So far no one has done this.

Figure 14.2b shows the band structure of sodium in the (011) direction which is perpendicular to the usual surface face. The solid lines are bands. Those below the chemical potential are occupied and those above are empty. Since electron wave vector $\vec{k}$ is conserved on a reduced band diagram, then optically induced transitions are vertical transitions between pairs of bands. Nonvertical transitions are also allowed, where wave vector is altered by scattering from impurities or phonons. These cause *Drude* absorption which is an important feature of the visible spectra. However, the Drude term declines rapidly at higher photon frequency. Indirect transitions become much less likely above $\hbar\omega = 10$ eV and contribute a negligible amount at high photon frequency.

One of the most interesting cases is the normal emission data of Jensen and Plummer (1985) for Na(110) shown in Fig. 14.10. This data should be compared to the band diagram shown in Fig. 14.2. There were two striking features of this data that were inconsistent with the nearly free electron picture of alkali metals. First, the observed band width (bottom of the band with respect to the Fermi energy) was 2.5 eV instead of 3.2 eV expected from theory (Chou et al., 1983). This is a 23% band narrowing compared to the 10% predicted by

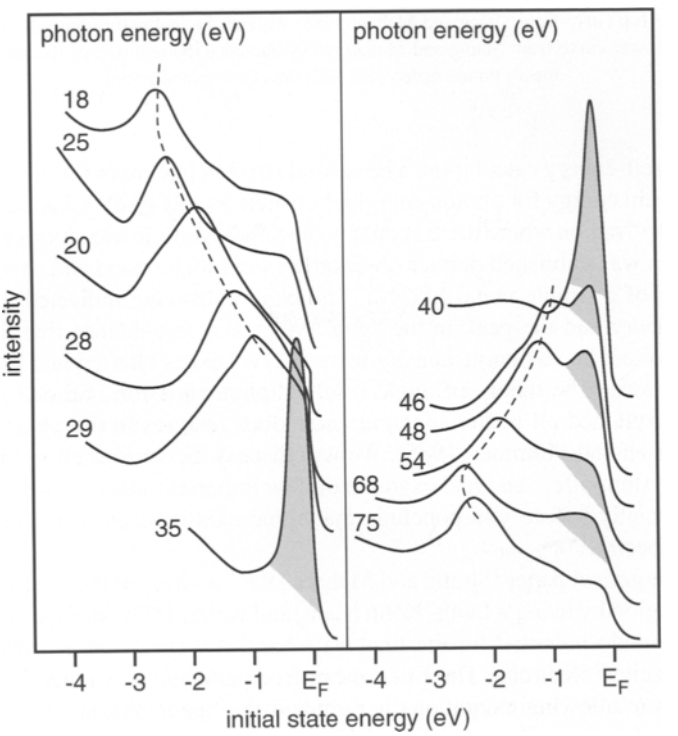


Fig. 14.10. Normal emission photoemission spectra from Na(110) as a function of photon energy (Jensen and Plummer, 1985). The shaded peaks near the Fermi energy are in the "gap" region.

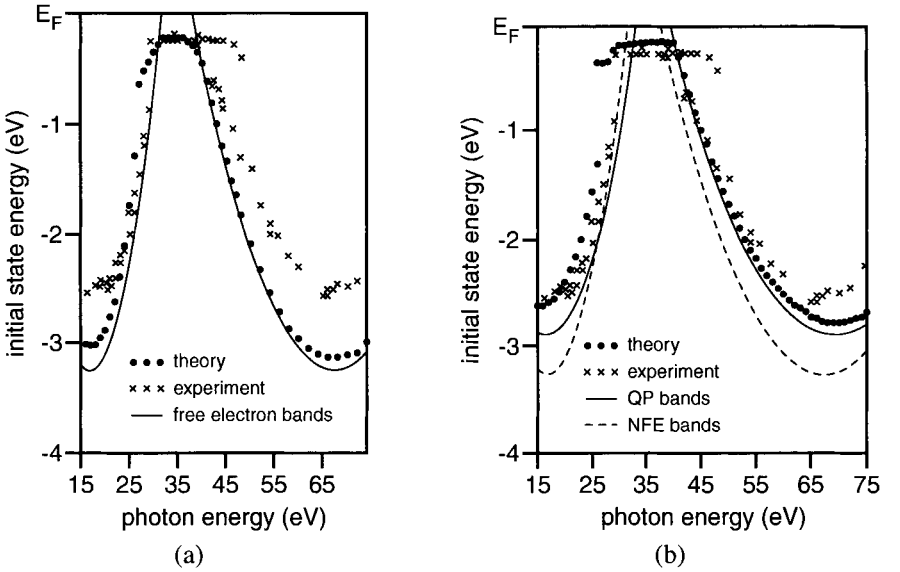


Fig. 14.11. Comparison of the calculated (Shung and Mahan, 1986; Shung et al., 1987) and the measured (Jensen and Plummer, 1985) peak positions as a function of wave vector in the (110) direction in Na. Points marked × are experimental. Top curve from Shung and Mahan (1986) without the real part of the self-energy but with the imaginary part. Lower curve from Shung and Mahan (1988) includes the real part of the self-energy. Here the theory points match well with the experimental points.

Hedin's RPA self-energy calculation. The second striking feature in the spectra is the sharp peak at the Fermi energy for photon energies between 30 and 40 eV (shaded in Fig. 14.10). This is the "gap" region where there should be no single particle transitions (see Fig. 14.2). When this data was published neither observation were understood and shed doubt on our understanding of a simple metal like Na. The band narrowing indicated inaccuracies in many-body theory and the peak in the "gap" was taken as evidence that the conduction band was distorted, i.e., a charge density wave (CDW) exists (Jensen and Plummer, 1985; Overhauser, 1985). The theory of angle-resolved photoemission outlined in this section successfully explained all of the apparent anomalous features in the photoemission data of Jensen (Jensen and Plummer, 1985). We will discuss the various effects in some detail because this system offers an ideal example of how important it is to understand what you measure, especially before you conclude that some exotic behavior is the origin of the 'anomalous' spectra.

The first theoretical paper (Shung and Mahan, 1986) addressed the intensity of the peak in the "gap" region by using a Lang–Kohn (Lang and Kohn, 1970) surface potential, a one-dimensional pseudo-potential for the final state band structure, and a realistic mean free path for the excited electrons. The finite mean free path caused a smearing in the direct transition picture allowing excitations to occur in the "gap" region and the surface potential generated surface photoemission that interfered with the bulk photoemission. The result of this first calculation is shown in Fig. 14.11a, where the peak in the photoemission spectra as a function of photon energy is plotted and compared to the data of Jensen (Jensen

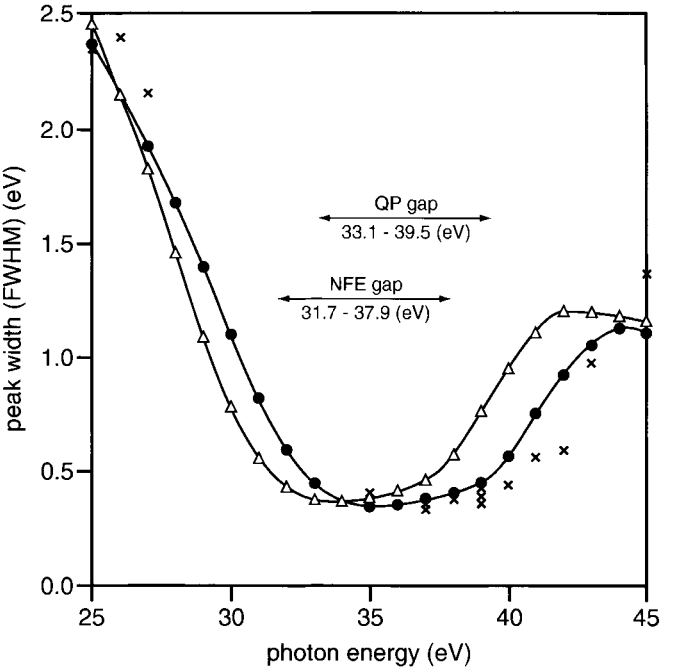


Fig. 14.12. The gap in the photoemission spectra of sodium for electrons whose initial state is near the Fermi surface. Experimental points labeled ×. The quasiparticle theory including self-energies, are labeled • and agree well with the data. The theory without the real part of the self-energies, labeled △, do not agree with the data on the position of the energy gap. From Allen et al. (1986) and Shung et al. (1987).

and Plummer, 1985) and Lyo (Lyo and Plummer, 1988; Lyo, 1988). The solid line is the prediction from free electron theory shown in Fig. 14.2a; in this theory there is no intensity in the photon energy region of the 'gap'. The finite mean free path, i.e., an imaginary part to the electron self-energy, allowed transitions to occur in the gap region. We will return to discuss the intensity in the 'gap' region. The difference between the free electron band bottom and the calculation originated from the interference of the surface and bulk photoemission. The second theory paper (Shung et al., 1987; Shung and Mahan, 1988) included the real and imaginary components for the self-energy $\Sigma(k, E)$ both for the hole state below the Fermi energy and the electron state above the Fermi energy. $\Sigma(k, E)$ was calculated using the Rayleigh-Schrödinger method (Shung et al., 1987) and differed slightly from the RPA results of Hedin (1965). The solid circles in Fig. 14.11b show the results of this calculation. The solid line marked QP bands is the calculated quasiparticle band structure consistent with Hedin's RPA calculation. The deviation of the theory from the QP bands is a result of the large imaginary part of the self energy in the final bands allowing non-vertical transitions and the interference between the surface and the bulk emission. The conclusion was that that the apparent band width narrowing in the data of Jensen (Jensen and Plummer, 1985) and Lyo (Lyo and Plummer, 1988; Lyo, 1988) could be explained by properly including $\Sigma(k, E)$.

In addition, these calculations produced a quantitative explanation of the intensity and width of the peak in the 'gap' region. Figure 14.2a shows that there is an energy gap in the predicted absorption spectra of electrons along the (001) direction in Na. The gap is caused by the fact that the Fermi wave vector is less than half of the reciprocal lattice vector and the Fermi surface does not touch the zone edge. The gap is the energy difference between the length of the two lines. There should be no current of photoemitted electrons, normal to the surface, for photon energies in this gap. Many experiments have been done to test this prediction. Figure 12 shows the photoemission peak width in sodium in the region of this gap. Points marked with an $\times$ are experimental data of Jensen and Plummer. The points marked with a $\triangle$ are the theoretical predictions if one includes the energy width $\Sigma_2$ but neglects the shift $\Sigma_1$. This theory does not line up well with the experimental points. The points marked with a $\bullet$ include the shift from $\Sigma_1$ as well as the width from $\Sigma_2$. These calculated points are in excellent agreement with the experimental points.

This shift in the observed gap is due to the change in the self-energy $\Sigma_1$ between the initial state at the fermi surface ($k = k_F$) and the final state ($k = 3.42k_F$). It had been predicted for many years that the self-energy of an electron from electron–electron interactions reduced in magnitude at large wave vector. Yet these photoemission experiments, as interpreted by Shung et al. (1987), were the first experimental verification. The magnitude of the decline, at this value of wave vector, confirms the theoretical prediction.

Another interesting experimental result in the gap region was a beam of photoemitted electrons which were narrow in energy and focussed normal to the surface. This beam is also well explained by the theoretical predictions, and is due to the finite mean free path of the electrons.

Potassium is also usually regarded as a free electron metal. The predictions for its photoemission are similar to sodium (Shung and Mahan, 1988). However, the experimental results in the gap region are quite different. Itchkawitz, Lyo, and Plummer (Itchkawitz et al., 1990; Itchkawitz, 1991) found that the photoemitted intensity *increased* in the gap region. This is contrary to the predictions of a nearly free electron model.

Overhauser (Overhauser, 1962, 1968, 1985; Overhauser et al., 1987) predicted years ago that the ground state of potassium had a deformation in its Fermi surface due to either a charge density wave (CDW) or to a spin density wave (SDW). Numerous experiments on potassium such as cyclotron resonance or neutron scattering have failed to find evidence for these excitations. Nevertheless, Ma and Shung (1994) pointed out that the gap intensity in potassium could be explained by postulating the existence of a CDW. Figure 14.13 shows their comparison between theory and experiment, which is obviously satisfactory. Again they find that the gap moves in frequency due to self-energy effects. However, the extra intensity comes from the CDW.

Recent LEED experiments (Itchkawitz et al., 1992) on potassium found that this metal had a misalignment of its outer layer of surface atom. Another interpretation (Wright and Chrzan, 1993) of the data is that the surface atoms have large anharmonic oscillations. However, the surface layer is clearly not well aligned with the bulk atoms. Since the photoemission experiment measures electrons emitted from only the first two atomic layers of atoms, the experiment is very sensitive to surface distortions. The success of Ma and Shung's model calculations leads to another speculation regarding the surface atoms: perhaps there is a surface CDW which exists only in the surface region. Photoemission from

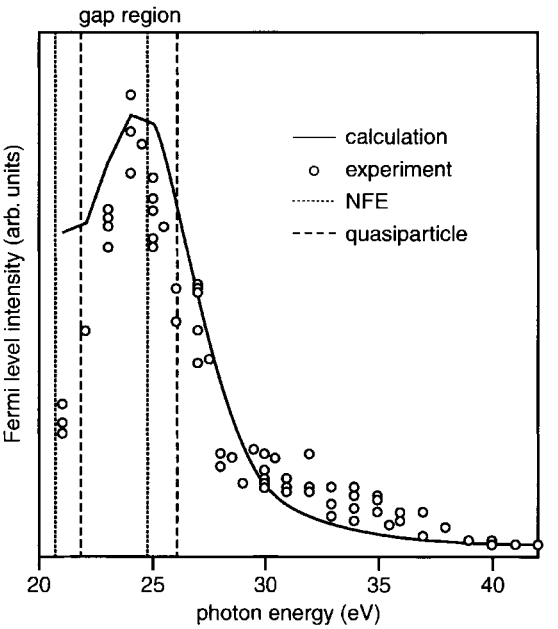


Fig. 14.13. The photoemission spectra of potassium for electrons whose initial state is at the Fermi surface. Nearly free electron theory predicts a gap which is not observed. Circles are data points showing the increase in intensity in the region of the gap. Solid line is theory of Ma and Shung (1994) showing effects of charge density wave on the spectrum.

potassium is obviously more complex than for sodium. Research is continuing into the properties of this amazing metal.

We end this section by discussing some of the systematic discrepancies that still exist between the calculated and measured photoemission spectra for the simple metals. First look at the comparison between the theory and experiment for Na shown in Fig. 14.11b. As you sweep photon energy you can reach the bottom of the band as several photon energies. The experimental data for all of the simple metals indicates that the measured band width is independent of photon energy. In contrast, the theory always predicts different binding energies for the bottom of the band at different photon energies. This is a consequence of the energy dependence of the surface-bulk interferences and the imaginary part of $\Sigma(k, E)$. Intimately related to this problem is the fact that the measured widths of peaks in the spectra do not agree with the calculations of the imaginary part of $\Sigma(k, E)$. The widths of the final (electron) bands can be measured by fixing the analyzer at the Fermi energy and sweeping the photon energy through a transition at the Fermi energy (Kevan, 1992). The width of the hole state at $k = 0$ can be measured directly from the width of the peak in the photoemission spectra. Table 14.2 shows a compilation of data for the simple metals (Watson, 1992). The width of the hole state at $k = 0$ is consistently larger than theory and the width of the electron state above the Fermi energy is consistently smaller than theory. This data is displayed in Fig. 14.14. The top panel is the hole state width and the

Table 14.2
Im $\Sigma(k, \xi_k)$ in eV for the simple metals as measured in photoemission (adopted from Watson, 1992)

| Metal | $\Sigma_2(k=0)$ | | $k/k_p$ | $\Sigma_2(k)$ | |
|---|---|---|---|---|---|
| | exp. | theory[a] | | exp. | theory[a] |
| Be[b] | 1.5 | 1.5 | | | |
| Al[c] | 1.4 | 1.3 | 0.85 | 1.45 | 1.2 |
| | | | 1.26 | 3.05 | 3.8 |
| | | | 1.48 | 3.15 | 4.5 |
| | | | 1.71 | 4.6 | 4.7 |
| | | | 1.82 | 5.15 | 4.7 |
| Mg[d] | 1.15 | 0.95 | 1.47 | 2.1 | 3.8 |
| | | | 1.61 | 2.5 | 3.95 |
| Li[e] | 0.7 | 0.5 | 2.02 | 2.25 | 3.45 |
| Na[f] | 0.6 | 0.5 | | | |
| K[g] | 0.4 | 0.35 | 1.91 | 1.6 | 2.65 |

$k_p$ is defined as the threshold wave vector for plasmon excitation in the free electron approximation.
[a]All theoretical values from Shung et al. (1987).
[b]Jensen et al. (1984b).
[c]Levinson et al. (1983).
[d]Bartynski et al. (1986).
[e]Watson (1992).
[f]Lyo (1988).
[g]Itchkawitz (1991).

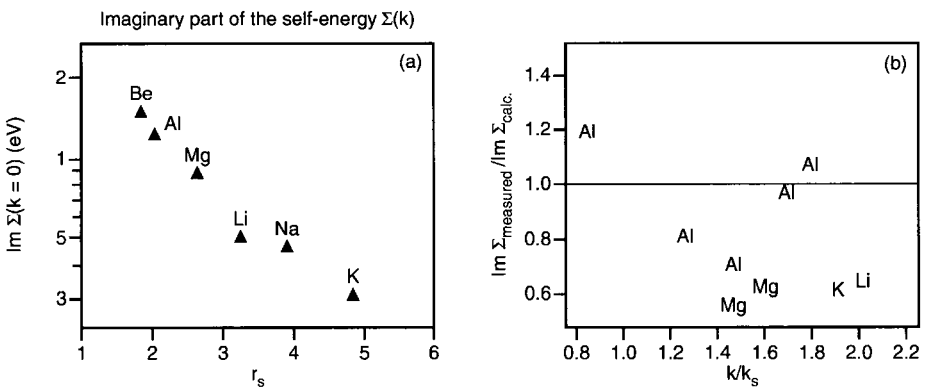


Fig. 14.14. Experimental results for the imaginary part of the electron self-energy as measured in photoemission (Watson, 1992).

bottom the electron state width. This data clearly indicates that there is something systematically wrong with the calculation of the energy dependence of the imaginary part of the self-energy. Figure 14.15 shows the calculated imaginary $\Sigma(k, E)$ for Li compared to a

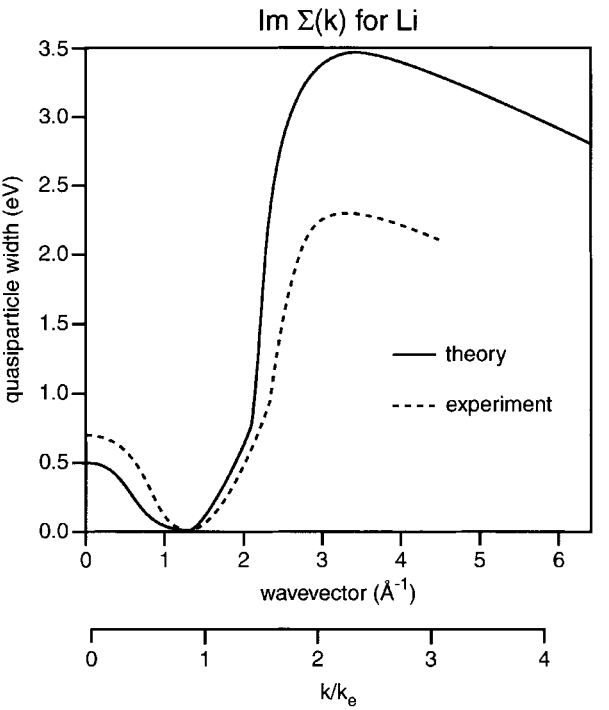


Fig. 14.15. Comparison between theory (Shung et al., 1987) and experiment (Watson, 1992) of the imaginary self-energy in lithium of an electron as measured in photoemission.

hypothetical self-energy consistent with the line-widths measured for Li (Watson, 1992). This difference is very important, since the imaginary part of the self-energy contributed to the shift of the theory in Fig. 14.11b from the quasiparticle bands upwards towards the data. If this functional form of the imaginary part of the self-energy is used in the calculation there will be a conspicuous discrepancy between the measured band width and the calculated band width, indicating that the real part of the self-energy calculated in the GWΓ (Fig. 14.8) is wrong. The game isn't over until the fat lady sings!

## 14.4. Electron–phonon interactions

The electron–phonon interaction also contributes to the self-energy of an electron. This dependence is usually not an important aspect of photoemission in simple metals. However, the electron–phonon interaction is important for other systems. As experimental resolution improves, the effects of phonons will be observed in simple metals. Here we review some of the properties of this interaction.

The interaction with phonons contributes to a self energy $\Sigma_p(E)$ which has real and imaginary parts (Grimvall, 1981). Note that we did not indicate a dependence upon wave vector. This self-energy only has nonzero values for electrons very near in energy to the

Fermi surface. So it is only important for electrons whose wave vector is near to the Fermi wave vector $k_F$. The energy of the phonons sets the energy scale of the self-energy. If the maximum phonon energy is $\hbar\omega_x = E_x$ then a useful approximation to the real part of the self-energy is

$$\Sigma_{p1}(E) = -E_x \ln\left(\frac{\lambda E(E+2E_x)+4E_x^2}{\lambda E(E-2E_x)+4E_x^2}\right). \tag{14.68}$$

Here, $\lambda$ is a dimensionless constant which gives the strength of the electron–phonon interaction (Grimvall, 1981; Mahan, 1990). The energy $E$ is measured with respect to the chemical potential. The above formula is valid at zero temperature. The real part of the self-energy decreases as the temperature is increased.

The energy scale $E_x$ should not be confused with the Debye energy. The latter is conventionally defined in regard to the low temperature heat capacity. For solids with many atoms per unit cell, the Debye energy is usually much smaller than $E_x$. The energy $E_x$ is small for simple metals: often only 10–20 meV. For cuprate superconductors $E_x = 90$ meV which is much larger. In these systems the electron–phonon self energy will extend over a larger range of frequency.

In photoemission, only electrons which are very near to the chemical potential will have a significant contribution from the electron–phonon interaction. The excited electrons which leave the solid will not have an important value of $\Sigma_{p1}$. Similarly, in inverse photoemission, only those final states near to the Fermi surface will have any effects due to phonons. One can also calculate the density of states using (14.2) in order to see whether there is structure due to phonons, which is done below. There is not much. It will be hard to see the real part of the self-energy of electrons from the interaction with phonons. Other experiments, such as cyclotron resonance, measure the properties of electrons right at the chemical potential. They are significantly changed by the interaction with phonons.

The imaginary part of the self-energy from phonons is more important in photoemission. For electrons whose energy is larger than $E_x$ then $\Sigma_{p2} = -i\pi E_x$. The imaginary self-energy is a constant. This result is for zero temperature. The answer increases at higher temperature. This feature is well known from the increase of electrical resistivity with increasing temperature. It contributes to the mean free path of electrons. Earlier we mentioned that it caused the Drude absorption observed in the visible spectra. In photoemission the electron leaving the metal may be scattered into other directions by the phonons. This will shift the electron energy by the small energy of the phonon. The biggest effect will just be the change in direction.

Undoubtedly the present emphasis in the photoemission community is the investigation of the Fermi surface. This interest increases with each improvement in energy resolution. It is driven in part by the discovery of the cuprates which are high temperature superconductors. The electron–electron contribution to the imaginary part of the self-energy vanishes at zero temperature at the Fermi surface. The observation in the cuprates that the line width does not vanish at the Fermi surface has led to speculation concerning possible non-Fermi liquid behavior. Other contributions to the line width such as impurity or alloy scattering do not vanish at the Fermi surface. Another equally important contribution is the electron–phonon part of the self-energy.

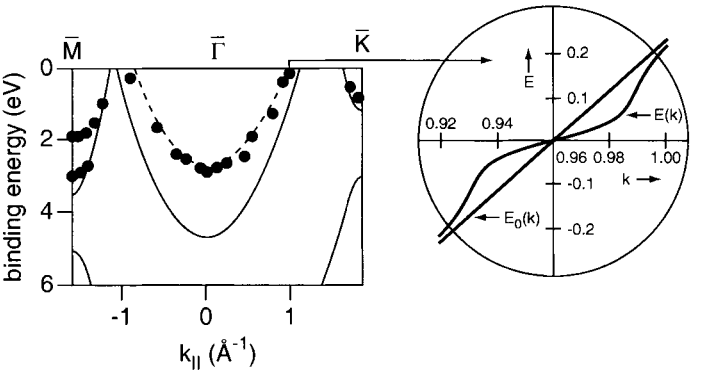


Fig. 14.16. Theoretical estimate of electron–phonon distortion of the surface state band on Be(0001) from Bartynski et al. (1985). The figure on the left is the measured surface state dispersion and the blow-up on the right is an estimate of the distortion of the band near the Fermi energy due to the electron–phonon contribution to the self-energy.

As an illustration, consider the electron–phonon self-energy for the (0001) face of metallic Be. In the bulk the electron–phonon coupling constant is (Grimvall, 1981) $\lambda = 0.24$. The small value is due, in part, to the small density of electron states at the Fermi energy. At the surface the electronic density of surface states is five times larger than in the bulk. A simple extrapolation gives $\lambda \sim 1$. This large value, coupled with the large Debye energy ($\theta_D \sim 1000$ K), could result in appreciable distortion of the surface state energy bands. If we assume that the self-energy depends only on energy $E$ and not on wave vector, then the integral (14.2) for the density of states can be evaluated analytically

$$N(E) = N(\mu)\sqrt{\frac{\Omega + \sqrt{\Omega^2 + \gamma^2}}{2}}, \tag{14.69}$$

$$\Omega = 1 + \frac{E + \Sigma_1(E)}{\mu}, \tag{14.70}$$

$$\gamma = \frac{\Sigma_2}{\mu}. \tag{14.71}$$

The relative change in the density of state due to the electron–phonon interaction is on the order $O(\lambda E_x/4\mu)$ which is small. This is indicated schematically in Fig. 14.16.

## References

Adawi, I., 1964, Phys. Rev. **134**, A788.

Allen, J.W., 1992, in: Synchrotron Radiation Research: Advances in Surface and Interface Science, ed. R.Z. Bachrach. Plenum, New York, p. 253.

Allen, J.W., S.-J. Oh, O. Gunnarsson, K. Schönhammer, M.B. Maple, M.S. Torikachvili and I. Lindau, 1986, Adv. Phys. **35**, 275.

Anderson, P.W., 1990, Phys. Rev. Lett. **64**, 1839; **65**, 2306.

Anderson, P.W., 1991, Physics Today, June, p. 60.
Anderson, P.W., 1994, Physica B **199/200**, 8.
Anderson, P.W. and Y.R. Ren, 1994, in: Proc. of Los Alamos Symposium on High Temperature Superconductivity, eds. K.S. Bedell, D. Coffey, D.E. Meltzer, D. Pines and J.R. Schrieffer. Addison–Wesley, p. 3.
Anderson, R.O., R. Claessen, J.W. Allen, C.G. Olson, C. Janowitz, L.Z. Liu, J.-H. Park, M.B. Maple, Y. Dalichaouch, M.C. De Andrade, R.F. Jardim, E.A. Erly, S.-J. Oh and W.P. Ellis, 1993, Phys. Rev. Lett. **70**, 3163.
Bartynski, R.A., R.H. Gaylord, T. Gustafsson and E.W. Plummer, 1986, Phys. Rev. B **33**, 3644.
Baym, G. and L.P. Kadanoff, 1961, Phys. Rev. **124**, 287.
Baym, G. and L.P. Kadanoff, 1962, Phys. Rev. **127**, 1391.
Ching, W.Y. and J. Callaway, 1975, Phys. Rev. B **11**, 1324.
Chou, M.Y., P.K. Lam and M.L. Cohen, 1983, Phys. Rev. B **28**, 4179.
Claessen, R., R.O. Anderson, J.W. Allen, C.G. Olson, C. Janowitz, W.P. Ellis, S. Harm, M. Kalning, R. Manzke and M. Skibowski, 1992, Phys. Rev. Lett. **69**, 808.
DuBois, D.F., 1959, Ann. Phys. **7**, 174; **8**, 24.
Eguiluz, A.G. and A.A. Quong, 1995, in: Dynamical Properties of Solids, eds. G.K. Horton and A.A. Maradudin. North-Holland, Amsterdam.
Freund, H.J., W. Eberhardt, D. Heskett and E.W. Plummer, 1983, Phys. Rev. Lett. **50**, 768.
Freund, H.J., E.W. Plummer, W.R. Salaneck and R.W. Bigelow, 1981, J. Chem. Phys. **75**, 4275.
Frota, H.O. and G.D. Mahan, 1992, Phys. Rev. B **45**, 6243.
Geldart, D.J.W. and S.H. Vosko, 1966, Can. J. Phys. **44**, 2137.
Geldart, D.J.W. and R. Taylor, 1970, Can. J. Phys. **48**, 155, 167.
Grimvall, G., 1981, The Electron–Phonon Interaction in Metals. North-Holland, Amsterdam.
Haldane, F.D.M., 1981, J. Phys. C **14**, 2585.
Hedin, L., 1965, Phys. Rev. **139**, A796.
Hedin, L. and S. Lundquist, 1969, in: Solid State Physics, Vol. 23, eds. F. Seitz and D. Turnbull. Academic Press, New York, p. 1.
Hedin, L. and B.I. Lundqvist, 1971, J. Phys. C **4**, 2064.
Hill, A.G., 1938, Phys. Rev. **53**, 184.
Hubbard, J., 1963, Proc. Roy. Soc. London Ser. A **240**, 539.
Itchkawitz, B.S., 1991, Ph.D. Thesis, University of Pennsylvania.
Itchkawitz, B.S., A.P. Baddorf, H.L. Davis and E.W. Plummer, 1992, Phys. Rev. Lett. **68**, 2488.
Itchkawitz, B.S., I.W. Lyo and E.W. Plummer, 1990, Phys. Rev. B **41**, 8075.
Jensen, E., R.A. Bartynski, T. Gustafsson and E.W. Plummer, 1984a, Phys. Rev. Lett. **52**, 2172.
Jensen, E., R.A. Bartynski, T. Gustafsson and E.W. Plummer, 1986, Phys. Rev. B **33**, 3644.
Jensen, E., R.A. Bartynski, T. Gustafsson, E.W. Plummer, M.Y. Chou, M. Cohen and G. Hoflund, 1984b, Phys. Rev. B **30**, 5500.
Jensen, E. and E.W. Plummer, 1985, Phys. Rev. Lett. **55**, 1912.
Kevan, S.D., 1992, Angle-Resolved Photoemission. Elsevier, North-Holland.
Lang, N. and W. Kohn, 1970, Phys. Rev. B **1**, 4555.
Levinson, H.J., F. Greuter and E.W. Plummer, 1983, Phys. Rev. B **27**, 727.
Louie, S.G., 1994, Surf. Sci. **299/300**, 346.
Lundqvist, B.I., 1967, Phys. Kond. Mat. **6**, 193, 206.
Lundqvist, B.I., 1968, Phys. Kond. Mat. **7**, 117.
Luttinger, J.M., 1960, Phys. Rev. **119**, 1153.
Lyo, I.W., 1988, Ph.D. Thesis, University of Pennsylvania.
Lyo, I.W. and E.W. Plummer, 1988, Phys. Rev. Lett. **60**, 1558.
Ma, S.K. and K.W.K. Shung, 1994, Phys. Rev. B **50**, 5004.
Mackinson, R.E.B., 1949, Phys. Rev. **75**, 1908.
Mahan, G.D., 1970, Phys. Rev. B **2**, 4334.
Mahan, G.D., 1990, in: Photoemission and Absorption Spectroscopy of Solids and Interfaces with Synchrotron Radiation, eds. M. Campagna and R. Rosei. North-Holland, pp. 25–40.
Mahan, G.D., 1990, Many-Particle Physics, 2nd edn. Plenum, New York.

Mahan, G.D., 1992, Int. J. Mod. Phys. B **6**, 3381.
Mahan, G.D., 1994, Comments Cond. Mat. Phys. **16**, 333.
Mahan, G.D. and B.E. Sernelius, 1989, Phys. Rev. Lett. **62**, 2718.
Mahan, G.D. and K.R. Subbaswamy, 1990, Local Density Theory of Polarizability. Plenum, New York.
Manzke, R., T. Buslaps, R. Claessen, M. Skibowski and J. Fink, 1989, Physica C **152–154**, 1381.
Matho, K., 1994, Physica B **199/200**, 382.
Mattis, D.C. and E.H. Lieb, 1963, J. Math. Phys. **6**, 3054.
Mitchell, K., 1934, Proc. Royal Soc. London Ser. A **146**, 442.
Northrup, J.E., M.S. Hybertsen and S.G. Louie, 1989, Phys. Rev. B **39**, 8198.
Olson, C.G., R. Liu, A.-B. Yang, D.W. Lynch, A.J. Arko, R.S. List, B.W. Veal, Y.C. Chang, P.Z. Jiang and A.P. Paulikas, 1990, Phys. Rev. B **42**, 381.
Overhauser, A.W., 1962, Phys. Rev. **128**, 1437.
Overhauser, A.W., 1968, Phys. Rev. **167**, 691.
Overhauser, A.W., 1985, Phys. Rev. Lett. **55**, 1916.
Overhauser, A.W., K.W.K. Shung and G.D. Mahan, 1987, Phys. Rev. Lett. **58**, 959.
Patthey, F., J.-M. Imer, W.-D. Schneider, H. Beck, Y. Baer and B. Delley, 1990, Phys. Rev. B **42**, 8864.
Quinn, J.J. and R.A. Ferrell, 1958, Phys. Rev. **112**, 812.
Rice, T.M., 1965, Ann. Phys. **31**, 100.
Shen, Z.X. et al., 1993, Phys. Rev. Lett. **70**, 1553.
Shung, K.W.K. and G.D. Mahan, 1986, Phys. Rev. Lett. **57**, 1076.
Shung, K.W.K. and G.D. Mahan, 1988, B **38**, 3856.
Shung, K.W.K., B.E. Sernelius and G.D. Mahan, 1987, Phys. Rev. B **36**, 4499.
Singhal, S.P. and J. Callaway, 1977, Phys. Rev. B **16**, 1744.
Singwi, K.S., A. Sjölander, M.P. Tosi and R.H. Land, 1970, Phys. Rev. B **1**, 1044.
Surh, M.P., J.E. Northrup and S.G. Louie, 1988, Phys. Rev. B **38**, 5976.
Tjeng, L.H., S.-J. Oh, E.-J. Cho, H.-J. Lin, C.T. Chen, G.-H. Gweon, J.-H. Park, J.W. Allen, T. Suzuki, M.S. Makivic and D.L. Cox, 1993, Phys. Rev. Lett. **71**, 1419.
Tiogo, F. and T.O. Woodruff, 1970, Phys. Rev. B **2**, 3958.
Vashishta, P. and K.S. Singwi, 1972, Phys. Rev. B **6**, 875.
Watson, G.M., 1992, Ph.D. Thesis, University of Pennsylvania.
Wright, A.F. and D.C. Chrzan, 1993, Phys. Rev. Lett. **70**, 1964.

This Page Intentionally Left Blank

# Author index


Aarts, J. 196, 428
Ababou, Y. 893
Abraham, D.L. 662
Abraham, D.L. *see* Hopster, H. 664
Abraham, D.L. *see* Kämper, K.-P. 665
Abraham, F.F. 86
Abukawa, T. *see* Bullock, E.L. 197
Abukawa, T. *see* Huff, W.R.A. 429
Achiba, Y. *see* Kimura, K. 744
Ackermann, B. 662
Adams, A.C. *see* Mrarka, S.P. 895
Adams, D.L. 86, 352
Adams, D.L. *see* Aminpirooz, S. 352
Adams, D.L. *see* Burchhardt, J. 353, 742
Adams, D.L. *see* Christensen, S.V. 353
Adams, D.L. *see* Jensen, V. 88
Adams, D.L. *see* Nielsen, H.B. 89
Adams, D.L. *see* Nielsen, M.M. 745
Adams, D.L. *see* Schmalz, A. 355, 950
Adams, D.L. *see* Stampfl, C. 355, 746, 951
Adams, J.A. *see* Yang, S.H. 208
Adawi, I. 947, 985
Ade, H. 380
Adler, D.L. 947
Adnot, A. 947
Aebi, P. *see* Fasel, R. 353
Aebi, P. *see* Stampfl, C. 356
Aers, G.C. 243
Agostino, R.G. *see* Fasel, R. 353
Ahlqvist, P. 947
Ahmad, S.B. *see* Mathon, J. 665
Akita, K. *see* Hiratani, Y. 894
Akita, K. *see* Taneya, M. 897
Alavi, A. 352
Albers, R.C. *see* Eriksson, O. 663
Albers, R.C. *see* MacLaren, J.M. 244
Aldao, C.M. *see* Trafas, B.M. 861
Aldao, C.M. *see* Waddill, G.D. 861
Aldau, C.M. 855
Aldén, M. 504
Alder, B.J. *see* Ceperley, D.M. 87, 197
Alemany, P. *see* Kádas, K. 201
Alerhand, O.L. 281
Alfonso, D.R. 196
Alig, R.C. 855
Allan, C.A.T. 662
Allan, D.C. *see* Alerhand, O.L. 281
Allan, D.C. *see* Li, Y.S. 89
Allan, D.C. *see* Payne, M.C. 89, 204, 355
Allan, D.C. *see* Teter, M.P. 90
Allan, G. 86
Alldredge, G.P. *see* Caruthers, E. 87, 505
Allen, J.W. 947, 985
Allen, J.W. *see* Anderson, R.O. 986
Allen, J.W. *see* Claessen, R. 505, 986
Allen, J.W. *see* Tjeng, L.H. 987
Allen, R.E. 855
Allen, R.E. *see* Beres, R.P. 197
Allenspach, R. 662
Allenspach, R. *see* Landolt, M. 665
Allison, W. *see* Rohlfing, D.M. 205
Allongue, P. 855
Allyn, C.L. 742
Alonso, M. 855, 893
Alonso, M. *see* Chassé, T. 428
Alonso, M. *see* Çimino, R. 856
Altarelli, M. 86
Altman, M.S. 86
Altmann, M. 504
Altmann, W. *see* Dose, V. 243, 663, 947
Altmann, W. *see* Goldmann, A. 243
Altmann, W. *see* Straub, D. 206
Alvarado, S.F. 662
Alvarado, S.F. *see* Carbone, C. 663

Alvarado, S.F. *see* Feder, R. 664
Alvarado, S.F. *see* Fuggle, J.C. 664
Alvarado, S.F. *see* Walker, T.G. 668
Alvarado, S.F. *see* Weller, D. 668
Alvarez, S. *see* Kádas, K. 201
Alves, J.L.A. 196
Amakusa, T. *see* Tochihara, H. 206
Amer, N.M. *see* Olmstead, M. 430
Amer, N.M. *see* Olmstead, M.A. 381
Aminpirooz, S. 352
Aminpirooz, S. *see* Burchhardt, J. 353, 742
Aminpirooz, S. *see* Schmalz, A. 355, 950
Amoddeo, A. *see* Chiarello, G. 947
Amoddeo, A. *see* del Pennino, U. 894
Ancilotto, F. 281
Andersen, D.G. 86
Andersen, J.N. 352, 353, 947
Andersen, J.N. *see* Adams, D.L. 86
Andersen, J.N. *see* Björneholm, O. 947
Andersen, J.N. *see* Burchhardt, J. 353, 742
Andersen, J.N. *see* Jensen, V. 88
Andersen, J.N. *see* Johansson, L.I. 507
Andersen, J.N. *see* Nielsen, H.B. 89
Andersen, J.N. *see* Nielsen, M.M. 745
Andersen, J.N. *see* Stenborg, A. 951
Andersen, O.K. 86
Andersen, O.K. *see* Das, G.P. 857
Andersen, O.K. *see* Methfessel, M. 89
Andersohn, L. 893
Anderson, A.B. *see* Mehandru, S.P. 203
Anderson, C.L. 855
Anderson, J. *see* Lapeyre, G.J. 745
Anderson, J. *see* Smith, R.J. 746
Anderson, J.R. *see* Williams, G.P. 431
Anderson, P.W. 281, 985, 986
Anderson, R.O. 986
Anderson, R.O. *see* Claessen, R. 505, 986
Anderson, R.W. 742
Anderson, S.G. 893
Anderson, S.G. *see* Seo, J.M. 896
Anderson, S.G. *see* Waddill, G.D. 861
Anderson, W.A. *see* Shi, Z.Q. 860
Andersson, C.B.M. *see* Håkansson, M.C. 429
Andersson, C.B.M. *see* Ölsson, L.Ö. 430
Andersson, S. 947
Andersson, S. *see* Harris, J. 744
Andreoni, W. *see* Ancilotto, F. 281
Andres, P.L. *see* Saiz-Pardo, R. 896
Andrews, A.B. *see* Kneedler, E. 508
Andrews, A.B. *see* Smith, N.V. 950
Andrews, J.M. 855
Andriamanantenasoa, I. 86
Andriotis, A.N. *see* Menon, M. 203
Andzelm, J. 86
Anger, G. *see* Rendulic, K.D. 355
Anisimov, A.N. *see* Farle, M. 663
Anno, M. 86
Antoniewicz, P.R. 353
Aono, M. 380
Aono, M. *see* Chiang, T.-C. 198
Aono, M. *see* Uchida, H. 861
Aoyagi, H. *see* Nakanishi, T. 666
Aoyagi, Y. *see* Hara, S. 199
Aoyagi, Y. *see* Nonoyama, S. 283
Apai, G. 742
Appelbaum, J.A. 86, 196, 281, 504
Arai, M. 196
Arakawa, H. *see* Ito, T. 895
Arbes, M. *see* Palm, H. 860
Arbman, G. *see* Nilsson, P.O. 509
Arbman, G.O. *see* Koelling, D.D. 88
Arcangeli, C. *see* Ossicini, S. 283
Arens, M. *see* Pahlke, D. 896
Arias, I. *see* Boszo, T. 742
Arias, T.A. *see* Payne, M.C. 204, 355
Aristov, V.Y. *see* LeLay, G. 430
Aristov, V.Yu. 196, 428
Arko, A.J. *see* Olson, C.G. 987
Arlinghaus, F.J. *see* Smith, J.R. 90
Arlinghaus, F.J. *see* Zhu, X.-Y. 668
Arlinghaus, F.K. *see* Gay, J.G. 88
Arrot, A.S. *see* Heinrich, B. 948
Artacho, E. 86
Aruga, T. 504, 947
Aruga, T. *see* Tabata, T. 206
Arvanitis, D. *see* Dunn, J.H. 663
Aryasetiawan, F. 196
Asano, S. *see* Fujitani, H. 857
Ashcroft, N.W. 86, 505, 662, 855
Aspnes, D.E. 196, 380
Asscher, M. 742
Asscher, M. *see* Peled, H. 745
Assmann, J. 380, 428, 855
Astaldi, C. *see* Rudolf, P. 950
Astaldi, S. 947
Astl, G. *see* Matthew, J.A.D. 508
Atlan, D. *see* Schmid, A.K. 667
Auer, P. *see* Finteis, T. 429

Auerbach, D.J. *see* Kleyn, A.W. 745
Auerbach, D.J. *see* Rettner, C.T. 746
Averill, F.W. 86
Avery, A.R. 428
Avouris, P. 893
Avouris, P. *see* Hasegawa, Y. 507
Avouris, P. *see* Lyo, I.W. 895
Avouris, P. *see* Schubert, B. 896
Avouris, Ph. 380, 893
Avouris, Ph. *see* Boszo, F. 893
Avouris, Ph. *see* Gumhalter, B. 744
Avouris, Ph. *see* Lyo, I.W. 895
Avouris, Ph. *see* Wolkow, R. 208, 283, 381

Babalola, I.A. *see* Petro, W.G. 860
Baberschke, K. *see* Dunn, J.H. 663
Baberschke, K. *see* Farle, M. 663
Baberschke, K. *see* Schulz, B. 667
Bachelet, G.B. 86, 196, 281, 855
Bachelet, G.B. *see* Scheffler, M. 205
Bachrach, R.A. *see* Uhrberg, R.I.G. 90
Bachrach, R.Z. *see* Brillson, L.J. 856
Bachrach, R.Z. *see* Bringans, R.D. 87, 197, 428
Bachrach, R.Z. *see* Olmstead, M.A. 89, 204
Bachrach, R.Z. *see* Uhrberg, R.I.G. 90, 207, 283
Bäck, W. *see* Engelhardt, H.A. 743
Backes, U. 428
Bacon, G.E. 662
Baddorf, A. *see* Heskett, D. 948
Baddorf, A.P. *see* Itchkawitz, B.S. 986
Bader, M. 742
Bader, R.F.W. 353
Bader, S.D. 86, 662
Bader, S.D. *see* Celotta, R.J. 663
Bader, S.D. *see* Falicov, L.M. 87
Bader, S.D. *see* Johnson, P.D. 664, 949
Bader, S.D. *see* Li, D. 949
Bader, S.D. *see* Liu, C. 665
Bader, S.P. *see* Qiu, Z.Q. 381
Badt, D. 196
Badziag, P. 196, 197
Baek, D.H. *see* Chung, J.W. 505
Baer, Y. *see* Lang, J.K. 949
Baer, Y. *see* Patthey, F. 987
Baerends, E.J. 86
Baerends, E.J. *see* Kirchner, E.J.J. 282
Baerends, E.J. *see* Kroes, G.J. 354
Baerends, E.J. *see* Ravenek, W. 89
Baeumler, M. 380
Bagus, P.S. 353, 742, 893
Bagus, P.S. *see* Hermann, K. 354, 744
Bagus, P.S. *see* Seel, M. 896
Baibich, M.N. 662
Baier, U. *see* Feder, R. 664
Baker, A.D. *see* Turner, D.W. 747
Baker, C. *see* Turner, D.W. 747
Bakshi, P. *see* Tsuei, K.-D. 381
Baldereschi, A. 197
Balerna, A. *see* Incoccia, L. 895
Balk, P. 893
Ballentine, C.A. *see* Chuang, D.S. 663
Ballu, Y. *see* Thiry, P. 431
Baltensperger, W. *see* Helman, J.S. 664
Bamming, M. *see* Nouvertné, F. 355
Bander, M. 662
Bansmann, J. 662
Bar-Yam, Y. *see* Kaxiras, E. 201
Baraff, G.A. *see* Appelbaum, J.A. 86, 196, 281
Baranowski, J.M. *see* Vogel, P. 861
Barber, M.N. 662
Barbieri, A. *see* Mizuno, S. 950
Bardeen, J. 86, 855
Bardeen, J. *see* Wigner, E. 91
Bare, S.R. *see* Hofmann, P. 744
Bare, S.R. *see* Stroscio, J.A. 746, 951
Bare, S.R. *see* Surmann, M. 746
Barker, R.A. 505
Barker, R.A. *see* Felter, T.E. 87, 506
Barman, S.R. 197, 428
Barnes, C.J. 353
Barnett, R.N. 86
Barnscheidt, H.-P. *see* Olde, J. 204
Barnscheidt, H.P. *see* Henk, J. 200
Barnscheidt, H.P. *see* Manzke, R. 203, 430
Baroni, S. 197
Baroni, S. *see* Bungaro, C. 505
Baroni, S. *see* Car, R. 197
Baroni, S. *see* Xie, J. 356
Barret, C. 855
Barrett, J.H. *see* Feldman, L.C. 87
Barrett, R.C. *see* Park, S.-I. 860
Barski, A. *see* Solal, F. 206
Bartels, F. 893
Bartelt, N.C. *see* Jonker, B.T. 949
Barth, J.V. *see* Schuster, R. 950
Barth, U.V. 662
Barthe, F. *see* Moison, J.M. 859

Barthés-Labrousse, M.-G. *see* Binns, C. 505, 947
Barton, J.J. 380
Barton, J.J. *see* Terminello, L.J. 381
Bartos, B. 742
Bartos, B. *see* Freund, H.-J. 743
Bartynski, R.A. 243, 505, 986
Bartynski, R.A. *see* Jensen, E. 507, 986
Bartynski, R.A. *see* Yang, S. 245, 951
Barzel, G. *see* Scheffler, M. 90, 205, 355, 950
Basilier, E. *see* Gelius, U. 381
Baski, A.A. 86
Baski, A.A. *see* Nogami, J. 89
Baski, A.A. *see* Richter, M. 90
Bass, J. 856
Bassani, F. 281
Bast, D. *see* Kliese, R. 895
Batchelor, D.R. *see* Aminpirooz, S. 352
Batchelor, D.R. *see* Schmalz, A. 355, 950
Batra, I.P. 86, 281, 428, 742, 893
Batra, I.P. *see* Abraham, F.F. 86
Batra, I.P. *see* Ciraci, S. 281
Batra, I.P. *see* Fong, C.Y. 282
Batra, I.P. *see* Himpsel, F.J. 200
Batra, I.P. *see* Horn, K. 744
Batson, P.E. 380
Baudelet, F. *see* Pizzini, S. 666
Baudoing, R. *see* Gauthier, Y. 664
Bauer, A. 856
Bauer, A. *see* Cuberes, M.T. 857
Bauer, A. *see* Ludeke, R. 859
Bauer, E. 505, 662
Bauer, E. *see* Grzelakowski, K. 506
Bauer, E. *see* Jalochowski, M. 949
Bauer, E. *see* Witt, W. 510
Bauer, F. 380
Bauer, G.E.W. *see* Schep, K.M. 244
Bauer, R.S. *see* Brillson, L.J. 856
Bauer, R.S. *see* Göpel, W. 199
Baumgarten, L. 86, 662
Baumgarten, L. *see* Ebert, H. 663
Baumgarten, L. *see* Starke, K. 667
Baumgarten, L. *see* Venus, D. 668
Bauschlieher, C.W. Jr. *see* Bagus, P.S. 742
Baym, G. 86, 986
Beaurepaire, E. *see* Boeglin, C. 662
Bechstedt, F. 86, 281
Bechstedt, F. *see* Grossner, U. 199
Bechstedt, F. *see* Käckell, P. 199, 201
Bechstedt, F. *see* Kress, C. 201
Bechstedt, F. *see* Schmidt, W.G. 205, 283, 431
Bechstedt, F. *see* Scholze, A. 205
Bechstedt, F. *see* Wenzien, B. 207, 208
Beck, H. *see* Patthey, F. 987
Becke, A.D. 86
Becker, G.E. *see* Cardillo, M.J. 87
Becker, G.E. *see* Hagstrum, H.D. 199
Becker, L. *see* Schmalz, A. 355, 950
Becker, R.S. 86, 197, 281, 856
Becker, R.S. *see* Alerhand, O.L. 281
Becker, R.S. *see* Kubby, J.A. 202
Beckmann, A. 947
Behm, R.J. 353, 947
Behm, R.J. *see* Brune, H. 505
Behm, R.J. *see* Coulman, D.J. 743
Behm, R.J. *see* Schuster, R. 950
Behm, R.J. *see* Wintterlin, J. 747
Behner, H. *see* Freund, H.-J. 743
Belkhir, H. *see* Themlin, J.-M. 206
Bell, L.D. 856
Bell, L.D. *see* Hecht, M.H. 858
Bell, L.D. *see* Kaiser, W.J. 858
Benbow, R. 380
Benbow, R. *see* Seabury, C.W. 746
BenDaniel, D.J. 856
Benedek, G. 947
Benedek, G. *see* Harten, U. 200, 282
Benedek, G. *see* Miglio, L. 203
Benesh, G.A. 86, 197, 243, 505, 947
Benesh, G.A. *see* Inglesfield, J.E. 507
Bennet, P.A. 428
Bennet, P.A. *see* Robinson, I.K. 205
Bennett, A.J. 86
Bennett, H.S. 86
Bennett, W.R. 947
Bennich, P. *see* Nilsson, A. 355
Benning, P.J. *see* Anderson, S.G. 893
Bensoussan, M. *see* Moison, J.M. 859
Bent, B.E. *see* Mate, C.M. 745
Bent, B.E. *see* Struck, L.M. 896
Beres, R.P. 197
Berger, A. 662
Berger, A. *see* Qiu, Z.Q. 381
Bergholz, R. *see* Gradmann, U. 664
Bergmark, T. *see* Gelius, U. 381
Bergter, E. *see* Gradmann, U. 664
Bermudez, V. 197, 428
Bermudez, V.M. *see* Long, J.P. 202

Bernardini, F. *see* Bertoni, C.M. 281
Bernardini, F. *see* Buongiorno Nardelli, M. 281
Bernardini, F. *see* Ossicini, S. 860
Berndt, W. 353
Bernholc, J. *see* Rapcewicz, K. 205
Bernholc, J. *see* Scheffler, M. 90
Bernholc, J. *see* Yi, J.-Y. 283
Bernholc, J. *see* Zhang, Z. 208
Bersuker, I.B. 505
Bertel, E. 742
Bertel, E. *see* Jacob, W. 949
Bertel, E. *see* Mack, J.U. 745
Bertel, E. *see* Memmel, N. 745, 950
Bertel, E. *see* Neumann, M. 745
Bertel, E. *see* Rangelov, G. 746
Bertel, E. *see* Schuppler, S. 244
Bertolini, J.C. 742
Bertolo, M. 742
Bertoni, C.M. 197, 281
Bertoni, C.M. *see* Buongiorno Nardelli, M. 281
Bertoni, C.M. *see* Calandra, C. 197, 281
Bertoni, C.M. *see* Di Felice, R. 281
Bertoni, C.M. *see* Manghi, F. 203, 282
Bertoni, C.M. *see* Marcellini, A. 282
Bertoni, C.M. *see* Margaritondo, G. 282, 895
Bertoni, C.M. *see* Ossicini, S. 860
Bertoni, C.M. *see* Palummo, M. 204
Bertoni, C.M. *see* Shkrebtii, A.I. 206, 283, 431
Besenbacher, F. *see* Pedersen, M.O. 355
Besenbacher, F. *see* Pleth Nielsen, L. 355
Besnard-Ramage, M.J. *see* Dujardin, G. 894
Besold, G. *see* Müller, K. 950
Bethe, H.A. 855
Bethune, P.S. *see* Terminello, L.J. 381
Bhargava, S. *see* O'Shea, J.J. 860
Bhargava, S. *see* Sajoto, T. 860
Biaggi, R. *see* del Pennino, U. 894
Biagini, M. *see* Ruocco, A. 896
Bianco, A. *see* Rudolf, P. 950
Biegelsen, D.K. 197, 281, 428
Biegelsen, D.K. *see* Uhrberg, R.I.G. 90
Bielański, A. 353
Bigelow, R.W. *see* Freund, H.J. 986
Billington, R.L. 86
Binasch, G. 662
Binnig, G. 281, 380, 428, 856
Binns, C. 505, 947
Birkenheuer, U. *see* Weinelt, M. 747
Bishop, A.R. 505
Bisi, O. *see* Bertoni, C.M. 197
Bisi, O. *see* Ossicini, S. 283, 860
Bjorken, J.D. 86
Björkquist, M. *see* LeLay, G. 430
Björneholm, O. 742, 947
Björneholm, O. *see* Stenborg, A. 951
Björqvist, M. *see* Göthelid, M. 894
Black, J.E. *see* Szeftel, J.M. 746
Blaha, P. *see* Finteis, T. 429
Blandau, H. *see* Over, H. 950
Blase, X. 281
Blase, X. *see* Hricovini, K. 200, 282
Blase, X. *see* Zakharov, O. 208
Blaudeck, P. *see* Frauenheim, Th. 199
Blöchl, P. *see* Das, G.P. 857
Bloom, S. *see* Alig, R.C. 855
Bludau, H. *see* Over, H. 355
Blügel, S. 662
Blügel, S. *see* Clemens, W. 947
Blügel, S. *see* Ebert, Ph. 199, 429
Blügel, S. *see* Engels, B. 429
Blügel, S. *see* Kobayashi, K. 201, 282
Blügel, S. *see* Rader, O. 355, 666
Blyholder, G. 353, 742
Bobo, J.-F. *see* Pizzini, S. 666
Bockstedte, M. 353
Bockstedte, M. *see* Gross, A. 354
Bode, S. 662
Boeglin, C. 662
Boeglin, C. *see* Venus, D. 668
Boehme, M. *see* Traving, M. 431
Boettger, J.C. 505, 947
Bogdány, H. *see* Stuhlmann, Ch. 206
Bogen, A. *see* Schnell, R.D. 205, 283, 896
Bogen, A. *see* Weser, T. 91
Bøgh, E. *see* Aminpirooz, S. 352
Bøgh, E. *see* Schmalz, A. 355
Bohm, D. 856
Bohnen, K.P. *see* Ho, K.M. 88
Bohr, J. 197
Bohr, J. *see* Feidenhans'l, R. 199
Bokor, J. *see* Haight, R. 199, 857
Boland, J. 281, 893
Boland, J. *see* Villarrubia, J.S. 897
Bonicke, I.A. *see* Pedersen, M.O. 355
Bonnel, D.A. *see* Rohrer, G.S. 205
Bonnet, J.E. *see* Aristov, V.Yu. 428
Bonnet, J.E. *see* Hricovini, K. 200, 282
Bonnet, J. *see* Le Lay, G. 858

Bonnet, J. *see* Sauvage-Simkin, M. 205
Bonzel, H.P. 742, 947
Bonzel, H.P. *see* Broden, G. 742
Bonzel, H.P. *see* Kiskinova, M. 745
Bonzel, H.P. *see* Pirug, G. 244, 950
Borgh, E. *see* Schmaltz, A. 950
Borgiel, W. *see* Nolting, W. 666
Boring, A.M. *see* Eriksson, O. 663
Bormet, J. 353
Bormet, J. *see* Wenzien, B. 356
Born, M. 353
Bornemann, T. *see* Huber, W. 744
Börnsen, N. *see* Palummo, M. 204
Borstel, G. 243, 662, 742
Borstel, G. *see* Goldmann, A. 243
Borstel, G. *see* Graß, M. 243
Borstel, G. *see* Schneider, R. 244
Borstel, G. *see* Thörner, G. 245
Borstel, G. *see* Wöhlecke, M. 668
Bortolani, V. 505
Boscherini, F. *see* Xu, F. 861
Boszo, F. 893
Boszo, F. *see* Avouris, Ph. 893
Boszo, T. 742
Böttcher, A. 353
Bouchard, A.M. 197
Bouilliard, J.C. *see* Rochet, F. 283
Bouldin, C.E. *see* Richter, M. 90
Bouzidi, S. 893
Bowman, L. *see* Newmann, N. 859
Bozack, M.J. *see* Muehlhoff, L. 203
Bozorth, R.M. 662
Bozso, F. *see* Avouris, Ph. 380
Bradshaw, A.M. 353, 505
Bradshaw, A.M. *see* Batra, I.P. 742
Bradshaw, A.M. *see* Berndt, W. 353
Bradshaw, A.M. *see* Bonzel, H.P. 742, 947
Bradshaw, A.M. *see* Hayden, B.E. 744
Bradshaw, A.M. *see* Hofmann, P. 354, 744
Bradshaw, A.M. *see* Horn, K. 354, 507, 744, 948
Bradshaw, A.M. *see* Klauser, R. 745
Bradshaw, A.M. *see* Kulkarni, S.K. 745
Bradshaw, A.M. *see* Lindner, Th. 745
Bradshaw, A.M. *see* Scheffler, M. 355
Bradshaw, A.M. *see* Stampfl, A.P.J. 431
Bradshaw, A.M. *see* Tüshaus, M. 747
Bradshaw, A.M. *see* Woodruff, D.P. 381, 747
Bram, Ch. *see* Schardt, J. 205
Bram, Ch. *see* Starke, U. 206
Brandes, G.R. *see* Horsky, T.N. 200
Brandt, O. *see* Ding, S.-A. 428
Braun, J. 947
Braun, J. *see* Graß, M. 243
Braun, J. *see* Schneider, R. 244
Braun, W. 742
Braun, W. *see* Alonso, M. 855
Braun, W. *see* Borstel, G. 742
Braun, W. *see* Chassé, T. 428
Braun, W. *see* McLean, A.B. 859
Braun, W. *see* Petersen, H. 666
Breitschafter, M.J. 742
Breitschafter, M.J. *see* Höfer, U. 744
Bremer, J.H. *see* Metzner, H. 895
Bressler, P. *see* Schneider, C.M. 667
Brillson, L.J. 87, 856
Brillson, L.J. *see* Chiaradia, P. 856
Brillson, L.J. *see* Margaritondo, G. 859
Brillson, L.J. *see* Viturro, R.E. 381, 861
Bringans, R.D. 87, 197, 428
Bringans, R.D. *see* Biegelsen, D.K. 197, 281, 428
Bringans, R.D. *see* Olmstead, M.A. 89, 204
Bringans, R.D. *see* Uhrberg, R.I.G. 90, 207, 283
Bringer, A. *see* Hillebrecht, F.U. 664
Brink, R.S. 87
Brivio, G.P. 353
Brockhouse, B.N. *see* Wood, A.D.B. 951
Brocks, G. *see* Ramstad, A. 205
Brodén, G. 742
Brodén, G. *see* Pirug, G. 244
Brodsky, M.B. *see* Grünberg, P. 664
Brommer, K.D. 197, 281, 428
Brookes, N.B. 663, 947
Brookes, N.B. *see* Schneider, C.M. 667
Brookes, N.B. *see* Smith, N.V. 667, 950
Brosseau, R. 742
Broto, J.M. *see* Baibich, M.N. 662
Broughton, J.Ch. *see* Brundle, C.R. 742
Browers, R. *see* Wood, A.D.B. 951
Brown, F. 856
Broyden, C.G. 197
Bruch, L.W. 353
Bruchman, D. *see* Ibach, H. 895
Brucker, C.F. *see* Brillson, L.J. 856
Bruhwiler, P.A. *see* Watson, G.M. 510, 951
Brundle, C.R. 742

Brundle, C.R. *see* Hermann, K. 744
Brundle, C.R. *see* Turner, D.W. 747
Brune, H. 505
Bu, H. 281
Buchel, M. 894
Bucher, E. *see* Finteis, T. 429
Bucksbaum, P.H. *see* Haight, R. 199
Bude, J. 856
Buhrman, R.A. *see* Fernandez, A. 857
Buhrman, R.A. *see* Hallen, H.D. 857
Bullemer, B. *see* Kulakov, M.A. 202
Bullett, D.W. *see* Stephenson, P.C. 90
Bullock, E.L. 197
Bullock, E.L. *see* Johansson, L.S.O. 282
Bungaro, C. 505
Buongiorno Nardelli, M. 281
Buongiorno Nardelli, M. *see* Bertoni, C.M. 281
Burchhardt, J. 353, 742
Burchhardt, J. *see* Christensen, S.V. 353
Burchhardt, J. *see* Nielsen, M.M. 745
Burchhardt, J. *see* Stampfl, C. 355, 746, 951
Burdick, G.A. 243
Burrows, V.A. 281, 856
Burstein, E. *see* Heinz, T.F. 381
Busch, G. 663
Buschow, K.H.J. 87
Buskotte, U. *see* Kuhlenbeck, H. 745
Buslaps, T. *see* Manske, R. 987
Butler, P.H. *see* Loucks, T.L. 508
Bylander, D.M. *see* Euceda, A. 506
Bylander, D.M. *see* Kleinman, L. 201
Bylander, D.M. *see* Zhu, M.J. 668

Cafolla, A.A. *see* Fowell, A.E. 857
Cafolla, A.A. *see* Shen, T.-H. 860
Calandra, C. 197, 281
Calandra, C. *see* Bertoni, C.M. 197, 281
Calandra, C. *see* Magri, R. 282
Calandra, C. *see* Manghi, F. 203, 282
Calandra, C. *see* Margaritondo, G. 282, 895
Calessen, R. *see* Finteis, T. 429
Callaway, J. 353
Callaway, J. *see* Ching, W.Y. 986
Callaway, J. *see* Rajagopal, A.K. 89
Callaway, J. *see* Singhal, S.P. 987
Callaway, J. *see* Wang, C.S. 91
Callcott, T.A. *see* Shek, M.L. 206
Calverie, P. *see* Sauvage-Simkin, M. 205
Cameron, S. *see* Ade, H. 380
Campagna, M. *see* Alvarado, S.F. 662
Campagna, M. *see* Busch, G. 663
Campagna, M. *see* Kisker, E. 381, 665
Campagna, M. *see* Landolt, M. 665
Campagna, M. *see* Weller, D. 668
Campell, C.T. *see* Over, H. 950
Campuzano, J.C. 353, 505
Canter, K.F. *see* Horsky, T.N. 200
Cao, R. 856
Cao, R. *see* Miyano, K.E. 859
Cao, R. *see* Spicer, W.E. 861
Capasso, C. *see* Anderson, S.G. 893
Capasso, C. *see* Seo, J.M. 896
Capasso, C. *see* Waddill, G.D. 861
Capasso, F. 856
Capozi, M. *see* Mascaraque, A. 895
Caputi, L.S. *see* Chiarello, G. 947
Car, R. 87, 197, 281, 353
Car, R. *see* Ancilotto, F. 281
Car, R. *see* Pasquarello, A. 896
Caragiu, M. *see* Seyller, T. 355
Carbone, C. 663, 947
Carbone, C. *see* Clemens, W. 947
Carbone, C. *see* Rader, O. 355, 666
Carbone, C. *see* Vescovo, E. 245, 668
Cardillo, M.J. 87
Cardona, M. 856
Cardona, M. *see* Shevchik, N.J. 431
Cardona, M. *see* Yu, P.Y. 431
Carelli, J. *see* Duke, C.B. 281
Carette, J.D. *see* Adnot, A. 947
Carey, G.P. *see* Sze, S.M. 861
Carlisle, J.A. 428, 856
Carlson, G.A. *see* Li, Y.S. 89
Carlsson, A. 947
Carlsson, A. *see* Lindgren, S.-Å. 949
Carra, P. 87
Carra, P. *see* Thole, B.T. 90
Carrière, B. *see* Boeglin, C. 662
Carstensen, H. 197, 428
Carter, C.H. *see* Davis, R.F. 198
Cartier, E. 856
Cartier, E. *see* Ludeke, R. 859
Caruthers, E. 87, 505
Catellani, A. 197
Caudano, R. *see* Rudolf, P. 896
Causá, M. *see* Pandey, R. 204
Cautero, G. *see* Rudolf, P. 950
Cederbaum, L.S. 742

Cederbaum, L.S. *see* Köppel, H. 745
Celinski, Z. 947
Celinski, Z. *see* Heinrich, B. 948
Celotta, R.J. 663
Celotta, R.J. *see* Pierce, D.T. 666
Celotta, R.J. *see* Siegmann, H.C. 667
Celotta, R.J. *see* Unguris, J. 667
Celotta, R.J. *see* Whitman, L.J. 283, 510
Ceperley, D.M. 87, 197
Cerrina, F. *see* Williams, G.P. 431
Cesarini, S. *see* Modesti, S. 895
Chabal, Y.J. 197, 281, 505, 894
Chabal, Y.J. *see* Bouzidi, S. 893
Chabal, Y.J. *see* Burrows, V.A. 281, 856
Chabal, Y.J. *see* Dumas, P. 198, 281, 894
Chabal, Y.J. *see* Higashi, G.S. 282
Chabal, Y.J. *see* Hirschmugl, C.J. 507
Chabal, Y.J. *see* Hricovini, K. 200, 282
Chabal, Y.J. *see* Prybyla, J.A. 509
Chabal, Y.J. *see* Reutt, J.E. 509
Chabal, Y.J. *see* Struck, L.M. 896
Chabal, Y.J. *see* Weldon, M.K. 897
Chaban, E.E. *see* Adler, D.L. 947
Chaban, E.E. *see* Chabal, Y.J. 197
Chaban, E.E. *see* Struck, L.M. 896
Chadi, D.J. 87, 197, 281, 428
Chadi, D.J. *see* Ihm, J. 88, 201
Chadi, D.J. *see* Katnani, A.D. 201
Chadi, D.J. *see* Mailhiot, C. 203, 282
Chadi, D.J. *see* Qian, G. 204, 283
Chadi, D.J. *see* Tromp, R.M. 90, 207
Chaiken, A. *see* Chen, C.T. 87, 663
Chakarian, V. *see* Lo, C.W. 895
Chambers, S.A. *see* Xu, F. 861
Chan, C.-M. *see* Van Hove, M.A. 245
Chan, C.T. 197
Chan, C.T. *see* Ding, Y.J. 281
Chan, C.T. *see* Wang, X.W. 510
Chan, S.-K. 505
Chandavarkar, S. *see* Adler, D.L. 947
Chandavarkar, S. *see* Fischer, D. 948
Chander, M. 894
Chander, M. *see* Rioux, D. 896
Chandesris, D. *see* Louie, S.G. 508
Chandesris, D. *see* Thiry, P. 510
Chang, C.C. *see* Mrarka, S.P. 895
Chang, C.S. 197
Chang, C.Y. *see* Lei, T.F. 858
Chang, J.J. *see* Cheong, B.H. 198
Chang, K.J. 198
Chang, K.J. *see* Park, C.H. 204
Chang, S. *see* Sorba, L. 896
Chang, S.C. *see* Duke, C.B. 198
Chang, Y. *see* Brookes, N.B. 663, 947
Chang, Y. *see* Garrison, K. 664, 948
Chang, Y. *see* Smith, N.V. 667, 950
Chang, Y.-C. *see* Aspnes, D.E. 380
Chang, Y.-C. *see* Li, G. 282
Chang, Y.-C. *see* Ren, S.-F. 283
Chang, Y.C. *see* Mailhiot, C. 202
Chang, Y.C. *see* Olson, C.G. 987
Chang, Y.J. *see* Turner, A.M. 667
Chao, Y.-C. *see* Karlsson, C.J. 429, 895
Chao, Y.-C. *see* Landemark, E. 202, 282, 430
Chao, Y.-C. *see* Uhrberg, R.I.G. 431
Charlesworth, J.P.A. 856
Chassé, A. *see* Schneider, C.M. 667
Chassé, T. 428
Chassé, Th. *see* Alonso, M. 855
Chassé, Th. *see* Evans, D.A. 857
Chassé, Th. *see* Ludwig, M.H. 859
Chatt, J. 742
Chaveau, D. *see* Guillot, C. 506
Chazelas, J. *see* Baibich, M.N. 662
Chelikowsky, J.R. 198, 428
Chelikowsky, J.R. *see* Corkill, J.L. 281
Chelikowsky, J.R. *see* Louie, S.G. 859
Chelikowsky, J.R. *see* Schlüter, M. 205
Chelnokov, V.E. *see* Ivanov, P.A. 201
Chen, C.J. 856
Chen, C.-L. 505
Chen, C.-T. 87, 505, 663, 947
Chen, C.-T. *see* Smith, N.V. 950
Chen, C.T. *see* Idzerda, Y.U. 88
Chen, C.T. *see* Modesti, S. 950
Chen, C.T. *see* Smith, N.V. 90, 244
Chen, C.T. *see* Tjeng, L.H. 987
Chen, H.-W. *see* Xu, F. 861
Chen, J. 663
Chen, L.Y. *see* Graham, A.P. 948
Chen, T.P. *see* Evans, D.A. 857
Chen, X.H. 198
Chen, Y. 428
Chen, Y. *see* Gu, C. 894
Cheng, C. 198
Cheng, C.C. *see* Yates, J.T. Jr. 897
Cheng, X.-C. 856

Cheong, B.-H. *see* Park, C.H. 204
Cheong, B.H. 198
Cherepkov, N.A. 663
Chevary, J.A. *see* Perdew, J.P. 89
Chiang, C. *see* Chadi, D.J. 197
Chiang, C. *see* Hamann, D.R. 88, 199
Chiang, S. 742
Chiang, S. *see* Larsen, P.K. 430
Chiang, T.-C. 87, 198, 428, 742
Chiang, T.-C. *see* Carlisle, J.A. 428, 856
Chiang, T.-C. *see* Eastman, D.E. 429, 857
Chiang, T.-C. *see* Himpsel, F.J. 429, 200
Chiang, T.-C. *see* Hirschorn, E. 429
Chiang, T.-C. *see* Hsieh, T.C. 507
Chiang, T.-C. *see* Ludeke, R. 859
Chiang, T.-C. *see* Miller, T. 203, 950
Chiang, T.-C. *see* Mueller, M.A. 950
Chiang, T.-C. *see* Rich, D.A. 89
Chiang, T.-C. *see* Rich, D.H. 89, 205
Chiang, T.-C. *see* Samsavar, A. 90
Chiang, T.-C. *see* Wachs, A.L. 207, 951
Chiang, T.T. *see* Spicer, W.E. 861
Chiaradia, P. 198, 380, 428, 856
Chiaradia, P. *see* Brillson, L.J. 856
Chiaradia, P. *see* Chiarotti, G. 428
Chiaradia, P. *see* Selci, S. 381
Chiarello, G. 947
Chiarotti, C. *see* Chiaradia, P. 380
Chiarotti, C. *see* Selci, S. 381
Chiarotti, G. 198, 428
Chiarotti, G. *see* Chiaradia, P. 198, 428
Chiarotti, G.L. *see* Lu, Z.-Y. 202, 430
Chikazumi, S. 663
Chin, K.K. *see* Cao, R. 856
Chin, M.A. *see* O'Shea, J.J. 860
Chin, M.A. *see* Rubin, M.E. 860
Chin, R.P. 198
Ching, W.Y. 986
Ching, W.Y. *see* Huang, M.-Z. 200
Ching, W.Y. *see* Xu, Y.-N. 208
Ching, Y.W. 505
Cho, A.Y. 428
Cho, E.-J. *see* Tjeng, L.H. 987
Cho, J. 198
Cho, J.-H. 353
Cho, K. 198, 281
Chodorow, M.I. 243
Chot, T. *see* Tam, N.T. 861
Chou, M.Y. 986
Chou, M.Y. *see* Jensen, E. 507, 986
Choyke, W.J. 198
Choyke, W.J. *see* Muehlhoff, L. 203
Choyke, W.J. *see* Yates, J.T. Jr. 897
Christensen, N.E. 198
Christensen, N.E. *see* Bachelet, G.B. 196, 855
Christensen, N.E. *see* Das, G.P. 857
Christensen, O.B. 353
Christensen, S.V. 353
Christman, S.B. *see* Burrows, V.A. 281, 856
Christman, S.B. *see* Chabal, Y.J. 197, 281, 894
Christman, S.B. *see* Prybyla, J.A. 509
Christman, S.B. *see* Reutt, J.E. 509
Christman, S.B. *see* Rowe, J.E. 896
Christmann, K. 742
Chrobok, G. 663
Chrost, J. 894
Chrstman, S.B. *see* Struck, L.M. 896
Chrzan, D.C. *see* Wright, A.F. 987
Chuang, D.S. 663
Chubb, S.R. 743
Chubb, S.R. *see* Soukiassian, P. 509, 951
Chulkov, E.V. 505
Chung, J.W. 505
Chung, J.W. *see* Altmann, M. 504
Chung, J.W. *see* Shin, K.S. 509
Chung, Y.W. *see* Parill, T.M. 204
Chye, P.W. *see* Lindau, I. 859
Chye, P.W. *see* Spicer, W.E. 860
Ciccacci, F. *see* Alvarado, S.F. 662
Ciccacci, F. *see* Crampin, S. 947
Ciccacci, F. *see* Selci, S. 381
Cimino, R. 856
Cimino, R. *see* Alonso, M. 855
Cimino, R. *see* Chassé, T. 428
Cin, M.A. *see* Sajoto, T. 860
Ciraci, S. 281
Citrin, P.H. 894
Citrin, P.H. *see* Adler, D.L. 947
Citrin, P.H. *see* Riffe, D.M. 509, 746, 950
Citrin, P.H. *see* Wertheim, G.K. 861
Clabes, J. 856
Claessen, R. 505, 986
Claessen, R. *see* Anderson, R.O. 986
Claessen, R. *see* Carstensen, H. 197, 428
Claessen, R. *see* Manske, R. 987
Claesson, D. *see* Carlsson, A. 947
Clarke, A. *see* Brookes, N.B. 663

Clarke, L.J. 87
Clarke, L.J. *see* De Vita, A. 281
Clarke, L.J. *see* Štich, I. 206 283
Clauberg, R. *see* Haines, E.M. 664
Clemens, H.J. *see* Linz, R. 859
Clemens, H.J. *see* Troots, D. 283
Clemens, W. 947
Clemens, W. *see* Rader, O. 666
Clemerns, H.J. *see* Bartels, F. 893
Clerjaud, B. 856
Cleveland, C.L. *see* Barnett, R.N. 86
Clinton, J. *see* Liebermann, L.N. 665
Coburn, J.W. *see* Winters, H.F. 897
Cochran, J.F. 663
Cochran, J.F. *see* Celinski, Z. 947
Cochran, J.F. *see* Heinrich, B. 664, 948
Coehoorn, R. 428
Cohen, M.H. *see* Wilke, S. 356
Cohen, M.H. *see* Zhang, S.B. 862
Cohen, M.L. 87
Cohen, M.L. *see* Chadi, D.J. 197
Cohen, M.L. *see* Chang, K.J. 198
Cohen, M.L. *see* Chelikowsky, J.R. 428
Cohen, M.L. *see* Cheong, B.H. 198
Cohen, M.L. *see* Chou, M.Y. 986
Cohen, M.L. *see* Garcia, A. 199
Cohen, M.L. *see* Ho, K.M. 282
Cohen, M.L. *see* Ihm, J. 88, 200, 201, 282, 858
Cohen, M.L. *see* Jensen, E. 507, 986
Cohen, M.L. *see* Kerker, G.P. 88
Cohen, M.L. *see* Larsen, P.K. 895
Cohen, M.L. *see* Louie, S.G. 89, 202, 859
Cohen, M.L. *see* Northrup, J.E. 203, 283, 430
Cohen, M.L. *see* Rubio, A. 205
Cohen, M.L. *see* Schlüter, M. 205, 896
Cohen, M.L. *see* Surh, M.P. 206
Cohen, M.L. *see* Yin, M.T. 91, 208
Cohen, M.L. *see* Zakharov, O. 208
Cohen, M.L. *see* Zhu, X. 208, 431
Cohen, M.L. *see* Zunger, A. 91
Colavita, E. *see* Chiarello, G. 947
Cole, M.W. *see* Bruch, L.W. 353
Coletti, F. *see* Bouzidi, S. 893
Collins, D.A. *see* Cheng, X.-C. 856
Collins, I.R. *see* Adler, D.L. 947
Collins, I.R. *see* Fischer, D. 948
Colombo, L. *see* Harten, U. 200, 282
Comin, F. *see* Fontes, E. 199
Comsa, G. *see* Kern, K. 508
Comtet, G. *see* Dujardin, G. 894
Connolly, J.W.D. *see* Dunlap, B.I. 87
Conrad, H. 743
Conrad, H. *see* Hemmen, R. 948
Cook, M.R. *see* Batra, I.P. 428
Cook, M.R. *see* Himpsel, F.J. 200
Cooper, B.R. 87
Copel, M. 894
Cord, B. *see* Courths, R. 743
Corkill, J.L. 281
Corkill, J.L. *see* Rubio, A. 205
Costello, C. *see* Ade, H. 380
Cotti, P. *see* Busch, G. 663
Cotton, F.A. 743
Couillard, J.G. *see* Davies, A. 857
Coulman, D.J. 743
Coulman, D.J. *see* Schneider, C. 746
Coulman, D.J. *see* Wintterlin, J. 747
Coulmann, D. *see* Höfer, U. 894
Courths, R. 243, 743, 947
Cousty, J. 505
Cowie, B. *see* Kerkar, M. 949
Cowley, A.M. 856
Cox, D.L. *see* Tjeng, L.H. 987
Cox, P.A. 505
Cracknell, A.P. 856
Cracknell, A.P. *see* Seghadat, A.K. 667
Craig, B.I. 198, 894
Craighead, H.G. *see* Davies, A. 857
Craik, D.J. *see* Tebble, R.S. 667
Cramm, S. *see* Incoccia, L. 895
Crampin, S. 947
Crampin, S. *see* MacLaren, J.M. 244
Crampin, S. *see* Nekovee, M. 244, 666
Crampin, S. *see* van Hoof, J.B.A.N. 510
Crapper, M.D. *see* Puschmann, A. 746
Crecelius, G. *see* Wertheim, G.K. 951
Creighton, J.R. 281
Creuzet, G. *see* Baibich, M.N. 662
Cricenti, A. *see* Chiaradia, P. 198, 428
Cricenti, A. *see* Mårtensson, P. 203, 430
Cricenti, A. *see* Selci, S. 381
Crombeen, J.E. *see* van Bommel, A.J. 207, 283
Crommie, M.F. 505
Crottini, A. 947
Crouser, L.C. *see* Swanson, L.W. 509, 510

Crowell, C.R. 856, 857
Crowell, C.R. *see* Anderson, C.L. 855
Crowell, C.R. *see* Sze, S.M. 861
Crowell, J.E. *see* Koel, B.E. 745
Crowell, J.E. *see* Tom, H.W.K. 951
Cuberes, M.T. 857
Cuberes, M.T. *see* Bauer, A. 856
Culbertson, R.J. 198, 894
Culbertson, R.J. *see* Chabal, Y.J. 197
Cullis, A.G. *see* Farrow, R.F.C. 429
Cullity, B.D. 663
Cupolillo, A. *see* Chiarello, G. 947
Curl, R.F. *see* Kroto, H. 895
Cvetko, D. *see* Crottini, A. 947

D'Evelyn, M.P. 743
Daams, J.M. *see* MacDonald, A.H. 89
Dabkowska, H.A. *see* van der Laan, G. 91, 667
Dabrowski, J. 198
Dai, H.-L. *see* Song, K.J. 950
Dai, H.-L. *see* Urbach, L.E. 951
Dal Pino, A. Jr. *see* Brommer, K.D. 281
Daley, R.S. *see* Hildner, M.L. 507
Dalichaouch, Y. *see* Anderson, R.O. 986
Dalmei-Imelik, G. *see* Bertolini, J.C. 742
Damon, R.W. 663
Daniels, R. *see* Brillson, L.J. 856
Darling, G.R. 353
Dartyge, E. *see* Pizzini, S. 666
Das, B. *see* Datta, S. 663
Das, G.P. 857
Datta, S. 663
Dau, F.N.V. *see* Baibich, M.N. 662
Daughton, J.M. 663
Daughton, J.M. *see* Pohm, A.V. 666
Daun, W. 947
Davenport, J.W. 743
David, R. *see* Irmer, N. 664
David, R. *see* Kern, K. 508
Davidson, B.N. 198
Davies, A. 857
Davis, H.L. 87, 505
Davis, H.L. *see* Itchkawitz, B.S. 986
Davis, L.C. *see* Bell, L.D. 856
Davis, L.C. *see* Hecht, M.H. 858
Davis, L.C. *see* Kaiser, W.J. 858
Davis, R.F. 198
Davis, R.F. *see* Chang, C.S. 197
Davison, S.G. 505
Daw, M.S. 857
Dayan, M. 198
de Andrade, M.C. *see* Anderson, R.O. 986
de Andrés, P.L. *see* Reuter, K. 860
de Andres, P.L. *see* Starke, U. 746
de Boer, F.R. *see* Miedema, A.R. 859
de Chatel, P.F. *see* Miedema, A.R. 859
de Gironcoli, S. *see* Xie, J. 356
de Groot, R.A. *see* Coehoorn, R. 428
de Rossi, S. *see* Crampin, S. 947
de Sousa Pires, J. 857
de Vita, A. 281
de Vita, A. *see* Štich, I. 283
Debe, M.K. 87, 505
Debe, M.K. *see* Marsh, F.S. 89
Debever, J.-M. *see* Themlin, J.-M. 206
Debever, J.M. *see* Bouzidi, S. 893
Dederichs, P.H. *see* Nordström, L. 666
Dederichs, P.H. *see* Zeller, R. 91
Deisz, J.J. 243
del Giudice, M. *see* Weaver, J.H. 861
del Pennino, U. 894
del Sole, R. *see* Manghi, F. 203
del Sole, R. *see* Shkrebtii, A.I. 206, 283, 431
Delley, B. 87, 281
Delley, B. *see* Li, Y.S. 89
Delley, B. *see* Ling, Y. 282
Delley, B. *see* Patthey, F. 987
Delley, B. *see* Tang, S. 90
Delley, B. *see* Ye Ling 91
Demuth, I.E. 743
Demuth, J.E. 198, 428, 857
Demuth, J.E. *see* Hamers, R.J. 88, 199, 381, 429, 894
Demuth, J.E. *see* Tromp, R.M. 90, 207, 431
Den Baars, S.P. *see* O'Shea, J.J. 860
Dench, W.A. *see* Seah, M.P. 667
Denecke, R. *see* Hillebrecht, F.U. 664
Deneuville, A. *see* Muret, P. 859
Dennis, P.N.J. *see* Farrow, R.F.C. 429
DePaola, R. *see* Eberhardt, W. 743
DePaola, R.A. 743, 947
DePaola, R.A. *see* Heskett, D. 744
Derry, T.E. 198
Derry, T.E. *see* Smit, L. 431
Desjonquères, M.C. *see* Guillot, C. 506
Desjonquères, M.C. *see* Legrand, B. 89

Desjonquères, M.C. *see* Spanjaard, D. 283, 355, 746
Desjonquères, M.C. *see* Treglia, G. 90
Deutsch, T. *see* Alavi, A. 352
Deutschmann, W. *see* Schottky, W. 860
Devreese, J.T. 198
Devreese, J.T. *see* van Camp, P.E. 207
Dewar, M.J.S. 743
Dhar, S. 505
Dharmadasa, I.M. 857
Dhesi, S.S. 429
di Bona, A. *see* Ruocco, A. 896
di Ciaccio, L. *see* Semond, F. 205
di Felice, R. 281
di Felice, R. *see* Buongiorno Nardelli, M. 281
di Felice, R. *see* Northrup, J.E. 204
di Felice, R. *see* Shkrebtii, A.I. 206, 283, 431
di Nardo, J.N. *see* Horn, K. 744
Di, W. 505
DiCenzo, S.B. *see* Wertheim, G.K. 431
Didio, R.A. 743
Diehl, R.D. 743, 947
Diehl, R.D. *see* Adler, D.L. 947
Diehl, R.D. *see* Fischer, D. 948
Diehl, R.D. *see* Kerkar, M. 949
Diehl, R.D. *see* Seyller, T. 355
Dieny, B. *see* Monsma, D.J. 665
Dijkstra, J. *see* Coehoorn, R. 428
DiNardo, N.J. *see* Demuth, J.E. 857
Ding, S.-A. 428
Ding, S.-A. *see* Barman, S.R. 197, 428
Ding, Y.J. 281
Dirac, P.A.M. 663
DiSalvo, F.J. *see* Smith, N.V. 431
DiSalvo, F.J. *see* Wilson, J.A. 510
Dittschar, A. *see* Kuch, W. 665
Dobson, P.J. *see* Larsen, P.K. 202, 430
Doering, D.L. *see* Semancik, S. 950
Dohrmann, T. *see* von dem Borne, A. 668
Domcke, W. *see* Cederbaum, L.S. 742
Domcke, W. *see* Eiding, J. 743
Domcke, W. *see* Köppel, H. 745
Domke, C. *see* Ebert, Ph. 199, 429
Domke, M. *see* Prietsch, M. 860
Donath, M. 243, 380, 663
Donath, M. *see* Borstel, G. 243
Donath, M. *see* Goldmann, A. 243
Donath, M. *see* Passek, F. 244, 666
Donath, M. *see* Schneider, R. 244
Dong, Q. *see* Johnson, P.D. 664, 949
Dong, Q.-Y. *see* Shek, M.L. 206
Dongqi, Li. *see* Johnson, P.D. 949
Doniach, S. 857
Donnelly, V.M. *see* Flammt, D.L. 894
Donoval, D. *see* De Sousa Pires, J. 857
Doppalapudi, D. *see* Dhesi, S.S. 429
Dornisch, D. *see* Rossmann, R. 205
Dose, V. 243, 505, 663, 947
Dose, V. *see* Borstel, G. 243
Dose, V. *see* Donath, M. 243, 663
Dose, V. *see* Goldmann, A. 243
Dose, V. *see* Graß, M. 243
Dose, V. *see* Jacob, W. 243, 507, 744, 949
Dose, V. *see* Memmel, N. 745, 950
Dose, V. *see* Nolting, W. 666
Dose, V. *see* Passek, F. 244
Dose, V. *see* Rangelov, G. 746
Dose, V. *see* Schneider, R. 244
Dose, V. *see* Starke, K. 244
Dose, V. *see* Straub, D. 206
Dose, V. *see* Thörner, G. 245
Dottl, L. *see* Dowben, P.A. 505
Douillard, L. *see* Aristov, V.Yu. 196
Douillard, L. *see* Semond, F. 205
Douillard, L. *see* Soukiassian, P. 206
Dovesi, R. 87
Dow, J.D. *see* Allen, R.E. 855
Dow, J.D. *see* Beres, R.P. 197
Dow, J.D. *see* Packard, W.E. 204
Dowben, P.A. 505, 743
Dowben, P.A. *see* Li, D. 508
Dowben, P.A. *see* Zhang, J. 951
Doyen, G. 505
Drabold, D.A. *see* Alfonso, D.R. 196
Drabold, D.A. *see* Yang, S.H. 208
Dragoset, R.A. *see* Whitman, L.J. 283, 510
Drathen, P. 429
Drchal, V. *see* Turek, I. 667
Dreizler, R.M. 281, 353
Drell, S.D. *see* Bjorken, J.D. 86
Droste, Ch. *see* Scheffler, M. 90, 205, 355, 950
Droste, R. *see* Walker, J.C. 668
Drouhin, H.J. 857
Drube, W. 198, 429
Drube, W. *see* Schäffler, F. 860
Drummond, W.E. 857
DuBois, D.F. 986
Dudde, R. 743, 947

Dudzik, E. 894
Dufour, G. *see* Poncey, C. 896
Dufour, G. *see* Rochet, F. 283
Dujardin, G. 894
Dujardin, G. *see* Semond, F. 205
Dujardin, G. *see* Soukiassian, P. 206
Duke, C.B. 198, 281, 429, 743, 857
Duke, C.B. *see* BenDaniel, D.J. 856
Duke, C.B. *see* Bennett, A.J. 86
Duke, C.B. *see* Holland, B.W. 88, 200
Duke, C.B. *see* Horsky, T.N. 200
Duke, C.B. *see* Kahn, A. 201
Duke, C.B. *see* Mailhiot, C. 202, 203, 282
Duke, C.B. *see* Meyer, R.J. 203
Duke, C.B. *see* Salaneck, W.R. 746
Duke, C.B. *see* Wang, Y.R. 207, 431
Dumas, P. 198, 281, 894
Dumas, P. *see* Bouzidi, S. 893
Dumas, P. *see* Hricovini, K. 200, 282
Duncauson, C.A. *see* Chatt, J. 742
Dunham, D. *see* Stöhr, J. 90, 381, 667
Dunlap, B.I. 87
Dunn, J.H. 663
Dunning, F.B. 663
Dunning, F.B. *see* Tang, F.-C. 667
Dünweg, B. 506
Durbin, T.D. *see* Lo, C.W. 895
Dürr, H. *see* Graß, M. 243

Eades, J.A. *see* Ma, Y. 202
Eaglesham, D.J. *see* Sullivan, J.P. 861
Eastman, D.E. 199, 429, 506, 857, 894
Eastman, D.E. *see* Chiang, T.C. 87, 198, 742
Eastman, D.E. *see* Himpsel, F.J. 200, 243, 429
Eastman, D.E. *see* Knapp, J.A. 381, 508
Eastman, D.E. *see* Koch, E.E. 858
Eastman, D.E. *see* Pandey, K.C. 204
Eastman, D.E. *see* Plummer, E.W. 746
Eastman, D.E. *see* van der Veen, J.F. 510
Eberhardt, W. 87, 243, 380, 506, 663, 743
Eberhardt, W. *see* Carbone, C. 663, 947
Eberhardt, W. *see* Clemens, W. 947
Eberhardt, W. *see* Freund, H.J. 743, 986
Eberhardt, W. *see* Heskett, D. 744
Eberhardt, W. *see* Horn, K. 744
Eberhardt, W. *see* Kevan, S.D. 508
Eberhardt, W. *see* Plummer, E.W. 244, 381, 509, 666, 745, 896
Eberhardt, W. *see* Rader, O. 355, 666
Eberhardt, W. *see* Salaneck, W.R. 746
Eberhardt, W. *see* Vescovo, E. 245
Eberle, K. *see* Schneider, C. 746
Ebert, H. 663
Ebert, H. *see* Schneider, C.M. 667
Ebert, H. *see* Venus, D. 668
Ebert, Ph. 199, 429
Ebert, Ph. *see* Engels, B. 429
Ebina, A. 199
Ebina, E. 199
Ebina, E. *see* Takahashi, T. 206, 431
Echenique, P.M. 243, 353, 947
Echenique, P.M. *see* Ortuno, M. 244
Eckardt, H. 663
Eckstein, W. *see* Müller, N. 666
Edamoto, K. 894
Edamoto, K. *see* Nishijima, N. 895
Ederer, D.L. *see* Shek, M.L. 206
Edmond, J.A. *see* Davis, R.F. 198
Edwards, D.M. 948
Edwards, P.M. *see* Liebermann, L.N. 665
Egelhoff, W.F. 380, 948
Egelhoff, W.F. *see* Bennett, W.R. 947
Eguiluz, A.G. 243, 986
Eguiluz, A.G. *see* Deisz, J.J. 243
Eguiluz, A.G. *see* Heinrichsmeier, M. 243, 507
Ehrenreich, H. 506
Ehrenreich, H. *see* Velicky, B. 510
Ehrlich, A.C. 948
Eichler, A. 353
Eiding, J. 743
Eigler, D. 380
Eigler, D. *see* Crommie, M.F. 505
Einstein, T.L. 506, 743
Eisenberger, P. *see* Citrin, P.H. 894
Eklund, E.A. *see* Cartier, E. 856
Elliot, G.S. *see* Smith, K.E. 509
Elliot, M. *see* Fowell, A.E. 857
Elliot, M. *see* Shen, T.-H. 860
Elliott, G.S. 506
Ellis, D.E. *see* Averill, F.W. 86
Ellis, D.E. *see* Baerends, E.J. 86
Ellis, D.E. *see* Delley, B. 87
Ellis, D.E. *see* Rosén, A. 90
Ellis, J. 948
Ellis, J. *see* Benedek, G. 947
Ellis, J. *see* Rohlfing, D.M. 205
Ellis, T.H. *see* Brosseau, R. 742
Ellis, W.P. *see* Anderson, R.O. 986

Ellis, W.P. *see* Claessen, R. 505, 986
Elmers, H.J. *see* Fritzsche, H. 664
Enderlein, R. *see* Bechstedt, F. 281
Eng, J. Jr. *see* Struck, L.M. 896
Engdahl, C. *see* Pleth Nielsen, L. 355
Engel, T. 353, 894
Engel, T. *see* Bauer, E. 505
Engel, T. *see* Engstrom, J.R. 894
Engelhardt, H.A. 743
Engelhardt, R. *see* Karlsson, U.O. 508
Engelhardt, R. *see* Magnusson, K.O. 202
Engelhardt, R. *see* Nicholls, J.M. 203
Engels, B. 429
Engels, B. *see* Ebert, Ph. 199, 429
Engstrom, J.R. 894
Engstrom, J.R. *see* Maity, N. 895
Enta, Y. 199, 429
Erbudak, M. 663, 857
Erickson, R.P. 663
Eriksson, O. 663
Erly, E.A. *see* Anderson, R.O. 986
Ernst, H. 506
Erskine, J. *see* Eberhardt, W. 243, 663
Erskine, J.L. 87, 243, 663
Erskine, J.L. *see* Chen, J. 663
Erskine, J.L. *see* Mulhollan, G.A. 665
Erskine, J.L. *see* Turner, A.M. 667
Ertl, G. *see* Bonzel, H.P. 742, 947
Ertl, G. 663, 743
Ertl, G. *see* Böttcher, A. 353
Ertl, G. *see* Brune, H. 505
Ertl, G. *see* Christmann, K. 742
Ertl, G. *see* Conrad, H. 743
Ertl, G. *see* Coulman, D.J. 743
Ertl, G. *see* Engel, T. 353
Ertl, G. *see* Grunze, M. 744
Ertl, G. *see* Kim, Y.D. 354
Ertl, G. *see* Over, H. 355, 950
Ertl, G. *see* Rotermund, H.H. 381
Ertl, G. *see* Schuster, R. 950
Ertl, G. *see* Stampfl, C. 356
Ertl, G. *see* Wintterlin, J. 747
Ertl, G. *see* Woratschek, B. 951
Ertl, K. *see* Donath, M. 243
Ertl, K. *see* Passek, F. 244
Ertl, K. *see* Schneider, R. 244
Ertl, K. *see* Starke, K. 244
Esaki, L. 948
Escudier, P. 663
Eshbach, J.R. *see* Damon, R.W. 663
Esser, N. *see* Pahlke, D. 896
Esser, N. *see* Resch-Esser, U. 896
Esteva, J.-M. *see* van der Laan, G. 91, 667
Estrup, P.J. 506
Estrup, P.J. *see* Altmann, M. 86, 504
Estrup, P.J. *see* Barker, R.A. 505
Estrup, P.J. *see* Chung, J.W. 505
Estrup, P.J. *see* Felter, T.E. 87, 506
Estrup, P.J. *see* Hildner, M.L. 507
Estrup, P.J. *see* Prybyla, J.A. 509
Eteläniemi, V. 894
Eteläniemi, V. *see* Michel, E.G. 895
Etgens, V.H. *see* Jedrecy, N. 201
Etienne, P. *see* Baibich, M.N. 662
Ettema, A.R.H.F. *see* Weitering, H.H. 861
Euceda, A. 506
Evans, D.A. 857
Evans, D.A. *see* Barman S.R. 197, 428
Evans, D.A. *see* Magnusson, K.O.M. 430
Evans, D.A. *see* Neuhold, G. 430
Evans, D.A. *see* Xue, J.Y. 431
Eyers, A. *see* Schäfers, F. 666

Fabisch, F.-J. *see* Duke, C.B. 743
Fadley, C.S. 380, 663
Fadley, C.S. *see* Saiki, R.S. 746
Fahsold, G. 663
Fahy, S. *see* Zhu, X. 208
Fain, S.C. *see* Diehl, R.D. 743
Fäldt, A. 948
Falicov, L.M. 87, 243, 663, 948
Fan, H. 663
Fan, L.-Y. *see* Troost, D. 861, 897
Fano, U. 506
Farge, Y. *see* Koch, E.E. 858
Farle, M. 663
Farnsworth, H.E. *see* Schlier, R.E. 90, 283, 431, 896
Farrell, H.H. 199, 894
Farrell, H.H. *see* Aspnes, D.E. 380
Farrell, H.H. *see* Larsen, P.K. 895
Farrow, R.F.C. 429
Fasel, R. 353
Fasel, R. *see* Stampfl, C. 356
Fasolino, A. 87, 506
Fathauer, R.W. *see* Bell, L.D. 856
Fathauer, R.W. *see* Kaiser, W.J. 858
Faul, J. *see* Zhang, X.D. 431

Fauster, R. *see* Fischer, N. 948
Fauster, T. 894
Fauster, T. *see* Fischer, N. 243, 664, 948
Fauster, T. *see* Fischer, R. 243, 948
Fauster, T. *see* Graß, M. 243
Fauster, T. *see* Himpsel, F.J. 200, 429, 894
Fauster, T. *see* Jacob, W. 243, 507
Fauster, T. *see* Nolting, W. 666
Fauster, T. *see* Steinmann, W. 244
Fauster, T. *see* Wallauer, W. 951
Fauth, K. *see* Finteis, T. 429
Fauxchoux, O. *see* Aristov, V.Yu. 196
Feder, R. 87, 663, 664
Feder, R. *see* Ackermann, B. 662
Feder, R. *see* Alvarado, S.F. 662
Feder, R. *see* Gradmann, U. 664
Feder, R. *see* Haines, E.M. 664
Feder, R. *see* Henk, J. 664
Feder, R. *see* Kirschner, J. 88, 665
Feder, R. *see* Rampe, A. 666
Feder, R. *see* Scheunemann, T. 666
Feder, R. *see* Tamura, E. 667
Feenstra, R.M. 199, 282, 429, 857
Feenstra, R.M. *see* Smith, A.R. 431
Feenstra, R.M. *see* Stroscio, J.A. 206, 861
Fegel, F. *see* Bansmann, J. 662
Fehlner, W.R. *see* Wilk, L. 510
Feibelman, P.J. 353, 380, 506, 948
Feibelman, P.J. *see* Levinson, H.L. 665
Feibelman, P.J. *see* Williams, A.R. 208
Feibelmann, P.J. 87
Feidenhans'l, R. 199
Feidenhans'l, R. *see* Adams, D.L. 86
Feidenhans'l, R. *see* Bohr, J. 197
Fein, A.P. *see* Feenstra, R.M. 199, 282, 429
Fein, A.P. *see* Stroscio, J.A. 206
Felcher, G.P. *see* Celotta, R.J. 663
Feldman, L. 87
Feldman, L. *see* Bennet, P.A. 428
Feldman, L. *see* Chabal, Y.J. 197
Feldman, L. *see* Culbertson, R.J. 198, 894
Felter, T.E. 87, 506
Felter, T.E. *see* Hildner, M.L. 507
Felton, R.H. *see* Sambe, H. 90
Fermi, E. 87
Fernandez, A. 857
Fernandez, A. *see* Hallen, H.D. 857
Ferrario, M. *see* Marcellini, A. 282
Ferrell, R.A. *see* Quinn, J.J. 987
Fert, A. *see* Baibich, M.N. 662
Fetter, A.L. 243
Feuerbacher, B. 506, 664
Feuerbacher, B. *see* Neuhaus, D. 509
Fiedler, M. *see* Kress, C. 201
Fimland, B.O. *see* Resch-Esser, U. 896
Fink, J. 743
Fink, J. *see* Manske, R. 987
Fink, R.L. *see* Mulhollan, G.A. 665
Finnis, M.W. 353
Finocchi, F. *see* Bertoni, C.M. 281
Finocchi, F. *see* Buongiorno Nardelli, M. 281
Finocchi, F. *see* Di Felice, R. 281
Finster, J. *see* Ranke, W. 896
Finteis, T. 429
Fiolhais, C. *see* Perdew, J.P. 89
Fiorentini, V. 199, 353
Fiorentini, V. *see* Oppo, S. 355
First, P.N. *see* Henderson, G.N. 858
Fischer, D. 948
Fischer, D. *see* Kerkar, M. 949
Fischer, N. 243, 664, 948
Fischer, N. *see* Fischer, R. 243, 948
Fischer, N. *see* Schuppler, S. 244
Fischer, Ø. *see* Niedermann, P. 860
Fischer, Ø. *see* Quattropani, L. 860
Fischer, R. 243, 948
Fischer, R. *see* Fischer, N. 243, 948
Fischer, T.E. *see* Erbudak, M. 857
Fischer, T.E. *see* Kelemen, S.R. 744
Fischetti, M.V. 857
Fischetti, M.V. *see* Cartier, E. 856
Fisher, D. 948
Fitton, B. *see* Feuerbacher, B. 506, 664
Flammt, D.L. 894
Flannery, B.P. *see* Press, W.H. 89
Fleszar, A. *see* Eguiluz, A.G. 243
Fleszar, A. *see* Heinrichsmeier, M. 243, 507
Fleszar, A. *see* Scheffler, M. 90, 205, 355, 950
Fleszar, A. *see* Wachutka, G. 207
Flipse, C.F.J. *see* Coehoorn, R. 428
Flipse, C.F.J. *see* van der Laan, G. 91, 667
Flodstrom, S.A. *see* Hansson, G.V. 506
Flodstrom, S.A. *see* Karlsson, U.O. 508
Flodström, S.A. *see* Magnusson, K.O. 202, 430
Flodström, S.A. *see* Nicholls, J.M. 203
Flodström, S.A. *see* Uhrberg, R.I.G. 207, 431, 897
Flodström, S.A. *see* Wang, Y.R. 207, 431

Floreano, L. *see* Crottini, A. 947
Flores, F. *see* García, N. 857
Flores, F. *see* Garcia-Vidal, F.J. 282
Flores, F. *see* Joyce, K. 508
Flores, F. *see* Louis E. 859
Flores, F. *see* Reuter, K. 860
Flores, F. *see* Rincón, R. 283
Flores, F. *see* Saiz-Pardo, R. 896
Flores, F. *see* Tejedor, C. 861
Florez, L.T. *see* Aspnes, D.E. 380
Florio, J.V. 199
Floyd, R.B. 857
Flynn, G.W. *see* Struck, L.M. 896
Fock, V. 87
Föhlisch, A. *see* Nilsson, A. 355
Folkerts, W. *see* Purcell, S.T. 666
Fondén, T. *see* Yang, S. 245, 951
Fong, C.Y. 282
Fontaine, A. *see* Pizzini, S. 666
Fontana, R.E. *see* Tsang, C.H. 667
Fontes, E. 199
Forbeaux, I. *see* Themlin, J.-M. 206
Forbes, S.G. 87
Ford, A.C. *see* Shen, T.-H. 860
Ford, W.K. *see* Duke, C.B. 198, 281
Forstmann, F. 506
Forstmann, F. *see* Pendry, J.B. 509
Forstmann, F. *see* Scheffler, M. 355
Fowell, A.E. 857
Fowell, A.E. *see* Shen, T.-H. 860
Fowler, R.H. 857
Fox, T. 743
Frahm, R. *see* Schütz, G. 90, 667
Franchini, A. *see* Bortolani, V. 505
Franciosi, A. *see* Sorba, L. 896
Frank, H.-J. Sagner 506
Frank, K.-H. 948
Frank, K.-H. *see* Bader, M. 742
Frank, K.-H. *see* Binnig, G. 856
Frank, K.-H. *see* Dudde, R. 743, 947
Frank, K.-H. *see* Heskett, D. 243, 948
Frank, K.-H. *see* Reihl, B. 244, 950
Frank, K.-H. *see* Watson, G.M. 510, 951
Frankel, D.J. *see* Schäfer, J.A. 896
Franklin, G.E. *see* Miller, T. 950
Franklin, G.E. *see* Rich, D.H. 89, 205
Frauenheim, Th. 199
Fredkin, D.R. *see* Liebermann, L.N. 665
Freeland, P.E. *see* Zegenhagen, J. 91
Freeman, A.J. 664
Freeman, A.J. *see* Fu, C.L. 87, 88, 664
Freeman, A.J. *see* Jansen, H.J.F. 88
Freeman, A.J. *see* Krakauer, H. 88, 508
Freeman, A.J. *see* Li, C. 89, 665
Freeman, A.J. *see* Ling, Y. 282
Freeman, A.J. *see* Ohnishi, S. 89
Freeman, A.J. *see* Posternak, M. 89
Freeman, A.J. *see* Redinger, J. 244
Freeman, A.J. *see* Soukiassian, P. 509, 951
Freeman, A.J. *see* Spiess, L. 206, 283
Freeman, A.J. *see* Tang, S. 90
Freeman, A.J. *see* Wan, C.S. 245
Freeman, A.J. *see* Wang, D.-S. 91, 668
Freeman, A.J. *see* Weinert, M. 91, 245, 668
Freeman, A.J. *see* Wimmer, E. 91, 208, 245, 356, 510, 668
Freeman, A.J. *see* Wu, R. 91
Freeman, A.J. *see* Wu, R.-Q. 668
Freeman, A.J. *see* Ye Ling 91
Freeman, R.R. *see* Haight, R. 199
Freeouf, J.L. 857
Freeouf, J.L. *see* Pandey, K.C. 204
Freeouf, J.L. *see* Tang, J.Y.-F. 861
Freeouf, J.L. *see* Wittmer, M. 861
Freitag, M.K. *see* Verheij, L.K. 897
Freund, H.-J. 380, 743, 986
Freund, H.-J. *see* Bartos, B. 742
Freund, H.-J. *see* Eberhardt, W. 743
Freund, H.-J. *see* Geisler, H. 743
Freund, H.-J. *see* Graen, H.H. 743
Freund, H.-J. *see* Greuter, F. 744
Freund, H.-J. *see* Grunze, M. 744
Freund, H.-J. *see* Heskett, D. 243, 948
Freund, H.-J. *see* Horn, K. 744
Freund, H.-J. *see* Kuhlenbeck, H. 745
Freund, H.-J. *see* Odörfer, G. 745
Freund, H.-J. *see* Saddei, D. 746
Freund, H.-J. *see* Salaneck, W.R. 746
Freund, H.-J. *see* Schmeisser, D. 746
Freund, H.-J. *see* Wambach, J. 747
Friday, W. *see* Pashley, M.D. 204, 283
Friedel, J. 506
Friederich, A. *see* Baibich, M.N. 662
Friend, C.M. *see* Liu, A.C. 745
Fritsche, L. *see* Eckardt, H. 663
Fritsche, L. *see* Noffke, J. 666
Fritzsche, H. 664
Frömter, R. *see* Schneider, C.M. 667

Frota, H.O. 986
Froyen, S. *see* Chang, K.J. 198
Froyen, S. *see* Northrup, J.E. 203
Fu, C.L. 87, 88, 664
Fu, C.L. *see* Li, C. 89
Fu, C.L. *see* Redinger, J. 244
Fu, C.L. *see* Wimmer, E. 356
Fu, J. 282
Fu, R.T. *see* Liu, J.N. 508
Fuchs, H. *see* Binnig, G. 856
Fuggle, J.C. 664
Fuggle, J.C. *see* van der Laan, G. 91, 667
Fujii, J. *see* Kakizaki, A. 665
Fujita, M. 429
Fujitani, H. 857
Fujiwara, K. 894
Fujiwara, T. *see* Arai, M. 196
Fukuda, Y. *see* Huff, W.R.A. 429
Fukukawa, Y. *see* Ito, T. 895
Fukutani, H. *see* Kakizaki, A. 665
Funke, P. 894
Fuoss, P. *see* Robinson, I.K. 205
Furthmüller, J. 199, 429
Furthmüller, J. *see* Finnis, M.W. 353
Furthmüller, J. *see* Grossner, U. 199
Furthmüller, J. *see* Käckell, P. 201
Furthmüller, J. *see* Kresse, G. 354

Gadeke, W. *see* Karlsson, U.O. 508
Gadzuk, J.W. 743, 857
Gadzuk, J.W. *see* Plummer, E.W. 509
Gaffner, G. *see* Broden, G. 742
Gallagher, M.C. *see* Fu, J. 282
Gallet, D. 282
Galli, G. *see* Catellani, A. 197
Galli, G. *see* Iarlori, S. 200
Galván, M. *see* Brommer, K.D. 281
Galwey, A.K. 506
Gambacorti, N. *see* Ruocco, A. 896
Ganduglia-Pirovano, M.V. 354
Ganduglia-Pirovano, M.V. *see* Hennig, D. 354
Ganz, E. 199
Gao, Q. *see* Yates, J.T. Jr. 897
Gao, X. 664
Garbe, J. *see* Venus, D. 668
García, N. 857
García, N. *see* Binnig, G. 856
García-Vidal, F.J. 282
García-Vidal, F.J. *see* Reuter, K. 860
García-Vidal, F.J. *see* Rincón, R. 283
Garcia, A. 199
Garcia, N. *see* Serena, P.A. 950
Garcia-Moliner, F. *see* Jaskolski, W. 949
Gardner, M. *see* Hiskes, J.R. 88
Garner, C.M. *see* Lindau, I. 859
Garrett, R.F. 243
Garrison, K. 664, 948
Garrison, K. *see* Johnson, P.D. 664, 949
Gartland, P.O. 88, 506, 948
Gartland, P.O. *see* Grepstad, T.K. 88
Gáspár, R. 88
Gauthier, Y. 664
Gay, J.G. 88, 664
Gay, J.G. *see* Smith, J.R. 90
Gay, J.G. *see* Zhu, X.-Y. 668
Gaylord, R.H. 506
Gaylord, R.H. *see* Bartynski, R.A. 505, 986
Gaylord, R.H. *see* Jeong, K. 507
Gaylord, R.H. *see* Kevan, S.D. 508
Gaylord, T.K. *see* Henderson, G.N. 858
Geisler, H. 743
Gelbel, Ch. *see* Binnig, G. 281
Geldart, D.J.W. 986
Gelius, U. 381
George, S.M. *see* Wise, M.L. 897
Gerber, Ch. *see* Binnig, G. 380, 428
Gerlach, R.L. 948
Gerstenblum, G. 894
Gerstenblum, G. *see* Rudolf, P. 896
Getzlaff, M. *see* Bansmann, J. 662
Ghiaia, G. *see* Karlsson, H. 429
Giarante, A. *see* Cimino, R. 856
Gibson, J.M. *see* Twesten, R.D. 207
Gidowski, G.E. *see* D'Evelyn, M.P. 743
Gierer, M. *see* Over, H. 355
Giesen, K. 243, 948
Giesen, M. *see* Hannon, J.B. 948
Giesen, M. *see* Klünker, C. 949
Gillan, M.J. *see* De Vita, A. 281
Gillan, M.J. *see* Štich, I. 283
Gimzewski, J.K. *see* Jung, T. 381
Giorgetti, C. *see* Pizzini, S. 666
Gironcoli, S.D. *see* Bungaro, C. 505
Girvan, R.F. 506
Gland, J.L. *see* Madix, R.J. 745
Gland, J.L. *see* Zaera, F. 747
Glander, G. *see* Tong, S.Y. 206, 431
Glanz, M. *see* Hofmann, P. 744

Glanz, M. *see* Schneider, C. 746
Glass, J.T. *see* Davis, R.F. 198
Glöbl, M. *see* Donath, M. 243
Glytsis, E.N. *see* Henderson, G.N. 858
Gnoc, T.C. *see* Poppendieck, T.D. 89
Godby, R.W. 199, 506
Godby, R.W. *see* Charlesworth, J.P.A. 856
Godby, R.W. *see* Palummo, M. 204
Godby, R.W. *see* White, I.D. 245
Goddard, W.A. *see* Redondo, A. 89
Godehusen, K. *see* von dem Borne, A. 668
Goedkoop, J.B. *see* van der Laan, G. 91, 667
Göhtelid, M. *see* LeLay, G. 430
Gokhale, M.P. 664
Gold, A.V. *see* Girvan, R.F. 506
Goldmann, A. 199, 243, 743
Goldmann, A. *see* Borstel, G. 243
Goldmann, A. *see* Dose, V. 243, 663, 947
Goldmann, A. *see* Jacob, W. 243, 507, 744
Goldmann, A. *see* Koke, P. 201
Goldmann, A. *see* Orr, B.G. 950
Golla, A. *see* Horn-von Hoegen, M. 894
Golovchenko, J. *see* Becker, R.S. 197, 856
Golovchenko, J. *see* Ganz, E. 199
Golovchenko, J. *see* Zegenhagen, J. 91
Golze, M. *see* Grunze, M. 744
Gonze, X. 199
Goodenough, J.B. 506
Goodman, A.M. 857
Goodman, D.W. 743
Goodman, D.W. *see* Peden, C.H.F. 355
Goodwin, E.T. 506
Göpel, W. 199
Göpel, W. *see* Henzler, M. 744
Göpel, W. *see* Munz, A.W. 203
Göpel, W. *see* Schäfer, J.A. 896
Gorczyka, I. *see* Christensen, N.E. 198
Gordy, W. 857
Gornik, E. *see* Heer, R. 858
Gossler, J. *see* Hofmann, P. 744
Gossman, H.J. 857
Göthelid, M. 894
Gotter, R. *see* Crottini, A. 947
Gradmann, U. 664
Gradmann, U. *see* Fritzsche, H. 664
Gradmann, U. *see* Korecki, J. 665
Gradmann, U. *see* Tamura, E. 667
Gradmann, U. *see* Waller, G. 668
Graen, H.H. 743, 744
Graen, H.H. *see* Neuber, M. 745
Gräf, D. 894
Graham, A.P. 948
Graham, G.W. *see* Schmitz, P.J. 667
Graham, W.R. *see* Melmed, A.J. 89
Graham, W.R. *see* Sullivan, J.P. 861
Graham, W.R. *see* Tung, R.T. 90
Grant, R.W. *see* Kowalczyk, S.P. 858
Grant, R.W. *see* Kraut, E.A. 858
Gräschus, V. 199
Gräschus, V. *see* Mazur, A. 203
Graß, M. 243
Graß M. *see* Schneider, R. 244
Graupner, R. 199, 429
Graupner, R. *see* Hollering, M. 200
Gray, L.G. *see* Dunning, F.B. 663
Green, M. 88
Greene, J.E. *see* Li, G. 282
Grehk, M. *see* Aristov, V.Yu. 428
Grehk, T.M. *see* LeLay, G. 430
Greiser, N. *see* Jedrecy, N. 201
Grepstad, T.K. 88
Greuter, F. 744
Greuter, F. *see* Eberhardt, W. 506, 743
Greuter, F. *see* Levinson, H.J. 244, 508, 986
Greuter, F. *see* Schmeisser, D. 746
Greve, D.W. *see* Smith, A.R. 431
Grey, F. *see* Feidenhans'l, R. 199
Grey, F. *see* Uchida, H. 861
Griffith, J.E. *see* Kubby, J.A. 202
Grimley, T.B. 282, 354, 506, 744
Grimvall, G. 986
Grioni, M. *see* Weaver, J.H. 861
Grobman, W.D. *see* Eastman, D.E. 506
Grobmann, W.D. *see* Lüth, H. 202
Grohndahl, L.O. 857
Gronsky, R. *see* Falicov, L.M. 87
Gross, A. 354
Gross, A. *see* Eichler, A. 353
Gross, E.K.U. *see* Dreizler, R.M. 281, 353
Grossner, U. 199
Grout, P.J. *see* Joyce, K. 508
Grub, A. *see* Hashizumi, T. 858
Gruenebaum, J. *see* Sahni, V. 90
Grünberg, P. 664
Grünberg, P. *see* Binasch, G. 662
Grünberg, P. *see* Purcell, S.T. 666
Gruncner, M. *see* Gräf, D. 894
Grunthaner, F.J. *see* Hecht, M.H. 858

Grunthaner, F.J. *see* Kaiser, W.J. 858
Grunze, M. 744
Grunze, M. *see* Freund, H.-J. 743
Grunze, M. *see* Schneider, C.M. 667
Grupp, C. 894
Grzelakowski, K. 506
Gsell, M. 354
Gsell, M. *see* Kostov, K.L. 354
Gu, C. 894
Gudat, W. *see* Carbone, C. 663, 947
Gudat, W. *see* Kisker, E. 381, 665
Gudat, W. *see* Plummer, E.W. 746
Gudat, W. *see* Rader, O. 355, 666
Gudat, W. *see* Vescovo, E. 245
Gudat, W. *see* Weller, D. 668
Guerney, B.A. *see* Tsang, C.H. 667
Guerney, R.W. 744
Guethner, P.H. *see* Mamin, H.J. 859
Guichar, G.M. 199
Guille, C. *see* Moison, J.M. 859
Guillot, C. 506
Guillot, C. *see* Thiry, P. 431, 510
Gumhalter, B. 744
Gumlich, H.E. *see* Weidmann, R. 207
Gunnarsson, O. 88, 199, 948
Gunnarsson, O. *see* Allen, J.W. 985
Gunnarsson, O. *see* Aryasetiawan, F. 196
Gunnarsson, O. *see* Das, G.P. 857
Gunnarsson, O. *see* Jones, R.O. 201
Gunnarsson, O. *see* Lundquist, B.I. 745
Gunnarsson, O. *see* Schönhammer, K. 431, 746
Gunnarsson, O. *see* Svane, A. 206
Gunnella, R. *see* Bullock, E.L. 197
Gunnella, R. *see* Johansson, L.S.O. 282
Günther, R. *see* Hricovini, K. 200, 282
Güntherodt, G. *see* Hartmann, D. 664
Güntherodt, G. *see* Hillebrands, B. 664
Güntherodt, G. *see* Nouvertné, F. 355
Güntherodt, G. *see* Rampe, A. 666
Güntherodt, G. *see* Weber, W. 668, 951
Gunton, J.D. *see* Kaski, K. 508
Gunton, J.D. *see* Rikvold, P.A. 509
Gurney, R.W. 354, 506, 948
Gustafsson, T. 744, 948
Gustafsson, T. *see* Allyn, C.L. 742
Gustafsson, T. *see* Andersson, S. 947
Gustafsson, T. *see* Bartynski, R.A. 243, 505, 986
Gustafsson, T. *see* Holmes, M.I. 507
Gustafsson, T. *see* Jensen, E. 507, 986
Gustafsson, T. *see* Nilsson, P.O. 509
Gustafsson, T. *see* Plummer, E.W. 746
Gutierrez, C.J. *see* Idzerda, Y.U. 88
Guttler, H.H. *see* Werner, J.H. 861
Guyot-Sionnest, P. 282
Gweon, G.-H. *see* Tjeng, L.H. 987
Gyftopoulos, E.P. *see* Hatsopoulos, G.N. 88
Gygi, F. 199
Gygi, F. *see* Catellani, A. 197
Gygi, F. *see* Iarlori, S. 200

Haak, H. *see* McLean, A.B. 859
Haas, C. *see* Coehoorn, R. 428
Haase, J. *see* Aminpirooz, S. 352
Haase, J. *see* Bader, M. 742
Haase, J. *see* Burchhardt, J. 353, 742
Haase, J. *see* Schmalz, A. 355, 950
Haber, J. *see* Bielański, A. 353
Haberern, K.W. 199, 282
Haberern, K.W. *see* Pashley, M.D. 204, 283
Haberland, H. *see* Woratschek, B. 951
Häberle, P. *see* Ding, S.-A. 428
Hafner, J. *see* Eichler, A. 353
Hafner, J. *see* Furthmüller, J. 199, 429
Hafner, J. *see* Käckell, P. 201
Hafner, J. *see* Kern, G. 201
Hage, F. *see* Giesen, K. 243, 948
Hagen, D.I. *see* Nieuwenhuys, B.E. 745
Hagstrom, S.B.M. *see* Allen, J.W. 947
Hagstrum, H.D. 199
Hagstrum, H.D. *see* Appelbaum, J.A. 281
Hagstrum, H.D. *see* Pandey, K.C. 283, 896
Hagstrum, H.D. *see* Pretzer, D.D. 896
Hagstrum, H.D. *see* Sakurai, T. 896
Hahn, Th. *see* Metzner, H. 895
Haight, R. 199, 857
Haight, R. *see* Baeumler, M. 380
Haight, R. *see* Culbertson, R.J. 894
Haines, E.M. 664
Håkansson, M.C. 429
Håkansson, M.C. *see* Khazmi, Y. 430
Håkansson, M.C. *see* Ölsson, L.Ö. 430
Haldane, F.D.M. 986
Halicioglu, T. *see* Takai, T. 206
Halilov, S.V. *see* Henk, J. 664
Halilov, S.V. *see* Scheunemann, T. 666
Hall, B.M. *see* Ormeci, A. 666
Hallen, H.D. 857

Hallen, H.D. *see* Fernandez, A. 857
Halse, M.R. 506
Hamada, N. *see* Terakura, I. 90
Hamann, D. *see* Stiles, M. 861
Hamann, D.R. 88, 199, 282
Hamann, D.R. *see* Appelbaum, J.A. 86, 196, 281, 504
Hamann, D.R. *see* Bachelet, G.B. 86, 196, 281
Hamann, D.R. *see* Feibelman, P.J. 380, 506
Hamann, D.R. *see* Mattheiss, L.F. 508
Hamann, D.R. *see* Tersoff, J. 431, 861
Hamawi, A. 506, 948
Hamers, R.J. 88, 199, 381, 429, 894
Hamers, R.J. *see* Tromp, R.M. 90, 207, 431
Hammer, B. 354
Hammer, L. *see* Starke, U. 206
Hammond, M. *see* Fahsold, G. 663
Hammond, M. *see* Schneider, C.M. 667
Hamza, A.V. 199
Hamza, A.V. *see* D'Evelyn, M.P. 743
Han, W.K. 506
Hanawa, T. *see* Oura, K. 896
Haneman, D. 88, 199, 282, 429
Hanke, W. *see* Deisz, J.J. 243
Hanke, W. *see* Eguiluz, A.G. 243
Hannon, J.B. 506, 948
Hannon, J.B. *see* Davis, H.L. 505
Hannon, J.B. *see* Klünker, C. 949
Hansen, W. *see* Bertolo, M. 742
Hansson, C.V. 381
Hansson, G. *see* Göpel, W. 199
Hansson, G.V. 199, 429, 506
Hansson, G.V. *see* Johansson, L.S.O. 201, 429
Hansson, G.V. *see* Karlsson, U.O. 508
Hansson, G.V. *see* Mårtensson, P. 203, 430
Hansson, G.V. *see* Nicholls, J.M. 203
Hansson, G.V. *see* Uhrberg, R.I.G. 207, 431, 897
Hara, S. 199
Harbison, J.P. *see* Aspnes, D.E. 380
Harm, S. *see* Claessen, R. 986
Harmon, B.N. *see* Koelling, D.D. 88
Harp, G. *see* Stöhr, J. 90, 381, 667
Harris, G.L. 199
Harris, J. 744
Harrison, N.M. *see* Jaffe, J.E. 201
Harrison, W. 88, 199, 200, 429, 506, 858
Harten, U. 200, 282, 507
Hartmann, D. 664
Hartmann, D. *see* Rampe, A. 666
Hartmann, D. *see* Weber, W. 668
Hartnagel, H.L. *see* Hashizumi, T. 858
Hartner, W. *see* Starke, U. 206
Hartree, D.R. 88
Hasegawa, H. *see* Hashizumi, T. 858
Hasegawa, Y. 507, 858
Hasegawa, Y. *see* Hashizume, T. 507
Hashimoto, S. *see* Jimenez, J.R. 858
Hashizume, T. 200, 507, 858
Hashizume, T. *see* Hasegawa, Y. 507
Hasselblatt, M. *see* Piancastelli, M.N. 430
Hasselström, J. *see* Nilsson, A. 355
Hathaway, K.B. *see* Falicov, L.M. 87
Hatsopoulos, G.N. 88
Hauser, J.R. 858
Hayakawaand I. Toyoshima, K. *see* Mizuno, S. 950
Hayashi, T. *see* Leung, K.T. 202
Hayden, B.E. 744
He, P. 948
Head-Gordon, M. 507
Heath, J.R. *see* Kroto, H. 895
Hebard, A.F. 894
Hebenstreit, J. 282
Hebenstreit, J. *see* Alves, J.L.A. 196
Hecht, M.H. 858
Hecht, M.H. *see* Bell, L.D. 856
Hecht, M.H. *see* Kaiser, W.J. 858
Heckenkamp, C. *see* Schäfers, F. 666
Hedin, L. 88, 200, 243, 282, 507, 744, 948, 986
Hedin, L. *see* Barth, U.V. 662
Hedin, L. *see* von Barth, J. 91
Heer, R. 858
Heiland, W. *see* Müller, N. 666
Heilmann, P. 88
Heim, D.E. *see* Tsang, C.H. 667
Heimann, P. 507, 948
Heimann, P. *see* Eastman, D.E. 429, 857
Heimann, P. *see* Himpsel, F.J. 200, 429
Heimann, P. *see* Schneider, C. 746
Heimann, P. *see* van der Veen, J.F. 510
Heine, V. 354, 507, 858
Heine, V. *see* Chan, S.-K. 505
Heine, V. *see* Cheng, C. 198
Heine, V. *see* Cohen, M.L. 87
Heine, V. *see* Payne, M.C. 355
Heine, V. *see* Robertson, I.J. 355
Heinemann, M. *see* Hebenstreit, J. 282

Heinrich, B. 664, 948
Heinrich, B. *see* Celinski, Z. 947
Heinrich, B. *see* Schmid, A.K. 667
Heinrich, M. *see* Ebert, Ph. 199, 429
Heinrichsmeier, M. 243, 507
Heinrichsmeier, M. *see* Eguiluz, A.G. 243
Heinz, K. *see* Chubb, S.R. 743
Heinz, K. *see* Heilmann, P. 88
Heinz, K. *see* Müller, K. 950
Heinz, K. *see* Reuter, K. 860
Heinz, K. *see* Schardt, J. 205
Heinz, K. *see* Starke, U. 206, 746
Heinz, T.F. 381
Heinzmann, U. *see* Irmer, N. 664
Heinzmann, U. *see* Schmiedeskamp, B. 667
Heinzmann, U. *see* Schäfers, F. 666
Helbig, R. *see* Pensl, G. 204, 430
Held, G. *see* Lindroos, M. 354
Held, G. *see* Narloch, B. 355
Hellner, L. *see* Dujardin, G. 894
Hellsing, B. *see* Carlsson, A. 947
Hellwege, K.-H. 200
Hellwig, C. *see* Paggel, J.J. 430
Helman, J.S. 664
Hemmen, R. 948
Henderson, G.N. 858
Hengsberger, M. *see* Finteis, T. 429
Henk, J. 200, 664
Henk, J. *see* Feder, R. 664
Henk, J. *see* Olde, J. 204
Henk, J. *see* Rampe, A. 666
Henk, J. *see* Scheunemann, T. 666
Henn, G. *see* Kulakov, M.A. 202
Hennig, D. 354
Hennig, D. *see* Andersen, J.N. 353
Hennig, D. *see* Methfessel, M. 244, 354
Henzler, M. 744, 894
Henzler, M. *see* Clabes, J. 856
Henzler, M. *see* Schulze, G. 283
Henzler, M. *see* Sinharov, S. 896
Herberg, W.-D. *see* Hillebrecht, F.U. 664
Herman, G.S. *see* Saiki, R.S. 746
Hermann, C. *see* Drouhin, H.J. 857
Hermann, K. 354, 744
Hermann, K. *see* Bagus, P.S. 353, 742
Hermann, K. *see* Batra, I.P. 742
Hermann, K. *see* Horn, K. 744
Hermanson, J. 664, 744
Hermanson, J. *see* Chen, Y. 428
Hermanson, J. *see* Heimann, P. 948
Hermanson, J. *see* Williams, G.P. 431
Hermanson, J. *see* Zhu, X.-Y. 668
Hermsmeier, B.D. *see* Stöhr, J. 90, 381, 667
Hernandez-Calderon, I. *see* Höchst, H. 200, 429
Herpin, A. 664
Herzberg, G. 744
Heskett, D. 243, 744, 948
Heskett, D. *see* DePaola, R.A. 743
Heskett, D. *see* Eberhardt, W. 743
Heskett, D. *see* Frank, H.-J. Sagner 506
Heskett, D. *see* Frank, K.-H. 948
Heskett, D. *see* Freund, H.-J. 743, 986
Heskett, D. *see* Greuter, F. 744
Heskett, D. *see* Shi, X. 950
Heskett, D. *see* Song, K.J. 950
Heskett, D. *see* Tang, D. 510, 951
Heslinga, D.R. 858
Hess, A.C. *see* Jaffe, J.E. 201
Hester, J.R. *see* Benesh, G.A. 505
Heuell, P. *see* Kulakov, M.A. 202
Heymann, G. *see* Ludwig, H. 859
Hibma, T. *see* Heslinga, D.R. 858
Hibma, T. *see* Weitering, H.H. 861
Hicks, J.M. *see* Urbach, L.E. 951
Hidaka, H. *see* Hiratani, Y. 894
Hidaka, H. *see* Taneya, M. 897
Higashi, G.S. 282, 894
Higashi, G.S. *see* Burrows, V.A. 281, 856
Higashi, G.S. *see* Chabal, Y.J. 281
Higashi, G.S. *see* Dumas, P. 281
Hijiya, S. *see* Ito, T. 895
Hildner, M.L. 507
Hill, A.G. 986
Hill, D.M. *see* Xu, F. 861
Hillebrands, B. 664
Hillebrecht, F.U. 664
Hillebrecht, F.U. *see* Jungblut, R. 665
Hillebrecht, F.U. *see* Roth, C. 666
Himpsel, F.J. 200, 243, 381, 429, 507, 664, 858, 894, 948
Himpsel, F.J. *see* Batra, I.P. 428
Himpsel, F.J. *see* Chiang, T.-C. 198, 428
Himpsel, F.J. *see* Drube, W. 198, 429
Himpsel, F.J. *see* Eastman, D.E. 199, 429, 857, 894
Himpsel, F.J. *see* Eberhardt, W. 380, 663
Himpsel, F.J. *see* Fauster, Th. 894

Himpsel, F.J. *see* Feibelman, P.J. 380, 506
Himpsel, F.J. *see* Fischer, R. 243, 948
Himpsel, F.J. *see* Giesen, K. 243, 948
Himpsel, F.J. *see* Heinz, T.F. 381
Himpsel, F.J. *see* Hollinger, G. 894
Himpsel, F.J. *see* Jung, T. 381
Himpsel, F.J. *see* Kaxiras, E. 895
Himpsel, F.J. *see* Knapp, J.A. 381, 508
Himpsel, F.J. *see* Landgren, G. 895
Himpsel, F.J. *see* Ludeke, R. 859
Himpsel, F.J. *see* Magnusson, K.O. 430
Himpsel, F.J. *see* Morar, J.F. 203
Himpsel, F.J. *see* Ortega, J.E. 204, 666, 950
Himpsel, F.J. *see* Rader, O. 355
Himpsel, F.J. *see* Schmeisser, D. 896
Himpsel, F.J. *see* Schnell, R.D. 205, 896
Himpsel, F.J. *see* Schäffler, F. 860
Himpsel, F.J. *see* Straub, D. 206, 244, 431, 951
Himpsel, F.J. *see* Terminello, L.J. 381
Himpsel, F.J. *see* van der Veen, J.F. 510
Hinarejos, J.J. *see* Chrost, J. 894
Hinch, B.J. *see* Rohlfing, D.M. 205
Hinkel, V. *see* Middelmann, H.-U. 430
Hinkel, V. *see* Sorba, L. 206, 431
Hinkel, V. *see* Wilke, W.G. 431
Hirabayashi, K. 200
Hiratani, Y. 894
Hirayama, T. *see* Dujardin, G. 894
Hirsch, G. 200
Hirsch, J.E. *see* Tang, S. 510
Hirschmugl, C.J. 507
Hirschorn, E. 429
Hirschorn, E. *see* Samsavar, A. 90
Hirschwald, W. *see* Grunze, M. 744
Hiskes, J.R. 88
Hiskes, J.R. *see* Wimmer, E. 91, 510
Hjeemberg, H. *see* Lundquist, B.I. 745
Hjelmberg, H. 354, 744
Hjelmberg, H. *see* Gunnarsson, O. 948
Ho, G.H. *see* Chen, C.T. 87, 663
Ho, K.M. 88, 282
Ho, K.M. *see* Ding, Y.J. 281
Ho, K.M. *see* Larsen, P.K. 895
Ho, K.M. *see* Louie, S.G. 89, 202
Ho, K.M. *see* Schlüter, M. 896
Ho, K.M. *see* Wang, X.W. 510
Ho, P.S. *see* Liehr, M. 858
Ho, W. *see* Stroscio, J.A. 746, 951
Höchst, H. 200, 429
Höchst, H. *see* Niles, D.W. 381
Hoeven, A.J. *see* Aarts, J. 196, 428
Höfer, U. 744, 894
Höfer, U. *see* Morgen, P. 895
Hoffmann, F. *see* Graham, A.P. 948
Hoffmann, F.M. *see* DePaola, R.A. 743
Hoffmann, F.M. *see* Eberhardt, W. 743
Hoffmann, F.M. *see* Heskett, D. 744
Hoffmann, F.M. *see* Hirschmugl, C.J. 507
Hoffmann, F.M. *see* Peden, C.H.F. 355
Hoffmann, F.M. *see* dePaola, R.A. 947
Hoffmann, M. *see* Jalochowski, M. 949
Hoffmann, R. 354
Hoffmann, R. *see* Schubert, B. 896
Hoflund, G. *see* Jensen, E. 507, 986
Hofmann, M. 664
Hofmann, M. *see* Chrobok, G. 663
Hofmann, P. 354, 744
Hofmann, Ph. *see* Surman, M. 746
Hofmann, Ph. *see* Stampfl, A.P.J. 431
Hohenberg, P. 88, 200, 282
Hohlfeld, A. *see* Horn, K. 507, 744, 948
Hohlneicher, G. *see* Saddei, D. 746
Holczer, K. 894
Holland, B.W. 88, 200
Holldack, K. *see* Schneider, C.M. 667
Hollering, M. 200
Hollering, M. *see* Graupner, R. 199, 429
Hollering, M. *see* Xue, J.Y. 431
Holling, P. *see* Horn, K. 744
Hollinger, G. 894
Hollinger, G. *see* Gallet, D. 282
Hollinger, G. *see* Himpsel, F.J. 381
Hollinger, G. *see* Morar, J.F. 203
Hollinger, G. *see* Schmeisser, D. 896
Hollins, P. *see* Horn, K. 507, 948
Hollins, P. *see* Kulkarni, S.K. 745
Hollins, P. *see* Tüshaus, M. 747
Holloway, S. *see* Darling, G.R. 353
Holloway, S. *see* Gadzuk, J.W. 743
Holmes, D.M. *see* Avery, A.R. 428
Holmes, M.I. 507
Holmström, S. 948
Hölzl, J. 243, 858
Holzwarth, N. *see* Plummer, E.W. 746
Hong, S.C. *see* Chung, J.W. 505
Hong, S.C. *see* Shin, K.S. 509
Hopkinson, J.F.L. 243
Hopster, H. 664

Hopster, H. *see* Abraham, D.L. 662
Hopster, H. *see* Alvarado, S.F. 662
Hopster, H. *see* Falicov, L.M. 87
Hopster, H. *see* Kämper, K.-P. 665
Hopster, H. *see* Pappas, D.P. 666
Hopster, H. *see* Walker, T.G. 668
Horikoshi, Y. *see* Yamaguchi, H. 431
Horinaka, H. *see* Nakanishi, T. 666
Horn, G. *see* Horsky, T.N. 200
Horn, K. 354, 381, 507, 744, 858, 948
Horn, K. *see* Alonso, M. 855
Horn, K. *see* Barman S.R. 197, 428
Horn, K. *see* Batra, I.P. 742
Horn, K. *see* Chassé, T. 428
Horn, K. *see* Cimino, R. 856
Horn, K. *see* Ding, S.-A. 428
Horn, K. *see* Eberhardt, W. 243, 663
Horn, K. *see* Evans, D.A. 857
Horn, K. *see* Gadzuk, J.W. 743
Horn, K. *see* Heskett, D. 948
Horn, K. *see* Hofmann, P. 354, 744
Horn, K. *see* Magnusson, K.O.M. 430
Horn, K. *see* Mariani, C. 745
Horn, K. *see* McLean, A.B. 859
Horn, K. *see* Middelmann, H.-U. 430
Horn, K. *see* Neuhold, G. 430, 950
Horn, K. *see* Paggel, J.J. 430
Horn, K. *see* Piancastelli, M.N. 430
Horn, K. *see* Scheffler, M. 355
Horn, K. *see* Sorba, L. 206, 431
Horn, K. *see* Wilke, W.G. 431
Horn-von Hoegen, M. 894
Horng, S.F. *see* Kahn, A. 858
Horsch, P. *see* von der Linden, W. 207
Horsky, T.N. 200
Hoshino, T. *see* Tsuda, M. 283
Hott, R. 200
Hou, Y. *see* Anno, M. 86
Houzay, F. *see* Moison, J.M. 859
Houzay, F. *see* Solal, F. 206
Hoving, W. *see* Purcell, S.T. 666
Hoyland, M.A. *see* van der Laan, G. 91, 667
Hrbek, J. *see* dePaola, R.A. 947
Hricovini, K. 200, 282
Hricovini, K. *see* Aristov, V.Yu. 428
Hricovini, K. *see* Boeglin, C. 662
Hricovini, K. *see* Le Lay, G. 858
Hricovini, K. 895
Hsieh, T.C. 507
Hsieh, T.C. *see* Wachs, A.L. 207, 951
Hsiung, L.M. *see* Jimenez, J.R. 858
Hu, P. 354
Hu, P. *see* Alavi, A. 352
Hu, W.Y. *see* Tong, S.Y. 206
Huang, D. *see* Uchida, H. 861
Huang, H. *see* Tong, S.Y. 206, 431
Huang, J.S.T. *see* Pohm, A.V. 666
Huang, J.Y. *see* Chin, R.P. 198
Huang, K. *see* Born, M. 353
Huang, K.-G. *see* Zegenhagen, J. 91
Huang, M.-Z. 200
Huang, T. *see* Fernandez, A. 857
Huang, T. *see* Hallen, H.D. 857
Hubbard, J. 664, 986
Huber, D.L. *see* Ching, Y.W. 505
Huber, W. 744
Huber, W. *see* Eiding, J. 743
Huber, W. *see* Steinrück, H.-P. 746
Huber, W. *see* Weinelt, M. 747
Hudeczek, E. *see* Wurth, W. 747
Huff, W.R.A. 429
Hüfner, S. 429, 664, 895
Hüfner, S. *see* Courths, R. 243, 743, 947
Hüfner, S. *see* Finteis, T. 429
Hughes, G. *see* Ludeke, R. 859
Hughes, G. *see* Morar, J.F. 203
Hughes, G. *see* Moriarty, P. 895
Hughes, G. *see* Schäffler, F. 860
Huijser, A. 200, 429, 858
Huijser, A. *see* van Laar, J. 207
Hulbert, S.L. 507
Hulbert, S.L. *see* Weinert, M. 510
Hulbert, S.L. *see* Woodruff, D.P. 245
Hulpke, E. 507, 948
Hulpke, E. *see* Ernst, H. 506
Hulpke, E. *see* Ernst, H.-J. 506
Humphreys, T.P. 200
Hund, F. 744
Hünlich, K. *see* Oepen, H.P. 666
Huodo, S. *see* Hashizume, T. 507
Hurych, Z. *see* Seabury, C.W. 746
Hüsken, H. *see* Käckell, P. 199
Hussain, I. *see* Leung, K.T. 202
Hutter, J. *see* Alavi, A. 352
Hwang, I.-S. *see* Ganz, E. 199
Hwu, Y. *see* Mao, D. 859
Hybertsen, M.S. 88, 200, 282

Hybertsen, M.S. *see* Becker, R.S. 86, 281
Hybertsen, M.S. *see* Northrup, J.E. 203, 283, 430, 987
Hybertsen, M.S. *see* Pasquarello, A. 896
Hybertson, M.S. 507
Hybertson, M.S. *see* Northrup, J.E. 509

Iarlori, S. 200
Ibach, H. 507, 664, 895, 948
Ibach, H. *see* Backes, U. 428
Ibach, H. *see* Daun, W. 947
Ibach, H. *see* Hannon, J.B. 948
Ibach, H. *see* Klünker, C. 949
Ibach, H. *see* Lehwald, S. 949
Ibach, H. *see* Rowe, J. 430
Ibach, H. *see* Stuhlmann, C. 206, 951
Ibach, H. *see* Szeftel, J.M. 746
Ichimiya, A. *see* Hashizume, T. 200
Ichinokawa, T. *see* Schmid, A.K. 667
Ide, T. 88
Ide, T. *see* Hashizume, T. 507
Ide, Y. *see* Tone, K. 897
Idzerda, Y.U. 88, 664
Idzerda, Y.U. *see* Chen, C.T. 87, 663
Idzerda, Y.U. *see* Hillebrecht, F.U. 664
Ignatiev, A. *see* Jona, F. 88
Ignatiev, A. *see* Lee, B.W. 89
Ihm, J. 88, 200, 201, 282, 429, 858
Illing, G. *see* Wambach, J. 747
Ilver, L. *see* Håkansson, M.C. 429
Ilver, L. *see* Qu, H. 205
Ilver, L. *see* Ölsson, L.Ö. 430
Imbihl, R. *see* Demuth, J.E. 857
Imer, J.-M. *see* Patthey, F. 987
Imry, Y. *see* Lang, N.D. 858
In-Whan, Lyo 948
In-Whan, Lyo *see* Avouris, Ph. 380
Incoccia, L. 895
Indelkofer, G. *see* Aristov, V.Yu. 428
Indlekofer, G. *see* Hricovini, K. 200, 282
Inglesfield, J.E. 88, 201, 243, 429, 507
Inglesfield, J.E. *see* Aers, G.C. 243
Inglesfield, J.E. *see* Benesh, G. 86, 197, 243, 505
Inglesfield, J.E. *see* Campuzano, J.C. 505
Inglesfield, J.E. *see* Nekovee, M. 244, 666
Inglesfield, J.E. *see* Schep, K.M. 244
Inglesfield, J.E. *see* van Hoof, J.B.A.N. 510
Inkson, J.C. 858
Ino, S. *see* Ma, Y. 202
Irmer, N. 664
Irmer, N. *see* Schmiedeskamp, B. 667
Ishida, H. 282, 507, 744, 948, 949
Ishida, H. *see* Shi, X. 950
Ishihara, N. *see* Nakanishi, S. 203
Ishii, T. *see* Chung, J.W. 505
Ishii, T. *see* Kakizaki, A. 665
Ishii, T. *see* Shin, K.S. 509
Ishikawa, H. *see* Ito, T. 895
Ishizawa, Y. *see* Anno, M. 86
Itchkawitz, B.S. 986
Ito, T. 895
Itoh, H. *see* Schmid, A.K. 667
Ivanov, I. 201
Ivanov, I. *see* Göpel, W. 199
Ivanov, P.A. 201
Iwami, M. *see* Tromp, R.M. 207
Iwan, M. *see* Mariani, C. 745
Iwata, S. *see* Kimura, K. 744
Iwatsuki, M. *see* Tochihara, H. 206

Jackson, J.D. 664
Jackson, K.A. *see* Perdew, J.P. 89
Jackson, M.D. *see* Thornton, J.M.C. 206
Jackson, T.N. *see* Woodall, J.M. 861
Jackson, W.D. 858
Jacob, P. *see* Gsell, M. 354
Jacob, W. 243, 507, 744, 949
Jacobi, K. 354
Jacobi, K. *see* Bertolo, M. 742
Jacobi, K. *see* Drathen, P. 429
Jacobi, K. *see* He, P. 948
Jacobi, K. *see* Hoffmann, P. 354
Jacobi, K. *see* Horn, K. 744
Jacobi, K. *see* Kübler, B. 202
Jacobi, K. *see* Ranke, W. 205, 896
Jacobi, K. *see* Zwicker, G. 208
Jacoboni, C. 858
Jacobsen, K.W. *see* Christensen, O.B. 353
Jacobsen, K.W. *see* Hammer, B. 354
Jacobsen, K.W. *see* Pleth Nielsen, L. 355
Jaeger, H.M. *see* Orr, B.G. 950
Jaffe, J.E. 201
Jager, K. *see* Purcell, S.T. 666
Jahns, V. *see* Rossmann, R. 205
Jaklevic, R.C. 949
Jakob, P. 744, 895
Jakob, P. *see* Kostov, K.L. 354

Jakob, P. *see* Schiffer, A. 355
Jakubith, S. *see* Rotermund, H.H. 381
Jalochowski, M. 949
Jamet, M. *see* Dujardin, G. 894
Jamison, K. *see* Rau, C. 666
Janak, J.F. 88, 354
Janak, J.F. *see* Moruzzi, V. 244, 665
Janda, K.C. *see* Sinniah, K. 283
Janietz, P. *see* Ludwig, H. 859
Janowitz, C. 201, 429
Janowitz, C. *see* Anderson, R.O. 986
Janowitz, C. *see* Claessen, R. 505, 986
Janowitz, C. *see* Henk, J. 200
Janowitz, C. *see* Manzke, R. 203, 430
Jansen, H.J.F. 88
Jansen, H.J.F. *see* Li, C. 89
Jardim, R.F. *see* Anderson, R.O. 986
Jaros, M. 858
Jaskolski, W. 949
Jaussaud, C. *see* Semond, F. 205
Jayaram, G. 201
Jedrecy, N. 201
Jedrecy, N. *see* Sauvage-Simkin, M. 205
Jenkins, S.J. 207
Jennings, P.J. 244, 354
Jennings, P.J. *see* Jones, R.O. 244, 949
Jensen, E. 507, 744, 986
Jensen, E. *see* Bartynski, R.A. 505
Jensen, E. *see* Seaburg, C.W. 746
Jensen, V. 88
Jeong, K. 507
Jeong, K. *see* Gaylord, R.H. 506
Jeong, S. *see* Cho, J. 198
Jepsen, D.W. *see* Demuth, I.E. 743
Jepsen, D.W. *see* Jona, F. 88
Jepsen, D.W. *see* Shih, H.D. 206
Jepsen, D.W. *see* Spanjaard, D. 509
Jepsen, O. *see* Jones, R.O. 244
Jezequel, G. *see* Ludeke, R. 859
Jezequel, G. *see* Solal, F. 206
Jiang, P.Z. *see* Olson, C.G. 987
Jimenez, J.R. 858
Jimenez, J.R. *see* Lee, E.Y. 858
Jin, C. *see* Rau, C. 666
Jing, Z. 201
Joachim, C. *see* Soukiassian, P. 206
Joannopoulos, J.D. *see* Alerhand, O.L. 281
Joannopoulos, J.D. *see* Brommer, K.D. 197, 281, 428
Joannopoulos, J.D. *see* Cho, K. 198, 281
Joannopoulos, J.D. *see* Ihm, J. 201, 429
Joannopoulos, J.D. *see* Kaxiras, E. 201, 282
Joannopoulos, J.D. *see* Lee, D.H. 202
Joannopoulos, J.D. *see* Mele, E.J. 859
Joannopoulos, J.D. *see* Needels, M. 203
Joannopoulos, J.D. *see* Payne, M.C. 89, 204, 355
Johal, T. *see* Dudzik, E. 894
Johansson, A. *see* Hedin, L. 200
Johansson, B. 949
Johansson, B. *see* Aldén, M. 504
Johansson, B. *see* Rosengren, A. 950
Johansson, H.I.P. *see* Johansson, L.I. 507
Johansson, L.I. 201, 507
Johansson, L.I. *see* Allen, J.W. 947
Johansson, L.S.O. 201, 282, 429, 895
Johansson, L.S.O. *see* Bullock, E.L. 197
Johansson, L.S.O. *see* Dudde, R. 947
Johansson, L.S.O. *see* Håkansson, M.C. 429
Johansson, L.S.O. *see* Karlsson, C.J. 895
Johansson, L.S.O. *see* Landemark, E. 202
Johansson, P. 507
John, P. *see* Hsieh, T.C. 507
Johnson, D.L. 201
Johnson, M.T. *see* Purcell, S.T. 666
Johnson, P.D. 244, 507, 664, 665, 949
Johnson, P.D. *see* Brookes, N.B. 663, 947
Johnson, P.D. *see* Garrison, K. 664, 948
Johnson, P.D. *see* Hulbert, S.L. 507
Johnson, P.D. *see* Li, D. 949
Johnson, P.D. *see* Smith, N.V. 667, 950
Johnson, P.D. *see* Weinert, M. 510
Johnson, P.D. *see* Woodruff, D.P. 245
Johnson, R.L. *see* Bohr, J. 197
Johnson, R.L. *see* Feidenhans'l, R. 199
Jona, F. 88, 895
Jona, F. *see* Barker, R.A. 505
Jona, F. *see* Batra, I.P. 428
Jona, F. *see* Himpsel, F.J. 200
Jona, F. *see* Shih, H.D. 206
Jona, F. *see* Yang, W.S. 91, 208
Jones, G.R. *see* Farrow, R.F.C. 429
Jones, H. 744
Jones, R.G. *see* Kerkar, M. 949
Jones, R.O. 201, 244, 949
Jones, R.O. *see* Gunnarsson, O. 199
Jones, R.O. *see* Jennings, P.J. 244
Jones, T.S. 744

Jones, T.S. *see* Avery, A.R. 428
Jones, W. 507
Jones, W. *see* Mott, N.F. 508
Jonker, B.T. 949
Jonker, B.T. *see* Idzerda, Y.U. 664
Jónsson, H. *see* Yan, H. 208
Joo, F. *see* Neuhaus, D. 509
Jordon, J.L. *see* Morar, J.F. 203
Jorgensen, W.L. 744
Joshi, A.W. *see* Jones, T.S. 744
Joshua, S.J. 665
Jostell, U. *see* Andersson, S. 947
Joyce, B.A. *see* Avery, A.R. 428
Joyce, B.A. *see* Larsen, P.K. 202, 430
Joyce, J.J. *see* Weaver, J.H. 861
Joyce, J.J. *see* Xu, F. 861
Joyce, K. 508
Joyce, S.A. *see* Whitman, L.J. 897
Jszeftel, M. *see* Lehwald, S. 949
Jugnet, Y. *see* Guillot, C. 506
Jugnet, Y. *see* Landgren, G. 895
Jung, Ch. *see* Paggel, J.J. 430
Jung, T. 381
Jungblut, R. 665
Jungblut, R. *see* Hillebrecht, F.U. 664
Jusko, O. *see* Moriarty, P. 895

Kachel, T. *see* Carbone, C. 663
Kachel, T. *see* Clemens, W. 947
Kachel, T. *see* Vescovo, E. 245
Käckel, P. *see* Wenzien, B. 207
Käckell, P. 199, 201
Käckell, P. *see* Wenzien, B. 207, 208
Kadanoff, L.P. *see* Baym, G. 986
Kádas, K. 201
Kadowaki, T. *see* Mizuno, S. 950
Kafader, U. *see* Sirringhaus, H. 860
Kahn, A. 201, 429, 858
Kahn, A. *see* Duke, C.B. 198, 281
Kahn, A. *see* Horsky, T.N. 200
Kahn, A. *see* Mao, D. 859
Kahn, A. *see* Meyer, R.J. 203
Kahn, A. *see* Stiles, K. 861
Kahn, A. *see* Wang, Y.R. 207, 431
Kahn, A. *see* Wu, C.I. 431
Kahng, D. *see* Sze, S.M. 861
Kaindl, G. *see* Bauer, A. 856
Kaindl, G. *see* Bode, S. 662
Kaindl, G. *see* Chiang, T.C. 742
Kaindl, G. *see* Cuberes, M.T. 857
Kaindl, G. *see* Prietsch, M. 860
Kaindl, G. *see* Starke, K. 667
Kaiser, W.J. 858
Kaiser, W.J. *see* Bell, L.D. 856
Kaiser, W.J. *see* Hecht, M.H. 858
Kaiser, W.J. *see* Henderson, G.N. 858
Kaiser, W.J. *see* Stroscio, J.A. 381, 896
Kakizaki, A. 665
Kakizaki, A. *see* Chung, J.W. 505
Kakizaki, A. *see* Shin, K.S. 509
Kalkoffen, G. *see* Eberhardt, W. 87
Kalla, R. *see* Pollmann, J. 204
Kalning, M. *see* Claessen, R. 986
Kamaratos, M. *see* Papageorgopoulos, A. 896
Kamata, A. *see* Kakizaki, A. 665
Kambe, K. 354
Kambe, K. *see* Hoffmann, P. 354
Kambe, K. *see* Jacobi, K. 354
Kambe, K. *see* Scheffler, M. 355
Kambe, K. *see* Stampfl, C. 356
Kamiya, I. *see* Hasegawa, Y. 507
Kamiya, I. *see* Hashizume, T. 507
Kamiya, Y. *see* Nakanishi, T. 666
Kampen, T.U. *see* Stockhausen, A. 896
Kämper, K.-P. 665
Kämper, K.-P. *see* Pappas, D.P. 666
Kane, E.O. 949
Kaneda, G. *see* Huff, W.R.A. 429
Kang, M.H. *see* Cho, J. 198
Kanski, J. *see* Håkansson, M.C. 429
Kanski, J. *see* Khazmi, Y. 430
Kanski, J. *see* Qu, H. 205, 430
Kanski, J. *see* Ölsson, L.Ö. 430
Kao, C.-T. *see* Mate, C.M. 745
Kao, C.M. 744
Kao, C.M. *see* Freund, H.-J. 743
Kao, C.T. *see* Asscher, M. 742
Kao, T.W. *see* Anderson, C.L. 855
Kaplan, R. 201
Kaplan, R. *see* Bermudez, V.M. 197
Kar, N. 88
Karis, O. *see* Nilsson, A. 355
Karlson, U.O. *see* Magnusson, K.O. 202
Karlsson, C.J. 429, 895
Karlsson, C.J. *see* Landemark, E. 202, 282, 430
Karlsson, H. 429
Karlsson, U.O. 508
Karlsson, U.O. *see* Göthelid, M. 894

Karlsson, U.O. *see* Håkansson, M.C. 429
Karlsson, U.O. *see* Karlsson, C.J. 895
Karlsson, U.O. *see* Karlsson, H. 429
Karlsson, U.O. *see* Khazmi, Y. 430
Karlsson, U.O. *see* LeLay, G. 430
Karlsson, U.O. *see* Magnusson, K.O. 430
Karlsson, U.O. *see* Nicholls, J.M. 203
Karlsson, U.O. *see* Qu, H. 205, 430
Karlsson, U.O. *see* Uhrberg, R.I.G. 207
Karlsson, U.O. *see* Ölsson, L.Ö. 430
Karnatak, R. *see* van der Laan, G. 91, 667
Karo, A. *see* Hiskes, J.R. 88
Karo, A.M. *see* Wimmer, E. 91, 510
Kaschner, R. *see* Finnis, M.W. 353
Kaski, K. 508
Kaski, K. *see* Rikvold, P.A. 509
Katayama, Y. *see* Tone, K. 897
Katnani, A.D. 201
Katnani, A.D. *see* Brillson, L.J. 856
Kato, I. *see* Ito, T. 895
Kato, T. *see* Nakanishi, T. 666
Katrich, G.A. 508
Katsumata, S. *see* Kimura, K. 744
Kauffmann, R.L. *see* Feldman, L.C. 87
Kaukasoina, P. *see* Fischer, D. 948
Kaukasoina, P. *see* Seyller, T. 355
Kaurila, T. *see* Uhrberg, R.I.G. 431
Kavanagh, K.L. *see* Talin, A.A. 861
Kavanagh, K.L. *see* Woodall, J.M. 861
Kawabe, M. 895
Kawabe, M. *see* Yong, J.C. 897
Kawabe, U. *see* Yamamoto, S. 861
Kaxiras, E. 88, 201, 282, 895
Kaxiras, E. *see* Alerhand, O.L. 281
Kaxiras, E. *see* Avouris, Ph. 380, 893
Kaxiras, E. *see* Lyo, I.W. 895
Kay, E. *see* Mauri, D. 665
Kaya, S. 665
Kelemen, S.R. 744
Kelly, M. *see* Chiaradia, P. 856
Kelly, M.K. *see* Brillson, L.J. 856
Kelly, P.J. *see* Ramstad, A. 205
Kelly, P.J. *see* Schep, K.M. 244
Kempa, K. 949
Kempa, K. *see* Tsuei, K.-D. 381
Kendelewicz, T. *see* Cao, R. 856
Kendelewicz, T. *see* Miyano, K.E. 859
Kendelewicz, T. *see* Newmann, N. 859
Kendelewicz, T. *see* Petro, W.G. 860
Kendelewicz, T. *see* Richter, M. 90
Kendelewicz, T. *see* Spicer, W.E. 861
Kennedy, P.J. *see* Hofmann, M. 664
Kent, A. *see* Niedermann, P. 860
Kerkar, M. 949
Kerker, G. 88
Kern, G. 201
Kern, K. 508
Kesmodel, L.L. *see* Mohamed, M.H. 950
Kesmodel, L.L. *see* Shen, Y. 950
Kessler, J. 665, 744
Kevan, S.D. 201, 244, 381, 430, 508, 949, 986
Kevan, S.D. *see* Dhar, S. 505
Kevan, S.D. *see* Di, W. 505
Kevan, S.D. *see* Elliott, G.S. 506
Kevan, S.D. *see* Gaylord, R.H. 506
Kevan, S.D. *see* Jeong, K. 507
Kevan, S.D. *see* Kneedler, E. 508
Kevan, S.D. *see* Peterson, L.D. 509
Kevan, S.D. *see* Rotenberg, E. 509
Kevan, S.D. *see* Smith, K.E. 509
Kevan, S.D. *see* Tersoff, J. 510
Kevan, S.D. *see* Wei, D.-S. 510
Kevan, S.D. 744
Khazmi, Y. 430
Kienle, P. *see* Schütz, G. 90, 667
Kikuchi, A. 858
Kilcoyne, A.L.D. *see* Woodruff, D.P. 747
Kilday, D. *see* Brillson, L.J. 856
Kilday, D. *see* Chiaradia, P. 856
Kilday, D.G. *see* Kahn, A. 858
Kilday, D.G. *see* Stiles, K. 861
Kim, C.Y. *see* Chung, J.W. 505
Kim, C.Y. *see* Shin, K.S. 509
Kim, H.J. *see* Davis, R.F. 198
Kim, H.W. *see* Chung, J.W. 505
Kim, J. *see* Fu, J. 282
Kim, J.S. *see* Mohamed, M.H. 950
Kim, J.S. *see* Shen, Y. 950
Kim, Y.D. 354
Kimura, K. 744
Kincaid, B.M. *see* Zegenhagen, J. 91
King, D. *see* Benesh, G.A. 947
King, D.A. 508, 895
King, D.A. *see* Campuzano, J.C. 505
King, D.A. *see* Debe, M.K. 87, 505
King, D.A. *see* Hofmann, P. 744
King, D.A. *see* Hu, P. 354
King, D.A. *see* Marsh, F.S. 89

King, D.A. *see* Surmann, M. 746
King-Smith, D. *see* Li, Y.S. 89
King-Smith, R.D. *see* Štich, I. 206, 283, 431
Kingdom, K.H. 88, 745
Kinoshita, T. *see* Chung, J.W. 505
Kinoshita, T. *see* Hillebrecht, F.U. 664
Kinoshita, T. *see* Kakizaki, A. 665
Kinoshita, T. *see* Shin, K.S. 509
Kinzel, W. *see* Kaski, K. 508
Kinzler, M. *see* Schneider, C.M. 667
Kipp, L. 201, 430
Kipp, L. *see* Janowitz, C. 201, 429
Kipp, L. *see* Olde, J. 204
Kipp, L. *see* Skibowski, M. 206
Kipp, L. *see* Traving, M. 431
Kirchner, E.J.J. 282
Kirchner, P.D. *see* Pashley, M.D. 204, 283
Kirkpatrick, S. *see* Velicky, B. 510
Kirschner, J. 88, 665
Kirschner, J. *see* Baumgarten, L. 86, 662
Kirschner, J. *see* Ebert, H. 663
Kirschner, J. *see* Fahsold, G. 663
Kirschner, J. *see* Feder, R. 87
Kirschner, J. *see* Gao, X. 664
Kirschner, J. *see* Heinrich, B. 948
Kirschner, J. *see* Kuch, W. 665
Kirschner, J. *see* Oepen, H.P. 666
Kirschner, J. *see* Plihal, M. 666
Kirschner, J. *see* Schmid, A.K. 667
Kirschner, J. *see* Schneider, C.M. 667
Kirschner, J. *see* Venus, D. 668
Kirz, J. *see* Ade, H. 380
Kishida, S. *see* Nakanishi, S. 203
Kisker, E. 381, 665
Kisker, E. *see* Carbone, C. 663
Kisker, E. *see* Feder, R. 664
Kisker, E. *see* Hillebrecht, F.U. 664
Kisker, E. *see* Jungblut, R. 665
Kisker, E. *see* Roth, C. 666
Kisker, E. *see* Tillmann, D. 667
Kiskinova, M. 745
Kittel, C. *see* Ruderman, M.A. 509
Klapwijk, T.M. *see* Heslinga, D.R. 858
Kläsges, R. *see* Rader, O. 355
Klaua, M. *see* Beckmann, A. 947
Klauser, R. 745
Klauser, R. *see* Hayden, B.E. 744
Klebanoff, L.E. 665
Klein, B.M. *see* Wang, C.S. 207
Klein, C.A. 858
Kleinman, L. 201, 354
Kleinman, L. *see* Caruthers, E. 87, 505
Kleinman, L. *see* Euceda, A. 506
Kleinman, L. *see* Phillips, J.C. 283
Kleinman, L. *see* Zhu, M.J. 668
Kley, A. *see* Bockstedte, M. 353
Kleyn, A.W. 745
Kliese, R. 895
Klimov, V.V. *see* Katrich, G.A. 508
Klitsner, T. 201
Klitsner, T. *see* Becker, R.S. 86, 197
Klitsner, T. *see* Li, Y.S. 89
Klünker, C. 949
Klünker, C. *see* Hannon, J.B. 948
Klyachko, D.V. 895
Knapp, J.A. 201, 381, 508
Knapp, J.A. *see* Chiang, T.-C. 198
Knapp, J.A. *see* Eastman, D.E. 894
Kneedler, E. 508
Kneller, E. 665
Knoppe, H. *see* Jalochowski, M. 949
Kobayashi, H. *see* Edamoto, K. 894
Kobayashi, K. 201, 282, 895
Kobayashi, K.L.I. 858
Koch, E.E. 858
Koch, E.E. *see* Dudde, R. 743
Koch, E.E. *see* Heskett, D. 243, 948
Koch, E.E. *see* Karlsson, U.O. 508
Koch, E.E. *see* Magnusson, K.O. 202
Koch, E.E. *see* Nicholls, J.M. 203
Koch, J. *see* Conrad, H. 743
Kochanski, G.P. *see* Yang, S. 245, 951
Koel, B.E. 745
Koelling, D.C. *see* MacDonald, A.H. 89
Koelling, D.D. 88
Koelling, D.D. *see* Krakauer, H. 88
Koelling, D.D. *see* Posternak, M. 89
Koenders, L. *see* Moriarty, P. 895
Koenders, L. *see* Troost, D. 283, 861, 897
Kogan, S.M. *see* Smith, D.L. 860
Kohler, B. 508
Köhler, U. *see* Andersohn, L. 893
Köhler, U.K. *see* Hamers, R.J. 199
Kohlhepp, J. *see* Fritzsche, H. 664
Kohn, W. 88, 201, 282, 354, 508, 665
Kohn, W. *see* Hohenberg, P. 88, 200, 282
Kohn, W. *see* Lang, N. 89, 244, 354, 949, 986
Kohn, W. *see* Lau, K.H. 508

Koinuma, H. *see* Ebina, A. 199
Koke, P. 201, 895
Koke, P. *see* Goldmann, A. 199
Koke, P. *see* Mönch, W. 203
Kolac, U. *see* Donath, M. 243
Kolac, U. *see* Dose, V. 243, 663, 947
Kolac, U. *see* Jacob, W. 243, 507
Kolasinski, K.W. *see* Kubiak, G.D. 202
Kollin, E. *see* Zaera, F. 747
Komeda, T. *see* Anderson, S.G. 893
Komeda, T. *see* Seo, J.M. 896
Kometer, K. *see* Memmel, N. 745
Kong, H.S. *see* Davis, R.F. 198
König, U. *see* Redinger, J. 244
Kono, S. *see* Bullock, E.L. 197
Kono, S. *see* Enta, Y. 199, 429
Kono, S. *see* Huff, W.R.A. 429
Kono, S. *see* Yokotsuka, T. 208
Konrad, B. *see* Weser, T. 91
Köppel, H. 745
Koranda, S. *see* Stöhr, J. 90, 381, 667
Korecki, J. 665
Korringa, J. 88
Korte, U. *see* Nouvertné, F. 355
Kosterlitz, J.M. *see* Altmann, M. 504
Kostov, K.L. 354
Kotani, A. 665
Koutecky, J. 745
Kowalczyk, S.P. 858
Kowalczyk, S.P. *see* Kraut, E.A. 858
Kowalczyk, S.P. *see* Ley, L. 202
Krahn, D.R. *see* Pohm, A.V. 666
Krakauer, H. 88, 508
Krakauer, H. *see* Posternak, M. 89
Krakauer, H. *see* Singh, D. 90, 509
Krakauer, H. *see* Wang, D.-S. 668
Krakauer, H. *see* Wimmer, E. 91, 245, 668
Krakauer, H. *see* Yu, R. 91
Krasovski, E.E. *see* Traving, M. 431
Kraus, P. 895
Kraut, E.A. 858
Kraut, E.A. *see* Kowalczyk, S.P. 858
Krebs, J.J. *see* Idzerda, Y.U. 664
Kress, C. 201
Kresse, G. 354
Kresse, G. *see* Furthmüller, J. 199, 429
Kresse, G. *see* Käckell, P. 201
Kresse, G. *see* Kern, G. 201
Kreuzer, H.J. *see* Sommer, E. 509
Krill, G. *see* Boeglin, C. 662
Kroes, G.J. 354
Kroto, H. 895
Krueger, S. *see* Mönch, W. 203
Krüger, P. 88, 89, 201, 202, 244, 282, 430, 895
Krüger, P. *see* Hirsch, G. 200
Krüger, P. *see* Landemark, E. 202
Krüger, P. *see* Lu, W. 202
Krüger, P. *see* Pollmann, J. 204
Krüger, P. *see* Rohlfing, M. 205
Krüger, P. *see* Sabisch, M. 205
Krüger, P. *see* Schröer, P. 205
Krüger, P. *see* Vogel, D. 207
Krüger, P. *see* Wolfgarten, G. 208
Kruse, C. *see* Finnis, M.W. 353
Kuball, M. *see* Resch-Esser, U. 896
Kubby, J.A. 202
Kubby, J.A. *see* Soukiassian, P. 90
Kubiak, G.D. 202, 244, 949
Kubiak, G.D. *see* Hamza, A.V. 199
Kubiak, G.D. *see* Sowa, E.C. 206
Kübler, B. 202
Kübler, J. *see* Oppeneer, P.M. 89
Kubler, L. 895
Kubo, R. 89
Kubota, M. *see* Hasegawa, Y. 507
Kubota, M. *see* Hashizume, T. 507
Kubota, T. *see* Kobayashi, K. 895
Kubota, Y. *see* Nishijima, N. 895
Kuch, W. 665
Kuch, W. *see* Gao, X. 664
Kuch, W. *see* Schneider, C.M. 667
Kuch, W. *see* Venus, D. 668
Kudrnovský, J. *see* Ganduglia-Pirovano, M.V. 354
Kudrnovsky, J. *see* Turek, I. 667
Kuhlenbeck, H. 745
Kuhlenbeck, H. *see* Bartos, B. 742
Kuhlenbeck, H. *see* Freund, H.-J. 743
Kuhlenbeck, H. *see* Geisler, H. 743
Kuhlenbeck, H. *see* Odörfer, G. 745
Kuhr, H.J. *see* Ranke, W. 896
Kuhr, J.-C. *see* Olde, J. 204
Kuk, Y. *see* Bennet, P.A. 428
Kuk, Y. *see* Culbertson, R.J. 198
Kuk, Y. *see* Hasegawa, Y. 858
Kulakov, M.A. 202
Kulkarni, S.K. 745
Kunz, C. *see* Eberhardt, W. 87

Kunz, C. *see* Incoccia, L. 895
Küppers, F. *see* Grunze, M. 744
Küppers, J. *see* Conrad, H. 743
Küppers, J. *see* Ertl, G. 663, 743
Küppers, J. *see* Woratschek, B. 951
Kupsch, M. *see* Weidmann, R. 207
Kurtin, S. 858

La Bate, E.E. *see* Sze, S.M. 861
La Femina, J.P. 282
Lægsgaard, E. *see* Pleth Nielsen, L. 355
Lacharme, J.P. *see* Andriamanantenasoa, I. 86
Laegsgaard, E. *see* Pedersen, M.O. 355
LaFemina, J.P. 202
Lagally, M.G. *see* Ching, Y.W. 505
Lagally, M.G. *see* Wang, G.-C. 510
Lagraffe, D. *see* Dowben, P.A. 505
Lam, P.K. *see* Chou, M.Y. 986
Lam, P.K. *see* Yu, R. 747
Lam, S.C. 244
Lambe, J. *see* Jaklevic, R.C. 949
Lambeth, D.N. *see* Falicov, L.M. 87
Lambrecht, W.R. 202, 430
Lampel, G. *see* Drouhin, H.J. 857
Lamson, S.H. *see* Messmer, R.P. 745
Land, R.H. *see* Singwi, K.S. 987
Landemark, E. 202, 282, 430
Landemark, E. *see* Johansson, L.S.O. 429
Landemark, E. *see* Karlsson, C.J. 429, 895
Lander, J. 89, 202
Landgren, G. 895
Landgren, G. *see* Chiang, T.-C. 198
Landgren, G. *see* Ludeke, R. 859
Landman, U. *see* Barnett, R.N. 86
Landolt, M. 665
Landolt, M. *see* Allenspach, R. 662
Lang, J.K. 949
Lang, N. 89, 244, 354, 508, 745, 858, 949, 986
Lang, N. *see* Williams, A.R. 208
Lang, P. *see* Nordström, L. 666
Langenbach, E. *see* Kirschner, J. 665
Langlais, V. *see* Themlin, J.-M. 206
Langmuir, I. 354, 508, 745
Langmuir, I. *see* Kingdon, K.H. 88
Langmuir, I. *see* Taylor, J.B. 356
Langreth, D.C. 508
Langreth, D.C. *see* Zhang, Z.Y. 510
Lannoo, M. *see* Allan, G. 86
Lanza, C. *see* Woodall, J.M. 861
Laperashvili, T.A. 858
Lapeyre, G.J. 745
Lapeyre, G.J. *see* Chen, Y. 428
Lapeyre, G.J. *see* Kulkarni, S.K. 745
Lapeyre, G.J. *see* Schäfer, J.A. 896
Lapeyre, G.J. *see* Smith, R.J. 746
Lapeyre, G.J. *see* Williams, G.P. 208, 431
Lapeyre, G.P. *see* Knapp, J.A. 201
Lapiano-Smith, D.A. *see* Terminello, L.J. 381
Lapujoulade, J. *see* Salanon, B. 509
Larsen, P.K. 202, 430, 895
Larsen, P.K. *see* Aarts, J. 196, 428
Larson, B.E. *see* Brommer, K.D. 197, 281, 428
Lassabatere, L. 202
Lathiotakis, N.N. *see* Menon, M. 203
Latta, E.E. *see* Conrad, H. 743
Lau, K.H. 508
Lau, K.H. *see* Kohn, W. 354
Laubschat, C. *see* Bauer, A. 856
Laubschat, C. *see* Prietsch, M. 860
Laux, S.E. *see* Fischetti, M.V. 857
Le Goff, E. *see* Dujardin, G. 894
Le Goues, F.K. *see* Liehr, M. 858
Le Lay, G. 282, 858
Le Lay, G. *see* Aristov, V.Yu. 428
Le Lay, G. *see* Mao, D. 859
Le Tranh Vinh *see* Aristov, V.Yu. 428
Leatherman, G.S. *see* Adler, D.L. 947
Lecante, J. *see* Guillot, C. 506
Lecante, J. *see* Louie, S.G. 508
Lecante, J. *see* Soukiassian, P. 509, 951
Lecante, J. *see* Thiry, P. 431, 510
Leckey, R.C.G. 430
Leckey, R.C.G. *see* Xue, J.Y. 431
Leckey, R.C.G. *see* Zhang, X.D. 431
Lee, B.W. 89
Lee, B.W. *see* Duke, C.B. 198
Lee, C.L. *see* Lei, T.F. 858
Lee, D.H. 202
Lee, D.H. *see* Ihm, J. 201, 429
Lee, E.Y. 858
Lee, E.Y. *see* Kaiser, W.J. 858
Lee, E.Y. *see* Rubin, M.E. 860
Lee, E.Y. *see* Schowalter, L.J. 860
Lee, E.Y. *see* Sirringhaus, H. 860
Lee, J.T. *see* Schaich, W.L. 244
Lee, K.-H. *see* Park, C.H. 204
Lee, M.-H. *see* Hu, P. 354

Lee, S. *see* Li, D. 508
Lee, S.K. *see* Chung, J.W. 505
Lee, S.K. *see* Shin, K.S. 509
Leelaprute, S. *see* Car, R. 197
Legrand, B. 89
Legvold, S. 665
Lehwald, S. 949
Lehwald, S. *see* Szeftel, J.M. 746
Lei, T.F. 858
Leibsle, F.M. *see* Hirschorn, E. 429
Leibsle, F.M. *see* Samsavar, A. 90
LeLay, G. 430
LeLay, G. *see* Aristov, V.Yu. 428
Lelay, G. *see* Göthelid, M. 894
Lennard-Jones, J.E. 745
Leonard, D. *see* Sajoto, T. 860
Lepselter, M.P. *see* Andrews, J.M. 855
Lessor, D.L. *see* Horsky, T.N. 200
Leung, K.T. 202
Leung, W.-Y. *see* Schmitz, P.J. 667
Levi, A.F.J. *see* Tung, R.T. 861
Levine, J. 89, 282
Levine, J. *see* Davison, S.G. 505
Levinson, H.J. 244, 508, 949, 986
Levinson, H.L. 665
Levy, F. *see* Thiry, P. 431
Levy, M. *see* Perdew, J.P. 355
Lewis, L.B. *see* Sinniah, K. 283
Ley, L. 202
Ley, L. *see* Cardona, M. 856
Ley, L. *see* Graupner, R. 199, 429
Ley, L. *see* Hollering, M. 200
Ley, L. *see* Straub, D. 206, 431
Ley, L. *see* Xue, J.Y. 431
Ley, L. *see* Zhang, X.D. 431
Ley, R. *see* Hillebrecht, F.U. 664
Li, C. 89, 665
Li, D. 282, 508, 949
Li, D. *see* Dowben, P.A. 505
Li, D. *see* Johnson, P.D. 664
Li, G. 282
Li, L. 202
Li, X.-P. 282
Li, Y.S. 89
Li, Y.Z. *see* Chander, M. 894
Li, Z.G. *see* Parkin, S.S.P. 666
Liang, X. *see* Adler, D.L. 947
Liberati, M. 665
Lieb, E.H. *see* Mattis, D.C. 987
Liebermann, L.N. 665
Liebl, H. *see* Engelhardt, H.A. 743
Liebsch, A. 354, 949
Liebsch, A. *see* Ishida, H. 949
Liebsch, A. *see* Kempa, K. 949
Liebsch, A. *see* Plummer, E.W. 746
Liebsch, A. *see* Song, K.J. 950
Liebsch, A. *see* Tsuei, K.-D. 381
Liehr, M. 858
Lilienkamp, G. *see* Jalochowski, M. 949
Liliental-Weber, Z. *see* Spicer, W.E. 861
Liliental-Weber, Z. *see* Waddill, G.D. 861
Lin, C.C. *see* Mednick, K. 895
Lin, D.S. *see* Hirschorn, E. 429
Lin, H. *see* Batra, I.P. 428
Lin, H.-J. *see* Chen, C.T. 87, 663
Lin, H.-J. *see* Idzerda, Y.U. 88
Lin, H.-J. *see* Tjeng, L.H. 987
Lin, H.F. *see* Rich, D.A. 89
Lin, H.F. *see* Rich, D.H. 89
Lin, J.-S. *see* Stich, I. 206, 431
Lin, J.-S. *see* Štich, I. 283
Lin, M.-T. *see* Kuch, W. 665
Lin, M.-T. *see* Venus, D. 668
Lin, T. *see* Tsang, C.H. 667
Lin, Z. *see* Khazmi, Y. 430
Lind, D.M. *see* Idzerda, Y.U. 664
Lindau, I. 381, 508, 859
Lindau, I. *see* Allen, J.W. 947, 985
Lindau, I. *see* Cao, R. 856
Lindau, I. *see* Miyano, K.E. 859
Lindau, I. *see* Petro, W.G. 860
Lindau, I. *see* Richter, M. 90
Lindau, I. *see* Spicer, W.E. 860, 861
Lindau, I. *see* Yeh, J.J. 861
Lindefelt, U. *see* Johansson, L.I. 201
Lindgren, S.-Å. 244, 508, 665, 949
Lindgren, S.-A. *see* Carlsson, A. 947
Lindgren, S.-A. *see* Hamawi, A. 506, 948
Lindgren, S.Å. *see* Svensson, C. 951
Lindner, H. *see* Bartos, B. 742
Lindner, Th. 745
Lindner, Th. *see* Horn, K. 507, 744, 948
Lindner, Th. *see* Klauser, R. 745
Lindner, Th. *see* Kulkarni, S.K. 745
Lindner, Th. *see* Woodruff, D.P. 747
Lindroos, M. 354
Lindroos, M. *see* Fischer, D. 948
Lindroos, M. *see* Seyller, T. 355

Ling, Y. 282
Linke, U. *see* Berger, A. 662
Linke, U. *see* Weber, W. 951
Linsday, R. *see* Johansson, L.S.O. 895
Linz, R. 859
Lipari, N.O. *see* Scheffler, M. 90
List, R.S. *see* Olson, C.G. 987
Litvin, D.B. 745
Liu, A.C. 745
Liu, C. 665
Liu, H. *see* Himpsel, F.J. 200
Liu, J.K. *see* Kaiser, W.J. 858
Liu, J.N. 508
Liu, L.Z. *see* Anderson, R.O. 986
Liu, R. *see* Olson, C.G. 987
Lizuka, Y. *see* Nagao, T. 950
Lloyd, D.R. *see* Dudzik, E. 894
Lloyd, D.R. *see* Netzer, F.P. 745
Lloyd, D.R. *see* Ramsey, M.G. 746
Lo, C.W. 895
Lo, C.W. *see* Shuh, D.K. 283
Lodder, J.C. *see* Monsma, D.J. 665
Loly, P.D. 949
Long, J.P. 202
Long, J.P. *see* Bermudez, V.M. 197
Lonie, S.G. *see* Eberhardt, W. 743
Lordi, S. *see* Ma, Y. 202
Loucks, T.L. 508
Louie, S.G. 89, 202, 508, 859, 986
Louie, S.G. *see* Becker, R.S. 86, 281
Louie, S.G. *see* Blase, X. 281
Louie, S.G. *see* Chan, C.T. 197
Louie, S.G. *see* Chelikowsky, J.R. 198
Louie, S.G. *see* Hricovini, K. 200, 282
Louie, S.G. *see* Hybertsen, M.S. 88, 200, 282
Louie, S.G. *see* Hybertson, M.S. 507
Louie, S.G. *see* Ihm, J. 200, 858
Louie, S.G. *see* Northrup, J.E. 203, 283, 430, 509, 987
Louie, S.G. *see* Rubio, A. 205
Louie, S.G. *see* Schlüter, M. 205
Louie, S.G. *see* Shirley, E.L. 206
Louie, S.G. *see* Surh, M.P. 206, 987
Louie, S.G. *see* Vanderbilt, D. 207
Louie, S.G. *see* Zakharov, O. 208
Louie, S.G. *see* Zhang, S.B. 862
Louie, S.G. *see* Zhu, X. 208, 283, 431
Louis, E. 859
Louis, E. *see* Tejedor, C. 861
Louis, S.G. *see* Kerker, G.P. 88
Lower, I. *see* Hulpke, E. 948
Lu, T.-M. *see* Wang, G.-C. 510
Lu, W. 202
Lu, Z.-Y. 202, 430
Lubinsky, A.R. *see* Duke, C.B. 198
Luchini, M.U. *see* Pick, S. 509
Lüdecke, J. *see* Hulpke, E. 507
Ludeke, R. 859
Ludeke, R. *see* Bauer, A. 856
Ludeke, R. *see* Chiang, T.-C. 198
Ludeke, R. *see* Landgren, G. 895
Ludeke, R. *see* Prietsch, M. 860
Ludeke, R. *see* Schäffler, F. 860
Ludwig, H. 859
Lundberg, M. *see* Gauthier, Y. 664
Lundgren, E. *see* Andersen, J.N. 352, 353, 947
Lundgren, E. *see* Burchhardt, J. 353, 742
Lundgren, E. *see* Johansson, L.I. 507
Lundqvist, B.I. 508, 745, 986
Lundqvist, B.I. *see* Gunnarsson, O. 88
Lundqvist, B.I. *see* Hedin, L. 88, 986
Lundqvist, B.I. *see* Hjelmberg, H. 354
Lundqvist, S. 202, 244
Lundqvist, S. *see* Gunnarsson, O. 88
Lundqvist, S. *see* Hedin, L. 200, 243, 507, 948, 986
Lundqvist, S.J. *see* Hedin, L. 88
Lungren, E. *see* Nielsen, M.M. 745
Luo, N.S. 949
Luo, Y.S. *see* Yang, Y.-N. 283
Lurie, P.G. 202
Luryi, S. 859
Lüth, H. 202, 282, 430
Lüth, H. *see* Buchel, M. 894
Lüth, H. *see* Matz, R. 381, 430
Luttinger, J.M. 986
Lutz, C.P. *see* Crommie, M.F. 505
Luutz, A.C. *see* Kleyn, A.W. 745
Lux-Steiner, M. *see* Finteis, T. 429
Lynch, D.W. *see* Olson, C.G. 987
Lyo, I.W. 895, 986
Lyo, I.W. *see* Avouris, P. 893
Lyo, I.W. *see* Itchkawitz, B.S. 986
Lyuksyutov, I. *see* Grzelakowski, K. 506

Mårtensson, N. *see* Dunn, J.H. 663
Mårtensson, N. *see* Stenborg, A. 951
Ma, C.Q. *see* Sahni, V. 90

Ma, S.K. 986
Ma, Y. 202
Ma, Y. *see* Chen, C.T. 87, 663
Ma, Y. *see* Modesti, S. 950
Maaref, H. *see* Barret, C. 855
Maase, J. *see* Puschmann, A. 746
Máca, F. *see* Scheffler, M. 90, 205, 355, 950
Máca, F. *see* Wachutka, G. 207
MacDonald, A.H. 89
MacDonald, A.J. 89
Macdonald, J.E. *see* van Silfhout, R.G. 207
Mack, J.U. 745
Mack, J.U. *see* Neumann, M. 745
Mackinson, R.E.B. 986
MacLaren, J.M. 244, 430
Madelung, O. *see* Hellwege, K.-H. 200
Madey, T.E. *see* Goodman, D.W. 743
Madey, T.E. *see* Semancik, S. 950
Madey, T.E. *see* Shinn, N.D. 746
Madey, T.E. *see* Thiel, P.A. 897
Madix, R.J. 745
Madix, R.J. *see* D'Evelyn, M.P. 743
Madix, R.J. *see* Liu, A.C. 745
Maggio-Aprile, I. *see* Quattropani, L. 860
Magnusson, K.O. 202, 430
Magnusson, K.O. *see* Neuhold, G. 430
Magnusson, K.O. *see* Wang, Y.R. 207, 431
Magri, R. 282
Mahajan, S. *see* Wilson, J.A. 510
Mahan, G.D. 986, 987
Mahan, G.D. *see* Frota, H.O. 986
Mahan, G.D. *see* Overhauser, A.W. 987
Mahan, G.D. *see* Shung, K.W.K. 987
Maierhofer, Ch. *see* Alonso, M. 855
Mailhiot, C. 202, 203, 282
Mailhiot, C. *see* Duke, C.B. 857
Maity, N. 895
Majewski, J.A. 203
Makivic, M.S. *see* Tjeng, L.H. 987
Malik, R.J. *see* Zegenhagen, J. 91
Malmström, G. *see* Rundgren, J. 244, 950
Mamin, H.J. 859
Mangat, P.S. *see* Semond, F. 205
Mangat, P.S. *see* Spiess, L. 283
Manghi, F. 203, 282
Manghi, F. *see* Bertoni, C.M. 197, 281
Manghi, F. *see* Calandra, C. 197, 281
Manghi, F. *see* Magri, R. 282
Manghi, F. *see* Margaritondo, G. 282, 895
Manion, S.J. *see* Bell, L.D. 856
Mankey, G.J. *see* Himpsel, F.J. 381
Mankey, G.J. *see* Ortega, J.E. 666, 950
Mante, G. *see* Olde, J. 204
Mantl, S. *see* Struck, L.M. 896
Manzke, R. 203, 430, 987
Manzke, R. *see* Carstensen, H. 197, 428
Manzke, R. *see* Claessen, R. 986
Manzke, R. *see* Henk, J. 200
Manzke, R. *see* Janowitz, C. 201, 429
Manzke, R. *see* Kipp, L. 201, 430
Manzke, R. *see* Olde, J. 204
Mao, D. 859
Mao, D. *see* Kahn, A. 858
Maple, M.B. *see* Allen, J.W. 985
Maple, M.B. *see* Anderson, R.O. 986
Maradudin, A.A. *see* Mills, D.L. 665
Marales De La Garza, L. *see* Clarke, L.J. 87
Marcellini, A. 282
March, N.H. 508
March, N.H. *see* Jones, W. 507
March, N.H. *see* Joyce, K. 508
March, N.H. *see* Lundqvist, S. 202, 244
March, R.N. *see* Wood, A.D.B. 951
Marcus, P.M. *see* Barker, R.A. 505
Marcus, P.M. *see* Batra, I.P. 428
Marcus, P.M. *see* Chubb, S.R. 743
Marcus, P.M. *see* Demuth, I.E. 743
Marcus, P.M. *see* Himpsel, F.J. 200
Marcus, P.M. *see* Jona, F. 88
Marcus, P.M. *see* Shih, H.D. 206
Marcus, P.M. *see* Spanjaard, D. 509
Marcus, P.M. *see* Yang, W.S. 91, 208
Marée, P.J.M. 203
Margaritondo, G. 282, 859, 895
Margaritondo, G. *see* Brillson, L.J. 856
Margaritondo, G. *see* Chiaradia, P. 856
Margaritondo, G. *see* Kahn, A. 858
Margaritondo, G. *see* Mao, D. 859
Margaritondo, G. *see* Rowe, J.E. 896
Margaritondo, G. *see* Schlüter, M. 896
Margaritondo, G. *see* Stiles, K. 861
Mariani, C. 745
Mariani, C. *see* Gadzuk, J.W. 743
Mariani, C. *see* del Pennino, U. 894
Mark, P. *see* Duke, C.B. 198
Mark, P. *see* Kahn, A. 201
Mark, P. *see* Meyer, R.J. 203
Markert, K. 745

Marks, D. *see* Heine, V. 354
Marks, L.D. *see* Jayaram, G. 201
Marliere, C. 950
Marsh, F.S. 89
Marsh, F.S. *see* Debe, M.K. 87
Marsi, M. *see* Mao, D. 859
Mårtensson, P. 203, 430
Mårtensson, P. *see* Johansson, L.I. 201
Mårtensson, P. *see* Johansson, L.S.O. 201
Mårtensson, P. *see* Karlsson, C.J. 895
Mårtensson, P. *see* Magnusson, K.O. 202
Mårtensson, P. *see* Nicholls, J.M. 203
Mårtensson, P. *see* Owman, F. 204
Martensson, N. 745
Martensson, N. *see* Stenborg, A. 951
Martin, R.M. *see* Boszo, T. 742
Martin, R.M. *see* Qian, G. 204, 283
Martin-Rodero, A. *see* Joyce, K. 508
Martins, J.L. 203
Martins, J.L. *see* Troullier, N. 207
Mascaraque, A. 895
Masri, P. 859
Massey, H.S.W. *see* Mott, N.F. 665
Massies, J. *see* Jedrecy, N. 201
Massies, J. *see* Sauvage-Simkin, M. 205
Masut, R. *see* Ababou, Y. 893
Mate, C.M. 745
Mate, C.M. *see* Chiang, S. 742
Mate, C.M. *see* Koel, B.E. 745
Mate, C.M. *see* Tom, H.W.K. 951
Materlik, G. *see* Eteläniemi, V. 894
Materlik, G. *see* Funke, P. 894
Materlik, G. *see* Michel, E.G. 895
Materlik, G. *see* Schütz, G. 90, 667
Matho, K. 987
Mathon, J. 89, 665
Mathon, J. *see* Edwards, D.M. 948
Mathon, J. *see* Liebermann, L.N. 665
Mathon, M. 665
Mattern, B. *see* Hollering, M. 200
Matthai, C.C. *see* Shen, T.-H. 90
Mattheiss, L.F. 508
Mattheiss, L.F. *see* Smith, N.V. 90
Matthew, J.A.D. 508
Matthew, J.A.D. *see* Porter, S.J. 666
Mattis, D.C. 665, 987
Mattson, J. *see* Johnson, P.D. 664, 949
Mattson, J.E. *see* Li, D. 949
Matz, R. 381, 430
Matz, R. *see* Lüth, H. 282
Maue, A.W. 508
Maurer, T. *see* Oppeneer, P.M. 89
Mauri, D. 665
Mauri, D. *see* Allenspach, R. 662
Maxwell, J.C. 665
May, F. *see* Dunn, J.H. 663
May, U. *see* Nouvertné, F. 355
Mayer, H. 665
Mayer, J.W. *see* Woodall, J.M. 861
Mayne, A. *see* Dujardin, G. 894
Mayne, A. *see* Semond, F. 205
Mayne, A. *see* Soukiassian, P. 206
Mazumdar, S. 508
Mazur, A. 203
Mazur, A. *see* Gräschus, V. 199
Mazur, A. *see* Ivanov, I. 201
Mazur, A. *see* Krüger, P. 202, 430
Mazur, A. *see* Larsen, P.K. 202, 430
Mazur, A. *see* Pollmann, J. 204
Mazur, A. *see* Sabisch, M. 205
Mazur, A. *see* Sandfort, B. 205
Mazur, A. *see* Sandfort, D. 283
Mazur, A. *see* Schmeits, M. 205, 283
McCants, C. *see* Spicer, W.E. 861
McClelland, J.J. 665
McConville, C.F. *see* Woodruff, D.P. 747
McCoy, B. 665
McElhiney, G. 745
McFeely, F.R. *see* Cartier, E. 856
McFeely, F.R. *see* Himpsel, F.J. 381
McFeely, F.R. *see* Ley, L. 202
McFeely, F.R. *see* McLean, A.B. 895
McFeely, F.R. *see* Morar, J.F. 203
McFeely, F.R. *see* Shuh, D.K. 283
McFeely, F.R. *see* Whitman, L.J. 897
McGee, N.W.E. *see* Purcell, S.T. 666
McGill, T.C. *see* Cheng, X.-C. 856
McGill, T.C. *see* Kurtin, S. 858
McGill, T.C. *see* Zur, A. 862
McGovern, I.T. *see* Dudzik, E. 894
McGovern, I.T. *see* McLean, A.B. 859
McGovern, I.T. *see* Thornton, G. 897
McGovern, I.T. *see* Williams, R.H. 897
McGrath, R. *see* Diehl, R.D. 947
McGrath, R. *see* Dudzik, E. 894
McGrath, R. *see* Thornton, G. 897
McGrawth, R.C. *see* Adler, D.L. 947
McKinley, J. *see* Kahn, A. 858

McLean, A.B. 859, 895
McLean, A.B. *see* Dharmadasa, I.M. 857
McLean, A.B. *see* Ludeke, R. 859
McIlroy, D. *see* Tang, D. 951
McMenamin, J. *see* Brillson, L.J. 856
McRae, E.G. 244, 354, 665, 950
McRae, E.G. *see* Bennet, P.A. 428
Mead, C.A. *see* Kurtin, S. 858
Meade, R.D. 430
Medeiros-Ribeiro, G. *see* Rubin, M.E. 860
Mednick, K. 895
Mednick, K. *see* Euceda, A. 506
Mehandru, S.P. 203
Mehra, V. *see* Pohm, A.V. 666
Mei, W.N. *see* Tong, S.Y. 206
Meier, F. *see* Pierce, D.T. 666
Meigs, G. *see* Chen, C.T. 87, 663
Meigs, G. *see* Idzerda, Y.U. 88
Meigs, G. *see* Modesti, S. 950
Meijer, C. *see* Terminello, L.J. 381
Meinel, K. *see* Beckmann, A. 947
Meinel, K. *see* Kuch, W. 665
Meinel, K. *see* Schneider, C.M. 667
Mele, E.J. 859
Mele, E.J. *see* Alerhand, O.L. 281
Mele, E.J. *see* Hannon, J.B. 506
Melmed, A.J. 89
Melmed, A.J. *see* Tung, R.T. 90
Memmel, N. 745, 950
Memmel, N. *see* Rangelov, G. 746
Men, F.K. *see* Tong, S.Y. 206, 431
Menon, M. 203
Menzel, D. *see* Breitschafter, M.J. 742
Menzel, D. *see* Engelhardt, H.A. 743
Menzel, D. *see* Gsell, M. 354
Menzel, D. *see* Hermann, K. 744
Menzel, D. *see* Hofmann, P. 744
Menzel, D. *see* Jakob, P. 744
Menzel, D. *see* Kostov, K.L. 354
Menzel, D. *see* Lindroos, M. 354
Menzel, D. *see* Narloch, B. 355
Menzel, D. *see* Schichl, A. 746
Menzel, D. *see* Schiffer, A. 355
Menzel, D. *see* Schneider, C. 746
Menzel, D. *see* Steinrück, H.-P. 746
Menzel, D. *see* Umbach, E. 747
Menzel, D. *see* Weimer, J.J. 747
Merino, J. *see* Garcia-Vidal, F.J. 282
Mermin, N.D. 665
Mermin, N.D. *see* Ashcroft, N.W. 86, 505, 662, 855
Merzbacher, E. 859
Messiah, A. 89
Messmer, R.P. 745
Messmer, R.P. *see* Freund, H.-J. 743
Messmer, R.P. *see* Kao, C.M. 744
Methfessel, M. 89, 244, 354
Methfessel, M. *see* Andersen, J.N. 353
Methfessel, M. *see* Fiorentini, V. 199, 353
Methfessel, M. *see* Polatoglu, H.M. 746
Metiu, H. *see* Boszo, T. 742
Metzner, H. 895
Meyer, E. *see* Ludwig, M.H. 859
Meyer, F. 895
Meyer, R.J. 203
Meyer, T. 859
Meyer-Ehmsen, G. *see* Braun, W. 742
Meyerheim, H.L. *see* Rossmann, R. 205
Meyerson, B.S. *see* Himpsel, F.J. 381
Michel, E.G. 895
Michel, E.G. *see* Chrost, J. 894
Michel, E.G. *see* Eteläniemi, V. 894
Michel, E.G. *see* Mascaraque, A. 895
Middelmann, H.-U. 430
Middelmann, H.-U. *see* Mariani, C. 745
Middelmann, H.-U. *see* Sorba, L. 206, 431
Middelmann, H.U. *see* Weidmann, R. 207
Miedema, A.R. 859
Miglio, L. 203
Miglio, L. *see* Harten, U. 200, 282
Miguel, J.J.D. *see* Schneider, C.M. 667
Mikkor, M. *see* Jaklevic, R.C. 949
Milchev, A. *see* Dünweg, B. 506
Miller, A.R. 354
Miller, D.L. *see* Fu, J. 282
Miller, T. 203, 950
Miller, T. *see* Carlisle, J.A. 428, 856
Miller, T. *see* Hsieh, T.C. 507
Miller, T. *see* Ludeke, R. 859
Miller, T. *see* Mueller, M.A. 950
Miller, T. *see* Rich, D.A. 89
Miller, T. *see* Rich, D.H. 89, 205
Miller, T. *see* Wachs, A.L. 207
Millet, P. *see* Dujardin, G. 894
Milliken, A.M. *see* Bell, L.D. 856
Mills, A.P. *see* Horsky, T.N. 200
Mills, D.L. 665
Mills, D.L. *see* Bander, M. 662

Mills, D.L. *see* Erickson, R.P. 663
Mills, D.L. *see* Gokhale, M.P. 664
Mills, D.L. *see* Ibach, H. 664, 948
Mills, D.L. *see* Lehwald, S. 949
Mills, D.L. *see* Ormeci, A. 666
Mills, D.L. *see* Szeftel, J.M. 746
Mills, D.M. *see* Plihal, M. 666
Minagawa, H. *see* Mizuno, S. 950
Miosga, H. *see* Heimann, P. 507, 948
Miranda, R. 745
Miranda, R. *see* Chrost, J. 894
Miranda, R. *see* Schneider, C.M. 667
Misawa, S. *see* Hara, S. 199
Missous, M. 859
Mitchell, G.E. *see* Madix, R.J. 745
Mitchell, K. 987
Mitchell, P.W. *see* Paul, D.M. 666
Mitchell, W.J. 354
Miyamoto, Y. 282, 895
Miyamoto, Y. *see* Nonoyama, S. 283
Miyano, K. *see* Cao, R. 856
Miyano, K. *see* Spicer, W.E. 861
Miyano, K.E. 859
Miyano, K.E. *see* Richter, M. 90
Miyano, K.E. *see* Shek, M.L. 206
Mizuno, S. 950
Mizuta, H. *see* Kotani, A. 665
Mizutani, T. *see* Ide, T. 88
Mock, J.B. *see* Zegenhagen, J. 91
Møartensson, P. *see* Feenstra, R.M. 282
Modesti, S. 895, 950
Modesti, S. *see* Astaldi, S. 947
Modesti, S. *see* Chen, C.T. 87, 663
Modesti, S. *see* Rudolf, P. 950
Mohamed, M.H. 950
Mohamed, M.H. *see* Shen, Y. 950
Moison, J.M. 859
Molinari, E. *see* Bertoni, C.M. 281
Molinari, E. *see* Manghi, F. 203, 282
Moll, J.L. *see* Drummond, W.E. 857
Molodtsov, S. *see* Bauer, A. 856
Mönch, W. 203, 430, 859, 895
Mönch, W. *see* Assmann, J. 380, 428, 855
Mönch, W. *see* Bartels, F. 893
Mönch, W. *see* Goldmann, A. 199
Mönch, W. *see* Koke, P. 201, 895
Mönch, W. *see* Kraus, P. 895
Mönch, W. *see* Linz, R. 859
Mönch, W. *see* Pankratz, J. 283
Mönch, W. *see* Stockhausen, A. 896
Mönch, W. *see* Troost, D. 283, 861, 897
Monnier, R. 89
Monsma, D.J. 665
Montgomery, V. *see* Srivastava, G.P. 206
Montgomery, V. *see* Williams, R.H. 861
Mook, H.A. *see* Paul, D.M. 666
Mookerjee, A. 508
Mookerjee, A. *see* Bishop, A.R. 505
Morán-López, J.L. *see* Falicov, L.M. 243
Morar, F. *see* Himpsel, F.J. 381
Morar, J.F. 203
Morar, J.F. *see* Landgren, G. 895
Morgante, A. *see* Crottini, A. 947
Morgen, P. 895
Morgen, P. *see* Höfer, U. 894
Moriarty, P. 895
Morikawa, Y. *see* Ishida, H. 949
Morikawa, Y. *see* Kobayashi, K. 201, 282
Morikawa, Y. *see* Shi, X. 950
Moritz, T. *see* Kostov, K.L. 354
Moritz, W. *see* Over, H. 950
Moritz, W. *see* Rossmann, R. 205
Moritz, W. *see* Stampfl, C. 355, 746
Morkoç, H. *see* Strite, S. 431
Morrison, J. *see* Lander, J. 89, 202
Moruzzi, V. 244, 665
Moser, H.R. *see* Eberhardt, W. 743
Mott, N.F. 508, 509, 665, 859
Moustakas, T.D. *see* Dhesi, S.S. 429
Mowrey, R.C. *see* Kroes, G.J. 354
Mrarka, S.P. 895
Muehlhoff, L. 203
Mueller, M.A. 950
Muir, W.B. *see* Heinrich, B. 948
Mulhollan, G.A. 665
Müller, C. *see* Dudzik, E. 894
Muller, F. *see* Heilmann, P. 88
Müller, J.E. *see* Hannon, J.B. 948
Müller, K. 950
Müller, K. *see* Bartos, B. 742
Müller, K. *see* Chubb, S.R. 743
Müller, K. *see* Schardt, J. 205
Müller, K. *see* Starke, U. 206
Müller, N. 666
Müller, N. *see* Erbudak, M. 663
Müller, S. *see* Schardt, J. 205
Müller, W. *see* Bagus, P.S. 353
Mundschau, M. *see* Bauer, F. 380

Muniz, R.B. *see* Edwards, D.M. 948
Munoz, M.C. *see* Perez-Diaz, J.L. 950
Munz, A.W. 203
Murano, K. 895
Murata, Y. *see* Aruga, T. 504, 947
Murata, Y. *see* Hasegawa, Y. 507
Murata, Y. *see* Hashizume, T. 507
Murata, Y. *see* Tabata, T. 206
Muret, P. 859
Murphy, R. *see* Plummer, E.W. 950
Murray, S.J. *see* Adler, D.L. 947
Muscat, J.P. 354, 509, 745, 950
Myers, H.P. *see* Fäldt, A. 948
Myrtle, K. *see* Heinrich, B. 948

Nagao, T. 950
Nagayoshi, H. 283
Nagayoshi, H. *see* Fujita, M. 429
Naitoh, M. 895
Naitoh, M. *see* Oura, K. 896
Nakada, T. 283
Nakagawa, K. *see* Marée, P.J.M. 203
Nakamura, S. *see* Nakanishi, T. 666
Nakamura, T. *see* Ito, T. 895
Nakanishi, S. 203
Nakanishi, T. 666
Nakashidze, G.A. *see* Laperashvili, T.A. 858
Nakashima, H. *see* Kobayashi, K.L.I. 858
Nannarone, S. *see* Chiarotti, G. 428
Nannarone, S. *see* Ruocco, A. 896
Nannarone, S. *see* Sorba, L. 896
Narayanamurti, V. 859
Narayanamurti, V. *see* O'Shea, J.J. 860
Narayanamurti, V. *see* Rubin, M.E. 860
Narayanamurti, V. *see* Sajoto, T. 860
Nardelli, M.B. *see* Rapcewicz, K. 205
Narloch, B. 355
Narusawa, T. *see* Kobayashi, K.L.I. 858
Nasu, K. *see* Liu, J.N. 508
Natoli, C.R. *see* Bullock, E.L. 197
Natoli, C.R. *see* Johansson, L.S.O. 282
Naumovets, A.G. 355
Navas, E. *see* Starke, K. 667
Neave, J.H. *see* Larsen, P.K. 202, 430
Neddermeyer, H. 895
Neddermeyer, H. *see* Badt, D. 196
Neddermeyer, H. *see* Heimann, P. 507, 948
Neddermeyer, H. *see* Kliese, R. 895
Needels, M. 203
Needels, M. *see* Brommer, K.D. 281, 428
Needels, M. *see* Payne, M.C. 204
Needles, M. *see* Brommer, K.D. 197
Needs, R.J. *see* Charlesworth, J.P.A. 856
Needs, R.J. *see* Cheng, C. 198
Needs, R.J. *see* Lam, S.C. 244
Needs, R.J. *see* Payne, M.C. 204
Needs, R.J. *see* Roberts, N. 205
Needs, R.J. *see* White, I.D. 245
Néel, L. 666
Nekovee, M. 244, 666
Nelin, C.J. *see* Bagus, P.S. 353
Nelin, C.J. *see* Hermann, K. 354
Nelson, J.S. *see* Klitsner, T. 201
Nelson, J.S. *see* Li, Y.S. 89
Nelson, J.S. *see* Wright, A.F. 208
Nelson, M.M. *see* Engstrom, J.R. 894
Nerlov, J. *see* Christensen, S.V. 353
Netzer, F.P. 745
Netzer, F.P. *see* Bertel, E. 742
Netzer, F.P. *see* Mack, J.U. 745
Netzer, F.P. *see* Matthew, J.A.D. 508
Netzer, F.P. *see* Neumann, M. 745
Netzer, F.P. *see* Ramsey, M.G. 746
Neuber, M. 745
Neuber, M. *see* Geisler, H. 743
Neuber, M. *see* Graen, H.H. 743
Neugebauer, J. 355, 509, 950
Neugebauer, J. *see* Bockstedte, M. 353
Neugebauer, J. *see* Bormet, J. 353
Neugebauer, J. *see* Northrup, J.E. 203, 204
Neugebauer, J. *see* Schmalz, A. 355, 950
Neugebauer, J. *see* Smith, A.R. 431
Neugebauer, J. *see* Stampfl, C. 356
Neugebauer, J. *see* Wenzien, B. 356
Neuhaus, D. 509
Neuhoff, G. *see* Barman S.R. 197
Neuhold, G. 430, 950
Neuhold, G. *see* Barman, S.R. 428
Neuhold, G. *see* Ding, S.-A. 428
Neuhold, G. *see* Magnusson, K.O.M. 430
Neumann, M. 745
Neumann, M. *see* Bartos, B. 742
Neumann, M. *see* Borstel, G. 742
Neumann, M. *see* Braun, W. 742
Neumann, M. *see* Freund, H.-J. 380, 743
Neumann, M. *see* Geisler, H. 743
Neumann, M. *see* Graen, H.H. 743, 744
Neumann, M. *see* Kuhlenbeck, H. 745

Neumann, M. *see* Netzer, F.P. 745
Neumann, M. *see* Neuber, M. 745
Neumann, M. *see* Odörfer, G. 745
Neve, J. *see* Lindgren, S.-Å. 949
Newman, N. 859
Newman, N. *see* Spicer, W.E. 861
Newns, D.M. 283, 745, 859
Newns, D.M. *see* Muscat, J.P. 354, 745, 950
Newns, D.M. *see* Stroscio, J.A. 206
Newns, D.N. *see* Muscat, J.P. 509
Newsam, J.M. *see* Li, Y.S. 89
Newstead, D.A. *see* Binns, C. 505
Ngoc, T.C. *see* Poppendieck, T.D. 204
Ni, W.-X. *see* Mårtensson, P. 203, 430
Nicholls, J.M. 203
Nicholls, J.M. *see* Magnusson, K.O. 202
Nicholls, J.M. *see* Mårtensson, P. 203, 430
Nicholls, J.M. *see* Perfetti, P. 204, 430
Nicholls, J.M. *see* Uhrberg, R.I.G. 207, 431, 897
Niedermann, P. 860
Niedermann, P. *see* Quattropani, L. 860
Niehus, H. *see* Böttcher, A. 353
Nielsen, H.B. 89
Nielsen, H.B. *see* Adams, D.L. 86
Nielsen, H.B. *see* Jensen, V. 88
Nielsen, K. *see* Christensen, S.V. 353
Nielsen, M. *see* Bohr, J. 197
Nielsen, M. *see* Feidenhans'l, R. 199
Nielsen, M. *see* Stampfl, C. 355, 746, 951
Nielsen, M.M. 745
Nielsen, M.M. *see* Aminpirooz, S. 352
Nielsen, M.M. *see* Burchhardt, J. 353, 742
Nielsen, M.M. *see* Christensen, S.V. 353
Nienhaus, H. *see* Pankratz, J. 283
Nieuwenhuys, B.E. 745
Niles, D.W. 381
Nilsson, A. 355
Nilsson, A. *see* Björneholm, O. 947
Nilsson, A. *see* Martensson, N. 745
Nilsson, A. *see* Stenborg, A. 951
Nilsson, P.-O. *see* Gustafsson, T. 948
Nilsson, P.O. 509
Nilsson, P.O. *see* Håkansson, M.C. 429
Nilsson, P.O. *see* Khazmi, Y. 430
Nilsson, P.O. *see* Qu, H. 205, 430
Nishigaki, S. *see* Naitoh, M. 895
Nishijima, M. *see* Edamoto, K. 894
Nishijima, M. *see* Kobayashi, K. 895
Nishijima, N. 895
Nishimori, K. *see* Nakanishi, S. 203
Nishiyama, A. 896
Noffke, J. 666
Noffke, J. *see* Eckardt, H. 663
Noffke, J. *see* Schneider, C.M. 667
Nogami, J. 89, 203
Nogami, J. *see* Baski, A.A. 86
Nogami, J. *see* Richter, M. 90
Nolting, W. 666
Nonoyama, S. 283
Nonoyama, S. *see* Miyamoto, Y. 282
Nordström, L. 666
Normn, D. *see* Thornton, G. 897
Norris, C. *see* Binns, C. 505, 947
Norris, C. *see* van Silfhout, R.G. 207
Nørskov, J.K. 355
Nørskov, J.K. *see* Hammer, B. 354
Nørskov, J.K. *see* Hjelmberg, H. 354
Nørskov, J.K. *see* Pedersen, M.O. 355
Nørskov, J.K. *see* Pleth Nielsen, L. 355
Northrup, J.E. 89, 203, 204, 283, 430, 509, 987
Northrup, J.E. *see* Biegelsen, D.K. 197, 281, 428
Northrup, J.E. *see* Bringans, R.D. 87
Northrup, J.E. *see* Smith, A.R. 431
Northrup, J.E. *see* Surh, M.P. 987
Northrup, J.E. *see* Uhrberg, R.I.G. 90, 207, 283
Nouvertné, F. 355
Nozaki, T. *see* Ito, T. 895
Nunes Rodrigues, W. *see* Kraus, P. 895
Nyholm, R. *see* Andersen, J.N. 352, 353, 947
Nyholm, R. *see* Johansson, L.I. 507
Nyrvkor, J.K. *see* Lundquist, B.I. 745

O'Brien, S.C. *see* Kroto, H. 895
O'Handley, R.C. *see* Chuang, D.S. 663
O'Shea, J.J. 860
O'Shea, J.J. *see* Rubin, M.E. 860
O'Shea, J.J. *see* Sajoto, T. 860

Ocal, C. *see* Bader, M. 742
Ocal, C. *see* García, N. 857
Odörfer, G. 745
Odörfer, G. *see* Graen, H.H. 743
Oehrlein, G.S. 896
Oepen, H.P. 666

Oepen, H.P. *see* Berger, A. 662
Oepen, H.P. *see* Schneider, C.M. 667
Ogata, H. *see* Fujiwara, K. 894
Oguchi, T. *see* Fu, C.L. 664
Oh, S.-J. *see* Allen, J.W. 985
Oh, S.-J. *see* Anderson, R.O. 986
Oh, S.-J. *see* Tjeng, L.H. 987
Ohba, Y.. 896
Ohdomari, I. *see* Hara, S. 199
Ohdomari, I. *see* Tsuda, M. 283
Ohki, Y. *see* Hiratani, Y. 894
Ohnishi, S. 89
Ohnishi, S. *see* Fu, C.L. 88
Ohnishi, S. *see* Weinert, M. 91
Ohno, T.R. *see* Gu, C. 894
Ohtani, H. *see* Chiang, S. 742
Oikawa, S. *see* Tsuda, M. 283
Okada, L.A. *see* Wise, M.L. 897
Okada, Y. *see* Yong, J.C. 897
Okazaki, M.J. *see* Onodera, Y. 89
Olde, J. 204
Olmstead, M.A. 89, 204, 381, 430
Olmstead, M.A. *see* Bringans, R.D. 87, 428
Olmstead, M.A. *see* Uhrberg, R.I.G. 90, 207
Olson, C.G. 987
Olson, C.G. *see* Anderson, R.O. 986
Olson, C.G. *see* Claessen, R. 505, 986
Ölsson, L.Ö. 430
Ölsson, L.Ö. *see* Håkansson, M.C. 429
Onchi, M. *see* Edamoto, K. 894
Onchi, M. *see* Kobayashi, K. 895
Onchi, M. *see* Nishijima, N. 895
Onda, N. *see* Stalder, R. 861
Onellion, M. *see* Dowben, P.A. 505
Onida, G. *see* Di Felice, R. 281
Ono, K. *see* Kakizaki, A. 665
Onodera, Y. 89
Onsager, L. 666
Oppeneer, P.M. 89
Oppenheimer, R. *see* Born, M. 353
Oppo, S. 355
Orlowski, B.A. *see* Janowitz, C. 201, 429
Ormeci, A. 666
Orr, B.G. 950
Ortega, J. 950
Ortega, J.E. 204, 666, 950
Ortega, J.E. *see* Himpsel, F.J. 381
Ortuno, M. 244
Osaka, T. *see* Nakada, T. 283
Osbourn, G.C. *see* Bouchard, A.M. 197
Oshima, C. *see* Anno, M. 86
Oshima, C. *see* Nagao, T. 950
Ossicini, S. 283, 860
Ossicini, S. *see* Buongiorno Nardelli, M. 281
Osterwalder, J. *see* Fasel, R. 353
Osterwalder, J. *see* Saiki, R.S. 746
Ottaviani, C. *see* Mascaraque, A. 895
Ottaviani, G. 860
Otto, A. *see* Persson, B.N.J. 509
Oura, K. 896
Over, H. 355, 950
Over, H. *see* Böttcher, A. 353
Over, H. *see* Kim, Y.D. 354
Over, H. *see* Stampfl, C. 355, 356, 746, 951
Overhauser, A.W. 987
Owman, F. 204
Owman, F. *see* Johansson, L.I. 201
Owman, F. *see* Karlsson, C.J. 895

Pabst, M. *see* Weinelt, M. 747
Pache, T. *see* Schneider, C. 746
Pache, T. *see* Steinrück, H.-P. 746
Packard, W.E. 204
Packard, W.E. *see* Tong, S.Y. 206, 431
Paggel, J.J. 430
Paggel, J.J. *see* Piancastelli, M.N. 430
Pahlke, D. 896
Paigné, J. *see* Thiry, P. 431
Palange, F. *see* Heinz, T.F. 381
Palm, H. 860
Palmberg, P.W. 355
Palmer, N.R. *see* Richardson, N.V. 746
Palmer, R.L. *see* Kern, K. 508
Palmour, J.W. *see* Davis, R.F. 198
Palmstrøm, C.J. 860
Palmstrøm, C.J. *see* Farrell, H.H. 199
Palummo, M. 204
Palummo, M. *see* Buongiorno Nardelli, M. 281
Panaccione, G. *see* Liberati, M. 665
Panaccione, G. *see* Poncey, C. 896
Panaccione, G. *see* Rochet, F. 283
Pandey, K.C. 89, 204, 283, 430, 896
Pandey, K.C. *see* Eastman, D.E. 894
Pandey, K.C. *see* Kaxiras, E. 201, 895
Pandey, R. 204
Pandey, R. *see* Jaffe, J.E. 201
Pane, M.C. *see* Stich, I. 206
Pang, A.W. *see* Walker, T.G. 668

Pang, Y. *see* Grünberg, P. 664
Pangher, N. *see* Aminpirooz, S. 352
Pankratov, O. 283
Pankratz, J. 283
Pantelides, S.T. *see* Pollmann, J. 204
Pantelides, S.T. *see* Scheffler, M. 90
Paolucci, G. *see* Woodruff, D.P. 747
Papaconstantopoulos, D.A. 509, 666
Papaconstantopoulos, D.A. *see* Idzerda, Y.U. 664
Papadia, S. 244
Papadia, S. *see* Yang, S. 245, 951
Papageorgopoulos, A. 896
Papagno, L. *see* Chiarello, G. 947
Papp, H. *see* McElhiney, G. 745
Pappas, D.P. 666
Pappas, D.P. *see* Tobin, J.G. 90
Parill, T.M. 204
Park, C.H. 204
Park, C.Y. *see* Chung, J.W. 505
Park, C.Y. *see* Shin, K.S. 509
Park, J.-H. *see* Anderson, R.O. 986
Park, J.-H. *see* Tjeng, L.H. 987
Park, K.-H. *see* Kakizaki, A. 665
Park, R.L. *see* Jonker, B.T. 949
Park, S.-I. 860
Park, S.-I. *see* Nogami, J. 203
Parkin, S.P. *see* Falicov, L.M. 87
Parkin, S.S.P. 666
Parr, R.G. 89
Parrinello, M. *see* Ancilotto, F. 281
Parrinello, M. *see* Car, R. 87, 197, 281, 353
Parrinello, M. *see* Iarlori, S. 200
Pashley, M.D. 204, 283
Pashley, M.D. *see* Haberern, K.W. 199, 282
Pashley, M.D. *see* Li, D. 282
Pasquarello, A. 896
Passek, F. 244, 666
Passek, F. *see* Donath, M. 243, 663
Pastore, R. *see* Chiarotti, G. 428
Pastori Parravicini, G. *see* Bassani, F. 281
Patchet, A. *see* Dudzik, E. 894
Pate, B.B. 204
Patel, J.R. *see* Fontes, E. 199
Patel, J.R. *see* Zegenhagen, J. 91
Paton, A. *see* Duke, C.B. 198, 281, 743
Paton, A. *see* Holland, B.W. 88, 200
Paton, A. *see* Horsky, T.N. 200
Paton, A. *see* Meyer, R.J. 203
Patrin, J.C. 896
Patrin, J.C. *see* Chander, M. 894
Patterson, M.H. *see* Dharmadasa, I.M. 857
Patthey, F. 950, 987
Patthey, L. *see* Bullock, E.L. 197
Paul, D.M. 666
Paul, J. 355
Paulikas, A.P. *see* Olson, C.G. 987
Pauling, L. 355
Pauly, Th. *see* Michel, E.G. 895
Payne, M.C. 89, 204, 355
Payne, M.C. *see* De Vita, A. 281
Payne, M.C. *see* Hu, P. 354
Payne, M.C. *see* Needels, M. 203
Payne, M.C. *see* Robertson, I.J. 355
Payne, M.C. *see* Štich, I. 283, 431
Peacock-Lopez, E. 509
Pearson, I. *see* Johnson, P.D. 949
Pearson, J. *see* Johnson, P.D. 664
Pearson, J. *see* Li, D. 949
Pearson, J. *see* Qiu, Z.Q. 381
Peatman, W. *see* Schäfers, F. 666
Pechman, R.J. *see* Rioux, D. 896
Peden, C.H.F. 355
Pedersen, M.O. 355
Pederson, J.S. *see* Feidenhans'l, R. 199
Pederson, M.R. *see* Perdew, J.P. 89
Pedio, M. *see* Mascaraque, A. 895
Pedio, M. *see* Sorba, L. 896
Pehlke, E. 283, 381, 430
Pehlke, E. *see* Tsuei, K.-D. 381
Peierls, R.E. 509
Peled, H. 745
Pendry, J. *see* Echenique, P.M. 947
Pendry, J. *see* Loly, P.D. 949
Pendry, J.B. 244, 509, 666
Pendry, J.B. *see* Echenique, P.M. 243, 353
Pendry, J.B. *see* Hopkinson, J.F.L. 243
Pendry, J.B. *see* MacLaren, J.M. 244, 430
Pendry, J.B. *see* Starke, U. 746
Pendry, J.N. 509
Pensl, G. 204, 430
Pentcheva, R. 355
Pentcheva, R. *see* Nouvertné, F. 355
Pepper, S. 204, 430
Percival, K.L. *see* Urbach, L.E. 951
Perdew, J.P. 89, 204, 355
Perdew, J.P. *see* Monnier, R. 89
Perdew, J.P. *see* Sahni, V. 90

Perez-Diaz, J.L. 950
Perfetti, P. 204, 430
Perfetti, P. *see* Manghi, F. 203
Perfetti, P. *see* Reihl, B. 205
Perkins, D.M. *see* Goodman, A.M. 857
Perlov, A. *see* Traving, M. 431
Persson, B. *see* Ishida, H. 949
Persson, B.N.J. 509
Persson, B.N.J. *see* Andersson, S. 947
Persson, B.N.J. *see* Demuth, J.E. 198, 428
Persson, C. *see* Johansson, L.I. 201
Persson, M. *see* Papadia, S. 244
Persson, M. *see* Salmi, L.-A. 950
Persson, M. *see* Stroscio, J.A. 951
Persson, M. *see* Yang, S. 245, 951
Persson, P. *see* Karlsson, U.O. 508
Persson, P.E.S. *see* Magnusson, K.O. 202, 430
Persson, P.E.S. *see* Uhrberg, R.I.G. 207, 897
Petersen, H. 666
Petersen, H. *see* Baumgarten, L. 662
Petersen, H. *see* Paggel, J.J. 430
Petersen, H. *see* Schneider, C.M. 667
Petersen, L. *see* Nielsen, H.B. 89
Petersen, M. 355
Petersen, M. *see* Wang, X.-G. 356
Peterson, H. *see* Baumgarten, L. 86
Peterson, L.D. 509
Petro, W.G. 860
Petroff, F. *see* Baibich, M.N. 662
Petroff, P.M. *see* Rubin, M.E. 860
Petroff, Y. *see* Hricovini, K. 200, 282
Petroff, Y. *see* Louie, S.G. 508
Petroff, Y. *see* Solal, F. 206
Petroff, Y. *see* Thiry, P. 431, 510
Pettit, G.D. *see* Woodall, J.M. 861
Peyerimhoff, S.D. 745
Pfandzelter, R. 666
Pfnür, H. *see* Lindroos, M. 354
Pfnür, H.E. *see* Rettner, C.T. 746
Phan, M.S. *see* Edwards, D.M. 948
Phaneuf, R.J. 204
Philip, P. *see* Sorba, L. 896
Philippe, L. *see* Dujardin, G. 894
Phillips, J.C. 89, 204, 283, 430
Phillips, J.C. *see* Andrews, J.M. 855
Phillips, J.C. *see* Pandey, K.C. 204
Phillips, R.A. *see* Girvan, R.F. 506
Piancastelli, M.N. 430
Pianetta, P. *see* Lindau, I. 859
Pianetta, P. *see* Richter, M. 90
Pick, S. 509
Pickett, W.E. 204, 244, 283
Pickett, W.E. *see* Davidson, B.N. 198
Piecuch, M. *see* Pizzini, S. 666
Piepke, W. *see* Tamura, E. 667
Pierce, D.T. 666
Pierce, D.T. *see* Celotta, R.J. 663
Pierce, D.T. *see* McClelland, J.J. 665
Pierce, D.T. *see* Siegmann, H.C. 667
Pierce, D.T. *see* Unguris, J. 667
Pierce, T.D. *see* Falicov, L.M. 87
Pignedoli, C.A. *see* Marcellini, A. 282
Pike, W.T. *see* Bell, L.D. 856
Pinchaux, R. *see* Jedrecy, N. 201
Pinchaux, R. *see* Louie, S.G. 508
Pinchaux, R. *see* Sauvage-Simkin, M. 205
Pinchaux, R. *see* Solal, F. 206
Pinchaux, R. *see* Thiry, P. 431, 510
Pines, D. 89, 509
Pinto, M.R. *see* Sullivan, J.P. 861
Pirug, G. 244, 950
Pirug, G. *see* Kiskinova, M. 745
Pizzagalli, L. *see* Soukiassian, P. 206
Pizzini, S. 666
Platow, W. *see* Farle, M. 663
Pleth Nielsen, L. 355
Pleyer, H. *see* Alvarado, S.F. 662
Pleyer, H. *see* Feder, R. 664
Plihal, M. 666
Ploog, K. *see* Ding, S.-A. 428
Plummer, E.W. 244, 381, 509, 666, 745, 746, 896, 950
Plummer, E.W. *see* Allyn, C.L. 742
Plummer, E.W. *see* Andersson, S. 947
Plummer, E.W. *see* Bartynski, R.A. 505, 986
Plummer, E.W. *see* Davis, H.L. 505
Plummer, E.W. *see* DePaola, R.A. 743
Plummer, E.W. *see* Didio, R.A. 743
Plummer, E.W. *see* Eberhardt, W. 243, 506, 663, 743
Plummer, E.W. *see* Freund, H.-J. 743, 986
Plummer, E.W. *see* Greuter, F. 744
Plummer, E.W. *see* Hannon, J.B. 506
Plummer, E.W. *see* Heskett, D. 744, 948
Plummer, E.W. *see* Horn, K. 744
Plummer, E.W. *see* In-Whan, Lyo 948
Plummer, E.W. *see* Inglesfield, J.E. 429, 507
Plummer, E.W. *see* Itchkawitz, B.S. 986

Plummer, E.W. *see* Jensen, E. 507, 986
Plummer, E.W. *see* Kuhlenbeck, H. 745
Plummer, E.W. *see* Levinson, H.J. 244, 508, 949, 986
Plummer, E.W. *see* Levinson, H.L. 665
Plummer, E.W. *see* Lyo, I.W. 986
Plummer, E.W. *see* Odörfer, G. 745
Plummer, E.W. *see* Salaneck, W.R. 746
Plummer, E.W. *see* Schmeisser, D. 746
Plummer, E.W. *see* Song, K.J. 950
Plummer, E.W. *see* Sprunger, P.T. 746
Plummer, E.W. *see* Urbach, L.E. 951
Plummer, E.W. *see* Waclawski, B.J. 510
Plummer, E.W. *see* Wang, J. 951
Plummer, E.W. *see* Watson, G.M. 510, 951
Plummer, F.W. *see* Tsuei, K.-D. 381
Pohm, A.V. 666
Polatoglu, H.M. 746
Polinger, V.P. *see* Bersuker, I.B. 505
Pollak, R.A. *see* Ley, L. 202
Pollmann, J. 204
Pollmann, J. *see* Göpel, W. 199
Pollmann, J. *see* Goldmann, A. 199
Pollmann, J. *see* Gräschus, V. 199
Pollmann, J. *see* Hirsch, G. 200
Pollmann, J. *see* Ivanov, I. 201
Pollmann, J. *see* Koke, P. 201
Pollmann, J. *see* Krüger, P. 88, 89, 202, 244, 282, 430, 895
Pollmann, J. *see* Landemark, E. 202
Pollmann, J. *see* Larsen, P.K. 202, 430
Pollmann, J. *see* Lu, W. 202
Pollmann, J. *see* Mazur, A. 203
Pollmann, J. *see* Rohlfing, M. 205
Pollmann, J. *see* Sabisch, M. 205
Pollmann, J. *see* Sandfort, B. 205
Pollmann, J. *see* Sandfort, D. 283
Pollmann, J. *see* Schmeits, M. 205, 283
Pollmann, J. *see* Schröer, P. 205
Pollmann, J. *see* Vogel, D. 207
Pollmann, J. *see* Wolfgarten, G. 208
Poncey, C. 896
Poncey, C. *see* Rochet, F. 283
Popma, T.J.A. *see* Monsma, D.J. 665
Popovic, S. *see* Hartmann, D. 664
Popovic, S. *see* Rampe, A. 666
Poppa, H. *see* Bauer, E. 505
Poppendieck, T.D. 89, 204
Porezag, D. *see* Frauenheim, Th. 199
Porter, S.J. 666
Porteus, J.O. 355
Posternak, M. 89
Posternak, M. *see* Krakauer, H. 88, 508
Poulin, S. *see* Ababou, Y. 893
Pouliot, R.J. *see* Klebanoff, L.E. 665
Poulopoulos, P. *see* Farle, M. 663
Powers, J.M. 204
Pracht, U. *see* Schneider, C.M. 667
Press, W.H. 89
Pretzer, D.D. 896
Prieto, P. *see* Liberati, M. 665
Prietsch, M. 860
Prietsch, M. *see* Bauer, A. 856
Prietsch, M. *see* Cuberes, M.T. 857
Prietsch, M. *see* Ludeke, R. 859
Prinz, G.A. *see* Chen, C.T. 87, 663
Prinz, G.A. *see* Falicov, L.M. 87
Prinz, G.A. *see* Idzerda, Y.U. 664
Pritchard, J. *see* McElhiney, G. 745
Proix, F. *see* del Pennino, U. 894
Prutton, M. 509
Prybyla, J. 509
Prybyla, J. *see* Altmann, M. 504
Puga, M.W. 204
Puga, M.W. *see* Tong, S.Y. 206
Pulay, P. 204
Pulm, H. *see* Grunze, M. 744
Purcell, S.T. 666
Puschmann, A. 746
Puschmann, A. *see* Bader, M. 742
Puschmann, A. *see* Höfer, U. 894

Qian, G. 204, 283
Qiu, Z.Q. 381
Qu, H. 205, 430
Quate, C.F. *see* Baski, A.A. 86
Quate, C.F. *see* Nogami, J. 89, 203
Quate, C.F. *see* Richter, M. 90
Quattropani, L. 860
Quattropani, L. *see* Niedermann, P. 860
Quinn, F.M. *see* Thornton, G. 897
Quinn, J.J. 860, 987
Quong, A.A. *see* Eguiluz, A.G. 986
Qvarford, M. *see* Andersen, J.N. 352, 947

Rabalais, J.W. *see* Bu, H. 281
Rader, O. 355, 666
Rader, O. *see* Carbone, C. 663, 947

Rader, O. *see* Clemens, W. 947
Rader, O. *see* Vescovo, E. 245, 668
Radermacher, K. *see* Struck, L.M. 896
Rado, G.T. 666
Radzig, A.A. 746
Ragavachari, K. *see* Stefanov, B.B. 896
Raghavachari, K. *see* Burrows, V.A. 281, 856
Raghavachari, K. *see* Higashi, G.S. 282
Raghavachari, K. *see* Struck, L.M. 896
Raghavachari, K. *see* Weldon, M.K. 897
Rahman, T.S. *see* Kern, K. 508
Rahman, T.S. *see* Lehwald, S. 949
Rahman, T.S. *see* Szeftel, J.M. 746
Raisanen, A. *see* Sorba, L. 896
Rajagopal, A.K. 89
Rajagopal, A.K. *see* Ramana, M.V. 89
Rajan, K. *see* Jimenez, J.R. 858
Ramaker, D.E. *see* Idzerda, Y.U. 664
Ramaker, D.M. *see* Long, J.P. 202
Ramana, M.V. 89
Rampe, A. 666
Rampe, A. *see* Hartmann, D. 664
Rampe, A. *see* Nouvertné, F. 355
Ramsey, M.G. 746
Ramstad, A. 205
Rangelov, G. 746
Rangelov, G. *see* Memmel, N. 745, 950
Rangelov, G. *see* Netzer, F.P. 745
Ranke, W. 205, 896
Ranke, W. *see* Chen, X.H. 198
Ranke, W. *see* Drathen, P. 429
Ranke, W. *see* Kübler, B. 202
Rapcewicz, K. 205
Rasing, Th. *see* Verheijen, M.A. 381
Ratliff, J.M. *see* Dunning, F.B. 663
Rau, C. 666
Rau, C. *see* Pfandzelter, R. 666
Rau, U. *see* Werner, J.H. 861
Rauscher, H. *see* Kostov, K.L. 354
Ravano, G. *see* Erbudak, M. 663
Ravenek, W. 89
Ray, K.B. *see* Davis, H.L. 505
Reaves, C.M. *see* O'Shea, J.J. 860
Rech, P. *see* Bode, S. 662
Redfield, A.C. 509
Redinger, J. 244
Redinger, J. *see* Rader, O. 355, 666
Redondo, A. 89
Reese, M. *see* Rampe, A. 666
Regenfus, G. *see* Chrobok, G. 663
Regenfus, G. *see* Hofmann, M. 664
Reggiani, L. *see* Jacoboni, C. 858
Reichardt, D. *see* Bechstedt, F. 86
Reichert, B. *see* Weinelt, M. 747
Reichmuth, A. *see* Benedek, G. 947
Reichmuth, A. *see* Hulpke, E. 948
Reihl, B. 205, 244, 950
Reihl, B. *see* Dudde, R. 947
Reihl, B. *see* Göpel, W. 199
Reihl, B. *see* Himpsel, F.J. 200
Reihl, B. *see* Johansson, L.S.O. 201
Reihl, B. *see* Manghi, F. 203
Reihl, B. *see* Mårtensson, P. 203, 430
Reihl, B. *see* Nicholls, J.M. 203
Reihl, B. *see* Perfetti, P. 204, 430
Reinecke, T.L. 509
Reinecke, T.L. *see* Tiersten, S.C. 510
Reining, L. *see* Palummo, M. 204
Remeika, J.P. *see* van der Laan, G. 91, 667
Ren, S.-F. 283
Ren, Y.R. *see* Anderson, P.W. 986
Rendulic, K.D. 355
Resch-Esser, U. 896
Resta, R. *see* Baroni, S. 197
Rettner, C.T. 746
Rettner, C.T. *see* Schweizer, E.K. 509
Reuter, K. 860
Reutt, J.E. 509
Rhead, G.A. *see* Sepulveda, A. 509
Rhoderick, E.H. 860
Rhoderick, E.H. *see* Missous, M. 859
Rhodin, T.N. *see* Billington, R.L. 86
Rhodin, T.N. *see* Dowben, P.A. 743
Rhodin, T.N. *see* Gerlach, R. L. 948
Rhodin, T.N. *see* Jensen, E.S. 744
Rhodin, T.N. *see* Seaburg, C.W. 746
Rice, T.M. 509, 987
Rich, D.A. 89
Rich, D.H. 89, 205
Richard, P. *see* Ebert, Ph. 199, 429
Richard, P. *see* Engels, B. 429
Richardson, B.E. *see* Fowell, A.E. 857
Richardson, B.E. *see* Shen, T.-H. 860
Richardson, N.V. 746
Richardson, N.V. *see* Jones, T.S. 744
Richardson, S.L. *see* Duke, C.B. 198, 281
Richmond, G.L. 950

Richter, M. 90
Richter, R. *see* Gay, J.G. 88, 664
Richter, R. *see* Zhu, X.-Y. 668
Richter, W. *see* Käckell, P. 199
Richter, W. *see* Pahlke, D. 896
Richter, W. *see* Resch-Esser, U. 896
Ricken, D. *see* Kulkarni, S.K. 745
Rieger, D. 746
Rieger, D. *see* Ludeke, R. 859
Rieger, D. *see* Miranda, R. 745
Rieger, D. *see* Schäffler, F. 860
Rieger, D. *see* Schnell, R.D. 205, 283, 896
Rieger, D. *see* Wegehaupt, T. 245
Rieger, M.M. *see* White, I.D. 245
Riess, H.J. *see* Giesen, K. 243, 948
Riester, T. *see* Reihl, B. 205
Riffe, D.M. 509, 746, 950
Rikvold, P.A. 509
Rikvold, P.A. *see* Dünweg, B. 506
Riley, C.E. *see* Puschmann, A. 746
Riley, J.D. *see* Hollering, M. 200
Riley, J.D. *see* Leckey, R.C.G. 430
Riley, J.D. *see* Xue, J.Y. 431
Riley, J.D. *see* Zhang, X.D. 431
Rincón, R. 283
Rincon, R. *see* Saiz-Pardo, R. 896
Rioux, D. 896
Rioux, D. *see* Niles, D.W. 381
Ristein, J. *see* Graupner, R. 199, 429
Riter, J.R. *see* Yean, D.H. 208
Ritke, C. *see* Pirug, G. 950
Ritsko, J.J. *see* Duke, C.B. 743
Ritter, M. *see* Wang, X.-G. 356
Ritz, A. *see* Matz, R. 381, 430
Riwan, R. *see* Cousty, J. 505
Riwan, R. *see* Soukiassian, P. 509, 951
Roadman, S.E. *see* Maity, N. 895
Robert, M. *see* Rau, C. 666
Roberts, N. 205
Roberts, N. *see* Payne, M.C. 204
Robertson, D.S. *see* Farrow, R.F.C. 429
Robertson, I.J. 355
Robertson, I.J. *see* Payne, M.C. 355
Robertson, W.D. *see* Florio, J.V. 199
Robinson, A.W. *see* Kulkarni, S.K. 745
Robinson, I.K. 205
Robinson, I.K. *see* Bohr, J. 197
Robinson, I.K. *see* Estrup, P.J. 506
Robinson, I.K. *see* Sauvage-Simkin, M. 205
Robinson, J.M. *see* Richmond, G.L. 950
Rochet, F. 283
Rochet, F. *see* Poncey, C. 896
Rochow, R. *see* Carbone, C. 663
Rodrigues, W.N. *see* Rochet, F. 283
Rodriguez, A. *see* Feder, R. 664
Rodriquez, C.O. *see* Methfessel, M. 89
Roetti, C. *see* Dovesi, R. 87
Rogozia, M. *see* Böttcher, A. 353
Rogozik, J. *see* Dose, V. 243, 663, 947
Rogozik, J. *see* Thörner, G. 245
Rohlfing, D.M. 205
Rohlfing, M. 205
Rohlfing, M. *see* Pollmann, J. 204
Rohlfing, M. *see* Sabisch, M. 205
Rohrer, G.S. 205
Rohrer, H. *see* Binnig, G. 281, 380, 428, 856
Roloff, H.F. *see* Heimann, P. 507
Ros, P. *see* Baerends, E.J. 86
Rösch, N. *see* Fox, T. 743
Rösch, N. *see* Memmel, N. 745
Rösch, N. *see* Schichl, A. 746
Rösch, N. *see* Weinelt, M. 747
Rose, H.B. *see* Hillebrecht, F.U. 664
Rose, H.B. *see* Roth, C. 666
Rose, M. *see* Dujardin, G. 894
Rosén, A. 90
Rosengren, A. 950
Rosenwinkel, E. *see* Miller, T. 203
Rosina, G. *see* Bertel, E. 742
Rosina, G. *see* Netzer, F.P. 745
Rosseinsky, M.J. 896
Rossi, G. *see* Liberati, M. 665
Rossmann, R. 205
Rostoker, N. *see* Kohn, W. 88
Rotenberg, E. 509
Rotermund, H.H. 381
Roth, C. 666
Roth, C. *see* Hillebrecht, F.U. 664
Roth, C. *see* Jungblut, R. 665
Röttger, B. *see* Kliese, R. 895
Roubin, P. *see* Guillot, C. 506
Roulet, H. *see* Poncey, C. 896
Roulet, H. *see* Rochet, F. 283
Rous, P.J. *see* MacLaren, J.M. 430
Rous, P.J. *see* Powers, J.M. 204
Rousseau, J. *see* Bertolini, J.C. 742
Rovida, G. *see* Nieuwenhuys, B.E. 745
Rowe, J.E. 430, 896

Rowe, J.E. *see* Bennet, P.A. 428
Rowe, J.E. *see* Chabal, Y.J. 197
Rowe, J.E. *see* Citrin, P.H. 894
Rowe, J.E. *see* Ibach, H. 895
Rowe, J.E. *see* Margaritondo, G. 282, 895
Rowe, J.E. *see* Schlüter, M. 896
Rowntree, P. *see* Klyachko, D.V. 895
Royer, W.A. *see* Hulbert, S.L. 507
Ruban, A. *see* Pedersen, M.O. 355
Rubin, M.E. 860
Rubio, A. 205
Rubio, A. *see* Zakharov, O. 208
Rubloff, G.W. *see* Lüth, H. 202
Ruckman, M.W. *see* Xu, F. 861
Rudd, J. *see* Heinrich, B. 948
Ruderman, M.A. 509
Rudolf, P. 896, 950
Rudolf, P. *see* Modesti, S. 895, 950
Rudolf, R. *see* Astaldi, S. 947
Rugar, D. *see* Mamin, H.J. 859
Ruggerone, P. *see* Benedek, G. 947
Ruggerone, P. *see* Harten, U. 200, 282
Ruggerone, P. *see* Kohler, B. 508
Ruggerone, P. *see* Luo, N.S. 949
Ruggerone, P. *see* Miglio, L. 203
Ruggerone, P. *see* Petersen, M. 355
Ruiz, E. *see* Kádas, K. 201
Rundgren, J. 244, 950
Rundgren, J. *see* Gauthier, Y. 664
Rundgren, J. *see* Lindgren, S.-Å. 949
Ruocco, A. 896
Russo, M. *see* Dunn, J.H. 663
Ruvalds, J. *see* Falicov, L.M. 663
Ryberg, R. 509
Ryu, J. *see* Davis, R.F. 198

Saalfeld, H. *see* Courths, R. 743
Saalfeld, H.B. *see* Kuhlenbeck, H. 745
Saalfeld, H.B. *see* Netzer, F.P. 745
Saalfrank, P. 950
Sabin, J.R. *see* Dunlap, B.I. 87
Sabisch, M. 205
Sabisch, M. *see* Pollmann, J. 204
Sacedón, J.L. *see* Alonso, M. 893
Saddei, D. 746
Sagawa, T. *see* Yokotsuka, T. 208
Sagner, H.-J. *see* Frank, K.-H. 948
Sagner, H.-J. *see* Watson, G.M. 510, 951
Sahni, V. 90
Sahu, D. *see* Altmann, M. 504
Saiki, R.S. 746
Saiz-Pardo, R. 896
Sajoto, T. 860
Sajoto, T. *see* O'Shea, J.J. 860
Saka, T. *see* Nakanishi, T. 666
Sakamoto, K. 896
Sakamoto, K. *see* Suto, S. 897
Sakamoto, T. *see* Enta, Y. 429
Sakisaka, Y. *see* Dowben, P.A. 743
Sakuma, E. *see* Hara, S. 199
Sakurai, T. 896
Sakurai, T. *see* Appelbaum, J.A. 281
Sakurai, T. *see* Hasegawa, Y. 858
Sakurai, T. *see* Hashizume, T. 200
Sakurai, T. *see* Pandey, K.C. 283, 896
Sakurai, T.. 896
Sakuri, T. *see* Hasegawa, Y. 507
Sakuri, T. *see* Hashizume, T. 507
Salahub, D.R. 90
Salamon, M. *see* Falicov, L.M. 87
Salaneck, W.R. 746
Salaneck, W.R. *see* Duke, C.B. 743
Salaneck, W.R. *see* Freund, H.J. 986
Salanon, B. 509
Saldin, D.K. *see* MacLaren, J.M. 430
Saldin, D.K. *see* Starke, U. 746
Salem, L. *see* Jorgensen, W.L. 744
Salmi, L.-A. 950
Salmi, L.-A. *see* Papadia, S. 244
Salvan, F. *see* Binnig, G. 856
Salvietti, M. *see* Gao, X. 664
Samant, M. *see* Nilsson, A. 355
Samant, M.G. 666
Samant, M.G. *see* Stöhr, J. 90, 381, 667
Sambe, H. 90
Sameth, R.L. *see* Hannon, J.B. 506
Samsavar, A. 90
Samsavar, A. *see* Hirschorn, E. 429
Samsavar, A. *see* Ludeke, R. 859
Samsavar, A. *see* Miller, T. 950
Samsavar, A. *see* Mueller, M.A 950
Samsavar, A. *see* Prietsch, M. 860
Samsavar, A. *see* Rich, D.A. 89
Samsavar, A. *see* Rich, D.H. 89
Sanada, N. *see* Huff, W.R.A. 429
Sanche, L. *see* Klyachko, D.V. 895
Sandell, A. 746
Sandfort, B. 205

Sandfort, B. *see* Mazur, A. 203
Sandfort, D. 283
Sands, T. *see* Palmstrøm, C.J. 860
Santaniello, A. *see* Ramsey, M.G. 746
Santoni, A. *see* Ludeke, R. 859
Santoni, A. *see* Shuh, D.K. 283
Santoro, G. *see* Bortolani, V. 505
Santoro, G. *see* Fasolino, A. 87, 506
Saris, F.W. *see* Tromp, R.M. 90, 207
Saunders, V.R. *see* Dovesi, R. 87
Saurenbach, F. *see* Binasch, G. 662
Sauvage, M. *see* Rochet, F. 283
Sauvage-Simkin, M. 205
Sauvage-Simkin, M. *see* Jedrecy, N. 201
Sawad, T. *see* Hashizumi, T. 858
Sawatzky, G.A. *see* van der Laan, G. 91, 667
Sawler, J. 666
Scandolo, S. *see* Lu, Z.-Y. 202, 430
Schäfer, J.A. 896
Schäfers, F. 666
Schäfers, F. *see* Baumgarten, L. 86, 662
Schäfers, F. *see* Petersen, H. 666
Schäfers, F. *see* Schneider, C.M. 667
Schaff, O. *see* Stampfl, A.P.J. 431
Schaffer, W.J. *see* Kowalczyk, S.P. 858
Schäffler, F. 860
Schäffler, F. *see* Ludeke, R. 859
Schaich, W.L. 244
Schaich, W.L. *see* Kempa, K. 949
Schardt, J. 205
Schärpf, O. *see* Hofmann, M. 664
Schattke, W. 205
Schattke, W. *see* Henk, J. 200
Schattke, W. *see* Olde, J. 204
Schattker, W. *see* Traving, M. 431
Schedel, T. *see* Ramsey, M.G. 746
Scheer, J.J. *see* van Laar, J. 207
Scheffler, M. 90, 205, 355, 950
Scheffler, M. *see* Alves, J.L.A. 196
Scheffler, M. *see* Andersen, J.N. 353
Scheffler, M. *see* Berndt, W. 353
Scheffler, M. *see* Bockstedte, M. 353
Scheffler, M. *see* Bormet, J. 353
Scheffler, M. *see* Bradshaw, A.M. 353, 505
Scheffler, M. *see* Burchhardt, J. 353, 742
Scheffler, M. *see* Cho, J.-H. 353
Scheffler, M. *see* Dabrowski, J. 198
Scheffler, M. *see* Eichler, A. 353
Scheffler, M. *see* Finnis, M.W. 353
Scheffler, M. *see* Fiorentini, V. 199, 353
Scheffler, M. *see* Ganduglia-Pirovano, M.V. 354
Scheffler, M. *see* Gonze, X. 199
Scheffler, M. *see* Gross, A. 354
Scheffler, M. *see* Hammer, B. 354
Scheffler, M. *see* Hebenstreit, J. 282
Scheffler, M. *see* Hennig, D. 354
Scheffler, M. *see* Hoffmann, P. 354
Scheffler, M. *see* Horn, K. 354, 744
Scheffler, M. *see* Kambe, K. 354
Scheffler, M. *see* Methfessel, M. 244, 354
Scheffler, M. *see* Neugebauer, J. 355, 509, 950
Scheffler, M. *see* Nouvertné, F. 355
Scheffler, M. *see* Oppo, S. 355
Scheffler, M. *see* Pankratov, O. 283
Scheffler, M. *see* Pehlke, E. 283, 381, 430
Scheffler, M. *see* Pentcheva, R. 355
Scheffler, M. *see* Petersen, M. 355
Scheffler, M. *see* Polatoglu, H.M. 746
Scheffler, M. *see* Schmalz, A. 355, 950
Scheffler, M. *see* Stampfl, C. 355, 356, 746, 951
Scheffler, M. *see* Wachutka, G. 207
Scheffler, M. *see* Wang, X.-G. 356
Scheffler, M. *see* Wenzien, B. 356
Scheffler, M. *see* Wilke, S. 356
Scheffler, M. *see* Xie, J. 356
Scheffler, M. *see* Yang, L. 356
Scheffler, M. *see* Yu, B.D. 356
Scheinfein, M.R. *see* McClelland, J.J. 665
Schell-Sorokin, A.J. *see* Demuth, J.E. 198, 428
Schep, K.M. 244
Scheunemann, T. 666
Scheunemann, T. *see* Henk, J. 664
Scheunemann, T. *see* Rampe, A. 666
Schichl, A. 746
Schichl, A. *see* Umbach, E. 747
Schief, H. *see* Benedek, G. 947
Schiffer, A. 355
Schlapbach, L. *see* Fasel, R. 353
Schlegel, B. 90
Schlier, R.E. 90, 283, 431, 896
Schlittler, R.R. *see* Jung, T. 381
Schlittler, R.R. *see* Reihl, B. 950
Schlögl, R. *see* Wang, X.-G. 356
Schlüter, M. 205, 860, 896
Schlüter, M. *see* Bachelet, G.B. 86, 196, 281
Schlüter, M. *see* Godby, R.W. 199, 506

Schlüter, M. *see* Hamann, D.R. 88, 199
Schlüter, M. *see* Ho, K.M. 282
Schlüter, M. *see* Larsen, P.K. 895
Schmalz, A. 355, 950
Schmalz, A. *see* Aminpirooz, S. 352
Schmalz, A. *see* Burchhardt, J. 353, 742
Schmeisser, D. 746, 896
Schmeits, M. 205, 283, 431
Schmid, A.K. 667
Schmid, P.E. 860
Schmid, P.E. *see* Liehr, M. 858
Schmidt, W.G. 205, 283, 431
Schmidt, W.G. *see* Kress, C. 201
Schmidt, W.G. *see* Scholze, A. 205
Schmiedeskamp, B. 667
Schmiedeskamp, B. *see* Irmer, N. 664
Schmitz, P.J. 667
Schneider, C. 746
Schneider, C. *see* Rau, C. 666
Schneider, C. *see* Venus, D. 668
Schneider, C.M. 667
Schneider, C.M. *see* Baumgarten, L. 86, 662
Schneider, C.M. *see* Ebert, H. 663
Schneider, C.M. *see* Gao, X. 664
Schneider, C.M. *see* Kuch, W. 665
Schneider, C.M. *see* Venus, D. 668
Schneider, R. 244
Schneider, R. *see* Graß, M. 243
Schneider, R. *see* Schuppler, S. 244
Schneider, W.-D. *see* Patthey, F. 950, 987
Schnell, R.D. 205, 283, 896
Schnell, R.D. *see* Miranda, R. 745
Schnell, R.D. *see* Rieger, D. 746
Schnell, R.D. *see* Weser, T. 91
Schober, O. *see* Christmann, K. 742
Scholl, D. *see* Mauri, D. 665
Scholze, A. 205
Schönhammer, K. 431, 746
Schönhammer, K. *see* Allen, J.W. 985
Schönhense, G. 667
Schönhense, G. *see* Bansmann, J. 662
Schönhense, G. *see* Schneider, C.M. 667
Schönhense, G. *see* Schäfers, F. 666
Schottky, W. 860
Schowalter, L.J. 860
Schowalter, L.J. *see* Jimenez, J.R. 858
Schowalter, L.J. *see* Lee, E.Y. 858
Schreiber, R. *see* Grünberg, P. 664
Schrey, F. *see* Sullivan, J.P. 861
Schrey, F. *see* Tung, R.T. 861
Schrieffer, J.R. *see* Einstein, T.L. 506, 743
Schröder, K. *see* Kisker, E. 381, 665
Schröder, K. *see* Weller, D. 668
Schröder-Bergen, E. *see* Chen, X.H. 198
Schroeder, K. *see* Ebert, Ph. 199, 429
Schroeder, K. *see* Engels, B. 429
Schröer, P. 205
Schröter, B. *see* Käckell, P. 199
Schubert, B. 896
Schubert, E.F. *see* Gossman, H.J. 857
Schug, C.A. *see* Weser, T. 91
Schuller, I.K. *see* Falicov, L.M. 87
Schulte, F.K. 90, 950
Schulte, F.K. *see* Hölzl, J. 243, 858
Schulz, B. 667
Schulz, H. *see* Rossmann, R. 205
Schulz, M. *see* Palm, H. 860
Schulz, R. *see* Gräf, D. 894
Schulze Icking-Konert, G. *see* Hannon, J.B. 948
Schulze, G. 283
Schumacher, D. *see* Persson, B.N.J. 509
Schuppler, S. 244
Schuppler, S. *see* Fischer, N. 243, 664, 948
Schuppler, S. *see* Fischer, R. 243, 948
Schuster, P. *see* Schneider, C.M. 667
Schuster, R. 950
Schuster, R. *see* Wintterlin, J. 747
Schütz, G. 90, 667
Schwartz, L.M. *see* Ehrenreich, H. 506
Schwarz, E. *see* Braun, W. 742
Schwarzacher, W. *see* Bennett, W.R. 947
Schweeger, G. *see* Hashizumi, T. 858
Schwegmann, S. *see* Böttcher, A. 353
Schwegmann, S. *see* Kim, Y.D. 354
Schwegmann, S. *see* Stampfl, C. 356
Schweizer, E. *see* Tüshaus, M. 747
Schweizer, E.K. 509
Schweizer, E.K. *see* Eigler, D.M. 380
Scott, G. *see* Duke, C.B. 198
Seaburg, C.W. 746
Seabury, C.W. 746
Seah, M.P. 667
Sears, M.P. *see* Li, Y.S. 89
Sebenne, C. *see* del Pennino, U. 894
Sebenne, C.A. *see* Guichar, G.M. 199
Sëbenne, C.E. *see* Andriamanantenasoa, I. 86
Seedorf, R. *see* Wilke, W.G. 431

Seeger, K. 860
Seel, M. 896
Segall, B. *see* Lambrecht, W.R. 202, 430
Segall, B. *see* Szmulowicz, F. 244
Seghadat, A.K. 667
Seip, U. *see* Grunze, M. 744
Seitz, F. 509
Seitz, G. *see* Borstel, G. 742
Seiwatz, R. 90
Seiwatz, R. *see* Green, M. 88
Seki, K. *see* Nicholls, J.M. 203
Selci, S. 381
Selci, S. *see* Chiaradia, P. 198, 380, 428
Selloni, A. *see* Ancilotto, F. 281
Selloni, A. *see* Manghi, F. 203
Selloni, A. *see* Takeuchi, N. 206, 431
Semancik, S. 950
Semond, F. 205
Semond, F. *see* Soukiassian, P. 206
Senf, F. *see* Incoccia, L. 895
Senftinger, B. *see* Donath, M. 243
Seo, J.M. 896
Seo, J.M. *see* Anderson, S.G. 893
Sepulveda, A. 509
Serena, P.A. 950
Sernelius, B.E. *see* Mahan, G.D. 987
Sernelius, B.E. *see* Shung, K.W.K. 987
Sesselmann, W. *see* Woratschek, B. 951
Sestovic, D. *see* Reuter, K. 860
Sette, F. *see* Chen, C.T. 87, 663
Sette, F. *see* Modesti, S. 950
Sette, F. *see* Smith, N.V. 90
Sette, F. *see* Thole, B.T. 90
Sexton, B.A. *see* Madix, R.J. 745
Seyller, T. 355
Shaikhutdinov, Sh.K. *see* Wang, X.-G. 356
Sham, L.J. *see* Godby, R.W. 199, 506
Sham, L.J. *see* Kohn, W. 88, 201, 282, 665
Shannon, V.L. *see* Richmond, G.L. 950
Shapiro, A.P. *see* Wachs, A.L. 207, 951
Shek, M.L. 206
Shen, G.D. *see* Ranke, W. 896
Shen, T.-H. 90, 860
Shen, T.-H. *see* Fowell, A.E. 857
Shen, T.C. 896
Shen, Y. 950
Shen, Y.R. *see* Chin, R.P. 198
Shen, Y.R. *see* Tom, H.W.K. 951
Shen, Z.X.. 987
Sheppard, N. 746
Sherman, M.G. *see* Sinniah, K. 283
Shevchik, N.J. 431
Shi, X. 950
Shi, X. *see* Tang, D. 951
Shi, Z.Q. 860
Shih, H.D. 206
Shih, H.D. *see* Jona, F. 88
Shih, Y.C. *see* Streetman, B.G. 861
Shima, N. *see* Ishida, H. 282
Shima, N. *see* Zhu, Z. 91, 431
Shimada, K. *see* Kakizaki, A. 665
Shimazaki, T. *see* Nagao, T. 950
Shimomura, M. *see* Huff, W.R.A. 429
Shin, K.S. 509
Shin, K.S. *see* Chung, J.W. 505
Shinn, N.D. 746
Shinoda, M. *see* Ito, T. 895
Shirley, D.A. *see* Apai, G. 742
Shirley, D.A. *see* Kevan, S.D. 381
Shirley, D.A. *see* Ley, L. 202
Shirley, D.A. *see* Leung, K.T. 202
Shirley, E.L. 206
Shirley, E.L. *see* Rubio, A. 205
Shirm, K.M. *see* Spiess, L. 283
Shirykalov, E.N. *see* Chulkov, E.V. 505
Shkrebtii, A.I. 206, 283, 431
Shkrebtii, A.I. *see* Di Felice, R. 281
Shkrebtii, A.I. *see* Takeuchi, N. 206
Shockley, W. 244, 509
Shoji, F. *see* Oura, K. 896
Shore, H.B. *see* Liebermann, L.N. 665
Shuh, D.K. 283
Shuh, D.K. *see* Lo, C.W. 895
Shuh, D.K. *see* Terminello, L.J. 381
Shung, K.W.K. 987
Shung, K.W.K. *see* Ma, S.K. 986
Shung, K.W.K. *see* Overhauser, A.W. 987
Siegbahn, K. *see* Gelius, U. 381
Sieger, M.T. *see* Carlisle, J.A. 428
Siegmann, H.C. 667
Siegmann, H.C. *see* Busch, G. 663
Siegmann, H.C. *see* Mauri, D. 665
Siegmann, H.C. *see* Pierce, D.T. 666
Sigino, O. *see* Yamauchi, J. 208
Silberman, J.A. *see* Haight, R. 199
Silcox, J. *see* Fernandez, A. 857
Silcox, J. *see* Hallen, H.D. 857
Silkin, V.M. *see* Chulkov, E.V. 505

Silverman, P.J. *see* Culbertson, R.J. 198, 894
Silverman, P.J. *see* Feldman, L.C. 87
Silverman, P.J. *see* Hasegawa, Y. 858
Silvestrelli, P.L. *see* Alavi, A. 352
Simmons, J.G. 860
Simpson, W.C. 896
Singer, K.E. *see* Missous, M. 859
Singh, D. 90, 509
Singh, D. *see* Perdew, J.P. 89
Singh, D. *see* Yu, R. 91
Singh, I. *see* Srivastava, G.P. 206
Singh, R. *see* Dhesi, S.S. 429
Singhal, S.P. 987
Singwi, K.S. 987
Singwi, K.S. *see* Vashishta, P. 987
Sinharov, S. 896
Sinniah, K. 283
Sirotti, F. *see* Liberati, M. 665
Sirotti, F. *see* Poncey, C. 896
Sirotti, F. *see* Rochet, F. 283
Sirringhaus, H. 860
Sirringhaus, H. *see* Lee, E.Y. 858
Sirringhaus, H. *see* Stalder, R. 861
Sitar, Z. *see* Davis, R.F. 198
Sizmann, R. *see* Chrobok, G. 663
Sjölander, A. *see* Singwi, K.S. 987
Skeath, P.R. *see* Spicer, W.E. 860, 861
Skelton, D. *see* Kneedler, E. 508
Skibowski, M. 206
Skibowski, M. *see* Carstensen, H. 197, 428
Skibowski, M. *see* Claessen, R. 986
Skibowski, M. *see* Henk, J. 200
Skibowski, M. *see* Kipp, L. 201, 430
Skibowski, M. *see* Manzke, R. 203, 430, 987
Skibowski, M. *see* Olde, J. 204
Skibowski, M. *see* Straub, D. 206, 431
Skibowski, M. *see* Traving, M. 431
Skottke-Klein, M. *see* Over, H. 950
Skriver, H. 355
Skriver, H. *see* Aldén, M. 504
Slade, M.L. *see* Brillson, L.J. 856
Slade, M.L. *see* Chiaradia, P. 856
Slade, M.L. *see* Viturro, R.E. 381, 861
Slagsvold, B.J. *see* Gartland, P.O. 88, 506, 948
Slagsvold, P.T. *see* Grepstad, T.K. 88
Slater, J.C. 90
Slater, L.J. 950
Slavin, A.J. *see* Feenstra, R.M. 199, 429
Slijkerman, W.F.J. *see* Hara, S. 199
Smalley, R.E. *see* Kroto, H. 895
Smeenk, R.G. *see* Tromp, R.M. 90, 207
Smilgies, D.-M. *see* Hulpke, E. 507
Smirnov, B.M. *see* Radzig, A.A. 746
Smit, L. 206, 431
Smit, L. *see* Derry, T.E. 198
Smit, L. *see* Tromp, R.M. 207
Smith, A.P. *see* Yan, H. 208
Smith, A.R. 431
Smith, D.J. *see* Parkin, S.S.P. 666
Smith, D.L. 860
Smith, D.L. *see* Daw, M.S. 857
Smith, D.L. *see* Zur, A. 862
Smith, G.D.W. *see* Melmed, A.J. 89
Smith, J.R. 90
Smith, J.R. *see* Gay, J.G. 88
Smith, J.R. *see* Zhu, X.-Y. 668
Smith, K.E. 509
Smith, K.E. *see* Dhesi, S.S. 429
Smith, K.E. *see* Di, W. 505
Smith, K.E. *see* Elliott, G.S. 506
Smith, K.E. *see* Kneedler, E. 508
Smith, N.V. 90, 244, 381, 431, 509, 667, 950
Smith, N.V. *see* Chen, C.T. 87, 505, 663, 947
Smith, N.V. *see* Garrett, R.F. 243
Smith, N.V. *see* Hulbert, S.L. 507
Smith, N.V. *see* Johnson, P.D. 244, 664, 665, 949
Smith, N.V. *see* Kevan, S.D. 508
Smith, N.V. *see* Larsen, P.K. 430, 895
Smith, N.V. *see* Woodruff, D.P. 245, 951
Smith, P.V. *see* Craig, B.I. 198, 894
Smith, P.V. *see* Zheng, X.M. 208, 283
Smith, R.J. 746
Smith, R.J. *see* Lapeyre, G.J. 745
Smith, R.J. *see* Williams, G.P. 208, 431
Smoliner, J. *see* Heer, R. 858
Sneh, O. *see* Wise, M.L. 897
So, E. *see* Kahn, A. 201
So, E. *see* Meyer, R.J. 203
Sob, M. *see* Turek, I. 667
Solal, F. 206
Soler, J.M. 90
Solt, K. *see* Niedermann, P. 860
Solt, K. *see* Quattropani, L. 860
Somers, J. *see* Horn, K. 507, 744, 948
Somers, J. *see* Lindner, Th. 745
Somers, J. *see* Woodruff, D.P. 747
Somerton, C. *see* Campuzano, J.C. 505

Sommer, E. 509
Somorjai, G.A. 90, 355, 746
Somorjai, G.A. *see* Asscher, M. 742
Somorjai, G.A. *see* Koel, B.E. 745
Somorjai, G.A. *see* MacLaren, J.M. 430
Somorjai, G.A. *see* Mate, C.M. 745
Somorjai, G.A. *see* Nieuwenhuys, B.E. 745
Somorjai, G.A. *see* Powers, J.M. 204
Somorjai, G.A. *see* Tom, H.W.K. 951
Somos, J. *see* Kulkarni, S.K. 745
Song, K.-J. 950
Song, K.-J. *see* Plummer, E.W. 950
Sonntag, B. *see* von dem Borne, A. 668
Sorba, L. 206, 431, 896
Sorba, L. *see* Middelmann, H.-U. 430
Sorensen, J.E. *see* Adams, D.L. 86
Soria, F. *see* Alonso, M. 893
Soukiassian, P. 90, 206, 509, 951
Soukiassian, P. *see* Aristov, V.Yu. 196, 428
Soukiassian, P. *see* Semond, F. 205
Soukiassian, P. *see* Spiess, L. 206, 283
Souteyrand, E. *see* Allongue, P. 855
Soven, P. *see* Bartynski, R.A. 243
Soven, P. *see* Kar, N. 88
Sowa, E.C. 206
Sowers, H. *see* Grünberg, P. 664
Spaarnay, M.J. *see* Meyer, F. 895
Spanjaard, D. 283, 355, 509, 746
Spanjaard, D. *see* Guillot, C. 506
Spanjaard, D. *see* Legrand, B. 89
Spanjaard, D. *see* Treglia, G. 90
Sparvieri, N. *see* Selci, S. 381
Spicer, W.E. 667, 860, 861
Spicer, W.E. *see* Cao, R. 856
Spicer, W.E. *see* Lindau, I. 381, 859
Spicer, W.E. *see* Miyano, K.E. 859
Spicer, W.E. *see* Newmann, N. 859
Spicer, W.E. *see* Petro, W.G. 860
Spicer, W.E. *see* Richter, M. 90
Spicer, W.E. *see* Wagner, L.F. 510
Spiess, L. 206, 283
Spindt, C.J. *see* Spicer, W.E. 861
Sprunger, P.T. 746
Srivastava, G.P. 206
Srivastava, G.P. *see* Humphreys, T.P. 200
Srivastava, G.P. *see* Jenkins, S.J. 207
Srivastava, G.P. *see* Williams, R.H. 897
Stagarescu, C.B. *see* Dhesi, S.S. 429
Stalder, R. 861
Stampfl, A.P.J. 431
Stampfl, A.P.J. *see* Hollering, M. 200
Stampfl, A.P.J. *see* Graupner, R. 199
Stampfl, A.P.J. *see* Xue, J.Y. 431
Stampfl, C. 355, 356, 746, 951
Stampfl, C. *see* Berndt, W. 353
Stampfl, C. *see* Burchhardt, J. 353, 742
Stapel, D. *see* Hannon, J.B. 948
Stark, J.B. *see* Robinson, I.K. 205
Starke, K. 244, 667
Starke, K. *see* Bode, S. 662
Starke, K. *see* Schneider, R. 244
Starke, U. 206, 746
Starke, U. *see* Schardt, J. 205
Starrost, F. *see* Traving, M. 431
Stefanov, B.B. 896
Stefanov, B.B. *see* Weldon, M.K. 897
Stegge, J.A.D. *see* Purcell, S.T. 666
Steierl, G. *see* Pfandzelter, R. 666
Steigenberger, U. *see* Paul, D.M. 666
Steimer, C. *see* Klünker, C. 949
Steiner, P. *see* Finteis, T. 429
Steiner, P. *see* Solal, F. 206
Steiner, P.-R. *see* Starke, U. 206
Steinhögl, W. *see* Kuch, W. 665
Steinkilberg, M. 746
Steinmann, W. 244
Steinmann, W. *see* Fischer, N. 243, 664, 948
Steinmann, W. *see* Giesen, K. 243, 948
Steinmann, W. *see* Rieger, D. 746
Steinmann, W. *see* Schnell, R.D. 205, 283, 896
Steinmann, W. *see* Schuppler, S. 244
Steinmann, W. *see* Wegehaupt, T. 245
Steinmann, W. *see* Weser, T. 91
Steinmüller, D. *see* Ramsey, M.G. 746
Steinrück, H.-P. 746
Steinrück, H.-P. *see* Eiding, J. 743
Steinrück, H.-P. *see* Huber, W. 744
Steinrück, H.-P. *see* Schneider, C. 746
Steinrück, H.-P. *see* Weinelt, M. 747
Stenborg, A. 951
Stensgaard, I. *see* Adams, D.L. 86
Stensgaard, I. *see* Pedersen, M.O. 355
Stensgaard, I. *see* Pleth Nielsen, L. 355
Stephan, U. *see* Frauenheim, Th. 199
Stephens, C. *see* McLean, A.B. 859
Stephenson, P.C. 90
Stephenson, P.C. *see* Binns, C. 505
Stepniak, F. *see* Rioux, D. 896

Stern, E.A. *see* Bennett, H.S. 86
Stern, E.A. *see* Erskine, J.L. 87
Stern, G. *see* Walker, J.C. 668
Stevens, K. *see* Horsky, T.N. 200
Stevens, K. *see* Wang, Y.R. 207, 431
Stewart, T. *see* Wood, A.D.B. 951
Štich, I. 206, 283, 431
Štich, I. *see* De Vita, A. 281
Stichler, M. *see* Gsell, M. 354
Sticht, J. *see* Oppeneer, P.M. 89
Stiles, K. 861
Stiles, K. *see* Horsky, T.N. 200
Stiles, K. *see* Kahn, A. 858
Stiles, M. 861
Stockhausen, A. 896
Stoffel, N.G. 206, 431
Stoffel, N.G. *see* Brillson, L.J. 856
Stoffel, N.G. *see* Hulbert, S.L. 507
Stoffel, N.G. *see* Kevan, S.D. 201, 430, 508
Stoffel, N.G. *see* Margaritondo, G. 859
Stöhr, J. 90, 381, 667
Stöhr, J. *see* Apai, G. 742
Stöhr, J. *see* Liu, A.C. 745
Stöhr, J. *see* Nilsson, A. 355
Stöhr, J. *see* Terminello, L.J. 381
Stoltze, P. *see* Pleth Nielsen, L. 355
Storjohann, I. *see* Incoccia, L. 895
Storz, R.H. *see* Haight, R. 199
Strasser, G. *see* Heer, R. 858
Strathy, I. *see* Eberhardt, W. 743
Strathy, I. *see* Heskett, D. 744
Straub, D. 206, 244, 431, 951
Straub, D. *see* Drube, W. 198, 429
Straub, D. *see* Ludeke, R. 859
Straub, D. *see* Magnusson, K.O. 430
Straub, T. *see* Finteis, T. 429
Streetman, B.G. 861
Streslicka, M. *see* Davison, S.G. 505
Strite, S. 431
Stroscio, A. *see* Whitman, L.J. 283
Stroscio, J.A. 206, 381, 746, 861, 896, 951
Stroscio, J.A. *see* Feenstra, R.M. 199, 429, 857
Stroscio, J.A. *see* Whitman, L.J. 510
Strozier, J.A. Jr. *see* Jona, F. 895
Struck, C.W. *see* Alig, R.C. 855
Struck, L.M. 896
Stucki, F. *see* Schäfer, J.A. 896
Studna, A.A. *see* Aspnes, D.E. 380
Stuhlen, R. *see* Hamza, A.V. 199
Stuhlmann, C. 206, 951
Stuhlmann, C. *see* Daun, W. 947
Stulen, R.H. *see* Sowa, E.C. 206
Stumpf, R. *see* Gonze, X. 199
Su, C. *see* Tang, D. 951
Su, C.Y. *see* Lindau, I. 859
Su, C.Y. *see* Spicer, W.E. 861
Subbaswamy, K.R. *see* Mahan, G.D. 987
Suda, Y. *see* Ebina, A. 199
Sudikono, J. *see* Avery, A.R. 428
Suga, S. *see* Venus, D. 668
Sugano, T. *see* Nonoyama, S. 283
Sugimoto, Y. *see* Hiratani, Y. 894
Sugimoto, Y. *see* Taneya, M. 897
Suhl, H. *see* Peacock-Lopez, E. 509
Sullivan, J.P. 861
Sullivan, J.P. *see* Tung, R.T. 861
Sumita, I. *see* Hashizume, T. 507
Sun, X. *see* Liu, J.N. 508
Sunjic, M. *see* Doniach, S. 857
Surh, M.P. 206, 987
Surkamp, L. *see* Bartels, F. 893
Surman, M. 746
Surman, M. *see* Klauser, R. 745
Surman, M. *see* Woodruff, D.P. 747
Surman, M. *see* van der Laan, G. 91, 667
Susa, K. *see* Yamamoto, S. 861
Suto, S. 897
Suto, S. *see* Sakamoto, K. 896
Suzuki, S. *see* Enta, Y. 199, 429
Suzuki, S. *see* Yokotsuka, T. 208
Suzuki, T. *see* Tjeng, L.H. 987
Suzuki, Y. *see* Huff, W.R.A. 429
Svane, A. 206
Svensson, C. 951
Svensson, C. *see* Carlsson, A. 947
Svensson, C. *see* Hamawi, A. 948
Svensson, C. *see* Lindgren, S.-Å. 949
Svensson, S. *see* Gelius, U. 381
Swanson, L.W. 509, 510
Swartz, L.-E. *see* Biegelsen, D.K. 197, 281, 428
Swartz, L.-E. *see* Uhrberg, R.I.G. 90
Swartzentruber, B.S. *see* Becker, R.S. 86, 197, 281, 856
Swartzentruber, B.S. *see* Bouchard, A.M. 197
Swiech, W. *see* Bauer, F. 380
Swiech, W. *see* Schneider, C.M. 667
Sze, S.M. 861

Sze, S.M. *see* Cowley, A.M. 856
Sze, S.M. *see* Crowell, C.R. 856, 857
Szeftel, J.M. 746
Szmulowicz, F. 244
Szotek, Z. 206
Szotek, Z. *see* Temmerman, W.M. 206

Ta, S.Y. *see* Shen, Y. 950
Tabata, T. 206
Tabe, M. 897
Taborelli, M. *see* Allenspach, R. 662
Taborelli, M. *see* Landolt, M. 665
Tache, N. *see* Chiaradia, P. 856
Takahashi, M. *see* Takayanagi, K. 206, 283, 431, 897
Takahashi, S. *see* Takayanagi, K. 206, 283, 431, 897
Takahashi, T. 206, 431
Takahashi, T. *see* Ebina, A. 199
Takahashi, T. *see* Ebina, E. 199
Takai, T. 206
Takayanagi, K. 206, 283, 431, 897
Takeuchi, N. 206, 431
Takeuchi, T. *see* Huff, W.R.A. 429
Taleb-Ibrahimi, A. *see* Aristov, V.Yu. 428
Taleb-Ibrahimi, A. *see* Grupp, C. 894
Taleb-Ibrahimi, A. *see* Himpsel, F.J. 381
Taleb-Ibrahimi, A. *see* Hricovini, K. 200, 282
Taleb-Ibrahimi, A. *see* Ludeke, R. 859
Talin, A.A. 861
Tam, N.T. 861
Tamm 510
Tamura, E. 667
Tamura, E. *see* Ackermann, B. 662
Tamura, E. *see* Feder, R. 664
Tamura, E. *see* Gradmann, U. 664
Tanaka, S. *see* Nishijima, N. 895
Taneya, M. 897
Taneya, M. *see* Hiratani, Y. 894
Tang, D. 510, 951
Tang, D. *see* Shi, X. 950
Tang, F.-C. 667
Tang, F.-C. *see* Dunning, F.B. 663
Tang, J.Y.-F 861
Tang, S. 90, 510
Tang, S.-T. *see* Spiess, L. 283
Tanishiro, T. *see* Takayanagi, K. 431
Tanishiro, Y. *see* Takayanagi, K. 206, 283, 897
Tark, J. *see* Haight, R. 199
Taylor, J.B. 356, 746
Taylor, R. *see* Geldart, D.J.W. 986
te Velde, G. *see* Kirchner, E.J.J. 282
Tebble, R.S. 667
Tejeda, J. *see* Shevchik, N.J. 431
Tejedor, C. 861
Telieps, W. *see* Bauer, E. 662
Temmerman, W.M. 206
Temmerman, W.M. *see* Szotek, Z. 206
Terakura, I. 90
Terakura, K. *see* Ishida, H. 507, 949
Terakura, K. *see* Kobayashi, K. 201, 282
Terakura, K. *see* Shi, X. 950
Terakura, K. *see* Terakura, I. 90
Terminello, L.J. 381
Terminello, L.J. *see* Leung, K.T. 202
Terminello, L.J. *see* McLean, A.B. 895
Terminello, L.J. *see* Shuh, D.K. 283
Terminello, L. *see* Whitman, L.J. 897
Tersoff, J. 431, 510, 861
Tersoff, J. *see* Feenstra, R.M. 199, 429
Teter, M.P. 90
Teter, M.P. *see* Li, Y.S. 89
Teter, M.P. *see* Payne, M.C. 89, 204, 355
Teukolsy, S.A. *see* Press, W.H. 89
Theis, W. *see* Chassé, T. 428
Theis, W. *see* Paggel, J.J. 430
Theis, W. *see* Wilke, W.G. 431
Theiss, S.K. *see* Ganz, E. 199
Themlin, J.-M. 206
Thiel, P.A. 897
Thiel, P.A. *see* Schmitz, P.J. 667
Thiel, R. *see* Tillmann, D. 667
Thieme, F. *see* Kessler, J. 744
Thiry, P. 431, 510
Thiry, P. *see* Hricovini, K. 200, 282
Thiry, P. *see* Louie, S.G. 508
Thiry, P.A. *see* Bouzidi, S. 893
Thiry, P.A. *see* Hricovini, K. 200, 282
Thole, B.T. 90, 667
Thole, B.T. *see* van der Laan, G. 91, 667
Thomas, H. *see* Mayer, H. 665
Thomas, H.R. *see* Duke, C.B. 743
Thomas, L.H. 90
Thomas, R.E. 951
Thomas, W.J.O. *see* Gordy, W. 857
Thompson, W.J. *see* Demuth, J.E. 857
Thomson, D. *see* Payne, M.C. 355
Thomson, D.I. *see* Robertson, I.J. 355

Thörner, G. 245
Thörner, G. *see* Borstel, G. 243, 662
Thornton, G. 897
Thornton, G. *see* Johansson, L.S.O. 895
Thornton, J.M. *see* Dharmadasa, I.M. 857
Thornton, J.M.C. 206, 897
Thuault, C.D. *see* Guichar, G.M. 199
Tiersten, S.C. 510
Tiller, W.A. *see* Takai, T. 206
Tillmann, D. 667
Tiogo, F. 987
Tischer, M. *see* Dunn, J.H. 663
Titterington, D.J. *see* Hopkinson, J.F.L. 243
Tjeng, L.H. 987
Tjeng, L.H. *see* Idzerda, Y.U. 88
Tobin, J.G. 90
Tochihara, H. 206
Tochihara, H. *see* Hasegawa, Y. 507
Tochihara, H. *see* Hashizume, T. 507
Tochihara, H. *see* Mizuno, S. 950
Toennies, I.P. *see* Ellis, J. 948
Toennies, J.P. 746
Toennies, J.P. *see* Benedek, G. 947
Toennies, J.P. *see* Bortolani, V. 505
Toennies, J.P. *see* Braun, J. 947
Toennies, J.P. *see* Ernst, H. 506
Toennies, J.P. *see* Graham, A.P. 948
Toennies, J.P. *see* Harten, U. 200, 282, 507
Toennies, J.P. *see* Luo, N.S. 949
Tokumoto, H.. 897
Tokutaka, H. *see* Nakanishi, S. 203
Tom, H.W.K. 951
Tomásek, M. *see* Pick, S. 509
Tommasini, F. *see* Crottini, A. 947
Tone, K. 897
Toney, M. *see* Bohr, J. 197
Tong, S.Y. 206, 431
Tong, S.Y. *see* Lee, B.W. 89
Tong, S.Y. *see* Puga, M.W. 204
Tong, S.Y. *see* van Hove, M.A. 91
Tonner, B.P. *see* Plummer, E.W. 746
Tonner, B.P. *see* Stöhr, J. 90, 381, 667
Topler, J. *see* Henzler, M. 894
Topping, J. 356, 510
Torikachvili, M.S. *see* Allen, J.W. 985
Tosatti, E. 90, 510
Tosatti, E. *see* Baldereschi, A. 197
Tosatti, E. *see* Car, R. 197
Tosatti, E. *see* Fasolino, A. 87, 506
Tosatti, E. *see* Iarlori, S. 200
Tosatti, E. *see* Lu, Z.-Y. 202, 430
Tosatti, E. *see* Takeuchi, N. 206, 431
Tosatti, E. *see* Yin, S. 668
Tosi, M.P. *see* Singwi, K.S. 987
Tove, P.A. *see* De Sousa Pires, J. 857
Trafas, B.M. 861
Traum, M. *see* Seabury, C.W. 746
Traum, M.M. *see* Smith, N.V. 431
Traving, M. 431
Treglia, G. 90
Treglia, G. *see* Guillot, C. 506
Treglia, G. *see* Legrand, B. 89
Trickey, S.B. *see* Boettger, J.C. 505, 947
Trioni, M.I. *see* Brivio, G.P. 353
Tromp, R. *see* Copel, M. 894
Tromp, R. *see* Himpsel, F.J. 200
Tromp, R. *see* Marée, P.J.M. 203
Tromp, R.M. 90, 207, 431
Tromp, R.M. *see* Batra, I.P. 428
Tromp, R.M. *see* Hamers, R.J. 88, 199, 381, 429, 894
Tromp, R.M. *see* Kaxiras, E. 895
Tromp, R.M. *see* Smit, L. 206, 431
Troost, D. 283, 861, 897
Troullier, N. 207
Troullier, N. *see* Martins, J.L. 203
Trucks, G. *see* Higashi, G.S. 282
Tsai, N.C. *see* Grunze, M. 744
Tsang, C.H. 667
Tsang, J.C. *see* Meyer, R.J. 203
Tsang, K.-L. *see* Shinn, N.D. 746
Tschudy, M. *see* Reihl, B. 205
Tsong, I.S.T. *see* Chang, C.S. 197
Tsong, I.S.T. *see* Li, L. 202
Tsong, T.T. *see* Chen, C.-L. 505
Tsu, R. *see* Li, G. 282
Tsubata, M. *see* Nakanishi, T. 666
Tsuda, M. 283
Tsuei, K.-D. 381
Tsuei, K.-D. *see* Adler, D.L. 947
Tsuei, K.-D. *see* Heskett, D. 948
Tsuei, K.-D. *see* Plummer, E.W. 950
Tsuei, K.-D. *see* Shi, X. 950
Tsui, D.C. 431
Tsukada, M. *see* Ishida, H. 282
Tsukada, M. *see* Uchiyama, T. 283, 897
Tsukada, M. *see* Zhu, Z. 91
Tsukuda, M. *see* Yamauchi, J. 208

Tsukuda, M. *see* Zhu, Z. 431
Tsvetkov, V.F. *see* Kulakov, M.A. 202
Tu, D.-W. *see* Duke, C.B. 198
Tucker, J. *see* Shen, T.C. 896
Tully, J.C. *see* Estrup, P.J. 506
Tully, J.C. *see* Head-Gordon, M. 507
Tung, R.T. 90, 861
Tung, R.T. *see* Hasegawa, Y. 858
Tung, R.T. *see* Melmed, A.J. 89
Tung, R.T. *see* Sullivan, J.P. 861
Turek, I. 667
Turner, A.M. 667
Turner, B.R. *see* Lee, E.Y. 858
Turner, D.W. 747
Tüshaus, M. 747
Twesten, R.D. 207
Tyc, S. 207
Tyson, J. *see* Walker, J.C. 668

Uchida, H. 861
Uchida, W. *see* Sakamoto, K. 896
Uchiyama, T. 283, 897
Udagawa, M.. 897
Ueda, K. *see* Murano, K. 895
Uhlenbrock, S. 747
Uhrberg, R.I.G. 90, 207, 283, 431, 897
Uhrberg, R.I.G. *see* Bringans, R.D. 87, 197, 428
Uhrberg, R.I.G. *see* Hansson, G.V. 199, 381, 429, 506
Uhrberg, R.I.G. *see* Johansson, L.S.O. 201, 282, 429, 895
Uhrberg, R.I.G. *see* Karlsson, C.J. 429, 895
Uhrberg, R.I.G. *see* Landemark, E. 202, 282, 430
Uhrberg, R.I.G. *see* Nicholls, J.M. 203
Uhrberg, R.I.G. *see* Olmstead, M.A. 89, 204
Ulloa, S.E. *see* Alfonso, D.R. 196
Umbach, E. 747
Umbach, E. *see* Breitschafter, M.J. 742
Umbach, E. *see* Höfer, U. 744, 894
Umbach, E. *see* Morgen, P. 895
Umbach, E. *see* Schneider, C. 746
Umbach, E. *see* Weimer, J.J. 747
Umbach, E. *see* Wurth, W. 747
Umeuchi, M. *see* Nagao, T. 950
Umezawa, K. *see* Oura, K. 896
Unguris, J. 667
Unguris, J. *see* Pierce, D.T. 666
Unno, T. *see* Ebina, A. 199
Unsworth, P. *see* Thornton, J.M.C. 206
Urbach, L.E. 951
Urban, K. *see* Ebert, Ph. 199, 429
Urban, K. *see* Engels, B. 429

Valeri, S. *see* Ruocco, A. 896
van Acker, J.F. *see* Andersen, J.N. 352, 947
van Bommel, A.J. 207, 283
van Camp, P. *see* Devreese, J.T. 198
van Camp, P.E. 207
van Daelen, M.A. *see* Li, Y.S. 89
van der Laan, G. 91, 667
van der Laan, G. *see* Hillebrecht, F.U. 664
van der Laan, G. *see* Thole, B.T. 90, 667
van der Veen, J.F. 510
van der Veen, J.F. *see* Derry, T.E. 198
van der Veen, J.F. *see* Eastman, D.E. 199
van der Veen, J.F. *see* Hara, S. 199
van der Veen, J.F. *see* Himpsel, F.J. 200
van der Veen, J.F. *see* Larsen, P.K. 202, 430
van der Veen, J.F. *see* Marée, P.J.M. 203
van der Veen, J.F. *see* Smit, L. 206, 431
van der Veen, J.F. *see* Tromp, R.M. 207
van der Veen, J.F. *see* van Silfhout, R.G. 207
van der Werf, D.P. *see* Heslinga, D.R. 858
van Doren, V.E. *see* van Camp, P.E. 207
van Hasselt, C.W. *see* Verheijen, M.A. 381
van Hoof, J.B.A.N. 510
van Hoof, J.B.A.N. *see* Schep, K.M. 244
van Hove, M.A. 91, 245
van Hove, M.A. *see* Lee, B.W. 89
van Hove, M.A. *see* MacLaren, J.M. 430
van Hove, M.A. *see* Mizuno, S. 950
van Hove, M.A. *see* Powers, J.M. 204
van Hove, M.A. *see* Somorjai, G.A. 90, 355, 746
van Hove, M.A. *see* Sowa, E.C. 206
van Kampen, D.G. *see* Klebanoff, L.E. 665
van Laar, J. 207
van Laar, J. *see* Huijser, A. 200, 429, 858
van Loenen, E.J. *see* Tromp, R.M. 207
van Rompay, M. *see* Moison, J.M. 859
van Rooy *see* Huijser, A. 858
van Rooy, T.L. *see* Huijser, A. 200, 429
van Rooy, T.L. *see* van Laar, J. 207
van Schilfgaarde, M. *see* Newmann, N. 859
van Siclen, C. DeW. 245
van Silfhout, R.G. 207

van Tooren, A. *see* van Bommel, A.J. 207
van Vleck, J.H. 510, 667
Vanderbilt, D. 207, 283
Vanderbilt, D. *see* Chan, C.T. 197
Vanderbilt, D. *see* Li, X.-P. 282
Vanderbilt, D. *see* Meade, R.D. 430
Vanderbilt, D.H. *see* Payne, M.C. 89, 204
Vandré, D. *see* Cuberes, M.T. 857
Varekamp, P.R. *see* Lo, C.W. 895
Varma, R.R. *see* Williams, R.H. 861
Vashishta, P. 987
Vassell, W.C. *see* Jaklevic, R.C. 949
Vazquez de Parga, A.L. 897
Veal, B.W. *see* Olson, C.G. 987
Velasco, V.R. *see* Jaskolski, W. 949
Velicky, B. 510
Venus, D. 667, 668
Venus, D. *see* Kuch, W. 665
Venus, D. *see* Sawler, J. 666
Venus, D. *see* Schneider, C.M. 667
Verheij, L.K. 897
Verheijen, M.A. 381
Versluis, L. 91
Verweyen, A. *see* von dem Borne, A. 668
Verwoerd, W.S. 91
Verwoerd, W.S. *see* Badziag, P. 197
Verwoerd, W.S. *see* Brink, R.S. 87
Vescovo, E. 245, 668
Vescovo, E. *see* Carbone, C. 663, 947
Vescovo, E. *see* Clemens, W. 947
Vescovo, E. *see* Rader, O. 355, 666
Vetterling, W.T. *see* Press, W.H. 89
Vickers, J.S. *see* Becker, R.S. 86, 197, 281
Vickers, J.S. *see* Kubby, J.A. 202
Victora, R.H. *see* Falicov, L.M. 87
Vidali, G. *see* Dowben, P.A. 505
Vielsack, G. *see* Yang, L. 356
Vigneron, J.P. *see* Scheffler, M. 205
Villarrubia, J.S. 897
Villarrubia, J.S. *see* Boland, J.J. 893
Villars, D.S. 747
Viswanath, Y. *see* Bauer, E. 505
Vitomirov, I.M. *see* Aldau, C.M. 855
Vitorimov, I.M. *see* Waddill, G.D. 861
Viturro, R.E. 381, 861
Viturro, R.E. *see* Brillson, L.J. 856
Viturro, R.E. *see* Chiaradia, P. 856
Vlieg, E. *see* Kirchner, E.J.J. 282
Vlieg, E. *see* Robinson, I.K. 205
Vogel, D. 207
Vogel, D. *see* Pollmann, J. 204
Vogel, P. 861
Vogl, P. *see* Majewski, J.A. 203
Vogt, B. *see* Schmiedeskamp, B. 667
Vögt, M. *see* Finteis, T. 429
von Barth, J. 91
von dem Borne, A. 668
von der Emde, M. *see* Evans, D.A. 857
von der Linden, W. 207
von Känel, H. *see* Lee, E.Y. 858
von Känel, H. *see* Meyer, T. 859
von Känel, H. *see* Sirringhaus, H. 860
von Känel, H. *see* Stalder, R. 861
von Münch, W. 207
von Muschwitz, C. *see* Hoffmann, P. 354
von Muschwitz, C. *see* Jacobi, K. 354
von Oertzen, A. *see* Rotermund, H.H. 381
Vos, M. *see* Trafas, B.M. 861
Vosko, S.H. *see* Geldart, D.J.W. 986
Vosko, S.H. *see* MacDonald, A.J. 89
Vosko, S.H. *see* Perdew, J.P. 89
Vosko, S.H. *see* Wilk, L. 510
Vosko, S.M. *see* MacDonald, A.H. 89
Vvedensky, D.D. *see* MacLaren, J.M. 244, 430
Vvedensky, D.D. *see* Thornton, G. 897

Wachs, A.L. 207, 951
Wachutka, G. 207
Wachutka, G. *see* Scheffler, M. 90, 205, 355
Waclawski, B.J. 510
Waddill, G.D. 861
Waddill, G.D. *see* Anderson, S.G. 893
Waddill, G.D. *see* Tobin, J.G. 90
Wagner, F. *see* Wang, X.-G. 356
Wagner, H. *see* Ibach, H. 895
Wagner, H. *see* Mermin, N.D. 665
Wagner, L.F. 510
Wagner, W. *see* Schütz, G. 90, 667
Wahi, A.K. *see* Miyano, K.E. 859
Wahlström, E. *see* Lindgren, S.-Å. 949
Wakita, T. *see* Suto, S. 897
Waldrop, J.R. 861
Waldrop, J.R. *see* Kraut, E.A. 858
Walecka, J.D. *see* Fetter, A.L. 243
Walker, J.C. 668
Walker, T.G. 668
Wall, A. *see* Sorba, L. 896
Wallace, R.L. *see* Shi, Z.Q. 860

Wallauer, W. 951
Walldén, L. 951
Walldén, L. *see* Carlsson, A. 947
Walldén, L. *see* Gustafsson, T. 948
Walldén, L. *see* Hamawi, A. 506, 948
Walldén, L. *see* Lindau, I. 508
Walldén, L. *see* Lindgren, S.-Å. 244, 508, 665, 949
Walldén, L. *see* Svensson, C. 951
Waller, G. 668
Waller, G. *see* Gradmann, U. 664
Waller, G. *see* Tamura, E. 667
Walmsley, D.G. *see* Floyd, R.B. 857
Walsh, A.D. 747
Waltenberg, H.N. 897
Walters, G.K. *see* Dunning, F.B. 663
Walters, G.K. *see* Tang, F.-C. 667
Wambach, J. 747
Wambach, J. *see* Geisler, H. 743
Wan, C.S. 245
Wandelt, K. *see* Gumhalter, B. 744
Wandelt, K. *see* Markert, K. 745
Wandelt, K. *see* Miranda, R. 745
Wandelt, K. *see* Schnell, R.D. 205, 896
Wandelt, R. *see* Schnell, R.D. 283
Wander, A. *see* Powers, J.M. 204
Wang, C. *see* Shen, T.C. 896
Wang, C.S. 91, 207
Wang, D. *see* Wu, R. 91
Wang, D.-S. 91, 668
Wang, D.T. *see* Pahlke, D. 896
Wang, D.T. *see* Resch-Esser, U. 896
Wang, G.-C. 510
Wang, G.-C. *see* Ching, Y.W. 505
Wang, G.C. *see* Celotta, R.J. 663
Wang, H. *see* Brosseau, R. 742
Wang, J. 951
Wang, J. *see* Alerhand, O.L. 281
Wang, X.-G. 356
Wang, X.W. 510
Wang, Y.C. *see* Chang, C.S. 197
Wang, Y.R. 207, 431
Wang, Y.R. *see* Duke, C.B. 198
Waskiewicz, W.K. *see* Robinson, I.K. 205
Wassdahl, N. *see* Nilsson, A. 355
Watababe, A. *see* Naitoh, M. 895
Watanabe, M. *see* Chung, J.W. 505
Watanabe, M. *see* Shin, K.S. 509
Watanabe, N. *see* Kobayashi, K.L.I. 858
Watanabe, S. 207
Watanabe, S. *see* Yamauchi, J. 208
Watson, G.M. 510, 951, 987
Watson, G.N. *see* Whittaker, E.T. 245
Wchutka, G. *see* Scheffler, M. 950
Weaire, D. *see* Srivastava, G.P. 206
Weast, R.C. 747
Weaver, J.H. 861
Weaver, J.H. *see* Aldau, C.M. 855
Weaver, J.H. *see* Anderson, S.G. 893
Weaver, J.H. *see* Chander, M. 894
Weaver, J.H. *see* Ding, S.-A. 428
Weaver, J.H. *see* Gu, C. 894
Weaver, J.H. *see* Patrin, J.C. 896
Weaver, J.H. *see* Rioux, D. 896
Weaver, J.H. *see* Seo, J.M. 896
Weaver, J.H. *see* Trafas, B.M. 861
Weaver, J.H. *see* Waddill, G.D. 861
Weaver, J.H. *see* Xu, F. 861
Weaver, J.S. *see* Yang, Y.-N. 283
Webb, M.B. 207
Webb, M.B. *see* Phaneuf, R.J. 204
Webb, M.B. *see* Poppendieck, T.D. 204
Webb, M.B. *see* Tong, S.Y. 206, 431
Webb, M.W. *see* Poppendieck, T.D. 89
Weber, E. *see* Spicer, W.E. 861
Weber, W. 668, 951
Weber, W. *see* Hartmann, D. 664
Weber, W. *see* Rampe, A. 666
Weber, W. *see* Wang, X.W. 510
Wedler, G. *see* Freund, H.-J. 743
Weertman, J.R. *see* Rado, G.T. 666
Wegehaupt, T. 245
Wehner, R.S. *see* Apai, G. 742
Wei, C.M. *see* Tong, S.Y. 206, 431
Wei, D.-S. 510
Wei, S.-H. *see* Martins, J.L. 203
Wei, S.-H. *see* Singh, D. 90
Wei, S.H. 207
Wei, S.H. *see* Yeh, Ch.Y. 208
Wei, S.H. *see* Zhang, S.B. 208
Weibel, E. *see* Binnig, G. 281, 380, 428
Weick, D. *see* Berndt, W. 353
Weidmann, R. 207
Weightmann, P. *see* Thornton, J.M.C. 206
Weill, T. *see* Nilsson, A. 355
Weimer, J.J. 747
Weimer, J.J. *see* Wurth, W. 747
Weinberg, W.H. *see* Mitchell, W.J. 354

Weinberg, W.H. *see* Sinniah, K. 283
Weinberg, W.H. *see* van Hove, M.A. 245
Weinberger, P. *see* Redinger, J. 244
Weinberger, P. *see* Turek, I. 667
Weindl, Ch. *see* Piancastelli, M.N. 430
Weinelt, M. 747
Weinelt, M. *see* Huber, W. 744
Weinelt, M. *see* Nilsson, A. 355
Weinert, M. 91, 245, 510, 668
Weinert, M. *see* Brookes, N.B. 663
Weinert, M. *see* Fu, C.L. 88
Weinert, M. *see* Jennings, P.J. 244
Weinert, M. *see* Smith, N.V. 244
Weinert, M. *see* Wimmer, E. 91, 245, 668
Weisel, M.D. *see* Peden, C.H.F. 355
Weiss, W. *see* Wang, X.-G. 356
Weitering, H.H. 861
Weitering, H.H. *see* Heslinga, D.R. 858
Weldon, M.K. 897
Weller, D. 668
Wells, A.F. 207
Wen, H.J. *see* Cuberes, M.T. 857
Wendin, G. 747
Wendt, S. *see* Kim, Y.D. 354
Wengelnik, H. *see* Badt, D. 196
Wensell, M. *see* Zhang, Z. 208
Wenzien, B. 207, 208, 356
Wenzien, B. *see* Bormet, J. 353
Wenzien, B. *see* Schmidt, W.G. 283
Wern, H. *see* Courths, R. 743
Werner, J.H. 861
Wertheim, G.K. 431, 861, 951
Wertheim, G.K. *see* Riffe, D.M. 509, 746, 950
Wertheim, G.K. *see* Smith, N.V. 950
Weser, T. 91
Wesner, D.A. *see* Weber, W. 668, 951
Westphal, C. *see* Bansmann, J. 662
Westrin, P. *see* Lindgren, S.-Å. 949
Westwood, D.I. *see* Fowell, A.E. 857
Westwood, D.I. *see* Shen, T.-H. 860
Wever, J. *see* Rossmann, R. 205
Whitaker, M.A.B. 668
White, C.W. *see* Himpsel, F.J. 200
White, I.D. 245
Whitman, L.J. 283, 510, 897
Whittaker, E.T. 245
Whitten, J.L. *see* Jing, Z. 201
Widdra, W. 897
Widdra, W. *see* Kostov, K.L. 354
Wiegerhaus, F. *see* Verheij, L.K. 897
Wigner, E. 91, 208
Wigren, C. *see* Björneholm, O. 947
Wigren, C. *see* Göthelid, M. 894
Wilhelm, W. *see* Schütz, G. 90, 667
Wilk, L. 510
Wilke, S. 356
Wilke, S. *see* Gross, A. 354
Wilke, W.G. 431
Wilke, W.G. *see* McLean, A.B. 859
Wilke., S. *see* Kohler, B. 508
Wilkinson, G. *see* Cotton, F.A. 743
Williams, A.R. 208
Williams, A.R. *see* Binnig, G. 856
Williams, A.R. *see* Knapp, J.A. 508
Williams, A.R. *see* Lang, N.D. 354, 508, 949
Williams, A.R. *see* Moruzzi, V. 244, 665
Williams, A.R. *see* Soler, J.M. 90
Williams, B.E. *see* Davis, R.F. 198
Williams, G.M. *see* Farrow, R.F.C. 429
Williams, G.P. 208, 431
Williams, G.P. *see* Hirschmugl, C.J. 507
Williams, G.P. *see* Lindner, Th. 745
Williams, G.P. *see* Struck, L.M. 896
Williams, M.D. *see* Newmann, N. 859
Williams, M.L. *see* Tsang, C.H. 667
Williams, R.H. 861, 897
Williams, R.H. *see* Dharmadasa, I.M. 857
Williams, R.H. *see* Fowell, A.E. 857
Williams, R.H. *see* Humphreys, T.P. 200
Williams, R.H. *see* McLean, A.B. 859
Williams, R.H. *see* Rhoderick, E.H. 860
Williams, R.H. *see* Shen, T.-H. 860
Williams, R.H. *see* Srivastava, G.P. 206
Williams, R.H. *see* Thornton, J.M.C. 897
Williams, R.S. *see* Talin, A.A. 861
Williams, R.W. *see* Apai, G. 742
Williams, S. *see* Ade, H. 380
Willis, R.F. *see* Feuerbacher, B. 664
Willis, R.F. *see* Fu, J. 282
Willis, R.F. *see* Himpsel, F.J. 381
Willis, R.F. *see* Ortega, J.E. 666, 950
Willis, R.F. *see* Rohlfing, D.M. 205
Wilson, A.H. 861
Wilson, J.A. 510
Wilson, J.M. *see* Lurie, P.G. 202
Wilson, R.J. *see* Chiang, S. 742
Wilson, R.J. 897
Wimmer, E. 91, 208, 245, 356, 510, 668, 951

Wimmer, E. *see* Andzelm, J. 86
Wimmer, E. *see* Fu, C.L. 88
Wimmer, E. *see* Li, Y.S. 89
Wimmer, E. *see* Ohnishi, S. 89
Wimmer, E. *see* Soukiassian, P. 509, 951
Wimmer, E. *see* Weinert, M. 91, 245, 668
Wincott, P.C. *see* Johansson, L.S.O. 895
Wincott, P.L. *see* Thornton, G. 897
Winkler, A. *see* Rendulic, K.D. 355
Winter, H. *see* Szotek, Z. 206
Winters, H.F. 897
Wintterlin, J. 747
Wintterlin, J. *see* Brune, H. 505
Wintterlin, J. *see* Coulman, D.J. 743
Wise, M.L. 897
Wissman, P. 510
Witt, W. 510
Wittmer, M. 861
Witzel, S. *see* Neuber, M. 745
Wöhlecke, M. 668
Wöhlecke, M. *see* Borstel, G. 742
Wohlfarth, E.P. 668
Woicik, J.C. *see* Richter, M. 90
Wold, A. *see* Coehoorn, R. 428
Wolf, D. *see* Rossmann, R. 205
Wolf, E.L. 861
Wolfframm, D. *see* Barman, S.R. 428
Wolfframm, D. *see* Xue, J.Y. 431
Wolfgarten, G. 208
Wolfgarten, G. *see* Goldmann, A. 199
Wolfgarten, G. *see* Koke, P. 201
Wolfgarten, G. *see* Krüger, P. 202, 430
Wolfgarten, G. *see* Pollmann, J. 204
Wolfram, D. *see* Barman, S.R. 197
Wolkow, R. 208, 283, 381
Wolkow, R. *see* Avouris, Ph. 893
Wöll, Ch. *see* Bortolani, V. 505
Wöll, Ch. *see* Harten, U. 200, 282, 507
Won-Kok Choi *see* Kneedler, E. 508
Wood, A.D.B. 951
Woodall, J.M. 861
Woodall, J.M. *see* Pashley, M.D. 204, 283
Woodruff, D.P. 245, 381, 747, 951
Woodruff, D.P. *see* Kerkar, M. 949
Woodruff, D.P. *see* King, D.A. 895
Woodruff, D.P. *see* Puschmann, A. 746
Woodruff, T.O. *see* Tiogo, F. 987
Woolf, D.A. *see* Fowell, A.E. 857
Woolf, D.A. *see* Shen, T.-H. 860
Woolf, D.A. *see* Thornton, J.M.C. 206
Woratschek, B. 951
Wright, A.F. 208, 987
Wrinn, M. *see* Li, Y.S. 89
Wu, C.I. 431
Wu, N.J. *see* Hashizumi, T. 858
Wu, R. 91
Wu, R. *see* Wang, D.-S. 91
Wu, R.-Q. 668
Wu, R.-Q. *see* Freeman, A.J. 664
Wu, T.T. *see* McCoy, B. 665
Wu, Y. *see* Stöhr, J. 90, 381, 667
Wurth, W. 747
Wurth, W. *see* Höfer, U. 894
Wurth, W. *see* Morgen, P. 895
Wuttig, M. *see* Rader, O. 355

Xia, L.Q. *see* Maity, N. 895
Xie, J. 356
Xing, G. *see* Rau, C. 666
Xing, Y.R. *see* Ranke, W. 896
Xiong, F. *see* Ganz, E. 199
Xiong, J.J. *see* Ihm, J. 201, 429
Xu, F. 861
Xu, F. *see* Aldau, C.M. 855
Xu, F. *see* Trafas, B.M. 861
Xu, G. *see* Puga, M.W. 204
Xu, G. *see* Tong, S.Y. 206
Xu, P. *see* Jayaram, G. 201
Xu, Y.-N. 208
Xue, J.Y. 431
Xue, Q.K. *see* Hashizume, T. 200

Yacoby, A. *see* Lang, N.D. 858
Yafet, Y. *see* Landolt, M. 665
Yakovkin, I.N. *see* Katrich, G.A. 508
Yalabik, M.C. *see* Rikvold, P.A. 509
Yamada, M. *see* Saiki, R.S. 746
Yamada, M. *see* Tone, K. 897
Yamaguchi, H. 431
Yamakaki, T. *see* Kimura, K. 744
Yamamoto, S. 861
Yamamoto, T. *see* Tabe, M. 897
Yamane, J. *see* Oura, K. 896
Yamauchi, J. 208
Yan, H. 208
Yang, A.-B. *see* Olson, C.G. 987
Yang, H. *see* Ding, S.-A. 428
Yang, L. 356

Yang, L.H. *see* Fong, C.Y. 282
Yang, S. 245, 951
Yang, S.H. 208
Yang, W. *see* Lu, W. 202
Yang, W. *see* Parr, R.G. 89
Yang, W.S. 91, 208
Yang, W.S. *see* Jona, F. 895
Yang, Y.-N. 283
Yarmoff, J.A. *see* Himpsel, F.J. 381
Yarmoff, J.A. *see* Lo, C.W. 895
Yarmoff, J.A. *see* Shuh, D.K. 283
Yarmoff, J.A. *see* Simpson, W.C. 896
Yarmoff, J.A. *see* Whitman, L.J. 897
Yates, J.T. *see* Goodman, D.W. 743
Yates, J.T. *see* Sinniah, K. 283
Yates, J.T. Jr. 897
Yates, T.E. *see* Boszo, T. 742
Yates, J.T. Jr. *see* Muehlhoff, L. 203
Yates, J.T. Jr. *see* Waltenberg, H.N. 897
Ye Ling 91
Yean, D.H. 208
Yeh, Ch.Y. 208
Yeh, J.J. 861
Yeh, J.L. *see* Meyer, R.J. 203
Yelon, A. *see* Ababou, Y. 893
Yeom, H.W. *see* Huff, W.R.A. 429
Yi, J.-Y. 283
Yin, M.T. 91, 208
Yin, M.T. *see* Chabal, Y.J. 197
Yin, S. 668
Ying, S.C. *see* Altmann, M. 504
Ying, S.C. *see* Chung, J.W. 505
Ying, S.C. *see* Graham, A.P. 948
Ying, S.C. *see* Han, W.K. 506
Ying, S.C. *see* Prybyla, J.A. 509
Ying, S.C. *see* Reinecke, T.L. 509
Ying, S.C. *see* Tiersten, S.C. 510
Ying, Z.C. *see* Wang, J. 951
Yndurain, F. 861
Yndurain, F. *see* Artacho, E. 86
Yndurain, F. *see* Louis, E. 859
Yokotsuka, T. 208
Yong, J.C. 897
Yoshida, K. 510
Yoshida, S. *see* Hara, S. 199
Yoshimori, A. *see* Fujita, M. 429
Young, I.M. *see* Farrow, R.F.C. 429
Young, K. *see* Kahn, A. 858
Yu, B.D. 356
Yu, P.Y. 431
Yu, R. 91, 747

Zaera, F. 747
Zahn, D.R.T. *see* Dudzik, E. 894
Zahn, D.R.T. *see* Evans, D.A. 857
Zakharov, O. 208
Zangwill, A. 747
Zangwill, A. *see* Redfield, A.C. 509
Zapol, P. *see* Jaffe, J.E. 201
Zapol, P. *see* Pandey, R. 204
Zare, R.N. 668
Zaremba, E. *see* Bruch, L.W. 353
Zartner, A. *see* Engelhardt, H.A. 743
Zartner, A. *see* Hofmann, P. 744
Zebisch, P. *see* Huber, W. 744
Zebisch, P. *see* Weinelt, M. 747
Zegenhagen, J. 91
Zegenhagen, J. *see* Resch-Esser, U. 896
Zehner, D.M. *see* Davis, H.L. 87
Zehner, D.M. *see* Didio, R.A. 743
Zehner, D.M. *see* Himpsel, F.J. 200
Zeller, R. 91
Zeller, R. *see* Nordström, L. 666
Zeller, R. *see* Schütz, G. 90, 667
Zeper, W.B. *see* Purcell, S.T. 666
Zhang, G. *see* Bortolani, V. 505
Zhang, G. *see* Harten, U. 507
Zhang, J. 951
Zhang, J. *see* Li, D. 508
Zhang, K. *see* Lu, W. 202
Zhang, L. *see* Dowben, P.A. 505
Zhang, S.B. 208, 862
Zhang, S.B. *see* Zhu, X. 208, 431
Zhang, X. *see* Ade, H. 380
Zhang, X. *see* Dunning, F.B. 663
Zhang, X. *see* Tang, F.-C. 667
Zhang, X.D. 431
Zhang, X.S. *see* Leung, K.T. 202
Zhang, Z. 208
Zhang, Z.Y. 510
Zharnikov, M. *see* Kuch, W. 665
Zheng, X.M. 208, 283
Zhilin, V.M. *see* Aristov, V.Yu. 428
Zhong, Q.M. *see* Heinrich, B. 948
Zhou, J. *see* Hashizume, T. 200
Zhu, M.J. 668
Zhu, X. 208, 283, 431
Zhu, X. *see* Blase, X. 281

Zhu, X. *see* Hricovini, K. 200, 282
Zhu, X. *see* Shirley, E.L. 206
Zhu, X.-Y. 668
Zhu, X.D. *see* Tom, H.W.K. 951
Zhu, Z. 91, 431
Zhu, Z. *see* Chiaradia, P. 380
Ziegler, A. *see* Graupner, R. 199, 429
Ziegler, A. *see* Hollering, M. 200
Ziegler, C. *see* Munz, A.W. 203
Ziegler, T. *see* Versluis, L. 91
Ziethen, C. *see* Schneider, C.M. 667
Ziman, J.M. 510
Zimmermann, P. *see* von dem Borne, A. 668
Zinn, W. *see* Binasch, G. 662
Zinn, W. *see* Müller, N. 666
Zubrägel, C. *see* Neuber, M. 745
Zuhr, R.A. *see* Feldman, L.C. 87
Zunger, A. 91, 862
Zunger, A. *see* Ihm, J. 201, 282
Zunger, A. *see* Perdew, J.P. 204
Zunger, A. *see* Wei, S.H. 207
Zunger, A. *see* Yeh, Ch.Y. 208
Zunger, A. *see* Zhang, S.B. 208
Zur, A. 862
Zwicker, G. 208

# Subject index


*ab initio* molecular dynamics 339, 342, 343
accumulation layer 421, 422
activation energy 676, 690
adatom 397, 399, 400, 402
adatom vibrations 146
adiabatic approximation 477, 484
adsorbate 365
adsorbate band structure 305, 308, 309, 322, 323, 327, 331
adsorbate dipole 288, 290, 315–319, 328, 329
adsorbate–adsorbate band 305
adsorbate–adsorbate bond 307, 318, 328, 329, 351
adsorbate–substrate bond 294, 309, 319, 335
adsorbates on Si(100)-(2 × 1)-like surfaces 259
adsorption 295, 317
– benzene 728
– chalcogenide 679
– CO 333, 693
– energy 295
– on III-V cleavage surfaces 261
– on Si(111) 253
– ordered 250
– site symmetry 722
Ag(111) 937
Ag/Fe(100) 938
Ag/Ge(111) 273
Ag/Ni(111) 938
Ag/Si(111) 272
Al 2p-level 943, 944
Al(001) 454–456, 459
Al(100) 228
Al(110) 228
Al(111) 228, 242, 454, 456, 459, 924
Al(111)/K 678
Al(111)/Na 906, 942, 944
Al/GaAs(110) 272, 274
alkali-metal adsorption 309–311, 313, 317, 324, 326, 329
alkali metal monolayers 916
alkali metals on semiconductors 267
alkaline earths on Mo(112) 448
alkalis on Cu(111) 466
allowed geometry 699, 739
anisotropic magnetoresistive (AMR) heads 518
Anderson–Grimley–Newns Hamiltonian 251, 672, 673
Anderson–Grimley–Newns model 294, 304
angle-resolved photoemission 363, 969
angular distribution pattern 696
anisotropy constants 552
antibonding states 294, 299, 302, 303, 307–309, 312, 313, 324, 333–335, 342
antisymmetric wave function 706
As–As bond 260
As–Ga bond 261
As/GaAs(111) 278
As–H bond 263, 275, 276
As/Si(100) 260
As/Si(111) 258, 280
As-trimer model 278
asymmetric dimer model 123, 259, 389
Au/Ge(111) 273
Auger electrons 376
Au/Si(111) 273
autocompensation 419

back-bond surface states 397, 412
$\pi$-backdonation 693
ballistic electron emission microscopy (BEEM) 831, 840, 847
– Bell–Kaiser model 812
– heterojunction studies 845
– hole injection 816
– electron beam divergence 811
– quantum mechanical transmission 818, 834
– transport model 809, 821
– UHV BEEM system 805
band bending 373, 374, 421, 422, 781, 792
band gap 107, 112, 127, 128, 176

band gap problem 970
band mapping 602
band narrowing 960
band structure 111, 322, 323, 675, 683
Bardeen limit 756
Bardeen model 272
Be(0001) 447–449, 451–458, 474
Be(0001)/Li 924
bending mode 255
benzene adsorption 728
beryllium 961
binding energy 945
bit 517
Bloch law 545, 581
Bloch states 305–308
Bloch theorem 26
Blyholder model 334, 335, 672, 693
bond-cutting model 297
$\pi$-bonded chain 394
$\pi$-bonded chain model 138, 142, 143, 146, 253
$\pi$-bonded $N_2$ 715
bond length 310, 351
bond nature 309
bond strength 304, 305, 310, 337, 346, 348, 349, 351
bond-length-conserving rotation relaxation 149, 173
bond-length-contracting rotation 149, 183
bonding state 294, 299, 300, 302, 303, 307–309, 312, 313, 335, 342
Born–Oppenheimer approximation 4, 294, 339, 476
Br 886
bridge bond 412
Brillouin zone 305, 307
broken bond 362, 365, 451
Broyden–Fletcher–Goldfarb–Shanno methods 26
buckling model 253
bulk band dispersion 929
bulk interband transition 600, 655
bulk semiconductors 370
bulk state 221, 222

C(111) 255
c(2 × 2)O/Ni(100) 679
c(2 × 2)S/Ni(100) 683
$C_2H_4$/Ni(110) 722
$C_2H_4$/Ni(111) 725
$C_{60}$ 892
$C_6H_6$/Ni(110) 735
$C_6H_6$/Ni(111) 729
$C_6H_6$/Os(0001) 733
$CaF_2$/Si (111) 367
Car–Parrinello method 34–38, 250, 252, 253, 255, 259, 263, 280
carbondioxide adsorption 718
catalysis 333, 337, 345, 350
$CH_3$/GaAs(100) 276
chalcogenide adsorption 679
charge density wave 477, 980
charge fluctuations 970
charge neutrality 352
charge rearrangement 414
charge transfer 291, 292, 300, 311, 313–316, 318, 321, 323, 327, 333, 374, 394, 913, 945
chemical activity 304, 337, 340
chemical bond 288–291, 293, 299, 303, 304, 307, 309–311, 314, 315, 318, 326, 335, 337, 343, 350, 351
chemical core level shift 374
chemical images 377
chemical potential 166
chemical reactions 373, 379
chemical reactivity 866
chemical shift 373
chemisorption 75, 251
Cl 886
$Cl_2$/Si(111) 258
Cl/Al(111) 309–311, 313, 314, 316
Cl–As bond 263, 264
Cl–Cl bond 258
Cl/Cu(111) 309, 310, 314
Cl–Ga bond 263, 264
Cl/GaSb(110) 263
Cl/InSb(110) 263
CO 964
CO adsorption 333, 693
CO/Ag(111) 694, 700, 701, 713
CO/Al(111) 700
CO/Co(0001) 699, 703
Co/Cu(001) 325, 331, 332
CO/Cu(001) 479, 480, 484
CO/Cu(001)
CO/Cu(011) 495
CO/Cu(111) 696, 700, 701
CO/H/Ni(1000) 738
CO/K/Cu(100) 738
CO/Ni(111) 696
CO/O/Pd(111) 741
CO/Pd(111) 696, 699
Co/Ru(0001) 334
(CO + O) on Ru(0001) 335, 336, 349
(CO + O) on Ru(001) 347, 349
CO tilt angle 711
$CO_2^-$ 718
$CO_2$/Fe(111) 718

$CO_2$/Ni(110) 718
$CO_2$/Pd(110) 718
$CO_2$/Re(0001) 718
CO(2 × 1)p2mg/Ni(110) 702, 705
CO(2 × 1)p2mg/Ni(110)/Pd(110)/Pt(110) 712
CO-2$\pi$–Ni-3d 703, 712
coherent potential approximation (CPA) 467, 475
coherent-forward-emission 699
collective excitations 367
complete scattering experiment 580
complex band structure 468, 470
compound semiconductors 149
computational methods 249
conduction band minimum 390, 422
conserving approximation 968
core level 313, 373, 374, 883
– binding energies 942
– photoemission 631
– shifts 944, 945
– spectroscopy 278, 785
corner hole 399
correlated dimers 390
corrugation 233
$CoSi_2$ film 799
$CoSi_2$/Si(111) 836
Coulomb energy 5
Coulomb potential 55, 57–59
covalent bond 288, 289, 299, 303–305, 310–315, 330, 341, 351
CP method 259
CPA method 476
cross section oscillations 936
crystal-field splitting 48
crystal-induced state 218
Cs(110) 270
Cs/Cu(111) 463, 929, 941, 945
Cu(001) 452, 456
Cu(100) 220, 224, 229, 230, 924
Cu(100)/Ca 906, 907
Cu(100)/Co 907
Cu(100)/Fe 907
Cu(100)/Na 907, 909
Cu(100)/Ni 907
Cu(111) 217, 231, 233, 438–445, 449, 452, 455, 456, 458, 463, 464, 467, 474, 476, 481, 494, 912, 913, 915, 937
Cu(111)/Cs 907, 909, 914
Cu(111)/K 905, 906
Cu(111)/Li 905, 906
Cu(111)/Na 905, 906, 914, 916, 917, 920, 923, 936
Curie temperature 543
Damon–Eshbach modes 548
dangling bond 116, 125, 152, 386, 419, 460, 462, 883
dangling bond band 399
Darwin term 532
dead layers 516
Debye length 755
defect model 764
delocalization model 766
density functional theory (DFT) 4, 98, 211, 249, 252, 265, 280, 292, 294, 299, 301, 302, 304, 312, 350
DFT-LDA 250, 257, 259, 263, 268, 269, 271, 280
DFT-LDA calculation 255, 265
density matrix 561
density of states 291, 524
depletion width 753, 755
depolarization 316–318
Dewar–Chatt–Duncanson model 673
diamond 405
dielectric function 109
difference density 292
differential reflectivity 367
dimer 386, 419
dimer-adatom-stacking fault 397
dimer-bond length 129, 130
dimer buckling 405
dimerisation 387
dipole approximation 596
dipole matrix elements 598
dipole moment 906, 907
dipole scattering 906
dipole–dipole interaction 316
dipole–image interaction 316
Dirac equation 14, 531, 561
dispersion 387, 388, 909, 910, 921, 935
disordered local moment model 627
dissociative adsorption 676
– anti-steering 345
– hydrogen 689
– steering 344, 345
$\sigma$-donation 693
donor–acceptor model for CO bonding 333, 334
double-group representations 529
dynamic charge 315, 316, 906, 907

effective-medium theory 297
effective midgap energy 422
effective radius 310
elbow plot 340–342
electron charge transfer 302
electron configurations 945
electron counting model (ECM) 274–278

electron counting rule 147, 178, 185, 419
electron energy loss 367
electron energy loss spectroscopy (EELS) 370, 903, 904, 907, 944
electron mean free path 372, 822, 830, 853, 937
electron reflectivity spectra 911
electron self-energy 979
electron stimulated desorption 264
electron–electron interaction 956
electron–hole pair continuum 480
electron–hole pair (exciton) 370, 373
electron–phonon interaction 444, 476, 477, 484, 983
electronegativity 147, 287, 302, 314, 315, 351
elemental semiconductor surfaces 122
Eley–Rideal mechanism 346, 347, 348
eliminating of forces 99
embedded atom method 212, 214, 239, 297, 455, 461
emission intensities 935
energy dispersion 674
energy minimization 419
energy shift 913
environmental conditions pressure 295, 337, 346, 348
– temperature 291, 318, 319, 324–326, 329, 332, 346, 348, 352
escape depth 372, 373
ethylene adsorption 722
even states 696
exchange–correlation 288, 298, 313, 351
– potential 5, 8, 10, 12, 23, 24, 55, 68, 211, 522
exchange interaction 515
exchange splitting 237, 523
exciton *see* electron–hole pair

Fano resonance 479
Fe(110) 238
Fermi contour 449, 453, 483, 492
Fermi golden rule 597
Fermi surface 444, 448, 449
ferromagnet strong 525
figure of merit 571
final state effects 402
flip process 588
fluctuating band theory 523
forbidden geometry 698, 739
formate/Cu(110) 720
Friedel oscillations 438, 941, 973
frontier orbitals 338, 341
frozen-potential approximation 304
full-potential linear augmented plane wave (FLAPW) method 21, 28–33, 39, 48, 54, 57, 63–68, 76, 77, 81–85, 252
fullerenes 376
fully relativistic formalism 534

Ga–As bond 264
Ga–H bond 263
GaAs 563, 755, 756, 773, 798, 867
GaAs(001) 275
GaAs(100) 275, 276, 368, 885
GaAs(100)/H 875
GaAs(100)/O 878
GaAs(110) 261, 263–267, 269, 270, 274, 275, 277
GaAs(110)/Br 892
GaAs(110)/Cl 892
GaAs(110)/H 873, 874
GaAs(110)/O 878
GaAs(110)/$SH_2$ 883
GaAs(111) 275, 278
GaAs/Si(100) 260
GaP 755, 756, 840
GaP(110)/$SH_2$ 883
gap states 788
Gaussian-type orbitals 38, 100, 107, 127
Ge(100) 261, 279, 402
Ge(100)/$NH_3$ 882
Ge(111) 272, 404
Ge(111)/Cl 890
Ge(111)/$H_2O$ 879
Ge(111)/I 890
Ge/GaAs(110) 277
generalized gradient approximation (GGA) 288, 289, 301, 351
germanium 867
giant magneto-resistance (GMR) 518
Gibbs free energy 295
glide plane 705, 709
gradient corrected density functionals 12, 13
grand canonical potentials 166, 167, 170
graphite 376
Green function 20, 42, 44, 45, 65, 102, 107, 109, 291, 294, 309, 312
Green-function techniques 252
Gurney model 469, 473, 474, 677
Gurney picture 328
GW approximation 107, 109, 111, 127, 136, 137, 144, 158, 159, 176, 242, 250, 257, 258, 280

H/Mo(011) 474, 482
H/Pd(111) 691
H/Si(111) 250, 256, 258, 274, 280
H–Si bond 255
H/Ta(011) 470, 475, 476

H/W(011) 474, 482, 484
$H_2$ 867
$H_2$/Ag(001) 341, 342
$H_2O$ 879
$H_2$/Pd(001) 341, 343
$H_2$/Rh(001) 343
halogens 886
Hamiltonian 526, 528
– Anderson–Grimley–Newns 251, 672, 673
– Hubbard-type 266, 280, 522
– Hubbard-type phonon 255
– Kohn–Sham 292
Hartree–Fock approximation 251
He atom scattering 903, 908, 928
Heisenberg model 544, 583
Helmholtz equation 315
– free energy 295
HF, aqueous solutions 883
HF method 259
highest occupied level 293, 302, 312
highest occupied molecular orbital (HOMO) 287, 333
Hohenberg–Kohn–Sham theorem 6
honeycomb-chained triangle (HCT) model 272, 273
hot electron effects 847
Hubbard
– bands 168
– model 522, 627
– repulsion 266
hybridization 532
– gap 532
– point 532
– $\sigma/\pi$ 710
hydrogen 867

ideal surfaces 116
image barrier 911
image barrier states 921
image charge density 320, 321
image effect 298, 316, 317, 320
image force 768, 772, 826
image plane 212, 237, 240, 298, 316, 320
image potential 211, 213, 218, 225, 237, 241, 910, 912
image potential surface states 211, 212, 218–220, 224, 239, 535, 610, 911, 926
impact scattering 587
incoming wave 972
index of interface behavior 758, 761
information density 517
information unit, bit 517
initial state effects 392
InP 867
InP(001) 277
InP(110) 791
InP(110)/$SH_2$ 883
interaction, 'through space' 675, 676
interface band structure 824
interface chemistry, core level spectroscopy 785
interface dipole 758, 768
interface states *see* also gap states 541, 612
interferences 981
interfering sources 937
interlayer coupling 585
intermixing 324
inverse photoelectron spectroscopy 594, 910
inverse photoemission 225, 359, 362, 363, 390, 911, 925, 926, 940
inversion layers 421
ionic bond 288–291, 303, 312, 315, 318, 327, 330
ionicity 121, 147, 149
ionization energy 301–303, 312
Ising system 583
island formation 324, 326, 329–331
itinerant ferromagnets 520, 623

Jahn–Teller distortion 491
– effect 736
– gap 389
– transition 132
Janak's theorem 10
jellium 19, 53, 54, 212
– edge 241, 242
– model 452, 463, 473

K/Cu(111) 465, 467, 468
K–Si bond 268
Kerr effect 371, 372
kinetic compensation 495
kink site 296, 297, 332
Kohn anomalies 487
Kohn–Sham approach 263
– eigenvalue 299, 302
– equations 7, 9, 10, 12, 24, 34
– Hamiltonian 292
Kondo resonance 955
Koopmans' theorem 301

Langmuir 671, 674
Langmuir–Gurney model 464
Langmuir–Gurney picture 303, 318
Langmuir–Hinshelwood reaction 346–349
lateral interactions 494

layer densities of states 105, 119
left–right asymmetry 569
Lennard-Jones 676
Li/Al(111) 309, 311
Li/Be(0001) 467, 468, 473–475
line shape analysis 391
linear combination of atomic orbitals (LCAO) method 263
LCAO-$X\alpha$ method 267
linear muffin-tin orbitals (LMTO) method 21, 22, 39, 252, 280
LMTO, full-potential (FP-LMTO) 32, 33
lithium 983
local atomic order 942
local density approximation (LDA) 8, 23, 98, 108, 112, 211, 288, 289, 298, 301, 302, 312, 351, 359, 442, 445, 453, 457, 969
local density of states 224
– approximation 377
local spin density functional theory 11
localized ferromagnet 520
long-range magnetic order 592
Lorentz–Lorenz dielectric function 967
loss energy 904–906
loss peak 904
low energy electron diffraction (LEED) 256, 379
– detector 572
– spin polarimeter 573
low-dimensional structures 370
lowest unoccupied molecular orbital (LUMO) 287, 333
Lucas mode 255
Luttinger liquid 955

macroscopic potential 421
magnetic 371, 373
magnetic circular dichroism (MCD) 82–84, 371, 379
magnetic dichroism 633, 636, 641–643, 647, 648
magnetic random access memory 519
magnetic size effects 584
magnetic stray field 553
magnetic systems 25
magnetization 371
magneto-crystalline anisotropy (MCA) 75, , 76–80, 84, 529, 533, 549
magneto-optical Kerr effect 76, 80
magnetoelastic anisotropy 552
magnetoelectronics 518
magnetoresistance 518
magnetostatic energy 553
magnons 543
majority states 525
many-body effects 442, 470
matrix element 937
metal-induced gap states (MIGS) 758, 759, 790
metal–GaAs interface 837
metallic bond 288, 289, 330
Mg(0001) 448
microscopy 377, 379
minority states 525
mirror plane 696
missing row reconstruction 685
Mo(001) 463, 490, 493
Mo(001)–2H 485
Mo(011) 463, 484
Mo(110)–H 488
molecular chemisorption 676
molecular orbitals 365
molecular oxygen 877
momentum conservation 819
Monte Carlo method 3, 9, 23, 25, 26, 85, 498, 830, 850, 852
Mott detectors 571
Mott model 756
Mott picture 766
Mott scattering 570
Mott–Hubbard insulator 266, 267, 271, 272, 280
magnetic random access memory (MRAM) 519
multilayer relaxation 66
multiple scattering theory 214, 216, 223, 227

$N_2$ 715, 880
$N_2$/Fe(111) 715
$N_2$/Ni(110) 716
$N_2$/Xe/Ag(111) 717
Na 2p-level 943
Na/Al(001) 302, 303, 319, 321–328
Na/Al(111) 309–311, 313, 314, 316, 325, 329–331
Na/Cu(111) 309, 310, 314
Na–Ga bond 270
Na–Si bond 269
Na/Ta(011) 475, 476
negative electron affinity 566
$NH_3$ 880
$NH_3$/Si(111) 258
Ni(100) 224, 240
Ni(100)/K 907, 909
Ni(110) 240
Ni(111) 240, 478
$NiSi_2$ 825, 850
$NiSi_2$/Si(100) 797
$NiSi_2$/Si(111) 764, 836
nitridation 880
non-adiabatic interactions 491
non-Fermi liquid behavior 955

non-flip process 588
non-linear phenomena 379
nonpolar (001) surface 179
nonpolar ($10\bar{1}0$) surface 149, 185, 191
nonpolar (110) surface 149, 172, 175, 183, 188, 190
Néel temperature 543

O/Al(111) 308
O/Ge(100) 261
O/Ru(0001) 302, 303
O/Ru(001) 347
O/Mo(011) 496–499, 501
O/W(011) 496, 500
odd states 696
one-step model 226
optical methods 367
optical second harmonic generation (SHG) 941
optical spin orientation 564, 637
optical sum frequency generation 369
optical surface spectroscopies 370
ordered adsorption 250
organ-pipe mode 908, 909
organic molecules 376
oscillatory magnetic coupling 938
oscillatory photoemission cross section 937
oscillatory thickness dependence 927
oscillatory work function 928
overlayer resonances 925
overlayer state 920, 926, 929, 932
oxidation of CO 345–350
oxidation of silicon 875
oxidation states at $Si/SiO_2$ interface 374

p(2 × 1)O/Cu(110) 685
p(2 × 2)S/Ni(100) 680
passivation 883
passivation (100) surfaces 275
Pauli equation 531, 561
Pauli matrices 561
Pb/Ge(111) 273, 274
Pb/Si(111) 273, 274
PBS *see* projected band structure
Peierls distortion 477, 490, 498, 501
perpendicular wave vector 929
$PH_3$ 883
phase condition 909–914, 929, 940
phase shift 293, 294, 910–912
phonon anomalies 451, 487
phonon scattering 826, 828
photoelectron 910
– diffraction 649
– microscope 379
– spectroscopy 594
photoemission 225, 226, 359–362, 594, 865, 913–915, 924, 926, 929, 931, 953, 971
– experiments on a sub-picosecond time scale 366
– inverse 360
– methods 780
– spectra 935
– spectroscopy 249
photoionization cross-section 680
physisorption 251, 288, 316
pinning 390, 422
plane wave 100, 107
plasmeron 964
plasmon 370, 372, 962, 963
plasmon excitation 373
point group 361
polar (0001) surfaces 160, 187
polar (001) surfaces 152, 183
polar (111) surfaces 160, 182, 183
polarization effects 887
polymers 373
potassium 980
potential barrier 293
potential energy surface (PES) 294, 337–345, 347, 352
power law 583, 584
preconditioned conjugate gradient 36
preconditioned conjugate gradient pseudopotential 38
precursor 875
precursor state 258
probing depth 363, 374
projected band structure (PBS) 104, 105
projected bulk band 396, 692
proper work function 921, 923
pseudopotential 15, 22, 23, 28, 34, 37, 47, 53, 72, 73, 85, 99, 113, 448, 451, 455
– method 249, 252, 255, 269, 270, 439, 458, 463, 467
– perturbation theory 68
– plane wave method 15, 20, 21, 33
– self-interaction correction (SIC) 113
– self-interaction and relaxation corrections (SIRC) 113, 115, 190, 192, 193
Pt(111) 488
Pt(111)/K 904–906

quantum defect 219, 343
quantum nature of adsorption 343
quantum nature of dissociation 343
quantum numbers 360
quantum well 933

quantum well state 541, 616, 911, 914, 920, 923, 925, 935, 937
quantum yield, electron–hole pair production 849, 852
quasiparticle 107, 359, 360, 362, 367, 956
quasiparticle band structure 107, 111, 127, 136, 137, 144, 159, 176, 970
quasiparticle energies 107

random phase approximation 962
reactivity 337, 338, 340, 345, 352
reconstruction 62–65, 69, 72
reconstruction energy 132
reconstruction W(001) surface 66
reconstruction-induced energy gain 132
refraction 299
relativistic correction 18
relativistic effects 14, 326
relaxation 62–65
relaxation effects 392
remotion of reconstruction 253
renormalization constant 964
renormalized atomic level 301, 302, 304
repeated slab method 20, 252
representations 529
resonance 220, 923–925
resonant overlayer states 937
rest-atoms 397, 399, 400, 402
Richardson constant 776, 777
rigid band model 466, 474
RKKY interaction 438, 494
rotational hindering 345
Ru(0001)/Cs 905, 906
Rydberg series 218, 220, 225, 911, 916
Rydberg state 911

satellite peak 964
satellite structure 680
Sb/GaAs(110) 265
Sb/InSb(111) 278
Sb/Si(111) 259
Sb–Sb bond 264
scalar-relativistic approach 15, 31
scanning tunneling microscopy (STM) 249, 260, 267, 270, 272, 273, 275, 277, 465, 865, 869
scanning tunneling spectroscopy 363
scattering potential 568
scattering-theoretical approach 100, 101
Schottky barrier 272
– ballistic electron emission spectroscopy 780
– capacitance 770
– formation 264, 272, 274
– height 756, 771, 773, 822
– internal photoemission 779
– model 272, 758
– thermionic emission 775
screening 392
screening charge 318, 320, 321, 352
Se/GaAs(110) 267
Se-passivated GaAs(001) 277
selection rule 364
self-energy 107, 109, 211, 212, 242, 955, 956
self-interaction 301, 302
self-interaction and relaxation corrections (SIRC) 113
self-interaction correction (SIC) 113
semiconductor surfaces 361, 364, 367
semiempirical method 249, 255
shape anisotropy 553
shape resonance 699
Sherman function 570
Shockley surface state 218, 219, 239
short-range magnetic order 592
Si 363, 378, 755, 756, 796, 867
Si/Al(111) 309–311, 313, 314, 316
Si/Cu(111) 309, 310, 314
Si(100) 259–261, 267
Si(100) As-passivated 279
Si(100)/Cl 890
Si(100)/F 891
Si(100)/H 872
Si(100)/$H_2O$ 879
Si(100)/K 268
Si(100)/O 877
Si(100)/S 882
Si(111) 250, 253–255, 258, 272, 273, 279, 865
Si(111) (2 × 1) 367
Si(111) (7 × 7) 367
Si(111)/Cl 884, 888
Si(111)/F 891
Si(111)/H 867, 868, 871, 884
Si(111)/$H_2O$ 879
Si(111)/$NH_3$ 880
Si(111)/O 875
Si(111)/$PH_3$ 883
Si(111)/$SH_2$ 883
$Si_2H_2$ 260
Si–H stretching mode 256
$SiH_2$ 260
Si–Si bond 260, 268, 269
Si–Si bond length 255
silicon nitride 880
single-group 529
$SiO_2$/Si interface oxidation states 374
Slater–Janak transition-state 301
Slater-type orbitals 42

Sm overlayers 945
sodium 958, 959, 980
spectromicroscopy 377
spin 561
spin density wave 980
spin-dependent confinement 618
spin-down states 525
spin filter 618
spin flip 545
spin fluctuations 970
spin lattice 543
spin magnetic moments 536
spin operator 561
spin–orbit interaction 76, 191, 486, 487, 528, 568
spin polarimeter 568
spin polarization 16, 361, 562
spin-polarized
– electron source 562
– electron spectroscopies 371
– photoemission 237
– quantum well states 938
spin quantization axis 527
spin-reorientation transition 556
spin-resolved Auger electron spectroscopy 633
spin-resolved photoemission 926, 938
spin-up 525
spin wave 543
spin wave dispersion 544
spin wave stiffness 544
spinors 527
step anisotropy 558
steric effect 345
sticking probability 343–345
Stoner criterion 523
Stoner excitation 545, 589, 592
Stoner–Wohlfarth model 522, 536, 623
stretching and bending vibrations 146
structure atomic 98
structure optimization 98
structure problem 98
subband energies 421
substitutional adsorption 287, 296, 317, 318, 323–332, 678
subsurface oxygen 346
sum rules 714, 966
supercell method 100
surface alloy 317, 324, 329, 331, 350, 466
surface anisotropy 554
surface band gap 396
surface barrier 211–213, 215, 226, 227, 234, 241, 293, 297, 299
surface bound states 104
surface Brillouin zone 104, 306
surface chemistry 376, 379
surface core level shifts 279, 391
surface corrugation 215
surface dipole 58
surface effect 972, 974
surface electronic states 535
surface electronic structure 370
surface energy 64, 67, 68, 213
surface Fermi level 390
surface lattice relaxation 68
surface magnetism 516
surface molecule 671, 673, 693
surface oxide 346, 350, 352
surface phase shift 972
surface phonons 147, 907
surface photoelectric effect 924, 925
surface photoemission 226
surface photovoltage effects 784
surface plasmon 370
surface reconstruction 67, 490
surface relaxation 408
surface resonance 45–47, 50, 104, 212, 216, 220, 221, 239, 410, 459, 535
surface states 45–47, 50, 211, 213, 214, 361, 363, 387, 535, 541, 605, 692, 867, 910–913
surface states, intrinsic 421
surface vacancy 325, 327, 329, 330, 332
symmetric wave function 706
symmetry 526
synchrotron radiation 249, 372

Ta(001) 463
Ta(011) 457–460, 462
test charge 212, 241
thermal desorption 871
three-step model 597
tight-binding 299, 341
– downward in models 458
– models 251, 675
– picture 299, 303, 305, 307, 308, 342
tilt angle CO 711
time-reversal symmetry 527
$TiTe_2$ 453
Tl/Cu(001) 500, 501
total energy 4, 32, 64, 65, 71, 84, 98
total-energy-and-force method 252, 255
transfer matrix 498
transition matrix element 600
transition state 337, 338, 341, 342, 348–352
transition-state, Slater–Janak 301
transmission probability 825
trimer models 165, 168
tunneling experiments 925
two-dimensional state 363

two-dimensional Brillouin zone 24, 27
two-photon photoemission 911, 916, 921

undulator sources 373
undulator-based synchrotron 377
UPS line width 695

vacuum level 218, 219, 225
vacuum potential 211, 213
valence band imaging 421
van der Waals bond 288
vector potential 226
vibration frequency 903, 905
vibrational electron energy-loss spectroscopy 264
vibrational energy 295, 340, 906
vibrational energy entropy 351
vibrational entropy 295
vibrational excitations 903–906
vibrational modes 908
virtual crystal approximation (VCA) 467, 474
volume effect 972, 974

W(001) 463, 479, 490–493
W(001)–2H 485
W(011) 463
W(110)–H 488
water 879
weak ferromagnet 525
work function 10, 11, 22, 48, 52–64, 213, 315–319, 326, 328, 329, 871, 921, 927
work function change 906, 907

X-ray circular dichroism 76
X-ray photoelectron spectroscopy (XPS) 373
X-ray photoemission spectroscopy 263
XY-model 583

zincblende 188